



AD-A280 384



The
American
Physical
Society



Proceedings of the 1993 Particle Accelerator Conference

DTIC
ELECTE
JUN 13 1994
S F D

Volume 3 of 5

Pages 1641-2545

This document has been approved
for public release and sale; its
distribution is unlimited.

30918
94-17987

Papers from the fifteenth biennial Particle Accelerator Conference, an international forum on accelerator science and technology held May 17-20, 1993, in Washington, D.C., organized by the Continuous Electron Beam Accelerator Facility (CEBAF), jointly sponsored by the Institute of Electrical and Electronics Engineers Nuclear and Plasma Sciences Society and the American Physical Society Division of Physics of Beams, and conducted with support from the U.S. Department of Energy, the National Science Foundation, and the Office of Naval Research.

DTIC QUALITY INSPECTED 1

94 6 10 097

**Best
Available
Copy**

1993 IEEE Particle Accelerator Conference

Abstracting is permitted with credit to the source. Libraries are permitted to photocopy beyond the limits of U.S. Copyright law for private use of patrons those articles in this volume that carry a code at the bottom of the first page, provided the per-copy fee indicated in the code is paid through the Copyright Clearance Center, 27 Congress Street, Salem, MA 01970. For other copying, reprint, or republications permission, write to the IEEE Copyright Manager, IEEE Service Center, 445 Hoes Lane, P.O. Box 1331, Piscataway, NJ 08855-1331. All rights reserved. Printed in the USA. Copyright © 1993 by The Institute of Electrical and Electronics Engineers, Inc.

IEEE Catalog Number: 93CH3279-7

Library of Congress Number: 88-647453

Additional copies of this publication are available from

ISBN Softbound: 0-7803-1203-1

Casebound: 0-7803-1204-x

Microfiche: 0-7803-1205-8

IEEE Service Center

445 Hoes Lane

Piscataway, NJ 08854-4150



The
American
Physical
Society

1993 Particle Accelerator Conference, Washington, D.C., 17-20 May

Conference Chairman
Christoph Leemann, *CEBAF*
Annie Soltys, Executive Assistant
Telephone: (804) 249-7575
E-mail: soltys@cebaf.gov
Fax: (804) 249-5024

18-May-94

Organizing Committee

M. Allen, *SLAC*
W. Barletta, *LLNL*
K. Berkner, *LBL*
D. Berley, *NFS*
J. Bisognano, *CEBAF*
R. Briggs, *SSCL*
Y. Cho, *ANL*
L. Costrell, *NBS*
M. Craddock, *U. of BC*
W. K. Dawson, *TRIUMF*
H. Edwards, *FNAL*
S. Holmes, *FNAL*
S. Krinsky, *BNL*
H. Lustig, *APS*
C. Roberson, *ONR*
S. Schriber, *LANL*
D. Sutter, *DOE*
S. Tazzari, *U. of Rome II & INFN*
M. Tigner, *Cornell*
W. T. Weng, *BNL*

Program Committee

J. Bisognano, Chair, *CEBAF*
Telephone: (804) 249-7521
E-mail: bisognano@cebaf.gov
H. Edwards, Deputy Chair, *FNAL*

Program Treasurer

Julie Leverenz
Telephone: (804) 249-7642
E-mail: leverenz@cebaf.gov

Conference Editor

Steven T. Corneliussen, *CEBAF*
Telephone: (804) 249-7582
E-mail: corneliussen@cebaf.gov

Editorial Assistant

Linda Carlton
Telephone: (804) 249-7690
E-mail: carlton@cebaf.gov
Fax: (804) 249-5024

DEFENSE TECHNICAL INFORMATION CENTER
BUILDING 5, CAMERON STATION
ALEXANDRIA, VA 22304-6145

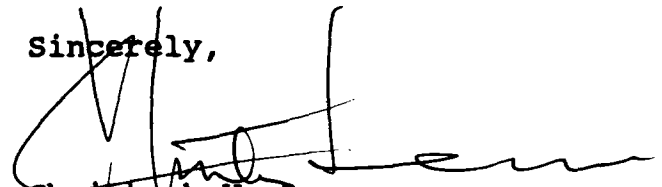
REF.: GRANT NO. N00014-93-1-0623

Dear Sir or Madam:

Enclosed please find two (2) copies of the Proceedings of the 1993 Particle Accelerator Conference (PAC93). The above-referenced \$15,000 grant from the Office of Naval Research helped fund the cost of publishing the Proceedings, enabling us to keep the registration fee to a minimum.

On behalf of the conference organizers and the more than 1300 participants, thank you for supporting PAC93.

Sincerely,



Christoph W. Leemann
Conference Chairman

cc: D. Galicki, IEEE

Five-Volume Contents

Each volume begins with this five-volume table of contents and ends with the five-volume author index. The chairmen's foreword and a list of conference organizers and staff appear as front matter in Volume 1. A list of conference participants precedes the author index in Volume 5.

Availability Codes	
Dist	Avail and/or Special
A-1	

Volume 1

Opening Plenary

Chair: J. Bisognano

HERA Operations and Physics — B. H. Wiik, U. Hamburg and DESY..... 1

Single-Particle Beam Dynamics

Chair: W. Weng

Nonlinear Beam Dynamics Experiments at the IUCF Cooler Ring (<i>Invited Paper</i>) — S. Y. Lee, Indiana University	6
The Preservation of Low Emittance Flat Beams (<i>Invited Paper</i>) — T. O. Raubenheimer, SLAC	11
Long-Term Stability Studies for CERN-LHC (<i>Invited Paper</i>) — W. Scandale, CERN	16
Emittance Growth in a Low Energy Proton Beam (<i>Invited Paper</i>) — J. A. Palkovic, SSCL	21
Proton Extraction from the CERN-SPS by a Bent Crystal — S. Weisz and the RD22 Collaboration; CERN	26
Longitudinal Tracking with Phase and Amplitude Modulated RF — D. D. Caussyn, M. Ball, B. Brabson, J. Budnick, J. Collins, V. Derenchuk, G. East, M. Ellison, T. Ellison, D. Friesel, B. Hamilton, H. Huang, W. P. Jones, S. Y. Lee, D. Li, S. Nagaitsev, X. Pei, T. Sloan, Y. Wang, IUCF; A. W. Chao, S. Dutt, M. Syphers, Y. T. Yan, P. L. Zhang, SSCL; M. G. Minty, SLAC; K. Y. Ng, FNAL.....	29
Measurement of Spin Motions in a Storage Ring Outside the Stable Polarization Direction — N. Akchurin, A. Bravar, J. McPherson, F. Olchowski, Y. Onel, U. Iowa; L. Badano, M. Conte, INFN Genova; A. Penzo, INFN Trieste; J. Hall, U. New Mexico; A. Pisent, INFN Legnaro; M. Pusterla, INFN Padova; T. Rinckel, Indiana U.; R. Rossmannith, CEBAF; H. Kreiser, U. Hamburg	32
A Clean Way to Measure Nonlinear Momentum Compaction Factor α_1 — J. P. Shan, I. Kourbanis, D. McGinnis, K. Y. Ng, S. Peggs, FNAL	35
Long-Term Tracking with Symplectic Implicit One-Turn Maps — Y. T. Yan, M. Li, M. J. Syphers, SSCL; P. J. Channell, LANL	38
Injection Method Using the Third Order Resonance at TARN II — M. Tomizawa, Y. Arakaki, K. Chida, S. Watanabe, T. Watanabe, T. Katayama, M. Yoshizawa, INS Tokyo; A. Noda, Kyoto U.	41
Effects of Tidal Forces on the Beam Energy in LEP — L. Arnaudon, F. Bordry, W. Coosemans, B. Dehning, K. Henrichsen, A. Hofmann, R. Jacobsen, J. P. Koutchouk, L. Lawson-Chroco, M. Mayoud, J. Miles, R. Olsen, M. Placidi, G. Ramseier, R. Schmidt, J. Wenninger, CERN; A. Blondel, Ec. Polytech. Paris; R. Assmann, MPI Munich; G. E. Fischer, C. Pan, SLAC; R. Olivier, Lausanne U.	44

Poster presentations:

The Appearance of Beam Lines — D. C. Carey, FNAL	47
Multipole Channel Parameters for Equalization of Beam Intensity Distribution — Y. K. Batygin, MEPI	50
Single Beam Effects Due to Errors in Crab Compensation — D. Sagan, Cornell	53
Lattice Design of the LANL Spallation-Source Compressor Ring — B. Blind, A. J. Jason, F. Neri, LANL	56
Optics Simulations of the 5 MeV NPBSE FOX Telescope — M. F. Reusch, D. L. Bruhwiler, Grumman Corp.	59
Longitudinal Kinetic Energy Spread from Focusing in Charged Particle Beams — N. Brown, M. Reiser, D. Kehne, D. X. Wang, J. G. Wang, U. Maryland	62
Numerical and Experimental Studies of Halo Formation Due to Mismatch in a Space-Charge-Dominated Electron Beam — D. Kehne, M. Reiser, U. Maryland; H. Rudd.....	65
Suppression of the Main LEP Coupling Source — J. Billan, J.-P. Gourber, J.-P. Koutchouk, V. Remondino, CERN	68
Applications of Matrix Optics to Acceptance Studies in Low-Beta Ion Linacs — K. Joh, J. A. Nolen, ANL	71
Analytical Evaluation of the Second Order Momentum Compaction Factor and Comparison with MAD Results — J. P. Shan, S. G. Peggs, S. A. Bogacz, FNAL	74
Chromaticity Compensation Scheme for the Main Injector — S. A. Bogacz, FNAL	77

Proceedings of the 1993 Particle Accelerator Conference

Accelerator Physics Analysis with Interactive Tools — J. A. Holt, L. Michelotti, FNAL	80
The 50 MeV Beam Test Facility at LBL — W. Leemans, G. Behrsing, K.-J. Kim, J. Krupnick, C. Matuk, F. Selph, S. Chattopadhyay, LBL	83
Knowledge Rule Base for the Beam Optics Program TRACE 3-D — G. H. Gillespie, P. K. Van Straagen, B. W. Hill, G. H. Gillespie Assoc.	86
Beam Dynamics Studies of Four-Gap Low-Beta Superconducting Resonators — J. A. Nolen, K. Joh, ANL	89
Third-Order Corrections to the SLC Final Focus — N. J. Walker, R. Helm, J. Irwin, M. Woodley, SLAC	92
Global Tuning Knobs for the SLC Final Focus — N. J. Walker, J. Irwin, M. Woodley, SLAC	95
Sigma Matrix Reconstruction in the SLC Final Focus — P. Raimondi, P. J. Emma, N. Toge, N. J. Walker, V. Ziemann, SLAC	98
Beam Based Alignment of the SLC Final Focus Superconducting Final Triplets — P. Raimondi, P. J. Emma, N. Toge, N. J. Walker, V. Ziemann, SLAC	100
A Design of a Quasi-Isochronous Storage Ring — S. Y. Lee, Indiana U.; K. Y. Ng, FNAL; D. Trbojevic, BNL	102
Optimization Method for Orbit Correction in Accelerators — E. Bozoki, A. Friedman, BNL	105
A Fast Model-Calibration Procedure for Storage Rings — W. J. Corbett, M. J. Lee, V. Ziemann, SLAC	108
Dynamic Accelerator Modeling — H. Nishimura, LBL	111
Procedure for Determining Quadrupole and BPM Offset Values in Storage Rings — W. J. Corbett, V. Ziemann, SLAC	114
Beam Based Alignment of the SLC Final Focus Sextupoles — P. Emma, J. Irwin, N. Phinney, P. Raimondi, N. Toge, N. J. Walker, V. Ziemann, SLAC	116
Analysis of Higher Order Optical Aberrations in the SLC Final Focus Using Lie Algebra Techniques — N. J. Walker, J. Irwin, M. Woodley, SLAC	119
Simulation Support for Commissioning and Operating the SSC Linac — F. W. Guy, J. W. Hurd, C. R. Chang, D. Raparia, C. Y. Yao, SSCL	122
The Provision of IP Crossing Angles for the SSC — Y. Nosochkov, SSCL; D. M. Ritson, SLAC	125
Interactive Simulation of LEB Commissioning Procedure on a Hypercube Parallel Computer — G. Bourianoff, M. Botlo, B. Cole, S. Hunt, N. Malitsky, A. Romero, SSCL	128
Localized Chromaticity Correction of Low-Beta Insertions in Storage Rings — M. Donald, R. Helm, J. Irwin, H. Moshhammer, SLAC; E. Forest, D. Robin, A. Zholents, LBL; M. Sullivan, U. Ca., SLAC	131
Amplitude Function Mismatch — M. J. Syphers, T. Sen, SSCL; D. A. Edwards, DESY/Fermilab	134
SSC Collider Arc Lattice — M. J. Syphers, E. D. Courant, A. A. Garren, S. K. Kauffmann, T. Sen, SSCL	137
Second Order Chromaticity of the Interaction Regions in the Collider — T. Sen, M. J. Syphers, SSCL	140
Chromaticity Correction for the SSC Collider Rings — T. Sen, Y. Nosochkov, F. Pilat, R. Stiening, SSCL; D. M. Ritson, SLAC	143
Effect of Power Supply Ripple on Emittance Growth in the Collider — T. Sen, M. J. Syphers, SSCL	146
The QBA Optics for the 3.2 GeV Synchrotron Light Source ROSY II — D. Einfeld, Res. Ctr. Rossendorf; M. Plesko, Sincrotrone Trieste	149
Dynamic Aperture of the 2.5 GeV Synchrotron Radiation Source LISA — D. Einfeld, Fachhochschule Ostfriesland; D. Husmann, U. Bonn; M. Plesko, Sincrotrone Trieste	152
Four-Cell Third-Order Achromats and Their Application to Multi-Pass Time-of-Flight Spectrometers — W. Wan, M. Berz, MSU-NSCL	155
An Automatic Finder of Field Defects in a Large A.G. Machine — A. Verdier, J. Chappelier, CERN	158
Automatic and Expert Systems for Orbit Analysis — A. Verdier, J. Chappelier, CERN	161
Symplectic Scaling, a DA Based Tool — G. H. Hoffstätter, M. Berz, NSCL-MSU	164
New Features in DIMAD — R. V. Servranckx, TRIUMF	167
A First Order Matched Transition Jump at RHIC — S. Peggs, S. Tepikian, D. Trbojevic, BNL	168
Comparison of Aperture Determinations on RHIC for Single Particles Tracked 10^6 Turns and 100 Particles, Having Randomly Generated Initial Coordinates, Tracked for 1000 Turns — G. F. Dell, BNL	171
Status of the Variable Momentum Compaction Storage Ring Experiment in SPEAR — P. Tran, A. Amiry, C. Pellegrini, UCLA; J. Corbett, M. Cornacchia, M. Lee, H.-D. Nuhn, H. Winick, D. Wu, SLAC; A. Hofmann, CERN; D. Robin, LBL	173
SSC High Energy Booster Resonance Corrector and Dynamic Tune Scanning Simulation — P. Zhang, S. Machida, SSCL	176
Transport Properties of the CEBAF Cavity — Z. Li, Coll. of William & Mary/CEBAF; J. J. Bisognano, B. C. Yunn, CEBAF	179

Each volume begins with this five-volume table of contents and ends with the five-volume author index. The chairman's foreword and a list of conference organizers and staff appear as front matter in Volume 1. A list of conference participants precedes the author index in Volume 5.

Stripper-Foil Scan Studies of the First-Turn Beam Loss Mechanism in the LAMPF Proton Storage Ring (PSR) — R. Hutson, D. Fitzgerald, S. Frankle, R. Macek, M. Plum, C. Wilkinson, LANL	366
Measurement of H^0 Excited States Produced by Foil Stripping of 800-MeV H^- Ions — J. Donahue, D. Clark, S. Cohen, D. Fitzgerald, S. Frankle, R. Hutson, R. Macek, E. Mackerrow, O. van Dyck, C. Wilkinson, LANL; H. Bryant, M. Gulley, M. Halka, P. Keating, W. Miller, U. New Mexico	369
Reducing Phase-Dependent Emittance Growth with Local Flattopping — R. E. Laxdal, T. Kuo, G. H. Mackenzie, L. Root, TRIUMF; A. Papash, INR Kiev	372
An Ion-Source Model for First-Order Beam Dynamic Codes — C. L. Fink, B. P. Curry, ANL	375
Lattice Design and Injection Issues for the 2 TeV SSCL High Energy Booster to Collider Injection Lines — F. Wang, R. Schailey, J. McGill, D. Johnson, SSCL; K. L. Brown, SLAC	378
Detailed Studies on the Beam Transfer Line from Linac to Low Energy Booster Synchrotron for the SSC — R. Bhandari, J. McGill, F. Wang, S. Penner, SSCL	381
200 GeV Beam Transfer Lines at the SSC — F. G. Mariani, J. McGill, SSCL; K. Brown, SLAC	384
Effect of Betatron Motion on the Septum Flux in Superslow Extraction at the SSC — B. S. Newberger, U. Texas, Austin; H.-J. Shih, SSCL; J. A. Ellison, U. NM	387
Study of Energy Ramping Process Applied to the LNLS Synchrotron Light Source (Brazil) — L. Jahnel, C. E. T. Gonçalves da Silva, Unicamp/LNLS Brazil	390
Extraction System Design for the SSC Low Energy Booster — X. Wu, R. York, U. Wienands, T. Hunter, S. Sheynin, SSCL	393
Tests and Analysis for SLC Damping Ring Data — J. E. Spencer, SLAC	396
RF Capture Studies for Injection into a Synchrotron — E. S. Lessner, Y. Cho, ANL	399
Results from Beam Diffusion and Collimation Measurements in Preparation for Fermilab Tevatron Crystal Extraction — G. Jackson, FNAL	402
Operational Experience with Third Harmonic RF Cavity for Improved Beam Acceleration Through Transition in the Fermilab Main Ring — C. M. Bhat, J. Dey, J. Griffin, I. Kourbanis, J. MacLachlan, M. Martens, K. Meisner, K. Y. Ng, J. Shan, D. Wildman, FNAL	405
New Method for Control of Longitudinal Emittance During Transition in Proton Synchrotrons — J. E. Griffin, FNAL (Ret.)	408
Remarks on the Differential Luminosity in the Weak Disruption and the Transition Region — H. Heydari, TUB Germany	411
Flat Beam Studies in the SLC Linac — C. Adolphsen, F.-J. Decker, J. T. Seeman, SLAC	414
Method to Evaluate Steering and Alignment Algorithms for Controlling Emittance Growth — C. Adolphsen, T. Raubenheimer, SLAC	417
Experimental Simulation of Ground Motion Effects — M. J. Syphers, A. W. Chao, S. Dutt, Y. T. Yan, P. L. Zhang, SSCL; M. Ball, B. Brabson, J. Budnick, D. D. Caussyn, J. Collins, V. Derenchuk, G. East, M. Ellison, T. Ellison, D. Friesel, B. Hamilton, H. Huang, W. P. Jones, S. Y. Lee, D. Li, S. Nagaitsev, X. Pei, G. Rondeau, T. Sloan, Y. Wang, IUCF; M. G. Minty, SLAC; W. Gabella, K. Y. Ng, FNAL; L. Teng, ANL; S. Tepikian, BNL	420
Bunch Coalescing Studies for the SSC — N. Mahale, Y. T. Yan, J. Ellison, SSCL	423
Compensation of RF-Induced Energy Spread in the CEBAF Injector Chopping System — M. G. Tiefenback, G. A. Krafft, CEBAF	426
The North Arc of the SLC as a Spin Rotator — T. Limberg, P. Emma, SLAC; R. Rossmanith, CEBAF	429
The Evolution of Tensor Polarization — H. Huang, S. Y. Lee, IUCF, L. Ratner, BNL	432
Even Order Snake Resonances — S. Y. Lee, Indiana U.	435
Wiggler as Spin Rotators for RHIC — A. Luccio, BNL; M. Conte, U. Genova	438
Taylor Map and Calculation of Equilibrium Polarization for Proton Storage Rings — V. Balandin, N. Golubeva, INR Moscow	441
Investigation of Spin Resonance Crossing in Proton Circular Accelerators — V. Balandin, N. Golubeva, INR Moscow	444
Electron Beam Depolarization in a Damping Ring — M. Minty, SLAC	447
SPINLIE: New Computer Code for Polarization Calculation — Yu. Eidelman, V. Yakimenko, BINP	450
IHEP Polarized Proton Beam — V. N. Zapolsky, Yu. A. Chesnokov, A. Dyshkant, N. A. Galyaev, V. I. Kotov, V. I. Kryshkin, R. A. Rzaev, R. M. Sulyaev, S. V. Tsarik, V. G. Zarucheisky, IHEP Moscow	454
Measurement of Longitudinal Beam Polarization by Synchrotron Radiation — I. P. Karabekov, Yerevan/CEBAF, R. Rossmanith, CEBAF	457

Proceedings of the 1993 Particle Accelerator Conference

The Status of Polarization Studies at HERA — <i>M. Böge, DESY</i>	460
Computer Assisted Accelerator Tuning — <i>J. K. Boyd, LLNL</i>	463
Pulse-to-Pulse Simulation of Orbit Feedback for JLC Final Focus System — <i>N. Yamamoto, K. Hirata, K. Oide, KEK</i>	466
Multi-Dimensional Beam Emittance and β -Functions — <i>J. Buon, LAL Orsay</i>	469
Observation of the Coalescing of Beam into an Asymmetric RF Bucket by Stochastic Cooling — <i>A. M. Halling, X. P. Lu, FNAL</i>	472
Effects of Transverse Coupling on Transverse Beam Size, Simulation and Measurements — <i>A. M. Halling, FNAL</i> ...	474
One of Methods to Extract Truncated Taylor Map for Orbital and Spin Motion in Proton Storage Rings — <i>V. Balandin, INR Moscow</i>	477
Skew Quadrupole Effects in the IBM Compact Synchrotron — <i>C. N. Archie, IBM Semiconductor R&D Ctr.</i>	480
A Simulation Study of Linear Coupling Effects and Their Correction in RHIC — <i>G. Parzen, BNL</i>	483
Eigenfunctions of the Transfer Matrix in the Presence of Linear Coupling — <i>G. Parzen, BNL</i>	486
Emittance and Beam Size Distortion Due to Linear Coupling — <i>G. Parzen, BNL</i>	489
Use of Regularization Method in the Determination of Ring Parameters and Orbit Correction — <i>Y. N. Tang, S. Krinsky, NSLS-BNL</i>	492
Automatic Differentiation of Limit Functions — <i>L. Michelotti, FNAL</i>	495
Corrector Ironing in the SLC Final Focus — <i>V. Ziemann, SLAC</i>	498
General Normal Form Procedure to Correct Tune-Shift and Non-Linear Chromaticity for Large Accelerators like the LHC — <i>M. Giovannozzi, F. Schmidt, CERN</i>	500
Review of Recent Optical Issues in LEP — <i>F. Ruggiero, CERN</i>	503
Emittance and Damping of Electrons in the Neighborhood of Resonance Fixed Points — <i>E. A. Crosbie, ANL</i>	506
Effects of the Third Order Transfer Maps and Solenoid on a High Brightness Beam — <i>Z. Parsa, BNL</i>	509
Simultaneous Cancellation of Beam Emittance and Energy Spread in the CEBAF Nuclear Physics Injector Chopping System — <i>H. Liu, J. Bisognano, CEBAF</i>	512
The Linkage of Zlib to TEAPOT for Auto-Differentiation Map Extraction and Nonlinear Analysis — <i>N. Sun, Y. T. Yan, F. Pilat, G. Bourianoff, SSCL</i>	515
Influence of the Ionization Loss in the Diagnostic Foil on the Phase Motion in the Phasotron — <i>O. N. Borisov, L. M. Onischenko, JINR, Dubna</i>	518

Lepton RF Linacs and Linear Colliders

Chair: Y. Kimura

Recent SLC Developments (<i>Invited Paper</i>) — <i>M. Ross, SLAC</i>	522
CEBAF Commissioning Status (<i>Invited Paper</i>) — <i>A. Hutton, CEBAF</i>	527
Overview of Linear Collider Designs (<i>Invited Paper</i>) — <i>R. H. Siemann, SLAC</i>	532
Progress Report on the TESLA Test Facility — <i>H. T. Edwards and the TESLA Collaboration, DESY/FNAL</i>	537
The CERN Linear Collider — <i>The CLIC Study Group, CERN</i>	540
The Next Linear Collider Test Accelerator — <i>R. D. Ruth, C. Adolphsen, K. Bane, R. F. Boyce, D. L. Burke, R. Callin, G. Caryotakis, R. Cassel, S. L. Clark, H. Deruyter, K. Fant, R. Fuller, S. Heifets, H. Hoag, R. Humphrey, S. Kheifets, R. Koontz, T. Lavine, G. A. Loew, A. Menegat, R. H. Miller, J. M. Paterson, C. Pearson, R. Phillips, J. Rifkin, J. Spencer, S. Tantawi, K. A. Thompson, A. Vlieks, V. Vylet, J. W. Wang, P. B. Wilson, A. Yermian, B. Youngman, SLAC; N. M. Kroll, UC San Diego; C. Nantista, UCLA</i>	543
High Power CW Linac in PNC — <i>S. Toyama, Y. L. Wang, T. Emoto, M. Nomura, N. Takahashi, H. Oshita, K. Hirano, Y. Himeno, PNC Japan; I. Sato, A. Enomoto, M. Ono, KEK</i>	546

Poster presentations:

A mm-Wave Planar Microcavity Structure for Electron Linear Accelerator System — <i>Y. W. Kang, R. Kustom, F. Mills, G. Mavrogenes, ANL; H. Henke, TU Berlin</i>	549
SCANUR: A Subcritical Reactor with Electron Linacs for Transmutation of Nuclear Wastes — <i>A. Krasnykh, Yu. Popov, V. Rudenko, L. Somov, JINR Dubna; L. Men'schikov, V. Prusakov, S. Subbotin, Kurchatov Inst., Moscow</i>	552
New Irradiation Field Shaping Systems of High Voltage Electron Accelerators for Industry — <i>A. S. Ivanov, V. P. Ovchinnikov, M. P. Svinin, N. G. Tolstun, Efremov Inst.</i>	555
A Versatile 2 MeV, 200 mA Compact X-Band Linac — <i>C. E. Clayton, K. A. Marsh, UCLA</i>	558

Each volume begins with this five-volume table of contents and ends with the five-volume author index. The chairman's foreword and a list of conference organizers and staff appear as front matter in Volume 1. A list of conference participants precedes the author index in Volume 5.

Proceedings of the 1993 Particle Accelerator Conference

Diffusion Phenomena in Simple Hamiltonian Systems: Some Analytical and Numerical Results — A. Bazzani, S. Rambaldi, G. Turchetti, U. Bologna; M. Giovannozzi, CERN	273
Particle Acceleration in Extremely Strong Electromagnetic Wave Fields — K. O. Thielheim, U. Kiel	276
Laser Powered Beam Conditioner for Free Electron Lasers and Synchrotrons — H. Liu, G. Neil, CEBAF	279
Tracking Studies of Insertion Device Effects on Dynamic Aperture in the APS Storage Ring — Y. Chae, U. Houston; E. A. Crosbie, ANL	282
Particle Diffusion from Resonance Islands in Aladdin at SRC — J. Liu, E. Crosbie, L. Teng, J. Bridges, D. Ciarlette, R. Kustom, D. Voss, F. Mills, M. Borland, ANL; K. Symon, U. Wisc. Madison; W. Trzeciak, SRC Stoughton	285
Alternating-Phase Focusing with Amplitude Modulation — L. Sagalovsky, J. R. Delayen, ANL	288
Full-Turn Symplectic Map from a Generator in a Fourier-Spline Basis — J. S. Berg, R. L. Warnock, R. D. Ruth, SLAC; É. Forest, LBL	291
Synchrotron Resonances Due to Crab Cavities — S. Kurokawa, KEK; D. Pestrikov, KEK/BINP Novosibirsk	294
Third-Order Bending Magnet Optics for Cartesian Coordinates — V. V. Andreev, I. P. Yudin, JINR Moscow	297
Effects of Plane Undulator (Wiggler) Fields on Beam Dynamics at Large Orbit Distortion — S. Efimov, E. Bulyak, Kharkov Inst.	300
Bunching Property of High Current Injector with Subharmonic Prebuncher in Linac — Z. Zhang, Y. Chen, CIAE China	303
Beam Transport Line of CIAE Medical Cyclotron and Its Magnetic Elements Design Studies — T. Zhang, C. Chu, M. Fan, CIAE China	306
Resonant Beam Extraction with Constant Separatrix — K. Hiramoto, M. Tadokoro, J. Hirota, M. Nishi, Hitachi Ltd.	309
The On-Line Control Software for BEPC Beam Transport Lines — X. Zhang, K. Wei, C. Zhang, IHEP China.....	312
About Extraction of 70-GeV Protons by a Bent Crystal from the IHEP Accelerator to the Proza Setup — A. A. Asseev, A. N. Vasil'ev, E. A. Ludmirsky, V. A. Maishev, S. B. Nurusev, Yu. S. Fedotov, IHEP Russia	315
Increase a Bent Crystal Extraction Efficiency by Means of Thin Internal Target — A. A. Asseev, E. A. Myae, S. V. Sokolov, Yu. S. Fedotov, IHEP Russia.....	318
Influence of Thin Internal Target on the Bent Crystal Extraction Efficiency — A. A. Asseev, S. V. Sokolov, IHEP Russia	320
Extraction of 50 GeV Protons from IHEP Accelerator by Bent Crystal — A. A. Asseev, V. A. Maishev, E. A. Myae, IHEP Russia.....	322
On Using the Thin Target at Extraction of Protons from the Accelerators by Bent Crystal — A. A. Asseev, IHEP Russia	324
A Digital Computer Program for the Simulation of Positive or Negative Particle Beams on a PC — J. E. Boers, Thunderbird Simulations	327
Antiproton Extraction in the Fermilab Antiproton Accumulator — M. Church, S. O'Day, FNAL	330
Beam Optics of LEB-MEB Transfer Line for Superconducting Super Collider — N. Mao, J. A. McGill, K. L. Brown, R. E. Gerig, SSCL	333
Acceleration and Bunching by a Gap — S. Kulinski, INFN-LNF	336
The New Slow Extraction System of the CERN PS — Ch. Steinbach, H. Stucki, M. Thivent, CERN	339
Simulation of Slow Extraction in the Main Injector — C. S. Mishra, F. A. Harfoush, J. Johnstone, FNAL	342
Stability of Beam in the Fermilab Main Injector — C. S. Mishra, F. A. Harfoush, FNAL	345
Correction Schemes to Improve the Dynamical Aperture of the Main Injector — C. S. Mishra, F. A. Harfoush, FNAL	348
Defining the Systematic and Random Multipole Errors for Main Injector Tracking — F. A. Harfoush, B. C. Brown, H. D. Glass, C. S. Mishra, S. Peggs, FNAL	351
Experience with the New Reverse Injection Scheme in the Tevatron — S. Saritepe, G. Goderre, J. Annala, B. Hanna, A. Braun, FNAL	354
Injection and Extraction Performance at the SIS/ESR Facility — H. Eickhoff, K. Blasche, U. Blell, B. Franzke, J. Pinkow, GSI Darmstadt	357
The AGS-Booster Complex for the g-2 Experiment and RHIC Injection — M. Tanaka, Y. Y. Lee, BNL	360
First-Turn Losses in the LAMPF Proton Storage Ring (PSR) — R. Hutson, R. Macek, LANL	363

Each volume begins with this five-volume table of contents and ends with the five-volume author index. The chairmen's foreword and a list of conference organizers and staff appear as front matter in Volume 1. A list of conference participants precedes the author index in Volume 5.

Global Coupling and Decoupling of the APS Storage Ring — Y. C. Chae, J. Liu, L. C. Teng, ANL	182
Conventional Collimation and Linac Protection — J. Irwin, R. Helm, W. R. Nelson, D. Walz, SLAC	185
Measurement of Beta-Function and Phase Using the Response Matrix — Y. Chung, G. Decker, K. Evans, Jr., ANL ..	188
MATCH 1.0: The Program for Analytical Matching of Insertion — I. P. Yudin, JINR Moscow	191
The Application Package DeCA for Calculating Cyclic Accelerators — P. I. Gladkikh, A. Yu. Zelinsky, M. A. Strelkov, Kharkov Inst.	194
Echo Effect in Accelerators — G. V. Stupakov, S. K. Kauffmann, SSCL	197
Tune Shift Effect Due to the Sextupole Longitudinal Periodic Structure in the Superconducting Dipole Magnets — G. López, S. Chen, SSCL	200
Decoupling Schemes for the SSC Collider — Y. Cai, G. Bourianoff, B. Cole, R. Meinke, J. Peterson, F. Pilat, S. Stampke, M. Syphers, R. Talman, SSCL	203
Matrix Nonlinear Beam Dynamics in Curvilinear Space-Time — A. Dymnikov, U. St. Petersburg; R. Hellborg, U. Lund	206
A Numerical Check of the Thermal Wave-Model for Particle-Beam Dynamics — R. Fedele, G. Miele, U. Napoli; F. Galluccio, INFN Napoli	209
Longitudinal Dynamics for Electrons in the Thermal Wave Model for Charged Particle Beams — R. Fedele, G. Miele, U. Napoli/INFN Napoli; L. Palumbo, U. Roma/INFN-LNF	212
Experimental Measurement of Dynamic Aperture at the Photon Factory Storage Ring — Y. Kobayashi, T. Mitsuhashi, A. Ueda, KEK; T. Yamakawa, Tohoku U.	215
Lattice and Dynamic Aperture of the Duke FEL Storage Ring — Y. Wu, V. N. Litvinenko, J. M. J. Madey, Duke ...	218
Synchrotron Coupling Effects in Alternating Phase Focusing — W. Cheng, R. L. Gluckstern, H. Okamoto, U. Maryland	221
Experimental Determination of a Betatron Difference Resonance — M. Ellison, M. Ball, B. Brabson, J. Budnick, D. D. Caussyn, J. Collins, V. Derenchuk, G. East, T. Ellison, D. Friesel, B. Hamilton, H. Huang, W. P. Jones, S. Y. Lee, D. Li, S. Nagaitsev, T. Sloan, Y. Wang, IUCF; A. W. Chao, S. Dutt, M. Syphers, Y. T. Yan, P. L. Zhang, SSCL; M. Minty, SLAC; K. Y. Ng, FNAL; L. Teng, ANL; X. Pei, BNL	224
Experimental Results of the Betatron Sum Resonance — Y. Wang, M. Ball, B. Brabson, J. Budnick, D. D. Caussyn, J. Collins, V. Derenchuk, G. East, M. Ellison, D. Friesel, B. Hamilton, H. Huang, S. Y. Lee, W. P. Jones, D. Li, S. Nagaitsev, T. Sloan, IUCF; A. W. Chao, S. Dutt, M. Syphers, Y. T. Yan, P. L. Zhang, SSCL; K. Y. Ng, FNAL; M. Minty, SLAC; X. Pei, BNL.....	227
Chromaticity Compensation and Dynamic Aperture Limitation of SIBERIA-2 — V. Korchuganov, E. Levichev, V. Sajaev, BINP	230
RF Voltage Modulation at Discrete Frequencies, for Application to Proton Extraction Using Crystal Channeling — W. E. Gabella, J. Rosenzweig, UCLA; R. Kick, IMSA; S. Peggs, BNL	233
Modification of the Short Straight Sections of the High Energy Booster of the SSC — M. Li, D. Johnson, P. Kocur, R. Schailey, R. Servranckx, R. Talman, Y. Yan, R. York, V. Yarba, SSCL	236
Dynamic Aperture of the Chromatically Corrected Collider Lattice — F. Pilat, Y. Nosochkov, T. Sen, R. Stiening, SSCL	239
An Optimized Formulation for Deprit-Type Lie Transformations of Taylor Maps for Symplectic Systems — J. Shi, U. Houston; Y. T. Yan, SSCL	242
Symmetric Integrable-Polynomial Factorization for Symplectic One-Turn-Map Tracking — J. Shi, U. Houston; Y. T. Yan, SSCL	243
Recent Results from the Dynamic Aperture Experiment at the SPS — W. Fischer, J. Gareyte, M. Giovannozzi, T. Risselada, W. Scandale, F. Schmidt, CERN	246
Higher Order Tune Derivatives Due to Low- β Insertions — A. Verdier, CERN	249
A Quasi-Isochronous Operation Mode for the LNLS UVX Storage Ring — L. Lin, C. E. T. Gonçalves da Silva, Unicamp/LNLS Brazil	252
Tracking Studies and Machine Performance Simulation of the SSC Low Energy Booster — X. Wu, R. York, R. Servranckx, S. Machida, J. F. Knox-Seith, U. Wienands, SSCL	255
Magnetic Correction of RHIC Triplets — J. Wei, R. Gupta, S. Peggs, BNL	258
Beam-Beam Modulational Diffusion in 2 1/2 Dimensions — T. Satogata, S. Peggs, BNL	261
Preparation of an Experiment to Investigate Nonlinear Beam Dynamics at the Storage Ring DELTA — M. Schürmann, U. Dortmund	264
Statistics of the Half-Integer Stopband — S. Dutt, F. Chautard, R. Gerig, S. Kauffman, SSCL	267
Stochastic Dynamics for Accelerators — A. Pauluhn, DESY	270

Five-Volume Contents

Emittance Measurements of the 4.5 MeV UCLA RF Photo-Injector — S. C. Hartman, N. Barov, S. Park, C. Pellegrini, J. Rosenzweig, G. Travish, R. Zhang, P. Davis, C. Joshi, G. Hairapetian, UCLA	561
Commissioning of the SIBERIA-2 Preinjector and First Beam Results — V. Korchuganov, G. Kulipanov, E. Levichev, O. Nezhevenko, G. Ostreiko, A. Philipchenko, G. Serdobintsev, E. Shaimerdenov, V. Ushakov, INP Novosibirsk; A. Kadnikov, Yu. Krylov, S. Kuznetsov, V. Ushkov, Yu. Yupinov, Kurchatov Inst.....	564
Emittance Measurement and Modeling of the ALS 50 MeV Linac to Booster Line — J. Bengtsson, W. Leemans, T. Byrne, LBL	567
Extended Version of an S-Band RF Gun — S. Park, C. Pellegrini, UCLA	570
Progress Report on the Commissioning of the Lisa 25 MeV SC Linac — F. Tazzioli, M. Castellano, M. Ferrario, S. Kulinski, M. Minestrini, P. Patteri, INFN-LNF; L. Catani, S. Tazzari, INFN Roma	573
The Plane Wave Transformer Linac Development at UCLA — R. Zhang, S. Hartman, C. Pellegrini, UCLA	575
Nanosecond MOSFET Gun Pulser for the CESR High Intensity Linac Injector — C. R. Dunnam, R. E. Meller, Cornell	578
Progress of PLS 2-GeV Linac — W. Namkung, I. Ko, M. Cho, C. Ryu, J. Bak, S. Nam, H. Lee, POSTECH	581
Lattice Design Principles for a Recirculated, High Energy, SRF Electron Accelerator — D. R. Douglas, CEBAF	584
Commissioning and Operation Experience with the CEBAF Recirculation Arc Beam Transport System — Y. Chao, M. Crofford, N. Dobeck, D. Douglas, A. Hofler, C. Hovater, G. A. Krafft, R. Legg, J. Perry, E. Price, S. Suhring, M. Tiefenback, J. van Zeijts, CEBAF	587
Linac Upgrade Plan for the KEK B-Factory — A. Enomoto, S. Anami, T. Kamitani, H. Hanaki, T. Shidara, I. Sato, KEK	590
Performance Characteristics of the Pulsed High Power Klystron Tube for PLS 2-GeV Linac — M. H. Cho, S. H. Nam, J. S. Oh, S. S. Park, H. S. Lee, J. S. Bak, I. S. Ko, W. Namkung, POSTECH	593
Electron Transport of a Linac Coherent Light Source (LCLS) Using the SLAC Linac — K. L. Bane, T. O. Raubenheimer, J. T. Seeman, SLAC	596
Phasing Schemes for the CEBAF Cavities — S. N. Simrock, R. Kazimi, G. A. Krafft, L. Merminga, L. Ninan, S. Witherspoon, CEBAF	599
Initial Data of Linac Preinjector for SPring-8 — S. Suzuki, H. Yoshikawa, T. Hori, K. Yanagida, A. Mizuno, K. Tamezane, K. Mashiko, H. Yokomizo, JAERI	602
Status of the Advanced Photon Source (APS) Linear Accelerator — M. White, W. Berg, R. Fuja, A. Grelick, G. Mavrogenes, A. Nassiri, T. Russell, W. Wesolowski, ANL	605
200 MeV RF Linac for Brookhaven National Laboratory — K. Whitham, H. Anamkath, S. Lyons, J. Manca, R. Miller, P. Treas, T. Zante, Titan Beta; R. Miller, SLAC; R. Heese, J. Keane, BNL	608
Design of the e^+/e^- Frascati Linear Accelerator for DaFne — K. Whitham, H. Anamkath, S. Lyons, J. Manca, R. Miller, T. Zante, P. Treas, D. Nett, Titan Beta; R. Miller, SLAC; R. Boni, H. Hsieh, S. Kulinski, F. Sannibale, B. Spataro, M. Vescovi, G. Vignola, INFN-Frascati	611
The Possibility of Introducing Additional Focusing Caused by the Circular Irises in Iris Loaded Accelerator Sections — M. Kurz, P. Hülsmann, H.-W. Glock, H. Klein, Inst. f. Ang. Physik	614
Disruption Effects from the Collision of Quasi-Flat Beams — P. Chen, SLAC	617
Accelerator and RF System Development for NLC — A. E. Vlieks, R. Callin, H. Deruyter, R. Early, K. S. Fant, Z. D. Farkas, W. R. Fowkes, C. Galloway, H. A. Hoag, R. Koontz, G. A. Loew, T. L. Lavine, A. Menegat, R. H. Miller, D. Palmer, C. C. Pearson, R. D. Ruth, S. G. Tantawi, P. B. Wilson, J. W. Wang, C. Yoneda, SLAC; N. Kroll, UCSD; C. Nantista, UCLA	620
Rise Time of the Amplitudes of Time Harmonic Fields in Multicell Cavities — H.-W. Glock, M. Kurz, P. Hülsmann, H. Klein, Inst. f. Ang. Physik	623
CLIC Drive Beam Generation by Induction Linac and FEL Experimental Studies for the CERN Linear Collider — R. Corsini, C. D. Johnson, CERN; J. Gardelle, J. Grenier, CESTA	626
Beam Instabilities Related to Different Focusing Schemes in TESLA — A. Mosnier, CE Saclay	629
A Large Aperture Final Focus System for TESLA — O. Napoly, CE Saclay	632
Chicane and Wiggler Based Bunch Compressors for Future Linear Colliders — T. O. Raubenheimer, P. Emma, S. Kheifets, SLAC	635
An "NLC-Style" Short Bunch Length Compressor in the SLAC Linac — J. T. Seeman, R. Holtzapple, SLAC	638
Multibunching Studies for CLIC — I. Wilson, W. Wuensch, CERN	641
Linear Collider Systems and Costs — G. A. Loew, SLAC	644
Application of the Monte Carlo Method to Estimate the Tenth-Value Thickness for X-Rays in Medical Electron Accelerators — J. Ródenas, G. Verdú, U. Politècnica, Valencia	647

Volume 1:	1-747
Volume 2:	748-1640
Volume 3:	1641-2545
Volume 4:	2546-3218
Volume 5:	3219-3933

Proceedings of the 1993 Particle Accelerator Conference

Burst-Mode Electron Gun Pulser for FEL with the ISIR Linac — K. Tsumori, Sumitomo Elect. Ind.; S. Okuda, T. Yamamoto, S. Suemine, S. Takamuku, Osaka U.	650
Positron Accumulation Ring for the SPring-8 Project — Y. Miyahara, JAERI-RIKEN	653

High-Current Accelerators

Chair: T. Fessenden

Induction Accelerator Development for Heavy Ion Fusion (Invited Paper) — L. L. Reginato, LBL	656
Generation and Focusing of High Energy, 35-kA Electron Beams for Pulsed-Diode Radiographic Machines: Theory and Experiment — R. L. Carlson, M. J. George, LANL; T. P. Hughes, D. R. Welch, MRC	661
Numerical Investigation of High-Current Ion Beam Acceleration and Charge Compensation in Two Accelerating Gaps of Induction Linac — N. G. Belova, Russian Acad.; V. I. Karas', Kharkov Inst.	664
The Light-Ion Pulsed Power Induction Accelerator for the Laboratory Microfusion Facility (LMF) — M. G. Mazarakis, D. L. Smith, L. F. Bennett, T. R. Lockner, R. E. Olson, J. W. Poukey, J. Boyes, Sandia Nat. Lab.	667

Poster presentations:

First Operation of the LELIA Induction Accelerator at CESTA — Ph. Eyharts, Ph. Anthouard, J. Bardy, C. Bonnafond, Ph. Delsart, A. Devin, P. Eyl, P. Grua, J. Labrousche, J. Launspach, P. Le Taillandier, J. de Mascureau, E. Merle, A. Roques, M. Thevenot, D. Villate, CEA-CESTA	670
An Induction Linac and Pulsed Power System at KEK — J. Kishiro, K. Ebihara, S. Hiramatsu, Y. Kimura, T. Ozaki, K. Takayama, D. H. Whittum, K. Saito, KEK	673
Design and Operation of Inductive Acceleration Modules for FEL with Controlled Voltage Ramp — S. Kawasaki, Saitama U.; H. Ishizuka, Fukuoka Inst.; A. Tokuchi, Nichicon Corp.; Y. Yamashita, S. Nakajima, Hitachi; S. Sakamoto, H. Maeda, M. Shiho, JAERI	676
Study on Induction Accelerator for Industrial Applications — Y. S. Cho, K. H. Baik, K. H. Chung, Seoul Nat. U.; B. H. Choi, Korea Atomic Energy Res. Inst.	679
Linear Induction Accelerators for Industrial Applications — M. I. Demsky, Yu. P. Vakhruhin, A. E. Baranovsky, A. A. Volzhev, A. P. Kuprianov, D. E. Trifonov, Efremov Inst.	682
High Power, High Brightness Electron Beam Generation in a Pulse-Line Driven Pseudospark Discharge — W. W. Destler, Z. Segalov, J. Rodgers, K. Ramaswamy, M. Reiser, U. Maryland	685
Experimental Study of Post-Acceleration and Transport of a Pseudospark-Produced Electron Beam — C. J. Liu, M. J. Rhee, U. Maryland	688
Compound-Lens Injector for a 19-MeV, 700-kA Electron Beam — T. W. L. Sanford, J. W. Poukey, J. A. Halbleib, Sandia Nat. Lab.; R. C. Mock, Ktech Corp.	691
Electron Flow in the SABRE Linear Induction Adder in Positive Polarity — J. R. Smith, Titan/Spectra; J. W. Poukey, M. E. Cuneo, D. L. Hanson, S. E. Rosenthal, M. Bernard, Sandia Nat. Lab.	694
Design and Progress of the AIRIX Induction Accelerator — J. de Mascureau, Ph. Anthouard, J. Bardy, C. Bonnafond, Ph. Delsart, A. Devin, Ph. Eyharts, P. Eyl, P. Grua, J. Labrousche, J. Launspach, P. Le Taillandier, E. Merle, A. Roques, B. Sacepe, M. Thevenot, D. Villate, CEA-CESTA	697
Nuclear Fusion of Protons with Ions of Boron — A. G. Ruggiero, BNL	700
Heavy Ion Fusion Injector Program — S. Yu, S. Eylon, W. W. Chupp, A. Faltens, T. Fessenden, E. Henestroza, R. Hipple, D. Judd, C. Peters, L. Reginato, H. Rutkowski, J. Stoker, D. Vanecek, LBL; J. Barnard, G. Caporaso, Y. J. Chen, F. Deadrick, A. Friedman, D. Grote, D. Hewett, LLNL	703
Ion Pulse Propagation Through a Previously Unfilled Electrostatic Aperture Lens Accelerating Column — H. L. Rutkowski, S. Eylon, D. S. Keeney, LBL; Y. J. Chen, D. W. Hewett, J. Barnard, LLNL	706
ILSE-ESQ Injector Scaled Experiment — E. Henestroza, S. Eylon, S. Yu, LBL; D. Grote, LLNL	709
One Dimensional Simulations of Transients in Heavy Ion Injectors — J. J. Barnard, G. J. Caporaso, LLNL; S. S. Yu, S. Eylon, LBL	712
Analysis of Beam Loading in Electrostatic Columns — G. J. Caporaso, J. J. Barnard, LLNL	715
Simulation of Transient Effects in the Heavy Ion Fusion Injectors — Y. Chen, D. W. Hewett, LLNL	718
Electrostatic Quadrupoles for Heavy-Ion Fusion — P. Seidl, A. Faltens, LBL	721
Simulation Studies of Space-Charge-Dominated Beam Transport in Large Aperture Ratio Quadrupoles — W. M. Fawley, L. J. Laslett, C. M. Celata, A. Faltens, LBL; I. Haber, NRL	724

Each volume begins with this five-volume table of contents and ends with the five-volume author index. The chairmen's foreword and a list of conference organizers and staff appear as front matter in Volume 1. A list of conference participants precedes the author index in Volume 5.

Three Dimensional PIC Simulation of Heavy Ion Fusion Beams: Recent Improvements to and Applications of WARP — D. P. Grote, A. Friedman, LLNL; I. Haber, NRL	727
Longitudinal Beam Dynamics for Heavy Ion Fusion — D. A. Callahan, A. B. Langdon, A. Friedman, LLNL; I. Haber, NRL	730
Correction of Longitudinal Errors in Accelerators for Heavy-Ion Fusion — W. M. Sharp, D. A. Callahan, J. J. Barnard, A. B. Langdon, LLNL; T. J. Fessenden, LBL	733
System Modeling for the Longitudinal Beam Dynamics Control Problem in Heavy Ion Induction Accelerators — A. N. Payne, LLNL	736
Development of FET-Switched Induction Accelerator Cells for Heavy-Ion Fusion Recirculators — M. A. Newton, W. R. Cravey, S. A. Hawkins, H. C. Kirbie, C. W. Ollis, LLNL	739
Parametric Studies for Recirculating Induction Accelerators as Drivers for Heavy-Ion Fusion — R. L. Bieri, Schafer Assoc.	742
A Fusion Device of the Continuous Electron Beam Confinement Used by the Accumulating Ring with the Continuous Injection — S. Gao, G. Qian, CIAE China	745

Volume 2

RF Structures

Chair: D. Reid

Operating Experience with High Beta Superconducting RF Cavities (<i>Invited Paper</i>) — H. F. Dylla, L. R. Doolittle, J. F. Benesch, CEBAF	748
Perpendicular Biased Ferrite-Tuned Cavities (<i>Invited Paper</i>) — R. L. Poirier, TRIUMF	753
SRF Cavities for Future Applications (<i>Invited Paper</i>) — D. Proch, DESY	758
Preparation and Testing of a Superconducting Cavity for CESR-B — D. Moffat, P. Barnes, J. Kirchgessner, H. Padamsee, J. Sears, Cornell	763
High Power Operation of Single-Cell 352-MHz Cavity for the Advanced Photon Source (APS) — J. F. Bridges, Y. W. Kang, R. L. Kustom, K. Primdahl, ANL	766

Poster presentations:

Development of Crab Cavity for CESR-B — K. Akai, J. Kirchgessner, D. Moffat, H. Padamsee, J. Sears, M. Tigner, Cornell	769
A New 3-D Electromagnetic Solver for the Design of Arbitrarily Shaped Accelerating Cavities — P. Arcioni, M. Bressan, L. Perregrini, U. Pavia	772
Design Study for the ELFA Linac — W. A. Barletta, LBL; G. Bellomo, INFN/ U. Milan; G. Gemme, R. Parodi, INFN Genova; V. Stagno, V. Variale, INFN Bari	775
The RF Cavity for DAFNE — S. Bartalucci, R. Boni, A. Gallo, L. Palumbo, R. Parodi, M. Serio, B. Spataro, INFN-LNF	778
Mechanical Results of the CEBAF Cavity Series Production — J. Mammosser, J. F. Benesch, CEBAF	781
Fabrication of Complex Mechanical Components — Y. Beroud, SICN	784
Measurements of Higher Order Modes in 3rd Harmonic RF Cavity at Fermilab — C. M. Bhat, FNAL	787
POISSON/SUPERFISH on PC Compatibles — J. H. Billen, L. M. Young, LANL	790
Radio Frequency Measurement and Analysis Codes — J. H. Billen, LANL	793
Progress on RF Superconductivity at Saclay — Groupe d'Etudes des Cavités Supraconductrices, CE Saclay and Institut de Physique Nucléaire, Orsay	796
A New Surface Treatment for Niobium Superconducting Cavities — B. Bonin, C. Henriot, C. Antoine, B. Coadou, F. Koechlin, J. P. Rodriguez, E. Lemaitre, P. Greiner, CE Saclay	798
Using the Panofsky-Wenzel Theorem in the Analysis of Radio-Frequency Deflectors — M. J. Browman, LANL	800
The Effects of Temperature and RF Power Level on the Tuning of the Water-Cooled SSC Low-Energy Booster Cavity — C. Friedrichs, LANL; G. Hulsey, SSCL	803
Superconducting Cavities for the LEP Energy Upgrade — G. Cavallari, C. Benvenuti, P. Bernard, D. Bloess, E. Chiaveri, F. Genesio, E. Haebel, N. Hilleret, J. Tuckmantel, W. Weingarten, CERN	806
TESLA Input Coupler Development — M. Champion, D. Peterson, T. Peterson, C. Reid, M. Ruschman, FNAL	809

Proceedings of the 1993 Particle Accelerator Conference

Computer Simulation and Cold Model Testing of CCL Cavities — C. R. Chang, C. G. Yao, D. A. Swenson, L. W. Funk, SSCL	812
Drive Linac for the Argonne Wakefield Accelerator — E. Chojnacki, R. Konecny, M. Rosing, J. Simpson, ANL	815
Choice of the RF Cavity for the SSC Collider — W. Chou, SSCL	818
High Field Conditioning of Cryogenic RF Cavities — M. Cole, T. Debiak, C. Lom, W. Shephard, J. Sredniawski, Grumman	821
Status of the SSC LEB RF Cavity — P. Coleman, F. Brandeberry, C. Friedrichs, Y. Goren, T. Grimm, G. Hulsey, S. Kwiatkowski, A. Propp, L. Taylor, L. Walling, SSCL; J. Averbukh, M. Karliner, V. Petrov, S. Yakovlev, BINP	824
RF Commissioning of the Superconducting Super Collider Radio Frequency Quadrupole Accelerator — R. I. Cutler, G. Arbique, J. Grippe, S. Marsden, O. Marrufo, R. Rodriguez, SSCL	827
Design of a Tuner and Adjustable RF Coupler for a CW 2856 MHz RF Cavity — M. S. de Jong, F. P. Adams, R. J. Burton, R. M. Hutcheon, T. Tran-Ngoc, AECL, Chalk River; A. Zolfaghari, P. T. Demos, MIT-Bates	829
A 2856 MHz RF Cavity for the MIT-Bates South Hall Ring — M. S. de Jong, F. P. Adams, R. J. Burton, R. M. Hutcheon, T. Tran-Ngoc, AECL, Chalk River; A. Zolfaghari, P. T. Demos, MIT-Bates	832
Cavity RF Mode Analysis Using a Boundary-Integral Method — M. S. de Jong, F. P. Adams, AECL, Chalk River ..	835
Design Considerations for High-Current Superconducting RFQ's — J. R. Delaven, C. L. Bohn, W. L. Kennedy, L. Sagalovsky, ANL	838
Commissioning of the CEBAF Cryomodels — M. Drury, T. Lee, J. Marshall, J. Preble, Q. Saulter, W. Schneider, M. Spata, M. Wiseman, CEBAF	841
Design and Fabrication of High Gradient Accelerating Structure Prototype at 36.5 GHz — V. A. Dvornikov, I. A. Kuzmin, MEPI Russia.....	844
The SSC RFQ-DTL Matching Section Buncher Cavities — T. Enegren, C. M. Combs, Y. Goren, M. D. Hayworth, A. D. Ringwall, D. A. Swenson, SSCL.....	846
Bulk Niobium Low-, Medium- and High-B Superconducting Quarter Wave Resonators for the ALPI Postaccelerator — A. Facco, J. S. Sokolowski, INFN Legnaro; I. Ben-Zvi, BNL; E. Chiaveri, CERN; B. V. Elkonin, Weizmann Inst.	849
A Numerical Method for Determining the Coupling Strengths and Resonant Frequencies of a Nonperiodic Coupled Cavity Chain — M. Foley, T. Jurgens, FNAL	852
Thermal Study of HOM Couplers for Superconducting RF Cavities — M. Fouaidy, T. Junquera, IPN Orsay; S. Chel, A. Mosnier, Saclay	855
Very Wide Range and Short Accelerating Cavity for MIMAS — C. Fougeron, P. Ausset, D. de Menezes, J. Peyromaure, G. Charruau, LNS-CE Saclay	858
Fundamental Mode Detuned Travelling Wave Accelerating Structure — J. Gao, LAL Orsay	862
Demi-Disc Travelling Wave Accelerating Structure — J. Gao, LAL Orsay	865
Analytical Formulae for the Coupling Coefficient β Between a Waveguide and a Travelling Wave Structure — J. Gao, LAL Orsay	868
Automated Bead-Positioning System for Measuring Impedances of RF Cavity Modes — D. A. Goldberg, R. A. Rimmer, LBL	871
Measurements of Higher-Order Mode Damping in the PEP-II Low-Power Test Cavity — R. A. Rimmer, D. A. Goldberg, LBL	874
Nonlinear Effects in Ferrite Tuned Cavities — Y. Goren, N. K. Mahale, L. Walling, T. Enegren, G. Hulsey, SSCL; V. P. Yakovlev, V. M. Petrov, BINP	877
Eddy Current Analysis for the SSC Low Energy Booster Cavity — Y. Goren, L. Walling, F. Brandeberry, N. Spayd, SSCL	880
Voltage Counter-Phasing in the SSC Low Energy Booster — Y. Goren, SSCL; T. F. Wang, LANL	883
An Update on High Peak Power (HPP) RF Processing of 3 GHz Nine-Cell Niobium Accelerator Cavities — P. Barnes, J. Kirchgessner, D. Moffat, H. Padamsee, J. Sears, Cornell; C. Crawford, FNAL; J. Graber, P. Schmüser, DESY	886
Microscopic Investigation of RF Surfaces of 3 GHz Niobium Accelerator Cavities Following RF Processing — P. Barnes, T. Flynn, J. Kirchgessner, J. Knobloch, D. Moffat, H. Muller, H. Padamsee, J. Sears, Cornell; J. Graber, DESY	889
A World Record Accelerating Gradient in a Niobium Superconducting Accelerator Cavity — P. Barnes, J. Kirchgessner, D. Moffat, H. Padamsee, J. Sears, Cornell; J. Graber, DESY	892

Each volume begins with this five-volume table of contents and ends with the five-volume author index. The chairmen's foreword and a list of conference organizers and staff appear as front matter in Volume 1. A list of conference participants precedes the author index in Volume 5.

Characterization of NSLS Accelerating Cavities Using Impedance Measurement Techniques — <i>S. M. Hanna, P. M. Stefan, NSLS-BNL</i>	895
In Search of Trapped Modes in the Single-Cell Cavity Prototype for CESR-B — <i>W. Hartung, Cornell; E. Haebel, CERN</i>	898
Envelope Equations for Transients in Linear Chains of Resonators — <i>H. Henke, M. Filtz, TU Berlin</i>	901
A Broad-Band Side Coupled mm-Wave Accelerating Structure for Electrons — <i>H. Henke, W. Bruns, TU Berlin</i>	904
Accelerator Structure Development for NLC — <i>H. A. Hoag, H. Deruyter, C. Pearson, R. D. Ruth, J. W. Wang, SLAC; J. Schaefer, Texas Inst.</i>	907
HOM Damping with Coaxial Dampers in a Pillbox Cavity Without the Fundamental Mode Frequency Rejection Filter — <i>Y. W. Kang, R. L. Kustom, J. F. Bridges, ANL</i>	910
Reduced Length Design of 9.8 MHz RF Accelerating Cavity for the Positron Accumulator Ring (PAR) of the Advanced Photon Source (APS) — <i>Y. W. Kang, J. F. Bridges, R. L. Kustom, ANL</i>	913
Higher Order Mode Damping System in the UNK RF Cavity — <i>V. Katalev, V. Kudryavtsev, I. Sulygin, IHEP</i>	916
Status and Outlook for High Power Processing of 1.3 GHz TESLA Multicell Cavities — <i>J. Kirchgessner, P. Barnes, J. Graber, D. Metzger, D. Moffat, H. Muller, H. Padamsee, J. Sears, M. Tigner, Cornell; L. Bartelson, M. Champion, C. Crawford, H. Edwards, K. Koepke, M. Kuchnir, H. Pfeffer, FNAL; A. Matheisen, M. Pekeler, P. Schmüser, DESY</i>	918
20 MV/m Accelerating Gradient with Heat Treatment of a Six Cell, 1.5 GHz Cavity for TESLA — <i>J. Kirchgessner, P. Barnes, W. Hartung, D. Moffat, H. Padamsee, D. Rubin, J. Sears, M. Tigner, Cornell; M. Hiller, Babcock & Wilcox; D. Saraniti, SLAC; Q. S. Shu, SSCL</i>	921
A New 50 MHz RF Cavity for Aladdin — <i>K. J. Kleman, SRC Madison</i>	924
Performance of a CEBAF Production Cavity After High-Temperature Heat Treatment — <i>P. Kneisel, M. G. Rao, CEBAF</i>	927
Suppression of Higher-Order Modes in an RF Cavity by Resistive Material — <i>T. Koseki, Y. Kamiya, ISSP Tokyo; M. Izawa, KEK</i>	930
A Coaxial-Type Accelerating System with Amorphous Material — <i>V. A. Krasnopolsky, MRTI Russia</i>	933
Applications and Comparisons of Methods of Computing the S Matrix of 2-Ports — <i>R. M. Jones, K. Ko, S. Tantawi, SLAC; N. Kroll, UCSD/SLAC; D. U. L. Yu, DULY Res.</i>	936
Construction of the CEBAF RF Separator — <i>A. Krycuk, J. Fugitt, A. Johnson, R. Kazimi, L. Turlington, CEBAF</i>	939
RF Cavity for the Medium Energy Booster for SSCL — <i>S. Kwiatkowski, J. Curbow, T. Enegren, A. Propp, SSCL; V. P. Yakovlev, V. M. Petrov, Budker Inst.</i>	941
New Achievements in RF Cavity Manufacturing — <i>G. Lippmann, K. Pimiskern, H. Kaiser, Dornier GmbH</i>	944
Analysis of Mechanical Fabrication Experience with CEBAF's Production SRF Cavities — <i>J. Mammosser, P. Kneisel, J. F. Benesch, CEBAF</i>	947
Microphonic Analysis of Cryo-Module Design — <i>A. Marziali, H. A. Schwettman, Stanford U.</i>	950
The Design of a Pill-Box Cavity with Waveguide HOM Suppressors — <i>A. Massarotti, G. D'Auria, A. Fabris, C. Pasotti, C. Rossi, M. Svandrlik, Sinc. Trieste</i>	953
Power Conditioning of the RF Cavities for ELETTRA — <i>A. Massarotti, G. D'Auria, A. Fabris, C. Pasotti, C. Rossi, M. Svandrlik, Sinc. Trieste</i>	956
High Power Test of a SLED System with Dual Side-Wall Coupling Irises for Linear Colliders — <i>H. Matsumoto, H. Baba, A. Miura, S. Yamaguchi, KEK</i>	959
Performance Tests of a Ferrite-Loaded Cavity Under Operation Conditions — <i>S. Papureanu, Ch. Hamm, A. Schnase, H. Meuth, Jülich</i>	962
CLIC Transfer Structure (CTS) Simulations Using "MAFIA" — <i>A. Millich, CERN</i>	965
Magnetron Sputtering Configuration for Coating 1.3 GHz Cavities with a Nb Film — <i>M. Minestrini, M. Ferrario, S. Kulinski, INFN-LNF; S. Tazzari, INFN Roma</i>	968
Accelerator Structure for Low-Energy Electron Beam — <i>A. V. Mishin, MEPI Moscow</i>	971
Higher Order Mode Dampers for the KAON Booster Cavity — <i>A. K. Mitra, TRIUMF</i>	974
Design and Fabrication of a Ferrite-Lined HOM Load for CESR-B — <i>D. Moffat, P. Barnes, J. Kirchgessner, H. Padamsee, J. Sears, M. Tigner, A. Tribendis, V. Veshcherevich, Cornell</i>	977
High-Beta Linac Accelerating Structure — <i>V. G. Andreev, G. I. Batsikh, B. I. Bondarev, B. P. Murin, MRTI</i>	980
Design of a 90° Overmoded Waveguide Bend — <i>C. Nantista, UCLA; N. M. Kroll, UCSD/SLAC; E. M. Nelson, SLAC</i>	983
Numerical Simulation of Coupler Cavities for Linacs — <i>C.-K. Ng, H. Deruyter, K. Ko, SLAC</i>	986

Proceedings of the 1993 Particle Accelerator Conference

TESLA Vertical Test Dewar Cryogenic and Mechanical Design — T. H. Nicol, D. E. Arnold, M.S. Champion, FNAL	989
Update of the TRISTAN Superconducting RF System — S. Noguchi, K. Akai, E. Kako, K. Kubo, T. Shishido, KEK	992
Cryostat for a Beam Test with the CESR-B Cavity — E. Nordberg, P. Barnes, R. Ehrlich, J. Kirchgessner, D. Metzger, D. Moffat, H. Muller, H. Padamsee, J. Sears, K. She, M. Tigner, Cornell; W. Fox, LANL; H. Heinrichs, U. Wuppertal	995
A Statistical Model for Field Emission in Superconducting Cavities — H. Padamsee, K. Green, W. Jost, B. Wright, Cornell	998
Design and Test of Prototype Cavities for the ELFA Linac — G. Bellomo, R. Parodi, G. Gemme, P. Fabbriatore, R. Musenich, B. Zhang, INFN	1001
Frequency Domain Determination of the Waveguide Loaded Q for the SSCL Drift Tube Linac — J. Petillo, W. Krueger, A. Mondelli, SAIC; J. Potter, AccSys Technology	1004
Some Operational Characteristics of CEBAF RF Windows at 2 K — H. L. Phillips, C. Reece, T. Powers, V. Nguyen-Tuong, CEBAF	1007
Photoemission Phenomena on CEBAF RF Windows at Cryogenic Temperatures — T. Powers, P. Kneisel, M. Vaidya, CEBAF	1010
Fabrication of the APS Storage Ring Radio Frequency Accelerating Cavities — K. Primdahl, J. Bridges, F. Depaola, R. Kustom, ANL; D. Snee, FNAL	1013
Performance of Production SRF Cavities for CEBAF — C. Reece, J. Benesch, P. Kneisel, P. Kushnick, J. Mammosser, T. Powers, CEBAF	1016
A New 15 MHz, 4 MV/m RF-Deflector for the Munich Heavy Ion Recoil Spectrometer (MRS)— K. Rudolph, P. Jaenker, U. Munich	1019
Superconducting Multicell Cavity Development Program at Los Alamos — B. Rusnak, G. Spalek, E. Gray, J. N. DiMarco, R. DeHaven, J. Novak, P. Walstrom, J. Zumbro, H. A. Thiessen, J. Langenbrunner, LANL ..	1021
L-Band Superconducting Cavities at KEK for TESLA — K. Saito, S. Noguchi, E. Kako, M. Ono, T. Shishido, T. Tajima, M. Matsuoka, H. Miwa, T. Suzuki, H. Umezawa, KEK	1024
Design of a HOM Damped Cavity for the ATF Damping Ring — S. Sakanaka, K. Kubo, T. Higo, KEK	1027
Measurement of Microwave Properties of X-Band Accelerating Structure Under Pulsed High-Power Operation at Liquid Nitrogen Temperature — A. J. Saversky, I. S. Shchedrin, MEPI Moscow	1030
RF Systems Engineering for the SSC Collider Rings — G. Schaffer, P. D. Coleman, R. E. Mustaine, J. D. Wallace, X. Q. Wang, Y. Zhao, J. D. Rogers, SSCL	1033
Impedance Calculations for a Coaxial Liner — M. Filtz, T. Scholz, TU Berlin.....	1036
Design of a High-Power Test Model of the PEP-II RF Cavity — H. D. Schwarz, R. A. Bell, J. A. Hodgson, J. G. Judkins, K. Ko, N. Kroll, C. K. Ng, R. P. Pendleton, K. Skarpaas, SLAC; G. Lambertson, R. Rimmer, LBL; M. S. deJong, T. Tran-Ngoc, F. P. Adams, M. G. Lipsett, W. Mellors, AECL	1039
Construction of a Superconducting RFQ Structure — K. W. Shepard, W. L. Kennedy, ANL; K. R. Crandall, AccSys Technology	1042
Niobium Coaxial Quarter-Wave Cavities for the New Delhi Booster Linac — K. W. Shepard, ANL; A. Roy, P. N. Potukuchi, Nuc. Science Ctr., New Delhi	1045
Design of High Power Model of Damped Linear Accelerating Structure Using Choke Mode Cavity — T. Shintake, KEK	1048
Suppression of Longitudinal Coupled-Bunch Instability Using Energy Storage Cavity in B-Factory RF System — T. Shintake, KEK	1051
A Two-Gap Booster Synchrotron RF Cavity — W. R. Smythe, D. C. Van Westrum, U. Colorado	1054
HOM (Higher-Order Mode) Test of the Storage Ring Single-Cell Cavity with a 20-MeV e^- Beam for the Advanced Photon Source (APS) — J. Song, Y. W. Kang, J. Kustom, ANL	1057
Performance of a 1500 MHz Niobium Cavity with 2K-LHe Channel Cooling — J. Susta, P. Kneisel, M. Wiseman, CEBAF	1060
Large Scale Production at Ansaldo of 352 MHz Niobium Coated LEP-CERN Cavities: Development Activities and First Results — A. Bixio, P. Gagliardi, M. Marin, S. Moz, W. Sciutto, F. Terzi, G. Zoni, Ansaldo	1063
RF Hardware Development Work for the CLIC Drive Beam — G. Carron, L. Thorndahl, CERN	1066
Accelerating Frequency Shift Minimization — A. V. Tiunov, V. I. Shvedunov, INP Moscow	1069

Each volume begins with this five-volume table of contents and ends with the five-volume author index. The chairmen's foreword and a list of conference organizers and staff appear as front matter in Volume 1. A list of conference participants precedes the author index in Volume 5.

Calculations and Model Measurements for the Euterpe Cavity — J. A. van der Heide, M. J. A. Rubingh, W. J. G. M. Kleeven, J. I. M. Botman, C. J. Timmermans, H. L. Hagedoorn, Eindhoven U. of Tech.	1072
APLE Accelerator Prototype Cavity Fabrication and Low Power Tests — A. M. Vetter, T. L. Buller, T. D. Hayward, D. R. Smith, V. S. Starkovich, Boeing D&S	1075
Mechanically Tuned Accelerating Resonators — F. A. Vodopianov, MRTI	1078
Industrial Fabrication of Superconducting Accelerators — D. Dasbach, R. Fleck, D. Kiehlmann, M. Peiniger, H. Vogel, Siemens AG	1080
Broadband Higher-Order Mode (HOM) Damper for SSC LEB Ferrite-Tuned Cavity — L. Walling, G. Hulsey, T. Grimm, SSCL	1083
Design of the Detuned Accelerator Structure — J. W. Wang, E. M. Nelson, SLAC	1086
Construction of an RF Cavity for the LNLS Synchrotron — D. Wisnivesky, IFGW/ Unicamp/LNLS Brazil; M. A. Remy, R. H. A. Farias, LNLS Brazil	1089
Field Emitted Electron Trajectories for the CEBAF Cavity — B. C. Yunn, R. M. Sundelin, CEBAF	1092
Study on TESLA Cavity Shape — D. Zu, J. Chen, Beijing U.	1095

Power Technology and Miscellaneous Subsystems

Chair: D. Reid

Regulation Loops for the Ring Magnet Power Supplies in the SSC Accelerator Complex (<i>Invited Paper</i>) — E. J. Tacconi, C. F. Christiansen, SSCL	1098
High Power CW Klystron® Amplifier for 267 MHz — M. B. Shrader, D. H. Preist, R. N. Tornoe, Varian	1103
Development of Multimegawatt Klystrons for Linear Colliders — G. Caryotakis, R. Callin, K. Eppley, T. Lee, K. Fant, R. Fowkes, H. Hoag, C. Pearson, R. Phillips, S. Tantawi, A. Vlieks, E. Wright, SLAC; E. Lien, Los Altos, CA; G. Miram, Atherton, CA	1106
CEBAF's New RF Separator Structure Test Results — R. Kazimi, J. Fugitt, A. Krycuk, C. K. Sinclair, L. Turlington, CEBAF	1109
Frequency-Domain Analysis of Resonant-Type Ring Magnet Power Supplies — J. M. S. Kim, U. Victoria; K. W. Reiniger, TRIUMF	1112
The Workshop on Microwave-Absorbing Materials for Accelerators — I. E. Campisi, CEBAF.....	1115

Poster presentations:

Analysis and Applications of Quadrature Hybrids as RF Circulators — S. M. Hanna, J. Keane, NSLS-BNL	1118
Flower-Petal Mode Converter for NLC — H. A. Hoag, S. G. Tantawi, H. Deruyter, Z. D. Farkas, K. Ko, N. Kroll, T. L. Lavine, A. Menegat, A. E. Vlieks, SLAC	1121
Development of an S-Band RF Window for Linear Colliders — A. Miura, Grad. U. for Adv. Studies; H. Matsumoto, KEK	1124
High Power Test of RF Window and Coaxial Line in Vacuum — D. Sun, M. Champion, M. Gormley, Q. Kerns, K. Koepke, A. Moretti, FNAL	1127
Mode Selective Directional Coupler for NLC — S. G. Tantawi, SLAC	1130
Window Design with MAFIA — W. Bruns, H. Henke, B. Littmann, R. Lorenz, TU Berlin.....	1133
Dead-Time Tuning of a Pulsed RF Cavity — P. Balleyguier, CEA, Bruyères le Châtel	1136
Frequency Control of RF Booster Cavity in TRIUMF — K. Fong, M. Laverty, TRIUMF	1139
The Phase Servo Tuner Control System of the ALS 500 MHz Cavity — C. C. Lo, B. Taylor, LBL	1142
The Low Level System for the ELETTRA RF Plants — A. Massarotti, G. D'Auria, A. Fabris, C. Pasotti, V. Rizzi, C. Rossi, M. Svandrik, Sinc. Trieste	1145
A Pulse Sequencer for the KAON Factory Beam Chopper — G. Waters, D. Bishop, M. J. Barnes, G. D. Wait, TRIUMF	1148
A Dual Frequency Resonator — P. Lanz, M. Lipnicky, M. Zach, TRIUMF	1151
The Los Alamos VXi-Based Modular RF Control System — S. P. Jachim, C. Ziomek, E. F. Natter, A. H. Regan, J. Hill, L. Eaton, W. D. Gutscher, M. Curtin, P. Denney, E. Hansberry, T. Brooks, LANL	1154
General Overview of the APS Low-Level RF Control System — J. D. Stepp, J. F. Bridges, ANL	1157
Operation of New RF Drivers for the Bevatron Local Injector — J. Calvert, J. Elkins, D. Howard, M. Hui, N. Kellogg, A. Lindner, R. Richter, LBL	1160
432-MHz RF Source for the JHP Proton Linac — M. Ono, S. Anami, H. Hanaki, Z. Igarashi, M. Kawamura, T. Kubo, C. Kubota, K. Kudo, E. Takasaki, T. Takenaka, KEK	1163

Proceedings of the 1993 Particle Accelerator Conference

Test Results of the AGS Booster Low Frequency RF System — R. T. Sanders, P. Cameron, R. Damm, A. Dunbar, M. Goldman, D. Kasha, A. McNerney, M. Meth, A. Ratti, R. Spitz, BNL	1166
Design and Test Results of a 600-kW Tetrode Amplifier for the Superconducting Super Collider — D. E. Rees, D. L. Brittain, LANL ; J. M. Grippe, O. Maruffo, SSCL	1169
Conceptual Design of the 26.7 MHz RF System for RHIC — J. Rose, D. P. Deng, R. McKenzie-Wilson, W. Pirkel, A. Ratti, BNL	1172
Operation of a High-Power CW Klystron with the RFQ1 Facility — J. Y. Sheikh, A. D. Davidson, G. E. McMichael, L. W. Shankland, B. H. Smith, AECL, Chalk River	1175
Design and Results of a 1.3 MW CW Klystron for LEP — E.-G. Schweppe, R. Bachmor, E. Demmel, Philips RHW	1178
Interleaved Wide and Narrow Pulses for the KAON Factory 1 MHz Chopper — G. D. Wait, M. J. Barnes, D. Bishop, G. Waters, TRIUMF	1181
Considerations Regarding the Efficiency of High Power RF Sources for Particle Accelerators — G. Clerc, C. Bearzatto, M. Bres, G. Faillon, Ph. Guidee, Thomson Tubes Elect.	1184
Initial Commissioning of High Power, Long Pulse Klystrons for SSC Injector Linacs — P. Collet, J. C. Terrien, Ph. Guidee, Thomson Tubes Elect.	1187
Simulation of Traveling-Wave Output Structures for High Power rf Tubes — K. R. Eppley, SLAC	1190
Upgrade of an RF Source of the Linac for the B-Factory Project — S. Fukuda, S. Anami, Y. Saito, S. Michizono, K. Nakao, I. Sato, KEK	1193
High-Power RF Pulse Compression with SLED-II at SLAC — C. Nantista, UCLA; Z. D. Farkas, T. L. Lavine, A. Menegat, R. D. Ruth, S. G. Tantawi, A. E. Vlieks, SLAC; N. M. Kroll, UCSD	1196
Rigid-Beam Model of a High-Efficiency Magnicon — D. E. Rees, P. J. Tallerico, LANL; S. J. Humphries, Jr., UNM	1199
High Power Operation Results of the X-Band SLED System — S. Tokumoto, H. Mizuno, KEK; O. Azuma, IHI Japan	1202
Automated Testing of a High-Power RF Microwave Tube — A. Young, D. E. Rees, A. Vergamini, LANL	1205
Two-Klystron Binary Pulse Compression at SLAC — Z. D. Farkas, T. L. Lavine, A. Menegat, A. E. Vlieks, J. W. Wang, P. B. Wilson, SLAC	1208
New Compact Mode Converters for SLAC RF Pulse Power Compression System — G. Luo, SRRC Taiwan	1211
Performance of Litton 805 MHz, 12 MW Klystrons — Q. Kerns, M. B. Popovic, C. Kerns, A. Moretti, FNAL	1214
Higher-Order Modes in the APS Storage Ring Waveguides — S.O. Brauer, R. L. Kustom, ANL	1217
The Design and Production of the Higher-Order-Mode Loads for CEBAF — I. E. Campisi, L. K. Summers, B. H. Branson, A. M. Johnson, A. Betto, CEBAF	1220
The High Level RF System for Transition Crossing Without RF Focusing in the Main Ring at Fermilab — J. Dey, C. M. Bhat, A. Crawford, D. Wildman, FNAL	1223
RF System of the CW Race-Track Microtron-Recuperator for FELs — V. Arbutov, S. Belomestnykh, A. Bushuyev, M. Fomin, N. Gavrilov, E. Gorniker, A. Kondakov, I. Kuptsov, G. Kurkin, V. Petrov, I. Sedlyarov, V. Veshcherevich, BINR, Russia.....	1226
Three Years of Operational Experience with the LEP RF System — S. Hansen, CERN	1229
Measured Performance of the GTA RF Systems — P. M. Denney, S. P. Jachim, LANL	1232
Improved RF System for Aladdin — K. J. Kleman, SRC Madison	1235
The ALS Storage Ring RF System — B. Taylor, C. C. Lo, K. Baptiste, J. Guigli, J. Julian, LBL	1238
The Upgrade Project for the RF System for the Brookhaven AGS — J. M. Brennan, D. J. Ciardullo, T. Hayes, M. Meth, A. J. McNerney, A. Otis, W. Pirkel, R. Sanders, R. Spitz, F. Toldo, A. Zaltsman, BNL	1241
Acceptance Test Performance of the Rocketdyne Radio Frequency Power System — M. Curtin, J. Hall, P. Metty, Rocketdyne; E. Gower, J. Manca, K. Whitham, Titan-Beta Corp.....	1244
The LEP II RF Power Generation System — H. Frischholz, CERN	1247
Overview and Status of RF Systems for the SSC Linac — J. Mynk, J. Grippe, R. I. Cutler, R. Rodriguez, SSCL	1250
Possibilities and Limitations for a Fully Digital RF Signal Synthesis and Control — H. Meuth, A. Schnase, H. Halling, Jülich	1253
RF System Analyses for the SSC Collider Rings — J. D. Rogers, P. D. Coleman, G. Schaffer, J. D. Wallace, X. Q. Wang, Y. Zhao, SSCL	1256
PEP-II Prototype Klystron — W. R. Fowkes, G. Caryotakis, T. G. Lee, C. Pearson, E. L. Wright, SLAC	1259

Each volume begins with this five-volume table of contents and ends with the five-volume author index. The chairmen's foreword and a list of conference organizers and staff appear as front matter in Volume 1. A list of conference participants precedes the author index in Volume 5.

Low Cost Concepts to Reduce the Voltage Ripple of the DC Power Supply — Y. Cheng, K. Liu, SRRC Taiwan	1262
Magnet Power Supply System for the ALS Storage Ring and Booster — L. T. Jackson, K. Luchini, I. Lutz, LBL	1265
Design and Development of Bipolar Power Supply for APS Storage Ring Correctors — Y. G. Kang, ANL	1268
Circuit Description of Unipolar DC-to-DC Converters for APS Storage Ring Quadrupoles and Sextupoles — D. G. McGhee, ANL	1271
PLL Subsystem for NSLS Booster Ring Power Supplies — J. Murray, Stony Brook; R. Olsen, J. Dabrowski, BNL	1274
Control and Performance of the AGS and AGS Booster Main Magnet Power Supplies — R. K. Reece, R. Casella, B. Culwick, J. Geller, I. Marneris, J. Sandberg, A. Soukas, S. Y. Zhang, BNL	1277
Hierarchical Modelling of Line Commutated Power Systems Used in Particle Accelerators Using Saber — J. A. Reimund, SSCL	1280
Independent Resonant System Tracking Considerations — K. W. Reiniger, TRIUMF	1283
Electrical Characteristics of the SSC Low-Energy Booster Magnet System — A. Young, B. E. Shafer, LANL	1285
Analysis and Design of a High-Current, High-Voltage Accurate Power Supply for the APS Storage Ring — M. Fathizadeh, ANL	1288
Design of the HIMAC Synchrotron Power Supply — M. Kumada, K. Sato, A. Itano, M. Kanazawa, E. Takada, K. Noda, M. Sudou, T. Kohno, H. Ogawa, S. Yamada, Y. Sato, T. Yamada, A. Kitagawa, J. Yoshizawa, T. Murakami, Y. Hirao, NIRS; S. Matsumoto, Dokkyo U.; H. Sato, T. Sueno, T. Kato, K. Endo, KEK; K. Utino, Tsukuba Tech.; Y. Takada, U. Tsukuba; A. Noda, Kyoto U.; T. Tanabe, S. Watanabe, INS; S. Koseki, H. Kubo, Hitachi	1291
A 2-Megawatt Load for Testing High Voltage DC Power Supplies — D. Horan, R. Kustom, M. Ferguson, K. Primdahl, ANL	1294
Energy Storage Inductor for the Low Energy Booster Resonant Power Supply System — C. Jach, SSCL; A. Medvedko, S. Petrov, INP Moscow; V. Vinnik, Y. Fishler, UETM Russia	1297
A High Power Water Cooled Resistor for the High Voltage Power Supply in the TRIUMF RF System — K. Jensen, G. Blaker, R. Kuramoto, TRIUMF	1300
Filament Power Supply Improvement of the TRIUMF RF System — A. K. Mitra, J. J. Lu, TRIUMF	1303
Advances in the Development of the Nested High Voltage Generator — R. J. Adler, R. J. Richter-Sand, North Star Res. Corp.	1306
High-Power Klystron Modulator Using a Pulse-Forming Line and Magnetic Switch — M. Akemoto, S. Takeda, KEK	1309
A Compact Modulator for RF Source Development — J. D. Ivers, G. S. Kerslick, J. A. Nation, L. Schachter, Cornell	1312
High Power Pulse Modulator for PLS Linac — S. H. Nam, M. H. Cho, J. S. Oh, S. S. Park, W. Namkung, POSTECH	1315
Pulse Modulator Developments in Support of Klystron Testing at SLAC — R. F. Koontz, R. Cassel, J. de Lamare, D. Ficklin, S. Gold, K. Harris, SLAC	1318
A Blumlein Type Modulator for 100-MW Class X-Band Klystron — H. Mizuno, KEK; T. Majima, S. Sakamoto, Y. Kobayashi, IHI Japan	1321
Noise Reduction Techniques Used on the High Power Klystron Modulators at Argonne National Laboratory — T. J. Russell, ANL	1324
Novel Gigawatt Power Modulator for RF Sources — I. Yampolsky, G. Kirkman, N. Reinhardt, J. Hur, B. Jiang, Integrated App. Physics Inc.	1327
Optimization of Speed-Up Network Component Values for the 30 Ω Resistively Terminated Prototype Kicker Magnet — M. J. Barnes, G. D. Wait, TRIUMF	1330
Test Results of the 8.35 kA, 15 kV, 10 pps Pulser for the Elettra Kickers — R. Fabris, P. Tosolini, Sinc. Trieste	1333
Preliminary Testing of the LEB to MEB Transfer Kicker Modulator Prototype — G. C. Pappas, D. R. Askew, SSCL	1336
A Novel Technique for Pulsing Magnet Strings with a Single Switch — R. J. Sachtshale, C. Dickey, P. Morcombe, Duke	1339
Linac Pulsed Quad Power Supply — L. Bartelson, FNAL	1342
The AGS New Fast Extracted Beam System Orbit Bump Pulser — J. S. Chang, A. V. Soukas, BNL	1345
Experimental Investigation of High Voltage Nanosecond Generators of Injection System for SIBERIA-2 Storage Ring — A. Kadnikov, Y. Matveev, BINP	1348

Proceedings of the 1993 Particle Accelerator Conference

Design and Preliminary Results for a Fast Bipolar Resonant Discharge Pulser Using SCR Switches for Driving the Injection Bump Magnets at the ALS — <i>G. Stover, L. Reginato, LBL</i>	1351
Design and Preliminary Testing of the LEB Extraction Kicker Magnet at the SSC — <i>D. E. Anderson, L. X. Schneider, SSCL</i>	1354
Development of a High Quality Kicker Magnet System — <i>J. Dinkel, B. Hanna, C. Jensen, D. Qunell, R. Reilly, FNAL</i>	1357
Consequences of Kicker Failure During HEB to Collider Injection and Possible Mitigation — <i>R. Soundranayagam, A. I. Drozhdin, N. V. Mokhov, B. Parker, R. Schailey, F. Wang, SSCL</i>	1360
High Efficiency Beam Deflection by Planar Channeling in Bent Silicon Crystals — <i>K. Elsener, M. Clément, N. Doble, L. Gagnon, P. Grafström, CERN; S. P. Møller, E. Uggerhøj, T. Worm, ISA-Aarhus; M. Hage-Ali, P. Siffert, Strasbourg</i>	1363
Extraction from the Fermilab Tevatron Using Channeling with a Bent Crystal — <i>G. Jackson, FNAL</i>	1366
2 TeV HEB Beam Abort at the SSCL — <i>R. Schailey, J. Bull, T. Clayton, P. Kocur, N. V. Mokhov, SSCL</i>	1369
Electrostatic Septa Design and Performance for Injection and Extraction to and from the MIT-Bates South Hall Ring (SHR) — <i>S. Sobczynski, R. Averill, M. Farkhondeh, W. Sapp, C. Sibley, MIT-Bates</i>	1372
Injection into the Elettra Storage Ring — <i>D. Tommasini, Sinc. Trieste</i>	1375
The Septum Magnets System of Elettra — <i>R. Fabris, F. Daclon, M. Giannini, D. Tommasini, P. Tosolini, Sinc. Trieste</i>	1378
High Voltage Vacuum Insulation in Crossed Magnetic and Electric Fields — <i>W. T. Diamond, AECL</i>	1381
Injection System for the SIBERIA-2 Storage Ring — <i>G. Erg, A. Evstigneev, V. Korchuganov, G. Kulipanov, E. Levichev, Yu. Matveev, A. Philipchenko, L. Schegolev, V. Ushakov, BINP</i>	1384
Fixed Target to Collider Changeover at A0 — <i>K. J. Weber, FNAL</i>	1387
Surface Resistivity Tailoring of Ceramic Accelerator Components — <i>S. Anders, A. Anders, I. Brown, LBL</i>	1390
Compensation of Field Shaking Due to the Magnetic Vibration — <i>Y. Cheng, C. Hwang, SRRC Taiwan</i>	1393
Superconducting Cavity Tuner Performance at CEBAF — <i>J. Marshall, J. Preble, W. Schneider, CEBAF</i>	1396
Test Results and Design Considerations for a 500 MHz, 500 kW Vacuum Window for CESR-B — <i>D. Metzger, P. Barnes, A. Helser, J. Kirchgessner, H. Padamsee, Cornell</i>	1399
An Experimental and Analytical Study of a Buoyancy Driven Cooling System for a Particle Accelerator — <i>B. Campbell, R. Ranganathan, SSCL</i>	1402
Collider Bypass Diode Thermal Simulations and Measurements for the SSCL — <i>C. Rostamzadeh, G. Tool, SSCL</i> ..	1405
Frequency-Feedback Tuning for Single-Cell Cavity Under RF Heating — <i>J. D. Stepp, J. F. Bridges, ANL</i>	1408
A Device of Amplitude and Phase Stabilization for the FEL Injector in the L-Band — <i>Q. Zhang, X. Wang, Y. Sun, S. Bu, M. Zhang, G. Su, CIAE China</i>	1411
A Jet Neutralizer Concept — <i>T. E. Horton, U. Mississippi</i>	1413
Modulator Upgrade of the KEK 2.5-GeV Linac — <i>T. Shidara, H. Honma, S. Anami, I. Sato, KEK</i>	1416
NSLS X-Ray Ring RF System Upgrade — <i>M. G. Thomas, R. Biscardi, W. Broome, S. Buda, R. D'Alsace, S. Hanna, J. Keane, P. Mortazavi, G. Ramirez, J. M. Wang, NSLS-BNL</i>	1419
A Wide Tuning Range Rf Cavity with External Ferrite Biasing — <i>X. Pei, BNL; S. Anderson, D. Jenner, D. McCammon, T. Sloan, IUCF</i>	1421
Longitudinal Rf Matching During AGS-RHIC Beam Transfer — <i>X. Pei, BNL</i>	1424
Photon Sources <i>Chair: J. Galayda</i>	
Commissioning and Performance of the ESRF (<i>Invited Paper</i>) — <i>J. L. Laclare and the Project Team, ESRF</i>	1427
Commissioning and Performance of the Advanced Light Source (<i>Invited Paper</i>) — <i>A. Jackson, LBL</i>	1432
Status of BESSY II, a High-Brilliance Synchrotron Radiation Source in the VUV to XUV Range (<i>Invited Paper</i>) — <i>D. Krämer, BESSY</i>	1436
A Superconducting Short Period Undulator for a Harmonic Generation FEL Experiment — <i>G. Ingold, L. Solomon, I. Ben-Zvi, S. Krinsky, D. Li, D. Lynch, J. Sheehan, M. Woodle, X. Z. Qiu, L. H. Yu, X. Zhang, NSLS-BNL; W. Sampson, M. Gardner, K. Robins, BNL; I. Lehrman, R. Heuer, J. Sheehan, D. Weissenburger, Grumman Corp.</i>	1439
UV-VUV FEL Program at Duke Storage Ring with OK-4 Optical Klystron — <i>V. N. Litvinenko, J. M. J. Madey, Duke; N. A. Vinokurov, BINP-Novosibirsk</i>	1442

Each volume begins with this five-volume table of contents and ends with the five-volume author index. The chairmen's foreword and a list of conference organizers and staff appear as front matter in Volume 1. A list of conference participants precedes the author index in Volume 5.

A 2–4 nm Linac Coherent Light Source (LCLS) Using the SLAC Linac — H. Winick, K. Bane, R. Boyce, G. Loew, P. Morton, H.-D. Nuhn, J. Paterson, P. Pianetta, T. Raubenheimer, J. Seeman, R. Tatchyn, V. Vylet, SLAC; C. Pellegrini, J. Rosenzweig, G. Travish, UCLA; D. Prosnitz, T. Scharlemann, LLNL; K. Halbach, K.-J. Kim, M. Xie, LBL	1445
The Vanderbilt University Compton Scattering X-Ray Experiment — P. A. Tompkins, C. A. Brau, W. W. Dong, J. W. Waters, Vanderbilt U.; F. E. Carroll, D. R. Pickens, R. R. Price, VUMC	1448
Observations of Effects of Ion Accumulation in the Maxwell Model 1.2–400 Synchrotron Light Source — R. P. Johnson (now at CEBAF), D. Y. Wang, Maxwell Labs; H. Bluem, LSU	1451
A Progress Report on the Laboratório Nacional de Luz Síncrotron (Brazil) — A. R. D. Rodrigues, C. E. T. Gonçalves da Silva, D. Wisnivesky, LNLS Brazil	1454
An Overview of the PLS Project — T. Lee, POSTECH	1457
Present Status of SRRC — E. Yen, SRRC	1460

Poster presentations:

SOLEIL, a New Synchrotron Radiation Source for LURE — M. P. Level, P. Brunelle, P. Marin, A. Nadji, M. Sommer, H. Zyngier, LURE; J. Faure, J. Payet, A. Tkatchenko, LNS	1465
Conceptual Design of a Compact Electron Storage Ring System Dedicated to Coronary Angiography — Y. Oku, K. Aizawa, S. Nakagawa, Kawasaki Heavy Ind.; M. Ando, K. Hyodo, S. Kamada, PF, KEK; H. Shiwaku, JAERI	1468
Report on DELTA, One Year Before Routine Operation — N. Marquardt, U. Dortmund	1471
Lattice Design for the 1.7-GeV Light Source BESSY II — E. Jaeschke, D. Krämer, B. Kuske, P. Kuske, M. Scheer, E. Weihrer, G. Wüstefeld, BESSY	1474
The Synchrotron Light Source ROSY — D. Einfeld, H. Büttig, S. Dienel, W. Gläser, H. Guratzsch, B. Hartmann, D. Janssen, H. Krug, J. Linnemann, W. Matz, W. Neumann, W. Oehme, D. Pröhl, R. Schlenk, H. Tyrroff, Res. Ctr. Rossendorf; Th. Goetz, M. Picard, U. Bonn; J. B. Murphy, BNL; M. Plesko, D. Tomassini, Sincrotrone Trieste; R. Rossmanith, CEBAF	1477
A Source of Synchrotron Radiation for Research and Technology Applications — E. Bulyak, V. Chechetenko, A. Dovbnya, S. Efimov, A. Gevchuk, P. Gladikh, I. Karnaukhov, V. Kozin, S. Kononenko, V. Likhachev, V. Lyashchenko, V. Markov, N. Mocheshnikov, V. Moskalenko, A. Mytsykov, Yu. Popkov, A. Shcherbakov, M. Strelkov, A. Tarasenko, Yu. Telegin, V. Trotsenko, A. Zelinsky, Kharkov Inst.; V. Bar'yakhtar, V. Molodkin, V. Nemoshkalenko, A. Shpak, Metallophysics Inst.	1480
Optimum Steering of Photon Beam Lines in SPEAR — W. J. Corbett, B. Fong, M. Lee, V. Ziemann, SLAC	1483
Establishment of a Tolerance Budget for the Advanced Photon Source Storage Ring — H. Bizek, E. Crosbie, E. Lessner, L. Teng, ANL	1485
Study of Transverse Coupled Bunch Instabilities by Using Non-Linear Taylor Maps for the Advanced Light Source (ALS) — M. Meddahi, J. Bengtsson, LBL	1488
Plans to Increase Source Brightness of NSLS X-Ray Ring — J. Safranek, S. Krinsky, NSLS-BNL	1491
A Design Concept for the Inclusion of Superconducting Dipoles Within a Synchrotron Light Source Lattice — M. W. Poole, J. A. Clarke, S. L. Smith, V. P. Suller, L. A. Welbourne, SERC Daresbury; N. A. Mezentssev, BINP Russia	1494
A Conceptual Design and Thermal Analysis of High Heat Load Crotch Absorber — I. C. Sheng, S. Sharma, E. Rotela, J. Howell, ANL	1497
Thermal Analysis of the Beam Missteering in APS Storage Ring — I. C. Sheng, J. Howell, S. Sharma, ANL	1500
Dynamic Response Analysis of the LBL Advanced Light Source Synchrotron Radiation Storage Ring — K. K. Leung, SSCL	1503
The Study of Seismic Vibration of SR Source "Zelenograd" — S. Kuznetsov, Kurchatov Inst.; E. Levichev, BINP	1506
Measurement of the Orbit Parameters at SOR-RING — H. Kudo, K. Shinoue, H. Takaki, T. Koseki, H. Ohkuma, Y. Kamiya, ISSP Tokyo	1509
Challenging Issues During ESRF Storage Ring Commissioning — A. Ropert, ESRF	1512
Upgrading to 500 mA of the Stored Beam Current at SORTEC 1-GeV Source Facility — M. Kodaira, N. Awaji, T. Kishimoto, K. Mukugi, M. Watanabe, SORTEC; T. Iida, H. Tsuchidate, Mitsubishi Corp.	1515
Performance of Upgraded SORTEC 1-GeV 500-mA SR Source Facility — T. Kishimoto, M. Kodaira, N. Awaji, K. Mukugi, M. Araki, SORTEC; Y. Kijima, M. Haraguchi, Mitsubishi Corp.	1518

Proceedings of the 1993 Particle Accelerator Conference

Design of Test Linac for Free Electron Laser — H. Kang, I. Ko, M. Cho, W. Namkung, POSTECH	1521
The Revised ELFA Project — E. Acerbi, F. Alessandria, G. Baccaglioni, G. Bellomo, C. Birattari, R. Bonifacio, I. Boscolo, A. Bosotti, F. Broggi, R. Corsini, L. De Salvo, D. Giove, C. Maroli, P. Pierini, N. Piovella, M. Pullia, G. Rivoltella, L. Rossi, G. Varisco, INFN/ U. Milan; P. Arcioni, M. Bressan, G. Conciauro, INFN Pavia; W. A. Barletta, LBL; G. Gemme, R. Parodi, INFN Genova; V. Stagno, V. Variale, INFN Bari.....	1524
Design and Construction of a Compact Infra Red Free Electron Laser CIRFEL — J. Krishnaswamy, I. S. Lehrman, J. Sheehan, R. L. Heuer, M. F. Reusch, R. Hartley, Grumman Aerospace Corp.	1527
Coherence and Linewidth Studies of a 4-nm High Power FEL — W. M. Fawley, A. M. Sessler, LBL; E. T. Scharlemann, LLNL	1530
Performance Characteristics, Optimization, and Error Tolerances of a 4 nm FEL Based on the SLAC Linac — K.-J. Kim, M. Xie, LBL; E. T. Scharlemann, LLNL; C. Pellegrini, G. Travish, UCLA	1533
X-Ray Beam Lines and Beam Line Components for the SLAC Linac Coherent Light Source (LCLS) — R. Tatchyn, P. Pianetta, SLAC	1536
Photon Pulse Filtering and Modulation Based on the Extreme Temporal Compression and Correlated Energy Spread of the Electron Bunches in the SLAC Linac Coherent Light Source (LCLS) — R. Tatchyn, SLAC	1539
Infrared (IR) vs. X-Ray Power Generation in the SLAC Linac Coherent Light Source (LCLS) — R. Tatchyn, SLAC	1542
Saturation of a High Gain FEL — R. L. Gluckstern, Maryland; S. Krinsky, BNL; H. Okamoto, Kyoto U.	1545
Numerical Studies of Strong Focusing in Planar Undulators — G. Travish, J. Rosenzweig, UCLA	1548
Generation of High Power 140 GHz Microwaves with an FEL for the MTX Experiment — S. L. Allen, C. J. Lasnier, B. Felker, M. Fenstermacher, S. W. Ferguson, S. Fields, E. B. Hooper, S. Hulse, M. Makowski, J. Moller, W. Meyer, D. Petersen, E. T. Scharlemann, B. Stallard, R. Wood, LLNL	1551
Burst Mode FEL with the ETA-III Induction Linac — C. J. Lasnier, S. L. Allen, B. Felker, M. E. Fenstermacher, S. W. Ferguson, S. D. Hulse, E. B. Hooper, M. C. Jackson, M. A. Makowski, W. H. Meyer, J. M. Moller, D. E. Petersen, S. E. Sampayan, B. W. Stallard, W. F. Fields, LLNL; K. Oasa, JAERI	1554
Design and Experiment of SG-1 FEL — Z. Hui, IEE China	1557
Electron Beam Quality Limitations and Beam Conditioning in Free Electron Lasers — P. Sprangle, G. Joyce, NRL; B. Hafizi, Icarus Res.; P. Serafim, Northeastern U.	1560
An Optical Approach to Emittance Compensation in FELs — G. R. Neil, H. Liu, CEBAF	1563
Ultrahigh-Brightness Microbeams: Considerations for Their Generation and Relevance to FEL — H. Ishizuka, Y. Nakahara, Fukuoka Inst. Tech.; S. Kawasaki, Saitama U.; K. Sakamoto, A. Watanabe, N. Ogiwara, M. Shiho, JAERI	1566
The Groove Guide: A Non-Conventional Interaction Structure for Microwave FEL Experiments — P. Arcioni, M. Bressan, G. Conciauro, U. of Pavia; F. Broggi, P. Pierini, INFN Milano	1569
First Undulators for the Advanced Light Source — E. Hoyer, J. Akre, J. Chin, B. Gath, D. Humphries, B. Kincaid, S. Marks, P. Pipersky, D. Plate, G. Portmann, R. Schlueter, LBL; W. Hassenzahl, LLNL	1572
Insertion Device Magnet Measurements for the Advanced Light Source — S. Marks, C. Cork, E. Hoyer, D. Humphries, B. Kincaid, D. Plate, A. Robb, R. Schlueter, C. Wang, LBL; W. V. Hassenzahl, LLNL	1575
Spectral Quality of ALS U5.0 Undulator and Field Error Effects — C. Wang, S. Marks, B. Kincaid, LBL	1578
Modeling and Measurement of the ALS U5 Undulator End Magnetic Structures — D. Humphries, K. Halbach, E. Hoyer, B. Kincaid, S. Marks, R. Schlueter, LBL	1581
Flux Shunts for Undulators — E. Hoyer, J. Chin, LBL; W. V. Hassenzahl, LLNL	1584
Design, Construction and Testing of Insertion Devices for ELETTRA — R. P. Walker, R. Bracco, A. Codutti, B. Diviacco, D. Mollo, D. Zangrando, Sinc. Trieste; C. Poloni, U. Trieste	1587
Performance Optimization of Pure Permanent Magnet Undulators — B. Diviacco, Sin. Trieste	1590
Magnetic Interaction Effects in ELETTRA Segmented Pure Permanent Magnet Undulators — B. Diviacco, R. P. Walker, Sinc. Trieste	1593
Planar Helical Undulator Sources of Circularly Polarized X-Rays — R. Carr, SSRL	1596
Polarized Wiggler for NSLS X-Ray Ring — A. Friedman, X. Zhang, S. Krinsky, E. B. Blum, NSLS-BNL; K. Halbach, LBL	1599
Magnetic Field Measurements of a Superconducting Undulator for a Harmonic Generation FEL Experiment at the NSLS — L. Solomon, G. Ingold, I. Ben-Zvi, S. Krinsky, L. H. Yu, NSLS-BNL; W. Sampson, K. Robins, BNL	1602

Each volume begins with this five-volume table of contents and ends with the five-volume author index. The chairmen's foreword and a list of conference organizers and staff appear as front matter in Volume 1. A list of conference participants precedes the author index in Volume 5.

Magnetic Performance of the NSLS Prototype Small-Gap Undulator — <i>G. Rakowsky, R. Cover, Rockwell;</i> <i>L. Solomon, NSLS-BNL</i>	1605
Design Considerations for a 60 Meter Pure Permanent Magnet Undulator for the SLAC Linac Coherent Light Source (LCLS) — <i>R. Tatchyn, R. Boyce, K. Halbach, H.-D. Nuhn, J. Seeman, H. Winick, SLAC; C. Pellegrini,</i> <i>UCLA</i>	1608
Adjustment and Measurement of a Hybrid Undulator — <i>B. Wu, Y. Ma, B. Liu, Z. Zhang, CIAE China</i>	1611
Coherent Radiation at Submillimeter and Millimeter Wavelengths — <i>M. Oyamada, R. Kato, T. Nakazato, S. Urasawa,</i> <i>T. Yamakawa, M. Yoshioka, M. Ikezawa, K. Ishi, T. Kanai, Y. Shibata, T. Takahashi, Tohoku U.</i>	1614
Suppression of Coherent Synchrotron Radiation in Conducting Boundaries — <i>R. Kato, T. Nakazato, M. Oyamada,</i> <i>S. Urasawa, T. Yamakawa, M. Yoshioka, M. Ikezawa, K. Ishi, T. Kanai, Y. Shibata,</i> <i>T. Takahashi, Tohoku U.</i>	1617
A Compact Tunable X-Ray Source Based on Parametric X-Ray Generation by Moderate Energy Linacs — <i>X. K. Maruyama, K. Dinova, D. Snyder, Naval Postgraduate School; M. A. Piestrup, Q. Li, Adelphi Tech.;</i> <i>R. B. Fiorito, D. W. Rule, NSWC</i>	1620
Fundamental and Harmonics of Thomson Backscattered X-Rays from an Intense Laser Beam — <i>C. Tang, NRL;</i> <i>B. Hafizi, Icarus Res.; S. K. Ride, UCSD</i>	1623
Generation of Intensive Long-Wavelength Edge Radiation in High-Energy Electron Storage Rings — <i>O. V. Chubar,</i> <i>N. V. Smolyakov, Kurchatov Inst.</i>	1626
The Radiation Emission by a High Energy Electron-Positron Pair and Ultrarelativistic Hydrogen-Like Atom Moving Through Thick Target — <i>A. V. Koshelkin, MEPI</i>	1629
Bremsstrahlung by the Bunch of Ultrarelativistic Charged Particles into a Thick Target — <i>A. V. Koshelkin, MEPI</i> ..	1632
Construction and Commissioning of the SRRRC Storage Ring — <i>Y. C. Liu, J. R. Chen, C. C. Kuo, SRRRC</i>	1635
Commissioning a Second Superconducting Wiggler in the Daresbury SRS — <i>M. W. Poole, J. A. Clarke,</i> <i>P. D. Quinn, S. L. Smith, V. P. Suller, L. A. Welbourne, Daresbury</i>	1638

Volume 3

Hadron RF Linacs, Cyclotrons, Radioactive Beams

Chair: *R. Pollock*

An Overview of Radioactive Beam Concepts (<i>Invited Paper</i>) — <i>J. M. D'Auria, TRIUMF</i>	1641
Heavy Ion Beam Accumulation, Cooling, and Experiments at the ESR (<i>Invited Paper</i>) — <i>B. Franzke, K. Beckert,</i> <i>F. Bosch, H. Eickhoff, B. Franczak, A. Gruber, O. Klepper, F. Nolden, P. Raabe, H. Reich, P. Spädtke,</i> <i>M. Steck, J. Struckmeier, GSI Darmstadt</i>	1645
The Research Center for Nuclear Physics Ring Cyclotron (<i>Invited Paper</i>) — <i>I. Miura, Osaka U.</i>	1650
The Fermilab 400-MeV Linac Upgrade (<i>Invited Paper</i>) — <i>C. W. Schmidt, FNAL</i>	1655
Use of the Holifield Facility 25-MV Tandem Accelerator in the Oak Ridge Radioactive Ion Beam Project — <i>C. M. Jones, R. C. Juras, M. J. Meigs, D. K. Olsen, ORNL</i>	1660
Realistic Modeling of Radiation Transmission Inspection Systems — <i>K. E. Sale, LLNL</i>	1663
Overview of Accelerators in Medicine — <i>A. J. Lennox, FNAL/Rush U.</i>	1666
Commissioning of the First Drift Tube Linac Module in the Ground Test Accelerator — <i>K. F. Johnson, O. R. Sander,</i> <i>W. H. Atkins, G. O. Bolme, S. Bowling, R. Cole, R. Connolly, P. Denney, J. Erickson, J. D. Gilpatrick,</i> <i>W. B. Ingalls, D. Kersteins, R. Kraus, W. P. Lysenko, D. McMurry, C. T. Mottershead, J. Power, C. Rose,</i> <i>D. P. Rusthoy, D. P. Sandoval, J. D. Schneider, M. Smith, G. Vaughn, E. A. Wadlinger, R. Weiss, V. Yuan,</i> <i>LANL</i>	1669
Acceleration and Isobaric Separation of Radioactive Ion Beams With the Louvain-la-Neuve Isochronous Cyclotrons — <i>M. Loiselet, N. Postiau, G. Ryckewaert, U. Catholique de Louvain; A. Morduev, R. Oganessian, JINR</i>	1672
Linear Accelerator for Plutonium Conversion and Transmutation of NPP Wastes — <i>I. M. Kapchinskiy, I. V. Chuvilo,</i> <i>A. A. Kolomiets, N. V. Lazarev, I. M. Lipkin, V. K. Plotnikov, I. A. Vorobjov, ITEP Moscow</i>	1675

Poster presentations:

Acceleration and Transverse Focusing of Ion Beams in Lineondutron — <i>E. S. Masunov, MEPI</i>	1681
Linac Design Study for an Intense Neutron-Source Driver — <i>M. T. Lynch, A. Browman, R. DeHaven, R. Jameson,</i> <i>A. Jason, G. Neuschaefer, P. Talerico, A. Regan, LANL</i>	1683

Proceedings of the 1993 Particle Accelerator Conference

Design and Operation of the HIMAC Injector — T. Murakami, H. Ogawa, S. Yamada, Y. Sato, T. Yamada, A. Kitagawa, J. Yoshizawa, S. Fu, T. Kohno, K. Sato, A. Itano, M. Kumada, E. Takada, M. Kanazawa, K. Noda, M. Sudou, Y. Hirao, Nat. Inst. of Radiological Sciences; O. Morishita, K. Sawada, Sumitomo Heavy Ind.	1686
Time-of-Flight Measurements of Absolute Beam Energy in the Fermilab Linac — M. B. Popovic, T. L. Owens, T. K. Kroc, L. J. Allen, C. W. Schmidt, FNAL	1689
Phase Scan Signature Matching for Linac Tuning — T. L. Owens, M. B. Popovic, E. S. McCrory, C. W. Schmidt, L. J. Allen, FNAL	1691
Operational Status of the Uranium Beam Upgrade of the ATLAS Accelerator — R. C. Pardo, L. M. Bollinger, J. A. Nolen, K. W. Shepard, P. Billquist, J. M. Bogaty, B. E. Clift, R. Harkewicz, F. H. Munson, J. E. Specht, G. P. Zinkann, ANL	1694
One Year Operation of the 7 MeV Proton Linac — T. Shirai, H. Dewa, H. Fujita, M. Ikegami, Y. Iwashita, S. Kakigi, H. Okamoto, A. Noda, M. Inoue, Kyoto U.	1697
The SSC Linear Accelerator — L. W. Funk, SSCL	1700
Finalized Design of the SSC RFQ-DTL Matching Section — M. Haworth, C. Combs, P. Datte, T. Enegren, W. Funk, Y. Goren, F. Guy, J. Hurd, G. Jamieson, D. Martin, A. Ringwall, R. Sethi, D. Swenson, SSCL; D. Barlow, R. Kraus, R. Meyer, LANL	1703
Accelerator Readiness Review Process for the SSC Linac — J. F. Tooker, T. Benke, L. W. Funk, V. Oliphant, SSCL	1706
Commissioning Status of the Continuous Wave Deuterium Demonstrator — P. Den Hartog, J. Dooling, M. Lorello, J. Rathke, Grumman Aerospace; J. Carwardine, D. Godden, G. Pile, Culham Lab.; T. Yule, T. Zinneman, ANL	1709
Design Study for a Superconducting Proton Linac From 20 to 100 MeV — T. P. Wangler, R. Garnett, F. Krawczyk, J. Billen, N. Bultman, K. Christensen, W. Fox, R. Wood, LANL	1712
Design Considerations for High-Current Superconducting Ion Linacs — J. R. Delayen, C. L. Bohn, B. J. Micklich, C. T. Roche, L. Sagalovsky, ANL	1715
Special Design Problems and Solutions for High Powered Continuous Duty Linacs — D. Liska, L. Carlisle, G. McCauley, LANL; S. Ellis, P. Smith, Grumman Aerospace	1718
Status of CIAE Medical Cyclotron — X. Zhang, Z. Li, M. Fan, CIAE China	1721
A 600 MeV Cyclotron for Radioactive Beam Production — D. J. Clark, LBL	1724
Development of a Compact Permanent Magnet Cyclotron for Accelerator Mass Spectrometry — A. T. Young, D. J. Clark, K. Halbach, W. B. Kunkel, K. N. Leung, C. Y. Li, A. Rawlins, R. D. Schlueter, M. E. Stuart, R. P. Wells, LBL; J. X. Yu, Beijing U.; K. J. Bertsche, SSCL	1727
Performance of H ⁺ /D ⁺ Cyclotron Using Internal Source — T. T. Y. Kuo, TRIUMF; G. O. Hendry, Cyclotron Inc.	1730
Operation of the TR30 "Industrial" Cyclotron — K. Erdman, R. Dawson, Ebco Tech./TRIUMF; B. Milton, N. Stevenson, TRIUMF	1733
The First Year with Electron Cooling at CRYRING — K. Abrahamsson, G. Andler, L. Bagge, E. Beebe, P. Carlé, H. Danared, K. Ehrnstén, M. Engström, Å. Engström, C. J. Herrlander, J. Hilke, J. Jeansson, A. Källberg, S. Leontin, L. Liljeby, A. Nilsson, A. Paál, A. Pikin, K.-G. Rensfelt, U. Rosengård, J. Starker, M. af Ugglas, Manne Siegbahn Inst. Stockholm	1735
Electron Cooling of Heavy Ions at GSI — M. Steck, K. Beckert, H. Eickhoff, B. Franzke, F. Nolden, P. Spädtké, GSI Darmstadt	1738
The Aarhus Storage Ring for Ions and Electrons ASTRID — S. P. Møller, Aarhus U.	1741
Recent Developments at the Gustaf Werner Cyclotron and CELSIUS — D. Reistad, Svedberg Lab.	1744
Ion Beam Acceleration and New Operation Modes at the TSR Heidelberg — M. Grieser, D. Habs, R.v. Hahn, B. Hochadel, C. M. Kleffner, J. Liebmman, R. Repnow, D. Schwalm, MPI Heidelberg; G. Bisoffi, INFN Legnaro; E. Jaeschke, BESSY; S. Papureanu, IFIN Bucurest.....	1747
A New Design for an EMIS-CYCLOTRON System, for Direct Production of Gaseous PET Radioisotopes — H. Ayvazian, Ion Beam App. Lab.	1750
The Chandigarh Variable Energy Cyclotron and Its Application for Trace Element Analysis Using PIXE Techniques — I. M. Govil, Panjab U.	1753
Proton Linacs for Boron Neutron Capture Therapy — A. J. Lennox, FNAL /Rush U.	1756
Modeling and System Specifications for an Integrated 3-D Proton Treatment Delivery System — J. W. Staples, B. A. Ludewigt, LBL	1759

Each volume begins with this five-volume table of contents and ends with the five-volume author index. The chairmen's foreword and a list of conference organizers and staff appear as front matter in Volume 1. A list of conference participants precedes the author index in Volume 5.

Five-Volume Contents

Shielding and Activation Study for Proton Medical Accelerators — <i>H. B. Knowles, J. L. Orthel, B. W. Hill, G. H. Gillespie Assoc.</i>	1762
Beam Dynamics Studies for Proposed Proton Therapy Facility — <i>D. Raparia, W. Funk, SSCL</i>	1765
Compact Protontherapy Unit Predesign — <i>D. Tronc, G.E.</i>	1768
High Energy Accelerator Technology in Radiology — <i>J. F. Crawford, B. Larsson, H. Reist, U. Zurich/PSI; L. Goldin, ITEP Moscow; H. Condé, K. Elmgren, E. Grusell, B. Nilsson, O. Pettersson, T. Rönqvist, U. Uppsala</i>	1771
The Neutral Particle Beam Space Experiment (NPBSE) Accelerator Designs — <i>C. C. Paulson, A. M. M. Todd, S. L. Mendelsohn, Grumman</i>	1774
The Continuous Wave Deuterium Demonstrator (CWDD) Design and Status — <i>A. M. M. Todd, Grumman; M. P. S. Nightingale, Culham Lab.; T. J. Yule, ANL</i>	1777
Beam Matching Section in the INS Heavy Ion Linac Complex — <i>K. Niki, S. Arai, Y. Hashimoto, H. Masuda, M. Tomizawa, K. Yoshida, INS Tokyo</i>	1780
A Heavy Ion Linac Complex for Unstable Nuclei — <i>S. Arai, M. Doi, Y. Hashimoto, A. Imanishi, T. Katayama, H. Masuda, K. Niki, Y. Takeda, N. Tokuda, M. Tomizawa, E. Tojyo, K. Yoshida, M. Yoshizawa, INS Tokyo; T. Hattori, Tokyo Inst. of Tech.</i>	1783
Interdigital-H Linac for Unstable Nuclei at INS — <i>M. Tomizawa, S. Arai, M. Doi, T. Katayama, K. Niki, M. Yoshizawa, INS Tokyo; T. Hattori, Tokyo Inst. of Tech.</i>	1786
SPIRAL: A Radioactive Ion Beam Facility at GANIL — <i>A. Joubert, R. Anne, P. Bertrand, MP. Bourgarel, C. Bieth, B. Bru, A. Chabert, M. Duval, R. Leroy, Ch. Ricaud, P. Sortais, GANIL</i>	1789
On Line Isotopic Separator Test Benches at GANIL — <i>R. Anne, B. Bru, A. Joubert, R. Leroy, M. Lewitowicz, P. Sortais, M. G. Saint Laurent, C. Tribouillard, GANIL; J. Obert, J. C. Putaux, IPN Orsay; C. F. Liang, P. Paris, CSNSM Orsay; N. Orr, J. C. Steckmeyer, LPC-ISMRA</i>	1792
The Outlook of MPC-10 Cyclotron Use for the Solution of Applied Problems — <i>S. T. Latushkin, V. V. Leonov, A. A. Ogloblin, L. I. Yudin, V. E. Yarosh, D. I. Yartsev, Kurchatov Inst.</i>	1795
ITEP Heavy Ion Alternating Phase Focusing Linac — <i>V. V. Kushin, N. A. Nesterov, I. O. Parshin, S. V. Plotnikov, ITEP Moscow</i>	1798

Accelerator Control Systems

Chair: *D. Gurd*

Sharing Control System Software (<i>Invited Paper</i>) — <i>P. Clout, Vista Systems</i>	1801
Control System Architecture: The Standard and Non-Standard Models (<i>Invited Paper</i>) — <i>M. E. Thuot, L. R. Dalesio, LANL</i>	1806
Anatomy of a Control System: A System Designer's View — <i>S. Magyary, LBL</i>	1811
Beam Position Monitor Data Acquisition for the Advanced Photon Source — <i>F. R. Lenkszus, E. Kahana, A. J. Votaw, G. A. Decker, Y. Chung, D. J. Ciarlette, R. J. Laird, ANL</i>	1814
New Tevatron Cryogenic Control System — <i>B. Lublinsky, J. Firebaugh, J. Smolucha, FNAL</i>	1817
Control Software for EUTERPE — <i>P. D. V. van der Stok, F. van den Berk, R. Deckers, Y. van de Vijver, J. I. M. Botman, J. L. Delhez, C. J. Timmermans, Tech. U., Eindhoven</i>	1820

Poster presentations:

Network Management of Real-Time Embedded Processors — <i>C. Kalbfleisch, S. Hunt, K. Low, D. Mathieson, SSCL</i>	1823
High Speed Serial Communications for Control Systems — <i>D. Mathieson, C. Kalbfleisch, S. Hunt, K. Low, SSCL</i>	1826
"BUBBANET": A High Performance Network for the SSC Accelerator Control System — <i>S. Hunt, C. Kalbfleisch, K. Low, D. Mathieson, SSCL</i>	1829
Gateway for Inter-Network Connection in the Pohang Light Source Control System — <i>S. C. Won, S. Kwon, POSTECH</i>	1832
The Star, a Dynamically Configured Dataflow Director for Realtime Control — <i>M. Bickley, J. Kewisch, CEBAF</i>	1835
The SSCL Linac Control System — <i>J. Heefner, C. Cuevas, S. Hunt, D. Murray, J. Sage, SSCL</i>	1838
Proposal to Use Failure Prediction as a Means of Meeting Availability Requirements at the SSC — <i>S. Sarkar, W. Merz, F. Meyer, SSCL</i>	1841
Control, Timing, and Data Acquisition for the Argonne Wakefield Accelerator (AWA) — <i>P. Schoessow, C. Ho, J. Power, E. Chojnacki, ANL</i>	1844

Volume 1: 1-747
 Volume 2: 748-1640
 Volume 3: 1641-2545
 Volume 4: 2546-3218
 Volume 5: 3219-3933

Proceedings of the 1993 Particle Accelerator Conference

The High Level Programmer and User Interface of the NSLS Control System — Y. N. Tang, J. D. Smith, NSLS-BNL; S. Sathe, AGS-BNL	1846
NSLS Control Monitor and Its Upgrade — S. Ramamoorthy, J. D. Smith, NSLS-BNL	1849
NSLS Control System Upgrade Status — J. Smith, S. Ramamoorthy, Y. Tang, J. Flannigan, S. Sathe, J. Keane, S. Krinsky, NSLS-BNL	1852
Digital Signal Array Processor for NSLS Booster Power Supply Upgrade — R. Olsen, J. Dabrowski, BNL; J. Murray, Stony Brook	1855
Control System for NSLS Booster Power Supply Upgrade II — R. Olsen, J. Dabrowski, BNL; J. Murray, Stony Brook	1858
Software Environment and Configuration for the DSP Controlled NSLS Booster Power Supplies — R. Olsen, J. Dabrowski, NSLS-BNL; J. Murray, Stony Brook	1861
Control Units for APS Power Supplies — O. D. Despe, C. Saunders, D. McGhee, ANL	1864
High Resolution ADC Interface to Main Magnet Power Supply at the NSLS — M. Bordoley, NSLS-BNL	1867
Design of the Advanced Light Source Timing System — M. Fahmie, LBL	1869
Ring Diagnostics and Consistency Test of the Model for the AGS Booster — A. Luccio, E. H. Auerbach, BNL	1872
Use of Design Codes for On-Line Beam Diagnostics at the MIT-Bates Accelerator — K. D. Jacobs, B. G. McAllister, J. B. Flanz, MIT Bates	1875
A Graphical User-Interface Control System at SRRC — J. S. Chen, C. J. Wang, S. J. Chen, G. J. Jan, SRRC Taiwan	1878
Machine Protection System Algorithm Compiler and Simulator — G. R. White, G. Sherwin, SLAC	1881
MPS VAX Monitor and Control Software Architecture — S. Allison, N. Spencer, K. Underwood, D. VanOlst, M. Zelanzy, SLAC	1884
The Continuous and Seamless Replacement of a Running Control System Succeeded — G.v. Egan-Krieger, R. Müller, J. Rahn, BESSY	1887
Control and Data Acquisition System of Electron Accelerator for Radiation Processing — W. Maciszewski, J. Lukasiewicz, W. Migdal, A. G. Chmielewski, Inst. of Nuc. Tech., Warsaw	1890
Expert System for Magnetic Systems Investigations — S. Lima, R. V. Poliakova, F. F. Nodarse, I. P. Yudin, JINR Moscow	1892
Orbit Correction Implementation at CEBAF — M. Bickley, B. A. Bowling, D. Douglas, A. Hofler, J. Kewisch, G. A. Krafft, CEBAF	1895
Controls Interface Protocols for the SSC Correction and 'DC' Magnet Power Supplies — S. Sarkar, J. Gannon, W. Merz, F. Meyer, SSCL	1898
Parametrization of the AmPS Magnets for the Control System — Y. Wu, G. van Garderen, R. Hart, J. van der Laan, R. Maas, F. Schimmel, NIKHEF-K	1901
Global Voltage Control for the LEP RF System — E. Ciapala, A. Butterworth, E. Peschardt, CERN	1903
Designing RF Control Subsystems Using the VXibus Standard — J. D. Stepp, F. C. Vong, J. F. Bridges, ANL	1906
Automated Measurement of Cavity Frequency and Cavity Tuning at CEBAF — R. Li, S. N. Simrock, B. C. Yunn, CEBAF	1909
A Beam Position Monitor Data Acquisition System for the New Fermilab 400 MeV Line — S. Lackey, J. Firebaugh, C. Johnstone, W. Marsh, J. Smolucha, K. Woodbury, FNAL	1912
A VME Based Quench Protection Monitor for the Tevatron Low Beta Quadrupoles — S. Lackey, C. Briegel, L. Chapman, R. Flora, K. Martin, FNAL; T. Savord, SSCL	1914
Experience with the TRIUMF Main Tank Vacuum Control System — S. Sarkar, D. P. Gurd, SSCL; J. C. Yandon W. Sievers, P. Bennett, P. Harmer, J. Nelson, TRIUMF	1916
Laser Power Stabilization in the TRIUMF Optically Pumped Polarized H ⁺ Ion Source — S. Sarkar, SSCL	1919
MPS Beam Control Software Architecture — K. Krauter, M. Crane, SLAC	1922
The CEBAF Analog Monitor System — K. Crawford, M. O'Sullivan, J. Perry, S. Simrock, CEBAF	1925
Techniques for Increasing the Reliability of Accelerator Control System Electronics — J. Utterback, FNAL	1928
WindoWorks: A Flexible Program for Computerized Testing of Accelerator Control System Electronic Circuit Boards — J. Utterback, FNAL	1931
Switching the Fermilab Accelerator Control System to a Relational Database — S. Shtirbu, FNAL	1934
The Impact of New Accelerator Control Software on LEP Performance — R. Bailey, A. Belk, P. Collier, M. Lamont, G. de Rijk, M. Tarrant, CERN	1937

Each volume begins with this five-volume table of contents and ends with the five-volume author index. The chairmen's foreword and a list of conference organizers and staff appear as front matter in Volume 1. A list of conference participants precedes the author index in Volume 5.

Five-Volume Contents

A Software System for Modeling and Controlling Accelerator Physics Parameters at the Advanced Light Source — <i>L. Schachinger, V. Paxson, LBL</i>	1940
Machine Physics Application Program for Control, Commissioning and Error Findings for Storage Rings — <i>H. P. Chang, C. H. Chang, C. C. Kuo, M. H. Wang, J. C. Lee, J. Y. Fan, H. J. Tsai, SRRC Taiwan; C. S. Hsue, SRRC/Nat. Tsing Hua U.</i>	1943
CATER: An Online Problem Tracking Facility for SLC — <i>R. C. Sass, H. Shoaee, SLAC</i>	1946
Ramping Control Using a Spreadsheet — <i>D. Y. Wang, R. P. Johnson (now at CEBAF), L. S. B. Ng, W. J. Pearce, Maxwell Labs</i>	1949
Easy and Effective Applications Programs Using DataViews — <i>E. S. McCrory, FNAL</i>	1952
The Graphic Environment for Transport Line Control and Beam Diagnostics — <i>S. Kuznetsov, Kurchatov Inst.</i>	1955
An I/O Subnet for the APS Control System: The BITBUS Universal Gateway — <i>G. J. Nawrocki, N. D. Arnold, M. G. Hoffberg, J. R. Winans, S. J. Benes, ANL</i>	1957
Status and Design of the Advanced Photon Source Control System — <i>W. McDowell, M. Knott, F. Lenkszus, M. Kraimer, N. Arnold, R. Daly, ANL</i>	1960
Controlling the Third Harmonic Cavity During Focus Free Transition Crossing in the Fermilab Main Ring — <i>M. A. Martens, FNAL</i>	1963
AMS: Area Message Service for SLC — <i>M. Crane, R. Mackenzie, D. Millsom, M. Zelazny, SLAC</i>	1966
Adding PCs to SLC Control System — <i>T. Lahey, S. Levitt, R. MacKenzie, N. Spencer, K. Underwood, SLAC</i>	1969
Precise System Stabilization at SLC Using Dither Techniques — <i>M. C. Ross, L. Hendrickson, T. Himel, E. Miller, SLAC</i>	1972
Thermal Stabilization of Low Level RF Distribution Systems at SLAC — <i>D. McCormick, M. Ross, T. Himel, N. Spencer, SLAC</i>	1975
 Lepton Circular Colliders, Synchrotrons, and Microtrons Chair: A. Sessler	
CESR Luminosity Upgrades and Experiments (<i>Invited Paper</i>) — <i>D. Rice, Cornell</i>	1978
LEP Status and Future Plans (<i>Invited Paper</i>) — <i>L. R. Evans, CERN</i>	1983
Challenges on the High Luminosity Frontier of e^+e^- Factories (<i>Invited Paper</i>) — <i>W. A. Barletta, LBL/UCLA</i>	1988
DAFNE, The Frascati F-Factory (<i>Invited Paper</i>) — <i>G. Vignola, INFN-LNF</i>	1993
Commissioning Results of the Amsterdam Pulse Stretcher/Storage Ring AmPS — <i>R. Maas, F. Kroes, J. van der Laan, G. Luijckx, J. Noomen, Y. Wu, NIKHEF</i>	1998
 <i>Poster presentations:</i>	
LEP Operation in 1992 with a 90° Optics — <i>R. Bailey, T. Bohl, F. Bordry, H. Burkhardt, K. Cornelis, P. Collier, B. Desforges, A. Faugier, V. Hatton, M. Jonker, M. Lamont, J. Miles, G. de Rijk, H. Schmickler, CERN</i>	2001
Status of TRISTAN-II Project — <i>S. Kurokawa, KEK</i>	2004
The Long Range Beam-Beam Interaction at CESR: Experiments, Simulations and Phenomenology — <i>A. B. Temnykh, INP Novosibirsk; J. J. Welch, D. H. Rice, Cornell</i>	2007
PEP-II Design Update and R&D Results — <i>W. Barletta, M. S. Zisman, LBL; R. A. Bell, J. M. Dorfan, SLAC</i>	2010
Commissioning and Operation of the LEP Pretzel Scheme — <i>R. Bailey, J. M. Jowett, W. Kalbreier, D. Wang, CERN</i>	2013
Progress of the LEP Energy Upgrade Project — <i>C. Wyss, CERN</i>	2016
Flat Beams in the SLC — <i>C. Adolphsen, T. Barklow, D. Burke, F.-J. Decker, P. Emma, M. Hildreth, T. Himel, P. Krejcik, T. Limberg, M. Minty, N. Phinney, P. Raimondi, T. Raubenheimer, M. Ross, J. Seeman, R. Siemann, W. Spence, N. Walker, M. Woodley, SLAC</i>	2019
The Damping Ring For Novosibirsk F- and B-Factories — <i>V. V. Anashin, S. E. Belomestnykh, A. A. Didenko, N. S. Dikansky, B. I. Grishanov, P. M. Ivanov, V. A. Kiselev, V. I. Kudelainen, N. A. Kuznetsov, V. A. Lebedev, B. L. Militin, S. I. Mishnev, V. V. Parkhomchuk, A. N. Voroshilov, M. N. Zakhvatkin, BINP, Russia</i>	2022
A Possible Redesign of the SLAC SLC Damping Rings — <i>T. O. Raubenheimer, R. Early, T. Limberg, H. Moshhammer, J. Spencer, SLAC</i>	2025
Update on the Argonne Positron Accumulator Ring — <i>M. Borland, ANL</i>	2028
Measurement on the SRRC 1.3 GeV Electron Booster Synchrotron Operation Parameters and the Ramping Behavior — <i>K. K. Lin, K. T. Hsu, T. S. Ueng, SRRC Taiwan</i>	2031

Volume 1: 1-747
 Volume 2: 748-1640
 Volume 3: 1641-2545
 Volume 4: 2546-3218
 Volume 5: 3219-3933

Proceedings of the 1993 Particle Accelerator Conference

1.3 GeV Electron Synchrotron — J. Modéer, Scanditronix	2034
Performance of the ALS Injection System — C. H. Kim, LBL	2036
Synchrotron of SPring-8 — H. Yokohara, H. Suzuki, T. Aoki, S. Yoneyama, Y. Ueyama, Y. Sasaki, T. Nagafuchi, S. Hayashi, H. Yokomizo, JAERI	2039
Further Study of JINR Tau-Charm Factory Design — E. Perelstein, V. Alexandrov, V. Antropov, O. Arkhipov, P. Beloshitsky, I. Bobylev, V. Kazacha, N. Kazarinov, A. Krasnykh, V. Mironov, D. Kaltchev, L. Onischenko, A. Sissakian, Yu. Smirnov, Ts. Vylov, JINR Dubna; V. Belov, B. Mudiugin, A. Popov, D. Serebrennikov, SRI St. Petersburg; I. Kvashonkin, E. Petrov, I. Umansky, Russian Inst., St. Petersburg ...	2042
A Versatile Lattice for a Tau-Charm Factory That Includes a Monochromatization Scheme (Low Emittance) and a Standard Scheme (High Emittance) — A. Faus-Golfe, U. Valencia; J. Le Duff, LAL Orsay	2045
DAFNE Interaction Region Design — M. Bassetti, M. E. Biagini, C. Biscari, M. A. Preger, G. Raffone, G. Vignola, INFN-LNF	2048
On an Asymmetric Correlated Flavor Factory — D. Cline, A. Boden, W. Gabella, A. Garren, X. Wang, UCLA	2051
Status of the MIT-Bates South Hall Ring Commissioning — J. B. Flanz, K. D. Jacobs, B. McAllister, R. Averill, S. Bradley, A. Carter, K. Dow, M. Farkondeh, E. Ihloff, S. Kowalski, W. Sapp, C. Sibley, D. Tieger, C. Tschalaer, A. Zolfaghari, MIT-Bates	2054
Current Status of the Design of the Kharkov Pulse Stretcher Ring PSR-2000 — S. Efimov, P. Gladkikh, Y. Grigor'ev, I. Guk, I. Karnaukhov, V. Kozin, S. Kononenko, V. Likhachev, V. Markov, N. Mocheshnikov, V. Moskalenko, A. Mytsykov, Yu. Popkov, A. Shcherbakov, M. Strelkov, A. Tarasenko, Yu. Telegin, A. Zelynsky, Kharkov Inst.; M. Nagaenko, Yu. Severgin, ESRI	2057
Moscow State University CW Race-Track Microtron Status — V. I. Shvedunov, A. S. Alimov, A. S. Chepurinov, O. V. Chubarov, I. V. Gribov, B. S. Ishkhanov, I. V. Surma, A. V. Tiunov, INP Moscow	2059
Optical Design of the 75-MeV Eindhoven Racetrack Microtron — G. A. Webers, J. L. Delhez, J. I. M. Botman, H. L. Hagedoorn, Eindhoven U. of Tech.	2062
Example Application for the Hamiltonian Description of an Azimuthally Varying Field Racetrack Microtron — J. L. Delhez, W. J. G. M. Kleeven, H. L. Hagedoorn, J. I. M. Botman, G. A. Webers, Eindhoven U. of Tech.	2065
A 100-MeV Racetrack Microtron — P. Lidbjörk, J. Åström, Scanditronix	2068
Electrostatic Quadrupole Focusing in the AGS g-2 Storage Ring — G. Bennett, R. Larsen, W. Morse, Y. Semertzidis, J. Yelk, BNL; Z. Liu, Boston U.	2070
Design of 8-GeV Rapid-Cycle Booster Synchrotron for the KEK B-Factory — S. Kurokawa, KEK; P. Zenkevich, ITEP Moscow	2073

Instrumentation and Beam Feedback

Chair: R. Shafer

Feedback Control of Coupled-Bunch Instabilities (Invited Paper) — J. D. Fox, N. Eisen, H. Hindi, I. Linscott, G. Oxoby, L. Sapozhnikov, SLAC; M. Serio, INFN Frascati	2076
Electro-Optical Technology Applied to Accelerator Beam Measurement and Control (Invited Paper) — R. J. Pasquinelli, FNAL	2081
RF-Synchronized Imaging for Particle and Photon Beam Characterizations (Invited Paper) — A. H. Lumpkin, ANL....	2086
Diagnostic Instrumentation System for the SRRC 1.3 GeV Synchrotron Radiation Light Source — K. T. Hsu, G. J. Jan, C. H. Kuo, K. H. Hu, SRRC Taiwan.....	2091
Overview and Status of Beam Instrumentation at the SSC — R. C. Webber, SSCL	2094
Performance of Advanced Light Source Particle Beam Diagnostics — J. Hinkson, LBL	2097
Damping in the Fermilab Booster — J. M. Steimel, Jr., D. McGinnis, FNAL	2100
Betatron Function Measurement at LEP Using the BOM 1000 Turns Facility — P. Castro, IFIC, Spain; J. Borer, A. Burns, G. Morpurgo, R. Schmidt, CERN	2103
Adaptive Cascaded Beam-Based Feedback at the SLC — T. Himel, S. Allison, P. Grossberg, L. Hendrickson, R. Sass, H. Shoaee, SLAC	2106
Design of the ALS Transverse Coupled-Bunch Feedback System — W. Barry, J. M. Byrd, J. N. Corlett, J. Hinkson, J. Johnson, G. R. Lambertson, LBL; J. D. Fox, SLAC	2109

Each volume begins with this five-volume table of contents and ends with the five-volume author index. The chairmen's foreword and a list of conference organizers and staff appear as front matter in Volume 1. A list of conference participants precedes the author index in Volume 5.

Poster presentations:

Results of Prototype Particle-Beam Diagnostics Tests for the Advanced Photon Source (APS) — A. H. Lumpkin, Y. Chung, E. Kahana, D. Patterson, W. Selley, A. Votaw, X. Wang, ANL	2112
Diagnostics Development for High Current Electron Accelerators at CESTA — J. de Mascureau, C. Bonnafond, A. Devin, E. Merle, G. Ployard, D. Villate, CESTA	2115
Beam Instrumentation for the SSC RFQ — P. Datte, G. Jamieson, R. Aiello, D. Beechy, A. Jones, D. Martin, J. Riordon, R. Webber, F. Wood, SSCL	2118
High Density Data Recording for SSCL Linac — A. L. VanDeusen, Allied Signal; C. Crist, SSCL	2121
Physic Requirements of Commissioning Diagnostics for SSCL Linac — J. W. Hurd, G. M. Arbique, C. E. Crist, F. W. Guy, M. Haworth, G. T. Leifeste, K. Saadatmand, SSCL; M. Krogh, K. McGinnis, D. Stittsworth, A. Vandeusen, S. Wright, Allied Signal	2124
Beam Diagnostic Layout Requirements for SSCL Linac — J. W. Hurd, F. W. Guy, G. Jamieson, D. Raparia, K. Saadatmand, SSCL	2127
SSCL Linac Commissioning Diagnostic Cart — C. E. Crist, L. W. Funk, J. W. Hurd, G. T. Leifeste, SSCL; M. Krogh, K. McGinnis, D. Stittsworth, A. Vandeusen, S. Wright, Allied Signal	2130
A Method for LEBT Automation — J. Sredniawski, L. Solensten, R. Schmidt, J. Porter, Y. Ng, C. Lom, Grumman; W. Newman, AMTEX	2133
Beam Energy Measurement Using the Hall C Beam Line — C. Yan, R. Carlini, D. Neuffer, CEBAF	2136
A Wide Range and High Speed Automatic Gain Control — E. J. Tacconi, C. F. Christiansen, SSCL/ UNLP Argentina.....	2139
A Beamline Design and Data Acquisition with the 20-MeV, 20-ps Electron Beam for the Higher-Order-Mode Studies of the APS SR-RF Cavities — J. Song, A. Nassiri, R. Daly, ANL	2142
A Bunch Killer for the NSLS X-Ray Electron Storage Ring — R. J. Nawrocky, U. Bergmann, D. P. Siddons, NSLS BNL	2145
The Mechanical Design of a Bunched Beam Stochastic Cooling Tank for the FNAL Tevatron — P. Hurh, G. Jackson, FNAL	2148
Design Study of Laser Compton Scattering with Relativistic Electron to Measure the Electron Beam Energy — I. Hsu, H. Chen, C. Cho, Y. Liu, Nat. Tsing Hua U.	2151
Transverse Beam Impedance Measurement: A New Coaxial Method — M. Cardito, F. Galluccio, R. Losito, M. R. Masullo, V. Vaccaro, INFN Napoli; G. Di Massa, U. Calabria	2154
A Novel Method of Noise Suppression in Beam Transfer Function Measurements — F. Caspers, M. Chanel, U. Oeftiger, CERN	2157
Beam Dispersion Measurements with Wire Scanners in the SLC Final Focus Systems — P. Emma, D. McCormick, M. C. Ross, SLAC	2160
Comprehensive Beam Jitter Study for the Commissioning of the Intermediate Matching Section and Drift Tube Linac at Ground Test Accelerator — D. S. Barr, J. D. Gilpatrick, LANL	2163
A New Method of Ion Beam Diagnostics — A. S. Artiimov, JINR Dubna	2166
Correlation Method of Measurements of Ion Beam Parameters — A. S. Artiimov, JINR Dubna	2169
The Compton Polarimeter at the SLC — G. Shapiro, S. Bethke, O. Chamberlain, R. Fuzesy, M. Kowitz, D. Pripstein, B. Schumm, H. Steiner, M. Zolotorev, LBL; P. Rowson, Columbia; D. Blockus, H. Ogren, M. Settles, Indiana; M. Fero, A. Lath, MIT; D. Calloway, R. Elia, E. Hughes, T. Junk, R. King, T. Maruyama, K. Moffeit, M. Petradza, M. Swartz, M. Woods, SLAC; G. Zapalac, Wisconsin	2172
Measurement of the Spin of a Particle Using Undulator Radiation — A. Luccio, BNL	2175
Quantum Geometrical Phase Signal of NLC Bunch Cross Section Carried by Virtual Photons — J. Shen, IHEP Beijing	2178
Response of Air-Filled Ion Chambers to High-Intensity Radiation Pulses — M. Plum, D. Brown, LANL	2181
The CEBAF Beam Loss Sensors — J. Perry, E. Woodworth, L. Meringa, S. Simrock, R. May, CEBAF; G. Stapleton, SSCL	2184
A Scintillating Fiber Beam Halo Detector for Heavy Ion Beam Diagnostics — M. A. McMahan, A. Assang, S. Herr, F. McCormack, G. Krebs, B. Feinberg, LBL	2187

Proceedings of the 1993 Particle Accelerator Conference

Development and Investigation of the 2 π Beam Loss Monitors for Super-High-Energy Accelerators, Part 1: Quad-BLM for "Warm" Machines — S. N. Lapitsky, I. A. Kurochkin, V. S. Seleznev, IHEP Russia	2190
The Design and Performance of a High Sensitivity Loss Monitor System for Use in the Fermilab Antiproton Rings — A. M. Halling, J. R. Zagel, A. Hahn, FNAL	2193
Abort Interlock Diagnostic for Protection of APS Vacuum Chamber — G. Decker, ANL	2196
Experience with Radiation Protection for a Silicon Vertex Detector at a Hadronic Collider — P. F. Derwent, D. Amidei, A. Dunn, T. Song, S. Vejck, U. Michigan; R. Crouch, R. Ducar, D. Herrup, FNAL; C. Haber, LBL	2199
Design of a New Generation of Collimators for LEP 200 — R. Jung, R. Perret, R. Valbuena, CERN	2202
Synchrotron Radiation Damage Test of Insulating Materials in the TRISTAN MR — H. Mitsui, R. Kumazawa, T. Tanii, T. Chugun, Toshiba Corp.; Y. Ohsawa, T. Ozaki, K. Takayama, KEK	2205
Insulating and Metal-Ceramic Materials for Particle Accelerators — Yu. P. Severgin, M. Z. Filimonov, Efremov Inst.	2208
The Advanced Light Source (ALS) Radiation Safety System — A. L. Ritchie, D. E. Oldfather, A. F. Lindner, LBL ..	2210
Radiation Measurements During Cavities Conditioning on APS RF Test Stand — D. M. Grudzien, R. L. Kustom, H. J. Moe, J. J. Song, ANL	2213
Application of a Simple Analytical Model to Estimate Effectiveness of Radiation Shielding for Neutrons — S. Frankle, D. Fitzgerald, R. Hutson, R. Macek, C. Wilkinson, LANL	2216
Monte Carlo Based Formula for Radiation Shielding Assessment in the Forward Direction — C. Wilkinson, D. Fitzgerald, S. Frankle, R. Hutson, R. Macek, LANL	2219
A High Reliability Oxygen Deficiency Monitoring System — R. Parry, G. Claborn, A. Haas, R. Landis, W. Page, J. Smith, SSCL	2222
Programmable Electronic Safety Systems — R. R. Parry, SSCL	2225
A Pseudo Real Time Tune Meter for the Fermilab Booster — G. Wu, V. Bharadwaj, J. Lackey, D. McGinnis, R. Tomlin, FNAL	2228
Measurement Techniques Using the Tektronix® 3052 DSP System — J. M. Steimel, Jr., D. McGinnis, FNAL	2231
Using Transient Waveform Recorders to Measure and Store Beam Parameters — R. E. Stege, Jr., R. K. Jobe, M. Ross, SLAC	2234
Tune Measurement in the APS Rings — W. Selley, E. Kahana, X. Wang, ANL	2237
Integrating Log-Ratio Position Processing for the Los Alamos Proton Storage Ring Extraction Line — T. W. Hardek, A. Band, LANL	2240
Betatron "Ping" Tune Measurement System for the IUCF Cooler Synchrotron/Storage Ring — B. J. Hamilton, M. S. Ball, T. J. P. Ellison, IUCF	2243
Tune Measurement in the NSLS Booster Synchrotron — E. B. Blum, R. Nawrocky, BNL	2246
A Realtime Feedback Microprocessor for the Tevatron — D. A. Herrup, L. Chapman, A. Franck, T. Groves, B. Lublinsky, FNAL	2249
A New Study of the Main Ring Physical Aperture — G. Wu, S. Pruss, D. Capista, FNAL	2252
Electron Beam Stability and Beam Peak to Peak Motion Data for NSLS X-Ray Storage Ring — O. Singh, BNL	2254
Test of Fast-Digital Beamline Feedback Control at the Photon Factory — N. Nakamura, T. Katsura, KEK	2257
Horizontal Movement of the Storage Ring Floor at the Photon Factory — T. Katsura, H. Nakamura, Y. Kamiya, KEK; Y. Fujita, Shimizu Corp.	2260
Closed Orbit Correction Using Singular Value Decomposition of the Response Matrix — Y. Chung, G. Decker, K. Evans, Jr., ANL	2263
Compensation for the Effect of Vacuum Chamber Eddy Current by Digital Signal Processing for Closed Orbit Feedback — Y. Chung, L. Emery, J. Kirchman, ANL	2266
Dynamic Closed Orbit Correction — Y. Cheng, SRRC Taiwan	2269
A Closed-Loop Photon Beam Control Study for the Advanced Light Source — G. Portmann, J. Bengtsson, LBL	2272
Global DC Closed Orbit Correction Experiments on the NSLS X-Ray Ring and SPEAR — Y. Chung, G. Decker, K. Evans, Jr., ANL; J. Safranek, I. So, Y. Tang, BNL; W. J. Corbett, R. Hettel, SSRL	2275
FFT-Oriented Feedback — F.-J. Decker, SLAC	2278
Issues of the Transverse Feedback Systems Design at the SSC — W. Chou, J. Peterson, SSCL	2281
A Digital Feedback System for Orbit Stabilization — A. Friedman, E. Bozoki, O. Singh, J. Smith, BNL	2284
Results from the AGS Booster Transverse Damper — D. Russo, M. Brennan, M. Meth, T. Roser, BNL	2286
Single Board Op-Amp Beam Position Monitors Electronics — M. Ball, T. J. P. Ellison, B. J. Hamilton, IUCF	2289

Each volume begins with this five-volume table of contents and ends with the five-volume author index. The chairmen's foreword and a list of conference organizers and staff appear as front matter in Volume 1. A list of conference participants precedes the author index in Volume 5.

Five-Volume Contents

A Single-Passage Beam-Position Monitor in the TRISTAN AR-to-MR Transport Lines — <i>T. Ieiri, M. Arinaga, KEK</i>	2292
Beam Position Monitoring System Using PIN Diode Switches — <i>K. Shinoe, T. Koseki, Y. Kamiya, ISSP Tokyo; N. Nakamura, T. Katsura, T. Ieiri, KEK</i>	2295
Performance of the CEBAF Arc Beam Position Monitors — <i>A. S. Hofler, B. A. Bowling, C. S. Higgins, P. K. Kloeppel, G. A. Krafft, K. L. Mahoney, CEBAF</i>	2298
The Million Turn Data Acquisition System BOSC — <i>A. Burns, W. Fischer, H. Jakob, I. Milstead, F. Schmidt, L. Vos, CERN</i>	2301
Beam Position Monitor Calibration for the Advanced Photon Source — <i>Y. Chung, G. Decker, E. Kahana, F. Lenkszus, A. Lumpkin, W. Sellyey, ANL</i>	2304
Self Triggered Single Pulse Beam Position Monitor — <i>J. L. Rothman, E. B. Blum, NSLS-BNL</i>	2307
A Prototype BPM Electronics Module for RHIC — <i>W. A. Ryan, T. J. Shea, P. Cerniglia, C. M. Degen, BNL</i>	2310
Dynamic Range Extension of BPM at the NSLS — <i>M. Bordoley, NSLS-BNL</i>	2313
Beam Position Monitoring in the 100-MHz to 500-MHz Frequency Range Using the Log-Ratio Technique — <i>F. D. Wells, R. E. Shafer, J. D. Gilpatrick, LANL</i>	2316
Beam Pinging, Sweeping, Shaking, and Electron/Ion Collecting, at the Proton Storage Ring — <i>T. Hardek, R. Macek, M. Plum, T.-S. Wang, LANL</i>	2319
Test Results of the SSC Log-Ratio Beam Position Monitor Electronics — <i>G. R. Aiello, M. R. Mills, R. E. Gonzalez, SSCL</i>	2322
RF Beam Position Monitors for the TESLA Test Facility — <i>R. Lorenz, TU Berlin</i>	2325
RHIC Beam Position Monitor Assemblies — <i>P. R. Cameron, M. C. Grau, W. A. Ryan, T. J. Shea, R. E. Sikora, BNL</i>	2328
Stripline Beam Position Monitor for the MIT-Bates South Hall Ring — <i>J. B. Flanz, R. Averill, E. Ihloff, K. D. Jacobs, D. Wang, A. Zolfaghari, MIT-Bates</i>	2331
Design and Operation of Button-Probe, Beam-Position Measurements — <i>J. D. Gilpatrick, J. F. Power, R. E. Meyer, C. R. Rose, LANL</i>	2334
Design and Calibration of Pickup-Electrodes for Beam Position Monitoring at SOR-RING — <i>K. Shinoe, Y. Kamiya, ISSP Tokyo; N. Nakamura, T. Katsura, KEK</i>	2337
The Position Monitor Using Stretched Wire Technique — <i>T. Mimashi, S. Kuroda, H. Nakayama, K. Oide, R. Sugahara, N. Yamamoto, KEK</i>	2340
An Over-Moded Stripline Beam Position Monitor — <i>J. G. Noomen, J. Bijleveld, F. Kroes, T. Sluijk, NIKHEF-K</i> ...	2343
Loss of Precision in Resonant Beam Position Monitors Due to Finite Q — <i>J. P. H. Sladen, W. Wuensch, CERN</i>	2346
Simulation of the ALS Longitudinal Multibunch Feedback System — <i>J. Byrd, LBL</i>	2349
Analysis of DSP-Based Longitudinal Feedback System: Trials at SPEAR and ALS — <i>H. Hindi, N. Eisen, J. Fox, I. Linscott, G. Oxoby, L. Sapozhnikov, SLAC; M. Serio, INFN</i>	2352
VXI Based Low Level RF System for Fermilab Linac Upgrade — <i>B. E. Chase, R. J. Pasquinelli, FNAL</i>	2355
Longitudinal Feedback in LEP — <i>J. P. Boiteux, P. Brown, E. Ciapala, H. Frischholz, G. Geschonke, J. C. Juillard, E. Peschardt, CERN</i>	2358
Performance of the Upgraded Stacktail Momentum Cooling System in the Fermilab Antiproton Source — <i>R. J. Pasquinelli, D. McGinnis, FNAL</i>	2361
Energy Vernier System for CEBAF — <i>G. A. Krafft, J. J. Bisognano, M. T. Crofford, J. C. Hovater, L. Merminga, S. N. Simrock, S. D. Witherspoon, CEBAF; K. Kubo, KEK</i>	2364
A Digital Approach for Phase Measurement Applied to Delta- i Tuneup Procedure — <i>G. R. Aiello, SSCL</i>	2367
RF Feedback for Beam Loading Compensation in the SLC Damping Rings — <i>P. Krejcik, P. Corredoura, M. Minty, R. Siemann, R. Tighe, SLAC; F. Pedersen, CERN</i>	2370
Simulation and Analysis of RF Feedback Systems on the SLC Damping Rings — <i>M. Minty, T. Himel, P. Krejcik, R. H. Siemann, R. Tighe, SLAC</i>	2373
Improved Impedance Reduction in the CERN SPS Superconducting Cavities for High Intensity Proton Operation — <i>D. Boussard, G. Lambert, T. P. R. Linnecar, CERN</i>	2376
Damping of Phase Errors at Injection in the LHC — <i>D. Boussard, E. Onillon, CERN</i>	2379
A Digital Beam Phase Loop for the Low Energy Booster — <i>L. K. Mestha, V. Brouk, R. C. Webber, J. Mangino, T. Uher, SSCL</i>	2382
General Time-Varying State-Space Control Model and Its Application for Transient Beam Loading Compensation — <i>L. K. Mestha, C. M. Kwan, SSCL; K. S. Yeung, UTA</i>	2385
A Digital Phase and Amplitude Feedforward Correction System — <i>D. Yu, P. Conway, DULY Res. Inc.</i>	2388

Volume 1: 1-747
Volume 2: 748-1640
Volume 3: 1641-2545
Volume 4: 2546-3218
Volume 5: 3219-3933

Proceedings of the 1993 Particle Accelerator Conference

Results of Adaptive Feedforward on GTA — C. D. Ziomek, P. M. Denney, A. H. Regan, M. T. Lynch, S. P. Jachim, L. E. Eaton, E. F. Natter, LANL	2391
Fast Bunch-to-Bunch Current Sampling in the Cornell Electron-Positron Collider — C. R. Dunnam, Cornell; K. B. Unser, CERN	2394
A Method for Measuring Dark Current Electron Beams in an RF Linac — X. K. Maruyama, T. Fasanello, H. Rietdyk, Naval Postgraduate School; M. A. Piestrup, Adelphi Tech.; D. W. Rule, R. B. Fiorito, NSWC	2397
High Bandwidth Beam Current Monitor — R. M. Baltrusaitis, C. A. Ekdahl, LANL; R. G. Cooper, E. Peterson, C. E. Warn, EG&G	2400
Rapid Measurements of Two-Dimensional Ion Beam Current Distribution for Pulsed Neutron Source — A. M. Tron, MEPI	2403
Short Bunch Length Detector for Ion Beam with High Bunch Density — A. M. Tron, V. V. Shako, MEPI	2406
Measurement of Bunch Time-Structure in KEK-PF — M. Tobiya, T. Kasuga, T. Takeo, T. Obina, K. Tamura, Hiroshima U.; T. Katsura, KEK	2409
A Fifth Harmonic RF Bunch Monitor for the ANL-APS Electron Linac — A. Nassiri, A. Grelick, ANL	2412
Characterization of Subnanosecond Heavy-Ion Bunches at the TASCC Superconducting Cyclotron — G. R. Mitchel, N. A. Towne, AECL	2415
Design, Implementation, and Results from a Longitudinal Phase Space Tomography (PST) Monitor in the Fermilab Main Ring — G. Jackson, FNAL	2418
An Electrostatic Sweep Plate Device for Emittance Measurement of Ion Beams to 2 MeV — T. W. Debiak, J. Porter, R. Heuer, I. Birnbaum, Grumman	2420
Length Monitor for 1 mm SLC Bunches — E. Babenko, BINP Novosibirsk; R. K. Jobe, D. McCormick, J. T. Seeman, SLAC	2423
Bunch Shape Monitor for SSCL Linac — J. W. Hurd, G. M. Arbiq, C. E. Crist, F. W. Guy, G. T. Leifeste, D. Raparia, K. Saadatmand, D. A. Swenson, SSCL; S. Esin, A. Feschenko, A. Stepanov, A. Mirzojan, INR Moscow	2426
A Field-Based Technique for the Longitudinal Profiling of Ultrarelativistic Electron or Positron Bunches Down to Lengths of ≤ 10 Microns — R. Tatchyn, SLAC	2429
Performance Limits of a Streak Camera in Real Time Three-Dimensional Measurement of Bunch Oscillation in LEP — E. Rossa, CERN; F. Tecker, RWTH Aachen; J. C. Mathae, ARP Strasbourg	2432
Bunch Length Measurements in the SLC Damping Ring — F.-J. Decker, T. Limberg, M. Minty, A. Ross, SLAC ..	2435
Virtual Photon Impulse of Bunch, Beam-pipe Response, Coherent RF Beamstrahlung; and BEPC Bunch Length, BES Jam, Virtual Acceleration — J. Shen, IHEP Beijing	2438
Development on Multistrip Monitor for Nonintercepting Measurement of Beam Geometric Moments — Y. Yin, TRIUMF	2441
Wire Scanner Data Analysis for the SSC Linac Emittance Measurement — C. Y. Yao, J. W. Hurd, J. Sage, SSCL	2444
Real-Time Spot Size Measurement for Pulsed High-Energy Radiographic Machines — S. A. Watson, LANL	2447
High Resolution Beam Monitoring with Optical Transition Radiation at 3 MeV Electron Energy — A. Specka, D. Bernard, R. Guirlet, F. Jacquet, P. Miné, B. Montès, R. Morano, P. Poilleux, LPNHE; F. Amiranoff, LULI; J. Morillo, LSI	2450
Beam Profiling with Optical Transition Radiation — D. W. Rule, R. B. Fiorito, NSWCDD	2453
Beam Emittance from Coherent Cherenkov Radiation in a Solid Dielectric — R. D. Richardson, R. C. Platt, SAIC; C. E. Crist, SNL	2456
A 10 μ m Resolution Secondary Emission Monitor for Fermilab's Targeting Station — P. Hurh, S. O'Day, R. Dombrowski, T. Page, FNAL	2459
Construction of a High Resolution Electron Beam Profile Monitor — J. Norem, J. Dawson, W. Haberichter, W. Novak, L. Reed, X-F. Yang, ANL	2462
Design Study of Beam Profile Monitor of Storage Ring by Using Synchrotron Radiation — I. C. Hs, T. H. Huang, Nat. Tsing Hua U./SRRC	2465
Limitations of a Residual Gas Ionization Beam Profile Monitor for the SSC Collider — R. Meinke, W. Nexsen, E. Tsyganov, A. Zinchenko, SSCL	2468
Full Cycle Beam Diagnostics with an Ionization Profile Monitor — A. Stillman, R. E. Thern, BNL	2471
Electron Beam Diagnostics by Means of Edge Radiation — O. V. Chubar, Kurchatov Inst.; E. S. Masunov, MEPI	2474
CEBAF Beam Viewer Imaging Software — B. A. Bowling, C. McDowell, CEBAF	2477

Each volume begins with this five-volume table of contents and ends with the five-volume author index. The chairmen's foreword and a list of conference organizers and staff appear as front matter in Volume 1. A list of conference participants precedes the author index in Volume 5.

Prototype Flying-Wire Beam-Profile Monitor — D. B. Barlow, C. M. Fortgang, J. D. Gilpatrick, R. E. Meyer, A. M. Rendon, D. S. Warren, M. D. Wilke, LANL	2480
Emittance Measurement and Data Analysis for the SSC Linac Injector Lab — J. E. Hébert, P. Datte, F. W. Guy, N. C. Okay, K. Saadatmand, J. Sage, D. M. Wetherholt, W. A. Whittenberg, SSCL	2483
Automatic Emittance Measurement at the ATF — X. J. Wang, R. Malone, K. Batchelor, I. Ben-Zvi, BNL	2486
Electron Beam Emittance Monitor for the SSC — E. Tsyganov, R. Meinke, W. Nexsen, S. Kauffmann, A. Zinchenko, A. Taratin, SSCL	2489
Measurement of Vertical Emittance at LEP from Hard X-Rays — H. Akbari, J. Borer, C. Bovet, Ch. Delmere, A. Manarin, E. Rossa, M. Sillanoli, J. Spanggaard, CERN	2492
Performance and Operational Experience of the LEP Synchrotron Light Telescopes — G. Burtin, R. J. Colchester, J. J. Gras, R. Jung, J. M. Vouillot, CERN	2495
High Sensitivity Beam Intensity and Profile Monitors for the SPS Extracted Beams — J. Camas, G. Ferioli, R. Jung, J. Mann, CERN	2498
High Density Harp for SSCL Linac — C. T. Fritzsche, M. L. Krogh, AlliedSignal; C. E. Crist, SSCL	2501
High Resolution Measurements of Lepton Beam Transverse Distributions With the LEP Wire Scanners — J. Camas, G. Crockford, G. Ferioli, C. Fischer, J. J. Gras, R. Jung, J. Koopman, J. Mann, CERN	2504
Beam Size Measurements with Noninterceptive Off-Axis Screens — F.-J. Decker, R. Brown, J. T. Seeman, SLAC ...	2507
Resolution Improvement in Beam Profile Measurements with Synchrotron Light — O. V. Chubar, MEPI	2510
The Orsay Spot Size Monitor for the Final Focus Test Beam — J. Buon, B. Delcourt, J. Jeanjean, F. Le Diberder, V. Lepeltier, P. Puzo, LAL Orsay	2513
Beam Monitor Utilizing Transition Radiation — Y. Jgawa, J. Choi, T. Suwada, T. Kamitani, T. Urano, K. Furukawa, S. Ohsawa, A. Enomoto, I. Sato, KEK	2516
Fermilab Main Ring Low Level RF System Modifications for Focus Free Transition Beam Tests — R. G. Scala, K. Meisner, FNAL	2519
RF Synchronous Transfer into Specific Buckets Between Fermilab Main Ring and Tevatron Accelerators — K. Meisner, FNAL	2522
Main Ring Bunch Length Monitor — K. Meisner, G. Jackson, FNAL	2525
A VX1/LabVIEW-based Beamline Tuner — W. Blokland, FNAL	2528
A Frequency-Domain Directivity Enhancement of Beam Position Stripline Detectors — E. L. Barsotti, FNAL	2531
The Control System of ROSY I — T. Goetz, M. Picard, U. Bonn; M. Plesko, Sinc. Trieste	2534
Measuring Emittance Using Beam Position Monitors — S. J. Russell, B. E. Carlsten, LANL	2537
On the Reliability of Measured Results by Non-Destructive Beam Profile Monitor — T. Kawakubo, E. Kadokura, KEK; T. Ishida, Mitsubishi Elect.	2540
Transverse Feedback System with Digital Filter — V. M. Zhabitsky, JINR; I. L. Korenev, L. A. Yudin, MRTI	2543

Volume 4

Advanced Accelerator Concepts

Chair: C. Joshi

R. R. Wilson Prize Lecture: Adventures with Accelerators (<i>Invited Paper</i>) — J. P. Blewett, BNL (ret.)	2546
Demonstration of Plasma Beat Wave Acceleration of Electrons from 2 MeV to 20 MeV (<i>Invited Paper</i>) — C. E. Clayton, K. A. Marsh, M. Everett, A. Lal, C. Joshi, UCLA	2551
Laser Wakefield Accelerator Experiments Using 1 ps 30 TW Nd:glass Laser — K. Nakajima, H. Nakanishi, T. Kawakubo, A. Ogata, KEK; Y. Kitagawa, H. Shiraga, R. Kodama, T. Zhang, K. Suzuki, Y. Kato, Osaka U.; Y. Sakawa, T. Shoji, Nagoya U.; Y. Nishida, N. Yugami, Utsunomiya U.; T. Tajima, U. Texas, Austin	2556
Photonic Band Gap Resonators for High Energy Accelerators (<i>Invited Paper</i>) — S. Schultz, D. R. Smith, UCSD; N. Kroll, UCSD/SLAC	2559
Update on the ATF Inverse Cherenkov Laser Acceleration Experiment — W. D. Kimura, L. C. Steinhauer, G. H. Kim, S. C. Tidwell, STI Optronics; I. Pogorelsky, K. P. Kusche, BNL/STI Optronics	2564
New Directions in RF Sources (<i>Invited Paper</i>) — L. Schächter, Cornell	2567
Criteria for Comparing the Suitability of Microwave Amplifiers for Driving TeV Linear Colliders — V. I. Granatstein, G. S. Nusinovich, U. Maryland	2572

Proceedings of the 1993 Particle Accelerator Conference

High Gradient Acceleration in a 17 GHz Photocathode RF Gun — S. C. Chen, J. Gonichon, L. C-L. Lin, R. J. Temkin, S. Trotz, B. G. Danly, J. S. Wurtele, MIT	2575
An Inverse Free-Electron-Laser Accelerator — A. S. Fisher, J. C. Gallardo, A. van Steenbergen, S. Ulc, M. Woodle, BNL; J. Sandweiss, Yale; J. Fang, Columbia U.	2578
Phase Control in High-Gradient Laser Particle Accelerators — L. C. Steinhauer, W. D. Kimura, STI Optronics	2581
<i>Poster presentations:</i>	
Beam Quality in a Cyclotron Autoresonance Accelerator — B. Hafizi, Icarus Res.; P. Sprangle, NRL; J. L. Hirshfield, Omega-P Inc.	2584
Superlattice Crystal Accelerator: Acceleration Beyond GeV/m — S. A. Bogacz, FNAL	2587
Design Study of a Microwave Driver for a Relativistic Klystron Two-Beam Accelerator — T. L. Houck, LLNL	2590
The Standing Wave FEL/TBA: Realistic Cavity Geometry and Energy Extraction — J. Kim, A. M. Sessler, LBL; H. Henke, TU Berlin; W. M. Sharp, LLNL	2593
The Argonne Wakefield Accelerator: Overview and Status — P. Schoessow, E. Chojnacki, W. Gai, C. Ho, R. Konecny, J. Power, M. Rosing, J. Simpson, ANL	2596
A Self-Consistent Theory of Ferromagnetic Waveguide Accelerators Driven by Electron Beams — H. S. Uhm, NSWC	2599
Wakefield Accelerator Driven by a Relativistic Electron Beam in a Ferromagnetic Waveguide — H. S. Uhm, NSWC	2602
Magnetic Field-Decay Accelerator Driven by a Relativistic Electron Beam in a Ferromagnetic Waveguide — H. S. Uhm, NSWC	2605
Three-Dimensional Simulation Analysis of the First Sections of a Standing-Wave Free-Electron Laser Two-Beam Accelerator — C. Wang, A. M. Sessler, LBL	2608
Reacceleration Experiment to Demonstrate the Concept of Efficiency Enhancement in a Relativistic Klystron Two- Beam Accelerator — G. A. Westenskow, T. L. Houck, LLNL	2611
Design Analysis for a 100-MeV Inverse Cherenkov Laser Accelerator — J. R. Fontana, UCSB; W. D. Kimura, L. C. Steinhauer, STI Optronics; I. Pogorelsky, BNL/STI Optronics	2614
An Inverse Free Electron Laser Driven Linear Collider Electron-Positron B-Factory — N. Barov, C. Pellegrini, UCLA; J. Sandweiss, Yale	2617
2.5D Numerical Simulation of Relativistic Electron Bunches (REB) Interaction with Underdense and Overdense Plasmas — O. V. Batishchev, Y. S. Sigov, Keldysh Inst.; V. I. Karas', Y. B. Fainberg, Kharkov Inst.	2620
Propagation of Short Electron Pulses in Underdense Plasmas — N. Barov, J. Rosenzweig, UCLA	2623
Numerical Simulations of Driving Beam Dynamics in the Plasma Wakefield Accelerator — G. Joyce, J. Krall, E. Esarey, NRL	2626
Self-Modulated-Laser Wakefield Accelerator — J. Krall, A. Ting, E. Esarey, P. Sprangle, NRL	2629
A 100 MeV Proof-of-Principle Laser Wakefield Accelerator Experiment — A. Ting, A. Fisher, R. Fischer, J. Grun, J. Krall, E. Esarey, P. Sprangle, NRL; D. Umstadter, G. Mourou, U. Michigan	2632
Recent Work on Short Pulse Laser-Plasma Accelerators — T. Katsouleas, T. C. Chiou, USC; W. B. Mori, C. Decker, UCLA; J. S. Wurtele, G. Shvets, MIT	2635
Plasma Lens Experiments at the Final Focus Test Beam — J. Norem, ANL; D. Cline, W. Gabella, P. Kwok, S. Rajagopalan, J. Rosenzweig, UCLA; B. Barletta, UCLA/LBL; R. Williams, Florida A&M; S. Chattopadhyay, W. Leemans, A. Sessler, LBL; G. Westenskow, LLNL; J. Wurtele, MIT; J. J. Su, NCU Taiwan; K. Nakajima, H. Nakanishi, A. Ogata, D. Whittum, KEK; I. Hsu, NTU Taiwan; D. D. Meyerhofer, U. Rochester; T. Katsouleas, P. Lai, R. Liou, USC; P. Chen, W. Craddock, C. K. Ng, J. Spencer, SLAC; Y. Nishida, Utsunomiya U.	2638
A Plasma Lens and Accelerator Based Upon Magnetically Driven Charge Separation — S. Robertson, U. Colorado	2641
The NRL X-Band Magnicon Amplifier Experiment — S. H. Gold, C. A. Sullivan, W. M. Manheimer, NRL; B. Hafizi, Icarus Res.	2644
Theoretical Investigation of Magnicon Efficiency — B. Hafizi, Icarus Res.; S. H. Gold, W. M. Manheimer, P. Sprangle, NRL	2647
First Test of the X-Band Pulsed Magnicon — O. Nezhevenko, I. Kazarezov, E. Kozyrev, G. Kuznetsov, I. Makarov, A. Nikiforov, B. Persov, G. Serdobintsev, M. Tiunov, V. Yakovlev, I. Zapryagaev, BINP Russia	2650

Each volume begins with this five-volume table of contents and ends with the five-volume author index. The chairmen's foreword and a list of conference organizers and staff appear as front matter in Volume 1. A list of conference participants precedes the author index in Volume 5.

Five-Volume Contents

TM-FEL With a Longitudinal Wiggler and an Annular Beam — L. Schächter, T. J. Davis, J. A. Nation, Cornell	2653
CARM and Harmonic Gyro-Amplifier Experiments at 17 GHz — W. L. Menninger, B. G. Danly, S. Alberti, C. Chen, E. Giguet, J. L. Rullier, R. J. Temkin, MIT	2656
Stability of Gyrotristrons — P. E. Latham, G. S. Nusinovich, J. Cheng, U. Maryland	2659
Optimum Operation of Gyrotristrons — P. E. Latham, G. S. Nusinovich, U. Maryland	2661
Large Orbit Gyroklystron Development at Los Alamos — R. M. Stringfield, R. M. Wheat, D. J. Brown, M.V. Fazio, J. Kinross-Wright, B. E. Carlsten, G. Rodenz, R. J. Faehl, R. F. Hoeberling, LANL	2664
Initial Operation of a High Power, K-Band, Harmonic Gyroklystron for Accelerator Applications — J. P. Calame, H. W. Matthews, W. Lawson, B. Hogan, M. K. E. Lee, J. Cheng, V. L. Granatstein, M. Reiser, C. D. Striffler, U. Maryland	2667
Design of a 100 MW, 17 GHz Second Harmonic Gyroklystron Experiment — W. Lawson, P. E. Latham, V. Specht, M. K. E. Lee, Q. Qian, J. P. Calame, B. Hogan, V. L. Granatstein, M. Reiser, C. D. Striffler, U. Maryland	2670
Some Concepts of Relativistic Gyroamplifiers for Particle Acceleration — G. S. Nusinovich, P. E. Latham, V. L. Granatstein, U. Maryland	2673
Experimental Progress Toward a 1 GW, 1 ms Pulse Length, High Current Relativistic Klystron — M. Fazio, B. Carlsten, R. Faehl, W. Haynes, T. Kwan, R. Stringfield, LANL	2675
Relativistic Plasma Klystron Amplifier in Connection with Application to High Gradient Accelerators — H. S. Uhm, NSWC	2678
Sheet-Beam Klystron RF Cavities — D. Yu, DULY Res. Inc.; P. Wilson, SLAC	2681
Beam-Wave Interaction in a Quasi-Periodic Structure — L. Schächter, J. A. Nation, Cornell	2684
Two-Stage, High Power X-Band Amplifier Experiment — E. Kuang, T. J. Davis, J. D. Ivers, G. S. Kerslick, J. A. Nation, L. Schächter, Cornell	2687
Long-Pulse, High-Power, X-Band Relativistic Traveling-Wave Tube Amplifier — T. Kimura, S. Alberti, B. G. Danly, R. J. Temkin, MIT	2690
Tapered Tube, Microsecond Electron Beam Gyrotron Backward-Wave Oscillators — R. M. Gilgenbach, M. T. Walter, P. R. Menge, T. A. Spencer, U. Michigan	2693
Quiet Start and Autotasking for PARMELA — J. Gonichon, S. C. Chen, L. C.-L. Lin, R. J. Temkin, MIT	2696
Waveguide Side-Wall Coupling in RF Guns — L. C.-L. Lin, S. C. Chen, J. Gonichon, S. Trotz, J. S. Wurtele, MIT	2699
A High-Current Micro-Pulse Electron Gun — F. M. Mako, W. Peter, FM Tech. Inc.	2702
Knife-Edge Thin Film Field Emission Cathodes — B. Lee, H. P. Demroff, M. M. Drew, T. S. Elliot, T. K. Mazumdar, P. M. McIntyre, Y. Pang, D. D. Smith, H.-J. Trost, Texas A&M	2705
The Oxidized Porous Silicon Field Emission Array — D. D. Smith, H. P. Demroff, T. S. Elliott, T. B. Kasproicz, B. Lee, T. K. Mazumdar, P. M. McIntyre, Y. Pang, H.-J. Trost, Texas A&M	2708
Study of Porous Silicon Morphologies for Electron Transport — Y. Pang, H. Demroff, T. S. Elliott, B. Lee, J. Lu, V. B. Madduri, T. K. Mazumdar, P. M. McIntyre, D. D. Smith, H.-J. Trost, Texas A&M	2711
Cold Test Measurements of a BWO Slow-Wave Structure — W. Main, Y. Carmel, K. Ogura, J. Weaver, S. Watanabe, U. Maryland	2714
Collective Accelerator with Variable Energy and Wide Spectrum of Accelerated Ions — R. Meshcherov, G. Batsikh, V. Krasnopol'sky, V. Rybalko, V. Sazhin, MRTI Moscow; A. Vasiliev, MAE Russia	2717
High Gradient Experiments with Nanosecond Pulses — V. Baglin, H. Haseroth, J. Knott, CERN; F. Chautard, SSCL	2720
Development of the Alternate Entry Port for the ATF — Z. Parsa, BNL	2723

Magnets, Cryogenics, and Alignment

Chair: J. Strait

Status of Superconducting Magnet Development (SSC, RHIC, LHC) (Invited Paper) — P. Wanderer, BNL	2726
Electrical Performance Characteristics of the SSC Accelerator System String Test (Invited Paper) — W. Robinson, W. Burgett, T. Dombeck, J. Gannon, P. Kraushaar, A. McInturff, T. Savord, G. Tool, SSCL	2731
Overview of the Final Focus Test Beam Alignment System — V. E. Bressler, R. E. Ruland, D. Plouffe, SLAC	2736
Long Term Experience with Cryoplant Operation for Superconducting Magnets and RF Cavities at CERN — D. Delikaris, J.-P. Dauvergne, P. K. Frandsen, F. Haug, G. Passardi, J.-M. Rieubland, J. Schmid, CERN	2739
Axial Variations in the Magnetic Field of Superconducting Dipoles and Quadrupoles — A. K. Ghosh, K. E. Robins, W. B. Sampson, BNL	2742

Volume 1: 1-747
 Volume 2: 748-1640
 Volume 3: 1641-2545
 Volume 4: 2546-3218
 Volume 5: 3219-3933

Proceedings of the 1993 Particle Accelerator Conference

Large Aperture Quadrupoles for RHIC Interaction Regions — R. Gupta, M. Anerella, G. Ganetis, M. Garber, A. Ghosh, A. Greene, A. Jain, S. Kahn, E. Kelly, E. Killian, G. Morgan, A. Morgillo, J. Muratore, A. Prodell, M. Rehak, W. Sampson, R. Shutt, P. Thompson, P. Wanderer, E. Willen, BNL	2745
--	------

Poster presentations:

Design of Superconducting Quadrupole Magnets for CEBAF's Hall A Spectrometer — R. Kreutz, E. Brüttsch, K. Dreher, H. Grüneberg, H. Lütkehaus, W. Nick, H. Peschel, B. Rzezonka, F. Sommer, P. Schäfer, Siemens AG	2748
Design of a Superconducting Wiggler for the PLS — B. K. Kang, Y. M. Koo, D. E. Kim, H. S. Seo, Y. U. Sohn, Pohang; P. D. Vobly, N. A. Mezentshev, G. N. Kulipanov, BINP	2751
Calculations of Magnetic Field for the End Design of the RHIC Arc Dipole — S. A. Kahn, R. C. Gupta, A. K. Jain, G. H. Morgan, P. A. Thompson, BNL	2754
Collider Scenario Implications of ASST Operation — A. D. McInturff, W. Burgett, M. Christianson, T. Dombeck, J. Gannon, D. Haenni, P. Kraushaar, M. Levin, M. McAshan, G. Mulholland, D. Murray, W. Robinson, T. Savord, R. Smellie, F. Spinis, G. Tool, J. Weisend II, J. Zatopek, SSCL	2757
Preliminary Analysis of Coil Wedge Dimensional Variation in SSC Prototype Dipole Magnets — D. Pollock, G. Brown, S. Dwyer, R. Gattu, D. Warner, SSCL	2760
SSC String Test Facility for Superconducting Magnets: Testing Capabilities and Program for Collider Magnets — P. Kraushaar, W. Burgett, T. Dombeck, A. McInturff, W. Robinson, V. Saladin, SSCL	2763
"B" Series RHIC Arc Quadrupoles — P. Thompson, M. Anerella, G. Ganetis, M. Garber, A. Ghosh, A. Greene, R. Gupta, A. Jain, S. A. Kahn, G. Morgan, A. Morgillo, J. Muratore, A. Prodell, M. Rehak, W. Sampson, P. Wanderer, E. Willen, BNL	2766
Fermilab-Built SSC Collider Dipoles Using Low Temperature Curing Insulation Systems With and Without Glass Tape — T. S. Jaffery, R. Coombes, A. Devred, J. DiMarco, T. Ogitsu, R. E. Sims, J. C. Tompkins, M. Wake, SSCL; R. Bossert, J. Carson, S. W. Delchamps, I. Gonczy, S. Gourlay, R. Hanft, M. J. Lamm, P. Mazur, D. Orris, J. Strait, FNAL	2769
Design and Tests of UNK Superconducting Correction Magnet Models — E. Rybakov, N. Bogatov, I. Dmitrieva, M. Kosyakin, Yu. Severgin, V. Fedorov, V. Shan'gin, Efremov Inst.; P. Chirkov, S. Kozub, K. Myznikov, V. Sychev, IHEP Moscow; A. Rychagov, V. Sytnikov, A. Taran, All-Union R&D Inst.	2772
Quench and Quench Protection for the SSC Collider Correctors — A. He, SSCL.....	2775
Variation in a_1 Saturation in SSC Collider Dipoles — R. C. Gupta, A. K. Jain, BNL	2778
Spool Pieces at the SSCL — T. Clayton, Y. Cai, R. Smellie, S. Stampke, SSCL	2781
Quench Simulations of the 40 mm Aperture SSC-Quadrupole Magnet Connected in Series with 50 mm Aperture SSC-Dipole Magnets — G. López, SSCL	2784
Effective Stress of the SSC 80 K Synchrotron Radiation Liner in a Quenching Dipole Magnet — K. K. Leung, Q. S. Shu, K. Yu, J. Zbasnik, SSCL	2787
Improved Cable Insulation for Superconducting Magnets — M. Anerella, A. K. Ghosh, E. Kelley, J. Schmalzle, E. Willen, BNL; J. Fraivillig, J. Ochsner, D. J. Parish, DuPont	2790
Treatment of the Results of Magnetic Mapping of the SIBERIA-2 Magnets — V. Korchuganov, E. Levichev, A. Philipchenko, BINP	2793
Prototype Quadrupole Magnets for the PLS Storage Ring — Y. M. Koo, D. E. Kim, Y. G. Nah, H. S. Han, B. K. Kang, K. H. Park, J. R. Yoon, H. K. Lee, J. E. Milburn, Pohang	2796
Magnetic Measurement Data of the Injector Synchrotron Dipole Magnets for the 7-GeV Advanced Photon Source — K. Kim, S. H. Kim, L. R. Turner, C. L. Doose, R. Hogrefe, R. Merl, ANL	2799
Magnet Measurement Facility for the 7-GeV Advanced Photon Source — S. H. Kim, K. Kim, C. Doose, R. Hogrefe, R. Merl, ANL	2802
Magnetic Measurements of the Storage Ring Quadrupole Magnets for the 7-GeV Advanced Photon Source — S. H. Kim, K. Kim, C. Doose, R. Hogrefe, R. Merl, ANL	2805
Design and Tests of the Injector Synchrotron Magnets for the 7-GeV Advanced Photon Source (APS) — K. Kim, S. H. Kim, K. M. Thompson, L. R. Turner, ANL	2808
Final Analysis of the ALS Lattice Magnet Data — R. Keller, LBL	2811
Design and Measurement of the Sextupole Magnet for the APS Storage Ring — L. R. Turner, K. M. Thompson, S. H. Kim, K. Kim, ANL	2814
A Pulsed Septum Magnet for the APS — L. R. Turner, D. G. McGhee, F. E. Mills, S. Reeves, ANL	2817

Each volume begins with this five-volume table of contents and ends with the five-volume author index. The chairman's foreword and a list of conference organizers and staff appear as front matter in Volume 1. A list of conference participants precedes the author index in Volume 5.

The ELETTRA Storage Ring Magnets — G. Petrucci, D. Tommasini, Sinc. Trieste/CERN	2820
Experience with the Source Evaluation Board Method of Procuring Technical Components for the Fermilab Main Injector — D. J. Harding, J. P. Collins, G. R. Kobliska, N. S. Chester, E. G. Pewitt, W. B. Fowler, FNAL ..	2823
Sextupole Magnets for the Fermilab Main Injector — D. J. Harding, N. Chester, R. Baiod, FNAL	2826
Design and Measurements of Prototype Fermilab Main Injector Dipole Endpacks — D. J. Harding, H. D. Glass, J.-F. Ostiguy, B. C. Brown, F. A. Harfoush, C. S. Mishra, FNAL	2829
Magnetic Measurement of Quadrupole and Sextupole Magnets for the MIT-Bates South Hall Ring (SHR) — D. R. Tieger, J. D. Zumbro, W. W. Sapp, MIT Bates	2832
A Permanent Magnet Dipole Correction Element for the Tevatron — J. E. Goodwin, T. Anderson, A. Franck, N. Gelfand, H. Jostlein, FNAL	2835
Precision Measurement of Transport Components — P. Tenenbaum, J. K. Cobb, D. R. Jensen, D. Sawyer, W. Wagner, H. V. Walz, S. H. Williams, SLAC	2838
Measurement and Adjustment of CIAE Medical Cyclotron Magnet — M. Fan, X. Zhang, T. Zhang, C. Liang, Q. Tao, Z. Zhao, C. Chu, T. Li, Y. Hu, Y. Chen, H. Zhang, H. Jia, C. Jiao, J. Liu, W. Zhang, C. Zhou, J. Jiao, Y. Hou, CIAE China	2841
Magnetic Measurement and Alignment of the ELETTRA Storage Ring Quadrupole, Sextupole and Steerer Magnets — D. Zangrando, R. P. Walker, Sinc. Trieste	2844
Measurement and Correction of the ELETTRA Storage Ring Dipole Magnets — R. P. Walker, D. Zangrando, Sinc. Trieste	2847
Magnet Costs for the Advanced Light Source — J. Tanabe, J. Krupnick, E. Hoyer, A. Paterson, LBL	2850
Automatic Bench for Precise Magnetic Measurements of Linac Multipole Focusing Elements — V. S. Skachkov, M. A. Kozchekin, R. P. Koujbida, V. I. Lulevich, A. V. Selin, O. S. Sergeeva, ITEP Moscow	2853
Measurements of Loma Linda Proton Therapy Gantry Dipoles — H. D. Glass, P. O. Mazur, J. W. Sim, FNAL	2856
Techniques for Measurement of Dipole Endfields with a Rigid Integrating Coil — H. D. Glass, FNAL	2859
Lamination and End Plate Design Studies of SSC Low Energy Booster Magnet Prototypes — N. Li, SSCL	2862
Design and Fabrication of a Multi-Purpose Panofsky Magnet — J. Budnick, T. Hall, D. Li, S. Y. Lee, IUCF	2865
Magnetic Septa Design and Performance for Injection and Extraction to and from the MIT-Bates South Hall Ring (SHR) — R. Averill, K. Dow, H. Enge, J. Flanz, E. Ihloff, M. Farkhondeh, C. Sibley, MIT-Bates	2868
Octupole Magnet Design for the 1/2 Integer Resonant Extraction of Electrons from the MIT-Bates South Hall Ring (SHR) — R. Averill, J. Flanz, E. Ihloff, D. Tieger, MIT-Bates	2871
Ramped Quadrupole Design and Performance for the MIT-Bates South Hall Ring (SHR) — R. Averill, J. Flanz, E. Ihloff, D. Tieger, MIT-Bates	2874
Lambertson Upgrade Program — K. J. Weber, FNAL	2877
Computer Studies of a Combined-Function Bend Magnet for a Proposed Redesign of the SLAC SLC Damping Rings — R. A. Early, T. O. Raubenheimer, SLAC	2880
Comparison of Computer Predictions and Magnetic Field Measurements for an Iron Spectrometer Magnet — G. T. Danby, J. W. Jackson, W. Meng, C. Spataro, BNL	2883
Design and Performance of the Dipole Magnet for the SRRC Storage Ring — C. H. Chang, H. C. Liu, G. J. Hwang, SRRC Taiwan	2886
Specific Features of Magnet Design for the Duke FEL Storage Ring — B. Burnham, N. Hower, V. N. Litvinenko, J. M. J. Madey, Y. Wu, Duke	2889
Dipole Design for the EUTERPE Storage Ring — J. I. M. Botman, C. J. Timmermans, B. Xi, H. Heller, H. L. Hagedoorn, P. Brinkgreve, E. Dekkers, J. Moerel, Eindhoven,	2892
Design of a Lambertson Injection Magnet for the RHIC Machine — E. Rodger, N. Tsoupas, J. Claus, H. W. Foelsche, BNL	2895
Combined AC Corrector Magnets — A. J. Otter, P. A. Reeve, TRIUMF; N. Marks, Daresbury	2898
Longitudinal Profile and Effective Length of a Conventional Dipole Magnet — J. Ostiguy, FNAL	2901
Magnetic Flux Shielding for the Muon g-2 Storage Ring Superconducting Inflectors — W. Meng, W. B. Sampson, M. Suenaga, BNL	2904
Three Dimensional Field Analysis for the AGS Combined Function Magnets — W. Meng, M. Tanaka, BNL	2907
Survey and Alignment Data Analysis for the ALS Storage Ring — R. Keller, LBL	2910
A Mechanical System for the Positioning of Accelerator Magnets — R. Viola, R. Martin, SSCL	2913
Preliminary Studies on a Magneto-Optical Procedure for Aligning RHIC Magnets — M. A. Goldman, R. E. Sikora, T. J. Shea, BNL	2916

Proceedings of the 1993 Particle Accelerator Conference

RHIC Survey and Alignment — F. X. Karl, R. R. Anderson, M. A. Goldman, F. M. Hemmer, D. Kazmark, Jr., T. T. Mroczkowski, J. C. Roecklein, BNL	2919
Effect of Magnet Sorting Using a Simple Resonance Cancellation Method on the RMS Orbit Distortion at the APS Injector Synchrotron — F. Lopez, R. Koul, F. E. Mills, ANL	2922
Optimal Magnet Sorting Procedure and Application to the APS Injector Synchrotron — R. K. Koul, F. Lopez, F. E. Mills, ANL	2924
Geodetic Concept for the Storage Ring EUTERPE — S. F. C. L. Wetzels, C. J. Timmermans, G. A. Webers, P. H. J. Schellekens, J. I. M. Botman, H. L. Hagedoorn, Eindhoven U. of Tech.	2927
Alignment of CEBAF Cryomodules — W. J. Schneider, J. J. Bisognano, J. Fischer, D. R. Douglas, K. Macha, J. Mammoser, W. Oren, J. Preble, J. Robb, M. Wiseman, CEBAF	2929
The Hydrostatic Levelling System (HLS) / Servo-Controlled Precision Jacks: A New Generation Altimetric Alignment and Control System — D. Roux, ESRF	2932
Control of Roll in Fiducialization of Quadrupole Magnets for the MIT-Bates South Hall Ring — M. Farkhondeh, K. A. Dow, W. W. Sapp, MIT Bates	2935
Survey and Alignment of the MIT-Bates South Hall Ring — M. Farkhondeh, K. A. Dow, W. W. Sapp, D. R. Tieger, MIT Bates	2938
Magnetic Measurement, Fiducialization and Alignment of Large Dipoles for the MIT-Bates SHR — M. Farkhondeh, K. A. Dow, W. W. Sapp, J. D. Zumbro, MIT Bates	2941
Pulsed Taut-Wire Measurement of the Magnetic Alignment of the ITS Induction Cells — J. G. Melton, M. J. Burns, D. J. Honabarger, LANL	2944
Application of Precision Mechanical Engineering Techniques to the Design of a Moderate Energy Beam Transport for the FAA Explosive Detection System — R. Lujan, K. Christensen, LANL	2947
The Final Focus Test Beam Laser Reference System — V. E. Bressler, R. E. Ruland, SLAC	2950
Thermal Modeling of Cryogenic Accelerator Structures — H. Muller, P. Smith, D. Walend, J. Kirchgessner, Cornell	2953
Cryogenics for the LEP200 Superconducting Cavities at CERN — D. Güsewell, M. Barranco-Luque, S. Claudet, W. K. Erdt, P. Frandsen, Ph. Gayet, J. Schmid, N. Solheim, Ch. Titcomb, G. Winkler, CERN	2956
Measurements of the Ground Motion Vibrations at the SSC — V. V. Parkhomchuk, BINP; V. D. Shiltsev, H. J. Weaver, SSCL	2959

Particle Sources, Beam Formation, and Matching

Chair: J. Fraser

Performance of Photocathode RF Gun Electron Accelerators (<i>Invited Paper</i>) — I. Ben-Zvi, BNL	2962
First Operation of a High Duty Factor Photoinjector — D. Dowell, K. Davis, K. Friddell, E. Tyson, C. Lancaster, L. Milliman, R. Rodenburg, T. Aas, M. Bemes, S. Bethel, P. Johnson, K. Murphy, C. Whelen, J. Adamski, D. Pistoresi, D. Shofstall, Boeing; G. Busch, D. Remelius, LANL	2967
Operation of the High Brightness LINAC for the Advanced Free-Electron Laser Initiative at Los Alamos — R. L. Sheffield, R. H. Austin, K. D. C. Chan, S. M. Gierman, J. M. Kinross-Wright, S. H. Kong, D. C. Nguyen, S. J. Russell, C. A. Timmer, LANL	2970
Performance of the SLC Polarized Electron Source with High Polarization — J. E. Clendenin, R. K. Alley, H. Aoyagi, J. C. Frisck, C. L. Garden, E. W. Hoyt, R. E. Kirby, L. A. Klaisner, A. V. Kulikov, C. Y. Prescott, P. J. Sáez, D. C. Schultz, H. Tang, J. L. Turner, M. Woods, A. D. Yermian, M. S. Zolotarev, SLAC	2973
Quantum Efficiency Measurements of a Copper Photocathode in an RF Electron Gun — P. Davis, G. Hairapetian, C. Clayton, C. Joshi, S. Hartman, S. Park, C. Pellegrini, J. Rosenzweig, UCLA	2976
High-Efficiency Target-Ion Sources for RIB Generation (<i>Invited Paper</i>) — G. D. Alton, ORNL	2979
Performance of SSC Linac Injector (<i>Invited Paper</i>) — K. Saadatmand, G. M. Arbique, F. Guy, M. Haworth, J. Hebert, J. Hurd, J. Lenz, N. Okay, D. Raparia, SSCL	2986
Proposal for a Pulsed Optically Pumped Polarized H ⁺ Ion Source for High Energy Accelerators — A. N. Zelenski, INR Moscow; C. D. P. Levy, P. W. Schmor, W. T. H. van Oers, G. Dutto, TRIUMF; Y. Mori, KEK	2991
Design and Performance of the Inter-RFQ Beam Transport and Matching Section for the SAIC PET Isotope Production Accelerator — W. D. Cornelius, SAIC	2994
Electron Cyclotron Resonance Sources of Multiply Charged Ions: Last Developments at Grenoble — G. Melin, F. Bourg, P. Briand, M. Delaunay, A. Girard, D. Hitz, P. Ludwig, T. K. Nguyen, M. Pontonnier, Grenoble	2997

Each volume begins with this five-volume table of contents and ends with the five-volume author index. The chairmen's foreword and a list of conference organizers and staff appear as front matter in Volume 1. A list of conference participants precedes the author index in Volume 5.

Poster presentations:

Design and Construction of a Full Copper Photocathode RF Gun — X. J. Wang, K. Batchelor, I. Ben-Zvi, D. Lynch, J. Sheehan, M. Woodle, BNL	3000
Streak Camera Measurements of Electron Bunch Length from a Copper Photocathode in an RF Gun — G. Hairapetian, P. Davis, M. Everett, C. Clayton, C. Joshi, S. Hartman, S. Park, C. Pellegrini, UCLA	3003
Possible Efficiency-Enhancement of Metal Photocathode for DISKTRON Electrostatic Accelerator — T. Tanabe, Y. Kawamura, K. Toyoda, RIKEN; D. Li, Changchun Inst., China	3006
Cold Test of Rocketdyne RF Gun — M. Lampel, Rockwell; R. Zhang, UCLA	3009
Design and Construction of a High-Duty-Factor Photocathode Electron Gun — I. S. Lehrman, I. A. Birnbaum, M. Cole, R. L. Heuer, E. Sheedy, Grumman; I. Ben-Zvi, K. Batchelor, J. C. Gallardo, H. G. Kirk, T. Srinivasan-Rao, BNL	3012
An Improved Thermionic Microwave Gun and Emittance-Preserving Transport Line — M. Borland, ANL	3015
Experience with a Radio Frequency Gun on the SSRL Injector Linac — J. N. Weaver, R. D. Genin, P. Golceff, H. Morales, J. Sebek, SLAC	3018
Design of a High Duty Cycle, Asymmetric Emittance RF Photocathode Injector for Linear Collider Applications — J. B. Rosenzweig, E. Colby, UCLA; G. Jackson, T. Nicol, FNAL	3021
Design of a High Brightness RF Photoinjector for the SLAC Linear Coherent Light Source — J. Rosenzweig, UCLA; L. Serafini, INFN Milan	3024
Performance of the SLC Polarized Electron Source and Injector with the SLAC 3 km Linac Configured for Fixed Target Experiments — A. D. Yeremian, R. K. Alley, J. E. Clendenin, J. C. Frisch, C. L. Garden, L. A. Klaisner, A. V. Kulikov, R. H. Miller, C. Y. Prescott, P. J. Saez, D. C. Schultz, H. Tang, J. L. Turner, M. B. Woods, M. Zolotarev, SLAC	3027
An In-Situ Photocathode Loading System for the SLC Polarized Electron Gun — R. E. Kirby, G. J. Collet, K. Skarpaas, SLAC	3030
High Voltage Processing of the SLC Polarized Electron Gun — P. Sáez, J. Clendenin, C. Garden, E. Hoyt, L. Klaisner, C. Prescott, D. Schultz, H. Tang, SLAC	3033
Study of Non-Linear Photoemission Effects in III-V Semiconductors — H. Tang, R. K. Alley, J. E. Clendenin, J. C. Frisch, C. L. Garden, E. W. Hoyt, R. E. Kirby, L. A. Klaisner, A. V. Kulikov, C. Y. Prescott, P. J. Sáez, D. C. Schultz, J. L. Turner, M. Woods, M. S. Zolotarev, SLAC; H. Aoyagi, Nagoya U.	3036
Photocathode Performance Measurements for the SLC Polarized Electron Gun — C. L. Garden, E. W. Hoyt, D. C. Schultz, H. Tang, SLAC	3039
Electron Quantum Yields from a Barium Photocathode Illuminated with Polarized Light — M. E. Conde, S. Chattopadhyay, K.-J. Kim, K.-N. Leung, A. T. Young, LBL; S.-I. Kwon, Kyonggi U.	3042
The 1992 Polarized Light Source — R. Alley, M. Woods, M. Browne, J. Frisch, M. Zolotarev, SLAC	3045
Operation of a Ti:Sapphire Laser for the SLAC Polarized Electron Source — J. Frisch, R. Alley, M. Browne, M. Woods, SLAC	3047
The Argonne Wakefield Accelerator (AWA) Laser System and Its Laser Pulse Shaper — W. Gai, N. Hill, C. Ho, P. Schoessow, J. Simpson, ANL	3050
CANDELA Photo-injector: The Drive Laser — P. Georges, P. Thomas, Inst. d'Opt. Theor. Appl., Orsay; B. Leblond, C. Travier, LAL Orsay	3053
A Flat-Cathode Thermionic Injector for the PHERMEX Radiographic Facility — T. Kauppila, L. Builta, M. Burns, W. Gregory, D. Honabarger, S. Watson, LANL; T. Hughes, Mission Res. Corp.	3055
The ALS Gun Electronics System — C. C. Lo, LBL	3058
Witness Gun for the Argonne Wakefield Accelerator — J. Power, J. Simpson, E. Chojnacki, ANL	3061
Parametric Studies with PARMELA to Improve SLC Performance — T. A. Jones, A. D. Yeremian, R. H. Miller, SLAC	3063
High Current, Low Energy Electron Beams Produced During the High Current Phase of a Pseudospark — T. Hsu, R. Liou, M. A. Gundersen, USC; G. Kirkman, Integrated App. Phys.	3066
Theoretical and Experimental Study of Pseudospark Electron Beam Generation — L. Pitchford, J. P. Boeuf, U. Paul Sabatier; V. Puech, U. de Paris-Sud; R. Liou, M. Gundersen, USC	3069
A Variable Pulse-Length Electron Beam From the Back-Lighted Thyatron — R. Liou, T. Hsu, G. Roth, M. Gundersen, USC; G. Kirkman, Integrated App. Phys.	3072

Proceedings of the 1993 Particle Accelerator Conference

One-Dimensional Simulation Studies of Breakdown and Electron Beam Generation Processes for a Hollow Cathode Pseudospark Discharge — S. Y. Cai, C. D. Striffler, U. Maryland	3075
A High Brightness Electron Beam Produced by a Ferroelectric Cathode — B. Jiang, G. Kirkman, N. Reinhardt, Integrated App. Physics	3078
The UV-FEL at the NSLS: Straight Injection Configuration — X. Zhang, J. C. Gallardo, BNL	3081
Progress on PEP-II Injection R&D — E. Bloom, F. Bulos, T. Fieguth, G. Godfrey, G. Loew, R. Miller, SLAC	3084
New Pre-Injector of the KEK 2.5-GeV Linac and Its Performance — S. Ohsawa, I. Abe, S. Anami, J.-Y. Choi, A. Enomoto, K. Furukawa, H. Hanaki, K. Kakihara, N. Kamikubota, T. Kamitani, H. Kobayashi, Y. Ogawa, T. Oogoe, I. Sato, T. Suwada, Y. Yamazaki, M. Yokota, KEK; A. Asami, Naruto U.	3087
Hydrodynamic Calculations of 20-TeV Beam Interactions with the SSC Beam Dump — D. C. Wilson, C. A. Wingate, J. C. Goldstein, R. P. Godwin, LANL; N. V. Mokhov, SSCL	3090
First Results Concerning a Crystal Radiator Dedicated to Positron Production by Photons from Channeled Multi-GeV Electrons — R. Chehab, T. Baier, P. Jean, LAL Orsay; X. Artru, M. Chevallier, R. Kirsch, J. C. Poizat, J. Remillieux, IPNL Lyon; A. Jejcic, J. Maillard, J. Silva, LPC Paris; E. Hourany, G. Renou, J. P. Didelez, A. Elayi, L. Rosier, IPN Orsay; V. N. Baier, V. M. Katkov, V. M. Strakhovenko, BINP Novosibirsk; K. Maier, MPI Stuttgart	3093
New Target Results from the FNAL Antiproton Source — S. O'Day, F. Bieniosek, K. Anderson, FNAL	3096
High Current Radioisotope Production with Solid Target System — W. Z. Gelbart, N. R. Stevenson, R. R. Johnson, J. Orzechowski, F. Cifarelli, TRIUMF; F. Nortier, NAC Faure	3099
Isospin Target-Ion Source Shielding — M. M. Barbier, Marcel Barbier Inc.	3102
Beam Raster System at CEBAF — C. Yan, J. Beaufait, P. Brindza, R. Carlini, W. Vulcan, R. Wines, CEBAF	3103
Monitoring Production Target Thickness — M. A. Oothoudt, LANL	3106
Beam Loss Handling at the SSC — I. S. Baishev, A. I. Drozhdin, N. V. Mokhov, SSCL	3109
Analytical Study of RFQ Channel by Means of the Equivalent Charges Model — V. M. Pirozhenko, O. V. Plink, MRTI	3112
Design of an 80-MHz RFQ Linac for Heavy Ions — O. Takeda, Y. Tanabe, K. Satoh, S. Kawazu, Toshiba; Y. Oguri, M. Okamura, T. Hattori, Tokyo Inst. of Tech.	3115
Operational Characteristics of a 100-mA, 2-MeV Radio-Frequency Quadrupole — K. F. Johnson, W. B. Cottingham, G. O. Bolme, C. M. Fortgang, W. Ingalls, J. Marquardt, D. P. Rusthoi, O. R. Sander, M. Smith, G. T. Worth, LANL	3118
Analysis of the End Regions of the CERN Lead-Ion 4-Rod RFQ — V. A. Andreev, ITEP Moscow; A. Lombardi, G. Parisi, INFN Legnaro; M. Vretenar, CERN	3121
90°-Apart-Stem RFQ Structure for Wide Range of Frequencies — V. A. Andreev, ITEP Moscow; G. Parisi, INFN Legnaro	3124
The SSCL RFQ System Integration — G. Arbique, A. Calo, C. Cuevas, P. Datte, D. Evans, J. Hurd, E. Marsden, K. Saadatmand, J. Sage, SSCL	3127
SSC Radio-Frequency-Quadrupole Beam: Comparison of Experimental and Simulated Results — F. W. Guy, J. W. Hurd, D. Raparia, K. Saadatmand, W. A. Whittenberg, SSCL	3130
Mechanical Integration of an RF Volume Source and Einzel Lens LEBT to the SSC RFQ — R. A. Valicenti, J. Lenz, N. C. Okay, L. Plesea, K. Saadatmand, SSCL	3133
Segmented Resonantly Coupled Radio-Frequency Quadrupole (RFQ) — L. M. Young, LANL	3136
Experiments with the High Current RFQ Prototype for GSI — A. Kipper, A. Schempp, H. Deitinghoff, J. Madlung, T. Ludwig, K. Volk, O. Engels, A. Firjahn-Andersch, H. Vormann, Inst. f. Angew. Physik	3139
Transport of Ions in RFQ-Accelerators — J. Dehen, W. Barth, A. Schempp, H. Deitinghoff, Inst. f. Angew. Physik	3142
An ESQ Lens System for Low Energy Beam Transport Experiments on the SSC Test Stand — S. K. Guharay, C. K. Allen, M. Reiser, U. Maryland; K. Saadatmand, SSCL	3145
Test of the Transport Properties of a Helical Electrostatic Quadrupole and Quasi-Octupole — L. Xiu, S. Ohnuma, K. Wang, U. Houston; C. R. Meitzler, Y. Xu, Sam Houston State U.	3148
Comparison of Experimental and Simulated Results for the SSC LEBT — J. W. Lenz, J. Hebert, N. Okay, D. Raparia, K. Saadatmand, SSCL	3151
Axial Magnetic Field Lens with Permanent Magnet — Y. Iwashita, Kyoto U.	3154
Design of a Merging Beamlet Pre-Accelerator for an Electrostatic Quadrupole Accelerator (ESQ) — C. F. Chan, M. C. Vella, LBL	3157
Low Energy H ⁻ Injector Design for SSC RFQ — C. F. Chan, K.-N. Leung, LBL	3160

Each volume begins with this five-volume table of contents and ends with the five-volume author index. The chairman's foreword and a list of conference organizers and staff appear as front matter in Volume 1. A list of conference participants precedes the author index in Volume 5.

Lithium Lens for Focusing Protons on Target in the Fermilab Antiproton Source — F. M. Bieniosek, K. Anderson, FNAL	3163
Injector Design for High-Current CW Proton Linacs — R. R. Stevens, Jr., J. D. Sherman, J. D. Schneider, LANL ...	3166
A High Power Long Pulse RF-Driven H ⁻ Source — J. W. Kwan, G. D. Ackerman, W. S. Cooper, G. J. deVries, K. N. Leung, R. P. Wells, LBL	3169
Initial Operation of the CW 8X H ⁻ Ion Source Discharge — H. V. Smith, Jr., P. Allison, C. Geislik, D. R. Schmitt, J. D. Schneider, J. E. Stelzer, LANL	3172
Volume H ⁻ Ion Source Development at LAMPF — R. L. York, D. Tupa, D. R. Swenson, R. Damjanovich, LANL	3175
Further Development with Heavy Ion Sources at Brookhaven National Laboratory's Tandem Van de Graaff Facility — M. J. Zarcone, D. B. Steski, K. S. Smith, P. Thieberger, BNL	3178
A Dual-Optically-Pumped Polarized Negative Deuterium Ion Source — Y. Mori, M. Kinsho, KEK	3181
The IUCF High Intensity Polarized Ion Source Project — M. Wedekind, R. Brown, V. Derenchuk, D. Friesel, J. Hicks, P. Schwandt, IUCF	3184
The High Current Ion Source System HOLCROSS — N. R. Lobanov, MEPI Moscow	3187
Positive Hydrogen Ion Beam Production by an RF-Driven Multicusp Source — K. N. Leung, D. A. Bachman, P. R. Herz, D. S. McDonald, L. T. Perkins, LBL; M. Olivo, PSI	3190
Measurements of Emittance and Species Fractions of a Positive Hydrogen Ion Beam Extracted from an RF-Driven Multicusp Source — G. Gammel, T. W. Debiak, S. Melnychuk, J. Sredniawski, Grumman	3193
A New Design of the Sputter Type Metal Ion Source and Its Characteristics of Ion Beam Extraction — W. Kim, B. H. Choi, J. T. Jin, K.-S. Jung, Korea Atomic Energy Res. Inst.; S. H. Do, Pusan Nat. Fishers U.; K. H. Chung, Seoul Nat. U.	3196
K ⁺ Ion Source for the Heavy Ion Induction Linac System Experiment ILSE — S. Eylon, E. Henestroza, W. W. Chupp, S. Yu, LBL	3199
On the Magnetic Compression and Guiding of Electron Beams in E.B.I. S. or E.B.I.T — J. L. Bobin, E. Mercier, UPMC Paris; G. Giardino, LPAN	3202
Choice of Hexapole Parameters for ECR Ion Source — V. P. Kukhtin, E. A. Lamzin, Yu. P. Severgin, S. E. Sytchevsky, Efremov Inst.	3205
Stripping Efficiencies for 277 MeV/amu Gold Beam on Copper Foils — T. Roser, BNL	3207
Management of High Current Transients in the CWDD Injector 200 kV Power System — J. A. Carwardine, G. Pile, AEA Tech. Culham Lab; T. E. Zinneman, ANL	3210
Design and Results of the Radio Frequency Quadrupole RF System at the Superconducting Super Collider Laboratory — J. Grippe, E. Marsden, O. Marrufo, SSCL; A. Regan, D. Rees, C. Ziomek, LANL	3213
Initial Operation and Beam Characteristics of the UCLA S-Band Photo-Injector — C. Pellegrini, N. Barov, P. Davis, G. Hairapetian, S. C. Hartman, C. Joshi, S. Park, J. Rosenzweig, G. Travish, R. Zhang, UCLA	3216

Volume 5

Multiparticle Beam Dynamics

Chair: M. Reiser

Methods of Impedance Calculation (<i>Invited Paper</i>) — R. L. Gluckstern, Maryland	3219
Space-Charge Calculations in Synchrotrons (<i>Invited Paper</i>) — S. Machida, SSCL	3224
Advanced Computers and Simulation (<i>Invited Paper</i>) — R. D. Ryne, LANL	3229
Measured Optimum BNS Damping Configuration of the SLC Linac — J. T. Seeman, F.-J. Decker, R. L. Holtzapple, W. L. Spence, SLAC	3234
Single Beam Phenomena in BEPC — Z. Y. Guo, X. Bai, G. X. Li, J. Qin, Q. Qin, G. Xu, C. Zhang, X. L. Zhang, Z. T. Zhao, IHEP, Academia Sinica	3237
High Intensity Bunch Length Instabilities in the SLC Damping Rings — P. Krejcik, K. Bane, P. Corredoura, F.-J. Decker, J. Judkins, T. Limberg, M. Minty, R. H. Siemann, SLAC; F. Pedersen, CERN	3240
Investigation on Relaxations in Electron Beams — A. Aleksandrov, N. Dikansky, N. Ch. Kot, V. Kudelainen, V. A. Lebedev, P. Logachov, BINP; R. Calabrese, G. Ciullo, V. Guidi, G. Lamanna, P. Lenisa, B. Maciga, L. Tecchio, B. Yang, INFN	3243
Studies of Multipass Beam Breakup and Energy Recovery Using the CEBAF Injector Linac — N. S. Sereno, L. S. Cardman, U. Illinois; G. A. Krafft, C. K. Sinclair, J. J. Bisognano, CEBAF	3246

Volume 1: 1-747
 Volume 2: 748-1640
 Volume 3: 1641-2545
 Volume 4: 2546-3218
 Volume 5: 3219-3933

Proceedings of the 1993 Particle Accelerator Conference

Poster presentations:

The Longitudinal and Transverse Beam Dynamics Simulation in the MMF Storage Ring — V. A. Moiseev, INR Moscow	3249
Control of Longitudinal Instabilities in the LEB — T. L. Grimm, P. D. Coleman, SSCL	3252
Simulation of the Transverse Dipole Mode Multibunch Instability for the SSC Collider — S. Chen, G. López, SSCL	3255
HOM RF Cavity Dampers for Suppressing Coupled Bunch Instabilities in the Fermilab Booster — D. Wildman, FNAL; K. Harkay, Purdue	3258
Longitudinal Instabilities in the MEB — J. A. Palkovic, SSCL	3261
A New Formulation of Longitudinal Coherent Instabilities — S. Y. Zhang, W. T. Weng, BNL	3264
Three-Dimensional Simulations for Accelerator Physics Using ARGUS — A. Mondelli, A. Mankofsky, J. Petillo, W. Krueger, C. Kostas, A. Drobot, SAIC; R. Ryne, R. K. Cooper, G. Rodenz, M. J. Browman, LANL	3267
A Higher-Order Moment Simulation Model — K. T. Tsang, C. Kostas, A. Mondelli, SAIC	3270
Collective Effects of the PLS 2 GeV Storage Ring — M. Yoon, J. Choi, T. Lee, Pohang	3273
Nonlinear Evolution of Longitudinal Bunched-Beam Instabilities — A. Gerasimov, FNAL	3276
Multi-Bunch Dynamics in Accelerating Structures Including Interaction with Higher Order Modes — M. Ferrario, F. Tazzioli, INFN-LNF; L. Serafini, INFN Milano	3279
Generation of Space-Charge Waves due to Localized Perturbations — J. G. Wang, D. X. Wang, D. Kehne, M. Reiser, U. Maryland	3282
Three Dimensional Multipole Decomposition of Fields — K. Hahn, LBL	3285
Multi-Bunch Beam-Break-Up Studies for a SWFEL/TBA — J. S. Kim, A. M. Sessler, LBL; D. H. Whittum, KEK; H. Henke, TU Berlin	3288
RF Noise Revisited: The Effect of Coherence — A. Gerasimov, FNAL; S. Y. Lee, Indiana U.	3291
TSD Versus TRL Calibration and Applications to Beam Impedance Measurements — M. Foley, P. Colestock, E. Barsotti, Jr., FNAL	3294
Recent Study of Beam Stability in the PSR — T. Wang, R. Cooper, D. Fitzgerald, S. Frankle, T. Hardek, R. Hutson, R. Macek, C. Ohmori, M. Plum, H. Thiessen, C. Wilkinson, LANL; E. Colton, DOE; D. Neuffer, CEBAF; G. Rees, RAL	3297
Impedance Budget and Beam Stability Analysis of the Fermilab Main Injector — M. A. Martens, K. Y. Ng, FNAL ..	3300
Trapped Ions and Beam Coherent Instability — P. Zhou, P. L. Colestock, S. J. Werkema, FNAL	3303
Comparison of the Coupled-Bunch Mode Theory to Experimental Observations in the Fermilab Booster — K. C. Harkay, Purdue; P. L. Colestock, FNAL	3306
Measurement of Trapped Ion Pockets and Control of Ion Instabilities in the Fermilab Antiproton Accumulator — S. J. Werkema, K. D. Fullett, P. Zhou, FNAL	3309
Study of Possible Energy Upgrade for the ALS and Modeling of the "Real Lattice" for the Diagnosis of Lattice Problems — M. Meddahi, J. Bengtsson, LBL	3312
Study of Coupled-Bunch Collective Effects in the PEP-II B-Factory — J. Byrd, LBL	3315
Study of Coupled-Bunch Collective Effects in the ALS — J. M. Byrd, J. N. Corlett, LBL	3318
Time Domain Solutions for a Coasting Beam with Impedance Feedback — M. Blaskiewicz, BNL	3321
Longitudinal Impedance and Stability Thresholds of the AGS Booster — M. Blaskiewicz, BNL	3324
Calculation of the Bunch Lengthening Threshold — X. T. Yu, J. S. Wurtele, MIT	3327
Computation of Longitudinal Bunched Beam Instability Thresholds — R. Baartman, TRIUMF; M. D'Yachkov, U. British Columbia	3330
Bunch Lengthening Observed Using Real-Time Bunch-Length Monitor in the TRISTAN AR — T. Ieiri, KEK	3333
Transverse Stability in Multibunch Mode for CLIC — G. Guignard, CERN	3336
Simulations of the Longitudinal Instability in the SLC Damping Rings — K. L. F. Bane, SLAC; K. Oide, KEK	3339
Multibunch Beam Break-Up in Detuned Structures — K. A. Thompson, C. Adolphsen, K. L. F. Bane, SLAC	3342
Longitudinal Head-Tail Instability in a Non-Harmonic Potential Well — B. Chen, A. W. Chao, SSCL	3345
Bunch Lengthening Effect and Localized Impedance — B. Chen, A. W. Chao, SSCL	3348
Experimental Reduction of Electron Beam Breakup Instability Using External Coupled Cavities — P. R. Menge, R. M. Gilgenbach, Y. Y. Lau, M. Walter, C. H. Ching, U. Michigan	3351
Beam Breakup in an Annular Beam — Y. Y. Lau, J. W. Luginsland, R. M. Gilgenbach, U. Michigan	3354

Each volume begins with this five-volume table of contents and ends with the five-volume author index. The chairman's foreword and a list of conference organizers and staff appear as front matter in Volume 1. A list of conference participants precedes the author index in Volume 5.

Five-Volume Contents

RF Focusing Effects and Multi-Bunch Beam Breakup in Superconducting Linear Colliders — <i>J. Rosenzweig, S. Hartman, J. Stevens, UCLA</i>	3357
Required Cavity HOM deQing Calculated from Probability Estimates of Coupled Bunch Instabilities in the APS Ring — <i>L. Emery, ANL</i>	3360
Measurement and Analysis of Transverse Beam Transfer Functions in the Fermilab Main Ring — <i>P. J. Chou, G. Jackson, FNAL</i>	3363
Observation of a Short Bunch Train Longitudinal Instability in the Fermilab Main Ring — <i>X. Lu, G. Jackson, FNAL</i>	3366
Suppression of Longitudinal Coupled-Bunch Instabilities by a Passive Higher Harmonic Cavity — <i>R. A. Bosch, C. S. Hsue, SRRRC Taiwan</i>	3369
The Longitudinal Coupling Impedance of a Slot on the SSC Collider Liner — <i>V. Thiagarajan, SSCL</i>	3372
Impedance of a Small-Gap Undulator Vacuum Chamber — <i>K. Bane, SLAC; S. Krinsky, NSLS-BNL</i>	3375
A Formula for the High Frequency Longitudinal Impedance of a Tube With Smoothly Varying Radius — <i>R. L. Warnock, SLAC</i>	3378
A Bench Set-Up for Low-Beta Beam-Current Test Measurements with COSY — <i>Ch. Günther, A. Schnase, H. Meuth, IKP Jülich; F. Caspers, CERN</i>	3381
A Generalized Model for Parametric Coupling of Longitudinal Modes in Synchrotrons — <i>P. L. Colestock, L. Klamp, FNAL</i>	3384
Longitudinal Coupling Impedance of a Cavity — <i>I. Gjaja, R. L. Gluckstern, U. Maryland</i>	3387
Transverse Impedance of an Iris in a Beam Pipe — <i>S. Jiang, R. L. Gluckstern, U. Maryland; H. Okamoto, Kyoto U.</i>	3390
RF Characteristics of the APS Storage Ring Isolation Valve — <i>J. J. Song, R. L. Kustom, ANL</i>	3393
Coupling Impedance of Vacuum Pumping Holes for the APS Storage Ring — <i>J. Zhou, J. J. Song, R. L. Kustom, ANL</i>	3396
Impedance Formalism for an Arbitrary Cumulative Instability — <i>X. T. Yu, J. S. Wurtele, MIT; D. H. Whitum, KEK</i>	3399
Longitudinal Impedance of a Prototype Kicker Magnet System — <i>H. J. Tran, M. J. Barnes, G. D. Wait, Y. Yan, TRIUMF</i>	3402
Beam Coupling Impedance Measurements and Simulations of a Beam Pipe Liner with Pumping Holes or Slots — <i>E. Ruiz, L. Walling, Y. Goren, N. Spayd, SSCL</i>	3405
Measurement and Computation of the Higher Order Modes of the ALS 500 MHz Accelerating Cavities — <i>J. N. Corlett, J. M. Byrd, LBL</i>	3408
Impedance Measurements of Components for the ALS — <i>J. N. Corlett, R. A. Rimmer, LBL</i>	3411
Advances and Applications of ABCI — <i>Y. H. Chin, LBL</i>	3414
On Coupling Impedances of Pumping Holes — <i>S. S. Kurennoy, SSCL</i>	3417
Using a Ceramic Chamber in Kicker Magnets — <i>S. S. Kurennoy, SSCL</i>	3420
An Analytical Treatment of Self Fields in a Relativistic Bunch of Charged Particles in a Circular Orbit — <i>J. L. Delhez, J. M. A. Hofman, J. I. M. Botman, H. L. Hagedoorn, W. J. G. M. Kleeven, G. A. Webers, Eindhoven U. of Tech.</i>	3423
Transverse Wake Fields in the CLIC Transfer Structure — <i>G. Guignard, G. Carron, A. Millich, L. Thorndahl, CERN</i>	3426
The LEP Impedance Model — <i>D. Brandt, K. Cornelis, V. Danilov, A. Hofmann, C. Juillard, E. Perevedentsev, E. Peschardt, E. Rossa, F. Tecker, D. Wang, B. Zotter, CERN; L. Rivkin, PSI</i>	3429
Impedance Calculations for the Improved SLC Damping Rings — <i>K. L. F. Bane, C.-K. Ng, SLAC</i>	3432
Broadband Impedance of Azimuthally Symmetric Devices in RHIC — <i>V. Mane, BNL</i>	3435
Software Development with Two Port Calibration Techniques for RHIC Impedance Measurements — <i>V. Mane, T. Shea, BNL</i>	3438
Resistive Wall Wake Function for Arbitrary Pipe Cross Section — <i>K. Yokoya, KEK</i>	3441
Impedance of a Perforated Liner and Its Impact on the SSC Collider — <i>W. Chou, T. Barts, SSCL</i>	3444
A Generalized Method for Calculating Wake Potentials — <i>O. Napoly, Saclay; Y. H. Chin, LBL; B. Zotter, CERN</i> ...	3447
The Interaction of a Beam With a Beam Line Higher-Order-Mode Absorber — <i>W. Hartung, K. Akai, J. DeFord, T. Hays, J. Kirchgessner, D. Metzger, D. Moffat, H. Padamsee, D. Rubin, M. Tigner, A. Tribendis, V. Veshcherevich, Cornell</i>	3450
Persistent Wakefields Associated with Waveguide Damping of Higher Order Modes — <i>N. M. Kroll, X. Lin, UCSD/SLAC</i>	3453

Volume 1:	1-747
Volume 2:	748-1640
Volume 3:	1641-2545
Volume 4:	2546-3218
Volume 5:	3219-3933

Proceedings of the 1993 Particle Accelerator Conference

Perturbation Theory of Broadband Impedances — <i>S. Heifets, SLAC</i>	3456
Broadband Impedance of the B Factory — <i>S. Heifets, SLAC</i>	3459
Study of a Detuned Accelerating Section With the Computer Program PROGON — <i>S. A. Heifets, S. A. Kheifets, SLAC</i>	3462
Estimation of Broad Band Impedance of the SPring-8 Storage Ring — <i>T. Nakamura, JAERI</i>	3464
Head-On and Long Range Beam-Beam Tune Shift Spread in the SSC — <i>G. López, SSCL</i>	3467
Beam-Beam Effects with Errors in the Crab Compensation — <i>D. Sagan, Cornell</i>	3470
A Strong-Strong Simulation on the Beam-Beam Effect in a Linac/Ring B-Factor — <i>R. Li, J. J. Bisognano, CEBAF</i>	3473
Some Aspects of the Long Range Beam-Beam Interaction in Storage Rings — <i>A. B. Temnykh, INP; J. J. Welch, Cornell</i>	3476
Experimental Study of Crossing Angle Collision — <i>T. Chen, SLAC; D. Rice, D. Rubin, D. Sagan, M. Tigner, Cornell</i>	3479
Beam-Beam Experiments in the Tevatron — <i>D. Siergiej, G. Goderre, FNAL</i>	3482
Beam-Beam Effects for the PEP-II B Factory — <i>M. A. Furman, LBL; J. R. Eden, U. Washington</i>	3485
Equivalent Equations and Incoherent Lifetime Calculated from e^+e^- Beam-Beam Simulation — <i>Y. Orlov, Cornell</i>	3488
Simulation of Beam-Beam Effects in Electron-Positron Rings — <i>K. Hirata, S. Matsumoto, KEK</i>	3491
Longitudinal Beam-Beam Effects in Circular Colliders — <i>M. Hogan, J. Rosenzweig, UCLA</i>	3494
Strong-Weak Beam-Beam Simulation with a Six Dimension Symplectic Code — <i>Y. Funakoshi, H. Koiso, KEK</i>	3497
Synchrotron Beam-Loading Stability with a Higher RF Harmonic — <i>T. F. Wang, LANL</i>	3500
Compensation of Bunch Position Shift Using Sub-RF Cavity in a Damping Ring — <i>K. Kubo, T. Higo, S. Sakanaka, KEK</i>	3503
Analytic Criteria for Stability of Beam-Loaded RF Systems — <i>S. R. Koscielniak, TRIUMF</i>	3506
Beam Loading Effect in SSCL Coupled Cavity Linac — <i>Yu. Senichev, R. Cutler, J. Hurd, D. Raparia, SSCL</i>	3509
The Ion Core Density in Electron Storage Rings with Clearing Electrodes — <i>E. V. Bulyak, Kharkov Inst.</i>	3512
Operation of the CEBAF Linac with High Beam Loading — <i>L. Merminga, J. J. Bisognano, C. Hovater, G. A. Krafft, S. N. Simrock, CEBAF; K. Kubo, KEK</i>	3515
An Idea of Dynamical Cooling of Electron Beam in SR Ring — <i>S. Kato, Osaka U.</i>	3518
The Principle of Ultra-Fast Automatic Cooling for Beams — <i>S. Gao, G. Qian, CIAE</i>	3521
On the Longitudinal Stability of Cooled Coasting Ion Beams — <i>S. Nagaitsev, IUCF</i>	3524
Crystalline Beam Ground State — <i>J. Wei, BNL; X. Li, Rutgers; A. M. Sessler, LBL</i>	3527
Confinement and Stability of a Crystal Beam — <i>A. G. Ruggiero, BNL</i>	3530
Bunched Beam Stochastic Cooling in the Fermilab Tevatron Collider — <i>G. Jackson, E. Buchanan, J. Budlong, E. Harms, P. Hurh, D. McGinnis, R. Pasquinelli, D. Peterson, D. Poll, P. Seifrid, FNAL</i>	3533
Longitudinally Space Charge Dominated Beams in a Synchrotron — <i>T. J. P. Ellison, S. S. Nagaitsev, M. S. Ball, D. D. Caussyn, M. J. Ellison, B. J. Hamilton, IUCF</i>	3536
High Density Plasma Source for Plasma Lens Experiments — <i>K. Nakamura, R. Liou, M. Gundersen, USC</i>	3537
Measurement of Escaping Ions in the Fermilab Antiproton Accumulator — <i>P. Zhou, P. L. Colestock, K. Junck, C. A. Crawford, FNAL</i>	3540
Experimental Demonstration of Plasma Lens Focusing — <i>G. Hairapetian, P. Davis, C. E. Clayton, C. Joshi, S. Hartman, C. Pelligrini, UCLA; T. Katsouleas, USC</i>	3543
Numerical Modelling of Time-Space Behavior of High-Current Relativistic Electron Beam in Plasma Waveguide — <i>V. I. Karas', Kharkov Inst.; N. G. Belova, Russian Acad.</i>	3546
IPROP Simulations of the GAMBLE II Proton Transport Experiment — <i>D. R. Welch, Mission Res. Corp.</i>	3549
Plasma Lens and Plasma Wakefield Acceleration Experiments Using Twin Linacs — <i>A. Ogata, H. Nakanishi, K. Nakajima, T. Kawakubo, D. Whittum, M. Arinaga, KEK; Y. Yoshida, T. Ueda, T. Kobayashi, Nucl. Eng. Res. Lab, Tokyo U.; H. Shibata, S. Tagawa, Res. Ctr. Nucl. Sci. Tech., Tokyo U.; N. Yugami, Y. Nishida, Utsunomiya U.</i>	3552
Plasma Focusing of the Final Test Beam — <i>S. Rajagopalan, UCLA</i>	3555
Emittance Growth in MEB and Its Control — <i>Y. Huang, S. Machida, R. Gerig, SSCL</i>	3558
Longitudinal Diffusion as Inflicted by Arbitrary Band-Width Random-Modulated Currents in Feeders of Detuned Cavities — <i>S. Ivanov, IHEP Moscow</i>	3561
Induced Beam Oscillations from Quadrupole Vibrations in the SLC Linac — <i>J. T. Seeman, R. L. Holtzapple, M. C. Ross, SLAC</i>	3564

Each volume begins with this five-volume table of contents and ends with the five-volume author index. The chairmen's foreword and a list of conference organizers and staff appear as front matter in Volume 1. A list of conference participants precedes the author index in Volume 5.

Effects of Magnetic Focusing on Longitudinal Emittance and Energy Dispersion of an Intense Short Accelerating Electron Pulse — <i>J.-M. Dolique, J. C. Coacolo, U. Joseph Fourier/CEA</i>	3567
Measurement and Reduction of Transverse Emittance Blow-Up Induced by Space Charge Effects — <i>R. Cappi, R. Garoby, S. Hancock, M. Martini, J. P. Riunaud, CERN</i>	3570
Transverse Emittance Growth in the Fermilab Antiproton Accumulator with High-Current Antiproton Stacks — <i>S. J. Werkema, D. W. Peterson, P. Zhou, FNAL</i>	3573
Transverse Tails and Higher Order Moments — <i>W. L. Spence, F.-J. Decker, M. D. Woodley, SLAC</i>	3576
Simulation of Emittance Dilution in Electron Storage Ring from Compton Backscattering — <i>L. N. Blumberg, E. Blum, BNL</i>	3579
Transverse Effects of Longitudinal Wakefields at High Dispersion — <i>F. Decker, SLAC</i>	3582
Error and Tolerance Studies for the SSC Linac — <i>D. Raparia, C. R. Chang, F. Guy, J. W. Hurd, W. Funk, SSCL; K. R. Crandall, AccSys</i>	3585
Emittance Growth Due to Dipole Ripple and Sextupole — <i>H.-J. Shih, J. A. Ellison, M. J. Syphers, B. S. Newberger, SSCL</i>	3588
Proton-Proton Scattering Contribution to Emittance Growth — <i>T. Garavaglia, SSCL</i>	3591
Source Size Variation and Ion Effects in the SRS at Daresbury — <i>J. A. Clarke, D. M. Dykes, S. F. Hill, E. A. Hughes, M. W. Poole, P. D. Quinn, S. L. Smith, V. P. Suller, L. A. Welbourne, SERC Daresbury</i>	3594
Global Trajectory Correction Algorithms in CLIC and Main Linac Alignment Tolerances — <i>C. Fischer, CERN</i>	3597
Lattice Scaling and Emittance Control in the CLIC Main Linac — <i>G. Guignard, CERN</i>	3600
Decoherence and Recoherence of Beam in Phase Space — <i>J. Shi, S. Ohnuma, U. Houston</i>	3603
Space-Charge-Induced Emittance Growth in an Elliptical Charged Particle Beam with a Parabolic Density Distribution — <i>T. P. Wangler, LANL; P. Lapostolle, A. Lombardi, CERN</i>	3606
Emittance and Luminosity Evolution During Collisions in the SSC Collider — <i>W. Chou, S. Dutt, T. Garavaglia, K. Kauffmann, SSCL</i>	3609
Emittance Growth in Displaced, Space-Charge-Dominated Beams with Energy Spread — <i>J. J. Barnard, J. Miller, LLNL; I. Haber, NRL</i>	3612
An Injection Scheme for the Brookhaven ATF Utilizing Space-Charge Emittance Growth Compensation — <i>J. C. Gallardo, H. G. Kirk, BNL</i>	3615
A Matrix Theory of the Motion of an Ellipsoidal Bunch in a Beam Control System with a Rectilinear Optical Axis and with Space Charge — <i>A. Dymnikov, U. St. Petersburg; R. Hellborg, U. Lund</i>	3618
Space-Charge Dominated Beam Envelope Transport with Rotatable Axes — <i>E. Y. Tsiang</i>	3621
Effect of Space Charge Forces on Particle Tracking and Generation of High-Order Maps — <i>D. L. Bruhwiler, M. F. Reusch, Grumman</i>	3624
Experimental Study of Longitudinal Dynamics of Space-Charge Dominated Parabolic Bunches — <i>D. X. Wang, J. G. Wang, D. Kehne, M. Reiser, U. Maryland; I. Haber, Naval Res. Lab.</i>	3627
Transition Crossing in the Fermilab Main Ring, Past and Present — <i>I. Kourbanis, K. Y. Ng, FNAL</i>	3630
Observation and Correction of Resonance Stopbands in the AGS Booster — <i>C. Gardner, L. Ahrens, J. W. Glenn, Y. Y. Lee, T. Roser, A. Soukas, W. van Asselt, W. T. Weng, BNL; Y. Shoji, KEK</i>	3633
The Stability of Ions in a Storage Ring in the Presence of Small Gap Insertion Devices — <i>E. Bozoki, BNL</i>	3636
Simulation of Space-Charge Dominated Beam Dynamics in an Isochronous AVF Cyclotron — <i>S. R. Koscielniak, TRIUMF; S. R. Adam, PSI Switzerland</i>	3639
Passage Through a Half-Integer Resonance Due to Space Charge for Different Initial Distributions — <i>A. Budzko, INR; Yu. Senichev, SSCL</i>	3642
Estimation of Collective Effects for the EUTERPE Ring — <i>B. Xi, J. I. M. Botman, J. van Laar, C. J. Timmermans, H. L. Hagedoorn, Eindhoven U. of Tech.</i>	3645
A Moment Method Laplace Solver for Low Energy Beam Transport Codes — <i>C. K. Allen, S. K. Guharay, M. Reiser, U. Maryland</i>	3648
Evolution of Hadron Beams Under Intrabeam Scattering — <i>J. Wei, BNL</i>	3651
Simulation Study of Ion Trapping in PLS Storage Ring — <i>J. Jung, I. Ko, POSTECH</i>	3654
Beam Halo Formation From Space-Charge Dominated Beams in Uniform Focusing Channels — <i>J. S. O'Connell, Booz, Allen & Hamilton; T. P. Wangler, R. S. Mills, LANL; K. R. Crandall, AccSys Tech.</i>	3657
Computer Simulation of the Maryland Transport Experiment — <i>I. Haber, Naval Res. Lab.; D. A. Callahan, A. B. Langdon, LLNL; M. Reiser, D. X. Wang, J. G. Wang, U. Maryland</i>	3660
Integrated Numerical Modeling of a Laser Gun Injector — <i>H. Liu, S. Benson, J. Bisognano, P. Liger, G. Neil, D. Neuffer, C. Sinclair, B. Yunn, CEBAF</i>	3663

Proceedings of the 1993 Particle Accelerator Conference

Halo Formation in Mismatched, Space-Charge-Dominated Beams — C. L. Bohn, J. R. Delayen, ANL	3666
Collective Effects in the VEPP-3 Storage Ring — S. A. Belomestnykh, A. N. Voroshilov, BINP	3669
Single Bunch Effects in the Daresbury SRS — L. A. Welbourne, J. A. Clarke, D. M. Dykes, S. F. Hill, E. A. Hughes, M. W. Poole, P. D. Quinn, S. L. Smith, V. P. Suller, SERC Daresbury	3672
The Effects of Coulomb Beam Interaction in Multiaperture Linac — A. I. Balabin, G. N. Kropachev, I. O. Parshin, D. G. Skachkov, ITEP Moscow	3675
Longitudinal Instability of an Induction Linac with Acceleration — L. Smith, E. P. Lee, LBL	3678
On Solvable Model with Synchrotron Mode-Coupling — D. V. Pestrikov, BINP/KEK	3681
On Limitations on Low- α Rings Performance Due to —Z-Instabilities — N. S. Dikansky, BINP Russia; D. V. Pestrikov, KEK	3684
On Landau Damping of Collective Beam-Beam Modes — D. V. Pestrikov, BINP/KEK	3687
Synchronous Phase Changes Due to the Gap in the Bunch Train — Z. Greenwald, M. Tigner, Cornell	3690
Simulation and Compensation of Multibunch Energy Variation in NLC — K. A. Thompson, R. D. Ruth, SLAC	3693
The Physical Mechanism of Ultra-Fast Automatic Cooling for Beams in the Six-Dimensional Emittance Space — S. Gao, G. Qian, D. Liang, H. Sun, CIAE China	3696
An Exact Expression for the Momentum Dependence of the Space Charge Tune Shift in a Gaussian Bunch — M. Martini, CERN	3699
Stored Beam Lifetime Evaluation Formulae for Electron Storage Rings — A. V. Makulkin, All-Russ. Res. Inst.	3702
A Simulation Study on Beam Bunching in the KEK 2.5-GeV Linac New Pre-Injector — T. Kamitani, J.-Y. Choi, A. Enomoto, S. Ohsawa, Y. Ogawa, T. Urano, T. Suwada, K. Furukawa, I. Sato, KEK	3705
New Outlooks on Bunched Beam Instabilities in Particle Accelerators: A Proposal for a Simple Method to Release a Potential Self-Consistent High Quality Beam — M. Bergher, LURE	3708
Experimental Study of Collective Effects in BEP Storage Ring with High Stored Current — V. Danilov, I. Koop, A. Lysenko, B. Milityn, I. Nesterenko, E. Perevedentsev, E. Pozdeev, V. Ptitsin, Yu. Shatunov, I. Vasserman, BINP	3711
Beam Coupling Impedances of Axial Symmetric Structures — W. Bruns, Technische Universität Berlin	3714

Hadron and e-p Colliders and Hadron Synchrotrons

Chair: D. Edwards

Accelerator Physics Issues at the SSC (Invited Paper) — G. F. Dugan, SSCL	3717
Fermilab Collider Upgrade: Recent Results and Plans (Invited Paper) — D. A. Finley, FNAL	3721
Operation of the Brookhaven AGS with the Booster (Invited Paper) — W. T. Weng, BNL	3726
Overview of Future Spallation Neutron Sources (Invited Paper) — G. H. Rees, Rutherford Appleton	3731
The Heavy Ion Synchrotron SIS: A Progress Report — K. Blasche, B. Franczak, B. Langenbeck, G. Moritz, C. Riedel, GSI	3736
Status of the PSR Improvement Program — R. J. Macek, D. H. Fitzgerald, M. Hoehn, R. Ryder, R. York, LANL	3739

Poster presentations:

First Experience with Colliding Electron-Proton Beams in HERA — R. Brinkmann, F. Willeke, DESY	3742
The Development of a Prototype Multi-MeV Electron Cooling System — D. Anderson, M. Ball, D. Caussyn, T. Ellison, B. Hamilton, S. Nagaitsev, P. Schwandt, IUCF; J. Adney, J. Ferry, M. Sundquist, Nat. Electr. Corp.; D. Reistad, Svedberg Lab.; M. Sedlacek, Alfvén Lab.	3745
The Bevalac Long Spill — C. M. Celata, S. Abbott, M. Bennett, M. Bordua, J. Calvert, R. Dwinell, D. Howard, D. Hunt, B. Feinberg, R. Force, R. Frias, J. Halliwell, J. Kalnins, S. Lewis, M. Nyman, L. Shalz, M. Tekawa, LBL; R. Solomons, RAFAEL, Israel	3748
Capture from Pair Production as a Beam Loss Mechanism for Heavy Ions at RHIC — B. Feinberg, A. Belkacem, R. Bossingham, H. Gould, LBL; W. E. Meyerhof, Stanford U.	3751
Acceleration of Deuteron Beam in the KEK Proton Synchrotron — Y. Mori, KEK	3754
Conceptual Design for a One Megawatt Spallation Neutron Source at Argonne — Y. Cho, J. Bailey, B. Brown, F. Brumwell, J. Carpenter, K. Crawford, D. Horan, D. Jerng, R. Kleb, A. Knox, R. Kustom, E. Lessner, D. McGhee, F. Mills, H. Moe, R. Nielsen, C. Potts, A. Rauchas, K. Thompson, ANL	3757
A Los Alamos Design Study for a High-Power Spallation-Neutron-Source Driver — A. J. Jason, R. A. Hardekopf, R. W. Macek, S. O. Schriber, H. A. Thiessen, R. Woods, LANL	3760

Each volume begins with this five-volume table of contents and ends with the five-volume author index. The chairmen's foreword and a list of conference organizers and staff appear as front matter in Volume 1. A list of conference participants precedes the author index in Volume 5.

Five-Volume Contents

On the High Intensity Aspects of AGS Booster Proton Operation — R. K. Reece, L. A. Ahrens, E. J. Bleser, J. M. Brennan, C. Gardner, J. W. Glenn, T. Roser, Y. Shoji, W. vanAsselt, W. T. Weng, BNL	3763
Results from Commissioning the AGS Booster Orbit System — E. Bleser, BNL	3766
The Effect of Global Survey Misalignment on the SSC — T. Garavaglia, N. Mahale, J. Peterson, SSCL	3769
Dealing with Abort Kicker Prefire in the Superconducting Super Collider — A. I. Drozhdin, I. S. Baishev, N. V. Mokhov, B. Parker, R. D. Richardson, J. Zhou, SSCL	3772
Design Status Report on the Collider Utility Straight Insertions — B. Parker, SSCL	3775
Current Design of the SSC Interaction Regions — Y. Nosochkov, A. Garren, T. Sen, R. Stiening, SSCL; E. Courant, BNL; D. M. Ritson, SLAC	3778
The Parameter Spreadsheets and Their Applications — R. Schwitters, A. Chao, W. Chou, J. Peterson, SSCL	3781
Lattice Studies for KAON Factory Accumulator and Booster Rings — A. Iliev, A. V. Budzko, INR-Troitsk; R. V. Servranckx, TRIUMF	3784
Reducing the Coupled-Bunch Oscillation in the Fermilab Booster by Optimizing RF Voltage — J. P. Shan, D. McGinnis, R. Tomlin, FNAL	3787
Beta Measurements and Modeling the Tevatron — N. M. Gelfand, FNAL	3790
The Status of the Fermilab Main Injector Project — D. Bogert, W. Fowler, S. Holmes, P. Martin, T. Pawlak, FNAL	3793
Constructing High Energy Accelerators Under DOE's "New Culture" for Environment and Safety: An Example, the Fermilab 150 GeV Main Injector Proton Synchrotron — W. Fowler, FNAL	3796
Performance and Comparison of the Different Coalescing Schemes Used in the Fermilab Main Ring — I. Kourbanis, G. P. Jackson, X. Lu, FNAL	3799
Operational Experience with Collimators in the Tevatron Collider — S. M. Pruss, FNAL	3802
Reliability of the Fermilab Antiproton Source — E. Harms, Jr., FNAL	3803
Multibunch Operation in the Tevatron Collider — J. A. Holt, D. A. Finley, V. Bharadwaj, FNAL	3806
Operational Experience with the Tevatron Collider Using Separated Orbits — G. Annala, FNAL	3808
Fermilab Antiproton Accumulator in the Main Injector Era — V. Visnjic, FNAL	3811
Study of Betatron Stochastic Cooling in Fermilab Antiproton Debuncher — V. Visnjic, M. Halling, FNAL	3814
Energy and Luminosity Limits of Hadron Supercolliders — W. A. Barletta, LBL/UCLA	3817
Ions Acceleration in the Synchrotrons with Constant RF of Electrical Field — V. P. Belov, Yu. P. Severgin, Efremov Inst.	3820
Ion Storage Ring of the INR Storage-Accelerating Complex — A. V. Dolinsky, A. I. Papash, S. N. Pavlov, A. T. Rudchik, A. E. Val'kov, I. N. Vishnevsky, A. V. Zhmendak, INR Kiev; V. P. Belov, A. A. Kapustin, V. S. Kashihin, A. M. Kokorin, A. A. Makarov, B. G. Mud'jugin, B. V. Rogdestvensky, Yu. P. Severgin, L. A. Schukeilo, M. N. Tarovik, Efremov Inst.	3822
A Compensated Dispersion-Free Long Insertion for an FFAG Synchrotron — P. F. Meads, Jr.	3825
Vacuum Technology Chair: D. Edwards	
Vacuum Technology for Superconducting Colliders (<i>Invited Paper</i>) — A. G. Mathewson, CERN	3828
Dynamic Vacuum in the Beam Tube of the SSCL Collider: Cold Beam Tube and Liner Options — W. C. Turner, SSCL	3833
Distributed Ion Pump Testing for PEP-II, Asymmetric B-Factory Collider — M. Calderon, F. Holdener, W. Barletta, D. Petersen, LLNL; C. Foerster, BNL	3836
High Capacity Getter Pump for UHV Operation — P. Manini, M. Marino, F. Belloni, M. Porro, SAES Getters	3839
<i>Poster presentations:</i>	
ELETTRA Vacuum System — M. Bernardini, F. Daclon, F. Giacuzzo, R. Kersevan, J. Miertusova, F. Pradal, Sinc. Trieste	3842
Vacuum Chamber and Crotch Absorber for the SPring-8 Storage Ring Vacuum System — K. Watanabe, S. H. Be, Y. Oikawa, H. A. Sakaue, C. Y. Xu, S. Yokouchi, Y. Wang, JAERI-RIKEN; S. Takahashi, Kobe Steel; M. Tsuchiya, IHI; Y. Yanagi, Hitachi	3845
SYNRAD, a Montecarlo Synchrotron Radiation Ray-Tracing Program — R. Kersevan, SSCL	3848
Vacuum System Design of the MIT-Bates South Hall Ring — E. Ihloff, R. Averill, J. Flanz, K. Jacobs, S. Sobczynski, D. Wang, A. Zolfaghari, MIT-Bates	3851
Design of Vacuum Chambers for Experimental Regions of Colliding Beam Machines — C. Hauviller, CERN	3854

Volume 1:	1-747
Volume 2:	748-1640
Volume 3:	1641-2545
Volume 4:	2546-3218
Volume 5:	3219-3933

Proceedings of the 1993 Particle Accelerator Conference

Distributed Non-Evaporable Getter Pumps for the Storage Ring of the APS — R. Dortwegt, R. Benaroya, ANL	3857
Test Fabrication of a Copper Beam Duct for the KEK B-Factory — Y. Suetsugu, K. Kanazawa, KEK	3860
FNAL Main Injector Quadrupole Vacuum Chamber — L. Sauer, FNAL	3863
FNAL Main Injector Dipole Installation Equipment — K. Moravec, F. Lange, J. Leibfritz, L. Sauer, FNAL	3864
Solvents and Pumpdown Characteristics of SRF Nb Cavities — M. G. Rao, P. Kneisel, H. F. Dylla, CEBAF	3867
Leak Checker Data Acquisition System — J. Payne, J. Gannon, SSCL	3870
Theoretical and Experimental Study of Sorption Processes on Non-Evaporable Getters St 707 — J. Miertusova, F. Daclon, Sinc. Trieste	3873
Photodesorption Experiments on SSC Collider Beam Tube Configurations — I. Maslennikov, W. Turner, SSCL; V. Anashin, O. Malyshev, V. Osipov, V. Nazmov, V. Pindyurin, A. Salimov, BINP; C. Foerster, C. Lanni, BNL	3876
The Heat Load of an 80 K Liner for the SSC — J. Maddocks, A. Yücel, SSCL	3879
Design of Large Aperture, Low Mass Vacuum Windows — W. J. Leonhardt, M. Mapes, BNL	3882
Observation and Analysis for Motions of Trapped Microparticles in the TRISTAN Accumulation Ring — H. Saeki, Japan SRRI; T. Momose, Miyagi; H. Ishimaru, KEK	3885
Overview of an 80 K Liner Design for Synchrotron Light Interception in SSCL Collider — Q.-S. Shu, W. Chou, D. Clark, W. Clay, Y. Goren, R. Kersevan, V. Kovachev, P. Kraushaar, K. Leung, J. Maddocks, D. Martin, D. Meyer, R. Mihelic, G. Morales, J. Simmons, G. Snitchler, M. Tuli, W. Turner, L. Walling, K. Yu, J. Zbasnik, SSCL	3888
Thermal Model and Associated Novel Approach for Synchrotron Radiation Liner with End Cooling — Q.-S. Shu, K. Yu, W. Clay, J. Maddocks, G. Morales, J. Zbasnik, SSCL	3891
Design of ECR Ion Source Vacuum Systems — J. Pivarc, JINR Dubna	3894
Development of Distributed Ion Pumps for g-2 Beam Vacuum System — H. C. Hseuh, M. Mapes, L. Snydstrup, BNL	3897
What Joining Method for the New Generation of Accelerators (SSC and LHC) — R. Gillier, Helicoflex; J. Montuclard, M. Lefrancois, Ch. Rouaud, LeCarbone-Lorraine, France	3900
Surface Treatments and Photodesorption of Oxygen Free Copper Used in an Accelerator — T. Kobari, M. Matumoto, S. Ueda, MERL Hitachi; M. Kobayashi, Y. Hori, KEK	3903
The DAFNE Main Ring Vacuum System — V. Chimenti, A. Clozza, H. Hsieh, G. Raffone, C. Vaccarezza, INFN-LNF	3906
Vacuum Tracking — V. Ziemann, SLAC	3909
 Closing Plenary Chair: W. Hess	
Future Accelerators in Japan — N. Toge, KEK	3912
LHC Progress and Status — G. Brianti and the LHC Machine Group, CERN	3917
Status of the SSC — R. J. Briggs, SSCL	3922
Design for Low Beam Loss in Accelerators for Intense Neutron Source Applications — R. A. Jameson, LANL	3926
Is There a Future for High Energy Accelerators? — M. Tigner, Cornell	3931

Each volume begins with this five-volume table of contents and ends with the five-volume author index. The chairmen's foreword and a list of conference organizers and staff appear as front matter in Volume 1. A list of conference participants precedes the author index in Volume 5.

An Overview of Radioactive Beam Concepts

John M. D'Auria

Department of Chemistry, Simon Fraser University
Burnaby, British Columbia, Canada V5A 1S6

Abstract

This report presents a status of the field of accelerated radioactive beams (RB). Following a review and comparison of the production methods, a brief description of the various low energy facilities, existing, or proposed, is given with some of the specifications. Emphasis is given to some of the outstanding technical problems existant for the ISOL (isotope separator on-line)/accelerator method of production.

I. INTRODUCTION

It is now well known that ion beams of almost any radioisotope can now be provided by modern accelerators over a wide range of energies and intensities. This has rejuvenated the field of nuclear physics while also providing additional research opportunities for other related disciplines including condensed matter physics, atomic physics, nuclear medicine and surface physics, among others. In this report a brief review of the methods of production will be given as well as a summary of the various facilities (existing and proposed) around the world. Particular attention will be given to low energy accelerated, radioactive beams facilities including a review of some of the technical challenges still remaining before a major facility of this type becomes operational.

II. METHODS OF PRODUCTION

There are two main methods by which accelerated or energetic beams of radioactive nuclides can be produced, namely, the projectile recoil fragmentation method (PF) and the ISOL/Accelerator approach. In the former, a very energetic heavy ion projectile transverses a thin low Z target material, resulting in the production of a wide range of projectile fragments with momenta similar to the incident beam. These products are emitted into a forward cone, dependent upon the projectile energy and can be captured by magnetic separators while elemental selection is obtained by taking advantage of energy loss in some thick wedge absorber. Additional details can be found elsewhere [1,2]. The ISOL method involves production of the desired radionuclide using energetic low Z projectiles, very low energy, eg., 30 MeV protons or even thermal neutrons. The target thickness is determined by the energy of the primary production projectile, or in some

cases, the reaction product recoil range. If a thick target is used, chemical methods lead to the release of the desired product from the target into an ion source. A gas jet system can be used with a thin target and in this case the products recoil out of a thin target; these are transported quickly to an ion source located far from the target. Regardless the resultant ion beam is extracted at some potential, generally less than 60 KeV and mass selectivity is then obtained by using a magnetic mass separator. Elemental (Z) selectivity is obtained by the combination of the target chemistry and the appropriate ion source. In some cases the production projectile only makes a limited number of products. Very high resolution magnetic mass separators can also be used to gain some additional final beam purity. Detailed description of this approach can be found elsewhere [3]. A third method involving transfer reactions with heavy ion projectiles at low energies and a superconducting solenoid to select a desired RB has been used to produce a limited number of beams of modest intensity [4]; this method will not be discussed further.

It is very difficult and can be misleading to provide a thorough comparison of these two very different methods in a brief format. In general PF can provide a wide range of RB of acceptable beams with energies higher than about 30 MeV/u while the ISOL method is better suited for RB with lower energies. Table 1 attempts to summarize some of advantages and disadvantages of each, but it is important to emphasize that indeed these approaches are complementary to each other, and that there is excellent physics to be done using each approach.

Projectile Fragmentation (PF) Facilities

There are a number of facilities in the world based on the PF approach which are either operating or planned. These are listed in Table 2 along with some of the facility parameters; additional information can be found in the indicated reference. These facilities are achieving significant results and have demonstrated clearly the importance of this science.

ISOL Based RB Facilities

At present there are no major operating RB facilities based upon the thick target ISOL method although there are one or two smaller systems in operation or being built. Table 3 presents information on the latter while Table 4

Table 1
Comparison of RB Production Methods
(optional conditions)

	<u>PF</u>	<u>ISOL Method</u>
Energy Range (MeV)	50-2000	0.2-10(+)
RB Delivery Time	$\sim \mu s$	≥ 50 ms
Momentum (%)	1-3	~ 0.1
Emittance (π mm mr)	~ 20	0.2-1.0
Production Luminosity	$\leq 10^{35}$	$\leq 10^{38}$
RB Intensities	$\leq 10^9$	$\leq 10^{12}$
Beam Purity	moderate	high

Further Advantages

<u>PF</u>	<u>ISOL</u>
No chemical requirements	Wide selection of RB
Simple production target	Easy energy variation
High collection efficiency	RB energies ≥ 0.2 MeV/u
Reliable operation	
Wide selection of RB	
Several major operating facilities	

Further Disadvantages

Production target thickness limited.	Intensity dependent on front end chemistry.
Deceleration difficult without losses and requires time.	Decay losses due to target delay.
	Radioactivity contamination requiring remote handling.
	Requires post-accelerator.

Table 2
Projectile Fragmentation Facilities
(existing or planned)

<u>Laboratory</u>	<u>Country</u>	<u>RB Energy</u>	<u>Reference</u>
<u>EXISTING</u>			
RIKEN/RIPS	Japan	100 MeV/u	5
GSI/FRS	Germany	0.5-2 GeV/u	6
GANIL/LISE	France	30-100 MeV/u	7
NSCL/A1200	USA	30-100 MeV/u	8
<u>PLANNED</u>			
CATANIA/FRS	Italy	50-100 MeV/u	9
LNL/ADRIA	Italy	.005-1 GeV/u	10
Dubna	Russia	20-500 MeV/u	11
Osaka	Japan	-	12

Table 3
ISOL Based RB Facilities
(existing*/funded)

<u>Facility</u>	<u>Country</u>	<u>Production System</u>	<u>Post Accel.</u>	<u>Ref.</u>
RIB/ Louvain*	Belgium	K=30 cyclotron Ep=30 MeV	K=110 Cyclotron	13
RIB/ Oak Ridge	USA	K=105 (ORIC) Ep \leq 80 MeV	Tandem (25 MV)	14
INS/ JHP prototype	Japan	K=68 cyclotron Ep=45 MeV	LINACS (RFQ,DTL) E \leq 1 MeV/u	15

Table 4
ISOL Based RB Facilities
(planned/proposed)

<u>Facility</u>	<u>Country</u>	<u>Production System</u>	<u>Post-Accel.</u>	<u>Ref.</u>
Arenas ³ Louvain	Belgium	K=110 cyc. (p,d,He)	SC LINAC	18
ISOLDE PRIMA	Swiss	Ep=1 GeV	LINACS	18
RAL	UK	Ep=0.8 GeV	LINACS/ISIS	18
RNB/ Moscow	Russia	Ep=0.6 GeV	LINACS or cyc.	18
PSI	Swiss	Ep=.59 GeV (gas-jet)	K=120	19
GANIL	France	H.I/100MeV/u	K=265	18
INFN/ Catania	Italy	H.I/50-80 MeV/u	Tandem (15 MV)	18
PIAFE Grenoble	France	n _{th} (Reactor)	K=88/160	18
ISAC/ ISL/TRIUMF	Canada	Ep=0.5 GeV	LINACS	20
Argonne	USA	E(¹² C)=1 GeV	LINACS	21
KEK/ JHP	Japan	Ep=1 GeV	LINACS	15

indicates the facilities in the proposal or planning stage. Detailed information can be found in the indicated reference.

Given the availability of operating PF facilities providing high energy RB and the lack of a major ISOL based system providing high intensity, low energy Rb, the focus of the remainder of this report will be on aspects of the latter systems.

Post-Accelerators for ISOL Facilities

There are a range of options available for accelerating the extracted radioisotopic ion beams from an ISOL system. At Louvain-la-Neuve where one of the first low energy beams was produced [13], a $K=110$ cyclotron was used to accelerate the first radioactive beam, ^{13}N . While there were some losses on injecting and extracting, nevertheless the cyclotron also acted as a high resolution mass spectrometer allowing for the separation of the desired beam of ^{13}N from the interferent, ^{13}C . The final beam energy was of the order of 1 MeV/u. At Oak Ridge a project has been funded to couple a front end ISOL device to a 25 MV Tandem accelerator [14]. The radioactive species are produced using the $K=105$ (ORIC) cyclotron, extracting them using ISOL technology, using a charge exchange cell to produce the needed negative ion beam and then accelerating these ions to energies of the order of 5 MeV/u. Chalk River (AECL) is also considering using a 30 MeV primary production cyclotron and a Tandem post-accelerator. This first stage can then be coupled to the TASC superconducting, high energy heavy ion cyclotron [22]. A number of laboratories are proposing the use of LINACS to provide the required acceleration. The ISL project calls for a combination of room temperature and superconducting LINACS as does the proposed ISAC facility at the TRIUMF laboratory in Canada [20,23]. Such devices are generally more user friendly and forgiving; essentially 100% of the beam is transmitted in the absence of any strippers. The first stage of such systems will need to include an RFQ LINAC to capture the low velocity ($\beta=0.0015$), heavy ions ($q/A < 1/60$) from the ISOL device; the velocity will also vary according to the mass. As mentioned below some study is needed to develop an efficient means to adjust the input velocities, given the need for constant injection velocity when using LINAC's. Demonstration of such an operating RFQ especially CW would be useful and studies are in progress at Argonne and TRIUMF.

III. TECHNICAL AREAS REQUIRING RESEARCH AND DEVELOPMENT STUDIES

While there do exist major PF facilities actively performing physics studies, there is still not a major ISOL based system. Aside from the obvious financial restraints, there do exist some technical questions which require

attention before a final system can be designed in detail. The smaller ISOL based facilities, while clearly clarifying important aspects, do not need to address some of the questions the design of a larger facility will precipitate. It should be noted that a number of these questions that an ISL facility will introduce were discussed at a special workshop held last year in Oak Ridge, and the proceedings will be available shortly [24] to provide further details than given below.

A. Primary Accelerator

The tentative specifications for the ISL foresee a primary beam accelerator for light ion (mainly protons) in the energy range of 0.5 to 1 GeV with a current of at least 100 μA . There are two accelerators in North America that can meet these specifications: LAMPF and TRIUMF. In the event that the ISL is not sited at these laboratories, a new primary beam machine would have to be built. This opens up different options and could include an isochronous H+ cyclotron, a FFAG (Fixed Field Alternating Gradient) machine, a ring cyclotron, or a fast cycling synchrotron. Less attractive options would be an H- or superconducting cyclotron or a LINAC for protons, although the latter accelerator is being considered as a source of high intensity, light ions such as ^{12}C [21].

B. Using High Intensity Production Beams

An important aspect to produce high intensity RB is to use high intensity, production beams. This introduces severe problems especially when these are projectiles with energies higher than a few hundred MeV. Beam heating in the target (as well as cooling) is not straightforward when dealing with beam currents up to 100 μA . In addition residual radioactivity levels, and potential contamination possibilities require hard solutions for these and for the problems associated with apparatus failure in high radiation fields and shielding needs to reduce external fields. Similar conditions do exist at present meson facilities, and relevant technology does exist. Joint projects are in progress at TRIUMF [25], LBL [26], and RAL [16] to demonstrate the operation of a thick target, ISOL device in a high intensity proton beam, and to explore solutions to the development of a fail-safe, remote handling system. From another perspective LAMPF is exploring the use of a thin target facility coupled to a gas jet transport system in proton beam currents of the order of milliamps [17]. This would minimize the radioactive contamination problems as well as reduce the shielding needed.

C. ISOL Ion Source Technology

Ion source systems are clearly important although a good deal is already known from considerable developments at the ISOLDE facility. Until now, ISOL devices have

produced only single charged ions, but multiple charged ions would be invaluable to minimize the cost of the post-accelerator. ECR (Electron Cyclotron Resonance) sources do produce such multiple charge beams efficiently, and there exists two such sources on-line at ISOL type systems at the TISOL facility [27] and at Louvain-la-Neuve [13]. Considerably more time must be devoted to systematic studies with such systems to understand more about this application and to develop the optimum system. Another new area of ion source technology developments is in the area of ISOL based, laser ion sources [28]. These can provide very pure radioisotopic ion beams and more information is needed on the universality of the approach as well as efficiency measurements.

D. Post-Accelerators

At present it is accepted that the LINAC is the optimal device to post accelerate the radioisotopic ion beams to some desired final energy. LINACs demonstrate high transmission and also the final energy can be increased at a later date in a straight forward manner. Given appropriate funding, this would be the preferred accelerator for the post accelerator of a major RB facility.

The low velocity ($\beta > 0.0015$) ions produced by the ISOL device will have q/A ratio of at least $1/60$ if not as small as $1/240$. It is believed that the best device to capture and provide some acceleration is an RFQ LINAC. While an 2.1 m in length prototype RFQ has been shown to accept low beta ions (with a q/A of $1/30$ and 1 keV/u) [29], further developments are needed. This device was a split vane RFQ, operating with a duty factor of about 10%. CW operation would be preferred to optimize transmission. In addition the front section of the RFQ required operation at a variable high potential to compensate for the varying masses of the different ions that come from the ISOL device. Finally there is a question about whether the LINACs including the RFQ should be superconducting or room temperature. With the technology developments around the world, it appears that SC LINAC structures are becoming more standard, but the RFQ does pose a challenge. Projects are initiating both at TRIUMF [30] and Argonne [31] on some of these questions.

IV. CONCLUSION

The field of radioactive beam science is now developing at an accelerating pace and has allowed the possibility of planning for experiments previously considered impossible. In turn, there is a strong need for more research and development studies in areas previously not considered important. A large number of scientists are quite interested in performing experiments with radioactive beams and accelerator scientists and engineers are strongly encouraged to turn their attention to addressing some of the questions being asked.

V. REFERENCES

- [1] G. Münzenberg, *Nucl. Instru. Meth.*, B70, 265 (1992).
- [2] B.M. Sherrill, *Proc. of 2nd Int. Conf. on Radioactive Nuclear Beams*, Th. Delbon ed., Louvain-la-Neuve, August 1991, p.3 (Adam Halger, 1992).
- [3] H.L. Ravn, *ibid*, p.85.
- [4] F.D. Becchetti, et al., *Nucl. Instru. Meth.*, B56/57, 554 (1991).
- [5] T. Kuber, et al., *Nucl. Instru. Meth.*, B70, 309 (1992).
- [6] H. Geissel, et al., *ibid*, B70, 286 (1992).
- [7] R. Anne and A.C. Mueller, *ibid*, B70, 276 (1992).
- [8] B.M. Sherrill, et al., *ibid*, B70, 298 (1992).
- [9] E. Migneco, et al., *Int. Workshop on Physics and Techniques of Secondary Nuclear Beams*, p.341 (Editor, Prentice, 1992).
- [10] G. Bisoffi, et al., *ibid*, p.437.
- [11] Y.T. Ognessian, *ibid*, p.377.
- [12] T. Shimoda, et al., *Nucl. Instru. Meth.*, B70, 320 (1992).
- [13] P. Van Duppen, et al., *Nucl. Instru. Meth.*, B70, 393 (1992).
- [14] J.D. Garrett and D.K. Olsen, "A Proposal for Physics with Exotic Beams at the HHIRF", Physics Div, ORNL, Feb. 1991.
- [15] T. Nomura, et al., *Nucl. Instru. Meth.*, B70, 407 (1992).
- [16] J.R. Bennett, Rutherford Appleton Lab, private communication, *Nature*, 362, 278 (1993).
- [17] D. Vieira, LAMPF, private communication.
- [18] H. Ravn, et al., "Comparison of radioactive ion beam intensities produced by means of thick targets bombarded with n,p, and heavy ions", CERN pre-print; to be submitted to *Nucl. Instru. Meth.*
- [19] H. Giggeler, et al., *Int. Workshop on Physics and Techniques of Secondary Nuclear Beams*, Dowdon, France, (Edition Frontiers) p.419 (1992).
- [20] L. Buchmann, et al., *Nucl. Instru. Meth.*, B26, 151 (1987).
- [21] J. Nolen, private communication.
- [22] H. Schmeing, private communication.
- [23] "The IsoSpin Laboratory, Research Opportunities with Radioactive Beams", *LALP*, 91-51.
- [24] *Workshop on Production and Use of Intense Radioactive Beams at ISL*, Oct. 1992, proceedings to be published.
- [25] J. D'Auria and J. Beveridge, private communication.
- [26] M. Nitschke, private communication.
- [27] L. Buchmann, et al., *Nucl. Instru. Meth.*, B62, 521 (1992).
- [28] H.L. Ravn, *Nucl. Instru. Meth.*, B70, 107 (1992).
- [29] S. Arai, et al., *ibid*, p.414.
- [30] H. Schneider, private communication.
- [31] K. Sheppard, private communication.

Heavy Ion Beam Accumulation, Cooling, and Experiments at the ESR

B. Franzke, K. Beckert, F. Bosch, H. Eickhoff, B. Franczak, A. Gruber, O. Klepper,
F. Nolden, P. Raabe, H. Reich, P. Spädtke, M. Steck, J. Struckmeier
GSI - Gesellschaft für Schwerionenforschung mbH
Postfach 110552, D-64220 Darmstadt, Germany

Abstract

The Experimental Storage Ring ESR — part of the heavy ion accelerator facility at GSI — started operation early in 1990. This paper informs about the progress achieved in accumulation, electron cooling and internal experiments with fully stripped heavy ions from O^{8+} to U^{92+} at energies between 90 MeV/u and 300 MeV/u. Rf-stacking combined with compression in phase space by electron cooling turned out to be a very effective accumulation technique. Maximum numbers of stored ions for heaviest ions are determined by the equilibrium between accumulation rate and beam loss rate due to radiative electron capture of cooler electrons. Beam currents for lighter ions up to Ar^{18+} are limited by coherent instabilities. First excellent results of internal experiments with cooled, circulating beams of either primary ions or of secondary nuclear fragments confirm that the combination of the heavy ion facility Unilac-SIS-FRS with the storage ring ESR offers unique possibilities for atomic, nuclear and accelerator physics.

1 HEAVY ION FACILITY AT GSI

1.1 The Unilac/SIS/FRS Complex

The first stage of the accelerator facility at GSI, the Unilac, accelerates heavy ions up to Uranium to variable energies in the range 1.4 to 17 MeV/u. In 1992 a new high charge state injector combining an ECR source with RFQ- and IH accelerating sections came in operation as an alternative to the old Wideröe pre stripper section. Now the Unilac is able to supply low energy experiments and the injection line for the heavy ion synchrotron SIS [1] in a fast time sharing mode, based on the 50 Hz macro-structure of the beam, with different ions species and different specific energies. The 18 Tm-machine SIS extended in 1989 the range of available ion energies to 2 GeV/u for Ne^{10+} and to 1 GeV/u for U^{72+} -ions. Up to the present, the SIS has accelerated many different ion species from d^+ to U^{72+} to energies between 100 MeV/u and 2 GeV/u. Maximum intensities of 2×10^{10} light ions as O^{8+} and more than 1×10^7 heaviest ions as Bi^{67+} per accelerating cycle have been attained by radial stacking of up to 40 effective turns [2] at the injection energy of 11.4 MeV/u. Up to three users can be supplied by the SIS with beams of strongly different energy in a time sharing mode from cycle to cycle. Slow, resonant beam extraction with up to

10 s spill duration may alternate likewise with fast bunch ejection using the same extraction line. Fast ejection is used mainly to supply the ESR in the “double shot” mode, in which two of the four SIS-bunches are transferred by two steps to rf-buckets of the half-sized storage ring [2].

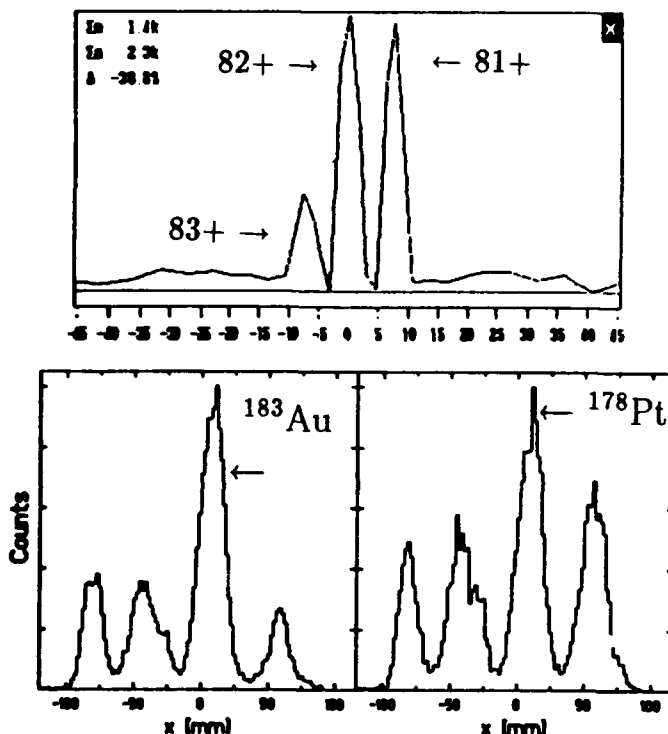


Figure 1: Typical distribution spectra after acceleration in SIS: for atomic charge states after one more stripping in 20 mg/cm² Cu of Bi^{67+} at 230 MeV/u (top) and for nuclear fragments of ^{197}Au at 950 MeV/u after a thick Al-target at different settings of the FRS.

Production of fully stripped ions with atomic numbers $Z \geq 36$ requires one more stripping in the transfer beam line. Alternatively, the transferred bunches may pass through a thick production target followed by the large FRragment Separator FRS [3]. By this way, separated beams of nuclear projectile fragments are delivered to ESR for injection, cooling and eventually accumulation. Examples for charge state distributions after the stripper and for nuclear fragment distributions after the production target and the FRS are displayed in fig. 1, beam transfer lines between the rings are shown in fig. 2.

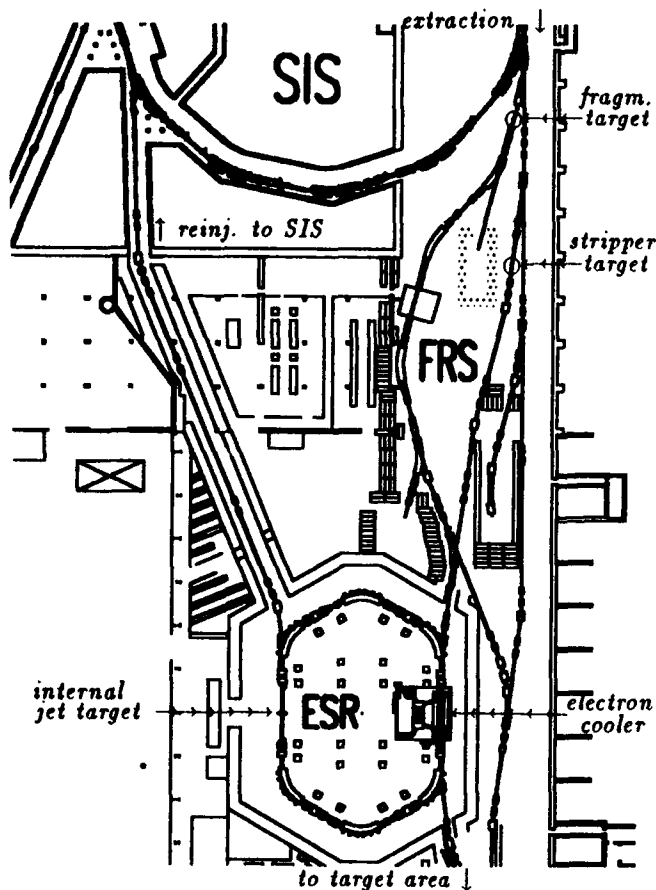


Figure 2: ESR with beam transfer lines from and to SIS.

1.2 Experimental Storage Ring ESR

The ESR design has been described in detail at past conferences [4], an impression of the ring structure is given in fig. 2. The following brief list may help to remind of most important ring features.

- The maximum bending power of 10 Tm allows storage of fully stripped ions at maximum energies between 560 MeV/u (U^{92+}) and 834 MeV/u (Nc^{10+}).
- Large acceptances in combination with flexible lattice optics are provided for beam accumulation, cooling of "hot" beams, storage of multi-component beams, and, not least, for beam injection and extraction.
- Electron cooling (EC) at variable beam energies from 30 to 560 MeV/u serves for beam brilliance as high as possible. It plays also an important role for beam accumulation and for internal experiments and facilitates the diagnosis of beam and lattice parameters.
- Special equipment is installed for investigations of interactions between cooled, circulating ions and internal gas jet atoms, free cooler electrons or laser beams.
- Acceleration or deceleration of cooled beams of fully stripped ions is in preparation for internal experiments at variable energy. Slow and fast extraction shall supply external experiments with highly brilliant beams.
- Beam diagnosis applies mainly modern Schottky and beam transfer function (BTF) techniques. Active damping

of coherent transverse beam oscillations has been practised already with some success. Emittances of circulating beams can be determined in a non-destructive way using several movable position sensitive particle detectors, which deliver transverse distributions of ions after radiative electron capture (REC) in the cooler or in the internal gas jet.

2 APPLICATION OF ELECTRON COOLING

Recent results of electron beam cooling at the ESR are presented in a separate contribution to this conference [5]. the importance of the EC device [5] for ring operation and internal experiments may be deduced from following selection of examples.

2.1 Beam Accumulation

Beam accumulation in the ESR is done by combining the conventional rf-stacking method with electron cooling. The electron energy is suitably switched between injection and stack levels. At first, the injected bunches are compressed in order to avoid beam loss during deceleration to the stack. This is shown in fig. 3 by two longitudinal Schottky scans at different times after injection. The coasting stack

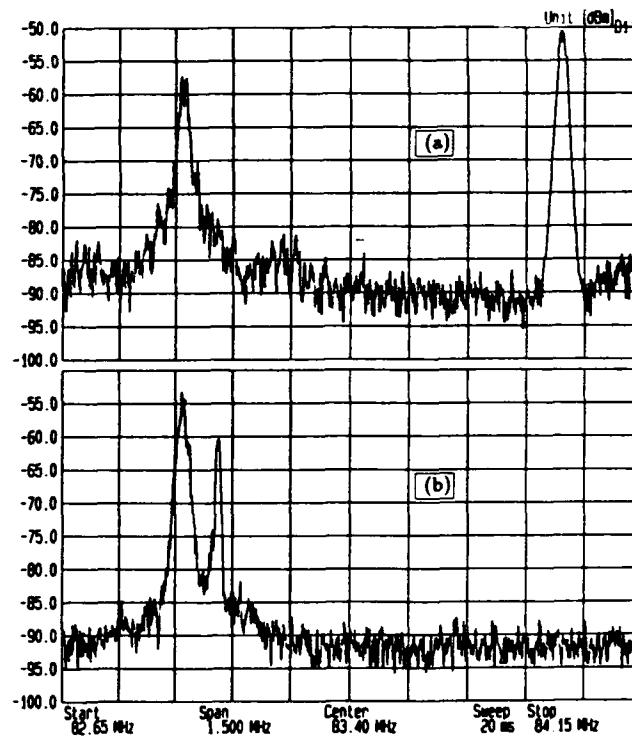


Figure 3: Combined Rf stacking and electron cooling demonstrated by longitudinal Schottky scans at different times t after bunch injection: (a) $t = 2000$ ms: cooled bunches are still on injection orbit (right) and modulate the coasting stack (left) due to somewhat faster circulation. (b) $t = 2050$ ms: bunches are decelerated to the stack, while the rf amplitude is decreased already.

is cooled in the time between subsequent stacking processes. Since the phase space is "cleaned" all the time, beam accumulation is limited by other effects rather than by phase space. One of the principle beam current limits for this technique is determined by the equilibrium between the REC rate in the electron cooler and the accumulation rate. For high- Z , high- q ions the REC rate ($\propto q^2$) is high and the primary intensity is relatively low, mainly because of repeated stripping in the Unilac, before injection to and after acceleration in SIS. With Au^{79+} at 270 MeV/u, for instance, a saturation current of 1.4 mA, corresponding to 6×10^7 stored ions, was attained recently. The observed REC loss rate of about $5 \times 10^{-4}/\text{s}$ is consistent with the injection of nearly 4×10^5 ions ($10 \mu\text{A}$) every 13 s. For cooled light ion beams ($Z \leq 30$), primary intensities are much higher and REC loss rates considerably lower. Up to now, the beam current is limited in this case to about 7 mA by coherent — mainly transverse — instabilities. Some success has been achieved already by an active feedback, the sources of high narrow band impedances in the frequency range 20 to 40 MHz, probably ferrite kickers, clearing electrodes with cables or the electrostatic septum, have to be found and deactivated in order to achieve essential beam current increase. For higher- Z ions, the coherent oscillations seem to be damped more and more by intra beam scattering (IBS), which increases the equilibrium momentum spread in cooled beams approximately $\propto Z$ (see fig. 4). A list of ion species, energies and beam currents stored and cooled in the ESR is given in table 1.

Table 1: Ions, energies and beam currents in ESR by April 1993. The major part of beam currents I_i (number of ions N_i) has been recorded during physics experiments and may not be considered as upper limits.

Ion	Energy	N_i	I_i
$^{18}\text{O}^{8+}$	150 MeV/u	1.1×10^9	2.0 mA
$^{20}\text{Ne}^{10+}$	250 MeV/u	2.6×10^9	7.0 mA
$^{40}\text{Ar}^{18+}$	250 MeV/u	4×10^8	2.0 mA
$^{58}\text{Ni}^{28+}$	250 MeV/u	1×10^9	6.0 mA
$^{84}\text{Kr}^{36+}$	150 MeV/u	1×10^8	0.9 mA
$^{129}\text{Xe}^{54+}$	250 MeV/u	4×10^8	6.0 mA
$^{163}\text{Dy}^{66+}$	297 MeV/u	1×10^8	2.0 mA
$^{197}\text{Au}^{79+}$	270 MeV/u	6×10^7	1.4 mA
$^{209}\text{Bi}^{82+}$	230 MeV/u	5×10^7	1.2 mA
$^{238}\text{U}^{92+}$	300 MeV/u	2×10^7	0.6 mA

At energies above 90 MeV/u the life time of fully stripped or few-electron ions is determined only by REC in the cooler. With an EC current of 1 A the life time of Ne^{10+} beam at 150 MeV/u is nearly 7 hours. Though REC rates increase approximately $\propto q$, comfortable life times of about 1 h have been achieved also for U^{92+} and Au^{79+} beams by applying low EC current, e.g. 100 mA, without major reduction of the beam quality, even if ion beam currents are in the mA-range. Beam loss due to residual gas interaction at pressures $\leq 10^{-10}$ mbar is negligible compared to

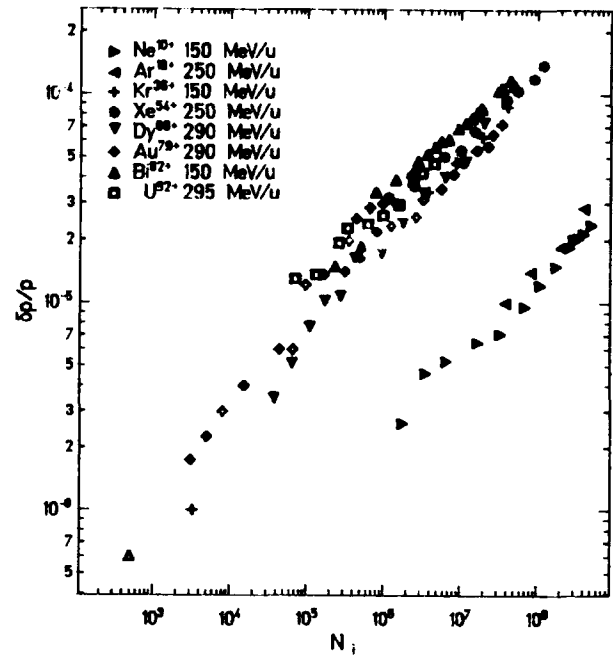


Figure 4: Equilibrium momentum spread $\delta p/p$ in electron cooled beams vs. number of stored ions N_i .

that caused by REC in the cooler. A quite different situation is expected at low energies of about 10 MeV/u or with partially stripped ions ($Z - q \gg 1$). For example, strongly reduced life times of 300 s were observed with Bi^{67+} at 230 MeV/u and only 10 s with Ni^{15+} at 150 MeV/u, due to electron stripping at an average residual pressure of about 5×10^{-11} mbar. In experiments with the internal gas jet target the beam life is dominated by charge changing processes in the target itself. With an Ar-jet of 6×10^{12} atoms/cm² thickness a beam of fully stripped Dy^{66+} ions at 290 MeV/u lived only 150 s, mainly due to REC of bound target electrons.

2.2 Multi-Component Beam Storage

The large momentum acceptance of the ESR and a special lattice optics with small dispersion on long straight sections makes it possible to store and cool simultaneously more than one charge state of an ion, e.g. two for Kr⁻, three for Au⁻, and even four for U⁻ ions. The secondary charge states are populated by sequential REC in the cooler and are fixed to at nearly the same velocity by the cooler. Therefore, the relative frequency differences are determined only by orbit length differences $\Delta C/C$ due to charge differences $\Delta q/q$:

$$\frac{\Delta f}{f_q} = -\frac{\Delta C}{C_q} = \frac{1}{\gamma_t^2} \frac{\Delta q}{q} \quad (1)$$

Charge states q are known exactly and mean Schottky frequencies of cooled beams can be measured with high accuracy. Hence, the transition point for the given lattice optics, γ_t , can be derived with an accordingly high precision, typically in the order of 1×10^{-4} .

Other effects producing multi component beams in the ESR itself are nuclear decay of stored primary nuclei and nuclear collisions in the internal gas jet target. There is also strong interest to inject and cool secondary beams of projectile fragments, aiming at precise mass determination for exotic nuclides. Electron cooling is the tool to reduce the momentum spread to extremely low values with a twofold profit. Both the spectral density in longitudinal Schottky spectra, i. e. the sensitivity, and the precision of mass determination are enhanced essentially. A precise determination of γ_t is of comparable importance for planned mass measurements as are reproducibility and stability of both the magnetic bending field and the accelerating voltage of the electron cooler.

2.3 Cooling of Radioactive Beams

Injection and cooling of radioactive beams from the FRS was demonstrated with fragments of ^{20}Ne at 250 MeV/u by means of longitudinal Schottky spectra recorded immediately after injection and cooling to equilibrium. Besides the strong band from the primary ^{20}Ne , two weak bands from the isotonic fragments ^{18}F and ^{14}N were clearly separated in the spectrum, though the intensity fraction of fragments was only about 2×10^{-3} . As in the case of different ionic charge states, all nuclei are cooled to the same velocity. Using a precise experimental value for γ_t the masses were determined with an relative error below 1×10^{-5} . Scans with higher resolution show that relative errors of peaks may touch the 10^{-7} range (see fig. 5). Even better precision should be attained by means of operating the ring near transition using a setting with low γ_t .

Compared to typical cooling times for primary beams of less than 1 s, electron cooling of ^{20}Ne fragment beams to equilibrium required between 10 s and 20 s. This time will be reduced hopefully by a factor of 10 after the planned installation of stochastic pre cooling.

2.4 Free Electron Target

The EC beam has been applied also as free electron target with variable energy, W_r , in the center of mass frame of ions. The energy is varied by suitably pulsing the accelerating voltage of the EC device or by applying a pulsed voltage of ± 5 kV to a drift tube in the cooling section. Both methods were combined in a recent experiment on di electronic recombination processes in order to increase the range for W_r . For this experiment, the desired beam of Li-like Au^{76+} has been breded from the primarily accumulated beam of He-like Au^{77+} . The rate of recombined Au^{75+} ions was then measured as a function of W_r by using one of the particle detectors mentioned above [8]. Other experiments using the cooler as free electron target are the investigation of REC by means of X ray spectra in coincidence with recombined particle detection and the study of laser induced electron capture (LIREC) to high n states, a process of simultaneous interaction between photons, electrons and highly charged ions.

3 INTERNAL TARGET EXPERIMENTS

3.1 Internal Gas Jet

The internal supersonic gas jet is produced by a Laval nozzle and a four stage differential pumping and skimming system. After crossing the interaction chamber in vertical direction over a free distance of 70 mm, the jet enters a four stage dump [7]. The jet diameter is less than 5 mm, the maximum thickness at the interaction point is presently about 6×10^{12} atoms/cm² for Argon and 2×10^{12} atoms/cm² for N_2 . The maximum UHV-pressure in surrounding chambers is in the low 10^{-9} mbar range and contributes approximately 1% to the total target thickness. It should be noted that the acceptances of the ESR are not affected by the jet target, i. e. there are no aperture limitations in ion beam direction.

Taking into account the numbers of stored ions given in table 1, the presently available luminosity for internal target experiments range from $1 \times 10^{27} \text{cm}^{-2} \text{s}^{-1}$ to $2 \times 10^{28} \text{cm}^{-2} \text{s}^{-1}$, depending on ion species and target gas. The design value of $1 \times 10^{30} \text{cm}^{-2} \text{s}^{-1}$ is hoped to be attained by improvements of the jet apparatus and by increasing ion beam currents.

3.2 Beam Target Interaction

The internal gas jet has been applied to measurements of REC- and stripping cross sections for various ions and for X-ray spectroscopy of H-like ions after REC in the target. It played also an important role for the investigation of a certain mode of nuclear decay (see below). The plot of fig. 5 demonstrates that Schottky spectroscopy is applicable for the analysis of nuclear interactions of electron cooled circulating heavy ions in the jet target. It was recorded after about 400 s interaction of a cooled $^{163}\text{Dy}^{66+}$ beam with an Ar-jet and subsequent switching off the jet. The highest (cut) band comes from the primary beam. Several small lines indicate secondary nuclides produced in the jet, which are stored and cooled simultaneously with the primary beam. The larger rightmost peak is explained below. The small $\delta p/p \approx 1.8 \times 10^{-6}$ indicates that, due to the momentum dispersion, the secondary components circulate on orbits, which are well separated from that of the intense primary beam, where they would be heated by IBS.

3.3 Decay of Stored Nuclei

There are some stable nuclides getting β^- -unstable as soon as the electron cloud has been stripped off. The low Q value of the decay forbids the emitted electron to escape from the nuclear Coulomb field. The electron is bound to innermost electronic shells. The first experimental proof of this bound state β^- decay (BBD) took place in 1992 at the ESR [9]. Primary $^{163}\text{Dy}^{66+}$ nuclei decayed during long term storage to H-like $^{163}\text{Ho}^{66+}$ ions, which have practically the same mass to charge ratio as the primary ions and, therefore, circulate on the same orbit as the primary

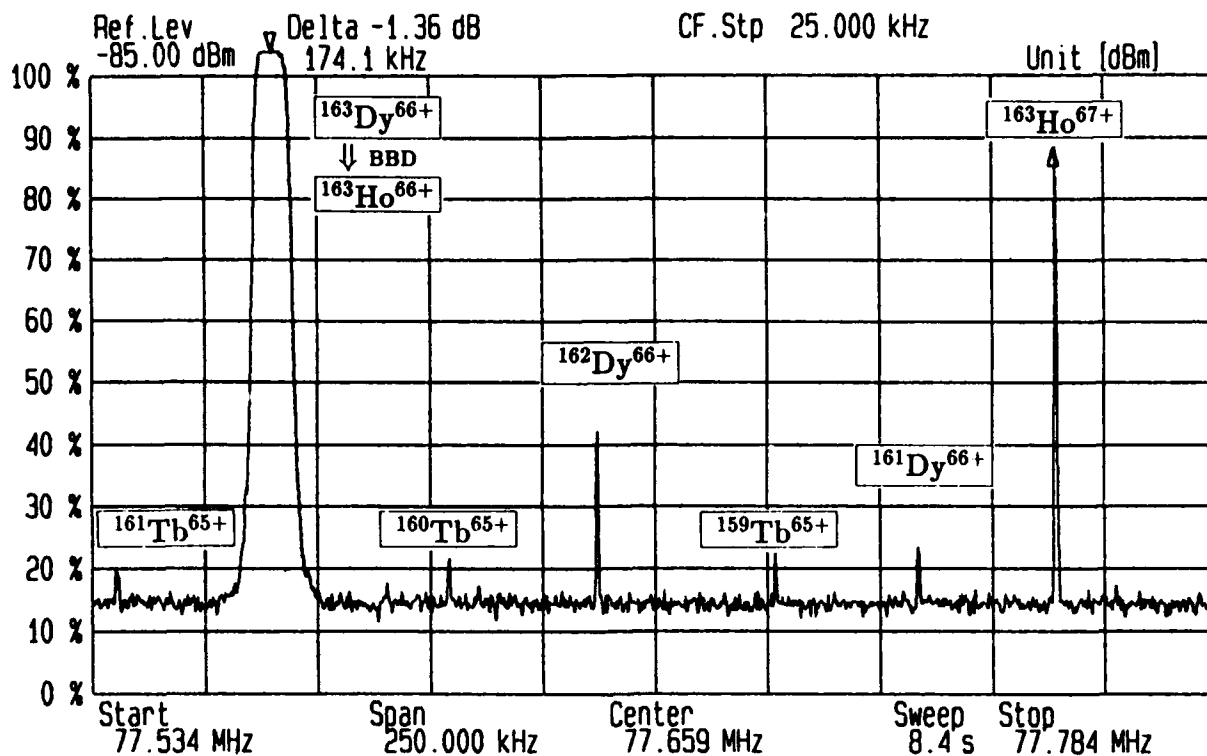


Figure 5: Longitudinal Schottky scan of stored and cooled nuclear fragments produced in ESR at 290 MeV/u in the internal gas jet from primary $^{163}\text{Dy}^{66+}$ (large cut band). The peak assigned to $^{163}\text{Ho}^{67+}$ — about 20000 out of 2×10^7 primary nuclei — results from bound-state β^- -decay (see text). Spectra with higher frequency resolution allow precise mass and cross production cross section measurements.

ions. Orbit separation was possible by stripping in the internal gas jet to fully stripped $^{163}\text{Ho}^{67+}$ nuclei, which were counted then by a particle detector. Alternatively, after removing the detector out of the aperture, the $^{163}\text{Ho}^{67+}$ were stored simultaneously with the primary beam and appeared as a separate band in the Schottky spectrum, which is visible in fig. 5 as the larger rightmost peak. The amount of daughter nuclei — or the peak height in the Schottky scan — normalized to the primary intensity, was measured as a function of storage time. However, the precise determination of the BBD life time τ_{BBD} required complementary measurements of nuclear and atomic cross sections for other charge states and isotopes. The value $\tau_{\text{BBD}}(\text{c.m.}) = 50 \text{ d} \pm 16\%$ was found by the detector method as well as by Schottky spectroscopy. Similar experiments are envisaged for $^{205}\text{Tl}^{81+} \rightarrow ^{205}\text{Pb}^{81+}$ with predicted $\tau_{\text{BBD}} \approx 100 \text{ d}$ and $^{187}\text{Re}^{75+} \rightarrow ^{187}\text{Os}^{75+}$ with $\tau_{\text{BBD}} \approx 10 \text{ y}$.

4 CONCLUSION AND OUTLOOK

The commissioning of the ESR is by far not complete and will probably never be completed as long as new ideas for experiments are created. But three years of commissioning, operation and internal experiments at the ESR confirm that the ring is a highly versatile instrument. It gives access to new physical systems and novel experimental methods with highest precision and, not least, with comfortable luminosity.

Next steps of more apparative developments are deceleration of fully stripped ions, “ramped” operation of the electron cooler at strongly different energies and installation of a stochastic pre-cooling for hot, radioactive beams. Our interests in beam physics are concentrated on investigations of current and quality limitations of electron cooled bunched and coasting beams, including investigations of impedances and IBS. Further experiments shall deal, e.g., with beam loss by charge changing processes and dielectronic recombination for electron rich ions, on-line monitoring of the beam target luminosity, and fast bunch compression methods for the production and investigation of hot, dense plasmas in solids.

5 REFERENCES

- [1] K. Blasche et al., these proceedings
- [2] H. Eickhoff et al., these proceedings
- [3] H. Geissel et al., Nucl. Instr. and Meth. **A282**, 247 (1989)
- [4] B. Franzke, Nucl. Instr. and Meth. **B24/25**, 18 (1987)
- [5] M. Steck et al., these proceedings
- [6] N. Angert et al., *Proc. of Europ. Part. Accel. Conf., Rome, 1988*, World Scientific (1989) p. 1436
- [7] A. Gruber et al., Nucl. Instr. and Meth. **A282**, 87 (1989)
- [8] W. Spies et al., Phys. Rev. Letters **69**, No. 19, 2768 (1992)
- [9] M. Jung et al., Nucl. Physics **A553**, 309c (1993)

The Research Center for Nuclear Physics Ring Cyclotron

I. Miura

Research Center for Nuclear Physics, Osaka University
10-1, Mihogaoka, Ibaraki, Osaka 567, Japan

Abstract

The main components of the new facility are a six sector variable energy ring cyclotron and a beam circulation ring linked to a high precision dual magnetic spectrograph system, a neutron TOF facility with a 100m neutron flight tunnel and a heavy ion secondary-beam facility.

The beams extracted from the RCNP AVF cyclotron are transported through one of the beam lines of the old facility and injected into the ring cyclotron. With this accelerator system, beams of p, d, ^3He , alpha and light-heavy ions are available in the wide range of energies of up to 400, 200, 510, 400 and $400 \cdot Q^2/A$ MeV, respectively. An emphasis is placed on the production of high quality beams to enable precise experiments.

These beams are extracted with single turn extraction mode with flat-topping. Beam energy width of 80 keV was achieved for 300 MeV proton. Energy resolution of 25 keV and 35 keV were obtained with high resolution spectrograph Grand Raiden by using dispersion matching for 300 MeV and 400 MeV proton inelastic scattering spectra, respectively. A very short polarized proton beam pulse of 150 ps was achieved for neutron TOF experiment.

I. INTRODUCTION

The Research Center for Nuclear Physics was founded in 1971, as a national user facility. A K=140 AVF cyclotron [1] and precise experimental apparatus were used during two decades by many researchers in Japan and abroad. After intensive design study of new facility, "RCNP Cyclotron Cascade Project" [2],[4] was proposed in 1985, to

extend the high precision studies into energy region above threshold energy of pion production.

In 1986 the proposal was accepted and the four years cyclotron construction contract was made with manufacturer in August 1987.

The main components of the new facility are a six separated spiral sector cyclotron (ring cyclotron) and beam circulation ring linked to a high precision magnetic spectrograph Grand Raiden ($p/\Delta p=39000, 54 \text{ kGm}$) and a Large Acceptance Spectrograph ($p/\Delta p=5000, 32 \text{ kGm}$), a neutron TOF facility with a 100m neutron flight tunnel and a heavy ion secondary beam facility, as shown in Fig. 1.

Installation of the ring cyclotron was started in February 1990, immediately after finish of the Ring Cyclotron Hall. On December 1991, the first extracted beam of 300 MeV protons was obtained [7]. Figure 2 shows the photograph of the ring cyclotron.

The new system of the ring cyclotron had been tested and many improvements were made for the initial trouble of operation. These systems work well now and efforts being continued to improve beam quality, intensity and stability of the ring cyclotron.

The ring cyclotron is energy quadrupler of the RCNP AVF cyclotron. Protons and alpha particles can be accelerated up to 400 MeV. Plan view of the ring cyclotron is shown in Fig. 3. Three single gap acceleration cavities are used in the ring cyclotron. Frequency range of the cavity

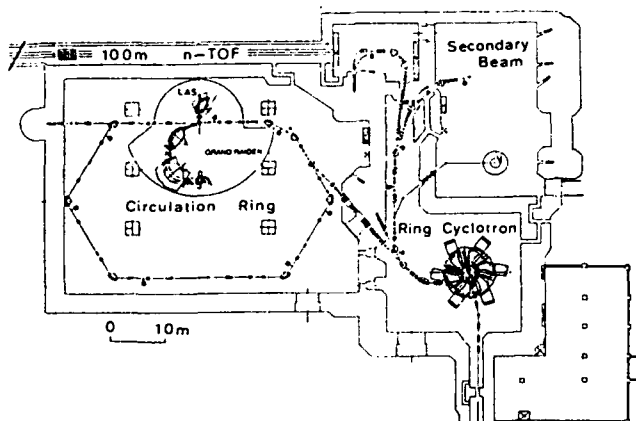


Fig. 1. Plan view of the new facility.

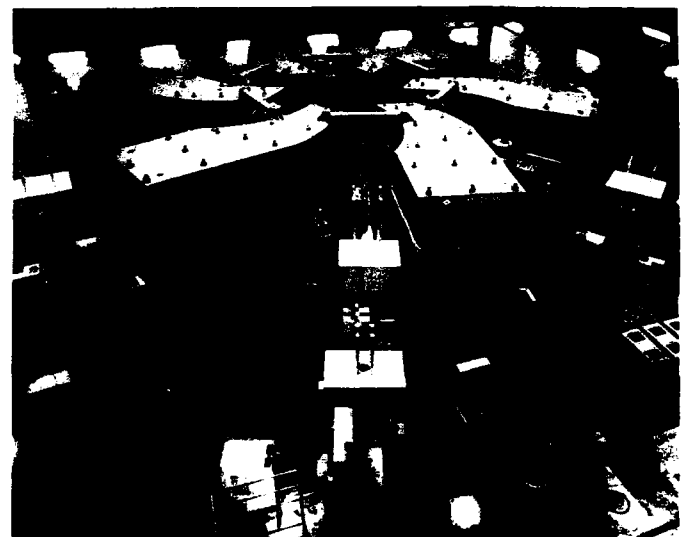


Fig. 2. Photograph of the RCNP ring cyclotron.

A 180°-single-dee acceleration cavity is used in the RCNP AVF cyclotron. The frequency range of the cavity is 5.5~19.5 MHz, and fundamental and 3rd harmonic acceleration modes are used. Figure 4 shows relation between orbital frequencies and acceleration frequencies in the AVF cyclotron and the ring cyclotron for various ions and energies. The characteristics of the cyclotrons are given in Table 1.

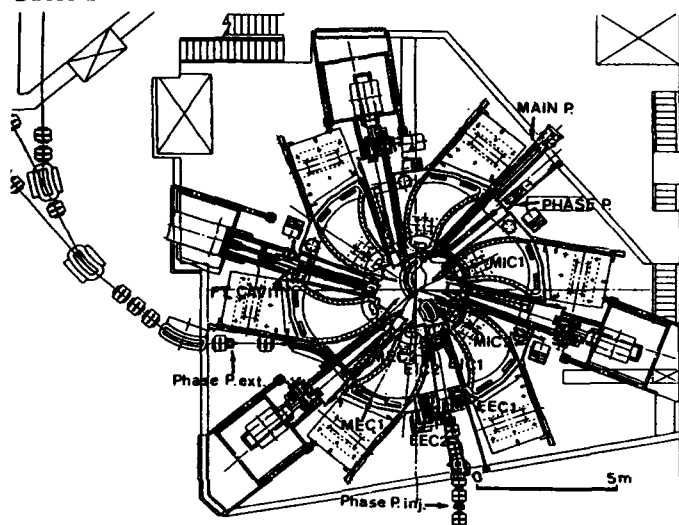


Fig. 3. Plan view of the ring cyclotron.

Table 1 Characteristic of cyclotrons

	AVF	Ring
No. of sector magnets	3	6
Sector angle	max 52°	22~27.5°
Injection radius(cm)		200
Extraction radius(cm)	100	404
Magnet gap(cm)	20.7 min	6.0
Max. Magnetic field(kG)	19.5	17.5
Proton max. energy(MeV)	84	400
Alpha particle energy(MeV)	130	400
³ He energy(MeV)	160	510
Weight of magnet(ton)	400	2200
Main coil magnet(kW)	450	440
No. of trim coils	16	36
Trim coil power(kW)	265	350
No. of cavities	1	3(Acc.) 1(FT)
RF frequency(MHz)	5.5~19.5	30~52 90~155
RF power(kW)	120	250×3 45

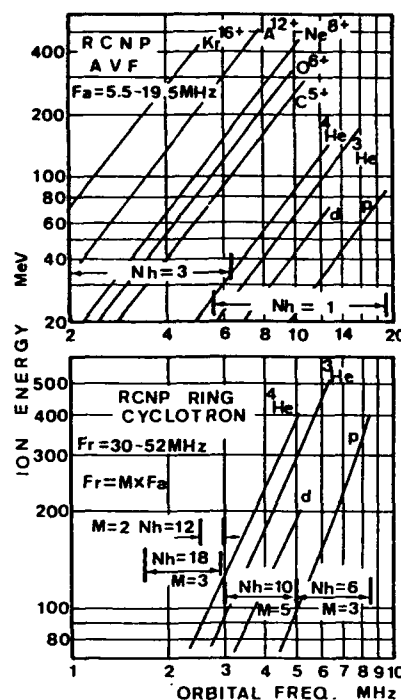


Fig. 4. Orbital frequencies, acceleration frequencies (Fa&Fr) and harmonic numbers of acceleration (Nh) in the RCNP AVF cyclotron and the RCNP ring cyclotron for various ions and energies. M is ratio of the acceleration frequency of the ring cyclotron to the AVF cyclotron.

The magnets of the six spiral sector ring cyclotron was designed by using computer code FIGER (artificial magnetic field distribution generator) and the results of model magnet study of the previous proposal [3]. Figure 5 shows calculated field distribution with the code. The sector magnets are designed as isochronous for 200 MeV proton acceleration without trim coil current. The measured magnetic field distribution are quite satisfactory [8].

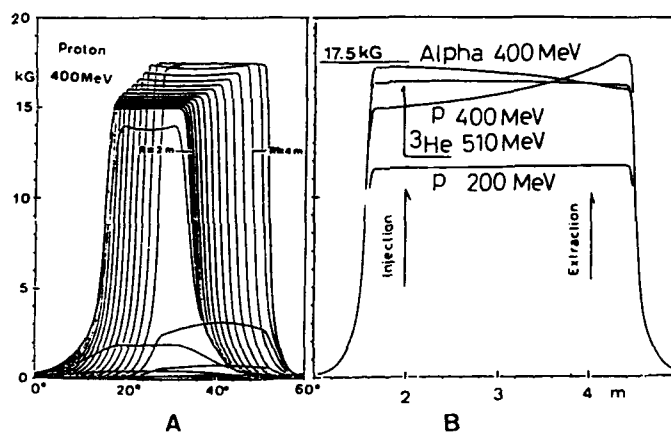


Fig. 5. A: Designed field distribution for 400 MeV proton.
B: Designed isochronous fields on hill center for various ions.

Figure 6 shows comparison between betatron frequencies calculated from the measured magnetic field and the designed one.

Figure 7 shows the structure of the spiral sector magnet. 36 pairs of trim coils are mounted on the pole faces by SUS mild-steel welded bolts. Each trim coil is insulated with alumina-ceramics coating. The radial pole edges are shaped stepwise to the Rogowski's curve. The carbon content of the forged poles and rolled iron yokes are 0.004% and 0.002%, respectively. The median plane of the sector magnets are aligned with accuracy of ± 0.2 mm. However, on 400 MeV proton beam acceleration, 30~50% of the accelerated beam was lost by axial oscillation driven with median plane error near $\nu_z=1$ resonance, on the orbit

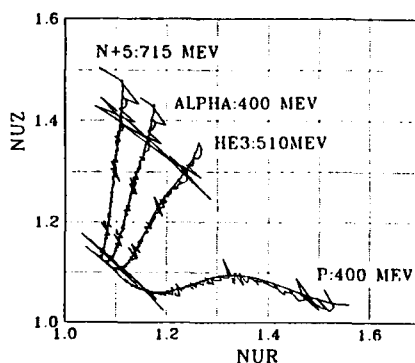


Fig. 6. Comparison between betatron frequencies calculated from the measured field and the designed one.

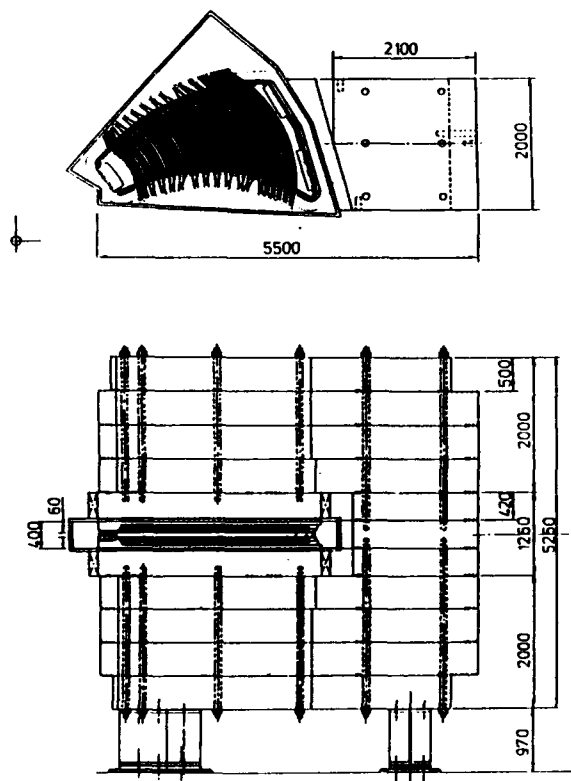


Fig. 7. Structure of the spiral sector magnet.

radius between 3 and 4 m. Three supplementary power supplies are installed to make median plan corrections by supplying different currents for the top and bottom of the auxiliary coil of the main coil on three individual sector magnets.

III. VACUUM SYSTEM

The vacuum chamber of the ring cyclotron consists of six magnet chambers, three acceleration cavity chambers, a flat-topping cavity chamber and two valley chambers as shown in Fig. 3. The gaps between these chamber are sealed by pneumatic expansion seals. These seals are working quite well [5]. The ring cyclotron is evacuated down to 1×10^{-7} Torr by six diffusion pumps with double chevron baffles (2,500ℓ/sec each eq.), three 16 inch cryopumps (6,500ℓ/sec each) with gate valve and six 20 inch cryopumps (10,000ℓ/sec each).

IV. ACCELERATION SYSTEM

Figure 8 and 9 show schematic drawing of the acceleration cavity and the flat-topping cavity. The walls of the cavities are made of stainless steel 50 mm in thickness with water cooled copper lining 5 mm in thickness. The walls can not withstand atmospheric pressure under evacuation, so these walls are supported by the magnet chambers. After full assembly of the ring cyclotron, full power test of the RF system and baking of the cavities were made [9]. The variable frequency acceleration cavity is tuned with a pair of rotatable plates. Figure 10 shows radial voltage distributions of the acceleration cavity and the flat-topping cavity. The beam phase compression factor is about 0.5.

The P.F power of the flat-topping cavity leaks easily to outside of the cavity, for asymmetric setting of the sliding shorts. RF shields of trim coil feed-through were set on the both side of the flat-topping cavity.

Acceleration frequency of the AVF cyclotron, generated by a frequency synthesizer, is used as clock signal of the ring cyclotron RF system. The clock signal is converted to acceleration, flat-topping, buncher, intermediate and various local frequencies. The intermediate frequency is used in phase control and auto tuning servo systems. Digital phase shifters, $0.03^\circ/\text{step}$, are working well on 455 KHz intermediate frequency. Achieved stability of cavity voltage and phase are now 10^{-4} and $\pm 0.1^\circ$, respectively.

A maximum acceleration voltage of 530 keV was achieved. The turn separation for 400 MeV proton acceleration at injection and extraction points are 10 mm and 3 mm, respectively.

improvement of capability on injection and extraction elements were made in 1992. These system is working satisfactory as designed.

VI. AVF CYCLOTRON

The 20° phase acceptance of the ring cyclotron correspond to 7° and 4° for the acceleration frequency of the AVF cyclotron, since the ratio of acceleration frequency of the ring cyclotron to that of the AVF cyclotron is 3 and 5 for proton and alpha acceleration, respectively.

For internal ion source, an internal phase slit [1] and a post-injector beam buncher [9] (energy modulator with energy selector) are used to limit the beam phase width. A new beam phase selector for axial injection mode was developed as shown in Fig. 11. Efficient phase selection was made down to about 3° .

In order to get high quality injection beam for the ring cyclotron, the six dimensional phase space volume of the injection beam is limited by various slits between the ion source and the ring cyclotron. The beam intensity reduction about 10^{-2} in the process is very serious for polarized beam and heavy ion beam. A new high intensity polarized proton and deuteron ion source, a new axial injection system and injector beam line for the polarized ion source and Neomafios will be installed in August 1994.

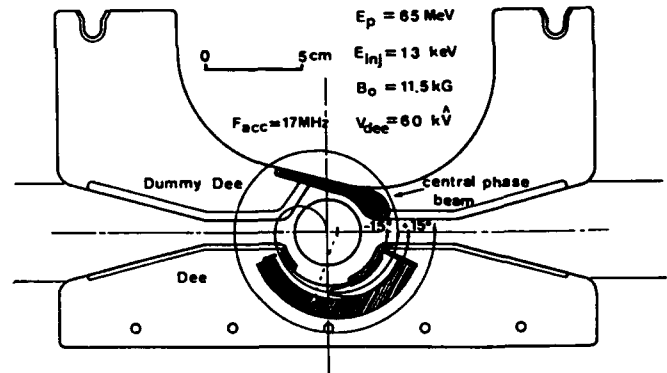


Fig. 11. Beam phase selector for axial injection mode of the AVF cyclotron.

Table 2. Parameters for 400 MeV beam

		Proton	α
Injection	MeV	63.6	86.3
MIC1 ΔB	Gauss	+1730	+1889.3
MIC2 ΔB	Gauss	+550	+551.1
EIC1/EIC2	kV/cm	80	59.1
EEC1/EEC2	kV/cm	70	38
Electrode gap	cm	1	1
MEC1 ΔB	Gauss	-900	-759.3
MEC2 B	kGauss	10	9.187

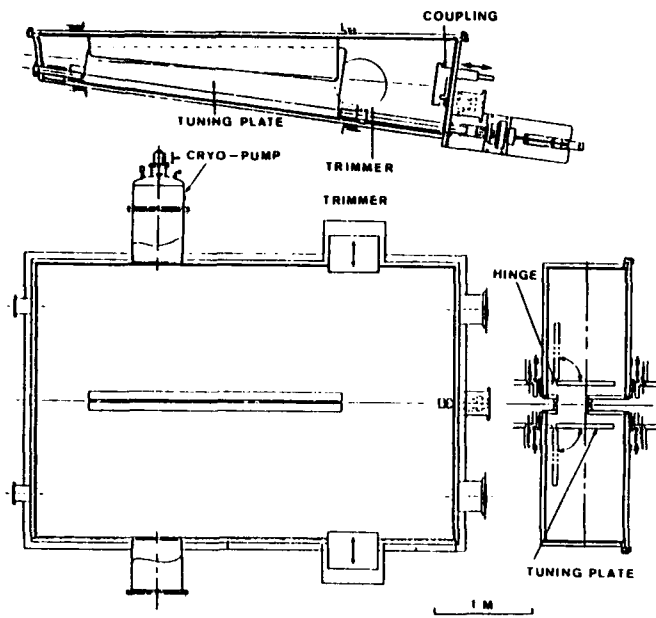


Fig. 8. Schematic drawing of the acceleration cavity.

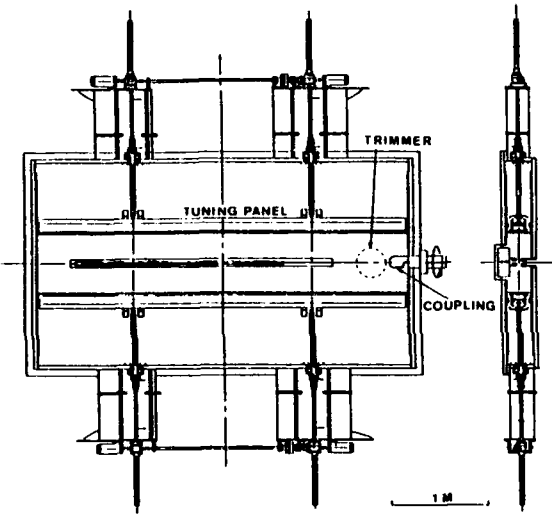


Fig. 9. Schematic drawing of the flat-topping cavity.

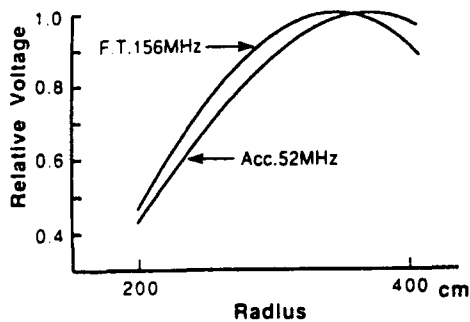


Fig. 10. Voltage distributions of the acceleration cavity and the flat-topping cavity.

V. INJECTION AND EXTRACTION SYSTEM

The maximum designed parameter of the injection and extraction system [6] are shown in Table 2. Various

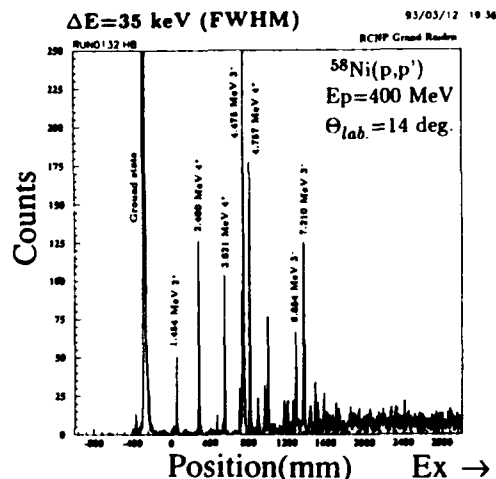
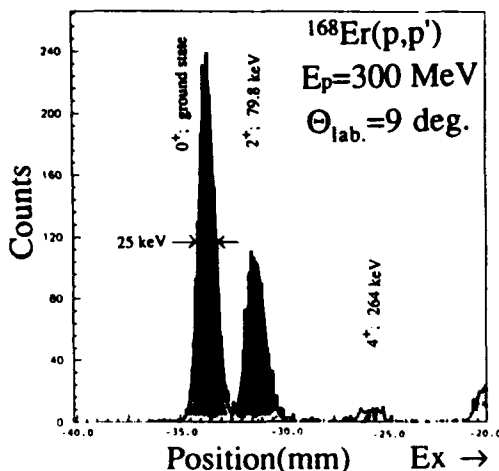


Fig. 12. Obtained Spectra. $^{168}\text{Er}(p,p')$ reaction at $E_p=300$ MeV and $^{58}\text{Ni}(p,p')$ reaction at $E_p=400$ MeV.

VII. BEAM DIAGNOSTIC SYSTEM

The commissioning of the ring cyclotron was made with various kind of beam diagnostic elements [10]. Efforts to get good S/N ratio for weak beam down to 1nA were made. A 30 Hz 5th order (30dB/Oct) low pass filter is used for beam current measurement.

For beam phase measurement, noise-free phase signal amplifier for acceleration frequency was used. 5/3 and 8/5 multiple of the acceleration frequency are used for phase measurement of proton and alpha, respectively. A crystal filter is used in IF amplifier of the phase signal amplifier to reduce noise. The output signals are averaged by a digital oscilloscope to reduce thermal noise. Relative phase between beams can be measured with this phase probe for beam current down to 1nA.

VIII. CONTROL SYSTEM

The old control system of the AVF cyclotron is used without any modification. The new computer control system [11] consist of a central computer (system controller, $\mu\text{VAX3500}$) and four sub-computers (group controller, $\mu\text{VAXII}+3\text{-rt-VAX1000}$). The control functions of the ring cyclotron are distributed to the five computers and many intelligent device-controllers. The new operator console of the ring cyclotron is installed near by the old operator console of the AVF cyclotron.

IX. ACCELERATED BEAMS

Polarized and unpolarized protons, deuterons and alpha particles were accelerated up to the designed maximum energies, 400 MeV, 200 MeV, and 400 MeV respectively. 450 MeV ^3He beam was also accelerated.

The beams are extracted with single turn extraction mode with flat-topping. Beam energy width of 80 keV was achieved for 300 MeV proton. Energy resolution of 25 keV

and 35 keV were obtained with high resolution spectrograph Grand Raiden, as shown in Fig. 12, by using dispersion matching for 300 MeV and 400 MeV proton inelastic scattering spectra, respectively [12]. A very short polarized proton beam pulse of 150ps was achieved for neutron TOF experiment.

X. REFERENCES

- [1] M. Kondo, "Recent Developments at the Osaka RCNP 230-cm Cyclotron and a Proposal for a New Ring Accelerator", IEEE Trans NS-26, 2, 1904-1911.
- [2] I. Miura, et al., "Proposal for Cyclotron Cascade Project", Proc. of the 11th Conf. on Cyc. and Their Appl., Tokyo (Japan) 1986, p.207.
- [3] I. Miura, et al., "A Computer Code FIGER", Proc. of the 4th Symposium on Acc. Science and Technology, RIKEN (Japan) 1982, p. 97, K. Hosono et al., Spiral Sector Magnet of RCNP Ring Cyclotron Project, RCNP Annual Report 1984.
- [4] H. Ikegami, "The RCNP Ring Cyclotron Facilities", Proc. of the 12th Conf. on Cyc. and Their Appl., Berlin (Germany) 1989, p.30.
- [5] A. Shimizu, et al., *ibid.* p.228.
- [6] A. Ando, et al., *ibid.* p.346.
- [7] I. Miura, et al., "Commissioning of the RCNP Ring Cyclotron", Proc. of the 13th Conf. on Cyc. and Their Appl., Vancouver (Canada) 1992, p.3.
- [8] K. Hosono, et al., *ibid.* p. 565.
- [9] T. Saito, et al., *ibid.* p. 538.
- [10] T. Itahashi, et al., *ibid.* p.491.
- [11] T. Yamazaki, et al., *ibid.* p.671.
- [12] M. Fujiwara, et al., RCNP, private communication.

The Fermilab 400-MeV Linac Upgrade

Charles W. Schmidt
Fermi National Accelerator Laboratory*
P.O. Box 500, Batavia, Illinois 60510

Abstract

The Fermilab Linac Upgrade will increase the linac energy from 201 MeV to 401.5 MeV. Seven accelerating modules, composed of 805-MHz side-coupled cells, will accelerate H^- beams from 116.5 to 401.5 MeV. The side-coupled structure (SCS) has been built, tuned, tested to full power, and placed in the linac enclosure along side the operating Linac. All seven accelerating modules, each containing four sections of sixteen cells, have been connected to 12-MW power klystrons and tested to full power for a significant period. The transition section to match the beam from the 201.25-MHz drift-tube linac to the SCS, consisting of a sixteen-cell cavity and a vernier four-cell cavity, has also been tested at full power. A new transport line from the Linac to the Booster synchrotron with a new Booster injection girder is to be installed. Removal of the last four Alvarez linac tanks (116.5 to 201 MeV) and beam-line installation of the Upgrade components is to begin in early June 1993 and should take about 12 weeks. Beam commissioning of the project will follow and normal operation is expected in a short period. In preparation for beam commissioning, studies are being done with the operating linac to characterize the beam at transition and prepare for phase, amplitude and energy measurements to commission the new linac. The past, present and future activities of the 400-MeV Upgrade will be reviewed.

Introduction

The present Fermilab Linac is an Alvarez-type drift-tube (DT) linac consisting of nine cavities operating at a frequency of 201.25 MHz that accelerates H^- ions to 201 MeV. The Linac operates for Booster injection at a maximum rate of 15 pulses-per-sec with a pulse length of 30 μ s and an intensity of 35 mA [1]. At present the Booster intensity is limited to approximately 3×10^{12} protons-per-cycle due to a large space charge tune shift during injection. Increasing the energy to 400 MeV should allow beams of higher brightness or intensity. Preserving this improvement through the following accelerators will give higher production rates for antiprotons, higher brightness and greater luminosity for colliding beams, and higher intensity for fixed-target experiments. The Main

Injector Project is intended to take full advantage of this improvement [2].

To achieve 400 MeV the present linac will be modified by removing the last four cavities and replacing them with 805-MHz side-coupled modules [3-6]. The 200-MeV DT linac will end at 116.5 MeV (Cavity 5) to inject into the side-coupled structure. The first section of the SCS is an 805-MHz transition module for longitudinally matching the beam into the first SCS accelerating module. Seven SCS accelerating modules will take the beam to 401.5 MeV. The new structure, which is 63.7-m long, about 3 m shorter than the old cavities, fits within the present enclosure allowing for a new transport line to the Booster. The SCS therefore operates at approximately three times the average accelerating gradient of the older linac.

The SCS is composed of seven modules, each assembled from four 16-cell sections and three bridge-couplers. Power for each module is fed to the center coupler. Each module is powered by a 12-MW, 805-MHz klystron. The nominal peak power for each module with 35 mA of beam is about 10 MW. The new structure is designed to accelerate up to 50 mA of beam.

General Design

Considerations for the project began in 1986 following studies and realization that the Booster was limited at injection and could be improved by increasing the Linac energy [2]. Several linac structures were reviewed and doubling of the Linac energy to give a significant improvement in the Booster appeared possible.

Two structures were carefully investigated through studies and by building models that were tested to high rf power. One, the disk-and-washer was considered for its efficiency and strong coupling however its mode structure and construction appeared uncomfortably complex [7,8]. The other, the side-coupled structure, appeared easier to build, better understood, and has a proven history as demonstrated at Los Alamos. The SCS was chosen.

The Project began in earnest in 1989 with approval from the DOE. Refinements of the basic design parameters were done using the SCS to achieve the desired energy within constraints of the present tunnel length. By dividing the accelerator into seven accelerating modules, each with four sections of sixteen cells, a solution was found that gave acceptable surface fields, divided the accelerator into sections that minimized the mechanical variables, gave

* Operated by the Universities Research Association, Inc. under contract No. DE-AC02-76CH03000 with the U.S. Department of Energy.

approximately equal power to each module, and achieved an acceptable transverse focusing condition (see Table 1) [9]. Studies on early prototype cavities gave an indication that a spark rate of one per thousand for the total structure could possibly be achieved [10] corresponding to an acceptable beam loss of 0.1%. Refinement of the nose-cone shape led to a significant reduction in the maximum surface field and surface area with little effect on the shunt impedance. This significantly reduced the sparking rate.

Table 1. General Design Parameters

Initial kinetic energy	($\beta=0.454$)	116.54	MeV
Final kinetic energy	($\beta=0.714$)	401.46	MeV
Beam current, design		50	mA
Repetition rate		15	Hz
Beam pulse length, design		<100	μ s
Length, with transition section		63.678	m
Transition cavities		2	sections
main section cells		16	cells
vernier section cells		4	cells
Accelerating cavities		7	modules
number of sections/module		4	sections
number of cells/section		16	cells
total accelerating cells (7x4x16)		448	cells
Bridge coupler length between sections		$3\beta\lambda/2$	
Module separation		$3\beta\lambda/2$	
Cavity bore radius		1.5	cm
Frequency		805.0	MHz
Accelerating phase		-32	deg
Average axial field		8.07-7.09	MV/m
Maximum surface field		36.8	MV/m
Kilpatrick number		1.42	
(1=26 MV/m @ 805 MHz)			
RF power/module, typical		<12	MW
copper losses		7.2	MW
beam power (50 mA beam)		2.0	MW
control and reserve		2.8	MW
Transverse focusing	FODO		
phase advance/FODO cell, average	79		deg
Quadrupole magnetic length		8.0	cm
poletip bore radius		2.0	cm
poletip field		4.6	kG

Mechanical Design

A mechanical design was chosen that would allow machining of cell segments from class 1 OFHC copper using computer controlled machines to give close tolerance and optimum surface finish. The copper was obtained from Hitachi Industries. The segments were assembled in successive steps by furnace brazing to form a section of sixteen cells (see Figure 1) [11].

All cells are identical within a section with the cell length corresponding to the average velocity for the section. The cell dimensions were computed using

the SUPERFISH code and tested for frequency using aluminum models. The modeling allowed for small corrections that could be fed into the final dimensions for the copper cells [12]. The design proved to be sufficiently accurate and reproducible that the final sections and modules required minimal tuning in their final stages [13,14].

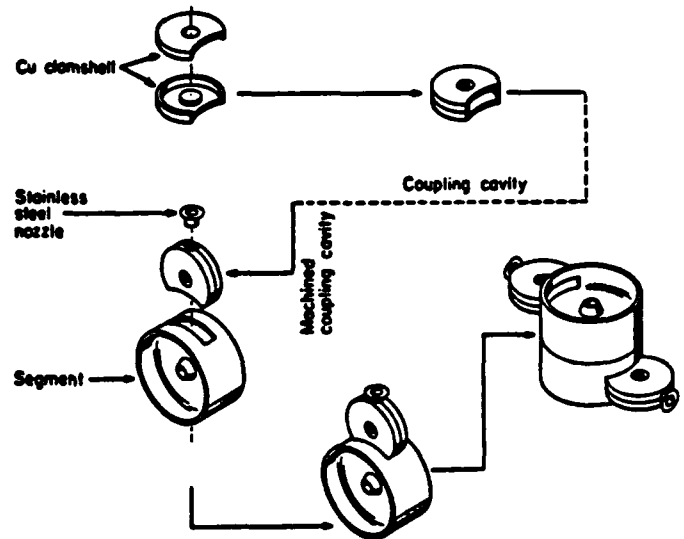


Figure 1. Side-coupled cavity construction.

The section ends and the bridge coupling cavities required special attention because of their different geometry and unique coupling flange. They require more tuning and specialized machining to arrive at the correct frequency.

Radio-Frequency Systems

Each of seven modules of the Linac Upgrade requires a 12-MW, 805-MHz rf system to power the cavities and accelerate beam. A 12-MW klystron is the center piece of each system powered by a charging supply and an SCR-switched PFN modulator through a 20:1 step-up transformer. The maximum klystron voltage is 180 kV at 15-Hz rate and a pulse length of 125 μ s. The pulsed current is 150 A. The klystron was developed by Litton Electron Devices (L-5859 klystron) for this project.

The rf output is controlled by the input rf drive to the klystron. With a gain of ~50 dB the input power is ~100 W from the low-level system. The low-level system, a VXI based system, monitors the module amplitude and phase to maintain set conditions for accelerating beam. Besides standard feed-back from the modules, learning programs using the error signal are used to improve the pulse wave-form [15].

The transition sections and a "debuncher" [16], an energy corrector in the transport line to the Booster, are powered by three smaller commercial 200-kW klystrons from Varian Associates.

Computer Controls

A new control system was installed for the Fermilab Linac and the Linac Upgrade. This control system was implemented for the Linac Upgrade and installed for the operating Linac in early 1992. It has been a very useful system. The system uses a Token-Ring network to interconnect several VMEbus crates (Local Stations) to each other and through a bridge to the central accelerator control system. The VME crates contain hardware to communicate with the network and control the Linac at 15-Hz rate. Local analog, digital, binary and timing control with the accelerator devices is accomplished by a "smart rack monitor" (SRM) containing a MC68332 microcontroller and interfaces to the VME crates via ARCnet links [17-19].

In addition to communicating with the Main Control Room consoles the Linac Local Stations support TCP/IP communications on Internet. This capability is used to communicate with Macintosh consoles located at the klystron control racks as well as with Macintosh and Sun workstations located in laboratories and offices of Linac personnel.

Diagnostics

The Linac Upgrade will incorporate several diagnostic devices to give the needed beam information for commissioning and operating the accelerator [20]. In the commissioning phase it is necessary to set the proper condition for transition of the beam from the 201-MHz DT linac to the 805-MHz SC linac, to set the correct amplitude and phase of each accelerating module, to center the beam in the aperture, and to measure the longitudinal and transverse properties of the beam especially at transition and output.

In the transition region there will be three horizontal and vertical wire scanners for measuring the emittance and Twiss parameters of the beam from tank 5 of the DT linac. This section will also contain two bunch length monitors of the secondary electron emission type [21] for measuring the longitudinal extent and density of the beam before and after the transition rotation.

In the accelerator sections the open spaces are only $3\beta\lambda/2$ between sections and modules or 14 cm to 40 cm from first to last section. In each section there is a quadrupole of 8.6-cm length and between modules there is also a vacuum valve. Because of the closeness, the diagnostic elements have been selected and designed to fit into the remaining space. An rf beam position monitor (BPM) is located within each quadrupole to give the horizontal and vertical beam centroid. Only alternate planes in which the beam is large will be used initially. The BPM's together with strategically located horizontal and vertical trim steering magnets will be used to center the beam. Where possible, there

are beam current toroids and beam wire scanners (about one per module). Similar devices will be located in the 400-MeV diagnostic line and the transport line to the Booster.

Resistive wall-current monitors will be used for measuring the relative beam phase for establishing the rf amplitude and phase in each module. The correct rf setting for a module can be determined by scanning the beam bunch phase some distance downstream of a module relative to a reference signal as the module phase is changed. Comparing the scanned signal for a full cycle to the theoretical curve will provide the rf phase and amplitude for the module. This phase-scan match method is similar to the delta-t method but somewhat simpler to implement [22-24].

Present Status

Presently all the accelerating modules have been built, tuned [25,26] and tested in a test concrete cave to shield for X-rays using the prototype klystron. They were run to full power for an extended period until the spark rate was acceptable [27]. The spark rate decreased to acceptable levels with approximately 4×10^6 pulses (<1 week).

Early last year the transition section and all seven accelerating modules were placed in the Linac enclosure along side the DT tanks they will replace. They were connected for vacuum, water cooling and control, and rf power and monitoring. As klystrons became available they were installed, and with the modules, operated at full power. All seven klystron rf stations and their respective modules have since been powered to full field, without beam, for an extended period [28]. This has given an opportunity to measure the characteristics of the rf systems, study the spark rate, and find early component failures and problems.

In general the system has performed well. Initial difficulties with the prototype klystron have not been seen in the final production klystrons. Of eight production klystrons only one had a problem due to poor vacuum and has been returned. It did operate at full power and could have continued operating. The other klystrons have all gone to full power in short time (~1 hour with experience) and continue to operate well. The klystrons now have a total of 25,000-hours operation with the longest being 7,000 hours (375×10^6 pulses). No production klystron has failed in service.

Problems have occurred with the charging transformers for the rf modulator power supplies. These are due to design and construction errors and will be repaired before the linac goes into commissioning.

The smaller klystrons for the transition cavities have also been installed and operated.

For the Upgrade the computer control system is fully operational and the operations group monitors and controls the Upgrade rf systems from the main

control room.

Installation and Commissioning

Commissioning of the Upgrade is to begin late this summer following installation of the beam line components and required approval. As a minimum, the installation will require removing the last four tanks of the DT linac and associated equipment, moving the side-coupled modules from their present position in the enclosure to their final beam line location, installing the quadrupoles, diagnostics and beam control components, aligning the modules and quadrupoles, and reconnecting or connecting all components. At the same time the Booster group will remove and replace the transport line and Booster injection girder to handle 400-MeV beams. All of this equipment has or will be tested without beam as fully as possible before installation. It is anticipated that installation will take ~12 weeks.

Before and during installation the Laboratory will conduct a DOE required "Accelerator Readiness Review" for the Upgrade project to obtain DOE approval for commissioning and later for routine operation [29].

Once the new accelerating structure, transport line and all necessary equipment are in place and fully operational, and all approvals are given, commissioning of the Upgrade with beam will commence. Initially, the beam current, pulse length and repetition rate will be set to a minimum but sufficient to observe beam. This will minimize the risk of damage and activation to the beam-line components during initial adjustments. Radiation safety protection to personnel areas outside the accelerator enclosure will be maintained by radiation monitors that will inhibit beam when indicated or by known sufficient passive shielding.

With low intensity, the quadrupoles will be set and adjusted to transport beam through the structure and to the dump. Beam current toroids, loss monitors, wire scanners, rf beam position monitors, and trim steering magnets will also be used to monitor and adjust the beam. With beam transported through the structure and to the dump, the output of DT tank 5 and the transition section can be studied and adjusted. Once an acceptable match is obtained the modules of the accelerating structure can be successively turned on and tuned. For tuning the module rf parameters a variation of the Los Alamos delta-t procedure, which has been termed the phase-scan match method, will be used. The phase-scan match method should be easier and sufficient for achieving our initial objective of accelerated beam. Beam time-of-flight and spectrometer momentum measurements will be used for necessary confirmation.

With low-intensity 400-MeV beam achieved, more

detailed studies can be done to improve the matching, steering and focus of the beam, improve the rf parameter settings, and slowly raise the intensity and duty-factor. During this time the Booster 400-MeV transport can be studied and tuned, and beam can be injected into the Booster.

Once sufficient 400-MeV beam is established to the dump and Booster transport line, the shielding at the high energy end of the linac enclosure can be reassessed for the new beam energy.

The commissioning period is anticipated to take about 5-6 weeks. Following commissioning the success of the program will be reviewed to obtain DOE approval for normal operation. The timely success of the installation and commissioning programs is important to the Laboratory's schedule and physics program. The second half of the present colliding beams (protons on antiprotons) program is to resume in the fall of 1993. It is obvious that the Linac Upgrade must be in operation for this to happen. Also, the increased intensity will be significant in reaching the antiproton production rate and the luminosity to carry out the physics program for this run.

Acknowledgments

As with any major project there are too many people to list individually, at least without missing some important contributors. I, and I am sure my close colleagues, express our appreciation to the many people at Fermilab and elsewhere that have worked on this effort and will see it through to completion.

References

- [1] L. J. Allen, Arlene J. Lennox and C. W. Schmidt, "Operational Experience with the Fermilab Linac", Proc. 1992 Linear Accel. Conf., Ottawa, (Chalk River-AECL-10728), p. 82.
- [2] Stephen D. Holmes, "Achieving High Luminosity in the Fermilab Tevatron", Proc. 1991 IEEE Part. Accel. Conf., San Francisco, (IEEE 91CH3038-7), p. 2896.
- [3] D. E. Young and R. J. Noble, "400-MeV Upgrade for the Fermilab Linac", Proc. 14th Int. Conf. on High Energy Accelerators, Tsukuba, Japan, (Aug., 1989). *Particle Accelerators*, 1990, Vol. 26, p. 205.
- [4] J. A. MacLachlan, "400 MeV Upgrade for the Fermilab Linac", Proc. 1989 IEEE Part. Accel. Conf., Chicago, (IEEE 89CH2669-0), p. 950.
- [5] Robert J. Noble, "The Fermilab Linac Upgrade", Proc. 1990 Linear Accel. Conf., Albuquerque, (Los Alamos, LA-12004-C), p. 26.
- [6] Robert J. Noble, "The 400 MeV Linac Upgrade at Fermilab", Proc. 1992 Linear Accel. Conf., Ottawa, (Chalk River-AECL-10728), p. 565.
- [7] A. Moretti *et al.*, "An 805 MHz Disk and Washer

- Structure for the Fermilab Linac Upgrade", Proc. 1988 Linear Accel. Conf., Newport News, VI, (CEBAF-Report-89-001), p. 143.
- [8] D. E. Young *et al.*, "An 805 MHz Disk and Washer Accelerating Structure with Coaxial Coupler for the Fermilab Upgrade", Proc. 14th Int. Conf. on High Energy Accelerators, Tsukuba, Japan, (Aug., 1989). *Particle Accelerators*, 1990, Vol. 26, p. 211.
 - [9] L. Oleksiuk, J. MacLachlan and F. Mills, "The Fermilab Upgrade Linac: Dynamics Design Process", Proc. 1990 Linear Accel. Conf., Albuquerque, (Los Alamos, LA-12004-C), p. 335.
 - [10] T. Kroc and A. Moretti, "Conditioning of High Gradient H⁻ Accelerating Cavities", Proc. 1990 Linear Accel. Conf., Albuquerque, (Los Alamos, LA-12004-C), p. 102.
 - [11] Michael P. May *et al.*, "Mechanical Construction of the 805 MHz Side Couple Cavities for the Fermilab Linac Upgrade", Proc. 1990 Linear Accel. Conf., Albuquerque, (Los Alamos, LA-12004-C), p. 105.
 - [12] Thomas G. Jurgens *et al.*, "The Determination of the 805 MHz Side Coupled Cavity Dimensions for the Fermilab Linac Upgrade", Proc. 1990 Linear Accel. Conf., Albuquerque, (Los Alamos, LA-12004-C), p. 108.
 - [13] Harold W. Miller *et al.*, "Tuning Methods for the 805 MHz Side-Coupled Cavities in the Fermilab Linac Upgrade", Proc. 1990 Linear Accel. Conf., Albuquerque, (Los Alamos, LA-12004-C), p. 111.
 - [14] Peter Steven Prieto *et al.*, "Side Coupled Accelerating Structure Automated Measurement System", Proc. 1990 Linear Accel. Conf., Albuquerque, (Los Alamos, LA-12004-C), p. 114.
 - [15] R. Pasquinelli and B. Chase, "VXI Based Low Level RF System for Fermilab Linac Upgrade", this conference.
 - [16] J. A. MacLachlan *et al.*, "Feed-Forward Compensation for Transient Beam Loading of the 805 MHz Debuncher for the Fermilab Linac Upgrade", Proc. 1990 Linear Accel. Conf., Albuquerque, (Los Alamos, LA-12004-C), p. 303.
 - [17] Elliott S. McCrory, Robert W. Goodwin and Michael F. Shea, "Upgrading the Fermilab Linac Local Control System", Proc. 1990 Linear Accel. Conf., Albuquerque, (Los Alamos, LA-12004-C), p. 474.
 - [18] S. Shutirbu *et al.*, "Smart Rack Monitor for the Linac Control System", Proc. 1991 IEEE Part. Accel. Conf., San Francisco, (IEEE 91CH3038-7), p. 1484.
 - [19] M. F. Shea *et al.*, "ARCNET as a Field Bus in the Fermilab Linac Control System", Proc. ICALEPCS, Tsukuba, Japan, (Nov. 1991) p. 291.
 - [20] Elliott S. McCrory, Glenn Lee and Robert C. Webber, "Diagnostics for the 400 MeV FNAL Linac", Proc. 1990 Linear Accel. Conf., Albuquerque, (Los Alamos, LA-12004-C), p. 456.
 - [21] Elliott S. McCrory, Charles W. Schmidt and A. V. Feschenko, "Use of an INR-Style Bunch-Length Detector in the Fermilab Linac", Proc. 1992 Linear Accel. Conf., Ottawa, (Chalk River-AECL-10728), p. 662.
 - [22] T. L. Owens *et al.*, "Tuning Procedures for the Fermilab Linac Upgrade", this conference.
 - [23] Thomas L. Owens and Elliott S. McCrory, "The Delta-T Tuneup Procedure for the Fermilab Linac", Proc. 1990 Linear Accel. Conf., Albuquerque, (Los Alamos, LA-12004-C), p. 721.
 - [24] M. B. Popovic *et al.*, "Time-of-Flight Measurements of Absolute Beam Energy in the Fermilab Linac", this conference.
 - [25] Zubao Qian *et al.*, "Final Module Tuning of the 805 MHz Side-Coupled Cavities for the Fermilab Linac Upgrade", Proc. 1992 Linear Accel. Conf., Ottawa, (Chalk River-AECL-10728), p. 422.
 - [26] Harold W. Miller *et al.*, "Tuning Summary for the 805 MHz Side-Coupled Cavities in the Fermilab Linac Upgrade", Proc. 1992 Linear Accel. Conf., Ottawa, (Chalk River-AECL-10728), p. 419.
 - [27] T. Kroc, A. Moretti and M. Popovic, "Fermilab Linac Upgrade - Module Conditioning Results", Proc. 1992 Linear Accel. Conf., Ottawa, (Chalk River-AECL-10728), p. 187.
 - [28] Q. Kems *et al.*, "Performance of Litton 805 MHz, 12 MW Klystron", this conference.
 - [29] DOE Order 5480.25.

Use of the Holifield Facility 25-MV Tandem Accelerator in the Oak Ridge Radioactive Ion Beam Project*

C. M. Jones, R. C. Juras, M. J. Meigs, and D. K. Olsen
Oak Ridge National Laboratory
P. O. Box 2008, Oak Ridge, TN 37831-6368

Abstract

The absence of time structure and the excellent beam and beam transport properties of tandem electrostatic accelerators make them an attractive choice for the acceleration of a large class of radioactive ion species produced with the ISOL technique. In this paper, considerations on the use of the Holifield facility 25-MV tandem accelerator in the ORNL Radioactive Ion Beam Facility now under construction will be presented. Preliminary beam parameter measurements which suggest that the 25-MV tandem accelerator can be used as an effective separator of isobaric contaminant beams will also be presented and discussed.

I. INTRODUCTION

The ORNL project [1,2] to produce medium-intensity, proton-rich, radioactive ion beams (RIBs) for astrophysics, nuclear physics, and applied research with the Holifield Heavy Ion Research Facility (HHIRF) accelerators is now in progress. Radioactive atoms will be produced by fusion reactions in an Isotope Separator On-Line (ISOL)-type target-ion source assembly using intense light ion beams from the Oak Ridge Isochronous Cyclotron. The radioactive atoms will be converted to negative ions either directly in one of several types of negative ion sources or by charge exchange following positive ionization. After acceleration to approximately 300 keV from a high-voltage platform, these negative ions will be injected into the HHIRF 25-MV tandem accelerator [3-5] for acceleration to higher energies. Beams up to mass 76 can be accelerated to energies greater than 5 MeV/nucleon. For some radioactive beams, intensities greater than 1 pA are possible.

While use of the existing HHIRF tandem accelerator was clearly dictated by its availability, it is also clear that tandem accelerators possess a number of attributes which make them an attractive choice for this type of application. The most important of these are a large phase space acceptance for the injected beam, good transmission efficiency, the absence of time structure, simplicity and reliability, the ability to accelerate singly charged injected beams with low initial velocity, and excellent accelerated beam quality. The latter property is

especially important because of its implications in regard to the use of radioactive beams in the research program and because high-quality accelerated beams create the potential for using the accelerator's energy-analyzing magnet as an isobar separator. The potential disadvantage of the tandem accelerator is the requirement to produce and inject beams of negative ions. In the remainder of this paper, some of these attributes as they apply to the HHIRF tandem accelerator will be discussed along with some more general considerations on the use of tandem accelerators.

II. INJECTED BEAM REQUIREMENTS

Two important injected beam parameters are minimum energy and maximum emittance. In the case of the HHIRF tandem accelerator, both of these parameters are strongly influenced by the fact that the tandem accelerator is equipped with a quadrupole lens in the low-energy acceleration tube at a position which is approximately one-third of the distance between the tube entrance and exit. With the use of this lens, the low-energy acceleration tube normalized acceptance is insensitive to injection energy if the injection system can provide a beam waist at the entrance of the low-energy acceleration tube which is approximately equal in diameter to the beam waist at the terminal stripper [6]. In practice, this condition cannot be satisfied over a wide range of injection energies because only one lens was provided between the image waist of the mass-analyzing magnet and the entrance of the low-energy acceleration tube [7]. This lens was positioned to provide good matching for beams of approximately 300 keV and cannot be easily moved because of its location with respect to the pressure vessel boundary.

The effect of lower injection energies was investigated by a series of measurements of overall optimized transmission efficiency for seven beams, typical of those expected for the RIB facility, at injection energies of 100, 200, and 300 keV. The essential result of these measurements is that transmission efficiency was reduced at 100 keV, but not at 200 keV, indicating that the tandem injection energy can be lowered to 200 keV without a significant effect on transmission efficiency.

Using the techniques discussed by Larson and Jones [6], it is possible to estimate the phase space

*Research sponsored by the U.S. Department of Energy under contract No. DE-AC05-84OR21400 with Martin Marietta Energy Systems, Inc.

"The submitted manuscript has been authored by a contractor of the U.S. Government under contract No. DE-AC05-84OR21400. Accordingly, the U.S. Government retains a nonexclusive, royalty-free license to publish or reproduce the published form of this contribution, or allow others to do so, for U.S. Government purposes."

acceptance of the low-energy acceleration tube as a function of terminal potential. With the assumption of a 9.5-mm-diameter terminal stripper and operation of the full, unshorted column, the calculated normalized phase space acceptance varies between 4.1π mm mrad $\text{MeV}^{1/2}$ at a terminal potential of 1 MV and 17.6π mm mrad $\text{MeV}^{1/2}$ at a terminal potential of 25 MV. These values of acceptance may be compared to the typical value of 8π mm mrad $\text{MeV}^{1/2}$ (80% fraction) measured for sources now being used with the tandem accelerator [8] and to the value of approximately 2π mm mrad $\text{MeV}^{1/2}$ estimated for the ISOLDE-type source planned for initial use with the RIB facility [9].

It should be noted that operation of the tandem accelerator with an unshorted column at low terminal potentials will require installation of a resistor-based voltage grading system [10]. It should also be noted that a new terminal potential stabilizer system developed at ORNL allows stable operation of the tandem accelerator using only a generating voltmeter to monitor the terminal potential. Since, in this mode, the beam is not used for terminal potential stabilization, there is no minimum injected beam intensity requirement for the tandem accelerator.

III. ACCELERATED BEAM ENERGY AND BEAM TRANSMISSION EFFICIENCY

Beam transmission efficiency for the tandem accelerator is the product of two factors: The first factor is a beam loss factor which describes transmission losses. This factor, which has been empirically determined from operating experience, depends on ion mass and the number and type of strippers, but is approximately independent of charge state. The second factor is the product of charge state fractions in the various strippers which may be employed.

For use as a RIB accelerator, it is assumed that (1) the tandem accelerator will be used only with a terminal stripper, (2) charge state distribution functions are accurately predicted by the semi-empirical parameterization of Sayer [11], and (3) use of a planned resistor-based voltage grading system [10] will enable operation at terminal potentials up to 26 MV. Maximum accelerated beam energies and corresponding transmission efficiencies, estimated with these assumptions, are shown in Fig. 1. With terminal gas stripping, beams of mass 52 can be accelerated to 5 MeV/amu with a total efficiency of 20%. With terminal foil stripping, beams of mass 76 can be accelerated to 5 MeV/amu with a total efficiency of 8%. In both cases, beams of lower masses can be accelerated to higher energies with total efficiencies approaching 50%.

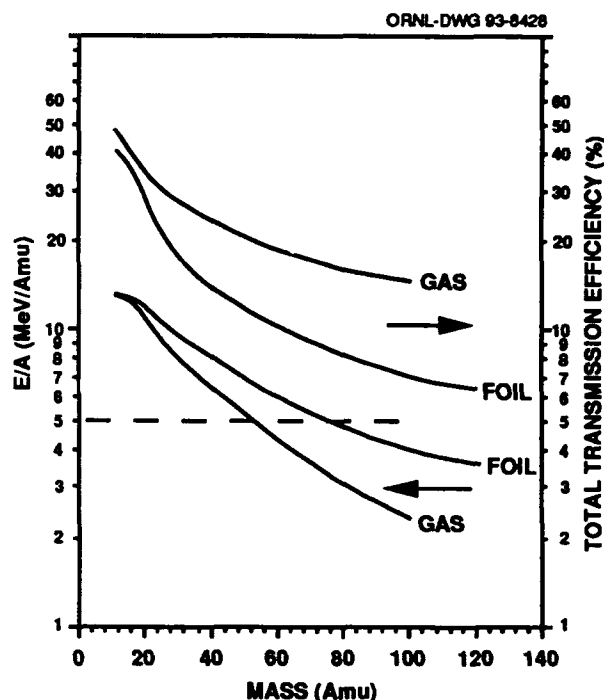


Fig. 1. Maximum beam energy per nucleon and total transmission efficiency of the most probable charge state for the tandem accelerator operated with gas and foil stripping with the terminal potential at 26 MV.

IV. ACCELERATED BEAM EMITTANCE AND USE OF THE ENERGY-ANALYZING MAGNET AS AN ISOBAR SEPARATOR

The high quality of tandem accelerator beams suggests the possibility of using the energy-analyzing magnet as an isobar separator. In the simplest mode, the accelerator would be operated using a generating voltmeter for terminal potential stabilization and ions of differing mass would be separated at the image plane of the energy-analyzing magnet, which, in the case of the HHIRF tandem accelerator, is a 90° double-focusing, $n = 0$ magnet with mass and energy dispersion = 3.35 m. In detail, there are several questions to be addressed: (1) What is the intrinsic energy spread of the beam; (2) What is the energy stability of the beam when operating with generating voltmeter stabilization; and (3) What is the emittance of the accelerated beam.

To address these questions, a series of measurements were made with ^{16}O , ^{32}S , and ^{58}Ni beams at energies which are typical of those expected for the new RIB facility. The essential results of these measurements may be summarized as follows:

- The apparent collective beam motion in the image-bending plane has a maximum amplitude of about 0.5 mm peak-to-peak with a dominant frequency of 2.3 Hz. This apparent collective motion appears to have at least two components:

1. A component which appears only in the image-bending plane and is thought to be due to tandem terminal voltage fluctuations.
2. A component which appears in both the object and image planes and is thought to be either an artifact of the measurement technique or real beam motion resulting from ion-optic component power-supply fluctuations.

Contributions of this apparent motion to beam size measurements were reduced by an averaging technique.

- Beam emittance for a 90% beam fraction is typically 0.3-0.5 π mm mrad for gas stripping and 1.0 π mm mrad for foil stripping.
- Beam widths for a 90% beam fraction in the image-bending plane are typically 0.5 to 1.0 mm for gas stripping and 1.4 mm for foil stripping.
- With the addition of a quadrupole lens upstream of the energy-analyzing magnet, beam widths for a 90% beam fraction in the range 0.2 to 0.3 mm are thought to be achievable with gas stripping. The corresponding mass resolution would be 1 part in 11,000 to 16,500. With a full-width-half-maximum criterion, the corresponding mass resolution would be 1 part in 16,000 to 24,000.
- More work is required to estimate achievable beam widths with foil stripping.

V. DISCUSSION

Without further modification, the HHIRF tandem accelerator can serve as an excellent RIB accelerator. Its acceptance and minimum injected beam energy requirements are well matched to the sources planned for the ORNL RIB facility; it has good final energy and transmission properties; and it produces high-energy accelerated beams with low emittance and energy spread. With a full-width-half-maximum criterion for mass resolution, the accelerator, as now configured, can provide mass resolutions of the order of 1 part in 6000 for terminal gas stripping and 1 part in 3000 for terminal foil stripping. With the addition of a quadrupole lens upstream of the energy-analyzing magnet, it is believed that the mass resolution with terminal gas stripping could be improved to the order of 1 part in 20,000. No reduction in beam intensity is required to achieve these resolution values.

The question can be asked as to whether other, smaller tandem accelerators should also be considered for use as radioactive ion beam accelerators. We believe the answer is yes, especially if used in the terminal gas stripping mode. While smaller tandem accelerators will have lower accelerated beam energies, their parameters will, in other respects, be similar or even more favorable than the HHIRF accelerator because acceptance and

transmission efficiency will, in general, improve as the length of the acceleration tubes is reduced [6]. The large acceptance and low injection energy requirements of tandem accelerators used in this application have recently assumed greater significance in the light of contributions by Shepard [12] and Talbert [13] who note that viable designs for the first stage of the ISL benchmark radioactive ion beam accelerator [14] capable of accelerating low-velocity, singly charged, high-mass ions have not yet been developed.

VI. REFERENCES

- [1] "A Proposal for Physics with Exotic Beams at the Holifield Heavy Ion Research Facility," eds. J. D. Garrett and D. K. Olsen (ORNL, February 1991).
- [2] "The ORNL Radioactive Ion Beam Project," D. K. Olsen, et al., Proc. of the Workshop on the Production and Use of Intense Radioactive Beams at the Isospin Laboratory, Oak Ridge, TN, Oct. 7-10, 1992, to be published.
- [3] C. M. Jones, et al., Nucl. Instr. and Meth. **A268**, 308 (1988).
- [4] J. K. Bair, et al., IEEE Trans. Nucl. Sci. **NS-22**, 1655 (1975).
- [5] C. M. Jones, Proc. 3rd Int. Conf. on Electrostatic Accelerator Technology, Oak Ridge, TN (Apr. 1981) p. 23.
- [6] J. D. Larson and C. M. Jones, Nucl. Instr. and Meth. **140**, 489 (1977).
- [7] W. T. Milner, et al., IEEE Trans. Nucl. Sci. **NS-22** (3), 1697 (1975).
- [8] G. D. Alton and J. W. McConnell, Nucl. Instr. and Meth. **A268**, 445 (1988).
- [9] G. D. Alton, et al., Nucl. Instr. and Meth. **A328**, 325 (1993).
- [10] D. L. Haynes, et al., Nucl. Instr. and Meth. **A320**, 400 (1992).
- [11] R. O. Sayer, Revue Phys. Appl. **12**, 1543 (1977).
- [12] K. W. Shepard, "Some Aspects of Linacs as Applied to the ISL Benchmark Facility," Proc. of the Workshop on the Production and Use of Intense Radioactive Beams at the Isospin Laboratory, Oak Ridge, TN, Oct. 7-10, 1992, to be published.
- [13] W. L. Talbert, "Considerations of the Low-Velocity Stage of a Radioactive Beams Accelerator," Ibid.
- [14] "The IsoSpin Laboratory (ISL) - Research Opportunities with Radioactive Nuclear Beams," North American Steering Committee for the IsoSpin Laboratory, Los Alamos report LALP 91-51.

Realistic Modeling of Radiation Transmission Inspection Systems*

Kenneth. E. Sale, Lawrence Livermore National Laboratory

L-41, P.O. Box 808

Livermore, CA 94550, USA

Abstract

We have applied Monte Carlo particle transport methods to assess a proposed neutron transmission inspection system for checked luggage. The geometry of the system and the time, energy and angle dependence of the source have been modeled in detail. A pulsed deuteron beam incident on a thick Be target generates a neutron pulse with a very broad energy spectrum which is detected after passage through the luggage item by a plastic scintillator detector operating in current mode (as opposed to pulse counting mode). The neutron transmission as a function of time information is used to infer the densities of hydrogen, carbon, oxygen and nitrogen in the volume sampled. The measured elemental densities can be compared to signatures for explosives or other contraband. By using such computational modeling it is possible to optimize many aspects of the design of an inspection system without costly and time consuming prototyping experiments or to determine that a proposed scheme will not work. The methods applied here can be used to evaluate neutron or photon schemes based on transmission, scattering or reaction techniques.

I. Introduction

Detection of hidden explosives and other contraband materials is a high priority in several branches of the government and civilian organizations. Examples of desired detection capabilities include sub-kilogram quantities of high explosive material in checked or carry-on airline luggage, illicit drugs in cargo containers, or a nuclear warhead entering or leaving the U.S. Other tasks in which nuclear interrogation methods may be of use include detection of land mines and the determination of whether a piece of ordnance contains a chemical warfare agent or only ordinary high explosives. Several nuclear physics based methods for detecting contraband have been proposed [1].

The technical problems that must be overcome to implement any of the proposed nuclear-based detection and identification schemes are formidable. Here only the detection of high explosives in checked airline luggage will be considered.

*Work performed under the auspices of the U. S. Department of Energy by the Lawrence Livermore National Laboratory under Contract W-7405-Eng-48

II. The Proposed Method

The detection scheme that is investigated here is based on fast neutron transmission. It, along with several other nuclear-based schemes are reviewed in reference [1]. A schematic view of the set-up that has been modeled is shown in Figure 1. A deuteron beam of about 5 MeV energy is incident on a Be target that is thick enough to stop it. A strongly forward peaked neutron beam with a wide energy range (0 to ~8 MeV) impinges on the item to be inspected. A neutron detector on the opposite side of the item detects the neutrons that are transmitted. A view of the system, generated by COG, is shown in Figure 1. The detector is a 0.5" thick piece of BC-401 scintillator in a boron loaded epoxy resin housing. The distance from the source to the detector is four meters and the suitcase is in the middle. Neutron energy can be inferred from the time-of-flight from the source to the detector. To identify the contents of the item it should be sufficient to infer the C, N and O densities. The neutron scattering cross sections for these elements have several strong narrow structures in the relevant energy range which can be used as signatures (the cross sections are shown in Figure 3). In a typical luggage item incident neutrons will be strongly scattered. Since the detector signal will be due to both transmitted neutrons and neutrons that have undergone one or more scatterings the detector signal is not simply the neutron source intensity times the transmission factor at the appropriate energy. One conclusion from the modeling that has been done is that the signal at the detector is larger with the inspected item in place than without it. This interference effect of neutrons arriving at the wrong time will make the interpretation of the measured signals extremely challenging. The inspection rate requirements for the system preclude the use of a neutron detector in the pulse counting mode. A source pulse with a Gaussian shape and a FWHM of 1 nS and a detector impulse response with an exponential fall with a time constant of 1 nS have been used in calculating the predicted signals.

III. Results

The Monte-Carlo coupled neutron-photon transport code COG [2] was used to model this system. As a first step toward understanding the functioning of the system very simple cases were simulated, namely a "suitcase" that was a solid block of a single material.

The geometry description part of the code is fully capable of handling a realistic, complicated luggage model. The materials studied were carbon, nitrogen, oxygen (all at a density of 2.25 g/cc) and the high explosive LXO40 at normal density. Figure 2 shows the effect of including multiple scattering for a solid carbon block, which is to move part of the signal strength to later times. In general, the later in time a cross section feature will fall, the more badly it will be corrupted by late-arriving neutrons.

Features in the cross section are clearly reflected in the signal when multiple scattered neutrons are eliminated (center plot of Figure 2). In the full calculation the correspondence is less clear.

Figure 3 shows the neutron scattering cross sections for the elements of interest and the predicted signal for a solid block of LXO40. Even in this extremely simplified model it is very difficult to identify clearly features in the signal that indicate the presence of the component elements. The possible utility of neural network methods to recover elemental densities from the measured signals are beginning to be looked at.

IV. Conclusions

It is clear that the nuclear interrogation method considered here, or any other, presents challenging technical problems, and that careful design of the measurement system and data interpretation methods will be necessary. Detailed accurate radiation transport modeling can be used to accurately and objectively assess possible substance detection schemes. These assessments and some optimizations of designs can be accomplished without costly and time consuming prototyping experiments (and without hazard control training or paperwork).

V. References

- [1] Lee Grodzins, "Nuclear techniques for finding chemical explosives in airport luggage", *Nucl. Inst. Meth.*, B57/57 (1991) 829-833
- [2] Thomas P. Wilcox, Jr. and Edward M. Lent, *COG- A Particle Transport Code Designed to Solve the Boltzmann Equation for Deep-Penetration (Shielding) Problems*, LLNL Report M-221-1

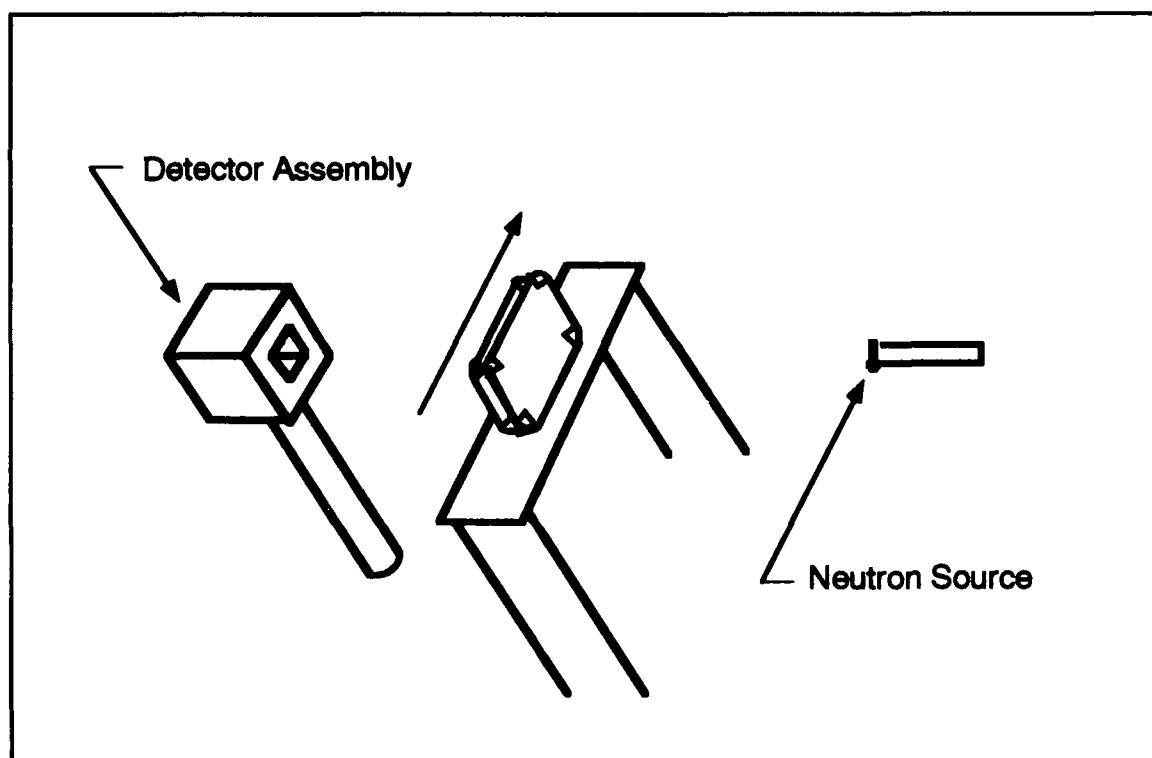


Figure 1. Perspective picture output of the the set-up modeled from the code COG.

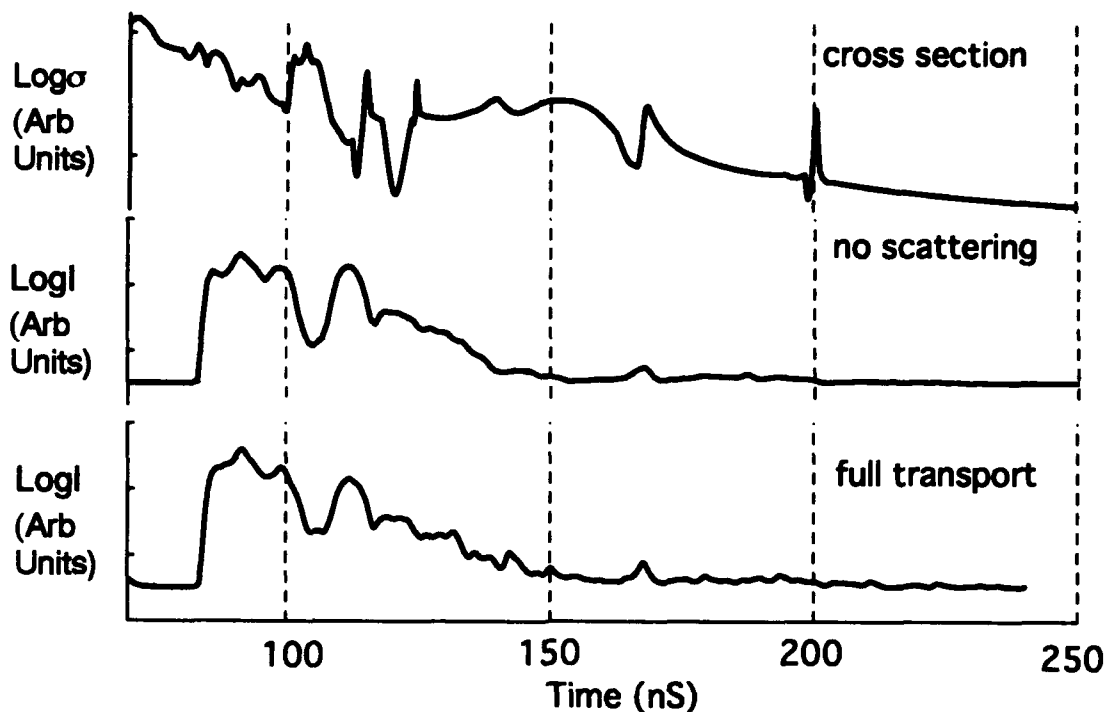


Figure 2. The top plot shows the log of the cross section for neutron scattering on C^{12} converted into a function of time. The center plot shows the calculated detector signal with multiple scattering suppressed. The third plot is of the total predicted signal. The signal predictions are convolved with a source pulse shape and a detector impulse response.

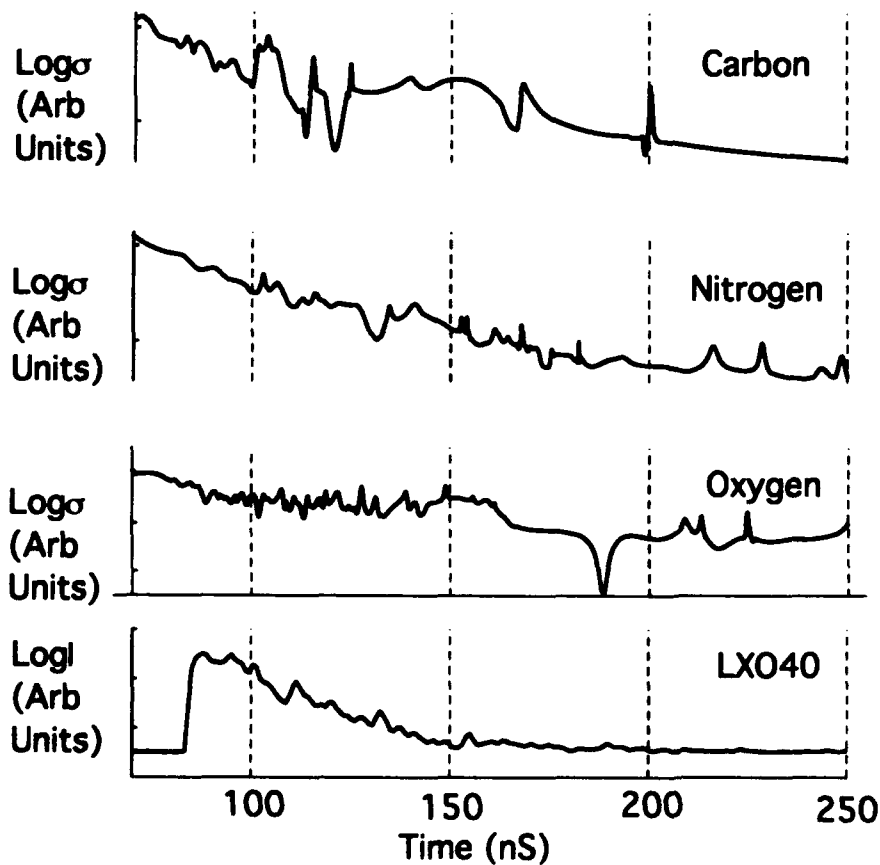


Figure 3. Logs of cross sections (converted from energy as the abscissa to time) for C^{12} , N^{14} and O^{16} are shown in the top three plots and the log of the predicted signal for a block of LXO40 in the bottom plot.

Overview of Accelerators in Medicine

Arlene J. Lennox

Fermi National Accelerator Laboratory* and Rush University
P.O. 500, MS 301, Batavia, Illinois 60510-0500 USA

Abstract

Accelerators used for medicine include synchrotrons, cyclotrons, betatrons, microtrons, and electron, proton, and light ion linacs. Some accelerators which were formerly found only at physics laboratories are now being considered for use in hospital-based treatment and diagnostic facilities. This paper presents typical operating parameters for medical accelerators and gives specific examples of clinical applications for each type of accelerator, with emphasis on recent developments in the field.

I. INTRODUCTION

Advances in diagnostic and therapeutic radiology have historically been coupled with advances in physics research. In many cases a new medical procedure is tried using equipment originally designed for physics research. Sometimes the medical use is parasitic to the physics use and at other times the equipment is turned over to medical researchers when it is no longer useful to physics researchers. Thus, when one studies, for example, a new form of radiation therapy it is possible to find several different types of accelerator being used for the same therapy.

When the therapy moves from the research stage to standard practice and it is time to design a dedicated, optimized system it is difficult to tell whether certain parameters are essential or simply there because the accelerator was designed for another purpose. It is also difficult for the accelerator designer to ascertain intensity requirements because medical accelerators are generally specified in terms of dose rate to a volume of tissue. This means that dosimetry techniques and the efficiencies associated with processes such as extraction, targeting, degrading, modulating and energy selection must be well understood before the machine can be designed.

In this presentation intensities and energies are discussed in terms of the current and particle type in the accelerator rather than dose rate and particle delivered to the patient. Typical operating parameters for accelerators which have been used for medical applications are given in Table 1. Design parameters for accelerators in the proposal or development stages are listed in Table 2.

II. ELECTRON ACCELERATORS

Conventional radiation therapy directs a beam of photons or electrons at a cancerous tumor. These beams are typically produced by betatrons, microtrons or radiofrequency electron linacs. Betatrons are gradually being replaced by electron linacs because the linacs can be mounted in a gantry which rotates a full 360° around the patient. State of the art electron linacs operate in two modes, a high intensity mode in

which electrons strike a tungsten target to produce photons for photon therapy and a low intensity mode in which electrons are directed to the patient for electron therapy. Racetrack microtrons provide electron beams for multiple treatment rooms. In this case the electrons are accelerated in the microtron and a beam transport system is mounted in the gantry. The controls systems for medical electron accelerators are becoming very sophisticated, allowing therapists to preprogram beam energy, collimator size and gantry angle so that these can be adjusted automatically by computer during a treatment.

Ordinary diagnostic x-rays are produced by 10-50 keV electrons striking a tungsten target. Normally these electrons are produced by a compact electron gun, but obtaining high quality images of cardiac blood vessels using the iodine K-absorption edge requires an intense monochromatic beam not available from a conventional x-ray machine. Electron synchrotrons operating at 2-3 GeV are a good source of this characteristic radiation for angiography.

III. CIRCULAR PROTON AND DEUTERON ACCELERATORS

Because of their mature technology it is not surprising that cyclotrons have been used for many medical applications. In particular, great strides have been made in producing isotopes for radiopharmaceuticals. For generating many isotopes it is no longer necessary to share a beam line with physics researchers because commercially available cyclotrons may be dedicated to this task. Hospital-based cyclotrons are also used for fast neutron therapy. At present, cyclotrons for proton and pion therapy are associated with physics laboratories, but increased interest in proton therapy has led to interest in developing hospital-based cyclotrons for proton therapy.

Synchrotrons for proton therapy can be found in both hospital and physics laboratory settings. Light ion therapy typically involves beams of helium, carbon, argon, silicon or neon ions and is available at synchrotrons associated with physics laboratories.

IV. PROTON AND ION LINACS

Recent advances in the technology of proton linacs, and particularly the use of 425 MHz radiofrequency systems, have made it possible to build smaller accelerators which are increasingly easier to maintain. For this reason linacs are beginning to compete with cyclotrons for isotope production and radiation therapies which involve a primary beam striking a production target to generate a secondary treatment beam. At present proton linacs at national laboratories are being used for fast neutron therapy and isotope production but it is possible to move these activities to the private sector by taking advantage of the new technology. Radiofrequency quadrupole

*Operated by the Universities Research Association, Inc., under contract No. DE-AC02-76CHO3000 with the U. S. Department of Energy.

Table 1
Medical Accelerator Applications Which Have Already Been Used Clinically

Accelerator	Application	Typical Kinetic Energy	Typical Average Current	Production Reaction
Electron Linac	Electron therapy	4-25 MeV e^-	100-500 nA	$e^- + W$
	Photon Therapy	4-25 MeV e^-	20-150 μA	
Microtron & Betatron	Electron Therapy	4-20 MeV e^-	100-500 nA	$e^- + W$
	Photon Therapy	4-50 MeV e^-	20-150 μA	
e^- Synchrotron	Angiography	2-3 GeV e^-	250 mA	Wiggler-extracted 33 keV γ
Cyclotron	Radioisotopes	10-100 MeV p	50-100 μA	p or d + Be p + Be or C
	Fast Neutron Therapy	50-75 MeV p or d	20-30 μA	
	Pion Therapy	500-600 MeV p	20-150 μA	
	Proton Therapy	70-185 MeV p	20-40 nA	
p Synchrotron	Proton Therapy	70-250 MeV p	20-40 nA	10^8 - 10^{10} ions/sec
	Light Ion Therapy	225-670 MeV/amu		
RFQ Linac	Injector for Synchrotron	2.0 MeV p	up to 150 μA	
Proton Linac	Fast Neutron Therapy	66 MeV p	30 μA	p + Be
	Radioisotopes	10 - 800 MeV p	50-1000 μA	p + Be or C
	Pion Therapy	800 MeV p	1 mA	
Light Ion Linac	Injector for Synchrotron	8 MeV/amu	70-250 μA	

(RFQ) linacs are competing with Cockcroft-Walton accelerators as injectors to drift tube linacs as well as synchrotrons. In fact, the compact size of an RFQ injector for a medical synchrotron contributes greatly to making hospital-based synchrotrons practical. Light ion linacs are being developed as injectors to light ion synchrotrons for both basic research and radiation therapy but the size and cost of these systems are likely to prohibit commercialization in the near future.

V. NEW APPLICATIONS

Recent renewed interest in boron neutron capture therapy (BNCT) for treating advanced brain tumors has led to interest in accelerator-generated epithermal (~ 10 keV) neutrons. Two approaches have been taken. The first produces the neutrons as near threshold as possible to minimize the amount of moderating material required. Because the production cross sections are relatively low near threshold this approach requires high current accelerators in the 2.5 - 5 MeV range. The second approach takes advantage of high yields from spallation sources at the expense of having to eliminate or moderate larger quantities of unwanted high energy spallation products. For a lithium production target the lower energy approaches use an RFQ or a tandem cascade accelerator. With a beryllium target a drift tube linac with an RFQ injector has been considered. For the spallation approach, both cyclotrons and linacs have been suggested. More details on accelerators for BNCT and relevant references are given in Table 2.

The increased demand for short-lived isotopes for positron emission tomography (PET) has led to the development of compact accelerators providing protons, deuterons, or $^3\text{He}^{++}$ with energies in the 4-10 MeV range. One approach uses a tandem cascade accelerator and the other combines three RFQ's in tandem. Both technologies promise to become competitive with the "baby" cyclotrons now in use for these isotopes. More information and references are given in Table 2.

Because proton linacs usually operate in a high current mode they are not well matched to the low currents needed for proton therapy. One way to safely use an H^- linac for therapy is to strip the H^- using a laser, strip the resulting H^0 using foils, and then direct the resulting protons to the therapy room. The proton intensity can be limited to nanoamps by limiting the power of the laser and the energy can be quantized by turning off the gradients in selected tanks. This scheme does not give the finely tunable energy variation obtainable with a synchrotron but passive scattering techniques can be used to make the final energy adjustments. It is a good method for physics laboratories with existing H^- linacs to provide parasitic beam for patient treatment or research in beam delivery and dosimetry techniques. Another approach to using proton linacs for proton therapy takes advantage of the existing technology for electron linacs. Protons are accelerated from 70 to 250 MeV using commercially available S-band radiofrequency power systems and accelerating cavities. The beam current is of the order of tens of nanoamps, which is

Table 2
Applications in Which the Accelerator and/or the Targeting System are in the Proposal or Development Stages

Accelerator	Application	Kinetic Energy	Average Current	Production Reaction	Reference
Cyclotron	BNCT*	70 MeV p	80 μ A	p + W	1
Proton Linac	BNCT	4 MeV p	??	p + Be	2
	BNCT	70 MeV p	180 μ A	p + W	3
	Proton Therapy	70-250 MeV H ⁺	10 - 40 μ A H ⁺ primary 20 - 40 nA p scattered	laser scattering	4
	Proton Therapy	70-250 MeV p	10 - 270 nA		5
RFQ Linac	PET ⁺ isotopes	8 MeV ³ He ⁺⁺	300 μ A		6
	BNCT	2.5 MeV p	30 mA	p + Li	7
Tandem Cascade	PET isotopes	3.7 MeV p or d	0.5-1.0 mA		8
	BNCT	2.5 MeV p	5 mA	p + Li	9
Coaxial Cascade	Angiography	600 keV e ⁻	1A for 10 msec	e ⁻ + BaB ₆ or CeB ₆	10

*Boron Neutron Capture Therapy

⁺Positron Emission Tomography

appropriate for proton therapy. Both approaches are discussed in the references in Table 2.

Clinical interest in cardiac angiography has led to development of a compact accelerator which generates 33 keV gamma radiation. The proposal referenced in Table 2 uses a 600 keV coaxial cascade accelerator to provide protons which strike a target containing barium or cerium hexaboride. Commercialization of this accelerator is consistent with the traditional approach to the development of medical accelerators, in which the medical procedure is tested using an accelerator built for basic research and then the technology is developed to move the procedure to a clinical setting.

VI. REFERENCES

- [1] J.F. Crawford, H. Reist, H. Conde, K. Elmgren, T. Roennqvist, E. Grusell, B. Nilsson, O. Pettersson, P. Stromberg and B. Larsson, "Neutrons for Capture Therapy Produced by 72 MeV Protons," in *Progress in Neutron Capture Therapy for Cancer*, B. J. Allen, D. E. Moore and B. V. Harrington, eds., Plenum Press, New York, 1992, pp. 129-132.
- [2] C-K. Chris Wang and Brian R. Moore, "On the Study of Energy Spectra and Angular Distributions of the Neutrons Emitted from a Beryllium Target Bombarded with 4-MeV Protons for Neutron Capture Therapy," *Proceedings of the Fifth International Symposium on Neutron Capture Therapy*, Columbus, Ohio, 1992.
- [3] Arlene J. Lennox, "Hospital-based proton linear accelerator for particle therapy and radioisotope production," *Nucl. Instr. and Meth. B56/57* (1991) pp. 1197-1200.
- [4] "Proton Therapy at the SSC - Conceptual Design Summary," *Superconducting Super Collider Laboratory Internal Report*, April 6, 1992.
- [5] R. W. Hamm, K. R. Crandall, J. M. Potter, "Preliminary Design of a Dedicated Proton Therapy Linac," *Proceeding of the 1991 Particle Accelerator Conference*, pp. 2583-2585.
- [6] W. Hagan, W. Cornelius, P. Young, M. Schulze, R. Little, K. Krohn, and J. Link, "A Helium-3 RFQ Accelerator for PET Tracer Production," *Proceedings of the IVth International Workshop on Targetry and Target Chemistry*, Paul Scherrer Institut Proceedings 92-01, August, 1992.
- [7] T. P. Wangler, J. E. Stovall, T. S. Bhatia, C. K. Wang, T. E. Blue, and R. A. Gahbauer, "Conceptual Design of an RFQ Accelerator-Based Neutron Source for Boron Neutron-Capture Therapy," *Proceedings of the 1989 Particle Accelerator Conference*, IEEE #89CH2669-0, pp. 678-680.
- [8] R. E. Shefer, R. E. Klinkowstein, B. J. Hughey, and J. J. Welch, "Production of PET Radionuclides with a High Current Electrostatic Accelerator," *Proceedings of the IVth International Workshop on Targetry and Target Chemistry*, Paul Scherrer Institut Proceedings 92-01, August, 1992.
- [9] R. E. Shefer, R. E. Klinkowstein, J.C. Yanch and G.L. Brownell, "An Epithermal Neutron Source for BNCT Using a Tandem Cascade Accelerator," in *Progress in Neutron Capture Therapy for Cancer*, B.J. Allen, D.E. Moore and B.V. Harrington, eds., Plenum Press, New York, 1992, pp. 119-122.
- [10] R. E. Shefer, private communication and Herbert L. Manning, Ruth E. Shefer, Robert E. Klinkowstein and Charles A. Mistretta, "A K α dual energy x-ray source for coronary angiography," *Med. Phys.* 18(5), pp. 880-893.

Commissioning of the First Drift Tube Linac Module in the Ground Test Accelerator*

K. F. Johnson, O. R. Sander, W. H. Atkins, G. O. Bolme, S. Bowling, R. Cole, R. Connolly,[†] P. Denney,[†] J. Erickson,[†]
J. D. Gilpatrick, W. B. Ingalls, D. Kersteins, R. Kraus, W. P. Lysenko, D. McMurry, C. T. Mottershead, J. Power,
C. Rose, D. P. Rusthoy, D. P. Sandoval, J. D. Schneider, M. Smith, G. Vaughn, E. A. Wadlinger, R. Weiss,[†] and V. Yuan
Los Alamos National Laboratory

P. O. Box 1663, MS H818, Los Alamos, NM 87545 USA

Abstract

The Ground Test Accelerator (GTA) [1] has the objective of verifying much of the technology required for producing high-brightness, high-current H^- beams. GTA commissioning is staged to verify the beam-dynamics design of each major accelerator component as it is brought online. The major components are the 35-keV H^- injector, the 2.5-MeV radio-frequency quadrupole (RFQ) [2], the intertank matching section (IMS) [3], the 3.2 MeV first $2\beta\lambda$ [4] drift tube linac (DTL-1) module, and the 24-MeV GTA with 10 DTL modules. Results from the DTL-1 beam experiments will be presented.

I. INTRODUCTION

This paper addresses the commissioning of the GTA DTL-1 module which was successfully completed in March 1993. The DTL-1 was designed to control emittance growth and to maintain high beam transmission and brightness. DTL-1 is the first of five $2\beta\lambda$ DTLs. The second five DTLs are $1\beta\lambda$ structures. The DTL was divided into 10 modules for ease of fabrication and drift-tube alignment. More details on the DTL and GTA are given in References [1], [2], and [3].

To evaluate the DTL-1's performance with beam, the commissioning plan encompassed numerous experiments. The DTL-1 position acceptance was measured both by displacing the beam and moving DTL-1. The DTL-1's output transverse and longitudinal phase-space distributions were measured versus the IMS permanent variable field quadrupole (VFQ) strengths, the IMS buncher rf amplitudes and phases, time in the macropulse, and the DTL rf amplitude and phase set points. The rf set points of the DTL-1 cavity were determined with beam by comparing measurements of the beam's energy and phase centroids with predictions. The x-ray energy spectrum from the cavity was measured versus cavity rf power. These data provide an independent verification of the rf amplitude set point [5]. Data were taken to obtain the effect of IMS steering and DTL-1 position on the DTL-1 output beam position centroids. These data can be used to determine an equivalent R transfer matrix for DTL-1. Jitter measurements were made of the beam current, position, energy, and phase [6]. RF studies were completed to assess the rf control system performance [7].

II. DTL EXPERIMENTS AND RESULTS

There were two principal GTA diagnostic [8] systems available for the DTL-1 commissioning. The first system was installed on a moveable plate (D-plate) and consisted of (1) two sets of slits and collectors for measuring horizontal and vertical transverse phase space, and position and angle centroids; (2) a toroid for measuring beam current; (3) three microstrip probes for measuring position, energy, and phase centroids; (4) a capacitive probe for measuring phase spread; and (5) Laser Induced Neutralization Diagnostic Approach (LINDA) [9] for measuring longitudinal phase space, and energy and phase widths. The D-plate was designed to commission, individually, the RFQ, IMS, and DTL-1.

The second system consisted of beamline diagnostics permanently installed on GTA. Two toroids, located in the entrance and exit endwalls of the RFQ, monitor beam transmission. Within the IMS beamline, there were (1) three microstrip probes; (2) a toroid; and (3) a video profile monitor (VPM) [10] for measuring transverse beam profiles and position centroids at the IMS exit.

Like the RFQ and IMS bunchers, the DTL-1 cavity conditioned rapidly to high power and operated reliably with few cavity breakdowns.

As expected, beam losses in the DTL-1 were small. Beam transmission was >98% (output current 35 mA). This high transmission was typical for most configurations of the IMS VFQs, buncher cavities, and permanent magnet quadrupole (PMQ) steerer settings. Significant transmission decreases occurred only for abnormal accelerator configurations, where beam losses were limited by the GTA Fast Protect system. The DTL-1 position acceptance for high transmission was ± 1 mm horizontally or vertically from the DTL center.

The microstrip probes are used in determining the rf set-points of DTL-1 using the phase-scan technique [11,12]. This technique uses the probes to measure beam energy and phase centroids versus the DTL-1 rf amplitude and relative phase. Single-particle simulations provide the shape signature for determining the rf amplitude set point. Figures 1A and 1B show simulation results and experiment data, respectively. The plotted points for each rf field correspond to a different input cavity phase. For a given cavity field, the input phase set point occurs at the zero normalized energy (Fig. 1A). The ~ 15 keV offset from zero in the data (Fig. 1B) is due to uncertainties with the absolute energy measurement calibration. Simulations and data exhibit the same counterclockwise rotation as the cavity power increases. Figure 2 shows the gap-voltage dependence of the slope of the

*Work supported and funded by the US Department of Defense, Army Strategic Defense Command, under the auspices of the US Department of Energy.

[†] Industrial Partner: Grumman Corporation

phase scan linear region. There is good agreement between data and simulations.

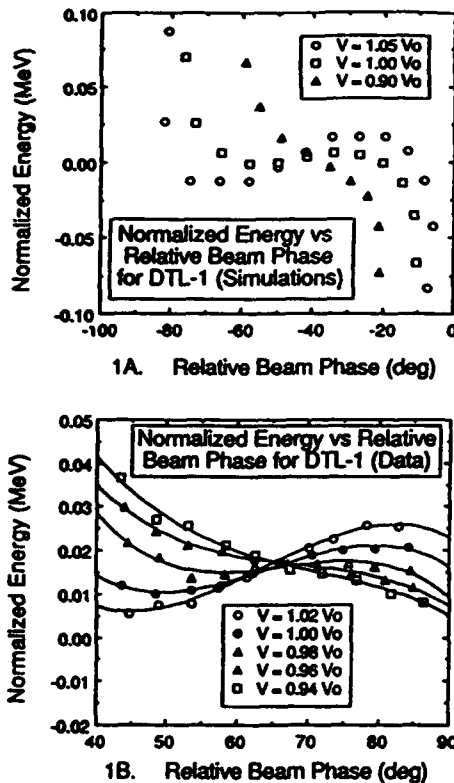


Figure 1. Normalized beam energy (design minus actual energy) versus the relative beam phase for DTL-1. V_0 is the design gap voltage. Relative phase is used to ease curve shape comparison.

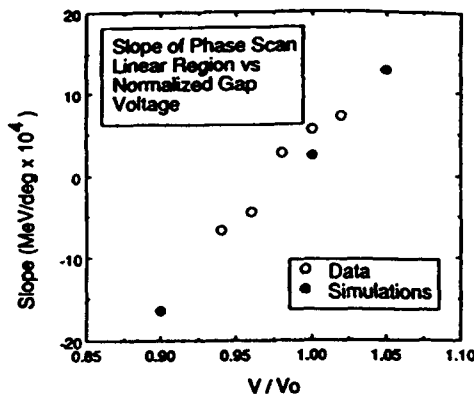


Figure 2. Slope of phase-scan linear region versus the normalized gap voltage V/V_0 .

We assume that the DTL rf cavity power P (kW) is related to the DTL gap voltage V (kV) through a relationship of the form $V = K\sqrt{P}$, where K is a proportionality constant determined by either experiment or theory. SUPERFISH calculations, using the measured Q of the DTL-1 cavity, give $K = 18.04$. From x-ray and phase-scan measurements, $K = 17.97$ and $K = 18.22$, respectively. The agreement between data and theory is $\sim 1\%$. Experimental and theoretical uncertainties are $\sim 3\text{--}5\%$.

The RFQ beam transmission varies during the macropulse [2], but the RFQ and IMS transverse phase-space distributions and the IMS transmission do not [3]. Measurements show that the DTL-1 beam transmission and output transverse phase-space distributions, including position centroids, do not change during the macropulse. The insensitivity of the mismatch factor MM [13] (i.e., the Courant-Snyder (CS) parameters or beam shape) to time is shown in Fig. 3.

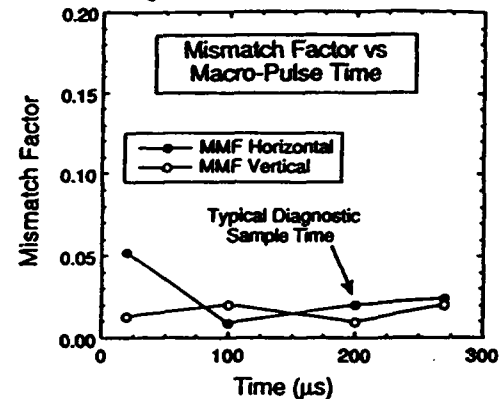


Figure 3. Horizontal and vertical MM versus time within the macropulse.

The DTL-1 output transverse phase-space distributions were measured as a function of the IMS transverse tune. Except for abnormal conditions (e.g., an IMS buncher off), the output CS parameters were insensitive to the tune. Their measured values were found to be near the ideal, design output values (Fig. 4) where a practical criteria of $MM < 0.3$ is considered good. Each run number in Fig. 4 corresponds to a particular IMS tune. Values of $MM \geq 0.4$ occurred for abnormal IMS configurations. The DTL-1 output emittances were independent of the DTL input and output CS parameters. No transverse/longitudinal coupling was observed for different IMS longitudinal tunes.

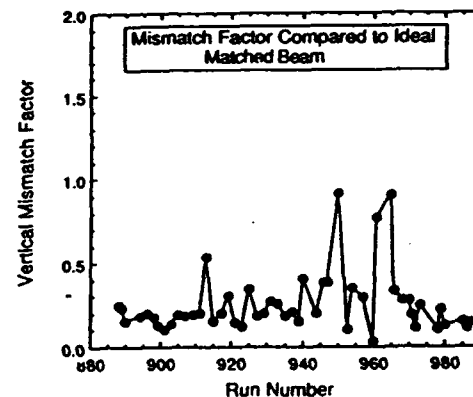


Figure 4. Vertical MM (DTL-1 output beam) between measurements and ideal beam.

The longitudinal DTL output phase-space distribution was measured versus IMS longitudinal tunes. As in the transverse case, the longitudinal emittance and CS parameters were insensitive to variations about the standard IMS tune. The CS parameters varied little from their ideal, design output values. Large deviations in the output emittance and CS parameters could be achieved for extreme IMS longitudinal tunes (e.g.,

operating the downstream IMS buncher in its debunch, acceleration, or deceleration modes).

The transverse and longitudinal phase-space distributions were measured as functions of the DTL-1 rf power and phase set points. The power and phase were varied from the optimum values by $\pm 10\%$ and ± 20 degrees, respectively. The longitudinal and transverse distributions were largely insensitive to DTL-1's amplitude and phase. For the transverse distributions $MM < 0.3$ for all set points.

A comparison of the DTL-1 output transverse and longitudinal emittances to those obtained out of the IMS during its commissioning indicates that there is little or no emittance growth through the DTL-1, as expected.

The DTL-1 output-beam-position centroids depend on the input centroids which were varied with IMS steering or DTL-1 entrance displacements. The data verified our IMS steering model. Analysis is underway to use these data to obtain an equivalent R transfer matrix for the DTL. The trace of the determined R matrix equals two times the cosine of the phase advance. The results will be compared to theory.

One PMQ steerer is attached to the exit of each DTL module for adjusting the position centroids at the next DTL module. Exercising the DTL-1 steerer resulted in expected changes in beam centroids.

For transverse phase-space measurements, a comparison was made between the standard slit and collector technique, which measures the full H^- beam, and the transverse LINDA [14] technique, which uses the same slit and collector to measure a photoneutralized portion of the H^- beam. The neutralization point is upstream (~ 32 cm) of the emittance gear slit. The two methods yield different results. The difference is real and is predicted by simulations that include the different space-charge effects between the neutralization point and the slit. Three experiments were made with different degrees of bunching. The more bunched the beam, the greater the difference between the techniques (Fig. 5). The two experimental techniques agree with predictions.

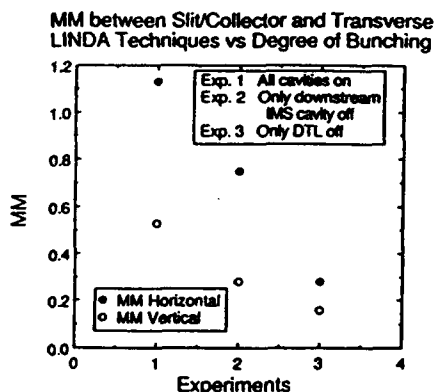


Figure 5. MM (between the two techniques) vs degree of bunching.

III. SUMMARY

DTL-1 is commissioned and fully operational. The injector, RFQ, IMS, and DTL-1 operations were reliable and stable, allowing for extensive beam measurements. High beam transmission was obtained with little or no transverse- and longitudinal-emittance growth through DTL-1. The

measured CS parameters are in good agreement with simulations as are the phase-scan data.

IV. ACKNOWLEDGEMENTS

The successful DTL-1 commissioning was made possible by the cooperation of many individuals throughout the Accelerator Technology Division of LANL. This includes the AT-10 injector section; AT-5 rf support; M. L. Milder and the GTA facility team; AT-8 software support; the AT-3 diagnostics section; R. Garcia and M. Shinas for LINDA support; and L. B. Dauelsberg and C. Vigil for beamline alignment.

V. REFERENCES

- [1] O. R. Sander et al., "Commissioning the GTA," 1992 Linear Accel. Conf. Proc., AECL Research, Chalk River Laboratories Report, AECL-10728 (1992), p. 535.
- [2] K. F. Johnson et al., "Commissioning of the Ground Test Accelerator RFQ," 1992 Linear Accel. Conf. Proc., AECL Research, Chalk River Laboratories Report, AECL-10728 (1992), p. 64.
- [3] K. F. Johnson, et al., "Commissioning of the Ground Test Accelerator Intertank Matching Section," 1992 Linear Accel. Conf. Proc., AECL Research, Chalk River Laboratories Report, AECL-10728 (1992), p. 61.
- [4] S. Humphries, *Principles of Charged Particle Acceleration* (John Wiley & Sons, New York, 1986), p. 456.
- [5] G. O. Bolme et al., "Measurement of RF Accelerator Cavity Field Levels at High Power from the Characteristic X-ray Emissions," in "Proc. 1990 Linear Accelerator Conf.," Los Alamos National Laboratory report LA-12004-C, March 1991, p. 219.
- [6] D. Barr and J. Gilpatrick, "Comprehensive Beam Jitter Study for the Commissioning of the IMS and DTL at GTA," these proceedings.
- [7] S. Jachim and P. Denney, "Measured Performance of the GTA RF System," these proceedings.
- [8] J. D. Gilpatrick et al., "GTA Beam Diagnostics for Experiments 1B through 2D," Los Alamos National Laboratory report LA-UR-91-341 (April 1991).
- [9] V. W. Yuan et al., "Measurement of Longitudinal Phase Space in an Accelerated H^- Beam Using a Laser-Induced Neutralization Method," Nucl. Instr. and Meth., A329 (1993) 381.
- [10] D. Sandoval et al., "Video Profile Monitor Diagnostic System for GTA," 1992 Linear Accel. Conf. Proc., AECL Research, Chalk River Laboratories Report, AECL-10728 (1992), p. 247.
- [11] K. F. Johnson et al., "Characterization of a Ramped Gradient DTL: Experiment and Theory," Proc. 1991 IEEE Particle Accelerator Conference, San Francisco, CA. (May 1991), p. 3017.
- [12] J. D. Gilpatrick et al., "Measurements and Performance of a Microstrip Beam Probe System," Proc. 1991 IEEE Particle Accelerator Conference, San Francisco, CA. (May 1991), p. 1136.
- [13] J. Guyard and M. Weiss, "Use of Beam Emittance Measurements in Matching Problems," Proc. 1976 Linear Accel. Conf., Atomic Energy of Canada, AECL-5677 (1976), p. 254.
- [14] R. C. Connolly et al., "A Transverse Phase-Space Technique for High-Brightness, H^- Beams," Nucl. Instr. and Meth., A312 (1992) p. 415.

Acceleration and isobaric separation of radioactive ion beams with the Louvain-la-Neuve isochronous cyclotrons

M. Loiselet, N. Postiau, G. Ryckewaert
Centre de Recherches du Cyclotron
Université Catholique de Louvain
2 Chemin du Cyclotron, B-1348 Louvain-la-Neuve, Belgium

A. Morduev, R. Oganessian
Flerov Laboratory, JINR, Dubna, Russia

Abstract

The paper reports on the results obtained for the production and acceleration of radioactive ions with the Louvain-la-Neuve cyclotrons. The specific problems of the separation of isobaric beams at low energy with a high efficiency is presented. Their consequences on the design of a cyclotron dedicated to the acceleration of radioactive beams are discussed.

I. INTRODUCTION

The Radioactive Ion Beam facility at Louvain-la-Neuve aims at the acceleration of unstable nuclei ($T_{1/2} \leq 2h$) in the low energy range (< 2.0 MeV per nucleon), which is of interest for cross section measurements of important reactions involved in astrophysical processes. It uses two cyclotrons coupled by an on-line ECR source to produce, ionize and accelerate the radioactive species. With this scheme, intensities of 10^6 particles per second (pps) for ^6He and up to 10^9 pps for ^{19}Ne have been obtained. Although the acceleration efficiency is low at these energies ($< 5\%$), it turns out that the high mass resolving power of a cyclotron is crucial to eliminate the isobaric contamination in a very efficient way. Results obtained so far will be presented and the main design feature of a new cyclotron dedicated to the acceleration and isobaric separation of radioactive ions will be discussed.

II. ACCELERATION OF RADIOACTIVE IONS IN CYCLONE

2.1. General layout

The general layout of the facility has been presented elsewhere [1]. The high intensity (200 μA) 30 MeV proton beam at a first cyclotron, CYCLONE 30, is used to produce large amounts of radioactive atoms in a target located in the wall which separates the two vaults. These are pumped out of the target through an Electron Cyclotron Resonance (ECR) ion source in which they are ionized. After a first analysis in a low resolution mass separator, ions with the same mass to charge ratio are injected in the second cyclotron, CYCLONE, which brings them to the required energy [1,2].

2.2. Acceleration and isobaric separation

Most of the elements that have been accelerated so far, have an isobaric contaminant coming either from the target or from the residual gas in the source. To achieve a high purity in the final beam, the cyclotron is tuned as a high resolution spectrometer and the intensity of the isobaric beam is considerably reduced after the acceleration and extraction processes. For isobars with a relative mass difference of 2×10^{-4} , like (^{19}Ne , ^{19}F) or (^{11}C , ^{11}B), an attenuation factor of the order of 10^6 is routinely achieved with only a minor reduction in the acceleration efficiency. More details about this were given elsewhere [3].

Table 1 summarizes the intensities and the maximum energy available for the various ions that have been delivered by CYCLONE. Most of them have been accelerated at energies between 0.6 and 2 MeV/Nucleon (which is the energy domain of interest for nuclear astrophysics) and intensities larger than 10^9 pps were obtained for $^{19}\text{Ne}^{2+}$. However, as soon as high charge states are provided by the ECR source, higher energies can be reached as it has been shown with $^{19}\text{Ne}^{4+}$ which was accelerated at 4.2 MeV/amu with an intensity of 5×10^8 pps.

Table 1
Intensities and energies of the radioactive beams which are presently available at the Louvain-la-Neuve facility

Element	$T_{1/2}$	q	Intensity (pps)	Max. Energy (MeV)
^6He	0.8 s	1+	$1.2 \cdot 10^6$	18
^{11}C	20 min	1+	$1.0 \cdot 10^7$	10
^{13}N	10 min	1+	$4.0 \cdot 10^8$	8.5
		2+	$3.0 \cdot 10^8$	34
^{18}Ne	1.7 s	3+	$4.2 \cdot 10^5$	55
^{19}Ne	17 s	2+	$1.9 \cdot 10^9$	23
		4+	$5.0 \cdot 10^8$	93
^{35}Ar	1.8 s	5+	$\sim 10^5$	79

III. DESIGN FEATURES OF A CYCLOTRON DEDICATED TO THE RADIOACTIVE BEAMS

The reasons which led to the decision to build a new cyclotron (provisionally called CYCLONE44) for the acceleration of radioactive isotopes of the light elements for the study of nuclear reactions of astrophysical interest have already been discussed elsewhere [2,3] and can be summarized as follows:

- its energy range: from 0.2 to 0.8 MeV/AMU, covering the astrophysically important region not accessible with CYCLONE (the lower limit is 0.56 MeV/AMU);
- its acceleration efficiency: one order of magnitude larger than the efficiency of CYCLONE allowing the study of nuclear reactions with smaller cross sections, e.g. those reactions involving alpha particles and short lived radioactive nuclei;
- its isobaric resolving power: 10^4 to allow the use of pure radioactive ion beams of very low intensity in the presence of large isobaric stable element beams;
- its availability and flexibility: for the production of radioactive nuclei, both CYCLONE30 (as in the actual case) and CYCLONE, with its greater variety of particles and higher energy but lower intensity will become available. The new dedicated cyclotron will be full time available for long term measurements.

The main characteristics of CYCLONE44, resulting from a detailed study of the experiments to be performed with it have been fixed now and are given in table 2.

Table2
Main characteristics of CYCLONE44.

Energy constant K (MeV)	44
Energy range (MeV/AMU)	0.2 - 0.8
Mass range	4 - 30
Maximum average field (T)	1.5
Extraction radius (m)	0.64
RF - system	2 Dees, var. angle
Frequency range (MHz)	12 - 17.5
Maximum Dee voltage (kV)	20
Harmonic modes	6 - 8
Injection	Axial
Extraction	Electrostatic

Description

The magnet has four sectors and a cylindrical return yoke, similar to CYCLONE30: such a design leads to a reduced size and a reduction in weight of about 25% for a given K-value, compared to the classical magnet. To further reduce the size and the power consumption, rather small hill and valley gaps have been chosen. Trimcoils will be located under the sectors and the accelerating electrodes will be located in opposite valleys. The most difficult area in obtaining isochronous fields is in the centre: the size of the axial hole is no longer small compared to the average gap and a smooth transition between the cylindrical centre plug and the sectors has to be realized at the earliest possible radius to assure vertical focusing. The magnet parameters are

given in table 3.

Table 3
Magnet parameters of CYCLONE44

Weight (Tons)	48
Height (m)	1.5
Outer diameter (m)	2.7
Pole diameter (m)	1.44
Hill gap (cm)	8
Valley gap (cm)	20
Sector angle (degrees)	48-58
Maximum hill field (T)	1.95
Maximum valley field (T)	1.0
Main coil: number of turns	364
maximum current (A)	500
maximum voltage (V)	105

Correction coils : circular, under sectors

The main challenge in the design of CYCLONE44 lies in the combination of two requirements: a high acceleration efficiency (from the ECR source for multiply charged ions with a relatively large emittance, through injection, acceleration and extraction) and a high resolving power for isobaric contaminant beams.

The resolving power of a cyclotron is proportional to the number of turns times the acceleration harmonic mode number [3], thus asking for low Dee voltage and high harmonic modes. On the other hand, a large acceleration efficiency can only be obtained if the axially injected low energy beam is perfectly matched to the cyclotron centre region acceptance, in six dimensional phase space. This requirement calls in turn for low harmonic modes, high injection voltage and high Dee voltage.

These conflicting requirements were partially circumvented in CYCLONE by adjusting the radial field profile to be non - isochronous resulting in an increased turn number. This method is not too satisfactory because difficult to control and leading to sensitive and unstable beams.

For CYCLONE44, harmonic modes 6 and 8 have been chosen and the option was taken to vary the Dee angle radially. Along the first turn, the Dee angle is close to the optimum for maximum energy gain and posts are used to reduce the transit times in the gaps. Then the Dee angle is gradually reduced with increasing radius. This way, the effective energy gain per turn is kept small to assure the required turn number (resp. 265 in H=6 and 200 in H=8). To provide maximum turn separation at extraction the Dee angle is allowed to increase to optimum during the last 10 cm before extraction radius. The exact profile of the acceleration electrode and gap has to be optimized carefully to preserve longitudinal beam quality: decreasing energy gain with radius increases bunch length, increasing energy gain shortens the bunch but both phenomena do not cancel totally [4].

Particles are injected with a magnetic bending radius of 35 mm in the isochronous field and deflected in the median plane on a centered orbit with a spiral inflector.

Extraction is performed using an electrostatic deflector eventually followed by a passive focusing channel if required. The turn separation at extraction is increased by an adjustable first harmonic field bump.

Good vacuum (10^{-7} range) is mandatory to minimize beam losses. The sectors and correction coils are in a primary vacuum to allow for light top and bottom covers of the vacuum chamber. The high vacuum in the acceleration chamber is obtained with diffusion pumps connected at the rear end of the Dee stem and with cryopumps connected through the return yoke.

The RF-system consists of two Dees connected together at the centre and coaxial resonators mounted vertically.

Figure 1 shows a schematic section through the midplane of the cyclotron.

IV. REFERENCES

- [1] G. Berger et al., "Acceleration and mass-separation of radioactive ion beams in an isochronous cyclotron", 1991 IEEE Particle Accelerator Conference, San Francisco, pp 2610-2612.
- [2] P. Decrock et al., "Production and acceleration of radioactive ion beams. Proceedings of the Second International Conference on Radioactive Beams, Louvain-la-Neuve, 1991, edited by Th. Delbar (Adam Hilger) pp 121-126.
- [3] G. Ryckewaert et al., "Radioactive ion beam production using the Louvain-la-Neuve cyclotrons", Proceedings of the 13th International Conference on Cyclotrons and their Applications, Vancouver, 1992, edited by G. Dutto and M.K. Craddock.
- [4] A. Chabert, private communication.

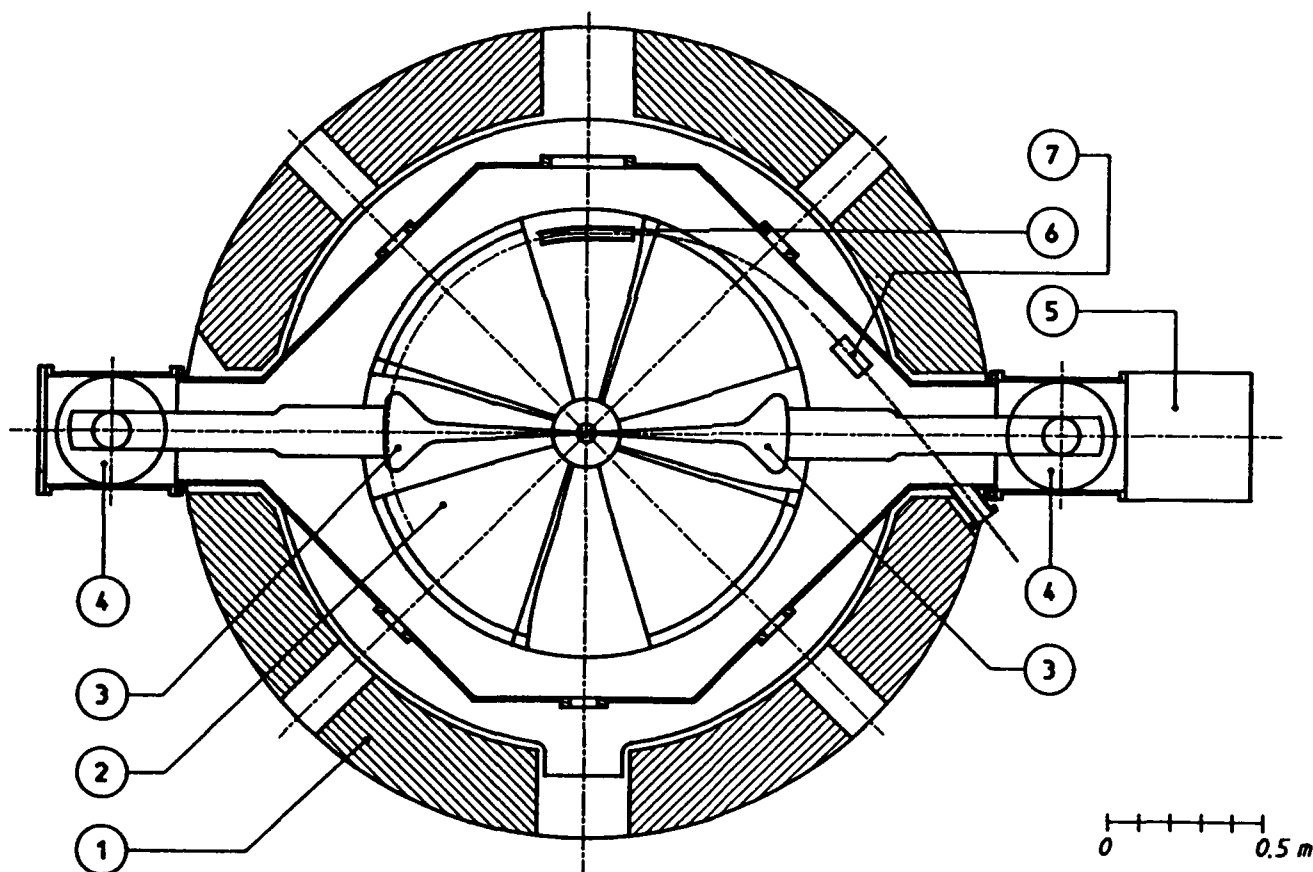


Figure 1

Schematic view of the midplane section of CYCLONE44

1. Magnet yoke 2. Sector 3. Accelerating electrode 4. Coaxial resonator 5. RF-amplifier 6. Electrostatic deflector 7. Passive magnetic channel - focusing

Linear Accelerator for Plutonium Conversion and Transmutation of NPP Wastes

I.M. Kapchinskiy*,

I.V. Chuvilo, A.A. Kolomiets, N.V. Lazarev, I.M. Lipkin, V.K. Plotnikov, I.A. Vorobjov
Institute for Theoretical and Experimental Physics, 117259, Moscow, Russia

I. INTRODUCTION

The conclusion of an agreement between Russia and the USA for significantly reducing the number of nuclear warheads has made the effective peaceful use of the stockpiles of weapons-grade plutonium a very urgent problem. Another relevant problem for all advanced countries is the transmutation of long-lived high level NPP wastes. One of the most promising ecologically pure and safe methods of plutonium conversion is to use it in subcritical accelerator-driven power reactors simultaneously for two aims – energy production and waste burning, as proposed last year by A. Favale [1].

The main parameters and engineering design of such a reactor are not reliably defined at present, so we do not know the optimal value of the proton energy and beam current. Nevertheless, the preliminary estimates [2,3] show that in any scenario the energy is in the range of 0.8–1.6 GeV and the beam current is 100–300 mA [1-3]. Estimates in projects of transmutation plants [4,5] show the values in the same ranges, although from common considerations in the last case the current must be closer to the upper limit.

The very high average beam power (hundreds of megawatts) involved requires construction of an accelerator with high efficiency (near 50%). This fact and the necessity of having extremely low beam losses make it possible to suppose that both tasks may be solved by the use of a CW linac only.

II. BASIC CONSIDERATIONS FOR LINAC SCHEME CHOICE

No doubt the most important criterion is the cost of construction and operation of the linac. However, it is hardly possible to determine the dependence of cost on even basic linac parameters at the beginning stage of design. So for elaboration of linac schemes and comparison of alternative variants one may assume:

- 1) the possibility of minimizing particle losses at extremely low permissible levels, particularly at the most radiation-sensitive places of the machine and at energies with the largest neutron yield;
- 2) ensured adequate removal of RF heat from accelerating structures upon the minimum linac length;
- 3) ensured adequate reliability;
- 4) ensured maximum efficiency;
- 5) the possibility of increasing beam current over the nominal value.

The permissible level of integral losses in the machine can be estimated according to those in the LAMPF and INR meson factory in Troizk, where at an average beam current about 1 mA they are of order 10^{-4} . Evidently, at the current of order 100 mA this value will be about 10^{-6} .

Because of very strong limitations on the particle losses, the requirements in transporting intensive beams along the whole tract are sharply increased, especially as one approaches the space-charge limit. This points to the necessity for detailed investigation into the problem of growth in the six-dimensional phase volume of the beam and defining the conditions which provide self-matching beam motion in the focusing channel, including particle acceleration.

Analytical solution of this problem is difficult to achieve and is possible only for some specific cases under the far going simplifying suppositions, which are not realized in practice. The widely used model of bunch in the view of uniformly charged ellipsoids, as has been shown in [6], cannot be self-matching in the field of conservative forces. So the application of this model for calculating the emittance growth and estimates of current limit requires caution. At present the most accurate method for calculating beam dynamics is computer simulation of the macroparticles. However, no existing computer codes are able to calculate beam halo and particle losses at the level of 10^{-6} - 10^{-7} and do not account for all factors leading to appearance of this halo [7]. One of the physical effects influencing beam quality is the dependence of the form of matching phase

volume on the correlation between Coulomb forces and forces of external field under non-microcanonical phase density distributions. As far as particles are accelerating this correlation is changing, that is may be regarded as adiabatic mismatching of beam with regular channel. Such mismatching may lead to production of beam halo, which is the main deliverer of losing particles. The influence of this effect under the loss level of 10^{-6} is not yet known. There exists a row of other effects, which influence under the same level of losses cannot be ignored. It is vital that the result of these effects show themselves not in the initial part of linac, but where they are most dangerous.

The above points out the necessity of calculating the linac with a sufficient reserve on beam current limit. The cost of the initial part of the accelerator structure is not large comparing with the cost of the main part of linac. So such reserve is admissible.

Construction decisions for accelerator structures essentially influence the choice of its scheme. These decisions cannot be accepted without examining such a complicated problem as heat removal from structure elements; apparently for solving this problem new original approaches will be required.

The considerations mentioned above allow us to admit as a lower limit the value of ~ 100 mA which guarantees acceptable efficiency and for a conservative upper limit, the Coulomb repulsion on order of 300 mA.

III. STRUCTURAL SCHEME AND THE MAIN DATA OF THE ITEP LINAC

The proposed scheme of one-channel linac is presented in Fig.1. The initial part of the accelerator is the RFQ structure, the intermediate part is the DTL with PMQs, and the main part is the DAW structure. This scheme is the result of further development of earlier published work [4,5].

The DAW structure, invented by V.G. Andreev [8], we proposed as main part of the linac. This structure has more wide dispersion characteristics and a higher shunt-impedance in comparison with SCS and ACS structures.

It seems to us that the DTL with PMQs is the most suitable for the intermediate part of the linac. Note that the PMQs allow us to decrease the diameter of the drift tubes and thus to increase the RF frequency and decrease active RF power losses.

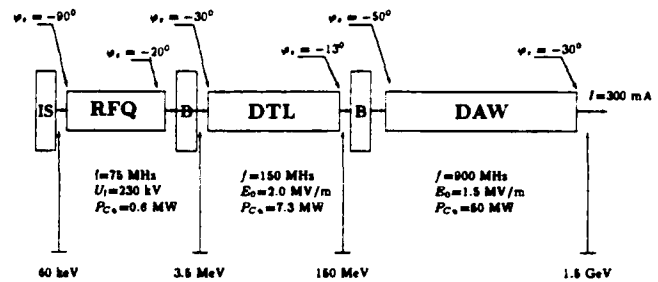


Figure 1: Block scheme of the linac.

However, the possibility of using PMQs must be confirmed by examination of their radiation resistance. The advantages of the RFQ for accelerating high current beams are well known.

The frequency of 900 MHz for the DAW structure is defined by the requirements of maximum efficiency. The frequency of 75 MHz is chosen for the RFQ in order to have a margin of the acceptance under nominal beam current 150 mA, suitable current limit (about 300 mA), and a decrease of emittance growth in the most dangerous parts of linac. The relatively low frequency of the RFQ allows us to realize a one-channel scheme for the linac. The frequency of the DTL is twice as high as that in the RFQ which simplifies the transverse matching of the beam at the input of the DTL.

To avoid particle losses between structures with frequencies 150 MHz and 900 MHz it is proposed to considerably decrease the absolute value of the synchronous phase according to the law

$$|\varphi_s| \sim W_s^{-1/4},$$

which must provide a more effective compression of the phase length of the bunch.

To provide adequate reliability let us set the value of the maximum RF electric field strength at the surface of the electrodes of the accelerating structures equal 160 kV/cm, that is 1.5 Kp criterion for a frequency of 75 MHz and a gap of 3 cm. In this case, for the minimum value of relative particle velocity 0.01131 the average value between adjacent electrodes is equal to 2.16 cm. With the field enhancement factor 1.47 for a four-vane RFQ structure [9,10] for defined parameters the value of the potential difference between the adjacent electrodes is equal to 230 kV/cm. Beam bunching is designed for quasi-stationary regimes. The value of the average field on the axis of DTL resonators was chosen to be 2.0 MV/m, and the aperture is 1.5 cm. The

value of the synchronous phase varies along the DTL from -30° to -13° . Calculations of the resonators were carried out by the RESALV code [11]. The total length of the DTL is 87 m. The value of the synchronous phase varies along the DAW structure from -50° to -30° . The average field on the axis was chosen to be 1.5 MV/m [12].

A. Matching Transitions in Linacs

Because neighboring sections in the proposed scheme are operating at different frequencies of RF field and with different types of focusing it is necessary to match the beam both in the transverse and longitudinal phase planes.

The special feature of space-homogeneous quadrupole focusing creates one more problem while matching the beam that we do not meet in linacs without RFQ. The problem is that the acceptance of the RFQ channel depends on time, and the parameters of normalized emittance of the beam in the regular channel are the same along the structure in any moment. The dependence of the beam emittance on the phase of RF field causes it to increase at the exit from the RFQ. And this increase will be larger the longer the phase width of the bunch. The calculations made for the ISTRA accelerator gives the value of the relation of the effective emittance at the exit from RFQ with phase length of 70° to the value of the current emittance of 1.70 for the focusing plane and 1.43 for the defocusing one. The computer simulation carried out in ITEP allowed us to work out the method of dynamically matching the space-homogeneous beam with the static space periodical channel [13]. (Under the dynamical matching we understand the conversion of the beam with time-dependent parameters into the beam with parameters that do not depend on time and vice versa.) If we have the beam crossover at the exit from RFQ for the synchronous particle the coordinates of the particles in the "head" and "tail" of the bunch while passing the output cross-section of the RFQ electrodes changes slightly, and the angles with longitudinal axis to a marked degree. The phase portraits for the particle in the "head" and "tail" of the bunch in this case deflects to different sides from the position of crossover on the phase plane, corresponding to the moment of passing of the synchronous particles through the output cross-sections of electrodes. The idea of the method is to create at the exit from the RFQ a short sector of sign-alternative RF field with the same frequency,

the phase of which is shifted relative to the phase of oscillation of the beam envelope for the defined value in order to compensate the deflection of the phase portraits for the particles in the "head" and "tail" of the bunch to the position of crossover. The influence of matching RF field does not change the frequencies of transverse oscillations of the particles, but its compensating effect is kept over a wide range of currents.

The possibility of preserving the transverse matching of the beam in connecting the RFQ and DTL channel was studied in [14] for different multiple frequencies of the RF field in the DTL. The results of this investigation show that for specific channels with the same length of focusing period and values of phase advance it is possible to realize the matching of the beam with the large phase differences of transverse oscillations of the particles over a wide range of currents. The higher quality of matching can be achieved by using in the DTL magnetic lenses with the maximum possible length. At the connecting point of the channels with the same frequencies of RF field, the transverse matching of the beam is possible only at the minimal frequency of transverse oscillations of the particles as most critical for beam losses by use of adiabatic matching horn. In any case the necessary condition of the direct connection of the channels is the presence of the crossover of the beam for the cross-section of the beam corresponding to the synchronous particle.

Equal frequencies of particle transverse oscillation (especially of a minimal frequency) at all the passages between the different parts of the linac and adiabatic changing of beam parameters in the focusing channels of the separate parts make it possible to construct the unified focusing channel throughout the linac in which the matching of the beam with the channel has no critical dependence on the beam current. The conditions of correctness of the adiabatic approximation defined in [14] and illustrated in Fig. 2 of the proposed scheme are proved for every part of linac. Such a design of the focusing channel carries the problem of matching the beam with the channel to the entrance of the RFQ. Methods and devices of matching the beam of the electrostatic injector and RFQ structure are well known today and have been tested at the working accelerators. Now preparations for the experimental test on the ISTRA-36 accelerator of the proposed ITEP method of dynamic matching are underway. Match-

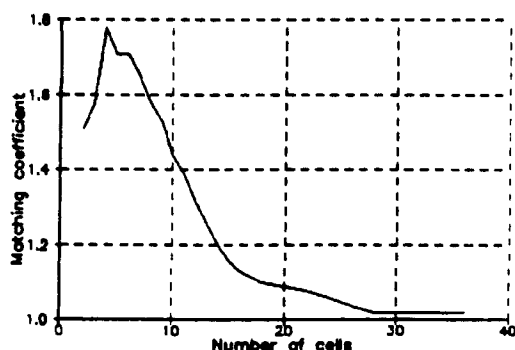


Figure 2: The dependence of matching coefficient on the number of RFQ cells for cosine law of RFQ electrodes mean radius variation in adiabatic matching horn.

ing of the RFQ with the Alvarez structure which works at the doubled frequency of RF field using the one gap buncher and the system of matching magnetic quadruple lenses at the drift space have been realized on the ISTRA-36 accelerator. Substitution of the one gap buncher for the quarter wave matching resonator on the part with RFQ with preliminary drift space [15] will let us connect both structures directly while preserving the transverse matching of the beam. The possibility of such a substitution is studied below.

To fully guarantee the absence of particle losses additional bunching of the beam between the RFQ and DTL with bunching factor 1.76 is needed. This result may be obtained by using a single-gap buncher with wavelength of 2 m or 4 m, effective voltage of 162.5 kV or 325 kV, respectively, and drift space of 80.4 cm. Between the DTL and DAW structures one may use the four-gap buncher with average field of 0.47 MV/m and wavelength of 2 meters. Use of a single-gap buncher in this case is impossible [12].

B. Current Limits and RF Power Losses in Linac Resonators

Current limits and transverse dimensions of the beam were calculated based on typical parameters of ion sources in the ITEP linac ISTRA-36: beam current = 150 mA and normalized emittance = 0.2 cm · mrad. Emittance growth along the linac was set partly taking into account of the experience with previous computer simulations for ISTRA [16] and partly analogical to values calculated in LANL. The values of current limits were calculated in smooth approximation to oscillation equations [17]. The minimum value of the current limit of 800 mA is at the

end of the RFQ and it is defined by longitudinal Coulomb repulsion due to decrease of the absolute value of the synchronous phase in the RFQ. Nevertheless, the presented value is 2.5 times higher than the maximum current of the beam. The matched beam size along the whole linac is below approximately one half of the aperture. As the taken value of input emittance is of an order of magnitude higher than the value adopted at LANL there is no reason to expect significant emittance growth in separate sections of the linac than the presented values. However, it is necessary to confirm this estimate by beam dynamics simulations.

As the total length of the RFQ is equal to 8.6 m the total losses in copper of the resonator are approximately 570 kW. Power consumption for acceleration is 1.03 MW.

Analysis of the calculation results [12] shows that the parameters of the DTL resonators are quite close to optimum from the point of view of efficiency. The obtained data show also that dissipation of RF power in the drift tubes is rather high (at the end of the last resonator each drift tube dissipates about 80 kW). Total RF power losses in the DTL resonators is 7.3 MW and total needed power is 51 MW.

For estimating RF power losses in the DAW resonators we use the data of MRTI for the INR meson factory: at an energy gain of 1 MeV/m the specific losses in copper are 0.04 MW/m. At a DAW structure length of 1246 m the losses will be 50 MW. Total power consumption in the DAW resonator is 455 MW.

The efficiency of the linac structures as a whole is ~80%.

IV. BRIEF ANALYSIS OF PROPOSED STRUCTURAL SCHEMES

The structural scheme of designing a high current linac has the same features in all the projects proposed by ITEP, MRTI, LANL and JAERI [4,5,12,18-23]. However, there are serious differences in the selection of such basic parameters as frequency and type of accelerating structures, energy of the beam at the passage between structures, beam current and so on. Because of the high price of accelerators and the difficulties of optimizing their characteristics and design, which depends on a large number of factors, a detailed discussion and estimation of different structural schemes and basic parameters of accelerators

becomes a necessary and important step in designing such a linac. There are enough data about the schemes of accelerators of LANL, MRTI and ITEP.

The main disadvantage of the LANL scheme is the possibility of the appearance of considerable deflection of the bunch's particles from the axis in the different parts along it after the beam convergence device. If we suppose that the deflecting field is sinusoidal, that the phase length of the bunch is 0.1 of the RF field period in the deflecting device, that it must work at a frequency of 350 MHz, that the deflecting angle in this device is 10° , and that the wavelength of transverse oscillations is 2 m, then the amplitude of coherent oscillations of the "head" and "tail" of the bunch will reach a value of 3 mm. As a result of nonlinearity of the field inside the focusing lenses, the coherent oscillations will quickly become noncoherent and emittance will be increased because of the appearance of the halo around the bunch, which will cause the loss of particles. Additional troubles can be expected because of the possibility of excitation inside the accelerating structure of the transverse modes of RF oscillations by the beam with periodical and multiple frequency deflections of the different parts of the beam from the axis of the structure.

At the same time the LANL scheme possesses some important merits. Among them, the simplicity of longitudinal matching while the bunches pass from one part of accelerator to another (only one change of frequency and only for two times), the filling in of all separatrices in accelerators with 700 MHz frequency, which decreases the peak current, and the ability to increase the shunt-impedance in the structure with the drift tubes at a frequency of 700 MHz due to the absence of lenses in tubes.

The scheme of the JAERI accelerator [22] for energy of 1.5 GeV and average current of 39 mA will be defined as the experience is gained while working on the prototype BTA-RFQ structures with energies of 0.1 - 2.0 MeV and the 10 MeV DTL with pulse current of 110 mA, $df = 10\%$ at a frequency of 201 MHz. Probably such a gradual approach to the development of such a large project is the most conservative.

The main disadvantage of the MRTI scheme [23] is the impossibility of correctly matching the channel with beam focusing by a longitudinal magnetic field of 7.6 Tl with the DTL; this mismatching causes large losses of particles, basically at a low energy. A

problem difficult to solve is created by placing the accelerating structure with the high heat extraction inside the superconductive solenoid, which will probably reduce the reliability of the accelerator. The merit of the scheme is the high ultimate current in the initial part if the difficulties with its design can be overcome.

The main disadvantage of the ITEP scheme is the very big difference (six times) between the frequencies in the DTL and DAW that forces a reduction in the synchronous phase along the DTL to low absolute value. Today this decision is not finally studied on particle losses. Among the merits of the ITEP's scheme is its simplicity and the possibility of transverse matching of the beam along all the linac in a wide range of currents, use of the structures tested in the working systems, and a good reserve in acceptance for the increase of the nominal current value.

Now we can see that all the proposed schemes have many common features, especially in the main part of the accelerator. The choice of DAW, SCS or ACS structures can be made after a detailed comparison of RF parameters and costs for construction and use, which can be done in a short time.

A much more difficult problem is the comparison of particle loss among the various accelerator schemes. There is no such data for losses of 10^{-6} - 10^{-7} today.

Comparison of the results is difficult also because different programs for accelerator design are used in the different accelerator centers. That is why the results can be compared only after calculation of the beam dynamics for all the proposed schemes using the same software package.

V. CONCLUSION

The analysis of the proposed structural schemes of the linacs and the results of estimates of the linacs' parameters shows us how impossible it is to choose definitively the optimal structural scheme today without some additional scientific and construction research. Some of the experimental investigations can be realized on the working accelerators LAMPF and ISTR-36. To test heat removal from the critical parts of CW accelerating structures a special experimental test stand should be constructed. Highly efficient and reliable CW power generators must be designed for this project.

To collect data about particle loss below the permissible integral level of $1.0 \cdot 10^{-6}$ it is necessary to

develop adequate programs for computing simulation of intensive beam dynamics along the whole accelerator, keeping in mind all the known factors that cause the beam's six-dimensional phase volume growth. For its minimization the investigations and solving of the problems connected with matching of the beam with the linac channel along its full length have to be done.

The parameters of the project proposed by ITEP can be corrected according to results of additional investigations and will be precise while studying the processes in the target and blanket of the accelerator.

The construction of such a large and expensive accelerator should be made step by step with the necessary corrections of design at the end of every step. It seems useful to start with the construction of a prototype of the initial part of CW linac, which will include all the elements that influence the beam quality.

The authors express their gratitude to Drs. T.E. Tretjakova, M.A. Kodzekin and V.S. Skachkov. The authors also wish to thank Prof. M. Reiser and Ms. C. Bellamy of the University of Maryland for their assistance with the final typing and editing of this manuscript.

*This paper is dedicated to the memory of Professor I.M. Kapchinskiy (1919-1993).

VI. REFERENCES

- [1] A. Favale et al., "Accelerator Based Conversion (ABC) for Utilization of Surplus Plutonium". White Paper, July 20, 1992.
- [2] G. Lawrence et al., "Overview of Los Alamos Power Accelerator Designs for ATW/ABC Applications". ATW/ABC Accelerator Workshop, Los Alamos, NM, November 16-20, 1992.
- [3] V.K. Plotnikov, "Main Considerations Related to ABC Project", *ibid.*
- [4] I.M. Kapchinskiy, "Choice of the Block-Scheme of 1-1.5 GeV, 300 mA Linear Accelerator", Proc. of the 1990 Linac Conf., LA-12004-C, Los Alamos, p.553.
- [5] P.P. Blagovolin et al., "High Current Ion Linacs for Transmutation of Long-Lived Wastes", *ibid.*, p.776.
- [6] I.M. Kapchinskiy, I.M. Lipkin, "On the Question of Density Distributions under Beams Autophasing in Linacs", Preprint ITEP 151, M., 1985.
- [7] T.P. Wangler, "Summary of Accelerator Aspects of the ATW/ABC Accelerator Workshop," Los Alamos, November 20, 1992.
- [8] V.G. Andreev, "The Geometry Determination for the Structure with Alternative Sign Accelerating Field of $\pi/2$ Type", Zh. Techn. Fiz., 1971, v. 41, N. 4., p. 788.
- [9] I.M. Kapchinskiy, "On the Choice of Method of Adiabatic Beam Bunching in the RFQ Linac", Preprint ITEP 64-90, M., 1990.
- [10] K.R. Crandall, "Effects of Vane-Tip Geometry on Electric Fields in Radio-Frequency Quadrupole Linacs", LA-9695-83, 1983.
- [11] I.M. Lipkin et al., "Codes for calculations and modeling for accelerator techniques (Summary of annotations)", M., 1992.
- [12] I.M. Kapchinskiy et al., "Linear Accelerator for Transmutation". Preprint ITEP 100-92, Moscow, 1992.
- [13] I.A. Vorobjov, A.A. Kolomiets, "Method of Dynamical Matching of RFQ's Charged Beam with Phase Length Lower than 180° ". Invention No. 1565336. Journal "Discoveries and Inventions" No. 34, 1991, p. 247.
- [14] I.A. Vorobjov, "Transverse Matching of RFQ's Beam with Closed Connected DTL", Preprint ITEP 4-93, M., 1993.
- [15] B.P. Murin et al., "Ion Linacs", v.1, M., Atomizdat, 1978.
- [16] I.A. Vorobjov et al., "Emittance Growth in ITEP RFQ Linac", Proc. 11th All-Union Acc. Conf., vol. 1, p. 506, 1989.
- [17] I.M. Kapchinskiy, "Theory of Resonant Linacs", M. Energoizdat, 1982.
- [18] G.P. Lawrence, "New Applications for High-Power Proton Linacs", ref. 4., p. 553.
- [19] R. A. Jameson et al., "Accelerator Driven Transmutation Technology for Radwaste and for Advanced Application to Power Production", LA-UR-91-2681, Los Alamos, 1991.
- [20] C.D. Bowman et al., "Nuclear Energy Generation and Waste Transmutation Using an Accelerator-Driven Intense Thermal Neutron Source", LA-UR-91-2601, Los Alamos, 1991.
- [21] S.O. Schriber, "Intense Proton Accelerator for Transmutation Neutron Source", LA-12205-C, Los Alamos, 1991, p. 261.
- [22] M. Mizumoto et al., "Intense Proton Accelerator Development Program", *ibid.*, p. 736.
- [23] G.I. Batskikh et al., "Linear Accelerator for Burner-Reactor", ref. 4., p. 581.

Acceleration and Transverse Focusing of Ion Beams in Lineondutron

Edward S. Masunov, Moscow Engineering Physics Institute, 115409, Moscow, Russia

Abstract

The main features of beam dynamics in linear accelerator with magnetostatic undulators (lineondutron) are discussed. Some expressions correlating the amplitude value of undulator and RF-fields under which the focusing and acceleration of particles take place in the absence of synchronism with the harmonics of RF-field are found. The configuration of magnetostatic and RF-field can be chosen to provide an effective bunching and acceleration of the beam.

I. INTRODUCTION

The idea to apply a combination of electrostatic field of undulator and radiofrequency field for acceleration and focusing of intense ion beams with low injection energy was discussed in [1], [2]. Employment of electrostatic undulator is useful for small values of initial particle velocity. The magnetostatic undulator may substitute instead of electrostatic one in case of high injection energy ($W > 100$ keV for proton beams).

In this paper we shall discuss the main features of beam dynamics in a lineondutron with magnetostatic undulator. In the evaluation of beam bunching and acceleration processes it is important to take into account the beam defocusing in a combined wave-undulator field. The motion equation of the particle may be written, using Lagrange function:

$$\frac{d}{dt} \vec{p} = e \vec{\nabla} (\vec{v} \cdot \vec{A} - \Phi), \quad (1)$$

where $\vec{p} = \vec{p} + e\vec{A}$ -- generalized momentum of particle, $\vec{A} = \vec{A}_r + \vec{A}_0$ -- the overall potential vector of RF-field and periodical magnetostatic field, Φ -- potential of electrostatic field.

II. LONGITUDINAL BEAM DYNAMICS

Let us see the beam dynamics in the magnetostatic undulator ($\Phi=0$) in the case, when no RF-field harmonics are synchronized with the beam. The trajectories of single beam particles in general case have complex nature, but they may always be represented as a combination of fast oscillations $\vec{r}(t)$ and slow variation $\vec{R}_c(t)$. Correspondingly, kinetic momentum of particle \vec{p} is represented as a sum of slowly varying and quickly oscillating components $\vec{p} = \vec{p}_c + \vec{\tilde{p}}$. By averaging over quick oscillations, from (1) we obtain an equation, which describes the slow evolution \vec{R}_c .

$$\frac{d}{dt} \vec{R}_c = - \frac{e^2}{2m\gamma} \vec{\nabla} \langle (\vec{A}_v + \vec{A}_0)^2 \rangle, \quad (2)$$

Taking into account only the fundamental space harmonics of the wave and undulator, the equation (2) can be rewritten in the form

$$\frac{d}{dt} (\gamma_c \vec{\beta}_c) = - \frac{\lambda}{8\pi\gamma_c} \vec{\nabla} U, \quad (3)$$

where the potential function

$$U = \vec{b}_v^2 + \vec{b}_0^2 - 2\vec{b}_v \cdot \vec{b}_0 \sin \psi. \quad (4)$$

Here $\vec{b}_{v,0} = e\vec{B}_{v,0}/2\pi mc$ -- the dimensionless amplitudes of the transverse components of the wave magnetic field \vec{B}_v and the undulator field \vec{B}_0 , $\vec{B}_{v,0} = \text{rot } \vec{A}_{v,0}$, $\psi = \omega \int dz/v - \tau - \psi_0$ -- the particle phase in a combined wave field, ω -- the frequency of RF-field, $\tau = \omega t$, ψ_0 -- the initial phase.

The normalized velocity of a synchronized wave is

$$\beta_s^{\pm} = \frac{v_s^{\pm}}{c} = \frac{\beta_v \lambda_0}{\lambda_0 \pm \beta_v \lambda_v}, \quad (5)$$

where β_v and λ_v -- the normalized phase velocity and RF-field wavelength, λ_0 -- the undulator period.

From (3) one can see that the longitudinal bunching and acceleration of the beam are possible even in the field of TE- or TEM-wave as a result of joint influence on the beam of non-synchronized RF- and undulator fields harmonics. The beam energy is increased due to RF-field energy.

At the given amplitudes the energy increase $\Delta\gamma = \Delta W/mc^2$ on the length λ_0 will be maximum, when the transverse symmetry (antisymmetry) planes over the magnetic field of the RF-wave and undulator coincide with the plane, along which the beam is injected. In this case for a synchronized particle

$$\Delta\gamma = \frac{\pi\lambda_0}{\beta_v \lambda_{\gamma_c}} b_v b_0 \cos \psi_s, \quad (6)$$

i.e. the acceleration rate is proportional to the amplitudes of RF- and undulator fields.

High level capture and good bunching of the beam may be obtained, provided one supplied the adiabatic growth of the values $b_v(z)$ and $b_0(z)$ along the longitudinal axis and corresponding increase of the undulator period λ_0 , to maintain the beam synchronism with a combined wave field.

III. TRANSVERSE FOCUSING OF BEAM

The choice of the functions $b_v(z)$ and $b_0(z)$ is not arbitrary because simultaneously with acceleration it is necessary to supply transverse focusing of the beam. Let us note that magnetostatic undulator with transverse deflection fields can always be treated as a device producing slalom beam focusing. The transverse RF-field of the wave can both focus and defocus the beam. A combined wave and undulator field, accelerating particles in the longitudinal direction, defocuses them in the transverse direction. Finally, the sum effect may be found only from the analysis of equation solutions (3). As one can see from (3) and (4), equilibrious trajectory may exist for all the particles of the injected beam, if two conditions for the injection plane are valid,

$$\bar{\nabla}_1(\bar{b}_v^2 + \bar{b}_0^2) = 0 \text{ and } \bar{\nabla}_1(\bar{b}_v \cdot \bar{b}_0) = 0. \quad (7)$$

In the simplest case, when the axis of magnetic undulator coincides with that of RF-system and the beam is injected along it, equalities (7) are validated automatically. In other cases an equilibrious trajectory exists, if the field amplitudes and their transverse gradients are connected by the relations

$$B_0 = \frac{\lambda_v}{\lambda_0} B_v, \quad \bar{\nabla}_1 B_0 = -\frac{\lambda_v}{\lambda_0} \bar{\nabla}_1 B_v. \quad (8)$$

This result may be used at high value of the aperture of the accelerating channel, because it allows to inject particles beyond the axis, closing the beam to the poles of undulators, in order to increase the efficiency of acceleration. Moreover, if the RF-field and undulator field have multiple symmetry (antisymmetry) planes, one can simultaneously accelerate several beams.

The condition of the transverse particle focusing may be obtained from (4), when the effective potential U_{eff} has the minimum. If the beam is injected on the axis, a focusing takes place for all particle phases, when

$$B_v < \alpha \frac{\lambda_0}{\lambda_v} B_0, \quad (9)$$

where $\alpha \approx 1$ and depends on field structure and beam phase size.

At low energy of injection in linecondutron the amplitude of the undulator field B_0 will be high because $\beta_v = \lambda_0/\lambda_v \ll 1$. The value B_0 may be decreased, if additional electrostatic field $\bar{E}_c^\perp = -\bar{\nabla}_1 \Phi(\bar{r}^\perp)$ is used. The equilibrious trajectory may exist for all particles of beam, when

$$\bar{\nabla}_1(\bar{B}_v^\perp \cdot \bar{B}_0^\perp) = 0 \quad (10)$$

and

$$\bar{E}_c^\perp = \frac{e\lambda_v^2}{8\pi m\gamma} \left(1 - \frac{\lambda_v^2 \bar{B}_v^{\perp 2}}{\lambda_0^2 \bar{B}_0^{\perp 2}} \right) \bar{\nabla}_1 \bar{B}_0^{\perp 2}. \quad (11)$$

IV. SOME EXAMPLES

The effective amplitude of the accelerating field $E_{eff} = T_b E_v$, where E_v is amplitude of RF-field, T_b is a parameter, proportional to the amplitude of undulator field,

$$T_b = \frac{eB_0\lambda_0}{4\pi mc\beta_v\gamma_c}.$$

For bunching and acceleration of nonrelativistic protons it is convenient to use RF-resonators, based on uniform longitudinal oscillators. When $\lambda_v = 3$ m, $\lambda_0 = 0.045$ m, we have $\beta_v = 1.5 \cdot 10^{-2}$, that corresponds to injection energy $W \approx 100$ keV. If $B_0 = 2$ T then $E_v = 90$ kV/cm and maximal increase of energy in such an accelerator: 1.4 MeV/m. The value E_v may be increased two times without variation of the acceleration rate, provided one decreases B_0 up to 1 T and introduces an additional transverse electrostatic field, value of which is not greater than $E_c \sim 20 - 30$ kV/cm.

V. CONCLUSION

Use of magnetostatic undulators to accelerate and to focus ion beams promises to be a very perspective practice. The necessity to use slowing-down systems is removed. RF-systems may be uniform ones that facilitates their tuning. By means of variation in the amplitude and in the period of the undulator field, there is a chance to provide high level capture factor of the beam and its effective bunching. Big opportunities are opened by applying linecondutron to accelerate quasi-neutral beams constituted by particles with the same Z/M ratio but with opposite signs of charge (for example, H^+ and H^-). Positively and negatively charged particles are accelerated in the same bunch. Therefore, when injecting quasi-neutral beam into such an accelerator, no difficulties arise related to limiting intensity due to the value of space charge.

VI. REFERENCES

- [1] E. Masunov, A. Novicov, "Application of electrostatic undulator for acceleration of intense ion beams", *Conference Record of the 1991 IEEE Particle Accelerator Conference*, Vol. 5, pp. 3177-3179.
- [2] E. Masunov, V. Leonov et. al., "A project of ion linear undulator accelerator with transverse RF-field", *Proceedings of the Third European Particle Accelerator Conference*, 1992, Vol. 1, pp. 572-574.

Linac Design Study for an Intense Neutron-Source Driver*

M.T. Lynch, A. Browman, R.DeHaven, R. Jameson, A. Jason, G. Neuschaefer, P. Tallerico, and A. Regan
Los Alamos National Laboratory
Los Alamos, NM 87545

*Supported by the US Department of Energy, Office of Defense Programs

Abstract

The 1-MW spallation-neutron source under design study at Los Alamos is driven by a linac-compressor-ring scheme that utilizes a large portion of the existing Los Alamos Meson Physics Facility (LAMPF) linac, as well as the facility infrastructure. The project is referred to as the National Center for Neutron Research (NCNR). A second phase of the proposal will upgrade the driver power to 5 MW. A description of the 1-MW scheme is given in this paper. In addition, the upgrade path to the substantial increase of beam power required for the 5 MW scenario is discussed.

I. Introduction

A proposal is being developed to modify LAMPF for use as a spallation-neutron source¹. The spallation source would require a 1 MW average beam as the input driver, with consideration being given for a future upgrade to 5-MW. The 1-MW driver would require that the LAMPF facility consistently and reliably provide 30 mA peak, 1.25 mA average current at 800 MeV. A large portion of the LAMPF accelerator can remain intact, but the front end of the accelerator would need replacement to be suitable for this application. This paper addresses the issues associated with the LAMPF linac and RF systems. Other papers at this conference address other parts of the spallation source^{1,2}.

II. The LAMPF Accelerator

The existing LAMPF accelerator consists of dual Cockcroft-Walton injectors (H^+ and H^-) with an output

energy of 750 keV. The current is chopped at a 201.25 MHz rate and then is accelerated to 100 MeV in a 201.25 MHz Drift Tube Linac (DTL). A side-coupled linac structure, operating at 805 MHz, accelerates the beam to the final energy of 800 MeV. A line diagram of the LAMPF accelerator is shown in Figure 1. Details of the LAMPF accelerator operation are listed in Table 1.

Table 1
LAMPF Accelerator Operating Parameters

Output Energy	800 MeV
Macropulse Rep Rate	120 Hz
Pulse Width	1 ms
Micropulse Rep Rate	201.25 MHz
Production Capability:	
Iavg during macropulse	17 mA, H^+
Duty Factor	10 %
Avg. Beam Power	1.4 MW
Experimental Operations:	
Iavg during macropulse	21 mA
(using 14 mA, H^+ ; and 7 mA, H^-)	

The baseline design for the neutron source driver completely replaces the Cockcroft-Walton injectors and the 201.25 MHz DTL. This section of the accelerator has been the most unreliable part of the accelerator in the recent past. The 805 MHz SCL would remain essentially intact.

III. Linac for the Intense Neutron Source

The linac for the proposed spallation source would use as

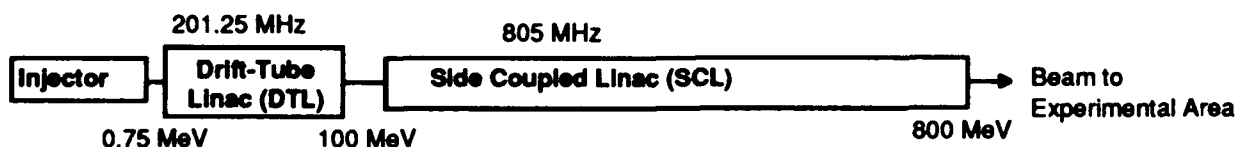


Figure 1. Line Diagram of the existing LAMPF Accelerator

much of the existing LAMPF accelerator as possible. Refer to Figure 2. The front end of LAMPF would be replaced with a 75 keV H⁻ injector, a 402.5 MHz RFQ and DTL to get the beam to 20 MeV, and a second DTL at 805 MHz to raise the energy to 100 MeV. The existing SCL would remain to accelerate the beam to 800 MeV for insertion into the storage rings¹. The RFQ has a relatively high output energy (~7 MeV). The DTL structures are all standard Alvarez DTL tanks. This front end uses relatively high gradients in order to fit into the existing LAMPF tunnel. The primary drawback to the use of high gradients is increased copper losses. The front end therefore operates at a lower efficiency (beam output power divided by RF power in) compared to an ideal structure with unlimited real estate.

IV. Beam Macropulse Structure and Repetition Rate

The storage ring design for this neutron spallation source has a one-time transit time of 671 ns. In order to allow time for kicker magnet rise-time, the beam must have a notch, so the beam time profile is 436 ns "on" and 235 ns "off". In order to obtain an average beam power of 1 MW, the average beam stored in the rings must be 1.25 mA (at 800 MeV). Assuming a 90% capture efficiency in the rings, the linac average output current must be 1.39 mA. Assuming a rep rate of 60 Hz and a macropulse length of 1.2 ms, the average current during the macropulse must be 19.5 mA. Given the chopping rate described above (65%), the peak current during the "on" time of the macropulse is 30 mA.

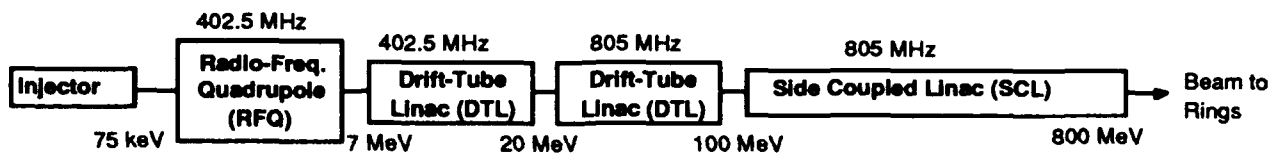


Figure 2. Line Diagram of the Proposed NCNR Driver Linac.

The SCL consists of 44 modules, each driven by a 1.25 MW klystron. Very little of this portion of the accelerator will need to be changed for the 1 MW driver. The primary changes would come in the low-level feedback/feedforward controls.

Structure power, beam power, and RF power requirements for the RFQ, DTL's, and SCL are shown in Table 2. The RF generator size for the new sections is nominally 1.25 MW based on the existing Ground Test Accelerator (GTA), LAMPF, and Ballistic Missile Early Warning System (BMEWS) klystron technology. Two-klystron modulators based on the GTA technology³ would be used for all new klystrons. Small RF generators (10 kW or less) are needed for matching section cavities between the RFQ and first DTL and between the two DTL's. These amplifiers will either be solid state (if the power is low) or triode or tetrode-based cavity amplifiers (if more than a few kW is needed).

The output beam is shared between two storage rings¹, one operating at 40 Hz and one at 20 Hz. This output requires that the injector be pulsed at a 120 Hz rate, but the RF in the accelerator cavities is pulsed only at the "syncopated" rate shown in Figure 3. The RF therefore must be capable of repeating at a 120 Hz rate but averages only 60 pulses per second.

V. The LAMPF SCL

There is one area of concern with the SCL. Some of the low energy modules are very long because four separate tanks are bridge-coupled together and driven by a single klystron. The measured group delay from the drive point to one end of the structure is about 1-μs in these modules, and the loaded Q of the structure is about 9000, giving a fill time of about 3.5 μs. It is therefore impossible for the RF feedback system to keep up with the chopping rate of the beam because the response time

Table 2
Sections of NCNR and Power Required

Section	Frequency (MHz)	# of Tanks	# of RF Modules	Beam Power (MW)	Structure Power (MW)	Total RF Power* (MW)	New?
RFQ	402.5	1	2	0.14	1.4	1.93	yes
DTL-1	402.5	2	2	0.25	1.23	1.85	yes
DTL-2	805	15	8	1.6	4.2	7.25	yes
SCL	805	104	44	13.7	27	51	no

*Total RF Power includes a 25% margin for control and losses

is so much slower than the chopping rate. Since the beam chopping pattern is repetitive and known, one could consider the use of feedforward and a large amount of RF overdrive to correct the beam chopping transients. However the long group delay of the structure precludes successful control. The RF cannot get from the drive point to the structure ends fast enough to react to the beam.

VI. Plans for Upgrade to 5 MW

The plans for upgrade to 5 MW are very sketchy at this point. The baseline accelerator for the 5 MW source has an output energy of 1.6 GeV and a current level of 75 mA. The pulse width and duty factor are unchanged. This accelerator would almost certainly require funneling at the

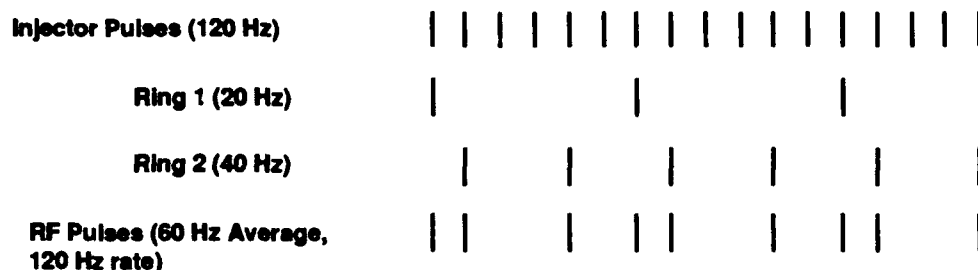


Figure 3. Distribution of pulses to the two rings for NCNR

Two items can ameliorate the beam loading problem due to a chopped beam. If the structure has enough stored energy, there will be a minimal drop in the structure field from the front to the rear of the pulse. Initial analysis of this variation in fields with NCNR currents shows a droop of 1.5% in one module during the "on" time of the beam. This is being investigated further to see if the beam transport system will carry the beam with this amount of energy variation.

Another solution being considered is to break the modules in half, and drive each half independently. Not all modules are large, so this would only be done on a few of the SCL modules. The RF system would still not be fast enough to respond at the chopping rate, but the droop per tank would be cut by a factor of 4 (droop is proportional to N^2 , N = number of cells).

An experiment is planned for early June, 1993, in which two different modules of the LAMPF accelerator will be operated with GTA style feedback controls. NCNR will require that LAMPF operate at what has historically been the limits of its capability. One of the problems has been beam spill at high operating currents. The major portion of the lost beam at LAMPF occurs during the beam turn-on transient. The GTA-style feedback controls allow precise setting of the feedback gains and have the capability of adaptive feedforward control⁴. The adaptive feedforward technique is an extremely powerful tool for the correction of repetitive, systematic errors. For more detail about the use and applications of adaptive feedforward refer to the paper by Ziomek⁵, et al, in these proceedings.

low energy end (between the two DTL's). The path to 1.6 GeV can go two ways. In the first, an afterburner (perhaps superconducting) would be added to the existing structure to raise the output energy from 800 MeV to 1600 MeV. This scheme assumes that operation at 1 MW has shown the capability for successful operation with 2.5 times more current. In the second scheme, the complete SCL structure and perhaps some of the DTL structures would be replaced with a new structure (perhaps superconducting).

VII. References

- [1] A. Jason, et al, "A Los Alamos Design Study for a High-Power Spallation-Neutron-Source Driver," these proceedings.
- [2] B. Blind, et al, "Lattice Design of the LANL Spallation-Source Compression Rings," these proceedings.
- [3] P.J. Talerico, et al, "Progress on the GTA 850-MHz RF System," LANL report number LA-CP-90-231, Proceedings of the NPB Technical Interchange Symposium, May 21-24, 1990.
- [4] S. Jachim, et al, "The Los Alamos VXI-Based Modular RF Control System," these proceedings.
- [5] C. Ziomek, et al, "Results of Adaptive Feedforward on GTA," these proceedings.

Design and Operation of the HIMAC Injector

Takeshi Murakami, Hirotugu Ogawa, Satoru Yamada, Yukio Sato, Takanobu Yamada, Atsushi Kitagawa,
Jun Yoshizawa, Shinian Fu, Toshiyuki Kohno, Kenji Sato, Akifumi Itano, Masayuki Kumada,
Eiichi Takada, Mitsutaka Kanazawa, Kouji Noda, Michio Sudou, and Yasuo Hirao
National Institute of Radiological Sciences
4-9-1 Anagawa, Inage-ku, Chiba 263, JAPAN

Osamu Morishita and Kenji Sawada
Sumitomo Heavy Industries, Ltd.
5-2 Sobiraki, Niihama, Ehime 792, JAPAN

Abstract

A heavy-ion synchrotron dedicated to medical use is under construction at the National Institute of Radiological Sciences, Japan. The injector system, comprising a PIG source, an ECR source, an RFQ linac, and an Alvarez linac of 100 MHz, accelerates heavy ions with a charge-to-mass ratio as small as 1/7, up to 6 MeV/nucleon. First operation of the injector system has shown satisfactory performance.

I. INTRODUCTION

A heavy-ion synchrotron, HIMAC (Heavy Ion Medical Accelerator in Chiba) [1], is under construction at the National Institute of Radiological Sciences (NIRS), Japan. HIMAC is the first heavy-ion accelerator dedicated to medical use in the world. Its design is based on the requirements of radiological treatments, referring to the research of biological effectiveness and clinical trials at LBL. Ions with atomic numbers between 2 (helium) and 18 (argon) are accelerated, and the maximum energy is 800 MeV/nucleon for ions with a charge-to-mass ratio (q/A) of 1/2, corresponding to a range of 30 cm in tissue. The reliability of the accelerator is of great importance.

The injector system [2] comprises two types of ion sources (a PIG source and an ECR source), an RFQ linac and an Alvarez linac of 100 MHz with three tanks. The beams extracted from the ion sources are transported through a low-energy beam transport line (LEBT), 7 m long, and injected into an RFQ linac. The Alvarez linac follows the RFQ linac and an interlinac transport line (LLBT), 1.9m long. The medium-energy beam transport line (MEBT) transports the accelerated beam to the synchrotron. The transport lines also include the beam diagnostic apparatus: Faraday cups, profile monitors, electrostatic pickup electrodes, etc. A 100 MHz debuncher cavity is installed in the MEBT line to suppress the energy spread to $\pm 0.2\%$.

The linac system accepts heavy ions with a q/A as small as 1/7 and has no charge strippers except for a stripper foil in the MEBT. The specifications of the injector system are summarized in Table 1.

The injector system has been completed and operation started in March, 1993.

Table 1. Specification of the injector system.

Ion species	$^4\text{He} \sim ^{40}\text{Ar}$
Charge-to-mass ratio	$\geq 1/7$
Ion sources	PIG & ECR
Frequency	100 MHz
Repetition rate	3Hz max
Duty factor	0.3% max
Acceptance	0.6π mm-mrad (normalized)
RFQ linac	
Input/Output energy	8 / 800 keV/nucleon
Vane length	7.3 m
Cavity diameter	0.59 m
Max surface field	205 kV/cm (1.8 Kilpatrick)
Peak rf power	260 kW (70% Q)
Alvarez linac	
Input/Output energy	0.8 / 6.0 MeV/nucleon
Total length	24 m (3 rf cavities)
cavity diameter	2.20 / 2.18 / 2.16 m
Average axial field	1.8 / 2.2 / 2.2 MV/m
Max surface field	150 kV/cm (1.3 Kilpatrick)
Peak rf power	840 / 830 / 770 kW (75%Q)
Focusing sequence	FODO (5.1 kG/cm max)
Output beam emittance	$\leq 1.5\pi$ mm-mrad (normalized)
Momentum spread	$\leq \pm 1 \times 10^{-3}$

II. ION SOURCES

Two types of ion sources (PIG and ECR) were chosen based on their reliability of operation, capability to produce the required intensities, and simple maintenance. The sources are placed on platforms to which a high voltage of 60 kV can be applied.

A. PIG Source

The PIG source is an indirectly heated (hot) cathode

type. The performance of the PIG ion source is shown in Table 2. The extraction voltage is 25 kV and the discharge power is 2-3 kW at peak and 1 W on the average. A typical value of the emittance is about 250π mm-mrad for both the x and y directions. The lifetime of the source is about two weeks, due to a low duty factor. The stability is satisfactory and no adjustments of the operation parameters are necessary for 24 hours.

Table 2. Beam intensities (in emA) extracted from the PIG ion source at a test bench. Underlined species have q/A values larger than 1/7. The intensities in parentheses may not be correct due to the mixed beam with the same q/A value.

Ion	Gas-flow (cc/min.)	Charge state							
		1 ⁺	2 ⁺	3 ⁺	4 ⁺	5 ⁺	6 ⁺	7 ⁺	8 ⁺
⁴ He	20 (He)	<u>3.5</u>	<u>3.0</u>						
¹² C	0.6 (CO ₂)	1.0	<u>3.5</u>	(3.0)	<u>0.6</u>	<u>0.02</u>			
¹⁴ N	0.6 (N ₂)		<u>2.0</u>	<u>2.5</u>	<u>1.2</u>	<u>0.2</u>			
¹⁶ O	0.6 (CO ₂)		2.0	<u>2.3</u>	(3.0)	<u>0.3</u>	<u>0.03</u>		
²⁰ Ne	1.1 (Ne)		2.0	<u>2.0</u>	<u>0.8</u>	<u>0.4</u>	<u>0.02</u>		
²⁸ Si*	0.3 (Ar)			0.4	<u>0.6</u>	<u>0.3</u>	<u>0.05</u>	<u>0.01</u>	
⁴⁰ Ar	0.2 (Ar)			1.5	1.9	1.8	<u>0.8</u>	<u>0.4</u>	<u>0.2</u>

*Produced by sputtering of a crystal with Ar ions.

B. ECR Source

The ECR source has a simple single-stage structure with microwaves of 10 GHz and 1.9 kW. The magnetic field for confinement consists of a 1T axial field produced by two solenoidal coils and a 0.8T radial field by a set of permanent sextupole magnets. A typical operational condition is a gas-flow rate of 5×10^{-4} Torr-l/sec and a vacuum of about 1×10^{-6} inside the plasma chamber. The performance of the ECR source is summarized in Table 3.

Table 3. Beam intensities (in eμA) extracted from the ECR ion source. See captions of Table 2.

Ion	Charge state								
	1 ⁺	2 ⁺	3 ⁺	4 ⁺	5 ⁺	6 ⁺	7 ⁺	8 ⁺	9 ⁺
¹ H	<u>1610</u>								
⁴ He	<u>1290</u>	(440)							
¹⁴ N	310	<u>350</u>	<u>250</u>	<u>240</u>	<u>160</u>	<u>23</u>			
¹⁶ O	290	250	<u>180</u>	(180)	<u>120</u>	<u>74</u>			
²⁰ Ne	360	210	<u>210</u>	<u>170</u>	(120)	<u>93</u>	<u>19</u>	<u>5</u>	<u>0.2</u>
⁴⁰ Ar	360	170	100	100	(100)	<u>100</u>	<u>100</u>	<u>120</u>	<u>61</u>

III. LINACS

A. RFQ Linac

The RFQ linac is a conventional type with four vanes. The cavity is mechanically separated into four tanks. The four vanes were placed in each tank independently and the four tanks were aligned precisely. The tanks are made of copper-plated mild steel, whereas the vanes are made of solid copper. The rf contact between the vanes and the tank walls is achieved by spring-rings made of silver coated stainless steel.

A rather low frequency of 100 MHz was chosen to obtain a sufficient focusing strength. The calculated transmission efficiency exceeds 90% for a DC beam with a focusing strength of $B = 3.8$. The longitudinal and transverse voltage distributions are controlled by 40 side-tuners. Those tuners were welded after the voltage distribution was tuned within errors of 4.9% in the longitudinal and 2.6% in the transverse directions.

The transverse phase matching between the RFQ and Alvarez linac is achieved by a quadrupole-magnet quadruplet and steering magnets installed in the LLBT.

B. Alvarez Linac

The linac tank, 24 m long in total, is separated into three independent rf cavities. The tanks are made of copper-clad mild steel, and the drift tubes are copper-plated stainless steel. Each drift tube is supported by horizontal and vertical stems, 3 and 5 cm in diameter, respectively. An overview of the RFQ and Alvarez linacs is given in Figure 1.

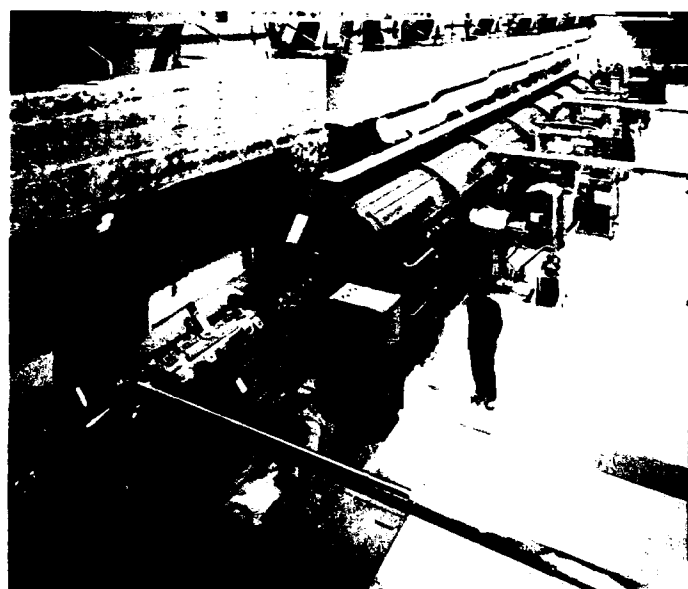


Figure 1. The RFQ and Alvarez linacs.

The number of unit cells is 106 and the gap-to-cell-length ratio is around 0.22. Every second drift tube is equipped with a quadrupole magnet. The Q-magnets have

laminated cores and are excited by pulse power sources with a flat-top-duty of 0.3% to reduce the thermal loads. The 54 quadrupole magnets were designed in four categories: 70, 90, 135, and 165 mm in length, and 5.1, 4.0, 2.7, and 2.2 kG/cm in field gradient.

The tolerance of alignment of the Q-magnets was estimated with the program PARMILA. The transverse emittance growth is not serious when the alignment error is ≤ 0.1 mm in the transverse direction, including the errors of rotation ($\pm 1^\circ$), tilt ($\pm 1^\circ$), and excitation ($\pm 0.5\%$). The accuracy was achieved by an alignment telescope and an optical target inside a bore hole of the tube. The tilt of the acceleration field was tuned with side-tuners, which were welded after the tuning, within an error of 2%. The calculation, however, showed that a phase difference larger than $\pm 3^\circ$ between three tanks had large effects on the beam quality. An automatic phase control system was therefore developed so that the phase stability could be measured to be better than $\pm 0.5^\circ/8h$.

Three sets of 1.4 MW amplifiers excite three cavities of the Alvarez linac. Each amplifier consists of a final stage and two driver stages (100 kW and 5 kW), which are equipped with power tubes of Siemens RS2074SK, RS2058CJ, and RS2032CL, respectively.

C. Control System

A control system consists of three hierarchical layers: a system control unit (SCU), a group control unit (GCU), and a universal device controller (UDC). The SCU of $\mu VAX3500$ mainly works as a man-machine interface. The GCU, comprising two $\mu VAX II$, directly controls the peripheral devices through the UDCs, which are 16-bit micro-computers installed in the devices. The SCU is connected through an ETHERNET to a central computer unit by which it communicates with other systems: a synchrotron system, a high-energy beam transport line, and a treatment control system. Another ETHERNET is installed to connect the SCU and the GCU. The UDCs are linked to the GCU with optical fiber lines. All devices are controlled at an operator console with four touch panels and three rotary encoders.

VI. PERFORMANCE OF THE LINACS

Installation of the injector system was completed in February, 1993. The beams of $^4\text{He}^+$ and $^{40}\text{Ar}^{3+}$ were successfully accelerated in the first operation about a month. The success of acceleration in a relatively short term made us confident of the reliability of the system. The typical parameters and characteristic values for the acceleration of $^4\text{He}^+$ ($q/A = 1/4$) are summarized in Table 4. The observed values of the transmission for the both linacs were satisfactory. Figure 2 shows the beam pulse shape after the

Alvarez linac. The beam intensity was stable within $\pm 3\%/2h$ without any changes in the operational parameters.

Table 4. Typical parameters and characteristic values for acceleration of $^4\text{He}^+$ ($q/A = 1/4$).

RFQ	
Injected beam intensity	190 μA
Extracted beam intensity	167 μA
Transmission of RFQ	88 %
Beam width	1 ms
Rf power	86 kW
Tank vacuum	1.0×10^{-7} Torr
Alvarez linac	
Injected beam intensity	167 μA
Extracted beam intensity	138 μA
Transmission of Alvarez	83 %
Repetition rate	1.3 Hz
Rf pulse width	1.2 ms
Rf power	270 / 390 / 270 kW
Tank vacuum	$0.9 \sim 1.0 \times 10^{-7}$ Torr

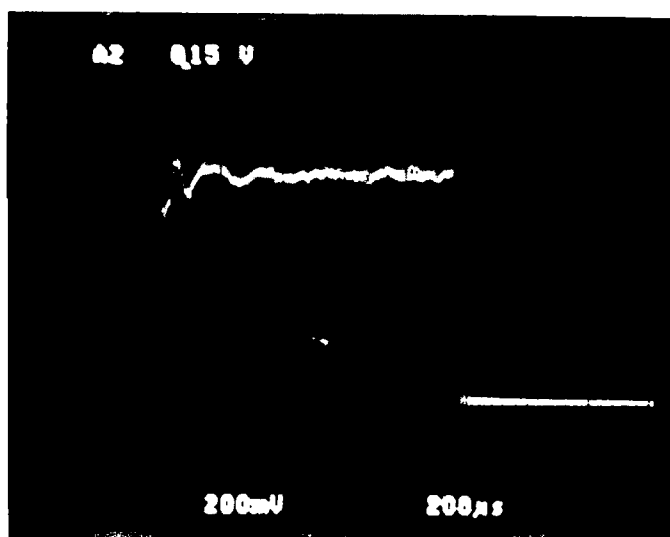


Figure 2. Observed beam pulse (output of a buffered amplifier) after the acceleration by Alvarez linac.

We would like to thank the crew of Accelerator Engineering Corporation of their skillful operation.

V. REFERENCES

- [1] Y. Hirao et al., "Heavy ion medical accelerator in Chiba," NIRS-M-89, HIMAC-001, 1 (1992).
- [2] S. Yamada et al., "Injector system of HIMAC," Proc. 1990 Linac Conf., Albuquerque, NM, USA, 593 (1990).

TIME-OF-FLIGHT MEASUREMENTS OF ABSOLUTE BEAM ENERGY IN THE FERMILAB LINAC

M.B. Popovic, T.L. Owens, T.K. Kroc, L.J. Allen and C.W. Schmidt
Fermi National Accelerator Laboratory*

ABSTRACT

Measurements have been made of the absolute energy of the fourth tank of our linac by measuring the time-of-flight of individual beam bunches passing between strip-line beam monitors at the entrance and exit of each tank of the linac. Accurate time-of-flight measurements are facilitated by the fact that the beam remains well bunched between strip-line monitors in the drift region beyond the fourth tank. Cable lengths were carefully measured using time-domain reflectometry. The data for tank 4 gave the time-of-flight over a 49.17 meter drift as 395.8 (± 0.5) nanoseconds. This translates into a measured β of 0.4155. The design[1] β for tank 4 is 0.4141. Further measurements on other linac tanks are planned, if machine time becomes available. In addition to determination of absolute beam energy, the time-of-flight data can be used for absolute energy calibration of the magnetic spectrometer system used for detailed energy analysis of the beam. We plan to implement this technique on the Linac Upgrade[2] to be installed in the summer of 1993.

EXPERIMENTAL CONFIGURATION

In this experiment it was important to identify signals produced from the same bunch at two different locations. The macropulse (train of beam bunches) for the Fermilab linac is produced by an electrostatic chopper which selects a portion of the DC beam from the preaccelerator. The initial state has one plate charged and one grounded which deflects the DC beam into a carbon disk. When beam is desired, the charged plate is grounded and the beam passes undeflected. To terminate the macropulse, the second plate is taken to the opposite polarity of the first plate so the beam is again deflected. The rise time of the thyratrons that switch the plates is such that the shortest macropulse is 50 to 100 nsec long which the buncher converts into approximately 10-20 micropulses.

A new circuit was devised out to produce the 3-4 micropulse burst used in these experiments. In the new circuit, one of the plates is disconnected from its corresponding thyatron and grounded. The other plate is given a DC bias so that its starting voltage is half its original value. When the thyatron fires, the voltage on the plate switches polarity. As the voltage passes through zero, a short section of beam (~ 20 nsec) passes down the beam line. The buncher then converts

the section of beam into 3 or 4 micropulses. Future experiments will attempt to produce single bunch micropulses by retuning the beamline and through strategic placement of apertures.

Figure 1 is an oscillogram from a Tek-7104 oscilloscope screen. The pulse train contains seven bunches. The larger amplitude pulse train comes from seven bunches pass

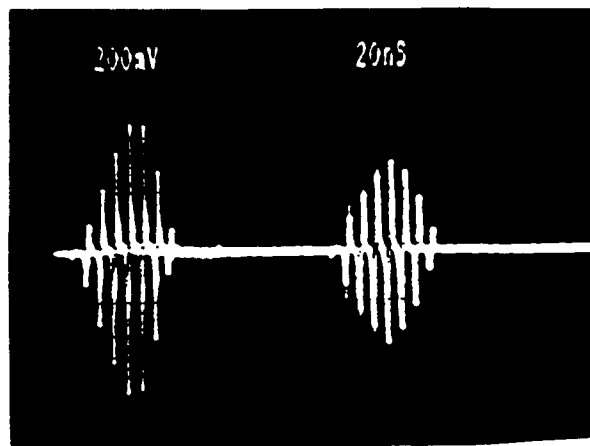


Figure 1.

ing the BPM detector at the entrance to tank 5. The second pulse train is produced by the same seven bunches passing BPM detector located at exit of the tank 7.

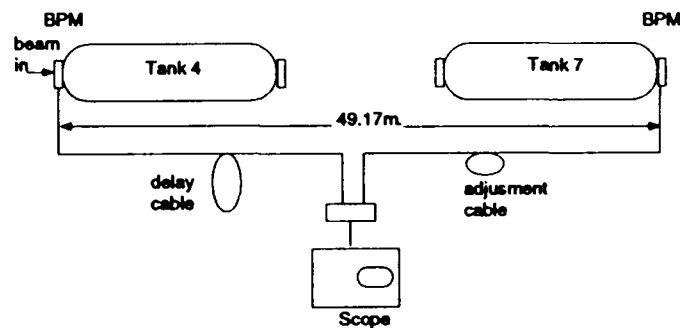


Figure 2.

The setup used in this experiment is shown schematically in figure 2. The delay and adjustment cables are used to insure that signals from two BPM detectors arrive at about the same time and that they can both be displayed on the scope screen with the shortest available time-base. This experiment was performed using a Tek-7401 scope. The time-base was 2nsec/div. The relative distance between two de-

* Fermilab is operated by the Universities Research Association under contract to the US Department of Energy.



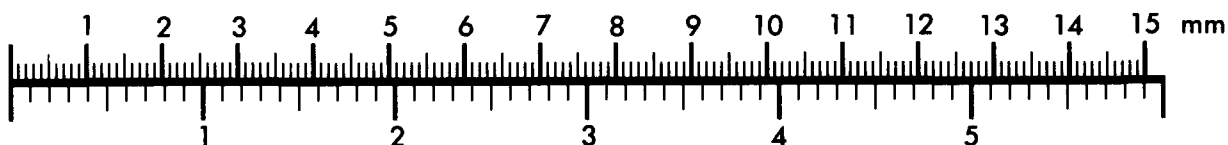
AIM

Association for Information and Image Management

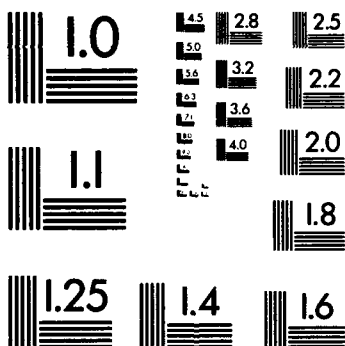
1100 Wayne Avenue, Suite 1100
Silver Spring, Maryland 20910

301/587-8202

Centimeter



Inches



tectors is known with a accuracy of ± 5 cm. We were able to read time interval between two signals with error of ± 0.5

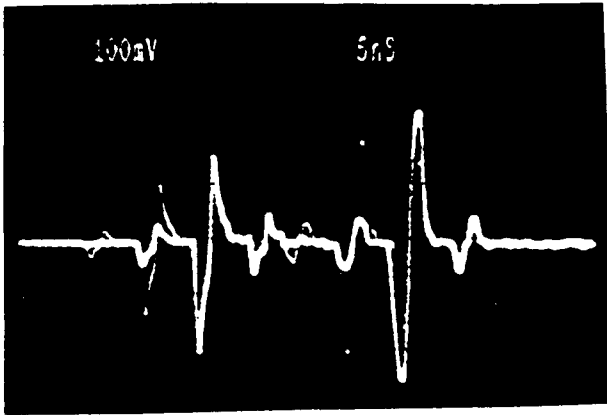


Figure 3.

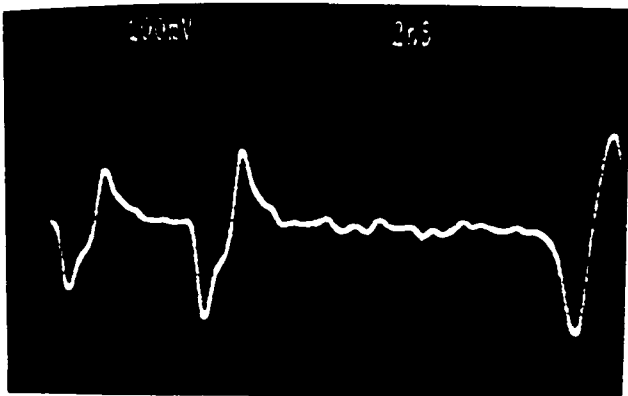


Figure 4.

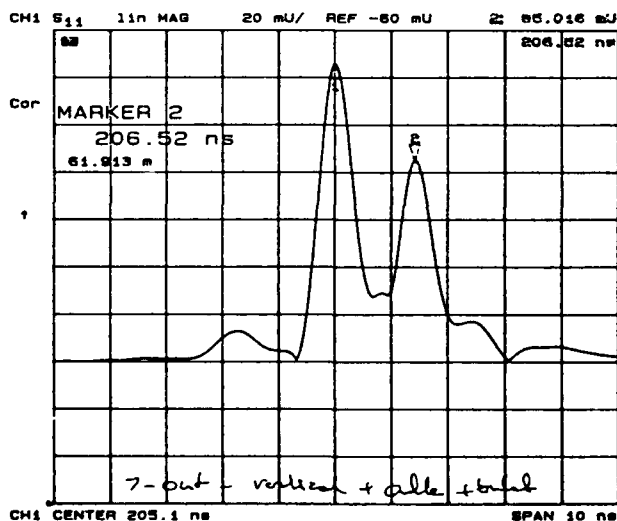


Figure 5.

nsec. Figures 3 and 4 show two signals on the scope screen with 5nsec/div and 2nsec/div time bases, respectively. Data

from figure 4 were used to determine β at exit of the tank 4.

The cable length or the time that the signal travels from BPM detector to the scope is measured using time-domain reflectometry. We have used an HP8753C network analyzer to determine cable length. Figure 5. is typical example of cable length measurement. Three peaks are associated with the cable connector on the detector, gap of the strip-line detector and termination of the strip-line, respectively. The marker position represents the time it takes for an impulse launched at the test port to reach a discontinuity and to return. Although the position of the marker is displayed with tenths of picosecond, HP documentation[3] is not clear concerning how errors are estimated. Using short cables whose lengths are known we have convince our self that errors are less than ± 0.5 nanosecond.

RESULTS AND CONCLUSIONS

The data for tank 4 gave the time-of-flight over a 49.17 (± 0.05) meter drift as 395.8 (± 0.5) nanoseconds. This translates into a measured β of 0.4155[1 ± 0.002]. The design β for tank 4 is 0.4141. We plan to implement this technique on the Linac Pugged to be installed in the summer of 1993. We will use wall current monitors for beam detection. Positions of detectors will be known to ± 0.5 am. We hope to measure time intervals up to ± 0.1 nsec using a Tetroxide Schedule transient waveform recorder.

REFERENCES

- [1] National Accelerator Laboratory, Design Report, July 1968.
- [2] CA.We. Schmidt, "The Forelimb 400-MeV Linac Upgrade", this conference.
- [3] HP8753C, "Operating Manual", Oct. 1989.

Phase Scan Signature Matching for Linac Tuning

T. L. Owens, M. B. Popovic, E.S. McCrory, C.W. Schmidt, and L.J. Allen
*Fermi National Accelerator Laboratory**
P.O. Box 500
Batavia, IL 60510, USA

Abstract

A conceptually simple method for tuning linac tanks has been tested on the Alvarez linac at Fermilab. Phases of beam-induced signals in stripline detectors are measured as tank phase is scanned over approximately 360 degrees. The stripline detectors are located downstream of the tank being tuned. The phase-scan curves have unique signatures that depend upon input beta and electric field. By matching theoretical curves of beam phase versus tank phase to measured curves, the important tuning parameters are determined. The tank parameters which are varied during curve matching include field amplitude, input beta, and relative tank-phase offset of the phase-scan curves. The actual phase of the tank fields relative to the design phase is found by noting the position of the actual tank phase along the phase-scan curve, once a curve match is obtained.

I. INTRODUCTION

The idea of comparing broad phase-scan signatures with theory to determine tank field amplitude, phase, and input beta was suggested at Fermilab a few years ago [1,2]. A similar idea was also proposed independently at the Los Alamos National Laboratory [3]. The early reports demonstrated that characteristic features of the phase-scan curves depend in unique ways upon input beta and tank electric field. References [4] and [5] are more recent papers which allude to the idea.

The phase-scan signature matching technique can be used to find all tuning parameters needed to center the beam in longitudinal phase space, including tank electric field, input beta, and tank phase. Originally, phase-scan signature matching was suggested as a means of coarse-tuning the Fermilab linac [1,2]. The classical delta-t procedure [6] was to be used for fine tuning.

One form of the delta-t procedure, which must be used on some of the linac tanks, assumes that the input energy equals the design value. This assumption can lead to errors in the procedure [2]. The phase scan signature

matching technique, on the other hand, makes no assumptions about any of the tank parameters. In addition, the phase-scan signature technique can be used even if the tank settings are far from design values. The delta-t procedure assumes that the tank settings are close to design values. Our recent results as well as results published by LANL [3] suggest that the phase-scan signature matching technique may provide accuracies of a few tenths of a percent.

The phase-scan signature matching technique will be one of the tools used to tune the new Linac Upgrade at Fermilab [7]. Commissioning is scheduled to commence in late summer of this year. Although the phase-scan technique by itself appears sufficiently accurate to properly position the beam in longitudinal phase space, we presently plan to use the delta-t procedure, and spectrometer measurements to confirm phase-scan signature matching results.

II. EXPERIMENTAL PROCEDURES

The basic idea behind the phase-scan measurements is illustrated in figure 1. In the figure, tank N is the tank being tuned. All upstream tanks are turned on and all downstream tanks are turned off. The rf power for tank N is initially turned off. The phase of the beam induced signals (beam phase) at a downstream monitor is then recorded. This zero-power beam phase reading is subtracted from all subsequent beam phase readings. The theoretical beam phases are similarly referenced to a zero-power phase (unaccelerated beam).

Radio-frequency power to tank N is next turned on, and the beam phase is recorded as a function of tank N phase. The tank phase is varied over approximately 360 degrees. The tank phase signal is derived from direct measurements of tank fields using pickup loops in the tanks. Phase detection for both the beam signal and the tank signal is performed using I&Q demodulators. This technique was first suggested to us by workers at the Los Alamos National Laboratory [8].

The detector output is periodic, repeating every time the input phase changes by 2π . The beam phase can vary over a range much greater than 2π radians, necessitating measures to eliminate potential ambiguities in the

* Fermilab is operated by the Universities Research Association under contract to the US Department of Energy.

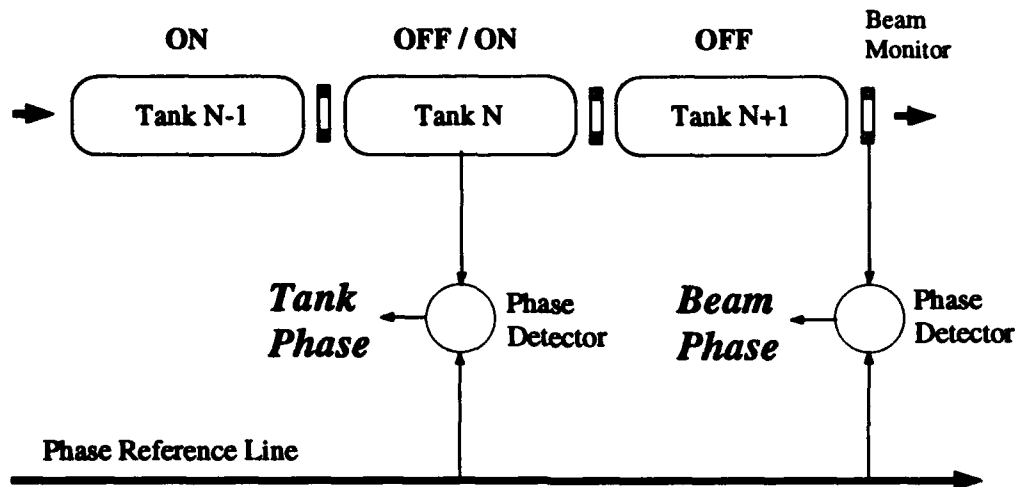


Figure 1. Schematic diagram of the phase-scan signature monitoring system.

raw data. The data analysis software keeps track of the number of 2π increments which occur in the phase scans and removes the ambiguities.

Tank phase is varied over approximately 360 degrees for at least two reasons. First of all, more complete comparisons between theory and experiment can be made. Secondly, verification can be made that the beam phase at 360 degrees of tank phase equals the beam phase at 0 degrees of tank phase. If the beam phases are equal at each extreme of tank phase, we can be sure that the software has properly tracked any 2π jumps in beam phase readings due to I&Q demodulator periodicity.

A special application program designed within the framework of the Fermilab ACNET accelerator control system, has been written to control and analyze the phase scans. After raw demodulator signals have been collected and converted to beam phase and tank phase, the operator can shift the whole phase-scan curve continuously along the tank-phase axis, and in 2π phase increments along the beam-phase axis.

The movement of the phase-scan curve follows the movement of a cursor placed directly on the graph. The cursor movement is controlled using a mouse. This provision allows the operator to manually line up the curve as closely as possible with a target curve that is superimposed on the graph of beam phase versus tank phase. The target curve is generated from the theory using design values for electric field and input beta for the tank.

Once the best manual curve fit to the target curve is obtained, a least-squares procedure is implemented to find the theoretical curve which best matches the measured data. The program first requests that the operator select up to 20 points along the phase-scan curve. The fitted curve will be through these selected points. With manual

selection of points, the operator can avoid curve fitting to particularly noisy regions or to regions where there may be beam loss. He is also free to select points in portions of the curves that are particularly sensitive to variations in electric field and input beta. By doing so, accuracy can be improved.

For least-squares curve fitting, the subroutine, MINUIT, from the CERN numerical library, is used. Three variable parameters are used in MINUIT. These include tank electric field, input beta, and offset of the measured tank phase. When a least-squares fit has been found, the program shifts the measured data by the calculated tank phase offset, and draws the theoretical least-squares curve through the measured points. The electric field and input beta derived from the least-squares fit are printed.

Finally, a marker appears on the phase-scan graph at the position of the current tank phase setting. The marker actively follows any tank phase adjustments. The operator can now adjust the tank phase to the appropriate position along the phase-scan curve. If the electric field and input beta equal design values, the proper tank phase setting will be zero on the phase scan curve, since we have referenced all phases to the design phase in the theory. Tank phases different from zero may be appropriate if electric field and input beta are not equal to design.

III. PHASE SCAN SIGNATURES

Figure 2 is an example of the phase-scan data that are obtained on tank 6 of the drift-tube linac at Fermilab. The faint solid line in the figure is the least-squares curve fit to the measured data. The fitted curve is nearly indistinguishable from the measured points in figure 2. The

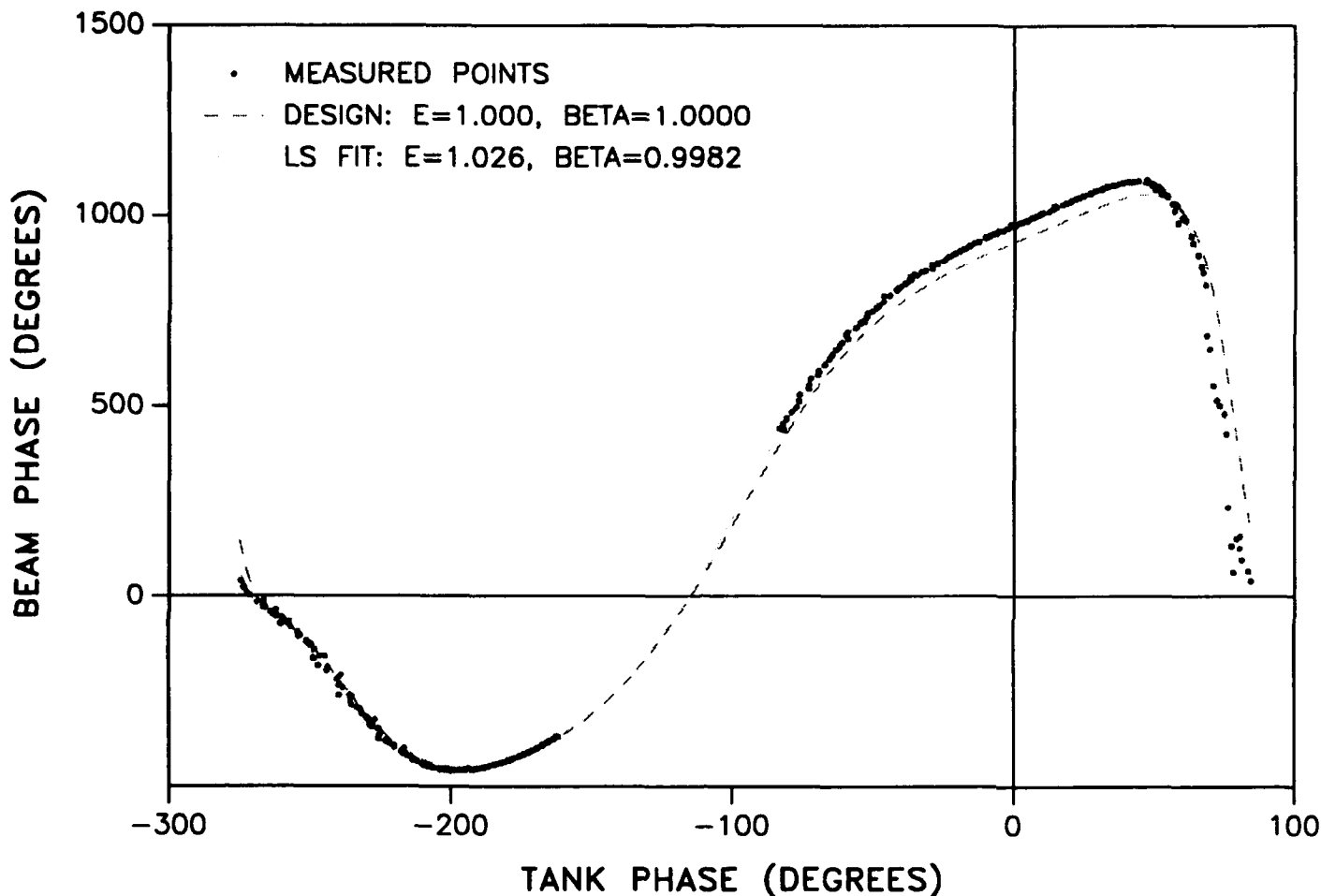


Figure 2. Phase-scan curves for tank 6 of the Fermilab drift-tube linac. Beam phase is measured 16.96 meters past the end of tank 6. Tank electric field (E) and beta (at input) are referenced to design values.

dashed line in figure 2, which deviates from the measured points, is the design curve. From the least-squares fitting procedure, the difference between design and measured phase-scan curves indicates that the tank electric field is 2.6% above the design value and the input beta is 0.18% below design.

IV. REFERENCES

1. T.L. Owens, "Phase and Amplitude Tuning Procedures for the Fermilab Linac," Fermilab Report TM-1713, Jan., 1991.
2. T. L. Owens and E. S. McCrory, "The Delta-T Tuneup Procedure for the Fermilab Linac Upgrade," in *Conference Record of the 1991 IEEE Particle Accelerator Conference*, May 6-9, 1991, pp. 3064-3066.
3. F. W. Guy and T. P. Wangler, "Least-Squares Fitting Procedure for Setting RF Phase and Amplitude in Drift-Tube-Linac Tanks," *ibid*, pp. 3056-3058.
4. P. N. Ostroumov, et. al., "Proton Beam Acceleration up to 160 MeV at the Moscow Meson Factory Linac," *ibid*, pp. 3067-3069.
5. T. L. Owens and M. B. Popovic, "Phase-Scan Signature Matching for Linac Tuning," Fermilab Report LU-186, Nov. 18, 1992.
6. K. R. Crandall, "The Delta-T Tuneup Procedure for the LAMPF 805 MHz Linac," LANL Report LA-6374-MS, June, 1976.
7. C. W. Schmidt, "The Fermilab 400MeV Linac Upgrade," this conference.
8. Olin Vandyck, LANL, private communication.

Operational Status of the Uranium Beam Upgrade of the ATLAS Accelerator

R.C. Pardo, L.M. Bollinger, J.A. Nolen, K.W. Shepard, P. Billquist, J.M. Bogaty, B.E. Clift,
R. Harkewicz, F.H. Munson, J. E. Specht, and G.P. Zinkann
Argonne National Laboratory
9700 S. Cass Avenue, Argonne, IL 60439-4843 USA

Abstract

The Positive-Ion Injector (PII) for ATLAS is complete. First beams from the new injector have been accelerated and used for experiments at ATLAS. The PII consists of an ECR ion source on a 350-kV platform and a low-velocity superconducting linac. The first acceleration of uranium for the experimental program has demonstrated that the design goals of the project have been met. Since the summer of 1992, the new injector has been used for the research program approximately 50% of the time. Longitudinal beam quality from the new injector has been measured to be significantly better than comparable beams from the tandem injector. Changes to the mix of resonators in the main ATLAS accelerator to match better the velocity profile for heavy beams such as uranium are nearly complete and uranium energies up to 6.45 MeV per nucleon have been achieved. The operating experience of the new ATLAS facility will be discussed with emphasis on the measured beam quality as well as achieved beam energies and currents.

INTRODUCTION

The ATLAS Positive-Ion Injector (PII) project was a development project with a goal of providing 6 MeV/nucleon beams of uranium ions as well as higher energies of other ions. ATLAS[1], the world's first application of RF superconducting technology for heavy-ion acceleration, was originally designed to use an existing electrostatic tandem accelerator as the injector for the superconducting linac. This injector was limited to providing beams with $A \leq 100$ due to stripper foil lifetimes and the total available voltage.

The Positive-Ion Injector[2,3] was proposed in 1985 to solve the limitation on ATLAS performance imposed by this tandem injector. The project is now complete and has been operating as an integral part of the ATLAS facility since April, 1992. During the past year, the new PII has met all of its design goals and in a number of important areas now routinely exceeds those goals. The specific goal of providing uranium beams at energies in excess of 6 MeV/A was achieved on February 9, 1993 when a beam energy of 6.45 MeV/A (1535.1 MeV) was achieved. Beam currents in excess of 4 pA at 6 MeV/A have been delivered to target during more recent runs.

In the remainder of this paper, specific performance parameters are reported and compared to expected performance. Near term future improvement plans are also discussed.

SYSTEM DESCRIPTION

The PII consists of two major components. An electron cyclotron resonance (ECR) ion source on a 350-kV platform provides high charge-state ions (charge-to-mass ratio ($Q/A \geq 0.1$)) to a new independently-phased superconducting resonator linac with a total effective voltage of approximately 12 MV. A floor plan of the PII is shown in Figure 1.

The PII ECR ion source[4] is the first ECR source to operate on a high voltage platform. Attention was given to minimizing power consumption while maintaining good performance for high charge-state ion production and to provide maximum flexibility for the production of beams from solids. The source operates with an RF frequency of 10 GHz. The high voltage platform design provides for the necessary source and beam transport utilities while maintaining a total voltage stability of $\Delta V/V \sim 10^{-4}$. Routine performance of the source for uranium ions using UO_2 source material is shown in Figure 2.

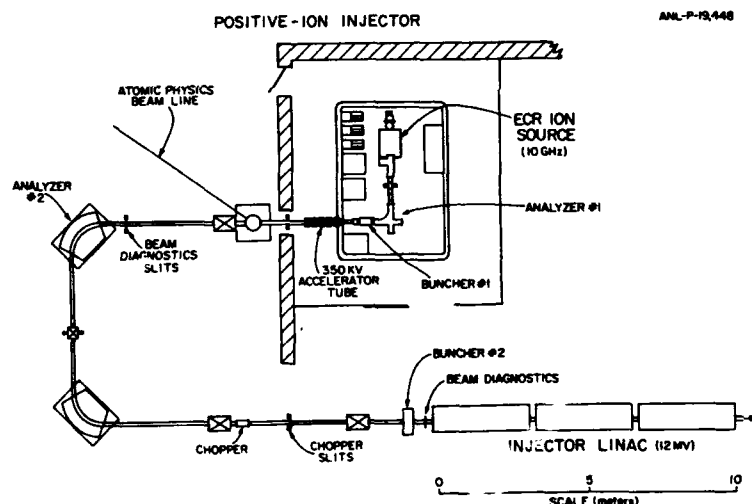


Fig. 1. Major elements of the Positive-Ion Injector.

The PII linac consists of 18 niobium superconducting quarter-wave resonators[5] (see Figure 3) of four different matched velocities. Superconducting solenoids are interspersed among the resonators for transverse focusing. The first resonator in the PII is designed for a matched velocity of $0.009c$ for ions with $Q/A=0.1$. The average accelerating gradient of the resonators in the PII linac section during recent operation has been 3.6 MV/m, corresponding to a surface field of 18 MV/m. This performance is a significant improvement over the design accelerating gradient of approximately 3 MV/m. Operation at these gradients has been reliable and trouble-free. Average power into the helium system under these conditions is about 6.5 watts per

resonator. An important contributor to this level of resonator performance is the significant improvement in the performance of the fast-tuning phase stabilization system (VCX) for these resonators[6].

The goal of the PII design was to develop a low-velocity linac system which combines broad Q/A ratio acceptance, excellent beam quality, increased beam current, and high total efficiency. These goals have been fully realized in the achieved performance of the PII.

OPERATING EXPERIENCE

The complete ATLAS-PII system began providing beams for the research program in April, 1992 and the facility became fully operational in July, 1992. Since then the PII has been used as the ATLAS injector more than 50% of the time and now nearly 80% of all beam time is provided by the PII. Nearly 1800 hours of research beam time has been provided during the past year. The system has been quite reliable with beam on-target 92% of the scheduled experimental time. Table I lists the beams which have been provided to the research program during that period.

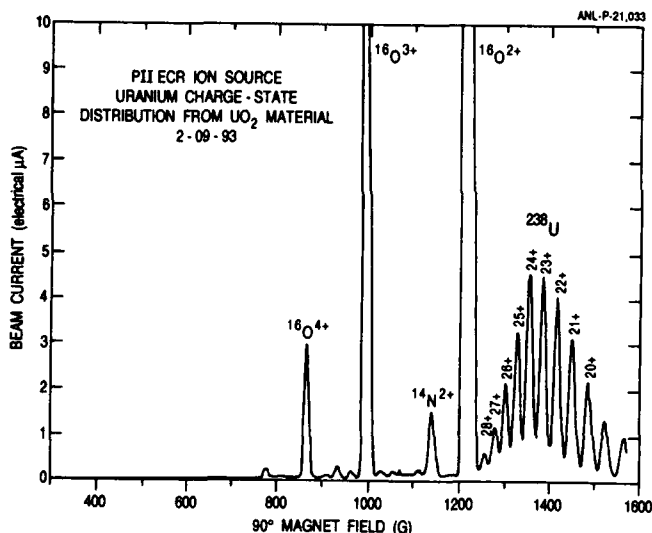


Fig. 2. Uranium charge-state distribution from ECR source.

Table I

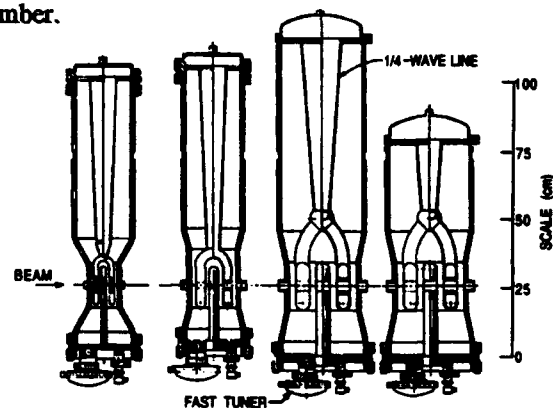
Properties of Beams Accelerated During First Year of PII Operation

Ion Species	PII Exit Energy (MeV)	Max. ATLAS Energy Used (MeV)	PII Long. Emit. (π keV·ns)
$^{20}\text{Ne}^{6+}$	33	160	
$^{27}\text{Al}^{5+}$	45	167	
$^{28,30}\text{Si}^{5,7+}$	43	161	12
$^{36,40}\text{Ar}^{10,9}$	62,69	260	8
$^{78,83}\text{Kr}^{16,15\&30}$	125	450,723	
$^{92,100}\text{Mo}^{15}$	153	440	
$^{132,136}\text{Xe}^{18}$	178	752	62
$^{208}\text{Pb}^{24\&39}$	248	1018	20
$^{238}\text{U}^{24\&39}$	300	1535	39

The longitudinal emittance (the area occupied in energy-time space) of beams from the Positive-Ion Injector was expected to be improved over that possible from the tandem injector, largely because of the reduced need for stripping for medium mass beams and improved beam transport optics. The transverse beam emittance was expected to be similar to that of beams from the tandem injector. Those expectations have been met. The longitudinal emittances of a number of the beams from the PII have been measured and are generally one half the values for beams of similar mass from the tandem. Table I lists the longitudinal emittance of a number of PII beams. The quoted value is the product of half-width half-maximum in units of π keV·ns.

URANIUM BEAM DEVELOPMENT

The first acceleration of uranium with the new Positive-Ion Injector(PII) of ATLAS was successfully accomplished during the week of July 27, 1992. A beam of 300-600 electrical nanoamps $^{238}\text{U}^{28+}$ was provided by the ECR ion source and accelerated by the PII linac to 293 MeV. This beam was stripped to a 42+ charge state and further accelerated to 1363 MeV (5.7 MeV per nucleon) by the ATLAS linac. Beam current after stripping and acceleration was 6 enA at the exit of the accelerator (for 300 enA injected). A second uranium run occurred in the first week of September.



TYPE	I ₁	I ₂	I ₃	I ₄
β	0.009	0.016	0.025	0.037
L _a (cm)	10.2	16.5	25.4	25.4
D (cm)	1.5	1.9	3.8	3.8
f (MHz)	48.5	48.5	48.5	72.75
F ₀ (MV/m)	4.5	3.0	3.0	3.0

Fig. 3. Resonators used in the Positive-Ion Injector..

A number of important techniques were demonstrated and refined in these early runs. The most important of these was the highly successful tuning of the 'booster' portion of the ATLAS linac with an analog beam from the tandem. In this case $^{34}\text{S}^{6+}$, which has the same charge-to-mass ratio as $^{238}\text{U}^{42+}$, was used. This analog beam technique is necessary because a number of charge states are now injected into the 'booster' portion of the linac and so,

tuning of a single selected charge state is not possible for this section of the linac before completion of the charge-state selector.

During the Fall and Winter, 1992 a major upgrade project to the existing ATLAS linac took place in order to achieve the goal of reliable operation of 6 MeV/A uranium with beams current of 5-10 pA. Six of the resonators in the ATLAS linac which had a matched velocity of approximately 0.15c were replaced with resonators whose matched velocity was 0.1c. This modification results in a significantly improved match to the velocity profile of low charge-to-mass ratio beams such as uranium. In addition, the improved fast tuner design was implemented for those devices.

The results of the improvements implemented in this period resulted in achieving a uranium beam energy of 6.45 MeV/A during February, 1993 with approximately 1pA on target. Additional improvements in the system have now resulted in subsequent runs in March and May yielding beam currents of 5-7 pA at 6.45 MeV/A for the experimental program. The increase in beam current was due to the use of lower charge states from the ECR ion source and from the stripping distribution. In the most recent run in May, 1993, charge state 24+ was selected from the source while charge state 39+ was selected from the stripping foil. The analog beam used for this situation was $^{60}\text{Ni}^{10+}$.

Stripper foil lifetime and charge-state distributions, which are very important to the performance of ATLAS for these very heavy beams, have been studied. Both carbon foils and self-supporting beryllium foils have been used. Beryllium foils exhibit a charge-state distribution peaked toward higher charge states as shown in Figure 4. This effect has been previously reported[7] and is due to reduced recombination cross-sections for the 'low-Z' materials. Foil lifetime for carbon stripping uranium at 300 MeV have been measured to average 175 pA-hours. Beryllium foil lifetime has not been as good with an average of 75-100 pA-hours.

Uranium Charge State Distribution

In Be and Carbon Foils @ 290 MeV

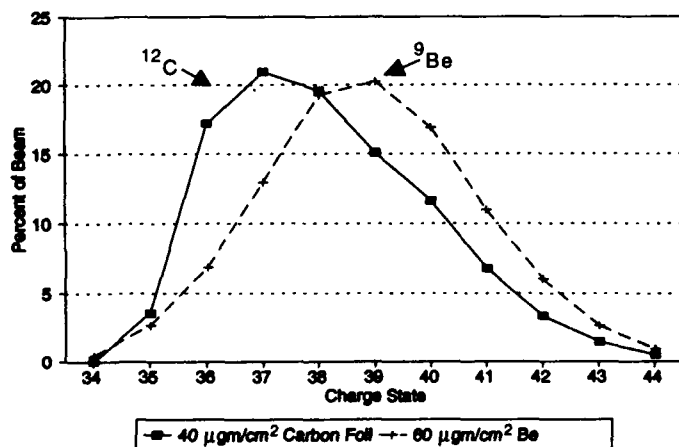


Fig 4. Stripped charge-state distributions from beryllium and carbon foils at 290 MeV.

Beam transmission through the PII linac was excellent for uranium. The total beam transmission through the PII linac was as high as 63%, including the bunching efficiency. Typical bunching efficiency is 60-70%, indicating that the transport efficiency of bunched beam through the PII is greater than 90%. Transmission through the ATLAS accelerator averaged 80-85%. The normalized transverse emittance of the uranium and lead beams has been measured to be between 0.2 -0.5 π mm-mr. This is two to three times greater than expected. We are investigating the cause of this emittance growth.

CONCLUSION AND SHORT TERM PLANS

The initial operation of the new PII-ATLAS system has met all of the project goals. Resonator and ion source performance meet or exceed all the specific goals. The system reliability, even during these early operational runs has been excellent.

A new charge-state selector system, which will select and deliver to the ATLAS linac a single charge-state from the PII stripper, is expected to be installed in the Fall, 1993. This will eliminate the need to tune the 'booster' section of the linac with a 'guide' beam and simplify setup for the heaviest of beams.

A new wet engine will be installed in September, 1993 on one of the refrigerators in the system to provide increased refrigeration capacity and to improve reliability. Resonator performance improvements may also be realized.

This research was supported by the US D.O.E., Nucl. Phys. Div., contract W-31-109-ENG-38.

REFERENCES

- [1] J. Aron, et al., Proceeding of the 1984 Linear Accelerator Conference, Seeheim, W. Germany, May 1984, GSI Report GSI-84-11, pp. 132 (1984).
- [2] L. M. Bollinger and K. W. Shepard, Proceeding of the 1984 Linear Accelerator Conference, Seeheim, W. Germany, May 1984, GSI Report GSI-84-11, pp. 217 (1984).
- [3] R. C. Pardo, L. M. Bollinger, and K. W. Shepard, Nucl. Instrum. and Methods, **B24/25**, 746 (1987).
- [4] R. C. Pardo, Nucl. Instrum. and Methods, **B40/41**, 1014 (1989).
- [5] K. W. Shepard, et al., Proceedings of the 1989 IEEE Particle Accelerator Conference, Chicago, IL, March, 1989, pp. 974 (1989).
- [6] N. Added, B. E. Clift, and K. W. Shepard, Proceeding of the 1992 Linear Accelerator Conference, Ottawa, Ont., August, 1992, pp. 181 (1992).
- [7] J.P. Rozet, et al., J. Phys. B., **22**, 33(1989).

One Year Operation of the 7 MeV Proton Linac

T. Shirai, H. Dewa, H. Fujita, M. Ikegami, Y. Iwashita, S. Kakigi, H. Okamoto, A. Noda and M. Inoue

Institute for Chemical Research, Kyoto University

Gokanoshō, Uji-city, Kyoto 611, Japan

Abstract

On the 7 MeV proton linac at ICR, the improvement of the beam transmission has been made. The measurement of the RFQ output beam was performed and the beam matching elements were designed and constructed to match the RFQ output beam to the acceptance of the Alvarez linac. The emittance is $42 \pi \cdot \text{m} \cdot \text{mrad}$ and $30 \pi \cdot \text{m} \cdot \text{mrad}$ in the x-x' plane and y-y' plane, respectively. The energy spread is 80 keV at 2 MeV. The matching elements consist of four permanent magnetic quadrupoles and a quarter wave-length resonator buncher. The RF power up to 5.0 kW has been safely fed into the buncher, which is well enough to provide a designed bunching voltage of 180 kV.

I. INTRODUCTION

At Institute for Chemical Research (ICR), 7 MeV proton linac consisting of an RFQ and an Alvarez cavities, has been constructed. The layout of the accelerator is shown in Figure 1. It is operated at 55 μsec pulse width, 180 Hz repetition rate. The operating frequency of 433 MHz is chosen to be more than twice higher than that of conventional proton linacs, so that the cavity size becomes compact and klystrons are available as RF power sources in this frequency range.

The first 7 MeV beam was accelerated about one year ago. The input RF power were 540 kW for RFQ and 320 kW for Alvarez cavity. The total transmission through two cavities

is measured to be 50 % [1]. This low transmission comes from the mismatching of the beam in the injection into the RFQ and Alvarez cavity. For the former, the final focus element in the injection line is prepared just before the RFQ [2]. For the latter, the beam matching elements between two cavities were designed and constructed, based on the beam measurements of the RFQ, such as a transverse emittance and an energy spectrum.

II. BEAM MEASUREMENTS OF THE RFQ

The transverse emittance and the energy spectrum were measured at the place for the beam matching section between the RFQ and the Alvarez linac. The measurement devices were developed to be compact for the limited space. The beam current is low for these measurements, usually about 200 μA .

A. Transverse emittance

The emittance monitor consists of a fluorescent screen (Desmarquest, AF995R) and movable slits. A schematic diagram of the monitor is shown in Figure 2 [3]. The x-slit and y-slit define the transverse position. The transverse spread of the beam is measured by the screen that is located downstream of the slits. Because of the high position sensitivity of the screen, we can get the high resolution of the transverse momentum. The distance between the slits and the screen is 315 mm. The resolution is 0.5 mm for the position and 1 mrad for the angle.

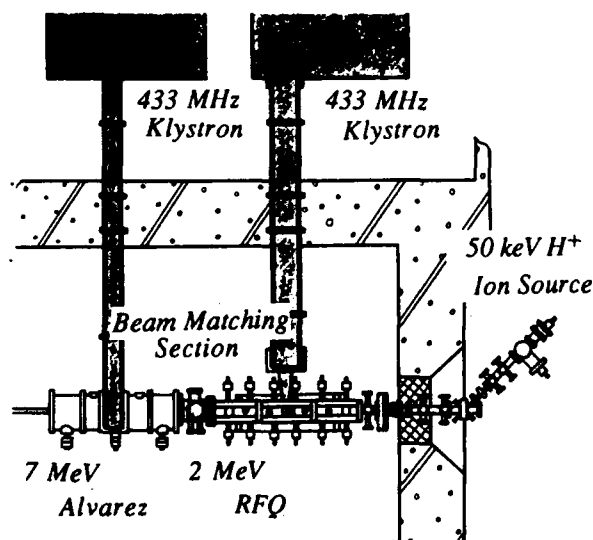


Figure 1. Layout of the accelerator system.

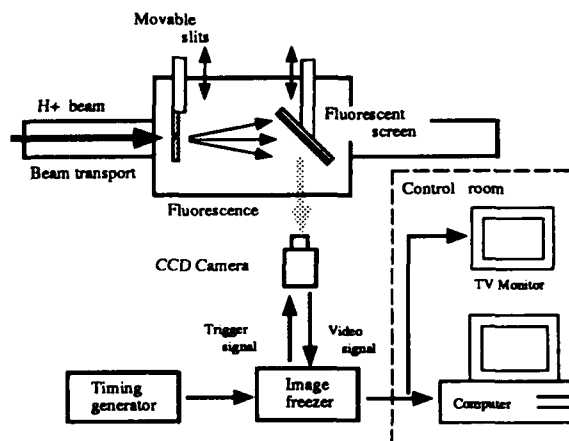


Figure 2. Schematic diagram of the beam emittance monitor system.

The screen can be also used for the profile monitor when the slits are extracted.

The fluorescent material is an alumina ceramic (99.5 % - Al_2O_3) in which a little chromium oxide is homogeneously doped. The fluorescence is observed by a CCD camera (PULNIX model TM720) which is placed 80 cm away from the screen. The camera is adjusted so that the output signal may be in proportion to the input light intensity. The shutter timing is synchronized to the pulse operation of the linac. The output signals from the CCD are digitized and stored by an image freezer. The digitized image is displayed on a TV monitor and transferred to a personal computer. It calculates the beam profile and the emittance.

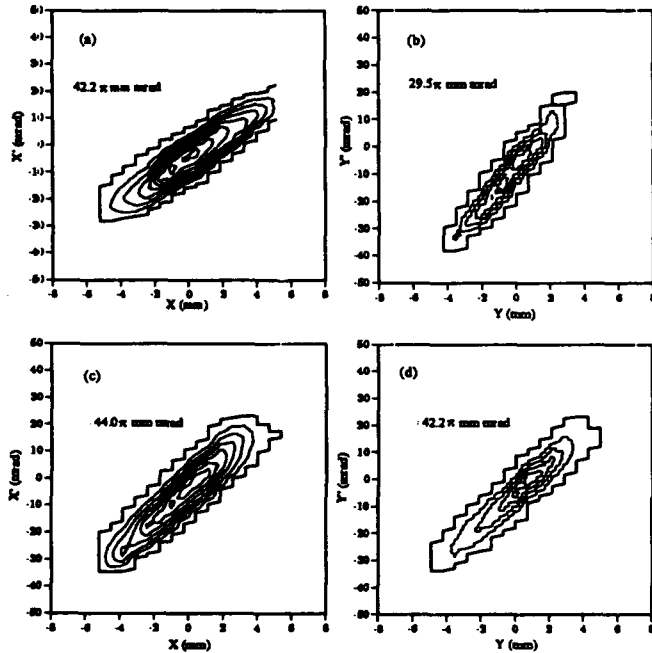


Figure 3. Measured 90 % emittance of the RFQ output beam.

(a), (b) : the input RF power of 540 kW,
(c), (d) : the input RF power of 370 kW.

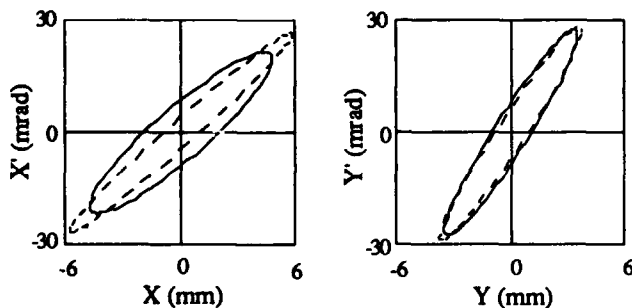


Figure 4. Comparison between the measured (solid line) and calculated (dotted line) emittance.

The measured results are shown in Figure 3. The emittance is for 90 % of the beam intensity and measured at 180 mm behind the vane end of the RFQ. The input RF power is 540 kW at (a), (b), which is the designed input power and 370 kW at (c), (d). Figure 4 shows the comparison between the measured emittance and the calculated one. The fluctuation of the emittance by the RF power level is within 2 % for the power level around the designed one.

B. Energy spectrum

A compact analyzing magnet was devised to measure the energy spread of the RFQ beam [4]. The cross section of the magnet is shown in Figure 5. It has C-shape and only the poles is in vacuum side, because the magnet had to be installed in the small space and in the vacuum. The yokes go through the vacuum flange made of stainless steel and the coil is located in the air side. It can generate the magnetic field of 1 Tesla at 8 mm gap through out 100 mm length. The deflection angle is 30 degree. The beam is detected by a Faraday cup with a collimator which is 210 mm away from the poles. The energy resolution is 1 % at 2 MeV.

The energy spectrum is shown in Figure 6. The input RF power is 540 kW. The FWHM of the energy spread is 80 keV. The result is consistent with the simulation.

III. BEAM MATCHING SECTION

The schematic view of the beam matching elements between RFQ and Alvarez linac are shown in Figure 7 [5]. The transverse beam matching is attained by four permanent magnetic quadrupole lenses (PMQs). They are compact compared with an electromagnet and the multiple elements can be installed in the limited space. The magnet material of the PMQ is Nd-Fe-B. The bore radius is 5.5 mm and the magnetic field

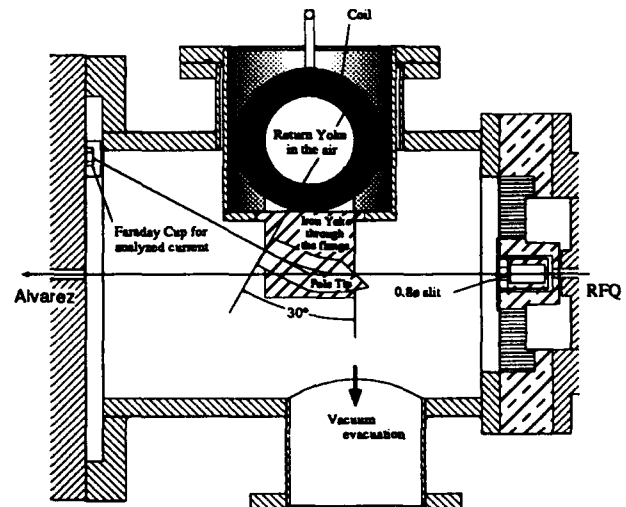


Figure 5. The cross section of the analyzing magnet.

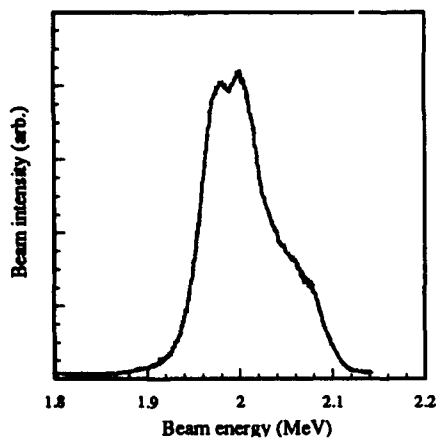


Figure 6. The energy spectrum of the RFQ output beam.

gradient is around 18.6 kGauss/cm.

The buncher matches the longitudinal beam distribution. It is a quarter wave-length resonator (QWR) and the resonance frequency is 433 MHz, which is the same as that of the linac system. It has merits of a high shunt impedance and a simple structure. The unloaded Q-value is 7400 and the shunt impedance is 8.8 M Ω . In the high power test, the RF power of 5.0 kW has been successfully fed after the 5 hours conditioning. The designed bunching voltage is 180 kV. The voltage was estimated from the maximum energy of the emitted X-ray and it was confirmed that the designed voltage can be obtained when the input RF power is 3.6 kW.

IV. SUMMARY

We have developed the compact analyzing magnet and the emittance monitor using the fluorescent screen. The transverse emittance and the energy spectrum of the RFQ beam

were measure by the devices. Based on the results and the simulation, the matching elements were designed and constructed to match the Twiss parameters of the beam between RFQ and Alvarez. They consists of the four PMQs and the QWR buncher. The designed RF power can be fed into the buncher.

The beam test of the linac system with the matching elements is in progress and the improvements of the injection line to the RFQ is also scheduled.

V. REFERENCES

- [1] T.Shirai et al., "Performance of the RFQ and Alvarez Linac at Kyoto University", Proc. of '92 European Particle Accelerator Conf, vol 1, pp. 560 (1992)
- [2] Y.Iwashita et al., "Axial Magnetic Field Lens with Permanent Magnet", these proceedings.
- [3] T.Shirai et al., "Study of Beam Profile Monitor for the Proton Linac", Bull. Inst. Chem. Res. Kyoto Univ., in print.
- [4] Y.Iwashita et al., "Operating Characteristics of the ICR Proton Linac", Proc. of '92 Linear Accelerator . Conf., pp. 746 (1992)
- [5] H.Dewa et al., "Design Study of a Beam Matching Section for the Proton Linac", Bull. Inst. Chem. Res. Kyoto Univ., 70, No.1, pp. 89 (1992)

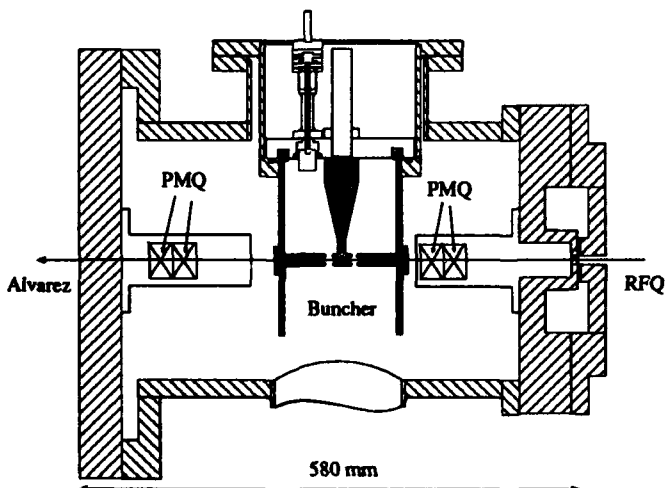


Figure 7. The cross section of the beam matching section.

The SSC Linear Accelerator

L. Warren Funk

Linac Group, Project Management Office, Superconducting Super Collider Laboratory*
2550 Beckleymeade Ave., Dallas, TX 75237

Abstract

The SSC linear accelerator will generate a 25 mA, 600 MeV, H^- beam with transverse normalized rms emittance less than $0.3 \pi \text{ mm} \cdot \text{mrad}$ in $9.6 \mu\text{s}$ pulses at a 10 Hz repetition rate. The Linac will ultimately have to operate with an availability for Collider filling in excess of 98%. In addition, the Linac will provide beams to service the Test Beams facility and may be delivering beam to a Proton Radiotherapy Facility. This paper presents an overview of the status of design, procurement, fabrication, civil construction, foreign contributions and commissioning plans, and directs the reader to additional details available in other presentations to this Conference.

I. INTRODUCTION

The main parameters of the SSC Linac [1-3] are given in Table 1. Negative hydrogen ions are accelerated so that 4-turn charge changing injection can be used in the Low Energy Booster [4] (LEB) to minimize emittance growth during the injection process. The energy and fundamental rf frequency of 428 MHz are chosen to make emittance growth due to space charge as small as possible in the linac, to make space charge tune shift at the start of the LEB cycle [5] manageable, to maintain the option of bunch-to-bucket transfer into the booster synchrotron by having an integer relationship between the linac rf frequency and that of the LEB at injection, and to allow use of klystrons, rather than gridded tubes in the rf supplies. Sufficient space has been provided in both the tunnel and the rf gallery for the additional equipment needed to increase the linac energy, if that route to higher luminosity is chosen. The transverse emittance and availability

specifications are derived from the overall complex requirements of $1 \pi \text{ mm} \cdot \text{mrad}$ at the collision point and availability to take data 80% of the time scheduled.

II. GENERAL DESCRIPTION

The linac consists of an rf-driven volume source and electrostatic low energy beam transport (LEBT), a 427.6 MHz radio frequency quadrupole (RFQ), a drift tube linac (DTL) operating at the same frequency as the RFQ and a specialized matching section to match the RFQ output beam into the DTL input acceptance. A coupled-cavity linac (CCL) operating at 1282.8 MHz is preceded by another matching section to take the DTL output beam and transform it into the acceptance of the CCL. Transition energies from one type of accelerator to another have been chosen to produce a cost-optimized high-performance design.

A FODO channel transports the beam to the start of the Linac-LEB transfer line and smoothly matches the CCL transverse optics to that of the transfer line. This space would be occupied by additional CCL modules as part of a linac energy upgrade. At the end of the transport line, an energy compressor cavity reduces the beam energy spread to $\leq 100 \text{ keV}$, as required by the LEB for preparation of beam for the Collider. The transfer line and LEB injection girder match the linac beam into the LEB, place it on the closed orbit and pass it through a stripper foil in an orbit bump.

Specific features have been incorporated in the CCL, the transport/transfer lines and the tunnel, to allow the Linac to provide beam to a proton radiotherapy facility under consideration for the West Campus [6].

Table 1
SSC Linear Accelerator Parameters

	RFQ	DTL	CCL
Frequency (MHz)	427.613	427.613	1282.84
Number of rf systems	1	4	9
Input Energy (MeV)	0.035	2.5	70
Output Energy (MeV)	2.5	70	600
Input Current (mA)	30	27	27
Output Current (mA)	27	27	27
Output Transverse Emittance (n,rms) ($\pi \text{ mm} \cdot \text{mrad}$)	≤ 0.20	≤ 0.21	≤ 0.25
Total rf power required/system (MW)	0.345	1.187-2.387	11.98-12.28
Total rf power available/system (MW)	0.6	4.0	20
Structure power/system (MW)	0.280	0.89-1.89	10.37-11.27
Peak surface field (MV/m; * sparking limit)	36; 1.8	28; 1.4	32; 1.0
Total length (m)	2.1863	24.366	112.41

III. CURRENT STATUS

Both the rf volume source and its cesiated surface source predecessor [7-9] produced beams with greater than specified brightness at the design operating conditions. The volume source is favored because it needs no cesium and is easier to condition. Engineering solutions for the higher gas load and electron contamination have been developed.

Several electrostatic LEBTs are being studied for use in the SSC Linac. Most experimental work has been done on a system comprised of a pair of Einzel lenses [10,11]. High voltages and emittance growth in this device due to its inherent non-linearity are seen as long-term problems which will probably lead to its replacement by an electrostatic quadrupole system [7,12,13], but for initial commissioning of Linac systems, the Einzel lens system will be used.

The RFQ was built for SSCL by Los Alamos National Laboratory, AT Division, and delivered to SSCL on schedule, in August 1992. It has been installed on the Injector Test Stand (Figure 1), integrated with its support systems, rf conditioned and operated [14] with beam. Its performance [15-19] has been excellent, and in agreement with simulation in all respects.

Detailed design of the RFQ-DTL matching section is complete, and construction is advancing on a schedule which will see all components delivered to SSCL in June for assembly and commissioning off-line in July and operation with beam in August [20,21].

Construction activities on the DTL are proceeding at full speed at AccSys Technology, Inc., with scheduled delivery of the first tank in mid-January 1994, and delivery of the fourth and final tank in May 1994. Measured characteristics of the permanent magnet quadrupoles has been significantly better than anticipated. Production of the 4 MW klystrons is complete, and fabrication of the modulator systems is proceeding on schedule [22].

Production of the CCL modulators and klystrons is equally well advanced. Detailed design of the resonant coupled cavity structures, carried out with major assistance from LANL, is now complete, and a close partnership with the Institute for High Energy Physics, Beijing, is being forged for the construction of this primary system [23,24]. The CCL modules will be the longest chains of side-coupled resonators ever operated. This has prompted more detailed studies of beam-loading and other transient effects, which have revealed several interesting phenomena [25,26].

Detailed design of the transport and transfer lines is also complete, and most of the major components have been ordered, or are being prototyped [27]. In addition, considerable progress has been made on the design of the LEB injection girder.

Commissioning of a linac, with its highly serialized configuration, extends over considerable time, and benefits from specialized instrumentation which can be used during commissioning, but which would not fit into the completed machine. Considerable progress has been made in planning for commissioning, including simulation support, and in the construction of special commissioning diagnostic equipment [28-33]. Of particular interest are the developments in the compact bunch shape monitor, being conducted in a collaboration with the Institute for Nuclear Research, Moscow.

Progress with civil construction has also been good. Construction of the tunnel is complete, and SSCL has taken beneficial occupancy. Detailed surveying and installation of beam absorbers is underway. Handover of the surface structures will take place in June, when work on HVAC and installation of a boom crane is complete. Electrical power is available on site, and installation of LCW systems, racks and cable trays will begin in June.



Figure 1. Injector Test Stand, showing ion source cart, RFQ and diagnostic chamber.

IV. FUTURE PLANS

Present plans call for commissioning of all parts of the Linac, up to and including the RFQ/DTL matching section, in the labs of the Central Facility in Waxahatchie during August and September 1993. Preparation of Linac buildings at the Injector Site to receive accelerator components is expected to be complete by October 1993. Transfer of operations to the new buildings is to take place in October and November, and these Injector subsystem are to be made operational during December and the first half of January 1994, in time for the arrival of the first DTL tank in the middle of that month. Rf power systems will begin arriving, at a rate of about one per month, in August of 1993, which should allow sufficient time for commissioning and sub-

system integration prior to the need to support cavity conditioning. Completion of DTL commissioning is anticipated in the fourth quarter of calendar 1993.

The first CCL module is expected from IHEP in December 1993. Modules are expected to arrive at an average rate of approximately one every six weeks. This allows a substantial block of time for final module alignment, tuning and rf conditioning before beam will be available for beam commissioning. Transport and transfer line installation is also expected to be complete by the end of calendar 1994.

IV. REFERENCES

- [1] L.W. Funk, "The SSC Linac", *Proceedings of the 12th International Conference on the Application of Accelerators in Research and Industry*, Denton, TX, November 1992, in press.
- [2] L.W. Funk, "The SSC Linac", *1992 Linear Accelerator Conference Proceedings, AECL-10728, Vol. 1, pp. 8-12*.
- [3] L.W. Funk, "The SSC Linac: Status of Design and Procurement Activities", *Supercollider 4*, J. Nonte, ed., Plenum Press, New York, 1992, pp. 833-9.
- [4] U. Wienands, et al., "Status of the SSC Low Energy Booster", these proceedings.
- [5] S. Machida, "Space Charge Effects in the SSC Low Energy Booster", *1991 Particle Accelerator Conference Proceedings*, pp. 383-5.
- [6] D. Raparia, L.W. Funk, "Beam Dynamics Studies for Proposed Proton Therapy Facility at the SSC", these proceedings.
- [7] K. Saadatmand, et al., "Performance of the SSC Magnetron Ion Source and LEBTs", *1992 Linear Accelerator Conference Proceedings, AECL-10728, Vol. 1, pp. 94-6*.
- [8] K. Saadatmand, N. Okay, "H-Source and LEBT R&D Activities at SSCL", these proceedings.
- [9] R.A. Valicenti, et al., "Mechanical Integration of an rf Volume Source and Einzel Lens LEBT to the SSCL RFQ", these proceedings.
- [10] J. Lenz, et al., "Comparison of Experimental and Simulated Results for the SSC LEBT", these proceedings.
- [11] J.S. Wagner, I. Shokair, D. Raparia, G.T. Leifeste, "BUCKSHOT Simulations for Neutralized H⁻ Beams in SSC LEBT", these proceedings.
- [12] S.K. Guharay, et al., "A Compact ESQ System for Transport and Focussing of H⁻ Beam from Ion Source to RFQ", *1992 Linear Accelerator Conference Proceedings, AECL-10728, Vol. 1, pp. 338-40*.
- [13] D. Raparia, "HESQ, a Low Energy Beam Transport for the SSC Linac", *1990 Linear Accelerator Conference Proceedings, LA-12004-C, pp. 405-7*.
- [14] J. Tooker, et al., "Operational Readiness Review Process for the SSC Linac", these proceedings.
- [15] K. Saadatmand, "Performance of SSC Volume H⁻ Ion Source, Preaccelerator and RFQ System", these proceedings.
- [16] G.M. Arbique, et al., "The SSCL RFQ System Integration", these proceedings.
- [17] R.I. Cutler, et al., "Rf Commissioning of the Superconducting Super Collider Radio Frequency Quadrupole Accelerator", these proceedings.
- [18] F. W. Guy, et al., "SSC Radio Frequency Quadrupole Beam: Comparison of Experimental and Simulated Results", these proceedings.
- [19] J.E. Hebert, et al., "Emittance Measurement and Data Analysis for the SSC Linac Injector", these proceedings.
- [20] M.D. Haworth, et al., "Initial Results from the SSC RFQ-DTL Matching Section", these proceedings.
- [21] T. Enegren, et al., "The SSC RFQ-DTL Matching Section Buncher Cavities", these proceedings.
- [22] J. Mynk, et al., "Overview and Status of the Rf Systems for the SSC Linac", these proceedings.
- [23] C. R. Chang, et al., "Computer Simulation and Cold Model Testing of CCL Cavities", these proceedings.
- [24] C.-G. Yao, C.R. Chang, "Status of SSC Coupled-Cavity Linac", these proceedings.
- [25] Yu. Senichev, "Some Features of Beam Interaction with $\pi/2$ Multicell Coupled Accelerating Structures", these proceedings.
- [26] Yu. Senichev, "Beam Loading Effects in the SSCL Couple Cavity Linac", these proceedings.
- [27] R. Bhandari, et al., "Detailed Studies on the Beam Transfer Line from Linac to Low Energy Booster Synchrotron for the SSC", these proceedings.
- [28] C.E. Crist, et al., "SSCL Linac Commissioning Diagnostic Cart", these proceedings.
- [29] F.W. Guy, et al., "Simulation Support for Commissioning and Operating the SSC Linac", these proceedings.
- [30] J.W. Hurd, et al., "Beam Diagnostic Layout Requirements for SSCL Linac", these proceedings.
- [31] J.W. Hurd, et al., "Physics Requirements of Commissioning Diagnostics for SSCL Linac", these proceedings.
- [32] J.W. Hurd, et al., "Bunch Shape Monitor for SSCL Linac", these proceedings.
- [33] D. Raparia, et al., "Error and Tolerance Studies for the SSC Linac", these proceedings.

Finalized Design of the SSC RFQ-DTL Matching Section*

M. Haworth, C. Combs, P. Datte, T. Enegren, W. Funk, Y. Goren, F. Guy,
J. Hurd, G. Jamieson, D. Martin, A. Ringwall, R. Sethi, D. Swenson
Superconducting Super Collider Laboratory
2550 Beckleymeade Ave., Dallas, TX 75237

D. Barlow, R. Kraus, R. Meyer
Los Alamos National Laboratory
P. O. Box 6300, Los Alamos, NM 87545

Abstract

The RFQ-DTL matching section has four variable field quadrupole magnets in a FODO lattice to match the 2.5-MeV, 27-mA, H^- beam from the RFQ to the acceptance space of the DTL, as well as to provide beam steering. In addition, there are two rf buncher cavities to provide longitudinal phase space tuning. An ensemble of beam diagnostics including input and output beam current toroids and beam position monitors, a wire scanner for beam profile measurements, a slit and collector device for beam emittance measurements, and a Faraday cup is used to quantify the matching section performance. The finalized design of the major components of the RFQ-DTL matching section is presented as well as the status of its construction.

I. INTRODUCTION

The SSC Linac [1] consists of an ion source and three different accelerating structures including a radio frequency quadrupole (RFQ), a drift tube linac (DTL), and a coupled cavity linac (CCL). In principal, the first DTL tank can be connected directly to the RFQ. However, the RFQ and the DTL have different beam acceptance spaces, and the resulting mismatch would lead to emittance growth in the beam. Also, any alignment error between the RFQ and the DTL could not be corrected, which again would lead to emittance growth. Given the stringent beam brightness requirements [1] for the SSC Linac, it was felt imperative to have a matching section to properly condition the beam from the RFQ into the first DTL tank.

The RFQ-DTL matching section has three principal elements (see Figure 1) with which to accomplish this task: (1) variable field permanent magnet quadrupole (VFPMQ) magnets for transverse focusing and beam steering, (2) double-gap RF buncher cavities for longitudinal phase space tuning, and (3) beam diagnostics to monitor the properties of the beam. The main design challenge is to fit the above elements into an axial distance of only 540 mm. The physics design [2] and preliminary mechanical design [3] of the

matching section have been presented in previous papers. Its design has now been finalized, and this paper will concentrate on the major components of that design as well as give an update on its construction.

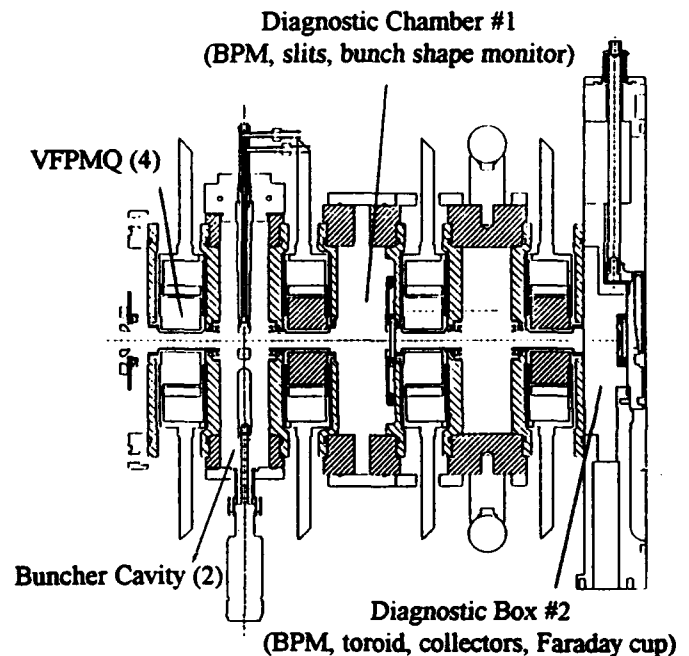


Figure 1. Side view of the RFQ-DTL matching section.

II. VARIABLE FIELD PERMANENT MAGNET QUADRUPOLES

The matching section has four VFPMQs in a FODO lattice with the first quad oriented to be horizontally focusing for the nominal 2.5-MeV, 27-mA, H^- beam exiting the RFQ. The main design features for these quads are shown in Figure 2. This concept was originally proposed by Halbach [4] and uses four mild steel pole pieces to shape the field, while its strength is varied by a 90° rotation of an outer ring of magnets. For the matching section VFPMQs, NeFeB magnet material is used while the hyperbolic pole tips are constructed using C-1006 carbon steel. Rotation of the outer ring is accomplished using a stepper motor driven worm gear, while a precision linear translation stage is used to move the

*Operated by the University Research Association, Inc. for the U.S. Department of Energy under contract No. DE-AC35-89ER40486.

VFPMQ by ± 2 mm in the focusing direction to obtain beam steering.

A prototype VFPMQ based upon the design in Fig. 2 has been built, although without the linear translation stages or any offset capability. A rotating coil [5] was used to measure the gradient-length (GL) product and harmonic content of the quad. The measured GL product shows excellent agreement with theory (see Figure 3). The measured harmonic content at maximum field strength was found to be less than 0.5% of the quadrupole field component at 80% of the aperture for each of the harmonics (up to $n=6$), which also agrees well with theory.

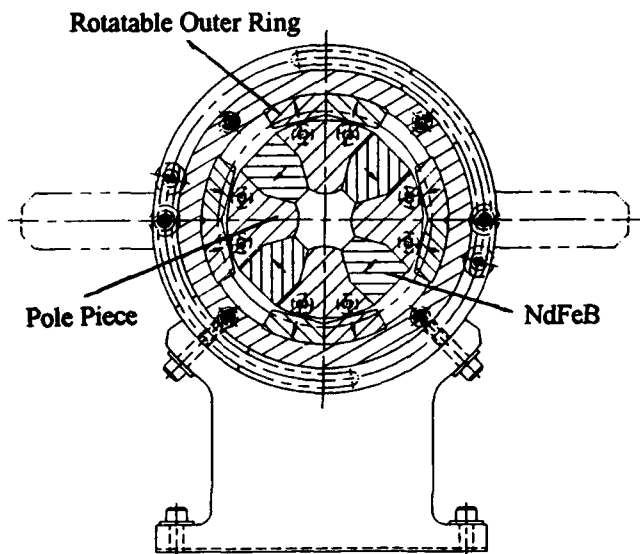


Figure 2. Design of the prototype VFPMQ.

III. RF BUNCHER CAVITIES

A cut-away view of one of the double-gap buncher cavities is presented in Figure 4. It is a quarter-wave rectangular copper cavity having a cylindrically shaped center conductor that supports a 16 mm I.D. drift tube through which the beam passes. Each gap in the cavity develops a voltage of 100 kV with a RF power input of 25 kW at the 428 MHz resonant frequency. The cavity $Q \approx 5000$, and its shunt impedance is 800 k Ω . A plug tuner provides coarse frequency adjustment over a 200 kHz range, while fine tuning of the cavity resonant frequency is obtained by temperature stabilizing the cavity walls and center conductor with low conductivity water from the RFQ temperature control unit (TCU).

Each cavity is powered by a 50 kW planar triode amplifier [6]. This power is transmitted down standard $1\frac{5}{8}$ -

inch rigid coax line and is coupled into the cavity through a tapered section which consists of a transition from $1\frac{5}{8}$ -inch to $\frac{7}{8}$ -inch coax line, an axial ceramic vacuum window, and a coupling loop inserted into the cavity. Specific details of the design of this tapered section are given in another paper [7].

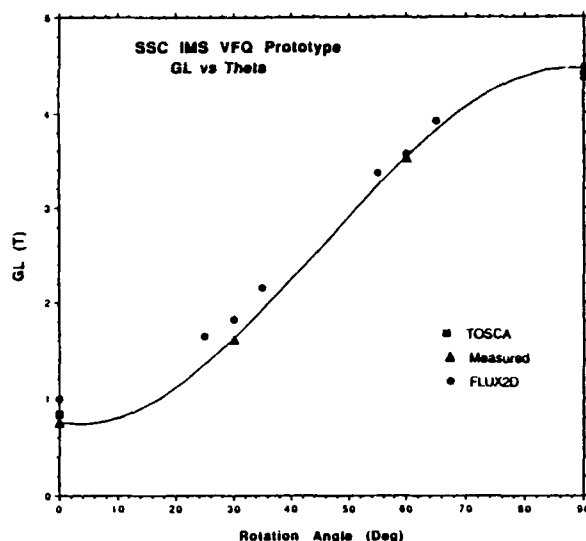


Figure 3. Comparison of measured GL product with computer results for prototype VFPMQ.

IV. BEAM DIAGNOSTICS

The performance of the RFQ-DTL matching section is quantified by an array of beam diagnostics (see Figure 1). This array consists of three beam position monitors (BPMs) for measuring the transverse displacement of the beam and its relative phase with respect to the buncher cavities, input and output current toroids to measure the total beam current, a 3-wire wire scanner to measure the x, y, and coupled x-y beam profiles, a segmented Faraday cup to measure beam position and current as well as to serve as a beam stop, and a separate x and y slit and collector to measure the transverse emittance of the beam. All of these diagnostics except the BPMs are actuated into place via actuators having better than 0.1 mm resolution. In addition, the slits and the Faraday cup are water cooled since they must withstand nearly the full power density of the 10 Hz beam.

Further details on these diagnostics can be found in Reference 8. The 128-wire collector array and its associated electronics [9] are in particular a unique design offering substantially improved resolution and enhanced data acquisition capabilities over past designs. Finally, two diagnostic ports in the matching section have been provided to accommodate a bunch shape monitor [10] now under development.

V. STATUS

Parts for the SSC RFQ-DTL matching section are scheduled to begin arriving in early June of this year. Bench testing of the device should commence in July, while beam commissioning is scheduled to begin at the SSC Central Facility in August. This fall, the ion source, RFQ, and RFQ-DTL matching section will be moved to the SSC Linac tunnel for installation and operation prior to delivery of the first DTL tank in early 1994.

VI. REFERENCES

- [1] L. W. Funk, "The SSC linac," *1992 Linear Accelerator Conference Proceedings*, Vol. 1, pp. 8-12.
- [2] R. C. Sethi *et al.*, "Design of the RFQ-DTL matching section for the SSCL linac," *1992 Linear Accelerator Conference Proceedings*, Vol. 2, pp. 483-485.
- [3] A. D. Ringwall and C. M. Combs, "SSCL RFQ to DTL input matching section," *1992 Linear Accelerator Conference Proceedings*, Vol. 1, pp. 235-237.
- [4] K. Halbach, "Conceptual design of a permanent magnet with adjustable strength," *Nuclear Instruments and Methods*, Vol. 206, pp. 353-354, 1983.
- [5] W. G. Davies, "The theory of the measurement of magnet multipole fields with rotating coil magnetometers," *Nuclear Instruments and Methods in Physics Research*, Vol. A311, pp. 399-436, 1992.
- [6] The planar triode RF amplifier is being built by AccSys Technology, Inc., Pleasanton, CA.
- [7] T. Enegren *et al.*, "The SSC RFQ-DTL matching section buncher cavities," these proceedings.
- [8] J. W. Hurd *et al.*, "Physics requirements of commissioning diagnostics for SSCL linac," these proceedings.
- [9] C. Fritsche *et al.*, "High density harp for SSCL linac," these proceedings.
- [10] J. W. Hurd *et al.*, "Bunch shape monitor for SSCL linac," these proceedings.

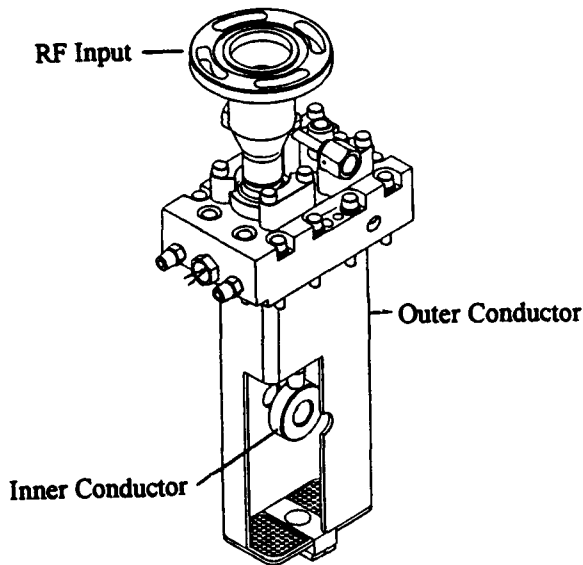


Figure 4. RF buncher cavity for RFQ-DTL matching section.

Accelerator Readiness Review Process for the SSC Linac*

J. F. Tooker, T. Benke, L. W. Funk, and V. Oliphant
Superconducting Super Collider Laboratory
2550 Beckleymeade Avenue, Dallas, TX 75237-3997 USA

Abstract

As each accelerator of the SSCL is prepared for operation, it must have an Accelerator Readiness Review (ARR) in order to begin high power RF or beam operation. This review validates the Safety Analysis Report (SAR) and demonstrates to an independent review panel that 1) the systems and equipment are in place and have been fully tested with satisfactory results; 2) systems and equipment are covered as necessary by written procedures that have been reviewed and approved; 3) those who carry out the activity are fully trained and qualified. The panel will then request that the SSCL Director give permission for operation. The Department of Energy must concur for operation to commence. The SSC Linac, a series of four accelerators, will be tested and commissioned in the Linac Tunnel in series starting in the fall of 1992 and ending in the spring of 1995. The Accelerator Readiness Review process will be described as it relates to the SSC Linac in order to support the staged commissioning.

I. INTRODUCTION

The SSC is a series of accelerators: Linac, Low Energy Booster, Medium Energy Booster, High Energy Boosters, and the Collider. An Accelerator Readiness Review must be held when each of these accelerators is fully prepared for commissioning or routine operation. This review validates the SAR and demonstrates to an independent review panel that each subsystem of the accelerator is in place and has been fully tested, the operating and maintenance procedures have been reviewed and approved, and that those who perform the operation and maintenance are fully trained and qualified.

The SSC Linac consists of a Linear Accelerator [1] and a Transfer Line that routes the beam to the Low Energy Booster. The Transfer Line also contains the main beam absorbers, that are needed for tuning of the Linear Accelerator and operation independent of the LEB. The Linear Accelerator is itself a cascade of four accelerators:

- 1) Ion Source (35 keV)
- 2) Radio Frequency Quadrupole (2.5 MeV)
- 3) Drift-Tube Linac (70 MeV)
- 4) Coupled Cavity Linac (600 MeV)

Plans for commissioning the Linac [2] have the Linac installed, tested, and beam commissioned in series. Prior to availability of the Linac Tunnel, the Ion Source through DTL Input Matching Section are planned to be tested and

commissioned in the Linac laboratory prior to installation and re-commissioning in the tunnel. Each of the four tanks of the Drift-Tube Linac will be installed and commissioned in sequence in the tunnel. This will be followed by the first module of the Coupled Cavity Linac and then the remainder of the Linac. The ARR process for the Linac is staged to support this commissioning and at the same time tailored to minimize the number of reviews, while demonstrating performance and verifying safety.

II. ACCELERATOR READINESS REVIEW

An ARR has four requirements:

- 1) validate the Safety Analysis Report
- 2) verify the subsystems are in place and fully tested
- 3) determine that the procedures are reviewed and approved
- 4) check that the personnel are fully trained and qualified.

To give accountability to the ARR process, a checklist was created. This checklist is a catalogue of the proof used to satisfy the four requirements of an ARR. It also includes spaces for signatures (of each item) from the Cognizant Engineer, Machine Leader, and the Readiness Review Committee. This checklist along with a letter from the Readiness Review Committee is sent through the lab management to the DOE compliance office with a request for a "Permit to Operate".

A. Safety Analysis Report

During the design process, hazard analyses are conducted to identify all potential safety hazards to equipment and personnel and to describe the manner in which the potential hazards and risks will be minimized. These are reviewed for adequacy during the design review process of the Linac. The SAR documents the identified potential hazards and presents the methods used to mitigate these hazards to the degree necessary to operate and maintain the Linac in a safe manner. Mitigation can be accomplished through adequate design safeguards, design safety features, development of operational safety procedures, planned training, and administrative controls. The SAR is reviewed and approved by the SSCL and DOE. All mitigation stated in the SAR must be validated as being in place prior to being given permission to begin commissioning the appropriate section of the Linac.

B. Subsystem Performance

A system engineering process has been incorporated into the SSCL that provides an orderly process for the documentation of the requirements in specifications, monitoring of the designs through reviews, and bringing the technical equipment into operation according to accepted test

*Operated by the University Research Association, Inc. for the U.S. Department of Energy under Contract No. DE-AC35-89ER40486.

plans and procedures. For the Linac [3] this has led to set of specifications, where the performance requirements for the various accelerators of the Linac and their subsystems have been specified. Through a series of design reviews presented by the SSCL engineering departments or outside vendors, the Linac Group monitors the development of the designs for the technical equipment. Acceptance test plans and procedures are written by the SSCL engineering departments or outside vendors and are reviewed by the Linac Group to ensure their adequacy for verification of the performance requirements of subsystems as stated in the specifications. The Linac Group verifies that the technical components and subsystems are then installed and tested according to the appropriate plans and procedures with satisfactory results.

The ARR committee verifies that the required testing has been performed with the resulting positive statement that appropriate subsystems are functioning properly and are ready to proceed to the next phase, such as beam operation. A walk-through of the area and equipment will be conducted by the committee as a final check to verify the configuration of the facility.

C. Procedures

The ARR committee verifies that the appropriate procedures are reviewed and approved. Each subsystem must have approved operation and maintenance procedures, normally written by the engineering departments.

RF conditioning and initial beam operation of a particular section of the Linear Accelerator are continuations of the acceptance testing. These are performed according to the approved acceptance test plans and procedures, normally written by the Linac Group, for those phases of operation. These are prepared before the ARR for anticipated testing and operation. In order to ensure proper review and control of either changes to these plans or future testing, measurements, and operation, a Machine Studies Management Plan for the Linear Accelerator [4] was developed. This document stipulates the process to control and review the machine studies, which retains the maximum amount of flexibility in order to plan and conduct them, while at the same time ensuring safety and quality.

D. Personnel

The personnel that will operate or maintain the equipment must be properly trained and qualified. Lists of trained personnel are provided at the ARR, as well as the required training and procedures needed to qualify future personnel.

III. LINAC ARR SEQUENCE

Commissioning of the Linac is staged so that each section of the Linac can be tested and characterized by a set of commissioning diagnostics located after it, prior to installation of the following section. This sequence is:

In the Linac Laboratory

Ion Source/Low Energy Beam Transport

RFQ

DTL Input Matching Section

In the Linac Tunnel

Ion Source -- DTL Input Matching Section

DTL Tank #1

DTL Tank #2

DTL Tank #3

DTL Tank #4 -- CCL Input Matching Section

CCL Module #1

CCL Modules #2 - #9 -- Transfer Line

During the installation and commissioning of the Ion Source through the first CCL module, CCL Modules #3 - #9 and the Transfer Line are installed, the various subsystems are tested, and the cavities are RF conditioned.

In order to support this staged commissioning, the ARR for the Linac has been divided into the following sequence:

In the Linac Laboratory

RFQ RF Conditioning

Ion Source -- RFQ Beam Commissioning

DTL Input Matching Section Commissioning

In the Linac Tunnel

Ion Source -- DTL Input Matching Section Re-commissioning

CCL #3-#9 RF Conditioning

DTL Tank #1 Commissioning

DTL Tank #2 Commissioning

DTL Tank #3 Commissioning

DTL Tank #4 - CCL Input Matching Section Commissioning

CCL Module #1 Commissioning

CCL Modules #2-#9 - Transfer Line Commissioning

Because of the availability of hardware, the RFQ ARR occurred in two phases. For the DTL Input Matching Section through CCL Module #1, there will be a single ARR for each, reviewing both high power RF conditioning and beam commissioning. To support the early high power RF conditioning of the CCL Modules #3 - #9, a separate ARR will be held to review the readiness of the subset of hardware needed for that activity.

To support the commissioning in the Linac laboratory, a SAR [5] was written for commissioning of the RFQ. It has been approved by the Department of Energy. An addendum to this SAR was issued covering the DTL Input Matching Section. For the commissioning in the Linac tunnel, a Preliminary Safety Analysis Report will be written that includes the Ion Source through CCL. The final SAR that also includes the Transfer Line is scheduled for completion in the fall of 1994.

The two ARR's for the RFQ have been held. SSCL management gave permission for each stage of operation and the Department of Energy approved. The RFQ is currently undergoing beam commissioning [6]. Preparations are beginning for the ARR on the DTL Input Matching Section, which is planned for this summer. The ARR for operation of the Ion Source through DTL Input Matching Section in the tunnel is planned for the fall of this year. Prior to the end of this year, approval to perform high power RF conditioning of the first CCL modules will be requested. Commissioning of the first DTL cavity will be requested early next year.

Permission to operate the entire Linear Accelerator into the main beam absorbers will be sought by the spring of 1995.

IV. CONCLUSION

A sequence of Accelerator Readiness Reviews has been established to support the *staged commissioning of the Linac* at the SSCL. An independent committee will validate the Safety Analysis Report and establish to its satisfaction that the accelerator, or that portion of it, is ready to operate. The committee will also verify that it will be operated and maintained safely, that the personnel are qualified to operate and maintain the accelerator, and that the controls and procedures are in place to ensure continued safe operation and training of future personnel.

V. REFERENCES

DOE 5480.25 Safety of Accelerator Facilities (Draft Guidance Section)

- [1] J. F. Tooker, "Parameter Overview of the SSC Linac," *1992 Linear Accelerator Conference Proceedings*, Vol 1, pp. 323-325.
- [2] J. W. Hurd, "Commissioning Plans for SSC Linac," *1992 Linear Accelerator Conference Proceedings*, Vol 2, pp. 462-464.
- [3] J. F. Tooker, "System Engineering in the SSC Linac," *1992 Linear Accelerator Conference Proceedings*, Vol 1, pp. 326-328.
- [4] SSCL Document No. AQA-1020001
- [5] SSCL Document No. DMP-000011
- [6] K. Saadatmand, "Performance of SSC Volume H⁺ Ion Source, Preaccelerator, and RFQ System," this conference

Commissioning Status of the Continuous Wave Deuterium Demonstrator*

P. Den Hartog, J. Dooling, M. Lorello, and J. Rathke

Grumman Aerospace Corporation, 1111 Stewart Avenue, Bethpage, NY 11714 USA

J. Carwardine, D. Godden, and G. Pile

Culham Laboratory, Abingdon, Oxfordshire, OX14 3DB UK

T. Yule and T. Zinneman

Argonne National Laboratory, 9700 S Cass Avenue, Argonne, IL 60439 USA

Abstract

Grumman Aerospace Corporation, Argonne National Laboratory, and Culham Laboratory are commissioning the Continuous Wave Deuterium Demonstrator (CWDD) in a facility at Argonne National Laboratory. CWDD is a high-brightness, high-current, 7.5-MeV negative deuterium accelerator. The 352-MHz rf accelerating cavities are cryogenically cooled with supercritical neon to reduce the rf power requirements. Installation of the accelerator into the Argonne facility began in May 1991, and first beam from the injector was extracted in February 1992. The accelerator and facility are described, and current status and future plans are discussed.

I. INTRODUCTION

Cryogenically cooled, high-brightness, negative deuterium accelerators have been proposed as part of a future defense system, either space-based or launched-on-demand, which could discriminate or destroy incoming ballistic targets. The Continuous Wave Deuterium Demonstrator (CWDD) has been developed to investigate some of the beam physics and accelerator engineering technologies required of such a system. The accelerator consists principally of a volume negative deuterium source designed to inject 92 mA at 200 keV into a 4-meter radiofrequency quadrupole (RFQ), a single-cavity intermediate matching section (MS), and a 2.6-meter ramped-gradient drift-tube linac (RGDTL). The injector and rf cavities are designed to operate cw or pulsed with an output current of up to 80 mA at 7.5 MeV (figure 1).

II. ACCELERATOR SUBSYSTEMS

The CWDD injector was designed and fabricated at Culham laboratory. A permanent-magnet suppressor and electrostatic collector at the source aperture limits the electron current. Additional reduction is obtained through the use of a pair of dipole magnets with rotating fields, incorporated into the triode accelerator, which sweep the electrons out of the beam before they reach the full 200 keV. Downstream, another pair of dipoles in the LEBT correct the steering introduced by the electron removal. The beam is focused to the RFQ match point by a solenoid lens. Beam centroid position and angle are monitored by a beam emission diagnostic (BED) that views hydrogen Balmer alpha radiation produced by the beam interaction with residual deuterium gas. Injector emittances are measured with an Allison scanner mounted in a removable diagnostic tank located between the injector and the RFQ.

The injector was assembled and operated prior to shipping and re-assembly at the Argonne site. After a suite of tests was

conducted to verify the installation, an engineering upgrade was initiated to eliminate power supply problems caused by breakdown induced transients at 200 kV[1]. The upgrade was completed in October 1992 and reliable, stable performance at 200 kV has now been demonstrated. To date, the maximum ion current from the source has been 20 mA. It has been shown that the introduction of cesium into the plasma discharge of a source can increase the current by a factor of two or more[2]. It is planned to modify the CWDD source to enable cesium experiments in late 1993.

The RFQ accelerates the D⁺ beam from 200 keV to 2.0 MeV. The mechanical design and fabrication approach is an extension of the techniques used for the Beam Experiment Aboard a Rocket (BEAR) RFQ built by Grumman for Los Alamos National Laboratory in 1988[3]. The CWDD RFQ is made from four one meter long segments; each machined from solid tellurium copper and electroformed into a four-vane assembly. The segments are bolted together to form the 3.96 meter (4.63λ at 352.2 MHz) structure. Unlike BEAR, which is un-cooled, the CWDD RFQ has extensive internal cooling passages to allow for removal of 161 kW (at QEF=4) of dissipated power during CW operation. The cavity structure has 48 parallel cooling passages to minimize thermal detuning effects. In addition, all ancillary components are actively cooled; including tuners, RF power couplers and end walls.

The CWDD RFQ has 76 fixed slug tuners distributed axially along the quadrants. The tuning process uses techniques and code developed at LANL. Automated beadpulls are run on the RFQ to determine the field profiles in the four quadrants. Data produced by the QUADPULL/QUADPLOT[4] software is then input to RFQTUNE[5], which uses perturbation theory to determine tuner movements necessary to correct the measured field profiles. Using this technique, the 76 tuner settings were determined in 5 iterations with a field quality of better than ±0.5% for the quadrupole and dipole components. Some retuning was required due to repairs made on the RF end walls. This tuning was done with the RFQ in the vacuum vessel with restricted access, therefore, only a limited number of tuners (10) were adjusted. The final field quality is ±1% quadrupole, 0 to -1% dipole 1 (1-3), and 0 to -1.5% dipole 2 (2-4). This is well within the specification value for field quality of ±5%.

In December 1992, the completed RFQ was installed into its cryostat. All instrumentation has been installed, cooling lines have been proof pressure tested, and drive loops and field pickups have been coupled. In July 1993, the rf drive lines will be installed and final alignment will be performed.

The room-temperature quality (Q) of the completed cavity, 7795, was better than the design goal of 6582 (70% of the SUPERFISH predicted value of 9403). This results in a drop

* This work was performed under contract to the U.S. Army Space and Strategic Defense Command, no. DASG60-88-C-0060 and under the auspices of the Department of Energy and funded by the U.S. Army Space and Strategic Defense Command.

in the total dissipation power in the RFQ from 161 kW to 136 kW during operation at cryogenic temperature.

The MS cavity has a 5-mm aperture, is 16 mm long, and is attached to the high-energy faceplate of the RFQ. Four samarium cobalt permanent magnet quadrupoles (PMQ) provide beam focusing. The axis of two of the PMQ's can be offset by stepping motors to provide beam steering. A 4-button capacitive pickup provides beam position, intensity, and phase spread information. Tuning of the cavity will be performed remotely at cryogenic temperature using a sliding-short tuner (SST).

The MS cavity has been fabricated, tested with low-level rf power, and will soon be installed on the RFQ. The SST has been designed but fabrication has not yet begun.

The 2.64 m long by 0.512 m diameter RGDTL is fabricated from a single extrusion of annealed OFHC copper. It is attached to the high energy faceplate of the MS and accelerates the 2.0 MeV D⁻ beam to 7.54 MeV. The accelerating field gradient is linearly ramped from 2.0 MV/m at the low energy end to 4.0 MV/m at the high energy end by detuning the end cells. Each of the 46 drift tubes contains a PMQ in a FOFODODO lattice.

The RGDTL cavity has been fabricated, cooling channels have been machined, and all of the drift tubes have been assembled. Procurement of the remaining components, including the post couplers, pickup loops, tuners, and cryostat is planned to begin in October 1993. Delivery to the Argonne site is scheduled for October 1994 and installation will be completed by December.

The 352.2 MHz RF System (cw or pulsed) was designed and manufactured by the GE Marconi Communications Systems Ltd.(GE-MCSL). It consists of two 1-megawatt amplifier subsystems with Valvo YK-1350 klystron output tubes, and one 25-kilowatt amplifier which uses a Thompson TH-571B tetrode. The 1-MW systems power the RFQ and RGDTL, and the 25-kw amplifier drives the MS. All stations have identical 100-kHz bandwidth analog phase and amplitude (APC/ALC) control loops with an accuracy of $\pm 1^\circ$ in phase and $\pm 1\%$ in amplitude. The tubes are driven by a master oscillator and solid state driver amplifiers. A mod-anode control system insures that the klystron collector dissipation never exceeds the YK-1350 maximum allowable limit of 900 kW.

Universal Voltronics Corporation (UVC) was subcontracted by GE-MCSL to design and manufacture the high voltage power supply equipment for the 1-MW systems. The power supplies can deliver up to 100 kV DC at 20 amperes. A crowbar, consisting of four ignitrons, reduces the power supply voltage to near zero in $\leq 10 \mu\text{s}$ to protect the klystrons in the event of a fault. Energy into a load fault is limited to approximately 40 joules.

Rf power is distributed to the RFQ and RGDTL through WR-2300 waveguide and to the MS by 6-1/8 inch coaxial line; A.N.T. Bosch Telecom Co. circulators are used to prevent reflected power from damaging the output tubes. An absorptive harmonic filter is placed between each klystron and circulator. The transmission lines for each of the 1-MW stations are terminated with "magic tee" power dividers for connection to the drive loops of the RFQ and RGDTL cavities.

All rf conditioning of the CWDD cavities will be performed at 26K. The CWDD cavities experience an upward

shift in resonant frequency of 1.1 MHz when cooled from room temperature to 26K, but the YK-1350 klystron has a 1-dB bandwidth of 1 MHz; implying that if the cavities were operated at 352.2 MHz at cryo temperature, then the klystron output would be about 3 dB down (from the peak output) at 351.1 MHz. Since the cavities must be conditioned to a power level of 1.4 times their anticipated dissipation, the cavities can only be conditioned at cryo temperature—unless the cavities are retuned. Experience at Grumman has shown that copper cavities can be conditioned for cw at cryogenic temperatures alone.

The rf systems have been installed in the facility and commissioning is underway. The 25-kW amplifier has been tested to 28 kW into an absorptive load and low power (100 W) phase and amplitude loop tests are scheduled for April, 1993. The HV systems for the 1-MW amplifiers were successfully tested into a resistive load at 446 kW and 91 kV. Testing of the 1-MW systems into absorptive loads will begin in May, 1993, but final testing of the rf systems into the cavities must await the completion of the cryogenic system, now scheduled for early 1994.

The HEBT is designed to allow configuration for operation with the RFQ and MS alone or with the RFQ, MS, and RGDTL. This permits testing of the RFQ and MS, as well as commissioning of the diagnostics, to proceed in parallel with the final assembly of the RGDTL. The HEBT contains a quadrupole (to expand the beam and thus reduce the power density at the beam stop), conical beamlines, instrumented graphite beam scrapers, a transverse emittance measurement system, and a set of three 4-button capacitive pickups that can measure the beam energy by a time-of-flight method.

The power density of the beam at the RGDTL output can be as high as 250,000 W/cm². This is reduced by a factor of 1000 by the beam expanding quadrupole and by the use of a V-shaped graphite beam stop. The beam stop is designed to dissipate 750 kW of heat for a 20 s pulse every 90 minutes.

The HEBT and beam stop have been installed into the CWDD vault. Final assembly of the instrumentation and diagnostics will be completed by July 1993.

Although the preferred cryogen would be liquid hydrogen, supercritical neon was chosen as a safer surrogate with scalable thermal properties. At full rf power, 78 kg/sec of 26K neon at 30 atmospheres absolute will be required to cool all three cavities. The major components of this system are a 4.7 kW helium refrigeration system, a supercritical pressure neon circulation loop, and a secondary gaseous/liquid neon loop. Although the entire accelerator system was designed to operate cw, a cryogenic system with sufficient capacity for continuous operation would have been too costly. Consequently, the accelerator test plan was structured to allow all of the required cw tests to be conducted in a series of 40 second or less "shots". The cryogenic system provides peak output during these shots followed by a variable length recovery period, depending on the thermal load. Those tests that do not require cw operation can be performed using a pulsed beam, lowering the refrigeration requirement. The recovery period is a maximum of 90 minutes for a shot of 40 seconds at full power loading. Pulsed operations can be conducted indefinitely, as long as the rf duty cycle does not exceed 0.75%.

The cryogenic system was designed by Cryogenic Consultants, Inc. and manufactured by Meyer Cryo Tech. All

of the components have been fabricated and the system is currently being installed. Procurement of the 150,000 standard cubic feet of neon required for operation will begin early in October 1993 and commissioning of the system will start in early 1994.

III. SUMMARY

The CWDD is a unique machine that will test the technology of cw, high brightness, cryogenically-cooled, D⁺ acceleration. All of the major components have been designed and fabricated; most have been assembled into the facility and beam has been available from the injector for more than a year. Operations of the RFQ will begin in early 1994 when the cryogenic system is completed. Installation of the RGDTL

will begin in late 1994 and operation of the full-energy accelerator will commence in early 1995.

- [1] J. Carwardine, G. Pile, and T. Zinneman, Proceedings of the 1993 IEEE Particle Accelerator Conf., Washington D.C., (May 1993).
- [2] K. N. Leung, Proceedings of the 1991 IEEE Particle Accelerator Conf., San Francisco, CA, (May 1991).
- [3] D. Schrage, et al., 10th Conference on the Application of Accelerators in Research and Industry, Denton, TX, (1988).
- [4] J. H. Billen, Proceedings of the 1993 IEEE Particle Accelerator Conf., Washington D.C., (May 1993).
- [5] L.M. Young, Proceedings of the 1990 Linear Accelerator Conference, Albuquerque, NM, (Sept. 1990).

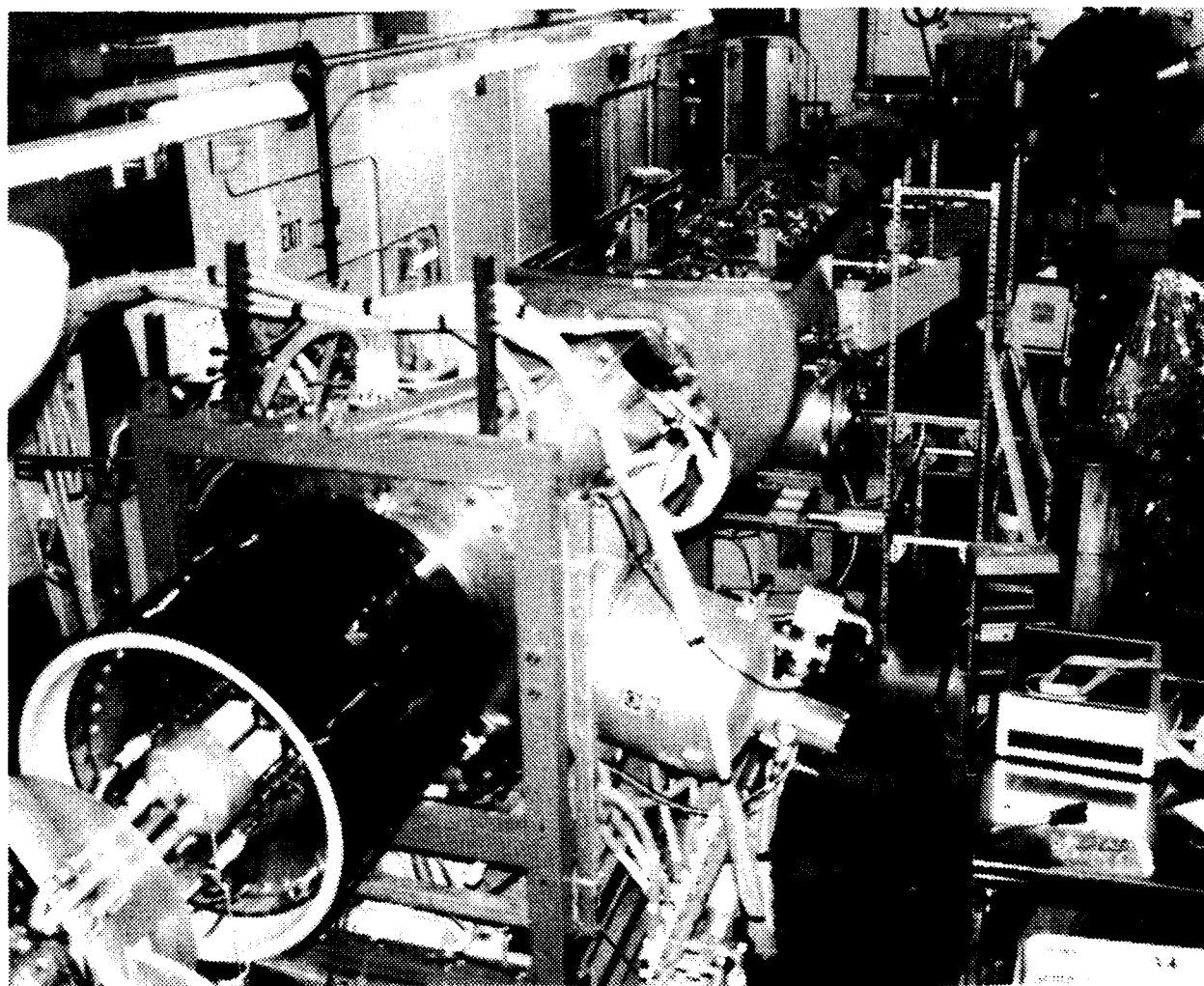


Figure 1. The CWDD accelerator showing the injector in the foreground, the RFQ in its cryostat with the lid removed, the HEFT, and the Beam Stop in the upper right corner. Vacuum insulated cryo lines will be connected to the large ports on the side of the RFQ.

DESIGN STUDY FOR A SUPERCONDUCTING PROTON LINAC FROM 20 TO 100 MEV*

T. P. Wangler, R. Garnett, F. Krawczyk, J. Billen, N. Bulman,
K. Christensen, W. Fox, and R. Wood
Los Alamos, National Laboratory, Los Alamos, NM 87545

I. INTRODUCTION

Advances in superconducting radiofrequency technology during the past 15 years have made possible the large-scale application of superconducting niobium accelerators. So far this development has been restricted to rather low-current electron and heavy-ion accelerators. In addition to the power savings, the improved capability of superconducting cavities to provide acceleration of high currents with low beam losses, which follows from the ability to use larger beam apertures without a large economic penalty from increased rf losses, could make superconducting proton linacs very attractive for high-intensity applications, where activation of the accelerator is a major concern. During the past year, at Los Alamos, we have been looking at a possible upgrade to the 800-MeV LAMPF proton accelerator, to provide higher intensity injection into a new storage ring for a new high-intensity pulsed neutron source. As part of this upgrade to the LAMPF accelerator, the entire linac below 100 MeV would be rebuilt to provide improved beam quality, improved reliability, and to include funneling at 20 MeV for higher beam currents. Both a room-temperature and a superconducting option are being considered for the section from 20 to 100 MeV. At present, this section is a 201.25 MHz room-temperature copper drift-tube linac (DTL). For this new upgrade scenario the frequency from 20 to 100 MeV was fixed at 805 MHz. The new duty factor is assumed to be 7.2%, and we will show some results at two currents, 30 mA and 150 mA, that span the range of interest. Our superconducting linac concept consists of individual multicell cavities, each driven by a klystron. Focusing would be provided by superconducting quadrupole lenses between cavities. In the remainder of the paper we describe our study to evaluate the potential of a superconducting proton linac section for this application, and address some of the many design choices.

II. ACCELERATING STRUCTURE STUDIES

Recently, at Argonne, a new niobium accelerating structure, called the spoke resonator¹ has been built and tested at high fields. This structure is suitable for acceleration of high-current beams at the intermediate velocities of interest. This structure is also equivalent to the slotted iris structure that was built many years ago for superconducting applications at Karlsruhe². The cavity that was tested resonated at 855 MHz, and was optimized for a particle velocity of 0.30 c. RF-tests were performed on the cavity and a high accelerating gradient of 7.2 MV/m, limited by magnetic quench, was obtained at a 4.2 K operating temperature. A peak surface electric field of 24 MV/m and a peak surface magnetic field of 560 G were obtained in the cavity. The accelerating gradient achieved in the test is already very attractive for a proton linac application.

For a proton linac it may be more economical to employ accelerating structures with more than two gaps. We have looked at two arrangements for the spokes, a) the ladder geometry where all the spokes are parallel, and b) the cross-bar geometry, where adjacent spokes are rotated by 90 degrees. We have studied the characteristics of both these structures at 805 MHz and at three different velocities, corresponding to 20, 60, and 100 MeV protons, using the 3D electromagnetic code MAFIA(Release 3.1). Figure 1 shows drawings produced by MAFIA for each of these structures. For these initial studies the spoke has been modeled as a rectangular bar of width = 6.0 cm with beveled edges to reduce the peak electric field, and thickness = $0.317 L_c$ along the axial direction, where $L_c = \beta\lambda/2$ is the cell length, and β and λ are the velocity and rf wavelength. The boundary conditions are defined for MAFIA on the transverse planes that pass through the center of the bars. For the π mode the electric fields are parallel to the boundary

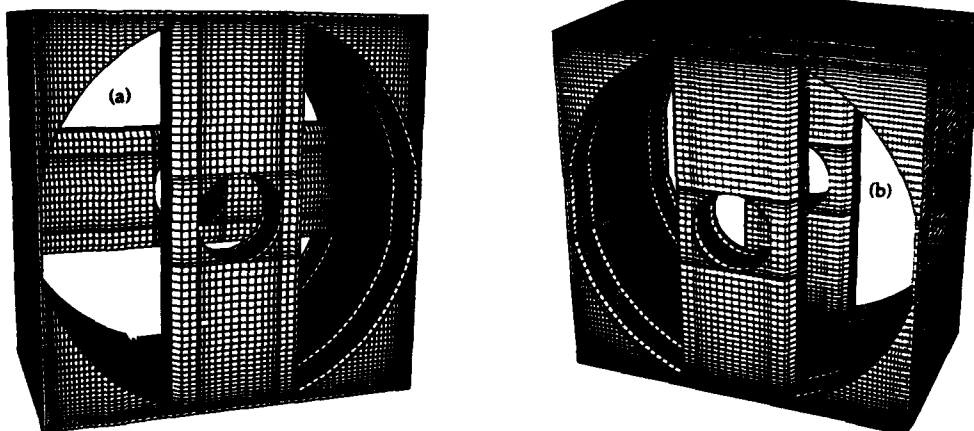


Fig. 1. Views of the multicell cavity structures designed for particles with velocity = 0.428 c produced by MAFIA. a) Cross-bar structure, b) Ladder structure.

*Work supported by Los Alamos National Laboratory Institutional Supporting Researches under the auspices of the United States Department of Energy.

plane. The cavity radius R was adjusted until the resonant frequency of the π mode was within 1% of 805 MHz. The results are shown in Table 1, where the cross-bar and ladder structures are designated as CB and L. The notation is: Q_0 is the unloaded quality factor, $R_s(\Omega)$ is the rf surface resistance, T is the transit-time factor, $k = (\omega_\pi - \omega_0) / \omega_{ave}$ is the intercell coupling factor defined in terms of the frequencies of the 0 and π modes, and their average frequency, $U(\text{mJ})$ is the stored energy within a length $\beta\lambda$, $E_p(\text{MV/m})$ is the peak surface electric field, and $B_p(\text{mT})$ is the peak surface magnetic field. The stored energy and field values are normalized so that the accelerating field $E_0T = 1 \text{ MV/m}$, where E_0 is the spatial average of the axial electric field. The coupling factor k is larger for the CB case but it is probably acceptably large for both structure types.

The peak surface field differences between the two structures are the result of 3D geometry effects. The peak surface electric fields generally occur at the edges of the bar even when the edges are beveled. For the CB structure the electric field lines that originate from the face of a bar tend to terminate preferentially along the edges of the adjacent perpendicular bar, and this concentration produces an enhanced peak surface field. Improvements in the spoke geometry should reduce E_p . The peak surface magnetic field is maximum where the bar intersects the cylindrical wall. For the CB structure the current and the magnetic field are not smoothly distributed around the bar, but are concentrated along the sides. For the L structure this results in the shortest path for the current. Although the optimization of the geometries is not completed, the smaller peak surface fields for the L structure makes this structure an attractive candidate.

We have also looked at the conventional 0-mode DTL structure. A disadvantage of the 0-mode structure is that the transit-time factor is reduced, because the axial field leaks into the drift tubes, when large apertures are required. We have considered an example in which the drift tubes will not contain a focusing quadrupole, and are designed with noses to compensate for the reduction in the transit-time factor caused by the large aperture. The DTL has been modeled as an azimuthally symmetric structure, and its properties have been calculated using the 2D electromagnetic code SUPERFISH. The results are also shown in Table 1. By comparison with the spoke-type structures, the DTL also has very strong intercell coupling, lower T , much larger E_p , and smaller B_p (but see footnote for Table 1).

III. BEAM DYNAMICS STUDIES

We present two examples³ from our study of superconducting linac solutions using the code CCLDYN. The

multicell cavities are generated for a fixed value of velocity β , all cells in the cavity have the same length $\beta\lambda/2$, and each cavity has a different β . The intertank spaces are chosen to allow adequate room for flanges, bellows, diagnostics, and quadrupole lenses. The beam current, averaged over an rf cycle, is assumed to be either 30 or 150 mA. The accelerating field E_0T as a function of beam energy was obtained from a polynomial fit to MAFIA calculations, and corresponds approximately to a constant peak surface electric field near 20 MV/m. We chose E_0T equal to 3.5 MV/m at 20 MeV, 5.1 MV/m at 60 MeV, and 5.5 MV/m at 100 MeV.

The two linac designs we have considered correspond to a 2.0-cm radial aperture and a fixed energy gain per multicell cavity equal to a) $\Delta W = 1.0 \text{ MeV}$, and b) $\Delta W = 3.33 \text{ MeV}$. The number of cells per cavity is determined by ΔW , E_0T , and the synchronous phase. Table 2 summarizes the parameters for the two examples. We interpret the results as follows. For design B the linac is shorter and has fewer components. However, for design B: a) the cavity input power coupler requirements are greater (The present state of the art for input power couplers represents a limit that is generally considered to be about 100 kW.), and b) the transverse aperture-to-rms beam size ratio is lower as a result of the reduced transverse phase advance per focusing period, leading to a larger beam envelope and indicating increased beam-loss potential. We consider that for 150 mA the transverse aperture to rms ratio is probably more than adequate for design A, and the longitudinal ratio is more than adequate for design B. In these designs with quadrupoles between all cavities, increasing the cavity energy gain and length increases the quadrupole period, which for fixed 80° transverse phase-advance per period, reduces the overall quadrupole focusing strength. However, it improves the overall longitudinal focusing, because of the reduced number of intertank spaces. The beam dynamics optimum in cavity energy gain lies somewhere between the two designs. Additional optimization would include the choices of aperture and synchronous phase.

It may be desirable from the point of view of reliability to restrict the number of gaps per cavity to only 2 or 3, so that failure of a single cavity would result in only a minor perturbation on the overall linac performance. We have not had time to explore this issue, but we note that the multicell cavities for the two designs presented here could be replaced by groups of two or three gap cavities. The beam dynamics results for this case should be similar to what has

Table 1 MAFIA results for cross-bar(CB) and ladder(L) structures in the π mode and DTL structure in 0 mode.

Type	β	$R(\text{m})$	$Q_0R_s(\Omega)$	T	k	$U(\text{mJ})$	$E_p(\text{MV/m})$	$B_p(\text{mT})^*$
CB	0.207	0.0745	63.7	0.782	0.58	16.9	6.16	24.9
CB	0.341	0.0845	85.0	0.776	0.46	17.6	4.14	16.4
CB	0.428	0.0891	93.3	0.771	0.40	21.4	3.86	14.6
L	0.207	0.0981	62.5	0.782	0.31	18.8	5.09	19.4
L	0.341	0.1000	86.5	0.777	0.30	18.3	3.58	13.6
L	0.428	0.1003	93.9	0.779	0.30	21.0	3.43	13.0
DTL	0.207	0.10	207.9	0.498	0.90	23.6	20.5	8.16
DTL	0.341	0.10	213.6	0.641	0.61	23.2	14.4	7.20
DTL	0.428	0.10	210.1	0.633	0.51	32.0	14.2	8.09

* For the DTL this does not include the factor of 2 stem enhancement.

Table 2 Comparison of 805 MHz, 20-100 MeV Superconducting Linac Designs

PARAMETER	DESIGN A	DESIGN B
Energy gain per cavity (MeV)	1.00	3.33
E_0T (MV/m)	3.5 to 5.5	3.5 to 5.5
Synchronous Phase (deg)	-40 to -35,	-40
Cells per Cavity	9 to 3	30 to 9
Number of Cavities	87	26
Cavity Lengths (m)	0.18 to 0.36	0.71 to 1.18
Cavity Input Power (kW)	30 (30 mA)	100 (30 mA)
	150 (150 mA)	500 (150 mA)
Intercavity Spacing	5.5 $\beta\lambda$ to 3.5 $\beta\lambda$	5.5 $\beta\lambda$ to 3.5 $\beta\lambda$
Aperture Radius(cm)	2.0	2.0
Transverse Aperture to Rms Beam-Size Ratio	14-25 (30 mA)	7-14 (30 mA)
	11-19(150 mA)	6-10 (150 mA)
Longitudinal Aperture to Rms Beam-Size Ratio	6-9 (30 mA)	12-13 (30 mA)
	5-6 (150 mA)	10-11(150 mA)
Focusing Lattice Type	Doublet	Doublet
Total Length(m)	62.0	36.9

been already presented in this paper, provided that the gaps required between cavities are small.

In Table 3 we show various power values at operating temperatures of both 2K and 4.2K. The peak rf power of 2.4 MW is determined by the beam power for an assumed 30 mA beam current. The average rf power is obtained by applying the 7.2% duty factor. The rf surface resistances are taken from measurements at 805 MHz on single-cell niobium elliptical cavities⁴ at $E_p = 20$ MV/m, and the surface resistance at 2K is lower than at 4.2K by a factor of 16.7. The rf power dissipation in the niobium structure has been obtained by using the parameters from the MAFIA calculations for the L structure. The static heat leak is estimated⁵ at 7 W/m of cryostat length, and the length is taken from the design A value of 62 m. Because the static heat leak is a continuous load, while the rf load is pulsed, the static effect is dominant at 2K and is comparable to the rf load at 4.2K. For this reason the large temperature dependence in the rf surface resistance does not produce a correspondingly large difference in the thermal power into the Helium. The refrigeration-efficiency⁶ difference favors the 4.2K temperature, mostly because of the temperature dependence of the Carnot efficiency factor. The net result is that the ac refrigeration power is about equal for the two operating temperatures. This conclusion would change in favor of 2K operation, if the accelerating field increased, if the duty factor increased, or if the static heat load decreased.

Table 3 Superconducting Linac Power Values

Operating Temperature	2K	4.2K
Beam current (mA)	30	30
Peak rf power(MW)	2.4	2.4
Average rf power (kW)	170	170
Niobium rf surface resistance (n Ω)	24	400
Peak rf power-niobium (W)	520	8600
Average rf power-niobium(W)	37	620
Static heat leak power (W)	430	430
Total power into Helium(W)	470	1050
Refrigeration efficiency	1/1200	1/530
AC power for refrigeration(kW)	560	560
AC klystron power(kW)	370	370
Total ac power (kW)	930	930

The ac power for the klystrons is calculated using an efficiency factor⁷ of 47%. The final conclusion is that at 30 mA the peak rf power required is 2.4 MW, and the total ac operating power (refrigeration plus klystrons) is just under 1 MW. The superconducting linac sections would reduce the peak rf power by 7.0 MW and the ac operating power by 0.8 MW, compared to the existing 201.25 MHz room-temperature copper DTL.

IV. ACKNOWLEDGMENTS

One of us, T.P.W., wishes to acknowledge several very productive discussions with Jean Delaysen and Cort Bohn from Argonne on superconducting linac issues. Discussions with Los Alamos colleagues Lloyd Young, George Spalek, Brian Rusnak, Joe Dimarco, Ed Gray, Mike Lynch, Don Reid, and Andy Jason have been very important. We would like to thank Bob Jameson, Andy Jason, and Jim Stovall for their support in carrying out this work.

VI. REFERENCES:

- [1] J. R. Delaysen, W. L. Kennedy, and C. T. Roche, "Design and Test of a Superconducting Structure for High-Velocity Ions", Proceedings of the 1992 Linear Accelerator Conference, Ottawa, Ontario, Canada, 24-28 August, 1992, AECL Report AECL-10728, p 695.
- [2] K. Mittag, "Superconducting Accelerator Structures for Medium Energy Protons", IEEE Trans. Nucl. Sci., Vol. NS-24, No. 3, 1156 (1977).
- [3] R. W. Garnett, "Example Beam Dynamics Solutions for a 20-100 MeV Superconducting Linac for LANSCE-II", Los Alamos Accelerator Technology Division Technical Note No. AT-1:93-099, April 15, 1993.
- [4] Brian Rusnak, Los Alamos, private communication.
- [5] C. H. Rhode and D. Proch, "Cryogenic Operation for Cavity Systems", Proc. of 4th Workshop on RF Superconductivity, KEK Report 89-21, KEK Laboratory, Tsukuba, Japan, August 14-18, 1989, p 751.
- [6] P. Lebrun, "Cryogenic Systems", Superconductivity in Particle Accelerators< CERN Accelerator School Proceedings, CERN 89-04, Hamburg, Germany, May 30-June 3, 1988, p 66.
- [7] Mike Lynch, Los Alamos, private communication.

Design Considerations for High-Current Superconducting Ion Linacs

J. R. Delayen, C.L. Bohn, B.J. Micklich, C.T. Roche, and L. Sagalovsky
Argonne National Laboratory, Engineering Physics Division
9700 South Cass Avenue, Argonne, Illinois 60439

Abstract

Superconducting linacs may be a viable option for high-current applications such as fusion materials irradiation testing, spallation neutron source, transmutation of radioactive waste, tritium production, and energy production. These linacs must run reliably for many years and allow easy routine maintenance. Superconducting cavities operate efficiently with high cw gradients, properties which help to reduce operating and capital costs, respectively. However, cost-effectiveness is not the sole consideration in these applications. For example, beam impingement must be essentially eliminated to prevent unsafe radioactivation of the accelerating structures, and thus large apertures are needed through which to pass the beam. Because of their high efficiency, superconducting cavities can be designed with very large bore apertures, thereby reducing the effect of beam impingement. Key aspects of high-current cw superconducting linac designs are explored in this context.

I. INTRODUCTION

Questions regarding the design of linear accelerators with high duty factor for the long-term production of high-current ion beams center as much on beam physics as on hardware. The pervasive concern is whether dynamical phenomena which generate a diffuse halo of beam particles can be sufficiently controlled to limit radioactivation induced by beam impingement to safe levels.¹ For example, as indicated in Section II below, the maximum tolerable amount of beam impingement is of the order of 0.03 nA/m for 1 GeV protons. The heat load associated with this level of impingement is 30 mW/m. The rf losses on a superconducting cavity will be ~20-40 W/m, and therefore radioactivation is by far the dominant concern related to beam impingement on superconducting structures. This concern is equally important for copper accelerators. Because shunt impedance is of less concern in superconducting cavities, they can be designed to operate at low frequency and with large bore-hole apertures to mitigate impingement. This constitutes additional degrees of freedom which are available in the design of high-current linacs. In Section III below, we provide four generic superconducting cavity geometries designed specifically for use in these high-current linacs.

II. LIMITS ON PERMISSIBLE RADIOACTIVATION

For a low-energy (35-40 MeV) deuteron accelerator, such as that being proposed for a d+Li neutron source for fusion materials testing, the most important reactions are the (d,p)

and (d,2n) reactions, with (d,n), (d, α), and other reactions being somewhat less important. The neutrons produced through (d,xn) reactions can also produce activation. Experiments have shown that neutron yield is higher in copper than in niobium by a factor of about two² at $E_d = 10-15$ MeV, and we use that assumption up through 40 MeV. This is consistent with the variations in (n,2n) cross sections such as shown by Barbier.²

Radionuclides produced from niobium have either very short or very long half-lives. Thus, the dose rate beginning a few hours after shutdown should be smaller relative to that from copper. For niobium, the dominant dose from direct D activation is due to ⁹³Mo^m (6.9 h). The neutron-induced activity in niobium is predominantly due to ⁹²Nb^m (10.13 d).

For copper, ⁶³Zn (38.3 m) and ⁶²Cu (9.8 m) dominate the dose rate at short times following irradiation. Of particular interest is ⁶³Zn (243.8 days), since this nuclide builds up over long irradiations and thus dominates the dose rate after several days for irradiation times of around 300 days. Other (d,p) and (d,2n) activities in Cu decay rapidly. At longer times following shutdown, ⁶⁴Cu (12.8 h) can also be important, as well as ⁶⁰Co (5.27 y) from ⁶³Cu(n, α) for long irradiation times.

Table 1. Dose rates in mrem/h at 30 cm distance from copper and niobium 35-MeV D accelerators for 1 nA/m current loss and 1 to 5 MV/m average gradient.

t_{sh}	Cu $t_{irr} = 30$ days	Nb $t_{irr} = 30$ days	Cu $t_{irr} = 300$ days	Nb $t_{irr} = 300$ days
0 h	21.	4.4	23.	4.4
1 h	5.7	4.2	7.4	4.2
8 h	2.0	3.1	3.8	3.1
24 h	1.0	2.2	2.7	2.2
30 d	0.43	0.31	2.1	0.31

Accelerator activation was estimated for a constant 1 nA/m current loss and an average gradient of 1 MV/m, with the results shown in Table 1. For 30 days irradiation time (t_{irr}), the copper dose is much higher for short time after shutdown (t_{sh}). The dose for niobium is higher from a few hours to a few days following shutdown (due to ⁹²Nb^m), while the copper is again higher at 30 days, although the difference is small. For an irradiation time of 300 days, the dose in copper is higher at all times following shutdown because of the ingrowth of ⁶³Zn. Dose rates are relatively insensitive to gradient, decreasing somewhat at higher gradient, assuming a constant deuteron loss per unit length; however, the amount of irradiated material will be greater for a lower gradient (longer accelerator).

For high-energy proton accelerators, neutron yields increase with higher Z for proton bombardment. The range

*Work supported by the U.S. Department of Energy under contract W-31-109-ENG-38 and by the Strategic Defense Initiative Organization.

of 1 GeV protons in both niobium and copper is of order 40 cm,³ and because the wall thickness of the cavities is much less than the range, radioactivation of niobium should be slightly more, but comparable to, that of copper. Thus, for a proton beam, the current loss in both niobium and copper needs to be less than 0.2 nA/m at 200 MeV, and less than 0.03 nA/m at 1 GeV, to be under 2.5 mrem/hr at a distance of 1 m from the linac one hour after shutdown.⁴

III. LARGE-BORE SUPERCONDUCTING CAVITIES

1. General considerations

Geometries of low-velocity superconducting resonators generally incorporate an inner conductor which provides a TEM-like accelerating mode.⁵ The center-gap to center-gap distance in these structures is of order $\beta\lambda/2$, where $\beta=v/c$ is the beam velocity, and λ is the rf wavelength. For velocities less than $\sim 0.1c$ and frequencies of several hundred MHz, this distance becomes too small for practical resonators, and this consideration is a principal motivator for superconducting RFQs which provide proton energies to ~ 8 MeV.⁶ For proton energies ranging from 8 MeV to 2 GeV, the corresponding velocity range is $\beta=0.1-0.9$. Superconducting resonators have recently been developed for frequencies in the range 350-850 MHz and optimized for velocities up to $\beta=0.3$. Off-line experiments with these structures have yielded high accelerating gradients.^{7,8} Of these structures, the easiest to fabricate is the spoke resonator shown in Fig. 1. This geometry is also modular, for several units can be stacked together to make a multigap cavity. For these reasons, we use the spoke as the baseline geometry for superconducting cavities to be used in high-current linacs.

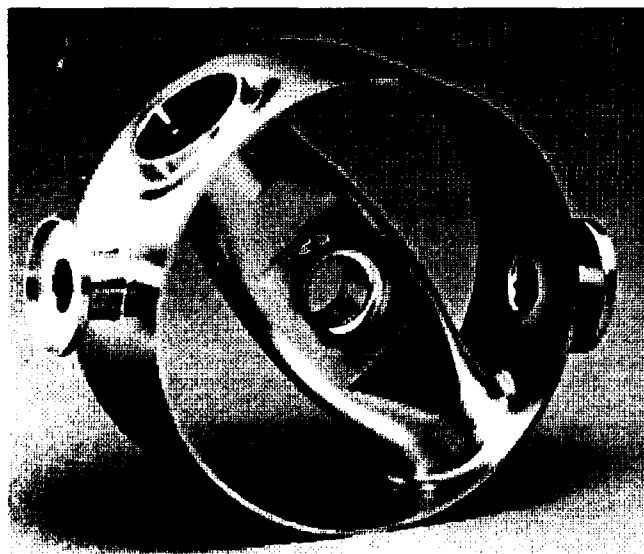


Figure 1. 850 Mhz, $\beta=0.28$, 2-gap spoke resonator prior to the welding of the end plates.

The choice of frequency hinges on a number of considerations. One of them is the ability to provide large-bore

apertures for the beam, and this favors lower frequencies and larger cavities. Large bores also provide lower transverse shunt impedances which reduce cumulative beam breakup. The availability of rf power is a second concern.

On the other hand, it has been inferred from numerical simulations that high frequencies mitigate emittance growth by lowering the charge per bunch.⁹ This is a major consideration when emittance preservation is crucial. For most of the high-current applications, however, emittance growth is a concern only in connection with halo formation and beam transport. A detailed understanding of the effects of bunching on high-current beams is a fundamental building block for the design of these linacs, and this will be the topic of future investigations.

One possible strategy for achieving high currents is to combine two beams by funneling them together at a relatively low energy, a process which doubles the rf frequency. To achieve large bores and use a common frequency for rf power amplifiers, we shall assume the linac operates at 350 MHz, and that prior to funneling, the frequency is 175 MHz.

2. Cavity geometries

As shown in the examples of Figs. 2 and 3, the spoke geometry can be adapted to span a wide velocity range. For high velocities it becomes more practical to introduce single-cell structures like that shown in Fig. 4, or multicell structures like that shown in Fig. 5. The properties of these large-bore geometries, which were calculated with MAFIA in the case of the spoke resonators and SUPERFISH in the case of the "elliptical" cavities, are given in Table 2 below. In the Table, resonators #1-#4 refer to the 175 MHz, $\beta=0.125$ spoke, the 350 MHz, $\beta=0.45$ spoke, the 350 MHz, $\beta=0.45$ single-cell, and the 350 MHz, $\beta=0.8$ two-cell, respectively.

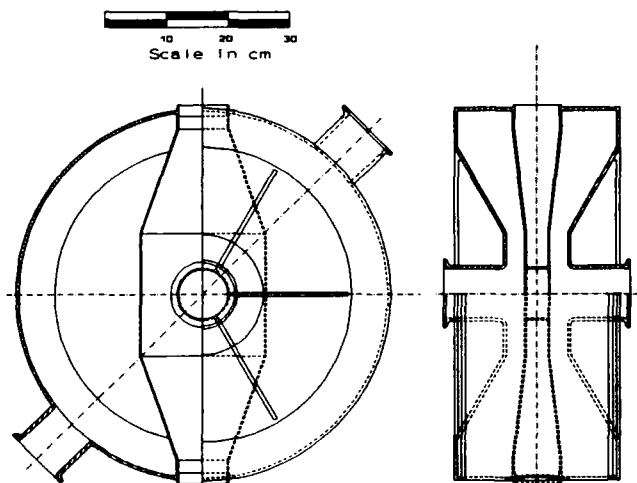


Figure 2. 175 MHz, $\beta=0.125$, 2-gap spoke resonator.

Compared to two-gap spoke resonators, two-cell "elliptical" cavities generally have higher shunt impedances and lower rf surface fields. They are also comparatively simple and easy to fabricate. However, for a given frequency, these structures are also much larger than the spoke, and are likely to be less mechanically rigid.

Table 2. Comparison of resonator properties.

	#1	#2	#3	#4
$B_p/E_{acc}[G/(MV/m)]$	122	125	41.6	35.9
R_{ab}^* ($10^3 M\Omega$)	1.3	1.5	1.2	6.7
R_{ab}/Q (Ω)	47.1	121	51.3	205
P (W) [†]	2.73	9.65	9.0	14.5
ΔV (MV) [†]	0.6	1.2	1.0	3.1
Diameter (cm)	60	38	74	76

*Assumes BCS R_s at $T = 4.2$ K, [†]At $E_{acc} = 6$ MV/m.

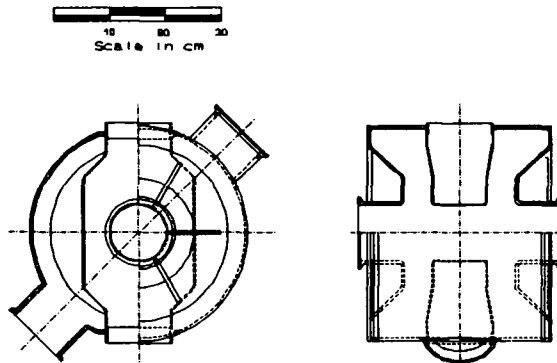


Figure 3. 350 MHz, $\beta=0.45$, 2-gap spoke resonator.

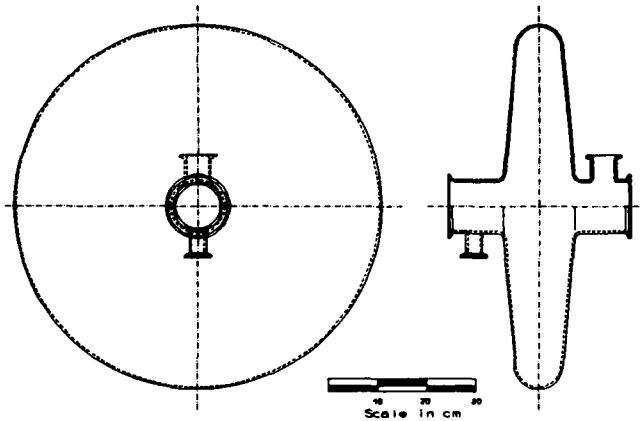


Figure 4. 350 MHz, $\beta=0.45$, Single-cell TM_{010} resonator.

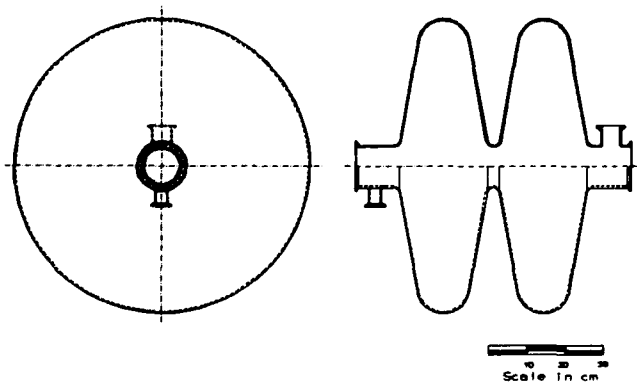


Figure 5. 350 MHz, $\beta=0.8$, 2-cell TM_{010} resonator.

It remains to be determined where to transition from the spoke geometry to multicell structures in a full linac design. It is also of interest to determine the optimum number of gaps or cells for each structure. Beam dynamics and the availability of rf power influence this question. The required lattice period of focusing elements will be shorter at lower velocities. A requirement that the linac be operable when one or more structures have failed will place an additional constraint on structure length. The amount of rf power which may be input to the cavity will be limited by the capability of the coupler, and this places the most stringent restriction on structure length in high-current linacs.

III. CONCLUSIONS

Radiofrequency superconductivity offers a number of advantages for high-current, high-duty-factor linacs, among these is the ability to open up the cavity apertures to mitigate beam impingement and its associated radioactivation. The cavities also may be expected to operate at a higher real-estate gradient than their normal-conducting counterparts. There are no known show-stoppers for rf superconductivity in these applications; the associated beam physics is beginning to be understood, appropriate accelerating structures have been designed.

An important uncertainty in the design of these linacs is the projected capability of rf power couplers. Coupler development and continued beam-physics research are key components of the development path. A more important and fundamental component, however, is a high-current ion-beam test of superconducting structures.⁷

IV. REFERENCES

- [1] C.L. Bohn and J.R. Delayen, "Halo Formation in Mismatched, Space-Charge-Dominated Beams", these Proceedings.
- [2] M. Barbier, *Induced Radioactivity*, North Holland (1969).
- [3] D.H. Perkins, *Introduction to High-Energy Physics*, (Addison-Wesley, Reading, MA, 1972), p. 29.
- [4] N.I. Golubeva, *et al.* "Problems of Beam Loss in Intense Ion Linear Accelerators", Proceedings of the 1988 Linear Accelerator Conference, p. 669 (1988).
- [5] J.R. Delayen, C.L. Bohn, and C.T. Roche, "Niobium Resonator Development for High-Brightness Ion Beam Acceleration", IEEE MAG-27, pp. 1924-1927, (1991).
- [6] J.R. Delayen, C.L. Bohn, W.L. Kennedy, L. Sagalovsky, "Design Considerations for High-Current Superconducting RFQ", these Proceedings.
- [7] J.R. Delayen, *et al.* "Recent Developments in the Application of RF Superconductivity to High-Brightness and High-Gradient Ion Beam Accelerators", *Proc. 5th Workshop on RF Superconductivity*, DESY Report No. M-92-01,
- [8] J.R. Delayen, W.L. Kennedy, and C.T. Roche, "Design and Test of a Superconducting Structure for High-Velocity Ions", *Proc. 1992 Linear Accelerator Conference*, AECL Report No. 10728, pp. 695-697 (1992).
- [9] T.P. Wangler, "High-Brightness Injectors for Hadron Colliders", in *Frontiers of Particle Beams: Intensity Limitations*, (Springer-Verlag, Berlin, 1992), pp. 542-561.

SPECIAL DESIGN PROBLEMS AND SOLUTIONS FOR HIGH POWERED CONTINUOUS DUTY LINACS*

D. Liska, L. Carlisle, and G. McCauley
Los Alamos National Laboratory
P.O. Box 1663, Los Alamos, NM 87545 USA

S. Ellis, T. Ilg and P. Smith
Grumman Aerospace
Bethpage, New York 11714

Abstract

Several high powered linac designs are being considered for various purposes including radioactive waste treatment, tritium production, and neutron factories for materials studies. Since the fractional beam losses must be in the 10^{-5} to 10^{-6} range and are clearly subject to operational variables, the design engineers are forced to develop concepts which combine maintainability under radioactivity conditions, high availability, and very high reliability while dealing with the operating parameters resulting from CW operation. Several design solutions to selected problems are presented.

I. INTRODUCTION

A common feature of the new class of high powered linacs being considered for such future tasks as radioactive waste transmutation, plutonium neutralization, tritium production, etc. is the unprecedented power carried in the beam. A typical design for a 1 GeV proton linac at 200 mA implies a beam power of 200 megawatts CW! An important task in designing such a linac is to safeguard the boretube from beam impingement by configuring the machine with a large aperture ratio (ratio of boretube diameter to rms beam diameter). This involves the use of short focussing lattices to tightly contain the beam, doublet focussing, and minimizing the structural variations, such as boretube diameter or lattice length changes. A second task in designing this sort of linac is to provide a mechanical

design which recognizes the major areas of potential operational difficulties such as multipactoring, RF and vacuum seal integrity, cooling channel durability and corrosion resistance as well as areas requiring relatively high maintenance so that accessibility and speed of maintenance in radioactive environments can be properly addressed.

II. THE APT POINT DESIGN AT LOS ALAMOS

Shown in Fig. 1 is a block diagram of the Los Alamos design for a high power linac. The same machine, or one closely related to it can be used for waste treatment (ATW) or conversion of plutonium (ABC). We call machines of this type AXY linacs. The linac is heavily beam loaded (79%) and will consume about 470 MVA to operate. It consists of two 100 mA H^+ injector lines feeding a funnel at 20 MeV which combines the two beams. The frequency of operation of the RFQ and DTL's in the injector lines is 350 MHz and downstream of the funnel the 200 mA beam is accelerated by RF structures operating at 700 MHz. Beyond the funnel the aperture ratio is gradually increased through the Bridge Coupled DTL (BCDTL), a new type of structure, and into the Coupled Cavity Linac (CCL). The aperture ratio through the CCL which comprises the bulk of the machine increases from 13 to 26:1. For comparison, the aperture ratio of LAMPF, the world's most powerful linac today is only 6:1.

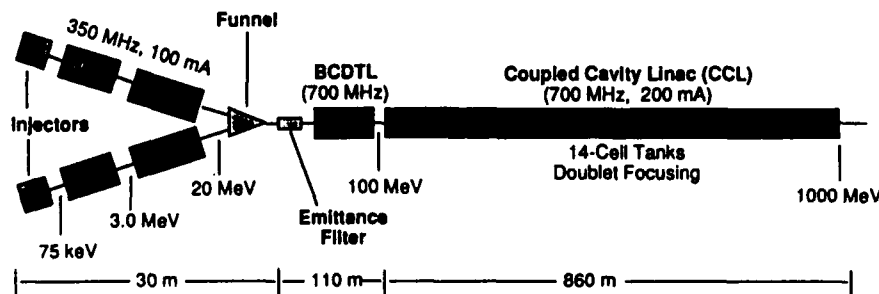


Fig. 1. High Power Linac Concept.

*Work supported by Los Alamos National Laboratory Program Development, under the auspices of the United States Department of Energy

III. ENGINEERING SOLUTIONS DEVELOPED IN THE APT DESIGN FOR HIGH POWERED STRUCTURES:

A) Innovative Accelerating Structures

In order to be able to use EMQ's in the DTLs, a high energy RFQ was required. A design was developed for a multi-sectioned RFQ to operate at 7 MeV (ref. 1). This 8 meter long unit actually functions as four independent 2 meter long RFQs thereby avoiding mode interference problems.

The other new structure is the BCDTL which is a multiple tank DTL with quadrupole doublet focussing in the intertank spaces much like a bridge coupled CCL. The BCDTL has large apertures at high frequency and solves many fabrication and operational problems associated with CCLs at low energy (refs. 2 & 3).

B) Radiation Hardening

Because of the potential for neutron damage to materials, essentially all the quadrupoles in the ATW point design are EMQ's with radiation resistant potting of the field coils. The technique proposed is shown in Fig. 2a-c. The coils are coated with a glass frit compound, fired to produce a glass coated surface and then potted in calcium aluminate cement (ref 4). In addition, quads are designed with demountable yokes so the coils can be removed if necessary.

Radiation hardening of the vacuum seals and knife-edge style RF seals are essential in an ATW type machine. We used the Helicoflex seal for most vacuum closures. Most of the Helicoflex beamline seals are used in conjunction with Helicoflex Quick Flanges which can be released and sealed from the aisle side of the machine with a single air drive screw. To assure high RF integrity, the RF joints throughout most of the machine are knife edges using a modified Conflat concept backed up by an independent Helicoflex seal enclosed in the same flange pair (Fig. 3).

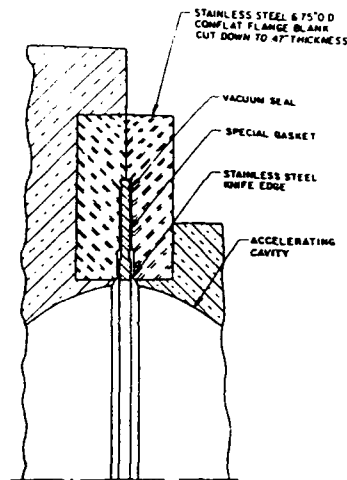


Fig. 3. Flange Design.

C) Modularization

ATW is modularized as illustrated in Fig. 4. The point design contains 403 modules of both BCDTL and CCL types requiring 366 1 MW klystrons. Modularization breaks the linac into manageable lengths for vacuum checkout and instrumentation. The modules are preassembled in the lab, aligned and checked out for vacuum, cooling and RF integrity. They are then transported to the tunnel and installed on 3-point support mounts and aligned to the tunnel alignment system. The beamline height is 1.47 meters which makes the modules convenient to work on. Most essential components are accessible from the aisle side, including the items most likely to need maintenance, i.e. the ion pumps and beamline components such as diagnostic devices located in the intertank spaces. Fig. 5 shows a typical doublet pair mounted as a module on two precision linear rails in the intertank gaps. Diagnostics, bellows, beamline vacuum valves and flanges are part of this modular



Fig. 2a. One of two copper coils that comprise a quadrupole magnet: note quadrupole complex nested winding, aluminum wrap.



Fig. 2b. Enameled quadrupole coil.



Fig. 2c. Encapsulated coil.

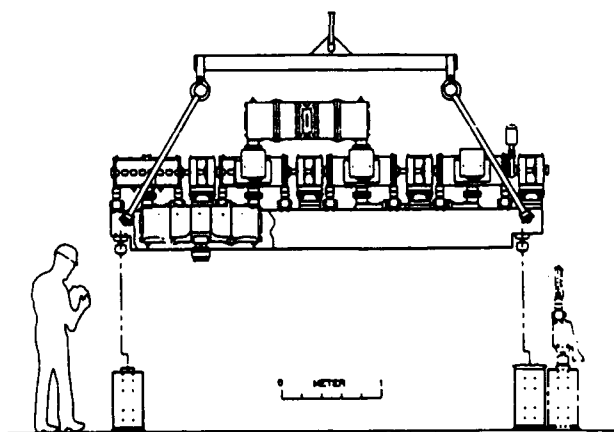


Fig. 4. Modular Linac Design.

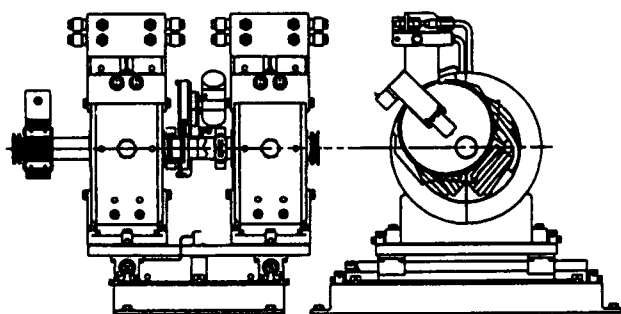


Fig. 5. Modular Doublet.

assembly. The doublet pair is critically aligned relative to the linear rails so that when the unit requires servicing it can be removed easily and mounted on a similar set of rails in the lab and then prealigned prior to re-installation on the beamline without the need for final alignment on-line.

D) Component Considerations

In the ATW point design the drift tubes were designed for changeout under potentially activated conditions by installing them on girders as shown in Fig. 6. The drift tube is "hard mounted", (sealed) by a single point RF knife edge and backed up by a silver plated Helicoflex vacuum seal. Alignment is critically set by means of a water cooled, heavy gauge copper flex membrane which is stressed, yielded and work hardened in the process. This method of hard socketing is necessary to withstand CW RF heating. If the knife edge or vacuum seal were to fail, the girder could be removed from the tunnel and work done on the failed drift tube.

The APT CCL is a 700 MHz cavity system which is sized to fit into existing hydrogen brazing facilities. A major concern is the careful selection of braze alloys to avoid galvanic corrosion along the cooling channel joints. The external manifolding that supplies the cooling is also critical since it will carry radioactive water which can not leak into the tunnel. In the APT design we used high vacuum (VCR) water fittings everywhere.

E) Tunnel Considerations

The final major consideration for the designers of AXI style linacs is the beamline tunnel itself. Even

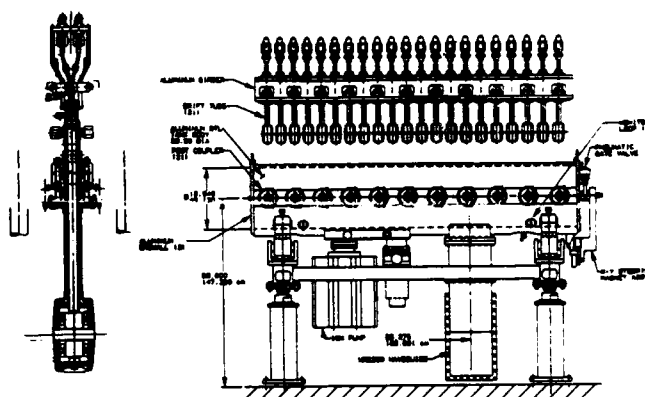


Fig. 6. Girder Mounted Drift Tubes.

though any given design will always assume hands-on maintenance as the design goal and the physics will always maximize such parameters as "aperture ratio", one must always consider future changes in personnel exposure limits, abnormal operation of the machine or degradation. For these reasons it is wise to allow for the possibility of remote maintenance. Two major features are incorporated in our ATW point design. One is the use of radio controlled bridge cranes in the tunnel to carry surveillance booms as an adjunct to the normal workhorse function. The other feature is a tunnel spacious enough to allow a high performance remote maintenance master-slave servo-manipulator system to work. One such system is MANTIS, used at CERN.

IV. CONCLUSIONS

The point design for the Los Alamos ATW linac has been conceived to be radiation hardened in spite of its careful design for extremely low beam loss. The use of modularization, self aligning quadrupole doublets and easy aisle-side maintenance adaptable to remote servicing has been promoted in anticipation of most of the maintenance problems we can foresee.

V. REFERENCES

- [1] Paper by Lloyd Young on high energy RFQ, to be presented at this conference?
- [2] Mechanical Features of a 700 MHz Bridge-Coupled Drift Tube Linac, D. Liska, et al. 1992 Linear Accelerator Conference Proceedings, Ottawa, Ontario, Canada, pp.148-150.
- [3] Design and Simulation of a Bridge-Coupled DTL Structure---, R.Garnett, et al. 1992 Linear Accelerator Conference Proceedings, Ottawa, Ontario, Canada, pp. 802-804.
- [4] Radiation-Resistant Encapsulation for Electromagnet Field Coils R.Blake, R.Greiggs, F. Gac., American Ceramics Society Bulletin, Vol 64 No. 8 August 1985.

Status of CIAE medical cyclotron

Xingzhi Zhang Zhenguo Li Mingwu Fan
China Institute of Atomic Energy
P.O. Box 275 (3), Beijing, 102413, PRC

Abstract

A 30 MeV compact cyclotron devoted to medical radioactive isotope production is being built in CIAE. It was originally designed by IBA, Belgium. Some major modifications of the design have been taken. In order to improve the performance of the machine, the magnet redesign and adjustment have to be taken. All equipments in control room are already in position. RF, power supplies, vacuum and water cooling system have been tested. The machine is being in final installation and ready for commissioning.

I. GENERAL DESIGN FEATURES

CIAE medical cyclotron is a fixed-field, fixed-frequency isochronous cyclotron accelerating H^- ions beam up to a maximum energy of 30 MeV and extracted beam intensity of 350 μA and low power consumption less than 100 KW.

Negative hydrogen ions are produced by an external multicusp ion source located above the cyclotron yoke [1].

The beam from ion source is injected axially and inflected in the median plane by an electrostatic helicoid inflector. It is then accelerated by two 30° dees electrodes while it is contracted to a fixed magnetic field. The two dees are located in the magnet valleys, allowing the magnet gap to be very small. The H^- ions are continuously accelerated until the beam passes through the carbon foil, the negative ions are stripped off their electrons, become positive. Continuously adjustable energy from 15 to 30 MeV is achieved by varying the radial position of the carbon foil.

Partially intercepting foils permit the extraction of two beams at the same time and will direct them to one of the two extraction beam lines.

The extracted beam passes through a 7 meter transport line to a solid target where a pneumatic carrier will

ship the isotope products from the station to an unload hot cell for radioisotope distribution.

This project with most of equipments made in China has been made significant progress. Various systems of the machine are installed in construction site separately and test results are satisfied.

II. THE MAGNET SYSTEM

The magnetic structure of Cyclone 30 has been specially designed to reduce the electrical power consumption combining the advantages of separated sector cyclotron and compact cyclotron. In order to meet the fabrication environment of China and to improve its performance, redesign was taken based on DE 3D program [2] and some structure modifications are made including:

- In original design, the upper and lower yokes are each separated into two pieces: base plate and base ring. In order to reduce mechanical work and loose the tolerance, the two separated pieces are combined together as one. The field stability and vacuum seal both are improved also.
- 54° angle four sector poles are rigidly fixed and sealed onto base plate by the grub screws with two polyflon material sealing rings.
- 8 positioner are used for positioning the upper yoke once it has to be lifted.

Now the magnet mapping is finished by means of a Hall probe controlled automatically. The required isochronous field related to R.F. phase shift and first harmonic are adjusted by azimuthal shimming of the pole edges. High quality isochronous field profile is obtained.

The measurement results are shown in Fig. 1, 2 and 3.

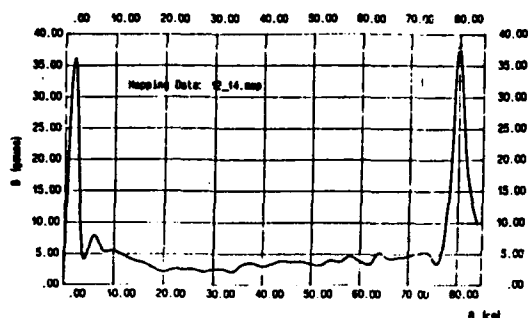


Fig. 1 Amplitude of first harmonic

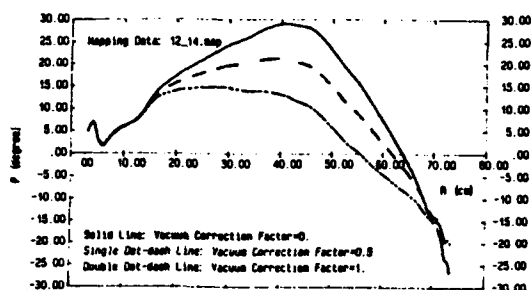


Fig. 2 Total phase shift with different vacuum corrections

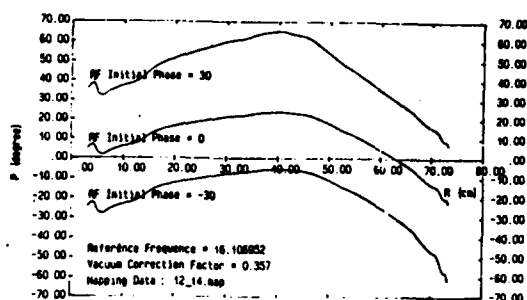


Fig. 3 Total phase shift with different RF initial phases

The isochronous field can be achieved using electrical power 7 KW only.

In addition, switching magnets, quadrupoles, steering magnets and corresponding power supplies are fabricated based on our own design. Their quality is same or better than the requested theoretically.

III. R.F. ACCELERATING SYSTEM

The R.F. accelerating system is made in Chinese manufacturer. The accelerating electrodes, the "dees" are

supported by stems inserted in the valleys. When the yoke lifted, the dees split into a lower and an upper parts. This configuration gives the acceleration system exceptional mechanical stability and does not require fragile insulators.

The dees are made of solid copper and are conduction cooled. This considerably reduces the risk of water-leakage inside the machine and thus the contamination risks.

The two 30° dees operate on the 4th harmonic mode with respect to the particle revolution frequency. To prevent any phase mismatch and to simplify the R.F. system, they are connected at the center below the median plane to leave room for the inflector.

The R.F. cavities are entirely located in the valleys. The R.F. power needed to obtain 50 KV of dee voltage is approximately 5.5KW per cavity. In addition, up to 15 KW of R.F. power are used for beam acceleration.

A single R.F. amplifier delivering 25 KW of power at 65.5 MHz is installed in the median plane and is capacitively coupled to the cavity. The variable load due to the beam behaves as a variable load resistor on the final tube, so the amplifier always operates at peak efficiency.

Zero-bias, grounded-grid triodes are used for the final 25 KW amplifier and 3 KW driver amplifier. This design gives the system absolute stability and eliminates the grid and screen grid power consumption. The R.F. system has been tested and the working frequency was measured. The result shows that Dee circuit coincides well with the results of magnetic mapping.

IV. VACUUM AND WATER COOLING SYSTEM

The vacuum chamber of cyclotron 30 is a cylinder made of aluminium alloy, sealed onto the magnet yoke by "O" rings. Some openings on the vessel for beam exit, stripper entry, R.F. feed etc. are isolated from ambient atmosphere by air-lock system and "O" rings.

Three types of pumps are used in the cyclotron. Roughing is performed by forepumps from 1000 mbar down to 10^{-2} mbar. High vacuum is maintained by two oil diffusion pumps (3000 l/s) from 10^{-2} mbar down to 10^{-6} mbar and by two cryogenic pumps (1500 l/s) to improve vacuum around 10^{-7} mbar adequate for extracting

beam above 350 μA . Cryopumps could also increase the pump-down speed in the cyclotron.

Demineralized water is used for machine cooling through manifold with stainless steel ball valves, flow controllers, distributing the water to all cooling circuits.

Temperature, resistivity and flow amount of water are used as control interlocks to guarantee the safety of the equipments.

All the vacuum and cooling system have been installed and tested for the machine operating properly.

V. CONTROL SYSTEM

The cyclotron and related equipments are controlled by a SIMATIC S5-135U programmable controller because of its reliability and its versatility. It also offers the possibility to expand and interconnect with other programmable devices. Normal operation of the cyclotron is entirely automatic, from cyclotron start-up to targetry and chemistry, requiring no operator during routine production. Color monitor displays graphically the operations.

A spillproof keyboard and two "virtual" knobs that can be used for preset the cyclotron parameters. To meet the control requirements of PLC, special interfaces are added in relevant devices. For examples, power distribution and power supplies, water and vacuum control and interlocks, beam measurement and displays... .. Now the whole control system are installed in control room, part of main functions has been tested, some with real devices and some with simulations. Overall hardware and software test will be done in final general testing.

VI. REFERENCES

- [1] Y. Jongen and G. Ryckewaert: "Preliminary Design for 30 MeV-500 μA H^- Cyclotron", Particle accelerator conf., Vancouver, B.C., I.E.E.E. Trans. science, Vol. NS-32, N° 5, PP. 2703-2705, October 1985.
- [2] Tianjue Zhang, Mingwu Fan: "Automatic mesh generation and graphic display for 3D finite element codes", Proc. of China-Japan Accelerator Symposium, 1990.

A 600 MeV Cyclotron for Radioactive Beam Production*

D. J. Clark

Nuclear Science Division, Lawrence Berkeley Laboratory
1 Cyclotron Road, Berkeley, CA, 94720, USA

Abstract

The magnetic field design for a 600 MeV proton cyclotron is described. The cyclotron has a single stage, a normal conducting magnet coil and a 9.8 m outside yoke diameter. It has 8 sectors, with a transition to 4 sectors in the center region. The magnetic field design was done using 1958 Harwell rectangular ridge system measurements and was compared with recent 3-dimensional field calculations with the program TOSCA at NSCL. The center region 4-8 sector transition focussing was also checked with TOSCA.

I. INTRODUCTION

The report on the IsoSpin Laboratory (ISL) [1] describes a "benchmark" reference design for a facility for the production of radioactive nuclear beams in North America. The primary accelerator is required to produce protons at an energy of .5-1.0 GeV and an intensity of 100 μ A, while a secondary accelerator will accelerate radioactive beams from the target to about 10 MeV/u. The primary accelerator can be a cyclotron such as the PSI ring or TRIUMF. Because of the high beam power an essential requirement for this cyclotron is that of minimizing the beam lost at high energy inside the cyclotron, to prevent component damage and reduce radiation exposures during maintenance. This in turn requires very high extraction efficiency either by good turn separation at extraction or by use of negative ions. This paper presents the magnetic field design of a primary cyclotron which minimizes cost while maintaining high extraction efficiency.

II. GENERAL FEATURES

The design choices are described in a previous paper [2]. The present design uses positive ions with very high extraction efficiency. This design has the advantage over a negative ion design of preventing the stripping loss activation of vacuum tank material, and using a higher magnetic field and thus a smaller radius. The advantage compared to a separate sector design is that the compact magnet requires only one main coil, and eliminates the injector stage. The choice of pole diameter size is a compromise between better turn separation for a large radius and lower cost for a small radius at higher magnetic field. The dees are placed in valleys so that the hill gaps can be made small, giving acceleration out to near the edge of the magnet, easier extraction and low magnet

*This work was supported by the Director, Office of Energy Research, Division of Nuclear Physics of the Office of High Energy and Nuclear Physics of the U.S. Department of Energy under Contract DE- ACO3-76SF00098.

power. Dees in the valleys at this energy require the resonators to be in the valleys also, since the radial length of the dees is the order of $1/4$ wavelength. The highest acceleration is required near extraction, so additional auxiliary dees are added there. The sector number can be 6 or 8 to get to 600 MeV. 8 is chosen to allow a transition from 8 to 4 sectors in the center with 2 main dees. The 4 sector center region gives better acceleration transit time factor and magnet flutter than an 8 sector design.

III. 4-8 SECTOR CENTER REGION

A magnetic field having a transition between different numbers of sectors has to be evaluated for adequate flutter to give axial focussing. Such a transition between 8 and 4 sectors was used by the Analogue II electron model [3] in 1961 at Oak Ridge, as pointed out by H. Blosser. The use of a transition from 6 to 3 sectors was proposed by AEG in 1962 [4], as pointed out by Joho.

To check the feasibility of a particular geometry of a 4-8 sector design, the magnetic field of a simple sector magnet representing the center region was calculated by F. Marti with the 3D program TOSCA [5]. The magnet is shown in Fig. 1. With a .1 meter gap in the hills, the pole radius is .75 m, compared to 3.4 m for the full 600 MeV beam. In Fig. 2 the magnetic flutter is plotted, showing the fast rise of the 4 sector region at the machine center, and the transition to the slower rising 8 sector region further out. The flutter drops at large radius due to the usual pole edge effect. The value of the axial focusing frequency Nuz is also plotted in Fig. 2, showing that there is adequate focusing from this configuration. Nuz could be increased at larger radius by having the transition further out. Nuz was calculated with the equilibrium orbit code CYDEG, a general form of the 88-Inch Cyclotron program CYDE, developed by J. Moehlis.

IV. MAGNETIC FIELD DESIGN

The present design for 600 MeV protons is shown in Fig. 3. As mentioned above it is a compact design using a single main coil. The maximum radius is about $3/4$ of that of the PSI ring design. The average magnetic field was assumed to be 12 kG at 600 MeV. The transition of 4-8 sectors can be seen in the center region.

For preliminary design one can use the simple formula for the axial focusing:

$$Nuz^2 = FSQ (1 + 2 \tan^2 Eps) - \mu'$$

where Nuz is axial frequency, FSQ is flutter, Eps is spiral angle and μ' is average field gradient. μ' is determined by the energy. To produce a Nuz of .3-.4 we need to have enough spiral and flutter at each energy to overcome the defocusing of the average field. In the previous paper [2] a sharp edge was assumed, with a valley field of zero. A better estimate is

tested in this paper. It uses some systematic magnetic field measurements on rectangular ridge systems by P. F. Smith of Harwell [6]. This work by Smith calculates the flutter and average gap for a range of average magnetic field of 6-20 kG, a range of ratio of hill width, p , to (hill + valley) width, λ , of .35-.80, and ranges of hill gap and hill depth. A design was tested using a p/λ of .5 at 600 MeV and using a spiral angle ϵ sufficient to make $N_{uz} = .35$. At lower energies p/λ was reduced to produce the proper isochronous field and ϵ was reduced to leave $N_{uz} = .35$. This calculation required considerable interpolation and extrapolation. The Smith measurements are on rectangular parallel ridges, but the correction suggested by him was used to calculate the spiral ridges used here. This consisted of measuring p and λ perpendicular to the edges of the spiral to give an effective reduced value. The valley depth was set at the coil height to make a simple design. Deeper valleys don't increase the flutter much.

The resulting hill shape is shown in Fig. 3. Spiral is required only at the outer radii. In Fig. 4 the values of ϵ and p/λ are shown. It was decided in this test to keep p/λ at .35 or larger, since this was the minimum value in the Smith report. ϵ is 0 below 100 MeV, slightly over half radius.

A TOSCA calculation was done on this design by F. Marti [5] to compare the values of average field and flutter with those predicted by Smith. Fig. 5 shows the comparison of average field. The field for the Smith case used the calculated average gap, and assumed the field is inversely proportional to the gap. In the Smith calculation the average gap depends on the field, so this comparison used the TOSCA field to calculate gap. The agreement is about .5 kG out of 10 kG, or 5%. The disagreement at the largest radius is due to the edge effect of the pole. An additional TOSCA run showed that the average isochronous field could be extended by increasing the hill radius, as expected. This field is approximately isochronous for the outer 1/3 of the radius. Inside that coils would have to be used to correct up to 3 kG error in the center. Alternatively the p/λ could be further reduced and the gap increased at smaller radii.

A similar comparison is shown for flutter, FSQ, in Fig. 6. There are two Smith curves. The one at small radius uses an approximation for small hill width to depth ratio, which applies at the center region. The last outer point of the Smith curve is again due to edge effects. The agreement of TOSCA and Smith are good enough for preliminary design.

The conclusion is that the Smith data can be used for first design, before running TOSCA, and can provide a guide to the hill geometry which can provide a required amount of axial focussing. However it needs interpolation and extrapolation to make use of the tables of data, and has some limitations of parameter range. The configuration used here and shown in Fig. 3 is just an example for evaluating the Smith data. For a final design we need up to 10 degrees more spiral at 300-600 MeV for focussing, a hill extension outward of about .1 m, and some adjustment of the average field in the smaller radii to reduce trimming coil power.

V. OTHER DESIGN FEATURES

The main dees operate at harmonic 4, 44 MHz, and extend in to the center. 1/4 wavelength of rf is 1.7 m, only about 1/2 the extraction radius, so the resonators must be in the valleys,

with vertical dee stems. 2 more dees can be added to reduce the number of turns from 2000 to 1000, at a dee voltage of 100 kV. Small auxiliary dees, indicated near extraction radius in Fig. 3, increase the energy gain/turn there and give the option of flat-topping for better turn separation. For acceleration they can operate at harmonic 8. For example, 4 dees at 250 kV, harmonic 8, would give about 2 MV/turn.

The ion source is assumed to be external, with an injection energy of about 50 kV. An external source allows bunching into the required phase width for turn separation at extraction.

VI. ACKNOWLEDGMENTS

The author wishes to extend thanks to W. Joho and H. Blosser for helpful discussions, and to Felix Marti for the TOSCA calculations of magnetic fields.

VII. REFERENCES

- [1] *The IsoSpin Laboratory (ISL)*, LALP 91-51, North American Steering Committee of the ISL, 1991.
- [2] D. J. Clark, "A conceptual design for a primary cyclotron for the ISL radioactive beam project," *Proc. 13th Int'l Conf. on Cyclotrons and Their Applications*, pp. 721-723, Vancouver, July 1992.
- [3] J. A. Martin and J. E. Mann, "Beam Characteristics in Cyclotron Analogue II," *Nucl. Instr. & Meth.* 18, 19 (1962), pp. 461-468.
- [4] W. Muller and W. Wolff, "Considerations on the Design of a Spiral Ridge Cyclotron for 450 MeV Protons," *Nucl. Instr. & Meth.* 18, 19 (1962), pp. 447-456.
- [5] Run by F. Marti, NSCL, Michigan State University.
- [6] P. F. Smith, "Further Measurements of the Magnetic Field Produced by Ridged Pole Pieces," *AERE A/R 2514*, A.E.R.E., Harwell, 1958.

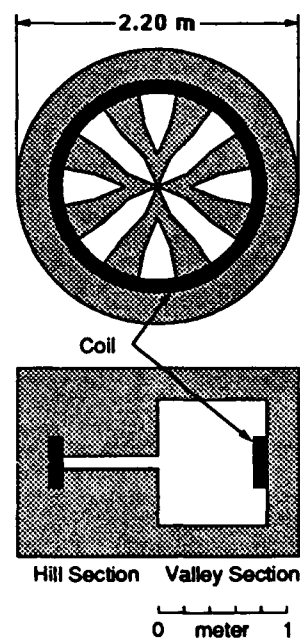


Figure 1. Magnetic model with 4-8 sector transition, for TOSCA calculation.

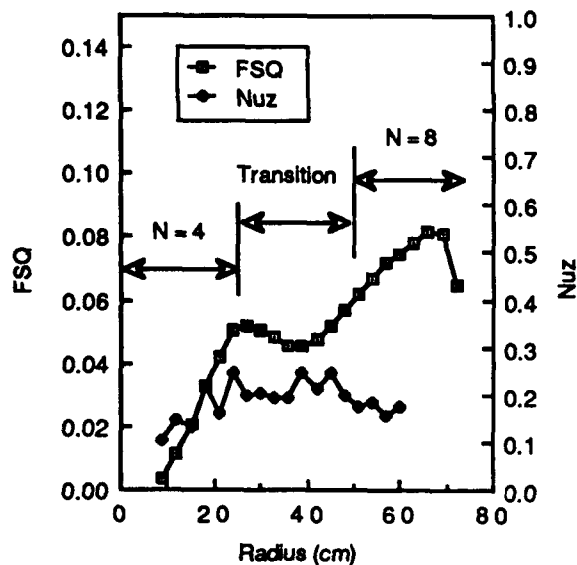


Figure 2. Flutter, FSQ, and axial focusing, Nuz, for 4-8 model using TOSCA calculation.

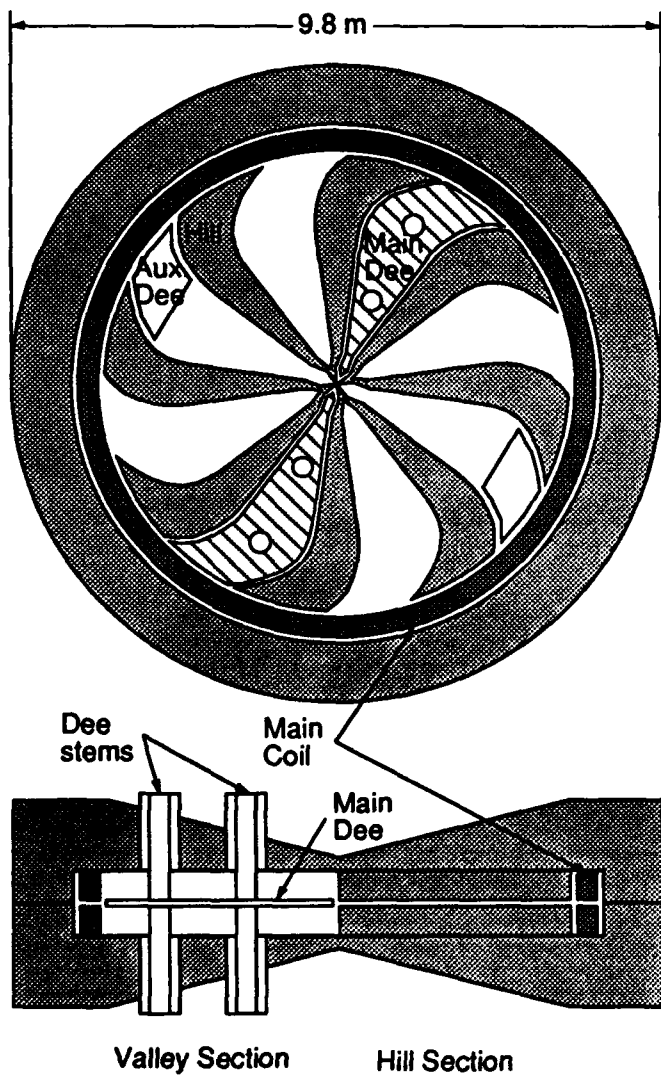


Figure 3. 600 MeV proton cyclotron, plan and elevation views.

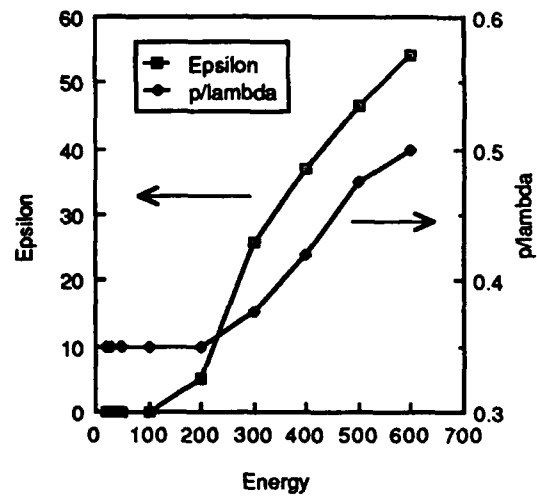


Figure 4. Spiral angle, epsilon, and hill fraction, p/λ for 600 MeV cyclotron.

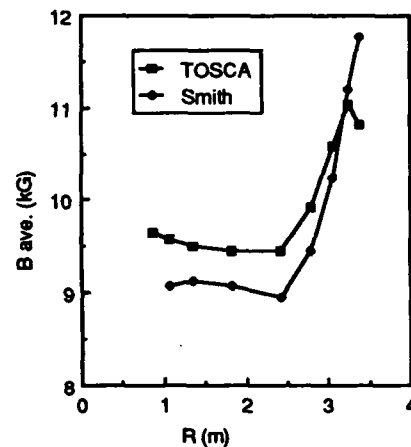


Figure 5. Average magnetic field, $B_{ave.}$, calculated by Smith tables and TOSCA.

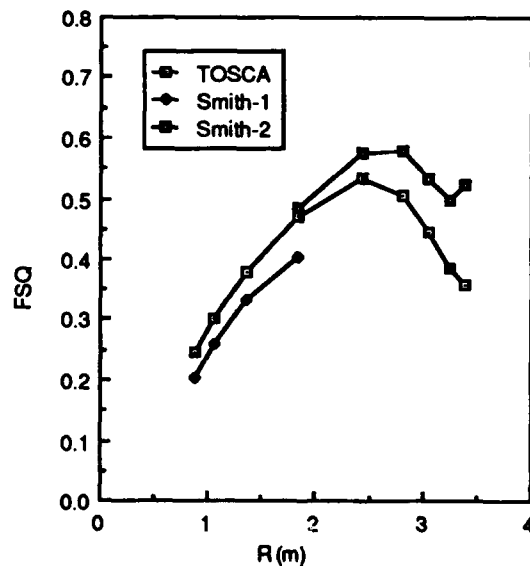


Figure 6. Flutter, FSQ, calculated by Smith tables and TOSCA.

Development of a Compact Permanent Magnet Cyclotron for Accelerator Mass Spectrometry*

A. T. Young, K.J. Bertsche[†], D.J. Clark, K. Halbach, W.B. Kunkel, K.N. Leung,
C.Y. Li, A. Rawlins, R. D. Schlueter, M.E. Stuart, R.P. Wells, and J.X. Yu^{††}
University of California,
Lawrence Berkeley Laboratory
Berkeley, California 94720, USA

Abstract

We describe the development of a new instrument for the detection of trace amounts of rare isotopes, a Cyclotron Mass Spectrometer (CMS). A compact low energy cyclotron optimized for high mass resolution has been designed and is under construction. The instrument has high sensitivity and is designed to measure carbon-14 at abundances of $< 10^{-12}$. A novel feature of the instrument is the use of permanent magnets to excite the iron poles of the cyclotron, giving a field uniformity on the order of 1 part in 10^4 . The instrument uses axial injection, employing a spiral inflector. The instrument is nearing completion, with most major components completed.

I. INTRODUCTION

Measuring the abundance of trace isotopic constituents has applications in many fields, such as archaeology, biomedicine, geology and geochemistry, and environmental research. In general, these applications require a very high sensitivity and selectivity. The combination of the samples being very dilute in the isotope desired ($< 10^{-10}$) and containing other atoms and molecules with almost the same atomic or molecular weight makes essential a detection scheme with high sensitivity and specificity (or resolution.)

One method of high-sensitivity detection is Accelerator Mass Spectrometry (AMS). In this technique, the sample of interest is ionized, and a charged-particle accelerator is used to detect single atoms of the isotope of interest. The first use of an accelerator as a mass analyzer was made in 1939 by Alvarez, who measured ^3He at natural abundance using a cyclotron. [1] The "modern" era of AMS began in 1977, when Muller proposed using a cyclotron for carbon and beryllium measurements [2,3], and the groups at the Univ. of Rochester, and McMaster Univ. demonstrated ^{14}C detection with tandem accelerators. [4,5] AMS has developed into a powerful tool for the detection of trace quantities of rare isotopes. Virtually all AMS is now performed on large tandem accelerators. Analysis of isotopes that are present in samples at a level of 1 part in 10^{15} has been achieved.

Recently, the original idea of using a cyclotron as the

accelerator has been revived, with the new wrinkle that the cyclotron be small and that the accelerating voltages be modest. In this incarnation, the technique has been dubbed Cyclotron Mass Spectrometry (CMS.) Here, the large tandem accelerator is replaced by a compact, low-energy cyclotron. Previous work at Lawrence Berkeley Laboratory (LBL) demonstrated the principle of these devices and showed that CMS can have much higher sensitivity than the scintillation methods used routinely in biomedical research for ^{14}C . [6,7] As a result, several small cyclotron mass spectrometers are now under development around the world. [8,9]

This paper describes the program now underway at LBL to improve the performance and operating characteristics of CMS. The design is discussed and the status of the construction of the CMS is given.

II. CMS DESIGN

A. System Considerations

The overall size of the machine is dictated by the species to be measured, the injection energy of the ion, and the mass resolution needed. For ^{14}C , a mass resolution of about 1800 is needed to separate ^{14}C from ^{13}CH . The resolution of a CMS is described by [7]

$$R \approx 3 \times n \times H, \quad (1)$$

where n is the number of orbits the particles make before extraction and H is the harmonic of the fundamental cyclotron frequency that the accelerating RF is operating on. For ^{14}C in a 1 T field, the fundamental frequency is 1 MHz. H might be 15, so that the minimum number of orbits would be 40. With modest energy gain per turn, ≤ 500 V, it is possible to achieve this figure with an extraction radius of ≤ 9 cm. We have conservatively designed the instrument for an extraction radius of 12 cm, corresponding to an energy of 50 keV.

Figure 1 shows a schematic diagram of the LBL CMS system. To improve the performance over existing devices, changes are being made in the ion source and the injection system. This will lead to enhanced sensitivity and increased sample throughput. In order to reduce the size, weight, and complexity of the system, the magnetic field of the cyclotron will be produced by permanent magnets rather than electromagnets. These improvements are described below.

B. Ion Source and Injection System

The ion source typically used in AMS is a cesium sputter ion source. However, at LBL, substantial experience has been obtained in developing negative ion sources for fusion and ion

* This work is supported by the U.S. Department of Energy, Office of Basic Energy Sciences, Division of Advanced Energy Projects, under contract No. DE-AC03-76SF00098

[†] present address: Superconducting Super Collider Laboratory, Dallas TX 75237

^{††} present address: Peking University, Beijing, PR China



Fig 1 Schematic diagram of the cyclotron mass spectrometer

implantation applications using magnetic multicusp sources.[10] In these devices, negative ions from gas phase precursors are formed directly in the discharge plasma. Recent experiments have shown that C^- can be formed in these sources as well. Further research is underway to optimize this type of source for C^- production. If successful, it will provide a simple to operate, high throughput source of negative ions without the need for the graphitization process used with sputter ion sources.

After production, the ions are transported to the cyclotron, where they are injected axially. Axial injection, in general, is very efficient in delivering the ions into the cyclotron midplane. We have designed a spiral inflector, an electrostatic channel which twists or "tilts" as it guides the ions down the axis of the machine and into the midplane. Figure 2 depicts the complicated shape of the inflector, showing the inner surfaces of the electrodes. The inflector shape has been optimized so that the emittance of the ion beam coming out of the inflector matches the acceptance of the cyclotron. This was accomplished using an ion trajectory program which

takes into consideration the spatial variation of the magnetic fields in the cyclotron for the inflector design and a second trajectory program which calculates the cyclotron midplane trajectories, including electrostatic focusing effects.

C. Magnet Design

A novel aspect of the cyclotron design is the use of permanent magnets to produce the magnetic field. This has two advantages. First, the overall size and weight of the magnet structure are reduced, as the magnet coils and power supplies are eliminated. Second, the electrical power and cooling requirements of the instrument are minimized. With permanent magnets, the CMS will be transportable and could be placed aboard aircraft, small boats, or in field locations. Their use will also reduce operational costs. The magnetic field in the midplane is 1 T. For high mass resolution, the orbits need to be isochronous; a flat magnetic field uniform to about 2 parts in 10^4 must therefore be maintained.

These parameters can be obtained by using permanent magnet material to energize soft iron poles pieces. This is shown schematically in Fig. 3. Magnet material, such as samarium cobalt, is placed in contact with the iron pole pieces. The iron concentrates and directs the magnetic flux to

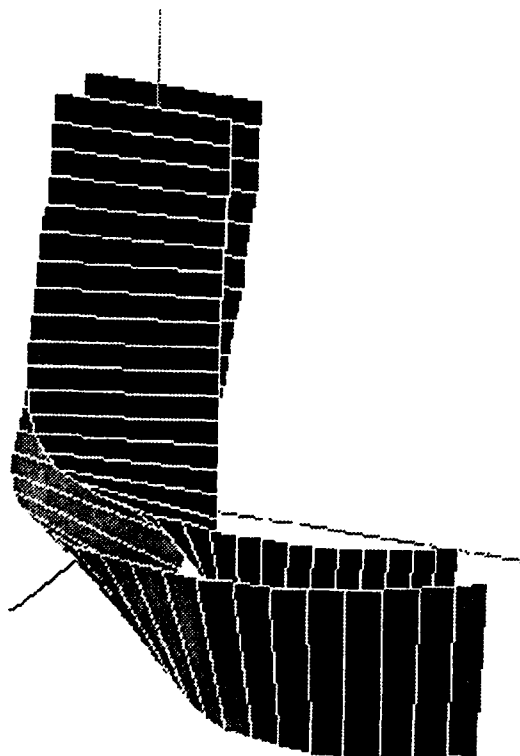


Figure 2 Spiral inflector used for axial injection

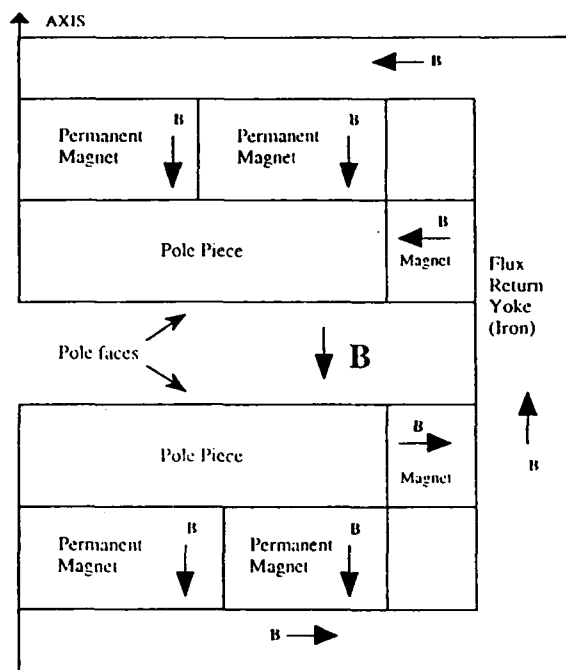


Figure 3 Schematic diagram of the design for the permanent magnet system.

the pole faces. For one pole, the magnets are oriented so that the magnetization vector points toward the pole face. For the other pole piece, the magnets are oriented so that the magnetization points away from the pole face. A magnetic flux return ('yoke') connects the magnets to complete the circuit. The midplane of the accelerator is placed between these poles. As shown in Fig. 4, calculations of the magnetic field using the computer program POISSON indicate that the field should be uniform to approximately ± 2 parts in 10^4 throughout the acceleration region, and ± 1 part for the majority of the trajectory.

III. PROJECT STATUS

The advanced CMS is being designed and optimized for use with ^{14}C . Some of the operating characteristics are shown in Table 1.

With one exception, all major subassemblies of the CMS have been fabricated, including the poles, yokes, pole spacer ring, and ion extraction channel. The exception, the spiral inflector, has been designed and is presently being fabricated. The CMS should be assembled by the fall of 1993, with demonstration of ^{14}C detection to follow.

Parameter	Description
Ion source	Magnetic multicusp
Species	Carbon 14
Injector type	Spiral inflector
Injection energy	5 keV
First orbit radius	4 cm
Extraction radius	12 cm
Extraction energy	< 50 keV
Pole face radius	15 cm
Pole gap	1.6 cm
Magnetic Field	1 T
Field Source	SmCo Magnets

Table 1 Cyclotron design Parameters

IV. CONCLUSIONS

Cyclotron mass spectrometry (CMS) is a potentially powerful analytical technique with applications ranging from studies of global warming constituents to the biological metabolism of pollutants and pathogens. A development program is now underway which will increase the sensitivity and improve operational characteristics, such as transportability and sample preparation, while at the same time reducing the cost of the instrument and its operation. These improvements will make CMS more widely available for routine analysis of trace materials.

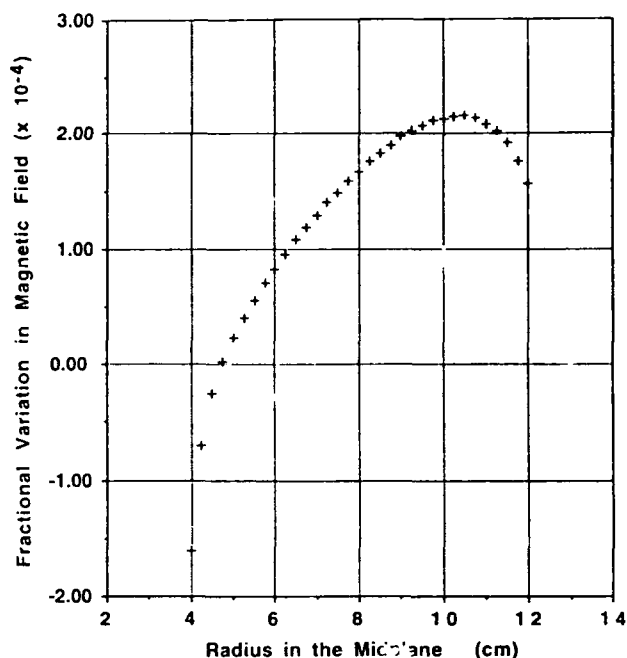


Figure 4 Fractional variation in the magnetic field from its mean value.

The authors would like to thank Bruce Milton of TRIUMF for help in obtaining and running some of the ion trajectory codes, and Wes Bethel of the Information and Computing Sciences Division of LBL for providing assistance with computer-generated graphics.

V. References

- [1] Litherland, A.E., in *Ann. Rev. Nucl. Part. Sci.* **30** 437-73 (1980).
- [2] Muller, R.A., *Science* **196** (1977) 489.
- [3] Muller, R.A., Stephenson, E.J., Mast, T.S., *Science* **201** (1978) 347.
- [4] Nelson, D.E., Korteling, R.G., and Stott, W.R., *Science* **198**, 507 (1977)
- [5] Bennett et al, *Science* **198**, 508 (1977)
- [6] Welch, J.J., Bertsche, K.J., Friedman, P.G., Morris, D.E., Muller, R.A., and Tars, P.P., *Nucl. Instr. and Methods* **B5** (1984) 230.
- [7] Bertsche, K.J., *Nucl. Instr. and Methods*, A301, (1991) 171.
- [8] Chen, M.B., Xu, S.L., Li, D.M., Zhabg, X.L., Chen, G.S., and Gao, W.Z., *Nucl. Instru. and Methods*, A297 (1990) 47.
- [9] Subotic, K.M., *J. Physics G - Nucl. and Part. Physics* **17S**, S363.
- [10] Leung, K.N., Anderson, O.A., Chan, C.F., Cooper, W.S., deVries, G.J., Hauck, C.A., Kunkel, W.B., Kwan, J.W., Lietzke, A.F., Purgalis, P., and Wells, R.P., *Rev. Sci. Instru.* **61** (1990) 9.

Performance of H^-/D^- Cyclotron Using Internal Source

Thomas T. Y. Kuo
TRIUMF, 4004 Wesbrook Mall, Vancouver,
B.C., V6T 2A3, CANADA
and

George O. Hendry
Cyclotron Inc., 3104 Redwood Road, Napa,
California, 94558, USA

Abstract

Over the past ten years, several models of H^-/D^- compact cyclotrons using internal source have been constructed and put into routine operation. This paper reports the performance of some of these machines. Detail description on individual cyclotron is omitted in order to give space for discussion on the design guideline and the criteria which warrant the high beam currents capability. It has been found that the design of the ion source and the central region (beam centering, axial focusing strength, puller voltage and RF phase acceptance, etc.) together with the design of the vacuum system determine the initial beam current capability. Subsequently, the magnet phase profile (energy gain per turn), magnet optics quality and the vacuum characteristics dictate the beam survival before extraction. Finally, the required beam quality after charge exchange in turn influences the design of the magnet structure. A thorough understanding on these coupled relationships between critical parameters is essential for the successful design of this type of cyclotron.

I. INTRODUCTION

Compact H^-/D^- cyclotrons in the 10-40 MeV range are widely used today for commercial isotope production and for PET scanning system in hospitals. Two types of these cyclotrons co-exist, namely, those that use an H^-/D^- cusp source with external injection and those that use an internal H^-/D^- source. At TRIUMF, both types are in operation at their peak performance, about 450 μA for the former and 240 μA for the latter. The H^-/D^- cyclotron using an internal source suffers from higher gas pressure thus higher stripping loss. The limited output from the internal source and the lower dee voltage used confine the beam current capability to about one-half of that obtainable from an external source system. However, these compact cyclotrons do find their usefulness in many medical facilities needing only 50-200 μA external beam currents. The compact internal source technology has been transferred through the authors of this report to several cyclotron manufacturers and about 30 H^- or H^-/D^- cyclotrons using such source are in service today worldwide.

These models are: CP-42 series including H^-/D^- CP-45, 11 MeV H^- RDS, 10 MeV $H^-/5$ MeV D^- Cyclone 10/5, 18 MeV $H^-/9$ MeV D^- Cyclone 18/9 and the 16.5/8.5 H^-/D^- cyclotron. Detail description of these cyclotrons has been reported elsewhere.

II. PERFORMANCE

EXTERNAL BEAM FROM SAMPLE H^-/D^- CYCLOTRONS

Facility	Beam Energy (MeV)	Target Curr. (μA)	Max. Ext. Curr. (μA)
TRIUMF CP-42	42 H^-	200	240
	30 H^-	240	300
M.D. Anderson CP-42	42 H^-	100	200
Amersham CP-42	42 H^-	200	240
	30 H^-	200	300
UCLA CP-45	45 H^-	100	150
	23 D^-	50 ^p	
CYCLONE 10/5	11 H^-	50	90
	5.5 D^-	40	80
CYCLONE 18/9	18 H^-	50 ^p	(250) ^a
	9 D^-	50 ^p	(180) ^a

p Projected
a at $r = 10$ cm

The external beam current available with various models are summarized in the table above. For CP-42 series 200 μA can be achieved throughout. Up to 300 μA has been obtained at 30 MeV at Amersham and at TRIUMF Applied Program facilities. Fig. 1 shows a section of recording of such event. Fig. 2 shows the recording of the endurance test for a CP-42, performed at Berkeley TCC for 100 hours uninterrupted extraction of 200 μA at about 38 MeV. Three attempts were made resulting a total of 300 hours of running such high beam power. Except for initial tuning at the beginning of the test, the entire operation was uneventful. As can be seen from Fig. 2 that the arc current

and vacuum were unchanged for the entire test. The RF amplifier was finetuned by operator about once per hour. Typical crowbar rate was about 2 per hour. As for the Cyclone 10/5, the routine beam requirement is only 50 μ A. The maximum achievable amounts to about twice as high, so the routine requirements are easily met.

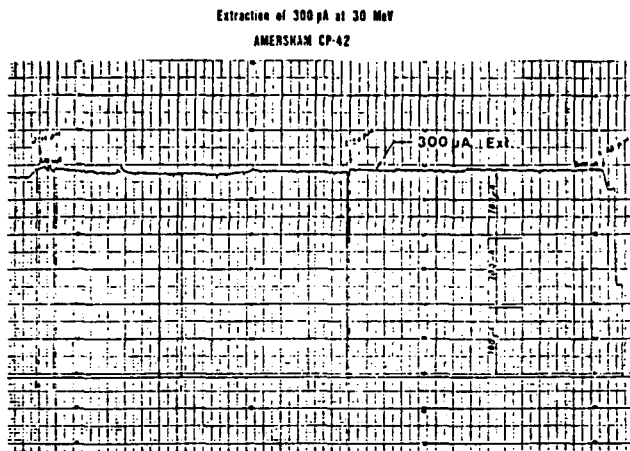


Fig. 1. Record showing the extraction of 300 μ A at 30 MeV from the Amersham CP-42.

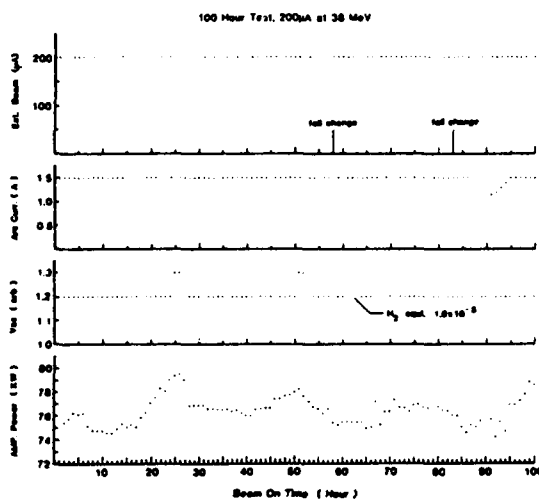


Fig. 2. Time dependence of cyclotron parameters over a period of 100 hours during high current extraction.

III. PHASE WIDTH and MAGNETIC FIELD

Since the extraction efficiency is always 100%, the emphasis of H^- cyclotron design is actually on the internal beam capability. As we shall point out later, within the present internal source technology the H^-/D^- ion density per unit RF phase is low in comparison with the corresponding proton beam. Ehlers [1] stated that the H^- ion density is emission limited, and that the intensity remains constant above 8 kV DC. This means that for cyclotron RF extraction the H^- beam current will be linearly proportional to the phase width achievable. One faces the

problem of how to optimize the phase width for the initial acceleration and how to maintain it until extraction.

For the first requirement, several contributing techniques can be utilized:

- Make the threshold dee voltage lower but operate the cyclotron at higher voltage if possible. Beam centering must be optimized.
- Minimize axial phase selection by using phase lagging and a proper cone field.
- Optimize the axial opening in the central region and make use of optimal electric focusing.
- Precision alignment of dee structure and ion source with respect to the magnet median plane. Also precision alignment of magnetic field symmetry about the geometrical mid-plane.

As for the second requirement, a very flat phase profile corresponding to a conservative energy gain per turn should be obtained. The designed or actually attainable energy gain per turn should be higher than the value used for the profile calculations. In addition, the best achievable vacuum should be provided. Fig. 3 shows the phase history in $\sin\phi$ for three CP-42 cyclotrons.

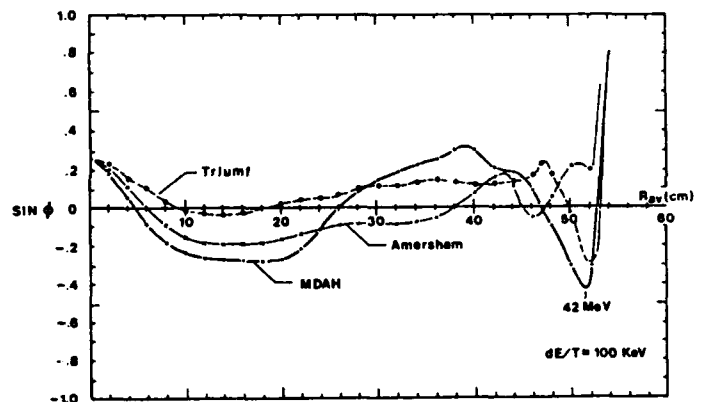


Fig. 3. Comparison of phase profiles in $\sin\phi$ between 3 CP-42 cyclotrons.

As can be seen in Fig. 3 that the magnet of Amersham CP-42 has the best field among these three whereas the one of M.D. Anderson the worst. Test records showed that extraction of 200 μ A at 42 MeV was relatively easy with the Amersham CP-42. No phase loss was observed when the matching RF frequency was found and used. In contrast, the same extraction test at MDAH was quite difficult. Although the extracted beam currents met the specification, the dee voltage and arc current required were much higher than those used for other CP-42s. Due to some difficulty in the dee supporting insulators, users of these cyclotrons reduce the dee voltage substantially making the energy gain per turn down to about 70-80 kV. The actual phase profiles will be much inferior to those shown in Fig. 3.

The characteristics of a resonance curve, $I(\text{beam})$ vs. $I(\text{mag})$, has been exploited to measure the phase width

at low energy. An example is shown in Fig. 4(a). The flat top region of the bell shape curve (solid) corresponds to the excursion of $\sin\phi$ of the beam bunch within the ± 1 boundary, while the fall-off slope represents the excursion out of the boundary. Since the total $\Delta\sin\phi$ is equal to 2, wider the width of the fall-off narrower the flat top. The $\Delta\sin\phi$ the beam occupies is larger. Furthermore, since $\Delta\sin\phi$ is invariant for an ideal phase profile, the ratio of fall-off width to flat top width should be the same for all radii.

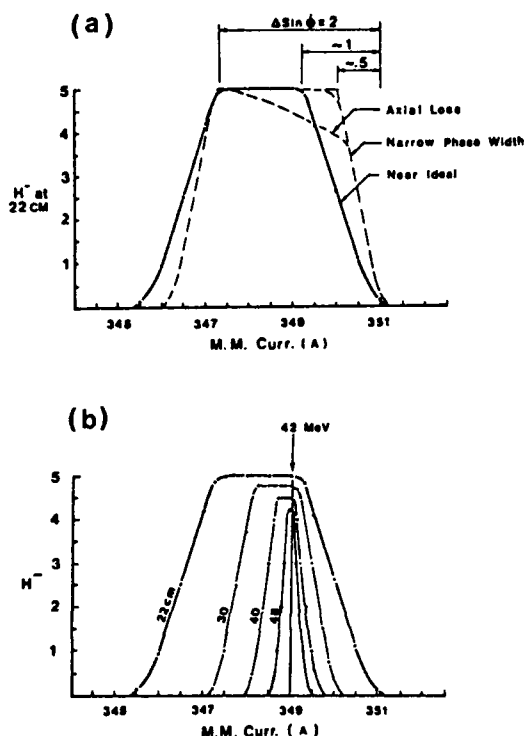


Fig. 4. Use of resonance curves for (a) central region and (b) phase profile optimization.

The quality of the resonance curve reflects the quality of the axial focusing at the initial stage of acceleration. A sloped top (dashed) indicates that axial loss occurs as the beam getting more phase advanced and being axially selected. The near ideal curve was obtained after various efforts to improve the axial focusing strength has been made following the guideline described earlier. The width of $\Delta\sin\phi$ occupied by the beam was also optimized to about one. The inferred phase width was about 60° .

A family of resonance curves at various radii can be plotted against a fixed RF frequency as shown in Fig. 4(b). This plot can be used to identify the extend of phase loss, gas stripping loss and axial loss. A number of these plots against a bandwidth of RF frequencies using an optimal dee voltage should be obtained in order to select an operating frequency which gives the best phase profile available.

IV. ION SOURCE and CENTRAL REGION

The performance of the internal H⁻/D⁻ source has been reported at the 1992 cyclotron conference. The optimum ion output and gas efficiency have been obtained by source

parameter optimization coupled with the central region optimization described in the last section. The coupled relationship between the source and the central region is also greatly improved. For example, four dimensional position adjustments optimize the initial orbit, the ion transit time from the source slit to the puller. This feature can also reduce the space-charge effect, minimize the initial vertical oscillation amplitude. The surface between the source and puller was shaped to provide axial electric focusing for the low energy ions during the first crossing. The careful surface treatment allowed a higher RF field between the gap without excessive flashovers. The sum of all these efforts provided us the beam capability of $600 \mu\text{A H}^-$ at $r=15 \text{ cm}$ (3.5 MeV). Routinely available beam currents has been about 450-500 μA with a lower dee voltage at a less than ideal condition.

V. SUMMARY

The capability of extracting 200-300 μA of proton beam from a compact H⁻/D⁻ cyclotron has been demonstrated. However, the highest potential for D⁻ beam was not explored except at low radius. The routinely available D⁻ currents at present is 50-100 μA from a somewhat compromised system. Due to limited space for writing, the importance of gas loading, cyclotron tank pressure and gas stripping loss were not discussed here. Reducing the gas loading into the acceleration chamber remains the greatest challenge for the internal H⁻/D⁻ source designers, but it also possesses the highest potential for improvement. In summary, the reported results were obtained with cyclotrons lacking either magnet profile perfection, or optimal dee voltage capability. It is possible that 450-500 μA of H⁻ can be accelerated to higher energy, say 30-40 MeV, with an internal source cyclotron if all deficiencies are removed, as this has been done in the case of external H⁻/D⁻ source cyclotrons.

VI. ACKNOWLEDGEMENT

The authors of this paper wish to thank Drs. M. Finlan and D. Lewis of Amersham International; J. Burgerjon, R. van den Elzen and J. Lofvendahl of TRIUMF applied Program; Dr. A. Zermeno and C. Brown of M.D. Anderson Hospital for their efforts and assistance in performing the tests for CP-42. Special thanks go to Drs. Y Jungen and S. Laycock, H. Marie and M. Abs of IBA; Dr. S. Lindback and J. Bergstrom of Scanditronic for adopting the internal source techniques and their invitation to join the efforts in making their cyclotrons work. The teaching of H⁻ acceleration from TRIUMF; the encouragement from Prof. Vogt, Drs. G. Dutto and P. Schmor of TRIUMF/UBC are greatly appreciated.

VII. REFERENCES

- [1] Ehlers, K.W., " Design consideration for high intensity negative ion source", Nuc. Instr. and Method, 32, (1965) p.811.

Operation of the TR30 "Industrial" Cyclotron

Karl Edman, R. Dawson
Ebco Technologies, TRIUMF

B. Milton, N. Stevenson
TRIUMF, 4004 Wesbrook Mall, Vancouver, B.C. V6T 2A3

Abstract

The 30 MeV TR30 cyclotron installed for Nordion has been in operation for two years. The use of industrial process controllers, the external H^- ion source and cryogenic pumping has made this machine easy to operate and reliable with extracted beams of 500 μA . The strong focussing properties of the magnet and low internal beam losses have reduced residual radiation fields so that there is negligible exposure to the operators during machine servicing. The main characteristics and features of the machine leading to a 98% accelerator availability are discussed in this paper. As well as this the extensions to the cyclotron allowing the acceleration of deuterons to 15 MeV are outlined.

I. INTRODUCTION

The TR30 cyclotron was designed to be an accelerator for the commercial production of isotopes and as such to be a highly reliable, low maintenance, automatically operated, and low residual activity system [1].

The basic design is for a compact magnet system with strong focussing of the particles to avoid losses during the acceleration process and using negative ions to give almost 100% extraction efficiency of the beam. The losses in the cyclotron are further minimized by the use of cryopumps to produce the vacuum in both the injection system and in the cyclotron itself. This reduces the losses due to stripping of the negative ions in the vacuum tank by eliminating residual contamination due to the presence of heavy molecules from the backstreaming of oil from the diffusion pumps.

The need to vent the cyclotron during servicing is obviated by the use of valves on both the ion source injection line and the stripper foil carriage mechanism so that routine maintenance can be carried out while maintaining a good vacuum in the tank. The life of the cryopumps is extended by this process and the "hard" vacuum established in the tank simplifies the operation of the rf system as well as improving the beam transmission.

II. OPERATION

Values extracted from a computer log record of the operating values of the various components of the system, while delivering two simultaneous beams down two external beam lines, are assembled in Table 1.

These values are taken from the hard copy output of the control system [2] which also continuously monitors and displays the input and output parameters of all of the system components on the color graphic display screens

as well as alpha numeric output. System set points can be altered by using a mouse pointer or by typing in new values by means of the computer keyboard. The control software is highly flexible and permits the operators to define macros which have greatly aided in the "turn on" and tuning procedures as well as in maintaining system stability.

Table 1 System parameters during dual beam operation.

RF power	35 kW
Main magnet power	33 kW
Beam current (29 MeV)	$2 \times 220 \mu A$
Extracted current	500 μA
Target collimator current	25 μA
Ion source arc current	15-20 A
Ion source arc power	~ 2 kW
Tank vacuum	3×10^{-7} torr
Total TR30 Facility (inc. processing areas and bldg. services) Power consumption	175 kW

The target system has been developed by NORDION to permit the operation of the system automatically by the use of the control computer and uses the same industrial control hardware and software that is used to control the cyclotron. Isotopes are transferred from the position of the irradiation to the processing hot cells by the use of a pneumatic transfer system [3]. The system has been developed over the course of the last 10 years of isotope production by NORDION and the performance of the system is shown in Fig. 1 where the production as a function of time from the commissioning of the TR30 cyclotron is displayed.

The servicing of the cyclotron is carried out in two different procedures. The first is the regular maintenance in

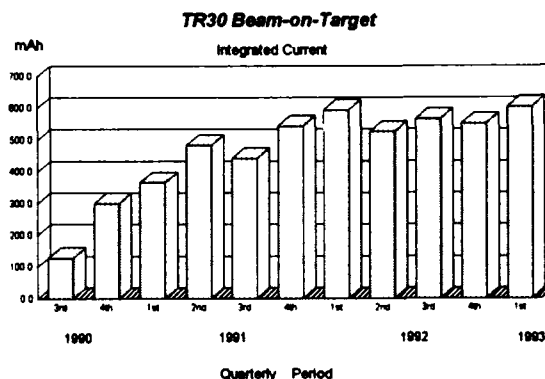


Fig. 1. Beam delivery by quarter.

which the tank is not vented and involves the ion source filament and the stripping foil carousel. The ion source filament is normally replaced once every 3 weeks. The duration of the operation is about 4 hours. The performance of the ion source is logged by the control system and the state of the filament is determined by the filament power required to produce a given output current from the system. The life of the stripping foil is between 20 and 50 mA hours of extracted beam. The multifoil cartridge is changed during a filament replacement when it is deemed necessary to have a spare foil ready for operation.

The second procedure is the regular yearly preventative maintenance in which the tank is vented and the state of the inflector and the injection optic elements are inspected as well as other parts of the system which are impacted by the beam. The dc beam injected during the operation of the system at high current is 5-6 mA and erosion of the lenses occurs under the high current conditions. This service normally requires one 8 hour shift. If it is deemed necessary the cryopumps are regenerated during this service period.

A graph of the availability of the cyclotron and of the various system failures is given in Fig. 2. It can be seen that the main problems associated with the system failures are associated with the high power targets that are being irradiated. As development of the targets continues the total availability of the system is expected to increase. A comparison of the radiation exposure of the operators per unit of charge delivered to the targets between the CP42 and TR30 operated by the same team is given in Fig. 3. The dramatic reduction is due to the decrease in beam

losses in the cyclotron with the external ion source and the clean vacuum in the tank.

III. DEUTERON OPERATION

To permit the operation of the cyclotron for the acceleration of deuterons, trim coils were added in the valleys of the magnet Fig. 4. The tuning stems on the resonators were extended by the use of a coaxial switch [4] to allow the rf system to be tuned to the 4th harmonic of the rotation frequency of the deuterons. By accelerating both the protons and the deuterons in the 4th harmonic mode the tuning of the cyclotron for protons and deuterons is greatly simplified. The magnet is shimmed for protons and isochronizing coils are only used during the deuteron operation. The rf voltage on the resonators is reduced by a factor of two so that the deuterons follow exactly the same orbits in the cyclotron as the protons but at 1/2 of the energy. The energy of the injected beam is also reduced to 1/2 of the proton energy. The maximum extracted deuteron beam current can be as much as 70% of the proton current using a common ion source. This cyclotron can be used as an extremely prolific source of neutrons for industrial neutron radiography as well as a deuteron accelerator for isotope production.

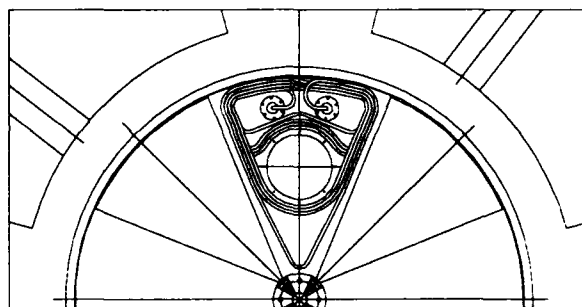


Fig. 4. Trim coils for deuteron operation.

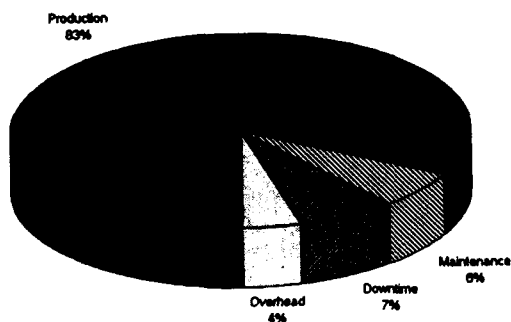


Fig. 2. TR30 operation system availability for 1993.

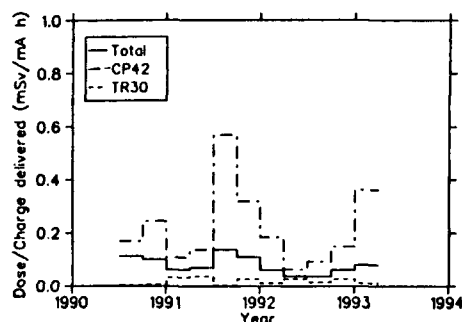


Fig. 3. Radiation levels in CP42 (solid line) and TR30 (dashed line).

IV. REFERENCES

- [1] B.F. Milton, *et al.* "First beam in a new compact intense 30 MeV H⁻ cyclotron for isotope production", *Proc. of the European Particle Acceleration Conference, Nice (1990)* p. 1812.
- [2] R. Keitel, *et al.*, "The TR30 control system - a case for off-the-shelf hardware", *Proc. of the 13th International Conf. on Cyclotrons and their Applications*, Vancouver, B.C. (World Scientific, Singapore, 1992) p. 685.
- [3] J.J. Burgerjon, *et al.*, "A high power target system for radioisotope production" *Proc. of the 11th International Conf. on Cyclotrons and their Applications*, Tokyo (1986) p. 634.
- [4] M. Eiche, *et al.*, "Dual frequency resonator system for a compact cyclotron" *Proc. of the 13th International Conf. on Cyclotrons and their Applications*, Vancouver, B.C. (World Scientific, Singapore, 1992) p. 515.

The First Year with Electron Cooling at CRYRING

K. Abrahamsson, G. Andler, L. Bagge, E. Beebe, P. Carlé, H. Danared, K. Ehrnstén, M. Engström, Å. Engström, C.J. Herrlander, J. Hilke, J. Jeansson, A. Källberg, S. Leontein, L. Liljeby, A. Nilsson, A. Paál, A. Pikin, K.-G. Rensfelt, U. Rosengård, J. Starker, and M. af Ugglas
Manne Siegbahn Institute of Physics, S-104 05 Stockholm

Abstract— The experimental program at CRYRING storage ring began shortly after the installation of the electron cooler in May 1992. The performance of the ion sources and the ring is reported. Results of electron cooling are reviewed and a method to improve the efficiency of electron cooling is presented.

I. INTRODUCTION

CRYRING is a low-energy synchrotron and storage ring equipped with electron cooling [1]. The ring receives light atomic and molecular ions from a plasmatron ion source (MINIS) or highly charged, heavy ions from an electron-beam ion source (CRYSIS). The ring has been running for experiments using light ions such as D^+ , H_3^+ , and $^3HeH^+$, but also Ar^{13+} has been accelerated and cooled. The EBIS source is regularly delivering beams for low-energy atomic-physics experiments using gas injection. It has also produced highly charged argon and xenon ions using injection of singly charged ions from an external ion source (INIS). Electron cooling has been applied both to atomic and molecular ions at energies between 290 keV/u (the injection energy in CRYRING) and 10.9 MeV/u [2]. By measuring the longitudinal drag force on the ions, the electron temperature has been determined to 0.1 eV transversally and around 10^{-4} eV or less longitudinally. We expect to reduce the transverse temperature a factor of 10 by using a magnetic field that is 10 times higher in the gun solenoid than in the rest of the electron cooler.

II. ION SOURCES

CRYSIS [3] has been running mainly with argon and xenon ions using gas injection. Ar has been produced in all charge states and Xe in charge states up to 49+. Atomic-physics experiments have used Xe ions in charge states up to 44+. Typical electron currents are between 150 and 300 mA and confinement times reach up to 5 s for the highest charge states. The ion source has also been used with ion injection. Injection of ions from an external ion source has several advantages compared to gas injection. The most important one is that the interior of the EBIS can be kept cleaner since no gas is adsorbed on the cold surfaces of its interior. This makes it easier to switch between different ions, also metallic ions can be used with

a suitable ion source. Unlike the gas, the ion current can easily be switched on and off, so that ions can be injected only for a very short time during the beginning of each ionization cycle. This results in a narrower charge-state spectrum. The ion injector is built as an isotope separator, which means that heavy elements, such as xenon, no longer have to be isotopically pure in order to allow separation between the high charge states. One can summarize the experience from using ion injection by saying that the output of CRYSIS is at least as good (concerning intensity and charge states) as with gas injection, while operation is considerably simpler.

The plasmatron ion source, MINIS, has recently been upgraded in order to improve the vacuum in the injection line. It has also been provided with an analyzing magnet.

III. RING

Since the installation of the electron cooler in May 1992, all major components of the ring are in operation. The layout of the facility is shown in figure 1. The RFQ and the electrostatic injection system were designed for ions with charge-to-mass ratios above 0.25. The range between 0.25 and 0.5 has been covered by ions such as D^+ , H_2^+ , $^3He^+$, H_3^+ , Ar^{13+} , D_2^+ , and $^3HeH^+$. All these ions have also been accelerated to full energy, $96(q/A)^2$ MeV/u, and

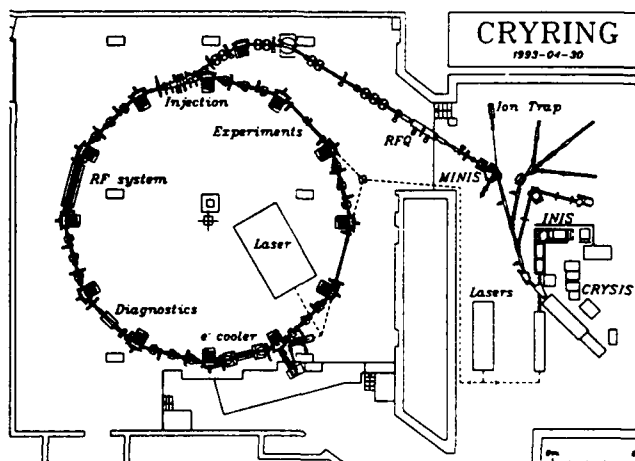


Fig. 1 Layout of CRYRING

cooled. The number of ions stored at full energy is typically between a few times 10^7 and 10^8 . For some cases, where the ion-source output is high, up to 2×10^9 ions have been stored. Four of the twelve straight sections in the ring have been baked to 250°C , and there the pressure is below 1×10^{-11} mbar (the lower limit of the vacuum gauges used at present). In the other straight sections the pressure is $1-3 \times 10^{-11}$ mbar. Most of the pumping speed is provided by NEG (Non-Evaporable Getter) pumps, and, to a lesser degree, by ion pumps [4]. Rest-gas analysis shows that the partial pressure of gases heavier than H_2 , mainly CH_4 and H_2O , constitutes about 10% of the total pressure.

For ions with large cross sections for electron loss in collisions against restgas molecules, such as the light molecules or He^+ , this pressure should give life times of around 30 s at the injection energy. Measured lifetimes are in the order of a few seconds, indicating that the true pressure is higher than the measured one or that the restgas composition is different from what has been measured. The lifetime for Ar^{13+} is even shorter due to the large capture cross section at the injection energy. Such lifetimes makes rapid acceleration necessary, in our case the acceleration to full energy is done in about 1 s. (Although the power supplies allow the ramping to be done in 150 ms, this fast mode has not been used yet.) At full energy the lifetime is 5–20 s for these ions. Bare ions have much longer lifetimes: for electron-cooled D^+ ions at 6 MeV/u, where single-scattering is the dominant loss mechanism, 21 h has been measured.

IV. ELECTRON COOLER

The electron cooler was assembled outside the ring during April of 1992 and tests with the electron beam were performed for a few weeks. Then the cooler was inserted into the ring and on the 20 May the electron beam was again turned on, and cooling of deuterons at 5.4 MeV/u was observed. A few weeks later, H_2^+ ions were cooled at the same energy. The momentum-cooling time is around 1 s for these ions and an electron current of 150 mA. The transverse cooling time has not been measured, but should theoretically be about 5 s, roughly the same as the lifetime of the beams. We have generally used electron currents between 100 and 150 mA. Higher currents gives a tune shift at injection energy that is so high that it has to be compensated with the ring quadrupoles. An alternative, which also has been used, is to turn off the electron beam during the injection and beginning of acceleration.

The relative momentum spread of the ion beam after cooling is usually $5-10 \times 10^{-5}$ and occasionally somewhat smaller. With Ar^{13+} , where the cooling is considerably stronger than for the light ions, 1.6×10^{-5} was recorded. The diameter of cooled D^+ beams has been measured with a position-sensitive channelplate detector located at the zero-degree extension after the electron cooler, which detects ions that have been neutralized in the cooler. A beam of 10^7 D^+ ions at 6 MeV/u created an image on the detec-

tor that had a width of 0.5 mm and a height of 0.25 mm (FWHM). Considering that the neutralized D beam had a certain divergence, the size of the stored beam should have been still somewhat smaller. The image size was sensitive to changes in the angle between ion and electron beams down to a few tenths of a milliradian.

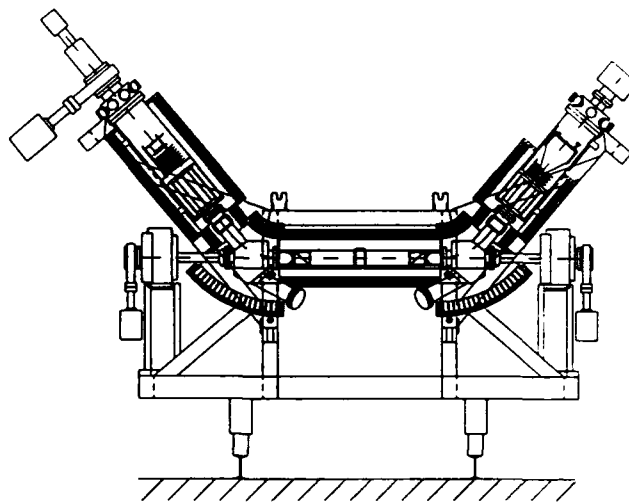


Fig. 2 Layout of the electron cooler

An interesting subject for study at CRYRING is electron cooling at very low ion energies. The reason is both that electron-cooler stacking in CRYRING would have to be performed at 290 keV/u (which thus is the injection energy) and that experiments have been suggested with heavy molecular ions where the maximum energy per nucleon is very low. Using an electron current of only 7 mA the goal to momentum-cool at the injection energy was reached with a beam of 2×10^9 H_2^+ ions. This energy corresponds to an electron energy of 170 eV. The momentum-cooling time was 3–5 s, which was about twice the lifetime of the ion beam. Schottky spectra of the cooled and uncooled H_2^+ beam at the 20th harmonic are shown in figure 3.

Through measurements of the longitudinal drag force that the electrons exert on the ions, the temperature of the electron beam could be obtained. The drag force was measured by cooling the ion beam, then shifting the electron energy by a small amount, and observing, using a spectrum analyzer, how fast the ion velocity changes toward the new electron velocity. Such measurements were made at three different charge-to-mass ratios using D^+ , H_3^+ , and D_2^+ . Since the longitudinal drag force depends both on the transverse and the longitudinal electron temperatures, both these could be estimated. The measured values followed the theoretical curve for a transverse temperature of 0.10 eV, corresponding to the cathode temperature of 900°C , and for a longitudinal temperature of the order 10^{-4} eV or less. Measurements could not be made at relative velocities low enough to resolve longitudinal temper-

atures lower than 10^{-4} eV. This longitudinal temperature is also consistent with measurements of the rate for radiative recombination of deuterons and electrons. This rate was measured at very low relative energies by sweeping the electron energy around the cooling energy according to a sawtooth function and was seen to increase even at energies below 10^{-4} eV.

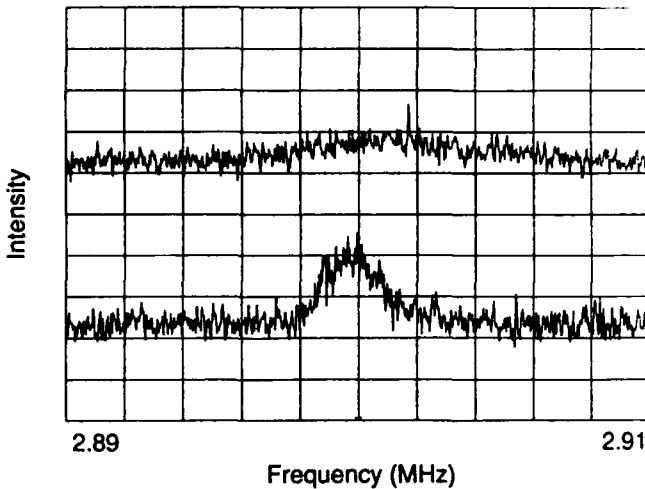


Fig. 3 Schottky spectra of cooled and uncooled H_2^+ at 290 keV/u

Stronger cooling forces, both longitudinally and transversally, would be obtained with a colder electron beam. A method for producing an electron beam that has a transverse temperature which is lower than the cathode temperature is to guide the electron beam through a negative magnetic-field gradient [5]. Since the ratio between transverse energy and longitudinal magnetic field for a charged particle is an adiabatic invariant under changes of the magnetic field strength, a smoothly decreasing field reduces the transverse temperature in proportion to the field decrease. If, as an example, the field in the gun solenoid is ten times stronger than in the rest of the cooler, the transverse electron temperature will decrease from 0.1 eV to 0.01 eV. The transverse energy spread will be transferred to the longitudinal motion. This will not be noticeable, however, after transformation to the moving system of reference—the longitudinal electron temperature will in general still be dominated by the longitudinal relaxation of the electron beam (transfer of potential energy due to the electron–electron interaction to kinetic energy).

The requirement that the electron motion is adiabatic with respect to the decrease of the field strength puts a limit to the electron energy for a given field gradient. In the case of the CRYRING cooler, a gradient can be obtained by having a strong field in the gun solenoid and a weaker field in the rest of the cooler. Calculations show that the transition region between the gun solenoid and the small solenoid below it allows a maximum electron en-

ergy of 30 keV when the field is 0.3 T in the gun solenoid and 0.03 T otherwise. Even at 60 keV there is a significant reduction in transverse electron energy.

The field gradient will increase the beam cross section with a factor equal to the ratio of field strengths. A new electron gun with a ten times smaller area is therefore under manufacturing for tests of this technique at the CRYRING cooler. It will be a scaled-down version of the present gun. It will thus have the same perveance as the present one and will give the same electron density in the cooling solenoid.

V. REFERENCES

- [1] K.-G. Rensfelt, "Status of the CRYRING project," in *PAC 91*, San Francisco, May 1991, p. 2814; K. Abrahamsson, G. Andler, L. Bagge, E. Beebe, P. Carlé, H. Danared, S. Egnell, M. Engström, A. Filevich, C.J. Herrlander, J. Hilke, J. Jeansson, A. Källberg, S. Leontein, L. Liljeby, A. Nilsson, A. Paál, K.-G. Rensfelt, U. Rosengård, A. Simonsson, J. Starker, and M. af Ugglas, "Status and Commissioning of CRYRING", in *EPAC 92*, Berlin, March 1992, p. 441; K. Abrahamsson, G. Andler, L. Bagge, E. Beebe, P. Carlé, H. Danared, S. Egnell, K. Ehrnstén, M. Engström, C.J. Herrlander, J. Hilke, J. Jeansson, A. Källberg, S. Leontein, L. Liljeby, A. Nilsson, A. Paál, K.-G. Rensfelt, U. Rosengård, A. Simonsson, A. Soltan, J. Starker, M. af Ugglas, and A. Filevich, "CRYRING—a synchrotron, cooler and storage ring" *Nucl. Instr. Meth.*, in press
- [2] H. Danared, "The CRYRING electron cooler," in *ECOOOL 90*, Legnaro, May 1990, p. 21
- [3] L. Liljeby and Å. Engström, "Status report on the Stockholm cryogenic electron beam ion source," in *Int. Symp. on Electron Beam Ion Sources and Their Appl.*, Upton, N.Y., 1988, p. 27.
- [4] L. Bagge, H. Danared, K. Ehrnstén, C.J. Herrlander, J. Hilke, A. Nilsson, and K.-G. Rensfelt, "The ultra high vacuum system of CRYRING", *Vacuum*, in press
- [5] H. Danared, "Fast electron cooling with a magnetically expanded electron beam", *Nucl. Instr. Meth.*, submitted

Electron Cooling of Heavy Ions at GSI

M. Steck, K. Beckert, H. Eickhoff, B. Franzke, F. Nolden, P. Spädtke
GSI

Postfach 110552
D-64220 Darmstadt

Abstract

Electron cooling of heavy ions has been studied at the storage ring ESR over the whole range of ions up to bare uranium. Systematic measurements of the ion beam temperature evidence a dependence on the particle number which proves an equilibrium between cooling and heating by intrabeam scattering. Measurements of the longitudinal intrabeam scattering rate and of the the longitudinal cooling force provide with information about the longitudinal cooling times. Small deviations of the longitudinal cooling time from the theoretically predicted A/Z^2 -dependence are found.

1 INTRODUCTION

The ESR storage ring at GSI [1] is part of an accelerator complex [2] which can deliver ion species over the entire range of masses and after acceleration in the heavy ion synchrotron SIS can produce bare ions up to uranium. These ions having emittances $\epsilon_{x,y} \approx 10 \text{ } \mu\text{mmrad}$ and a momentum spread $\Delta p/p \approx 10^{-3}$ are injected into the storage ring ESR and can be cooled by the electron cooling system to a phase space density which is typically by 5 to 6 orders of magnitude larger than that of the uncooled beam after injection. This implicates the possibility to accumulate particles in the storage ring. Multiplication factors in excess of 100 are routinely achieved by a combination of rf stacking and cooling resulting in a maximum ion current of 7 mA. The beam lifetime of the cooled heavy ion beams under ultra high vacuum conditions is limited by radiative electron capture [3]. Therefore a high efficiency of the cooling system is desirable in order to reduce the ion beam losses by operation of the electron cooler at low electron currents. The achievable multiplication factors by cooled beam accumulation are also affected as for highly charged ions they are determined by a balance between the injection rate and the capture loss rate.

2 ELECTRON COOLER PARAMETERS

The large range of ion masses and charges as well as the possibility to decelerate the ions in the ESR require a large flexibility of the electron cooling system. A system was designed which allows independent choice of electron energy, electron current and magnetic guiding field [4]. For sim-

plicity of operation the magnetic field in the present experiments was chosen in the range $B_0 = 0.7 - 1.1 \text{ kG}$. The lowest electron beam energy for cooling was 50 keV, the highest energy was 165 keV, since the maximum energy is presently limited by high voltage breakdown in the air filled Faraday room at approximately 190 kV. Reconstruction of the causing components is under way. No significant dependence of the cooling efficiency on the energy and magnetic field in this regime has been observed.

The electron current determines the cooling power which is directly proportional to it. The maximum electron current for continuous cooler operation was 1 A since for higher currents unreliable operation is caused by electron beam instabilities most likely due to discharges. For experiments with highly charged ions operation with high electron currents is undesirable in most applications as the beam lifetimes drops to a few minutes. To achieve fast cooling during injection of hot ion beams or to extract the stored ion beam by the electron capture process higher currents might be requisite. Reconstruction of the drift tubes which surround the electron beam on its way from the gun to the collector and modifications of the gun and collector geometry are expected to improve the high current performance. In the low current regime efficient cooling with currents of a few mA was observed, even a current of 1 mA was found to be sufficient to stabilize the ion beam against heating from scattering in the residual gas. Therefore in experiments with continuous electron cooling storage times on the order of days are feasible.

For optimized cooling a fine adjustment of the angle between electron and ion beam is necessary. Minimum transverse emittances of the ion beam indicate the optimum situation, although in this case the longitudinal momentum spread is not minimum necessarily. An increased heating by intrabeam scattering from the strongly compressed transverse to the longitudinal degree of freedom explains this contradiction.

3 EQUILIBRIUM BETWEEN COOLING AND INTRABEAM SCATTERING

In the static operational mode of storage and cooling at constant energy the ion beams are cooled to equilibrium temperatures which are determined by a balance between all heating sources and the cooling power of the electron

cooling system. As the ESR is operated under ultrahigh vacuum conditions ($p \leq 10^{-10} \text{ mb}$) scattering in the residual gas is negligible. For cooled ion beams of high phase space density the main heating process is intrabeam scattering.

This has been proven by systematic measurements of the longitudinal momentum spread and the transverse emittances as a function of the number of stored ions. The momentum spread was measured by Schottky noise or BTF analysis. Position sensitive wire chambers detecting ions after recombination with electrons in the cooling section provided a non-destructive method to measure beam profiles using the down charged ions which are spatially separated in dispersive sections of the storage ring [5].

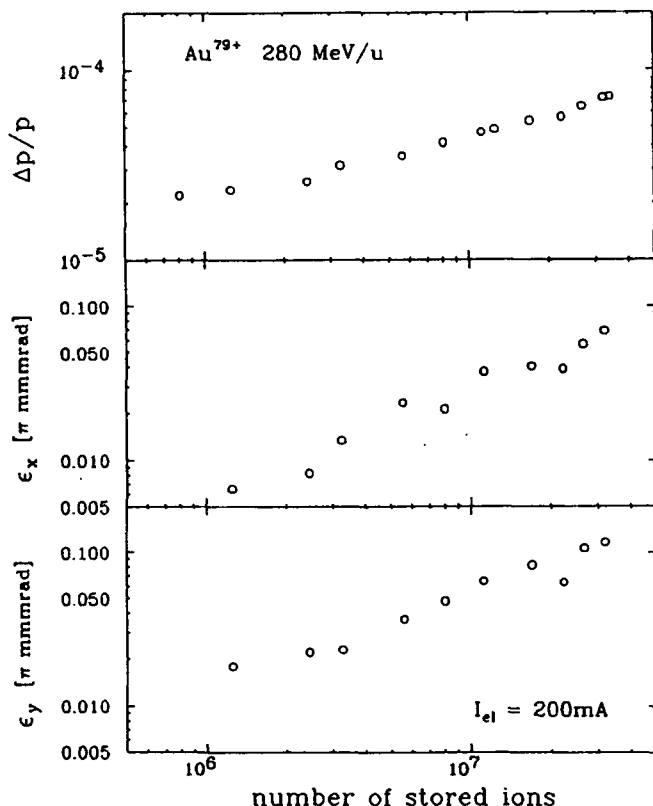


Figure 1: Momentum spread and emittances of a cooled Au^{79+} 280 MeV/u beam as a function of the number of stored particles.

The equilibrium beam properties of a beam of bare gold ions at 280 MeV/u cooled by a 200 mA electron beam are shown in Fig. 1. The temperatures - longitudinal and transverse as well - increase with the number of stored ions N . The longitudinal momentum spread shows a $N^{1/3}$ -dependence, whereas horizontal and vertical ion beam emittances grow with $N^{2/3}$. This is in good agreement with previous results for the equilibrium momentum spread of a xenon beam, but in small disagreement for the transverse degree of freedom which was increasing with $N^{1/2}$ [3]. Considering that particularly the transverse degrees of freedom are sensitive to small alignment errors of

the electron beam this effect may be accountable for the discrepancy.

During many experiments with cooled heavy ions the dependence of the momentum spread on the ion beam intensity was monitored parasitically by Schottky noise analysis (Fig. 2). Due to the experimental requirements the cooling electron currents vary, but all measurements show the $N^{1/3}$ -increase of the momentum spread with the number of stored ions, only for very small particle numbers the dependence seems to approach $N^{1/2}$. The separation of the light ions from the heavier ones is likely to be caused by some complication in the analysis of the Schottky noise. Due to the high phase space density the light ions show collective beam behaviour which aggravates the interpretation of the spectrum. Schottky noise analysis in this case can result in a momentum spread which deviates from that obtained by BTF analysis by up to a factor of two. The Schottky noise analysis results in systematically lower values for the momentum spread, but proves the $N^{1/3}$ -dependence.

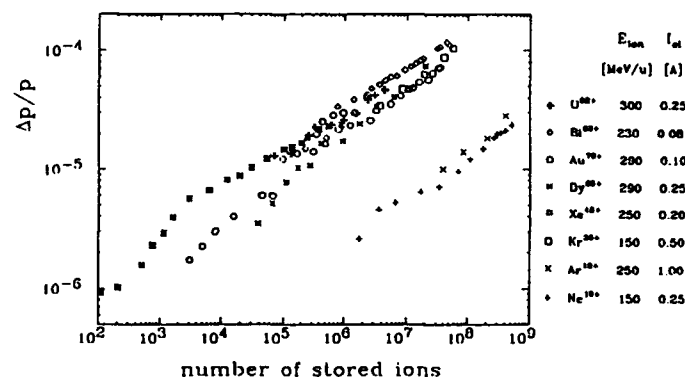


Figure 2: Dependence of ion beam momentum spread as a function of the number of stored ions. Electron currents and ion beam energies are indicated.

The observed equilibrium beam temperatures can be well founded in the framework of the intrabeam scattering theory giving indirect evidence of the prevalence of this heating mechanism for cooled heavy ion beams [6]. This was also confirmed by variation of the electron current and the good agreement between experimental and theoretical cooling rates.

4 LONGITUDINAL INTRABEAM SCATTERING RATES

The heating effect by intrabeam scattering was directly observed by a measurement of the longitudinal beam distribution after stopping cooling instantaneously. The energy of the electron beam can be detuned by stepping of the accelerating voltage ($\Delta V = 5 \text{ kV}$) within milliseconds to an energy which causes a momentary interruption of the cooling action. The high voltage step was used as a trigger signal to start a fast Fourier analyzer (minimum sweep time 8 ms) with a variable delay after the trigger signal. In Fig. 3 the momentum spread of a 0.9 mA Dy^{66+} beam

at 290 MeV/u which was cooled by an electron beam of $I_{el} = 500$ mA is shown as a function of the delay time between the high voltage step and the start of the analyser sweep. The time derivative of the momentum spread growth reflects the instantaneous heating rate.

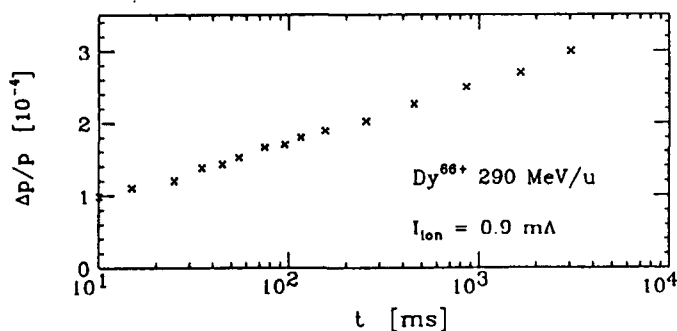


Figure 3: Momentum spread of an intense Dy^{66+} beam at 290 MeV/u as a function of the time between interruption of cooling and start of the spectrum analyzer sweep.

From the initial value of the growth rate the longitudinal cooling rate of the electron beam in equilibrium can be concluded which results in a cooling time $\tau = 17$ ms (normalized to $n_e^* = 1 \cdot 10^6 \text{ cm}^{-3}$ and a relative cooler length $\eta_c = 0.0185$). Similar measurements with less intense beams of Au^{76+} , Pb^{82+} and U^{91+} resulted in cooling times $\tau = 5 - 8$ ms. As the difference in the A/Z^2 -ratio in these measurements is almost negligible the difference may be explained by a dependence of the cooling time on the intensity and phase space density of the ion beam. Measurements with simultaneous observation of the transverse degree of freedom will give more detailed information of the transverse heating rate and of the Z- and A-dependence of the cooling time.

5 LONGITUDINAL COOLING FORCE AND COOLING TIME

The measurement of the longitudinal cooling force can be separated into two regimes. For large relative velocities ($v^* \geq 10^4 \text{ m/s}$) the cooling force descends and can be easily measured by fast stepping of the accelerating voltage of the electron beam. The action of the detuned electron energy can be consequently monitored by fast Fourier analysis of the motion of the ion beam towards the velocity that is determined by the electron velocity. In contrast to this the cooling force at small relative velocities ($v^* \leq 10^4 \text{ m/s}$) is expected to increase directly proportional to the relative velocity up to a certain maximum. This linear increase of the cooling force corresponds to a constant cooling time which is on the order of milliseconds and therefore not accessible by the high voltage stepping method. Therefore the approach to heat the ion beam simultaneously with rf noise and to determine the cooling force from the particle distribution was applied [7].

The results of both methods for Ne^{10+} and Bi^{82+} ions

are displayed in Fig. 4 with the straight line indicating the smoothed cooling force curve from the heating method and the discrete data points originating from the high voltage step method. For easiness of comparison the results are normalized to an electron density $n_e^* = 1 \cdot 10^6 \text{ cm}^{-3}$ proving a strong increase of the cooling force with the ion charge.

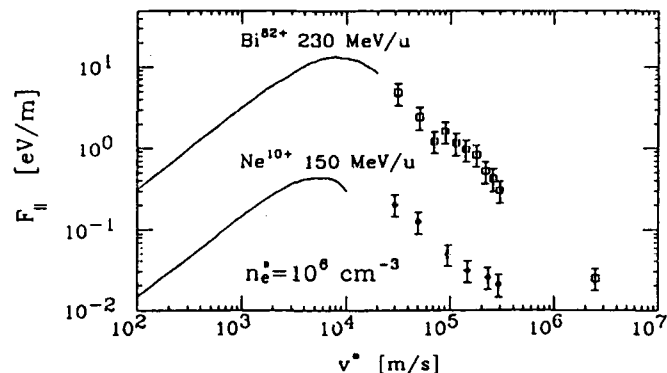


Figure 4: Cooling force as a function of the longitudinal relative velocity for Ne^{10+} at 150 MeV/u and Bi^{82+} at 230 MeV/u normalized to $n_e^* = 1 \cdot 10^6 \text{ cm}^{-3}$. Data points were determined by high voltage stepping, straight lines are smoothed data from measurements of the particle distribution with heating by rf noise.

From these cooling force measurements a cooling time $\tau_c = 2.4$ ms for Ne^{10+} and $\tau_c = 0.9$ ms for Bi^{82+} (normalized to $n_e^* = 1 \cdot 10^6 \text{ cm}^{-3}$) was derived for the linear part of the cooling force. The improvement for the heavier ion however is a factor of 2.5 smaller than expected from the Z^2 -scaling of the cooling force. Further studies under well controlled conditions are necessary to prove whether this is a deviation from the standard theory as predicted for highly charged ions or whether it is related to differences in the transverse beam size caused by small misalignments between electron and ion beam.

6 ACKNOWLEDGEMENT

We gratefully acknowledge support from F. Bosch, M. Jung, O. Klepper, C. Kozhuharov, R. Mooshammer in the operation of the charged particle detectors.

7 REFERENCES

- [1] B. Franzke, Nucl. Instr. Meth. B24/25 (1987) 18
B. Franzke et al., these proceedings
- [2] K. Blasche et al., Part. Acc., 1990, Vol. 32, pp. 83-90
- [3] M. Steck et al., Proc. of the 3rd Europ. Part. Acc. Conf., Berlin 1992, pp. 827-829
- [4] N. Angert et al., Proc. of the 2nd Europ. Part. Acc. Conf., Nice 1990, pp. 1374-1376
- [5] F. Bosch, Nucl. Instr. Meth. A314 (1992) 269-276
- [6] I. Hofmann et al. Proc. of the 3rd Europ. Part. Acc. Conf., Berlin 1992, pp. 783-785
- [7] H. Poth et al., Nucl. Instr. Meth. A287 (1990) 328-332

The Aarhus Storage Ring for Ions and Electrons ASTRID

Søren Pape Møller
Institute for Synchrotron Radiation
University of Aarhus
DK-8000 Århus C, Denmark

Abstract

ASTRID is a storage ring/synchrotron for ions and electrons. Results from the first 3 years of commissioning and running will be presented. A wide range of both positive and negative ions (both atomic and molecular) varying in mass from ${}^3\text{He}$ to C_{70} (Buckminsterfullerene) have been stored in the ring. The physics has been centered around laser-cooling, lifetime measurements of metastable ions and electron recombination. The ring is 2×3 months a year operational as a 580 MeV synchrotron radiation source ($\lambda_c = 35 \text{ \AA}$), with stored currents (presently) around 150 mA. Initially beam-loading problems in the rf-cavity hindered large currents, but a fast feedback loop has circumvented this problem. Presently the current is limited by the injection rate at 100 MeV and the lifetime of the beam, at high currents influenced by ions trapped in the beam.

I. THE FACILITY

ASTRID is the first facility which combines a storage ring for ions with a synchrotron-radiation source [1-3]. The motivation for this was to make a relative expensive piece of equipment available to a wider user community.

The layout of the storage ring with injectors is shown in fig. 1. The electron injector is placed in a separate well-shielded cave. There is no radiation shielding around the storage ring; hence the ring hall is evacuated during filling of the ring. Scrapers in the ring are left close to the electron beam to give a well-defined beam dump.

A. The injectors

Ions are preaccelerated in an isotope separator using a very stable ($\text{RMS} < 1 \text{ V}$) 200 kV high-voltage supply. A variety of ion sources for both positive and negative ions can be used with the separator to produce singly-charged ions and molecules of almost any type. A charge exchange cell has been installed after the separator magnet to produce negative ions by electron capture in a Na, K or Cs vapour. Differential pumping in the injection beamline separates the high-pressure ion source (10^{-2} torr) from the ring vacuum (10^{-12} torr).

A pulsed (10 Hz) race-track microtron has been built to produce the 100 MeV electrons for the storage

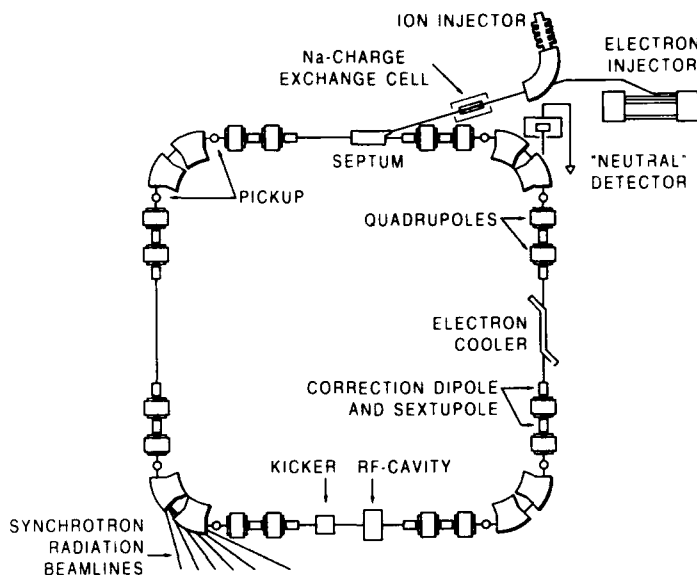


Figure 1. Layout of the storage ring with injectors.

ring. The RF system is operating at 3 GHz. The resonant energy gain is 5.3 MeV corresponding to 19 turns.

B. The storage ring

The "ring" is a square as formed by two 45° bending magnets, excited by a common coil, in each corner. The lattice functions for ASTRID are shown in fig. 2. The quadrupoles are grouped in four families, so that the dispersion in two opposite straight sections can be varied continuously between 0 and 6 m without change of the tunes. In fig. 2 is shown the dispersion in ASTRID with four superperiods, and with two superperiods giving two dispersion-free straight sections.

Two families of 8 sextupoles are available for chromaticity corrections. Superimposed on the air-cored sextupoles are 8 horizontal and 8 vertical correction dipoles. Furthermore 4 horizontal correctors are available as back-leg windings on the main dipoles.

The vacuum system is designed for the 10^{-12} torr region, as required for long storage times of the ions. Hence the system has been vacuum fired and is prepared for a 300° C in-situ bake-out. There is installed a total of 20 ion pumps and 24 sublimation pumps in the ring. Presently the system has only been baked to 150° C, resulting in an average pressure around 10^{-11} torr.

Two different RF systems are used. For the ions, a

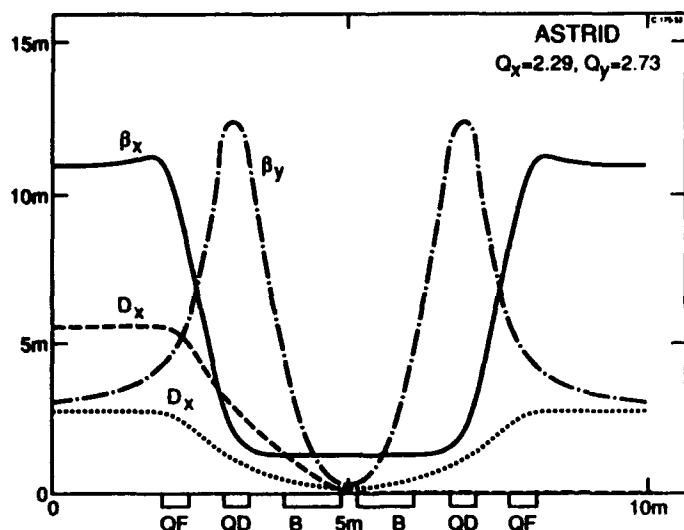


Figure 2. Lattice functions of ASTRID.

ferrite-loaded cavity operating in the 0.5-3.3 MHz region is available, giving a maximum voltage of 2 kV. For the electrons, a capacitively loaded coaxial TEM cavity operating at 104.9 MHz is used. This cavity was fabricated in steel, which was then copper plated. The obtained Q is around 9000.

Table 1
Parameters of ASTRID

Magnetic rigidity	1.87 Tm
Circumference	40 m
Ions	
Injection energy	<200 keV
Hor., vert. tune	2.29 2.73
Hor., vert. chromaticity	-3.4 -7.5
Momentum compaction	0.053
RF system	0.5-3.3 MHz 2 kV
Injected currents	1 pA - 10 μ A
electrons	
Injection energy	100 MeV
Hor., vert. tune	2.208 2.640
Hor., vert. chromaticity	-4.3 -7.1
Momentum compaction	0.068
Design current	200 mA
Electron energy	580 MeV
Horizontal emittance	0.14 mm mrad
Critical energy, wavelength	0.36 keV 35 \AA
Energy loss/turn	8.3 keV
Beam lifetime (Touschek)	16 hours
Number of bunches	14
RF system	105 MHz 125 kV

Ions and electrons are injected with a magnetic septum (dc) and a kicker placed diametrically opposite. For the ions, the electrostatic kicker excited by a square pulse injects one turn. For the electrons, a magnetic kicker excited by a half-sine pulse is used to

accumulate electrons. The dc septum has a maximum bending power of 1.3 Tm and an effective thickness of 11 mm. This rigidity allows injection of heavy ions and also extraction of a low-intensity 580-MeV electron beam.

The kicker and RF-system are the only components being exchanged when swapping between electron and ion operation.

Clearing electrodes covering around half the circumference are installed in the ring to reduce ion-trapping effects.

A variety of diagnostics is installed, including 10 horizontal and vertical position pick-ups, scintillation screens, Schottky pick-ups, beam-current transformer, beam scrapers and synchrotron-radiation detectors.

The control system is based on a NORD main computer with PC's as consoles. Autonomous function generators are used for all dynamical parameters for acceleration and similar operations.

II. RUNNING ASTRID WITH IONS

Since the start up of the facility many different ions have been stored in the ring; a list is given in table 2.

Table 2
Atomic and molecular ions stored in ASTRID

$^4\text{He}^+$	$^6\text{Li}^+$	$^7\text{Li}^+$	$^{16}\text{O}^+$	$^{20}\text{Ne}^+$	$^{40}\text{Ar}^{++}$
$^{151}\text{Eu}^+$	$^{166}\text{Er}^+$				
H_2^+	$^{13}\text{CO}^+$	$^{12}\text{CO}^{++}$	$^{13}\text{CO}^{++}$	C_{60}^+	C_{70}^{++}
C_{70}^+					
$^3\text{He}^-$	$^4\text{He}^-$	$^9\text{Be}^-$	$^{12}\text{C}^-$	$^{16}\text{O}^-$	$^{19}\text{F}^-$
$^{35}\text{Cl}^-$	$^{40}\text{Ca}^-$	$^{56}\text{Fe}^-$			
$^4\text{He}_2^-$	$^{12}\text{C}_2^-$	OH^-	C_{60}^-	C_{70}^-	

The stored ion beams had rigidities between 7 MeV/c for 6 keV $^4\text{He}^-$ and 260 MeV/c for 50 keV $^{12}\text{C}_{60}^-$.

The lifetime at injection energy of stored beams of positive ions was limited by the vacuum, typically a few 10^{-11} torr, giving lifetimes around ten seconds. Injected currents for the positive ion beams were in the 1-10 μ A range. A large fraction of the runs with positive ions have been for laser cooling experiments [4] with Li^+ and Er^+ .

The lifetime of a negative ion beam is determined by rest gas stripping, intrabeam stripping and field stripping (in the bending magnets) [5,6]. A new stripping mechanism has been identified for loosely bound ions. Black-body radiation can ionize ions with small electron affinities like Ca^- and He^- [7]. Furthermore some ions are metastable and autoionize on timescales around a msec. In fig. 3 is shown the decay

of a stable and a metastable beam. The slow components are due to restgas interactions. The energy of the stable beam has been chosen so that the two beams have the same rigidities, to avoid adjustments of the ring magnets between the two measurements. A storage ring, acting as a very long beamline, is ideal

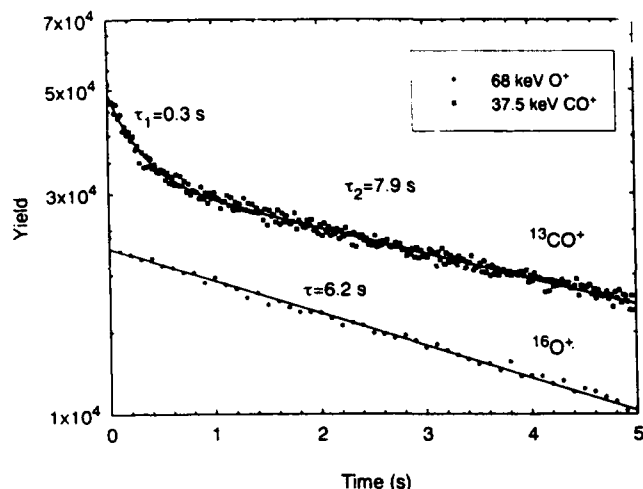


Figure 3. Decay of a stable and an unstable beam.

for such fundamental lifetime measurements.

Most negative ions can only be produced in small quantities, leading to currents in the pA-nA range. Hence they can only be observed with 'neutral' detectors monitoring the decay of the stored beam by counting neutralized ions at the end of the straight sections. An electron multiplier, a semiconductor and a microchannel-plate detector (as in fig. 3) have been used in ASTRID for this purpose.

The first electron cooling/recombination experiments have started. The electron beam has an energy of 0.5-2 keV, requiring ion energies above 1 MeV/a.m.u. Ions can now be accelerated from 0.15 MeV up to 6 MeV in one cycle, whereas higher energies requires change of harmonic number and two acceleration cycles.

III. RUNNING ASTRID WITH ELECTRONS

The 100-MeV race-track microtron routinely delivers 10-15 mA pulses of 1 μ sec width. This 3 GHz beam is injected into the ring and captured by the 105 MHz RF system. The current captured per injection is around 1-5 mA, and the optimal injection frequency is around 0.2 Hz, to be compared to transverse damping times of 4 secs. This rather low injection frequency is caused by the rather thick septum used. During the early commissioning it was realized, that beam loading in the rf-system [8] limited the maximum accumulated current to 1-2 mA per bunch for rf-voltages around 8 kV. In our case this limitation can not be cured by running with a higher rf power, since a good accumulation efficiency is needed owing to the

low injection frequency. A rf power of less than 10 kW is needed to keep the bucket height smaller than the ring acceptance (1%). Hence an amplifier feedback system was built, which reduce the effective cavity impedance as seen by the beam [8]. This feedback system has raised the beam-loading threshold to 20 mA per bunch. The largest current accumulated to date is 210 mA, well below this threshold.

Up to 160 mA can be accelerated to 580 MeV during 1 min. without significant losses. Above this current, large losses occur. The reason for these losses is currently being investigated. The lifetime at high current at 580 MeV is around 80 minutes, determined by the high pressure (few 10^{-8} torr.). No decrease in this pressure has been observed after a conditioning of the vacuum system to 12 A hours. Coupled bunch oscillations are observed at high energy with large circulating currents. The beam size has been measured using the optical part of the synchrotron radiation at 580 MeV. The horizontal and vertical beam size at the entrance to the dipole have been measured to 0.73×0.10 mm²(RMS). From this we deduce a coupling of 1.4 %, and an increase in the horizontal beam size of around 60 % owing to the bunch oscillations.

IV. FUTURE PLANS

The coming laser cooling experiments will be performed on Mg⁺, which can be cooled in the ground state using UV photons. A wide program with negative ions and molecular ions is planned. One program is a continuation of the lifetime measurements. Another is electron recombination/detachment studies using positive/negative ions and molecules. Also photo-excitation experiments are planned.

Two synchrotron-radiation beamlines are currently in use, i.e. a x-ray microscope and a PGM monochromator (SX-700) for the 11-2300 eV range for surface physics. The third beamline, a large acceptance (20 mrad) high-resolution SGM monochromator for the 30-600 eV region is presently being commissioned.

Several longer term improvements are being discussed, among others we mention installation of insertion devices (wiggler/undulator) in the ring combined with new monochromators, new ion sources and an induction accelerator.

V. REFERENCES

- [1] S.P. Møller, Proc. 1st Eur. Part. Acc. Conf., Rome 1988, p. 112.
- [2] S.P. Møller, Proc. of the 1991 IEEE Part. Acc. Conf., San Francisco 1991, p. 2811.
- [3] S.P. Møller, Proc. 3rd Eur. Part. Acc. Conf., Berlin 1992, p. 158.
- [4] J. Hangst et al., Proc. of the 1991 IEEE Part. Acc. Conf., San Francisco 1991, p. 1764.
- [5] L.H. Andersen et al., Phys. Lett. A **162** (1992) 336.
- [6] M. Chanel et al., Phys. Lett. B **192** (1987) 475.
- [7] T. Andersen et al., Phys. Rev. **47** (1993) 890.
- [8] F. Pedersen, IEEE Trans. Nucl. Sci. **NS-32** (1985) 2138.

Recent developments at the Gustaf Werner Cyclotron and CELSIUS

D. Reistad
The Svedberg Laboratory
Box 533, S-751 21 UPPSALA, Sweden

Abstract

The Gustaf Werner cyclotron, which usually operates in isochronous mode, is used as a synchrocyclotron for high energy protons. In addition to its internal PIG ion source, it has been equipped with two external ion sources, an ECR source for heavy ions and a source for polarized protons and deuterons. The CELSIUS ring is used for intermediate-energy physics with thin internal targets. A major concern is to keep the experimental background small. The electron cooling system is helping this task, but is not yet very useful at the injection energy. The reasons behind this are becoming clear. A long shutdown in the fall of 1993 will bring further enhancements to both accelerators.

I. INTRODUCTION

The The (=Theodor) Svedberg Laboratory (TSL) in Uppsala, Sweden, is a Swedish national accelerator centre. It operates an EN tandem accelerator with maximum terminal potential of 6 MV, and the Gustaf Werner cyclotron with the CELSIUS cooler ring.

TSL "shall promote research by making available facilities for accelerator-based investigations, and by carrying out such research with its own resources." (Quotation from the laboratory statutes).

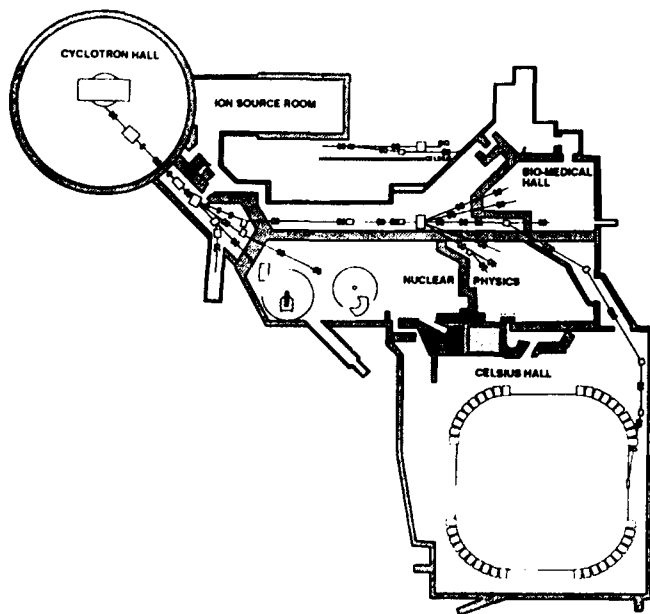


Fig. 1. The Gustaf Werner cyclotron complex. The CELSIUS ring has a circumference of 82 m.

The Gustaf Werner cyclotron complex is shown in fig. 1. The cyclotron [1,2], which has several different modes of operation, delivers beams of light and heavy ions for fixed target nuclear physics experiments, radionuclide production for hospital and scientific use, proton therapy, and acts as injector to the CELSIUS ring.

The CELSIUS ring [3] is used for physics experiments using stored ion beams interacting with very thin internal targets [4]. An electron cooling system is used to reduce the experimental background by increasing the stored beam lifetime.

II. THE GUSTAF WERNER CYCLOTRON

The Gustaf Werner cyclotron, initially built in the forties and early fifties as a (fixed-energy) 185 MeV proton synchrocyclotron with cylinder-symmetrical poles, converted during the eighties to a variable-energy multi-purpose sector-focused cyclotron, is now in use for a wide range of applications. It operates both as an isochronous cyclotron ("CW mode") and as a synchrocyclotron ("FM mode"). Its k -value 192, so it accelerates non-relativistic ions to an energy of $192 \times Q^2/A$ MeV. The maximum energy for protons is 180 MeV, limited by saturation in the cyclotron magnet, power limitation in the extraction septum, and band-width and power limitations in the high-frequency system.

The three-sector geometry of the magnetic field provides sufficient vertical focusing during isochronous operation (when the magnetic field must satisfy $\langle B(r) \rangle \propto \gamma(r)$), except for protons above 105 MeV and for the highest energies of ^3He , when frequency modulation is necessary.

The cyclotron is now used during 15 eight-hour shifts per week. The ion species and the energy are changed frequently in order to satisfy the various needs of the users.

The cyclotron has been in operation in CW mode with an internal PIG ion source for light ions since 1987. In this mode the accelerating frequency is tunable between 12.25 and 24.5 MHz. Acceleration has been done using the harmonic numbers one and two. The maximum dee voltage is 50 kV.

In this mode the cyclotron accelerates the molecular ions H_2^+ and D_2^+ in order to inject protons and deuterons with stripping injection in CELSIUS, as well as He^+ in order to store alpha particles with the same method. Then the ion source is pulsed, with pulse length 8 ms. The peak accelerated beam current is up to 100 μA with H_2^+ and up to 30 μA with D_2^+ and He^+ .

Radionuclide production is performed with 60-100 MeV protons with beam currents up to 10 μA .

The PIG ion source used in CW operation has a double-arc anode. This permits operation both with harmonic number one and two without changing the position of the source. The gas supplies to the two arcs are connected with each other. Especially during acceleration of the molecular ions used for stripping injection in CELSIUS, which are susceptible to break-up by collisions with the rest gas, it is necessary to avoid gas load from the arc that is not in use. Therefore, a dummy is mounted instead of the slit at that side. This is done by pulling out the source through an air lock. Since such changes have turned out to occur quite frequently a new design is underway, in which the two gas volumes are separated. This will significantly reduce the number of times that the internal source has to be pulled out, in order to change the slits.

Synchrocyclotron operation with an internal PIG source has been operational since 1991. Beam stretching is often used to provide a beam (macroscopic) duty factor of about 50 %. This is achieved by reducing the df/dt and the accelerating voltage during extraction. The pulse repetition frequency is presently up to 300 Hz. The accelerated beam current is about 2 nA/Hz at energies below 160 MeV and 1 nA/Hz at 180 MeV.

Synchrocyclotron acceleration is performed with harmonic number one and the frequency in the range between 17 and 24.5 MHz. The power tubes are operated as "broadband" amplifiers with bandwidth up to 2.2 MHz and dee voltages up to about 16 kV.

The PIG ion source used during operation in the FM mode is more compact than the one used in CW mode. This is necessary, due to the smaller dee voltage.

III. THE EXTERNAL ION SOURCES

Two external ion sources, an ECR source for heavy ions and an atomic-beam source for polarized protons and deuterons, have been installed at the cyclotron. The sources are placed outside the cyclotron hall next to an area for atomic-physics experiments, where heavy ion beams directly from the ECR source are used.

A. The ECR ion source

The ECR ion source [5], which was built in collaboration with the University of Jyväskylä, Finland, is based on the design of the room-temperature ECR source at NSCL, MSU, East Lansing, Michigan [6]. The source is vertically mounted and has a plasma chamber of 14 cm diameter and total length of 82 cm, surrounded by a sextupole of NdFeB permanent magnets, giving 0.27 T on the edge of the plasma chamber. An axial field of up to 0.52 T on the axis of the plasma chamber is obtained by 9 circular coils excited by four power supplies. To make the operation of the source more stable and reproducible [7], the original two-stage source has been rebuilt to a one-stage version with axial injection of the gas and of the 6.4 GHz microwave power. The gas supply to the ion source is provided through a line connected to the

main gas and mixing gas bottles and regulated by two stepping-motor driven needle valves. The gases are chosen from a manifold of small bottles placed close to the source.

The ion source itself has been run with the noble gases up to xenon and with hydrogen, nitrogen, and oxygen. Hydrogen, helium, oxygen, nitrogen and krypton ions have also been accelerated through the cyclotron.

Heavy-ion beams have been brought directly from the ECR source to atomic physics experiments, and through the cyclotron for nuclear physics experiments, both with fixed targets and in the CELSIUS ring.

B. The Ion Source for Polarized Protons and Deuterons

The ion source for polarized protons and deuterons was built by Balzers/Pfeiffer at Asslar, Germany, with installation in Uppsala and beam tests during the first half of 1992. The source is based on the atomic-beam method, with state selection accomplished by multipole magnets and radiofrequency transitions. The dissociation of the molecules is obtained by a 27 MHz rf. discharge in a water-cooled Pyrex tube. The atoms then pass a nozzle, cooled to 30 K by a two-stage closed-cycle cryogenerator, to form an atomic beam. The geometry of the focusing sextupole and quadrupole magnets is optimized to give a high transmission to the center of the ionizer region. Radio-frequency transitions between different hyperfine-structure magnetic substates provide the required polarization of the beams. The rf. loops are located both between and after the focusing magnets. The differentially pumped beam source and the atomic-beam unit are built into one housing including an integrated turbomolecular pump system. This configuration ensures a high pumping speed close to the beam region.

The ion source is equipped with an ECR ionizer in which the plasma is confined axially and radially by a pair of solenoid magnets and a permanent sextupole magnet, end excited by microwave power at 2.45 GHz.

In April 1993 the first polarized protons were accelerated in the cyclotron. The degrees of positive and negative polarization of the extracted 100 MeV proton beam were measured to be 0.55 and -0.45 by a polarimeter based on pd scattering.

C. The beam transport system and injection

The ion beams from the two external ion sources are brought to a common horizontal beam line, which takes them to the top of the cyclotron, where they are bent down axially through a hole, drilled through the upper yoke and pole of the cyclotron magnet. Einzel lenses and magnetic quadrupoles are used as focusing elements in the beam transport system. Magnetic dipoles are used for bending the beam. In the vertical part within the upper cyclotron magnet, solenoids are used as focusing elements.

A spiral inflector bends the ion beam into the median plane of the cyclotron.

A buncher is installed to improve the transmission through the cyclotron, which has been as high as 10 % for protons. When the buncher was turned off, the proton transmission went down to 2 %.

IV. CELSIUS

Protons, deuterons, alpha particles and oxygen ions have been stored, accelerated, and exposed to internal targets in CELSIUS. The highest stored beam intensities are 4×10^{11} , 4×10^{10} , 1×10^{10} , and 3×10^8 of protons, deuterons, alpha particles and oxygen ions respectively. Transmission from the injected intensity (with static magnets and without rf.) to accelerated (up to 2.1 GeV/c per charge) beam intensity is typically 25 – 50 %, due to the difference between the phase space area of the maximum rf. bucket which fits inside the CELSIUS momentum acceptance and the total longitudinal emittance of the injected beam from the cyclotron, and to losses during acceleration.

Since the dipole magnets of CELSIUS are not laminated [8], acceleration is performed slowly. This is acceptable for the use of the ring for physics experiments with very thin internal targets due to the long life-time of the stored beams. The machine cycle, which is used during physics runs, is typically five minutes long, with four minutes flat top, and a total of one minute spent for decrease and increase of the magnetic field and for injection.

Many experiments to be carried out at CELSIUS are devoted to studies of reactions with small cross sections. Such measurements require a very low background. A system of 11 pairs of plastic scintillator detectors, which is placed around the ring, has proven very useful to guide the operator while tuning the ring [3]. In addition, one pair of detectors is placed on the straight line going through the axis of the electron cooler, in order to measure the rate of atomic hydrogen, which is produced while cooling protons. This is used as an aid while tuning the electron cooling system. Two detectors, placed at each side of the cluster-jet target, have also been added to the system. These detect protons, which are elastically scattered in the target, and are used as a luminosity monitor.

At low energies (around 300 MeV) the background has been improved by trimming the beam with mechanical scrapers. The mechanical scrapers have not been useful at high energies.

The electron cooling system is used to improve the lifetime of accelerated beams. This is especially important to reduce the experimental background. A recent example (May 1993) is that the lifetime of 280 MeV alpha particles interacting with a neon target of $1.6 \times 10^{13} \text{ cm}^{-2}$ was increased from 40 s to 600 s by electron cooling.

A problem, which has made the electron cooling system less beneficial, particularly at the injection energy, where it should be possible to use electron cooling for accumulation, is that there is a rapid loss of stored beam intensity immediately during the first moment of exposure of the stored beam to the electron beam. We have called this effect "electron heating." Recent measurements indicate, that it is due to non-linear resonances, which are driven by the electrical field from the electrons. The diameter of the electron beam is smaller

than the size of the stored beam before acceleration. These investigations continue.

V. NEAR FUTURE PLANS

There will be a long shutdown of the Gustaf Werner cyclotron and the CELSIUS ring during the period from August through October 1993. During this period, large cryo-panels will be installed inside the cyclotron, and cryogenic chevron baffles will be installed above the oil diffusion pumps of the cyclotron. This is intended to improve the vacuum in the cyclotron by one order of magnitude to become better than 10^{-5} Pascal (10^{-7} mbar) during operation with the external ion sources and a few times 10^{-5} Pascal during operation with the internal PIG source. This will improve the high-voltage characteristics of the cyclotron and the transmission of heavy ions. At the same time, a new control system will be implemented on the cyclotron [9]. This is the first step toward a unified control system for both CELSIUS and the cyclotron.

At CELSIUS, the shutdown will be used for measures to further reduce the experimental background. One of these will be to replace the vacuum chambers in the quadrupoles in order to increase the aperture near the internal target locations. The shutdown will also be used to mount a new collector on the electron cooling system. The collector is expected to have a collection efficiency which is exceeding that of the present collector, and is going to be built by the Budker Institute of Nuclear Physics in Novosibirsk, Russia, according to principles developed there [10].

VI. REFERENCES

- [1] S. Holm, Proc. 13th Int. Conf. on Cyclotrons and their Applications, Vancouver, Canada, July 6-10, 1992, p. 106.
- [2] B. Lundström, B. Holmgren, *ibid.*, p. 553.
- [3] D. Reistad et al., *ibid.*, p. 266.
- [4] C. Ekström, Proc. 19th INS Symp. on Cooler Rings and their Applications, Tokyo, Japan, Nov. 5-8, 1990, p. 228.
- [5] C. Ekström et al., Rev. Sci. Instr. 63 (1992) 2878.
- [6] T.A. Antaya, Z.Q. Xie, Jül-Conf-57, 1986, p. 72.
- [7] T.A. Antaya, J.Phys.Collo. C1 50 (1989) 707.
- [8] G. Norman, D. Reistad, O. Johansson, Proc. 2nd European Particle Accelerator Conference, Nice, France, June 12-16, 1990, p. 881.
- [9] K. Gajewski, L. Thuresson, O. Johansson, Proc. Int. Conf. on Accelerators and Large Experimental Physics Control Systems, Tsukuba, Japan, 11-15 November, 1991. p. 78.
- [10] A.N. Sharapa, to be published.

Ion Beam Acceleration and New Operation Modes at the TSR Heidelberg *

M. Grieser, D. Habs, R. v. Hahn, B. Hochadel, C.M. Kleffner,
J. Liebmann, R. Repnow, D. Schwalm

MPI für Kernphysik
W-6900 Heidelberg, Germany
G. Bisoffi

INFN, Legnaro, Italy
E. Jaeschke
BESSY, W-1000 Berlin, Germany
S. Papureanu

IFIN Bucharest, Romania

Abstract

A newly designed radio frequency cavity was used at the storage ring TSR in Heidelberg to accelerate stored $^{12}\text{C}^{6+}$ ($E_0 = 73.3$ MeV) beams. It was possible to accelerate about 90% of the stored particles by more than a factor of three in kinetic energy ($E_{fin} \approx 240$ MeV). A new operating mode of the machine close to the transition energy was also investigated. Up to $10 \mu\text{A}$ $^{12}\text{C}^{6+}$ and protons could be stored, however the beams were susceptible to longitudinal instabilities. For 21 MeV protons ($\gamma = 1.02$) a γ_{tr} parameter of 1.04 could be reached. A new method to produce a beam of polarized ions, based on spin selective attenuation by a polarized atomic hydrogen target was successfully proved with 23 MeV protons. To minimize losses of the beam particles the TSR was operated in the low-beta- mode. After one hour a beam polarization of 0.014 was achieved.

1 INTRODUCTION

The Test Storage Ring TSR [1] installed at Max Planck Institut für Kernphysik is used for accelerator, atomic and nuclear physics experiments. The 55.4 m circumference ring with the maximum rigidity of 1.5 Tm receives heavy ions up to iodine from a 12 MV Van de Graaff and a normal conducting RF linac combination. Electron cooling is used to reduce the phase space of the stored beam and for accumulation [2], which resulted in stored intensities up to 18 mA $^{12}\text{C}^{6+}$ ions ($3 \cdot 10^{10}$ particles). In table 1 the achieved intensities and lifetimes are listed for various ion species. The lifetimes were measured in the range of $4 \cdot 10^{-11}$ mbar. For protons a lifetime of 60h could be reached. To study dissociative recombination processes [3] between molecules and electrons, HD^+ ($E=2$ MeV) molecular ions were stored with a beam lifetime of 5s at $1 \cdot 10^{-10}$ mbar.

2 BEAM ACCELERATION

For acceleration and deceleration of ions a $\lambda/4$ resonator [4] filled with 20 ferrite rings was developed. The variation

Table 1: *Energies, currents and lifetimes of some ion beams stored in the TSR.*

Ion	Energy [MeV]	Intensity [μA]	Lifetime [sec]
p	21	3300	220000
$^7\text{Li}^+$	13	12	48
$^9\text{Be}^+$	7	2	16
$^{12}\text{C}^{6+}$	73	18000	7500
$^{28}\text{Si}^{14+}$	115	960	540
$^{32}\text{S}^{16+}$	195	1500	450
$^{35}\text{Cl}^{17+}$	202	650	370
$^{63}\text{Cu}^{26+}$	510	110	240
$^{80}\text{Se}^{25+}$	480	110	204

of the resonance frequency is realized by changing the permeability of the ferrites with a d.c. magnetic field, created by an external magnetic quadrupole shown in figure 1.



Figure 1: *The ferrite loaded quadrupole resonator.*

Each magnetic pole has a coil of 5 windings. In contrast to conventional design the magnetization coils are completely outside the rf- field of the resonator. The resonator can be operated in a frequency range of 0.8 to 7 MHz. This resonator was used to accelerate stored $^{12}\text{C}^{6+}$ ($E_0 = 73.3$ MeV) beams without phase feedback loop. It

*Work supported by BMFT under contract No. 08HD525I

was possible to accelerate the stored particles by more than a factor of three in kinetic energy ($E_{fin} \approx 240$ MeV) corresponding to an increase of the revolution frequency of 0.7707 MHz to 1.394 MHz with particle losses of less than 10%. Consider into account saturation effects all magnetic fields were changed synchronously. Particle losses during the acceleration depends on the resonator voltage. Figure 2 shows the fraction of ions stored after the acceleration.

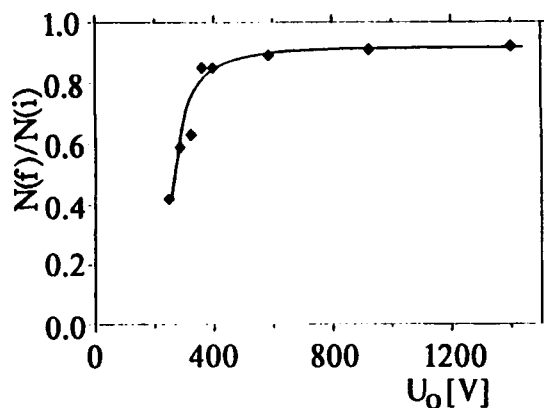


Figure 2: Fraction of ions stored after acceleration from 73.3 MeV to 240 MeV for different acceleration voltages.

The maximum attainable energy for $^{12}\text{C}^{6+}$ was about 300 MeV corresponding to a rigidity of 1.44 Tm. Electron cooling was applied at a carbon energy of 130 MeV to decrease the momentum spread after acceleration from $8 \cdot 10^{-3}$ to $1.5 \cdot 10^{-4}$. With electron cooling a horizontal and a vertical beam diameter of about 1 mm was obtained.

3 THE LOW-BETA MODE

The application of internal atomic beam targets or storage cells demands a β -function at the position of the target to be as small as possible to increase the acceptance angle: In order to achieve these requirements the TSR is operated in the low-beta mode. This mode was used to produce a polarized proton beam ($E=23$ MeV). The new polarization method is based on spin selective attenuation in a polarized target [6]. Electron cooling was used to compensate heating and energy losses in the target. The longitudinal B-field (0.02 T) in the cooler was compensated with two correction solenoids. The target consists of a Teflon coated storage tube of 11 mm diameter and 250 mm length, cooled at 100 K. To determine the target density the deceleration of the stored proton beam without electron cooling was measured. A typically value of $6 \cdot 10^{13} \text{H}_1/\text{cm}^2$ for a target polarization of 0.8 was achieved. The beam lifetime of the protons was about 5 h without and about 30 minutes with polarized gas. These measurements result in an acceptance angle at the target of 4 mrad. A proton beam of typically 0.8 mA was accumulated with electron cooling stacking. After one hour storage time a polarization of the remaining beam (about $100 \mu\text{A}$) of 0.014 could be measured [6].

The calculated horizontal (β_x) and vertical (β_y) β -functions and the dispersion function (D) of the low-beta-mode obtained with the computer code MAD [5] are shown in figure 3. The calculations predict β -functions of $\beta_x=0.8\text{m}$ and $\beta_y=0.8\text{m}$ at the target position.

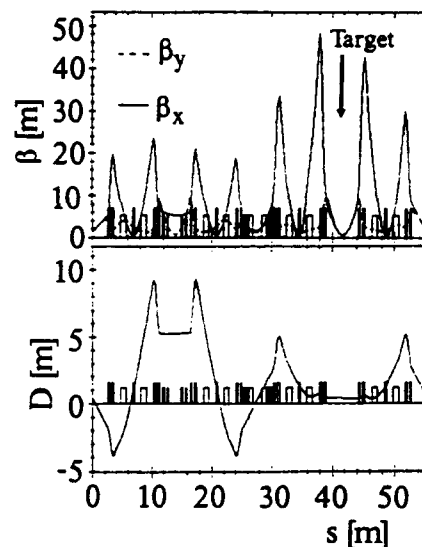


Figure 3: Calculated β -functions and dispersion of the low-beta mode.

4 OPERATION OF THE TSR CLOSE TO THE TRANSITION ENERGY

A new operation mode close to transition energy was also investigated, since for sufficient small currents and strong cooling intra beam scattering (IBS) is expected to be strongly suppressed, as already observed for protons in the NAP-M storage ring at Novosibirsk [7]. This is especially of great interest for the laser cooling experiments performed at the TSR.

This mode can be obtained by increasing the dispersion function in the dipole magnets up to 8.8 m. The calculated dispersion function and the β functions are shown in figure 4. The properties of this mode were investigated in a few beam times with $^{12}\text{C}^{6+}$ (63 MeV, 73 MeV) and protons (21 MeV). Table 2 shows a comparison between typically measured and calculated ring parameters. $\bar{\beta}$ is the average value of the β -function of a quadrupole family. This measurements were done at $\gamma_{tr}=1.1$.

The measured value of the dispersion function $D(s)$ at the location of the beam profile monitor was $D_{BPM} = 6\text{m}$ compared to the theoretically value of 8.8 m calculated with the computer code MAD [5], thus, confirming the need of generally much bigger values for $D(s)$ than for the standard operation mode at $\gamma_{tr} = 3.1$.

Using a beam profile monitor and a Schottky pick-up equilibrium values of the emittances and the momentum spread for an electron cooled 63 MeV $^{12}\text{C}^{6+}$ beam and a 21 MeV proton beam were measured. The transverse blow-up of the ion velocity distribution after switching off the elec-

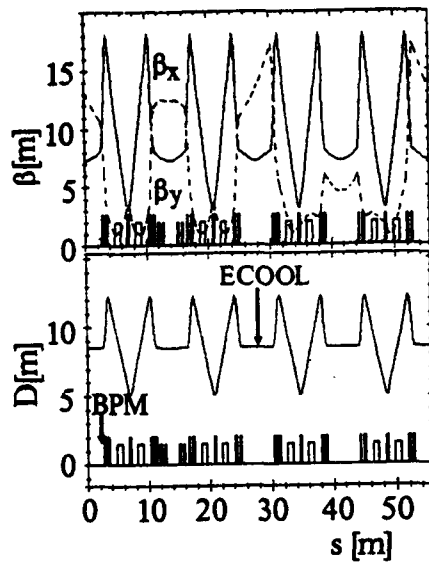


Figure 4: Calculated Twiss parameters of the mode with $\gamma_{tr} \approx 1$.

Table 2: Calculated and measured Twiss parameters of the mode with $\gamma_{tr} \approx 1$.

	Experiment	Theory
Q_x	1.1	1.11
Q_y	3.39	3.42
γ_{tr}	1.1	0.99
$\beta_{x,1}, \beta_{y,1}$ [m]	3.7, 12.3	8.6, 13.5
$\beta_{x,2}, \beta_{y,2}$ [m]	8.9, 5.4	18.2, 4.7
$\beta_{x,3}, \beta_{y,3}$ [m]	2.4, 2.3	3.0, 2.5
$\beta_{x,4}, \beta_{y,4}$ [m]	21.4, 3.9	18.2, 3.0
$\beta_{x,5}, \beta_{y,5}$ [m]	10.1, 7.9	8.6, 8.6

tron cooler was also investigated to determine IBS heating rates. Experimental data were compared with theoretical predictions by calculating the equilibrium and blow-up with a suitable IBS computer code [8], which describes the measurements in the standard mode very well. In the γ_{tr} -mode however, the measured equilibrium emittances were about one order of magnitude higher in the case of 63 MeV $^{12}\text{C}^{6+}$ and 21 MeV protons than predicted by the calculations. The experimental blow up of the horizontal and vertical emittances after switching off the electron cooler are also much too high than predicted by IBS. These measurements are shown in figure 5 together with the theoretical curve.

One reason for this strong heating could be a first order resonance as a requirement for the operation near the transition energy is $Q_x \approx \gamma_{tr} \approx 1$, where Q_x is the horizontal tune. Because of the large dispersion function in the cooler section ($D=8.8$ m) it was very difficult to optimize the electron cooler. These insufficiencies can be avoided

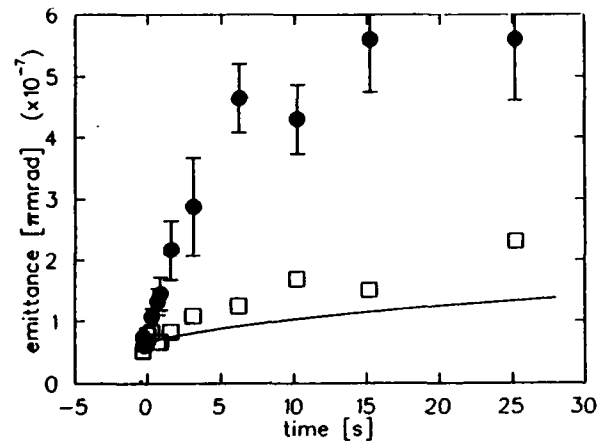


Figure 5: Experimental horizontal (●) and vertical (□) blow-up of 21 MeV protons, measured at $7 \mu\text{A}$.

with an improved ring setting.

5 ACKNOWLEDGMENT

We would like to thank the technicians of MPI for their work which made these experiments at TSR possible.

6 REFERENCES

- [1] E. Jaeschke, D. Krämer, W. Arnold, G. Bisoffi, M. Blum, A. Friedrich, C. Geyer, M. Grieser, B. Habs, H. W. Heyng, B. Holser, R. Ihde, M. Jung, K. Matl, R. Neumann, A. Noda, W. Ott, B. Povh, R. Repnow, F. Schmitt, M. Steck, E. Steffens, The Heidelberg Test Storage Ring for Heavy Ions TSR, 1988 European Particle Accelerator Conference, Rome, vol. 1, p. 365
- [2] M. Grieser, D. Habs, R. v. Hahn, C. M. Kleffner, R. Repnow, M. Stampfer, E. Jaeschke and M. Steck, Advanced Stacking Methods Using Electron Cooling at the TSR, 1991 IEEE Particle Accelerator Conference, San Francisco, vol. 5, p. 2817
- [3] P. Fork, M. Grieser, D. Habs, A. Lambert, R. Repnow, D. Schwalm, A. Wolf, D. Zajfman, Dissociative Recombination of Cold HD^+ at the Test Storage Ring, Physical Review Letters, Volume 70, Number 4, p. 426
- [4] M. Blum, M. Grieser, E. Jaeschke, D. Krämer, S. Papureanu, A New Type of Acceleration Cavity for the Heidelberg Test Storage Ring, 1990 European Particle Accelerator Conference, Nice, vol. 1 p. 955
- [5] Ch. Iselin, The MAD program, Proceedings of Computing in Accelerator Design and Operation, Berlin 1983
- [6] E. Steffens, Test of Spin Filter for Stored Protons and Implications to Polarise Antiprotons, 10. Symposium on High Energy Spin Physics, Nagoya, 1992 (in print)
- [7] N. S. Dikansky, D. V. Pestrikov, Ordering Effects in Coulomb Relaxation of a Cold, Proceedings of ECOOL 1984, Karlsruhe, p. 275
- [8] R. Giannini, private Communication, 1993

A New Design for an EMIS - CYCLOTRON System, for Direct Production of Gaseous PET Radioisotopes

Henrik AYVAZIAN
Ion Beam Applications Laboratory
Nuclear Research Center for Agriculture and Medicine
P.O.Box 4395, Karaj 31585, Iran

Abstract

A new scheme for direct production of ^{11}C ($T_{1/2}=20\text{min}$) and ^{15}O ($T_{1/2}=2\text{min}$) for medical purposes is studied as a future plan in IBAL. A broad sheet beam of separated stable isotopes ($120\times 10\text{mm}$) is converted into an almost cylindrical synchronous bunched beam of high intensity (100mA) and is accelerated in a low energy single cavity RF accelerating unit, in order to lengthen the Mean Free Path (MFP) of the separated ions. The resulting beam is directed into a special Target Ion Source (TIS) and is exposed to a cyclotron beam of protons (deuterons) with relatively high intensity (500 μA). The bunching unit is in-tune with that of the cyclotron injection device, in order to achieve effective results of radioisotope production. The high concentration of produced radioisotopes are extracted and directed into a strong analyzing magnet to prevent transportation of target gas and/or undesired impurities into medical areas. The beam line, including focusing magnets, apertures, the special ion source and vacuum system are explained in brief. Finally a comparison is given between the conventional and the new design.

I. INTRODUCTION

The main idea of going for the new system comes from the problems that usually occurs when a radiochemical lab becomes a necessity in short lived medical radioisotope production sites. Eliminating this, and offering a direct gaseous usage of the main PET radioisotopes, viz. ^{11}C and ^{15}O , seems to be a method with a reasonable cost, since in the new method, except for the TIS, all neutron polluted areas are omitted.

In a typical Electro-Magnetic Isotope Separator (EMIS) designed for separation of light elements, ion currents higher than 100 mA is available for highly abundant isotopes, and for those of lower abundance, a minimum of 1mA is a reasonable figure. If the separated beam is cut into intense bunches of ions, then each bunch is regarded as a time-lapsed target, seen from the proton beam point of view. This requires bunching frequencies, harmonically, of the same order as the proton beam; i.e. two beams should be properly in-tune.

Outcome of this scheme is a secondary ion beam of desired radioisotopes, which is stopped in a decelerating chamber, then pumped out with efficiencies less than 30% (^{11}C is stopped and oxidated in the same chamber).

This non-standard on-line configuration is capable of easy switching between $^{14}\text{N}(\text{d},\text{n})^{15}\text{O}$, $^{14}\text{N}(\text{p},\alpha)^{11}\text{C}$ and $^{15}\text{N}(\text{p},\text{n})^{15}\text{O}$ reactions by applying a slight change in separator's magnetic field. This, optimises the occupancy of the cyclotron beam, and offers a selective production of ^{13}N and ^{18}F , as well, provided that ^{18}O -enriched source is used to feed the EMIS. In this case, either of $^{16}\text{O}(\text{p},\alpha)^{13}\text{N}$ and $^{18}\text{O}(\text{p},\text{n})^{18}\text{F}$ reactions could be selected. This versatility is a promising factor, although drastic production rates are not expected.

II. BEAM LINE

The main beam line consists of two parts: The stable and radioactive beam sections. Optics-wise it is sected into DC and bunched parts (fig. 1), therefore, some focusing characteristics are different for quadrupoles in the latter section.

Since, delicate focusing is not required for isotope production, obviously, higher order focusing elements are omitted.

A: Beam converter

Design of a sheet-to-cylinder beam converter is the dominant focusing task in the DC part. The undesired shape of the sheet beam (mostly a bended rectangle) is transfigured, using an electrostatic set of crescent-like electrodes, followed by a rectangular slit. A series of doublet-triplet is used for reshaping the beam.

B: Bunching, Pre-acceleration

Proton (deuteron) beams in typical dedicated radioisotope production cyclotrons are bunched with frequencies up to 60 MHz. If a Harmonic frequency of 15 MHz is chosen as the bunching frequency of the separator ion beam, then each concentrated group of ions will be bombarded with 4 consecutive bunches of protons. This number can be raised to desired figures, by appropriate selection of the bunching mode.

A 15 MHz tuned single cavity RF accelerator with an energy of 100 Kev is an ideal choice for this purpose, since it is also quite easily available. Such a unit is used as a booster pre-accelerator, in order to extend the MFP of the ions before they are exposed to the cyclotron beam.

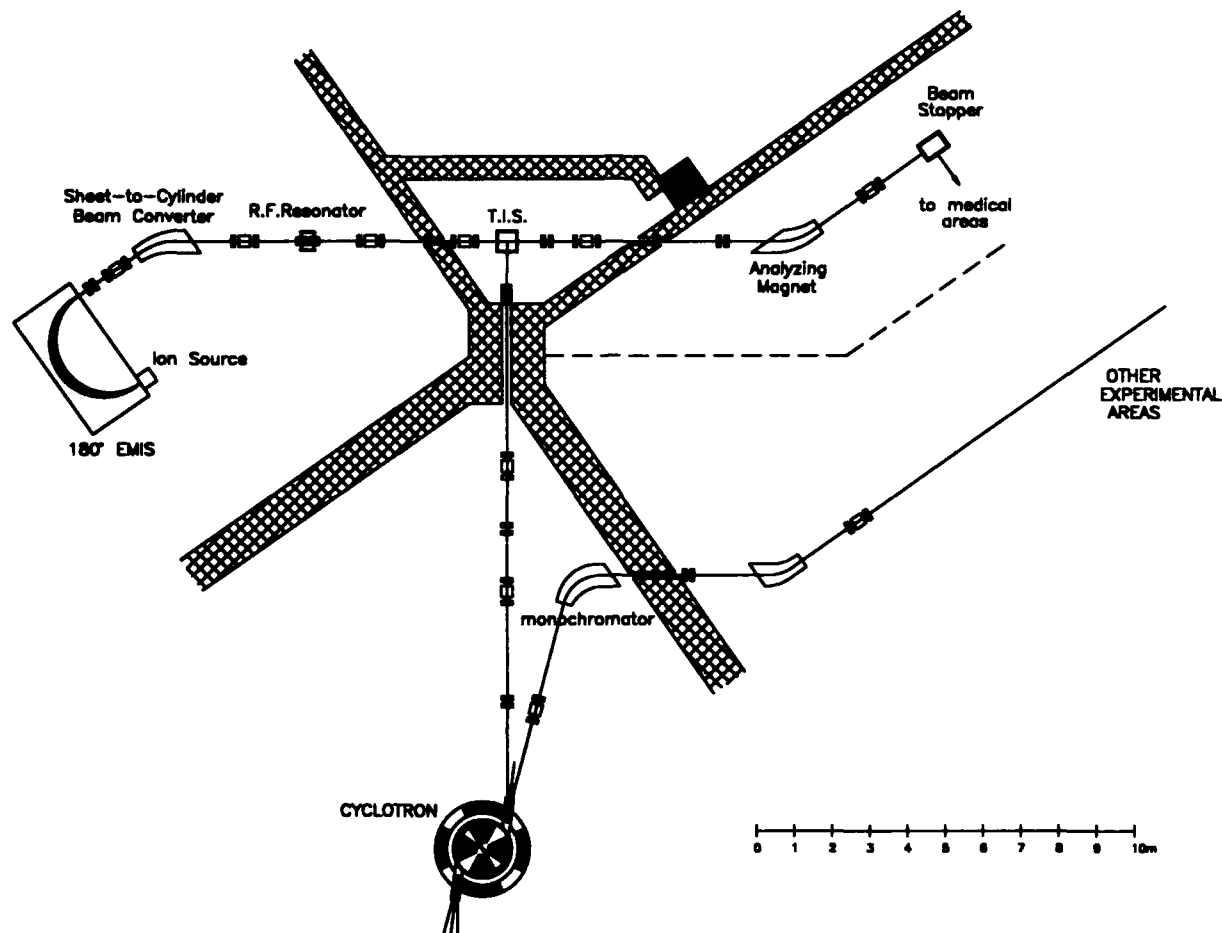


Fig.1 General layout of the new EMIS-CYCLOTRON scheme for production of PET nuclides

C: Target Ion Source

The ion-proton junction is the point where the concept of the new method is realized. A modified Jvaskylä ion guide (fig. 2) is used as the TIS for the system [1,8]. In the original ion guide a skimmer is used to trim the excess of the feed gas, in the ionization chamber. In the modified version the skimmer is drawn out, since the feeding of the source is supplied from the separator beam and a skimmer will cause remarkable loss of ions. The exit hole of the primary injection stage is widened so that the beam flow is made easier and overheating of the ion guide is avoided.

A vacuum pump is attended to the proton-stopper end of the source, to collect recombined H atoms from the ionization chamber, and to maintain the pressure drop caused by the difference in the vacuum systems of the ion and the

proton beam lines.

Since the element range is not varied for the separator beam, the extraction efficiency is dedicatedly upgraded to 30%, therefore, higher rates of production is achieved in this specially modified ion guide.

D: Vacuum System

The pressure gradient, caused by the difference in the vacuum systems used in three different beam lines (i.e. the DC beam, the bunched ion beam and the proton beam), has to be balanced by rather tricky methods.

Normally the gas pressure in a separator hardly goes lower than 10^{-4} Pa, where in a bunched ion beam line it should be kept lower than $5 \cdot 10^{-6}$ Pa, at least, to obtain good beam-transport conditions. In this sense the reshaping of the DC

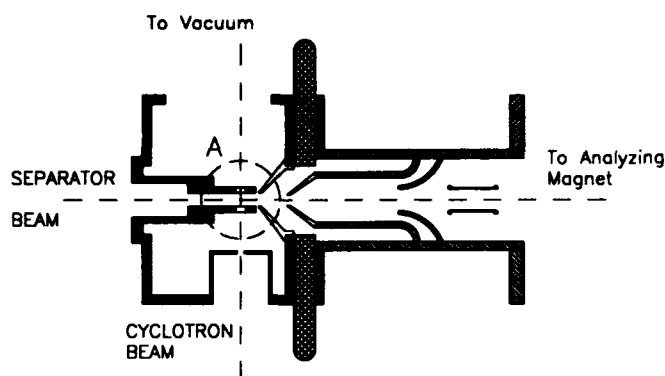


Fig. 2 Schematic drawing of the modified Jvaskylä ion guide used as the special Target Ion Source.

beam doesn't help much, since the beam area remains unchanged. The entrance and exit slits of the RF resonator are functioning as orifices to maintain the pressure drop in this section.

The second point of pressure drop lies in the TIS, where two beam lines of different vacuum qualities are crossing. The second trick is to choose the entrance slit of the cyclotron beam such that it acts like an orifice. However, some limitations in focusing of the proton beam in the vicinity of the TIS should be considered.

III. A BRIEF COMPARISON

The idea of consecutive on-line production of radioisotopes is not unknown, either in classic ISOL facilities [2] or in modern compact systems, recently tested for production of short lived radioisotopes for nuclear astrophysics research [3,4,5]. The production-separation sequence is common between all previous designs.

Compared to a double cyclotron arrangement for production of ^{11}O , ^{13}N , ^{15}O and ^{18}F , the production costs are reduced by replacing one of the complicated cyclotrons, with an economically designed mass separator and an RF resonator, in the present design. The production-separation sequence is reversed, in the new design, so that the neutron polluted areas are minimized, which requires lower costs for separation of the radionuclides.

Remarkable costs of radiochemical labs either in modern single-cyclotron systems [6] and in older systems, using radioisotope generators [7], are eliminated.

The special TIS is designed for limited range of radionuclides, therefore the efficiencies could be pushed to higher limits compared to conventional complicated tubular gas targets [8].

IV. ACKNOWLEDGEMENTS

I would like to acknowledge my colleagues in IBAL, specially our director Mr. M.Karbassforoushan. I express my special gratitude to Dr. K.Halbach and my brother Abraham and his Wife Helen; without their support this work would not be presented.

V. REFERENCES

- [1] J.ÄRJE et al, Nucl. Instr. and Meth., A 247,(1986)431.
- [2] H.L.RAVN, "Radioactive Ion Beams available at On-Line Mass Separators", Proc. of the 11th Int. Conf. on EMIS and technics related to their application ed. W.L.Talbert, (1986)72.
- [3] M.ARNOULD et al, "Production and acceleration of Radioactive Ion Beams at Louvain-La-Nouve", Proc.of the 10th Conf. on the applications of Accelerators in research and industry, eds. J.L.Duggan, I.L.Morgan, (1988)498.
- [4] Y.JONGEN et al, " A two-Cyclotron concept for the production of Radioactive Beams", Proc. of the 1989 IEEE Particle Accelerator Conf., p.1620.
- [5] G.BERGER et al, " Acceleration and Mass Separation of Radioactive Ion Beams in an Isochronous Cyclotron", Proc. of the 1991 IEEE Particle Accelerator Conf., p.2610.
- [6] J.R VOTAW and R.J.NICKLES, "Radionuclide Production for Positron Emission Tomography : Choosing an appropriate Accelerator", the same Conf. as ref. [3], p.1093.
- [7] Y.YANO, "Radioisotope generators for short lived Positron Emitters applicable to Positron Emission Tomography", the same Conf., p.1105.
- [8] R.D.HICHA et al, " Design of Target Systems for production of PET nuclides", the same Conf., p.1110.

THE CHANDIGARH VARIABLE ENERGY CYCLOTRON AND ITS APPLICATION FOR TRACE ELEMENT ANALYSIS USING PIXE TECHNIQUES.

I.M. GOVIL,
Department of Physics, Panjab University, Chandigarh, INDIA.

Abstract

The paper describes the details of the Chandigarh Variable Energy Cyclotron and its application to trace element analysis using PIXE Technique. The various samples of water and Air of Chandigarh and nearby regions have been analyzed using 2-4 MeV Proton beam from this Cyclotron. The importance of the analysis of a few Biological and Archeological samples has also been discussed. The application of this technique is also being exploited for identification of forged ancient coins.

I. INTRODUCTION

The Variable Energy Cyclotron at Chandigarh [1] has now been functioning with resolved beams of protons, deuterons, alphas and He-3. The beams of protons of energy from 1 to 5 MeV, deuterons of 4 MeV, alphas from 7 to 8 MeV and He-3 upto 11 MeV have been obtained at the target. This paper describes the various features of the cyclotron and the characteristics of the accelerated particles. The recent use of this machine for trace element analysis using Proton Induced X-ray Technique has also been discussed.

II. MAIN FEATURES OF THE CYCLOTRON

The machine at Chandigarh is adapted and built out of the components of the variable energy cyclotron at the University of Rochester, Rochester, New York, USA. It is single Dee classical cyclotron with arrangement for variable frequencies from 10 to 20 MHz, and a main magnetic field upto a maximum of 14 K Gauss. This permits the variability of the energy of the various accelerated ions. The layout plan of the whole set-up is shown in figure 1. Figure 2 shows the variation of the typical beam currents of the various ions at different radii from the center of the cyclotron. Figure 3 and 4 shows the gamma-ray and charged particle spectra taken with protons on the specpure Al target. The γ -ray spectra were taken at 90° to the beam direction with the help of 50 cc Ge(Li) detector to avoid broadening of the peaks due to Doppler shift and charged particle spectra were taken with 300 μ m thick silicon surface barrier detector.

III. EXPERIMENTS WITH MACHINE

At present three types of experiments are being done with this machine which are described below.

(A) In-beam spectroscopy using proton and He³ induced reactions.

In these experiments, we have studied the angular distribution of resulting γ -rays from the excited nuclei formed by (p,p')

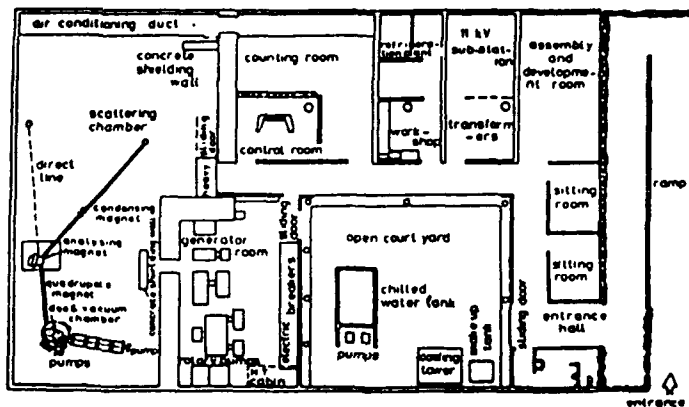


Figure 1. General layout plan of the cyclotron laboratory.

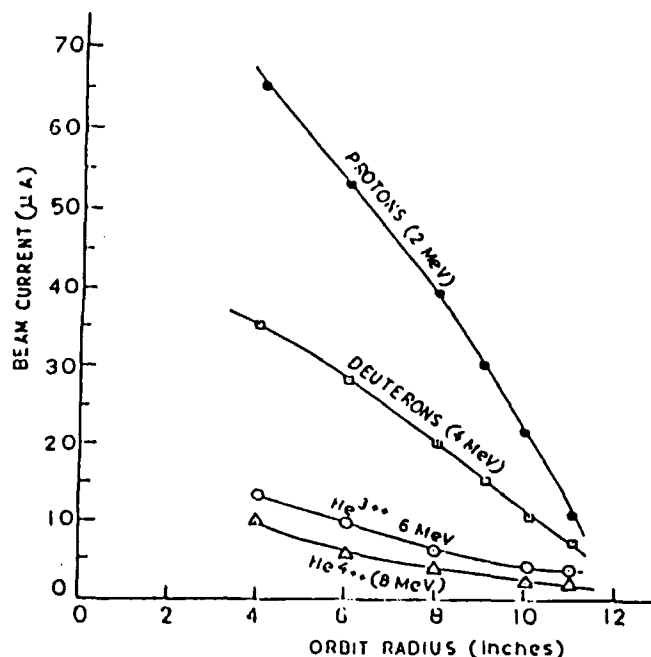


Fig. 2. VARIATION OF INTERNAL BEAM CURRENTS INSIDE THE CHAMBERS

γ), (p,n γ), (p, $\alpha\gamma$) reactions and similarly with alphas by (α ,p γ), (α ,n γ) and (α , α' , γ) reactions. The angular momentum and lifetimes of various excited states are measured using the computer code CINDY and DSAM technique[2-4].

(B) Coulomb Excitation

The phenomena of Coulomb excitation takes place when protons or α -particles interact with the target nucleus with the energy lower than the Coulomb barrier. Many cases of Coulomb excitation have been studied and reported in literature[5-6] using protons as projectiles.

(C) Proton Induced X-ray Emission Technique

In this technique, the interaction between target material and the incident beam of Protons or Alphas results in the emission of X-rays. These X-rays are then detected by a Si(Li) detector at liquid Nitrogen temperature. The energies and intensities of the characteristic X-rays gives the information about the presence and the concentration of the trace element in the target material.

Figure 5 shows the PIXE spectrum of NBS standard Spinach sample. The analysis of spinach standard shows the presence of Al, Cl, K, Ca and Fe. Out of these K has maximum relative percentage of 63.48% followed by Ca (30.65%), Cl (3.83%), Fe (1.38%) and Al (0.66%). These results are in agreement with the standard data and hence allows the confidence in our results.

SPECTRUM OF SPINACH

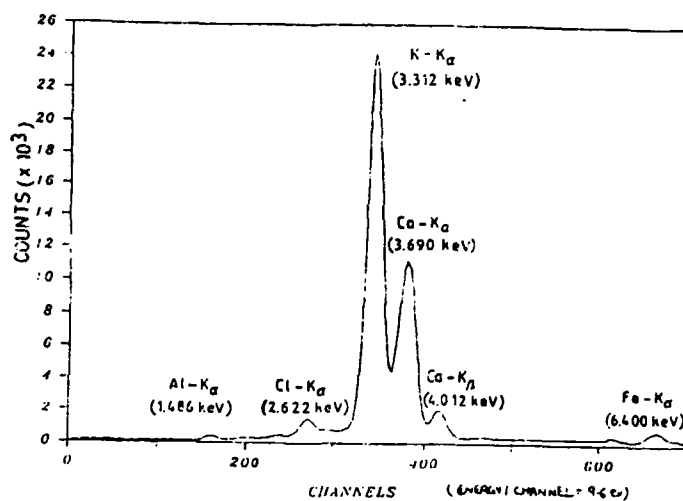


Fig. 5

WATER 1

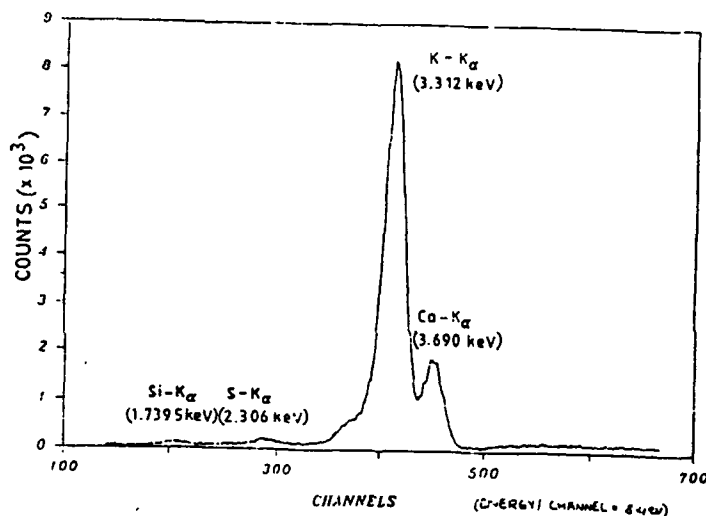


Fig. 6

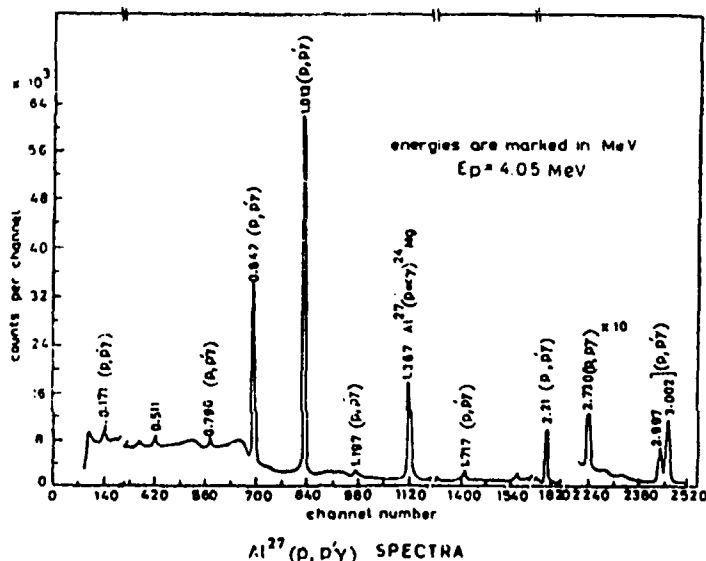


Figure 3 Typical gamma rays spectra due to ²⁷Al (p, p' γ) at E_p = 4.05 MeV.

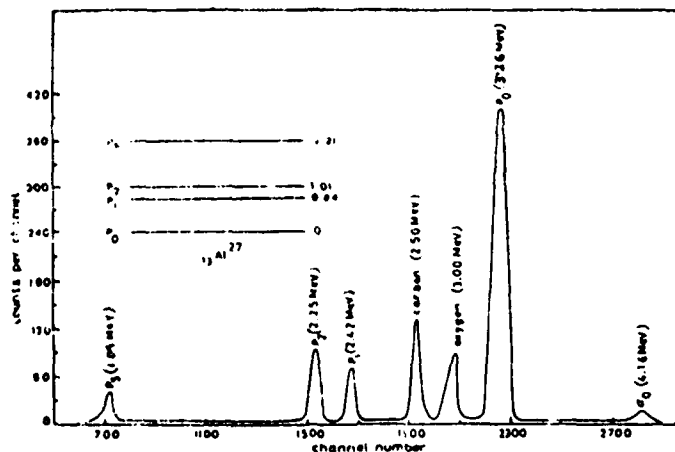


Figure 4 Proton spectrum from ²⁷Al (p, p' γ).

As a first case, this technique was used to study the water pollution of the different places in Patiala District in India[7]. The PIXE spectrum of typical two water samples are shown in Figure 6-7. The Table 1 shows various pollutants and their relative percentage in there two samples. In all the samples, the common pollutants are found to be K, Ca, S with the relative percentage of K as maximum. Element K, Ca, S, Cr, Fe are essential for many deficiency disease is known for each but may not always result from an inadequate diet. Co is physiological active only in the form of vitamin B₁₂. In addition to these Mn, V, Ni, Si have been shown by highly artificial isolator system to be essential for animals. Human deficiency disease is not known for many of these minor trace elements. Therefore, trace element analysis of water samples using PIXE technique is quite useful in the diagnosis of various types of diseases in animals and human beings.

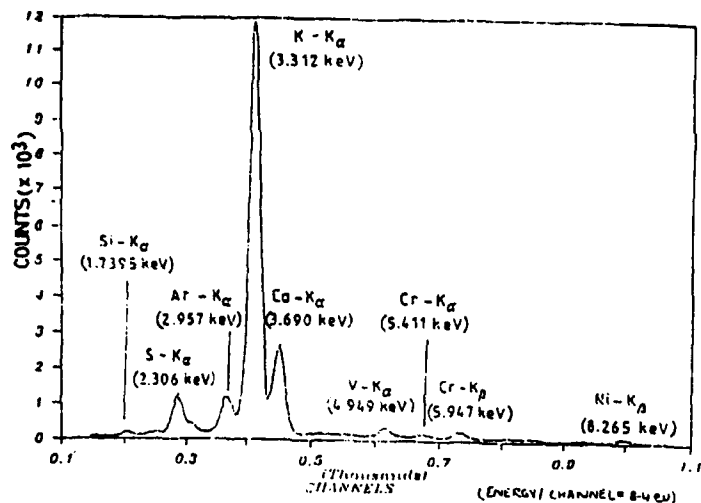


Fig.7

This technique is also being used for the study of Ancient coins, pottery and other artifacts of Archaeological importance with a special emphasis on the identification of forged Indian coins.

RELATIVE PERCENTAGE OF METALLIC POLLUENTS PRESENT IN WATER SAMPLES

Water Sample	Metallic pollutants present	A (mass per unit area of pollutants in $\mu\text{g}/\text{cm}^2 \times 10^6$)	Relative % of pollutants
1. (Kila Chonk)	Si	0.0021	.80
	S	0.0035	1.33
	K	0.2347	89.34
	Ca	0.2224	8.53
2. (Ragho Mazra)	Si	0.0013	0.61
	S	0.0087	4.11
	Ar	0.0103	4.87
	K	0.1455	68.76
	Ca	0.0286	13.52
	V	0.0023	1.09
	Cr	0.0098	4.63
	Ni	0.0051	2.41

1. Chandigarh Variable Energy Cyclotron
I.M.Govil & H.S.Hans, Proc. Ind. Acad. Science (Engg. Sc.):
Vol.3, 237(1990).
2. Structure of Se^{75} .
G.P.Sahota, V.K.Mittal, S.D.Sharma, H.S. Sahota, G.Singh, S.S.Datta and I.M.Govil:
Physical Rev. C44,987(1991).
3. Gamma-Ray spectroscopy in Pd^{103}
K.C.Jain, S.S.Datta, D.K.Avasthi, I.M.Govil and V.K.Mittal:
Physical Rev. C35,534(1987).
4. Study of Low lying levels in Ni^{59}
V.K.Mittal, D.K.Avasthi and I.M.Govil:
J. Phys. G9,91(1983).
5. Coulomb excitation studies in Antimony isotopes.
K.C.Jain, G.Singh, S.S.Datta and I.M.Govil:
Physical Rev. C40,5(1989).
6. Coulomb excitation of Cs^{133} with protons.
K.P.Singh, D.K.Avasthi, I.M.Govil and H.S.Hans:
Can. Jour. Phys. 63,483(1985).
7. Non destructive trace element analysis by PIXE
Rasmi Rawat, M.Phil Thesis (1989).

Proton Linacs for Boron Neutron Capture Therapy

Arlene J. Lennox
Fermi National Accelerator Laboratory* and Rush University
P.O. 500, MS 301, Batavia, Illinois 60510-0500 USA

Abstract

Recent advances in the ability to deliver boron-containing drugs to brain tumors have generated interest in ~4 MeV linacs as sources of epithermal neutrons for radiation therapy. In addition, fast neutron therapy facilities have been studying methods to moderate their beams to take advantage of the high cross section for epithermal neutrons on boron-10. This paper describes the technical issues involved in each approach and presents the motivation for undertaking such studies using the Fermilab linac. The problems which must be solved before therapy can begin are outlined. Status of preparatory work and results of preliminary measurements are presented.

I. INTRODUCTION

Despite the efforts of many researchers, the prognosis for a patient diagnosed with an inoperable advanced brain tumor (glioma) is dismal. The difficulty with using radiation therapy is that the tumor propagates by sending out microscopic clusters of cells close to the main body of the tumor. Even when the gross tumor is killed by radiation these clusters continue to grow. If a large margin is included around the gross tumor it is possible to destroy the clusters, but the process causes unacceptable damage to the healthy tissue in which the clusters are embedded. Hence, it is advantageous to sensitize the tumor cells to radiation without sensitizing the healthy cells. One way to sensitize the tumor is to introduce into the body a compound containing boron-10. Depending on the exact nature of the carrier, boron-10 will be absorbed by various parts of the body, including the tumor. However, healthy brain tissue will not absorb the compound because it is protected by the blood-brain barrier. When the brain is exposed to neutron radiation the large cross section for interactions between thermal neutrons and boron-10 will result in a larger dose to tumor than healthy tissue. This form of radiation therapy is called boron neutron capture therapy (BNCT).

In recent years the Department of Energy has been supporting research in the development of boron pharmaceuticals, and a number of drugs are ready or nearly ready for clinical trials. In addition, several reactors have been modified to provide neutrons for early clinical trials [1] and work is proceeding on a tandem cascade accelerator [2]. However, much remains to be done in developing accelerator sources needed to make BNCT more widely available. Because of the high currents needed to achieve adequate dose rates, proton linacs are well suited for this application.

*Operated by the Universities Research Association, Inc., under contract No. DE-AC02-76CHO3000 with the U. S. Department of Energy.

II. PRODUCTION NEAR THRESHOLD

The present consensus is that the optimum neutron energy for BNCT is in tens of keV. In this energy range neutrons will penetrate the skull and be thermalized by the time they reach the tumor. One approach is to produce neutrons at an energy as close as possible to the keV range in order to minimize the need for moderating material. Recent progress in the technology of radiofrequency quadrupole (RFQ) linacs and the 1.8 MeV production threshold for the ${}^7\text{Li}(p,n){}^7\text{Be}$ reaction have led to the hope that a 2.5 MeV RFQ could accelerate protons which would strike a lithium target to produce the neutrons [3]. Despite a great deal of interest in this approach, the critical problems remain unsolved. Estimates of the average proton current required for acceptable dose rates range from 5 to 30 milliamperes [2],[4]. This uncertainty is largely due to uncertainties in the relative biological effectiveness (RBE) of neutrons in tissue at these energies. Current requirements decrease with increasing RBE, but until at least one prototype is constructed the RBE's cannot be measured. In addition, a moderating system must be incorporated to accommodate the fact that the neutrons produced in this reaction are too energetic. A number of moderating schemes have been proposed but they cannot be evaluated until an accelerator becomes available. Finally, the problem of cooling the lithium target is unlikely to be solved within reasonable economic constraints, and the safety issues related to using lithium in a clinical environment are formidable.

The difficulties associated with a lithium target have led to interest in using a beryllium target. Beryllium has a higher melting point than lithium, is easier to cool, and has been used successfully in clinical fast neutron therapy facilities. The neutron production threshold for protons impinging on a beryllium target is 2.2 MeV and the yield becomes comparable to a lithium target yield at about 4 MeV. Using 4 MeV protons and a beryllium target produces even more energetic neutrons than the system described above. Monte Carlo studies indicate that the spectrum can be moderated to reduce the high energy component [5] but no work is being done on designing a 4 MeV proton source for BNCT. It is believed that a 4 MeV RFQ is impractical and that a drift tube linac (DTL) is required. Use of a DTL with a beryllium target will solve the technical issues associated with the target but the questions relating to specifying an appropriate proton current remain unanswered. The most economical approach is to identify an existing 4 MeV accelerator and use it and a prototype moderating system to measure RBE's and dose rates. Such experiments would provide the data needed to extrapolate to the DTL operating parameters with confidence. This step is critical for the continued evolution of compact neutron sources for BNCT.

III. SPALLATION SOURCES

The targeting schemes described above attempt to produce neutrons at low energies to minimize moderation requirements at the expense of requiring high primary beam currents. An alternate approach is to build a spallation source for which relatively low currents produce large neutron fluxes at high energies requiring a great deal of moderation. Researchers at Paul Scherrer Institute have been using a 72 MeV cyclotron to test target and moderating systems [6]. They have the advantage of access to an existing accelerator and have actually used a number of heavy targets with various moderating schemes to measure neutron spectra and photon contamination. Their 80 microampere beam is believed adequate to produce an acceptable dose rate but a 70 MeV linac operating at about 200 microamperes would be an ideal proton source for this approach. Operating parameters for a multipurpose 70 MeV medical proton linac have been described elsewhere [7].

IV. FAST NEUTRON THERAPY BOOST

The neutron therapy facility (NTF) at Fermilab uses a Be target and 66 MeV protons from a DTL to produce fast neutrons for radiation therapy. NTF conducted clinical trials treating gliomas with fast neutrons from 1979 until 1989. In many cases patients experienced remarkable, but temporary improvement. Autopsies showed that neutrons were successful in killing the tumors and that the patients died from necrosis of nearby healthy tissue [8]. With the existing fast neutron beam it is not possible to establish a therapeutic window for a long-term cure - that is, enough dose to destroy the tumor without causing unacceptable damage to neighboring healthy tissue. However, it is possible that a dose enhancement of as little as 10 or 20% from the introduction of boron into the tumor would open the therapeutic window.

The cross sections for neutron- ^{10}B interactions decrease with increasing energy, so it is not expected that boron would enhance the dose due to the higher energy neutrons. However, preliminary phantom studies at NTF using Fricke dosimetry and gold foils show a peak in the thermal component at 5 to 10 cm in tissue. These studies also show that introduction of one inch of iron into the beam has little effect on the thermal component at shallow depths but reduces it by 20% deeper in tissue [9]. Further studies must be done to measure the absolute thermal flux and to determine whether an iron filter can be used to limit the thermal dose to distal healthy tissue. One possibility for enhancing the thermal component is to introduce 20-30 cm of D_2O into the beam. In evaluating this technique one must consider not only the resulting energy spectrum but the possible loss of collimating ability. Fast neutron therapy relies on collimation to reduce healthy tissue dose. Epithermal and thermal beams scatter throughout the entire brain regardless of upstream collimation. Hence, the goal is to shift the NTF energy spectrum downward to enhance the probability of thermalization in tissue while perturbing the beam's angular distribution as little as possible.

Previous attempts to measure the energy spectrum of this beam have been hampered by the 200 MHz beam

structure. The beam arrives at detectors in one-nanosecond micropulses, five nanoseconds apart for a total of 57 microseconds, and this pattern is repeated 15 times per second. This structure and the ~8 meter neutron flight path have precluded the use of time-of-flight techniques. In addition, the types of detectors normally used with Bonner spheres experience saturation effects with these instantaneous dose rates. To address this issue studies are being conducted on a beam chopper which would allow individual micropulses to be accelerated through the linac at a 15 Hz rate [10]. These studies include not only the design of the chopper but also the installation of diagnostics which are sensitive to the relatively low currents transmitted by the chopper. Once the chopper is working the energy spectrum will be measured and it will be possible to use existing computer codes to design an energy degrader.

In addition to measuring the energy spectrum it is necessary to develop dosimetry techniques to study the relative contribution of fast and thermal neutrons to the total dose as a function of depth in a phantom. This must be done for the existing beam so that it can be compared to a newly designed degraded beam. Techniques will include foil activation studies, Fricke dosimetry, measurements with miniature tissue equivalent detectors and appropriate thermoluminescent detector systems. Finally, biophysical studies with boronated cell culture systems and rodent tumors must be done to check the efficacy of using boron-10 to enhance tumor dose from the NTF beam. Similar biophysical studies at a fast neutron facility in Essen have shown the dose enhancement in animals to be greater than expected from calculations based on conventional dosimetry [11]. Hence, the results of the biophysical studies are very important in establishing a prescribed dose to humans.

V. CONCLUSIONS

Present schemes for accelerator-produced neutron beams for BNCT use trade-offs between lower yield reactions with neutron energies as close as possible to epithermal energies and higher yield reactions with higher energy neutrons. Proton linacs play an important role in both scenarios. However, before linacs can be used for BNCT a great deal of work must be done. In some cases it would be good to use data from existing lower current accelerators to obtain the information needed to design practical systems.

VI. REFERENCES

- [1] Rolf F. Barth, Albert H. Soloway, Ralph G. Fairchild and Robert M. Brugger, "Boron Neutron Capture Therapy for Cancer", *Cancer*, Vol. 70, No. 12, 1992.
- [2] R. E. Shefer, R. E. Klinkowstein, J.C. Yanch and G.L. Brownell, "An Epithermal Neutron Source for BNCT Using a Tandem Cascade Accelerator," in *Progress in Neutron Capture Therapy for Cancer*, B. J. Allen, D.E. Moore and B. V. Harrington, eds., Plenum Press, New York, 1992, pp. 119-122.
- [3] M. A. Lone, A. M. Ross, J. S. Fraser, S. O. Schriber, S. A. Kushneriuk, and W. N. Selander, "Low Energy

$^7\text{Li}(p,n)^7\text{Be}$ Neutron Source (Canutron)," Chalk River Laboratories, Internal Report AECL-7413, April, 1982.

- [4] T. P. Wangler, J. E. Stovall, T. S. Bhatia, C. K. Wang, T. E. Blue, and R. A. Gahbauer, "Conceptual Design of an RFQ Accelerator-Based Neutron Source for Boron Neutron-Capture Therapy," *Proceedings of the 1989 IEEE Particle Accelerator Conference*, IEEE #89CH2669-0, pp. 678-680.
- [5] C-K. Chris Wang and Brian R. Moore, "On the Study of Energy Spectra and Angular Distributions of the Neutrons Emitted from a Beryllium Target Bombarded with 4-MeV Protons for Neutron Capture Therapy," *Proceedings of the Fifth International Symposium on Neutron Capture Therapy*, Columbus, Ohio, 1992.
- [6] J.F. Crawford, H. Reist, H. Conde, K. Elmgren, T. Roennqvist, E. Grusell, B. Nilsson, O. Pettersson, P. Stromberg and B. Larsson, "Neutrons for Capture Therapy Produced by 72 MeV Protons," in *Progress in Neutron Capture Therapy for Cancer*, B. J. Allen, D. E. Moore and B. V. Harrington, eds., Plenum Press, New York, 1992, pp. 129-132.
- [7] Arlene J. Lennox, "Hospital-based proton linear accelerator for particle therapy and radioisotope production," *Nucl. Instr. and Meth. B56/57* (1991) pp. 1197-1200.
- [8] K. R. Saroja, JoAnne Mansell, F. R. Hendrickson, Lionel Cohen, and Arlene Lennox, "Failure of Accelerated Neutron Therapy to Control High Grade Astrocytomas," *Int. J. Radiation Oncology Biol. Phys.* Vol 17 pp. 1295-1297.
- [9] L. Wielopolski, unpublished.
- [10] T. Kroc, private communication.
- [11] Wolfgang Sauerwein, *Proceedings of the Fifth International Symposium on Neutron Capture Therapy*, Columbus, Ohio, 1992.

Modeling and System Specifications for an Integrated 3-D Proton Treatment Delivery System*

John W. Staples and Bernhard A. Ludewigt
Lawrence Berkeley Laboratory
1 Cyclotron Road, Berkeley, California 94720

Abstract

Beam scanning in proton radiotherapy facilities imposes stringent requirements on the accelerator and beam transport system performance. We will report on a study of the interrelationship between the beam quality presented to the scanning system and the quality of the dose delivered to the desired target volume. The constraints on the accelerator will be quantitatively specified so the clinical specifications will be met.

I. INTRODUCTION

The use of proton accelerators for radiotherapy allows full three-dimensional conformal treatment of a tumor volume by sweeping a pencil beam transversely and longitudinally, filling the volume to the desired dose. Scanning the beam transversely by magnetic deflection and longitudinally by changing the accelerator energy allows optimal shaping of the dose distribution in the target volume and minimizing the dose outside. This can be achieved with full electronic computer control without mechanical beam modifying devices such as scattering foils, range shifters or collimators. The longitudinal dose distribution is given by the Bragg curve, which peaks at the distal end, followed by a small tail due to energy straggling. The transverse size of a single pencil beam spreads as the beam proceeds toward the distal Bragg peak, widening the transverse falloff downstream and reducing the dose along the axis for any one beamlet.

The raster scanning method chosen here uses velocity modulation instead of intensity modulation of the beam. This offers the following advantages:

- No modulation of the accelerator intensity is required.
- The good dynamic range provides the high occupation function values required at the edges of the dose volume.
- The non-periodic line scan rate minimizes the effect of periodic ripple modulation of the beam intensity from the accelerator.

Velocity modulated scanning requires that the accelerator beam intensity fluctuations and position, angular and energy modulation be within prescribed limits in order to meet the accuracy requirement of the dose prescription. A simulation was performed, filling a dose volume with beam subject to the above beam errors, and also subject to slew rate limitations of the scanner itself.

*This work was supported in part by the Lawrence Berkeley Laboratory by funds from the Director's Office and by the National Institutes of Health grant #CA56932

II. DEFINING THE PROTON BEAM

The model pencil proton beam includes small-angle scattering, energy straggling and losses due to nuclear interactions. The spread out Bragg peak (SOBP) requires beams of several energies to be overlaid to produce a smooth longitudinal dose profile and to minimize the entrance dose. Scattering spreads the beam, and nuclear interactions attenuate the beam along the path (the dosage effect of nuclear interactions is not taken into account in these simulations). The Bragg peak is broadened by energy straggling, the peak is shifted upstream, direction, and a small distal tail is produced.

To facilitate the simulation calculation, the energy deposition function and rms beam width of pencil beams over the entire energy range are pre-calculated, using the usual scattering and energy straggling formulae[1]. Each beam starts with transverse betatron and energy spread parameters characteristic of the beam emerging from a realistic accelerator and beam transport system: $\pi\epsilon_{x,y} = 4\pi$ cm-mrad, $\beta_{x,y} = 1$ meter, $\alpha_{x,y} = 0$, and negligible energy spread.

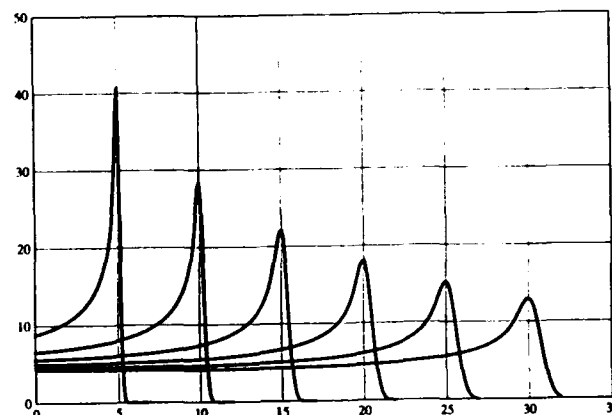


Figure 1. Energy Loss Function

Figure 1 shows the energy loss along the beam axis for ranges from 5 to 30 cm in water. The energy loss is integrated over the x and y planes transverse to the direction of motion, and attenuation due to nuclear interactions is included.

III. OPTIMIZATION PROCEDURE

The dose distribution D is a three-dimensional convolution of a density function F with the beam distribution P : $D(x,y,z) = F \otimes P$. An optimization procedure is needed to determine how the target volume is best filled by pencil beams assuming no restrictions are imposed by the scanning system or the accelerator. The procedure consists of finding the function F which delivers the required dose to the target

volume while maximizing the lateral and distal falloffs. We have used an optimization procedure developed by Brahme[2] and by Lind[3]. The function F is approximated through an iteration process

$$F_0 = D_0$$

$$F_{n+1} = C[F_n + a(D_0 - F_n \otimes P)].$$

Here, D_0 is the desired dose distribution, C is a constraint operator guaranteeing non-negative occupation function amplitude, and a is a convergence speed parameter.

This method of determining the occupation function F has two advantages over other optimization methods:

- F is non-negative,
- D is never smaller than the desired dose D_0 within the treatment volume at the scanned points.
- The dose outside the treatment volume is minimized.

The function F is the irradiation or Bragg peak density defined throughout the volume and describes the amount of beam deposited in the volume with the center of the Bragg peak at a particular location. F can also be viewed as a beam occupation distribution which can be directly used to control a voxel scanning system.

As an illustration, a one-dimensional example is given. A gaussian beam irradiates a line segment to give a uniform dose for $0 \leq x \leq 50$ and no dose for $50 < x \leq 100$. Figure 2 shows the beam half-profile (dashed), the occupation function (solid line), the time spent along the line segment by the beam, the inverse of the scanning velocity, as it sweeps. Note that the occupation function has a peak at the edge and oscillates within the dose area. This occupation function assures that full dose (dot-dash) is given inside the required dose volume, and the width of the fall-off is minimized.

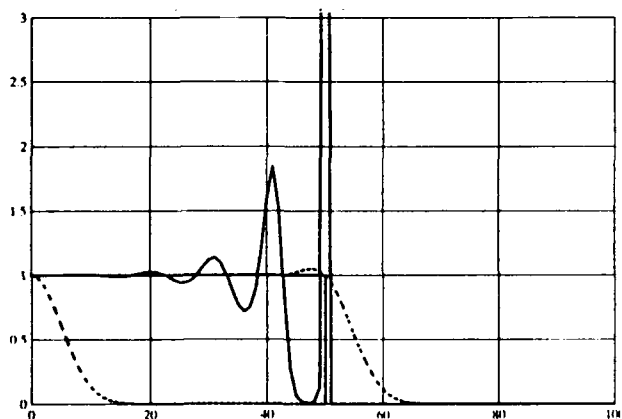


Figure 2. Dose, Occupation Function

We have simulated a raster scanner system in which each layer of target volume is transversely scanned as shown in Figure 3.

The idealized dose distribution without imperfections was first determined for a fixed raster scanning pattern consisting of zig-zag pattern with a 10 mm separation at the

turn-around points. The accelerator and beam transport system energy is changed for each layer. Typically, layers are separated in range by 5 mm and as many as 60 layers may be used.

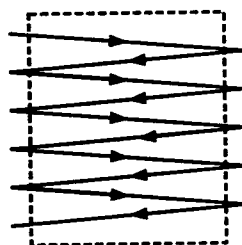


Figure 3.

The sweep velocity is modulated to vary the pixel dose. The raster pattern is conserved by keeping the ratio of the horizontal and vertical sweep velocities constant. This pattern requires the smallest slew rate to cover the dose area. The maximum slew rate requirement of the scanning magnets is specified at 10 times the average, with no lower limit to provide high dose capability to selected pixels, particularly at the edges.

For simulation of the raster scan the density function F is defined along the zig-zag scan lines only and is determined by an iteration procedure as described above. The linear sweep velocity is the inverse of the occupation function F for each voxel on the scan line. The calculations were done on a 1 mm transverse grid with a 5 mm longitudinal spacing. About 20 iterations are necessary for F to converge.

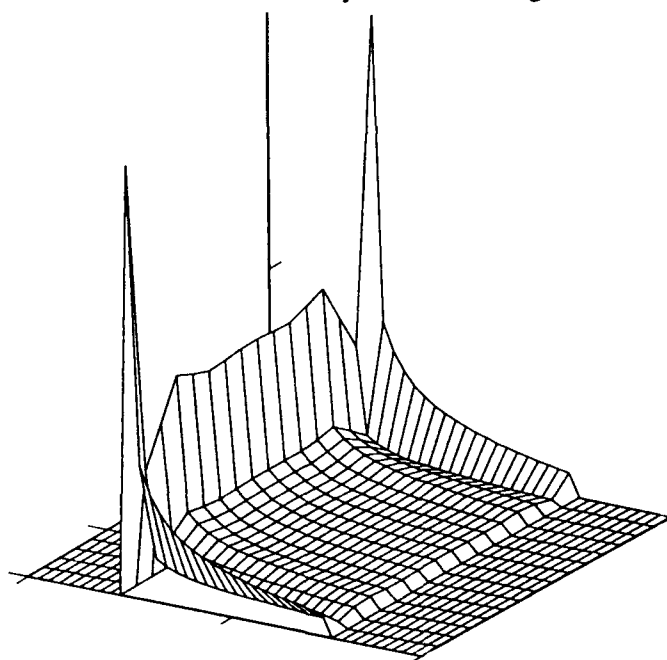


Figure 4. Bragg Peak Density Function F

Figure 4 shows the optimized Bragg peak density function on a plane perpendicular to the scan plane and through the central axis of the radiation field.

IV. SENSITIVITY TO FLUCTUATIONS

The goal of this study is to evaluate the dose distribution subject to imperfections in the scanned beam such as intensity fluctuations and scanning system limitations.

We have simulated the actual dose distribution with limited maximum slew rate of the sweep magnets and with realistic fluctuations in the accelerator beam intensity. The maximum sweep rate capability is specified at 10 times the average sweep rate, which satisfies the requirement of the occupation function calculated in the treatment planning process.

The perturbed dose distribution using F was then calculated by imposing maximum slew rates on the scan velocity and introducing beam intensity fluctuations.

The accelerator beam intensity fluctuation is defined within a moving time window[4]. Ripple, intensity spikes and random variations are averaged within a moving time window. This reflects the integrating effect of a finite beam width as it moves along its path. In our example, a beam with an rms size of 3–8 mm moves over a 1300 mm path in one second. The maximum fluctuations within the window are:

Window	Fluctuation
200 μ sec	$\leq \pm 20\%$
100 μ sec	$\leq \pm 100\%$
<25 μ sec	$< 5 \times 10^6$ in 25 μ sec

For a moving time window shorter than 25 μ second, the number of particles permitted in an intensity spike is limited as shown. Full r.f. modulation of the beam is permitted, as it will occur at a megaHertz rate, and r.f.-on spill simplifies the synchrotron beam spill monitoring function.

Figure 5 shows the dose distribution for a $\pm 20\%$ intensity fluctuation within a 200 μ second traveling window, a scanner slew rate limitation of 10 times the average rate, and with an additional 180 Hz ripple modulating the intensity by 30%. This distribution differs by no more than 3% from a dose distribution with no perturbations and unlimited scanner slew rate.

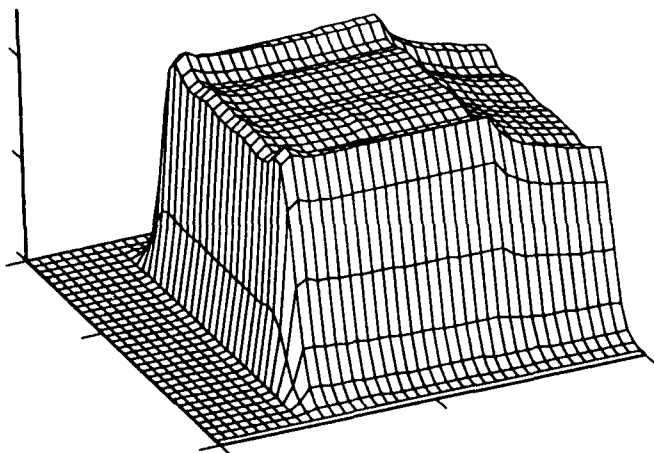


Figure 5. Dose Distribution with Nominal Perturbations

Additional perturbations were applied to the beam and limitations applied to the maximum scanning rate. The table lists the effect on the dose distribution in each of these cases.

The fluctuation σ defines the random intensity variations within a 25 μ second window. When $\sigma = 0.35$, the $\pm 20\%$ variation integrated in a 200 μ second window is achieved.

The error indicated is the maximum deviation at any one point of the achieved dose distribution with the added fluctuations or scanner slew rate limitation from the distribution with no fluctuations.

Simulation Parameter	Error
Max sweep velocity = $2 \times$ average	2%
Max Sweep velocity = $1.2 \times$ average	40%
Fluctuation $\sigma = 0.35$ and 30% 180 Hz ripple	3%
Fluctuation $\sigma = 1.05$ and no a.c. ripple	4%
Fluctuation $\sigma = 0.35$ and 100% 180 Hz ripple	7%
Fluctuation $\sigma = 0.35$ and 30% 60 Hz ripple	7%
Fluctuation $\sigma = 0.35$ and 100% 60 Hz ripple	19%

V. CONCLUSIONS

This simulation study shows that a 3-D dose distribution can be delivered by a velocity modulated raster scanning system without the use of an intensity modulator or collimator. Velocity modulation serves well for distributing a pencil beam as required by the occupation function which peaks at the outside edges. A maximum sweep velocity of several times the average seems to be sufficient. Depending on the beam diameter, target volume size and sweep velocity, effects of beam intensity fluctuations and ripple are washed out to a large degree due to the large overlap of beam between different scan lines and layers and the non-periodic line scan rate.

Acknowledgements

The authors would like to thanks Bill Chu, Tim Renner and Jose Alonso for helpful discussions.

VI. REFERENCES

- [1]. For example, Section 16.07D in *A Physicist's Desk Reference*, AIP (1989)
- [2]. A. Brahme, P. Källman and B. K. Lind, *Optimization of Proton and Heavy Ion Therapy Using an Adaptive Inversion Algorithm*, *Radiotherapy and Oncology*, 15: 189-197 (1990)
- [3]. B. K. Lind, *Properties of an Algorithm for Solving the Inverse Problem in Radiation Therapy*, *Inverse Problem* 6: 415-426 (1990)
- [4]. W. T. Chu, J. W. Staples, B. A. Ludewigt, T. R. Renner, R. P. Singh, M. A. Nyman, J. M. Collier, I. K. Daftari, H. Kubo, P. L. Petti, L. J. Verhey, J. R. Castro and J. R. Alonso, *Performance Specifications for Proton Medical Facility*, LBL Report LBL-33749, March 1993

Shielding and Activation Study for Proton Medical Accelerators

H. B. Knowles*, J. L. Orthel, and B. W. Hill

G. H. Gillespie, Associates, Inc.**, P. O. Box 2961, Del Mar, CA 92014

Abstract

A preliminary study has reviewed much of the pertinent data on the required radiation shielding and radioactivation processes associated with the operation of a 70-250 MeV proton accelerator to be used for cancer therapy. As a result, a "tool kit" has been prepared for designing appropriate shielding and evaluating radiation hazards from activation around such accelerators. It includes general principles, a simple desktop computer program for preliminary facility design and the use of the LCS Monte Carlo program. The anticipated integration of the ORIHET program with LCS will provide detailed activation information.

I. INTRODUCTION

One new accelerator for proton radiation therapy is already operational at the Loma Linda University Medical Center, and two more are in the late planning stage. These are expected to have similar proton beams: average currents up to 20 nA and energies from 70 to 250 MeV. The LLUMC facility can be used as a paradigm for studying radiation protection, even though other facilities may include different types of accelerators and facility designs.

The technical concerns include: a) Projected changes in limits on radiation exposure for both occupational personnel and the general public, together with the possible impact of proposed new quality factors for neutrons. b) Identification of source terms for fast neutrons (and gamma rays) with respect to location, intensity, directionality, and energy spectrum. Accelerator physics input and experience are needed. c) Verification of the attenuation properties of shielding materials for the radiation of concern, principally neutrons, by experimental and theoretical methods. d.) Determination of the reduction of dose equivalent by ducts and mazes needed in a radiation therapy facility. e) Evaluation of the radioactivation hazard especially that which occurs in the treatment rooms and can affect clinical personnel.

II. RADIATION EXPOSURE

The existing annual limits on dose equivalent in California (this study was commissioned for a California site) are:

- 5.0 rem (50 mSv) for occupational radiation workers
- 0.5 rem (5 mSv) for the general public

The limit for the general public will soon be reduced to 0.1 rem, without changing the radiation worker limit. However, it is believed that the latter will also soon be reduced to 2 rem, under the urging of the ICRP and NCRP. The ICRP has also issued a recommendation for a change (generally, an increase) in the neutron quality factor[1]. Because so many conversion data were available using only the present values, these have been retained in this study, but an estimate of the effect of instituting the new values has been made.

*H. B. Knowles, Physics Consulting, consultant to G. H. Gillespie, Associates, Inc.

**This work was supported in part by the Lawrence Berkeley Laboratory through the National Institutes of Health grant #CA56932.

III. NEUTRON SOURCES

The highest energy protons will cause the greatest hazard. Two recent experimental studies near 250 MeV have been used to test computer simulations. Siebers' work was done at 230 MeV and measured both energy deposition (absorbed dose) and quality factor, by simultaneously performing microdosimetry[2]. Meier obtained the raw neutron spectrum from targets struck by both 113 MeV and 256 MeV protons[3,4]. These data were compared to predictions made by LCS[5]. A best fit was found (for all data) by using the combination of cascade mechanism, multistage preequilibrium model and nuclear evaporation called "LAHETprq2". This appears to predict neutron fluxes accurately (within a factor of two) and may provide still better values of dose equivalent, when used together with fluence-to-dose-equivalent tables of Belogorlov[6]. Pearlstein has devised an analytic expression for the quantity $d^2\sigma/dE d\Omega$ that can be used to estimate a neutron yield and spectrum in an arbitrary direction[7]. The spectra so obtained are "harder" than those from a thick target, and thus lead to overestimating shielding requirements.

IV. ATTENUATION IN SHIELDING

Siebers' experiment included neutron attenuation in concrete, and used the LCS code (with the prq2 switch) to calculate attenuation, so that it could be compared to measured values. A "zero-depth source term", called H_0R^2 , can also be calculated and compared to experiment by the equation:

$$HR^2 = H_0R^2 \exp\left(-\frac{s}{\lambda}\right) \quad (1)$$

in which λ is the attenuation length in the shield material (here, concrete), s , the thickness of the shield, H or H_0 the dose equivalent per stopping proton and R the distance from the neutron source to the observation. We have redone the calculations of Siebers, and find no results that differ significantly from his. These are presented in Table 1, where they are compared to Siebers' experimental values in comparable directions. The attenuation of dose equivalent, H , is emphasized because this is the single parameter of concern.

Both the zero depth source term and the attenuation length increase with angle to the beam, θ . The calculations slightly overestimate both parameters and therefore give conservative values. We have also compared the Siebers values (at the $\theta = 0^\circ$ and 90° directions) to those calculated from the work of Braid, *et al.*[8]. They are in good agreement in the "forward" direction, but, in the "lateral" direction, both the zero-depth source term and the attenuation length are significantly larger than the calculated values obtained by both Siebers and ourselves. The comparison of λ requires that the distance be given in areal density (kg/m^2) because of the unusually low density of the concrete used in the Siebers experiment ($1.88 \text{ g}/\text{cm}^3$). The calculated dose-equivalent attenuation lengths in Table 1, which we recommend, are in very reasonable agreement with the well-established neutron attenuation lengths in concrete[9]. It is well established that other shielding materials (earth, iron, high-density concrete) can replace concrete if substituted on the basis of areal density, except that a sufficient thickness of hydrogenous

Table 1. Zero-Depth Source Intensities and Attenuation Lengths from Siebers 230 MeV Data

θ	Experimental		θ	LCS Calculated	
	$H_0 R^2$ (Sv·m ²)	λ_{eff} (kg/m ²)		$H_0 R^2$ (Sv·m ²)	λ_{eff} (kg/m ²)
0°	$(8.6 \pm 0.8) \times 10^{-15}$	910 ± 30	0-10°	$(6.6 \pm 0.4) \times 10^{-15}$	991 ± 28
22°	$(4.6 \pm 0.5) \times 10^{-15}$	876 ± 34	10-30°	$(5.0 \pm 0.2) \times 10^{-15}$	1040 ± 21
45°	$(2.1 \pm 0.2) \times 10^{-15}$	746 ± 24	40-50°	$(2.3 \pm 0.1) \times 10^{-15}$	894 ± 21
90°	$(6.9 \pm 0.8) \times 10^{-16}$	519 ± 21	85-95°	$(1.0 \pm 0.2) \times 10^{-15}$	534 ± 26

material must be on the personnel side of the shield.

V. ATTENUATION IN MAZES AND DUCTS

While plug doors are commonly used in physics-oriented accelerator facilities, they are undesirable in a therapy facility because of possible adverse reactions of patients. It is also noted that the treatment room at the end of a maze (which must be large enough to pass a hospital gurney) is a copious source of radiation: the patient is in reality a beam dump and other losses occur in the beam transport system. Numerous investigations of radiation transport through mazes have done using various Monte Carlo codes. Experiments have also been performed, often using simple fission neutron sources [10,11,12,13]. This is a fairly satisfactory substitute for the neutron fluxes induced by a high-energy proton beam, because most of the dose equivalent transmitted through maze is carried by low-energy neutrons. Thermal neutrons are generated by collisions with the walls and tend to build up as the maze is traversed. All investigators found this effect. In addition, Vogt examined the effect of varying the water content of the concrete walls, and found it to be significant[11].

We explored dose-equivalent attenuation in a three-legged maze (Fig. 1.) using LCS. The neutron "source", a beam stop intercepting 250 MeV protons, was centered on the

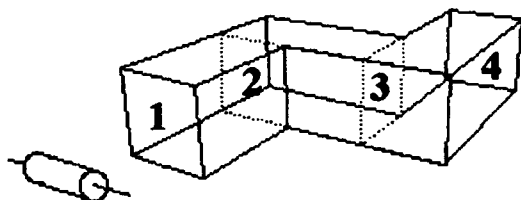


Fig. 1. Maze problem geometry. Protons impinge on a cylindrical target in the foreground, producing radiation. The dose equivalent is tabulated for each of the four windows.

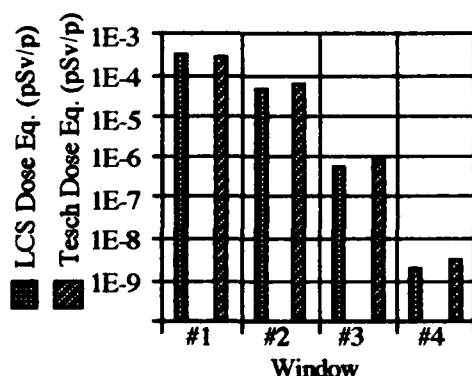


Fig. 2. Predictions for neutron dose equivalent in sample maze problem.

first leg, and also offset from the centerline. At each of four successive Windows, the neutron fluence per stopped proton and the dose equivalent per proton was determined. The analytic expressions for attenuation developed by Tesch were also used[13]. These are as follows: in the first, centered leg, the attenuation is simply given by an inverse-square dependence along the maze centerline, with a factor of 2 for dose equivalent buildup in the walls:

$$H(r_1) = \frac{2H_0 R^2}{r_1^2} \quad (2)$$

while in the second leg, there is an attenuation factor which must be used to multiply the dose equivalent value obtained from Eq. (2) at the end of the first leg. If r_2 is the centerline distance along the second leg, this attenuation factor is $f(r_2)$:

$$f(r_2) = \frac{\exp(-(r_2 / 0.45) + B \exp(-(r_2 / 2.35))}{1 + B} \quad (3)$$

where the quantity B is related to the cross-sectional area of the maze A by

$$B = 0.022 A^{1.3} \quad (4)$$

Subsequent legs are measured in distances r_3, r_4 , etc., along the maze centerline and the attenuation has the same form as given in Eq. (3) for the second leg. Tesch also determined, empirically, that the second-leg attenuation must be multiplied by a factor of two for a high-energy (accelerator beam stop) source. These recipes were compared to the LCS calculations for the maze geometry of Fig. 1, and the comparisons appear in Fig. 2. There is agreement within a factor of 2. The more realistic case of the off-centerline source was also examined and will be discussed below.

Ducts, defined here as shield penetrations with an average diameter of 30 cm or less, are needed for power, cooling, and other utilities. The principal vector of dose equivalent is, again, low-energy neutrons, and their transport behavior in ducts has been understood for at least 40 years by the nuclear power industry[14].

VI. ACTIVATION

Radionuclides are principally produced by high energy protons and by low-energy neutrons, especially those that thermalize and capture. The model of the cascade-evaporation process in LAHET predicts some residual radionuclides, although its accuracy has been questioned. A plot of the radionuclide distribution produced per proton by 230 MeV protons on concrete appears in Fig. 3. An improved prediction would result when LCS is linked with ORIHET[15]. The equivalent CINDER90 code has already been integrated with LCS but has not been released.

There is special concern about the clinical personnel who must tend the patients after treatment. Typically, a brief 1-2 min. irradiation is followed by a 15-20 min. interpatient time. It can be shown that the clinical staff are likely to receive more dose equivalent from radionuclides with half lives of the order of the interpatient time than from shorter- or longer-lived activities, provided that the latter have not been allowed to build up over a long time. Components with such long decay times would of course be routinely replaced, but nature has been unkind in the matter of radionuclides created in the body itself: there is a high production of the radionuclide

^{11}C , which decays by positron emission with a 20.4 minute half-life.

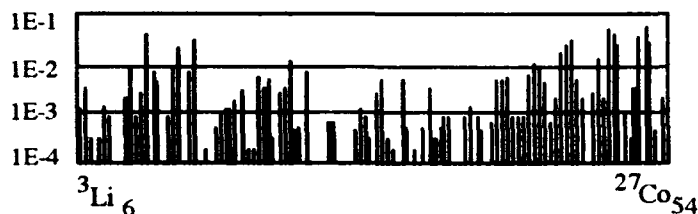


Fig. 3. Number of isotopes produced in concrete per incident proton (vertical axis) versus isotope, from the LAHET code. The incident proton energy is 230 MeV, and all cascade particles down to 20 MeV contribute to production.

Sullivan[16] observes that the statistical distribution of half-lives from proton bombardment of iron or copper varies as $1/(\text{half-life})$. An average of the number and energies of the gamma-rays produced is then used to estimate the effects. When the total dose equivalent to clinical personnel during one interpatient period was determined, assuming an iron or copper component of the beam "nozzle" and a loss of 10 nA of protons in 20g/cm^2 of material, it was found that, at a distance of 1 meter, the dose equivalent would be 0.57 mrem. A more detailed, conventional calculation for equivalent loss in aluminum gave a result of about one-quarter of this value of dose equivalent, supporting the well-known fact that aluminum is a better material than iron or copper in terms of activation.

VII. THE PTFshield PROGRAM

PTFshield is a simple program that operates on a desktop computer. It is intended for first-order scoping of shielding and maze design, to be supplemented if necessary by LCS computations. It includes: 1) the Pearlstein model for neutron source terms as functions of beam energy and angle, or, the thick-target Meier data (interpolated or scaled); 2) the empirical attenuations found by Braid, *et al.*; 3) the neutron-fluence-to-dose tables of Belogorlov, *et al.*; 4) the Tesch maze attenuation relations, Eqs. (2) and (3), are used to estimate both centered and non-centered sources.

VIII. SUMMARY AND CONCLUSIONS

Much that is published about shielding and activation in the energy domain below 250 MeV is self-consistent, and a great deal of this information can be represented by a limited number of analytic expressions, or at least, simple calculations. However, the LCS code system is a very powerful and reliable computational tool for more detailed exploration of the problems associated with shielding of such an accelerator. When ORIHET (or CINDER) are included, the expanded code system will also determine activation from high energy particles.

REFERENCES

- [1] "1990 Recommendations of the ICRP", ICRU Publication 60.
- [2] J. V. Siebers, "Shielding Measurements for a 230 MeV Proton Beam", Ph. D. Thesis, University of Wisconsin, Madison, 1990.
- [3] M. M. Meier *et al* "Differential Neutron Production Cross Sections and Neutron Yields from Stopping-

Length Targets for 113-MeV Protons", Nucl. Science and Engin. **102**, 332 (1990).

- [4] M. M. Meier *et al*, "Neutron Yields from Stopping-Length Targets for 256-MeV Protons", Nucl. Science and Engin. **110**, 299, (1992).
- [5] R. E. Prael, "Model Cross Section Calculations using LAHET", Los Alamos Publication LA-UR-3404, Oct. 1992.
- [6] E. A. Belogorlov and V. T. Golavachik, Nucl. Instr. Meth. **199**, 563, (1982).
- [7] S. Pearlstein, "Systematics of Neutron Emission Spectra from High-Energy Proton Bombardment," Nucl. Science and Engin. **95**, 116 (1987).
- [8] T. H. Braid *et al*, "Calculations of Shielding for Large Cyclotrons," IEEE Trans. Nucl. Sci. **NS-18**, 821 (1971).
- [9] R. H. Thomas and G.R. Stevenson, *Radiological Safety Aspects of the Operation of Proton Accelerators*, IAEA Technical Report Series No.283, Vienna, 1988, p.283, Fig. A4.2.
- [10] P. J. Gollon and M. Awshalom, "Design of Penetrations in Hadron Shields", IEEE Trans. Nucl. Sci. **NS-18**, 741, (1971).
- [11] K. Goebel *et al*, "Evaluating Dose Rates due to Neutron Leakage through the Access Tunnels of the SPS", LAB II-RA/Note/75-10, CERN, Geneva, June 25, 1975.
- [12] H. Vogt, "Monte Carlo Calculations of the Neutron Transmission through the Access ways of the CERN Super Proton Collider", CERN 75-14, Laboratory Radiation Group, Geneva, November 6, 1975.
- [13] K. Tesch, "The Attenuation of the Neutron Dose Equivalent in a Labyrinth through an Accelerator Shield", Particle Accelerators **12**, 169 (1982).
- [14] *Reactor Shielding Design Manual*, Ed., T. Rockwell, III, McGraw-Hill, New York, NY (1956), pp.261-287.
- [15] A. G. Groff, "A User's Manual for the ORIGEN2 Computer Code", ORNL/TM-7175, July 1980.
- [16] A. H. Sullivan, *A Guide to Radiation and Radioactivity Levels near High-Energy Particle Accelerators*, Nuclear Technology Publishers, Ashford, UK (1992), pp.103 ff.

Beam Dynamics Studies for Proposed Proton Therapy Facility

D. Raparia and W. Funk
Superconducting Super Collider Laboratory*
2550 Beckleymeade Ave., Dallas, Texas 75237

Abstract

A proton therapy facility is proposed at the Superconducting Super Collider (SSC). The facility will use proton beam from SSC Linac. The SSC Linac can provide the discrete intermediate energies of 70, 110, 157, 210, 268, and 329 MeV by drifting the beam in the high-energy end of the Linac, which is not exited with rf power. 250 MeV is expected to be the maximum energy needed for therapy. This paper summarizes beam dynamics studies for different energies.

I. INTRODUCTION

The linear accelerator (LINAC) [1] is the first injector in the chain of four injectors for the Superconducting Super Collider (SSC). The SSC Linac will provide up to 600 MeV beams. The main beam parameters out of the SSC Linac are listed in Table 1. The availability of H^- beams of suitable energy and current at the end of Linac offers an attractive opportunity for a medical facility for proton therapy. At the request of Southwestern Medical Center, Particle Accelerator Corporation (PAC) in collaboration with Lawrence Berkeley Laboratory (LBL) and Aguirre Association Inc. has done tradeoff studies of several options, all of which would parasitically use the H^- beams accelerated by the SSC Linac [2], [3]. They have recommended to treat patients with the Linac beam directly after passing through a series of devices to reduce its intensity appropriately. This approach provides a treatment time of less than two minutes and a dose controllability of a factor of ten below the desired dose uniformity. The dose control requires a system time response of only 0.1 second, which is easily achievable.

II. BEAM FORMATION AND TRANSPORT SYSTEMS

As shown in Table 1, the Linac operates in the so called 'collider fill' mode and 'test beam' mode. The most demanding mode from injector point of view is 'test beam' mode. The scenario for 'test beam' mode to use the Linac beam for medical use is as follows. The LEB cycle time is 0.1 seconds and each LEB 'batch' is injected into the Medium Energy Booster (MEB). The MEB takes

*Operated by the Universities Research Association, Inc. for the U.S. Department of Energy, under contract No. DE-AC02-89ER40486

Collider Fill Mode	
Current	21 mA
Pulse length	9.6 μ sec
Proton per Macropulse	1.26×10^{12}
Trans. Emittance (n,rms)	$\leq 0.3 \pi$ mm mrad
Rep. Rate	10 Hz
Test Beam Mode	
Current	21 mA
Pulse length	48 μ sec
Proton per Macropulse	6.30×10^{12}
Trans. Emittance (n,rms)	$\leq 0.3 \pi$ mm mrad
Rep. Rate	10 Hz

Table 1: The SSC Linac Beam Parameters

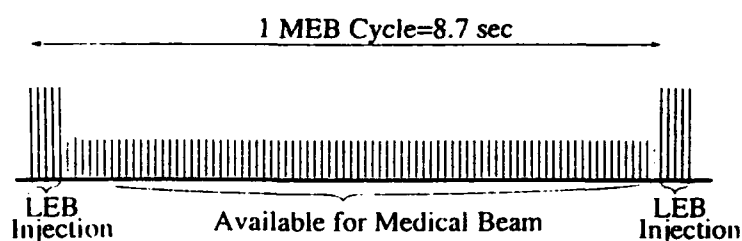


Figure 1: Linac Pulse Structure

six batches from the LEB and accelerates the total injected beam to full energy (199100 MeV) in a period of 8.7 seconds. During this MEB acceleration process, the Linac and LEB are in a standby mode and available for medical use. If the MEB accelerated beam is used to inject into the High Energy Booster (HEB), which has a cycle time of 516 seconds, the availability of the linac beam for the medical application is grater. Thus in the test beam mode, the Linac as available for 8.2 seconds out of every 8.7 seconds, give or take a possible pulse on each end of the 8.2 sec that might be used in ramping quadrupole magnets for their medical values. The therapy beam can be interleaved with LEB injection pulses. The pulse availability in time is shown schematically in fig 1.

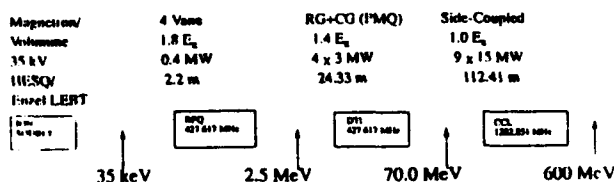


Figure 2: SSC Linac Block Diagram

A schematic layout for the SSC Linac is shown in figure 2. The Drift Tube Linac (DTL) will accelerate the beam up to 70 MeV. The Coupled (side) Cavity Linac will take this beam and accelerate up to 600 MeV. The CCL has 9 modules powered by 9 Klystrons. By delaying the rf power into the CCL modules, the energies available for medical use are shown in Table 2. CCLDYN [4] simulations have shown that it is possible to drift a lower energy beam through higher-energy modules in the CCL, which are not excited with rf power during the passage of the beam. The beam cavity interaction for an unexcited module is not important because beam has a time structure of 428 MHz and the CCL cavity resonance frequency is 1283, the third harmonic of the beam. Moreover the field in the cavity which is excited by the beam will have the a random phase with respect to the beam, therefore on the average the beam will not be affected when it passes through the RF unexcited cavities. However, it is necessary to lower the excitation of quadrupoles for the lower energy beam if the beam is to remain well-enough focused to pass through the small beam apertures of the modules without loss. The quadrupole gradients for the discrete intermediate energies are shown in Table 2. Figure 3 shows the 70 MeV beam profiles for energy spread, phase spread and beam size, through the CCL. The quadrupole gradient required is down to 10.0 T/m whereas for normal operation quadrupole strength is 31 T/m. Figure 4 shows energy spread, phase spread and beam size for 250 MeV through the CCL. The quadrupole gradient needed for this is 31 T/m for modules 1 through 4 and 20 T/m for modules 5 through 9.

The quadrupole magnets are made of laminated steel so that they can be rapidly pulsed (0.1 sec) to lower values to accommodate lower-energy beams. The maximum energy needed for therapy is 250 MeV.

The beam for therapy will be diverted to the proton therapy facility in the Linac-LEB transfer line between the Q1, Q2 doublet and the Q3, Q4 doublet with help of a three magnet bump. The schematic layout of these magnets is

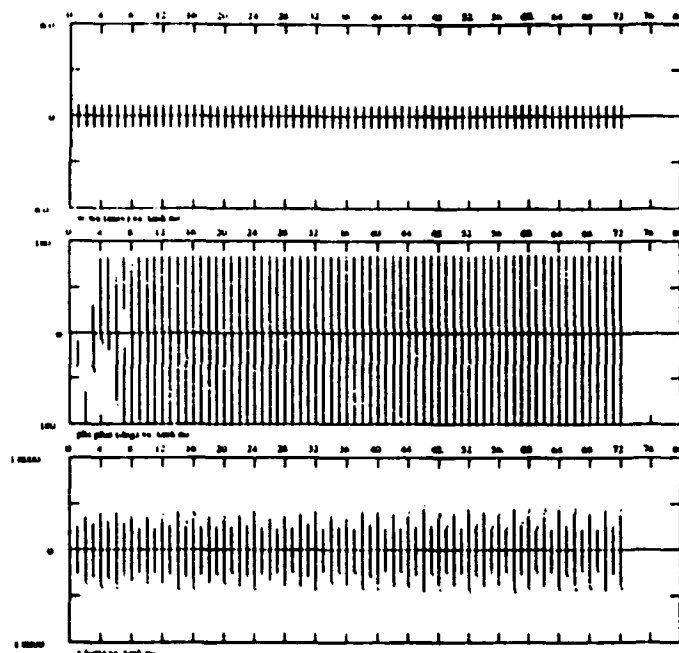


Figure 3: 70 MeV Beam size, phase and energy profiles as beam traverses the CCL

Table 2: Available beam energy for proton therapy.

Energy MeV	RF Excited		RF Unexcited	
	Module No	G (T/m)	Module No	G (T/m)
70	-	-	1-9	10.0
110	1	31.0	2-9	12.0
157	1-2	31.0	3-9	14.4
210	1-3	31.0	4-9	16.8
267	1-4	31.0	5-9	19.2

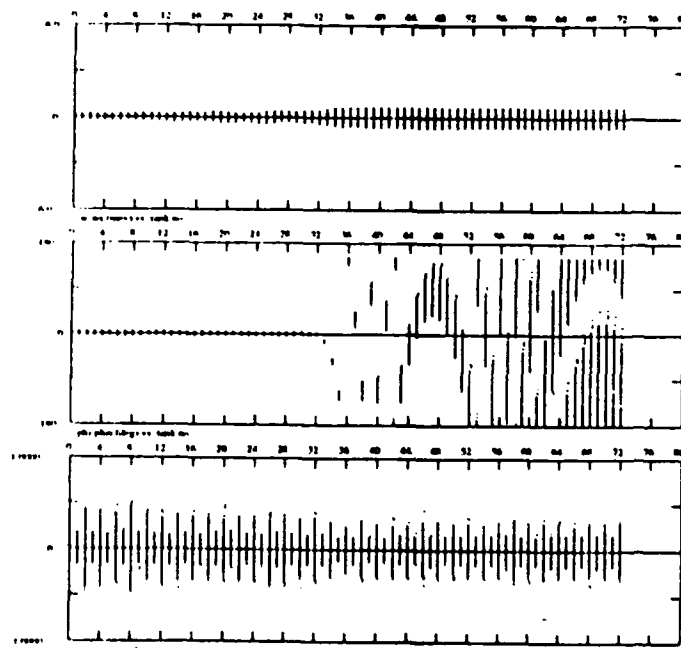


Figure 4: 250 MeV Beam size, phase and energy profiles as beam traverses the CCL

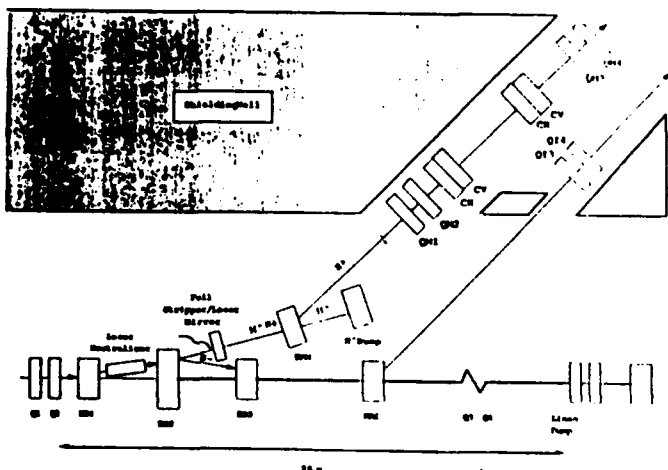


Figure 5: Schematic Layout of Bump Magnets

shown in figure 4.

The bump magnet BD1 bends the H^- beam 5.59 deg away from the Linac axis to provide enough transverse space for the second bump magnet BD2 and longitudinal space for a device to neutralize a small portion of beam. A cw laser LS installed as shown before the second bump magnet is sufficient to neutralize a small fraction of the H^- beam. It is also fail-safe. The second bump magnet bends the H^- beam back toward the Linac axis (thus BD2 has twice the bend angle of other bump magnet) while the H^0 beam passes through the magnet undeflected. Third bump magnet BD3 bends the H^- back onto the Linac axis. A stripping foil is placed in the H^0 beam beyond the second bump magnet to provide an H^+ beam.

III. CONCLUSIONS

The SSC linac can provide the required energy and more than adequate intensity for the proton therapy. The only change which has been made in the Linac design to accomodate the proton therapy beam is the laminated quadrupole magnet.

We would like to thank to Jun Wu for his help in making the figures, and Frank Guy for reading the manuscript.

IV. REFERENCES

- [1] L. W. Funk, "The SSC Linear Accelerator," these proceedings.
- [2] "Proton Therapy at the SSC," Conceptual Design Summary, April 1992
- [3] B. A. Prichard, "A Proposed Proton Therapy Facility at the SSC," to be published in the Twelfth International Conference on the Application of Accelerators in Research & Industry, Nov 2-5, 1992.
- [4] K. R. Crandall, Private Communication.

COMPACT PROTON THERAPY UNIT PREDESIGN

Dominique Tronc

General Electric Medical Systems - Europe
Rue de la Minière, BP 34, 78 533 Buc Cedex, France

Abstract

Conceptual guidelines lead to treatment unit descriptions based on (i) 3 GHz traveling wave acceleration in 4 sections of 10.5 m total length fed by 2 klystrons, (ii) treatment cell which moves with a 270° dipole for large SAD, low weight, single optical component. RF structure for test is reviewed.

I. INTRODUCTION

Radiotherapy uses beams of electrons cheaply produced by RF linac at 3 GHz. One would like to take advantage of the existing industrial basis to accelerate protons of low & variable velocity & high rigidity. Following earlier proposals based on proven solutions [1-3] we propose innovations as simpler accelerating RF geometries [4-5], improved focusing [6], an original combination between head optics & treatment bed & access [7]. A very compact therapy unit predesign which delivers an high quality beam emerges. It is able to spread proton uses within hospitals.

II CONCEPTUAL GUIDELINES

1. High frequency of 3 GHz increases simultaneously the shunt impedance and the maximum permissible field gradient.
2. Acceleration in traveling wave removes the coupling cells: simultaneous acceleration & focusing becomes feasible.
3. Use of forward or backward waves magnetically coupled in a new way increases the acceleration efficiency. Figure 1 shows the half cross-sections for two adjacent cells in two cases. Reference [4] quantify the gain.
4. Minimal length is fixed by maximum allowable field gradient (3 GHz RF high peak power is available). It minimizes size/ cost and alleviate the synchronism problem.
5. RF auto-focusing by alternate dephasing of the bunch to the RF wave is obtained in the simplest manner: using groups of cells of same length. However the effect remains modest and must be complemented by quadrupolar magnetic FODO or innovative helical focusing [6].
6. Optical transport components between the linac and the treatment head vanishes. Switching from one treatment room to the other does not requires a dedicated magnet when they follow each other along the beam axis.
7. Enge 270° dipole at room temperature has excellent optics. It allows a very large Source to patient Axis Distance (SAD): focus in two planes and in energy occur at $2.74 \times$ curvature radius from the dipole exit.
8. Bending can precede the transformation from the narrow beam to distributed one. This reduces dipole weight and structural cost.
9. Energy stabilisation is achieved by beam analysis within the required narrow bandwidth ($\pm 0.3\%$). Neutrons are controlled as beam loss occurs opposite to the patient.
10. Patient moves symmetrically to the magnet inside a treatment cell which is a part of the rotating head. This non-isocentric choice (as made at PSI, Villigen, Switzerland) allows reproducible error at the level of the rollers rotation mechanism, the linac-head colinear adjustment being electronically controlled.
11. The treatment cell is a chamber large enough (2.5 m dia.) to allows bed rotations and human assistance at set-up location.
12. The rotating part has low weight (<10 tons) and its mechanical structure can be best designed as hollow rolled metal box.
13. The patient crosses the wall protection, takes an elevator, installs in a treatment chamber: he sees, without trauma, a "segmented corridor" of rather constant cross-section.

14. The neutron protection uses diaphragms plus nearby absorbers at phase selection at the end of the first linac sub-section, at radial selection at the end of the linac, at energy analysis. Patient protection from thermal neutrons is helped by chamber walls made of hydrogenous material.

II TREATMENT UNIT DESCRIPTIONS

Two designs are based on available subcomponents or [foreseeable ones]. Figure 2 shows the instrument block diagram:

1/ Beam line:

1.1/ 50kV source + 4 MeV RFQ, 3.5 m length [150kV proton source + preaccelerator made of 3 gaps DTL inside each TW cell at 3 GHz, 1 m]

1.2/ 4 TW waveguides, 10.5 m length. Each waveguide is fed by one klystron arm, the first waveguide is made of two segments in serie. The expected shunt impedance is [4]: $Z_{TT} \approx 200 \beta \approx 100 \text{ M}\Omega/\text{m}$ avrg. or $70 \text{ M}\Omega/\text{m}$ including dynamics, load loss etc.

1.3/ Doublets, adjustment dipoles, current monitors. [low energies: supercon. solenoidal focusing or sub-sections bridging + quads]

2/ RF sources:

2.1/ 0.5 or 0.75 GHz

2.2/ Twin modulator 100 Hz 4.5 μs [Single modulator 3 μs]

2.3/ 2 klystrons TH 2132 42 MW 20kW

[1 klystron 85 MW 30kW]

Energy gain is given by:

$$V = (PZL)^{0.5} = (80 \times 70 \times 10.5)^{0.5} = 242 \text{ MeV.}$$

With T transit factor, d nose to nose distance $\approx 2\pi/3$, l cell length = $5\pi/4$ in the direct coupling $3\pi/4$ case, see [4] & fig.1, E_s peak field on surface, E_z on-axis field, V full energy, L total length:

$$E_s = \frac{1}{T} \times \frac{1}{d} \times \frac{E_s}{E_z} \times \frac{V}{L} = \frac{1}{0.8} \times \frac{5\pi/4}{2\pi/3} \times 2.5 \times \frac{242}{10.5}$$

$$E_s = 135 \text{ M V/m}$$

2.4/ waveguides + phasors Φ 20 MW 180°

3/ Therapy fixed head:

3.1/ 270° Enge dipole, curvature radius 1.3 m B_r max 1.8T, hollow ring of reduced cross-section 0.15 m side, weight 2 tons

3.2/ 50 kW DC source stab. 5 10-4

3.3/ Hall Bz measurement and current monitor

3.4/ Beam medicalisation components easily located in a truncated cone of 3.5 m height

3.5/ Beam optical + radiological simulations

4/ Therapy mobile head:

4.1/ Components of 3/

4.2/ Rotating hollow structure to insure dipole to bed center of rotations rigidity. 3.5 m radius for large treatment room of dia. 2.5 m. Limit of 3.0 m minimum (due to dipole).

5/ Controls & commands:

5.1/ The linac is energy controlled with help of Bz measurement and current monitor (the dipole selects a $\pm 0.3\%$ energy window inside the accelerated spectrum of $\langle \pm 1\% \rangle$)

5.2/ The energy change from nominal to -25% is obtained on section no.4 by TW asynchronism, end to head, produced by 2.4/ phasor rotation over 180°. Lower energy levels are obtained on section no.3 by phase rotation of the klystron amplified signal then by its suppression etc.

III IMPLEMENTATION STRATEGY

A test must be performed to confirm our simulations of efficiency and dynamics on the most critical low energy acceleration part. It uses backward wave at $-\pi/4$ coupling ($7\pi/4$ required bunch cell to cell dephasing).

The first waveguide subdivides into two segments designed to accelerate from 4 MeV to 12 MeV (x3) and then to 36 MeV (x9). Elegant simplification occurs as: (a) constant group velocity is possible with a moderate field decrease as the cell shunt impedances increase when the RF power decreases, (b) groups of 6 to 10 cells of same length introduces a back and forth dephasing of the accelerated bucket with respect to the wave at the mid-plane of each cell. This RF autofocusing is however limited to a narrow 10° phase acceptance band.

Provision must be made to superimpose magnetic focusing. Taking advantage of the absence of (side) coupling cells, adjustable FODO seems relevant for test. In the future fixed helical quadrupolar geometry could be used. To this must be added the proton source of 4 MeV and a standard S-band RF source of 20 MW.

III REFERENCES

- (1) A J Lennox, Hospital-based proton linear accelerator for particle therapy and radioisotope production, Fermilab-pub-90/217, 1990.
- (2) R W Hamm and al., Preliminary design of a dedicated proton therapy linac, Part. Accel. Conf., San Francisco, 1991, 2583.
- (3) M P S Nightingale and al., Booster linear accelerators for proton therapy, Linear Accel. Conf., Ottawa, 1992
- (4) D.Tronc, Traveling wave acceleration of protons, Nuclear Instr. & Methods, A327 (1993) 253.
- (5) Patent F 91 09292
- (6) Patent F 92 06290
- (7) Patent F 93 03152

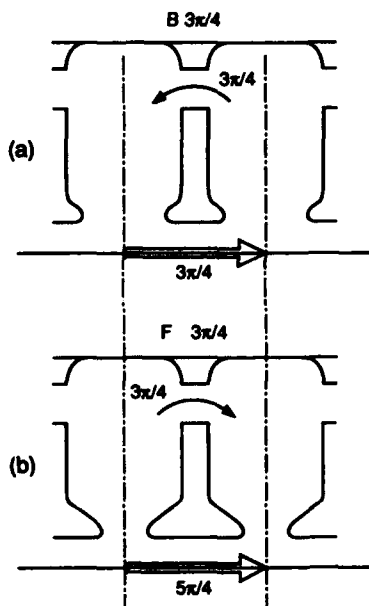


Figure 1. Half-views of adjacent TW cells for two cases: (a) RF coupling $3\pi/4$ backward accelerates high velocity protons with same on-axis delay value [already used for electrons] (b) same coupling forward can accelerate lower velocity ones delayed by $2\pi - 3\pi/4 = 5\pi/4$.

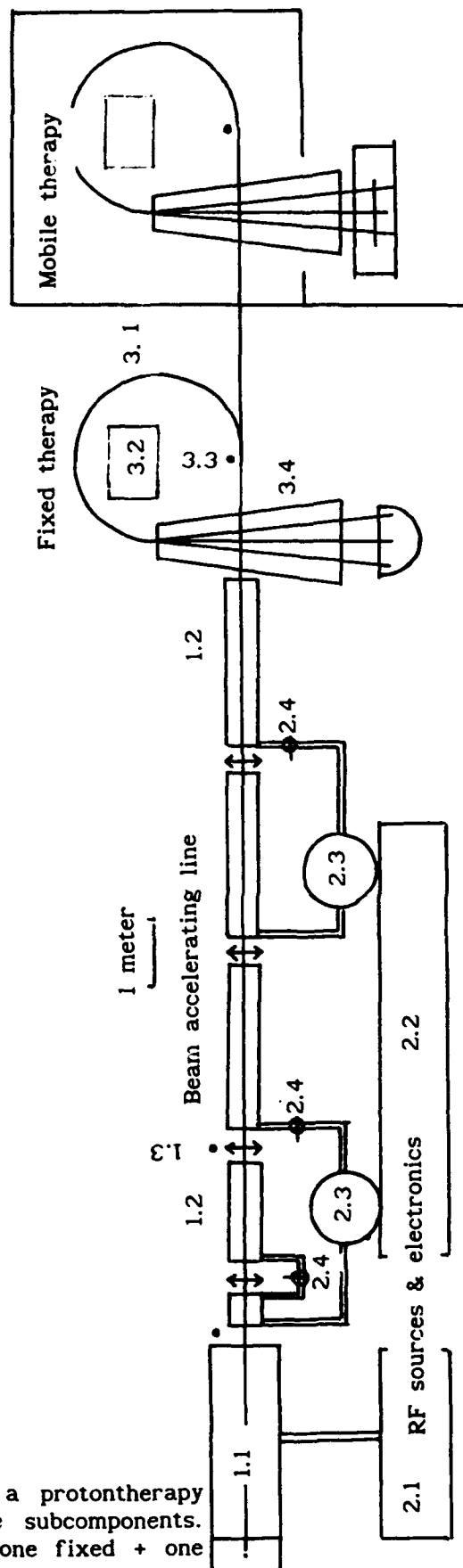


Figure 2. Block diagram of a protontherapy instrument made of available subcomponents. Total length 25 m including one fixed + one mobile treatment facilities.

High Energy Accelerator Technology in Radiology

J. F. Crawford, B. Larsson, H. Reist, IMR, University of Zurich, and PSI, Switzerland;

L. Goldin, ITEP, Moscow, Russia;

H. Condé, K. Elmgren, E. Grusell, B. Nilsson, O. Pettersson, T. Rönqvist, ISV, University of Uppsala, Sweden.

Abstract

Radiation treatment of cancer dates back about 100 years. Today, mega-voltage electron accelerators are used routinely to irradiate many kinds of tumours. About two thirds of all cancer patients receive at least some radiation. More recently, other kinds of particles have come into use, some already on a more or less routine basis: neutrons, pions, protons and other light ions. Experience with some of these particles at PSI is described. As an illustration, a concept for advanced accelerator-based therapy is described; it consists of a 2.5 MeV RFQ injector, a 70 MeV linac, a 250 MeV H^- synchrotron, and a 2.1 GeV electron ring operated as a synchrotron light source. Possible niches for high energy technology are identified.

INTRODUCTION

At present, about two out of three cancer patients receive at least some radiation[1]. In the longer term, there is concern throughout Europe, and in particular in the EEC countries, about the growing human toll of the disease, and the increasing strain that it is placing on health and welfare facilities. In 1985 about three-quarters of a million people died of it in the EEC alone. Given present-day costs, improved (and cheaper) treatment methods are becoming increasingly important.

One promising line of attack involves the use of accelerators. PSI, with its expertise in all the fields involved in this multi-disciplinary effort, and its national and international contacts, is very well placed to contribute to the R & D effort, and to some degree to routine treatments. However, the main goal is to develop hardware and techniques that can be transferred to the lower-technology environment of hospitals, clinics, etc., not only in the developed world.

THE PIOTRON - IRRADIATION WITH π^- S

One of the most technologically advanced forms of therapy is irradiation with negative π^- s, which has been tried at all three pion factories: PSI, LAMPF & TRIUMF. The principle of the technique is that as a π^- comes to rest in tissue, it will react with one of the heavier nuclei (C, N, O...). If the π^- s can be brought to rest in a tumour, the reaction products will preferentially irradiate the tumour. At PSI about 500 patients have been treated, starting in 1980 with a superficial melanoma case.

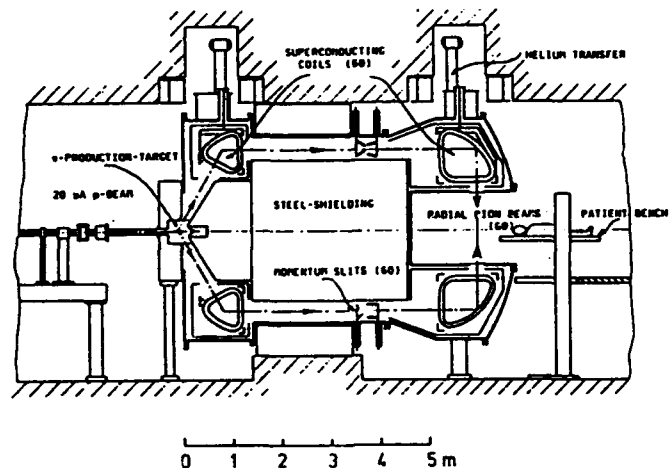


Figure 1: The Piotron at PSI

The beam-line, the most sophisticated yet built, is known as the 'Piotron', and is shown in Figure 1. A full description can be found in references[2,3]. In brief, a beam of up to 20 μ A of 600 MeV protons from the PSI Main Ring impinges on the π^- production target. Among the many particles produced, π^- s at near 60° are collected and deflected parallel to the axis of the Piotron by a toroidal arrangement of super-conducting coils. After passing through the momentum slits, the π^- beams are bent by a second toroid, towards the patient, who is supported within a water bolus.

With appropriate selection of the rigidity, and hence the range, of the π^- s, most of them will come to rest near the focus, forming a 'hot spot' 40-50 mm in diameter. Treatment consists of moving the patient inside the water bolus in such a way that the hot spot is scanned through the tumour, sparing as much as possible the healthy tissues nearby.

The technique has been tried on many tumours, and is almost routine for large (typically some kg) abdominal sarcomas of complicated shape. The usual dose is 33 π^- Gy delivered in 20 fractions. The 5-year local control rate is 60% for the sarcoma cases, which cannot for various reasons be treated by conventional radiation, chemotherapy or surgery. There are however some drawbacks:

- About 10^5 protons at 600 MeV are required to deliver 1 π^- to the tumour; this corresponds to about 0.5

Gy-kg per minute at 20 μ A.

- The RBE under treatment conditions is not as high as expected from the very early studies made at low dose rates to low doses, usually on plants, in the π^- beams that were available before the advent of the pion factories.

The RBE has in any case been less useful than the ability to make the dose distribution conform to the tumour shape.

OPTIS - TREATMENT OF RETINAL MELANOMAS

Optis, the 72 MeV PSI beam-line dedicated to the treatment of retinal melanomas, is a simpler device, based on earlier work in the USA. It is based on the principle that a heavy particle, as it comes to the end of its range in matter, deposits an increasing amount of energy per unit track length - the so-called Bragg peak. Eye tumours are typically 15 mm thick as seen by the protons, each of which will therefore deposit a few tens of MeV in the tumour.

The proton beam from injector 1 is shaped to match the tumour by a combination of scattering, collimation and range shifting. The dose is 60 Gy (cobalt equivalent), delivered in four fractions of 15-30 seconds each by a nA beam. This technique is well suited to routine therapy, as evidenced by the 200 or so patients treated in 12 weeks of operation each year. Some results are shown in Figure 2.

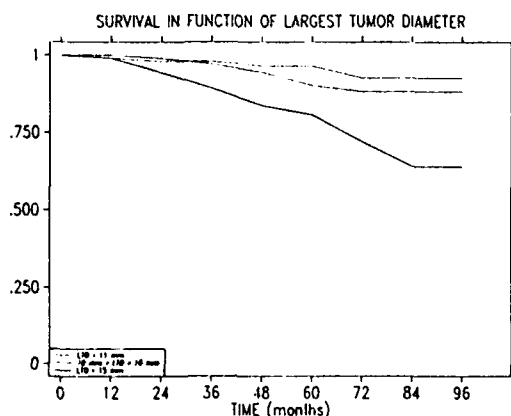


Figure 2: Some results of retinal melanoma irradiation.

PROTON IRRADIATION OF LARGE TUMOURS

A great deal has been learned from a decade's experience of treating some 500 patients in the Piotron, especially about 3-dimensional treatment planning. Much of this experience is being applied to proton irradiation of large tumours - the Proton Therapy Project (PTP). Scanning is done magnetically, by range shifting, and by moving the patient, in that order. Installation of the device has begun.

The proton beam spot is significantly sharper than the π^- beam spot in the Piotron. One can therefore match the treatment volume more precisely, sparing better the healthy tissue near the tumour. It is felt that this will more than compensate for the lower RBE of protons as compared to π^- s. In consequence, the proton beam is expected to be as good or better than the π^- beam.

At PSI the protons are made by slowing down 600 MeV particles from the Main Ring. An accelerator of the size needed to produce beams at the 200-250 MeV required, although a large and expensive device, would be within the budget of a large hospital if sufficiently good results could be demonstrated.

EXPERIENCE AT UPPSALA

Biological experiments and radiotherapy with 185 MeV protons from the synchrocyclotron at what is now the The Svedberg Laboratory (TSL) began in the 1950's. The accelerator, now rebuilt, can be operated at fixed frequency to deliver 100 MeV protons, or with variable frequency up to nearly 200 MeV.

A treatment room equipped with a narrow proton beam unit for therapy of small intracranial targets is in operation at TSL. Patients are seated in front of a fixed horizontal beam line. Titanium markers permanently implanted in the patient's *tabula externa* are used for the precise location of the patient with X-rays for each treatment fraction. To date, 14 patients have been treated with 100 MeV protons, most for arterio-venous malformations. In addition, 20 eye melanoma cases have been treated with 72 MeV protons, using a technique very similar to the PSI one discussed above.

BORON NEUTRON CAPTURE THERAPY (BNCT)

This is a promising technique for the treatment of gliomas and other brain tumours, and for certain other cancers[4]. It is based on the large cross-section (4 kbarn) for thermal neutron capture by ^{10}B : if the latter is concentrated in a tumour, the tumour cells will be preferentially irradiated by the short-range reaction products; healthy tissue nearby will be largely spared.

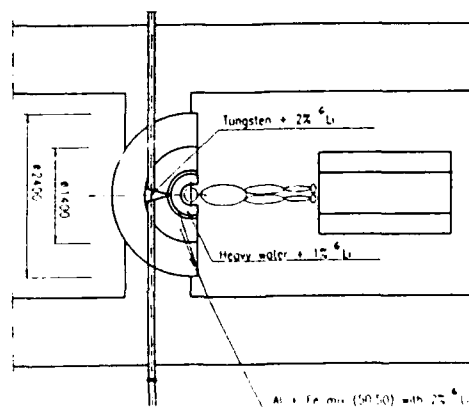


Figure 3: A possible BNCT layout

Concentrations of ~ 30 ppm_w of ^{10}B in the tumour, and neutron fluxes of $10^9 \text{ cm}^{-2} \text{ s}^{-1}$ at keV energies are needed, for a total treatment time of a few hours, fractionated as required. Because reactors face such problems of public acceptance, accelerator-produced neutrons are very attractive. A dedicated spallation source, based on a $100\mu\text{A}$ proton beam from Injector 2, is under intensive study at PSI; a possible layout is shown in Figure 3.

A POSSIBILITY FOR THE FUTURE

Table 1 lists some parameters of a possible accelerator complex which is described elsewhere[5]. It consists of several parts:

1. A 2.5 MeV RFQ injector, intended for
 - (a) Feeding the 70 MeV injector linac
 - (b) Low energy BNCT, neutrons being produced by the $^7\text{Li}(p,n)^7\text{Be}$ reaction
2. A 70 MeV linac, intended for
 - (a) Feeding the synchrotron
 - (b) Nuclide production, as at PSI today
 - (c) Eye irradiation, again as at PSI today
 - (d) BNCT, in a double-patient facility, using spallation neutrons
3. A 250 MeV H^- synchrotron, intended for the irradiation of large, deep-seated tumours in five beam-lines, three of which are equipped with gantries in which patients can be irradiated isocentrically. One beam-line is available for experiments.

4. (In a later option, if required by future radiological developments.) A 2.1 GeV electron ring, built on a different level and intended for the generation of keV X-rays for imaging and treatment. The ring might also be able to accelerate carbon ions, in the first instance for intracranial irradiations.

The facility, able to treat several thousand patients each year, would cost about as much as a jumbo-jet; it would be small enough to be installed at a large university hospital, or at PSI. A related study is under way in Italy, by the Progetto Adroterapia ('TERA') group at the Como campus of the University of Milan.

ACKNOWLEDGEMENTS

A paper of this kind relies very heavily on information kindly provided by those active in fields related to the authors' own. Particular thanks are due to the Piotron, Optis and PTP teams at PSI, to Scanditronix, Sweden, and to the TERA group, Como.

REFERENCES

- [1] A. Vermorken, S124, Proceedings of EPAC 90 (2nd European Particle Accelerator Conference, Nice, 12-16 June 1990); Editions Frontières, Gif-sur-Yvette, France.
- [2] J. Zellweger, G. Vecsey and I. Horvath. *Advances in Cryogenic Engineering*. Volume 25 (1980) 232.
- [3] G. Vecsey, *Pion and Heavy Ion Radiotherapy: Pre-Clinical and Clinical Studies*, New York, Elsevier North Holland, 1982.
- [4] Proceedings of the 4th International Symposium on BNCT, Sydney, Australia, 4-7 December 1990; Plenum Publishing, New York.
- [5] B. Larsson, Antrittsvorlesung 'Strahlung als Heilmittel', University of Zürich, 30 November 1991.

Table 1: Accelerator Specifications for a Medical Facility

RFQ Injector

Energy	2.5	MeV
Beam Current (pulse)	20-30	mA

Linac

Energy	70	MeV
Beam Current (pulse)	40	mA
Energy Spread (FWHM)	± 0.1	%
Emittance (normalized rms)	0.15π	mm.mrad
Max beam pulse width	215	μsec
Pulse repetition rate	1-120	Hz
Max average beam current	1000	μA
Accelerator weight	7.5	ton
Accelerator length	ca 25	m
Input power		
at $100 \mu\text{A}$ average current	100	kW
at $1000 \mu\text{A}$ average current	650	kW

Synchrotron

Particle type: H^-		
Energy	60-250	MeV
Intensity	10^{11}	p/s
Extraction time	30	μsec
Repetition rate	5	Hz
Accelerator diameter	16	m
Power consumption	100	kW
Particle type: $^{12}\text{C}^{6+}$		
Ring diameter	20	m
Dipole field	1.3	T
Max energy	260	MeV/A

The Neutral Particle Beam Space Experiment (NPBSE) Accelerator Designs

C. C. PAULSON, A. M. M. TODD, and S. L. MENDELSON
Grumman Space Systems
4 Independence Way
Princeton, N. J. 08540-6620

Abstract

Accelerators that are designed to operate in a space environment are more strongly constrained by hardware envelope size, power consumption and cooling requirements than are equivalent ground based systems. The challenges presented by these constraints have resulted in the development of novel features in the Neutral Particle Beam Space Experiment (NPBSE) accelerator designs, which may also find application in ground systems. We will describe both the low power 2.0 MeV RFQ and 5.11 MeV ramped gradient DTL designs. The initial DTL cell is suitably phased as a compactor to provide longitudinal matching and the first four DTL PMQs have different strengths to obtain transverse matching. Minimum beam momentum spread is essential to the minimization of chromatic aberrations in the downstream optics components but drift space for beam expansion prior to compaction is highly limited. We therefore shift to positive synchronous phase in the tail of the DTL to minimize the required pre-compaction drift length. These and other accelerator design details will be described.

I. INTRODUCTION

The NPBSE accelerator is a 425 MHz, 12.5 m straight beamline designed to deliver a 5 MeV neutral hydrogen beam with a divergence of 30 mrad. Table 1 provides a component parameter summary of the beamline. In this table, the power figures in parentheses are the projected RF unit sizes.

Component	W(MeV)	L(m)	P(kW)	P _{thermal} (kW)
Injector	0.035	0.820	50	50
RFQ	2.000	1.587	234(300)	183
Drift	-	0.028	-	-
RGDTL	5.110	1.721	291(300)	210
Optics	-	6.520	42(60)	42
Total	5.110	10.676	617(660)	485

Table 1. Component Parameter Summary

The 35 keV injector system was designed at Culham Laboratories[1]. It and the RFQ are complete at a level suitable for near term fabrication. The RFQ feeds a single tank, ramped gradient, $\beta\lambda$ FO-DO DTL to accelerate the beam to the 5 MeV output energy[2]. To minimize length and total power consumption, the two novel features have been incorporated in to the DTL. They are: a direct coupling

scheme between the RFQ and DTL with transverse and longitudinal beam matching accomplished within the initial few cells of the DTL; and the incorporation of much of the post DTL drift into the DTL thus achieving the required momentum compaction and eyepiece matching while minimizing overall length. Positive cell phasing is used in the final four DTL cells to stretch the bunch and increase the energy spread within the DTL such that momentum compaction can be achieved in as short a distance as possible. These techniques are described in section III. The output optics is described in reference 3.

II. RFQ

Due to the requirements of the space mission, the RFQ has been designed to minimize RF power consumption and length. This has been effected by using a relatively narrow "BEAR like" aperture (0.255 cm at the choke point) with an inter-vane potential of 68.4 kV (at the choke point) which leads to a current limit of approximately 73 mA. In this design, the length reaches the output energy in 2.25λ . It has a nominal transmission of 94% with output emittance values of 0.01080π cm-mrad and 0.06943 MeV-deg. The design and operation of the RFQ is summarized in table 2.

Particle mass	1.0084 amu	Frequency	425 MHz
Rest Energy	939.293MeV	Wave Length	70.54 cm
Max. modulation	2.306	Radius of Curv.	$3/4 r_0$
Min Vane Aper.	0.163 cm	Inter-vane Pot.	68.4/78.9 kV
Ave. Aper.	0.255/294 cm	Peak Sur. field	37.06 MV/m
Min. Long. ρ	0.604 cm	Kilpatrick factor	1.83
Nom. Input I	28.0 mA	RF Cav. power	182.5 kW
Transmission	92.1 %	RF Beam power	51.2 kW
Phase Adv.	$19.7^\circ / 5.7^\circ$	Sync. Phase	-27.1°

Table 2. RFQ Design Parameter Summary

III. RGDTL

Table 3 is the cell table for the RGDTL. This device accelerates the beam to an output energy of 5.1105 MeV. It has 32 cells at a mean synchronous phase of -27.1° . The two unusual features of the DTL are shown in this table. The direct DTL to RFQ coupling is seen in the initial three cells (four magnets). (There is also a small 2.8 cm drift between

Cell No.	Energy out (MeV)	Beta out (cm)	Cell Len (cm)	Gap Len (cm)	Drift Tube Length			Quad Len	Eff. Quad Grad (kG/cm)	Eo (MV/m)	ϕ_s (deg)	Match. Param. [EoT/ β]	Total Len (cm)
					1st Half (cm)	2nd (cm)	Total (cm)						
in	2.0003	0.0652				0.9428	1.8855	2.50	-23.6721				
1	2.0003	0.0652	4.5962	1.1012	0.9428	2.5462	4.2851	2.50	25.8609	2.2753	-90.0	26.954	4.5962
2	2.0736	0.0669	4.6380	1.1150	1.7389	1.7749	3.5407	2.50	-25.0869	2.2993	-27.1	27.037	9.2342
3	2.1492	0.0681	4.7217	1.1430	1.7658	1.8021	3.5950	2.50	25.4118	2.3200	-27.1	26.863	13.9559
4	2.2270	0.0694	4.8064	1.1714	1.7928	1.8295	3.6494	2.50	-24.5000	2.3411	-27.1	26.696	18.7624
5	2.3071	0.0706	4.8921	1.2004	1.8199	1.8570	3.7038	2.50	24.5000	2.3625	-27.1	26.536	23.6544
10	2.7456	0.0770	5.3361	1.3538	1.9668	2.0061	4.0046	2.50	-24.5000	2.4757	-27.1	25.808	49.4361
15	3.2527	0.0837	5.8071	1.5217	2.1132	2.1546	4.2993	2.50	24.5000	2.5990	-27.1	25.079	77.5188
20	3.8363	0.0908	6.3049	1.7041	2.2745	2.3183	4.6244	2.50	-24.5000	2.7330	-27.1	24.451	108.0363
25	4.5055	0.0984	6.8306	1.9014	2.4341	2.4801	5.9890	2.50	24.5000	2.8783	-27.1	23.812	141.1267
26	4.6507	0.0999	6.9391	1.9427	3.5090	1.4687	4.3500	2.50	-24.5000	2.9134	+27.1	23.758	148.0659
27	4.7998	0.1015	7.0490	1.9846	2.8813	2.9353	5.4797	2.50	24.5000	2.9445	+27.1	23.587	155.1148
28	4.9531	0.1031	7.1600	2.0271	2.5444	2.5919	5.1716	2.50	-24.5000	2.9760	+27.1	23.450	162.2748
29	5.1105	0.1039	7.2722	2.0702	2.5797	2.6277	5.2553	2.50	24.5000	3.0080	+27.1	23.350	169.5471
out	5.1105	0.1039			2.6277								

Table 3. Ramped Gradient DTL Cell Table

the RFQ output and the first DTL magnet.) Longitudinal matching is effected by phasing the first DTL cell at -90° . Transverse matching is obtained varying the first four DTL drift tube permanent magnet quadrupoles (PMQs). In this manner a relatively current independent match has been achieved. A direct comparison of beam envelopes in Trace-3d shows the beam well matched to the DTL in all three of the phase space planes.

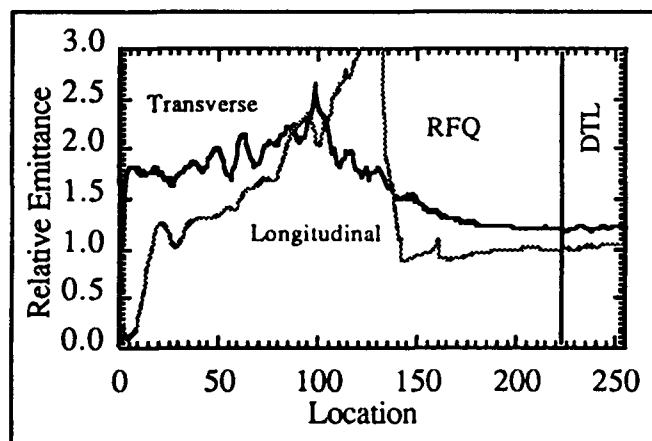


Figure 1. System Emittance Growth

The relative emittance growth through the accelerator components is shown in figure 1 and Figure 2 shows the same growth through the DTL. Due to the small vertical scale used in figure 2, the effect of the positive cells on the longitudinal emittance can easily be seen. The additional small continuous growth throughout the DTL in the longitudinal emittance is attributed to the small negative slope seen in Table 3 in the matching parameter $[E_0 T/L]$. This

arose due to a system redesign that was driven by a need to increase the value of the RFQ longitudinal radius of curvature from approximately 0.4 cm to the final value of 0.604 cm.

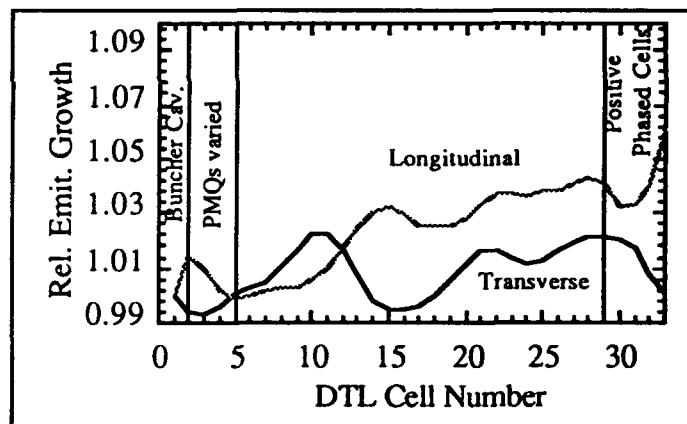


Figure 2. DTL Emittance Growth

The pre-stretching of the beam is necessitated by the fact that there is virtually no length available for pre-compaction drifting following the DTL. Therefore the beam is stretched in both phase and energy prior to the 425 MHz compaction by utilizing a $+27^\circ$ phasing in the last four DTL cells. The output momentum spread achieved in this manner is:

$$\delta p/p \sim 6.6 \times 10^{-4}.$$

Figure 3 show the beam brightness through the DTL with varying RFQ input parameters. The parameter space spanned by the input beams runs from the nominal case to the extreme case of 64 mA at 0.013π cm-mrad. (The beam input values for the 7 cases may be found in Table 4.) All curves

in Figure 3 are basically flat with the differences entirely attributable to the current limit of the RFQ. This indicates that the DTL design is relatively insensitive to the input beam parameters.

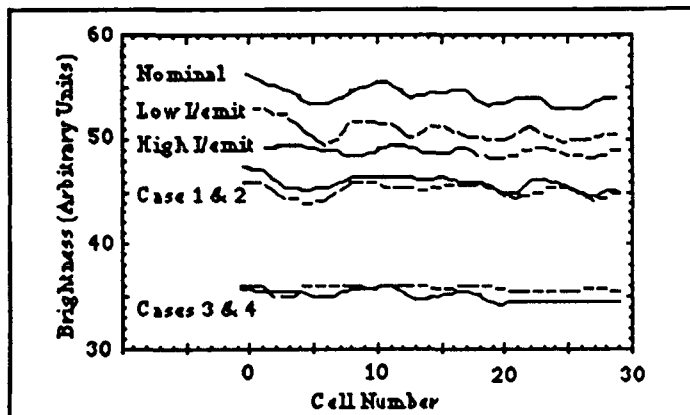


Figure 3. Brightness Through DTL

	Current (mA)	Emit. (π cm-mrad)
Nominal Input	28	0.009
Low Current/Emit. Input	15	0.006
High Current/Emit. Input	40	0.012
Case 1 (90% value)	47	0.009
Case 2 (90% value)	51	0.010
Case 3 (90% value)	54	0.012
Case 4 (90% value)	64	0.013

Table 4. RFQ Input Parameters

The irregular phasing of the first cell and the final four cells in the design has led to some difficulty. The phasing changes are effected by changing the distance between gaps from one cell to the next. However, the center-to-center spacing of the PMQ lattice does not change. It is maintained in order to minimize the effect of the phase change on the beam transverse properties. This results in the PMQs being offset to the end of the drift tubes and therefore being shorter with higher field gradients. At both ends, the PMQs still require some minor but readily achievable redesign. Presently the largest problem seems to be the low energy end-plate PMQ which will probably have to use an inner radius of 0.4 cm to fit in the drift tube.

The stretching of the beam in the high energy end is effected by phasing the final four cells at $+27^\circ$ rather than -27° . The use of the same angle minimizes the impact on the final energy. A study was made to determine the how many cells could be phased in this manner before there is a significant emittance growth in the beam output. The system

was run with zero through 6 cells phased in this manner. The results are shown in Figure 4. Although more positive cells were desired, it was concluded that the maximum stretching that could reasonably be accomplished without significantly affecting beam performance was 4 cells.

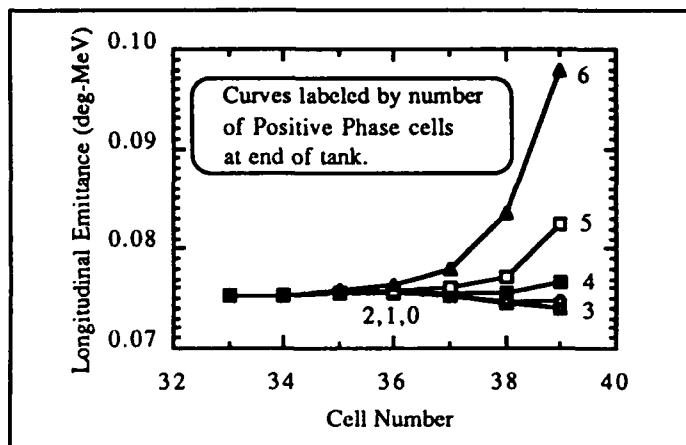


Figure 4. Effect of Positive Phasing on Beam Performance

IV. CONCLUSIONS

The physics design of the NPBSE 5 MeV accelerator has been presented. The standard concepts of device matching were revisited in the design which uses novel concepts for the entrance & exit matching in the DTL. These techniques have proven to be very successful. Off nominal analyses have begun and have shown the accelerator to be exceptionally robust in coping with inputs far from the nominal values. The use of the DTL cells for matching have proven to be workable over a parameter range far in excess of anything that would have been anticipated.

V. ACKNOWLEDGMENT

This work supported by the U.S. Army Space and Strategic Defense Command under contract number DASG60-90-C-0103.

VI. REFERENCES

- [1] M. Nightengale; priv. comm.
- [2] A.M.M. Todd; "Applications of Proton and Deuteron Accelerators"; to appear in Nuclear Instruments and Methods B, April 93.
- [3] M. F. Reusch and D. L. Bruhwiler; "Optics Simulations of the 5 MeV NPBSE FOX Telescope"; these proceedings

The Continuous Wave Deuterium Demonstrator (CWDD) Design and Status†

A. M. M. Todd, M. P. S. Nightingale¹, T. J. Yule² and the CWDD team
Grumman Space Systems Division,
4 Independence Way, Princeton, N. J. 08540, U. S. A.

Abstract

The design of the Continuous Wave Deuterium Demonstrator (CWDD) and the status of the fabricated hardware is presented. The CWDD is a high brightness, 352 MHz, CW linear accelerator designed to deliver a 7.54 MeV, 80 mA D⁻ beam at a transverse normalized rms emittance of 0.11π mm-mrad and a longitudinal rms emittance of 0.20π mm-mrad. End-to-end beam dynamics analysis for nominal and off-design conditions is described. The tuning and predicted operational performance of the as-built device are also discussed. These results all indicate that the present design can meet the output performance specifications in the presence of combined errors at the limits of the specified engineering tolerances. Preliminary injector operations have been conducted at AEA Technologies, Culham Laboratory and at Argonne National Laboratory, where the CWDD is sited. Initial RFQ beam experiments at Argonne are projected for early 1994. DTL installation and commissioning will be completed in 1995.

I. INTRODUCTION

The Continuous Wave Deuterium Demonstrator (CWDD) is a high brightness, unfunneled, 352 MHz, CW linear accelerator designed to deliver a 7.54 MeV, 80 mA D⁻ beam with a transverse normalized rms emittance of 0.11π mm-mrad and a longitudinal rms emittance of 0.20π mm-mrad. The device, which has been built by Grumman and principal subcontractor AEA Technology, Culham Laboratory with the assistance of the Los Alamos National Laboratory, is sited at the Argonne National Laboratory. The purpose of CWDD is to demonstrate automatic control of a cryogenic, CW, high brightness deuterium accelerator. Figure 1 is a component schematic that illustrates the principle design point performance parameters that characterize the CWDD beamline. Powers are room temperature (RT) values.

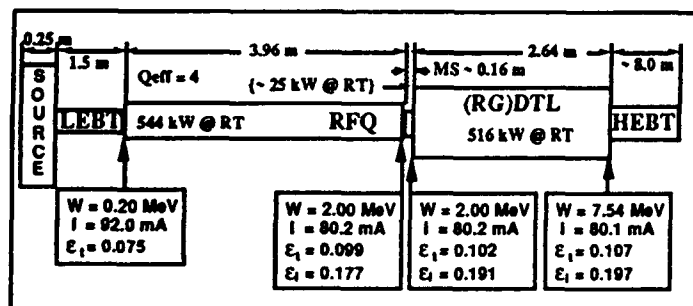


Figure 1. CWDD component schematic and key parameters.

† Supported by the U.S. Army Space & Strategic Defense Command under Contract Number DASG60-88-C-0060.

1 AEA Industrial Technology, Culham Laboratory, Abingdon, Oxon. OX14 3DB, U. K.

2 Argonne National Laboratory, 9700 S. Cass Avenue, Argonne, IL 60439

Figure 2 demonstrates that in an end-to-end source-to-dump beam dynamics simulation, CWDD target performance values for transverse and longitudinal emittance (the identified horizontal lines) are met at the end of the DTL accelerator where the performance will be characterized.

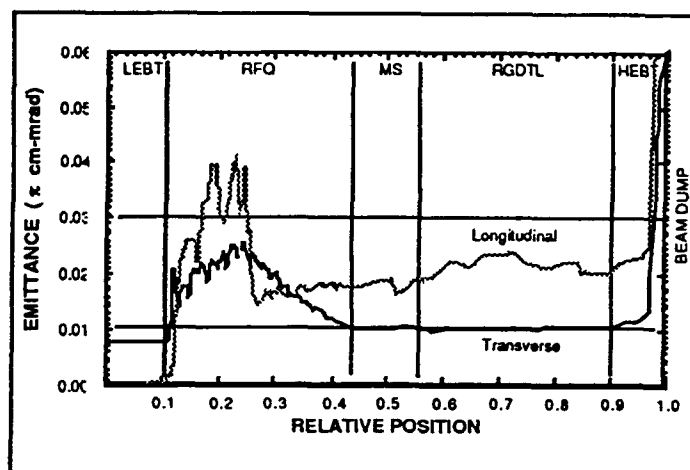


Figure 2. End-to-End CWDD Beam Dynamics Simulation.

The goal of the CWDD physics design was to meet the output performance targets for energy, current, transverse and longitudinal emittance. Below, we describe the beam dynamics of each beamline component and the current status of the associated hardware.

II. INJECTOR

The principal physics issue for the CWDD injector is the ability of the Culham negative ion volume source to meet the required CW performance specifications of both the nominal 90 mA current at 0.150π mm-mrad, and 50 mA at the nominal 0.075π mm-mrad emittance. Additional areas of concern are stripping and emittance growth of the negative ion beam in the accelerator column and LEBT, and problems associated with the electron component extracted from the source. An electron suppression technique to reduce the extracted electron component, and a novel electron trapping technique that uses rotating dipoles to spread the electron power load on the dump are used.

Both analytical calculations and numerical modeling using the SCHAR code have been used to model emittance growth within the LEBT solenoid and drift spaces. The resultant emittance growths for the 50 mA, 0.075π mm-mrad case are $3.7 \pm 0.5 \%$ due to aberrations for an aligned solenoid with a K-V beam distribution, as shown on the right of Figure 3, and $2 \pm 1 \%$ due to space charge at an effective LEBT current of 1 mA. Monte Carlo calculations have been performed for stripping within the DC accelerator using an axisymmetric computer code. Assuming a gas temperature of 700 °K throughout the accelerator, the derived pressure profiles suggest that between 24% and 34% of the negative ions will

be stripped for the range of source and accelerator operating parameters envisaged. The AXCEL code has been used to confirm, as shown on the left of Figure 3, that the DC accelerator will operate correctly as the initial LEBT lens, and that the first gap potential needed to obtain the required output beam can be varied by changing the length of the second grid.

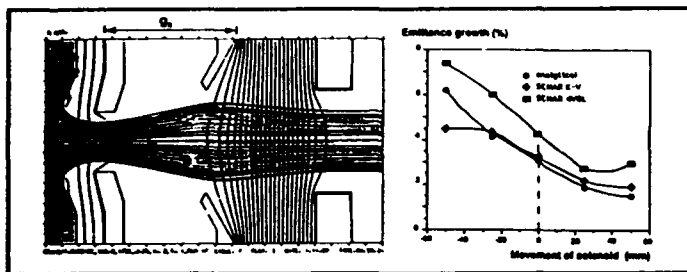


Figure 3. AXCEL & SCHAR Accelerator & LEBT Analysis

III. RFQ

The principal design parameters of the CWDD RFQ, which is shown in Figure 4, are listed in Table I. In designing the accelerator, the Kilpatrick factor was set to 1.8. Scoping studies that traded length, transmission, current limit and emittance growth were performed. Input and output RFQ energies together with the aperture, synchronous phase and energy at the internal RFQ breakpoints between the shaper, gentle buncher and accelerating sections were used to drive these trades and generate the Table I parameters.

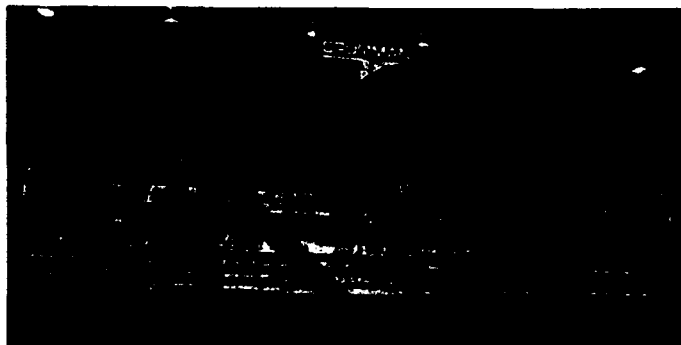


Figure 4. The CWDD RFQ.

The accelerator features include end stabilizers and a constant minimum aperture, a , where the average vane aperture, r_0 , varies to reduce the length of the structure accelerating section by maintaining the accelerating field with β at a constant peak surface electric field (PSEF). The vanes have a constant radius ($3/4 r_0$), except in the accelerator section where the radius increases to maintain the desired resonant frequency. This yields an enhancement factor of 1.26 which has been factored into the Kilpatrick value and PSEF.

The outstanding issues for the CWDD RFQ are the longitudinal field stability of the 4.6λ device, where conventional wisdom recommends the length be maintained under 4λ , the 13% current loss and the control consequences of very high beam loading in the CW cryogenic device, and the ratio of the design current to the accelerator current limit, which is slightly higher than the 50% rule of thumb.

The high RFQ input energy is driven by deuterium operation, the high current performance requirement and the resultant high RFQ current limit. Additional advantages of

high injector output energy are reduced LEBT stripping, and improved margin with respect to LEBT instability.

Table I. CWDD RFQ Design Parameters.

Injection Energy	0.200	MeV
Output Energy	2.004	MeV
Input Current	92.0	mA
Output Current	80.2	mA
Transmission	87.1	%
Current Limit	140.	mA
Final Synchronous Phase	-33.0	degree
Initial (Final) Intervane Voltage	87.7 (92.0)	kV
Maximum Vane Modulation	1.625	
Peak Surface Field	33.7	MV/m
Vane Length	3.96 (4.64)	m (λ)
Kilpatrick Factor	1.80	
Enhancement Factor	1.26	
Minimum Vane Aperture	0.257	cm
Initial (Final) Average Aperture	0.328 (0.337)	cm
Minimum Longitudinal Radius	3.499	cm
Admittance	1.153	π mm-mrad
Input Transverse Emittance	0.075	π mm-mrad
Output Transverse Emittance	0.099	π mm-mrad
Output Longitudinal Emittance	0.175	π mm-mrad
Transverse Phase Advance ($I=0$)	6.6 (17.7)	degree
Longitudinal Phase Advance ($I=0$)	5.4 (13.1)	degree

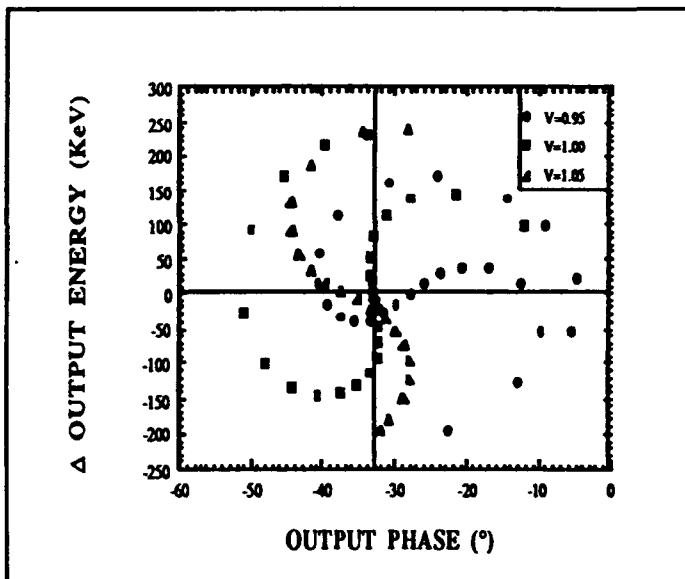
Table II. CWDD Tolerance Criteria Summary

Location	Type	Criterion
Injector to RFQ Interface	Beam Axis Misalignment	$\langle x \rangle \leq \pm 0.20$ mm
	Beam Angular Misalignment	$\langle x' \rangle \leq \pm 3.0$ mrad
	Transverse Beam RMS Size	$\langle r \rangle \leq \pm 5\%$ ($\pm 10\% < 5$ msec)
	RMS Convergence Angle	$\langle r' \rangle \leq \pm 2.5$ mrad
	Beam Energy Offset	$\Delta W \leq \pm 1\%$ or ± 2 keV
Internal RFQ	RF Amplitude	$\Delta V \leq \pm 1\%$
	RF Phase	$\Delta \Phi \leq \pm 1^\circ$
	Vane Machining Errors	$\Delta r \leq \pm 1$ mil
MS to RGDTL Interface	Axis Misalignment	$\langle x \rangle, \langle y \rangle \leq \pm 0.20$ mm
	Axis Angular Misalignment	$\langle x' \rangle, \langle y' \rangle \leq \pm 3.0$ mrad
	Beam Energy Offset	$\Delta W \leq \pm 5$ keV
	Buncher RF Amplitude	$\Delta V \leq \pm 1\%$
	Buncher RF Phase	$\Delta \Phi \leq \pm 1^\circ$
Internal RGDTL	RF Amplitude	$\Delta V \leq \pm 1\%$
	RF Phase	$\Delta \Phi \leq \pm 1^\circ$
	PMQ Field Strength	$\Delta K \leq \pm 5\%$ ($\pm 1\%$ random)
	PMQ Tilt : Roll	$\Delta \theta \leq \pm 1\% : \pm 0.5\%$
	PMQ Transverse Alignment	$\Delta r \leq \pm 2$ mils

The impact of interface or engineering tolerance variation is traced through the entire downstream beamline. The tolerance criteria selected reflect a specified acceptable deterioration in the RGDTL output beam performance. Our guideline sought to keep the design point transmission above 86.5%, the transverse emittance growth under 5%, and the longitudinal emittance growth under 10% for off-design conditions. Additionally, we have verified that the other scenarios, in particular the potentially damaging 90 mA, 0.0150 π cm-mrad CW scenario, and the impact of higher order field components in the RFQ, can be accommodated by the engineering design also under this maximum combined

DTL tuning diagram which will be used to set the accelerator RF phase and amplitude.

Figure 5 schematically illustrates the matching section, which consists of a single buncher cavity and three PMQs (permanent magnetic quadrupoles). PMQ alignment steering uses the two magnets straddling the buncher. The MS delivers a satisfactorily matched beam to the RGDTL over the anticipated range of operating conditions. The output of this system is a parallel beam suitable for immediate diagnosis.



V. HEBT, BEAM DUMP AND DIAGNOSTICS

V. HEBT, BEAM DUMP AND DIAGNOSTICS

Beam spill is the principal HEBT and beam dump physics issue. However, beam dynamics analysis indicates that it is not a serious concern for the present design over the spectrum of anticipated operating conditions. The effectiveness of the HEBT transverse emittance diagnostic and the various fast shut down diagnostics are critical. Figure 7 shows the Injector, RFQ and HEBT as presently installed at Argonne.

Figure 7. The present installed CWDD beamline at Argonne.

VI. CONCLUSIONS

The RGDTL employs a constant $g/L = 0.2$ for all cells which results in near optimal values for the transit time factors but complicated the manufacture. The resonant frequency is established by varying the face angles from cell to cell over the range of $\sim 1.0^\circ$ to $\sim 5.0^\circ$. The low input energy is the minimum that leads to an acceptable engineering design for the first drift tube. This lower DTL input energy permits a higher initial DTL accelerating field which is desirable for controlling longitudinal emittance and yields a more efficient ramp section. The maximum Kilpatrick factor is 1.4 at the high energy end of the accelerator. The accelerating field is ramped from ~ 2.0 to ~ 4.0 MV/m in the 47 cell RGDTL. The linear ramp will be imposed in the single tank by detuning the DTL end cells. We used a constant ramp defined by a fixed longitudinal focusing prescription that maintains the bunch length.

We adopted a FO-FO-DO-DO lattice structure to reduce the required PMQ gradient to achievable levels. The zero current transverse phase advance in the $4\beta\lambda$ structure ($\sim 70^\circ$) does not exceed the beam stability boundary (90°). Although the tolerances and available space are tight, from the standpoint of the required magnetic properties and from mechanical or thermal design considerations, the drift tubes and the PMQs can be successfully engineered.

Finally, various commissioning analyses have been completed. For instance, Figure 6 illustrates the calculated

The 352 MHz CWDD has been designed to deliver a 7.54 MeV, 80 mA CW D^- beam with normalized rms emittance values of 0.11 and 0.20 π mm-mrad in the transverse and longitudinal planes respectively. Nominal and off-design analysis of the device have been completed, and commissioning support analysis is in progress. Injector acceptance tests will be completed in August 1993, first RFQ experiments are scheduled for early 1994, and the DTL will be installed and commissioned in 1995.

Beam Matching Section in the INS Heavy Ion Linac Complex

K. Niki, S. Arai, Y. Hashimoto, H. Masuda, M. Tomizawa and K. Yoshida
Institute for Nuclear Study, University of Tokyo
3-2-1 Midori-cho, Tanashi-shi, Tokyo 188, Japan

Abstract

The beam transport system between a 25.5-MHz split-coaxial RFQ and a 51-MHz interdigital-H linac has been designed. This transport system is composed of a charge stripper, a 25.5-MHz rebunching cavity and two quadrupole doublets. A 170-keV/u beam passes through the stripper and its charge state is increased up to a charge-to-mass ratio greater than 1/10. The rebuncher causes an aberration of the longitudinal beam profile due to its non-linear accelerating field. In order to contain the distorted beam profile by the aberration in the acceptance of the IH, the rebunching cavity must be operated at 25.5 MHz. We have carried out a beam trace by taking account of the aberration and the effects of the increase of the charge state, the energy-loss, the straggling and the scattering in the stripper, and compared its results with the design assuming a linear system.

I. INTRODUCTION

Exotic nuclei arena (E-arena) project, the acceleration of the unstable nuclei beams from an isotope separator on-line (ISOL), is proposed in the Japanese Hadron Project (JHP). A prototype E-arena project at Institute for Nuclear Study is proceeding since 1992. We are constructing two linacs: a 25.5-MHz split coaxial RFQ (SCRFAQ) and a 51-MHz interdigital-H (IH) linac. The former accelerates unstable nuclei up to 170 keV/u, and the latter up to 1 MeV/u at maximum. The minimum charge-to-mass ratio (q/A) is 1/30 at the SCRFAQ and 1/10 at the IH linac; hence, a charge stripper is necessary. For the charge stripping and the beam matching between the linacs, we have designed a beam transport system, as shown in Fig. 1. The design procedure is reported in this paper.

II. ACCEPTANCE OF THE IH LINAC

The acceptances of the IH linac is shown in Fig. 2. We designed the transport system so that the beam profiles match to the solid ellipses in the figure. The parameters of these

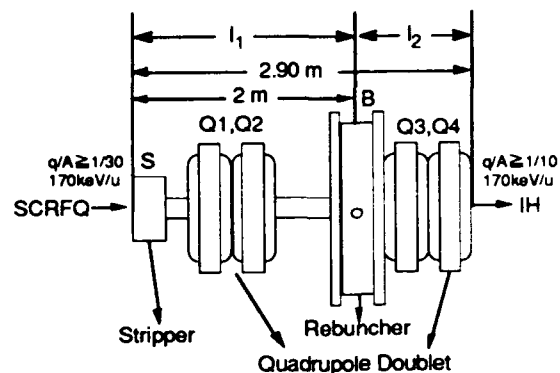


Figure 1. The schematic view of the transport system

ellipses are listed in Table 1, where the emittance parameters of the beam at the exit of the SCRFAQ are also listed. The acceptances of the IH linac is larger these ellipses, as indicated by the dots and open circles in the figure. The normalized area of the solid ellipses in the $x-x'$ and $y-y'$ space are about 2.4π mm-mrad. The normalized emittances from the SCRFAQ are 0.6π mm-mrad. The solid ellipse area in the $\Delta\phi-\Delta T$ space is

Table 1

(a) Ellipse parameters in $x-x'$ and $y-y'$ space

	$x-x'$		$y-y'$		$x-x', y-y'$ ϵ_{norm} (π mm-mrad)
	β (m)	α	β (m)	α	
RFQ _{out}	0.3858	-1.379	0.4238	1.431	0.6
IH _{in}	0.8	2.8	0.8	2.8	2.4

(b) Ellipse parameters in $\Delta\phi-\Delta T$ space

	$\Delta\phi-\Delta T$ (51MHz)		
	$\delta\phi$ (deg)	δT (keV/u)	ϵ (π keV/u-deg)
RFQ _{out}	30.0	2.5	75
IH _{in}	19.3	10.3	200

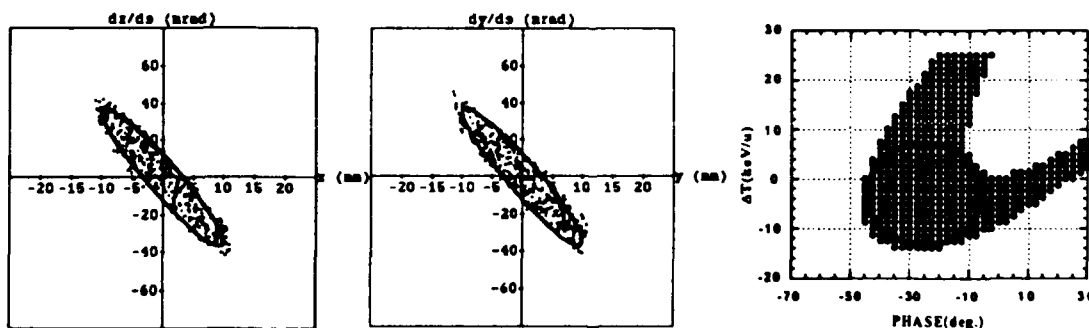
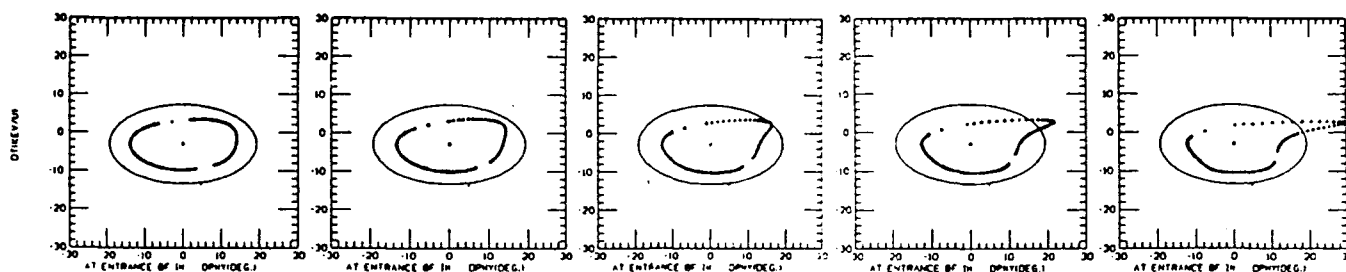


Figure 2. Emittance profiles at the input of the IH linac. The dots ($x-x'$ and $y-y'$ spaces) and open circles ($\Delta\phi-\Delta T$ space) indicate the acceptances of the IH linac. The solid lines are the ellipses to which the beam profiles are to be matched by the design. See the ellipse parameters in Table 1.



(a) (1.0 m, 0.6 m) (b) (1.5 m, 0.75 m) (c) (2.0 m, 0.9 m) (d) (2.5 m, 1.05 m) (e) (3.0 m, 1.2 m)
Figure 3. The beam profiles at the entrance the IH linac (a $10\text{-}\mu\text{g}/\text{cm}^2$ stripper and a 25.5-MHz rebuncher). (l_1, l_2)

about 200π keV/u-deg and the emittance from the SCRFQ is about 75π keV/u-deg.

III. CHARGE STRIPPER

We designed this transport system by using $^{12}\text{C}^+$ ions as a beam from the SCRFQ, because they have larger energy-loss and -straggling per nucleon in the stripper than other ions with a q/A less than $1/10$ [3]. The energy loss is about 6 keV/u and the straggling is about ± 1 keV/u in rms when the 170-keV/u beam through a carbon foil with a thickness of $10\text{ }\mu\text{g}/\text{cm}^2$. The charge states after the stripper are 1.7% (1+), 23% (2+), 57% (3+), 18% (4+) and 0.7% (5+) [4]. In order to make the energy loss and the straggling small, a thin stripper foil is preferable. However, for the handling safely and the achievement of the complete charge equilibrium state, a thick foil would be better. The thickness of $10\text{ }\mu\text{g}/\text{cm}^2$ is enough to achieve the equilibrium charge state. The thickness of $5\text{ }\mu\text{g}/\text{cm}^2$ may be enough. The two thickness are considered as the candidates.

IV. LONGITUDINAL MATCHING

When a single buncher is used for the beam matching in

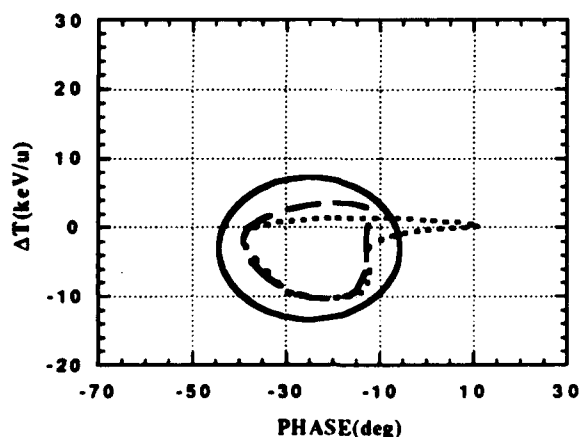


Figure 4. The dashed and dotted lines indicate the beam profiles obtained by the 25.5-MHz rebuncher and the 51-MHz one, respectively. These profiles are with l_2 of 0.9 m and the $10\text{-}\mu\text{g}/\text{cm}^2$ stripper. The solid line is the acceptance of the IH linac.

the longitudinal phase space, the optimized condition is determined by the following parameters: the emittance at the SCRFQ output ($\delta\phi, \delta T$), the position and the thickness of the stripper foil, the position and the frequency of the rebuncher, and the acceptance of the IH linac ($\delta\phi, \delta T$). The voltage and the phase of the buncher are uniquely determined as functions of these parameters when the longitudinal matching is satisfied between the SCRFQ and the IH linac. In these parameters, the position of the stripper foil is determined at 10 cm after the SCRFQ, because the transverse emittance-growth in the stripper foil is proportional to the beam size and the position where the beam size is relatively small is just behind the SCRFQ. Consequently the free parameters are the thickness of the stripper foil, the position and the frequency of the rebuncher.

As discussed in Sect. 3, the thickness of the stripper foil might be 5 or $10\text{ }\mu\text{g}/\text{cm}^2$. The operating frequency of the rebuncher should be 25.5 or 51 MHz, the frequencies of the linacs. Since a linear accelerating field would cause no distortion of the beam profile, the lower frequency is better. However, the higher frequency can easily keep the size of the cavity small. Finally we have four possibilities about the thickness of the stripper foil and the frequency of the rebuncher. In each case, the position of the rebuncher (the distance l_1 between the SCRFQ and the rebuncher) gives the longitudinal beam profile at the entrance of the IH linac and the distance l_2 between the rebuncher and the IH linac. As a result, we chose the combination of a $10\text{-}\mu\text{g}/\text{cm}^2$ stripper and a 25.5-MHz rebuncher. Figure 3 shows the beam profiles obtained with this combination. When l_2 is longer than 0.9 m, the distortion of the beam profile is greater. The longest l_2 in which the beam profile can be contained completely in the acceptance of the IH linac is about 0.9 m. In this case l_1 is 2.0 m and the beam profile is in Fig. 3-(c). Figure 4 indicates the beam profiles obtained by means of the 25.5-MHz rebuncher and the 51-MHz one. The profile with the frequency of 25.5 MHz is better due to the smaller aberration. Though the beam profile with the $5\text{-}\mu\text{g}/\text{cm}^2$ stripper is better than $10\text{ }\mu\text{g}/\text{cm}^2$, the rebuncher with the frequency of 25.5 MHz is still necessary. The result from the longitudinal design study is that the rebuncher with the frequency of 25.5 MHz is required and l_2 is less than about 0.9 m. As setting beam monitors and quadrupole magnets and etc., l_2 would better have a enough space and must be considered with the further studies of the transverse matching.

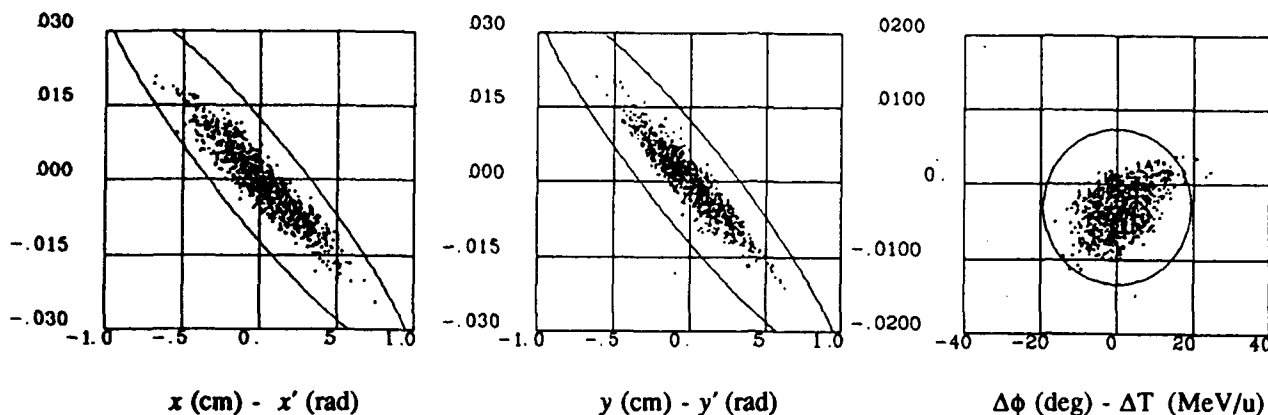


Figure 5. The emittance profiles at the exit of this transport system. The dots are obtained by using TRACEP. V_{eff} and G_Q s are optimized for ions of $^{12}\text{C}^{3+}$ after the stripper. The solid ellipses are the goaled profiles at the IH linac entrance.

V. TRANSVERSE MATCHING

As mentioned in Sect. 2, the normalized beam acceptances of the IH linac are 2.4π mm-mrad. The solid lines in Fig. 2 have the ellipse parameters of the β of 0.8 m and the α of 2.8. In order to match the beam profiles to these ellipses, the position and field gradient (G_Q) of the quadrupole magnets are determined by using the program MAGIC. The position, the voltage and the phase of the rebuncher are determined by the matching condition in the longitudinal phase space. As the result, the rebuncher has defocusing force expressed by the following matrix:

$$\begin{pmatrix} 1 & 0 \\ -\delta & 1 \end{pmatrix}, \quad \delta = \frac{\pi(q/A)V_{\text{eff}}}{m_u c^2 \beta^3 \gamma^3 \lambda} \sin \phi_s,$$

where $V_{\text{eff}} = (\text{gap voltage}) \times (\text{transit time factor})$, m_u is the atomic mass unit, c is velocity of light, β is the relativistic velocity of the ions, γ is the Lorentz factor, λ is the free space wavelength, ϕ_s is the synchronous phase. Using the ellipse parameters at exit of the SCRfQ and the entrance of the IH linac, and the above matrix for the rebuncher, the position and G_Q s are determined. The result of these studies is that one quadrupole triplet is not enough to optimize the transverse matching. Two quadrupole doublets are necessary. Especially one set of doublet must be placed just before the IH linac, because the strongly focused beam must be inject to the IH linac in the both x and y plane. Consequently the spacing between the rebuncher and the IH linac must be greater than about 0.9 m for setting the doublets. Then l_2 is determined to be about 0.9 m.

VI. RESULTS AND SUMMARY

Using parameters determined in the above studies, we take a trace of $^{12}\text{C}^{3+}$ ions with the program TRACEP. The parameters are optimized for ions with a charge state of 3+ after the stripper. Figure 5 indicates the emittance profiles at the exit of this transport system. The solid lines in Fig. 5 are the same ellipses as ones in Fig. 2. The profiles show a good matching to these ellipses. At the stripper, we take into account of the effects of the energy straggling and the

scattering. As a result, the emittance-growth rate of the beam is about 1.6 in the horizontal plane and about 1.2 in the vertical one. In the longitudinal phase space the emittance-growth rate is about 1.4.

The non-linear accelerating field of the rebuncher causes an aberration in the longitudinal beam focusing. The rebuncher working at 25.5 MHz is required to reduce the distortion of the beam profile. Setting the rebuncher near the IH linac is also required ($l_2 \leq 0.9$ m). For the transverse matching of the beam, one quadrupole doublet must be placed just before the IH linac. A space longer than 0.9m is necessary to set a doublet between the rebuncher and the IH linac ($l_2 \geq 0.9$ m). Therefore, the distance between the rebuncher and the IH linac is determined to be 0.9 m and the total length of this transport system is 2.9 m. As the rebuncher with a frequency of 25.5 MHz, a spiral loaded cavity [5,6] is being developed to keep the size of the resonator small.

VII. ACKNOWLEDGMENT

The simulation works were executed by using the computer FACOM M-780 of INS computer room. We thank the staff at the computer room for their support.

VIII. REFERENCES

- [1] S. Arai *et al.*, these proceedings.
- [2] M. Tomizawa *et al.*, these proceedings.
- [3] J. Lindhard *et al.*, Mat. Fys. Medd., 33 (1963) 14.
- [4] K. Shima *et al.*, NIFS DATA-10, Jan. 1991.
- [5] P. Z. Peebles *et al.*, Particle Accelerators, 6 (1975) 201.
- [6] A. Schempp *et al.*, Nucl. Instr. and Meth., 135 (1976) 409.

A Heavy Ion Linac Complex for Unstable Nuclei

S. Arai, M. Doi, Y. Hashimoto, T. Hattori^{*}, A. Imanishi, T. Katayama, H. Masuda, K. Niki, Y. Takeda, N. Tokuda, M. Tomizawa, E. Tojyo, K. Yoshida, and M. Yoshizawa
Institute for Nuclear Study, University of Tokyo, Tanashi, Tokyo 188, Japan
^{*}Tokyo Institute of Technology, Ohokayama, Meguro, Tokyo 152, Japan

Abstract

A heavy ion linac complex for unstable nuclei is under construction at INS. The linac complex consists of a 25.5-MHz split coaxial RFQ (SCRFFQ), a charge-stripper section, and a 51-MHz interdigital-H (IH) linac. The SCRFFQ with modulated vanes, 0.9 m in diameter and 8.6 m in length, accelerates ions with a charge-to-mass ratio (q/A) greater than 1/30 from 2 to 170 keV/u. The stripper is a carbon foil. The IH linac, 1.34 m in diameter and 5.54 m in total length, comprises four cavities and three magnetic quadrupole triplets placed between cavities, accelerates ions with $q/A \geq 1/10$, and varies the output energy continuously in the range 0.17 ~ 1.05 MeV/u. The duty factor of the linac complex is 30% for $q/A = 1/30$ ions.

1. INTRODUCTION

A short-lived nuclear beam acceleration facility, which is a prototype for the exotic nuclei arena (E-Arena) of the Japanese Hadron Project (JHP), has been under construction since fiscal year 1992 at INS. This facility aims to carry forward the R&D of isotope separator on-line (ISOL) and heavy ion linac as well as the studies on nuclear astrophysics, structure of unstable nuclei, etc. The facility is composed of an SF cyclotron, an ISOL and a 1-MeV/u heavy ion linac. The layout of the facility is shown in Figure 1. The radioactive nuclei, produced by bombarding a thick target with a 40-MeV 10- μ A proton beam from the existing cyclotron at INS, are ionized in an ion source, mass-analysed by means of the ISOL and transported to the heavy ion linac through a 50 m long beam line. The linac is an accelerator complex composed of a 25.5-MHz split coaxial RFQ (SCRFFQ) with modulated vanes, a charge-stripper section, and a 51-MHz interdigital-H (IH) linac. The SCRFFQ accelerates ions with a charge-to-mass ratio (q/A) greater than 1/30 from 2 to 170 keV/u. The beam from the SCRFFQ is charge-stripped by a carbon foil, and is transported to the IH linac through two magnetic-quadrupole doublets and a 25.5-MHz rebuncher cavity. The IH linac accelerates ions with $q/A \geq 1/10$ up to 1.05 MeV/u. The output-beam energy is variable between 0.17 and 1.05 MeV/u. The duty factor of the linac complex depends on q/A of the ions: nearly 100% at $q/A \geq 1/16$, and

given by $270 \times (q/A)^2$ at $1/17 \geq q/A \geq 1/30$. The main parameters of the linac complex are shown in Table 1.

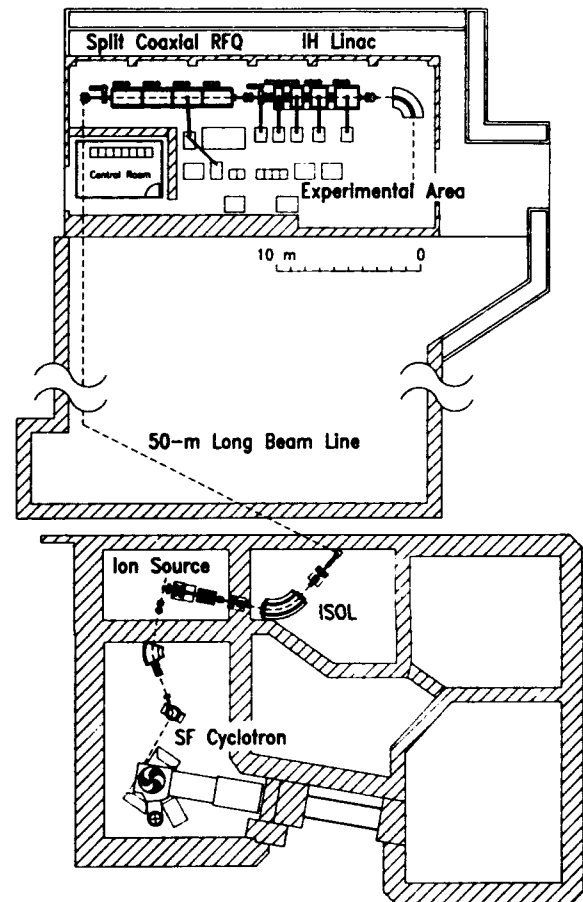


Figure 1. Layout of the radioactive-beam acceleration facility.

Table 1
Main parameters of the heavy-ion linac complex

Input energy	2 keV/u
Output energy (variable)	170 ~ 1046 keV/u
Energy spread (half width)	2 ~ 5%
Beam emittance (normalized)	0.67π mm·mrad
Intensity (radioactive nuclei)	$10^7 \sim 10^{11}$ ions/s
Charge-to-mass ratio (q/A)	$\geq 1/30$
Mass number	≤ 60
Duty factor (for $q/A=1/30$)	30%
Repetition rate	20 ~ 1000 Hz
Total length	17 m

II. SPLIT COAXIAL RFQ

The accelerating cavity, 0.9 m in diameter and 8.6 m in length, is under construction. Main parameters of the SCRFQ are listed in Table 2. This SCRFQ is an extended version of a prototype model (25.5 MHz, $q/A \geq 1/30$, $1 \rightarrow 45.4$ keV/u, 0.9 m in diameter, 2.1 m in length). The design of the new SCRFQ is based on the experience gained through the operation of the prototype [1]. The 8.6 m long SCRFQ comprises four unit cavities, whose structure is nearly same as that of the prototype. We fabricate three unit cavities and connect them together with the prototype cavity.

Table 2
Main Parameters of the 25.5-MHz SCRFQ

Frequency (f)	25.5 MHz
Charge-to-mass ratio (q/A)	$\geq 1/30$
Kinetic energy (T)	$2 \rightarrow 172$ keV/u
Normalized emittance (ϵ_N)	0.6π mm-mrad
Vane length (L)	8.585 m
Number of cells (radial matcher)	172 (20)
Kilpatrick factor (f_K)	2.49
Intervane voltage (V)	108.6 kV
Mean bore radius (r_0)	0.985 cm
Min. bore radius (a_{\min})	0.539 cm
Margin of bore radius (a_{\min}/a_{beam})	1.2
Focusing strength (B)	5.5
Transmission efficiency (for $q/A = 1/30$ ions):	
at 0 mA input	91.4%
at 1 mA input	90.6%
at 2 mA input	90.2%
at 5 mA input	83.2%

The modifications and improvements introduced to the new SCRFQ are as follows. 1) The duty factor for $q/A = 1/30$ ions was 10% at the prototype, whereas 30% at the new RFQ. For such a high-duty operation with a maximum peak power of 350 kW, we have thickened the water cooling pipes of the cavity. Furthermore, the vane coupling rings installed in the prototype have been removed, because they caused appreciable shift of the resonant frequency in high-power operations. 2) The energy of the input beam is 1 keV/u at the prototype, whereas 2 keV/u at the new RFQ. Since the beam emittance has become smaller, the beam transport from the ISOL to the SCRFQ will be easier. 3) As for the vane-tip geometry of the prototype, the transverse radius of curvature is constant at the mean bore radius, $\rho_T = r_0$ (0.946 cm) [2]. At the new RFQ, however, ρ_T is variable in the low-energy part (up to the center of the 76th cell), and $\rho_T = r_0$ (0.985 cm) in the high-energy part. The vanes in the first unit

cavity are machined by means of a three-dimensional cutting technique; the cutter is a ball-end-mill. A two-dimensional cutting technique is applied to the other vanes; the cutter edge is shaped to the transverse cross section of the vane tip. 4) For the both vane-tip geometries, we have made a correction on the aperture parameter a and modulation m (A_{10} correction). These parameters were optimized in the beam dynamics design by using the PARMTEQ program. In the PARMTEQ simulation, the electric field is derived from the two-term potential function by Kapchinskii and Teplyakov. The actual electric field generated by the vanes is, however, different from that used in the simulation; particularly, the A_{10} coefficient is different. The A_{10} term is important among the multi-pole terms, because it is the principal term yielding the acceleration field. Through acceleration tests on the prototype RFQ without A_{10} correction, we verified that the A_{10} correction is indispensable to $\rho_T = r_0$ vanes.

III. INTERDIGITAL-H LINAC

The IH linac, 1.34 m in diameter and 5.54 m in total length, comprises four cavities and three quadrupole triplets, as illustrated in Figure 2 [3]. The main parameters of the IH linac are listed in Table 3.

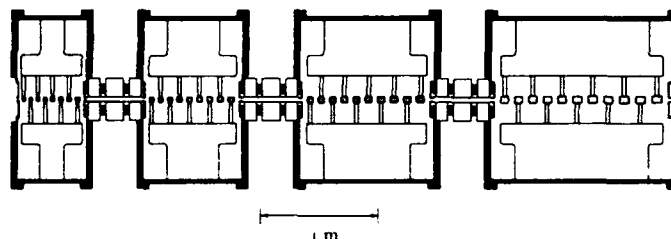


Figure 2 Schematic view of the IH linac.

Table 3
Main parameters of the IH linac

Cavity number	I	II	III	IV
Resonant frequency (MHz)	51	51	51	51
Min. charge-to-mass ratio	1/10	1/10	1/10	1/10
Synchronous phase (deg)	-25	-25	-25	-25
Max. output energy (keV/u)	292	471	721	1046
Cavity diameter (m)	1.34	1.34	1.34	1.34
Cavity length (m)	0.59	0.84	1.15	1.53
Number of cells	9	10	11	12
Max. gap voltage (kV)	200	250	315	370
Effective shunt impedance (MΩ/m)	751	510	345	244
Max. peak power (kW)	5	11	22	40

The IH linac has the following characteristics: 1) it accelerates ions from a very low energy of 170 keV/u; 2) synchronous phase is chosen at -25° to assure the stable longitudinal motion in spite of the strong transverse rf defocusing force in the accelerating gaps; 3) to obtain high shunt impedance, a π - π mode is adopted as an accelerating periodic structure, and no transverse focusing element is installed in the drift tubes; 4) the IH linac is divided into four cavities to set the transverse focusing elements locally, and to vary the output energy easily; 5) the output energy is continuously varied by changing the rf power and the phase in a last cavity of the working ones.

The quadrupole triplet is placed in short space of 47.5 cm to make the decrease of the longitudinal acceptance small. As a result, the longitudinal acceptance is 200π keV/u-deg, which is nearly three times as large as the predicted beam emittance from the SCRFQ. The transverse emittance of the radioactive beams is estimated to be less than 0.1π mm-mrad. However, an acceptance larger than this value is required, considering the emittance growth at the charge stripper and the acceleration of stable nuclei from other ion sources. The acceptance of 2.4π mm-mrad is achieved by selecting the bore radius of quadrupole triplets as 20 mm. The quadrupole triplet, 9, 14 and 9 cm in pole length, requires high field gradient such as 55 T/m at maximum. The axial length of the four cavities is shorter than or near the diameter needed for a resonant frequency of 51 MHz. To estimate the rf characteristics, an equivalent circuit analysis was performed. The analysis predicts that diameters of the four 51-MHz cavities are kept in the same size by adjusting the radius of the drift tubes of each cavity in the range of 2~4 cm, and by adjusting the sizes of magnetic flux inducers.

IV. CHARGE STRIPPER SECTION

By considering budgetary and space limitations, we designed a compact stripper section, 3 m in total length, as shown in Figure 3 [4].

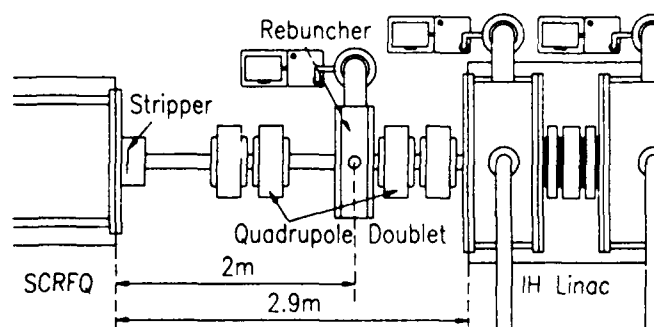


Figure 3. Layout of the stripper section.

In the design of the stripper section, a $^{12}\text{C}^+$ ion beam is used, because $^{12}\text{C}^+$ ion has larger energy-deposit and energy-straggling per nucleon in the stripper than other ions. The energy loss is about 6 keV/u and the energy straggling is about ± 1 keV/u when the beam with an energy of 170 keV/u passes through a carbon foil, $10 \mu\text{g}/\text{cm}^2$ in thickness.

Since the transverse emittance-growth in the stripper is proportional to the beam size, the stripper is placed just behind the SCRFQ, where the beam size is relatively small. The emittance-growth rate of the beam is about 1.6 in the horizontal plane and about 1.2 in the vertical one. The longitudinal matching of the beam is done by means of a rebuncher cavity. It is convenient for matching that the position of the rebuncher is near to the SCRFQ, because the debunching due to the drift space becomes small. The distance between the SCRFQ and the rebuncher is uniquely determined as a function of the distance between the rebuncher and the IH linac, when the longitudinal matching is satisfied. As a result, the distance between the SCRFQ and the rebuncher is determined to be 2 m, since the space longer than 0.9 m is necessary to set a doublet between the rebuncher and the IH linac.

V. STATUS AND PERSPECTIVE

Two unit cavities and a 350-kW power amplifier for the 170-keV/u SCRFQ were constructed in fiscal year 1992. Construction of a unit cavity, conversion of the prototype and whole assembling will be performed this year. By using a half scale model cavity, the rf characteristics of the IH linac are being investigated. On the basis of the model studies, the cavities and the rf power amplifiers will be constructed this year. The design of the charge stripper section was almost completed. As the rebuncher, a spiral loaded cavity working at 25.5-MHz is being developed.

VI. ACKNOWLEDGMENTS

The authors express their thanks to T. Nomura and M. Kihara for their encouragement. This work is supported by Accelerator Research Division, High Energy Physics Division, and Nuclear Physics Division of INS. The computer works were done on FACOM M780 in the INS Computer Room.

VII. REFERENCES

- [1] N. Tokuda *et al.*, INS Rep. 897, 1991.
- [2] K. R. Crandall, LA-9695-MS, 1983.
- [3] M. Tomizawa *et al.*, these proceedings.
- [4] K. Niki *et al.*, these proceedings.

Interdigital-H Linac for Unstable Nuclei at INS

M. Tomizawa, S. Arai, M. Doi, T. Katayama, K. Niki, M. Yoshizawa
Institute for Nuclear Study, University of Tokyo
3-2-1 Midori-cho, Tanashi-shi, Tokyo, 124, Japan
T. Hattori

Research Laboratory for Nuclear Reactors, Tokyo Institute of Technology,
Ohokayama, Meguro-ku, Tokyo 152, Japan

Abstract

In the prototype facility of the Exotic-arena at INS, unstable nuclei with a charge-to-mass ratio greater than 1/10 is accelerated from 170 to 1046 keV/u by an interdigital-H linac. Designed IH linac consists of four acceleration tanks and three sets of quadrupole triplets placed between tanks. Output energy is continuously variable by changing rf power and phase of the last operating tank. A high shunt impedance is expected from an equivalent circuit analysis. The rf measurement on the low power models is now in progress. Preliminary results of the tank-4 model shows that a resonant frequency and a shunt impedance roughly agree with the design values.

I. INTRODUCTION

The construction of the prototype facility of the Exotic-arena proposed in the Japanese Hadron Project(JHP) started at INS in 1992[1-3]. In this facility, unstable nuclei accelerated up to 170 keV/u by a split coaxial RFQ is charge-exchanged by a stripper up to a charge-to-mass ratio (q/A) greater than 1/10, and further accelerated by an interdigital-H linac[4,5]. Design of the interdigital-H (IH) type linac has been performed in 1992. Designed IH linac has the following characteristics. (1) It accelerates the heavy ions from low energy (170 keV/u). (2) Synchronous phase is selected as -25 deg to assure the stable longitudinal motion in spite of the strong transverse rf defocusing force in the accelerating gaps. (3) To obtain high acceleration efficiency, a π - π mode is adopted as a periodic structure, and no transverse focusing element is installed in the drift tubes. (4) The IH linac is divided into four tanks. Transverse focusing elements are placed between tanks. (5) The output energy is continuously variable from 170 to 1046 keV/u by tuning the rf power and phase.

The view of the designed IH linac is shown in Figure 1.

The parameters of the designed IH linac are listed in Table 1.

II. BEAM DYNAMICS

The resonant frequency of the IH linac is chosen to be twice as high as that of the SCRFQ. To keep the phase spread small, the length of drift spaces where Q-magnets are placed should be as short as possible. The length of the drift spaces is taken to be 47.5 cm. In this case, longitudinal acceptance of 200π keV/u-deg is obtained, which is nearly three times as large as the predicted beam emittance from the SCRFQ. The transverse emittance of the unstable nuclei is small, estimated to be less than 0.1π mm-mrad[6]. But an acceptance larger than this value is required because of an emittance growth at the charge stripper. The acceptance of 2.4π mm-mrad (transmission 97%) is achieved by setting the bore radius of quadrupole magnets at 20 mm (the emittance of the SCRFQ is estimated to be 0.6π mm-mrad). Figure 2 shows the calculated longitudinal and transverse beam traces. In this calculation, longitudinal and transverse emittance at the entrance of the tank-1 are taken to be 200π keV/u-deg and 1.7π mm-mrad, respectively.

The output energy of the IH linac can be continuously varied by tuning the rf power and phase in the last tank of operating ones. The variation of output energies results from separating the IH linac into several tanks. Figure 3 shows the output energy and its spread as a function of the gap voltage. Longitudinal emittance at the entrance of the tank-1 is taken to be 200π keV/u-deg. For example, if a certain energy in the range from 471 to 721 keV/u is needed, the gap voltage of tank-3 is varied without operating tank-4. The energy spread ($\pm\Delta T/T$) is $\pm 2\sim 6\%$ except at the exit of tank-1. Its spread, however, can be made smaller by adjusting the rf phase as well as the gap voltage.

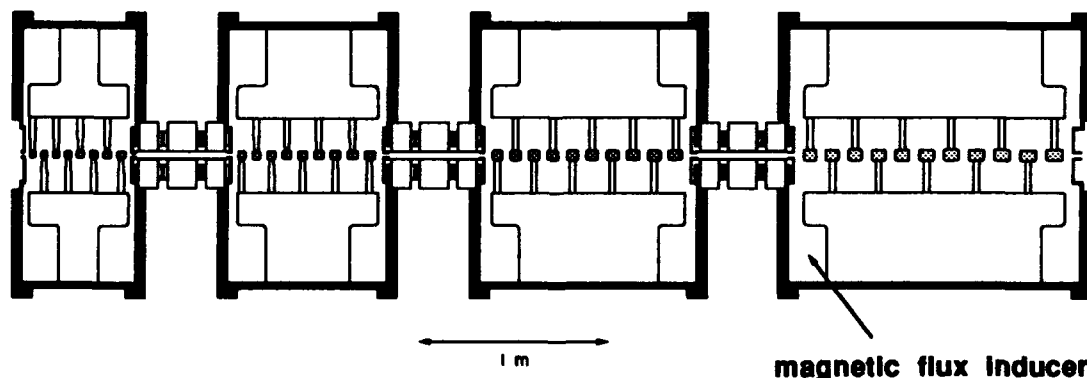


Fig.1 View of the desined IH linac.

Table 1 Parameters of designed IH linac.

	tank-1	tank-2	tank-3	tank-4
resonant frequency (MHz)	51	51	51	51
charge-to-mass ratio	$\geq 1/10$	$\geq 1/10$	$\geq 1/10$	$\geq 1/10$
energy (keV/u)	170 ~ 292	292 ~ 471	471 ~ 721	721 ~ 1046
velocity β (%)	1.91 ~ 2.50	2.50 ~ 3.18	3.18 ~ 3.93	3.93 ~ 4.74
synchronous phase (deg)	-25	-25	-25	-25
tank diameter (m)	1.34	1.34	1.34	1.34
tank length (m)	0.59	0.84	1.15	1.53
cell number	9	10	11	12
acceleration gradient (MV/m)	2.73	2.73	2.72	2.65
effective shunt impedance (M Ω /m)	751	510	345	244
maximum peak power (kW)	5.1	11	22	40

III. QUADRUPOLE MAGNETS

To obtain large transverse acceptance, the bore radius of quadrupole magnets was chosen to be 20 mm. High field gradient (5.5 kG/cm at maximum) is required to focus the beam. Further, compact sizes are required to be placed in the 47.5 cm long drift space. Design of the quadrupole magnets

was performed by the computer code TRIM. The parameters of the quadrupole magnets are shown in Table 2. To obtain high field gradient, pure iron with a low amount of carbon will be used as the material of poles and yokes. From the calculation, 10000 A-T is necessary to attain the field gradient of 5.5 kG/cm. To save the cost of the power supplies, the size of hollow conductors used as the coils of magnets was chosen to keep the maximum current in 300A. As a result, the coil has two lines for water cooling per pole. One set of the quadrupole triplets is now under construction. Effects of the adjacent quadrupole magnets and the saturation of the magnetic field in the pole will be investigated by field measurements.

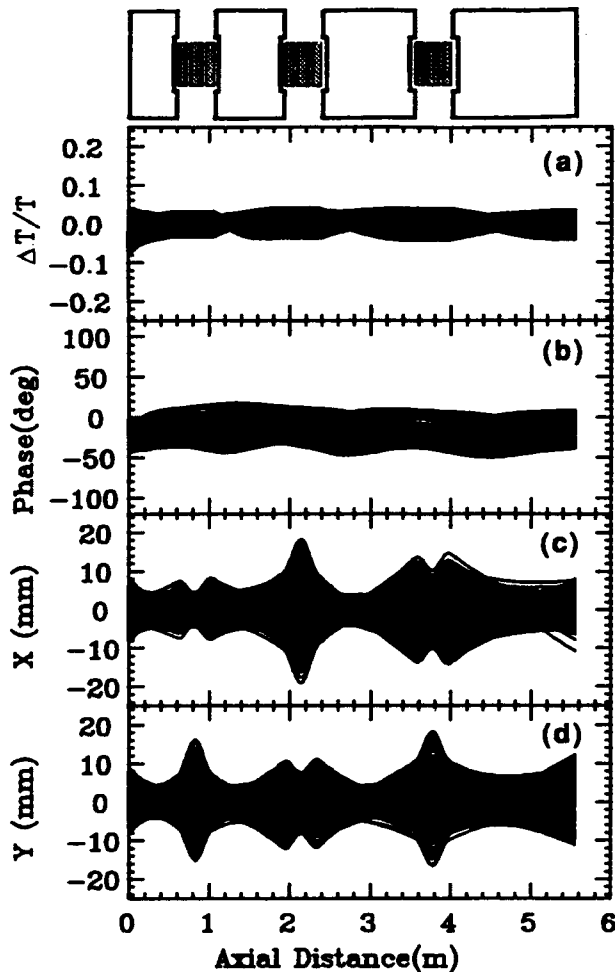


Fig.2 Calculated beam profile.

IV. RF CAVITY

A. Cavity Design

Axial length of the four cavities is shorter than or near the diameter needed for resonant frequency of 51 MHz. To estimate the resonant characteristics, an equivalent circuit analysis was performed. In this analysis, the capacitance in each cell was partially calculated by the computer code SUPERFISH. The inductance of each cell was approximately obtained by assuming uniformity of the magnetic flux[7]. The equivalent circuit composed of these cells is terminated by a circuit composed of the capacitance and inductance of end

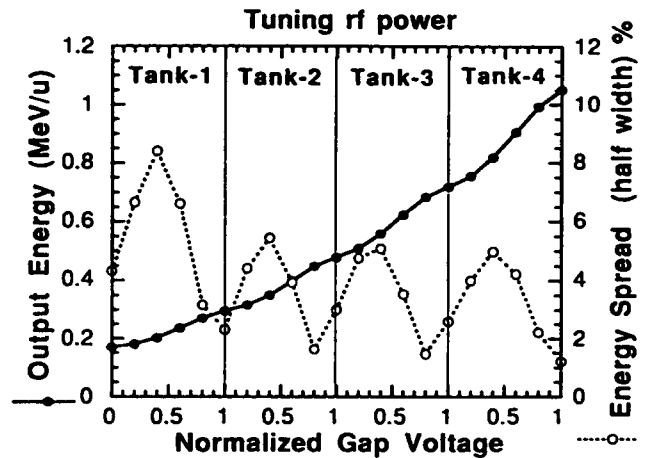


Fig.3 Output energy and its spread as a function of normalized gap voltage.

Table 2 Design parameters of quadrupole triplet.

	QS 1	QL	QS 2
bore radius (cm)	2	2	2
pole length (cm)	9	14	9
max. B' (kG/cm)	5.5	5.5	5.5
max. current (A)	300	300	300
max. power (kW)	9.3	11.2	9.3

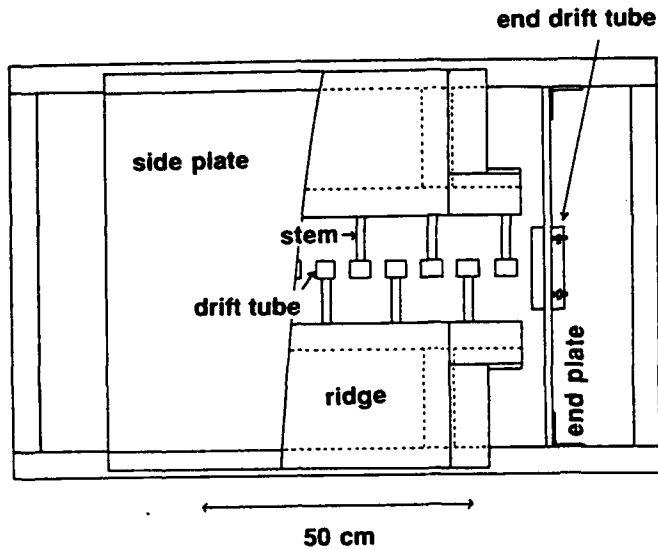


Fig.4 1/2 scale model of the tank-4.

spaces. In our case, the end capacitance as well as the end inductance depends on the size of the magnetic flux inducers. These sizes were chosen to resonate the closed equivalent circuit at 51 MHz. The analysis predicts that the diameters of four 51 MHz-tanks are kept in the same size (134 cm) by adjusting the radius of the drift tubes of each tank in the range of 2~4 cm, and by adjusting sizes of the magnetic flux inducers. Predicted effective shunt-impedances are shown in Table 1 together with maximum peak powers. In this table, the reduction factor of 0.6 is included in the shunt impedances and the consumption powers. This factor is due to the surface roughness of conductor and the contact resistance.

B. Low Power Models

On the basis of the analysis described in (a), 1/2 scaled low power models for the tank-1 and tank-4 were constructed. Schematic drawing of the tank-4 model is shown in Fig.4.

The rf measurements are now in progress. In a preliminary result, the resonant frequency of 106 MHz (the design value is 102 MHz) was obtained for the tank-4 model. Figure 5 shows the field distribution of the tank-4 model measured by the bead perturbation method. Shunt impedance of the tank-4 estimated from this field measurement is about 230 M Ω /m for the practical use machine, which roughly agrees with that by the equivalent circuit analysis. The field distribution and the resonant frequency will be optimized by increasing the area of the magnetic flux inducer.

In these models, the end drift tubes were designed to be movable to the axial direction. In practical use machine, the

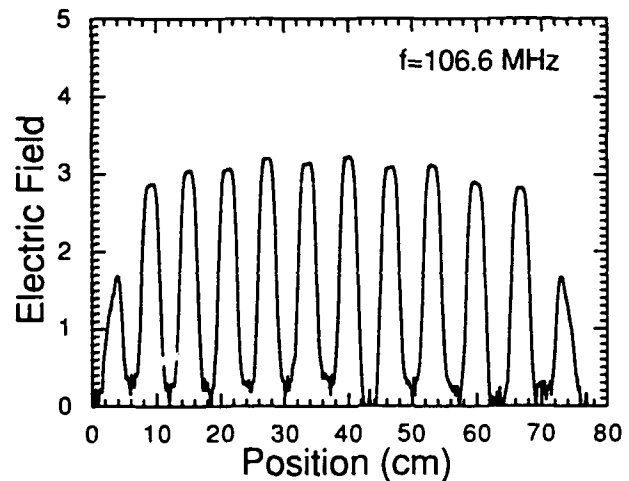


Fig.5 Measured field distribution of the tank-4 model.

end plate of the end drift tubes is slightly bent by vacuum pumping of the tanks. The effect of this bend on the rf characteristics of the cavity will be investigated.

V. SCHEDULE

The tests on the model cavities will be completed in summer 1993. Two of four acceleration tanks and all of four rf amplifiers for the practical use will be constructed in the fiscal year 1993. The remaining two tanks will be constructed together with two sets of the quadrupole triplets in the fiscal year 1994. First beam test is planned in the fiscal year 1995.

VI. ACKNOWLEDGEMENT

We would like to thank T. Morimoto for useful advices with the design of the cavity models. We are also grateful to R. Nagai for the help with the drawings of the models.

VII. REFERENCES

- [1] T. Yamazaki, INS-Report-763 (1989).
- [2] T. Nomura, INS-Report-780 (1989).
- [3] M. Tomizawa et al., INS-Report-953 (1992).
- [4] S. Arai et al., these proceedings.
- [5] K. Niki et al., these proceedings.
- [6] T. Nomura, Private communication.
- [7] S. Arai, INS-JHP-20 (1991), in Japanese.

SPIRAL: A Radioactive Ion Beam Facility at GANIL

A. Joubert, R. Anne, P. Bertrand, MP. Bourgarel, C. Bieth, B. Bru, A. Chabert,
M. Duval, R. Leroy, Ch. Ricaud, P. Sortais and the project group

GANIL
BP 5027, F-14021 CAEN Cedex

Abstract

The SPIRAL project makes use of the very high intensity ion beams soon available at GANIL (over 10^{13} pps at 95 MeV/u from He to Ar) to produce radioactive nuclei by the ISOL method. The facility will consist of a production target situated close to an ECRIS specially designed for this purpose, a very low energy beam line, a $k=265$ compact cyclotron as postaccelerator (2 to 20 MeV/u according to the Q/A factor), a medium energy beam line transferring the radioactive beams into the existing experimental rooms through the α spectrometer. The whole facility will be installed at the end of the existing machine.

I. INTRODUCTION

From the first experiments at GANIL, fragmentation reactions have been used to produce and study exotic nuclei. Such a research made use of the large intensities obtained through the whole accelerator system. It was realized that these beams could also be used to produce nuclei at rest in thick targets and to adapt the ISOL method to primary heavy ion beams.

This program is now under consideration with the project of a RIB facility here presented and a strong effort of R&D concerning the production and the ionization of secondary elements has been set up [1].

Such a program can only be conducted if the GANIL accelerator is able to deliver very intense beams. The first part of this operation is almost completed [2] and over 10^{13} pps of light ions (He to Ar) are already available at the exit of the injector cyclotron. The second part, which consists in injecting, accelerating and transferring such beams up to the high energy beam line, has partially been funded this year. So more than 10^{13} pps (~ 5 kW of beam power) at full energy (95 MeV/u) will routinely be obtained by the end of 1995.

After various versions [4] our final project for a RIB facility called SPIRAL (Séparateur et Postaccélérateur d'Ions Radioactifs produits en Ligne) is described below.

II. TARGET AND ECRIS SYSTEM

Having decided to look at a RIB facility based on a heavy ion primary beam and a high charge state ion source, we soon began an important R & D program to investigate the possibilities of this solution and to get some experience on the target and associated ECR devices.

A first rather crude test bench [1] was built and gave the first results in 92. Using a 95 MeV/u, ^{20}Ne beam and a MgO target, radioactive isotopes in charge states 1 to 4 have been produced (^{18}F , ^{19}F , ^{23}Ne , ^{24}Ne , ^{13}N ...). The yields for the

various isotopes were, at the target level, in the range of 10^9 to 10^7 pps per μA of primary Ne beam.

These encouraging results lead us to conceive a new efficient test bench now under construction [1] with the goal to run it by the end of this year.

It will really be the prototype of the target-ECRIS system of our project allowing us to study all the technical problems involved : target behaviour under high power, permanent magnet ECR in a high radiation field, coupling of the target to the ECR, remote handling problems and so on.

III. THE POST-ACCELERATOR

Our choice of a compact cyclotron is based on the following main reasons :

- First of all, using a high charge state ion source allows us to consider a cyclotron.

- Second, the energy range to be covered (≈ 2 to 20 MeV/u) and the charge over mass ratio as given by the ECRIS (≈ 0.1 to 0.35) are typical of a compact cyclotron whose beam characteristics satisfy rather well the requirements of the physicists. Moreover, a cyclotron is by itself a powerful mass analyser and will deliver rather pure beams, a prime quality in RIB physics.

- Third, GANIL has a good knowledge about cyclotrons and a large experience in their design and operation so that no more than 4 years after funding will be needed to deliver a first beam. Moreover, this new facility will fit in the loose end of the existing building still lowering the cost of an already rather cheap solution.

A. The working chart

The goal being to provide the $A \approx 100$ ions produced by the ECRIS with $Q/A \approx 0.15$ at an energy ≈ 6 MeV/u, we thus obtain :

$$(\bar{B} \cdot \bar{r})_{\text{ejec}} = 2.344 \text{ T.m} \quad (K = 265)$$

The magnetic rigidity of the present high energy beam lines being 2.88 T.m, the cyclotron beams will be accepted without any problem in our experimental areas.

Choosing a mean ejection radius of 1.5 m results in a conservative $B_{\text{max}} \approx 1.56$ T and in the working charts displayed on the figures 1 and 2. The limits seen on these figures are related to the values chosen for the max and min mean field (0.75 - 1.56 T), the max voltage on the 2 dees (≈ 100 kV), the lowest ion source extraction potential (≈ 10 kV) and the revolution frequency range (≈ 1.92 to 7.25 MHz).

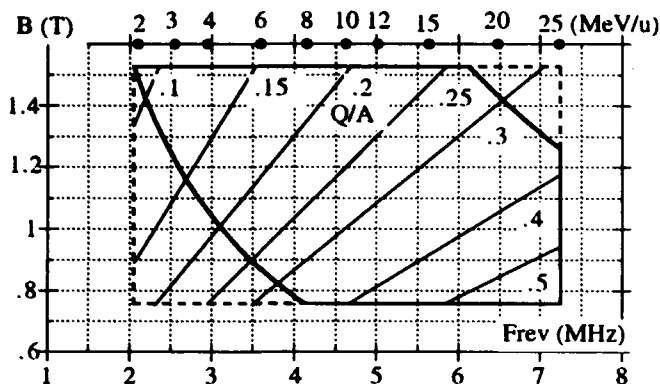


Figure 1. Working chart.

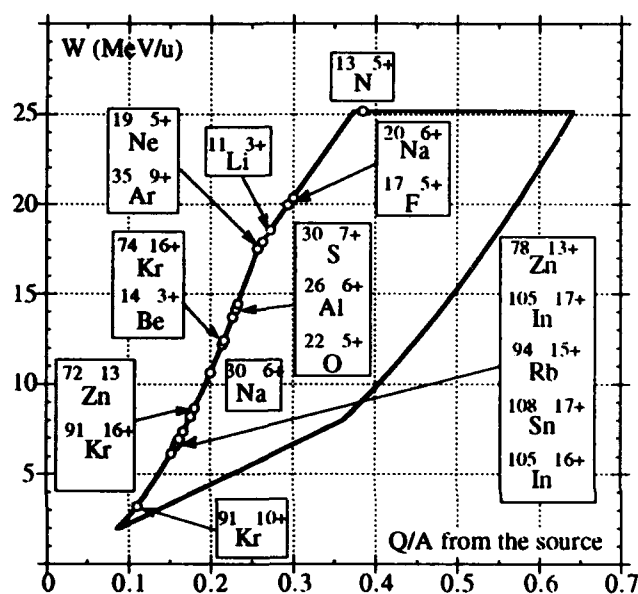


Figure 2. Energy range.

B. Description of the cyclotron

. The RF system covers the f_{rev} range using the harmonics 2-3-4 and 5 with $9.6 \leq f_{rf}$ (MHz) ≤ 14.5 . Such an RF frequency range leads to a rather compact resonator : external diameter ≈ 1.2 m, length ≈ 1.3 m, internal coaxial line diameter ≈ 0.25 m and displacement of the short circuit ≈ 0.70 m. The power dissipated at 100 kV turns out to be as low as ≈ 40 kW. Using two 40° dees and choosing to accelerate all the ions whatever their output energy with a constant turn pattern, the number of turns will be ≈ 250 and the turn separation at ejection ≈ 3 mm.

. The magnet will be built using 4 independant yokes and common circular poles (3.5 in diameter) equipped with 4 straight 45° sectors. Hill and valley gaps are respectively 12 and 30 cm allowing an easy fitting of the 2 dees and giving a good flutter.

Using TOSCA code, we have refined the magnet geometry so that the maximum correction required is as low as ± 200 gauss, the gradients being ≤ 5 G/cm. Circular trim

coils (≈ 10) located on the poles and giving $7.5 \cdot 10^{-2}$ G/AT and $2.5 \cdot 10^{-3}$ G/cm/AT, will be used to shape the field within the required tolerances. The inner region ($r \leq 20$ cm) where the sectors join the central plug is still to be refined.

. The central geometry (axial injection and Mueller type inflector) is under study with the goal to work out a fixed injection pattern suited for the 4 harmonics we will use. Our first studies concerning the beam centering and its 6D matching lead to fine results for $h = 2 - 3$ (above the heavy ion Coulomb barrier) and $h = 4$. In the case of $h = 5$ (≤ 3 MeV/u) the same geometry can still be used but the acceptance and so for, the intensities will be reduced.

. The extraction system is quite conventional including one electrostatic deflector located in a valley (≤ 60 kV/cm) followed by two magnetic channels (gradient compensation). A field bump will be used to increase the turn separation.

C. The beam characteristics

Using either the multiparticle code NAJO or the newly written one LIONS [3] we have simulated the beam behaviour in this cyclotron.

. Beam transmission : using similar central region and injection line (6D matching) as for our present GANIL injector [2], we can expect similar transmissions e.g $\geq 40\%$ from the ion source analyzed beam to the cyclotron extracted one (we have obtained a 75% record transmission in our injector).

. Beam emittance : injecting a matched beam, 80π mm.mrad in each transverse plane and $\pm 6^\circ$ in phase width, leads in front of the extraction system to a monochromatic transverse emittance $\approx 8.5 \pi$ mm.mrad and to an energy dispersion of $\pm 3.5\%$. In these conditions, the extracted beam will contain parts of the 3 last accelerated turns and so the characteristics of the extracted beam will be lowered. However, it seems possible, at least for $h = 2 - 3$ to bunch the injected beam in a $\pm 3 - 4^\circ$ phase width, in this case due to the low energy spread ($\leq \pm 1\%$) a single turn extraction is possible and the extracted beam qualities are much improved ($\Delta W/W \leq 1\%$, emittances $\leq 10 \pi$ mm.mrad).

. Mass analysis : besides the usual analyser following the ECRIS which eliminates most of the contaminants, (see IV), the cyclotron will select Q/A within 3.5 to $1.5 \cdot 10^{-4}$ depending upon the harmonic. These values should be sufficient for most of the experiments ; if not, we will put a thin target at the object point of the α spectrometer, which will select the right component within some 10^{-5} taking advantage of the difference in the energy losses of the various ions (isobars) through the foil. The resulting beam will of course suffer of the target crossing (mean energy, emittances and energy dispersion), nevertheless good characteristics could be restored, the price being to be paid on the intensity. This method will be limited to ions of $A \leq 80$ at $W \geq 6$ MeV/u.

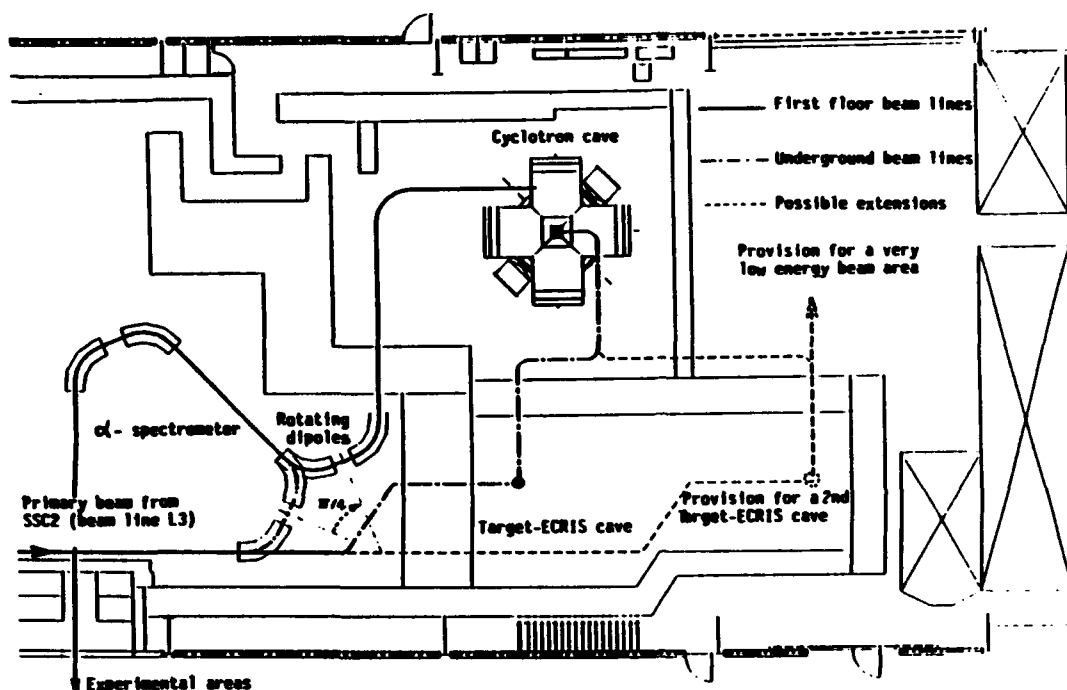


Figure 3. Layout of the SPIRAL facility

IV. THE BEAM LINES

The layout of the RIB SPIRAL facility is shown on the figure 3. As we see, we need to study and to build three beam lines.

. The primary beam line from the SSC2 output to the target will be the prolongation of L3. From the object point of the α spectrometer, the primary beam ($B_p \leq 2.88 \text{ T.m}$) goes straight through the first α dipole and is bent down to the heavily shielded production target cave (-3m) using an antisymmetrical achromatic deviation and a two quadrupole doublet system devoted to the transverse matching of the beam on the target. The beam spot is adjustable from ± 2.5 to $\pm 13 \text{ mm}$ for transverse emittances ranging from 2.5 to $6 \pi \text{ mm.mrad}$. This primary beam line $\approx 13 \text{ m}$ in length could be extended to a second target cave using the same optics.

. The low energy beam line ($B_p \leq 0.05 \text{ T.m}$) from the ECRIS extraction to the cyclotron inflector is $\approx 19 \text{ m}$ in length. It can be divided into two main parts :

- The first part includes an achromatic magnetic mass spectrometer system followed by a matching section to the second part. The optics [1] will insure a $m/\delta m$ resolution of 250 for a $80 \pi \text{ mm.mrad}$ radial emittance. Such a resolution is quite enough as far as the cyclotron injection is concerned, anyway it would be almost impossible to exceed the cyclotron resolution at this level in order to fulfil the physics requirements. The second dipole will accommodate the beam from the second ECRIS if any, it can also be crossed without any deviation to feed a very low energy beam area under discussion (atomic and astro physics).

- The second part similar to the one used on our present injector is devoted to the 6D matching on the first accelerated orbit of a $80 \pi \text{ mm.mrad}$, $\pm 6^\circ$ in phase beam as accepted by the cyclotron.

. The high energy beam line ($B_p \leq 2.344 \text{ T.m}$) extends from the cyclotron exit to experimental caves through the analyzing section of the α -spectrometer (to do so the first 2 dipoles of the α -spectrometer can be rotated by 45°). The acceptance of this line will amount at least to $10 \pi \text{ mm.mrad}$ and $\pm 3\%$ in energy dispersion. We will have to build $\approx 21 \text{ m}$ of new line divided into a first part allowing a betatronic isochronisation of the cyclotron beam and a second one to be used for the transversal matching of the beam at the α - spectrometer object point.

V. CONCLUSION

The proposal will greatly enlarge the possibilities opened at GANIL in the field of radioactive ion beam physics at low and medium energy. Moreover, this new facility can be built without disturbing the classical use of GANIL.

Due to its rather low cost ($\leq 100 \text{ MF}$), to the short delay involved (≤ 4 years) and to the available experimental facilities we can really expect that this project will be funded and so be confident in the future of our laboratory.

VI. REFERENCES

- [1] - P. Sortais et al, "An On Line Isotopic Separator Test Bench at GANIL", this conference.
- [2] - Ch. Ricaud et al, "Commissioning of the New High Intensities Axial Injection System for GANIL", 13th. Int. Conf. on Cyclotrons and their Applications, Vancouver, Canada, July, 1992.
- [3] - P. Bertrand "Le programme LIONS, version 1.0", Int report, GANIL.
- [4] - M.P. Bourgarel et al, "Proposals for a Radioactive Ion beam Facility at GANIL", NIM in P.R. A328 (1993) 321-324.

On Line Isotopic Separator Test Benches at GANIL

R. Anne, B. Bru, A. Joubert, R. Leroy, M. Lewitowicz, P. Sortais, M.G. Saint Laurent, C. Tribouillard

GANIL

BP 5027, 14021 CAEN Cedex, France

J. Obert, J.C. Putaux,

C.F. Liang, P. Paris

IPN

CSNSM

91406 Orsay Cedex, France

91406 Orsay Cedex, France

N. Orr, J. C. Steckmeyer

LPC-ISMRA

6, Bld du Maréchal Juin, 14050 Caen Cedex, France

Abstract

A first version of isotopic separator on line test bench has been built in order to test the feasibility of the production of radioactive species from 96 MeV/u of ^{20}Ne impinging a thick target of MgO. This test bench was equipped with a very compact ECR ion source (Nanogan) entirely made from permanent magnets and operating at 10 GHz.

We succeeded in producing and ionizing $^{18}\text{Ne}^{2.4+}$; $^{19}\text{Ne}^{1,2,3,4+}$ and $^{23,24}\text{Ne}^{1+}$.

We then decided to build a new more performing separator (SIRa) allowing the use of different types of ion sources. It will be completed by the end of 1993.

I. INTRODUCTION

From the first experiments at GANIL, fragmentation reactions have been used to produce and study exotic nuclei. Such a research made use of the large intensities obtained through the whole accelerator system. It was realized that these beams could also be used to produce nuclei at rest in thick targets and to adapt the ISOL method to primary heavy ion beams.

This program is now under consideration with the project of a RIB facility (SPIRAL project [1]).

An important R&D program has been implemented from mid 1991 to investigate the use of high energy ion beams provided by the GANIL facility to produce radioactive atoms by the ISOL method.

We present the first version of isotopic separator and the results we got with it in 1992. We are now building a new isotopic separator called SIRa (Séparateur d'Ions Radioactifs) which is thereafter described.

II. THE FIRST ON-LINE SEPARATOR

The challenge is to continuously separate the produced nuclei from a huge amount of target nuclei and transfer them into the gas phase to the plasma of a ECR ion source. Such a transfer process is only governed by element specific diffusion, desorption and chemical processes.

A - The target box

The target box, the same as the one constructed by the ISOCELE group at Orsay [2], has been connected to a new compact ECR ion source specially designed for that purpose [3]. Fig.1 shows a schematic cut of the target chamber and its coupling to the source. The target is mounted on the rear flange of the target box and placed in a nickel container.

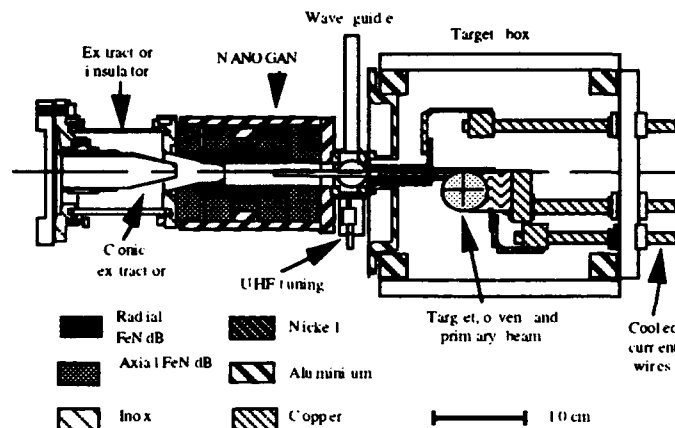


Figure 1. Cut of the target-ECRIS system.

The container is a 7.5 cm long cylinder heated by ohmic power up to 1200°C maximum. It is put at the source potential (15 to 20 kV). The transfer tube (25 cm long, 5mm inner diameter), also made of Ni, is welded on the container and inserted into the inner copper tube of the source.

B - The Nanogan source

The ionizer is a very compact ECR ion source (called Nanogan), entirely made of Fe.Nd.B permanent magnets for both radial and axial magnetic confinement. Its dimensions are 17 cm long and 13 cm diameter. This ECR ion source needs a rather small amount of microwave power: < 100W at 10 GHz.

C - The separator

Due to the short requested duration of realization and the limited budget allotted, the separator has simply been made up of available components: a 102° bending magnet (acceptance figure 150 π .mm.mrad), allowing a maximum mass resolution of 10^{-2} , a diagnostic box (with horizontal slits and beam profile monitor) followed by two electrostatic quadrupole doublets.

D - The detection system

The collection chamber at the end of the separator beam line is equipped with a Faraday cup and the tape transport system coming from ISOCELE experiment [2]. It is operated in primary vacuum, except for the collection point placed in secondary vacuum.

The collected ions are periodically moved to one of the two different detector locations. In the first one, two NaI detectors detect in coincidence the two gammas produced by the β^+ annihilation. At the second one, there are a plastic scintillator and a Ge detector.

III - RESULTS AND DISCUSSION

Table 1 gives the measured parameters of different isotopes detected.

As predicted "light" Neon (^{19}Ne , ^{18}Ne) coming from projectile fragmentation process together with "heavy" Neon (^{23}Ne , ^{24}Ne) coming from target fragmentation have been observed. Charge states higher than 1^+ have been obtained (Ne^{3+} , Ne^{4+}) which corresponds to suitable Q/A values for postacceleration in the cyclotron of the SPIRAL project.

The last column but one of table 1 gives the production yield corrected from transmission and ionization efficiencies in order to compare real and calculated values.

This table shows also the rather poor transmission factor of this separator since the overall efficiency was only around 3,5 %. Nevertheless, tests made off-line with Nanogan operated with stable ions and calibrated leak have shown that a total ionization efficiency of 40 % was obtained in real experimental conditions.

	Separator		ECR I. S.		Target	
	Yield meas. pps/pμA	Trans. eff. %	Yield extract. pps/pμA	Ion. eff. %	Yield prod. pps/pμA	Yield Calc. pps/pμA
$^{19}\text{Ne}^{1+}$	$4.8 \cdot 10^7$	3.5	$1.4 \cdot 10^9$	25	$5.6 \cdot 10^9$	
$^{19}\text{Ne}^{2+}$	$8.9 \cdot 10^6$	3.5	$2.5 \cdot 10^8$	7.5	$3.3 \cdot 10^9$	
$^{19}\text{Ne}^{3+}$	$1.6 \cdot 10^6$	3.5	$4.6 \cdot 10^7$	4	$1.2 \cdot 10^9$	
			$\Sigma 1.7 \cdot 10^9$	40	$4.3 \cdot 10^9$	$1.3 \cdot 10^{10}$
$^{18}\text{Ne}^{2+}$	$1.9 \cdot 10^6$	3.5	$5.4 \cdot 10^7$	7.5	$7.2 \cdot 10^8$	
$^{18}\text{Ne}^{4+}$	$1.9 \cdot 10^5$	3.5	$5.4 \cdot 10^6$	3.5	$1.5 \cdot 10^8$	
			$\Sigma 2.7 \cdot 10^8$	40	$6.8 \cdot 10^8$	$2.7 \cdot 10^9$
$^{23}\text{Ne}^{1+}$	$6.3 \cdot 10^5$	3.5	$1.8 \cdot 10^7$	25	$7.2 \cdot 10^7$	$5.0 \cdot 10^8$
$^{23}\text{Ne}^{1+}$	$1.5 \cdot 10^5$	3.5	$4.3 \cdot 10^6$	25	$1.7 \cdot 10^7$	$1.0 \cdot 10^8$
$^{13}\text{N}^{1+}$	$3.8 \cdot 10^5$	3.5	$1.1 \cdot 10^7$	1(?)	$1.1 \cdot 10^9$	$1.5 \cdot 10^9$

Table 1. Experimental results for on line isotope production with ^{20}Ne primary beam at 95 MeV/u on a MgO thick target. (*) Assum. $I_{\text{Ne}^{1+}} = 4 \times I_{\text{Ne}^{2+}}$ and $I_{\text{Ne}^{2+}} = 2 \times I_{\text{Ne}^{3+}}$ like ^{19}Ne .

The first version of separator has been useful for bringing out unacceptable drawbacks :

- the optics of the primary beam was not well under control (non achromatic focusing point),
- the detection system, located inside the experimental room, was not enough shielded from background noise and slow neutrons. As a consequence, the primary beam had to be pulsed which resulted in strong pressure variations in the source,
- the overall separator performance (resolution and transmission efficiency) was rather poor and not enough well controlled.

IV. THE NEW SEPARATOR

From 1992, September, a new separator called SIRa (Séparateur d'Ions Radioactifs) is under construction, according to the following specifications :

- the target will be put at the normal focusing point in the experimental room (achromatic point) ;
- the secondary beam line will be more sophisticated in order to have the possibility of creating an object point upstream the 90° dipole magnet, whatever the type of source in operation ;
- the collection point as well as the detectors will be installed outside of the room and concrete blocks added so as to strongly damp the background noise.

A - Target box

A new target box is under design. An internal mechanism will automatically withdraw the transfer tube from the ECR source so as to shut 3 insulating vacuum valves (contamination problem). So the used target will be kept under vacuum in a confined volume, easy to be handled.

B - The source

A new source, called Supermanogan, is under study.. Its commissioning is expected in mid 1994. That is why the first ECR source of SIRa will be a classical one (Caprice type 10 GHz), already available at GANIL.

V. BEAM OPTICS OF SIRa

A. Primary beam

The beam radius on the target (T on figure 2) can be varied from 4 to 15 mm (for emittances ranging from 2.5 to $6\pi \text{ mm.mrad}$) by means of a magnetic quadruplet. 2 steerers, 2 beam profile monitors (1 behind the quadruplet, 1 in front of the target) and a Faraday cup allow to adjust the beam on the target.

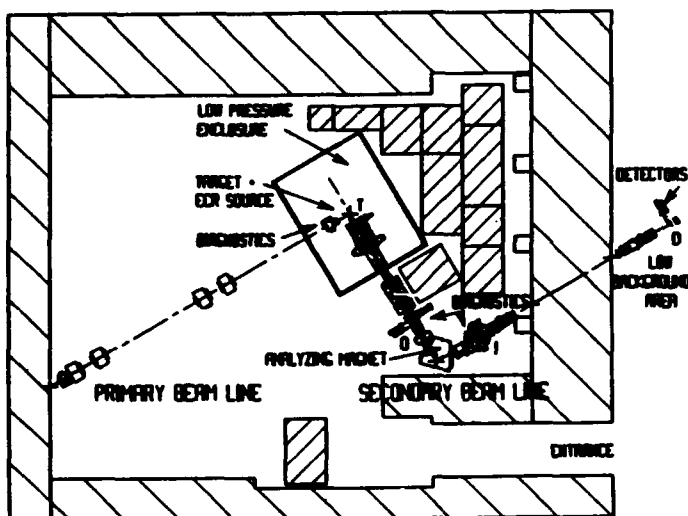


Figure 2. Layout of SIRa

B. Isotopic separator

The on-line isotopic separator follows the ECRIS ; it can be divided into two parts:

A matching section composed of a solenoid and a magnetic triplet to focus the beam at the object point O of the analyzing magnet. For an emittance of $150 \pi \text{ mm.mrad}$ (corresponding to the acceptance) and beam dimensions of $\pm 3 \text{ mm}$ at the source puller the radial size at O can be adjusted between ± 1.5 and $\pm 10 \text{ mm}$. The type of source can easily be

changed -provided that the solenoid remains close to it- by adjusting the distance between the solenoid and the triplet.

The maximum rigidity of the line of 0.136 T.m corresponds to the maximum field of the existing dipole.

The characteristics of the elements are :

- Solenoids : max field = 6800 G, magnetic length = 400 mm, bore diameter = 70 mm.
- Quadrupoles (which provide in addition a dipolar component for a steering purpose) : max gradient 3.5 T.m, magnetic length = 210 mm, bore diameter = 80 mm.

. An analyzing section composed of:

- A 90° double focusing dipole (max field = 3400 G., radius of curvature = 400 mm, gap height = 70 mm, max radial extent in the vacuum chamber = ± 120 mm, pole face rotation 27°, tilt of the focal plane with respect to the axis 27°).
- A sextupole (max field = 700 G, magnetic length 170 mm, bore diameter = 140 mm) is placed 230 mm in front of the dipole entrance to correct geometrical aberrations.

The calculated mass resolution is $4 \cdot 10^{-3}$ for an emittance of 80 π mm.mrad (see figure 3) ; the ZGOUBI code (4) was run with 200 particles uniformly filling a 4D hyperellipsoid ; a measured field map is used. A better resolution can be obtained by achieving a lower radial angle matching and then cutting with the slits located at 0. Vertical slits, as well as radial ones, can be used for stopping unwanted charge states.

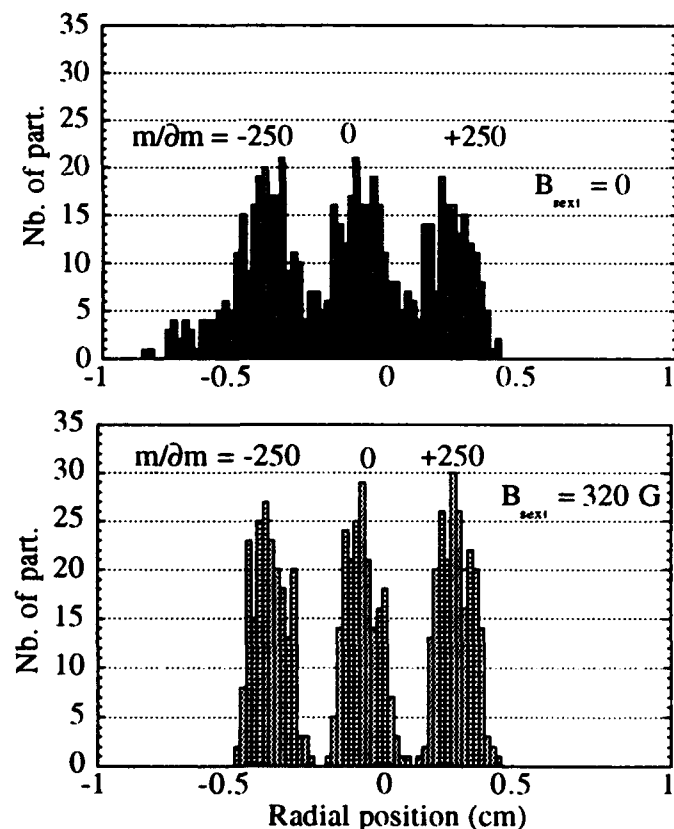


Figure 3. Mass resolution without and with sextupole

A special box for diagnostics is placed around the image point I. It contains a vertical wire moving parallel to the focal

plane, 2 radial slits moving in the plane, a beam profile monitor and a faraday cup. The tilt of the first 3 diagnostics can be manually adjusted.

Transport to the detector:

A set of electrostatic quadrupole doublet and triplet is used to transport the whole emittance on the detector D located in a very low background area. The beam diameter at D is 10 mm. Since there is independant power supply per electrode for each quadrupole, horizontal and vertical steering can be achieved. The quadrupole characteristics are : max voltage = 2.5 kV,

SIRa - FROM SOURCE PULLER TO DETECTION POINT -
FIRST ORDER ENVELOPES $\Delta m/m = \pm 4 \cdot 10^{-3}$
Em-H=150.00 V=150.00 π mm.mrad $\Delta W/W = 0.200$ pm
27/04/93 12.13.04 FICH. DON. -GSD2S12N-

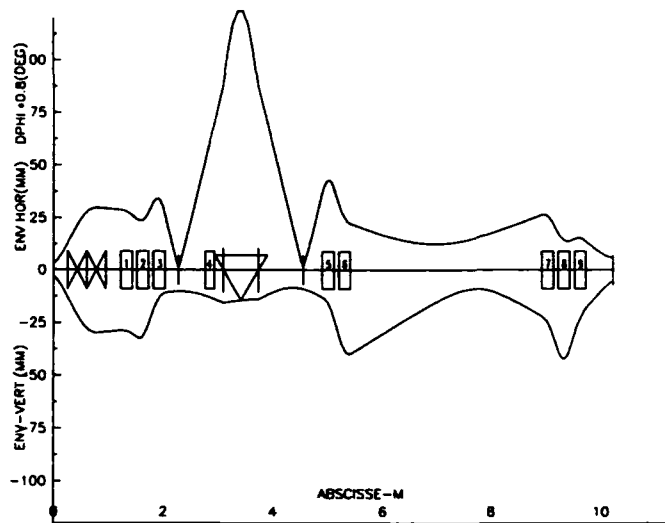


Figure 4. Beam envelopes from source to detector

VI. CONCLUSION

The first version of separator has allowed to establish the basic feasibility of the "ECR Source-close-to-target" concept for efficiently producing high charge state radioactive ions by the ISOL method.

With the new separator SIRa, high charge state and good transfer efficiencies are expected in a first step with gaseous radioactive ions like ^{19}Ne , ^{35}Ar or ^{78}Kr . First tests will take place by the end of this year.

In a second step, alkaline ions like ^{21}Na or ^{25}Na will be progressively tested together with a variety of research studies in the field of radioactive beam production.

VII. REFERENCES

- [1] - A. Joubert et al, "SPIRaL, A Radioactive Ion Beam Facility at GANIL, this conference.
- [2] - P. Paris et al, "Development of the Orsay High Current On-Line Separator ISOCELE", NIM 139 (1976) 251-256.
- [3] - P. Sortais et al, "NANOCHAN : An Ultra Compact ECRIS for On-Line and High Voltage Applications, ECR Ion Source Workshop, Groningen, 1993, May, 6-7.
- [4] - F. Méot and S. Valéro, ZGOUBI User's Guide, Saturne., note LNS/GT/90/05.

THE OUTLOOK OF MPC-10 CYCLOTRON USE FOR THE SOLUTION OF APPLIED PROBLEMS.

S. T. Latushkin, V. V. Leonov, A. A. Ogloblin,
L. I. Yudin, V. E. Yarosh, D. I. Yartsev
Russian Research Centre "Kurchatov Institute",
Moscow, 123182, Russia

ABSTRACT.

The compact isochronous MPC-10 cyclotron is now under construction at REC KI. It has been especially designed to operate as part of positron-emission tomography centre. The main cyclotron parameters are given, the opportunity to use it for solving some applied problems not related with PET is considered in the report.

INTRODUCTION.

At present the REC KI is being mounted the MPC-10 cyclotron, designed for negative hydrogen ions acceleration. The tests and adjustment of its various systems are being carried out. This cyclotron was especially designed as a part of positron-emission tomography centre. Thus the main cyclotron parameters were determined by the requirements for production of ultrashort-lived radionuclides C-11, N-13, O-15 and F-18, in the amounts measured in Curies (Table 1).

Table 1. The main parameters of MPC-10 cyclotron.

Accelerated particles	H ⁻
Extracted particles	H ⁺
Beam energy (max)	10 MeV
Beam current (max)	50 nA
Operating frequency	23 MHz
Harmonic mode	1
Pole diameter	80 cm
Magnetic field	1.5 T
Extraction radius	31 cm
Method of extraction	charge exchange
Extraction efficiency	100%
Number of extracted beams	2
H ⁻ ion source	PIC, internal

However, it seems to be expedient to consider some other applications for the accelerator of this type, installed at the scientific physical centre and operating at PET only part time, thus increasing the accelerator efficiency factor.

The study of wear and corrosion resistances for the metallic details of various machines by the thin-layer activation method is one of the promising field of MPC-10 cyclotron application. The essence of this method, as known, is as follows. The detail region under its wear resistance study is irradiated by the beam of accelerated particles penetrating into the detail surface layer and react with the metal nuclei, producing various γ -radioactive isotopes. Thus for the ironmasonry under irradiation by protons with the energy higher than 6 MeV the most preferable reaction is $^{56}\text{Fe}(p,n)^{56}\text{Co}$ with production of ^{56}Co radioactive isotope, which has a half-life period of 77.3 days, convenient for studying the wear resistance and a lot of intensive lines of short-wave γ -radiation. Then the operation of the mechanism in on-line regime is investigated at the test bench or directly during the exploitation process. Either the decrease in operating detail activity due to the attrition of the surface layer, or the increase in the activity of

lubricant, where the wear products accumulate is registered with, as a rule, NaI gamma-detectors.

The main advantages of the thin layer activation method are:

- 1) an opportunity to investigate the wear process dynamics without disassembling the machine;
- 2) an opportunity to determine the wear resistance of surface having complicated geometry;
- 3) high sensitivity;
- 4) economic efficiency: in the wear studies by the thin-layer activation method, one can save up to 80% of expenses and up to 90% of time in comparison with other methods of wear studies [1].

The MPC-10 cyclotron is designed for acceleration one type of particles, therefore, irradiation mode of metal, which the surface layer is activated by protons, is proposed. First of all, it is an iron which remains to be the main material the machine detail manufacture.

The activated layer thickness, which determines the possibility of wear studying by thin layer activation method, depends on the proton energy and on the angle of beam incidence upon the detail surface. Moreover, with the increase of the proton energy the Co isotope yield rises that allows one to reduce the detail irradiation time and hence to reduce the expenses on activation. However, at the energies exceeding 12 MeV reactions with productions of other isotopes has begun, which considerably reduces the method efficiency or even excluded the possibility of its application. Thus, the best proton beam energy for activating steel and iron is about 12 MeV. The activated layer thickness can be varied in a wide range (30-300 nm) due to the choice of beam incidence angle upon the detail surface. Changing the activation depth may also be effected by varying the proton energy from 9 to 12 MeV.

Such proton beam energies will make it possible to activate the details made of copper, titanium, chromium and others with the maximal activation depth of 250-300 nm, that turns out to be quite sufficient for the majority of problems in the wear study in mechanical engineering.

The maximal intensity of the beam which activates the experimental detail, as a rule, is determined by the conditions of cooling the irradiated detail region. The local heating in the irradiated area should not result in an essential change in the mechanical properties in this region. The typical beam intensity values for activation are not more than 1 nA.

Thus, the MPC-10 cyclotron completely satisfies the requirements for proton beam intensity from the point of view of its usage for the activation of the thin layer, but the maximal beam energy, taking into consideration energy losses at the output foil window turns out to be insufficient.

The second promising implementation the MPC-10 cyclotron can find in the neutron radiography method: for the non-destructive control of various products and materials in the atomic power production, in propulsion and rocket technologies, in the fields related with the creation of new materials and compositions.

The neutron radiography technique is based on the dependence of the substance-neutron interaction cross-sections on neutron energy and on the characteristics

of a substance. The main peculiarity is the clearly pronounced leap-character of the general behaviour of the effective cross-sections of thermal neutrons interaction with nuclei unlike in the interactions of gamma and X-ray radiation with matter. The total cross-sections of some isotopes reach very high values and it often turns out that the neighbouring nuclei have a many-times smaller cross-section. As a result, one can control the content of a number of elements in the products of complicated chemical structure by a degree of neutron flux attenuation. The essence of the neutron radiography technique is as follows: an object under study is examined with the penetrating collimated beam of thermal neutrons and, at the same time, the neutron flux distribution beyond the object is registered by the detector. The nuclear reactors are mainly used for NR as a powerful sources of thermal neutrons. They can provide high fluxes of thermal neutrons: $\sim 10^6$ neutrons/cm²s beyond the collimator. Accelerators (cyclotrons) can also be used for production of neutrons for NR. In this case the most preferable reaction is $\text{Be}^9(p,n)\text{B}^9$. As a result of this reaction, the neutron yield is maximal, and since the neutrons of a lower energy are produced, the process or their further thermalization is more effective.

The advantages of using the cyclotron as compared to the reactor are evident:

- neutron generation stops with switching off the cyclotron beam, i.e. the neutron source is controlled;
- the system is compact and easily to operate;
- there is considerable gain in electric power.

In particular, the NR studies with baby-cyclotrons, as neutron sources, have already been done in Japan for a long time [2].

If one turns to the NPC-10 cyclotron with the increase of the maximal energy of the extracted proton beam up to 12 MeV the neutron flux from the point source (Be-target) will be equal about $2 \cdot 10^{11}$ neutron/mkA^{1/2}s [2]. With the increase of the beam current up to 200 mA, the thermal neutron flux density after the collimator can be equal about 10^6 neutrons/cm²s, i.e. is approaching in its value the similar value for the reactors.

From the above-said one can conclude that it is necessary to increase the maximal energy of the extracted beam up to 12 MeV in the near studies and in the NR-technique, as well as to increase the beam current up to 200 mA (for NR) for an effective the NPC-10 cyclotron using.

ION ENERGY INCREASING.

The increasing of the maximal energy of H⁺ ions, accelerated at the NPC-10 cyclotron, from 10 to 12 MeV requires increasing the magnetic rigidity from 0.456 to 0.5 Tm that is expected to be attained both due to the average magnetic field raising and due to extraction radius raising. The magnetic field will be increased up to ~ 1.55 T; its further increase turns out to be unexpedient because of the abrupt growth of the required magnet main coil ampertages (due to the saturation of the magnetic circuit iron) that reduces the accelerator efficiency. Moreover, an essential increase of the magnetic field will lead to the necessity of the magnetic structure geometry considerable changing due to the changing of the radial field shape and the decrease of the flutter, determining the vertical focussing of ions.

The isochronous magnetic field profile is being formed up to the radius of about 30 cm. Thus the acceleration of H⁺ ions at the last revolutions takes place in the region of magnetic field edge, in radii from 30 to 33 cm, where the stripping foil to obtain the energy of 12 MeV must be located. Despite the phase shift of about 30°, which the particles will get, they will not leave the accelerating phase.

The extraction of H⁺ ions with the energy of 12 MeV is expected to be performed into the same channels as the 10

MeV particles. This will be attained due to suitable selection of the stripping foil position by the azimuth. Besides, moving the stripping foil by the radius and azimuth one can vary the energy of extracted protons from 9 to 12 MeV.

The increase of the accelerating structure resonance frequency up to 23.7 MHz, corresponding to the magnetic field will be attained due to some structural peculiarities of the resonance system.

The NPC-10 resonance system design provides the possibility of tuning its frequency from 23 to 25 MHz by changing the dees different in area; the possibility of fine tuning the resonator frequency by changing the gap between the dee and the cover is also provided. Finally, the capacitive trimmers - remotely driven - will allow one to adjust and to stabilize the resonator frequency under operating conditions. All this excludes the necessity in the insertion of a complicated system of movable short-circuited plates.

In order to increase the resonance system operation stability, the artificial capacitive link between the resonance lines is provided. The connection is supplied with an additional capacity between the rods of resonance lines.

The NPC-10 resonance system has been numerically simulated and studied with a full scale mock-up at the frequencies of 23 and 25 MHz. The measurements have demonstrated full agreement between the calculation and simulation. The resonator quality factor has been measured, $Q \sim 2250$.

The industrial broadcasting transmitter PKN-20 providing up to 25 kW in the operating frequency range is expected to be used for the resonator excitation. In accordance with the calculations and measurements, this power is a priori sufficient for providing the cyclotron operating conditions.

ION SOURCE.

An internal radial ion source has been chosen for the NPC-10 cyclotron. Initially, the ion source, PIC type, with self-heated cathodes, was manufactured and one was tested at the special test bench. At this ion source was obtained a beam H⁺ ions with energy 15 keV, at the current 1 mA, at the gas flow 9.5 cm³/min ($B = 0.6$ T). Unfortunately, the designed ion source had two main drawbacks: a) hard discharge ignition and frequent breakdowns along the insulator surfaces in the process of ignition; b) short life time of a cathode under operating conditions, moreover, for application of the NPC-10 in the method of neutron radiography, one should increase ion current, extracted from the source, without increasing (better reducing), the gas admission to the source. In connection with the above-said, we have started the investigation of an ion source with directly-heated cathode [3]. In order to increase the cathode and the reflector life-time they have been made of low-sputtered, electrically-conducting ceramics (initially, the cathodes were made of tantalum). This allowed us to increase a few-times life-time of the ion source and provided the reliable operation of the insulator. Moreover, the H⁺-ion beam current was increased up to 1.3 mA, at gas flow $Q = 8$ cm³/min, that was related with a finer discharge adjustment to the optimal operating mode. The insertion of molybdenum non-cooled converter in the extraction slit zone allowed to increase the ion beam current up to 2 mA in constant arc regime ($U_{acc} = 230V$, $I_{acc} = 3.5$ A, $B = 0.85$ T), at the energy 14 keV and $Q = 8$ cm³/min. The dependences of H⁺-ion yield on the gas flow to the ion source and on the extraction voltage under operating conditions are given in Fig.1 and Fig.2. At present, some studies are done in order to find out the mechanism of the converter effect upon the ion yield from the source. It seems to be important to determine whether the H⁺-ions are mainly produced upon the converter surface or in the volume discharge zone, meanwhile

the converter assists in their drift to the extraction slit. If the assumption that main roll in this process is played the volumetric ion production and the drift of charged particles are corroborated, this will allow us to increase ion current (up to 4-6 mA) or without reduction in the beam current, to reduce the gaseous loading on the cyclotron and to increase ion source life-time by the geometry optimisation of the converter, and a discharge chamber with extraction slit.

REFERENCES.

1. V.Beichtold, P.Fehsenfeld, H.Schweickert, Proc. 11th Int. Conf. on Cyclotrons and their Applications, Tokyo, 1987, p.p. 593-596.
2. E.Hiraoka, Proc. 11th Int. Conf. on Cyclotrons and their Applications, Tokyo, 1987, p.p.587-592.
3. K.Prelec, Proc. Int. Ion Engineering Congress, Kyoto, 1983, p.p.47-58.

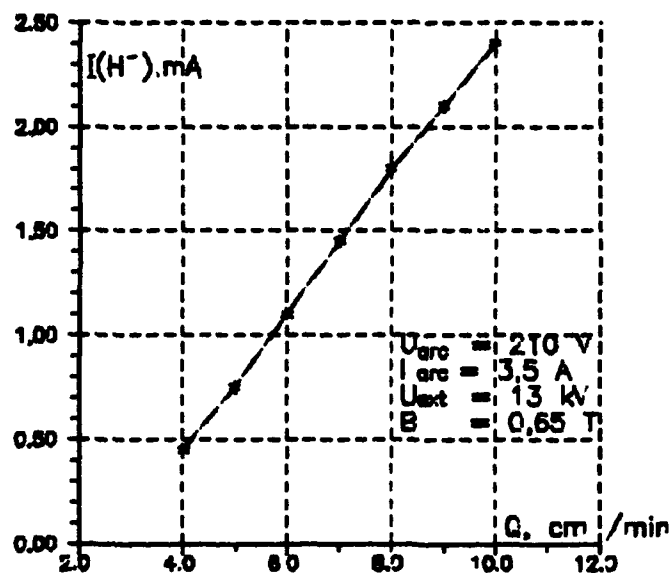


Fig 1 Dependence ion beam current on hydrogen flow

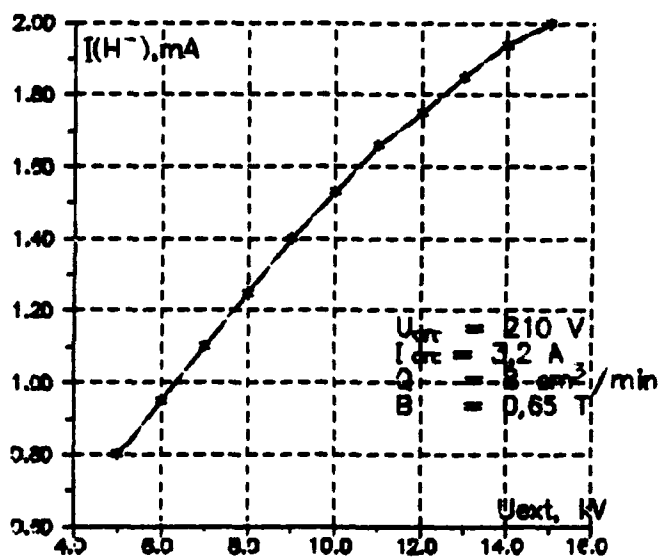


Fig 2 Dependence ion beam current on extraction voltage

ITEP Heavy Ion Alternating Phase Focusing Linac

V.V.Kushin, N.A.Nesterov, I.O.Parshin and S.V.Plotnikov
ITEP,Bolshaja Chermomushkinskaja 25, 117259 Moscow, Russia

Abstract

The experimental RF heavy ion linac with charge to mass ratio up to $1/46$ has been built to demonstrate some possibilities of the compact alternating phase focusing (APF) accelerator structure with high energy gain speed. The first experience on molybdenum and tungsten ions acceleration to 0.31 MeV/amu is considered. The linac consists of 90 kV electrostatic injector with the MEVVA ion source and 6m Wideroe-type drift tube APF 18.4 MHz resonant structure.

1 INTRODUCTION

Ever increasing interest of different branches of science and technology in accelerated heavy ions urges intensive investigations at ITEP applied linacs department in direction of creating accelerators to adequate up-to-date industrial facilities which make use of compact to the utmost utility and not expensive accelerators.

In conventional self-phasing RF accelerator structures ions are affected strongly by defocusing accelerating field forces. In low charged heavy ion linacs these forces are strong throughout the whole accelerator because of low speeds of velocity gain. It makes a typical RF self-phasing heavy ion linac for the energy of $1\text{-}2 \text{ MeV/u}$ a huge and complicated machine which would be comparable with proton one for energies of tens and ever hundred MeV. In APF linacs self-phasing is replaced by alternating-sign phasing to avoid RF defocusing almost entirely at the cost of some accelerated current decreasing. The transverse and longitudinal focusing forces are produced by RF accelerating field by means of appropriate arranging the drift tubes and accelerating gaps length in such systems. So there is no need in any external focusing arrangements, accelerating field amplitudes may be increased up to $5\text{-}10 \text{ MV/m}$ and the linac channel length decreased by a factor of $10\text{-}20$ therefore. For some scientific and industrial problems APF linac advantages may be overrading.

In the late 1980s APF short 148.5 MHz linac sections for ions with charge to mass ratios $1/2$ and $1/4$ have been built and investigated [1-3]. Those works proved APF structures possibilities to reach very high energy gain speed (up to 7.5 MeV/m and more), reliability and relative technological simplicity. Since 1990s APF linac opportunities for very heavy ions are considered at ITEP too.

2 ACCELERATOR DESIGN

The 18.4 MHz APF heavy ion linac for the energy of 310 keV/amu has been constructed and put into operation

at ITEP. It consists of 90 kV electrostatic injector with MEVVA-type ion source and 6m Wideroe-type accelerating structure.

For heavy metal ion production the MEVVA-type ion source developed at ITEP [4]. The source is operated in pulse mode and able to deliver metal ion beams of moderately charged up to some tens mA and offers a large variety of elements.

The twin transmission line (Wideroe-type) accelerating structure with drift tubes is located inside the 6m stainless steel vacuum tank of 0.7 m in diameter which offers the service of external resonator surface too (see fig.1). The vacuum tank consists of six 1 m length and 6 mm wall thickness identical tubings joined together. Every tank has four large ports for a vacuum pumping, view windows and RF power driving, tuning and monitoring. The 50 uniform diameter drift tubes are arranged along the 5.5 m resonator accelerating channel. All the drift tubes are supported by stems mounted by turns on the two longitudinal resonant electrodes (copper pipes). The longitudinal positions of the drift tubes was defined by calculations and ensured by precise alignment. The drift tubes stems are bolted to the longitudinal resonant electrodes. Every drift tube stem has special technological circle tooth and is supplied with copper foil to provide reliable RF contacts with the longitudinal electrodes. All drift tubes alignment is occurred by picking out suitable foil thickness. The resonator forced cooling was absent at that experimental stage because of high values of pulse period-to-pulse duration ratio (10000 and more). The APF linac technical parameters are listed in table 1.

Table 1: APF Linac Experimental Parameters

Accelerated ions	Mo, W
Minimum charge to mass ratio(q/A)	$1/46$
Input energy	1.9 keV/amu
Output energy	310 keV/amu
Frequency	18.4 MHz
Max.electric field on the axis	10.2 MV/m
Current pulse length	$20\text{-}150 \text{ ncs}$
Q-factor	2000
Shunt impedance	82 MOhm
Aperture radius	$5\text{-}16 \text{ mm}$

The gap field gradients are tilted from 4.0 to 10.2 MV/m on the initial 1.5 m length and kepted approximately constant then up to the channel exit.

The measured voltage distribution differed strongly from calculated one in some places along the accelerator

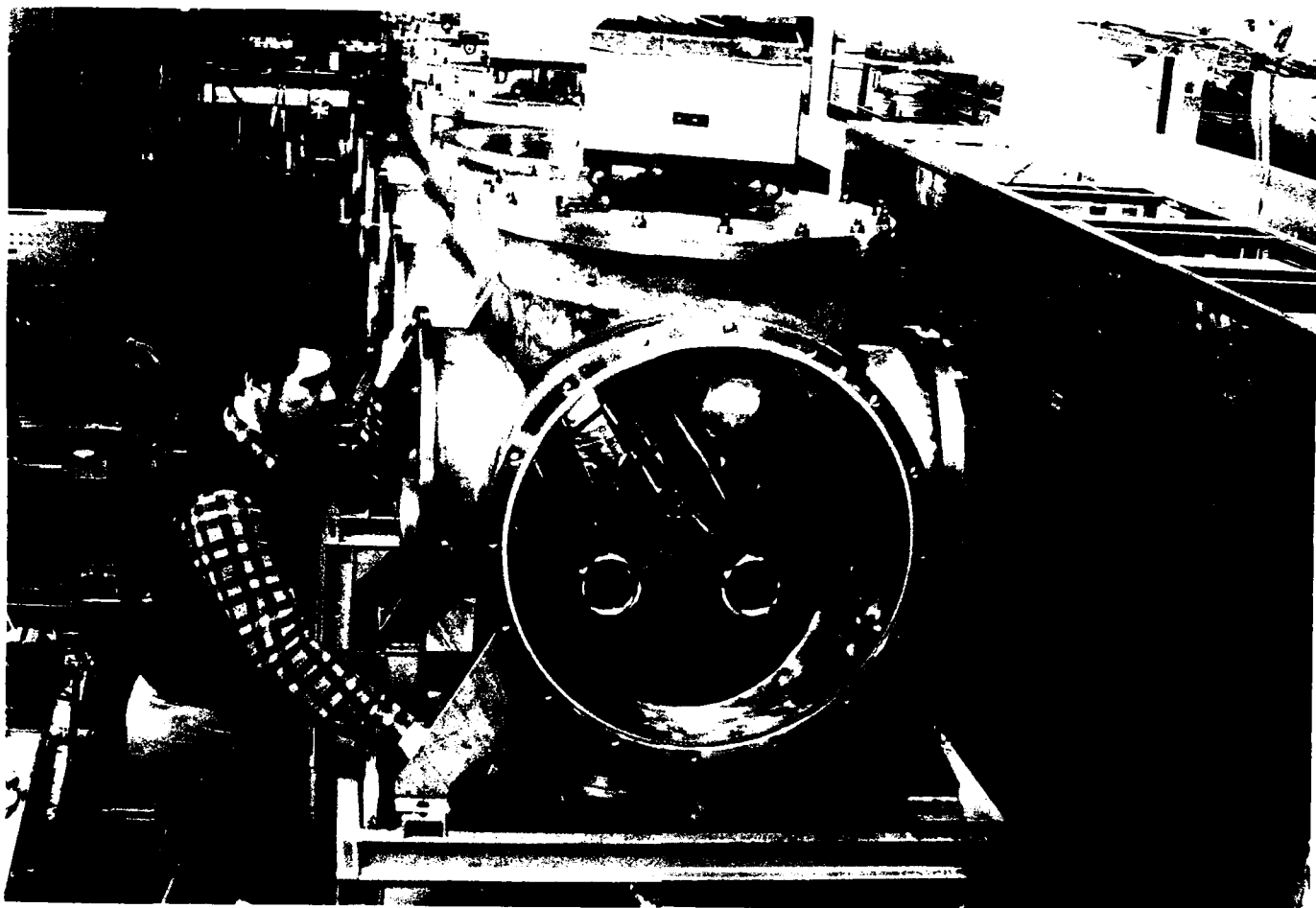


Figure 1: 18.4 MHz APF accelerating structure

axis. So the adjustments have been made by changing some gaps and drift tubes length at some input and intermediate accelerating periods.

3 FIRST EXPERIMENTS

Here, the aim was twofold. In the first place the main technical details with APF linac technological systems operating in independent modes and than their joint working with different ion species acceleration modes have been studied. The design charge to mass ratio(q/A) had been adopted as $1/46$ which corresponded with tungsten(W_{184}^{+4}) ions acceleration. But the different species such as W^{+3} , Mo^{+3} and Mo^{+4} ions have also been accelerated by appropriate changing injection voltage and RF power consumption levels. So accelerated ion species were within the range from $1/24$ (for Mo_{96}^{+4} ions) to $1/46$. The total pulse RF power consumption level varied from 0.7 to 2.0 MW.

The 18.4 MHz RF system provides a 0.2 ms peak pulse power up to 2.5 MW and contains the driver and final amplifier with the positive feedback coupling loop to work at self-excited mode. The RF power is fed through a cable to the cavity.

The accelerator vacuum system comprised of two ro-

tary pumps, eight 500 l/s turbomolecular and ten 400 l/s electrocharging pumps which promised to get the working vacuum 3.10^{-4} Pa.

The accelerated W^{+4} ions intensity reached 5.10^8 ions/pulse at the first stage.

The other special purpose program was to investigate different modes of thin polymer films irradiation for particle-track membranes(PTM) producing technology development[5]. The accelerated heavy metal (Mo and W) ion beams have been used for PTF thin films irradiations. Heavy ion intensities varied over the wide range from 10^6 to 5.10^8 ions/pulse. The type PTF film photo after the tungsten ion irradiation and etching processes is shown at fig.2.

4 ACKNOWLEDGMENTS

The authors would like to express their thanks to V.S.Artemov, V.L.Baranov, I.B.Barsukov, I.V.Chuvilo, D.D.Iosseliani, O.A.Ivanov, V.S.Kosjak, T.V.Kulevov, J.N.Kuzmin and A.I.Velitchko for useful discussions, support and help in putting the accelerator into operation.

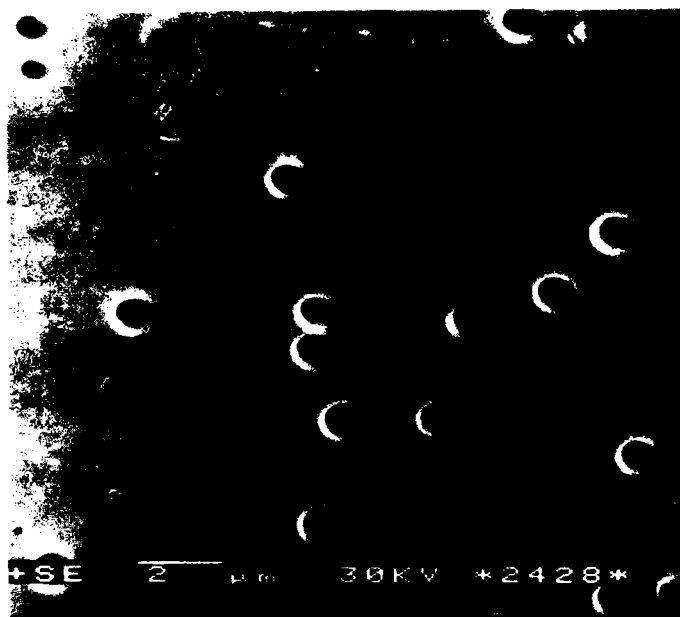


Figure 2: Polymer film after tungsten ion bombarding and etching

5 REFERENCES

- [1] I.V. Chuvilo et al., "APF Accelerating Structures for Light and Heavy Ions", In *Proceedings of the I European Particle Accelerator Conference*. Vol.1, pp. 78-80, Rome, 1989.
- [2] I.V. Chuvilo et al., "Acceleration of Helium Ions in the APF Structure and the Linac I-2 for Injection into 10 GeV Synchrotron", *Proc. 1988 Linac Conf.*, CEBAF-Report-89-001, Newport News, June 1989, pp. 146-148.
- [3] S.V. Plotnikov, "Rectangular-type H-resonator Accelerating Structures for Alternating Phase Focusing Ion Linac", *Pribory and tehnika eksperimenta*, vol.1, 1990, pp. 41-44.
- [4] V.A. Batalin et al. "Vacuum Ark Source of Metal Ions", *Preprint ITEP 91-37*, Moscow, 1991.
- [5] C. Bieth et al. "Industrial Applications of Heavy Ions Beams at Ganil", in *Proceedings of the I European Particle Accelerator Conference*. Vol.1, pp. 189-191, Rome, 1989.

Sharing Control System Software

Peter Clout

Vista Control Systems, Inc.

134 B Eastgate Drive, Los Alamos, NM 87544 USA

Abstract

Building a custom accelerator control system requires effort in the range of 30–100 person-years. This represents a significant investment of time, effort, and risk, as well as challenges for management. Even when the system is successful, the software has not yet been applied to the particular project; no custom control algorithms, either engineering or physics-based, have been implemented; and the system has not been documented for long-term maintenance and use. This paper reviews the requirements for sharing software between accelerator control system projects. It also reviews the three mechanisms by which control system software has been shared in the past and is being shared now, as well as some of the experiences. After reviewing the mechanisms and experiences, one can conclude there is no one best solution. The right software sharing mechanism depends upon the needs of the client site, the client resources available, and the services the provider can give.

I. PROBLEMS WITH DEVELOPING CONTROL SYSTEM SOFTWARE

Sharing software is a solution; the problem is the risk, cost and time taken to develop the control system software. Before any application to the accelerator in question, the control system software represents an investment of between 30 and 100 or more person-years [ref. 1]. Multiplying this figure by any developed country's average programmer's salary with overheads easily turns this into multi-million dollar investments for just one part, albeit important, of the overall control system. If one then adds in the maintenance, support and improvement of the software over the life of the accelerator, the number can easily be multiplied by factors of between two and five to obtain the lifetime cost.

Clearly, such expenditures should not be entered into without examining the alternatives.

Apart from cost, the risk of the software being incomplete or insufficient at the time it is needed is also a serious issue.

For the accelerator field as a whole, this problem is getting bigger simply because the number of accelerators is growing as new accelerator applications are developed. As evidence for this one only has to plot the growth in the attendance of the conferences such as this one. One recent estimate [ref. 2, 3] for providing desirable and reasonable control system user facilities at the major accelerators world-wide adds up to in excess of one billion dollars over ten years. The inference is that

unless changes are made, only a fraction of the requirements will be met.

II. THE VALUE OF SOFTWARE

Software is intellectual property and each piece of software represents a solution to a problem or a component of a solution to a problem. Like other forms of intellectual property, the value of a piece of software is derived from

1. Understanding of the problem.
2. Analyzing the problem and its requirements towards a solution.
3. Literacy with the techniques and skill with the associated tools to be used.
4. Effort expended to provide the particular solution.

The first three could be thought of as setting the hourly rate and the last item being the multiplier that sets the cost of a solution.

Software also represents a value to the user. This value is measured by the overall satisfaction with the system. Basically, what is the cost of not having that piece of the solution? There is another component of the cost of software—risk. This is the risk that the software solution to the problem will either simply not be working when needed or will not fulfill one or more of the requirements. Custom-developed software represents the highest risk with the level of risk being determined by the size and track record of the team working on the problem.

III. DIFFICULTIES IN ACCELERATOR CONTROL SYSTEMS DEVELOPMENT

Accelerator control systems are large in the number of channels, complex in the engineering and physics of the process and uncertain in the sudden appearance of new requirements. All these factors are greater than they are in industrial systems. In developing a control system, or any other system, one cannot reduce the complexity of the system to a level below the basic complexity of the application.

From the first operation of the accelerator, one can confidently expect that the requirements on the control system will grow rapidly and in unpredictable ways as the understanding of the physics of the accelerator is developed and confirmed and the needs of operations understood. There will be the need to incorporate into the control system some of the basic physics codes that were written for accelerator design rather than accelerator operations. There will also be the need to incorporate control algorithms developed during the R&D phase and also during operations.

If the architecture and design of the control system hardware and software are not structured, open and flexible, then expanding requirements will be harder and harder to meet and the result will be a nightmare to maintain. Very often, small control systems are required at the R&D stage of a project. The ability to make a version of the final system available early on will save work and simplify project integration.

IV. REDUCING THE COST AND RISK OF ACCELERATOR CONTROL SYSTEM DEVELOPMENT

Table 1 lists some of the accelerator control system software sharing. It will be seen that there has been an increasing pace of software sharing in recent years as the advantages come to be appreciated and the complexity of the requirements and the basic tools of computing increased rapidly (compare the Plot-10 graphics library with Xlib!). The industry has developed software development methodologies and tools to support these methodologies. These help to combat the complexity of the requirements and reduce the development time for the solution.

Tools are also being developed to assist with the implementation of the design. Some of these are general-purpose tools (Visual Basic, Object Vision, OBLOG, OBLOG CASE, Data-views, SL-GMS, IDL, etc.) which reduce the writing of code, and others are specific application shells or toolboxes (Factory Link, LabView, VXL, Wonderware, Vsystem, Basestar, RTAP and so on). Each application shell or toolbox is targeted at a particular class of applications and allows the user to start developing the specific application as soon as the initial design is complete. One can expect this picture to change rapidly in the future.

V. ISSUES IN SHARING SOFTWARE

A. Architecture

The general hardware and software architecture of the system will determine how easily the shared software will fit. This section discusses some of the issues of the operating system interface and the application interface.

1. Computer, Operating Systems, Graphics and Networking Choices

It is unfortunately still true that it is a substantial job to port a system developed using the full facilities of one choice of hardware and software to a different family of choices. Improvements in this area are slow but they are occurring (UNIX, POSIX), although other market forces like Macintosh, MSDOS and Windows/NT confuse this improvement.

2. Application Interfaces

a. I/O Hardware

In many of the more recent software architectures, this interface is standardized so that the applications do not need to know about the exact details of the hardware connection. Some form of standardized hardware access is a requirement if software is to be shared. This can be by using protocols such as are being developed and used by the European Physical Society Group on Experimental Physics Control Systems, or by using a real-time database or, indeed, both.

b. Software Data Bus

This is a software data interface for communication between the software components of the system. This can include a real-time database and embedded features such as alarming, data conversion and the storing of secondary information about each item of data. Mechanisms such as pipes and local and remote procedure calls are very simple mechanisms that know nothing about the application. Many systems have built specific control system functions and communications on top of these primitives.

c. User Interface

Different user interface environments can make the use of software from another institute difficult. Clearly, the ASCII terminal interface is common to nearly all systems (remember EBCDIC?) but there are a number of graphics interfaces in use, although the two rather different low-level interfaces, X-windows with Motif and MS-Windows, are presently the primary software interfaces.

d. Operating System Services

Programs directly use many services of the operating system for which they are written. In this case there is often considerable re-engineering to be done to port the program to another operating system. Here, even UNIX does not help as each UNIX supplier has modified UNIX for their particular view of their users' needs. The POSIX set of standards will be a great improvement once they are all finally agreed upon and commercially available. It is unfortunate that the POSIX standard most needed for accelerator controls, the real-time extensions, is the one that is yet to be agreed.

The other operating system interface issue is the file system. If one considers the three primary operating systems as MS-DOS (and Windows), UNIX (in its many different flavors) and OpenVMS (on the VAX and the Alpha/AXP) then one has three different naming conventions and restrictions and three very different sets of file structure capability.

B. Support and Maintenance

All software needs support and maintenance. This is either provided in-house for the personnel costs involved, or it is pro-

vided by the supplier of the software for a fee. If no support is available, it will still be a cost to the user because of the effort to get systems working and working effectively. Either way it will be a cost to the user. For this reason, no software is free.

C. Control

One of the reasons for the call for "open" systems is so that users can feel in control of the system. Control means that regardless of the unexpected requirements that arise during the life of the system, the system can be adapted and grown to meet those requirements. This is, of course, vital in research.

D. Documentation

No software is complete until the documentation is written. Experience here has been that this job is often not started until the need is more than pressing. For software to be shared and successfully used at another site, good documentation is required.

VI. STAGES OF SOFTWARE SHARING

Using software engineering techniques, the results of any stage of control system implementation can be shared in order to reduce effort and improve quality. Clearly, the more stages that are shared, the more cost and risk are reduced. These stages are

1. The concepts of the system and the understanding of the problem
2. The analysis of the problem
3. The design of the solution
4. The implementation of the solution, the basic system without the specific application
5. The complete implementation including the application

The ability to share stage one and stage two are only constrained by the type of accelerator and its operation requirements (such as the need for super-cycles).

Sharing the design of the solution will require accepting some constraining technical choices, such as networks, computer and operating system and so on. However, this is not such a strong constraint at the design phase as it is in the last two phases when actual executable code is shared.

Depending on the software engineering tools used, non-executable code can be shared in the analysis and design phases.

VII. METHODS AND EXPERIENCES IN SHARING COMPLETE ACCELERATOR CONTROL SYSTEM SOFTWARE

To date there have been three methods of sharing software. These are "As-is," Collaboration and Commercial. Each is de-

scribed below, with some of the advantages and disadvantages listed. Table 1 lists some of the known software sharing experiences in the accelerator control system field.

Table 1: Software Sharing

Originator	First Distribution Date	Receiving Institutes	Method
CERN/SPS	1970	DESY, KEK	"As-Is"
HMI [ref. 4]	1978	CRL, KFA	"As-Is"
FNAL [ref. 5]	1984	NSCC, Loma Linda	"As-Is"
HMI [ref. 4]	1985	CRL*	Collaboration
LANL/PSR	1985	KFA	"As-Is"
SLAC [ref. 6]	1986	BEPC, IHEP* Duke U., Oxford Instruments	"As-Is"
LANL/TCS	1987	TRIUMF, BNL, CRPP, CERN/LEAR, GSI, PSI, HMI, GA	"As-Is"
CEBAF	1989	Bates, SSC, LLNL, etc	"As-Is"
VCS	1990	Various	Commercial
LANL [ref. 7]	1990	ANL/APS, Duke U., LBL, SSC	Collaboration

*Application Programs Also Used

Also included for comparison is the case of an institute developing their own system, the "roll-your-own" method. The list is ordered in decreasing cost, development time and risk. Where costs and effort are mentioned, they are for the basic system to the point that it is being implemented for a particular project and they do not include any application effort.

A. Roll-Your-Own Method

Here the institute develops their own system using basic computing tools.

Advantages

1. Complete control of the software function.
2. Free choice of computers, displays and I/O system.

Disadvantages

1. Considerable initial development cost, \$2.2-20M.*
2. Considerable risk.
3. Highest support and maintenance cost, 4-20 people, \$300K-\$4M/yr.*

* Programmers are assumed to cost between \$75K/yr at salary plus overhead and \$200K/yr. at salary, overhead and burden costs.

B. "As-Is" Method

Here the complete software, including sources, and any documentation is provided from another institute on an "as-is" basis. Recipients then have to develop and support the software on their own, thus the software provides a substantial initial start to a project. Of course, the recipient can call for either free or paid help from the source institute of the software and, in practice, this has often been given. However, the people who wrote the software initially usually have to respect the schedules and demands of their home institute first; therefore, the external requests usually create added pressure with little recognition or reward.

Advantages

1. Significant design and implementation work are saved. This is probably valued at about 60% or more of the "roll-your-own" cost.
2. Experience from another project is used initially.
3. Receiving institute has full control of further development.
4. Considerable risk reduction, the amount depending on the further development required.

Disadvantages

1. Local continuing support and development costs incurred. This can easily add 4-20 people to the staffing requirements at a cost of \$300K-\$4M/yr*
2. Local variations of the "as-is" software are usually developed, inhibiting further sharing between the institutes.
3. Software developed for in-house use is not usually engineered to be easily installed by other sites. Thus, there will be a steep and costly learning curve.
4. Distribution of the software adds a load on the writers of the software in the form of preparing and making distributions and answering support requests. This is not often offset by recognition or reward from their home institute.
5. Restricted, if any, choice of computers and I/O system.

C. Collaborations

In this form of software sharing, one institute takes the lead and provides the initial software that is then further developed by a group of institutes under some form of common management. The key requirement of a collaboration is that the control system software remains one system with no local variants. If local variants develop then the relationship is likely to move from a collaboration to an "as-is" relationship.

Advantages

1. Sharing of development costs.
2. Broader experience feeds into the requirements for new releases.

3. Considerable risk reduction.

Disadvantages

1. Cost of local support and development team, 3-8 people at a cost of between \$225K-\$1.6M/yr.*
2. Complexity and expense of management between different institutes to keep the software common. Frankly, this is an achievement in a single group or institute! This management issue also results in a loss of local control for development decisions and relies on goodwill between the members.
3. Restricted, if any, choice of computers and I/O system.

D. Commercial Systems Developed for Accelerator Controls

In this software sharing model, a company, through normal commercial arrangements, effectively becomes the control system software group for the customers. Experiences with institutes using commercial control systems developed initially for industrial applications has been poor because of the additional requirements of physics research applications that are uncommon in industry. My company is the only example that has started with the physics market for developing, selling and supporting a control system toolbox. As far as I am aware, no other company has more than a single control system sale active in this market.

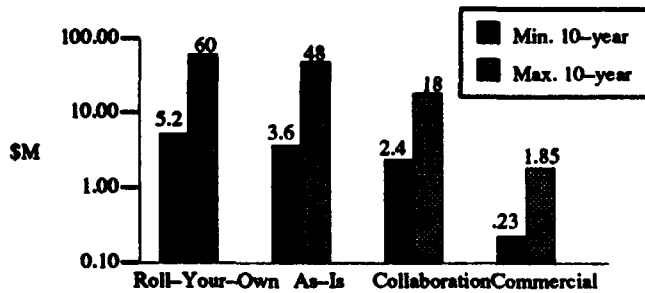
Advantages

1. Minimal support and development costs, a fraction of a person locally and \$4.5-50K/yr support and maintenance charges to the supplier, total, 23-150K/yr.*
2. Considerable risk reduction that is essentially complete if the products meet the requirements as demonstrated before the sale.
3. Support is available and of good quality because of broad support experience of the company personnel and the direct reward to the company and the employees of the company for good product and support.
4. The company normally controls the key sources, ensuring compatibility and the ability for customers to share code between themselves.
5. Company can and is motivated to provide application help at critical times to customers.
6. Product is engineered for distribution and installation and documentation is provided.

Disadvantages

1. Initial license cost, in the range of \$30K to \$350K.
2. Control depends on the documented "openness" of the product.
3. Issues of the company failing have to be addressed.
4. Restricted choice of computers and I/O system.

Figure 1 illustrates the minimum and maximum costs likely to be incurred by each method over a ten year period.



Note: Logarithmic Scale

Figure 1: 10-Year Control System Software Costs

It should be noted that the commercial solution has an order-of-magnitude cost advantage. This is because of the efficiencies of commercial operations and the economies of scale, as well as engineered, tested and documented software.

VIII. SHARING SOFTWARE COMPONENTS OF A SYSTEM

For this to be successful, the interfaces as listed above have to be the same or the differences must be manageable. If the data bus is common, the problem is almost completely solved and some agreement here would greatly facilitate software sharing. The other interfaces will be as influenced by the market forces as by our community.

Experiences here have been to successfully use some of the physics beam analysis codes within a control system and to use commercial products for a part of a control system. Past results here have been mixed, usually because the commercial products chosen were developed for small industrial applications.

IX. PLANNING FOR THE FUTURE

The accelerator controls community has a choice. It can let the commercial products develop and use them as it can or it can be proactive in influencing the commercial developments. In parallel with the first option of commercial laissez-faire, the community can continue to develop its own systems and share them as before. The basic problem with this approach is that it will greatly slow the development of commercial solutions that are focused on the class of applications represented by accelerator control systems. There are two ways to influence commercial developments. One is for the community to be a significant customer of one or more software companies and the second is for the community to develop broadly applicable standards and to purchase products based on those standards.

The developments one might look for in a commercial package that is specifically designed for accelerator control are interface packages for incorporating some of the standard physics

codes, control programs for accelerator specific tasks and so on.

X. SUMMARY

Methods of sharing software, either in analysis and design stages or in the complete system, have been defined with the advantages and disadvantages explored. Is there one right solution? Currently, I think that the answer is no. It depends on the number and skills of the programmers available to the project. If resources are scarce, then a commercial solution is the only solution. If ample resources are available and the institute wants complete control and will accept the risks, then an "as-is" solution or "roll-your-own" solution is indicated. Between these two extremes sits a collaboration such as the EPICS collaboration.

The important aspect of the choice is to understand that a choice is being made and there are advantages and disadvantages to each choice. Equally important is to defer making any component or personnel decisions until the overall strategy is decided. If one starts by hiring systems programmers, one has already eliminated some choices. Equally, computer, operating system and I/O subsystem decisions will restrict the choices for the most expensive and risk-prone component of the control system, the software.

XI. ACKNOWLEDGEMENTS

I would like to acknowledge the review and constructive criticism of the draft of this paper by Peter Lucas of Fermilab, and Axel Daneels and Berend Kuiper of CERN.

XII. REFERENCES

- [1] A. Daneels, "Current Trends in Accelerator Controls: The Issue of Accelerator Software, Particle Accelerators, 1990," *Proc XIV Intl. Conf. on High Energy Accelerators*, Vol. 29, p. 875, Tsukuba, Japan, Gordon and Breach Publ.
- [2] B. Kuiper, Private Communication
- [3] B. Kuiper, "Issues in Accelerator Controls," *Proc XIV Intl. Conf. on High Energy Accelerators*, Vol. 29, pp. 602-611, Tsukuba, Japan, Gordon and Breach Publ.
- [4] Winfried Busse, Private Communication
- [5] Peter Lucas, Private Communication
- [6] Sam Howry, Private Communication
- [7] L.R. Dalesio, M.R. Kraimer, and A.J. Kozubal, "EPICS Architecture," *Proc. Intl. Conf. on Accl. and Expt. Phys. Contr. Sys.*, Nov. 1991, KEK, Tsukuba, Japan, KEK Proceedings 92-15

Vsystem is a trademark of Vista Control Systems, Inc. Other products mentioned might be trademarks and are mentioned for identification purposes only.

Control System Architecture: The Standard and Non-Standard Models*

M. E. Thuot, L. R. Dalesio, Los Alamos National Laboratory

Abstract

Control system architecture development has followed the advances in computer technology through mainframes to minicomputers to micros and workstations. This technology advance and increasingly challenging accelerator data acquisition and automation requirements have driven control system architecture development. In summarizing the progress of control system architecture at the last International Conference on Accelerator and Large Experimental Physics Control Systems (ICALEPCS) B. Kuiper asserted that the system architecture issue was resolved and presented a "standard model".[1] The "standard model" consists of a local area network (Ethernet or FDDI) providing communication between front end microcomputers, connected to the accelerator, and workstations, providing the operator interface and computational support. Although this model represents many present designs, there are exceptions including reflected memory and hierarchical architectures driven by requirements for widely dispersed, large channel count or tightly coupled systems. This paper describes the performance characteristics and features of the "standard model" to determine if the requirements of "non-standard" architectures can be met. Several possible extensions to the "standard model" are suggested including software as well as the hardware architectural features.

I. INTRODUCTION

Advances in computer technology, changes in the computer marketplace, and demanding control requirements [2] have motivated control system architecture development. The reduction in prices of powerful, user-friendly, networkable workstations coupled with the ever increasing cost and complexity of software stimulated new designs with a philosophy of control system evolution rather than totally new design, even on entirely new facilities[3]. This evolutionary design philosophy includes standardized structures

**Los Alamos National Laboratory is operated by the University of California under contract W-7405-ENG-36 for the U. S. Dept. of Energy.*

and the use of open software standards to provide much greater flexibility to expand the size and automation of a system, to accommodate new high performance platforms, to reuse software developed previously, and to share software developed by other laboratories and industry. "The recent and continuing efforts of standardization at all levels on protocols and other interfacing conventions means that the plugged in equipment and other gadgets may be exchanged for newer versions, using entirely different internal technologies, which may then increase performance" [1] or functionality of the entire control system. These changes have driven the designers of computer control systems toward a standardized modular architecture.

II. THE STANDARD MODEL

The standard model employs a workstation/personal computer as the operator station, a local area network for data communications and front end micro-computers connected to the accelerator through signal conditioning and/or remote input/output interfaces. In a recent literature review, over three dozen systems world-wide were identified as employing this standard architectural model.

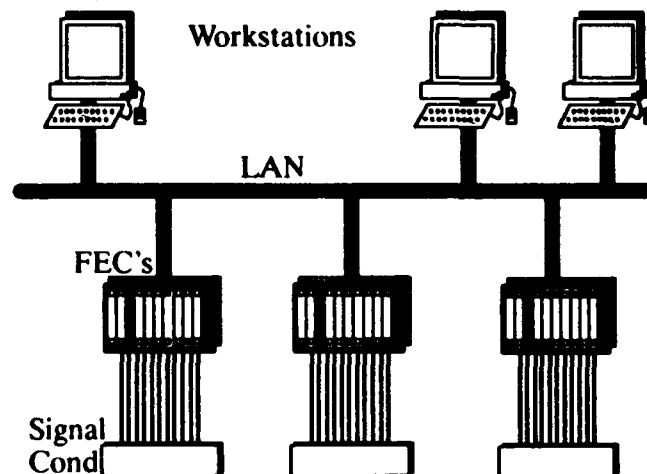


Figure 1. Three basic components of the standard model: the operator interface, data communication, and the front-end computers.

The operator interface provides the operator with a current view of the control process, historical data, alarm information, and a number of physics

models to help maintain and predict the operation of the machine. The communication layer provides data transport between the distributed front-end computers and between the front end and the operators. The front-end computers provide distributed intelligence for data acquisition, data conversion, supervisory control, interlock enforcement, closed-loop control and sequential control.

III. OPERATOR INTERFACE FACTORS

The most important factors in selecting an operator interface are: performance, user-friendly interface, cost to configure and maintain displays. To monitor a process, 10 Hz updates to the operator offer feedback in real-time (human perception). Responses at less than 10Hz may be acceptable in many cases. Feedback to an operator action should also occur within 100 milliseconds to give the operator an immediate feedback that the action has occurred. Most modern operating systems (UNIX, VMS, etc.) on moderate performance workstations can provide an off-the-shelf platform that supports this level of performance. Slower system response could result in the operator giving multiple commands to take the same action, not to mention operator frustration. To take full advantage of a windowing environment, display call-up needs to occur quickly, less than 100 milliseconds is optimal, up to four seconds may be acceptable. When the delay is too long, the operator will resort to multiple dedicated displays. This will increase the system cost and overhead. The workstations may also support physics modeling codes that provide higher level data analysis and interpretation. These codes may take many seconds to run. The operator station needs to have adequate computational performance to provide the operator with adequate response from physics modeling codes – ideally in under four seconds.

Consistency in the operator interface is required to reduce the number of interactions the operator needs to learn to monitor and control the many diverse processes. This can be done by minimizing the number of interactions available, by standardizing the meaning of symbols and colors and by consistent display layout.

Display configuration and maintenance cost is based primarily on the quality of the tools

provided to create the operator interface displays. An interactive display builder will provide the quickest creation and modification of displays with the highest reliability as it will only entail interactive editing of graphical objects. Hard coded displays will take the longest to create with the highest cost as they will require editing, compilation, debugging and activation to verify position, color, and shape, and function.

IV. DATA COMMUNICATION FACTORS

The communication layer has several features of importance: reliability, throughput, cost, and connectivity. The most widely used communication media is 802.3 standard Ethernet using TCP/IP. It provides a data communication rate of approximately 350K bytes per second per subnet. (35% utilization of a 10 Mbit media to reduce the collision rate). Throughput per node can be enhanced through the use of routers and bridges to isolate traffic on any subnet. The cost for an Ethernet communication interface is less than \$500 per node and in many cases interfaces are included on the front end controller CPU board. Higher bandwidth network technology like FDDI is also available. Using TCP/IP, FDDI has an approximate 8 Mbyte throughput (80% of the 100 Mbit media; token ring does not need a collision margin). The cost per node is approximately \$5,000. It is possible to mix FDDI and Ethernet using commercial bridges and routers. Efficient protocols, intelligent buffering, blocked message construction, and data compression can also help reduce the communication utilization. Buffering must not however, introduce excessive latency for operator notification (100 milliseconds or more).

The physical layer is only one aspect of network/system performance; there is also the use of a communication layer. The communication layer provides a means to isolate the various functional modules of an application, for example, isolating details of the data acquisition function from the data archiving function. If there is no imbedded knowledge of the location of some piece of data, system growth or re-configuration will only impact the portion of the application that is being modified. If there is embedded knowledge, a slight modification could cause a perturbation in the entire control network. B. Kuiper warned designers "to take appropriate measures to safe guard the upper part of the

control system from importing the intricacies and diversity of the far front-end". [1]

There are two primary methods of moving data between nodes of a network: polling data into a target node and notification on change of state. Polled updating of a centralized data node or display is conceptually simple, provides redundant data for improved data security, and consumes a lot of front end computer cycles and network bandwidth. Polling requires the continuous communication of all data channels, so higher update rates use more network bandwidth, while lower rates increase the latency between a change of state and operator notification. Polling improves the data security, but makes acquisition of beam synchronous data in a generalized way more difficult. Variability in data latency in polled data systems will have a deleterious effect on the stability of closed loop control.

In contrast, notification on change of state significantly reduces the needed communication bandwidth for discrete (binary) variables and slow analog signals with reasonable deadbands. Beam diagnostics data however, may need to be sent on every sample. Notification on change requires guaranteed delivery of notifications, where polling may to some degree, compensate for a lost message. Event driven acquisition, a variant of notification of change, is an efficient method to provide stable closed loop control data. The best system design will support both time driven and notification on change to balance data communication efficiency and to insure data integrity.

Connectivity is extremely important in providing maximum flexibility for control and monitoring. There are important cases where front-end controllers need information from each other to provide optimization, closed-loop control and sequential control. A lack of point to point connectivity will result in added latency for these inter-computer control strategies and may result in an inability to provide needed control.

V. FRONT END COMPUTER FACTORS

The most important aspects for the front-end computers are performance and ease of configuration. Single board computers running a real-time operating system provide a high performance, general use environment. In a

physical memory mapped environment, no operating system overhead will be added for paging or swapping virtual memory. Response to outside stimuli can occur in less than five microseconds when action can be provided in an interrupt routine and about thirty microseconds when a context switch is required. The use of a configuration database or class library can provide an easy to configure and more reliable application since the base software for all front-end controllers is identical. For example, in the EPICS control system software being produced by a collaboration of Los Alamos, Argonne, Lawrence Berkeley and Superconducting Super Collider Laboratory, [5] processing an input has been timed at about 80 microseconds per signal (read, convert, check for alarms, notification on change of state). It is easy to achieve 10 Hz closed loop operation of hundreds of control loops in the EPICS operating environment. 100 Hz operation of 10s of control loops is also possible. Kiloherz bandwidth closed loop control using DSPs and MHz operation using wide bandwidth hardware feedback is also possible using a VME/VXI front end controller backplane to monitor and control setpoints at slower rates. The ability to reduce data in the front-end controllers allows the system computational requirements to be distributed over many front-end computers. Moving the data conversions, closed-loop control, interlocks and sequential control closest to the physical I/O provides the highest performance possible. It also improves reliability by reducing the number of control system components required to maintain control in any local area.

Signal conditioning and field instrumentation must be selected for performance, cost, and reliability. There is a wide variety of field instrumentation techniques available. Using the backplane of the front end computer for communication to the field instrumentation provides the highest throughput. This is very useful for high repetition rate and short latency responses like those required for beam instrumentation. There are also a variety of commercial field buses that provide wider distribution of the I/O, better environmental tolerance, and short instrumentation cable runs. Industrial buses can also provide I/O redundancy, hot swap, and convenient field cable connections.

This significantly reduces installation and maintenance cost and down time.

It is worth mentioning the need to correlate data taken in an accelerator. Three system design approaches are: distribute the data acquisition and provide a correlation identifier, e.g., a time stamp, control the data collection rate by triggering data acquisition system wide, or collect all of the data at a single point. In the case where the data is identified with a time stamp as belonging to a unique event, data collection can run at the rate of the data source event. In the case where the data is taken in complete synchronous sets at one time, the data acquisition is synchronous in the entire system and therefore can only be gathered at a rate limited by the availability of a complete data set. Finally, in the case where the data is collected to a single node, the limiting factor is predominantly the transfer and processing rate in that node and a further limitation is that all data in the synchronous set must be connected to that node.

VI. NON-STANDARD MODELS

There are a number of system design problems that are not optimally addressed by the standard model as defined above. Many of these issues can be addressed as extensions to the standard model however. Three will be addressed as examples of the flexibility of this basic architecture: large area and high signal count systems, requirements for fast global system data access, and the distribution of control system data to a large multiple node user community.

The SSC has an estimated 445,000 signals distributed over a fifty mile ring. There will be five machines separated into fifteen sectors: linac (1), low energy booster(1), medium energy booster(1), high energy booster(2) and collider ring(10), where each sector must be capable of independent operation. Reliability, performance, and cost are major issues. The control system availability must exceed 99.3% to meet operational goals. To meet stringent reliability and wide area requirements telephone communication network technology was selected to provide each front end computer with communication links.[6] As with the more common Ethernet LAN, this wide area network provides point to point capability between

front-end computers within a sector as well as the ability to configure a direct connection to any other sector. All of the front-end computers are connected to a high speed router in the sector and a high speed router in the main control room through a 155 Mbps OC3 communication link. This maintains the original standard model node concept of point-to-point communication and uses routers for sub-net isolation. It replaces the Ethernet and FDDI technology typical of the standard model, with broad bandwidth area high reliability telecommunications gear. An extra level of flexibility is also provided since at each controller node multiple T1 (1.54 Mbps) channels may be allocated for data intensive functions, like archiving.

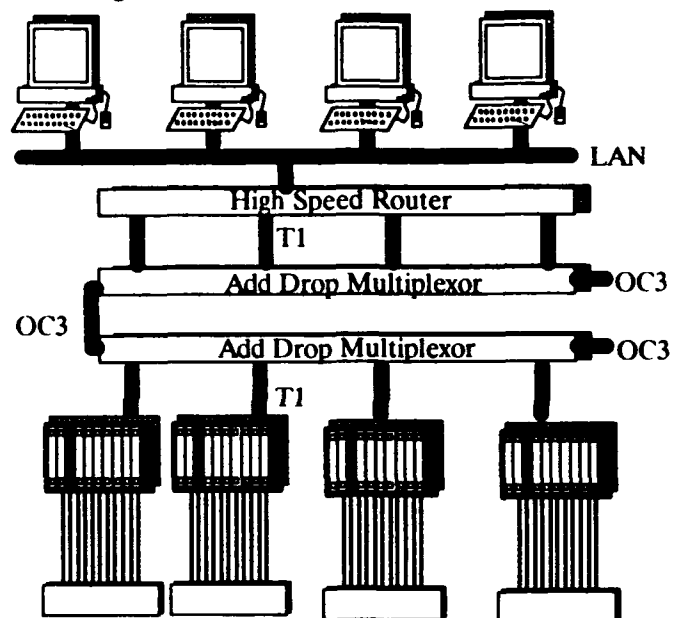


Figure 2 – SSC Architecture with additions to the standard model.

The global control beam steering problem at APS requires collecting beam position (BPM) data and providing feedback control at 4Khz. This performance issue is addressed by using an additional data communication path in a reflected memory scheme to each of 20 VME BPM controllers to provide position readback for all BPMs to all 20 controllers within 50 microseconds.[7] A correction is formulated by individual digital signal processors that solve the correction matrix for magnet control. The additional communication bus overlays the standard model control network that provides general monitoring and supervisory control.

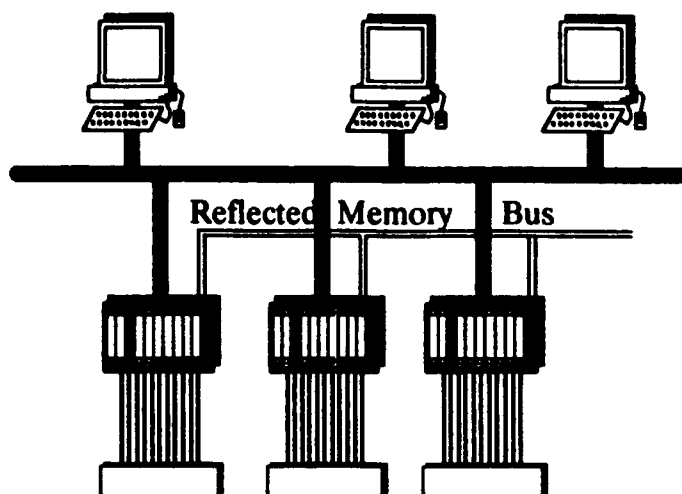


Figure 3 - APS Architecture with Global Data Path

With many user facilities, there is a need to send status information to a large number of users. In the standard model systems, this would place a high burden on the front-end computers for duplicating information to non-critical locations. With the addition of a data gateway, a minimal load is added to the standard model control network, while providing isolation for the control network from the user demand for data. There is an additional latency added to this data, a possible throughput bottleneck, and the potential for a single point of failure. If this function was part of the machine control, these three limitations would be of paramount importance. However, for providing status monitoring, these limitations are not critical.

VII. CONCLUSION

The standard model architecture has been used very successfully on dozens of distributed control systems with thousands of data channels. It provides performance, flexibility and cost benefits when implemented with present workstation, LAN and VME/VXI microprocessor technology. Standardization of network protocols (TCP/IP), open software standards, communication layer protocols, [4] workstation operating systems, and POSIX compliant real-time operating systems provide the ability to expand the size and automation of a system as requirements change, the ability to accommodate new high performance platforms as technology advances and most importantly, to share and re-use software.

The standard model has demonstrated an ability to meet demanding requirements by accommodating overlays of alternate technology while leaving the basic structure and function unchanged. This ability to adapt gives the software designer some level of assurance that programs designed for a local application may indeed find extensive use at other facilities using standard model architectures.

VIII. ACKNOWLEDGEMENTS

The authors gratefully acknowledge the direct contributions and many productive discussions with the members of the EPICS co-development collaboration. We specifically thank M. Knott, M. Kraimer, and F. Lenkszus at Argonne National Laboratory, S. Lewis at Lawrence Berkeley Laboratory, D. Gurd, D. Murray and S. Hunt at the Superconducting Super Collider Laboratory and J. Hill and A. Kozubal at Los Alamos National Laboratory.

IX. REFERENCES

- [1] B. Kuiper, "Issues in Accelerator Controls", Proceedings of International Conference on Accelerator and Large Experimental Physics Control Systems", (ICALEPCS '91), Tsukuba, Japan, November 1991, pp. 602-611.
- [2] R. Humphrey, "Lessons from the SCL for Future LC Control Systems", Proceedings of ICALEPCS '91, Tsukuba, Japan, November 1991, pp. 14-18.
- [3] W. McDowell, et. al. "Standards and the Design of the Advanced Photon Source Control System", ICALEPCS '91, Tsukuba, Japan, November 1991, pp. 116-120.
- [4] J. Hill, "Channel Access: A Software Bus for the LAACS", ICALEPCS '89, Vancouver, BC, Canada, October 1989, pp. 352-355.
- [5] L. Dalesio, et. al. "EPICS Architecture", ICALEPCS '91, Tsukuba, Japan, November 1991, pp. 278-282.
- [6] S. Hunt, et. al. "BubbaNet" - A High Performance Network for the SSC Accelerator Control System", these proceedings.
- [7] F. Lenkszus, et. al., "Data Acquisition of Beam Position Monitor for the Advanced Photon Source", these proceedings.

Anatomy of a Control System; A System Designer's View*

S. Magyary

Lawrence Berkeley Laboratory, University of California
1 Cyclotron Road, Berkeley, California 94720 USA

Abstract

The ADVANCED LIGHT SOURCE (ALS) control system is quite unconventional in its design and implementation. This paper will discuss the system design considerations, the actual implementation, hardware and software costs, and the measured performance across all layers of the system.

I. INTRODUCTION

Three interrelated factors continue to drive accelerator control system design. The first is the ongoing evolution of semiconductor technology leading to rapid improvements both in speed as well as density of processors and support circuitry. The second is the ubiquitous presence of the personal computer (PC), the third is the revolution in software due to the large installed base of PC-s.

[1] As silicon systems continue to shrink in size and increase in speed and complexity, concepts that would have been prohibitive a few years ago are quite feasible now. A device controller that might have taken a half a rack in the 1960-s, a large chassis in the 1970-s, a VME or Multibus crate in the 1980-s can now be handled by a single 3U high Eurocard. This allows us to consider, once again, the viability of building, rather than buying, device control hardware.

[2] On the computer front, the downsizing of mainframes, minicomputers and workstations continues. While this downsizing has resulted in PC-s becoming a commodity item, it also has led to increased competition among manufacturers. Only the most efficient, large volume producers and those capable of extremely fast design cycles (to keep up with the rapid changes in processor technology) are able to survive due to the large investments required for R/D and fabrication facilities.

[3] A similar trend is now developing in software. Software is finally entering the phase where proprietary and expensive operating systems and large custom programs will not be viable. Very large volume sales will be required in order to sell software for low prices and at the same time afford the cost of development. (i.e. database prices that used to be > \$1000 are now in the \$100-s range).

I felt these three items were far more important than the peripheral issues (such as the 8086 vs. 68000, RISC vs. CISC, or minicomputer vs. PC) that dominated when we began construction. Therefore, in doing system design, after assessing the functional and performance requirements of the ALS (taking into account budgets and schedules), I tried to anticipate the impact of the three items above on the control system. This is particularly important on the software side, since an increasing fraction of control system costs and manpower goes toward software, often leading to cost over-runs and excessive staffing requirements.

*This work was supported by the Director, Office of Energy Research, Office of Basic Energy Sciences, Materials Sciences Division, of the U.S.DOE, under Contract No. DE-AC03-76SF00098.

The resultant system architecture is shown in fig. 1; detailed description of system functionality and implementation is documented in refs. 1, 2 and 3. The device control level (layer 1) controls the accelerator devices while layers 2 and 3 connect device control and the operator interface (layer 4). Layer 5 is for the networking and development resources.

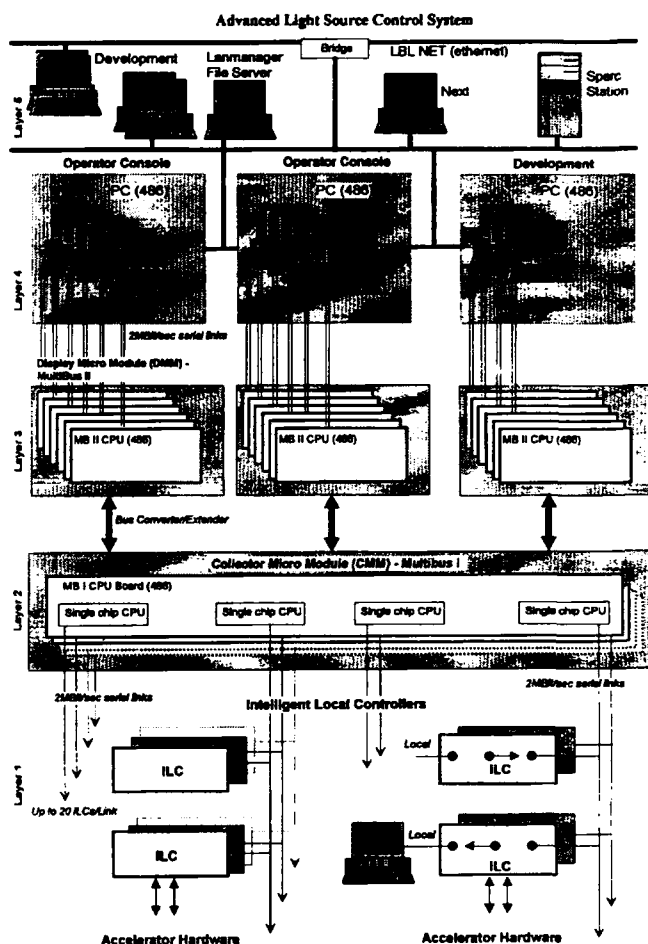


Figure 1. ALS Control System Architecture

II. SYSTEM ARCHITECTURE

A. Distributed Device Control (Layer 1).

The conventional ("bus" based) approaches to the device control problem was either to have a VME/Multibus chassis to which the signal cables are dragged from a large number of devices, or to have STD/Gespac crates (connecting to a few devices) communicating with VME/Multibus systems. I chose an approach which has the benefits of the STD/Gespac without the need for VME/Multibus; the result is the Intelligent Local Controller (ILC, see fig. 2). Designed at LBL (manufactured by outside vendors) it is an evolutionary step toward the single chip (or at least a few chip) solution. Such a custom controller was

economically feasible only if we could find a significant commonality among the control requirements of the accelerator devices (power supplies, Beam position monitors (BPM), vacuum devices, oscilloscopes, etc.) so that ILC-s could be built in volume and thereby recover the development costs. At the same time I wanted functional advantages that would result in overall reduction in system/maintenance costs over the alternate "bus" based solutions. These advantages are: reduced cabling (a costly item) leading to a cleaner installation (fewer trays, less wiring to document), device control isolation and local control (since one ILC is responsible for one device, failure analysis is simple), control built into devices (smart instruments such as a BPM), and flexibility in device/controller placement. The ILC-s also eliminate the need for multi-card systems (and their noise sensitive digital buses) while providing better analog signal handling (lower noise) by allowing placement next to or in the device to be controlled. Power consumption is a mere four watts, resulting in reduced chassis power and cooling requirements, and sufficient computer power is built into the ILC so it meets the performance requirement of any device it controls.

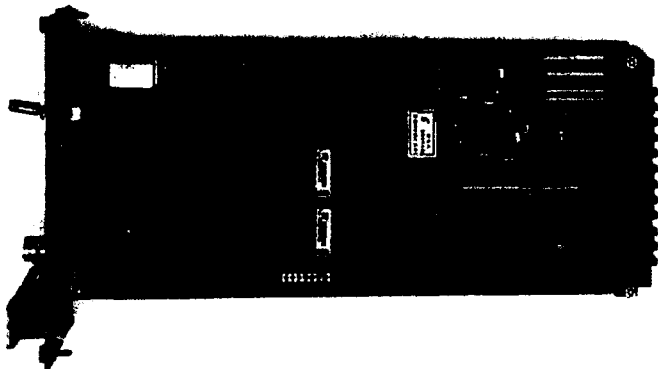


Figure 2. ILC

Two generations of ILC-s were built (175 of version I, 500 of version II), with respective costs of \$650 and \$1000. The added cost of version II is due to the resolution (nominally 16 bit) of the A/D converters, larger memory size and higher performance. Currently 400 ILC-s operate the accelerator; at full system implementation 500-600 ILC-s will be in use.

B. Communications (Layers 2,3).

When we began construction, the communication part of most control systems was handled by a few Token Ring or Ethernet based links. I chose a "star" type "shared memory" (the CMM, see figs. 1,3) approach to allow many parallel links to feed a centralized memory where data from many devices can be accessed quickly using a parallel bus. This type of "shared memory" system has the advantage that it can behave as a "router" (star-like routers are now coming into vogue for increased communications bandwidth) but in addition allows data to be "cached" for multiple access by a number of users without continually requesting data on the bandwidth limited links. Accelerator control systems are well suited to a "shared memory" architecture since data access is inherently asymmetric, i.e. for normal operation many devices need to be monitored by

numerous users (increasingly by people in their offices), but few devices are allowed to be controlled.

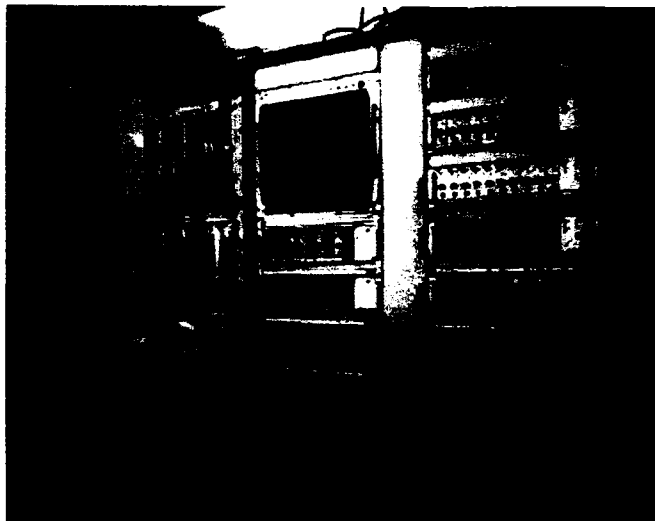


Figure 3. CMM, DMM-S, and Fiber Optic Links

Each of our currently installed 41 links runs at 2 Mbits/sec, for a total communications bandwidth of 82 Mbits/sec. The CMM has 7 CPU-s to support the links, with an expansion capability for up to 11 CPU-s to support 88 links. About 1400 data (average of 80 bytes) packets/sec are transmitted on each link. This amounts to an average of about 15 updates/sec of the active part of the entire accelerator database. The need for these high performance links is driven by the nature of distributed device control that de-emphasizes processor bandwidth with a concomitant increase in communications requirements. A control loop that used to be contained in a single chassis (VME or Multibus) now may be spread over a dozen device controllers; therefore the problems of feedback loops migrate from being a CPU performance issue (in a bus based system) to a communications issue among distributed device controllers.

The high communications bandwidth ensures that we meet the performance and deterministic response requirements of the feedback loops. Determinism means that data access is strictly a function of the number of links, devices on a link and the packets/sec/link and not dependent on user driven (i.e. what is being displayed on a console) system load. The need for Determinism also led to a communications system that, rather than being message driven (conventional approach) is instead controlled by data update needs that are prioritized at the device (i.e. ILC) level. Since communications is often the limiting factor with many commercial devices (i.e. IEEE-488 link to a scope, or RS-232 link to a stepper motor), we want to limit data traffic to those devices, especially if multiple users want (often simultaneously) the same data.

For very fast data transfer, ILC-s can additionally communicate with each other directly up to about 2000Hz. This should be sufficient for the fast feedback loops that are expected to require a rate of about 200 Hz.

The DMM-s (see figs. 1,3), which access the shared memory, can act as a database, task or "permission" server for the operator stations. The DMM-s, using the "shared

memory" deterministic behavior of the CMM, can also act as a timing synchronization system. Since all the data arrives and leaves from one central location, it is possible to software synchronize the ILC-s without resorting to hardware timing signals. For the ALS a clocking system of 50 Hz could be done entirely in software, saving additional cost by eliminating the need for a hardware based timing and event tagging system. We used a software event tagging system, combined with a simple hardware interrupt distribution, to synchronize data access to 96 BPM-s from the operator station (PC-s). Such synchronization could be even faster if the software was executed in the DMM-s, where access to the data is at MULTIBUS bandwidth speeds.

C. Human Interface and Network. (Layers 4,5)

At the time of conceptual design, the most controversial part of the control system was the use of PC-s as the operator station (see fig. 1).

However, with the huge numbers of PC-s installed world wide (> 150 million) and the success of WINDOWS (30 million copies, and growing at the rate of 1 million/month), my prediction has paid off. With the imminent arrival of WINDOWS NT even large modeling applications can be accommodated. All of our current 16 bit applications already run unmodified on a beta version of WINDOWS NT (after writing a hardware interface Dynamic Link Library) with no change in the look and feel of the operating environment. The ubiquitous presence of WINDOWS has resulted in a rapidly exploding field of development tools (Visual Basic, Turbo Pascal for Windows, Visual C++, Toolbook, etc.) in addition to a large number of commercial applications (Designer, Excel, Word for Windows, Access, etc.). With the large sales volumes involved, prices of this software is rapidly declining (approaching commodity pricing) while features (Object Linking and Embedding [OLE], multimedia support etc.) and ease of use increases. This has resulted in a system to which many different individuals could contribute, depending on the level of their programming experience, thereby breaking the stranglehold imposed by systems that require "professional" programmers exclusively.

We use two dedicated links (identical in hardware to the CMM to ILC link) from each PC to communicate with a matching CPU in the DMM.; we achieve 1250 database accesses/sec for each PC. This currently is limited by processor speeds in the PC and the DMM; the link bandwidth will limit us to a maximum of 3000 accesses/sec/link. The 15 PC-s currently in use allow an aggregate of about 18,000 accesses/sec; however this is still a small fraction of the bus bandwidth that the CMM/DMM have available. When the Storage Ring was brought on line no degradation occurred in the data access to the existing parts of the accelerator. The PC-s can be upgraded to "PENTIUM" based systems thereby giving workstation ("RISC") like performance to the operator stations and even higher data access rates.

A conventional Ethernet interface (layer 5) allows the PC-s to communicate with a file server, workstations and other networked computers. We have provided for Remote Procedure Call based access to the database by UNIX based workstations (SUN, NEXT, IBM RS 6000). We note

that recently many UNIX (and even Mac) based manufacturers are porting their operating systems to PC-s, as well as trying to provide WINDOWS compatible emulators, but with the arrival of Windows NT on the PC-s, workstations will not be required (they were needed for the large modeling applications that were too large for WINDOWS).

III. SCHEDULE, COST, STAFFING AND FUTURE OPTIONS

Over a period of 4.5 years \$4.8 million (estimated escalated cost at beginning of construction was about \$5.3 million) was spent on the control system. Of this cost, about 35% was for hardware, the remainder went for manpower (primarily software development) costs. An average of 5 people were required during the construction period; this includes software, coordination and management. The control system was on schedule and at no time delayed commissioning in any significant way, and can be maintained (due to its modularity) and software improvements added (for the currently needed functionality of the ALS) with a minimal staffing requirement of about 2 FTE-s.

The specifications, set out at the beginning of construction, have been exceeded in every category. The ILC-s are faster, more accurate and consume less power than anticipated; the CMM can handle more CPU-s and links. More DMM-s are in use than promised, and the PC front ends are more powerful and versatile.

Future improvements could complete the transference of WINDOWS based applications to WINDOWS NT, use network Dynamic Data Exchange to integrate application behavior among the many PC-s, and use OLE to allow an object based approach to application use and interaction. When Futurebus+ based systems become readily available, one could consider using them to replace the DMM/CMM. The use of an ATM or SONET based fiber optic system for the serial communications would allow replacement of the many parallel links with a single cable.

IV. ACKNOWLEDGMENT

The author would like to express his appreciation to the many people involved in making this control system a success. In particular D. Meaney, B. Brokloff, of operations, M. Fahmie, P. Molinari of Electronics, M. Chin, C. Timossi of controls, H. Nishimura of physics, H. Lancaster of Electrical Engineering, and R. Yourd of ALS project management.

V. REFERENCES

- [1] Magyary et al., "Advanced Light Source Control System," Lawrence Berkeley Laboratory, LBL 26028 and Proc 1989 IEEE Particle Accelerator Conf, Chicago (IEEE Publishing, New York, 1989).
- [2] Magyary et al., "Advanced Light Source Control System," Nuclear Instruments and Methods in Physics Research, A293 (1990) 36-43, North Holland.
- [3] Magyary et al., "Status Report on the Advanced Light Source Control System," ICALEPS Tsukuba, Japan, (1991).

Beam Position Monitor Data Acquisition for the Advanced Photon Source*

Frank R. Lenkszus, Emmanuel Kahana, Allen J. Votaw, Glenn A. Decker, Youngjoo Chung, Daniel J. Ciarlette, Robert J. Laird
Advanced Photon Source, Argonne National Laboratory, Argonne, IL 60439

Abstract

This paper describes the Beam Position Monitor (BPM) data acquisition scheme for the Advanced Photon Source (APS) storage ring. The storage ring contains 360 beam position monitors distributed around its 1104-meter circumference. The beam position monitor data acquisition system is capable of making turn-by-turn measurements of all BPMs simultaneously. It is VXI-based with each VXI crate containing the electronics for 9 BPMs. The VXI Local Bus is used to provide sustained data transfer rates of up to 13 mega-transfers per second to a scanner module. The system provides single-bunch tracking, bunch-to-bunch measurements, fast digital-averaged positions, beam position history buffering, and synchronized multi-turn measurements. Data is accessible to the control system VME crates via an MXI bus. Dedicated high-speed ports are provided to supply position data to beam orbit feedback systems.

I. INTRODUCTION

The BPM data acquisition system requirements are:

1. Measure beam position both during injection at 2 Hz and during closed orbit.
2. Provide single bunch tracking around the ring.
3. Measure position of different bunches at each BPM turn-to-turn.

4. Measure position at each BPM on each turn (3.6 microseconds for the storage ring).
5. Provide averaged beam position for higher accuracy.
6. Provide a beam history for each BPM .

Major design goals included:

1. Minimize front panel connections by using available VXI backplane lines.
2. Design the system so that BPM data acquisition will operate autonomously upon power on with no set-up/intervention by the control system.

Figure 1 shows one of 20 storage ring control nodes. Each node contains the control and BPM electronics for two storage ring sectors. The nodes are interconnected via the controls local area network (LAN) and a high-speed fiber optic ring. The BPM electronics are contained in two VXI crates with each crate containing the BPM signal processing electronics for a sector. An MXI bus connects the controls VME crate to the BPM VXI crates and a VME orbit feedback crate. The control system can set the data acquisition mode of each BPM and read, on demand, beam intensity and averaged or raw beam position.

II. METHOD

Figure 2 is a block diagram of a BPM VXI crate. The

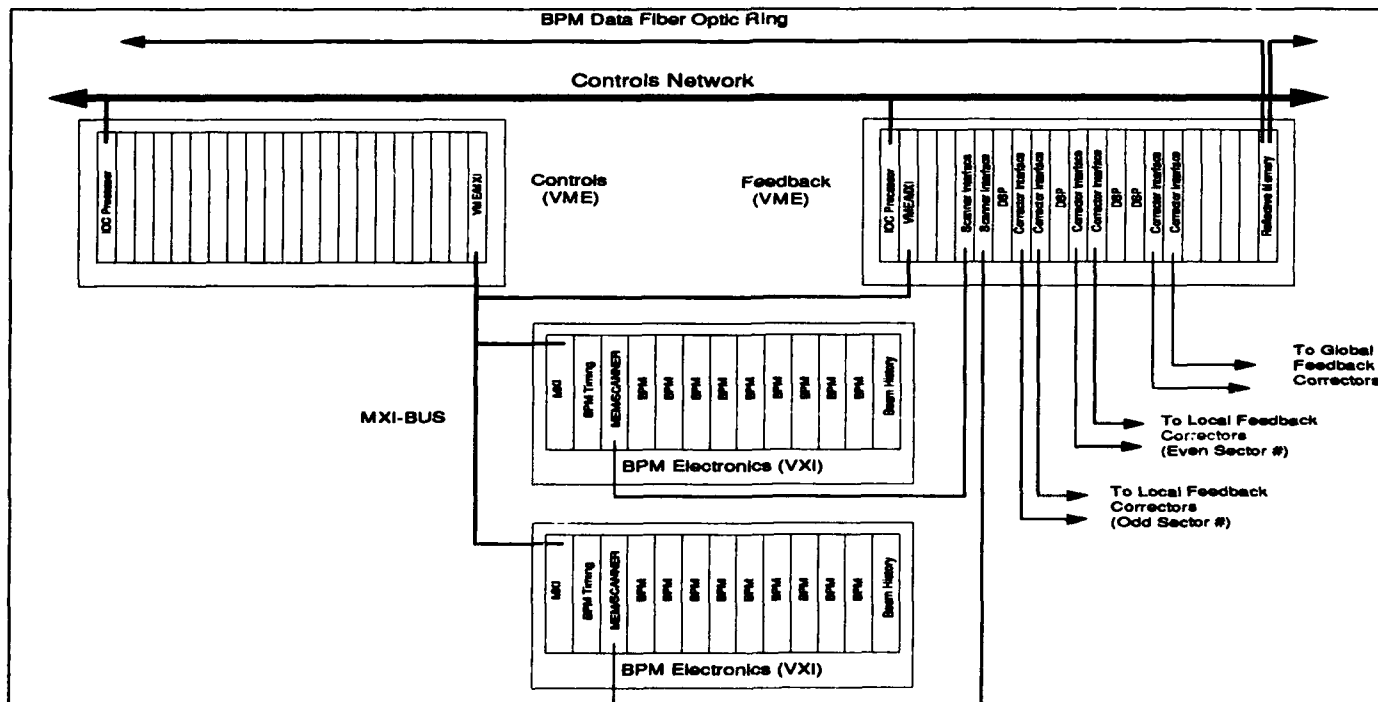


Figure 1. Typical Storage Ring Node

***Work supported by U.S. DOE Office of Basic Energy Sciences, under Contract No. W-31-109-ENG-38.**

The submitted manuscript has been authored by a contractor of the U.S. Government under contract No. W-31-109-ENG-38. Accordingly, the U.S. Government retains a nonexclusive, royalty-free license to publish or reproduce the published form of this contribution, or allow others to do so, for U.S. Government purposes.

VME bus lines have been omitted for clarity. The 12 VXI Local Bus lines are daisy chained through each BPM module (SCDU - Signal Conditioning and Digitizing Unit) and terminated at each end to form a 12-bit data bus. The eight VXI bus TTL Trigger lines are used for control, status, and BPM module readout select.

The Memory/Scanner module sequentially selects each BPM module at a fixed scanning rate sufficient to ensure that

indicated by the Status/X/Y line) on the rising edge. The Summary Status is the OR of BPM module error status bits. The BPM Select, Data Strobe, New Data, and Status/X/Y signals are located on the VXI TTL Trigger lines. Our measurements indicate that greater than 13 Mtransfers per second are achievable using backplane transceiver logic (BTL) drivers and receivers.

Each module in the BPM system is designed to default to

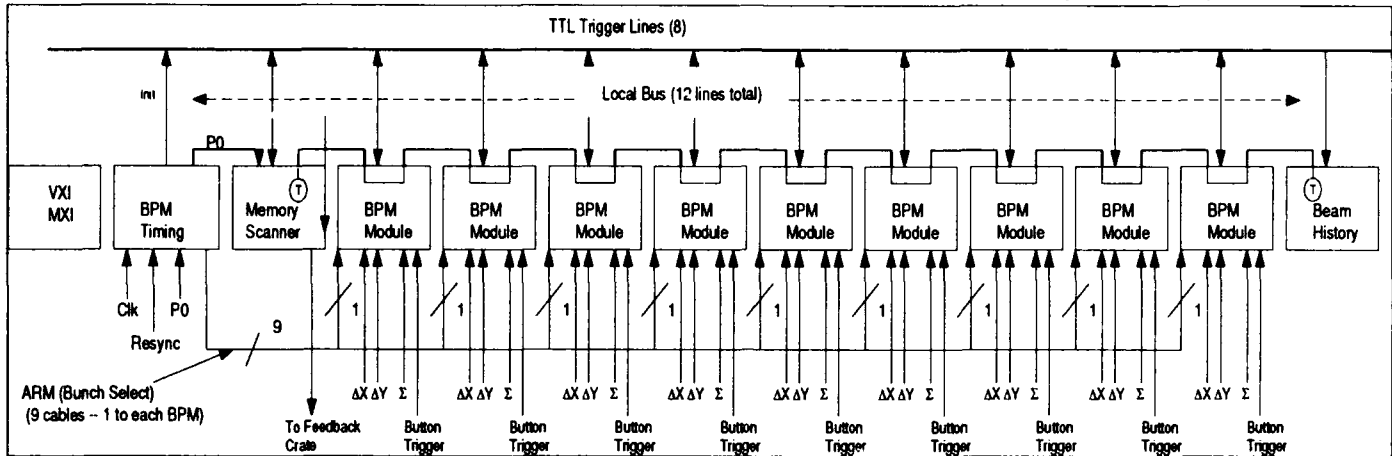


Figure 2. BPM Data Acquisition Block Diagram

each BPM module will be scanned at least once per turn. For the storage ring, a scanning rate of 13 Mtransfers per second will access each BPM three times per turn. If an addressed module has new data available, it sequentially places the beam intensity followed by the position on the Local Bus lines and asserts a New Data signal to indicate the presence of data. The BPM module also drives an additional time multiplexed signal to indicate a summary module status and whether the X or Y position is currently being transferred. The BPM module is capable of digitizing only the X or the Y position on any given turn. The control system may set each BPM to measure X or Y only or alternate between X and Y on successive turns. The Memory/Scanner accepts the data on the Local Bus lines when New Data is signalled by a BPM module.

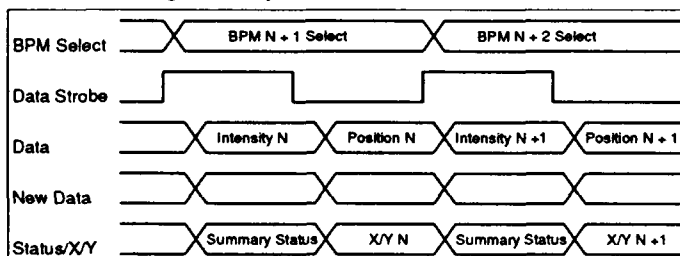


Figure 3. Data Transfer Over the Local Bus

Figure 3 shows the data transfer cycle over the VXI Local Bus. Transfers are synchronous, with timing controlled by a Data Strobe signal driven by the Memory/Scanner. A 4-bit BPM module readout address is output by the Memory/Scanner module on the positive edge of the Data Strobe. If the addressed module has new data, it responds by driving the Data lines, New Data, and the Status/X/Y lines. If New Data is asserted, the Memory/Scanner module accepts intensity data on the falling edge of Data Strobe and position (either X or Y as

a running condition on power up; i.e. on power up data collection begins after a short initialization phase without intervention by the control system. The control system can alter the default power on operation through the MXI/VXI bus.

III. MODULE DESCRIPTIONS

BPM Module

Each BPM module [1] provides the signal conditioning and analog-to-digital conversion for a 4-button BPM. An on-board mono-pulse receiver accepts sum and difference signals from a front-end filter comparator located at the button pickups and outputs beam intensity and normalized position. Two channels of 12-bit digitization are provided. One channel digitizes intensity while the second channel digitizes position. The position channel may be programmed to digitize X only, Y only, or alternate X and Y on successive turns. A digitization cycle takes approximately 900 ns.

Each BPM module accepts a Bunch Select (ARM) signal and a button trigger signal. The Bunch Select signal is generated by the BPM timing module and acts as a gate for the button trigger signal, which is a fast trigger derived from the button pickups. The trigger circuitry will run in a "free run" mode if the ARM signal is disconnected or held active. In this mode the BPM module triggers on the "next" button trigger signal after completing a digitization cycle. This mode will be used during injection.

In addition, a signal derived from the button trigger signal is available on the front panel for use with other equipment.

Memory/Scanner

The Memory/Scanner controls the BPM data acquisition by driving BPM module select lines and the Data Strobe. This module provides a programmable box car averager for each

BPM X and Y position. In addition, a high speed fiber optic port provides a BPM position data stream to the orbit feedback crate.

At power up, the Memory/Scanner module sequentially initializes the readout addresses of the BPM modules and begins sequential scanning.

BPM Timing

The BPM timing module generates a bunch select (ARM) signal for each of the BPM modules. The bunch select signals are generated by arbitrary bit-pattern generators running at 117 MHz. This provides a time resolution of 8.5 ns. Each bit-pattern generator has a 4-kbyte memory which is loaded by the control system to select a bunch pattern.

The timing module also provides a "Bunch 0" reference (P0) and a "Resync" signal which is used to selectively synchronize BPM modules.

At power on the timing module forces all bunch select signals active. This causes each BPM to run in "free run" mode.

Beam History

The Beam History module provides storage memories for each BPM. It captures data transfers on the Local Bus and stores time-stamped intensity and position information. The time stamp is based on a turns counter driven by the bunch 0 reference from the BPM timing module. The 32k by 32-bit memories operate as first-in first-out (FIFO) buffers and are capable of storing ~50 milliseconds of storage ring BPM data.

Each FIFO may be operated in fill and stop mode or circular mode. The fill and stop mode will be used to collect data during machine experiments. In this mode the FIFO for each participating BPM is initially cleared. Data collection begins upon receipt of the Resync signal from the BPM timing module and ceases upon FIFO full.

In the circular mode, each FIFO fills and then overwrites the oldest data point with new data. Since the BPM modules are triggered by a beam-derived signal, digitizing ceases upon loss of beam. The FIFOs therefore will contain the beam history prior to beam loss. The circular mode will be useful in diagnosing beam loss events.

IV. ORBIT FEEDBACK SYSTEMS

As shown previously in Figure 1, each storage ring node has a VME feedback crate. The distributed feedback system architecture relies heavily on a technology known as reflective memory. Reflective memory can be defined as a network of replicated shared memory. Reflective memory has the following features:

1. Any node can write to reflective memory.
2. All nodes see the same reflective memory image (data is replicated in every reflective memory.)
3. Reflective memory is designed for real-time performance -- latency is minimized.
4. No processor involvement is required for network initialization or operation.
5. Data is transferred (replicated) by merely writing to

memory -- actual transfer is handled by hardware.

Reflective memories are connected in a fiber optic ring. With presently available commercial hardware, sustained data transfer rates of 6.2 to 26 Mbytes per second are achievable. A network may consist of up to 256 nodes. At 26 Mbytes/sec up to 300m spacing between adjacent node is allowed.

The 20 orbit feedback crates distributed around the 1104-meter storage ring circumference are networked with reflective memories. Each crate receives local BPM data from the Memory/Scanners. The BPM position data is averaged by a programmable boxcar averager located in the feedback crate. Forty X and forty Y BPMs will be selected to provide global position information. An additional two X and two Y BPMs will be used for each installed insertion device beamline and an additional two Y BPMs for each installed bending magnet beamline. The beamline position data may come from rf BPMs or X-ray BPMs or some combination of both. All BPM data used for orbit correction is written to reflective memory. For the fully populated ring with 34 insertion devices and 34 bending magnet beamlines, a total of 284 positions will be used for orbit feedback. With 26-Mbyte-per-second memories, the position data will propagate around the storage ring in less than 50 microseconds. The planned feedback system sample rate will be 4 kHz [2].

Within each feedback crate, Digital Signal Processors (DSPs) use the feedback position data to calculate corrector values for the two local sectors. The global position data is used to calculate local corrector values assigned to the global feedback system. For reasons beyond the scope of this paper and related to overall feedback stability, the corrector calculations for the local beamlines use both global position data and position data associated with the local beamline.

The use of reflective memory greatly facilitates a distributed feedback system by making all BPM data required for orbit feedback available to all distributed feedback processors. Also, since each feedback node calculates corrector values for its two sectors, the need to distribute computed corrector values around the storage ring is eliminated.

V. STATUS

At the time of this writing, a prototype BPM timing module is under test. A contract to build the BPM modules to a performance specification is in place with prototypes due in June. The Memory/Scanner module detailed design is complete and is currently in CAD. Design of the Beam History module is underway. Proof of concept tests for the feedback systems are scheduled to take place at SSRL.

VI. REFERENCES

- [1] E. Kahana, "Design of Beam Position Monitor Electronics for the APS Storage Ring", *Proceedings of the 3rd Accelerator Beam Instrumentation Workshop*, CEBAF, Newport News, VA, 1991.
- [2] Y. Chung, L. Emery, J. Kirchman, "Compensation for the Effect of Vacuum Chamber Eddy Current by Digital Signal Processing for Closed Orbit Feedback," these proceedings.

New Tevatron Cryogenic Control System.

B. Lublinsky, J. Firebaugh, J Smolucha, FNAL.*

Abstract

We are updating the Tevatron's cryogenic control systems (FRIGs) to provide a more powerful, flexible and robust architecture based on Intel's 80386 microprocessor. The objective of an individual FRIG is to: perform data acquisition and control for over 1000 dedicated data points; produce alarms in the case of abnormal functioning of equipment; run PID closed loops for the cryogenic hardware; program and run finite state machines, thus automating operations such as cooldown, warm-up and so on; and fulfill fast data logging for any particular set of parameters of interest.

1. INTRODUCTION

The physical characteristics of the Tevatron's cryogenic hardware require a highly distributed control system. From the cryogenic point of view the entire ring is partitioned into six physical sectors; with each sector containing four satellite refrigerators and an associated compressor. In the current implementation each satellite system is driven by a dedicated Intel SBC386/116 single board computer. These FRIG execution processors reside in a Multibus II chassis. One chassis can support up to 8 FRIG systems servicing the same sector. The Multibus II environment provides a centralized interface to Fermilab's control system (ACNET) as well as a variety of support services (Tevatron clock, Ethernet, and Token Ring), while simultaneously supporting a private, protected execution platform for each 80386 based FRIG. An embedded DOS PC is used for system initialization and diagnostics. The 80386 execution processors are decoupled from the actual cryogenic hardware by a layer of 80186 based I/O processors. Communications between the execution processors and I/O processors are implemented through an ARCnet based small area network.

2. INTERPROCESSOR COMMUNICATIONS.

In a highly distributed system like FRIG, one of the primary factors driving software development is the question of how to handle interprocessor communications. Obvious considerations include the desire for deterministic network traffic, topological flexibility, and overall system robustness. We decided to implement communications on the basis of a reflective memory paradigm, dedicating a block of memory in each processor to serve as an interprocessor shared memory and supplying supporting services. The scheme provides for a periodic update of the 80386's reflective memory with data read from each of the I/O processors. Since the cryogenic system is generally considered to be fairly slow (1-2 Hz), we also decided upon an update frequency of 15 Hz. This makes the network load quite predictable and establishes a uniform facility for acquiring actual hardware data. Using a higher update frequency

allows simplification of the timing problems in the reflective memory updates and error checking mechanisms. Settings, due to their infrequent and unsolicited nature, are serviced on demand. In this case we use a special handshaking mechanism (with retries) to ensure that all setting requests are reflected to the appropriate I/O processor. Another, less obvious, advantage of the periodic communications scheme associated with reflective memory is that it provides a very straightforward mechanism for support of the system's heartbeat. In the current implementation, communications between processors have to occur within a predetermined amount of time. Silence on the part of any processor indicates a serious problem, allowing special measures to be initiated by any one of the network peers.

In order to achieve proper functioning of reflective memory it is necessary to provide identical device mappings in all participating machines. This is trivial if we have a fixed set of devices connected to each I/O processor. However, one of the primary design goals was to provide a greater level of flexibility within the system. Ideally, we should be able to change the hardware configuration of each I/O subsystem with a minimum of effort. In order to provide that level of flexibility, at boot time we download configuration files from the embedded DOS PC into each of the 80386 processors. These files inform each execution processor of how many I/O processors he needs to communicate with, along with the specific hardware configuration for each one. The execution processors, in turn, relay the information to each of their associated I/O processors upon request. The reflective memory in each of the participating processors is built on the basis of this information. The configuration files are maintained as standard ASCII script files. They can be edited either in the field or remotely through any of the standard network utilities.

The actual software that supports reflective memory is implemented as a task called Virtual I/O Bus (VIOB), and it runs in all participating machines. It is based on an in-house developed network protocol (YAKNET), layered on top of the basic ARCnet communication facilities. Besides evening up the length of all ARCnet messages, this layer features packeting and depacketing, task to task communications, and prioritized message passing. The last feature allows us to send rather long messages without delaying short, important ones. Also, instead of using a processor specific interrupt to service ARCnet communications, we are using high frequency (100 Hz) polling. This allows us to use the same software on all processors within the system.

3. 80186 SOFTWARE.

The interprocessor communication scheme allowed us to define the responsibilities of each processor in the system, thus simplifying the software within the 80186 I/O processors. Instead of using a commercial embedded kernel we developed a preemptive task scheduler driven by a combination of timing and hardware interrupts. The scheduler features several interrupt levels with selectable priorities and background execution. Tasks in the system append themselves

* Operated by the Universities Research association under contract with the U. S. Department of Energy.

to the necessary interrupt at startup, and the provision exists for each task to be able to dynamically change the interrupt it is appended to. We were able to put enough intelligence in the tasks themselves so that they can change their own priorities and frequencies. Also, a high level task can make decisions regarding the priority and frequency of a lower level task. This feature is especially important if we decide to change the system configuration on the fly. It is also useful in the case of special hardware events. For example, in the event that the I/O processor loses communications with its associated 80386, it can reschedule itself to send a 1 Hz "Init me" request, rather than do 15 Hz reflective memory updates. Within a given interrupt level the tasks are executed in the order in which they have been appended. One more mechanism incorporated in the kernel is a message passing facility, supporting intertask communications.

The major task divisions within the I/O processors are organized around four prioritized timer interrupts with the following rates: 1000 Hz for real time kernel services and fast data logging (SNAPSHOTS); 100 Hz for network communication services (YAKNET) and system console support; 15 Hz for general data acquisition services (VIOB); and 1 Hz that is used primarily for updating system statistics. The fast data logger maintains 10 seconds worth of circular buffers for as many as sixteen individual ADC channels without exceeding 10% of the available system bandwidth. Data logging can be initiated on request and stopped either by the receipt of any specified Tevatron clock event, or by the occurrence of a user-definable hardware event. After data is transferred to the 80386, data logging can be restarted.

Much effort was also devoted to developing adequate debugging facilities. For instance, each I/O processor includes a second RS232 port dedicated to a PC hosted, interrupt driven monitor. The monitor provides access to the system at the highest kernel level; and was instrumental in debugging the initial versions of the task scheduler and during the installation in the field. Each I/O processor also includes a bank of user-definable LED's and front panel switches reserved exclusively for diagnostic purposes.

4. 80386 SOFTWARE.

One can view the 80386 software as three major layers (Fig1), each of which is implemented using the services of the previous layers. At the lowest level we have chosen the MTOS operating system because it provides a large variety of system services. OOC++, an intermediate layer, serves as a system kernel with two major functionalities: support of object handling and message passing mechanisms within the system, and support of standard ACNET communications. Introduction of this layer enables us to simplify the overall organization of the total system. The highest layer is the cryogenic specific software dedicated to data acquisition, closed loops and Finite State Machines (FSMs).

OOC++ is implemented on the basis of the C++ binding and memory management technique, and provides support for multiple class inheritance, polymorphism and encapsulation. It features dictionaries of defined classes and instances of these classes (objects), and an object to object message passing facility. OOC++ provides a uniform communication protocol between software objects within the 80386, and adds significantly to the flexibility of the whole system. It allows

us to create software objects that support certain types of messages regardless of their source and to use them interchangeably within the system. The object identifier (OID) becomes part of the message and informs the kernel about the message destination.

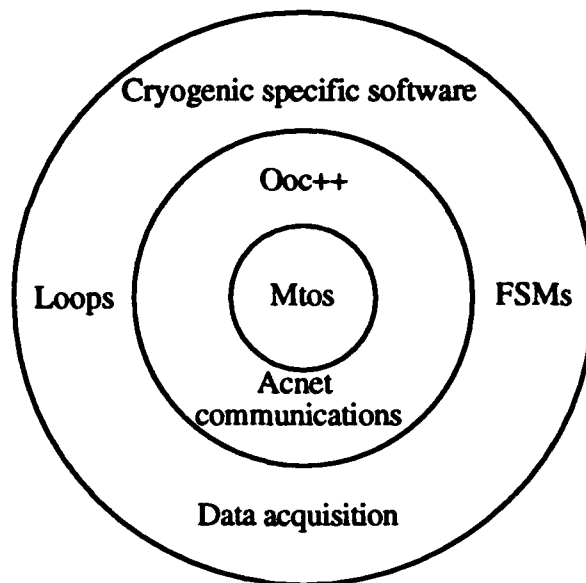


Fig. 1 Internal Organization of 386 software.

The system kernel supports several ACNET communication protocols. Standard ACNET communication support is based on four main tasks: RETDAT, SETDAT, READER and WRITER. The first two serve to receive requests to read data and control hardware, respectively. The latter two provide replies back to the ACNET system for both reading and control. RETDAT can accept two types of requests: periodic and one-shots. For periodic requests a cancel message from the network should arrive in order to stop the replies. Replies for RETDAT requests are shipped to ACNET via READER and consist of the specified requested data, collected by the local system. Usually each RETDAT request creates a list object that generates replies and submits them to READER. SETDAT can accept only one-shot requests and fulfills hardware control. The status of the hardware control operations is shipped back to ACNET through WRITER. Access to internal software objects is done on the basis of message type (type of the ACNET request) and OID of each object involved with the request. All of the internal message passing necessary for ACNET support is done through OOC++. Additional ACNET communication protocols are provided to support alarm processing and fast data logging.

The cryogenic specific software itself can be partitioned into three major layers.

The lowest is the data acquisition layer, which consists of the device drivers for the hardware used in the cryogenic system. Each driver is built as a class that supports all ACNET messages needed for a particular device. These messages can be reading, setting, reading of setting, basic status, basic control, analog and digital alarms. This layer allows the use of standard ACNET parameter pages and application programs that utilize data acquisition services; it also serves as a base for all upper layers. Access to the actual

hardware for this layer is provided through reflective memory, supported by the previously described VIOB task.

The second layer is closed loop control. Presently we are supporting only relay-like control and PID control with its variations (PI, PD, P, I and D). This layer operates at its own frequency (currently 1 Hz) under control of its own monitor. Besides the control itself, this layer supports access from VAX based applications for configuration and tuning of the control loops. Configuration of the loops refers to the ability: to start or stop a control loop; to change its frequency using 1 Hz granularity; to assign a loop input to any value in the system, including the output of another loop; and to assign a loop output to any controllable device in the system. Tuning of the loop refers to the ability to change the values of the loop coefficients, including zeroing them out, thus allowing a change of the control strategy. The current version of the FRIG software can support up to 32 loops. Future plans are to incorporate into this layer special control algorithms for the cryogenic plants with large dead times and to add adaptive control algorithms.

The uppermost layer of cryogenic software is the finite state machines (FSMs), driven by the state of the cryogenic hardware. This layer is implemented to provide support for various discrete control algorithms necessary for the operating of cryogenic equipment. Rather than having these algorithms hard coded we have provided cryogenic engineers with the capability to program their own discrete algorithms without changing microprocessor software. The present version of the software can support up to 32 FSMS, each containing up to 16 states. Each state can contain up to 8 action rules, (hardware and software settings) when the state is entered, and up to 8 transition rules, defining possible transitions from this state based on the conditions of the hardware and software.

Features of this implementation are:

- several FSMs can run concurrently in a FRIG system;
- FSM transition rules can involve a great deal of "special" calculation;
- all FSMs and special calculations are "reprogrammable" through VAX based applications.

In order to satisfy these requirements several additional software classes, which serve as a basis for FSMs were introduced into the system:

- operations - doing special calculations on the basis of measured parameters;
- actions - doing setting and/or control on one or several appropriate devices;
- timers - doing time measurements inside the system.
- storages - storing useful constants for special calculations.
- states - states of the FSMs, containing action and transition rules.

All of the mentioned classes are tunable from VAX based applications and can be used not only inside the FSMs, but elsewhere inside the system, as inputs and outputs of loops, on parameter pages, etc.

5. EMBEDDED PC SUPPORT.

The present version of FRIG software is using a PC/AT exclusively for booting/downloading of the embedded 386 based software. Two major functions are available in the FRIG loader routine:

- download code and default parameters to the microprocessors.
- restart all embedded 386.

Downloading of the default parameters adds flexibility to the created software and allows to make changes by simple rebooting of the system without any additional software work. Another feature provided by default parameters is the possibility for a FRIG system to come up aware of what the system is and what it should be doing, without depending on the central VAX for obtaining of this information.

The default parameters downloading allows to define default parameters for:

- hardware configuration;
- loops;
- FSMs and its elements.

All of the default parameters are implemented as human readable ASCII files that can be easily accessed and changed by any available PC based editor.

Two additional provisions implemented on the PC/AT are remote reboot and file transfer service. The first uses the specialized hardware allowing remote reboot of the PC/AT and the whole Multibus II chassis using a common purpose CAMAC digital I/O module. This feature allows us to hook a dedicated I/O module to one of the existing CAMAC Front-Ends and incorporate remote reboot into one of the applications. File transfer service is built on the basis of standard Ethernet protocol support and FTP software. When the system is rebooted, by means of a specialized script, invoking the loader, the FTP server task is invoked, thus enabling file transfers to the PC from the central VAX.

Future plans for PC software include moving it to the Windows environment to make a nicer interface with the loader, and implementation of a sector-wide PC based watchdog system.

6. CONCLUSION.

The described control system is fully implemented and has been working in several installations around the ring for the last two months. Full conversion to the new cryogenic control system is planned for this summer. Besides future plans mentioned within the paper, we are thinking about incorporating a Micro VAX into the system to provide ring wide intelligence and coordination of the individual control systems described in this paper.

7. ACKNOWLEDGMENTS.

The authors are thankful to M. Glass for numerous consultations on the MTOS operating system and 80386/80186 software, and suggestions concerning system implementation. T. Groves, L. Chapman, B. Hendricks and W. Krakar made many useful suggestions to improve interactions with FRIG application programs.

Control Software for EUTERPE

P.D.V. van der Stok[†], F. van den Berk[†], R. Deckers[†], Y. van de Vijver[†],
J.I.M. Botman[‡], J.L. Delhez[‡] and C.J. Timmermans[‡].

Eindhoven University of Technology

[†]Department of Mathematics and Computing Science

[‡]Department of Technical Physics

P.O. Box 513, 5600 MB Eindhoven, Netherlands

Abstract

This paper describes the software design of the EUTERPE synchrotron radiation facility. Applications are developed as a set of separate programs. Services are exported from these programs and can be used by other programs. The programs are built from classes following the object oriented programming paradigm. Objects are created from these classes when the programs are distributed over a set of processors.

The objects of the applications, which represent existing accelerator related objects, also profit from standard facilities provided by the control system software, like: adaptable acquisition and user dependent object views (e.g. B-field for physicist and power-supply for engineer).

This approach makes the application software independent of the underlying control system structure. Applications do not see if the underlying structure is 1-, 2- or 3-layered. Accordingly, the mapping of the application software to the hardware can be postponed until the last moment. Once installed, the control system structure can be adapted to new performance and flexibility requirements without consequences for the application software.

I. INTRODUCTION

The Eindhoven University of TEchnology Ring for Protons and Electrons (Euterpe) is currently being designed and constructed at the physics department of the Eindhoven University of Technology (EUT). The accelerator is designed for the production of synchrotron radiation extending from the infrared to the ultraviolet [1]. Apart from radiation production, the ring will also be used to study beam dynamics and to assist in the teaching of accelerator physics. In the same spirit the design for the control system for the ring has been started. The design should not be limited to the most cost effective way to control the accelerator, but it should support accelerator control in general. The object oriented method is investigated for its applicability to accelerator control. Claims about reusability, maintainability and simplicity [2] can be evaluated. In

this paper a summary of the main results is presented. A more detailed treatment is found in [3]. The verification of the object orientation claims is only possible in a later stage when the control system is actually used and modified.

II. REQUIREMENTS

The requirements on accelerator control are motivated by (1) the experimental nature of the installations, the distribution of the accelerator over a large area, (2) the often conflicting wishes of different user groups and (3) synchronous actions of different accelerator components. Less essential are the short time range of many phenomena and the wish to access the equipment from personal computers situated at widely dispersed locations.

The experimental nature of the installations leads to changes in the type and amount of equipment to be controlled. Also changing operational conditions require that the relations between different components are frequently modified. The *flexibility* of the control system that allows additions and removals of pieces of equipment without major control system shutdowns is a major requirement.

During the lifetime of the accelerator, components break down and are replaced by other components. For a high availability of the accelerator, online modifications to the equipment should be possible with a minimum of effort or modifications to the application programs. Consequently, the *reconfiguration* of the equipment and the associated control system components should be possible.

The physical distribution of the accelerator components makes it attractive to group equipment at a number of locations and to control this equipment from computers situated at these same locations. The wish to control all the equipment from one central control room and provide some controlled access from individual workstations necessitates the *distribution* of the control system.

The different groups that build, maintain and operate the accelerator have widely different views on the same pieces of equipment. An engineer is interested in bit patterns, a physicist in current and field values. Consequently, a piece of equipment should offer *multiple views* for an efficient manipulation by a heterogeneous population.

Accelerator components are grouped to construct higher level components. Several magnets can be grouped to produce a higher order harmonic magnetic field; a phase and a strength are the only required attributes of such a group. At a lower level, the individual magnets still need to be controlled by individual settings. At a lower level yet the magnets are composed of a power-supply, the magnet status equipment and the timing equipment. *Multilevel access* is a characteristic of accelerator control. Dependent on the situation, groups of equipment or individual pieces of equipment need to be accessed.

Applications can be invoked concurrently on different computers. Many different applications often need values from the same pieces of equipment (e.g. the beam current). The *atomicity* of groups of actions by the control system has the results that: (1) the concurrent access to the same piece of equipment by different applications needs to be organized such that no invalid results are returned to the applications and (2) when a series of actions or acquisitions is done, it is important that the results concern the same time period and that all actions are completely executed or not at all.

III. DISTRIBUTION

The distribution of the applications over the computers is not usually supported by object oriented languages. Therefore, an extension to C++ has been developed called DEAL [4]. This language allows the system designer to define *programs* that contain all elements which constitute one inseparable piece of coding. A *Process* (instance of a program) can export the procedures of classes and objects which are visible to all code in the process. Other processes can use these exported procedures and objects. Procedures of other processes are invoked with the Remote Procedure Call (RPC) paradigm [5]. These concepts are shown in more detail in Fig. 1. In process (circle) A two objects (rectangles with rounded angles) O1 and O2 are present. The procedures (ellipses) O1.PO and O2.PO are invoked simultaneously from process B, while an unspecified process NN is invoked from O2 in A.

The processes allow the separation of the control system software into independent programs, which at a later stage can be loaded on the target hardware. This strategy makes the software as independent as possible of the underlying hardware-structure. However, at a lower level hidden to the application program writer, the operating system should know the physical locations of the processes.

During the design of the software architecture, knowledge about possible distribution configurations is nevertheless required. When only one program that contains the complete control-system information is developed, the later distribution of the program necessitates that it is split into smaller programs. When the programs are split into functional parts (e.g. one program for all quadrupole power supplies) and a geographical split is re-

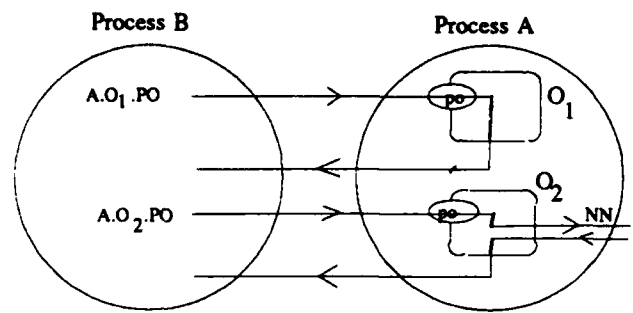


Figure 1: Processes and objects

quired later, the program splitting needs to be redone. It is important to realize as well that every time an object in another process is invoked, time-consuming parameter-copying and process-switching occur. The control-system designer should verify that program splits are both functional (i.e. reflect the structure of the accelerator) and efficient (i.e. no unnecessary overheads are incurred during execution).

IV. MULTI-LEVEL AND -VIEW ACCESS

The datamodule concept, as successfully defined at CERN [6], is eminently supported by object oriented languages via inheritance. In Fig. 2, a diagrammatic representation of the classes is shown. A rectangle represents a class and the arrows represent inheritance relations. Visible procedures and objects are drawn on the class (rectangle) edge and internal (hidden) ones are drawn inside the class. The *equipment* class (e.g. power-supply) inherits from the different views and the *Device* class. The *Device* class contains one (or more) object(s) of the interface class that represent the interface card(s). General facilities which are always needed act upon the device such as: e.g., enable, disable. Access protection can be defined by adding procedures not shown in Fig. 2 which handle protection and access rights. The code for such an equipment class can then be written by the person responsible for that particular piece of equipment without bothering him with the less interesting other details already defined in the class *Device*. The equipment class with all its views is exported from the enveloping process. In the application process that uses the equipment the object of the equipment class is accessed with the view that suits the application.

The above *multi-view* access is complemented with a *multi-level* access. A family constitutes a piece of equipment to be controlled by an operator. It can be composed of a power-supply, one or more magnets and a timing module. At the family level, modifications to magnets are defined in Gauss or other relevant units. At the lower

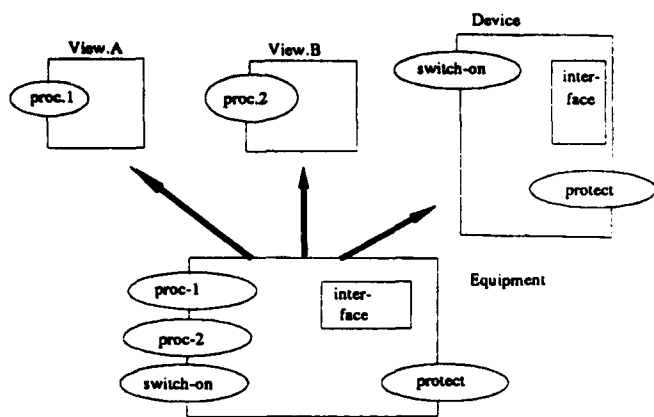


Figure 2: Inheritance from views

equipment level access can be defined in Amps or just bit patterns depending on the view of the user. At the lowest interface-level, the access is purely done in bit patterns. At a higher level, families can be grouped to construct accelerator parameters such as bumps or Q-values.

V. ATOMICITY

When a periodic access to the same equipment is required by multiple applications, it is more efficient to access the equipment at the highest required rate and to store the values in memory. For example, the reading of Pick-Up electrodes can be done every millisecond locally in one computer. The different applications can then read those values concurrently from memory and select the appropriate ones. When all applications access the equipment directly, the accesses to the equipment have to be strictly serialized to prevent inconsistencies and even equipment damages. These sequential equipment accesses each take longer than the simple memory location accesses. To reduce message overhead, multiple acquisition values can be sent in one message. An advantage is that the data read by different applications are identical and lead to the same result in applications executing concurrently at different locations.

The observer object has been introduced to support this approach. It consists of an action that has to be executed on a piece of equipment and a period that defines the invocation rate. Different rates for different applications can be defined. The observer object orders the rates and returns the corresponding values to the correct applications. Data are stored in shared objects that are read by the application. An action may return one result from a single ADC access or multiple results as provided by a transient recorder. When reading the values, the application needs to specify the first and last value and the total number of values it wants to read.

Two modes of the observer object exist. A single access mode, where only the latest result consisting of one or

more values is returned and an averaging mode, where the average of a series of values is returned.

When applications concurrently read the values from observer stations, two problems may occur: (1) while the application reads a set of values of one observer station, the same observer station can be activated one or more times, thus overwriting the shared object and leading to inconsistent results and (2) when the values from related observer stations are read (e.g. a set of pick-up stations), these values are not automatically related in time. Concurrency control algorithms based on time-stamping assure that consistent results are returned to the invoking process [7]. Consequently, applications read data from sets of equipment which are produced over the same time period and multiple data from the same equipment will concern one continuous time interval.

The same concurrency algorithms also assure that modifications to related equipment are executed at roughly the same times and to all equipment involved. When actions on the same equipment are required by two conflicting applications, either both actions are executed sequentially, or one of the actions will fail with an error message that the equipment setting is also modified by another application.

REFERENCES

- [1] J.I.M Botman, Boling Xi, C.J. Timmermans, and H.L. Hagedoorn. The EUTERPE facility. *Review of Scientific Instruments*, 63(1):1569-1570, January 1992.
- [2] Bertrand Meyer. *Object-oriented Software Construction*. Prentice/Hall Int., 1988.
- [3] F. van den Berk, R. Deckers, and Y. van de Vijver. Object oriented development of the control system for EUTERPE. Technical Report ISBN 90-5282-249-2, Instituut vervolgoedingen-TUE, 1993.
- [4] D.K. Hammer and O.S. van Roosmalen. An Object-Oriented Model for the Construction of Dependable Distributed Systems. In *Proceedings of the International Workshop on Object Orientation and operating Systems*, Paris, september 1992.
- [5] A.D. Birrel and B.J. Nelson. Implementing Remote Procedure Calls. *ACM Transactions on Computer Systems*, 2(1):35-59, February 1989.
- [6] M.C. Crowley-Milling. The Data Module, the missing link in high level Control Languages. In *Proceedings of the 3rd International conference on Trends in On-line Computer Systems*, Univ. of Sheffield, March 1979.
- [7] P.D.V. van der Stok and A.E. Engel. Shared Data Concepts for DEDOS. In *Proceedings of the 10th IFAC workshop on Distributed Computer Control Systems*, Semmering, Austria, September 1991.

Network Management of Real-Time Embedded Processors

C. Kalbfleisch, S. Hunt, K. Low, D. Mathieson
SSC Laboratory *
2550 Beckleymeade Ave.
Dallas, Texas 75237

Abstract

The Superconducting Super Collider Laboratory is a complex of particle accelerators being built in Ellis County, Texas. It will have a dedicated global communications network that will deliver control messages and provide for general data acquisition. This network will connect thousands of computer nodes over a very large geographic area. In order to meet the demanding availability requirements being levied on the system, it will need comprehensive network management. A large number of the computer nodes are embedded systems that traditionally do not support network management services. This presents unique challenges to standard network management practices. The Simple Network Management Protocol, SNMP, is widely accepted by industry as a tool to manage network devices. In this paper we will examine the performance characteristics and usefulness of an SNMP agent in a real-time environment.

I. Network Management Historical Perspective

The Internet Activities Board (IAB) has spent considerable time focusing on standards for network management. In 1987 a group of engineers implemented the Simple Gateway Management Protocol (SGMP). Around the same time, the OSI network management documents specified CMIP over TCP (CMOT). (CMIP is the OSI Common Management Information Protocol, and TCP is the Transmission Control Protocol). These two groups met to determine if a consensus could be reached on a network management approach. The result of the meeting was that the SGMP protocol would be extended to address the needs of network devices other than gateways. It would be called the Simple Network Management Protocol (SNMP). This was to become the short term solution for network management in the community while a second group worked on the OSI approach as a long term solution. A third group was to design a common framework for network management so as to make the migration from SNMP to CMOT easier. By the fall of 1989 a number of vendors had implementations of SNMP installed, and it became the de facto operational standard for network management of TCP/IP based networks[1].

II. Structure of Management Information

*Operated by the Universities Research Association, Inc., for the U.S. Department of Energy under Contract No. DE-AC02-89ER40486.

The Structure of Management Information (SMI) was initially deployed in order that the SNMP and the CMOT camps would have a common framework for identifying managed objects[2]. A collection of managed objects is referred to as a Management Information Base (MIB)[3]. Essentially the SMI specifies a syntax for defining MIBs in Abstract Syntax Notation One (ASN.1) macros and a base group of object types. Complex object types can be created using ASN.1. Additionally, a set of Basic Encoding Rules (BER) are defined to translate the ASN.1 instances into serialized octet strings that can be sent out onto a network.

Objects are defined with an associated Object Identifier (OID) in a tree structure. There are four branches in the tree that are of primary interest; Directory, Management, Experimental and Private. The Directory subtree is reserved for future use with the OSI network management model. The Management subtree is used to define objects in the Internet standard MIB. This consists of objects that are expected to be available on managed nodes running the Internet suite of protocols. The latest version of this MIB is referred to as MIB-II[4]. It contains 171 objects in a number of groups that are identified as System, Interfaces, Address Translation, IP, ICMP, TCP, UDP, EGP, transmission and SNMP. Each group is considered optional, but if any object in a group is implemented, then the whole group must be implemented. The Experimental subtree is used for conducting Internet experiments. The Private subtree allows any enterprise to register with the Internet community and build their own MIBs. MIBs developed by the SSC Lab fall into this category.

III. What is SNMP?

SNMP has become widely implemented in the network community as the accepted de facto standard network management protocol. Agents supporting SNMP are provided by many network device vendors. In addition, many workstation vendors provide an SNMP agent either as part of their standard operating system release or through third party vendors.

SNMP provides four operations: Get, GetNext, Set, and Trap[5]. It requires a connectionless transport service to be provided. TCP/IP implementations of SNMP use the User Datagram Protocol (UDP) as the transport mechanism. Community names provide for minimal authentication access to a managed nodes MIB. Different community names can be used for Get and Set to provide read-only access to some users and read-write access to others. Get

and Set operate on a specified OID. GetNext returns the OID and value of the next object in the MIB. This allows a Network Management Station (NMS) to "walk" through a managed nodes MIB by repeatedly issuing GetNext calls to that node. Traps are the means that the managed node can report that an event has occurred or some threshold has been passed.

Many commercially available NMSs are available that use SNMP. NMS provides a user interface to the SNMP objects and allows for data collection, MIB browsing, trap handling and maintaining graphical maps of the network. The NMS can draw conclusions on the health of the network and its associated devices based on the MIB data it collects. Additionally, SNMP applications can be purchased or written to manipulate the data in a number of ways. e.g. a meter to show the network or CPU utilization of a particular device.

IV. SNMP Agent for Real-Time Systems

In order to provide SNMP services for real-time systems, SNMP agent software was purchased in source form. This software is the SNMP Universal Agent[6]. C source code is provided to implement the SNMP agent, and sample MIB interfaces which simulate MIB-II and the experimental Uninterruptible Power Supply (UPS) MIB. Each MIB adheres to a defined Agent-MIB interface so that new MIB modules can be added. This code was ported to VxWorks[7], a real-time operating system, by SSC Lab engineers.

VxWorks provides many data structures that contain data relevant to the status of the network. A mapping of this data to the MIB-II objects was performed by SSC Laboratory personnel resulting in a near complete implementation of MIB-II under VxWorks.

V. SSCL Real-Time MIB

With the standard MIB-II objects in place, it is apparent that extensions are needed in order to manage real-time systems. Objects that are not part of any existing standard MIB are desired. For instance, from the central management station, it may be desirable to change a nodes configuration, determine the current software version, modify the state of tasks in the system, determine the CPU load or even reboot the system.

A MIB was designed to address these unique requirements for management of real-time systems, referred to as the SSCL Real-Time MIB. There are four main groups in the MIB: Real-Time Operating System (RTOS), SNMP Daemon (SNMPD), CPU Idle (IDLE) and System.

The RTOS group contains objects relevant to each real-time operating system that the agent may be ported to. For example, a VxWorks sub-group could contain objects representing system memory usage, system tasks and boot parameters. The current implementation allows the VxWorks boot parameters to be interrogated and modified using SNMP. Due to the distribution of real-time systems at the SSC over many miles, this functionality could be invaluable.

The SNMPD group contains information relevant to the tasks used to support SNMP on the target. These objects include the version of the Agent core, version of the Operating System Port, and the task priority of the daemon task. The task priority is settable using SNMP.

The CPU idle group contains information regarding the utilization of the CPU. Objects provide the CPU percent idle at various time intervals as well as a user settable time interval. The values can be queried to monitor the system performance.

The system group is intended to monitor and control the real-time system as a whole. It contains objects that allow the user to start reboot sequences or abort reboot sequences to a target. When these values are set, SNMP Traps can be sent to a NMS to advise that the system is being rebooted. These traps contain the system being rebooted, how long until the reboot will occur and which system caused the reboot to occur.

VI. SSCL T1 MIB

The communications for the SSC controls system will consist largely of point-to-point links to satisfy the throughput and response time requirements[8]. These point-to-point links will be provided directly into the real-time system by means of a fractional T1 interface. This interface is being developed by the SSC to implement standard protocols such as HDLC, PPP, and TCP/IP. Some of these interfaces are already managed by standard MIBs defined by the Internet community. Where applicable, those MIBs will be used to manage the point-to-point links. In addition to that, a SSCL T1 MIB will be designed to implement direct driver level statistics about the T1 interfaces. This MIB will allow network managers to determine the operational status of the interfaces, and verify that the T1 communications are set up properly in accordance with ADM and SONET equipment used to transport the T1. For example, the T1 channels involved in a point-to-point link could be verified.

VII. Real-Time Performance issues

When real-time systems are operational, there are essentially three types of operations: Interrupt Service Routines (ISR), real-time tasks, and non real-time tasks. The goal of the real-time operating system is to schedule the real-time tasks in a deterministic nature. The non real-time tasks are tasks that are generally not mission critical (e.g. a user level shell), they may use the remaining CPU time, or if there is no remaining time, they are postponed until CPU resources are available.

Since the SNMPD task is not mission critical to the embedded system, but rather provides support information to the management station, it is considered part of the non real-time group of tasks. To address this issue, the SNMPD task has been designed to run at any priority level. The system designer assigns a priority when the SNMPD task is initialized, or also while it is running through the use of SNMP.

The local CPU utilization is only one concern for the impact of the SNMP task on the real-time system. The other consideration is the bandwidth requirement added to the network. In the SSC control system, each real-time system will have a fractional T1 interface. This means that a given system will have a dedicated bi-directional network bandwidth between 64 kbps and 1.554 Mbps. (i.e. the total bandwidth is available for transmitting and receiving data simultaneously). Although the exact traffic patterns for the SNMP data are not known at this time, estimates can be made based on experience using an existing NMS to manage ethernet networks. The NMS could query a node at some user configurable rate for the network utilization, CPU utilization and a few other parameters. This total of about 15 objects could be sufficient to determine if the system is functioning.

It is estimated that each object requires a packet of 128 bytes to be transmitted on the network with a response of the same size. Based on this packet size, SNMP would require 1920 bytes for a complete data acquisition cycle. If the polling period is set to one minute, then the theoretical bandwidth of a 64kbps channel is 480KB/minute, and the bandwidth of a T1 is 11.7MB/minute. The SNMP traffic is then 0.39 percent of the 64 kbps channel or only 0.016 percent of the full T1.

VIII. Future directions

The Real-Time MIB will be expanded to provide additional functionality in terms of Operating System configuration, utilization and task maintenance. Some of these areas will be threshold monitoring for various portions of the MIB including sending out SNMP traps when the CPU utilization passes certain thresholds. It is desirable to be able to set task priorities, interrogate memory, and possibly to use SNMP to implement some debug capabilities for the real-time system. Each of these areas are under investigation.

In the areas of network management protocols, the Internet Engineering task force is nearing completion of the next generation of SNMP, SNMP Version Two, commonly referred to as SNMPv2. SNMPv2 addresses manager-to-manager communications, bulk data transfer, and security enhancements. It is widely expected to be the replacement for SNMPv1. Because of this development, plans are already in place to move the SSC Lab real-time SNMP Agent to SNMPv2 compatibility.

It is not clear if or when the SSC control system network will migrate to an OSI-based network, but we believe that CMOT for real-time systems is feasible.

IX. Conclusions

SNMP seems quite well suited for managing real-time systems in the SSC Lab control system. It provides a common management protocol for traditional network devices as well as UNIX systems, real-time systems and possibly

other control system components. SNMP's wide vendor acceptance provides a common ground for network management. This allows the SSC to manage its devices while still using commercial network management packages. With a sufficiently advanced NMS, proactive network management should be feasible. The background work put in by the Internet community will allow following the direction of the community as the standards migrate to newer versions of technology. This will certainly provide some interesting challenges in implementing the network management of the SSC controls system network.

References

- [1] M. Rose, *The Simple Book*, Prentice-Hall, Inc., 1991, ISBN 0-13-812611-9.
- [2] M. Rose and Keith McGlohrrie. *Structure and Identification of Management Information for TCP/IP based Internets*, May 1990.
- [3] M. Rose and Keith McGlohrrie. *Concise MIB Definitions*, Request for Comments 1212, March 1991.
- [4] M. Rose and Keith McGlohrrie. *Management Information Base for Network Management of TCP/IP-based internets: MIB-II*, Request for Comments 1213, March 1991.
- [5] J. Case, M. Fedor, M. Schoffstall, J. Davin, *A Simple Network Management Protocol (SNMP)*. Request for Comments 1157, May, 1990.
- [6] Paul Freeman Associates, 14 Pleasant Street, P.O. Box 2067, Westford, MA 01886.
- [7] Wind River Systems, Inc., 1010 Atlantic Ave., Alameda, CA 94501.
- [8] S. Hunt, C. Kalbfleisch, K. Low, D. Mathieson, "BUBBANET" - A High Performance Network for the SSC Accelerator Control System, these proceedings.

High Speed Serial Communications for Control Systems

D. Mathieson, C. Kalbfleisch, S. Hunt, K. Low
SSC Laboratory *
2550 Beckleymeade Ave.
Dallas, Texas 75237

Abstract

The Superconducting Super Collider Laboratory is a complex of accelerators being built in Ellis County, Texas. The SSCL control system consists of front-end processors and their associated control points remotely distributed from the Central and Regional control rooms. Control messages passing between these locations require timely (deterministic) distribution. A prototype network consisting of point-to-point links utilizing commercial T1 (1.544 Mb/s) communication boards has been implemented. These dedicated communication links will replace networking services traditionally provided for by shared medium networks like Ethernet(IEEE 802.3) and FDDI(IEEE 802.5). A seamless migration will be achieved by using packet encapsulation based on PPP(Point-to-Point Protocol, RFC 1171). All other networking functions including routing and reliable delivery are still being handled by the usual internet services. A distributed control system that currently uses Ethernet for communication is being re-implemented using these point-to-point links. We will report on throughput measurements, timing constraints and ease of transition to a point-to-point network.

I. INTRODUCTION

The Superconducting Super Collider imposes particularly strict requirements for the data networks used in the control and monitoring of accelerator equipment. These requirements are due to the large size of the site and the large number of control points and the complexity of the equipment being controlled [1].

II. SONET AND T1

A high speed optical telecommunications technology called SONET [2] will be used to carry data between control computers. The SONET (Synchronous Optical Network) standard [3] was developed by the ANSI accredited T1X1 committee, and provides cost-effective, flexible networking using the principles of direct synchronous multiplexing. The use of synchronous multiplexing allows multiplexing of low-speed signals directly onto a high speed backbone without the need for intermediate multiplexor stages. This functionality is integrated with digital switching technology in the Add-Drop Multiplexor

(ADM), the device that will be used extensively to connect systems directly to the optical backbone via lower speed T1 (1.54Mbit) links. The network management software built into the ADM allows the creation of logical point-to-point links between any two systems throughout the entire network. In addition to this flexibility SONET is also extremely reliable with every ADM having 100% redundancy including power-supplies and optics, which is important when one considers the availability requirements of the network.

III. THE POINT-TO-POINT PROTOCOL

The SONET backbone provides the basic point-to-point connectivity between systems, but in order that application software may use this network a networking protocol has to be used. We have selected the Internet Point-to-Point Protocol. The Point-to-Point Protocol(PPP) [4] provides a method for transmitting datagrams over serial point-to-point links. PPP is comprised of three main components:

A. Encapsulation

PPP uses HDLC [5] as a basis for the encapsulation.

B. Link Control Protocol

In order to establish communications over a point-to-point link, each end of the PPP link must first send Link Control Protocol (LCP) packets to configure, test the data link, and negotiate optional facilities.

C. Network Control Protocol

A family of Network Control Protocols [6] (NCPs) are used in establishing and configuring different network-layer protocols. After the link has been established, each host must then send NCP packets to choose and configure one or more network-layer protocols. Once each of the chosen network-layer protocols has been configured, datagrams from each network-layer protocol can be sent over the link.

IV. IMPLEMENTATION

A. Hardware

The hardware currently in use is a commercial VME ISDN card manufactured by Rockwell-CMC that contains intelligent ISDN hardware (Brooktree 8071) capable of generating HDLC formatted frames on any combination

*Operated by the Universities Research Association, Inc., for the U.S. Department of Energy under Contract No. DE-AC02-89ER40486.

of DS0 time slots. In the future we will use a T1 interface built onto a daughter-board conforming to the Greensprings Industry Pak (IP) specification. Several VME-based CPU manufacturers have provided interfaces for Industry Pak's, notably Motorola with their MVME162 which is capable of carrying up to 4 Industry Pak's, each capable of providing a separate T1.

B. Software

In the current implementation on the PPP used at SSCL all of the LCP and NCP have been omitted, since there is no need for the initial configuration and testing of links that will be established indefinitely. During the Boot phase of a system there has been some interest in using LCP in place of a 'bootp'-like protocol when discovering initial configuration options such as the IP-address, since LCP has the ability to propagate this information to remote hosts. Additionally since we need to communicate with commercial PPP implementations within routers, there is a possibility we may need to adhere more strictly to the standard. Device drivers have been written for SunOS (although not using STREAMS for portability reasons), LynxOS and VxWorks [7]. The implementation for VxWorks is to support EPICS (Experimental Physics Industrial Control System) which will be used for the control of all of the technical systems associated with the accelerator complex.

V. EPICS

EPICS has influenced many of the design decisions made during the development of the device driver. EPICS assumes an Ethernet-like network architecture with all hosts able to communicate with any other host. More importantly EPICS assumes the existence of a broadcast facility over all the nodes in the system. It was for this reason that additional functionality had to be built into the driver to allow broadcast messages to be forwarded between nodes. The prospect of forwarding broadcast messages would cause network designers to break out in a cold sweat. We hope that the ability to forward broadcasts will only be used as an interim solution, since the danger of 'broadcast-storms' on a network with as many as 2500 nodes is very real.

VI. T1 COMMUNICATION

The software has been designed in such a way as to allow a single host to use any fraction of its available bandwidth to communicate with another host.

As can be seen from Diagram 1, the T1 frame from each of the four hosts, A thru D, are split into several channels. Within the ADM, each channel can be routed to either another host connected to the same ADM or onto the optical link, from where it will be removed by another ADM. If a host wishes to communicate with another host which does not have a direct point-to-point link via an ADM, the IP forwarding/routing mechanism will pass the message on to

the recipient host via a host that has a point-to-point link both the sender and the recipient. Obviously this form of 'relayed' communication is slow and non-deterministic, and thus only non-critical data would take this path.

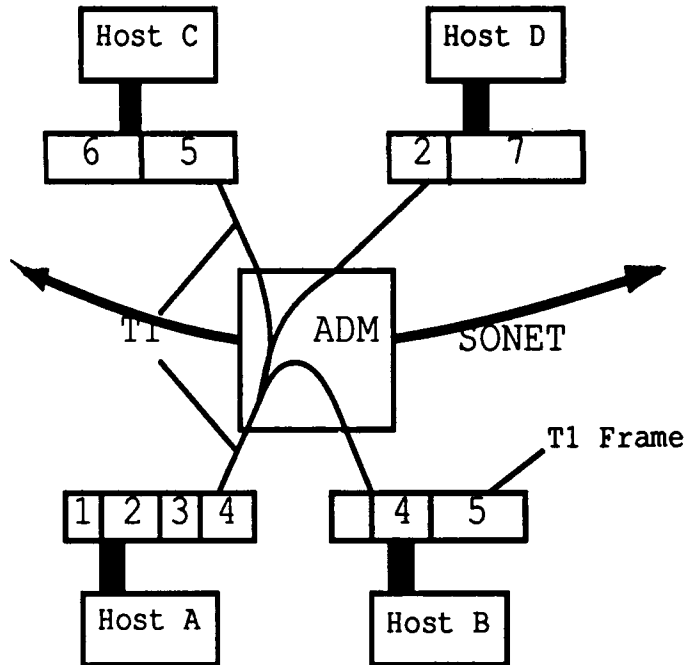


DIAGRAM 1

VII. T1 \Rightarrow LAN IP ROUTER

It is a requirement that every host be able to communicate with any other on the network. In order to make this possible commercial routers will be used. Most hosts will dedicate a fraction of their bandwidth to a direct communication channel with a router, and, in turn, all routers will be connected together using a high speed backbone (possibly FDDI). In this way any host can talk to any other host with the minimum number of 'hops'.

VIII. NETWORK MANAGEMENT

A. SONET Network Management

Nearly 5% of the SONET data stream is allocated to providing advanced network management and maintenance.

B. SNMP

The Simple Network Management Protocol (SNMP), is a standard method of managing networks from a single console. SNMP allows the remote manipulation of MIBs (Management Information Bases) which hold information about each node on a network. These MIBs hold information about network interfaces, CPU idle time, operating system, etc. In addition, the network administrator may modify values within the MIB to reset statistics or mark interfaces up or down. The description of these MIBs is given in Abstract Syntax Notation 1 (ASN.1) and we are developing a MIB to monitor specific aspects of a SONET

network, not covered by the standard MIBs, such as line bit-error rates [8].

IX. PERFORMANCE

Two areas of network performance are of highest concern to SSC: determinism and throughput.

A. Determinism

One of the reasons for choosing a point-to-point network over more traditional networking technology is the need for deterministic network performance. Shared media networks, such as FDDI and Ethernet, although common in other research centers, fail to provide reliable throughput. In accelerator control systems much of the traffic is 'bursty' with many systems triggered on the same 'event'. This type of traffic is not handled well by shared media networks where all systems compete for the same resource, leading to catastrophic failure unrelated systems due to network congestion. With a point-to-point network, all systems have a pre-determined available bandwidth, which, although usually less than the peak bandwidth available on a shared media network, is completely unaffected by other network users. We have conducted several tests to illustrate the improved determinism of a point-to-point network (1.54Mbit T1) over a more traditional Ethernet. In our test we used four identical systems. Three of the systems, the 'slaves', received a trigger from the fourth, the 'master', after which they sent a data packet to the master using the TCP/IP protocol, as used by EPICS. On Ethernet, normal Ethernet encapsulation was used, and on the T1 network the data was carried using PPP.

Table 1: Performance Measurements

No. Hosts	σ Message Delay (μ s)	
	T1	Ethernet
1	220.86	168.26
2	220.20	459.96
3	221.95	777.80

As one can see from the table above, the T1 network performance was unaffected by the number of systems using the network, and the packet arrival time was well bounded. The Ethernet performance, however, demonstrated the contention problems of a shared media network.

B. Throughput

The measurable network performance is unfortunately adversely affected by the current implementation of the T1 interface in the form of a separate intelligent VME card. Taking this into account, we have been encouraged by the performance of the current implementation. We have observed 85% of the maximum theoretical throughput with very little load on the host CPU. These figures are

likely to improve with the introduction of a daughter board T1 implementation since much of the buffer manipulation, which seems to be the bottle-neck with the current version, will be more more efficient with a local bus. In addition, the external T1 board has no DMA capability, and the CPU, a Motorola 68020, is much less powerful than that available on the Motorola MVME162.

X. CONCLUSIONS

As future network protocols and traffic types emerge, the Point-to-Point Protocol should be able to carry them. If not, the HDLC framing used by the PPP is the same as that used by emerging standards such as ATM, which means that the network infrastructure will not need to be changed to carry other HDLC traffic as well. The use of high speed point-to-point networking is a departure from more traditional accelerator control systems. This decision has enabled us to design a flexible, cost-effective networking solution that will meet the demanding requirement of such a large complex. In addition, the extensibility of SONET technology, coupled with the long lifetime of telecommunications hardware, means that the network will be able to grow to meet any future requirements of the control system.

References

- [1] S. Hunt, C. Kalbfleisch, K. Low, D. Mathieson, "BUBBANET" - A High Performance Network for the SSC Accelerator Control System, these proceedings.
- [2] American National Standard for Telecommunications - Digital Hierarchy - Optical Interface Specification (Single-Mode), ANSI T1.106-1988.
- [3] American National Standard for Telecommunications - Digital Hierarchy - Optical Interface Rates and Formats Specification, ANSI T1.105-1988, ANSI T1.105-1990.
- [4] Simpson, W. A., *The Point-to-Point Protocol*, RFC 1331, May 1992.
- [5] International Organization For Standardization, ISO Standard 3309-1979, *Data communication - High-level data link control procedures - Frame structure*, 1979.
- [6] McGregor, G., *The PPP Internet Protocol Control Protocol (IPCP)*, RFC 1332, May 1992
- [7] Wind River Systems, Inc., 1010 Atlantic Ave., Alameda, CA 94501.
- [8] C. Kalbfleisch, S.Hunt, K. Low, D. Mathieson, *Network Management of Real-Time Embedded Processors*, these proceedings.

'BUBBANET' - A High Performance Network for the SSC Accelerator Control System

S. Hunt, C. Kalbfleisch, K. Low, D. Mathieson
SSC Laboratory *
2550 Beckleymeade Ave.
Dallas, Texas 75237

Abstract

The Superconducting Super Collider Laboratory imposes particularly strict requirements on data networks used in the control and monitoring of accelerator equipment. These requirements are a consequence of the large size (approximately 100 km of accelerators), large number of control points (544,000), and the complexity of the equipment. An overview of the technical systems to be monitored and the projected data rates is presented, emphasizing systems with stringent data communications requirements. We can characterize these requirements in terms of expected network traffic, network throughput or average latency. Analysis of these traffic patterns as applied to different network architectures will aid in identifying the essential components of the final network architecture which meets or exceeds these requirements. We will report on the design decisions and initial results of performance tests on the controls communications network.

1 Introduction

BUBBANET (Bidirectional Underground Big Big Accelerator NETWORK) is the data communications network to be used to control the accelerators of the Superconducting Super Collider Lab (SSCL). The SSCL consists of a series of proton accelerators being built around the town of Waxahachie Texas. It will consist of a 600 MeV Linear Accelerator (Linac), a 12 GeV synchrotron (LEB), a 200 GeV synchrotron (MEB), a 2 TeV Superconducting Synchrotron (HEB) and a dual counter-rotating 20 TeV Superconducting Collider.

2 Accelerator Control System

The SSC accelerator control system is classified into Beam related controls (RF, Magnet Power supplies, Beam Instrumentation) and Process Controls (Cryogenics, Vacuum, Low Conductivity water). The process controls will not be considered in this document. The SSC Accelerator Beam Controls uses a suite of software tools, originally developed at Los Alamos National Laboratory (LANL), and further enhanced at Argonne National Laboratory (ANS) called EPICS [1]. In addition to LANL and the SSCL, EPICS is also used for controls at Argonne National Laboratory (APS), Lawrence Berkeley Laboratory

*operated by the Universities Research Association, Inc., for the U.S. Department of energy under Contract No. DE-AC02-89ER40486

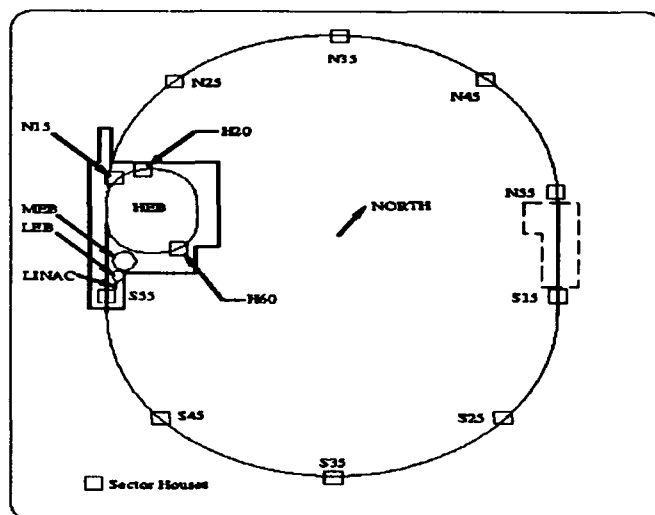


Figure 1: SSCL Accelerators

(ALS), DESY (Tesla) and at Duke University (Free Electron Laser). EPICS has two classes of system, Real-Time VME or VXI systems called Input-Output Controllers (IOCs), and Workstations running UNIX. The SSC ac-

Table 1: SSC Control requirements

Machine	IOCs	Control Points	Size	Cycle Time
LINAC	54	6,000		.1s
LEB	106	23,000	500m	.1s
MEB	120	27,000	4km	3s
HEB	250	58,000	11km	12s
COLL	1450	430,000	87km	3000s

celerator control system is comprised of Front-End Electronics Crates, Supervisory Control Crates and Back-End Crates. The Front-End IOCs provide the first level of control of the technical systems. Supervisory Control IOCs provide real-time control and act as data concentrators for a number of Front-End crates. Back-End systems (Unix Workstations and IOCs) provide high level functions such as operator interface, alarm handling and archiving. The three levels are not, however, enforced. Back-end computers can read data from a Front-End IOC without passing through a Supervisory Crate CPU.

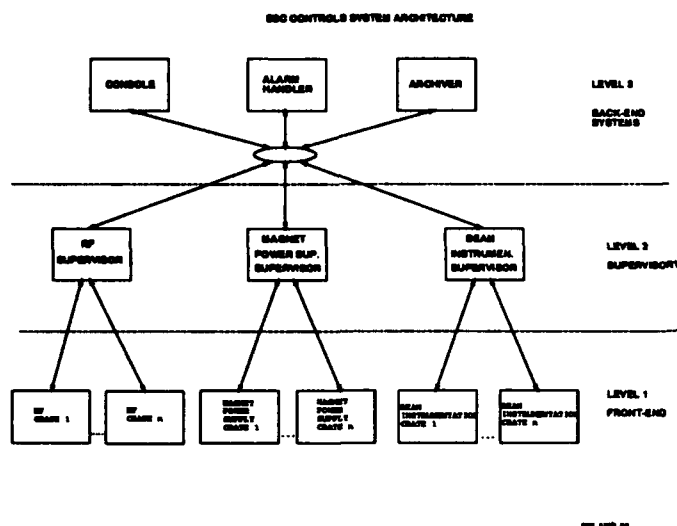


Figure 2: Control system data flows

3 Communications Requirements

The control system has half a million control points and two thousand computer nodes spread around one hundred kilometers of network. The availability requirement for the communication system is less than 10 hours unscheduled down time per year.

Accelerators are characterized by having much of the demand for network bandwidth being concurrent, at times such as injection. At other times, such as during coast, the networks are relatively quiet.

Systems for power control, including Kicker magnets, Corrector Magnets, Ring Magnets and Quench Protection, will have a supervisor crate monitoring a number of slave VME crates at data rates of up to 64 kbits/sec. Ring Magnets and Quench Protection also require deterministic communication with 1ms maximum response time over distances of up to 40km.

RF control crates will be grouped for each machine at a single location. At that location a supervisor will control the groups of three crates required to control each cavity. Data rates are 1 M bit/sec per cavity to the RF supervisor for that machine.

Beam Instrumentation will also have a supervisor, acting mainly as a data concentrator, to avoid each user simultaneously asking for data from the many crates supplying beam information data. Each of the Beam Instrumentation crates requires up to 64 kbit/sec bandwidth.

Total network traffic is greater than 1 Gbit/sec (peak). Much of the data-flow is hierarchical, with little data flow between a front end computer node and its peers.

Because of these factors it was required to design a network infrastructure which provided high reliability, long lifetime and deterministic performance, used commercial components, and had bandwidth management, performance monitoring, fault analysis, and extensibility.

4 Local Area Networks

Commonly used Local Area Networks used to link computers do not meet the requirements of the SSCL. CSMA networks like Ethernet are not deterministic, and are limited in distance and bandwidth. Higher speed token passing networks, such as FDDI, are limited by the single token causing deteriorating response times as network size and number of nodes increases. When sending short packets over large FDDI rings, as is often the case in a control system, actual realisable bandwidth is much less than the theoretical maximum, down to 1% when transmitting 60 byte packets over a 100km ring.

Newer networking technology, such as Asynchronous Transfer Mode (ATM) and Scalable Coherent Interface (SCI), may be appropriate in the future, but are not yet mature, or even stable.

5 BUBBANET Infrastructure

The BUBBANET infrastructure is a layered communication system designed to meet the present and evolving needs of the SSC accelerator controls network users. It is designed on a number of layers designed to be complementary but allowing future requirements to change one layer without modifying the others.

5.1 Fiber optic cable

The first layer in the BUBBANET will be an installed infrastructure of single-mode fiber optic cable. Single-mode fiber was chosen for a number of reasons. Using present day technology, it has a much higher information carrying capacity than multi-mode fiber or coaxial cable. Its latent information carrying capacity is very high, allowing future upgrading of electronics to provide more bandwidth without installing more fiber. Modern single-mode fiber is more resistant to damage by ionizing radiation than multi-mode fiber. Fiber optic cable takes up much less volume than coaxial cable. Single-mode fiber is cheaper than multi-mode or coaxial cable.

5.2 SONET

Synchronous Optical Network (SONET), has been chosen as the transport service running over the single-mode fiber. It is a standard for the transport of Time Division Multiplexing (TDM) channels over high bandwidth links. SONET multiplexors are available from many vendors, at data rates from OC1 (50 Mbits/sec) to OC48 (2 Gbits/sec). SONET has a number of advantages over older generations of multiplexors. It is an International Standard, compatible (at 150 Mbits/sec and above) with Europe. It does not have a practical bandwidth limit; new technology can increase the maximum bandwidth of equipment while still retaining compatibility with the standard. It has a very rich set of built-in network management facilities for monitoring and provisioning (setting up of the

network). Being synchronous, low speed data streams can be extracted without disturbing other traffic. A multiplexor providing this 'in line' de-multiplexing is called an add-drop multiplexor (ADM). Slow speed channels (time-slots) can be rearranged in the high speed data-stream, allowing grouping or redirecting of individual channels without switching. This is termed grooming.

5.3 T1

SONET links will link all equipment locations, but the control system interface to the VME equipment crates will not be at SONET rates. The SONET network infrastructure will carry T1 TDM channels operating at 1.544 Mbits/sec. Interface to all VME equipment crates will be at this rate. Each of these T1 interfaces can itself transport 24 of the 64 Kbit/sec point-to-point channels [2]. Each of these channels can have, by using SONET grooming, a different destination. As each of these channels uses a dedicated time-slot on the TDM data-stream, it provides a deterministic response time required by systems such as magnet power supply controllers. This also suits the classical hierarchical controls that characterize many of the SSC systems.

5.4 Higher Level Protocols

The T1 byte-stream is formatted into HDLC frames on each Channel, thus adding the required structure to format 'messages' and providing a checksum. Although point-to-point transport meets many requirements, including low response time dedicated links over the entire geographic area of the complex, some systems require the ability to select, at run time, data from any of the two thousand crates in the control system. To meet this requirement, the links use the Internet Point to Point Protocol (PPP) which is used to set up a TCP/IP service. Thus, with the addition of nodes acting as routers, full connectivity is obtained, and the standard EPICS communication paradigm (which uses TCP) is supported. Commercial routers are available from industry which support PPP protocol over channelized T1 which are compatible with BUBBANET.

6 Performance Testing

A prototype BUBBANET communication system has been built, consisting of SONET Add-Drop Multiplexors, Commercial VME channelized T1 interfaces, and drivers for VxWorks, Lynx and SunOS. Performance has been measured and compared against SSC requirements. Operating under the VxWorks real-time operating system, BUBBANET achieves an application to application response time of 1ms. and throughput per node approaches 200 K bytes/sec with no degradation under maximum load conditions. This meets all the requirements for the SSC control system. BUBBANET has also been successfully tested with the EPICS software that will be used for the

EPICS CHANNEL ACCESS
TCP
IP
PPP
HDLC FRAMING
CHANNELIZED T1
SONET TRANSPORT
SINGLE MODE FIBER

Figure 3: BUBBANET Layers

control system. The first Accelerator to use BUBBANET will be the Linac, to be installed in July.

7 Other Services

The infrastructure of BUBBANET is not restricted to Controls Data Communication. T1 links will also be used to transport live video, and a Message Broadcast System. Live video will use JPEG data compression, to reduce the bandwidth of the video signal for transport over a 1.544 M bit/sec T1 link. Live video will be used in the Personnel Access Safety System for surveillance and for Beam Instrumentation for the transmission of the image of phosphor screens in the beam pipe. The Message Broadcast System [3] will be used to transport timing and synchronization messages around the accelerator complex.

8 Conclusions

The use of international standards and commercial equipment on a layered communications infrastructure, has enabled BUBBANET to be rapidly developed. BUBBANET meets the very demanding requirements of the SSC for reliability, throughput, and response time. The use of SONET has allowed other services such as live video and timing to share the infrastructure.

References

- [1] L.R. Dalesio, M. R. Krammer, A. J. Kozubal, *EPICS Architecture*, International Conference on Accelerator and Large Experimental Physics Control Systems, Tsukuba Japan, 1991.
- [2] D. Mathieson, S. Hunt, C. Kalbfleisch, K. Low, *High Speed Serial Communications for Control Systems*, these proceedings.
- [3] K. Low, R. Skegg, *Prototype Message Broadcast System for the Superconducting Super Collider, PAC91*.

Gateway for Inter-Network Connection in the Pohang Light Source Control System

S.C. Won, S. Kwon
Pohang Accelerator Laboratory,
POSTECH, P.O. Box 125,
Pohang 790-600, Korea

Abstract

The control system for the Pohang Light Source(PLS), under construction, is a large scale distributed computer control system which can manipulate approximately 7000 signals. It has a hierarchical structure with two heterogeneous data communication networks. The upper level network is a baseband Ethernet to link operator console computers with Subsystem Control Computers. The lower level network is a MIL-STD-1553B multidrop field bus which connects each Subsystem Control Computer with VME based local controllers. In this control system structure, frequent modification of local control software during system commissioning and maintenance periods requires repeated installations of developed software on the local controllers, which are distributed along the 280 circumference of the storage ring. This paper describes the construction of a software gateway which is a specific kind of network server, to interconnect the two different networks so that an operator in the upper level network is able to access any low level local control computer transparently.

1. INTRODUCTION

The Pohang Light Source(PLS) control system has a hierarchical structure with distributed intelligence and autonomous processing units as shown in Fig.1.

The hierarchy consists of four layers with different roles. The four layers are the computing service layer, the human interface layer, the subsystem control layer and the machine interface layer. The computing service layer is the UNIX based host computers for mathematical modeling system simulation and off-line data analysis. The human interface consists of six console computers equipped as graphical engineering workstations. These console computers are linked with the host computer and the subsystem computers via Ethernet. The Subsystem Control Computers(SCC) are microprocessor assemblies in a standard VMEbus crate and the drive Machine Interface Unit(MIU) clusters through the 1 Mbit/sec MIL-STD-1553B serial multidrop field bus. Each MIU, which is also based on the VMEbus and the Motorola 680x0 microprocessor family, can use various protocols to interface with machine components.

In order to develop an integrated and standardized software for such a large scale distributed control system, a powerful software development environment providing necessary development tools should be arranged.

The software development system consists of a development host, mass storage devices, printers, and communication network to the target systems. The development host uses X-windows as graphics basis, and is equipped with various development tools, utilities, and libraries. All SCC's and MIU's should be able to share these resources

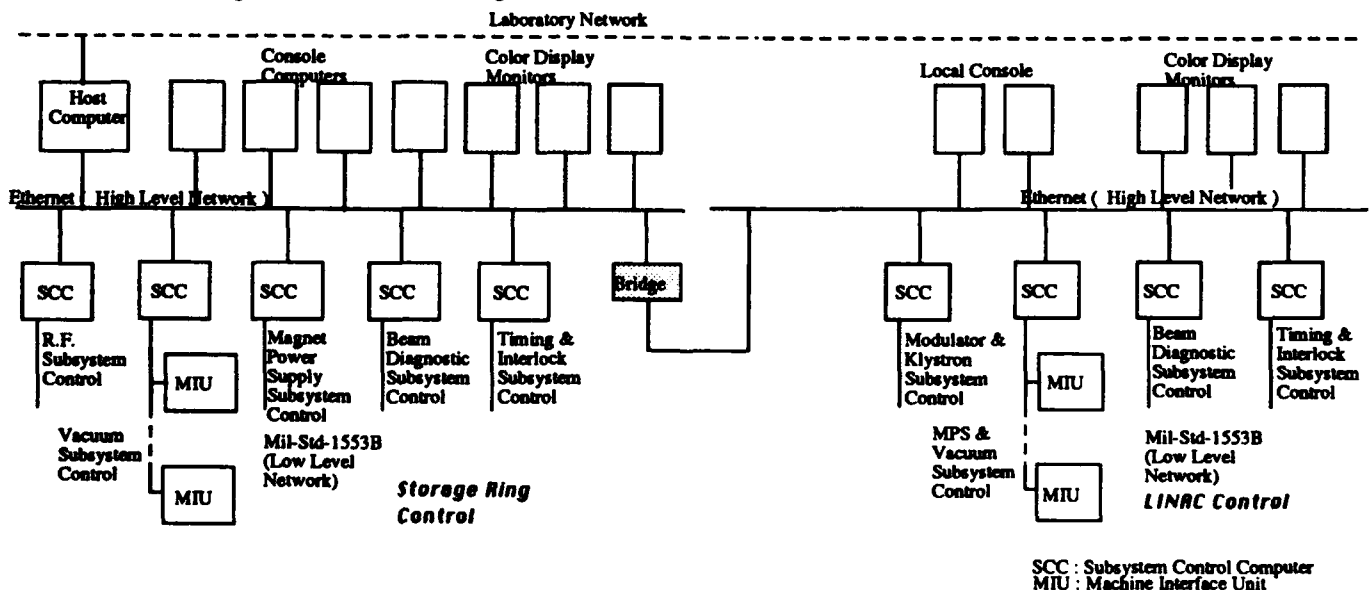


Fig1. PLS Control System Architecture

through the network, so that developed software can be downloaded to the target system, tested and modified remotely.

However, the PLS control system has two heterogeneous data communication networks. The upper level network uses a baseband Ethernet to link operator console computers and development workstations with SCC's. The lower level network is a MIL-STD-1553B multidrop field bus which connects each SCC with it's MIU's. MIL-1553B is used because of it's deterministic behavior, standard chip, noise immunity and galvanic insulation. Development hosts in the upper level network cannot access MIU's in the lower level network transparently. One way to solve this problem is to construct a software gateway on the SCC to interconnect the two different networks.

2. GATEWAY FOR INTERNETWORK

A gateway is a system that interconnects two or more distinct networks so that computers on one network are able to communicate with computers on another network. Considering the OSI 7-layer model, we have to choose the layer at which a gateway operates, depending on the type of translation and forwarding done by the gateway. In the PLS control system, one of the goals of the internetwork connection is to support remote login and file transfer services from the Ethernet based development host to MIUs on the MIL-STD-1553B field bus. Adoption of a standard protocol suite such as TCP/IP enables us to reduce software development efforts.

Fortunately, the SCC's and the MIU's run Microware System's OS-9 as their operating system. Currently, OS-9 supports TCP/IP protocols and provides an Ethernet network device driver. Furthermore, the UNIX based host computer on Ethernet uses TCP/IP for it's communication protocol. Under the TCP/IP protocol suite, interconnection of two networks is simple and straight forward. If we have an internet of Ethernet and MIL-STD-1553B that both use TCP/IP protocols, no translation of protocols is required. Instead, the gateway only needs to forward packets from one network to another. The IP layer is responsible for this forwarding of packets. Each IP packet contains enough information(i.e., its final destination address) for it to be routed through the TCP/IP internet by itself. Another advantage of a TCP/IP gateway is that OS-9 supports a socket library for network programming, which we can use to develop communication software through the MIL-STD-1553B.

Fig. 2 shows the structure of the TCP/IP gateway which was implemented for the PLS system. The implemented gateway, which was installed on an SCC, has two network interfaces under the IP layer. One is an Ethernet interface and the other is a MIL-STD-1553B interface. The MIL-STD-1553B interface, which corresponds to a data link layer and physical layer in the OSI model, has the hardware characteristics shown in Tables 1 and 2.

Development Host

SCC

ILC

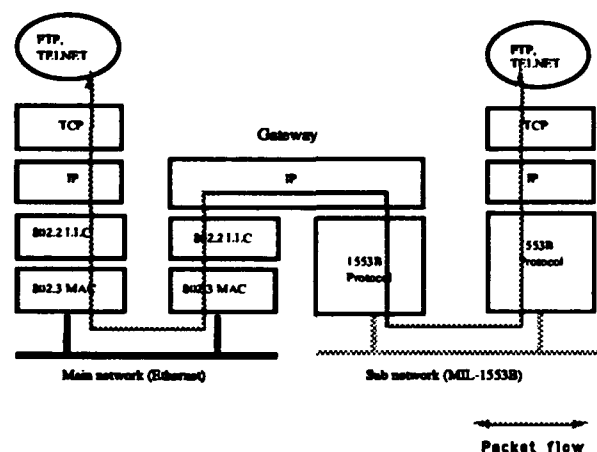


Fig2. TCP/IP Gateway

Framing	Invalid Manchester Coding
Flow Control	Subsystem busy bit in Status word
Error Control	Status Response, Parity bit for each word
Link Management	Bus Controller, C/R

Table1. MIL-STD-1553B Data Link Layer

Application	DoD Avionics
Data Rate	1 Mbps
# of Data bits/Word	16
Word Length	20 bits
Transmission Technique	Half Duplex
Operation	Asynchronous
Encoding	Manchester Biphase
Bus Cabling	Transformer
Bus Control	Single or Multiple
Transmission Media	Twisted pair shield

Table2. MIL-STD-1553B Physical Layer

3. NETWORK DEVICE DRIVER FOR OS-9

OS-9 has a modularized I/O structure. It has four levels of modularity including the kernel, file managers, device drivers, and device descriptors. The kernel maintains the I/O system for OS-9. It provides the first level of I/O service by routing system call request between processes,

the appropriate file managers, and device drivers. Since the network interface software is embedded in this modularized, layered structure, our major concern was focused on the network file manager, IFMAN, which all the network drivers should interact with.

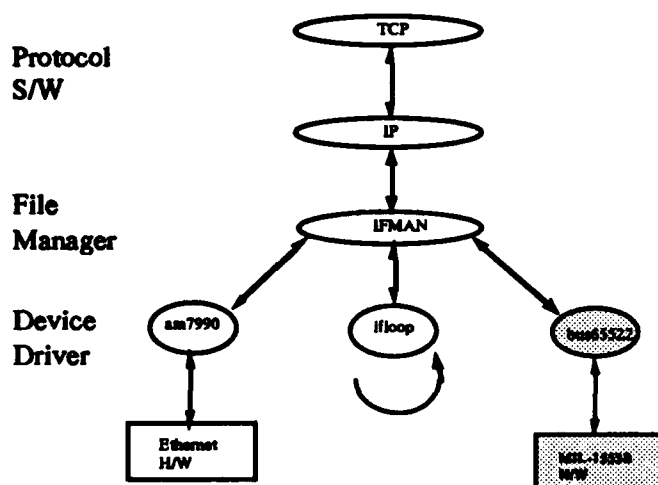


Fig3. OS-9 TCP/IP Software

Fig. 3 shows the network interface software structure in OS-9. IFMAN is below the IP layer and above the NIF(Network InterFace) which correspond to the device driver and the descriptor. In order to interface the DDC BUS 65522 II MIL-STD-1553B network hardware, a device driver, "bus65522", and the corresponding descriptor "mil0", was developed. The device descriptor is a small table which contains network information, such as the Maximum Transfer Unit(MTU), the IP address, the physical address of the port, and initialization data. In Fig. 3, the shaded part represents the new driver attached to the existing OS-9 network system. The major jobs for development of "bus65522" were MIL-STD-1553 bus control, address resolution and packet fragmentation. MIL-STD-1553B consists of a Bus Controller(BC), Remote Terminals(RT) and a twisted shielded pair wire data bus. Unlike Ethernet, on which every node has a unrestricted access rights to the main bus, MIL-1553B reserves exclusive access rights to the BC only. Therefore we must include a polling process on the BC to recognize the individual RT's. The polling process gathers information about bus requests from RT's and maintains this data on it's local table, so that the BC controls data flow for all transmissions on the bus. The other issue during development of "bus65522" was address resolution. Application software such as TELNET uses a logical address(IP address), while the network driver needs a RT address for the actual transmission. We managed this problem by using host ID field in the IP address as the RT address, for simplicity. An-

other problem we considered was packet fragmentation. The MTU of the Ethernet is 1500 bytes and that of MIL-STD-1553B is 64 bytes, therefore a large Ethernet packet should be segmented into smaller packets for transmission on MIL-STD-1553B. However, fortunately, the IP protocol was developed considering this situation, and we let the IP layer handle packet fragmentation and reassembly internally.

4. CONCLUSION

For implementation of the PLS control system software development environment, a TCP/IP gateway was constructed on the SCC. It interconnects the upper level network, Ethernet, and the lower level MIL-STD-1553B field bus. To check remote login function of the implemented gateway, a TELNET service test was performed. It was proven that an operator at the host computer can access any MIU transparently. Also, the FTP service was tested by sending a 67796 byte file to one of the MIU's. Even though the transmission speed was rather slow due to the protocol conversion overhead, the file was successfully transferred. After the test, the developed gateway was installed on the SCC and has been used by the PLS software team satisfactorily. An operator at a console computer can download developed software to a local controller for remote testing and debugging. Also, using a set of in-house developed local controller access services, we can run application tasks on the console computers. We expect the gateway to serve as a platform for various applications to MIL-STD-1553B internetworking.

5. REFERENCE

- [1] S.C. Won, "Status Report on Control System Development for PLS", Invited talk EPS ICALEPCS '91 Tsukuba, Japan, Nov. 1991.
- [2] S.C. Won, Jae W. Lee and Juno Kim, "Computer control system for PLS", Proc. of the 4th Asia Pacific Physics conference, Seoul, Korea, Aug. 1990, pp. 1114-1117
- [3] J.C.Shu and M.T.Liu, "An approach to indirect protocol conversion", Computer Networks and ISDN Systems, Vol.21, pp.93-108, 1991.
- [4] P.E Green,Jr., "Protocol conversion", IEEE Trans. Commun., Vol.34, pp.257-268, 1986
- [5] S. Alfonzetti, S. Casale, and A. Lonbardi, "Internetworking between telex and OSI system," Comput. Commun., vol.12, pp.17-24, Feb.1988.
- [6] F.M.Burg and N.Di Iorio, "Networking of networks: Internetworking according to OSI," IEEE J. on Select. Areas Commun., vol.7, pp.1131-1142, 1989

The Star, a Dynamically Configured Dataflow Director for Realtime Control*

M. Bickley and J. Kewisch

Continuous Electron Beam Accelerator Facility

12000 Jefferson Avenue, Newport News, VA 23606-1909 USA

Abstract

The CEBAF accelerator is controlled by an automated system consisting of 50 computers connected to machine hardware and another 20 to 30 computers used for displaying machine data. The control system communication software must manage the inter-machine communication of these computers. Each of the different segments of software that make up the machine control system is treated as data sources and data sinks, with a single process mediating the transfer of all data between any data source/data sink pair. The mediating process is called the Star. This dynamically configured process keeps track of all available machine data posted by data sources and of all data requested by data sinks. Data transmission rates through the Star are kept low by sending only data that is requested by other control software, and then only when the value of the data changes. The system is entirely response-driven, with the Star process taking action only at the request of either a data source or a sink. The software for the communication is written using standard C code and TCP/IP sockets, making the communication software platform independent.

I. INTRODUCTION

The control system in place at CEBAF in the fall of 1991 used reflected memory to transport data between the data sources and data sinks. The machine information that was produced at the data sources was stored in a block of shared memory. This block of shared memory was copied from the data source machines to the data sink machines by custom software which ran continuously, cycling constantly. Some fraction of the total CPU time on every machine was devoted to performing this operation. In addition, all applications which used the data were forced to poll the appropriate memory locations in order to determine if the value of the data had changed.

Although this technique was effective for small systems, it became a burden as the amount of machine data to be transferred increased. Once the complete CEBAF injector was installed, the cryomodule that are part of the injector increased the volume of machine data dramatically. The increase in machine data caused a corresponding increase in the time taken to pass the blocks of shared memory over the network. This resulted in a significant increase in response time to operator input. It was clear that as more of the accelerator was installed, the performance of the system would degrade so much that the machine would be very painful to operate. A new data transfer paradigm was needed.

II. A COMMUNICATIONS PARADIGM

* Supported by DOE contract DE-AC05-84ER40150.

In order to create the new data transfer paradigm, the strengths and weaknesses of the existing system were examined. The following requirements of the communication protocol were deemed necessary for the new software:

- The communications should be connection-based, so it would be clear at either end of a connection when the other end had been closed. This would greatly simplify the bookkeeping associated with the data transfer.
- The database organization associated with data transfer should be dynamically allocated. It should be clear when new machine data sources are added to the system and are available to data sinks.
- The complexities of the network transfer should be concentrated on a single computer. This increases the average size of the network packets, making the network data transfers more efficient. It also minimizes the CPU effort devoted to communications on the data source and data sink computers.
- The data flow should be based on a single request-multiple reply query protocol. This minimizes the overhead associated with maintaining a data flow channel.
- Data should be transferred only as it changed. It made no sense to burden the communication software with the delivery of data that provided a data sink with no additional information.
- The communications software should be as general as possible, to simplify porting to new computer platforms.

In order to fulfill the desired requirements of the communications paradigm, the logical topology to use is a star. This organization, with a single central computer, allows the total system throughput to be governed by the performance of that computer. The central computer (which was named, rather simply, the "Star") could be a system with as much CPU horsepower as was needed to adequately handle the expected load of the complete accelerator.

III. FUNCTION OF THE STAR

The Star computer is fundamentally just a manager of the dataflow between the data sources and the data sinks. Its principal task is to forward data requests from data sinks to data sources, and to forward data responses from the sources back to the sinks. In addition, the intelligence for the control of data traffic is kept in the Star. This allows the sources and sinks to be ignorant. The data source does not have to keep track of the destination of all of the data flowing out, and the data sink does not have to be aware of the source of the data that comes into it.

In order to accomplish the management of the dataflow, the Star keeps three interrelated data structures. The

first data structure is a hash table that contains a reference to every piece of data available from any data source. The second is a sink table, used to associate the current data sinks with the data sources from which the data items originate. The third data structure is a source table, which associates the current data sources with the data sinks that have made requests for data values.

The hash table associates with each table entry an identifier that indicates from which data source the relevant data item originates. The hash table is used when a data sink makes a request for a data element. If the data element is found in the hash table then a request for the data value is forwarded to the appropriate data source. If the data element is not found in the hash table, then the data sink is informed that the data is not available.

Once a data value has been requested by a data sink process and the data element is found in the hash table, the data sink table and data source table must be altered. The sink table is used to keep track of which data elements have been requested by which sinks. In the event that one of the sinks terminates, this table is used to identify those data elements which the data sink had requested.

The other data structure, the source table, is similar to the sink table. The source table is used to keep track of which data elements are being supplied by each data source. In the event that a data sink process terminates, this table is used to inform the associated data sinks that the requested data elements are no longer available. In addition, the source table is used to track how many requests have been made for each data element. When a data element is requested by multiple sinks, only a single request is made of the responsible data source. It is not until the data is no longer needed by any sink that the request for data from the source is terminated.

IV. TESTING OF THE STAR

It was necessary to make a good estimate of the ultimate load on the Star once the complete CEBAF accelerator was installed and running. This was done by extrapolation from the portion of the machine in use at that time, the injector. There were a total of 10,000 data channel read backs in use, and of those 10,000 approximately 13% changed per second. The cycle rate of the control algorithms on the data source computers was 3 Hz, but the plan was to increase the rate to 10 Hz. Once the performance of the data sources was enhanced, it was expected that the number of data source changes per second would triple, resulting in about 40% of the read backs changing per second.

Furthermore, on a typical CEBAF display page, there are about 100 data channels, of which 40 are set points and the other 60 are read backs. Taken together with the fact that a change rate of 40% of the total number of read backs per second was predicted, the anticipated system load was 24 changes per second per display page. The completed accelerator was expected to have a total of 100 display pages in use at any time, giving an expected system load of 2,400 changes per second.

Preliminary testing of the Star computer was performed using an HP720 computer. Software was written which functioned as a simple data source, where the total volume of data out of the data sources was controllable in

each of two ways. First, the interval between data transfers was variable, at rates up to 20 Hz. Second, the number of data points sent per transfer was variable, from 100 to 1000 data values. Each data value consisted of a floating point value, of length 4 bytes. The data sinks used for the testing were the same graphical display software used in the normal control of the accelerator.

For the testing, the number of data values sent per transfer from each of 9 artificial data sources was varied from 100 to 1000. For each transfer volume, the transfer rate was increased from 1 Hz to either the maximum transfer rate of 20 Hz, or until the system saturated. System saturation is the point at which the Star computer can no longer keep up with total volume of traffic, so buffer overflow occurs. For each volume/rate pair the average time between the issuance of a new value by a data source and its receipt by a data sink was measured. The performance of the Star computer with respect to signal load was linear for all tests, with system one-way travel time ranging from 0.0025 to 0.08 seconds as the signal load increased from less than 1,000 changes per second to 24,000 changes per second. At the upper end of the range, above 24,000 changes per second, the one-way travel time degraded worse than linearly. Once the upper limit of 27,000 changes per second was reached, the system broke down completely, with buffer overflow in the Star. See Figure 1.

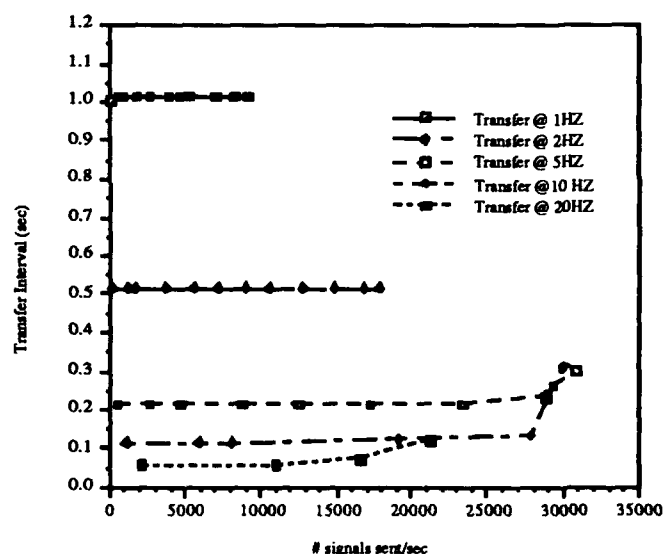


Figure 1. Data transfer interval vs. # signals sent.

The testing demonstrated that on an HP720 computer, rated at 56 MIPS, the Star process could support a dataflow rate of 10 times the expected load of the complete accelerator. Similar testing was done with different computers in order to determine if the performance of the Star process scaled with the performance of the computer. The most extensive testing was done with an HP835 computer. The results of the testing, along with an extrapolation of the expected performance from an HP735 computer, are shown in Figure 2.

The Star process, running on an HP735 computer rated at 125 MIPS, should support a dataflow rate of 25 times the expected load of the CEBAF control system. Given these

favorable test results, the Star process was implemented as part of the CEBAF control system, and was used for the commissioning of the CEBAF North Linac and East Arc from August of 1992 until April of 1993.

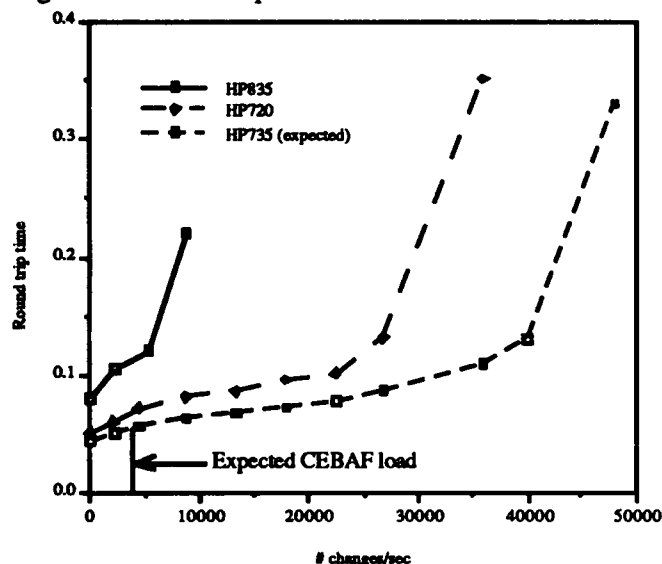


Figure 2. Round trip time vs. changes/sec for different computers.

V. OBSERVED PERFORMANCE

Performance statistics for the Star were kept during the commissioning period mentioned above. There were two goals of the data collection during this time. The first goal was a demonstration that the signal load extrapolations made when examining the injector were valid when scaling the system to include more of the CEBAF accelerator. The second goal was a measure of how the system performed in a real-world situation. It was necessary to find out if the system performed as expected, and also to see if other Ethernet traffic affected the performance of the Star. The data that was tracked during the commissioning consisted of two elements. The first element was the total volume of data traffic through the Star computer, and the second was the average data round trip time.

The traffic volume through the Star process was trivial to measure. A counter, which was incremented as each data item passed through the system, was added to the Star software. After ten seconds had passed, the total data load measured was saved, and the counter was reset. The system load was tracked over time and compared to the average data round trip time.

Determining the average round trip time was a more complicated procedure. Two simple programs were written, one a data source and one a data sink. The data source was a source for only one data item. The data sink was a sink for that one item. The data sink started a timer, then requested the value of the data item. When the value of the data was received, the data sink made a request to the Star that the value of the item be changed. This sort of request is akin to a machine operator turning a knob or otherwise changing a machine set point. The data source changed the value of the data item, then sent the new value to the data sink. When the

updated value was received by the data sink (indicating the request had been honored) the sink requested a different new value. The data sink made a total of fifty change requests, then stopped the timer. The total time elapsed then included a total of fifty round-trip passages of the data through the Star. The data sink waited five seconds after completion of the measurement and started the process over.

During a typical month of commissioning, from January 2 to January 29, 1993, the total data load and average data round trip time measurements were recorded. This data is reflected in Figure 3.

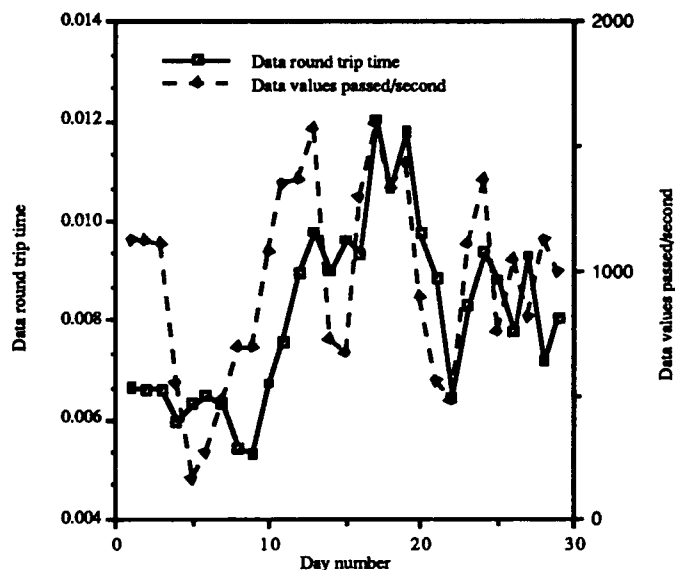


Figure 3. Observed Star performance.

During this running period, approximately 25% of the CEBAF accelerator hardware had been installed, and 12 of the expected 50 display consoles were in place. The average data load during the period was slightly more than 1,000 data elements per second, with peaks as high as 2,000 data elements per second. The data round trip time under these loads was always well under 0.1 seconds, and typically was under 0.02 seconds. The measured load was greater than was expected when extrapolating from the injector, as mentioned in section IV, but was still well within the capabilities of the Star process running on the HP720 computer used during the commissioning.

It appears that the completed accelerator will have a signal load of 4,000 data elements per second, with peaks as high as 8,000 per second. Given this updated data traffic information, the Star process running on an HP735 computer will be capable of supporting 5 times the expected peak load and 10 times the typical load when controlling the finished CEBAF accelerator.

VII. REFERENCES

- [1] R. Bork, C. Grubb, G. Lahti, E. Navarro, J. Sage, T. Moore, "CEBAF Control System," CEBAF-PR-89-013

The SSCL LINAC Control System

J. Heefner, C. Cuevas, S. Hunt, D. Murray, J. Sage

Superconducting Super Collider Laboratory*
2550 Beckleymeade Ave., Dallas, TX 75237

I. INTRODUCTION

The SSCL Linear Accelerator (LINAC) consists of an Ion Source, Low Energy Beam Transport (LEBT), Radio Frequency Quadrupole (RFQ), Drift Tube LINAC (DTL), Coupled Cavity LINAC (CCL), CCL Transport and LINAC to Low Energy Booster (LEB) Transfer Line. The Ion Source generates H⁺ ions and accelerates them to 0.035 MeV. The LEBT transports and matches the beam to the input of the RFQ. The RFQ bunches and accelerates the beam to 2.5 MeV. The DTL and CCL accelerate the beam to 70 and 600 MeV, respectively. The Transfer Line routes the beam from the CCL Transport Line to the LEB.

The Ion Source/LEBT, RFQ, DTL and CCL support systems consist of vacuum, cavity temperature control, beam instrumentation, RF power, and magnet subsystems. Each of these sections is capable of stand-alone operation.

The SSCL Global Accelerator Control System (GACS) is a standard multi-layered system. Figure 1 illustrates the six levels of functional hierarchy used to specify and describe the GACS. Level 6 provides information exchange services. No true control functions are performed at this level. This level is used to provide a pathway for the exchange of information between the Control System and SSCL computer services. Level 5 is the machine integration level of the system. At this level, controls for all SSCL machines, i.e., LINAC, LEB, MEB, HEB and Collider, are integrated into a single unit. This level includes a central control room for operations. Level 4 is the machine control level. At this level all module level controls are integrated into an SSCL machine, in this case the LINAC. Level 3 is the LINAC module controls. The function of Level 3 is to tie the various subsystem controls together into stand-alone modules, i.e., Ion Source, RFQ, etc. Level 2 controls are defined as those which logically combine a group of front-end systems into a control unit. Subsystem controls such as vacuum and RF are performed at this level. Level 1 is the front-end controls. This level provides interconnections between sensors and controls, signal conditioning, I/O module interfaces, front-end processors and local operator stations used for system maintenance and commissioning.

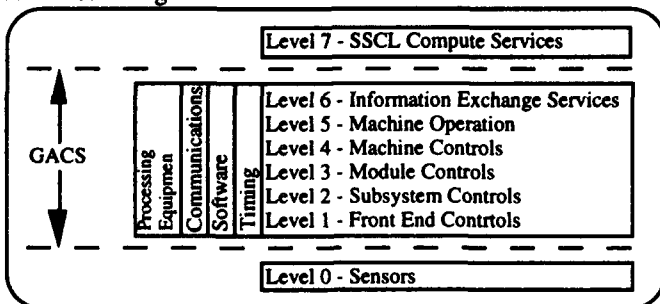


Figure 1. GACS Levels

II. LINAC CONTROL SYSTEM ARCHITECTURE

A. Communications

Figure 2 is a block diagram of the LINAC controls communications infrastructure.

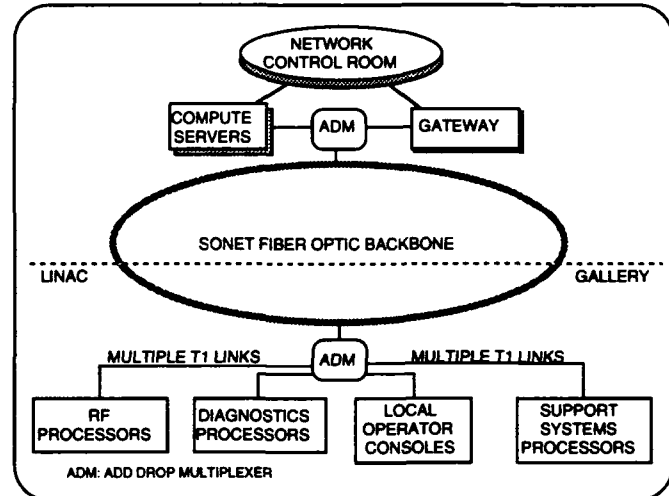


Figure 2. LINAC Communications Infrastructure.

The communications backbone is a SONET fiber optic network that interconnects the LINAC Gallery and the Accelerator Main Control Room (AMCR). Add-Drop Multiplexer (ADM) equipment is installed in the LINAC Gallery and the AMCR to interface the SONET backbone with T1 telecommunications links. Communication interface modules are provided to interface the T1 links from the ADM with the front-end equipment in the Gallery. Communications gateway equipment is provided at the AMCR to connect the ADM to the standard communications network of the AMCR.

B. Front End Systems

The SSCL has chosen EPICS (Experimental Physics and Industrial Control System) as the front-end control software. The primary hardware supported by EPICS is VME and VXI based. Commercial and custom modules mounted in VME and VXI crates are used to interface the control system to the various sensors and systems of the LINAC.

A minimum of four operator workstations, used for checkout and commissioning, will be located in the Ion Source, DTL, CCL and Transfer Line sections of the LINAC Klystron Gallery. The operator workstations will have a direct connection to a SONET backbone through an ADM or a commercial router. In addition, each workstation will act as a data server for the section of the LINAC to which it is connected. This will be accomplished by additional Ethernet connections to the building Network. In this manner, additional workstations may be connected and obtain access to the LINAC Control System.

*Operated by Universities Research Association, Inc., for the U.S. Department of Energy under Contract No. DE-AC35-89ER40486.

C. Machine Synchronization

The LINAC Control System provides synchronization of the front-end processors used to control each of the LINAC sections. The system is capable of delivering synchronizing messages to the processors within a 10-millisecond window before the start of each LINAC pulse. Typical messages will indicate the operating mode of the machine, i.e., LEB injection, medical facility operation, test beam operation, etc. The Global Controls Message Broadcast System (MBS) is used to provide this capability. The message indicating that the LEB is ready for a LINAC pulse will originate in the LEB Control System and be passed to the LINAC Control System by the MBS. LEB Injection will be the top priority mode of operation and will override all other LINAC operating modes.

D. Control Room Systems

The LINAC compute servers shown in Figure 3 and described below are located in the AMCR.

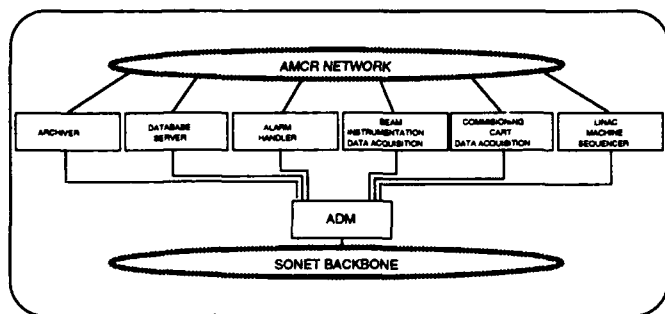


Figure 3. LINAC Compute Server.

LINAC Archiver – This computer performs the functions of archiving machine settings and slow (10 Hz) status information, along with operator actions.

LINAC Alarm Handler – The LINAC alarm compute server is used to log and alert the operator of any alarm conditions.

LINAC Database Server – The LINAC database server is used for storing and loading control application tables and software, and saving/restoring machine configurations.

LINAC Data Acquisition – Data acquisition here is defined as blocks of data read from various systems, often at high rates. This is data that may require further analysis and is of a type not covered by the data archiver. The primary subsystems that supply this type of data are the LINAC beam instrumentation system and the LINAC "Commissioning Cart." The LINAC Control System will supply a compute server or servers with sufficient compute capacity to perform analysis of data and sufficient disk capacity to archive the data. Analysis and storage of the data will be limited to that required for proper LINAC operation.

III. OPERATIONAL SEQUENCES AND CONTROL

The levels of control described in the preceding sections can be used to describe the types of control sequences and applications used within the LINAC Control System.

LINAC CONTROL APPLICATION (LEVEL 4)

The state machine for the LINAC can be described using sequential function charts (SFC) common in many industrial control systems. Each instance of an SFC is considered to be

an application. The highest level of control in the LINAC is the actual machine sequence that leads to a beam pulse. In turn, each module of the LINAC would have a control application and each subsystem of each module would have an application. Devices within each subsystem can even have applications. The LINAC Control Application SFC is shown in Figure 4. Each state and transition event is described in the following text.

OFF State – Control power to the VME/VXI crates, CPUs, racks and operator consoles is on. Code is executing in the LINAC Control System CPUs. Beam Permit is "Off".

Event A – The operator or an automatic sequence has commanded that the LINAC start.

Start-up State – The operator or an automatic sequence has issued the "start LINAC" command. In this state the operator will be able to direct the desired destinations for the beam (i.e., LEB, Medical, DTL Tank 1, etc.). When this state is entered from the OFF state, the operator will be prompted. The logic will then issue the appropriate start-up commands to the various LINAC modules. All modules required for each destination will be commanded to start.

Event B – The LINAC modules ready status is equal to the required module ready status.

Event F – The LINAC "off" command has been issued.

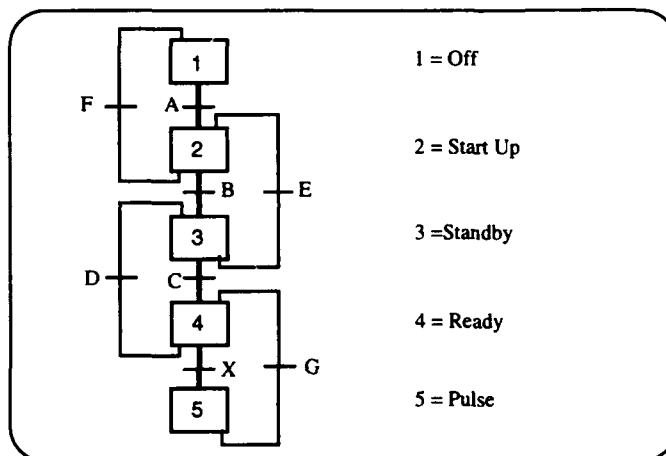


Figure 4. LINAC Control Application.

LINAC Standby State – In this state, the ready status of the LINAC modules is equal to the ready status for the anticipated beam destinations. This is a hold state, waiting for an operator or automatic sequence command to commence LINAC beam operations.

Event C – The LINAC "Go to Ready" command has been issued.

Event E – The LINAC module ready status is "not ready".

LINAC Ready State – In this state the "beam ready" status of each LINAC module is compared with the required module status for the particular pulse destination. In effect, this allows a Beam Permit for the pulse. If the beam ready status equals the required module ready status, the Beam Permit is granted. If the beam ready status does not meet the required status the timing delay for the RFQ is set and the LEBT chopper is not pulsed. The timing pulse for the other LINAC RF modules is not affected.

Event X – The Beam Permit for the pulse has been granted.

Event D – The LINAC modules ready status is less than required.

LINAC Pulse State – The LINAC pulse command is given to the ion source. The proper timing for the LEBT, RFQ and other LINAC modules is set such that beam is accelerated. Note that the LINAC state will cycle between Pulse and Ready on a pulse-to-pulse basis, even when the LINAC is running to the same location on every pulse.

Event G – The LINAC pulse is complete.

Implied Events – For the sake of clarity, the implied transitions from one state to another have been omitted from the drawing. These events would be operator or automatic sequence events that would command the LINAC state to a lower state than it is presently in. For example, the LINAC can be manually moved from the READY state to the STANDBY state by the operator. The LINAC can also be switched completely off from any state by the operator.

MODULE CONTROL APPLICATION (Level 3)

Each module of the LINAC (Source, RFQ, DTL, etc.) will have a module level control application. The purpose of this application is to transition the module from the OFF state to the MODULE READY state. In this state the module is ready for beam. The module level application SFC for the DTL Input Matching Section (IMS) is shown in Figure 5. It is a representative example of the application used for each module. The module states and transition events are described in the following text.

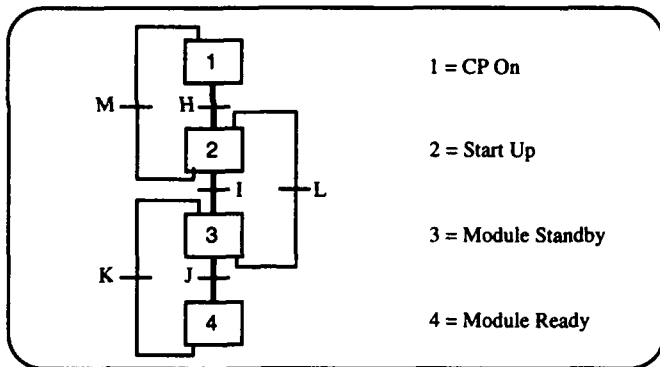


Figure 5. LINAC DTL IMS Module Application.

Module Control Power On State – This is the lowest state that a module control system can reach. In this state the control power is turned on to the VME/VXI crates, processors, racks, etc. Code is executing in the module control CPUs.

Event H – The "module start" command is received from the LINAC Application.

Event M – The "module off" command is received.

Module Start-up State – In this state the module control application will command its various subsystems to begin turning on and preparing for beam. Vacuum systems will begin the pumpdown process, the Temperature Stabilization System (TSS) will begin to function and regulate cavity temperature, magnets will move to their nominal beam positions (focus and steering), RF systems will turn on, etc.

Event I – All module subsystems are ready for beam.

Event L – All module subsystems are not ready for beam.

Module Standby – All module subsystems are ready and operational. This is a hold state, waiting for an operator or

automatic sequence command to move the LINAC to beam operations. In this state the module status is reported as "Ready" to the LINAC Application.

Event J – The "Go to Beam Ready Command" is received.

Event L – All subsystems are not ready.

Module Beam Ready – All module subsystems are ready. In this state the module status is reported as "Beam Ready" which also implies "Ready".

Event K – Subsystems are not "beam ready".

Implied Events – For the sake of clarity, the implied transitions from one state to another have been omitted from the drawing. These events would be operator or automatic sequence of events that command the module to a lower state.

SUBSYSTEM CONTROL APPLICATION (Level 2)

Each subsystem of the module will have a subsystem level control application. The purpose of this application is to transition the subsystem from the OFF state to the SUBSYSTEM READY state. In this state the subsystem is ready for beam. The subsystem level application SFC for the DTL IMS vacuum system is shown in Figure 6. It is a representative example of the application used for each subsystem. The subsystem states and transition events are described in the following text.

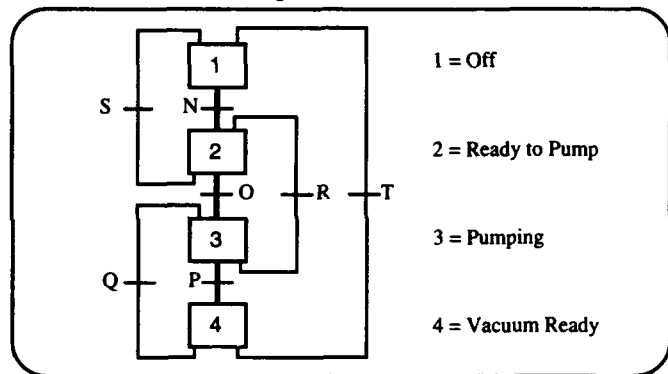


Figure 6. LINAC DTL IMS Vacuum Application.

Vacuum System Off State – The vacuum system is in the off state. Ion gauges and ion pumps are turned off and gate valves are closed.

Event N – The vacuum system is manually roughed down. This event occurs when the Convectron gauge pressure is measured to be less than 10^{-2} Pa.

Vacuum System Ready to Pump State – Ion gauges are on, Ion Pumps are off, and gate valves are closed.

Event O – The "Pump" command has been received from the module control application.

Event S – The Convectron gauge pressure is above 10^{-2} Pa.

Vacuum System Pumping – Ion gauges, and Ion Pumps are on. Gate valves are closed.

Event P – The DTL IMS Ion Gauge pressure is less than 10^{-5} Pa.

Event R – The DTL IMS pressure is greater than 10^{-4} Pa.

Vacuum Ready State – Ion pumps, Ion gauges are on. Gate valve enables have been granted.

Event Q – The DTL IMS pressure is greater than 10^{-5} Pa.

Event T – The "vacuum off" command has been received from the module application.

Proposal to use Failure Prediction as a Means of Meeting Availability Requirements at the SSC

Surajit Sarkar, William Merz, Frank Meyer.

Superconducting Super Collider Laboratory*
2550 Beckleymeade Avenue, Dallas, Texas, 75237

Abstract

The SSC is a complex of six accelerators with a large number of components and high availability requirements. In a number of accelerator subsystems, for example the Collider Correction Magnet Power Supplies, availability requirements cannot be met with non-redundant architectures. Cost and practicality considerations preclude the use of multiply redundant architectures as viable options. The possible use of failure prediction as a means of meeting the high availability requirements of the Collider Corrector Power Supply subsystem is described and the implications on the SSC Central Control System is discussed.

I. INTRODUCTION

The SSC complex of six accelerators is currently estimated to have about 540,000 control and monitor points[1]. The large number of control and monitor points reflects the number of devices and components which are involved in the proper operation of these accelerators. The availability requirements placed on these accelerators and therefore on the devices and components is high. For example the required Collider availability of 0.80 translates to an availability requirement of 0.997 for the Collider correction magnet power supply system. Comparable availability figures have been achieved at Fermilab, a complex of accelerators the largest of which is about one tenth the size of one of the two SSC collider rings, however, only after many years of operation.

For a system consisting of a network of components the system reliability is evaluated by applying well known combinatorial rules as determined by network topology and by the individual component reliabilities[2]. Very roughly, the Mean Time Between Failure, MTBF, of a system 's', with 'n' identical components having component MTBF_c is given by $MTBF_s = MTBF_c / n$. The MTBF decreases (or the system failure rate increases) in proportion to the number of components. The standard approaches to improving the system reliability are: (1) to increase the component reliability or (2) to favorably alter the system / sub-system topology by adding redundancy to (weak or) less reliable links.

The problem arises in systems with a large number of components. For such systems it may not be possible to increase component reliability to meet the availability requirements. The avenues of using redundant architectures may not be cost effective and those of using multiply redundant architectures may not be practical. This problem is aggravated as the numbers increase.

Two examples related to the Collider correction magnet power supply operation are the Collider correction magnet power supply system and the power supply controller to power supply fibre optic link components.

Even with singly redundant architectures[3] achieving a Collider correction magnet power supply system MTBF of ten days (or one run period) requires an increase of component power supply MTBF from the current industry standards, in the range of 50,000-100,000 hours to a figure somewhat greater than 1 million hours MTBF - a ten to twenty fold increase.

Using selected devices for the power supply controller fibre-optic links, with component typical MTBF in the range of about 4 million hours, the 24,000 optical transmitters and receivers to be used in the SSC correction, 'DC', and ring magnet power supply controllers will have a combined MTBF of 6.5 days. This is less than the ten day running period.

From the above two examples it becomes clear that for systems with a large number of components increasing the MTBF of well designed sub-systems or good components, which may already be state-of-the-art limited, becomes increasingly difficult to the point of requiring the achievement of unattainable MTBFs.

MTBF gains for redundant systems do not scale directly as the number of systems when repair is constrained to scheduled maintenance periods. They are further degraded due to the additional components and methods required to switch over to the non failed system. Buying more reliable components, using redundancy and component derating as means of increasing system MTBF have cost implications which may pose limitation on system design for reliability. For example the 'reliability allowance' included in cost estimates for the collider corrector power supply systems do not allow redundancy and power supply controller costs have been estimated using commercial not high reliability components.

While cold spares may reduce the mean time to repair a sub-system and consequently increase system availability it cannot compensate for the lost time required to reach the given operational state aborted by the particular failure.

The MTBF is a statistical figure. By definition for a constant failure rate, ie. an exponential distribution of failures, the probability of surviving one MTBF without failure is 37%. For a system MTBF of one run period, most failures will happen before this time interrupting a run. User frustration will likely scale as the frequency of stopped runs.

From the above arguments we conclude that: '*what is required is failure free system operation for the duration of each run and not a high over all system MTBF*' - with a failure being defined as anything that causes beam quality degradation sufficient to require a dump.

II. FAILURE PREDICTION

The method proposed here to address the above requirement is the use of 'quantitative' prediction of failures. The assumptions are that we have a scheduled 4 day shutdown following a ten day run period. If all failures can be anticipated and taken care of during the scheduled shutdown,

*Operated by the Universities Research Association, Inc., for the U.S. Department of Energy under Contract No. DE-AC02-89ER40486.

unscheduled downtime is nil. The effective system uptime is 100% or equivalent to a system with an infinite MTBF.

Our premise here is that if some of the failure modes of a component are not instantaneous, but rather are a result of the progression of degradation of some parameter(s), then it should be possible to monitor those parameters and from the progression of monitored states predict, with some associated probability, that a piece of equipment is going to fail within a certain time period.

Failure modes with the highest frequency can be identified and the characterized such that one can predict component failure to some required degree of temporal accuracy. Such components can then be replaced during a shutdown period or scheduled maintenance so as not to contribute to system downtime figures. Components known to be partially marginal (or those for which, the temporal bracketing achievable is known to be less accurate) may be removed from critical subsystems and placed into operation in the less critical or easily accessible areas which incur a smaller Mean Time to Repair (MTTR) or system down-time per failure.

In searching the literature we find that the idea of being able to detect failures exists in the industry, though somewhat qualitatively, under the name of Condition Monitoring. What is proposed here is an extension of these basic principles to add a temporal domain to the analyzed data so as to allow us to bracket the failure to some predetermined window of time in which failures will happen with some given probability. This probability multiplied by the cost of such a failure (in terms of lost beam production) gives us a factor determining the urgency, or the requirement to replace, given the cost of reaching that stage of operations. The probability of failure, the cost to reach that stage in operations and the cost of potential loss of operation as a function of stage of operation are all continuously changing variables and need to be dynamically evaluated against the real cost of component replacement.

The idea proposed here is generally applicable to large systems. Conveniently failure prediction becomes useful for systems where it becomes necessary to use or rely on such methods: those with a large number of components. Systems with large numbers of similar components require less running hours to gather the statistical data needed to characterize the failure modes. Failure modes with the highest frequency - those that can cause the most operational grief - provide data (and so can be characterized) quicker. This proposal can be extended to the not so large systems, which however have critical mission requirements, as described in section V.

A. Implementation

In practice a combination of methods will have to be used. In any system routine Failure Modes and Effects Analysis (FMEA) will identify the critical areas and actions required to mitigate them. Quantitative failure prediction is proposed to be used as an adjunct to the above procedures, in cases where requirements cannot be met by such methods alone, in cases where exceptional availability is required during run periods, or in mission critical systems where even single failures cannot be tolerated and cost is not a constraining factor.

For each system it is necessary to determine what fraction of components can fail before system operation is affected. For the 'DC' and corrector power supply to controller fibre-optic links, failures do not affect the operation of the 'DC' PS operation as long as no beamline energy or steering changes

are required. Injector and possibly collider corrector failures during the 20 hour collider flat-top may also be tolerable. The effect of single point failures[5] and the possibility of compensation using adjacent (sets of) correctors[4] is being explored. In the case of the controller to power supply fibre-optic links implementation of failure prediction using parasitic trending of link Bit Error Rates is being explored - system cost here is the specification of appropriate link protocol[6].

The practical implementation of these techniques must proceed in the stages. Initial task will be the identification of failure modes followed by the implementation in stages of condition monitoring, qualitative and quantitative failure prediction, to the generation of dynamically evaluated component replacement cost factor projected as a function of time, for particular failure modes with operator prompting programs being implemented later.

III. METHODS

The parameters used as indicators of failure may be analog, digital or complex types derived by processing other parameters as described below.

A. Analog Parameters

Typical analog parameters envisaged for example in a power converter was h_{FE} of pass transistors in regulator banks. At a recent conference it was confirmed that this is indeed a parameter which showed degradation in failing power converter amplifier pass banks[7]. In switched mode power converters for example the occurrence of spikes have been seen as precursors to failure[8] although they have not been used in the manner proposed here of characterization and failure prediction.

B. Digital Parameters

Some of the parameters may be digital signals say from relay contact closures, logic signals or composite digital signals from interlock processing equipment.

It may seem that digital signal failures are not predictable or are sudden. Looking more closely for example a relay may have some contact bounce associated with closure. It is possible to characterize this bounce and see if this changes with time - or as a function of other factors such as operating current or ambient temperature.

Discreet logic signals are digital only in that a categorization has been imposed on analog characteristics: for example for TTL signals a logic level of 0 encompasses 0-0.4V and some associated node currents. Logic state transitions are digital (only) above a range of time granularity. Variations in any of these parameters can be used for failure mode identification. Examples are given in reference[9].

C. Complex Parameter Types

Adding a level of complexity one could explore the behaviour 'surface' (along the lines of control surface for a dynamical control system) of multi-parameter failure modes, such as ambient temperature and operating current versus the contact bounce, and contact opening time versus the bounce for a relay. A fraction of such failure data may be non-stationary and may require specialized techniques[10] for processing. The caveat of course is that this must be only for systems where this is indeed of sufficient importance - how ever in

such large systems and where other restrictions do not hinder this may be a possible technique to consider. The plotting of behaviour surfaces for visual feature detection or the use of Neural nets for feature extraction may be required. With the perfection of these techniques relatively inexpensive integrated hardware to carry out these functions could be developed and the evaluation and implementation of complex processing functions could be easier. The use of Fuzzy logic to implement estimation algorithms on the extracted features and implement decision trees to inform Central controls of impending failures or of required actions such as abort or change particular component within predicted time are all possible. The use of built in test vectors in front end electronics allows the possibility in controls electronics of predicting chain failures which may not become critical before a certain time.

IV. CONSEQUENCES OR REQUIREMENTS FOR THE CONTROL SYSTEM

To implement Quantitative Failure Prediction (QFP) the Global Accelerator Control System (GACS) must allow for the collection and analysis of requisite data - the characteristics of both of which are not fully defined at this stage. Data for QFP will have to be collected either 'passively' from accelerator sub-system and component data monitored routinely, or 'actively', where the data collection process requires the modification of mode of operation of the sub-system or device under test from the normal accelerator operation modes, between acceleration cycles. The monitoring of specific controls equipment, the use of specialized techniques such as statistical or syntactic pattern recognition[11] techniques and the possible use of neural nets[12] and fuzzy logic in decision processes and their impact on the GACS processing hardware, controls software and the effects (of additional hardware and system software) on system reliability all need to be addressed. The addition of processing capacity at the 'rear-end' or Main Control Room computers is relatively easy. Number of component systems are relatively small and good accessibility guarantees a small mean time to replace. Capacity additions to the GACS communications are also relatively easy but are not expected to be required.

Typically Front End Electronics components and sub-systems have the largest numbers and are most difficult to change or upgrade later in the implementation cycle and must be appropriately designed. Changes have ripple effects on downstream equipment such as sensors and controllers. Reliability of front end electronics needs to be considered in detail. The use of front end equipment buses with the capability to isolate failed cards and with kernels which allow dynamic task allocation between crate level processors allows the problem at the equipment crate level to be mitigated. The problem of failures at the front end electronics signal conditioning and interface level can not be addressed by the methods used above and a possible solution is QFP. With time as such methods are frequently used library of standard techniques will be developed which can be reused with relatively lower cost and effort impact.

V. DISCUSSION

A. Status

Few systems are currently being analyzed with reference to controls requirements for failure detection or prediction. The

redeeming factor is that at present only systems having relatively small number of components are being interfaced to the GACS. However, the definition of techniques required for failure prediction, from this stage would have allowed all systems to be similar with the attendant benefits of inventory reduction and maintenance streamlining.

For the 'DC', correction and pulsed power supply controls we are considering these options when feasible within limited available effort.

B. Cost Implications

The use of high reliability components and testing methods increases the cost of systems conservatively by a factor of 10 times for initial purchases and all future replacements. If the use of failure prediction allows the use of relatively inexpensive components then there can be definite long term cost gains associated with the use of such techniques.

The initial cost of implementation of failure prediction is in the systems analysis effort and currently in the development of implementation techniques. Only the hooks required for the specialized data acquisition hardware and software needs to be provided initially with modules being populated or incorporated as required. For the 'DC' and corrector power supply controllers the additional costs for hardware were found to be negligible.

C. General

Quantitative failure prediction can be useful for mission critical systems such as space flight where even single 'unprotected' failures can be critical. In case of not so large systems, data required for failure characterization can be acquired by using an extended set of components during the system design and commissioning periods - assuming that cost is not a constraining factor.

System availability requirement allocations may require a re-evaluation based on the modified system properties with the incorporation of failure prediction.

VI. REFERENCES

- [1] 'SSC Global Accelerator Control System Preliminary Design Requirements Review', SSC Internal Documents, September 9th, 1992.
- [2] 'Electronic Reliability Design Handbook', Military Handbook, MIL-HDBK-338-1A, vol. I, October 1988.
- [3] F. Meyer, 'Impact of Reliability Requirements for the Collider Correction Power Systems', SSC internal note, May 5th, 1992.
- [4] S. Sarkar, 'Compensation for Failed Collider Correctors', SSC internal note, December 9th, 1992.
- [5] G. Bourianoff, 'Accelerator Simulation activities at the SSCL', SSC laboratory publication number SSCL-N-811, January, 1993.
- [6] S. Sarkar *et al*, 'Controls Interface Protocols for the SSC Correction and 'DC' Magnet Power Supplies' These proceedings.
- [7] M. Fatizadeh, private communication, Panel Discussions on Power Supply Controls, IEEE Nuclear Science Symposium, Orlando, FL, October, 1992.
- [8] H. Isch, private communication, Panel Discussions on Power Supply Controls, IEEE Nuclear Science Symposium, Orlando, FL, October, 1992.
- [9] K. Liu, J. Gentler, 'Monitoring the Condition of Feedback Control Systems', Proceedings IEEE International Symposium on Intelligent Control, p-51, Arlington, VA, August, 1988.
- [10] A. Moore, S. McLaughlin, 'Spectral Estimation of Nonstationary Time Series', Proceedings 6th International Conference on Digital Processing of Signals in Communications, Loughborough, UK, p-36, September, 1991.
- [11] R.J. Hamilton *et al*, 'Syntactic Techniques for Pattern Recognition on Sampled Data Systems', IEE Proceedings on Computers and Digital Techniques, p-156, Vol. 139, No. 2, March, 1992.
- [12] M. Chow *et al*, 'A neural Network Approach to Real-Time Condition Monitoring of Induction Motors', IEEE Transactions on Industrial Electronics, p-448, Vol. 38, No. 6, December, 1991.

Control, Timing, and Data Acquisition for the Argonne Wakefield Accelerator (AWA)

P. Schoessow, C. Ho, J. Power, E. Chojnacki
Argonne National Laboratory, Argonne, Illinois 60439

Abstract

The AWA [1] is a new facility primarily designed for wakefield acceleration experiments at the 100 MV/m scale, which incorporates a high current linac and rf photocathode electron source, a low emittance rf electron gun for witness beam generation, and associated beamlines and diagnostics. The control system is based on VME and CAMAC electronics interfaced to a high performance workstation and provides some distributed processing capability. In addition to the control of linac rf, laser optics, and beamlines, the system is also used for acquisition of video data both from luminescent beam position monitors and from streak camera pulse length diagnostics. Online image feature extraction will permit wakefields to be computed during the course of data taking. The linac timing electronics and its interface to the control system is described.

Introduction

The design of the AWA control system is based in part on experience gained at the Advanced Accelerator Test Facility (AATF), and also on more extensive data acquisition systems used for high energy physics experiments. The goal of the AWA system is to provide easy selection and adjustment of accelerator and beamline parameters, as well as the online analysis of diagnostic and physics data. Other necessary functions are the storage and recall of working parameter sets and the automatic monitoring of component performance (and flagging of deviations from preselected tolerances). The control system must also be sufficiently flexible to permit expansion for subsequent phases of the AWA project.

At the core of the system is an HP-750 RISC workstation using the UNIX operating system. The workstation is interfaced to VMEbus via a high speed bus adaptor with dual port RAM. A 68030 CPU board on the VMEbus handles command requests from the workstation and provides auxiliary processing capabilities.

Most of the control and monitoring functions are handled through a VME-CAMAC parallel bus interface. Video signals from beam position monitors and from the streak camera, comprising the actual physics data from the experiment, are acquired using a high resolution VME-based frame grabber. A block diagram of the AWA control system is shown in figure 1.

HP Workstation

The HP-750 workstation provides the user interface to the AWA control system, data analysis and display, and data storage. User input to the control software can be

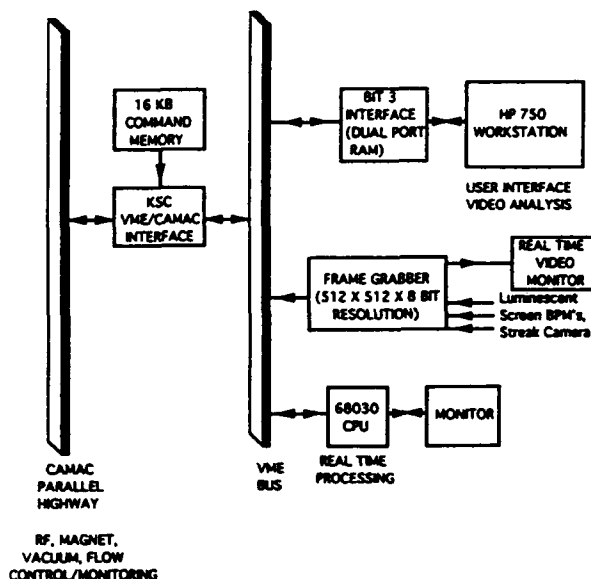


Figure 1: Block diagram of the AWA control and data acquisition system.

made using either a mouse, keyboard, or knob panel. The AWA control software is being developed in-house and is based upon the Motif graphical user interface. The various codes comprising the system are written in C and FORTRAN77.

Experience with the AATF control system [2] demonstrated the importance of rapid online image data analysis for wakefield measurements. This procedure (for each frame in a delay scan) consists of fitting edge data to a model of the background, performing a background subtraction, and extracting moments of the resulting 2D beam intensity distribution. The high floating point performance of the HP-750 will enable this analysis to be accomplished in real time.

VMEbus and CAMAC Systems

The interface between the HP workstation and the VMEbus is provided by a Bit3 Model 487 bus adaptor. Communications are handled primarily via the adaptor's 1 MB dual port RAM, which appears transparently as a shared memory space accessible from both the workstation and the VMEbus. Memory access conflicts are arbitrated by the adaptor itself.

In general the workstation does not directly control devices on the VMEbus. Rather, the control processes on the

HP write commands to a queue in dual port RAM. The queue is then serviced by the Heurikon V3D 68030 CPU board, which issues the command to the appropriate VME device. Another section of dual port RAM is used to store data read back from VME devices for use by monitoring and display processes on the workstation.

The bus adaptor also provides the option of bypassing the dual port RAM and addressing the VMEbus directly from the HP workstation. This is desirable for large data transfers like video images, since the V3D does not support block transfer modes.

The V3D board uses the OS9 operating system. Software is written in C and 68030 assembly language. The V3D board can act autonomously to control the system for hardware testing and diagnostics, and will be used if required to service interrupts generated from the VMEbus.

The interface to CAMAC from the VMEbus is provided by a Kinetic Systems Model 2917 interface card. The interface incorporates an 8k Word command memory, and can autonomously execute a programmed command list without processor intervention. All control and monitor functions with the exception of image acquisition are currently performed in CAMAC.

Accelerator Controls

In order to minimize the problem of rf noise pickup, all rf system control and monitoring signals are carried by fiber optic cables. Analog signals are encoded by the repetition rate of an optical pulse train, using voltage to frequency (V/F) converters. Digital signals (such as fault and status indicators) are encoded simply as the presence or absence of light (DFO).

The cards provided by the rf system vendor to perform these functions were designed to be compatible with signals provided by standard CAMAC modules. DFO out cards are controlled by contact closures provided by a CAMAC output register, while DFO in cards are read by an input gate module. Analog levels are provided to the V/F cards by CAMAC DAC's, and readout of the F/V cards by ADC's. A 12 bit resolution is adequate for both DAC's and ADC's.

Other functions handled by the CAMAC system include stepping motor controls for phase shifters and wavefront shaper [3], and beamline magnet power supply control and readback. Adjustment of linac cooling water temperatures and cavity temperature monitoring will also be implemented.

Master Trigger/Timing Module

The master trigger is a custom designed CAMAC card which provides the signal that triggers the laser and rf systems to begin their firing sequences, allowing the repetition rate and delay of the trigger pulse to be programmed. A zero crossing detector is used to synchronize the trigger to the 60 Hz line signal to provide shot-to-shot stability

of experimental apparatus. The triggering phase with respect to the line is also adjustable. A second trigger output is provided, with additional delays of up to 33 ms, programmable in 1 μ s increments.

The card allows the rep rate of the trigger pulse to be specified as 30, 15, 10, 5, 2, 1 Hz or single shot. The module also supports a local control mode which allows adjustments directly from knobs on the front panel. The output voltage pulses from this module are converted to optical pulses by a separate module for transmission to the laser and rf systems.

Imaging

Images from luminescent screen beam position monitors and streak camera based temporal diagnostics are captured using an Imaging Technology FG-100 video digitizer board with 512x512x8 bit resolution. The frame buffer can store 4 digitized images simultaneously. A real time (passthru mode) display of the digitized video signal is provided on a dedicated monitor. False color enhancement of images is available if desired.

An imaging software package (xframe) on the HP workstation has been developed. Xframe is used to retrieve image data from the FG-100 frame buffer for analysis, display and storage on disk (in either raw, GIF, or Postscript format). Some examples of the xframe image analysis features are found in reference [3].

An important function of the control system is to provide the sequencing of wakefield measurements. In a delay scan, the drive-witness delay is varied in programmable increments (typically a few ps) by simultaneously adjusting the witness gun rf phase and laser injection phase. For each delay an image is acquired of the witness bunch on a phosphor screen in the spectrometer focal plane. The frame is then transferred to the HP for storage and analysis as described above. The performance of the wakefield analysis software has been verified with AATF wakefield data.

Acknowledgement

This work is supported by Department of Energy, High Energy Physics Division under the contract W-31-109-ENG-38.

References

- [1] P.Schoessow et al., these proceedings
- [2] P.Schoessow, proceedings of the 1989 IEEE Particle Accelerator Conference, pp.1629-1630
- [3] W.Gai, J.Simpson, N.Hill, C.Ho, P.Schoessow, these proceedings

The High Level Programmer and User Interface of the NSLS Control System *

Y.N. Tang, J.D. Smith and S. Sathe†

National Synchrotron Light Source, Brookhaven National Laboratory, Upton, NY 11973

Abstract

This paper presents the major components of the high level software in the NSLS upgraded control system. Both programmer and user interfaces are discussed. The use of the high-speed work stations, fast network communications, UNIX system, X-window and Motif have greatly changed and improved these interfaces.

1 Introduction

The NSLS control system is undergoing a major upgrade and phase II has been completed [1, 3]. Many new capabilities and features have been brought in by the upgrade.

- The fast ethernet communication replaced the slow serial links and the powerful work stations are replacing the old central hosts and terminals. Many programs run 10 to 20 times faster than before. The ring down time for injection becomes much shorter. Many advanced diagnostic tools such as the real time orbit display are emerging.
- The graphical user interface is replacing the traditional textual interface. The X window and Motif have completely changed its look and feel.
- The UNIX excellent programming environment have greatly shortened the life cycle of the software development. Eight major libraries and more than 60 programs have been developed or converted since we started the project at the beginning of 1992.
- The rich set of the UNIX utilities and its flexible file system have helped us in developing a powerful interpreter and NSLS standard file format.
- The reliability of the system is very much enhanced. For example, there are many history processes running in the background at different scheduled frequencies. They never stopped and have not missed any scheduled readings under normal conditions.

Many people in the NSLS Department contributed to this project. Our special thanks go to S. Krinsky and John Keane. Without their encouragement, support and guidance, today's success of the upgrade would not be possible. Thanks also go to the ring managers N. Fewell and S. Kramer and many other people for their support and many very helpful suggestions, opinions and ideas. All members of the computer controls group made their contributions.

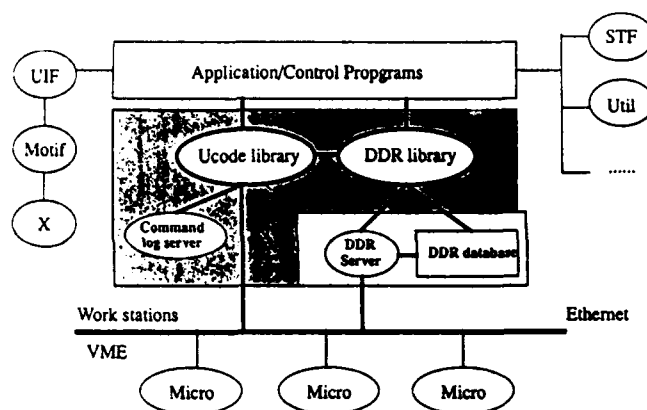
*Work performed under the auspices of the U.S. Dept. of Energy under contract no. DE-AC02-76CH00016.

†Ms. Sathe now in the AGS Department

2 Overview of Work station Software

The upgraded control system is a distributed system and its software consists of three layers (Fig. 1). The VME micros, which control the hardware, constitutes the lower layer. The high level applications talk to these micros through ethernet by calling functions in the ucode (user code) library. The controllable and/or readable system parameters and hardware signals are called devices, which are stored in a home made database — DDR (Device Data Record). The applications access the DDR database through the DDR library. The ucode and DDR constitute the middle layer of the control software.

Figure 1



3 Major Components of System Software

3.1 The DDR Database

We use logical and composite devices, whose records contain logically related parameters such as the setpoint, read-back, command and device states, tolerance, high and low limits, error flag, error mask, lock status, in-process flag etc. A parameter mask field in the record masks out the parameters not used for a device.

Using logical records, which is a key to a high-capacity and high-speed control system, drastically reduces the number of devices in our system and the network traffic. We have about 5100 devices now and it may increase to 10000 in the near future. If we did not use the compos-

ite records, the device number might be 10 times or more larger.

The DDR database keeps the addresses and other important parameters of all devices in the system. Any program accessing devices must consult DDR at first. The whole database is loaded into memory (now 0.5 Mbytes) at run time for the fast execution.

A complete set of DDR utilities has been built. A graphical browser/builder allows users to build, inspect, search, sort, save and print the DDR or displayed pages. The DDR library provides the programmer interface.

3.2 The Ucode Library

The ucode library is the interface between the high level programs and low level micros. Every program must call ucode functions when accessing devices. This library was carefully designed and developed because of its importance and is still evolving.

- To achieve high data rates is one of our major goals in the system upgrade. The UDP protocol is used to reduce the overhead caused by the TCP protocol. The reduction of the overhead in the network transport increases the effective bandwidth of the network. Though we spent much effort in the library and real-time monitor [2] to make the communication reliable, this effort is many times rewarded by the benefits we gained. For example, a program may read a set of devices at a 120 Hz rate or more. If the TCP protocol were used, we could only make about 70 Hz.
- To make the library as robust and easy to use as possible has been always emphasized because it is not only used by programmers, but also used by physicists, engineers and others. Generally, one ucode function is enough to write any settable fields of any number of devices or read any field, a commonly-used combination of fields or the whole records of any number of devices from any number of micros. The ucode automatically call functions in the DDR library and divides the user request in multiple packets (a UDP packet consists of at most 1024 bytes) if necessary. The implementation details are completely hidden and ucode does all the "dirty work" and decodes all the read back data. For example, it not only gives the state code of devices, it also encodes the code into "ON", "OFF" or whatever is appropriate. We provide both C and Fortran versions. A physicist or engineer needs only several hours to learn how to use it.
- For each ucode call of reading or writing devices, the ucode uses an internal buffer which is filled with the access status code for each device upon the completion of the call. The code is either SUCCESS (0) or an error number. If the function returns an error,

one may acquire this buffer to check which devices went wrong and what went wrong and get an encoded message for each device.

- The ucode allocates and keeps all accessed devices in device lists. If the same set of devices are accessed again, the ucode does not need to search the DDR database once more.
- The ucode uses a special algorithm to assign each process an access class. Every process may read devices. However, whether a process may set devices or not depends on its access class and the system class at that time. Every device may be locked. Once a device is locked, no one may write to it unless it is unlocked at first. All the write command will be logged into a disk file¹.

3.3 The UIF Toolkit

The User InterFace Toolkit (UIF) based on X and Motif has been developed and it has greatly sped up the development of graphical software, which constitutes a major portion of the important programs in the system.

The toolkit provides a consistent look and feel to the operators by providing a standard Menubar with the standard buttons namely Help, Tools and Quit. Other buttons on the menubar are user configurable. Below the menubar is the drawing area where the user can draw various graphics objects, plot graphs *etc.* The toolkit provides higher level abstractions such as a Matrix and a Plot. With the Matrix, it is very easy to create tabular displays. It has some features of a spreadsheet.

The toolkit provides a rich set of User Interface tools such as popup and pulldown menus, various kinds of buttons, lists, directory and file browsers, scrollbars, controls specific switch panels, text input areas, standard error popups, confirmation boxes *etc.*

All the X fonts and colors are available to the user. The toolkit deals with the graphics at an individual object level and lets the user interact with it. The user can group a number of such objects and can save them in a file.

The timer events are integrated with the toolkit. One can create an animation effect using this feature.

4 Orbit Monitoring and Display System

In addition to a complete and big set of orbit measurement, comparison, display, correction and history data collection and display programs, the following new features have been added in the upgraded system.

¹we are developing a command log server to make the command log process more efficient and centralized.

- Real-time orbit graphical display: this is a sophisticated program which has numerous options. However, its greatest feature lies in the real time display with 4 to 6 Hz display rate, which is limited by the drawing speed of the X graphics. One may see the orbit moving or changing almost spontaneously when doing orbit correction or sending local bumps. It is one of the most useful tools in the system used in the studies and daily operations.
- Fast orbit history: this is another very useful tool. The fast history daemons run in the background and read a user-specified set of monitors at the user-specified rate (between 5 to 20 Hz). Several hours (specified by users) of the most recent readings are stored in a circular ring buffer. The program will dump a portion of or the whole buffer to disk files upon request, which is made through a signal sent by another process. The dumped data are in the NSLS standard file format and a general plot program then is used to look at and browse the data set. Many interesting phenomena have been detected by using the fast orbit history.

5 Standard File System and General History

In order to make the important data files transparent through the whole control system and to develop a general history and display program, we developed the standard file system.

A file in the standard format has a file header and segment headers which contain all the necessary information for application programs to read and display the file without prior knowledge. A C function library and several programs to inspect and display the data in the files of the standard format have been developed. The library functions provide an easy way to create, write, update, edit, search and read standard files. For example, One may read/write any rows or columns in the file or read/write any columns by their physical types or labels.

The standard file system now is used in many programs. One of its major use is in the general history system. Anyone may start his own history to record a certain set of devices at certain rate and write data to a specific directory in the standard file format. A general history graphical display may read and display any history files. At first, the display program gets all the device names from the segment header and prompts user to select some devices to display. Then it reads the data by device name or by column index. There are many other options in the program.

The ring managers and many users have started their own history processes. The general history system is widely and fully used in the Department.

6 The Interpreter

An interpreter has been developed by using the UNIX yacc utility. Since it was developed, more than 200 macros have been written by physicists, ring managers, control personnel and beam line users. These macros are used in the every day operations such as ramping, feedback controls, local and angle bumps, orbit corrections and other kinds of monitoring and controlling functions.

The interpreter may be executed interactively or run prewritten macros. It has all the read/write/control functions used in the control system plus many mathematical and scientific functions. It offers an unlimited layers of control flows and loops (both C- and Fortran-style if, while, for and *etc*) and macros may be nested to 16 layers deep. It has its own set of input/output functions, and the UNIX cursor and window package is implemented into it. In addition to the normal data types and float and character arrays, it has special data types to allow reading and writing control system parameters easily. For example, there is an array type for device names. The quotation marks are not needed when assign a device name to a variable. The built-in macro utility lets users list, inspect, edit and execute macros very easily. One may execute any shell commands and existing programs from the interpreter.

7 summary

We have presented the major components and features of the high level software. The upgraded system has been successfully installed and used in operations and is promising. Physicists, engineers and operators appreciate it very much. There are many important components and programs such as graphical save/restore, pretune, soframp, bramp, runramp, automenu *etc*, which are not mentioned in the text.

Now we are evaluating commercial databases. The DDR naming server is under development. The phase III upgrade will start soon. We hope a more capable and more intelligent control system will emerge on the completion of the whole upgrade process.

I. REFERENCES

- [1] J.D. Smith, *et al.*, this proceeding (1993).
- [2] S. Ramamoorthy, *et al.*, this proceeding (1993).
- [3] J.D. Smith, *et al.*, System Upgrade, NSLS, BNL (1990).
- [4] There are many technotes written by members of the Computer Group on separate pieces of software. They are too many to list.

NSLS Control Monitor and its Upgrade*

Susila Ramamoorthy and J.D.Smith
National Synchrotron Light Source, Brookhaven National Laboratory
Upton, New York 11973

Abstract

The NSLS Control Monitor is a real-time operating system designed for the microprocessor subsystems that control the machine hardware in the NSLS facility. Its major functions are to control the hardware in response to the commands from the host computers, monitor hardware status and report errors to the alarm handler. The software originally developed for the Multibus micros has been upgraded to run on the VME-based systems. The upgraded monitor provides ethernet communication with the new system and serial link with the old system. The dual link is the key feature for a smooth and nondisruptive transition at all levels of the control system. This paper describes the functions of the various modules of the monitor and future plans.

1. Introduction

The microprocessor subsystems controlling the machine hardware in the National Synchrotron Light Source facility are driven by a realtime operating system referred to as NSLS Control Monitor. As in any control system, the monitor performs hardware control, data acquisition and closed loop algorithms in real-time. It provides a standard interface to the control commands and data requests from the high level application programs on the host computers. The functional blocks of the upgraded monitor software, the current status and future plans are reported.

2. Upgrade Goals

The control system designed in 1978 was upgraded to meet the increasing demands on data acquisition rates and CPU power and to provide better diagnostics. The original system used Multibus-1 with 8 bit Intel 8080/85 CPU single board computers. A realtime multitasking monitor developed in-house is used for low level equipment control. The communication with host computers uses a serial link at 19.2 kbaud. The serial link, 16 bit address space, assembly language programming and absence of floating point co-processors were the major limitations. The architecture, hardware and software components have been changed. The micros and the host workstations have been connected by ethernet in a distributed network.[Ref. 1,2]. As part of the upgrade, the Multibus micros have been replaced by VME based 32-bit computers with an ethernet controller. The software has been upgraded to be compatible with the hardware changes. A goal of the upgrade is to make the transition smooth with no impact on machine operations.

This was realized by modifying the communication software which provides simultaneous access to both the new and old systems.

3. Hardware Configuration

The minimum hardware required to run the control monitor on a microprocessor system are a VME-based 68020 CPU with ethernet controller, 1 megabyte battery backed-up ram and the General Purpose Light Source (GPLS) board which has timers, serial ports, bus-interrupter module, video display generator, diagnostic LEDs and software selectable switches. Further hardware requirements are dependent on the equipment to be controlled. The hardware I/O interfaces include analog and digital cards in the VME crate, bus extenders, GPIB and RS-232/422 and Camac interfaces.

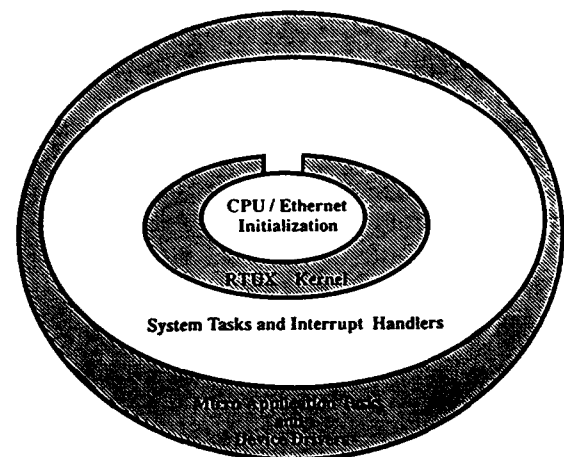


Fig. 1. Monitor Software Layers

4. Software Overview

The software consists of a set of system and application tasks and interrupt handlers. It provides an easy environment for developing application-specific modules in the micro. The Control Monitor is organized in logical layers as shown in Fig 1. The real-time kernel initializes the CPU and the Ethernet hardware thereby making the monitor software CPU/Ethernet hardware independent. The monitor system software initializes a few peripheral chips on the CPU for its own purpose. The system tasks are responsible for the management of the system hardware (GPLS board

*Work performed under the auspices of the U.S.Department of Energy.

peripherals). This isolates the system hardware and the real-time kernel from the micro application tasks. The application tasks use device drivers and system services to control and monitor the hardware. The interface between the system and the application software has been defined in such a way that any modification and upgrade at the system level will not require rewriting of the micro application tasks.

In addition to the software modules, the monitor has a device database in memory which is accessed by both the system and micro application tasks. The software views the various hardware signals (analog and digital) of the equipment as a set of logical devices. The database is a collection of data structures representing the logical devices. A standard device Format is used. This contains a number of fields for various information about a device (readback, setpoint, tolerance, limits for setpoint and alarms, digital command and states, and error status). The format also supports calibration and four data arrays. The devices can be a simple analog/digital input/output type or a composite type consisting of more than one simple type. A physical device with various types of signals can be represented by a group of simple logical devices or by a composite logical device. The device need not necessarily represent hardware. There can be soft devices that may be used by control algorithms. The device format has a configuration mask to indicate applicable fields and commands for a device. The database also includes all the pertinent hardware information such as its type, address etc. All the devices are treated in a similar fashion as far as updating or retrieving commands from the database. The host computers refer to a logical device by a descriptive name. The Device Data Record library (DDR) at the host computer translates the name to a physical address. (For serial link this is a serial line ID and device number. For ethernet link it is node name and device number). Thus the high level software controls and acquires data from the machine hardware using names and a set of standard commands without any knowledge of its location or the internals of the hardware. The micro application software and the device driver modules take care of all the details.

5. Software Components.

Fig 2 illustrates the software components, their interaction and the data flow.

5.1 Real-time Kernel

The processor runs RTUX, a real-time operating system developed by Emerge Systems Inc. in Florida. This is a fast, memory resident real-time kernel with the interrupt latency time in range (10-12 μ sec) for 20 MHz CPU. The task switching time is approximately 40 to 50 μ sec. The kernel supports multitask control, memory management, interrupt handling utilities, event handling, message queuing, intertask communications. The RTUX-ethernet clerk (Network package) provides the standard socket level abstraction. Software development is carried out in a standard Motorola UNIX development system using the C language.

The program can be downloaded into the target system and debugged using the RTUX tool ANALYZ. The rombuild utility generates an executable image that can be burned into prompts.

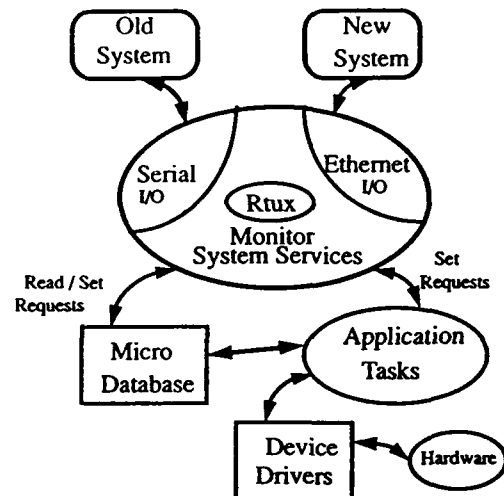


Fig. 2, Software Components.

5.2 Monitor System software.

This module is standard for all the micros and consists of multiple system tasks and interrupt handlers. It provides system timing (1 millisecond resolution) and uses RTUX primitives to synchronize and coordinate the activities of the various tasks. The important features of the system module are described below:

A. Initialization module.

The monitor initializes the necessary timing, display and serial port hardware, sets up interrupt handlers for timing, video, console and serial IO functions. After initialization, the application tasks are spawned.

B. Communication management

This is the most important activity of the system tasks. It receives operator messages in a standard format for all micros and updates the micro database fields. Since the high level applications can use serial or ethernet link during the conversion period it is imperative that the micros should accept requests via any link.

The serial server uses interrupt handlers for message I/O and provides handshake on every message. The message can have up to 64 bytes and contains only one request or reply per device.

For ethernet, the message headers and device packet formats have been carefully designed for future enhancements. UDP protocol with message size 1024 bytes per packet is used. Multiple read requests or commands or replies are packed in one message, resulting in low network traffic. The communication model supports both server and client roles. The server receives commands from host computers or any micro in the network. The client software pro-

vides micro to micro communication facility. Both the application and system tasks use the client services to acquire data from or to control any device on a different node. Handshake is provided for all messages. Integrity of the messages is checked and duplicate and out of sequence messages are identified and appropriate actions taken. Valid messages are disassembled into individual packets and passed to the command decoder. The decoder returns a reply which may be the requested data or acknowledgement. All the replies are assembled into a single message in the same order as received and returned to Ethernet IO module.

C. Command Decoder

The device commands are divided into two types, READ and SET. The READ requests are handled by the monitor system task. It builds the requested reply packets using the current values from the device database which is updated at rates of more than 10 Hz. There are more than 20 set commands for setpoints, limits, arrays and digital state control. Most of the set commands are handled by the system. The monitor uses the configuration mask before updating the Database fields. A setpoint command for an ON/OFF type is automatically discarded. All the necessary checks such as limits check, lock/unlock status check etc. are carried out before updating the command field. The application tasks are notified only for a few commands (setpoint, digital state control, device reset and new array) for further low level control.

D. Error And Alarm Reporting

The monitor provides services for alarm check, tolerance check and error reporting to the micro application tasks. The device error messages are sent asynchronously to an Error processor system on the network using micro to micro communication. Error flags are latched in the device records to prevent error storms. A new Set or Reset or device Error Clear command will unlatch the error. If the device is no longer in error, an ERROR RESET message is sent to the Error Processor. During the transition, a switch was provided to select the error reporting either through the serial or ethernet link. The system has the option to inhibit error reporting on an individual device basis or on a micro basis by selecting the error disable switch.

E. Diagnostic statistics

The monitor provides a display for the system statistics such as number of devices in error, number of spurious bus interrupts, transmission errors, message traffic and the time the system has been up etc.

F. Display management

Cable TV compatible ASCII display is a new feature added to the upgraded micros. There are 4 switch selectable hardware display pages. One hardware page can multiplex up to 8 software selectable pages. The display page can be controlled either by a push-button panel connected to the micro or by a remote command. Both system and application tasks generate displays for diagnostics and for continuous monitoring of device parameters and status without

imposing any load on the network.

5.3 Micro Application Tasks

This software is responsible for all the control and monitoring of the low level hardware. It sets up the application-specific device database and initializes it either with default parameters or from the battery backed up ram. The device control may be as simple as setting a bit in a bit/io card or setting a DAC or may involve control of a group of devices synchronously or sequentially, or may require a complicated software algorithm. The application tasks use the appropriate device drivers to accomplish the commands. The tasks also monitor the hardware signals at 10 Hz or more and update the database and generate application-specific video displays. The application tasks can use periodic timer interrupts provided by the system clock to trigger data acquisition. They use the system services for getting interrupts from an external source or from a slave on the VME bus.

6. Conclusions

The initial goals of the micro upgrade have been completed. All the 70 Multibus micros have been converted to 50 VME-based systems. New features such as video displays and optional recovery from battery backed up ram on start-up have been extremely useful from the operations and diagnostic points of view. The dual communication allowed us to carry out the workstation and the micro upgrade activities with practically no impact on the machine operations. During this period, the prime objective has been conversion to VME micros with ethernet link. Future plans include more device types which will support multivalued setpoint or readback devices and automatic device configuration module from a file image representing the device parameters and hardware information. A Device Name server to furnish various information such as the micro location, record number, calibration constants etc. is being planned. The monitor will provide a real time Name server to micro application tasks to access device information. An optional watchdog timer and a facility to save crucial parameters when AC failures occur, have been tested for future additions. Plans to boot the software from the rom image on a battery backed up ram is being tested.

7. Acknowledgement

The authors express their gratitude to S.Krinsky and J.Keane for their support and encouragement during this period. We thank S.Kramer and N.Fewell for helpful suggestions and W.Rambo and his group for the technical support.

8. References

- [1] J.Smith *et al.*, "NSLS Control System Upgrade Status," *These Proceedings*, 1993.
- [2] Y.N.Tang *et al.*, "The High Level Programmer and User Interface," *These Proceedings*, 1993.

NSLS Control System Upgrade Status *

J. Smith, S. Ramamoorthy, Y. Tang, J. Flannigan, S. Sathe, J. Keane, S. Krinsky
National Synchrotron Light Source, Brookhaven National Laboratory, Upton, NY 11973

Abstract

The NSLS control system initially installed in 1978 has undergone several modifications but the basic system architecture remained relatively unchanged. The need for faster response, increased reliability and better diagnostics made the control system upgrade a priority. Since the NSLS runs continuously, major changes to the control system are difficult. The upgrade plan had to allow continuous incremental changes to the control system without having any detrimental effect on operations. The plan had to provide for immediate improvement in a few key areas, such as data access rates, and be complete in a short time. At present, most accelerator operations utilize the upgraded control system.

1 Introduction

The NSLS initial control system design included a pair of Data General computers and multibus micros. A VAX, Apollos and VME micros were added later. The result was a system with a mixture of equipment that was unreliable, slow and difficult to maintain. The NSLS realized that a major improvement to the control system was necessary. It had to be complete in a very short time utilizing existing manpower.

The first step focused on converting from serial communications to Ethernet communications, replacing the multibus hardware and adding high speed workstations. The goal was to convert from the old system (fig. 1) to the new system (fig. 2). Although many new functions were envisioned for the control system, the focus was on making the basic architecture change and other improvements were postponed until this was accomplished.

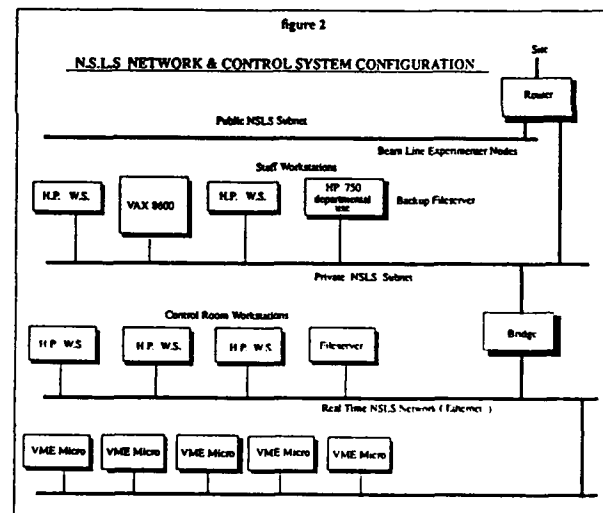
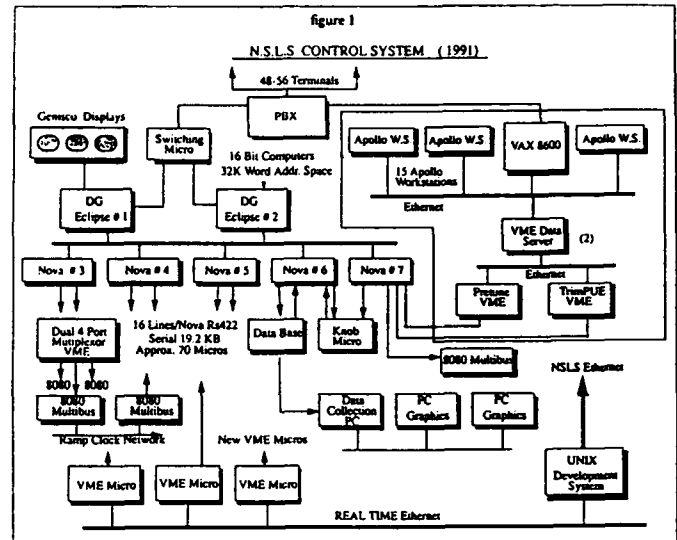
Key to the smooth transition is a module in the monitor which allows simultaneous computation with old serial lines and new Ethernet.

The immediate goals were to:

- convert all Multibus micros to VME.
- remove Data General and Nova computers.
- remove VAX computer from the control system.
- provide a graphical interface to programs.
- add Ethernet to existing VME micros.
- upgrade several existing micros.
- add several new micro systems.

*Work performed under the auspices of the U.S. Dept. of Energy under contract no. DE-AC02-76CH00016.

- Remove the Apollo Domain workstations.



2 Original Control System

The control system (figure 1) in late 1991 consisted of two Data General 16-bit computers that communicate with five Nova computers over a high speed (100k to 300k words) DG proprietary parallel bus. Each Nova computer is connected to sixteen micros using 19k baud serial lines. The Nova computers act as store and forward processors and buffer the data to accommodate the differences in speed between the serial and parallel lines. All messages contain source and destination addresses. The Novas determine the destination ports from the message headers. This gives a micro to micro communications capability which is used

for fast update of micro displays, knob control of devices and provides for device access from the VAX and Apollo computers.

When the Xray ring was upgraded the simulation and modeling programs could not run on the DG computers. To quickly integrate the department VAX computer into the control system, a Unix VME server was installed to provide a communications path from Ethernet to the serial links. Later Apollo workstations were added in the same manner. Graphic programs for orbit plotting and diagnostics were provided on the Apollo computer. The VAX and Apollo programs were slow because dual serial lines are used to access micro data.

Since 1988 all new control micros added have been VME system. In early 1992 there were about fifty five multibus and twenty VME systems. It was important to convert all multibus micros since many parts are no longer available. When including the test and development micros the total number of micros exceeded the number of Nova lines so the NSLS used multiplexors to increase the number of serial lines.

Each computer system used a different operating system. The DG's used AOS, the VAX used Ultrix and the Apollos used the Domain operating system. VME micro software development is done on a Motorola Unix system. All the multibus micros were written in assembly language and use an NSLS developed operating system. New VME micros were written in C and utilize a commercial operating system (RTUX).

The NSLS does not use a standard field bus. Each system uses the most appropriate interface method. Systems may use a parallel bus, serial bus, GPIB, Camac or other interface system. Conversion of the micros required modifications to the interface hardware to be compatible with VME systems.

3 New Control System Design

The new computer control system is shown.(figure 2). All the VME micros are connected via Ethernet to all the control room workstations. The Apollo workstations are shown upgraded to HP/700 series workstations. The operator terminal is a high performance workstation with sufficient memory and a local disk to give fast response. Several operator workstations are shown in addition to a file server and backup file server. Uninterruptible power supplies are provided for key systems. The low power consumption of workstations make UPS backup economical.

The file server will run programs that periodically take a snapshot of the data and provide a history capability. It also stores all the system files needed for day to day operations. Files are automatically copied to the backup file system periodically.

The performance of workstations has increased dramatically over the last few years. The new HP workstations are rated at over 10 times the performance of the Apollo work-

stations which substantially decreases the response time to operator requests.

In some cases several multibus micros were combined into one VME micro. The increased power of the VME system allows more functions to be programmed into one system. In the upgrade fifty five multibus micros were reduced to about thirty VME systems. In one case eight multibus micros were combined into one VME system. This eliminated a clock system needed to synchronize the multibus systems. Micros were combined so that related data could be collected in one micro. This minimizes Ethernet traffic and more functions can be done locally in micros. Some systems have several VME crates connected with Bus Repeaters and some have multiple CPUs.

Each new micro has a multipage TV compatible display some of which go to the CATV system. Presently there are over twelve TV displays continuously being updated. Since the displays are generated by micros very little of the network bandwidth is used. The memory mapped displays are a great diagnostic aid for realtime programmers.

4 Micro Changes^[1]

The key to a smooth upgrade was a design modification made to the Micro monitor. All VME application software is designed around the NSLS monitor. The monitor does the functions common to all systems. The application program will deal with hardware and software requirements unique to a particular system.

The monitor handles all the messages from the serial lines. It interprets the messages and calls the application programs as needed. For example, all read requests are handled by the monitor. A new system module was added to the monitor that handles Ethernet communications. This module operates in parallel with the serial communications module. Messages can be received simultaneously from different computers over the serial and Ethernet links. The micro applications programmer does not need to know the source of the message. The goal is to allow all existing micro application code to continue running while new applications were written using the Ethernet communications.

By relinking existing micro application code with the new monitor, all twenty existing VME systems obtained Ethernet communication while each maintained a compatible serial interface.

Fast communications was a requirement in the new system. New additions to the monitor allow reading a group of devices with one message whereas with serial communications only one message per device was allowed. Depending upon the data format twenty or thirty devices can be read from a micro with one message.

In analyzing the old system, we found that the average data rate was up to 450 messages per second. Much of the traffic was needed to update displays or for micro to micro communications. In the new system, more functions are

done in the micros which minimizes Ethernet traffic.

Two multibus micros would have required significant engineering effort to convert to VME. Special NSLS hardware was incorporated into the multibus micros and there was not sufficient manpower available to upgrade the system. To prevent these micros from holding up the conversion process a VME interface micro was built that controls the multibus systems. In such a case the multibus systems act as peripherals to the VME system. These two systems will be converted to VME systems soon.

The micros can send unsolicited error messages when an error is detected. These messages are sent over the serial link to an error process. The monitor was modified so that the setting of a switch in the VME crate will route the message to an error process on Ethernet. When the last micro is converted to VME, the Ethernet Error Processor will be enabled.

5 Workstation Software^[2]

All the programs written for the DG, VAX and Apollo had to be ported to the HP workstations. This consists of over 100 programs and several hundred interpreter programs.

All programs written for the VAX, Apollo and DG utilized a user interface library (Ucode) to isolate the communications hardware from the application programmer.

To minimize the time needed to convert programs to Ethernet a Ucode library was written which is compatible with the Ucode library for serial interface. This simplified the porting of old programs from the DG, VAX and Apollo.

Many changes were made in the interface library. Options were made to allow reading a group of devices with one message. The device name size was increased from eight to fifteen characters. Programs were combined to give a more efficient user interface and there was an increased use of graphics. Realtime orbit displays and realtime orbit history programs were added. The orbit history normally runs at five Hz but can run at up to twenty Hz. The system will support fifty Hz or higher, depending upon the cpu used, but the micros presently have an arbitrary limit of 20 Hz. Only critical programs were modified to collect data at fast rates. For the comint digital feedback system, a 200 Hz data rate is planned^[3].

There are many terminals scattered around the building near the equipment. Some programs had to be accessible via ASCII terminals so that technicians had remote access from equipment locations scattered around the building. For some programs the interface had to be

6 Present Status

All programs are now running on the HP workstations and all but two micros have been converted to VME. The last two micros are ready for testing. Essentially all accelerator operations are run with the new system.

7 Conclusion

The conversion from old to new system was completed faster than expected. One reason for this has been management involvement in the plan. Clear goals were defined and remained relatively unchanged throughout the project. During the upgrade many requests for improvements were made but there was strong support for limiting change requests and maintaining an appropriate level of effort on the conversion process.

The modular design of the Micro and host system software facilitated the upgrade. Interface libraries were used for communications and graphics software. Much of the conversion could be done by making changes to system libraries. In early program development attention was paid to evolving standards and portability. With the NSLS monitor, modifying or building new micros is relatively easy.

Now that the conversion is nearing completion the next phase of the upgrade can be started. The operator interface will be improved, a commercial database will be used, commercial GUI software will be tried, an upgraded monitor with provision for automatic code generation will be installed, hardware and software to time-synchronize all micros and workstations will be added, a real time name-server for micros will be added, FDDI links for the file server and control room workstations are planned and more logical device types will be added.

8 Acknowledgements

The authors would like to acknowledge the support given by many staff members including: S. Kramer, N. Fewell, H. Langenbach, R. Rose, A. Friedman, J. Dabrowski, P. Pearson, the Computer Support Group, R. Church and the NSLS control room operators.

I. REFERENCES

- [1] S. Ramamoorthy and J.D. Smith, this proceeding (1993).
- [2] Y.N. Tang, J.D. Smith and S. Sathe, this proceeding (1993)
- [3] A. Friedman *et al.*, this proceeding (1993)

Digital Signal Array Processor for NSLS Booster Power Supply Upgrade*

R. Olsen, J. Dabrowski,
National Synchrotron Light Source, Brookhaven National Laboratory
Upton, New York 11973

J. Murray
SUNY Stony Brook
Stony Brook, New York 11794

Summary

The booster at the NSLS is being upgraded from 0.75 to 2 pulses per second. To accomplish this, new power supplies for the dipole, quadrupole, and sextupole have been installed. This paper will outline the design and function of the digital signal processor used as the primary control element in the power supply control system.

INTRODUCTION

The booster power supply controllers operates in the z domain (1). Since many functions were required to be performed in parallel using interrupt frequencies from 180 Hz to 92.160 KHz, it was clear that parallel processing would be required. In addition, the uneven distribution of real-time required in the various circuit nodes implied a processing element where the processors could be assigned on an as-needed basis. This paper outlines the design and function of the Digital Signal Array Processor (DSAP) designed to be used for the booster power supply upgrade.

PRELIMINARY DESIGN REQUIREMENTS

The choice of VMEbus for the control system and a 6U, 160 mm format for the host processor dictated the size of the processor module. Downloading and supervision was to be performed by means of the VMEbus, thereby using up a considerable portion of the available bandwidth. Therefore, the VSB (VME secondary bus) is employed for interprocessor communications. Communication between the DSAP and application modules such as the trigger generator (TGEN), servo data I/O channel (SDIC), or phase locked loop (PLL) takes place over a board to board internal bus (the P3 connector). Thus, a DSAP module would normally be mated with an application module. Reliability and fault diagnosis dictated that the static RAM be provided with error detection and correction (EDAC). The need to provide a wide range of processing capability and the relative complexity of the I/O structure dictated the use of a mother board holding the I/O

bus hardware and a minimal number of DSP elements, while using a mezzanine board to hold an array of DSP elements which may be added as required. In the immediate case, the processor used is the TMS320C31, however, another processor, such as a special purpose FFT engine could be employed.

I/O CONTROL

Since I/O takes place over the VME and VSB bus, we use a 68030 as a bus controller, a Newbridge Microsystems CA91C078 as the VMEbus interface, and the PLX VSB1400 and VSB2000 as the VSBbus master and slave respectively. The CA91C078 provides all interface functions to the 68030 such as interrupt handling, local bus requestor, mailbox, VMEbus DMA, and address decoding, with no glue logic required. In addition, it provides the address mapping for the VSBbus master. The 68030 bus functions are closely enough matched to the VSBbus protocol so as to require a bare minimum of glue logic. A serial port is provided mainly to assist in debugging the I/O controller using a local monitor and a debugger resident on a PC. A math coprocessor is provided to allow DSP functions to be performed locally during idle time. The 68030 is provided with 128K by 32 bit words of SRAM (CYM1836) which is error corrected (IDT49C465). VSBbus DMA is provided by a TMS320C31. Programming for this function resides in the internal 2K RAM.

SIGNAL PROCESSING

The signal processing functions of the mother board take place in a pair of TMS320C30's (Node 0,1). As may be seen from Fig. 1, they are connected in a symmetrical arrangement, and communicate with the I/O controller by means of a dual-port memory on the primary bus. Each DSP is provided with 128K words of fast SRAM (CYM1836) which is error corrected (IDT49C460). This is more than adequate to hold the operating system plus application programs. Each DSP provides for four external interrupts. Level 0 is reserved for the operating system, levels 1 and 2 are for applications and appear on the P3 connector, while level 3 is reserved for handling errors from the associated

*Work performed under the auspices of the U.S. Department of Energy, under contract DE-AC02-76CH00016.

EDAC. Nodes 0,1 may be synchronized by means of the interconnected flags XF0,1 using the SIGI assembler instruction.

GLOBAL BUS

The processor nodes 0,1 communicate with a global resource by means of their expansion bus. Each processor bids for the bus for each transaction. Arbitration is performed by means of a synchronous state machine (CY7C330). This global resource consists of 2K x 32 SRAM for direct interprocessor communication, two 2K x 32 pages for communication to the mezzanine processors, and an 8K x 32 page for communication with the application modules.

INITIAL PROGRAM LOADING AND EMULATION

It may be observed from Figs. 1 and 2 that the DSAP consists of a cluster of processor nodes which communicate by means of shared multi-port memory. No hardware is provided to load program directly to the memory from the VMEbus. This architecture, and its attendant great saving in hardware complexity was made feasible by using the emulator port provided on each TMS320C3X device. The emulator port consists of a five wire interface; the clock, serial data out, serial data in, and control bit 0 and 1, and conforms to IEEE 1149.1. This local emulation bus is controlled by means of a local test bus controller (74ACT8990). The TBC is a 16 bit device requiring a 5-bit address and is mapped into the VMEbus in A16 D16 short I/O address space using a dedicated VME slave interface (VME2000). The Emulator Porting Kit (2), is a software package which runs on the host processor and interacts with the user through a series of windows. It provides for downloading and uploading of files, as well as full facilities for program debugging such as reading and writing registers, single stepping, and breakpoints. Since the 68030 is not provided with an emulator port, the TMS320C31 used for VSB DMA/block transfer acts as an emulator interface to the SRAM providing the program IPL function.

MEZZANINE BOARD

Although the mother board contains substantial processing power, in several instances it was not sufficient. To provide processing power on an as-needed basis, and also provide the flexibility of using processors other than the TMS320C3X family for special applications, the majority of processors are located on the mezzanine board. Communication with the mezzanine board is by means of two 2K x 32 memory pages one page each for the odd and even processor clusters. These processors are IPL'd by means of the emulator bus. If a processor other than TMS320C31's where to be used, a single

TMS320C31 would be provided as an IPL port, in the same manner as is used for the 68030.

ERROR HANDLING

As noted above, each block of processor memory is equipped with EDAC. An error occurring in the I/O process area generates an interrupt to the VMEbus by means of the CA91C078. An error in node 0,1 is handled by a routine which resides in internal RAM. The error data is deposited in the dual-port memory, and an interrupt is generated to the I/O controller. The error message is then passed to the system host. Error messages are communicated on the mezzanine bus by means of a serial data link as shown in Fig. 3. A simple packet network scheme has been provided to allow direct interprocessor communication of process control messages. The serial ports are provided on the chip, and implementation of this scheme required only the interconnections between the chips.

HARDWARE IMPLEMENTATION

The DSAP consists of a 6U, 160 mm, single width module. The printed wiring board is 18 layer with 12 signal, 3 power, and 3 ground planes, ~110 mil thick, with reliefs milled into the front side to provide 0.062 inch card guides and to recess the P1 and P2 connectors and the front panel mounts sufficiently to provide 110 mil clearance at the back side. Line width is 5 mil with 5 mil space, vias are blind and through hole and use 30 mil pads and 14 mil drill. The majority of components are SMT with the notable exception of the CA91C078 which is a 299 pin PGA and the processors. All PGA's are mounted on side 1 while SMT's are mounted on both sides. Two 9-pin D connectors are mounted on the front panel for the two RS-232 serial ports. Fourteen front panel LED's display control and status information. The module address is selected by means of two hexadecimal switches (1 of 256). All other control functions are performed by means of the VMEbus slave interface.

ACKNOWLEDGEMENT

The authors wish to express their great appreciation to J. Rubino, J. Boheneck, and C. Neuls of the NSLS electrical drafting group for their expert assistance in the difficult task of placing and routing the printed wiring board employed in the construction of the DSAP module.

REFERENCES

- [1] R. Olsen, J. Dabrowski, J. Murray, "Dipole Power Supply for National Synchrotron Light Source Booster Upgrade IEEE Nuclear Science Symposium, Orlando, FL, Oct. 25-31 1992, p. 572-574.
- [2] Texas Instruments

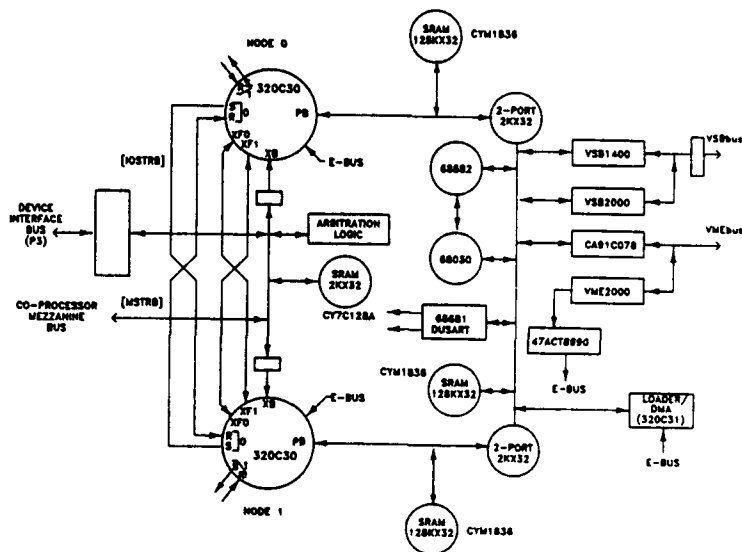


Fig. 1

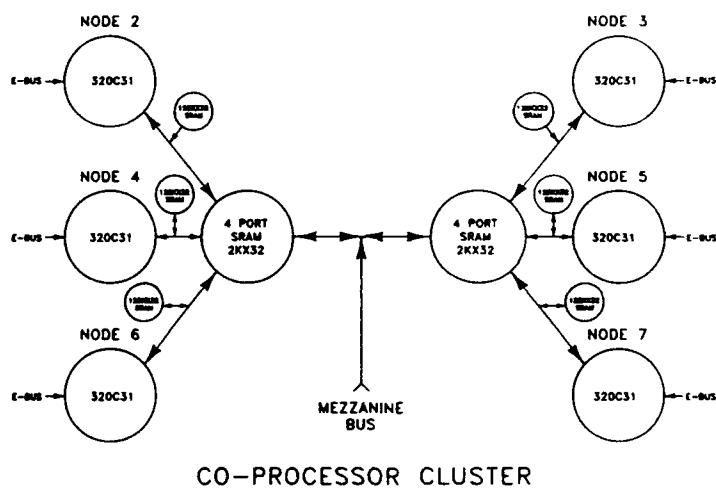


Fig. 2

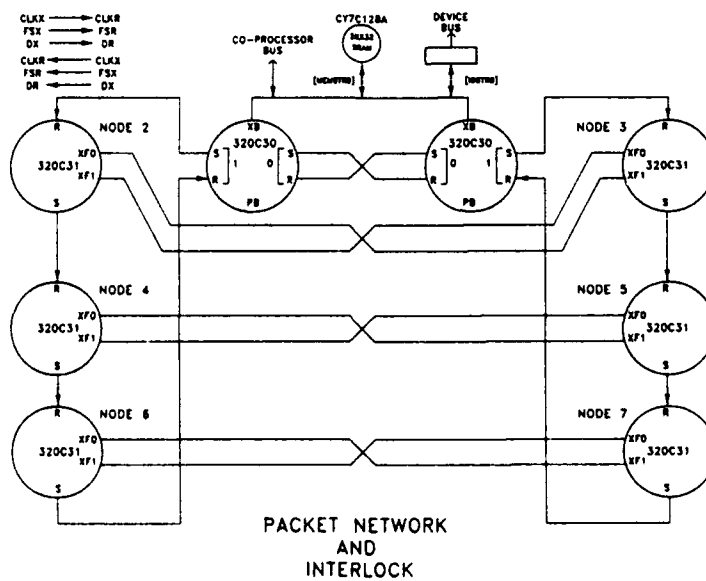


Fig. 3

Control System for NSLS Booster Power Supply Upgrade II*

R. Olsen, J. Dabrowski,
National Synchrotron Light Source, Brookhaven National Lab
Upton, NY 11973 USA

J. Murray
New York State University at Stony Brook,
Stony Brook, NY 11794 USA

Summary

The booster at the NSLS is being upgraded from 0.75 to 2 pulses per second by means of the installation of new dipole, quadrupole, and sextupole power supplies. Here we outline the design of the power supply control system.

INTRODUCTION

Due to the complex nature of the control functions required in these power supplies(1), it was decided early on that the control system would be based on digital signal processing. Since this would produce a system configuration which would be difficult to debug using normal techniques, a design for test philosophy was adopted at the outset. This paper outlines the global design of the control system, and how the test facilities are implemented.

SYSTEM DESIGN

The control system consists of a VMEbus crate which holds the signal processing elements, and one VME crate which holds the gate drivers. The processor crate is equipped with two P1 and one P2 backplanes. The gate driver crate is not provided with either bus, but is wire wrapped. The two crates are connected together by means of a 61 conductor cable. Fig.1 shows the arrangement of circuit packs in the processor crate and the bussing scheme.

The first four slots are reserved for the NSLS control system interface. A remote ramp generator crate receives compressed ramp files, and a local processor converts this to sampled data points which are transferred by means of an optical fiber bus extender to the ramp memory located in the ramp generator. During power supply ramping, this data is read cyclically, and transferred over the VSBbus for processing in the servo. It will be noted that the ramp generator serves as the communication link between the two systems. The ramp generator contains a 2K x 16 page of dual port ram.

*Work performed under the auspices of the U.S. Department of Energy, under contract DE-AC02-76CH00016.

The NSLS control system is able to turn the power supply on or off, and is able to control the ramps by writing into this memory page. The power supply controller passes status information by means of the same memory.

The power supply interlock and status is controlled by means of a PLC. This communicates with the processor on the ramp generator by means of an RS-232 link. The PLC in addition to its interlock functions, monitors the temperature of each transformer in the power supply by means of platinum RTD's buried in the windings. This temperature data is made available to the NSLS control system to allow for fault prediction.

DESIGN FOR TEST

The previous article (2) describes how use is made of the JTAG IEEE 1149.1 test bus for downloading and debugging the processor module. This approach was not used on the application modules. Instead, the more direct means communicating over the VMEbus is used. Each application module has two bus accesses. Real time data is passed over the internal P3 bus, while test data is passed over the VMEbus. Registers which are associated with test functions only appear only on the VMEbus, while data registers appear on both. In this way, for development purposes, the device may be used for real time applications over the VMEbus, and test programs may be run on the host processor and communicate with the module directly, bypassing the necessity of first downloading to a DSP, and then communicating over the internal bus. Since a VME slave may be constructed using six 300 mil DIPs, this is a simple and economical approach.

CIRCUIT PACK TESTING

In order to demonstrate the application of the design for test philosophy, we may consider the trigger generator.

The function of the trigger generator is to provide the 32 gate drive pulse trains required to trigger the thyristors in the power supply(3). This function is accomplished by means of a state machine consisting a number of counters, look-up tables, and decoding logic, driven by a 5.89 MHz clock. The primary test functions provided were the facility to disable the real-time clock, and substitute a clock which is generated

under program control, and the provision of read ports for the values contained in the various entities comprising the state machine. The module is placed in the test mode by setting a bit in the mode control register. Setting a bit in the diagnostic control register disables the real-time clock, while setting an additional bit enables the test simulation clock. Additional control bits allow counters and registers to be reset or loaded with defined values. The default values on power up are for normal operating mode. Debugging during the design process was accomplished by writing a C program which ran on the host PC, and which used function keys to define load/reset functions. Registers were displayed on the terminal in various colors, and in patterns which clearly showed the interrelations. The clock was incremented either by defining the number of pulses, or by single-stepping. In this way, the state machine was initialized to a known state, then single stepped to verify that subsequent states were as predicted. This feature proved its worth by allowing an obscure error in a look-up table to be quickly identified and corrected.

For production and subsequent equipment maintenance, a program will be written which will step through a defined sequence, and compare inputs to outputs. In this way it will be possible to diagnose the majority of errors quickly, and without resorting to test equipment. This may be done without removing the circuit pack from the control bin by simply taking the system off-line, and loading the test program to the host.

SYSTEM TESTING

A failure mode which can cause damage to the power supply during operation is the misfiring of one or more thyristors. This may be caused by insufficient or complete loss of gate drive. This failure will produce high output ripple, and in the case of the dipole supply, will bring the 10 KW filter damping resistor to red heat in very short order. Although the filter current is monitored by an over-current relay, a backup is provided by measuring the gate current and drive voltage in each thyristor, to determine if it falls within prescribed limits. This allows a soft failure to be tracked and corrected before it becomes a hard failure.

This diagnostic capability is achieved by providing a current transformer in each gate drive channel. A multiplexer in the gate driver circuit pack selects the appropriate channel, and transmits the analog signal to the gate driver controller. An A/D converter digitizes the voltage and stores the result in a memory. This memory is read over the VMEbus interface by the host.

In this way, the host may continually monitor the gate drive parameters. The voltage waveform is also made available on a BNC connector so that it may be monitored on an oscilloscope. During commissioning, a test routine allows the selection of thyristors under operator control.

CONCLUSION

The implementation of a control system based on digital signal processing techniques involved a substantial degree of effort. However, it was anticipated that results would be obtained which could not be achieved with an analog system. This has proven to be the case. Initial testing of a prototype of the feed-forward portion of the servo on the old booster dipole power supply (2,4), resulted in a factor of 20 decrease in acquisition time and a factor of 5 increase in tracking accuracy. The feed-forward system is representative of many of the control functions which must be executed in this type of system. Transfer functions of arbitrary complexity may be implemented by cascading simple routines. Many of our filters have been realized by cascading IIR filter sections such as that shown in Fig. 2

REFERENCES

- [1] J. Murray, R. Olsen "Proc. 1992 IEEE Regional Controls Conference, July 24-25, 1992 Polytechnic University of Brooklyn, NY, pp. 85-88.
- [2] R. Olsen, J. Dabrowski, M. Murray "Digital Signal Array Processor for NSLS Booster Power Supply Upgrade," these proceedings.
- [3] R. Olsen, J. Dabrowski, J. Murray, "Control System for NSLS Booster Power Supply Upgrade", Proc. 1992 IEEE Nuclear Science Symposium, Oct. 25-31, pp. 572-574.
- [4] E. Blum, R. Nawrocky, "Tune Measurement in the NSLS Booster Synchrotron.

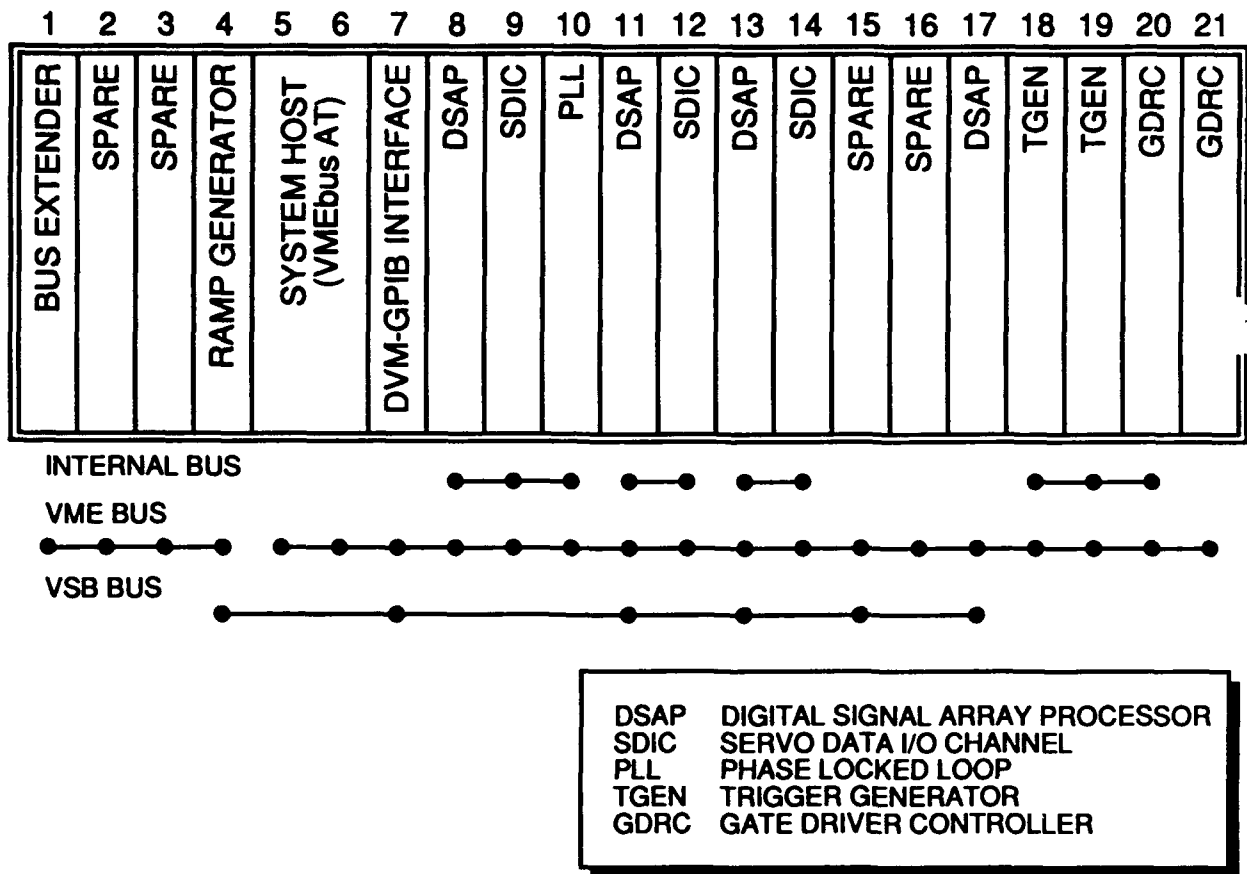


Figure 1. Slot Assignments in Control Crate

```

*
* REGISTERS USED AS INPUT: R2, AR0, AR1, BK
* REGISTERS MODIFIED: R0, R1, R2, AR0, AR1
* REGISTER CONTAINING RESULT: R0
*
* CYCLES: 11          WORDS: 8
*
* FILTER
*
*      .global  IIR1
*
IIR1      MPYF3      *AR0,*AR1,R0
*
*              ; a2 * d(n-2) -> R0
*      MPYF3      *++AR0(1),*AR1--(1)%,R1
*              ; b2 * d(n-2) -> R1
*
*      MPYF3      *++AR0(1),*AR1,R0 ; a1 * d(n-1) -> R0
*      ADDF3      R0,R2,R2          ; a2*d(n-2)+x(n) -> R2
*
*      MPYF3      *++AR0(1),*AR1--(1)%,R0 ; b1 * d(n-1) -> R0
*      ADDF3      R0,R2,R2          ; a1*d(n-1)+a2*d(n-2)+x(n) -> R2
*
*      MPYF3      *++AR0(1),R2,R2 ; b0 * d(n) -> R2
*      STF        R2,*AR1++(1)%
*
*              ; Store d(n) and point to d(n-1).
*
*      ADDF      R0,R2          ; b1*d(n-1)+b0*d(n) -> R2
*      ADDF      R1,R2,R0      ; b2*d(n-2)+b1*d(n-1)+b0*d(n) -> R0
*
* RETURN SEQUENCE
*
* RETS                      ; Return

```

Figure 2.

Software Environment and Configuration for the DSP Controlled NSLS Booster Power Supplies*

R. Olsen, J. Dabrowski
National Synchrotron Light Source, Brookhaven National Laboratory
Upton, New York 11973 USA

J. Murray
SUNY Stony Brook
Stony Brook, New York 11794 USA

Summary

The booster at the NSLS is being upgraded from 0.75 to 2 pulses per second by means of the installation of new dipole, quadrupole, and sextupole power supplies. The control system of these power supplies employs general purpose digital signal processing modules, and therefore, software support is required. This paper outlines the development system configuration, and the software environment.

INTRODUCTION

At the beginning of this project, it was realized that the single largest task would be the writing of the system software. We therefore wished to make the maximum possible use of commercially available software packages. The design process was driven, to a considerable degree, by what software could be purchased. The hardware modules, for example, were designed to have a multiple I/O capability, being equipped with a VME interface in addition to the internal bus(1). In this way, early operation of various sub-systems could be achieved by using equipment on hand, without the necessity of waiting for other system components. A VME format DSP module was purchased to allow for software development, and initially, real time data transfer was done over the VMEbus rather than the VSBbus. Although it did not have enough power to execute more than one task at a time, this processor was, non-the-less an invaluable development tool.

SYSTEM HARDWARE CONFIGURATION

The control system components are mounted in a 21 slot 6U VME crate. The slot functions for the dipole system are allocated as follows(2).

1. interface to NSLS control
2. spare
3. spare

*Work performed under the auspices of the U.S. Department of Energy, under contract DE-AC02-76CH00016.

4. ramp generator
5. |
6. | host processor (PC-386)
7. DVM interface (current feed-back)
8. signal processor 1
9. A/D (60 Hz phase reference)
10. phase locked loop
11. signal processor 2
12. A/D's (supply voltage, filter current)
(100 volt supply)
13. signal processor 3
14. A/D's (supply voltage, filter current)
(1000 volt supply)
15. spare
16. spare
17. signal processor 4
18. trigger generator
19. trigger generator
20. gate driver controller
21. gate driver controller

The partitioning of system functions is shown in Fig. 1. The system host is a VME format PC-386 equipped with VGA and an 80MB SCSI hard drive. A PC was chosen as the system host, since all the development tools are available in a PC version, and they are relatively inexpensive. A 386 processor is more than adequate, since its function is only to download, initialize, and monitor for error interrupts. During normal operation, neither a display nor a keyboard are equipped. On power-up, a .BAT file initializes the downloading sequence of the signal processors and starts program execution.

SYSTEM SOFTWARE CONFIGURATION

The signal processing functions which are performed are, for the most part, filters. Although some of these filters may have many poles, and have very stringent performance requirements, they are all constructed by cascading simple biquads. An example of a single biquad is shown in (9).

For system functions, such as the phase locked loop, which operate at low sampling rates (2-60Hz interrupts), the bulk of the code is written in C, and SPOX(7) is used as the

operating system. This allows us to implement filters simply using system level functions to create arrays for coefficients, data and delay nodes, without having to consider low level detail. Functions which require high sampling rates are generally less complex, and are written in assembler and serviced by a simple interrupt handler. On the DSAP module (3), SPOX is run in node 0 to perform data streaming for module to module data transfers in conjunction with the 68030 I/O controller. Processes which run at high sample rates would generally be relegated to the mezzanine board. In the case of the phase locked loop which has only two discrete functions, the loop program runs in node 0, while node 1 runs a ten pole constant phase filter with a sampling rate of 10 KHz which filters the output of the phase reference A/D converter and conditions the signal to the format required by the phase comparator. In this case, the mezzanine is not equipped.

PROTOTYPING OF FEED FORWARD SYSTEM

The booster dipole power supply employs a feed forward system to improve tracking accuracy(4). This system employs digital data storage and analog signal processing. In order to gain an immediate improvement in booster performance, it was decided that a prototype of the digital feed forward block which had been developed(5) for this project would be constructed and installed on the old power supply. To accomplish this, we made use of the fact that the SDIC (servo data I/O channel) had a VME interface in addition to the internal bus, and also that a D/A converter had been provided for test purposes. A transition module was constructed to take the place of the old feed forward module in the regulator NIM bin. This module supplies the start of cycle strobe, clock, and error signal, and receives the feed forward correction voltage which is summed into the analog voltage feed back loop.

An adjacent VME crate holds a VME AT, a purchased DSP module with a VME interface, and an SDIC. The control program was written in C, and runs at an interrupt rate of 720 Hz. Initialization is as described above. This system resulted in a factor of 20 decrease in acquisition time, and a factor of 5 increase in tracking accuracy.

Measurements(6) indicate a improvement in booster tune, and we now observe a considerable improvement in pulse to pulse stability as well as increased booster current.

DEBUG ENVIRONMENT

The system host PC is provided with compilers for the 80386, 68030, and TMS320C3X processors. In this way, an application program may be written in C and compiled to run on any of the three processors. Programs are written to be bus independent, and a bus specific driver is written for each processor type as required.

The first level of debugging was related to hardware in application modules such as the trigger generator and servo data I/O. This was accomplished by writing test programs in C and running them on the PC. Liberal use of color in the displays greatly facilitated the development effort. These programs read and write registers, and in addition to providing application specific functions, could be made to loop in order to facilitate trouble shooting with test instruments.

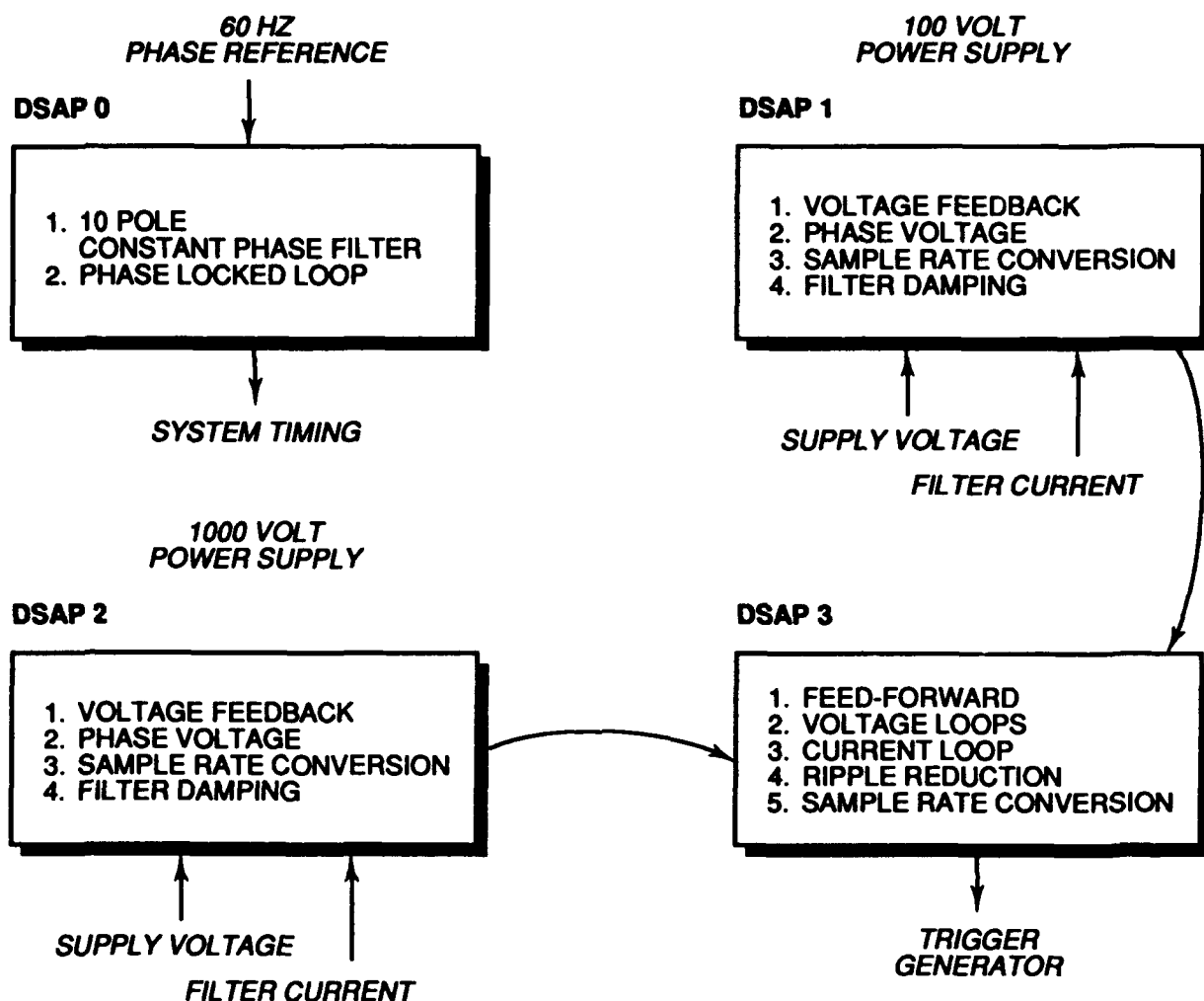
At the second level, an application was written and run on the purchased DSP module. This communicated with the application directly over the VMEbus, or through an adapter module which mapped VME A16 D16 to the A32 D32 of the P3 internal bus. In this way, a program could be run on a TMS320C30 with a VME interface, then by changing the driver, transferred to a DSAP module where communication takes place over an internal module to module bus or the VSBbus.

The third level of debugging is that of the DSAP module. This debug facility was designed around two commercially available products. The TMS320C3X system is designed around the Emulator Porting Kit(7) and is described in (3). The 68030 system consists of a monitor which is resident in SRAM, and a debug controller which runs on a PC-386. The two systems communicate over a serial port. The monitor is down loaded to SRAM by means of the TMS320C31 loader/DMA on the 68030 bus(3). In the case of the DSAP, the EPK runs on the system host, while the 68030 debugger runs on a stand alone PC. In this way, the 68030 I/O processor and a DSP node may, for instance, be single stepped simultaneously, to check message passing between the two processors. Both systems provide extensive window based facilities which allow manipulation of memory and processor registers.

OPERATING ENVIRONMENT

During normal operation, all process initialization is done via the test bus controller/emulator bus. In this instance, we invoke not the EPK, but a program whose only function is to load executable files to a given starting address. The system load resides on a hard disk, but we envisage converting to a WORM drive before the equipment is placed in permanent service. The hard drive will be retained for further development work and to trap errors as required, but would be powered down when not in use.

Since each DSAP module is equipped with a test bus controller IC, system problems may be resolved by using the on-board emulation rather than resorting to external test equipment.



SYSTEM SOFTWARE CONFIGURATION

Fig. 1

REFERENCES

- [1] R. Olsen, J. Dabrowski, J. Murray "Control System for NSLS Booster Power Supply Upgrade" these proceedings.
- [2] For an outline of each module function see R. Olsen, J. Dabrowski, J. Murray, "Dipole Power Supply for National Synchrotron Light Source Booster Upgrade" 1992 IEEE Nuclear Science Symposium Conference Record, p. 572.
- [3] R. Olsen, J. Dabrowski, J. Murray, "Digital Signal Array Processor for NSLS Booster Power Supply Upgrade" these proceedings.
- [4] B. B. Culwick, R. E. Olsen, "Application of a Digital Trigger Generator to NSLS Booster and Storage Ring Power Supplies; Proceedings, 1983 Particle Accelerator Conference, IEEE Transactions on Nuclear Science.
- [5] J. Murray, R. Olsen, "A Differential - Decay Control for Ramped Magnet Current" Proc. 1992 IEEE Regional Controls Conference, Polytechnic University of Brooklyn, NY, pp. 85-88.
- [6] E. Blum, R. Nawrocky, "Tune Measurement in the NSLS Booster Synchrotron" these proceedings.
- [7] Spectron Microsystems.
- [8] Texas Instruments
- [9] TMS320C3X User Guide pp. 11-56

Control Units for APS Power Supplies*

O.D. Despe, C. Saunders, D. G. McGhee
Argonne National Laboratory, Argonne, Illinois 60439

Abstract

The Advanced Photon Source (APS) accelerator facility is made up of five major subsystems in addition to the linac: the positron accumulator ring (PAR), low energy transport (LET), booster synchrotron (SYNCH), high energy transport (HET), and the storage ring (SR). Each subsystem has multiple magnet and power supply combinations, some requiring multiple modes of operation. These magnet and power supply combinations are computer controlled and monitored. The power supply control unit (PSCU) is the first layer of hardware and software directly above the power supply itself and is described in this paper. The description includes the basic philosophy for each mode of operation and how it influences the topology and means of implementing control. The design of the analog reference blocks (ARBs) influenced the design of other custom functions as well as the feedback controls for vibration and other dynamic corrections. The command set supported by the PSCU is discussed.

I. INTRODUCTION

Four basic ideas form the control philosophy that determined the design of the power supply control unit (PSCU): 1) buy commercial rather than build, 2) use optical/fiber transmission for digital signals, 3) use differential twisted shielded pairs for short off-card analog transmission, and 4) control analog reference via pulses to an UP/DN counter feeding the reference digital-to-analog converter (DAC) to improve noise rejection. The PSCU is the first layer of hardware and software above the power supply itself. A typical rack with eight power supplies is controlled by one PSCU. Each PSCU is connected to the host computer via a two-tiered local area network (LAN) (see Figure 1).

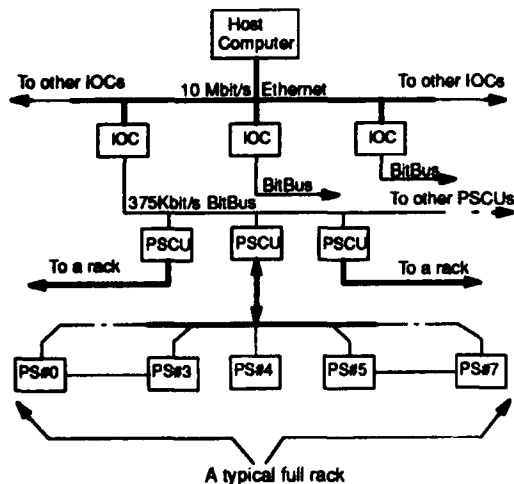


Figure 1. APS Control Hierarchy

* Work supported by the U.S. Department of Energy, Office of Basic Energy Sciences under Contract No. W-31-109-ENG-38.

The host computer is connected via a 10-Mbit/sec Ethernet LAN to VME-based Input/Output Controllers (IOCs) distributed around the accelerator facility. The IOCs are connected to the PSCUs and other field instruments by a 375-Kbit/s master-slave BitBus network. Each PSCU is connected to the power supplies it controls via custom cabling. The Ethernet and BitBus networks are implemented with optical fibers. All digital signals from and to the PSCU are optically coupled to improve noise immunity. To reduce the number of cables between the PSCU and the controlled power supplies, serial transmission of digital signals is used. Analog signals with 10-bit or less resolution are transmitted and received differentially using twisted pairs. A key function block is the analog reference block (ARB) located in the remote DAC/ADC board (see Figure 2). This design results from implementation of the fourth idea of the control philosophy, i.e. analog reference should change only as a result of counting UP/DN pulses to assure smooth changes in the reference voltage.

1.1 Hardware

The PSCU is a 680xx microprocessor-based system housed in a 16-slot Eurocard chassis using a G-6-64/G-96 compatible bus. A 250-watt, built-in power supply provides ± 12 V and +5 V power to the chassis. The compatible cards (commercially produced by GESPAC Inc. [1] of Mesa, AZ and custom-made (see *) by ANL) for a typical full rack configuration are:

Items	# of Cards
CPUCard with memory	1
BitBus Adapter	1
Differential input analog card	2 (32)
Opto Coupled digital In	2 (64)
Opto Coupled digital out	2 (64)
16-bit timer card *	2 (4)
Arbitrary Fnc Gen (AFG) *	2 (4)
ADC/DAC Intf *	1 (8)

1.10 CPU Cards (GESSBS6-A, Gesmpu-30H)

The booster synchrotron has four types of dynamic supplies, namely: dipole, quadrupole, sextupole, and correction supplies. A MC68030 25-MHz CPU board Gesmpu-30H is used for these. All other supplies use an MC68000 16-MHz CPU board Gessbs6-A.

1.11 BitBus Adapter

This card is the interface to the 375-Kbit/s network between the IOCs and all PSCUs. This master/slave network implementation was chosen for its simplicity but with a standard communication protocol (transparent error correction).

1.12 Differential ADC (GESADC-3)

This unit provides 16 analog channels with differential inputs. It is built around an Analog Devices AD576 (12-bit ADC)

and a unity gain, high voltage, common mode instrumentation amplifier (Burr Brown INA117). Its conversion time is 35 μ s.

1.13 Digital Inputs (GESINP-2A)

Thirty-two optically coupled digital signals are connected to this unit via two 26-pin connectors. The nominal input level required is 12 volts for a HIGH and 0 volt for a LOW. Isolation is rated at 1500 V.

1.14 Digital Outputs (GESOUT-3A)

Thirty-two optically coupled digital signals are output from this unit via two 26-pin connectors. It has a power-on reset only. Resetting the CPU board will not affect its output states. The open collector output lines can drive up to 100 mA. The voltage rating of the output transistor is 24 V. Isolation is rated at 1500 V.

1.15 Timer Card (Custom)

Two 9513 counter chips together with an 8-bit digital I/O for control and monitoring are provided. This card generates a programmed number of pulses for four power supplies. The power supplies can be programmed individually, generating the pulses upon receiving the software command (SyncMode=0), or as a group, waiting for an external trigger (SyncMode=1) before delivering the pulses. This card also provides the two quadrature clock pulse trains used by the pulse width modulated (PWM) chopper supplies. Its output consists of differential line drivers for optical couplers to provide isolation and reduced interference pickup.

1.16 ADC/DAC Interface (Custom)

This unit accepts pulse train input from up to eight remote ADCs/DACs. This allows the monitoring of analog signals of higher precision than that provided by the GESADC-3 described earlier, such as transducer or shunt signal. It enables the readback of the reference DAC's digital input. This card also allows selection of the control source for the DAC's input from the PSCU or some other external source (such as the Diagnostics group).

1.17 Arbitrary Function Generator (Custom)

The design of this arbitrary function generator (AFG) card is based on the design described in a paper published in the 1991 PAC Proceedings entitled "Arbitrary function generator for APS injector synchrotron correction magnets," [2]. The design is constrained by the way the analog reference block works. The idea is to control gating of the UP/DN pulses to the DAC counter in order to direct the analog output of the DAC to follow the desired function. The information that determines if a pulse is allowed to reach the UP/DN counter as well as the direction (up/dn) information is stored in a first-in-first-out (FIFO) memory of the appropriate depth.

It is worth mentioning that only two bits of information are needed to encode a point in the waveform for any DAC resolution compared to a full n-bit requirement for the conventional AFG design. As a consequence, the standard 9-bit FIFO can store information for four channels. This card is used to generate the reference analog voltage required by the dynamic supplies of the injector synchrotron.

1.2 Software Modules

The embedded application software that runs in the PSCU is a multi-tasking program written in the C language under Microware's OS-9 operating system. The modules that make up the application are the **main**, **my_defs.h**, **pscu_9513.h**, **shmem.h**, **rs232**, and **bitbus** modules. These modules, when compiled and linked together, produce the executable code burned into the application EPROMs.

1.20 main This module initializes the hardware and software states of the PSCU. It creates the shared data block **shmem** and also forks (creates) the two tasks **rs232** and **bitbus**.

1.21 my_defs.h This module contains defined constants global to the program, such as board ID numbers, control port, and data port addresses for all cards in the PSCU.

1.22 pscu_9513.h Constants for programming master registers as well as counter mode registers for all timers are contained in this module.

1.23 shmem.h This is the data module created by **main** as part of program startup. It is a global module.

1.24 rs232 and bitbus These are the two tasks that support the full operation of the PSCU. The **rs232** module supports the use of RS232-C for local control of the PSCU after local control is granted by the host while **bitbus** is intended for normal operation.

1.3 Command Set

All commands are associated with a power supply number. The standard command syntax of a PSCU command is: **command** <power supply #> <argument0 argument1 ...argumentn>. Below is a partial listing of the commands.

table {
rampto	<ps> <value>	Ramp <ps> to <value> where <value> is a decimal integer (i.e. 9000).
setrate	<ps> <ramprate>	Set ramp rate divider of <ps> to <ramprate> where <ramprate> is an integer
setbyte	<ps> <hexval>	Set control byte of <ps> to <hexval> where <hexval> is a hex byte (i.e. 8f).
getsb	<ps>	Print hex byte content of input port.
showstate	<ps>	Print summary of <ps> database contents.
calibrate	<ps>	Calibrate precision ADC of <ps>.
getrb	<ps> <rb>	Perform A/D conversion and print result in hex format where <ps> is 0-7 (-1 means all), <rb> is 0-4 (-1 means all). 0 means precision ADC (5 chars printed), 1-4 means 12bit ADC (4 chars printed).
getdac	<ps>	Print hex value of hardware DAC input.
setaf	<ps> <npts> <time value pairs>	Set arbitrary function for <ps> with <npts>

time value pairs. <time value pairs> are the data points to specify.

setbias <ps> <bias>

Set arbitrary function for <ps> to <bias> bias value.

II. GENERAL OPERATION

Figure 2 shows the typical magnet power supply control chain that starts from the VAX or SUN host, to the IOC, to the power supply control unit, down to the regulator and signal conditioning block. The PSCU communicates to each power supply using optically coupled digital signals and differential shielded twisted pairs for analog signal transmission.

The BitBus command packet transmitted to the PSCU contains the node address (rack number), the command code, power supply number ID, and the required parameter bytes appropriate for the command as well as the bytes required for the host communication protocol. The node address selects one of the 221 cabinet racks on top of the storage ring tunnel. Each rack has one PSCU that handles the operation and monitoring of six to eight magnet/power supply pairs.

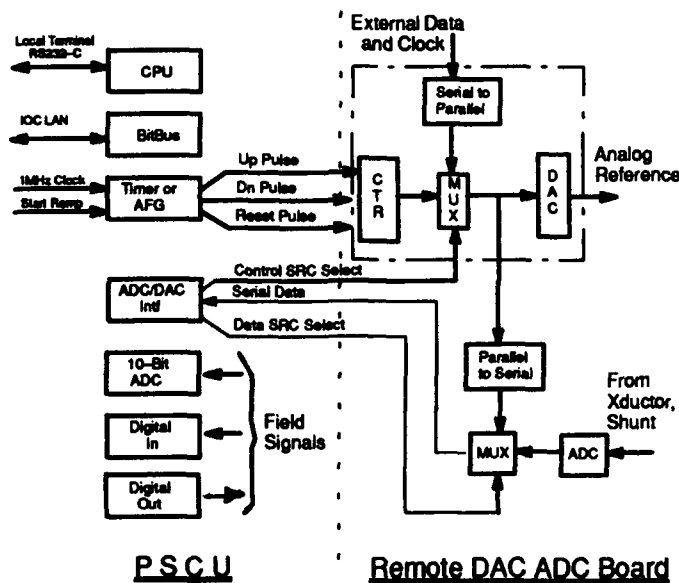


Figure 2. Signals between PSCU and a Typical Power Supply

When a command is received from the host via the LAN, the PSCU receives an interrupt from the communication hardware. The message is sent according to a specific format, decoded into its various components (command, power supply #, and appropriate parameter values), and used by the embedded PSCU software to execute the command. All commands received are compared to a table of commands supported by the particular PSCU; an invalid command results in a null operation.

III. CONCLUSION

The control unit designed for the APS power supplies tried to follow the control philosophy outlined: buy rather than build, use optical/fiber coupling for digital signal transmissions and differential twisted shielded pairs for short off-card analog transmission, and control analog reference via UP/DN pulses to a counter feeding the reference DAC. For certain functions, the desired features can only be supplied by custom design as in the cases of the Timer card, ADC/DAC interface card, and the AFG card. However, custom design has allowed the use of dense, electrically programmable logic devices (EPLD) [3] that has resulted in reduced component counts which should, in turn, improve overall system reliability.

IV. REFERENCES

- [1] GESPAC, Inc. 1987 G-64/G-96 Data Book Interfaces.
- [2] O. D. Despe, "Arbitrary Function Generator for APS Injector Synchrotron Correction Magnets," 1991 IEEE Particle Accelerator Conference Proceedings, Vol. 3, p. 1461, 1991.
- [3] Altera Corporation, 1990 Data Book.

High Resolution ADC Interface to Main Magnet Power Supply at the NSLS*

Mordechai Bordoley
NSLS Department, Brookhaven National laboratory
Upton, NY 11973

Abstract

Previous readings of DCCT were limited to 11 bits of resolution with large offsets and drifts, providing inaccurate data. The current design overcomes this limitation by using Analog Device's AD7703 20 bit serial output ADC to digitize the main magnet DCCT at the power supply, and transmit the data serially at 2KHz over to the VME controller.

I. INTRODUCTION

The new system was designed to interface seven main magnet power supply DCCT's for the X-ray ring, and eight power supplies for the VUV ring with their respective VME controllers. To prevent disturbance of the power supplies, each with its own carefully balanced isolated DC supply, any signal leaving the power supply must be isolated. In addition, the distance between the analog signal source and the VME must be kept to a minimum.

The new approach satisfies the above criteria by digitizing the DCCT analog signal at the power supply and transmitting the digitized signal serially via an opto-isolator. On the VME side the received signal passes through additional opto-isolators and the serial data is converted to a parallel format. This method achieves isolation from the power supply source, high noise immunity of the transmitted signal, and insensitivity to cable length. It requires only a few wires for transmission, and eliminates ground loop noise in the VME.

II. DIGITIZER

The main components of the digitizer are the input instrumentation Amplifier (AD620), a precision reference (LT1019-2.5) and a 20 bit sigma delta ADC (AD7703). The ADC is a sigma delta converter which has a built-in 6 pole low pass gaussian filter. The cut-off frequency is a function of the ADC crystal clock input. With a 2Mhz clock, the cut-off is set to 5 Hz and the rejection at 60 Hz is 90dB. The output of the ADC is in serial format: clock signal, data signal and a ready signal. This format interfaces directly with shift registers without additional hardware. In the circuit these outputs are first opto-isolated, then buffered through a differential line driver. Figure 1 shows the block diagram of the digitizer box.

The ADC can be self-calibrated by raising an input bit. The self calibration procedure measures the ground potential and the reference level, and recalculates the gain coefficient which is stored in the ADC. The ADC is configured to operate continuously, with a transmission rate of 2KHz.

In the implementation of the circuit, high precision resistors with low temperature coefficients were used to set the gains. No potentiometers were used, thus rendering the circuit very stable. Each channel was calibrated and the slight offset and gain were corrected in the VME software. Calibration is effected by injecting a precise voltage source to the ADC inputs and modifying the coefficient in the computer data base to correct for any errors.

III. VME BOARD

Each VME board accepts 4 individual channels, where each signal first passes through an

*Work performed under the auspices of the U.S. Department of Energy.

AD620

OP077

AD7703
20 BITS
ADC

LT1019
-2.5

VREF.

CLOCK

DATA

READY

INPUT
0-10V

ANALOG
IN

OFFSET
FILTER
AMP.

CALIBRATE
IN.

HCPL-2231
OPTO-ISOLATOR

CAL

TO VME CRATE

LINE
DRIVER

BUFFER

IV. RESULTS

The graph displays the ADC voltage output over 300 samples at a 3Hz rate. The y-axis, labeled 'ADC voltage out', ranges from 4.99992 to 4.99998. The x-axis, labeled 'Samples # (@ 3Hz rate)', ranges from 0 to 300. The data points are connected by a line, showing a noisy signal that fluctuates around a mean value of approximately 4.99995. The noise is characterized by sharp, frequent spikes and dips, with the signal staying mostly within the range of 4.99994 to 4.99997.

V. CONCLUSION

1868

Design of the Advanced Light Source Timing System*

M. Fahmie

Lawrence Berkeley Laboratory, University of California
1 Cyclotron Road, Berkeley, CA 94720 USA

Abstract

The Advanced Light Source (ALS)[1] is a third generation synchrotron radiation facility, and as such, has several unique timing requirements. Arbitrary Storage Ring filling patterns and high single bunch purity requirements demand a highly stable, low jitter timing system with the flexibility to reconfigure on a pulse-to-pulse basis. This modular system utilizes a highly linear Gauss Clock with "on the fly" programmable setpoints to track a free-running Booster ramping magnet and provides digitally programmable sequencing and delay for Electron Gun, Linac, Booster Ring, and Storage Ring RF, Pulsed Magnet, and Instrumentation systems. It has proven itself over the last year of accelerator operation to be reliable and rock solid.

I. INTRODUCTION

ALS consists of an Electron Gun with a gated 125 MHz repetition rate. The gun injects into a 3 GHz 50 MeV Linac providing acceleration to the injection energy of the 500 MHz Booster Synchrotron. A Peaking Strip and Gauss Clock track the slope of the Booster Bend Magnet ramp, providing field-derived triggers for the various injection systems.

The 1 Hz Injection/Booster system allows up to twelve 500 MHz buckets to be bunched, accelerated and stored each cycle. When extracting beam from the Booster, an array of fast pulsed magnets are individually triggered by programmable digital timers, referenced to the Gauss Clock, so that their extraction fields coincide with the arrival of beam.

The timing system features a very flexible Storage Ring loading scheme that targets accelerated bunches into Storage Ring buckets as defined by a spreadsheet-based control program. The targeted buckets can be re-targeted on a cycle-to-cycle basis, and can be loaded into any combination of Storage Ring buckets and in any order.

II. HARDWARE

We use Eurocard 3U modules for most of our low level construction. We found no difficulty passing high speed logic signals across the 96-pin DIN connector using adjacent pins and differential format. One double rack was reserved for timing system components, of which 40% is available for future development.

Test points are brought to SMA connectors on the front panel and are individually buffered. ECL signals leaving a module are always differential and routed in twisted pairs.

To control temperature rise, each module was limited to four watts dissipation. No blowers are used, so cooling is entirely by conduction & convection.

*This work was supported by the Director, Office of Energy Research, Office of Basic Energy Sciences, Materials Sciences Division, of the U.S. Department of Energy under Contract No. DE-AC03-76SF00098.

III. LOGIC FAMILY SELECTION

An early problem was the choice of a logic family. The timing system frequently uses 500 MHz clock frequencies, and even when lower frequencies are used, preservation of edge resolution is crucial. Conventional TTL logic is totally incapable of performing in this area; even conventional ECL logic is pushed beyond its capabilities. Gallium Arsenide logic was available, but costs were quite high. A variant of ECL called ECLiPS (ECL in PicoSeconds)[2] was introduced by Motorola that fit our needs. ECLiPS handles speeds almost three times as high as conventional ECL and dissipates half the power. It uses conventional ECL logic levels and is packaged in a 28-pin PLCC surface mount package.

IV. PC BOARD DESIGN

Due to the very high edge speeds (300 ps) of ECLiPS, the printed circuit layout must follow guidelines similar to UHF RF designs[3]. All signal lines are configured as 50 Ohm strip lines or microstrip lines and are terminated at their destinations. Low impedance ground planes and power planes help maintain good noise margins. A four-layer board with one signal plane was adopted for simple designs and a six-layer board with two signal planes is used for more complex layouts.

FR-4, a glass epoxy based substrate, was chosen for economy. The dielectric constant is not tightly controlled, but is quite adequate for this service. True "RF grade" substrates tend to have high dielectric constants, which increase the propagation delays, and are significantly more costly.

V. CONTROL SYSTEM

The control system in use at the Advanced Light Source is based on a custom-designed controller, the ILC (Intelligent Local Controller) [4, 5]. An ILC is installed in each timing system bin that requires real-time external control. Timing system modules are designed with addressable registers so that they can be programmed from an ILC 8 bit I/O port. Addressing is done via a second 8 bit port and up to 16 four byte registers can be serviced by a single ILC.

VI. TIMING SCHEME

Timing for the ALS is based on three epochs. These separate epochs are necessary because the Booster Bend Magnet is driven by an unregulated voltage. Current (and field) will rise at the L/R time constant (0.71 sec.) of the magnet.

Epoch 1 is driven by a line sync'd clock at the Booster rep-rate, nominally 1 Hz. Its function is little more than "Phasing On" the Booster Bend Magnet power supply, and some long lead-time, low criticality systems.

Epoch 2 is defined by the Bend Magnet reaching the field strength necessary to bend the injected 50 MeV electrons around the Booster Ring. This point is determined by measurement of the magnetic field with the Gauss Clock system. Epoch 2 is the basis of timing for the Electron Gun, Linac, and Booster Injection Kicker.

Epoch 3 is defined by the Bend Magnet reaching the field strength consistent with the desired final booster energy, nominally 1.24 Tesla @ 1.5 GeV. The Gauss Clock system, again, provides the signal. Epoch 3 is the basis of timing for extraction from the Booster and injection into the Storage Ring, including kickers, septum, and bump magnets. The Booster Bend Magnet ramp is terminated several milliseconds after Epoch 3.

VII. CLOCKS

There are 4 clocks utilized in the timing system, all but one (line sync) are derived from the 500 MHz (499.654 MHz to be precise) RF Master Oscillator:

60 Hz - Derived from power line, used to establish basic repetition rate of the machine.

Booster Ring Orbit Clock (BROC) - 4 MHz (500 MHz/125), 250 ns. This is the period of one revolution of an electron in the Booster Ring.

Storage Ring Orbit Clock (SROC) - 1.523 MHz (500 MHz/328), 657 ns. This is the period of one revolution of an electron in the Storage Ring.

Coincidence Clock (COIC) - 12.19 KHz (500 MHz/(125*328)), 82 us. Marks the beginning of the pseudorandom intersection pattern of the Booster and Storage Ring Buckets. More on this later.

VIII. GAUSS CLOCK SYSTEM

Booster Ring injection and extraction timing are primarily dependent upon the field in the Booster Bend Magnet. The magnet power supply is turned on at the beginning of each Booster cycle (Epoch #1) and the current is allowed to ramp up on the magnets' L/R time constant. It is not possible to predict, with the required accuracy, just when the field will be proper, because the power supply voltage is unregulated and residual magnetism is left in the magnet core. The Gauss Clock system provides real-time magnetic field tracking and a set of programmable trip points, which can be set in absolute Gauss via an ILC.

The timing system is composed of:

Peaking Strip—A RF-excited sensing coil array[6] wound on a Permalloy strip is used to detect when the Bend Magnet field reaches 100 Gauss.

Pickup Coil—A one-turn shielded loop wound around the pole of one of the 24 series-connected Bend magnets. The voltage induced into the loop is directly proportional to the rate of rise of the magnets field.

Voltage to Frequency Converter—An amplifier and highly linear Quartz controlled V/F converter convert the loop voltage to a logic compatible pulse rate in the 1 to 2 MHz range.

Programmable Counter Modules—24 bit programmable downcounters that, when preset by the ILC, will output a pulse when the downcount reaches zero.

At magnet turn-on time, there exists some unknown residual field in the magnet core; this field adds to the field induced by the now-ramping magnet current. When this sum is sufficient to counteract a bias field set up in the peaking strip, an inversion of the magnetization in the Permalloy strip occurs. A short output signal results. The bias field is set so that this inversion occurs at about 100 gauss.

When the Peaking Strip signals that the Bend Magnet field has crossed 100 Gauss, the Counter modules begin counting the output of the V/F converter. The counters are, in fact, integrating the rate of rise, and the count, at any instant, is proportional to the absolute field (less the 100 Gauss starting point). A bank of these counters, each preset to look for its dedicated field intensity, count in parallel, providing triggers for injection, extraction, Booster Bump magnet triggering, and instrumentation. One counter provides a burst of 100 equi-gauss spaced sampling pulses used to control tracking of focusing and corrector magnets with the Booster Bend magnet.

IX. INJECTION LINE TIMING

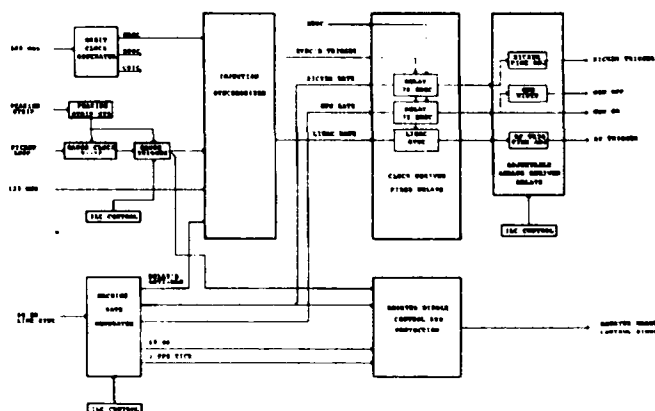
The Injection system must produce gated bursts of electron bunches at a 125 MHz rate. The bursts may contain one to twelve bunches, and will nominally occur at one burst per second. The bunch width is nominally two nanoseconds.

Burst gate timing is dependent on:

1. Desired repetition rate.
2. Booster Bend Magnet attaining injection field.
3. Phase of Booster Ring Orbit Clock (BROC).
4. Phase of 125 MHz RF signal.

The last two dependencies exist so that an electron burst, when steered into the Booster, will always begin in bucket #1 (thus greatly simplifying the task of timing for transfer into a selected bucket in the Storage Ring). When all four conditions are met, a synchronized trigger results. This is Epoch 2. This trigger will fire the Electron Gun[7], start the RF system, and trigger the Injection Kicker magnet so that the beam arrives just as the Kicker reaches its flattop region. The Buncher and Linac RF system is triggered about 16.5 us prior to beam arrival at the Buncher. Its timing system[8] generates the individual gates for RF system components.

Booster Injection Timing



Each of these functions must have versions of the Epoch 2 trigger to compensate for pre-trigger requirements and electron time of flight. The gross delays are achieved by digital countdown of the BROCC period while fine adjustment delays are done with an Analog Devices AD-9500 very fast analog timer chip.

X. TARGETING THE STORAGE RING

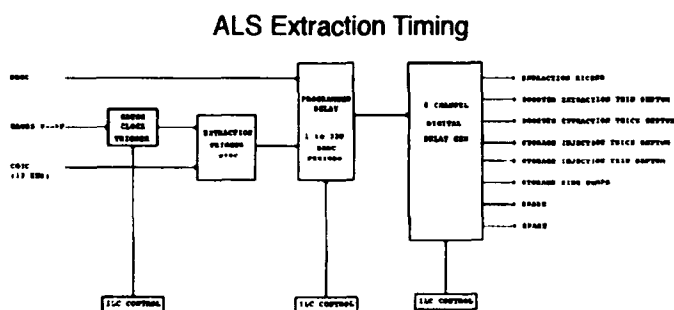
Imagine, for a moment, the Booster and Storage rings as a pair of intersecting mechanical gears. The Booster gear has 125 teeth, corresponding to its 125 beam buckets, and the Storage gear has 328 valleys. Now paint the current intersection of the Booster tooth and Storage valley white, this will mark bucket #1 of each ring.

Each time the Booster gear revolves, tooth #1 will intersect a different Storage gear valley, 1, 126, 251, 48, 173, etc., each valley is offset 125 from the last. This series continues un repeating until Booster tooth #1 has met all 328 Storage gear valleys (328 Booster revolutions). This is the period of the COIC clock.

Discarding the gear analogy, you see that once Booster Ring beam has reached the desired energy, it can be injected into any Storage Ring bucket simply by delaying injection by "n" BROCC periods from COIC. "n" is derived from an equation which is a function of the target bucket number (1-328). A programmable up counter is loaded by the ILC with 2's complement of "n."

$$n = (21 \times t) \text{ modulus } 328$$

where "r" is the target bucket in the Storage Ring and "n" is the required number of Booster Ring revolutions after COIC necessary to line up the Booster beam with the target bucket.



Storage Ring loading requirements mandate an agile control scheme. Accelerated beam will be placed into Storage Ring orbit at positional offsets (buckets) that may vary from pulse to pulse. An "Intelligent Local Controller" (ILC) is dedicated to controlling this process and is provided with a 1 Hz (Epoch 1) interrupt to insure lockstep with Booster cycles.

A Storage Ring loading pattern table is downloaded to the ILC from an EXCEL spreadsheet application. This table has an entry for each Booster cycle, and may include;

- A. Target Bucket number.
- B. Beam Dump trigger.
- C. Idle Mode command.
- D. Flow commands such as START, STOP, PAUSE, REPEAT, etc.

The ILC interrupt steps the table to the next entry and sends appropriate commands to the hardware.

The loading table is prepared off-line and stored on disk; the operator simply chooses a table from the list and tells the Accelerator Control system to load and start it. The table will execute until it encounters a Stop command or is manually terminated.

XI. ACKNOWLEDGMENTS

The author would like to acknowledge the valuable assistance of:

Dr. Radloff (DESY) and his assistant Mr. Burfeindt for sharing their adaptation of the Peaking Strip developed from the work K. Endo and H. Sasaki (University of Tokyo), and C.C. Lo (LBL) who further adapted it for use in ALS.

J. Zelter (LBL) for the lesson in the use of the Euclidian Algorithm, allowing me to better understand the target bucket equation which I derived empirically.

S. Magyary (LBL) and J. Zelter (LBL) for their work creating the software that exercises my hardware.

Allen Geyer (LBL), without whose help it would all be just a drawer full of drawings!

XII. REFERENCES

- [1] "1-2 GeV Synchrotron Radiation Source Conceptual Design Report," Lawrence Berkeley Laboratory, Pub 5172, July 1986. (Available from Lawrence Berkeley Laboratory, 1 Cyclotron Rd., Berkeley, CA 94720).
- [2] Motorola, Inc., "ECLiPS Databook," DL-140, Rev. 1.
- [3] Motorola, Inc., "MECL System Design Handbook," HB-205, Rev 1.
- [4] S. Magyary, et al, "Advanced Light Source Control System," IEEE Particle Accelerator Conference, March 1989.
- [5] S. Magyary, "Anatomy of a Control System: a System Designers View," to be presented in this conference.
- [6] K. Endo, H. Sasaki, "A Modified Peaking Strip Method for Measurements of Slowly Varying Low Field," Report SJC-A-70-5 Institute for Nuclear Study, University of Tokyo.
- [7] C. C. Lo, "The ALS Gun Electronics System," to be presented in this conference.
- [8] C. C. Lo, "Low Power RF System for ALS Linac," IEEE Particle Accelerator Conference, May 1987.

Ring Diagnostics and Consistency Test of the Model for the AGS Booster*

Alfredo Luccio and Elliot H. Auerbach
AGS Dept., Brookhaven National Laboratory
Upton, NY 11973

Abstract

From a systematic analysis of readings of the beam position monitors in the AGS Booster ring, combined with the transfer matrices between a few locations in the ring, calculated with MAD [1], the consistency of the model of the lattice has been tested. This technique has enabled us to (i) detect errors in the machine that subsequent survey during shutdown has confirmed, and (ii) to measure the actual circulating beam momentum offset. The method has proved rather general and convenient for accelerator diagnostics as part of a model-based accelerator control system and extensions are suggested.

I. INTRODUCTION

We had two motivations for this work. The first was specific: to find the displacement of the closed orbit and its angle and the momentum offset of the beam in the AGS Booster in order to calculate correct orbit bumps for injection, extraction and so on. The second was general: to set up a model based [2] algorithmic tool to search systematically for errors in the machine lattice and to check the agreement between the real machine and the model. For this, we have used the orbit data, that is, the values of the orbit displacement at each of the 22 orbit position monitors in the ring. In this work we have considered the effect of orbit measurement errors only as "noise". Indeed, the purpose of the present paper, for lack of space, is mainly to show the principles of operation of the tool and to describe a few examples of application to the AGS Booster.

II. THEORETICAL BASIS

Consider three beam position monitors, or BPM's: i, j, k . Here, beam position readings are

$$(x_i, x_j, x_k). \quad (1)$$

At BPM locations, the model (MAD) gives dispersions and their derivatives

$$(\eta_i, \eta_j, \eta_k); (\eta'_i, \eta'_j, \eta'_k). \quad (2)$$

The transfer between BPM- i and BPM- j is described by

$$\begin{bmatrix} x \\ x' \end{bmatrix} - \frac{\delta p}{p} \begin{bmatrix} \eta \\ \eta' \end{bmatrix} = \mathbf{M}^{(i,j)} \begin{bmatrix} x \\ x' \end{bmatrix} - \frac{\delta p}{p} \begin{bmatrix} \eta \\ \eta' \end{bmatrix}, \quad (3)$$

with the (unknown) momentum offset of the beam $\delta p/p$,

and transfer matrices between BPM's, whose elements are expressed in terms of the machine's Twiss functions α, β, ϕ

$$\mathbf{M}^{(i,j)} = \begin{pmatrix} A & B \\ C & D \end{pmatrix}. \quad (4)$$

Eq.(4) gives

$$\begin{cases} C^{(i,j)} x_j = x'_i - D^{(i,j)} x'_j + F^{(i,j)} \delta p/p \\ C^{(j,k)} x_k = x'_j - D^{(j,k)} x'_k + F^{(j,k)} \delta p/p \\ x_i - A^{(i,j)} x_j = B^{(i,j)} x'_j + E^{(i,j)} \delta p/p \\ x_j - A^{(j,k)} x_k = B^{(j,k)} x'_k + E^{(j,k)} \delta p/p \end{cases} \quad (5)$$

with the definitions

$$\begin{aligned} E^{(i,j)} &= \eta_i - A^{(i,j)} \eta_j - B^{(i,j)} \eta'_j \\ F^{(i,j)} &= -\eta'_i + C^{(i,j)} \eta_j + D^{(i,j)} \eta'_j \end{aligned} \quad (6)$$

Eqs.(4) are four to be solved for the four unknown quantities, the beam angle at the chosen PUE's and momentum offset

$$(x'_i, x'_j, x'_k; \delta p/p). \quad (7)$$

Among several possibilities, let us choose the following strategy. Survey all PUE's in the ring in groups of three, as follows

$$1,2,3 \quad 2,3,4 \quad 3,4,5 \quad \dots$$

and solve the system (5) for each group, in turn. If the machine is perfect and agrees with the model, there will be an unique solution for

$$\delta p/p \quad x'_1 \quad x'_2 \quad x'_3 \quad x'_4 \quad \dots$$

Otherwise, if one obtains different values when calculated in two different groups, it means that inside either group something is wrong, like a localized unexpected kick or an erroneous reading in a monitor. In the former case, to represent the machine with Eq.(4), the appropriate correction should be found and inserted in the transfer matrices.

The procedure can be extended to analyze other locations in the machine, that we label with the index m , other than BPM's. Once angles and momentum offset are established for a group of three monitors, using the transfer matrix between any one of them and m , one can predict position and angle

$$x_m, x'_m$$

at the new location. If at m there is no monitor, we will not know whether these values reflect the reality, but we know that, if at m there is anything unpredicted with the machine (or the model), the above quantities calculated from different groups of BPM's will be different. In particular, they will be different if calculated by the same group by a clockwise or counter-clockwise transformation along the machine.

It is easy to recognize if the error is due to a kick or to a monitor misreading. In the former case, there will be a different result when the calculation is performed with two groups of three that have an *interval* in common, and then we will search for the kick in that interval. In the latter case, the result will be different if calculated with two groups that have a *monitor* in common.

The eventual kick $\delta x'$ can be found in the following way. As a specific example, assume that results at m due to groups

* Work supported by the U.S. Department of Energy.

(1,2,3), (2,3,4), (3,4,5) and then (6,7,8), (7,8,9) give the same result at m , while groups (4,5,6) and (5,6,7) give a different result. This may mean that there is an unknown kick between BPM's 4 and 5, since the latter two groups have this interval in common.

Now, since a *partial* solution of Eq.(5) can be written as follows

$$\begin{pmatrix} x'_u \\ x'_v \\ \delta p/p \end{pmatrix} = P^{(j)} \begin{pmatrix} x_i \\ x_j \\ x_k \end{pmatrix} \quad (8)$$

with the indices u and v being any two of i, j, k . The elements of P for a "good" triplet must be identical with the ones for a "bad" triplet, corresponding to the *same* data x . These elements can be expressed, after inverting the matrix in Eq.(5), in terms of the Twiss functions and, for the "bad" P 's, must contain the unknown kick. Finally, a system of equations is obtained (that we omit here for lack of space), that explicitly yields the kick, position and strength, in terms of the model (Twiss functions) and the measured BPM data.

Another approach, convenient with fast workstations, is to fit the analysis of the measured data with an iterative series of MAD runs, containing varied kicks and/or simulated monitor reading errors. The results presented in the next section rather reflect this methodology.

III. RESULTS

Fig.1 represents the analysis of difference orbits in the AGS Booster measured at 22 BPM's (two are physically missing), with an horizontal kick of about 2 mrad given to the beam in a position between BPM's E4 and E6, actually very close to E6. We have plotted the resulting momentum offset and the position and angle at BPM C2 as a function of the data triplet used, referred for convenience to the position of the central BPM of the triplet.. The curves show a sharp bump in the E4-E6-E8 region.

We have somewhat reproduced the results with MAD (Fig.2), applied a 2 mrad kick in the same location.

Fig.3 and 4 represent the analysis of orbit data with a forced momentum offset of $\pm 1.5 \cdot 10^{-3}$.

Finally, we mention that a similar analysis performed on the bare orbit during the 1992 operating year of the machine showed possible errors in the F6-region. A subsequent survey confirmed magnet misalignment there and ring inspection found an erroneous electrical connection in the coils wrapped around the vacuum chamber that are used to correct for eddy current multipoles.

IV. REFERENCES

- [1] Ch.Iselin, J.Niederer, CERN/LEP-TH/88-38, Geneva (1988).
- [2] A.Luccio, "Algorithms and Modelling for the AGS Booster", *Nucl. Inst. & Meth A293*, p.460 (1990)

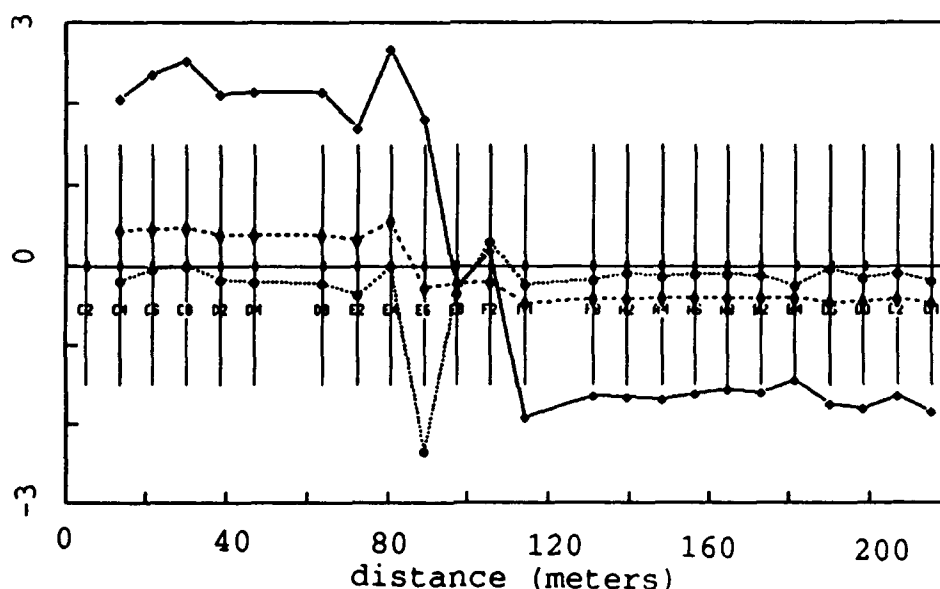


Fig.1. Analysis of difference orbits in the AGS Booster with a kick of 2 mrad applied at location E6. Data calculated at C2 from successive BPM triplet data. The solid curve represents x [mm], the dashed curve x' [mrad] and the dotted curve dp/p [10^{-3}].

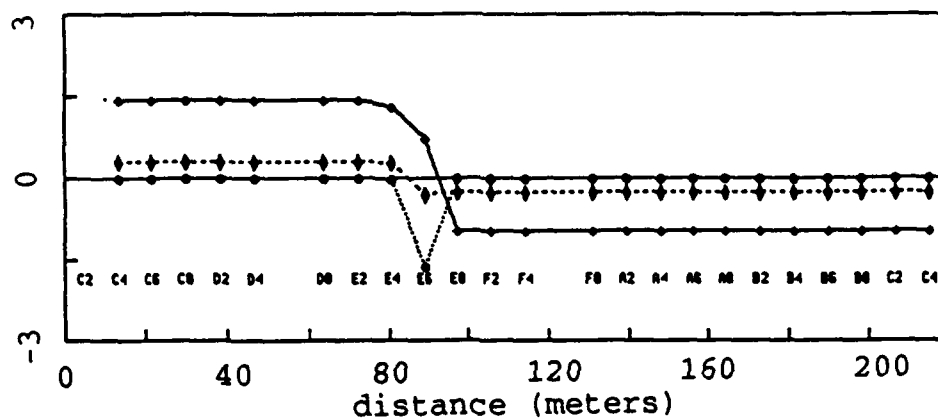


Fig.2. MAD simulation of the effect on the orbit by a 2 mrad kick localized at E6. Same conventions as in Fig.1.

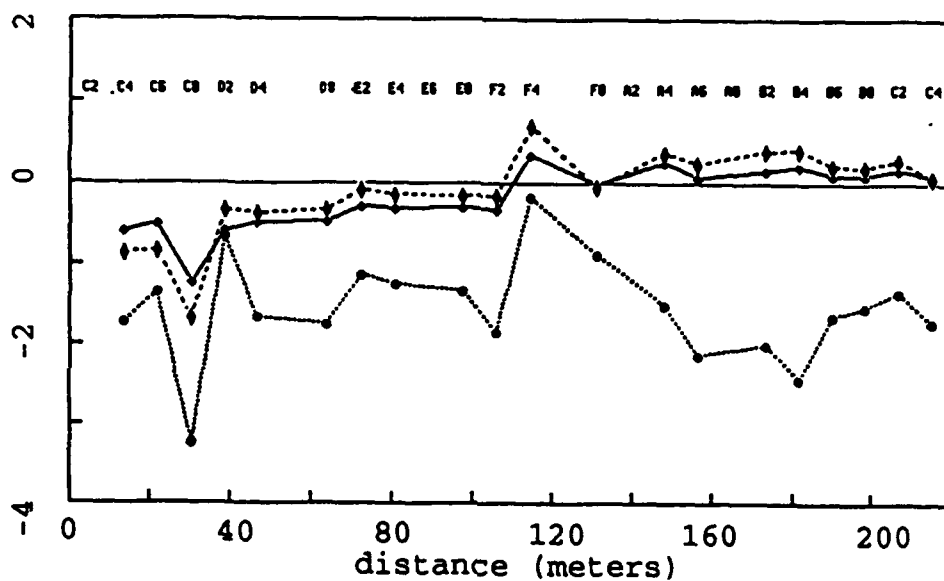


Fig.3. Analysis of difference orbits when the beam momentum was offset by $-1.5 \cdot 10^{-3}$.

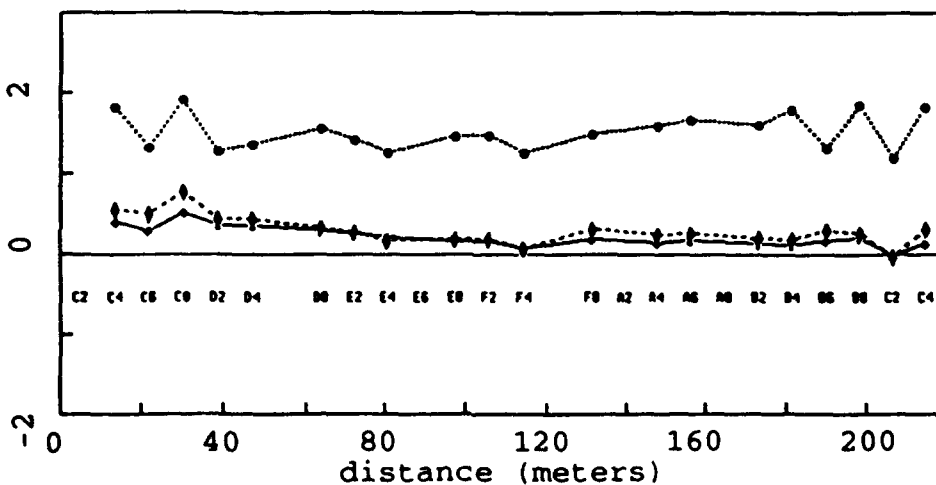


Fig.4. Analysis of difference orbits when the beam momentum was offset by $+1.5 \cdot 10^{-3}$.

Use of Design Codes for On-Line Beam Diagnostics at the MIT-Bates Accelerator*

K. D. Jacobs, B. G. McAllister, and J. B. Flanz
MIT Bates Linear Accelerator Center
P.O. Box 846, Middleton, MA 01949

Abstract

The MIT-Bates Accelerator Center consists of a one GeV electron linac with a beam recirculation system, and a storage ring which was initially commissioned in early 1993. For proper operation of this facility, on-line beam measurements and analysis are important. To this end we have developed codes for simulating and measuring beam optics and the transverse beam phase space. One of the beam optics simulators is an extension of the DIMAD based simulator which originated at CEBAF. It has been modified to include the capability of directly reading the machine magnetics values and thereby predict the beam envelope, as well as automatically set up the desired theoretical beam phase space. Two types of on-line transverse phase space measuring codes are in operation. It is envisioned that these phase space measurement systems will eventually be linked with the optics simulator to allow semi-automatic beam tuning procedures. Another code for automatically measuring optical matrix elements has been in use for several years. A description of the codes, their bases and their operation are presented here.

I. Introduction

The MIT Bates Accelerator Center has recently begun commissioning the South Hall Ring (SHR)[1]. This 1 GeV 190 m circumference ring is filled from the 1 % duty factor electron linac. It is designed to provide high duty factor beams to targets internal to the ring and also to external targets, for nuclear physics experiments. Proper operation of the beam lines and the ring, including maintaining the high quality of the beam, requires achieving the proper optical matrix elements and matching the phase space of the beam to the beam line or ring design phase space.

In order to accomplish this matching, we use computer programs to automatically measure the transfer matrix elements and the transverse phase space of the beam at various points along the beam line. An optics simulation program is then used to set the beam line magnetic elements to achieve the proper phase space match. These programs are, to varying degrees, extensions and modifications of programs used in the design of the ring and beam lines. Each of them operates interactively, and is interfaced with the control system and instrumentation, to provide real-time tuning capability.

II. Ring Controls and Instrumentation

The Ring Control System (RCS) comprises a number of distributed Local Area Computers (LACs) and workstations interconnected by Ethernet[2]. The LACs control

and monitor all beam line devices, as well as collect data from instrumentation such as beam position monitors and wire scanners. Available data is sent out on the network at a rate of 4 Hz. The workstations are used for displaying this data, for operator interface, and to run application software such as that described here. Thus, the applications have access to all information on the present state of the beam and magnetic elements. In addition, the applications can control the magnetics and instrumentation.

III. Phase Space Programs

We use two independent techniques for measuring the transverse phase space of the beam. The first uses the beam size measured at three locations along the beam line. It has the advantage of not perturbing the beam transport, but its precision suffers when measuring small emittance beams in certain optics configurations. The second technique involves measuring the beam size at a fixed location as a function of the strength of an upstream quadrupole. Although this perturbs beam transport, and tends to be slower than the three profile method, it is able to make good measurements over a wider range of phase space. In addition, this method can be used in situations where it is not possible to measure the beam size at three different locations.

A. Three profile method

By measuring the horizontal and vertical beam sizes at three different locations along a beam line, the transverse phase space in both planes can be determined. We are using an extension of an earlier technique[3] which allows for general beam transport between the three locations. Beam sizes are measured using wire scanners driven by stepper motors. The horizontal beam size at location i is $x_i = \sqrt{\beta_i \epsilon}$ where

$$\beta_i = R_{11}^2(i)\beta_0 - 2R_{11}(i)R_{12}(i)\alpha_0 + R_{12}^2(i)\gamma_0 \quad (1)$$

is the β function at location i , and $R_{lm}(i)$ is the lm component of the transfer matrix R from location 0 to location i . The beam emittance is ϵ . The variables β_0 , α_0 and γ_0 are the Twiss parameters at location 0. At locations 1, 2 and 3, then,

$$\begin{pmatrix} \beta_1 \\ \beta_2 \\ \beta_3 \end{pmatrix} = M \begin{pmatrix} \beta_0 \\ \alpha_0 \\ \gamma_0 \end{pmatrix}, \quad (2)$$

where

$$M = \begin{pmatrix} R_{11}^2(1) & -2R_{11}(1)R_{12}(1) & R_{12}^2(1) \\ R_{11}^2(2) & -2R_{11}(2)R_{12}(2) & R_{12}^2(2) \\ R_{11}^2(3) & -2R_{11}(3)R_{12}(3) & R_{12}^2(3) \end{pmatrix} \quad (3)$$

Using $\epsilon\beta_i = x_i^2$ and inverting the matrix M , Eq. 2 can be solved to give $\epsilon\beta_0$, $\epsilon\alpha_0$ and $\epsilon\gamma_0$. Thus β , α and γ at

*Work supported by the U.S. Department of Energy

location 0 can be determined by measuring the beam size x and three different locations, knowing the transfer matrices from the three locations to location 0, and using $\epsilon = \sqrt{(\epsilon\beta_0)(\epsilon\gamma_0) - (\epsilon\alpha_0)^2}$. Standard propagation of errors is used to calculate the precision of the measurement.

The core of the program used to make these measurements is based on a design program used to determine the optimal locations of the wire scanners. We have added a graphical user interface for data display and control of the wire scanners. Figure 1 shows the user interface for this application. Displayed are the raw and processed data from the wire scanners, and the wire scanner control parameters. In order to calculate the phase space, the application program reads the settings of the magnetic elements along the beam line and calculates the appropriate transfer matrices. Combining the beam widths and the transfer matrices, the phase space can be calculated, along with the precision of the measurement. The resulting horizontal and vertical phase space ellipses are then displayed. A complete set of beam profiles is typically acquired in 10-30 seconds. Processing of the data takes 1-2 seconds.

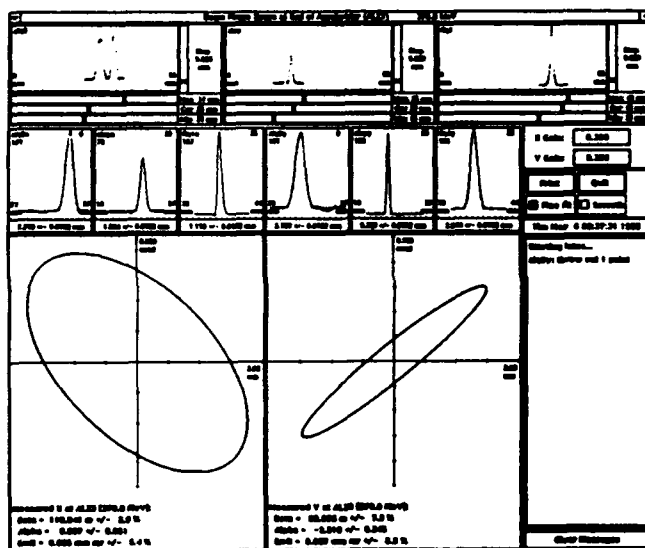


Fig. 1: User interface for measuring the transverse phase space using three beam profiles.

This application, written in C and using Motif, gives a real time measurement of the beam transverse phase space. The wire scanners scan on a continuous basis, sending out data at the end of each scan. Any change in the setting of a beam line element is recognized by the program and taken into account. Thus, the most current data available is displayed. There is an option for saving all raw data on disk, for later replay. In addition, the measured phase space can be projected to any point along the beam line.

B. Varying quadrupole method

By varying a quadrupole in the beam line and observing the beam size at a point downstream, the transverse phase space may be determined for a point upstream of the quadrupole[4]. This method is normally used for one

plane at a time. The beam size is measured with a wire scanner, as in the three profile method.

The square of the beam size at the wire scanner (σ_{11} in x and σ_{22} in y) is determined by the beam sigma matrix σ'' at a point upstream by

$$\sigma_{11} = R_{11}^2 \sigma''_{11} + 2R_{11}R_{12} \sigma''_{12} + R_{12}^2 \sigma''_{22} \quad (4)$$

for x , and similarly for y . The R_{ij} are the elements of the beam transfer matrix between the upstream location and the wire scanner.

A weighted least-squares fit of the square of the beam size as a function of quadrupole settings is made, yielding the complete beam sigma matrix. From this the beam emittance ϵ and the Twiss parameters β and α are given by $\epsilon = \sqrt{\sigma_{11}\sigma_{22} - \sigma_{12}^2}$, $\beta = \sigma_{11}/\epsilon$, and $\alpha = -\sigma_{12}/\epsilon$ in the x plane. Similar expressions hold in the y plane.

This application is written in C, using Motif for the user interface, which is shown in Fig. 2. The wire scanner controls and the profile display are identical to those used in the three profile application. The transfer matrix is calculated for each setting of the quadrupole, reading the settings of the beam line elements from the network. The measured data points and the function fitted to them are plotted, and the phase space ellipse is displayed, as projected to any point in the beam line. Acquisition of each beam profile to determine the beam width typically takes a few tens of seconds. One complete scan of the quadrupole, to make one phase space measurement, may take 5-10 minutes. Data analysis requires only a few seconds.

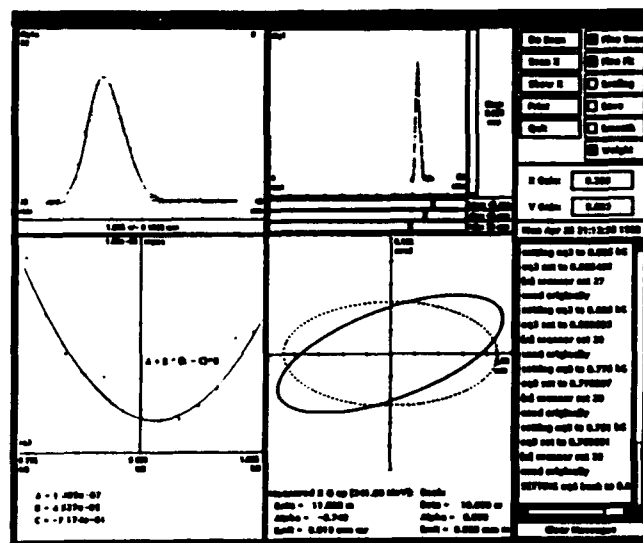


Fig. 2: User interface for measuring the transverse phase space by measuring the beam size as a function of the strength of an upstream quadrupole.

IV. Optics Simulator

This application is based on the beam line simulation code DIMAD[5] and a graphical interactive interface to it developed at CEBAF[6]. This interface, based on the X Window System, is itself an extension of the original

DIMAD text-based interactive interface allowing graphical display of the computed results, and the manipulation of beam line element settings using graphical display objects.

The program has been further modified for use as an on-line diagnostic and machine tuning tool. An interface to the RCS allows the settings of beam line elements to be incorporated into the simulation in real time. Selected elements may also be set by the application from calculations based on data supplied by the user. A graphical display of the beam beta functions for the modeled beam line is provided.

There are two basic modes of operation. In the first, the parameters of the beam phase space at the beginning of the beam line are specified by the user, along with a set of desired beam parameters at some other point in the beam line, usually the end. A selected group of elements are then used as parameters in a least squares fitting procedure, with the desired beam parameters as the fitting conditions. The calculated settings for the beam line elements can then be applied directly from the program on command from the user. This allows a complex beam line to be tuned in a simple and deterministic fashion.

In the second mode of operation, the actual settings of all the beam line elements are continuously read from the RCS, and the simulation is performed based on them. This allows a real-time display of the beam line tune, as elements are adjusted by the operator. The display update rate is limited by the computation of the beam line transfer matrices and thus by the number of elements in the beam line. For beam lines with 20-30 elements, updates can be provided about once a second on a mid-range workstation.

The graphical interface, shown in Fig. 3, is written in C, using DECwindows for the user interface. The CEBAF code has been modified and extended to incorporate new functions, and some features have been deleted. DIMAD is written in FORTRAN, and modifications were made to it at CEBAF to allow access to data and functions from the C interface code. We have made further modifications and additions, particularly to the least squares fitting routines.

V. Transfer Matrix Element Measurements

The operation of some beam lines depends on the proper set-up of the optical matrix elements. To verify that this has been achieved, we have developed an automatic OPTICS measurement system. This application uses steering dipoles to independently vary the position and angle in x and y of the beam entering the beam line. The beam positions at downstream BPMs are then measured, and the resulting optical matrix elements are calculated and displayed.

The graphical interface, shown in Fig. 4, is written in C, using X10. There is provision to interact with the program as the data is taken, or to allow the program to operate automatically. The results are used to modify the quadrupole and dipole trim settings in the beam line to obtain the desired optics.

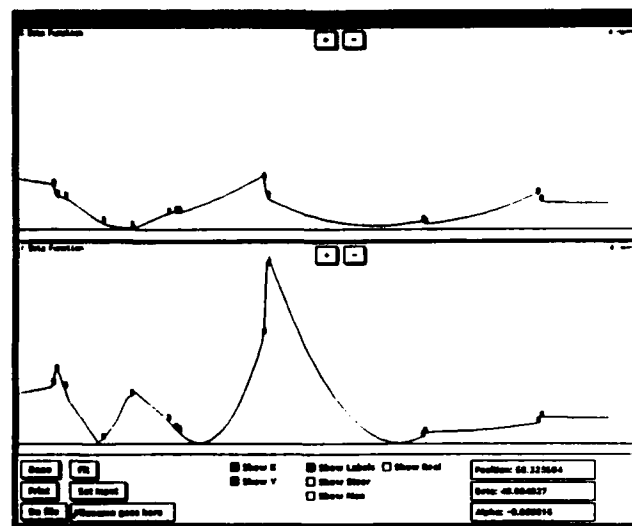


Fig. 3: User interface for the DIMAD optics program.

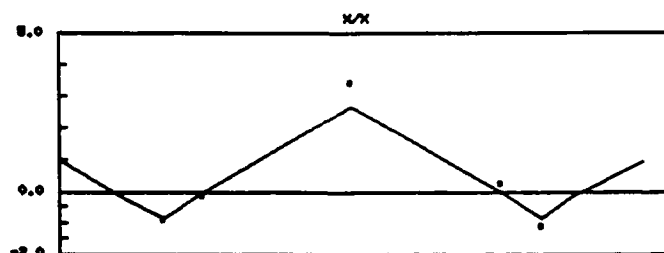


Fig. 4: Sample result from the OPTICS program. The solid lines indicate the desired optics, the points are the measured optics.

VI. References

- [1] J. B. Flanz, et al., "Status of the MIT Bates South Hall Ring," these proceedings.
- [2] T. Russ, A. Carter, Z. Radouch, and C. Sibley, "The Bates Pulse Stretcher Ring Control System Design," *Conference Record of the 1989 IEEE Part. Accel. Conf.*, Vol. 2, p. 85.
- [3] K. D. Jacobs, J. B. Flanz and T. Russ, "Emittance Measurements at the Bates Linac," *Conference Record of the 1989 IEEE Part. Accel. Conf.*, Vol. 2, p. 1526.
- [4] M. C. Ross, N. Phinney, G. Quickfall, H. Shoaee and J. C. Sheppard, "Automated Emittance Measurements in the SLC", SLAC Pub. 4278, March 1987.
- [5] R. V. Servranckx, et al., "User's Guide to the Program DIMAD", SLAC Report 285 UC-28, May 1985.
- [6] M. H. Bickley and D. R. Douglas, "DIMAD Based Interactive Simulation of the CEBAF Accelerator", CEBAF PR-91-011, May 1991.

A Graphical User-Interface Control System at SRRC

J. S. Chen, C. J. Wang, S. J. Chen and G. J. Jan*

Synchrotron Radiation Research Center
Hsinchu 30077, Taiwan, R. O. C.

* Department of Electrical Engineering, National Taiwan University
Taipei 10764, Taiwan, R. O. C.

Abstract

A graphical user interface control system of 1.3 GeV synchrotron radiation light source was designed and implemented for the beam transport line (BTL) and storage ring (SR). A modern control technique has been used to implement and control the third generation synchrotron light source. Two level computer hardware configuration, that includes process and console computers as a top level and VME based intelligent local controller as a bottom level, was setup and tested. Both level computers are linked by high speed Ethernet data communication network. A database includes static and dynamic databases as well as access routines were developed. In order to commission and operate the machine friendly, the graphical man machine interface was designed and coded. The graphical user interface (GUI) software was installed on VAX workstations for the BTL and SR at the Synchrotron Radiation Research Center (SRRC). The over all performance has been evaluated at 10Hz update rate. The results showed that the graphical operator interface control system is versatile system and can be implemented into the control system of the accelerator. It will provide the tool to control and monitor the equipments of the radiation light source especially for machine commissioning and operation.

I. INTRODUCTION

A third generation synchrotron radiation light source has been constructed and commissioned at current stage in SRRC. It includes a turn-key electron injector (50MeV Linac and 1.3 GeV booster synchrotron), a BTL and a SR with triple bending achromat lattice [1]. Two level hierarchical computer hardware systems were linked by

Ethernet and four layers software structures were configured to simplify the architecture of the control system. High performance workstations have been used as operator consoles and VME crate based intelligent local controllers (ILC) have been used to interface field level equipments. In order to access and control devices and equipments on the BTL and SR easily, a graphical operator interface technique was implemented on the control system of the synchrotron radiation facility at SRRC. This simple, flexible and expandable control system was used to commission the BTL and the SR of SRRC. Large than 10 mA stored beam and several tenth minutes lifetime was achieved quickly within short commissioning period.

II. HARDWARE SYSTEM CONFIGURATION

Two level hierarchical hardware architecture were adopted for the control system at SRRC [2]. The open system configuration ensure the expandability of the control system. The hardware system configuration of the control system at SRRC is shown in the Figure 1. Top level computers include a process computer which is VAX Systems 4000-500 supermini computer, several workstations (VAXstation 3100-76 and VAXstation 4000-60) running under VMS and one DECstation 5000-200 run under Ultrix acts as a file server for intelligent local controllers (ILC). Multiple ILCs at bottom level are use to interface with the field devices. Both level computers are linked by Ethernet network. The control local area network is also connected to the control system of 1.3 GeV full energy electron injector and laboratories wide network through multi-port router. All ILCs are used to monitor or control the equipment on the BTL and SR.

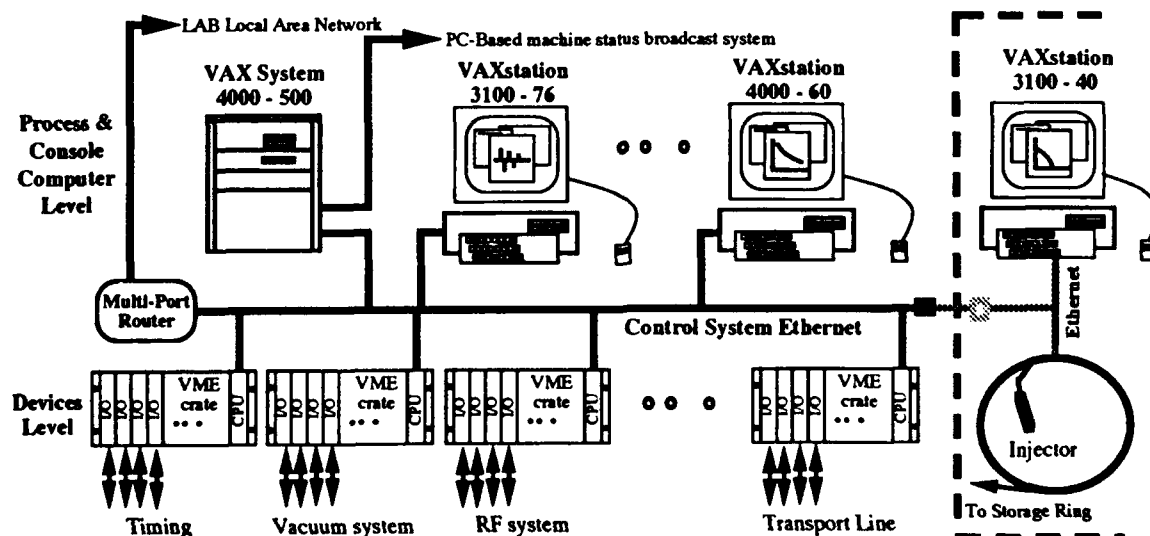


Figure 1. Hardware configuration of the control system at SRRC.

The ILC is VME crate based system which includes Motorola MVME-147 CPU board and variety of interface cards. The MVME-147 CPU board consists of 68030 microprocessor, 68882 floating point coprocessor, 4M byte on board memory and Ethernet interface. The ILCs are connected to the hardware devices or equipments via parallel or serial input/output (I/O) as well as IEEE-488 bus interface. Data acquisition, open or closed loop control functions of the equipment are handled by ILCs. A device, such as magnet, pulse magnet, vacuum gauge/ion pump current or valve, RF controller, diagnostic instrumentation, can be accessed from operator console. The update rate of the dynamic data from ILCs to console computer is about 10Hz.

III. SOFTWARE SYSTEM

Software system has been developed by SRRC staffs using C language under VMS environment. The software is structured into four layers and is shown in Figure 2, there are device access, network access, database access, and applications. Real time database of the control system for the BTL and SR facilities at SRRC has been implemented and tested successfully. Modularized software designed approach ensured flexibility, expandability and maintainability of the system.

The device access processes are run on ILCs. The PSOS+ real time multitasking kernel provides the ILCs with task scheduling, memory allocation, event handling and message queueing. The PNA+ network package provides socket interface in TCP/IP protocols. Those software package are purchased from commercial available products. The control tasks and various I/O drivers as well as application programs were implemented at SRRC and are successful running on ILCs. In order to develop all the necessary software on ILC, VAX machine is used as a host and connected to the target ILC via Ethernet. Microtec cross C compiler, cross assembler, and S-record linker which are installed on the VAX machines are developing tools. The XRAY+ running on VAX is used to aid the software debugging. The developed software are downloaded in S-record format file to the desired target ILC to start the running activity on it. All ILC software package has been developed by two man-years and the result is quite successfully.

The network access software is in charge of the data exchange between console level computer and ILCs. The TCP/IP protocol is used to provide an open environment.

The console level computers are running under VAX/VMS environment. The function of the process computer and workstation is slightly different. The process computer keeps the system-wide static database and maintains it. At the system start-up, each workstation requests and receive a copy of the static database from the process computer to achieve consistency. Each console computer then has all database information necessary to process dynamic

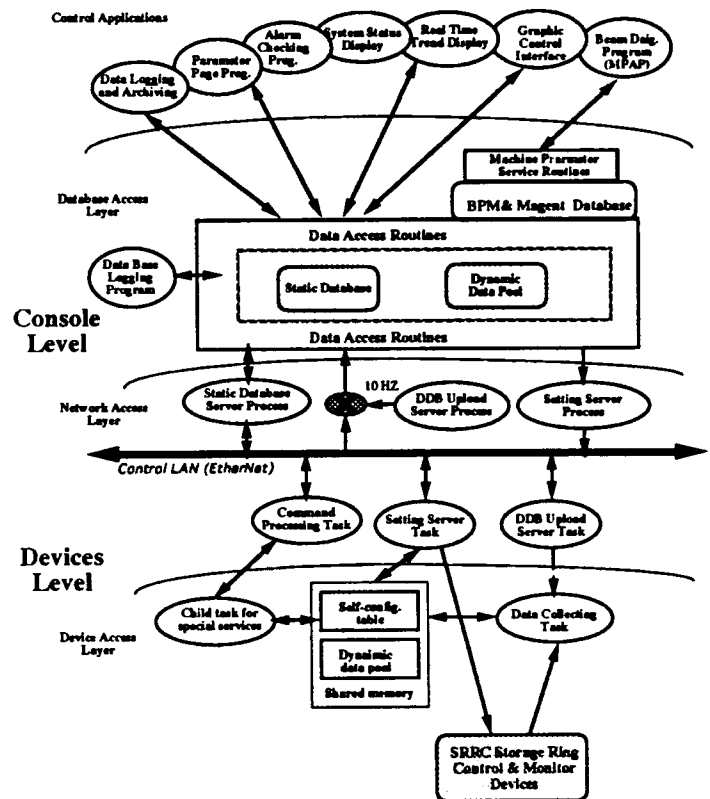


Figure 2. Block diagram of the software system

database frames received from ILCs. The upload command is broadcasted by an ILC which connects to 10Hz injection trigger signal then each ILC broadcast its dynamic database after receiving the command. The workstations are mainly for operator interface to operate the machine. All of the console level computers can be expanded easily without increasing the network traffic load.

The central database which includes the static and dynamic database are created on the console level computers. It is used as data buffer between the low level tasks at ILCs and console level applications. The application programs get equipment parameters or machine parameters directly from database rather than from ILCs. Many applications are coded and run at console computer, such as data logging/archiving, alarm checking, real-time multiple trend and correlation plot display as well as machine modeling programs.

The novel man machine interface technique is used to develop a graphical operator interface control system. The graphic user interface software was developed based on X-window/Motif. The graphic editor program was developed and used to edit the display pattern of the machine component and built up the relationship between the component and the static database. Those pattern file is stored in the hard disk by using ASCII file format. The console program reads those ASCII file and make a connection between the component pattern and dynamic database. This program is also capable of

the data reading, setting and display of linked devices. Operator interface pages on workstation can be a simple spread sheet, a control panel of a subsystem shown as Figure 3 or object oriented form as show in Figure 4. The sub-system or components on BTL and SR can be accessed from workstation by mouse and keyboard. Multiple software knobs, multiple file trend display and correlation plot functions are also available. This man machine interface makes the machine commissioning or routine operation more easily and friendly.

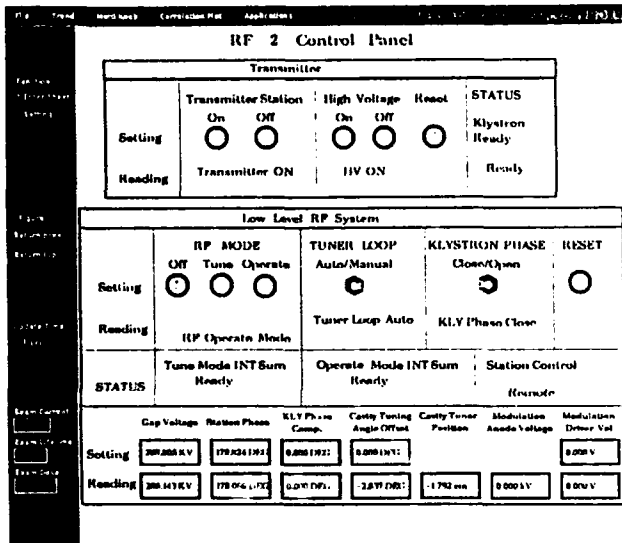


Figure 3. RF system control panel interface

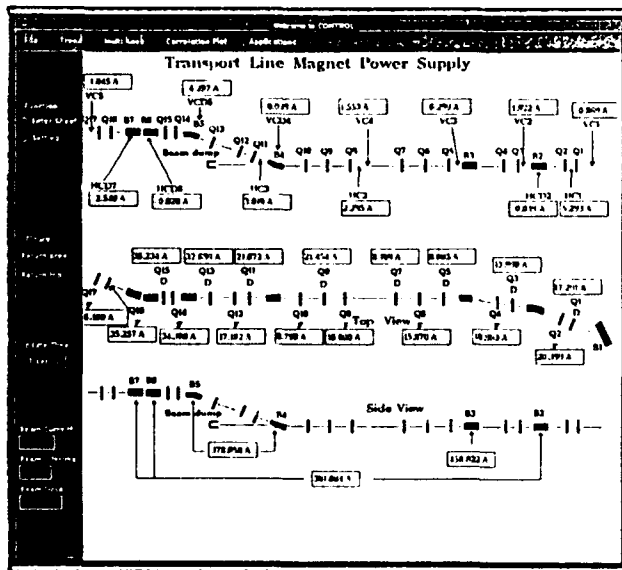


Figure 4. Transport line power supply control interface

IV. SUMMARY

Graphical oriented man-machine interface has been implemented on the control system for 1.3 GeV synchrotron radiation light source at SRRS successfully. It demonstrated that graphical operator interface of the control system are

helpful for commissioning of the machine. Most of the design specifications has been achieved. The turning and modification of the control system now is under way to improve the system performance.

V. ACKNOWLEDGEMENT

The authors would like to express his sincere appreciation to R. W. Goodwin and Mike Shea of FNAL, D. Klotz at ESRF and T. Katsura at KEK-PF for their helpful comments. Finally, special acknowledges to David Rice at CESR for his help.

VI. REFERENCE

- [1] C. S. Hsue, C. C. Kuo, J. C. Lee, and M. H. Wang "Lattice Design of the SRRS 1.3 GeV Storage Ring", IEEE Proc. of the Part. Accel. Conf., 2670 (1991).
- [2] G. J. Jan, "Control System at the Synchrotron Radiation Research Center", IEEE Proc. of the Part. Accel. Conf., 1380 (1991).

Machine Protection System Algorithm Compiler and Simulator *

Gregory R. White

Gregory Sherwin

Stanford Linear Accelerator Center, Stanford University, Stanford CA 94305

ABSTRACT

The Machine Protection System (MPS) component of the SLC's beam selection system, in which integrated current is continuously monitored and limited to safe levels through careful selection and feedback of the beam repetition rate, is described elsewhere in these proceedings.

The novel decision making mechanism by which that system can evaluate "safe levels", and choose an appropriate repetition rate in real-time, is described here. The algorithm that this mechanism uses to make its decision is written in text files and expressed in states of the accelerator and its devices, one file per accelerator region. Before being used, a file is "compiled" to a binary format which can be easily processed as a forward-chaining decision tree. It is processed by distributed microcomputers local to the accelerator regions. A parent algorithm evaluates all results, and reports directly to the beam control microprocessor.

Operators can test new algorithms, or changes they make to them, with an online graphical MPS simulator.

PROBLEM STATEMENT AND RATIONALE

The Machine Protection System (MPS) monitors, in real-time, potential autogenic operational hazards of the Stanford Linear Collider (SLC). These include the ambient radiation of the beam-pipe and its devices, vacuum, water and other critical parameters throughout the accelerator.

The MPS's purpose is to limit the integrated current of the beam to any part of the accelerator to safe levels, while continuing to deliver beam with the desired parameters to the rest of the machine; that is, to be minimally invasive. The extent to which the current is lowered should be just enough to make the SLC's operation secure, but not so low as to make the cause of the problem untraceable. If, for instance, a collimator is causing a hazardous radiation shower in one section of the SLC, MPS should tell the software system that selects beam configurations to lower the current in that sector. MPS must return the beam to its desired current and configuration automatically, as soon as it detects that the fault has been ameliorated.

OVERALL SOLUTION METHOD

Other papers in these proceedings describe the MPS system in general [1] and two of its subsystems[2][3]. Here we summarize the overall solution strategy, so as to put the MPS Algorithm Compiler and Simulator in context.

Devices and parameters deemed critical to the operation of the SLC are connected via MIL-1553 to a VME based micro-

*Work supported by the Department of Energy, contract DE-AC03-76SF00515

processor local to an accelerator region. These microprocessors compute an MPS "algorithm". The algorithm processors or "AP"s are arranged in a two tier hierarchy, there being one Supervisor AP whose inputs are the outputs from the other APs and whose output is fed directly to the beam control computer, which then adjusts the next beam's parameters. This process is repeated with each beam pulse. See figure 1.

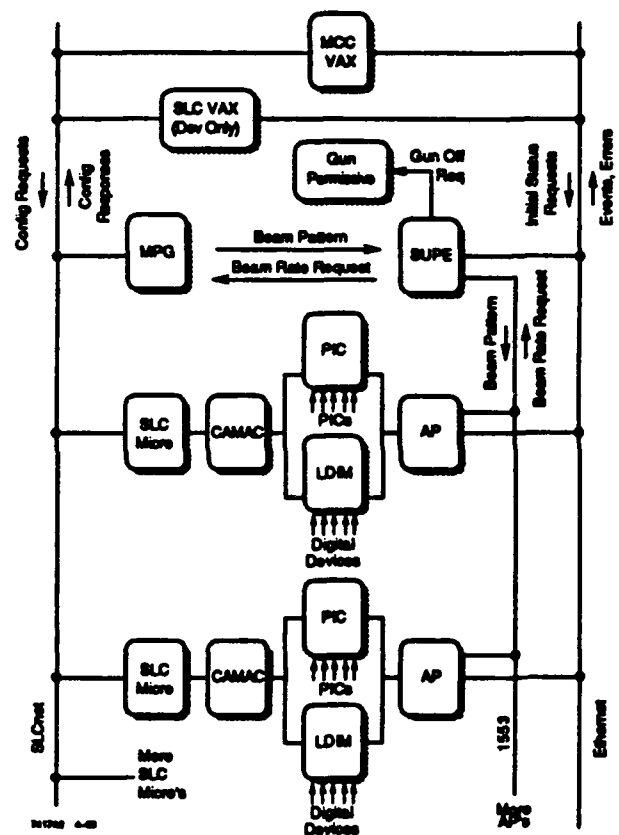


Figure 1: MPS Data Interconnection Diagram

Since the devices which form the input to an algorithm, and the available re-configurations of the accelerator which form the output, are different for each sector of the SLC, a different algorithm must be developed and tested for each algorithm processor. For that reason, the algorithm "compiler" and "simulator" software were developed. They are two distinct programs, their relationship being analogous to the compilers and debuggers used in conventional programming.

The following describes first the algorithm compiler (MPSL) and then the simulator (MAS).

ALGORITHM COMPILER

First a computer language was developed in which the following could be formally expressed: i. the states of devices ii. the state of the accelerator, that is, where there is currently intended to be beam, and iii. possible alternative accelerator configurations, principally with regard to repetition rate. A device "state" is a device name in equality or inequality with one of the values that device can report. A well formed algorithm then describes, for all expected states of the accelerator in a region, the conditions under which some specified alternative machine configurations should be adopted.

```
AP = AP92
ALG = "Demonstration for PAC 93"

/*
** Algorithm contains one beampath, consisting of two bgrp names.
*/
BEAM = "SLC5LD" | "BBA"

RATE = "FULLRATE" /* Full rate everywhere */
      "LIMIT_HI" /* E- beam in arc/ff limited to 10 Hz */
      "LIMIT_FS" /* E+ beam in arc/ff limited to 10 Hz */
      "LIMIT_FF" /* Beams in both arcs limited to 10 Hz */

STOPCH = MPST.AP92.1."PROT" == "UNPRCTD" &
        MPST.AP92.2."PROT" == "UNPRCTD"
        ("A Stopper's OUT or MOVING")

NEWRATE = "ZERORATE" /* Absolute minimum needed to run SLC */
        VACV.L131.114."VALVE" == "CLOSED" &
        PICS.L131.102."CABLE" == "OK"
        ,
        NEWRATE = "LIMIT_HI"
        PICS.L131.102."THRESH_D" == "OK" |
        PICS.L131.111."THRESH_A" == "OK" &
        PICS.L131.112."THRESH_A" == "OK"
        ,
        NEWRATE = "FULLRATE"
        /* default */

STOPCH = MPST.AP92.1."PROT" == "PROTECTD" ("STOPPER IN")
NEWRATE = "ZERORATE"
/* default */

RATE = "LIMIT_HI" /* Beam everywhere limited to 10 Hz. */
STOPCH = MPST.AP92.1."PROT" == "UNPRCTD"
NEWRATE = "ZERORATE"
        VACV.L131.114."VALVE" == "CLOSED" &
        PICS.L131.102."CABLE" == "OK"
        ,
        NEWRATE = "LIMIT_LO"
        PICS.L131.102."THRESH_D" == "OK"
        ,
        etc etc.
```

Figure 2: Extract from an MPS algorithm for an AP

AN MPS ALGORITHM'S STRUCTURE

In the SLC timing system, a "beamcode" describes a beam in terms of the accelerator devices necessary to propagate that beam, and the times in relation to a fiducial that those devices must fire. "Beamcode modifiers" define the repetition rate of a beamcode, and in great part, where in the accelerator complex beam from that beamcode can go. A Regional Beamcode "group" is a set of beamcodes for running the accelerator for a particular experiment. Call a disjunction of these groups then, a "beampath".

To identify exactly where beam in a given pulse will wind-up, one needs to add a statement of the states of the beam stoppers. Call a conjunction of stopper states a "stopper configuration".

Then, for some disjunction of beampaths, for some disjunction of stopper configurations and for some target repetition rate, a single Boolean expression in the states of local devices is sufficient to specify whether that target rate can be adopted.

An algorithm is a list of expressions in local devices, one for each repetition rate possible in each of the beampath/stopper

configuration possibilities. Once loaded with an algorithm, an Algorithm Processor, within one beam-pulse (8.333 msec), determines which beampath and stopper configuration are in effect on that pulse, and starts to evaluate the expressions specifying the safety of each available repetition rate. It does this from first to last, until it finds an expression which is false, at which point it concludes that the associated rate is the highest it can recommend. This means there is one last repetition rate per clause which is always true (has no expression) and specifies the highest possible repetition rate in that part of the accelerator.

ALGORITHM COMPILER FUNCTION

The primary function of the compiler is to translate each expression into a bit-mask on the MIL-1553 port data that each device sends to its AP. The compiler prepares the data on a per port basis. It provides a bit-mask for the location of interesting data, and a second mask for the values of that data were the associated expression to be true. The compiler acquires the information about how the devices are wired from the SLC database.

The output binary file is isomorphically very similar to the input file. In addition it contains some information to help the AP configure its data acquisition process optimally.

ALGORITHM SIMULATOR

The function of the MPS algorithm simulator (MAS) is to verify that recently developed MPS algorithms will perform as intended. The simulator tests the software integrity of the algorithms by providing the capability to simulate any possible state of the accelerator and its associated hardware devices. To accomplish this, the software attempts to simulate virtual devices, and their trip conditions, to verify that the algorithm performs according to design. Other beam and accelerator characteristics are also simulated as inputs.

The great number of variables which the simulator controls requires an extensive configuration procedure. This procedure includes the selection of APs, algorithms, states for various devices, beam groups, rate-limiting kinds, and states for stopper devices (ie. stopper configurations). In addition to this complexity, the software is event-driven (via individual button pushes and item selections from lists) and not procedural, and therefore much of the simulator software is exposed directly to the interface-level software. This creates software vulnerability issues.

To prevent improper or incomplete selections and to keep track of the current configuration state of the simulator, the program implements a state-machine using global variables. Once the simulator is properly configured, the user can execute a simulation and view the results and/or dump them to a file. At the core of the simulator processing is the same algorithm loading and evaluation software used in the algorithm processors to determine device trips and requested machine states. Configuration information is converted into the equivalent of MIL-1553-level raw port data and beam data, as input to the AP's evaluation software. All input conditions and processing results are presented in the simulator output.

The simulator is designed so that the user can then make minor modifications to the simulator configuration and repeat the simulation. File inputs and outputs are also provided for most

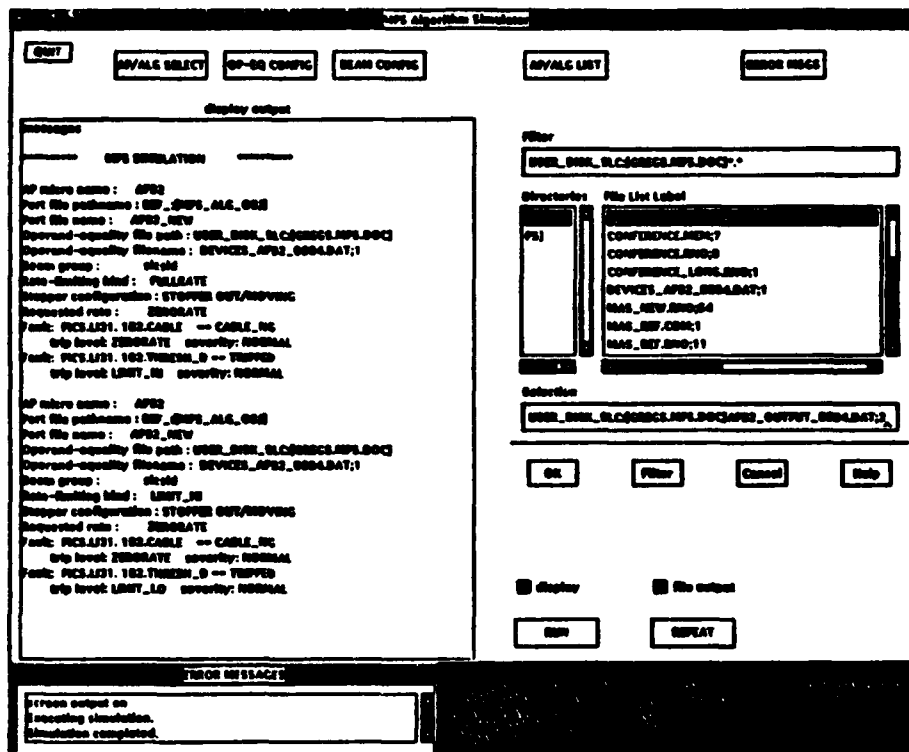


Figure 3: Algorithm simulator screen showing the result of a test when two devices were tripped

of the configuration data to simplify setup for re-simulations performed at a later time.

Since the MPS system is designed with devices subordinate to APs, which in turn are subordinate to a supervisor AP, there are several levels of operation which the simulator can perform. At the most basic level, devices are configured as inputs to a single AP. Additionally, individual APs can be configured as inputs to a simulation of the Supervisor and its algorithm. At the most complex level, devices can be configured as inputs to APs, which in turn are used as inputs to the Supervisor, hence simulating the entire MPS system from devices up to the Supervisor.

The simulator has a MOTIF user-interface consisting of various buttons, display windows, and selectable lists. To begin a simulation, the user must first select a mode of operation: the simulation of a single AP (which may or may not be a supervisor) and its direct inputs, or the simulation of the entire MPS system (a supervisor at the device-level). Once this selection is made, the user chooses an MPS algorithm and its associated AP from available choices presented in respective lists. From this selected algorithm file, a list of beam parameters and devices relevant to the AP is accessed and used to prepare their respective configuration portions of the simulator.

With an AP and an algorithm selected, the user can configure beam characteristics and virtual devices. Beam groups and rate-limiting kinds are activated for the simulation through selectable lists and button options. For devices, the user is presented with a list of devices and their currently configured states (ie. operand-equalities) to be used as input to the currently selected algorithm. To minimize the configuration effort, all devices are initialized to healthy states. Upon selection of any device, the user is presented with a list of possible states

to configure the device to. To enhance the possible use of the simulator as a diagnostic tool, the user also has the option of configuring the list of devices to the states that exist on the running MPS system.

Once the simulator is configured, the user presses a button to execute the simulation and to acquire output. As illustrated in Figure 3 (cool screen capture), the output includes the algorithm processor name, the algorithm path and file names, the name of the saved file of operand-equality configuration data (if applicable), the beam group and rate-limiting kind, the stopper configuration, the requested rate resulting from algorithm processing, and individual device faults along with their trip levels and severities. Since a single simulation can be configured with multiple beam groups, rate-limiting kinds, APs and algorithms, the output is formatted by grouping the results for each combination of these inputs as if they were individual simulations.

The simulator has proved to be a useful tool in debugging the MPS software. Since the simulator used the same algorithm loading and evaluation software used in the real MPS system and was dependent upon the integrity of the MPS compiler, it served as a top-level software test platform from which to find and correct software errors in a variety of MPS software areas.

REFERENCES

- [1] R. Chestnut *et al.* Machine Protection System for the SLC. *These proceedings.* 1993.
- [2] S. Allison *et al.* MPS VAX Monitor and Control Software Architecture. *These proceedings.* 1993.
- [3] K. Krauter, M. Crane. MPS Beam Control Software Architecture. *These proceedings.* 1993.

MPS VAX MONITOR AND CONTROL SOFTWARE ARCHITECTURE*

S. Allison, N. Spencer, K. Underwood, D. VanOlst, M. Zelanzky
Stanford Linear Accelerator Center, Stanford University, Stanford, CA 94309 USA

Abstract

The new Machine Protection System (MPS) now being tested at the SLAC Linear Collider (SLC) includes monitoring and controlling facilities integrated into the existing VAX control system [1]. The actual machine protection is performed by VME micros which control the beam repetition rate on a pulse-by-pulse basis based on measurements from fault detectors. The VAX is used to control and configure the VME micros, configure custom CAMAC modules providing the fault detector inputs, monitor and report faults and system errors, update the SLC database, and interface with the user. The design goals of the VAX software include a database-driven system to allow configuration changes without code changes, use of a standard TCP/IP-based message service for communication, use of existing SLCNET micros for CAMAC configuration, security and verification features to prevent unauthorized access, error and alarm logging and display updates as quickly as possible, and use of touch panels and X-windows displays for the user interface.

Introduction

The new MPS [1] can be broken into three separate hardware subsystems each responsible for a piece of the overall machine protection:

Beam control

The beam control subsystem [2] is resident in VME micros located close to beam monitoring devices within the machine. The beam control micros acquire data on a pulse-by-pulse basis from CAMAC modules using MIL-1553 serial protocol, process the data using a downloaded MPS algorithm file, and send the resultant beam repetition rate to a SLC micro called the master pattern generator (MPG). The algorithm file used for data processing contains logic which dictates the repetition rate to be adopted based on which devices are currently tripped. Beam control micros are also known as algorithm processors (APs).

The APs also send trip information and error messages up to the VAX and respond to VAX control and status requests. Communication with the VAX is achieved using the TCP/IP-based area message service (AMS) [3]

SLC micros

Functionality has been added to the existing SLC micros to also configure MPS CAMAC modules and periodically verify that the CAMAC hardware is consistent with the requested settings in the database. The MPG, a special SLC micro, has been enhanced to provide the current repetition rate to the beam control micros and acquire and

process the resultant rate requested by these micros. The communication link with the VAX and the SLC micros is SLCNET, a high-speed polled network developed at SLAC.

VAX monitor and control

The existing VAX control system has been enhanced to provide MPS monitoring and control. New and existing programs have been developed or enhanced for MPS and include the SLC control program, MPS controller, MPS event manager, MPS status display handler, and the error manager. Data flow between VAX processes and the interface between these processes and the beam control and SLC micro subsystems are shown in Fig. 1.

SLC Control Program

The SLC Control Program (SCP) provides a user interface for many SLC control functions and has been upgraded to handle MPS requests. There is one SCP process for each user, and each process gets input from a keyboard and touch panel and provides output to a high resolution color-graphic display and standard terminal. If the SCP is run on a VAX workstation, all input/output uses an X-windows interface.

When the SCP receives a MPS user request, it prepares and sends a message to the MPS controller process using a VMS mailbox and waits for a return message indicating whether the request was implemented successfully or not. User requests include:

1. Change MPS State—MPS may be turned on or off.
2. IPL AP—one or all AP's may be booted.
3. Download Algorithm—after an algorithm is changed and recompiled, the user may request that it be downloaded to the AP.
4. Bypass/Unbypass Device—when a beam monitoring device is determined to be unreliable, the user may override the current device state with a bypass value and unbypass the device after it has been fixed.
5. Configure CAMAC Module—settings in the CAMAC module including threshold and filter values may be changed in the database and the module configured with the new values.
6. Save and Load MPS Configuration Files—a snapshot of the current MPS database information may be saved or restored.

Each MPS user request is associated with a privilege level where lower privilege levels correspond to relatively harmless actions like verification and higher privilege levels correspond to more disruptive actions like downloading new algorithms. Each privilege level is mapped to a VMS account name, and when the user makes a request, the appropriate account name and password must be entered before mail is sent to the MPS controller.

* Work supported by Department of Energy contract DE-AC03-76SF00515.

display shows verification errors detected in any MPS subsystem in enough detail to allow easy diagnosis and correction.

MPS Controller

The MPS controller process is the overall coordinator of all MPS subsystems. It services all MPS requests from other VAX processes including user requests from the SCP and halt requests from the error manager, and deals with CAMAC configuration errors sent by the SLC micros through PARANOIA, a process that receives asynchronous SLCNET messages. It periodically checks the health of the MPS by verifying that the networks and micros are still active, sending verification requests to the micros and checking their responses for validity and consistency, and checking the status of other MPS VAX processes. If any error is found, MPS is halted either immediately or after an appropriate number of warning messages are output depending on the severity of the error. All verification errors are updated in the MPS manager global section and reported to the standard error handler for logging and broadcasting to all SCPs,

The controller is also the keeper of the database and updates information pertaining to overall MPS state and status, the status and configuration data for each AP, information about each bypassed item, and the configuration data for each CAMAC module. On user request, current MPS configuration data from the database is saved to a file or loaded back into the database. When a user request causes the CAMAC configuration data to change in the database, SLCNET messages are sent to the affected SLC micros to update the CAMAC hardware. The controller periodically checks that the current data in the database matches the values in the "ideal" or golden configuration file.

When the user requests a change in MPS state, the controller sends AMS messages to the APs and SLCNET messages to the MPG in the sequence required to produce a smooth transition to the on or off state. When a new algorithm needs to be downloaded to an AP, the controller checks the algorithm for validity, copies it from the library to the production directory, updates the database, and sends a message to the AP to read in the new file. When the user requests an AP IPL, the controller halts MPS, resets the AP hardware, spawns a subprocess to load the AP with an image residing on the VAX, updates the database, sends a message to the AP with algorithm and bypass information, and turns MPS back on.

When a device is bypassed, the controller updates the database with the device identification, bypassed state, and time at which the bypass expires. When the device is unbypassed, the entry in the database is erased. For both actions, the controller sends a message to the affected AP containing the location and value of the bypassed bits in the raw data acquired from the CAMAC modules. When a bypass expires, the controller automatically unbypasses the associated device.

MPS Event Manager

The MPS event manager receives and processes event buffers from the event task on an AP and updates the MPS manager global section with current faults, repetition rate, and status of the AP. There is one event manager process for each AP in the system, and each event manager writes to its own slice of the global section. The AP sends an event buffer both periodically (i.e., every 5 s) and whenever it either finds a trip or has an error that results in a rate change. Each event in the event buffer contains the raw data read from the CAMAC modules, indication of which CAMAC modules could not be read, the current rate broadcast to the AP, the new rate requested by the AP, and the AP status. Events are buffered by the AP to prevent a flood of AMS messages when rate-changes happen at a very high frequency.

The event manager runs the raw data through the same algorithm as the AP but unlike the AP, which must process and send results at a very high rate, the event manager has the time and access to the database to do extra processing. It translates faults which are just bits to the AP to device and state names that are understandable to the user. The CAMAC module name and location are determined for any port which could not be read by the AP. The current and requested rate integer values are translated to meaningful character strings. Since the event manager uses the same algorithm and data as the AP, it also checks that it gets that same results as the AP, providing extra verification of AP functionality.

Error Manager

The error manager is a simple process which receives error message buffers sent using AMS from any micro task and then forwards these messages to the standard SLC error handler for logging, display, and broadcasting to the SCPs. Error messages are buffered on the micro side to prevent a flood of AMS messages when a flood of errors are experienced by the micro. If an error is associated with a particular SCP process, that SCP identification is included in the buffer so that the error is sent to just that SCP instead of all SCPs. If a fatal error is detected from an AP, error manager also sends mail to the MPS controller to halt MPS.

References

- [1] S. Clark, *et al.*, "Smart Machine Protection System," in Proceedings from the International Conference on Accelerators and Large Experimental Physics Control Systems, Tsukuba, Japan, SLAC-PUB-5688 (1991).
- [2] K. Krauter and M. Crane, "MPS Beam Control Software Architecture," these proceedings, SLAC-PUB-6149.
- [3] M. Crane, *et. al.*, "AMS: Area Message Service for SLC," these proceedings, SLAC-PUB-6166 (1993).

The Continuous and Seamless Replacement of a Running Control System Succeeded

G. v. Egan-Krieger*, R. Müller*, J. Rahn*

Berliner Elektronenspeicherring-Gesellschaft für Synchrotronstrahlung m.b.H.
(BESSY), Lentzeallee 100, D-14195 Berlin, FRG

Abstract

A continuous replacement and upgrade procedure for the control system of the running light source BESSY has been proposed in 1990 [3]. Today we can present the components of the 'final' system. The concept has shown to be practicable and flexible. Technically improved solutions unforeseeable at start time of the conversion and not available before 1991 could be utilized even in the main turnover phase. The intended goals have been achieved: Beam time has not been affected by the conversion process. Developmental and operational experiences show that the system will supply us with key components for the control of BESSY II.

Introduction

The 'Berliner Elektronenspeicherring-Gesellschaft für Synchrotronstrahlung m.b.H.' (BESSY) operates an 800 MeV storage ring dedicated to the generation of synchrotron light in the VUV and soft X-ray region [1].

A cautious and smooth modernisation scheme for the aged control system [2] of the fully equipped and continuously running light source BESSY has been introduced in 1990 [3]. Since then step by step the electronically cascading interface system attached to a central minicomputer system has been exchanged 'in the fly' by a DCE (*distributed computing environment*). Application programs have been ported to a modern workstation platform. Progressive replacement of all system components led us to the current phase of finishing and clean up.

Prerequisites and schedule of the modernisation concept [3] as well as the features of our graphical user interface management system (UIMS) [4] have already been described. Purpose of the present paper is to point out those modifications of the original approach, that have shown to be advantageous and describe specific solutions, that could be of general interest.

Configuration Overview

The new system consists of four stationary operator consoles (See fig. 1). Two of them are the workstation console displays of HP Apollo 9000/730 machines and two are fast, but otherwise

'dumb' 19" X-terminals. One mobile console, an elder 17" X-terminal, can be used at the location of equipment that has to be repaired or where diagnostics have to be performed.

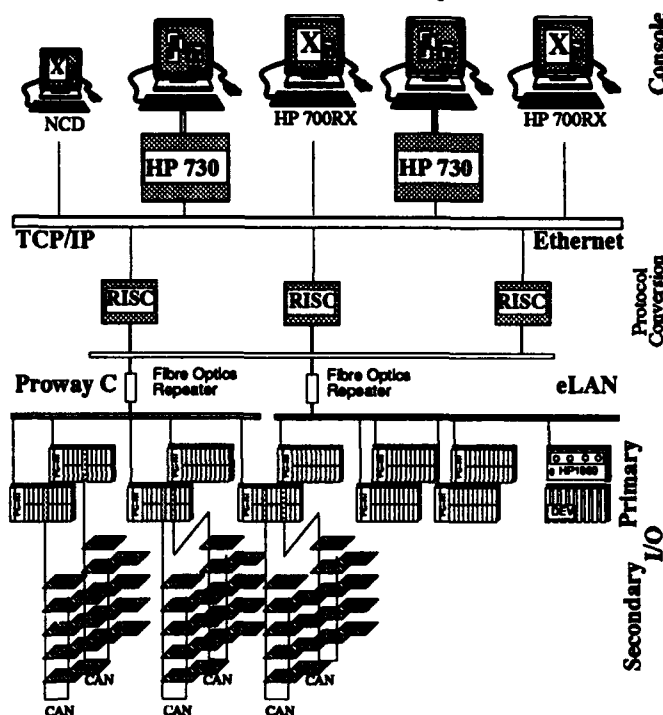


Figure 1: Sketch of the Hardware Configuration

Three unexpensive RISC workstations with minimal configuration provide protocol conversion from TCP/IP (IEEE 802.2) on the presentation and command level to Proway C (IEEE 802.4, IEC 955) on the process field bus 'eLAN' (See [3]).

Attached to three segments of the Proway C fieldbus are about twenty micro processor nodes (crates) with 312 slots. Node masters are IBM-AT compatible boards (See 'Interface Node Master'). On the parallel bus (ECB) they control both standard I/O interface cards and gateway controller boards to lower level field bus systems, the *Controller Area Networks* (CAN) [5]. In total eight CAN configurations allow to equip the electronics of about 50 power supplies with an embedded controller (See 'Low Level Field Bus').

The new hardware configuration not only replaces (nearly) all aged interfaces. In addition, a 20% increase of the number of remote controlled devices is achieved. About 50 pieces of

*eMail: egan@acc.bessy.de, mueller@bessy.de, rahn@bessy.de

equipment formerly handled by local buttons, potentiometers, wheel switches and digital voltmeters are now attached to the computer system.

Software Architecture

The completely transparent transition from the old control system to a flexible, modern one imposes severe restrictions on any possible solution. More software modules are needed and the architecture is more complicated than in a newly designed system.

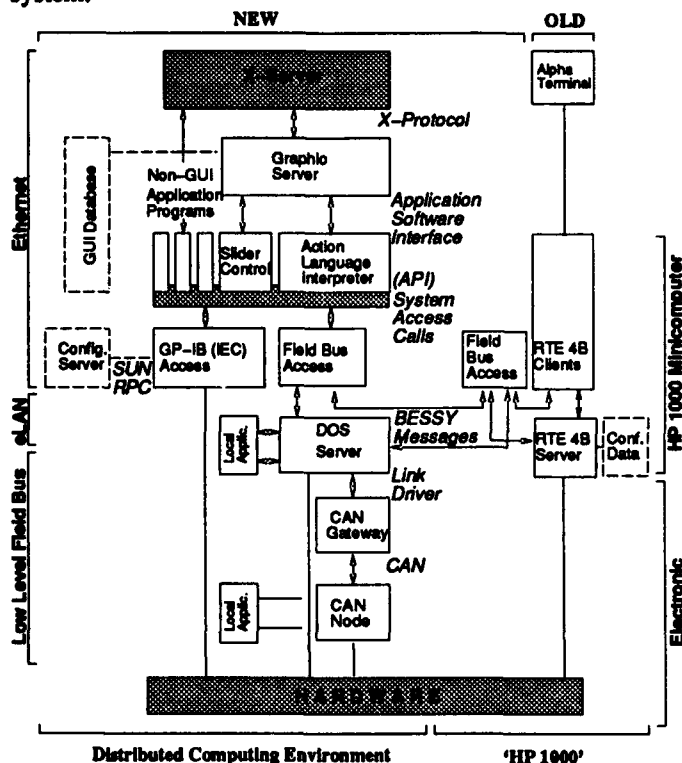


Figure 2: Sketch of the Software Architecture

The new control system is based on six very different protocol layers (See fig. 2). As the operator clicks a button of the *Graphical User Interface* (GUI) at one of the console displays up to seven server programs have to communicate until that event is converted into the hardware action the operator had in mind. Nevertheless the total response time stays within the order of 100 ms. This period of time is basically due to the moderate performance of the field bus 'eLAN'.

Despite that complexity any program that has to drive or control a piece of equipment has to use an application program interface (API) from a library of system access calls. That central software interface allows to keep the application code transparent and independent from the current field level configurations.

Programmable Control Application

Complex driving programs written in a sequential language (BASIC, FORTRAN) and programmed by sets of configura-

tion data are difficult to modify and maintain. Properties of the hardware and exception handling are usually spread all over the code.

We try to minimize these problems with an object oriented approach [7]: According to hardware specifics and driving methods devices correspond to classes in the code, usually derived from the obvious generic structures (e.g. power supply, valve, etc.). A built in interpreter section allows to attach device name to device class, form lists of devices, do simple arithmetical and logical operations, parse input and write output files. That provides the desired flexibility to the sets of configuration data.

Interface Node Master

As a new technical solution a board equipped with an Intel i386DX processor became available in April '91. It is 100% IBM-AT compatible and runs MS-DOS 5.0. It fits with its ISA and ECB bus connectors into a dual bus crate.

This board implies so many advantages that our developments for the system envisaged so far (MC 680x0 running OS 9) [3] have been frozen.

- The equipment server software existing for CP/M (Z80) systems [3] is much easier and faster ported to the more similar DOS (i386) system than to OS 9 (MC 680x0).
- In addition to the ECB bus IO cards standard PC hardware becomes accessible by the ISA slots. This makes it easy to utilize inhouse expertise for PC systems. Solutions from outside the controls group can be integrated into the control system with little extra work.
- More ECB bus slots per crate (26 instead of 16) provide better flexibility.
- Whenever required the hardware allows to replace DOS by a realtime UNIX kernel or another powerful realtime operating system like Lynx OS.

The equipment server code fits into modern object oriented concepts (object description, data, methods). Software interfaces within this server foresee to treat local application programs and requests from the fieldbus on an equal basis. Vacuum and high frequency surveillance, lifetime monitor etc. that run presently on stand alone PC-AT systems will be integrated into the server at this point.

Low Level Field Bus

The fast and robust CAN (*controller area network*) [5] has been developed for trucks and cars and is available as unexpensive firmware [6]. Its efficient protocol (Iso/DIS 11898) is based on priority drive bus arbitration. Messages are not sent to specific addresses. Nodes broadcast data objects that are received and evaluated by all participants where the objects are meaningful. A mechanism to notify data requests is part of the protocol. CAN supplies very flexible solutions for the common problem to treat analogous signals at the location of the devices and transport the data to the higher level micro computer.



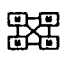

CAN	Profibus
ISO/OSI Level 2	ISO/OSI Levels 1, 2, 7
	
Multimaster	Multimaster/Master-Slave
	
Messageoriented	Point to Point
unlimited user 32 user for RS 485	32 user per Segment
1 Mbit/s for 40m (approx. 40 KBit/s for 1000 m)	500 Kbit/s for 200m (93,75 KBit/s for 1200m)
CSMA/CR	Token Passing with Polling
RS 485, fiberoptic possible	RS 485, fiberoptic
Extremely reliable data transfer	Excellent for large amount of data.
Free priorities	Two priorities
Deterministic at the highest priority level. Very fast.	Deterministic but not always suitable for fast realtime applications.
Simple Wiring	Simple Wiring
Decentralized mounting of modules possible	Decentralized mounting of modules possible
CAN - Controller Area Network Bosch/Intel	BMFT-Project German DIN 19245 standard
Low-Cost	Low-Cost
Excellent choice for semi-open systems	Easy system-expansion. Excellent choice for open systems.
Many Chip-Manufacturer have committed for CAN.	No chip-set available

Figure 3: CAN compared to MAP conformal Profibus

We have defined and implemented a small protocol layer between DOS Server and CAN gateway that allows to establish a stable and fault tolerant link between Proway C node master (i386) and CAN gateway (Z84xx) (Link Driver in fig. 2). A device server running on the embedded controller (Z84xx) of a CAN node has been designed and realized. The required communication protocol (on top of the CAN bus protocol) between CAN gateway and 'slave' node has been implemented (CAN in fig. 2). Matching of these modules has been tuned and the Proway C-CAN microprocessor system as a whole runs stable.

The determination of the beam position for the fast orbit measurement and correction system currently under development at BESSY will take place locally at the pick up stations. The application software that converts signal strength to the electron beam position information will run on the embedded controller of a CAN 'slave' node (See fig. 2).

Measuring Devices

Varying command sets and limitations to bus cable length require specific solutions for the control of measurement equipment on the GP-IB bus (IEEE 488, IEC 625). We use separate GP-IB

controller units that give bus access to any computer equipped with a serial line interface (RS 232 C).

Serial line interfaces on the console computers attached to a GP-IB controller unit are handled by dedicated server programs. A configuration server (See fig. 2) supplies the actual mapping of device names to serial line server responsible for the appropriate GP-IB segment. The API library routine then opens a *rpc*-connection to the GP-IP access server that mediates the exchange of commands and replies with the device.

Summary

With the new system maintenance will be no problem for a long period of time. Nearly no extra machine time has been needed for installation, testing and debugging. From graphical entities to device servers object oriented programming methods have been used at all levels. The modern man machine interface based on the X window system has been intuitively learned by the operators and is widely accepted. Application programs could be drastically improved and are much easier maintainable on the modern platform.

During the start phase of BESSY II we are immediately in a position to control hardware at the level of the magnet or vacuum laboratories. For the operation of the light source BESSY II it is at least a core system. Superfluous modules that have been necessary for the current control system conversion (like the Proway C field bus) have to be removed.

Synchronisation of application programs and database structures have to be introduced. Simulation programs have to give decision and control support. Sophisticated driving programs have to compensate correlated interactions (e.g. of undulators scanning at different speed). For the storage ring components different levels of privacy have to regulate access permissions and protection.

References

- [1] S. Bernstorff et. al., Physica Scripta, 36, 15 (1987)
- [2] G. v. Egan-Krieger, W.-D. Klotz and R. Maier, IEEE Transactions on Nuclear Science, NS-30, 2273 (1983)
- [3] G. v. Egan-Krieger, R. Müller, Proceedings of the 2nd European Particle Accelerator Conference, Nice, pp. 872-874, 875-877 (1990)
- [4] R. Müller, H.-D. Doll, I. J. Donasch, H. Marxen, H. Pause, Conference Record of the 1991 IEEE Particle Accelerator Conference, San Francisco, pp. 1311-1313 (1991)
R. Müller, Proceedings of the 3rd European Particle Accelerator Conference, Berlin, pp. 1167-1169 (1992)
- [5] Road Vehicles - Interchange of Digital Information - Controller Area Network (CAN) for High Speed Communication, Document Iso/DIS 11898, International Standardization Organization (1991)
- [6] INTEL 82526, Serial Communication Controller, Architectural Overview, Order Number 270 678-001 (Jan. 1989)
Philips PCA 82C200, Stand-alone CAN-Controller, Product Specification (Oct. 1990)
- [7] R. Lange, Diploma Thesis, FB 20, TU-Berlin, in preparation

Control and Data Acquisition System of Electron Accelerator for Radiation Processing

Wiesław Maciszewski, Janusz Łukaszewicz,
Wojciech Migdał, Andrzej G. Chmielewski
Institute of Nuclear Chemistry and Technology
03-195 Warsaw, Dorodna 16, Poland

Abstract

In the INCT a Pilot Plant for Food Irradiation started the operation November 1992. The plant is equipped with linear electron accelerator. To improve the operation it was decided to equip the accelerator with computerized system of the control and data acquisition. It is based on IBM PC/AT computer and the BITBUS interconnection system.

I. INTRODUCTION

In the Pilot Plant for Food Irradiation, new accelerator facility is installed. This is Russian made industrial electron linac "Elektronika 10-10" with electron energy of 10MeV and mean power of the beam up to 10kW [1]. The main parts of the accelerator are RF magnetron power generator, travelling wave type accelerating structure, high power pulse modulator, an electron gun and control system. To assure more effective operation of the accelerator and for its more convenient inspection, it was decided to equip the accelerator with computerized system of the control and data acquisition. Such a system will be very useful for the assurance of the irradiation process quality. The system is based on IBM PC/AT computer and the BITBUS interconnection system possessing distributed control modules [2, 3].

II. REQUIREMENTS FOR THE SYSTEM

The task of the system on its first stage of realization was supervising selected parameters of the accelerator, and memorizing/visualizing their current values in the form convenient for inspection of the accelerator operation by the operator. The second stage will be full automatization of accelerator operation. After realization of the second stage of the system we will be able to assure full automation of accelerator operation including the reaching selected parameters of the accelerator and their stabilization with a closed feedback loop. To do it, considerable modification of electronic systems of accelerator is needed. Starting the second stage of realization of the system is planned to be

done after finishing the warranty period for the accelerator. To attain practical realization of the system sixteen analog signals taken from the electronic circuits of the accelerator should be processed. The list of signals to be processed is as follows:

- 1 - straight beam current
- 2 - bended beam current
- 3 - bending magnet current
- 4 - scanning magnet current
- 5 - mean magnetron current
- 6 - magnetron voltage
- 7 - magnetron frequency deviation
- 8 - HF power level
- 9 - magnetron solenoid current
- 10 - accelerator solenoid current, section I
- 11 - accelerator solenoid current, section II
- 12 - accelerator solenoid current, section III
- 13 - gun voltage
- 14 - velocity of the conveyor
- 15 - vacuum level
- 16 - mains voltage

III. SYSTEM DESCRIPTION

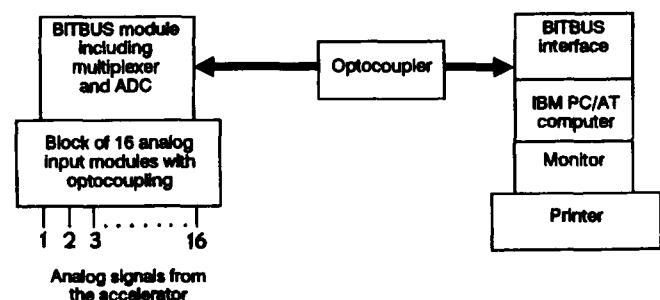


Fig.1. Block diagram of the system of data acquisition

The block diagram of the system of data acquisition is shown in fig. 1.

Analog signals from the accelerator are delivered to the block of sixteen analog modules with optoisolation. Next, these signals are fed to the BITBUS analog module which includes multiplexer and analog-to-digital converter. This module realizes sequential ADC conversion of the signals and their preliminary processing. Digital signals are transmitted to the computer by means of BITBUS data way. Operation of the system is based on appropriate software, which may be divided into three following parts:

1 - local software of analog module responsible for carrying out the measurements, their results memorizing and preliminary processing inside the module;

2 - data base, which ensures to storage operational parameters of the accelerator and various data of the plant's activity, for example registration of customers, write out the cheques and certificates of radiation treatment. Apart from this, data base allows to define all parameters of measuring channels, which gives the operator the possibility of adjusting the voltage on a given measuring output and related physical parameter of the accelerator;

3 - controlling software, written in C language, which allows the current inspection of the accelerator parameters

and directs the transmission of information through the BITBUS data way, participating in data exchange between analog module and data base.

IV. CONCLUSIONS

The system of data acquisition (stage 1) has been connected to the "Elektronika 10-10" rf linac and preliminarily tested. In consequence considerable improvement in the inspection of the accelerator was obtained.

Further development of the system (stage 2) for the extension its ability in the control and stabilization of important accelerator parameters is under consideration.

V. REFERENCES

- [1] Linear Electron Accelerator "Elektronika 10-10", *Technical Description*, Moscow (1991).
- [2] The BITBUS Interconnect Serial Control Bus Specification, *Intel Corp.*, order number 280645-001 (1988).
- [3] Distributed Control Modules, *Intel Corp.*, order number 230973-004 (1988).

Expert System for Magnetic Systems Investigations

S. Lima, R.V. Poliakova, F. Fernandez Nodarse, I.P. Yudin,
Joint Institute for Nuclear Research
141980, Dubna, Moscow Region, Russia

Abstract

The paper deals with development of the conception and main functions of the system based on knowledge for magnetic systems investigations. The use of distributed artificial intelligence and cooperating systems is discussed. Some applications are presented.

I. INTRODUCTION

Distributed problem solving architectures can now also give benefits for intelligent advice giving and problem solving systems, as they might be used in accelerator operation and design. At point of view of the solution methods, this task was defined as a problem characterized by incomplete and inexact data, the use of heuristic knowledge for defining part of the values of the model parameters and its following solution. A Computer Aided Assistants (integrated expert systems) have been developed to solve this tasks using the architecture of cooperating distributive systems. Data are used with user feedback to provide the modeling and to change the solution. Multilevel problem solving scheme is used. The comparison of the different solutions for the tasks or subtasks carries out using a problem solving model with the use of qualitative model. It describes the system regimens.

II. ACCELERATOR OPERATION AND CONTROL SYSTEMS

Accelerator operation is a task demanding technical competence, experience, diagnostic skill and judgement. The essential ingredients in any kind of accelerator control system are: timing system, equipment interfaces, networks, computers, software. The operator has to handle large amounts of information coming from several different kinds of systems, coordinate and use a limited number of tools simultaneously, make a general judgment of the situation, and take reasonable decisions. Therefore, as soon as reliable computers were available and the accelerators complicated enough, a part of the operator's duties was off-loaded onto computers. This formulation already implies that there are several layers of control objectives (hierarchical structure):

- reflexive controls (simple servo and regulatory controls or simple sequential and interlocking digital devices). It is a rule to keep reflexive control away from the top layers and for this, modern microprocessors can be very good tools. Here the major portions of the real-time programs run.

- reactive controls (adaptive control, failure diagnostics, safety systems and multivariable controls). They are the realm of the distributed computerized control system today.
- tactical controls. Using digital models of the analogous process, "accelerator" physicists try to optimize the controls and the machine. At this level it should be possible to try (in the model) different optical configurations of the accelerators and the corresponding changes in magnet settings.
- strategic controls. These would be the scheduling of the run times, selecting optimum energies to run at, and related topics.

The subdivision into decision layers as in a hierarchically ordered system is not followed in all existing accelerator control systems. A modern accelerator control system contains distributed intelligence for reflexive and, if possible, reactive control tasks. The hierarchy of control is realized in layers of hardware interconnected by networks. The lowest layers takes care of reflexive controls, the up-most layer of tactical or strategic controls. The interfaces to the process are in some way standardized to ease both commissioning and maintenance. Real-time operating software has to be switched coinciding with external signals. Many levels of timing precision can be distinguished. This observation leads unavoidably to the idea of local electronics at the device in question and a bus to transport information to some intelligent controller. Not all information flows to the control room through the computer networks. Analog signals, TV pictures and in particular interlock circuits go via other routes.

The analysis of the tasks of an operator show that there are different levels of involvement/ expertise necessary during the operation of the accelerator. Task-dependent knowledge is more useful in problem solving. These levels can be described in the following way:

- Training and testing.
- Operation in normal conditions. The basic tasks for the operator are monitoring the performance and adjusting parameters in case of slight fluctuations to optimize the operation.
- High level breakdown, i.e. troubleshooting of high level faults like false parameter setting, an entirely broken element, drifts, etc. These faults should be seen as breakdowns that can be diagnosed on a conceptual level that needs no reasoning about the control system.

- Low level breakdown, i.e. troubleshooting of low level elements/ modules of the control system like wrong data in equipment driver tables or faulty electronic interface modules which are only resolved by a controls specialist.

III. CONCEPTION AND MAIN FUNCTIONS

The use of artificial intelligence and workstations in the accelerator operation and design has become standard practice [1]. Most expert system (ES) tools used in this field comprise an inference engine, a knowledge acquisition system, a knowledge base, an explanation system and a user interface. Applied knowledge usually takes the form of "assistant" programs (CAA - Computer Aided Assistant).

ES may be used to integrate a big program complex oriented to modeling the accelerator, for example in the design of the modification of the spectrometrical magnet SP-40 at the EXCHARM facility [2]. This problem solving system (CAA) assists the user during the following steps: to prepare the input data, to integrate and store the information required, to model the different solutions, to select the best solution, and to check the solution. During the modeling the heuristic knowledge may play a big role. A prototype of this CAA has developed using blackboard architecture and network workstations.

The blackboard-system essentially consists of three components: blackboard data structure (BB), knowledge sources (KS) and control modules (CM). BB-systems emphasize the use of multiple cooperating subESs, or KSs. The purpose of BB (global solution database) is to hold computational and solution data needed and produced by the subsystems. The BB was segmented into distinct levels of abstraction. It also describes the problem solving strategies and programs. Each KS is a small knowledge based problem solver, and its internal processes have only local effects, rather than causing potential interactions with the rest of the system. KSs assist to the user in the selection of the problem solving strategies. The problem solving behavior of a BB-system is determined by the KS application strategy encoded in the control modules. Basically the CM determines the blackboard region to focus on and the particular KS to work on that region. Graphic tools are included.

The following tasks were important for ES oriented to accelerator operation and control: on-line data processing (analog and digital data); finding heuristic methods of diagnosis from human expert (surface knowledge); modeling, and calculations (deep knowledge); local checks using oscilloscopes, measurement tool, etc. (off-line information); visual checks and unmeasured information; logbook, chart, and drawing checks; wave from diagnosis; and Case Base storage (indexing, learning).

The goal of the accelerator operation and control can be achieved if the identified tasks cooperate with each other. Well defined autonomous tasks like alarm monitoring and treatment, equipment access, optimization, management

of archives, beam diagnosis, and control system diagnosis, can be regarded in the context of accelerator operation as loosely coupled cooperating agents. They can perform tasks independently of each other and can send requests to other agents to work on the common goal of accelerator operation. The cooperational features on top of these subtasks must include the capability of reasoning on the current state of the task, the current state of other tasks, and how the interaction between these tasks influences the control within any particular task.

The increasing complexity of accelerator control systems raises the need for distributed processing systems. A high degree of physical distribution and modularity and the need for continuous modifications and updates can easily make such evolving complex systems inconsistent. These kinds of problems are the subject of Distributed Artificial Intelligence (DAI). Distribution of the intelligence allows one to free the host from trivialities. Once freed from the reflexive control, it can support the operator effectively maximizes reliability and efficiency. Effective partitioning maximizes reliability and efficiency. A closed loop works properly only if all time constants are adequately chosen and this applies also if a man is part of the loop. The user interface has to be user friendly. To be effective, the system has to perform three functions on the incoming data stream:

- a reliable and accurate collection, fast enough in real time, is mandatory;
- the vast amount of data, possibly created in this way, has to be reduced and concentrated; and
- each system user, operator and maintenance technician, has to have the possibility of accessing the bits, the equipment or physics parameter that they need in real time, without interruption or excessive time lag.

Software clearly depends on the architecture of the control system. The software includes data preparation and data acquisition modules (build up configuration, compute optics & beam parameters, trim model output); databases (reference data set, target data set, current data set, accelerator description); hardware interface modules (initialize/ set/ increment hardware, read accelerator parameters, measure beam parameters); feedback modules (compute modifications); and learning mechanism (archive/ improve accelerator description, update when improved). The console programs at the accelerator may be generally classified in three main groups: study programs (modeling: accelerator physics - model beam dynamics); model programs (accelerator component description - compute machine/ beam parameters - accelerator parameters description); and real-time application programs (calculate/ set/ read/ adjust accelerator parameters, measured/ read parameters).

The CAA AOC for accelerator operation and control includes the following basic components: accelerator's CAA, operator's CAI (Computer Aided Instruction), operator's CAA (that assists the operator during the operation in

normal conditions), diagnostic ESs (that assist the operator during the high and low level breakdown), DBMS, and help, utilities and interface programs.

The control system (CS) gives the possibility of accessing the different accelerator elements in a standard way.

Drift in parameters and optimization is checked by a subsystem of the operator's CAA, using the applications software for measurements and control actions. Test which change control values are passed through it.

The control system scans the equipment and produces an unfiltered alarm list. The alarm expert subsystem of the operator's CAA can be considered as an intelligent interface to the control system and its alarm system in particular and could be responsible for processing alarm data for the operator. Then it will reduce the feedback loop via the operator, by eliminating useless, misleading and unnecessary information.

The operator's CAI is an ES oriented to training and to testing their technical competence and experience.

The ES for diagnosing hardware and software problems in the modules of the control system is mainly based on deep knowledge, and uses DBMS to instantiate the models used in a session. The path of the control parameter goes via several front end computers (network workstations), transmission systems and microcomputers, and was piloted by generic and specific software for the equipment control.

The ES for diagnosing problems concerning the accelerator and the beam includes a data acquisition module that acquires and judges information about beam parameters. It reduces the uncertainty in the acquisition.

The equipment diagnosis expert system verifies the hypotheses developed by the expert system for diagnosing problems.

The information about the layout and function of the accelerator and control system is stored in the database (DBMS). It also serves to fill information into local and on-line data storage. In operation it can be used for checking reality against design intentions, mostly for software modules, and for storage of reference data for well defined operational situations. The distributed database contains the translation table, the current values, set points and actual values for each piece of equipment, conversion factors, end point settings and many other parameters.

The user interface module coordinates information from the different subsystems and takes care of the presentation to the user. The operator interface includes the use of interactive menus, spreadsheets and distributed windows.

A framework [3] for integration of cooperating distributed systems in process supervision, design (modeling) and control applications in the accelerator was developed. The Cooperation Layer, that provides the means for cooperation, is decomposed into several components. The Intelligent System (IS) incorporates subtasks of the problem. The Monitor is the control instance and connects the ISs or semi-autonomous processing elements to the Cooperation Layer. Using the knowledge sources, the Planning and Coordination Module supervises all cooperational behavior

like situation assessment and planning. The Communication Modules and the Session Layer do all message passing between systems. The Information Management Module (DBMS) provides a distributed information access mechanism to support the remote access and sharing of information among systems and it is in close connection with the Acquaintance Models (AM) and the Self Model (SM). The SM Model represents a system's own capabilities, needs and interests. The AM stores similar information about other systems of the cooperating community in which the system itself is interested. The accelerator's CAA provides (integrates) the functions of the Cooperation Layer and Session Layer. This framework may also be used for each intelligent system.

These CAAs integrate systems based on knowledge, databases, spreadsheets, graphic tools and other utilities. It also provides a user-friendly interface. This conception was developed using network workstations for the MT-25 microtron [4] at JINR to help microtron operator in the preparation, start, technical fault search and adjust, run (operation), turn off and maintenance processes.

IV. CONCLUSION

Computer Aided Assistants based on knowledge and characterized by good ergonomic conditions, user-friendly interfaces and adequate response time make more easy the work, reduce the training time and the number of user mistakes. They use symbolic manipulation and numerical methods, heuristic knowledge and specialized graphic tools.

The proposed architecture of cooperating distributed systems increases the performance and power of such systems specially of the cooperating heterogeneous on-line systems for operating an accelerator. It covers the whole range of diagnosis, process optimization, recovery actions and unified presentation to the operator. This has emerged from the careful study of the accelerator operation at the JINR.

V. REFERENCES

- [1] M. Lee, S. Clearwater, "GOLD: Integration of Model-based Control Systems with Artificial Intelligence and Workstations," (SLAC-PUB-4396, August 1987).
- [2] E.P. Zhidkov et al., "Mathematical Modeling of Some Modification of Spectrometrical Magnet SP-40," *JINR Communication* P11-92-490, Dubna, 1992.
- [3] ARCHON - Architecture for Cooperating Heterogeneous On-line Systems Status Report (compiled by S. Becker, J.Ehlers), *ESPRIT Conference Week 1990*, and *Technical Report No.9* (ESPRIT - Project 2256 ARCHON) 9-1990.
- [4] V.G. Ivanov et al., "Automated Workstation for Microtron MT-25. Conception and main functions," *JINR Communication* P10-91-302, Dubna, 1991.

Orbit Correction Implementation at CEBAF*

M. Bickley, B. A. Bowling, D. Douglas, A. Hofler, J. Kewisch, G. A. Krafft
Continuous Electron Beam Accelerator Facility
12000 Jefferson Avenue, Newport News, VA 23606-1909 USA

Abstract

CEBAF has recently performed automated beam orbit control in real time. This effort was achieved by exploiting the capabilities of the TACL control system, using the newly implemented STAR network, which easily yielded the required data transfer density needed. Also involved in this effort was the On-Line Envelope code OLE, which provided first-order transfer matrices that reflected the current machine optics. These tools made the implementation of the specific orbit-correction algorithms easier and increased reliability. The implemented algorithms include beamthreading, orbitlocks with 2 correctors/2 monitors, most-effective corrector, and n -corrector/ n -monitor correction.

I. INTRODUCTION

The CEBAF superconducting accelerator^[1] is a recirculating cw electron linac consisting of a 45 MeV injector linac, two 0.4 GeV main linacs, a recirculator, and a beam switchyard. Each beam can be recirculated up to five times for a final energy of 4 GeV. In both arcs, beamlines tuned to specific energies transport the different-energy beams between linacs; at the end of each arc, the beams are recombined and made collinear for reinjection and further acceleration. There are 1400 correction magnets and 550 beam position monitor devices.

The large magnitude of correction elements at CEBAF requires automated beam orbit control for proper accelerator operation. A requirement therefore exists to develop algorithms which will automatically correct beam position and optical parameters. Tools have been developed to greatly assist in this development. CEBAF has recently implemented the STAR network protocol, which has vastly improved the data transfer speed and ease of obtaining current operational values. A machine model has been developed, known as the On-Line Envelope (OLE), which uses real time magnet currents and RF cavity settings, computing ideal optics and transfer matrices. These values are delivered to the orbit correction applications by the STAR and reflect the current running state of the accelerator.

With the use of these tools, it is quite easy to implement various correction methods. CEBAF has just successfully completed the high-power and east arc tests, and some orbit correction techniques have been tested. This paper will discuss these methods, as well as others that have been implemented in code and are ready for real beam testing.

II. STAR DATA DIRECTOR

In TACL^[2], the STAR^[3] is a request-based entity

responsible for signal data communications among applications. In general, signals represent readbacks and setpoints for hardware and software controls that are created in TACL logic sets. Although these signals are updated each logic cycle, the STAR communicates signal updates only for those requested by applications such as other logic sets, TACL display pages, and stand-alone simulations. Signal value changes are recorded and maintained in shared memory on the front-end computers, known as locals. When a signal is requested by an application, the STAR sends out a request to the logic set that owns the signal. After checking the shared memory on the front-end computer, the logic set sends the update to the STAR which, in turn, passes the data to the application originating the request.

In this scheme, stand-alone simulations (like OLE) operate like logic sets on front-end computers in that they write to shared memory, but the aspect that looks at shared memory and communicates with the STAR is managed by programs called spy programs. These programs use standard STAR protocols to communicate with the STAR, but they are customized to read the shared memory generated by the simulation and package the information into an acceptable signal format for the STAR.

Application programs, like orbit correction codes, attach to the STAR by a single function call. Data value setting and retrieval are accomplished by the use of other easy-to-use function calls. The STAR is implemented using Berkeley Sockets under TCP/IP protocol, which allows attachment from any other computer located on the network which are routable to the computer executing the STAR code. The STAR maintains a list of computers and valid users which have write permission—all other connections can only receive data. This feature allowed testing of application program execution and logical flow without the fear of contaminating data values and, possibly, consequential machine damage.

III. ON-LINE ENVELOPE

CEBAF originally developed the OLE^[4] program, which quickly computes first-order machine Twiss parameters, in order to model and correct the beam envelope. The design goal of OLE was to develop a machine model which would use real-time machine settings, such as magnet currents and RF cavity amplitudes and phase, and generate beta functions and phase advance values at various points around the lattice, with updates taking less than one second to compute and post. With the combined use of efficient programming techniques and modern fast computers, this goal was easily achieved.

OLE starts the calculation by obtaining magnet optical strengths, obtained directly from the magnet LOGIC for each element, which develops the calculation based on beam

* Supported by U.S. DOE contract DE-AC05-84ER40150

energy and excitation curves for that element. Also inputted are cavity amplitude and phase settings, obtained from the RF LOGIC. Initial alpha and beta values used are derived from emittance measurements and back-propagated to the beginning of the lattice for use by OLE.

OLE performs first-order optics calculations using 2×2 matrix formulation for calculating the machine beta function at a point, by the use of orthogonal trajectories:

$$\begin{pmatrix} X_1 & X_2 \\ X'_1 & X'_2 \end{pmatrix} = \begin{pmatrix} \sqrt{\beta} \cos \phi & \sqrt{\beta} \sin \phi \\ -\frac{\alpha}{\sqrt{\beta}} \cos \phi - \sqrt{\beta} \phi' \sin \phi & -\frac{\alpha}{\sqrt{\beta}} \sin \phi + \sqrt{\beta} \phi' \cos \phi \end{pmatrix}$$

where ϕ is the arbitrary initial phase angle, usually set to zero, and α and β are initial amplitude functions. Transfer matrices of the familiar form used for propagating $(X \ X')$ are used for the above trajectories. The transfer matrix used for the accelerating cavities was developed at CEBAF and is basically a particle-tracing algorithm which numerically adjusts a model of the electric field, matching the energy gain measured in the RF controls system. The matrix contains focusing effects which the particles experience in the CEBAF cavities.

The Twiss parameters can be found by:

$$\begin{aligned} \beta &= R_{11}^2 + R_{12}^2 \\ \alpha &= -R_{11}R_{21} - R_{12}R_{22} \\ \phi &= \tan^{-1} \left(\frac{R_{12}}{R_{11}} \right) \end{aligned}$$

These parameters can be used to produce transfer matrices of the familiar form:

$$M(s1, s2) = \begin{pmatrix} \frac{\sqrt{\beta_2}}{\beta_1} (\cos \Delta\phi + \alpha_1 \sin \Delta\phi) & \sqrt{\beta_1 \beta_2} \sin \Delta\phi \\ \frac{(1 + \alpha_1 \alpha_2) \sin \Delta\phi + (\alpha_2 - \alpha_1) \cos \Delta\phi}{\sqrt{\beta_1 \beta_2}} & \frac{\sqrt{\beta_2}}{\beta_1} (\cos \Delta\phi - \alpha_2 \sin \Delta\phi) \end{pmatrix}$$

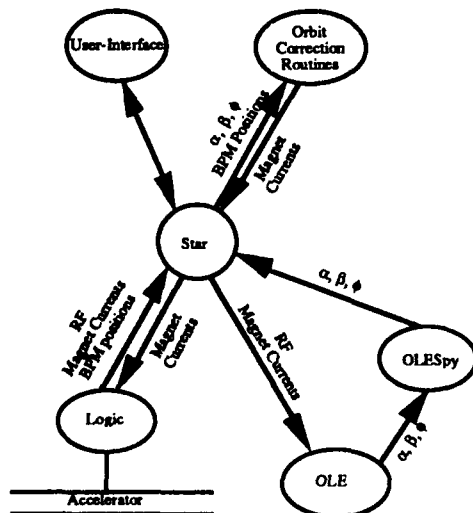


Figure 1. OLE-STAR Block Diagram

OLE constantly checks for changes in the magnet or RF values and recomputes new parameters when changes occur. The resulting Twiss parameters are posted on the STAR for use by all application programs via the OLEspy program (figure 2). The use of OLE results in a method of predicting orbit corrections for the current machine settings without user interaction, simplifying implementation and increasing reliability.

IV. ORBIT CORRECTION METHODS

Using the above tools made implementation of orbit correction algorithms very simple, allowing the person developing the code to concentrate mostly on the algorithm, not the implementation. Most orbit correction techniques read beam position monitor data, compute a correction, and set changes in corrector strengths. The STAR allows the global reading of various monitor data in one function call, passing back an array of values. Corrector strengths, in optical units as a function of energy and set current, are generated at the local computer level and are transferred by the STAR in an identical manner. Similarly, in one function call, Twiss parameters generated by OLE for all invoked corrector and monitors are delivered, and transfer matrices between elements are easily created.

CEBAF has recently attempted automatic steering for the first time. The first tested algorithm was beamthreading, which employs one corrector and one monitor, with the goal being to predict and correct the beam orbit. The algorithm implemented was to predict a kick which would locally correct the orbit at a downstream point:

$$\Delta K_1 = \frac{-\Delta X_{\text{monitor}}}{\sqrt{\beta_{\text{corrector}}} \sqrt{\beta_{\text{monitor}}} \sin(\phi_{\text{monitor}} - \phi_{\text{corrector}})}$$

The denominator is the M_{12} transfer matrix, which describes a downstream change in displacement from an upstream kick. OLE computations had been verified previously by comparing results with DIMAD, TRANSPORT, and PETROS simulation codes, and by predicting beam sizes through several quadrupoles and comparing with real beam emittance measurements. The other factors involved that were tested included the calibrations of the beam position monitors, which were determined from test stand data, and the computation of optical strength from magnet current and beam momentum measurement.

The beamthreading algorithm, as implemented, uses one monitor and one corrector and performs the correction, iterating if necessary, and then moves to the next corrector/monitor pair. This method, although slow, is simple and results in a properly zeroed orbit. It has the added advantage of easily testing the model against the real machine, as well as testing the monitor and corrector devices.

The above equation was applied in the spreader and arc section of the machine during the east arc commissioning tests, which were recently completed. The energy at this point

was 130 MeV, and the testing was performed using pulsed beam operation, using the beam position monitors in pulsed configuration. The results were very encouraging, with the achieved correction within 10 percent of zero position with one application.

With the success of the beamthreading method, the algorithm was expanded to use two correctors and two monitors. This effectively corrects the slope and displacement of the beam and will result in a beam with zero slope and zero displacement, and is known as an orbit lock. If one wishes to maintain a given orbit in an area of the machine, this method snapshots the initial beam position monitor readings and declares these values as the zero reference trajectory. Subsequent readings are subtracted from these values to find differences in position. The equation of the lock is of the form:

$$\begin{bmatrix} \sqrt{\beta_{c1}\beta_{m1}} \sin(\phi_{m1} - \phi_{c1}) & \sqrt{\beta_{c2}\beta_{m1}} \sin(\phi_{m1} - \phi_{c2}) \\ \sqrt{\beta_{c1}\beta_{m2}} \sin(\phi_{m2} - \phi_{c1}) & \sqrt{\beta_{c2}\beta_{m2}} \sin(\phi_{m2} - \phi_{c2}) \end{bmatrix} \begin{bmatrix} \Delta_{k1} \\ \Delta_{k2} \end{bmatrix} = - \begin{bmatrix} \Delta_{x1} \\ \Delta_{x2} \end{bmatrix}$$

This was employed in the region after the north linac immediately preceding the east arc spreader. The result obtained were that expected for this method, with the orbit returning back to the zero-defined trajectory after execution of the lock program. The program was made to execute when the orbit measured exceeded a set tolerance, which allowed the orbit downstream of the lock to remain stable regardless of the upstream orbit. This lock is desirable when one performs dispersion measurements in the spreader region while altering a parameter in the injector or linac, to maintain a constant trajectory preceding the spreader dipole.

The next natural extension of the above is to expand to many correctors and many monitors. For N correctors and N monitors, the equation takes the form of a square matrix as above with N equations which can be solved directly. For some cases occurring in the CEBAF arcs, there are more correctors than monitors. This results in an underdetermined equation system, which can be solved using singular-value decomposition. These correction methods have been coded but have not been tested with actual beam.

Other correction methods have been implemented, such as the Micado method (most-effective corrector), beam bumps, least squares correction of several correctors and several monitors, and entrance angle and displacement adjustment for multi-pass linac operation. These methods, however, have not yet been beam-tested.

To assist in the debugging of orbit correction methods, as well as other computer-assisted optics adjustments, a simulation reflecting the CEBAF lattice has been developed[4]. This simulation operates similarly to the OLE code, reading real-time magnetic strengths and RF parameters and computing a central trajectory orbit, with this orbit replacing the beam position monitor readings in the real machine. The orbit correction codes operate on the machine as designed and the simulation reacts to the corrections as

would real accelerated beam. Therefore, the codes can be thoroughly debugged and tested for proper operation before being put into service.

V. REFERENCES

- [1] H. Grunder, "The Continuous Electron Beam Accelerator Facility", 1988 *Linear Acc. Conf. Proc.*, pp. 3—8.
- [2] R. Bork, C. Grubb, G. Lahti, E. Navarro, J. Sage, T. Moore "CEBAF Control System." CEBAF-PR-89-013.
- [3] M. Bickley and J. Kewisch. "The Star, a Dynamically Configured Dataflow Director for Realtime Control." These Proceedings.
- [3] A. Barry, *et al.*, "OLE: Fast On-Line Display of the CEBAF Beam Envelope" CEBAF-TN (internal document).
- [4] J. Kewisch, *et al.*, "Accelerator Simulation and Operation Via. Identical Operational Interfaces", *Conference Record of the 1991 Particle Accelerator Conference*.

Controls Interface Protocols for the SSC Correction and 'DC' Magnet Power Supplies

Surajit Sarkar, Jeff Gannon, William Merz, Frank Meyer.

Superconducting Super Collider Laboratory*
2550 Beckleymeade Avenue, Dallas, Texas, 75237

Abstract

The control, monitoring and diagnostic requirements of power supply systems determine the required functionality (or transactions) and response of the interface protocol. Advances in technology allow increased functionality of front end control equipment and therefore relatively sophisticated interfaces are required. The protocols to be used must be capable of supporting functionality upgrades. The command response type protocols standardized on earlier are no longer adequate. This paper describes the interface protocol to be used between the SSC Corrector and 'DC' magnet power supplies and their respective controllers. Factors affecting protocol definition and constraints placed by cost and availability considerations are described as well as an implementation strategy.

I. INTRODUCTION

Magnet power supply control requirements for the SSC Global Accelerator Control System (GACS) are determined by many factors. The SSC Global Accelerator Control System must support the operation of the 10 hz cycling LINAC and the Low Energy Booster (LEB) on the one hand, while at the same time it must be capable of supporting the 20 hour flat-top operation of the collider. Special requirements are additionally imposed by the large number of devices involved, the large distances spanned and by the demanding availability requirements placed on the collider.

The SSC GACS interfaces to sub-system' controls for major systems such as the RF and Cryo. The interface to the magnet power supply controls is at the sub-system level for the Ring magnet and the Kicker magnet power supply systems, while for the 'DC', the Pulsed and the Corrector magnet systems[1] it is at the equipment interface level.

Figure 1 is a representation of the generic GACS equipment level interface to magnet power supply systems. The

lers or IOCs. The IOCs talk to VME crate based power supply controllers which are connected to power supply interfaces by fibre optic links. The power supply interfaces hide power supply particulars such as type (bulk or power converter), reference resolution and output current level, from the controller. Configurations can differ from that shown in figure 1. For example each of the LINAC 'DC' power supplies will be independent. There will be no shared bulk power supply.

In the above controls architecture the interfaces between the GACS, the Crate IOC, the power supply controller and the power supply all need to be defined (the power supply to magnet interconnect is defined elsewhere). The earlier choice of EPICS as the controls software platform for the SSC GACS defines primary interaction of the GACS with the Crate IOC. The physical interface between the IOC and the power supply controller is the VME crate backplane. The data transfer protocols between the IOC and the equipment (in this case power supply) controller level affects GACS characteristics such as process synchronization and are to be defined elsewhere. An instance of this interface is to be described for the LINAC 'DC' power supply controllers in reference [2]. This paper discusses the equipment control protocol between the power supply controller and the power supply for the SSC Corrector, Pulsed and 'DC' Magnet power supplies.

A. Requirements

Design goals are to reduce the number of controllers types and to use common protocol format across Machines and power supply types. The control protocols chosen must be capable of supporting as subset the collected requirements of the Corrector, Pulsed and 'DC' power supply controls.

Details of protocol such as command and data formats for the various power supply types depend on the required functionality (control, monitoring and diagnostic) for each of these types and are described elsewhere, for example[3].

The GACS interfaces to the power supplies through three control levels. The protocol must allow the use of power supply interfaces that do not require local intelligence, reducing the software and maintenance support required.

The protocol must support timely delivery of command & data and the synchronization of actions across the site. For the LEB correctors a reference update rate of 10 khz with a delivery accuracy of $\pm 2 \mu\text{s}$ is required.

The protocol must allow expansion to include foreseen requirements such as: the use of special methods for meeting the high availability requirements of the SSC accelerator complex[4], or the expected use of these controllers for other applications requiring either set-point controllers or ramp generators synchronized to the machine cycle, eg. the ramp generators required for the Beam Loss Monitor Bias supplies and tune kickers.

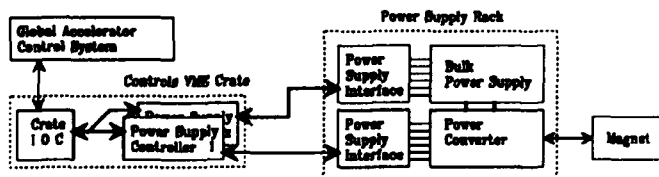


Figure 1: Power Supply Controls Block Diagram

boundary between the GACS and the magnet power supply system is the link between the power supply (equipment) controller and the power supply. The GACS interfaces to processors at the VME crate level called Input Output control-

* Operated by the Universities Research Association, Inc., for the U.S. Department of Energy under Contract No. DE-AC02-89ER40486.

B. Choice of Protocols

Various alternative protocols were explored including the SSC Message Broadcast system (MBS) protocol[5]. Advantages would have been common hardware components and reusable support software. However the $\pm 5 \mu\text{s}$ message granularity (as determined the 1.54 Mhz T1 carrier and the MBS frame definition) would not meet the delivery accuracy requirement. The MBS variable length frame left open the possibility of timing inaccuracies exceeding tolerances being inadvertently introduced at a later date.

A command response type protocol is inappropriate since it would require intelligence at the power supply interface for interpreting received commands. A free running protocol, in which status information is continuously returned, was chosen. Requirement for delivery accuracy was met by specifying fixed frame size, with each frame delivering a specific command or reference data and by specifying required link speed. Delivery requirements for other high speed applications may be met by using higher speed links limited by the minimum packet size that can be used.

II. CONTROLS INTERFACE PROTOCOLS

Functionally the interface can be considered as a layered system along the lines of the ISO Open Systems Interconnect model, which consists of the applications, the presentation, the

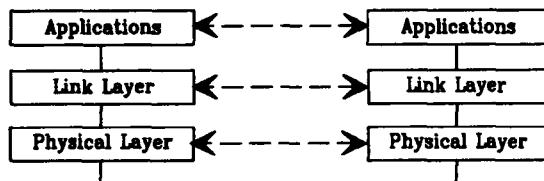


Figure 2: Power Supply Control Protocol Layers

session, the transport, the network, the data link and the physical layer. The power supply controller to power supply link is a point to point link. The presentation, the session, the transport and the network layers can be considered null since corresponding functionality requirement does not exist or is minimal. Figure 2 is a data flow diagram showing the physical data paths and the logical interconnects. The functionality of each of the layers (except the physical interface) may be implemented in either hardware or software. The following sub-sections discuss the functionality and implementation choices for the each of the layers.

A. The Application level protocol

Protocol data flows for the ramped and the set-point controllers are as described below. Correction magnets reference (and optionally command information) is sent from the power supply controller to the power supply interface every $100 \mu\text{s}$ for the LEB correctors (1 mS for all other machines), during normal operations. Reference and commands received at the power supply interface are loaded into predetermined registers. Receipt of a reference value triggers a series of events overseen by a hardware timing controller at the power supply interface. The digital reference value is converted and sent as an electrically isolated analog reference to the power supply. After a predetermined delay to allow for settling times of interface electronics the timing controller orchestrates the acquisition of analog readback parameters and status informa-

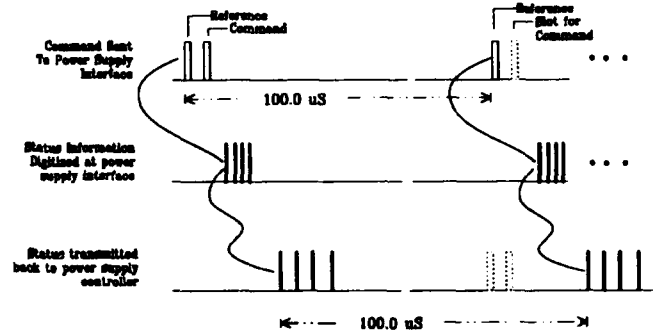


Figure 3: Corrector PS Controller / Interface Data Flow

tion from the power supply. The acquired values are digitized and then sent back to the power supply controller as shown in figure 3. Corrector power supplies are not necessarily switched off during machine maintenance and monitoring is required. In the absence of reference update stream for periods exceeding 0.4 seconds, the power supply interfaces go into a second mode of generating status information continuously at a 10 khz rate for the LEB (1 khz for all other machines). This mode is also activated in case of link failure.

The protocol for the 'DC' power supply controls is similar except that the reference values are sent to the power supply infrequently, usually at multiples of a 0.1S interval. The status information required for monitoring power converter performance is required to be readback at a 1 khz rate and is

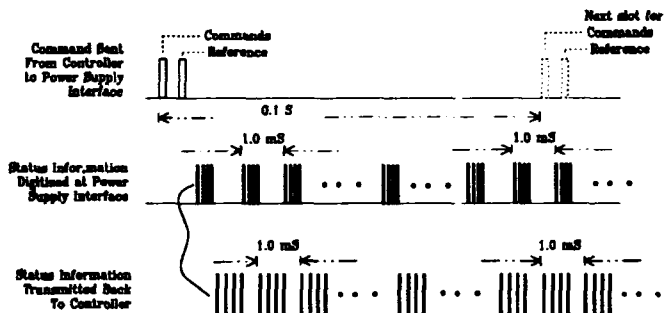


Figure 4: 'DC' PS Controller / Interface Data Flow

generated asynchronously as shown in figure 4.

The application level protocol format consists of fixed length, byte serial frames with a type field, indicating command or data, followed by one or more data fields. Commands are identified by a one in the most significant bit position and data by a zero. The following two bits identify the power supply types. The last five bits specify command number. All analog values are transferred as 16 bit values. Bipolar data is sent as sign plus 15 bit magnitude.

B. Link Level Protocol

Link level framing is asynchronous 8 bit plus parity with one start bit and one stop bit. Maximum intra frame byte separation allowed is $51.2 \mu\text{s}$ or 256 bit periods. Link state is initialized on time out. Explicit link management commands such as link initialize have not been specified in order to keep the link simple. For the slowest controller processor this corresponds to 512 instructions. This requirement is very easy to meet for the power supply interface electronics.

C. Physical interface

The physical interface between the power supply controller and the power supply interface is a bi-directional, bit serial, digital fibre optic link. The interface specification details media and optical signalling levels based on required Bit Error Rates (BER) as discussed later. A digital fibre optic link was chosen for the usual reasons of common mode isolation and immunity to electromagnetic interference.

A Total Output Deviation (TOD)[6] tolerable for power supplies is specified based on machine operation requirements. A digital interface allowed us to allocate a small, predetermined part of the TOD set by quantization error due to selected data word length or resolution in the controller. The rest of the allowable TOD is available to the power supply electronics. Problems of controls ADC / DAC drift and noise pickup are reduced. Location of error source is easier.

The Link encoding is bi phase mark. This is a modification of the bi-phase encoding used for the Fermilab machine data transmission link[7]. The mark condition corresponds to a fibre optic transmitter LED off condition and purports to lengthen the LED lifetime. Encoder and decoder implementation requires very few components and present strategy is to use popcorn logic followed by encapsulation using Field Programmable Gate Arrays.

III. ERROR DETECTION AND CORRECTION

A. Link Level

At the link level, an analysis was done about the expected number of errors under normal operating conditions for the 'DC' and the corrector magnet power supply. Fibre optic link BER depends on the optical loss budget and the receiver SNR. Using calculated BER of 1 in 10^{12} , expected errors for the 'DC' controller were about 1 per 300 shifts - with a shift defined as a 14 day running period. This was considered low and as such explicit error detection and correction in hardware was not felt to be necessary and was not planned to be done initially.

The link BER will be monitored on-line for link fibre optic component characterization and for failure prediction[4]. This is to address the combined 6.5 day MTBF of the ~24,000 fibre optic link components to be used on site.

Additional error sources are power supply and coupled noise in the controller and the power supply interface, the serial to parallel (and vice versa) conversion and the encoding / decoding done at each end of the link. End-to-end and link measurements to characterize actual BER achieved are therefore required to estimate actual errors expected.

B. Application Level

At the application level, effect of link errors on power supply operation need to be considered. Misinterpretation of Commands due to link errors can cause unacceptable down time for example by turning off a power supply which may then require some time for orderly turn on.

Given the calculated link error rates the command format encoding for all power supplies, interfaces and controllers is double bit. The likely hood of adjacent double bit errors is expected to be orders of magnitude lower than single bit errors and need to be characterized.

The effects of error on the reference output values for the 'DC' and the corrector magnet power supplies are some what different. The DC power supply references are sent infrequently such as few times per second. The expected errors in this is low and can for the time being be neglected. For the correctors drastically different values will be filtered out by power supply compliance limitations. Additional checking in may be imposed, in controller firmware, to allow some fractional change based on past values. This detail is yet to be determined.

C. Loose Packetization

Error checking at the application level frames is intended to be defined as the method of 'loose packetization', as an extension of application level framing. This would be a computed checksum for a group of (variable length) frames bracketed by a start checksum frame command and an end checksum frame command with the checksum transmitted as two bytes of data. These techniques are to be developed and will become useful by the time they are required for collider operations.

IV. DISCUSSION

The choice of protocols is driven by a number of factors such as the SSC Global controls architecture and machine operational requirements. Details of the protocol are decided by a tradeoff between implementation cost, component and resources availability. All of the specifications are evolving. The first specification is for a group of about 70 LINAC 'DC' power supplies. Future refinements of the design will be based on experience with this set. Presently encoders and decoders are being designed, BER testing is being setup, and methods to implement measurement of BER during controller operation are being looked into. Prototype controllers are expected to be made by the summer.

V. ACKNOWLEDGEMENT

The Authors would like to acknowledge the advice and support of D.P. Gurd and R. Winje, and the help of J. Payne and E. Faught in the process of protocol definition and building of prototypes.

VI. REFERENCES

- [1] W. Merz, F. Meyer, S. Sarkar, 'Correction Magnet Controls at the SSC', IEEE NSS conference proceedings, p596, Orlando, FL, Oct., 1992.
- [2] 'LINAC 'DC' Power Supply Controller Specification', SSC ref. ABM-2000004.
- [3] 'LINAC 'DC' Power Supply Controls Interface Specification', SSC ref. ABM-200002, March '93.
- [4] S. Sarkar, W. Merz, F. Meyer, 'Proposal to use failure prediction as a means of meeting availability requirements at the SSC', These proceedings.
- [5] K. Low, R. Skegg, 'The Prototype Message Broadcast System for the Superconducting Super Collider', IEEE NSS conference proceedings, p355, Arlington, VA, Oct. '90.
- [6] W. Merz, 'LEB Correction Element PDRR', SSC internal document, Dec. '91.
- [7] D.C. Beechy and R.J. Ducar, 'Timing and Data Distribution Systems at the Fermilab Accelerator', *Nuclear Instrumentation Methods in Physics Research*, vol. A247, p231, North-Holland, Amsterdam, '86.

Parametrization of AmPS magnets for the control system

Y. Wu, G. van Garderen, R. Hart, J. van der Laan, R. Maas, F. Schimmel

NIKHEF -K, P.O. Box 41882, 1009 DB Amsterdam, the Netherlands

Abstract

Parametrization of the AmPS magnets (dipoles, quadrupoles, sextupoles and steering coils) has been performed by precisely measuring the field integrals of each magnet type as function of the excitation current. In order to guarantee a good accuracy of the measurements the used Hall probe was carefully calibrated. These magnet data have been imported into the machine-simulation program DIMAD and a complete refit has been made for various machine properties like the achromatic curved section, the tune, the chromaticity, etc. The algorithms have been implemented in the control system and were calibrated against the beam energy. From the start of the commissioning (spring 1992) the calculated settings and the measurement results proved to be in good agreement: guiding the first beam through the ring took only a few minutes. Also the first measurements of the betatron tune are in agreement with the calculated value using the parametrization of the ring magnets. Furthermore local closed orbit bumps can be generated in the following regions: the injection area, the extraction area, the r.f. cavity area and the internal target area. The performance of this program also indicates the magnet settings are correct.

I. INTRODUCTION

The first commissioning of AmPS (Amsterdam Pulse Stretcher) ring at NIKHEF has been performed in spring 1992 and recently AmPS delivered a 1.5 μ A beam with a duty factor of ~30% for nuclear physics experiments. The evolution of its performance is described in [1][2]. The construction of AmPS has been described elsewhere[3]. There are 32 dipoles, 68 quadrupoles and 32 sextupoles, as well as 4 extraction sextupoles and 32 combined steering magnets installed in AmPS. It is built for improving the duty factor of 0.1% from linac to ~100% from the pulse stretcher ring. For proper computer control of the power supplies, the parametrization of the magnets is necessary. The main parameters of those magnets and the measurement results of these magnets have been shown in[4]. However, the integral field of the quadrupoles and sextupoles, and the magnetic field as function of the excitation current were not known. A few of each type of magnets, such as ring dipoles, the quadrupoles, the sextupoles, and the steering magnets, therefore, have been measured thoroughly. The final measurement result has been implemented to the program DIMAD[5] to refit the parameters of the machine properties such as tune, chromaticity, etc. Parametrization, which was based on the measurement results from those magnets, was calculated in order to provide enough information for a central computer control of AmPS. The successful start of the commissioning proved that a good

parametrization steered the beam through the ring with some ease.

II. MEASUREMENT PREPARATION.

The tools which were available for measurement were a DTM-141 Hall probe (Group 3 Technology) and a precise position x-y-z measurement setup. In order to obtain a high accuracy, the following calibration were made.

The accuracy of the Hall probe for the magnetic field was calibrated by an NMR in the magnetic field region of 0.3 – 1.0 T.

The temperature dependence of the Hall probe has been measured with a Tektronix-thermometer. The temperature-dependent coefficient is $1.77 \cdot 10^{-5}$ T/°C.

This Hall probe was used to measure the quadrupole field along the axial direction in order to obtain its integral field. The position of the Hall probe was read out within an accuracy of 0.01 mm with the x-y-z measurement setup. In order to improve the accuracy of the integral field of the multipoles the sensitive center of the Hall probe was calibrated with the x-y-z setup. By rotating the Hall probe 180° in the center of the quadrupole it turned out that the sensitive center of the Hall probe had a 0.4 mm offset with its mechanical center. With the correction of this offset the measurement result gave a better result for the quadrupole and the sextupole.

III. PARAMETRIZATION OF THE MAGNETS.

Measurement results for the ring dipoles[4] indicated that there is deviation of the integral field $\int B dl$ between the 32 dipoles (which is about $\pm 0.3\%$). Since they will be connected to one power supply, the parametrization has to take into account of this fact. A few dipoles were measured and a mean value of their integral field has been taken for the parametrization. In the mean time an NMR probe was used to calibrate the central magnetic field. The integral field is not the linear function of the excitation current and a slight saturation occurs when a high excitation current is applied were observed for ring dipoles. Therefore, a polynomial fitting program was used to obtain the coefficients of the dipole integral field. The dipole field as function of the excitation current as well as the beam energy is implemented in the control system. There is an additional dipole located outside the ring and an NMR probe is installed in the gap of the dipole to track the performance of the 32 ring dipoles.

There are three types of quadrupoles, which have aperture diameters of 71mm, 95mm and 144 mm respectively.

There is one type of sextupole installed in the ring and its aperture diameter is 80 mm. One of each magnet type has been measured for the integral field. Every quadrupole and sextupole has been measured by rotating coils and the results indicated that the higher-order components in the quadrupole are less than 0.1% for radii up to 0.8r and 1% for sextupoles^[4]. The integral field was therefore measured in the 0.6r region in order to obtain the relative high accuracy. The optical strengths ($K_{q/s}$) of the quadrupoles and sextupoles are converted to the excitation current as function of the beam energy.

The measurement results of the multipoles show that the effective length of the magnets with respect to their design value is somewhat different, see table 1:

Table 1: The effective length of the magnets, where Q is quadrupole and S is sextupole. The number is the diameter. First column is the design value and the second column is the measurement result.

	L_{de} [mm]	L_{mea} [mm]
Q71	210	213
Q95	290	296
Q144	290	323
S80	150	142

The beam energy was calibrated by an analytic bending magnet with the aid of a secondary emission monitor in the tune-up line at the end of the linac, which gives an accuracy of the beam energy of 0.1%.

The measurement results were imported into the program DIMAD^[5] to refit the required optical properties of AmPS, such as achromatic transform in the curved section, tune and chromaticity. The new parameters of the magnets are used as the input for the control system.

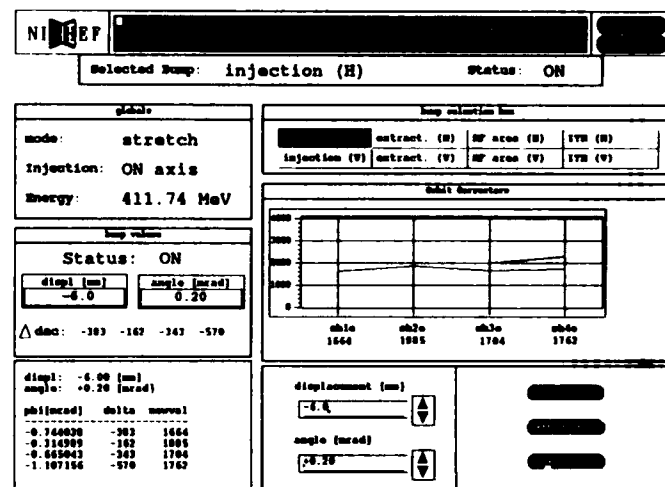
With this effort when the commissioning started at spring of 1992, it only took a few minutes to guide the first beam through the ring. Measurement of the machine betatron tune yields $\nu_x = n.38$ and $\nu_y = n.21$ which is in a good agreement with the design value.

There are 32 pairs of steering magnets in AmPS for orbit correction purpose. Their integral field has also been measured in both the vertical and the horizontal direction. The excitation current is as function of both the bending angle and the beam energy. This is implemented in the control system as well.

IV. PARAMETRIZATION OF MACHINE PROPERTIES.

In order to be able to adjust the machine parameters promptly, chromaticity adjustment and tune adjustment are also implemented in the control system. Two quadrupole families are chosen for the tune adjustment, and two sextupole families are chosen for the chromaticity adjustment. A precalculated table is implemented in a graphic setup to make it user friendly. An example of this setup is shown below.

Besides the program for tune and chromaticity control, local bump programs for the injection area, the extraction area, RF cavity area and the internal target area are implemented also. There are four pairs of steering magnets chosen in each concerned region. According to the request from the user, such as an angle or a displacement in the local area, the program will calculate the required current for each steering magnets as function of the beam energy, and then it will be executed. With this facility one can easily adjust the closed orbit at the injection or extraction area with one's interest or fit the request from the ring condition.



V. CONCLUSION.

The commissioning experience in the past period proved that the careful parametrization of the ring magnets and the machine properties are worth to do and it provides convenient tools for adjusting ring parameters as well as helping to understand the performance of the operation during the commissioning period.

VI. REFERENCES.

- [1] R. Maas, e.a. Commissioning Results of the Amsterdam Pulse Stretcher/Storage Ring AmPS. in the Proc. of this conf.
- [2] G. Luijkx, e. a. The Amsterdam Pulse Stretcher, first commissioning results. Proc. HEACC '92, Hamburg, p. 464
- [3] G. Luijkx, e.a. Status of the Amsterdam Pulse Stretcher project (AmPS). Proc. of the 2nd European Particle Accelerator Conference (EPAC '90) p. 589
- [4] H. Boer Rookhuizen, e.a., Magnetic Devices of the Amsterdam Pulse Stretcher Ring AmPS. Proc. of IEEE Particle Accelerator Conference (San Francisco, California, May, 1991) p. 2366
- [5] R. V. Servranckx e.a. Users Guide to the Program DIMAD SLAC-285, May 1985.

Global Voltage Control for the LEP RF System

E. Ciapala, A. Butterworth and E. Peschardt
CERN, 1211 Geneva 23, Switzerland

Abstract

The LEP RF system is installed as independent 16 cavity units. In addition to the eight copper cavity units originally installed 12 units with super-conducting cavities are being added for the LEP200 energy upgrade. The total RF voltage determines the synchrotron tune (Q_s) and must be controlled precisely during energy ramping. Local function generators in each of the RF units are pre-loaded such that when triggered simultaneously by ramp timing events transmitted over the general timing system the total voltage varies to give the Q_s function required. A disadvantage is that loss of RF in a unit at any time after the loading process cannot be corrected. As the number of RF units increases automatic control of the total RF voltage and its distribution around LEP becomes desirable. A global voltage control system, based on a central VME controller, has recently been installed. It has direct and rapid access to the RF units over the LEP time division multiplexing system. Initial tests on operation and performance at fixed energy and during energy ramping are described, as well as the implementation of a Q_s loop in which Q_s can be set directly using on-line synchrotron frequency measurements.

I. INTRODUCTION

The RF system of LEP is made up of individual RF units. For the first phase of LEP and operation up to 50 GeV 128 room temperature coupled cavity assemblies have been installed in the form of eight individual RF units. Each unit consists of 16 cavities and two 1 MW klystron power sources, high voltage power supply, low level and digital controls. For the LEP200 upgrade to energies approaching 90 GeV a further 192 super-conducting (SC) cavities will be installed. These will be arranged as an additional 12 RF units using as far as possible the same type of infra-structure, but with one klystron per unit, making a total of 20 RF units. Furthermore for high beam intensities the SC cavity units may be equipped with two klystrons per unit, each driving a group of eight cavities, each group thereby operating independently.

The method originally envisaged for control of the total RF voltage was based simply on the individual control of the voltage of each unit [1]. For energy ramping the total RF voltage must increase according to a pre-determined function such that the synchrotron tune Q_s is maintained throughout the ramp. To achieve this each RF unit was equipped with its own RF voltage function generator. These are pre-loaded with calculated values prior to the ramp and triggered simultaneously by ramp events transmitted over the LEP general machine timing (GMT) system. This system works

satisfactorily provided that all units continue to contribute the expected voltages during the ramp. It cannot cope with unexpected changes in the state of individual RF units due to interlock trips. Some form of overall and automatic control of RF voltage is clearly desirable and becomes increasingly important with the large number of RF units for LEP200.

A software global voltage control system running on a central workstation was implemented last year. This was used successfully to maintain fixed voltage (at injection or at top energy) but could not be made fast enough for ramping. The limitation was due to the time required to get commands and status information to and from the equipment inside the RF units. Access from PCR to the main 'Data Manager' (DM) which controls the RF unit over the Ethernet connection used for remote control takes around 50 ms. Access from the DM to the 'Equipment Controller' (EC) [2] which interfaces the equipment of the low level RF of the unit (one of 23 such ECs) over IEEE bus takes a further 50 ms. These times can not be predicted exactly and can be considerably increased depending on network activity and on IEEE bus activity inside the RF unit.

Ideally the performance of the overall system should be limited only by the response of the RF voltage control loop inside the RF unit. This loop has been designed such that the RF voltage can be ramped at a rate of 5% of maximum per second, this being at least an order of magnitude greater than that required during energy ramping. If the RF voltage is to be maintained to a precision of 0.1 % then the system must be capable of acting on each unit at least every 20 ms. Guaranteed access times can be obtained only by dedicated connections. In LEP the most economical way of implementing these is over the time domain multiplexing (TDM) system. It connects all the interaction points (IPs) of LEP and the control room via fibre optic links and is the backbone for the Ethernet and Token Ring networks and timing systems. Commercial equipment exists to multiplex various types of analogue and digital signals over TDM systems. The transmission and reception of analogue signals directly to a hardware based central controller would provide fast overall response but would lack flexibility. The use of a computer based central controller and the transfer of data over the TDM to the RF units can provide more than adequate speed for this and also the possibility of directly transferring additional low level RF system information useful for global voltage control, such as loop states and RF phase settings.

A global RF voltage control system making use of the TDM system in this way has recently been installed. The system hardware and software is described and the results of an initial test made at the end of 1992 presented.

II. THE GLOBAL VOLTAGE CONTROL SYSTEM

A. System configuration

A block diagram is shown in Figure 1. The central controller is situated in the Prevessin control room (PCR). TDM channels at 2 MBit/s have been allocated for each of the points of LEP where RF is already installed (IPs 2 and 6) or will be installed (IPs 4 and 8). Serial line multiplexers at the end of each TDM link provide individual connection between the central controller and the RF units at each point. In the PCR connection is by sets of RS232 lines, one for each unit. In the underground klystron gallery where the distances are up to 500 metres the connection to the remote RF units is by RS485 differential transmission.

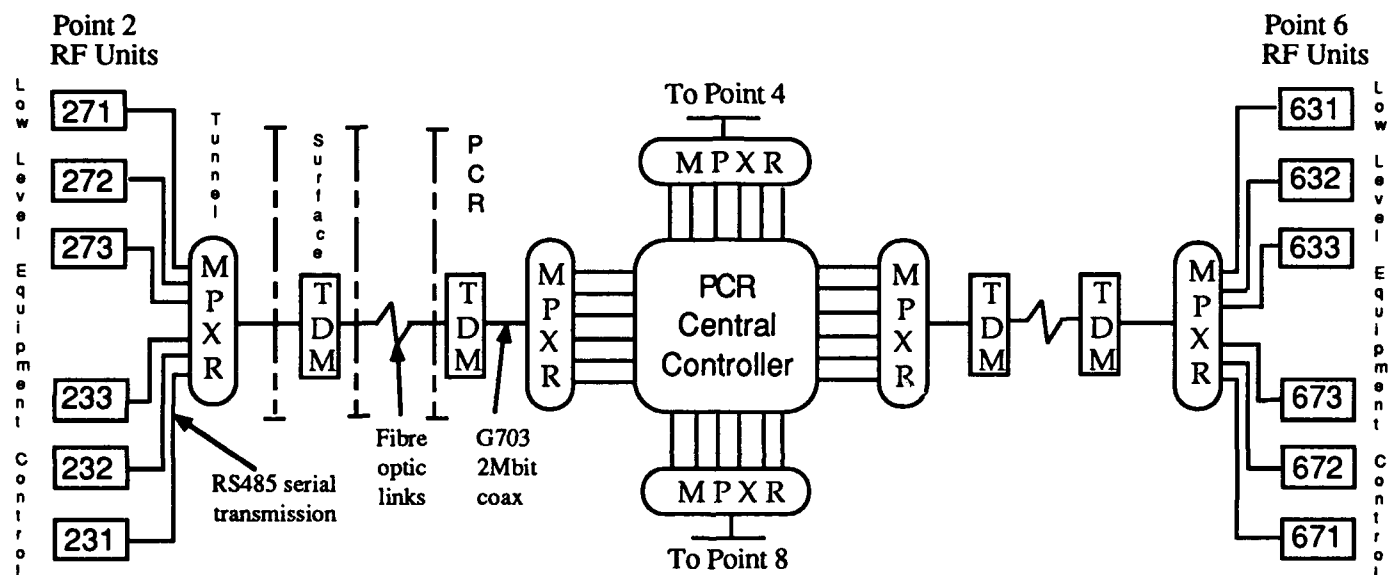


Figure 1. RF Global voltage control system - overall layout.

B. Central controller

The central controller is a VME crate containing a 68030 based CPU module. An intelligent IO module carries the multiple serial IO controllers for communication with the RF units. The OS/9 operating system is used and the global voltage control is implemented as a 'C' language program which continuously monitors all the RF units and sets RF voltages depending on equipment states and the desired modes of operation.

C. Multiplexing equipment

The CCITT G703 standard is used for the TDM equipment of LEP. Multiplexing equipment in the form of crates allowing a range of up to 16 interfaces of different types, each using 32 kBit of the 2 Mbit per channel, was obtained from industry. The global voltage system uses serial interfaces of RS232 and RS485 types but other interfaces allowing the transmission of analogue signals are used on spare channels,

for example the analogue signal representing the synchrotron motion of the beam from tunnel equipment to the PCR.

D. RF unit interface

The serial RS485 line is connected to the low level EC of the RF unit. This EC contains the interfaces which allow the setting of RF voltage and phase, the reading of the detector sum of all cavity voltages and the state of the voltage control loop. The global voltage control system can set values and read information in the same way as the DM over the GPIB but this must be independent of all other processes and with higher priority. The RF voltage is set to the value required by a linear software ramp at a pre-determined rate. The existing EC software is however based on single task operation with a single interrupt level and the condition of absolute priority

was difficult to implement. For this as well as other reasons the Low Level equipment controller has been fitted with a 68000 type processor module and VME to G64 converter such that interrupt driven multi-tasking software can be used. This was not completed in time for the initial test described later but will be installed for the final operational system this year.

III. OPERATION

The system can be considered to have different modes of operation depending on the reference used for the total voltage. In addition the distribution of voltage on the various units is determined by requirements of RF symmetry around the machine.

A. Modes of operation

- Fixed RF voltage - The reference is a value fixed by software. This mode is applicable to injection and coast.

- **RF voltage ramp** - For energy ramping the RF voltages corresponding to each of the individual energy ramp vectors are loaded into a table in the central controller. The reference voltage during the ramp is derived from the table using a vector interval counter triggered by the events of the GMT.

- **Q_s loop** - Readings of synchrotron frequency (f_s) can be derived from acquisition and processing of the synchrotron frequency spectrum from a phase detector which compares RF and bunch signals. If Q_s is specified as reference, either fixed or varying according to the ramp, the loop can adjust RF voltages to maintain the required value. This requires rapid, accurate and reliable measurements of f_s .

B. RF voltage distribution

The voltages which can be provided by the various units are not identical. The SC units produce more voltage than the copper cavity units, for the SC units the voltages may not all be the same and during operation certain units may be down or unable to provide their nominal voltage. The distribution of the RF voltages making up the total has to be arranged according to the voltages available and to the degree of symmetry required. The RF 'current data set,' (CDS) a table containing information on RF unit states and voltage limits, is kept up to date during operation. When this is changed the updated table is sent to the central controller. Symmetry conditions can be specified by the operator and the system will maintain these as long as the available voltage at each point or individual unit permits. The following conditions are allowed for :

- **Asymmetrical** - All units maintained at the same fraction of their individual maximum voltage. This allows ramping to maximum voltage with all units reaching maximum at the same time, without symmetry considerations
- **IP symmetry** - Equal voltages from RF on either side of the IP, all units at each side having the same fraction of their maximum.
- **Symmetrical** - Equal voltages at opposite interaction points, This can be with or without IP symmetry.

Since the symmetry conditions are stored in array form any possible configuration can be used.

IV INITIAL TEST WITH BEAM

A first test with beam was carried out on the RF global voltage control system just before the start of the LEP annual shutdown in November 1992. Switching the system on with seven RF units running brought the voltage to the set fixed voltage reference of 50 MV. Switching on of another RF unit was correctly compensated by the system. This is shown in

Figure 2. A relatively slow rate of RF ramp was set in the low level equipment.

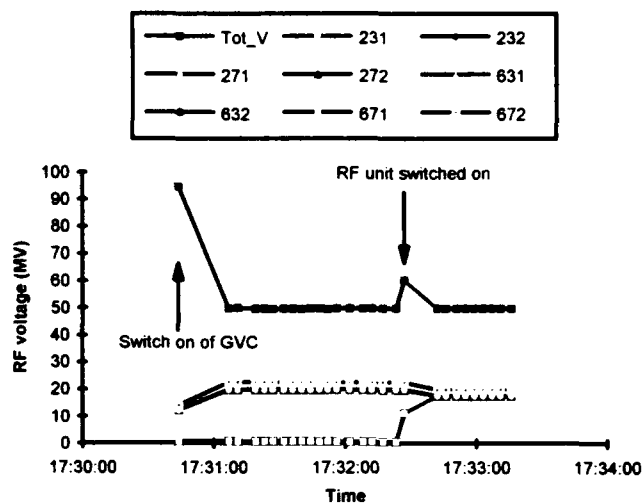


Figure 2. Switch on of system with seven RF units followed by switch on of new RF unit

Over long term operation, however, and during ramping, occasional delays in communication over the serial channels hampered operation. This was caused by interference with other activities at the level of the low level ECs. This should be resolved by the improvements previously described. The tests showed the feasibility of the Q_s loop. Response was slow, however, due to the time taken to make accurate measurements with the spectrum analyzer. A more rapid synchrotron frequency detector using FFT methods is in preparation.

V CONCLUSIONS

A global RF voltage system capable of meeting the requirements of LEP operation has been installed and initial tests carried out. Some modifications to resolve problems discovered during these tests are being carried out and further tests will be done soon with the aim of having the system fully operational during 1993.

VI ACKNOWLEDGEMENTS

The provision of the TDM channels by the SL-CO group and the assistance of specialists in the group is gratefully acknowledged.

REFERENCES

- [1] P. Brown, E. Ciapala, S. Hansen, E. Pescherdt, J. Sladen, "The LEP Radio-Frequency Low Power System," IEEE Trans. Nucl. Sci. NS-32, p. 2037 (1985)
- [2] E. Ciapala and M. Disdier, "A Dedicated Multi-Purpose Digital Controller for the LEP RF System," Conference Record of the 1987 Particle Accelerator Conference, Washington, Vol. 1, pp. 520-522.

Designing RF Control Subsystems using the VXIbus Standard*

Jeffrey D. Stepp, Frederick C. Vong, James F. Bridges
Argonne National Laboratory
9700 S. Cass Avenue, Argonne, IL 60439 USA

Abstract

Various components are being designed to control the RF system of the 7-GeV Advanced Photon Source (APS). The associated control electronics (phase shifters, amplitude modulators, phase detectors, automatic tuning control, and local feedback control) are designed as modular cards with multiple channels for ease of replacement as well as for compact design. Various specifications of the VXIbus are listed and the method used to simplify the design of the control subsystem is shown. A commercial VXI interface board was used to speed the design cycle. Required manpower and actual task times are included. A discussion of the computer architecture and software development of the device drivers which allowed computer control from a VME processor located in a remote crate operating under the Experimental Physics and Industrial Controls Software (EPICS) program is also presented.

1. INTRODUCTION

RF field parameters must be precisely regulated in order to confine and accelerate the APS positrons. Precision RF instruments control and monitor the RF field parameters. Sophisticated computer controls and diagnostics are necessary to support remote supervision and operation of the RF instrumentation. A modular RF control system has been implemented using the architecture of the VMEbus Extension for Instrumentation (VXIbus). Features include broadband backplane analog interconnections, precision timing signals, EMI/RFI compatibility, standardized configuration, and communication protocols. RF and control, signal conditioning, signal processing, and interface circuitry can be housed in the same module. Additional features include modular instrument-on-a-card applications and synchronization of many instrument channels. A VXIbus backplane interface links the modules to a controlling microprocessor for high-speed signal acquisition and data processing [1].

This paper describes the implementation of the APS low-level RF control system using the VXI architecture. It outlines how control system development was done with minimum staffing and with an off-the-shelf VXI interface module. Advantages of the VXI architecture are increased equipment density, eliminated cabling, and simplified system integration.

Using a register-based VXIbus interface, we can divide the function of a "complete instrument" into a number of VXIbus modules such as signal acquisition, signal processing, and control functions. Processing capabilities can thus be remote from the acquired data. This is then a shared-resource environment

in which one or more processors do all the processing for the entire system [2].

The interface module uses most of the VXIbus features, including module self-test functions, module slot identification, failed-module inhibit capability, and the dynamic configuration of a module's base address.

II. DESCRIPTION

The Bruel & Kjaer Type 3154 VXI User Module is a single-slot, C-size, Extended Register Based device, with which one can design and build a VXIbus module without designing a customized VXIbus interface. The following features of the B & K module were used to design the associated control electronics (phase shifters, amplitude modulators, phase detectors, automatic tuning control, and local feedback control) with multiple channels:

- an isolating, low-noise analog power supply
- digital power supply lines
- 3 TTL trigger lines
- a 10-MHz clock line
- 4 isolated input/output 16-bit ports from VXIbus interface registers for control purposes [3].

Approximately one-half of a C-size VXI PC board is available for user circuitry. This space was used to hold the RF modules, associated A/D and D/A converters, and timing and interface circuitry. Power and cooling are done by the VXI mainframe. See Figure 1.

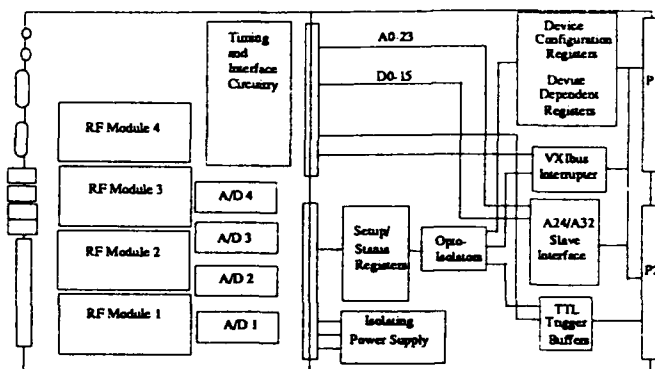


Figure 1. VXI Module block diagram.

The services of one full-time engineer, one full-time technician, one part-time draftsman, and one part-time software engineer were used over a period of six months to design and build one low-level RF system with four VXI modules.

VXIbus Interface

The register-based protocol defines the conventional method of VMEbus data transfers to address-mapped configuration and control registers. Each VXIbus module contains a set of 32 I/O registers through which the configuration, control, and sig-

*Work supported by the U.S. Department of Energy, Office of Basic Sciences, under contract W-31-109-ENG-38.

nal access are made for the module. Standard VXIbus configuration registers are included in these 64 bytes. These registers identify the device, its address space, and some status and control for the module. All binary, analog, and timing signals required for RF modules are represented as 16-bit data registers. The registers represent channels of analog control and monitor signals which access the RF electronics.

The register-based VXIbus interface is located in every VXIbus module. It controls the data cycle, interrupt cycle, and backplane handshaking with the VME processor card. This interface contains the backplane buffers, VXI configuration registers, and the timing signal generator. The module has additional VXIbus features that are not used in the VMEbus environment, including module self-test functions, module slot identification, failed-module inhibit capability, and the dynamic configuration of a module's base address.

Timing and Triggering

Each module contains a local timing circuit that synchronizes the operation of the RF control electronics. The VXIbus controller buffers external timing signals and drives the backplane ECL trigger, TTL trigger, and clock signals (ECLTRGn, TTLTRGn, CLK10). A local timing circuit on each VXI module uses the backplane signals to generate five variable-delay, variable-width pulses, providing all timing triggers and windows to control the RF electronics on the module. In this manner, the timing signals on all modules within an entire mainframe are synchronized to a common gating signal within 20 ns accuracy and jitter.

Electromagnetic Compatibility

Four areas of electromagnetic compatibility that are covered in the VXIbus specification are conducted noise, far-field radiation, near-field magnetic radiation, and electric-field radiation. Conducted noise is reduced by bypass capacitors located on all IC supply leads and also close to the backplane power pins. Far-field radiation is reduced by adequate ground planes on the PC boards, RF circuitry shielding, and the metallic VXI module enclosure. Near-field magnetic radiation is reduced by limiting the inductance paths of current loops. Additional shielding can be inserted between modules by the mainframe manufacturer. Electric-field radiation is limited by the grounded metallic module enclosure.

III. COMPUTER-BASED CONTROL SYSTEM

A computer-based control system has many advantages. A well-designed system can reduce staffing requirements. The system can be reconfigured easily when hardware and software modifications are made. Controls can be added in piecemeal fashion. Different computers located in separate areas or buildings can readily communicate through a local area network. Data can be easily archived and made instantly accessible to various workstation users simultaneously [4].

The APS control system is derived from the Experimental Physics and Industrial Control System (EPICS), which was developed by Los Alamos National Laboratory and Argonne National Laboratory. EPICS is a software system with which en-

ables the user to readily develop control software in a simple and flexible environment.

The hardware for the test system, shown in Figure 2, consists of a workstation, a VME system, and a VXI system. The workstation runs the UNIX operating system with the X-windows graphical user interface (GUI). The operator communicates with the control system using a Sun workstation. The operator interface (OPI) running on the workstation communicates with the VME system through the Ethernet local area network using the TCP/IP protocols. The OPI, based on the X-windows GUI, configures the text and graphical representation of the data and interactive data entry for the test system. The VME system input/output controller (IOC) functions as a front-end computer doing the real-time control, data conditioning, and data acquisition. The IOC is running on top of the VxWorks real-time kernel. The VXI system is connected as a subsystem to the VME system through the MXIbus. This configuration is essentially based on the EPICS system architecture [5].

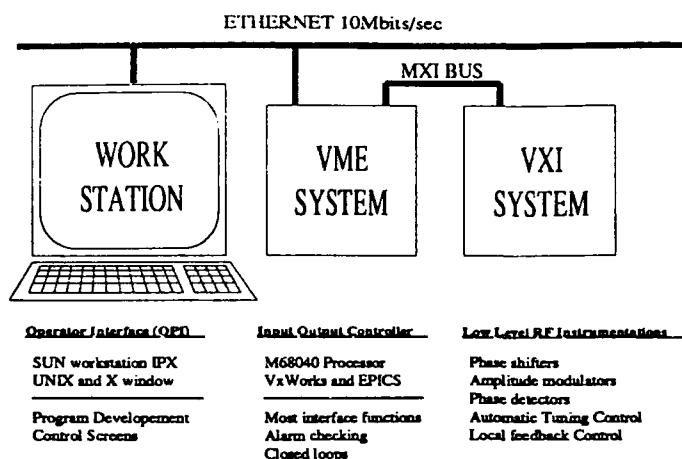


Figure 2. VXI control system hardware.

The heart of an IOC is a memory-resident database. Each signal is represented by a record. A record contains several fields that describe the operating range, conversion factor, scanning mechanism, and different alarm trigger levels. The database is made using the Database Configuration Tool (DCT) running on the workstation. The database is downloaded to the VME system during run time.

A primary EPICS concept is that each hardware-specific routine, such as the device driver, is isolated from the IOC core software by a record and device support layer (see Figure 2). The database of the IOC core communicates with the hardware via the record and device support layer and the hardware's device driver [6]. A device driver is needed for each new piece of hardware.

The VXI instrument prototypes can be classified into two categories: analog input record and analog output record. The block diagram of the device support and device driver routines is shown in Figure 3. Two device support entry tables (DSET) are shown in the block diagram, one for the analog input record and one for the analog output record. The main difference between them is the DSET of the analog input record has the

'read_ai' entry but the analog output record has the 'write_ao' entry. The items in the entry tables are predefined in EPICS.

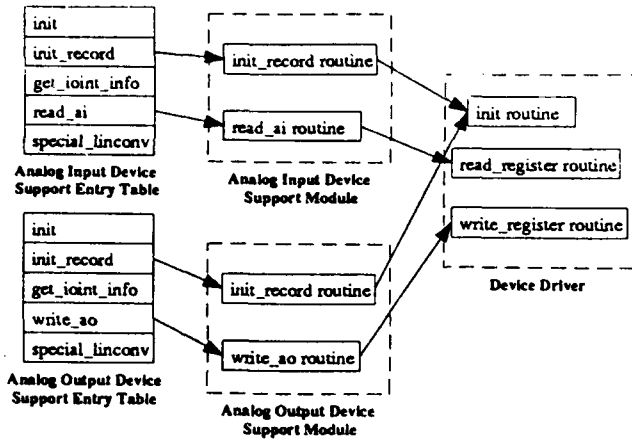


Figure 3. Device Support Layer.

The 'read_ai' routine for the analog record first calls the device driver 'read_register' routine to get the raw value, then converts the raw value into proper form according to the corresponding record conversion setting defined in the database. The value is returned in the proper form and raises an alarm if an error is reported by the 'read_register' routine of the device driver. The 'write_ao' routine reverses the process of the 'read_ai' routine. It converts the value passed by the record into the hardware data format according to the corresponding record conversion setting, calls the write_register routine, and passes along the data, and raises an alarm if an error occurs.

Device Driver Implementation

Our prototype VXI instrumentations are based on the Bruel & Kjaer Type 3154 User Module as the VXIbus interface. Each module has the same set of isolated input/output 16-bit ports; therefore, only a single device driver is needed. The device driver has three routines—for hardware initialization, read operations, and write operations.

During system power-up, the EPICS VXI resource manager initializes all the standard VXI tests, such as module self-test, module slot identification, dynamic configuration of a module's base address, and inhibiting failed modules. The initialization routines of the device driver first calls the resource manager to obtain the base address of the module specified by the signal assignment in the database and then calculates the ad-

dress of the corresponding register. If this is an input operation, the initialization routine sets up the associated ports for a strobe operation by setting the corresponding bit of the Strobed/Transparent Configuration Register in the User Module. Finally, the routine reports any errors to the calling routine.

For read and write operations the routines are fairly straightforward. The read routine peeks the associated register and returns the value to the calling routine. Similarly, the write routine pokes the associated register with the value passed by the calling routine.

ACKNOWLEDGMENTS

The authors wish to thank Terry Smith and Christine Verdicto for their part in integrating the system. We also wish to thank the ASD/APS Controls Group for providing the application code, writing the EPICS database, and designing the interface control panels.

REFERENCES

- [1] C. Ziomek, "Interfacing RF Control Electronics to the VXIbus for the Ground Test Accelerator," Proc. Neutral Particle Beam Tech. Symp., San Diego, CA, May 21-24, 1990.
- [2] C. Ziomek, "Accelerator RF Instrumentation Implemented with the VXIbus," ATE & Instrumentation Conference, Anaheim, CA, Jan. 15-17, 1991.
- [3] "User Module Type 3154 Hardware Users Guide," Bruel & Kjaer A/S, Naerum, Denmark, 1992, 1-2.
- [4] A. J. Kozubal, L. R. Dalesio, J. O. Hill, and D. M. Kersiens, "Run time environment and applications tools for the Ground Test Accelerator Control System," in *Accelerator and Large Experimental Physics Control Systems*, D. P. Gurd and M. Crowley-Milling, eds. 288-291, (ICALEPCS, Vancouver, BC, Canada, 1989).
- [5] M. Kraimer, "Experimental Physics and Industrial Control System (EPICS) Input / Output Controller (IOC) Application Developer's Guide," EPICS Manual, pp. 41-57, March 1992.
- [6] R. T. Daly, F. C. Vong, M. R. Kraimer, "The APS Radio Frequency Test Stand Control System," Real Time '91, Computer Applications in Nuclear Particle and Plasma Physics, Julich, Germany, 25-28 June, 1991.

Automated Measurement of Cavity Frequency and Cavity Tuning at CEBAF*

Rui Li, Stefan N. Simrock and Byung C. Yunn
CEBAF, 12000 Jefferson Ave., Newport News, VA 23606

Abstract

We propose a method here which allows the measurement of the cavity resonance frequency in a frequency range up to ± 5 kHz from the operating frequency. This is achieved by phase modulation of the incident signal with noise to drive the cavity with a broad band spectrum. The cavity resonance frequency can then be determined from the response signal of the field probe, which has a narrow frequency spectrum due to the high loaded Q of the cavity of 6.6×10^6 , corresponding to a cavity bandwidth of 125 Hz.

Introduction

The cavity tuning algorithms as presently implemented in the CEBAF RF control system rely on the accuracy of the detuning angle measurements. It is measured as the phase difference between the incident and transmitted RF power and due to hardware limitations not accurate at low-power levels, i.e., if the cavity is detuned by several bandwidths or at very low gradients. Phase offsets are changing as functions of temperature and power level or replacement of control modules. In many instances cavities need to be tuned manually after accelerator shutdown. In this study, we propose a method to measure the cavity resonance frequency by driving the cavity with a noise spectrum. This is achieved by modulating the phase of the incident signal with a band-limited pseudo-random signal. The cavity resonance frequency can then be determined from the response signal of the field probe, which has a narrow frequency spectrum due to the high loaded Q of the cavity of 6.6×10^6 , corresponding to a cavity bandwidth of 125 Hz. The presently used hardware allows the measurement of the cavity frequency in a range up to ± 5 kHz from the operating frequency.

Layout of the Scheme

The principle of the scheme is shown in Fig. 1. A signal $V_1(t) = |V_1|e^{-i\omega_0 t}$ from the master oscillator (A) is sent to a vector modulator (B), where $V_1(t)$ is modulated by a pseudo random signal $x(t) = e^{i\phi(t)}$. The power spectrum of $x(t)$ is required to be a positive constant for $|f| < 5$ kHz and to be zero outside this frequency region. The output signal from (B) $V_{in}(t) = V_1(t)x(t)$ is then sent to the cavity (C), which excites the cavity at its resonance frequency f_c (assuming $|f_c - f_0| < 5$ kHz with $f_0 = \omega_0/2\pi$). A sample of the accelerating field $V_c(t)$, as the response to the incident signal $V_{in}(t)$, is detected by the probe coupler. Then at the vector demodulator (D) the signal $V_c(t)$ is multiplied by a

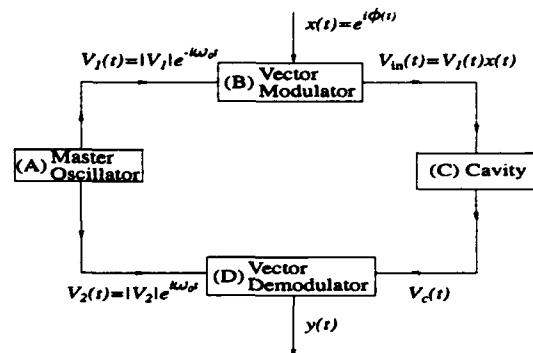


Figure 1: Layout of the cavity resonance frequency measurement scheme.

reference signal $V_2(t) = |V_2|e^{i\omega_0 t}$ from the master oscillator to generate a baseband signal $y(t) = V_2(t)V_c(t)$. Our task is to generate a bandwidth-limited signal $x(t)$ at the vector modulator (B), and then set a scheme to detect the cavity resonance frequency f_c from the signal $y(t)$ output from the vector demodulator (D).

Generation of a Bandwidth-Limited Random Signal

First, a real ideal bandwidth-limited signal $u(t)$ for $0 < t < T$, whose power spectrum $S_{uu}(\omega)$ satisfies

$$S_{uu}(\omega) = \begin{cases} S_0 & |\omega| < \omega_b \\ 0 & |\omega| > \omega_b \end{cases}, \quad (1)$$

is generated using the sampling theorem [1]:

$$u(t) = \sum_{n=-N_1}^{N_2} u(nT_b) \frac{\sin \omega_b(t - nT_b)}{\omega_b(t - nT_b)} \quad (0 < t < T) \quad (2)$$

with $T_b = 2\pi/\omega_b$. Here $u_n = u(nT_b)$ are uniformly distributed in the range $(-1, 1)$, and n runs from $-N_1$ to N_2 , with $(T_1, T_2) = (-N_1T_b, N_2T_b)$ fully covering the time range $t = (0, T)$.

Let u and v be both ideal bandwidth-limited real pseudo-random processes independently generated using Eq. (2), and define a complex signal $w(t)$

$$w(t) = u(t) + iv(t). \quad (3)$$

It can be shown that $w(t)$ is an ideal bandwidth-limited signal. We can write $w(t)$ in terms of the amplitude and the phase

$$w(t) = |w(t)|e^{i\phi(t)}. \quad (4)$$

*Supported by D.O.E. contract #DE-AC05-84ER40150

Numerically it turns out that the signal formed from the phase variation of $w(t)$ only, namely,

$$x(t) = e^{i\phi(t)} = w(t)/|w(t)| \quad (5)$$

is also a good approximation of a bandwidth-limited signal. This is shown in Fig. 2.

Response Signal from the Cavity

The analysis for the output signal $y(t)$ of the overall system is given in this section.

The pseudo random signal $x(t)$ is multiplied by the signal $V_1(t)$ from the master oscillator at the vector modulator (B), producing an incident signal $V_{in}(t)$ to the cavity,

$$V_{in}(t) = V_1(t)x(t). \quad (6)$$

The cavity (C) acts like a forced oscillator with characteristic resonance angular frequency ω_c and damping constant α . For an input signal $V_{in}(t)$, the cavity probe will detect a gradient $V_c(t)$ which satisfies

$$\ddot{V}_c + 2\alpha\dot{V}_c + \omega_c^2 V_c = \lambda V_{in}(t) \quad (7)$$

with λ containing the proper units. Assuming $V_c(0) = \dot{V}_c(0) = 0$ and applying Laplace transform to Eq. (7), we get

$$\begin{aligned} V_c(t) &= \frac{\lambda}{\omega_c'} \int_0^t e^{-\alpha(t-t')} \sin \omega_c'(t-t') V_{in}(t') dt' \\ &\approx \frac{\lambda}{\omega_c} \int_0^t e^{-\alpha(t-t')} \sin \omega_c(t-t') V_{in}(t') dt' \end{aligned} \quad (8)$$

with $\omega_c' = \sqrt{\omega_c^2 - \alpha^2}$. Here the relation $\alpha/\omega_c = 1/2Q_c \ll 1$ is used in Eq. (8) (Q_c is the effective quality value of the cavity). The response signal $V_c(t)$ from the cavity is then multiplied by $V_2(t)$ from the master oscillator at the vector demodulator (D), which gives

$$y_1 = V_2(t)V_c(t). \quad (9)$$

Combining Eqs. (6), (8) and (9), we get

$$y_1(t) = \frac{\lambda V_2(t)}{\omega_c} \int_0^t e^{-\alpha(t-t')} \sin \omega_c(t-t') V_1(t') x(t') dt'. \quad (10)$$

Together with $V_1(t) = |V_1|e^{-i\omega_0 t}$ and $V_2(t) = |V_2|e^{i\omega_0 t}$, one obtains

$$y_1(t) = a_1 \int_0^t e^{-\alpha(t-t')} e^{i\omega_0(t-t')} \sin \omega_c(t-t') x(t') dt'. \quad (11)$$

Here $a_1 = \lambda|V_1V_2|/\omega_c$ is a constant. Denote $\tilde{\omega}_c$ as the cavity resonance frequency relative to ω_0 , $\tilde{\omega}_c = \omega_c - \omega_0$, and assume the overall output signal $y(t)$ from the vector demodulator (D) extracts from $y_1(t)$ only the part containing the difference of the frequencies. It then yields

$$y(t) = a \int_0^t e^{-\alpha(t-t')} e^{-i\tilde{\omega}_c(t-t')} x(t') dt' \quad (12)$$

with constant $a = a_1/2i$. By taking the first derivative of $y(t)$ in Eq. (12) with respect to t , one can readily show that

$$\dot{y}(t) + (\alpha + i\tilde{\omega}_c)y(t) = a x(t). \quad (13)$$

Given ω_c , and thus knowing $\tilde{\omega}_c$, we can numerically integrate Eq. (13) to obtain $y(t)$ in terms of $x(t)$ as the simulation of the response signal of the whole system.

Let the Fourier transform of the processes $x(t)$ and $y(t)$ be $X(\omega)$ and $Y(\omega)$ respectively,

$$X(\omega) = \int_{-\infty}^{\infty} x(t)e^{-i\omega t} dt \text{ and } Y(\omega) = \int_{-\infty}^{\infty} y(t)e^{-i\omega t} dt. \quad (14)$$

From Eq. (13) one gets

$$Y(\omega) = \frac{aX(\omega)}{-i(\omega - \tilde{\omega}_c) + \alpha}. \quad (15)$$

The power spectra for the two processes are related by

$$S_{yy}(\omega) = \frac{|a|^2 S_{xx}(\omega)}{(\omega - \tilde{\omega}_c)^2 + \alpha^2}. \quad (16)$$

Power Spectrums

It shows below that an estimate of the cavity resonance frequency can be yielded from the proper averaging over the power spectrum of the output signal $y(t)$.

In real measurements, the signal lasts only for a finite time period. The Fourier transform of the process $y(t)$ for $0 < t < T$ is

$$Y(\omega) = \int_0^T y(t)e^{-i\omega t} dt. \quad (17)$$

It can be shown that

$$|Y(\omega)|^2 = \int_{-T}^T e^{-i\omega\tau} T(1 - \frac{|\tau|}{T}) \langle R_{yy}(\tau) \rangle_T d\tau, \quad (18)$$

where $\langle R_{yy}(\tau) \rangle_T$ is the finite time correlation function

$$\langle R_{yy}(\tau) \rangle_T = \frac{1}{T - |\tau|} \begin{cases} \int_0^{T-|\tau|} y(t)y^*(t+|\tau|) dt & (\tau < 0) \\ \int_0^{T-\tau} y^*(t)y(t+\tau) dt & (\tau > 0). \end{cases} \quad (19)$$

Applying a convolution to the integral in Eq. (18), one has

$$|Y(\omega)|^2 \approx \frac{1}{2\pi} \int_{-\infty}^{\infty} T \left(\frac{\sin(\omega - \omega')T/2}{(\omega - \omega')T/2} \right)^2 S_{yy}(\omega') d\omega'. \quad (20)$$

Here it is assumed $\langle R_{yy}(\tau) \rangle_T \approx R_{yy}(\tau)$, and $S_{yy}(\omega)$ is the power spectrum

$$S_{yy}(\omega) = \int_{-\infty}^{\infty} R_{yy}(\tau) e^{-i\omega\tau} d\tau \quad (21)$$

with the correlation function $R_{yy}(\tau)$ obtained by averaging over infinite random ensembles

$$R_{yy}(\tau) = \langle R_{yy}(\tau) \rangle_{t \rightarrow \infty}. \quad (22)$$

The expression of $|Y(\omega)|^2$ in Eq. (20) corresponds to viewing the actual spectrum $S_{yy}(\omega)$ through a spectral window $W_T(\omega)$

$$W_T(\omega) = \frac{T}{2\pi} \left(\frac{\sin \omega T/2}{\omega T/2} \right)^2, \quad (23)$$

which provides a resolution of $\delta\omega = 2\pi/T$ [2]. Note $\lim_{T \rightarrow \infty} W_T(\omega) = \delta(\omega)$.

The above results can be further generalized to view $S_{yy}(\omega)$ at any resolution $\delta\omega > 2\pi/T$ by setting a cut-off to the correlation time range. Given T_M ($T_M < T$), the spectrum with resolution $\delta\omega = 2\pi/T_M$ is obtained by changing the integration range in Eq. (18) from $(-T, T)$ to $(-T_M, T_M)$,

$$[|Y(\omega)|^2]_{\delta\omega=2\pi/T_M} = \int_{-T_M}^{T_M} e^{-i\omega\tau} T_M \left(1 - \frac{|\tau|}{T_M}\right) \langle R_{yy}(\tau) \rangle_T d\tau \quad (24)$$

$$\approx \int_{-\infty}^{\infty} W_{T_M}(\omega - \omega') S_{yy}(\omega') d\omega'. \quad (25)$$

Combining Eq. (25) with Eq. (16), one gets

$$[|Y(\omega)|^2]_{\delta\omega=2\pi/T_M} \approx |a|^2 \int_{-\infty}^{\infty} \frac{W_{T_M}(\omega - \omega') S_{xx}(\omega')}{(\omega' - \tilde{\omega}_c)^2 + \alpha^2} d\omega'. \quad (26)$$

Note $[|Y(\omega)|^2]_{\delta\omega=2\pi/T_M}$ samples $S_{xx}(\omega)$ at the frequency $\omega = \tilde{\omega}_c$ with width $\Delta\omega = \alpha$ and resolution $\delta\omega = 2\pi/T_M$.

When the resolution $\delta\omega$ of $[|Y(\omega)|^2]$ is comparable with the bandwidth $\Delta\omega$, the fine structures of $S_{xx}(\omega)$ in Eq. (26) are smoothed out, giving rise to a well-behaved peak for $[|Y(\omega)|^2]$ centered at $\omega = \tilde{\omega}_c$. This can be achieved by choosing $T_M = 1/\alpha$. The cavity resonance frequency can then be determined by the frequency corresponding to the center of the peak in $[|Y(\omega)|^2]_{\delta\omega=2\pi\alpha}$.

Numerical Results

In the current problem we intend to have low-pass filtered signal $x(t) = e^{i\phi(t)}$ for $0 < t < 10$ ms. The required bandwidth limit is $f_b = 5$ kHz ($f_b = \omega_b/2\pi$) and thus $T_b = 100$ μ s. Two uniform random series u_n and v_n were generated for $n = (-200, 300)$, or $t = (-20, 30)$ ms, and $x(t)$ with the time interval $\Delta t = 10$ μ s is evaluated for $0 < t < 10$ ms using Eqs. (2), (3) and (5). Figure 2 shows that $x(t)$ is a very good approximation of an ideal bandwidth-limited process. The simulation of the cavity response signal was obtained by numerical integration using Eq. (13), with given relative cavity resonance frequency $\tilde{f}_c \equiv f_c - f_0$. By setting the cut-off time $T_M = 1/\alpha = 1.4$ ms in Eq. (24) (for $Q_c = 6.6 \times 10^6$), the power spectrum of $y(t)$ is obtained as shown in Fig. 3. It shows that the central peak is well behaved and centered right at the given \tilde{f}_c . The residual spectrum away from the central peak is caused by the remaining oscillations of the factor $W_{T_M}(\omega - \omega')$ in Eq. (26).

The above simulation shows that the cavity resonance frequency can be revealed from the location of the central

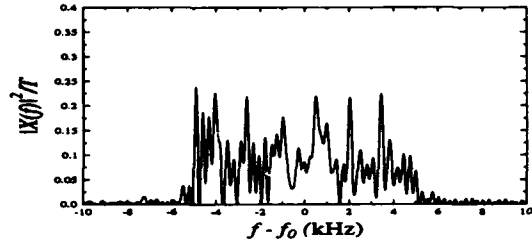


Figure 2: Power spectrum for the input signal $x(t)$.

peak of the properly averaged power spectrum $|Y(\omega)|^2$ for the output signal $y(t)$. For the particular problem we are interested in, the cavity quality number Q_c is high enough that the output signal $y(t)$ is a sinusoidal signal with varying amplitude. The frequency of $\text{Re}[y(t)]$ or $\text{Im}[y(t)]$ determines the frequency offset from the operating frequency, and the direction of rotation of the vector $y(t)$ indicates whether it is a positive or negative frequency offset. The validity of the scheme presented in this paper is currently under test by experiments.

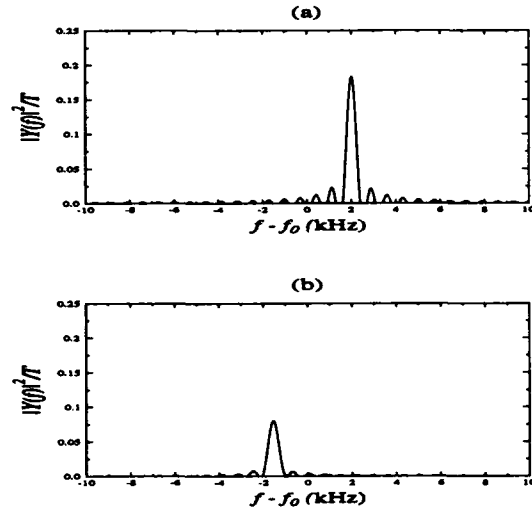


Figure 3: Power spectrum for the output signal $y(t)$ for (a) $\tilde{f}_c = 2$ kHz and (b) $\tilde{f}_c = -1.6$ kHz.

Acknowledgement

We wish to thank J. Bisognano for valuable discussions. The information provided by P. Gupta is also gratefully acknowledged.

References

- [1] A. Papoulis, *Probability, Random Variables, and Stochastic Process*, 1965.
- [2] G. M. Jenkins and D. G. Watts, *Spectral Analysis and its Applications*, 1968.

A Beam Position Monitor Data Acquisition System for the New Fermilab 400 MeV Line

S. Lackey, J. Firebaugh, C. Johnstone, W. Marsh, J. Smolucha and K. Woodbury,
F.N.A.L.*

Abstract

A VME based data acquisition system has been designed and installed for use in the new 400 MeV line connecting the Linac and Booster at Fermilab. Position information is digitized at rates up to 5 MHz during the entire beam pulse. Triggering can be accomplished by any of several mechanisms, including beam synchronized clock events, Tevatron clock events or an external trigger based on the chopper power supply trigger. Scaling and averaging are done locally. The results are returned to the ACNET control system via the Token Ring network.

I. INTRODUCTION

The Fermilab Linac is being upgraded to deliver 400 MeV beam to the Booster¹. This requires a redesign of the transfer line into the Booster. The new transfer line will include beam position monitors. This paper will describe the hardware and software included in the data acquisition system for the beam position detectors in the 400 MeV transfer line.

There are a total of 26 beam position detectors each of which have both horizontal and vertical pick-ups. Some of these are actually located in the Booster and are used in the Booster BPM system as well.

The position and intensities are digitized at a 5MHz rate during the beam pulse. The length of the beam pulse will vary depending on the number of turns injected into the Booster. A single turn of Booster beam requires a 2.8 microsecond pulse. Individual samples are available for display as well as the average position, position sigma and average intensity for each beam pulse.

Unlike the other beam position monitor systems at Fermilab, the scaling of the position signals as well as averaging is done locally in the microprocessor. Also, any offsets needed are applied at the microprocessor level.

II. HARDWARE

A. Overview

The digitization is accomplished in two VME crates each of which includes a processor board, system services module², memory board, Token Ring³ interface board, universal clock decoder board and several digitizer boards.

The system services module is a Fermilab designed board that includes a bank of dot matrix displays, led displays and switches for diagnostic purposes. The switches are also used to set the token ring address for the crate. The SSM board has a multi-function peripheral chip which is used to generate interrupts from external signals.

The universal clock decoder is a Fermilab designed board that decodes Tevatron and Beam Sync clock events. The on board state machine is programmed to produce the proper VME bus interrupts in response to clock events. Process scheduling interrupts are also provided by the U.C.D. board.

B. Digitization

The digitizer boards are the four channel, 5 MHz quick digitizer boards⁴ designed at Fermilab which are now commercially available. The position signals are digitized with 12 bits of resolution and several intensity signals are also digitized. Each digitizer board has 512 Kbytes of memory available. Therefore, 64,000 position or intensity samples can be stored from each detector before the information is overwritten..

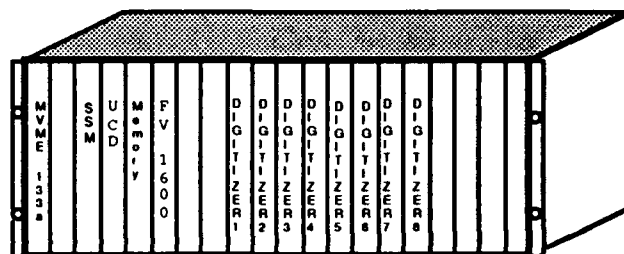


Figure 1. Beam Position Monitor Crate

C. Timing

The digitizers are gated on with a pulse that is derived from the chopper power supply trigger and conditioned by intensity. In this way, the beam position is monitored for the entire length of the beam pulse no matter how many turns are injected into the Booster. On the falling edge of the gate signal, a VME interrupt is generated causing the digitized data to be read.

In the case of the detectors surrounding the Booster injection point the gate pulse is active during the first turn in Booster. We will also attempt to read the position information from the detectors in the circulating beam for as long as there is sufficient 200 MHz structure. These detectors are digitized on an additional channel with a different gate pulse. The additional gate pulse is delayed by one turn and the length of the gate is determined by a timer.

III. SOFTWARE

A. Microprocessor

In addition to a commercial operating system, there are several pieces of code written in house for these systems. These include Object Oriented Communications⁵, the ACNET⁶ and Token Ring interfaces, as well as the code that

* Operated by Universities Research Association under contract with the U.S. Department of Energy

reads the digitizers. Each of these tasks is written in C and runs under control of the operating system.

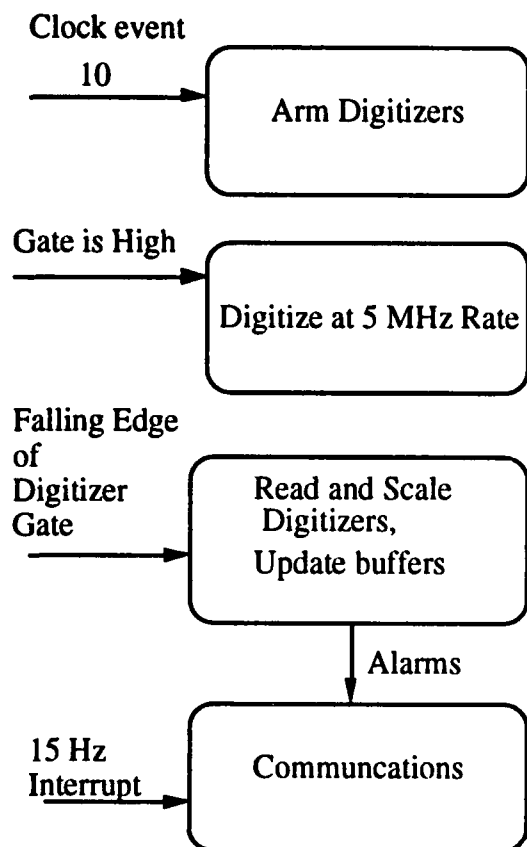


Figure 2. Beam Position Monitor Operation

The task that reads the digitizer boards is connected to the interrupt generated by the falling edge of the gate signal. The purpose of this task is to average and scale the positions, calculate the standard deviation of positions, average and scale the intensities, and record the date, time and memory location

of the raw data.

A buffer including the date, time and memory location of the position data for the last 4000 Booster cycles is kept. This allows detection of beam position drifts over time.

In addition, position information is checked against variable limits. If the limits are exceeded, alarms are sent to the control system.

B. Application Program

The position information is transmitted to the accelerator controls system by way of Token Ring, and an application program will display the information in graphical form as well as numerically.

The positions are displayed in map form along with the respective magnets to facilitate tuning of beam position along the line as well as injecting properly into the Booster.

IV. ACKNOWLEDGMENTS

The authors would like to thank T. Zuchnik and R. Mraz for assembling and installing the equipment and J. Lackey for pointing us in the right direction.

V. REFERENCES

1. C. Schmidt, invited paper this conference.
2. D. Beechy and G. Mayer, "Design and Implementation of a VMEbus System Services Card", Proceedings of the 1989 IEEE Particle Accelerator Conference, Vol. 3, pp. 1695-1697.
3. The Institute of Electrical and Electronics Engineers, Inc., 802.5 Token Ring (Wiley Interscience, 1985).
4. M. Shea, et.al., "Fairly Quick VMEbus Digitizer, internal report # FAA-617.
5. L. J. Chapman, "Object-Oriented Communications", Proceedings of the 1989 IEEE Particle Accelerator Conference, Vol. 3, pp. 1631-1632.
6. C. Briegel, G. Johnson and Lin Winterowd, "The Fermilab Acnet Upgrade", Nuclear Instruments and Methods in Physics Research, Vol. A293 (1990) pp. 235-238.

A VME Based Quench Protection Monitor for the Tevatron Low Beta Quadrupoles

S. Lackey, C. Briegel, L. Chapman, R. Flora, K. Martin, and T. Savord*, F.N.A.L.**

Abstract

A VME based quench protection monitor system has been designed and installed at both low beta locations in the Tevatron. Fixed-target and collider mode operations have been successful. One VME based system protects all of the high current circuits in each building rather than one Multibus I system per circuit as is the case for other Tevatron quench protection monitors. The software has been written in C for portability and flexibility for possible use with other magnet systems. Object oriented communications with the ACNET control system are made via the Token Ring network.

I. INTRODUCTION

When the new low beta quadrupoles were installed at the B0 and D0 straight sections of the Tevatron¹, the quench protection system was re-designed. Each low beta insertion now consists of five individual circuits. One of the five circuits includes a trim supply which requires that circuit be treated as two independent circuits.

II. HARDWARE

The quench protection monitor hardware is comprised of a standard VME crate with a 400 watt power supply, a Motorola MVME133a-20 processor board, a Formation FV1600 token-ring interface board and a four mega-byte ram board. In addition to the purchased boards, several in-house designed boards are used. These include three scaler boards a control board and a global functions board. The entire crate, as well as some supporting hardware, is powered by an uninterruptable power source which can supply 120 volts ac to the system for approximately 20 minutes.

The hardware external to the VME crate is the same hardware that is used for the rest of the Tevatron.² The voltage to frequency convertors were re-packaged to allow more channels per crate. The heaters in two of the circuits required ganging of heater firing units in order to supply the required energy. External current sharing resistors had to be added to the heater firing units in these circuits. Figure 1 shows the quench protection monitor and how it is connected to the external hardware.

The three scaler boards are identical. They are VME versions of the scaler boards used in the Multibus I systems. These boards have 30 channels each as opposed to the 40 channels on a Multibus I scaler board. For the low beta systems, 30 channels each allows each scaler to be dedicated to a specific type of voltage to frequency convertor. These being the ± 10 volt, the ± 200 milli-volt, and the ± 100

volt range voltage to frequency convertors.

The control board is a digital I/O board that inputs status from and sends qpm status to the low beta power supplies. The heater firing units are also monitored and controlled by this card.

The global functions card is another digital I/O board which monitors and controls external systems such as the refrigeration system, the beam abort system, the correction element power supplies and the uninterruptable power source. The global functions card supplies the VMEbus interrupts which trigger the quench detection and protection software routines. The interrupts are synchronized by a phase locked loop which provides 60 Hz, 360 Hz and 720 Hz line-locked signals. The 60 Hz signal is used to trigger the quench detection software and the 360 Hz or the 720 Hz are jumper selectable to trigger the quench protection code which determines the levels output to the external hardware.

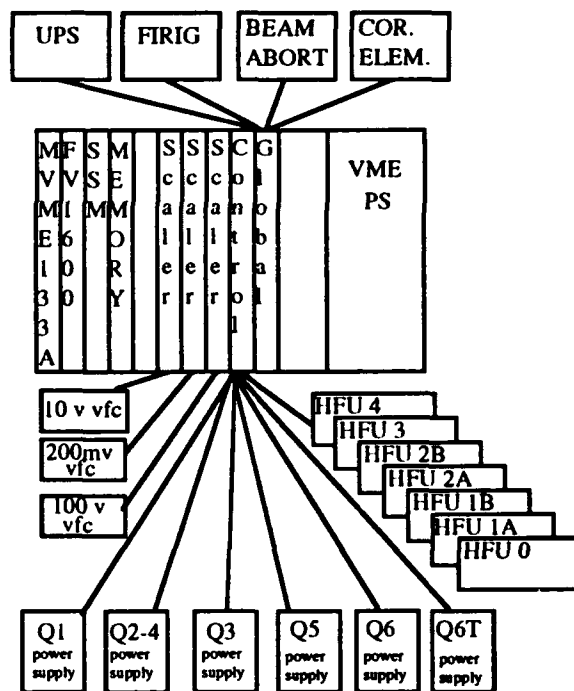


Figure 1. Low Beta Quench Protection System

III. SOFTWARE

The software includes both a purchased operating system and in-house code written in the C language. The actual quench detection and protection software run above the operating system as interrupt service routines which are unknown to the operating system. The communications software, Object Oriented Communications³, and the interface to ACNET are comprised of tasks running under the auspices of the operating system.

* Currently with the S.S.C.L.

** Operated by the Universities Research Association under Contract with the U.S. Department of Energy.

In order to make the system flexible, the number of circuits, quench detection units and quench protection units are defined at compilation time. A quench detection unit refers to the section of the circuit between voltage taps and a quench protection unit is the group of magnets whose heaters will be fired if a quench develops in any of its quench detection units.

The actual algorithm used to determine if a quench has occurred is the same as used in the Tevatron and Switchyard quench protection monitors. A 'relative' di/dt value is calculated based on the assumption that the circuit is superconducting and all voltages are inductive. This 'relative' di/dt value is used to calculate the expected voltage for each quench detection unit. The actual value of the voltage is compared to the expected value. Any differences are assumed to be caused by a resistance. If the absolute value of the voltage difference is greater than 0.25 volts, a quench is detected. As an additional check, the current is monitored, the actual di/dt is calculated and compared to the 'relative' di/dt . If these values are not in agreement, the system will not allow the magnets to be powered.

The actions of the system are controlled by masks which can easily be configured to accomplish the required responses. Although there are basic functions that cannot be masked out, such as firing of heaters or de-energizing the circuit in the case of a quench. These masks are altered slightly depending on the operational mode of the Tevatron, collider or fixed target.

While operating, the quench protection monitor maintains a circular buffer of all status, voltages and currents that can be accessed in the event of a quench.

When the Tevatron is running in the fixed target mode, the magnets are re-configured in the tunnel. In order to

facilitate the change-over from one mode to another, the proper masks and parameters are stored in files which can be downloaded to the quench protection monitors. The monitors default to the collider mode. To account for magnets that are disconnected in the fixed target mode, the inductance values and the power lead resistance values are set to zero for the missing magnets. In this way, the monitoring cables do not have to be disturbed.

IV. OPERATIONAL EXPERIENCE

The low beta quench protection monitors have been installed since November of 1990. The initial installation consisted of all circuits at B0 and only one circuit at D0. The fixed target physics run began July 16, 1991. This configuration remained until the end of the fixed target physics run in January of 1992. By the middle of April 1992, all of the remaining circuits had been installed and tested.

These systems have been running with very little downtime since the beginning of the present collider run.

IV. REFERENCES

- ¹K. Koepke, M. J. Lamm and G. S. Tool, "The D0 Low Beta Power and Quench Protection System", Proceedings of the 1989 IEEE Particle Accelerator Conference, Vol. 1, pp. 515-517.
- ²R. Flora, J. Saarivirta, G. Tool and D. Voy, "The Energy Saver/Doubler Quench Protection Monitor System", IEEE Trans. on Nucl. Sci., Vol. NS-28, No. 3, pp. 3289-3291 (1981).
- ³L. J. Chapman, "Object-Oriented Communications", Proceedings of the 1989 IEEE Particle Accelerator Conference, Vol 3, pp. 1631-1632.

Experience with the TRIUMF Main Tank Vacuum Control System

S. Sarkar[†], J.C. Yandon, W. Sievers, P. Bennett, D.P. Gurd[†], P. Harmer, J. Nelson.
TRIUMF, 4004 Wesbrook Mall, Vancouver, B.C., Canada. V6T 2A3.

Abstract

The TRIUMF Main Tank Vacuum Control System was upgraded in 1984. The earlier system, which consisted of a collection of hardwired relay logic boxes housed in three standard instrumentation racks, was replaced with a compact and flexible microprocessor-based control system. The user interface, previously distributed over the three racks, was consolidated into a single hardwired control and mimic panel. Since 1984, the Main Tank Vacuum System has undergone a series of changes in configuration and vacuum pumping hardware with necessary changes being implemented in the control system logic. Corresponding changes to the user interface were sometimes difficult to implement and in time exhausted the spare input / output capacity which had been built in to the panel. The availability of inexpensive personal computers with adequate graphics capability and the ease of modifying, or adding to a programmable user interface precipitated the retirement of the hardwired panel and its replacement by a PC-based graphics user interface. System configuration, safety considerations, the hardware and the software implementation using the 'C' programming language are described. The evolution of the control system and its performance, both over the years and in adapting to the vacuum system changes, are discussed.

I. INTRODUCTION

The TRIUMF Main Tank Vacuum System (MTVS) pumps the cyclotron vacuum tank from atmospheric pressure to an operating pressure of $4 \cdot 10^{-8}$ torr [1]. The pressure is measured in the range from 760 to 10^{-3} torr by broad range Pirani gauges and in the range from 10^{-3} torr to 10^{-8} torr by broad range ionization gauges. The pumping system is

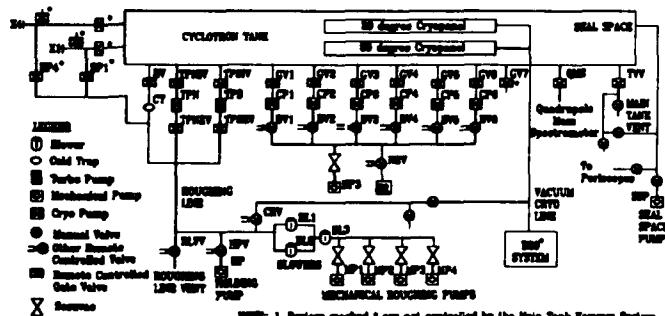


Figure 1: The TRIUMF Main Tank Vacuum System

composed of a number of pump groups, shown schematically in figure 1. Each group is a sub-system consisting of pumps, valves, vacuum gauges and pump condition indications.

† Presently at SSC Laboratory, 2550 Beckleymeade Ave., Dallas, TX., 75237.

The mechanical pumps (MP1-4) and Rootes blowers (BL1-3) reduce the pressure from atmosphere to 10^1 torr. The turbo pumps (TPN and TPS) further reduce the pressure to 10^{-3} torr. The cryogenic pumping system, consisting of six cryo pumps (CP1-6) and two cryo panels, brings about the final reduction in pressure to $4 \cdot 10^{-8}$ torr.

The pumps operate efficiently over limited but overlapping ranges of pressures and are used in stages, to pump down the cyclotron tank from atmospheric pressure. Inadvertent operation with out of range, fore or backing, pressures can cause pump damage or contamination of the vacuum system. Pressure measurements are used to monitor the operation of the vacuum system and to provide interlock setpoints for the safe operation of the pumps. Temperature measurements are used to monitor the operation of the cryo systems and utilize RTDs, thermocouples and hydrogen bulbs. Auxiliary devices such as the holding pump, the seal space pump and the N₂ purge system are used to maintain backing vacuum, to maintain tank seal at low pressure and to regenerate the auxiliary cryo pumps respectively.

Prior to 1984 the function of providing system status information and protective device operation interlocks for the MTVS devices was implemented by in-house built, relay-based logic boxes. Commercial gauge controllers and readout controllers used for pressure and temperature measurements usually provided a single mechanical set point contact closure for use in the interlock logic. All of these boxes were distributed over three standard relay racks. Interlock logic was determined in part by the logic boxes, in part by the point-to-point wiring of control signals between boxes at the rear of the racks and in a small number of cases by an operator forming a part of the loop. Though only simple interlocks could be implemented with the relay logic, verification, documentation, addition and change of logic were cumbersome processes. System operation was through control switches and status indicators on the boxes spread over the three racks.

The control system was upgraded in 1984 to address the limitations of the earlier system. A concurrent goal was to produce a compact, generic vacuum control system design to eliminate the need to individually 'engineer' controls for the various beamlines' vacuum systems at TRIUMF. A relatively compact control system would allow the inclusion in centralized controls of devices previously left with independent manual controls and local readouts only, due to limits in the rack space allocated to vacuum system controls.

II. CONTROL SYSTEM

The use of a microprocessor based architecture for interlock controls and the use of 'C' as the programming language for these processors were both new at TRIUMF in 1983, though it has been commonly used since.

Considerations of safe operation of a microprocessor based Main Tank Vacuum Control System (MTVCS) were addressed: by specifying the use of hardwired first level protection of all devices with potential for major damage - such as the use of differential pressure switches to interlock all Cyclotron Tank gate valves, and by requiring the MTVCS microprocessors to re-evaluate MTVS interlocks and regenerate all device operation permissives quicker than every 200 mSec.

Figure 2 is a block diagram of the MTVCS as it stands today. Two TRIMAC [2] 8085 based CAMAC Auxiliary Crate Controllers (ACCs) were used for control of the MTVS based on an estimate of the number of analog and digital points to be monitored and controlled, the update rate requirements specified above and expected system growth. The two TRIMACs were functionally partitioned to handle analog signal

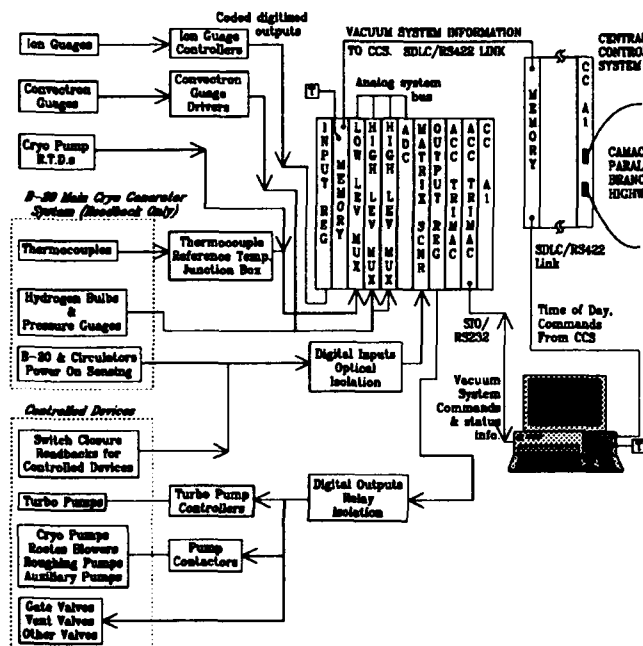


Figure 2: Main Tank Vacuum Control System Block Diagram.

processing and to carry out digital I/O and control operations. Communications between the Trimacs is via a shared (reflective) memory also accessible to the TRIUMF Central Control System (CCS). This allowed monitoring of vacuum control system and for remote operations described later.

A. Hardware

Features which make this system robust, compact and flexible, allowing generic application, are the use of a matrix scanner with opto-isolation (instead of relays) for inputs and the use of a general purpose analog input system.

High density (large number of I/O points per crate) was achieved by using single slot form factor Joerger Quad (24 bit) output registers and GEC Canada 256 (upgradeable to 512) point matrix scanner for digital output and input respectively.

The matrix scanner is itself a Z-80 microprocessor based module which provides features useful for interlock control systems. Input debounce processing, logic sense and masking are each software selectable on a per point basis. Further the (A) CC can read instantaneous point status, be interrupted (LAM) or polled (test LAM) for time tagged point status

changes, read from a queue of time tagged point status changes or a mix of these modes under software control. These facilities have many implications for interlock system implication one of which is the use of time tagged point status information for diagnostics and trending in large systems.

Analog signals were interfaced using the Quantrol ADC and MUX system which can handle a maximum of 256 analog channels and can interface to a range of analog signals with integral first line signal conditioning. Signal conversion and linearization were done in software. Together this reduced the need to use various external boxes to interface and 'linearize' the different analog inputs.

B. Software

Prior to 1984 existing microprocessor-based systems at TRIUMF were programmed in assembly language. Migration to higher level languages such as FORTRAN was being explored. 'C' with its rich set of bit manipulation primitives was a natural choice for the implementation of interlock control systems. The 'C' preprocessor allowed specification of interlock logic in an english like, human readable form which were easy to understand and modify. The facility for data structures and pointers allowed for the generation of software routines useable for classes of devices. Structures provide the natural grouping of related information while pointers associated with these structures allow easy manipulation of these related information eg. a device analog pressure has associated with it the type of gauge used, linearization and data conversion information, physical location, set points and associated units.

The Digital TRIMAC program was structured such that by changing Camac configuration data, by generating English language equivalents for device state information (utilizing preprocessor directives) and by using these equivalent statements in interlock logic specification the program could be easily 'ported' to control other vacuum systems.

In the Analog TRIMAC an ASCII file was used to define all analog channels to be scanned by the system and to specify channel details such as conversion factors, units, filtering to be done on the raw signal. Changes to the analog system required only this file to be updated. The Analog TRIMAC program was translated in to FORTRAN to deal with early version 'C' compiler problems. The natural device structuring possible in 'C' was unimplementable in the FORTRAN version. Subsequent updates to the Analog TRIMAC program entailed changes to multiple tables and keeping track of table data relationships.

III. USER INTERFACE

A generic (vacuum) interlock control system design capable of supporting configuration changes requires a soft or reconfigurable user interface. Intended implementation target, a low cost 'Personal Computer' (PC), with adequate graphics display resolution, would run tasks to receive system status information from the TRIMAC ACC, generate & update graphics display and send vacuum system control commands merged from keyboard and mouse to the TRIMAC ACC for execution.

In 1983 an established PC meeting the above requirements was unavailable. User acceptance of the soft user interface concept was low.

A. local Interface

Initial user interface was implemented using a conventional hardwired mimic and control panel. The Main tank vacuum system devices were drawn on the panel with multiple LEDs used to indicate status of the device. Push buttons placed in proximity were used for device control functions. Spare buttons and LEDs had been added to the panel to cope with vacuum system additions and changes. These were able to carry through for a number of years but changes or additions were usually difficult since to the control system were made difficult due to the need to

By 1987 the hardwired display had been in service for 3 years and was out of space for additions. Reliability was low due to mechanical wear out. Modifications were becoming costly. A backup panel was estimated to cost \$5K and at this time it was cheaper to implement a PC based user interface. The user interface was replaced in 1988 with a 'soft' interface consisting of IBM PC/XT with a floppy disk and a EGA display. The hardwired panel, retained as backup only, was removed in 1989.

B. Remote Operation

The MTVCS was designed with remote operations capability with commands / status communications from and to the CCS via a shared CAMAC memory. This feature has been used to date only for remote monitoring of the system. The importance of this feature was for addressing the design goal of a generic vacuum control system design capable of addressing all vacuum systems at TRIUMF. In particular the secondary channel controls require centralized vacuum system controls because of shared pumping system but require distributed operator controls or consoles at each of the channel operational areas. The remote vacuum system control commands were to be funneled in to the MTVCS via the CCS. This would be useful in cases such as secondary channel controls were 'soft' user interfaces at the various counting room locations could control beam line vacuum system devices by communicating with the CCS computer to send information to this control memory allowing independent control stations for a central vacuum control system.

IV. IMPLEMENTATION

The entire system was implemented in 1.2 years elapsed time with 4 man-years of effort. This included 1 man year spent in verifying existing system and making bridge connectors to allow upgrading of system with minimum disruption of operation. Software effort totaled about 6 man-months equally divided among software design, development and coding.

There were initial teething problems with the early 'C' compilers available. The situation improved in time, with the availability of stable and relatively complete implementations of the 'C' language cross-compilers for the Intel 8085 processor running under DOS on an IBM PC.

V. SYSTEM UPGRADES

Initially the Main Tank Vacuum System utilized 5 diffusion pumps along with associated liquid nitrogen (LN₂) cold traps to maintain operating vacuum. The diffusion pumps and LN₂ traps were replaced one at a time by cryo pumps, an

additional turbo pump was added and the Roughing system pumping configuration was changed in a series of upgrades.

Hardware and Software changes to the control system associated with the above upgrades required on average 1-2 man-months of effort spread over 3 months of which the software component was typically 15-20 man days. The system has proven very flexible. Minor additions and changes are made routinely and easily.

The Soft user interface initially programmed in BASIC was later converted to 'C'.

VI. CONCLUSION

We started out with the goal of providing a flexible and compact control system. The MTVCS has been able to provide an interlock and control system for 256 input and 182 output points for a cost of about \$27000, including additional cabling costs required because the vacuum system was being upgraded. It has worked well since 1984 and has been able to adapt to a changing system with relative ease and with little additional expenditure. The Rad Hard valve controls and the Extraction Probes housing vacuum controls for beamline 1 and beamline 4 were incorporated using two TRIMACs and a few I/O modules housed in the same CAMAC crate. In 1991 control programs for the Rad Hard valves and the Extraction Probes were transferred to the MTVCS digital TRIMAC. The current system utilizes one and a half racks including space for some gauge controllers. In the nine years of operation the system has proven highly reliable.

VII. ACKNOWLEDGEMENTS

The authors would like to thank Dr. W.K. Dawson for his advice, D. Harrison, J. Stewart and E. Osberg who helped out during system installation and commissioning, and last but not least B. Evans and D. Morris who have maintained the Fortran version of the analog trimac program.

VIII. REFERENCES

- [1] J.C. Yandon, "Vacuum Production in the TRIUMF Accelerator", *Proceedings of the National Research Council of Canada Div. of Phy. Vacuum Production Workshop*, pp. 75-79, Ottawa, Ont., Oct., 1989.
- [2] *TSM-1005 Main Tank Vacuum Control System Manual*, Vancouver, B.C., TRIUMF, Feb., 1989.
- [3] *ACC-160108 Trimac Auxiliary Crate Controller Reference Manual*, Toronto, Ontario, GEC Canada, Dec., 1984.

Laser Power Stabilization in the TRIUMF Optically Pumped Polarized H⁻ Ion Source

S. Sarkar*

SSC Laboratory, 2550 Beckleymeade Avenue, Dallas, TX., 75237.

Abstract

Power stabilization of the lasers, used in the TRIUMF optically pumped polarized ion source prior to 1991, was crucial to maintaining the laser wavelength and hence nuclear polarization. Output power of the dye lasers was dependent on a number of variables, including the relative drift between the transmission peaks of the birefringent filter and the etalon used to tune each dye laser. The power control system used a program running in a CAMAC crate based PC/AT to control the birefringent filter. Heuristic algorithms implemented to control power and their performance in the steady state and the wavelength shifting modes are described.

I. INTRODUCTION

The current system used at TRIUMF for optically pumping the polarized H⁻ ion source is different. However the stabilization of laser power in the previous system represented a challenging class of problems with parallels in many other areas and is of general interest. This paper describes the implementation of heuristic algorithms for control of processes which are badly characterized, for which there are many unknowns and which fall in to the category that cannot be easily formulated as a classical controls problem. This implementation shows that heuristic methods can provide solutions to such problems even in the presence of extremes of noise.

Three tuneable CW dye lasers pumped by Argon lasers were used (until early 1991) to optically pump sodium vapor cells in the TRIUMF Optically pumped polarized H⁻ ion source and has been described in reference[1,2]. A fourth CW dye laser was used as a probe to measure the sodium polarization. The laser system was used in two modes. For final ion source polarization in either the spin up or the spin down state the lasers were all operated at a single frequency. When the ion source was operated in a spin flipping mode the lasers were operated in a wavelength shifting mode with the operating frequency of the lasers tuned to the absorption bands of the sodium vapor in the hot cells. To maintain stable polarization the frequency and the power of the laser system must be maintained within required tolerances[3]. The lasing frequency is determined by factors such as the combined transmission characteristics of the solid etalon and the bi-refracting filter, the laser system gain and the pump laser power. Although the bi-refracting filter is used to control power, it is loosely coupled to the output frequency, until it is tuned to adjacent etalon transmission peaks - and causes the laser to mode hop.

The goal of the laser power stabilization program is to maximize and maintain dye laser power for the single frequency laser operation, to maintain constant power ratio for two frequencies in the wavelength shifting mode of operation, and

*Previously at TRIUMF, 4004 Westbrook Mall, Vancouver, BC, Canada. Work performed 1989 - 1990.

to prevent mode hopping in both the single frequency and wavelength shifting modes of operation.

II. SYSTEM CHARACTERISTICS

The task of stabilizing the power of the dye lasers was made difficult for a number of reasons. The laser output power changes randomly due to thermal drifts caused by convection currents within the laser housing, by bubbles in the dye jet, by jet pressure and shape fluctuations and by Argon pump laser power and incident angle changes. The dye laser output is noisy. Dye breakdown with operation adds to the laser noise which at times is greater than 50% of peak amplitude.

The problem was further complicated by implementation details of the bi-refracting filter controls. There was no optical encoder to provide position readback on the bi-refracting filter motor drives due to space limitations within the laser housing, there was backlash on the spring loaded motor drive which also had different loading for travel in the forward and the reverse direction.

To further complicate matters change in the controlled variable (output power) depended on the relative position of the bi-refracting filter and the etalon. Neither of these positions were measurable even relatively in this system. The output power versus frequency envelope shape changed with time and between the edges of adjustment favoring particular modes the system simultaneously lased at two frequency bands - (Although the output power was not changed markedly).

Initially an attempt was made by others to implement degenerate power stabilization in an analog circuit along with closed loop frequency control implemented using feedback from a spectrometer which gave the laser frequency reading accurate to 1 GHz. This was abandoned when it was found difficult to cope with drive backlash and to keep track of laser power changes. An attempt was made to cast the process as a classical controls problem with the intention of implementing it on the I4 laser control Micro-VAX processor - since maximization of laser power was thought to be a slow and simple process. This was abandoned as some of the system complications mentioned above became apparent.

III. ALGORITHMS

The laser power stabilization processes used modified versions of the hill climbing algorithm to cope with laser noise and drift and for the two modes of operation.

A. Hill Climbing Algorithm

In a simple hill climbing algorithm (figure 1) the operating point is stepped in a given direction and the power change δp determines direction of motion in the succeeding step: if $\delta p < 0$ the direction is reversed, else direction of motion is unchanged. The system is stepped continuously and oscillates

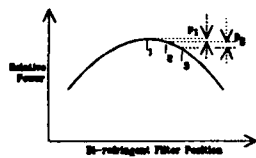


Figure 1: Ideal Power versus frequency characteristics.

for the ideal amplitude versus position relationship shown in figure 1.

In reality the power v/s frequency envelope shape is quite different. Figure 2 shows the power v/s frequency characteristics for one of the dye lasers as measured by keeping the

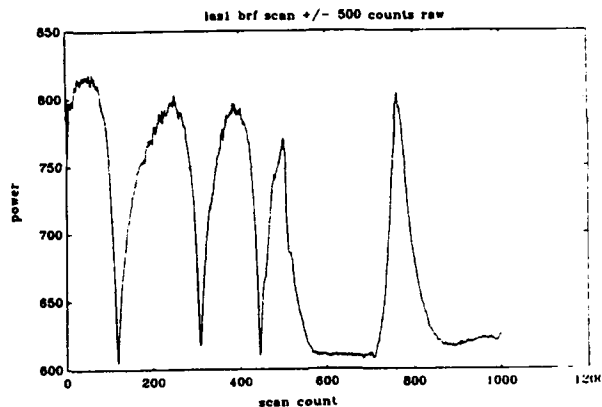


Figure 2: Real Power versus Frequency envelope

etalon constant and stepping the bi-refractive filter 500 steps in one direction and then back 500 steps. This characteristics varied from laser to laser and for the same laser with time and as the operating point changed.

B. Single Frequency mode

The modification required to the hill climbing algorithm for the single frequency mode of operation was to account for the apparent 'hill shape changes' caused by laser drifts and by laser noise. Noise affects the peak finding process. After a direction reversal and retraverse of the peak a simple algorithm is confused by either falsely reaching the peak value too quickly or in not reaching the peak at all. The solution in this case was to traverse the peak more than two times, if the maximum value for the last traverse was off by more than a given percentage, from the previous traverse. If after three traverses power was different from last activation and if after this peak power matched on two successive traverses, then the peak power was updated to the new value, as also the activation threshold which is a percentage of the peak power.

C. Wavelength Shifting Mode

There were two categories of operation for the wavelength shifting mode - slow for shifts at a maximum of once per minute and fast at a 100 hz. The slow mode of operation was implemented first since it was easier to implement etalon controls for slow frequency shifting. However, this was the most difficult task for power stabilization process since it was

not possible to distinguish between bi-refractive filter drift and laser power changes while sitting at one of the two operating frequencies. This is addressed by using partial correction at each state.

Operation in the wavelength shifting mode is different from the single frequency mode, since the algorithm is required to maintain the bi-refractive filter transmission slope (not peak) on the operating frequencies. Power is expected to increase or decrease as a function of direction. Taking a step in the wrong direction increases error and the time to recover from this condition. Since operation time at each frequency is limited one has to maximize the time at the optimum power level or maintain correct power ratio between the two operating states as setup. Two modes of operation in the wavelength shifting mode was allowed. Based on initial selection the program either equalizes the power in the two states, or tries to maintain the power ratio from start of run.

Ideally the laser output power is expected to increase or decreases monotonically as a function of birefractive filter position due to its transmission characteristics. Had this been the case, at any operating point the direction of bi-refractive filter motion for increasing or decreasing power would be fixed. The 'direction-map' for the bi-refractive filter movement for increasing power was not expected to be constant over the range of operation due to the large number of variables determining the output power at any given setting and the drift in these parameters. An algorithm was used to dynamically build and alter the 'direction-map' at any given operating point. It had built in hysteresis against noise in that a change in direction would be recognized only after a selectable number of consecutive direction errors.

IV. IMPLEMENTATION

The 14 laser control system has been described in reference [4]. The laser power is sensed using photo diodes and is digitized using a 32 channel auto-ranging ADC with rudimentary signal filtering. The software was implemented for the three pump plus one probe laser as a single tasking program run on an IBM PC/AT. The laser power read task was implemented as an independent DOS terminate and stay resident task triggered off the system clock to allow timed sampling. Raw power data was filtered to remove high frequency noise initially using a straight averaging filter and later with a finite impulse response filter. Low frequency noise along with short term laser power drift could not be filtered.

The program was implemented over a period of about 1 year and was approximately 6600 lines of 'C' code. This could have been reduced by about 30% but would have required additional effort and made the maintainability of the program more difficult.

V. RESULTS

The program performed better than initial requirements for the single frequency mode of operation. The program first maximized the power - with sizeable increases in power frequently seen over that achieved by manual tuning - and then maintained power at the maximum possible for a given pump laser power. The program was able to keep the output power at maximum with pump power variations of greater than 25% seen for periods exceeding two to three days (figure 3) as against a requirement for stable operation of eight hours.

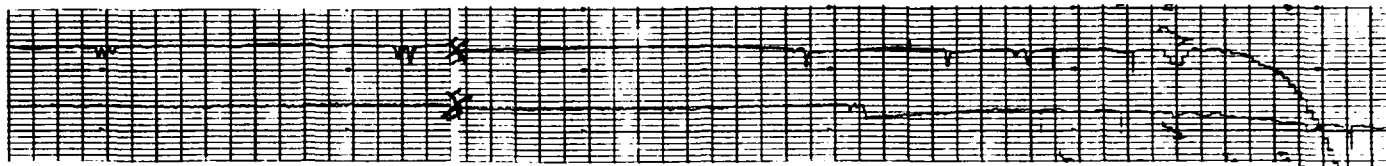


Figure 3: Power Stabilization in Single Frequency Mode of Operation

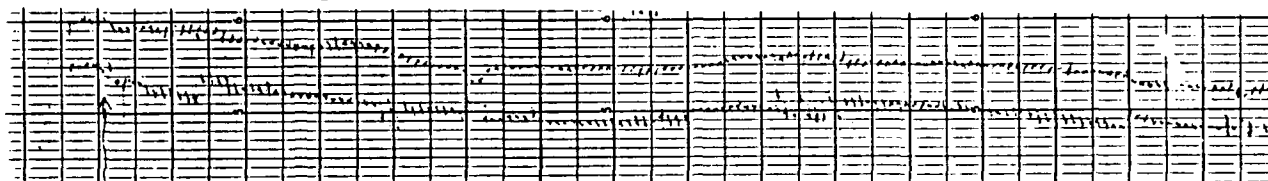


Figure 4: Power Stabilization in the Wavelength Shifting Mode - Laser with Average Noise

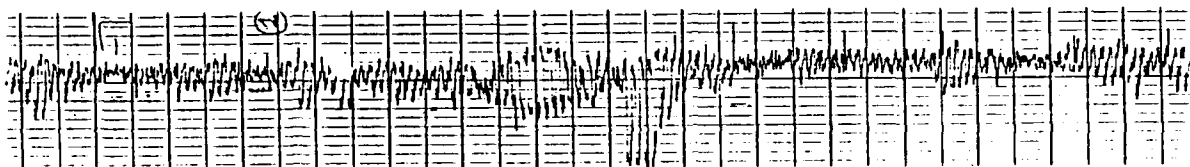


Figure 5: Power Stabilization in Wavelength Shifting Mode - Laser with extreme noise.

In the wavelength shifting mode the performance is close to that required. The laser power was held within required limits without mode hop for the required eight hours (figure 4) except for the most noisy laser where periods of six to seven hours were achieved (figure 5). Hysteresis dead band was increased to reduce system activation but this caused operation with power divergent to the dead-band limits. With the expected changeover to Titanium sapphire lasers, noise is expected to be lower and these programs or simpler versions should be able to meet or exceed requirements for operation in the wavelength shifting mode.

VI. DISCUSSION

The choice of slow spin flip operation to simplify the frequency stabilization process was not optimum from the system point of view. The power stabilization process was made difficult since laser power variations and bi-refractive filter drifts could not be distinguished before a long elapsed time. The solution generated was to carry out a partial correction at each stage and then verify against perceived drifts for the bi-refractive filter and laser power variations in the other frequency state - power variations cause similar changes in the laser power whereas bi-refractive filter causes complementary changes. For the quick spin-flip operation this is not a problem, however the correction algorithm must optimize straddling many frequency state changes.

This type of control problem is ideally suited to software implementation the control cycle is slow but the algorithm is sufficiently complex and undeterminable and has enough variables such that a hardware implementation becomes difficult. The results point out a class of problems that are hard to analyze using classical controls theory but can be solved heuristically.

The lasers are not too difficult to tune manually - the question is where is the pitfall in translation to an automated system? First the perception that manual tuning is easy needs to be verified. Performance of manual tuning needs to be logged over a period of time to allow comparison against the performance of an algorithm. One part of the comparison

exists and that is for single frequency mode of operation the algorithm was able to better adjust for peak power as evidenced by the consistent increases in power after a manual maximum had been achieved: conclusion is that in the case of simple well directed tasks involving magnitudes or maintaining a parameter within tolerance limits an algorithm based on digital measurements performs better than the human analog. However where more qualitative information is involved such as evaluating when a mode hop is likely to occur or what is the past history of the laser system settings or factors such as the hill shape for a particular laser and the expected range of tuning - the simple algorithms fail against manual tuning because they do not include the complexity, the adaptiveness, and learning or the capability to switch to new algorithms of the human. However the human approach suffers (usually) from a lack of trace of the procedures done. In translating human operations to algorithms the hidden processes need to be first observed, then the important ones need to be selected, followed by translation and implementation as wrappers for the simple (kernel) control programs. Examples being the implementation of the three traverse peak finding wrapper for noise compensation for the hill climbing algorithm and the implementation of partial optimization to prevent against over compensation in the slow spin-flip mode of operation.

VII. ACKNOWLEDGEMENTS

The author would like to thank Dr. W.K. Dawson for his advice and acknowledge the help of Paul Schmor, Phil Levy and others with understanding the operational and controls requirements of the ion source and the laser system and for their many suggestions.

VIII. REFERENCES

- [1] L. Buchmann *et al*, "Operational Experience With The TRIUMF Optically Pumped Polarized H⁺ Ion Source", conference proceedings, IEEE Particle Accelerator Conference, San Francisco, CA, May 1993.
- [2] C.D.P. Levy *et al*, "The Laser System of the Optically Pumped Ion Source at TRIUMF", paper presented at the International Workshop on Polarized Ion Sources and Polarized Gas Jets, Tsukuba, February 12-17, 1990.
- [3] C.D.P. Levy *et al*, "Recent results from the TRIUMF optically pumped polarized ion source", AIP conference proceedings, 8th International Symposium in High Energy Spin Physics, Minneapolis, Minnesota, September, 1988.
- [4] R. Chan *et al*, "The Preliminary Laser Control System for the TRIUMF Optically Pumped Polarized Ion Source", *IEEE Trans. Nucl. Sci.*, vol. 36, no. 1, pp. 798-800, Feb. 1989.

MPS BEAM CONTROL SOFTWARE ARCHITECTURE*

K. Krauter and M. Crane

Stanford Linear Accelerator Center, Stanford University, Stanford, CA 94309 USA

Abstract

The new Machine Protection System (MPS) now being tested at SLAC has a beam control subsystem resident in processors located close to the beam monitoring devices within the machine. There are two types of beam control micros: Algorithm Processors (AP's) which collect and evaluate data from monitoring devices, and a Supervisor (SUPE) which collects and evaluates data from all the AP's. The SUPE also receives the global machine beamcode indicating beam presence, and passes it on to the AP's. The SUPE receives the beamcode pattern from the Master Pattern Generator (MPG) via a shared-memory communication link. MIL-1553 serial communication is used between the SUPE and the AP's, and between the AP's and the monitoring devices. Multitasking software is used to allow high priority handling of data evaluation and low priority handling of host/user interfacing and event reporting. Pipelining of data between acquisition and evaluation and reporting is used to accommodate the processing capacity, while still supporting full processing at the 360Hz broadcast rate of the beamcode pattern.

1. MOTIVATION

The beam control subsystem of MPS does the actual per-beam data acquisition, data processing, and resultant beam control. Data from beam monitoring devices is acquired on a per-beam basis and processed to determine whether a machine-endangering condition (fault) has been detected. If a fault is found, then the data processing produces a result which indicates the rate at which the beam may be operated safely given the presence of the fault. When the fault is corrected, through steering or some other correction, the processing produces a result which requests that the beam operate at full rate again. If a fatal error internal to MPS occurs, the beam is completely disabled until the fatal flaw is corrected. The full functionality is documented elsewhere [1].

The per-beam data acquisition must be done at the same rate as the beam frequency, and it must be done as soon as possible after the beam has passed a given beam monitoring device, in order to acquire timely per-beam data such as material temperature and radiation level. The acquired data must be processed at the same frequency as well, in order to respond immediately to changes in per-beam data. High speed processors and communications and a fast realtime operating system are therefore required in the beam control VME crates.

Processor and communication limitations necessitate the placement of several beam control micros along the

length of the accelerator machine, each acquiring a subset of available per-beam data. These are called Algorithm Processors (APs) because they process acquired data by passing it through a logic machine called an algorithm. An algorithm is a list of tests dictating the level at which the beam may operate for each state detected by the beam monitoring devices [2]. Each AP produces a single result indicating the level at which the beam may safely operate in that AP's region of the machine. The results of all the APs are sent to the SUPE, a special consolidating AP. The SUPE processes the APs' results by passing them through a supervisor-level algorithm, producing a single result which is used to control the beam.

A secondary function of the beam control subsystem is to keep the operators in the main control center apprised of the machine status. Both APs and the SUPE report periodically which beam monitoring devices faulted and what beam level changes (events) have resulted. These reports are handled in the main control center VAX by the MPS code located there.

2. HARDWARE ARCHITECTURE

The beam monitoring devices have always been configured and read through CAMAC interfaces and SLAC's SLCNET network. MPS adds an additional serial MIL-1553B interface to these same devices which connects them to their respective APs. The APs are connected to the SUPE via MIL-1553B also, and the SUPE is connected to the beam controlling Master Pattern Generator (MPG) via a shared memory interface.

The AP and SUPE hardware consists of a 6-slot completely enclosed fan-cooled VME crate, each with a processor card and some number of 1553 cards. The SUPE also has a card for the MPG interface. The processor card is, currently, a Force CPU-30 68030 with ethernet. The VME-based 1553 card is adapted from work done at Fermilab. The SUPE-to-MPG shared memory interface is Bit-3 which is commercially available.

Both the APs and the SUPE are connected to the main control center VAX by LEBNET (Linac Ethernet Backbone NETWORK). Figure 1 illustrates the hardware layout.

3. SOFTWARE ARCHITECTURE

The beam control micros use multitasking to support both high frequency per-beam processing together with low frequency user request interfacing and event reporting. Each of the Tasks on the micro generally has a corresponding Manager on the VAX [3]. The operating system chosen for the micros was pSOS+, in part because it had the best VMS cross development environment.

All communication between the micro MPS tasks and the VAX MPS managers is over TCP/IP through the new Area Message Service (AMS) which makes software access

* Work supported by Department of Energy contract DE-AC03-76SF00515.

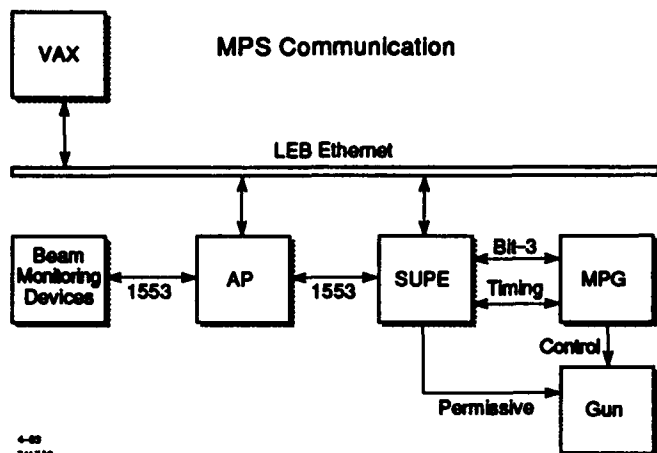


Figure 1. Hardware layout.

to the ethernet appear identical to the already existing software access to SLCNET [4]. The Slow Task also makes direct NFS calls to acquire algorithm description files from the VAX. There are two rules about I/O on the micro which dictate much of the architecture. Per-beam code may not do time-consuming ethernet I/O, and high volume small size message traffic must not be allowed to congest the ethernet. Per-beam data acquisition and processing is the highest priority task in the micro, doing the most important job—controlling the beam. Only when the micro is waiting between beams may it receive and answer ethernet requests, or ship events or error reports on the ethernet. Congestion is avoided by enforcing a minimum time interval between ethernet sends in each task. If a task is requested to send up a new event or error before this minimum time has elapsed since the last send, then the request is buffered up until the time interval has elapsed.

The micro Slow Task runs in the micro constantly and handles requests from the Slow Manager (also called the MPS controller) on the VAX, such as downloading MPS algorithms and reporting micro status. When the Slow Manager requests MPS be made operational, the micro Fast Task is started up to do per-beam processing.

The Fast Task spins off data acquisition I/O requests at up to 120 times per second, and does data processing in parallel. Always accompanying the Fast Task is the Event Task. Whenever the Fast Task detects a beam level change result (an event) from the data processing, the event is passed to the Event Task. The Event Task buffers the event as necessary and sends the event buffer to the Event Manager on the VAX, where the events are processed into displays and summarizations.

The Milcom Task waits for requests from the Fast Task to begin a data acquisition cycle. Since the configuration of the beam monitoring devices read by an AP is unchanging, the data acquisition commands can be prepared in advance and executed in a timely way on a per-beam basis.

Any errors or messages which the micro (Slow, Fast, Event, or Milcom Tasks) would like to report directly to

the operators at the main control center are passed to the micro Error Task. The Error Task buffers the error as necessary and sends the error buffer to the Error Manager on the VAX. See Fig. 2 for a task data flow schematic.

4. FAST TASK

The Fast Task must complete a number of functions between each beam pulse that occurs on the machine. The original design assumed the worst case of the beam coming at 360Hz, allowing 2.7 ms between beam pulses for the Fast Task to complete a full processing of beam pulse data. It was quickly recognized that 2.7 ms was not enough time in which to sequentially acquire the data and process it and report on it. This was enough time only if the Fast Task were able to start the data acquisition and data processing at the start of the cycle and run them in parallel. The Fast Task accomplishes this with a two-stage data pipeline in which the data acquired in one cycle isn't processed until the next cycle.

The two-stage data pipeline is further complicated by the fact that the APs and the SUPE also represent a form of pipelining in that the APs must fully process their data and pass their results up to the SUPE before the SUPE may begin processing those results and pass its own result up to the MPG. The flow of the data must then be as follows. An AP starts a data acquisition cycle in cell ZERO of the pipeline. The AP starts the data processing on that same data in cell ONE, and at the end of cell ONE sends the result up to the SUPE. The SUPE starts a data acquisition cycle in cell TWO, acquiring the result data sent up from the APs in cell ONE. The SUPE starts the data processing on that same data in cell THREE, and at the end of cell THREE sends the result up to the MPG. Therefore a final beam controlling request from the SUPE is not generated until four beam pulse cycles after that beam has occurred. Figure 3 shows the pipeline synchronization.

Only after the Fast Task has completed the result reporting at the end of its second stage may it finally send status information up to the main control center VAX. This is done at the end of the second stage of the pipeline.

An Interrupt Service Routine (ISR) has been set up on the SUPE to awaken the Fast Task whenever the machine timing system determines that a beam pulse is going to occur; at this time the SUPE expects new beam pattern data to be issued to it from the MPG. An ISR has also been set up on each AP to awaken their Fast Tasks whenever the SUPE is broadcasting new beam pattern data to the APs. There is an ISR which detects when an individual piece of beam monitoring device data has been received, moving the Milcom Task through its data acquisition cycle.

5. FUTURE

A couple learning experiences have occurred during the testing of MPS. MPS has not been able to meet the design goal of operation at 360Hz since there is just too much processing to do: internal error handling, the algorithm processing itself, operating system overhead etcetera. MPS

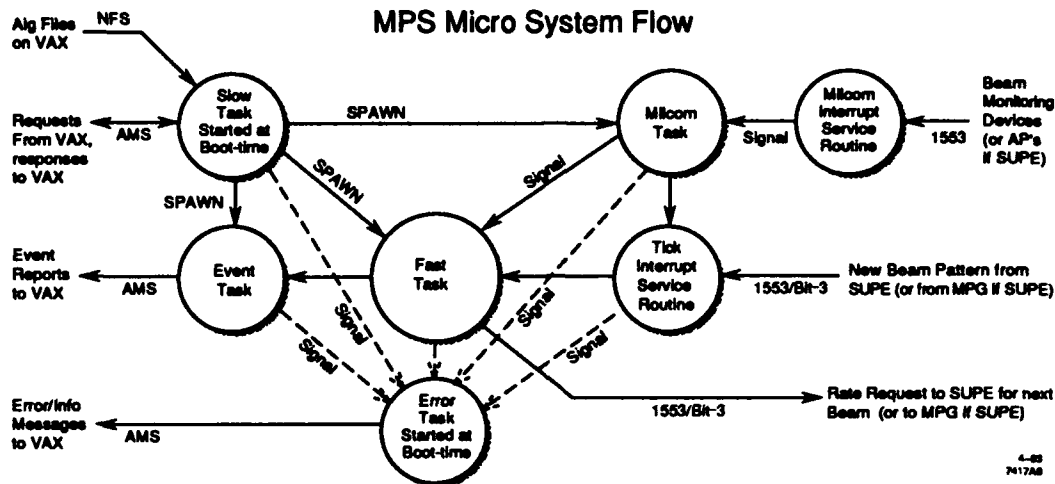


Figure 2. Task dataflow.

Table I. Fast task functional unit timing survey.

8252 μ s	total time between beam ticks (120 Hz)
6548 μ s	total time waiting for the next beam tick
1672 μ s	total time processing one beam tick
228 μ s	delay data acquisition until after beam passage
656 μ s	SUPE broadcasting new pattern info to APs
72 μ s	shifting the pipeline
292 μ s	starting a data acquisition cycle
200 μ s	milcom 1553 port reads (two ports in this case)
300 μ s	milcom task overhead per data acquisition cycle
1500 μ s	processing a small algorithm
96 μ s	sending the result to the MPG
144 μ s	reporting the results to the VAX

will be commissioned to run at 120Hz, although it has been tested at 180Hz. Future design enhancements include the Fast Task executing on its own CPU; however, MPS is presently not required to run at greater than 120Hz. Table I shows the big time consumers in the fast task.

The speed and priority at which the Fast Task must execute caused some multitask management challenges, wherein all other tasks must be prepared to be preempted by the Fast Task even if they aren't ready.

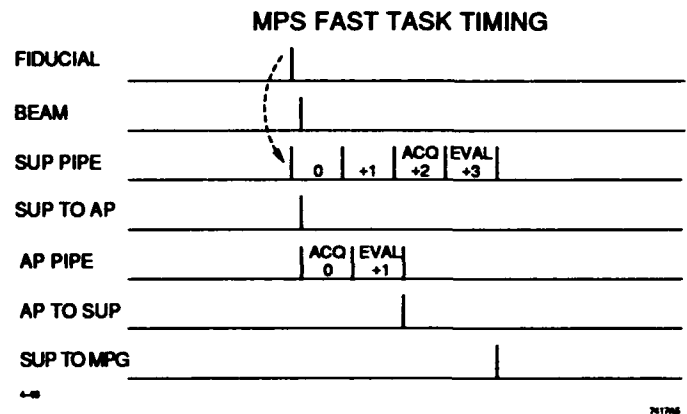


Figure 3. Pipeline.

References

- [1] S. Clark, et. al., "Smart Machine Protection System," in Proceedings from the International Conference on Accelerators and Large Experimental Physics Control Systems, Tsukuba, Japan, SLAC-PUB-5688 (1991).
- [2] G. White and G. Sherwin, "Machine Protection System Algorithm Compiler and Simulator," these proceedings, SLAC-PUB-6159 (1993).
- [3] S. Allison, et. al., "MPS VAX Monitor and Control Software Architecture," these proceedings, SLAC-PUB-6155 (1993).
- [4] M. Crane, R. McKenzie, D. Millsom, M. Zelazny "AMS: Area Message Service for SLC," these proceedings, SLAC-PUB-6166 (1993).

The CEBAF Analog Monitoring System*

K. Crawford, M. O'Sullivan, J. Perry, S. Simrock
Continuous Electron Beam Accelerator Facility
12000 Jefferson Avenue, Newport News, VA 23606-1909 USA

Abstract

The purpose of the analog monitoring system (AMS) is to provide CEBAF operators the ability to monitor voltage signals from the RF control modules, beam loss monitors, and other dedicated systems from the accelerator service buildings with a 10 MHz (-1 dB), bandwidth. The signals are presented at the AMS receiving crate in the Machine Control Center (MCC). The system, when completed, will allow the operator to monitor any 4 signals from available channels in each location. At present these locations provide 800 signals in each of the linacs, 16 signals in each of the arcs, 120 signals in the injector, and 16 signals in the beam switchyard. This provides a total capacity of 1768 signals, with an upgrade ability of 3740 total signal capacity.

I. INTRODUCTION

The analog monitoring system is distributed in a zone architecture throughout the accelerator, (Figure 1), where a station zone is defined as the 8 RF control modules that control the field gradients in the cavities.

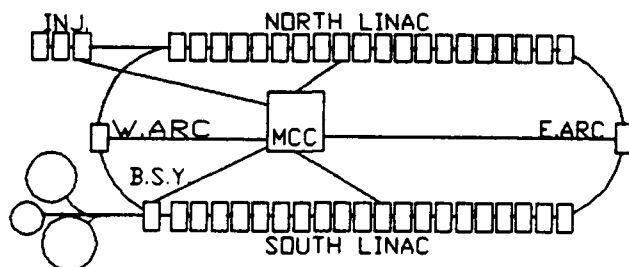


Figure 1. AMS Zone Locations

One AMS station will be located at each RF station. Each AMS's permanently connected inputs monitor the RF systems measured phase (PMES), phase vector modulator drive voltage (PASK), measured gradient (GMES), and gradient modulator drive voltage (GASK). In addition to the RF System inputs the AMS station has eight input channels to monitor the accelerators beam loss monitor signals (BLM) from 0 to 5 V, and to allow connection to any ± 10 V signal for observation. The AMS has the capability to expand and to monitor up to an additional 28 inputs, bringing the total capacity up to 68 input channels per crate. In the standard configuration, the AMS will provide the minimum requirement of 40 input channels (32 RF control module inputs, 8 BLM inputs), and eight output channels.

The system zones are divided into six groups: North

linac, South Linac, East Arc, West Arc, Beam Switch Yard (BSY) and the Injector. The linac areas are subdivided into two groups of 8 and 11 AMS stations. To link the accelerator to the MCC a specially configured AMS station called a concentrator crate is used. The concentrator crate links the analog signals from all of its assigned AMS standard crates and sends the selected output channel to the MCC through an analog fiber optic transmitter (Figure 2).

The concentrator crate also receives and transmits serial fiber optic control data to and from the MCC. The concentrator crate receives commands through the fiber optic serial link and distributes the control data through an RS-485 serial link to all of the connected AMS standard crates for channel selection commands.

The MCC concentrator receives 24 channels of analog data from the 6 system zones and routes them to 24 BNC type connectors on the monitoring panel located in the MCC. From the monitoring panel the operator can connect signals into a four channel oscilloscope for signal display or connect the signals into a four channel, 1 MHz data acquisition card.

II. SYSTEM DESCRIPTION

The analog monitoring system is composed of three main sub-systems. Together these sub-systems provide a means of selecting a desired input signal, routing the selected signal to the MCC, and conditioning the signal for observation in the MCC. These three sub-systems are:

- A. AMS standard crate
- B. AMS concentrator crate
- C. MCC concentrator system

A. AMS Standard Crate

The AMS standard crate, Figure 3, performs two functions: it inputs selected analog signals from connected instrumentation and routes them to the concentrator, and allows subsequent AMS signals to pass through a daisy chain to the AMS concentrator crate. Equipment and instrumentation interface is accomplished by two types of analog signal modules. The input module (AMIC) is an eight channel signal input module that serves to input and condition the RF control module signals, and the variable gain module (AMVG) is a four channel signal input module that serves to input and condition BLM or other desired signals. In addition to a high input impedance the AMVG modules have user defined gains from unity to $\times 10$. Each of the AMS standard crates is configured with four AMIC modules and two AMVG modules. Once a signal is selected for observation at the MCC the

* Supported by U.S. DOE contract DE-AC05-84ER40150

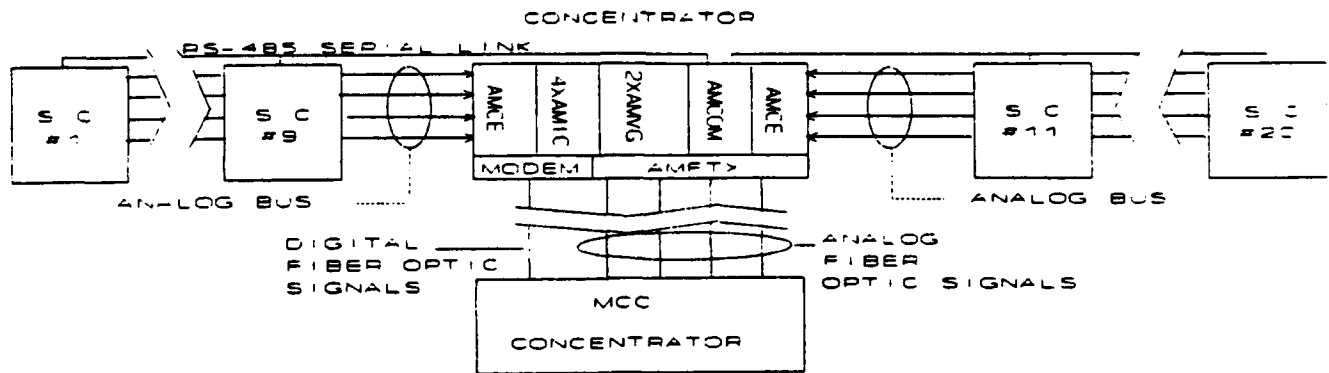


Figure 2. AMS Zone Architecture

appropriate module is programmed to place the connected signal on the "analog bus".

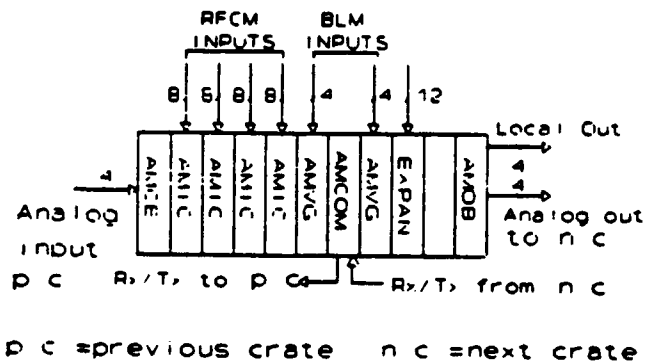


Figure 3. AMS Standard Crate

This bus is made up of four dedicated wires with multiple switches that span 1/2 the length of a system zone terminating into a concentrator crate. The switching action is accomplished through 64 T matrix type video crosspoints. Once a signal is selected the AMS closes the appropriate semiconductor switches to complete an electrical path from the desired input signal to the analog bus, through intermediate AMS standard crates (effectively bypassing these crates) to the appropriate channel of the AMS Concentrator Crate. The signal is then sent via an analog fiber optic transmitter to the MCC for conditioning and observation. The interconnection of the selected signals through a daisy chain architecture is achieved through the cable equalizer module (AMCE). This module accepts four differentially driven inputs from a previous AMS standard crate and restores any frequency dependent losses that have occurred in the RG-58 connection cable by a passive cable equalizer network at the input of the AMCE module. In the event an AMS standard crate is being bypassed the AMCE will place its output on the analog bus, effectively connecting the crate input to the crate output. This mode, bypass mode, allows a signal originating from the end of the linac to pass through the daisy chain architecture with good signal isolation from crates in the serial path to the termination point, the

concentrator crate.

The output section of the standard crate is comprised of an output buffer module (AMOB). This module is a four channel differential output driver capable of driving 100 mA with a small signal bandwidth > 15 MHz. Each of the AMOB modules in an AMS standard crate differentially drives eight RG-58 cables approximately 60 feet to the upstream AMS standard crate's AMCE module. This architecture repeats itself until the signal path terminates into an AMS concentrator crate.

System communication is accomplished through an RS-485 serial link connected to all of the standard crates. This link provides bi-directional communication to/from the concentrator. This serial link programs the standard crate to place the selected analog signal on the analog bus defined by the program code that contains the card address (similar to the CAMAC card addressing scheme), input channel, and output channel information. In addition to the serial link for remote control of the standard crate, the system offers local control through an RS-232 port on the communication and control module (AMCOM) to observe selected signals locally as accessed through the front panel of the AMOB module. The AMCOM module is based around a MC68701 microcontroller. This controller has 4K PROM on chip for the system program that controls RS-485 communication, card addressing, input/output selection, start-up routines, and confirmation echoing.

B. AMS Concentrator Crate

The concentrator crate is a specially configured standard crate that has three basic functions: input analog signal data, to convert and transmit analog fiber to optic data to the MCC, and to act as a node controller for all of the connected AMS standard crates. The substitution of a fiber optic transmitter (AMFTX) in place of an AMOB module (Figure 2) allows the concentrator crate to output optical signals instead of an analog signal. The concentrator crate is made from a standard crate by the addition of this module, an additional AMCE module to terminate two linac sections, and a fiber optic data modem. This modem receives commands from the MCC and presents the data to the communication module (AMCOM). This module

acts as the crate controller by interpreting commands, echoing the program code for signal selection through the RS-485 serial link, and transmitting confirmation codes back to the MCC Concentrator.

C. MCC Concentrator System

The Machine Control Center is the central node from which the user can select any one of 1768 connected signals from anywhere around the accelerator. The controller for this system utilizes a 486DX, 33 MHz PC based computer equipped with an EISA bus supporting both a GPIB interface and a four-channel, 1 MHz data acquisition board. The MCC concentrator system is composed of three major components. These are:

1. 486DX PC
2. Fiber optic receiver
3. AMS buffer crate

1. 486DX PC

The rack-mounted PC is equipped with Labview software configured as graphical interface for input channel selection from all of the six system zones. In addition to AMS system control the computer functions as both a GPIB controller for a rack-mounted digital storage scope located at the AMS operators panel, and a data acquisition system capable of single channel operation at 1 MHz or four channel operation at 250 kHz.

2. Fiber Optic Receiver

The analog fiber optic receiver is a 24-input rack-mounted receiver with power supply manufactured to a 3U eurocrate specification by Meret Optical, Inc. The system is designed as a modular receiver with plug-in type four-channel optical receiver cards. The transmitter/receiver system from Meret provides 20 MHz, -3 dB bandwidth, with 2% signal linearity and a -8 dB optical loss budget. The electrical output of the receiver module is presented to the AMS buffer module for final signal conditioning before being presented to the user panel.

3. AMS Buffer Module

The buffer module provides the necessary gain and rolloff to restore the analog signal to the unity gain level and to reduce broadband noise figures above 10 MHz from excessively degrading signal fidelity. The output of the buffer module is presented to an oscilloscope for signal observation, or presented to the input of the data acquisition board mounted in the PC.

III. SPECIFICATIONS

System Specifications:

Required System Performance at MCC

Input range	+/-10 V
Output range	+/-10 V
Noise level	<35 mV rms
-1dB bandwidth	10 MHz
THD	<0.6%
Crosstalk	>60 dB
Gain accuracy	<5%

Fiber Optic System Performance

Link noise	3 mV
Link linearity	2%
Input/output impedance	50 Ω
Pulse response time	20 nsec
SNR (peak signal to rms noise)	48 dB
Maximum overshoot	10%
Operating wavelength	820 nm
Loss budget	-8 dB (50 μ m fiber)

IV. ACKNOWLEDGEMENTS

We wish to thank C. Settles, C. Robert, M. Augustine, L. Beckett, B. Vignato, and D. Griffith for their many hours of consultation and assistance.

Techniques for Increasing the Reliability of Accelerator Control System Electronics

Jeff Utterback

Fermi National Accelerator Laboratory*
POB 500, MS 307, Batavia, IL 60510 USA

Abstract

As the physical size of modern accelerators becomes larger and larger, the number of required control system circuit boards increases, and the probability of one of those circuit boards failing while in service also increases. In order to do physics, the experimenters need the accelerator to provide beam reliably with as little down time as possible. With the advent of colliding beams physics, reliability becomes even more important due to the fact that a control system failure can cause the loss of painstakingly produced antiprotons. These facts prove the importance of keeping reliability in mind when designing and maintaining accelerator control system electronics.

I. RELIABLE HARDWARE DESIGN

In order to produce reliable circuit boards, the boards must be designed with reliability in mind. Components with high rates of failure must be avoided and good hardware design practices must be followed.

A. Chip Sockets

It is wise to avoid using chip sockets unless absolutely necessary. At Fermilab, chip sockets have been known to corrode after a few years in service. The corrosion is not visible from the exterior of the socket, but can be seen on the legs of the chip when removed. The reason for the corrosion is not definite but it may be caused by a reaction between two dissimilar metals.

When corrosion occurs, the socket loses contact with the legs of the chip causing an intermittent failure which is hard to diagnose. The failure will suddenly clear up if the chip is physically disturbed because it reestablishes contact with the socket. This type of thing is very confusing to a repair technician who can't understand how he suddenly fixed the board by simply touching some pins with a scope probe.

The faulty contact usually occurs on the ground pin of a chip socket because the ground pin carries the most current. The corroded joint acts like a resistive connection. Voltage drops of up to 3 volts have been observed between the chip's ground pin and the board's ground plane. Obviously, I.C. chips will not function properly when their ground pin is not held at ground potential.

To avoid socket unreliability, it is wise to solder all chips directly to the circuit board unless the chip is subject to change, such as an EPROM or a programmable logic device. If a socket is necessary, only a high quality socket should be used. It is better to spend some extra money on a high quality socket than to have reliability problems in the future.

B. Polarized Capacitors

Polarized electrolytic capacitors are a high failure item.

They should be avoided unless absolutely necessary. After a few years in service a polarized capacitor may develop an internal short. At Fermilab, shorted capacitors have been known to cause blown fuses, power supply failures, and in some cases circuit board fires.

Many designers use polarized capacitors as a rule of thumb in the power supply section of a circuit board. The rule of thumb should be closely examined to see if an alternative component, such as an I.C. regulator, or an unpolarized capacitor can be substituted. Of course in some designs there is no viable alternative to using a polarized capacitor. In these cases the designer should spend some time finding capacitors which have a good history of reliability.

C. Components which Need Calibration

In order to produce a reliable circuit board, it is wise to avoid components which need calibration. Components which need calibration are a maintenance headache and if calibration is not done on a regular basis, the performance of the circuit board will degrade or the circuit board may fail in service.

Some designers use variable resistors to set timing or voltage thresholds. After a period of time, the resistor may need to be calibrated to keep the circuit performing well. Also, there is some danger that the position of the variable resistor may be disturbed by someone mishandling the board.

If possible use components which need no calibration. For timing circuits substitute "delay line" I.C.s in place of "one-shots". For comparators, use zener diodes in place of variable resistors.

D. Protected Inputs and Outputs

A circuit board often produces an output which drives an external device or relies on some input signal from another circuit board. The board designer can not trust the external peripherals to perform correctly. The board must be designed with protected inputs and outputs.

In order to perform reliably the inputs should be able to withstand an overvoltage and the outputs should be able to withstand a short circuit. Otherwise, the board may have a high rate of failure, especially when being newly installed with untried external peripherals. There are several devices available which provide protection, such as optically coupled input I.C.s and short circuit protected output drivers.

At Fermilab, a circuit board is quite often designed for one purpose and ends up being used for several different purposes. The inputs and outputs should be protected for all contingencies because the board may be used in a situation that it was never designed to be used in.

E. Component Specifications

In order to produce a reliable circuit board, it is wise to study and heed the component minimum and maximum specifications. Specifications such as maximum input frequency, maximum operating temperature, and minimum

*Operated by the Universities Research Association under contract with the U.S. Department of Energy.

input voltage are determined by the manufacturer and should not be taken lightly. Sometimes designers ignore the specifications during the prototype phase only to find out that the components fail when subjected to adverse conditions in service.

It is wise to avoid components that are brand new on the market and have not yet been proven reliable. It is more fun to use the latest and greatest thing, but designing for reliability dictates the use of tried and true components. Sometimes a circuit is designed around a component that is so new, it only exists on a marketing advertisement. This is known as a "Vapor Component", and can cause frantic redesign efforts when it fails to materialize.

F. Built in Diagnostic Aids

When designing a circuit board it is wise to include built in diagnostic aids. Things such as LEDs, test points, and terminal ports can be invaluable to a repair technician when diagnosing a failure in the repair lab or in the field.

Sometimes a systematic failure will occur in the field. Diagnostic aids on the front panel of a circuit board can be the difference between a one minute simple solution or a half day ordeal.

LED indicators are a cheap, simple, and valuable way to indicate the state of the circuit board. They can be used for indicating the presence of input signals, the state of the CPU, and any other status information. Test points are valuable for checking the presence of voltages on the board and for looking at important signals with an oscilloscope. If the board contains a CPU, it may be wise to include a front panel RS-232 port so that diagnostic information can be exchanged with the CPU using a terminal.

II. RELIABLE SOFTWARE DESIGN

Many circuit boards designed for use in accelerator control systems have on board microprocessors. Several techniques can be used when designing the microprocessor software to improve the reliability of the circuit board.

A. Self Tests

Self tests should be incorporated into the software so that the circuit board can proclaim its own readiness to be put to use. Self tests can improve the reliability of circuit boards by finding components which have failed, and by finding components which are soon to fail. Self tests are fast, accurate and complete. They make life much easier for the repair technician.

Self tests are usually performed upon power up or reset. If the self test finds a problem it must have some way to proclaim the error. This can be as simple as sounding a beep, or lighting a light. The self test should not only proclaim the error but also give some information about the nature of the error. One simple way to do this is by flashing a code on an LED. For example, flash pause flash pause means the RAM is dead. Flash flash pause flash pause means the I/O chip is dead. It is also a good idea to proclaim the results of the self test in a status register. This will allow diagnosis from a remote location provided the status register is not the broken component.

When the self test routines are written, keep in mind that the self test must be able to run with a minimum of working components. The self test can not assume that the RAM is working, so it must be able to run completely from PROM without using the stack. The self test should be designed to run with only the CPU and the PROM working.

Self tests should be performed on all components that the CPU has access to. RAM tests can be done using some systematic scheme which writes to and reads from every address location. RAM tests should check for bad data bits as well as bad address lines. It is wise not to write the same data to every location because a stuck address line could be overlooked.

The PROM itself can be tested by doing a check sum self test. When the PROM is burned, the check sum can be manually entered and burned into the last address. During the self test, the CPU adds up the contents of the entire PROM and compares it with the last location.

Other miscellaneous components should also be tested. Command/Status registers can be tested by writing some data and reading it back to confirm. DAC/ADC pairs can be tested by writing a value to the DAC and reading it back on the ADC. Some items such as a "write only" register are hard to test. The software designer should work with the hardware designer to make the hardware self testable.

B. Signs of Life

Hardware and software should be designed as reliably as possible, but in the event of an unforeseen glitch or bug, the CPU may malfunction. These malfunctions can cause the CPU to go senile, (lose the data in memory) go crazy, (execute data instead of instructions) become compulsive, (execute an infinite loop) or die (cease to run at all). It is wise to add special hardware to detect a malfunctioning CPU and to show the state of the CPU to the outside world. This hardware can then be used to find problems and improve the reliability of the hardware and software.

One way to determine the health of a CPU is to check its pulse. At Fermilab, it is common practice to include a heartbeat circuit on smart circuit boards. The CPU must periodically access the heartbeat circuit in order to keep the heartbeat LED on and the heartbeat status bit asserted. If the heartbeat circuit times out, it indicates that the CPU is malfunctioning.

A similar scheme to the heartbeat circuit is the watchdog circuit. The watchdog detects the death of the CPU when it fails to be periodically fed (accessed). When the watchdog gets hungry it bytes (resets) the CPU. When designing a watchdog it is wise to make it a finicky eater. The periodic access should be a specific data code written to a specific address. If the watchdog ignores the data and depends only upon a chip enable, the CPU may still be able to randomly feed the watchdog even if it is in a "crazy" state.

Another diagnostic aid used at Fermilab is called Age. The CPU keeps a running total of the time elapsed since it was last reset. The age can then be read from a register by anyone interested. Age is useful for determining reliability. If a smart circuit board keeps resetting every day or two, steps

should be taken to improve its reliability. A reliable smart board should be able to run for several months without resetting. Anything over 6 months is hard to achieve due to the inevitable lightning glitches and AC power failures.

C. Exceptions and Interrupts

All CPUs provide a way for external hardware to request service from the software. This is known as exception processing and is used quite frequently in control system electronics. Due to its complicated nature, incorrect exception processing is the source of a great many reliability problems in smart circuit boards.

Most smart boards do not utilize all of the CPU's available interrupt and exception vectors. The software designer should not leave the unused vectors blank. This may cause the CPU to go astray if one of the unused exceptions unexpectedly occurs. It is wise to provide a graceful return from each and every exception vector in order to improve the reliability of the circuit board. Another good idea is to somehow make it known when an unexpected exception occurs. This will allow the designers to track down problems with the design.

Most CPUs provide a nonmaskable interrupt input. If this interrupt occurs, the program must stop what ever it is doing and service the interrupt. It is wise to use this interrupt only for catastrophic events such as impending power failure. It is not a good idea to use this interrupt for mundane tasks such as servicing a timer. The software becomes very complicated when dealing with nonmaskable interrupts and this complication leads to bugs and unreliability. The complications are caused by nonmaskable interrupts occurring at a point in the program when the CPU can not afford to be interrupted. It is best to use maskable interrupts in most situations so the software can choose to delay servicing them if the CPU is busy in a critical part of the program.

D. Good Programming Practice

In order to produce reliable software, it is important to use good programming practices. With the advent of high level languages, this is just as important as it was with assembly language. Document routines with comments to make the purpose and operation known. Split the program up into small routines with a specific purpose. This makes the program less complicated and enables code reuse. Use good naming conventions for routines and variables. Long names are encouraged in high level languages to make the program self documenting.

III. MAINTENANCE

After the hardware and software design is finished and the circuit board is in use, the reliability of the board depends on efficient trouble shooting and good failure tracking. If the circuit board has a high rate of failure, attention should be devoted to making changes for improving the reliability.

A. Tracking Failures

It is a good idea to keep a record of failures for electronic circuit boards. The record can be used to track reliability

and to aid in repairing boards with similar types of failure. The record should include all pertinent information such as the date of failure, location of failure, and the board's serial number. The record should also include the failure symptoms and the diagnosis.

There are several commercial database programs available which are ideal for keeping records of failure. They have customizable data entry screens and hardcopy report generation. The database programs also have nice information searching facilities which work great for finding failure trends. The database operator can do queries such as "Show me all the boards which failed in January of 1991." or "Show me all the boards which have failed due to a shorted capacitor."

B. Computerized Test Station

In order to produce a circuit board with a high degree of reliability, the board must be tested comprehensively during the design phase. Also, failures which occur while in service must be diagnosed quickly. A computerized test station is a good way to meet these goals.

Most modern control system circuit boards reside in a commercial bus crate such as CAMAC, VME, or Multibus. The circuit boards are designed to send and receive data to and from a bus master over the bus backplane. In order to test a circuit board, there must be some way to talk to the board over the bus backplane.

At Fermilab, it is common practice to connect a PC computer to a test crate via a PC to bus interface. Interface hardware can be obtained from commercial companies who specialize in this area, most notably BiT3 Computer Corp.* Programs, which run on the PC, can then be written to test circuit boards. PC computers are the obvious choice because they are readily available, relatively inexpensive, and have a wide selection of compilers and programming aids to choose from.

Programs written to test a circuit board should be flexible and easy to use. The tests should generally keep repeating until halted by the operator. Constantly repeating tests are valuable for providing stimulus when using an oscilloscope for diagnosis.

Sometimes a circuit board may develop an intermittent failure. This type of failure is very hard to diagnose because it may take hours or days for the board under test to fail. The computerized test station is very valuable for finding intermittent failures because it can perform tests, unattended, 24 hours a day, and create a log of failures for the repair technician.

Sometimes when a board fails in the field it may seem to work fine when tested in the repair lab. If this happens the tests must be made more rigorous in order to find the problem. Long term computerized tests may be needed. Technicians should not be content to put a board back into service without first finding and fixing the reported error.

*BiT3 Computer Corp. 8120 Penn Avenue South, Minneapolis, MN, 55431-1393 Phone (612) 881-6955

WinDoWorks

A Flexible Program for Computerized Testing of Accelerator Control System Electronic Circuit Boards

Jeff Utterback

Fermi National Accelerator Laboratory*
POB 500, MS 307, Batavia, IL 60510 USA

Abstract

Since most accelerator control system circuit boards reside in a commercial bus architecture, such as CAMAC or VMEbus, a computerized test station is needed for exercising the boards. This test station is needed for the development of newly designed prototypes, for commissioning newly manufactured boards, for diagnosing boards which have failed in service, and for long term testing of boards with intermittent failure problems. WinDoWorks was created to address these needs. It is a flexible program which runs on a PC compatible computer and uses a PC to bus crate interface. WinDoWorks was designed to give the user a flexible way to test circuit boards. Each test is encapsulated into a window. By bringing up several different windows the user can run several different tests simultaneously. The windows are sizable, and moveable. They have data entry boxes so that the test can be customized to the users preference. The windows can be used in conjunction with each other in order to create super-tests. There are several windows which are generic. They can be used to test basic functions on any VME (or CAMAC) board. There are other windows which have been created to test specific boards. New windows for testing specific boards can be easily created by a Pascal programmer using the WinDoWorks framework.

I. MOTIVATION

Most modern accelerator control system circuit boards reside in a commercial bus crate such as CAMAC, VMEbus, or Multibus. Due to the nature of the bus architecture, an intelligent bus master is required to exercise the boards in the crate. An intelligent bus master is a circuit board which either has an on board CPU or is controlled by a remote computer.

When developing a newly designed circuit board, commissioning a newly manufactured circuit board, or diagnosing a board which has failed, some sort of testing facility is required. A minimum testing facility configuration consists of a test crate, a bus master, and a computer program which allows a human to conduct various tests on the circuit board of interest.

The test software should be easy to use and flexible enough for the operator to devise tests in unique ways in order to solve particular problems. The test software should have basic functions such as reading from and writing to an address, as well as more sophisticated tests for exercising

overall circuit board functions. The test software should have tests which constantly repeat so as to provide stimulus when using an oscilloscope to diagnose a failure. It should also be able to run unattended for long periods of time so that intermittent failures can be found.

When investigating suitable computer programs for conducting tests, very few commercial products were found. The products which are available, such as VMEbug [1] are rather tedious to use and limited in capabilities. When no suitable commercial programs could be found for testing circuit boards, WinDoWorks was created.

II. HARDWARE

The original WinDoWorks test station was configured to test newly designed VMEbus circuit boards. Later, a CAMAC version of the test system was also created.

A. VMEbus Test Station

The hardware for the VMEbus test station consists of a VME crate, a Bit3 PC to VMEbus adaptor [2], and a PC/AT compatible computer with mouse.

A PC computer is used in the test station because they are readily available, relatively inexpensive, and have a wide selection of software tools available. Also, the PC's color graphics and mouse helps to make a nice user interface.

The Bit3 PC to VMEbus adaptor consists of a circuit board which goes into one of the PC's expansion slots, another circuit board which goes into the VME crate, and an interconnecting cable. The Bit3 interface has several command and status registers to configure and use the system. A program running on the PC can access any address on the VME crate using a paged memory mapping scheme.

The Bit3 board which resides in the VME crate acts as a bus master to access all other boards in the crate. It can also be configured to be the "slot one controller". All types of bus cycles can be performed including interrupt acknowledge cycles. Both normal and "short I/O" address space can be accessed. The VME address modifier can be set to any value using a command register.

B. CAMAC Test Station

The hardware for the CAMAC test station consists of a CAMAC crate, a Tevatron Serial Crate Controller [3], a TSCC Link Driver [4], a PC to Link Driver interface card [5], and a PC/AT compatible computer with mouse.

The PC/AT was chosen for the same reasons as in the VMEbus test station, and to keep the standard human interface that users had become accustomed to using with the VMEbus test station. The TSCC and Link Driver are

*Operated by the Universities Research Association under contract with the U.S. Department of Energy.

standard Fermilab equipment used for all CAMAC crates in the field. The PC to Link Driver interface card was designed at Fermilab for the sole purpose of creating flexible modern CAMAC test stations. It resides in a PC expansion slot and is connected to the Link Driver via ribbon cables.

A program running on the PC uses registers on the interface card to invoke the standard CAMAC function codes. In this manner, the PC can send commands to or read data from the circuit boards in the crate.

III. SOFTWARE

The program which runs on the PC was written in Pascal using the Turbo Pascal [6] compiler and development environment. The program also makes use of a windows programming package called MetaWINDOW [7].

Because of the differing nature between CAMAC and VME two separate versions of the software have been created. The user interface is the same on both versions but the hardware drivers and test windows are necessarily different. In order to avoid confusion the rest of this paper will be constrained to the discussion of the VMEbus version.

A. User Interface

WindoWorks was created with a modern "mouse and windows" user interface. The interface eliminates the need for tediously typing in commands. It utilizes pull down menus and scroll boxes.

Each test is encapsulated into a window. The user can create and delete window tests at will. The windows are moveable and sizeable. Most of the test windows only need a small area on the CRT. This allows the user to run several tests at the same time or in conjunction with each other. The tests running in the windows generally keep repeating until stopped by the user. This feature is useful when stimulus is needed while diagnosing a problem with an oscilloscope. The windows execute their tests in a round robin fashion. Usually the tests execute fast enough so that all windows appear to be running simultaneously.

Once a suite of windows has been set up and configured, the entire setup can be saved on the hard disk. This allows for quick retrieval of preconfigured setups.

B. Generic Windows

Several test windows have been designed so that they would be useful for testing any VMEbus circuit board. These windows test basic functions which are common to all VMEbus boards. The generic VMEbus windows include the Hex Memory Dump Window, the Binary Memory Dump Window, the Memory Test Window, the Block Fill Window, the Write Burst Window, the Watcher Window, the Matcher Window, the Interrupt Acknowledge Window, and the Text Window.

The Memory Dump Window is the most used of all the generic windows. The Memory Dump Window constantly reads an area of memory and displays it in the window. The user chooses the starting address and the size of the memory

block displayed. The memory block size is chosen by changing the size of the window. The user can display one byte of data by making the window very small or several hundred bytes by making the window large. The user can choose to display the data in bytes, words, or longwords, in hex or in binary. If any data changes in the memory, the new value is immediately displayed in the window. The user can also write new data to a specific address by simply clicking the mouse on the data of interest. After choosing the data location to alter, the user can type in new data, or scroll the data up and down by using the left and right mouse buttons. The Memory Dump Window is useful for testing basic circuit board read and write functionality. It is also useful for watching the progress of other test windows such as the Memory Test Window or the Block Fill Window. Since the Memory Dump Window runs constantly, the user can diagnose problems with an oscilloscope without having to keep entering read commands like some commercial test programs require.

The Memory Test Window writes data to a user specified block of memory and then reads the data back to verify the write-read functionality. If the read back process finds an error, an error message is displayed in the window with the offending address and data. The user can specify byte, word, and longword access. The user can also specify one of 3 test schemes. The first scheme writes the same user specified value to each location on each pass. The second scheme writes the same value to each location, but chooses a new random value on each successive pass. The third and most stalwart scheme writes a different random value to each location on every pass. Each of the three schemes can be useful depending on the particular problem that is being diagnosed.

The Block Fill Window writes user specified data to a block of memory. This window is useful for finding write cycle problems and for initializing memory or command registers. The window continues to keep writing the block of data over and over until stopped by the user so that diagnosis can be done. This window can be used in conjunction with the Memory Dump Window to verify that the data was successfully written.

The Write Burst Window writes user specified data to a single user specified address. The user can choose exactly how many times the data is written, from 1 to infinity. This can be useful when testing a circuit which produces a signal each time a command is written. The user may need to verify that a precise number of signals occur in conjunction with the number of commands sent.

The Watcher Window continuously reads one user specified address. The window will display the number of times the data changed and will also display the highest and lowest data value ever read from that location. This window has a wide range of uses and is very useful for diagnosing intermittent problems.

The Matcher Window continuously reads one user specified address and compares the data read to a user specified value. If the data read matches the value, the window increments a

counter and displays the number of occurrences when the data matched the value of interest. The user can use "don't care" X's in the value to allow more flexibility. There is a hex and a binary version of this window.

The Interrupt Acknowledge Window is used for debugging boards which generate interrupts. When a board in the crate produces an interrupt, the window performs an interrupt acknowledge cycle and then displays the vector returned by the interrupting board.

The Text Window is used for documenting the users test setup. After a set of windows are created and configured for testing, the user may document the test setup by entering text into one or more Text Windows. The entire test setup can then be saved on the hard disk so that it may be recalled at a later date. The text windows serve as an aid to understanding the tests which were previously configured.

C. Special Windows

The generic windows can be quite useful for testing circuit boards and in some cases the generic windows are all that is needed, but for special purpose circuit boards, special purpose test windows are often desired. Special purpose test windows can be created by a Pascal programmer using the WindoWorks frame work. A programmer may use the generic windows as a template for creating windows to test specific circuit boards.

Some examples of special purpose windows which have been created are:

- A window to display and change the dots on a board with a dot matrix display.

- A window to run long term bit errors tests on a transmitter-receiver pair.

- A window to configure the registers of a video chip.

- A window to display the time and date read from a clock calendar chip.

D. Using Windows Together

One of the nice features of WindoWorks is that the windows can be used in conjunction with each other to perform super-tests. Each window provides a basic building block which gives the user power to create unique tests in order to solve particular problems. For example, the user can watch the outcome of the Memory Test Window with the Memory Dump Window. The user may want to use the Watcher Window to see if the Write Burst Window had the desired effect. It is amazing how creative the user becomes when using WindoWorks to test and diagnose hardware. Sometimes the user is able to create tests which were never envisioned by the software designer.

E. Long Term Tests

It is often necessary to run long term tests on circuit boards in order to catch intermittent failures or to determine error rates. The long term tests must be able to run unattended, for days or weeks at a time. If an error occurs when no human is present the test program must be able to keep a log of failures.

WindoWorks has the capability to be used for long term tests. Several of the generic windows display and hold errors that occur. The PC's hard disk makes a convenient place to keep a log of failures. Error log text files can easily be created and updated by the WindoWorks program so the user can read the file at his leisure.

F. Future Upgrades

WindoWorks was originally created before the advent of Microsoft Windows [8]. Since the popularity of MS Windows 3.1 is now evident, it may be wise to port the WindoWorks program to the MS Windows format. There are several new programming packages that propose to help a programmer develop MS Windows applications. Using MS Windows may be advantageous because of its standard GUI and its true multitasking ability.

IV. REFERENCES

[1] VMEbug is a trademark of Motorola Inc. Microcomputer Division, 2900 South Diablo Way, Tempe, Arizona 85282 VMEbug is a program which runs from PROM on Motorola VMEbus CPU boards. It uses a dumb terminal for the user interface. VMEbug was designed for downloading and debugging programs which run on the CPU board, but it is often used to exercise circuit boards in the crate when no other debugging facility is available.

[2] BiT3 Computer Corp. 8120 Penn Avenue South, Minneapolis, MN, 55431-1393 Phone (612) 881-6955

[3] R. Ducar, "Tevatron Serial Crate Controller," *Fermilab Controls Hardware Release No. 2*, (1981)

The Tevatron Serial Crate Controller (TSCC) was designed at Fermilab and is used in all of the CAMAC crates in the Fermilab Tevatron control system.

[4] R. Ducar, "TSCC Link Driver," *Fermilab Controls Hardware Release No. 8.1*, (1987)

The TSCC Link Driver (TSLD) was designed at Fermilab to accommodate the user with a convenient parallel interface to the serial protocol demanded by the TSCC.

[5] The PC to Link Driver Interface card was designed at Fermilab by R. Marquardt, J. Smolucha, and J. Zagel.

[6] Turbo Pascal is a registered trademark of Borland International, Inc. 4585 Scotts Valley Drive, Scotts Valley, CA 95066

[7] MetaWINDOW is a trademark of Metagraphics Software Corporation, 4575 Scotts Valley Drive, POB 66779, Scotts Valley, CA 95066

[8] Microsoft, and MS are registered trademarks, and Windows is a trademark of Microsoft Corporation.

Switching the Fermilab Accelerator Control System to a Relational Database

S. Shtirbu (shtirbu@fnal.fnal.gov)
Fermi National Accelerator Laboratory¹
P. O. Box 500
Batavia, IL 60510

Abstract

The accelerator control system ("ACNET") at Fermilab is using a made-in-house, Assembly language, database. The database holds device information, which is mostly used for finding out how to read/set devices and how to interpret alarms. This is a very efficient implementation, but it lacks the needed flexibility and forces applications to store data in private/shared files. This database is being replaced by an off-the-shelf relational database (Sybase²). The major constraints on switching are the necessity to maintain/improve response time and to minimize changes to existing applications. Innovative methods are used to help achieve the required performance, and a layer seven gateway simulates the old database for existing programs. The new database is running on a DEC ALPHA/VMS platform, and provides better performance. The switch is also exposing problems with the data currently stored in the database, and is helping in cleaning up erroneous data. The flexibility of the new relational database is going to facilitate many new applications in the future (e.g. a 3D presentation of device location). The new database is expected to fully replace the old database during this summer's shutdown.

I. INTRODUCTION

The accelerator control system is using a made-in-house, hierarchical, based on indexed files, client-server, database manager (called DBM). The current implementation is in use since 1985 [1&2]. The implementation uses code-based protocol (e.g. in order to read setting information one needs to know the code associated with the setting property). In the past eight years there were very few changes made in the database, the reason being the complexity of providing new functionality since both the client and the server sides have to be changed to support new features, which is an expensive ordeal, especially due to the usage of Assembly language. The lack of flexibility in the central database forces many applications to create their own representation of data stored in the database (by reading the whole database and storing the information in new files, or by analyzing the changes made in the database). A great deal of other device-related information ends up in private/shared files, and even in source code. The inconsistency in interfaces and sources of information creates an unmanageable situation (a device might be deleted from the central database, but information related to the device and dependencies on the device are still present in private/shared files, and hidden inside applications). In addition, there is no trivial mechanism to query the database in ad-hoc fashion, and

as a result, there are many inconsistencies even in the central database. Even with all these problems, the database provides good service to the control system, since problems are rectified when encountered.

The advantages of a relational database, supporting the ANSI SQL protocol, over the above, are overwhelming: on-line changes in table structure, ad-hoc queries, ability to enforce referential integrity, and many others. But relational databases have one major deficit - they are much slower than a customized, application dependent, Assembly language, implementation. Fortunately, CPU performance is improving fast, and can help relational databases achieve sufficient performance.

Switching from one database to another is not a simple task. The existing data has to be loaded to the new database. Existing query protocols have to be supported. Existing tools which directly accessed the database files, DBM audit files, or DABEL files (DABEL was the language used to insert/update DBM) must be converted to use a new interface (or rewritten). A new device entry/manipulation tool, that can support the new fields in, and different organization of, the new database has to be written.

II. RELATIONAL DATABASE PERFORMANCE[3]

We tested several products. The performance tests were done on parameter page queries (which probably are the most common queries in our environment, though not the most complex ones). Conversion programs were written to take DBM files and generate ASCII, ready for load (i.e. first normal form), version of them. This way we could load our real data to the database, and get meaningful benchmarks. There are many benchmarks available in the literature, but the results they report vary widely, and none of them seems to resemble the type of activities in real-time environments. We also realized a major problem regarding I/O. DBM did cache information from the files, and so do most databases in the market. But the caching algorithm used by most relational databases is LRU (least recently used), and is not aware of the logical meaning of the data. Therefore, one might wipe out all the cached information by querying a large, relatively low usage, table (e.g. we have a table holding all the last settings sent to devices). There is only one way to overcome this problem, and that is to provide enough memory to allow the whole database to reside in cache. It is not very hard to do, since our database is small in database terms (less than 30 MB). We realize that the size is going to increase drastically over time (we have over 300MB of shared files), but for the time being, it is feasible to put enough memory in the server machine to provide full caching (in the future, we might move large, non critical, tables to a separate server node).

In our testing, we discovered a major problem with most relational databases - the client library is very slow. The

¹ Operated by the Universities Research Association, Inc. under contract with the U.S. Department of Energy.

² Sybase is a registered trademark of Sybase Inc.

reason the client's performance is very important to us is that the users see only response time - they do not care where the time was spent, and our need for a gateway to the DBM protocol provided us with a unique opportunity to tie the performance of both the server and the client.

Our testing proved that using a relational database is feasible for our control system. The product we chose was Sybase, which had the best performance overall (simple and complex queries).

III. DBM-SQL GATEWAY

As mentioned above, we have to support existing applications with the least impact. The most natural way to use relational databases is to use their client libraries (or pre-compilers which produce the calls to the client libraries). This solution can not work for us since we have database clients residing in front-ends, running real-time kernels -- and no vendor has client libraries available for pSOS, MTOS or even VxWorks... One way to resolve this problem with minimal impact is to build a layer seven gateway. This gateway receives (via ACNET, our home grown protocol) requests using the DBM protocol, translates the request to optimized SQL, calls the applicable client library routines to retrieve the data, translates the replies to DBM protocol, and sends the reply back to the requester. As far as existing applications programs and other DBM clients are concerned - nothing has changed, even devices added to the database after the switch to Sybase will be fully accessible by existing applications.

Our gateway also supports SQL requests from applications. The major benefit of doing so is providing a very simple interface for applications to access the database: all an application needs to provide is the applicable SQL statement, and the address of an array of structures where the data retrieved from the database should be put. The application (or other clients) need to call only one procedure. In addition, using the gateway to interact with the database simplifies monitoring and management of database access, and allows us to implement diverse security/priority schemes (e.g. based on client's node id). The applications can also benefit from multiple asynchronous requests and packeting of large requests/replies provided by the client's access routine. Hiding the vendor's client library routines from the user also removes the dependency on a specific vendor's interface, and drastically simplifies switching to another vendor's ANSI SQL server in the future (not that we see a need for that).

The gateway is multi-threaded, to optimize SQL server utilization. Currently, the gateway runs on the SQL server's machine, but that is not required. The gateway is going to support TCP/IP and UDP access to the database in the future (in addition to ACNET).

IV. UPDATING DEVICES

DBM uses a special device update utility (called DABEL). This utility parses text files containing keyed values. The utility does not support interactive changes. Updates are done directly on the physical files.

The new database is adding many fields and tables (DBM has tables that store unstructured information that have to be spread between multiple structured tables). It is clear that the

effort needed to change DABEL to support the changes in the underlining database is not worth the effort.

Instead, an interactive device entry application is on the works (Lee Chapman is responsible for this effort). The interactive utility is a regular application. This application uses multiple windows and some graphical displays to assist in inserting or updating a device. Thanks to its interactive nature, this application eliminates the mystery from updating devices, and allows one to make changes to the information stored for a device and run an application on another window to see the impact the changes had. The user can easily compare the characteristics of two devices, and copy any property from one device to the other. In the future, this utility will be enhanced to provide logical assistance in entering devices (e.g. it will become aware of correct device entry requirements for different types of devices).

V. AUDIT

DBM has a basic audit facility. The audit trail is based on the DABEL tokens used for updating a device, and can keep track of whom updated what property, and when. The information is stored in a separate file, and a special interface is used to access it. The new database is expected to provide a better audit trail.

The new audit trail keeps track of changes at the field level, and stores the **previous value** of each modified field. Since the audit information is available from the device update application, recovery from erroneous changes becomes trivial.

VI. BACKUP & RECOVERY

Relational databases tend to be very good when recovery is concerned. They support rollback of transactions, and can tell which transactions were complete when the machine loses power, and roll them forward.

We intend to keep a backup database server, used mainly for development and complex reports. The backup server is going to be at most 10 seconds off the operational database, using a Sybase tool called Replication Server. The backup database will maintain multiple copies of the database, to allow logical recovery of information (existing databases do not support recovery at the table level from a backup file).

VII. SUPPORTED TOOLS

Following are examples of issues that need to be addressed when one is switching databases, in order not to lose existing functionality:

DBM has a simplistic report generating tool, mainly for CAMAC devices. The tool was written years ago, and was never updated to support emerging driver types. This tool has a temporary replacement, which replicates the functionality, supports new device types, and is two orders of magnitude faster. The intent is to make this tool part of an application page, in which the user can even choose the data fields desired in the report.

There is a special application used by operations to decide which properties of which devices are important for machine operations, to be able to tell if a restore went smoothly for all the important properties. To generate the data for this

application, once a week, DBM files are scanned to learn about changes. The support for this application is now available in the database, and the information is automatically updated when changes are made.

There is a special utility to load changes in devices from the linac control system (written by William Marsh). The linac control system has its own device database, which is considered the source of information about linac devices. The utility produces DABEL files, and has been converted to generate the needed SQL to update the relational database.

VIII. DEPLOYMENT

Unfortunately, DBM and the new database can not co-exist. Loading all DBM files into the relational database takes close to a weekend, and is done infrequently. We are almost ready for the switch (only the device entry application is not finished yet). A great deal of testing took place, with actual applications, and the results were satisfactory (the performance tests were done on VAX station 4000/60 which is 7 to 10 times slower than the AXP platform). The actual switch is expected to take place before the end of the accelerator shutdown, this summer.

There is a somewhat surprising side-benefit we are already enjoying, even though we have not switched databases yet. Since the first time data was loaded from DBM files to the Sybase database, the relational database has been used to find erroneous device entries, provide ad-hoc reports, and even find bugs in DBM (which went unnoticed for years). The availability of a good ad-hoc access to the data (using the SQL interface provided by Sybase) also is substituting the need for code development.

IX. EXPANSION

What is the future of using the new database in the Fermilab control system? We hope to move as much as possible private and shared data used by applications into the database. The major justification for that is the simplification of maintenance of both applications and of the data used by them. Other benefits are: improved performance, improved integrity, better control over content and size, better security mechanisms, simplified system management.

Many new applications, taking advantage of the dynamic nature of the new implementation, are also expected. Questions that could not have been answered before without writing complex programs, are now a SQL query away. New tables are designed and are waiting for data (e.g. geographical location of devices, to be used for simplified alarm analysis and other graphical representations). Many of the improvements in the Fermilab control system in the next few years are expected to be related to, and benefit from, the new database.

X. CONCLUSION

Switching real-time control systems to relational databases is possible and very beneficial. The benefits include: simplification of application maintenance, and improved consistency and integrity of the data stored. The same benefits

business applications enjoyed for the past two decades, are now readily available to real-time applications.

XI. REFERENCES

- [1] A. Waller, "The Fermilab Accelerator Control System Database", in *Proceedings of the Second International Workshop on Accelerator Control Systems*, Los Alamos, NM, October, 1985, pp. 251-258.
- [2] S. Sommers, et al, "An Editing and Reporting System for Fermilab's Accelerator Controls System Database", in *Proceedings of the Second International Workshop on Accelerator Control Systems*, Los Alamos, NM, October, 1985, pp. 259-263.
- [3] S. Shtirbu, "Using a Relational Database in a Real-Time Environment", in *Proceedings of the fifth Sybase User Meeting & Training Conference*, San Jose, CA, April, 1993.

The Impact of New Accelerator Control Software on LEP Performance

**R. Bailey, A. Belk, P. Collier, M. Lamont, G. de Rijk and M. Tarrant
CERN**

CH-1211 Geneva 23, Switzerland

Abstract

After the first year of running LEP, it became apparent that a new generation of application software would be required for efficient long term exploitation of the accelerator. In response to this need, a suite of accelerator control software has been developed, which is new both in style and functionality. During 1992 this software has been extensively used for driving LEP in many different operational modes, which include several different optics, polarisation runs at different energies and 8 bunch operation with Pretzels. The software has performed well and has undoubtedly enhanced the efficiency of accelerator operations. In particular the turnaround time has been significantly reduced, giving an increase of around 20% in the integrated luminosity for the year. Furthermore the software has made the accelerator accessible to less experienced operators. After outlining the development strategy, the overall functionality and performance of the software is discussed, with particular emphasis on improvements in operating efficiency. Some evaluation of the performance and reliability of ORACLE as an on-line database is also given.

1. Brief history of the project

In response to requests from many areas, not least the LEP operators themselves, during the summer of 1990 the authors began considering what was required of application software for routine operation of LEP. Later in the year and into 1991, these ideas were developed, resulting in a rather detailed structured analysis of the required functionality by spring 1991.

The data flow diagrams and data dictionary of this analysis formed the basis of software design and data modelling work which was undertaken between March and September 1991. In parallel with the latter stages of this, database requirements were investigated which resulted in a definition of the structure of the on-line data and the choice of ORACLE as the on-line database for driving LEP.

We were thus in a position from autumn 1991, after one year of analysis and design work, to undertake module coding and database implementation. This activity of course continued through implementation and testing ready for first use for operations in spring 1992.

2. The major tasks performed

The software is divided broadly into four distinct parts, each interacting directly with the on-line database. These software packages are either driven through interfaces running under the standard SPS/LEP console manager [1], or through commands from other software. This last facility allows the operator to control the run by using a task sequencer to drive the new software. Before discussing these four pieces of software it is necessary to understand something of the underlying data organisation.

2.1 Data organisation

The accelerator is divided into around 30 different systems. Within each of these systems the data is organised in a hierarchy, consisting of physics parameters at the highest level, descending through hardware magnitudes (which in the case of magnetic systems is the field strength) to hardware settings such as currents. It is these hardware settings that are loaded into the machine. For the most part the operator wants to interact with the machine in terms of physics parameters, with propagation down through the hierarchy to the hardware settings being taken care of by the software. Data for each system is described as amplitude versus time functions, reflecting the need to take LEP from injection energy, through an energy ramp to physics energy and through a vertical beta* squeeze to the physics optics.

The multitude of hardware elements are also grouped into around 20 different element groups. This makes it easier to interact with the hardware independently of any physics interest, such as during start-up when one wants to load lots of equipment, or during periods of equipment problems. The way in which the operator can interact with any piece of equipment depends on the equipment type (power converter, kicker etc.), and this interaction is completely data driven from the database.

2.2 Settings Generation

The overall task performed here is to take the output of the MAD program and to build settings in a suitable format for running the machine. That is to say, this software produces all the data that the other applications require. The operator selects which energy ramp and beta* squeeze he wants to be used to make up a LEP run. Once having

defined this, he can create on the database a specification that describes how he wants to run the machine. This run specification is used to create the full set of functions that are needed to effect the mode of operation required. A major part of this is to combine the ramp and squeeze functions to produce functions that define how the machine parameters vary from the injection point right through to the physics settings. These data form the full image of the machine.

In order to work more efficiently on the machine when in a static state, we have introduced the notion of a time slice of the machine settings. The most frequent examples of this are the settings for accumulation or for physics, but should the operator choose to introduce a breakpoint at which to stop in the middle of the ramp or squeeze for whatever reason, a corresponding set of machine settings is automatically produced.

2.3 Drive Hardware

This software provides a uniform way of sending all requisite equipment settings to the relevant hardware. There are two basic areas of applicability; either to load settings to the vast majority of equipment, or to load setting changes to the hardware group affected by a trim. This functionality is possible because of the structure of the data, allowing one to drive physics systems, hardware groups or individual pieces of equipment.

2.4 Trim Actual Settings

At a given breakpoint a time-slice of the active machine functions exists, called the actual settings. These can be trimmed either in terms of physics parameters or at the hardware magnitude or hardware setting level. Again a key feature is a unified interface for making trims to any system and at any level.

While making trims at a certain breakpoint, a complete history of the changes made is kept, enabling the operator to go back to some previous state of the machine. Before leaving the breakpoint the operator has the option of incorporating the changes that he has made into the functions. There is now considerable versatility in the way in which this incorporation is made. When the incorporation is finished, the actual setting trim history is archived and all actual setting trims removed.

2.5 Trim Functions

This offers the ability to trim physics parameters, hardware magnitudes of hardware settings defined as functions of time in the machine settings. This is presently done manually through a single graphical interface, but we have foreseen the possibility to feedback measured parameters, thereby providing an auto trim

facility. The same program, without the interface, is used to incorporate the actual trims made at a breakpoint.

In much the same way as for actual settings trimming, a complete history of all function trims is kept, enabling the operator to back out to some previous point in time. This is true whether the trim is made by hand, by auto trim or by incorporate.

3. Software performance during operation

The major applications described, and others, communicate with each other via the on-line database. They are all essentially data driven, enabling new systems or equipment groups to be added without writing new code. For these reasons the structure of the data is of utmost importance, not least in terms of the performance of the software.

3.1 Choice of ORACLE

There are many databases available, most of them commercially. Why choose ORACLE, which has little or no history of on-line implementation? There are several reasons;

- Complete set of integrated software tools
- Available on a wide variety of platforms
- Professional support available
- Full RDBMS available
- High level query language, SQL

Apart from these considerations we were mostly worried about performance. Several benchmark tests were made, such as the time taken to perform a chromaticity trim, requiring some 20 functions to be modified on the database. These tests showed that for the frequently used applications, the response time was the order of seconds which is considered to be acceptable. Other pieces of software, such as generating the reference settings, can take up to a minute but since they are only run at the beginning of an operational period lasting weeks, this is not a problem. Indeed throughout the whole of the year, the database performed well enough for the needs of operations. It also proved to be extremely reliable.

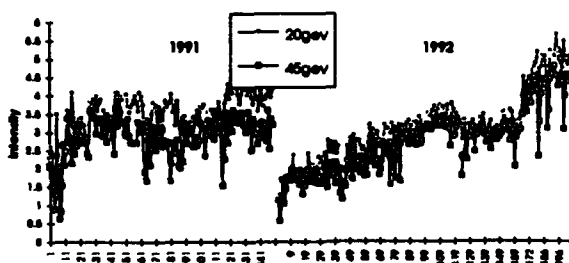
3.2 Settings management

LEP was required to perform in a variety of different ways during 1992. For routine operation several different optics were used early in the year before the optimum one was established. Each new optics meant generating new settings (ramps and squeezes) and optimising them with beam. During this the new software performed well, leading to a significant reduction of the amount of time required to commission a new optics. Towards the end of the year this was achieved in a few hours whereas in 1991

it always took the best part of a day.

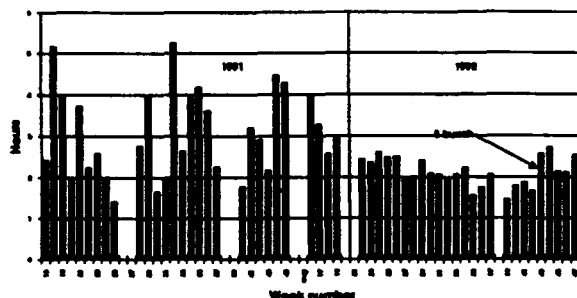
Furthermore, once a ramp had been commissioned it was much easier to keep track of any variation in the machine with time. Such variations led in previous years to a reduction in the efficiency of accelerating beam from the injection energy to physics energy, a figure of 75% being a typical weekly average. In 1992 this figure was often over 90%, see figure 1.

Figure 1 - Intensities at 20 and 45 GeV



The time spent going from physics conditions, through cycling the machine, accumulation of beam current, ramping and squeezing and back into physics also plays an important part in the LEP performance. In 1991 the mean time for this was over 3 hours for the 150 coasts made. In 1992 this was reduced to 2 hours 10 minutes over the 200 coasts made (Figure 2). In other words some 200 hours of physics time, out of 1700 achieved, was gained through this improvement.

Figure 2 - filling time in 1991 and 1992



3.3 Machine tuning and run analysis

The majority of running in 1992 was with a low emittance optics to maximise the luminosity. The price to pay for this was that the machine parameters had to very closely monitored and controlled throughout a physics run, which lasted typically around 10 hours. Particularly during the first hour or two of physics the operations team would be required to make many changes to key physics parameters such as beam sizes, betatron tunes and the closed orbit. All these changes could be achieved through a standard

interface, allowing quick and clear actions on the machine.

Many of the changes made were empirical trims, and the facility to revert back to any previous machine state, provided by the trim history, proved extremely useful.

In the longer term the trim histories proved valuable in post-analysis of different runs. It was possible to correlate changes in beam behaviour with trims made on the machine. It should be stressed that the choice of ORACLE again proved to be justified here, enabling these correlations to be developed interactively on the database.

3.4 MMI

Finally a word on the ease of use of the applications. In previous years, routine operation of LEP had been performed essentially by the engineer on shift. It had proved very difficult to delegate tasks to technicians, partly because of the complexity of operation but also because of the way the information was presented to him. With the new software in use during 1992, less experienced operators have felt much more comfortable and have been able to work effectively on the machine.

4. Conclusions

The new applications software for driving LEP has made an important contribution to the operation of the machine during 1992. The estimated gain in integrated luminosity is of order 20%. The look and feel of the software has made the accelerator more accessible to less experienced operators.

5. References

- [1] Experience with workstations for accelerator control at the CERN SPS
A. Ogle et al, Proceedings of Accelerator Controls Conference, Vancouver 1989

A Software System for Modeling and Controlling Accelerator Physics Parameters at the Advanced Light Source *

L. Schachinger and V. Paxson
Lawrence Berkeley Laboratory
Berkeley, CA 94720

Abstract

We describe a software system used at the Advanced Light Source for accelerator physics studies and accelerator control. The system consists of a number of Unix processes that can be connected together in modular ways. Processes communicate using messages with a common data format, but processes do not know where their messages come from or go to, making each process easily replaceable by others using different algorithms, measurement techniques, or models. Some of the controls and correction functions we have implemented using the system are closed-orbit correction, continuous tune display, and Fourier analysis of turn-by-turn beam position monitor (BPM) data.

INTRODUCTION

Over the lifetime of an accelerator, and particularly in the commissioning phase, programs which measure and correct machine parameters can change significantly. For instance, at the ALS our current orbit correction algorithm is the local bump method, but we plan to implement an algorithm based on Singular Value Decomposition in the near future. As diagnostics come on line and are better understood, preferred methods for measuring a particular parameter change. Currently we use a model to calculate tunes from magnet currents, but soon we will read the tunes from a spectrum analyser, or perform an FFT of turn-by-turn data from the BPM's. These circumstances cry out for a modular, flexible approach, so that new correction algorithms or measurement techniques can be substituted and compared easily.

TOOLBOX PHILOSOPHY

We have long advocated a "toolbox" approach to building accelerator simulation and control software[1]. This approach emphasizes building applications by plugging together modular, single-function programs. The goal is

*Work supported by Director, Office of Energy Research, Office of Basic Energy Sciences, Materials Sciences Division, U.S. Department of Energy under Contract Number DE-AC03-76SF00098.

to avoid monolithic, buggy, hard-to-maintain applications, and instead to stress having the flexibility to rapidly piece together new applications as the need arises.

Crucial to this approach is the modularity of the individual programs that comprise the toolbox. Each of these programs must be wholly self-contained; if we are to be able to connect the programs together in unforeseen ways, the programs must not assume anything about what other programs they might communicate with.

We can achieve this degree of modularity by making the programs *event-oriented*. By event-oriented, we mean that we write programs in terms of events they receive, telling them what to do; and events they generate, publishing the results of whatever they did. Each event is a name (e.g., "compute tune") and a value (typed data associated with the event). Event values can be quite large, as programs may have to communicate a large amount of data (e.g., computed β_x and β_y values at every BPM and corrector).

Programs do not know anything about where the events they receive came from, nor where the events they generate go to. In this way, programs remain completely modular. By making the events generated by one program become the events received by another, we can forge a new application from the two programs even though neither was written with any knowledge of the other.

THE GLISH SOFTWARE BUS

An environment for connecting together these sorts of modular programs is sometimes called a *software bus*, in analogy with hardware busses that enable independently-designed hardware components to communicate. The software bus we use, called *Glish*[4], was designed with accelerator applications in mind.

While programs are written for use with Glish in an event-oriented style, Glish does not limit the names of the events used by a program nor the structure of the associated data. At first this might seem like granting the program writers too much freedom, since how can the programs communicate if they don't agree on data formats and naming conventions?

The answer lies in Glish's chief strength: Glish provides an interpreted scripting language, similar to that used in

shell programming, for piecing together applications from individual Glish programs. These scripts not only specify which programs to run, but can dynamically control what should be done whenever any of the programs generates a particular event. Here, "what should be done" includes possibly routing the event to another program (perhaps renaming it), and modifying the event's associated data. Thus Glish offers a powerful sort of "glue" that we can use both to connect disparate programs, and to overcome their incompatibilities. If, for example, we want to use programs written with different physical units, or sign conventions, or data structures, a Glish script can readily provide on-the-fly conversion between the two programs, without requiring any modification of any source code.

A final benefit of Glish is that it supports transparent networking. Glish programs can run on different hosts and never know that their events travel over a network.

ORBIT CORRECTION APPLICATION

One of our principle simulation and control applications for the ALS is *orbit correction*. The present application we describe here evolved from that described in [3].

On the face of it, correcting the orbit of an accelerator is a simple task. Given the machine's current trajectory, calculate the corrector settings necessary to flatten the trajectory; apply the new settings; and we're done. So simple that we might be tempted to write a single program to deal with the entire task.

In reality, though, many other factors enter into the application, and greatly complicate it. Correctors or monitors may be broken, disabled, or untrustworthy. We might need to use different hardware to read the first turn trajectory, before beam is stored, than the closed orbit, and a different correction algorithm in the two cases. We might want to average the position readings over a variable number of turns. Beam position monitors (BPMs) have offsets due to engineering errors, correctors have calibration factors for converting between radians of angle and amperes of current. We may have to apply corrections in steps, to avoid risking beam loss from overzealous correction. We may be able to use nominal phase and beta information for the accelerator, or want to calculate more precise values. Our "goal orbit" may change from a flat trajectory for stored beam, to a betatron oscillation when injecting.

Finally, we want a *single* application that can correct the orbit for both the ALS booster and the storage ring, taking into account all of the above factors. And we want to use this same application on-line, correcting the actual orbit, off-line for simulation using a modeling program instead of the actual hardware, and with data we previously archived, to try alternative correction strategies.

Figure 1 shows how we built the orbit correction application using Glish. The boxes along the left and right edges represent different Glish programs, all of which connect to the central software bus. The dotted box at the

bottom represents static information that the Glish interpreter reads from data files and disseminates to those programs needing it.

The "Simulation / Accelerator" box represents one of two programs: either our modeling program (Teapot), for simulating orbit correction, or access to the actual accelerator hardware, for on-line orbit correction. The Glish script picks which of these two programs to use based on the script's run-time arguments.

Arrows indicate the events received and produced by each program. Note that there is *not* necessarily a one-to-one correspondence between an event produced by one program and an event sent to another program. Sometimes the Glish script itself deals directly with these events. For example, while the User Interface might request the current trajectory using a "get orbit" event, the Glish script decides whether to pass that event along to Simulation / Accelerator as a "get closed orbit" event, or whether to use the separate program for First Turn BPM Readouts. In the latter case, the script must send several different events to the program, one first to trigger the hardware, and then ones to read the X, Y, and signal sum values. Each of these elicits a separate event in response.

Picking between these two sources for the current orbit illustrates a key point: the system can accommodate two very different ways of getting the beam position data, and it does so transparently to all of the other programs involved in the application.

The orbit-correction application achieves all of the goals outlined above: we use it for both the ALS booster and the storage ring, both on-line, off-line to examine archived data, and off-line for simulation. A considerable amount of the application is done directly in the Glish script: converting between the units and sign conventions used by the different programs, incorporating BPM offsets and corrector calibration factors, averaging trajectories over multiple turns, applying fractional corrections, modifying first-turn readings based on the signal sum values, computing trajectory and correction statistics, and enforcing "fixed status" (e.g., "always off") for devices whose status is erroneously reported by the hardware.

TURNPLOT APPLICATION

Another application we built using Glish is *turnplot*, a program for analyzing beam position data[2]. Turnplot is structurally simpler than orbit correction, but maintains the property that it can be run on either the ALS booster or the storage ring, using either live hardware readings, tracking data produced by a modeling program, or previously archived data. Turnplot can analyze either a single, full turn of data (taken at each BPM), or an orbit scanned over every *n*th turn at a specified BPM.

Turnplot can display tracking data as a turn-by-turn point plot, as a phase space plot, or as X/Y data. In addition, we can FFT tracking data to identify probable X, Y,

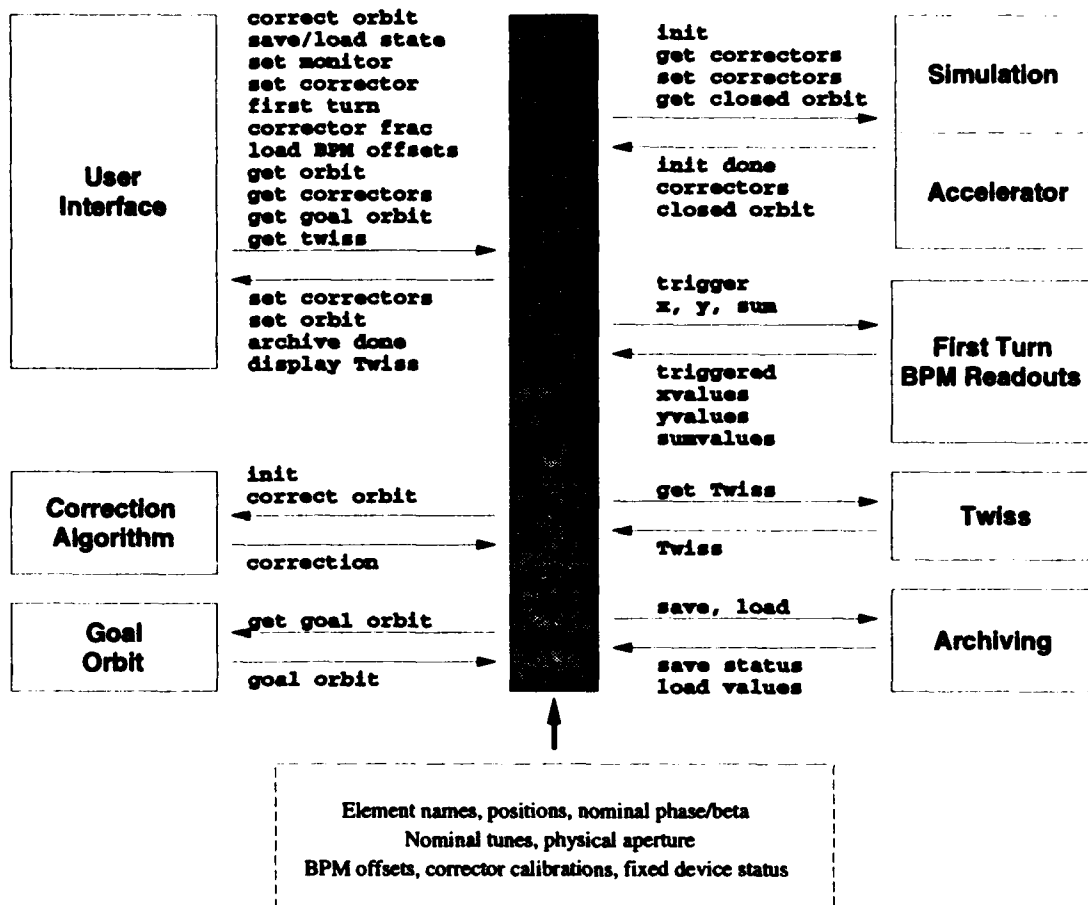


Figure 1: Structure of Orbit Correction Application

and synchrotron tunes, display harmonics associated with those tunes, select alternate FFT peaks if a peak found automatically appears unlikely, and display resonance plots for the identified tunes.

asuring tunes, and by reading turn-by-turn data from all the BPM's while exciting a betatron oscillation), one to measure and correct dispersion, and one to measure and correct linear coupling.

TUNEPLLOT APPLICATION

A third application is *tuneplot*, for analyzing and controlling the machine tune. Tuneplot displays the current tune values on a resonance diagram. Like turnplot, tuneplot has no knowledge of where the tune values come from, so they can be changed transparently, including using a spectrum analyzer, the BPM hardware, and values computed from the present magnet currents. Because whenever tuneplot is sent a "tune read back" event it updates its display, we can use tuneplot to continuously display the tune, computed in "real time", without the program having any special provision for such a display.

FUTURE WORK

Other applications planned and in progress are one to measure and correct chromaticity, another to measure and correct betas (both by varying quadrupole strengths and mea-

REFERENCES

- [1] V. Paxson, C. Aragon, S. Peggs, C. Saltmarsh, and L. Schachinger, "A Unified Approach to Building Accelerator Simulation Software for the SSC," Proc. 1989 IEEE Particle Accelerator Conf., Chicago, IL.
- [2] V. Paxson and L. Schachinger, "Turnplot: A Graphical Tool for Analyzing Tracking Data," Proc. 1991 IEEE Particle Accelerator Conf., San Francisco, CA.
- [3] J. Bengtsson, E. Forest, H. Nishimura, and L. Schachinger, "Modeling in Control of the Advanced Light Source," Proc. 1991 IEEE Particle Accelerator Conf., San Francisco, CA.
- [4] V. Paxson and C. Saltmarsh, "Glish: A User-Level Software Bus for Loosely-Coupled Distributed Systems," Proc. 1993 Winter USENIX Conf., San Diego, CA.

Machine Physics Application Program for Control, Commissioning and Error Findings for Storage Rings

H. P. CHANG[†], C. H. CHANG[†], C. C. KUO[†], M. H. WANG[†],
J. C. LEE[†], J. Y. FAN[†], H. J. TSAI[†], and C. S. HSUE^{*†},
SRRC [†], Hsinchu Science-based Industrial Park, Hsinchu, Taiwan, R. O. C.
and

Department of Physics*, National Tsing Hua University, Hsin-Chu, Taiwan, R. O. C.

Abstract

We have developed a Machine Physics Application Program (MPAP) package for control, commissioning and error finding to be used on the SRRC storage ring with user friendly graphic interface. The program gives on-line machine parameters as well as Twiss functions together with the machine elements in graphic form. It supported the following capabilities: machine modeling, orbit corrections and adjusting, tune adjustments, error findings for the misalignment and strength setting, etc. The code is written in ANSI C and can be imported to both VAX and UNIX operating systems which support the standard X-window/Motif. The arrangements of the code is in such a way that the interface with the on-line Control Data Base can be easily implemented for use on any machine. It can be used both for on-line control and/or for off-line analysis.

1. Introduction

To aid the commissioning and operation of the 1.3 GeV electron storage ring dedicated for synchrotron radiation we have developed a Machine Physics Application Program (MPAP) package using ANSI C combined with X-window/Motif which provides friendly user graphic interfaces in real operations.

Since only ANSI C are used in the coding, the program can be compiled and run in both VMS and UNIX machines. This flexibility will allow the program to be used in the VMS machines, which is being used in the control system at SRRC at this moment, and in the UNIX machines which becomes more and more popular among the accelerator communities around the world.

The package can be used both for on-line control and for off-line analysis. For the on-line version, an interfacing program linked the Machine Physics Application Programs directly with the Control Data Base. Because of the module structure of the programming, implementation of the program on other machines is straightforward.

2. Overview of MPAP

Fig. 1 shows the essential structure of the package. The package is composed of several individual modules. Intercommunications between different modules are facilitates

The MPAP's Routine Library and GUI are supported for all MPAP package.
The CDBS/MPAP interface is supported for "Online Control" on VAX/VMS,
since SRRC's control system is only available on VAX/VMS currently.

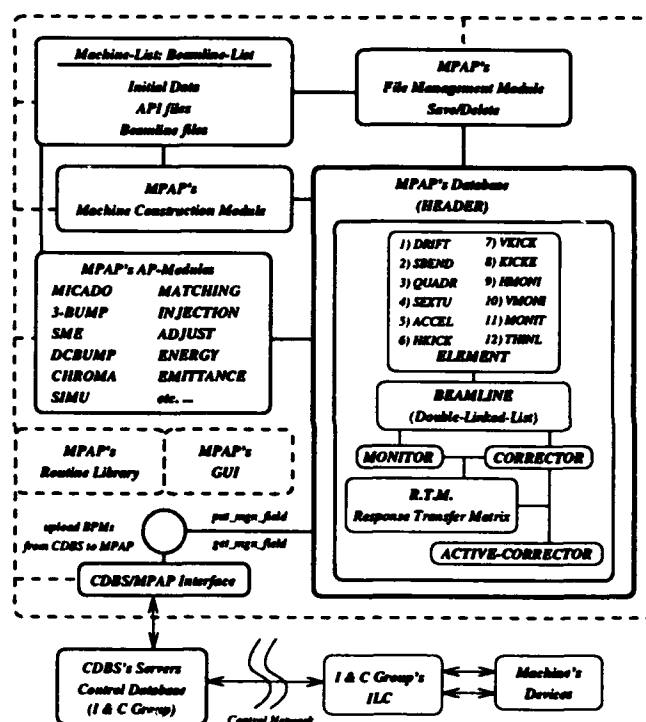


Figure 1: The structure of SRRC/Beam Dynamics Group's MPAP.

by various text files. The program is started by reading the appropriate Beamline files which contains the relevant machine element data for the beamline to be studied. A control panels provide the possibilities of switching among different selections of the relevant data. Convenient file management facilities are provided for saving and restoring of the data for future analysis. The necessary data such as the BPM readings and the current settings can also be obtained directly from the Control Data Base(CDBS) directly.

Currently supported facilities include: machine modeling, machine parameters and Twiss functions calculation, orbit corrections for both transport lines and storage rings, chromaticity calculation and adjustments, adjustment of

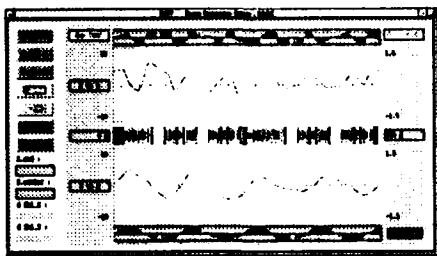


Figure 2: The COD of SRRC Storage Ring before vertical correction (RMS-Vertical = 2.405 mm).

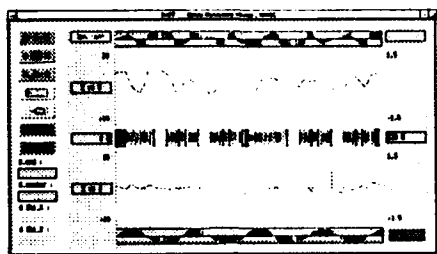


Figure 3: The COD of SRRC Storage Ring after vertical correction with SME method (RMS-Vertical = 1.028 mm).

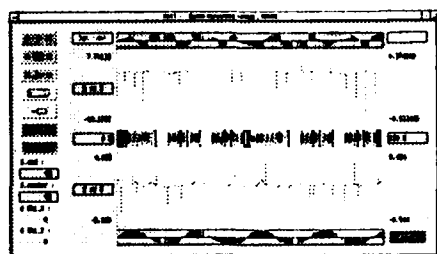


Figure 4: The best COD of SRRC Storage Ring currently with Energy = 1.3026 GeV (RMS-Horizontal = 0.4915 mm; RMS-Vertical = 0.2823 mm).

launching conditions, emittance measurements, etc. Control panel and the graphical display of the relevant quantities are provided for each of the application modules. Relevant machine parameters and Twiss functions are calculated and exhibition in graphic form for easy apprehension. We will demonstrate the MPAP in detail for an explicit usage on orbit correction in SRRC commissioning in the next section.

3. Orbit Correction

Currently there are three methods of orbit corrections are available: MICADO[1], beam bump method, and also SME (which automatically includes bounds on the current settings). Fig. 2 shows an output panel for orbit correction. The upper half and the lower half of the panel exhibits in graphical form the BPM readings of the Closed Orbit Distortions(COD) in the horizontal and the vertical plane respectively. The middle region shows the corresponding machine elements. The appropriate machine

parameters (such as the Corrector-to-BPM response functions may be obtained directly from the control panel.) Zooming for the machine elements and for the COD values as well as the setting values of the correctors are achieved by suitable clicking of the mouse on the panel. Shown on the top part and the bottom part of the panel are the graphical exhibition of the corresponding tunes in each plane. In this example, the behavior of the vertical BPM errors are very similar to the phase advance of the machine, indicating that a single corrector could be very effective in reducing the errors. This is in Fig 3. which shows the results of the vertical BPM errors after applying a single corrector. In agreement with theoretical calculation, the RMS of the COD errors in the vertical plane is reduced from 2.41 mm down to 1.03 mm by application of a single corrector indicated in the panel by the single bar. The values of the corrector strength is given by the length of the bar.

To further reduce the rms of the COD values, we may use the package to find the desired settings for the correctors. After the setting values of the correctors which produce satisfactory trajectories have been found we may use the package to set the combined settings of correctors in the machine. If necessary, we can divide the settings in a desired number of steps (with fixed ratios between) and watch directly the response of the BPM values step by step. Fig 4. shows the results after such an application. The RMS values of the COD errors in the horizontal plane and the vertical plane is 0.49 mm and 0.28 mm respectively. The bars shown represents the strengths of the correctors.

4. Error Findings

Error finding facilities of the package are still in the process of developing and improvement. However since we may use the package to obtain the relevant parameters and Twiss functions, and these values can be checked with the observed behavior of the machine to detect possible errors of the machine settings. For example, in the process of correcting the COD values, if the BPM readings did not improve at each substeps of corrector settings, it will indicate that there is probable some setting errors.

In a more quantitative example, we may subtract the BPM readings of the COD errors after each correction from the those values before correction and compare the difference of these BPM values with the calculated response function from the package. It is worthwhile to remember that the linear contributions of alignment errors has been eliminated by the subtraction process. Fig. 5 and Fig 6 shows such a comparison for vertical orbit correcting and horizontal orbit correcting respectively. The agreement in the vertical plane is almost perfect. This means that the modeling for the vertical beta functions and the BPM readings are essentially correct. However, in the horizontal plane, the real response functions of the machine has an overall factor of about 1.7 comparing with the calculated ones. From the expression of the COD increments

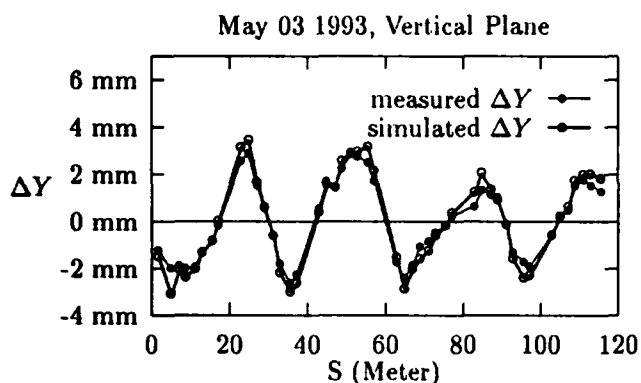


Figure 5: Comparison of the measured ΔY and simulated COD change by the correctors with specified strengths.

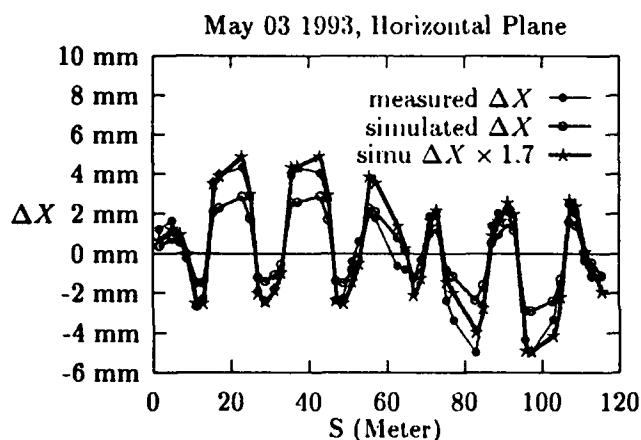


Figure 6: Comparison of the measured ΔX and simulated COD change as well as $(1.7\times)$ simulated COD change by the correctors with specified strengths.

at the monitors

$$\Delta x_m = \sum_k \frac{\sqrt{\beta_k \beta_m} \delta_k}{2 \sin \pi \nu} \cos(\pi \nu - |\phi_k - \phi_m|) \quad (1)$$

where β_k and β_m are the values of the beta functions at the correctors and monitors respectively, we find that the most probable source of the errors are due to errors of tune values. The major reason of this error comes from an energy error. A subsequent readjustment of the machine settings using this information brought the model in close agreement with most of the experimental results such as tune measurements and beta function measurements in the commissioning of SRRC storage ring and is very close to the original design[2].

5. Summary

The MPAP package developed by SRRC has been successfully applied in the commissioning of the SRRC 1.3 GeV electron storage ring dedicated for synchrotron radiation in Taiwan which has just finished construction and installation. The module of the package should allow the package to be easily used in any accelerators.

6. Acknowledgements

We have been aided by various friends around the accelerator communities for various advices and suggestions. One of the author, C. S. Hsue would like to take this opportunity to thank Dr. Martin Lee who convinced him of the importance of the application programs in the early stage while we were busy in designing and studying various issues of the SRRC storage ring in Taiwan.

References

- [1] B. Autin, Y. Marti, *Closed Orbit correction of A. G. machines using a small number of magnets*, CERN ISR-MA/73-17 (1973).
- [2] C. S. Hsue, C. C. Kuo, J. C. Lee and M. H. Wang, *Lattice Design of the SRRC 1.3 GeV Storage Ring*, 1991 IEEE particle Accelerator Conference, p. 2670.

CATER: AN ONLINE PROBLEM TRACKING FACILITY FOR SLC*

Robert C. Sass, Hamid Shoaee

Stanford Linear Accelerator Center, Stanford University, Stanford, CA 94309 USA

Abstract

An online facility has been developed for SLC to organize and simplify the management of all problems encountered in the operation of the accelerator. CATER (Computer Aided Trouble Entry and Reporting) may be used to make the initial entry of a problem, to enter one or more solutions to a problem, to modify or closeout a problem, to generate a variety of pre-defined reports giving status and statistical summaries, and to allow anyone to browse the database. All phases of CATER can take place on the operator console, workstations, or on any ANSI compatible terminal. The user interface is designed around a menu driven windowed environment with a large amount of context sensitive help information to alleviate the need for consulting user documentation. Currently, the CATER database contains information on more than 30,000 problems entered since it went online in January of 1988. The features of the software and some implementation details will be presented.

INTRODUCTION

In the early days of SLC operation, hardware and software problems were reported and tracked by the "yellow-sticky" and other paper-based methods. It was apparent early on that some more reliable method of tracking the many machine problems was needed. The initial attempt to implement a problem tracking software system failed mostly because of a lack of user acceptance. For the second attempt, it became clear that like a good business, the system had to cater to the needs of the users first if it was to be accepted. CATER was thus designed with the following general requirements:

1. Above all it had to be easy to use with a minimum of instruction and keystrokes.
2. It had to run on any of the terminals then in use at SLAC.
3. It had to keep all problems in a database for historical analysis.
4. It had to be fairly easy to modify so it could adapt to changes in the physical accelerator and management structure.

GENERAL FEATURES

At any point, a given problem is either Unsolved (has no solution), Solved (has one or more solutions) or Closed (solved and a supervisor agrees that it's fixed). Thus from the main menu there are separate CATER functions to report, solve and close a given problem. Also from the main menu are additional functions to modify existing unclosed problems or solutions, generate canned reports and browse the database.

For consistency, the operation of all screens in CATER is as similar as possible. Figure 1 shows the hardware problem report screen as it appears when reporting a new problem which we'll use to show the operations common to all screens.

CATER - Report a Hardware Problem

Your Userid : [BAS] Date/Time : 6-MAY-1993 08:58
Your Name : [Glenn Horton-Smith]
Urgency : [Immediate] Computer Assigned :
(I) Immediate Problem Number :
(S) Scheduled
(L) Later
Area : [LINAC]
Subsystem : [MICRO]
Micro : [FB31] Primary & Unit :
Shop - Main : [CTL] Shop - Alternate :
Problem description. (CR) next line and (TAB) validate description.
FB31 Matrix board is not working correctly. Horizontal and vertical timing of video output is wrong.

Control Menu: Cancel menu, Get help, Rewrite screen, Entry Mode, Overstrike, Insert/Overstrike, Move in field, Next field, Previous field, Record problem

Figure 1. Hardware problem report screen

1. All allowable control options are highlighted at the bottom of the screen. Control key sequences are used for most control options because there is little overlap in function key mappings between the various terminals and emulators on which CATER can be run.
2. Online help is available for every field. This help information includes any validation which is performed. If the field is limited to a set of specific entries, the help lists them and the minimum keystrokes required for each entry.
3. Within a field the user can edit the text using the arrow keys and switching the entry mode to insert or overstrike.
4. The user can move back and forth to the next or previous field as many times as desired until all data is entered satisfactorily. Until the user enters CTRL-Z to execute the function, the cancel option (CTRL-C) is always available which returns to the previous menu without making any database changes.

PROBLEM REPORTING

Again refer to Figure 1, the hardware problem report screen. The software screen is similar but with different fields after "Urgency". For the problem and solution entry forms there are some additional items of note:

1. Required fields are enclosed in brackets. CATER insists that you make a valid entry in these fields.
2. Initial default values are entered. For the hardware problem report this includes the users id, name and problem priority.
3. Both the problem report and solution forms have a 10 line free form description field used to describe the problem or solution. As in single line fields, the arrow keys and entry mode can be used to do simple editing. For this multi-line field, carriage-return goes to the next line as you would expect. The TAB or CTRL-B must be used to go to the next or previous field respectively.

* Work supported by Department of Energy contract DE-AC03-76SF00515.

An interesting historical anecdote reveals how important it is for any widely used system to adapt to the user's needs. The initial system had two lists of supervisors; one for hardware problems and one for software. After a problem was entered, it was mailed to the appropriate list. It turned out that the hardware people were usually in the field and rarely read electronic mail and so their problems were just stacking up! While the specific printer details have evolved over the years, we automatically print new hardware problems, email software ones and everybody's happy.

Except for the distribution list, the email of software problems has remained unchanged since CATER's initial release. Hardware problem distribution on the other hand, has been modified several times, reflecting organizational and personnel changes. At the present time a hardware problem is assigned to a default shop based on several problem criteria. The reporter can change the default if desired and when the problem is entered it is immediately printed on that shop's printer. This has served to expedite the solution of hardware problems since most problems go directly to those responsible for fixing them without the necessity of logging in to the computer system.

SOLVING A PROBLEM

Once a problem has been completely or partially fixed, the solver enters a solution into the database. Any number of solutions can be entered for a given problem. Figure 2 shows the solution entry of a previously solved hardware problem. As with the problem entry, there are a set of required fields and some default values are supplied.

CATER - Hardware Problem Report Information

CATER - Hardware Problem Solution Information

CATER - Solution to Hardware Problem Active

Your Userid : [PMIPAT] Date/Time 6-MAY-1993 09:13
 Your Name : [Patrick Conroy]
 Hours to Solve : [] Problem Number 31659
 Solution was : [] Solution Number
 (A) Adjust/repair, (R) Replace, (E) Enhance/Modify, (N) No trouble found
 Exchange Unit-FRU :
 Old serial number :
 New serial number :
 Documentation : [Unknown]
 Schematic number :
 Ready-to-Close Y/N:[Yes]
 Solution description: <CR> next line and <TA3> to validate description.

[PF1] Buries top window [PF2] Toggles thru solutions

[F1] Cancel menu [F2] Entry Mode : Overstrike [F3] Next field
 [F4] Get help [F5] Insert/Overstrike [F6] Previous field
 [F7] Rewrite screen [F8] Move in field [F9] Record solution

Figure 2. Hardware problem solution entry screen

In this case there have been previous attempts to solve the problem and while entering yet another solution you have immediate access to the initial problem entry and all solutions to date. By using the PF1 and PF2 keys as indicated, you can expose the buried problem and solution windows and scroll through all previous solutions. If this is the first solution entry to a previously unsolved problem, the problem status automatically changes from Unsolved to Solved.

MODIFYING PROBLEMS AND SOLUTIONS

It is frequently useful to modify the fields of an existing problem or solution. Additionally, not all fields in a problem description (such as who is assigned to fix it) are available to the initial reporter. The modify function allows supervisors to change any field in an existing, Un-closed problem. Typical reasons for modifications include:

- Add to the problem description.
- Change the person or shop to which the problem is assigned.
- Change the problem's urgency

When the modified problem is entered into the database, the modifier has the option of re-distributing the modified problem in the same way as if it were initially entered. This again allows the immediate notification of maintenance personnel of any change in a problem's status.

CLOSING PROBLEMS

When a problem has been solved to everyone's satisfaction, a supervisor is responsible for officially closing it. Figure 3 shows the closeout screen.

CATER - Hardware Problem Report Information

CATER - Hardware Problem Solution Information

Solved by PATR PAT REARDON
 Hours to solve 1.00 Date solved 4-MAY-1993 23:00
 Solution type Adjust/Repair Problem number 31656
 Exchange module NONE Solution number 1
 Old serial number
 New serial number
 Documentation Unknown
 Schematic Number

Solution description.
 20-8 FOUND KLYS FIL AT MAX CURRENT, MIN VOLTAGE. TESTED MODULATOR WITH KLYS LOAD TEST UNIT, FOUND KLYS FAULTY. INFORMED AMRF.

CATER - Closeout a Problem

Your Userid : [JLM] Closeout Date 5-MAY-1993 09:48
 Your Name : [Eusty Mumfrey]

[PF1] Buries top window [PF2] Toggles thru solutions

[F1] Cancel menu [F2] Entry Mode : Overstrike [F3] Next field
 [F4] Get help [F5] Insert/Overstrike [F6] Previous field
 [F7] Rewrite screen [F8] Move in field [F9] Close problem

Figure 3. Problem closeout screen

As before, the report and all solutions are available for immediate review by burying windows and scrolling through multiple solutions. The user's id and name are filled in and validated against a list of authorized closers before the status of the problem is officially changed to Closed in the database.

REPORTS & DATABASE BROWSING

Figure 4 shows the first level report screen.

```

CATER - Report Summary Options

(H) Hardware Compose-it-Yourself Summary
(S) Software Compose-it-Yourself Summary
(Q) Quit and Return to Task Selection Menu

Pre-Defined Cater Management Reports:

Hardware Reports          Misc Reports
-----
(1) Immediate/Unsolved   (11) PEP/SPEAR
(2) Open                 (12) 24 Hour
(3) Solved/Unsolved      (13) Beam Time Lost
(4) Unsolved             (14) Feedback/Unsolved
(5) Closed               (15) BPM/Unsolved
                        (16) Micro/Unsolved
Software Reports          (17) Magnet/Unsolved
-----
(6) Immediate/Unsolved   (18) Klystron/Unsolved
(7) Open                 (19) Track Facility
(8) Solved/Unsolved      (20) Radio/Communications
(9) Unsolved and         (21) Solution Documentation
    'Solved-Do-Not-Close'
(10) Closed
Type 'H' or 'S' to get Help for CATER reports.
  
```

Figure 4. First level report screen

If you enter one of the numbers, CATER generates the appropriate pre-defined report on a printer of your choice. This is submitted as a batch job and returns immediately so you can do other CATER work while it's printing. If you enter 'H' or 'S', you get a "compose-it-yourself" screen for browsing the database. Figure 5 shows the hardware browsing screen. There are several things to note about this screen:

1. You can direct the output to a printer, have it displayed on your screen or written to a file for disposition as you choose.
2. The output format can be an abbreviated one liner for each selected problem, a full display of the problem and all solutions or the data can be written to a file in an 'export' format, suitable for incorporation into a PC spreadsheet or database.
3. You can enter selection criteria for any of the problem or solution fields augmented with the operators listed at the bottom of the screen. This allows almost unlimited read access to the database in a simple manner.

IMPLEMENTATION

CATER was implemented in late 1987 before workstations and GUI interfaces were available or popular at SLAC. Indeed, many of the CATER users still use VTXXX compatible terminals or emulators which are located throughout the accelerator to access the system. The basic tools used to construct CATER were:

1. SMG, a set of screen management routines.

```

CATER - Hardware Compose-It-Yourself Summary Report

Report Options

Printer Name : One          Format : Line
Report Filename:

Problem Report Search Criteria

Problem Number :          Report After Date :
Status :              Report Before Date :
Urgency :              Modify After Date :
Area :                Modify Before Date :
Micro :               FixEst After Date :
Subsystem :           FixEst Before Date :
Primary - Unit :      Close After Date :
Ready-to-Close :      Close Before Date :
Documentation :        Assigned to :
Beam Lost :           Reported by :
Problem Code :         Modified by :
Est Fix Hours :        Closed by :
Disposition :          Shop - Main :
Num Solutions :         Shop - Alternate :
Description :

Problem Solution Search Criteria

Solved By :              Solve After Date :
Solution Type :          Solve Before Date :
Old Serial Num :         Hours to Solve :
New Serial Num :         Schematic Number :
Exchange Module :
Description :

The selected criteria have matched Problems or Solutions.

[Ctrl-C] Cancel menu  [Ctrl-H] Entry Mode : Overstrike  [Ctrl-N] Next field
[Ctrl-L] Get help    [Ctrl-I] Insert/Overstrike  [Ctrl-P] Previous field
[Ctrl-W] Write screen [Ctrl-M] Move in field      [Ctrl-R] Make report

Operators:  [ ] and  [ ] or  [ ] less than  [ ] greater than  [ ] not  [ ] missing
  
```

Figure 5. Hardware browsing screen

2. Rdb, DEC's relational database and associated tools, precompilers etc..
3. VAX "C" programming language.

The SMG routines are fairly low level so the CATER program has a set of data structures which define the screen layouts, fields and their validation. This means that the screens are decoupled from the database so when new database fields are added, they must also be manually added to the appropriate screens. This is the most tedious and error prone aspect of CATER software maintenance. We considered migrating to Oracle a few years ago to make maintenance easier. We ultimately decided against this approach since it would have substantially changed CATER's "look-and-feel" and some of the fine control we exercise over the screen was difficult to reproduce under Oracle.

In general, Rdb has been satisfactory for our purposes. It offers a precompiler for executing fixed queries like we use for problem & solution entry or modification. For the browsing screens, we compose a query "on-the-fly" from the fields and operators entered and pass that to Rdb for interpretation. This is somewhat slower but gives us complete freedom to formulate queries at run time.

Retrieval performance for the browsing screens has been a bit of a problem as the database has grown. The indexes are defined around the set of fields most often referred to when scanning open (Unsolved or Solved) problems and with a little care, retrieval performance is generally satisfactory averaging 1-10 seconds depending on the complexity of the query. At the present time, of the more than 30000 problems in the database, only about 1% are open so historical queries which look at a large number of closed problems can take a minute or more. For this reason, those people compiling historical statistics usually export a large selection of records into a PC tool and do the analysis there.

To date our reliability has been excellent; we have not lost a single problem or solution in CATER's operating history.

Ramping Control Using a Spreadsheet

D. Y. Wang, R.P.Johnson*, L.S.B. Ng, W.J. Pearce

Brobeck Division of Maxwell Laboratories, Inc., 4905 Central Ave. Richmond, Ca. 94804

*Now at CEBAF, Newport News, Virginia

Abstract

The model 1.2-400 synchrotron light source built by Maxwell Laboratories for Louisiana State University uses a 200 MeV injector. After injection and accumulation, the beam is ramped up to 1.3 GeV in less than 30 seconds. During ramping, the dipole magnet waveform must be synchronized with those of 3 families of quadrupoles, 2 families of sextupole, 24 trims and the RF voltage. A commercially available spreadsheet program (20/20) incorporating lattice physics, magnet calibrations and flexible curve fitting was used to generate the necessary waveforms. These are downloaded to two list processors, auxiliary CAMAC crate controllers, which control the 31 DAC channels. The spreadsheet approach was cost effective in terms of programming effort, yet still enabled quick changes to the ramp path allowed cycling of all magnets to standardize magnet settings and provided for easy graphical feedback. The implementation of the ramping spreadsheet and experience with its usage will be described.

I. Introduction

The MLI model 1.2-400 synchrotron light source has been described in detail elsewhere [1]. After beam is injected and accumulated, the beam energy is ramped up from 0.2 GeV to the flattop energy of 1.2-1.3 GeV in less than 30 seconds. During ramping, 31 control currents must be incremented in synchrony. In addition, at the end of a store after the beam is dumped, all magnets must be brought back to a standard state by cycling of the magnet currents. Given these requirements, a convenient method of generating and modifying these control current waveforms was essential for commissioning.

The user interface chosen was a spreadsheet program, 20/20, produced by Access Technology, Inc. This spreadsheet ran on a Vax Station under Decwindows. The spreadsheet

format is well-suited for generating the large number of points which make up magnet waveforms during ramping. The logic of the calculations is linear, progressing from input to output without any branching. Moreover, the interface is user friendly. A "mouse" enables rapid paging through data and entry of values into selected cells. Lastly, graphs of the magnet waveforms which are calculated or read back from ADC's are readily displayed for diagnostic purposes.

In section A, the spreadsheet design requirements are discussed. In section B, the spreadsheet structure is described, showing how a configuration of the synchrotron is defined. Section C contains a brief recount of the operating experience..

B. Spreadsheet Design Requirements

The organization of the ramping spreadsheet is driven principally by two considerations.

The most important consideration for the spreadsheet design was governed by the requirement of providing enough flexibility so that quite general ramping waveforms could be generated with minimal user input. The user only needs to enter a small number of configurations at different energies along the ramp which has been found by experience or theory.

Subsequent automatic calculations join these configurations and divide the waveforms into many fine steps. To do this, each configuration is associated with a time up the ramp and also a "slope". This "slope" value is actually the desired tangent of the curve at that time normalized to the slope of a straight line connecting two configurations and varies between 0 and 1. A cubic fit is then used to join between configurations; it allows four

degrees of freedom which enables the values and slopes to be matched.

A ramp cycle for the dipole current is shown in figure 1 to illustrate the curve fit. The smooth transitions at the beginning and top of the ramp, obtained by specifying zero slopes, minimize beam losses that may occur due to eddy current induced effects. In this illustration, the flattop time is only about 5 seconds. During operation, the ramp waveform is actually halted at flattop and reinitiated only when a dump is desired, allowing beam to be stored for as long as the beam lifetime.

After beam is dumped, the ramp waveform takes all magnet control currents down to zero and brings it up to the injection level. This was the standardization cycle used.

Ramp Cycle

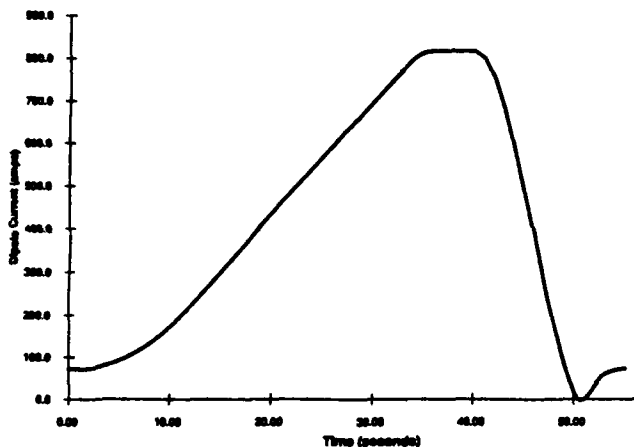


Fig. 1

The other major consideration in the spreadsheet design was that a machine configuration must be easily understood in terms of lattice parameters such as beam energy, betatron tunes or chromaticities. A machine configuration is completely defined by the set of 31 set-points for 30 magnets and RF voltage at a particular time.

But the representation of a particular magnet set-point is not unique. For example, the settings of the focusing and defocusing quadrupoles in the lattice can be shown as currents in units of amperes or alternatively they can be defined completely by the betatron tune values.

Using the latter representation assumes a much more detailed knowledge of the machine. As a first step, one needs the beam energy and quadrupole gradients in term of dipole current and quadrupole current settings. This come from previously measured calibration curves. Then it must be assumed that the synchrotron behaves sufficiently closely to the ideal lattice that a quadrupole perturbation is linearly related to a change in tune. The calibration curves may have errors and the synchrotron may not behave like the ideal lattice. But the utility of this representation, which was the one chosen for entering values into the spreadsheet, is that ideally, various parameters remain constant independent of beam energy up the ramp. Deviations point to anomalies.

C. Spreadsheet structure:

The spreadsheet structure is illustrated in figure 2 which shows only the top left corners of each section of the spreadsheet. As discussed in section B, configurations are entered into the Lattice Parameters Representation. In this representation, the variables are the beam energy, betatron tunes, chromaticities, and orbit correction deflection angles. These define the currents of the dipole, the focusing and defocusing quadrupole families, the focusing and defocusing sextupoles, and all trims which form the "Currents Representation". (The current waveform for the achromatic quadrupole family is scaled directly to the beam energy.)

Only 15 machine configurations are entered for the entire ramp cycle. After the curve fitting process, 141 expanded configurations in currents are generated. By use of power supply calibrations, these are converted into DAC settings. At this stage, timing offsets between the various magnets can be introduced. These offsets account for the different time lags in various power supplies.

A custom macro outputs this file to disk. A stand-alone program further expands the 141 configurations into 15000 configurations by linear interpolation. The final ramp waveform has this many fine steps. When each step is advanced, a momentary tune error can occur since magnet currents are updated with small relative delays, but no larger than 20

microseconds. With so many steps, the largest tune deviation is limited to 0.002. The final ramp waveform is loaded into list processors. These are CAMAC crate-controllers which load the data into appropriate devices when triggered.

Lattice Parameters Representation				
	Time(s)	E(GeV)	tunex	tuney
	0.00	0.11	3.260	1.168
	2.00	0.11	3.260	1.168
	5.00	0.14	3.260	1.168

Currents Representation				
slope	time	Ibm(A)	Iqf	Iqd
0.00	0.00	72.5	21.5	16.5
1.00	2.00	72.5	21.5	16.5
1.00	5.00	92.1	27.3	21.0

Expanded Configurations (currents)				
	time	Ibm(A)	Iqf	Iqd
	2	72.5	21.5	16.5
	2.3	73.7	21.8	16.8
	2.6	75.1	22.2	17.1
	2.9	76.6	22.7	17.4

Expanded Configurations (DAC counts)				
	time	Ibm(A)	Iqf	Iqd
offset(ms)		60	66	77
	200	3912	4221	4272
	230	3979	4292	4344
	260	4053	4371	4424
	290	4135	4458	4513

Figure 2 Spreadsheet Structure

D. Operational Experience

The spreadsheet ramping program has been used extensively to generate different ramp cycles during the commissioning of the MLI model 1.2-400.

During the first successful ramp only a few microamperes survived at 1.2 GeV out of an accumulated current of a few milliamps. Subsequently the ramping efficiency has improved dramatically. For example, out of 200 mA accumulated, more than 90% survives up the ramp. This was mainly the result of better vacuum.

The first successful ramps were done by directly scaling all other magnet currents with respect to the dipole current. The intentional timing offsets used to compensate for the time lag between power supplies proved to cause large beam losses and were deleted. For ramping up to 1.4 GeV, the dipole calibrations

which show saturation behaviour at energies above 1.3 GeV had to be incorporated.

The betatron tunes are constant up the ramp in the spreadsheet. But measurements using a network analyzer show that the horizontal tune moved over a range of ± 0.05 during ramping. In any case, the optimum tunes in the spreadsheet were (3.203, 1.453) versus (3.260, 1.168) for the theoretical lattice.

These discrepancies were mainly due to problems with the calibrations of the power supplies which drifted after the initial tests. It was not surprising that the spreadsheet structure was soon augmented with a section which transformed a configuration in the currents representation, found by trial and error, into the lattice parameters representation.

In terms of the original design, the most successful feature was the use of the standardization cycle shown in figure 1. It has to be run if beam is to be accumulated at injection energy.

Summary:

Despite all the problems encountered during operation, the spreadsheet interface for ramping control is still to be recommended. Indeed, its flexibility is proven by how readily changes were made to handle the problems encountered. The graphical interface was very useful in the debugging phases. But most importantly, for a cost of about \$1K plus 100 hours of initial programming effort, there is no other platform that can provide this degree of ramping control.

REFERENCES:

- [1] M.A. Green et al., NIM A291, 464 (1990).
B.C. Craft et al., NIM B40/41, 379 (1989)
R. C. Sah, NIM B56/57, 379 (1991)
D. Y. Wang et al., San Francisco:PAC, 2727 (1991)
R.P. Johnson et al., Berlin:EPAC, 197 (1992)
P. Letellier et al., Berlin:EPAC, 575 (1992)

EASY AND EFFECTIVE APPLICATION PROGRAMS USING DATAVIEWS

Elliott S. McCrory
Fermi National Accelerator Laboratory*
Batavia, IL 60510, USA

Abstract: The commercially-available product DataViews [1] is being used for a simple and effective applications program builder for the new Fermilab Linac Control System [2]. This product consists of a "view" editor, a thorough set of object-oriented graphics subroutines and a convenient method for incorporating your own data acquisition into the system. There are many advantages to this package, most significantly the modularity and effectiveness of the graphics and of the data acquisition schemes.

First, the programmatic structure of the DataViews product is described. Then a brief description of the Fermilab Linac control system is presented. A few of the programs developed using DataViews are described, especially a simple application-builder program. Finally, some operational experience is presented.

THE DATAVIEWS PACKAGE

Quoting from the VI Corporation manuals on DataViews:

DataViews is a set of tools for building graphical user interfaces for complex software applications. The main tools are DV-Draw, the graphical editor for building the visual interface, and DV-Tools, the library routines for building the programmatic control of the interface [3].

The DataViews package is available on virtually all workstations, in particular, Sun and VAX (VMS).

DV-Draw is used to edit the following aspects of the view: the character of the interface; the method by which the data are obtained; the graphs which are displayed; the way in which the graphs and the geometry of the graphics change according to the values for the data (the dynamics); user-input methods; and some limited prototyping methods. DV-Draw creates a binary file commonly referred to as a view.

DV-Tools provides the programmatic interface to the package. Anything which can be done in DV-Draw can be accomplished through DV-Tools. The use of the DataViews package which seems the most robust and

useful is to generate the layout of graphs, geometry, input objects and dynamics in DV-Draw, and to use the DV-Tools routines to respond to the user interrupts, do some special data gathering and act on the various events the program encounters.

The DataViews package has been extended, through their Function Data Source methodology, to include data acquisition from the Fermilab Linac control system. "Linac Scalar Devices" appears on the DV-Draw Data Source menu under the "Function Data Source" data source type and allows the user to observe these data in DV-Draw (for quick plotting without programming) or from a more sophisticated application using DV-Tools. It is not, in general, necessary for the DV-Tools programmer to worry about data collection.

A measure which some people use to determine the level of sophistication of a software system is the time it takes to modify that system. It required approximately two weeks of effort for one physicist to learn the DataViews Function Data Source methodology and implement "Linac Scalar Devices" into the system. VI Corp provides two examples of Function Data Sources with their product, which helped this physicist very much.

The performance of an application program which uses DataViews is generally limited to 5 Hz or slower, depending on the complexity of the view. (This is observed on a Sun SPARCstation 2 workstation with GX graphics.) It is believed that a true graphics accelerator would greatly enhance this performance.

THE LINAC CONTROL SYSTEM

The Linac control system is fully documented elsewhere [2]. Briefly, we have twenty VME local control stations (LCSs), connected together on the IEEE 802.5 (4 MB) Token Ring communicating with each other, with Macintosh consoles and with Sun Microsystems workstations (running, among other things, DataViews).

A large set of C++ classes for Linac data acquisition and control have been built at Fermilab. Acquisition of large amounts of data (in excess of 500 frames of 100 bytes of answers per second) has been demonstrated on a single SPARCstation 2 using these classes.

* Operated by the Universities Research Associations, Inc., under contract with the U.S. Department of Energy, contract number DE SC02 76CH03000

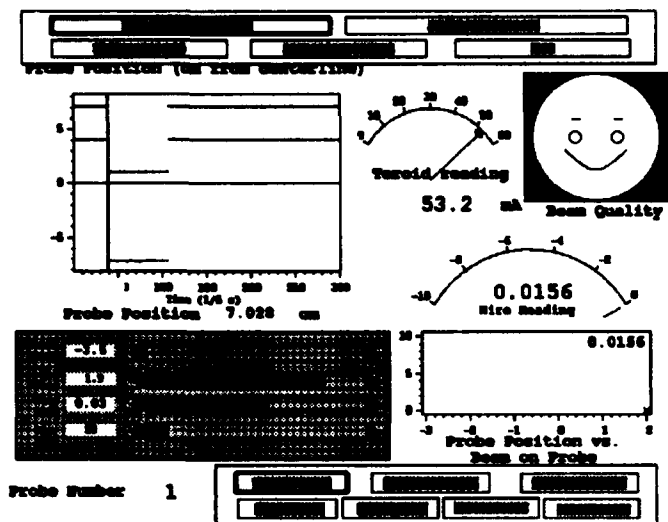


Figure 1, The low-energy emittance control program.

The pertinent classes to mention here are the *Device* and the *Request* classes. A *Device* instance handles all of the information connected with the 16-bit analog devices in the Linac control system, for example, the reading, setting, nominal, tolerance, title, units, conversion constants, sibling channels, etc. The *Request* class handles everything associated with getting data back from a LCS at a repetitive rate. In particular, a *Request* instance can handle 15 Hz data returned from an LCS for a *Device* or for a list of *Devices*.

The DataViews "Linac Scalar Data" uses the *Device* and *Request* classes to return the scalar data for that device or those devices to the DV application, either DV-Draw or DV-Tools.

THE DATAVIEWS/LINAC PROGRAMS

Two of the more sophisticated applications written using the DataViews package are described here.

The first application is for the low-energy emittance measurement and calculation programs (*emit* and *show_analysis*, respectively) [4]. When the program begins, the screen shown in Figure 1 is displayed. (Note: These program are normally viewed on a color monitor; some of the quality of the display has been lost in the translation to a form suitable for this paper.) From there, the user can select the emittance probe to run and the limits on the motion of the probe. The progress of the probe and some information on the returned data are displayed. The C++ program is responsible for (1) responding to user interrupts and setting the emittance run parameters and for (2) launching the emittance measurement program (another C++

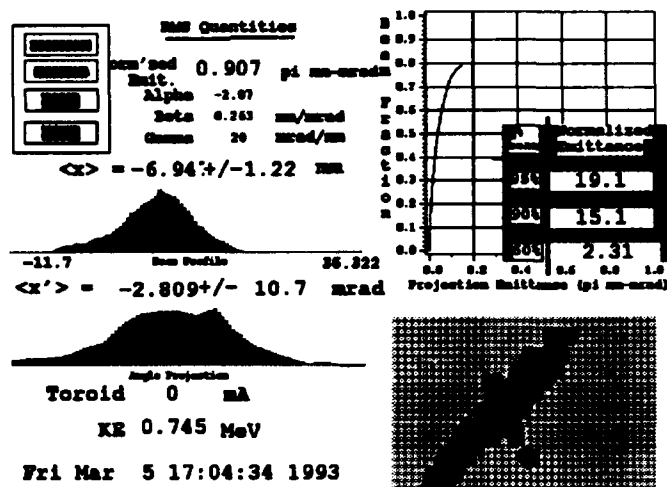


Figure 2, The low-energy emittance display program

program on the SPARCstation 2). DataViews is responsible for gathering the data for the displays and for making the displays. When the emittance measurement is completed, the user asks to analyze the data. The *emit* program then launches an analysis program and, when that completes, it launches *show_analysis*. A screen for *show_analysis* is shown in Figure 2. This program is essentially a DataViews example program supplied with the product, modified for the 4-button input field in the upper left corner of the display. The C++ program only reacts to user input; DataViews handles the rest. (These program was conceived and initially written by M. Allen, presently of the SSC, with substantial modifications by the author and by J. Palkovic, also now at the SSC.)

The second program is intended to be a general program for a synaptic display for a system. The user would set up a view with DV-Draw to graphically represent his/her system in any way desired. There are some restrictions on the names of the graphical and data objects in the view. When the user interrupts on an object which is bound to a piece of data obtained from the Linac control system, the program creates a popup box containing the information on this datum as provided by the *Device* structure. The program also shows database information for binary information.

The program can switch the view from one rf system to another (there are eleven rf systems in the new Linac) by changing the value of a datasource variable called "System Number." This change is made possible by the fact that all database names for the 805 MHz Linac systems have a digit in the second character position of the name field which is the RF system at which

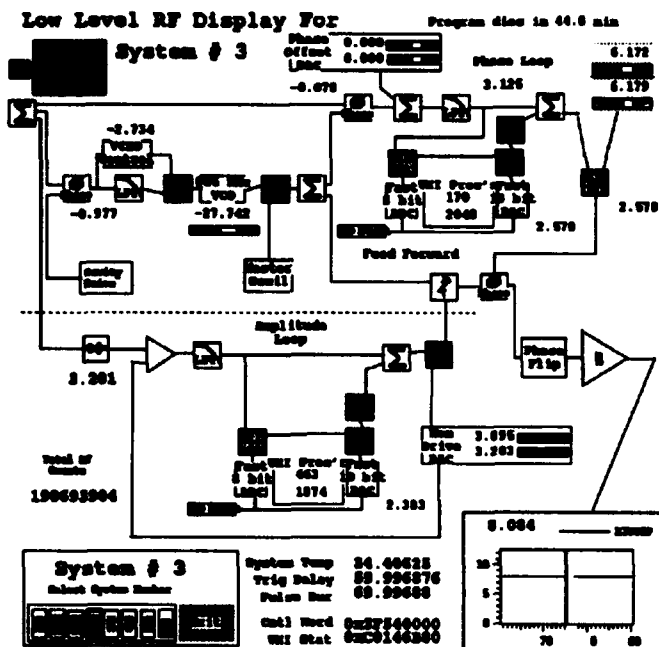


Figure 3, The low-level rf display program

that device is located. For example, M5MODV is the MODulator Voltage at system 5.

The clever user can add dynamics to the objects which have binary data for their dynamics, for example, show a closed switch when the value is greater than 0.5 (e.g., a value of 1), and an open switch when the value is less than 0.5 (e.g., a value of 0).

Five applications have been built using this applications builder for the 400 MeV Linac Upgrade. The most complicated application is for the low-level RF system, and the image of this program is shown in Figure 3. This view takes advantage of the dynamics possible with this program: note the switches which change position according to the value of a binary datum. Also (not shown), readings which are out of tolerance are red. The same application with a view for the overview of a single klystron is shown in Figure 4. Note the database description box. The other three programs are synaptic displays for the cavity water system, an overview of ten of the klystron systems and a simple flow-diagram for the modulator sub-system.

OPERATIONAL EXPERIENCE

The DataViews package has been very useful and effective. There has only been one physicist/programmer working on this project. DataViews makes it possible for a small group to produce high-quality graphical applications quickly and easily.

The engineers in the Linac Upgrade project have been particularly happy with these applications. This is

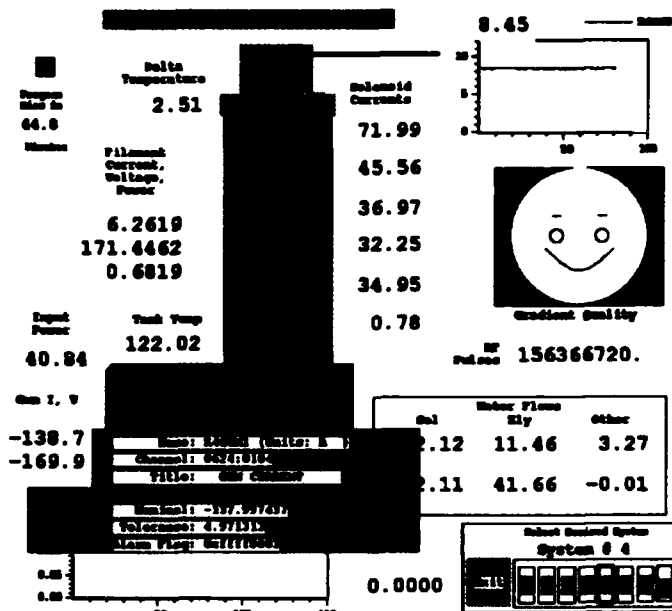


Figure 4, The klystron-overview display program; note the popup database description.

because they have produced Macintosh-generated block diagrams for their systems, which were easy to cast into DataViews with the dynamics attached.

The major limitation on the production of these displays has been (1) the artistic complexity of creating a satisfactory display and (2) the fact that very few people in the Linac Dept. have learned to use DV-Draw.

The Controls Group in our Accelerator Division does not have the liberty to experiment with these sorts of products on-line. Their top priority is to present a coherent and integrated look-and-feel to the Operations Staff. This sort of integration of the DataViews package would require a lot more effort than has been put in so far.

CONCLUSION

DataViews has been demonstrated to provide a simple and powerful means by which a small group of applications programmers can produce a very sophisticated graphics user interface for an accelerator.

REFERENCES

- [1] DataViews is a registered trademark of V.I. Corporation, Northampton, MA 01060.
- [2] "Upgrading the Fermilab Linac Control System" E. McCrory, et al., in Proceedings of the 1990 Linear Accelerator Conference, Albuquerque, pp 474-477.
- [3] DV-Tools Reference Manual for Release 8.0, September 1, 1990, VI Corporation, page Introduction-1.
- [4] Part of the work for John Palkovic's Dissertation: "Gabor Lens Focusing and Emittance Growth in a Low Energy Proton Beam," University of Wisconsin-Madison, July 22, 1991

The Graphic Environment for Transport Line - Control and Beam Diagnostics

S.Kuznetsov,
Kurchatov Institute, Moscow 123182, Russia

Abstract

This paper describes a computer program that is used in control of beam transport line from preinjector to booster ring of dedicated synchrotron radiation source "Siberia-2" (Kurchatov Institute, Moscow). The program combines the control of magnet structure, beam simulation and on-line beam monitoring. A graphical interface and mouse input provide an easy select and control of magnet elements. The program computes the beam transport using a first-order matrix formalism. The instantaneous display of the computed beam trajectories provides the necessary feedback to the user. The program displays information from beam position monitors in specific graphical window. The dialog windows contain list of elements, control buttons and list box with the real currents of power supplies. The operator interface and beam simulation are written in C++ language under MS-Windows.

I. INTRODUCTION

The dedicated synchrotron radiation source "Siberia" includes linac injector, small storage ring booster (450 MeV), main storage ring (2.5 GeV) and two transport lines. It is comfortable, when operator has interactive access to magnet elements control, beam diagnostic and simulation of electron-optical beam lines. Also, at the beginning stage of beam alignment procedure, the magnet structure of storage ring can be presented as transport line. The presented program allows to calculate particle motion trajectories and beam envelope. The program applies at commissioning stage and makes simple beam modeling "help", but difficult to use for development and optimization magnet system.

II. BEAM SIMULATION AND GRAPHICAL INTERFACE

The beam transport line structure consists of element's sequence. For each element user can to define name, type,

drift, magnet structure parameters and graphical image properties. The following element types are taken: bending magnets (in X and Z planes), drift spaces, quadrupoles (no skew), orbit correctors, beam position monitors. The special element type is a functional group of elements. The functional group allows to change some values of structure elements simultaneously. For example, independent control of displacement and slope of beam center at the end of transport line requires two correctors[1]. At that, kick of each corrector can be calculated:

$$A1 = K11*Y + K12*Y'$$

$$A2 = K21*Y + K22*Y'$$

where Y, Y' displacement and slope at X or Z planes.

The data base files (*.dbf) describe the beam transport line structure and functional group's spreadsheet. The program menu item "File" defines standard file exchange procedures. Beam transport line structure displays in graphical window after reading data base files. At any time user can be select structure part from list of elements. The beam position and envelope are calculated for three hundred points in selected part of magnet structure. This allows to increase accuracy for short part of structure (one or two elements) and to plot graphics in detail.

User sets initial conditions X, X', Z, Z', dp/P for computing the particle motion trajectories. To compute beam envelope Twiss parameter's phase plane ellipse α , β and emittance ϵ are defined. The program menu item "Options" contains edit control window and "listbox" with initial condition parameters. The first-order matrix method applies for computation[2]. Figure 1 shows modeling results for electron beam trajectories in the transport line from linac to booster storage ring "Siberia-1".

The trajectories are displayed in red and blue colors for X and Z planes. The "begin" and "end" values of displacement and slope present in digital form. The "Control" dialog box window may be used for new setting of elements (Fig. 2). Window contains special control buttons and listbox with the beam transport line elements. The mouse input is used for element and value of increase selection. User can to change element setting by "+", "-", "Return" buttons and defines new values of increase. When the optical structure is changed, program computes new trajectories. In the graphical window new

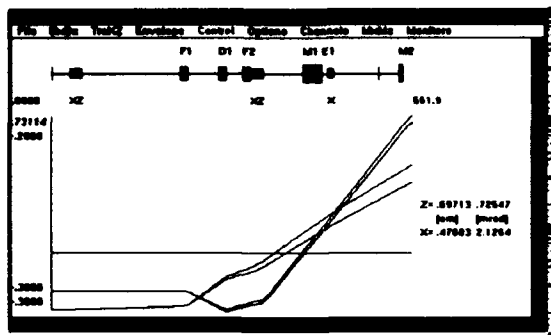


Figure 1: The beam trajectories in the transport line from linac to booster ring "Siberia-1".

trajectories display in dark color, previous in light. If user edits the initial conditions X , X' , Z , Z' or dp/P in trajectory's simulation mode the new calculations are performed. The beam trajectories are presented in Fig. 1 after user changes the strength quadrupole $F1$ and initial displacement in X and Z planes non zero. User can to edit element, which is not presented in the graphical window, and the new computed results can also be displayed. Similarly, the beam envelope mode allows to control and display transport line optical structure.

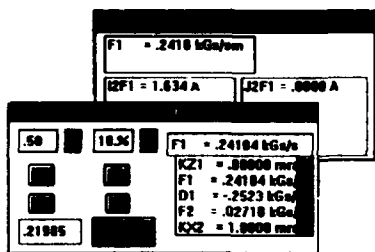


Figure 2: The console windows.

III. ON-LINE CONTROL AND DIAGNOSTIC

The special data base describes control and monitoring channels. File defines names, coefficients, service information for power supplies system for each magnet element. In the case of menu item "Channels" is selected, the program performs operative control of power supplies as well as the beam simulation. The window "Channels" shows list of control and measurement parameters for element or functional group. Program is realized data exchange with the control computer, sends steering currents of power supplies and reads actual values of current. At background of Fig.2 on-line control window is presented.

The additional graphical window displays beam position monitors information. Position monitors can be selected

from transport line structure using "Monitors" menu. The color marker plots beam position in X , Z plane. The program presents calculated X , Z values for each monitor, and the real beam displacement values can be read from diagnostic control computer. These values are displayed in different colors. If the profile grid monitors are used in transport line, the control computer sends center of gravity and measured profile width of beam. In this case, real beam position may be display in ellipse form at X , Z plane. Figure 3 shows program results for two selected beam position monitors.

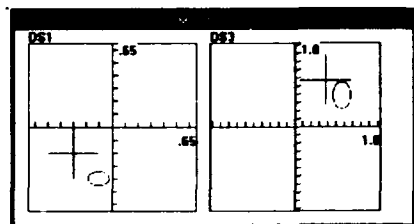


Figure 3: Calculated and measured beam position monitors information.

IV. APPLICATION

The program has been used to operate with transport line from 65 MeV linac to the storage ring "Siberia-1". Interactive graphic provides effective operator environment for commissioning. It is planned also to control transport line from booster ring to the 2.5 GeV main storage ring "Siberia-2". MS-Windows and C++ development environment allows to create "window-oriented" user interface.

REFERENCES

- [1] E.Levichev, The Beam Transport Lines for "Siberia" Complex. *BINP Internal Report*, 1991 Novosibirsk.
- [2] K.L. Brown, R.V. Servranckx, Optical modules for circular accelerator design. *NIM A258 (1987)*, pp.480-502.

An I/O Subnet for the APS Control System – The BITBUS Universal Gateway*

G. J. Nawrocki, N. D. Arnold, M. G. Hoffberg, J. R. Winans, S. J. Benes
Argonne National Laboratory
Advanced Photon Source
9700 South Cass Avenue
Argonne, Illinois 60439

Abstract

The Advanced Photon Source (APS) control system is based on a distributed topology of microprocessor-based Input/Output Controllers (IOCs). Since the cost effectiveness of placing an IOC near every point where an interface to the control system is required may be prohibitive, I/O subnets implemented via message passing network protocols are utilized. For greatest flexibility, such a subnet must support connections to equipment via discrete I/O points, connections to standard interfaces such as GPIB and RS232, and be a practical network for custom-designed interfaces to intelligent equipment. This paper describes the BITBUS Universal Gateway (BUG), a device which supports the different interfaces mentioned above with a connection to a single BITBUS distributed subnet. The BUG utilizes an interchangeable set of circuit boards, which allow for a commonality among interface points, and the ability to use commercially-available modules for I/O. This approach also circumvents several limitations of GPIB and RS232, which restrict their use in industrial, electrically harsh environments, via an implementation of the BITBUS protocol over optical fibers.

I. SUBNETS IN THE APS CONTROL SYSTEM

The APS control system provides for VME-based Input/Output Controllers (IOCs) to be distributed throughout the facility and interconnected via Ethernet to one another and also to UNIX-based Operator Interface (OPI) consoles. Although this distributed architecture allows for intelligent processors near the major subsystems, I/O subnets are frequently required to interface directly to the equipment and communicate I/O information to the nearest IOC. [1]

II. CURRENT INTERFACE PROBLEMS

Currently GPIB (IEEE-488) and RS232 interfaces are being used to interface instruments to the APS control system. These interfaces have severe limitations when used in an industrial, non-office type environment for computer control systems. GPIB offers no error detection mechanisms, no ground isolation, and severe distance limitations. Although both fiber optic and twisted pair extenders are available for GPIB they are cost inefficient. RS232 offers no ground isolation, severe distance limitations, and exists with a single node master/slave topology. Again, extenders and multidrop RS232 network solutions are available, however, their repeated use can be expensive.

*Work supported by U.S. Department of Energy, Office of Basic Energy Sciences under Contract No. W-31-109-ENG-38.

Basic binary and analog I/O have obvious distance and noise immunity problems when interfaced to a control system. Currently the Allen-Bradley 1771 series I/O modules provide remote interfacing for these types of signals in the APS control system. Although effective, it is best used for a multitude of signals as its use becomes cost prohibitive when used with just a few raw binary or analog signal points. An additional complication with the Allen-Bradley solution is that the network and I/O chassis are proprietary designs of Allen-Bradley. Modules cannot be customized to meet the unique requirements of the APS control system.

III. THE BITBUS SUBNET

An ideal subnet for the APS control system should provide a distributive, homogeneous solution to differing control interface topologies. The design should be based upon a non-proprietary commonly accepted network which provides the ability to communicate control signals to multiple nodes, over distances up to several hundred meters, and in electrically harsh environments. The subnet must provide a "gateway" for GPIB, RS232, and raw binary and analog I/O signals. BITBUS[†] was selected as the subnet of choice for this type of interface to the APS control system. [1]

IV. THE BITBUS UNIVERSAL GATEWAY

To implement BITBUS as a subnet in the APS control system, a BITBUS slave node was developed to meet the previously defined criteria. This instrument has taken the form of the BITBUS Universal Gateway, or BUG.

A. Hardware Description

The BUG acts as a slave node on the BITBUS subnet and provides a communication link between BITBUS protocol and other computer-signal interfaces such as GPIB, RS232, and discrete binary and analog I/O (see Figure 1). The BUG is housed in a commercially available plastic enclosure measuring 2.25H x 5.08W x 5.25L. Located on this small enclosure are connections to the BITBUS subnet, I/O points, and power supply. There are red and green CPU status LEDs, and a series of eight diagnostic LEDs which can be written with a byte of data for additional status indication. Power is generally supplied by a small "calculator type" wall plug adapter or brick type power supply. The entire part cost for each BUG node is under \$400.

B. The BITBUS Interface Board

The BITBUS interface board is the BUG's link to the BITBUS subnet. Communication over the BITBUS subnet in the APS control system is self clocked at a speed of 375Kb/s. Original

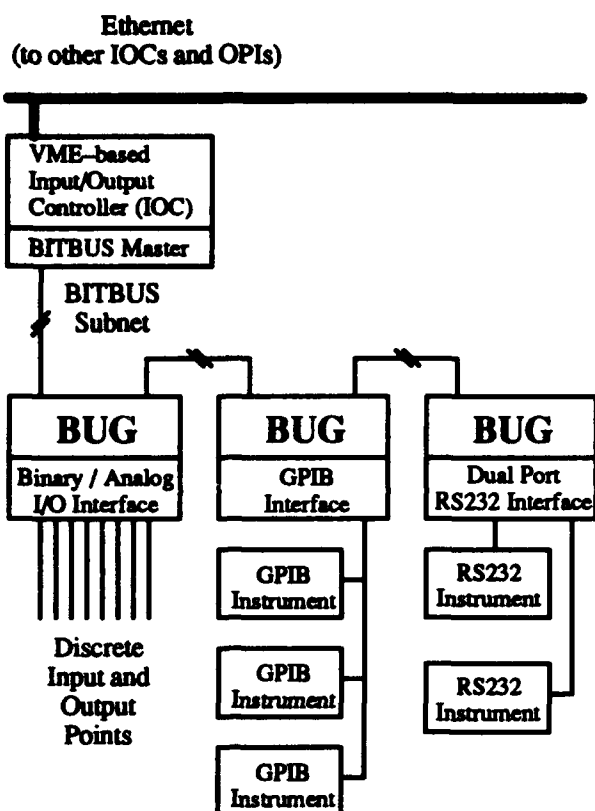


Figure 1. BITBUS Subnet at the Advanced Photon Source

nally this separate board for the BITBUS interface was chosen so that communication could be implemented over either a "twisted pair" RS485 subnet, or a fiber optic interface. The RS485 subnet has been abandoned at the APS in favor of the more noise immune and cost effective fiber optic interface.

The fiber optic BITBUS interface card is constructed using transmitters and receivers with AT&T ST type connectors. These bayonet-style connectors provide a simple and accurate fiber connection. The BUGs in a fiber optic BITBUS subnet are connected in a daisy chain configuration, linked from the VME IOC BITBUS master, and serially one after the other with duplex (two fibers per cable) fiber optic cable. The APS BITBUS fiber optic subnet utilizes standard 62.5/125 μ m fiber optic cable.

C. The BITBUS Controller (CPU) Board

The CPU board is the middle board of the BUG three-board configuration. It contains the Intel 8044 BITBUS enhanced microcontroller, data memory, code memory, and additional support circuitry. The 8044 provides both the processing and communication ability of the BUG. Unique firmware for each type of interface resides in the external code memory of the BUG. The external code memory of the BUG uses either a 256Kbit RAM chip, or an identical size (E)PROM chip. The type of memory is selected by a configuration jumper. Software may be downloaded over the BITBUS link to the external code RAM, which is useful for BUG software development. When suitable code is developed, a PROM, or EPROM may be created for more permanent use.

D. The I/O Board

The I/O board is the BUG's interface to the controlled equipment. The I/O board interface was chosen to be the iSBX[†] (single board extension) bus. Since the iSBX bus is an Intel and IEEE standard (IEEE 959-88) there are many such I/O boards commercially available. These boards, however, can often be made "in house" at a fraction of the cost of commercially available products. Currently at the APS there has been "in house" design of both hardware and software for the following boards: a single port GPIB interface with the ability to control 15 GPIB instruments, a dual port RS232 interface, and a discrete binary and analog signal interface with 16 optically isolated binary inputs, eight optically isolated binary outputs, four 12-bit analog inputs, and two 12-bit analog outputs.

E. The Interface to the APS Control System

The BITBUS subnet interface to the APS control system is accomplished through the BITBUS master. The master is a modified BITBUS node with an interface to the VME host computer bus. Currently the BITBUS subnet master in the APS control system is the Xycom XVME-402 VME module modified for use with the APS BITBUS optical fiber subnet.

V. THE GPIB BUG AT THE APS

A basic timing study was done on GPIB message passing over the BUG link compared to GPIB message passing using the National Instruments GPIB 410 VME module. The GPIB instruments being controlled were four identical Hewlett Packard 34401A digital multimeters. The four multimeters were initially connected directly to the GPIB 1014 VME module and a series of read-back commands were sent to them. Next, the four multimeters were connected to a single BUG which in turn was connected to the VME IOC via the BITBUS subnet. The BUG showed no significant decrease in data throughput for this read command.

Next, two BUGs were connected to two multimeters each, and placed on the same BITBUS subnet. Following that, four BUGs were each connected to one multimeter each and placed on the same BITBUS subnet. There was an increase in read-back command data throughput in each case. The single BUG per multimeter configuration even showed faster read-back data throughput times than the single GPIB 1014, four multimeter configuration. This increase in read-back data throughput is due to the fact that when a GPIB instrument is sending data back to the control system using the GPIB bus, it takes command of the bus, thereby allowing no other instruments to use the bus until it is finished. The remaining instruments must wait in turn for the previous instrument to send its data back to the control system before they may respond. When multiple BUGs are used, the per instrument distribution on the GPIB bus decreases. Commands and responses may be sent to, and read back from, multiple BUG-isolated GPIB instruments at the same time. The BUG will in turn relay the data to the control system. Since the BITBUS subnet does not need to wait for individual node responses before commands are sent out, data throughput increases.

The multimeter used for the timing study was a relatively quick responding instrument. Far more significant increases in

data throughput were evident when instruments, which upon receiving a command take several seconds to complete a calculation or data read before replying, were isolated behind GPIB BUGs on the BITBUS subnet.

A disadvantage to using the BUGs was discovered when interfacing to GPIB instruments that send several hundred data bytes back to the control system in response to a single read command. The current implementation of the VME BITBUS master limits each BITBUS message to 13 data bytes. When an instrument such as an oscilloscope was connected to a BUG and a waveform was sent back to the control system, the limited message size required a multitude of BITBUS messages to be sent to the control system as the result of a single read command. This, combined with the limited speed of the BITBUS subnet, produced a bottleneck.

The BUG, in its current state, is not recommended for such large data transactions. Fortunately, the vast majority of instruments in the APS control system respond with fewer than 50 bytes as the result of a single read command. For these applications the BUG is well suited.

Simple GPIB write commands that implement instrument control and require no response are a different issue. The GPIB 1014 VME interface is almost eight times faster than an individual BUG interface for sending this type of command. However, the data throughput for GPIB write commands remains constant on the GPIB 1014 regardless of the number of GPIB instruments added to the link. Write commands to GPIB instruments, isolated behind GPIB BUGs, show a near linear increase in data throughput as GPIB instruments connected individually to BUGs are added.

VI. THE RS232 BUG AT THE APS

In addition to the multidrop and distance extension abilities of running RS232 over BITBUS, another advantage was discovered. RS232 instruments are often very different in both their command sets and how they respond to commands. For instance, some instruments may or may not echo each received byte back

to the control computer. Some units respond to commands after a carriage return, others need the command placed in parentheses. A variety of instruments return data with a carriage return and/or line feed, others use odd termination or data return framing characters. For these specialized cases, unique software for each type of controlled instrument may be created for the BUG. Despite this additional software design work, there are distinct advantages to allowing a universal version of RS232 software to reside at the point of the control system IOC.

The BUG can also be given the ability to remove worthless data bytes or interpret data sent by an RS232 instrument into a more concise package to be sent to the control system. For these reasons, the RS232 BUG is currently the only recommended method for RS232 instrument interfacing to the control system.

VII. CONCLUSION AND FUTURE PLANS

The BUG has proven itself as an extremely popular method of GPIB, RS232, and discrete I/O signal interfacing to the APS control system. Already in this early stage of construction at the APS, as many as 35 BUGs are in operation in various test stands and sections of the accelerator. Optimization of the BUG hardware and software will continue by reducing the size of the BUG to a two-board configuration due to the exclusive use of the fiber optic BITBUS interface, investigating faster VME BITBUS masters, possibly increasing the size of the BITBUS message to greater than 13 bytes, and adding more supported I/O modules.

VIII. REFERENCES

- [1] N.D. Arnold, G.J. Nawrocki, R.T. Daly, M.R. Krammer, W.P. McDowell, "I/O Subnets for the APS Control System," *Proceedings of the 1991 IEEE Particle Accelerator Conference*, pp. 1496-1498, 1991.

† BITBUS and iSBX are registered trademarks of Intel Corporation and its affiliates.

Status and Design of the Advanced Photon Source Control System

W. McDowell, M. Knott, F. Lenkszus, M. Kraimer, N. Arnold, R. Daly

Advanced Photon Source, Argonne National Laboratory

9700 South Cass Avenue Argonne, Illinois 60439

Abstract

This paper presents the current status of the Advanced Photon Source (APS) control system. It will discuss the design decisions which led us to use industrial standards and collaborations with other laboratories to develop the APS control system. The system uses high performance graphic workstations and the X-windows Graphical User Interface (GUI) at the operator interface level. It connects to VME/VXI-based microprocessors at the field level using TCP/IP protocols over high performance networks. This strategy assures the flexibility and expansibility of the control system. A defined interface between the system components will allow the system to evolve with the direct addition of future, improved equipment and new capabilities.

I. INTRODUCTION

The APS accelerator control system is a distributed system consisting of operator interfaces, a network, and interfaces to hardware.

The operator interface is a UNIX-based workstation with an X-windows graphical user interface. The workstation may be located at any point on the facility network and maintain full functionality. The user has the ability to generate and alter control displays and to access the alarm handler, the archiver, interactive control programs, custom code, and other tools.

The TCP/IP networking protocol has been selected as the underlying protocol for the control system network. TCP/IP is a commercial standard and readily available from network hardware vendors. Its implementation is independent of the particular network medium selected to implement the controls network. In the development environment copper Ethernet is the network medium; however, in the actual implementation a fiber-based system using hub technology will be utilized. The function of the network is to provide a generalized communication path between the host computers, operator workstations, input/output crates, and other hardware that comprise the control system.

The crate or input/output controller (IOC) provides direct control and input/output interfaces for each accelerator subsystem. The standard crate uses either the VME or VXI standards, a Motorola 68040 processor, network communications, and a variety of signal and sub-network interfaces. The 68040 processor provides the crate with the intelligence to allow it to run its software autonomously with respect to all other devices in the system. The software running in the crate hides hardware dependencies from the high-level software running on the workstation. There are approximately 45 crates used in the accelerator control system with plans for about 50

additional crates controlling insertion devices. A real-time operating system, VxWorks, is run in the crate central processing unit (CPU) to provide the basis for the real-time control.

Design challenges for the group implementing the APS controls included protecting investment from rapid obsolescence and designing into the system the ability to quickly incorporate improved equipment and software. The APS approach to the solution to these problems is to use a distributed control system and standards, to provide "tools" to the greatest extent possible instead of custom programming, and to collaborate with other laboratories and groups whenever possible.

II. STANDARDS

The use of standards allows vendor independence, a migration path for future advances in technology, and the use of commercially available "tools" when these tools meet requirements. A modular approach to design supports both hardware and software modularity in crates, workstations, I/O modules, etc. Standards also make it possible to share accelerator control software and collaborate with other laboratories. Before hardware standards, each facility designed and built its own hardware. This custom hardware also required custom software. Today, most new facilities are selecting hardware based upon industrial standards and thus sharing software has become possible.

III. COLLABORATION

The advantages of collaboration are obvious. Collaboration reduces the need to start from scratch when a majority of the system requirements are not unique. Collaboration also takes advantage of existing "tools" that meet standard requirements and has the effect of freeing up staff to work on "non-standard" requirements. EPICS collaborators now include Los Alamos National Laboratory, Lawrence Berkeley Laboratory, and the Superconducting Supercollider Laboratory.

Prior to the Accelerator Control Toolkit Workshop in 1988 [1] the APS controls group had decided to examine existing control systems with the aim of determining if they could be used at APS. After studying several systems we decided to pursue a collaboration with the AT-8 group at Los Alamos National Laboratory (LANL).

APS received the first version of the LANL Ground Test Accelerator Control System (GTACS) software in late 1988, the controls and computing group at Argonne APS, with the cooperation of Los Alamos AT-8, suggested and implemented several changes to the structure of the core software which facilitated the incorporation of many different hardware devices without recompiling the complete code. This new, extensible, version of the code was then named EPICS (Experimental Physics and Industrial Control System) to distinguish it from the original GTACS. GTACS is still in use at Los Alamos and

*Work supported by U.S. DOE Office of Basic Energy Sciences under contract no. W-31-109-ENG-38.

several other sites.

Argonne, with the cooperation of Los Alamos, has taken a lead role in developing and applying EPICS tools. Los Alamos has taken the role of coordinating the development efforts between laboratories as well as maintaining and improving sections of the system software. The Advanced Photon Source control system has been completely developed using EPICS tools. The original applications at APS were the radio frequency (RF) test stand and the linac test stand. Today the linac itself is being installed and is completely controlled by the EPICS system. As a further example of the APS commitment to EPICS, it has been decided that EPICS will be the system used to develop and run all ANL-developed experimental beamlines and front-end devices at the APS.

Continuing development of the software is foreseen. APS plans to improve the system by adding new functionality when required by applications. We expect other laboratories will also add functionality to the system.

IV. GENERAL DESIGN FEATURES OF EPICS

EPICS-based control systems include operator interfaces which consist of multi-screen UNIX workstations using a graphical user interface based on the X-windows Motif model. The selection of a workstation implementation based on X-windows for the operator interface allows field instruments, video tools and the interface for controls and data acquisition, and the software development effort to take place in the same environment. It is now possible to locate consoles in offices, labs, seminars, and wherever they are required in the field. The operator can select by list, diagram, flow chart, and map as well as the more standard text-based selection menus. The workstation supports external software interfaces including: Wingz, Nodal, Mathematica, accelerator modeling codes, Fortran, C, and any application software a physicist may write. Auxiliary displays using X-window terminals and projection and large screen displays in the main control room and seminar rooms are easily implemented using commercial equipment.

V. SPECIFIC EPICS FEATURES

EPICS provides a number of tools for creating a control system. This minimizes the need for custom coding and helps ensure uniform operator interfaces.

An arbitrary number of IOCs and operator interfaces (OPIs) can be supported and, as long as the network is not saturated, no single bottleneck is present. If a single IOC becomes saturated, its functions can be spread over several IOCs. Rather than running all applications on a single host, the applications can be spread over many OPIs.

A. EPICS Core Software

EPICS consists of a set of core software and a set of optional components. The core software, i.e. the components of EPICS without which EPICS would not function, are: channel access-client and server software, database scanners-monitors, the database configuration tool (DCT), and the source/release control. All other software components are optional.

B. Channel Access

Channel access provides network-transparent access to IOC databases. It is based on a client-server model. Each IOC provides a channel access server which is willing to establish communication with an arbitrary number of clients. Channel access client services are available on both OPIs and IOCs. A client can communicate with an arbitrary number of servers. [2]

C. Database

The heart of an IOC is a memory-resident database together with various memory-resident structures describing the contents of the database. EPICS supports a large and extensible set of record types, e.g. ai (Analog Input), ao (Analog Output), etc. Each record type has a fixed set of fields. Some fields are common to all record types and others are specific to particular record types. Every record has a record name and every field has a field name. The first field of every database record holds the record name, which must be unique across all IOCs attached to the same TCP/IP subnet. A number of data structures are provided so that the database can be accessed efficiently. Because they access the database via database access routines, most software components do not need to be aware of these structures.

D. Database Access

With the exception of record and device support, all access to the database is via the channel or database access routines. Database scanning is the mechanism for deciding when to process a record. Four types of scanning are possible: periodic, event, I/O event, and passive.

A request can be made to process a record periodically; a number of time intervals are supported. Event scanning is based on the posting of an event by any IOC software component. The I/O event scanning system processes records based on external interrupts. An IOC device driver interrupt routine must be available to accept the external interrupts.

E. APS-Developed EPICS Tools

The Motif-based Display Editor/Manager Tool (MEDM) allows staff to easily create, configure, and modify displays and then activate and connect displays to actual hardware. The display editor portion of MEDM provides process connections via an interactive display editor/control. Editing/drawing commands are used to build displays with little or no custom programming required to build applications. Process connections to the data are entered as process variable name and field name; no other knowledge of the hardware configuration is required. This tool allows the designer to modify any aspect of the display element, as well as copy, align, and group display elements. Standard drawing tools can be used to create backgrounds which can then be imported into MEDM via GIF files. The alarm handler provides the ability to display alarm messages in a hierarchical manner. The backup and restore tool (BURT) stores and retrieves data from selected channels. A database configuration tool (DCT) allows the application designer to configure the run-time database. The knob manager (KM) allows the operator to attach physical knobs to process variables.

Third party software now interfaced to EPICS via channel access calls include Wingz, Nodal, DevTest, Mathematica and an interpretative version of C. An automatic cavity conditioning system has been developed using a Mathematica routine running under EPICS.

VI. SYSTEM FEATURES

The equipment interface or input/output controller is based on VME/VXI standard and uses a Motorola 68040 microprocessor for control and a fast, real-time kernel, VxWorks, as the operating system. No local disk drive is required in this system. The software image can be down-loaded from a file server or from on-board PROM. The system also supports task priorities and interrupts as well as custom code. The APS control system will use about 45 such crates. More than twenty VME input-output modules are currently supported. Others will be supported as they become available and desirable.

Most information preprocessing is performed at this level. Sequential and control-loop operations can be performed. In this way, maximum benefit is gained from the many IOC processors operating in parallel.

Hardware I/O can be generalized into several types: analog and binary I/O, stepper motor, and sub-network connections. Hardware records contain information for run-time processing including scaling, engineering units, hardware address, and scanning information. The process database contains parameters such as scan requirements, address of I/O, engineering unit conversions, alarm limits, control parameters, current value, etc. for each defined process variable. Records can be linked together to implement complex algorithms. The database scanner scans database records and updates dynamic fields (i. e. value, alarm status, severity, etc.). Data conversions including linear, piecewise linear, and value-to-state are supported. Alarm checking for limit violations, state violations, hardware communication errors, and alarm severity is supported. Binary and analog I/O are provided through the database. Analog input can be smoothed, and analog output can be either incremental or positional and the output rate of change can be specified. Multi-bit (16 states) and single binary I/Os are supported.

All I/O fields can be connected to a hardware device or another database element (calculator, PID, fan-out to several devices). Timing signals, motion control, and transient digitizers are supported through the database.

Stepper motor records can get desired position/velocity input from user or other data, provide positional or velocity mode operation, provide position feedback through an encoder or another database record, and allow simple closed-loop position maintenance. Limit switches are supported through indexers or other database records.

General purpose calculations, a PID algorithm, and a signal selector are supported to provide closed-loop control and data filtering. The calculation record supports up to six sets of input, C language expressions, algebraic operations, relational operations, boolean operations, and trigonometric functions. The PID algorithm allows a user interface optional database

connection for setpoint, proportional, integral, and derivative gains; incremental or positional output; and anti-windup and reset on the integral term.

VII. NETWORKS AND SUBNETS

The communication network will be a combination of FDDI, Ethernet over fiber, and Ethernet over copper. Future plans call for the introduction of 100 MB Ethernet and ATM when these protocols have been standardized. The cable plant will be installed using fiber with a hub and spoke topology. All fibers will terminate in the main control room. This technique will allow APS to tailor network bandwidth as required by the application running in a particular IOC.

Subnets can be driven from the IOC. GPIB, RS-232, and Bitbus [3] are presently supported. These subnets allow various instruments and low-cost, few-point interfaces to be connected and controlled. The Bitbus can be used to make remote, multidrop connections to GPIB and other interface subsystems.

VIII. PRESENT STATUS

All seven of the linac IOCs are now installed and have been successfully tested. All subnets have been installed and are being tested. The linac timing system installation and testing is complete. Local consoles, implemented with X-terminals, are now operational in the klystron gallery. File servers and OPIs have been installed in the injector control room to support linac commissioning. An FDDI link between the Building 362 development area and the injector control room has been installed and is operational. This allows continued controls development and supports network growth into the final APS site. Positron accumulator ring (PAR) installations will start in June 1993.

EPICS tools in development include a graphical process-variable links tool which will reduce the complicated process of creating and documenting multi-parameter control processes. A generalized drag-and-drop process has been developed to facilitate the transfer of process-variable names between EPICS tools. The sequencer tool has been ported from the IOC to the OPI using a Posix threads library.

IX. REFERENCES

- [1] Accelerator Automation Application Toolkit Workshop, sponsored by AT Division and MP Division, Los Alamos National Laboratory and CERN, Geneva, 31 October - 4 November, 1988.
- [2] J. O. Hill, "Channel Access: A Software Bus for the LAACS," in *Accelerator and Large Experimental Physics Control Systems*, D. P. Gurd and M. Crowley-Milling, Eds., ICLAEPCS, Vancouver, B. C., Canada, pp. 288-291, 1989.
- [3] G. J. Nawrocki, N. D. Arnold, M. G. Hoffberg, J. R. Winans, S. J. Benes, "An I/O Subnet for the APS Control System, The BITBUS Universal Gateway," these proceedings.

Controlling the Third Harmonic Cavity During Focus Free Transition Crossing in the Fermilab Main Ring

M.A. Martens

Fermi National Accelerator Laboratory, P.O. Box 500, Batavia, Illinois 60510*

Abstract

Crossing transition with an additional third harmonic cavity [1] in the Fermilab Main Ring requires techniques which are different from those used previously at Fermilab. The implementation of these new techniques has involved the addition of new components to the low level RF system [2] and a new applications program to control these new components. After an introduction to the basic theory, this paper describes the applications program and its relation to the low level RF hardware.

I. INTRODUCTION

The use of a third harmonic cavity during the focus free transition crossing has required additional low level hardware and new controls. This paper describes the basic theory of focus free transition crossing as well as the basic low level and controls. Details of the low level are described elsewhere [2]. An applications program was also written to control the hardware used and is discussed briefly in the final section.

II. BASIC THEORY

Implementing the third harmonic transition scheme involves controlling the amplitudes, phases, and frequencies of the 53 MHz and 159 MHz cavities during a short time near the transition crossing [3]. During this time the beam is accelerated using a third harmonic cavity (159 MHz) in addition to the normal 53 MHz cavities. By choosing phases of 90 and 270 degrees for the 53 MHz and 159 MHz RF voltages and adjusting the ratio of amplitudes, V_1 and V_3 , it is possible to produce an RF waveform which is approximately constant for several nanoseconds. The ratio of the amplitudes, $V_3 \cong 0.129V_1$, is chosen to optimize the width and uniformity of the flat portion of the waveform. The particles in the bunch are accelerated by this flat portion of the voltage waveform and therefore all the particles

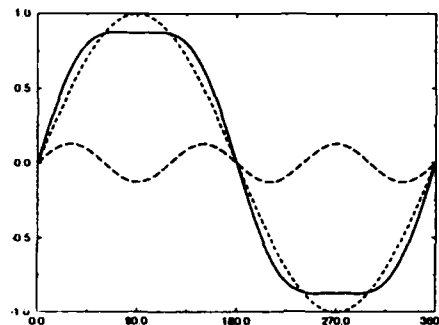


Figure 1: First and third harmonic waveforms combined to give a nearly constant waveform for several nanoseconds. During transition the beam is at the center of the flat portion of the waveform.

are accelerated at the same rate. This is illustrated in figure 1.

Since the acceleration rate is determined by the Main Ring ramp rate, the voltages of the 53 MHz and 159 MHz cavities must also satisfy the relationship

$$V_{acc} = \dot{E}/f_{rev} = V_1 - V_3 = (1 - .129)V_1 \quad (1)$$

where \dot{E} is the Main Ring ramp rate in MeV/sec and f_{rev} is the revolution frequency. Given a time in the Main Ring cycle and using information from the programmed energy ramp, the ramp rate and revolution frequency can be calculated. The voltages V_1 and V_3 are then uniquely determined.

To provide the correct voltages for the transition crossing means using some new techniques and new LLRF hardware in addition to the 159 MHz cavity. In normal Main Ring operation (without the third harmonic cavity) the phase of the RF cavity is controlled by a feedback loop using the radial position error as an input. This keeps the accelerating voltage at the correct value, $V_{acc} = V_1 \sin(\Phi_s)$ by adjusting the phase angle assuring that the beam has the correct energy.

When using the third harmonic cavity scheme, however, the phases of V_1 and V_3 are fixed at 90 and 270 degrees. Therefore the usual radial position phase feedback cannot

*Operated by Universities Research Association, Inc. under contracts with the U.S. Department of Energy

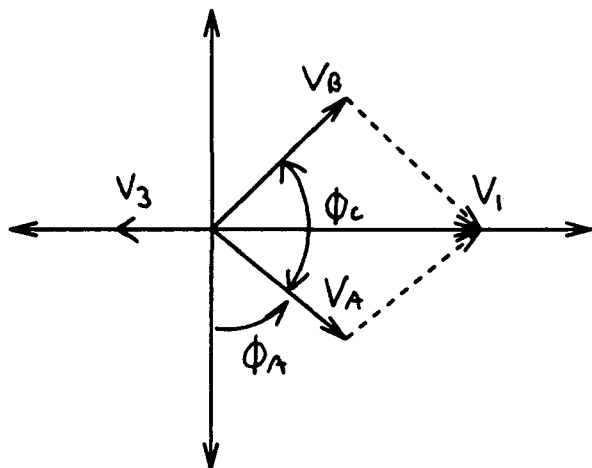


Figure 2: Relationship between different vector voltages during transition. By adjusting the cone angle Φ_c the amplitude of V_1 can be adjusted without changing its phase.

be used. Instead, the amplitude of the 53 MHz voltage, V_1 , is modulated in response to errors in the radial position of the beam. To accomplish the amplitude modulation, the 53 MHz cavities are divided into two groups, the A and B groups, and the phase of each group is controlled individually. The net 53 MHz voltage is then the vector sum of the A and B group voltages.

$$\vec{V}_1 = \vec{V}_A + \vec{V}_B. \quad (2)$$

To simplify matters it is assumed that the amplitudes of the A and B group cavities are the same, $V_A = V_B$, and that the phases of the cavities are such that $\Phi_B = 180 - \Phi_A$. A cone angle, Φ_C , is also defined as the angle between the A and B groups of cavities

$$\Phi_C = \Phi_B - \Phi_A. \quad (3)$$

The relation of these components is shown in figure 2. Using these definitions, equation 2 simplifies and the amplitude of the 53 MHz RF is given by

$$V_1 = V_A \sin \Phi_A + V_B \sin \Phi_B \quad (4)$$

$$= 2V_A \cos(\Phi_C/2) \quad (5)$$

With the cavity phases and amplitudes as described, the accelerating voltage is maintained at the correct value by modulating the cone angle in response to the radial position error. If the accelerating voltage is too large then the cone angle is increased and as a result the net 53 MHz voltage is decreased. The change in the accelerating voltage is given by $\Delta V_{acc} = -V_A \sin(\Phi_C/2) \Delta \Phi_C$.

Having described the basic theory, the next section describes some of the hardware installed to implement the scheme.

III. LLRF HARDWARE

In order to implement the third harmonic transition crossing scheme, some new hardware and LLRF modules were

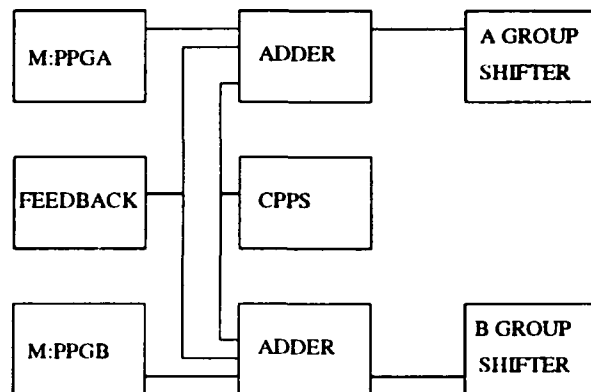


Figure 3: Schematic of the low level phase control of the RF cavities.

designed and installed. This section schematically describes that part of the hardware to which the applications program relates. When designing the LLRF modifications and the applications program for the third harmonic experiment the general philosophy was to leave as much of the present LLRF undisturbed as possible making it easier to return to normal operations when the third harmonic experiments are completed.

Since the transition crossing scheme lasts for several milliseconds, the voltages and phases on the 53 MHz and 159 MHz cavities must be programmed as a function of time. This is accomplished by using a set of CAMAC 465 and CAMAC 467 Ramp Controller modules. The 465/7 cards are programmable voltage ramps as a function of time with a time resolution of 100 μ s. The relationship of these cards to the LLRF and to the operation of the transition crossing is described below.

In normal Main Ring operations the phases of the A and B group cavities are controlled via the Counterphase Shifter modules. Usually these modules are driven by the Counterphase Program Select (CPPS) module. For the third harmonic experiment, however, a digital adder box was built and installed. The Adder box is placed between the CPPS module and the Shifter modules. This box has three 12 bit digital inputs and one 12 bit digital output for each of the A and B group cavities. The output is the digital sum of the three inputs. One of the inputs is the output of the CPPS. (Therefore, if the other two inputs are zero the Main Ring is operated as normal.) The second input is the digital output of a CAMAC 467 card labeled M:PPGA. This card is programmed to shift the phase of the A cavities to their desired positions during the transition crossing. The third input is from the radial position feedback loop. This input goes to both the A and B inputs of the digital adder box but with opposite signs. (See figure 3.) Therefore any input from the radial position error has the effect of opening or closing the cone angle.

During transition crossing experiments, the normal transition phase jump from the CPPS is disabled. The outputs of M:PPGA and M:PPGB start at zero degrees before the

transition crossing. When the third harmonic transition scheme is initiated the M:PPGB "jumps" and M:PPGA is adjusted to give the correct cone angle. After the transition crossing is completed, the M:PPGA "jumps" and both M:PPGA and M:PPGB output the same value until the end of the Main Ring cycle. Having both M:PPGA and M:PPGB set to some value after the transition jump serves the same purpose as the transition phase jump that the CPPS supplies during normal Main Ring operations.

Also during normal Main Ring operations, the amplitude of the 53 MHz cavities are controlled by the output of a CAMAC 365 Ramp Controller module labeled M:M3APG. In order to control the amplitude of the 53 MHz cavities during the transition crossing, the output of a CAMAC 465 card labeled M:DHV1 is summed with the output of the 365 M:M3APG card and the summed output is used to drive the cavities. The hardware was configured in this manner to facilitate the return of operations back to the normal mode. By adding the M:DHV1 card the amplitude of the 53 MHz cavities can be controlled without modifying the programmed voltage for normal operations.

The amplitude of the 159 MHz cavity is controlled by a CAMAC 465 card and by feedback control. The output of the 465 card labeled M:HV3PG provides the feed forward part of the amplitude control. The frequency of the 159 MHz is controlled by a 159 MHz oscillator which is essentially a frequency tripler of the 53 MHz signal. The amplitude feedback and frequency control are described elsewhere.

Another function of the applications program is to control the current in the ferrite tuner of the 159 MHz cavity. This current is controlled using another CAMAC 465 card M:FBI3. A table of current versus time is entered by the user into the program which then loads the 465. Since this data is saved in a disk file, it can be conveniently recalled and reloaded as needed.

IV. APPLICATIONS PROGRAM

An applications program was written using the standard library of controls subroutines used at Fermilab. The program makes the computations outlined in section II then loads the CAMAC 465/7 cards accordingly. As a dependent variable we chose the cone angle. Therefore the program is set up to input the cone angle for various times during transition and make calculations based on the cone angle and the programmed ramp rate and RF curves.

The program also controls the bias current to the tuner for the third harmonic voltage. This is done by loading a table of bias currents versus time. The program then loads the appropriate values to a ramp controller card. In addition the program controls various timers to turn on and off things like feedback loops and power amplifiers. All of this data can be saved in a file for use at a later time.

REFERENCES

- [1] C.M. Bhat et. al. , "Operational Experience with the Third Harmonic RF for Improved Beam Acceleration through Transition in the Fermilab Main Ring", These Proceedings.
- [2] B. Scala et. al. , "Fermilab Main Ring Low Level RF System Modification for Focus Free Transition Beam Test", These Proceedings.
- [3] J. Griffin, "A new method for control of longitudinal emittance dilution during transition crossing in proton synchrotrons", These Proceedings

AMS: Area Message Service for SLC

M. Crane, R. Mackenzie, D. Millsom, M. Zelazny

*Stanford Linear Accelerator Center, Stanford University, Stanford CA 94305 **

Abstract

The Area Message Service (AMS) is a TCP/IP based messaging service currently in use at SLAC. A number of projects under development here at SLAC require an application level interface to the 4.3BSD UNIX socket level communications functions using TCP/IP over ethernet. AMS provides connection management, solicited message transfer, unsolicited message transfer, and asynchronous notification of pending messages. AMS is written completely in ANSI 'C' and is currently portable over three hardware/operating system/network manager platforms, VAX/VMS¹/Multinet², PC/MS-DOS³/Pathworks⁴, VME 68K/pSOS/pNA⁵. The basic architecture is a client-server connection where either end of the interface may be the server. This allows for connections and data flow to be initiated from either end of the interface. Included in the paper are details concerning the connection management, the handling of the multi-platform code, and the implementation process.

1. Introduction

The principal reason for developing the AMS was to provide network services to hardware and software which was not already supported by the Stanford Linear Collider (SLC) control system. The initial demand for AMS came from a specific project, the Machine Protection System (MPS) and was soon followed by projects being developed off-line and off-site by various collaborators. In attempting to satisfy the need to access the SLC control system and database by diverse projects, the following requirements were specified.

1. The message service shall be able to be implemented on a variety of hardware and software platforms and should be easy to port to new configurations when needed. The platforms to be supported initially were VAX/VMS, Motorola 680X0/pSOS, PC/MS-DOS.

2. The message service shall rely on readily available hardware, software and protocol support. This was seen to have the following advantages: new implementations

would be easier to generate, projects being developed at other sites would get easier access to the appropriate hardware and software, using widely used protocols would allow off-site developers to connect to the control system remotely for testing purposes and developers would be able to test their software off-site in the same network environment as the production environment.

3. The network services must be able to be integrated into the existing SLC network software.

4. The services shall not impose a particular paradigm: for example, server-client, master-slave. Applications shall select which ever paradigm was appropriate for them.

5. The services shall provide a flexible naming scheme which was suitable in a real-time environment.

6. AMS shall not issue error messages. Instead it shall simply return status to the caller.

2. Overview

It was decided that Ethernet and TCP/IP would provide the underlying physical, network and transport layers and that the package would rely specifically on TCP as the transport layer. Thus AMS consists of a layer between the application program and TCP/IP: calls made by the application to send and receive data to other tasks are translated into the appropriate TCP calls to set up connections and send or receive data. The application is oblivious to the connection management being undertaken on its behalf.

AMS provides two types of transfers, synchronized and unsynchronized. A synchronized message expects a reply which is bound specifically to that message. An unsynchronized request is like a reliable datagram. No reply or acknowledgement is expected at the application level although the TCP protocol provides reliable delivery.

AMS provides asynchronous notification of arrival of a message or a reply to a message. At present it is only implemented on the VAX platform. Other implementations can provide this if the operating system allows and it is required by the applications.

AMS provides peer to peer services. That is, any process can initiate or receive a data transfer at any time. If a process attempts to send data to a process to which a connection has not yet been established, AMS transparently sets up the connection. If a connection crashes, AMS attempts to re-establish the connection when the next message is sent. Thus, AMS provides the appearance of connection-

*Work supported by the Department of Energy, contract DE-AC03-76SF00515

¹VAX and VMS are trademarks of Digital Equipment Corporation

²Multinet is a trademark of TGV, Inc

³MS-DOS is a trademark of MicroSoft Corp.

⁴Pathworks is a trademark of Digital Equipment Corporation

⁵pSOS and pNA are trademarks of ISI

less network services by hiding the connection management from the application.

A name translation service is provided so that local name table maintenance is not necessary. This service can be provided from more than one source, to avoid having a single point of failure, and it allows for dynamic address assignment so that in the event of a system failure the translation for a name, 'ONLINE' for example, can be re-assigned to the address of the current online host. This name server currently runs only under VMS.

A naming convention is used to allow the application program to send and receive messages to AMS peers using ASCII node and task names. In this convention the node name corresponds to the IP address and task name corresponds to the TCP port number. The translation of these node and task names to IP addresses and port numbers is provided by the name server.

3. Connection Management

One design goal of AMS is to hide connection management from the user providing peer to peer networking in keeping with the current SLC control system message service. Each AMS peer which uses AMS has a server socket to passively accept connection requests and a client socket to actively connect a client socket to a target AMS peer. AMS initialization is performed by calling AMS_INIT with a number of configuration arguments such as the maximum size of the messages to be sent/received, the maximum number of nodes to connect to, lists of AMS peer names to send or receive from, etc. The initialization routine: allocates memory space to use at run time; sets up a linked list of records which track the status of each connection; sets up the local server socket to accept incoming connections; allocates a client socket for each possible remote connection; tries to connect to each possible remote peer; registers the peer with the name server; and then returns to the user. To remove AMS from a process the AMS_KILL routine is used which closes all allocated socket structures including the server socket, frees the AMS allocated memory space and removes the AMS peer from the name server.

During runtime the code checks to see if there are any outstanding incoming connection requests at the server port and connects them as required. If a data send is required and there are no connections to the peer, AMS tries to set up a connection to the peer and complete the data transfer.

4. Message Transfer

The calling interface provides two modes for sending messages, "synchronized" and "unsynchronized". Synchronized mode provides a mechanism by which a sending task can bind an outbound message with a specific reply. If a reply to a synchronized message is not received within a specified timeout but is later generated by the receiver,

because, for example, the receiver's host is slow or the function requested takes a long time, it will be discarded. Thus, an application can be sure that a synchronized reply really "belongs" to the message last sent. It also ensures that the reply comes from the instantiation of the task which received the message. Unsynchronized mode provides a simple message transfer without regard to synchronization and without regard to the current instantiation of the receiving task. Thus two unsynchronized messages could be received by different sequential executions of the same task.

Synchronized messages are supported by the services AMS_SEND_SYNCH, AMS_SEND_REPLY, AMS_GET_REPLY and AMS_RECEIVE. Synchronized messages are sent by calling the routine AMS_SEND_SYNCH. This allows the caller to send multiple synchronized messages in the one call and primes the message service to expect replies. Message destinations are identified uniquely by the triplet (node, task, command) and only one outstanding message to a specific triplet is allowed at any time.

Once a synchronized message has been sent, it can be "cancelled" by receipt of a reply from the target or a timeout where the timeout period for a reply starts after AMS_GET_REPLY has been called. After sending a synchronized message, the sender can receive a reply by calling AMS_GET_REPLY. This service allows the caller to specify a list of messages sent using one or more previous calls to AMS_SEND_SYNCH. In AMS_GET_REPLY a timeout can be specified after which any replies to the messages specified are discarded. In addition, for each message in the list, a status is returned which specifies the fate of the reply. Once a timeout has expired, a new message can be sent to the same triplet. In this case it is possible that the receiver is still holding onto messages from a previous "send". In fact, messages can "stack up" in the receiver and will be presented to the application in the order received. If a receiver replies to messages which have been timed-out, the replies are discarded by AMS at the sender end.

Replies are sent using the service AMS_SEND_REPLY. AMS checks that replies correspond with synchronized messages previously received and for given node/task, it always generates replies to the earliest synchronized message received.

Unsynchronized messages are supported by the services AMS_SEND, AMS_RECEIVE and AMS_RECEIVE_NOWAIT. To send an unsynchronized message, the routine AMS_SEND is called.

To receive the next available message, AMS_RECEIVE or AMS_RECEIVE_NOWAIT is called. These routines return both synchronized and unsynchronized messages. It is up to the application to decide which type of message it has received. The "nowait" version provides a mechanism for asynchronous notification under VMS.

AMS_RECEIVE_NOWAIT will set up an Asynchronous System Trap (AST) for when a message arrives unless there is already a message waiting. When a message arrives, the AST set up by AMS_RECEIVE_NOWAIT will copy

the message into the user's buffer, remove its own internal copy, set the user's event flag and call the user's AST.

5. Name Server

The name server process currently runs on the VAX platform only. It has a hardcoded, well known IP port and IP address but future plans include the ability to move the server from node to node. TCP/IP was chosen for the server connection protocol since there was already a base of TCP code implemented for AMS. This will eventually change to UDP to allow less network overhead, quicker response, and the ability to use multicast features. The server simply loops accepting new connections from AMS clients, servicing name translation requests and closing the connections. Utilities to support server diagnostics and routine shutdown and startup procedures are in development now.

The AMS name server client code resides along with the rest of the AMS code in each platform's libraries. The client connects to the name server, sends a name translation request to the name server, and returns. There are no special features in these client operations.

6. Security

Security is required to protect an AMS peer from receiving connections from unauthorized clients. Extra connections including accidental and malicious attempts to talk to a peer are not allowed. Each peer provides a list of permitted peers to AMS at initialization time. This list is checked at connect time to ensure that the incoming peer is valid and permitted. The notion of a ALL* (or total wildcard) is used to tell AMS that any peer may be connected and received/sent to. The use of ALL* bypasses the use of the permitted peer list, but does check the name server to validate the peer name. The name server is the central place where security is checked. Before a peer is recognized it must register with the name server. After it has registered, other peers may attempt connections to it. When AMS no longer exists for a particular node, the peer can be removed from the name server by calling AMS-KILL.

7. Implementation

All of the AMS source code is stored on the VAX/VMS system using the Digital Equipment Corporation Code Management System (CMS) as the code management tool. This allows multiple programmers to work on the same bits of code with a minimum of conflicts. The code is shared amongst the differing platforms by using a special include file, one for each platform. This include file provides a means to translate file names, differing function return codes and differing function call names. Very few 'C'

language #ifdef statements are actually used in the code which makes maintenance and readability much easier.

The first goal in the implementation process was to get a simple connect and data passing skeleton up and working. The requirement was to implement the basic connection philosophy as the foundation for the send/receive portions of the code. AMS_INIT was the first routine to be coded along with the multi-platform include files. VAX to VAX were the first connections, followed by the 68K to VAX. The MS-DOS port followed soon after to ensure that the multi-platform coding philosophy was correct. After connections were established, the passing of data was the next step. The send routines were simple since it is an active type of transaction. Receive was more difficult because of the polling nature of time independent data receives. The TCP socket select call was implemented along with buffer allocation routines to allow receiving data with a minimum of CPU overhead. Studies of CPU and network performance were done soon after the initial releases of AMS. It was found that each VAX process using AMS consumed substantial CPU time calling the TCP select call to see if any new data was available. The no.wait receive routines were then coded specifically for the VAX platform to cut this CPU time down. The name server was the last part of the project to be implemented. Previous to this time, all AMS peer names were stored in hard coded tables internal to AMS.

8. Future Plans

There are plans to improve AMS as the user base grows. The most important plan is to change the name server communications from TCP to UDP. This will reduce network traffic and server node CPU usage. There also needs to be failover procedures in software to gracefully handle the transfer of the SLC control system from on VAX to another with the AMS impact being the node location of the name server and the translation of the node names "PRODUCTION" and "DEVELOPMENT" which are used by the AMS peers to distinguish between the SLC VAX'es. There are also a number of diagnostic tools to support the name server which need development.

AMS is currently being used by a number of development projects here at SLAC and has had nearly a year of satisfactory service. It has proven itself to be a reliable messaging service and has met all of its design goals. The first production release of projects using AMS are due in the very near future.

Adding PCs to SLC Control System

T. Lahey, S. Levitt, R. MacKenzie, N. Spencer, K. Underwood

*Stanford Linear Accelerator Center, Stanford University, Stanford CA 94305 **

Abstract

The SLAC Controls Department has interfaced IBM-Compatible PCs to the SLC Control System, for use by the Final Focus Test Beam (FFTB) experimenters, who are building new accelerator equipment and developing and testing it at their home institutions. They will bring the equipment to SLAC and integrate it into the control system using a new software package. The machine physicists and operators will use the existing SLC control system applications and database device types to control and monitor the equipment. The PCs support a limited control environment: they run DOS and exchange messages with the existing control system via TCP/IP over ethernet, using the new SLC Area Message Service. This mechanism will also allow SLC to implement other commercial device controllers that can communicate over ethernet and run the same software interface code.

Introduction

Final Focus Test Beam (FFTB) is an international collaboration that will run this year at Stanford Linear Accelerator Center (SLAC). The collaborating institutions are providing instrumentation and control computers that they are bringing from their home institutions and connecting to the existing Stanford Linear Collider (SLC) accelerator control system.

This paper describes the method used to connect this instrumentation to the SLC control system so that the operator interface from the control room matches the existing control system.

Justification

PCs were chosen for the control computers because they can be used in a standalone mode to develop instrumentation, they are commonly available, and they have good development tools. The international collaborators can develop the instrumentation at their home institutions, and bring their instruments and PC to SLAC.

*Work supported by the Department of Energy, contract DE-AC03-76SF00515

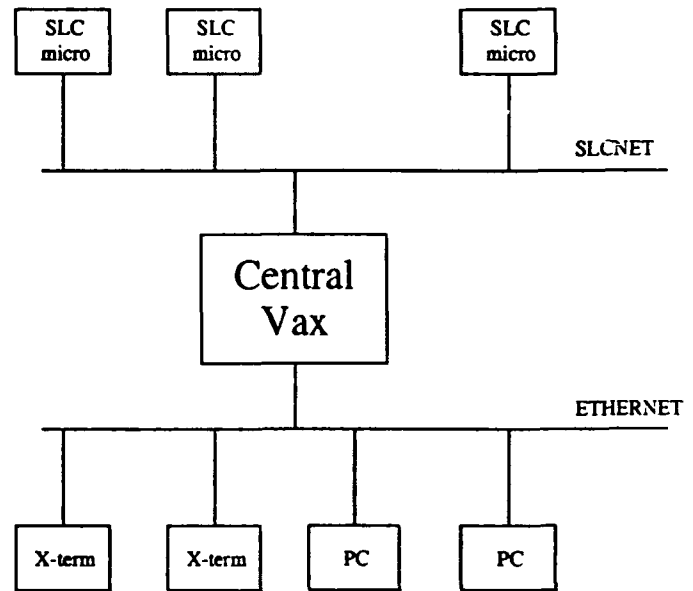


Figure 1: Adding PCs via ethernet to SLC Control System

Additions to SLC Control System

The existing SLC control system generally consists of:

- a SLC Control Program (SCP) that operators use from an X-windows compatible terminal.
- the database describing accelerator devices.
- a host VAX on which we run the SCP, database, and other applications.
- standard SLC 80386 micros that run the Intel RMX operating system, and are geographically distributed throughout the accelerator to control and monitor the accelerator devices.
- the SLCNET proprietary network and network software.

An FFTB PC is a IBM PC-compatible that runs MS-DOS, and communicates with the VAX over ethernet using

the TCP/IP protocol. Figure 1 shows the PC added to the SLC control system.

FFTB experimenters bring accelerator instrumentation that is controlled by a PC-compatible computer. The PC runs a program that receives and processes device commands. The program is built from experimenter software linked to a SLAC-developed library.

SLAC Controls has written a PC library that provides the basic micro services and device support, a VAX-resident Database Server (FFTB-DBS) that allows a PC to access the SLC database, and a VAX-resident Network Server (A_SERVER) that redirects messages to the PCs from existing SCP and applications.

The network software is SLAC's Area Message Service (AMS) [1] that resides on the VAX and PCs and sends messages using commercial TCP/IP software: TGV's Multinet on the VAX, and DEC's TCP/IP on the PCs.

To support FFTB, we have not modified the SCP, other application programs, or the database device types.

Figure 2 shows the software components.

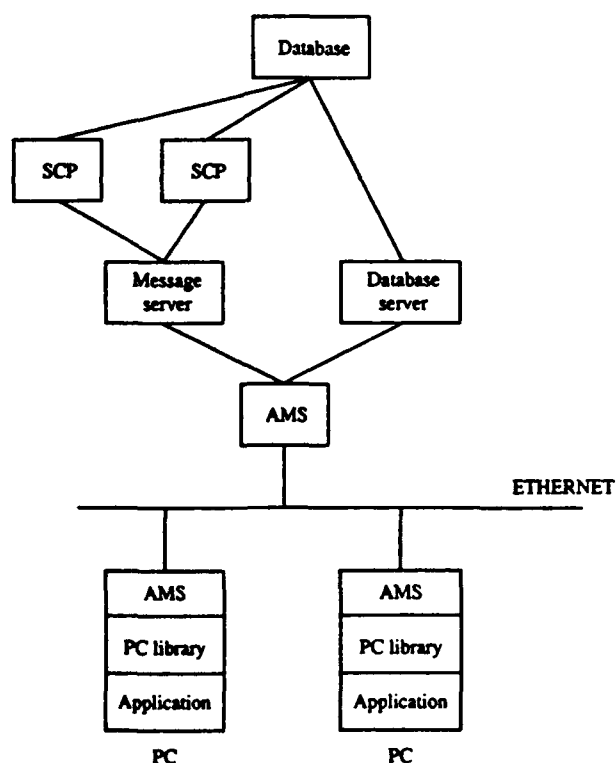


Figure 2: Software Components for FFTB PC

To add an FFTB PC to the control system, we identify the standard SLC device-types needed for the instrumentation, define the FFTB devices in the database, and define the PC as an FFTB PC.

Using PCs, KEK provides FFTB quadrupoles and a quadrupole-support table, and Beam Size Monitor instrumentation. A SLAC/DESY group provides FFTB beam-line alignment instrumentation.

Alternate Platform

The main use of this package is on a PC-compatible. The FFTB package can also run as a process on the VAX, emulating the functionality of a remote micro. An initial implementation of this VAX process, called a VAX-based micro, is presently used to control FFTB magnet mover devices. The movers are physically connected to standard SLC micros, and were initially developed and tested with a standalone VAX program. To integrate these movers into the control system, the FFTB package runs as a VAX-based micro, controls the mover devices and supports device commands issued from the SCP. The VAX-based micro sends messages to standard SLC micros to control the physical hardware, performs special transformations that are specific to the FFTB movers, and replies to the SCP commands.

The VAX-based micro is also used to test PC software.

Functionality of a PC

To use a PC to control devices, the PC must support a subset of the standard SLC micro functionality. This includes:

- devices in the database: the PC supports a subset of standard SLC devices. The PC emulates all the necessary characteristics of these device types, updating all values in the database for the given device type. A PC owns database units to describe any instruments that are connected to the PC.
- communication with SCPs, supporting existing application messages.
- periodic events to trigger updates of PC device values in the database.

The PC program acts both as a server and a client. It is a server to the SCP, processing SCP messages that contain device control or monitor command. To support the SCP message, the PC must get and put device values from/to the SLC database that resides on the VAX. The PC is then a client to the database server, requesting get/put operations of values in the database.

The SLAC-written PC library hides many of the details of the SLC micro and its integration within the control system. The interface with experimenter-written code is well-defined [2] and simpler than similar interfaces in standard SLC micros.

The PC library contains device-specific functions for the supported device types. The experimenter initializes a device buffer, and then gets/puts values from/to the database

for devices via the device buffers. For each device buffer, the experimenter provides the address of their routine which will do the physical device I/O and command processing. The PC library and database server support four device buffer types: actuator, analog, digital, and general.

A PC uses: actuator buffers to get/put database values for magnets and power supplies, analog buffers for floating point values, digital buffers for digital states (bits), and general buffers to get device values for any other type of device in the database.

The PC library contains a main function that initializes the network, and then enters a loop that dispatches SCP messages to the experimenter-written code for processing, dispatches commands to experimenter-written code requesting a periodic update of devices values to the database, and calls the user each loop execution.

The experimenter also writes three pre-defined functions: `USER_INIT` to initialize their hardware and actuator, analog, digital, and general device buffers; `USER_CODE` to execute periodic functions needed each program loop; and `USER_STOP` to shut-down their application.

The PC can get values from the database for devices in any part of the accelerator. The PC must maintain current values for devices that it owns in the database.

PCs do not receive SLC timing interrupts. Timing signals are generated by standard SLC micros, and delivered directly to hardware that is connected to the PC.

Database Server

The VAX-resident database server, `FFTB_DBS`, provides access to the database via device buffers. It performs device buffer initialization, get and put of values via device buffers, cancellation of device buffers, protection of database access to allow a PC to write to only its own database devices, and other important support functions. The database server contains critical information to access the database. PCs do not directly access database values, thus protecting the database. The server allows easy control of database access.

Message Server

The VAX-resident message server, `A_SERVER`, dispatches all communications between SCPs and PCs. When the SCP or other application program calls the existing message service, and wants to communicate with a node connected to ethernet, the message is routed to this server. `A_SERVER` sends/receives messages via AMS to the ethernet nodes. We updated the existing SLC message functions to recognize a node that is connected to ethernet, and to redirect the message to `A_SERVER`.

Both `FFTB_DBS` and `A_SERVER` use a list of legal nodes, providing security for which nodes can connect to the control system via AMS.

The number of available DOS TCP/IP connections is a critical resource. We have used a single message server to reduce the number of connections between a PC and the SCPs and other VAX applications.

Project Status and Futures

We are close to completion of this project. The FFTB experiment will use PCs and VAX-based micros this summer and autumn to measure the alignment of movers, control and monitor quadrupole-support table, measure beam size, and control the movers.

For future projects, this package can be used to connect smart instruments to the control system. We have started to migrate this package to an HP Unix system for control and monitoring of smart instrumentation. The AMS network is already implemented on the HP platform. We plan to compile and link the PC library on the HP platform, define database devices and control the instruments from the existing SCP and other applications. We can add additional device commands to control/monitor the smart devices.

Using this package for VAX-based micros, we support unique devices that exist in small numbers. When device support is added to a standard SLC micro, it is generally added to all the micros in the control system. When the support is complicated and requires prototyping, or it is needed in only one part of the accelerator, we can now implement the micro that controls the devices, in a VAX-based micro or in a PC.

References

- [1] M. Crane *et al*, AMS: Area Message Service for SLC. *These proceedings, SLAC-PUB-6166 (1999)*.
- [2] T. Lahey *et al*, SLC PC-VAX Link for FFTB: PC Users Manual. *SLAC Controls Department Software Manual (November 1992)*.

PRECISE SYSTEM STABILIZATION AT SLC USING DITHER TECHNIQUES

M. C. Ross, L. Hendrickson, T. Himel, E. Miller
Stanford Linear Accelerator Center
Stanford, California 94309

Abstract

A data acquisition method has been developed at the SLAC Linear Collider (SLC) that provides accurate beam parameter information using sub-tolerance excitation and synchronized detection. This is being applied to several SLC sub-systems to provide high speed feedback on beam parameters such as linac output energy spread. The method has significantly improved control of the linac energy spread. The linac average phase offset (ϕ), used to compensate the effects of longitudinal wakefields¹, is adjusted ± 1 control bit (about 0.18° S-band or 20% of tolerance), in a continuous fashion. Properly coordinated beam energy measurements provide a measure of the derivative of the accelerating voltage ($dE/d\phi$). The position of the beam on the RF wave can thus be determined to $\pm 0.3^\circ$ in about 5 seconds. The dithering does not contribute significantly to the energy jitter of the SLC and therefore does not adversely affect routine operation. Future applications include control of the interaction region beam size and orientation.

I. Introduction

Linear colliders require very tight control of beam parameters such as energy spread and emittance. Typical beam feedback loops in widespread use at SLC stabilize the beam centroid to a previously recorded position or energy. Beyond this, optimization or minimization 'feedback' is required that does not restore the beam to any previous setting but instead moves it as required in order to reach an optimum as defined with respect to a well defined signal. These loops then perform many routine tasks presently delegated to operators and the operators task becomes one of monitoring their performance.

Typical application of minimization loops is in the control of phase space volume or orientation. Limitations in instrumentation, namely the lack of ubiquitous single pulse beam size monitors, require indirect means of measuring phase space volume. A novel technique has been tested at SLC that provides accurate control of indirectly monitored parameters through narrow band signal averaging. At SLC, two examples of

this are the average linac RF phase offset, (ϕ), and the skew, waist and chromatic corrections applied to the interaction region beam spot.

While centroid parameters can be easily detected and corrected locally, beam size parameters may not be correctable locally because the source of error may not be locally identifiable or correctable. However, such errors can grow and become more difficult to correct if not corrected as locally as possible². Perhaps the most important reason for local feedback is that the transfer function between the detector and the corrector is likely to be more stable. In other words, global variables such as storage ring capture or luminosity should not be used to provide signals to loops which have controls that are far away.

At the SLC we have applied a dither technique for beam size optimization. With this technique small changes are applied to key devices and the associated response is separately measured. The sign of the small signal response is required, in general, to indicate which way the control should be varied. The narrow band technique can be used to reduce measurement statistical and systematic errors.

II. Technique

The technique is an improvement over previously established correlation procedures³ since it uses a sub-tolerance excitation and measures only the local slope. The luminosity lost in the process can be easily estimated in the case where the luminosity depends quadratically on the control.

Let :

S_y = the standard deviation of a single measurement of the quantity to minimized

$S_{\frac{\Delta y}{\Delta x}}$ = the standard deviation of a single dithered slope measurement

S_{ave} = the standard deviation of the average of N dither measurements

S_{des} = desired standard deviation of averaged dither measurements

Δx = total amount of the dither

*Work supported by Department of Energy contract DE-AC03-76SF00515.

m = number of beam pulses per half dither measurement (up for m and down for m)

N = number of dither measurements averaged

f = repetition rate of the accelerator (120Hz for SLC)

Then the error for a single dither measurement is:

$$S_{\frac{\Delta y}{\Delta x}} = \frac{\sqrt{\frac{2}{m}} S_y}{D_x}$$

and the error for N dither measurements:

$$S_{ave} = \sqrt{\frac{2}{mN}} \frac{S_y}{D_x}$$

Total time to make a measurement of accuracy S_{des} :

$$N = \frac{2S_y^2}{mS_{des}^2 \Delta x^2}$$

Loss in luminosity, assuming a quadratic behavior of the luminosity around present state:

$$\Delta f(Ldt) = \frac{S_y^2}{2fS_{des}} \frac{\partial^2 L}{\partial x^2} \bigg|_{x_0}$$

The loss in luminosity is fixed for a given desired accuracy. Using a large number of small steps or a small number of large steps is equivalent. This is only true for linear response. Furthermore the accuracy depends on the beam stability during the measurement.

The technique relies on the broadly based, powerful, synchronized data acquisition of the SLC control system. In the scheme adopted for this purpose, synchronizing codes are broadcast to all SLC remote data acquisition computers. The codes serve to prepare and start the sequence, guaranteeing that the control device is adjusted and the data collected on the correct pulse. Data can be acquired from throughout the complex providing a mechanism for correlation studies. In the feedback central processor, the signal is analyzed against the excitation and the response is estimated. Figure 1 shows a diagnostic, with ten times the normal excitation, used to test the system. It is clear from the figure that the nominal excitation of 0.18° gives a negligible contribution to the energy jitter.

III. Application and Results

Table 1 lists some of the applications of minimization feedback in the SLC. The first two rows outline the average phase stabilization. We will now describe this application.

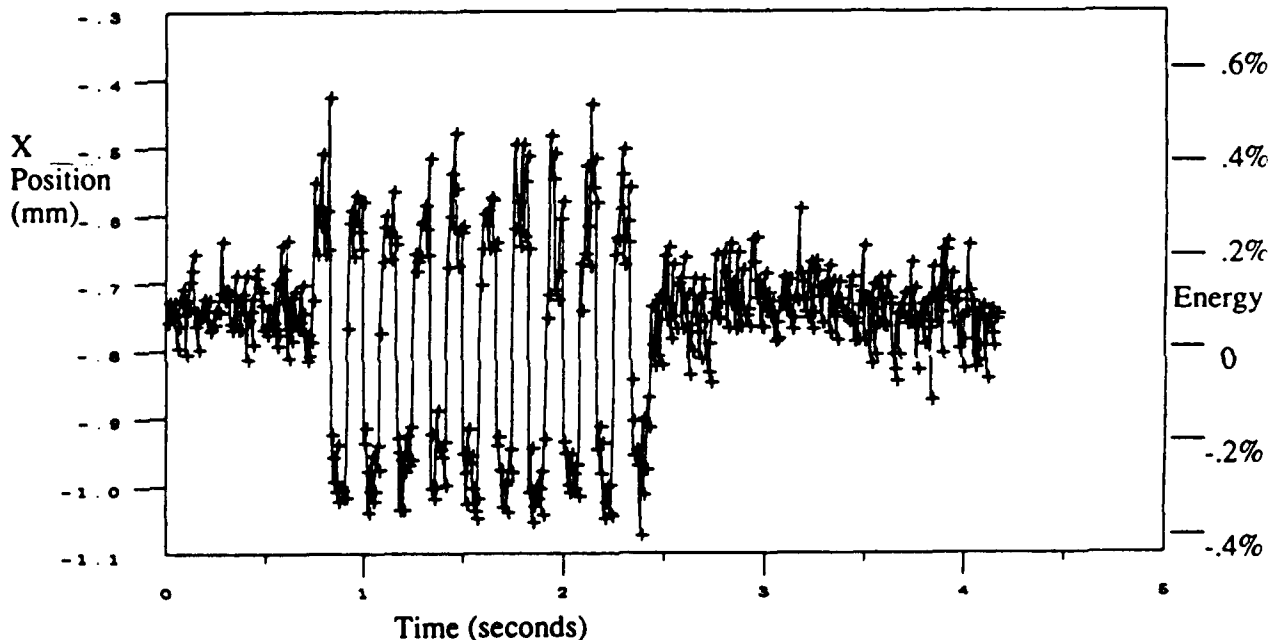


Figure 1. Energy measurements taken on 500 successive pulses showing the dither control. For this diagnostic test, the dither amplitude is 10 times the nominal 0.18° .

Loop	Method	Control	Sensor	Dither step size
Linac ϕ off	$dE/d\phi$	Phase shifter	BPM's - high η	0.2'
Injector ϕ off	$dE/d\phi$	Phase shifter	BPM's - high η	0.1'
Ring Extraction Kicker Timing	change in x correlated with kicker timing	Thyratron trigger timing	Linac BPM's	Natural Thyratron jitter, ~ 0.1 ns rms
IP Waist	Fast Luminosity Monitor	Final triplet lens	Deflection angle and luminosity monitor	enough to drop L by $\sim 5\%$
IP Skew	Fast Luminosity Monitor	Skew quadrupole	Deflection angle and luminosity monitor	enough to drop L by $\sim 5\%$
IP Chromatic	Fast Luminosity Monitor	Sextupoles	Deflection angle and luminosity monitor	enough to drop L by $\sim 5\%$
IP Dispersion	Fast Luminosity Monitor	chromatic corr. quad	Deflection angle and luminosity monitor	enough to drop L by $\sim 5\%$

Table 1. The first minimization loops to be implemented at SLC. The last 4 are an extension of existing automated interaction region (IP) tuning.

V. References

The single, high peak current bunch in the SLC linac requires strong beam loading compensation for longitudinal wakefield compensation. The slope of the accelerating RF is used for compensation with the bunch typically placed 5 to 10' ahead of the crest. The energy spread and the tails of the energy spread distribution must be minimized to achieve optimum performance of the downstream chromatic corrections and to reduce detector backgrounds. The problem is that the optimum is poorly defined by the wire scans of the profile itself. Assuming constant intensity and bunch length, the optimum phase offset (ϕ_{off}) is constant and by determining ϕ_{off} from $dE/d\phi$, the derivative of energy with respect to phase we can more accurately place the bunch on the RF. The feedback loop will dither the beam with a 30Hz cycle period, ± 1 digital to analog converter least significant bit, and apply the control at an update rate of 0.1Hz. Note that for the narrow band technique, different dithering frequencies are required if multiple loops operate at once.

IV. Conclusion

The narrow band dither technique will have application in other machines⁴. It has the promise of providing accurate data that is not possible to acquire in more conventional look and adjust schemes. Ultimately, this technique may be used to remove some of the load of the operators.

¹ K. L. Bane et al., "Measurements of Longitudinal Phase Space in the SLC Linac," Proceedings of the Second European Particle Accelerator Conference, p. 1762 (1990).

² J. Seeman, et.al., 'The Introduction of Trajectory Oscillations to Reduce Emittance Growth in the SLC Linac', Proceedings of the XVth International Conference on High Energy Accelerators', Hamburg, 1992.

³ L. Hendrickson, et.al., 'The Correlation Plot Facility in the SLC Control System', Proceedings of the 1991 IEEE PAC.

⁴ R. Schmidt, 'Real Time Applications', Presented at the First European Workshop on Beam Instrumentation and Diagnostics for Particle Accelerators', Montreux, Switzerland, May 1993.

Thermal Stabilization of Low Level RF Distribution Systems at SLAC*

D. McCormick, M. Ross, T. Himel, N. Spencer
Stanford Linear Accelerator Center

ABSTRACT

Analysis of SLC accelerator operator activity, in particular control system knob turns, indicated poor thermal stability performance of the low level RF distribution system in the SLC injector and positron production complex. Daily drifts of up to 15° S-band delay, about 30 times the tolerance, were observed. In this paper we describe the tool used to track down and quantify operator knob turn activity, the low level RF distribution stabilization systems, and some fixes used to correct the problem. In order to identify poorly performing components, a beam timing or phase monitor diagnostic has been developed. Initial results from it will be presented.

INTRODUCTION

The SLC RF distribution system has evolved from the original SLAC design. The original system consists of a main drive line running the length of the linac with couplers at the beginning of each of the 30 sectors. The portion of the RF that is coupled out of the main drive-line at the start of each sector is amplified by a sub-booster, and distributed along a sub-drive line to each of the eight klystrons. Temperature

stabilization of the main and sub-drive lines is only partially effective, and diurnal phase changes correlated with temperature have been a source of instability. For SLC, temperature stabilized phase reference lines¹ have been added to each sector. These reference lines provide a reference phase to each klystron in a sector. The injector and positron production complex have been fitted with a number of these phase reference lines and a marked increase in the phase stability has been observed. However, operators must still apply diurnal phase adjustments to the electron injector and the positron capture klystrons to maintain injection of electrons and positrons into the damping rings. Two software packages; Error Log and SLC History Buffers² are used to help determine which RF devices require the most adjustment. Some of the phase stability problems have been traced to poor temperature stabilization of coaxial cables. A low cost coaxial cable temperature stabilization system has been developed to fix identified problems.

SOFTWARE TOOLS

KNOB TURNS

The SLC control system is used to control all phase shifters in the RF distribution system. An operator wishing to adjust the phase of an RF device, selects the appropriate phase shifter and assigns it to a knob. The knob is turned to adjust the phase the desired amount. A control system program called ERROR LOG creates an entry in a file each time the knob is turned. The entry consists of a time stamp, the knob name, the identification number of the control console where the knob was assigned, and the value of the device. The entries can be collected for any period of time up to a year and printed out. Figure 1 shows the knob turns for a 24 hr. period. The first six entries are phase shifters. The large number of knob turns for these devices indicate stability problems with the corresponding portions of the RF distribution systems.

HISTORY BUFFER

The SLC History Buffer is another software tool. Every three to six minutes the data returned from most devices is saved. The data can be plotted vs. time, or vs. the data from other devices. The data can be plotted for the last few minutes, or the last year. The history buffer data is used to look for correlation's between phase changes in RF devices and temperature. When the phase of a device is dependent on several parameters, including temperature, the history buffer data of the known parameters can be subtracted away revealing any remaining temperature correlation. Figure 2 shows a portion of the injector RF distribution system. The CIDM_PHAS PAD (phase and amplitude detector) provides a measurement of the phase between the injector klystron RF and SB 0 (sub-booster 0) RF. The SB 0 PAD measures phase changes made by its phase shifter. Phase changes measured by the CIDM_PHAS PAD should be due only to adjustments of the CIDM_PHAS phase shifter and the SB 0 phase shifter. Figure 3a shows history buffer readings of the CIDM_PHAS PAD. Figure 3b shows the same data after subtracting out the phase changes made by operators adjusting the CIDM_PHAS phase shifter. If the RF distribution system were perfect, the remaining phase changes should be due entirely to changes in

KNOB TURNS OVER FOUR HOUR INTERVALS

KNOB	6-10	10-14	14-18	18-22	22-2	2-6	COUNT
POSPHAS	89	105	106	105	112	70	587
NLTRPHAS	35	55	68	63	24	4	249
DR02 PH 6	12	20	20	22	30	50	154
PHSRMP	17	35	14	13	21	34	134
EP02 S 700	35	22	18	10	24	4	113
CIDM_PHAS	24	32	9	6	5	—	76
YP@NINJ	24	11	8	5	6	1	55
XP@NINJ	28	10	7	5	3	1	54
X@NINJ	20	11	8	8	5	1	53
Y@NINJ	20	9	9	5	6	1	50
EP_Y_MM	—	6	4	4	3	—	17
EPYNG_MR	—	6	4	3	3	—	16
EPXNG_MR	—	5	3	—	4	—	12
EXPV36	—	—	—	—	—	10	10
PXPV36	—	—	—	—	—	10	10
NUY@NDR	1	—	—	—	—	—	9
EP_X_MM	—	3	3	—	3	—	9
NUX@NDR	1	—	—	—	—	—	8
Y@SINJ	—	2	—	2	4	—	8
K20-4A DRV	—	—	—	—	7	—	8
XP@SINJ	—	—	1	1	4	—	7
LI11YPOSE+	—	—	—	7	—	—	7
X@SINJ	—	—	1	1	3	—	6
DR11 AM 1	—	—	2	—	—	—	6
YP@SINJ	—	—	—	1	3	—	6
NLTRENGYE	—	—	5	—	—	—	6
DR01 AM 1	—	—	3	—	—	—	5
PHBMIV 10	—	—	—	5	—	—	5
1-1BPAU	—	—	2	—	—	—	4

Figure 1: Knob turns made by the operators over a 24 hr. period are shown above. The first six are knobs that control RF phase shifters in the electron and positron production areas. The large number of knob turns for these devices, indicates phase poor stability in the their respective RF distribution systems.

* supported by DOE contract DE-AC03-76SF00515

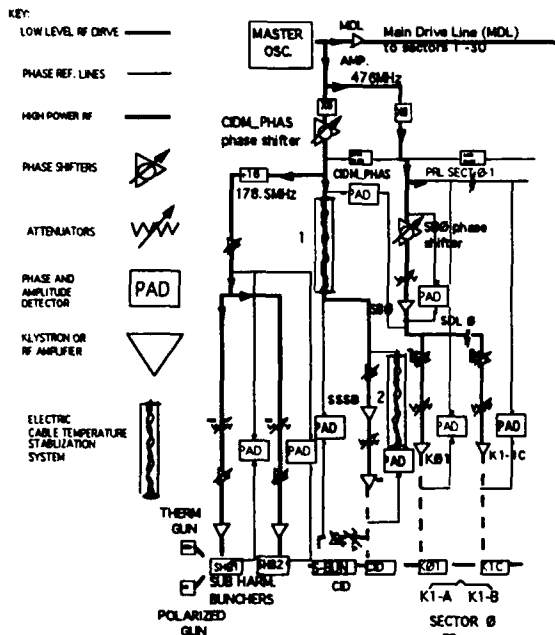


Figure 2: Electron injector RF distribution system. Operators adjust CIDM_PHAS and SB 0 phase knobs to maintain injection into the north damping ring. Two 2.5m sections of the RF distribution system have been fitted with a electric cable temperature stabilization system (shown with the numbers 1&2 above). This has improved the stability of the system.

the phase of sub-booster 0. In figure 3c, the data from the SB 0 PAD is subtracted from the data in figure 3b. A remaining diurnal phase change is clearly seen. These two sections of the RF distribution system are being investigated to determine the cause of this phase error.

PHASE REFERENCE LINE IMPROVEMENTS

An inspection of the phase reference lines in the injector revealed two 2.5 m sections and a number of smaller lengths that had no temperature stabilization. The phase reference lines are "phase stabilized" lengths of Andrews LDF4-50 coaxial cable. The phase change calculated from Andrews phase stability documentation³, indicated that the 5m of unstabilized cable should have an S-band phase shift of 0.04 deg./°F. For the 30°F temperature change shown in figure 4a, the 5m of unstabilized cable should contribute 1.25 degrees to the observed 8.5 deg. S-band phase change. At the end of the 1992 run these two 2.5m sections of cable were fitted with the electrical stabilization system described below. History buffer data showing the correlation between temperature and phase for the 1992 and 1993 runs are shown in figure 4. Stabilizing the 5m of cable, reduced the temperature phase correlation by 14%. This is in good agreement with the predicted change of 15%.

TEMPERATURE STABILIZATION OF COAXIAL CABLES

For SLC, the control of propagation delay in the phase reference lines has been accomplished by placing the cables inside double wall tubing with temperature-stabilized water flowing between the walls¹. Hot and cool water are mixed so that the temperature at the pump output was kept constant. A new system that operates well above the ambient temperature and requires only the input of heat has been developed.

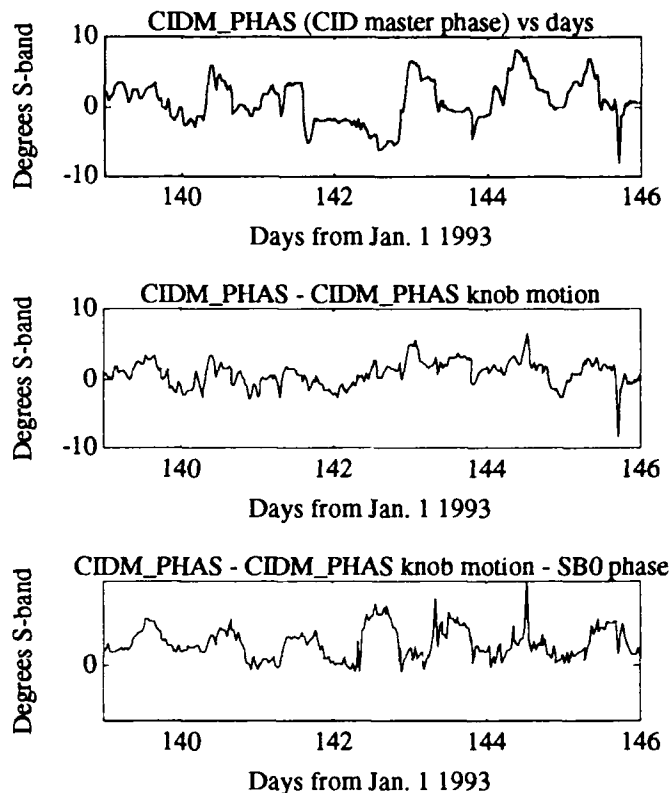


Figure 3: Figure 3a (Top) is history buffer data from CIDM_PHAS PAD. Figure 3b (middle) is CIDM_PHAS PAD data minus CIDM_PHAS knob turns. Figure 3c (bottom) is data from figure 3b minus SB 0 PAD data. The remaining diurnal phase variations indicate temperature instabilities in the low level RF distribution system.

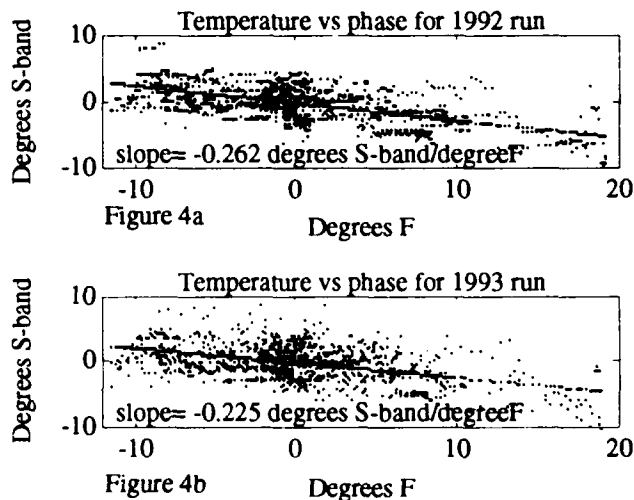


Figure 4: Figure 4a shows the temperature phase correlation between the injector air temperature and CIDM_PHAS PAD readings for the 1992 run. Two electric cable temperature stabilization systems were added (see figure 2) before the 1993 run. Figure 4b shows the resultant 14% reduction in the temperature phase correlation.

In this scheme, control of the propagation delay of coaxial

cables is accomplished by maintaining an average cable temperature. If the temperature drops in a section of cable producing a decrease in propagation delay, the entire cable temperature is raised slightly to produce an increase in delay that cancels the original change. A sensor described below measures the cable's average temperature. Heater tapes are used to heat the cable to its operating point and produce the small temperature changes which control its propagation delay. The coaxial cables, the sensor, and heater tapes are covered with semi-rigid foam insulation. A cut away drawing of the system is shown in figure 5.

Measuring the average temperature of the cable with a single sensor distributed over the entire cable was determined to be more effective and less costly than many discrete sensors. A distributed RTD (resistance temperature detector) running the length of the cable was developed. A prototype sensor was constructed by sandwiching eight strands of 36 gauge enameled copper wire between two pieces of flexible cloth backed tape. The number and gauge of the strands can be varied so that when connected in series and in parallel, the resistance is 100 ohms at 0 °C. Minco Corp. manufactures distributed RTDs and can supply units up to 80ft. in length.

Heat for the system is provided by self-regulating heater tapes manufactured by Raychem Corp. This product consists of two parallel conductors with a resistive material between them. As the temperature of the tape increases the resistance of the material between the conductors also increases reducing the current flow through the tape. This self regulating feature prevents thermal runaway in the event of a temperature controller malfunction. This product has an output of 32.8 watts/m at 10 °C. As the temperature of the cable is raised to its normal operating point of about 43 °C, the output of the heater tape falls to 12 watts/m. A double helix of this material is wrapped around the cable assembly with a pitch of one revolution/m, giving a total of 24 watts/m for both heater tapes. The insulating foam jacket has an inside diameter of 7.6cm and a wall thickness of 2.5cm. Using the foam's R value of 5.2 and a maximum temperature differential of 50 °C, the heat loss through the insulation is 20 watts/m.⁴ The distributed RTD is connected to a standard temperature controller whose setpoint is adjusted above the highest expected air temperature. The controller applies power to the heater tapes to increase the average temperature of the coaxial cable. After the average temperature of the cable reaches the setpoint, the power is cycled on and off by the controller to keep the temperature constant.

PERFORMANCE OF STABILIZED COAXIAL CABLES

The performance of the temperature stabilized cable was evaluated by measuring its propagation delay. A TDR (time

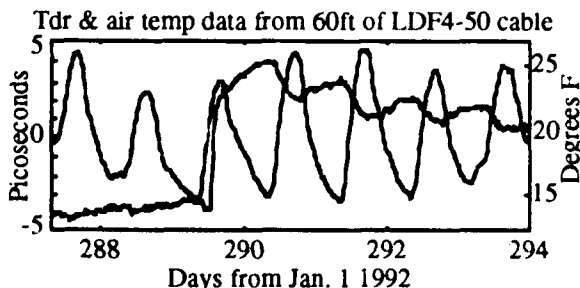


Figure 6: TDR (time domain reflectometry) data of temperature stabilized cable, along with outside air temperature. While the temperature stabilization system was active, the change propagation delay of the 20m cable was 0.3ps. The system was turned off around noon on day 289.

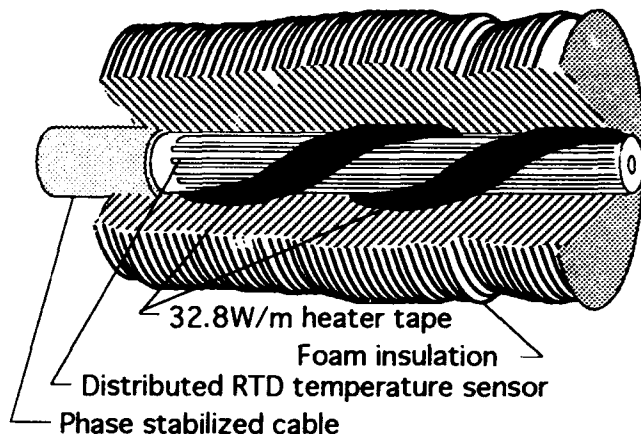


Figure 5: Cut away of a section of temperature stabilized cable. The distributed RTD (resistance temperature detector) runs the length of the cable and is connected to a temperature controller which then measures the average temperature of the cable. The controller cycles power to the heater tapes to maintain this temperature.

domain reflectometer) was connected to a 10 meter piece of temperature controlled cable and the round trip travel time of the pulse was measured over several day/night periods. Results of this test are shown in figure 6. The calculated temperature change of the cable while the temperature stabilization system was functioning is about ± 0.35 °C. This is based on the 20m path length of the TDR pulse, the 0.042ps/m °C temperature coefficient for the cable and the 0.3ps propagation delay change observed in figure 6. Tests on other pieces of stabilized cable have indicated that the temperature controller used is affected by the temperature variations in the klystron gallery. Tests with other controllers are planned for the future.

CONCLUSIONS

Software tools have been developed to help locate and quantify stability problems in the SLC low level distribution system. Knob turn software has identified the systems that show the greatest instability and History Buffers have been used to demonstrate the magnitude of the temperature phase correlation's. Initial installations of electric cable temperature stabilization systems have proved to be reliable and effective at maintaining the average temperature of the cables at ± 0.35 °C

ACKNOWLEDGMENTS

I would like to thank Heinz Schwarz for the original RF distribution drawing.

REFERENCES

- [1] K. Jobe et al, "Test Results of Sector 9 Phase Reference Line," SLAC Signal Pass Collider Memo #177, 1982
- [2] Ralph Johnson, "Stanford Linear Collider History Data Facility," Proceedings of the 1989 IEEE Particle Accelerator Conference, Vol. III, p. 1716.
- [3] Andrew Corporation, "Phase Performance of Helix Coaxial Cables," Andrew Corporation document SP30-14 July 24, 1992, pp. 4-6
- [4] IEEE Standards Board, "IEEE Recommended Practice for the Testing, Design, Installation, and Maintenance of Electrical Resistance Heat Tracing for Industrial Applications", ANSI/IEEE Std 515-1983, pp. 27-30

CESR* Luminosity Upgrades and Experiments

David Rice for the CESR Operations Group

Newman Laboratory of Nuclear Studies, Cornell University, Ithaca, NY 14853

Abstract

The Cornell Electron Storage Ring (CESR) has provided over 2.5 fb^{-1} integrated luminosity on the $Y(4S)$ resonance and nearby continuum, facilitating measurements of B meson decays. In order to seek out rarer events, the luminosity of the storage ring must maintain a geometric growth. The luminosity upgrade program of CESR provides this growth capability while utilizing many of the developments in technology and accelerator physics required for later upgrade to an asymmetric B factory. All upgrades incorporate approximately the same per-bunch parameters as in CESR's present operation. The next step in the upgrade replaces the individual bunches with "bunch trains," or closely spaced groups of bunches treated as a single bunch by the pretzel separation scheme. The higher beam currents will require improvements to the RF, vacuum, feedback, and injector systems. Separation at the parasitic interaction points near the main interaction point is provided by a small horizontal crossing angle. Machine experiments have been conducted to determine criteria for separation at parasitic crossings and measure the effects of small crossing angles on beam-beam dynamics, as well as study other topics related to the upgrade program.

I. INTRODUCTION

Since the commissioning of CESR in 1979, the CLEO and CUSB experiments at Cornell have been a primary source of experimental data on B meson decays. Several of the important observations first made at CESR are:

- $Y(4S)$ resonance
- First evidence for B mesons
- $b \rightarrow c$ decays
- First measurement of B mass
- $b \rightarrow u$ decays
- $B^0 \rightarrow \psi K_S$
- higher order loop decays of B mesons
- $B^0 \rightarrow \pi^+ \pi^-$

where the last four processes provide direct evidence for the existence of CP violation and channels for its observation in B decays.

The primary goal of the laboratory is the detailed exploration of B meson decays, and particularly the characterization of CP violation. At this time the most direct path appears to be through neutral B decays which requires the

relativistic boost of an asymmetric collider. Thus the CESR B asymmetric B factory is the principal goal of the laboratory.

As much of the technology required for an asymmetric B factory is related to the large beam currents and closely spaced bunches, also needed for upgraded CESR operation, carrying out an upgrade program for CESR is a conservative yet timely approach to an asymmetric B factory. Accordingly we have planned a phased upgrade to CESR which will provide increased luminosity to satisfy near term physics needs, will establish a solid technical basis for CESR B operation, and will be compatible with the commissioning of CESR B as soon as possible after approval.

II. PRESENT CESR STATUS

The CESR facility has been described in detail in several documents [1,2,3,4]. The accelerator facility is located on the side of a small valley, providing convenient access to the accelerator tunnel which is approximately 15 m below the surface level. The storage ring and former 12 GeV electron synchrotron share a 3.3 m diameter tunnel with a circumference of 768 m. A 300 MeV linac provides a $2.5 \mu\text{s}$ long stream of bunches to the synchrotron which accelerates these bunches to as much as 8 GeV. Thus full energy injection of nearly all bunches stored in one beam in CESR is possible.

The storage ring itself is capable, in principle, of operating from 3 to 8 GeV. However, because of the strong interest in B physics, performance has been optimized in the range of 4.7–6.0 GeV beam energy. Independent power supplies[5] for the 102 quadrupoles and 84 sextupoles provide great flexibility in optics implementation which has proven invaluable for both operations and machine studies.

CESR operates with a single interaction point (accommodating the CLEO detector) and 7 bunches per beam. The bunches collide head-on, but electrons and positrons follow separate (horizontal) closed orbits for approximately 88% of the circumference to provide separation at the 13 parasitic crossing points. These orbits, or "pretzels," are established by 4 electrostatic separators. A schematic plan view showing the pretzel orbits is shown in Figure 1.

A list of the principal operating characteristics of CESR may be found in Table 1 (later in this document). Several parameters merit special note.

We have found by extensive machine studies [6] that, while the vertical beam-beam parameter, ξ_V , falls as β_V^* approaches the bunch length, σ_1 , the best luminosity (proportional to ξ_V / β_V^*) is found when $\beta_V^* \approx \sigma_1$.

β_V^* itself is less than 2.0 cm. Beam size and chromaticity are limited by the use of 1.22 m long permanent magnet quads

* Work supported by the US National Science Foundation.

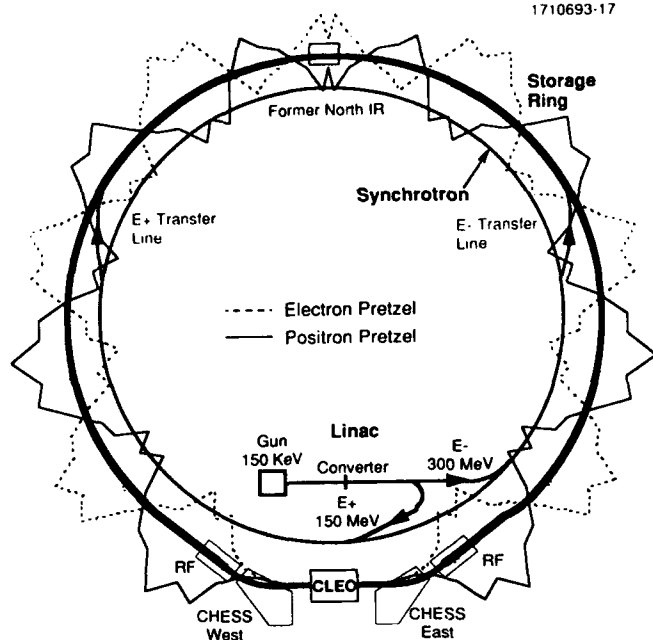


Figure 1. Schematic layout of CESR and injector complex. Pretzel orbits for 7 bunch operation are superimposed on the CESR ring.

with a gradient of approximately 15 T/m. Energy flexibility is provided by an adjacent electromagnetic quad.

The charge per bunch is modest, minimizing blowup of vertical emittance by the beam-beam effect. During machine studies with 1 bunch/beam, up to 3×10^{11} e/bunch have been collided.

The vertical beam-beam parameter, ξ_V , reaches 0.04 during high energy physics. ξ_H is also around 0.04 during physics runs, and somewhat higher during single bunch machine studies.

III. UPGRADE PATH

The luminosity of a colliding beam machine is often parameterized in terms of total beam current and factors determining the luminosity per bunch:

$$L = 2.17 (1+r) E_{\text{beam}} \frac{\xi_V}{\beta_V^*} I_{\text{beam}} \quad (1)$$

where L is luminosity in units of $10^{32} \text{ cm}^{-2} \cdot \text{s}^{-1}$, r is the beam aspect ratio at the ip, E_{beam} the beam energy (GeV), ξ_V the beam-beam parameter, β_V^* the vertical focussing function at the i.p. (m), and I_{beam} the current per beam (A).

Here E_{beam} is determined by the physics and we will continue to use flat beams (r small) to avoid background problems and optics designs which are difficult to implement. Of the remaining three parameters, we choose to concentrate initially on increasing total beam current, I_{beam} . After looking at the accelerator physics and engineering problems associated with each of these three parameters, we feel that the largest potential gain lies in the total beam current. Short of a breakthrough in understanding of the beam-beam effect, ξ_V is

unlikely to be increased much beyond 0.06, and may be adversely affected by changes made in β_V^* or I_{beam} . Reducing β_V^* will require reducing the bunch length proportionately. These changes will increase chromaticity (Q'), RF voltage requirements, and higher order mode (HOM) losses, all of which are undesirable and, in turn, affect limits on ξ_V and I_{beam} .

Having chosen to increase I_{beam} , there remains the decision of how to distribute the additional current. The HOM losses, at constant bunch length, scale as $I_{\text{bunch}} \times I_{\text{beam}}$, so these will increase as I_{beam}^2 if the current per bunch is increased, but only as I_{beam} if we increase the number of bunches and keep the bunch current constant. A more fundamental limit results from beam-beam effects. The horizontal beam-beam parameter, ξ_H , increases linearly with I_{bunch} . In the case when ξ_V has reached a saturation limit, the vertical emittance increases with bunch current, causing the beam lifetime to decrease (and often the detector background to increase) beyond some limiting current. For these reasons we choose to increase the number of bunches in CESR.

Assuring sufficient separation of counter-rotating bunches at all parasitic crossing points is the most fundamental consideration in planning the distribution of additional bunches. The most obvious option is to increase the number of "loops" in the pretzel orbit shown in Figure 1 by increasing the horizontal betatron tune, Q_H . This option results in stronger sextupoles which reduces the dynamic aperture of the machine and increases the difficulty of balancing optics distortions from the off-center orbits of the pretzel through the sextupoles. An increase from 7 to 12 bunches per beam may be possible by this approach.

A more attractive option [7] is to use each pretzel loop to separate multiple parasitic crossings. This leads to grouping the additional bunches in "trains." Thus several trains of 2 to 5 bunches each could be separated using a pretzel scheme resembling that currently used. We have studied options capable of accommodating as many as 45 bunches per beam arranged in 9 trains, each with 5 bunches.

There is an additional complication with this approach. The closely spaced bunches in each train create parasitic crossings very close to the main interaction point (i.p.), posing a difficult separation problem. The bunches could be separated at these parasitic crossings if a small crossing angle is used at the i.p. The pretzel orbits near the IR are shown for both present (7 bunch) layout and for a bunch train with crossing angle layout (9x3 bunches) in Figure 2.

IV. UPGRADE PLAN

We are following a phased approach to the CESR luminosity upgrade. There are several reasons for this. Operational reliability is maximized by relatively short shutdowns to install hardware for each phase and the option to go back to a previous configuration is available. We get practical experience with equipment and optics configurations with fewer bunches and lower currents before adding the complications of more parasitic crossings and higher currents. The beam current is increased gradually, accommodating the

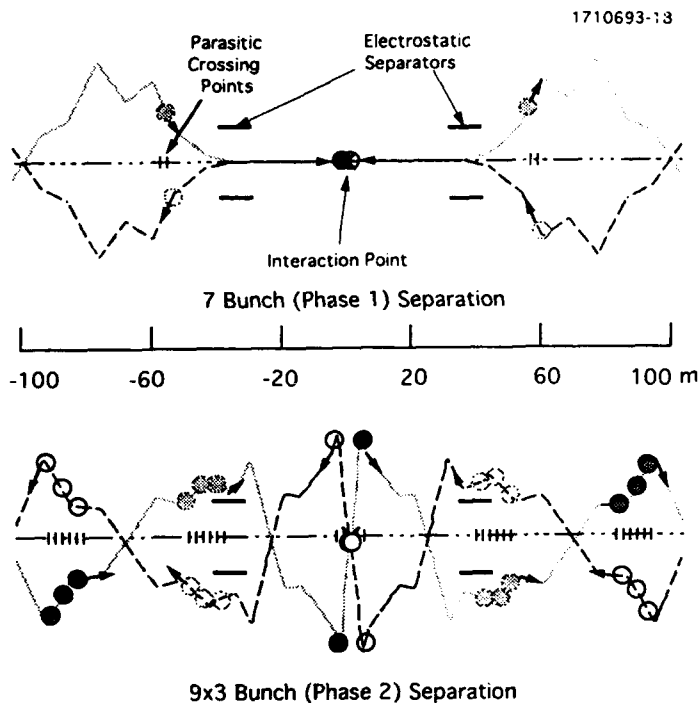


Figure 2. Pretzel separation plan near the IR. The present 7 bunch layout is shown in the top view. The 9x3 bunch train with a ± 2.5 mr horizontal crossing angle is shown in the bottom view. The scales' aspect ratio is highly distorted.

conditioning of RF cavities and separators into the schedule. The gradual increase of current is also compatible with systematic identification and replacement of any individual vacuum system components which exhibit excessive HOM losses.

The present configuration of CESR is identified as Phase I of the luminosity upgrade plan. The major components of Phase I are: 1) conversion from 2 to 1 interaction point, 2) upgrade of the linac instrumentation to increase its intensity and reliability, and 3) replacement of the original 14 cell RF cavities with 5 cell cavities of similar geometry. The original RF cavities in CESR were designed for 100 mA/beam maximum current. The new 5-cell "Mk III" cavities are designed for 300 mA/beam. The measured peak luminosity in this configuration is $2.5 \times 10^{32} \text{ cm}^{-2}\text{s}^{-1}$ and maximum beam current is ≈ 100 mA/beam.

Phase II equipment construction has been approved and commissioning will take place in early 1994 at the same time as the CLEO inner detector will be upgraded by the installation of a silicon strip vertex detector. [8] 27 bunches per beam will circulate in 9 bunch trains. The bunch spacing within a train will be 28 ns or 14 CESR RF wavelengths.

Several pieces of accelerator equipment will be replaced or modified:

- New electrostatic separators will be installed which are expected to have 1/3 the HOM losses of the present ones.

- Vacuum chambers and pumps within ± 15 m of the i.p. are being replaced to maintain particle backgrounds at present levels even with 3x increase in beam current.
- A wideband transverse feedback system has been tested in CESR which will provide bunch-by-bunch feedback in both planes with bunch spacings as low as 10 ns.
- The master timing system will be replaced with a system that will accommodate all likely combinations of bunch spacing.
- A new gun modulator has been installed which will provide bunches at full charge (10^{11} e^-) at a spacing of 14 ns.
- The IR quadrupoles will be reconfigured to provide more horizontal aperture to accommodate the ± 2.5 mr crossing angle pretzel orbits during injection.
- The CHSS beam stops and windows for wiggler lines are being upgraded to handle the higher beam power.

The design luminosity in the Phase II configuration is $6 \times 10^{32} \text{ cm}^{-2}\text{s}^{-1}$ at a current of 300 mA/beam.

A comparison of the parameters for Phase I and Phase II is made in Table 1. We use a conservative value of 0.03 for ξ_v although we expect to eventually reach 0.04 as is our present experience. Note also that the emittance and current per bunch are lower in Phase II operation.

Table 1. Principal parameters for current CESR operation (Phase I) and upgrade operation in 1994 (Phase II)

Parameter	Phase I	Phase II	Units
E_0	5.30	5.30	GeV
Peak Luminosity	0.25	0.6	$10^{33} \text{ cm}^{-2} \text{ sec}^{-1}$
n_b (bunches/beam)	7	9x3	
r (aspect ratio at i.p.)	0.014	0.023	
N	2.24	1.75	$10^{11} \text{ e}^-/\text{bunch}$
i_b (current/bunch)	14.0	11.0	mA
I_{beam} (current/beam)	0.10	0.30	Amps
ξ_v (beam-beam param.)	0.04	0.03	
ξ_h " " "	0.04	0.04	
$2\pi R$ (circumference)	768.43	768.43	m
σ_h^* (beam size at i.p.)	550	430	μm
σ_v^* " " " "	8	10	μm
β_h^* (focus funct at i.p.)	1.00	1.00	m
β_v^* " " " "	18	17	mm
σ_l (bunch length)	18	17	mm
ϵ_h (emittance)	3.0	1.9	$\times 10^{-7} \text{ m}$
α_p (momentum comp.)	1.54	1.13	$\times 10^{-2}$
Q_s (synchrotron tune)	0.06	0.055	
Q_h (betatron tune)	8.57	10.57	

The bunch train concept can be taken to the beam current limit of the CESR vacuum chamber, estimated to be around 500 mA/beam at 5.3 GeV. In order to handle the total storage ring current of 1 ampere, many components will have essentially the same specifications as for the CESR-B asymmetric B factory [9]. Therefore, to a large extent, the two programs have identical R&D agenda. The principal components for both projects are:

- Single cell superconducting RF cavities will be required to handle the very high currents and maintain low beam impedance. The design is identical for both upgrade or CESR-B.
- Copper vacuum chambers with high pumping speeds from NEG and TiSP pumps will be needed in the hard-bend regions of CESR. In CESR-B the whole vacuum system will be of a similar design.
- Some arc vacuum chamber components will be replaced in CESR to accept 1A of total stored current. The design for these components will again be similar to those in CESR-B.
- CESR Phase III interaction region uses both permanent-magnet and superconducting technologies for the first vertically focussing quads. CESR-B uses a superconducting quad with compensating solenoids.
- CESR will use a ± 2.5 mr uncompensated crossing angle, while CESR-B will use a ± 12 mr crab compensated crossing angle.

With 500 mA/beam in 45 bunches, the luminosity will be between 1 and $2 \times 10^{33} \text{ cm}^{-2}\text{s}^{-1}$ depending on the extent to which ξ_V and β_V^* can be further optimized. CESR-B will reach $3 \times 10^{33} \text{ cm}^{-2}\text{s}^{-1}$ with 0.87 A in the 8 GeV beam and 2 A in the 3.5 GeV beam.

V. UPGRADE R&D ACTIVITIES

There is no operational experience with bunch trains and a small horizontal crossing angle in existing or past e^+e^- storage rings. Therefore it is necessary to understand the accelerator physics aspects of this mode of operation through analytic methods, computer simulation, and machine experiments. We will discuss several of the accelerator experiments at CESR in the remainder of this report.

Some of the recent areas of experimental study are:

- Single beam stability of bunch trains in CESR
- Comparison of injection performance with a computer model [10]
- Dynamic aperture and beam-beam performance with small β_V^* and large Q_H . [11]
- Ion and dust trapping phenomena [12,13]
- Comparison of measured with simulated detector background from both synchrotron radiation and lost particles [14]
- Beam-beam effects with a crossing angle [15]

- Long range beam-beam interaction and separation criteria for optics design [16]

The last two of these will be discussed in more detail below.

A. Crossing Angle

The independently controlled quadrupoles and sextupoles in CESR make it possible to use the pretzel electrostatic separators to create a horizontal crossing angle at the i.p. Adjustment of separator voltages causes a horizontal separation at the i.p. for injection. The crossing angle may be adjusted from 0 to ± 2.8 mrad.

These experiments were carried out with the 1.5 tesla experiment solenoid turned on to eliminate the overhead of ramping the solenoid and readjusting compensation. Since a crossing angle of 2.5 mr is over 5 times the rms angular spread from natural beam emittance, the sensitivity to errors in compensation the relevant coupling terms is increased a comparable amount. Effects such as this are usually removed by operator tuning over periods of several days to weeks. This was not possible in the limited time available for machine studies.

ξ_V was calculated from Bhabha scattering measurements for different crossing angles. The results appear in Figure 3. Part of the $\sim 15\%$ drop at -2.5 mrad is from the orbit distortion as can be seen in the square points representing magnetically induce orbit distortions (which result in head-on collisions but with orbit distortions of comparable magnitude). Most of the remaining drop is probably a result of imperfections in the solenoid compensation as described above.

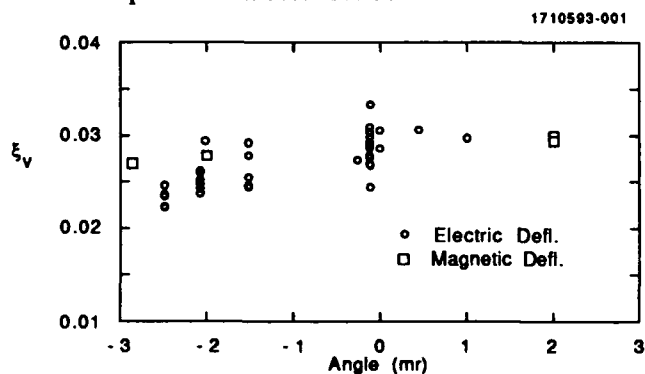


Figure 3. ξ_V vs. horizontal crossing angle. The data represented by square markers were taken using a magnetic orbit distortion without crossing angle.

Beam lifetime is also important for integrated luminosity. A sensitive measurement of lifetime effects may be made by inserting a movable aperture or "scraper" into the vacuum chamber and recording beam lifetime as a function of its position. Measurements in the vertical plane show no influence of crossing angle on particle distribution. In the horizontal plane some effect may be seen (Figure 4), but small changes in betatron tune cause the crossing angle induced blow up to disappear (11 mA, $Q_H=8.59$). More detailed studies [17]

of resonances and crossing angles confirm the picture that the primary effect of a small crossing angle is to drive isolated resonances which are avoidable with proper choice of operating point.

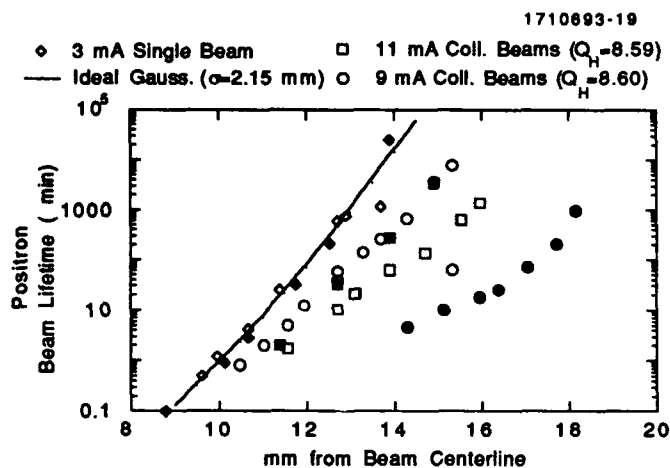


Figure 4. Beam lifetime due to movable aperture for single and colliding positron beams. The result for an ideal gaussian charge distribution is shown by the solid line. The open points were measured with head-on collisions, the solid points were measured with ± 2 mrad crossing angle.

B. Long Range Beam-Beam Effects

We have had experience at CESR with no parasitic crossings (single bunch operation), and $n=4, 12$, and 13 parasitic crossings with 3 and 7 bunches per beam. The required separation between beams has increased more slowly than \sqrt{n} , which would be expected if the effects of the crossings added but were uncorrelated. However, with the possibility of 89 parasitic crossings and tightened optics constraints, a better understanding of the relevant physics and an analytic formulation of separation criteria for optics optimization is needed.

While initial measurements at CESR suggested a "hard-core" model of the parasitic interaction (counter-rotating beam acted like a scraper), using a fixed limit on the long range tune shift experienced by a zero-amplitude particle fit the current dependence of separation better. (All measurements were done for a beam lifetime of 60-100 minutes.) However, the appropriate value of tune shift varied from one crossing point to another.

Recently a phenomenological approach has been taken to finding an appropriate separation criterion. Measurements of separation vs. beam current were made in 11 different configurations. Several plausible forms of separation criteria were used to fit the data. Finally the residual scatter about the fit curve was reduced to an r.m.s. spread. The aforementioned criteria were among the worst fits. Several scaling relations were found which had about half the r.m.s. scatter. These are discussed in detail in another paper in this conference[16].

VI. CONCLUSION

A. Summary

The demands of the high luminosity colliders and "factories" being planned today will push many of the older accelerator design techniques close to, and possibly beyond their limits. Innovation and a systematic design approach coupling analytic, simulation, and experimental techniques is the most effective way to answer these challenges.

CESR is not only an effective physics production machine, but is also an ideal platform for carrying out experiments in accelerator physics. An optimum size and the flexibility offered by independent magnet control contribute to these qualities.

The upgrade described here will assure a continuation of the past trend in CESR luminosity (doubling every two years) and address many of the issues of asymmetric B factories.

B. Acknowledgements

The dedicated technical staff and accelerator operations group made the impressive performance record of CESR possible. All members of the accelerator operations group contributed to the measurements described here. Several members of the CLEO collaborating institutions have been very active in accelerator development areas; their capable help is gratefully acknowledged.

VII. REFERENCES

- [1] M. Tigner, *IEEE Trans. Nucl.Sci.* NS-24, 1849 (1977)
- [2] D. Morse, *XI Int. Conf. on High Energy Accel.* 26 (1980)
- [3] R. Littauer, *IEEE Trans. Nucl.Sci.*, NS-32, 1610 (1985)
- [4] S. Herb, J. Kirchgessner *IEEE 87CH2387-9*, 130 (1987)
- [5] D. Hartill, D. Rice, *IEEE Trans. Nucl.Sci.* NS-26 4078 (1979)
- [6] L. Shick, D. Rubin, *IEEE 91CH3038-7*, 470 (1991)
- [7] R. Meller, Cornell internal note CON 90-17 (1990)
- [8] J. Alexander *et al.*, *Nucl. Instr. & Meth.* A326, 243 (1993)
- [9] M. Tigner, *AIP Conf. Proc.* 214, 561 (1990)
- [10] D. Rice, F. Tian, *SLAC-400*, 242 (1992)
- [11] T. Pelaia, Cornell note CBN 91-13 (1991)
- [12] D. Sagan, Cornell note CBN 91-2 (1991)
- [13] D. Sagan, Cornell note CBN 92-12 (1992)
- [14] H. Yamamoto, *BFWS 93*, Tsukuba, Japan, Nov, 1992.
- [15] D. Rubin, *et al.*, *Nucl. Instr. & Meth.* A330, 12 (1993)
- [16] S. Temnykh, *et al.*, presented at IEEE/APS Part. Acc. Conf., Washington, D.C. (1993)
- [17] T. Chen, *et al.*, presented at IEEE/APS Part. Acc. Conf., Washington, D.C. (1993)

LEP Status and Future Plans

Lyndon R. Evans

European Organization for Nuclear Research (C.E.R.N.), CH - 1211 Geneva 23, Switzerland

Abstract

At the end of 1992, LEP completed its fourth year of operation, producing more than 28 inverse picobarns of integrated luminosity in each of the four experiments and a total of three million hadronic Z^0 s. For the first time the machine operated for physics with a new high-tune optics producing the smaller transverse emittance eventually needed for future operation at higher energy. As well as gaining valuable experience with this optics the luminosity lifetime could be improved by using wigglers to control the evolution of beam emittance during a run. In addition, the so-called 8-bunch "pretzel" scheme was commissioned, allowing the number of bunches per beam to be increased from four to eight towards the end of the year. Present performance limitations are discussed and future plans for increasing both the energy and luminosity are described. Many details of the topics mentioned here may be found in [1] and in contributed papers to this conference.

I. INTRODUCTION

In its fourth year of operation, the CERN Large Electron Positron (LEP) collider ran for 138 days for physics data taking, producing 28.6 inverse picobarns of integrated luminosity and a total of 3 million hadronic Z^0 s summed over the 4 experiments (Figs. 1 and 2).

The peak luminosity achieved was $1.15 \cdot 10^{31} \text{ cm}^{-2} \text{ s}^{-1}$, about 15% higher than in 1991 and less than 20% below the design luminosity at 45 GeV. The average daily integrated luminosity of 206 inverse nanobarns was most 40% higher

than achieved the previous year, mainly due to the very good luminosity lifetime. The limiting vertical beam-beam tune shift parameter was about 0.03 with 0.04 achieved under the very best conditions.

For most of the year, LEP ran as in the past with four counter-rotating bunches of electrons and positrons per beam. During the last month of operation the so-called "pretzel" scheme was commissioned. Electrostatic separators are used to horizontally separate the beams around most of the machine circumference in order to allow the number of bunches per beam to be doubled without exceeding the beam-beam limit.

A significant change compared with previous operation was the move to a new high-tune optics [2] (90° phase advance per cell compared with 60° in 1991). This change was made for three main reasons

- The 90° optics produces a smaller natural beam emittance allowing the possibility of controlled blow-up in order to remain at the beam-beam limit throughout a physics run, the luminosity thus decreasing proportional to the current and not to the square of the current
- The new optics was designed to cover machine development requirements, in particular the development of the 8-bunch pretzel scheme and energy calibration by resonant depolarization as well as normal operation. This made the use of machine development time much more efficient.
- The higher tune optics is necessary in order to achieve useful luminosity for future operation above the W-pair production threshold since the natural emittance increases like the square of the energy.

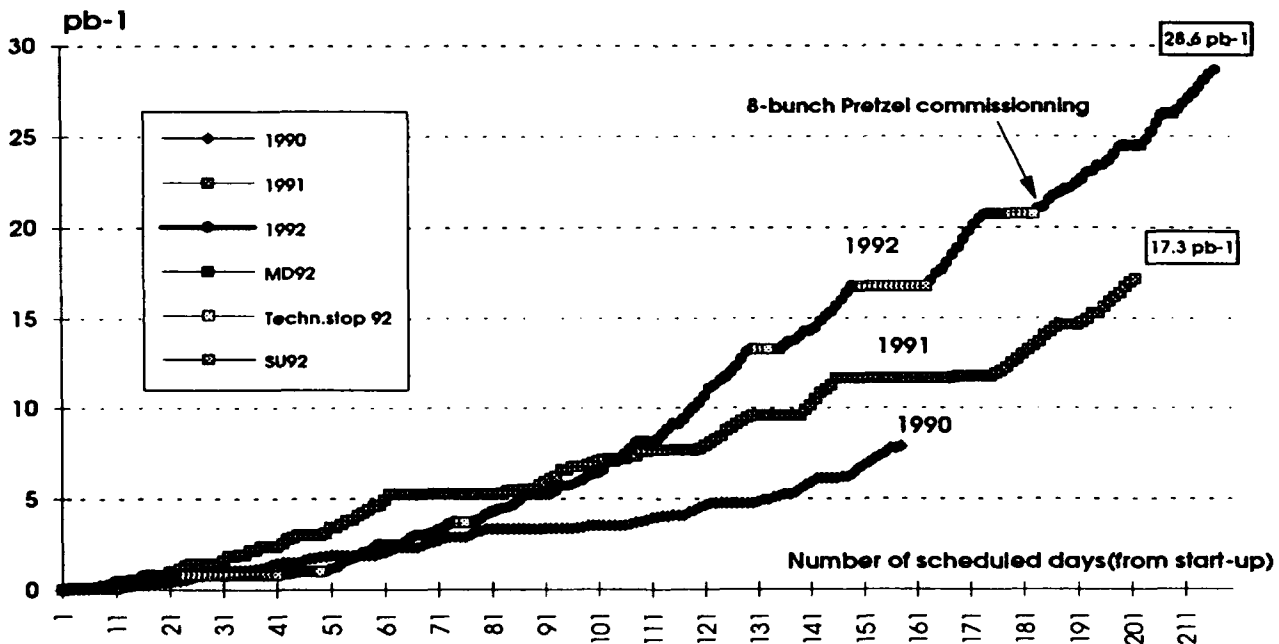


Fig. 1 Integrated luminosity per year 1991-1992

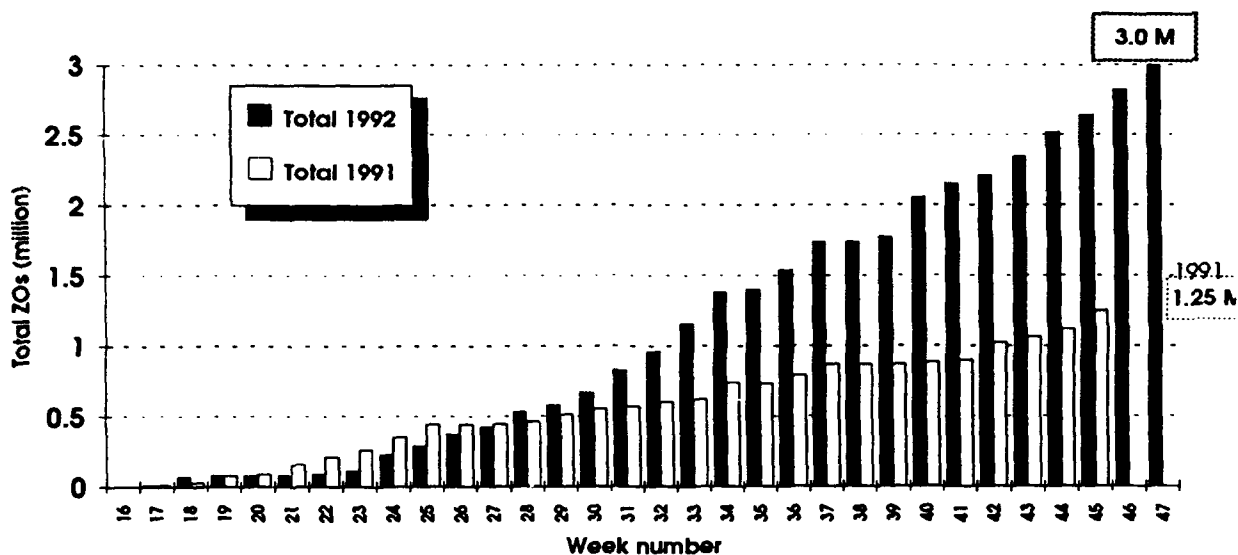


Fig. 2 Number of Z^0 s detected in the four LEP experiments in 1991 and 1992

II. PERFORMANCE LIMITATIONS

The luminosity of an electron-positron collider is limited by three main parameters, the total circulating current, the maximum attainable beam-beam tune shift parameter and the minimum value of the vertical beta function at the interaction point.

2.1 The Beam Current

LEP suffers from both longitudinal and transverse instabilities. Turbulent bunch lengthening occurs but is of no consequence. Longitudinal dipole mode instabilities are damped by a 1 GHz feedback system [3] using cavities provided to CERN by the DESY laboratory.

LEP is the first machine in which higher head-tail modes can be observed directly using a novel streak camera to display the three-dimensional charge distributions of individual bunches on successive turns [4]. The chromaticity must be kept slightly positive in order to damp the classic mode $m=0$. However, for too strong chromaticity, mode $m=1$ is observed with a threshold behaviour when the growth rate exceeds the damping rate. The threshold depends in a complicated way on the bunch length. Moderately increasing the bunch length with wigglers couples the bunch spectrum to the machine impedance, dominated by the radio-frequency cavities, more efficiently and actually increases the growth rate. Above about 18 mm bunch length the growth rate once more decreases. The threshold also depends on the value of the chromaticity, which must be reduced to a small but positive value in order to keep mode $m=0$ stable as the current is increased. With Q' less than about 4 units, this instability does not limit the bunch current.

The most fundamental limitation to the maximum single bunch current is as predicted many years ago, the fast head-tail or transverse mode-coupling instability (TMCI). The threshold for the onset of this instability is given by

$$I_b = \frac{2\pi Q_s E}{e \sum_i \beta_i k_i (\sigma_z)}$$

where Q_s is the synchrotron tune, E the beam energy, β_i is the betatron amplitude function at the location of the i th transverse impedance driving the instability and k_i is the transverse loss factor of the impedance, which decreases with increasing bunch length.

The natural bunch length (σ_z) at the 20 GeV injection energy for the 90° lattice is less than 5 mm and the TMCI threshold is consequently much lower than with the 60° ($\sigma_z = 20$ mm) lattice. Lengthening the bunch increases the threshold of this instability as expected theoretically. Figure 3 shows the predicted threshold current [5] as a function of bunch length compared with a few measured points. The bunch lengthening was achieved using powerful wigglers. Single bunch currents of around 0.65 mA are presently achieved with a bunch length of about 20 mm and a synchrotron tune of 0.085. During machine studies the threshold has been increased to 0.8 mA by increasing Q_s to 0.13.

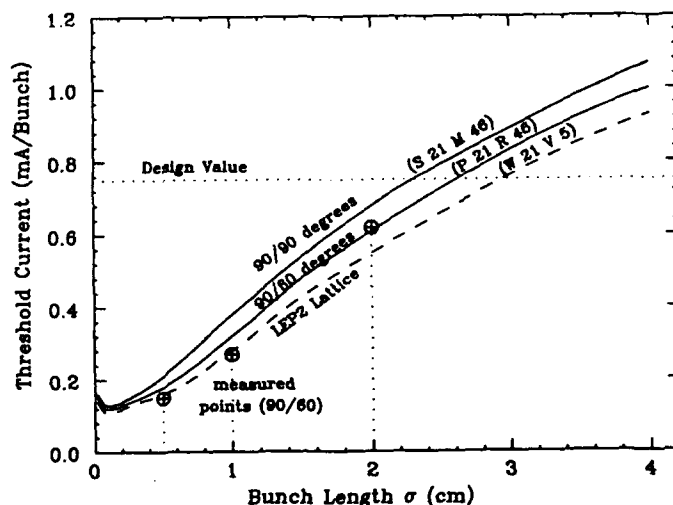


Fig. 3 Predicted TMCI threshold currents for various LEP lattices with some measured points. The slight dependence on lattice phase advance is due to the different β values in the RF cavities.

2.2 Beam-beam Limits

Although the bunch current can exceed 0.65 mA for a single beam under normal conditions, with two beams the current is limited to 0.55 mA. During injection and accumulation, the two beams are separated vertically at all eight collision points using electrostatic separators. This current limitation is most probably linked to the long range beam-beam interaction although the exact mechanism has not yet been clarified.

During collision, the maximum achievable beam-beam tune shift has been steadily increased since the early days of LEP commissioning by careful choice of integer and non-integer tune values and by the gradual correction of optical errors, phase advance between collision points, residual dispersion at the interaction points and residual separation between the two beams. With the small natural emittance (12 nm) of the 90° phase advance lattice, the beam sizes must be artificially increased with "emittance" wigglers before the beams are brought into collision otherwise they are lost. Achieving the highest possible tune shift is still an inexact science, requiring small empirical adjustments of critical parameters, particularly the closed orbit. The maximum tune shift still varies somewhat from run to run and shows some slight current dependence (Fig. 4) [6].

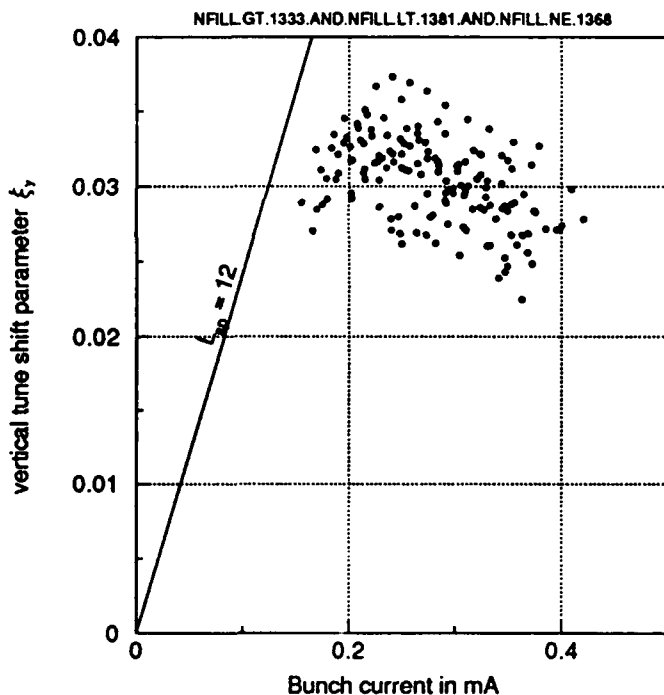


Fig. 4 ξ_y dependence on current over a number of physics runs.

A great advantage of the high tune lattice is that the beam size reduces with decreasing current so the tune shift can be kept close to the limit throughout the duration of a physics run, generally about 10 hours. Figure 5 shows an example [7] of a fill which was kept much longer than this due to trouble with the injectors. For the first half of the store the luminosity decreased approximately proportionally with beam current, indicating a more or less constant beam-beam tune

shift. During the last hours the machine was no longer beam-beam limited so the luminosity decay was faster. This ability to stay at the beam beam limit means that the daily integrated luminosity is higher than expected from the original design even though the peak luminosity is slightly lower.

Although the two-beam current limit is 550 μ A, the bunch intensity for physics runs is limited to below 450 μ A in order to keep the background in the experiments under control. The horizontal aperture is collimated to about 45 nm for clean conditions.

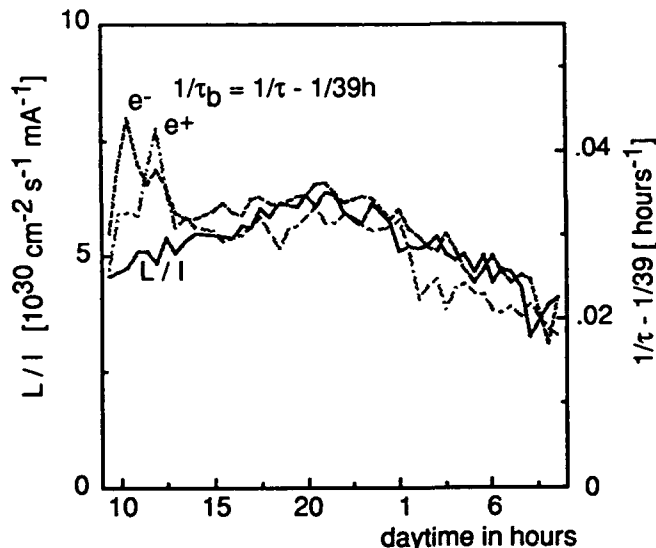


Fig. 5 L/I and inverse beam lifetime over a long run. For the first 10 hours, L/I is constant or slightly increasing. Later the beam-beam tune shift is no longer saturated and L/I decreases.

2.3 Beta Function at the IP

The minimum β^* at the IP is limited by the very high beta values in the insertion quadrupoles, producing large chromatic aberrations and closed orbit errors due to small displacement of these quadrupoles. In addition it has been shown [8] that a combination of spurious vertical dispersion and orbit errors in these quadrupoles can result in a rapid reduction in the vertical damping partition number. Up to now, LEP has run with $\beta_H^* = 1.2$ m, $\beta_V^* = 0.05$ m. Below this value the machine gets to be much too sensitive to the above mentioned effects.

The problem of keeping the background due to soft photons for large emittance beams can be alleviated by making a weaker horizontal focusing into the IP. At the end of the year a new optics with $\beta_H^* = 2.5$ m was tried and should allow colliding beams with significantly more than 400 μ A per bunch.

III. 8-BUNCH PRETZEL

Further substantial increase in luminosity at 45 GeV can only be achieved by increasing the number of bunches per beam. Going from 4 to 8 bunches means that the beams must be separated at all unwanted crossing points. In order to

achieve this a scheme similar to those already used successfully at Cornell and at the CERN and FNAL proton-antiproton colliders has been implemented [9]. Electrostatic separators are used to make global horizontal orbit distortions in opposite directions for electrons and positrons between each experimental collision point (Fig 6).

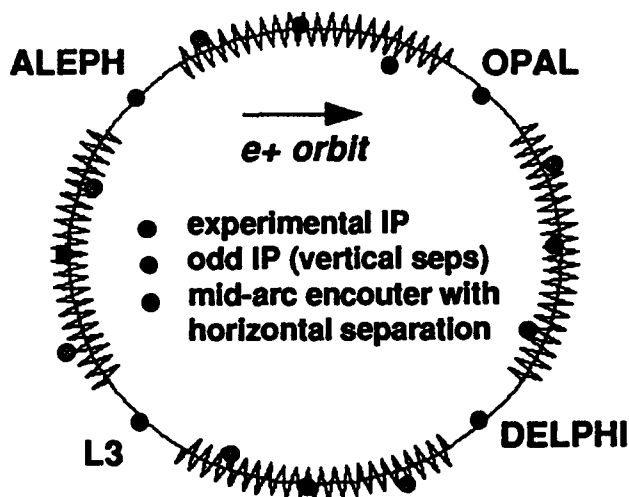


Fig. 6 Schematic representation of the orbits in the LEP pretzel scheme.

Early experience with horizontal separators in the high synchrotron radiation environment of LEP indicated a very high spark rate in the presence of the beams. Further investigation showed that the spark rate was strongly correlated with the polarity of the high voltage electrode [10]. For the normally used negative polarity, which avoids dark current in the high voltage circuit, the spark rate was found to be intolerably high whereas for positive polarity, it was reduced to an acceptable level. The exact mechanism has yet to be understood but it is felt that the positive polarity alleviates the problem of charging of the ceramic insulators by stray electrons.

During the January 1992 winter shutdown the full pretzel scheme consisting of 8 horizontal separators recuperated from the SPS proton-antiproton collider together with a number of sextupoles for independent tune control of the two beams was installed. Commissioning started in June 1992 and 8-bunch operation was implemented for physics during the last 5 weeks of the run. The main objective was to reach "break even", the same integrated luminosity with 8 bunches per beam as with 4, by the end of the year. This was achieved quite rapidly, the peak luminosity exceeding that achieved with 4 bunches by about 15%. This now provides a solid base on which to make further progress.

IV. POLARIZATION

The first observation of a small but significant level of transverse polarization was made in 1990. In 1991, polarization levels of between 10% and 20% were achieved. This level was perfectly adequate to allow precise energy calibration by resonant depolarization with a precision of better than 1 MeV at 45 GeV.

The high tune optics used in 1992 was designed to allow transverse polarization on the Z-pole under operational conditions in order to exploit more fully the possibility of systematic precision energy calibration during physics runs. However, three attempts to find polarization on this optics did not succeed. After extensive tests of the polarimeter it was concluded that the main reason was that the quality of the vertical orbit correction was insufficient, about 0.7 mm rms, due to the fact that the 90° optics allows four pickup measurements per betatron wavelength instead of six with the 60° optics of 1991, where 0.5 mm rms was routinely achieved.

During machine studies when the old optics was reloaded, polarization was quickly observed and calibration at two different beam energies was successfully performed [11]. However, transfer of calibrations between different optics is delicate so another hybrid optics which could eventually be used operationally was commissioned, with a phase advance of 90° in the horizontal plane in order to retain the small natural emittance but with the vertical phase advance reduced to 60° per period in order to optimize the orbit correction. Again, polarization was quickly observed and energy calibrations extensively performed. In addition, the depolarising effect of the ALEPH solenoid was compensated with dipole π -bumps in the arcs each side of the solenoid. This was an important step towards the final goal of energy calibration under full data taking conditions. Finally the pretzel was switched on and a useful amount of transverse polarization was still retained.

For a long time the extreme precision of energy calibration made available with polarized beams has revealed small but significant drifts in beam energy as a function of time. It had been postulated that these variations could be explained by small changes in the circumference of LEP due to the combined tidal effect of the sun and the moon deforming the earth's crust. An experiment was therefore performed to track the variation of the LEP energy over a 36 hour period coincident with strong tidal activity. A peak to peak energy variation of about 9 MeV, corresponding to a change in the 27 km circumference of about 1 mm, was indeed measured [12]. The cyclic nature of the phenomenon could be easily observed (Fig 7) and the measured results were found to be in good agreement with the theoretical prediction. This 18 MeV variation in the centre of mass energy is now the dominant factor in the determination of the Z^0 mass.

V. FUTURE PLANS

Over the next few years it is foreseen to increase both the energy and luminosity of the machine.

The energy upgrade will allow operation above the W-pair threshold for physics from the beginning of 1995. The cross section for W-pair production rises sharply above 82 GeV and a beam energy of at least 87 GeV is required in order to ensure a reasonable rate. At this energy, the synchrotron radiation loss per turn is 1.6 GeV and therefore a minimum circumferential RF voltage of 1900 MV is required. This will necessitate the installation of 192 superconducting cavities around the four even interaction points, 32 cavities each around points 2 and 6 where the copper cavities are presently installed and 64 cavities each at two new acceleration points 4 and 8. These cavities will be powered by twelve 1.3 MW klystrons, 16 cavities per klystron, operating at 352 MHz.

LEP TidExperiment

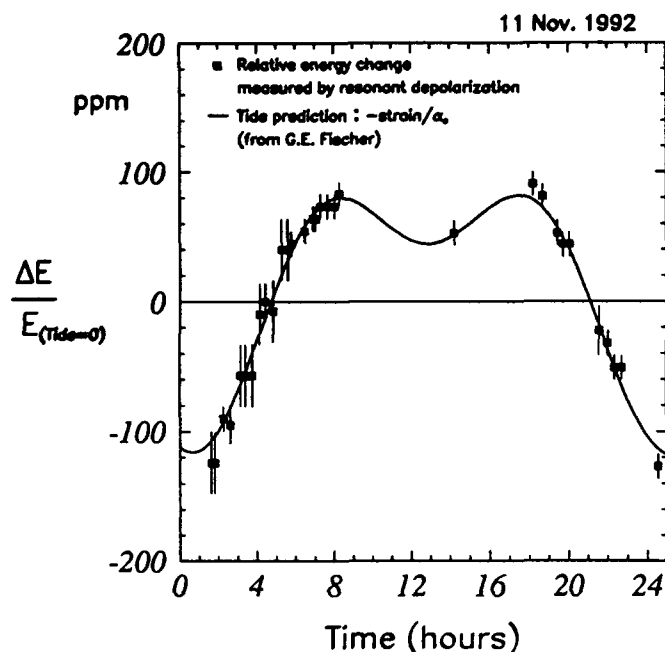


Fig. 7 Energy variation over a 24-hour period compared with the expectation.

The cooling of the cavities requires the installation of 4 cryoplants, each with a cooling capacity of 12 kW at 4.5 K.

The first set of 32 cavities at point 2 consists of 8 prototype Nb sputtered copper cavities made at CERN and 24 Nb sheet cavities, four prototypes and 20 industrially produced series units. All cavities have achieved or exceeded the specified gradient of 5 MV/m with a quality factor of $3 \cdot 10^9$.

LEP points 4, 6 and 8 will all be equipped with Nb sputtered copper cavities with a nominal gradient of 6 MV/m and a Q of $4 \cdot 10^9$. So far, 29 cavities fulfilling the above specification have arrived at CERN.

As well as the radio-frequency, major upgrades are needed on many other systems. A number of changes of the original lattice are needed because quadrupoles run out of focusing strength above 65 GeV and also because the length of the RF cells increases. The present superconducting quadrupoles need to be replaced by new ones with the gradient increased from 36 T/m to 55 T/m. The project also requires major modifications to vacuum, power converters and civil engineering. A more detailed presentation of the LEP2 project is given elsewhere in these proceedings [13].

At high energy, luminosity is of critical importance since the cross section for W-pair production is about three orders of magnitude lower than that at the Z-pole. In addition, the natural emittance at 90 GeV is a factor of 4 larger than at 45 GeV so the unperturbed tune shift for 0.5 mA per bunch is about 0.014, well below the saturation value.

Several measures are envisaged to increase the current per bunch. Firstly the injection energy into LEP will be raised from 20 GeV to around 22 GeV when a second superconducting cavity module is installed in the LEP injector (the SPS). This will raise the TMCI threshold by 10% as well as providing faster damping in LEP. Secondly it is envisaged to

reduce the transverse impedance of LEP by removing the copper radiofrequency system, which is the main contributing element to the TMCI current limitation, and to compensate for the lost circumferential voltage by installing 32 additional superconducting cavities which, in view of their much larger iris diameter, have considerably lower impedance. Further bunch lengthening by varying damping partition numbers or with a higher harmonic cavity is under study as well as the possibility of operating at a higher synchrotron tune. It is predicted that these measures will allow the TMCI threshold to be raised to around 1 mA per bunch.

Studies have shown that background control in the experiments will become a serious problem in LEP2 because of the higher photon flux and the larger natural beam emittance. One option under serious consideration is to move to a low emittance lattice with a phase advance even higher than 90° , at the same time providing higher luminosity and better background control [14]. The fact that such flexibility exist says much for the quality of the original optical design of LEP.

In addition to the above measures, pretzel operation will be actively pursued over the next two years, with 8-bunch operation at 1 mA per bunch at 90 GeV and an initial luminosity above $5 \cdot 10^{31} \text{ cm}^{-2} \text{ s}^{-1}$ as an objective. RF power considerations and higher mode losses will then start to play an important role.

VI. CONCLUSIONS

LEP is now operating close to its design peak luminosity and with a better than expected luminosity lifetime. The main limitations to machine performance are now well understood and plans are underway to substantially improve the luminosity on several fronts. The LEP2 energy upgrade project is making progress and regular operation at energies above the W-pair production threshold is foreseen for 1995.

VII. ACKNOWLEDGEMENTS

This article is a brief review of the work done by many dedicated people in the accelerator and technical sector at CERN. More detailed contributions on specific items can be found elsewhere in these Proceedings.

VIII. REFERENCES

- [1] J. Poole (Ed.), "Proc. Third Workshop on LEP Performance", Chamonix 1993, CERN SL/93-19(DI), 1993.
- [2] R. Bailey et al, these proceedings.
- [3] E. Peschardt et al, these proceedings.
- [4] E. Rossa et al, these proceedings.
- [5] B. Zotter, Proc. European Particle Accelerator Conference, Berlin 1992, p. 273.
- [6] H. Burkhardt, in [1].
- [7] H. Burkhardt, in [1].
- [8] E. Keil, in [1].
- [9] R. Bailey et al, these proceedings.
- [10] W. Kalbreier et al, in [1].
- [11] M. Placidi, in [1].
- [12] L. Arnaudon et al, these proceedings.
- [13] C. Wyss, these proceedings.
- [14] J.P. Koutchouk, in [1].

CHALLENGES ON THE HIGH LUMINOSITY FRONTIER OF e^+e^- FACTORIES

William A. Barletta

*Lawrence Berkeley Laboratory
and*

Dept. of Physics, University of California at Los Angeles

ABSTRACT:

For phi factories, tau-charm factories, and B factories to meet their respective luminosity goals, the circulating currents that typify e^+e^- colliders must be raised an order of magnitude. At the same time the beam size at the interaction point must be decreased. The approaches to realizing these conditions include increasing the charge per bunch, increasing the number of bunches in the collider, increasing the crossing angle for rapid bunch separation, tilting the bunch with respect to the direction of motion at the interaction point ("crab-crossing"), and minimizing the β function at the interaction point. The technological challenges implied by such strategies include the development of 1) novel rf-cavity designs to suppress higher order modes and to provide large rf-voltages for longitudinal focusing, 2) a new generation of powerful feedback electronics to control multi-bunch instabilities, and 3) vacuum chambers and pumping schemes suitable for operation with very high levels of synchrotron radiation. In high current colliders the design of the interaction region poses special problems of allowing rapid beam separation and avoiding excessive scattering of background radiation into the detector.

I. GENERAL CONSIDERATIONS

In recent years most accelerator laboratories throughout the world have conducted detailed studies of the design of high luminosity electron-positron colliders at a variety of center of mass energies. Commonly referred to as "factories", these machines generally have been considered to be storage ring colliders, although the low energy end of linear colliders has been studied as top and Higgs factories. Of all such studies only one, the Frascati phi factory DAΦNE, is an approved construction project. Other efforts – most notably the B-factory efforts at SLAC/LBL/LNL, at Cornell, and at KEK – are still restricted to the R&D phase. While designs of tau-charm, Z, and top factories have been focused on equal beam energies, proposals for phi factories have also considered the use of unequal beam energies [1]. Indeed all recent conceptual design studies of B factories (at CERN, DESY, KEK, Cornell, and SLAC) are based on the use of unequal beam energies (asymmetric B factories). This paper reviews the accelerator physics and technology issues that are central to the design of high luminosity lepton colliders with particular attention paid to the interaction region, vacuum and rf-systems.

The common features of all factory designs follow from the basic scaling of luminosity with beam energy, E,

average current I, tune shift, ξ , aspect ratio, r, and β -function at the interaction point. With equal tune shifts for both beams, the peak luminosity is

$$\mathcal{L} = 1.3 \times 10^{33} \left(\frac{\xi(E)}{0.03} \right) \left(\frac{I}{2 \text{ A}} \right) \left(\frac{1 \text{ cm}}{\beta_y^*(E)} \right) \left(\frac{E}{1 \text{ GeV}} \right) (1 + r) \text{ cm}^{-2} \text{ s}^{-1}$$

This scaling equation along with required ranges of time-average luminosity is illustrated in Figure 1. The dark gray curve assumes that β^* scales with \sqrt{E} and $\beta^* \approx 1 \text{ cm}$ at 5 GeV. To take advantage of the small β^* possible at low beam energy requires operating the collider with very short bunches, as has been proposed for a quasi-isochronous phi factory at UCLA. [2] If the minimum practical value of β^* is limited to 1 cm, then the scaling of luminosity with energy is follows the bottom of the gray band.

There is no strong evidence that the maximum achievable tune shift has any strong dependence on the beam energy. Though there has been theoretical speculation that the maximum head-on tune shift may be as large as 0.1 for round beams, there is no experimental evidence for this assumption, especially in the case of colliders with many, closely spaced bunches, for which the long-range tune spread is non-negligible. Consequently, most factory designs have assumed a "conservative" value of $\xi = 0.3$.

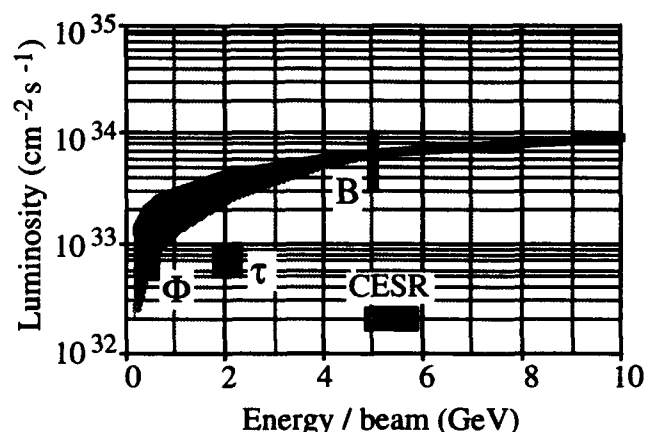


Figure 1. Luminosity scaling with beam energy and the requirements for flavor factories.

Especially for B-factories, the control of synchrotron radiation generated by the beam separation process seems to preclude the use of round beams; all B factory designs now

have adopted flat beam scenarios. Moreover, studies of IR optics indicate that the minimum practical β^* is larger for round beam designs than flat beam designs.

As the physics goals of the flavor factory determines the range of operating energies, the only quantities available for adjustment by the designer are the average current and β^* . With the exception of Φ -factory designs by UCLA (SMC) and Novosibirsk, all of the e^+e^- factories have assumed the following common characteristics: 1) two rings with one or more common interaction regions (I^*); 2) an average beam current in each ring of ~ 2 Amp, 3) a number of bunches $\sim 10^3$ to keep the single bunch current well within existing practice, 4) flat beams - the apparent gain with round beams cannot be realized due to background problems and optics design practicalities. In contrast, both the UCLA and Novosibirsk Φ -factory designs rely on single, compact rings with 4 - 6 T dipoles and few, very short bunches.

II. INTERACTION REGION DESIGN

The large number of bunches in e^+e^- factories requires rapid separation of the beams outside interaction region to avoid the deleterious effects of parasitic, near-collisions. In the case of asymmetric colliders the separation need not rely on the beams crossing at a finite angle. Indeed, the separation can be accomplished by purely magnetic means as typified by the PEP-II design [3], which employs a S-shape, magnetic separation scheme. Such configurations with head-on collisions have the advantage of maximizing the beam-beam tune shift without risking the excitation of synchro-betatron resonances and without the introduction of additional rf-cavities for beam manipulation. The price of purely magnetic separation is the use of several shared optical components, some of which are of unusual design. The septum quadrupole of PEP-II exemplifies a difficult, specialty magnet for the IR. In the design of the shared optics, special attention must be paid to the minimization of the synchrotron radiation fans that can lead to detector backgrounds and excessive operating pressure near the IR.

For the tau-charm factory and symmetric Φ -factory, the typical approach is to consider a first phase design based on proven beam separation approaches; in the second phase the effective luminosity is increased by modifying the IR (and ring lattice) to include crab-crossing, monochromatization, or longitudinal polarization of the beams. In phase 1, beam separation is performed via a shallow crossing angle or by electrostatic separators. Consequently, the bunch spacing cannot be as close as is possible with an energy asymmetry or with crab-crossing. Achieving sufficient luminosity during phase one depends, therefore, on maximizing the single bunch luminosity; i.e., by maximizing the single bunch peak current and minimizing β^* .

A further challenge for the design of the tau-charm factories is the exceedingly narrow width of the J/ψ at 3.1 GeV. For the collider to access this state with high efficiency Zohrlentz [4] has proposed a monochromatization scheme. In this scheme the dispersion at the IR is non-zero

in the horizontal plane. The sign of the dispersion is opposite for the two beams so that electrons of slightly higher energy collide with positrons of slightly lower than average energy and vice versa. The center of mass energy is then always $2E$. The emittance is made small so that the beam size (and tune shift) is set by the energy spread and the dispersion. In that case luminosity scaling equation above does not apply. An example of a two stage approach including monochromatization [5] is given in Table 1.

Table 1. Characteristics of tau-charm factory with Phase 2 optimized for J/ψ production

Characteristic	Phase 1	Phase 2
Energy (GeV)	2	1.5
β at IP, (β_x^*, β_y^*) (m)	(0.2, 0.01)	(0.01, 0.15)
Energy spread in CM	4×10^{-4}	6×10^{-5}
Emittance, ϵ_x, ϵ_y (nm)	110, 2.6	10, 2
Number of bunches	30	30
Bunch spacing (m)	12	12
Particles/bunch	1.4×10^{11}	8×10^{10}
Tune shift	0.039	0.015
Long. impedance (Ω)	≈ 0.13	≈ 1
Luminosity ($\text{cm}^{-2}\text{s}^{-1}$)	10^{33}	4×10^{32}

Including radio frequency deflecting cavities located at a betatron phase angle of $(n + 1/2)\pi$ on each side of the collision point allows rapid separation of the beams via the crab-crossing scheme [6], [7]. The crab-cavities introduce a time-dependent transverse kick that tilts the bunches with respect to the beam trajectories so that the collisions take place head-on. The crossing angle of the beam trajectories can then be large enough to reduce the number of magnets common to both beams to a single quadrupole. This approach, adopted for CESR-B and for the second phase of DAFNE, allows for greater flexibility in the choice of beam energy and greater ease in suppressing the generation synchrotron radiation near the IR. The voltage in the crab cavity is related to the "crab angle", rf-wavelength, and the magnitude of the beta function at the cavity by

$$V_{\perp \text{ crab}} = \frac{\theta_{\text{crab}} \lambda_{\text{rf-crab}} (E/e)}{4 \pi \sqrt{\beta^*} \beta_{\text{crab}}}$$

Typical peak voltages in the crab cavities are 1 - 4 MV.

The "crab-crossing" scheme has never been tried in practice. Considerable effort in designing and testing superconducting crab-cavities [8] has been conducted at Cornell in collaboration with KEK. Foreseen difficulties include the maintenance of tight tolerances on the phase and voltage of the rf in the cavities; another disadvantage of crab crossing is that the cavities add to ring impedance. Both the voltage and phase tolerances are proportional to the beam radius at the interaction point; the voltage tolerance also varies with the square root of the damping decrement. Hence, crab-

crossing provides an additional reason for the use of wigglers or wiggler lattices in low energy rings.

III. RF CHALLENGES

The rf-systems challenges of flavor factories derive from two considerations: 1) maintaining a short bunch length through strong longitudinal focusing, 2) restoring the large amount of energy lost through higher order modes and copious synchrotron radiation. Both these requirements imply that the cavity must have as large a shunt impedance as possible at the fundamental. As the circulating current in all factories range from ≈ 1 to 5 Amps, coupled bunch instabilities will be excessively strong unless the shunt impedance is low at all other frequencies.

Unless the bunch length, σ_z , is appreciably less than β^* (the depth of focus), the actual luminosity will be reduced due to the "hourglass" shape of the bunch at the interaction point and due to synchrotron coupling effects. Consequently factory designs generally have required that $0.2 < \sigma_z < 1.5$ cm. As the bunch length scales as

$$\sigma_z \propto \left(\frac{\alpha_1}{V_{RF} f_{RF}} \right)^{1/2}$$

where α_1 is the first order momentum compaction, flavor factories generally require a large rf-voltage, even at low beam energies for which the radiated power is not large. As high power tubes are readily available at ≈ 500 MHz, all proposed projects have opted for frequencies in this range, leaving V_{RF} as the only free parameter. Despite the broad range of RF-voltages for the various projects (see Table 2), the simultaneous need to minimize the higher order mode impedances has led almost all the projects to adopt designs with a large voltage per cavity (1.5 - 2 MV).

Table 2. RF parameters for various flavor factories

Project	L (10^{33})	Type	V_{RF} (MV)	f_{RF} (MHz)	σ (cm)	P_{SR} (MW)
SMC	1	NC	0.1	486	0.1	0.1
DAΦNE	0.2 - 1	NC	0.25	≈ 357	3.0	0.05
INP	> 1	NC		≈ 700	0.5	0.05
StCF	1	SC	12	400	0.8	0.06
JINR	1	?	3.1	257.5	0.8	0.06
BFI	1	SC	13	498	2	3.1
CESR-B	3	SC	35	500	1	4.5
DESY	3	NC	17	500	1	2.4
INP	5	NC/SC	15.4	500	0.7	3.8
KEK	2	NC/SC	48	508	0.5	4.6
PEP-II	3	NC	19	476	1	5.3

Especially in small rings such as CESR where space is at tight, high voltage operation makes superconducting cavities an attractive option, despite the lack of any experience with operating such cavities at high fields under heavy beam loading. A further practical difficulty is

protecting the superconducting cavities from virtually all the synchrotron radiation generated in the dipole arcs. For superconducting cavities, widening the beam pipe so that the cavity supports only the fundamental accelerating mode can reduce HOMs. The Cornell design extends this concept by adding a specially designed fluted wave-guide tube [9] to transmit the two lowest frequency modes (TM_{111} and TM_{110}) outside the cavity to ferrite rf-absorbers located outside the cryostat. A problem peculiar to crab-cavities is the need to attenuate fundamental mode which is at a lower frequency than the desired deflecting mode.

Room temperature cavities can satisfy all requirements by extending the nose cone to increase the gradient to 4 MV/m. The price is increased power dissipation in the cavity walls (up to ≈ 150 kW in PEP-II) and large Q for the superior modes. SLAC/LBL, LNF, and KEK have been studying the suppression of the superior modes through the addition of waveguides attached to the sides of the cavities. The waveguides must be positioned carefully to couple to all the unwanted modes without strong suppression of the fundamental accelerating mode. Calculations and low power tests confirm the validity of this approach for reducing the Q of the most dangerous modes below 100. At this level, coupled bunch instabilities can be controlled by a suitable feedback system. Indeed for $Q_{HOM} \gg 100$ the growth can be more rapid than change in beam phase, thus precluding efficient feedback control. The design of a high power cavity is complicated by the frequency shifts (≈ 130 MHz) caused by the deformation of the copper cavity under the high thermal and mechanical loads. Both approaches to supplying rf-power require the development of high power klystrons and windows that can pass ≈ 500 kW reliably.

An alternative to using large RF-voltages is to design the lattice to have a very small value of α_1 . As the maximum current to avoid the single bunch microwave instability is also proportional to α_1 , this approach will decrease the luminosity unless the second order momentum compaction and the damping time are simultaneously made small enough that radiation damping prevents the bunch-lengthening. This approach has been analyzed by Pellegrini and Robin [10], [11] as the basis of a quasi-isochronous design for the proposed UCLA Φ factory.

IV. FEEDBACK CONTROL OF INSTABILITIES

Despite the suppression of the Q of the superior modes to values < 100 , the large number of bunches and high average current make factories susceptible to virulent multi-bunch instabilities. Those modes with growth times shorter than a radiation damping time must be controlled with active feedback system.

The heavy beam loading combined with a sizable gap in the bunch pattern (to avoid ion trapping) requires detuning the cavity by so that the beam presents a matched load to the rf-drive. The shift,

$$\Delta f/f \sim I (R/Q) N_{cell};$$

hence, the detuning can lead to driving the first ($m=1, n=1$) longitudinal, coupled-bunch mode. For room temperature

cavities the dipole oscillation must be controlled by a feedback loop on the low-level rf-drive. The use of superconducting cavities can avoid this difficulty as Q is very large and the number of cells can be minimized; hence the detuning frequency can be much smaller.

Other longitudinal, coupled-bunch modes can be controlled via a digital, bunch-by-bunch feedback system. A down-sampling technique of updating the correction signal every n^{th} revolution allows the feedback to operate closer to the Nyquist limit and reduces the number of computations by n^2 . A prototype for PEP-II [11] that employs commercially available signal processors has been tested at SLAC and will be installed on the Advanced Light Source at LBL. A similar system will be used in DAΦNE. Such bunch-by-bunch feedback systems are also essential to preserve the emittance in the SSC and LHC.

Digital feedback systems are also envisioned to control transverse, coupled bunch modes, including the transverse resistive wall instability. Even with feedback, the resistive wall mode grows so rapidly in the low energy rings that the beam tube must have a conductivity much higher than that of stainless steel.

IV. VACUUM IMPLICATIONS

While currents >1 Amp are not unprecedented in rings, they are much larger than found in existing e^+e^- colliders. Hence, factories will be characterized by large thermal loads on the vacuum chamber walls and large dynamic gas loads. Moreover, factories require operating pressures <10 nTorr in the dipole arcs. To meet these unprecedented demands, the characteristics of vacuum systems of colliders at the luminosity frontier must evolve markedly from those of existing rings. Thermal loads due to synchrotron radiation, which were typically in the range of 1 - 5 kW/m, have been pushed to 10 - 40 kW/m, introducing both cooling and thermal fatigue difficulties. Whereas the material of choice for vacuum chambers was commonly stainless steel, it is now Al (with an outer Pb cladding) or Cu (or a Cu alloy). Thus, the vacuum engineer faces new and unfamiliar fabrication and cost issues. The are summarized in Table 3.

Table 3. Materials for e^+e^- factory vacuum chambers

	Al	Cu	SS
Photo-desorption	+	++	++
Self-shielding	-	++	++
Thermal conductivity	+	+ to ++	-
Strength	+	- to +	++
Ease of fabrication	++	+	++
Experience	++	+	++
Cost	\$	\$\$	\$\$

Whereas typical photon fluxes have been 5×10^{17} photons/s/m, B factories will generate $\approx 10^{19}$ photons/s/m. Hence, the vacuum chamber must be characterized by a low design value of the photo-desorption efficiency, η_F , $\approx 10^{-6}$. As the scrubbing of the vacuum chamber by the radiation is

the principal means of reaching very low η_F , the initial value of η_F must be small and the clean-up rate rapid to keep the commissioning time less than hundreds of hours.

Pumping speeds in the dipole arcs, S_d , which are 100 - 300 L/s/m in existing storage rings, will be increased to values as large as 3000 L/s/m for CESR-B and SMC. Providing so much distributed pumping strongly affects the choice of the type of pumps and the chamber design. For $S_d > 1000$ L/s/m, the chamber will not have the traditional oval shape. Rather, a complex shape including an ante-chambers is likely to be adopted despite the adverse impact on ease of fabrication, on costs, and on magnet designs.

The complexity of the vacuum system design is exemplified by the arcs of the low energy ring (LER) of CESR-B. The arcs are a wiggler lattice composed of dipoles with a 20 m bend radius interleaved with -98 m reverse bends. The arrangement of the magnets, the relative distribution of synchrotron power, the relative η_F , and the relative distributed gas load are displayed in Fig. 2. Because of the strong variation in power loading, the desorption coefficient suffers equally strong fluctuations. The gas load, which is proportional to the product of these two functions, is much smoother; hence, the phrase "eta-leveling". [13]

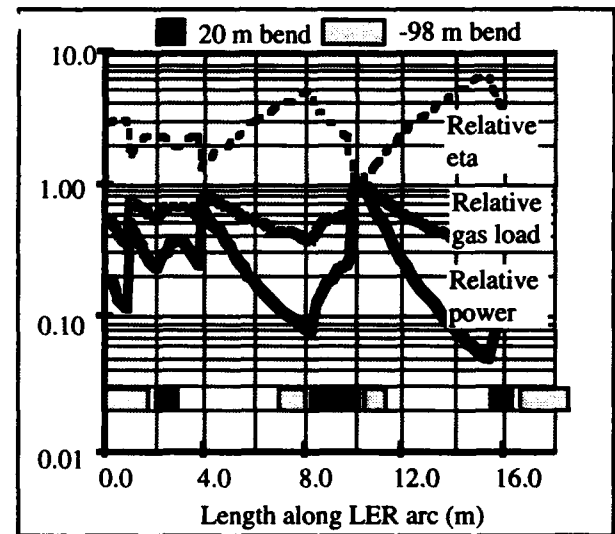


Figure 2. Relative desorption characteristics in dipole arcs of the CESR-B LER. 1.0 corresponds to $\eta = 1.7 \times 10^{-6}$, $Q = 2.3 \times 10^{-6}$ Torr-l/s/m and $P = 10.4$ kW/m.

The arc is pumped with a combination of TiSPs and NEG, each of which require regeneration at differing intervals. The system requirement is formulated in terms of the average pressure along the arc. Figure 3 illustrates the degree to which the requirement is met as the pumps approach their capacity and require regeneration. From such curves, one calculates an appropriate regeneration scenario.

The vacuum system in the interaction region of e^+e^- factories poses a confluence of conflicting physics and engineering difficulties. Space is at a premium because the beams must be separated rapidly into their respective rings, because detector components are desirable where one might wish to locate pumps, and because beam-pipe conductance

can be expected to be small. The rapid beam separation can produce several tens of kilowatts of radiation which must be deposited on photon dumps near the IR, generating a moderately large distributed gas load. Handling the gas load would be routine were it not that the background pressure especially in the incoming beamlines must be $\ll 1$ nTorr. The desorbed gas is a direct source of backgrounds because the electrons that scatter from the beam can readily be transported into the detector. Controlling this lost particle background is an extremely difficult and important problem for all high luminosity electron-positron colliders.

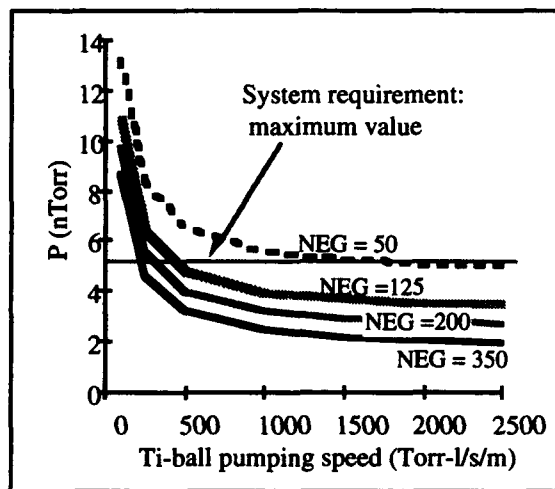


Figure 3. Variation of $\langle P \rangle$ in the CESR-B LER

One approach that minimizes pumping would employ a differentially-pumped ante-chamber to house the photon dump. In such a design, illustrated schematically in Fig. 4, most of the gas is removed by TiSPs. The gas that leaks through the low conductance duct into the beam chamber is pumped by two rows of NEG modules. The regeneration intervals for the NEG and TiSPs in the interaction region of PEP-II are ≈ 2 months and ≈ 1 week respectively.

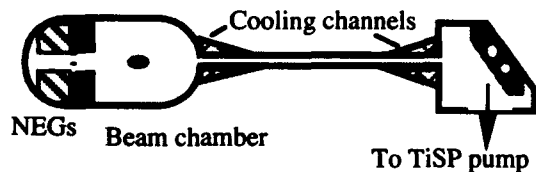


Fig. 4. Differentially-pumped chamber in the PEP-II HER beamline of upstream of IR. The duct is 11×300 mm

V. CONCLUDING COMMENTS

To meet the electromagnetic impedance budget, factory designs will require beamline components to have a $(Z/n)_{\text{eff}} \approx 1 \Omega$ – lower than typically found in storage rings. In the case of the tau-charm or Φ factory, in which the single bunch luminosity must be maximized, $(Z/n)_{\text{eff}} \sim 0.1 \Omega$. The compact Φ factory designs of UCLA and Novosibirsk have the additional difficulty that the ring impedance will be dominated by the vacuum impedance,

because of the very small radius of the machine. Coherent synchrotron radiation may therefore be a substantial component of the total beam losses, even exceeding the incoherent synchrotron radiation. Large losses are especially trouble-some in miniaturized rings as the interaction region may absorb as much as 1 kW/m of the coherent radiation.

Most factory designs include specialized components such as wigglers to decrease the damping time and increase the natural beam emittance. Given the high currents, such wigglers can generate enormous, localized thermal and/or gas loads. Although such specialized beamline components do not appear to produce insurmountable problems, engineering the practical realizations can be costly.

Proposed e^+e^- factories present a challenging task to the accelerator designer. As the single bunch physics of most designs is similar to that in existing colliders, the major challenges derive from the large number of bunches that yield a high average current. Most major sub-systems will be pushed to unprecedented levels of performance and of reliability. The benefits of accelerator development for high luminosity will be realized not only in flavor factories, but also in hadron supercolliders.

ACKNOWLEDGMENTS

The author thanks Alexander Zohrents (LBL) for his critical comments. This work was partially supported by Lawrence Berkeley Laboratory for the U. S. Dept. of Energy under contract No. DE-AC0376SF00098.

References:

- [1] W. A. Barletta, R. Berg, A. Boden, C. Buchanan, D. Cline, C. Pellegrini, "A Linear Collider Phi Factory and Beam Dynamics Test Machine", Proc. of the International Workshop on CP Violation, Blois, (May, 1989)
- [2] C. Pellegrini et al. "A Superconducting Mini-collider for the Copious Production of Phi Mesons", Proc. IEEE Particle Accelerator Conference, (San Francisco, 1991)
- [3] "Investigation of an Asymmetric B Factory in the PEP Tunnel" LBL PUB-5263, March, 1990
- [4] A., Zohrents, Polarized J/ψ Mesons at a Tau-Charm Factory with a Monochromator Scheme, CERN SL/92-27(AP), June, 1992
- [5] J. M. Jowett, et al., "The Tau-Charm Factory", Proc. High Energy Accelerator Conf., Hamburg, (1992)
- [6] R. B. Palmer, SLAC Pub-4707 (1988)
- [7] K. Oide and K. Yakoya, Phys. Rev., A40, 315, (1989)
- [8] Akai et al., Proceedings of "B Factories - State of the Art", Stanford, April, 1993
- [9] M. Tigner for the CESR-B Accelerator Group, *ibid.*
- [10] D. Robin, *ibid.*
- [11] C. Pellegrini and D. Robin, "Energy Density Enhancement in Quasi-Isochronous Storage Rings", Proc. of IEEE Particle Accelerator Conf., San Francisco, 1991
- [12] G. Oxoby et al., "Bunch-by-bunch Feedback for PEP-II", SLAC Pub-6035, January, 1993
- [13] W. A. Barletta, "Modeling vacuum systems in high current storage rings", Proc. of IEEE Particle Accelerator Conf., San Francisco, 1991

DAΦNE, The Frascati Φ-factory

The DAΦNE Project Team*

presented by G. Vignola

INFN Laboratori Nazionali di Frascati - C.P. 13 - 00044 Frascati (Roma) - Italy

Abstract

The e^+e^- Φ-factory DAΦNE is presently under construction in Frascati. It is designed as a double ring system with a maximum number of 120 bunches/beam. The short term luminosity goal is $L=1.3 \cdot 10^{32} \text{ cm}^{-2} \text{ sec}^{-1}$ with 30 bunches. The strategy, adopted to achieve such a luminosity, is common to many factory designs : high current, many bunches and separate rings. The technical problems are complicated by the relatively low energy of the beams. A general overview of the project and the most significant technical solutions adopted for DAΦNE are presented.

I. INTRODUCTION

The construction of DAΦNE in the Frascati National Laboratories (LNF), has been approved and fully funded by the National Institute of Nuclear Physics (INFN) in June 1990, while the engineering design phase has started in January 1991.

The layout of the new accelerator complex (housed in the buildings where ADONE and its injector Linac have been running until the last April) is shown in Fig. 1.

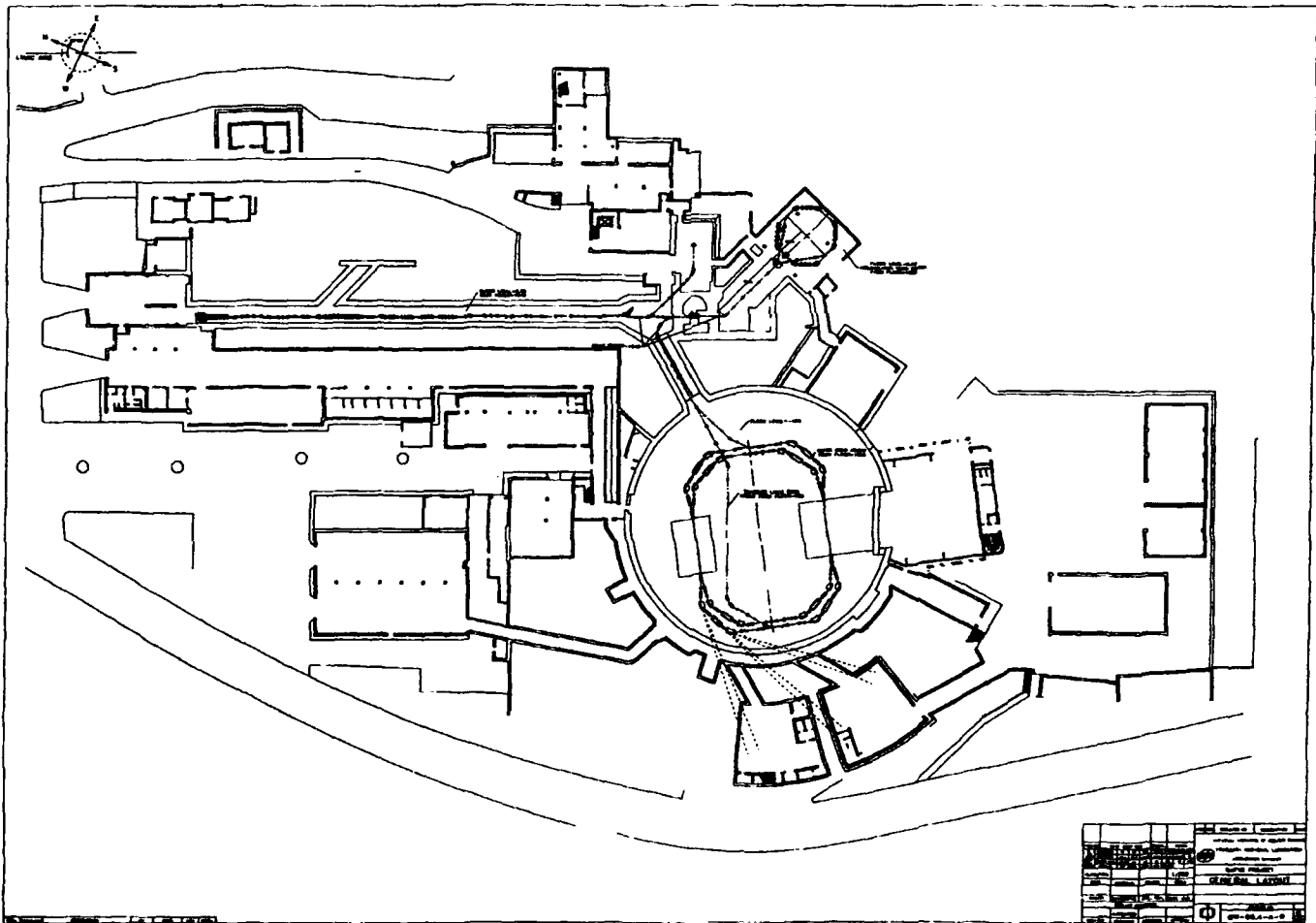


Figure 1. DAΦNE complex layout.

* G. Vignola, S. Bartalucci, M. Bassetti, M.E. Biagini, C. Biscari, R. Boni, A. Cattoni, V. Chimenti, A. Clozza, S. De Simone, A. Drago, G. Di Pirro, A. Esposito, S. Faini, A. Gallo, A. Ghigo, S. Guiducci, Y. He, H. Hsieh, J. Lü, C. Marchetti, M.R. Masullo, M. Migliorati, C. Milardi,

M. Modena, L. Palumbo, R. Parodi, L. Pellegrino, M. Pelliccioni, M. Preger, G. Raffone, C. Sanelli, F. Sannibale, M. Serio, F. Sgamma, B. Spataro, A. Stecchi, L. Trasatti, C. Vaccarezza, M. Vescovi, S. Vescovi, J. Wang, M. Zobov.

It consists of an e^+e^- Linac, a damping ring used for both beams, rather long transfer lines to cope with the necessity of using existing buildings, and a twin rings collider with two interaction points. All the accelerators are designed for the same working energy of 510 MeV.

The first interaction region is dedicated to a large detector KLOE [1]. This detector has been approved and funded by INFN and it is in the construction phase. The major physics aim of KLOE is the observation of direct CP-violation in K_L decays, i.e. the measurements of ϵ'/ϵ with accuracy in the 10^{-4} range. In order to achieve such a result a luminosity $L=5 \cdot 10^{32} \text{ cm}^{-2}\text{s}^{-1}$ integrated over an effective year of 10^7 seconds is required.

The second interaction region is assigned to a smaller size detector, FINUDA [2], for hypernuclear physics.

The installation of three beam lines for soft X-rays [3] is planned.

The start of the commissioning, with 30 bunches, is scheduled for the beginning of 1996 with a short term luminosity goal of $1.3 \cdot 10^{32} \text{ cm}^{-2} \text{ s}^{-1}$. The target luminosity $L \sim 5 \cdot 10^{32} \text{ cm}^{-2} \text{ s}^{-1}$ should be achieved in a period of ~ 2 -3 years of operation by pushing up the current and, at same time, by fine-tuning all the machine parameters.

II. INJECTOR COMPLEX

The injector complex of DAΦNE consists of an e^+e^- Linac, a damping ring and transfer lines.

The Linac [4] is an S-band structure with a SLED type pulse compression system capable of accelerating electrons up to 800 MeV at 50 pps. In the positron mode of operation, a first section is used to accelerate electrons to 250 MeV.

The electron beam is focused by a quadrupole triplet onto a high Z converter, positron are collected by 5 T tapered flux concentrator and accelerated to the nominal operating energy of 510 MeV. The design positron current is larger than 30 mA in a 10 ns pulse within $\pm 1\%$ energy spread and 10^{-5} m-rad emittance. The Linac construction has been committed to industry and it is in progress in U.S. Installation at LNF will begin in early 94 and the Linac is expected to be operational for the end of the same year.

The design of the transfer lines has been completed, and the contract awarded to an Italian firm. Installation will begin in the first months of 1995.

The damping ring has been adopted to avoid injection saturation due to the large current to be stored in the collider, to improve the longitudinal acceptance for the Linac beam, and to deliver low emittance and low energy spread beams to the main rings. With this arrangement, injection requirements to the main ring lattice are strongly reduced. A compact 4 period structure, with a total length 1/3 of the main rings, and vanishing dispersion at the injection/extraction septa, allows injection of both electrons and positrons in the single bunch mode at 50 Hz repetition rate. Extraction will be performed at the optimum current level for injection into the main rings, typically at ~ 1 Hz. Detailed specifications have been sent out for bid, and the tenders from potential vendors are under evaluation. The contract for complete construction and installation will be awarded next June. Commissioning will be performed in the second half of 1995.

III. MAIN RINGS

The magnetic layout of DAΦNE is shown in Fig. 2. Its

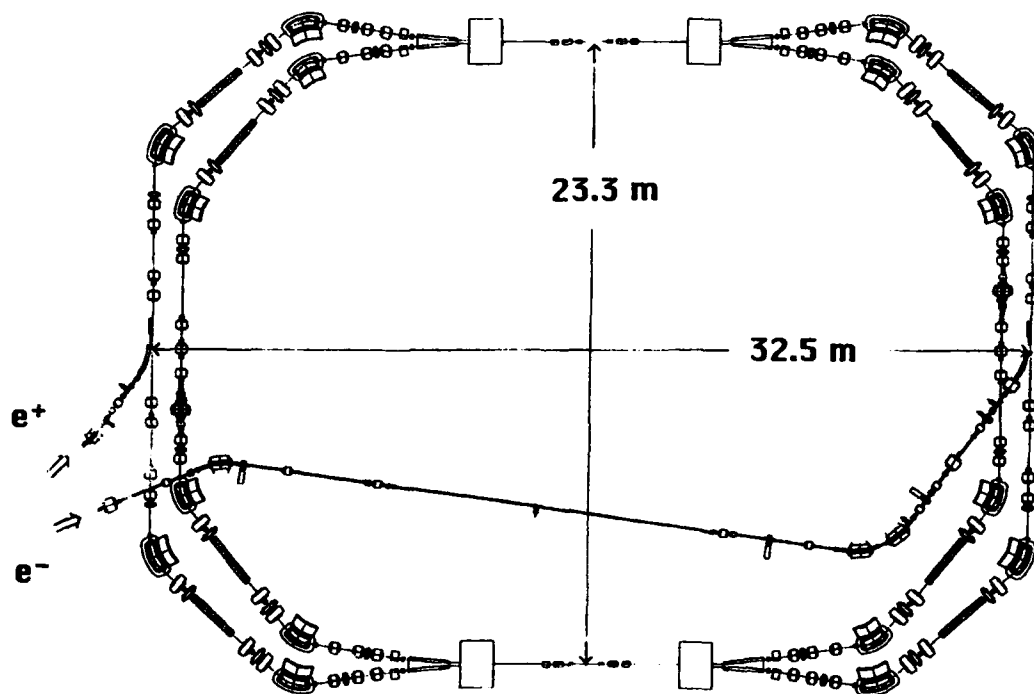


Figure 2. DAΦNE magnetic layout.

main features, in order to achieve the design luminosity, are based on well proven accelerator physics: the large luminosity improvement is reached with the same interaction conditions of already operating colliders, by increasing the number of colliding bunches up to the RF harmonic of the revolution frequency and by reducing the number of interaction points with the adoption of a double ring scheme.

The large stored current required by this scheme is the major technical challenge of DAΦNE: the vacuum system must hold a heavy gas load, due to the intense synchrotron radiation, and the beam stability can be destroyed by multibunch instabilities, so that careful design of the RF cavity and vacuum chamber are necessary to avoid high order oscillation modes, and, in any case a powerful feedback system is required. The main ring design is based on conventional technology and well established physics parameters (see Table 1).

Table 1. DAΦNE Parameter List

Beam Energy (MeV)		2×510
Luminosity ($10^{32} \text{ cm}^{-2} \text{ sec}^{-1}$)		1.35 ($\rightarrow 5.40$)
Bunches per ring per species		30 ($\rightarrow 120$)
Particles/bunch		$8.9 \cdot 10^{10}$
Luminosity lifetime (hr's)		2 + 3
Single ring circumference		97.69 m
Filling time (min.)		< 2 (topping up)
Time between collisions (ns)		10.9 ($\rightarrow 2.7$)
Crossing half-angle (mrad)		10 + 15
Interaction Point (IP)		1 or 2
Interaction Region Length		2×10 m
Free space @ IP		± 46 cm
β -function @ IP :	H	4.5 m
	V	4.5 cm
Beam r.m.s. dimension @ IP :	H	2.1 mm
	V	21 μm
Beam-beam tune shift per crossing :	H	.04
	V	.04
β -tune :	H	5.18
	V	6.15
Natural Chromaticity :	H	- 9.2
	V	- 20.6
Momentum compaction		.005
Dipoles per ring		8
Wigglers per ring		4
Quadrupoles per ring		51
Sextupoles per ring		16
Peak magnetic field (T) :	Dipoles	1.2
	Wigglers	1.8
Energy loss/turn (keV)		9.3
Relative natural r.m.s. energy spread		$4 \cdot 10^{-4}$
Natural emittance (mm·mrad)		1.0
RF frequency (MHz)		368.25
RF harmonic number		120
Peak RF voltage (kV)		250
Synchrotron frequency (kHz)		21.4
Z/n (Ω)		1.0
r.m.s. bunch length (cm)		3.0
Damping time (msec) :	τ_s	17.8
	τ_x	36.0
	τ_y	35.7

Flat beams ($\kappa=.01$) are foreseen at the IP, so that only one betatron function must be in the range of few centimeters, thus avoiding large contributions to the chromaticity and strong non linear correction fields.

The electron and positron beams are stored in two separated rings laying in the same horizontal plane with horizontal crossing in two interaction regions at an angle of ± 12.5 mrad. The lattice of each ring consists of 4 achromats, each housing a 2 m long, 1.8 T normal conducting wiggler to increase and finely tune the beam emittance, and to increase radiation damping, which compensates for the low operating energy, as suggested by beam-beam interaction models and simulations. The straight sections at 90° with respect to the interaction regions are used for injection, RF and feedbacks.

The main rings optics (frozen) shows satisfactory dynamic aperture (see Fig. 3).

The engineering design has been completed for all the major components and the procurement phase is in progress. The installation of the main rings is scheduled for the end of 1995.

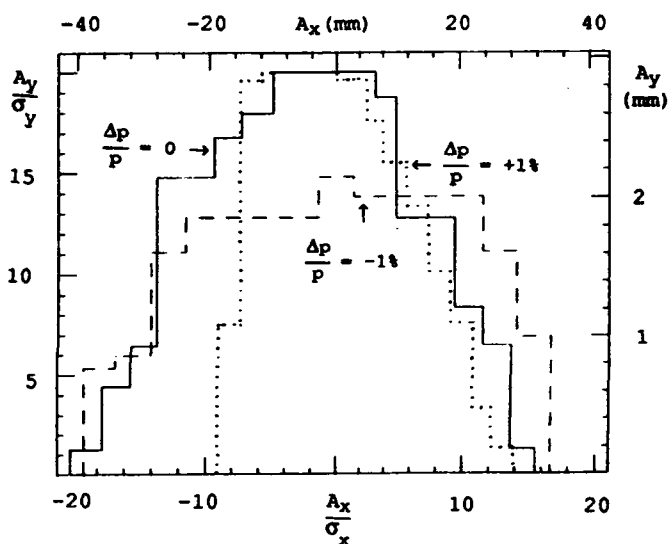


Figure 3. Dynamic Aperture @ IP with 8 families of sextupoles

IV. INTERACTION REGIONS

Careful study has been dedicated to the interaction regions (IR), where a solenoidal field of 0.6 T is required by KLOE and 1.5 T by FINUDA. A new compensation scheme, including compensating superconducting solenoids and rotation of the low-b permanent magnet quadrupoles has been developed to accurately decouple the betatron normal modes at the IP.

Three different IR's have been designed [5], one without longitudinal fields for commissioning purposes, the others to accommodate KLOE and FINUDA experiments, under the conditions of complete transparency with respect to the rest of the ring (i.e. with the same transfer matrix). In Fig. 4 a detail of the KLOE IR is shown.

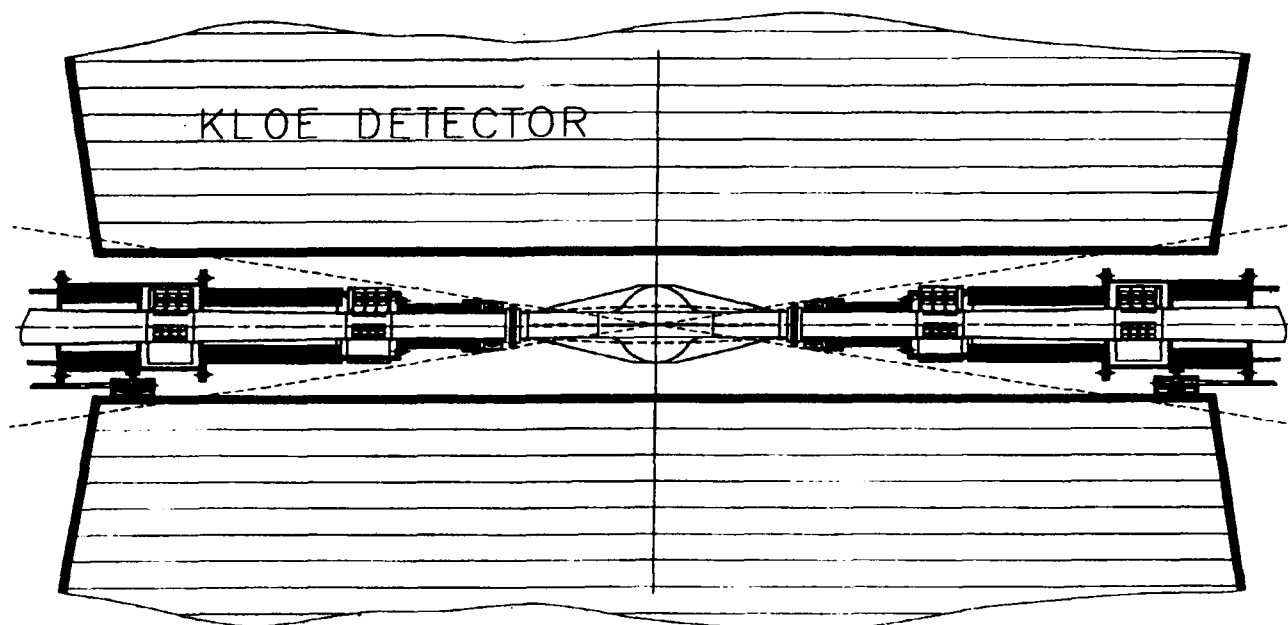


Figure 4. KLOE Interaction Region.

V. VACUUM SYSTEM

The DAΦNE vacuum system[6] is dimensioned to keep the average operating pressure ~ 1 nTorr with 5 A of circulating current.

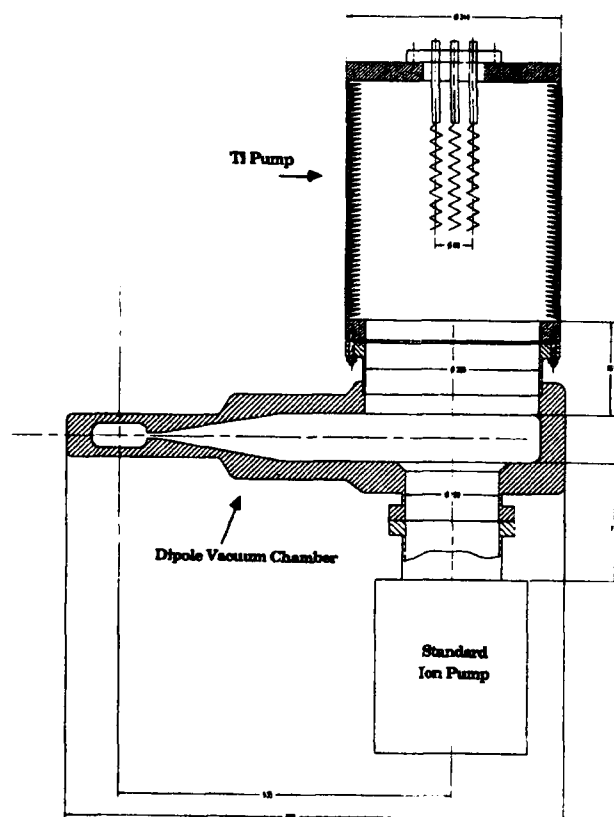


Figure 5. Dipole vacuum chamber cross section.

A design, similar to ALS, has been adopted for the vacuum vessel, consisting of two chambers connected through a narrow slot. The beam is stored in the first one, while the synchrotron radiation photons hit the wall of the second (the antechamber), after traveling through the slot. The chamber has been designed in such a way that $\approx 95\%$ of the photon flux is concentrated on a limited number of copper absorbers in the antechamber. More than 90% of the gas load is removed by titanium sublimation pumps, while sputter ion pumps are used to get rid of those gases which cannot be pumped by the sublimators. Figure 5 shows a cross section of the vacuum chamber in the bending magnet. Measurements performed on a full scale prototype indicate that, at full current operation, a new layer of Ti must be deposited on the wall of the sublimator vessel once a week.

VI. RF CAVITY

The DAΦNE RF cavity [7] has been designed with the aim to reduce significantly the shunt impedance of the longitudinal high order modes (HOM) which are responsible of multibunch instabilities. The main features of the resonator are large and tapered beam tubes, which allow the HOM's to propagate out of the cavity, and an elliptical profile, to avoid multipacting.

An intense R&D program has been carried out to couple off and damp the HOM impedance by applying to the cavity walls three ferrite-loaded waveguides (WG) at 120° . In alternative to the ferrite loads under vacuum, we are studying a broadband transition from WG to coaxial. This design would allow to dissipate the HOM power on external $50\ \Omega$ loads, with enormous advantages from all points of view.

The measurements, performed on a cold prototype, have been very encouraging, so we have frozen the cavity shape.

Figure 6 shows the engineering design. In addition to the rectangular waveguide ports, there is provision for round ones, which will be used for the main coupler, tuner, vacuum pumps and diagnostics. Conventional loops or antennas tuned to most harmful HOM's can also be installed.

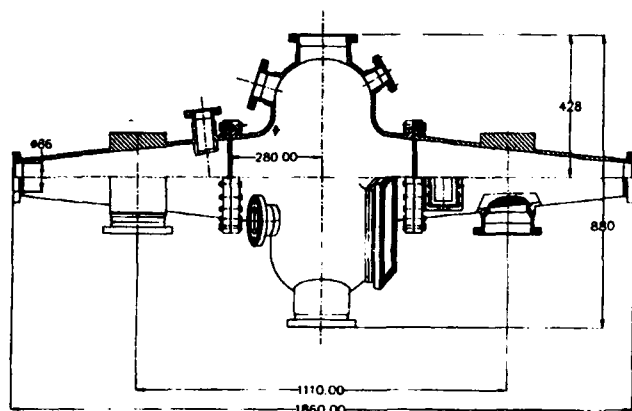


Figure 6. RF cavity engineering design.

The final prototype, electro-formed copper, will be available next fall. The only open problem is the choice between ferrites and broadband transition: at this moment the solution with transitions is preferred, and a major effort is being devoted to carry out the complete engineering design.

VII. LONGITUDINAL FEEDBACK SYSTEM

We recognize that longitudinal multibunch instabilities can put a severe limit on the current intensity and luminosity achievable in DAΦNE.

Even if the HOM's in the accelerating cavities are heavily damped, the probability for a damped HOM to cross a coupled bunch mode frequency is large and, because of the relatively large current, the rise-time of the unstable modes can be faster than the natural damping time. Therefore, a powerful active feedback system capable of damping all the coupled modes and the injection transients [8] is necessary.

In the framework of a collaboration on feedback systems for the next generation of factories with intense beams and a large number of bunches with the SLAC/LBL B-Factory group, a bunch by bunch, time-domain feedback largely based on Digital Signal Processors (DSP) is under development. In fact, the design specifications are such to fulfill the ultimate performance specifications of ALS, PEP-II and DAΦNE [9, 10]. The first complete DSP feedback system is being realized for the ALS (2.2 ns bunch spacing).

Each bunch is treated as a separate oscillator: a bank of DSP filters operating in parallel compute the correction kick signals to be applied to each bunch by means of a power amplifier and a kicker, according to the measured phase errors, which are uniquely detected and digitized.

The main advantage of such a system is that the same DSP can process several bunches, thus reducing the hardware

complexity. Moreover, it is possible to take advantage of the relatively low synchrotron frequency ($\sim 1/140$ of the revolution frequency) and reduce substantially the sampling rate at which the synchrotron phase is detected. This results in less complex filters and reduces the overall data rate and computational load in the DSP section [10].

A proof-of-principle experiment with a down-sampled DSP feedback has been carried out at SPEAR with a single bunch, to measure the system performance and to get some operational experience [11]. A small scale (few bunches), full-functional prototype board to be used for tests at ALS is being developed at SLAC [12].

According to simulations, ~ 500 W of large band-width power are enough to damp out a 100 ps offset of the injected bunch with the other 29 at the full design current [8].

VIII. ACKNOWLEDGMENTS

The DAΦNE machine project periodically undergoes a review by an international Committee of experts. I like to thank warmly A. Hutton (Chairman), F. Bonaudi, D. Boussard, J.P. Delahaye, A. Wrulich for their collaboration and advice throughout all the steps of this ambitious project.

I am also pleased to acknowledge all the technical personnel of the LNF Accelerator Division for their enthusiastic commitment to this Project, and Mrs. P. Possanza for her outstanding secretarial support.

IX. REFERENCES

- [1] The KLOE Collaboration, "KLOE: A general purpose detector for DAΦNE", LNF-92/019 (IR), April 1992.
- [2] M. Agnello et al., "FINUDA: A detector for nuclear physics at DAΦNE", to be published.
- [3] A. Balema et al., "DAΦNE-L: Proposta per l'utilizzazione di DAΦNE come sorgente di luce di sincrotrone", LNF-91/083 (IR), October 1991.
- [4] K. Whitham et al., "Design of the e^+e^- Frascati Linear Accelerator for DAΦNE", these Proceedings.
- [5] M. Bassetti et al., "The Design of the DAΦNE Interaction Region", these Proceedings.
- [6] V. Chimenti et al., "The DAΦNE Vacuum System", these Proceedings.
- [7] S. Bartalucci et al., "The RF Cavity for DAΦNE", these Proceedings.
- [8] M. Bassetti et al., "DAΦNE Longitudinal Feedback", Proceedings of EPAC 92, Vol. 1, p. 807 (1992).
- [9] J. D. Fox et al., "Feedback Implementation Options and Issues for B factory Accelerators", SLAC-PUB 5932, LBL 33092, September 1992.
- [10] G. Oxoby et al., "Bunch-by-Bunch Feedback for PEP-II", SLAC-PUB 6035, January 1993.
- [11] H. Hindi et al., "Analysis of Bunch-by-Bunch DSP Based Longitudinal Feedback System: Trial at SPEAR", these Proceedings.
- [12] J. D. Fox et al, SLAC, private communication.

Commissioning results of the Amsterdam Pulse Stretcher/ Storage Ring AmPS

R. Maas, F.Kroes, J. van der Laan, G. Luijckx,
J. Noomen, Y. Wu

NIKHEF-K, P.O. Box 41882, 1009 DB Amsterdam, the Netherlands.

Abstract

AmPS has been built to enhance substantially the main specifications of the 1 % duty factor 550 MeV electron accelerator facility MEA. The maximum energy will be raised to 0.9 GeV while the duty factor increases from 1 % to approximately 100 %. To this purpose the ring AmPS was added to the facility. Simultaneously the linac was upgraded both in current and energy. Two modes of operation for the ring are implemented: a Pulse Stretcher mode with 3 turn injection creating an external beam, and a Storage Mode with multi turn injection for internal target physics. The commissioning of the ring started in April 1992. Within two months 10 % duty factor beams could be delivered for electron scattering experiments. Meanwhile the performance of the machine has been improved dramatically. The actual performance of the ring is presented and is compared with the initial design goals.

I. INTRODUCTION

At NIKHEF-K electron scattering experiments for nuclear physics research are carried out. A 500 MeV electron linac delivered typically 50 μ A beams of 1%-duty factor to the experimental area. Since coincidence scattering experiments (e,e'X) got more emphasis, the available low duty factor became a serious handicap to carry out these type of experiments. With the addition of the Pulse Stretcher AmPS to the facility, in conjunction with an increase of the linac energy to 900 MeV (zero-current; beamloading 2.6 MeV/mA), it will be possible to deliver near-CW beams in the energy range 250-900 MeV to the experimental area.

The maximum peak current of the linac will be 80 mA; at this value a degradation of the energy spread is expected: $\Delta p/p \approx 1-2\%$. Such an energy spread will exceed the momentum acceptance of the ring. Therefore an Energy Spectrum Compressor (ESC) has been installed between linac and AmPS. At the present low values of the injection current (typically 10 mA), the linac + ESC system delivers beams with energy spread of typically 0.03% (FWHM).

Another option is the Storage Mode: in this case the circulating beam is not extracted, but used in conjunction with an internal target (e.g. gas jet) to carry out scattering experiments. The present 2856 MHz RF system can be used to store a beam at energies up to about 550 MeV. In order to be able to store beams at the maximum energy, a 476 MHz RF system will be installed during the winter of '93-'94.

II. PULSE STRETCHER

AmPS was originally designed as a Pulse Stretcher. The basic design of the machine has been described in [1]; an overview of the AmPS project is given in [2]. The main parameters of the Stretcher are summarized in Table 1.

Table 1
Main parameters of AmPS in Stretcher Mode

Energy, min-max	250-900	MeV
circumference	211.62	m
current (injected)	80	mA
current (extracted)	65	μ A
injection frequency	400	Hz
injection duration	3	turn
RF-frequency	2856	MHz
momentum compaction α	0.027	
harmonic number h	2016	
horizontal tune ν_x	8.300	
vertical tune ν_y	7.21	
horizontal chromaticity χ_x	-15.0	
vertical chromaticity χ_y	+ 0.2	
synchr. loss (@900 MeV)	17.6	keV/turn

In order to slowly extract the beam from the machine, third integer resonance extraction is used. As non-linear elements four extraction sextupoles are used (AmPS has basically a four-fold symmetric lattice). The extraction is accomplished by phase-modulating the RF voltage of the cavity. The non-synchronous motion, in combination with the large negative value of the chromaticity, effectively brings the tune close to the resonant value. The unstable particles are intercepted by an electrostatic (wire) septum and from there directed into the extraction channel.

Commissioning experiments have been performed at a beam energy of $E = 410$ MeV, and an injected (peak) current of 10 mA. Since we started with single-turn injection, only one injection kicker needed to be used. The injection frequency was reduced to 50 Hz in order to avoid too much radiation. The average current under these circumstances (single-turn injection) is $\bar{i} = (f_{inj} \times \hat{i}_{inj}) / f_{rev} = 0.35 \mu$ A

The proper location of the injection septum is $x=+16.5$ mm off-axis in order to create the proper conditions for extraction (see [1]). From the Storage Mode runs, see Section III, the septum was still in on-axis position. Rather than changing its position, we created a local bump in the closed orbit around the injection location of -16.5 mm.

During the extraction time (20 ms at $f_{inj} = 50$ Hz, which corresponds to appr. 28000 rev's) a phase shift is applied to the RF voltage, such that the phase shift increases as the extraction progresses. This procedure 'shakes' the particles out of the bucket, and once out, the synchrotron losses carry the particles into the unstable part of the phase space (the chromaticity has a large negative value). Since the extraction depletes the population of the bucket, the phase shift per unit of time has to increase as the extraction progresses in order to ensure a constant extracted current. The total phase shift during the extraction was about 1400 degrees.

Currently the phase shifts are defined by linear interpolation between only 16 points over the whole extraction cycle, thus making careful adjustment of the phase shifts not possible. Software is being developed to divide the extraction cycle into 1000 different regions, allowing fine tuning on a almost turn-by-turn basis. When passing the $\phi = 360^\circ$ point, the phase is quickly (120 ns, corresponding to less than 1/5 th of a turn) restored to zero. Details about this phase shift procedure can be found in [3]. Since the energy spread of the injected beam is so small, only 4–5 kV RF voltage is needed to generate a bucket large enough to capture the injected pulses. Indeed, it was quickly found that too large an RF voltage inhibits the extraction process.

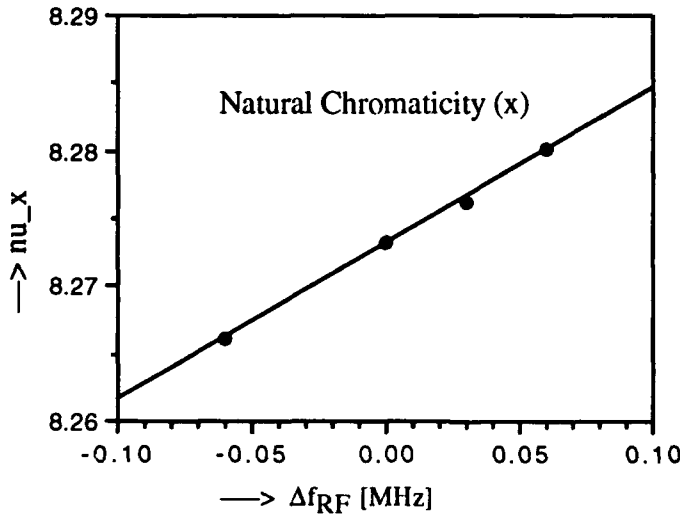


Fig.1 Relation between Δf_{RF} ($f_{RF} = 2856$ MHz) and χ_x for zero-sextupole strength (natural chromaticity): $\chi_x = -9.03$.

The extracted beam was directed into a small Faraday Cup, about 25 m distance from the extraction point. Close to the Faraday Cup a scintillator was placed. By inserting a beam

viewer a few meter upstream of the scintillator, the time structure of the extracted beam could be observed. The current in the ring was measured with a parametric current transformer (pct) from Bergoz. The horizontal tune was measured by applying a FFT algorithm on the signal of a stripline monitor. This method is possible because in Stretcher Mode the beam is injected off-axis in the horizontal plane. The vertical tune was measured by storing the beam, and then applying a small fast ($< 0.7 \mu s$) vertical kick by a specially-designed kicker. Once adjusted to $\nu_y = 7.22$, this value was not changed anymore.

The chromaticity, defined as $\chi_z = \Delta \nu_z / (dp/p)$, $z = x, y$, was measured by varying the RF frequency and observing the resulting tune change:

$$\chi_z = -\alpha \cdot f_{RF} \frac{\Delta \nu_z}{\Delta f_{RF}}, \quad z = x, y \quad (1)$$

where α is the momentum compaction. Eq. (1) was used to check the parametrization of our chromaticity control. Fig. 1 gives an example of such a measurement.

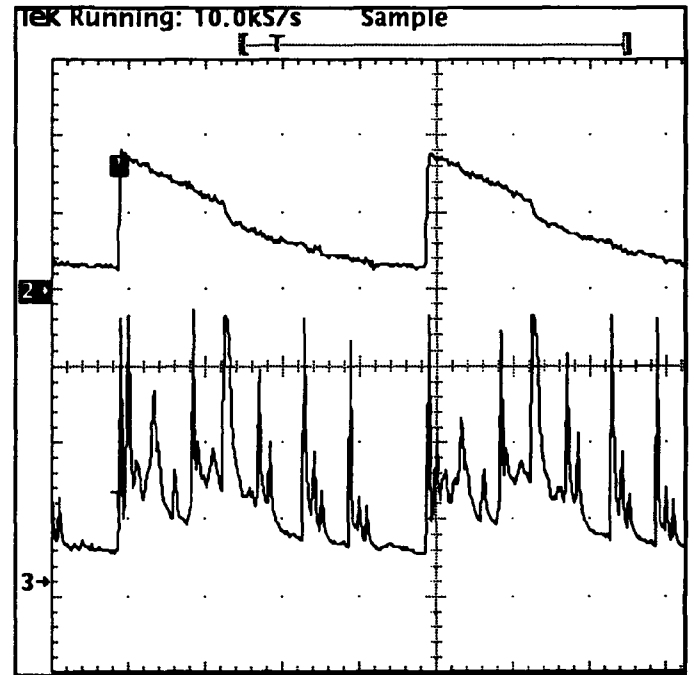


Fig.2 Ring current (top) and scintillator signal (bottom) during two injection/extraction cycles. Injection frequency is 50 Hz; the ring current is 20 mA (two-turn injection).

The proper conditions for extraction were first checked by applying constant RF, and observing the light from one of the four available synchrotron monitors. RF capture was accomplished by slightly retuning the field of the

ring dipoles. Once this was set, the RF was phase modulated. The extracted beam was first observed on some view screens in the extraction channel. From this information it was possible to make a better phase space match in y between incoming beam and machine. The extracted current was optimized by optimizing RF parameters and extraction sextupoles settings.

more-turn injection

By switching on the second injection kicker and increasing the length of the injected beam pulse to $1.4\ \mu\text{s}$, the doubling of the circulating current, see Fig. 2, indicated that two turns got injected. The obvious extension to three-turn injection (the design goal) could not be tested yet due to (a software-related) inability to extend the MEA beampulse beyond $1.4\ \mu\text{s}$. Finally the injection frequency was increased to 200 Hz; under these conditions the max. extracted current was $2.5\ \mu\text{A}$, which means an extraction efficiency exceeding 90 %. No attempt has been made yet to measure the emittance of the extracted beam.

Particles captured inside the bucket can also be expelled from it by changing the RF power level during extraction (amplitude modulation, AM). This method was tried briefly and produced a very 'clean' signal on the scintillator. Due to machine problems this short experiment could not be repeated. This method will be tried again later on.

III. STORAGE MODE

In Storage Mode each quadrant of AmPS is tuned identically (as opposed to Stretcher Mode, where the injection area is tuned slightly different). Experiments were also carried out at $E = 410\ \text{MeV}$. The storage time at $V_{\text{RF}} = 40\ \text{kV}$ and $i = 10\ \text{mA}$ was $\tau = 2.5\ \text{min}$. Since this storage time is approximately equal to the Touschek lifetime ($f_{\text{RF}} = 2856\ \text{MHz}$), no serious attempts were made to improve this. The beam behaviour as observed by the synchrotron ports indicated that probably quite some higher harmonics were picked up by the beam.

As we were virtually not able to determine the trajectory of the closed orbit, this is not too surprising. By moving the horizontal tune close to 8.33, we were able to store three distinct beams: these beams are probably trapped in the three islands adjacent to the three unstable fixed points. Being so close to the resonance reduces the stable part of the phase space to zero, so there is no room any more for the 'central' beam.

IV. CONCLUSIONS

The results obtained so far in Stretcher Operation indicate that the machine behaves as expected. It seems important that we improve our (non-interfering) monitoring system in order to measure – and correct – the closed orbit. The two fast injection kickers and the associated timing system work quite well as we succeeded in two-turn injection without any additional adjustments.

The results in Storage Mode so far are encouraging; but only when we attempt to store higher beam currents at higher energies (using the new 476 MHz system) might we learn more about the behaviour of AmPS. For internal target physics experiments the lifetime obtained so far is already sufficient to carry out meaningful experiments.

V. REFERENCES

- [1] R. Maas and Y. Wu, *Optics of the Amsterdam Pulse Stretcher*, In Proc. 1989 IEEE Particle Accelerator Conf., p. 1698, 1989.
- [2] G. Luijckx et al., *The Amsterdam Pulse Stretcher Project (AmPS)*, In Proc. 1989 IEEE Particle Accelerator Conf., p. 46, 1989.
- [3] F.B. Kroes, E. Heine, T.G.B.W. Sluijk, *A fast amplitude and phase modulated RF source for AmPS*, In Proc. 1991 IEEE Particle Accelerator Conf., p. 684, 1991.

LEP Operation in 1992 with a 90° optics

R. Bailey, T. Bohl, F. Bordry, H. Burkhardt, K. Cornelis, P. Collier, B. Desforges, A. Faugier, V. Hatton, M. Jonker, M. Lamont, J. Miles, G. de Rijk and H. Schmickler

CERN

CH-1211 Geneva 23, Switzerland

Abstract

The optics for physics operation in LEP was changed from 60° to 90° at the start of 1992 with a view to improved Z^0 production, preparation for future operation at higher energies and the use of the same optics in machine developments. The developments included running LEP with twice the number of bunches and using resonant depolarisation for energy calibration. Perturbation to steady operation was felt at the start of the year but was soon overcome as the benefits of smaller emittances were realised. The peak luminosity increased to $1.15 \cdot 10^{31}$ and the luminosity lifetime improved. New operational software halved the time taken between dumping one coast and the start of data taking on the next. The 8+8 bunch operation was introduced as routine operation for the last month. Overall, there was an increase in integrated luminosity from 17.6 inverse picobarns per experiment in 1991 to 28.6 in 1992. Along with improvements in detector efficiency, almost 3 million hadronic Z^0 s were recorded by the four experiments, an increase from 1.27 million in 1991.

1. Introduction

LEP was operated for the whole of 1992 with a phase advance per cell of 90° compared to 60° in previous years. This optics was designed to produce low emittance beams for physics while also being suitable for operation with Pretzels, for polarisation studies and in the longer term for LEP2. After initial difficulties with the commissioning, performances easily surpassed those of previous years.

The whole of the year's running was at the Z^0 peak, mostly with 4 bunches in each beam. Towards the end of the year, however, and following a substantial program of machine development throughout the year, the machine was operated with 8 bunches per beam circulating on Pretzel orbits [1].

2. Filling and preparation for physics

The procedure for filling LEP during 1992 was much the same as in previous years [2]. Bunches of 20 GeV positrons and electrons supplied by the SPS are injected into LEP during a 4.8s slot in the 14.4s SPS supercycle.

Accumulation is achieved by repetitive injection of this kind, typically over about 30 minutes. Accumulation rates were similar to 1991, but the total beam currents achieved during 1992 were somewhat less than in the previous year (See Table 1 for details). This comes from the fact the LEP intensity is presently limited not by single beam phenomena, but rather by beam-beam excitation of transverse instabilities. With lower emittance beams, the threshold for these effects is lower.

In previous years two different ways of getting from the 20 GeV machine into physics conditions have been used. During the early years of operation, beams were first ramped in energy and then squeezed in beta* γ at the experimental interaction points. Towards the end of 1991 running, these two actions were combined, resulting in a simultaneous energy ramp and beta* squeeze. This meant that at the end of the energy ramp, which presently takes around 7 minutes, the machine was already set to the physics optics, and a considerable amount of time was saved in this way. In 1992, with the low emittance optics, the combined ramp and squeeze was never mastered and it was necessary to fall back to separating these two functions. This did not in fact incur much overhead, since the machine was being driven by new applications software which made it possible to run through a separated ramp and squeeze in just 12 minutes [3]. Indeed, over the whole year, the turnaround time between physics runs was almost halved compared to the previous year. Furthermore the amount of beam lost during ramping the machine was significantly less than in previous years (Fig 1). This was due partly to a slightly smaller 20 GeV intensity to start with, but also the new software ensured the integrity of the ramp settings much more than in previous years.

Figure 1 - Intensities at 20 and 45 GeV

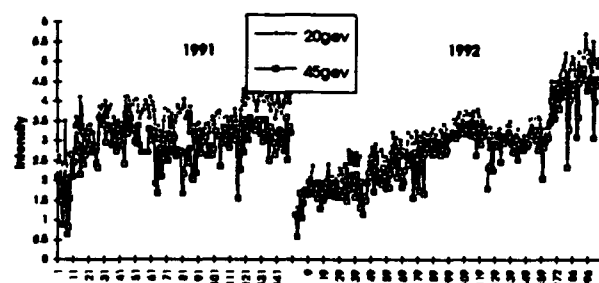


Table 1 - Comparison between the 4 years of LEP running

		1989		1990		1991		1992		
Total hours scheduled	Hrs.		3107		3433		4002		4883	
Hours scheduled for commissioning	"		1284		0		0		501	
Hours scheduled for setting-up	"		48		240		243		509	
Hours scheduled for MD	"		454		689		997		935	
Hours scheduled for physics	"		1321		2504		2762		3439	
Hours of beam in coast	"		469		1048		1242		1742	
Efficiency	%		35		43		45		51	
			peak	avg.	peak	avg.	peak	avg.	peak	avg.
Total current accumulated 20Gev(4+4)	mA		2.85	2.2	4.2	3.1	4.3	3.5	4.5	3.2
Total current accumulated 20Gev(8+8)	mA								5.7	4.7
Current in collisions 45Gev(4+4)	mA		2.64	1.66	3.6	2.5	3.7	2.8	4	2.4
Current in collisions 45Gev(8+8)	mA								5	4.2
Initial luminosity cm-2 s-1 *	10 ³⁰		4.25	1.59	11	5.1	10		11	
Integrated luminosity	pb-1			1.74		12.1		18.9		28.6
Beta at the experiments (v)	cm		7	7	4.3	7 & 5	4.3	7.5 & 5		5&7
Filling time	h:mm		0:50	7:35	1:20	6:57	01:20	03:07	00:50	02:12
Coast duration	h:mm		12:45	5:00	22:35	7:30	27:00	08:00	26:30	08:35
Total number of coasts			97		143		154		199	
Percentage of coasts lost	%		35		33		36		36	

3. Tuning during physics

While running with low emittance beams in collision is of course good for luminosity, it caused problems due to the large beam-beam effects induced. These effects were so large that it proved impossible to maintain good lifetimes after bringing low emittance beams into collision when the total current in the machine exceeded 2 mA. It proved necessary to blow up the transverse emittance with wigglers before bringing the beams into collision. With this mechanism in use the currents in physics were slowly increased throughout the year, eventually reaching levels comparable with previous years. The big advantage during 1992, however, was that throughout the physics coast it was possible to gradually reduce the wigglers to reduce the beam size as the intensity fell, thereby maintaining luminosity levels. While this procedure proved very productive, it meant that machine conditions were often changed, and the operators had to optimise parameters frequently through the run.

Instantaneous luminosity levels achieved in this way were much the same as in previous years, with best performances in the region of $10^{31} \text{ cm}^{-2} \text{ s}^{-1}$. However by maintaining luminosity levels for longer through the run, the integrated daily and weekly rates were higher. Figure 2 shows the evolution of the integrated luminosity throughout the year compared to 1990 and 1991. Figure 3 compares data from the last 2 years in terms of the number of Z^0 detected by the four experiments. Here the increase is more pronounced due to increased efficiency in the detectors and to the fact that all the 1992 running was on the peak while in 1991 energy scanning was performed.

Figure 2 - Integrated luminosities

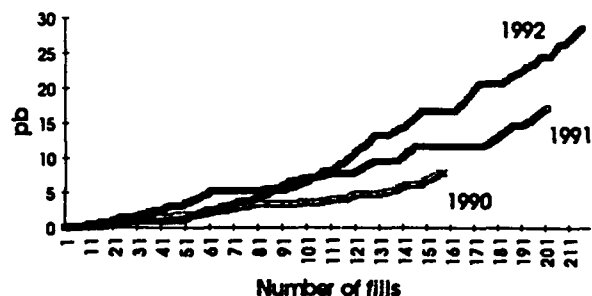
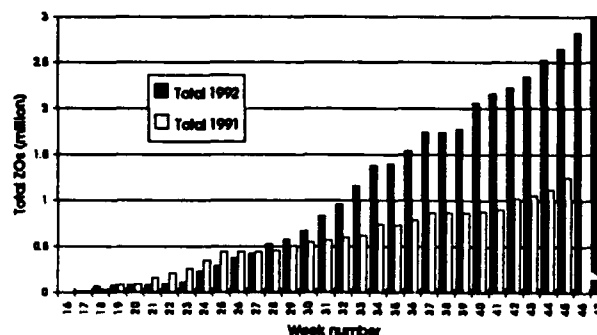


Figure 3 - Z^0 Production



4. 8 bunch operation

For the previous years' running and for most of 1992, LEP has been operated with 4 bunches per beam. Unwanted beam collisions, of which there are 8 during filling and preparation for physics, and 4 during physics, are avoided by a local vertical separation scheme [4]. In order to go to 8 bunches per beam a horizontal Pretzel scheme, developed during 1991 and 1992, was introduced into routine operations for the last four weeks of running [1].

Filling 8 bunches per beam in LEP was achieved with no change to the injectors. Instead the LEP RF synchronisation was flipped back and forth on successive SPS supercycles, filling alternatively normal and 'Pretzel' bunches. Towards the end of the year this was achieved in an automatic way.

The maximum bunch intensities achieved during Pretzel operation were about 70% of those achieved during normal four bunch running. With 8 bunches per beam there are extra long-range encounters in the middle of the arcs, which further limit the accumulated current. The mechanism appears to be the same as that limiting the current in the four bunch case, but at a lower threshold.

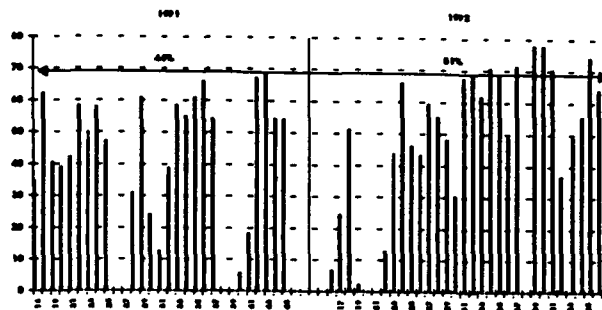
The overall operational efficiency was little affected by 8 bunch operation. Even with the filling scheme described above, accumulation times were only slightly higher than with 4 bunches per beam. Ramp and squeeze efficiencies were also comparable to those achieved with four bunch running. However a further factor of 70% was observed in the luminosities achieved for a given bunch current. This probably came from a combination of beam blow-up and a residual horizontal miscrossing at the experimental interaction points.

These two factors of 70% combined to cancel out the gains coming from having twice the number of bunches in the machine. Nevertheless the break-even point was reached early in the 8 bunch operation, and as more experience was gained throughout the few weeks of running, peak luminosities were seen to gradually increase. The highest luminosity ever seen in LEP was $1.2 \cdot 10^{31} \text{ cm}^{-2} \text{ s}^{-1}$, achieved during 8 bunch operation.

5. Efficiency during operations

The LEP efficiency is defined as the number of hours with beams in coast divided by the number of hours scheduled for physics. Since LEP has to be filled, ramped squeezed and prepared before physics can start, this figure can never reach 100%. The efficiency has been slowly increasing since the start of LEP (see Table 1), and in 1992 was above 50% for the first time. During later running this figure was higher, even during the 8 bunch operation at the end of the year (Figure 4).

Figure 4 - Operational efficiency



The overall efficiency of LEP operation benefited from running with a single optics through the year. Transition from physics to machine study periods and back were more efficient than in previous years. In particular the development of the Pretzel operation on the same optics used for physics was particularly beneficial.

The percentage of coasts lost, rather than intentionally killed, was 36%, a value very similar to that of the three previous years (see Table 1).

5. Summary

The average integrated luminosity measured by the four LEP experiments in 1992 was 28.6 inverse picobarns. The peak luminosity observed in any of the 199 fills made was $1.2 \cdot 10^{31} \text{ cm}^{-2} \text{ s}^{-1}$, achieved during Pretzel running. All running was at the peak, which together with an improved efficiency of the experiments resulted in a total of 3.0 million hadronic Z^0 s recorded in all experiments.

6. References

- [1] Commissioning and operation of the LEP Pretzel scheme
J. M. Jowett et al., these proceedings
- [2] Three years operational experience with LEP
V. Hatton et al., paper presented at the 1992 European Particle Accelerator Conference, Berlin
- [3] The impact of new accelerator control software on LEP performance
R. Bailey et al., these proceedings
- [4] Commissioning and operating experience with the electrostatic beam separation system of LEP
W. Kalbreier et al, paper presented at the 1990 European Particle Accelerator Conference, Nice

Status of TRISTAN-II Project

Shin-ichi Kurokawa and TRISTAN-II Accelerator Task Force
National Laboratory for High Energy Physics, KEK
1-1 Oho, Tsukuba, Ibaraki, 305 Japan

Abstract

TRISTAN-II (B-Factory) project at KEK aims at constructing an accelerator complex which enables us to detect the CP-violation effect of B-mesons. It is a 3.5 x 8 GeV electron-positron collider in the existing TRISTAN tunnel. The eventual luminosity goal is $10^{34} \text{ cm}^{-2}\text{s}^{-1}$. Progress of design work and present status of R&D are reported.

I. INTRODUCTION

The design of the B-Factory at KEK has converged to that on the basis of existing TRISTAN[1], hence the name TRISTAN-II: Two rings of the TRISTAN-II are to be installed in the existing TRISTAN tunnel and the infrastructure of TRISTAN should be maximally utilized. The 2.5 GeV electron linac will be upgraded to 8 GeV in order to inject 3.5 GeV positrons and 8 GeV electrons directly into TRISTAN-II and to produce a sufficient positrons necessary for TRISTAN-II.

We plan to increase the luminosity of the B-Factory in two steps[2]. We first employ a small-angle ($\pm 2.8 \text{ mrad}$) crossing scheme (step 1). In this step we cannot fill the whole bucket with beam, since we need a length for separation of electrons and positrons to avoid spurious collisions; therefore, every fifth bucket is filled with beam. Three meter bunch spacing in this case is long enough to install beam separation equipment, such as separation dipole magnets. The luminosity of step 1 is $2 \times 10^{33} \text{ cm}^{-2}\text{s}^{-1}$. In the second step, we fill every bucket with beam by introducing a large-angle crossing ($\pm 10 \text{ mrad}$) with crabbing[3,4]. The luminosity will be increased by a factor 5 to $10^{34} \text{ cm}^{-2}\text{s}^{-1}$. The machine parameters for both steps are essentially unchanged except the bunch spacing and the total current. The same lattice is used for both steps with minor changes of the interaction region. The main parameters are given in Table 1. The values in parentheses correspond to those for step 1.

As shown in Fig.1 the detector will be installed at Fuji Experimental Hall of TRISTAN, which is occupied now by VENUS detector. The superconducting solenoid magnet and outer-layer ion structure of VENUS will be used for the B-Factory detector with some slight modifications; inner part of the detector will be completely renewed. Electrons and positrons are injected from the upgraded linac to TRISTAN-II at straight sections on both sides of the collision point. Figure 2 illustrates the cross sections of the tunnel for TRISTAN-II.

II. RF SYSTEM

A. Normalconducting RF cavity

To prevent the coupled bunch instabilities we need a special cavity which has small HOM impedance. We have been studying a two-cell damped cavity[5], which was first

proposed by R. B. Palmer[6]. The basic idea of the damped cavity is that the HOM field is guided to waveguides attached to the side of the cavity through slots cut on the disk between cells; the cutoff frequency of the waveguide is set higher than the fundamental accelerating mode frequency.

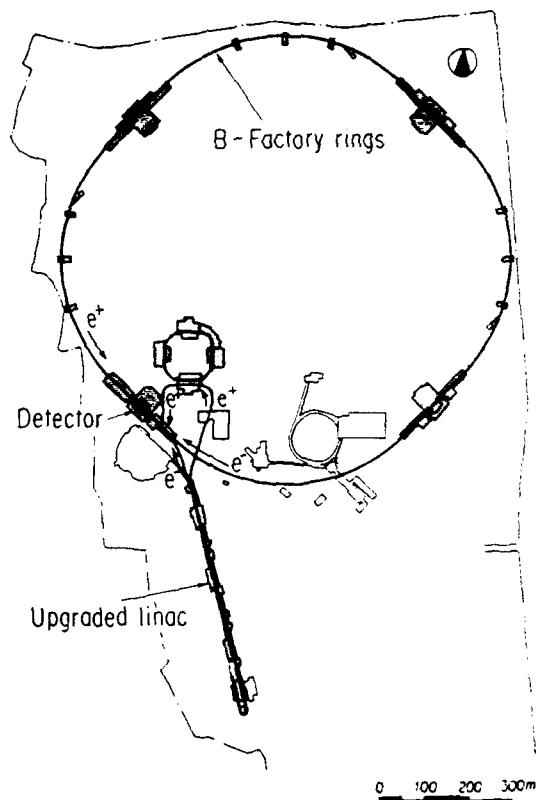


Fig. 1. Layout of TRISTAN-II within the KEK site.

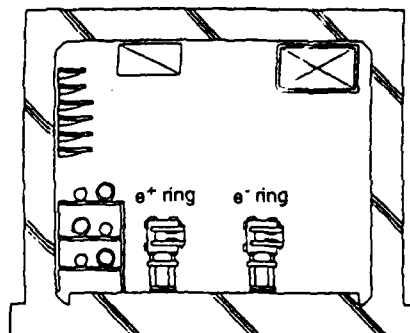


Fig. 2. Cross sections of the tunnel for TRISTAN-II.

Table 1 Main parameters of TRISTAN-II

	LER	HER	
Energy	3.5	8.0	GeV
Circumference	3018		m
Luminosity	$1 \times 10^{34} (2 \times 10^{33})$		$\text{cm}^{-2}\text{s}^{-1}$
Tune shifts	0.05/0.05		
Beta function at IP	1.0/0.01		m
Beam current	2.6 (0.52)	1.1 (0.22)	A
Natural bunch length	0.5		cm
Energy spread	7.8×10^{-4}	7.3×10^{-4}	
Bunch spacing	0.6(3.0)		m
Particles/bunch	3.3×10^{10}	1.4×10^{10}	
Emittance	19/0.19		10^{-9}m
Synchrotron tune	0.064	0.070	
Betatron tune	~ 39	~ 39	
Momentum compaction	8.8×10^{-4}	1.0×10^{-3}	
Energy loss/turn	0.91	4.1	MeV
RF voltage	20	47	MV
RF frequency	508		MHz
Harmonic number	5120		
Damping decrement	2.6×10^{-4}	5.1×10^{-4}	
Bending radius	15.0	91.3	m
Length of bending magnet	0.42	2.56	m

Values in parentheses are for step 1.

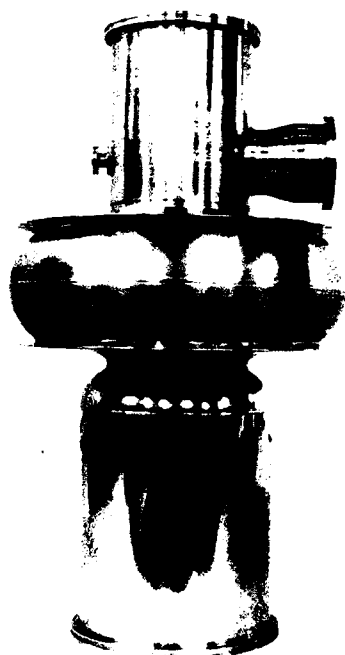


Fig. 3 Full-size Nb model cavity.

The first prototype damped cavity has been completed and a low-power test is now under way. Q-values of the most dangerous modes, TM110- π and TM011- π , were found to be as small as 41 and 14.

As an alternative of the two-cell damped cavity, the design of the choke-mode cavity[7] is under way at KEK.

B. Superconducting RF Cavity

After having determined the optimized shape of the cavity by computer calculation a full-size aluminum model was manufactured and resonance spectra of the cavity were measured with and without ferrite absorbers (TDK IB-004). The loaded Q values of most modes were ~ 100 or less with absorbers, except two harmless quadrupole modes, TM210 and TE211.

A full-size Nb model with this optimized shape was constructed (see Fig. 3) and tested in a vertical cryostat. The maximum accelerating field obtained was 11 MV/m with the Q value of 10^9 (see Fig. 4).

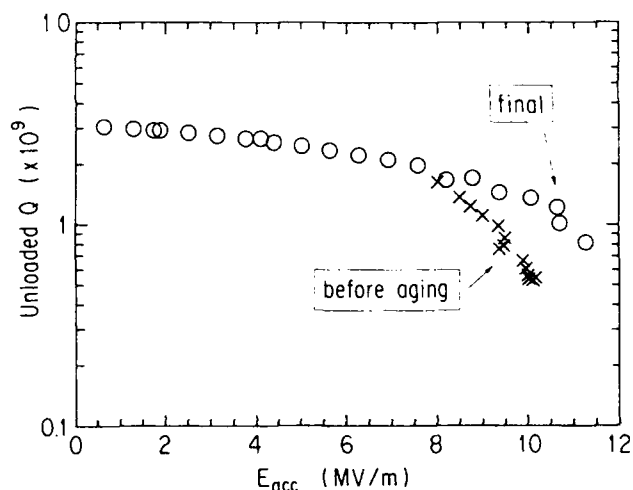


Fig. 4. The result of the vertical test of the prototype Nb cavity.

C. Energy Storage Cavity

Extremely heavy beam loading to the cavity, together with the small revolution frequency, leads to a quite violent longitudinal coupled-bunch instability due to the fundamental mode of accelerating cavities. The most straightforward way to avoid this instability is to employ superconducting cavities, since a large storage energy mitigates the beam loading. T. Shintake of KEK proposed to add an energy storage cavity to the accelerating cavity cell[8]. This storage cavity effectively enlarge the stored energy and makes the cavity system stronger against beam loading; no RF feedback[9] is necessary even for normal conducting cavities. We are investigating the feasibility and applicability of the idea to TRISTAN-II.

III. VACUUM SYSTEM

A trial model duct was fabricated. The duct is straight and 3.7 m long and consists of a beam channel (100 mm in width and 50 mm in height), a pump channel and a cooling channel. The duct material is Oxide Free Copper provided from HITACHI Cable, Ltd. Each channel was independently

extruded in a circular pipe shape with a proper size and then extracted to its design shape. They were welded each other by EBW. The thermal gas desorption rate and photodesorption coefficient of the duct were measured[10].

IV. SEPARATION DIPOLE MAGNET

The separation superconducting dipole magnets will be installed close to the vertex detector and the precision drift chamber. In order to reduce the leakage field, this magnet has two layers of $\cos\theta$ windings[11]. As shown in Fig. 5, the leakage field from the longitudinal end part of the magnet at the detector is less than 50 Gauss.

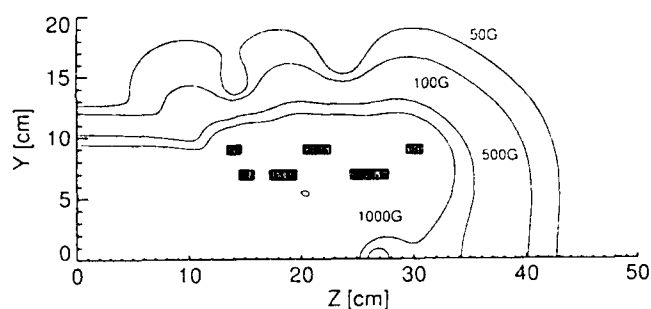


Fig. 5. Leakage field near the longitudinal end part of the separation superconducting dipole.

V. LINAC UPGRADE

Present 2.5 GeV linac will be upgraded by adding accelerating structures and changing 20 MW klystrons to 60 MW ones. SLEDs are used to increase the field gradient. After this upgrade, the linac can accelerate 8 GeV electrons, which will be injected directly into HER. Positrons are produced by 4 GeV electrons and accelerated up to 3.5 GeV before being injected directly to LER. If we assume a normalized yield of positrons to be 2%/1 GeV electron, the intensity of positrons produced by 4 GeV electrons of 4×10^{10} per pulse amounts to 3.2×10^9 per pulse; this corresponds to 1000 sec injection time to LER.

VI. MACHINE STUDY PLAN

A. Beam Test of RF Cavities and Feedback Systems at the TRISTAN AR

Three-month long beam test is planned to be held in spring of 1995 by the use of TRISTAN Accumulation Ring (AR). We plan to store more than 500 mA electron beam in AR with a multibunch mode at 2.5 GeV. The bunch spacing is 10 nsec and the total number of bunches amount to 128. To accumulate this high current, the existing APS type RF cavities will be removed temporally from the ring and a normal conducting damped cavity and a single cell superconducting cavity will be installed. The transverse and the longitudinal feedback systems will be also installed. An IR beam pipe close to the one used for TRISTAN-II will be installed to check the heating due to the beam.

B. Dynamic Aperture Study

We plan to adopt the non-interleaved sextupole scheme for the purpose of keeping enough (transverse) dynamic aperture[12]. Since this sextupole scheme has never been adopted in real machines, we must be very careful introducing this scheme. We have a plan to carry out a machine study on this scheme in this autumn at TRISTAN which needs a dedicated machine time of about a month. Measured and calculated dynamic aperture will be compared.

VII. PROSPECTS

TRISTAN-II project at KEK is regarded as the third phase of TRISTAN. After having pursued the energy frontier by increasing the beam energy from 25 GeV to 32 GeV, the TRISTAN has stepped into its second phase from February 1990, where we put the stress on accumulating as large an integrated luminosity as possible at a modest energy (29 GeV). The goal is to accumulate 300 pb^{-1} integrated luminosity. By the end of 1994 this goal will be reached. We envision that construction of TRISTAN-II will start from April 1994 and by the end of 1998 the commissioning will take place.

VIII. REFERENCES

1. Y. Kimura, Proceeding of the Second European Particle Accelerator Conference, p.23 (1990).
2. B-Physics Task Force, Accelerator Design of the KEK B-Factory, KEK Report 90-24 (1991).
3. K. Oide and K. Yokoya, Phys. Rev. A40, p.315 (1989).
4. K. Akai et al., Proceedings of B Factories, the State of the Art in Accelerators, Detectors and Physics, SLAC-400, p.181 (1992).
5. M. Suetake et al., ibid. p.189.
6. R. B. Palmer, SLAC-PUB-4542 (1989).
7. T. Shintake, Jpn. J. Appl. Phys. 31 p.1567 (1992).
8. T. Shintake, in these proceedings.
9. F. Pedersen, Proceedings of B Factories, the State of the Art in Accelerators, Detectors and Physics, SLAC-400, p.192 (1992).
10. Y. Suetugu, in these proceedings.
11. S. Kurokawa et al., Proceedings of B Factories, the State of the Art in Accelerators, Detectors and Physics, SLAC-400, p.331.
12. H. Koiso, ibid. p.86 (1992).

The Long Range Beam-Beam Interaction at CESR — Experiments, Simulation and Phenomenology *

Alexander B. Temnykh[†], James J. Welch and David H. Rice, Wilson Lab, Cornell U., Ithaca NY

Introduction

A direct route to higher luminosity at colliding beam storage rings is to increase the average beam current by increasing the number of bunches in each beam. However, as the number of bunches increases, so does the number of crossing points where bunches from opposing beams may interact destructively. The most obvious result of these long range interactions, (often seen at CESR), is poor beam lifetime. An increasingly important issue is then how to determine the minimum separation required for adequate lifetime [2] [3]. We have conducted fairly extensive experiments at CESR to measure the minimum separation using a variety of different optics, crossing points, beam currents, and energies. In all cases we found that if the opposing beam current is large enough, we can adequately fit the minimum separation to a function proportional to the square root of the opposing beam current. However, if the opposing beam current is instead quite small, reasonable lifetime may be obtained with no separation at all. Tracking simulations give similar results. We also found that the minimum required separation depends significantly on the beta functions at the crossing points. A number of phenomenological models/criteria suitable for use in designing optics have been evaluated against the experimental data and the results are reported here. Some traditional models did not fare well in this evaluation.

Experiments

The basic technique used to study the long range interaction was to fill selected noncolliding bunches and reduce the separation at the crossing points until a poor (≈ 50 minutes) lifetime was observed. The value of the separation obtained represents the minimum necessary (but not sufficient) for acceptable lifetime. Almost always, a small $\approx 10\%$ increase in the separation above the measured minimum was sufficient to obtain very long lifetimes.

In most tests, only one bunch from each beam was filled. In these cases the effects of the long range beam-beam interactions at *two* crossing points are combined. In general, the separation distances, beam sizes, beta functions,

etc., were different at the two crossing points, though often the effects from one crossing point dominated. In other tests, one bunch was filled against two or three noncolliding bunches in the opposite beam. For each test, only the overall separation amplitude was adjusted so the individual separation distances at the different crossing points were changed proportionally.

Four completely different lattices were used for the experiments, with varying beta functions, tunes, sextupole distributions, emittances and in the case of optics D of table 1, slightly different energy. We tested several crossing points by filling different combinations of bunches. The theoretical values of the optical functions for each of the one on one bunch configurations used in the tests are given in table 1.

For each configuration, the minimum separation was measured over a range of opposing beam currents. An example of the current dependence of the minimum required separation is given in figure 1. A best fit curve, assuming the minimum separation is proportional to the square root of the current, is superposed on the plot. This choice of fitting does a somewhat better job than a simple linear fitting when applied to all the data, though in this case the difference is small. It does not fit well if the current is reduced to the point where it is possible to obtain head-on collisions, but such currents are generally less than the design currents.

Simulation

We simulated some of the experimental data by tracking using the BEAMBEAM element in the MAD program [1]. Sextupoles were included and betatron and synchrotron tunes were adjusted to the measured values.

Lifetime is not simulated directly. Instead the tracking efforts were aimed at finding out what kinds of dynamics come into play when the long range interaction becomes strong. To make sure that all kinds of modulation were excited we used initial amplitudes in all three dimensions: vertical, horizontal and synchrotron, and used four particles with different initial synchrotron phases. Most of the study involved initial amplitudes of 3.2σ . If there was an aperture at 3.2σ in any dimension, a gaussian beam would have about a 50 minute lifetime. The number of turns

*Work supported by the National Science Foundation

[†]On leave from BINP, Novosibirsk

Table 1: Design values of crossing point optical parameters for each of the test configurations are listed. Subscripts 1,2 refer to crossing points locations on opposite sides of the ring. The separation distances, s_1 , s_2 , are the millimeters of separation obtained when the separation amplitude is 1000 units. The horizontal beam size σ_x is in millimeters, while the rest of the betatron functions are given in meters. The relative energy spread δ , is about 6.3×10^{-4} for all lattices.

Set	Optics	β_{x1}	β_{y1}	η_1	σ_{x1}	s_1	β_{x2}	β_{y2}	η_2	σ_{x2}	s_2
1	A	5.9	27.9	1.6	1.6	11.2	8.7	31.4	1.8	1.89	12.0
2	A	13.6	16.2	3.0	2.65	17.5	24.9	8.9	2.7	3.05	18.4
3	B	16.0	16.8	2.0	2.19	8.8	14.5	26.9	3.4	2.74	13.4
4	C	18.9	18.2	2.5	2.64	10.9	12.4	19.7	2.3	2.27	10.7
5	C	30.4	10.6	2.8	3.20	16.7	15.1	13.9	3.0	2.66	13.5
6	C	12.9	23.6	2.1	2.21	10.4	9.0	21.2	1.6	1.83	10.9
7	D	19.7	24.0	2.4	2.57	10.4	18.4	18.1	1.6	2.25	15.0
8	C	13.5	87.9	0.0	1.64	7.2	7.3	12.2	0.2	1.21	8.3
9	C	99.7	25.21	0.1	4.47	17.5	35.0	10.3	0.5	2.66	16.8
10	C	12.9	23.6	2.1	2.21	9.20	9.0	21.2	1.6	1.83	10.45
11	C	13.5	87.9	0.0	1.64	7.2	7.3	12.2	0.2	1.21	8.3

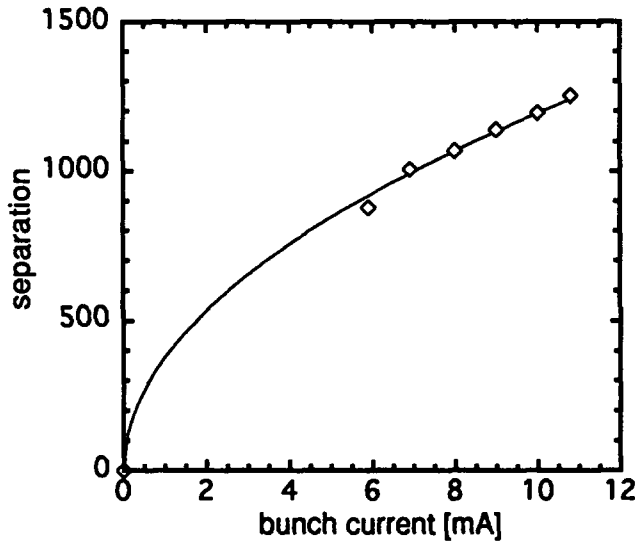


Figure 1: The minimum separation amplitude obtained for different opposing beam currents is plotted. 1000 units of separation corresponds roughly to a typical maximum separation of ± 10 mm. In this case one bunch in each beam is colliding at two points with optical properties defined in table 1.

tracked was 2000 which corresponds to substantially less than the radiation damping time.

In figure 2 we show an example of results of a simulation corresponding to data set 5 in table 1 for an opposing beam current of 10 mA. In particular we plot the vertical amplitude as a function of the turn number. At the larger separation amplitude of 1300 units, tracking gives no discernible growth in vertical amplitude. When the separation is reduced to 1000 units, tracking shows an unstable vertical amplitude and growth rate sufficient to take the average tracked particle out near the vertical physical

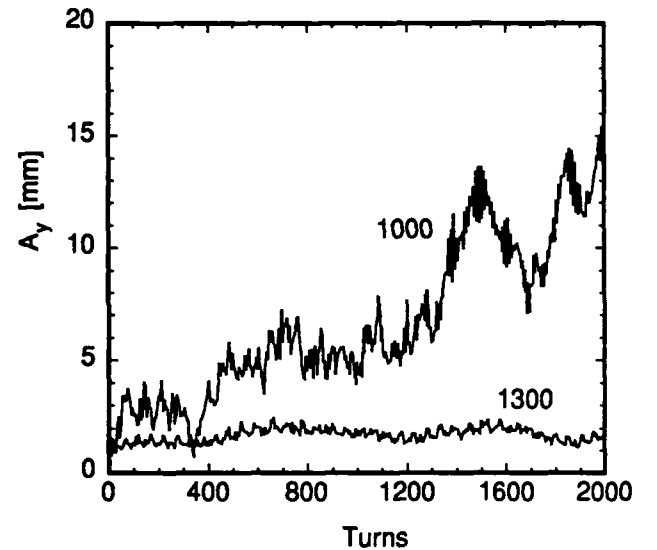


Figure 2: The maximum vertical amplitude of four test particles was tracked for 2000 turns with two different separation amplitudes. At 1300 units of separation the vertical amplitude is stable, while at 1000 units, the amplitude grows rapidly to near the machine aperture.

aperture of the machine. Experimentally we observed that at 1200 units the beam had a 50 minute lifetime, but when the separation was reduced/increased the lifetime rapidly decreased/increased. This comparison was made against several of the machine studies results with similar results.

In the simulations, the horizontal and synchrotron amplitudes never exhibited large instabilities. Only the vertical amplitude seems to be seriously affected by the long range beam beam interaction.

Table 2: The predictive abilities of various phenomenological models, labeled A through K, for determining the minimum separation amplitudes for good lifetime are compared in this table. The models were applied to experimental results obtained from 11 different configurations of crossing points and lattices. In this table X_i refers to the distance in millimeters between beam centerlines at crossing point i , and ξ_i is the long range tune shift parameter. The free parameters n_σ , C , and C' are adjusted for best-fit.

	DESCRIPTION	BEST FIT at 10 mA	RMS
A	$X_i \geq n_\sigma \sigma_{xi} + C \sqrt{\beta_{xi} \beta_{yi}}$	$n_\sigma = 2.0$ $C = .31$	0.124
B	$X_i \geq n_\sigma \sigma_{xi}$	$n_\sigma = 4.5$	0.255
C	$X_i \geq C$	$C = 11.0$	0.203
D	$\xi_i \leq C, x \text{ or } y$	$C = 0.0019$	0.212
E	$\sum \beta_{yi} \sigma_i^2 / X_i^2 \leq C$	$C = 1.61$	0.112
F	$X_i \geq C + n_\sigma \sigma_{xi}$	$C = 7.4$ $n_\sigma = 1.6$	0.190
G	$X_i \geq C + C' \sigma_{xi} \sqrt{\beta_{yi}}$	$C = 2.75$ $C' = 0.73$	0.120
H	$\sqrt{\sum \xi_i^2} \leq C$	$C = 0.0021$	0.192
I	$X_i \geq n_\sigma \sigma_{\beta xi}$	$n_\sigma = 5.50$	0.227
J	$X_i \geq C + C' / \sigma_{xi}$	$C = 11$ $C' = 0.0$	0.203
K	$\sum \beta_{yi}^2 \sigma_i^4 / X_i^4 \leq C$	$C = 3.00$	0.144

Phenomenology

A number of phenomenological models describing separation criteria for good lifetime were constructed. They were checked against the results of the machine experiments for a beam current of 10 mA. Only the one-on-one bunch data were used in this comparison and the results are shown in table 2. All models implicitly assume the tunes were adjusted to get away from destructive resonances, as was done in the experiment.

The models are compared on the basis of the root mean square deviation of the predicted minimum separation amplitude from the actual obtained in machine studies, normalized to the actual separation amplitude. All models assume either one or two free parameters which were varied to obtain the minimum RMS. The best performing of the models, E, gives a best-fit RMS of .11 (11%), which is about as well as we can expect given the limited accuracy with which we know the actual optical functions at the crossing points. The worst of the models give an RMS more than 20%.

The two-parameter models seek to describe the data by requiring the separation at all crossing points be greater than an amount which depends on an effective core size and the distance between the test beam and the core edge. This is motivated by the rapid increase in the vertical beam-beam deflection for particles which pass close to the center

of the opposing beam [4]. The best performing "variable core" models, A and G, require greater separation at points with larger β_y and larger σ_x . The worst performing core models, F and J, do not have any β_y dependence.

The one-parameter models are of two types. Models E, J and K add up the effects from all crossing points, while the other one-parameter models simply require that the separation distance at all crossing points be greater than some model dependent number. Model E gives more weight to points with high β_y and large beam sizes.

Two models previously used extensively in design criteria at CESR are D and I. Model D requires all long range tune shift parameters be less than a fixed value, and model I requires at least some fixed number of betatron sigma between beam centers. These models are among the worst at describing machine performance. In fact they predict a minimum separation amplitude which in some data is in error by a factor of two.

Conclusions

The correlation of the tracking results with machine studies data is very encouraging. However, such tracking can only be used to check a lattice design, and is too cumbersome to be used in the optimization programs that are used to generate a lattice. In this regard, we are pleased to see that some phenomenological models can give reasonably good prediction of required separation, at least for the range of parameters we have been able to test. Further experimental work will extend the range to include larger and smaller beta functions, and examine more of the effects of multiple bunches per beam. For one-on-one bunch configurations models A, E and B are about equally good. A lattice designer might use any of these for optimization and check the results against tracking. He should keep in mind a small ($\approx 10\%$) increase in separation will be needed to get from the marginal 50 minute lifetime predicted by the models to long lifetimes acceptable for running conditions.

References

- [1] MAD — Methodical Accelerator Design, Version 8.1 from CERN
- [2] B. Goddard, W. Herr, J. M. Jowett, M. Lamont, *Measurements of minimum pretzel separation as a function of energy*, SL-MD Note 67, Nov 1992
- [3] Alexander B. Temnykh, James J. Welch, *Some Aspects of the Long Range Beam-Beam Interaction in Storage Rings*, CBN 92-13, Nov. 1992.
- [4] Alexander B. Temnykh *Tune Spread and Tune Shift for the Long Range Beam-Beam Interaction* CBN 93-1, March 1993.

PEP-II Design Update and R&D Results

William Barletta and Michael S. Zisman
Accelerator & Fusion Research Division
Lawrence Berkeley Laboratory, Berkeley, CA 94720 U.S.A.
and

Robert A. Bell and Jonathan M. Dorfan
Stanford Linear Accelerator Center
Stanford, CA 94309 U.S.A.

for the SLAC/LBL/LLNL PEP-II Design Group*

Abstract

We describe the present status of the PEP-II asymmetric B factory design undertaken by SLAC, LBL, and LLNL. Design optimization and changes from the original CDR are described. R&D activities have focused primarily on the key technology areas of vacuum, RF, and feedback system design. Recent progress in these areas is described. The R&D results have verified our design assumptions and provide further confidence in the design of PEP-II.

1. INTRODUCTION

The conceptual design for the PEP-II asymmetric B factory, carried out as a collaboration of SLAC, LBL, and LLNL, was completed in February, 1991 [1]. The design goal for PEP-II, which comprises a high-energy ring (HER) of 9 GeV e^- and a low-energy ring (LER) of 3.1 GeV e^+ , is to provide a luminosity of $\mathcal{L} = 3 \times 10^{33} \text{ cm}^{-2} \text{ s}^{-1}$. Since the conceptual design report (CDR) was completed, the design has continued to evolve and R&D is being carried out in the technological areas of vacuum, RF, and feedback. The main design changes and R&D results are summarized here.

2. DESIGN OVERVIEW

The two-ring PEP-II facility will be located in the 2200-m circumference PEP tunnel, with the new LER mounted atop the HER. The HER reuses most of the components from the existing PEP ring. The injector for the rings makes use of the present SLC injector, which routinely provides $3 \times 10^{10} e^\pm$ per pulse at 120 pps (compared with a PEP-II design requirement of $0.2\text{--}1 \times 10^{10} e^\pm$ per pulse). With this injection system, the estimated top-off time for the operating collider is 3 minutes, and the time to fill the rings from zero current is about 6 minutes. A summary of the main PEP-II parameters is given in Table 1.

*Work supported by the Director, Office of Energy Research, Office of High Energy and Nuclear Physics, High Energy Physics Division, U.S. Dept. of Energy, under Contract Nos. DE-AC03-76SF00098 (LBL), DE-AC03-76SF00515 (SLAC), and W-7405-Eng-48 (LLNL).

Table 1. Main PEP-II Parameters.

	LER	HER
Energy, E [GeV]	3.1	9
Circumference, C [m]	2200	2200
ϵ_y/ϵ_x [nm-rad]	2.6/64	1.9/48
β_y^*/β_x^* [cm]	1.5/37.5	2.0/50.0
$\epsilon_{0x,0y}$	0.03	0.03
f_{RF} [MHz]	476	476
V_{RF} [MV]	5.9	18.5
Bunch length, σ_t [mm]	10	10
Number of bunches, k_B	1658 [†]	1658 [†]
Damping time, $\tau_{x,y}$ [ms]	40.3	37.2
Total current, I [A]	2.14	0.99
U_0 [MeV/turn]	1.14	3.6
Luminosity [$\text{cm}^{-2}\text{s}^{-1}$]	3×10^{33}	

[†]includes gap of $\approx 5\%$ for ion clearing

3. DESIGN OPTIMIZATION

3.1 Lattice Design

The main changes with respect to the CDR design involve the LER lattice. To increase the emittance contribution and radiation damping from the arcs (thereby reducing the dependence on wigglers), the LER arc dipole length has been reduced from 100 cm to 45 cm. Increasing the width of the LER vacuum chamber to provide additional conductance has made this solution acceptable. The LER arcs now provide half of the required damping decrement and half of the required emittance for the LER.

We have also increased the symmetry of the LER by making the magnet arrangement mirror symmetric about the interaction point (IP), as described in Ref. [2]. We have examined the concept of "local" chromaticity correction in which sextupoles are located in the interaction region (IR) straight section itself to control the chromaticity generated by the IR quadrupoles. This approach reduces the higher-order chromaticity that must otherwise be controlled with the arc sextupoles alone. Finally, we reduced β_y^* and β_x^* in the HER to 2 cm and 50 cm respectively and the design

luminosity is now reached with a lower current of 0.99 A in the HER and a smaller emittance of 64 nm-rad in the LER.

Based on beam-beam simulations of the injection process [3], we have now adopted a vertical injection scheme for the rings. This keeps the injected beam well away from the stored beam in the other ring at the parasitic crossing points and thus minimizes the beam blowup during injection. Horizontal injection is still an acceptable option but leads to more blowup and thus potentially more detector background.

3.2 IR Design

The PEP-II IR design is based on an "S-bend" geometry, as illustrated in Fig. 1. Compared with the CDR design, we now have fewer magnets (2 vs. 3 IR quadrupoles) and a stronger B1 separation dipole (tapered for maximum strength and minimum interference with the detector solid angle). This configuration, in combination with the reduced emittance in the LER, leads to larger horizontal separation at the parasitic crossing points (11.8σ vs. 7.6σ). Only the Q1 quadrupole is common to both HER and LER. The Q2 magnet is a conventional septum quadrupole acting only on the low-energy beam.

As part of the IR design procedure, we have adopted criteria against which any proposed design is tested. For example, we design for an aspect ratio of $\sigma_y/\sigma_x \geq 0.04$. This minimizes the potential loss in luminosity associated with the beams being tilted at the IP. Another criterion is to use a "graded aperture" whereby the acceptance at the IR is 15σ , that in the adjacent straight sections is 12.5σ , and that in the arcs is 10σ . This ensures that particle losses will preferentially occur far from the detector. As with all B factory projects, we carry out extensive studies of detector backgrounds [4].

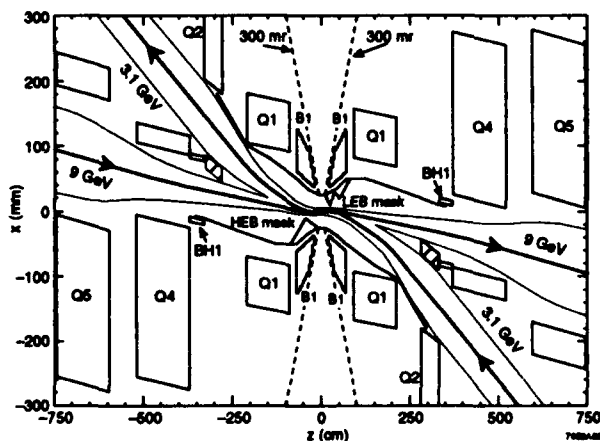


Fig. 1. PEP-II IR layout (anamorphic plan view).

4. R&D PROGRESS AND PLANS

R&D activities permit us to verify design choices and optimize design parameters. Results of the R&D activities are continually folded back into the project design. Examples of this include the down-sampling feature added to

the multibunch feedback system [5], the detailed calculations of the higher-order mode (HOM) damping and thermal loading of the RF cavities [6], the simplified approach to the HER vacuum chamber design [7] and the improved support system resulting from shortcomings which were apparent from our mockup.

4.1 Vacuum System

We have carried out extensive photodesorption studies using the VUV ring at BNL [8]. Initial studies used copper bars to choose acceptable materials for the chamber, and subsequently an actual chamber was studied to examine fabrication and cleaning issues. Chamber production is being studied in detail to determine optimum fabrication, cleaning, and assembly techniques. We are also preparing a series of tests on the pumping speed of distributed ion pumps (DIPs) to optimize the pumping cell design and verify the pumping speed of our chosen configuration.

The status of this work [7] is that materials choices have been made (C10100 copper for the chamber body and C10300 copper for the cooling bar), and the required photodesorption coefficient, $\eta \leq 2 \times 10^{-6}$, has been achieved after an equivalent PEP-II photon dose of only 25 A-hr. A DIP test facility, utilizing an actual PEP dipole, has been fabricated, with pumping tests to be completed in the next few months. Over 70 m of arc chamber extrusions, both dipole and quadrupole chambers, have been procured along with the cooling bar extrusions. The chambers meet tolerances and are acceptable in all respects. Electron-beam welding techniques have been developed for attaching the cooling bar to the chamber body. A fixture has been built which bends the dipole chambers to the required sagitta.

In the next six months, we plan to use the prototype HER extrusions to carry out a realistic fabrication sequence which will result in a complete arc cell vacuum assembly. Impedance measurements of the various chamber components will also be performed.

4.2 RF System

The R&D goals of the RF system program have included fabricating a low-power test cavity and measuring its HOM properties. In addition, tests to verify the efficacy of the proposed waveguide damping scheme have been carried out, resulting in damping of the most dangerous longitudinal HOM (TM011) to $Q \sim 30$ (compared with a desired reduction to $Q < 70$). A program of three-dimensional thermal and mechanical stress calculations for the RF cavity has been carried out in collaboration with the AECL Chalk River Laboratory (CRL) to devise a suitable cooling scheme for the high-power cavity [9]. This cavity is in final design with fabrication to commence soon. A high-power test stand that will be used for the cavity tests (150 kW design goal) and window tests (500 kW design goal) is now available, powered by a 500-kW modified PEP klystron retuned to 476 MHz. These tests will be carried out in the upcoming year.

Considerable emphasis has been placed on the development of an RF feedback system to avoid driving coupled-bunch instabilities with the fundamental mode. A detailed simulation model of the RF feedback system has been carried out in collaboration with CRL and the results are very promising [10]. The design of a 1.2-MW, 476-MHz klystron is well under way, with materials on order for fabrication, and full-power testing planned in the next eighteen months.

4.3 Feedback System

The feedback system R&D in the past year has concentrated on optimizing the design of the longitudinal system. In addition to carrying out simulations with realistic parameters, actual system tests have been performed with beam, using the SPEAR ring at SLAC [11] and the Advanced Light Source (ALS) at LBL. These measurements verify that the system performs properly and understandably under "combat" conditions. In addition, the data have allowed us to verify, in detail, the validity of our simulation package. Our simulations have shown that the down-sampled design is both simple and effective, and that realistic noise and bunch-to-bunch coupling in pickup and kicker do not degrade system performance. At the present time a full prototype longitudinal and transverse systems are being designed. These prototypes will be installed and tested at the ALS beginning in November 1993.

4.4 Magnets and Supports

In the past year we have completed a full-cell hardware mockup of the PEP-II rings and performed mechanical stability and alignment tests. Based on this work, we intend to modify the LER support structure for better alignment line-of-sight. As mentioned, the vacuum system and its supports will be included in this setup. A prototype LER quadrupole will be fabricated and measured to ensure it meets field-quality requirements.

5. SUMMARY

Major progress has been made on the PEP-II design in the past year. Technical uncertainties have been successfully eliminated and no significant new problems have been uncovered. R&D activities are also well under way and have resulted in important design improvements. The issues being studied by the PEP-II team are of great interest to the entire new generation of colliders and storage rings, including B , Φ , τ -charm factories, hadron colliders (SSC, LHC) and new generation light sources.

The PEP-II project has a strong design team combined with an excellent site from which to mount it. We are looking forward to receiving soon the go-ahead to begin construction.

REFERENCES

- [1] An Asymmetric B Factory Based on PEP, Conceptual Design Report, LBL PUB-5303, SLAC-372, CALT-68-1715, UCRL-ID-106426, UC-IIRPA-91-01, February, 1991.
- [2] D. Robin *et al.*, "Local Chromaticity Correction Scheme for the PEP-II Low-Energy Ring," Proc. of International Workshop On B-Factories, Tsukuba (KEK), Japan, Nov. 17-20, 1992; to be published
- [3] Y. H. Chin, "Effects of Parasitic Beam-Beam Interaction During the Injection Process at the PEP-II B Factory," Proc. of Conference on B Factories: The State of the Art in Accelerators, Detectors and Physics, Stanford, April 6-10, 1992, SLAC-400, November, 1992, p. 130.
- [4] M. K. Sullivan, "Interaction Region Proposal for the PEP-II Upgrade," Proc. of Conference on B Factories: The State of the Art in Accelerators, Detectors and Physics, Stanford, April 6-10, 1992, SLAC-400, November, 1992, p. 255.
- [5] H. A. Hindi *et al.*, "Downsampled Bunch-by-Bunch Feedback for PEP-II," Proc. of Conference on B Factories: The State of the Art in Accelerators, Detectors and Physics, Stanford, April 6-10, 1992, SLAC-400, November, 1992, p. 216.
- [6] R. Rimmer, "RF Cavity Development for the PEP-II B Factory," Proc. of International Workshop On B-Factories, Tsukuba (KEK), Japan, Nov. 17-20, 1992; to be published
- [7] C. Perkins, "Research and Development for the PEP-II Vacuum System," Proc. of International Workshop On B-Factories, Tsukuba (KEK), Japan, Nov. 17-20, 1992; to be published
- [8] C. Foerster, *et al.*, "Desorption Measurements of Copper and Copper Alloys for PEP-II," to be published in Proc. of 12th Intl. Vacuum Congress 8th Intl. Conf. on Solid Surfaces, October 12-16, 1992, The Hague.
- [9] M. S. de Jong and T. Tran-Ngoc, "Design of Highly Beam-Loaded, Normal-Conducting RF Cavities," Proc. of Conference on B Factories: The State of the Art in Accelerators, Detectors and Physics, Stanford, April 6-10, 1992, SLAC-400, November, 1992, p. 150.
- [10] F. Pedersen, "RF Cavity Feedback," Proc. of Conference on B Factories: The State of the Art in Accelerators, Detectors and Physics, Stanford, April 6-10, 1992, SLAC-400, November, 1992, p. 192.
- [11] G. Oxoby, *et al.*, "Bunch-by-Bunch Feedback for PEP-II," Proc. of International Workshop On B-Factories, Tsukuba (KEK), Japan, Nov. 17-20, 1992; to be published.

[1] An Asymmetric B Factory Based on PEP, Conceptual Design Report, LBL PUB-5303, SLAC-372, CALT-

Commissioning and Operation of the LEP Pretzel Scheme

R. Bailey, J.M. Jowett, W. Kalbreier and D. Wang*,
CERN
CH-1211 Geneva 23

Abstract

From its start-up in 1989, LEP ran, as designed, with 4 bunches per beam and flat orbits. After 4 days of commissioning activity in October 1992, the regular mode of operation became 8 bunches per beam, thanks to a horizontal separation scheme of the "pretzel" type. Here we describe this transition, starting from the final stages of the machine studies which preceded it and concluding with the performance achieved by the end of 1992 and the factors limiting it. Some of the important steps were: the redistribution of betatron phase advance, minimisation of tune-splits between the beams, chromaticity changes, reduction of residual separations at the interaction points when running for physics at the Z^0 energy, optimisation of pretzel separations at injection and in collision, and equalisation of the bunch currents. A number of changes to operational procedures and instrumentation were made. It was shown that, with a suitable optics, the full beam polarization could be preserved on pretzel orbits. This allowed energy calibration by resonant depolarization and a measurement of the energy shift on pretzel orbits.

I. LEP OPERATION WITH PRETZEL SCHEME

Feasibility studies and preparatory machine experiments connected with the LEP pretzel scheme have been described in previous papers [1, 2, 3]. Here we report on the final commissioning of the scheme for a first period of physics data-taking. It is intended to become the regular mode of operation of LEP from now on. Considerably more detail can be found in [5].

In 1992 the full set of 8 separators was available and the 4 spare arc sextupoles were installed in non-experimental straight sections to allow a partial compensation of the tune-split between the beams due to imperfections.

The low-emittance ($\mu_x = \mu_y = 90^\circ$ in the arc cells) optics used throughout the year was designed with the pretzel scheme in mind. Some preliminary studies [3] were made during the year to study the problems of injection into 8 bunches per beam, energy ramping and "squeezing" to the luminosity optics with $\beta_y^* = 5$ cm. Then, during one week of intense activity in October, the pretzel scheme was commissioned as the regular operational mode of LEP for the last 4 weeks of the 1992 run. The break-even point in luminosity, compared with the previous 4-bunch operation, was reached within 3 days.

Figure 1 shows the configuration of electrostatic sep-

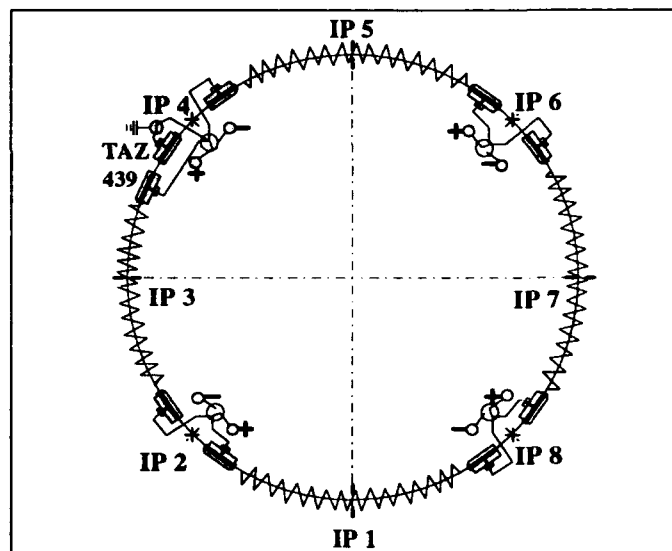


Figure 1: Schematic layout of the horizontal electrostatic separators for the pretzel scheme as it was in 1992. Local vertical separation bumps are used at the 8 IPs.

arators for the pretzel scheme. The circumference can be divided into 4 quadrants between the experiments (even-numbered IPs), each containing a single pretzel bump with horizontal betatron phase advance $\Delta\mu_x = 20 \times 2\pi$ between the two separators. Although the main separator pairs are on the same high voltage supplies their electrode gaps can be remotely adjusted to provide some independent variation of their electric fields. (Two additional trim separators have now been installed to adjust beam separations independently at all 4 IPs in 1993 (DW in [5]).)

A. Injection and Intensity Limits

While filling LEP it is important to keep the individual bunch intensities, I_b , approximately equal. This is all the more true with pretzels when different values of I_b can generate different long-range beam-beam kicks, resulting in each bunch having its own closed orbit, tune and tune-spread depending on the sequence of beam-beam kicks it experiences. Unequal intensities also generate a richer spectrum of coherent beam-beam modes and extremely complex dynamic behaviour can result.

It was possible to fill all 16 bunches automatically: the 4 "normal" bunches on one SPS supercycle were followed by 4 interleaved bunches (displaced by $C/8$) on the subsequent SPS supercycle. However, for technical reasons, the bunch current equalisation system (used regularly

* Visitor from IHEP, Beijing

with $k_b = 4$) could only act on 4 bunches of each beam. This forced us to adopt tricky strategies, filling one set of bunches at a time, which become increasingly difficult near the intensity limit where the lifetime is reduced.

To identify the source of the intensity limits at injection, several tests were done with the separators at 79 kV across 12 cm, giving pretzel amplitudes in mid-arc of about 9 mm. With a single beam (e^+ or e^-), 8 bunches of $I_b \gtrsim 500 \mu\text{A}$ could be accumulated. With two beams of 4 bunches crossing at the IPs (other conditions kept identical), the limit was around $I_b \simeq 450 \mu\text{A}$. Both of these are similar to the limits without pretzel orbits. However when 4 electron bunches were injected against 4 positron bunches, displaced in time so that encounters occurred in mid-arc, the single bunch current limit fell to $I_b \simeq 300 \mu\text{A}$. Although there has been no opportunity for detailed study, the limiting mechanism appears to be the coupling of the $m = 0$ and $m = -1$ head-tail modes, as it is with $k_b = 4$, but occurring sooner because of the mid-arc beam-beam encounters acting rather like an additional impedance.

For most of the operational period the separator voltage was set to 90 kV at injection, raising this limit to $325 \mu\text{A}$. Going higher could lead to beam loss, probably due to the significant e^+e^- tune-split (typically of order 0.01) which could only be partially controlled with what was in effect a single sextupole family. In addition it was necessary to adjust the chromaticities as a function of pretzel amplitude to maintain head-tail stability.

B. Transition to Physics Conditions

Somewhat surprisingly, ramping and squeezing 16 bunches with pretzel orbits posed no particular problems with the low-emittance optics. Typically the separator voltage was ramped linearly from 90 to 120 kV while the beam energy changed from 20 to 45.6 GeV. However the beams were very sensitive going into collision, and time had to be spent carefully correcting (e^+e^- average) orbits and tunes before colliding to get good lifetimes and background conditions in the experiments. During these adjustments the current would fall, and inequalities among bunches would have a chance to set in, before physics conditions were declared.

C. Corrections to the Optics

At both 20 and 45.6 GeV, it was necessary to measure and correct the phase advance errors through the arcs which would otherwise cause non-closure of the pretzels (JMJ in [5]). This was done using the multi-turn acquisition of the orbit, from which the phase errors could be deduced by harmonic analysis to an accuracy approaching 1° . Phase advance corrections inside each pretzel were applied by scaling a pre-matched set of quadrupoles around the odd-numbered IP and produced exactly the intended effect. Compensating phase adjustments to keep the tune constant were applied in the low- β insertions, outside the pretzels. Typical errors were up to 12° in a quadrant. Direct correction of the β -functions was not attempted.

D. Luminosity

In tests at the end of a fill with $k_b = 4$, it was found that simply turning on the pretzel separators to 120 kV, would cause the measured luminosity to drop to 50–60 % of the level without pretzels. With $k_b = 8$, it was difficult to reduce the separators below this value without a loss of beam lifetime. Backgrounds in the experiments were perfectly acceptable.

Fine "Vernier" adjustment of the vertical beam separation at the IP, recovered some 15 % of this deficit. As explained above, only limited horizontal steering was possible (Figure 1) by varying the separator gaps. This was done around two IPs, recovering a further 10 % of the missing luminosity, but with the complications of inter-dependent settings. Finally the specific luminosity with pretzels was 75 % of that without. Non-symmetric settings around IP8 increased the luminosity. The vertical settings and the pretzel separator gaps were left at their optimum during the early physics runs.

Attempts were made to reduce the separator voltages during some pilot physics fills, but it was found that below 115 kV the experimental background rose.

A programme of detailed studies by experiment and simulation of parasitic beam-beam effects in combination with the head-on collisions was started with a view to understanding the energy-dependence of separation requirements for LEP2. In these experiments it was found possible to go to small or zero separation (for sufficiently low I_b) by careful adjustments of tunes, orbit and vertical separation. The results will be reported elsewhere [4].

E. Electrostatic Separators

The 8 electrostatic separators ZX are unipolar and operate at fields $\simeq 1 \text{ MV m}^{-1}$ across gaps of 12 cm. In the test area TAZ (Figure 1), both separators have an insulated ground electrode for current and spark measurements. Without beam the spark rate of the separators is negligible, $< 10^{-4} \text{ h}^{-1}$. With beam, the synchrotron radiation from the main bends dramatically increases the spark rate for negative polarity; for positive polarity it remains acceptable (WK in [5]).

With positive polarity, no breakdowns were observed in the 7 standard separators in 1370 hours. Discharges were detected on the ground electrode of the special TAZ separator at normally distributed breakdown intervals of $1.9 \pm 0.1 \text{ h}$. At 45.6 GeV some 30 % of events had a coincident HT signal indicating a discharge across the gap. These did not cause any beam loss or "background spikes" for the experiments.

With positive polarity sparks are only produced when the ground electrode is insulated. We therefore believe that the screening effect of the positive electrode prevents the HT insulators from being charged by photoelectrons produced by synchrotron radiation. An insulator at the ground electrode can, however, be charged, and subsequent de-trapping of these charges may trigger breakdown. For negative polarity the photoelectrons can charge the HT insulators, leading to breakdown.

Bunches per beam, k_b	8	4	Units
Average I at 20 GeV	4.8	3.0	mA
Best I at 20 GeV	5.6	3.8	mA
Average I into physics	4.5	3.0	mA
Best I into physics	4.8	3.5	mA
Average peak L	9	8	$10^{30}\text{cm}^{-2}\text{s}^{-1}$
Best peak L	11.5	10	$10^{30}\text{cm}^{-2}\text{s}^{-1}$
Typical ξ_y	.025	.035	
Best ξ_y	.028	.0375	
$\langle L \rangle$ over fill	21	20	$\text{nb}^{-1}\text{h}^{-1}$
Best for fills > 6 hours	32	27	$\text{nb}^{-1}\text{h}^{-1}$
Fraction of fills lost	9 %	40 %	

Table 1: Comparison of performance achieved with the pretzel scheme in its operation so far (32 fills) and that achieved in the last 141 fills with $k_b = 4$; "Average" means average over the fills; I , the sum of the currents in both beams, is quoted at injection energy (20 GeV) and after ramping and "squeezing" to physics conditions with $\beta_y^* = 5$ cm; $\langle L \rangle$ denotes the average luminosity over a fill.

F. Performance Summary

Table 1 compares average and peak performances between $k_b = 8$ and $k_b = 4$.

Although the total current brought into physics conditions has increased by 50 %, the 25 % drop in the attainable beam-beam tune shift results in only a 10 % in luminosity.

The number of fills lost fell dramatically in comparison to $k_b = 4$ operation. Of the 3 lost only 1 was for unknown reasons. With $k_b = 4$, about half of the losses were never explained. The difference may arise from the value of I_b .

II. POLARIZATION WITH PRETZEL

One of the main reasons for choosing a purely horizontal pretzel separation for LEP was so as not to exclude the possibility of polarized beams. While it is clear that a vertical or helical separation scheme would depolarize strongly and that a perfect horizontal scheme would not, it was difficult to demonstrate that residual coupling would not be enough to depolarize the beam. Accordingly an experimental test was made on a pretzel optics with $\mu_x = 90^\circ$, $\mu_y = 60^\circ$, with the results shown in Figure 2. (It had not been possible to obtain polarization on the regular 1992 optics.)

Although a discrepancy remains between prediction and measurement of the energy shift due to the pretzel (JMJ in [5]), this result opens up the possibility of energy calibration by resonant depolarization in conditions as close as possible to those of physics data-taking and should help to improve the precision of measurement of the Z-boson mass and width.

III. CONCLUSIONS

After its successful start, the pretzel scheme must now go on to increase the luminosity of LEP.

At 20 GeV it is important to overcome the current limitation. An increased separation should be feasible with a

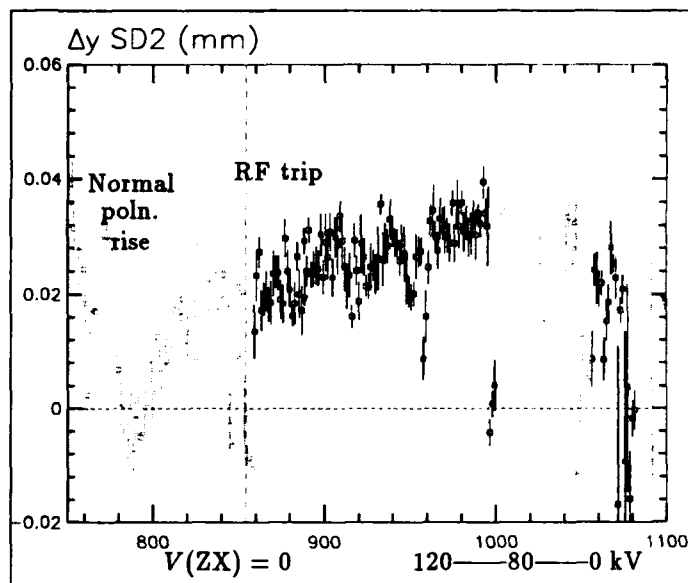


Figure 2: Transverse polarization, P , as pretzel orbits were switched on and then off again, following an period in which the polarization was allowed to rise normally with flat orbits. An asymmetry $\Delta y = 0.05$ mm corresponds to a polarization level of 10 %. Resonant depolarizations (indicated by pairs of vertical dashed lines) were performed during a period of some 15–20 min, at the end of the experiment, in which the pretzel separator voltage was reduced from its maximum back to zero.

new set of achromatic sextupoles which will provide complete control of the the e^+e^- tune-split. A comprehensive bunch equalisation system is a necessity.

With higher currents, the requirements for control of the tunes and chromaticities (to keep both $m = 0$ and $m = 1$ head-tail modes stable) become more stringent.

Additional separators and sextupoles will facilitate correction of the defects of the machine. Reducing the separator fields in physics under carefully controlled conditions will help to reduce the effects of pretzel orbits.

Acknowledgements Many of our colleagues in CERN made valuable contributions to the commissioning of the pretzel scheme.

IV. REFERENCES

- [1] J.M. Jowett, "More bunches in LEP", Proc. 1989 IEEE Particle Accelerator Conf., Chicago, (1989) 1806.
- [2] "Report of the Working Group on High Luminosities at LEP", E. Blucher, J.M. Jowett, F. Merritt, G. Mikenberg, J. Panman, F. Renard, D. Treille (Eds.), CERN Report, 91-02 (1991).
- [3] W. Kalbreier *et al*, "The Pretzel Separation Scheme in LEP", Proc. XVth Internat. Conf. on High-Energy Accelerators, Int. J. Mod. Phys. A (Proc. Suppl.) 2A (1993) 401.
- [4] J.M. Jowett, W. Herr, to be published.
- [5] J. Poole (Ed.), Proc. 3rd Workshop on LEP Performance, CERN SL/93-19 (DI), Chamonix, 1993.

Progress of the LEP Energy Upgrade Project

Carlo Wyss
CERN-AC
CH - 1211 Geneva 23

Abstract

Beams approaching 90 GeV are expected in LEP in 1995; to this end, 192 superconducting accelerating cavities will be installed. The LEP energy upgrade also requires a low-emittance optics, layout modifications, new machine components, powerful cryoplants and a general upgrade of the LEP infrastructure, which will have to distribute and cool away about twice the present energy requirements. The programme was launched in December 1989 and by now major milestones have been achieved. The progress achieved in the various activities are presented, with the aim of providing a view of the programme goals and status.

I. INTRODUCTION

The LEP collider has been designed [1] to allow its upgrade from an initial energy of about 50 GeV per beam (Phase 1) to an optimum energy near to 90 GeV, the ultimate limit being set at 125 GeV by the magnet system. To run LEP at high energy in an economical way, 352 MHz SC cavities (SCC's) have been developed [2] since the beginning of the LEP design. Various schemes [3] for the energy upgrading by adding SCC's were worked out; the one retained consists of 32 SCC's added to each of the LEP Pts 2 and 6, where the copper cavities are presently installed, and of the installation of 64 SCC's at each of the Pts 4 and 8, where new RF accelerating stations are being created. A pilot project for the installation of a first set of 32 SCC's at the LEP Point 2 was launched in 1988. In December 1989 a programme [4] termed LEP 200 was started, aiming at upgrading the beam energy above the W pair production threshold.

II. OPTICS AND LATTICE MODIFICATIONS

A low-emittance optics, achieved by increasing the phase advance in the arcs from 60° to 90° , is necessary to maximise luminosity by approaching the beam-beam limit. In this way a luminosity of about $1.1 \cdot 10^{31} \text{cm}^{-2}\text{s}^{-1}$ is expected around 87 to 90 GeV, assuming 0.5mA/bunch and 4 bunches per beam. Such an optics [5] has successfully been used for regular LEP operation during 1992. Furthermore the 90° optics is also well suited for the 8-bunch scheme ("pretzel" scheme) also commissioned in 1992 [6], aiming at increasing luminosity by a factor two.

A number of geometry modifications of the original LEP lattice are necessary at the even and odd points of LEP, because of quadrupole magnets running out of focusing strength above 65 GeV and because of an increase in length of the SC RF cells, due to the longer length of the SCC's assemblies. All the relevant studies [7] have been completed, the layout of the odd

IP's has already been modified during the 1992/1993 winter shutdown.

III. THE SC ACCELERATING SYSTEM

3.1 SC cavities

The SCC's [8] are installed in LEP as 4-units modules, 11.285 m long. The first set of 32 SCC's, at Pt2, consists of eight prototype Nb sputtered cavities (two modules) made at CERN and 24 Nb sheet cavities (six modules), out of which four are prototypes made in 1989, and 20 are series units, delivered by industry during the years 1991 and 1992. For these cavities, a nominal gradient of 5 MV/m with a quality factor of $3 \cdot 10^9$ was specified.

This performance has been achieved and exceeded by the Nb sputtered prototype units and by all the 20 series Nb sheet SCC's, the last of which has been accepted by October 1992 (7 MV/m have consistently been attained with Q values between 2 and $3 \cdot 10^9$). The three SCC prototype modules operated in LEP during 1991 could not be fully conditioned to nominal performance before their installation because of difficulties that were later traced back to insufficient conditioning of the power couplers. In LEP they were run with beams up to an average of 3.7 MV/m, delivering a total voltage of up to 76 MV. Uneven excitation of the four SCC's of a module, because of geometry tolerances, has been overcome by the design of an adjustable power coupler, required anyhow for optimum coupling at higher beam intensities. The RF conditioning of the main couplers (MC's) has turned out to be a key step, among others, in view of achieving the specified performances. To ensure efficient and safe conditioning, the MC's have been fitted with diagnostics like vacuum gauges and electron pick-up antennas. Mastery of contamination during assembly is as another key issue; contamination monitoring techniques as used for the production of VLSI circuits are at present being used at CERN to gain a deeper insight in this matter. In view of gaining experience and introducing the necessary modifications, the assembly at CERN of the series Nb sheet SCC modules has been slowed down; the first module of this kind, driven at 5 MV/m for 12 hours during lab tests, has been installed at LEP Pt2 this April.

LEP Pts 6, 8 and 4 will be equipped with Nb sputtered SCC modules, to be delivered fully assembled by industry. A nominal gradient of 6 MV/m with a quality factor of $4 \cdot 10^9$ has been specified for this type of SCC's. At the time of writing 29 SC bare cavities (17% of the total quantity) fulfilling the specifications, have been delivered by the three manufacturers, to which SCC's and module delivery were entrusted by contract in October 1990. After the

acceptance test at CERN, the bare SCC's are shipped back to the manufacturers', for assembly into modules. The measurement of the first module delivered by industry shows that nominal performance has been achieved by two SCC's, the other two being slightly below, but that some contamination and irregular patterns in the LHe distribution to the HOM couplers prevent the whole module from being conditioned to nominal performance. These difficulties are being corrected and there is confidence that by September 1993 two Nb-film modules will be installed at LEP Pt6.

The series production of SCC units is now taking off and it is expected to be completed by end 1994; provided that the present difficulties with SCC's modules are solved in the next months, it is hoped to nearly complete during the 93-94 winter shutdown the installation of SCC modules at Pts 2 and 6, and possibly install a few modules at least at Pt 8.

3.2 RF power and control

Twelve new RF units are required for the 192 SCC's. Each unit consists of a 1.3 MW klystron and circulator, the waveguide distribution system and 22 racks of electronics for the controls, low and high power. (The present copper system consists of eight RF units.) The contracts for klystrons, circulators and waveguides have been adjudicated in September 1991, the end of these deliveries is expected by end 1993. Control electronics, RF amplifiers, power meters, temperature stabilised fibre optics for RF reference distribution and associated transmitting equipment have also been ordered in 1991; all the corresponding deliveries have been completed.

The new RF units at Pts 2 and 6 are ready, the four new units at Pt8 will be completed by this summer, those at Pt 4 will become available during 1994.

A central control of the total 20 RF units, which will be available in 1994, will be ensured by a global RF control system, designed to adjust synchrotron tune and to keep an optimum RF balance; this system is already operational [9] for the presently available accelerating cavities.

3.3 Cryogenics

At each of the even LEP Points there is a cryoplant [10] with an initial cooling power of 12 kW at 4.5 K and an ultimate one of 18 kW. These cryoplants consist of a surface upper cold box for the 300 K to 20 K temperature range, connected by vertical transfer lines in the machine shafts to an underground lower cold box for the 20 K to 4.5 K range. The corresponding contracts were adjudicated in December 1990; their execution is progressing close to the contractual planning, i.e. the cryoplants at Pts 6 and 8 have been installed during the last five months and are now being commissioned. They show an inverse efficiency (power from the grid/cooling power at 4.5 K) better than 230 W/W, which is the best ever achieved. The cryoplants at Pts 2 and 4, at present being installed, will be commissioned by October 1993 and February 1994, respectively.

Two 6 kW cryoplants have been delivered and are at present routinely operated. One has been installed

underground for cooling the SCC's at Pt2 during 1992 and 1993, and the other one equips the SM18 cryogenic test facility, where the acceptance tests of the SC cavities and LHC magnet development work are taking place.

The installation of the He transfer lines for supplying the SCC's at Pts 2, 6 and 8 has been completed; the installation of those at Pt4 will take place during the next winter shutdown. The delivery of all other components for the cryogenic system (e.g. high and low pressure storage vessels, piping for He gas) will be completed by this summer.

IV. COLLIDER COMPONENTS AND INFRASTRUCTURE

4.1. Magnets, separators, vacuum, instrumentation, power converters

The present SC quadrupoles at the even IP's will be replaced at earliest during the 1993-1994 shut-down by new ones [11], having the same outer overall dimensions, but with a magnetic field gradient increased from 36 to 55 T/m. A prototype magnet has successfully been tested in November 92 and the series production has started.

The 24 steel-concrete cores of the original injection dipoles saturated as from 70 GeV and have been replaced by classical steel laminated cores during the 92-93 shut-down.

To keep sufficient beam separation during acceleration up to 100 GeV, two additional electrostatic separators, identical to those already in operation, will be added at each of the even IP's. The vacuum tanks and the electrodes for these eight new separators have all been delivered, their assembly is taking place at CERN, installation is foreseen for the 94-95 shutdown.

The performance of the vacuum system in presence of the high energy synchrotron radiation has been extrapolated from various measurements [12], and a beam-gas lifetime of about 20 hours is expected. The modifications of the odd and even IP's, and that of the RF straight sections, require that about 130 vacuum chambers for drift spaces and quadrupole magnets be manufactured or modified. The aluminium vacuum chambers are modified at the CERN workshops, whereas the stainless steel chambers have been ordered to industry. The odd IP's and some RF straights at Pt6 (total length about 2 km) have been modified during the 92-93 shut-down. The RF cells at Pts 4 and 8 (700 m), and the even IP's (240m, 80 vacuum chambers) will be modified during the 93-94 and 94-95 shutdowns. In total some 17 km of the LEP vacuum system will have been opened to air and baked out again. The cooling of the vacuum system is likely to be upgraded during the 94-95 shutdown; it will then cope with up to 32 MW of synchrotron power, i.e. 1.6 kW/m (electron and positron beams of 6 mA each at 95 GeV will radiate about 28 MW of synchrotron power). This cooling upgrade will be achieved by changing from series to parallel the water flow in the cooling channels of the vacuum chambers. The lead shielding along the beam

path will be completed at about 2700 locations also during the 94-95 shutdown.

The major modifications to the beam instrumentation equipment concern the addition or the replacement of collimators[13], to cope with the higher energy deposition by synchrotron radiation. Out of the sixteen collimators in the arcs, shielding the even IP's from off-momentum particles (the absorbing material has changed from aluminium to tungsten) eight are already installed at positions compatible with the 90° optics. To shield the SC cavities from synchrotron radiation, sixteen new collimators will be installed during the 93-94 shutdown at the outer ends of the RF straight sections.

The original magnet power converters (PC's) were designed for operation up to 65 GeV; those for LEP 200 are foreseen for a maximum beam energy of 100 GeV. For the LEP bending magnets, the new PC's (2 x 9.7 MW) have been delivered in October 1991. Because of difficulties with the new large thyristor units, their installation has eventually taken place in the 92-93 shut-down. All the magnet PC's are now ready in their LEP200 configuration; their total number has increased from 758 to 868 units and the installed power from 18 to 50 MW. Ten new klystron power converters (40 A, 100 kV), identical to those already in use for the present RF system, are necessary. The corresponding contracts were placed in March 1991, their delivery was completed this March.

4.2 Power distribution, cooling, civil engineering

The power distribution system required major extensions at Pt 2, where the main dipole PC's are located, and at Pts 4 and 8, where the new RF units are situated (4 x 4.2 MW at each point). The cryoplants need about 3 MW from the grid at each of the even points, where the power converters (2 x 1.1 MW) for the arc quadrupoles are also situated. Additional power is also necessary for all the other magnet PC's, for the new RF units at Points 2 and 6, for cooling and ventilation and other services. To cope with these requirements, 50 MVA power links (10 km of trenches) from the Préveessin 400 kV/66 kV station (where a second 400 kV/66 kV, 110 MVA transformer has been installed) to Points 4 and 8 have been realised in 1991. Extensions of the 66 kV substations at Points 2, 4 and 8 with new 38 MVA transformers are operational since this April. All contracts for power distribution equipment, harmonic filters, reactive power compensation, HV and LV switchgear have been completed. To cope with the increase in power dissipation, the number of cooling towers has been increased from four to six at Pts 2 and 6, and from one to five at Pts 4 and 8 (Pts 2 and 6 need additional cooling capacity because of the presence of the copper RF system and resistive experimental magnets). Major extensions of the air and water cooling facilities are needed at Points 4 and 8, because of the new RF units. All the activities related to the cooling system will be finished by June 1993.

New klystron galleries (2 x 2 x 230 m) have been excavated at Pts 4 and 8 for housing the RF units. At Point 8, the UA83 and UA87 galleries are completely

equipped. At Pt 4 one gallery has been delivered for installation early May, the second one will follow by early June 93. The five new sound-proofed compressor buildings (5 x 600 m²) are in service. At Pts 4 and 8 the extensions of the rectifier halls (2 x 300 m²) and the water pump stations (2 x 170 m²) have also been delivered to schedule and are already equipped. The twelve new cooling towers described above have been made out of concrete, as are the original ones, and were delivered by December 92.

V. SUMMARY

A high energy optics for LEP is well in hand. The operation of three prototype SCC modules in LEP during 1991 has allowed to gain precious experience, necessary for improving hardware and operational procedures. Concerning SCC's from industry, the transfer of know-how and the begin of series production have required about two years, during which development of power and HOM couplers has been necessary in order to cope with the anticipated higher beam intensities of up to 1 mA/bunch x 8 bunches/beam [14]. All activities for machine components and infrastructure are in regular progress.

LEP operation at beam energies above the W pair production threshold is foreseen in 1995.

VI. ACKNOWLEDGEMENTS

In such a short article it is unfortunately not possible to describe or even mention all the Project activities. The ingenuity, determination and untiring efforts of all those contributing to the success of the LEP Energy Upgrade Programme are gratefully acknowledged.

VII. REFERENCES

- [1] LEP Design Report, CERN-LEP/84-01
- [2] E. Picasso "Development of RF Superconducting Cavities for Large Storage Rings" *Proc. 20th Int. Conf. on High Energy Physics*, Madison, 1980.
- [3] Ph. Bernard et al "Upgrading of LEP energies by superconducting cavities", CERN/LEP-DI/86-29
- [4] C. Wyss "The LEP Energy Upgrade Programme", *Particle Accelerator Conference, San Francisco 1991*
- [5] R. Bailey et al "LEP Operation in 1992 with a 90° Optics", this Conference
- [6] R. Bailey et al "Commissioning and Operation of the LEP Pretzel Scheme", this Conference
- [7] D. Brandt "Lattice Modifications for the LEP Energy Upgrade", *EPAC 1992*, Vol. 1, pp. 403-405
- [8] G. Cavallari et al "Superconducting Cavities for the LEP200 Energy Upgrade", this Conference
- [9] E. Ciapala et al, "Global Voltage Control for the LEP RF System", this Conference
- [10] M. Barranco-Luque et al "Status of Cryogenics for the LEP200 Project", *ICEC14*, Kiev, June 92
- [11] T. Taylor et al "Design of the Superconducting Quadrupoles for the LEP200 Low-beta Insertions", *12th Intern. Conf. on Magnet Technology, Leningrad*, 1991
- [12] J.-P. Bojon et al "Experience with the Operation of the LEP Vacuum System and its Performance for LEP200", *EPAC92*, Vol. 2, pp. 1564-1566
- [13] R. Valbuena et al "Design of a New Generation of Collimators for LEP200", this Conference
- [14] L. Evans "LEP Status and Future Plans", this Conference

Flat Beams in the SLC*

C. Adolphsen, T. Barklow, D. Burke, F.-J. Decker, P. Emma, M. Hildreth, T. Himel, P. Krejcik, T. Limberg, M. Minty, N. Phinney, P. Raimondi, T. Raubenheimer, M. Ross, J. Seeman, R. Siemann, W. Spence, N. Walker, M. Woodley
*Stanford Linear Accelerator Center
Stanford, California 94309*

ABSTRACT

The Stanford Linear Collider was designed to operate with round beams [1]; horizontal and vertical emittance made equal in the damping rings. The main motivation was to facilitate the optical matching through beam lines with strong coupling elements like the solenoid spin rotator magnets and the SLC arcs.

Tests in 1992 showed that 'flat' beams with a vertical to horizontal emittance ratio of around 1/10 can be successfully delivered to the end of the linac [2]. Techniques developed to measure and control the coupling of the SLC arcs [3] allow these beams to be transported to the Interaction Point (IP). Before flat beams could be used for collisions with polarized electrons, a new method of rotating the electron spin orientation with vertical arc orbit bumps [4] had to be developed.

Early in the 1993 run, the SLC was switched to 'flat' beam operation. Within a short time the peak luminosity of the previous running cycle was reached and then surpassed. The average daily luminosity is now a factor of about two higher than the best achieved last year.

In the following we present an overview of the problems encountered and their solutions for different parts of the SLC.

I. FLAT BEAMS IN THE DAMPING RINGS

The SLC was designed to operate with 'round' beams where horizontal and vertical beam emittance are equal ($\epsilon_x = \epsilon_y$). Electron/positron storage rings naturally produce 'flat' beams where $\epsilon_x \gg \epsilon_y$. Round beams had to be produced by operating the SLC damping rings on the linear coupling difference resonance:

$$\nu_x - \nu_y = n \quad (1)$$

With round beams, the horizontal and vertical tunes in the electron and positron damping rings were $(\nu_x, \nu_y) = (8.28, 3.28)$ and $(\nu_x, \nu_y) = (8.18, 3.18)$. Alignment and field errors in the rings resulted in a resonance width of roughly $\Delta\nu = 0.01$. The normalized rms emittances were $\gamma\epsilon_x \approx \gamma\epsilon_y = 1.5 \times 10^{-5}$ m-rad.

To generate flat beams, the betatron coupling was reduced by separating the tunes by $\Delta\nu = 0.2$. The vertical dispersion due to residual errors was reduced by choosing the vertical tune close to half integer. Currently, the electron and positron rings are operating with horizontal and vertical tunes of (8.28, 3.43) and (8.18, 3.38), respectively. The difference between the

electron and positron ring tunes is historical. For normal SLC operation, simply splitting the horizontal and vertical tunes is sufficient; producing beams with normalized rms emittances of $\gamma\epsilon_x = 3 \times 10^{-5}$ m-rad and $\gamma\epsilon_y = 0.3 \times 10^{-5}$ m-rad.

The vertical emittance could be reduced further with more sophisticated coupling and dispersion correction. However, in the electron damping ring, the beam is stored for only 2.4 damping times and thus the extracted vertical emittance is limited by the injected emittance. Emittance dilution in the bunch compressor after the damping rings, where the bunch length is compressed from roughly 10mm to 1mm, prevents the realization of significant improvements.

Further reduction of the vertical emittance was achieved during an experiment in 1992 where the electron damping ring was operated with a longer store time (and lower beam repetition rate). Vertical orbit bumps through the sextupoles were used to correct the betatron coupling and vertical orbit bumps in the insertion quadrupoles to correct the vertical dispersion. With these bumps, the vertical rms emittance was reduced to $\gamma\epsilon_y \approx 0.05 \times 10^{-5}$ m-rad, a 1.7% emittance coupling ratio.

Under typical SLC operating conditions both the electron and positron vertical emittance at linac injection (after the bunch compressors) are $\gamma\epsilon_y \approx 0.4 \times 10^{-5}$ m-rad. The horizontal emittances are $\gamma\epsilon_x \approx 3.6 \times 10^{-5}$ m-rad. These values are quite stable with fluctuations primarily arising from orbit changes in the bunch compressor which generate vertical dispersion.

II. FLAT BEAMS IN THE LINAC

The acceleration of both bunches (e^- and e^+) in the linac from 1.19 to 47 GeV requires precision measurements, tight component tolerances and operational controls to maintain the 10 to 1 emittance ratio of the compressed damping ring beams.

Emittance measurements are made at three locations along the linac (at 1.2, 15, and 47 GeV) using three sets of four wires scanners. The resolution for the normalized emittance is 0.05 - 0.1×10^{-5} m-rad. Typical vertical rms beam sizes at 47 GeV are 35 to 60 μm .

The required alignment tolerances are tight: the quadrupole rolls are corrected to 0.1 mrad, the quadrupoles and the beam position monitors are aligned to better than 100 μm , and the accelerating structures are aligned to about 300 microns (all rms). The linac support girders are mechanically clamped to reduce component vibration [5] to below 100 nm.

Transverse wakefield damping (BNS) is used in the first two-thirds of the linac to control emittance growth from beam trajectory jitter. Klystron phasing with an accuracy of 0.5

* Work supported by Department of Energy contract DE-AC03-76SF00515

degrees produces a small energy spread (0.3 % rms) at 47 GeV. Along the linac, eight transverse feedback groups (x, x', y, y' for two bunches) maintain the trajectory to about 50 μm with an update rate of 30 HZ.

Finally, the emittance growth from residual dispersion and wakefield effects is reduced by cancellation using "trajectory bumps" along the linac[6]. The transverse feedbacks are used to generate and close these bumps. They are tuned to control emittance and beam tails throughout the linac. About 8 to 12 bumps are in use at any given time with amplitudes of order 100-200 μm and lengths of 200 to 800 m. Most of these bumps are reasonably stable over several weeks, however, fine tuning (10%) is often done to track hourly and diurnal changes. For vertical emittances of the order of 0.5×10^{-5} m-rad, bump control at the 25 μm level is needed.

Emittance and Twiss parameters in key parts of the accelerator are measured automatically by the SLC control system every 30 minutes and recorded in long term history buffers for analysis as seen in Figure 1.

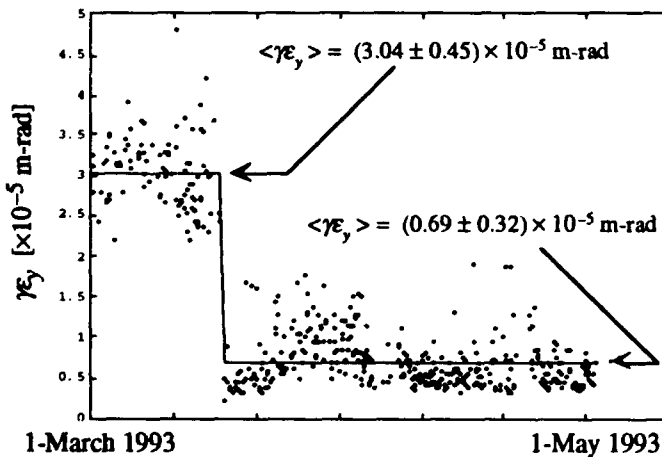
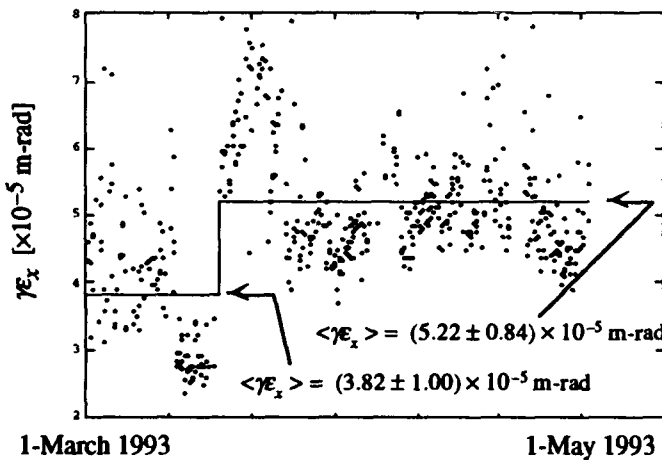


Figure 1. Horizontal (upper) and vertical (lower) invariant emittances for positrons as a function of time (March 1st to May 1st, 1993) at 47 GeV. The beams were made flat for collisions on March 17. The variations with time come from changing accelerator conditions and emittance optimization by the accelerator operators.

We observe from this data that a vertical invariant emittance in the range of $0.5\text{-}0.8 \times 10^{-5}$ m-rad can be maintained over long times during collisions at 3×10^{10} particles per bunch with 25 to 100% enlargement along the linac. The horizontal emittance can be maintained at $4.0\text{-}6.0 \times 10^{-5}$ m-rad with 20 to 50% increase along the linac.

During tests in 1992, vertical emittances of about 0.15×10^{-5} m-rad have been produced at 47 GeV at low beam intensity (1×10^{10}) and long store time in the damping ring [2].

III. FLAT BEAMS IN THE COLLIDER ARCS

The SLC Collider Arcs were designed with rolled achromatic sections to follow existing terrain elevations of the SLAC site [1]. In the presence of optical errors, the rolls generate coupling and vertical emittance growth due to synchrotron radiation. A well tested and refined optical correction algorithm [3] has been developed which measures and cancels both the net coupling and the local coupling in the arcs to within design tolerances. This is aided by an early hardware modification, known as 'rollfix', which distributes the roll transitions over several magnets [7] to improve the coupling cancellation in the presence of phase errors and also reduce the vertical emittance growth due to synchrotron radiation. Table 1 below summarizes the expected normalized emittance increase due to the synchrotron radiation of a perfect arc, with and without "rollfix", in both planes for each arc.

	e- Arc		e+ Arc	
$\gamma \Delta \epsilon$ [10^{-5} m-rad]	X	Y	X	Y
with out rollfix	1.22	0.25	1.19	0.27
with rollfix	1.30	0.07	1.13	0.12

Table 1. Synchrotron radiation emittance growth (10^{-5} m-rad) per plane of each arc before and after the implementation of "rollfix".

With this emittance growth and the full 4×4 measured arc transfer matrix, the flat beam emittance dilution in the arcs was estimated to be $\leq 20\%$. For incoming vertical linac emittances of $\sim 0.5 \times 10^{-5}$ m-rad, the importance of the "rollfix" improvement is clear. In practice, the actual transport of flat beams through the arcs required little or no additional coupling correction beyond that already applied for round beams. The beam emittances at the end of the arcs were measured [12] and found consistent with the emittance growth cited above.

A new important achievement for flat beam running was the use of the north collider arc as a spin rotator by taking advantage of the strong resonance between the spin tune and the vertical betatron tune. A novel method was developed to perform arbitrary spin vector rotations with closed vertical betatron oscillations [4]. This method was very successfully tested and implemented early in 1993 so that the RTL and linac solenoid spin rotator magnets remained turned off for the entire 1993 luminosity run. If these solenoids were still used for the spin handling, a significant amount of new hardware (8 skew quads) and new tuning techniques would have been necessary to compensate for the beam rotations and preserve beam emittance.

IV. FLAT BEAMS IN THE FINAL FOCUS

Several new problems arise when considering the measurement and tuning of flat beams in the SLC Final Focus Systems. Beam-beam deflections [9] used to measure IP beam sizes and luminosity have, in the past, been fitted with a simplified round beam deflection curve. Fitting this curve to data from flat beam deflections (for present SLC parameters) produces a systematic underestimation of the luminosity of up to 25%. A correct flat beam deflection fit was developed to more accurately measure beam sizes and luminosity. Fig. 2 shows a vertical deflection scan and the fitted quadratic sum of the e^- and e^+ vertical beam sizes.

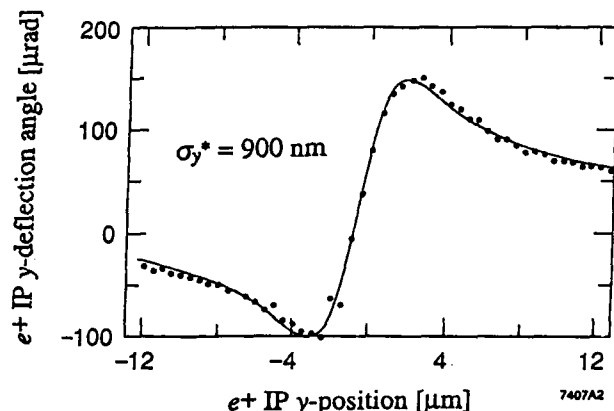


Fig 2. Flat beam-beam vertical deflection scan which measures the quadratic sum of the e^- and e^+ vertical beam sizes. The individual vertical beam sizes are $<0.9 \mu\text{m}$. The horizontal beam sizes (not shown) are typically $2.2\text{--}2.5 \mu\text{m}$.

To correct residual coupling at the IP, each Final Focus employs just two skew quadrupoles. This is sufficient for equal emittances, but for a general solution four skew quadrupoles are necessary. By comparing a model of the linear optics of the combined arcs and final focus systems with the measured 4×4 arc transfer matrices, the existing Final Focus coupling correction was found to be adequate given the small residual arc coupling.

Third order optical calculations were required to determine the optimal IP beam divergences (β^*) for each plane. For round beams and 0.3% rms uniform energy spread the minimum beam size is achieved with a divergence of $\sim 300 \mu\text{rad}$ rms in both X and Y. For present SLC flat beams (ϵ_x/ϵ_y @IP = $6.0/0.6 \times 10^{-5}$ m-rad), the optimal divergences are $350 \mu\text{rad}$ in X and $110 \mu\text{rad}$ in Y. This optics was established for flat beam collisions.

Beam-beam disruption is estimated to contribute about 10% [10] to luminosity with present SLC beam parameters (3×10^{10} particles per bunch, $\sigma_z \sim 0.75$ mm). An upgrade of the final focus optics is scheduled for completion before the 1994 SLC/SLD physics run. The new optics will substantially reduce the limiting third order aberrations and allow a smaller β_y^* (~ 1 mm) at an optimal vertical IP beam divergence of $245 \mu\text{rad}$. With these parameters, a vertical beam size of 350 nm is expected [11]. This will increase luminosity by a factor of 2.4 from geometry alone, with an

additional 40% expected from the beam-beam pinch enhancement [10] (3.5×10^{10} particles per bunch, $\sigma_z = 0.6$ mm) giving a total improvement factor of 3.5.

V. CONCLUSIONS

Operating the SLC with flat beams has been very successful. The average luminosity doubled from $1.7 \times 10^{29} \text{ cm}^{-2} \cdot \text{sec}^{-1}$ ($18 Z_0/\text{hr}$) with round beams to $3.0 \times 10^{29} \text{ cm}^{-2} \cdot \text{sec}^{-1}$ ($32 Z_0/\text{hr}$) with flat beams. Operational problems were modest and the improvement was achieved within a few days. Peak luminosities beyond $40 Z_0/\text{h}$ have been observed. At present, the integrated luminosity has reached a total of $\sim 20,000 Z_0$'s, nearly doubling the entire 1992 round beam run with 11,000.

Spin manipulation in the arcs has been successful and stable; the electron polarization at the IP is currently averaging $>60\%$.

VI. ACKNOWLEDGMENTS

The authors would like to thank the SLC operations and maintenance staff for their hard work and support.

VII. REFERENCES

- [1] *SLC Design Book*, SLAC (December 1984).
- [2] C. Adolphsen, F.-J. Decker, and J. Seeman, *Flat Beam Studies in the SLC Linac*, Proceedings of 1993 Part. Accel. Conf., Washington, D.C., 1993.
- [3] T. Barklow, *et al.*, *Review of Lattice Measurement Techniques at the SLC*, Proceedings of the Advanced Beam Dynamics Workshop, Corpus Christi TX 1991, AIP Particles and Field Series 48.
- [4] P. Emma, T. Limberg and R. Rossmanith, *The North Arc of the SLC as a Spin Rotator*, Proceedings of 1993 Part. Accel. Conf., Washington, D.C., 1993.
- [5] J. Seeman, R. Holtzapple, and M. Ross, *Induced Beams Oscillations from Quadrupole Vibrations of about 2 Microns in the SLC*, Proceedings of 1993 Part. Accel. Conf., Washington, D.C., 1993.
- [6] J. Seeman, F.-J. Decker, and I. Hsu, *The Introduction of Trajectory Oscillations to Reduce Emittance Growth in the SLC Linac*, XV Int. Conf. on HE Accel., Hamburg, Germany, 1992, p. 879.
- [7] P. Bambade, *et al.*, *Rollfix — An Adiabatic Roll Transition for the SLC Arcs*, Proc. Particle Accelerator Conference, Chicago, Illinois (March 1989).
- [9] P. Bambade, *et al.*, "Observation of Beam-Beam Deflections at the Interaction Point of the SLAC Linear Collider", *Physical Review Letters*, Vol 62, No 25, p 2949, June 1989.
- [10] P. Chen, *Disruption Effects from the Collision of Quasi-Flat Beams*, Proceedings of 1993 Part. Accel. Conf., Washington, D.C., 1993.
- [11] N. Walker, *et al.*, *Third-Order Corrections to the SLC Final Focus*, Proceedings of 1993 Part. Accel. Conf., Washington, D.C., 1993.
- [12] P. Raimondi, *et al.*, *Sigma Matrix Reconstruction in the SLC Final Focus*, Proceedings of 1993 Part. Accel. Conf., Washington, D.C., 1993.

THE DAMPING RING FOR NOVOSIBIRSK Φ - AND B-FACTORIES

V.V.Anashin, S.E.Belomestnykh, A.A.Didenko, N.S.Dikansky, B.I.Grishanov,
P.M.Ivanov, V.A.Kiselev, V.I.Kudelainen, N.A.Kuznetsov, V.A.Lebedev,
B.L.Militsin, S.I.Mishnev, V.V.Parkhomchuk, A.N.Voroshilov, M.N.Zakhvatkin
Budker Institute of Nuclear Physics
630090, Novosibirsk, Russia

Abstract

The Damping Ring is designed to provide the accumulation, cooling and extraction of electron and positron beams at energy of 510 MeV with the particle production rate 2×10^{10} per second for injection into Φ -factory and (after additional acceleration) B-factory. The lattice consists of four symmetrical quadrants. The magnetic field polarity doesn't change by changing the particle sort. To provide a short bunch length ($\sigma \approx 5$ mm) two warm cavities of 800 kV total RF voltage are used. The single turn injection scheme with the orbit bump and horizontal kick is used. In this report the general parameters and features of the Damping Ring are presented. The state of the ring design and construction is discussed.

1 INTRODUCTION

The study and design of new generation electron-positron colliders with ultra high luminosity, Φ - and B-factories are carried out presently in Novosibirsk [1,2,3]. These new facilities will require a large intensity of injected beams. The new injection complex constructed now in BINP should solve this task. It will deliver electron and positron beams with the production rate 2×10^{10} particles per second with energy of 510 MeV for injection into the Φ -factory and, with maximum energy of 8.5 GeV for injection into the B-factory. The injection complex includes the $e^- - e^+$ linac at energy of 510 MeV [3], the Damping Ring of the same energy and main linear accelerator. After acceleration in the linac the electron and positron beams are accumulated alternately in the Damping Ring. They are cooled there due to SR damping, decreasing transverse and longitudinal sizes, and are extracted from the Damping Ring for injection into Φ -factory or the acceleration up to the maximum energy 8.5 GeV. A short description of the Damping Ring project for this program is presented in this report.

2 GENERAL PARAMETERS

The electron-positron linac produces short particle bunches with repetition frequency of 50 Hz. In the case of positrons a number of particles in each bunch is small, and many bunches have to be accumulated to achieve the required intensity. The electron and positron beams are injected in the ring by two different transfer lines. Polarity of ring magnets is not changed, so the electrons and positrons are

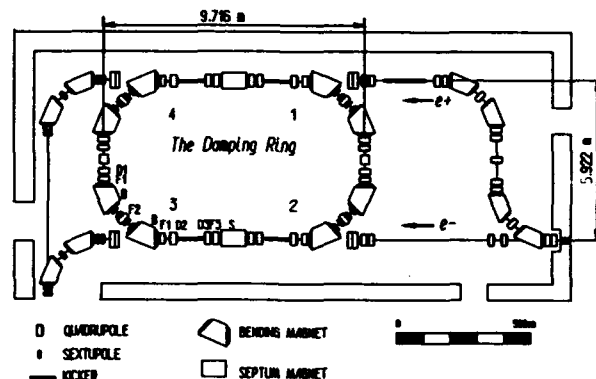


Figure 1: The Damping Ring layout

injected in opposite directions at the opposite straight sections. The energy of accumulator is not changed at operation. The basic mode of operation includes an injection of 40 positron pulses in the same bucket, cooling them due to SR damping and extraction. One cycle duration is 1 s. It is possible to increase the extraction frequency up to 4 Hz. To decrease the horizontal betatron damping time the redistribution of horizontal and longitudinal dampings is provided by the use of bending magnets with field gradient (lattice with combined functions). It allows to reach the horizontal betatron damping time, which determines the injection efficiency, two times smaller than the injection period. At the gradient of bending magnets equal to 4 T/m the horizontal damping portion number is approximately equal to the longitudinal one, $G_h \approx G_s \approx 1.53$. The basic parameters of the Damping Ring are presented in Table 1. The disposition of the accumulator and transfer lines are shown in Figure 1.

3 LATTICE AND MAGNETS

The lattice of the Damping Ring is symmetrical relatively two axes passing through the centers of short and long straight sections and consists of four quadrants. Each quadrant includes the basic magnets and correctors with DC feeding and the group of pulsed magnets, which provide a beam extraction. One quadrant includes two bending magnets and seven quadrupoles. The lattice design

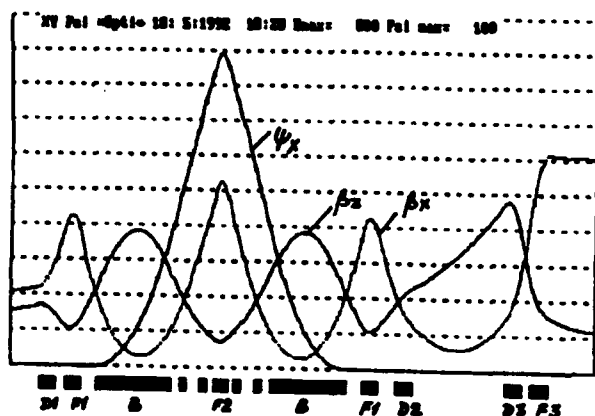


Figure 2: Betatron and dispersion functions

provides the zero dispersion function in the straight sections and the horizontal betatron phase advance between two kickers equal to π . The betatron and dispersion functions of one quadrant are shown in Figure 2. The parameters of the Damping Ring magnets are given in Table 2. Two families of sextupoles for the vertical and horizontal chromaticity correction are used. They are placed symmetrically between bending magnets. Each family includes eight sextupoles.

4 RF SYSTEM

The RF-system is designed to solve the next tasks: 1) capture of the electron and positron bunches coming from the linac; 2) compensation of the energy loss caused synchrotron radiation (5.3 keV/turn); 3) formation of the short bunches for injection in the Φ -factory and the main linac.

The RF frequency has been chosen equal to 700 MHz, what corresponds to the 64-th harmonic of a revolution frequency. To obtain the short length of bunches ($\sigma = 5$ mm) the RF-system with high voltage has to be used. For longitudinal coupling impedance of the vacuum chamber ($Z_n/n \simeq 1 \text{ Ohm}$) and for the given bunch length the calculation determines the required RF voltage of 800 kV. In this case the longitudinal acceptance of the accumulator dE/E is equal to 2.3%, what provides a sufficient bucket height to capture the linac pulses. The energy spread of injected positrons has been designed equal to ± 0.01 . The energy spread of incoming electrons is smaller. Two warm cavities should provide the required RF-voltage. The parameters of the RF-system are given in Table 3.

5 INJECTION AND EXTRACTION

There are two identical injection and extraction systems for the two sorts of particles. A vertical 20° Lambertson type septum with a constant magnetic field and two kickers with horizontal kick are used for the injection. Both kickers are placed symmetrically relatively to the center of long straight section. The first kicker pushes the accumulated bunch to the septum magnet edge. At the same time the linac bunch appears on the other side of the sep-

Table 1: The Damping ring parameters

Energy (MeV)	510
Circumference (m)	27.401
Number of particles	2×10^{10}
Beam current (mA)	35.5
RF frequency (MHz)	700
injection frequency (Hz)	50
extraction frequency (Hz)	1-4
Energy loss/turn (keV)	5.3
Momentum compaction	0.028
Horizontal tune ν_x	4.78
Vertical tune ν_z	2.86
Synchrotron tune ν_s	.021
Horizontal chromaticity S_x	-7.66
Vertical chromaticity S_z	-4.94
Horizontal damping time (ms)	11.3
Vertical damping time (ms)	17.5
Longitudinal damping time (ms)	11.9
Horizontal r.m.s. acceptance (mrad cm)	10
Vertical r.m.s. acceptance (mrad cm)	4
Input beam parameters:	
Horizontal r.m.s. emittance (mrad cm)	1.5
Vertical r.m.s. emittance (mrad cm)	1.5
Energy spread	0.01
Output beam parameters:	
Horizontal r.m.s. emittance (μ rad cm)	2.3
Vertical r.m.s. emittance (μ rad cm)	0.5
Energy spread	0.0007
Bunch length (cm)	0.5

Table 2: Parameters of magnets

Bending magnet				
Number	8			
Field strength* (T)	1.52			
Field gradient (T/m)	4.0			
Magnetic length (m)	0.88			
Gap height* (mm)	36			
Quadrupoles	number	Insc. radius	Gradient	Length
		mm	(T/m)	m
F1	8	30	22.67	0.18
D1	4	30	-10.88	0.18
F2	4	30	20.31	0.18
D2	4	40	-5.64	0.20
F3	4	40	14.17	0.20
D3	4	40	-15.13	0.20

* — at the central orbit

Table 3: RF parameters

RF frequency (MHz)	700
Harmonic number	64
Total voltage (kV)	800
Synchrotron tune ν_s	.021
RF power (kW)	70
Energy loss/turn (keV)	5.3
Energy acceptance dE/E	0.023
Number of cavities	2
Quality factor	21000
Beam current (mA)	35.5

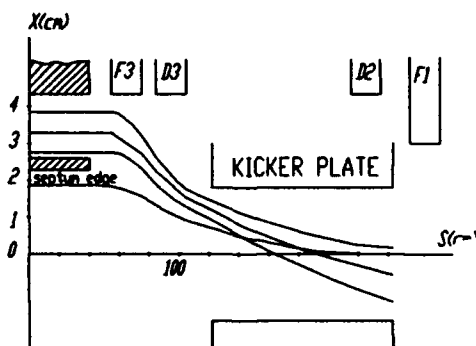
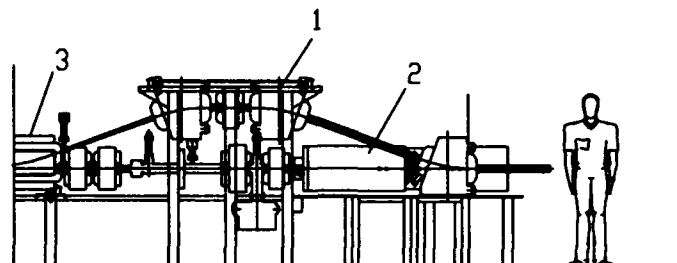


Figure 3: Beam layout at the injection

tum edge, which makes the linac bunch travel parallel to the accumulated bunch. The betatron oscillations are canceled by a kicker downstream of the injection septum, so the accumulated bunch follows again the central orbit, a new bunch has small betatron oscillations. The horizontal betatron phase advance between kickers is equal to π . The injection is repeated after approximately double damping time of the horizontal betatron oscillation. After several injections an extraction takes a place, using the same septum magnet. A pair of pulse correctors displaces a closed orbit to the edge of the septum magnet and the fast kicker extracts the bunch from the Damping Ring. Then new injection again takes a place. Each kicker consists of two 110 cm length plates, each of them provides a 60 kV pulse. The expected full rise and fall times are equal to 80 ns, what is less than a revolution period. The injection and extraction kick instabilities are less than 1%. The beam layout at the injection is shown in Figure 3.

6 BEAM TRANSFER LINE FROM LINAC TO DAMPING RING

To transfer the electron and positron beams from linac to the Damping Ring two different transfer lines are used (see Figure 1). After the linac the positron bunch has rather large energy spread, so to have an effective injection one should decrease it. Taking into account a small bunch length the transformation in the longitudinal phase space have been suggested for use before injection. In this case



1 - transfer line magnet
2 - ring magnet
3 - septum magnet

Figure 4: Beam transfer to the Damping Ring

during movement in a specially designed beam line the bunch length increases due to energy spread, what produces the energy modulation along the bunch length. The downstream linac type accelerator section is used to cancel this modulation that decreases the initial energy spread of the bunch. It is possible to vary the energy modulation of the bunch length over a wide range. Specially designed three 20° vertical magnets together with the septum magnet produce the achromatic beam transfer from the transfer line to the Ring (see figure 4). To separate the electron and positron beams an input dipole magnet is used. For a change of particle sort from positrons to electrons it has to be switched off.

7 STATUS

At present time the design of magnets and cavities of the Damping Ring is finished, the prototypes of magnets are in the production. By the end of this year the construction of the building for the Damping Ring housing has to be finished.

References

- [1] L.M.Barkov et al., "Status of the Novosibirsk Phifactory project", IEEE Particle Accelerator conference, San-Francisco, USA, 1991.
- [2] V.E.Blinov et al., "B-factory with Monochromatization and Vertical Separation", Conference on B-factories: "The State of Art in Accelerators, Detectors and Physics", SAC, May 1992.
- [3] N.S.Dikansky et al., "Novosibirsk B - factory: Status and perspectives" XV-th International Conference on High Energy Accelerators, Hamburg, Germany, July 1992.

A Possible Redesign of the SLAC SLC Damping Rings*

T. O. RAUBENHEIMER, R. EARLY, T. LIMBERG, H. MOSHAMMER, J. SPENCER

Stanford Linear Accelerator Center, Stanford University, Stanford, CA 94309

Abstract

We describe a possible replacement for the SLC damping rings that would generate beams with normalized horizontal emittances of $\gamma\epsilon_x = 9 \times 10^{-6}$ m-rad when uncoupled; this is more than three times smaller than that generated by the current rings. The primary difference between the new design and the current ring is the arc cell structure; the insertion regions, the kickers, and the RF are essentially unchanged. The new cell uses a single combined function bending magnet, roughly 70 cm in length, to replace the two bends, defocusing quadrupole, and defocusing sextupoles in the current FODO cell; the focusing quadrupole and sextupoles, used in the current cell, are also used in the new structure. The length of the new cell is identical to that of the current cell and thus nine of these new cells would simply replace the nine FODO cells in each arc of the rings.

Introduction

In this paper, we will describe a possible replacement for the Stanford Linear Accelerator (SLC) damping rings. The SLC damping rings [1] are very compact storage rings, operating at 1.19 GeV with a circumference of 35.28 meters. They have transverse damping times of 3.5 ms and equilibrium rms emittances of $\gamma\epsilon_x = 3 \times 10^{-5}$ m-rad. The rings are composed of 18 FODO bending cells plus two insertion regions for injection/extraction, kickers, and RF.

Although the equilibrium emittance of the SLC damping rings is very small, given the recent performance of the SLC, we can consider the possibility of transporting even smaller emittances to the IP [2]. The minimum emittance at the IP is set by the synchrotron radiation emittance growth through the SLC arcs. In normalized units, this is roughly $\gamma\epsilon_x \approx 1.3 \times 10^{-5}$ and $\gamma\epsilon_y \approx 0.1 \times 10^{-5}$ m-rad. These emittances will be added to the emittances at the end of the SLC linac and thus we used these values as a goal for the emittances of a future damping ring; one has diminishing returns when achieving values significantly smaller.

We will first discuss the constraints on the replacement ring and then we will describe the lattice and the bending magnets. Next, we describe the dynamic aperture limitations and a possible correction scheme, and finally, we discuss other possible upgrades to the SLC damping rings.

Emittance Reduction and Lattice Choice

When considering a replacement, one is constrained to the same energy, the same, or faster, damping times, and roughly the same circumference as the SLC damping

rings. The energy is constrained by the required rotation of the electron polarization before injection into the ring, the damping times are needed to damp the injected emittances while operating at 120 Hz, and the circumference is determined by the size of the damping ring vaults. Thus, there are only three possible ways of reducing the emittances: (1) use damping wigglers to decrease both the damping times and the emittances, (2) use combined function bending magnets to change the horizontal damping partition, also decreasing the damping times and the emittances, and (3) use a more efficient cell structure with smaller dispersion to reduce the quantum excitation and thus the emittance.

Unfortunately, wigglers are not very effective at reducing the emittance. Roughly four meters of 5T superconducting wiggler with a 15 cm period would be needed to reduce the damping time and emittance by a factor of two. In addition to the severe operational difficulties with such a device, the wigglers would increase the longitudinal emittance an unacceptable amount.

This leaves the latter two choices, changing the damping partitions and/or using a more emittance efficient lattice. We chose a combination: increasing the horizontal damping partition to roughly 1.7 while decreasing the quantum excitation in the cells. Many emittance efficient cell structures have been developed such as the Chasman-Green, Triple Bend Achromat (TBA), and Theoretical Minimum Emittance (TME) structure. Unfortunately, all of these structures require more physical space than is available; they are not very compact. For example, 12 Chasman-Green cells, using 24 bending magnets, could be used to generate the desired emittance, but to keep the quadrupole strengths reasonable, we found that the ring circumference would have to double. Alternately, 16 TME cells, using 16 bending magnets, could also generate the desired emittance, but again the ring circumference nearly doubled.

Thus, we chose to use a FODO type structure where all of the vertical focusing is performed in a combined function bending magnet located between the horizontally focusing quadrupoles; we refer to this as a FOOF structure. [3,4] The cell structure is similar to the TME structure in that the horizontal dispersion and horizontal beta function are minimum at the center of the bending magnet and, with the parameters we have chosen, the equilibrium emittances are comparable; 20 FOOF cells are needed to achieve the same emittance as 16 TME cells. This structure was actually suggested as a replacement for the SLC damping rings in 1989, but this option was not studied seriously until recently.

Lattice

The new ring is illustrated schematically in the bottom half of Fig. 1 while the current SLC rings are shown in the top half. As described, the FOOF lattice structure

* Work supported by Department of Energy, contract DE-AC03-76SF00515.

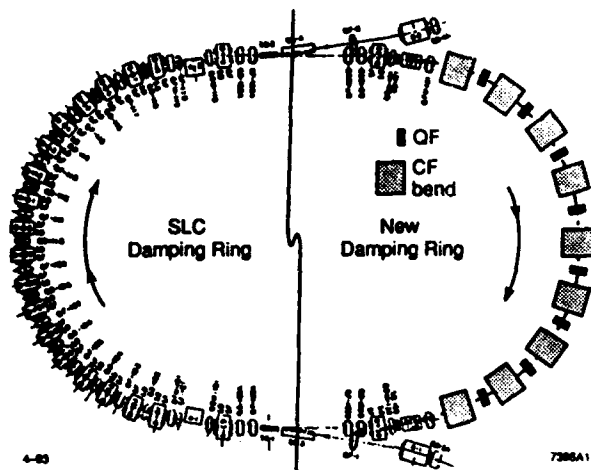


Fig. 1 Schematic of the current SLC damping ring (upper half) and a new damping ring design (lower half). The arc cells of the SLC rings are replaced in the new design while the injection/extraction, RF, and kicker regions remain the same.

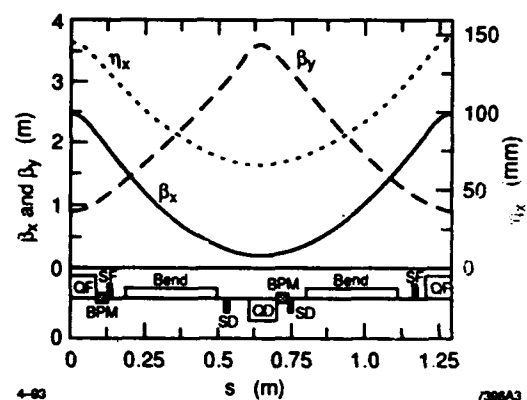
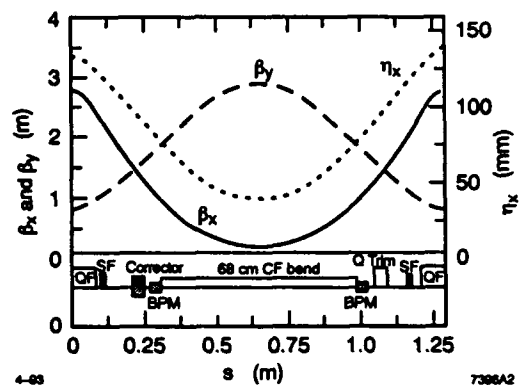
Table 1. Damping ring parameters.

	\bar{B}_0 [kG]	τ_x [ms]	J_x	τ_y [ms]	$\gamma\epsilon_x$ [mm-mrad]
SLC	20.24	3.5	1.0	3.5	30
new	18.34	2.0	1.7	3.5	9

consists of a focusing quadrupole and a defocusing combined function bending magnet. The cell length chosen to be equal to that of the SLC damping ring FODO cells, 1.29 meters, and the cell tunes were chosen close to those of the current rings: $\nu_x \approx 0.37$ and $\nu_y \approx 0.13$; this is close to the optimal focusing to minimize the emittance.

Thus, nine of the new arc cells simply replace nine of the original FODO arc cells. The original focusing quadrupoles are reused and the injection/extraction insertion regions are not changed. The chromatic correction is performed using the focusing permanent magnet sextupoles in the present rings and a defocusing sextupole gradient in the bending magnets. Thus, a single combined function bending magnet, roughly twice the length of the present bending magnets, replaces two bends, a defocusing quadrupole, and the defocusing sextupoles. Additional, dipole correctors and trim quadrupoles are needed for orbit correction and control of the tunes and a new vacuum chamber is required.

The lattice functions of the new cells and the original FODO cells are compared in Figs. 2 and 3. The beta functions are similar in the two cells, but the dispersion, and thus the quantum excitation, is significantly smaller in the new cell. Parameters of the present SLC damping rings and the new damping ring are listed in Table 1. The equilibrium emittance in the new ring is over a factor of three smaller than that in the present rings. This is due



Figs. 2 and 3 Lattice functions in an arc cell of the new damping ring (top) and the SLC rings (bottom); the cell length is the same in both.

to both the change in the damping partition from the defocusing gradient in the bending magnets and the smaller dispersion in the bending magnets.

Combined Function Bending Magnet

The combined function bending magnet is described in detail in Ref. 5. It is 68 cm long with fields of $B_0 = 18.33$ kG, $dB_y/dx = -140$ kG/m, and $d^2B_y/dx^2 = -4770$ kG/m². The gap was chosen to be equal to the aperture in the focusing quadrupoles, 1.3 cm radius, which is larger than the current bending magnets; this would allow a constant radius vacuum chamber without the aperture transitions that can increase the ring impedance.

To achieve good fields without differential saturation of the magnet pole, we chose to design the bending magnet with Vanadium Permendur poles. This allows one to change the ring energy without changing the normalized quadrupole and sextupole components of the bend. Another advantage of the long bends with permendur poles is that the fringe fields are small. The SLC bending magnets are constructed from saturated iron and are relatively short and, although the peak field is roughly 20.2 kG, the fringe fields reduce the rms bending field to less than 18 kG.

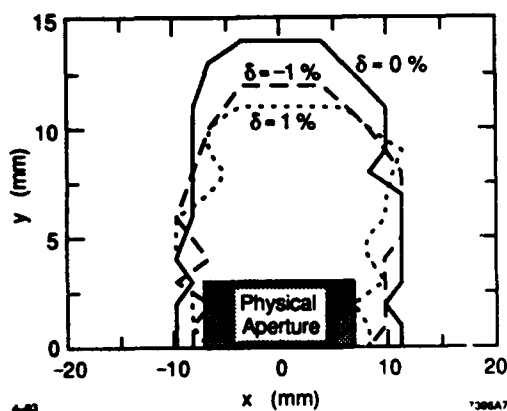


Fig. 4 Dynamic aperture in the new damping ring design at the injection point for initial energy deviations of 0% and $\pm 1\%$. Particles were tracked for 1000 turns with synchrotron oscillations and alignment errors.

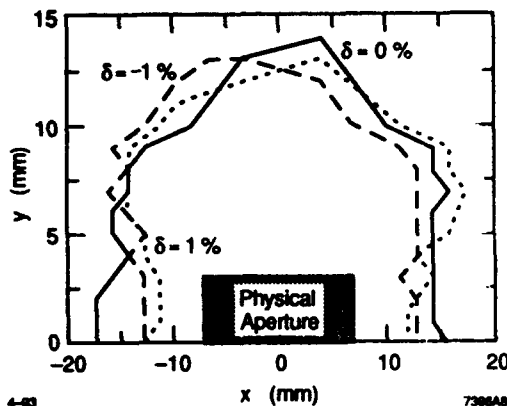


Fig. 5 Dynamic aperture in the new damping ring with an octupole field of $K_3L = 1000 \text{ m}^{-3}$ added to each focusing quadrupole; synchrotron oscillations and alignment errors were included.

Thus, the synchrotron radiation power and therefore the vertical damping times from the SLC and the new bending magnets are roughly equal, even though the SLC magnets have peak fields that are 10% higher.

Dynamic Aperture

The dynamic aperture in the new ring is slightly poorer than in the current SLC rings. This arises because of the additional sextupole field that is needed to correct the chromaticity since the dispersion is smaller and because of the octupole-like terms that arise in the combined function bending magnet. Despite the reduction, the dynamic aperture is still larger than the physical aperture. This is illustrated in Fig. 4 where the aperture was calculated with the alignment and field errors and synchrotron oscillations.

Although this aperture should be sufficient, it is possible to increase it by adding octupoles; this is true for both the SLC and the new damping ring. The prime limitation on the aperture is the horizontal tune shift with amplitude. This can be corrected with octupoles fields in the focusing quadrupoles. The dynamic aperture is plotted in Fig. 5 where an integrated octupole field of 1000 m^{-3} was added to the QF magnets; alignment and field errors and synchrotron oscillations were included. This octupole field could be generated with either permanent magnets or by shimming the quadrupole poles 10 mils.

Alternate Upgrades

There are two primary problems with the design we have described: time and money. There are two upgrades that may be more attractive since they are much faster, cheaper and less disruptive to implement even though they only offer half the emittance gain. These require modifying the present SLC bending magnets to change the horizontal damping partition to roughly 1.7. The dispersion is not changed, but, with the additional damping, the horizontal emittance is reduced by a factor of 1.7. The damping partitions could be changed by adding a gradient to the bends or by changing the edge focusing of the bending magnets.

Conclusions

We have described a possible upgrade for the SLC damping rings which entails replacing the present bending magnets with longer combined function magnets. The new rings have the same circumference and generate the same amount of synchrotron radiation as the present rings, but have an equilibrium horizontal emittance that is a factor of three smaller. The emittance is reduced by increasing the horizontal damping partition and by reducing the quantum excitation in the bending magnets. Finally, we are pursuing two other possible upgrades. Although they only achieve half the emittance reduction, they are cheaper and easier to implement. These will be described in subsequent reports.

References

- [1] G. Fischer, W. Davies-White, T. Fieguth, H. Wiedemann, "A 1.2 GeV Damping Ring Complex for the Stanford Linear Collider," *Proc. of the XIIth Int. Conf. on High Energy Acc.*, Fermilab, IL (1983).
- [2] C. Adolphsen, *et. al.*, "Flat Beams in the SLC," contributed to this conference.
- [3] This lattice had been independently studied by J. P. Delahaye of CERN and T. Raubenheimer of SLAC in 1988 and was discussed at the "Workshop on Future Linear Colliders" at SLAC in December 1988; it is being used in the KEK ATF damping ring project [4].
- [4] J. Urakawa, *et. al.*, "The Damping Ring of Accelerator Test Facility for Linear Collider," *Proc. of the XVth Int. Conf. on High Energy Acc.*, Hamburg, Germany (1992).
- [5] R. Early and T. Raubenheimer, "Computer Studies of a Combined Function Bend Magnet," contributed to this conference.

Update on the Argonne Positron Accumulator Ring*

Michael Borland

Argonne National Laboratory, 9700 So. Cass Ave., Argonne, IL 60439

Abstract

The injector for the Advanced Photon Source incorporates a 450-MeV positron accumulator ring (PAR) to decrease the filling time with the 2-Hz synchrotron. In addition to accumulating positrons from the linac, the PAR damps the beam and reduces the bunch length. The PAR lattice has been redesigned to use zero-gradient dipoles, while retaining essentially the same damping partition. Extensive simulations have been performed to set tolerances that will give high capture efficiency, in spite of the large momentum spread of the incoming positron beam.

I. INTRODUCTION

The Advanced Photon Source [1] (APS), now under construction at Argonne National Laboratory, is a 7 GeV positron storage ring. It is served by a full-energy injector consisting of a 2 Hz synchrotron, a positron accumulator ring [2] (PAR), and an electron/positron linac [3].

The concept behind the PAR is the same as for the PIA accumulator at DESY [4]: to compensate for the low efficiency with which positrons are created and captured in the linac, many positron macro-pulses are accumulated to make a single bunch for acceleration in the synchrotron.

The APS linac is operated at 60 Hz, and hence the maximum increase in the charge per synchrotron ramp is a factor of 30. The actual improvement is less because the 30 ns linac macropulse length is too long for the synchrotron's 352 MHz RF system, so that time must be allowed for damping. This pulse length is not a problem with the PAR's 9.78 MHz first-harmonic RF system.

Figure 1 illustrates the PAR operating cycle. During the first 400 ms, 24 consecutive positron pulses are accumulated and damped. At 1/60 s after injection of the last pulse, a 12th-harmonic RF system is activated, to compress the bunch length. After damping for 83 ms, the positrons are ejected.

II. DESIGN ISSUES

The principle issues in the design of the PAR are the need for large momentum acceptance and rapid damping.

The damping rates are proportional to the ring circumference and to the bending radius of the dipoles [5], indicating that a small circumference and bending radius are required. A circumference of 30.6667 m was chosen, 1/12 that of the synchrotron. The bending radius, ρ , was chosen to be approximately 1 m.

Positron pulses are accumulated at 60 Hz, so a horizontal damping time of the order of 1/60 s is desirable. Faster horizon-

tal damping allows a larger injection kicker bump, reducing the amplitudes of newly injected particles and thus the required good field region in the magnets.

In PIA and the original PAR design, a non-zero dipole field index was used to increase J_x to speed horizontal damping. The current PAR design instead uses non-sector edge angles, making the dipole easier to construct, particularly given the small ρ .

Simulations [3] of the positron linac predict a momentum spread of $\pm 1\%$ and an emittance of $6.6 \mu\text{m}$ for 95% of the beam. The dispersion in the PAR is quite large, giving a maximum dispersive contribution to the 95% beam size of ± 32 mm. Coupled with the residual betatron oscillation of the injected beam, this requires a large (± 60 mm) horizontal good field region.

Of particular concern was the beam dynamics modeling of the dipoles. Tunes, chromaticities, and damping partition numbers were calculated by single-turn integration/tracking with various fringe-field models [6], giving good agreement with second-order matrix methods. Long-term tracking employed 4th order canonical integration with the exact Hamiltonian [7], with extra sextupoles added to compensate the chromatic effect of the lack of nonlinear edge terms.

III. MACHINE PARAMETERS

A MAD-format [8] lattice listing follows. The dipole has approximate residual sextupole and edge-integral values, based on magnet simulations. The sextupoles are also used for horizontal and vertical steering. Beam position monitors are located at every quadrupole. Because of the strong vertically focusing dipole edges, all quadrupoles are horizontally focusing. Quadrupole Q3, nominally unpowered, will be used in adjusting the tunes.

Figure 2 shows the Twiss functions for one quarter of the PAR, while Table 1 lists some important parameters.

```
L1: DRIFT, L=1.731675
S1: SEXTUPOLE, L=0.2, K2=0.0
L2: DRIFT, L=0.08
LQB: DRIFT, L=0.24
Q1: QUADRUPOLE, L=0.23, K1=1.786022448154
B: SBEND, L=0.8, ANGLE=-0.785398163397,
  E1=-0.445, E2=-0.445, K2=0.1375,
  HGAP=0.0225, FINT=0.41
Q2: QUADRUPOLE, L=0.23, K1=2.295915530046
L3: DRIFT, L=1.47
SD: SEXTUPOLE, L=0.2, K2=5.95873739969822
Q3: QUADRUPOLE, L=0.23, K1=0.0
Q4: QUADRUPOLE, L=0.23, K1=2.270174600496
L5: DRIFT, L=0.325
SFH: SEXTUPOLE, L=0.1, K2=-1.65546424863732
```

* Work supported by U.S. Department of Energy. Office of Basic Energy Sciences under Contract No. W-31-109-ENG-38.

QUADRANT: LINE= (L1, S1, L2, Q1, LQB, B, LQB,
Q2, L3, SD, L2, Q3, LQB, B, LQB,
Q4, L5, SFH)
PAR: LINE= (2* (QUADRANT, -QUADRANT))

IV. INJECTION AND EJECTION

Injection and ejection utilize a single pulsed 1.5-kHz transformer septum and three fast kicker magnets. Two of these later form a closed injection bump, while all are used for ejection. The nominal parameters of the kickers are 80 ns rise and fall times, and an 80 ns, 430 G flat-top (the revolution time is 102 ns).

The large incoming momentum spread makes optimization of injection more involved than is usual:

- The incoming beam must not scrape the outside septum wall. This requires $x_i - m_i > A_s + \Delta A_s$, where x_i is the incoming beam centroid, $2 m_i$ the incoming 95% beam size, A_s the inner septum wall position, and ΔA_s the septum thickness (2 mm).
- In order to take the incoming beam "across" the septum, one requires $x_b > x_i + m_i - A_s$, where x_b is the kicker bump height.
- The incoming beam must not scrape the aperture in the SFs, requiring

$$x_b \geq x_i + m_i + (|\delta|_{\max} |\eta_{SF}| - A_{SF}) \sqrt{\frac{\beta_i}{\beta_{SF}}},$$

where β_i is ring β_x at the injection point and $\delta = \Delta p/p$. (The dispersion at the injection point is neglected here and throughout.)

- The last previously injected bunch (which is not fully damped) must not scrape the inside septum wall when the kickers are fired, requiring

$$x_b \leq \frac{A_s - D_x (x_i + m_i)}{1 - D_x}$$

where $D_x = e^{-\Delta T/\tau_x}$, with $\Delta T = 1/60$ s.

These equations were used to find the minimum kicker strength that satisfies all constraints. Using the lattice parameters from Table 1, $A_{SF} = 60$ mm (previously chosen), and using the emittance and energy spread for the incoming beam gives $A_{sept} = 20$ mm and $x_b = 11.6$ mm. (These results allow 1 mm clearances, not shown in the equations.)

V. TOLERANCE STUDIES

Extensive numerical studies have been carried out in order to find tolerances that maintain good injection efficiency and dynamic aperture. Various limits were established on the allowable departure of the as-built machine from the model, and tolerances were set to ensure a 95% probability of not exceeding these limits. In evaluating the effect of any error, the simulations included the effect of appropriate corrective strategies. More specifically, the following procedure was used:

1. *Set tolerances on errors affecting the linear optics.* The criteria for setting these tolerances was to maintain beta-beats below 10%, eta-function errors below 0.2 m, and linear emittance coupling of less than 10%. The corrective strategy consisted of adjusting the tunes back to the ideal values using Q3 and Q4. Examples of errors involved are quadrupole strength errors and dipole yaw.
2. *Add tolerances on errors affecting the chromaticity.* The criterion is that the maximum strength of the sextupoles not be exceeded. The additional corrective strategy consisted of adjusting SD and SF to return the chromaticities to zero. Examples of errors involved are sextupole strength variations, unexpected sextupole terms in the bending magnet, and quadrupole yaw.
3. *Add tolerances on errors affecting the closed orbit.* The criteria are that the steering magnet strength limit not be exceeded and that the residual orbits be less than 1 mm. The additional corrective strategy consisted of correcting the closed orbit. Examples of errors involved are dipole strength variations, quadrupole positioning errors, and geomagnetic fields.
4. *Add tolerances on errors affecting the dynamic aperture.* The criterion is that the dynamic aperture be outside the physical aperture for $|\Delta p/p| \leq 1\%$. The dynamic aperture is limited by multipole errors in the magnets, and hence the tolerances being set are on these errors.

As implied, each stage of the procedure includes errors at the tolerance levels set in all previous stages. Hence, in the final stage, the dynamic aperture is evaluated in the presence of all categories of errors. For each stage, final simulations with all appropriate errors and corrective strategies were done for a large number of random machines (between 50 and 500, depending on the time required for each machine). Space does not permit a presentation of the tolerance values, but they are well within achievable values.

Because of the time required for dynamic aperture runs, the simulations had all error multipole strengths at the tolerance limits, with randomized signs for both normal and skew components. This allowed evaluation of a set of worst-case dynamic apertures. Under these pessimistic conditions dynamic aperture was found to be outside the physical aperture for $-1\% \leq \delta \leq 0.8\%$; for $0.8\% \leq \delta \leq 1.0\%$, approximately 95% of the physical aperture was stable. The addition of a momentum compression system before the PAR is under consideration in order to ameliorate this problem, which may reduce injection efficiency.

After completion of these tolerance studies, injection simulations were performed using idealized kicker waveforms and initial beam phase-space, and including the effects of transport line errors. These indicate that capture efficiencies greater than 95% should be obtained.

Table 1
PAR Lattice Parameters

Circumference	30.6667	m
Energy	450	MeV
Tunes: $\nu_x \nu_y$	2.170, 1.217	
Largest β_x, β_y, η_x	4.70, 13.71, -3.21	m
β_x, β_y, η_x at injection pt	2.00, 9.80, 0.0054	m
Momentum compaction	0.247	
τ_x, τ_δ	20.8, 14.7	ms
J_x, J_δ	1.242, 1.758	
Energy loss per turn	3.56	keV
ϵ_0	0.36	$\pi \cdot \mu\text{m}$
σ_δ	0.041	%

RF: 1st, 12th harm.

Voltage	40, 30	kV
Synchronous phase	174.89, 0	deg
Synch. tune	1.86, 5.90	$\times 10^{-3}$
RMS bunch length	0.884, 0.280	ns

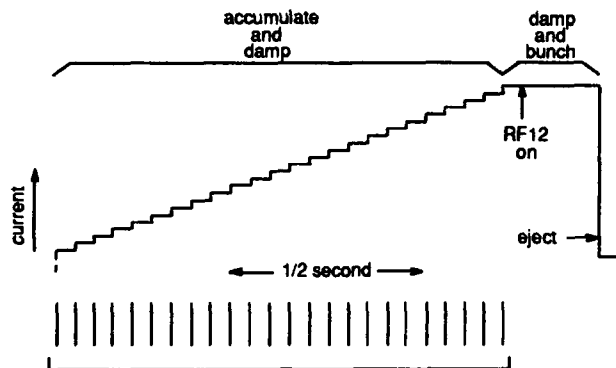


Figure 1
PAR operating cycle

VI. ACKNOWLEDGEMENTS

The author is pleased to acknowledge valuable discussions with and suggestions from E. Crosbie, L. Emery, J. Galayda, F. Mills, and L. Teng.

V. REFERENCES

- [1] "Advanced Photon Source Conceptual Design Report," ANL-87-15, 1987.
- [2] E. A. Crosbie, "The Positron Accumulator Ring for the APS," in *Proceedings of the Particle Accelerator Conference*, March 1989.

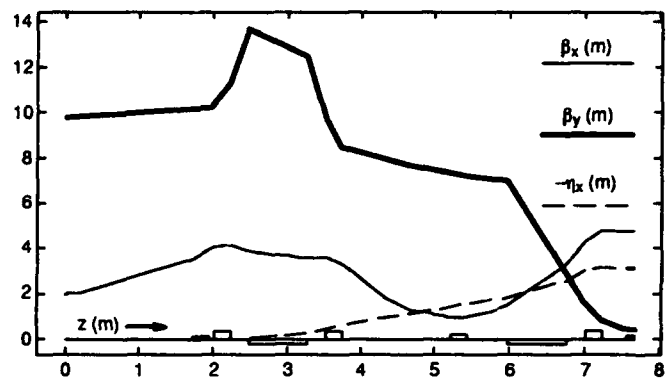


Figure 2
Twiss parameters for PAR

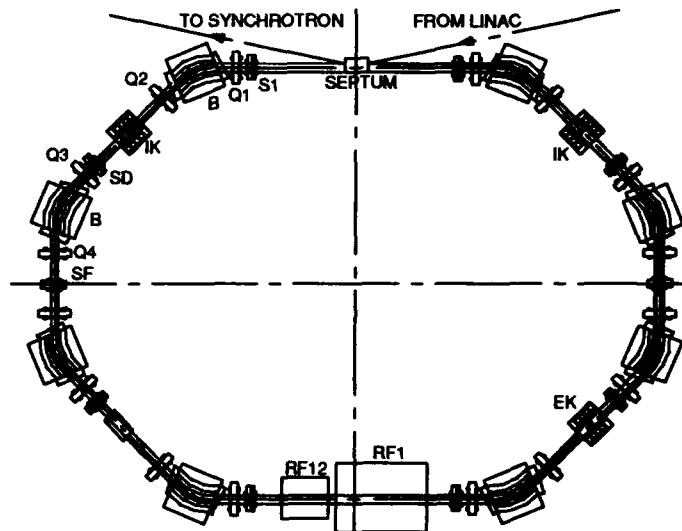


Figure 3
Plan view of the PAR

- [3] A. Nassiri, et. al., "The Linac Injector for the ANL 7 GeV Advanced Photon Source," in *Proceedings of the Linear Accelerator Conference*, September 1990.
- [4] A. Febel, G. Hemmie, "PIA, The Positron Intensity Accumulator for the PETRA Injection," *IEEE Transactions of Nuclear Science*, Vol. NS-26, pp. 3244-3245, June 1979.
- [5] M. Sands, "The Physics of Electron Storage Rings," SLAC-121, 1970.
- [6] M. Borland. Private communication.
- [7] E. Forest, "Canonical Integrators as Tracking Codes," in *Physics of Particle Accelerators*, No. 184, pp. 1106-1136, 1987.
- [8] H. Grote, F. C. Iselin, "The MAD Program," CERN/SL/90-13(AP), 1990.

Measurement on the SRRC 1.3 GeV Electron Booster Synchrotron Operation Parameters and the Ramping Behavior

K. K. Lin, K. T. Hsu, T. S. Ueng
Synchrotron Radiation Research Center
No. 1, R & D Road IV, Hsinchu Science-Based Industrial Park
Hsinchu 30077, Taiwan, R. O. C.

Abstract

The booster operation parameters, such as synchrotron tune, betatron tune, momentum compaction factor, betatron function etc. were measured at injection energy, 50 MeV, and compared with the calculated results. The synchrotron tune shift was done by varying the applied cavity voltage, and the betatron tune shift was observed by changing the current on the quadrupole magnets. The measured results of booster beam emittance and energy spread during acceleration were based on the beam size measurement from the emitted synchrotron light. Possible maximum emittance and energy spread were obtained directly from the measured data, assuming the corresponding calculated betatron and dispersion functions at the point of observation were correct. The measured results were also compared with the theoretical expectation.

INTRODUCTION

The SRRC booster was manufactured and delivered by Scanditronix AB, Sweden in July 1992 [1]. The booster rf system was provided by the SRRC rf group. In order to understand the booster performance characteristics, the operation parameters were measured at various aspects and compared with the designed values.

OPERATION PARAMETERS

These experiments were carried out at injection energy, 50 MeV, with energy spread set at $\pm 0.5\%$.

Synchrotron Tune and Momentum Compaction Factor

The electron beam signal was picked-up with a stripline monitor and analyzed with a spectrum analyzer. Synchrotron tune was measured by observing the sideband of the revolution signal. Using the following relation, the momentum compaction factor was determined to be 0.57 compared with the calculated 0.58.

$$f_s^2 = f_r^2 [e \cdot h \cdot \cos f_s \cdot \alpha \cdot V_{rf}] / [2\pi E], \text{ where}$$

f_s : synchrotron oscillation frequency;
 f_r : revolution frequency, 4.167 MHz;
 e : electron charge;
 h : harmonic number, 120;
 f_s : synchronous phase;
 V_{rf} : peak rf voltage;
 E : electron beam energy;
 α : momentum compaction factor.

The measured result is shown in figure 1. The experimental uncertainty were few percent on E and about 10% on both f_s and V_{rf} .

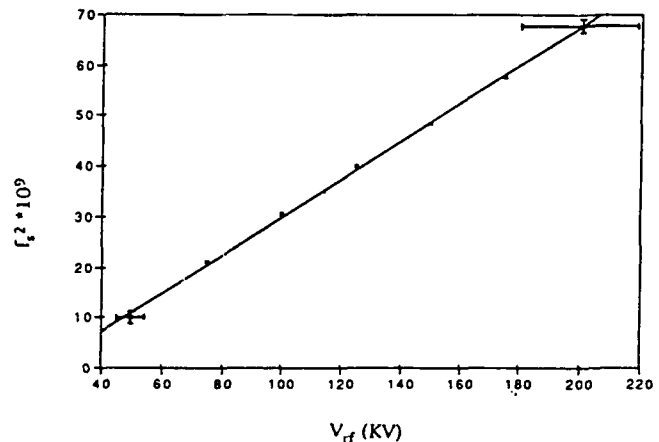


Figure 1. Synchrotron frequency verses rf cavity gap voltage. The fitted slope is 3.77×10^{-5}

Betatron Tune and Tune Diagram

A tracking generator was used as an excitation source in order to perturb the beam for betatron tune measurement. The betatron tune was first set to the designed value, then both focusing and defocusing quadrupole families were adjusted to look for the tuning range. Typical display on the spectrum analyzer is shown in figure 2, with $V_x = 4.4$, $V_z = 2.43$. The uncertainty in the tune fractional part was estimated to be 0.02.

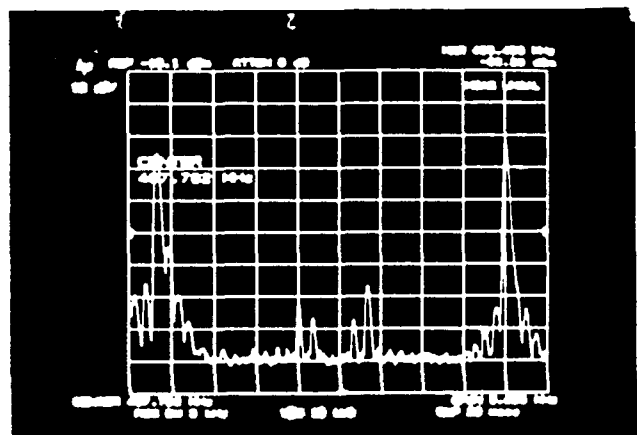


Figure 2. Typical operation tune signal. The highest peaks on both sides are the revolution signal of 4.167 MHz apart. Two pairs of secondary peaks around the center are the betatron tune signals of $V_x = 4.4$, $V_z = 2.43$. The horizontal scale is 0.5 MHz/div.

By using the associated quadrupole strengths in the experiment, the measured ones agree with the calculated tunes from MAD [2] or PATRICIA [3]. The observed tuning range for $\nu_{x,z}$ were

$$4.33 < \nu_x < 4.44, \text{ and}$$

$$2.33 < \nu_z < 2.44.$$

The corresponding tune diagram is given in figure 3, and the indicated resonant lines satisfy

$$m \nu_x + n \nu_z = k,$$

where m , n , and k are integers. The measured tuning range shows that the beam survives while crossing the coupling resonant line and was limited by the stop band on $\nu_{x,z}$.

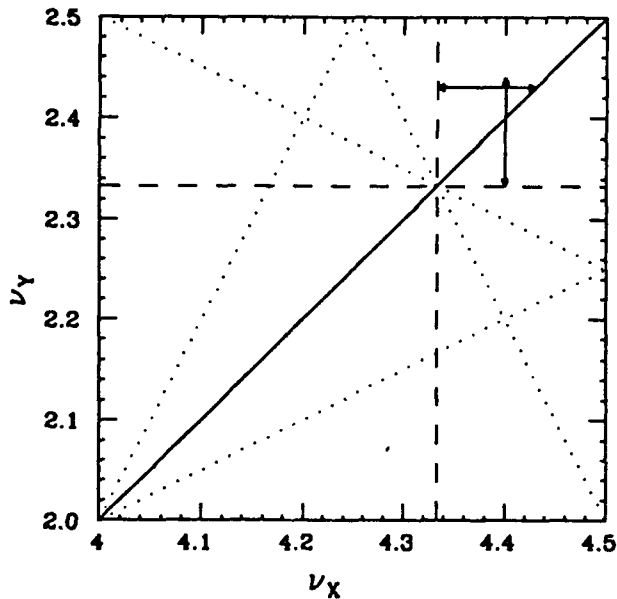


Figure 3. The tune diagram of the booster. Tuning range for both ν_x and ν_z are also indicated.

Betatron Functions

The betatron functions were measured by changing the quadrupole current and observing the associated tune shift. The measurement was carried out with operating tune $\nu_x = 4.4$, $\nu_z = 2.43$. The lattice in one superperiod of the booster consists of one bending magnet, two quadrupoles (FQ, DQ), and two correction magnets. The correction magnet consists of steering, quadrupole, and sextupole windings. The measurement of betatron function at certain location was done by adjusting the strength of each quadrupole families and observing the associated tune shifts. This gave an averaged betatron function at the quadrupole locations. Also, by changing the individual quadrupole component driving current in the correction magnet and observing the corresponding tune shifts, betatron function at that particular corrector location can be obtained. The measured betatron function was determined from the following relation,

$$\Delta \nu_{x,z} = (1/4\pi) \cdot \beta_{x,z} \cdot k.l. (\Delta I/I),$$

where $\Delta \nu$ is the observed tune shift, k stands for the quadrupole strength, l represents the magnet effective length,

and ΔI is the current change which moves the tune. The measured results in two consecutive sections of the booster is also shown in figure 4. The major cause of the measurement uncertainty is due to the tune shift estimation. In figure 4, for those data which give high beta values, the uncertainty is in the range of 25%. For low beta values, the uncertainty is about 80%.

Booster Beta Functions

$$(\nu_x = 4.4, \nu_z = 2.43)$$

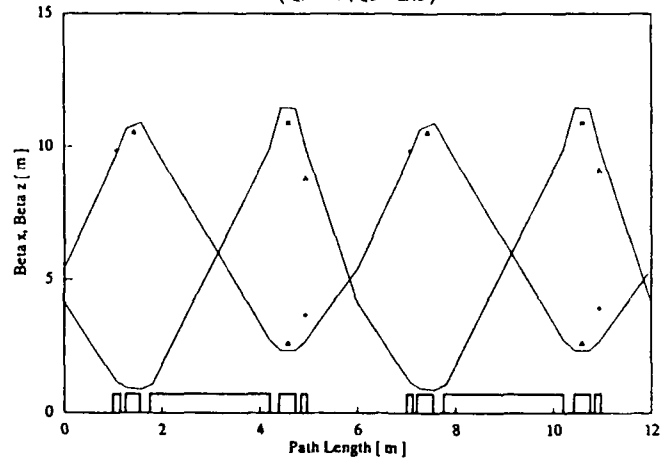


Figure 4. Both calculated and measured betatron functions in two consecutive superperiods.

RAMPING BEHAVIOR

Beam size, Horizontal Emittance, and Energy Spread

The measured beam emittance and energy spread during acceleration were based on the beam size measurement from the emitted synchrotron light, assuming the corresponding calculated betatron and dispersion functions at the point of observation were correct. The measured results were compared with the theoretical expectation.

The emitted synchrotron light was collected by a CCD camera with resolution of 22 μm in vertical and 11 μm in horizontal directions. It is assumed that the measured photon spot size is the same as the corresponding electron beam size in this case [4]. Both beam emittance(ϵ) and energy spread($\Delta E/E$) contribute to the beam size(σ) with the relation

$$\sigma = [\epsilon \cdot \beta + (\eta \cdot \Delta E/E)^2]^{1/2},$$

where β and η are the corresponding betatron and dispersion functions at the emission source respectively.

During the acceleration period, the competition among processes such as adiabatic damping, radiation damping, and quantum excitation leads to ever changing values for dynamic parameters of the electron beam as a function of time. The measured beam emittance and beam energy spread variation during acceleration period are shown in figure 5 and figure 6 together with the theoretical expectation [5]. In figure 5, at every measurement step, the emittance was obtained by making use of the calculated lattice parameters, such as $\Delta E/E$ at that particular energy, and the calculated β and η . The upper limit of the emittance (ϵ_{max}) was obtained by assuming that emittance was the only contribution factor to

beam size. The experimental results show that the adiabatic and radiation dampings give major contribution to emittance damping in the early stage of acceleration, while quantum excitation effect is responsible for emittance growth as the beam energy becomes higher. The contract required emittance specification is also indicated in the figure. In figure 6, it also indicates that the energy spread variation is caused by similar damping processes as have been described above.

the Synchrotron Radiation Research Center, December, 1988. (c) K. K. Lin, K. C. Cheng. SRRC/U/IM/89-01. Rev.(1), January, 1989.

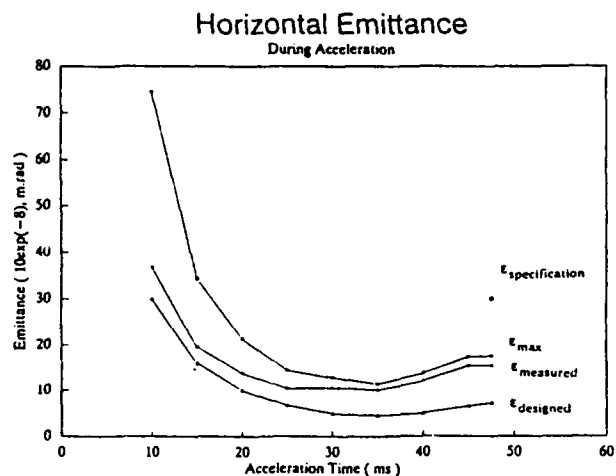


Figure 5. Emittance variation as a function of acceleration time. Ramping period is 50 ms. Repetition rate is 10 Hz.

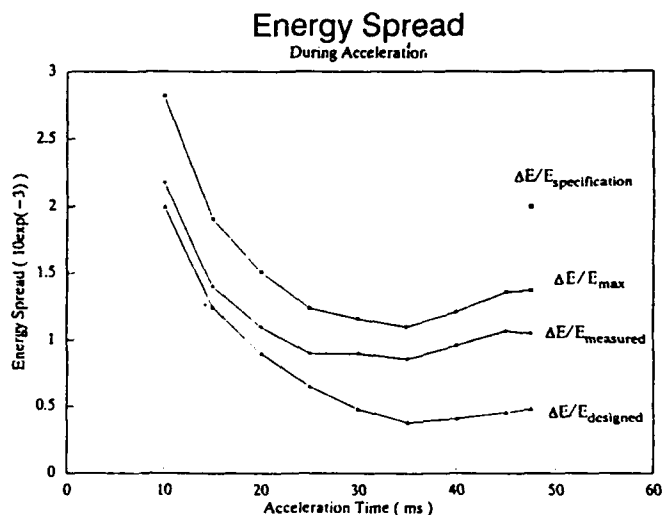


Figure 6. Energy spread variation during ramping period.

REFERENCES

- [1] J. Modeer, project manager, Scanditronix AB, "1.3 GeV Electron Synchrotron" in this conference, Pb12.
- [2] F. C. Iselin, The MAD Program Reference Manual, CERN-LEP-TH/85-15, May 1985.
- [3] H. Wiedemann, Users Guide for Patricia version 85.5, SSRL ACD-NOTE 29, May 1985.
- [4] A. Hofmann, F. Meot, Nuclear Instruments and Methods 203(1982)483-493.
- [5] (a) K. K. Lin, K. C. Cheng, Nucl. Sci. J. 25(4), p.227-246, August, 1988. (b) Scanditronix AB, Conceptual Design Report of a 1.3 GeV Electron Beam Injection System for

1.3 GeV Electron Synchrotron

Jonas Mod  r

Scanditronix AB, Husbyborg, 75229 Uppsala, Sweden

Abstract

The performance of a 1.3 GeV electron booster synchrotron installed at SRRC, Hsinchu Taiwan R.O.C. is described. The system comprises a 140 keV gun, a 50 MeV linac and a 1.3 GeV 10 Hz synchrotron. Beam performance: Multibunch mode > 20 mA 200 ns pulse single bunch mode > 50 mA 1.8 ns. It was commissioned in June 1992.

I. INTRODUCTION

In 1988 Scanditronix received an order for a 1.3 GeV Electron beam injector system for Synchrotron Radiation Research Center Taiwan. The order was for a turn-key system including a 50 MeV Linac as preinjector. The RF-system was built by the SRRC RF group.

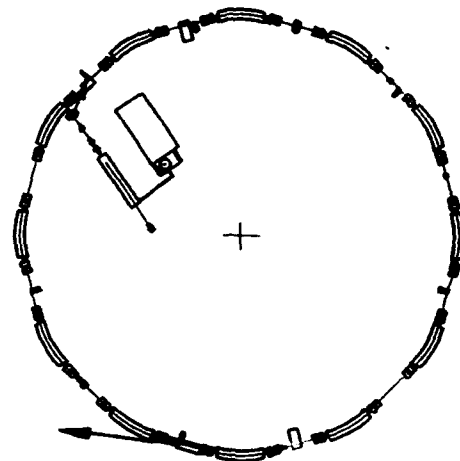
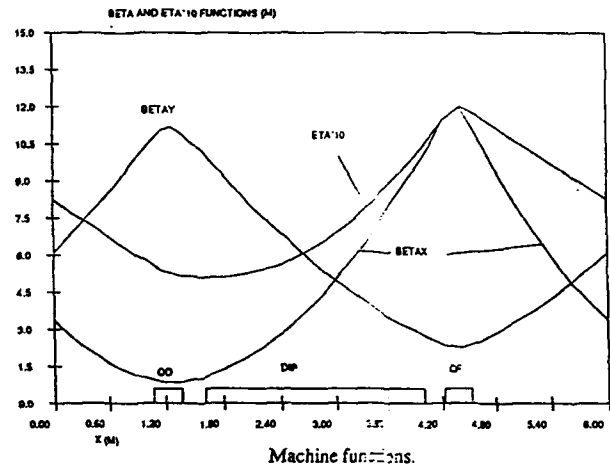
II. PARAMETER LIST

The most important synchrotron parameters are summarized below. [1]

Max energy	1.3 GeV
Circumference	72 m
RF-freq.	500 MHz
Hor. emittance	$3 \cdot 10^{-7}$ mrad
Energy spread	$2 \cdot 10^{-3}$
β_x max	11.97 m
β_y max	11.04 m
η max	1.20 m
Hor nat chromaticity	-5.65
Vert nat chromaticity	-3.67
Momentum compaction factor	0,058
Multi bunch	
Pulse length	100 ns min
Current	5 mA
Single bunch	
Pulse length	< 2 ns
Current	40 mA

III. LATTICE

The lattice is of FO DO type. It consists of twelve cells. Each cell consists of one dipole, two quadrupoles and two sextupoles. The betafunctions are shown in the following figure.



IV. PREINJECTOR

The preinjector consists of a 140 kV gun, SLAC type, and a 50 MeV Linac structure delivered by HRC [2]. The specification for the Linac system:

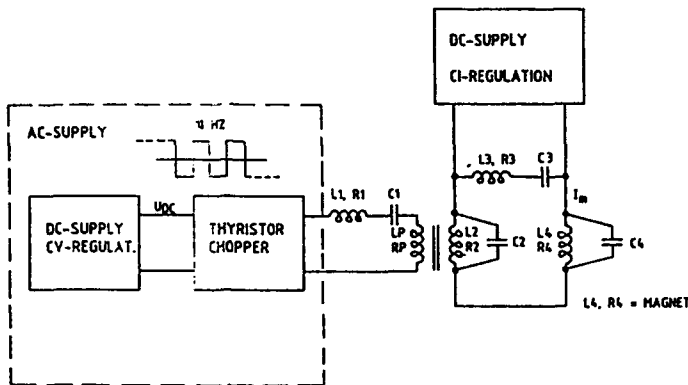
Energy	50 MeV
Frequency	2997.9 MHz
Multibunch	
Pulse length	< 500 ns
Current	30 mA
Single bunch	
Pulse length	1.8 ns
Current	220 mA

V. INJECTION

The injection is single turn. A twenty degree septum magnet in one straight section positions the beam on axis on the following straight. At the crossing point an extremely test kicker, less than 50 ns fall time, kicks the beam on orbit.

VI. MAGNET SYSTEMS

Three separate White circuits are used. One for the dipoles and one each for quadrupole families. The principle diagram for the White circuits is shown below. The AC-supplies is of the GTO type.



	<u>DQ</u>	<u>FQ</u>	<u>Dipole</u>
DC-current	90 A	145 A	1070 A
AC-current	22 A	70 A	540 A
Magnet peak current	162	257 A	1920 A
Tracking	$< 3 \cdot 10^{-3}$		

VII. EXTRACTION

Three bumper magnets in adjacent cells creates a local bump at the extraction septum entrance. A fast kicker, less than 50 ns rise time, kicks the beam across the septum. The timing of the extraction kicker is synchronized to the injection kicker. In that way the gap in the bunch train caused by the injection kicker fall time is used for the extraction kicker rise time.

VIII. MEASUREMENTS

All designed parameters have been achieved and some generously exceeded dc.

At the exit of one of the dipoles a mirror is placed looking upstream. The light from the dipole is with some optics fed to a CCD camera. The CCD camera can be triggered at any time during the ramping. Assuming that the β -functions are correct the emittance and energy spread can be calculated. This measurements are described in [3].

The extracted pulse in the long pulse mode has been measured by three independent methods; a Faraday cup, a Bergoz Fast Current Transformer and a Q-electrode. The short pulse was measured by a Faraday cup, a Q-electrode and a fast ceramic gap.

	<u>Specification</u>	<u>Design value</u>	<u>Measured</u>
Emittance	$3 \cdot 10^{-7}$	< 1	1.5
Energy spread	$2 \cdot 10^{-3}$	0.5	1
Long pulse			
Pulse length	100 ns	200 ns	200 ns
Current	5 mA	> 5 mA	20 mA
Short pulse			
Pulse length	2 ns	2 ns	2
Current	40 mA	40 mA	> 55

IX. ACKNOWLEDGEMENT

Consultants for the design are Prof. M. Eriksson and Dr. L-J Lindgren MAX-lab, Lund, Sweden.

The collaboration with the RF group from SRRC has been very good.

X. REFERENCES

- [1] Conceptual Design Report for the 1.3 GeV Booster, Scx AB.
- [2] J. Haimson, B. Mecklenburg
Proc. PAC 1991 Page 3183
- [3] K.K Lin, K.T. Hsu, T.S.Veng
Measurements on the SRRC 1.3 GeV booster, this conference.

Performance of the ALS Injection System*

Charles H. Kim

Lawrence Berkeley Laboratory, University of California
Berkeley, CA 94720 USA

Abstract

We started commissioning the Advanced Light Source (ALS) storage ring on January 11, 1993. The stored beam reached 60 mA on March 24, 1993 and 407 mA on April 9, 1993. The fast pace of storage ring commissioning can be attributed partially to the robust injection system. In this paper we describe the operating characteristics of the ALS injection system.

I. INTRODUCTION

The ALS injection system [1] consists of an electron gun, a 50 MeV linear accelerator, a 1.5 MeV booster synchrotron and three beam transfer lines (GTL, LTB, and BTS), as shown in Figure 1. Accelerator installation began with the beneficial occupancy of Building 6 in January, 1990. Linac [2] reached the design energy of 50 MeV in December, 1990 and the design current of 125 mA in November, 1991. Booster installation [3] was finished in May, 1991 and the booster rf system in December, 1991. The booster reached the design energy of 1.5 GeV in January, 1992 and design current of 15 mA in February, 1992. Full energy beam was extracted from the booster in April, 1992. The injection system has been running reliably since September, 1992, after some technical problems associated with the magnet power supplies were corrected. The BTS beam transfer line was installed on January 11, 1993 and the beam was successfully transferred to the storage ring on the first day.

The filling time to 460 mA measured on April 30, 1993, was about 14 minutes. That was without any optimization. We expect a significant improvement in filling time as we reduce the linac energy spread and the storage ring injection efficiency. The repetition rate of the injection system is 1 Hz.

II. GUN AND GTL BEAM TRANSFER LINE

The 120 keV electron gun has a triode geometry. An rf voltage with a frequency of 125 MHz (synchronous with the 500 MHz storage ring rf system) and an amplitude of 0 - 70 Volt is applied between the cathode and the grid. The rf voltage is biased up to 30 V dc to produce shorter pulses. We recently upgraded the gun electronics to add the single-bunch-mode capability and reduce the gun timing jitter. Pulse duration is now about 2 nsec fwhm and number of electrons is ≤ 3 nC/bunch. Electron gun current is monitored with a wall current monitor.

Bunchers consists of a 125 MHz subharmonic buncher, a 500 MHz subharmonic buncher, and a 3 GHz traveling wave

buncher. We tune the amplitudes and phases of the bunchers carefully while monitoring the bunch shape using LEP buttons at the 25 MeV point. We do not have fast enough beam diagnostics to directly measure the bunch length at this time. Computer simulations show that the total bunching factor should be about 50 at the optimum condition. The linac can be characterized as a high peak-current, low duty-factor machine.

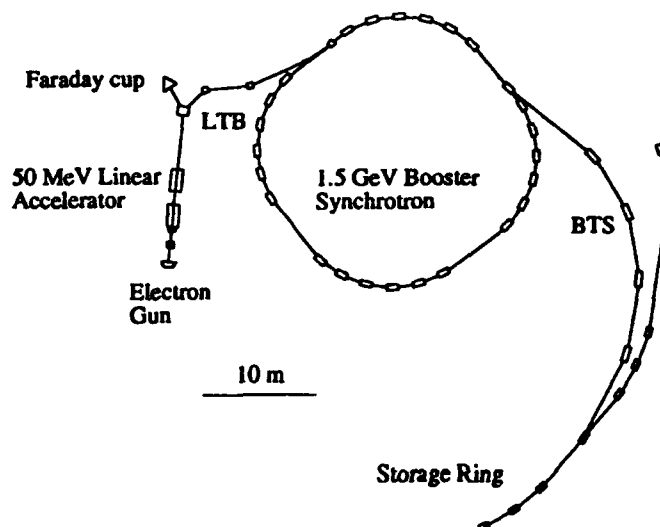


Figure 1. ALS Injector

We monitored the beam size and shape in the LTB line just after the first bending magnet, where energy dispersion is large. If the bunching system is tuned well, we can see well-separated individual bunches on the screen.

III. LINAC

The linac consists of two 2-meter, 3-GHz, disk-loaded waveguides with a constant-impedance structure for the 2p/3 mode [4]. Beam parameters at the linac exit, measured for optimized operating conditions, are summarized in Table 1.

Table 1.

Charge	0.8 nC/bunch
Energy spread (dE/E)	
single bunch	0.2%
multi-bunch	0.6%/bunch
Beam Emittance [5] (ss')	
Vertical	3.2×10^{-7} m-rad
Horizontal	3.3×10^{-7} m-rad

*This work was supported by the Director, Office of Energy Research, Office of Basic Energy Sciences, Materials Sciences Division, of the U.S. Department of Energy under Contract No. DE-AC03-76SF00098.

A computer simulation [6] and a beam loading consideration in the waveguides indicate that beam loss should most likely occur before the electrons reach the first wave guide. The measured emittances agree well with the simulations.

Large energy spread in multi-bunch mode is caused by beam loading in the wave guides. A beam loading compensation scheme using the fast-phase-switching technique was tested successfully [2]. Because the booster energy acceptance is $\pm 1\%$, only 4 linac bunches can be accepted to the booster at a time without beam loading compensation. This mode of operation has been good enough for the storage ring commissioning so far. We expect to use the beam loading compensation scheme more routinely in the future.

IV. LTB BEAM TRANSFER LINE AND BOOSTER INJECTION

Beam matching from the 50 MeV linear accelerator to the booster and steering are done in the LTB beam transfer line for a maximum beam capture in the booster. Injection to the booster is via a fast kicker magnet utilizing the well-established single-turn, on-axis injection technique. The injection kicker magnet has a 100 nsec flat top ($< \pm 0.5\%$), with a fall time of about 150 nsec. The flat top time window is long enough to inject 13 linac bunches into the booster. Booster orbit time is 250 nsec. Beam transfer efficiency from linac to booster is typically about 75%. Most of the beam loss occurs during the first 200 msec after injection.

A peaking coil installed in one of the booster dipole magnets triggers the electron gun, linac, and the injection kicker magnet. The peaking coil also triggers a Gauss clock, which then starts to generate a series of pulses at given dipole field intervals. The Gauss clock is used to trigger and moderate other booster instrumentations such as rf ramping and beam position monitors.

V. BOOSTER SYNCHROTRON

The booster consists of 24 dipole- and 32 quadrupole-magnets in a missing-magnet FODO-lattice configuration with a super periodicity of 4. The booster lattice parameters and the operating point are summarized in Table 2.

Dipole magnets are connected in series to a SCR-switched power supply and run freely at a repetition rate of 1 Hz. Acceleration to 1.5 GeV in the booster takes 0.34 seconds. The focusing (defocusing) quadrupoles are connected in series to a power supply which tracks the excitation current of the dipole magnet. The core nonlinearities such as remnant magnetic fields at low fields and core saturation at high fields cause large tune-shifts during acceleration. Tune-shifts make machine operations very susceptible to resonant beam losses during the first 100 msec of the ramping. We were able to correct the tune-shift to < 0.02 by applying programmable correction voltages to the quadrupole power supplies at certain Gauss clock intervals.

Spontaneous betatron oscillations were observed during the first 1 msec after injection. We can excite horizontal betatron oscillations using the extraction kicker magnet at any time 50 msec after injection. Tunes were measured by (1)

analyzing the beam position monitor signals in the Fast-Analog-to-Digital (FAD) [7] mode, or (2) using a Tektronics 3052 spectrum analyzer. In the FAD mode BPMs provide beam-position information for 1024 turns. The Tektronics 3052 spectrum analyzer can provide, for example, a 100 msec record of spectra in 200 msec steps.

Table 2. Booster Lattice Parameters

Circumference [m]		75
Revolution Frequency [MHz]		3.997
Betatron Tune	Horizontal	5.80
	Vertical	2.79
Synchrotron Freq (kHz)	injection	256
	extraction	44
Momentum Compaction		0.046
Chromaticity	Horizontal	-8.31
	Vertical	-4.69
Quadrupole kL [1/m]	Focusing	0.787
	Defocusing	0.471
Sextupole kL [1/m ²]	Focusing	0.867
	Defocusing	0.989
Radiation Loss at 1.5 GeV [keV/turn]		112
Natural Energy Spread at 1.5 GeV [%]		0.064
Radiation Damping at 1.5 GeV [msec]	Horizontal	6.68
	Vertical	6.72
	Energy	3.37

for quadrupoles $k = (dB/dx) / [Br]$

for sextupoles $k = (d^2B/dx^2) / 2 [Br]$

Ramping the rf amplitude was programmed by specifying the rf amplitude values at Gauss clock intervals. Under the best condition the synchrotron frequency was 256 kHz at injection and 44 kHz at extraction. Many higher order synchrotron harmonics were observed under this condition, which may mean quadrupole and sextupole modes were present.

The booster has 20 sextupole-magnets for chromaticity corrections and 32 corrector-magnets for orbit corrections. Sextupole- and corrector-magnet power supplies are designed to track the dipole field in a way similar to the way the quadrupole fields do. Sextupoles have not been necessary for and have had no effects on booster operations so far. We expect that sextupoles may be necessary in the future, when the booster current is higher (which may induce some instabilities).

Orbit correction was successful in improving the capture efficiency [7]. The booster circumference is about 5 mm larger than designed and closed orbit is distorted to the first order by the dispersion function [8].

VI. BOOSTER EXTRACTION AND BTS TRANSFER LINE

When the beam is accelerated to the extraction energy, the following sequence of events occurs. Three extraction

bump magnets are turned on to form a 10 mm local bump near the extraction septum magnet. The bump is slow enough for the extraction kicker magnet to wait up to 82 msec for the correct storage ring rf bucket to line up with the booster rf bucket. We can thus program the storage ring fill pattern by programming the kicker timing.

We measured the beam emittance of the extracted beam by measuring the horizontal and vertical beam sizes in the BTS line where the beta functions are known. The results are: $e_x = 2.5 \times 10^{-7}$ m and $e_y = 0.1 \times 10^{-7}$ m rms unnormalized. The measurements agree with the theory very well.

VII. INSTRUMENTATION AND CONTROL

The accelerator instrumentation [9], [10] played the roles of our eyes and ears in commissioning and operating the accelerator. We had adequate accelerator instrumentation in most parts of the accelerator. The cost of the instrumentation is small compared with other costs and was well worth it for the saved time and effort during commissioning. We felt that we could have used more diagnostics such as BPMs and steering magnets in the GTL line. More diagnostics at the linac exit such as total charge monitors and high speed diagnostics are becoming commercially available. This will make further commissioning more enjoyable. ALS accelerator instrumentation is summarized in Table 3.

Table 3. Summary of ALS accelerator instrumentation.

	GTL	Linac	LTB	Booster	BTS
WCM	1	-	-	-	1
Faraday cup	-	-	1	-	-
DCCT	-	-	-	1	-
Scintillator	2	2	6	5	7
BPM (buttons)	2	1	-	32	-
BPM (TWE's)	-	1	7	3	6

Scintillators were used for focussing and steering of the beam in the linac and in the beam transfer lines. They are also used for calibrating magnets using the electron beam as a probe.

Because of their non-destructiveness of the beam and the high speed with which data can be processed, various types of beam position monitors are extensively used throughout the ALS accelerator system. Fast and simultaneous measurements of the beam positions and the relative intensities at different locations in the accelerator are very important for tuning and feedback stabilizing of accelerators. BPM's were used for tuning the beam transfer lines, injection and first-turn studies in the booster synchrotron and the storage ring, tune measurements, closed orbit measurement and correction, feedback stabilization, etc. A BPM system consists of an array of beam pickup electrodes, a set of high-quality coaxial cables, a bin of processing electronics, and a controlling computer. Careful preparation and testing of the hardware and software were necessary for each of these applications.

The BPMs were an indispensable part of our instrumentation, and we have learned a great deal during our commissioning about how to use them and interpret the data properly.

The booster is controlled by the ALS control system. It utilizes the intelligent local controllers (ILC's) which are highly distributed and centrally connected to collector micro-modules via fiber optical links. Operator interface is via a number of personal computers (six 486/PC's at present) using mostly commercially available software and development tools. Applications have been developed jointly by the ALS control systems group and the accelerator systems group.

VIII. ACKNOWLEDGMENTS

Material presented in this paper is the result of a cooperative work performed by the ALS project team and the Accelerator Systems Group. I want to thank Mr. Alan Jackson for his leadership and encouragement. Many helpful discussions with Center for Beam Physics staff at the Lawrence Berkeley Laboratory are gratefully acknowledged.

IX. REFERENCES

- [1] "Injection System Design for the LBL 1-2 GeV Synchrotron Radiation Source," F. Selph, A. Jackson, and M.S. Zisman, Proceedings of the 1987 IEEE Particle Accelerator Conference, Washington, D.C., page 446 (1987).
- [2] "Operating Experience with ALS Linac," F. Selph and D. Mossoletti, Proceedings of the 1991 IEEE Particle Accelerator Conference, San Francisco, page 2978 (1991).
- [3] "Commissioning Experiences of the ALS Booster Synchrotron," C. Kim, Proceedings of the 1991 IEEE Particle Accelerator Conference, San Francisco, page 2691 (1991).
- [4] "LBL Injector Linac Design Study," H. Hoag, LBL report LSAP 010 (1987).
- [5] "Emittance Measurement and Modeling of the ALS 50 MeV Linac to Booster Line," J. Bengtsson, W. Leemans, and T. Byrne, in these proceedings.
- [6] "Simulation of Emittance Growth in the ALS Pre-injector," C. Kim, Proceedings of the Linear Accelerator Conference, CEBAF, October 3-7, 1988. Also Lawrence Berkeley Laboratory Report, LBL-25891 (1988).
- [7] L. Schachinger, private communications.
- [8] H. Nishimura, private communications.
- [9] "Performance of ALS Particle Beam Diagnostics," J. Hinkson, in these proceedings.
- [10] "ALS Instrumentation Overview," C. Kim and J. Hinkson, Proceedings of the Accelerator Instrumentation Workshop, Lawrence Berkeley Laboratory, October 27-30, 1992.

Synchrotron of SPring-8

Hiroto Yonehara, Hiromitsu Suzuki, Tsuyoshi Aoki, Syoji Yoneyama, Yasuo Ueyama,
Yasushi Sasaki, Teruyasu Nagafuchi, Soichiro Hayashi and Hideaki Yokomizo

JAERI-RIKEN SPring-8 Project Team

JAERI, Tokai-mura, Naka-gun, Ibaraki-ken, 319-11, Japan

Abstract

The specification and the layout of the synchrotron of SPring-8 were decided. The synchrotron is designed to accelerate electron or positron beams from 1 GeV to 8 GeV with the repetition cycle of 1 Hz. The injection method of the 1-GeV beam from the linac is adopted to be single-turn technique with on-axis into the synchrotron. The input power of 250 kW into the cavity was achieved in 1991, and the rise time of less than 100 nsec in kicker was succeeded in 1992. The construction of the synchrotron is started in the fiscal year of 1993, and it will be accomplished in 1997.

1. INTRODUCTION

Parameters of the synchrotron are listed in Table 1. A single-turn technique with on-axis is adopted as beam injection method from the linac to the synchrotron. For the single-bunch mode-operation in the storage ring, the 8 buckets of the synchrotron will be filled and ejected by the injection and extraction of 8 times, respectively. The interval of the two buckets which are neighborhood is 160 nsec. Then the rise time and fall time of less than 100 nsec in kicker is required in order to carry out the operation of the 8-buckets single-bunch for the single-bunch mode-operation in the storage ring. The synchrotron is located outside the storage ring and is constructed on ground having a grade level about 9 m lower than that of the storage ring. This necessitates a long beam transfer line about 300 m. Figure 1 shows the layout of the injector system.

Table 1 Parameters of the synchrotron

Injection energy	1 GeV
Maximum energy	8 GeV
Circumference	396.12 m
Repetition time	1 sec
Natural emittance (8 GeV)	230 nm.rad
Momentum spread (8 GeV)	1.26×10^{-3}
Number of cells/periodicity	40/2
Nominal tune (ν_x/ν_y)	11.73/8.78
Natural chromaticity (ξ_x/ξ_y)	-14.4/-11.5
Radio frequency	508.58 MHz
Harmonic number	672
Radiation loss (8 GeV)	12.27 MeV/turn

2. GENERAL DESCRIPTION

A. Lattice Design

The synchrotron has a twofold-symmetric lattice composed of 40 FODO cells. There are 30 normal cells, each having two bending magnets. Two straight sections are provided for injection, extraction and acceleration of the beam. The straight sections consist of these cells with no bending magnet. RF cavities and the devices for injection and extraction are installed into empty-dipole cells. The dispersion function at the straight section is suppressed by removing a bending magnet from a normal cell (dispersion-suppression cell) and selecting the optimum value for the horizontal tune suppress dispersion at the exit of the residual bending magnet. Horizontal and vertical tune values are 11.73 and 8.78,

respectively. The natural chromaticities are $\xi_x = -14.4$ and $\xi_y = -11.5$. To correct the chromaticities, each normal cell contains a focusing and defocusing sextupole near the focusing and the defocusing quadrupole, respectively.

B. Injection and Extraction

At the injection energy of 1 GeV, a single-turn with on-axis technique is adopted as the standard injection method to provide good injection efficiency of the beam into the synchrotron. Two septum magnets and two kicker magnets are used for the on-axis injection. After leaving two septum magnets, the injected beam is inflected to the reference orbit by the focusing quadrupoles. Before entering the reference orbit of the synchrotron, the beam is kicked and placed smoothly in the reference orbit by the kicker magnets.

The duration when the kicker magnets are excited must be shorter than 300 nsec. Thus, the kicker waveform has 100-nsec rise-time, 40-nsec flat-top, and 100-nsec fall-time. For the operation with the long pulse mode, another PFN circuit for the kickers is used to generate a long flat-top. Figure 2 shows a short pulse waveform of the prototype kicker magnet for injection. Figure 3 shows a cross-sectional view of the kicker magnet.

The aperture of the vacuum chamber in the normal cells is determined by the size of the injected beam and the injection method. Substituting maximum beta and dispersion functions; $\beta_x = 16.7$ m, $\beta_y = 17.9$ m, $\eta = 1.0$ m, a maximum COD; $COD_x = 9.0$ mm, $COD_y = 7.5$ mm, and beam quality; $1.0 \mu\text{mm.mrad}$, $\Delta P/P = 0.01$ into the following equations;

$$BSC_x = (\epsilon_x \beta_x)^{1/2} + (2\Delta P/P)\eta + COD_x$$

$$BSC_y = (\epsilon_y \beta_y)^{1/2} + COD_y$$

The beam-stay-clear results in $BSC_x = 33.5$ mm and $BSC_y = 11.7$ mm. Presently the physical half aperture is designed to be $A_x = 40$ mm, $A_y = 15$ mm, to accommodate both cases.

The 8-GeV electron- or positron-beam is extracted from the synchrotron with four septum magnets, three kicker magnets and four bump magnets. The magnetic rigidity of these magnets is large but the empty space available for these magnets is limited, thus bump orbit must be used to assist the kicker and septum magnets.

C. Magnets

The magnets of the synchrotron are 64-dipole magnets, 80-quadrupole magnets, 60-sextupole magnets and 80-correction magnets. The core of each magnet is stacked with 0.5 mm thick, silicon steel laminations. The dipole magnet has a C type core and assembled by lamination stacking; this is curved with parallel end plates. The pole width is 140 mm with lateral shims 7.5 mm wide by 1 mm high. The pole length is 2870 mm. The maximum field strength of dipole magnets is 0.9 T. The Bohr radius and the length of the quadrupole are 70 mm and 0.57 m. And those of sextupole are 100 mm and 0.15 m. Quadrupole and sextupole magnets are constructed with two-piece core-structure. The maximum field strength of these magnets are 15 T/m and 200 T/m², respectively.

D. Power Supplies for the Magnets

Power supplies for the magnets provide the pulsed current of 1 Hz. The waveform of the pulsed current has 150-msec flat-bottom, 450-msec rise-time, 150-msec flat-top and 250-msec fall-time. For the dipole magnet two 24-pulse thyrister-converters are used to reduce the direct current ripple. These two converters are connected in series to reduce the reactive power. One transfers the power from the mains to the magnet load and the other backs into the mains. A DC filter is installed which is composed of a passive filter and an active filter to bring the ripple down further. For the quadrupole and sextupole magnet, a 24-pulse and a 12-pulse thyrister converter are used, respectively. Transistor power supplies are used for correction magnets.

E. Vacuum System

The synchrotron has two types of vacuum chambers: an ordinary type which has a race-track cross-section with 1.5-mm wall-thickness and a rib-reinforced type that has 0.3-mm wall thickness with a race-track cross-section. The ordinary-type chambers are installed in the quadrupole magnets and the rib-reinforced-type chambers are in the dipole magnets. Both chambers are made of 316L stainless steel. The aperture of 80x30 mm² is requested. Under the condition of the present duct-aperture and the pressure of 1×10^{-6} Torr, the beam lifetime determined by the residual gases is estimated to be 100 sec at 1 GeV. Although it is sufficiently long compared to the lifetime, we have decided the design pressure should be less than 1×10^{-6} Torr throughout the synchrotron because of the gross reliability of the vacuum system.

F. RF System

The synchrotron uses 508.58 MHz RF system, the same frequency as that for the storage ring. The total required RF power is 1.69 MW. Two 1-MW KEK-type klystrons are used as the power source and provide for eight five-cell cavities. The RF power from a klystron is divided equally into the four cavities using three magic-T splitters. The required RF voltage is increased linearly during the ramping from 8 MV to 18.7 MV. The effective RF voltage is changed by controlling the phases of RF between two klystrons, keeping the output power of the klystrons constant. The phase differences between the two klystrons, 131 and zero degrees, correspond to the total RF voltages, 8 and 18.7 MV, respectively, at the constant klystron output power of 845 kW each.

Dissipation of RF power occurs mainly at the cavity walls, since the beam loading is very low because of the maximum beam current of 10 mA in the synchrotron. The design requirement for the cavity is to realize high shunt impedance to reduce the wall losses. A multi-cell type cavity, that consists of 5 cells was chosen. The cavity has inductive coupling slots. A large coupling-factor is required to stabilize the accelerating field against disturbances of the temperature-rise. A cross-sectional view of the prototype five-cell cavity is shown in figure 4. The total length is 1700 mm and the outer diameter is 492 mm. The cavity is constructed with OFHC copper with cooling channels machined into every component. The effective shunt impedance is about 21 M Ω /m. The maximum input power is 250 kW.

G. Beam Monitors

Table 2 shows beam monitors installed in the synchrotron. Beam position is measured at 80 locations around the synchrotron at every quadrupole magnet. Each beam-

position monitor(BPM) consists of a set of four button electrodes mounted on the wall of the vacuum chamber. The signals from each BPM are transmitted through low-loss, high-frequency cables to the detector circuits via fast pin-diode switches. For real-time measurements of beam position during ramping, 4 detector circuits are used for 80-BPMs. Movable and rigid fluorescent screens are installed to see the position of the injection and extraction beam. The intensity of the beam current is measured by several types of current transformers. Horizontal- and vertical-beam excitation-electrodes are installed at the injection section to determine the tune values and the tune shift during acceleration.

Table 2 Beam monitors of the synchrotron

monitor type	quantity
Current transformer for short pulse	2
DCCT	1
BPM	80
Fluorescent screens	14
Photon monitor	1
RF-KO	1
Beam loss monitor	5

H. Beam Transport System

The injector system is located outside the storage ring and is at a lower elevation by about 9 m than the storage ring. It is necessary to construct a long beam-transport line(about 300 m) with vertical bending magnets. Thirteen bending magnets, 42 quadrupole magnets and 21 correction magnets are used in this beam transport line. The vacuum chamber of this transport line is made of stainless steel pipe with the inside diameter of 36 mm. The vacuum system is designed so that the pressure anywhere in the beam transport line will not exceed 1×10^{-5} Torr.

I. Timing System

To operate the accelerator complex of this facility, two systems for timing coordination are necessary. The first system is associated with beam transfer from the linac to the synchrotron. The second system is associated with beam transfer from the synchrotron to the storage ring. The RF systems of the synchrotron and the storage ring will be operated by the 508.58 MHz frequency of a master oscillator and the harmonic numbers of 672 and 2436, respectively. Since the time width of each RF bucket is 2 nsec, the timing accuracy required for beam transfer from the synchrotron to the storage ring must be less than 100 psec to suppress the beam loss due to the synchrotron oscillation of the injected beam. For single-bunch operation, it is necessary to select any one of the 2436 buckets as the single filled bucket in the storage ring into which the bunched beam from the synchrotron is transferred. Two concepts for the timing systems are being considered. One concept uses a synchronous timing table which has low jitters(lower than 100 psec) and the other utilizes a phase control loop which has the accuracy of lower than 1 degree. The transfer line of the timing signal and the RF frequency consists of the optical fiber and the EO/OE transmitter and receiver which has low jitters and temperature dependence.

3. CONCLUSION

The specification of the synchrotron were decided. The construction of the synchrotron is started in the fiscal year of 1993, and it will be accomplished in 1997.

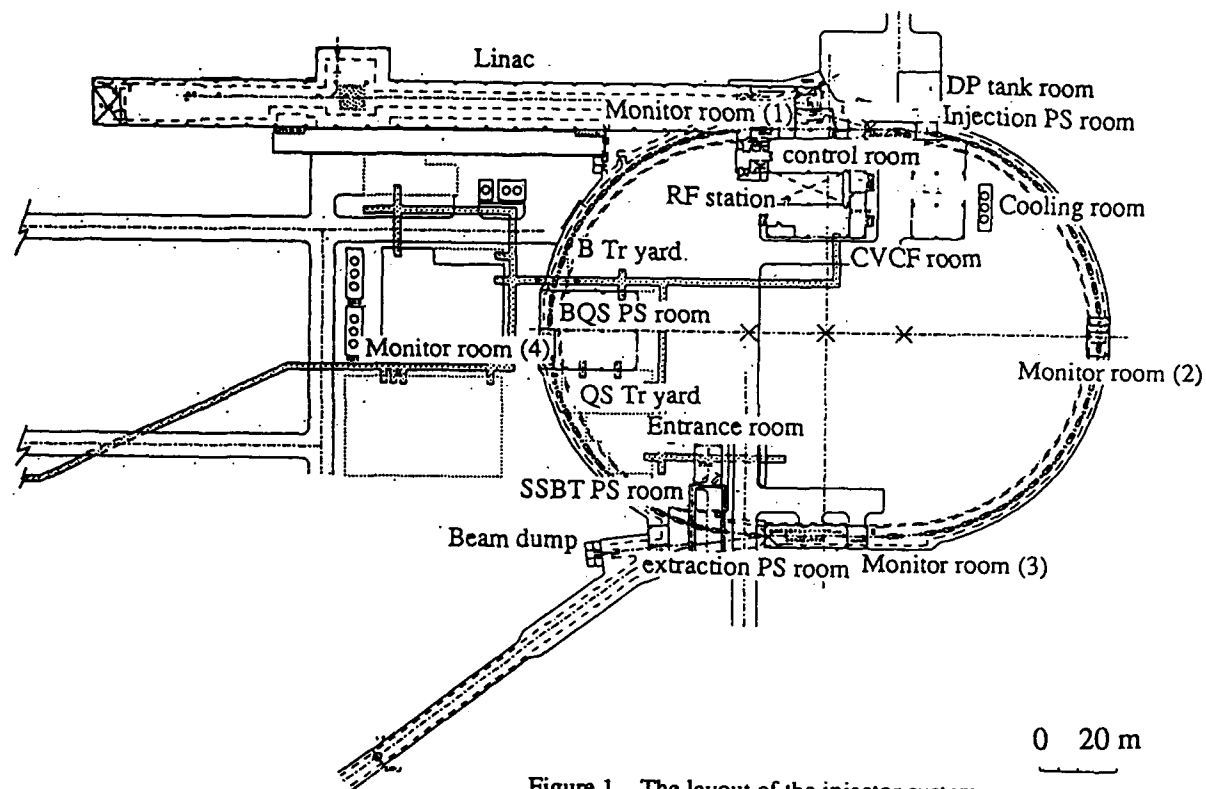


Figure 1. The layout of the injector system

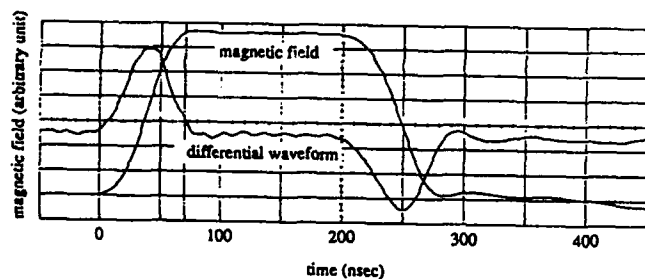


Figure 2. The short pulse waveform of the prototype kicker magnet

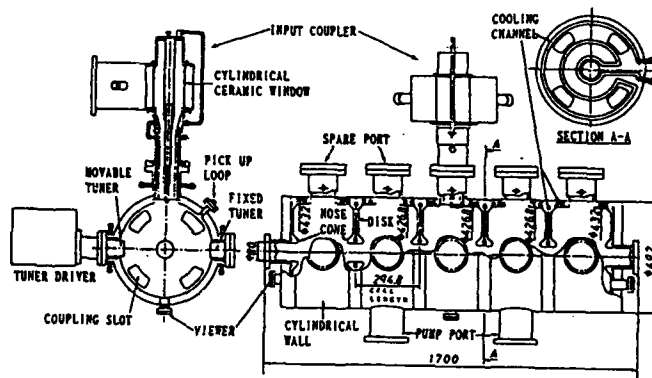


Figure 4. The cross sectional view of the prototype five-cell cavity

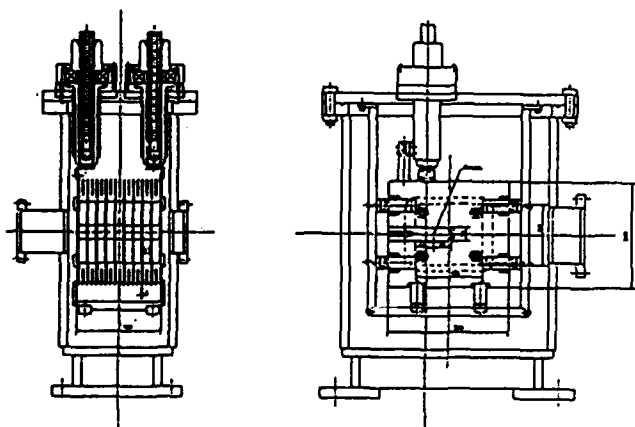


Figure 3. The cross sectional view of the kicker magnet for injection

FURTHER STUDY OF JINR TAU-CHARM FACTORY DESIGN

E. Perelstein, V. Alexandrov, V. Antropov, O. Arkhipov, P. Beloshitsky,
L. Bobyleva, V. Kasacha, N. Kazarinov, A. Krasnykh, V. Mironov,
D. Kaltchev, L. Onischenko, A. Sissakian, Yu. Smirnov, Ts. Vylov

Joint Institute for Nuclear Research, Dubna, Russia

V. Belov, B. Mudiugin, A. Popov, D. Serebrennikov

Scientific Research Institute of Electrophysical Apparatus, St. Petersburg, Russia

I. Kvashonkin, E. Petrov, I. Umansky

Russian Institute of Powerful Radioconstruction, St. Petersburg, Russia

I. INTRODUCTION

At present there are several proposals of the magnet lattices suitable the standard and monochromatization regimes for tau-charm factory [?], [?], [?]. In this paper the main features of the design using versatile lattice are discussed. The beam and machine parameters and a short description of some factory systems are presented to illustrate the design feasibility.

II. MAGNET LATTICE OF TCF

Now we have changed magnet lattice of tau-charm collider. The previous one [?] was based on conventional flat beam scheme. The new lattice [?] is versatile and allows to use both standard scheme and monochromatization one. To have the possibility of a use both schemes the versatile lattice should to fulfil few conditions. Two of them are of most importance. The first is a possibility to change an emittance approximately in 20 times: from $300 \div 400$ nm for the conventional scheme up to $15 \div 20$ nm for the scheme with monochromatization. The second is a necessity of a change polarity in micro-beta quadrupoles. The last condition is a consequence of a fact one wants to gain in energy resolution without loss of a luminosity in the case the monochromatization is made in the vertical plane.

The big change of an emittance is achieved by use of different phase advances in a regular cell for conventional scheme and monochromatization scheme and by appropriate use of wigglers. In high emittance lattice (conventional scheme) 60° phase advance is used in a regular cell. Two variants of wigglers switching to increase an emittance compared with those generated in bending magnets are now under consideration. In the first variant Robinson wigglers reduce horizontal damping partition number J_x from 1 to 0.6. Robinson wiggler consists of 4 blocks each of 0.23m long. It is necessary 4 such wigglers located close to each of 4 dispersion suppressors with gradient $G=4.3\text{T/m}$ and magnetic field $B=0.35\text{T}$. Four dipole wigglers each of 1.0m long with magnetic field $B=1.9\text{T}$, located in first half cell of suppressor, produce an additional increase of emittance. The magnetic elements location and lattice functions in this variant are shown in Fig. 1. In the second variant the dipole wigglers only are used to increase an

emittance. The magnetic field in dipole wigglers is 2.6T in this case.

When comparing two variants (Table 1) one sees the first one is preferable from the point of view smaller RF voltage is needed to keep bunches short. On the other hand, in the second variant damping times are smaller that is important for the injection and beam-beam effects. The final choice can be done after comprehensive study problems mentioned above and others such as multibunch instabilities, broadband impedance restriction etc.

For monochromatization scheme, the horizontal phase advance is 90° in a regular cell. Dipole wigglers are switched off. Robinson wigglers are switched on in a way to reduce an emittance by increasing horizontal damping partition number J_x from 1 to 2. The value of gradient in wiggler is $G=7.3\text{T/m}$ and magnetic field $B=1.9\text{T}$. The dispersion suppressor is made flexible enough to cancel dispersion in both 60° lattice and 90° one.

To make a small beta's at interaction point (I.P.) $\beta_x^* = 0.30\text{m}$ and $\beta_y^* = 0.01\text{m}$ two quadrupoles are used instead of triplet [?]. When changing polarities in quads for monochromator optics (Fig. 2), the values of beta's become $\beta_x^* = 0.01\text{m}$, $\beta_y^* = 0.15\text{m}$ and vertical dispersion $D_y^* = 0.36\text{m}$. The preliminary vertical separation is made by vertical separator. The vertical distance between beam axis in parasitic I.P. is $24\sigma_y$ for conventional scheme and $11\sigma_y$ for monochromatization scheme.

The chromaticity correction is made now for high emittance lattice. With 60° phase advance per regular cell 6 sextupole families have been used to correct chromatic properties. The solution have been found provides $\pm 1.8\%$ of energy acceptance. The beam lifetime for conventional scheme is defined by beam-beam bremsstrahlung predominantly and, to some extent, by neutral gas scattering. With longitudinal acceptance 1.8% and average pressure in vacuum chamber of $2 \cdot 10^{-7}$ Pa it is of 5 hours. The beam lifetime for monochromatization scheme is defined by Touschek effect and depends strongly on dynamic aperture. Its estimate gives $1 \div 3$ hours [?], [?]. The main parameters of tau-charm collider are presented in Table 1.

		Monochrom. scheme	Standard Var.1	scheme Var.2
Energy, GeV	E	2.0	2.0	2.0
Luminosity, $\text{cm}^{-2}\text{sec}^{-1}$	L	$8.0 \cdot 10^{32}$	$9.2 \cdot 10^{32}$	$9.4 \cdot 10^{32}$
C.M. energy resolution, MeV	σ_w	0.14	1.8	2.4
Circumference, m	C	378	378	378
Natural emittance, nm	ϵ_0	15.1	388	393
Bending radius in arc, m	ρ	11.5	11.5	11.5
Damping times, msec	$\tau_x/\tau_y/\tau_z$	19/39/39	43/25/11	19/19/9.7
Momentum compaction	α	$7.85 \cdot 10^{-3}$	$1.63 \cdot 10^{-2}$	$1.63 \cdot 10^{-2}$
Energy spread	σ_E	$7.18 \cdot 10^{-4}$	$6.23 \cdot 10^{-4}$	$8.50 \cdot 10^{-4}$
Total current, mA	I	441	516	536
Number of bunches	k_b	30	30	30
RF voltage, MV	V	5	10	16
RF frequency, MHz	f_{RF}	476	476	476
Harmonic number	q	600	600	600
Energy losses per turn, kV	U_0	131	200	262
Bunch length, mm	σ_s	7.83	6.93	7.47
Longitudinal impedance, Ohm	$ Z_n/n $	0.18	0.21	0.42
Beta functions at LP., m	β_x^*/β_y^*	0.01/0.15	0.30/0.01	0.30/0.01
Vertical dispersion at LP., m	β_y^*	0.36	0.	0.
Beam-beam parameters	ξ_x/ξ_y	0.040/0.029	0.04/0.04	0.04/0.04

Table 1: List of parameters of tau-charm collider

	N	AC A	DC A	R m Ω	L mH	Power kW
Dipoles	48	585	865	11	6.0	1700
Quads I	36	565	865	10	1.8	1200
Quads II	36	565	865	3	0.23	300
Sext. I	30	86	140	8.4	1.6	30
Sext. II	30	115	185	8.4	1.6	40

Table 2: Booster Power Supply Dates

III. MAGNET SYSTEM

According to the factory cyclogram [?] the booster repetition rate is 25 Hz. The ceramic booster vacuum chamber is designed here and the white-circuit type of the resonant scheme of booster power supply is adopted. The compensation of the pulse loss is realized by the isolation reactors from the special pulse power supplies. The design dates of the booster power supply are presented in Table 2.

There are a three subsystems for the system of the power supply of the tau-charm factory storage ring. They feed: 1) superconducting quadrupoles and dypole wigglers; 2) septum magnets; 3) dipoles, quadrupoles, sextupoles, Robinson wigglers. The third group has a big energy capacitance and is quit expensive. It consists of 160 dipole magnets, 8 vertical bend magnets, 16 wigglers, 234 quads and 112

arc sextupoles. There are a 48 group for the power supply to this system. Each chain has got a separate power source. The prototype of the power source is DC Sources that have been designed at Institute of Electrophysical Apparatus (St.Petersburg) and "Electrotechnic" firm (Tallin, Estonia). The parameters of this power sources allow to get the driving range $(0.6-1.0) \cdot P_{nom}$ with stability coefficient $\pm 10^{-5}$.

The cores of the storage ring magnet is made from the laminated electrical steel (type 2212) with thickness of 1.5 mm. The main ring dipoles have C-shape with the dimensions 440x580 mm with the gap of 60 mm. and will be made from laminated electrical steel (type 2411) with thickness of 0.5 mm.

IV. VACUUM SYSTEM

The beam particle bremsstrahlung in the residual gas atmosphere contributes to the beam lifetime. For the typical residual gas composition (70% H₂, 20% CO, 10% CO₂) and the pressure $2 \cdot 10^{-7}$ Pa vacuum lifetime is about 30h. The gas loading is defined mainly by synchrotron radiation (SR) desorbtion. The photodesorbtion coefficient is adopted to be equal to $\eta = 10^{-6}$ [mol/phot], that corresponds to the dose of 50 A·h [?]. Providing the chemical cleaning and heating of the vacuum chamber the outgassing rate of aluminum doesn't exceed $g = 10^{-9}$ [m·Pa/sec], that much less then stimulated desorbtion.

The vacuum chamber of tau-charm factory is manufactured from aluminum and designed in such a manner that SR goes through next straight section and is absorbed at the bending magnet end (Fig. 2). The vacuum volume at the bending magnet region is divided on two parts: the beam chamber and the antechamber. The chamber aperture is 49×64 mm and it isn't varied along the whole chamber length. The gap between the beam chamber and antechamber has been chosen to fulfil the condition of 95% SR passing through. The SR absorber is made as water-cooling couplers tube with extended surface. The absorbers have the outlet SR extracting windows for the user purposes.

The stimulated outgassing per a bending magnet is equal to $8 \cdot 10^{-8}$ [m³·Pa/sec]. Using the combined pumps with the pumping speed 0.4 m³/sec, one gets the pressure about $2 \cdot 10^{-7}$ Pa at the absorber location. The additional pump is used for the pumping of the remaining part of vacuum volume and provides the pressure at the level $2 \cdot 10^{-8}$ Pa.

V. RF SYSTEM

To compensate energy beam losses and to keep bunches short 500 MHz superconducting RF cavities is planned to use. The total value of SR and HOM losses at energy $E = 2.0$ GeV is of order 300 kW and the maximum RF voltage is of 16 MV for one ring. The voltage amplitude and phase tolerances are defined by beam quality demands. The fluctuations in voltage amplitude enhance beam spread. Putting the tolerable increase of beam spread 5% one gets limitation for RF voltage fluctuations $\Delta V/V \leq 5 \cdot 10^{-3}$. The phase shift between RF modules excites the synchrotron oscillations. Putting restriction for their amplitude to be ≤ 1 mm, one gets $|\delta\phi_s| \leq 1^\circ$.

The RF power supply scheme for tau-charm factory is grounded on the principle of separate supply of each cavity like [7]. The main questions are the choice of an adequate final stage amplifier and the feeder line design. Klystrons developed at "SVETLANA" (St. Petersburg) satisfied tau-charm factory requirements and have the following parameters: output power - 80 kW, frequency - 500 MHz, efficiency - 0.58, amplification - 45 dB, collector voltage - 16 kV, collector current - 8.6 A.

Each feeder line includes a ferrite circulator with a ballast load, that allows to refuse from phase shifter using. The effective automatic phase control is provided by the electronic phase shifter in a preliminary stage of a RF amplifier. The main coaxial feeder connecting a circulator output and a cavity input has the cross section dimensions 160×70 mm and the wave impedance 50 Ohm. Thus the RF power supplier consists of 4 independent FR lines with the total output power 320 kW.

REFERENCES

- [1] A. Faus-Golfe and J. Le Duff "A Versatile Lattice for a Tau-Charm Factory That Includes Monochromati-

zation Scheme" (LAL-RT/92-01, Orsay, 1992)

- [2] Alexander Zholents "Polarized J/ψ Mesons at a Tau-Charm Factory with a Monochromator Scheme" (CERN SL/92-27(AP), 1992)
- [3] Paul Beloshitsky "A Magnet Lattice for a Tau-charm Factory Suitable for Both Standard Scheme and Monochromatization Scheme" (LAL-RT/ 92-09, Orsay, 1992)
- [4] E. A. Perelstein e.a. "JINR Tau-Charm Factory Study" (Proceeding of XV International Conference on High Energy Accelerators, Hamburg, 1992)
- [5] M. V. Danilov e.a. "Conceptual Design of Tau-Charm Factory in ITEP" (Proceeding of XV International Conference on High Energy Accelerators, Hamburg, 1992)
- [6] M. Bernardini "Vacuum System for ELETTRA of Synchrotron Trieste" (Proceedings of the SR Vacuum Workshop, Wako-shi, Saitama, Japan, 1992, p.272)
- [7] B. Barish e.a. "Tau-Charm Factory Design" (SLAC-PUB-5180, Stanford, 1990)

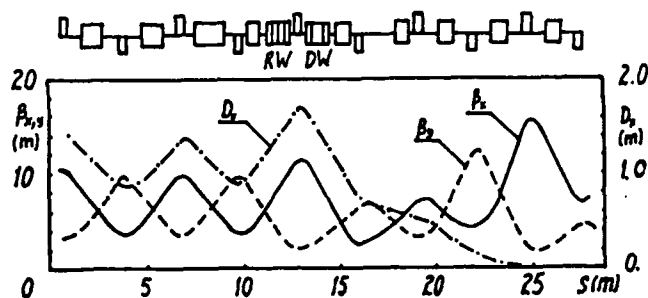


Fig. 1. Lattice functions in regular cell and dispersion suppressor.

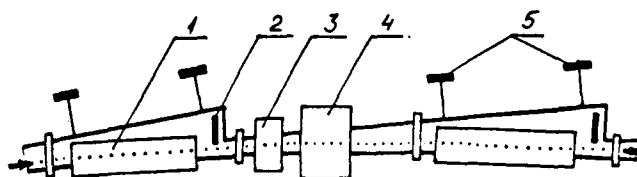


Fig. 2. Periodic cell scheme (1-dipole, 2-SR absorber, 3-sextupole, 4-quadrupole, 5-pumps).

A Versatile Lattice for a Tau-Charm Factory that includes a Monochromatization Scheme (Low-Emittance) and a Standard Scheme (High-Emittance)

A. Faus-Golfe* and J. Le Duff
Laboratoire de l'Accélérateur Linéaire
Centre d'Orsay Bat. 200, 91405 Orsay FRANCE

Abstract

A versatile lattice for a tau-charm factory working at 4 GeV center of mass energy with $10^{33} \text{ cm}^{-2} \text{ s}^{-1}$ luminosity is considered in this paper. The main goal of this study due to absence of experience in this kind of features, is the possibility to use easily the same lattice for either monochromatization (low-emittance) scheme or standard (high-emittance) scheme. This monochromatization scheme permits to reduce the spread of collision energies at the interaction point to the level of 0.1 MeV. In this paper we consider a low-emittance arc (10^{-8} m rad) typical from synchrotron radiation lattices and the passage from low-emittance to high-emittance (10^{-7} m rad) is obtained by detuning of the low-emittance arc.

I MONOCHROMATIZATION AND EMITTANCE

From [1] and [2] we can deduce that a non-optimized monochromatization scheme gives a factor gain λ in energy resolution, Σ_w , but a loss by the same factor in luminosity.

Assuming that $D_{y-}^* = -D_{y+}^* = D_y^*$ and $D_{x-}^* = -D_{x+}^* = 0$ we obtain:

$$L = \frac{L_0}{\lambda} ; \Sigma_w = \frac{\sqrt{2}E_0\sigma_\epsilon}{\lambda} \quad (1)$$

with

$$\lambda \simeq \frac{\sigma_\epsilon D_y^*}{\sigma_{\beta y}} ; L_0 = \frac{k_b f_r N_+ N_-}{4\pi\sigma_{\beta y}^* \sigma_{\beta x}^*} \quad (2)$$

where λ is the gain factor, L_0 the total luminosity with zero dispersion at the interaction point, σ_ϵ denotes the relative energy deviation of each beam, E_0 the nominal energy per beam, k_b the number of bunches per beam, f_r the revolution frequency, N_{\pm} the number of particles in each bunch and $\sigma_{\beta xy}^*$ the betatron size at the interaction point (IP).

To achieve a factor λ in energy resolution, without loss in total luminosity, it is necessary to optimize the beam parameters as described in the following.

The total luminosity can be defined as a function of beam-beam parameters, ξ_{xy} :

$$L = \frac{\gamma I}{2er_e} \left(\frac{\xi_x}{\beta_x^*} + \frac{\xi_y}{\beta_y^*} \right) \quad (3)$$

where I is the total beam current, r_e the classical electron radius, $\gamma = E_0/mc^2$ and β_{xy}^* the values of beta functions at IP.

*On leave from IFIC, Univ. of Valencia-CSIC

The beam-beam effect for the case of a large dispersion at the IP was analysed in [5] and the following recommendations were pointed out.

- Beams in collision must be flat.
- Dispersion must be in a plane where beams are wide (easier matching).
- The beam-beam parameters for a plane with dispersion must be less than 0.04 and for a plane without dispersion approximately 0.04.

With these requirements if we have $D_y^* \neq 0$ and $D_x^* = 0$ then $\sigma_x^* \ll \sigma_y^*$ and $\xi_y \ll \xi_x$. From the first look to equation 3 it seems that decreasing ξ_y should result in a fall of the luminosity but if one takes $\beta_x^* \ll \beta_y^*$ the total luminosity is given essentially by:

$$L \simeq \frac{\gamma I}{2er_e} \left(\frac{\xi_x}{\beta_x^*} \right) \quad (4)$$

To preserve ξ_x with enlarged σ_y^* one should increase N (but the possibility to increase N is limited by the coherent stability requirements) or reduce σ_x^* but the latter requires a low-emittance lattice. These requirements for the typical parameters of the Tau-Charm factory ($E_0 = 2.0$ GeV, $\beta_x^* = 0.01$ m, $\xi_x = 0.04$, $N = 1.2 \cdot 10^{11}$) set a limit on the maximum value of the horizontal emittance at the level of $\epsilon_x \simeq 1.2 \cdot 10^{-8}$ m rad. This emittance is the typical emittance of synchrotron radiation machines of the third generation.

From [6] we can deduce that a luminosity at the level of $L \simeq 10^{33} \text{ cm}^{-2} \text{ s}^{-1}$ for a standard scheme with a flat beam, requires the horizontal emittance at 2.0 GeV to be of the order of $\epsilon_x \simeq 3.4 \cdot 10^{-7}$ m rad.

As analysed previously a total luminosity at the level of $L \simeq 10^{33} \text{ cm}^{-2} \text{ s}^{-1}$ for both standard and monochromatization schemes requires to vary the emittance over a wide range from $\epsilon_x \simeq 1.2 \cdot 10^{-8}$ m rad up to $\epsilon_x \simeq 3.4 \cdot 10^{-7}$ m rad, i.e. a versatile lattice.

With this philosophy and with FODO cells in the arc two studies [3] and [4] have been proposed. In our case the idea is to use DBA or TBA cells in the arc optimized for low-emittance and the high emittance is achieved by detuning this low-emittance lattice.

II VERSATILE LATTICE

To describe the lattice one can divide it in three sections: interaction region, arc (DBA or TBA) and utility insertion. The versatile lattice has been designed in such a way

that with some additional quadrupoles in the interaction region and changing the strength of the quadrupoles it is possible to pass from monochromatization optics to standard optics. This is precisely the main goal of this study, ie. the possibility to use easily the same lattice for either monochromatization and standard scheme.

Two different arcs DBA and TBA have been studied with the same interaction region. The description of the interaction region, the different arcs and the utility section is accomplished in the following sections.

A Interaction region

Standard choice of optics in the micro-beta insertion for a Tau-Charm factory design is used in both schemes (monochromatization and standard) [3] and [4]. The distance between the first superconducting quadrupole and the IP is kept at 0.8 m to locate the detector, but the distance between the first and the second quadrupole has been reduced to avoid the growth of the high beta function in this region, which is responsible for the high vertical chromaticity in this kind of lattices.

The parameters of the micro-beta insertion and the lattices functions in this region for the two schemes are shown in table 1 and on figures 1-4.

B Arc: DBA

In this first study we have taken a DBA cell in the arc with a doublet in the dispersive section and a triplet in the non-dispersive section to have more flexibility in matching of the optics, since the same lattice is used for both low and high emittance arcs.

For the monochromatization scheme the arc has been optimized to obtain $\epsilon_x = 2 \cdot 10^{-8}$ m rad (10 periods) at $E_0 = 2.0$ GeV with $J_x = 1.0$. The change from low-emittance ($\epsilon_x = 2 \cdot 10^{-8}$ m rad) to high-emittance ($\epsilon_x = 3 \cdot 10^{-7}$ m rad) is achieved by decreasing the strength of the quadrupoles in the dispersive doublet and a mismatch of the dispersion in the achromat. This mismatch implies that $D_x \neq 0$ and $D'_x = 0$ between cells hence it is necessary to rematch the dispersion at the entrance and exit of the arc; this is done by independent quadrupoles.

The performances and the lattice functions of half a ring for both schemes are shown in table 1 and on figures 1 and 2.

C Arc: TBA

For the second study we have used a TBA cell in the arc with six quadrupoles by half cell, three in the dispersive section and three in the non-dispersive section. This high number of quadrupoles permits to have more flexibility in matching the optics.

As in the previous case the arc has been optimized to have $\epsilon_x = 2 \cdot 10^{-8}$ m rad (12 periods) at $E_0 = 2.0$ GeV with $J_x = 1.0$, the change from low-emittance to high-emittance being achieved in the same way as in the previous case.

The performances and the lattice functions of half a ring for both schemes are shown in table 1 and on figures 3 and 4.

Table 1: Performances for both schemes and both arcs

		Monochr.	Standard	
		Low-Emit	High-Emit	GeV
E_0		2.0	2.0	GeV
β_x^*		0.01	0.3	m
β_y^*		0.15	0.01	m
D_y^*		0.32	0.0	m
κ		0.067	0.033	
ξ_x		0.04	0.04	
ξ_y		0.035	0.04	
DBA	σ_e	$5.42 \cdot 10^{-4}$	$5.42 \cdot 10^{-4}$	
	ϵ_x	$1.93 \cdot 10^{-8}$	$2.97 \cdot 10^{-7}$	m rad
	ϵ_y	$1.28 \cdot 10^{-9}$	$9.91 \cdot 10^{-9}$	m rad
	C	321.687	321.687	m
	$k_b f_r$	27.957	27.957	MHz
	N_b	$1.31 \cdot 10^{11}$	$1.1 \cdot 10^{11}$	
	I_b	0.585	0.49	A
	L	$1.09 \cdot 10^{33}$	$8.97 \cdot 10^{32}$	$\text{cm}^{-2}\text{s}^{-1}$
	λ	12.545	1.0	
	Σ_w	0.122	1.533	MeV
TBA	σ_e	$6.81 \cdot 10^{-4}$	$6.81 \cdot 10^{-4}$	
	ϵ_x	$1.9 \cdot 10^{-8}$	$2.86 \cdot 10^{-7}$	m rad
	ϵ_y	$1.27 \cdot 10^{-9}$	$9.52 \cdot 10^{-9}$	m rad
	C	387.008	387.008	m
	$k_b f_r$	27.886	27.886	MHz
	N_b	$1.23 \cdot 10^{11}$	$1.05 \cdot 10^{11}$	
	I_b	0.551	0.470	A
	L	$1.01 \cdot 10^{33}$	$8.43 \cdot 10^{32}$	$\text{cm}^{-2}\text{s}^{-1}$
	λ	15.834	1.0	
	Σ_w	0.122	1.926	MeV

D Utility section

This section has almost the same length as the insertion region. It is made of regular FODO cells and it is designed to house the RF cavities, the beam instrumentation devices and to locate additional sextupoles to help the correction of chromaticity should it be necessary.

The lattice functions in this region for both schemes and both cases are shown on figures 1-4.

III REFERENCES

- [1] J.M. Jowett "Feasibility of a monochromator scheme in LEP" (CERN LEP Note 544, 1985)
- [2] A. Faus-Golfe and J. Le Duff "A versatile lattice for a Tau-Charm factory that includes a monochromatization scheme" (LAL/RT 92-01, February 1992)
- [3] A. Zholents "Polarized J/Ψ mesons at a Tau-Charm factory with a monochromator scheme" (CERN SL / 92-27)
- [4] P. Beloshitsky "A magnet lattice for a Tau-Charm factory suitable for both standard and monochromatization scheme" (LAL/RT 92-09, July 1992)
- [5] A.L. Gerasimov, D.N. Shatilov and A. Zholents "Beam-Beam effects with a large dispersion function at the interac-

- [6] J. Gonichon, J. Le Duff, B. Mouton and C. Travier "Preliminary study of a high luminosity e^+e^- storage ring at a CM energy of 5 GeV" (LAL/RT 90-02, January 1990)

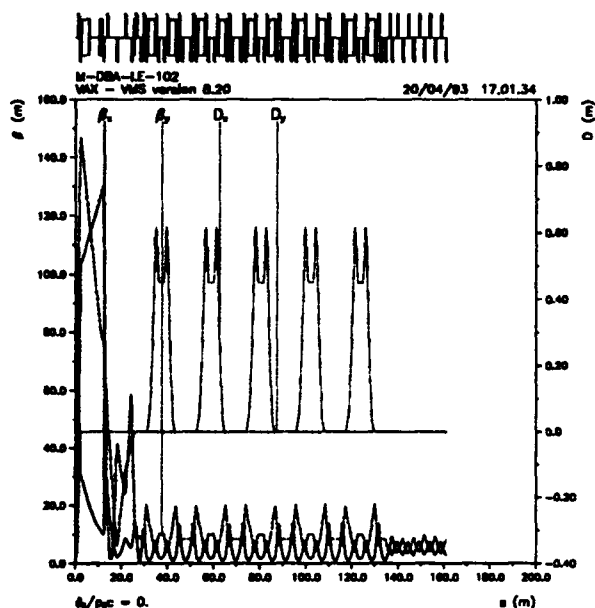


Figure 1: Lattice functions of half a ring for monochromatization scheme, arc DBA

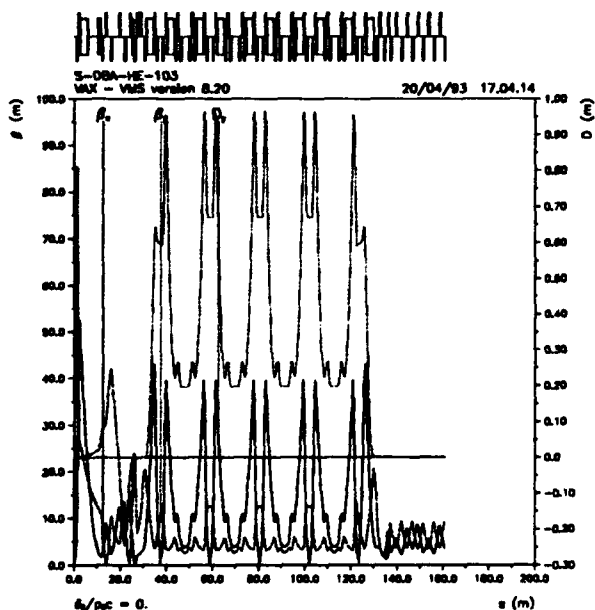


Figure 2: Lattice functions of half a ring for standard scheme, arc DBA

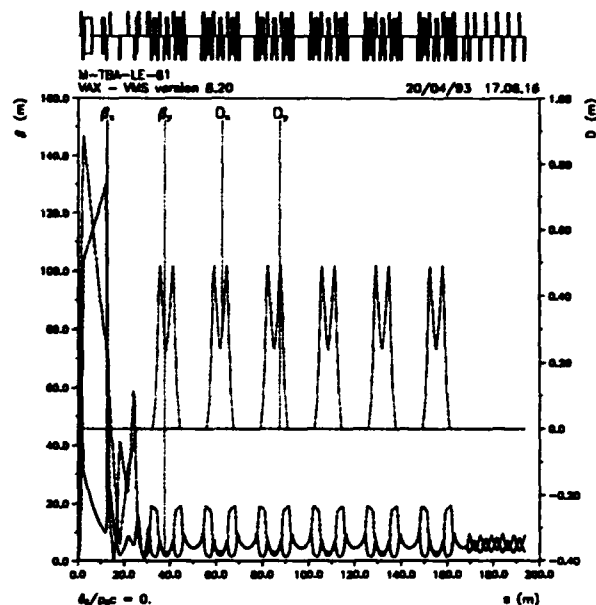


Figure 3: Lattice functions of half a ring for monochromatization scheme, arc TBA

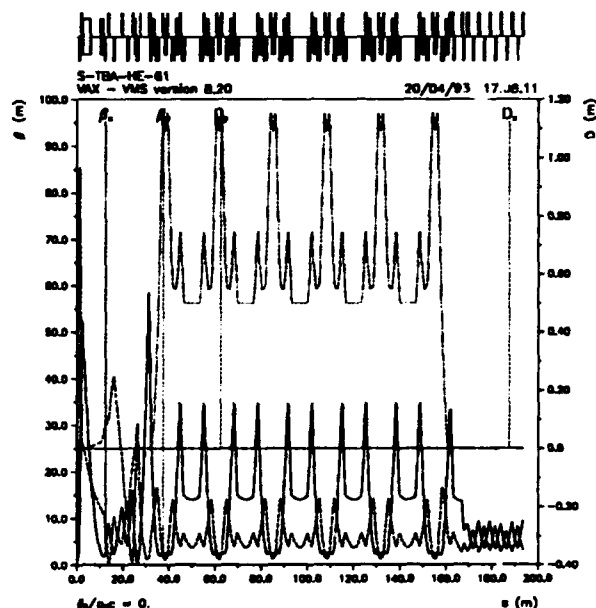


Figure 4: Lattice functions of half a ring for standard scheme, arc TBA

DAΦNE Interaction Region Design

M. Bassetti, M.E. Biagini, C. Biscari, M.A. Preger, G. Raffone, G. Vignola
INFN - LNF C.P. 13 00044 Frascati

Abstract

The strategy adopted in designing the DAΦNE Interaction Regions is presented, and the basic theory for the novel compensation scheme of the high field detector solenoid is discussed. A preliminary mechanical design is also illustrated.

I. INTRODUCTION

DAΦNE, the Frascati Φ factory [1], is a double ring collider with a maximum number of 120 stored bunches. In order to avoid parasitic crossings near the Interaction Point (IP), the beams cross at a horizontal angle of 25 mrad, whose harmful effects are overcome by a large horizontal beam size at the IP. To achieve the target luminosity, $L = 5 \times 10^{32} \text{cm}^{-2} \text{s}^{-1}$, the betatron coupling should not exceed 1%. In the following we call Interaction Region (IR) the part of DAΦNE shared by the two rings, which corresponds to a total length of 10.1 m. In the IR the two beams follow separate trajectories and they pass off axis in all the magnetic elements crossing only at the IP.

One IR is dedicated to the KLOE [2] experiment, and the other one to FINU.DA. [3]. Three different IR lattices have been designed: two for the experiments and one for commissioning. The latter consists of two conventional quadrupole triplets. The total IR first order transport matrix is the same for the three designs, thus allowing to interchange the three IRs with minor changes in the regular ring lattice. FINU.DA., an experiment to study Hypernuclei, K-nucleon and K-nucleus at very low energy, has been approved lately and its design is still in a very preliminary stage. We will describe in the following the KLOE IR. The KLOE detector is designed primarily to detect direct CP violation in K^0 decays. Its main features are: a cylindrical structure surrounding the beam pipe consisting of a vertex chamber, a large tracking device, an electromagnetic calorimeter and a solenoidal magnet, in order of increasing radius, as shown in Fig. 1.

The magnetic field, $0.6 \text{T} \times 4.32 \text{m}$, has a strong effect on the beam, due to the relatively low energy of DAΦNE (0.51 GeV). Since a very large solid angle is required, the machine components must be installed within a cone of 9° maximum half-aperture. The small vertical β value at the IP is obtained with a permanent magnet quadrupole triplet on each side. A sophisticated compensation scheme, including the rotation of the low- β quadrupoles, has been adopted to locally decouple horizontal and vertical betatron motions.

II. ROTATING FRAME METHOD

The main effect of a solenoidal magnetic field is to focus and to couple the horizontal and vertical betatron phase spaces. In the following we refer to the 4-dimensional (x, x', y, y') phase space. To decouple the transverse planes the skew quadrupole method [4] needs 4 skew quadrupoles. In fact 4 is the difference between the 10 degrees of freedom of a general coupled 4×4 symplectic matrix and the 6 of an uncoupled block diagonal one. In our case, to decouple the normal modes at the IP, both the matrices corresponding to half IR before and after the IP must be block diagonal, so that 8 skew quadrupoles should be necessary.

The Rotating Frame Method (RFM) [5] in principle block diagonalizes a matrix with only 2 independent parameters. This scheme cannot be exactly applied when the quadrupoles are immersed in the detector longitudinal field as it is in DAΦNE. Nevertheless, the residual coupling can be corrected by adopting a generalization of the Guignard scheme.

A uniform solenoid, with a longitudinal field B_z , can be identified, from the optical point of view, by its length l_s and its normalized gradient k_z :

$$k_z = \frac{B_z}{2 B \rho}$$

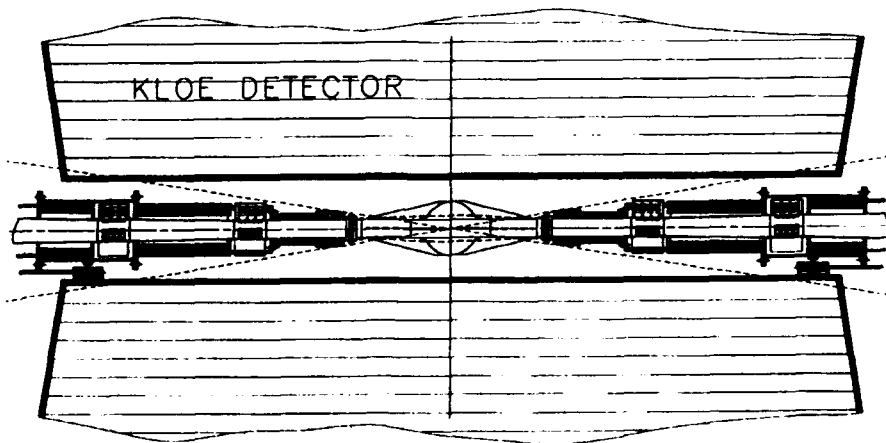


Figure 1. KLOE Interaction Region.

Its transport matrix P_S can be expressed [5] as the product of a rotational and a focusing part:

$$P_S = R(\theta_r) \cdot F(\theta_r)$$

where $\theta_r = k_z l_s$.

The R matrix rotates the transverse plane around the longitudinal direction by an angle θ_r :

$$R = \begin{pmatrix} I \cos \theta_r & I \sin \theta_r \\ -I \sin \theta_r & I \cos \theta_r \end{pmatrix}$$

where I is the 2x2 identity matrix. This rotation couples the radial and vertical phase spaces. F is a diagonal block matrix:

$$F = \begin{pmatrix} A & 0 \\ 0 & A \end{pmatrix}$$

being A the 2x2 matrix:

$$A = \begin{pmatrix} \cos \theta_r & \frac{1}{k_z} \sin \theta_r \\ -k_z \sin \theta_r & \cos \theta_r \end{pmatrix}$$

Given the block diagonality of F, $FR = RF$. The F matrix focuses both transverse motions. So, once fixed θ_r , the focusing action of a solenoid strongly depends on its length.

In the following we limit our considerations to one half of the KLOE IR. The rules of the RFM are two:

- 1) The total rotating angle must vanish:

$$\int_{IR} B_z ds = 0$$

A compensator solenoid at the end of the IR, with an angle θ_r opposite to the half detector one, satisfies this condition.

- 2) Each quadrupole must be rotated exactly by the angle:

$$\theta(z) = \int k_z dz$$

where the integral is calculated from the IP to its longitudinal position. This means that each quadrupole should be rotated as an helix, which cannot be easily accomplished. Practically the best one can do is to rotate each quadrupole by the angle corresponding to its longitudinal midpoint.

In order to compute the matrix belonging to quadrupoles immersed in a longitudinal field, each quadrupole is represented as a large number of equally spaced thin lenses, interleaved with small uniform solenoids. The resulting IR matrix exhibits, as expected, a small residual coupling which must be corrected, the design coupling being very small. In order to perfectly diagonalize our system we need 4 more parameters: we choose three independent supplementary rotations, $\delta\theta_i$ ($i = 1, 2, 3$), of the three quadrupoles, plus a correction $\delta\theta_c$ of the compensator field. The quadrupole rotations θ_i , the rotation inside the compensator and their respective small corrections

are shown in Table I. The angle associated to the KLOE field is assumed to be positive.

Table I - IR element rotations

Elements	θ	$\delta\theta$
Q1	+5.66°	+0.31°
Q2	+10.15°	+0.02°
Q3	+14.80°	+0.27°
Compensator	-21.84°	+0.12°

Finally, the complete IR layout, proceeding from the left to the right side of KLOE, is as follows:

- a compensator rotating the phase plane by $\theta_c + \delta\theta_c$,
- three quadrupoles rotated by $-(\theta_i + \delta\theta_i)$,
- the IP,
- three quadrupoles with $\theta_i + \delta\theta_i$,
- a compensator with $\theta_c + \delta\theta_c$.

Superimposed is the KLOE solenoidal field which rotates the normal modes by $-2\theta_c$.

The optical functions and the horizontal and vertical beam trajectories in half IR are plotted in Fig. 2. The optical functions are computed in a frame following the rotation or the normal betatron modes.

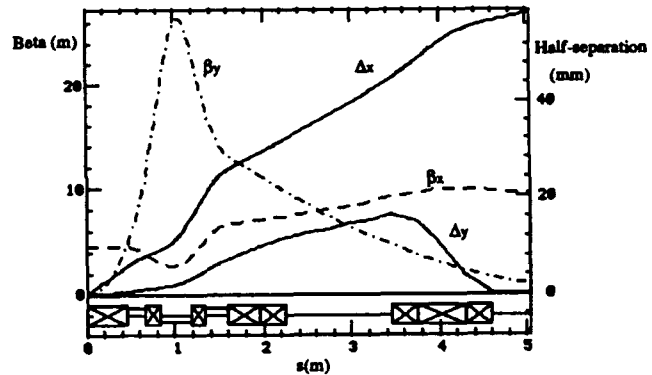


Figure 2. Optical functions and beam trajectory in KLOE IR.

III. LINEARITY STUDIES

In order to study the linearity of our scheme, taking into account that relatively low energy beams pass off axis in the magnetic elements, a half method has been applied to a preliminary design of the compensator solenoid field [6]. In our IR's lattice design the solenoidal field on the axis is approximated by uniform field slices. In this model the transverse field thin lenses are linear, and the longitudinal field does not depend locally on the distance from the solenoid axis. Therefore the total matrix does not depend on the initial conditions, which is of course an approximation. An analytical formula for the field $B_z(0, z)$ on the solenoid axis has been obtained by fitting the numerically computed field. Given the field $B_z(0, z)$, in cylindrical symmetry, the field in the region delimited by the iron and the magnet coils can be calculated

from the expansion [7]:

$$B_z(r,z) = \sum_{n=0}^{\infty} (-1)^n \frac{B^{[2n]}(0,z)}{(n!)^2}$$

$$B_r(r,z) = \sum_{n=1}^{\infty} (-1)^n \left(\frac{r}{2}\right)^{2n-1} \frac{n B^{[2n-1]}(0,z)}{(n!)^2}$$

where $B^{[2n]}(0,z)$ is the $2n$ -th order derivative of $B_z(0,z)$. Derivatives up to the fifth order have been retained. These expressions have been used to track large amplitude particles by simply integrating the Lorentz force equations. Fig. 3 shows, as an example, the vertical angle of the trajectory as a function of the initial horizontal position. We have verified that the system is linear up to ≈ 10 cm from the beam axis, providing a good safety margin for the divergent trajectories of electrons and positrons in the IR. For our design values, the obtained trajectories agree very well with the results of tracking through uniform field slices, so we are confident that the method used in the calculation of the optical effects in the IR is correct.

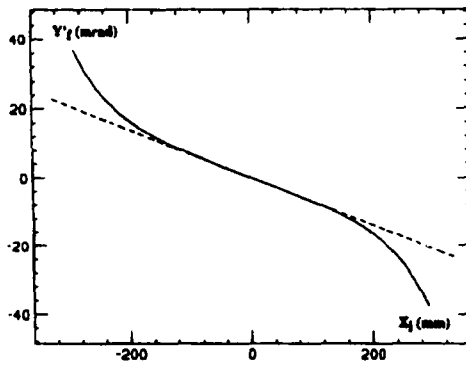


Figure 3. Vertical trajectory slope vs. horizontal initial position.

V. MECHANICAL DESIGN

The IR beam pipe is about 0.7 m long and the cross-section diameter ranges from 68 mm to 200 mm in the interaction region; 0.5 mm thick pure beryllium has been chosen to provide a very good transparency, in terms of radiation lengths, and scattering angle. The use of beryllium is the "crucial part" of the design as preventive maintenance has to be minimized as well as the risks during weldings, brazings or handlings of components close to the IR beam pipe. An inner, very thin, beryllium strip shields the outer chamber to prevent the rf power losses which can lead to huge thermal loads. The inner strip is one-side brazed or simply free to minimize its thermal stresses. Two rigid copper end flanges brazed onto the beryllium tube should prevent the buckling and make handling of the chamber easier; at the same time the flanges may house two cooling rings (water or freon heat sinks) which keep the wall temperatures below a given limit.

An outer additional "inert gas" cooling must surround the chamber when the machine is running in order both to avoid contact with air and to cool the chamber in the case of possible overheating due to an accidental disruption of the inner rf

shield. For this last reason a smoothly tapered outer shape of the beryllium chamber is preferred to a spherical one even if the buckling safety factor is much lower. The possible above mentioned overheatings are strongly dependent upon both the shape of the chamber and the beam parameters and can cover a potentially very wide range of power losses; such hard and uncertain working conditions must be carefully checked to assure the safety norms otherwise an alternative material for the outer chamber must be considered.

The inner 50 μ m rf shield has a small outward curvature to prevent the synchrotron radiation to illuminate this very thin strip. A finite element analysis on the thin strip can not be easily carried out without experimental data as the commonly used failure criteria (as the maximum strain energy or the maximum shearing stress) lose their effectiveness when applied to beryllium foils; even if at a first sight the thermal stresses are small, a thermo-structural study as well as a thermal fatigue life expectancy must be carefully estimated in extreme working conditions before going on with the design. Because of the reasons herein described the design of the IR beam pipe is still in a preliminary stage.

The remaining part of the beam pipe is made of copper for its good thermal conductivity and is shielded by a multi-layer super-insulation material in order to protect the surrounding permanent magnets during baking and to make the latter easier.

The low- β triplet support barrel allows remote control of its degrees of freedom (vertical and horizontal positions and roll, pitch and yaw angles). It will be made of a rigid composite material in order both to minimize the amount of material inside the detector and to obtain an acceptable bending at its end; it will be simply supported in two points: one inside the detector, right on the end of the tracker cone, the other outside the detector near the compensator solenoid. This support must be split across its diameter or divided into three pieces to allow beam pipe and permanent magnets installation.

Each quadrupole is confined with two aluminium collars. The space between the ion pumps and the magnet ends allows TIG welding to close the vacuum chamber after the quadrupoles have been introduced around the pipe; of course this assembly requires great deal, and splitting of the permanent magnets into two parts is advisable in spite of the need for larger collars. The water cooled trim coils are mounted inside the inner collar of the permanent magnets and follows the rotation of the triplet support; the space at the ends of the coils needs a limited reduction in coil length resulting in lesser turning ability. Careful study on the size of the components and the assembly sequence must be carried out to fulfill proper alignment requirements; improvements on the design are still in progress.

VI. REFERENCES

- [1] G. Vignola, Ib4, this conference.
- [2] The KLOE Collaboration "KLOE, a general purpose detector for DAΦNE" LNF Internal Note LNF-92/019(IR), April 1992.
- [3] T. Bressani "Nuclear Physics at DAΦNE" - Workshop on Physics and Detectors for DAΦNE, Frascati, April 9-12, 1991, p.475.
- [4] G. Guignard, CERN ISR-MA/75-23.
- [5] M. Bassetti, DAΦNE Int. Note, to be published.
- [6] C. Sanelli, private communication.
- [7] G. Bowden, "Fringe field representations of IP magnets", Asymmetric B-factory Collider Tech. Note 046 (1991).

On an Asymmetric Correlated Flavor Factory

D. Cline, A. Boden, W. Gabella, A. Garren, X. Wang
Center for Advanced Accelerators, Physics Department
University of California Los Angeles
405 Hilgard Ave., Los Angeles, CA 90024

Abstract

There are distinct physics advantages to using asymmetric ϕ factories to test and study CPT and CP violation. However, several beam dynamics issues remain to be addressed, especially for the effects of a high energy linac beam on a low energy target (most likely a storage ring or a recirculator structure). We present a preliminary discussion of collider concepts, especially with regard to the creation of high luminosities.

I. INTRODUCTION

Flavor Factories (e^+e^-) are now established as an important component of the experimental equipment required to study elementary particles in the future, with emphasis on the study of CP violation, search for CPT violation and the detailed measurement of the parameters of the CKM matrix. To date, only two types of Flavor Factories have been studied: Symmetric (ϕ and Charm- τ Factories) and Asymmetric (B-Factories with a ratio of 3:1 for the high energy and low energy beams). We believe there will be a need for very asymmetric flavor factories (VAFF) where the ratio of beam energies may vary up to 20:1 [1, 2]. An example of such a factory is the Asymmetric ϕ Factory where the major innovation is to give the K_S^0 "beam" a Lorentz boost γ of a factor of (3-10).

Very asymmetric collisions could be useful for ϕ Factories, Z^0 Factories, and 2nd Generation B-Factories. To our knowledge no systematic study of VAFF has been carried out to date. In this report, we first discuss some of the scientific motivation for VAFF, including the collision kinematics. We then discuss the various types of colliders, especially with respect to resulting luminosity and beam-beam interaction dynamics.

II. KINEMATICS OF VAFF

The key goals of ϕ factories are:

1. Measurement of $[\epsilon'/\epsilon] \sim 10^{-4}$;
2. Search for CP violation in other decays, such as $K_L^0 \rightarrow \gamma\gamma$;

3. Search for possible CPT violation at a very sensitive level,

$$\left(\frac{M_{K^0} - M_{\bar{K}^0}}{M_K} < 10^{-18} \right)$$

All of these goals require the study of K_S^0 mesons and a detector with extremely good resolution, and are documented in many studies at UCLA, Frascati, KEK and Novosibirsk. We have previously proposed an asymmetric ϕ factory[1] to simplify these measurements and have also carried out extensive calculations for the proposed UCLA (Symmetric) Φ Factory [3]. In this note we compare the kinematics of symmetric and asymmetric ϕ factories and show how the experimental precision can be increased and the detector simplified for the latter case.

We consider the ϕ factory configuration shown in Fig. 1 where a 2 GeV/c e^- linac beam collides with a stored 130 MeV/c e^+ beam. A scintillating fiber Pb detector covering the angular region of $\pm 60^\circ$ is assumed for the purpose of reference. This will lead to a sharply reduced detector cost compared to that for a symmetric ϕ factory.

The major problem of studying K_S^0 's at a symmetric ϕ factory is the very short decay length compared with the experimental resolution of final states, such as

$$K_S^0 \rightarrow \pi^0 \pi^0, \quad (1)$$

$$K_S^0 \rightarrow \gamma\gamma. \quad (2)$$

Fig. 2 shows the decay length distribution for symmetric and asymmetric collision energies. All new tests of quantum mechanics at ϕ factories require the insertion of some material into the beam in order to perform the measurement[4]. An asymmetric ϕ factory allows inserts of 1-2 cm of material and thus provides unique ways to test quantum mechanics.

Another comparison concerns the energy distribution of the photons from reaction (1) above. We expect reaction (2) to give similar results. A symmetric ϕ factory has a very low energy tail on the photon distribution. It is difficult to detect photons with energy below 100 MeV and even more difficult those below 50 MeV with high efficiency. Also, the energy resolution improves as the photon energy increases. In Fig. 3(a) we compare the photon energy spectra for symmetric collisions. Fig. 3(b) shows the photon energy distribution for asymmetric collisions and for angles less than 60° with respect to the high energy beam direction. The combination of extended decay

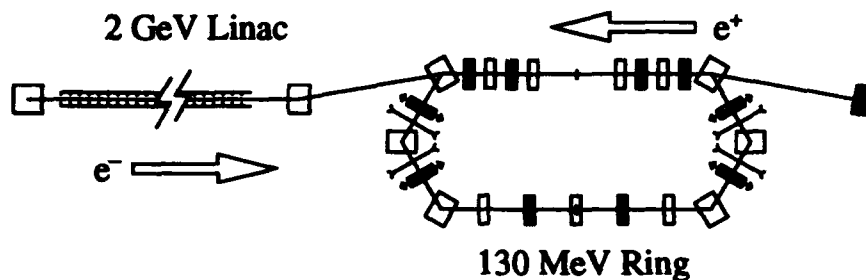


Fig. 1. Possible layout of an asymmetric ϕ factory.

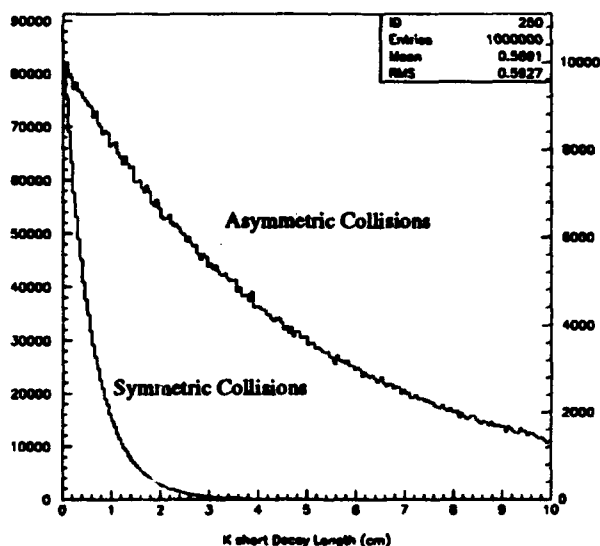


Fig. 2. Decay length for the K_s particle for symmetric and asymmetric collision energies. In asymmetric case, the particles are significantly boosted. Symmetric data uses the left ordinate, asymmetric data the right.

length and harder photon spectrum considerably increases the advantage of an asymmetric ϕ factory, and allows a relatively simple and inexpensive detector which we estimate will cost approximately 10% as much as the 4π detector proposed for the UCLA Symmetric ϕ Factory.

III. VARIOUS ASYMMETRIC COLLIDER CONCEPTS

There are three generic collider designs for creating very asymmetric collisions between e^- and e^+ bunches with high luminosity. These are linac-on-ring, linac-on-linac, and ring-on-ring colliders. For this discussion, we assume a high energy electron beam and a low energy positron beam. This is advantageous for the production of positrons. The details of each design type is quite involved. Here we wish

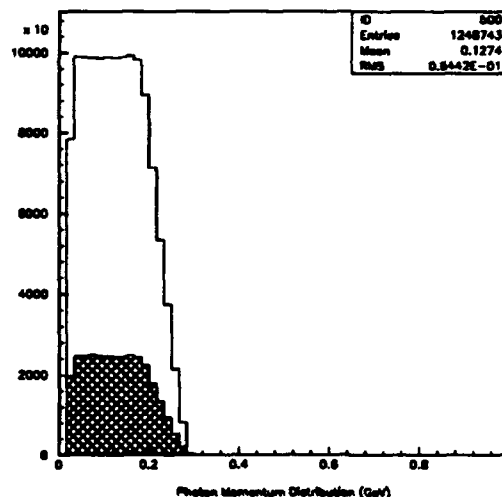


Fig. 3(a). Distribution of photons from $K_0 \rightarrow \pi^0 \pi^0$ for the symmetric case. Photons accepted into the $\pm 60^\circ$ calorimeter are indicated in the shaded region.

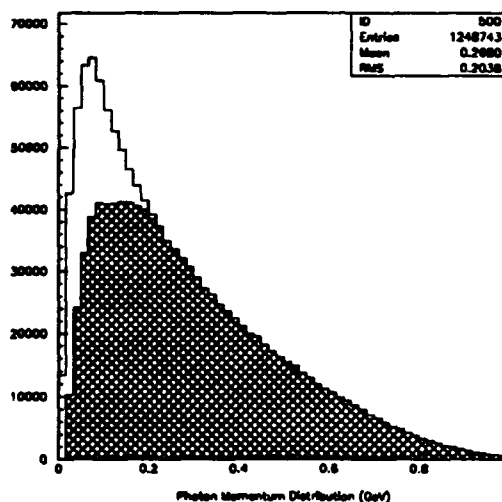


Fig. 3(b). Distribution of photons from $K_0 \rightarrow \pi^0 \pi^0$ for an energy asymmetry of 20:1. Photons accepted into the $\pm 60^\circ$ calorimeter are indicated in the shaded region.

Table 1. Linac-on-Ring ϕ Factory Parameters			
		e^+ Ring	e^- Linac
E	GeV	0.13	2
s_B	m	9	9
I	Amps	0.77	0.0018
ϵ_x, ϵ_y	nm	10, 2	1, 1
β_x, β_y	cm	0.65, 0.13	6.5, 0.26
ξ_x, ξ_y		0.05, 0.05	13.8, 2.78
$r = \sigma_y/\sigma_x$			0.2
L_0	$\text{cm}^{-2} \text{s}^{-1}$		10^{33}
L	$\text{cm}^{-2} \text{s}^{-1}$	0.2×10^{33}	

to suggest some strengths and weaknesses of each, especially with regards to creation of high luminosities ($L \approx 10^{33} \text{ cm}^{-2} \text{s}^{-1}$) at the mass of the ϕ ($E_{\text{cm}} = 1020 \text{ GeV}$).

The linac-on-ring option may be the most economical. New technologies make the the 2 GeV linac seem reasonable, as would be a 0.13 GeV ring. The converse, beam collisions from a high energy e^+ ring on a lower energy e^- linac have been studied as an option for B-Factories [5, 6]. Some work suggests an instability would develop in the ring beam from jitter in the linac beam, for the high energy ring case [7], which would also be a problem for the low-energy ring case.

For collisions in the low-energy ring, the luminosity is limited by the beam-beam tune shift of the positron beam. Table 1 gives some parameters used to give an approximate luminosity of $10^{33} \text{ cm}^{-2} \text{s}^{-1}$. The variation of the longitudinal distribution during the collision, the "bow-tie" effect, for $\sigma_x \sim 1 \text{ cm}$, decreases this to $0.2 \times 10^{33} \text{ cm}^{-2} \text{s}^{-1}$. The luminosity without this effect is given by

$$L_0 = 2.17 \times 10^{34} \xi^+ (1+r) (EI/\beta_y^*)^+ \text{ cm}^{-2} \text{s}^{-1} \quad (3)$$

where ξ is the beam-beam tune shift, r is σ_y/σ_x , E is the energy in GeV, I is the current in Amps, β_y^* is given in cm, and the beams sizes are transversely matched. To regain this lost factor, short bunches are desired such that σ_x/β_y^* is of the order unity. Using the smaller energy asymmetry of 10:1 and doubling the β_y^* would decrease the bow-tie effect and increase the luminosity. Smaller bunch lengths might also be possible in the ring using strong RF and/or a lower momentum compaction factor.

The parameters in Table 1 push the state of the art in several places. The emittances for the e^+ bunch in the ring are small for such a high current, low energy beam. Also the frequency with which the linac must deliver electrons to the interaction point is quite large. This could be achieved with many bunches in the linac for a single RF fill time, by using a superconducting linac. A microtron accelerator might also be used to deliver low current, small emittance bunches with a 9 m spacing.

The linac-on-linac option, or linac-on-ring with collisions outside the ring, would avoid the above beam-beam tune shift limit on the positron beam. This allows the linac intensity to increase, however the lost collision frequency drastically decreases the luminosity. This assumes that

the positrons are created and damped after each collision. Efficient, effective recirculation of the positrons after collision would increase the collision frequency increasing the luminosity.

For the ring-on-ring, the luminosity is reduced because the positron current must be lowered in order to keep the electron tune shift below 0.05. The positron current is limited to 0.0138 Amps giving a luminosity of $L \approx 2.6 \times 10^{31} \text{ cm}^{-2} \text{s}^{-1}$, where all the other parameters are the same as in Table 1.

We have not made an attempt to do more than discuss superficially the different options for a ϕ factory with an energy asymmetry of 20:1. However, the particle physics that can be accomplished at an asymmetric ϕ factory is compelling and complimentary to the program at the Frascati symmetric ϕ Factory. No real conclusions can be made now about the best kind of collider to use, though it is clear that all the options presented above would need to push technological limits to reach the desired luminosity of $10^{33} \text{ cm}^{-2} \text{s}^{-1}$.

REFERENCES

- [1] D. Cline, "A New Concept for an Asymmetric ϕ Factory to Test CPT and Study K_s^0 Mesons", in the *Proceedings of the XXVI International Conference on High Energy Physics*, Dallas, August, 1992; D. Cline, "Asymmetric ϕ Factories to Test CPT and Quantum Mechanics", to be published by World Scientific Press (1993).
- [2] *Workshop on Asymmetric ϕ Factory Design*, UCLA, October (1992); *Workshop on Asymmetric Flavor Factory Design*, UCLA, April (1993).
- [3] David S. Robin, *Quasi-Isochronous Storage Ring Colliders: Energy Density Enhancement as a Route to High Luminosity*, UCLA Ph. D. Thesis, UMI-92-15742-mc, 1991.
- [4] P. Eberhard and S. Chattopadhyay, "Asymmetric ϕ Factories—A Proposed Experiment and its Technical Feasibility", in *Proceedings of the 15th International Conference on High Energy Accelerators*, Hamburg, Germany, July, 1992.
- [5] P. Grosse-Weismann, "Colliding a Linear Electron Beam with a Storage Ring Beam", *Nucl. Instrum. Methods*, A274, 21 (1989).
- [6] B. Norum, "Studies of a Linac-Ring B-Factory", talk presented at *Workshop on Asymmetric Flavor Factory Concepts*, UCLA, April 2, 1993.
- [7] C. D. Johnson, "The Incoherent Beam-Beam Effect in Linear-on-Ring Colliders", in *Proceedings of the IEEE Particle Accelerator Conference*, San Francisco, California, May, 1991.

Status of the MIT-Bates South Hall Ring Commissioning*

J.B. Flanz, K.D. Jacobs, B. McAllister, R. Averill, S. Bradley, A. Carter,
K. Dow, M. Farkondeh, E. Ihloff, S. Kowalski, W. Sapp, C. Sibley, D. Tieger,
C. Tschalaer, A. Zolfaghari
MIT-Bates Accelerator Center
P.O. Box 846, Middleton MA 01949 USA

I. INTRODUCTION

The MIT-Bates South Hall Ring construction project is now nearly complete. At this time the Energy Compression System, the SHR Injection Line and the South Hall Ring itself are complete. The SHR Extraction Line is complete but has not been connected to the ring. Commissioning with beam of the completed beam lines has been started.

The MIT-Bates South Hall Ring (SHR) is an electron storage ring used with the 1 GeV Bates electron accelerator [1] to increase the effective duty factor and luminosity. A beam can be stored for use with an internal target, thus allowing for high duty factor, high luminosity experiments. External beams with high duty factor can be obtained using resonant extraction. References [2] and [3] describe some aspects of the SHR design features. A layout of the 190m circumference ring and associated new beam lines is shown in figure 1.

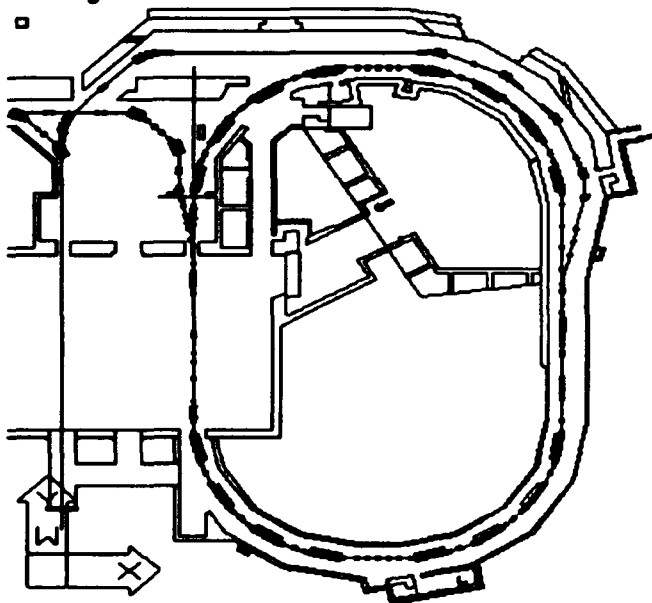


Figure 1. SHR Layout, Injection from the left.

The new systems associated with the SHR include the Energy Compression System (ECS)[4], the Injection line, and the Extraction line. We have commissioned the

ECS, the new injection line and the SHR without Rf. This includes transporting beam, measuring beam phase space parameters, using critical injection elements including a high voltage electrostatic septum, and a fast beam kicker, and storing a beam in the SHR.

II. Injection Line Commissioning

The injection line directs the beam to the ring and prepares the beam phase space for appropriate SHR injection. It uses two achromatic bends and a phase space telescope as shown in figure 1. The instrumentation in the injection line allows automatic phase space measurements and adjustment for optical matching to the ring.

Beam has been transported through the injection line to the ring. The phase space has been measured and adjusted with the appropriate quadrupoles [5]. The method of phase space measurement includes the vary quad technique [6], and using three lutes within the beam line [7]. Part of the commissioning studies has been devoted to understanding the sensitivities of these measurements. The measurements have verified a beam emittance of 0.02π mm-mrad at 330 MeV, with beta functions below 100 meters.

III. ECS Commissioning

The ECS uses a four dipole chicane and accelerating section to convert energy spread to phase spread thereby reducing the beam energy spread and energy centroid fluctuation. Thus far there has been one shift devoted to ECS commissioning. The results in that time have been very encouraging. A target was used at a location with high dispersion (10cm/%) to observe the beam spot. The beam was transported through the ECS without complication. The resulting beam spot is shown in figure 2 below. The energy defining slits were set to allow

transmission of a beam with energy spread of 0.4%. The beam spot on target was consistent with that.

Turning on the Rf power to the appropriate level for energy compression resulted in a reduction of the beam spot size as shown in figure 3.

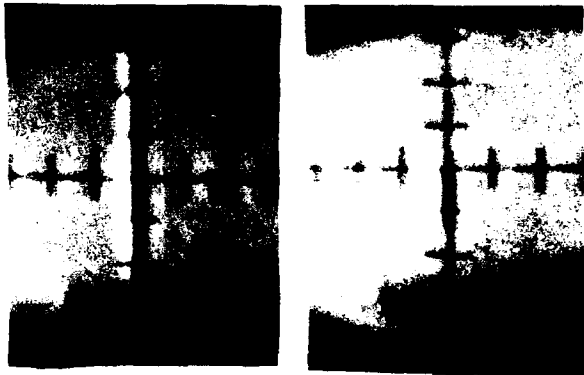


Figure 2 and 3. Dispersed beam spot without and with ECS Rf

The final energy compressed beam spot size was consistent with about 0.04% full energy spread. However this spot size was also consistent with the monochromatic beam spot size. This was proven by reducing the opening of the energy defining slits without seeing a further reduction in the beam spot size.

IV. SHR Commissioning

The SHR has sufficient hardware and controls for initial beam injection and storage studies. This includes one magnetic and one electrostatic septum for injection, and a fast (20nsec) kicker with a 1.3 usec flatop. Ten button type BPMs and ten low impedance stripline type BPMs [8] were installed along with 11 TV flip targets. There were six sets of BPM electronics. Without Rf, it was expected that the storage time would be determined by synchrotron radiation losses. At the 330 MeV injected beam energy and a $\pm 0.8\%$ energy aperture, this corresponds to roughly 23000 turns or about 15 msec of beam storage time.

A. First Turn

Transporting beam for the first turn was straightforward. All quadrupoles were set at design values. Once the dipole values were set in the first 90° arc, the dipoles in the other arcs were set to the same values. The beam was transported easily (with

minimal steering corrections) to each screen. It was found that in one arc, three quadrupoles (out of 85 installed in the ring) were incorrectly wired. The entire procedure lasted a few hours and the beam was successfully transported through one turn.

B. Storage

The first turn was accomplished using a pair of steering correctors to obtain the required kick. Even so, the first turn beam immediately appeared to circulate three turns (with some beam loss). With a small adjustment of the closed orbit (ring correction dipoles) the beam circulated for several turns.

When the kicker was activated and properly timed, the beam stored for several milliseconds. With appropriate matching of the beam energy and the SHR dipole settings and closed orbit adjustments, the beam was stored for a time consistent with synchrotron radiation losses or about 30,000 turns. The total procedure lasted several hours.

Examination of the beam storage behavior with the instrumentation available proved useful. Figures 4, 5 and 6 below, show the stored beam using three different monitors. One of these monitors was a toriod current transformer. This measured the AC component of the current in the ring. Another monitor used was a BERGOZ DCCT which had a response time of several microseconds and measured the DC current. The third was a BPM which was sensitive to the rf structure of the beam and responded only as long as the rf structure was sufficient. The SHR has a momentum compaction of 0.029 and therefore it was not expected that this signal would last long.

The DCCT showed a constant current stored in the ring until the synchrotron energy losses caused the beam to be lost on the walls in the region of large dispersion. The toriod showed no visible losses in the first hundreds of turns. The toriod did indicate a pulse shortening (which was reduced when using the ECS). This may be indicative of a time dependence of beam energy in that region. The current output from the BPM lasted for a few milliseconds, longer than had been expected. However this is not inconsistent with; a) a smaller energy spread of the beam within a single pulse

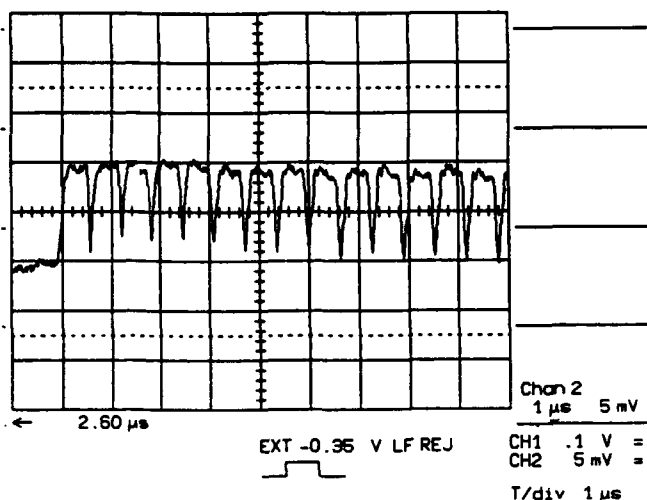


Figure 4. Toroid signal of stored beam current for first several turns.

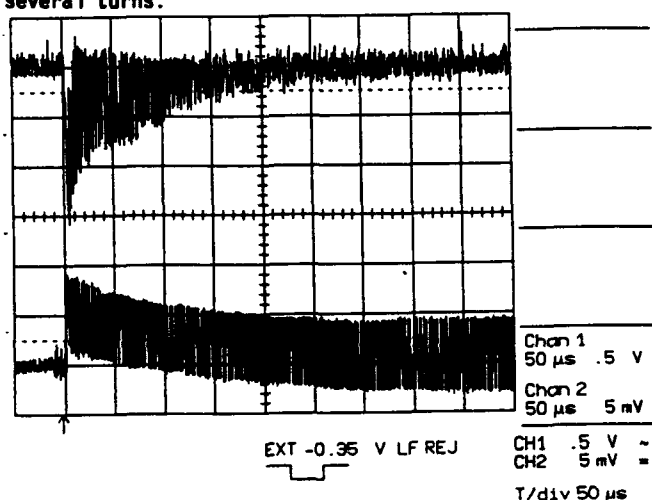


Figure 5. Upper trace is beam current signal from stripline BPM, lower trace is current signal from toroid.

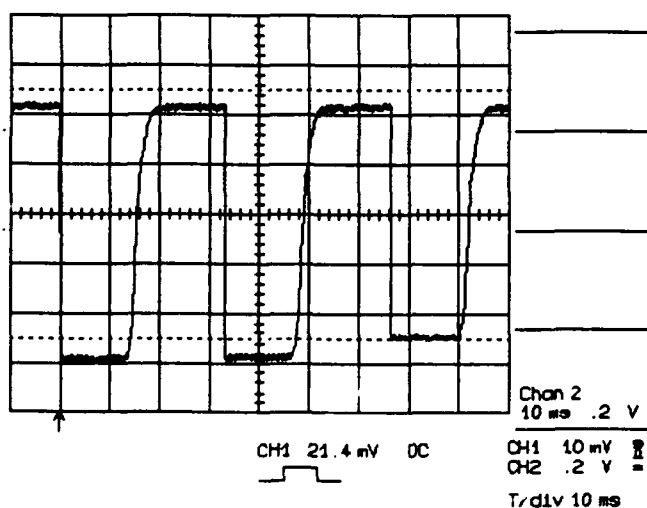


Figure 6. Current signal of Stored Beam from DCCT for three successive injections.

than the average energy spread integrated over many pulses (as the energy spread is normally characterized) or b) a larger component of the charge located in a smaller part of the longitudinal phase extent of the beam. Tests were made with up to 40 mA peak injected current.

V. Plans

The ring rf cavity has recently been completed and delivered. When installed storage times will no longer be limited by synchrotron losses and can be measured. The second fast kicker which will allow two turn injection is nearly completed. Within a few months, this will allow commissioning with the full design 80 mA. The SHR octupoles are currently under test and the extraction septa are also under construction. Within a few months the first extraction studies should commence.

VI. References

- * Work supported by the US Department of Energy
- [1] J. Haimson, Linear Accelerators, eds., P. Lapostolle and A. Septier (North-Holland, Amsterdam, 1970) ch B.3.2.
- [2] J.B. Flanz et. al., Proceedings 1989 IEEE Particle Accelerator Conference p34, (1989).
- [3] J.B. Flanz and C.P. Sargent, IEEE Trans. Nucl. Sci., Vol NS-32, No. 5 p 2444 (1985).
- [4] J.B. Flanz, P.T. Demos, K.D. Jacobs and A. Zolfaghari, Proceedings 1991 IEEE Particle Accelerator Conference p601, (1991).
- [5] K.D. Jacobs, B. McAllister and J. Flanz, These Proceedings.
- [6] M.C. Ross, N. Phinney, G. Quickfall, H. Shoaee, and J.C. Sheppard, SLAC-PUB-4278, March 1987
- [7] K.D. Jacobs, J.B. Flanz and T. Russ, Proceedings 1989 IEEE Particle Accelerator Conference p1526, (1989).
- [8] J.B. Flanz et. al. These Proceedings.

CURRENT STATUS OF THE DESIGN OF THE KHARKOV PULSE STRETCHER RING PSR-2000

S. Efimov, P. Gladkikh, Yu. Grigor'ev, I. Guk, I. Karnaukhov, V. Kozin, S. Kononenko, V. Likhachev, V. Markov, N. Mocheshnikov, V. Moskalenko, A. Mytsykov, Yu. Popkov, A. Shcherbakov, M. Strelkov, A. Tarasenko, Yu. Telegin, A. Zelynsky

Kharkov Institute of Physics and Technology, 310108 Kharkov, Ukraine

M. Nagaenko, Yu. Severgin

Efremov Scientific Research Institute of Electrophysical Apparatus 189631, St.-Petersburg, Russia

Abstract

Structural and engineering designs of the PSR-2000 are completed on the whole. Stands for investigations magnetic, vacuum, RF elements as well as some experimental units are constructed. In the design, the first stage of realization is determined. It will allow us to obtain a continuous electron beam with energy of 1.5 GeV and average current of 5 μ A, and to start nuclear investigations in the existing experimental hall. Engineering and technological problems are discussed in this report.

I. INTRODUCTION

The currently central problem of the accelerator physics and engineering is the production of continuous electron beams of energies ranging from a few MeV to several GeV. Such beams are required for investigating the subnuclear degrees of freedom in the nucleus. The design work for the pulse stretcher ring PSR-2000 at the output of the operating at Kharkov 2GeV electron linac [1] was started several years ago. The basic design parameters of the setup have been given in [2,3]; the operation of the PSR-2000 in mode of low radiation emittance as a source of synchrotron radiation has been considered in [4]. By the present time the engineering aspect of the design is completed.

II. GENERAL DESCRIPTION AND DESIGN PARAMETERS

The magnet lattice of the PSR-2000 consists of four superperiods ensuring the achromaticity of straight sections. Each superperiod comprises 8 dipole and 12 quadrupole magnets. To compensate the chromaticity, each arc section has 4 sextupole lenses, and each straight section comprises one sextupole lens to adjust the amplitude and the phase of the 16th harmonic of the sextupole field during a slow extraction at the third-order resonance. The detuning of betatron oscillations and adjustment of the angle of extraction are corrected by means of pulsed quadrupole and sextupole lenses. The achromatic and chromatic regimes of slow extraction were optimized by the use of the DeCA package [5]. The beam injection to the ring is carried out with septum magnets bringing the beam on the reference orbit perturbed by three pulsed bump magnets. The reference orbit in the two planes was corrected with 30 dipole correctors.

The RF system is based on 4 sections, each consisting of Ω -shape cell. The operating frequency is 699.3MHz, the

power of each of four klystrons is 100 kW, the accelerating voltage is 3 MV. The beam parameters are monitored by pickup stations, RF and magnetoinduction transducers, against synchrotron radiation, etc. The basic structural material of the vacuum chamber is an aluminum alloy. The chamber is elliptical in the cross section, the semiaxes being 70 and 19 mm. In the dipole magnets of the storage ring the chamber with an antichamber is used. The PSR-2000 design incorporates the arrangement of an internal jet target with an appropriate detecting equipment, the systems of photon tagging and monochromatic gamma-photon beam production through Compton interaction of laser light with the electron beam. The main parameters of the PSR-2000 are presented in Table 1.

Table 1

Parameter	Stretching mode	Low rad. emittance mode
Beam energy, GeV	0.5...3.0	0.75...2.5
Stored current, mA (multibunch mode)	140	400
Average current, μ A	30	-
Emittance, mrad		
-horizontal	10^{-7}	$(2...15) 10^{-8}$
-vertical	10^{-8}	$(2...15) 10^{-9}$
Duty factor	0.9	-
Energy spread, %	0.1	-
Momentum compaction factor	0.048	0.021
Orbit length, m	214.78	214.78

The report on the state of the setup design has been presented at the European Particle Accelerator Conference EPAC-92 [6], but for the last year the project has undergone substantial changes due to the following circumstances. The realization of the project in its full scale would require, apart from the construction of the PSR-2000, the updating of the linear accelerator now in service and the construction of new experimental halls. In this connections, two stages are allowed for the implementation of the project. The first stage provides for a continuous beam of energy up to 1.5 GeV and a current up to 5 μ A. This can be reliably attained by using the linear accelerator-injector and the existing facilities in the operating experimental halls. The setup is mounted in a

skeleton-type structure, which also comprises two halls for conducting synchrotron radiation experiments. The design of the structure is such that it allows its subsequent development as needed. Besides, we have adopted in the project the concept of a demontable biological shield. This allows us to start the commissioning of the facility at a shield thickness of 1m, with its further build-up as the beam intensive grows. In the sections where the beam losses exceed the average value, the local shield is built. The general arrangement of the PSR-2000 units at the 1st stage is shown in Figure 1.

III. CURRENT STATUS OF THE PSR-2000

The development of the 1st stage of the PSR-2000 construction is completed. All equipment necessary for commissioning the setup is devised. Test beds are created to investigate magnetic systems, vacuum and RF systems as well as diagnostics tools. Pilot samples of the 699.3 MHz RF klystron with a meanpower of 100 kW as well as the vacuum chamber of beam transport lines and straight sections of the ring are made. Machine-tool attachment are made to fabricate the dipole-magnet vacuum chamber. The scale models of beam diagnostics components are made.

IV. CONCLUSION

The design work in extent necessary for realizing the scope of the 1st stage is completed. Now the pilot components are being fabricated, though at not such a good pace as desired, this being due to many economical difficulties. The realization of the project will depend on how successfully the problems of financing the setup construction and fabrications of the equipment will be solved.

V. REFERENCES

- [1] V.A.Vishnyakov, A.N.Dovbnya, G.K.Dem'yanenko, et al. Kharkov electron linac as an injector for a stretcher ring. Proc. of the III Linear Acc. Conf., Stanford, 1986, p. 576-580.
- [2] V.F.Boldyshev, V.A.Vishnyakov, P.I.Gladkikh, et al. A design of 3GeV CW Electron Accelerator Facility. Proc. IEEE Part. Acc. Conf., Washington, D.C., 1987, New York, 1987, p. 883-886.
- [3] P.I.Gladkikh, V.Yu.Gonchar, Yu.N.Grigor'ev, et al., PSR-2000. The Pulse Stretcher Ring for the Kharkov Electron Accelerator. Preprint KhFTI 90-22, Moscow, Atominform, 1990, 34p.
- [4] S.V.Efimov, P.I.Gladkikh, Yu.N.Grigor'ev, et al. PSR-2000. The Mode of Low Emittance Operation. The Program of SR Investigations, Rev. of Sci. Instr., v.63, N1(part IIA), 1992, p.385-388.
- [5] A.Zelinsky, P.Gladkikh, M.Strelkov, et al., New version 3.3 of the DeCa code. Proc. EPAC-92, v.1, p.685-687.
- [6] S.Efimov, P.Gladkikh, Yu.Grigor'ev, et al., The Pulse Stretcher Ring PSR-2000. Current Status. Proc. EPAC-92, v.1, p.453-455.

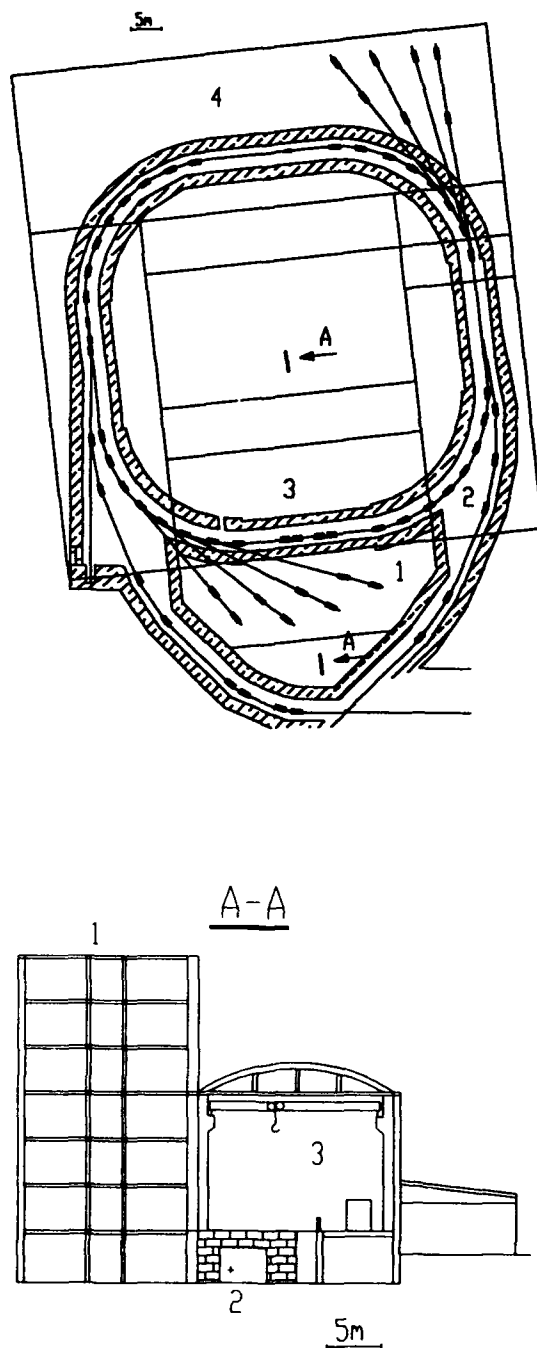


Figure 1. Layout of the PSR-2000. 1 - laboratory with underground synchrotron radiation hall; 2 - PSR-2000 ring; 3 - main hall; 4 - synchrotron radiation hall.

Moscow State University CW Race-Track Microtron Status

V.I.Shvedunov, A.S.Alimov, A.S.Chepurinov, O.V.Chubarov, I.V.Gribov, B.S.Ishkhanov,
I.V.Surma, A.V.Tiunov.

INSTITUTE OF NUCLEAR PHYSICS, MOSCOW STATE UNIVERSITY
119899 MOSCOW, RUSSIA

I. INTRODUCTION

Continuous wave (CW) race-track microtron (RTM) with the maximum output energy of 175 MeV and beam current 100 mcA is under construction at the Institute of Nuclear Physics of Moscow State University [1]. The main parameters of the RTM are listed in Table 1, its plan view is shown in fig. 1.

Table 1. The main parameters of the RTM

Injection energy	6 MeV;
Energy gain per pass	6 MeV
Maximum number of passes	27
Output energy	24-175 MeV
Energy spread	$10^{-3} - 10^{-4}$
Transverse beam emittance	0.05 mm \times mr
Maximum current	100 mcA
Increase of orbit circumference per turn	1 λ
Distance between end magnets	10 m
End magnet field	1.027 T
End magnet weight, each	18 t
Length of linac	6.24 m
Effective shunt impedance	78 MOhm/m
Number of klystrons	12+1
RF frequency	2450 MHz
Total rf power consumption	205 kW

II. RTM DESCRIPTION.

The cw RTM consists of the following main systems: injector, consisting of electron gun, chopper-buncher, capture section and preaccelerator; injection transport line; main linear accelerator located between two 180° end magnets; rf system; cooling and thermoregulating system; beam monitors; control system.

The electron gun beam with the energy of 100 keV passes through the chopper-buncher system and then is accelerated in the capture section and preaccelerator up to the energy of 6 MeV. The 6 MeV beam enters the main linac. After the first acceleration up to 12 MeV the beam is reflected and accelerated in the opposite direction up to 18 MeV. Then the beam enters the first orbit of recirculation. This scheme allows us to provide sufficient beam clearance from the linac on the first orbit. Compensation of beam displacement, because of the influence of the injection magnet M8 and mirror magnets M9, M10, is achieved by means of correct choice of effective lengths and fields of M11 and M12 magnets.

Electron gun [2] consists of a large anode and focusing electrodes confined in a cylinder with the diameter of 300 mm made of magnetic steel which serves as a magnetic shield and vacuum vessel. High voltage and heating current are supplied through a special cable with high voltage conjunction. Cathode, made of impregnated tungsten, has a 3.2 mm diameter of active surface. Measured beam emittance at the energy of 100 keV is 5.8 mm \times mr [3]. Maximum beam current is 10 mA, high voltage stability ± 0.1 keV.

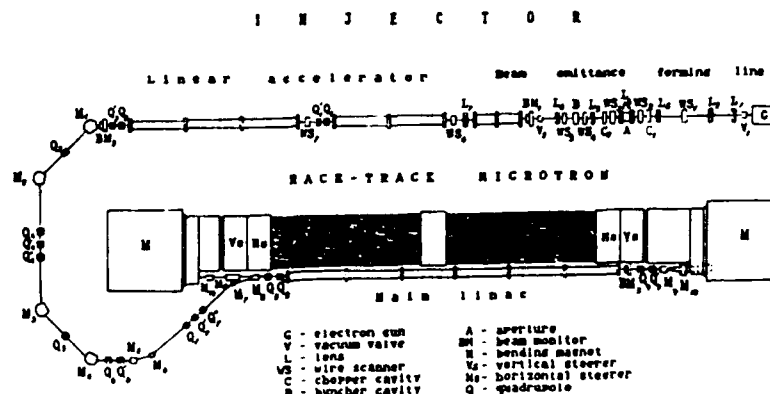
The beam parameters are controlled by wire scanners [4], luminescent screens and by rf beam position, current and phase monitor [5].

Chopper - buncher system is intended for forming electron bunches of 10^0 bunch length, ± 2 keV energy spread, 4 - 5 mm \times mr transverse emittance, and 100 mcA mean current from 100 keV continuous electron beam [6].

Two types of accelerator structures were tested for RTM project - an on-axis coupled structure and a disk and washer structure (DAW) with radial stems. The results of

Fig. 1.

Plan view of the cw race-track microtron.



investigation of DAW structure are described in ref. [7]. During these investigations the problem of parasitic modes was solved, but considerable reduction of effective shunt impedance ZT^2 of this structure because of the radial stems makes it difficult to use this structure for cw machines.

An on-axis coupled structure was adopted for RTM project. The calculated values of the quality factor and the effective shunt impedance $Q=17500$, $ZT^2=92$ MOhm/m, respectively [8,14]. This calculation doesn't take the influence of the coupling slots into account.

The schematic view of a standard accelerating section, which is comprised of 17 accelerating and 16 coupling cells, is shown in fig. 2. The section is cooled through 40 circumferential 4 mm-diameter channels bored along the axis on the periphery of the cells; the rf power input cell is cooled separately. For field control, a rf probe, located at the rf power input cell, is used. Plungers for resonant frequency tuning are absent.

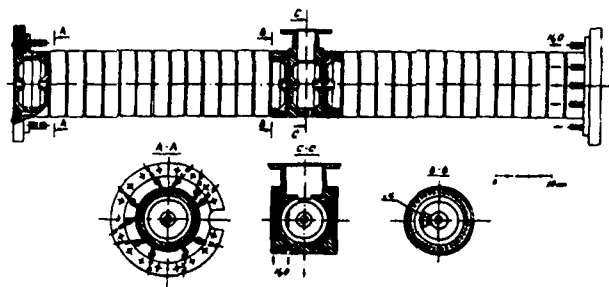


Fig. 2. Construction of accelerating section.

The first neighbour coupling constant of 4.4 % was obtained with the coupling slots located at the cavities' webs, one slot for each web, having an azimuthal span of 55.6° . The orientation between adjacent coupling slots is 180° . The tuning of the cells was carried out by lathe turning before brazing and by deforming the webs of the detuned cavities after brazing. Total number of fabricated sections with $\beta=1$ is 11. The measured effective shunt impedance for all the sections is 78 ± 3 MOhm /m and intrinsic quality factor is $15\,000 \pm 500$.

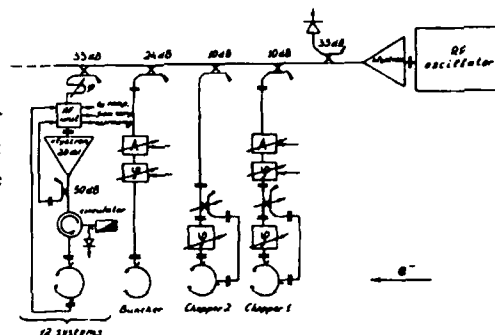
A block diagram of the rf power supply system [9] is shown in fig.3. The reference signal, which is generated at the rf frequency of 2449.600 MHz by a stabilized oscillator excites a 3 kW klystron. The klystron output power level may be changed by a computer controlled attenuator. Chopper cavities C1, C2 and the buncher B are excited from the reference signal line through directional couplers with 10 dB, 10 dB, and 24 dB attenuation, respectively. The klystrons supplying the accelerating sections are excited through directional couplers with 33 dB attenuation.

Each of the rf power supply channels, one for each accelerating section, has a phase shifter, a rf unit, a klystron, a circulator with water dielectric load, and a directional coupler for controlling incident wave.

The rf unit is made up on the basis of microstrip rf devices such as a p-i-n attenuator, a phase shifter in the

Fig. 3.

Block-diagram of the RF power supply system:
 ψ - phase shifter,
 A - attenuator.



form of a meander line on a ferrite layer, two phase detectors combined with phase shifters for selecting the phase detectors operating points, several diodes, a 5 W rf amplifier and other rf devices. The rf unit forms the klystron input signal as well as signals for phase, amplitude and resonant frequency control systems of the linac, made as local analog computer control subsystems. An important function of the rf unit is to ensure a simple and straightforward start-up of the accelerating sections [10].

The basic klystron parameters are listed in table 2.

TABLE 2

Operating frequency	2450 MHz
Maximum output power	22 kW
Gain	40 dB
Efficiency	55 %
Beam voltage	10 kV
Beam current	4 A
Focusing	By permanent magnets

The construction of bending magnet is shown in fig.4. It consists of main yoke, reverse field yokes, poles, separated from the main yoke by homogenizing air gap, the main coils, and reverse field coils. Sheems are placed in air gaps between main yoke and poles. The configuration and mass of main yoke, position of reverse field yokes, thicknesses of air gaps, sheems and poles were optimized by "FEM12B" code [11]. The height of poles' gap was chosen to be 60 mm in order to leave enough space for

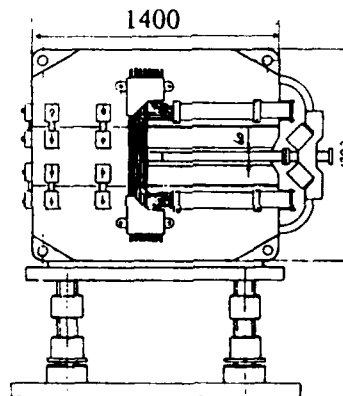


Fig. 4. Construction of bending magnet.

vacuum chamber and correcting plates. The size of poles is 1500x700 mm. Magnets were fabricated from steel 10. Vacuum chambers were made of aluminum alloy. Special computer controlled coordinate table with Hall probe was designed for field measurements. The accuracy of probe movement by step motors in two directions is about 0.05 mm. The measurements of field uniformity are in progress.

Control system is described elsewhere [12]. The function of the control system of the microtron is to support means for an easy programming of accelerator's behavior, when being adjusted, and to meet requirements of experimental work. Local feedback loops are needed to control parameters of RF accelerating sections.

Performance of the 6 MeV injector is described in ref [13]. The injector linac (fig.1) comprises a capture section consisting of 17 accelerating cells of a biperiodic on-axis coupled structure with tapered β , and five accelerating sections of 17 accelerating cells each with $\beta=1$. The beam is focused by a solenoidal lens, L7, and a quadrupole pair, Q1 Q1'. In order to measure the beam energy and energy spread, a 45° dipole magnet is used. Fig.5 shows the beam photos after three accelerating sections, at the exit of the linac, and after the dipole magnet. In the last case, the beam energy was 6.2 MeV. The beam dispersion of 3.5 mm corresponds to the energy spread of ± 20 keV. The minimum energy spread of ± 15 keV was obtained at the energy of 6 MeV.

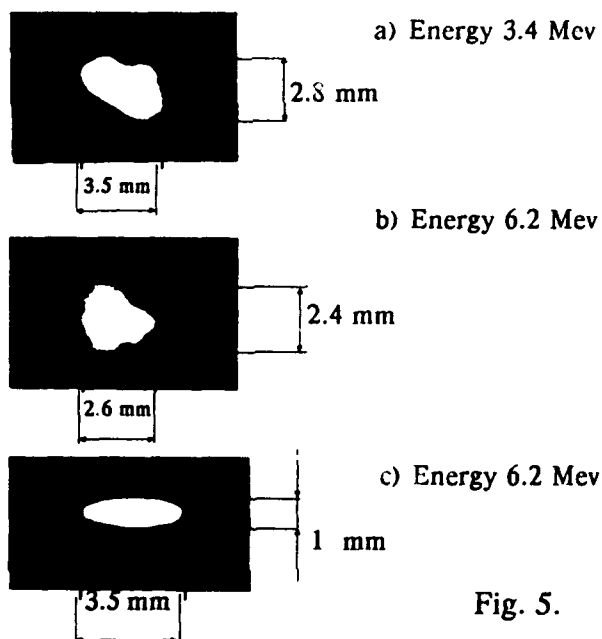
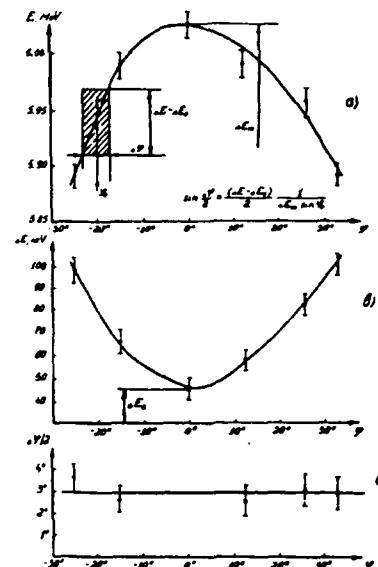


Fig. 5.

The dependence of beam dispersion from the last section accelerating phase was used to estimate the electron bunch phase length. Since, as far as such a bunch has a finite phase length, an additional energy spread occurs when the bunch is shifted relative to the last section accelerating field maximum. Fig.6 shows : a) beam energy,

Fig. 6. Calculated and measured dependencies of
a) energy of the beam;
b) energy spread of the beam;
c) phase length of the bunch, upon the phase of the last accelerating section.



versus the accelerating phase of the last section. The estimated bunch phase length is $6 \pm 2^\circ$.

REFERENCES :

- [1] Yu.I.Gorbatov et al. CW race-track microtron of the Institute of Nuclear Physics of Moscow State University (Physical Principles), MSU Editorial Board (1984), (IN RUSSIAN).
- [2] B.S.Ishkhanov et al., Radiotekhnika i Elektronika, V.31, no.1(1986)156 (IN RUSSIAN).
- [3] B.S.Ishkhanov et al. Priory i Tekhnika Eksperimenta, No.3 (1987) 24 (IN RUSSIAN).
- [4] I.V.Gribov et al. Priory i Tekhnika Eksperimenta, No.4(1989)37 (IN RUSSIAN).
- [5] A.S.Alimov et al. Priory i Tekhnika Eksperimenta, No.3 (1989) 28 (IN RUSSIAN).
- [6] A.S.Alimov et al. Nucl. Instr. and Meth. A278 (1989) 379.
- [7] V.K.Grishin et al. Nucl. Instr. and Meth. A255 (1987) 431.
- [8] V.K.Grishin et al. Preprint IHEP 84-116, Serpuchov 1984. (IN RUSSIAN)
- [9] A.S.Alimov et al. Proc. of the XI All-Union Meeting on Charged - Partical Accelerators, Dubna (1989) 230 (IN RUSSIAN).
- [10] A.S.Alimov et all. Start up procedure for cw multisection linear accelerators. USSR Patent No. 1709887, 1990.
- [11] V.K.Grishin et al. Preprint IHEP 86-145, Serpuchov 1986. (IN RUSSIAN)
- [12] I.V.Gribov et al. Proc. of the XI All-Union Meeting on Charged-Partical Accelerators, Dubna (1988) 132 (IN RUSSIAN).
- [13] A.S.Alimov et al. Nucl. Instr. and Meth. A326 (1993) 243.
- [14] A.S.Alimov et al. Nucl. Instr. and Meth. A328 (1993) 385.

Optical design of the 75 MeV Eindhoven Racetrack Microtron

G.A. Webers, J.L. Delhez, J.I.M. Botman, H.L. Hagedoorn
Eindhoven University of Technology
P.O. Box 513, 5600 MB Eindhoven
The Netherlands

Abstract

A 75 MeV racetrack microtron is being designed and constructed at the Eindhoven University of Technology. This microtron will serve as injector for the storage ring EUTERPE. The microtron contains two inhomogeneous bending magnets which are rotated in the median plane. In this paper we will present the optical design of the machine using a first order matrix theory to describe the focusing forces, including fringe field effects. Optimization of the machine acceptance in the horizontal and vertical plane yields the optimum shape of the magnet poles, which are currently under construction. The results from matrix theory are verified by numerical orbit tracking using the measured field map. Also an analysis of the effect of alignment errors will be given.

I. INTRODUCTION

At the Eindhoven University of Technology, a 75 MeV racetrack microtron (RTME) is being designed and constructed (see Figure 1). This microtron will serve as injector for the electron storage ring EUTERPE [1]. A similar RTM (25 MeV) is simultaneously being built for a FEL project [2]. The electrons are injected from a 10 MeV medical linac into the microtron and are accelerated in a 2998 MHz standing wave cavity with an accelerating voltage of 5 MeV. Two phase-locked 2.2 MW magnetrons will be used to power the 10 MeV injector linac and the cavity separately. This will be sufficient to accelerate 10 mA current. From numerical simulations it is seen that the accepted momentum spread $\Delta p/p$ is about 1% at injection (10 MeV), which is reduced to 0.15% at extraction (75 MeV).

The magnetic field consists of 2-sector magnets, separated by a drift space of 0.99 m. The dimensions of the magnets are $50 \times 150 \times 45 \text{ cm}^3$. The gap and magnetic field in sector I and II are respectively, 20 mm, 0.51 T and 17 mm, 0.60 T. This field increase is realized by pole shaping. Due to the magnet design there is a field dip, i.e. the magnetic field in the center is lower than the field near the edges. The magnets are rotated at an angle τ in the median plane to obtain proper 360° bending [3]. The dashed curve in the orbit pattern in Figure 1 shows where the high field region II will end, such that the exit angle at extraction is 2τ . The number of orbits is 13 and the orbit separation is 60.6 mm, which is sufficient for beam monitoring and steering.

At the front of the magnets, clamps are mounted to shield the magnetic field in the drift space.

The vacuum system will be made of aluminium and consists of a central vacuum chamber, two wedged shaped chambers and the vacuum boxes in the magnets. A 400 l/s turbo pump will be connected to the central vacuum chamber to obtain a pressure in the 10^{-6} mbar regime.

In the center of the microtron a correction magnet (CM) will be placed to correct the bending angle of each orbit separately. For beam diagnostics we will use Beam Position (BP) monitors.

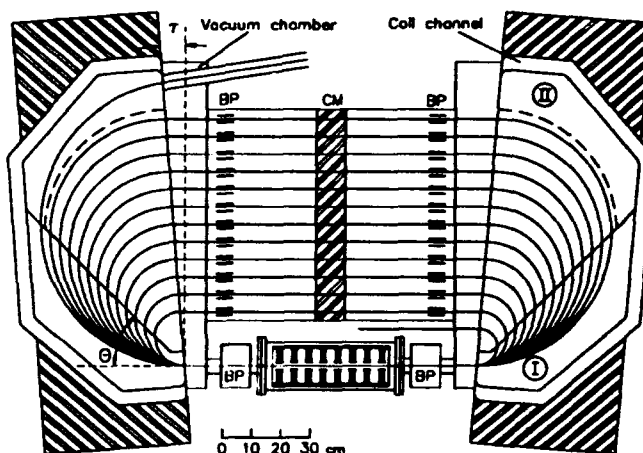


Figure 1: Median plane view of the Eindhoven Racetrack Microtron

Table 1: Main RTME parameters

RF frequency	2998 MHz
Drift length	0.99 m
Injection energy	10 MeV
Extraction energy	75 MeV
Accelerating voltage	5 MV
Number of orbits	13
Magnetic field (sector I/II)	0.51 T / 0.60 T
Mode number	2
Orbit separation	60.6 mm

The 2-sector configuration is described by the ratio $a = B_{II}/B_I$ and the angle θ between the boundary, separating sector I and II, and the cavity axis. The tilt angle τ is related to a and θ by the condition of 360° bending. The injection energy, accelerating voltage and magnetic field are related by the isochronism condition, i.e. the

path length of each orbit is an integer multiple of the RF wave length λ . The path length difference between two successive orbits is $h\lambda$ with h the mode number. In the case of the RTME we have chosen $h=2$ in order to limit the number of orbits and to have a sufficient orbit separation.

II. TRANSVERSE MOTION

The shape of the magnetic field is determined by the parameters a and θ . To estimate the optimum \hat{a} and $\hat{\theta}$, we optimized the machine acceptance using a first order matrix theory including the defocusing effect of the fringe fields [3]. Using a drift length of 0.99 m, we found $\hat{a}=1.17$ and $\hat{\theta}=45^\circ$ ($\tau=4.5^\circ$) which yields a horizontal acceptance of about 100 mm.mrad and a vertical acceptance of about 50 mm.mrad. The vertical acceptance is mainly limited by the mismatch in phase space between the injection orbit (10 MeV) and the first orbit (15 MeV), but this can easily be compensated by placing a quadrupole in the center of the microtron. The defocusing effect in the horizontal plane is small, but even this can be compensated by using a quadrupole doublet.

From the numerical calculations it is seen that the horizontal acceptance is (almost) not affected by a momentum spread $\Delta p/p$ in the range of -1%..1%.

As a check, we performed numerical orbit calculations and estimated the horizontal and vertical tunes ν_x and ν_z . As input we used a field map, generated from field profiles in 2D cross sections of the magnet. We used the analytical tool of conformal mapping [4] to estimate these profiles. In Figure 2 we plotted ν_x and ν_z versus energy for each orbit separately. In the range 20..70 MeV we see a good agreement between the theoretical results and the results obtained from numerical orbit tracking using the computer code HIATT [5]. The discrepancy in ν_x at lower energies is probably caused by the fringe fields which force a deviation of the reference orbit.

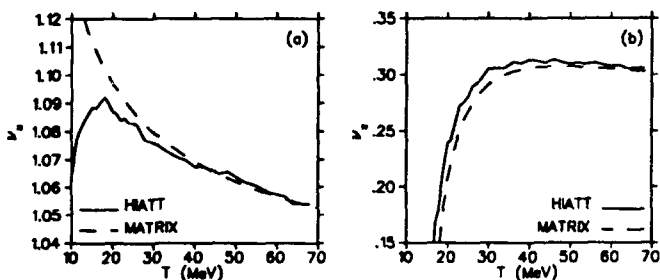


Figure 2: (a) ν_x and (b) ν_z versus kinetic energy T from numerical orbit tracking (solid) and 1st order matrix theory (dashed)

To estimate the effect of the realistic 3D magnetic field distribution we used the computer code RELAX3D [6] which solves the potential distribution, i.e. the magnetic field distribution for non-saturated cases. The results of this code for 2D cross sections are in good agreement with Conformal Mapping, but the accuracy of the 3D results

is limited by the number of mesh points, and will not be used therefore.

III. LONGITUDINAL MOTION

An important feature of a microtron is the longitudinal focusing effect which is obtained by proper timing of the injection process with respect to the RF wave in the cavity. To study the longitudinal motion, we solved numerically the difference equations. In Figure 3a we plotted the phase ϕ and energy spread ΔT at injection, which correspond to an extraction energy which is close (within 1%) to 75 MeV. In Figure 3b we plotted the corresponding phase space at extraction. Here we used a synchronous phase $\phi_s=9^\circ$ which gives a maximum separatrix area (area occupied in phase space at injection) of about 30 deg% at 10 MeV. The dashed curve is the separatrix as derived by a Hamiltonian derivation of the equations of motion.

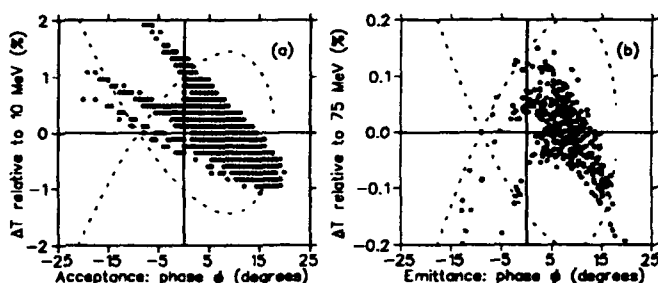


Figure 3: Longitudinal phase space at (a) injection (10 MeV) and (b) at extraction (75 MeV) with $\phi_s=9^\circ$

So far we neglected the effect that the relativistic velocity $\beta < 1$. Including this effect, the stable region in phase space at injection shifts towards smaller ΔT -values by 0.4%, but the separatrix area does not change.

Factors that may disturb the longitudinal motion are (i) path length deviations due to the field dip (3%) in the center of the magnet and (ii) (time-dependant) cavity voltage variations. The effect of the field dip is (partly) compensated by a (small) increase of the magnetic field. The remaining path length error is less than 6 mm and shows some oscillatory behaviour versus energy. From numerical simulations we see that the separatrix area is almost not affected by this remaining path length deviation. This implies that no isochronism corrections are required so we only need a central correction magnet for proper orbit bending.

Similar calculations have been performed for a cavity voltage variation $\Delta V/V$. For a constant voltage variation we find $\Delta V/V \leq 2\%$ is allowed in the case of the RTME. Including a harmonic voltage variation with frequency Δf and amplitude $\Delta V/V$, we find a maximum $\Delta V/V \approx 0.7\%$ at $\Delta f=1$ MHz and a maximum $\Delta V/V=0.3\%$ at $\Delta f=20$ MHz. Note that the latter affects each micro pulse since the revolution time is about $0.14 \mu s$ (7 MHz). Expected voltage variations, due to cavity tuning errors and generator power variations, are in the order of 1%.

IV. MEASUREMENTS

At this moment, the 2-sector magnets are available for magnetic field measurements. The measuring equipment consists of a Hall probe, mounted on a computer controlled X-Y table. In order to check the transverse optics, we measured the field map of one magnet in a mesh of 70x110 cm with mesh sizes of 10 mm in both directions. From numerical orbit tracking we see that the exit angles are about 30 mrad due to the field dip. This effect is (partly) compensated by adjusting τ to 3.6° . In this case, we find $\nu_x \approx 0.31$ and $\nu_z \approx 1.1$ in the range 20..70 MeV, which is in agreement with the design values. To obtain the matrix for a full acceleration process of 13 orbits, we estimated the transfer matrix for each orbit separately and added the matrix describing the cavity. The corresponding horizontal and vertical acceptance are plotted in Figure 4. Here the injection energy is varied while the extraction energy is fixed at 70 MeV, the last full orbit. The solid curves refer to the design values while the dashed ones are derived from the measured field map and we see a very good agreement.

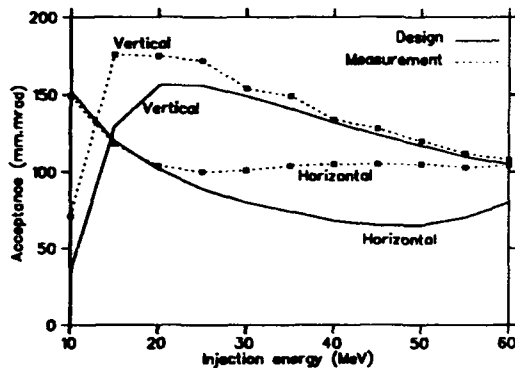


Figure 4: Horizontal and vertical acceptance versus injection energy. The extraction energy is fixed at 70 MeV

To check the numerical orbit tracking results, we used the Hall probe as reference particle and measured directly the orbit and its gradient. The tunes ν_x and ν_z estimated from these measurements are in agreement with the results given above.

V. MISALIGNMENTS

To study the effect of misalignments we used the description of Lobb [7] and extended this model to mechanical errors specific for our 2-sector geometry (δa , $\delta \theta$). Limiting ourselves to the horizontal motion, it is seen that δa (in the order of 1%) has by far the largest effect. In order to compensate an asymmetric δa (i.e. left and right magnet) we need for each magnet a separate correction possibility. A symmetric δa is easily compensated by choosing a different τ . This is still possible since the vacuum chamber is not constructed yet.

Compared to the alignment errors, the field dip of about 3% gives by far the largest contribution to the path length, total bending angle and exit position. Due to the small

gap it is not profitable to use correction coils inside the magnets and therefore we investigate the use of one central correction magnet. Since the effect on the longitudinal motion is small, we only need a correction magnet to bend at most 40 mrad at 45 MeV in the horizontal plane. Since we want to have the possibility to control each orbit separately, we designed an array of 12 (iron cored) magnets. A (part of the) cross section is shown in Figure 5 where the dots represent the designed beam center. Using a bending length of 12 cm and a gap of 2 cm, the maximum field is about 500 Gauss to correct for the field dip. From POISSON [8] calculations we have seen that the homogeneity in the center of each pole is about 0.5% within 10 mm. The magnetic field drops to about 1% in the neighbouring cell.

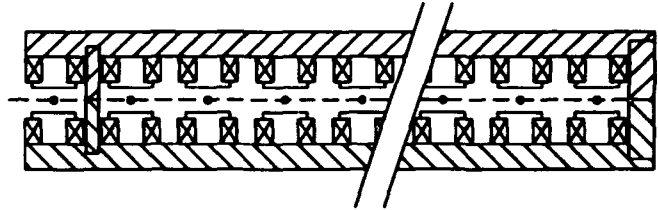


Figure 5: Designed central correction magnet

To estimate the optimum correction strengths we used the Least Squares Minimization method. It is found that, after one full turn, the path length difference with respect to the unperturbed case, is less than 2 mm, the orbit shift is less than 1 mm and the angle with respect to the cavity axis is less than 1 mrad, in the range 10..75 MeV.

VI. CONCLUSIONS

In this paper, we described the layout of a 75 MeV race-track microtron. The optical design is discussed and the effect of alignment/construction errors is mentioned. Magnetic field measurements have been done to check the theoretical design and a good agreement is found.

VII. REFERENCES

- [1] B. Xi et.al. - Nucl. Instr. and Meth. B68 (1992) 101-104
- [2] J.I.M. Botman et.al. - Nucl. Instr. and Meth. A318 (1992) 358-363
- [3] J.L. Delhez et. al. - Nucl. Instr. and Meth. B68 (1992) 96-100
- [4] G.A. Webers et. al. - Nucl. Instr. and Meth. B68 (1992) 83-86
- [5] G.A. Webers - 'HIATT users manual, TUE (1992)
- [6] C.J. Koest and F.W. Jones - 'RELAX user guide and reference manual', Computing document of Triumf, Vancouver, Canada (1988)
- [7] D.E. Lobb - Nucl. Instr. and Meth. 87 (1970) 59-72
- [8] M.T. Menzel and H.K. Stokes, 'User's guide for the POISSON/SUPERFISH Group of Codes', LA-UR-87-115 (1987)

Example Application for the Hamiltonian Description of an Azimuthally Varying Field Racetrack Microtron

J.L. Delhez, W.J.G.M. Kleeven, H.L. Hagedoorn, J.I.M. Botman and G.A. Webers,
Eindhoven University of Technology, P.O. Box 513, 5600 MB Eindhoven, Netherlands.

Abstract

A useful method for obtaining stable transverse motion in a (racetrack) microtron is the application of bending magnets with an azimuthally varying field (AVF) profile. A Hamiltonian theory has been set up to describe the reference orbit as well as the optical properties in both transverse directions for an AVF magnet with an arbitrary field profile. We recapitulate the main analytical results of the Hamiltonian theory and compare these to the results of numerical calculations for a relevant example AVF profile.

I. INTRODUCTION

For cyclotrons, it is well known that simultaneous horizontal and vertical orbit stability as well as isochronism can be achieved by subjecting the beam to an azimuthally varying magnetic field. We apply similar ideas to a (racetrack) microtron, i.e. we superimpose an azimuthally varying field (AVF) profile on the main average magnetic field of the bending magnets. When such magnets are designed properly, quadrupoles in the drift space and solenoids on the cavity axis are no longer needed to focus the beam.

As the modulation of the magnetic field is assumed to be small, a first order solution for the particle motion has been derived. In this paper, we will compare these analytical results with numerical calculations in order to verify the first order equations and to examine higher order effects.

II. ANALYTICAL RESULTS

In this section, we recapitulate the main analytical results, obtained in reference [1]. A schematic overview of the geometry is given in Fig. 1. We consider a bending magnet in a polar coordinate system (r, ϑ, z) . The median plane is the $z = 0$ plane. A test particle is injected into the magnet at the origin of the righthanded coordinate system (r, ϑ, z) . The median plane field B_z (pointing in the positive z direction) is assumed to depend only on ϑ and is split into a constant main field B_0 and a flutter profile $f(\vartheta)$

$$B_z(\vartheta) = B_0[1 + f(\vartheta)], \quad |f(\vartheta)| \ll 1, \quad 0 \leq \vartheta \leq \frac{1}{2}\pi.$$

We assume $f(0) = (df/d\vartheta)_0 = 0$. The pole edge where the beam exits the magnet is located at $\vartheta = \frac{1}{2}\pi$. Via a suitable choice of the vector potential, the magnetic field is incorporated in a relativistic Hamiltonian describing the

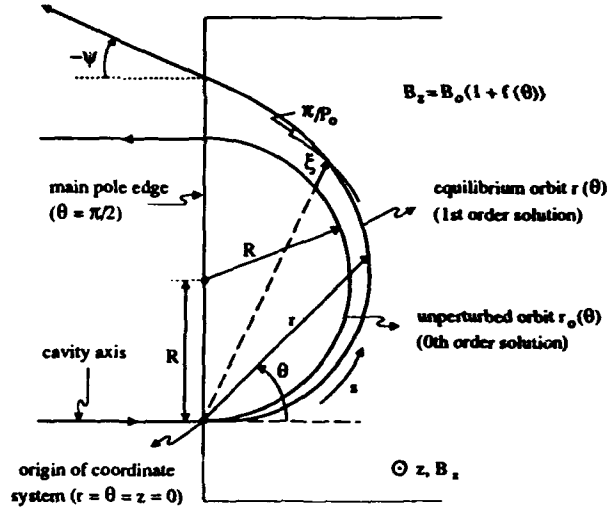


Figure 1: Schematic overview of the considered geometry.

median plane particle motion with ϑ as independent variable. From the solution for the equilibrium orbit up to first order we can derive expressions for the exit angle ψ (defined as the angle relative to the pole boundary normal vector) and orbit length s through the magnet. We obtain

$$\psi = -2 \int_0^{\pi/2} f(\vartheta) \cos(2\vartheta) d\vartheta,$$

$$s = R \left\{ \pi + \psi - 2 \int_0^{\pi/2} f(\vartheta) d\vartheta \right\},$$

where R is the reference radius, defined as $R = P_0/(eB_0)$, with e the electron charge and P_0 the total kinetic momentum. The angle ψ should normally be chosen zero for the sake of closed orbits.

The linear, transverse oscillations with respect to the equilibrium orbit, either horizontally (x) or vertically (z), are derived from Hamiltonians and can be expressed as phase space transfer matrices M_x and M_z

$$\begin{pmatrix} y \\ y' \end{pmatrix}_\vartheta = M_y(\vartheta) \begin{pmatrix} y_0 \\ y'_0 \end{pmatrix}, \quad y \in \{z, x\}, \quad y' = dy/ds.$$

In the present paper, we only consider the trace of the transfer matrices as a function of azimuth. These read

$$\text{Tr}^x(\vartheta) = 2 + [a - \frac{1}{2}(dF/d\vartheta)]\vartheta,$$

$$\text{Tr}^z(\vartheta) = 2 \cos(2\vartheta) - 2[G + \frac{1}{2}(dF/d\vartheta)] \sin(2\vartheta),$$

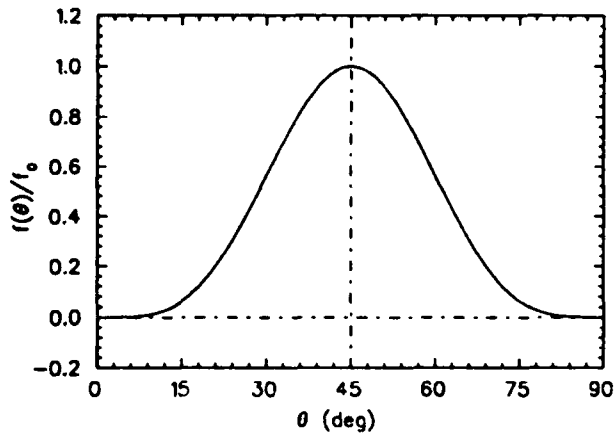


Figure 2: Shape of the applied AVF modulation.

with

$$F(\vartheta) = \frac{1}{\sin^2(\vartheta)} \int_0^\vartheta f(t) \sin(2t) dt, \quad G(\vartheta) = \int_0^\vartheta g(t) dt,$$

$$g(\vartheta) = 2f - 2F - \frac{1}{2 \tan(\vartheta)} \frac{df}{d\vartheta} - \frac{1}{8} \frac{d^2 F}{d\vartheta^2},$$

$$a(\vartheta) = - \int_0^\vartheta \left[\frac{2}{\tan(\vartheta)} \frac{df}{d\vartheta} - \frac{1}{2} \frac{d^2 F}{d\vartheta^2} \right] dt.$$

By evaluating the above expressions at $\vartheta = \pi/2$, we can find the matrix traces $\text{Tr}_{\pi/2}^y$ for half the revolution

$$\text{Tr}_{\pi/2}^x = 2 + \frac{1}{2} \pi \bar{a}, \quad \text{Tr}_{\pi/2}^y = -2,$$

with

$$\bar{a} \equiv a(\pi/2) = - \int_0^{\pi/2} \frac{2f(\vartheta)}{\sin^2(\vartheta)} d\vartheta.$$

Using the mirror symmetry of the equilibrium orbit (assuming $\psi = 0$), we can also derive the traces Tr_π^y for a full revolution through a 'classical' microtron (no drift space). We obtain in first order

$$\text{Tr}_\pi^x = 2 + 2\pi \bar{a}, \quad \text{Tr}_\pi^y = 2.$$

III. NUMERICAL CALCULATIONS

In order to check the above analytical first order results, exact numerical calculations have been done for various profiles. In this paper, we consider one specific profile and examine the effect of its amplitude on exit angle, orbit length and focusing properties in both transverse planes. The profile we consider is

$$f(\vartheta) = f_0 \sin^4(2\vartheta),$$

being a smooth hill ($f_0 > 0$) or valley ($f_0 < 0$), centered around $\vartheta = \pi/4$, see Fig. 2. For this specific profile, we obtain with our first order theory

$$\psi = 0, \quad s = \pi R(1 - 3f_0/8), \quad \bar{a} = -\pi f_0,$$

$$\text{Tr}_{\pi/2}^x = 2 - \frac{1}{2} \pi^2 f_0, \quad \text{Tr}_\pi^x = 2 - 2\pi^2 f_0.$$

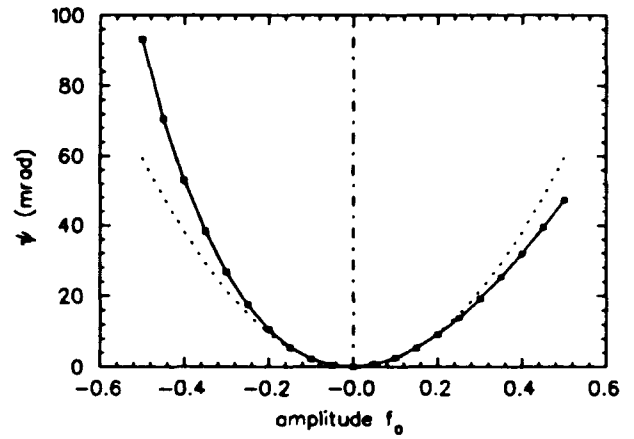


Figure 3: Exit angle ψ as a function of f_0 .

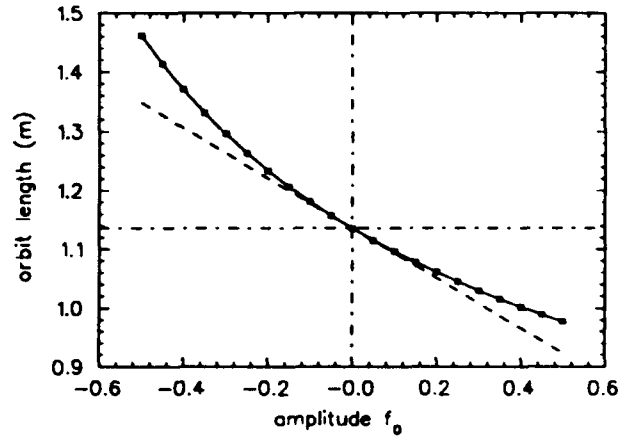


Figure 4: Orbit length s as a function of f_0 .

For the numerical calculations we consider the interval $-0.5 < f_0 < 0.5$ as to get a good view on effects higher order in f_0 . All calculations were done for $P_0 = 20$ MeV/c electrons and $B_0 = 0.19$ T.

Fig. 3 shows the exit angle ψ as a function of f_0 as obtained from numerical calculations. The curve has been fitted with a fifth order polynomial in f_0 . It turns out that there is no first order term, fully in accordance with our first-order result $\psi = 0$. The dotted curve represents only the second order term of the polynomial. From this we infer that a second order theory could give a much more accurate expression for the exit angle, hence also a more accurate condition for keeping the orbits closed.

In Fig. 4, the total orbit length is plotted against f_0 . The dashed, sloping line represents our first order result. It convincingly touches the numerical curve in $f_0 = 0$. The difference between both curves increases with increasing $|f_0|$, but once again, we see that this difference could be highly reduced by a second order description, as required for the sake of the isochronism condition.

The linear transverse motion in both transverse directions was numerically calculated as a function of azimuth. From the resulting matrices, the trace as a function of azimuth was extracted, its zero order part removed and the

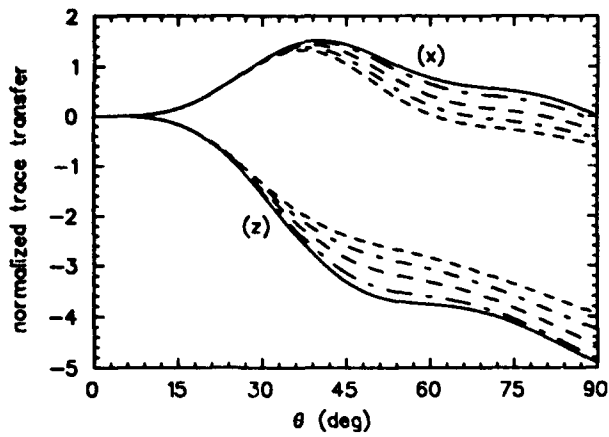


Figure 5: Normalized horizontal and vertical trace as a function of azimuth ϑ through a single magnet.

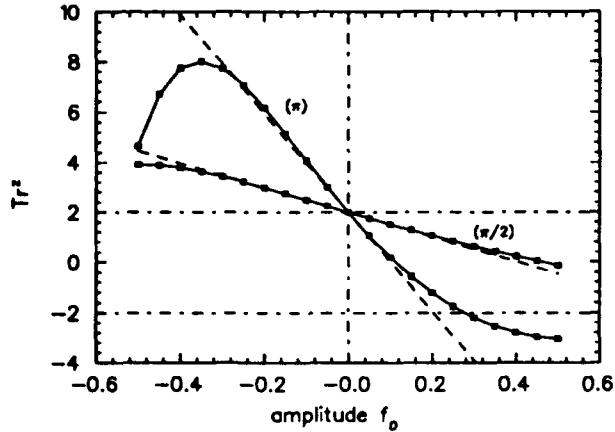


Figure 6: Vertical traces Tr^2_π , $Tr^2_{\pi/2}$ as a function of f_0 .

remaining part divided by the amplitude f_0 . The resulting curve (the 'normalized trace') is in first order independent of f_0 , hence any f_0 dependency represents higher order terms. The drawn lines in Fig. 5 are the normalized horizontal and vertical traces as a function of azimuth as derived from the first order theory. The dashed lines are the result of the numerical calculations for the cases $f_0 = 0.1, 0.3, 0.5$ and 0.7 . The higher order deviation gets larger with increasing f_0 , but the overall shape of the curves is retained and the values at $\vartheta = \pi/2$ are still very close to the first order result.

In Fig. 6, the matrix trace for vertical motion as a function of amplitude is shown. The two drawn curves represent the numerical results for half an orbit through a microtron (labeled $\pi/2$) as well as for a full orbit (π). The dashed lines represent our first order analytical results. The agreement for half the orbit is excellent over the entire amplitude range. For the full orbit, higher order effects become significant for amplitudes larger than 0.3. It is interesting to note that the numerically obtained curve for Tr^2_π bends back to the stable region for $f_0 < -0.3$; this means that for $f_0 \approx -0.55$, vertical motion can be stable again, but it is governed by higher order effects in f_0 and

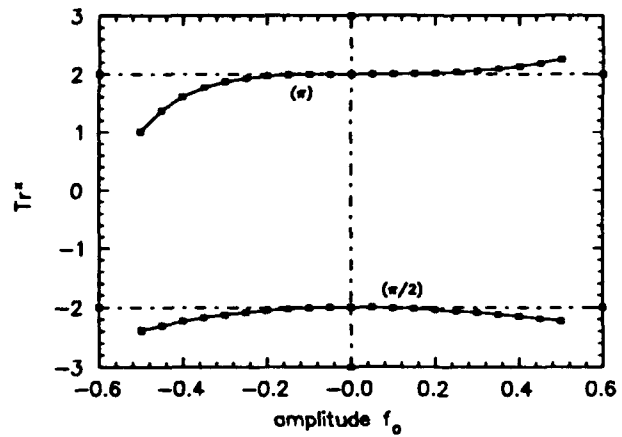


Figure 7: Horizontal traces Tr^2 as a function of f_0 .

therefore very sensitive to small changes in f_0 .

In Fig. 7, the matrix traces for horizontal motion as a function of amplitude are drawn. For half the orbit, we see that there is a weak second order contribution that moves the trace value outside the stable region for either sign of f_0 . For the full orbit, it was predicted by the first order theory that there could be no second order effect of f_0 on the trace [1]. Indeed, we see that the curve of Tr^2_π is antisymmetric around f_0 . A least squares fit of the results with a fifth order polynomial in f_0 proved that no second order term is present in the curve.

Combining the results of Fig. 6 and 7, we see that, for the present profile, simultaneous horizontal and vertical beam stability in a 'classical' microtron is not possible with small values of f_0 . This same conclusion has been derived in general for the case of a racetrack microtron (with driftspace) in reference [1]. As a solution, we rotate the bending magnets of the racetrack microtron through the median plane (but keeping the orbits closed), thus introducing additional quadrupole effects at the magnet entrance and exit. For a classical microtron (no drift space) this solution cannot be used.

IV. CONCLUSIONS

We have compared the analytical results of our first order description of the azimuthally varying field (racetrack) microtron with numerical results for one specific AVF profile. The analytical theory shows excellent agreement with the numerical calculations up to first order. Second order effects could be important for determining the exit angle and orbit length, but focusing properties are sufficiently accurate in first order for flutter profile amplitudes up to 30%.

V. REFERENCES

- [1] J.L. Delhez and W.J.G.M. Kleeven, "Canonical Treatment of an Azimuthally Varying Field Racetrack Microtron," submitted to *Particle Accelerators*.

A 100 MeV Racetrack Microtron

P. Lidbjörk, J. Åström
Scanditronix AB, Husbyborg, 75229 Uppsala, Sweden

Abstract

The Scanditronix 100 MeV racetrack microtron is described. Examples of design data and measured performance are given.

I. INTRODUCTION

The racetrack microtron is an excellent choice as injector for electron synchrotrons and storage rings [1]. It is compact, easy to operate and offers a combination of high beam current with small emittance and very good energy resolution. The Scanditronix RTM100 racetrack microtron is a 19 orbit machine with a final energy of 100 MeV. It is based on the design of the Scanditronix RTM50, (with energies 10-50 MeV found in MM50 systems for radiation therapy) and was developed from accelerator concepts at University of Lund [1] and The Royal Institute of Technology in Stockholm [2]. Up to this time two RTM100 have been delivered and commissioned.

II. INJECTION AND FIRST ORBIT GEOMETRY

The electrons are supplied from a cylindrical Pierce-type gun, at injection voltages up to 100 kV. The current emitted from the cathode is approximately 1 A, but the anode aperture is limiting the current from the gun to about 200 mA, when operating in saturated space charge mode. The injection beamline consists of three focusing solenoids and an achromatic bending system, consisting of two 45° dipole magnets and a quadrupole, deflecting the electrons from the gun into the linac. The injection line can also be supplied with a 1 kW RF buncher system with an accelerating voltage of 30 kV, operating at 500 MHz. The RTM100 incorporates the reversed orbit geometry [3], where the electrons after the first pass through the linac are displaced by a magnet system and then directly reflected back into the linac by the main dipole. The acceleration phase during the first pass can be independently adjusted by sliding the linac along its axis, without affecting the phase for subsequent orbits. This also avoids any problem for the first orbit to clear the linac structure.

III. EXTRACTION

The extraction is carried out by deflection of the beam 5° into the extraction channel by a small dipole magnet in the last orbit. The extracted pulse current is 15 mA.

IV. TRANSVERSE STABILITY

The main dipole field in the RTM100 is 1.1 T, resulting in a final orbit radius of 0.3 m. The main dipoles are equipped with active field clamps producing a reversed field in the fringe field region [4], which together with a small gradient (2.4 %/m) in the main dipole field provide the vertical stability. The horizontal focusing is achieved by a quadrupole on the linac axis. The Twiss parameters after the extraction magnet were calculated to

$$\beta_x = 12 \text{ m and } \alpha_x = 0 \text{ in the horizontal plane and} \\ \beta_y = 4.1 \text{ m and } \alpha_y = 0.26 \text{ in the vertical plane}$$

(with an estimated accuracy of 10 - 20 %). Since the focusing is rather weak in the higher orbits the beam is sensitive for dipole errors, but these errors are easily corrected by small dipoles placed in the return orbits. In the RTM100 there are horizontal correction magnets in every return orbit and dipoles for vertical correction in every second orbit.

V. LINAC AND RF SYSTEM

The linac is of the sidecoupled standing wave type with $1/2 + 7 + 1/2$ cavities, operating in the $\pi/2$ mode. RF-power is supplied from an 5 MW klystron operating at 3 GHz. The resulting energy gain is 5.26 MeV per orbit. The beam pulse width is continuously variable between 0.1 - 1.2 μs with a pulse repetition frequency of up to 10 Hz with the present modulator, but can easily be increased with an upgraded modulator (up to 5 μs and 300 Hz as in the Scanditronix RTM50, 50 MeV racetrack microtron).

VI. EMITTANCE AND MOMENTUM SPREAD

The emittance was found by measuring the beam profile of the synchrotron light observed from the beam inside one of the main dipoles, which together with the calculated Twiss parameters resulted in the following values for the horizontal emittance: $(0.10 \pm 0.04)\pi \text{ mm mrad}$, and for the vertical emittance: $(0.20 \pm 0.06)\pi \text{ mm mrad}$.

The momentum spread was measured using a 45° bending magnet and a slit system. The beam was focused on the slit by a quadrupole doublet and the current collected on the beam stop after the slit was integrated. The result found from this measurement was $\Delta p/p = (1.0 \pm 0.1) \cdot 10^{-3}$.

VII. SUMMARY OF DATA FOR THE SCANDITRONIX RTM100

Electron energy (MeV)	100
Main dipole field (T)	1.1
Beam pulse current (mA)	15
Pulse length (μ s)	0.1-1.2 (5)
Pulse rep. freq. (Hz)	0.1-10 (300)
Hor. emittance (mm mrad)	$(0.10 \pm 0.04) \pi$
Vert. emittance (mm mrad)	$(0.20 \pm 0.06) \pi$
Momentum spread (%)	0.10 ± 0.01

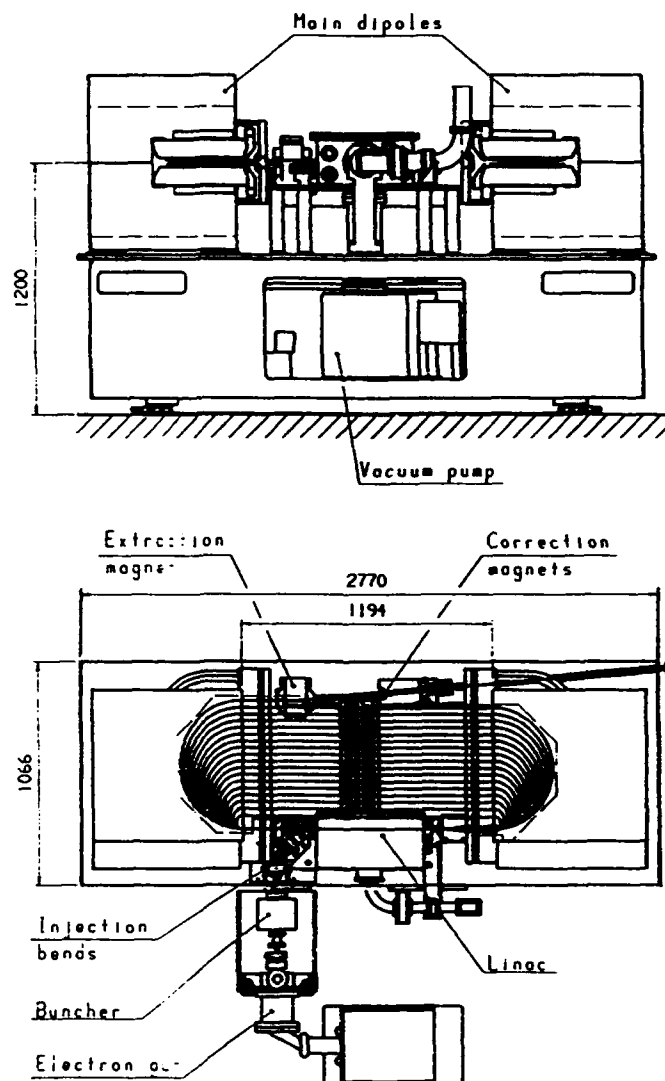
Numbers in parenthesis for pulse length and pulse repetition frequency refer to a system with an upgraded modulator.

VIII. REFERENCES

- [1] M. Eriksson, IEEE Trans. NS-30, No. 4 (1983) 2070.
- [2] S. Rosander, M. Sedlacek and O. Wernholm, Nucl. Instrum. Methods 204 (1982) 1.
- [3] R. Alvinsson and M. Eriksson, Royal Inst. of Tech., Stockholm, Report TRITA-EPP-76-07 (1976).
- [4] H. Babic. and M. Sedlacek, Nucl. Instrum. Methods 56 (1967) 170.

ACKNOWLEDGEMENTS

The authors would like to thank Ö. Hansen for valuable information and helpful discussions during the preparation of this manuscript.



Side and top view of the RTM100

ELECTROSTATIC QUADRUPOLE FOCUSING IN THE AGS g-2 STORAGE RING*

G. Bennett, R. Larsen, W. Morse, Y. Semertzidis, J. Yelk

AGS Department, Brookhaven National Laboratory

Associated Universities, Inc., Upton, New York 11973

Z. Liu, Physics Department, Boston University, Boston, MA 02215

Abstract

Electrostatic quadrupole focusing is to be used in the high precision measurement of the anomalous magnetic moment of the muon, AGS Experiment 821. The final design uses planar rather than hyperbolic electrodes, and the field is pulsed to minimize the effect of trapped electrons. The mechanical design is described. Performance in a 1.5T magnetic field at less than 10^{-6} Torr is reviewed.

I. INTRODUCTION

Experiment 821 at the AGS will measure the magnetic moment of the muon to unprecedented precision.[1] Muons at 3.094 GeV/c will be contained in a superconducting storage ring with a magnetic field of 1.45T homogeneous and controlled to 1 part in 10 million. At that momentum the effects of electric fields are null to first order so that focusing is provided by electrostatic quadrupoles without compromising magnetic field homogeneity.

Design requirements include conflicts such as low stopping power (low density, thickness, and atomic number) to allow efficient detection of the electrons from muon decay, yet mechanical strength for precise positioning and shape, and high stopping power to scrape the tails of the muon distribution. Magnetic permeability must be low. Good vacuum properties are also required.

The crossed electric and magnetic fields cause "trapping" of electrons with maximum energy equal to electrode voltage. These trapped particles oscillate between and circulate about the electrodes, causing further ionization with charge build up and ultimately, breakdown with potentially destructive consequences for the electrodes and insulators. Trapping is a major design consideration.

Pulsed electrostatic quadrupole focusing was used in the previous measurement of the muon g-2 at CERN. The asymmetric electrodes were hyperbolic in form and operated at 5 and 38 kV. The problems of electron and ion trapping were analyzed thoroughly.[2]

II. MECHANICAL DESIGN AND ANALYSIS

The layout of the storage ring is shown in Fig. 1. The quadrupoles subtend 39 degrees per quadrant. The electrodes are fabricated in modules about 13 degrees long. The vacuum chamber sections are each 28 degrees in azimuth with interstitial bellows sections of 2 degrees free of electrodes. Each

vacuum chamber carrying electrodes has feedthroughs.

Note the scalloping of the inner wall of the vacuum chamber for placement of the electron detectors signaling muon decay.

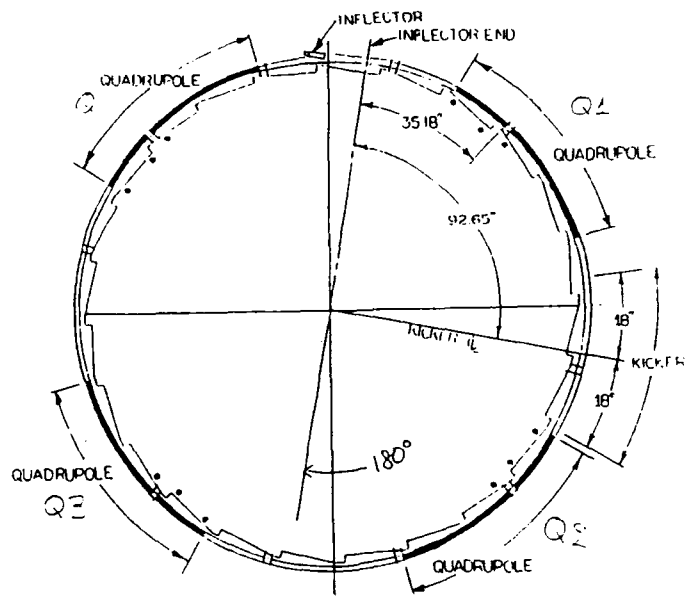


Fig. 1. Plan view of the storage ring showing quadrupoles and other major components.

A major simplification is the concept of flat electrodes. [3] Because of the fourfold symmetry all multipoles vanish except the 4, 12, 20 ... poles, and the 12-pole can be made arbitrarily small by choice of the electrode dimensions. A cross section through the quadrupoles is seen in Fig. 2. The electrodes are supported by an aluminum cage with sturdy corner rails, solid plates on top and bottom, and thin strips forming the sides. The cages and electrodes can be precisely assembled before installation in the vacuum chambers. Final positioning in the chambers utilizes adjustment screws.

Analysis of the electric fields was performed using the two dimensional modeling code POISSON to assay voltage instability, positioning errors, and various other geometrical changes.[4] The resulting allowed tolerances are shown in Fig. 3. Table I shows the relative multipole content up to 28 pole for the ideal geometry of Fig. 2 (columns 2 and 3), for the case with the maximum inward extension of the scalloped vacuum chamber inner radius wall (columns 4,5) with two diagonally opposite corner rails missing (columns 6,7), with the upper and lower plates at maximum inward displacement, 0.5 mm, while the side plates have the maximum displacement outward, 0.75 mm, plus the inner vacuum chamber wall

* Work performed under the auspices of the U.S. Department of Energy.

has maximum inward extension (columns 8,9). All these conditions are seen to be acceptable.

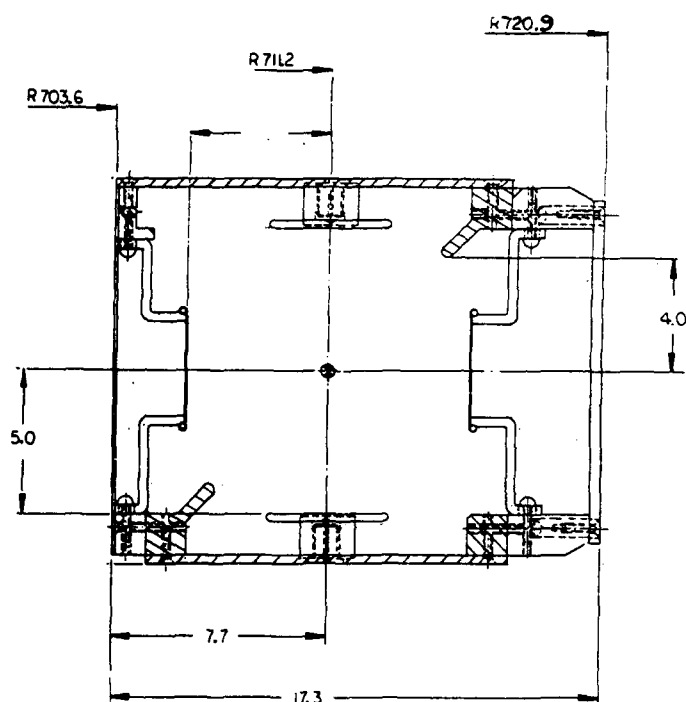


Fig. 2. Cross section through the vacuum chamber showing the cage assembly, quadrupole electrodes, and insulators.

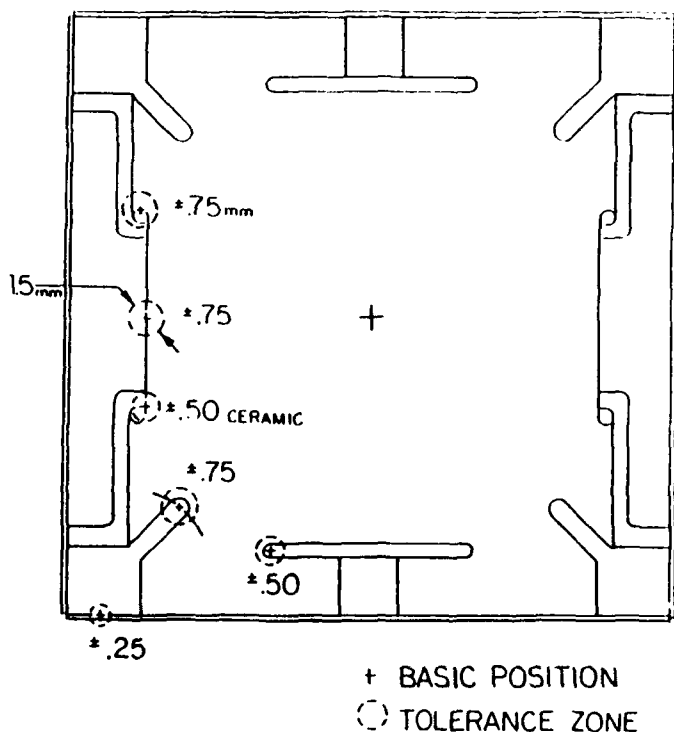
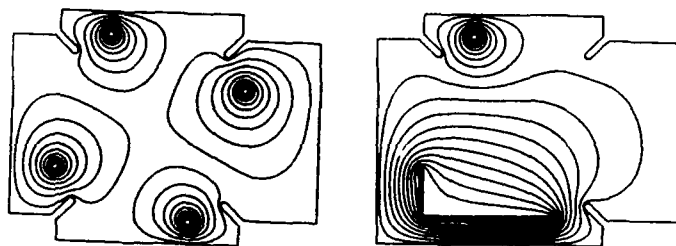


Fig. 3. Construction tolerances for the quadrupole assemblies.

The connections from electrodes to the feedthroughs shown in Fig. 4 were designed to interrupt the trajectories of the trapped particles, channeling them to grounded structures in the vacuum chamber



k	AN(K)	BN(K)	k	AN(K)	BN(K)
1	1.48	-0.05	1	-13.17	-53.20
2	22.11	19.50	2	-0.55	16.86
3	0.71	0.00	3	-3.25	5.19
4	1.02	0.03	4	2.44	0.02
5	0.26	0.11	5	5.60	-0.79
6	-6.12	4.02	6	-2.26	-0.21
7	0.03	0.13	7	-0.75	-1.67
8	0.20	0.02	8	-0.02	0.26
9	-0.05	0.07	9	-0.19	1.29
10	-1.02	-1.53	10	-0.03	-0.44
11	-0.05	0.00	11	0.50	-0.11
12	0.04	0.10	12	-0.04	0.03
13	-0.02	-0.03	13	-0.32	-0.06
14	0.38	-0.26	14	0.11	-0.02

Fig. 4. Cross sections through the interconnections from electrodes to feedthroughs showing equipotential contours and multipoles.

III. ELECTRICAL PARAMETERS

The electric gradient required to achieve a desired focusing index n , is

$$|dE/dr| = nvBo/Ro$$

where v is the muon velocity, Bo the magnetic field, and Ro the muon orbit radius. The potential on the plates is then

$$V = dE/dr (r_m^2 / 2f)$$

where the field index, n is 0.139, the orbit radius is 1.112 m, r_m is 48 mm, half the separation of the quadrupole plates, and f is the fraction of the azimuth subtended by the electrodes, 0.4. The resulting plate potentials are thus ± 22.6 kV.

The capacitance of each electrode was calculated to be 54 pF/m,[5] or about 250 pF per electrode per quadrant. Other electrical parameters include:

Voltage stability	$\pm 1\%$
Pulse duration	1 ms
Maximum jitter	100 ns
Minimum pulse interval	25 ms
Stored energy per electrode	.08 J

Pulsing the quadrupoles is another means of reducing the effects of trapped particles.

Solid state high voltage switches[6] have been used to date to test the design in vacuum and evaluate the measures taken to minimize trapping. A section of the quadrupoles 6 degrees in length was tested in a vacuum chamber at 5×10^{-7} Torr in a magnetic field of 1.5 T. After conditioning the electrodes were tested to more than 10,000 pulses at 28 kV with polarities appropriate to muons of both signs with no sparking or breakdown with pulse durations of 1 to 3 msec!

Since the trapped electrons oscillate at an angular frequency

$$\omega = \sqrt{2eV/mr_m^2}$$

where e and m are the charge and mass of the electron. For V , the electrode potential, at 28 kV the electron frequency is about 330 MHz. We have measured this frequency using an rf oscillator and amplifier capacitively coupled to the electrodes, observing a resonant build up at the appropriate frequency. This technique can be used to measure the effective field strength in the presence of trapped electrons.

V. REFERENCES

- [1] L.M. Barkov et al., "The Anomalous Magnetic Moment of the Muon," Proc. of the 9th International Symposium on High Energy Spin Physics. Nov. 1990.
- [2] W. Flegel and F. Krienen, "Pulsed Electrostatic Focusing for the CERN Muon Storage Ring," NIM **113** (1973) 547-560.
- [3] S.R. Mane, "Electrostatic Quadrupole Design," Brookhaven National Laboratory Internal Report g-2 #103, Feb. 1992, unpublished.
- [4] Y. Semertzidiz, "Quadrupole Tolerances, Rails and More," Brookhaven National Laboratory Internal Report g-2 #149, April 1992, unpublished.
- [5] S.R. Mane, "Quadrupole Capacitance," Brookhaven National Laboratory Internal Report g-2 #150, April 1992, unpublished.
- [6] Behlke, A.G. Model HTS 301 from Euroteck Inc., Morganville, New Jersey.

TABLE I

Multipole Analysis of the Electrostatic Field for Various Geometries. An's are the normal and Bn's the skew components. Amplitudes shown are percent of the normal quadrupole compoent for the ideal geometry, column 2.

k	Ideal Geometry		Inner wall at min radius		2 corner rails missing		Side plates out top and bottom in inner wall at min radius	
	An	Bn	An	Bn	An	Bn	An	Bn
1	0.14	0.10	-0.08	0.02	0.18	0.07	2.48	1.71
2	100.00	0.09	100.16	-0.42	100.04	-0.22	100.18	-0.50
3	-0.11	0.04	0.04	0.02	-0.14	0.01	0.86	-0.60
4	-0.54	-0.02	-0.92	-0.09	-0.76	-0.08	-0.94	-0.04
5	-0.05	-0.04	0.05	-0.01	-0.07	-0.03	0.01	-0.01
6	-0.02	0.00	-0.19	0.15	-0.04	0.12	-0.18	0.16
7	0.01	0.02	0.00	-0.01	0.02	0.03	-0.24	0.18
8	0.03	0.01	0.12	0.06	0.09	0.07	0.10	0.03
9	0.01	0.00	-0.01	0.00	0.01	-0.01	-0.25	-0.16
10	-2.67	-0.02	-2.59	-0.02	-2.64	-0.04	-2.61	0.00
11	0.02	-0.02	-0.01	0.00	0.02	-0.02	-0.07	0.05
12	0.08	0.00	0.08	-0.02	0.07	-0.02	0.09	-0.02
13	0.00	0.01	0.00	0.00	0.00	0.01	0.02	0.01
14	0.25	0.25	0.00	0.25	0.24	0.00	-0.25	-0.01

Design of 8-GeV Rapid-Cycle Booster Synchrotron for the KEK B-Factory

Shin-ichi Kurokawa and Pavel Zenkevich*
KEK, National Laboratory for High Energy Physics
1-1 Oho, Tsukuba, Ibaraki, 305 Japan

Abstract

An 8-GeV rapid cycle booster synchrotron was designed as possible injector for the KEK B-Factory.

I. INTRODUCTION

We should have an injector to supply 8 GeV electron beams to the high-energy ring (HER) of the KEK B-Factory[1]. Constructing a rapid-cycle booster synchrotron is an attractive option, since this scheme enables us to accelerate electrons to 8 GeV rather easily. Positrons will be injected directly into the low energy ring of the B-Factory; moderate upgrading of the present 2.5 GeV linac to 3.5 GeV is necessary. According to the two options of the KEK B-Factory**, (1) to dig a new tunnel of 1.5 km circumference and accommodate two rings in this tunnel, or (2) to install the two rings in the existing TRISTAN tunnel, the size of possible booster synchrotrons becomes different. In the former case half of the booster is placed in the B-Factory tunnel, while the other half in a bypass tunnel (see Fig. 1); the total length of the booster is 1071.6 m (long booster). In the latter case the booster is accommodated in a special tunnel of 600 m circumference (short booster), since the TRISTAN tunnel (3000 m circumference) is too large for the booster.

Required parameters of the booster are:

injection energy	3.5 GeV
extraction energy	8.0 GeV
repetition rate	50 Hz
intensity	10^{10} electrons/bunch

The booster is operated in a single-bunch mode. The parameters of the injected beam from the linac are:

transverse emittance	1.5×10^{-7} m
energy spread	2.5×10^{-3}
bunch length	a few mm

Below we mainly consider the long booster.

II. LINEAR LATTICE

A. Long Booster

The booster has two-fold symmetry and two long (60 m) straight sections. One of the straight sections is used for RF stations and the other for injection and extraction. The magnetic lattice for the long booster consists of two arcs, four

dispersion suppressors and two long straight sections. The betatron tune is 16.33. One arc cell consists of one F-type and one D-type combined function magnets. Dispersion suppressors are located between arcs and straight sections to match the dispersion function. Each dispersion suppressor has two quadrupole lenses; one of which is shifted from its periodical position in order to suppress beatings of the β -function. Phase shift of one cell in arcs and in dispersion suppressors is 60 degree. Nine quadrupole magnets in a straight section are placed at the periodical position. Their strength is symmetrical with respect to the center of the straight section. The phase shift of a cell in the straight section is chosen to be 90 degree in order to avoid the intrinsic resonance of the sixth order excited by the fifth-order non-linearity and to suppress beating of the β -function in the straight sections.

Combined-function lattice results in antidamping in the horizontal direction. Due to the large bending radius of magnets, the growth of the horizontal emittance during acceleration is tolerable (see Fig. 3).

The advantage of the combined function type lattice is that most part of arcs are occupied by combined-function magnets with a small cross section. Whole magnet can be inclosed in a vacuum vessel; this further reduces the cross section of the magnet because the gap of the magnet can be reduced by the thickness of vacuum chamber wall.

Lattice of the final part of the arc, the dispersion suppressor and the straight section is shown in Fig. 2.

B. Short Booster

The magnetic lattice of the short booster is in principle the same as that of the long booster; however, the use of combined-function magnets for arcs is precluded since antidamping nature of the lattice would result in too large horizontal emittance for the B-Factory. Only separated function lattice can be employed in this case. Parameters of both boosters are given in Table 1.

III. COHERENT INSTABILITIES

A. Impedances

The main source of the longitudinal impedance is steps at the entrance and exit of the combined-function magnets where the aperture changes. The impedance of the step Z_{step} is given by

$$Z_{\text{step}} = \frac{Z_0}{\pi} \ln \frac{b}{a}$$

where Z_0 is the impedance of vacuum, and a and b are the vertical aperture of the magnet and that of the beam pipe between magnets[3]. The total impedance $|Z_{11}/n|$ of the ring becomes,

* On leave from ITEP, Moscow.

** The design has been converged to that based on existing TRISTAN. Two rings will be installed in the TRISTAN tunnel. The 2.5 GeV linac will be upgraded to 8 GeV instead of constructing a booster. See Ref. [2].

$$\left| \frac{Z_{11}}{n} \right| \sim \frac{2NZ_{\text{step}}}{R/a},$$

where N is the number of magnets in the ring and R the average radius of the ring. If we substitute $a = 1.5 \times 10^{-2}$ m, $b = 0.15$ m, $N = 190$, $R = 170$ m, we get $|Z_{11}/n| = 9.3 \Omega$. Taking into account the presence of other impedance sources, we take 10Ω as the total impedance. Transverse impedance is estimated to be $16.6 \text{ M}\Omega/\text{m}$ by the use of the formula,

$$|Z_{\perp}| = \frac{2R}{a^2} \left| \frac{Z_{11}}{n} \right|.$$

B. Longitudinal Microwave Instability

The threshold for this instability is given[4] by

$$N_b \leq \frac{(2\pi)^{3/2} \frac{E}{e} \sigma_p^2 \sigma_z \alpha}{e c \left| \frac{Z_{11}}{n} \right|}.$$

where N_b is the number of particles in a bunch, E the beam energy, e the electron charge, σ_p the energy spread of the beam, σ_z the bunch length, and α the momentum compaction factor.

By substituting the values at injection and extraction given in Table 1, we get $N_b < 1.2 \times 10^{11}$ (at injection) and $N_b < 1 \times 10^{10}$ (at extraction).

The longitudinal microwave instability may appear near the end of acceleration; however, this instability only increases the longitudinal emittance and does not cause any particle losses.

C. Head-Tail Instability

The tune shift and the growth rate of the lowest head-tail (synchrotron) mode can be approximated in a frame of the broadband resonator model by the following expressions[5]

$$\Delta v = \frac{e R^2 I_B |Z_{\perp}|}{4\sqrt{2} v E \sigma_z}, \quad \frac{1}{\tau} = -\frac{e c^2 I_B |Z_{\perp}| \xi}{4\sqrt{2} \alpha E \omega_{\text{res}} \sigma_z},$$

where I_B is the bunch current, v = the betatron tune, $\xi = \left(\frac{\delta v}{v}\right)/\left(\frac{\delta E}{E}\right)$ the chromaticity, and ω_{res} = the resonant frequency of the broadband resonator ($\omega_{\text{res}} = \omega_c$; ω_c is the cutoff frequency). Taking into account that $I_B = eNc/2\pi R$ and $\omega_c = c/a$ and substituting $N_b = 10^{10}$, $|Z_{\perp}| = 16.6 \text{ M}\Omega/\text{m}$, $\alpha = 5.1 \times 10^{-3}$, $\xi = -19$, $v = 16.33$, $\sigma_z = 3.3 \times 10^{-2}$ m for $E = 3.5$ GeV and $\sigma_z = 1.23 \times 10^{-2}$ m for $E = 8.0$ GeV we obtain

	injection	extraction
Δv	0.02	0.023
$\tau(\text{ms})$	0.523	0.446

The beam intensity is below the threshold of the transverse mode-coupling instability (this instability occurs when $\Delta v \simeq v_s$, v_s is the synchrotron tune). On the contrary the head-tail mode (the lowest synchrotron mode) is dangerous and has to be suppressed by chromaticity compensation.

For a separated-function lattice chromaticity correction is rather straightforward by adding sextupole magnets. For a combined-function lattice the simplest way is to create an artificial nonlinearity in magnets by making special shape of poles.

IV. TUNE ADJUSTMENT

Tunes are adjusted by changing the strength of quadrupole magnets in the straight sections. Eighteen magnets in the straight sections are grouped into 10 focusing quadrupoles and 8 defocusing quadrupoles. Necessary variation of quadrupole magnet strength for changing tunes by 0.1 is smaller than 5% and beating of the β -function in the arc is negligible.

V. REQUIRED APERTURE

During acceleration the emittance of the beam varies due to radiation damping, adiabatic damping and quantum excitation. Figure 3 shows this change. Since the emittance is maximum at injection, the required aperture becomes maximum at injection. By assuming that the maximum closed orbit displacement is 10^{-2} m in both directions, we get apertures A_x and A_y shown below.

	F-magnet	D-magnet	Q-lense
A_x	31.2	22.4	15.1
A_y	10.8	15.1	15.1

VI. ACKNOWLEDGEMENT

One of the author (P.Z.) would like to thank professor K. Oide and Dr. S. Matsumoto for their help in using SAD.

VII. REFERENCES

- [1] S. Kurokawa, K. Sato and E. Kikutani, "Accelerator Design of the KEK B-Factory", KEK Report 90-24, March 1991.
- [2] S. Kurokawa, these proceedings.
- [3] S. A. Heifets and S. A. Kheifets, "Coupling Impedance of Modern Accelerators", AIP Proceedings 249, p.150.
- [4] M. S. Zisman, "Influence of Collective Effects on the Performance of High-Luminosity Colliders".
- [5] T. Le Duff, "Current and Current Density Limitations in Existing Electron Storage Rings", Nuclear Instruments and Methods, A239 (1985) pp.83-101.

Feedback Control of Coupled-Bunch Instabilities*

J. D. Fox, N. Eisen, H. Hindi, I. Linscott, G. Oxoby, and L. Sapochnikov
Stanford Linear Accelerator Center, Stanford University, Stanford, CA 94309 USA
and
M. Serio, INFN Laboratori Nazionali, Frascati

Abstract

The next generation of synchrotron light sources and particle accelerators will require active feedback systems to control multi-bunch instabilities [1,2,3]. Stabilizing hundreds or thousands of potentially unstable modes in these accelerator designs presents many technical challenges.

Feedback systems to stabilize coupled-bunch instabilities may be understood in the frequency domain (mode-based feedback) or in the time domain (bunch-by-bunch feedback). In both approaches an external amplifier system is used to create damping fields that prevent coupled-bunch oscillations from growing without bound. The system requirements for transverse (betatron) and longitudinal (synchrotron) feedback are presented, and possible implementation options developed. Feedback system designs based on digital signal-processing techniques are described. Experimental results are shown from a synchrotron oscillation damper in the SSRL/SLAC storage ring SPEAR that uses digital signal-processing techniques.

I. A CLASSICAL ANALOGY

The dynamics of coupled-bunch motion can be illustrated by the mechanical analog of coupled pendulums. In Figure 1 this analogy is applied to the charged particle bunches in a storage ring, with each pendulum representing the oscillatory motion (synchrotron or betatron) of a bunch. The coupling springs represent the impedances of the accelerating cavities and vacuum structures. Bunch_{i+1} and subsequent bunches are driven from the excitations of bunch_i, much as pendulum_i drives pendulums_{i+1} through the coupling springs [4].

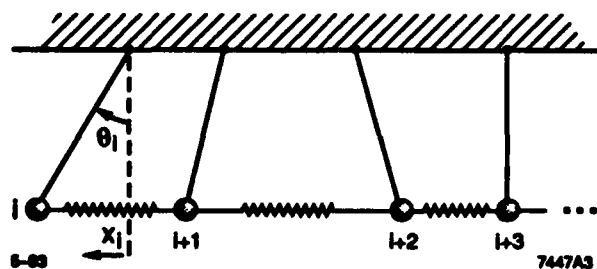


Figure 1. Coupled pendulum analogy.

In a storage ring with many bunches and many external higher-order mode resonators, the resulting motion can be found by coherently summing the driving terms and considering the periodic excitation due to the orbit of the particles [5,6]. Unstable, growing oscillatory motion can result, in which the motion of a few bunches can excite an unstable normal mode. These instabilities can be controlled by reducing the magnitude and number of external, parasitic higher-order modes, carefully controlling the resonant frequencies of the parasitic resonators to avoid coupling to the beam, and by adding damping to the motion of each bunch.

External beam-feedback systems do the latter. In the analogy of Figure 1, they act to add dashpots to each pendulum. Each bunch can be thought of as a harmonic oscillator obeying the equation of motion

$$\ddot{x} + \gamma \dot{x} + \omega_0^2 x = f(t),$$

where ω_0 is the bunch synchrotron (longitudinal) or betatron (transverse) frequency, $f(t)$ is an external driving term and γ is a damping term. An external feedback system acts on the beam, contributing to this damping term, and allowing control of external disturbances $f(t)$ driving the beam.

II. TIME DOMAIN VS. FREQUENCY DOMAIN PROCESSING

The action of the feedback system can be understood in either the time or frequency domains [7]. If each unstable normal-mode frequency is identified, a single narrow-band feedback channel for each mode can be implemented. Such a system consists of a frequency-selective filter (with tailored phase characteristics) and feedback power amplifier for each mode. For a given mode the feedback system acts to generate a driving term which counteracts the excitation from an external resonator. N modes are simply treated as N parallel feedback systems. However, if there are potentially thousands of unstable modes, or the external resonator frequencies or strengths change over time, this narrowband frequency-domain processing is not very attractive or manageable.

The time-domain approach treats each bunch as an independent oscillator coupled to its neighbors through an external driving term. Such a bunch-by-bunch system implements a logically separate feedback system for each bunch in a multibunch accelerator [8,9,10]. In this scheme the coupling to multiple bunches is lumped into a single $f(t)$ driving term in Equation 1.

* Work supported by Department of Energy contract DE-AC03-76SF00515.

Table 1 Parameters of the Boosters

	Long Booster	Short Booster	
Injection energy	3.5	GeV	
Ejection energy	8.0	GeV	
Inj. trans emittance	1.5×10^{-7}	m	
Inj. energy spread	2.5×10^{-3}		
Circumference	1071.6	599.2	m
Number of cells	94	70	
Phase shift cell	60°	60°	
Betatron tunes ($\nu_x = \nu_y$)	16.33	11.66	
Superperiodicity	2	2	
Length of period	11.4	8.56	m
Length of straight section	57	42.8	m
Bending magnet			
whole number	162	116	
in main lattice	154	108	
in suppressors	8	8	
length	4.56	2.58	m
k_1^*	± 0.0564	0	m^{-2}
k_2^* (F magnet)	0.0193	0	m^{-3}
k_2^* (D magnet)	0.0264	0	m^{-3}
bending radius	116	43.9	m
Quadrupole lense			
whole number	26	140	
in straight sections	18	18	
in suppressors	8	8	
length	0.6	0.6	m
k_1^* (max)	0.455	0.616	m^{-2}
Natural chromaticity	-18.9	-13.0	
Momentum compaction	5.12	10.54	$\times 10^{-3}$
RF frequency	508		MHz
RF Voltage	10	20	MV
Energy loss per turn	3.16	8.96	MV
Damping partition numbers			
T_x	-0.8216	0.9801	
T_y	1.0007	1.004	
T_z	3.8209	2.0195	
Synchrotron tune			
E = 8.0 GeV	0.0401	0.0602	
E = 3.5 GeV	0.0643	0.0965	
Final emittance			
ϵ_x	11.5	17.7	10^{-8} m
ϵ_y	4.1	0.59	10^{-8} m
ϵ_z	0.86	1.75	10^{-8} m
Bunch length			
E = 3.5 GeV	3.2	2.5	cm
E = 8.0 GeV	1.3	2.3	cm
Energy spread			
E = 8 GeV	6.6×10^{-4}	7.6×10^{-4}	

$$* k_1 = \left(\frac{\partial B_y}{\partial x} \right) / (B\rho), \quad k_2 = \left(\frac{\partial^2 B_y}{\partial x^2} \right) / (B\rho)$$

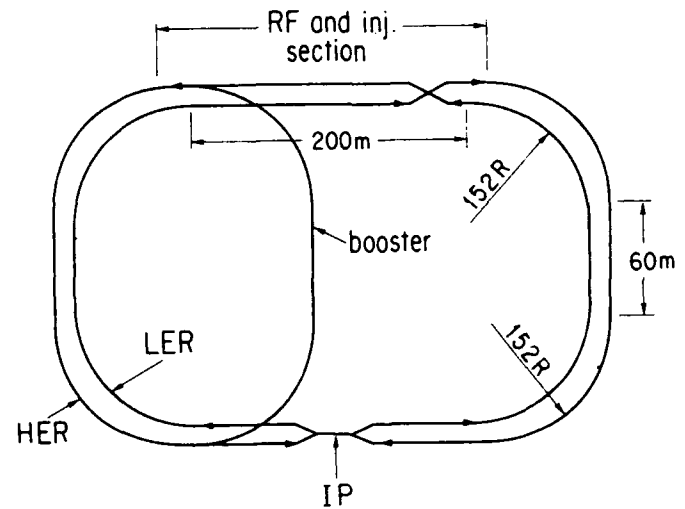


Fig. 1 Layout of booster and B-Factory.

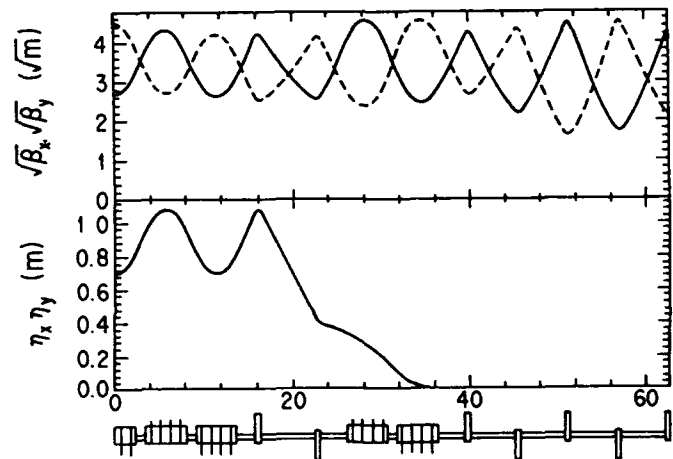


Fig. 2 Lattice of the final part of the arc, the dispersion suppressor and the straight section.

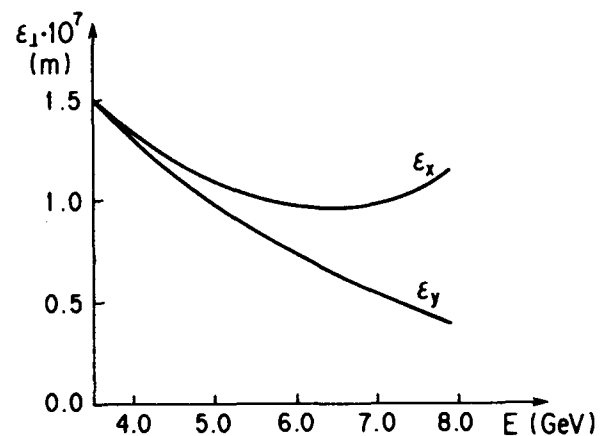


Fig. 3 Change of emittance with energy.

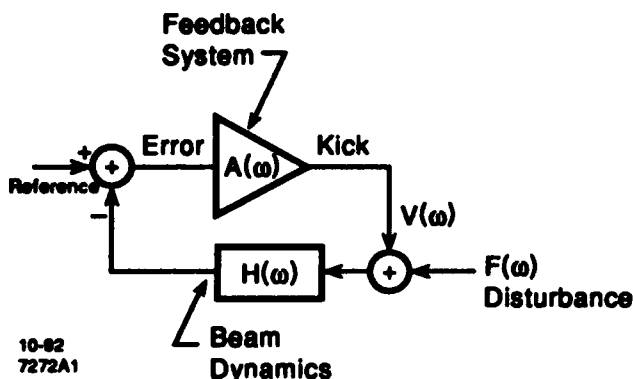


Figure 2. Conceptual diagram of a feedback system $A(\omega)$ acting to stabilize a system $H(\omega)$.

It is important to realize that the input and output signals are identical for both time- and frequency-domain processing. The output signal of a time-domain system contains all the unstable-mode frequency information found at the output of an all-mode frequency-domain system. The approach being implemented cannot be identified if the processing electronics are hidden. The advantage to the time-domain (bunch-by-bunch) approach is the potential to implement a more compact processing block for systems with thousands of bunches and insensitivity to exact knowledge of unstable mode frequencies.

III. FEEDBACK CONTROL

Figure 2 shows a summing node that generates an error signal, a feedback amplifier with complex gain $A(\omega)$, a second summing node that adds an external driving term $F(\omega)$, and a beam-dynamics block with complex transfer function $H(\omega)$.

A disturbance $F(\omega)$ applied to the system is reduced by the feedback amplifier by the amount

$$\frac{H(\omega)}{1 + A(\omega)H(\omega)}.$$

As the dynamics of the beam $H(\omega)$ are determined by accelerator design, the challenge to the feedback designer is to specify $A(\omega)$ so that the loop is stable, the response to disturbances $V(\omega)$ is bounded, and the transients are well damped.

Both longitudinal and transverse feedback systems can be described by Figure 2. For the transverse case, the input set point is the desired-orbit mean coordinate, and the output signal is applied via a transverse electrode assembly which acts with a transverse kick on the beam. For the longitudinal case, the set point refers to the desired stable-bunch phase or energy, and the correction signal is applied to the beam to change the bunch energy [26].

One fundamental difference between longitudinal and transverse accelerator feedback systems is the ratio of the oscillation frequency ω_0 to the revolution (sampling) frequency ω_{rev} . If $\omega_{rev} \geq 2\omega_0$, the Nyquist sampling limit is not exceeded and spectral information is not lost. As synchrotron frequencies are typically lower than revolution frequencies, the sampling process does not alias the longi-

tudinal oscillation frequency. However, in the transverse case, betatron frequencies are greater than revolution frequencies, and the sampling process aliases the oscillation to a different (aliased) frequency. Thus, the transverse signal processing must operate at an aliased frequency, and be capable of operating over a range of aliased frequencies representing the machine betatron-tune operating range. A general-purpose processing block for transverse feedback may be implemented using two beam pickups $\pi/2$ apart in betatron phase, and combining these signals in a quadrature phase shifter. This approach allows flexibility in the location of the kicker with respect to the pickups, and allows adjustment for machine tune via scaling of the quadrature coefficients [11].

IV. SIGNAL PROCESSING OPTIONS

The feedback path $A(\omega)$ in Figure 2 has several functions:

- Detect the bunch oscillation.
- Provide a $\pi/2$ phase shift at the oscillation frequency.
- Suppress DC components in the error signal.
- Provide feedback loop gain at ω_0 .
- Implement saturated limiting on large oscillations.

These requirements are met by a differentiator, or a bandpass filter centered at the oscillation frequency ω_0 , with some specified gain and a $\pi/2$ phase shift at ω_0 . DC rejection of the filter is necessary to keep the feedback system from attempting to restore a static equilibrium position to an artificial set point. The filter should also reject signals above the oscillation frequency to prevent noise or other high-frequency signals from being mixed down into the filter passband and impressed onto the beam. The limiting function allows injection (and large-amplitude excitation of the injected bunch) while still damping neighboring bunches in a linear regime. The saturated processing has been shown to suppress the growth of coherent instabilities from injection-like initial conditions [12].

For systems with thousands of bunches, an efficient processing approach is to take advantage of the inherent sampling at ω_{rev} , and implement the filter as a discrete time filter of either finite impulse response (FIR) or infinite impulse response (IIR) forms. A FIR filter is a convolution in the time domain

$$Y_k = \sum_{n=0}^{m-1} C_n X_{k-n}$$

where Y_k is the filter output on sample k , X_k is the filter input on sample k , and m is the length of the filter (or number of past input samples used to generate an output).

There are many possible forms of filter that are adequate for the beam feedback task [19]. Pure delays and differentiator or bandpass functions can be specified to implement the required $\pi/2$ phase shift. One possible filter is a differentiator using two taps spaced roughly $\pi/6$ of an oscillation cycle apart. If the tap spacing is $\pi/2$ of the synchrotron period, a two-tap bandpass filter can be created.

Choosing among the many possible filters requires trade-offs in signal-to-noise (the differentiators emphasize high frequencies) and in the complexity of the filter.

These filters can be realized by several approaches. All-analog approaches are possible, in which the required feedback filter is implemented as a transversal filter comprised of several stages of tapped delay lines. Dispersion and losses in the delay line must be matched to the filter properties. For example, a full oscillation-period longitudinal filter for a PEP-II-like facility (136 kHz ω_{rev} , 7 kHz ω_s) with 4 ns spacing between the bunches would require a total delay time of roughly 140 μ s with a signal bandwidth of greater than 125 MHz, or a τB product of 2×10^4 . Only optical delay $\tau B_{max} = 10^6$ lines allow adequate bandwidth-delay product to implement the PEP-II filter. Longitudinal filters for the SSC or LHC machines, with their several Hz synchrotron frequencies and 60 MHz bunch-crossing frequencies look even more challenging, requiring τB products of greater than 10^6 for a full-period filter.

In contrast, digital signal-processing techniques look very attractive as the means to implement these feedback filters. One interesting feature of the time-domain processing scheme is that the feedback process uses only information from a particular bunch to compute the feedback signal for that bunch. It is therefore possible to implement a parallel processing strategy and spread the high sampling-rate bunch information among several slower computing blocks.

For longitudinal feedback ω_{rev} is typically much higher than the oscillation frequency ω_s , and it is possible to implement a downsampled processing channel. In a downsampled scheme the information about a bunch's oscillation coordinate is only sampled once every n revolutions, and a new correction signal only updated once every n crossings [13]. This approach reduces the number of multiply-accumulate operations in the filter by a factor of $1/n^2$. Table 1 shows the aggregate filter complexity (in MACS/sec) for downsampled five-tap filters and non-downsampled two-tap filters for five accelerator facilities. The advantage of downsampling in reducing the aggregate MAC rate is clearly seen. The filter complexity linearly scales with the MAC rate in terms of storage required and speed of the operations. Large facilities with low synchrotron frequencies are especially good candidates for downsampled processing. For example, the SSC design, with a 3.4 kHz revolution frequency and a 4–7 Hz synchrotron frequency, samples the bunch information 500 to 850 samples per cycle, or 250–400 times the Nyquist limited rate. The downsampled processing technique allows the use of arrays, or "farms," of commercial single-chip DSP microprocessors to compactly implement feedback systems for thousands of bunches. This approach is particularly well-matched to the commercial activity in digital signal-processing microprocessors.

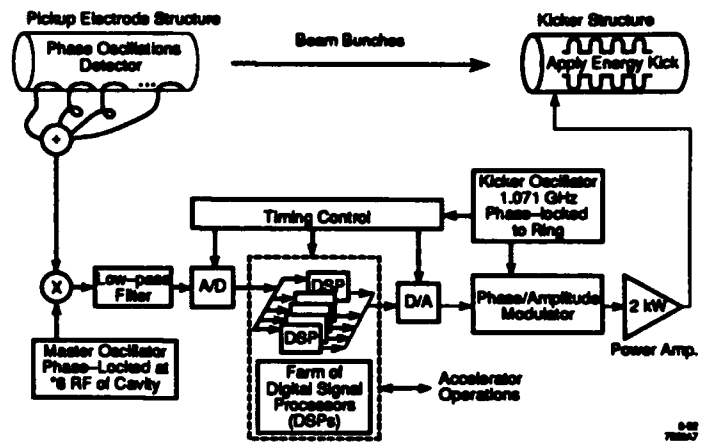


Figure 3. Block diagram of the PEP-II longitudinal feedback system.

Table 1.
Filter Complexity for Five Accelerators.

Parameter	PEP-II	ALS	DAΦNE	SSC	LHC
Number of bunches	1746	328	120	17424	5940
$\tau_{revolution}$ (sec)	7.3 E-6	6.6 E-7	3.2 E-7	3 E-4	9 E-5
$\tau_{synchrotron}$ (sec)	1.4 E-4	7.9 E-5	2.6 E-5	.24	1.3 E-2 (min) 4.8 E-2 (max)
τ_s/τ_r	19.2	121	79.8	814	150 (min) 540 (max)
Filter MACS/sec 2 TAP non-downsampled	5E8	1E9	7.4 E8	1.2 E8	1.3 E8
Downsampling Factor	4	24	16	161	30 (min) 108 (max)
Filter MACS/sec Downsampled 5 TAP	3E8	1E8	1.2 E8	2 E6	1 E7 (min) 3 E6 (max)

V. OPERATION OF A DSP FEEDBACK SYSTEM AT SPEAR AND ALS

Figure 3 shows the essential components of the PEP-II longitudinal-feedback system in development at SLAC [14,15]. This design was selected for use by the PEP-II B factory, the LBL Advanced Light Source (ALS), and the Frascati ϕ factory DAΦNE [16]. A prototype system was constructed incorporating an eight-tap stripline comb generator, a master-phase reference oscillator, a phase detector, 250 MHz A/D and D/A stages, and an AT&T 1610 DSP microprocessor.

The prototype feedback system was tested in September 1992 using the SPEAR storage ring at SLAC, and in April 1993 on the ALS at LBL [17]. For this experiment the beam was sensed via a button-type BPM electrode and processed by the prototype B factory front end. The DSP feedback signal was used to control a phase shifter acting on the rf cavity phase, which closed the loop around

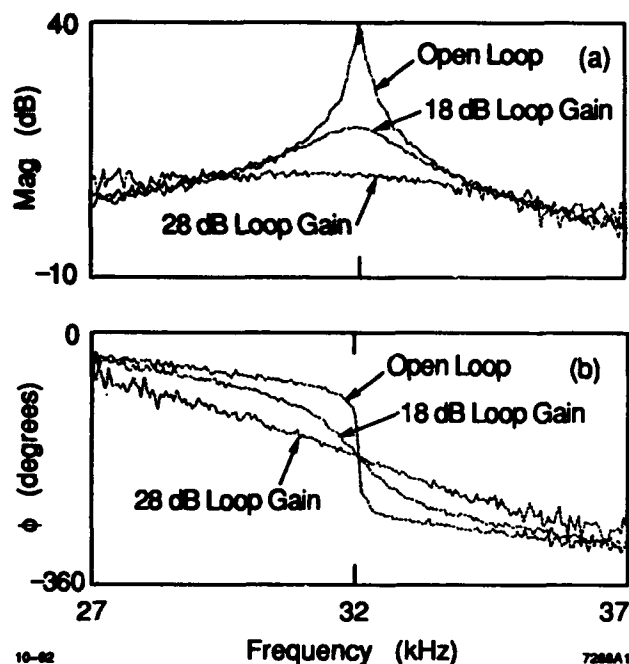


Figure 4. Magnitude(a) and phase(b) response for a single bunch for open-loop and closed-loop gains of 18 and 28 dB. The associated Q factors are 200 (open loop), 20 (18 dB) and 5 (28 dB).

the stored beam. The feedback filters used in these experiments are the same type proposed for PEP-II (five-tap FIR bandpass filter), with a downsampling factor of eight (SPEAR) or thirty-one (ALS).

The SPEAR and ALS storage rings do not have a wideband kicker of the type proposed for PEP-II [18]. The systems implemented used one of the two main rf accelerating cavities to apply corrections to the beam. As the bandwidths of the rf systems are limited to 40 kHz and 20 kHz, it is not possible to implement true multibunch feedback systems. Therefore, all of the closed-loop measurements were performed using a single stored bunch demonstrating the behavior of a single bunch acted upon by a digital feedback system. An additional series of open-loop measurements were made with the rings filled with multiple bunches, which allows multi-bunch coupling to be observed but not controlled.

Figures 4a and 4b show the magnitude and phase responses of the SPEAR beam-transfer function for an open-loop configuration, and for closed-loop gains of 18 and 28 dB. In this figure the open-loop response shows a weakly damped harmonic oscillator as described by Equation 1, with a Q of 200. The natural damping present in this case is due to Robinson damping as well as radiation damping. We see in the figure the action of the feedback system to increase the damping term in Equation 1, and lower the Q of the harmonic oscillator. The configuration with 28 dB of loop gain barely displays any resonant behavior ($Q = 5$), and suggests that the transient response of the combined system will damp in a few cycles.

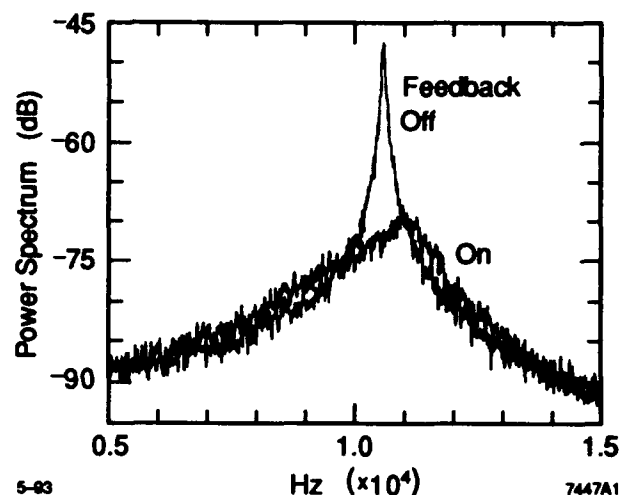


Figure 5. ALS power spectra for open loop and 31 dB loop gain.

Figure 5 presents power spectra of the ALS bunch motion for single-bunch operation with the feedback system operated open loop and with 31 dB loop gain. In this measurement a broadband noise source is used to excite the beam through the rf cavity. The figure shows a 28 dB reduction in the magnitude of the synchrotron oscillation due to the external damping provided by the feedback system.

The time response of the system can be observed in Figure 6. In this experiment the feedback loop is opened, and a gated burst at the synchrotron frequency is applied via the rf cavity. This excitation burst drives a growing synchrotron oscillation of the beam. The excitation is then turned off and the feedback system loop closed. Figure 6a shows the free decay of the SPEAR beam in which the damping-time constant (e folding time) in the absence of feedback is 2 ms. Figure 6b shows the damping transient of such a gated burst for a 33 dB loop-gain configuration which reduces the damping time constant to 40 μ s.

To quantify the equilibrium noise performance of the damping system the rms bunch phase was measured at the completion of the damping transient. These measurements reveal that the residual beam motion is roughly 2.5 mR at 358 MHz (3% of the 1.4 cm bunch length), corresponding to a time jitter of 1 ps. The quantizing interval for the system as configured at SPEAR was 2.7 mR, indicating that the feedback system acted to damp excitations and noise to within the front-end quantization interval.

VI. SUMMARY

Multibunch feedback systems may be understood as electronic systems which add damping to the motion of particles in an accelerator. The systems may be designed using frequency- or time-domain formalisms. An example system which uses digital signal processing has been tested at SPEAR and the ALS. These system measurements have shown the operation of all the essential detection and processing components required for the PEP-II longitudinal-feedback system. The fast front-end circuits were demon-

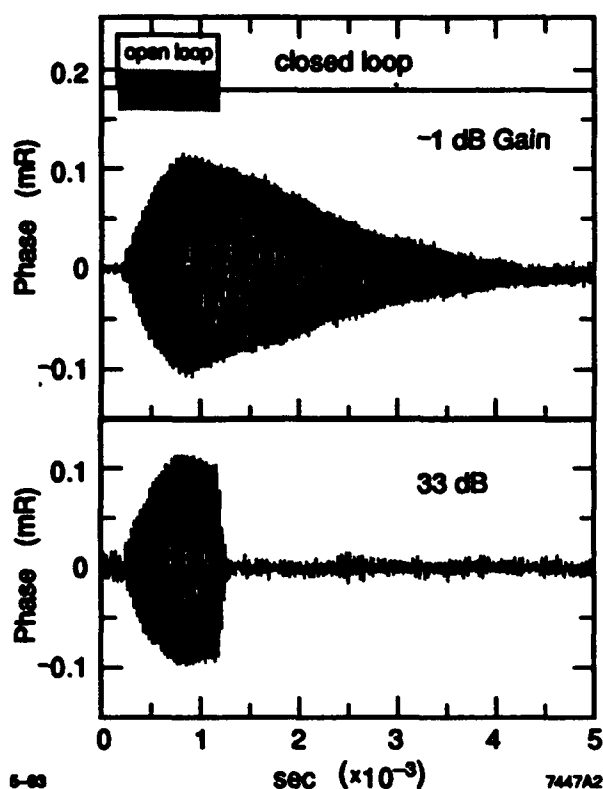


Figure 6. Time response of a SPEAR excited bunch—open-loop response in 8a, 33 dB loop gain in 8b.

strated with the required 4 ns bunch spacing, and the digital signal-processing filter proved for linear and saturated modes. The digital filter-signal processing provides a very flexible and general-purpose feedback system which is easily configured to operate for varied operating facilities.

ACKNOWLEDGEMENTS

The ideas discussed in this paper reflect the contributions of many people at SLAC, LBL, INFN Frascati and the Stanford Electrical Engineering Department. The ideas and contributions of Flemming Pedersen (CERN) during his 1992 visit to SLAC deserve special mention and thanks. Bob Genin, Bob Hettel, Walt Barry, John Byrd, John Corlett, Glen Lambertson and the SPEAR and ALS operations groups provided expertise and enthusiasm for the machine physics runs. The authors also thank George Caryotakis, Jonathan Dorfman, Andrew Hutton, Alan Jackson and Mike Zisman for their support of the PEP-II feedback research and development activities.

REFERENCES

- [1] "PEP-II, An Asymmetric B Factory—Design Update," Conceptual Design Report Update, SLAC, 1992.
- [2] B Factory Accelerator Task Force, S. Kurokawa, K. Satoh and E. Kikutani, Eds. "Accelerator Design of the KEK B Factory," KEK Report 90-24, 1991.

- [3] "CESR-B Conceptual Design for a B Factory Based on CESR," CLNS Report 91-1050, Cornell University, 1991.
- [4] Fetter, A. and J. Walecka, "Theoretical Mechanics of Particles and Continua," McGraw Hill, New York, 1980.
- [5] Lambertson, G. "Control of Coupled-Bunch Instabilities in High-Current Storage Rings," Proceedings of the 1991 IEEE Particle Accelerator Conference, pp. 2537-2541.
- [6] Pellegrini, C. and M. Sands, "Coupled-Bunch Longitudinal Instabilities," SLAC Technical Note PEP-258, 1977.
- [7] Pedersen, Flemming, "Multibunch Feedback— Transverse, Longitudinal and RF Cavity Feedback," Presented at the 1992 Factories with e^+/e^- Rings Workshop, Benalmadena, Spain, November 1992.
- [8] Kohaupt, R. D., "Theory of Multi-Bunch Feedback Systems," DESY 91-071, 1991.
- [9] D. Heins et al., "Wide-Band Multi-Bunch Feedback Systems for PETRA," DESY 89-157, 1989.
- [10] M. Ebert et al., "Transverse and Longitudinal Multi-Bunch Feedback Systems for PETRA," DESY 91-036, 1991.
- [11] J. Byrd et al., "ALS Transverse Multibunch Feedback System," Proceedings of the 1993 IEEE Particle Accelerator Conference, May 1993.
- [12] D. Briggs et al., "Computer Modelling of Bunch-by-Bunch Feedback for the SLAC B Factory Design," Proceedings of the IEEE Particle Accelerator Conference, 1991.
- [13] H. Hindi et al., "Down-Sampled Bunch-by-Bunch Feedback for PEP-II," B Factories: The State of the Art in Accelerators, Detectors, and Physics, SLAC Report 400, p. 216.
- [14] D. Briggs et al., "Prompt Bunch-by-Bunch Synchrotron Oscillation Detection by a Fast-Phase Measurement," Proceedings of the Workshop on Advanced Beam Instrumentation, KEK, Vol. 2, p. 494, 1991.
- [15] G. Oxoby et al., "Hardware and Software Implementation of the Longitudinal Feedback System for PEP-II," Proceedings of the 1993 IEEE Particle Accelerator Conference, May 1993.
- [16] M. Bassetti, O. Coiro, A. Ghigo, M. Migliorati, L. Palumbo, and M. Serio, "DAFNE Longitudinal Feedback," Proceedings of the Third European Particle Accelerator Conference, Berlin, Germany, 1992, p. 807.
- [17] H. Hindi et al., "DSP-Based Longitudinal Feedback System: Trials at SPEAR and ALS," Proceedings of the 1993 IEEE Particle Accelerator Conference, May 1993.
- [18] J. Byrd, J. Johnson, G. Lambertson, and F. Voelker, "Progress on PEP-II Multibunch Feedback Kickers," B Factories: The State of the Art in Accelerators, Detectors, and Physics, SLAC Report 400, p. 220.
- [19] J. Fox et al., "Multibunch Feedback—Strategy, Technology, and Implementation Options," Proceedings of the 1992 Accelerator Instrumentation Workshop, Berkeley, CA, 1992.

Electro-Optical Technology Applied to Accelerator Beam Measurement and Control

Ralph J. Pasquinelli

Fermi National Accelerator Laboratory *

P.O. Box 500, Batavia, IL 60510

ABSTRACT

Recent improvements in optical components have provided another choice for signal processing for beam instrumentation and feedback. Signal transmission utilizing the low insertion loss of optical fibers has been attractive for years. Today optical amplifiers are available in several wavelength ranges. These amplifiers provide photon to photon gain, eliminating the need to down convert signals back to baseband for regenerative repeaters. New temperature stabilized fibers virtually eliminate transmission delay variation, a feature that can be critical for synchronizing distribution of timing signals. Optical attenuators, filters, couplers, and isolators are also readily available making signal processing similar to RF/Microwave engineering. The presentation will discuss these components and techniques while referring to a new optical storage ring that will be used to make a notch filter for Bunched Beam Cooling in the Fermilab Tevatron.

I. INTRODUCTION

Optical signal processing is now a viable alternative for implementing instrumentation in accelerators. Many of the new machines are either very large in size or very exacting in timing precision, old machines can also benefit from the improved performance of optical fibers and components.

Signal transmission around huge accelerators has typically been done with standard coaxial cable. Information bandwidth has increased over the years extending into gigahertz bandwidths. The long lengths coupled with wide bandwidth leads to high insertion loss and dispersion on standard coax. Single mode fiber optics and narrow line width lasers open up a new gateway to high data rates over long hauls with a minimum of loss and virtually no dispersion.

II. FIBER OPTICS VS COAXIAL TRANSMISSION LINES

A single mode optical fiber has a bandwidth capacity of 100 GHz per kilometer, far in excess of the modulators available today. The insertion loss ranges from 0.35 dB per kilometer at 1310 nanometers to 0.15 dB per kilometer at 1550 nanometers. There are two main types of fibers, the standard fiber has a zero dispersion wavelength of 1310 nanometers and dispersion shifted fiber with a zero at 1550 nanometers. The line width of the transmitter light source and its operating wavelength determine the maximum useful bandwidth transmission length product. Cost of signal mode fiber is approximately 25 to 50 cents per meter.

In contrast, coaxial cable must be chosen by examining the transmission bandwidth, allowable link loss, and available funds. Larger coax has lower loss, higher cost, and limited bandwidth due to higher mode propagation. Smaller coax has

*Operated by the Universities Research Association under contract with the U.S. Department of Energy

the advantage of increased bandwidth and lower cost, but at the expense of high losses. In all wide band use of coax, it is important to take into account the effects of dispersion. As can be seen in Figure 1, a length of 1/2 coax that is 100 feet long not only has a gain slope versus frequency, but also nonlinear phase characteristics due to dispersion.

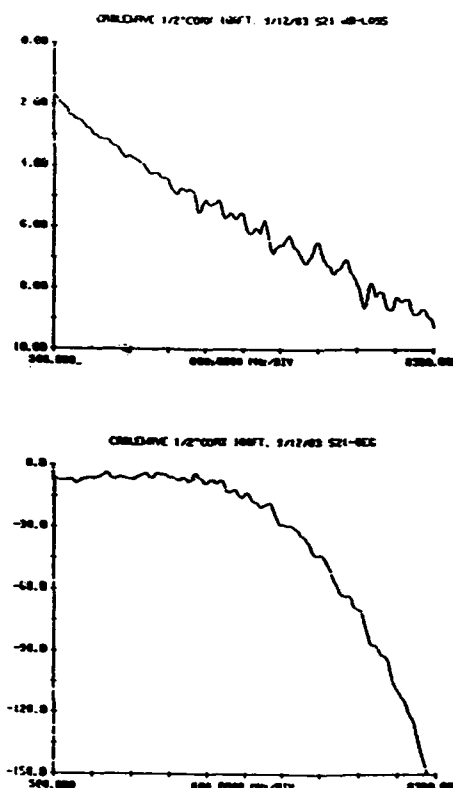


Figure 1. Amplitude and phase response for 100 feet of 1/2 in foam coax measured 0.5 to 8.5 GHz.

For very stringent timing conditions, a specially fabricated single mode fiber with very low temperature coefficient is available[1]. The fiber is jacketed in a special polymer coating that reduces the temperature dependent propagation characteristics dramatically while maintaining the low insertion loss and wide bandwidth characteristics of standard single mode fiber. Figure 2 shows the comparison of this special fiber and standard fiber versus temperature.

Most communication systems use amplitude modulation of the optical carrier for information transfer. Another possibility in some applications would require coherent signal transmission such as in interferometers. Due to polarization sensitivity, coherent systems rely on polarization maintaining

fibers and components. These fibers have elliptical cores which help preserve polarization. Couplers, polarizers and other components are available. [2]

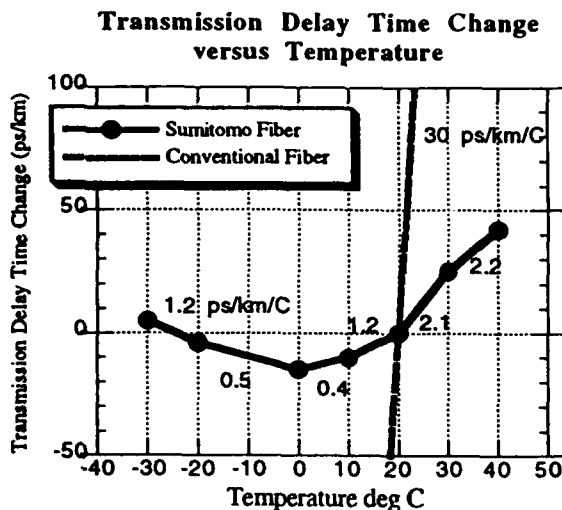


Figure 2. Transmission delay time change versus temperature for conventional and temperature stabilized single mode fiber optic

III. COMPONENTS

Instrumentation in the RF/Microwave frequency ranges has always required more than just a good transmission medium. Other components such as couplers/splitters, isolators, filters, switches, attenuators, transmitters, receivers, amplifiers, etc. are necessary. All of the above devices are now available in fiber optic form.

Fiber optic couplers/splitters are available over a wide range of coupling values. The advantage over their microwave counter parts is that the directivity of these components routinely exceeds 60 dB. Fanout splitters with 2 to 16 outputs are catalog items.

Isolators utilizing the faraday rotation of the light rays can provide 40 plus dB of reverse isolation. This is an important consideration in conjunction with laser transmitters. A laser transmitter outfitted with an isolator can afford a higher percentage of output coupled light with out fear of back reflections that might otherwise damage the laser. The end result being higher transmitter power and longer transmission length capability.

Manually and voltage tuned Fabry-Perot bandpass filters are available. They are typically used for separating different wavelength carriers in wavelength division multiplexing systems. Band limiting noise is also a use with optical amplifiers.

Programmable MxN switch matrices with switching times typically 15 ms or less are standard. Most switches have back reflections of 55 dB typical. Attenuators with continuous

tuning range of 30 dB are available in manual and voltage tuned versions.

The bandwidth of transmitters and receivers has increased steadily over the last few years. Transmitter bandwidths of 15 GHz employing amplitude modulation of laser diode current are standard. Receiver bandwidths exceed 20 GHz. Due to the low input impedance of the laser and photo diodes, resistive matching networks are used to achieve the broad bandwidths. Lossy matching yields a typical insertion loss of 40 dB, but is flat across the band as shown in figure 3. [3] If a bandwidth greater than 15 GHz is necessary, external Mach-Zender interferometer modulators are capable of bandwidths in excess of 20 GHz.[4]

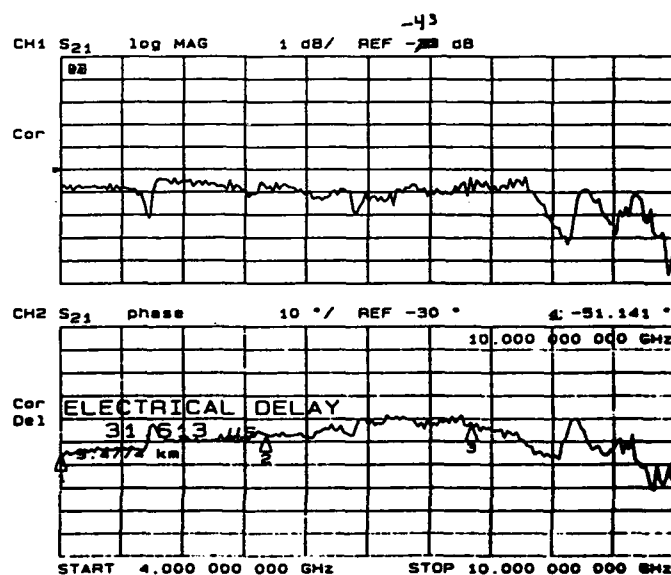


Figure 3. Broad band optical link with 6.44 km of fiber measured from 4-10 GHz.

Perhaps the most important innovation of the last decade is the optical amplifier. Long transmission links such as the trans- Atlantic fiber required electronic repeaters every 40 to 60 kilometers. This meant decoding and re-modulating the signal some 125 times. With an optical amplifier, the information never leaves the photon domain. There are two types of optical amplifiers, a solid state version which operates at 1310 nm, and an Erbium doped fiber version which operates at 1550 nm.

The solid state amplifier (SOA) [5] is basically a diode laser biased below the critical current. The reflective facets are replaced with anti reflective coatings. Incoming photons stimulate emission in the diode amplifier producing 10 to 15 dB of bi-directional gain. The draw back of these amplifiers is the high broad band noise output. They typically are used with some type of bandpass filter.

Erbium doped fiber amplifiers (EDFA) [6] are lengths of rare earth single mode fiber that are pumped with a diode laser of a different wavelength. The pumping causes a population inversion that releases stimulated emission from incoming photons. These amplifiers are substantially quieter than the

solid state units and are capable of more gain and output power. This coupled with the lower insertion loss of fiber at 1550 nm has allowed transmission links that require repeaters at intervals of 200 km. The trans-Pacific link will be installed with Erbium amplifier technology.

For now, finding the rare earth that will make a fiber amplifier at 1310 is still a research project. Most of the installed fiber systems operate at 1310 nm so there is keen interest in fiber amplifiers at this wavelength.

IV. EXAMPLE OF OPTICAL SIGNAL PROCESSING

One example of signal processing using many of the mentioned components is a special correlator notch filter that is required for Bunched Beam Stochastic Betatron Cooling in the Fermilab Tevatron[7][8]. This filter is designed to provide a recursive notch filter operating 4-8 GHz that has a "brick wall" amplitude transfer function with flat phase between notches, see figure 4. The filter is designed to reduce the longitudinal spectral lines from the bunched beam signal (figure 5) without degrading the amplitude and phase of the betatron schottky signal sidebands. Notch frequency stability of 0.1 part per million is desired.

A simplified block diagram of the filter is shown in figure 6. If the optical storage ring can be built to have unity gain, the Q becomes infinite, thus leading to the desired brick wall transfer function. [9] As was pointed out earlier, optical fiber has very low insertion loss, but not zero. In addition, there is insertion loss in the input and output couplers. The length of fiber used to make this filter is 4.5 kilometers in length which corresponds to a transmission signal delay of 21 microseconds, i.e. the revolution time of the beam in the Tevatron. The insertion loss of the optical fiber alone is 2 dB.

Our filter uses the Sumitomo temperature stabilized fiber to achieve the frequency stability mentioned earlier. Figure 7 shows the storage ring Q as a function of optical loop gain.

Before the availability of optical amplifiers, such rings were made by putting a repeater within the loop thus requiring demodulation and regeneration. At wide microwave frequencies this presents a degradation in signal to noise ratio. The solid state optical amplifier used in this filter is polarization insensitive, an important requirement. The slightest twist of any part of the fiber causes the polarization to change dramatically. If the loop gain is not maintained close to unity, the filter will have low Q. If the gain exceeds unity, you have an optical oscillator on your hands that could damage the amplifier.

Due to the high output noise of the amplifier, a tunable bandpass filter is placed after the amplifier. The amplifier has gain in both directions and the laser transmitter is sensitive to back reflections. An isolator is installed to reduce reverse loop gain.

The dynamic range of the optical transmitter/receiver is 55 to 60 dB. This is insufficient dynamic range for this filter application hence a parallel microwave path provides the short leg of the correlator filter. The spectral width of the laser transmitter source is of importance with such long delays. To avoid any coherence length problems, one would like a wide spectral source. Distributed feedback lasers[10] produce very narrow line widths that can lead to carrier interference in the loop. We are using a Fabry-Perot laser which has a line width of 10 MHz.

Figure 8 is a gain and phase plot of the actual filter performance. Narrower frequency span data shows the notch depth to be in excess of 30 dB. Figure 9 shows the dynamic range of the filter.

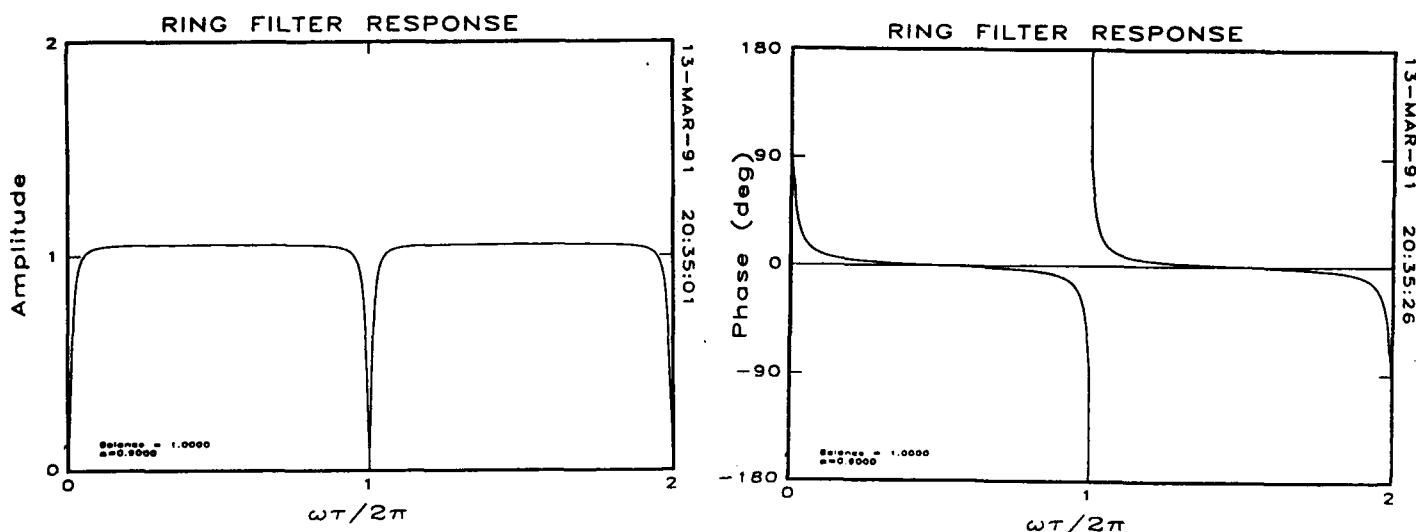


Figure 4. Ideal amplitude and phase characteristics for a storage ring correlator notch filter.

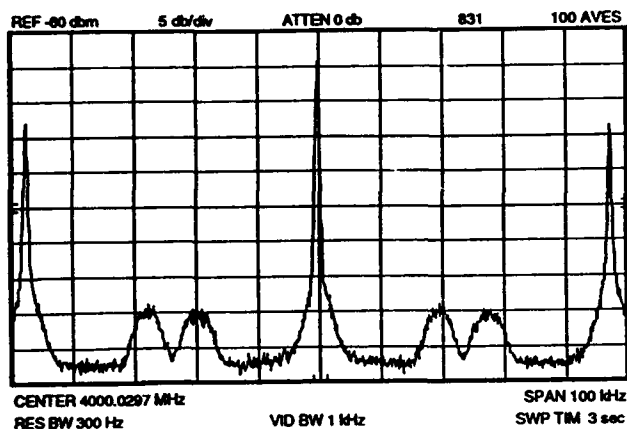


Figure 5. Typical Tevatron vertical bunched beam spectrum at 4 GHz as measured by the vertical proton pickup.

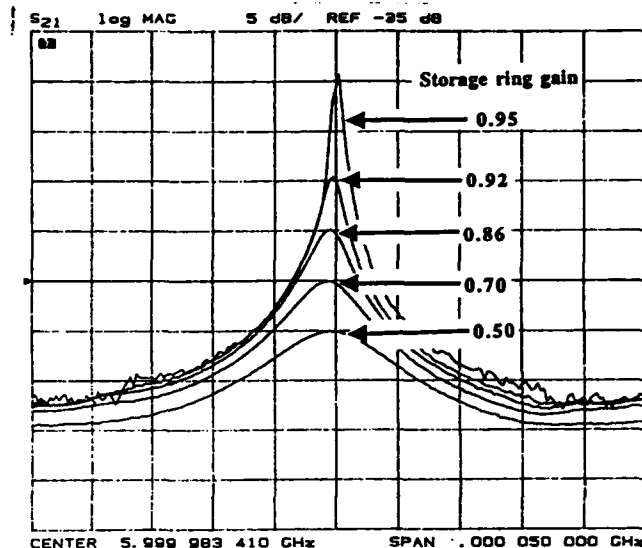


Figure 7. Variation of optical storage ring Q as a function of loop gain.

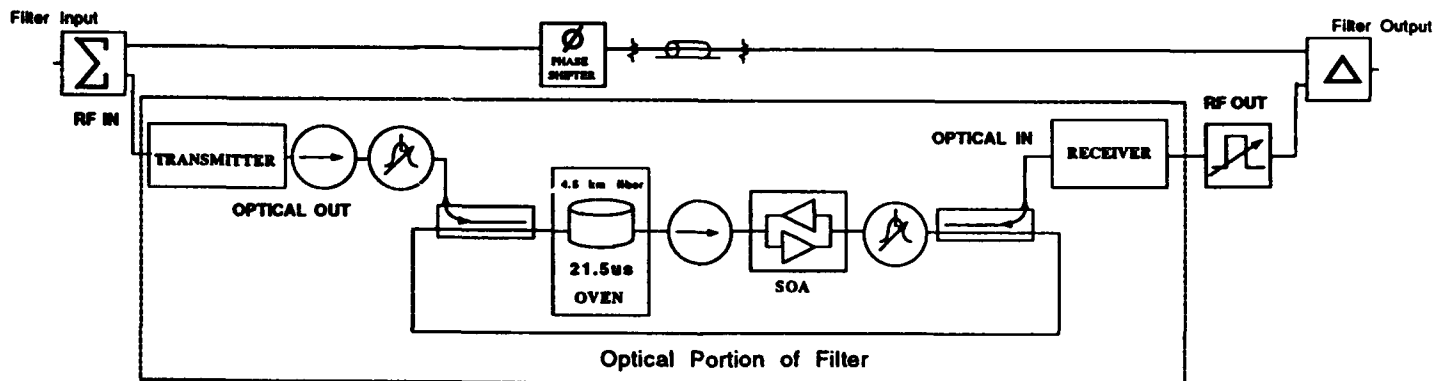


Figure 6. Block diagram of optical storage ring correlator notch filter

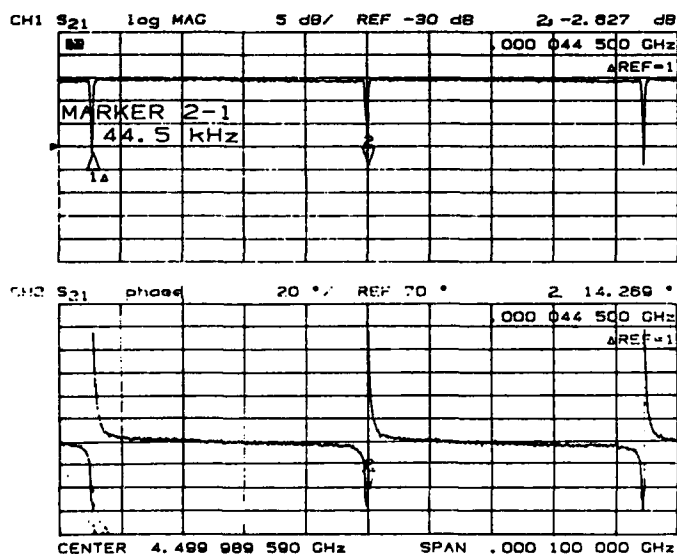


Figure 8. Amplitude and Phase plot of actual filter performance.

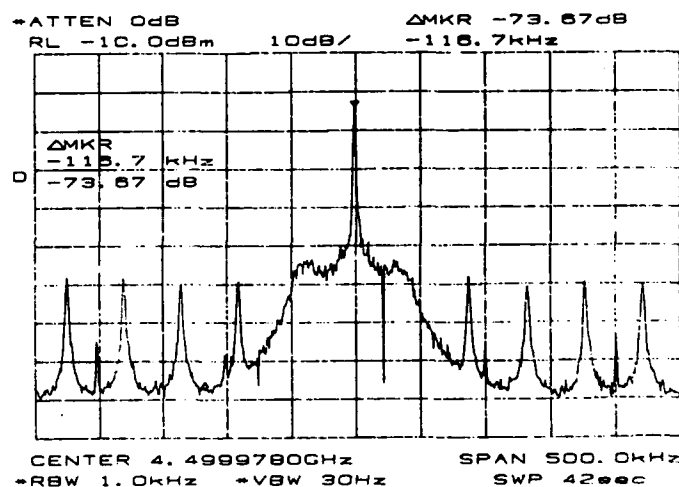


Figure 9. Dynamic range performance of actual filter. Filter is narrow band swept by network analyzer and plotted on wide band with spectrum analyzer. Peaks are noise floor of optical portion of correlator filter.

V. CONCLUSIONS

We have successfully used optics to create a filter for a feedback system that could only be fabricated in the optical domain because of the limitation of microwave transmission lines and devices. Four such filters must be fabricated for the full Tevatron Bunched Beam Stochastic Cooling systems. Future plans are to extend the cooling bandwidth to 8-16 GHz. Because of the wide bandwidth capacity of the fiber optics, only the transmitter and receiver will need to be replaced.

VI. ACKNOWLEDGMENTS

I would like to thank Gerry Jackson for his efforts of doing the theoretical calculations associated with the filter design and Ernie Buchanan for his diligent handiwork in filter construction. He has spent many hours with strands of the angel hair fibers.

VII. REFERENCES

- [1] S. Tanaka, "Phase Stabilized Optical Fiber cable", Sumitomo Electric Industries, Ltd.
- [2] R.B. Dyott, S.M. Bennet, "The Properties of Elliptically Cored Polarization Holding Fibers" Andrew Corporation, Presented at Workshop on Fiber Optics for Missile Applications, Huntsville, AL., May 12-14, 1992.
- [3] Ortel Corporation, Data sheets 5515B Optical Link, Alhambra, CA.
- [4] *Fiber Optics Handbook*, Hewlett Packard, 2nd edition pg. 110-112, 1988.
- [5] BT&D Corp., Solid State Optical Amplifiers, Wilmington, DE.
- [6] J. Hecht, "Laser action in fibers promises a revolution in communications", *Laser Focus World*, Feb. 1993, pg. 75-81.
- [7] R.J. Pasquinelli et al., "Optical Correlator Notch Filters for Fermilab Debuncher Betatron Stochastic Cooling", *Proc. of 1989 IEEE Particle Accelerator Conf.*, pg 694-696.
- [8] G. Jackson, "A Test of Bunched Beam Stochastic Cooling in the Fermilab Tevatron Collider", *Proc. of 1991 IEEE Particle Accelerator Conf.*, pg 1758-1760.
- [9] B. Moslehi, J.W. Goodman, "Novel Amplified Fiber-Optic Recirculating Delay Line Processor", *Journal of Lightwave Technology*, Vol. 10, No. 8, August 1992, pg. 1142-1147
- [10] J. Hecht, "Long-Wavelength diode lasers are tailored for fiber optics", *Laser Focus World*, Aug. 1992, pg. 79-89.

RF-Synchronized Imaging for Particle and Photon Beam Characterizations*

A. H. Lumpkin
Advanced Photon Source
Argonne National Laboratory
9700 S. Cass Avenue, Argonne, IL 60439

Abstract

The usefulness of imaging electro-optics for rf-driven accelerators can be enhanced by synchronizing the instruments to the system fundamental frequency or an appropriate subharmonic. This step allows one to obtain micropulse bunch length and phase during a series of linac bunches or storage ring passes. Several examples now exist of the use of synchroscan and dual-sweep streak cameras and/or image dissector tubes to assess micropulse scale phenomena (10 to 30 ps) during linac and storage ring operations in the U.S., Japan, and Europe. As space permits, selections will be presented from the list of phase stability phenomena on photoelectric injectors, micropulse bunch length during a macropulse, micropulse elongation effects, transverse Wakefield effects within a micropulse, and submicropulse phenomena on a stored beam. Potential applications to the subsystems of the Advanced Photon Source (APS) will be briefly addressed.

I. INTRODUCTION

Significant advantages for imaging instrumentation used for diagnostics and experiments on rf-driven accelerators can be realized if the electro-optics are synchronized to the accelerator fundamental frequency or a subharmonic of the master oscillator. This step allows one to obtain bunch length and phase during a series of linac beam bunches or storage ring turns. Over the last few years synchroscan and dual-sweep techniques using streak cameras [1-3] and/or image dissector tubes [4] have been used to assess micropulse scale phenomena (10 to 30 ps) during linac and storage ring operations in the U.S., Japan, and Europe. Space constraints will limit discussion to selections from the list of phase stability phenomena on a photoelectric injector, micropulse bunch length variation during a macropulse, micropulse elongation effects, transverse Wakefield effects within a linac micropulse, and head-to-tail bunch instabilities in a stored beam. Potential applications to the subsystems of the Advanced Photon Source (APS) will be addressed. Although the number of examples is not large, the applications described cover the gamut of rf-accelerators one might encounter within this conference's purview.

*Work supported by the U.S. Department of Energy, Office of Basic Energy Sciences, under Contract No. W-31-109-ENG-38.

II. BACKGROUND AND PROCEDURES

In some of the earlier attempts on using single-shot streak cameras to assess the micropulse bunch length of beams from a variety of linac configurations, one encountered triggering jitter from the standard pulse generators at that time as well as the internal streak camera timing jitter. The first area we solved by using a synchronous delay unit developed at EG&G (SBO) that referenced itself to the 108.3-MHz subharmonic and then allowed time delays with low jitter for triggering the streak camera. Basically at that time, we dropped the ± 100 ps jitter to about ± 20 ps [5]. Practically speaking, this meant the streak image stayed localized in the 400-ps field-of-view instead of bouncing up and down by one fourth the viewed scene on the time axis. Within the free-electron-laser (FEL) community where I was working at that time, the need for phase stability of the e-beam relative to the oscillator cavity caused us to look at a tradeoff. As seen in Table 1 (Hamamatsu C1587 mainframe), one can significantly

Table 1 Summary of Streak Camera Module Properties

Module*	Temporal Resolution (FWHM, ps)	Phase Jitter (FWHM, ps)	Phase Jitter (rms, ps)
Fast Sweep (single)	< 2	10 - 15	4 - 6
Synchroscan (M 1954)	6 - 8	4	1.7
Synchroscan (M 1954-10)	~ 3 - 4	2	~ 0.8

reduce the streak camera internal jitter by using the synchroscan mode. In this mode, the 108.3-MHz rf signal is injected directly into the camera's sweep circuitry so the plates are driven at the rf frequency and with much lower timing jitter [2]. The temporal resolution was reasonable in the Hamamatsu M1954 system (8-10 ps), but was improved in the M1954-10 unit with 3-4 ps (FWHM) resolution and an rms jitter <1 ps.

Additionally, once in the synchroscan mode, one could synchronously sum the signals from a series of micropulses (such as from optical transition radiation (OTR)) in a linac or turns in a storage ring. To obtain some knowledge of evolution within these much longer timescales, the orthogonal set of plates in the tube were given a time-dependent ramp (Fig. 1). This allows micropulse phenomena to be tracked during macropulse timescales. We identified a number of

phenomena that previously were difficult to assess. These included observation of the time structures of the field-emission electrons reported at the last PAC [6], and a number of transient phase phenomena in photoinjectors, linacs, and potentially in storage rings. The work here uses visible-UV imaging, but could be extended in principle to the VUV, XUV, and x-ray regimes. The techniques directly apply where a conversion mechanism transforms the particle beam information into the detectable photon field. Descriptions of many of these results are given in more detail elsewhere [3]. I will concentrate on data from the rf-linac driven FEL programs at Los Alamos and Boeing, which include the first dual-sweep results on a drive laser for a photoinjector and for linac-driven FELs. It should be noted that work in Japan was the first on a storage ring [1], while additional effort with a different dual sweep camera has been going on at CERN by E. Rossa in 1990-93. [7]

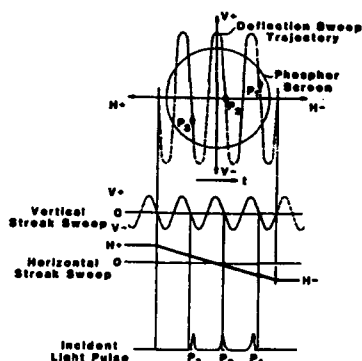


Figure 1 A schematic of the dual-sweep streak techniques.

III. EXAMPLES OF RESULTS

As discussed earlier, the usefulness of these techniques can be graphically demonstrated by measurements made in various stages of the production and use of a charged-particle beam in an accelerator system. Possible uses include the experimental area, a FEL wiggler, injection into a storage ring and its undulators, etc.

A. Photoinjector Drive Laser

Laser phase jitter was not identified as an issue in an early configuration of the 1-MeV photoinjector at Los Alamos because the jitter was much less than the ~ 60 ps bunch length. However, phase stability issues soon became evident in the next configuration of a 6-MeV photoinjector, followed by a second 12-MeV accelerator [8]. In these operations of the 1300-MHz rf cavity and with drive laser bunch lengths of 5-15 ps, drive laser phase jitter shot-to-shot directly impacted particle beam stability shot-to-shot (macropulse-to-macropulse). Because there has been increased activity in the use of these devices, it is appropriate to remind the accelerator community of the obvious: you need a stable laser. The mode-locked Nd:YLF oscillator configuration at Los Alamos is shown in Fig. 2. Although details will not be presented here of its

operation, several references exist [9]. We actually looked at both the fundamental, $\lambda=1.053 \mu\text{m}$, before and after the pulse compressor as well as the final doubled-frequency component after the KTP crystal which was delivered to the photocathode.

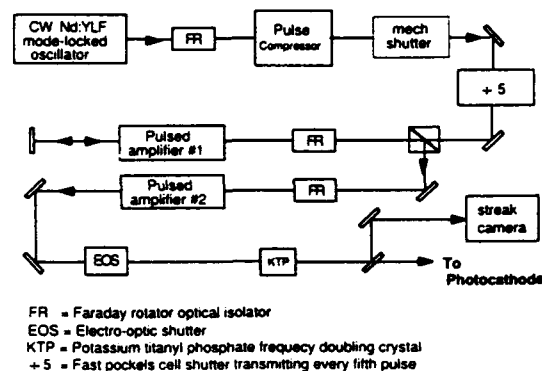


Figure 2 Schematic of modelocked Nd:YLF drive laser on the Los Alamos photoinjector.

The initial data that we saw were synchroscan streak images on the video monitor that moved (jittered) on the time axis more than the pulse length. There, of course, was a discussion over whether this image jitter was due to streak camera timing jitter or laser jitter. We resolved this by playing back from the encoded video record into the digitizer a series of consecutive macropulses and displaying them in sets of four. In this case (Fig. 3), the horizontal axis is the time axis, and the motion of the center of the profile is evident (macropulse integrated). From the same set of video-encoded

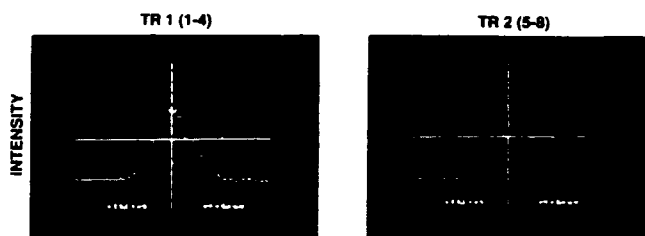


Figure 3 Drive laser micropulse temporal profiles for 8 consecutive macropulses taken using the synchroscan streak camera.

data we analyzed the electron spectrometer images at the end of the linac for the same 16 macropulses and tracked the e-beam energy. As seen in Fig. 4, a strong correlation is observed between the relative drive laser phase jitter and the e-beam energy. A sensitivity of about $0.1\% \Delta E/\text{ps}$ at 17 MeV was observed which was in reasonable agreement with PARMELA simulations. [10, 11] This was cross-checked against a deliberate change of a NARDA phase shifter on the drive laser where a 14-ps shift resulted in a 1.5% energy change. In fact, in our limited field-of-view of the energy in the spectrometer, for the larger phase jitters (>5 ps) the energy shifted out of view! Further corroboration of the phase jitter in the drive laser was seen when an active Lightwave phase

feedback unit was incorporated into the laser system, and these effects were significantly reduced as shown in Fig. 32 of Ref. 3.

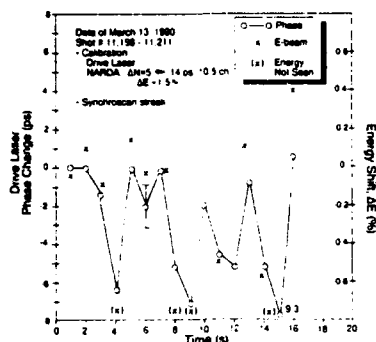


Figure 4 Comparison of observed drive laser phase jitter and e-beam energy for the same 16 macropulses.

This was a shot-to-shot (intermacropulse) phenomenon, but there were additional intra- or submacropulse effects in the drive laser that occurred in the 10- μ s domain. These also were sufficient to affect FEL operations within a macropulse. In this case, the dual sweep feature of the camera was used. Eight time-samples were selected for analysis across the nominal 20- μ s-long macropulse. Both single and 20-macropulse averages were used. The nominal bunch length was still 7-10 ps. In Fig. 5, for some data (File 9) the phase

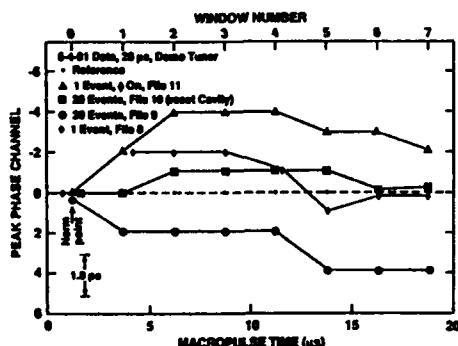


Figure 5 Submacropulse phase slew effects in the drive laser 20- μ s long macropulse.

of the laser drifted about 4 ps (which would be 0.4% ΔE at 17 MeV and 0.8% $\Delta \lambda$ at 10 μ m) during the macropulse. Resetting the cavity (File 10) resulted in stable behavior within the error of the measurement (~ 1 ps), as referenced to the normalization line. More details are in Ref. 11.

B. Photoinjected Linac

Just as the timing (relative to the rf field) of the release of the electrons from the photocathode may be expected to cause an energy effect, it also is related to transit time through the photoelectric injector (PEI) accelerator first cell and the rf bunching across the micropulse available from the field gradient. Figure 6 shows our measurement at 17 MeV on the

observed bunch length and transit time. In the dual images we "simultaneously" detected (1) a split-off fraction of the drive laser light beam just before the photocathode and (2) the subsequent electrons at 17 MeV via a Cherenkov converter. Figure 7 shows the variation of this phenomenon as a function of drive laser phase. The elongation due to space change forces increases as the effective field gradient is reduced. The PARMELA simulation by B. Carlsten (solid line) is in good agreement [8].

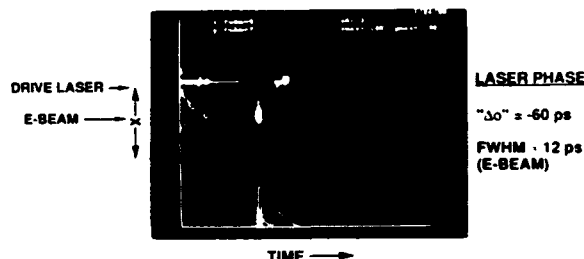


Figure 6 Streak images of the drive laser and e-beam micropulses for one laser phase setting.

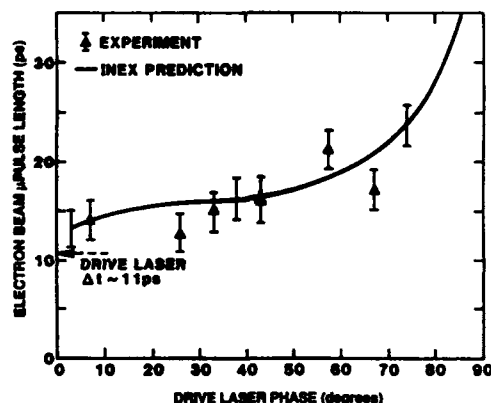


Figure 7 Plot of observed e-beam bunch length versus drive laser relative phase. The drive laser bunch length was monitored at 11 ps.

C. 110-MeV Linac

The next example is from operations a few years ago on the 110-MeV linac injected with electrons from a thermionic-gun with rf buncher system (at Boeing in Seattle, WA). This linac beam was used to drive a visible FEL oscillator experiment. The output spontaneous emission or lasing from the 5-m wiggler was optically transported to a streak/spectrometer system [12]. During the course of the various configurations of the experiment including a ring-resonator mode, the electron-beam bunch length was shown to vary during the macropulse. As shown in Figs. 8 and 9, the bunch length FWHM started at ~ 25 ps and was reduced to ~ 10 ps (as was its intensity) by the end of the 100- μ s-long macropulse. Since FEL gain is strongly dependent on peak current, inefficient operations resulted. The e-beam problem was traced to the combination of an rf phase slew, an energy slew, and a nonachromatic bend in the beam transport.

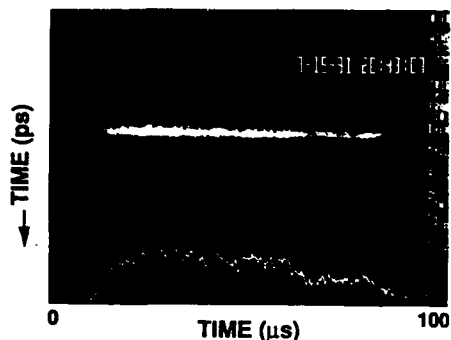


Figure 8 Dual-streak image of the e-beam micropulse bunch length variation during the 100- μ s long macropulse.

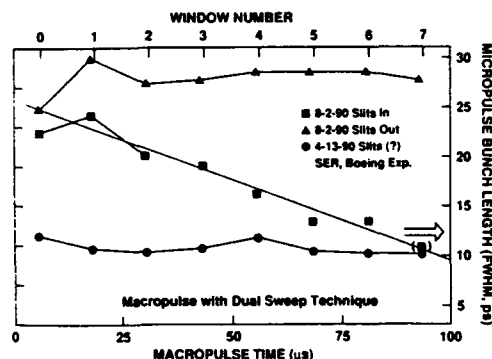


Figure 9 Eight-window samples analyzed on the macropulse time axis from Fig. 8 showing the 25- to 10-ps bunch length variation in the 8-2-90 data (squares).

Another example of dual-sweep data is shown in Fig. 10 involving the FEL output. The laser intensity was strongly modulated during the macropulse while we simultaneously measured the ~ 8 -ps (FWHM) lasing micropulse. The modulation was correlated with an e-beam energy centroid modulation measurement (using a stripline BPM in a dispersive location) and traced to the rf system (the pulse-forming network). When the rf system was corrected, significant improvement in e-beam parameter stability and FEL quality resulted [13].

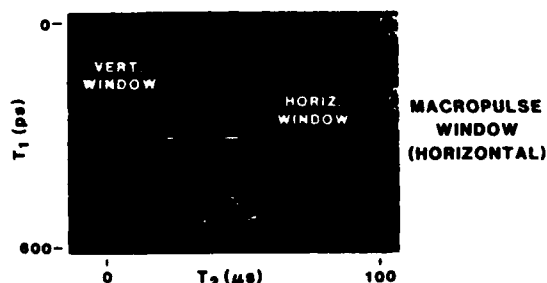


Figure 10 Dual-sweep streak image of the Boeing visible FEL output showing intensity modulation during the macropulse.

D. Transverse Wakefields

In most applications for low-emittance beams, it is not sufficient to generate them; you must preserve the beam as you

transport it. As an example, off-center transport through subsequent linac tanks can degrade the beam. An example is shown from the 40-MeV linac at Los Alamos [14]. Figure 11 shows the experimental setup where a synchroscan streak camera was used to view the forward lobes of the optical transition radiation (OTR) foil at station #4 after the fourth tank (D). Another OTR screen after Tank C was used to determine the position entering Tank D. Steering magnets were used to change the beam offset as it went through Accel. D to screen 4. In Fig. 12, for $Q=5$ nC per micropulse, the time-resolved x-profile is shown for different steering/offset conditions. The images are the synchronous sum of the micropulses in one macropulse, and one can see that the direction of the head-to-tail kick changes on the micropulse time scale as the beam is steered differently through Tank D. In fact, Fig. 12 a,b shows one can actually compensate for the transverse kick and reduce the observed time-averaged spatial x-profile FWHM from 0.8 mm to 0.4 mm. More detailed discussion is given elsewhere in this conference [15].

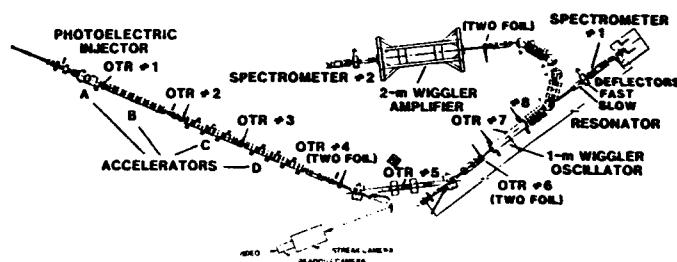


Figure 11 Experimental setup for the synchroscan streak camera on the Los Alamos 40-MeV linac. The forward OTR radiation from the screen after Tank D is detected.

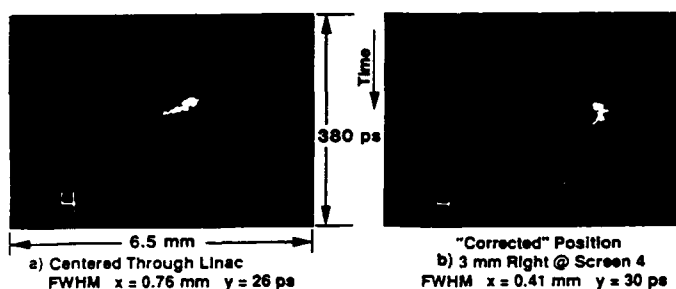


Figure 12 Synchronous sum of submicropulse streak data exhibiting "head-to-tail" kick changes with steering through the linac.

Similar phenomena have been detected at SLAC and more recently at LEP by E. Rossa using a dual-sweep streak camera. Figure 13 is a reproduction from the CERN work illustrating the head-to-tail transverse effect in LEP [7]. The micropulse time scale is horizontal and the vertical axis is related to the transverse spatial projection. The "tilts" of some of the bunch projections imply the head-to-tail kicks varied on different turns.

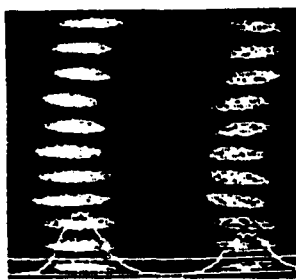


Figure 13 Reproduction of dual-sweep data from the LEP experiment by E. Rossa, et al. [7] showing head-to-tail kicks in a single bunch over 11 turns. The left set is y-t (sideview) and the right set is x-t (top) view.

E. Potential Applications at APS

At APS the undulator test line will involve a low-emittance beam in a small bore linac structure. Potential transverse Wakefield effects such as described earlier will be considered. In the 7-GeV storage ring, we have revisited the possibility of longitudinal instabilities and how to measure them. A workshop was held on this topic in 1989 specifically for the APS storage ring [16]. L. Emery's recent simulations using the impedance file prepared for the APS storage ring indicates that in addition to bunch length changes, the longitudinal phase space could vary as a function of time [17]. Variation of the projection on the time axis after injection and during damping for different currents should be directly measurable by the dual-sweep streak techniques. Additional work is needed to simulate how this phenomenon might carry over to the transverse phase-space projections.

IV. SUMMARY

In summary, a number of diagnostic applications are noticeably enhanced by using rf-synchronization techniques for the streak camera systems. Both synchroscan and dual-sweep features are important. The synchroscan allows the synchronous sum of pulses to be done with good temporal resolution, and it also allows the use of less bright conversion mechanisms (such as OTR) to be used in intercepting beam experiments. The dual-sweep allows the tracking of ps-phenomena over much longer time scales on a linac macropulse or many turns in a circular accelerator. The techniques have been applied successfully to both particle and photon beams on the submicropulse, submacropulse, or single pass mode. They have been applied to rf-linacs driving FELs and should be useful to linacs injecting damping rings or storage rings (as well as the rings). It is expected they will be applied to the subsystems of the APS, and hopefully be eventually extended to study the x-ray beams from the APS.

V. ACKNOWLEDGEMENTS

The author acknowledges the staff and technicians at the Los Alamos FEL facility (M. Wilke, S. Apgar, J. Early, D. Feldman, P. O'Shea, et al.) and the Boeing FEL facility (D. Dowell, P. Johnson, A. R. Lowrey, K. Davis) for their assistance during operations and experiments; the Simulation group (M. Schmitt, B. Carlsten, et al.) at Los Alamos for many useful discussions; M. Couprie of Orsay for information on the Super-ACO experiment; E. Rossa of CERN for discussions of his dual-sweep system; and L. Emery of Argonne for his recent simulation of APS longitudinal phase space effects.

V. REFERENCES

- [1] Kazuhisa Nakajima, and Atsushi Ogata, "Variation of Longitudinal Beam Profile During Acceleration in Tristan Main Ring," *6th Symposium of Accel. Sci. and Tech.*, Tokyo, Japan, Oct. 27-29, 1987.
- [2] Y. Tsuchiya, et al., SPIE Vol. 693 Highspeed Photography, Videography and Photonics IV, p. 125 (1986).
- [3] Alex H. Lumpkin, "Advanced Time-Resolved Imaging Techniques for Electron-Beam Characterization, *AIP*, No. 229, p. 151 (1991), and references therein.
- [4] M. Couprie, et al., *NIM A318*, p. 59 (1991).
- [5] A. H. Lumpkin, et al., *NIM A285*, p. 17-22 (1989).
- [6] Alex H. Lumpkin, et al., *Proceedings of the 1991 PAC*, Vol. 3, p. 1967 (1991).
- [7] E. Rossa, et al., "Real-time Measurements of Bunch Instabilities in LEP in Three Dimensions Using a Streak Camera," CERN, 92-SL-155.
- [8] A. H. Lumpkin, et al., *NIM A304*, p. 379-385 (1991).
- [9] J. W. Early, et al., *NIM A318*, p. 381-388 (1992) and references therein.
- [10] B. E. Carlsten (Los Alamos National Laboratory), private communication, 1990.
- [11] Alex H. Lumpkin and James W. Early, *NIM A318*, p. 389-395 (1992).
- [12] A. H. Lumpkin, et al., *NIM A296*, p. 169-180 (1990).
- [13] D. H. Dowell, et al., *NIM A318*, p. 74-80 (1992).
- [14] Alex H. Lumpkin and Mark D. Wilke, "Time-Resolved Electron Beam Characterizations with Optical Transition Radiation," presented at the *14th International Free-Electron Laser Conference*, Kobe, Japan, Aug. 23-28, 1992.
- [15] P. G. O'Shea, et al., "Measurement of Single-Bunch Transverse Wakefield Effects in an Electron Linac," these proceedings.
- [16] Proceedings of the Impedance and Bunch Instability Workshop, Argonne National Laboratory, Argonne, Illinois, Oct. 31-Nov. 1, 1989, ANL/APS/TM-5 (April 1990).
- [17] L. Emery (Argonne National Laboratory), private communication, May 1993.

2091

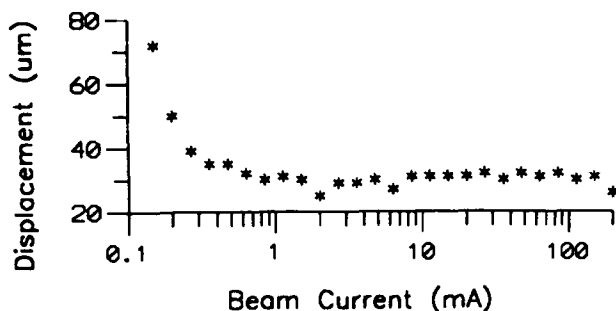


Figure 3. Current dependent drift of the measured beam position.

B. Intensity monitor

Bergoz's parametric current transformer (PCT) is used to measure average beam current with resolution better than 1 μ A (1 sec integration window). The output of PCT are digitized by 16 Bits ADC module on VME crate at current stage. The ADC card will be changed to high resolution DVM for high precision measurement. High frequency components of beam current are observed by a fast current transformer (FCT) with rise time better than 1 ns. The beam filling structure at injection phase and routine operation can be observed by FCT.

C. Stripline electrodes and excitation electrodes

Two linear tapered stripline [4] electrodes were used to measure transverse motion and time structure as shown in Figure 4 (a). The linear tapered preserve wide bandwidth feature with slightly large amplitude ripple than ideal exponential taper (6 dB from 300 MHz to 6 GHz) [5]. Easy fabrication was the main reason to choose linear tapered stripline from mechanical point of view. Typical beam response of the linear tapered stripline measured by using 20 GHz sampling oscilloscope are shown in Figure 4 (b), the bunch length less than 100 psec (FWHM) are observed when the gap voltage of RF cavity is 300 kV.

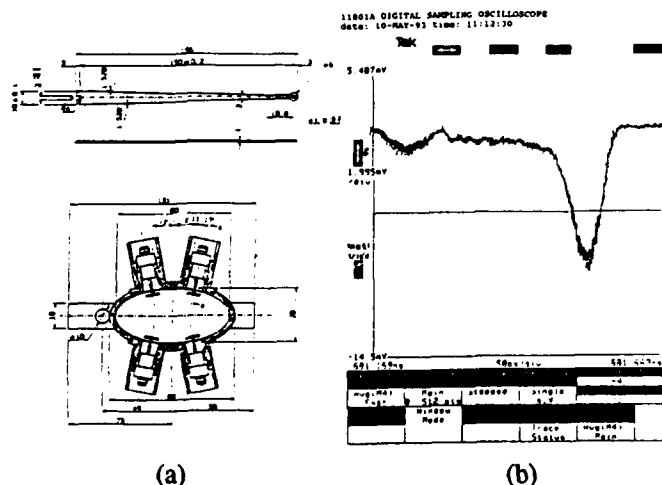


Figure 4. (a) Structure of the linear tapered stripline, (b) Beam response of the linear tapered stripline.

One set excitation electrodes which is composed by four electrodes mounted on skew position of circular vacuum chamber as a magnetic kicker. The excitation electrode is used to excite transverse beam motion or to damp transverse instability if necessary.

D. Tune measurement

Two methods are adopted to measure betatron tune currently. One is using RF knockout technique by using the combination of stripline electrodes, excitation electrodes and spectrum analyzer/tracking generator. The alternate approach are using one of the kickers to provide about 1 mrad kick angle, and Fourier analysis turn-by-turn beam position motion by oscilloscope as shown in Figure 5. The synchrotron turn are observed from the synchrotron sideband near the harmonics of the revolution frequency.

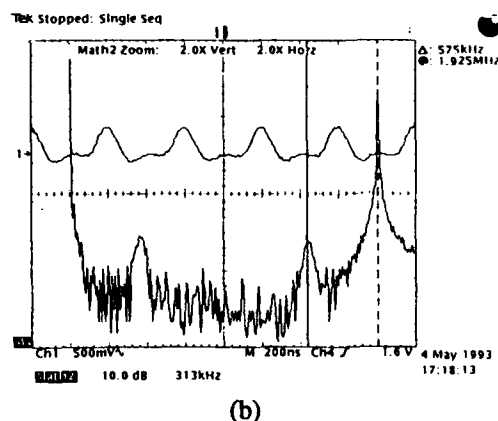
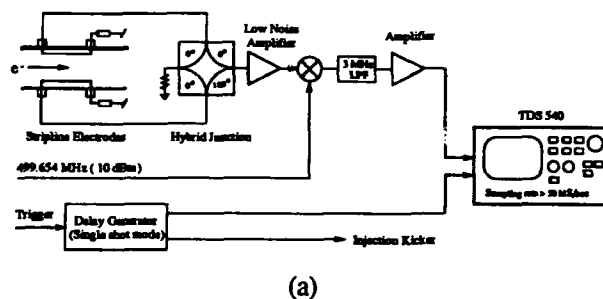


Figure 5. (a) Betatron tune measurement setup, (b) Typical spectrum of the betatron oscillation.

E. Screen monitor

Injection conditions and first turn behaviours of the storage ring are study by the aid of eight fluorescent screens. The screen is mounted on the linear motion feedthrough driven by stepping motor. CCD cameras are use to observe fluorescent light.

F. Synchrotron radiation monitor

The synchrotron radiation output from one bending magnet was used to measure the transverse profile by XC-

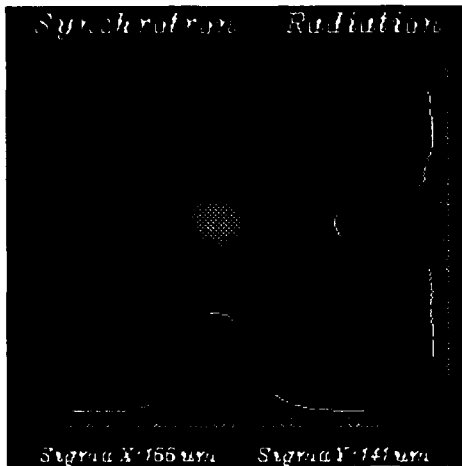


Figure 6. Preliminary result of synchrotron radiation profile measurement, no correction on depth of field and diffraction effect.

77RR high resolution CCD camera. The video signal are captured by frame grabber to extract the transverse profile information. Figure 6 are the the preliminary results of profile measurement. Line scan CCD camera, quadrature diode array, position sensitive detector will be used to measure beam motion. Optical sampling oscilloscope with resolution about 10 psec will be used to measure averaged bunch length.

III. TRANSPORT LINE DIAGNOSTICS

The diagnostic devices of the transport line consist of beam position monitors, current monitors, screen monitors and secondary emission monitor. Seven stripline beam position monitors are used to measure electron beam position. The accuracy of the BPM is better than ± 0.5 mm. Output of the front-end electronics for BPM are shown in Figure 7. The transmission efficiency of the transport line are measured by Bergoz's fast current transformer as shown in Figure 8.

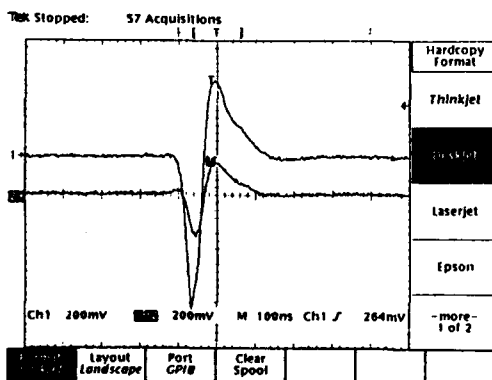


Figure 7. BPM front-end electronics output, upper trace is the response of the left electrode, the lower trace is the right electrode response.

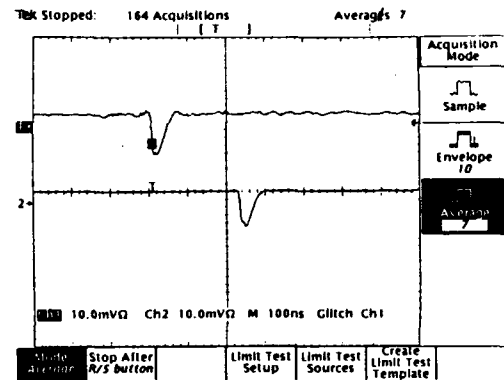


Figure 8. Beam response of the FCT, upper trace is the response of FCT which is located at upstream of the transport line, the lower trace is the downstream FCT response.

Transverse beam profile and spatial position are observed by six screen monitors. The design of the screen monitor are same as the storage ring. One secondary emission monitor will be used to measure transverse profile.

IV. CONCLUSION

The commissioning of the storage ring is under way. From the preliminary beam test results shown that most of the diagnostic devices are work functionally as the design specifications. Improvement and reinforcement of the diagnostics system will be continued.

V. ACKNOWLEDGEMENT

We are thankful to T. Katsura (KEK-PF), J. Hinkson (ALS), F. Loyer (ESRF), T. Linnecar (CERN) for their helpful suggestion.

VI. REFERENCE

- [1] "SRRC Design Handbook", Synchrotron Radiation Research Center, 1989.
- [2] G. J. Jan, and K. T. Hsu, "Beam diagnostic instrumentation of the synchrotron radiation research center", Proc. of the Workshop on Advanced Beam Instrumentation, KEK, Tsukuba, pp.60, April 22, 1991.
- [3] G. J. Jan and K. T. Hsu, "Beam Position Measurement System for SRRC", IEEE Proc. of the Part. Accel. Conf. San Francisco, 1157 (1991).
- [4] Private communication with J. Hinkson of ALS and T. Linnecar of CERN-SL.
- [5] T. Linnecar, "The High Frequency Logitudinal and Transverse Pickup Used in the SPS", CERN-SPS /ARF/78-17, (1978).

Overview and Status of Beam Instrumentation at the SSC

Robert C. Webber
Superconducting Super Collider Laboratory*
2550 Beckleymeade Avenue, Dallas, Texas 75237 USA

Abstract

An overview of beam instrumentation requirements at the SSC and a status report on work progress is given. Small transverse emittance beams, ranging in energy from 30 KeV to 20 TeV, must be commissioned, measured, and diagnosed. Instrumentation plans and current design and development efforts for BPMs and other systems are presented. Monitors and electronics soon to be delivered for use in the Linac are described. Design of the Linac systems has been done with requirements and applications in the synchrotrons in mind and thus should provide a basis for design of much of that hardware. The useful commonality of design across the machines is discussed.

I. INTRODUCTION

Instrumentation for one Linac, three booster synchrotrons, the two Collider rings, associated transfer lines, and the test beams facility must be provided to commission and operate the Super Collider [1]. With the wide range of beam energies encountered within the SSC complex, nearly every imaginable type of instrumentation has potential application, from the traditional slit and collector emittance measuring unit for 2.5 MeV H-minus ions to exotic schemes for profile measurement of the 20 TeV proton beams. The many kilometers of accelerator and beamline ensure that all types of traditional instrumentation will exist in large quantities. Yet, budgetary limitations and the sheer magnitude of the task require concentration on a sound baseline suite of instrumentation. Table I provides an approximate instrumentation count.

II. PLANS, ACTIVITIES AND STATUS

A. BPM Mechanics

BPM designs are a focus of current activity. Open-circuited microstrip type designs are planned for use through the drift tube section of the Linac and center-tapped 'button' style monitors for the side-coupled Linac sections. External mechanical constraints, rather than beam or signal characteristics, drive the choice of two different design styles. Linac BPMs are in fabrication at this time.

Throughout the synchrotrons and transfer lines, plans call for stripline type pick-ups which are shorted at one end. The stripline design has been chosen to obtain adequate signal

strength for low intensity commissioning of the superconducting rings, while maintaining well controlled impedances presented to the beam. The shorted-end design halves the number of signal feedthroughs required relative to an externally terminated design and eliminates reliability concerns of an internally terminated design. Additionally, the shorted-end pick-up exhibits no directionality, permitting it to be used in the HEB where beams circulate opposite directions from one cycle to the next and in the LEB where mechanical constraints require pick-up installation in alternating longitudinal orientations.

The HEB and Collider BPMs, located within the cryogenic spool pieces, must be designed to operate reliably and predictably at 4°K and through numerous temperature cycles [2]. It is anticipated that a common design will satisfy the requirements and constraints of those two machines, though plans call for both two and four electrode versions in the Collider. An early version prototype Collider BPM exists and procurement of prototypes of the current design is underway. The possibility of a warm beam tube liner for synchrotron radiation absorption within the cold Collider vacuum tube strongly impacts aspects of BPM design. Efforts are underway to identify a design that satisfies beam impedance and heat leak requirements without sacrificing position measurement performance.

B. BPM Electronics

Considerable development effort has been expended toward the use of logarithmic video detecting amplifiers in beam position processing circuitry [3]. Current plans are to use such circuits, operating in the 47-60 Mhz band, for Linac and LEB BPMs. Identical circuitry will form the core for both systems, though the Linac signals first require a 428 to 60 Mhz frequency conversion stage. Experience acquired during development of the log-amp electronics for those applications will determine its suitability for use in the common BPM electronics design required for the MEB, HEB, and Collider. A prototype of this circuitry has been tested with real beam signals at the FNAL Booster and its performance [4] compares favorably with the AM-PM circuits employed there. The log-amp processing method offers the wide instantaneous dynamic range and "automatic" normalization provided by the AM-PM method, while offering advantages including simplicity of implementation, relaxed phase matching requirements of the input signals, and wider input signal bandwidth acceptance. Signals from BPM pick-ups in the Linac will also be used as beam phase and time-of-flight monitors. A novel phase measurement method has been developed to meet the accuracy

* SSC operated by the Universities Research Association Inc. for the U.S. Department of Energy under Contract No. DE-AC35-89ER40486.

Table 1
Quantities of Beam Instrumentation Required in SSC Accelerators

Instrument	Linac	LEB	MEB	HEB	Collider	Transfer and Test Beam Lines
Planes of Beam Position Measurement	78	180	218	330	2320	142
Beam Loss Monitors	22	90	206	330	3000	175
DC current monitor	-	1	1	1	2	-
Wideband and Fast (video bw) current monitor	20	2	2	3	4	37
Beam Phase Monitor	39	1	1	1	2	8
Diagnostic Kickers	-	H&V	H&V	H&V	2 X H&V	-
Wire Scanners	32	-	1	-	-	10
Assorted Profile Monitors	2	3	9	6	6	36
Assorted Misc. Monitors	-	-	-	6	12	20

and dynamic range requirements demanded in this application [5].

Turn-by-turn position data acquisition is planned for each BPM location in each synchrotron. A VXI circuit board has been designed to provide the required digital processing and interface circuits and to accommodate a plug-in module for the log-amp analog signal processing circuitry [6]. A single board is designed to process two planes of position measurement. It digitizes both position and sum signals for each plane and has on-board memory to store up to 64K samples of each signal. Programmable averaging capability of up to 2048 turn-by-turn positions is also featured for closed orbit measurements. Memory freeze capability is included for quench and beam abort post-mortem analysis.

The concept of a plug-in module for the analog circuitry permits the same board to be used with little modification for other applications, such as beam loss monitors. Discussions have been held with numerous electronics manufacturing companies, large and small, in preparation to contracting for design assistance with this board. The quantities required force us to address industrial production and quality issues, especially in the areas of manufacturability, reliability, and testing. The plan is for development of a product suitable to our needs which may be made commercially available.

C. Profile Monitors

The small beam emittance, 1π mm-mrad normalized rms, and tight budget for allowable emittance growth through the accelerators make transverse beam size and profile measurements both essential for diagnosis of emittance blowup problems and difficult to accomplish. Accurate determination of beam sizes as small as 100 microns must be made in the high energy machines.

In the Linac and up to the LEB, traditional stepper motor

driven wire scanners will be used [7]. They will be mounted at 45° to allow both horizontal and vertical measurements to be made at one location with a single device. Such instruments are already in use on the ion source and RFQ [8]. For longitudinal profile measurements in the Linac, a 'Feschenko style' bunch length monitor is being built [9].

Multi-wire harps are expected to be used as transverse profile monitors in most transfer lines, where single pass profile measurements are required due to long machine cycle times. The HEB to Collider transfer lines may be exceptions where required beam size resolution is difficult to achieve with harps. Also, the tolerance of the Collider superconducting magnets to energy deposition from scattered particles from such intercepting monitors may limit their usefulness in those lines. Ionization monitors, optical transition radiation monitors, and monitors employing a transverse probe beam have been suggested as possible solutions for this application. Little concentrated effort has yet been spent considering the merit, feasibility, or design of such devices.

In the synchrotrons, the baseline method for profile measurement is envisaged to be the flying wire. Design details for flying wire systems at the SSC have not yet been addressed. Such a device is believed to be quite adequate for the MEB and HEB rings. In the LEB there is concern that the fly time of the wire through the beam is unacceptably long compared to expected dynamic variation of beam parameters. Some effort has been spent investigating a suitable design for an ionization profile monitor for that application. In the Collider, the wire-beam interaction time can be shorter than a single turn. However, there are concerns there about emittance growth, energy deposition effects of scattered particles, and luminosity lifetime degradation if the wire is used with a full intensity beam during a colliding beams store. There have been efforts

in the Collider group to assess the relative merits of numerous other, less obtrusive methods for continuous emittance monitoring in the Collider [10]. Schemes utilizing synchrotron light, ionization, and both neutral and electron probe beams have been considered [11], [12], [13]. The current view of that group is that an electron probe device is the most attractive alternative. Efforts are underway to initiate an R&D project for such a device.

D. BLMs

Reliable beam loss monitoring systems are required for commissioning, operations, and diagnostics purposes, as well as for machine protection and quench prevention in the superconducting rings. The baseline design is still use of FNAL style ion chambers or BNL style proportional chambers regularly spaced around the rings, typically near the quadrupole locations. There has been some investigation of solid state detectors, including PIN diodes and HgI₂ and CdTe based devices, as possible alternatives. Of these, the HgI₂ device offers the highest radiation damage threshold and lowest leakage current.

III. COMMONALITY ACROSS MACHINES

The goal of commonality of design across machines is a necessary and desirable objective in a project of SSC scale. Manpower resources, budget, and schedule all contrive to limit the number of unique designs that may be produced. Yet, performance requirements, space constraints, and aperture requirements demand that the individual details, especially of the mechanics, of each application not be ignored. This is especially true in the low energy end of the Linac, which is now being designed, where space is scarce and instrumentation performance requirements are exacting.

Each of the synchrotrons has a unique beam tube aperture and/or cross-section resulting in different BPM pick-up designs, except perhaps for a common HEB / Collider design. Differences of beam size, relevant measurement time scales, and machine operating tolerance for beam loss and emittance blowup all affect instrumentation design decisions.

Signal processing electronics is an area in which we find more practical commonality over larger scales. System functional requirements, as well as beam bunch intensities and time structures, throughout the MEB, HEB, and Collider rings are quite similar, permitting use of a single BPM electronics design throughout. We also expect beam loss monitoring electronics hardware to be common across at least the high energy machines.

Resources are stretched much more by the number of designs than by the production quantity of any one design. Nevertheless, final designs must be compatible with mechanical reality, and provide credible and useful information on the beam parameters they are intended to measure. This forces the need for continual compromises.

IV. SUMMARY

Many activities covering a broad range of beam instrumentation issues and designs are underway at the SSC

with contributions from various corners of the laboratory organization. There are simultaneous efforts to design and build the 'bread and butter' instrumentation essential to any accelerator and to develop strategies for coping with the unique instrumentation problems posed by the small emittance and high energy beams of the SSC. There is a continuous struggle to achieve the economy of scale possible by commonality of design while sacrificing as little performance as possible in any particular application.

V. REFERENCES

- [1] Superconducting Super Collider Laboratory Site-Specific Conceptual Design Report, SSC Laboratory Report No. SSCL-SR-1056, (1990).
- [2] D. Martin, "Instrumentation Issues at the SSC," Proceedings of the Second Annual Accelerator Instrumentation Workshop, Batavia, Illinois, AIP Conference Proceedings No. 229, ISBN 0-88318-832-1 (1990).
- [3] R. Aiello, "Log-ratio Technique for Beam Position Monitor Systems," to be published in AIP Proceedings of the Fourth Annual Accelerator Instrumentation Workshop, Berkeley, California (1992).
- [4] R. Aiello and M. Mills, "Test Results of the SSC Log-Ratio Beam Position Monitor Electronics," to be published in proceedings of 1993 Particle Accelerator Conference.
- [5] R. Aiello, "A Digital Approach for Phase Measurement Applied to Delta-t Tune-up Procedure," to be published in proceedings of 1993 Particle Accelerator Conference.
- [6] A. Jones, "VXIbus Register Based Beam Position Monitor," SSCL Pre-print 153, 1992, to be published in AIP Proceedings of the Fourth Annual Accelerator Instrumentation Workshop, Berkeley, California (1992).
- [7] J. Hurd, et al., "Beam Diagnostic Layout Requirements for SSCL Linac," to be published in proceedings of 1993 Particle Accelerator Conference.
- [8] R. Aiello, et al., "Beam Instrumentation for the SSC RFQ," to be published in proceedings of 1993 Particle Accelerator Conference.
- [9] J. Hurd, et al., "Bunch Shape Monitor for SSCL Linac," to be published in proceedings of 1993 Particle Accelerator Conference.
- [10] W. E. Nexsen, et al., "Minimal Interference Beam Size/Profile Measurement Techniques Applicable to the Collider," draft SSCL note, April, 1993.
- [11] E. Tsyganov, et al., "Electron Beam Emittance Monitor for the SSC," SSCL Pre-print 179, December, 1992, to be published in proceedings of 1993 Particle Accelerator Conference.
- [12] R. Richardson, et al., "Beam Profile Measurement Using Thin Molecular Beams," to be published in proceedings of 1993 Particle Accelerator Conference.
- [13] E. Tsyganov, et al., "Limitations of a Residual Gas Ionization Beam Profile Monitor for the SSC Collider," SSCL-602, November, 1992.

PERFORMANCE OF ADVANCED LIGHT SOURCE PARTICLE BEAM DIAGNOSTICS*

J. Hinkson

Accelerator and Fusion Research Division
Lawrence Berkeley Laboratory
University of California
Berkeley, California 94720

Abstract

The Advanced Light Source (ALS), a third-generation synchrotron radiation facility, is complete. The particle beam diagnostics have been installed and tested. The beam injection systems have been running for two years. We have performance data on beam position monitors, beam intensity monitors, scintillators, beam collimators, a 50 Ω Faraday cup, and broad-band striplines and kickers used in the linac, transport lines, and the booster synchrotron. The single-turn monitoring capability of the booster beam position monitoring system has been particularly useful for studying beam dynamics. Beam diagnostics for the storage ring are being commissioned. In this paper we describe each instrument, show its performance, and outline how the instruments are controlled and their output data displayed.

I. INTRODUCTION

Recently, the commissioning performance goals of the ALS storage ring were met. Multi-bunch beam intensity has reached 460 mA. Single-bunch current has exceeded the 8 mA specification by a factor of three. Beam lifetime is dominated by vacuum chamber pressure and is increasing as synchrotron light scrubs the many photon stops. At 100 mA, the lifetime is about 1 hour. The commissioning process went very rapidly. Instrumentation played a critical role.

II. BEAM INTENSITY MONITORS

A. Wall Current Monitors

Two identical monitors are installed, one near the electron gun, and the other in the 1.5 GeV beam transport line connecting the booster and storage rings. The monitor near the electron gun is described. The function of this device is to measure the amplitude and duration of the RF-modulated beam emitted from the electron gun. Beam energy at this location is 120 keV. The gun emits from 1 to 20 beam bunches, 2 ns FWHM, spaced at 8 ns, at a 1 Hz repetition rate. Peak current is between 1 and 2 A.

The wall current monitor requires a gap in the beam pipe to intercept the beam image (wall) current. This is provided by a commercially available ceramic insulator fitted to 114 mm diameter flanges on a 64 mm diameter beam pipe. The ceramic insulator is approximately 25 mm long and is coated with a thin layer of chromium on the vacuum side. This coating protects the ceramic from the beam and somewhat damps wave guide modes (important only in the high-energy transport line beam monitor). The

resistance of the metalization is 60 Ω . Twenty, 39 Ω , low-inductance, leadless resistors are installed symmetrically around the outside of the ceramic gap. The resistors are soldered to soft copper rings, which are strapped to the metal beam pipe on each side of the gap. The total resistance across the gap is about 1.9 Ω .

With a single tap on the resistor belt we noticed undesirable beam position sensitivity during the early part of each bunch. By tapping the resistor belt at four equally spaced locations and summing the voltages in three, 180-degree hybrid combiners, the position sensitivity is considerably reduced. The summed output of the hybrids is displayed on an SCD1000 scan-converter oscilloscope via 60 feet of 0.25 inch Helix cable. The ALS control system collects oscilloscope trace data over the General Purpose Interface Bus (GPIB) and displays the trace in the control room at 1 Hz. At the oscilloscope input the final sensitivity including cable and hybrid response is about 2.5 V/A.

High frequency response of the wall current monitor is dominated by the gap resistance and shunt capacitance of 20 pf. In our monitor the response is reduced by 3 dB at 4.2 GHz. The beam bunch spectra at the electron gun do not extend beyond about 1 GHz. The upper limit of the hybrid response is 2 GHz. The oscilloscope response is down 3 dB at 1 GHz. There is sufficient high frequency response in the system to show relevant beam bunch structure.

Low frequency response of the wall current monitor is dominated by system inductance. The beam pipe is grounded in many locations, creating a low-frequency short circuit across the gap. The limited inductance in these short circuits causes a noticeable baseline tilt in the oscilloscope response when we observe many bunches at 8 ns intervals. The calculated total inductance across the gap resistance is 130 nH. We intend to improve low-frequency response with external frequency compensation circuits.

B. Faraday Cup

This device is used to measure total beam charge in the 50 MeV transport line between the linac and booster. A passive, impedance matched RC network integrates the cup voltage for presentation on a remote digitizing oscilloscope. The wave form is displayed in the control room. We hoped the cup's 50 Ω construction would yield frequency response high enough to resolve adjacent S-band beam bunches. Our aim was to make a straightforward sub-harmonic buncher tuning aid. A rise time of 100 ps or less in a single-shot system was necessary. The best cup rise time we have observed is about 300 ps due to the lumped capacitance of a ceramic gap on the end of the cup. See Figure 2. Although the cup does not have the frequency response we desire, it does accurately quantize total beam charge. One interesting

*This work supported by the Director, Office of Energy Research, Office of Basic Energy Sciences, Materials Sciences Division of the U.S. Department of Energy, under Contract No. DE-AC03-76SF00098

feature of this design is the ceramic break. It supports the coaxial center conductor and permits having an air dielectric. We are not required to use a vacuum coaxial feedthrough. Assembly is quite easy.

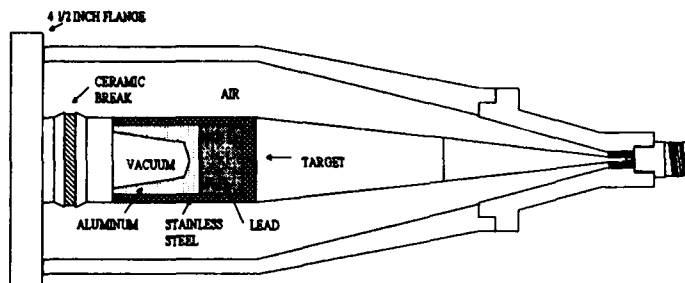


Fig. 2: Drawing of 50 MeV, 50 Ω Faraday Cup

Recently we tested 11 mm electrostatic pickup buttons (Ceramex, type ESRF) installed near the cup for their suitability as bunch monitors. The results are encouraging. With the linac bunchers detuned we can observe small adjacent S-band buckets on an SCD5000 oscilloscope. This instrument is a 5 GHz single-shot digitizer with an effective sampling rate of 200 Gs/s. When the bunchers are properly tuned we observe a large single bunch. System rise time is about 100 ps. Some objectionable ringing is seen following the bunch signal. This may be due to button response and/or wake fields produced in nearby beam pipe discontinuities.

C. DC Current Transformer (DCCT)

A Holec DCCT with 100 mA full-scale sensitivity is used in the booster synchrotron. This device has adequate time response to measure average beam current during the booster acceleration cycle (350 ms). Unfortunately, the DCCT electronics are quite sensitive to RF. Our DCCT core shield resonates at 40 MHz, the 10th harmonic of the booster revolution frequency, and couples RF energy to the core windings. RF filters installed in the cable between the DCCT cores and the electronics have helped reduce the effects of RF pickup. The filters have upset the DCCT sense circuits somewhat. As a result we see interference at 55 Hz (the core modulation rate) equivalent to 100 μ A beam current. With a single 1 mA bunch in the booster we also see RF interference upsetting the DCCT feedback circuits.

A Bergoz parametric current transformer is installed in the storage ring. This instrument has two ranges, 10 mA and 1 A full scale (10 V). It also has a di/dt output of -10 mA/s/V (on the 1 A range). Noise and offsets sampled at 1 Hz are equivalent to a few micro amperes of beam, well within ALS requirements. The DCCT shield is a very complex device based on a LEP design [1]. The shield resonates in a $\lambda/4$ coaxial mode at 40 MHz. Beam impedance measurements [2] predict 5.5 W will be lost in the shield at 50 mA beam current in a single bunch. So far, DCCT core temperature measurements at all levels of beam current have revealed no temperature rise. We have observed no RF effects on the DCCT performance. The cores and electronics are well shielded. A nearby corrector magnet has sufficient leakage fields to cause objectionable DCCT offsets. We installed a soft iron shield around the DCCT enclosure to eliminate the problem.

In order to corroborate storage ring DCCT readings, a calorimetric experiment was conducted [2] to determine average beam current. The cooling water temperature rise in a photon stop

intercepting a known fraction of the total synchrotron light was measured at 300 mA beam current. The calculated average current from this measurement was 280 mA.

The storage ring DCCT has three output signals, wide-band, low-pass filtered, and di/dt. The wide-band and di/dt signals are fed to a digitizing oscilloscope for control room display. The low-pass filtered and di/dt outputs are fed to 16-bit digitizers in the control system. Computer displays show current plotted against time and calculated beam lifetime.

III. BEAM POSITION MONITORS

Beam position monitors (BPMs) [3] are installed in 96 locations in the storage ring, 32 locations in the booster synchrotron, and in 15 places in the linac and transport lines. A detailed description of the BPMs is beyond the scope of this paper. A brief description of storage ring BPMs and their performance to date follows. A block diagram of the BPM electronics is shown in Figure 2.

Each BPM pickup array consists of four button-style electrodes. The electrodes are connected to individual super-heterodyne receivers via Heliax cable. The 500 MHz component of the bunched beam spectrum is selected and mixed down to 50 MHz. A broad-band pseudo-synchronous detector converts the signals to base band. The detected signal is fed to three circuits, a video monitor, a fast Analog-to-Digital (A/D) converter, and a 1 kHz low-pass filter. The filtered signal is digitized for calculation of beam position by the difference-over-sum method. These calculations are performed by the on-board Intelligent Local Controller (the basic input-output module for the ALS computer control system). The fast A/D data are fed to first-in-first-out memory where up to 1024 turns of beam data are stored.

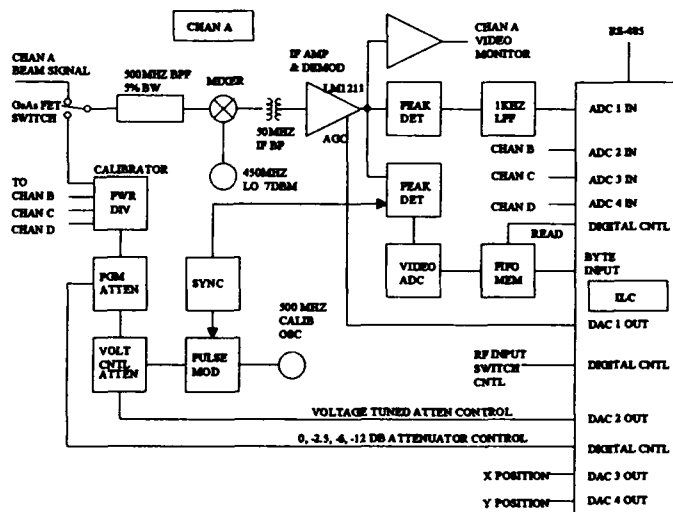


Fig. 2: One of four BPM channels.

When the fast digitizers are stopped, we recover the single-turn data from one or all BPMs. These data are useful for tune measurements, single-shot closed orbit measurements, and other transient beam phenomena. It was these fast A/Ds that helped us discover a defective quadrupole magnet in the storage ring lattice. We were having great difficulty getting more than a few turns of beam. Only when single-turn BPM data were compared with the lattice model [4] did we know where to look for the culprit. A quick

magnet repair was performed, and beam circulated with little tuning.

The BPMs require internal measurement of differential gain and offsets in order to make repeatable measurements to the required 30 mm. For reasons discovered just recently the storage ring BPMs would not perform an internal calibration sequence. Even so, the averaged beam position readings with stored beam made closed orbit corrections possible to 0.5 mm rms. With BPM calibration working we expect better than 0.1 mm performance.

IV. SCINTILLATORS AND TV

Throughout most of the ALS project we use scintillators made of high-purity alumina doped with chrome. They are referred to as Chromox 6 fluorescent screens and are produced by Morgan Matroc Ltd. in the U.K. The scintillators are UHV compatible and, in over three years of service, we have seen no signs of beam damage. Two zinc oxide scintillators are installed near the electron gun. We found the Chromox 6 scintillators were not usable in this location. Apparently, lack of a conducting substrate caused the scintillators to charge as they stopped the low-energy beam. A distorted image and some flashing resulted.

Early on, with weak beams, we had difficulty obtaining enough light from Chromox 6 for our CCD TV cameras. This was due to camera optics, number of electron bunches, and rather diffuse beams. TV image frame-grabbing and image enhancement helped. At the suggestion of a visiting colleague [5] we removed the infrared filter from the CCDs and obtained a huge increase in camera response. The scintillators produce strong infrared with a long response tail. The CCDs are quite sensitive at those long wavelengths.

Our efforts have been to commission the accelerator, and consequently, there has been little attention paid to improving the TV systems. We intend to study scintillator response and determine ways to optimize the scintillator and TV systems for best performance.

V. BROAD BAND STRIPLINES

Two broad band stripline pickups [6] are installed in the booster synchrotron. They are referred to as traveling wave electrodes (TWE). They were intended to be part of a fractional tune measurement system. The pickups have good frequency response and adequate coupling to the beam. The kicker however does not have sufficient coupling. We have been unable to excite detectable betatron motion in booster beam with as much as 70 W driving the kicker. We feel this is due to a rather large tune spread. The booster sextupoles that would reduce the tune spread are not needed for satisfactory beam acceleration. Our plan is to run the sextupoles and attempt more tune measurements. If we are unsuccessful, we will install a more robust kicker.

It is worth noting that booster fractional tune measurements are easily done with the BPM single-turn response and multi-turn data storage. At injection we determine fractional tune by performing an FFT on 1024 sequential turns. At higher energies, when the beam is damped, we excite it with the extraction kicker at low fields and again use the BPM data to determine tune.

We have no striplines, TWEs, or transverse kickers installed in the storage ring at this time. Consequently, accurate fractional tune measurements have been difficult to obtain when we have a stable, damped beam. We have had some limited success tickling the beam horizontally using one of three arrays of LEP BPM buttons, a 100 W power amplifier, and a tracking generator/spectrum analyzer combination. These buttons are not meant to be kickers. They will be used as pickups for transverse and longitudinal damping systems. We are able to use the single-turn capability of the BPMs to determine tune to 0.01 when the beam is unstable (at injection and at high current). A Tektronix 3052 fast spectrum analyzer displaying BPM spectra or an FFT performed 1024 turns of BPM data show similar results. We plan to install the transverse damping system kickers this year and will use them to excite a damped beam in the future. We expect we will achieve 0.001 tune resolution then.

VI. BEAM COLLIMATORS

Adjustable two-jaw beam collimators are installed in the low-energy diagnostics line off the linac and in the line between the linac and booster. A single collimator is used in the diagnostics line and defines a vertical slit. Two collimators in the booster line define a beam aperture. The 50 MeV beam is stopped with 0.5 inch tantalum plates. Stepper motors position the plates with 10 μ m resolution. Absolute position encoders read position to a few microns.

VII. CONCLUSION

The diagnostics are working well enough to commission and run the accelerators. Some improvements are needed. BPM resident software will be changed to take advantage of the device's ability to calibrate offsets and correct detector nonlinearity. We currently have no way of measuring total beam charge at the exit of the booster. We plan to install an integrating current transformer there. More work will be done on the wide band linac bunch monitor.

VIII. REFERENCES

- [1] K. Unser, personal communication to author.
- [2] K. Kennedy, personal communication to author.
- [3] J. Hinkson, "Advanced Light Source Beam Position Monitor," *AIP Conference Proceedings No. 252 on Accelerator Instrumentation, Particle and Fields Series* 46, pp. 21-41.
- [4] J. Bengtsson, M. Meddahi, "Elementary Analysis of BPM Data for the ALS Storage Ring," LBL CBP Tech Note 003, March 1, 1993.
- [5] J.C. Denard, personal communication to author.
- [6] J. Hinkson, "A Wide Band Slot-Coupled Beam Sensing Electrode for the Advanced Light Source (ALS)," *Conference Record of the 1991 IEEE Particle Accelerator Conference*, Vol. 2, pp. 1234-1236

Damping in the Fermilab Booster

James M. Steinel Jr. & Dave McGinnis
Fermi National Accelerator Laboratory*
P.O. Box 500, Batavia, IL 60510 USA

Abstract

A working prototype of a narrow band longitudinal phase damper has been developed and tested on the Fermilab Booster. This paper will discuss the design and results of the damper as well as problems associated with designing dampers for fast frequency sweeping accelerators. Results for wide band, longitudinal dampers and transverse dampers will also be discussed.

I. INTRODUCTION

The upgrade of the Fermilab Linac from 200MeV to 400MeV will reduce the losses in the Booster due to space charge effects, but the increased beam current will cause greater coupled bunch mode instabilities. Strong coupled bunch modes exist even at present beam current levels. To suppress the coupled bunch modes, bunched beam dampers were designed.

A generic damper configuration is shown in Figure 1. The damper reduces beam oscillations via negative feedback. This paper discusses the different types of damper systems designed and tested on the Fermilab Booster. These include: narrow band and wideband longitudinal dampers, and wideband transverse dampers.

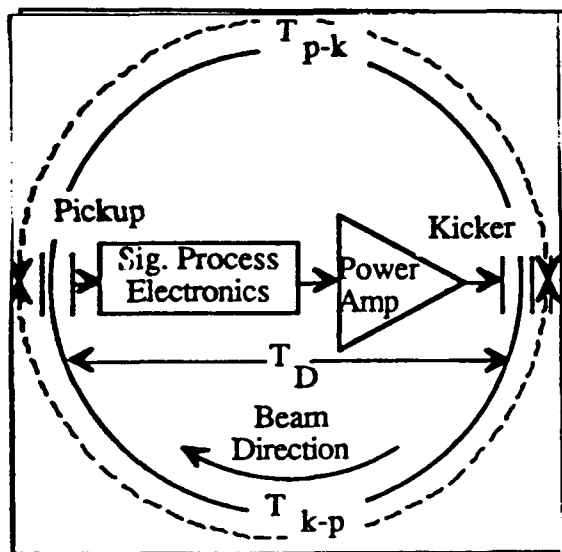


Figure 1. Simple schematic of a damper system.

II. NARROWBAND VS. WIDEBAND

The frequencies of the coupled bunch modes are located around the rotation harmonics, and the number of coupled

bunch modes equals half of the RF buckets [1]. A narrowband damper damps one coupled bunch mode, while a wideband damper damps all coupled bunch modes. There are advantages and disadvantages to both.

A. Noise Power and Processing Requirements

The gain requirements of a damper system are determined by the instability growth rate [2]. With the gain set, the power requirements of the damper are determined by the noise power, and the power of rotation and RF harmonics on the output signal. The high power, linear, RF amplifiers are the most expensive part of the system, so the cost of the system becomes proportional to the output power required.

A narrowband damper blocks all frequency components outside the range of the single coupled bunch mode frequency. This makes the noise power very small and reduces the amount of output power required, but it only damps one mode. If more than one mode is unstable, multiple narrowband dampers must work in parallel. This not only increases the output power requirements, but it also increases the processing cost. A separate processor will be needed for every unstable mode.

Only one wideband damper processor is needed to damp all of the coupled bunch modes, but the noise power is much greater than in the narrowband system. Consequently, the wideband damper will require more powerful amplifiers than the narrowband damper for a given damper gain.

If there are only a few unstable coupled bunch modes, a few narrowband systems would be the most cost effective. But, if there are many unstable coupled bunch modes, a wideband system would be most cost effective by reducing processor costs.

B. Phase Error and Delay

The RF accelerating voltage in the Booster must ramp from a frequency of 30MHz to 53MHz in a cycle time of 33ms, and the non-linear frequency ramp has a peak slope of 2GHz/s near the beginning of the cycle. The revolution period varies from 2.8μs to 1.59μs. To maintain feedback on the proper bucket, the processing system must handle 1.21μs of delay change quickly.

An error in delay from pickup to kicker will have a greater effect on the wideband damper than the narrowband damper. The narrowband damper sees the error in delay as a phase shift which is easily compensated. An error in delay for a wideband damper may cause a reduction in gain for higher frequency modes or even drive them unstable.

III. WIDEBAND TRANSVERSE DAMPER

The Fermilab Booster uses a directional stripline pickup to detect the transverse error signal for the damper. The

*Operated by the University Research Association, Inc. under contract with the US Department of Energy.

signals from the two plates (top and bottom for vertical; inner and outer for horizontal) are combined in a 180° hybrid. The difference signal is processed, split with another 180° hybrid, amplified, and sent to a directional stripline kicker. The processor must maintain the proper phase relationship, bucket offset, and common mode rejection for effective damping.

A. Timing and Delay

Maintaining proper bucket delay is one of the most difficult problems in designing a wideband damper system for accelerating beam. The revolution period gets shorter as beam accelerates, and the total electrical delay from pickup to kicker must match the beam transit time. One way around this problem is to sample the beam digitally and delay the digital signal for a number of clock pulses. The system designed for the Booster is shown in Figure 2.

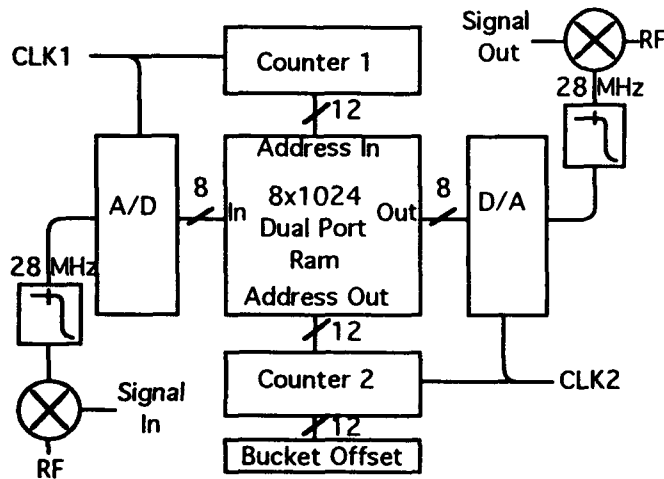


Figure 2. Digital Delay Block Diagram

The beam signal is mixed with the RF frequency, filtered, and enters an A/D converter. From the converter, the data is stored in a fast dual port memory at the address specified by the top counter. The data is then sent to the D/A converter when the bottom counter matches its memory address. The difference in value between the two counters is the bucket delay. The signal from the D/A is filtered and mixed with the RF frequency before it is sent the kickers. Mixers are required because of the frequency response of the pickup and amplifiers.

Each of the clock signals is tied to the Booster VCO which must be phase locked to the beam. The signal will be sampled at the exact frequency needed to damp all of the coupled bunch modes according to Nyquist sampling.

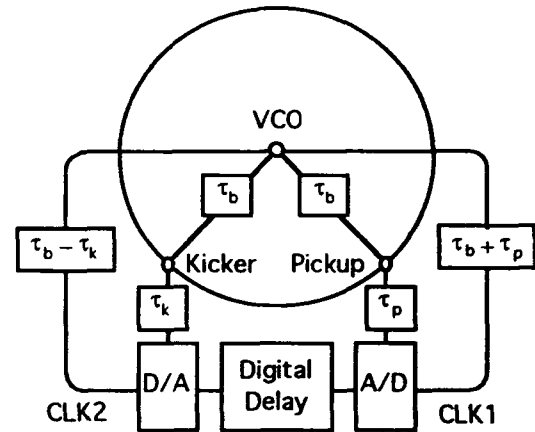
As long as the initial bucket delay is set correctly, taking into account beam velocity and fixed delay, the digital system will remain locked to the beam and provide proper bucket delay. Figure 3 shows the timing conditions for the system. As the beam accelerates, more of the bucket delay is stored in the fixed cable delays, τ_p and τ_k . The bucket delay of the digital delay must be reduced. Because of the difference in delay from the VCO to the A/D trigger and the D/A trigger,

an increase in frequency will trigger the D/A counter more than the A/D counter according to:

$$\int_0^t f_{rr}[t' + \tau_k] dt' - \int_0^t f_{rr}[t' - \tau_p] dt' \quad (1)$$

The number of buckets stored in the fixed delay increases by the exact same amount, so the bucket delay stays matched.

Another possibility for a digital delay is a FIFO memory. This method works very well for storage rings and ultra relativistic accelerators, but it runs in to problems with sweeping accelerators because of its fixed memory length. Even a FIFO with an adjustable pointer will have trouble when the D/A tries to read a signal at the same time the A/D is shifting the memory. The A/D can write to the dual port memory while the D/A simultaneously reads from it, giving the dual port memory more flexibility than the FIFO.



τ_b = Delay from VCO to Beam
 τ_k = Delay from D/A to Kicker
 τ_p = Delay from A/D to Pickup

Figure 3. Transverse Damper Timing Diagram

B. Noise Power

Because the system is wideband, the noise power is much higher than for a narrowband system. Also, the noise floor is increased by the digitization noise of the system[3]. The A/D converter is 8 bits wide and will have a dynamic range of 48dB.

This transverse damper system has two features which suppress fundamental frequencies. First, the system uses the difference signal from a stripline pickup. Ideally, the pickup would only detect changes in displacement and cancel out all common mode signals. Second, the sampling process of the digital delay filters out all of the RF harmonics of the signal.

IV. NARROWBAND LONGITUDINAL DAMPER

The Booster longitudinal damper uses the same stripline pickup used by the transverse damper, but it uses the sum of

the signals from the plates instead of the difference. The phase of this signal is compared to the phase of the RF, processed, amplified, and sent to a wideband cavity. In the case of the narrowband damper, the processing must filter out a single coupled bunch mode frequency, and track that frequency throughout the cycle[4].

A. Mode Tracking

The frequency of a coupled bunch mode is a linear function of the RF frequency. A direct digital synthesizer creates a sine wave with a frequency which is some rational number less than 1 times its input frequency. Thus, a direct digital synthesizer is perfect for tracking the coupled bunch mode frequency with a sweeping RF.

Figure 4 shows the layout of the Booster narrowband longitudinal damper processor. The processor is a tracking notch filter, where the notch is located at a revolution harmonic. The revolution harmonic, around which damping occurs, is chosen by the user through the DDS. An equation for determining the DDS ratio is:

$$\text{DDS ratio} = \frac{\text{mode\#} + \text{harmonic \#}}{\text{harmonic \#} \times 4} \quad (2)$$

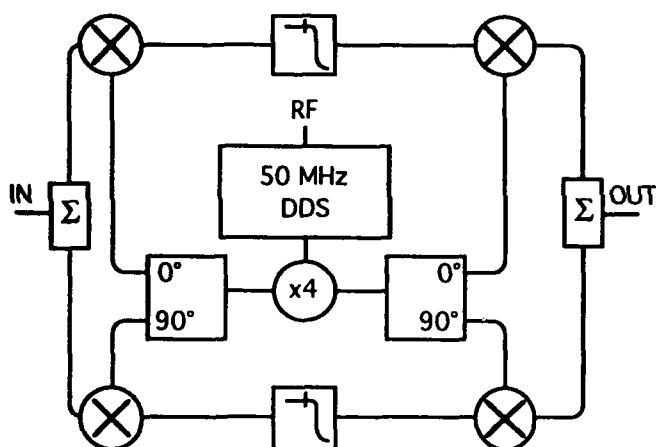


Figure 4. Narrowband Longitudinal Damper Processor

This ratio can be set using any terminal emulator with an RS232 port. A frequency quadrupler is used to track modes at the peak response of the pickup. The filters in the baseband portion of the processor have a bandwidth of 5 kHz and this keeps the noise bandwidth much lower than the wideband damper. The low bandwidth also rejects the fundamental frequency except for the leakage through the mixers.

Results from the narrowband damper are shown in Figure 5.

V. WIDEBAND LONGITUDINAL DAMPER

The wideband longitudinal damper system tested in the Booster is an energy damper. It uses the horizontal stripline detector in difference mode at a high dispersion point. The energy signal is then processed, amplified, and sent to a wide bandwidth cavity. A wideband longitudinal damper requires almost the same kind of processing that a wideband transverse damper requires. The wideband system has not been tested with the digital delay, however. Instead, a system of switching cable delays was used which did not provide adequate common mode suppression for effective damping. This test led to the design of the digital delay, and future

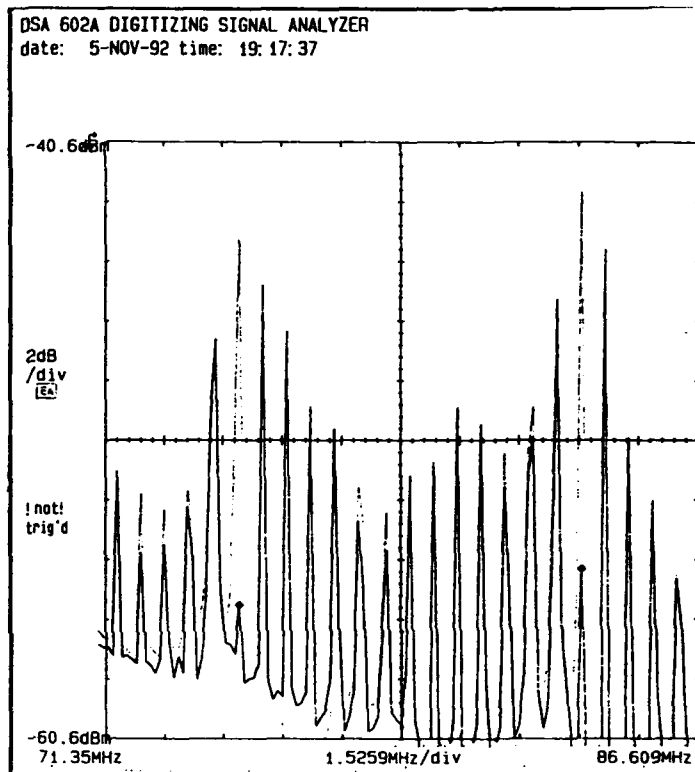


Figure 5. Effect of dampers on coupled bunch mode #35.
RF = 52.8MHz, DSA ratio = (35 + 84)/(4*84)

designs of the digital delay are planned for the longitudinal damper.

VI. ACKNOWLEDGMENTS

The authors would like to thank Ken Koch, Barry Barnes, and Steve Conlon for their work in building the processing equipment and maintaining the power systems.

VII. REFERENCES

- [1] J. L. Laclare, "Bunched Beam Coherent Instabilities," *Cern Accelerator School CERN 85-19*, pp. 289-294.
- [2] D. P. McGinnis, "Coupled Bunch Mode Instabilities Measurement and Control," *Conference Proceedings of the 1991 AIP Accelerator Instrumentation Workshop*, 78.
- [3] L. Vos, "Transverse Feedback System in the CERN SPS," *Conference Proceedings of the 1991 AIP Accelerator Instrumentation Workshop*, 185.
- [4] McGinnis, pp. 79-81

Betatron function measurement at LEP using the BOM 1000 turns facility

P.Castro, IFIC -Instituto de Física Corpuscular, University of Valencia-, E-46100 Burjassot, Valencia, Spain
J.Borer, A.Burns, G.Morpurgo, R.Schmidt, CERN SL Division, CH-1211 Geneva, Switzerland

Abstract

A new method for measuring the beta function around LEP is presented. The method uses phase difference measurements between three adjacent beam position monitors to obtain the value for the beta function at the monitors and in their neighbourhood, e.g. at interaction points, electrostatic separators etc. The phase differences are obtained from measuring coherent betatron oscillations for 1024 turns at the 504 beam position monitors. After a discussion of the accuracy of the method the measured values for the beta function are compared with the theoretical values for different lattices. In regular parts of the lattice (e.g. arcs) the beating of the beta function measured using this method agrees well with the beating obtained by another method using a fit of the phase over 15 monitors.

I. INTRODUCTION

During 1992 on several occasions the optics mismatch was measured at LEP using the phase difference measurements realised by the BOM (Beam Orbit Measurement system) 1024 turns facility. In this report a new method to obtain the experimental values of the beta and alpha functions from these phase difference measurements is presented. The accuracy of this technique has been studied by obtaining the error in the phase measurement and its good performance proved by comparing the results with other methods. This method is used for checking the machine optics, however a very precise measurement of the beta function will be very helpful at the radiation source for the exact calibration of emittance monitors, at Beam Position Monitors (BPM) for their calibration, at Interaction Points (IP) and at Electrostatic Separators (ES).

II. PHASE MEASUREMENT AT LEP

The 1024 turns beam position measurement at each BPM is used in combination with the LEP Q-meter. The Q-meter measures the fractional part (q) of the betatron tunes by exciting and observing coherent transverse oscillations in the horizontal and vertical planes with a single dedicated beam position monitor [1]. To measure the phase, one specific bunch is excited in one plane (horizontal or vertical) with a frequency close to the betatron tune. The amplitude of the bunch oscillations depends on the proximity of the exciting frequency to the tune and on the strength of the excitation. For a precise measure of the phase of these oscillations, the beam must be excited to high amplitude to gain in signal to noise ratio. The maximum amplitude is limited by the machine aperture but also the presence of non-linear elements (like sextupoles

etc.) constrains the maximum due to non-linear fields. These oscillations are then sampled at each BPM for 1024 turns (i.e. during 91 msec) (see fig. 1). When the condi-

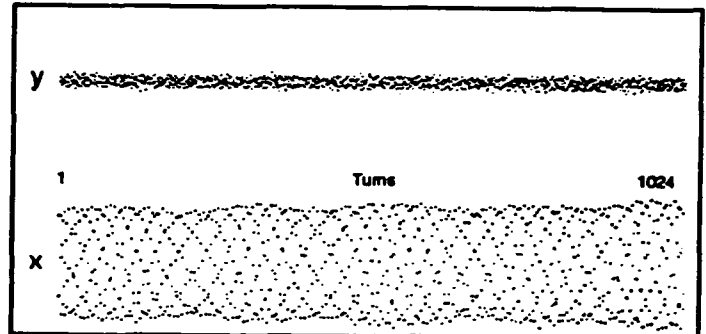


Figure 1: Single BPM recording the excited horizontal beam motion (scale: 8 mm peak to peak, time=88.9 μ sec/turn)

tions of the machine are stable, a constant amplitude of a few millimeters is observed in the plane of excitation. Applying harmonic analysis we obtain the amplitude A and the phase μ of these oscillations at each BPM:

$$A = \frac{2\sqrt{C^2 + S^2}}{N} \quad \mu = -\cot\left(\frac{S}{C}\right)$$

where $N = 1024$ and

$$C = \sum_{i=1}^N x_i \cos(2\pi i q) \quad S = \sum_{i=1}^N x_i \sin(2\pi i q)$$

Because the amplitude obtained is proportional to $\sqrt{\beta}$, one can compare the measured values of the amplitudes at the BPMs with the expected ones and deduce β . Unfortunately this method depends on the calibration factor of each BPM. However, the phase differences are measured with high precision and there is no systematic error since the phases are independent of individual monitor calibration errors.

III. PHASE ERROR MEASUREMENT

With constant amplitude, the error of the phase is proportional to the noise of the position signal of the BPM. Using harmonic analysis we obtain the following expression for the error:

$$\sigma_\mu = \frac{1}{A} \sqrt{\frac{2}{N}} \sigma_x \quad (1)$$

with:

N : the number of the samples (1024),

A : amplitude of the signal, and

σ_s : the estimate of the BPM error [3]; it is calculated on the basis that both contributions (the electronic noise and the numerical error of the ADC) are superimposed:

$$\sigma_s \approx \sqrt{\sigma_{Num.Error}^2 + \sigma_{Electr.Noise}^2} = 0.07mm$$

On 40 occasions with different optics, tunes and excitation amplitude the phase difference was measured and the position data from each BPM recorded. In the following we discuss the results of the phase error obtained for these 40 data sets and compare these results with the error values expected shown above. First of all, the frequency of the oscillations is determined by taking the frequency with the maximum amplitude response using harmonic analysis. A precise value of the oscillation frequency is necessary to compute the phase, because the phase result is very sensible to small changes on the frequency selected for the harmonic analysis.

To calculate the error of the phase the procedure is to repeat the same measurement several times and obtain the sigma. In order to estimate the error in the phase measured at the BPMs, the technique used is to take segments of n points (n smaller than 1024, e.g. 512 or 256) from the first point and sliding it over the entire measurement of 1024 points. Applying harmonic analysis gives $(1025 - n)$ phase values. The sigma of these phase results have been found to be 10 or 50 times higher than the expected phase error. In some cases, oscillations of the phase of 50 Hz (probably due to power supplies noise) have been observed in the results.

However, taking two BPM signals from the same data set and calculating the phase difference between them, the dispersion of the results decreases drastically and corresponds to the predicted phase accuracy (see fig. 2). Whatever ef-

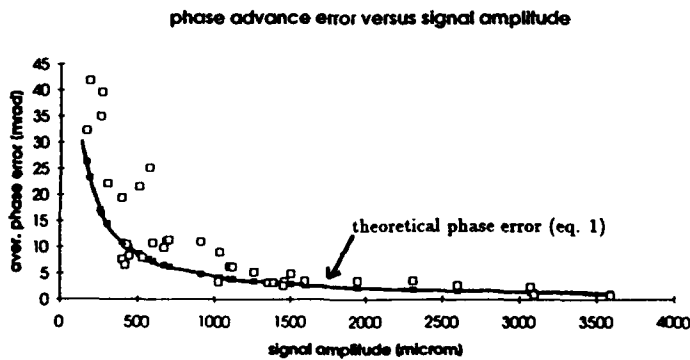


Figure 2: Phase difference error average

fect introduces a change in the oscillations (e.g. 50 Hz noise, changes in the natural tune etc) it is seen by all BPMs, and the phase difference is not very sensitive to beam perturbations. To summarise, a determination of the oscillation frequency with an accuracy less than $\sim 10^{-5}$ and an oscillation amplitude of at least 1 mm are needed to compute, through the Harmonic Analysis, the phase difference with an error of 4-5 mradians.

IV. BETA FUNCTION MEASUREMENT

Once the phase differences have been measured between all BPMs around LEP, the beta and alpha functions are obtained using the following method.

Let M be the transfer matrix of a charged particle from one point s_1 to another s_2 :

$$\begin{pmatrix} x \\ x' \end{pmatrix}_2 = \begin{pmatrix} m_{11} & m_{12} \\ m_{21} & m_{22} \end{pmatrix} \begin{pmatrix} x \\ x' \end{pmatrix}_1 \quad (2)$$

where x is the particle's displacement from the beam center and x' the angle and the elements m_{ij} can be expressed as [2]:

$$\begin{pmatrix} \cos \mu + \alpha_1 \sin \mu & \beta_1 \sin \mu \\ -\gamma_1 \sin \mu & \cos \mu - \alpha_1 \sin \mu \end{pmatrix} \quad (3)$$

where β is the beta function, $\alpha = -\frac{1}{2} \frac{d\beta}{ds}$, $\gamma = (1 + \alpha^2)/\beta$ and μ is the phase difference defined as:

$$\mu = \int_{s_1}^{s_2} \frac{ds}{\beta(s)} \quad (4)$$

This matrix M is easily obtained by multiplying successively the transfer matrices for each existing element (drift space or quadrupole) between s_1 and s_2 . The matrix elements of the first row

$$\frac{m_{11}}{m_{12}} = \frac{\cos \mu + \alpha_1 \sin \mu}{\beta_1 \sin \mu} \quad (5)$$

show the relationship between the optics parameters β and α at s_1 and μ the phase difference between s_1 and s_2 . The phase difference is provided by the BOM 1024 turns facility and the matrix coefficients are calculated from the layout between two BPMs and reading the magnet strengths of the quadrupoles. Consequently, in equation (5) there are two unknown variables: α and β . Therefore, a set of three consecutive BPMs is selected.

Let m_{11} and m_{12} be the elements of the first row of the transfer matrix from monitor 1 to monitor 2 and N_{11} and N_{12} be the similar elements for the transfer matrix from monitor 1 to monitor 3, then the equations are:

$$\beta_1 \frac{m_{11}}{m_{12}} = \cot \Psi_{12} + \alpha_1 \quad (6)$$

$$\beta_1 \frac{N_{11}}{N_{12}} = \cot \Psi_{13} + \alpha_1 \quad (7)$$

with Ψ_{ij} : the phase difference between BPMs j and i . Finally it yields:

$$\beta_1 = \frac{\cot \Psi_{12} - \cot \Psi_{13}}{(m_{11}/m_{12}) - (N_{11}/N_{12})} \quad (8)$$

$$\alpha_1 = \frac{(N_{11}/N_{12}) \cot \Psi_{12} - (m_{11}/m_{12}) \cot \Psi_{13}}{(m_{11}/m_{12}) - (N_{11}/N_{12})} \quad (9)$$

Alternatively, knowing the theoretical values of beta and the phase difference (by other programs like MAD), the expression of the experimental $\beta(ezp)$ yields as the ratio

between the measured $\cot \Psi_{12} - \cot \Psi_{13}$ and the theoretical one:

$$\beta_{1(exp)} = \beta_{1(theo)} \frac{\cot \Psi_{12(exp)} - \cot \Psi_{13(exp)}}{\cot \Psi_{12(theo)} - \cot \Psi_{13(theo)}} \quad (10)$$

and one easily deduces the equivalent expression for alpha. The method is limited for a regular structure such as the FODO cells in the arcs of LEP when the optics has a phase difference of 90 degrees between consecutive BPMs. In this case, $\cot \Psi$ is zero and β can not be calculated.

V. BEATING OF THE BETA FUNCTION MEASUREMENTS

During last years run, LEP was operated mainly using 90 degrees lattice optics and only a few times in special Machine Development (MD) schedules the 60° lattice optics was used. In the following pictures all the results are shown as the ratio between the experimental value of beta obtained by this method and the theoretical beta calculated with the MAD model [4]. Figure 3 shows the vertical beta function for 60° lattice at the BPMs obtained by this method (line and crosses) compared to the beta beating obtained by fitting [5] the measured phase difference over 15 BPMs (white boxes) in the arc between Interaction Point 2 (IP2) and IP3. The latter method makes the hy-

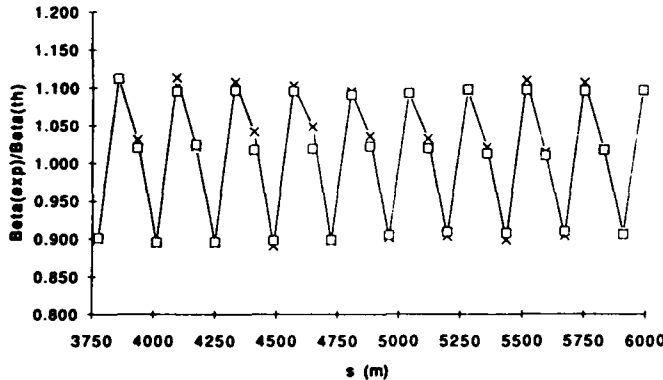


Figure 3: Comparison between beta beating fit method and the value of beta obtained with eq. 8

pothesis that the optics mismatch between the predicted and the measured phase difference is due to beta beating, while the former makes no assumption. The small difference between the results shows that almost all the effect seen is due to beta beating.

Figure 4 shows the beta function calculated at some of the beam instruments at LEP and in fig. 5 at the horizontal electrostatic separators. These values of beta are calculated from the ones obtained at the closest BPM around the instrument.

beta measurement at Beam Instrumentation

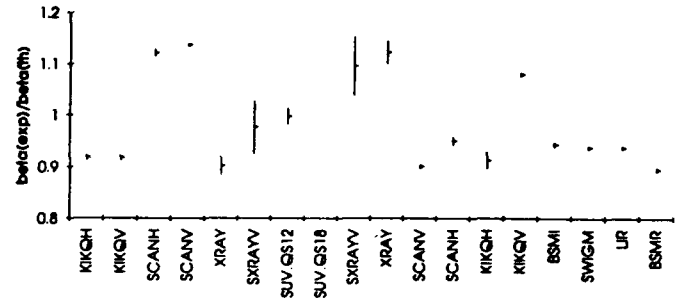


Figure 4: Vertical beta function measured at Beam Instrumentation (90° lattice, 46 GeV)

beta measured at horizontal electrostatic separators

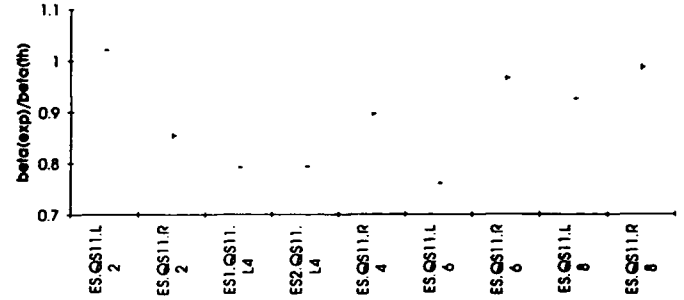


Figure 5: Horizontal beta function measured at Horizontal Separators (90° lattice, 46 GeV)

VI. CONCLUSION

From the BOM 1024 turns measurement the phase error is typically about 4-5 mrad for a signal of 1 mm of amplitude and 1024 points. An algorithm applied to three consecutive BPMs gives the local values of the betatron function assuming no magnetic error between the three BPMs. Apart from when the phase difference between BPMs is 90°, the value of beta is determined with a precision better than 5 % in general. From the same algorithm the alpha function is also calculated and both alpha and beta values can be transported from the BPMs to other points of interest such as at emittance monitors, radiation source instruments, electrostatic separators and interaction points.

VII. REFERENCES

- [1] K.D.Lohmann et al.; Proc. EPAC, Nice, France June, CERN/SL/90-32 (BI) 1990
- [2] E. D. Courant and H. S. Snyder; *Theory of the Alternating-Gradient Synchrotron*; Annals of Physics, Vol. 3, 48 (1958).
- [3] J. Borer; *BOM system hardware status*; Proc. of the Third Workshop on LEP Performance, CERN SL/93-19 (DI), Chamonix, January 10-16, 1993.
- [4] F.C. Iselin; *The LEP Model Interface for MAD*; Proc. of ICALEPCS'91, Tsukuba; CERN SL/91-41 (DI), 1991.
- [5] A. Burns; *BOM Software*; Proc. of the Second Workshop on LEP Performance, Chamonix, January 19-25, 1992.

Adaptive Cascaded Beam-Based Feedback at the SLC*

T. Himel, S. Allison, P. Grossberg, L. Hendrickson, R. Sass, H. Shoae
Stanford Linear Accelerator Center, Stanford University, Stanford, CA 94309 USA

Abstract

The SLC Linear Collider now has a total of twenty-four beam-steering feedback loops used to keep the electron and positron beams on their desired trajectories. Seven of these loops measure and control the same beam as it proceeds down the linac through the arcs to the final focus. Ideally each loop should correct only for disturbances that occur between it and the immediate upstream loop. In fact, in the original system each loop corrected for *all* upstream disturbances. This resulted in undesirable over-correction and ringing. We added MIMO (Multiple Input Multiple Output) adaptive noise cancellers to separate the signal we wish to correct from disturbances further upstream. This adaptive control improved performance in the 1992 run.

I. INTRODUCTION

The SLC presently has twenty-four steering feedback loops running [1]. Seven of these loops are placed one after the other along the linac.

A typical loop measures and controls eight states: the position and angle of the electron beam in both the horizontal and vertical directions and the same for positrons. The loop measures these states using ten beam position monitors (BPMs). Each monitor gives the horizontal and vertical position for electrons and positrons. Hence, there are a total of forty measurements.

Each feedback loop is designed using our knowledge of accelerator optics and the state-space formalism of control theory. The linear quadratic Gaussian (LQG) method is used to design optimum filters to minimize the rms disturbance seen in the beam. Since there is a fair amount of white noise in the incoming beam disturbance, this filter averages measurements of about six beam pulses. Hence the typical loop corrects most of a step change in six pulses.

A problem exists with the system as described so far. Seven loops in a row examine the same beam. Figure 1 depicts the beam trajectory in the region of two of these loops. Figure 1a shows the trajectory on the first pulse after a sudden disturbance (such as an operator adjusting a dipole magnet strength) upstream of the two loops. The plot of transverse beam position as a function of distance along the linac shows the sine-like trajectory caused by the focusing quadrupole lenses. At this time, the loops have not made a correction. Figure 1b shows the trajectory on the next pulse. To keep this example simple, the loops were set to completely fix an error detected in one pulse instead of in six. The first loop completely corrected the original disturbance. The second loop also made a correction, which was unnecessary because the first loop cor-

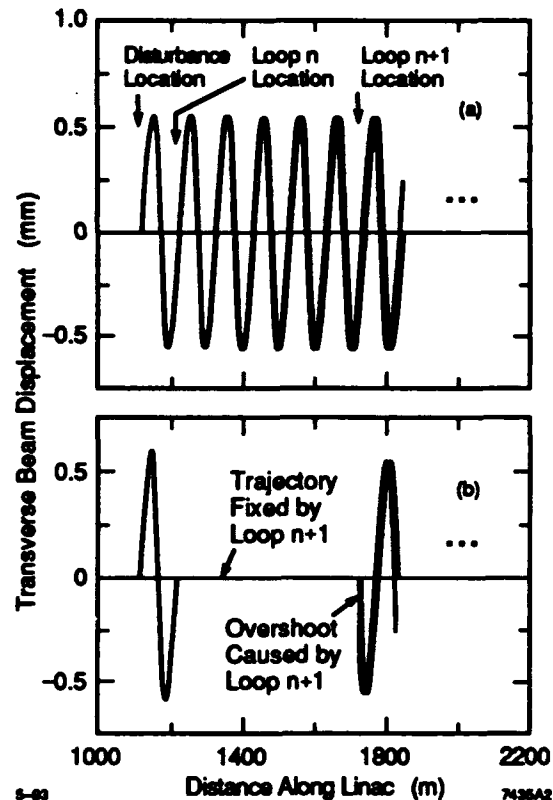


Figure 1. Feedback's response to a disturbance. The beam trajectory shown is on the first pulse (a) and second pulse (b) after a sudden disturbance is introduced. The response of the two feedback loops shows the need for the adaptive noise cancelling system.

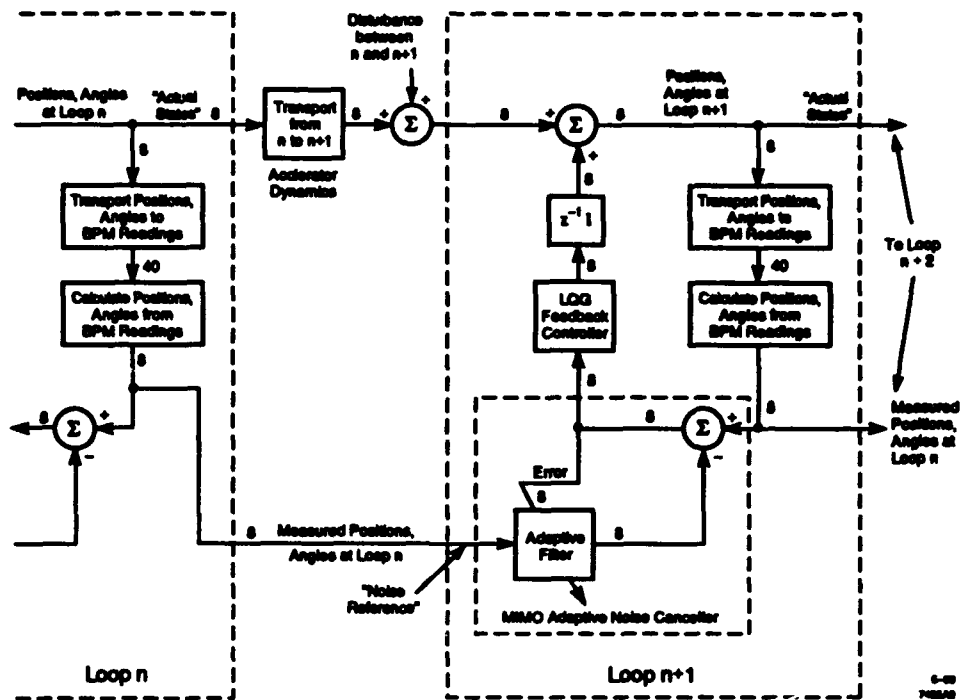
rected for the disturbance. Of course, on the next pulse the second loop would correct its error but the damage has been done, the loops have overshoot the mark for a pulse. The problem gets much worse with seven loops in a row. The overshoot can be reduced by having each loop respond more slowly but the system still overshoots and then rings for many pulses. The system is stable and the ringing gradually dies out, but the overall response of the loops is not optimal, hence the beam positions and angles have a larger rms than need be.

The proper solution is to have each loop correct only for disturbances which happen between it and the next upstream loop. This would completely eliminate the overshooting caused by multiple loops correcting for the same disturbance.

ADDING A MIMO ADAPTIVE NOISE CANCELLER

An individual loop (say loop $n+1$) has only a few local BPMs to detect disturbances in the beam. It has no way to tell how far upstream the disturbance occurred. Since we want loop $n+1$ to correct for disturbances downstream of

* Work supported by Department of Energy contract DE-AC03-76SF00515.



2. Adaptive MIMO noise canceller added to the typical feedback loop.

loop n , but not upstream, the upstream disturbances can be thought of as noise. Hence an adaptive noise canceller can be used to solve our problem.

A block diagram of the cascading of information from one loop to the next is shown in Figure 2. The bold lines represent information carried by the beam and the bold boxes represent transfer functions which are part of the plant (accelerator). The non-bold items represent items implemented as part of our feedback system.

The line in the upper left labeled "Positions, angles at loop n " represents the eight states. Since loop n is responsible for maintaining these states at their desired set points (which are typically zero since we want the beam to move in a straight line down the center of the linac), as far as loop $n+1$ is concerned, these states are noise. Loop n reads some BPMs and calculates the positions and angles from their readings. It uses the numbers for its own feedback loop, and sends them via a communications link (labeled "Measured positions, angles at loop n ") to loop $n+1$, that uses them as its noise reference signal for its adaptive noise canceller.

Similar information is carried to loop $n+1$ by the beam itself. Between the two loops, the beam executes a betatron oscillation so that positions and angles transform into each other. This is represented by the box labeled "Transport from n to $n+1$," and represents the accelerator, dynamics between the two loops. It is very important to note that our problem is static; the transport of this beam pulse does not depend on the positions and angles of the previous beam pulse. Hence, the box can be represented as a simple 8×8 matrix.

In addition to the simple transport of the beam, an additional "Disturbance between n and $n+1$ " may be added.

This disturbance could be due to a klystron tripping off or an operator adjusting a magnet. Loop $n+1$ is intended to correct this kind of disturbance so that it corresponds to the signal that we want the noise canceller to extract.

The last box that needs an explanation is the "LQG Feedback Controller." This box represents the controller feedback loop $n+1$. The controller now takes as its input the output of the MIMO adaptive noise canceller, which represents our best estimate of the "Disturbance between n and $n+1$." That is precisely what we want loop $n+1$ to correct. The output of the controller controls the dipole magnets that steer the beam between n and $n+1$. Hence its output is shown summed into the positions and angles of the beam transported from loop n .

In summary, before the implementation of the adaptive noise canceller, the series of seven feedback loops over-corrected for deviations in the position and angle of the beam because each feedback loop acted independently, and all feedback loops applied a correction for the same disturbance. MIMO adaptive noise cancellers allow each loop to separate disturbances that happen immediately upstream from those that occur upstream of the previous loop. This action cures the over-correction problem.

ADAPTIVE CALCULATION

Before delving into the details of the adaptive calculation, it is worthwhile to ask why adaptation is necessary at all. What is varying? The box labeled "Transport from n to $n+1$ " in Figure 2 is what varies. It accounts for the sine-like trajectory, caused by the focusing magnets, that the beam follows as it travels down the accelerator. For example, if loop $n+1$ is 90° of the betatron (sine-like) oscillation downstream of loop n , then a position offset at loop

n becomes an angle at loop $n+1$, and an angle transforms into a position. The transformation is critically dependent on the number of betatron oscillations between the loops. This is parameterized as the *phase advance* where 360° of phase advance corresponds to one full oscillation. Figure 1 shows two loops separated by $5 \times 360^\circ$ of phase advance, the average for the loops in the SLC. The dotted line in Figure 1a shows a betatron oscillation where the focusing strength is incorrect by 1 percent, an error typical of the real linac. Note that the position and angle at the second loop are quite different due to the 1 percent error. This significant variation of the "Transport from n to $n+1$ " forces the use of an adaptive method for the noise canceller.

The updates of the weights in the adaptive filter are made using the Sequential Regression (SER) algorithm [2]. The equations used in the SER algorithm are explained in Reference [2].

Basically the inverse of the input correlation matrix is estimated. This estimate is used to scale the inputs so that all the eigenvalues of the correlation matrix of the scaled inputs are equal to one.

Using the SER method, the calculation of the weights becomes unstable for a short time if the beam jitter suddenly increases. During the time it takes for the estimate of the inverse of the input correlation matrix to converge to the new value, the weights diverge rapidly. This problem and the solution were found in simulation: not to update the weights if the inverse correlation matrix is receiving large updates.

After testing the algorithms with the computer simulation we implemented them in the SLC control system.

EXPERIENCE ON THE REAL ACCELERATOR

First we turned on just the adaptive algorithm. The results were not used to control the beam. After confirming that the matrices had converged to reasonable values, we turned on the noise cancelling system. As shown in Figure 3 the response to a step disturbance in the beam trajectory was greatly improved with the startup of the adaptive noise-cancelling system.

Over the next few weeks we varied the learning rate to find the optimum value that would allow the adaptation to converge rapidly without having too much noise introduced by the adaptive process. We settled on a learning rate of 0.001 and an adaptive update rate of 10 Hz. A convergence time of about 100 seconds resulted. The system ran for several days with learning rates of 0.1 and 0.01 and was completely stable, but with these higher learning rates more random noise showed in the adaptive matrix elements.

The adaptive noise-cancelling addition to the fast feedback system has been running stably in seven locations on the SLAC linear collider for over six months. Probably the best measure of its robustness and stability is that operators have made no middle of the night phone calls asking for help to recover from a problem. In fact there have been

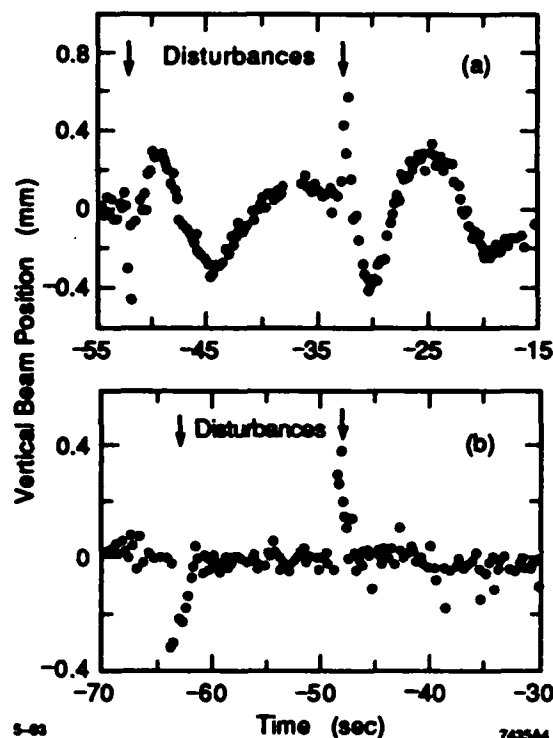


Figure 3. Response of a chain of six feedback loops to a sudden disturbance in the incoming beam. In part (a) adaptive noise cancelling is off so there is a ringing caused by the over correction of many loops. In part (b) adaptive noise cancelling is on, so the whole chain of loops responds like a single loop. In fact, the first loop did all the work to correct the beam and the downstream loops did virtually nothing.

no significant problems with the system. Adaptive noise cancelling has significantly improved the performance of our feedback systems and helped us achieve our goals of accelerating two beams over a distance of three kilometers, pointing the beams at each other, and then colliding them head on so they pass through each other even though they have a radius of only $2 \mu\text{m}$ at the collision point.

In fact we have received an unexpected bonus from the adaptive calculation. The adaptive weights can be interpreted as measurements of the beam transport matrix from one loop to the next. These measurements are recorded on disk and can be displayed. Such data shows a typical variation of over 30 degrees which is about 1 percent of the total phase advance between the two loops. We have made many checks and convinced ourselves that this variation is caused by a real variation in the focusing strengths in the linac (typically due to rf phase and energy changes). Accelerator physicists are using this data to identify and try to fix the cause of the changes in focusing strength. This would make a still more stable accelerator.

REFERENCES

- [1] F. Rouse et al., "A Database-Driven Fast Feedback System for the Stanford Linear Collider," *Nuc. Instrum. Meth.* A316:343-350, 1992.
- [2] B. Widrow and S. Sterns, *Adaptive Signal Processing*. New Jersey: Prentice-Hall, 1985

Design of the ALS Transverse Coupled-bunch Feedback System*

W. Barry, J. M. Byrd, J. N. Corlett, J. Hinkson, J. Johnson, G. R. Lambertson
Lawrence Berkeley Laboratory, Berkeley, CA 94720 USA

J. D. Fox

Stanford Linear Accelerator Center, Stanford, CA 94309 USA

Abstract

Calculations of transverse coupled bunch growth rates in the Advanced Light Source (ALS), a 1.5 GeV electron storage ring for producing synchrotron radiation[1], indicate the need for damping via a transverse feedback (TFB) system. We present the design of such a system. The maximum bunch frequency is 500 MHz, requiring that the FB system have a broadband response of at least 250 MHz. We describe, in detail, the choice of broadband components such as kickers, pickups, power amplifiers, and electronics.

INTRODUCTION

Because of the high beam current and large number of bunches at the ALS, coupled-bunch instabilities are predicted to be one of the limiting factors in achieving the design beam intensity while maintaining good beam quality[2]. The instabilities are driven by the RF cavity dipole higher order modes (HOMs) and the resistive wall impedance of the vacuum chamber. We have designed a TFB system to damp beam oscillations to an acceptable level. General ALS parameters relevant to the system are listed in Table 1.

FEEDBACK REQUIREMENTS

The proposed TFB system is a so-called bunch-by-bunch system because each bunch is acted upon independently. This requires that the system bandwidth be at least one half the bunch frequency to encompass all possible coupled-bunch mode frequencies. This bandwidth requirement poses the most difficult design restrictions on the system.

The TFB system can, in principle, be operated in any one of many frequency bands (0-250 MHz, 250-500 MHz, etc.). In order to minimize expensive wideband high-power driver amplifier power, we chose to kick in the 0-250 MHz frequency band, where the impedance of a stripline-pair kicker is greatest. In addition, the fastest growing CB modes are driven at low frequency by the resistive wall impedance, where the kicker impedance is maximum. The lowest frequency unstable mode is assumed to be no lower than 150 kHz.

The amount of voltage kick/turn and gain required in the system is determined by the driving impedances, total beam current, and transverse oscillation amplitude. In order to damp an oscillation, the TFB system must be capable of providing a transverse voltage kick equal to the

Parameter	Description	Value
E_b	Beam energy	1.5 GeV
C	Circumference	196.8 m
f_{rf}	RF Freq.	500 MHz
N	Number of bunches	328
I_0	Total DC beam current	0.4 A
σ_t	RMS bunch length	3.9 mm
$Q_{x,y}$	Horizontal betatron tune	14.28, 8.18
$\beta_{x,y,cav}$	$\beta_{x,y}$ at cavity	11.5 m, 5 m
$Z_{\perp,RW}$	max. RW impedance	2 M Ω /m
$Z_{\perp,HOM}$	max. HOM impedance	4 M Ω /m

Table 1: ALS parameters used for calculations.

beam induced voltage. Neglecting radiation damping, this voltage is given by

$$V_b = I_0 \Delta x Z_{\perp} \quad (1)$$

where Δx is the transverse oscillation amplitude of a coupled-bunch mode.

Kicker power is provided to deliver a transverse kick of 1.6 kV/turn; this will damp a CB mode oscillation with amplitude up to 1 mm. The ALS injector system injects beam at a 1 Hz rate in bursts of ~1% of the full beam current. The injected beam has ~10 mm horizontal offset from the design orbit. To damp this, the transverse kick is applied until it is damped below the 1 mm saturation level of the system whereupon the feedback becomes proportional to beam excursions. In the few milliseconds this requires, CB growth is arrested before it exceeds the 1 mm limit.

FEEDBACK SYSTEM DESIGN

General Description

A general diagram of the TFB system is shown in Figure 1. The system is identical in both transverse planes. Two transverse (x,y) pickup signals located ~90° apart in betatron phase are added together with appropriate coefficients to produce a 90° betatron phase shift between the pickup signal and the kicker for arbitrary kicker location and betatron tune. The electronics systems consist of two microwave receivers for detecting horizontal and vertical moment ($I_0 \Delta x$), a system (shown as two variable attenuators) for mixing the signals from the two pickup stations, a delay, and a power amplifier for driving the kicker. Detection of the transverse moment rather than position makes the FB damping rate current dependent. Except

*This work was supported by the Director, Office of Energy Research, Office of Basic Energy Sciences, Materials Sciences Division, of the U.S. Department of Energy under Contract No. DE-AC03-76SF00098.

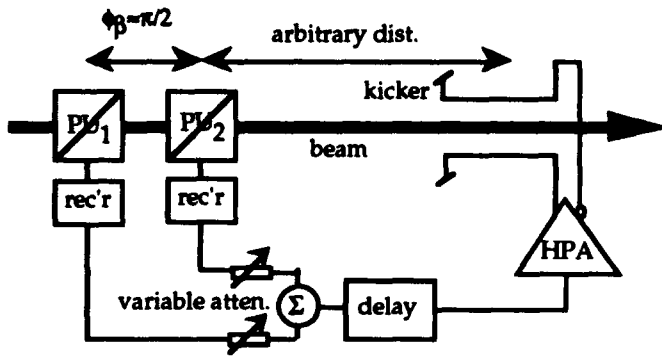


Figure 1: General arrangement of the transverse FB system.

for increased difficulty in calibrating the system, this does not affect the ability of the system to stabilize the beam. Separate amplifiers and kickers are used for each transverse plane. The system uses entirely analog components, although future upgrades include a digital delay. Appropriate interfaces to the accelerator control system are not shown.

Pickups

A set of four LEP-style beam button pickups[3] are used as the transverse detectors at each pickup location. Each button has a measured pickup impedance of $\sim 1 \Omega$. For their arrangement in the vacuum chamber, transverse pickup impedance is $\sim 1 \Omega/\text{cm}$. With ALS peak bunch currents in excess of 10 A, the pickups provide ample signal. Each button has been loaded with ferrite and reduced in size to suppress high frequency resonances[4] observed in bench measurements. Observations of the button signals during ALS storage ring commissioning show adequate bunch-to-bunch isolation to reduce coupling through the TFB system.

In contrast to the kicker operation, position detection is performed at 3 GHz (the sixth harmonic of the RF). This frequency band was chosen because the button pickups are most sensitive in this region. As indicated below, the front end receivers detect beam position at this frequency and subsequently demodulate the position signals to baseband for driving the kickers.

Kickers and Amplifiers

Each transverse kicker is a pair of 50Ω quarter-wave striplines at 250 MHz operated in difference mode. The kicker parameters are listed in Table 2.

The power required to damp the amplitude Δx is, using V_b from Eq. 1, given by

$$P_k = \frac{V_b^2}{2R_k} \quad (2)$$

indicating that we require $>250 \text{ W}/\text{plane}$. One drawback of kicking in the baseband is the problem of obtaining power amplifiers (500 W cw each) which have good linearity and phase characteristics over this relatively wide

Parameter	Description	Value
Z_{inp}	Input impedance	50Ω
$2b$	Plate separation	7.2 cm
l	Kicker electrical length	30 cm
g	Coverage factor	1.1
$R_{k,DC}$	Kicker impedance at DC	8.9 k Ω
$R_{k,250}$	Kicker impedance at 250 MHz	3.6 k Ω
n_k	Number of kickers/plane	1
P_T	Min. amplifier power	350 W

Table 2: Transverse stripline kicker parameters.

frequency range (0.1–250 MHz). Presently, several manufacturers of such amplifiers have submitted proposals and bids, procurement of one of these is expected to take place during the next several weeks. Available amplifiers are solid-state with $>57 \text{ dB}$ gain.

RF Electronics

The most intricate, and perhaps most interesting electronics in the system, are the 3 GHz front end receivers, shown in more detail in Figure 2. Bunch to bunch position variations due to coupled bunch instabilities result in amplitude modulation of the sixth harmonic 3 GHz beam signal (carrier) detected by the button pickups. The pickup signals are routed to the receivers via accurately phase-matched coaxial cables. In addition, the receiver inputs employ adjustable delay lines for trimming of the phase match between channels. The button signals are first bandlimited with $\pm 250 \text{ MHz}$ bandpass filters centered at 3 GHz, allowing for double sideband AM detection. Given the fact that the system bandwidth is limited to 250 MHz (baseband) by the power amplifiers, the bandpass filters were chosen so as not to exceed this bandwidth in order to maximize signal to noise. In addition, the bandpass filters prevent intense spikes from individual bunches from reaching the ensuing gain stages. Apart from the adjustable attenuators, whose function is described below, the remaining portions of the receivers simply sum and difference the button signals to produce x and y position signals. The x and y signals are demodulated to baseband with a 3 GHz local oscillator locked to the storage ring RF. As a practical note, the microwave hybrids for performing sums and differences have been purchased as an integrated package, commonly known as a monopulse comparator. With no significant increase in cost, the integration of the hybrids yields better phase and amplitude balance compared to using separate components. Demodulation components consist of standard mixers and 250 MHz low pass filters.

In order to reject signals due to closed orbit offsets, the receivers employ feedback loops which eliminate slowly varying position signals by setting the gains of each button signal so that the beam appears to be effectively centered in the button array. At the outputs of the x and y channel low pass filters, low frequency error signals are detected via

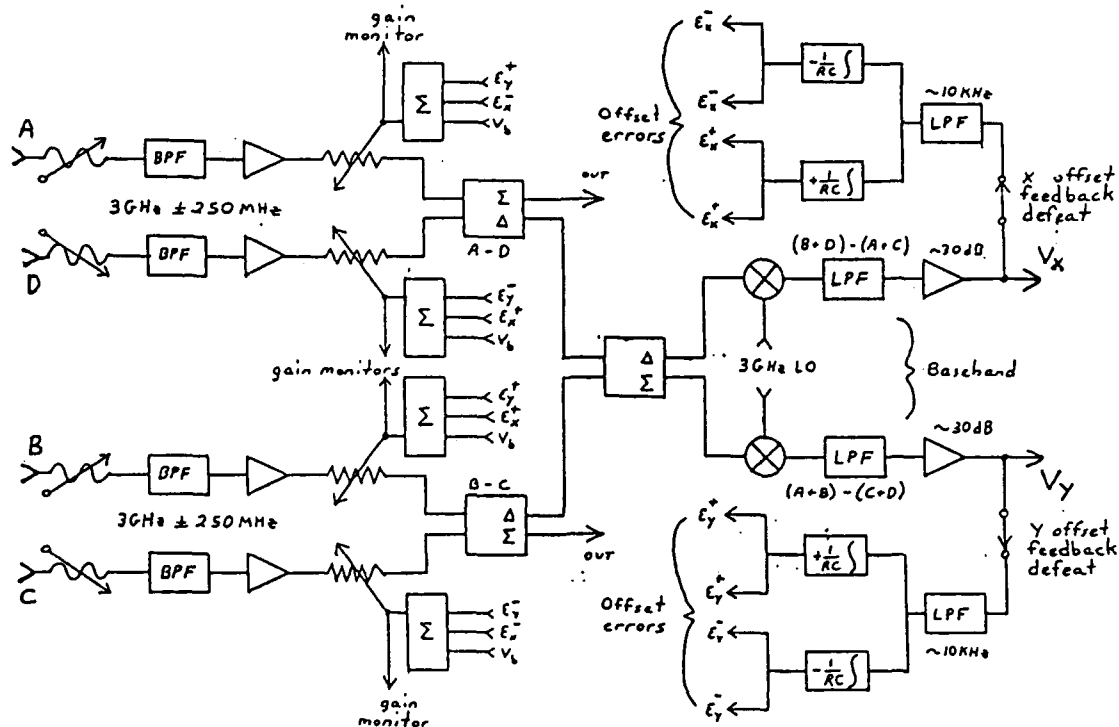


Figure 2: Receivers used in the transverse FB system.

extremely narrow band low pass ($<10\text{ kHz}$) filters. These signals, with the aid of the integrators, are used to drive variable attenuators in the RF legs of the signal paths for each button. The action of the feedback is such that the attenuator settings vary in a way that keeps the $<10\text{ kHz}$ frequency components of the x and y output signals at zero. In addition, the closed-orbit feedback loops are configured as to not change the system gain. The narrow bandwidth of the feedback allows the higher frequency components of the position signals (betatron oscillations) to pass undisturbed to the kickers. With this 10 kHz bandwidth, it is conceivable that position signals due to magnet power supply ripple can be zeroed. The variable attenuators are simply RF mixers configured in "attenuator" mode. That is, the DC coupled IF ports of the mixers are driven by error currents from the integrators resulting in controlled attenuation of the RF signals passing from the RF to LO ports. In this application, it is important that the control current does not greatly alter the phase characteristics of the RF signals. At present, various mixers are being evaluated for this applications.

Returning to Figure 1, the signals from each receiver are combined in proportions dictated by the Twiss parameters at the two pickups and the phase advance between the two pickups and the kicker. These parameters are determined by an on line computer program from quadrupole current measurements. Horizontal and vertical correction signals are then sent to the power amplifiers and kickers via ~ 1 turn delay. For commissioning of the system, the delay

(approximately 600 nsec) will consist of a coaxial cable.

CONCLUSIONS

We have designed a TFB system to damp coupled-bunch oscillations in the ALS. Currently, RF electronics are being delivered, the amplifiers are being ordered, and the stripline kickers are being constructed for installation in summer of 1993. The entire system should be installed and operational within a year.

The authors would like to thank the SLAC Feedback Group for many useful discussions and members of the Center for Beam Physics at LBL for their general support and encouragement.

REFERENCES

- [1] *1-2 GeV Synchrotron Radiation Source-CDR*, LBL PUB-5172 Rev., July 1986.
- [2] J. Byrd and J. Corlett, *Study of Coupled-bunch Collective Effects in the ALS*, these proceedings.
- [3] J. Borer, *Instrumentation and Diagnostics Used in LEP Commissioning*, proceedings of the 1990 Accelerator Instrumentation Workshop, Batavia IL, AIP Proc. 229.
- [4] W. Barry, *Broad-band Characteristics of Circular Button Pickups*, proceedings of the 1992 Accelerator Instrumentation Workshop, Berkeley CA, LBL-32939, UC-406, Oct. 1992.

Results of Prototype Particle-Beam Diagnostics Tests for the Advanced Photon Source (APS)*

A. H. Lumpkin, Y. Chung, E. Kahana, D. Patterson,
W. Sellyey, A. Votaw, and X. Wang
Argonne National Laboratory
9700 S. Cass Avenue, Argonne, IL 60439 USA

Abstract

The Advanced Photon Source (APS) will be a third-generation synchrotron radiation source (hard x-rays) based on 7-GeV positrons circulating in a 1104-m circumference storage ring. In the past year a number of the diagnostic prototypes for the measurement of the charged-particle beam parameters throughout the subsystems of the facility (ranging from 450-MeV to 7-GeV positrons and with different pulse formats) have been built and tested. Results are summarized for the beam position monitor (BPM), current monitor (CM), loss monitor (LM), and imaging systems (ISYS). The test facilities ranged from the 40-MeV APS linac test stand to the existing storage rings at SSRL and NSLS.

I. INTRODUCTION

The Advanced Photon Source (APS) will be a third-generation synchrotron radiation user facility with one of the world's brightest x-ray sources in the 10-keV to 100-keV regime [1]. Its 200-MeV electron linac, 450-MeV positron linac, positron accumulator ring (PAR), 7-GeV injector synchrotron (IS), 7-GeV storage ring, (SR), and undulator test lines (UTL) will also provide the opportunity for development and demonstration of key particle beam characterization techniques over a wide range of parameter space. Some of these values overlap or approach those projected for fourth generation light sources as described at a recent workshop [2]. The Accelerator Systems Division (ASD) Diagnostics Group is responsible for the design, procurement, testing, and operation of all the diagnostic systems on the injector rings, their transport lines, the storage ring, and the undulator test lines. Descriptions of these plans using electrical conversion and optical conversion techniques and initial results from some prototype diagnostics tested on the linac test stands operating at 20 and 45 MeV, and the storage rings at SSRL and NSLS are presented briefly. These are supplemented by more detailed reports given at the 1992 Accelerator Instrumentation Workshop [3-8] and elsewhere at this conference. A brief outline of the undulator test line parameters and diagnostics is also presented.

*Work supported by the U.S. Department of Energy, Office of Basic Energy Sciences, under Contract No. W-31-109-ENG-38.

II. BACKGROUND

Space precludes providing a complete description of the accelerator facilities for the APS but some background information is needed. The baseline electron source is a thermionic gun followed by a 200-MeV linac operating at an rf frequency of 2.8 GHz, and a maximum macropulse repetition rate of 60 Hz. The base injector (gun, bunchers, and 45-MeV accelerating structure) was operated April through June 1992 as the injector linac test stand [9]. The design goals include 14-ps-long micropulses, separated by 350 ps in a 30-ns macropulse with a total macropulse charge of 50 nC. The 200-MeV linac beam will be focused to a 3-mm spot at the positron-production target. The target yield is about 0.0083 positrons per incident electron with a solid angle of 0.15 sr and an energy range of 8 ± 1.5 MeV. The positrons will then be focused by a pulsed solenoid and about 60% of them will be accelerated to 450 MeV. Commissioning of these two linacs is to be completed by December 1993. The 450-MeV positrons are injected into the horizontal phase space of the PAR at a 60-Hz rate. As many as 24 macropulses can be accumulated as a single bunch during each 0.5-s cycle of the injector synchrotron. The injector (or booster) synchrotron accelerates the positrons to 7 GeV at which energy they can be extracted and injected into the designated rf bucket of the storage ring. A schematic of the APS accelerators which lists the number of diagnostic stations is given in Ref. 3.

Several features of the subsystems are provided in Table 1. The peak current, bunch length, and charge per pulse are given for the low energy transport (LET) lines between the linac and the PAR and the PAR and synchrotron, respectively. The high energy

Table 1. APS Parameters for Beam Diagnostics

	LET 1	LET 2	HET
PEAK CURRENT	8 mA	11.9 A	28.9 A
BUNCH LENGTH	30 ns	0.29 ns	122 ps
INTENSITY PER PULSE	1.5×10^8 positrons	2.2×10^{10}	2.2×10^{10}
CHARGE PER PULSE	240 pC	3.5 nC	3.5 nC
PULSE RATE	60 Hz	2 Hz	2 Hz

transport (HET) parameters are also provided. The revolution time, bunch length, and average currents are provided in Ref. 3 for the rings. Due to the low emittance of the beam, the B_M resolution in the SR and the number (360) of units is a challenge.

III. Prototype Diagnostic Results

The basic charged-particle beam parameters such as beam position, profile, current, bunch length, energy, and beam loss are to be addressed. Both intercepting and nonintercepting techniques are used. Some of the systems had initial results from their prototypes on the APS linac test stand in the Spring of 1992 as described previously [3,6,7]. Other tests have been performed on the ANL Chemistry Department linac at 20 MeV, the Los Alamos APEX facility at 40 MeV, and the storage rings at SSRL and NSLS in the year prior to this conference.

A. Beam Position Monitors

The major component of the beam position monitor (BPM) plans involves rf BPM pickup elements and their associated electronics. The button feedthrough for the storage ring main chamber (~10-mm-diameter button) and the insertion device chamber (~4-mm-diameter button) have been designed. Over 1800 standard buttons have been received and tested mechanically and electrically. A number of them are installed in the first set of vacuum chambers in a staging area. In addition to these, there will be intercepting beam profile screens and the use of synchrotron radiation from at least one bending magnet in each of the rings.

The BPM electronics have been designed for single turn capability in the storage ring and injector synchrotron. For these two rings the prototypes of the rf front end and the monopulse receiver that uses the AM/PM conversion technique have been tested in the laboratory and with input from BPMs at SSRL. Figure 1 shows the results of data obtained in a 20-bunch mode and using the signals from the SSRL striplines. The observed linearity and the resolution were scaled to APS conditions satisfactorily [4].

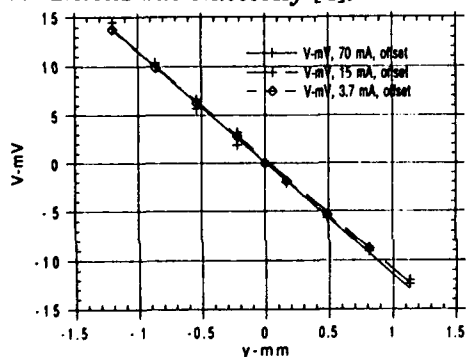


Figure 1 BPM Prototype Electronics Test at SSRL.

Another extensive program involves our orbit feedback design developments. Both AC global and local feedback aspects are involved. Results of a DC test at NSLS of the singular value decomposition (SVD) algorithm for global feedback were encouraging. A noticeable improvement in the rms orbit error relative to the reference orbit was obtained, a reduction from 137 μ m to 61 μ m. This is described in more detail in a separate paper at this conference [10].

B. Beam Current Monitor

Monitoring of the current/charge in the transport lines and rings will generally be based on use of fast current transformers manufactured by Bergoz and in-house electronics. Because the pulse structure of the electron linac will be representative of beam in the linac-to-PAR transport line, or LET1, the prototype current monitor (CM) was tested on the APS linac test stand as reported previously [6]. More recently, the integrating current monitor (ICM) was tested on the ANL Chemistry Department linac. Measurement capability of the charge (5 nc) in a 25-ps FWHM bunch was demonstrated successfully. Sum signals in the BPMs will also provide relative beam intensity measurements.

C. Beam Loss Monitor

The loss monitor (LM) system which will cover the entire extent of beamlines and accelerators was tested as a prototype. A gas-filled coaxial cable acting as an ionization chamber was installed along the length of the APS linac test stand. Results from tests at 25-40 MeV were reported elsewhere [7]. More recently the system was installed in the first 30 m of the SSRL storage ring after the injection point. Initial data were obtained under purposely poor injection efficiency conditions. The trace showed losses as negative-going pulses on the first few passes around the ring. DC tests were also performed and compared successfully to the SSRL DCCT under various stored beam lifetime conditions.

D. Imaging System

The beam imaging system (ISYS) can be applied to several aspects of the beam profile tasks. These can relate to beam spatial profiles, energy, or bunch length depending on the location in the beam transport (dispersive or nondispersive) or the nature of the imaging system (standard camera, gated camera, or streak camera). Initial tests included use of a VME-architecture-based video digitizing system linked to a Sun workstation. We have recently had the Los Alamos GTA video system adapted to the APS EPICS environment [11]. Sample data from the use of a demo, gated camera at SSRL (collaboration with Jim Sebek and Bob Hettel) show the ability to image a single bunch from a single pass in the storage ring. A

short gate, ~ 30 ns, was used and the gate delay was adjusted to step the active window off the back edge of the beam bunch pattern. The signal levels for $N = 0$, 1, and 2 bunches were clearly evident (Fig. 2).

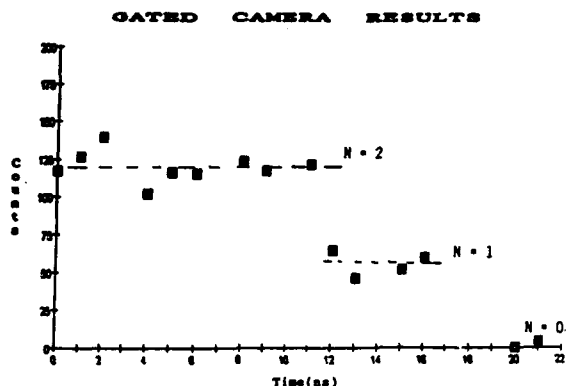


Figure 2 Gated camera results show observation of single bunch ($N=1$) possible.

IV. UNDULATOR TEST LINES

The undulator test lines are being considered at 650 MeV and 7 GeV. In the first case, the tungsten positron conversion target will be retracted and the 450-MeV linac rephased to accelerate the electrons to 650 MeV. A key point here would be the switch to the rf thermionic gun which is projected to provide normalized, edge emittance of about 10π mm rad, a few orders of magnitude colder than the standard thermionic gun [12]. This gun also may allow micropulse bunch lengths of less than 1 ps to be attained via filtering and magnetic compression techniques. The emittance at 200 to 650 MeV will be measured in a straight 10-m-long section that bypasses the PAR. Cross-comparison of several techniques, including three-screen, two-screen, optical transition radiation (OTR) interferometry [13], and quadrupole field scan, is planned. Bunch length will be determined by a streak camera using either OTR [8] or some other prompt mechanism. Many of the critical beam parameters identified in the 4th Generation Light Source Workshop [2] will be approached by the proposed undulator test line electron beam.

V. SUMMARY

In summary, key charged particle beam parameter characterizations are being addressed at the APS. Due to the diverse parameter space involved, a number of complementary intercepting and nonintercepting beam techniques are being employed and most prototypes have now been tested. In the rings, of course, the nonintercepting techniques are dominant. Additionally, the undulator test line

initiative will address measurement of high brightness beams, their emittance-preserving transport, and their interactions with undulators in a parameter space which will be of interest to the designers of the next generation of light sources.

VI. ACKNOWLEDGMENTS

The authors are indebted to the Diagnostics Group technicians (J. Crissup, L. Erwin, P. Nemenyi, and A. Pietryla) for their technical support; to G. Mavrogenes and J. Galayda for their support; to the linac test stand operations crew including R. Fuja, W. Berg, and W. Wesolowski for beam time; and to R. Hettel, J. Sebek, and J. Corbett of SSRL for their collaborations.

VII. REFERENCES

- [1] D. E. Moncton, E. Crosbie and G. K. Shenoy, "Overview of the Advanced Photon Source," *Rev. Sci. Instrum.*, **60**, (7), July 1989.
- [2] Proceedings of the Fourth Generation Light Source Workshop, Feb. 24-27, 1992, Stanford, California, SSRL 92-02.
- [3] A. H. Lumpkin, et al., "Overview of Charged-Particle Beam Diagnostics for the APS," *Proceedings of Fourth Accelerator Instrumentation Workshop*, October 27-30, 1992, Lawrence Berkeley Laboratory, Berkeley CA, AIP Conference Proceedings (in press).
- [4] E. Kahana and Y. Chung, "Test Results of a Monopulse Beam Position Monitor for the Advanced Photon Source," *ibid.*
- [5] A. J. Votaw, "Preliminary Design of the Memory Scanner for the Advanced Photon Source," *ibid.*
- [6] X. Wang, "Design and Initial Tests of Beam Current Monitoring Systems for the APS Transport Lines," *ibid.*
- [7] D. R. Patterson, "Preliminary Design of the Beam Loss Monitor System for the Advanced Photon Source," *ibid.*
- [8] A. H. Lumpkin and M. D. Wilke, "Further Time-Resolved Electron-Beam Characterizations with Optical Transition Radiation," *ibid.*
- [9] G. Mavrogenes, et al., *Proceedings of the Linac Conference*, Ottawa, Canada, August 24-28, 1992.
- [10] Y. Chung, et al., "Global DC Closed Orbit Correction Experiments on the NSLS X-ray Ring and SPEAR," these proceedings.
- [11] M. Zander and R. Wright, Los Alamos National Laboratory, "EPICS Video Manual," April 1993.
- [12] M. Borland, "An Improved Thermionic Microwave Gun and Emittance-Preserving Transport Line," these proceedings.
- [13] D. Rule and R. Fiorito, NSWC, Collaborative study in process, May 1993.

J. de Mascureau, C. Bonnafond, A. Devin, E. Merle, G. Ployart, D. Villate

Commissariat à l'Energie Atomique, Centre d'Etudes Scientifiques et Techniques d'Aquitaine

B.P. 2

33114 LE BARP - FRANCE

Abstract

Some applications of the Induction Accelerators require high quality electron beams and among them we are mainly interested in Free Electron Laser (FEL) experiments and the achievement of the AIRIX high performance Radiographic Hydrotest Facility. In both cases small emittance and energy spread are needed to fulfill the experimental requirements. Beam diagnostics have been developed in order to allow a better knowledge of the main parameters and hence to optimize it. Since pulsed Accelerators, and namely Induction Linacs, have essentially time dependant characteristics, it is necessary for most of the diagnostics to be time resolved. We describe the emittance measurement which uses the Cerenkov radiation from a thin window on a gated camera to record and process the image of a pepper-pot. A new electron magnetic spectrometer is presented which includes high energy resolution optical fibers and streak camera recording. Other diagnostics are discussed such as beam position measurements.

I - INTRODUCTION

In high current electron accelerators, such as Induction Linacs, mechanical and magnetic alignment is a key topic for the beam transport and the emittance conservation along the accelerator. Small amplitude misalignments can be the cause of aberrations and instabilities that prevent the beam from being properly transported and focused. For high current (kA), low energy (few MeV) pulsed devices, only beam position monitors (BPM) using B-loops can be used as non-destructive diagnostics. Other diagnostics that stop the beam are needed to measure the beam emittance, the beam contour and position, the energy spectrum of electrons. They often use optical observation of the Cerenkov radiation from a thin target placed on the beam path. At higher energies, over 10 MeV, it may be helpful to consider the Optical Transition Radiation (OTR) as a powerful and non-destructive beam diagnostic.

Some experimental devices and first results are presented. The beam facilities devoted to these developments are the LELIA Induction Accelerator,

the EUPHROSYNE pulsed electron generator, and the ALEXIS RF accelerator (for OTR studies).

II ALIGNMENT

The alignment of charged particles accelerators has two components : mechanical alignment and magnetic alignment.

A - Mechanical alignment

On the LELIA accelerator we have used a device with a He-Ne laser and position detectors located on the mechanical axis of each part of the accelerator. It allows to measure gaps between an ideal straight line and the actual axes of the cells with an accuracy of 50 μm over a 30 m machine.

B - Magnetic alignment

The magnetic coils allowing the beam to be guided into the accelerator are mechanically bound to the cells. Magnetic axis of each coil is checked in translation and rotation by the use of the stretched wire technique. It allows to point out offsets of 50 μm and tilts of 10 μrad . Only tilts in rotation can be eliminated by the help of steering coils.

C - AIRIX Alignment

We are currently studying procedures for assembling the cells and achieving the whole accelerator alignment.

The problem of marking the difference between mechanical and magnetic axis should be solved by the assembling technique of the different parts of the accelerator and the use of homogenizer rings [1] mechanically centered in the coils. References, carrying back the magnetic axis to the outside of the structures, will make possible a dynamic realignment of the accelerator.

III - EMITTANCE MEASUREMENTS

This diagnostic has been performed to measure time resolved electron beam transverse emittance by using the pepper-pot technique. Characteristics of the

beams are typically 1 to 3 kA and 1 to 6 MeV for a pulse duration around 50 nsec. The beam entering the pepper-pot is screened by a plate which holds a set of holes regularly spaced in the two transverse directions of the beam. The emerging beamlets, after travelling a drift length L , strike the analysis plane (silica window) for electron-photon Cerenkov conversion. But here care has to be taken of the spatial resolution connected with the thickness of the interaction target. The transverse emittance is then defined as the trace space area divided by π occupied by the beam in one direction. This area is determined by analyzing the beamlet distribution. Thus, emittance can be measured in the two transverse directions simultaneously.

The mechanical parameters of the diagnostic have been calculated with the help of an envelope code. For the design of the AIRIX emittance meter at $E = 4$ MeV, $I = 3$ kA and $\varepsilon = 100\pi$ mm mrad we obtained the values indicated on the figure 1. This experimental set up consists in :

- a vacuum tank with the selection and analysis planes
- a CCD camera (with gating from 3 nsec to 300 msec) located 90° from the beam axis to record the beamlet distributions. This camera is packed in a lead box inside a Faraday cage to shield it from X rays and electromagnetic radiations,
- a computer in order to analyze the pepper-pot image and calculate the emittance value. An image processing has been performed.

This apparatus is currently being tested with the EUPHROSYNE generator before being put on the LELIA beam. It will then be used for the measurement of the emittance of the AIRIX injector electron beam.

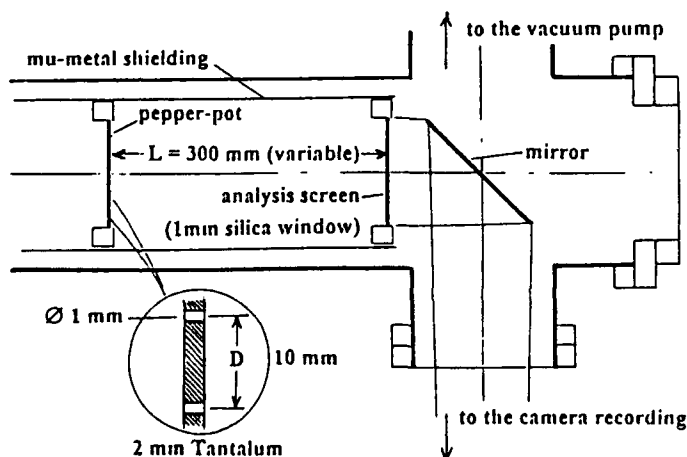


Figure 1 : AIRIX emittance layout

IV - SPECTROMETER

A magnetic spectrometer is being tested which allows to analyze the electron energy versus time between 1 and 10 MeV.

Its principle is founded on a 180° magnetic deviation obtained with the help of an electromagnet. The magnetic field is measured by a Nuclear Magnetic Resonance probe giving an absolute accuracy around 10^{-5} .

The analyzing plane can be equipped with different detectors such as a film (no more time resolved measurements in this case), a set of 28 Faraday cups allowing, over an energy range of $0.5E$, resolutions of $\Delta E/E = 2\%$ and $\Delta t = 3$ nsec, and two sheets of 100 optical fibers. (see Figure 2)

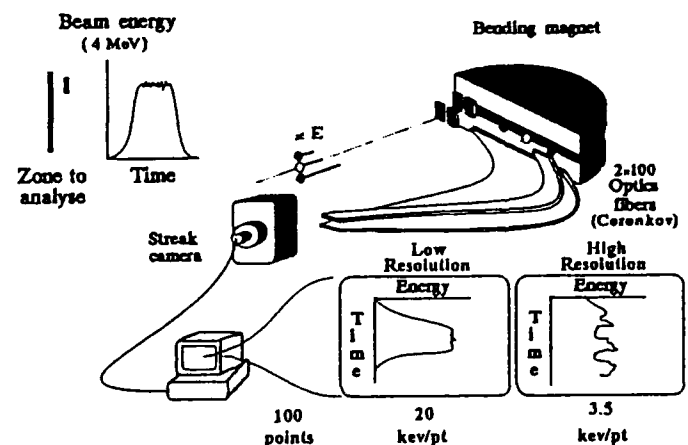


Figure 2 : Spectrometer

In this last case, the Cerenkov radiation emitted by electrons into the fibers is guided to a streak Camera which allows a continuous time analysis with a 1 nsec resolution. For the first sheet of fibers the resolution is $\Delta E/E = 0,5\%$, over an energy range of $0,5E$. The second sheet with fibers placed side by side provides a resolution $\Delta E/E = 0,1\%$ over a $0,1E$ energy range.

The electron path has been numerically simulated by following the particles in the actual field given by a magnetic cartography of the air gap.

Calibration of the whole is achieved at low energy ($\approx 0,6$ MeV) thanks to a Cs-Ba β source and a counting system.

V - BEAM POSITION

A - B_θ loops

Determination of the electron beam position is obtained from measurements given by 4 loops influenced by the B_θ field generated by the beam.

A beam calibration, using a wire (which simulates the beam) gives the result when centring is perfect and then when a few millimeters off-axis displacement is imposed.

The voltage pulse delivered by each loop is proportional to the time derivative of current. The intégration is mathematically obtained. This can be the cause of errors due to the evaluation of the continuous level of offset. It would probably be better to process the signal after being integrated in a high bandwidth (2 GHz) integrator allowing to observe fast fluctuations of the beam centroid. An other way of improving the diagnostic could be the use of calibrated beam instead of a wire.

B - Optical measurements

Spatial profile and position of the beam in the pipe are analyzed. Electron-photon converters allowing to obtain an " image " of the beam are inserted in the guiding channel. They often use Cerenkov radiation from a thin target. Such measurements have been achieved on the LELIA injector at 1.3 MeV using a fast gated camera giving a 5 nsec time resolution. As an alternative, the use of a streak camera can provide a continuous analysis of a transverse diameter of the beam with a time resolution around 1 nsec.

VI - OPTICAL TRANSITION RADIATION

It occurs when a charged particle crosses the interface separating two mediums having different dielectric indices[2-4]. As a first advantage this radiation is emitted as well forward than backward in visible lobes distinctly orientated. It can provide measurements of beam position and profile, but in addition it can give access to the beam energy since the angular separation of the lobes presents a $1/\gamma$ variation. An other advantage is the result of the nature of this radiation, depending only on the index variation. It allows a thin membrane to be used as target with only few perturbation in the beam transport.

We have an RF accelerator with a 13 to 20 MeV energy and a 400 mA intensity in macropulses of 5 μ sec duration (ALEXIS). An experiment has been installed to study OTR in this energy range and first results are interesting. We anticipate a useful application of these techniques to the high energy part of the future AIRIX Accelerator.

VII - OUTLOOK

These diagnostics appear directly connected with the development of the AIRIX program. In particular

the new time-resolved energy spectrometer and the emittance meter described above are intended for measurements of the beam characteristics of the AIRIX injector (4 MeV-3.5 kA - 60 nsec) now under construction . They are planned for the optimization of the beam in the PIVAIR milestone [5] before the completion of the AIRIX Accelerator.

VII - REFERENCES

- [1] M.J. Burns et al,
Magnet Design for the DARHT Linear
Induction Accelerators
Proceedings of the 1991 IEEE Particle
Accelerator Conference, p. 2110-2112
- [2] L. Wartski et al, J. Appl. Phys. 46
p. 3644 (1975)
- [3] D.W.Rule, R.B. Fiorito et al,
Nucl. Instr. Method A 296 (1990) 739-743
- [4] A.H. Lumpkin, R.B. Feldman et al,
Nucl. Instr. Method A 318 (1992) 415-421
- [5] Design and progress of the AIRIX Induction
Accelerator
J. de Mascureau et al
Proceedings of the same conference

Beam Instrumentation For The SSC RFQ

P. Datte, G. Jamieson, R. Aiello, D. Beechy, A. Jones, D. Martin, J. Riordon, R. Webber, F. Wood
Superconducting Super Collider Laboratory*
2550 Beckleymeade, MS-4005, Dallas, TX 75237 USA

Abstract

A detailed description of the SSC RFQ beam instrumentation is presented. Most of the instrumentation is located in the RFQ end walls. The upstream end wall contains a segmented Faraday cup, a segmented aperture and a wire scanner. The down stream end wall contains a segmented aperture and wire scanner. Two current toroids are used to measure the transmission through the RFQ. The output of the RFQ is a low emittance, pulsed 2.5 MeV H^+ beam with peak current of 25 mA and maximum pulse length of 35 μ s. Typical beam data are shown with the emphasis being on instrumentation performance.

I. INTRODUCTION

The RFQ instrumentation consist of two current toroids, a segmented Faraday cup, two wire scanners and two segmented apertures. All of the instruments except the current toroids are actuated instruments and mounted in the end walls. Of the two current toroids one is up stream and one is down stream of the RFQ. The toroids have been electrically matched to allow for proper transmission measurements during commissioning. The wire scanners are placed up and down stream of the RFQ to measure the beam profile and position information. Also up stream is the segmented aperture and the segmented Faraday cup which will define a maximum beam size and measure the beam position and current respectively. Down stream is a segmented aperture which defines the beam size entering the Drift Tube Linac (DTL) matching section. Figure 1 shows the RFQ with the instrumentation mounted.

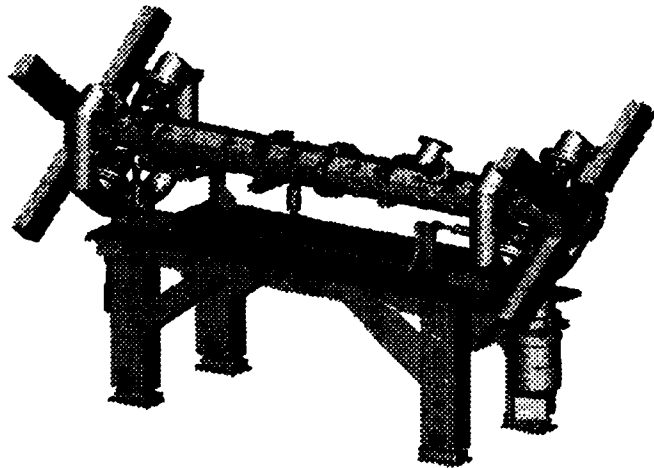


Figure 1. RFQ with end wall actuator mounted instrumentation.

II. DESCRIPTION OF THE BEAM INSTRUMENTS

The entrance end wall contains the segmented aperture and Faraday cup which can be used as separate instruments or as a system with 1 mm spacing between them. The segmented sections of each instrument can be monitored independently. Beam positioning is accomplished by producing equal current on all four segments. By placing the aperture and Faraday cup in the beam line at the same time, beam size and position can be obtained. When the instruments are at the beam line center, the operator can steer the beam into the RFQ by monitoring the current on the individual wedges. Once the segments have equal current values, the Faraday cup can be removed to allow for beam transmission into the RFQ. A second aperture is used in the exit end wall of the RFQ to define the maximum beam size into the DTL matching section. The transmission through the RFQ is measured by two matched current toroids. A 195 mm OD toroid surrounds the ion source low energy beam transport and is mounted just upstream of the RFQ entrance end wall. A matched toroid is mounted in a temporary diagnostic chamber at the exit of the RFQ. When the two current toroid waveforms are superimposed, the ratio is the total current transmission through the RFQ as a function of time. The wire scanners located at both the entrance and exit end walls are designed to have three separate wires that are electrically isolated to cover X, Y, and 45° . The profile is measured by stepping the wire through the beam and recording the current on each wire. By plotting the position and the measured current at each step location, the profile can be determined[1-2].

The electronics to read out the sensing instrumentation consists of a preamplifier, an integrator, and a waveform digitizer which all reside in a VME crate. The Faraday cup and aperture electronics are designed to measure a voltage produced by the beam current flowing through the preamplifier's input impedance. A fixed gain stage to matches the full scale input to the waveform digitizer when a beam current of 25 mA is being measured. The wire scanner electronics measures the signal current through an active transimpedance-difference circuit. A VME programmable 2 gain selectable second stage is used to match the full scale input of the waveform digitizer based on the dynamic range requirements of the beam current. The current toroid preamplifier measures a voltage that is produced by the current toroid and has a fixed gain based on the selected transformer's sensitivity (V/A). The circuit also produces an integrated output which can be digitized with an ADC. Figure 2 shows a digitized waveform from the integrator card with the integrated signal superimposed. The waveform is 35 μ s long and both were digitized at 200ns per point.

*Operated by the University Research Association, Inc., for the U.S. Department of Energy under contract No. DE-AC35-89ER40486

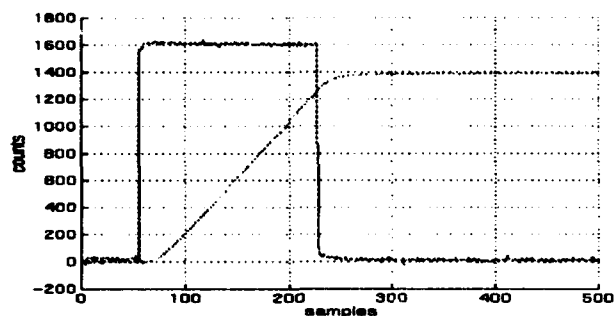


Figure 2. Digitized 35 μ s pulse and integrated output.

The waveform digitizer has a analog bandwidth of 11 MHz and a sampling rate of 5 MHz. The VME board was designed by Mike Shea (FERMI LAB) and Alan Jones (FERMI LAB/SSCL) and is now commercially available from OMNIBYTE CORP, VMIC, and JOERGER ENTERPRISES INC. The electronic specifications for each analog VME board are shown in table 1.

Table 1
RFQ instrumentation specifications

VME Board	Bandwidth	Input Channels	Input Range
Faraday Cup	DC - 10 MHz	4	5 - 50 mA
Wire Scanner	DC - 10 MHz	3	.25 mA - 5 mA
Current Toroid	DC - 10 MHz	4	0 - 100 mA
Digitizer	5MHz	4	± 1 V

Figure 4 shows a single channel of the Faraday cup preamplifier card. The first stage is a buffered difference circuit. The second stage is a gain stage with a low pass filter of 3dB @ 10 MHz designed to produce a 4 volt output into 50 ohms with a 100 mA input current. Figure 3 shows a functional diagram of the Faraday cup circuit. The output is passed to the integrator card where both the waveform and integrated waveform are then digitized. A biasing circuit for control of secondary emission which occurs when the beam interacts with the intercepting material is connected to the input of the amplifier. Secondary emission from beam intercepting monitors can be difficult to understand at low energies. Problems with biasing of instrumentation at 35 keV were observed at the LEBT and have disappeared at 2.5 MeV. A more detailed discussion of these issues can be found in ref [3]. When the bias supply is connected, the circuit no longer has DC response.

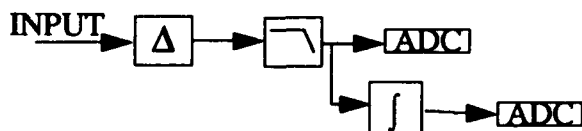


Figure 3. Faraday cup functional circuit.

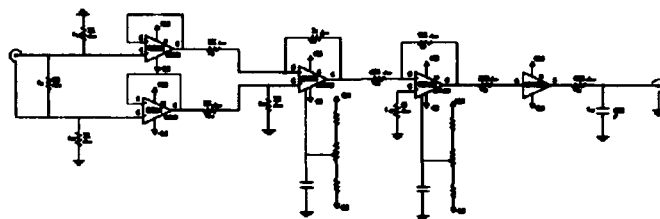


Figure 4. Circuit diagram for a Faraday cup channel.

The wire scanner and segmented aperture circuits have the functionality. The current toroid electronics has the preamplifier and integrator circuit on the same board. Figure 5 shows the down stream segmented aperture head without the actuator. The intercepting material is made of Graphite and is insulated from the copper housing by KAPTON film.

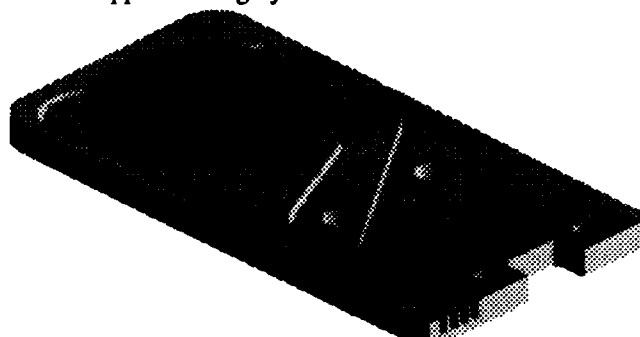


Figure 5. Down stream segmented aperture.

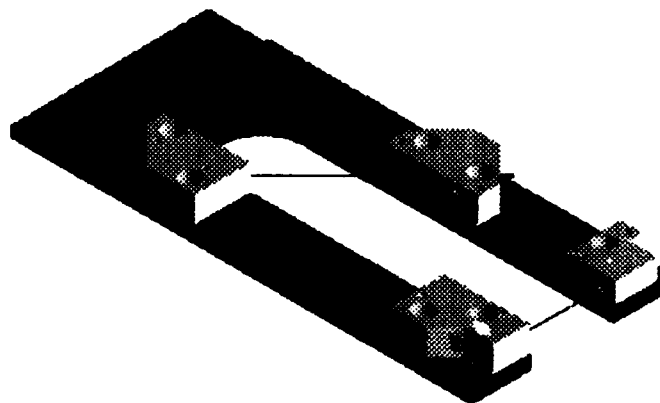


Figure 6. Three channel wire scanner.

Figure 6 shows the wire scanner head without the actuator. The wires are located in a ceramic block and held in place by gold plated pins. The pins have a jewelers sapphire in the tip which locate the wire in the housing. The wire is crimped with 50 grams of tension and the signal is read out through a flex circuit on the back side of the frame. If wire heating by the beam will be a problem at this energy a future design will have a spring mechanism for maintaining tension on the wires.

Figure 7 shows a typical waveform produced by the test pulse circuit for the current toroid electronics. Here a test pulse is injected into the current toroid located in the vacuum chamber and the induced pulse through the transformer and 16 meters of cable is digitized and displayed. This graph shows the rise time of the test pulse to be much less than the rise time of the actual beam (see figure 9) and therefore the electronics is not the limiting factor in this measurement.

III. PERFORMANCE WITH BEAM

The first beam through the RFQ was achieved on April 8, 1993. Examples of signals from the entrance and exit current toroids of the RFQ are shown in figures 8 and 9. The entrance current toroid has 2 and 4 MHz pickup from the RF volume source which is located 0.5 meters away. The coupling mechanism for this signal is unclear. The small notch at 15 μ s corresponds to the start of plasma formation, at this point the RF noise changes from 2 to 4 MHz. In figure 9 the average input current waveform can be seen after software filtering. The RFQ unfiltered output current is shown for comparison.

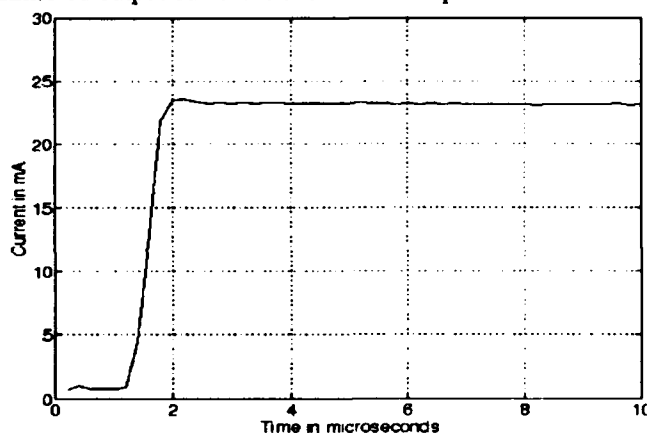


Figure 7. Test pulse for the current toroid.

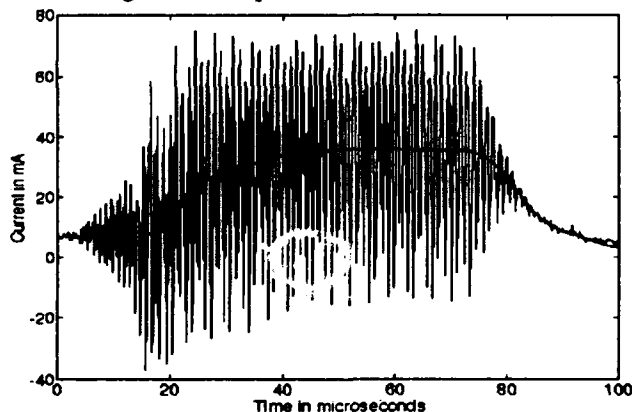


Figure 8. Input current toroid waveform.

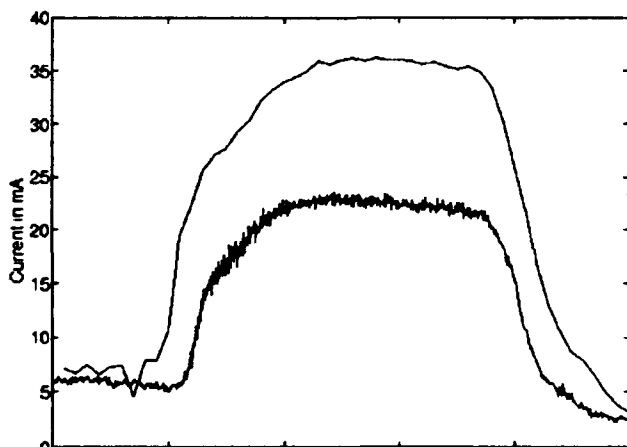


Figure 9. Input and output current toroid waveform.

IV. CONCLUSION

Our plan is to continue commissioning the RFQ instrumentation in the next 4 months. We have to bring the apertures, Faraday cup and wire scanners on line. Damage to the instrumentation at the output of the RFQ due to the 2.5 MeV beam will be the major concern. It is expected at maximum current density, that the wire from the wire scanner will not survive a single beam pulse. Single beam pulse damage can not be mitigated by water cooling. At 2.5 MeV the beam has a diameter of about a millimeter at the location of the instruments and is absorbed in a layer approximately 50 μ m deep. The aperture has an opening angle designed to minimize single shot damage by maximizing the surface area hit by the beam. The toroid at the present time is closely matched to the input toroid. When the matching section from the RFQ to the DTL is installed this toroid will be replaced with a small toroid mounted on an actuator (see Figure 10) and installed in the RFQ end wall.

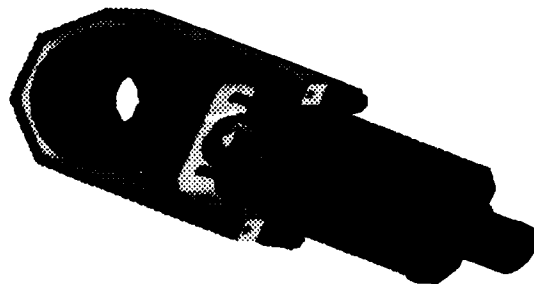


Figure 10. Current toroid head.

V. ACKNOWLEDGEMENTS

The authors would like to thank the individuals involved in the testing and the installation of these devices. Monica Chavez, Mike Gargiulo, and Wayne Johnston, Rita McDermott for their long hours in the lab during all phases of the operation.

VI. REFERENCES

- [1] R. Jung, "Beam Intercepting Monitors", CERN/LEP-BI/89-36.
- [2] R. Fulton et al., "A High Resolution Wire Scanner For Micron-Size Profile Measurements at the SLC", *NIM A274* (1989) pp. 37-44.
- [3] AIP Conf. Proc. 212, (1989) EDITORS: Edward R. Beadle Vincent J. Castillo Brookhaven National Laboratory, pp.143-144.
- [4] AIP Conf. Proc. 229, (1990) EDITORS: Elloit S. McCrory Fermi National Accelerator Laboratory, pp.88-105.

HIGH DENSITY DATA RECORDING FOR SSCL LINAC

Alan L. VanDeusen
AlliedSignal Inc., Kansas City Division¹
2000 E. Bannister, Kansas City, MO 64141-6159 USA

Charles Crist
Superconducting Super Collider Laboratory²
2550 Beckleymeade Avenue, Dallas, TX 75237

Abstract

The Superconducting Super Collider Laboratory and AlliedSignal Aerospace have collaboratively developed a high density data monitoring system for beam diagnostic activities. The 128 channel data system is based on a custom multi-channel high speed digitizer card for the VXI bus. The card is referred to as a Modular Input VXI (MIX) digitizer. Multiple MIX cards are used in the complete system to achieve the necessary high channel density requirements. Each MIX digitizer card also contains programmable signal conditioning, and enough local memory to complete an entire beam scan without assistance from the host processor.

I. BACKGROUND

A compact 128 channel data system was needed for performing beam diagnostic activities. To accurately profile the expected beam pulse, the 128 channels would have to be sampled simultaneously every 50 nSec for a period of up to 50 uSec. There was not anything commercially available that could perform this function within the allocated 24" rack space. In addition to the high number of channels to be digitized, the incoming current signals had to be converted to a voltage and amplified to the proper level before being recorded. Manufacturing costs and development time of the system were also considered important due to schedule and cost constraints. The time allocated for development and manufacture of the first board was targeted at 16 weeks.

II. EARLY DEVELOPMENT

Preliminary design and layout activities revealed that eight 20 MHz channels of data per VXI board was the practical limit. Higher levels of integration could yield slightly higher channel counts, but the increase in development time and cost would become significant. Even in the eight channel board layout, very little room remained for signal conditioning. At this point we decided to split the board functions between generic digitizing functions and signal conditioning functions. The entire main board or 'motherboard' would contain the 8-channel digitizing functions and the control interface. The 'daughterboards' were then assigned the exclusive tasks of signal conditioning. There is just enough room inside a VXI

module to allow the daughterboards to be stacked on top of motherboard.

III. MOTHERBOARD DESIGN

Digitizing

The motherboard consists of eight independent channels. Each channel has its own flash converter and 256K memory (128K samples). The flash converters are 10-bit, 20 MSPS devices that were selected for their power-consumption, performance and cost parameters. The memory is high-speed CMOS static RAM using 128K x 8 chips. A Programmable Logic Device (PLD) is used to control data acquisition, triggering and timing for all eight channels.

Timing

The PLD controls the timing and memory usage on the board. To optimize the memory for performing beam scans, the memory is divided into 100 records of 1K each. After the board is armed, each trigger pulse initiates a 1024 point digitized record covering 50 uSec. After the record is complete, the card remains armed and ready for the next trigger. After trigger pulse number 100, the card will automatically disarm and ignore further trigger pulses. If fewer than 100 pulses are desired, a starting record other than zero may be pre-loaded into the current record counter. For example, loading a 99 into the current record counter would allow only one record to be taken before disarming.

The PLD may be put into an alternate single shot trigger mode. This mode effectively makes each record one sample long. Since each trigger pulse takes only one reading (instead of 1024), then 102,400 individual readings can be taken. The PLD used is an electrically erasable Altera 7032 device in an on board socket. It can be easily removed and reprogrammed for different memory or timing configurations.

Clock and Trigger Modes

To give the board maximum flexibility for use in multiple board systems, several clock and trigger options are available. The clock may be jumper selected from one of three sources; 1) A front input clock connector, 2) an on board 20 MHz crystal oscillator, or 3) the clock may be taken

off the VXI local bus. Option 3 is provided so that multiple cards on a VXI backplane can be synchronized with the first card in the series.

The trigger to initiate a data record can also be jumper selected from a number of different sources. Again the VXI local bus or VXI trigger bus can be used as a trigger source.

Daughterboard Interface

The motherboard also provides the necessary interface signals, power, and connectors to the daughterboards. Each channel on the daughterboard is individually programmable. The following signals are provided for each channel on the daughterboards through the interface connector;

1. +5, -5, +12, -12, GND power.
2. Four digital control lines.
3. One 12-bit DAC voltage (-1 to +1).
4. Differential input from front panel.
5. Differential output to A/D converters.
6. Differential calibration input from front panel.

VXI Interface

The simple VXI register based interface is used for all board control and data transfer operations. The interface chip and design were purchased from Hewlett Packard as part number Z2492A. The data from the eight channel local memory bus are mapped to eight registers in the VXI A16 address space. The local address pointer can be loaded and incremented through a control register. All the data is then read across the VXI bus by reading all eight channels and then incrementing the local address pointer.

The register based interface was selected over a message based interface because of the higher transfer rate. Further improvements to the transfer rate could occur if the local memory could be mapped directly into the VXI A32 address space. This was not done on this design due to the delivery time and development cost constraints.

IV. DAUGHTERBOARD DESIGN

Requirements

The eight channel motherboard is designed to accept four daughterboards, with two channels on each board. The function of the daughterboard is to convert low level current signals into the $\pm .5$ volt signal for the motherboard. To cover the expected range of values, the amplifier supplies a full scale output ($\pm .5$) for inputs of 10 μ Amps to 10 mAmps. The amplifier also needs to have a high enough frequency response to follow an input rise-time down to 100 nSec. These electrical parameters have to fit within the size allowed by the enclosure, and use only the power and signals supplied by the motherboard.

Amplifier Design

In order to maximize the resolution of the 10-bit A/D converter, the amplifier has to have enough ranges to keep the maximum signal level in the upper part of the A/D range. The higher the signal can be to full scale, the greater the resolution. A two stage amplifier was designed to handle these requirements.

Stage one of the amplifier is a differential current to voltage (I>V) converter that covers three decades. The three ranges of one decade each, are achieved by switching different scaling resistors into the feedback of the I>V stage. A relay is also included on the daughterboard so that a calibration signal can be routed directly to each amplifier. All the relays are controlled by the four digital control bits provided for each channel.

The second stage of the amplifier contains a voltage programmable amplifier. The gain can be varied from 1 to 10 using the ± 1.0 volt DAC voltage from the motherboard. This effectively yields a continuously variable I>V converter over the entire three decade range. This does not occur without some sacrifices.

The second stage does not have a consistent voltage vs gain curve from channel to channel. This requires that each channel have some calibration factors that are determined during calibration. In addition to the gain variations, there is a large offset at the amplifier output. The offset is consistent at a particular gain setting, but varies as the gain is changed. The good thing is that both of these undesirable characteristics are repeatable. To handle this in our checkout software, we selected nine discreet gain settings for the second stage. For each gain, the DAC value for the proper gain and an OFFSET value are stored. These are determined through application of a DC calibration signal and stored on a disk file. During data collection, when a gain range is selected, the exact DAC value for that channel and gain is written to the motherboard DAC for that channel. When the data is read in, the OFFSET value is added to the data so that it is corrected. This was all performed within some low level device drivers written in C. Once the driver routines were completed, this manipulation became invisible to the application program. By using a programmable voltage source, software was written that determined the two calibration factors for each of 25 selected gain settings. Because of the calibration relays on the daughterboard, the calibration process is completely automated and takes about one minute for an 8-channel system.

V. SUMMARY

The motherboard serves as a general purpose eight channel 20 MSPS digitizer. By adding a different daughterboard design, an entirely different set of inputs can be digitized. The daughterboard is easily changeable and can be as simple as a jumper wire, if the input signal is already in the $\pm .5$ volt range.

The daughterboard is a continuously variable gain I>V converter that can supply a full scale input to the motherboard for any current input from 10 μ Amp to 10 mAmp.

Multiple 8-channel MIX digitizer modules can provide up to 96 channels of 20 MSPS current monitoring in a single VXI rack. Using two VXI racks, the 128 channel beam monitoring system was accomplished with eight empty VXI slots available for additional instrumentation.

¹Operated for the U.S. Department of Energy under Contract Number DE-AC04-76-DP00613.

²Operated by the University Research Association, Inc. for the U.S. Department of Energy, under contract No. DE-AC35-89ER40486.

Physics Requirements of Commissioning Diagnostics For SSCL Linac*

J. W. Hurd, G. M. Arbique, C. E. Crist, F. W. Guy, M. Haworth, G. T. Leifeste, K. Saadatmand
Superconducting Super Collider Laboratory
2550 Beckleymeade Avenue, Dallas, TX 75237

M. Krogh, K. McGinnis, D. Stittsworth, A. Vandeusen, S. Wright
Allied Signal, Kansas City Plant
2000 East 95th Street, Kansas City, MO 64141

Abstract

Commissioning diagnostics are described in terms of the beam physics requirements of the SSCL linac. Commissioning diagnostics include current monitors, beam position monitors, spectrometer, foil scattering experiment, wire scanners, Faraday cups, and bunch shape monitors. Two DOE integrated contractors, the Superconducting Super Collider Laboratory and Allied Signal, Kansas City Plant, are developing the commissioning diagnostics. The need to measure bright, short linac beam pulses requires special design considerations. High density harps and collectors with up to 50 wires per cm and 128 wires total, and fast, 3.5-MHz amplifiers have been developed. The diagnostics will be first used and tested during beam commissioning of the RFQ.

I. INTRODUCTION

The Superconducting Super Collider Laboratory (SSCL) is currently constructing and commissioning a 600 MeV linac to serve as the injector into a series of synchrotron accelerators [1]. The final structure will be a pair of 53 mile circumference synchrotrons providing colliding proton-proton beams, each at 20 TeV.

The linac [2] consists of an ion source, three distinct accelerator structures, and matching sections to transport the beam between structures. The rf accelerating structures are a Radio Frequency Quadrupole (RFQ), four Drift Tube Linac (DTL) tanks, and nine Coupled-Cavity Linac (CCL) modules, each with eight tanks. The general beam parameters are shown in Table 1. It is important to note the peak current, emittance requirements, and short pulse length of the linac beam. These characteristics, along with the high reliability requirement, provide the unique characteristics for the SSCL linac which drive the commissioning and development program.

Table 1
SSCL Linac Description

Length	143 m
Output Energy	600 MeV
Output Current	25 mA peak
Pulse Rate	10 pulses per second
Pulse Length	2 to 35 μ sec
Transverse Emittance	$<0.3 \pi$ mm-mrad, rms, norm.
Longitudinal Emittance	$<7.0 \cdot 10^{-7}$ eV-sec
Frequency	427.617 MHz

* Operated by the URA for the USDOE, under contract No. DE-AC35-89ER40486.

II. COMMISSIONING PLAN

The SSCL linac is to be commissioned in stages [3]. The current plans calls for installation and commissioning in a serial approach for each of the following sections: a) Ion Source, b) RFQ, c) DTL Input Matching Section (IMS), d) DTL tank 1, e) DTL tank 2, f) DTL tank 3, g) DTL tank 4 and CCL Input Matching Section (IMS), h) CCL module 1, and i) CCL modules 2-9 and the transfer line to the LEB. Currently, the H^- Ion Source and the RFQ are being operated at the Central Facility laboratory building near Waxahachie. The linac tunnel is near completion and the first DTL tank is scheduled for delivery in January.

III. COMMISSIONING DIAGNOSTICS

Commissioning diagnostics for the SSCL linac consists of a suite of instruments on a diagnostic cart which will be placed at the end of each section as it is being commissioned, and the standard set of operational diagnostics which are located between rf tanks and in matching sections [4, 5]. In addition there are stand alone diagnostics such as the spectrometer and x-ray detector.

Table 2 describes the diagnostic cart instrumentation. The primary function of each type of instrument is indicated. Some diagnostics could measure other variables. For example, a Slit and Collector Emittance Measurement Unit could measure total current if calibrated absolutely, but the SSCL emittance unit measures relative current only. A description of some of the devices and the design considerations for the SSCL commissioning diagnostics follows.

Slit-and-Collector Emittance Measurement Unit - The system measures the phase space distribution of the beam in the $x-x'$ plane and the $y-y'$ plane. A graphite slit measures the position of the beam, and a multi-wire collector measures the angular distribution. The collector is a sandwich design of copper and mica after a design used at LAMPF. The collector has 128 "wires" spanning 24.7 mm (0.13 mm wire width + 0.07 mm mica width).

Each channel of the 128 wires goes to a separate amplifier-ADC-memory array. The amplifier is bipolar and deferential with continuous gain ranges from 10 mA to 10 μ A full scale. The amplifier has a 10-MHz bandwidth at the lowest gain and approximately a 1-MHz bandwidth at the highest gain. The ADC digitizes at up to 20 MHz. Each time the board is triggered, 1000 data points are digitized during the beam pulse and stored in memory. Memory for each channel can hold up to 100 sets of data. The board was designed and built by a joint effort between SSCL and Allied Signal, Kansas City [6].

The required dynamic gain range is determined by the following method. Consider a transverse phase space distribution in the $x-x'$ plane given by

$$\rho(x, x') = \frac{I}{2\pi\epsilon_{rms}} e^{-\left(\gamma x^2 + 2\alpha x x' + \beta x'^2\right)/2\epsilon_{rms}}, \quad [1]$$

where I is the total beam current,

α , β , and γ are the standard Twiss parameters,

ϵ_{rms} is the unnormalized rms emittance,

x is the position coordinate, and x' is the angle coordinate.

The signal on any wire, $I_s(x_0, x'_0)$ is given in terms of the position of the slit, x_0 , the angular position of the wire, x'_0 , the slit width, Δx , the angular wire width $\Delta x'$, and the secondary electron emission coefficient, C_s , as

$$I_s(x_0, x'_0) = \frac{C_s I \Delta x \Delta x'}{2\pi\epsilon_{rms}} e^{-\left(\gamma x_0^2 + 2\alpha x_0 x'_0 + \beta x_0'^2\right)/2\epsilon_{rms}}. \quad [2]$$

The peak signal is given for

$x_0 = 0$, and $x'_0 = 0$, by

$$I_s(0, 0) = \frac{C_s I \beta_r \gamma_r \Delta x \Delta x'}{2\pi\epsilon_{n,rms}}, \quad [3]$$

where β_r and γ_r are the standard relativistic notation,

$\epsilon_{n,rms}$ is the normalized rms emittance.

Table 2
Commissioning Diagnostics and Primary Function

DEVICE	FUNCTION								
	Beam Current	Transverse Centroid	Transverse Width	Transverse Phase Space Distribution	Phase Centroid	Energy Centroid	Phase Width	Energy Width	Longitudinal Acceptance Width
Current Monitor Toroid	X								
Faraday Cup	X								
Segmented Faraday Cup	X	X							
Segmented Aperture		X							
Beam Position Monitor		X			X				
Wire Scanner		X	X						
Slit-Collector Emittance		X	X	X					
Spectrometer						X		X	
Absorber-Collector							X		X
Bunch Shape Monitor					X		X		X
Elastic Scattering						X		X	
X-ray Detector									X

Table 3 gives an estimate of some of the peak wire currents expected for the SSCL linac. Table 3 indicates that the highest gain needed is 10 μ A. The lowest gain needed is when the collector is run in the beam with no slit in front of it.

Table 3 Peak Signal Level On Collector Wires At Different Locations Along Linac As Indicated By Energy. Slit Is In Beam.				
$I_s(0,0)$ - maximum expected collector wire signal				
T - kinetic energy				
C_s - estimated secondary emission coefficient				
$I = 25$ mA $\epsilon_{n,rms} = 0.2$ mm mrad				
$\Delta x = 0.1$ mm				
$I_s(0,0)$ (mA)	T (MeV)	β_r, γ_r	$\Delta x'$ (mrad)	C_s
0.015	0.03	0.0086	0.85	1
0.32	2.5	0.073	0.44	5
0.0078	70	0.39	0.10	0.1
0.0054	600	1.3	0.042	0.05

The maximum signal current is then

$$I_s(x=0) = \frac{C_s I \sqrt{\beta_r \gamma_r} \Delta w}{\sqrt{2\pi\beta\epsilon_{n,rms}}} \quad [4]$$

where Δw is the wire width.

Table 4 shows the expected peak wire current for various locations along the linac.

The wire spacing, number of wires, and separation between the slit and collector are another important design parameter. The maximum and minimum angular spread of the beam (full width) can be estimated as

Table 4 Peak Signal Level On Collector Wires At Different Locations Along Linac As Indicated By Energy. Slit Is Not In Beam.				
$I_s(0,0)$ - maximum expected collector wire signal				
T - kinetic energy				
C_s - estimated secondary emission coefficient				
$I = 25$ mA $\epsilon_{n,rms} = 0.2$ mm mrad				
$\Delta w = 0.127$ mm				
$I_s(0)$ (mA)	T (MeV)	β_r, γ_r	β (mm/mrad)	C_s
1.8	0.03	0.0086	0.02	1
8.6	2.5	0.073	0.2	5
0.13	70	0.39	2.0	0.1
0.06	600	1.3	6.5	0.05

$$W'_{max} = 2 \frac{\epsilon_n}{\beta \gamma x_{min}}, \text{ and}$$

[5]

$$W'_{min} = 2 \frac{\epsilon_n}{\beta \gamma x_{max}}.$$

Table 5 shows the values for the estimated maximum and minimum angular spread of the beam along the linac assuming $\epsilon_n = 0.2$ mm mrad.

Table 5
Estimated Minimum And Maximum Full Widths and
Number of Wires Needed

	W' _{min} (mrad)	W' _{max} (mrad)	n	x _{min} (mm)	x _{max} (mm)	$\beta, \gamma,$
LEBT	4.6	31.	34	1.5	10.	0.0086
DTL IMS	0.68	11.	78	0.5	8.	0.073
CCL IMS	0.10	2.0	100	0.5	10.	0.39
TRSPT	0.031	0.62	103	0.5	10.	1.3

If one wishes to obtain at least 5 data points across the minimum angular space, than the space between wires is needed is $w' = W'_{\min}/5$. The number of wires needed to span the maximum angle space is

$$n = W'_{\max}/w' = 5 W'_{\max}/W'_{\min} \quad [6]$$

Based on equation 6, table 5 shows the minimum number of wires, n, needed at various locations along the linac. To make a general wire collector for all regions and assuming a 20% safety factor, the collectors need approximately 120 wires. This is close to the "computer" number 128, which we chose for the design.

The maximum physical size of the collector should be no larger than twice the beam pipe diameter for the case where the collector moves with the slit, and the physical wire spacing is limited by engineering considerations. For the SSCL linac commissioning, copper with a 0.127 mm width and mica with an approximate 0.066 mm width (including packing factor) were used to make the collector. Given the separation, L, between the slit and collector imposed by the linac lattice, a 0.193 mm separation between wires, and a 24.7 mm overall collector width then the actual values for W'_{min} and W'_{max} are shown in table 6. These values compare favorably with the requirements shown in table 5.

Table 6
Actual Values For W'_{max} and W'_{min}

	L (mm)	W' _{min} (mrad)	W' _{max} (mrad)	n
LEBT	150	1.3	165	128
DTL IMS	300	0.64	82	128
CCL IMS	8800	0.022	2.8	128
TRSPT	30000	0.006	0.82	128

Harp - Harps are multi-wire devices much like collectors, but with high transmission. Harps are better at high energies than the collectors described because harps produce less ionizing radiation. They can be used as collectors for high energy emittance scans as well as fast, accurate position measuring devices. Harps take a full profile in one pulse and at low energies they can be used with a collector downstream to accurately measure the beam position at two points along the beam line. SSCL is working with Allied-Signal to produce high density harps on ceramic boards. The harps will have 128 wires over approximately 48.8 mm with 0.033 mm thick wires. The harps use the same amplifiers as the Emittance Measurement Unit. Details of the SSCL harp are describe elsewhere at this conference [7].

Wire Scanner - Standard wire scanners are being developed for commissioning of the SSCL linac. In the commissioning

diagnostics, three wire scanners will be separated by some drift at the end of the diagnostic cart. Each wire scanner will have three wires to reconstruct the RMS emittance of the beam. For more details see [7], [8], and [9].

Bunch Shape Monitor - An important new diagnostic for linac commissioning and operation is the bunch shape monitor. The version for the SSCL will have better than 6 psec resolution. The results for the first version developed by the Institute of Nuclear Research are presented at this conference [10].

Absorber-Collector - The absorber-collector pair is used to measure the beam current above some energy level as an upstream rf module is being scanned. The design of the absorber is such that it will stop the unaccelerated beam, while the beam captured in the acceptance fish will pass through the absorber to the collector. Table 7 shows the basic design for the absorbers. Calculations were done, including the effects of straggling [11], to show the relation of the absorber-collector phase scan measurement data and the phase and amplitude of the rf cavity. This method will be used to determine the course adjustment of the rf cavity.

Table 7
Design Thickness of Absorber

	Design Output Energy (MeV)	Absorber range (MeV)	Thickness of Cu Absorber (mm)
Tank 1	13.4	12	0.332
Tank 2	32.9	28	1.427
Tank 3	51.6	46	3.396
Tank 4	70.3	64	6.056

VIII. REFERENCES

- [1] *Site-Specific Conceptual Design Report*, SSCL Report SSCL-SR-1056, July 1990.
- [2] L. W. Funk, "The SSC Linac, 1992 *Linear Accelerator Conference Proceedings*," Vol. 1, pp. 8-12.
- [3] J. W. Hurd et. al., "Commissioning Plans for SSC Linac," 1992 *Linear Accelerator Conference Proceedings*," Vol. 2, pp. 462-464.
- [4] J. W. Hurd et. al., "Beam Diagnostic Layout Requirements for SSCL Linac," these proceedings.
- [5] R. Aiello, et. al., "Beam Instrumentation for the SSC RFQ," these proceedings.
- [6] A. L. VanDeusen, et. al., "High Density Data Monitoring for SSCL Linac," these proceedings.
- [7] C. Fritsche, et. al., "High Density Harp for SSCL Linac," these proceedings.
- [8] C.Y. Yao, et. al., "Wire Scanner Data Analysis for the SSCL Linac Emittance Measurement," these proceedings.
- [9] C. E. Crist, et. al., "SSCL Linac Commissioning Diagnostic Cart," these proceedings.
- [10] J. W. Hurd, et. al., "Bunch Shape Monitor for SSCL Linac," these proceedings.
- [11] J. Siegrist, "Impact of Range Straggling in the Absorber-Collector Phase Scan," internal SSCL memorandum, March 31, 1993.

Beam Diagnostic Layout Requirements for SSCL Linac*

J. W. Hurd, F. W. Guy, G. Jamieson, D. Raparia, K. Saadatmand
Superconducting Super Collider Laboratory
2550 Beckley Trade Avenue, Dallas, TX 75237

Abstract

A basic set of diagnostics is needed to commission, tune, and monitor the operation of the SSCL linac. This set of diagnostics has been refined in the final stages of design of the linac. Planned diagnostics include current monitors, Faraday cups, beam loss monitors, beam position monitors, wire scanners, absorber-collector phase scan units, slit and collector emittance measurement units, and longitudinal bunch shape monitors. The diagnostics are described and their placement along the linac is given. The use of the diagnostics for tuning the linac is described. The first set of diagnostics will be installed with the RFQ, with additional diagnostics installed with each linac section.

I. INTRODUCTION

The Superconducting Super Collider Laboratory (SSCL) accelerator complex [1] is currently under construction in North-Central Texas, near Dallas. In the first stage an H^+ beam is accelerated to 600-MeV by a conventional linac [2]. The beam is then accelerated by a series of synchrotrons to form two counter circulating 20-TeV proton beams that collide at defined intersection regions. The colliding beams produce high energy physics events that act as probes for observing the interaction of the fundamental particles in nature. The linac consists of an ion source, three distinct accelerator structures, and matching sections to transport the beam between structures.

An important aspect of the SSCL linac is the required brightness of the beam and subsequent requirement for low emittance. The design of the linac has been driven by the need to limit the emittance growth. Therefore, the periodic lattice structure and phase advance is held constant as much as possible through the linac. In addition, the beam is accelerated as quickly as possible to limit effective emittance growth at low energies due to space charge. The result is a linac with very short matching sections. Short matching sections are very good for limiting emittance growth, but they do not leave much room for diagnostics. It is difficult to characterize the beam without sufficient diagnostics, and without a well characterized beam, the matching section lenses cannot be adjusted properly to match the beam into the next section of linac. The resulting mismatch leads to an effective emittance growth due to non-linear fields and transverse-longitudinal coupling. To correct this problem, great effort has been expended to justify and develop diagnostics which will fit in the limited matching section region and between accelerator tanks, and to include space where future diagnostics will be located when the need arises.

* Operated by the University Research Association, Inc. for the U.S. Department of Energy, under contract No. DE-AC35-89ER40486.

II. DIAGNOSTIC LAYOUT

The diagnostics for the SSCL linac are specified in table 1. They consist of the standard linac diagnostics. A brief description follows.

Table 1
List of SSCL Linac Diagnostics

Location	Diagnostic
Low Energy Beam Transport	1 Segmented Faraday Cup 1 Segmented Aperture 1 Current Monitor Toroid 1 Wire Scanner
DTL Input Matching Section	1 Segmented Faraday Cup 1 Segmented Aperture 1 Current Monitor Toroid 1 Wire Scanner 1 Slit & Collector EMU 1 Bunch Shape Monitor 3 Beam Position Monitors
DTL Inter-Tank Spaces (per space)	1 Current Monitor Toroid 1 Wire Scanner 2 Beam Position Monitors
CCL Input Matching Section	1 Absorber-Collector 2 Current Monitor Toroids 3 Wire Scanners 3 Beam Position Monitors 1 Slit & Collector EMU 1 Bunch Shape Monitor 1 Absorber-Collector
CCL Inter-Tank Spaces (per module of 8 tanks)	1 Current Monitor Toroid 1 Wire Scanner 2 Beam Position Monitors 8 Beam Diagnostics Boxes 3 Current Monitor Toroids 8 Wire Scanners 6 Beam Position Monitors
Transport Line	1 Bunch Shape Monitor 9 Current Monitor Toroids 10 Wire Scanners 10 Beam Position Monitors

A. Slit and Collector Emittance Measurement Unit

The linac slit and collector Emittance Measurement Unit measures the phase space distribution of the beam in either the horizontal or vertical plane of the beam. The slit measures the position of some fraction of the beam and the collector measures the angular distribution of beam for that particular position. By stepping the slit and collector across the beam, the distribution in position-angle space is measured. The first and second moments of the distribution give the centroids, Twiss parameters, and emittance of the beam in the plane of measurement.

B. Wire Scanner

Wire Scanners measure beam intensity in the horizontal or vertical plane as a function of position. The measurement lacks the angular information the slit and collector Emittance Measurement Unit provides, but wire scanners are less complicated, less expensive, and do not have to completely stop the beam, so they are more useful at high energies. Three wire scanner measurements can be used in series to reconstruct the RMS Twiss parameters and emittance of the beam. Wire scanners can also be used to measure x-y correlations.

C. Beam Position Monitor

Beam Position Monitors measure the centroid of the beam. They are non-intercepting, so they do not interfere with the beam. Transverse and longitudinal centroid measurements can be made with Beam Position Monitors. The beam position monitors will be used to steer the beam, to tune the rf using the Δt method [3] or the least squares method [4], and they will be used as an on-line measure to monitor the beam during operation.

D. Current Monitor Toroid

Current Monitor toroids are also non-intercepting diagnostics which measure the total current passing through them. They are used to measure transmission and monitor the beam during operation. Current monitors with high frequency response can be used to monitor the turn-on transient of the beam. The signal can be fed forward to the rf drive loops to provide additional power for the beam in the rf accelerator loops.

E. Faraday Cup

Faraday cups also give total beam current, and they fully intercept the beam, thus they can be used as beam stops. Care must be taken to make the beam stops thick enough to stop all the beam, provide enough cooling to dissipate the average beam power, and select proper materials and shape to handle the instantaneous heat deposited in each micro-pulse.

F. Absorber-Collector

Absorber-Collectors are used to measure the longitudinal characteristics of the beam. The absorber is made to stop all beam below design energy, and the collector measures the beam current that passes through the absorber. In this way the accelerated and unaccelerated parts of the beam can be separated. The acceptance of the upstream rf cavity can be scanned in phase across the beam, and the beam captured in the acceptance fish is measured as a function of phase. The width and relative phase of the acceptance fish is measured and some information concerning the phase width of the beam can be gained by differentiating the signal.

G. Bunch Shape Monitor

A new device being developed at the SSCL and other laboratories is the Bunch Shape Monitor [5]. The Bunch

Shape Monitor is analogous to a longitudinal wire scanner. It can measure the longitudinal profile of the beam. A more complete review is given elsewhere at this conference [6].

III. FUNCTION

The primary functions of the SSCL linac diagnostics are to tune and monitor the beam for delivery to the Low Energy Booster and the Proton Therapy Facility. Initially, the diagnostics will be used to commission the linac and carry out linac development necessary to meet full design specifications.

The SSCL linac has a short beam pulse, from 2 μ sec to 35 μ sec with an expected rise time of up to 100 nsec. The beam tune is space-charge dependent, especially at the lower energies. It is therefore necessary to know the current and longitudinal characteristics as a function of time. Examples of time dependent beam characteristics are given in references [7] and [8]. Averaging over any beam time dependence would smear out the measured emittance. The apparent increase in beam size would cause errors in the estimates of space charge forces. The reduced tune shift would result in errors in the machine simulations. Specifications for most diagnostics call for a frequency response capable of observing 100 nsec rise times on the beam signals, zero to full scale.

A. Transmission

One of the most fundamental characteristics of the linac beam is the transmission. The SSCL linac is designed to deliver 25 mA peak beam with a 30 mA input beam. The RFQ should have a capture of 80% to 100%. Losses along the rest of the linac should be less than a few percent. Current Monitor Toroids along the beam line will be used to monitor beam transmission. During development, they will be used to map out the physical aperture of the linac. Transmission contours as a function of steering and transverse match will be generated using the toroids. Faraday cups are used to stop the beams at low energies. The ion source can be run and its current monitored while downstream linac elements are off.

B. Transverse Tune

To limit emittance growth it is important to keep the beam as small and uniform in size as possible as it traverses the linac. This is done by designing the linac as a periodic strong focusing lattice and matching the beam into the periodic structure. One method of measuring the transverse phase space distribution of the beam is to use the slit-and-collector Emittance Measurement Unit. The unit measures the Twiss parameters and the emittance of the beam. The emittance growth is monitored as a function of some other machine parameter to investigate and optimize the tune space of the linac. The measured beam parameters are used as inputs to tuning algorithms that adjust quadrupoles and match the beam. The slit-and-collector do not give the x-y correlation of the beam. The emittance measurement unit also gives centroid and relative intensity information. Patterns in the phase space distribution can be recognized to help give indications of higher order aberrations, space charge effects, and aperture restrictions.

Wire scanners are used to measure the width of the beam. There is no angular information as with the slit and

collector. By measuring the width for three different upstream lens settings or at three different positions along the beam line, one can solve for the RMS phase space parameters of the beam as long as the linear problem is non-singular. For larger numbers of measurements, least squares techniques can be utilized. Wire scanners are more practical at higher energies than slit-and-collector emittance measurement units. Wire scanners do not have to stop the beam. At higher energies, the slit produces ionizing radiation that creates noise on the downstream collector. The drawback to wire scanners is that they integrate over the angle dimension of phase space and the details of the angular distribution cannot easily be recovered except in an RMS sense. At low energies, wire scanners can also be used where there is not sufficient drift to use the slit and collector. At the SSCL, a three wire scanner is being developed, one wire in x, one in y, and a third wire at 45 degrees. The third wire will be used to help measure possible x-y correlation introduced by the Helical Electrostatic Quadrupole[9] or rotated quadrupoles.

Beam position monitors are the third transverse measurement diagnostic. These are non-intercepting devices which makes them the best candidates for on-line beam monitoring. Measurement capabilities are practically limited to centroid measurements only and they are usually less accurate than wire scanner measurements. Because they do not have to be stepped across the beam, beam position monitors can give results on a much faster "real time" basis as the steering is being adjusted. Beam position monitors can also be used to give intensity data. When used at a high dispersion point, the position of the beam is coupled to the momentum, and thus the beam position monitors can be used to monitor the beam energy.

C. Longitudinal Tune

The Bunch Shape Monitor in longitudinal space is analogous to the wire scanner in transverse space. It measures the intensity as a function of phase (proportional to time) along the longitudinal dimension of the micro-bunches. By measuring for three or more different points in longitudinal space, one can reconstruct the longitudinal RMS phase space for the beam. The longitudinal emittance can be measured and the beam matched longitudinally in this manner. The phase of the upstream rf cavity can be scanned and the bunch shape measured as a function of cavity phase. The result gives an estimate of the bucket width from which the cavity amplitude and phase can be inferred.

Another method of measuring the bucket width is by using an absorber-collector. By differentiating the resulting signal an estimate of the bunch width can be made, but this method is not as accurate or as direct as the bunch shape measurement. The absorber-collector phase scan method, along with beam loading measurements, is used to make the course adjustments to the rf phase and amplitudes.

The beam position monitors at SSCL will be used to measure the longitudinal as well as transverse center of the beam. In transverse phase space the beam position monitor signal is proportional to the transverse centroid of the beam. In longitudinal phase space the phase is that of the 428-MHz Fourier component of the beam [10]. Once the rf cavity is set approximately with absorber-collector phase scans or beam loading scans, the classical Δt and least squares phase scan

techniques [11] will be used to tune the rf cavities using the phase information.

IV. CONCLUSION

The SSCL linac will have the full suite of diagnostics used at other comparable linear accelerators such as the Moscow Meson Factory and the Los Alamos Meson Physics Facility. To successfully control the emittance growth in the SSCL linac, it is necessary to have a full set of diagnostics to perform measurements outlined. Some restrictions such as permanent magnet quadrupoles eliminate the use of certain diagnostic techniques such as "quad unrolls." To limit emittance growth, transport sections have been made as short as possible, eliminating space for diagnostics. To work in this new and restricted environment, not only must standard diagnostics be made more compact, but new diagnostics requiring less longitudinal space may need to be developed [12]. The short pulse lengths at SSCL force the requirement for diagnostic bandwidths on the order of 3.5 MHz to observe the time dependent behavior of the beam.

VII. REFERENCES

- [1] *Site-Specific Conceptual Design Report*, SSCL Report SSCL-SR-1056, July 1990.
- [2] L. W. Funk, "The SSC Linac, 1992 Linear Accelerator Conference Proceedings," Vol. 1, pp. 8-12.
- [3] K. R. Crandall, "The Δt Tuneup Procedure for the LAMPF 805-MHz Linac," Los Alamos Scientific Laboratory Report LA-6374-MS, June 1976.
- [4] F. W. Guy and T. P. Wangler, "Least-Squares Fitting Procedure for Setting RF Phase and Amplitude in Drift-Tube-Linac Tanks," *Conference Record of the 1991 IEEE Particle Accelerator Conference*, Vol. 5, pp. 3056-3058.
- [5] A. V. Feschenko and P. N. Ostroumov, "Bunch Shape Measuring Technique and Its Application for an Ion Linac Tuning," *Proceedings of 1986 Linac Conference*, pp. 323-327.
- [6] J. W. Hurd et. al., "Bunch Shape Monitor For SSCL Linac," these proceedings.
- [7] E. McCrory et. al., "Observation of Transverse Instabilities in the FNAL 200-MeV Linac," *Proceedings of 1988 Linac Conference*, pp. 182-184.
- [8] J. W. Hurd, "Solution to the Transverse Phase Space Dependence Problem with LAMPF's High Intensity H^+ Beam," *Proceedings of 1983 Particle Accelerator Conference*, IEEE Trans. Nucl. Sci., Vol. NS-30, No. 4, pp. 2487-2489, (1983).
- [9] D. Raparia, "HESQ, A Low Energy Beam Transport for the SSC Linac," *Proceedings of 1990 Linac Conference*, pp. 405-407.
- [10] R. Aiello, "A Digital Approach for Phase Measurement Applied to Delta-t Tuneup Procedure", these proceedings.
- [11] F. W. Guy and J. W. Hurd, "Procedures for Setting RF Phase and Amplitude in the SSC Drift-Tube-Linac Tanks," *1992 Linear Accelerator Conference Proceedings*, Vol. 1, pp. 196-198.
- [12] D. Swenson and M. Andrews, "Performance of a Wire Shadow Emittance Scanner", these proceedings.

SSCL Linac Commissioning Diagnostic Cart

C.E.CRIST, L.W.FUNK, W.HURD, G.T.LEIFESTE

Superconducting Super Collider Laboratory*

2550 Beckleymeade Avenue, Dallas, TX 75237

M.KROGH, K.MCGINNIS, D.STITTSWORTH,

A.VANDEUSEN, S. WRIGHT,

Allied Signal Inc., Kansas City Division§

P.O. Box 419159, Kansas City MO 64141-6159

Abstract

A portable diagnostic system is under development and construction for use in commissioning the SSCL LINAC. This system is being used during the construction of the LINAC, and will be used to commission each section of the accelerator as assembled. The diagnostic system consists of a portable ultra high vacuum system, high speed actuators, high density (128 channel) diagnostic heads, x-ray detectors, and high density VXI 128 channel amplifier arrays. Various innovative designs will be described. These designs led to high density wire spacing, high frequency, wide bandwidth, low cost amplifiers, and compact systems. State of the art manufacturing techniques were employed as a result of the joint interaction between the SSCL and Allied-Signal.

Introduction

The SSCL LINAC diagnostic cart is an experimental station that is designed as a flexible platform on which an experimenter will configure various components to perform experiments. One such experiment was for the Bunch Shape Monitor for the SSCL LINAC [1].

The over all system consists of a portable platform, high vacuum chamber and vacuum system, precision actuators, diagnostic heads, electronic packages, and support systems.

The system is designed to allow high speed measurements of the H^- beam in order to minimize the effects of radiation production due to the interaction of the beam and diagnostic heads, and to measure pulse to pulse instability of the beam.

System Components

The Cart

The portable platform is a wheel mounted aluminum test stand with locking feet. The platform is 1 meter wide, 2 meter long, and 1 meter tall, with 3 individual equipment bays. Two of the equipment bays are configured to accept standard 19 inch rack mounted packages on both sides, while the third contains the high vacuum pump, vacuum pump controller, vacuum gauges, air and water meters and controls. While the present system contains a 500 liter per second vacuum pump, the cart will accept vacuum pumps that exceed 2000 liter per second. The diagnostic chamber is constructed from 10 inch diameter knife edge flanges with

*Operated by the University Research Associates for the United States Department of Energy under contract No. DE-AC35-89ER40486.

§ Operated by Allied-Signal Aerospace Co. Kansas City Division for the United States Department of Energy under prime contract No DE-AC04-76-DP00613

8 inch diameter tubing and 4 1/2 inch diameter knife edge flanges with 2 1/2 inch diameter tubing. The chamber is mounted over the first bay of the diagnostic cart. Mounting of a viewing port or diagnostic is possible on any of the 10 inch flanges perpendicular to the beam and all of the 4 1/2 inch flanges. See figure 1.

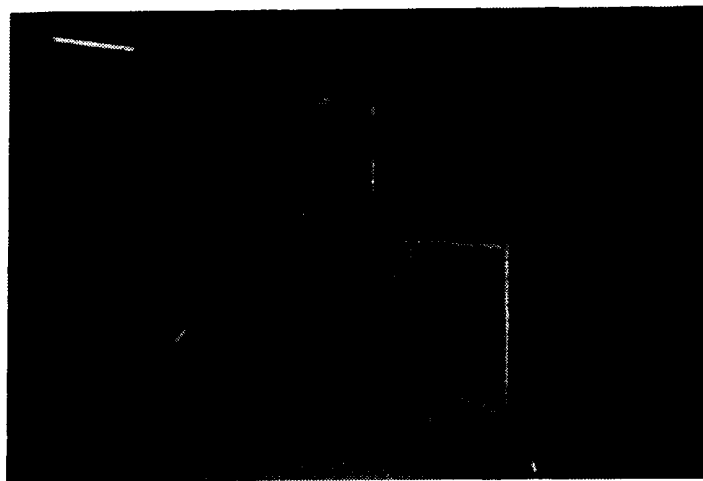


Figure 1.

The SSCL LINAC diagnostic cart connected to the exit end of the RFQ.

Actuator

Several of the diagnostics used with the commissioning cart during commissioning of the Linac are actuator mounted. One of the actuators used is configured to position a diagnostic head, such as a slit, collector, wire scanner, or harp. These actuators have a foot print of 80 mm by 130 mm and allow diagnostic heads with more than 128 signal wires and liquid cooling lines mounted on 2 1/8 inch knife edge flange to be positioned into the beam. The actuator will position a diagnostic head to each data position within 50 milliseconds. An example of one of the actuators used on the diagnostic cart was constructed by a team of engineers from the SSC and Allied-Signal's Kansas City Plant.

The submitted manuscript has been authored by a contractor of the U.S. Government under Contract No. DE-AC35-89ER40486. Accordingly, the U.S. Government retains a nonexclusive, royalty-free license to publish or reproduce the published form of this contribution, or allow others to do so, for U.S. Government purposes.

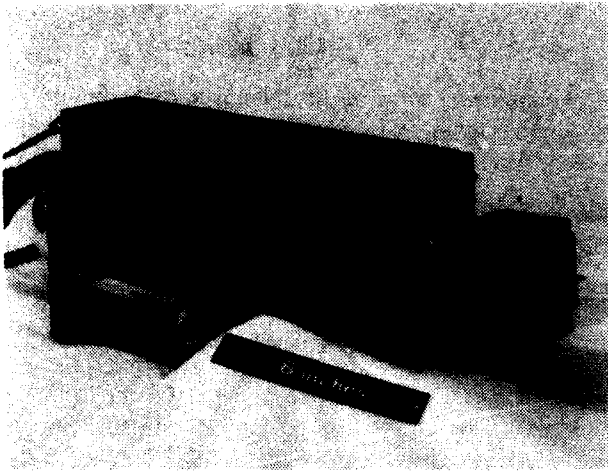


Figure 2.

Diagnostic Cart Actuator with a 128 element collector attached.

Diagnostic Heads

Slit and Collector

Utilizing the interchangeable diagnostic head feature of the actuator, a set of diagnostic heads has been designed and constructed. These diagnostic heads include a slit and collector, wire scanner, and harp. Each element of the slit can be electrically isolated from each other and biased separately all electrical connection can be made outside the vacuum system. The collector's design allows for the 128 electrically isolated copper elements to thermally connect to the collector's copper frame. Each collector element is 50 mm wide, 0.1 mm thick and 20 mm deep. Electrical isolation is achieved by utilizing 0.1 mm thick natural mica or mica paper. See figure 3.



Figure 3

The collector contains 128 copper elements that are .1mm thick with .09 mm thick natural mica or mica paper.

Wire Scanner and Harp

With the need for higher resolution in profile measurements for the SSCL LINAC, [3] the concept of utilizing hybrid microcircuit (HMC) technology was chosen in the design of the diagnostic cart's wire scanner and harp. See figure 4. Using this process for the design and construction of a wire scanner, a harp with 128 individual 33 μ m diameter carbon wires with calibration resistors is under construction with the Department of Energy's manufacturing center in Kansas City, MO.

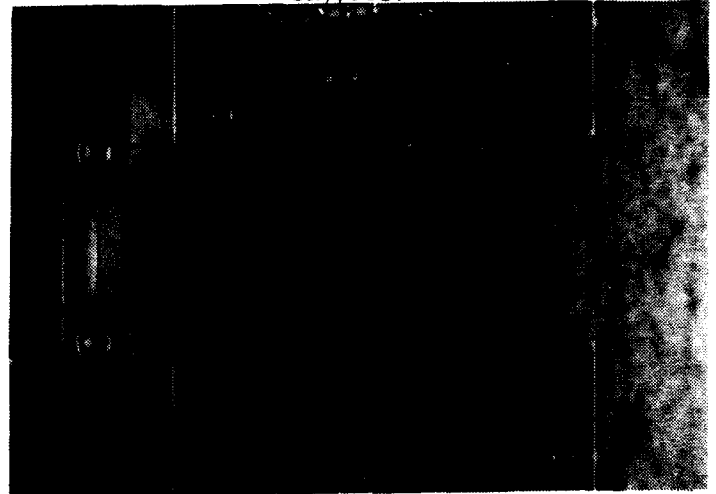


Figure 4.

Diagnostic Cart Wire Scanner fabricated using HMC technology with wire bonding.

High Density VXI Amplifier Array

In order to integrate a diagnostic head with 128 wires an amplifier array was needed. The solution selected was an eight channel 20 million samples per second (MSPS). Using this approach, an entire 128 channel amplifier array was constructed into a VME Extension for Instrumentation (VXI) system. See figure 5

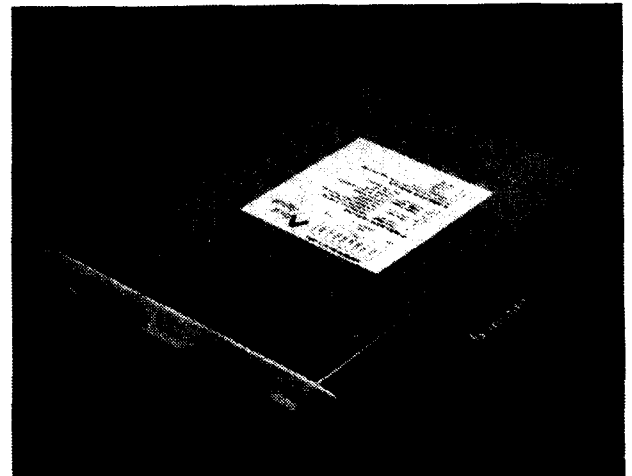


Figure 5

The Modular Input VXI digitizer contains 8 bipolar channels.

This amplifier circuit is designed to accept a bipolar differential current signal from $10\ \mu\text{A}$ to $10\ \text{mA}$. For maximum flexibility the circuitry for this module is divided into two separate functions; the mother board and daughter board. See figure 6 and 7. The mother board contains all of the digital signal function including the buffer circuitry to the VXI interface, memory, 10 bit analog to digital converters and the interfaces to the daughter boards, while, the daughter board contains all analog signal conditioning and amplifying the current signal for a wide variety of diagnostic heads

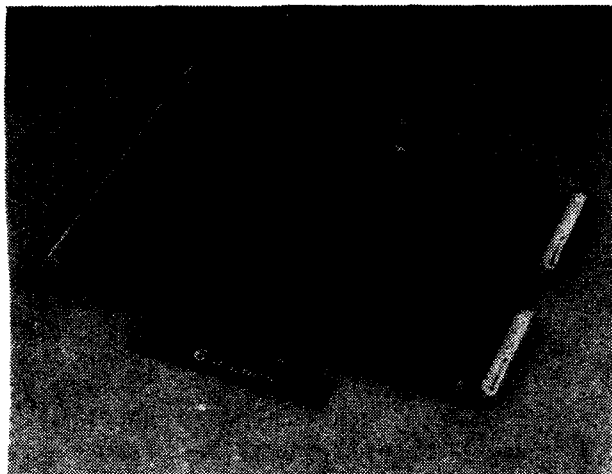


Figure 6

The MIX mother board can accept four daughter boards.

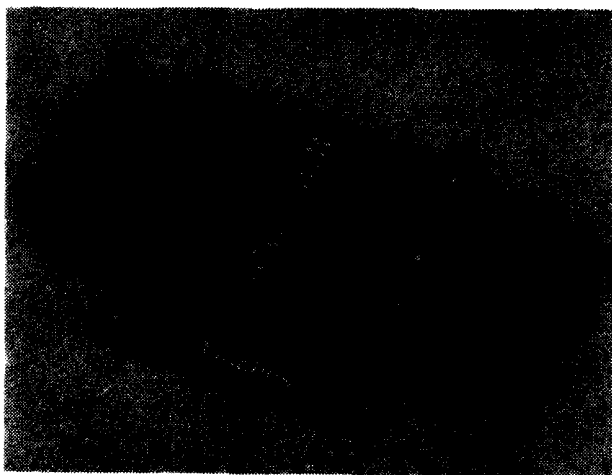


Figure 7.

Each daughter board contains circuitry for two differential channels of $\pm 10\ \mu\text{A}$ to $10\ \text{mA}$

Conclusion

We are using some of the diagnostic tools on the commissioning cart, developed at the SSCL and other laboratories for the LINAC and the SSCL. Early results of the LINAC commissioning were aided as a result of this needed platform and many improvements to the LINAC diagnostics will be facilitated with this flexible research tool.

Acknowledgments

Frank Ross, Jonathan Watts, Noel Okey, Scott Volz and Matthew B. Lawson of the Superconducting Super Collider Laboratory and Paul Quirk, Betty Shannon, Ken Reeves, Jim Reilly, Jim Thomas, John White, Mark Alexander, and Craig Fritsche of Allied-Signal are acknowledged for their support and effort on these and other diagnostic cart projects.

References

- [1] J.Hurd et. al., "Bunch Shape Monitor for SSCL LINAC", these proceedings.
- [2] C. Fritsche et. al., "High Density Harp for SSCL LINAC", these proceedings.
- [3] A. VanDeusen et. al., "High Density Data Monitoring for SSCL LINAC", these proceedings.
- [4] J.Hurd et. al., "Physics Requirements of Commissioning Diagnostics for SSCL LINAC", these proceedings.

A METHOD FOR LEBT AUTOMATION*

J. Sredniawski, L. Solensten, R. Schmidt, J. Porter, Y. Ng, C. Lom
Grumman Aerospace Corporation
Bethpage, NY 11714 USA
W. Newman
AMTEX Computer Systems
Islip Terrace, NY 11752 USA

I. INTRODUCTION

A generic method of Low Energy Beam Transport (LEBT) automatic tuning is under development that can be applied toward any pulsed beam accelerator using a radio frequency quadrupole (RFQ) with an adjustable solenoid-type LEBT. The purpose of this control scheme is to self-optimize the beam transport through the RFQ for any operating condition of the accelerator. This system is useful for an accelerator that operates over a range of currents. For a constant current machine, the system is useful to dynamically correct any drifts with time. This system is being developed on a beamline that uses a dual solenoid LEBT; however, the same system can also be used on a beamline with a single solenoid. This paper describes the mechanical and electrical design of the system and the algorithms used for the tuneup.

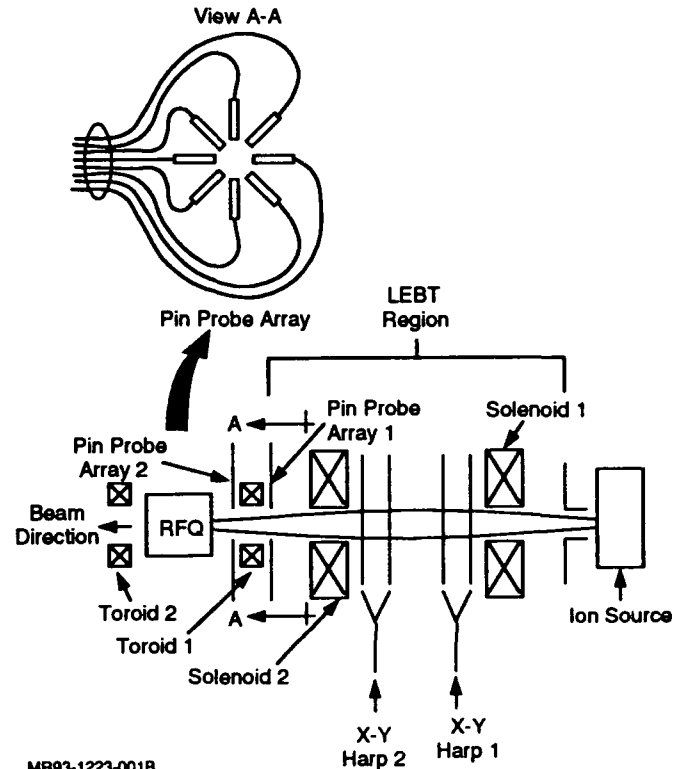
II. SYSTEM DESCRIPTION

The beamline diagnostics arrangement and controls are shown in Figure 1. The harps used for a pre-optimization algorithm are located between the two solenoids. For a single solenoid system, the harps should be located upstream and downstream of the solenoid.

The two sets of pin probes located near the RFQ input aperture are made from 60 mil tungsten wire. Wire was used instead of flat scraper blades because of the required uniformity between probes needed to obtain accurate signals. In addition, the tips of the pin probes were ground for uniform shape. A current measuring toroid is positioned between the pin probe arrays for measurement of the RFQ input beam (Ref 1). Figure 2 is a photograph showing this diagnostic arrangement. The pin probes nearest the RFQ are located so that when the beam is properly matched, they would barely see the edge of the beam halo. A protective cover is provided over the front of the first pin probe array to shield the delicate signal wire connections.

The electronics signal conditioning for both the harps and the pin probes are very similar. Shown in Figure 3, each harp wire or pin probe is connected to a current-to-voltage converter stage. Additional stages provide voltage gain and filtering functions. The signals are stored in the sample-and-hold amplifiers until they can be read by the channel multiplexer into the analog-to-digital converter. The digitized signals are then processed by the computer as part of the analysis, control, and display system.

*This work was conducted under Grumman IR&D project 7256-2709.



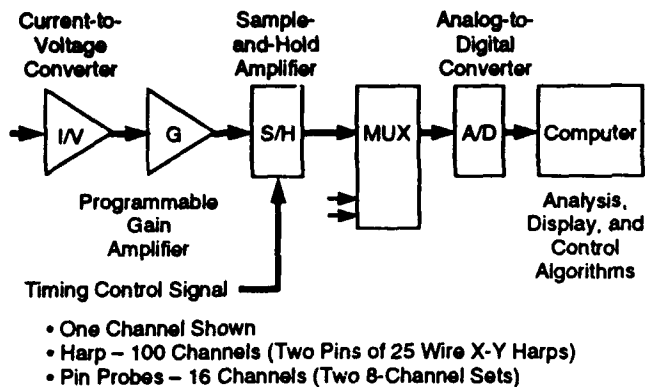
MR93-1223-001B

Figure 1. Schematic of LEBT diagnostics.



MR93-1223-002
921901-7

Figure 2. Pin probe array at RFQ entrance.



MR93-1223-003B

Figure 3. Harps and pin probes block diagram.

III. OPERATION

A logic flow chart of the control system operation is shown in Figure 4. The LEBT optimization algorithm consists of the following four states:

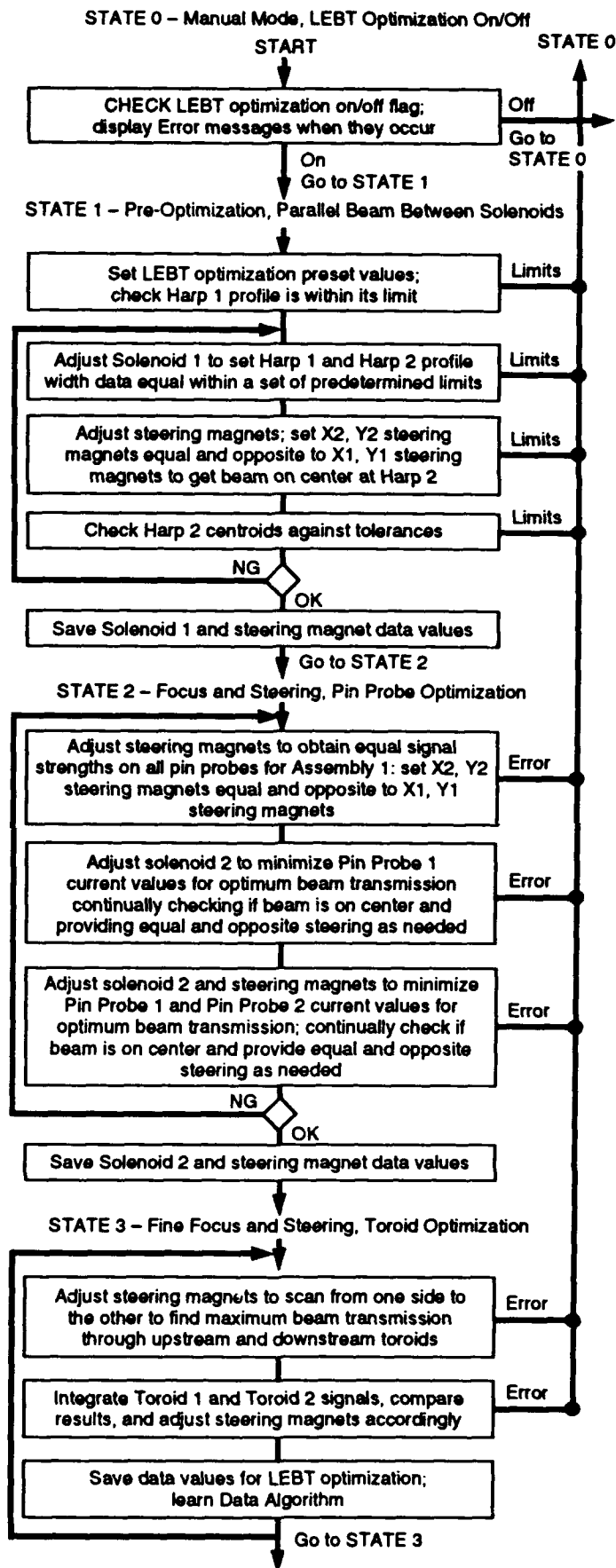
- State 0 – Manual mode, LEBT optimization on/off control
- State 1 – Pre-optimization, harp signal interface
- State 2 – Focus and steering, pin probe signal interface
- State 3 – Fine steering, toroid signal interface.

A. Pre-Optimization (State 1)

The pre-optimization step uses the harps to set up the initial beam focus from the first solenoid and to perform any gross steering that may be required. This is accomplished by analyzing the X and Y profiles and positions from the harp data as displayed in Figure 5. In the case of a two solenoid system as presently used, the current of the first solenoid is ramped until the total beam width of the downstream beam, as seen by harp two, is essentially the same as the beam width defined by harp one. This produces a parallel beam between the two solenoids. A similar condition can be set up with a single solenoid as well. It can be seen from Figure 5 that the downstream beam profile is not as peaked as the upstream profile. This is a normal condition for a low energy transported beam and is of no consequence since the control algorithm only uses the total beam width at this point. The control sequence now examines the crude centroid position of the beam in the second harp and makes any minor steering adjustments that are necessary to position the beam approximately on downstream center. This starting condition is necessary to be able to achieve a useful signal on the pin probes. If the beam is too big and unfocused at the RFQ entrance, the signals on the pin probes will be very low and essentially the same on each probe wire.

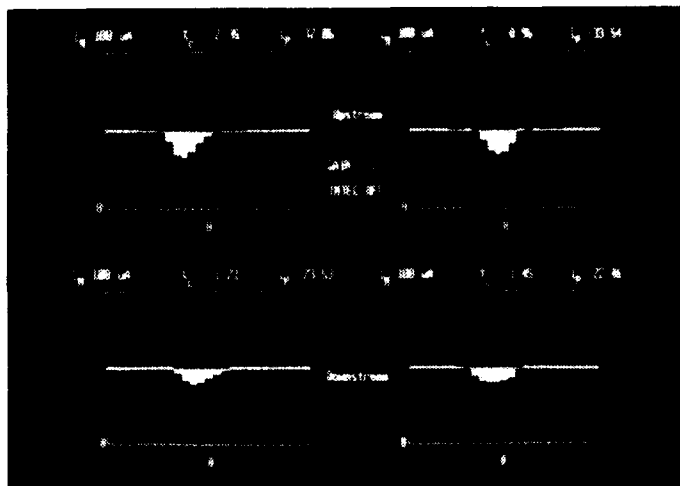
B. Focus and Steering (State 2)

For all of the following steps, the set point of the first solenoid is kept constant at the value previously defined. For a single solenoid system, the solenoid current will not be permitted to drop below the value previously defined. At this point, the current of solenoid two is ramped, while the signals on the first pin probe array are monitored for beam size, as shown in Figure 6. The intent is to make the beam disappear from the pin signals. A mild amount of steering correction is also applied to maintain the beam on center, as indicated by the magnitude of the relative pin



MR93-1223-005C

Figure 4. Control system logic flow chart.



R93-1223-006
930312-6

Figure 5. Harps for parallel beam pre-optimization.

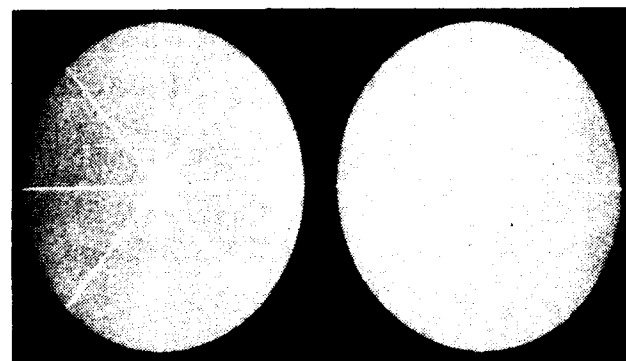
signals. These loops are nested so that a flip-flop between them is continually in process. This is due to the rotational effects of a solenoid system. Once the signals on the first pin probe drop below a set threshold, the second and more fine pin probe array is used to continue the above process. This is done until all the pin probe signals go essentially to zero, plus or minus a set tolerance band. The tolerance band must be established on the actual beamline installation by experimentation, since it may be sensitive to factors such as installation tolerances, EMI of the installed system, etc.

C. Fine Steering (State 3)

At this point, the pin probes and harps have been used to the best of their potential, yet the optimum beam transport through the RFQ may still not have been obtained. A very fine raster algorithm is now employed to literally hunt and peck the beam steering in a random pattern while observing the RFQ transmission by means of the upstream and downstream current toroids. A series of limits in each direction are attempted and stored in a dynamic data file which is used to peak the transmission value. This is all done for constant RFQ field amplitude, which is the extent of the LEBT control logic. If the radio frequency (RF) field or the beam current are changed in any significant way, the control logic is such that a series of checks for all of the previously described sequences and conditions is initiated once again.

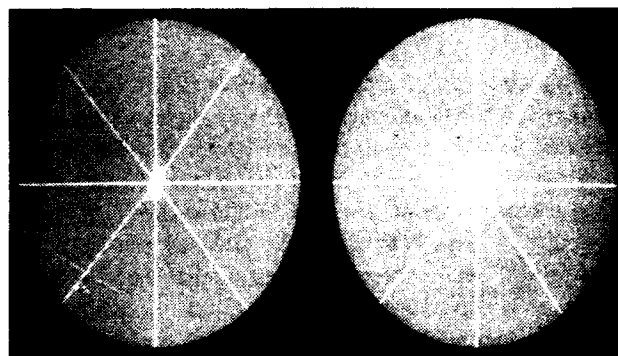
IV. CONCLUSIONS

The diagnostics described have been implemented and tested at Grumman on the front end of a pulsed beamline. So far, using the man in the loop to carry out the control logic flow, LEBT tuneup has been successful. We are now coding the steps for final implementation and qualification. This approach of automating the man in the loop has been used in the past on our ion source control system to provide a reliable automatic optimization technique (Ref 2). Future work will include automation of the



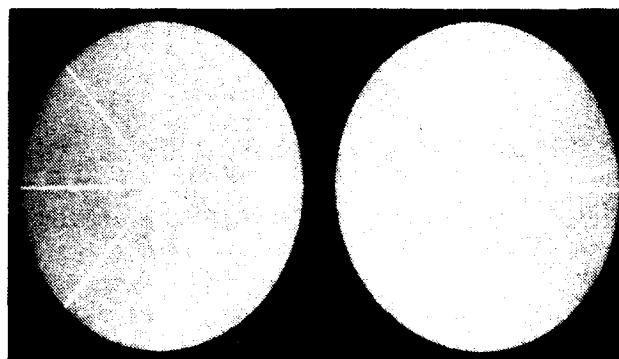
930312-5

(A) Parallel beams



930312-4

(B) Partially focused



930312-2

Pin Probe 1

Pin Probe 2

(C) Fully focused

R93-1223-007

Figure 6. Beam configurations.

RF amplitude and phase of the various accelerating structures downstream of the RFQ.

V. REFERENCES

- [1] J. F. Power, "Compact Cryogenic Toroid for Beam Current Measurement," *NPB Symposium*, Monterey, CA (July 1989).
- [2] Y. Ng, et al., "Automatic Optimization of the Output Beam from a Small Pulsed Volume Source," *NPB Symposium*, San Diego, CA (April 1990).

Beam Energy Measurement Using the Hall C Beam Line

C. Yan, R. Carlini, D. Neuffer
Continuous Electron Beam Accelerator Facility
12000 Jefferson Ave., Newport News, VA 23606

Abstract

We propose to use the curved transport line into Hall C to measure the beam energy. With only dipoles powered, this transport arc has a dispersion of 12 cm/%. We propose to insert pairs of wire scanners at the entrance and exit of the arc to measure beam position and direction. These measurements, together with a calibrated dipole field, obtain an absolute beam energy measurement with $\sim 10^{-3}$ accuracy, according to error analyses. In operational mode, arc quads and sextupoles are powered to obtain a second order achromat with a dispersion of 2.1 cm/% at the arc center. A wire scanner at the arc center then obtains a relative energy measurement of $\sim 10^{-4}$ accuracy.

I. INTRODUCTION

The Hall C beam line is sketched in Figure 1. The arc section of this beam line consists of 8 dipoles, 12 quads, 8 sextupoles, and 8 beam correctors (4 vertical and 4 horizontal). These dipoles bend the beam by a total of 34.3° , and the full 41.6 m long arc transport is designed to form a second-order achromat. We now describe the beam energy measurement method which uses that arc as proposed in refs. [1], [2], and [3]. For the absolute energy measurement only the dipoles are switched on (quads, sextupoles and correctors are off). The current in the calibrated bending magnets, which are serially connected, is varied to set the beam position to be along the center of the dipoles. The position and direction of the beam entering the arc section are measured by a pair of high resolution harps (wire scanners). The position and direction of the beam at the exit of the arc are determined by another pair of calibrated harps. From the initial position and direction measurements, the final position measurement, and the calibrated dipole field, the beam momentum can be determined. Thus the method requires accurate position measurements at the harps and an accurate determination of

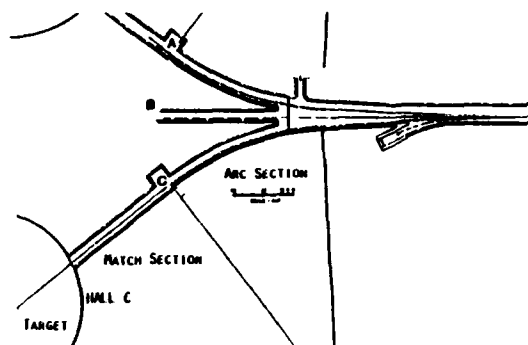


Figure 1: Hall C beam transport line.

the magnetic field integral $\int Bdl$ as a function of the current I in the arc dipoles. Accurate position measurements depend on the alignment accuracy, which can be reduced to errors on the order of $100 \mu\text{m}$. Accurate field determination will require a new calibrating set of careful absolute field measurements on two (or a few) reference dipoles. In the following sections we will discuss the error analyses of these measurements. After setting an absolute energy scale with the dipoles, the quadrupoles and sextupoles are then energized to the values required for achromatic transport, and the correctors will be used to center the beam. The magnets are then fixed in strengths. Variations in beam energy can then be measured as variations in beam position at the midpoint, which has a dispersion of 2.1 cm/%. Thus, in this mode, measurable position shifts of $100 \mu\text{m}$ corresponding to relative energy shifts of 0.5×10^{-4} . As this relative measurement is not dependent on calibration errors, relative energy measurements will be substantially more accurate than the absolute determination.

II. OPERATIONAL PRINCIPLES AND OPTICAL CHARACTERISTICS OF THE ARC SPECTROMETER

An initial beam position and direction Δx and $\Delta x'$ are measured by the initial pair of harps with respect to their surveyed centerlines. The arc magnetic field is calibrated to bend a beam of a central energy P_0 the reference angle of 34.3° from harp center to harp center. The beam position

*This work was supported by the U.S. Department of Energy, under contract No. DE-AC05-84ER40150.

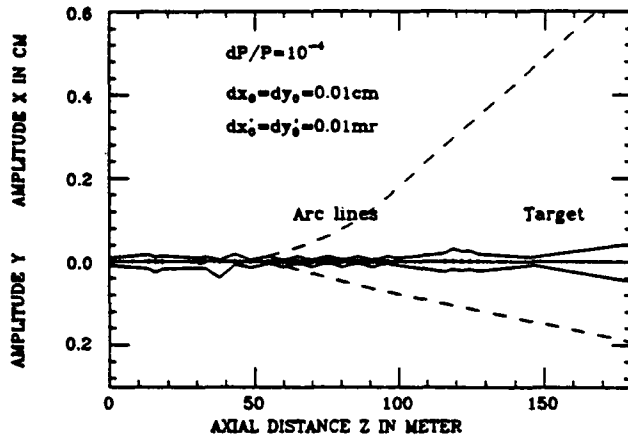


Figure 2: Beam envelope along Hall C beam line

Table 1: The major first order matrix elements of an N -dipole systems

N	ϕ ($^\circ$)	Size (cm)	R_{11}	R_{12}	$D = R_{16}$ (m)
1	4.2875	0.022	0.9064	2.0234	-0.1422
2	8.5750	0.033	1.1015	3.0322	-0.6734
3	12.863	0.045	1.2965	4.0410	-1.5938
4	17.150	0.060	1.4916	5.0498	-2.9032
5	21.438	0.078	1.6866	6.0586	-4.6017
6	25.725	0.099	1.8817	7.0675	-6.6894
7	30.013	0.124	2.0767	8.0763	-9.1608
8	34.300	0.152	2.2718	9.0851	-12.032

X_{final} at the final harp then obtains a measured energy offset of:

$$\Delta P = \frac{P_0}{\eta} (X_{final} - \Delta x - \Delta x' L) \quad (1)$$

where L is the arc length (41.6 m) and η is the dispersion at the exit of the arc (-12.03 m). The errors in the various measured quantities, calibrations, and surveying will determine the actual energy measurement error; these error sources are discussed in the next section. In normal (achromatic) operation the beam remains tightly confined. The design beam envelope along the Hall C beam line is shown in Figure 2. The initial conditions are beam widths of $\delta x = \delta y = 0.01$ cm, $\delta x' = \delta y' = 0.01$ mrad. The solid line describes the beam envelope sizes in the normal transport conditions. In absolute energy measurement mode, the arc quads are off. The beam therefore is enlarged through the arc, as shown in the dashed lines in Figure 2, in which all downstream quads are also switched off. Table 1 shows beam transport elements through the 8-dipole arc. Note that the dispersion D increases as N^2 , where N is the dipole location number. Maximum dispersive effect is therefore found by using the entire arc.

III. ERROR ANALYSIS

The proposed measurement method is planned to obtain absolute energy measurements at the $\delta E/E \approx 10^{-8}$ level. Analyses to support an estimate of errors at this level are required. An initial error analysis was obtained by [3] and the same methods were also used to study variations and changes in the proposed energy measurement configuration. In this section we describe the error analysis methods, including estimates of the expected error sources, and report results of the analyses. The various error sources and their estimated contributions include:

A. Initial harp location and direction

Surveying errors at each location should be on the order of 100 μ m. However, with an entrance harps separation of 1m, this implies an initial direction error of 100 μ rad. This 100 μ rad error translates into a 0.5 cm position change at the end of the arc, where the dispersion is about 12 m. Thus this error alone would give $\delta p/p = 0.4 \times 10^{-3}$; it is the largest estimated source in the error analysis [3]. Subsequent to that study, it was decided to increase the initial harp separation to 2.5 m. That reduces the initial direction error to 40 μ rad and the subsequent contribution to $\delta p/p$ is 2×10^{-4} .

B. Final harp location

In the error analysis, it was assumed that a random 20 μ rad missteering occurs every 10.4 m (an assumed intermediate monument location), and this accumulates to obtain a displacement at the end of the 41.6 m arc. This corresponds to a mislocation of 200 μ m at every arc cell. It somewhat overshoots the estimate of an rms total error of 200 μ m displacement at the end of the arc, after smoothing. The total effect on the beam is an rms error of $\delta p/p = 0.05 \times 10^{-4}$.

C. Location, orientation errors, and variations in dipole integrated fields

Placement errors are assumed to be on the level of 1 mm; they have little effect. A 1 mrad roll error is also included; it changes vertical positions but does not greatly change horizontal (energy measurement plane) locations. A random dipole-to-dipole bend variation of 2.5×10^{-4} rms was also assumed. This adds a rms energy error of slightly more than 10^{-4} .

D. Quad and steering magnet effects

In the absolute energy measurement mode, the quads and steerers are assumed to be off. Remanent fields could add some bending and therefore some error to the energy measurement. In the initial analysis, these are assumed to be negligibly small (contributing errors less than 10^{-4} of the dipole bends), and are not explicitly included. In recent

Table 2: Error analysis from DIMAD simulation

N	L = 1 m	L = 2.5 m
	$\delta E/E$	$\delta E/E$
1	4.0×10^{-3}	2.3×10^{-3}
2	2.1×10^{-3}	1.0×10^{-3}
4	1.14×10^{-3}	0.44×10^{-3}
8	0.50×10^{-3}	0.23×10^{-3}

experimental tests, the remanent field contribution to the $\int B dl$ was found to be less than 5×10^{-5} .

E. Beam size effects

It was assumed that the beam size at the entrance to the arc was less than $100 \mu\text{m}$ by $10 \mu\text{rad}$. The beam size would then be less than 1.5 mm at the end of the arc, and would add a width of 10^{-4} to the final harp position uncertainty.

F. Field normalization error

An important error which was not explicitly included in simulations [3] is the error in mean magnetic field (as a function of current) in the dipoles. This absolute normalisation will have to be obtained by a new set of careful absolute measurements on two or a few sample dipoles. Current measurements are absolute at only the 0.01 level. We assume this absolute calibration can be done to better than the 5×10^{-4} level and expected a 2.5×10^{-4} error level. The various error sources were combined with random error generation using the transport program DIMAD, an established, debugged transport code which is also the basic tool used in the CEBAF transport design. However, it is not optimised for error analysis and it has the disadvantage that every evaluation requires a separate run, and therefore it cannot be used to develop large-statistics random variation studies. In the analysis [3], 10 random error seeds were run and obtained error estimates of 3×10^{-4} to 6×10^{-4} . The analysis indicates that an absolute beam energy measurement at the 1.0 to 1.5×10^{-3} level is obtainable with high confidence.

IV. OPTIONS FOR THE ARC SPECTROMETER

Some variations on the measurement technique were explored. Variation of the placement of the final harp was considered. The 34.3° arc has 8 dipoles, and the final harp could be located after any one of these. Error analyses for 1, 2, 4, and 8-dipole configurations were simulated using the same methods, and the results are summarised in Table 2.

Now a shorter configuration would permit more accurate alignment. However the dominant error is the initial missteering and the resulting displacement increases linearly with N_D , the number of dipoles. The energy-dependent displacement is proportional to the dispersion D , which increases as N_D^2 , so the energy error $\delta E/E$ decreases as $1/N_D$. Accumulation of random errors also decreases as $1/\sqrt{N_D}$. Thus, the longer arc is favored. The error analysis actually uses only three harps. The proposed configuration includes three pairs of harps: pairs at the beginning, center, and end of the arc. The harps at the center provide an energy measurement with the transport quads on and the arc tuned to the achromatic mode (360° phase advance), when the dispersion has a 2 m maximum at the center. This measurement will be calibrated by the proposed absolute energy measurement. The center harps will also provide an additional $N_D=4$ measurement in the absolute energy calibration, which will be an important consistency check. The final harp pair will also provide an independent evaluation of beam direction, and can be used as a consistency check and to reduce steering error effects by $\sqrt{2}$. The proposed method will also be capable of obtaining relative energy measurements with great accuracy. In that mode the field normalisation error is inapplicable and missteering effects are reduced (by the strong focusing and 180° entrance to arc center phase advance). The dominant error should be harp misalignment and measurement uncertainties. The sum of those errors should be less than $\delta x \sim 0.2 \text{ mm}$. The resulting error in $\delta E/E$ (relative) will be on the level of $\delta x/D \sim 10^{-4}$.

V. SUMMARY

The results of the simulations and analyses discussed above indicate that it is possible to make an absolute beam energy measurement to an accuracy of about 10^{-3} . The hardware components and the optical tuning of arc are unchanged from the original beam line design. As the precision beam position probe, the upgraded CEBAF "Superharp", is developed and tested, a special alignment technique for the superharps must be carefully considered and implemented. Also at least two of the production arc dipole magnets must be mapped to obtain an absolute field integral measurement with an accuracy of 2.5×10^{-4} .

REFERENCES

- [1] C. Yan, R. Carlini, J. Napolitano, D. Neuffer, CEBAF-R-92-003, March 25, 1992.
- [2] D. Neuffer, C. Yan, R. Carlini, CEBAF-TN-92-054, November 24, 1992.
- [3] R.V. Servranckx, CEBAF-TN-92-044, September 29, 1992.

A Wide Range and High Speed Automatic Gain Control

Eugenio J. Tacconi[†] and Carlos F. Christiansen[†]
 Superconducting Super Collider Laboratory*
 2550 Beckleymeade Avenue, MS 4004
 Dallas, Texas 75237

Abstract

Automatic gain control (AGC) techniques have been largely used since the beginning of electronics but in most of the applications the dynamic response is slow compared with the carrier frequency. The problem of developing an automatic gain control having simultaneously high dynamic response and wide control range is analyzed in this work. An ideal gain control law, having the property that the total loop gain remains constant independent of the carrier amplitude, is obtained. The resulting AGC behavior is compared, by computer simulations, with a linear multiplier AGC. The ideal gain control law can be approximated by using a transconductance amplifier. A practical circuit that has been used at CERN in the radiofrequency loops of the Booster Synchrotron is presented. The circuit has high speed and 80 dB gain control range.

I. INTRODUCTION

In standard automatic gain controls the dynamic response is slow compared with the carrier frequency. When it is necessary to develop an AGC presenting simultaneously high dynamic response and wide control range, some stability problems arise due to the inherent non linear behavior of the control loop.

A simplified schematic diagram of an AGC is shown in figure 1, where P represents the controlled amplifier, A the power amplifier, D the amplitude detector, F a low pass filter and C a cascade compensator. The AGC has to regulate the amplitude of the output voltage V_o following the reference voltage V_{ref} . The amplitude of the carrier voltage V_{in} is the main perturbation to be rejected.

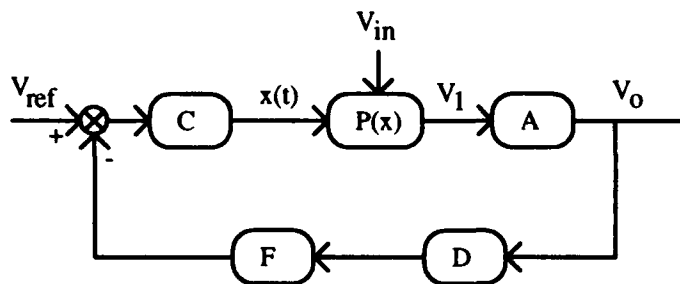


Figure 1. AGC Block Diagram

* Operated by the Universities Research Association, Inc., for the U.S. Department of Energy under Contract No. DE-AC35-89ER40486.

[†] On leave from Leici, UNLP, Conicet, Argentina

The gain of the controlled amplifier is a function of the control voltage $x(t)$. Thus, the control system is non linear and gain loop and stability are usually dependent on the operating point. The system has to be designed in order to be stable for the maximum loop gain and a poor dynamic behavior is obtained for low gain operating points. The effect of the gain control law on the loop gain variation range is analyzed in the next section.

II. GAIN CONTROL LAW

The output of the variable gain amplifier is given by:

$$V_1 = V_{in} \cdot P(x) \quad (1)$$

Thus, its equivalent gain depends on the operating point and is given by:

$$p = \frac{dV_1}{dx} = V_{in} \cdot \frac{dP(x)}{dx} \quad (2)$$

From figure 1, the loop gain LG can be expressed by:

$$LG = C \cdot p \cdot A \cdot F \cdot D \quad (3)$$

Expressions (2) and (3) show that the loop gain is usually dependent on the carrier amplitude (V_{in}). This is apparent when a linear multiplier type of control amplifier is used.

Linear Multiplier

In this case, the gain control law is:

$$P(x) = V_{in} \cdot k \cdot x \quad (4)$$

where k is a constant. Equation (3) becomes

$$LG = C \cdot k \cdot V_{in} \cdot A \cdot F \cdot D \quad (5)$$

Thus, the loop gain is directly proportional to the carrier amplitude. For having adequate stability over the whole amplitude range a low frequency dominant pole compensation is generally used. Then, when the carrier amplitude is reduced, the AGC constant time is proportionally increased.

The time domain system behavior is shown in figures 2 and 3, where the input carrier signal and the regulated output for two different operating points are represented. Figure 2 shows a good dynamic response, obtained when the carrier signal has maximum amplitude. Nevertheless, if the carrier signal amplitude is reduced (figure 3), the AGC constant time is increased resulting a slow time domain response.

The system behavior is highly dependent on the gain control law of the controlled amplifier. Different controlled amplifiers have been proposed in the literature [1], [2].

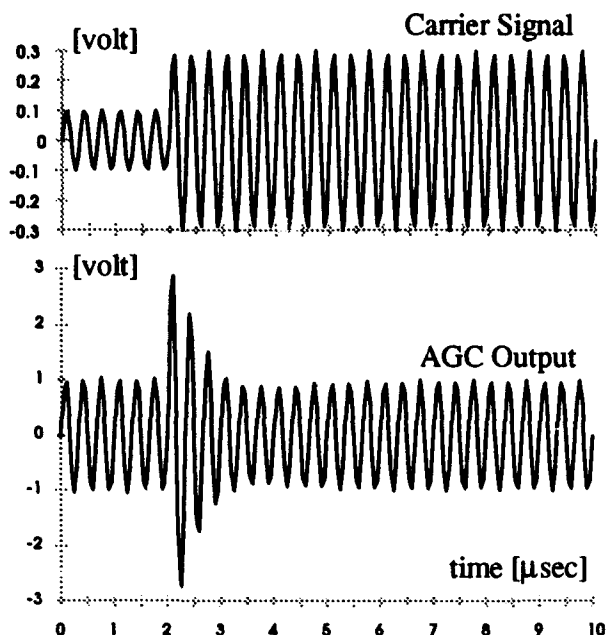


Fig. 2. Transient behavior of a linear multiplier AGC.
Carrier amplitude, 0.1V to 0.3V

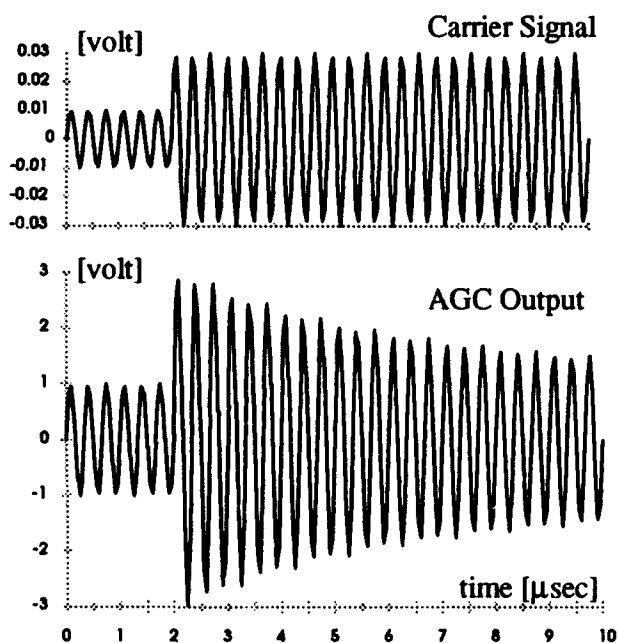


Fig. 3. Transient behavior of a linear multiplier AGC.
Carrier amplitude, 0.01V to 0.03V

Ideal Control Law

Our aim is to derive a gain control law which gives, for a constant output amplitude, a constant loop gain independent of the carrier amplitude.

The purpose of an AGC is to obtain an output signal with a given constant amplitude. Let us call this output amplitude V_o^o .

$$V_o^o = V_{in} \cdot P(x) \cdot A|_{V_o=V_o^o} = A \cdot V_1^o \quad (6)$$

For a constant p , a constant loop gain is obtained.

$$p = \frac{dV_1}{dx} \bigg|_{V_1=V_1^o} = \frac{V_1^o}{P(x)} \cdot \frac{dP(x)}{dx} = K_1 \quad (7)$$

where K_1 is an arbitrary constant. From equations (6) and (7) it is

$$P(x) = K_2 \cdot \exp\left(\frac{K_1 \cdot A}{V_o^o} \cdot x\right) \quad (8)$$

where K_1 and K_2 are arbitrary constants.

Thus, by imposing a loop constant gain, independent of the carrier amplitude, the control law of an ideal controlled gain amplifier has been deduced (expression (8)).

$$LG = C \cdot K_1 \cdot A \cdot F \cdot D \quad (9)$$

An AGC using this control law will present a dynamic behavior that changes with the amplitude value of the output voltage but, that is independent of the carrier amplitude. The input carrier presents a wide amplitude range while the regulated output amplitude is usually constant.

The computer simulation results of an AGC with an exponential control law are shown in figures 4 and 5. In order to compare the behavior of both AGCs, the cascade compensator has been designed for having similar relative stability than for the case of figure 2.

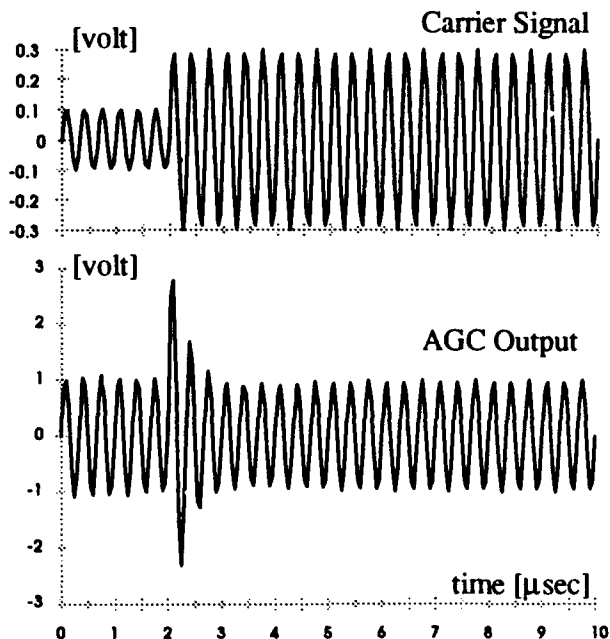


Fig. 4. Transient behavior of an exponential law AGC.
Carrier amplitude, 0.1V to 0.3V

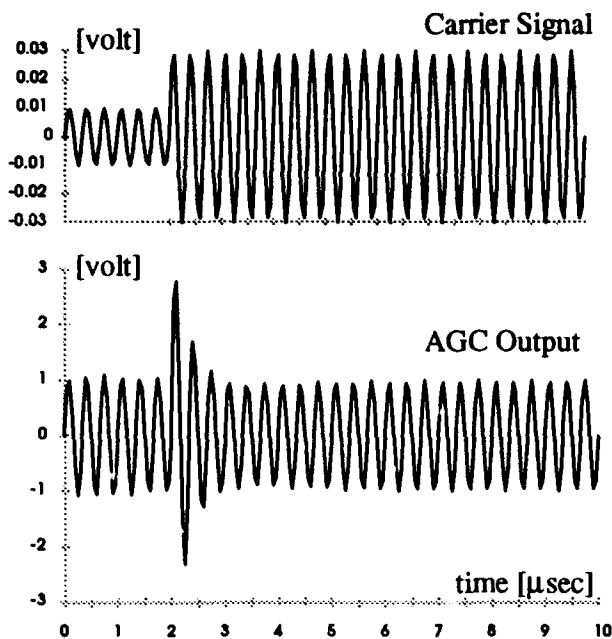


Fig. 5. Transient behavior of an exponential law AGC.
Carrier amplitude, 0.01V to 0.03V

The simulations have been carried out under the following conditions: the power amplifier A and the feedback loop have unitary gain, the amplitude detector is a quadratic detector, the filter F presents a single pole at 0.5 MHz and the compensator C has a dc gain of 10^4 having a single pole at 30 Hz.

Equation 9 shows that the loop gain is constant over the whole AGC range. Thus, the AGC constant time is also constant and independent of the carrier amplitude. This feature is shown in Figures 4 and 5 where the AGC dynamic response continues been the same although the carrier amplitude has been reduced in 20 dB. The advantages of the method are clearly seen by comparing figures 3 and 5.

III. CIRCUIT IMPLEMENTATION

An exponential law gain control can be approximated by a transconductance amplifier [3]. In this case, the gain control law is expressed by:

$$P(x) = c_1 / \left[1 + \exp\left(\frac{x - c_2}{c_3}\right) \right] \quad (10)$$

where c_1 , c_2 and c_3 are constants and $x \geq c_2$.

$$p = -\frac{V_1^o}{c_3} \left[\exp\left(\frac{x - c_2}{c_3}\right) \right] / \left[1 + \exp\left(\frac{x - c_2}{c_3}\right) \right] \quad (11)$$

From equations (3) and (11), the loop gain variation is limited to less than 6 dB over the whole control range. If the AGC range is 40 dB, the 3 dB corner frequency changes 100

times for a linear multiplier AGC and less than 2 times for a transconductance amplifier AGC. Thus, by using a transconductance amplifier, an AGC with a dynamic behavior almost independent of the carrier amplitude is obtained.

An AGC having these characteristics has been designed and implemented at CERN for the radiofrequency loops of the Booster Synchrotron. For this application, it was necessary to regulate a radiofrequency signal with an amplitude range of 80 dB and frequencies comprised between 3 MHz and 9 MHz. The AGC requirements included minimum phase rotation and fast AGC time response. The problem was solved by using two AGCs in cascade connection. Each AGC presents a control range of 40 dB and a constant time of less than 1 μ s [4]. The circuit was implemented with a commercial transconductance amplifier gain controller (MC1590) having a 60 dB AGC range. The amplitude detector is a full-wave mean value rectifier, the passive filter F presents a corner frequency at 8 kHz and the cascade compensator C is a dc amplifier with a single-pole at 1 MHz. The total open loop transfer function has a dc gain of 50 and the closed loop bandwidth is 0.4 MHz.

IV. CONCLUSIONS

An automatic gain control having simultaneously a high dynamic response and a wide control range has been analyzed in this work. It has been deduced that an exponential control law AGC presents a constant loop gain, independent of the carrier amplitude. The computer simulation results show the advantages of the method. For practical applications, the exponential gain control can be approximated with a transconductance amplifier. For designing a high speed AGC, a transconductance controlled gain amplifier must be consider over other commercial AGC. The characteristics of an AGC of this type, used in the radiofrequency loops of the Booster Synchrotron at CERN, are also presented.

V. REFERENCES

- [1] D. V. Mercy, "A Review of Automatic Gain Control Theory", *The Radio and Electronic Engineer*, Vol. 51, No. 11/12, pp. 479-590, (1981).
- [2] I. M. Filanovsky and V. A. Piskarev, "Automatic Gain Control by Differential Pair Current Splitting", *Int. Journal Electronics*, Vol. 62, No. 2, pp. 243-250, (1987).
- [3] Brent Trout, "A High Gain Integrated Circuit RF-IF Amplifier with Wide Range AGC", *Application Note AN-513*, Motorola.
- [4] E. J. Tacconi, "Amplificateur a Large Gamme Dynamique, Fiable Bruit et Commande Automatique de Gain pour le Systeme de Controle RF du Faisceau PSB", *CERN PS/BR No. 85-3*, (1985).

A Beamline Design and Data Acquisition with the 20-MeV, 20-ps Electron Beam for the Higher-Order Mode Studies of the APS SR-RF Cavities*

J. SONG, A. NASSIRI and R. DALY
Advanced Photon Source, Argonne National Laboratory
9700 S. Cass Ave. Argonne, IL 60439, USA

The submitted manuscript has been authored by a contractor of the U. S. Government under contract No. W-31-109-ENG-38. Accordingly, the U. S. Government retains a nonexclusive, royalty-free license to publish or reproduce the published form of this contribution, or allow others to do so, for U. S. Government purposes.

ABSTRACT

A beamline has been designed and assembled to use the ANL Chemistry Division 20-MeV electron linac for the testing of higher-order mode excitation and damping in RF cavities. The beamline consists of two sections (a beam collimating section with a 1.5"-OD vacuum line, and a cavity test section with a 3"-OD vacuum line), separated by two double aluminum foil windows. The beam diagnostics consist of a stripline beam position monitor, integrating current transformers, fluorescent screens, and a Faraday cup. EPICS (Experimental Physics and Industrial Control System) is used for beamline control, monitoring, and data acquisition. Also described is the diagnostic system used for beam image capture and analysis using EPICS-controlled hardware and PV-WAVE software. The RF cavity measurement will be described in a separate paper [1].

I. INTRODUCTION

The 20-MeV linac beam at the Argonne Chemistry Division was used to measure the RF properties of the single-cell cavity and WR 2300 waveguide system. The primary reason for building this test facility is to measure those HOMs near and above the cutoff frequency of the beampipe. These modes cannot be easily calculated well because of strong geometric effects. Bench measurements cannot be easily related to beam-induced effects. The 20-MeV chemistry electron beam is good for testing because of the similarities of pulse shape and charge to those of the APS storage ring bunch. Comparison of the linac beam and the APS storage ring bunch parameters are given in Table 1.

Table 1 Main Beam Parameters for the APS-SR System and the Chemistry Linac.

	7-GeV APS Storage Ring			20-MeV Linac
Mode	single	Nominal	Maximum	single to 60 Hz
# of bunch	1	20	60	
average current	5 mA	100	300	>1.5 μ A
peak current	700 A			> 625 A
bunch length (FWHM)	27.5 ps	50	72.5	25 - 40 ps
total # of particles	1.2X10 ¹¹	2.3x10 ¹²	6.9X10 ¹²	>1.5X10 ¹¹
total charge	18.5 nC			1 - 20 nC
natural emittance	8.2 x 10 ⁻³ mm-mrad			10 mm-mrad

Higher-order modes (HOMs) of the SR single cell cavity are studied by sending the beam on-axis and off-axis of the cavities, and the HOM dampers can be tested.

II. BEAMLINE SYSTEM

The Argonne Chemistry linac is an L band (1.3 GHz) traveling wave accelerating structure [2]. The linac beamline exits through an Al foil window (5"), followed by a beam collimator (2' long, and 3/16" diameter). After tuning the linac for an optimized beam condition, the collimator is removed to provide a maximum beam current through the cavity section.

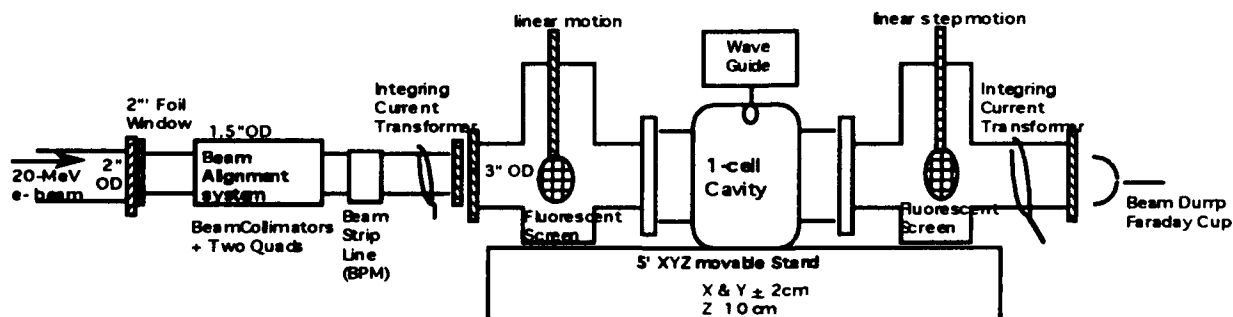


Fig. 1 Schematics of the Beamline to Test HOMs of the APS/SR RF Cavity

*Work supported by U.S. Department of Energy, Office of Basic Sciences, under Contract W-31-109-ENG-38.

Our beamline consists of two sections (a beam collimating section with a 1.5"-OD vacuum line, and a cavity test section with a 3"-OD vacuum line, separated by two double Al foil

windows as shown in Fig. 1. The collimating section consists of a water-cooled collimator (3/4" long and 1/8" diameter) and 2" Al foil window to get a small size beam (3 mm diameter). The energy loss and the beam divergence angle through the double 2" Al foil windows were calculated to be 30 keV and 1.8 degree, respectively [3]. The double Al foil window system was adopted to prevent the beamline from possible vacuum break, using a differential pressure between the two foil windows.

The beam focusing is provided by two quadrupole magnets (length = 8 cm, bore radius $a = 2.5$ cm, focal length $f = 30$ cm). To confine beam inside the beam pipe, a solenoid coil ($L_S = 7$ mH, $Q = 23.7$, and $R = 1.7 \Omega$) is used. The beam diagnostics used in the first section include a beam stripline and an integrating current transformer.

The second section of the beamline includes the RF cavity, two fluorescent screens, an integrating current transformer, and the beam dump.

The second section is movable with respect to the first section by ± 2 cm in the X and Y directions and 10 cm along the beamline to have a beam off-center of the cavity. To align the beamline, many three-point adjustment mounts were used and a He-Ne laser beam was used to check the alignment. The vacuum was about 1×10^{-4} Torr.

III. BEAM DIAGNOSTICS SYSTEM

The beam diagnostics consist of an APS/linac beam position monitor (Stripline-type) (BPM), two integrating current transformers (ICT), two fluorescent screens (FS), and a Faraday cup (FC).

The BSL or BPM consists of four equal-length electrodes ($\ell = \lambda/4$, $\lambda = 10.5$ cm) [4]. The monitor provides a triggering signal for the rest of the diagnostics in the beamline.

Two ICTs measure total beam current: one upstream of the cavity and the other downstream of the cavity. The ICT, manufactured by Bergoz, is based on toroids and responds with a fast pulse signal as short as ten picoseconds. The ICTs are mounted through the vacuum ceramic break and confined in a Cu housing to avoid disrupting the return current. In-house high speed beam signal processing electronics provides a DC level output proportional to the peak current or the total charge for the digitizer input. The calibration is done with a short electronic pulse (FWHM = 140 picoseconds) using the wire method. More detailed description of the 'Gate' electronics and their measurements can be found in the reference [5].

A fluorescent screen monitors relative beam position and spot size of an electron beam. A chromium doped alumina ($Al_2O_3:Cr$) ceramic screen inserted into the beamline is monitored by a video camera. The fluorescent screen housing is mounted to the air-actuator to insert and retract from the beamline. The resulting image is captured using a frame grabber and stored into memory. The camera was shielded to prevent possible noise due to radiation. Reconstruction and analysis of the stored image are performed using PV-WAVE [6].

The beam dump serves as a Faraday cup with a 50 Ω termination. Even though the FC does not respond as fast as ICT, it certainly gives a signal that is proportional to the total beam current at the end of the beamline. To reduce the secondary electron emission, and the radiation outside the beam

dump due to the high energy beam, the FC is well shielded with lead.

IV. CONTROL & DATA ANALYSIS

The EPICS (Experimental Physics and Industrial Control System) control system is used for control and data collection. The hardware configuration is shown in Figure 2. The operator interface (OPI) is a SUN workstation running the UNIX operating system.

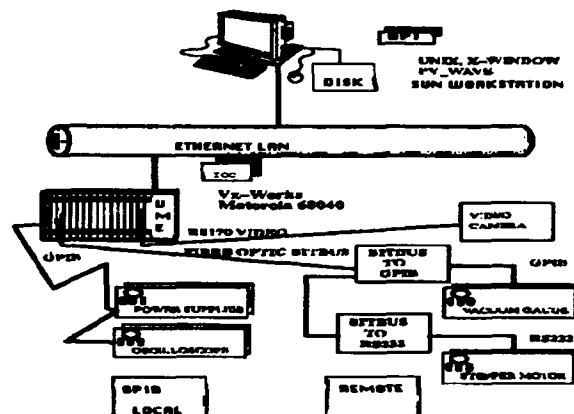


Fig. 2 System Control and Data Analysis, using VME-based with SUN Workstation

Control panels displayed on the SUN and configured with the EPICS Motif Edit Display Manager (MEDM) tools are used to control a frame grabber system, a stepping motor positioner for the fluorescent screen, the power supplies for the vertical and horizontal focusing quadrupole magnets, and a sampling oscilloscope. Monitors for the sampling scope waveform and the vacuum readings are also displayed on operator control panels.

The SUN workstation communicates with a VME based Input/Output Controller (IOC) through an Ethernet LAN. The VME crate contains a Motorola MVE167 single board computer and through VME communication modules is responsible for direct instrument control. For instrumentation close to the VME crate (i.e., sampling oscilloscope and quadruple power supplies) direct GPIB communication is used. For instrumentation remote from the VME crate, a fiber optic BITBUS communication link is used. The BITBUS protocol signal is converted to a GPIB protocol for interfacing to the vacuum gauge, and to an RS232 protocol for interfacing to the stepper motor positioner. These protocol converters were developed at Argonne for the Argonne APS control system. The IOC runs the Vx-Works real-time kernel and the EPICS IOCCORE software.

The frame grabber is used to capture images of the beam from a camera. The camera views a fluorescent screen placed at an angle of 45 degrees with respect to the camera. The frame grabber is a VME based MaxVideo 10 system with DigiMax frame grabber and RoiStore video memory. The captured image data is stored in a disk file for off-line analysis.

The data analysis program (PV-WAVE) provides background subtraction, compensation for the viewing angle of the

fluorescent screen, and calculation of the beam position and full-width half and tenth maximum values. Pseudo color displays are provided for the raw and compensated images. X and Y beam profile displays are also provided.

V. MEASUREMENTS AND RESULTS

The beam emittance was measured with the collimating system of the first section of the beamline. The image of the beam profile was captured with the first FS, while varying the magnetic field of the two quadrupole magnets. A typical image pattern is exhibited in Fig. 3. The top-left photo is a 2-D pattern plot and the bottom-left is a 3-D plot. The top-right is an X-profile and the bottom-right is a Y-profile, respectively. Analyzing the beam image pattern, one can get FWTM versus strength of a focusing magnet as presented in Fig. 4. The measured emittance, ϵ_x and ϵ_y , are 9.20 and 3.72 mm mrad, respectively [7].

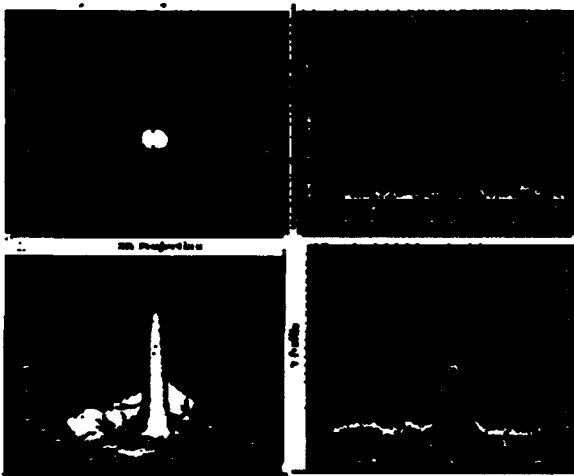


Fig. 3 Typical Beam Profile with the focused beam

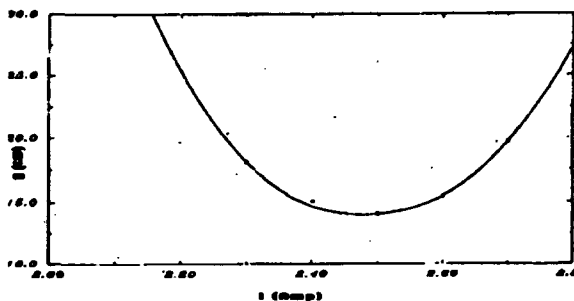


Fig. 4 Beam Profile Width (FWTM) with Various Current in Q2.

The data with ICT is shown in Fig. 5: The left one is the ICT output signal with 100 mV/Div, 20 ns/Div and the right one is a DC output with Gate, 200 ns/Div, 200 mV/Div. The total charge is about 5.0 nC and the sensitivity of both ICTs (one with 1.5" OD and the other with 3" OD) is about same within 5% of each other.

The signals from the BSL and FC are shown in Fig. 6: The bigger signal is from the BSL and the smaller signal is from the FC with 2 ns/Div, 5 V/Div. The total current trans-

mission is about 87% when it ends at the beam dump. The time delay between the two signals signifies the time of flight of the beam between the BSL and the FC, which is about 5.5 ns.

The RF cavity measurement was done with two H-loops and E-probes, and will be discussed in a separate paper [1].

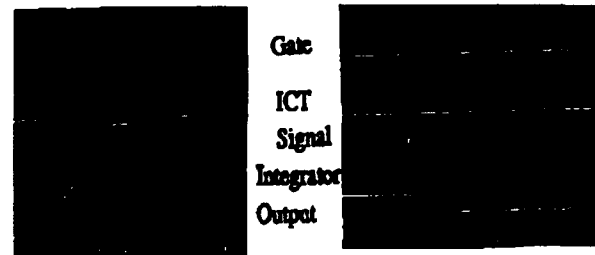


Fig. 5 ICT output signal and its gated DC signal.

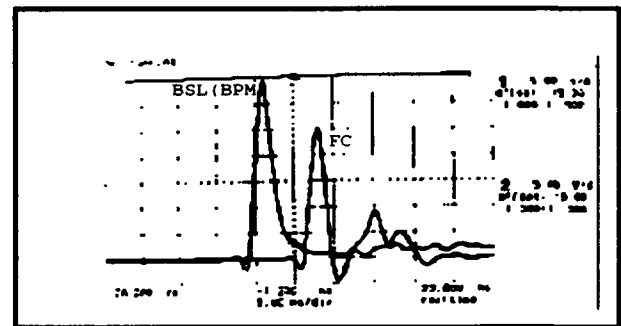


Fig. 6 Signal from BSL and FC, with 2 ns/Div, 5 V/Div.

VI. ACKNOWLEDGMENTS

The authors would like to thank Bill Berg, Don Ficht, Eric Landahl, Ed Wallace, Fred Vong, Bill Wesolowski, and Portia Young for their technical support and allowing their beam diagnostics use.

VII. REFERENCES

- [1] J. Song, et al., "HOM (Higher-Order Mode) Test of the Storage Ring Single-Cell Cavity with a 20-MeV e^- Beam for the Advanced Photon Source (APS)" in these proceedings.
- [2] G. Mavrogenes, "Beam Measurements on Argonne Chemistry Linac for Collider Injector Design," 11th International Accelerator conference, Geneva, Swiss, 1980.
- [3] A. Nassiri, "Stopping Power and Scattering Angle Calculations of Charged Particle Beam Through Thin Films," ANL/APS LS-165, March, 1991.
- [4] R. Fujia, et al., "The APS Linac Beam Position Monitors and Electronics," submitted to 1992 Accelerator Instrumentation Workshop, LBL Berkeley, CA, Oct. 27-30, 1992.
- [5] X. Wang, "Design And Initial Tests Of Beam Current Monitoring Systems For The APS Transport Lines," submitted To 1992 Accelerator Instrumentation workshop, LBL Berkeley, CA, Oct. 27-30, 1992.
- [6] W. Berg, et al., "Fluorescent Screens and Image Processing for the APS Linac Test Stands," submitted to 1992 Accelerator Instrumentation Workshop, LBL Berkeley, CA, Oct. 27-30, 1992.
- [7] Y. Qian, et al., private communication.

A BUNCH KILLER FOR THE NSLS X-RAY ELECTRON STORAGE RING*

R.J. Nawrocky, U. Bergmann, and D.P. Siddons

National Synchrotron Light Source, Brookhaven National Laboratory, Upton NY 11973

Abstract

In the NSLS x-ray electron storage ring, which operates at a harmonic number of 30, the beam may be stored in many different bunch patterns. The minimum spacing between bunches is approximately 19 nsec. While most of the experimenters are primarily interested in photon flux, some experiments are sensitive to bunch spacing. Time resolved nuclear resonance scattering experiments, for example, need pulses of x-rays spaced of the order of 100 nsec apart and a very low noise floor (10^{-6}) between pulses. Perhaps even more important than the level of the background is that it be reproducible and homogeneous in time. It has been found in practice that a small number of electrons always get trapped in the "empty" rf buckets during injection into the storage ring and remain as low level stray bunches. These extra bunches produce an unacceptable temporally localized, non-reproducible background which is difficult if not impossible to correct for. A "bunch killer" system based on the rf knock-out technique has been developed and installed on the ring to remove the unwanted bunches. We describe the operation of this system and present experimental results to illustrate its effectiveness.

I. INTRODUCTION

The NSLS x-ray storage ring operates with an accelerating rf frequency $f_{rf} = 52.88$ MHz and a harmonic number $n = 30$. The ring energy is ramped after injection from 750 MeV up to approximately 2.5 GeV. The machine is usually filled with 25 consecutive bunches. Some fraction of the machine operation is devoted to special fill patterns, usually single or five bunch modes. This provides the capability for performing time-resolved experiments in the nanosecond range. For example, nuclear resonance scattering experiments [1] need to maintain a very low background (a factor of 10^{-6}) between consecutive light pulses spaced some 100 nsec or more apart.

In practice we find that some electrons get trapped in the "empty" rf buckets during injection which in effect raises the background. This noise, which is time-localized and typically different from fill to fill, is difficult to correct for. It should be noted that at the present time the very low level stray bunches can only be observed by the synchrotron radiation that they produce using photon counting x-ray detectors after the beam has been stored and ramped up in energy. The low level stray bunches can not be readily seen with conventional rf beam pick-ups or visible light monitors.

* Work performed under the auspices of the U.S. DOE.

After a preliminary investigation, it was concluded that removing the unwanted bunches after filling would require less effort than cleaning up the injection process itself.

The low background requirement prompted the development of a "bunch killer" system. This system uses a stripline kicker to induce large coherent vertical oscillations in the unwanted bunches at the betatron frequency [2] until they collide with the vacuum chamber wall and are lost. The kicker is driven by a gated, swept rf signal which is synchronized with the stored bunch pattern. The rf amplifiers driving the kicker are limited in output power, so that the stray bunches can only be knocked out at low energy. The kickers are driven sinusoidally at a single frequency within a betatron sideband which is only a few kHz wide. Because this frequency can vary from fill to fill by as much as ± 175 kHz (± 0.05 tune units), the frequency of the excitation is modulated back and forth across its nominal value (see Fig. 1). In the x-ray ring, the fractional part of the vertical tune, q , is nominally equal to 0.36 and the available stripline is best coupled to the beam in the 100 MHz range. As a result, the kicker is driven at the frequency of the upper betatron sideband of the 60th revolution harmonic ($60 f_0$) which is 106.4 MHz.

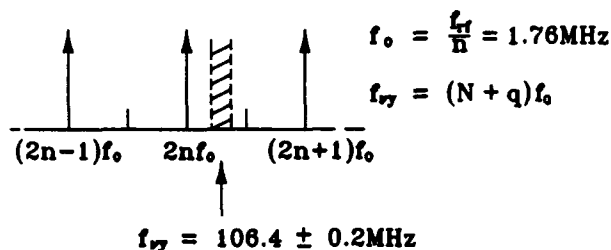


Fig. 1. Vertical betatron frequency during injection.

The bunch killer system has been installed and used in routine operations; photon counting data indicate that the system is effective in removing stray bunches to a level where they can no longer be distinguished from the random background noise. The system requires a minimum of intervention from the machine operator and is now being upgraded for completely automatic operation.

II. SYSTEM DESCRIPTION

A block diagram of the system is shown in Fig. 2. The kicker drive signal from a 106.4 MHz VCO is gated on and off by means of a double balanced mixer. The IF input of

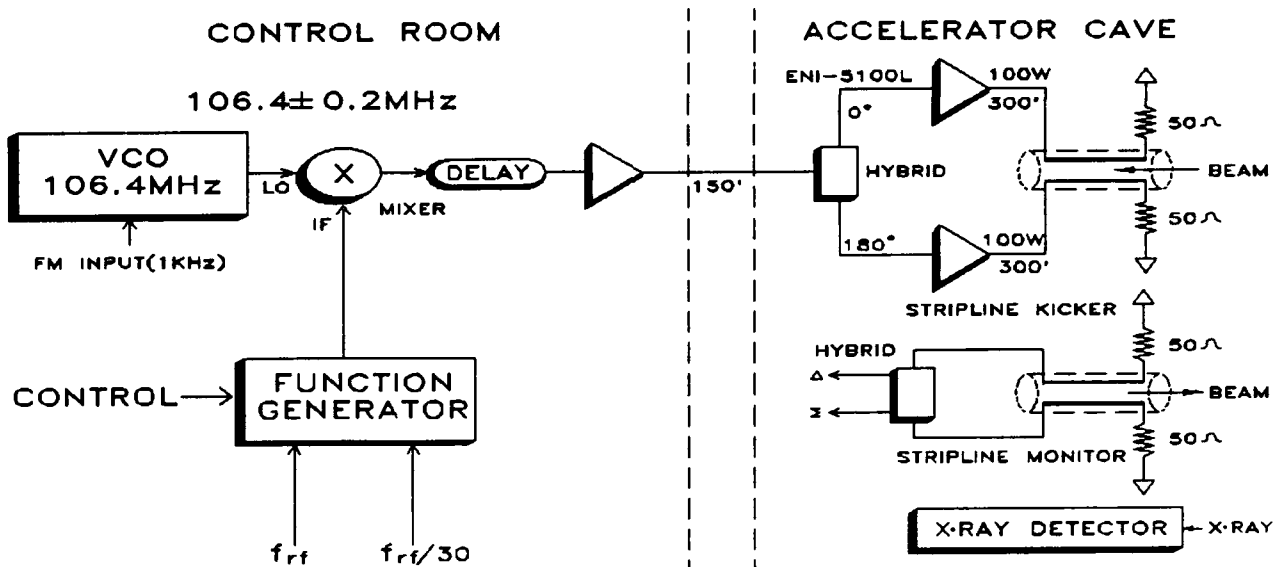


Fig. 2. System block diagram

the mixer is driven by a programmable function generator (PFG). The PFG, which also provides a bias to the mixer input for clean gating of the VCO signal, is synchronized with signals at f_{rf} and $f_{rf}/30$. The PFG has several modes of operation tailored to the various bunch patterns of interest which can be selected by the computer control system. The mixer output is split and amplified by two 100 Watt rf power amplifiers (ENI Model 5100L) to drive the stripline differentially. The gated drive and a sum signal proportional to beam intensity derived from another rf stripline are monitored with a fast digital oscilloscope. The kicker is driven at 106.4 MHz because it is best coupled to the beam in this frequency range.

As mentioned earlier, the tune of the machine may vary from fill to fill by as much as ± 0.05 units. The resonance line, however, is narrow (a few kHz), and the amplifiers driving the kicker are limited in power. This means that we must drive with a single frequency within the betatron sideband to excite the resonance. To simplify the process of finding the correct frequency during operations, we modulate the output of the 106.4 MHz oscillator by ± 200 kHz at 1 kHz rate. The transverse oscillations are induced in the beam by sweeping back and forth through the resonance. The excitation of these oscillations by the kicker is counteracted to a small degree by radiation damping. Since the radiation damping time constant at low energy is of the order of two hundred msec, the excitation is sufficiently strong to build up the amplitude of the oscillations and drive the stray particles into the vacuum chamber wall.

To demonstrate the operation of the bunch killer, we first generated an artificially "bad" five bunch fill and then removed the unwanted bunches by turning the system on, as shown in Fig.3. The lower trace of Fig.3a shows the bunch

pattern with small intermediate bunches as observed with the rf stripline monitor. The upper trace in the same figure is the gated rf drive which is to be applied to the kicker electrodes. Since there are arbitrary delays introduced in various signal paths, it is necessary to compensate for them by trial and error until the correct phase relationship between the drive and the bunch pattern is found. With the correct delay established and the drive signal connected to the kicker, the intermediate bunches are reduced to a point where they can no longer be observed with the rf pick-up. This is shown in the lower trace of Fig.3b. Since the bunch spacing is only 19 nsec, the jitter

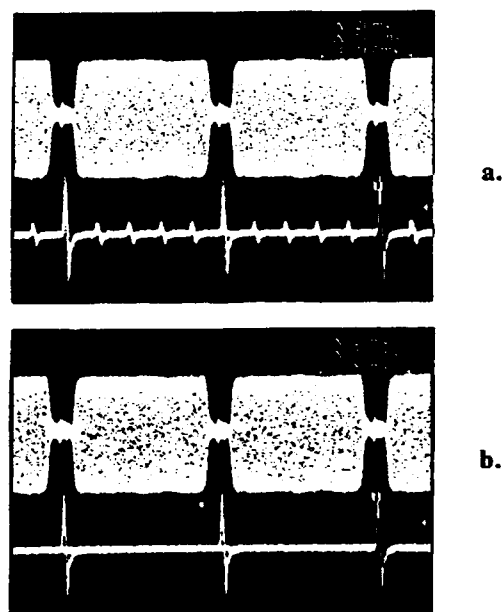


Fig. 3. Mixer output and beam pick-up signal with kicker off (a), and with kicker on (b).

between the kicker excitation and the beam pattern must be controlled to a few nsec so as not to affect the desired bunches. This has been readily achieved in the NSLS system as can be seen in Fig. 3 where the waveforms are the envelopes of many oscilloscope traces.

III. EXPERIMENTAL RESULTS

As previously mentioned, the level of the unwanted bunches is typically too low to be detected by the rf pick-up detectors. The best technique so far is to use the set-up for nuclear resonance experiments as a diagnostic. This uses a fast plastic scintillator detector which is usually employed to probe the decay of nuclei excited by synchrotron radiation. A block diagram of the detector is shown in Fig. 4. An x-ray emitted by a stray bunch and registered by the detector starts a time-to-analog converter (TAC). A legitimate beam pulse signal (the prompt) derived from a fast photo-diode looking at synchrotron light stops the TAC. The TAC output, which is proportional to the time delay between the two events, is digitized and stored in the computer memory. The process is repeated for a large number of events and the distribution is plotted as a function of the delay. Results for a five bunch fill with and without the bunch killer are shown in Fig. 5. Fig. 5a shows the presence of stray bunches at 19 nsec and at 38 nsec after the prompt. The level of these bunches is roughly 100 times the expected signal level for the nuclear resonance experiment. With the bunch killer turned on, stray bunches can not be distinguished from the background (Fig. 5b).

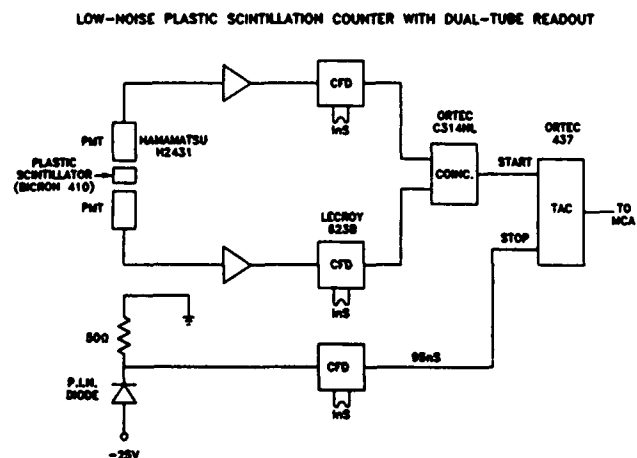


Fig. 4. The x-ray detector.

IV. ACKNOWLEDGEMENTS

The function generator used in the NSLS bunch killer was designed and constructed by J. Tallent. The authors would like to thank Dr. E. Blum for reviewing the manuscript.

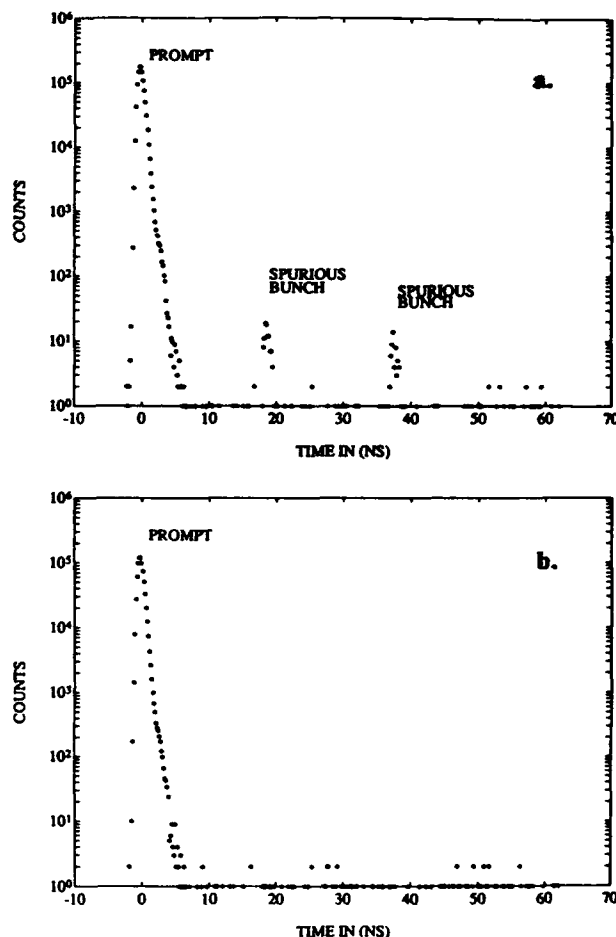


Fig. 5. Typical detector output with bunch killer off (a), and with bunch killer on (b).

V. REFERENCES

- [1] U. van Buerck, et al., "Nuclear forward scattering of synchrotron radiation", *Physical Review B*, Vol.22, No.10, 6207 (1992).
- [2] E. Wilson, "Transverse beam dynamics", in *Proceedings of CAS*, P. Bryant and S. Turner ed., CERN 85-19, Vol.1, 64 (1985).

The Mechanical Design of a Bunched Beam Stochastic Cooling Tank for the FNAL Tevatron

P. Hurh, G. Jackson

Fermi National Accelerator Laboratory*, Batavia, Illinois 60510

Abstract

The stringent alignment required for successful bunched beam stochastic cooling in FNAL's Tevatron necessitates the design and manufacture of a complex vacuum compatible mechanical alignment system. The design presented uses remote motion control to provide a positioning system with four degrees of freedom for placing two symmetric pickup loop arrays about the proton beam and with two degrees of freedom for aligning the arrays relative to each other. The system provides a 7.62 cm aperture between arrays during injection and a 1.90 cm aperture during operation while maintaining alignment between arrays within 50 μm . The system also allows precise remote longitudinal adjustment between pickup arrays with .002 μm resolution via a piezoelectric crystal inchworm motor in vacuum. Discussion includes the manufacture and installation of four complete pickup and kicker systems in the FNAL Tevatron.

I. INTRODUCTION

Stochastic cooling of proton and antiproton bunched beams in the Tevatron requires the careful design of a precise alignment and positioning system for the proper placement of two microwave loop arrays (per tank) symmetrically about the circulating beams. This high level of symmetric alignment is necessary to achieve the stringent electrical balances required to successfully filter out common mode noise [1]. The precision alignment criterion in addition to the requirements of vacuum compatibility, smooth electrical transitions of beam tube current through the tanks, and actual physical size constraints pose severe design challenges for the mechanical engineering design of the tanks.

A. Positional Alignment and Movement Criteria

The loop arrays for both kicker and pick-up tanks are constructed of flexible, glass impregnated PTFE circuit board attached to stiff, flat aluminum backing plates. During operation, the array plates are ideally located symmetrically on either side of the beam, each at a distance of 9.5 mm from beam center. The absolute distance between the arrays is not crucial (± 2.5 mm) provided the arrays can be centered on the beam symmetrically within 0.13 mm. In addition, during beam injection into the Tevatron, the array plates must allow for a physical beam line aperture of 7.62 cm. Thus the criteria for array plate motion is set at 0.13 mm resolution and at least 2.86 cm travel per plate perpendicular to beam axis.

The alignment of paired array plates to each other is also of great concern. The plates should be flat within 50 μm and parallel to each other within 0.5 mm. Locationally, the centerline of the planar loops on each array plate must be aligned parallel to the loops on the facing plate, and the beam axis, within 0.5 mm.

The longitudinal alignment (along beam axis) of the array plates to each other is of primary importance in the pick-up tanks because any small misalignments could produce unsymmetric signal delays causing errors in common mode rejection [1]. Requirements for alignment in this direction are not precisely

known due to the uncertainty of the effect upon the filtering electronics, however real time remote control of the longitudinal position of the boards with a tight resolution of approximately 1 μm should alleviate any problems associated with longitudinal misalignment.

The precise alignment required at the operating aperture should also be repeatable within 50 μm after the array plates are cycled through the entire aperture range necessary for injection. This positional repeatability will allow the cooling system to come back up on line as soon after injection as possible without any delays for realignment.

Finally, the entire array assembly of each tank should possess the capability to be remotely positioned relative to the beam so that errors from the theoretical (surveyed) beam center to actual beam center can be zeroed out easily during initial operation. This requires alignment drives to position the tanks horizontally and vertically plus rotationally about the vertical and horizontal axes (pitch and yaw) with a resolution of 0.13 mm and travel of at least ± 1.3 cm.

B. Other Design Criteria

In order to reduce unwanted higher order microwave modes created by the bunched beam image current discontinuities, it is necessary to provide a smooth transition path for the current from the upstream beam tube to the ground plane of the loop arrays and back to the downstream beam tube. In addition, the design of the tank should incorporate microwave absorbing material surrounding the beam line in an attempt to damp out any microwave ringing caused by the effective cavity of the interior surface of the surrounding vacuum tank.

The locations of the bunched beam stochastic cooling systems in the Tevatron pose great limitations on overall tank dimensions. The limiting dimensions for one tank (pick-up or kicker) are 56 cm in the vertical and horizontal directions and 140 cm in the longitudinal (beam axis) direction with a beam line center height of 26.7 cm.

Lastly, the materials and design of both pick-up and kicker tanks should be vacuum compatible since they are installed directly into the Tevatron's vacuum system. The requirement for vacuum in the Tevatron is less than 10^{-8} torr.



Figure 1. Vertical Cooling Tank on Stand.

* Operated by the Universities Research Association under contract with the U.S. Department of Energy.

II. DESIGN AND CONSTRUCTION

Both pick-up and kicker tanks are constructed of a stainless steel (304) 30.5 cm diameter tube capped on both ends with 35.6 cm diameter conflat type vacuum flanges. The central tube portion is modified to provide flat surfaces for the array insertion drives and to comply with physical size constraints (see fig. 1 & 2). Additional feedthrough ports are provided around the entire periphery of a tank for electrical connections, ion pumps and the array insertion drives. The entire length of a tank, including dog-leg bellows at either end to allow for remote tank motion, is 110.5 cm.

A. Array Insertion and Longitudinal Drive Systems

In order to facilitate the range in aperture required for operation and injection, a plunging-type insertion drive system for the array plates is utilized. Although this type of design, which allows for relative motion between the two array plates, inherently introduces clearances and therefore increased tolerances into the alignment system, it is necessary to allow the capability of signal amplitude adjustment, via adjusting each plate's distance from the beam.

Each 15.2 cm by 38.1 cm aluminum array plate of each tank array plate pair is inserted via a dedicated independent drive. However, each array plate is also registered to its mating plate through tightly toleranced stainless steel guide shafts. Figure 2 shows a cross-section of an insertion guide shaft and drive assembly. Clearance between the guide shaft and mating bushing is 25 μm . The guide shaft is coated with 38 μm of a PTFE based surface coating, to reduce friction and eliminate galling in the sliding connection.

The array plates are registered to each other in two locations, near the upstream and downstream edges of the array plates. This arrangement ensures the even and stable motion of the arrays relative to each other. In order to alleviate binding due to the overconstraint of using two full guide shafts, the upstream guide shaft has a full circular cross-section to register the plates positionally while the downstream guide shaft has a diamond shaped cross-section, oriented perpendicular to the beam line (so that only two opposite sides of the shaft contact the bushing wall), to register the plates rotationally. In addition, to allow relative motion between the guide shaft locations, the downstream guide shaft and bushing are connected to their respective array backing plates with a belleville spring loaded connection plate. This special connection plate allows longitudinal slipping to occur during the 150°C vacuum bake-out without losing rotational alignment.

Linear motion is transferred from the exterior of the tank to the interior array plates via a conventional welded bellows feedthrough. On the atmosphere side, a lubricated bronze bushing is used to locate the guide shaft/array plate assembly relative to the vacuum tank (see fig. 2). Actual linear motion is achieved by exterior mounted worm drive assemblies and low friction ball screws driven by a standard DC stepping motor. Backlash associated with the worm drives is virtually eliminated by the pre-loading effect of the vacuum pressure. Each drive assembly is mounted within a vacuum flange for easy assembly.

Initial alignment and registration of each pair of array plates is achieved before assembly by pinning the array plates together with an alignment fixture. The alignment fixture is removed only after the array plates have been securely mounted within the tank to the insertion bellows. The same alignment fixture is used for surveying the precise location of the array plates to exterior mounted tooling balls.

Submicron longitudinal alignment of the pick-up tank array plates, relative to each other, is achieved through the use of a piezo-electric crystal motor. This motor utilizes an inchworm

type series of crystal expansions and contractions to move one array with respect to the other. In figure 2, the top array plate is actually mounted (hung) beneath a second aluminum plate. This guidance plate is attached rigidly to the insertion drives and provides mounting positions for three small, Teflon-S coated, guide shafts. Bushings attached to the top surface of the array plate mate (with 38 μm clearance) to the shafts on the guidance plate to allow longitudinal motion of the top array plate relative to the guidance plate (and lower array plate). The motion is provided by the inchworm motor which rides on a ceramic shaft also mounted on the guidance plate. The inchworm motor (made by Burleigh Instruments [2]) is only capable of 1.5 kg of load, so the entire drive system is tweaked manually until the top array plate glides effortlessly on the guidance plate's mounted shafts.

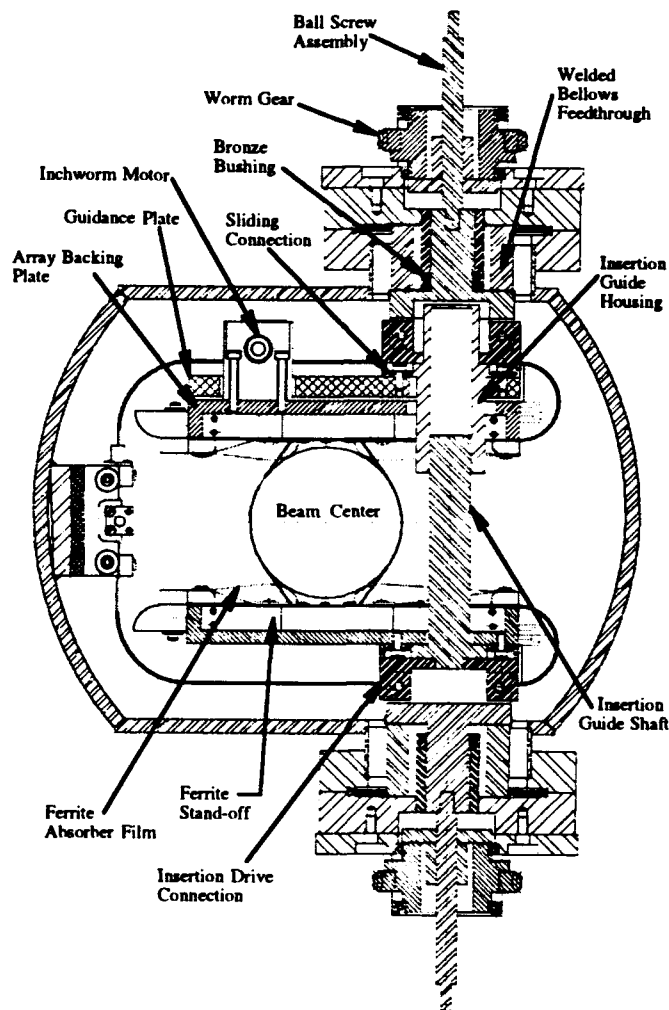


Figure 2. Cross-section view of array insertion drive assembly.

B. Array Board/Absorber Design

The loop array circuit boards are connected to the aluminum backing plates via several ferrite absorber standoffs. These standoffs help eliminate unwanted microwave ringing in the concave area created between the array backing plates and the backs of the array circuit boards (see fig. 2). To damp out ringing created by the cavity of the tank itself, loops, or pillows, of carbon coated polyimide film were attached to the array boards on each side of the pick-up/kicker loops (see fig. 2). These loops of film fill the gaps between the faces of the loop array boards when the boards are at the narrow aperture required for operation.

Smooth electrical transition from the up and downstream beam tubes to the array boards is achieved by the use of beryllium-copper foil (0.25 mm thick) and commercially available Be-Cu finger stock. The foil is formed into a transition piece with a cylindrical shape on one end and two flat tabs on the other (see fig. 3). The cylindrical end is outfitted with the fingerstock and fitted into a neighboring beam tube and the flat tabs are fastened tight to each loop array ground plane. The fingerstock keeps positive spring loaded pressure on the interior wall of the beam tube for good electrical transmission without hindering the array plates' insertion movements.

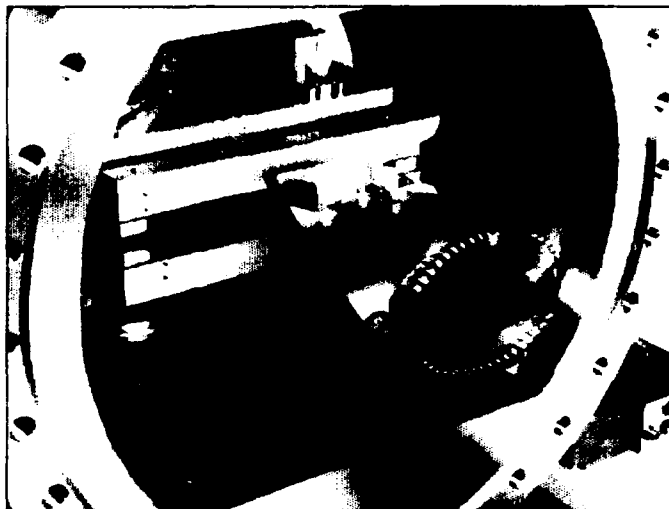


Figure 3. Interior end of tank, showing transition foil assembly.

In the pick-up tanks, the transition pieces are modified to accommodate the longitudinal motion of the inchworm drive system. Figure 3 shows the modification, a sliding interface foil tab and mating aluminum housing, designed to provide a smooth transition for the image current while allowing array longitudinal movement.

C. Vacuum Design

All materials used in the design of the bunched beam cooling tanks are vacuum compatible. Materials include 6061 aluminum, 304 stainless steel, beryllium-copper foil, PTFE surface coating, glass impregnated PTFE circuit board, polyimide film, and high absorption nickel ferrite. All blind holes and trapped volumes are vented to ensure quick pump down. Stainless steel screws which engage stainless steel threads are gold plated to avoid galling. All stainless steel is degassed at 850°C to remove the hydrogen content before machining. An additional 150°C bake is performed on the installed tanks to remove any water content adsorbed during installation. Two 20 l/s diode pumps are used on each tank to achieve an ultimate pressure of 10^{-9} torr.

D. Tank Stand Design

The geometrical space constraints of the Main Ring tunnel required the design of two separate stands. One for tanks oriented for stochastic cooling in the vertical direction and one for tanks oriented for cooling in the horizontal direction. Both designs use conventional gear and sliding v-block designs driven by standard DC stepping motors to achieve remote motion in four degrees of freedom. The stands are capable of translations perpendicular to the beam line in the vertical and horizontal directions and rotations about the horizontal and vertical axes. Detailed discussion of these stand designs is beyond the scope of this paper, suffice to state that the stand designs satisfy the travel and resolution requirements described earlier to initially align the array assemblies with respect to the actual beam centerline.

III. DESIGN RESULTS

Table 1 shows the results of the described tank design in terms of alignment parameters. All motions desired are provided at the resolutions, tolerances, and repeatability required for successful bunched beam cooling.

After the construction of one prototype tank of this design, it was noted that the inchworm motor guides were binding intermittently, especially after the 150° vacuum bake-out. After careful analysis, it was determined that the array plate and guide shaft assembly was coupled to the vacuum tank walls to a greater extent than predicted. The vacuum tank wall deflections due to vacuum pressure loading (0.20 mm) was enough to cause binding in the close fitting inchworm motor guides. In order to decouple the interior assembly from the exterior vacuum jacket, the bronze bushings in the bellows assembly have been removed. This results in allowing the interior components to keep their close alignment by floating with respect to the exterior vacuum tank walls. The locating function of the bronze bushings was found to be redundant since the clearance on the ball screw drives is much tighter than previously perceived (within 50 μ m). In addition, the transition foil sliding connection shown in figure 3 was redesigned to decrease the friction loading on the inchworm motor. The redesign incorporates a flexible foil tab to allow longitudinal inchworm motion. These changes result in a free moving inchworm drive system even directly after the 150°C bake-out.

Alignment Parameter	Required Value	Actual Value Achieved
Array Insertion Drive		
Travel	2.858 cm	2.858 cm
Resolution	0.127 mm	5.3 E-4 mm
Repeatability	50.8 μ m	50.8 μ m
Longitudinal (Inchworm) Drive		
Travel	+/- 1.6mm	+/- 3.2mm
Resolution	1 μ m	2 nm
Repeatability	NA	NA
Array Plate Relative Alignment		
Parallel (XZ)	0.508mm	0.279mm
Parallel (YZ)	0.508mm	0.152mm
Location (X)	+/-0.127mm	+/-0.076mm

Table 1. Critical Alignment Criteria Satisfaction.

The design described here has been built and tested in prototype form successfully. All drive systems move smoothly and with the tolerances, resolutions, and repeatability required. Presently four complete systems (8 tanks total) are being constructed and should be ready for installation in the FNAL Tevatron during the 1993 shutdown.

IV. ACKNOWLEDGMENTS

The author would like to thank the following FNAL personnel who contributed to the design and construction of the Tevatron bunched beam stochastic cooling mechanical tank system: L. Brown, R. Brown, J. Budlong, D. Cobb, C. Foster, H. Gusler, R. Joseph, H. Landers, N. Lesniewski, J. Misek, D. Poll, D. Snee, M. Tarkowski, and G. Waver.

V. REFERENCES

- [1] G. Jackson, et al., "Bunched Beam Stochastic Cooling in the Fermilab Tevatron Collider," these proceedings.
- [2] Burleigh Instruments, Inc. Burleigh Park, Fishers, New York 14453.

Design Study of Laser Compton Scattering with Relativistic Electron to Measure the Electron Beam Energy*

Ian Hsu, Hone-Cheng Chen, Chen-Lien Cho, and Yuen-Chung Liu*

*Institute of Nuclear Science, National Tsing-Hua University and
Synchrotron Radiation Research Center
Hsinchu, Taiwan 30043, R.O.C.*

Abstract

This paper presents the design study of a system to measure the electron beam energy in an accelerator. The method of Compton scattering between laser photons and relativistic electrons was used. By knowing the backscattered photon energy, the electron beam energy can be deduced. The scattering mechanism between the laser photons and the relativistic electrons was well known. The optical system for the laser light was design to match the laser beam with the electron beam in order to enhance the backscattered photon flux. The implementation of the system in the electron beam transport line in SRRC and the optimization method will be discussed. A CO₂ laser was chosen to produce 3 MeV backscattered photons that will be detected with a high purity germanium detector(HPGe). The reason of using HPGe and the predicted results will be presented. Under this study, a 0.5 % energy measurement accuracy was expected.

I. INTRODUCTION

Compton backscattering of the laser light from relativistic electrons can produce quasi-monochromatic photon beam. The energetic photon beam can be used for the investigation of photonuclear reaction, the calibration of the detectors, and electron beam diagnostics^[1]. Here we use the method of Compton scattering and design a system to measure the electron beam energy.

II. THEORY

The kinematics associated with the scattering is discussed by many papers. The process is shown in fig.1.



fig. 1 The schematic drawing of the process of Compton scattering

The scattered photon energy k_2 from laser photons of energy k_1 in lab. frame is ^[2]

$$k_2 = \frac{k_1(1 - \beta \cos \theta_1)}{1 - \beta \cos \theta_2 + k_1(1 - \cos \chi)/E_e} \quad (1)$$

and can also be expressed as

$$k_2 = \frac{4\gamma^2 k_1}{1 + \frac{4k_1^2}{m^2} + \gamma^2 \theta^2} \quad (2)$$

where $\chi = \theta_2 - \theta_1$, $\beta = v/c$ with v and c the velocities of the electron and the laser light, θ is the angle between the laser and the scattered photons, and E_e is the electron energy. The Klein-Nishina formula shows the differential cross section $d\sigma$ for the head on collision, after the Lorentz transformation, is rewritten as ^[3]

$$d\sigma = \frac{\pi r_0^2}{2} \frac{m^2}{k_1 E_e} \left[\frac{m^4}{4k_1^2 E_e^2} \left(\frac{k_2}{E_e - k_2} \right)^2 - \frac{m^2}{k_1 E_e} \left(\frac{k_2}{E_e - k_2} \right) + \frac{E_e - k_2}{E_e} + \frac{E_e}{E_e - k_2} \right] dk_2 \quad (3)$$

where r_0 is the classical electron radius, and m is the electron rest mass. The photon yield Y per pulse is given by

$$Y = \frac{2N_e N_p \sigma d}{A c \tau} \quad (4)$$

where N_e and N_p are the number of electrons and laser photons per pulse, d is the average interaction length, A is the larger one of the transverse beam size of the electron beam and the laser beam, and τ is the shorter one of the pulse length of the electron beam and the laser beam. σ is the total cross section of photons and electrons.

III. SYSTEM DESIGN

The system was designed to induce the Compton scattering effect and to measure the backscattered photon energy. A pulsed CO₂ laser with high peak power was chosen to produce the backscattered photons with maximum energy 3.03 MeV and to match the repetition rate of electron beam in transport line of SRRC. The schematic drawing of the whole system was shown in fig. 2.

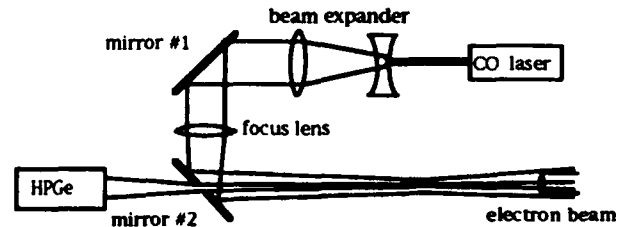


fig. 2 The designed experimental setup

A. Optical System

The laser beam was designed to pass a beam expander, a mirror, a focus lens, and a mirror with a hole. The hole was there to clear the path of the backscattered

photons to the detector. We chose a suitable expanded beam size to decrease the laser beam loss due to the hole on the second mirror. An expander with suitable expanding rate was chosen to increase the backscattered photon number. After a series of calculation, the functional dependents of the laser beam size at different location $w(z)$ on the focal length and the location of the focus lens is shown below.

$$w = \sqrt{\frac{A^2 + (Az + B)^2 \frac{\lambda^2}{\pi^2 w_0^4}}{[A \times (Cz + D) - (Az + B) \times C] \frac{1}{w_0^2}}} \quad (5)$$

where w is the laser beam size, A, B, C, D are the values of the entries of the transformation matrix (also called as ABCD matrix) of the system which we are considering. λ is the laser wavelength, w_0 is the original laser beam waist, and z is the longitudinal position with origin at the location of the focus lens. The dependent of the focal length and the location of the focus lens are through the ABCD and the z . The comparison of the laser beam size change for different focal lengths was shown in fig.3.

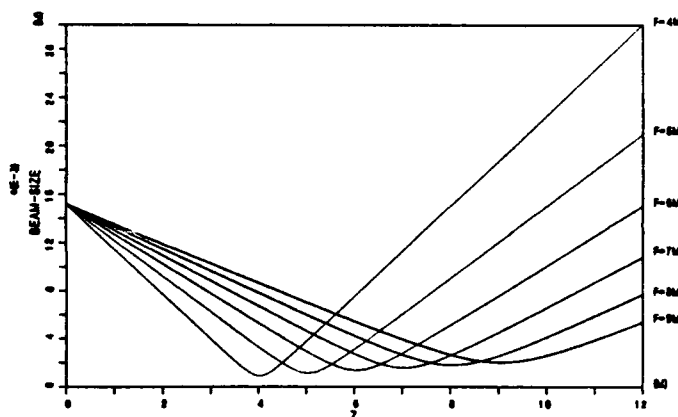


fig. 3 laser beam size vs. longitudinal location z

For the beam profile change of the Gaussian beam and the effect of the hole on the mirror, we correct eq. (4) to

$$Y = \frac{2P\sigma N_e}{k_1 c} \int_{z_1}^{z_2} \left(\bar{A} - \frac{A_h}{A_e} \right) \frac{dz}{\pi w^2} \quad (6)$$

where P is the power of the laser light, σ is the total cross section of Compton scattering, w is the radius of the laser light. A_h is the transverse beam size of the lost laser beam which was due to the hole on the mirror #2 and A_e is that of the electron beam. \bar{A} is the smaller one of 1 and A_l/A_e , where A_l is the transverse beam size of the laser beam, and z_1 to z_2 is the interaction region of the laser beam and the electron beam. The 3D plot of the photon yield vs. the expanding rate of the expander and the focal length of the focus lens was shown in fig. 4. The optimum condition was chosen as that the expanding rate is triple and focal length is 6 meter.

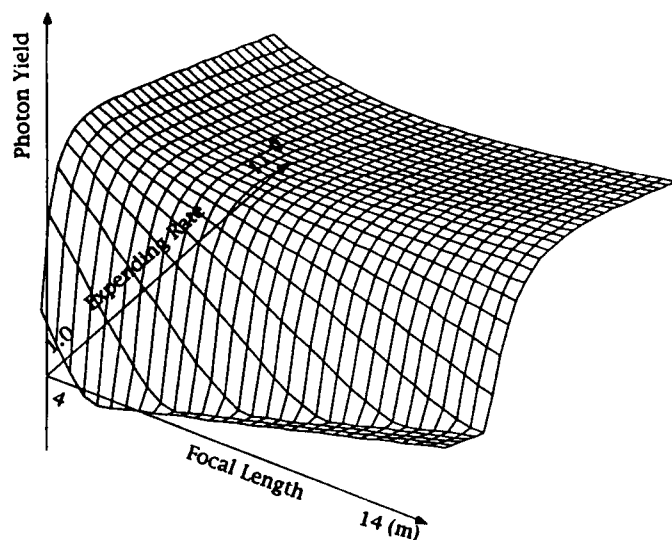


fig. 4 Photon yield vs. the expanding rate and the focal length

B. Detection System

The detection techniques of high energy photon of 1 MeV order of magnitude is universally applied. The coaxial HPGe detector was chosen for the reason of good detector resolution, therefore increasing the accuracy of the beam energy measurement. However at the same time, the detection efficiency of the coaxial HPGe is lower than that of other types. The definition of the intrinsic efficiency of HPGe is

$$\epsilon_{int} = \frac{\text{detected_photon_number}}{\text{photon_number_into_the_detector}} \quad (7)$$

rewrite as

$$\epsilon_{int} = \epsilon \times \frac{A}{A_a} \quad (8)$$

where ϵ is the absolute efficiency of HPGe, A and A_a are the area of source to detector sphere and the HPGe front surface respectively. The empirical formula of relative efficiency of HPGe was shown as [4]

$$\begin{aligned} \log \epsilon &= \text{const.} + S \log E + C(\log E)^2 \\ S &= a \log(V_{ac}) + b \end{aligned} \quad (9)$$

where E is the gamma ray energy, $a=0.6246$, $b=-2.136$, V_{ac} is the active volume of HPGe, S is the slope of the efficiency curve, and $C(\log E)^2$ is the second order corrected term. The empirical formula is useful in the range up to 3.55 MeV. By those theoretical calculations, we plotted the scattered photon energy vs. photon number as shown in fig. 5. Finally we can estimate the detected backscattered photon number by taking the detector efficiency into account.

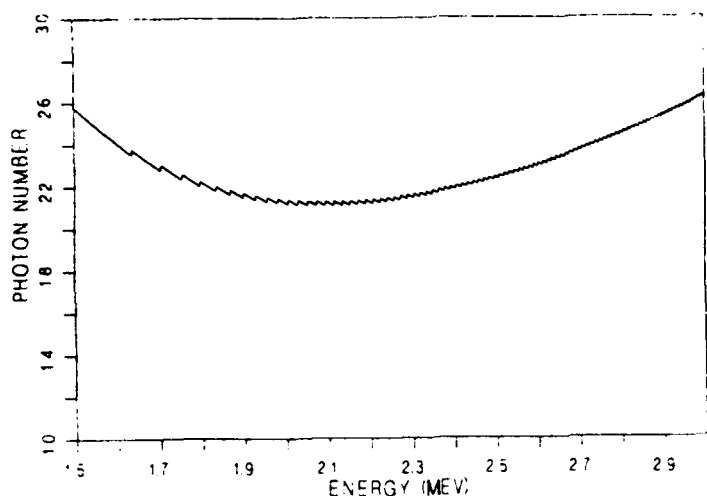


fig. 5 Theoretical results of scattered photon energy vs. photon number.

C.. Error Analysis

In our study, we take the effects of the electron beam energy spread ΔE_e , the line broadening of CO₂ laser Δk_1 , and the resolution of HPGe, Res , into account to predict the backscattered photon energy spread Δk_2 by the square root sum :

$$\frac{\Delta k_2}{k_2} = \sqrt{\left(\frac{2\Delta E_e}{E_e}\right)^2 + \left(\frac{\Delta k_1}{k_1}\right)^2 + (Res)^2} \quad (10)$$

The calculated value of the backscattered photon energy spread at 3.03 MeV is 0.5%.

The energy uncertainty of the 1.3 GeV electron beam is to be 0.25%.

IV. DISCUSSION

During these studies, we simplified the condition of the processes. The above results are under the following assumptions :

- (1) The electron beam moves in the center of the orbit.
- (2) The alignment of the laser beam to the electron beam was well done.
- (3) The effect of the electron beam divergence was not taken into account because the scattered photon energy of the non-head-on collision is smaller than that of the head-on collision. Therefore, the electron beam divergence will cause the decrease of the maximum energy photon number. The result is that the sharpness of the maximum energy spectrum will become dull.

V. REFERENCE

- [1] R. Rossmanith and R. Schmidt, Laser Diagnostics in High Energy Accelerators, *DESY M-81/24* (1981)
- [2] T. Yamazaki, et al., Generation of Quasimonochromatiz Photon Beams from Compton Backscattered Laser Light at ETL Electron Storage Ring. *IEEE Trans. Nucl. Sci.* 32 (1985) 3406-3408
- [3] F. R. Arutyuanin and V. A. Tumanian, The Compton Effect on Relativistic Electrons and the Possibility of Obtaining High Energy Beams, *Phys. Lett.* 1 April (1963) 176-178
- [4] Cao Zhong, Empirical Relation between Efficiency and Volume of HPGe Detectors, *Nucl. Instr. and Meth.* A262(1987) 439-440

*Supported by the National Science Council of ROC, Contract NSC 81-0417-E-007-545 and SRRC, ROC.

Department of Physics, National Tsing-Hua University, Hsinchu, Taiwan 30043, ROC

Transverse Beam Impedance Measurement. A New Coaxial Method.

Michele Cardito, Giuseppe Di Massa*, Francesca Galluccio, Roberto Losito,
Maria Rosaria Masullo, Vittorio G. Vaccaro

Istituto Nazionale di Fisica Nucleare - sez. di Napoli

Mostra d'Oltremare, Pad. 20 - 80125 Napoli, Italy.

* Dip. Elettrico Univ. della Calabria - 87036 Rende (CS), Italy.

Abstract

Coupling bunch and μ -wave instabilities can strongly affect the beam behavior in cyclic accelerators. Stability conditions depend not only on the beam characteristics, but also on its interactions with the surrounding environment. Transverse coupling impedance and transverse kick are two parameters usually used, in frequency and time domain respectively, to study this kind of interaction. A new procedure of measurements is proposed in order to calculate the transverse impedance.

I. INTRODUCTION

A Φ Factory machine, DAΦNE [1], has been proposed at the National Lab. of INFN of Frascati - Italy- (a general talk is presented elsewhere at this conference). The goal of this accelerator is to reach a luminosity of $10^{32} \text{ cm}^{-2} \text{ sec}^{-1}$ at 510 MeV. To achieve this requirement high currents, short bunch lengths, long lifetimes and high stable beam are required. All these requirements are strictly related to the design of the whole machine and they can be affected by intrabeam scattering, μ -wave instabilities, coupled bunch instabilities, whose thresholds are linked to the vacuum chamber geometry, to RF cavity properties depending on the interaction of the bunch with the surrounding structure (coupling). A problem of great importance is to keep both longitudinal and transverse machine impedances at a low value. This means that all the accelerator components like kickers, bellows, etc. that can give a big contribution to the total impedance, have to be carefully designed and tested before the installation. From this the necessity of a laboratory method to measure impedance follows, which has to be used as a feedback on the design of the machine elements.

We propose to use the coaxial wire method [2] instead of the frequency perturbation one [3], because of the low quality factor (Q) linked to the low impedance to be measured in our components. The technique transforms the Device Under Test [DUT] in a coaxial line by putting in two wires [4],[5],[6]. In this paper a proper procedure has been developed in order to deembed the transverse impedance due to the DUT.

II. IMPEDANCE CALCULATION

The measurement is performed by means of a two-wire transmission line located on the axis of the beam. The line has a resistance R_0 , an inductance L_0 and a capacitance C_0 per unit length. The device under test (DUT), by means of the coupling, produces an extra term $\zeta = R + jX$, so that the propagation constant of the line becomes

$$k_d = \sqrt{(\omega L_0 - jR_0 - j\zeta) \omega C_0} \quad (1).$$

As a consequence, the scattering parameter, referred to the characteristic impedance of the line, becomes:

$$S_{12}^{\text{od}} = \exp(-j k_d L) \quad (2)$$

where L is the total length of the line.

If the same measurement is performed replacing the DUT with a smooth pipe of uniform cross section, the scattering parameter becomes:

$$S_{12}^{\text{or}} = \exp(-j k_r L) \quad (3).$$

where

$$k_r = \sqrt{(\omega L_0 - jR_0) \omega C_0} \quad (4).$$

If the distributed impedance ζ , induced by the device, is small compared to the quantity $(R_0 + j\omega L_0)$, we may linearize the propagation constant k_d as a function of ζ and get

$$S_{12}^{\text{od}} / S_{12}^{\text{or}} = \exp(-\zeta L / 2 Z_0) \quad (5).$$

where the characteristic impedance Z_0 is

$$Z_0 = \sqrt{\frac{(R_0 + j\omega L_0)}{j\omega C_0}} \quad (6).$$

Finally the transverse impedance is

$$Z_T = 2 \frac{c}{\omega} \frac{Z_0}{\Delta^2} \ln(S_{12}^{\text{or}} / S_{12}^{\text{od}}) \quad (7).$$

where Δ is the distance between the two wire centers of the line.

III. THE MEASURING TECHNIQUE PHILOSOPHY

Allowing for the scattering matrix S , we see, according to its definition, that this quantity is a function of a reference impedance Z_c :

$$S = (Z - Z_c I)(Z + Z_c I)^{-1} \quad (8).$$

This can be better seen, in the case of a symmetrical device, from the expression of the scattering parameters as a function of the hybrid parameters:

$$S_{12} = \left[\frac{h_{12}}{2Z_c} \left(1 - \frac{Z_c}{Z_0} \right)^2 + h_{11} + j\sqrt{1 - h_{11}^2} \right]^{-1} \quad (9)$$

$$S_{11} = S_{22} = \frac{h_{12}}{2Z_0} \left[1 - \left(\frac{Z_c}{Z_0} \right)^2 \right] S_{12} \quad (10).$$

Most measuring devices give the values of the scattering parameters calculated on the basis of the equations (9) and (10) with $Z_c = 50 \Omega$.

On the other hand, if the value of Z_c can be set equal to the characteristic impedance Z_0 of the two wire transmission line, then the scattering parameters take the form

$$S_{12}^0 = h_{11} - j \sqrt{1 - h_{11}^2} \quad (11)$$

$$S_{11}^0 = S_{22}^0 = 0 \quad (12)$$

In this case, and only in this case, the scattering parameter S_{12}^0 can be correctly interpreted as the phasor $\exp(-j\theta)$, whose complex angle is the phase lag and the attenuation of a progressive wave along the wires (see eqs. 2,3).

In order to measure correctly the scattering parameters, we adopt the following procedure:

- i) we measure the entire scattering matrix S^c for a configuration formed by the two spacers, directly connected, and the two adaptors, as depicted in figure (1a);
- ii) we measure the entire scattering matrix S for a configuration formed by the device, two spacers and two adaptors, as depicted in figure (1b).

It has been shown [7] that the scattering parameter S_{12}^0 referred to the characteristic impedance Z_0 can be calculated according to the formula

$$S_{12}^0 = \frac{1}{2S_{12}^c S_{12}} \left\{ \frac{1}{2} (|S^c L - L S| - |S^c - S|) + \right. \\ \left. - j \sqrt{|S^c L - L S| |S^c - S|} \right\} \quad (13),$$

where L is $\begin{pmatrix} 1 & 0 \\ 0 & -1 \end{pmatrix}$

Applying this procedure to both the device under test and the reference pipe, we may obtain S_{12}^{od} and S_{12}^{or} by plugging in eq. (13) S^d and S^r respectively. Finally resorting to eq. (7), we get an accurate evaluation of the transverse impedance. Conversely, errors could arise, if one adopts the standard procedure, namely using eq. (9).

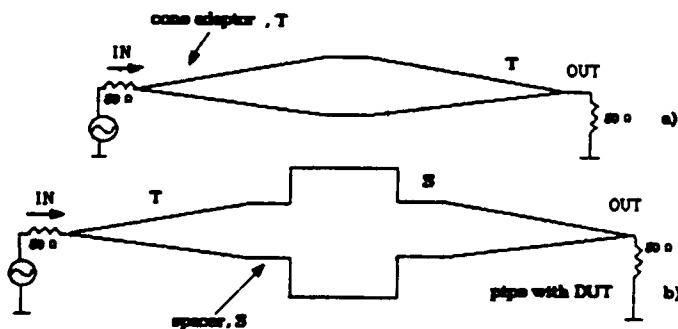


Figure 1. Schematic diagram of experimental set-up: a) cone adaptors; b) test structure.

IV. EXPERIMENTAL RESULTS

The measurements were performed on a Accumulator kicker prototype 90 cm long and with a diameter of 20 cm (fig.2). The pipe used for the spacers (5 cm each) has an elliptical shape, as the real vacuum chamber will have, with two semiaxis of 5.2 cm and 1.75 cm respectively. Two cones, 50 cm long, have been used to slowly match the elliptical tube to the N connectors on both ends. Two 1 mm wires, spaced 10 mm, were stretched in the tube center. An elliptical tube, same spacer shape, of a total length equal to the kicker plus the two spacers has been used as reference pipe inserted between the tapers.

For the data acquisition and for the remote control of the instrumentation an Hp 9000/300 computer has been used connected to the measurement system (Network Analyzer (N.A.), Sweep Oscil., etc.) through an Hp-IP bus. Transmission measurements have been performed in the frequency range between 1 and 500 MHz.

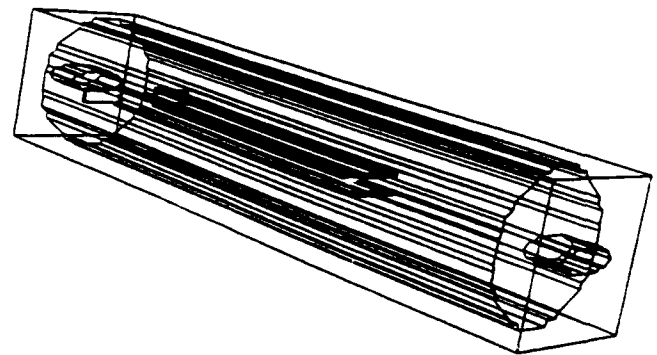


Figure 2. Accumulator kicker

The transverse impedance, calculated by means of the present procedure is reported under fig. (3), while the one calculated by means of the standard method is reported in fig. (4). Comparing the two results the following comments are in order:

a) the resonances appearing in fig. (3) are those foreseen from numerical simulation; however the spike close to 330 MHz cannot be explained. We have reasons to believe that this arises from the ambiguity in the numerical calculations in the square root in eq.(13).

b) the coupling resistance, calculated by means of the present procedure, is positive except in a very small frequency range (see above), while the one calculated by the standard methods exhibits negative values in wide range of frequencies;

c) the discrepancy is even more relevant when we calculate the transverse kick, where the resistance is weighted by the inverse of frequency, as the value is wrong at low frequencies.

d) from the FFT analysis, shown in fig. (5), we learn that the multiple reflections have been largely suppressed.

Finally it has to be pointed out that the goodness of the results is very sensitive to the matching of the feeding line to the adaptors, as the large amount of experimental data has shown. The results are even better if the matching is done by

means of a resistive lumped circuit, improving in this way the signal-noise ratio by reducing the contribution of multiple reflections.

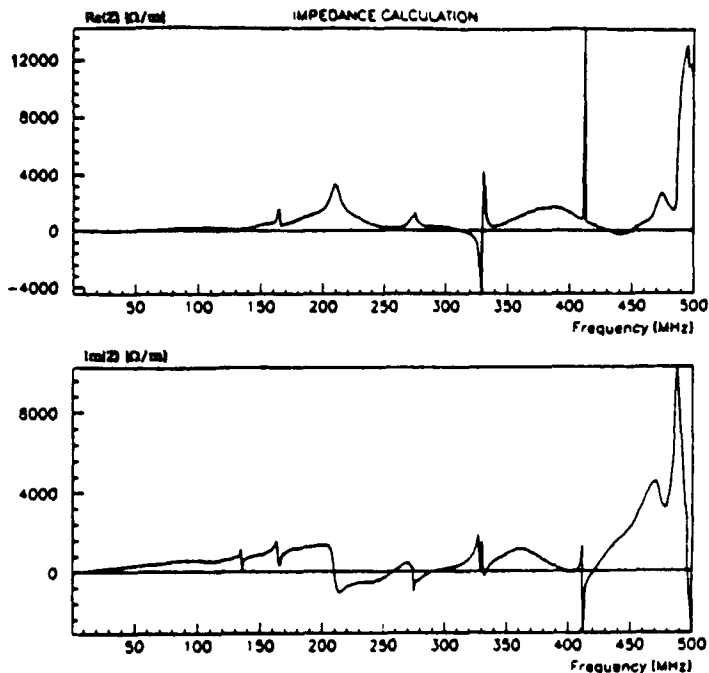


Figure 3. Transverse impedance calculated by present method.

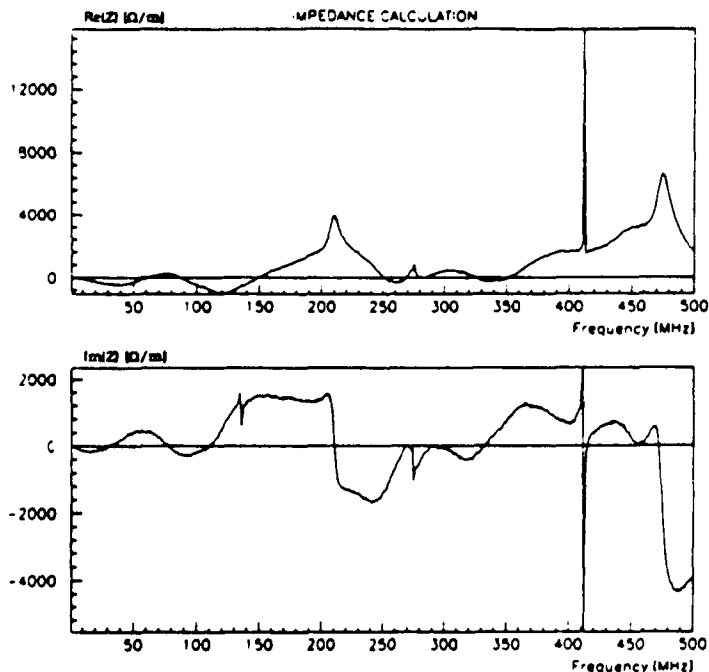


Figure 4. Transverse impedance calculated by standard method.

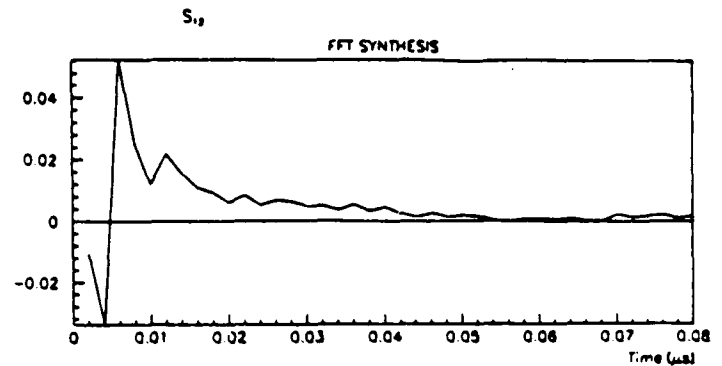


Figure 5. Time domain FFT of the kicker transmission coefficient calculated by present method.

Table (1) shows the values of the transverse kick [8] calculated from the measurements obtained with the present method and the ones produced by computer simulations [9], for different bunch lengths σ . The agreement looks interesting.

σ [cm]	4	6	8	12
k (exp.) [V/pCm]	12.27	11.20	9.96	7.50
k (sim.) [V/pCm]	16.95	11.88	9.26	6.40

Table 1. The transverse kick. Comparison between measured data and numerical simulations.

V. REFERENCES

- [1] *PROPOSAL FOR A Φ -FACTORY*, LNF-90/031(R), Frascati, Italy, 1990.
- [2] M. Sands, J. Rees: "A bench measurement of the energy loss of a stored beam to a cavity", PEP-95, 1974.
- [3] L.C. Maier, J.C. Slater, "Field strength measurements in resonant cavities", *Journal of Applied Physics*, Vol. 23, pp.68, 1952.
- [4] F. Caspers: "Beam impedance measurement by wire method using a synthetic pulse technique", *IEEE Trans. Nucl. Science*, vol. NS-32, pp. 1914, 1985.
- [5] L.S. Walling, D.E. McMurry, D.V. Neuffer, H.A. Thiessen, "Transmission-line impedance measurements for an advanced hadron facility", *Nuclear Instruments and Methods in P.R.*, A281, pp. 433-447, 1989.
- [6] G. Di Massa, M.R. Masullo, "Beam impedance measurements using a synthetic pulse technique", in *EPAC European Particle Accelerator Conference*, Nice, France, June 1990.
- [7] V. G. Vaccaro: Private communication.
- [8] L. Palumbo, V.G. Vaccaro, "Wake field measurements", LNF Report 89/035 (P), May 1989.
- [9] The Mafia collaboration, "MAFIA User Guide", Desy Report, May 1988.

A Novel Method of Noise Suppression in Beam Transfer Function Measurements

F. Caspers, M. Chanel, U. Oeftiger
CERN, CH-1211 Geneva 23

Abstract

Beam transfer functions (BTF), giving the frequency domain response of the beam to an external excitation, are widely used to measure the impedance of the beam environment, to analyse stability conditions and to determine the true momentum distribution in spite of strong signal shielding in dense, cooled beams. A problem encountered in low intensity (antiproton and rare ion) storage rings is the unwanted noise on the BTF signal.

We have developed a method of noise suppression which may be viewed as gating in time domain: Transforming (by software) the BTF into time domain, cutting off the tail after the response decayed and going back into frequency space we obtain a significantly cleaner signal. The tail of the time response contains information on beam and system noise which can be treated separately. Results obtained on the low energy antiproton ring LEAR are discussed.

I. THE TIME GATING TECHNIQUE

A. The time gating technique and its application to BTF measurements

Definitions:

- $A(t)$ = digitized time trace containing the excitation signal
- $B(t)$ = digitized time trace containing the beam response signal
- $B_{corr}(t)$ = part of the beam response, which is correlated to the excitation signal
- $B_{nosc}(t)$ = part of the beam response, which is not correlated to the excitation signal
- $\tilde{A}(\omega)$ = discrete (complex) Fourier transform of $A(t)$ [1]

The fast Fourier transformer, which is used here to measure the frequency response of the beam to a band-limited noise excitation, digitizes the two time traces $A(t)$ and $B(t)$. The two data sets are then Fourier transformed into frequency domain and the ratio

$$S(\omega) = \frac{\tilde{B}(\omega)}{\tilde{A}(\omega)}$$

is displayed as the frequency response function [2] (Fig. 1). The beam response consists of a signal contribution $B_{corr}(t)$, which is correlated to the excitation and which represents the BTF proper, and of non-correlated signal contributions $B_{nosc}(t)$, which are due to noise. The measurement data $S(\omega)$ can be transformed back into time domain by a software implemented inverse Fourier transform:

$$\tilde{S}^{-1}(t) = \frac{\tilde{B}_{corr}(t)}{\tilde{A}(t)} + \frac{\tilde{B}_{nosc}(t)}{\tilde{A}(t)}$$

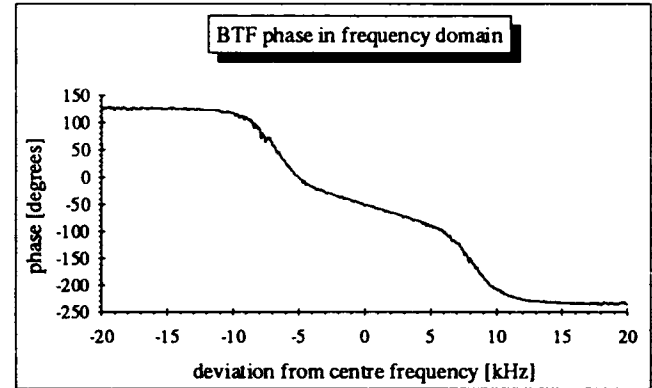
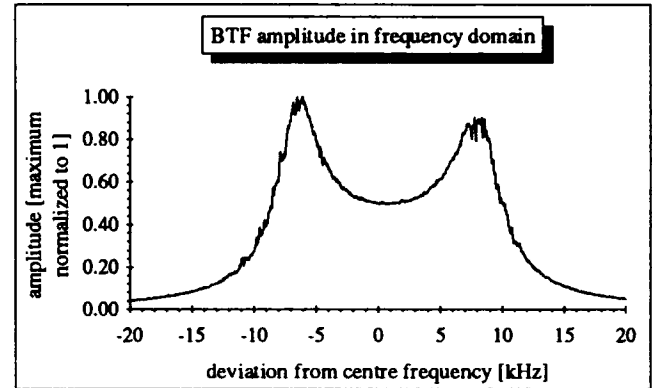


Figure 1. $S(\omega)$ of a longitudinal BTF measurement with a coasting beam of $7.6 \cdot 10^9$ protons at 200 MeV/c in LEAR, revolution frequency = 0.796 MHz, centre frequency = 42.17 MHz, $(\Delta p/p)_{FWHM} = 1.6 \cdot 10^{-4}$

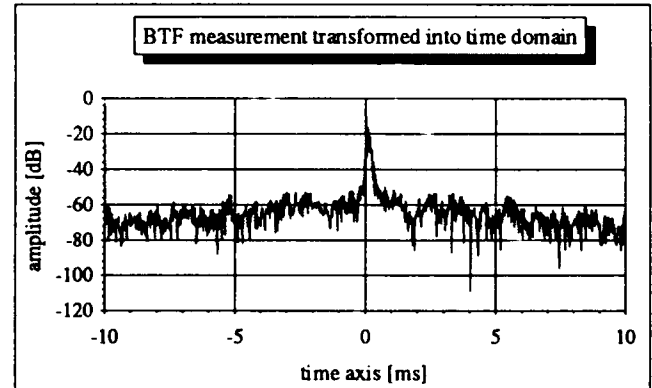


Figure 2. The inverse Fourier transform of the BTF represents the beam response to an impulse excitation.

In time domain the correlated part of the signal represents the response of the beam to an impulse excitation. For the damped system this response decays rapidly, whereas the non-correlated part is distributed over the whole time interval (Fig. 2).

It is possible to separate the two signal contributions by applying a weighting function to the data in time domain [3]. This procedure, which is used to leave the information included in a specified time interval unchanged and which suppresses signal contributions outside this time window, is called time gating. By applying a weighting function with a special shape (Hanning window) one avoids unwanted weighting effects, which are due to discontinuities at the borders of the time gate. This technique is implemented in certain network analysers and frequently used to separate and suppress reflection contributions from the required signal [4],[5],[6].

B. Suppression of the non-correlated signal contributions

Once the time interval including the correlated information is established and the time gating is performed (Fig. 3), the Fourier transform into frequency domain leads to a significantly cleaner BTF signal (Fig. 4):

$$S_{gated}^{corr}(\omega) \approx \frac{\bar{B}_{corr}(\omega)}{\bar{A}(\omega)} \equiv BTF$$

C. Analysis of the non-correlated signal

It is also possible to suppress the correlated information included in the specified time interval. The remaining non-correlated signal can be Fourier transformed to analyse its frequency domain behavior.

The resulting spectrum consists of noise from the electronics and most importantly in the present case from the beam itself, divided by the amplitude of the excitation signal. If the power of the exciting signal is constant over the frequency range of the measurement, this signal represents the Schottky signal, that would have been observed without exciting the beam:

$$|S_{gated}^{nonc}(\omega)| \approx \frac{|\bar{B}_{nonc}(\omega)|}{|\bar{A}(\omega)|} \equiv \text{Schottky power spectrum}$$

Direct Schottky measurements using a spectrum analyser are often done just before or after a BTF measurement, because the knowledge of both makes it possible to calculate the coupling impedance of the beam with its environment and to reconstruct the true momentum distribution [7],[8]. The comparison of the Schottky-like signal with the Schottky measurement is a tool to check, if the cooling (electron or stochastic) of the beam was in an equilibrium state during both measurements and to optimize the excitation strength for the BTF measurement.

Fig. 5 gives the stability diagrams derived from the longitudinal BTF data either directly smoothed in frequency

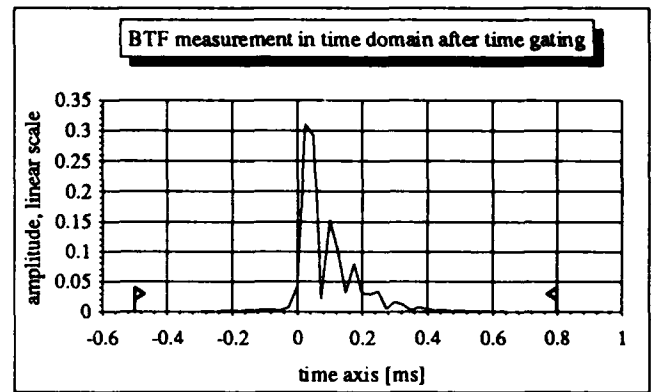


Figure 3. In time domain an interval can be specified, in which the coherent response is present. The information outside - which is due to noise - is suppressed. This procedure is called time gating.

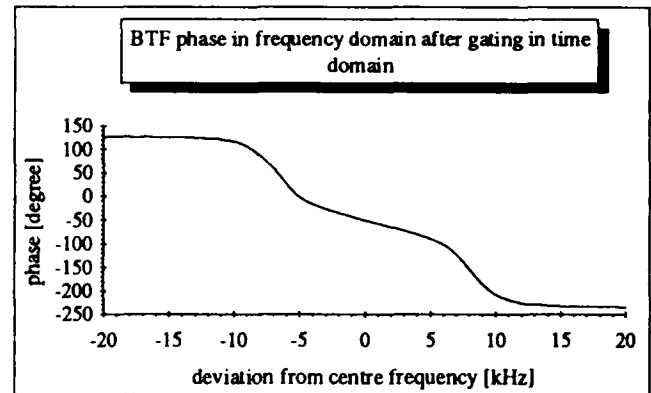
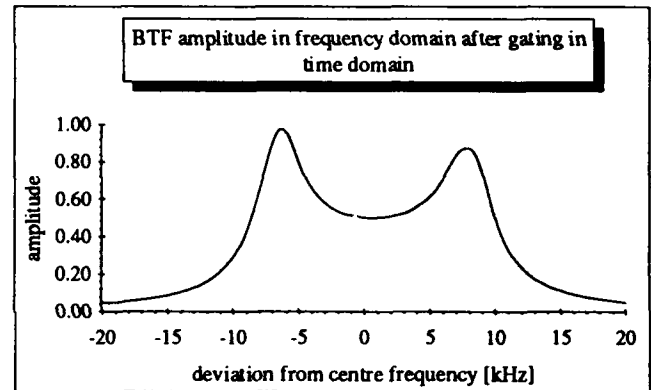


Figure 4. Gating in time domain and transforming back into frequency domain leads to a significantly cleaner BTF. Analysis of the signal outside the time gated range shows that its main contribution is due to beam Schottky noise.

domain or cleaned by time gating. One notes the difference near the "shaft" of the stability curve. In many situations beam stability is highly sensitive to this shaft region, which is obtained with higher accuracy by gating out the noise on the BTF. To avoid unwanted weighting effects in this region the width of the time gate has to be large compared to the damping time τ of the beam response (typically 10τ).

II. CONCLUSION

The application of the time gating technique allows an efficient separation of the BTF signal from noise.

The suppression of the beam Schottky noise is of great importance. Using time gating, the BTF excitation strength can be decreased, measurements can be performed with beams of lower intensity, and the stability conditions of the beam can be determined with high precision.

By comparing the Schottky-like non-correlated signal contribution with a normal Schottky measurement, the excitation strength can be controlled.

Apart from the narrow band measurements, broad band BTF data from the CERN antiproton machines have been cleaned using the time gating technique to adjust e.g. the stochastic cooling systems.

III. ACKNOWLEDGEMENTS

We would like to thank J. C. Perrier and D. Williams for the development of the hardware and D. Möhl for numerous discussions.

IV. REFERENCES

- [1] Robert A. Witte: "Spectrum and Network Measurements", Prentice Hall, Inc., New Jersey 1991 (ISBN 0-13-826959-9)
- [2] Takeda Riken Company: "TR 9405, Performance and Feature of Digital Spectrum Analyzer", Application Note No. 4-2E
- [3] U. Oeftiger and F. Caspers: "Gating in time domain as a tool for improving the signal-to-noise-ratio of beam transfer function measurements", CERN Internal Note 1992, PS/AR/NOTE 92-19,
- [4] C. Offelli and D. Petri: "Weighting Effect on the Discrete Time Fourier Transform of Noisy Signals", *IEEE Trans. Instrum. and Meas.*, IM 40, No. 6, Dec. 1991, pp. 972-981
- [5] O. M. Solomon, Jr.: "The Effect of Windowing and Quantization Error on the Amplitude of Frequency-Domain Functions", *IEEE Trans. Instrum. and Meas.*, IM 41, No. 6, December 1992, pp. 932-937
- [6] Hewlett and Packard Company: "HP 8753 B Network Analyzer, System Operating and Programming Manual", HP Part Number 08753-90122
- [7] U. Oeftiger: "Measurements of Beam Properties and Beam Environment in LEAR and COSY using RF Excitation Methods", Thesis to be published
- [8] J. Bosser, M. Chanel, R. Ley, D. Möhl, U. Oeftiger, G. Tranquille: "Electron Beam Cooling and Beam Instability Studies at LEAR", *Proceedings of Workshop on Heavy Ion Storage and Cooler Rings*, Smolenice, June 1st-5th, 1992, to be published, preprint CERN/PS 92-45 (AR)

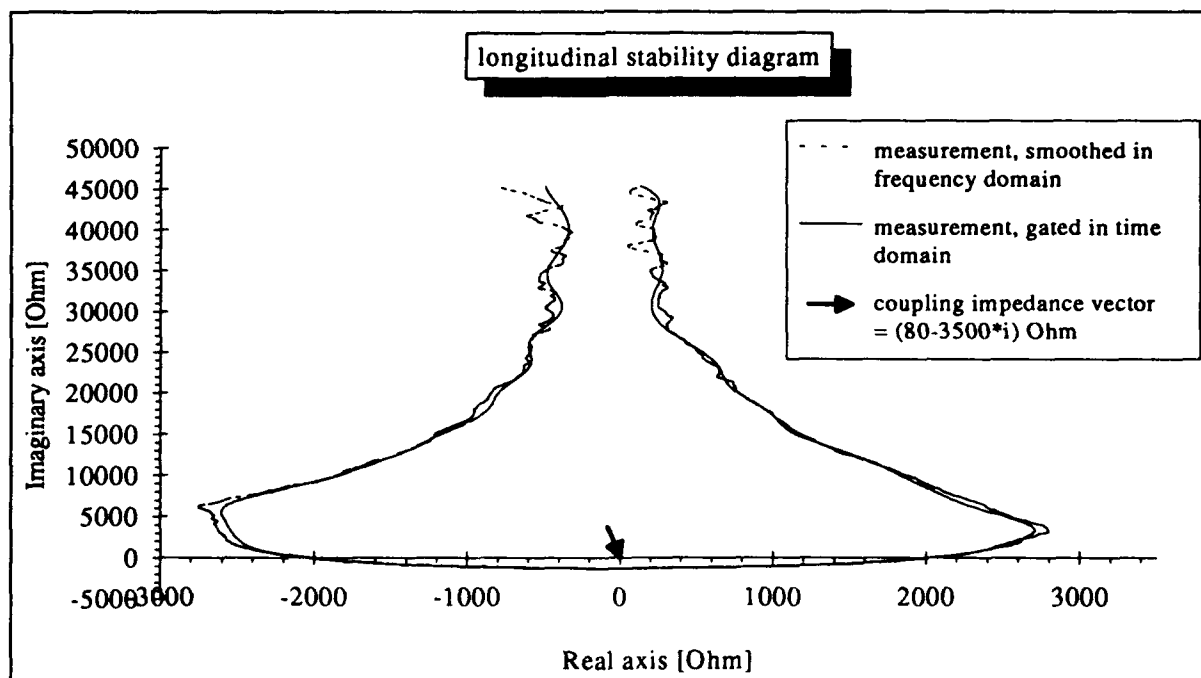


Figure 5. In this "stability diagram" the beam response of figure 1 and figure 4 is shown in the complex plane rather than in an amplitude and phase diagram. The effect of time gating becomes important at low particle numbers and low excitation strength.

Beam Dispersion Measurements with Wire Scanners in the SLC Final Focus Systems*

P. Emma, D. McCormick, M.C. Ross
Stanford Linear Accelerator Center
Stanford, California 94309

ABSTRACT

A method is described to make a direct measurement of the horizontal and vertical momentum dispersion of the electron and positron beams as they pass through the chromatic correction sections (CCS) of the SLC final focus systems. The method is advantageous since it cleanly separates betatron components of the beam size from dispersive components, can be measured during standard colliding beams machine conditions in a minute or two, and directly measures the energy-position correlation within the beam.

I. INTRODUCTION

A dispersion measurement in circular accelerators usually requires sampling an off-energy orbit with beam position monitors. The cyclic boundary conditions provide a closed dispersion function which is measurable by observing the beam centroid. In linear colliders, however, varying the beam energy at some point in the beam line and observing downstream beam centroid positions measures the position/energy transfer matrix element (e.g. R_{16}) from the point of energy change to the orbit observation point. If a dispersion source exists upstream of the energy variation point, its contribution to the total dispersion function will not be measured. Since it is usually important to remove all energy-position correlations to minimize the transverse beam size, a beam centroid based correction technique as used in circular machines may not fully correct the total beam dispersion. Furthermore, other sources of beam energy spread (e.g. synchrotron radiation in the SLC collider arcs) produce energy-position beam correlations¹ which are not measured with a simple beam centroid observation technique.

In the SLC final focus, residual dispersion at the interaction point (IP) has normally been corrected by varying the beam energy at the end of the linac and setting quadrupoles of the final focus dispersion matching section to cancel the correlated transverse beam motion at the beam position monitors² (BPM). Because of the strong magnification of the sine-like betatron phase in the final focus and the demagnification of the cosine-like phase, the resolution of the angular IP dispersion, η'^* (sine-like), using the BPMs is very good, but the resolution of the spatial IP dispersion, η^* (cosine-like), is very poor. Therefore, η^* is actually corrected by minimizing the IP beam size with closed trajectory bumps in the sextupoles of the CCS, or more recently, with four small CCS correction quadrupoles³. Unfortunately, the BPM method actually corrects the R_{26} transfer matrix element from

linac to IP and the R_{26} is not necessarily equal to the total IP energy-angle correlation, η'^* .

The actual η'^* , and a finite beam energy spread, produces larger angular divergence at the IP (larger beam size at the final triplet) which may increase detector backgrounds through bremsstrahlung of the more intense focusing. In order to compensate for increased detector backgrounds the total divergence must be reduced with upstream final focus beta matching quadrupoles. This divergence reduction has the undesirable effect of increasing the beam size at the IP (increase of β^*). For this reason the actual η'^* must be minimized. Therefore it is useful to find a fast, direct method to measure the energy-position correlations in the beam which are present under normal machine operating conditions.

II. APPLICATION TO THE SLC

The most useful place to measure the total accumulated beam dispersion in the SLC is in the final focus just before the beams are squeezed down to transverse sizes of $\sim 2 \mu\text{m}$. In order to provide separation of betatron beam size components from dispersive components some section with bending is necessary. The nominal bending and optical symmetries of the final focus CCS (Fig 1) are ideal for this purpose.

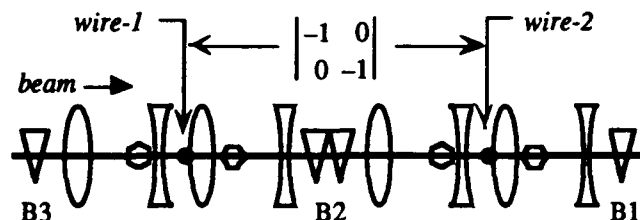


Fig 1. Schematic of the chromatic correction section of the final focus system with wire scanner locations indicated (sextupoles are drawn as hexagons). The interaction point (not shown) is located downstream of bend B1 by a betatron phase advance of π .

Wire scanners at the two points in the CCS where the horizontal dispersion is a maximum are used to compare the beam sizes at these two locations. In order to cancel geometric aberrations, the 4×4 linear transfer matrix between nested sextupole pairs is $-I$. This $-I$ matrix between the first wire scanner (*wire-1* in Fig 1) and second wire scanner (*wire-2*) ensures equal beta functions at the two wires.

$$\beta_{x1} = \beta_{x2} \equiv \beta_x, \quad \beta_{y1} = \beta_{y2} \equiv \beta_y \quad (1)$$

Propagating the horizontal dispersion function from wire-1 to wire-2 yields

$$\eta_{x1} + \eta_{x2} = R_{16} \equiv 2\bar{\eta}_x \quad (2)$$

where the transfer matrix element R_{16} ($=540 \text{ mm}$) from wire-1 to wire-2 is solely defined by the local lattice (B2 horizontal bending dipoles in Fig 1). Similarly, an incoming

* Work supported by Department of Energy contract DE-AC03-76SF00515

mismatched component of the dispersion function, $\Delta\eta$, including all upstream sources of position-energy correlation, will propagate freely through the final focus.

$$\Delta\eta_{x1,y1} = -\Delta\eta_{x2,y2} = \Delta\eta_{x,y} \quad (3)$$

Here $\Delta\eta_{xi,yi}$ is the residual spatial component of the dispersion at wire- i .

These beta and dispersion functions contribute to the beam sizes at the wire scanners in different ways. Writing the transverse position of a particle at each wire location, using the $-I$ matrix between them, and expressing the random fractional energy deviation as $\delta = \delta E/E$ ($=\delta p/p$ for these ultra-relativistic electrons/positrons) yields

$$\begin{aligned} x_1 &= x_\beta + (\bar{\eta}_x + \Delta\eta_x)\delta \\ x_2 &= -x_\beta + (\bar{\eta}_x - \Delta\eta_x)\delta \\ y_1 &= y_\beta + \Delta\eta_y\delta \\ y_2 &= -y_\beta - \Delta\eta_y\delta \end{aligned} \quad (4)$$

where x_β, y_β are betatron position components at wire-1 which reverse sign through the $-I$ transfer to wire-2. These betatron components may also be expressed in terms of the transverse beam emittances, ϵ_x and ϵ_y (all random variables throughout are assumed to have zero mean).

$$\langle x_\beta^2 \rangle = \epsilon_x \beta_x, \quad \langle y_\beta^2 \rangle = \epsilon_y \beta_y \quad (5)$$

Since $\Delta\eta_{x,y}$ includes all position-energy correlations, then by definition x_β and y_β will not be correlated with δ (i.e. $\langle x_\beta \delta \rangle = \langle y_\beta \delta \rangle = 0$). The beam sizes at the wires are then

$$\langle x_1^2 \rangle = \epsilon_x \beta_x + (\bar{\eta}_x^2 + 2\bar{\eta}_x \Delta\eta_x + \Delta\eta_x^2) \langle \delta^2 \rangle, \quad (6)$$

$$\langle x_2^2 \rangle = \epsilon_x \beta_x + (\bar{\eta}_x^2 - 2\bar{\eta}_x \Delta\eta_x + \Delta\eta_x^2) \langle \delta^2 \rangle, \quad (7)$$

$$\langle y_1^2 \rangle = \epsilon_y \beta_y + \Delta\eta_y^2 \langle \delta^2 \rangle = \langle y_2^2 \rangle. \quad (8)$$

From the difference of (6) and (7), and knowledge of the beam energy spread, comes the mismatched component of the horizontal dispersion, $\Delta\eta_x$. However, the vertical beam sizes at wire-1 and wire-2 are always equal (8) since there is no vertical bending between wires. So measurement of the vertical beam profile is not as useful to measure dispersion. The vertical dispersion can, however, be measured by observing the X-Y coupling it generates in the presence of the nominal horizontal dispersion. The X-Y coupling is measured by taking advantage of the 3-wire orientations of the available SLC wire scanners⁴. The best resolution of $\Delta\eta_{x,y}$ is achieved using a horizontal scan direction (given wire orientations on the support fork of Fig 2).

The leftmost wire in Fig 2 (*U-wire*) scans the beam profile along $u = (x + y)/\sqrt{2}$. The rightmost wire (*V-wire*) scans along $v = (x - y)/\sqrt{2}$. All other SLC wire scanner installations are rotated 45 degrees to Fig 2 such that X, Y, and U beam profile scans are made⁴.

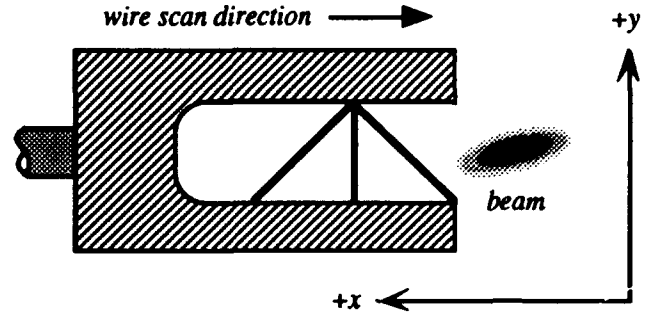


Fig 2. Horizontally installed SLC wire scanner viewed in the beam direction. Leftmost wire is the *U-wire*, center is the *X-wire*, and rightmost is the *V-wire*.

With this horizontal scan direction, the beam profile is measured along the X-axis, as well as the U and V-axis.

$$\langle u^2 \rangle = \frac{1}{2} (\langle x^2 \rangle + \langle y^2 \rangle) + \langle xy \rangle \quad (9)$$

$$\langle v^2 \rangle = \frac{1}{2} (\langle x^2 \rangle + \langle y^2 \rangle) - \langle xy \rangle \quad (10)$$

From (4), the X-Y coupling term at each wire is

$$\langle x_1 y_1 \rangle = \langle x_\beta y_\beta \rangle + \Delta\eta_x \Delta\eta_y \sigma_\delta^2 + \bar{\eta}_x \Delta\eta_y \sigma_\delta^2, \quad (11)$$

$$\langle x_2 y_2 \rangle = \langle x_\beta y_\beta \rangle + \Delta\eta_x \Delta\eta_y \sigma_\delta^2 - \bar{\eta}_x \Delta\eta_y \sigma_\delta^2, \quad (12)$$

with $\langle x_\beta y_\beta \rangle$ as the observable phase of the betatron component of X-Y coupling, and $\sigma_\delta^2 = \langle \delta^2 \rangle$. Using (6) through (12) yields an over determined linear system relating the discernible beam size components to the six measured beam profiles at the two wires.

$$\begin{pmatrix} \sigma_{x1}^2 \\ \sigma_{u1}^2 \\ \sigma_{v1}^2 \\ \sigma_{x2}^2 \\ \sigma_{u2}^2 \\ \sigma_{v2}^2 \end{pmatrix} = \begin{pmatrix} 1 & 1 & 0 & 0 & 0 \\ .5 & .5 & .5 & 1 & 1 \\ .5 & .5 & .5 & -1 & -1 \\ 1 & -1 & 0 & 0 & 0 \\ .5 & -.5 & .5 & 1 & -1 \\ .5 & -.5 & .5 & -1 & 1 \end{pmatrix} \times \begin{pmatrix} \epsilon_x \beta_x + (\bar{\eta}_x^2 + \Delta\eta_x^2) \sigma_\delta^2 \\ 2\bar{\eta}_x \Delta\eta_x \sigma_\delta^2 \\ \epsilon_y \beta_y + \Delta\eta_y^2 \sigma_\delta^2 \\ \langle x_\beta y_\beta \rangle + \Delta\eta_x \Delta\eta_y \sigma_\delta^2 \\ \bar{\eta}_x \Delta\eta_y \sigma_\delta^2 \end{pmatrix} \quad (13)$$

The spatial components of the mismatched dispersion are then

$$\Delta\eta_x = \frac{(2\sigma_{x1}^2 + \sigma_{u1}^2 + \sigma_{v1}^2 - 2\sigma_{x2}^2 - \sigma_{u2}^2 - \sigma_{v2}^2)}{12\bar{\eta}_x \sigma_\delta^2}, \quad (14)$$

$$\Delta\eta_y = \frac{(\sigma_{u1}^2 - \sigma_{v1}^2 - \sigma_{u2}^2 + \sigma_{v2}^2)}{4\bar{\eta}_x \sigma_\delta^2}, \quad (15)$$

where the notation σ^2 has replaced expectation brackets and the energy spread, σ_δ , must be known from other measurements. In practice, a weighted fit using (13) and the measurement errors is employed.

III. RESOLUTION AND ERRORS

For reasons described in the introduction, a tolerance may be specified on η'^* . The present background limited IP divergence, $\hat{\sigma}_\theta$, is 300-350 μrad rms. Given typical SLC IP energy spread, σ_δ , of $\sim 0.2\%$ rms, a tolerance on $|\eta'^*|$ of ≤ 50 mrad limits the related transverse IP beam size increase, σ_{IP}/σ_{IP0} , to $\leq 5\%$.

$$\frac{\sigma_{IP}}{\sigma_{IP0}} = \frac{\hat{\sigma}_\theta}{\sqrt{\hat{\sigma}_\theta^2 - \eta'^*{}^2 \sigma_\delta^2}} \leq 1.05 \quad (16)$$

Due to the $n\pi + \pi/2$ ($n = 1, 2$) betatron phase advance from the CCS wire scanners to the IP, $\Delta\eta_{x,y}$ at wire-1 translates into $\eta'^*_{x,y}$ through the R_{12} ($= -3.2$ m) and R_{34} ($= -1.2$ m) matrix elements from wire-1 to IP.

$$\eta'^*_x = \frac{\Delta\eta_x}{R_{12}}, \quad \eta'^*_y = \frac{\Delta\eta_y}{R_{34}} \quad (17)$$

The resolution of the IP angular dispersion from (14), (15), and (17) is

$$\sigma_{\eta'_x} = \frac{\sigma_R \sqrt{4\sigma_x^2 + \sigma_u^2 + \sigma_v^2}}{3\sqrt{2} R_{12} \bar{\eta}_x \sigma_\delta^2}, \quad (18)$$

$$\sigma_{\eta'_y} = \frac{\sigma_R \sqrt{\sigma_u^2 + \sigma_v^2}}{\sqrt{2} R_{34} \bar{\eta}_x \sigma_\delta^2}, \quad (19)$$

with σ_R as the CCS wire scanner instrumental resolution (~ 50 μm), and σ_x , σ_u , and σ_v as the measured beam profiles at the wires (in this case assumed equal at both wires for simplicity). From the approximate SLC CCS beam parameters

$$\begin{aligned} \beta_x &= 2000 \text{ m} & \beta_y &= 300 \text{ m} \\ \epsilon_x &= 600 \mu\text{m}\cdot\mu\text{rad} & \epsilon_y &= 400 \mu\text{m}\cdot\mu\text{rad} \\ \sigma_\delta &= 0.2 \% & \sigma_x &= 1.2 \text{ mm} \\ \sigma_u &= \sigma_v = 0.9 \text{ mm} & \bar{\eta}_x &= 270 \text{ mm} \end{aligned} \quad (20)$$

and assuming matched conditions and no large betatron X-Y coupling, the resolutions from (18) and (19) are

$$\begin{aligned} \sigma_{\eta'_x} &= 9 \text{ mrad} (< 50 \text{ mrad}), \\ \sigma_{\eta'_y} &= 35 \text{ mrad} (< 50 \text{ mrad}). \end{aligned} \quad (21)$$

The horizontal dispersion resolution is more than sufficient, however the vertical resolution is just adequate. Allowing for poorly matched conditions, coupling, and reasonably larger emittances produces resolutions which may increase by up to a factor of 2. Several repeated measurements, as the matching is improved, may be necessary in this case.

A systematic mis-scaling between the two wire scanners of 5%, given actual matched conditions (20), produces a tolerable 10 mrad apparent η'_x . This same mis-scaling produces no

error for η'_y . An achievable relative roll error between wire-1 and wire-2 of $\leq 1^\circ$ produces an apparent $|\eta'_y|$ of ≤ 8 mrad.

Turtle⁵ tracking calculations have shown no significant systematic error in the measurement of $\eta'^*_{x,y}$ produced by local sextupole aberrations (< 1 mrad), or by full scale tuning of the nearby IP dispersion correction quadrupoles (< 8 mrad).

IV. CORRECTION SCHEME

The actual correction algorithm requires a scan of the CCS wires, and the use of (13) and (17) to fit for $\eta'^*_{x,y}$. Next the X and Y beam sizes at the IP are minimized with the small CCS correction quadrupoles (using beam-beam deflections⁶ to measure the beam sizes) and these quadrupole settings are used to calculate the existing residual $\eta'^*_{x,y}$. The values of residual angular and spatial IP dispersion are then back-propagated to the final focus dispersion matching section (upstream of the CCS). A non-linear fitting program² is then used to calculate the new settings of the dispersion matching section quadrupoles in order to cancel the residual angular and spatial IP dispersion, and the CCS correction quadrupoles are reset to zero. The IP beam sizes are finally minimized one more time with the CCS correction quadrupoles to fine tune the beam.

With the residual dispersion corrected at the wires, (13) may also be used to fit for the betatron X-Y coupling term, $\langle x\rho y\rho \rangle$, which would otherwise be improperly measured in the presence of significant residual dispersion.

V. ACKNOWLEDGMENTS

The authors are grateful to Eric Bong for mechanical support in the design and installation of the wire scanner hardware and Nick Walker and Pantaleo Raimondi for many useful discussions. We are also grateful to Leeanne Yasukawa and Linda Hendrickson for software support.

VI. REFERENCES

- [1] W. Spence, *Private Communication*.
- [2] C.M. Hawkes and P.S. Bambade, "First Order Optical Matching in the Final Focus Section of the SLAC Linear Collider", *Nucl. Inst. and Meth. A274* (1989) 27.
- [3] P. Emma, "Minimizing Residual Dispersion at the SLC Interaction Point", (to be published)
- [4] M.C. Ross, *et.al.*, "Wire Scanners for Beam Size and Emittance Measurement at the SLC", *Proceedings of the 1991 IEEE Particle Accelerator Conference*, p.1201, May 1991
- [5] D.C. Carey, K.L. Brown, Ch. Iselin, "Decay Turtle", SLAC-246, March 1982.
- [6] P. Bambade, *et.al.*, "Observation of Beam-Beam Deflections at the Interaction Point of the SLAC Linear Collider", *Physical Review Letters*, Vol 62, No 25, p 2949, June 1989.

Comprehensive Beam Jitter Study for the Commissioning of the Intermediate Matching Section and Drift Tube Linac at Ground Test Accelerator*

D. S. Barr, J. D. Gilpatrick,
Los Alamos National Laboratory
MS H808, Los Alamos, NM 87545

Abstract

An experiment on the Ground Test Accelerator (GTA) for the Neutral Particle Beam (NPB) at Los Alamos commissioned the intermediate matching section (IMS) and a single 3.2-MeV drift tube linac (DTL). A diagnostic platform or D-plate was used at the output of the DTL in order to measure various beam parameters. The D-plate and other diagnostic devices located in the IMS, provided measurement of the horizontal and vertical beam position, current, energy, and output phase. These instruments were installed to perform a complete beam jitter analysis based on the current beamline configuration to better understand the causes of any jitter sources as well as to prepare for the initial design of future feedback control systems. The study explored all types of jitter for various beamline configurations. Both interpulse jitter (jitter from pulse to pulse) and intrapulse jitter (jitter within each macropulse) were investigated. Spectral and statistical time analyses were used. Spectral analysis was employed to gain an understanding of the spectral contributions of various jitter sources to determine the degree of correction possible. Statistical time analysis gave a good overall representation of the jitter magnitude and allowed easy comparison of jitter for different beamline configurations, as well as an easy method for determining consistent problems.

I. INTRODUCTION

Jitter data were collected during the GTA Experiment 2A run in October and November of 1992. The beamline consisted of an H⁻ ion source and injector, followed by an RFQ (Radio Frequency Quadrupole), an IMS used to match the RFQ output to the DTL input in the transverse and longitudinal phase space), a DTL, and a D-plate. The D-plate contained various diagnostic devices, including three microstrip beam probes (MBP), a toroid, three Faraday cups, and a slit and collector (for transverse emittance measurements). The measurements utilized six MBPs, four toroids, and a Faraday cup [1]. MBP #1, #2, and #3 were located in the IMS, while MBP #4, #5, and #6 were located on the D-plate. The MBPs on the D-plate were separated by drifts, thus allowing beam trajectory angle and time-of-flight energy measurements. Toroids #1 and #2 were located just before and after the RFQ, toroid #3 was located in the IMS, and toroid #4 was located on the D-plate. The DTL output phase measurements were

*Work supported and funded by the US Department of Defense, Army Space and Strategic Defense Command, under the auspices of the US Department of Energy.

obtained by comparing the phase of the DTL electric fields to the phase of the MBP #4 signal. Both the MBPs and the toroids produce measurements of the beam current. The MBP current measurements (referred to as intensity) produces an output proportional to the peak bunch current at any given point in time. The toroid measures the average beam current integrated over time. Note that the data presented here are just a subset of the total data taken.

II. MEASUREMENT DESCRIPTION

Intrapulse data, which are composed of multiple data points taken within a single macropulse were taken. Using a 4-channel, 12-bit digitizer, we were able to take data at 5 megasamples per second. A 2.0-MHz analog filter was used on the input of the digitizer to remove any aliased frequency spectra. Each macropulse was roughly 300 μ sec long, and therefore 1500 points per macropulse were taken. We collected 25 consecutive macropulses on each of the four digitizer channels for many different accelerator configurations. Various combinations of beam position, current, energy, and DTL output phase were taken synchronously. Data presented were taken with all cavities and devices operating in-time (the RFQ, both IMS cavities, and the DTL), and with the steering quads set to their nominal design values.

III. PROCESSING OF DATA

A brief description of the algorithm used to produce the power spectrum plots is given below:

- 1) Conversion from raw digitizer counts to appropriate units (ma, mm, MeV, degrees)
- 2) Removal of data points outside the macropulse
- 3) Removal of dc component
- 4) Data was windowed using Von Hann window
- 5) The FFT of the data was taken
- 6) The magnitude of the data was taken
- 7) Each value was divided by the number of data points
- 8) The magnitude of each value was squared
- 9) Each value of the spectrum was scaled for energy lost in windowing and display of one-sided spectrum
- 10) The deterministic noise components created by the digitizer were removed
- 11) The ensemble average of the various spectra was taken
- 12) The square root was taken to get the root-mean square (rms).

IV. DATA ANALYSIS

Figures 1-6 show the rms ensemble averages of the power spectrum of 25 consecutive macropulses for the intrapulse data. Table 1 lists each of the measurements along with the average mean and standard deviation for the 25 consecutive macropulses. The mean is the ensemble average of time averages for each macropulse. The standard deviation is the square root of the ensemble average of the time-variance of each macropulse [2], [3]. The mean and standard deviation of each interpulse data set is also given in Table 1.

V. RESULTS AND CONCLUSIONS

In most of the position measurements there is an interesting clump of frequency spectra located around 1.95 MHz. These spectra show up in the microstrip intensity measurement, but not in any of the others. Because the microstrip intensity measurements are dependent on beam position and the toroid measurements are not, it can be inferred that this is a beam position phenomenon.

There is a fairly clear peak at about 0.95 MHz in all of the position and current measurements except the first toroid (not shown). Because this is the only device preceding the RFQ, it can be inferred that this peak is caused by the RFQ. There is an interesting peak at 0.55 MHz, which is seen in plots of the toroid, the energy, and the phase.

Note the large degree of low-frequency movement in most of the plots. Doubtless some of this is leakage from the dc component, but most of it is real beam jitter. It can be seen that the intrapulse energy and phase jitter are small, typically 0.048% $\Delta W/W$ and 0.23 degrees in phase. The intrapulse current jitter was measured typically at less than 1%.

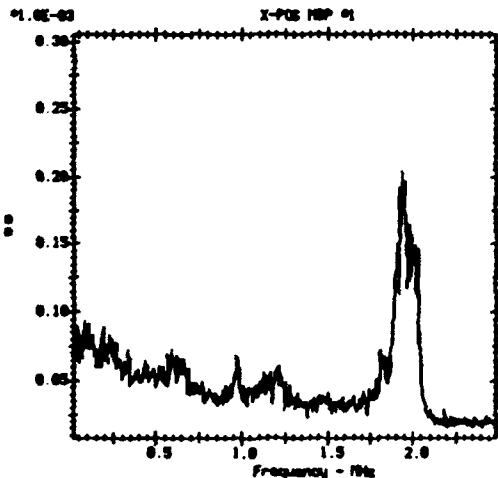


Figure 1 - Averaged Power Spectrum

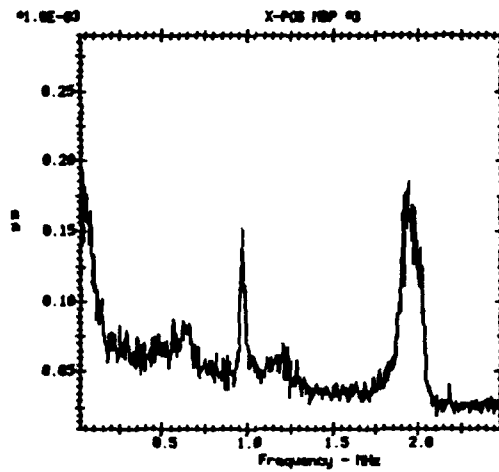


Figure 2 - Averaged Power Spectrum

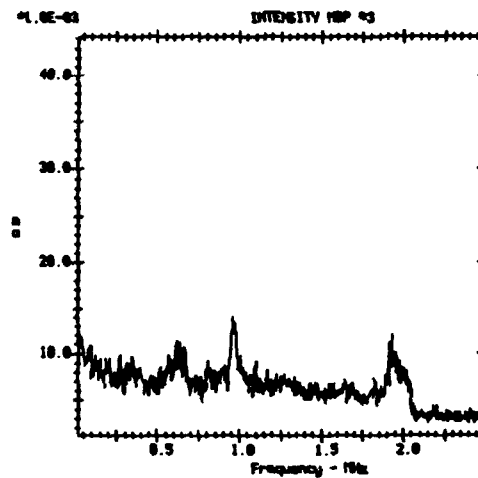


Figure 3 - Averaged Power Spectrum

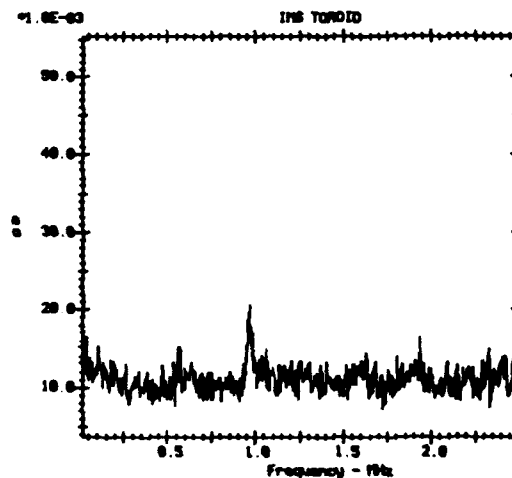


Figure 4 - Averaged Power Spectrum

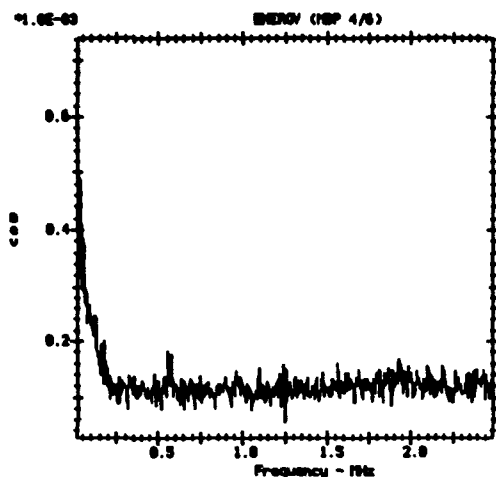


Figure 5 - Averaged Power Spectrum

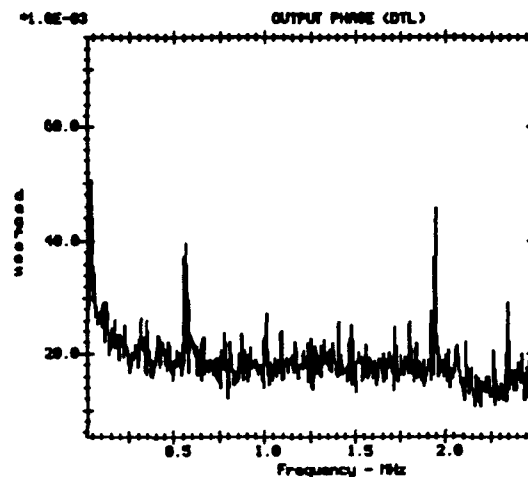


Figure 6 - Averaged Power Spectrum

Table 1
Time-Data Statistics for Intrapulse Data

Measurement Device	Mean	St. Dev.
Horizontal position at MBP #1	341.427 μm	0.564 μm
Horizontal position at MBP #3	61.377 μm	0.611 μm
Intensity at MBP #3	33.641 ma	0.190 ma
Current at toroid #3 (IMS)	32.544 ma	0.326 ma
Energy from MBP #4 to #6	3.173 MeV	1.525 Kev
DTL output phase	60.826 degrees	0.232 degrees

VI. REFERENCES

- [1] J.D. Gilpatrick, F.D. Wells, R. Martinez, K.F. Johnson, R.E. Meyer, S. Lloyd, J.F. Power, G.H. Neuschaefer, R.B. Shurter, "Measurements and Performance of a Microstrip Beam Probe System," *1991 Particle Accelerator Conference Proceedings*, San Francisco, CA, May 6-9, 1991, Los Alamos National Laboratory LA-UR-1428.
- [2] F.G. Stremler, *Introduction to Communication Systems*, 2nd edition, Addison-Wesley Publishing Company, Reading, Mass., 1982, p. 170.
- [3] W.H. Press, B.P. Flannery, S.A. Teukolsky, W.T. Vetterling, *Numerical Recipes: The Art of Scientific Computing*, Cambridge University Press, Cambridge, England, 1986, p. 484.

A New Method of Ion Beam Diagnostics

A.S. Artiomov
Laboratory of High Energies, JINR
141980, Dubna, Russia

Abstract

In the considered method of ion beam diagnostics, information on beam parameters is taken out via fast neutral particles produced in definite quantum states in a specially shaped target before the bending transport line area. The target is formed so that these particles follow the ion velocity in magnitude and in direction with accuracies required for measurements. The beam parameters are determined in a convenient area outside the transport line by means of a compact magnetic analyzer and electrons produced from selective photoionization of the used quantum state of the fast neutral particles. The realization of such diagnostics in the area of charge-exchange $H^- \rightarrow P$ injection of meson factory storage ring is considered.

1. INTRODUCTION

A charge-exchange method of particle flux control in the modern accelerators and the storage rings is broadly used. By using negative ions at the beginning of a beam transport line and forming charge-exchange targets at various transport line areas a convenient separation of high energy beams can be realized. A charge-exchange process in a target always leads to some flux of fast neutral particles (A^0) which follow the ion velocity in magnitude (in relative units) and in direction (in rad) with high accuracies. At present various methods of nonperturbative diagnostics on high-energy H^- beams, where information on the beam parameters is taken out via the fast H^0 atoms, are proposed [1-5]. The disadvantages of these methods are a long drift distance in time-of-flight measurements of the energy spectrum [2] or the large mass and size characteristics of the magnetic analyzers when the H^0 detachment to protons is used in the measurements [1,4]. A new method of ion beam diagnostics proposed by the author [6] and considered in this paper allows to avoid these difficulties.

2. METHOD

For ion beam diagnostics based on the fast neutral particles A^0 a compact apparatus can be created if information on the ion energy spectrum then is passed to electrons. A maximum accuracy of this transformation can be realized for the neutral particles in a definite quantum

state in an optimum shaped photon target. A quantum state, photon polarization and their frequency ω in the particle rest frame are chosen so as to achieve a necessary accuracy of the information transfer to the electrons and a required ratio of photoionization probabilities of the used and other quantum states. A kinematic analysis of an electron detachment after the photon absorption by the fast neutral particle $A^0(n)$ in the quantum state " n " (photoionization) shows that, depending on the photon polarization, the created electron follows the particle energy (in relative units) and momentum direction with accuracies:

$$\Delta E_e/E_e \leq \frac{2\beta\gamma}{(\gamma-1)C} \cdot \sqrt{2(\omega - \epsilon_n)},$$

$$\Delta\theta_e[\text{rad}] \leq 2 \cdot \frac{\sqrt{2(\omega - \epsilon_n)}}{\gamma\beta C}, \quad (1)$$

where we use the atomic units ($e = m_e = \hbar = 1$), $E_e = E_0/M_0$; β and γ are relativistic beam parameters, M_0 and E_0 are the mass and energy of the neutral particle, $\omega = \omega_0\gamma(1 - \beta \cdot \cos\eta)$, ω_0 is the photon energy in the laboratory frame, η is the lab. angle between the particle and photon momenta, C is the speed of light, ϵ_n is the photoionization threshold of the quantum state " n ". Taking into account a maximum cross section of a photoionization near the threshold ϵ_n , the best accuracy of an information transfer on ion beam parameters to the electrons is achieved for

$$(\omega - \epsilon_n)_{\min} \approx \gamma\omega_0 \{ |\Delta\beta \cdot [\beta(1 - \beta\cos\eta)\gamma^2 - \cos\eta]| + |\beta\sin\eta \cdot \Delta\theta_i| \}, \quad (2)$$

where $\Delta\beta$, $\Delta\theta_i$ are the spreads of the particle (ion) velocities in value and direction, respectively.

As an example, we estimate potentialities of such diagnostics for the H^- beam in the area of the charge-exchange injection at meson factories. Usually, for a high ($\approx 99\%$) efficiency of the $H^- \rightarrow P$ transformation carbon foils are used. As a result of the H^- destruction the H^0 atoms ($\approx 1\%$) in various quantum states are produced. A relative number of the H^0 atoms in the quantum state " n " (δ_{on} , $n = 1, 2, \dots$) depends on the H^- ion energy, thickness and material of the stripping target [7,8]. A flux

of the fast H^0 atoms leaves the ion beam after the stripping foil in a transport line area with a bending magnet. Except a charge separation in the magnetic field a destruction of some quantum states of the H^0 atoms takes place. Taking into account the $H^0(n)$ -photoionization cross sections (see for example [9]), for a transfer of the information on beam parameters from the fast H^0 atoms to the electrons conveniently to use quantum states "1s" and "2s" which dominate in the H^0 flux. Conditions of an optimum photoionization of the 1s- and 2s-quantum states are obtained as a result of the Monte Carlo simulation of the elementary acts of the electron creation from the ns -quantum state of the A^0 . The correspondent probability distributions of the electrons in the spaces of transverse momenta ($P_x/P_0, P_y/P_0$, where $P_0 = \sqrt{2(\omega - \epsilon_n)}$) and energy (E_e) in the laboratory frame (the own distributions) are obtained. The results of the simulation show that for a transfer of information on the transverse beam emittance, for example in the (X, X') -plane, to electrons with a maximum accuracy, the photon target must be polarized in the (Y, Z) -plane of the Cartesian coordinate system (X, Y, Z) with the Z -axis in the direction of the A^0 flux. $X' = dX/dZ$ is the ion trajectory slope proportional to the transverse momentum P_x . The corresponding own distribution of electrons $f(P_x, P_y)$ at $\eta = \pi/4$ and $3\pi/4$ is shown in Fig.1. For other angles η similar distributions

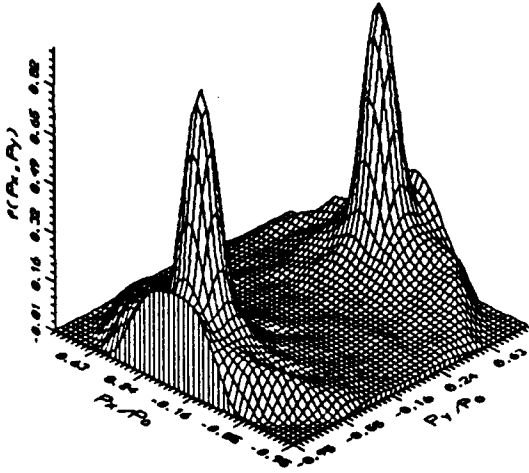


Figure 1: The own distributions of electrons in the (P_x, P_y) -space for the $A^0(ns)$ -atom photoionization ($\eta = \pi/4, 3\pi/4$, optimum photon polarization).

but with a various distance between the maxima along the P_y -axis are obtained. The measurement accuracy of X' in the considered diagnostic method determined by the half-width of the distribution $\varphi(P_x) = \int f(P_x, P_y) dP_y$ is independent of η and equals

$$\Delta X'_{rad} \approx \frac{\sqrt{2(\omega - \epsilon_n)}}{4\gamma\beta C}, \quad (3)$$

The measuring apparatus is supposed to integrate the electron distribution along the P_y -axis not perturbing information in the (X, X') -plane. Unlike the above-

mentioned condition, a maximum accuracy of the information transfer on the longitudinal beam emittance and the ion energy spectrum to electrons is achieved when the planes of the photon polarization and the $A^0(ns)$ -photon interaction are mutually perpendicular. The corresponding own energy distribution of electrons in dimensionless units $XS = [E_e - (\gamma - 1)C^2]/(0.1\gamma\beta C P_0)$ is shown in Fig.2 and independent of η . It is easy to see that the

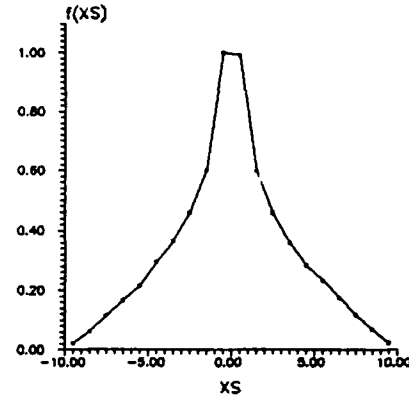


Figure 2: The own energy distribution of electrons for the $A^0(ns)$ -atom photoionization (optimum photon polarization).

accuracy in determining the ion energy by electrons in relative units is equal to

$$\Delta E_e/E_e \approx \frac{0.4\beta\gamma}{(\gamma - 1)C} \cdot \sqrt{2(\omega - \epsilon_n)}. \quad (4)$$

The photon targets necessary for the diagnostics of the H^- beams with various energies are simply realized when the information on the beam parameters is received through the H^0 atoms in the 2s-quantum state ($\epsilon_2 = 3.395$ eV). In this case, e.g. forming the optimum photon target by means of N_2 -laser ($\omega_0 = 3.678$ eV) at $\eta = 58^\circ$, the accuracies of measurements $\approx 10^{-2}\%$ in energy and $\approx 3 \cdot 10^{-5}$ rad in X' can be obtained for the H^- beam with $E_i = 600$ MeV, $\Delta\beta/\beta \approx \pm 10^{-3}$ and $\Delta\theta_i \approx \pm 10^{-3}$ rad at the Moscow Meson Factory Linac (MMFL). For the more energetic ions with $E_i \geq 800$ MeV (LAMPF), the information on the beam can be obtained from the intense flux of the H^0 atoms in the 1s-quantum state ($\delta_{01} \approx 50\delta_{02}, \epsilon_1 = 13.599$ eV). For this, the optimum photon target is simply realized by means of a fourth-harmonic radiation of a Nd:YAG-laser ($\omega_0 = 4.6595$ eV). But in this case the accuracies of the measurements of the beam parameters are about twice worse than in the above-considered case.

3. APPARATUS

For measuring the electron flux parameters and determining through them the corresponding ion beam parameters a compact multifunctional apparatus which is proposed in [10] can be used. The apparatus based on a dipole magnet (MA) with a homogeneous field and inter-polar distance D_m sufficient to pass unhindered all the

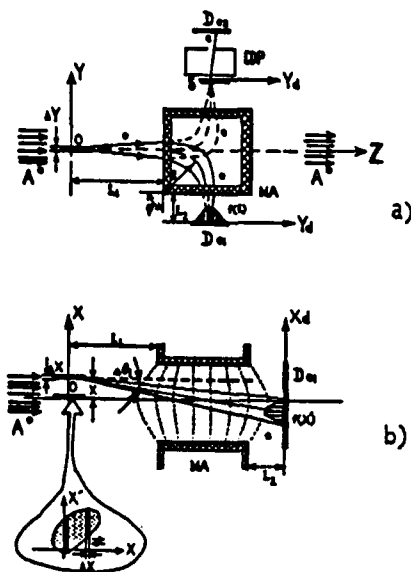


Figure 3: Schematic of measurement apparatus.

electrons produced from a photoionization of the fast neutral particles (see Fig.3).

The ion energy spectrum and longitudinal beam emittance measurements are performed according to a scheme (Fig.3a) well known for magnetic analyzers where, instead of a diaphragming slit of the analyzer, a band-type photon target (O) is formed. The energy spectrum of the ions is determined according to the spatial distribution of the electron flux density along the Y_d -axis on the detector D_{e1} . Electrons with momenta needed for the phase analysis are operatively separated by means of the diaphragm S, when a sign and value of the analyzer magnetic field are changed. The longitudinal emittance of the ion beam is determined according to a combination of the spatial distributions of the selected electrons on the detector D_{e2} after the cavity dispersed in phase (CDP), e.g. with a circularly polarized rf -field [11].

For measuring the transverse emittance in the (X, X') -plane and the X -profile of the neutral particle flux (and through them of the ion beam in the charge-exchange target area), the band-type photon target is localized within the (Y, Z) -plane and moves in parallel along the X -axis (Fig.3b). A computer simulation of the influence of boundary fields, inaccuracies in adjusting and manufacturing of the magnetic dipole shows that electron distributions on the detector D_{e1} along the X_d -axis are described by the expression

$$X_d = a \cdot X + b \cdot X', \quad (5)$$

where "a" and "b" are determined only by parameters of the analyzer chosen and can be defined in control experiments by means of a testing electron beam. The ion distribution in the (X, X') -plane can be reconstructed according to the X_d -distributions of the electrons on the detector for controllable characteristics of the photon target

(defining a probability of an electron generating) and its position in the space (X) . At the same time the functional dependence of the integral electron flux on the detector upon the target position defines the beam profile along the X -axis. For a short time interval (e.g. during a laser pulse) a certain information on the ion distribution over the (X, X') -plane can be obtained by means of several band-type photon targets fixed in space, created and separated from each other along the X -axis by diaphragming a laser radiation. The distance between them (δX) is defined by a condition of the electron distributions overlapping on the detector along the X_d -axis.

The required diagnostics of the above considered H^- beam at the MMFL can be realized during a time of $\tau_m \approx 1$ s by means of the $H^0(2s)$ atoms, pulsed photon target (≈ 300 kW/pulse, N_2 -laser) synchronized with the beam and apparatus (see Fig.3) with $\varphi = \pi$, $R = 200$ mm, $L_1 = L_2 = 0$, $D_m = 40$ mm, spatial resolution of the detectors $\Delta d \approx \Delta Y \approx \Delta X \approx 0.1$ mm, $\delta X \approx 1.3$ mm and projection of the target area (where the electrons are collected from) onto the Z -axis $\Delta Z_t \leq 20$ mm (energy spectrum, profile, transverse emittance) or $\Delta Z_t \leq 1$ mm (phase analysis, longitudinal emittance). A value of magnetic field of such an electron analyzer is $H = 110$ Oe. For a precise operation of the apparatus spatial position of the band-type photon target should be controlled with accuracies of $\delta(X) \approx \delta(Y) \leq 0.1$ mm, $\alpha(X) \approx \alpha(Y) \leq 3$ mrad. Moreover, the background magnetic fields H_b should be well shielded off, as well as required accuracy of the magnetic field magnitude H in the analyzer ($H_b \approx \delta H \leq 3 \cdot 10^{-4} H$). In a charge-exchange area at the LAMPF ($E_i = 800$ MeV) the above considered apparatus allows to realize more operative diagnostics of the beam (through the intensive flux of $H^0(1s)$ atoms) and without detriment to the measurement accuracy.

REFERENCES

- [1] Stephen L.Kramer, D.Read Moffett, *IEEE Trans. Nucl. Sci.*, NS-28, 2174(1981).
- [2] W.B.Cottingham et al., *ibid*, NS-32, 1871(1985).
- [3] K.Saadatmand, K.F.Johnson, J.D.Schneider, *IEEE Part. Accel.Conf., San Francisco, California, May 6-9, 1991*, Vol.3, p.1183.
- [4] R.C.Connolly, D.P.Sandoval, *ibid*, p.1237.
- [5] R.C.Connolly et al., *Nucl. Instr. Meth.*, Vol.A312, 415(1992).
- [6] A.S.Artemov, Avtor. Svid. SSSR, No.1679878, G01T1/36, 1989.
- [7] A.K.Kaminsky, R.A.Meshcherov, M.I.Popova, *Trudy MRTI*, Vol.22, 215(1975).
- [8] H.Gillespie, *Nucl. Instr. Meth.*, Vol.B10/11, Pt.1, 22(1985).
- [9] C.F.Barnett, J.C.Ray, *ORNL-3113*, 1963.
- [10] A.S.Artemov et al., *IEEE Part.Accel.Conf., San Francisco, California, May 6-9, 1991*, Vol.3, p.1573.
- [11] E.S.Zlunitsin et al., *VANT. Ser.: Tekn. Fiz. Eksp.*, No.2(28), 37(1986).

Correlation Method of Measurements of Ion Beam Parameters

A.S.Artiomov

Laboratory of High Energies , JINR
141980, Dubna, Russia

Abstract

A correlation method of nonperturbative control on the ion energy spectrum, beam profile and transverse emittance in a bending transport line area, is suggested. The method is based on measurements of the cross-correlation function between a flux of photons or particles from a probing target pseudorandomly modulated in time, and that of fast information-carrier convoy particles produced in the target and recorded at a drift distance. Characteristics of the apparatus used to realize the proposed diagnostic method by means of time-integrated correlometers based on charge-coupled devices, are considered for a source of H^- ions.

1. INTRODUCTION

For high-brightness ion accelerators it is important to obtain information on beam parameters not affecting them appreciably during measurements (nonperturbative diagnostics). For this purpose in a bending transport line area fast neutral or charged convoy particles can be used. These particles are produced as a result of ion destruction or the charge-exchange process in a specially shaped target which is practically transparent for a beam (for H^- beams see [1-5]). The target is formed so that these information-carrier convoy particles (IN-particles) follow the ion velocity in magnitude (in relative units) and in direction (in rad) with accuracies required for measurements. These accuracies can be estimated by $\leq (\mu_o I_o / M_i E_i)^{0.5}$ where μ_o is the reduced mass of the IN-particle and the remaining part of the ion in its destruction or the ion

and electrons in their recombination, I_o is the affinity energy, M_i and E_i are the ion mass and energy, respectively. In sources, for example of negative ions, the probability of IN-particle generation (η) in residual gas can be quite considerable (for the neutral IN-particles $\eta_r \approx 0.2 - 0.4$). In this case, using the well known methods [1-5] for any density of a probing target, it is impossible to separate directly information on beam parameters from a flux of background IN-particles on a detector. The correlation method of nonperturbative measurements of ion beam parameters considered in this paper allows one to overcome these difficulties.

2. METHOD

The correlation method of nonperturbative measurements of the ion energy spectrum has been previously proposed [6,7]. It is based on the use of test IN-particles produced in a target, pseudorandomly modulated in time, and detected at drift distance L . To measure the transverse beam emittance, for example in the (Y, Y') -plane (see Figure), one or a few thread-type targets parallel to the (X, Z) -plane can be formed in front of a bending transport line area. If the ion beam current is invariable during measurements, the spatial X -dimension of the target must be required for reproducing target time modulation by the flux Ψ_{pn}^o of test IN-particles

$$\Psi_{pn}^o(t) = \text{const}_{(n)} \cdot I_n^o(t), \quad (1)$$

where I_n^o is the flux of photons or particles in the n -target. The targets are fixed in space

and separated from each other along the Y -axis. When one target is used, it moves in parallel along the Y -axis. Taking into account (1), the autocorrelation function of the flux of test IN-particles on a m -detector is equal to

$$\begin{aligned} R_{nm}^{pp}(\tau) &= \int_{-\infty}^{+\infty} \Psi_{pn}^o(t) \cdot \Psi_{pn}^o(t - \tau) dt = \\ &= \sum_{k=-\infty}^{+\infty} \delta(\tau - kT). \end{aligned} \quad (2)$$

The pulsed characteristic $h_{nm}(t)$ of the drift distance from the n -target to the m -band-type detector ($Y' = fix$) is related to the velocity (V) distribution of IN-particles ($t = L/V$) in the $n-m$ direction and, hence, to the energy spectrum of ions. The fluxes of IN-particles in the n -target area (Ψ_n^o) and on the m -detector (f_{nm}^o) are related by the convolution

$$\begin{aligned} f_{nm}^o(t) &= C_m \cdot \int_0^{+\infty} h_{nm}(\tau) \cdot \Psi_n^o(t - \tau) d\tau, \\ \sum_m C_m &= 1, \end{aligned} \quad (3)$$

where $\Psi_n^o = \Psi_{bn}^o + \Psi_{pn}^o$, Ψ_{bn}^o is the flux of background IN-particles produced in the residual gas. Taking into account the independence of Ψ_{bn}^o and Ψ_{pn}^o and measuring the cross-correlation function between the fluxes of target particles or photons and IN-particles on the detector

$$\begin{aligned} R_{nm}^{\gamma o}(\tau) &= \int_{-\infty}^{+\infty} I_{nm}^{\gamma}(t) \cdot f_{nm}^o(t - \tau) dt = \\ &= B_{nm} \cdot \int_0^{+\infty} h_{nm}(t) \cdot R_{nm}^{pp}(\tau + t) dt = \\ &= B_{nm} \cdot \sum_{k=0}^{+\infty} h_{nm}(\tau - kT), \end{aligned} \quad (4)$$

we obtain the pulsed characteristic of the drift distance in the $n-m$ direction ($I_{nm}^{\gamma} \propto I_n^{\gamma}$). Using normalization $\int h_{nm}(\tau) d\tau = 1$, we get from the B_{nm} -matrix information on the ion distribution

in the (Y, Y') -plane and thus on the beam Y -profile and transverse emittance.

In reality, we must form such targets when convolution (4) of h_{nm} and R_{nm}^{pp} does not change the supposed $h_{nm}(t)$ -function. In accordance with [8], this condition means that a periodically replicating element of the autocorrelation function of the I_n^{γ} -flux must have a sufficiently narrow shape in time with width $\Delta \ll \tau_{max}$, where $h_{nm}(\tau) = 0$ for $|\tau| \geq \tau_{max}$, and its period T must meet the condition $T > 2 \cdot \tau_{max}$. Correlation methods measure a useful signal with a background which is several orders of magnitude more than the signal. Thus, measuring $R_{nm}^{\gamma o}(\tau)$ by " $n \times m$ " correlometers, the energy spectrum and distribution of ions in the (Y, Y') -plane can be controlled without perturbation of beam parameters.

3. APPARATUS

Nonperturbative measurements of ion beam parameters, for example in a source of H^- ions, can be realized according to the scheme shown in Figure. It is analogous to the previously proposed one [7], but it contains " n " identical photon targets (I_n^{γ}) and photon detectors (D_n^{γ}), " $n \times m$ " correlometers (C_{nm}) and band-type detectors (D_{nm}^o) of fast H^o atoms. When probing targets are formed by diaphragming radiation with an optimum polarization and a wavelength of $\lambda = 10600 \text{ \AA}$ from the Nd:YAG laser with synchronized modes (see Fig.a,b), the test H^o atoms follow the H^- velocity in magnitude (in relative units) and in direction (in rad) with accuracies of $\sim 4 \cdot 10^{-3} \cdot (E_i[\text{keV}])^{-0.5}$. The series duration of pseudorandom radiation pulses is $T_s \approx 100 \text{ ns}$ and the width of the autocorrelation function is $\Delta \approx 50 \text{ ps}$ [9]. Thus, such photon targets due to H^- photodetachment can efficiently generate test IN-particles (H^o) and allow one to measure pulsed characteristics of the drift distance $h_{nm}(\tau)$ which are fairly short in time. At present, potentialities of the above diagnostics are mainly limited by the fast action of correlometers. The cross-correlation function $R_{nm}^{\gamma o}(\tau)$ between the

THE COMPTON POLARIMETER AT THE SLC*

G. Shapiro, S. Bethke, O. Chamberlain, R. Fuzesy, M. Kowitt, D. Pripstein,
B. Schumm, H. Steiner, and M. Zolotorev
Lawrence Berkeley Laboratory
1 Cyclotron Road, Berkeley, CA 94720, USA

P. Rowson
Columbia University
538 West 120 Street, New York, NY 10027 USA

D. Blockus, H. Ogren, and M. Settles
Indiana University
Bloomington, IN 47405 USA

M. Fero and A. Lath
Massachusetts Institute of Technology
Cambridge, MA 02139 USA

D. Calloway, R. Elia, E. Hughes, T. Junk, R. King, T. Maruyama,
K. Moffeit, M. Petradza, M. Swartz, and M. Woods
Stanford Linear Accelerator Center
P. O. Box 4349, Stanford, CA 94309 USA

G. Zapalac
University of Wisconsin
1150 University Avenue, Madison, WI 53706 USA

Compton scattering provides a fast and accurate measurement of the longitudinal polarization of electron beams available at linear colliders. At the SLC, green (532 nm) circularly polarized light from an Nd:YAG laser, frequency doubled, collides nearly head-on with electrons after they have passed the e^+e^- interaction point but before they have encountered any dipole bending magnets.

Unique to this application, the recoil electrons, rather than scattered photons, are detected, after being momentum analyzed by the bending magnets nearest to the interaction point. Thus we achieve spatial separation of several centimeters between electrons from scattering at different Compton angles.

The analyzing power of Compton scattering of 2.34 eV photons from 45.6 GeV electrons is 75% at full backward scattering. The analyzing power is zero at 90 degrees in the electron rest frame, and data from this channel helps us correct for luminosity variations in the electron-photon collisions.

The Compton polarimeter is capable of measuring the electron beam polarization to within a few percent of itself. Statistical accuracy of better than 1% in the absolute beam polarization is achieved routinely in runs of three minutes duration, with the laser firing at 11 Hz.

*This work was supported by the U.S. Department of Energy.

Figure 1 shows the Compton Light Source and the Compton Electron Detectors in relation to the e^+e^- Interaction Point within the SLD detector, and to the nearest bending magnet in the south final focus region of the SLAC Linear Collider.

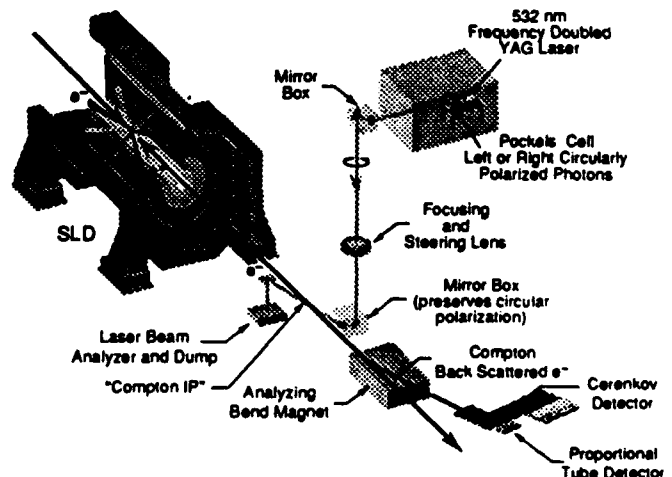


Fig. 1. The Compton Polarimeter

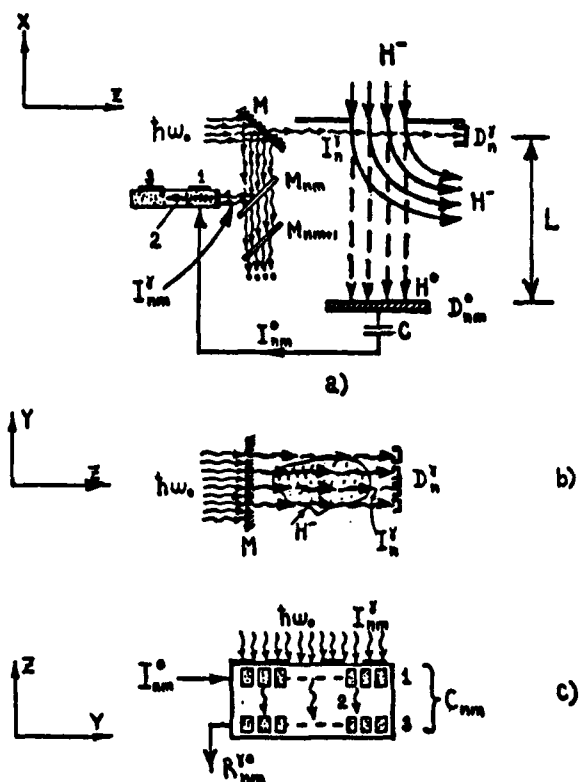


Figure : Schematic of measurement apparatus.

photon flux I_{nm}^{γ} from a partly reflecting M_{nm} -mirror and current $I_{nm}^0 \propto f_{nm}^0$ from the D_{nm}^0 -detector can be measured by means of a time-integrated C_{nm} -correlometer based on charge-coupled (CC) linear structures [7,10]. As a result of the waveguide propagation of photons through GaAs CC-linear structure 1 (see Fig.a,c), the I_{nm}^0 -current modulates the flux I_{nm}^{γ} by the photoelectric absorption effect within a $\approx 100\%$ dynamical range of modulation. An instantaneous spatial distribution of charges over the pixels of this structure corresponds to the discrete-in-time representation of the shape of a I_{nm}^0 -current signal. After the modulation, photon flux 2 is detected by silicon CC-linear structure 3. The spatial distribution of charges accumulated there during the measurement time T_m corresponds to the discrete-in-time presentation of the $R_{nm}^{\gamma 0}$ -function. Fairly large I_{nm}^{γ} -fluxes of photons provide the needed charge within the pixels of the detected CC-linear structure du-

ring a short time within a pulse of the ion beam. The $R_{nm}^{\gamma 0}$ -functions can be read out during intervals between target switchings or between ion beam pulses and taking into account the guiding frequency of modulating structures 1.

As estimates for the source of H^- ions with an energy of $E_i \approx 20$ keV, $L \approx 100$ cm and the average power density of laser radiation within the duration of a series of pulses $I_n^{\gamma} \approx 4 \cdot 10^5$ W/cm² ($\Psi_{bn}/\Psi_{pn} \approx 10^2$), the proposed apparatus allows one to realize nonperturbative measurements of beam parameters during $T_m \geq T_s \approx 100$ ns with accuracies, e.g., of $\approx 0.4\%$ in energy and of $\approx 2 \cdot 10^{-4}$ rad in Y' .

References

- [1] Stephen L.Kramer, D.Read Moffett, *IEEE Trans. Nucl. Sci.*, NS-28, 2174 (1981).
- [2] W.B.Cottingham et al., *IEEE Trans. Nucl. Sci.*, NS-32, 1871 (1985).
- [3] K.Saadatmand, K.Johnson, J.Schneider, *IEEE Part. Accel. Conf., San Francisco, California, May 6-9, 1991*, Vol.3, p.1183.
- [4] R.C.Connolly, D.P.Sandoval, *ibid*, p.1237.
- [5] R.C.Connolly et al., *Nucl. Instr. Meth. A*, Vol.312, p.415 (1992).
- [6] A.S.Artiomov, *Avtor. Svid. SSSR* No.298206, G01T1/36, 1988.
- [7] A.S.Artiomov, *IEEE Part. Accel. Conf., San Francisco, California, May 6-9, 1991*, Vol.3, p.1576.
- [8] Methodes et techniques de traitement du signal et applications aux mesures physiques. Tome 1, par J.Max, Paris, 1981.
- [9] Ultrashort Light Pulses (picosecond techniques and applications), Edited by S.L.Shapiro, New York, 1977.
- [10] R.H.Kingston, *Proc. IEEE*, Vol.72, p.954 (1984).

The Compton Light Source consists of the laser, the evacuated transport line, and hardware and optics for laser beam circular polarization, steering, focusing and diagnostics. The laser is a commercially available SpectraPhysics GCR-11 frequency doubled Nd:YAG laser. The laser pulse width is 7 ns (FWHM), and has a pulse energy of about 45 mJ. The laser is pulsed once every 11 SLC machine cycles. (The SLC operates at 120 Hz.) The laser beam passes through a prism polarizer and Pockels cell combination to circularly polarize the beam. The sign of the circular polarization, determined by the polarity of the high voltage applied to the Pockels, is normally set pulse-to-pulse following a pseudo-random pattern.

Before exiting the laser room, and entering the evacuated transport line, the beam diameter is expanded to 2 cm in order to maintain collimation over the 40-meter pathlength to the Compton interaction point. The beam transport line between the Pockels cell and the Compton interaction point consists of evacuated straight sections connected by 4 sets of phase compensated mirror pairs, 4 windows, and a focusing/steering lens. The compensated mirror pairs preserve the polarization of the photon beam upon reflection. The transport line windows were measured to have negligible birefringence. The 5-meter focal length lens focuses and steers the laser beam onto the electron beam. After leaving the SLC vacuum, the beam is monitored for intensity, steering and polarization. The electron and photon beams cross at an angle of 10 milliradians. At the Compton interaction point, the RMS beam sizes are approximately 350 microns for the electron beam, and 500 microns for the photon beam.

The Compton Cerenkov detector consists of a nine-cell gas threshold Cerenkov counter viewing a retractable 1.4-radiation-length lead radiator. Each $1 \times 1.5 \times 20$ cm mirrorized Cerenkov channel is filled with non-scintillating gas (beta-butylene) at atmospheric pressure, and is viewed by a 1-cm diameter phototube. The mirrorized aluminum walls are thin (250 microns) to minimize showering in the scattering plane. The Cerenkov light collection efficiency is estimated to be over 50%. The electron energy threshold for producing Cerenkov light is 10 MeV, providing good immunity to low energy backgrounds. The phototubes are operated at low gain (100,000) to ensure a linear response function.

The Compton Proportional Tube Detector consists of 16 proportional counter tubes of inside diameter 3.9 mm embedded in a 5-radiation length radiator. The sensitive area of the detector is 60 mm in the horizontal plane by 6 mm in the vertical plane. In order to maintain a linear response, they are operated at very low gain (50-100). The detector is heavily shielded except for a narrow region in the scattering plane. This reduces susceptibility to beam related backgrounds.

Since the laser is pulsed once in 11 machine pulses, the ten intervening pulses provide an accurate measurement of the background. The background in both detectors is due principally to beamstrahlung photons produced at the SLC

interaction point. The signal-to-noise ratio is typically 5-10 for the Cerenkov detector and 1-2 for the Proportional Tube detector.

Figure 2 shows the raw asymmetry as a function of channel in each of the two Compton electron detectors. The data are for a typical three-minute run at a time when the beam polarization exceeded 60%. The raw asymmetries are as high as 45% in the backward scattering channels.

Any channel in either of the two detectors, with large analyzing power, can be used to measure the beam polarization, if the analyzing power for that channel is well understood. The detector position and spectrometer momentum scale are determined from measurements of the kinematic endpoint of the Compton recoil electron energy spectrum, and from the zero-asymmetry point. Corrections to the analyzing power of each channel are made for the finite width of the channel, and for showering in the pre-radiator and channel walls.

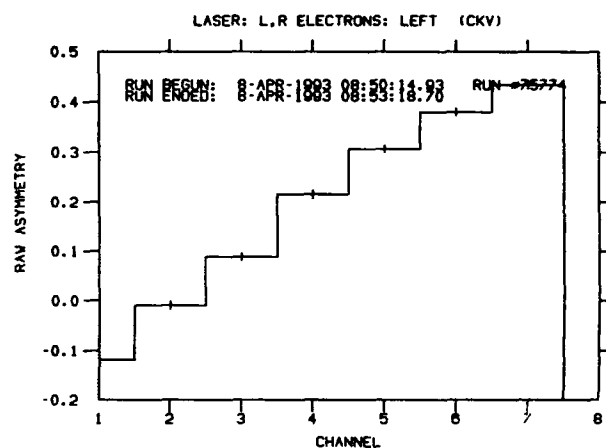


Fig. 2A. Raw asymmetry as a function of channel in the Cerenkov detector.

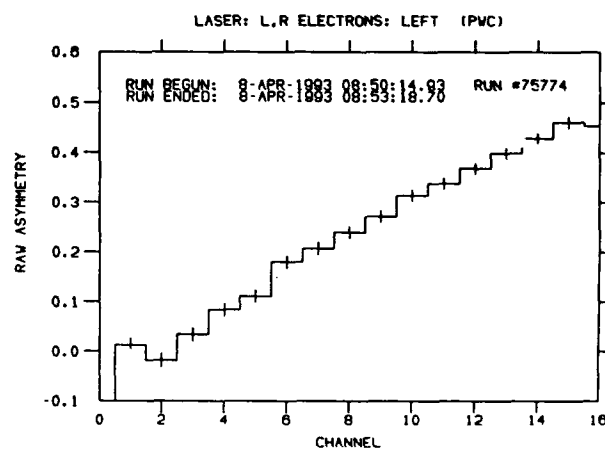


Fig. 2B. Raw asymmetry as a function of channel in the proportional tube detector.

Limits have been placed on the various sources of systematic error associated with the measurement of the electron polarization. The circular polarization of the laser beam at the interaction point is known to within 2.0%. The detector linearity is understood to within 1.5%. Interchannel consistency contributes to the systematic uncertainty at the level of 0.9%. Uncertainties in the Compton recoil energy scale, and corrections for electronic noise are both at the 0.4% level. The total systematic uncertainty of the polarization measurement to the recent SLD measurement of the left-right cross-section asymmetry in Z Boson production [1] was 2.7%. Improvements can be made that will further reduce this contribution to the systematic error.

Performance of the SLC continues to improve. Figure 3 shows the polarization measurement nearest to the production of each Z Boson in the year since polarized beams have been accelerated at the SLC. The first 11,000 Z's, produced from April to September of 1992, were with

beams whose polarization averaged 22%. The run that began in March, 1993, had polarization in the 55% range at first. This was increased to more than 60% when the wavelength of the laser at the electron source was adjusted.

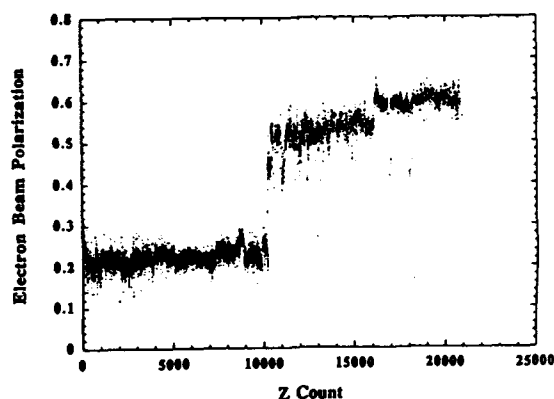


Fig. 3. Beam Polarization for 1992 and 1993 SLD Data

[1] K. Abe et al. (SLD collaboration), Physical Review Letters 70, 2515 (1993).

Measurement of the Spin of a Particle Using Undulator Radiation*

Alfredo Luccio
AGS Dept, Brookhaven National Laboratory
Upton, NY 11973

Abstract

Use of many period wigglers to rotate the spin of particles in accelerators has been proposed [1]. An added advantage of this scheme is that a spectrum of synchrotron radiation will be produced that contains a contribution due to the spin, so that the device can be effectively used as spin polarimeter, with advantages compared to Compton backscattering methods. Results are presented for two high energy proton storage rings: RHIC and the SSC.

I. INTRODUCTION

We have proposed to build spin rotators with two transverse wigglers of many poles with fields perpendicular to each other, longitudinally shifted. Wiggler spin rotators can also be used as beam diagnostic tools, allowing measurements of the beam size and spin polarization from observation of the synchrotron radiation spectrum. Beam diagnostics can be done with the SR spectral continuum from bending magnets, however the spectrum of wigglers being the result of interference presents a characteristic line structure and therefore has a higher specific brightness.

Spin polarization can be measured by Compton backscattering of laser light by the particle beam. The physical mechanism of photon production by wiggler radiation and backscattering is the same, and lead to comparable results. However, also laser backscattering produces a continuum and many of the nice properties of the enhanced wiggler spectrum are lost.

II. ELECTRIC AND MAGNETIC DIPOLE SYNCHROTRON RADIATION

A particle of mass m and charge e is accelerated in a magnetic field B . The frame of reference is shown in figure 1. The preferred direction of motion is along z (k). The radial direction is x (i), the vertical direction is y (j). In a given point of space the radiated power flux is given by the Poynting theorem [2]

$$\frac{dP}{d\sigma} = E \times B \quad ; \quad \frac{dP}{d\Omega} = \frac{R^2 E^2}{\mu_0 c} \quad (1)$$

with R the distance between charge and field point. If we only retain the "radiation" term in the expression for the field E (i.e. the term $\propto 1/R$), it is

$$RE = \frac{\mu_0}{4\pi} ec |A(t)|; \quad 4\pi \frac{dP}{d\Omega} = \frac{\mu_0}{4\pi} e^2 c |A(t)|^2 \quad (2)$$

$$A = \frac{n \times \left[(n - \beta) \times \frac{d\beta}{dt} \right]}{[1 - n \cdot \beta]^3} \quad (3)$$

where A is the vector potential,

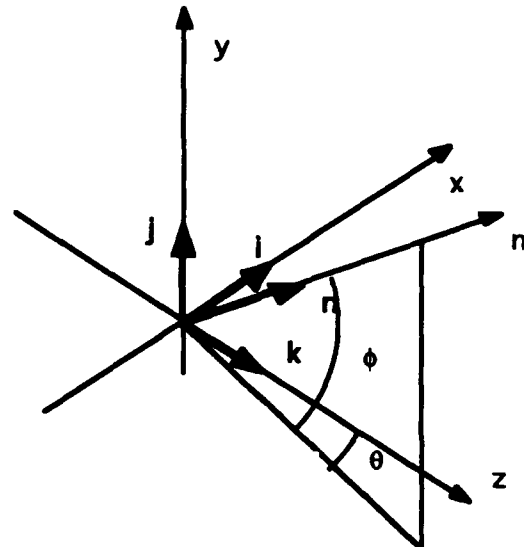


Fig. 1. The unit vector n points towards the observation point.

and the energy radiated by the particle in a time interval Δt is

$$4\pi \frac{dW}{d\Omega} = \frac{\mu_0}{4\pi} e^2 c \int_{\Delta t} |A(t)|^2 dt \quad (4)$$

To calculate the spectrum, replace t with the retarded time t_R in the integral of Eq. (4) and apply Parseval's Theorem, then, introducing the source current I [amp], obtain for the number of photons emitted per second, per unit solid angle and per unit photon energy interval

$$\frac{d^2 n}{d\Omega d(\hbar\omega)} = \frac{\alpha I}{2\pi e} |A(\omega)|^2 \quad (5)$$

(α is the fine structure constant).

If we assume that the energy of the particle remains constant, in Eq.(3), the particle velocity β and its time derivative are calculated from the equation of motion

$$\frac{d\beta}{dt} = \beta \times \Omega \quad ; \quad \Omega = \frac{eB}{m\gamma} \quad (6)$$

In far field (Fraunhofer), the radiation will be calculated along the direction defined by the unitary vector n , with angles θ and ϕ . Vector potential components A_p , parallel to the horizontal plane and perpendicular to n , and A_σ , perpendicular to n and to A_p are

$$A_p = A \cdot [j \times n]; \quad A_\sigma = A \cdot \{[j \times n] \times n\} \quad (7)$$

Explicit expressions are of the form

$$A_p = \frac{1}{D^3} P \cdot \Omega \quad ; \quad A_\sigma = \frac{1}{D^3} S \cdot \Omega \quad (8)$$

with P and S some vector expressions, and

$$D = 1 - \beta \cdot n \quad (9)$$

The "usual" synchrotron radiation is the radiation of an oscillating electric dipole in the external magnetic field. If the

* Work supported by the U.S. Department of Energy

particle has a magnetic moment μ proportional to the spin s (in units $\pm 1/2$)

$$\mu = \frac{ge}{mc} \frac{\hbar}{2} s \quad (10)$$

where s is the particle spin in the particle rest frame (PRF), magnetic dipole radiation will appear.

In the LAB frame, the spin transforms as follows

$$S = s + \frac{\gamma^2}{\gamma+1} (\beta \cdot s) \beta. \quad (11)$$

The particle spin, in its precession in an external magnetic field, adds to the radiation field of Eq. (3) a contribution

$$A^{(s)}(t) = \frac{1}{(1-\beta \cdot n)} \frac{d}{dt} \left[\frac{n \times [S + n \times (\beta \times S)]}{(1-\beta \cdot n)} \right] \quad (12)$$

and the total radiation field will be

$$A^{(r)}(t) = A(t) + \eta A^{(s)}(t), \quad (13)$$

$$\eta = g \frac{\gamma^2}{\gamma+1} \frac{\hbar \omega}{4mc^2} \equiv \frac{g\gamma}{4} \frac{\hbar \omega}{mc^2}. \quad (14)$$

Eq. (14) shows that at a given photon energy the contribution of the spin to the radiation density is inversely proportional to the mass of the particle.

Perform the time derivative in Eq.(12) and find

$$A^{(s)}(t) = \frac{D[(\dot{\beta} \cdot s)n \times \beta + (\beta \cdot s)n \times \dot{\beta}] + (\beta \cdot s)(\dot{\beta} \cdot n)n \times \beta + \frac{\beta \cdot \dot{s}}{D^2} n \times \beta}{D^3} \quad (15)$$

where the first term contains the spin and the second its time derivative.

The spin s precesses in an external magnetic field, according to the BMT equation

$$\frac{ds}{dt} = C_1 s \times \Omega + C_2 (\beta \cdot \Omega)(s \times \beta) \quad (16)$$

$$C_1 = 1 + G\gamma; \quad C_2 = -\frac{G\gamma^2}{1+\gamma}; \quad G = g - 2. \quad (17)$$

If only a transverse magnetic field ($\Omega_x = 0, \Omega_y \neq 0$) is present and the beam has no emittance, for observation *on axis*

$$\begin{aligned} A_p &= B\Omega_y & A_\sigma &= 0 \\ A_p^{(s)} &= 0 & A_\sigma^{(s)} &= -F[C_1\theta_b s_x + s_z]\Omega_y \end{aligned} \quad (18)$$

with the positions

$$\begin{cases} F = 1 + \gamma^2(\Delta\theta^2 + \Delta\phi^2) \\ B = 1 - \gamma^2(\Delta\theta^2 - \Delta\phi^2) \end{cases}; \begin{cases} \Delta\theta = \theta - \theta_b \\ \Delta\phi = \phi - \phi_b \end{cases} \quad (19)$$

Eq.(18) shows that on axis the spin dependent radiation is polarized in a direction parallel to the magnetic field.

The spectrum is obtained by a Fourier transform of the vector potential of Eq. (18). In an undulator with N periods (lines of width $1/N$), write the magnetic field as

$$\Omega_y = \Omega_0 \sin \omega_0 t; \quad \omega_0 = \frac{2\pi c}{\lambda_0}, \quad (20)$$

with λ_0 the undulator period. In this field, an approximate expression for the instantaneous angle of the trajectory is

$$\theta_b = \frac{k}{\gamma} \sin \omega_0 t; \quad k = \frac{e}{2\pi mc} \lambda_0 B = \frac{\gamma}{c} \lambda_0 \Omega_0. \quad (21)$$

The first Eq. (18) yields

$$A_p(t) = (1 - \gamma^2 \theta_b^2) \Omega = \Omega_0 (1 - k^2 \sin^2 \omega_0 t) \sin \omega_0 t \quad (22)$$

showing that the spin independent radiation field only contains odd harmonics on axis (in this simplification, only 1 and 3).

The fourth Eq.(13) for the spin dependent radiation field is

$$A_\sigma^{(s)}(t) = -(1 + \gamma^2 \theta_b^2) [C_1 \theta_b s_x + s_z] \Omega. \quad (23)$$

After integration of the BMT, e.g. if we assume example that the beam is totally x polarized at the entrance in the magnetic field, we obtain an expression also containing only odd harmonics.

A first competitor that can make the observation of the spin dependent radiation difficult is the *finite emittance* of the beam. In this case, a contribution A_σ also appears on axis, but in the *even* spectral harmonics. The ratio is

$$\frac{A_\sigma^{(s)}}{A_\sigma} = \frac{2\eta}{\gamma} \sqrt{\frac{\beta_y}{\epsilon_y}} \quad (24)$$

with ϵ_y and β_y are the emittance and the twiss function. This may impose a limit on beam emittance, and shows that it is convenient to make the beam vertically parallel and wide.

Another competing effect in the odd harmonics and in the σ polarization is due to undulator field imperfections, since a small $\delta\Omega_x$ field residual component with the *same periodicity* of the main field will again produce an unwanted A_σ on axis. A signal to noise ratio of the order of one is obtained when

$$\frac{\delta\Omega_x}{\Omega_y} \leq \eta = \frac{g\gamma}{4} \frac{\hbar \omega}{mc^2}. \quad (25)$$

This is of the order of 10^{-5} for protons, thus to measure the proton spin the contribution to the field errors in phase with the field should be very small. Using the random walk argument through N periods [3], we find an upper limit of the error in phase of the order of

$$\left(\frac{\delta\Omega}{\Omega} \right)_{\text{in phase}} = \frac{1}{\sqrt{N}} \left(\frac{\delta\Omega}{\Omega} \right)_{\text{random}} \quad (26)$$

III. COMPTON BACK SCATTERING

The fundamental frequency of undulator radiation is

$$\omega_1 = \omega_0 \frac{2\gamma^2}{1 + \frac{1}{2}k^2 + \gamma^2(\Delta\theta^2 + \Delta\phi^2)}. \quad (27)$$

Compare this with the radiation obtained by scattering of laser light by a charged particle beam (head-on collisions)

$$\hbar\omega_s \approx \hbar\omega_L \frac{2(1+\beta)\gamma^2}{1 + 2(1+\beta)\gamma \frac{\hbar\omega_L}{mc^2} + \gamma^2\theta_s^2} \quad (28)$$

with ω_s and ω_L the frequency of the scattered and laser radiation, and θ_s the angle of the back scattered photon.

Let us treat the radiation from an undulator as a scattering process of a photon and a charged particle. In the PRF, the

undulator is seen as an incoming e.m. wave, since Relativity builds up an electric field from the static magnetic field of the undulator. (Note that this equivalent wave does not travel at the speed of light, but at the lower speed βc).

The intensity of the back scattered radiation is related to the luminosity of the process as

$$n_s = \frac{N_p N_L}{\Sigma} f \sigma \quad (29)$$

with n_s the number of back scattered photons per unit time, N_p and N_L the number of particles and primary photons contained in the volume of interaction, Σ the common cross section of the particle and laser beams, f the frequency of encounters, and σ the scattering cross section.

The radiation cone has a half-aperture defined by

$$\gamma\theta \approx 1. \quad (30)$$

If the particles have a spin, the scattering cross section can be written as follows [4]

$$\sigma = \sigma_0 \pm \sigma_1 P_L P_p \cos \phi \quad (31)$$

where σ_0 is the scattering cs for the unpolarized beam, σ_1 the spin dependent scattering cs, P_L the polarization of the laser, P_p the particle spin and ϕ the scattering angle relative to P_p . It can be shown that the unpolarized cross section is symmetric around the axis of scattering with a maximum there

$$\sigma_0|_{\max} = 2r_0^2 \quad ; \quad r_0 = \frac{\mu_0 e^2}{4\pi m} \quad (32)$$

(r_0 the classical radius of the proton), and that the polarized cross section is anti symmetric about the axis of scattering with maxima at angles determined by

$$\gamma\theta_s = \frac{1}{\sqrt{3}}. \quad (33)$$

The ratio between maximum polarized cross section to maximum unpolarized is

$$\frac{\sigma_1|_{\max}}{\sigma_0|_{\max}} = \frac{3\sqrt{3}}{16} \xi = \frac{3\sqrt{3}}{4} \gamma \frac{\hbar\omega_L}{mc^2}. \quad (34)$$

A comparison of the ξ parameter of Eq. (34) for laser scattering with the η parameter of Eq. (14) shows that the relative intensity of the polarized to unpolarized radiation is of the same order, as it should.

In the scattering of virtual undulator photons, the number of primary photons to enter in Eq. (29) can be calculated by dividing the magnetic energy by the energy of a photon

$$\frac{\epsilon_0 c^2 B_0^2}{2\hbar\omega_0} V \quad (35)$$

with V the volume of the particle beam bunch. Both for undulator radiation and BS, the intensity of the observed radiation is inversely proportional to the square of the mass of the particle.

IV. CONCLUSIONS

The spin polarization of the beam can be measured by synchrotron radiation or by Compton backscattering of laser light. The physical principles are similar for the two modes, with some important differences.

Undulator radiation shows the line structure of a diffraction pattern, with characteristic polarization properties.

Compton BS produces a wide spectrum of radiation, correlated to the observation angle. If the undulator radiation is interpreted as a scattering of virtual photons, the expression for the luminosity shows that the number of undulator photons in the interaction region can be very large, since each photon (of frequency ω_0) is much smaller than a laser photon (of frequency ω_L).

Tables 1 and 2 show the order of magnitude of some of the quantities in selected machines. We have considered two proton machines: RHIC and SSC.

Table 1. Undulator and Laser Parameters.

mc^2 [MeV]	938
r_0^2 [m ²]	5.58
r_0^2 [m ²]	2.36 10 ⁻³⁶
<u>undulator</u>	
λ_0 [m]	0.20
B_0 [T]	3.2
N	20
$k =$	0.05086 $\lambda_0 B_0 = 0.0326$
$\hbar\omega_0$ [eV]	6.20 10 ⁻⁶
<u>Laser scattering</u>	
ND-Yag, 10 mJ, 1 KHz, $\lambda_L = 532$ nm	
$\hbar\omega_L$ [eV]	2.33

Table 2. Proton Colliders.

	RHIC	SSC
γ (= GeV)	270 (250)	2.1 10 ⁴ (20 TV)
emittance	9	0.05
[10 ⁻⁹ π m-rad]		
current	10 ¹¹ /bunch	7.3 10 ⁹ /bunch
beta [m]	100	100
<u>undulator radiation</u>		
$\hbar\omega_1$ [eV]	4.4 (5 th harm)	5.6 10 ³
$\frac{d^2n}{d\theta d\phi}$ [1/sec-rad ²]	6.5 10 ²²	4.1 10 ²⁶
η , Eq. (31)	1.8 10 ⁻⁶	0.17
<u>backscattering</u>		
$\hbar\omega_s$, max	66 MeV	4.2 GeV
ns [1/sec]	0.030	7.2 10 ³
ξ , Eq. (81)	2.6 10 ⁻⁶	2.1 10 ⁻⁴

IV. REFERENCES

- [1] A.Luccio, M.Conte, these Proceedings
- [2] J.D.Jackson "Classical Electrodynamics" Wiley, NY (1962)
- [3] N.M.Kincaid, J. Opt. Soc. Am B2 (1985) 1294
- [4] D.B.Gustavson et al., Nucl. Inst. Meth. 165 (1979) 177

Quantum Geometrical Phase Signal of NLC Bunch Cross Section Carried by Virtual Photons

Jing Shen

Institute of High Energy Physics, Academia Sinica.
19 Yu Quan Road, P. O. Box 918, Bin 6, Beijing 100039 P. R. C.

Abstract

Richter pointed out that the final focus for NLC pose a very difficult challenge. The cross section of bunch at interaction point is about $\sigma_x \sigma_y = 60 \text{ nm} \times 2 \text{ nm}$. It is too small to measure by EEE methods. Hence, The new conceptions of beam — beam deflection and inverse Compton gamma modulation are developing respectively at SLAC and KEK in the scope of orthodox quantum mechanics. Here we pointed out that the cross section information of bunch can be carried by the quantum geometrical phase of a test beam across the bunch which is modulated by the virtual photons of bunch. It is beyond the orthodox quantum mechanics, standard of IEC, ANSI, IEEE,

GB and presented by EM potential $[A, i\sqrt{\epsilon_0 \mu_0} \varphi]$ of bunch. The EM potential signals of unpolarized bunch signals have similar formula of $\sigma_x \sigma_y = a^2 \exp[P_1 \theta / N]$, where $P_1 = -P_m = -8h/\mu_0 e^2 v$ is a magnetic constant for rarefied bunch, $P_1 = P_e = 4\pi e_0 hc/e^2$ is a electric constant for dense bunch. Since NLC beam is always polarized, the magnetic potential flux line of bunch spin are concentric circles surrounding the bunch axis. It can be measured remotely. Hence, $\sigma_x \sigma_y = SH^2 N / \theta$, where $S = 3\mu_0 \alpha \mu_B e / 32h = \text{Constant}$, σ_x is bunch length, H is the distance of detection beam, θ is quantum geometrical phase, N is partical number of a bunch. It can be measured by electron, neutron or atom beam interferometers, including superconductive ring interferometers.

I. Introduction

Richter pointed out in 1989 that the final focus system for the NLC (Next generation Linear Collider) pose a very difficult challenge. One of the most difficult problems is measuring the beam size at the interaction point. None now exists except for beam deflection system. [1, 2] Hitherto, physical methods of Beam — Beam Deflection and Inverse Compton Gamma Modulation have been developing at SLAC and KEK in the scope of orthodox quantum mechanics, [3 — 5] and standards of IEC, ANSI, IEEE, GB.

In the point of view of EEE technique, the bunch size measurement of NLC demands time — spatial resolution of fs and pm. It exceeds the recent technical ability of EEE. Therefore, it is a physical problem, which will promote the development of EEE.

II. Quantum Signal Dynamics

The particle distance in NLC is equal approximately to the radius of positronium. Hence, bunch signal of NLC is a special problem of QED field with geometric shape of bunch and boundary condition of beampipe. However, it is beyond orthodox QM.

Here we pointed out that the information of a bunch can be carried by the quantum geometrical phase of a test beam across the bunch side. It is an effect beyond orthodox quantum mechanics, and presented by EM potential A of a polarized bunch spin as well as $[A, i\sqrt{\epsilon_0 \mu_0} \varphi]$ of bunch.

To modulate and demodulate a QED signal of both real and virtual photons as well as electrons for the purpose of carrying NLC bunch size information, we have analyzed subtle discrimination in the four kinds of quantization theory. [6, 7] Therefore, we suggest that

- (1) abandon the quantization of wave — particle unification which is the standard quantum conception of recent ANSI/IEEE std 100 — 1988, because it neglects virtual photons, which are the bunch signals actually;
- (2) abandon the carnonical quantization of QED signal field, because it is not covariant though it is the standard form of orthodox QED theory;
- (3) adopt quantization of path integral of gauge field;
- (4) extend the quantization of path integral in state space from flat Hilbert space to a curved Riemann — Hilbert space to reform the basic conception of cybernetics, where the measurable and controllable problems of object like bunch is the first fundamental conception of all.

It is covariant, and deal with both virtual and real photons. Furthermore, the state transfer equation of bunch signal splits into two parts: the dynamic equation and the geometric phase equation. The late has not yet been used as a signal equation in ANSI/IEEE std 100 — 1988, GB3100 — 86, IEC 50 (121) 1978, ISO 31 — 5: 1979, ISO 31 — 6: 1992, but it carries the information of bunch size. Hence, It can be used to measure the bunch cross — section $\sigma_x \sigma_y$ of the NLC bunch.

III. Quantum Geometric Phase of Virtual Photon of Bunch

Let Φ_i is the state transfer matrix in an ordinary flat Hilbert space of orthodox quantum theory, then the extended state transfer matrix in a curved Riemann Hilbert space is Φ which equals Φ_i multiplied by Φ_e . Hence, we have

$$\Phi = \Phi_e \cdot \Phi_i \quad (3.1)$$

where the phase factor of state vector is

$$\Phi_e = \exp[-i\theta(x)] \quad (3.2)$$

and the phase angle is

$$\begin{aligned} \theta(x) &= \frac{e}{h} \oint A_\mu(x) dx \\ &= \frac{e}{h} \oint [A, i\sqrt{\epsilon_0 \mu_0} \varphi] \cdot d[x, ict] \\ &= \frac{e}{h} \left[\oint A(x) \cdot dx, -\sqrt{\epsilon_0 \mu_0} \int_A^B (\varphi_B - \varphi_A) dl \right] \end{aligned}$$

$$= \frac{e}{h} [F_m - \frac{i}{c} V l] \quad (3.3)$$

where

θ : the angle increment of a parallel displacement loop of a state vector in the curved state space, [0];
 $A(z)$: the magnetic potential of bunch, [W/m];
 F_m : the magnetic flux of bunch, [W];
 φ_A, φ_B : the electrical potential of bunch at position A and B, [V];
 l : the effective bunch length, [L].

IV. Bunch Cross Section Information Carried by Potential and Readout by Quantum Geometric Phase

A. Flight Coaxial Cavity

Approximately, the VLE virtual photon in wakefield looks like a inner conductor which extend the bunch [6]. It is π multiple longer than bunch length. Hence, the flight coaxial approximation of bunch — beampipe system of Wang — Leow [7] can be considered as a first order. If we choose $4\sigma_z$ of bunch to be the inner current then its actual length is $4\pi\sigma_z$, because the following wakefield of VLE mode is a displacement current which extends the bunch current length to

$$l = 4\pi\sigma_z \quad (4.1.1)$$

Thus, the mutual inductance L and capacitance C are approximately expressed by

$$L = 4\pi\sigma_z \frac{\mu_0 \ln \frac{a}{\sqrt{\sigma_z \sigma_y}}}{4\pi} \quad (4.1.2)$$

$$C = 4\pi\sigma_z 2\pi\epsilon_0 / \ln \left(\frac{a_i}{\sqrt{\sigma_z \sigma_y}} \right) \quad (4.1.3)$$

and the bunch current as a δ function is

$$I_b = \frac{Nev}{4\sigma_z} \delta(t - t_0) \quad (4.1.4)$$

and its magnetic flux and electric potential difference

$$F_m = I_b L = NevL / 4\sigma_z \quad (4.1.5)$$

$$\varphi_B - \varphi_A = V = Q/C = Ne/C \quad (4.1.6)$$

where

$\sigma_x, \sigma_y, \sigma_z$: standard deviation of bunch width, height, and length, [L];

N : the particle number in bunch, [0];

v : the bunch velocity, [LT⁻¹];

a : the radius of beampipe, [L];

a_i : the radial distances of potential detectors, [L].

B. Magnetic Potential Signal of Unpolarized Bunch Cross Section

From (4.1.2), we have

$$\sigma_x \sigma_y = a^2 \exp \left[- \frac{2L}{\sigma_z \mu_0} \right] \quad (4.2.1)$$

Substitute (4.1.5), (3.3) into (4.2.1)

$$\sigma_x \sigma_y = a^2 \exp \left[- P_m \theta / N \right] \quad (4.2.2)$$

$$P_m = \frac{8h}{\mu_0 e^2 v}, [0] \quad (4.2.3)$$

$$h = 1.05457266(63) \times 10^{-34} \text{ Js}$$

$$e = 1.60217733(49) \times 10^{-19} \text{ C}$$

$$\mu_0 = 4\pi 10^{-7} \text{ H/m}$$

$$\epsilon_0 = 8.854187817 \times 10^{-12} \text{ F/m}$$

$$v = c = 299792458 \text{ m/s}$$

$$\therefore P_m = 43.62$$

$$\theta = \frac{N}{P_m} \ln \frac{a^2}{\sigma_x \sigma_y} \quad (4.2.4)$$

If $N = 10^2$, then $\theta \approx \pi$, that means it is suitable merely to the very rarefied bunch.

C. Electric Potential Signal of Unpolarized Bunch Cross Section

Substituting (4.1.3) and (3.3) into (4.1.6), we have

$$\sigma_x \sigma_y = a_i^2 \exp [P_e \theta / N] \quad (4.3.1)$$

where

$$P_e = 16\pi^2 \epsilon_0 h c \sigma_z / e^2 l = 4\pi \epsilon_0 h c / e^2, [0] \quad (4.3.2)$$

$$\therefore P_e = 1.370 \times 10^{14}$$

If $N = 4.3 \times 10^{14}$ then $\theta = \pi$ that means it is good for very dense bunch.

D. Polarized Signal of Bunch

The magnetic induction on the bunch axis is

$$B_z = \mu_0 M = \mu_0 \lim_{\Delta V \rightarrow 0} \frac{\sum m_i}{\Delta V} \quad (4.4.1)$$

$$\sum m_i = N \alpha \mu_B \quad (4.4.2)$$

$$\Delta V = \frac{4}{3} \pi (2\sigma_x) (2\sigma_y) (2\sigma_z) \quad (4.4.3)$$

where

M is the magnetization of bunch, [A/m];

m_i is the magneton of bunch electron, [Am²];

$$\mu_B \text{ is Bohr magneton} = 9.27401541 \times 10^{-23} \text{ J/T} \\ = 5.78838263 \times 10^{-11} \text{ MeV/T}$$

$$\alpha = 1.001145358 \pm 0.000000005$$

Hence,

$$\sigma_x \sigma_y = \frac{3\mu_0 \alpha \mu_B N}{32\pi \sigma_z B_z^2} \quad (4.4.4)$$

Unfortunately, B_z^2 is difficult to measure because it is at the bunch axis

However

$$\therefore |B_z^2| \pi H^2 = |A_\varphi^2| 2\pi H \quad (4.4.5)$$

$$\therefore A_\varphi^2 = \frac{h\theta}{e2\pi H} \quad (4.4.6)$$

$$\therefore B_z^2 = \frac{h\theta}{\pi e H^2 Z_0} \quad (4.4.7)$$

where, A_φ^2 is concentric circles surrounding the bunch axis. It can be measured remotely like measuring the magnetic flux and electric potential, Z_0 is unit vector in direction of axis. H is the distance of detector from the bunch axis. Hence, substituting (4.4.7) into (4.4.4), we have

$$\sigma_x \sigma_y = \frac{3\mu_0 \alpha \mu_B N e}{32 h \sigma_z \theta} H^2 \quad (4.4.8)$$

$$\sigma_x \sigma_y \sigma_z = S H^2 N / \theta \quad (4.4.9)$$

$$S = \frac{3\mu_0 \alpha \mu_B e}{32 h} = 1.659906733 \times 10^{-15} \text{ meter} \quad (4.4.10)$$

$$\theta = S N \frac{H^2}{\sigma_x \sigma_y \sigma_z} \quad (4.4.11)$$

$$\text{If } N = 10^{10}, \text{ then } S N = 1.66 \times 10^{-5}$$

$$\text{If } \sigma_x = 60 \text{ nm}, \sigma_y = 2 \text{ nm}, \sigma_z = 60 \text{ nm}, H = 36.9 \text{ nm}, \text{ then } \theta = \pi$$

That means, the distance between test beam and bunch is about 40nm, then $\theta = \pi$. It is available to carry out by atom interferometers for the intermediate density bunch.

E. Magnetic Field of Bunch Motion

The magnetic field strength of bunch motion is

$$H_p = \frac{I_b}{2\pi H} = \frac{Nev}{4\sigma_p H} [\text{A/m}] \quad (4.5.1)$$

$$= 1.71 \times 10^7 [\text{A/m}],$$

where $N = 10^{10}$, $H = 1.17\text{cm}$. It is equivalent to $B_p = \mu_0 H_p = 21.48\text{T}$

Hence, it is an extreme strong jamming for the electron interferometer, therefore, the neutron or atom interferometers may be used.

F. Wake Field Effect

The wakefield effect will reduce B_p from 21T to about 7T. [6] Furthermore, If $\sigma_s = 600\mu\text{m}$, then $B_p = 0.7\text{T}$, hence it is easy to be shielded by Meissner effect.

The wakefield effect also happens to A_p^0 . It lengthen the interference time and benefits the method of interference. If the $\sigma_s = 60\mu\text{m}$, then the interference time is lengthened from 0.8ps to 2.4ps.

Thus, we can obtain the bunch cross section by three ways of magnetic flux F_m , electric potential V , and polarization potential A_p^0 . All of these three quantities can be measured remotely by the phase shifts θ of probe beam interferometers which are composed of electron beam, neutron beam, or atom beam etc.

V. Bunch Length Information

$\sigma_s \approx 60$ micron, It is about $1 - 2 \times 10^2$ times long of the wave length of Cerenkov radiation in an optical fiber close to the bunch. Hence σ_s can be measured by waveguiding Cerenkov radiation [9] which is also in the response range of optical interferometers. [10] or by non-linear optical method. [11]

VI. Instrumentation

θ may be measured directly by electron or atom beam interferometer through EEE quantities of $[F_m, -\frac{i}{c}V]$ of A_p^0 with SI unit of $[\text{Webb}, -i\text{Volt} \cdot \text{sec}]$.

The bunch length of NLC is designed as 60 micron, Thus, the signal duration is 0.4—0.8ps. It is lengthened by wakefield to 2.4 ps and just in the response range of coherent technique of recent electron [12] and atom [13, 14] interferometers. We analyze subtle discrimination this subject as the bunch signal dynamics. [6, 7]

VII. Virtual Photons and Accelerator

Hitheto, the $[E, cB]$ is always used in accelerator physics to deal with accelerating, bending, focusing, observing, monitoring and measuring. It complies with standards of IEC, ANSI, IEEE, GB etc, but it loses some abilities of EM field. For example, [15]

$$E = -\frac{q}{4\pi\epsilon_0} \left[\frac{R_0}{R^2} + \frac{R}{c} \partial_t \left(\frac{R_0}{R^2} \right) + \frac{1}{c^2} \partial_t^2 R_0 \right] \quad (7.1)$$

to be the acceleration field, people used first term of static for

van de Grooff, (1931) or Cockcroft—Walton (1932) accelerators. People used third term of real photon for Wideroe proton linac (1929), Hanson electron linac (1947), Lawrence cyclotron (1931), Kerst betatron (1941), and Veksler—McMillan Synchrotron (1945); and also modern colliders of e^+e^- , $p\bar{p}$, pp and ep . People usually forgot second term of virtual photon for accelerator. Here we used A_p instead of $[E, cB]$ to research accelerators. A_p composed of virtual and real photons which include more properties. Some of new conceptual designs about detection and acceleration worked out by the author are in preparing. [16] The geometrical information of bunch is one of them.

Thanks to Prof. M. H. Ye and Prof. Z. P. Zheng.

VIII. References

- [1] B. Richter, "SLC Statuts and SLAC Future Plans" *SLAC - PUB-5075*, Aug. 1989 (E/A).
- [2] J. M. Paterson, "Next Generation Linear Collider", Address on Opening Conference of Accelerator Physics Symposium of PASC, IHEP, Beijing June 8, 1991.
- [3] Yu—Chiu Chao and Pisin Chen "Higher Order Effects in Beam—Beam Deflection" *SLAC - PUB-5221*, Jan. 1992. (A).
- [4] R. D. Ruth, "The Development of NLC at SLAC", *SLAC - PUB-5729*, Feb. 1992 (A).
- [5] T. Shintake, "Laser—Compton Spot Size Monitor, Proc. of the 3rd Workshop on JLC, KEK Proc. 92—13 Dec. 1992.
- [6] Jing Shen, "Bunch Signal Dynamics I: Charge, and Virtual Photon Sources, Beampipe Responses, Coherent Beamstrahlung; VTA, VTEM, VTE, VTM, VLE, RTE, RTM Modes of Signal", *BIHEP-DE-92-02*, Jan. 1. 1992.
- [7] Jing Shen, "Theoretical Base of NLC Bunch Size Measurement—Quantum Geometrical Information and General Relativistic Cybernetics, Bunch Signal Dynamics II", *BIHEP-DE-92-03*, April. 1. 1992.
- [8] J. W. Wang and G. A. Leow, *SLAC-PUC-2830*, Oct. 1981 (A).
- [9] A. I. Akhiezer, *Nuovo Cim*, Series 10. 3, Suppl. (4). 591, (1956).
- [10] R. C. Eckardt and C. H. Lee, *Appl. Phys. Lett.* 15, PP. 425—427, (1969).
- [11] Jing Shen, "Ultra Short Bunch Length Measurement—Nonlinear Optical Effect of Bunch Virtual Photon", *BIHEP-DE-93*, in printing, 1993.
- [12] R. A. Webb and S. Washburn, *Phys. Today*. 41. 12, PP. 44—53, Dec. 1988.
- [13] D. W. Keith, C. R. Ekstrom, A. Turchette, and D. E. Pritchard, *Phys. Rev. Lett.* 66, 2693 (1991).
- [14] M. Kasevich, and S. Chu, *Phys. Rev. Lett.* 67, 181 (1991).
- [15] E. J. N. Wilson, "Accelerators for the Twenty—First Century—A Review", *CERN90-05*, 1990.
- [16] Jing Shen, "Virtual Photon Impulse of Bunch, Beampipe Response, Coherent RF Beamstrahlung; and BEPC Bunch Length, BES Jam, Virtual Acceleration", 1993 *IEEE-APS Particle Accelerator Conference*, Washington D. C. Mar. 1993.

Response of Air-Filled Ion Chambers to High-Intensity Radiation Pulses

Michael Plum and David Brown
Los Alamos National Laboratory

Abstract

Ion chambers are one of the most popular types of detectors used for beam loss-monitor systems. To provide a foundation for the development of future loss-monitor systems, and to fully characterize the ion chambers in use at LAMPF, we have studied the response of air-filled cylindrical ion chambers to high-intensity, short-duration radiation pulses. The most intense pulses were about 180 rad in 250 ns (the equivalent steady-state dose rate was about 700 Mrad/h). We filled our chambers with nitrogen gas at 760 Torr and air at 600 Torr. The ion chambers were driven into extreme nonlinear response. We hope these data will be used to design loss-monitor systems based on air-filled ion chambers, thus eliminating the need for gas-flow systems and/or air-tight ion chambers.

I. INTRODUCTION

Most loss-monitor detectors at the Los Alamos Proton Storage Ring (PSR) facility are ion chambers filled with nitrogen gas at 1 std. atm. The idea behind this combination of gas and pressure is, if the ion chamber leaks, and the gas is exchanged for air at local pressure (about 80% of 1 std. atm.), the sensitivity of the ion chamber will decrease by about 20%. This 20% change is small enough that the safety of the system will not be seriously compromised, yet large enough that we can detect it with a radioactive source check.

The main advantage of using ion chambers filled with air at local pressure is that one would not have to worry about leaks or gas-handling systems. The disadvantages are:

- 1) the response becomes nonlinear at smaller radiation pulses;
- 2) to control the sensitivity of the ion chamber, one may vary the volume of the gas, but not the pressure;
- 3) the sensitivity of the ion chamber may change in proportion to local barometric changes;
- 4) possible undesirable effects due to water vapor migrating into the ion chamber gas. We have not yet studied these effects.

At the Los Alamos Meson Physics Facility (LAMPF), the function of the PSR is to compress the proton beam from the 800-MeV linear accelerator. A typical pulse of about 600 μ s is compressed to just 250 ns. The PSR is therefore an ideal source for short, intense pulses of radiation. On the other hand, monitoring beam losses from such a beam is a challenging task for some types of detectors, for example, those based on photomultiplier tubes.

II. EXPERIMENTAL SETUP

To determine the suitability of air-filled ion chambers for use at LAMPF, we conducted two sets of measurements – one in the Fall of 1991, and one in the Fall of 1992. For the first data set, we steered the PSR beam into the side of the beam pipe. Two ion chambers, one of the usual type filled with nitrogen gas at 1 std. atm., and one filled with air at local pressure, were placed about 1 m transversely from the beam pipe. For the second data set, beam was directed onto a beam plug in the PSR extraction line, and the ion chambers were placed directly alongside the plug. We chose this scenario because it is the worst-case test available at the PSR (not including actually directing the beam through the ion chamber). The location of the beam plug is such that it can intercept either beam from the linac or beam from the PSR. This gives us some flexibility on the length of the beam pulse, and therefore on the duration of the radiation pulse. For our 1992 tests the linac beam pulse length was set to 800 μ s.

As shown in Fig. 1, the active volume of our ion chambers is contained between two concentric cylinders. The outer diameter of the center electrode is 1.59 cm, the inner diameter of the HV shell is 4.19 cm, and the active volume is about 180 cm³. When filled with nitrogen gas at 1 std. atm. the sensitivity is 56 nC/rad, and when filled with air at local pressure (600 Torr) the sensitivity is 44 nC/rad. The data shown are for -1 kV and -2 kV applied to the outer cylinder. We use negative voltages because we have empirically found that negative voltages result in a more linear ion chamber response. The center electrodes of the ion chambers were connected to 0.22- μ F integrating capacitors, followed by a digitizing scope with a 1-M Ω input impedance.

III. DATA

As shown in Table 1, the 1992 data set, with beam directed onto a beam plug, offered considerably more intense radiation pulses. In Figs. 2 and 3 we plot the ion-chamber output divided by the intensity of the radiation pulse (nC/rad, or sensitivity). Such a plot should give a straight horizontal line when the ion chamber is operating in its linear region. The plot should then descend towards zero as the ion chamber begins to operate in its nonlinear region. From the figures we see that the ion chambers were clearly driven into the nonlinear response region.

As expected, the plots show that at higher voltages the ion chamber response remains linear up to higher-intensity radiation pulses, and that the sensitivity of air at local pressure is about 20% lower than nitrogen at 1 std. atm. The latter is due to the 760 vs. 600-Torr pressure difference. We also see that the response of the air-filled ion chamber becomes nonlinear at lower-intensity pulses than the nitrogen-filled ion chamber. This could be due to the large electronegativity of oxygen. Neutral oxygen atoms tend to

attract electrons to form negative ions, which combine with the positive ions to reduce the ion chamber output.

IV. CONCLUSIONS

We have measured the response of air-filled and nitrogen-filled ion chambers to high-intensity radiation pulses. The most intense pulses drove the ion chambers well into the nonlinear region. We found that, compared to the nitrogen-filled ion chamber, the response of the air-filled ion chamber becomes nonlinear at lower-intensity radiation pulses. Although the ion chamber responses were highly nonlinear for high-intensity radiation pulses, they did not exhibit any other failure modes. We hope our data can be used to develop other loss monitor systems that are simpler and more reliable through the use of air at local pressure as opposed to pure gas under pressure. If air can provide sufficient sensitivity, and if nonlinear response for high-intensity pulses is not a problem, then the advantages of air-filled ion chambers should be considered.

Table 1. Intensity and duration of radiation pulses incident on the ion chambers.

Data set	Intensity of radiation pulse	Duration
1991	0.036 to 2.3 rad	250 ns
1992	1.0 to 160 rad	250 ns
1992	1.3 to 260 rad	800 μ s

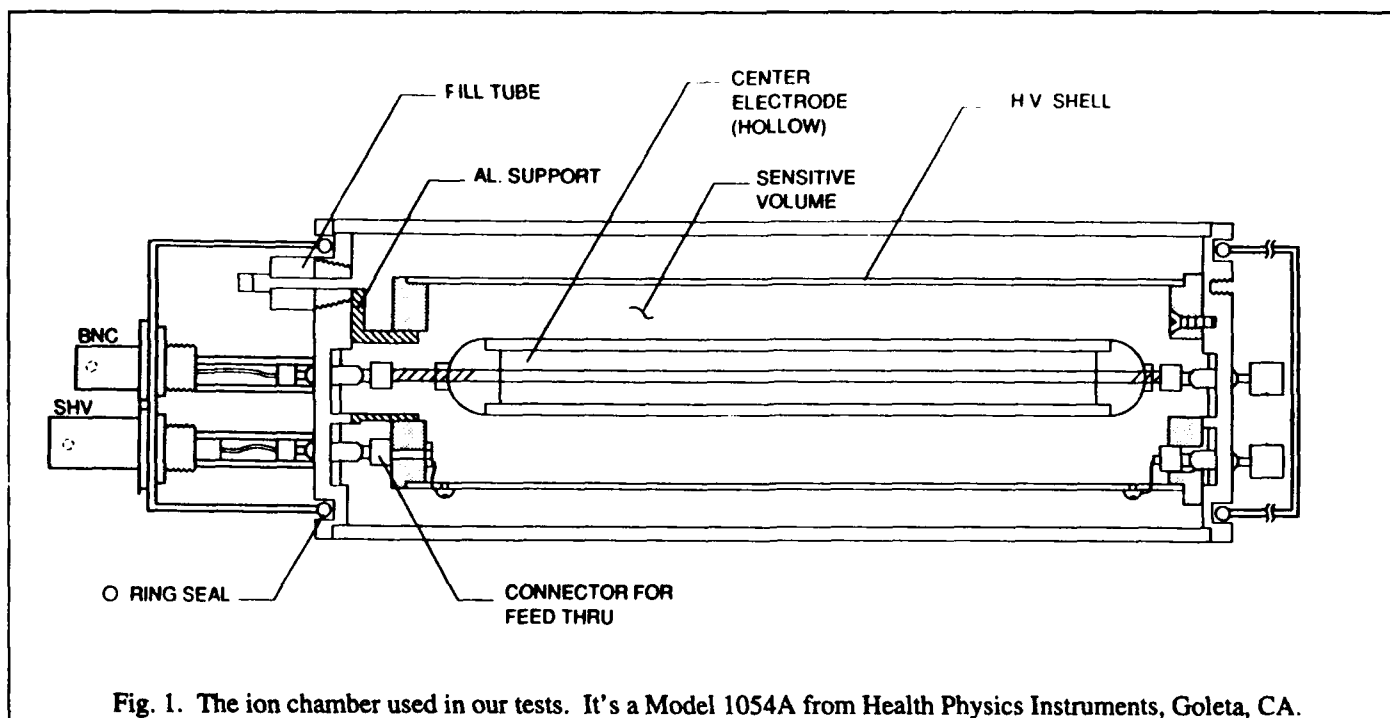


Fig. 1. The ion chamber used in our tests. It's a Model 1054A from Health Physics Instruments, Goleta, CA.

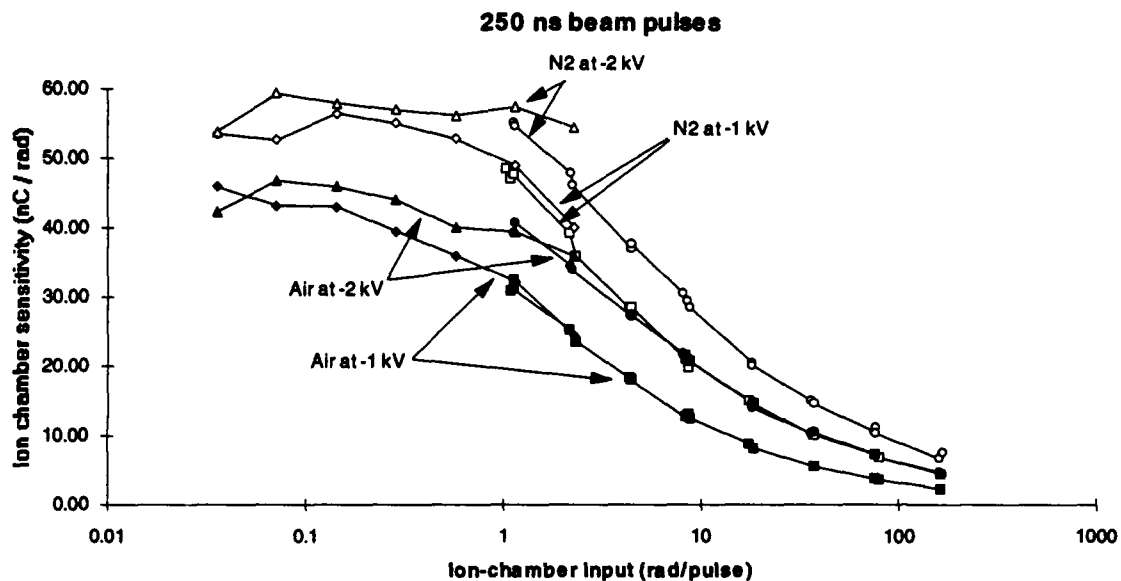


Fig. 2. 250-ns beam pulses. Data from the 1991 and 1992 tests. The air-filled ion chamber begins to become nonlinear at about 0.2 rad, and the nitrogen-filled ion chamber begins to become nonlinear at about 0.5 rad. The difference in sensitivity at low radiation pulses is due to the difference in gas pressure.

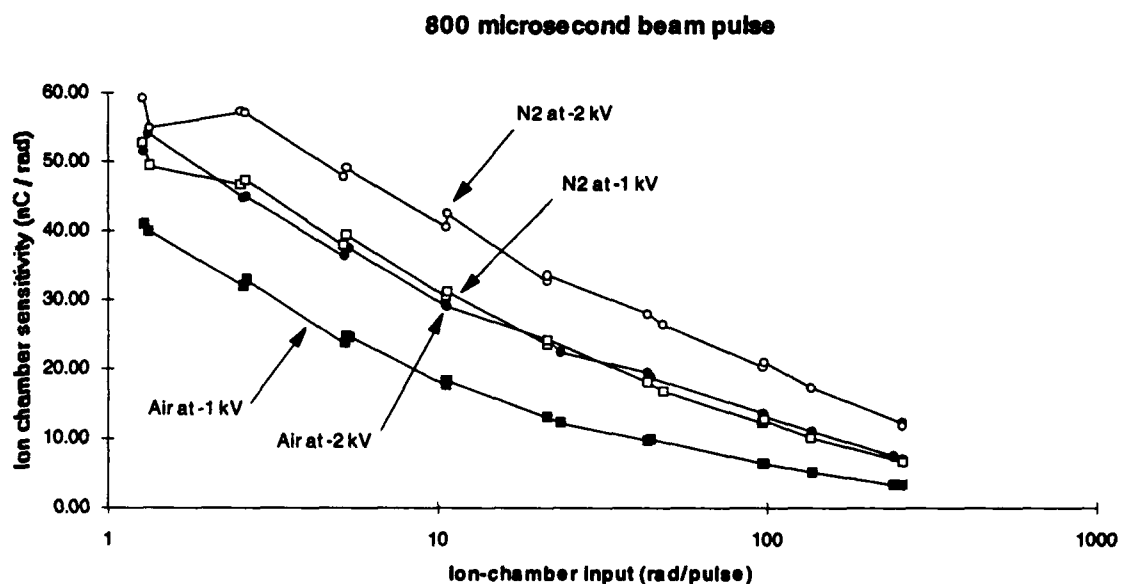


Fig. 3. 800- μ s beam pulses. Both the air-filled and nitrogen-filled ion chamber are nonlinear even at the lowest radiation pulse tested. For a given ion-chamber input (rad/pulse), the ion-chamber output (nC/rad) is higher for the 800- μ s beam pulse than for the 250-ns beam pulse.

The CEBAF Beam Loss Sensors*

J. Perry, E. Woodworth, L. Merminga, S. Simrock, R. May, G. Stapleton†
Continuous Electron Beam Accelerator Facility
12000 Jefferson Avenue, Newport News, VA 23606-1909 USA

Abstract

The CEBAF beam can burn through the vacuum wall in approximately 100 μ s. We have developed an inexpensive beam loss sensor that will unambiguously detect a true beam loss and shut off the beam within this time without tripping on moderate interference from other sources. We have incorporated a full system test into the system, with provision for direct replacement of faulty sensors without adjustment.

We describe the sensors, the signal processing design, system test results, and characterization procedures.

I. INTRODUCTION

The CEBAF beam will carry 200 μ A of current in its 100 μ m diameter, enough to burn through the accelerator vacuum wall in time of the order of 100 μ s [1, 2]. The beam loss monitors (BLM's), as the last resort for protection of the accelerator, must operate much faster than this time to allow time for the fast shutdown system [3] to shut the beam off before damage occurs. The time scale allocated to the BLM system is 10 μ s. The size of the CEBAF accelerator (7/8 mile circumference) means either that many BLM's must be installed or that each must protect a large area.

II. SENSORS

The speed requirement ruled out most ion chamber configurations quite early in the process. Although several labs have designed ion chambers to operate in this time range, we felt that photosensitive devices offered a more likely direction for highly sensitive, low-cost beam loss sensing. Geoffrey Stapleton presented the possibility of darkened photomultipliers, which were known to be sensitive to cosmic ray pulses. The mechanism is scintillation and Cherenkov radiation in the glass envelope of the tube [4, 5], and extension to beam loss monitoring by detection of the radiation shower from beam interaction with nearby matter was highly successful.

Extensive testing showed that for beam loss monitoring one of the least expensive photomultipliers, the venerable 931B, was preferable, as it is among the highest in electron gain available. Since we did not need the features which make photomultipliers expensive, such as transparent or high-efficiency photocathodes, or large size, we selected this tube as the basis of our sensor.

The variation of tube gain with cathode voltage is convenient because it allows us to shift the detection range (discussed later) to suit various conditions. The disadvantage

is that the high-voltage system hardware that we selected cost more than all the rest of the hardware together. We are investigating alternative high-voltage supplies for the needed expansion of the system as the rest of the accelerator comes on line.

The tubes are built into a housing made of ABS plastic, which has proved to be a consistently effective, inexpensive light barrier which does not impose much shielding even from lower-energy x-rays. Electrical interference is occasionally present when we must route the cabling near a fluorescent lamp, but even here we lose at most only the lowest decade (5 nA–50 nA) of the system's signal.

Since an undetected beam loss event could cause burn through of a cavity costing several hundred thousand dollars to repair reliability is a critical consideration. We incorporated into the control module [6] a test command signal which drives a light-emitting diode in the sensor. This tests the entire beam loss channel from high-voltage supply through the sensor and signal conditioning to the fault detect circuit.

The LED's within the sensor heads are calibrated precisely against reference tubes; then each tube to be used as a BLM is checked for current output at a specific cathode voltage when it is installed into the sensor head (figure 1). The light generates a current corresponding to about 80% of the four decade logarithmic scale (10% of the equivalent linear scale) of the sensor. This is well within the normal operating range of the sensors.

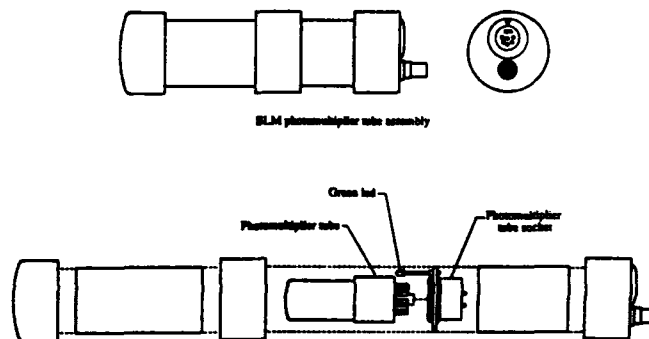


Figure 1. BLM Sensor

In extensive testing we found the best location to be well away from the beam line, since shielding by the many magnets of the CEBAF beam transport system is worst near the beamline. This gives the further benefit of reducing activation of the metallic parts of the sensor (discussed later). In the accelerator segments we attach the sensors to the cable tray, approximately five feet above the beam line, and in the recirculation arcs we attach them to the ceiling about eight feet to one side of the beam lines.

* Supported by U.S. DOE contract DE-A05-84ER40150

† Now at SSC Laboratory

III. SIGNAL PROCESSING

Since the photomultiplier is a very low noise device under normal conditions, and the radiation environment at CEBAF during normal running is rather low, the large dynamic range available from the tube (<5 nA to >100 μ A) gave us the possibility of using the full range of the tube to survey a much larger area of the accelerator than is reasonably possible with linear signal conditioning. For this reason, we incorporated logarithmic signal conditioning, using $V_{out} = k \log(I_{in})$ to measure the radiation level signal.

The log converter was designed as a dual converter followed by a differential amplifier (figure 2). The first converter is biased at 5 nA, the maximum dark current (specified at 1000 V) for the 931B, and converts to voltage the input current from the tube plus the 5 nA bias. The second converter has a variable bias to allow us to offset the baseline output and thermal drifts of the first converter. The log conversion elements (the base-emitter junction of a high-gain, low-noise transistor) are thermally connected so that thermal drifts are well compensated.

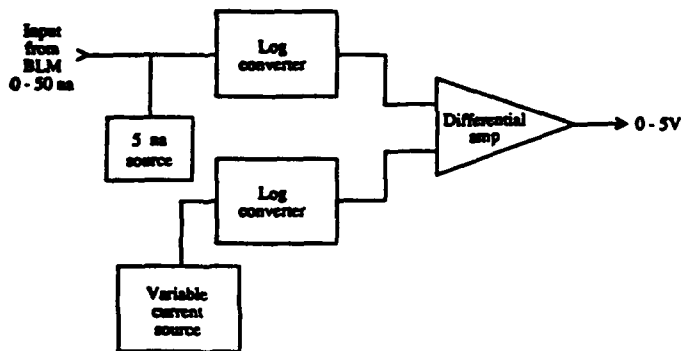


Figure 2. Signal Conditioner Block Diagram

Finally, the differential amplifier shifts the difference between the two converter outputs to a zero baseline, and amplifies the output to scale four decades of current (5 nA–50 μ A) to the 0–5 V level for the fault detect and data acquisition circuitry. The output amplifier is slowed to a 4 μ s rise time to avoid triggering on the short pulses characteristic of cosmic radiation.

IV. EXPERIENCE

In setting up the BLM's for operation, we set up the beam for 1 μ A beam current in a 100 μ sec wide pulse; this was deemed a completely safe condition for a beam driven directly into any component of the accelerator. We then drove the beam out of the beam line in all directions at many locations, concentrating on locations and angles our operations experts considered likely and/or particularly sensitive targets of errant beam. We set the cathode voltage and trip levels for reliable trip on the smallest signals found.

We tried first for fully redundant coverage of the accelerator. This proved to be impossible in some areas of the accelerator with the present density of BLM's. Where it was

not possible, we tried for full coverage, and succeeded in all areas except the injector: here, we are forced to depend upon a correctly set up beam passing through protected locations before it can arrive at an unprotected location. This is generally considered a safe assumption.

The BLM's were initially attached to the beam line. Early tests showed two problems: first, local beam loss completely saturated the sensors even with very low cathode voltages of 100 V, and second, distant loss events were completely shielded by the many magnets and other equipment in the transport system. We could not fully protect the cryomodules with their expensive superconducting cavities.

We solved these problems by moving the sensors well away from the beam line as described above. Experience has shown that CEBAF's running radiation levels are below the threshold of the BLM system's detection; we could therefore take advantage of the property of a true loss event which generates a long pointed ellipsoid of high-level radiation downstream of the loss event. Since the log conditioners allow us to work effectively with the full range of the photomultipliers, we are able to detect the lower signal levels characteristic of distant beam loss events and still not damage the tubes with overloading due to strong local loss signals. Figure 3 shows a plot of the signal versus angle of loss at a BLM in the vicinity of an accelerator cryomodule.

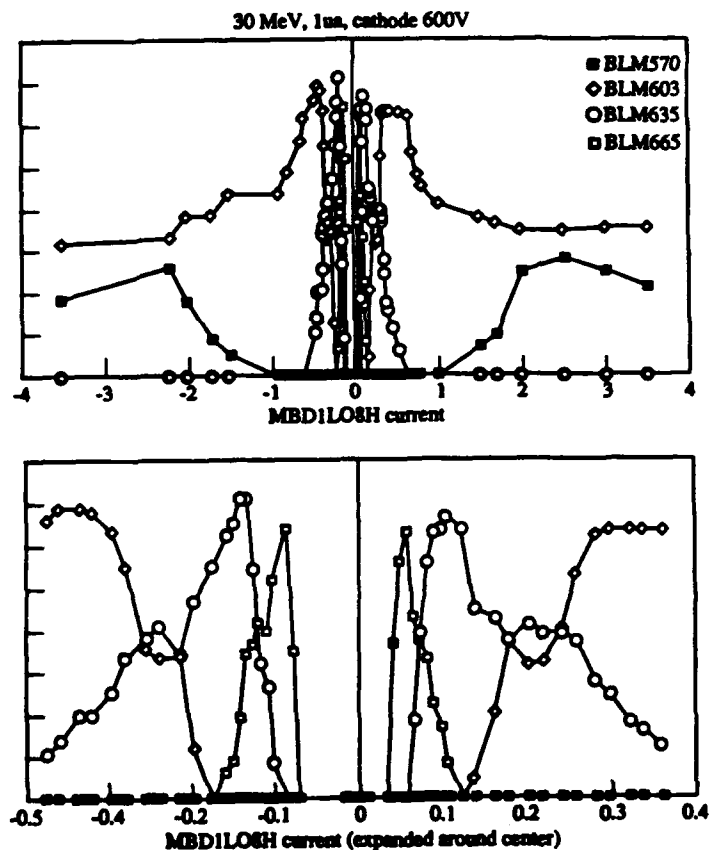


Figure 3. Beam Loss Signal vs. Corrector Magnet Current

The upper plot shows the reduction of signal level as the beam is directed at very large angles away from the beam line and the sensors. BLM 570 is actually upstream of the magnet being tested: in this 30 MeV test, one may observe that there is rather little backscatter.

The lower plot is expanded around the center of the upper plot. BLM #665 is 30 M downstream and one can see that it is effective for very small angles of loss, where the beam is lost far downstream of the disturbing magnet. BLM #635 is the next nearer BLM. Note that both BLM #635 and BLM #603 show the effect of magnet shielding at +0.2A and -0.3A. Note also that sensing overlaps from one sensor to the next at approximately midscale, which corresponds to 1% of an equivalent linear full scale. It would be impossible to protect the accelerator fully with linear signal conditioning.

Later tests showed an increasing pulse noise at the lower end of the sensors' range which limited sensitivity for higher voltages. This noise has been of concern since it was first noticed in late 1992. The photomultipliers were originally of very low noise, showing few pulses above the 15 nA level. The 70 that were in the accelerator have shown increasing spurious pulse levels up to 400 na that required that they be moved to the higher-energy sections of the accelerator and replaced with new tubes for the lower-energy sections.

It is not yet clear whether the pulse noise derives from activation of the tubes or from helium contamination due to residual helium in the accelerator tunnel. For several months, they were attached to the beam line, and subject to direct irradiation from errant beam. Further, our superconducting accelerator requires great quantities of helium for its operation, and a certain amount of that helium is always present in the tunnel atmosphere. Helium is suspect because it diffuses into the tube through the glass envelope, corrupting the vacuum.

We are testing a number of tubes for both possibilities. We have already determined that after the sensors were moved away from the beam line in February 1993 they generally showed a marked decrease in spurious pulse level and frequency; this argues for radioactive interference from the metallic elements of the photomultiplier tube. We have in fact confirmed that the worst offenders are contaminated with ^{57}Co and ^{58}Co , among other radioactive isotopes. We are having a set of the tubes tested for helium contamination.

V. CONCLUSIONS

In the accelerator the BLM sensors have so far performed adequately. They reliably detect beam loss at distances exceeding 20 m when energy is above 100 MeV at 1 μA current; at reduced energy (i.e., reduced beam loss radiation power level), pulse noise from the photomultipliers causes spurious trips if the tubes are not selected for low pulse noise. Recent tests show a diminution of this pulse noise that augurs well for the future when BLM's are placed away from the beam line.

At the low energies of the injector, the present BLM's are

inadequate: careful selection of photomultipliers and placement of sensor assemblies are required to get even partial coverage of critical locations. We are actively exploring methods of completing the coverage of the injector.

The concept of using darkened photomultipliers has proved to be an inexpensive, effective method of detecting beam loss in the higher-energy segments of the CEBAF accelerator.

III. REFERENCES

- [1] P. K. Kloeppel, "On the Temperature Effects of High Current, Low Emittance Beams," CEBAF-TN-85-018, Nov. 1985.
- [2] C. K. Sinclair, "Time Response Requirement for the BLM/FSD System," CEBAF-TN-92-046, Oct. 1992.
- [3] J. Perry, E. Woodworth, "The CEBAF Fast Shutdown System," CEBAF-PR-90-015, or, *Proceedings of 1990 Linac Conference*, p. 484, Sept. 1990.
- [4] A. T. Young, "Cosmic Ray Induced Dark Current in Photomultipliers," *Review of Scientific Instruments* 37, p. 1472, Nov. 1966.
- [5] S. N. Makeev *et al.*, "Variation of Photomultiplier Anode Current for Continuous and Pulsed Gamma Radiation," transl. in *Instrum. & Exp. Tech. (USA)*, Vol. 29, No. 1, pt. 2, Jan.-Feb. 1985, pp. 182-185.
- [6] J. Perry, E. Woodworth, "The Beam Loss Monitors at CEBAF," CEBAF-PR-90-022, October 1990, or, *Proceedings of the Second Annual Accelerator Instrumentation Workshop*, p. 294, October 1990

A Scintillating Fiber Beam Halo Detector for Heavy Ion Beam Diagnostics

M.A. McMahan, A. Assang, S. Herr, F. McCormack, G. Krebs, and B. Feinberg
Accelerator and Fusion Research Division, Lawrence Berkeley Laboratory
1 Cyclotron Road, Berkeley, CA 94720

Abstract

A prototype beam halo detector of scintillating fibers has been designed in order to detect beam halo problems at an early stage in the tuning process. The results of initial characterization of the fibers are presented and issues of electronics and readout discussed.

I. INTRODUCTION

The Bevalac at Lawrence Berkeley Laboratory (LBL), before its closure in February of 1993, was a weak-focussing synchrotron injected by the SuperHILAC linac. The Bevalac had the capability of running protons (up to 5 GeV) through uranium (up to 960 MeV/nucleon). This wide range of beams and energies caused unique problems in beam diagnostics, which were exacerbated by the large size of the beam in the accelerator and the method of extraction.

A particularly nasty diagnostic problem was the measurement of beam halo, whether caused by the extraction process, scraping on apertures, or charge-changing in the poor vacuum. The halo could be several orders of magnitude less than the peak beam intensity and thus undetectable during the tuning process using the standard Bevalac wire chambers. Yet this halo could wreak havoc with experimenters' detectors, sometimes causing insurmountable background problems. In one celebrated case, a low energy heavy ion run (the worst conditions for extraction problems as well as vacuum problems), a satellite beam 14° removed from the main beam made it through a whole beam line and into delicate detectors, bypassing both collimator systems and the target assembly along the way.

Because of experiences like these, a project was embarked upon to first, characterize the beam halo and try to understand what was the predominant cause, and then, to set up a diagnostic system for beam halo which the operators could use as part of the tuning process. The idea was eventually to have halo detectors in every beam line. Initial tests were done and a prototype detector built before the closure of the Bevalac. This detector will be described in the remainder of this paper.

II. THE HALO DETECTOR

Requirements

The main requirement of the beam halo detector was the ability to detect a large range of beam intensities, particles, and energies. This requirement made the wire chamber system useless for beam halo. For example, Figure 1 gives the calculated energy loss as a function of energy for ions ranging from protons to gold ($Z=79$). The energy loss of an ion in a 1 mm. scintillator ranges from 10000 MeV for gold at low energies down to near 0.1 MeV for protons at high energies. Coupling this with a perhaps factor of 1000 in beam intensity

between the main beam and the halo, one can imagine the magnitude of the problem.

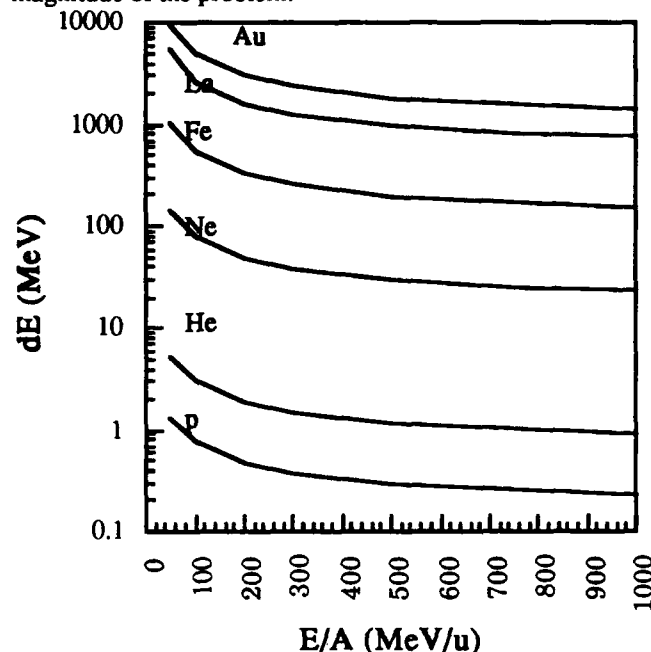


Figure 1. Calculated Energy Loss in 1 mm. scintillating fiber

Other considerations were that the chosen detector should be a high-count rate, radiation resistant, device which would integrate well into the wire chamber readouts for tuning purposes. Plastic scintillator was settled on early as the detector material of choice because it will take relatively high rates and is less subject to radiation damage than other material, as well as being inexpensive and versatile. Recent technological advances have made a variety of plastic scintillating fiber readily available. These fibers are beginning to be widely used in high energy physics as well as space applications. [1] Using fibers, a detector could be made that looked like a Bevalac wire chamber, mounting on the same hardware, but covering the larger dynamic range necessary to tune on beam halo.

The Detector

The design of the prototype detector is shown in Figure 2. Because most of the wire chambers in the beam lines have wire spacings of 6 mm. in an 8" beam pipe, a similar geometry was chosen for the scintillating fiber detector. Twelve fibers were used in each of two planes (horizontal and vertical) separated by approximately 1 cm. The fibers were spaced 6 mm. apart in the central beam region, with 12 mm. spacing in the outer halo regions, giving a total coverage of 10 cm. Each scintillating fiber was coupled on the edge of the mount to an optical fiber of the same composition and diameter. The coupling was done with a layer of optical

grease. The optical fibers were brought out of the vacuum through an epoxy-filled feedthrough. For the initial tests, each fiber was coupled directly to a photomultiplier tube (PMT).

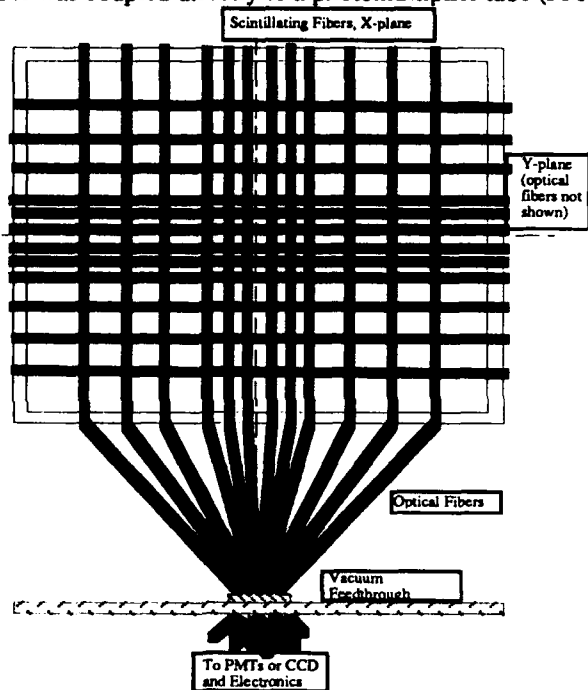


Figure 2. Prototype Detector

The Fibers

Initial tests were done with several scintillating fibers of varying diameter; some were square in cross section and some round. We settled on using 1 mm. diameter round BCF-10 fiber, a blue-emitting fiber with a polystyrene core and PMMA cladding made by Bicon Corporation. [2] The 1 mm. diameter was thick enough so that the individual fibers could be mounted in a rigid fashion. The fibers were tested with a

laser beam, an electron source, and in several test runs with different beams.

Electronics and Data Acquisition

A computer acquisition system was developed for these tests based on a Macintosh FX [3] running National Instrument's Labview acquisition software [4] to read signals from standard CAMAC modules over a GPIB interface. This acquisition proved to be slow but adequate for these tests. The output from the PMTs were taken into an Charge-to-Digital Converter (QDC) and converted to a pulse height. A sample spectra is shown in Figure 3 for a 300 MeV/nucleon Au beam passing through the fiber, with a calculated energy loss of approximately 2300 MeV. The background was negligible in these runs, consisting only of low pulse height counts in the PMTs, and easily discriminated out.

The use of individual PMTs with 24 channels of electronics added a layer of complexity to the detector that was counter to the goal of a user-friendly device for operator tuning. For the next step, it was planned to read all the fibers out into a charge-coupled device (CCD). One could then either use a frame-grabber board in the Macintosh to digitize the CCD output and convert it into a beam profile, or the CCD output could be displayed directly on a video monitor in the Control Room. Similar systems have been used in biological and space applications. [1,5] For this application a low resolution but large dynamic range CCD chip would be necessary. It was not clear whether an image intensifier would be needed in order to meet the dynamic range requirements. If it were, it would add significantly to the cost. In order to try to answer this question, many of the initial tests on the prototype detector were designed to get an estimate of the light output of the fibers and the transmission through the detector to the PMT. These tests and calculations are described in the next section.

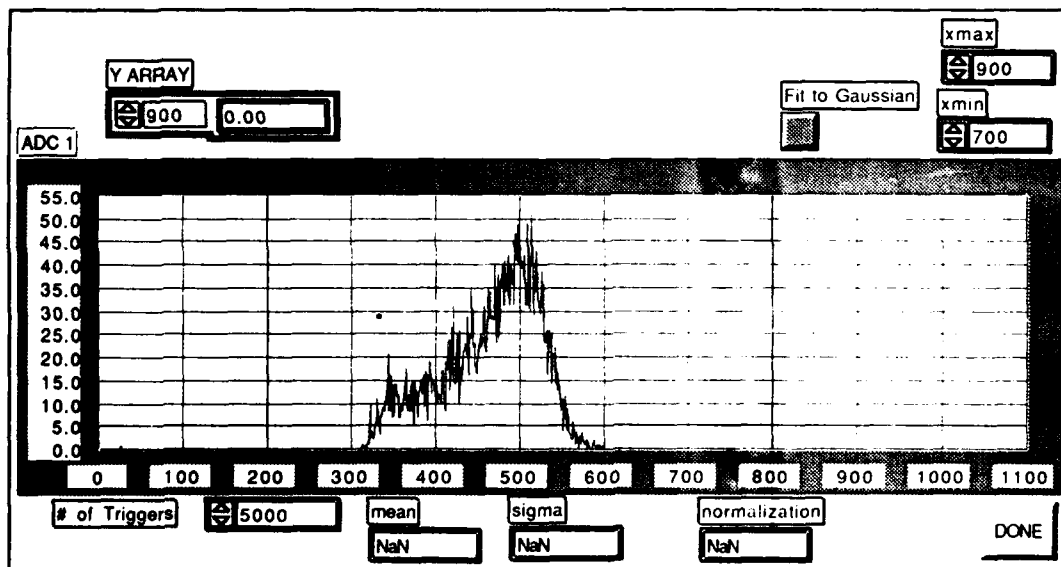


Figure 3. Online data for 300 MeV/nucleon Au going through a fiber in the central region of the prototype detector. The PMT high voltage was HV=-2000 V.

III. Transmission Calculations

In order to assess whether or not one can obtain sufficient dynamic range with these fibers to make a good halo detector, as well as whether an image intensifier would be needed for use with a CCD, tests were made comparing the response with a heavy beam to that of an electron source, and estimates were made of the transmission of light from the particle passing through the fiber to the PMT. Figure 4 shows a schematic of the transmission of the light from the fiber to the PMT, with the expected losses noted. An additional complication is the fact that the scintillation mechanism for heavy ions is different than that for electrons, and exhibit a Z dependence. This can be estimated from earlier studies of the response of plastic scintillators to heavy ions [6], if the assumption is made that the response is to first order independent of the particular scintillator material.

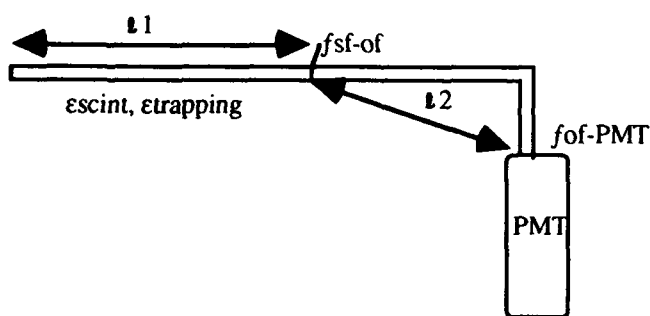


Figure 4. Schematic of transmission losses in fiber detector.

The measured light output of the detector, L_d , then, is given by the light output of the scintillating fiber for a heavy ion, L_{HI} , multiplied by the various transmission loss factors, multiplied by the gain of the PMT:

$$L_d = L_{HI} * \epsilon_{trapping} * (1 - A_{l1}) * f_{sf-of} * (1 - A_{l2}) * f_{of-PMT} * G_{PMT} \quad (1)$$

where $\epsilon_{trapping}$ is the percentage of total light piped down the fiber. A_{l1} and A_{l2} are the attenuation factors for the lengths of the scintillating fiber and optical fiber, respectively, f_{sf-of} is the fraction of light transmitted through the scintillating fiber/optical fiber interface, f_{of-PMT} is the fraction of light transmitted from the optical fiber to the PMT, and G_{PMT} is the gain of the PMT. $\epsilon_{trapping}$, A_{l1} , and A_{l2} are properties of the fibers and are given in the data sheet from Bicron Corp. [2] f_{sf-of} , f_{of-PMT} , and G_{PMT} can be estimated or measured using an electron source.

An attempt was made to measure directly the transmission to the PMT using a 1 MeV electron source; unfortunately, the losses are large enough so that the signal is in the noise by the time it reaches the PMT. (This immediately implies that this detector is limited to particles heavier than protons, where the energy loss is greater than 1 MeV. It will probably also not work with helium, since the

energy loss from Figure 1 is around 1 MeV, and the light output is decreased for a heavy ion relative to an electron of the same energy loss. [7])

An estimate of the transmission from Eqn. 1 can be made, knowing the attenuation lengths A_{l1} and A_{l2} are equal and given by the manufacturer as 2 meters for a 1/e drop in light, and $\epsilon_{trapping}$ is given by the manufacturer as 3.4% (it may be higher since one end of the fiber was made reflective). The scintillation efficiency of the fiber is quoted by Bicron to be 2.8% for electrons or minimum-ionizing particles, that is, 2.8% of the energy is converted into light. The scintillation photons have an average energy of 3 eV. [2] Therefore with a 1 MeV electron, ≈ 9000 photons are made, of which 350 make it to the end of the fiber. $l_1 + l_2$ was approximately 0.5 meters, so the attenuation in the fiber is small. The coupling between the scintillating fibers and optical fibers should be near 100% efficient as the two sets of fibers are well matched in size and composition. So we can estimate that 300 photons, or 900 eV of light make it through the fibers. The coupling to the PMT was not good for these tests, as the PMTs were much larger than is optimum to couple to a 1 mm. fiber. Coupling the fibers to a CCD should be more efficient. For Au at 300 MeV/u, the energy loss in the fiber is 3000 MeV, so $\approx 10^6$ photons should make it to the PMT., not taking into account decrease in light output for Au relative to electrons, which isn't known at these energies.

IV. Conclusion

A prototype scintillating fiber detector was built and tested with heavy ions at the Bevalac. In addition to the Au beam results shown here, the detector was used to look at La and Ne beams. These beams were easily seen with the detector, but because of efficiency problems, one detector will not cover the full range of ions and energies run at the Bevalac. A second detector could be made with thicker fibers for the light ions. This detector appears to be a useful device for this application. The use of CCD readouts rather than PMTs would make it more portable and straightforward to use. An image intensifier would probably be necessary in the halo regions (not the central beam regions) to obtain the dynamic range that is desirable.

References

- [1] A.J. Davis, et al., "Scintillating Optical Fiber Trajectory Detectors", *Nucl. Instr. and Methods A276*, 347 (1989).
- [2] Bicron Corporation, Newsbury, Ohio
- [3] TM Apple Computer, Inc., Cupertino, CA
- [4] TM National Instruments, Inc., Austin, TX
- [5] M. LeBlanc, et. al., "SOFI: A Scintillating Optical Fiber Imager", *Nucl. Instr. and Methods A273*, 583 (1988).
- [5] M.A. McMahan, "The Response of Scintillators to Heavy Ions - I. Plastics", *IEEE Trans. on Nucl. Sci.* **35**, 42(1988).
- [6] J.B. Birks, "Theory and Practice of Scintillation Counting", (Pergamon, Oxford, 1964).

This work was supported by the Director, Office of High Energy Research, Division of Nuclear Physics of the U.S. Department of Energy under Contract DE-AC03-76SF00098.

DEVELOPMENT AND INVESTIGATION OF THE 2π BEAM LOSS MONITORS FOR SUPER-HIGH ENERGY ACCELERATORS.

part 1. QUAD – BLM for 'warm' machines.

S. N. Lapitsky, I. A. Kurochkin, V. S. Seleznev.

Institute for High Energy Physics,
Protvino, Moscow region 142284, Russia

Abstract

Described are the results on examination in the 70 GeV proton circulating beam of beam loss monitor (BLM) called QUAD, having been developed for the UNK-I. The specific feature of QUAD is its special design: quasi- 2π geometry of sensitive volume and installation directly on the accelerator beam pipe for increasing its sensitivity to the beam loss and reproducibility. The significant advantages of QUAD (air-filled, diaphragm-type, four-module ion chamber) against the traditionally remotized from the accelerator beam pipe BLM's have been proved. Experimental results are presented together with the computer simulation ones for investigated and for the TeV beam energies.

I. INTRODUCTION

In [1] the package of BLM's, developed for the UNK project on the basis of common approach to their design, was described. The advantages of these BLM's, having quasi- 2π geometry of sensitive volumes and placed directly on the accelerator beam pipe, against the traditional ones were put forward on the basis of computer simulation results and the experience of beam loss monitoring in a high-intensity 70 GeV extracted proton beam. Nevertheless, some questions on this approach efficiency on circulating beam remained to be answered. The first industrial batch of QUAD's has been manufactured. The devices were tested, and the results are presented in this article.

II. QUADs TESTING IN THE U-70 CIRCULATING BEAM.

First of all, the effectiveness of the proposed concept on BLM's design in the 70 GeV circulating proton beam was examined with QUAD's in comparison with the traditional BLM's: Ar-filled Ion Chamber (ArIC) and Scintillating BLM (Sc). The performance of 'local' BLM's — QUAD's, installed directly on the accelerator beam pipe, and the 'remote' ones — ArIC and Sc., removed from the beam at a distance of about 1 m, has been investigated for the cases of local and remote sources of beam loss. Within the 'remote' class of BLM's, different types of them were compared: with- and without the inner amplification of signal. Analysing the data, we compared our results with

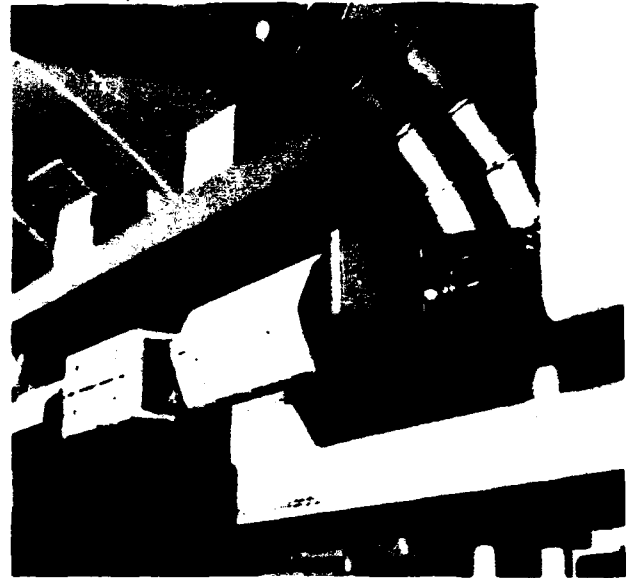


Figure 1: Common view of QUAD, installed on its duty position at the UNK-I ring.

[2], where the performance of 'remote' BLM's in a high energy proton beam was studied in detail. The obtained results completely agreed with conclusions of [2] for this class of BLM's. Briefly about the objects of the study:

- QUAD is a diaphragm-type, four-module, air-filled parallel-plate ion chamber with working gap 4mm and total active volume 0.9 litre, which corresponds to sensitivity $0.35 \mu\text{A}/\text{rad}\cdot\text{s}^{-1}$. It is very handy in use device, self-tuning and -fixing directly on the accelerator beam pipe with any size and shape in the aperture ranging from 30 to 215mm. It needs only 60 mm of free space along the beam pipe to be installed and may be used in single, two- or four-channel operational mode. Other details are given in [1]. Fig. 1 presents the common view of the device, installed on its duty position in UNK-I ring.
- ArIC is an Ar-filled, 1.5 litre volume, parallel plate IC with 6 mm working gaps.
- Sc. — includes 10 cm^3 plastic scintillator, connected by means of a 1.2 m polished tube with a photomultiplier (PM), and placed in the median plane of the accelerator inside. Fig. 2 presents the scheme of BLM's study in the circulating beam. QUAD1 was installed upstream the septum magnet and QUAD2, ArIC and Sc. — downstream. Q1 and Q2 were installed on the 220 mm beam pipe at 3.5 m distance from one another.

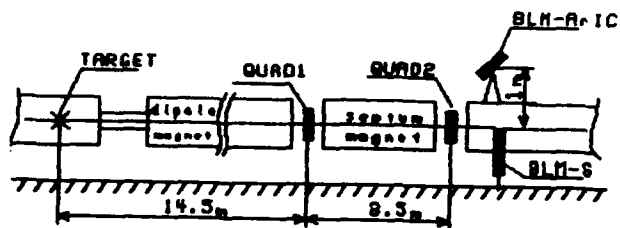


Figure 2: Scheme of BLM's study on U-70 circulating beam.

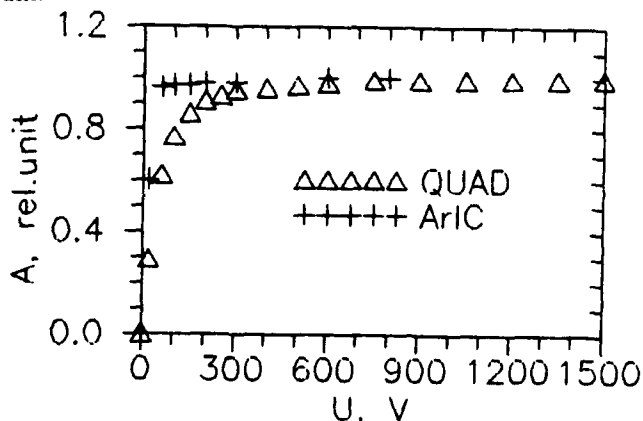


Figure 3: Bias curves of ArIC and QUAD in the radiation fields of about 1.0 and 60.0 krad·s⁻¹ respectively.

ArIC was placed on the top of magnet block 1 m vertically, and Sc. — in the median plane 0.75 m inside the accelerator. The partition of Septum magnet was considered as a local beam loss source and thick Internal Target 18 m ahead — as a remote one. The first question, we had to answer, was the correctness of our choice of Air for filling the IC-type BLM. Fig. 3 demonstrates the excellent performance of air-filled QUAD in the 60 krad·s⁻¹ radiation field, the hardest one, expected at the future machines.

We also calibrated the QUAD2. In its real position the specific response of Q2 to the beam loss on Septum magnet was $0.52 \cdot 10^{-3}$ pA/prot.·s⁻¹, which agreed within 30% with the computer simulation results for real conditions and approximately agreed with the results of computer simulation in the TeV-energy region for the case of linear extrapolation in energy scale, corroborated for BLM's in [2]. The results on relative study of sensitivity, reproducibility and correlations of different BLM's are summarized in table 1. First of all, one can see the significant superiority in sensitivity of Q2 against the ArIC. It should be noticed, that in order to express the Q2 and ArIC relative sensitivity in correct terms, factor 20 from the table for local loss should be additionally multiplied by 3 (one should take into account the difference in their volumes and sensitive media). As a result, the total gain in sensitivity due to the geometric factor only, is about 60 for 70 GeV lost protons. Under real conditions of future machines the additional strong attenuation factor of shielding matter will take place. Sum-

Table 1: BLM's relative sensitivities, reproducibilities and correlations

Specification of used Marks						
I-Beam Int.	1-Q1	11-.25Q1	2 Q2			
Local source of beam loss – Septum Magnet.						
Statistical parameter	Pair of objects for stat. processing					
	1-21	11-2	11-3	11-4	2-3	21-3
mean ratio	0.47	0.04	0.71	—	20.1	9.1
$\sigma_r(\%)$	1.6	6.0	3.7	6.3	0.6	1.1
correl.	0.63	0.76	0.88	0.70	1.00	0.96
Remote source of beam loss – Internal Target.						
Statistical parameter	Pair of objects for stat. processing					
	1-21	11-2	11-3	11-4	2-3	—
mean ratio	2.0	0.5	7.2	—	14.0	—
$\sigma_r(\%)$	0.5	1.0	11.6	11.6	7.3	—
correl.	1.00	1.00	0.52	0.53	0.46	—

Specification of used Marks						
I-Beam Int.	21-.75Q2	3-ArIC	4-Sc.			
Local source of beam loss – Septum Magnet.						
Statistical parameter	Pair of objects for stat. processing					
	2-4	21-4	3-4	1-I	21-I	4-I
mean ratio	—	—	—	—	—	—
$\sigma_r(\%)$	5.2	4.2	5.3	14.7	44.7	39
correl.	0.62	0.80	0.61	0.12	0.42	0.48
Remote source of beam loss – Internal Target.						
Statistical parameter	Pair of objects for stat. processing					
	2-4	—	3-4	1-I	21-I	—
mean ratio	—	—	—	—	—	—
$\sigma_r(\%)$	7.4	—	0.7	0.7	0.9	—
correl.	0.45	—	0.98	1.00	1.00	—

marizing all, we can conclude, that 'local' IC in the simple charge collection mode of operation provides the same sensitivity to the local beam loss as the 'remote' BLM with inner amplification of signal.

Conclusion 1: to be sensitive, BLM should be 'local'.

The accuracy (reproducibility) of Q2 and ArIC were in the case of local beam loss the same, to an accuracy of 0.5%, which also agree with [2], and their correlation coefficient was 0.999! On the contrary the accuracy and correlations have been dramatically lost, if we use Sc. monitor with inner amplification of signal.

Conclusion 2: inner amplification of signal is a great disadvantage of any BLM.

Mark '21' in the table is used for Q2 with a weakly violated geometry: one of four modules, namely – inner in the median plane, was switched off. Result: sensitivity decreased twice and accuracy deteriorated twice as well.

Conclusion 3: in the case of local loss the 'local' BLM should have 2π geometry of sensitive volume. With energy growth this demand becomes rigidier. Some other conclu-

sions can be extracted from this table, for example: beam halo weakly correlates with beam intensity.

Now let consider the case of remote source of beam loss. The situation changes. The 2π geometry of 'local' BLM isn't necessary now to provide the desired 0.5 – 1.0% reproducibility. Mark '11' in the table is used for Q1 with a strongly violated geometry: only one of four modules, namely – inner in the median plane, was switched on. But one can see no loss in accuracy, the sensitivity decreased only, proportionally to the active volume decreasing. One can see also the excellent correlations between Q1, Q2 and Intensity on the target on one hand and on the other hand – nice correlation between 'remote' BLM's and bad between them and QUAD's.

Conclusion next: in the case of remote beam loss, 'local' and 'remote' BLM's indicates different sources. Q1,2 indicates Intensity of remote loss, but ArIC and Sc. – ? May be the equilibrium background in the accelerator tunnel, because of their excellent correlation and relative reproducibility. In any case they are useless to signal the dangerous situation for strong remote beam loss.

Finally we can conclude that air-filled QUAD is very sensitive, precise, handy and flexible in use BLM, absolutely adequate for different applications in high-energy "warm" machines in addition to its primary function. While it is very sensitive and reproducible, it can be used in the multichannel operational mode for alignment of some accelerator equipment, scrapers for example, for beam halo study, ... The only advantage of Sc. BLM against the IC ones is its very fast response to the instantaneous loss – in the ns range. But it is hard to imagine, where this advantage possibility may be taken in the beam loss monitoring.

One can see, that some results in table 1 are contradictory and the table needs to be completed with some data. So, we are planning to complete the set of 'remote' BLM's with an extended IC, similar to the one, used in [2]: fabricated from spirally insulated, air dielectric coaxial cable. The reason is, that the extended 'remote' BLM (but in proportional operation mode, which is worse, see concl. 2 and in addition a rather complex intercalibration problem needs to be solved in this case), has been now announced as the main competitor to our proposals both for 'warm' and SC machines, see part 2 of this work. [3]. We are also going to provide these measurements with more accurate loss and beam intensity monitoring. The 'Sc.' BLM also should be modified to be compatible with the electronics we used for IC monitors: a current to frequency converters [4]. We will try also to complete our experimental set-up with a shielding matter between Septum magnet and 'remote' BLM's in order to simulate correctly their real environment in the future high-energy 'warm' machines.

III. CONCLUSIONS

The main conclusion: the right way on the designing of BLM's with 2π -geometry of their sensitive volumes for

the beam loss monitoring on super-high energy machines is proved in all principal points by means of experimental study on circulating and extracted 70 GeV proton beams. The proposed IC-types BLM's combine a capability for high dose rates with a sensitivity and precision, which allow the interpretation of minute perturbations that may signal the onset of a failure. They will provide very sensitive, reproducible, reliable and handle beam loss monitoring to be used in addition to their main specification as a diagnostic tool for beam halo study at extremely low levels, starting from 10^4 – 10^5 protons in sub-TeV region of energy, and in some other applications. This paper is the first half of a common work and is devoted to the beam loss monitoring in the 'warm' machines. The second one, to be presented at this Conference also, is devoted to the case of beam loss monitoring in the SC accelerators.

Although the main address of our activity are the SC accelerators-colliders, the high-energy, high-intensity "warm" machines also need an effective tool for beam loss monitoring, and, on the other hand, they may be considered as the excellent test-site to accumulate experience in BLMS use in different applications. Unfortunately this work can't be carried out completely in our existing 70 GeV machine, where we found only several places for QUAD installation, although it needs only 60 mm of free space along the beam pipe to be installed. So, we are waiting for the commissioning of UNK-I, 400 GeV proton ring, to test the declared new possibilities of BLMS, based on the QUAD's. [5].

The authors are very grateful to A.E.Yakutin for his assistance in operating with liquid helium, Dr. V.I.Terekhov and I.V.Krupchenkov for the electronics we used in measurements, Drs. N.V.Mokhov and A.A.Aseev for the instructive discussions on the subject, and F.M.Solodovnik for his help in data processing.

IV. REFERENCES

- [1] S. N. Lapitsky, I. A. Kurochkin, N. V. Mokhov and V. S. Seleznev, *Proceed. of XV-th Int. Conf. on High-Energy Accel., HEACC'92*, Hamburg, July 20-24, 1992, pp. 242-244.
- [2] F. Hornstra, *Preprint DESY HERA 89-02*, 1989.
- [3] J. Bosser, C. Bovet, L. Burnod, et al., *Proceed. of Workshop on Advanced Beam Instrumentation*, 1, Tsukuba, 1991, p. 85.
- [4] Yu. B. Bushnin, V. S. Seleznev and V. I. Terekhov, *Preprint IHEP 83-103*, Protvino, 1983, (Russian).
- [5] S. N. Lapitsky, A. F. Lukyantsev, V. S. Seleznev, et al., *Proceed. of 3-rd European Conf. on High-Energy Accel., EPAC'92*, Berlin, March 24-28, 1992, pp. 1052-1057.

The Design and Performance of a High Sensitivity Loss Monitor System for use in the Fermilab Antiproton Rings

Alfred Mike Halling, James R. Zagel, Alan Hahn
Fermi National Accelerator Laboratory[†]
P.O. Box 500, Batavia, IL 60510-0500

ABSTRACT

As part of a general laboratory cleanup of hazardous materials from the accelerator enclosures we have replaced the liquid scintillator based paint can type beam loss monitors with improved loss monitors based on plastic scintillator. This paper describes the design of these counters and their performance in the PBAR source.

I. HARDWARE DESIGN

New loss monitors for the antiproton source at Fermilab have been constructed and installed. These are based on NE102 plastic scintillator, and have been designed to be sensitive to single lost particles and short lived nuclear decay products. Figure 1 shows the design of the scintillator and light guides.

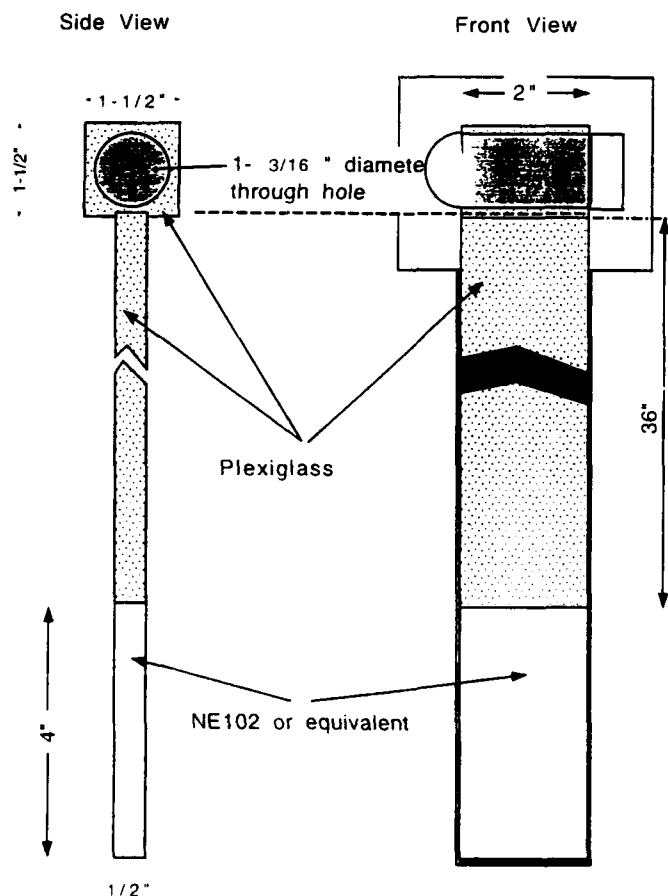


Figure 1. Loss monitor light guides and scintillator.

[†] Operated by the Universities Research Association, Inc under contract with the U.S. Department of Energy.

The 4" x 2" x 1/2" pieces of scintillator are glued to 36" long lucite light guides. The light guides are used to keep the phototubes away from the stray fields and particles near the beam pipe. A small lucite coupling attachment is glued to the top of the light guide to hold the side view RCA 4552 photomultiplier tubes. The RCA 4552 photomultiplier tubes, which are recycled from the paint can detectors, are an excellent tube for this application because the solid photocathode is a much more rugged than a head on phototube. Figure 2 shows a photograph of the light guide with a phototube inserted into the coupling attachment.



Figure 2. Photograph of loss monitor light guides. A phototube is shown inserted in the coupling attachment.

The base of the phototube was modified to have a smaller standing current than the original paint can loss monitors. We use a 100 μ A resistive voltage divider, which should protect the phototube from being damaged by large losses.

The entire assembly shown in Figures 1 and 2 is housed in a gray PVC schedule 80 pipe, as is shown in Figures 3 and 4. This inexpensive housing has proven to be very durable.

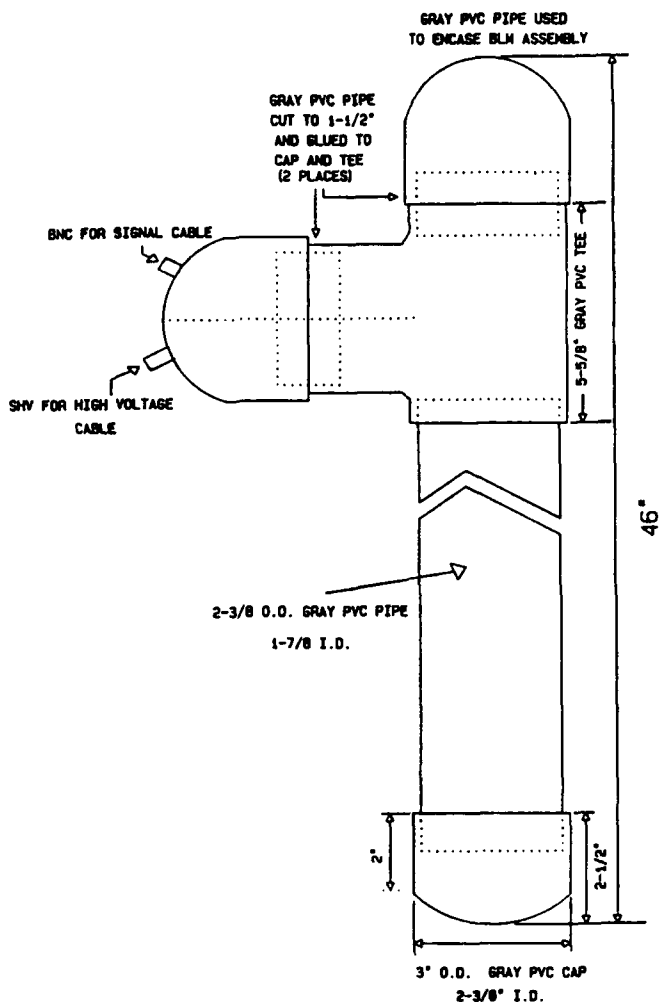


Figure 3. Drawing of PVC loss monitor housing.

II. READOUT

The loss monitors are read out using obsolete equipment from the HEP equipment pool. We use LeCroy 612A photomultiplier amplifiers with 20 db gain to amplify the signals from the phototubes. These signals are then fed into discriminators and readout with CAMAC scalars. Figure 5 shows a block diagram of the readout system. We have a large number of different types of discriminators, most have a 100 mv threshold. We most often left the CAMAC scalars counting continuously, and cleared them at a 1 HZ or 15HZ rate.

III. PREDICTED AND MEASURED SIGNAL SIZE

Paint can type loss monitors are much more sensitive to beam loss than ion chambers. We have measured signal sizes about 7000 times larger from "paint can" loss monitors with respect to ion chambers. This is due to the large gain of the photomultiplier tube. In the PBAR source we often have very

small beam currents, so the sensitivity to very small losses is desired.

We estimate the signal size for minimum ionizing particles as follows. The dE/dx energy loss in the scintillator is about 1.9 MeV/cm. The light yield of plastic scintillator is about 1 photon per 100 eV. We estimate that about 10% of the light from the scintillator is captured by the light pipe, and about 20% of this captured light shines on the photocathode. The quantum efficiency of the photocathode is about 10%, and the phototube gain is about 5×10^5 . Combining all these factors gives a signal size of about 10^8 electrons in about a 20 ns pulse, or about a 40 mv pulse into 50 ohms. This is too small for our discriminators to detect without amplification, but with amplification these signals are easily seen.



Figure 4. Photograph of PVC loss monitor housing.

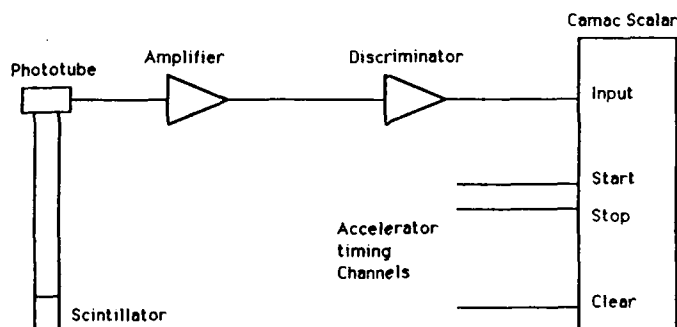


Figure 5. Loss monitor readout block diagram.

The actual counters give about 20 mv signals before amplification from 1.2 MeV gammas from a Co^{60} source. This demonstrated level of sensitivity allows the loss monitors to be sensitive to both minimum ionizing tracks and short lived radioactive states produced by interacting beam.

IV. PERFORMANCE IN THE BEAM

During a recent studies period we tested the usefulness of the loss monitors for determining the location of aperture restrictions. To demonstrate that the loss monitors could locate obstructions in the beam we measured the loss monitor counting rates in both the accumulator and debuncher storage rings as a scraper was slowly inserted into the beam. Figure 6 is a reproduction of our loss monitor display program taken during one of these tests. The figure shows a three piece linear representation of the debuncher storage ring, with the lattice beta functions and the beam pipe size shown for reference. The counting rates in the loss monitors are displayed on top. There are large losses just downstream of the scraper, while the other loss monitors in the ring show no signals. This test and others showed that the loss monitors could determine the location of aperture restrictions.

In real practice the locations of aperture restrictions in the accelerators were found by injecting 8 GeV/c protons, then heating the beam slowly by applying white noise through the transverse damper system. The location of aperture restrictions was observed where the loss monitors counted the highest. The improved loss monitors proved to be a useful tool during the last studies period for improving the aperture of the two storage rings in the PBAR source.

V. ACKNOWLEDGMENTS

We would like to thank Doris Dick, Judy Sabo and Marvin Olson for their parts in the fabrication and installation of the loss monitors.

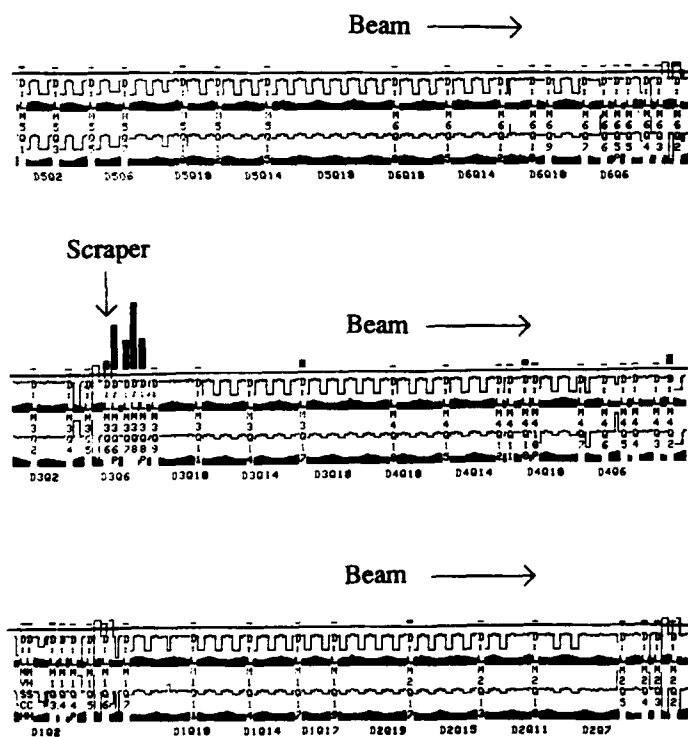


Figure 6. Debuncher loss monitor rates while scraper at the location shown is slowly inserted.

Abort Interlock Diagnostic for Protection of APS Vacuum Chamber*

Glenn Decker
Advanced Photon Source,
Argonne National Laboratory, Argonne, IL, 60439

The Advanced Photon Source (APS) vacuum system has been designed to be passively safe from bending magnet radiation heating at positron beam currents up to 30 mA. Above this value, certain components may be damaged from vertical beam missteering, although work is proceeding to raise the safe current threshold. Because of this, a system for preventing the misalignment of high power density beams is required. This report details a system for protection from dipole radiation only. Work on a system for ID radiation is continuing.

I. INTRODUCTION

Radiation from bending magnets is emitted in fans emanating from the positron beam as it follows a nominally circular trajectory through each of the 80 dipole magnets in the storage ring. The nominal power emitted due to bending magnet radiation is 1.6 MW at a beam current of 300 mA. The distribution of radiated power with vertical angle above the accelerator midplane is quite accurately described by a Gaussian distribution with an rms width given by $\sigma = 0.608 / \gamma$, where γ is the relativistic factor, equal to 13,700 for the APS beam energy of 7 GeV. Therefore $\sigma = 44 \mu\text{rad}$, and the power per unit solid angle in the midplane, averaged over horizontal angles is $dP/d\Omega = 1.6 \text{ MW} / 2\pi / 1000 / (2\pi)^{1/2} \sigma = 2.3 \text{ kW/mrad}^2$ at 300 mA.

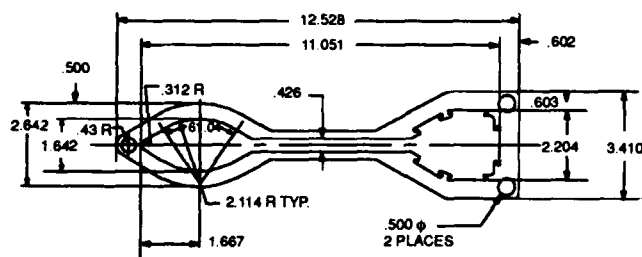


Figure 1. Cross Section of Storage Ring Vacuum Chamber.

The positron beam is confined to move within the storage ring vacuum chamber extrusion, whose cross section is shown in Figure 1. Each sector is broken down into six vacuum chamber sections. Bellows are located between storage ring vacuum chamber sections and allow a certain amount of mechanical com-

pliance between chambers to facilitate small motions for alignment purposes. Located within each bellows assembly is an rf liner which yields a smooth electrical transition from one vacuum chamber section to the next and must be shadowed from synchrotron radiation at all power levels. The shadowing is accomplished by small tapered spacers which are attached inside the upstream and downstream flanges of all chambers. These spacers will be subjected to synchrotron radiation heating during beam missteering conditions and, in fact, are responsible for the beam intensity limitation during commissioning. Above 100 mA curved vacuum chamber sections can be damaged by synchrotron radiation. This occurs when the beam is parallel-translated vertically by an amount greater than 5 mm (see Figure 1). The bellows spacers and curved chambers are the only components at risk from vertically missteered dipole radiation.

Shown in Table 1 are values for horizontal and vertical acceptances for various phases of storage ring operation. For commissioning, the entire storage ring vacuum chamber will by and large have the cross section shown in Figure 1. Following commissioning, insertion devices will be installed in two stages. Initially, chambers with a 6-mm vertical half aperture will be installed (Phase I), and mature operation (Phase II) entails the installation of insertion device vacuum chambers with a 4-mm half aperture.

Once one has the values for the acceptances given in Table 1, it is a simple matter to find the maximum position and angle caused by a global closed orbit distortion anywhere around the ring.

II. BEAM ABORT INTERLOCK

The beam abort interlock associated with beam missteering is part of the overall machine protection system (MPS), which encompasses all mechanisms which can potentially damage the machine. Common to all MPS input is a method for turning off the beam; at the APS the chosen method is to momentarily interrupt the rf system. This ensures that the beam will lose energy and spiral inwards, to be totally lost in less than 300 microseconds [1]. This process can be made even faster and the loss localized by placing a horizontal aperture limitation, or scraper, at a location of large horizontal dispersion [2].

Table 1. APS Storage Ring Acceptances

	Acceptance A, mm-mrad	Limiting Aperture a, in mm	β (m) at limiting aperture
Vertical, commissioning	20.4	20.85	21.3
Vertical, Phase I	3.36	6	10.7
Vertical, Phase II	1.50	4	10.7
Horizontal	74.2	42.3	24.1

* Work supported by U.S. Department of Energy, Office of Basic Energy Sciences, under Contract W-31-109-ENG-38.

The submitted manuscript has been authored by a contractor of the U.S. Government under contract No. W-31-109-ENG-38. Accordingly, the U.S. Government retains a nonexclusive, royalty-free license to publish or reproduce the published form of this contribution, or allow others to do so, for U.S. Government purposes.

The proposed diagnostics for detecting a potentially damaging beam missteering condition are tungsten wires strung inside the vacuum chamber in pairs, one wire above and one below the beam axis. Bringing the wire ends out of the vacuum system through a vacuum feedthrough, a resistance measurement can easily be made and translated directly into a temperature measurement. Shown in Figure 2 is a plot of resistivity vs. temperature for tungsten. At high temperatures, the dependence is almost linear.

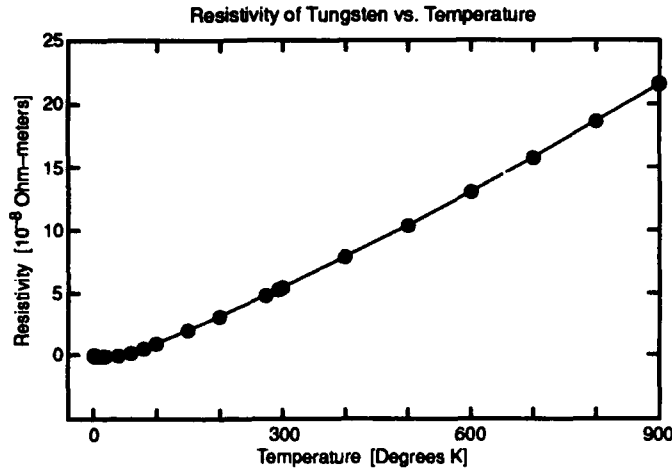


Figure 2. Variation of Tungsten Resistivity with Temperature.

The tungsten wires will be incorporated into a total of 80 accelerator absorbers located downstream of dipole sources. Shown in Figure 3 is a schematic of a radiation absorber assembly with two tungsten wires strung behind it such that the radiation strikes the wires at an angle of 4.5 degrees, approximately 80 mrad. The figure indicates that the wires will heat up if photons strike the absorber between 3.5 and 5 mm vertically from the nominal positron beam midplane. Because the beam has some width, the centroid of the photon beam will be effectively limited to lie between 3.0 and 5.5 mm, since 2σ is about 0.5 mm

Shown in Figure 4 is a positron phase space plot showing the limitations imposed by the wires. The figure is a projection of vertical phase space as viewed from the downstream end of a dipole magnet. One can extend this concept and map all 80 pairs of wires onto the same plot. What results is the 160-sided polygon producing an effective vertical acceptance limit of $A = 0.45$ mm-mrad. This means that global orbit distortions will be limited by the interlock system to vertical displacements no larger than $\sqrt{\beta A} = 2.9$ mm at $\beta = 19.0$ meters and angles no larger than $\sqrt{\gamma A} = 0.2$ mrad inside the dipole. What remains are the effects of purely local orbit distortions, which are generally too weak to cause the beam to strike any at risk components without first striking a downstream wire monitor.

III. CALCULATION OF WIRE TEMPERATURE

Recall that the accelerator vacuum system is deemed to be passively safe from dipole radiation at beam currents below 30 mA. At currents less than this, it is desirable to inhibit the action

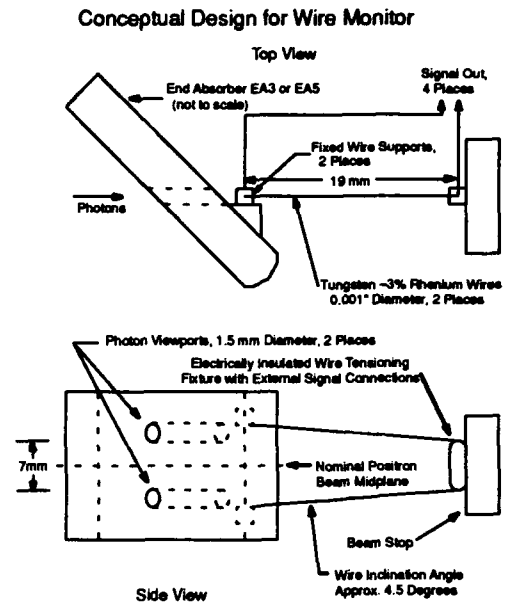


Figure 3. Concept for Interlock Diagnostic Built into a Radiation Absorber.

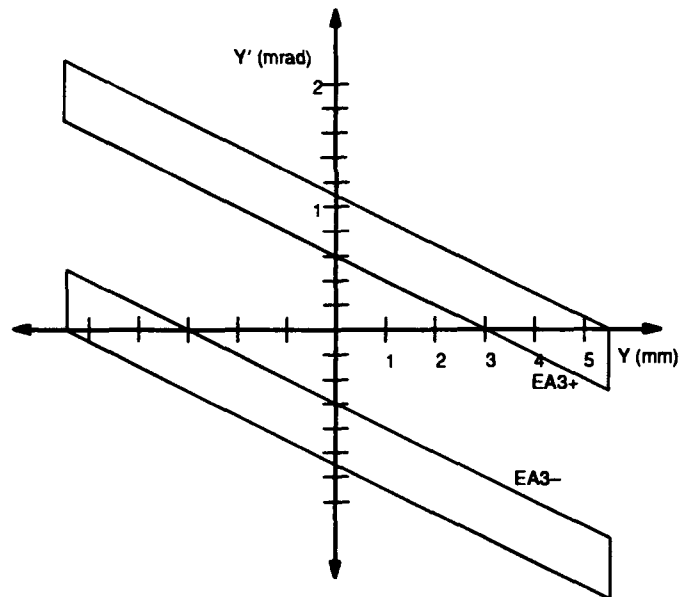


Figure 4. Projection of EA3 Wires onto Positron Phase Space at Downstream End of AM.

of the interlock, e.g. for the purpose of orbit studies. Therefore, in order to have a margin of safety, the tungsten wires must be able to withstand direct irradiation from bending magnet sources for sustained periods of time at beam currents up to 30 mA, and much higher if possible.

The primary mechanism for cooling of the wire is black body radiation. One can solve for the equilibrium wire temperature, arriving at

$$T_{\text{wire}}^4 = T_{\text{ambient}}^4 + \frac{A_p}{A_s} \frac{1}{\sigma \epsilon L^2} \frac{dP}{d\Omega} \quad (1)$$

where T_{wire} and T_{ambient} are the wire and ambient temperature in degrees Kelvin respectively, σ is the Stefan-Boltzmann constant, and ϵ is the wire surface emissivity. For reference, $(1/L^2) dP/d\Omega = 27.2 \text{ Watts/cm}^2$ peak for each milliamp of positron beam current at $L = 5.3$ meters, corresponding to the typical source – wire distance.

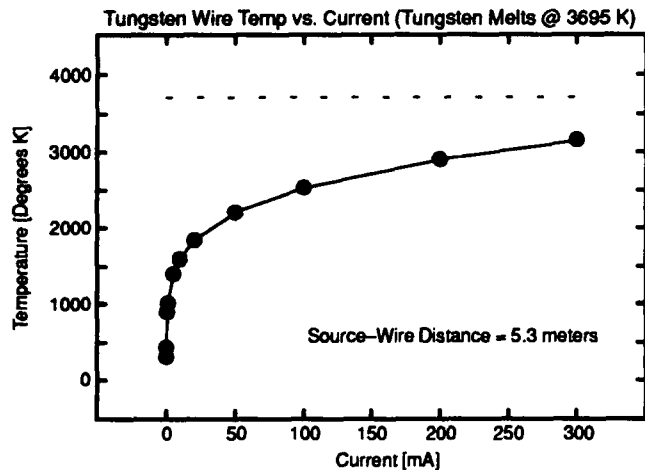


Figure 5. Wire Temperature vs. Positron Beam Current.

One interesting aspect of the above result is that the wire temperature is independent of the wire gauge, depending only on the ratio A_p/A_s , which, for a round wire inclined at an angle θ , is just $A_p/A_s = (\sin \theta)/\pi$. Shown in Figure 5 is a plot of wire temperature vs. positron beam current, inclined with respect to the nominal positron orbit midplane at an angle of 80 mrad. In generating Figure 5, a linear dependence of the emissivity ϵ with temperature, approximating measured values, was used, resulting in a fifth-order polynomial for T . Despite the variation of power with vertical angle, it turns out that the peak temperatures for beam currents exceeding 30 mA very closely follow the behavior shown in Figure 5 in a simulation including a Gaussian distributed power density and conductive cooling. This is due to the fact that heat conduction through the wire ends has a relatively small effect.

IV. TIME RESPONSE

In addition to the ability to withstand high photon fluxes without being damaged, the wire monitors must have the capability to respond very quickly. Although no components can be damaged in times shorter than a few seconds, the potential exists for the photon beam to sweep past the wire monitors so quickly that not enough energy gets deposited to produce a measurable resistance change.

The worst case situation occurs when a global orbit distortion moves the photon beam close to a wire and then a maximum amplitude local bump is applied. The maximum value of a vertical parallel translation bump inside a dipole magnet is 3.6 mm, and from Figure 4 it can be seen that the beam must move 2.5 mm

to get past the viewport, i.e. 69% of a full strength local bump. The L/R time constant of the vertical correctors is 82 ms to reach $(1-1/e) = 63\%$ of full strength. In other words, the wires must respond significantly faster than 82 ms to prevent a local bump from sweeping the photon beam past the wire undetected.

The relation determining the time rate of change of temperature does not depend on radiative heat loss at all, since we are most concerned with the time period when the wire is still relatively cool. The relation is given by

$$\frac{dT}{dt} = \frac{1}{\rho C_p L^2} \frac{dP}{d\Omega} \frac{4 \sin \theta}{\pi d}, \quad (2)$$

where $\rho = 19.3 \text{ g/cm}^3$ is the density of tungsten, $C_p = 0.133 \text{ J/g/}^\circ\text{K}$ is the heat capacity, and d is the wire diameter, assuming the wire is uniformly illuminated.

For a 50-micron-diameter wire, Eq. (2) yields 6500°K/sec at a beam current of 30 mA, otherwise known as 216°K/sec/mA , for $\theta = 80 \text{ mrad}$, $L = 5.3$ meters. A 100°K temperature rise at 30 mA thus requires a time period of 15.4 milliseconds. Because the wire is not uniformly heated along its entire length, one should conservatively use the total volume of the wire rather than just the volume of wire being hit by radiation, as was done in Eq. (2). This reduces the response time by at most a factor of 5, i.e. a 100°K temperature rise in 72 milliseconds. This is still faster than the L/R time constant of the magnets.

For the resistance measurement, care must be taken to limit ohmic heating. For a 35-mm-long, .002"-diameter tungsten-3% rhenium alloy wire, the room temperature resistance is 1.7 ohms, but rises rapidly if ohmic heating exceeds a few milliwatts. This limits the applied current to between 20 and 30 mA, producing 50 to 100 millivolts of signal, which should be easily detected.

V. CONCLUSIONS

A simple method for the detection of vertical missteering of dipole magnet radiation in the APS storage ring for use in a beam abort interlock has been developed. The method uses 50-micron-diameter tungsten alloy wires as resistive temperature sensing devices to directly detect the presence of photon beams off axis. These wires can withstand direct irradiation from bending magnet radiation conservatively at beam currents up to 100 mA, and are significantly below their melting temperature even at 300 mA. Their response time is faster than 72 milliseconds at 30 mA of beam current, the lowest current at which the interlock will be activated. By integrating the wires into the design of water-cooled radiation absorbers, their alignment with respect to the beam is simplified. The wire resistance is in the range of 1 to 2 ohms and can be measured with an applied current between 20 and 30 mA without causing an unacceptable temperature rise from ohmic heating.

VI. REFERENCES

- [1] L. Emery, private communication, APS Internal Note.
- [2] L. Teng, private communication, APS Internal Note.

Experience with Radiation Protection for a Silicon Vertex Detector at a Hadronic Collider

P.F. Derwent, D. Amidei, A. Dunn, T. Song, S. Vejckik

University of Michigan, Ann Arbor MI 48109

R. Crouch, R. Ducar, D. Herrup

Fermi National Accelerator Laboratory, Batavia IL 60510

C. Haber

Lawrence Berkeley Laboratory, Berkeley CA 94720

Abstract

The Collider Detector at Fermilab (CDF) incorporates a Silicon Vertex Detector (SVX) in the study of proton antiproton collisions at the Fermilab Tevatron Collider. We describe here our experience with SVX radiation protection issues during the commissioning and subsequent operation of the Collider. We outline the catalog of typical accelerator loss mechanisms, the radiation dose associated with each, and our eventual protection strategy in each case. We map the total radiation dose received by the SVX in space as well as in time. We also discuss measured radiation damage to the SVX, and its correlation with the independently measured radiation dose.

1 Introduction

The CDF SVX is a high precision Silicon Microvertex tracking detector [1] installed as part of the CDF experiment at the Fermilab Tevatron Collider. It is the first Silicon Microvertex detector installed at a hadron collider. It is used for the study of short lived particles produced in the proton antiproton collisions at the Tevatron [2].

The SVX detector is built of high quality single sided DC coupled silicon detectors in a four inch technology, connected to a custom VLSI chip developed at Lawrence Berkeley Laboratory [3]. The SVX chip contains 128 channels of low noise charge amplification, sample and hold, and comparator latch circuitry followed by a digital section which allows readout of only those channels in which the integrated charge exceeds an injected analog threshold level. The chip was fabricated using a 3 micron CMOS technology, a radiation "soft" technology. The high cross section at a hadron collider means that this device will be exposed to a large radiation dose coming from the physics processes.

The inner most layer of the SVX detector is located 3 cm from the beam axis. The high loss conditions of a hadron collider, in conjunction with the radiation softness of the SVX detector, led to the design and implementation of a dedicated loss mon-

itor system to protect the SVX against accidental radiation dose. This system was designed to be part of the general Tevatron control system, including inputs to the abort network [4].

2 Expected Radiation Damage

During the 1988-89 Tevatron collider run, measurements of the radiation were made in the CDF collision hall. These records showed a rate of approximately $900 \text{ rads}/\text{pb}^{-1}$ during the early stages, which declined to the level of $300 \text{ rads}/\text{pb}^{-1}$ as the run continued. At the start of the 1992-93 Tevatron Collider run, the expected 25 pb^{-1} of delivered luminosity would lead to an integral dose of 12 krad, which is enough to have an impact on the device performance. Based on these numbers, we adopted an upper limit of 15 krad as a goal for the 1992-3 Tevatron Collider run.

In addition, various accelerator "accidents" can deposit large radiation doses in the SVX. These accidents range from abort kicker prefires (5 μsec time scale) to sparks in electrostatic separators (1 msec time scale, or 50 turns) to trips of correction elements (100 msec time scale). The Tevatron lattice contains two low- β insertions, at D0 and CDF. In the injection lattice, $\beta^* = 1.7 \text{ m.}$, and $\beta_{\text{max}} = 100 \text{ m.}$, and in the low- β lattice, 0.5 m. and 1200 m. Thus, oscillations induced anywhere in the ring can lead to losses at the low- β insertions, and the SVX in particular.

3 Protection System

Radiation backgrounds are monitored with two systems, located approximately 2.8 m from the interaction region in both the proton and antiproton directions, at a distance of 5 cm from the beam axis. Silicon diodes are used to measure the minimum ionizing particle rates and ionizing dose levels are measured with Tevatron Beam Loss Monitors (BLMs) [5]. Rate information is processed via 3 digital ratemeters with integration on 10 turn (5 kHz), 100 turn (500 Hz), and 10,000 turn (5 Hz)

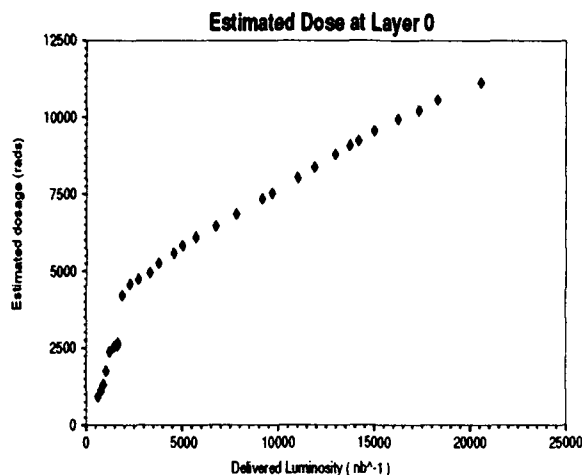


Figure 2: Extrapolated inner layer radiation dose as a function of delivered luminosity.

5 Total Damage Estimates

As displayed in Figure 2, the BLM and TLD data imply a total of approximately 12 krad delivered to the SVX inner layer with 18 pb^{-1} of delivered luminosity. In Figure 3, we show the average change in gain for the 4 layers of the SVX. The changes in gain show a similar radial dependence to what has been measured with the TLDs, though the overall change in gain is inconsistent at the factor of two level with the other measures. The total change in noise at the inner layer predicts a radiation dose of 13 krad at this point in time. Both the gain and noise have changed linearly with the delivered luminosity (except for the early commissioning period), which is indicative of damage caused by the flux of particles coming from the beam collisions and not from accidents.

6 Conclusions

We have designed and built a system to monitor the Tevatron losses in the vicinity of the CDF SVX and operated it through the 1992-3 Tevatron Collider run. We have received a total dose consistent with expectations from luminosity related causes, with a small addition due to Tevatron accidents. Significant accidents have only occurred in situations where the Tevatron lattice was perturbed and not at well understood operating points. We wish to emphasize that the total dose is small compared to what one might have expected at a hadron collider. We have demonstrated that it is possible to achieve relatively "lossless commissioning" and clean running conditions in the hadron collider environment.

Acknowledgements

We wish to thank the members of the Fermilab Accelerator Operations Group for assistance dur-

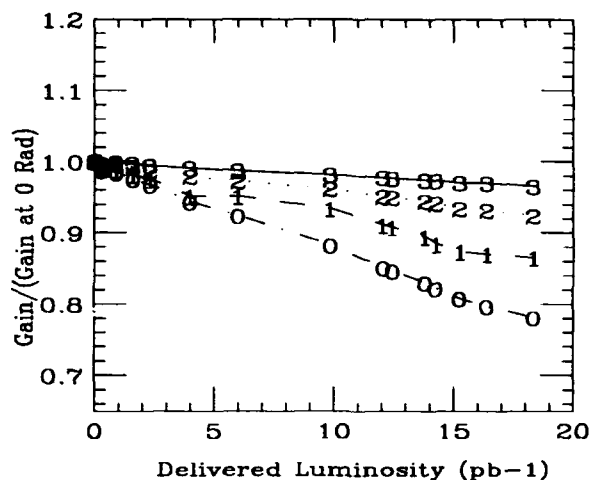


Figure 3: The *in situ* measured change in gain as a function of delivered luminosity, for the 4 layers of the SVX (0 is the inner most layer, 3 the outermost layer).

ing the 1992-3 Tevatron Collider run and Kathy Graden and Dave Boehnlein of the Fermilab Radiation Physics Staff Group for help with the TLD measurements.

References

- [1] W.C. Carithers, et al., NIM A 289, 388 (1990).
- [2] H. Wenzel, in *QCD and High Energy Hadronic Interactions*, proceedings of the XXVIIIth Rencontres de Moriond, Les Arcs, France, March 1993, ed. by J. Tran Thanh Van (to be published).
- [3] S. Kleinfelder, et al., IEEE, Tr.Nucl.Sci., NS-35,n.1, 171 (1988).
- [4] D. Bogert, et al., in Proceedings of IEEE Particle Accelerator Conference, p2204, Washington, D.C., March 1981.
- [5] R. Shafer, et al., in Proceedings of the International Conference on High Energy Accelerators, Fermi National Accelerator Laboratory, Batavia, IL, August, 1983.
- [6] D. Beechy and R. Ducar, in Proceedings of the International Workshop on Accelerator Control Systems, p231, Los Alamos, NM, October 1985.

Design of a new generation of collimators for LEP 200

R. Jung, R. Perret, R. Valbuena
European Organization for Nuclear Research (CERN)
CH-1211 Geneva 23, Switzerland

Abstract

One hundred and twenty six movable collimator blocks have been installed for the first phase of LEP. They have proved indispensable for providing good conditions for data taking of the experiments and gave no problems for running LEP. Sixty four additional movable blocks are planned to be added for the second phase of LEP (LEP 200 project). The collimators will consist of copper blocks with tungsten inserts or of spherical tungsten blocks. Their design is adapted to maintain the original low RF loss factor of 0.06 V/pC at the nominal aperture with reduced variations over the entire useful stroke.

I. INTRODUCTION

For the first phase of LEP, one hundred and twelve movable collimator blocks have been installed around the four even intersection points housing the large LEP experimental detectors. Fourteen other collimator blocks were installed around crossing point 3 in order to define the LEP aperture. The blocks are grouped into one, two or four jaw collimators depending on their function and space available, and are designed to match cruciform, round or elliptical neighbouring vacuum chambers for minimum RF losses. Most of these collimators are installed in long straight sections where they experience only a small amount of synchrotron radiation (SR) power or in the arcs with the SR striking only the outer wall of their vacuum tank. These collimators were designed so that they could withstand the increased radiation when doubling the LEP beam energy (LEP 200 project), except two horizontal and the three vertical aperture limiting collimators which for economical reasons were made similar to the collimators used for protecting the experiments. All these collimators have been in operation since the 1989 LEP start-up. They have been very effective for providing good data taking conditions for the experiments, have given no problem to operate LEP and have proven very reliable.

Eight more collimators were quickly designed, manufactured and three installed in 1992 to protect a horizontal separator used in the pretzel scheme when SR originating in the arc dipoles was thought to be a major problem for the scheme. They have been used since then to make long term studies for preparing the operational use of the scheme. It was finally found that it was not necessary to install the five other collimators of this type at the present beam energy. The exercise proved very valuable as prototype work for the next generation of collimators.

The additional requests for the LEP 200 project are the following: sixteen two-jaw horizontal collimators for a small circular vacuum chamber (100 mm) to protect the superconducting cavities and the horizontal separators from the arc

synchrotron radiation, sixteen one-jaw horizontal collimators for an elliptical chamber (131 mm x 70 mm) to protect the machine luminosity detectors from off-momentum particles, and the replacement of three vertical and two horizontal two-jaw collimators for an elliptical chamber for defining the LEP aperture. These collimators will be submitted to the full power of the SR generated in the arcs, i.e. 900W per meter of trajectory. There is a pending request for another eight horizontal two-jaw collimators with a large circular aperture (180 mm) to provide additional protection for the experiments.

II. DESIGN CONSTRAINTS FOR LOW RF LOSSES AND HIGH SYNCHROTRON RADIATION POWER DEPOSITION

As for the first generation of collimators [1], great care has been taken to minimise the RF losses in the collimators and to limit their variation over the useful stroke of the blocks. This is achieved by minimising the changes in the vacuum enclosure seen by the beam when entering and leaving the collimator. The most economical means to achieve this for the large number of items considered is to provide a rectangular shaped vacuum tank in which the blocks are moving with a maximum gap of 1 mm between tank walls and block and to have a tapered transition between the connecting vacuum chamber and the limited aperture defined by the blocks. As the blocks are movable, this taper is defined so as to minimise the disturbance over the full useful stroke. Calculations have been made with the method described in [1], the results of which were confirmed by bench measurements. The loss factor for the 100 mm circular aperture horizontal two jaw collimator is given in Figure 1.

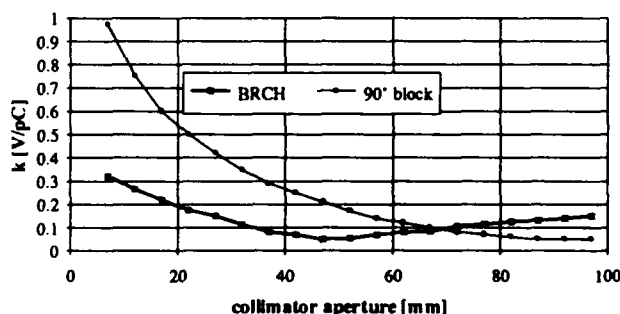


Fig. 1: Loss factor for a circular aperture two-jaw collimator, with (BRCH) and without (90°) RF tapers

The second and new constraint for these collimators was the possibility to be submitted to an intense SR power deposition. The vacuum constraint imposes a maximum temperature in operation well below the bake-out temperature of 150°C. For

the vertical and inner one-jaw horizontal collimators it imposes a copper SR absorber inside the stainless steel tank to absorb the 900 W/m SR generated by a 6 mA beam at 100 GeV. For the horizontal collimators, the situation is more critical as the outer block intercepts the SR coming from a long length of beam trajectory. With the previous beam parameters, the power intercepted by the outer block can be as high as 10 kW at a half aperture of 15 mm for an elliptical vacuum chamber at the exit of the main dipoles. In order to keep a low loss factor and to distribute the SR power deposition over the largest surface, blocks with a double taper have been designed (type BRCH, see Fig. 1 and 5). The power deposition coming from the RF losses is negligible compared to that from the SR. Nevertheless all surfaces exposed to the beam are cooled. Finally the collimators have to be submitted to a bake-out at 150°C and have to use stainless steel for all parts in contact with the LEP demineralized cooling water to avoid corrosion effects.

III. THERMAL AND MECHANICAL STRESS CALCULATION RESULTS

An intensive use of Finite Element Modelization (FEM) programs has been made in order to evaluate the steady temperature field in the collimator blocks when heated by SR. The amount of energy deposition depends on the position of the horizontal outer block w.r.t. the beam orbit and of the material traversed, i.e. copper and tungsten. The calculations were made for the separator and superconducting cavity protection collimators BRCH which are the most critical case.

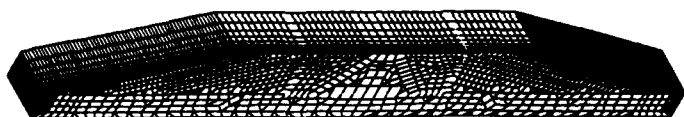


Fig. 2: FEM modelization of half of a collimator jaw of type BRCH

Only one half of the jaw was considered for the FEM because of the symmetry plane on which appropriate boundary conditions of zero flux were applied. In order to simulate as accurately as possible the non-uniformity of the power deposition, a mesh of seven thousand 8-node cubes or 6-node prisms was generated: Fig. 2.

The heat source was defined for each volume by taking into account the SR deposition calculated from the convolution of the energy deposition as a function of depth and material with the beam size. The total power deposited in the jaw is equal to 5 kW. This heat has to be removed by water cooling for which only the rear surface of the block is available. As the surfaces in contact with the cooling water have to be made of stainless steel, the whole rear surface had to be taken as exchange surface, so as to compensate for the bad heat conduction properties of the stainless steel. The cooling circuit is machined into two stainless steel plates

brazed onto the copper block. As the available water pressure drop is of six bars, and taking into account the cooling duct shape, the average water cooling flow was predicted to be equal to 20 l/min in each circuit. The convective heat transfer coefficient can be computed using the Colburn formula and is found to be equal to $L=0.02 \text{ W} \times \text{mm}^{-2} \times ^\circ\text{C}^{-1}$. The calculated isothermal lines are presented in Fig. 3. The highest temperature is found in the median plane of the block with a maximum temperature of 108°C. There is also a hot spot of 95°C in the tungsten block. The copper part had to be extended before the tungsten in order to decrease this temperature. The average block temperature is equal to 70°C.

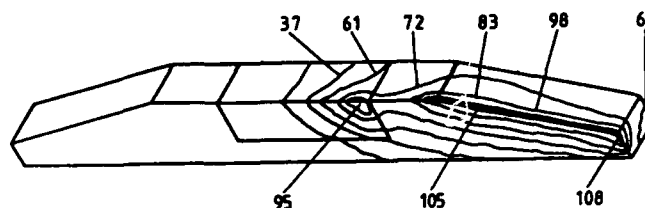


Fig. 3: Isothermal lines of the BRCH block

It is well known that parallelepipedic tanks are not adapted to vacuum vessel design. It was necessary to check that the wall deformations under vacuum will remain within acceptable limits. The FEM structure analysis code CASTEM was used to compute the tank stresses and deformations. Because of the three symmetry planes of the tank, only one eighth of the tank was modelled. The mesh was made of one thousand 20-node cubic elements.

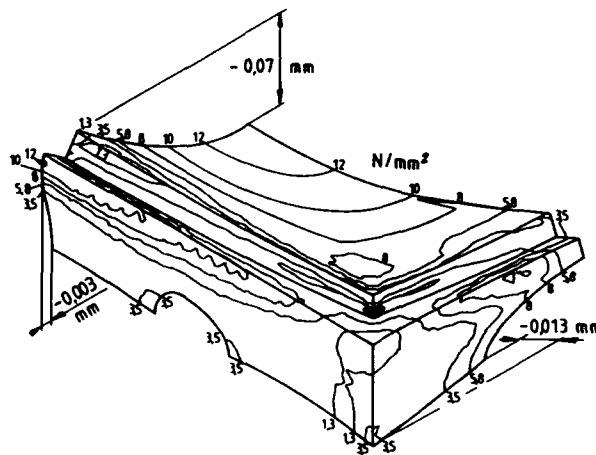


Fig. 4: Tank deformation (x1000) and isostress lines

The result of the deformation calculation is presented in Fig. 4, where the deformations are magnified a thousand times. The maximum deformation of 70 μm occurs as expected at the centre of the largest face of the tank. The maximum equivalent von Mises stress is equal to 18 N/mm^2 , which is acceptable.

IV. MECHANICAL DESIGN AND PROJECT STATUS

There are three main subassemblies in a collimator:

- the mobile blocks for defining the aperture
- the vacuum vessel
- the auxiliary elements, e.g., the block guiding system, the water cooling circuits, the support.

The collimator blocks are of three types: tungsten blocks with a spherical surface polished to optical quality, copper blocks with tungsten inserts, either flat or spherical, and copper blocks only when the SR power deposition is too high and when copper alone is acceptable as an absorber. Tungsten lengths of 100 and 175 mm are used for best photon and electron absorption, and spherical surfaces have been asked for on some collimators in order to have always the block surface tangent to the particle trajectory whatever errors occur in beam orbit and collimator alignment. Copper blocks are used in the horizontal aperture limiting secondary collimators which are submitted to the full SR power of the arcs and where the particle absorption is less critical. The tungsten used is a sintered alloy containing 95% of tungsten and 5% of copper. OFHC copper is used for its better brazing properties. As mentioned earlier, the constraints on the BRCH blocks were the most stringent ones and request a more complex construction: Fig. 5.

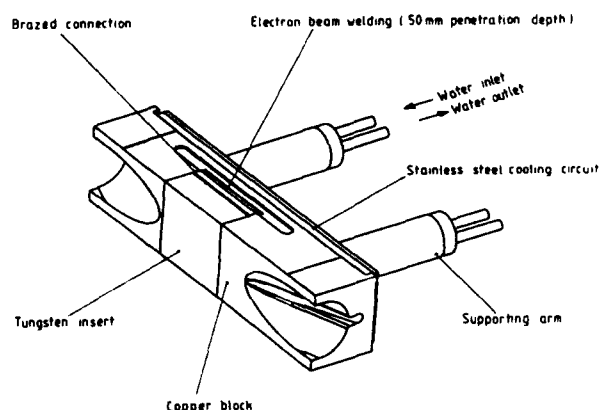


Fig. 5: BRCH collimator block with double input taper, tungsten insert and at the rear, the supporting tubes

The main absorber is a 100 mm long tungsten block. This block is brazed onto a 13 mm thick OFHC copper plate in order to provide the best thermal contact. On the other hand, there is a 450 mm long base OFHC copper block which provides the RF matching transitions to the 100 mm diameter circular vacuum chamber, has a stainless steel machined cooling circuit brazed to its rear surface and absorbs the less energetic SR before the final absorption in tungsten. The two blocks are joined together through a final operation consisting of a full depth electron beam welding in order to guarantee minimum deformation of the finished block.

The dimensions of the vacuum vessel depend on the surrounding vacuum chamber and on the block length. They do not exceed $460 \times 300 \times 120 \text{ mm}^3$. The tank is an e-beam welded stainless steel structure made of 6 mm thick plates. It is rigidified in order to minimise the deformations when

under vacuum by brazing to the largest walls a 12 mm thick plate. The water cooling circuit is machined in it. All stainless steel parts in contact with vacuum have been fired up to 900°C to remove any hydrogen and well defined cleaning procedures have been used before final assembly to reach the operating pressure of 10^{-8} Pa .

The blocks are connected to the tank with welded disk bellows and fixed to a support fitted with precision bearings sliding on circular shafts for best precision. Each block is driven by a stepping motor with a $2.5 \mu\text{m}$ resolution and its position is checked independently with a resolver geared to the motor. The main support is made of aluminium and includes on its upper part alignment references for precise positioning in the tunnel. Spring compensators are fitted to most of the blocks to compensate the weight and the atmospheric pressure due to the bellows in order to reduce the load of the stepping motors.

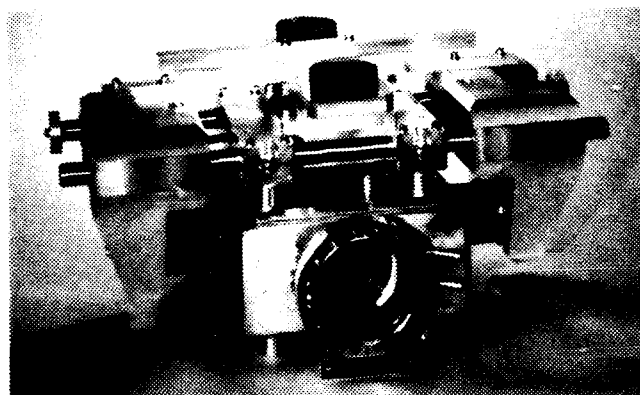


Fig. 6: Horizontal two-jaw collimator ready for installation

A series of seventeen one-jaw spherical tungsten collimators have been built in industry, and five vertical and three horizontal two-jaw collimators for aperture limitation have been built at CERN. Nine of these collimators have been installed during the 1992/93 winter stop. The order for the complex seventeen separator protection collimators BRCH has been placed with industry and the preseries collimator is expected for May 1993. The design for the additional horizontal experiments protection collimators is finished and ready to go out for production, depending on the final go-ahead.

V. ACKNOWLEDGEMENTS

Acknowledgements are due to G. Burtin for his contributions to the design, to J.P. Corso for the detailed design of the collimators, to J.P. Claret, N. Mezin, M. Souchet, B. Trincat and all other members of the CERN workshops for their good collaboration in the construction and reception of the various collimators.

VI. REFERENCES

- [1] F. Bertinelli, R. Jung: Design and construction of LEP collimators, Proc. 1987 Accelerator Conf., Washington DC

SYNCHROTRON RADIATION DAMAGE TEST OF INSULATING MATERIALS IN THE TRISTAN MR

H. Mitsui, R. Kumazawa, T. Tanii, and T. Chugun
Toshiba Corporation

2-4 Suehiro-cho, Tsurumi-ku, Yokohama-shi, 230 Japan

Y. Ohsawa, T. Ozaki, and K. Takayama

National Laboratory for High Energy Physics in Japan (KEK)

1-1, Ohno, Tsukuba-shi, Ibaraki-ken, 305 Japan

Abstract

Irradiation test of typical insulating materials for an accelerator magnet was carried out, using actual radiation in the TRISTAN MR (main ring) which was operated at the highest radiation level in the accelerator society. Physical and chemical degradations of the insulating materials due to irradiation are quantitatively reported in this paper. Some suggestions on future insulating material and its manufacturing method are given.

I. INTRODUCTION

TRISTAN is an e^+e^- colliding beam accelerator with the collision energy in a range of $\sqrt{s} \approx 60$ GeV. The MR was first operated in October 1986 at the beam energy of 25 GeV. Since then the beam energy has been increased step by step from 25 GeV to 30 GeV by employing RF accelerating cavities [1]. Thereafter the radiation damage on accelerator components, such as signal cable for beam monitors, power cable for vacuum pumps, various electric circuit components, and exciting coil of magnets, has become increasingly serious [2].

Systematic studies of the radiation damage on electrically insulating materials used for particle accelerators are found in the literature [3]; meanwhile, same kind of tests were carried out in the TRISTAN MR [4] several years ago. However, the irradiation dose was limited below 100 MGy for both cases. Radiation damage beyond this level is currently of big concern in the accelerator society because irradiation beyond 100 MGy is likely to occur in localized regions of the existing machines. Under such a situation, results of the first systematic studies performed in this dose level are released.

II. SPECIMENS

Three types of insulating materials for an exciting coil as shown in Table 1 were chosen for the current study. Type A is the so-called VPI (vacuum-pressure-impregnation) insulation system which consists of glass-cloth reinforced mica-paper tape impregnated with epoxy resin. Type B is a resin-rich insulation system which is manufactured in the atmosphere, by molding BT (bismaleimide triazine) resin preimpregnated glass-cloth, by means of heat shrinkable tape. Type C is another resin-rich insulation system which is manufactured under vacuum, by molding polyimide preimpregnated glass-cloth, with an asphalt compound.

For the purpose of knowing a change in their electrical

properties such as $\tan \delta$, an aluminum bar with cross-section of 6(mm) x 25(mm) and total length of 160(mm) was covered with each of these materials in the same manner as actual coils. To measure a change in their mechanical properties, on the other hand, samples were formed in a laminate by molding the tapes in the same manufacturing process as that of the bar coils. The plate sizes were 2 mm in thickness, 25 mm in width and 100 mm in length.

Table 1 Insulation constitution of test specimens.

Type	Material	Manufacturing process	Applied machine
A	Epoxy/mica/ E glass	VPI	TRISTAN main ring
B	BT resin/S glass	Heat shrinkable tape-molding	PS ring
C	Polyimide/T glass	Vacuum-asphalt pressure- molding	None

E glass : Electric grade glass
S.T glass: Boron-free glass

III. TEST BENCH

All of test specimens were put in a radiation box located in the steering magnet of the normal section where the dose of $3.7-6.5 \times 10^4$ Gy/h, consisting of direct synchrotron radiation and its secondary, was seriously high in the MR. The dose has been calibrated with the thermo-luminescence dosimeter method [2] by employing a test beam with well monitored energy and current.

The samples taken out of the irradiation box at some fixed time period were subjected to the tests explained in the following section.

IV. TEST RESULTS AND DISCUSSIONS

In Fig. 1, the magnitude of BDV (breakdown voltage) of the bar coils are shown as functions of dose. Fig. 2 shows the relationship between flexural strength of the laminate and dose. Fig. 3 is the relative dose dependence of residual BDV and flexural strength. The dose for halving BDV and flexural strength, which is usually used as criteria for insulation design, is listed in Table 2. In the case of type B, the degradation of the residual BDV appears in the lower dose compared to that

of the mechanical property; this is contrary to the popular view. At the highest irradiation level of 167 MGy, type A including mica reveals the highest BDV but the lowest flexural strength among three samples. In addition, it shows large swelling; it is understandable from speculation that the epoxy resin adjacently placed to the glass-cloth is decomposed into gas and the amount of gas increases with dose.

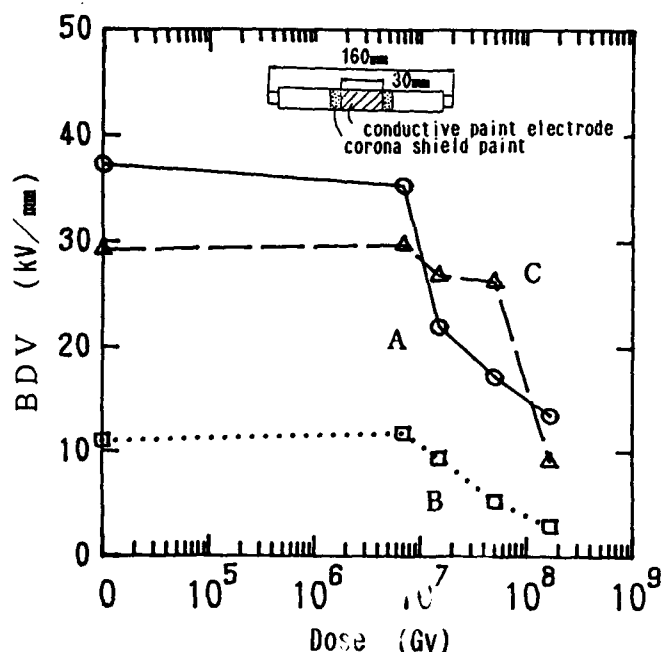


Fig. 1 Relationship between BDV of bar coils and dose.

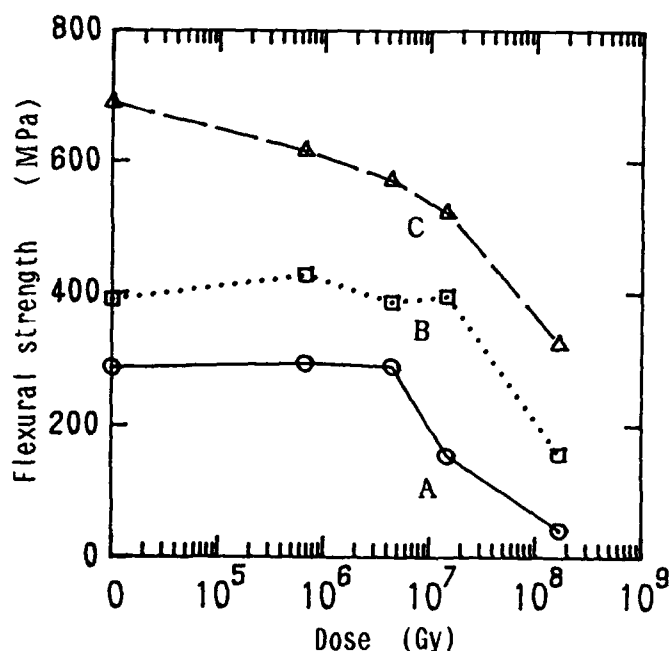


Fig. 2 Relationship between flexural strength of laminates and dose.

Table 2 Irradiation dose for halving BDV and flexural strength obtained from Fig. 3.

Type	BDV	Flexural strength
A	3.3×10^7	1.9×10^7
B	4.6×10^7	1.1×10^8
C	1.1×10^8	1.3×10^8

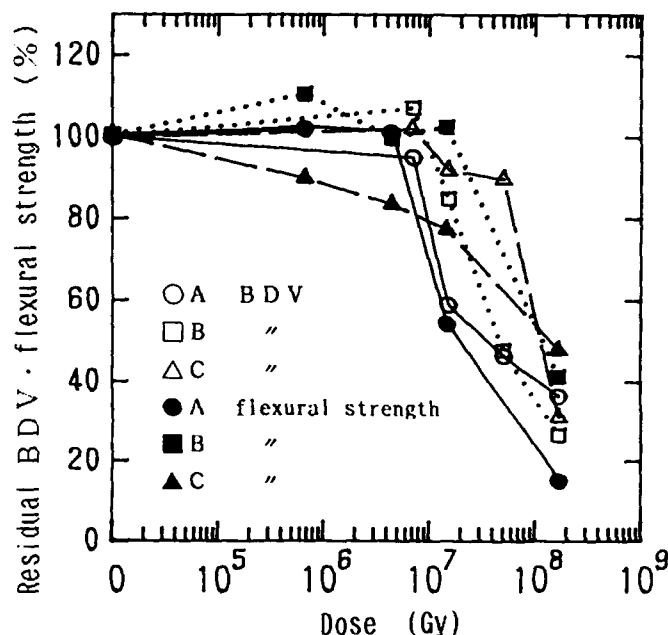


Fig. 3 Dose dependences of residual BDV and flexural strength obtained from the results shown in Fig. 1 and Fig. 2

Let's compare type B and type C which are the glass-cloth reinforced resin-rich insulations without mica. Type C is apparently superior to type B with respect to the BDV and flexural strength, as seen in Figs. 1 and 2. This can be attributed to the existence of voids in the insulating materials. The oxidation tends more to develop in the void contained insulating materials than in the void-free one. Type C is void-free because it was processed in vacuum by the asphalt-compound molding technique. type B was processed in the atmosphere by the heat shrinkable tape molding technique; therefore it contains voids.

It should be pointed out that in type B sample voids generate more easily than in type C with irradiation, as discussed below. Fig. 4 shows $\Delta \tan \delta$ characteristics as a function of dose. Where, $\Delta \tan \delta = (\tan \delta @ 3kV - \tan \delta @ 0.5kV)$. The parameter $\Delta \tan \delta$ is known to reflect partial discharges in void. It is reasonable to regard $\Delta \tan \delta$ as a measure of the amount of voids. As seen in Fig. 4, $\Delta \tan \delta$ increases with dose in the lower dose region in type B than in type C. This suggests that due to gas evolution by decompositions of the resin by irradiation, delaminations of the insulating materials

occurred to generate voids. The down in $\Delta \tan \delta$ at 167 MGy for type B is supposed that the puncture of the insulation occurred due to the increase of pressure in the closed void, and the void became open to the atmosphere resulting in decrease in volume.

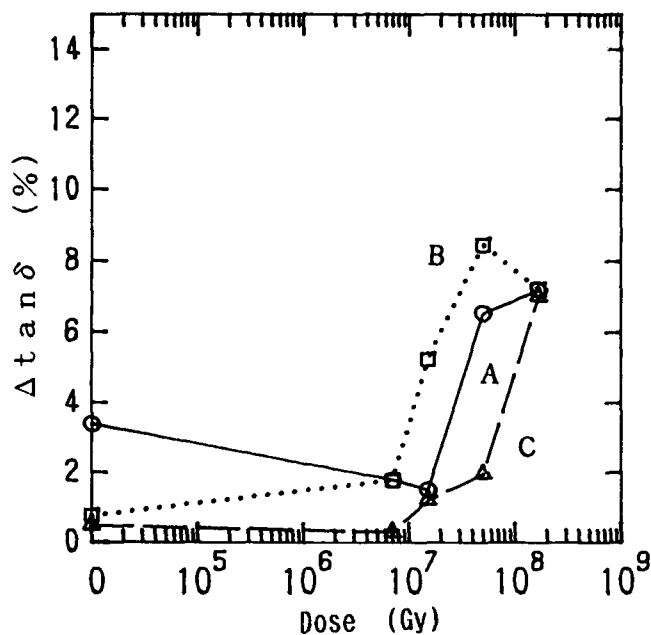


Fig. 4 Dose dependence of $\Delta \tan \delta$ of bar coils.

Fig. 5 shows the relationship between carbonyl absorbance and dose for all samples. Their features, except for the magnitude, are similar to each other. The carbonyl

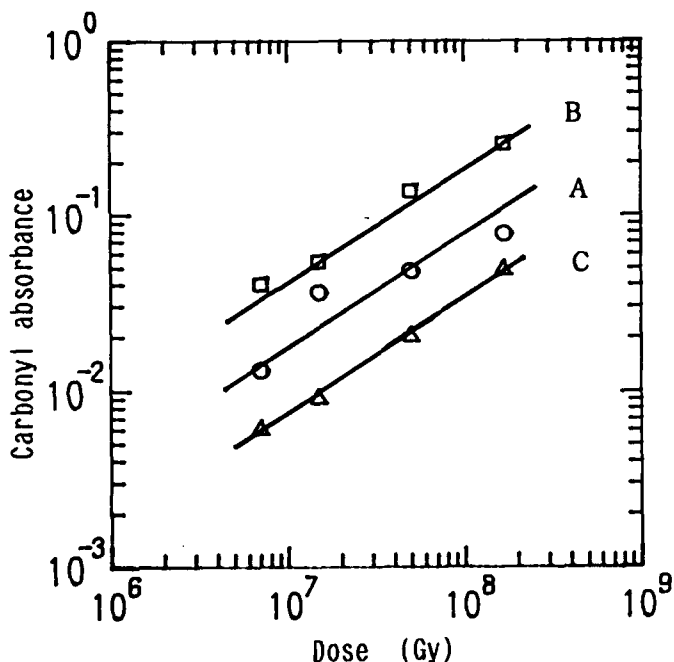


Fig. 5 Relationship between carbonyl absorbance and dose.

absorbance is apparently proportional to dose. The increase of the carbonyl group should originate from the oxidation reactions and scissions of molecules of resin which are caused by the radiation. As seen in Figs. 4 and 5, the characteristics of samples for carbonyl absorbance qualitatively coincide with that for $\Delta \tan \delta$. Thus, carbonyl absorbance can be regarded as a useful index giving the size of chemical decomposition.

The authors arrived at a speculation that these oxidation reactions and delaminations degraded insulating materials, and thus decreased BDV and flexural strength; the voids took essential roles in the process.

V. CONCLUSIONS

From the irradiation tests of typical insulating materials for magnet, using actual radiation in the TRISTAN MR (up to 167 MGy at the highest), the following were made clear.

- (1) Epoxy/glass-cloth/mica-tape insulation processed by the VPI method has higher BDV by the aid of mica tape; however its flexural strength remarkably degrades at the higher dose.
- (2) The insulation processed by the asphalt pressure molding method under vacuum is far superior both in electrical stability and mechanical rigidity to the insulation processed by the heat-shrinkable tape molding method.
- (3) The insulation processed by the heat-shrinkable tape molding method shows that the decrease in the BDV appears at a lower dose than for the flexural strength; this fact is contrary to the popular view.
- (4) Carbonyl absorbance is a useful index to measure the size of chemical decomposition caused by irradiation.

As a concluding remark, studies of the manufacturing process as well as insulating materials themselves are, indeed, important in order to develop the higher radiation-resistant insulation.

VI. REFERENCES

- [1] Y. Kimura et al., Proceedings of the 6th Symposium Accelerator Science and Technology, Tokyo, 1987, pp15-17.
- [2] T. Momose et al., European Particle Accelerator Conference, Rome, 1988
- [3] P. Beynel et al., CERN 82-10 (1982)
- [4] T. Ozaki et al., Proc. AC89, 2015-2017 (1989)

Insulating and Metal-Ceramic Materials for Particle Accelerators

Yu.P. Severgin, M.Z. Filimonov
D.V. Efremov Scientific Research Institute
of Electrophysical Apparatus
189631, St.-Petersburg, Russia

Abstract

The properties of nitride and oxide ceramic materials, which find application for structural elements of accelerating facilities, are analyzed. The construction versions and technological aspects for manufacturing of the magnetic coils with current-leading buses made from copper or aluminum are considered. The designs of metalloceramics-based vacuum ceramic chambers, current leads and other elements of accelerating facilities are presented.

I. CERAMIC MATERIALS AND SOLDERS

Ceramic facilities are favoured for application in accelerating facilities because of their low susceptibility to ionizing radiation and an exceptional combination of mechanical, electro- and thermophysical properties. The methods of ceramic technology facilitate the manufacturing of products based on nonmetallic refractory compounds with a specified phase and chemical composition and structure, which determine the required properties and operational characteristics. Refractory nonmetallic silicon, aluminium or

full-scale constructions a series of experiments on manufacturing of scale models have been undertaken. A permanent gap between the magnet coil turns and a rigid joint of coil turns into a monoblock unit are provided by structural spacers from ceramics on the basis of silicon nitrides and aluminium oxide. During coils assembly two variants if joining the ceramic spacers with copper conductors have been tested: soldering by metallic solders and glueing by an epoxy compound with a filler. The main problem to be solved in soldering was a considerable difference in thermal expansion coefficients of soldered materials (thermal expansion coefficient of copper is $19.3 \cdot 10^{-6} K^{-1}$; silicon nitride — $2.2 \cdot 10^{-6} K^{-1}$; aluminium oxide — $4 \cdot 10^{-6} K^{-1}$). The investigations were performed in two directions: metallization of ceramics based on plastic materials and subsequent soldering by low-temperature solders, as well as high-temperature soldering by active solders.

High-temperature soldering without pre-metallization by active solders with a compensator from plastic materials showed promise in developing the soldering technology. A solder based on titanium and niobium with a silver additive and a fluoroplastic interlayer has been tested. Soldering of copper buses with plates from silicon nitride and aluminium oxide has been performed. Solder is strong, weld is plastic spread of the solder is good. This method of joining provides the required ruggedness of the construction, but the control over electrical insulation between the turns is required, as the solder may spread over ceramics. It is necessary to weigh out the amount of the solder and to grind solder traces on the ceramics ends after soldering. The method of joining the copper buses with ceramics by an epoxy compound with a boron-nitride filler is free from the above disadvantage. Vacant gaps were filled with a lute from modified liquid glass or an epoxy compound with fillers from boron nitride or silicon nitride powders. Then the coils were wrapped with glass cloth and impregnated with a decorative protection layer.

Table 1: Properties of refractory nonmetallic nitrides

Parameter	Materials		
	silicon nitride	aluminium nitride	boron nitride
Bending strength, MPa	600-800	100-400	150-200
Compression strength, MPa	2500	500-1500	300
Decomposition temperature, K	2170	2720	2970
Thermal conductivity, W/m K (at 293 K)	25-60	40-140	15-30
Thermal expansion, $10^{-6} K^{-1}$	2.2	4.0	0.5-1.7
Electric resistance, Ohm.cm (at 293 K)	$1 \cdot 10^{15}$	$1 \cdot 10^{13}$	$2 \cdot 10^{13}$
Electric strength, KV/mm	12	5-8	2-4
Swelling after irradiation, % ($\phi \sim 10^{21} n^0/cm^2 s$)	0.3	—	—

boron nitrides fall in a class of nonpolar dielectrics. High energy of directed bonds of atoms in grids contributes to stability of properties of these materials, rather large value of the forbidden zone width (4.6 eV for boron nitride; 6.2 eV for aluminium nitride and 4.1 eV for silicon nitride) determine a high value of electric resistance (up to $10^{16} Ohm \cdot cm$) and the total combination of the above characteristics determine their high radiation resistance.

To develop the assembly technology of coils structural elements and to evaluate the possibility to manufacture

II. DIELECTRIC COVER OF ALUMINIUM CONDUCTORS

Among the adaptable to streamlined production methods is the method of aluminium anode oxidation in chemically moderate-active electrolytes. The fact, the coating and substrate are chemically similar, results in formation of a low-stressed system resistant to mechanical and thermal conductivity of up to 30 W/m K. The growth of oxide films results from inner oxidation processes practically not changing the product geometry. Oxide films with 100 μm

endure without damages thermal loads of up to 600 K.

Anodizing of aluminium buses in the oxalic acid solution allowed oxide films with a thickness of up to 100 μm to be obtained. Electrical strength of the coating amounted to 3 kV. Electroinsulating varnishes and siloxane sealing compounds were used as an additional electric insulation monolithic seal and moisture-protection coatings. Glyptal epoxy and organosilicon varnishes were chosen for testing. The best results were obtained with glyptal varnishes, thin films of which (80-100 μm) were applied to the aluminium buses with an oxide coating. Adhesion of films to the substrate is satisfactory. Electrical strength amounted to 25 kV/mm. For sealing compounds used to impregnate the constructions with narrow deep gaps (of accelerator coils type) critical is toughness determining the impregnability of a material. Sealing compounds based on liquid low-molecular siloxane rubber possess stable easy-to-manufacture properties with long-duration operation in a wide temperature range, preserve elastic properties for 2500 hours at 500 K, they are water-repellant, wet aluminium and its alloys well, have an electric strength of 6 kV/mm.

Model units compressing 9 and 18 aluminium buses were manufactured. Before being assembled the buses were anodized to obtain an oxide film 100 μm thick and impregnated by glyptal varnish. Then the buses with an assured gap (1 mm) were placed in a casing or fixed between each other by ceramic spacers 1 mm thick and the assembly was potted with a sealing compound. Tests for electric strength of the coils scale model showed the turn-to-ground and turn-to-turn insulation to withstand voltages of more than 6 kV.

In the technology of building up the protection coatings on aluminium and its alloys tested was the enamelling method based on a partial melting of glass powder uniformly distributed over the product surface. To apply dielectric coating to aluminium buses a low-fusible lead-borate glass ($T_{\text{melt}} \sim 720\text{K}$) with a thermal expansion coefficient of $\sim 13 \cdot 10^{-7} \text{K}^{-1}$ was chosen. The coating width amounted to 0.5-0.6 mm. The tests revealed, that the enamel coating had an electric strength of 8-10 kV per coating width.

III. METALLOCERAMIC COMPONENTS OF ACCELERATING FACILITIES

A number of metalloceramic units and components, such as vacuum ceramic chambers, electric decouplings, current leads etc, is used in accelerating facilities. To manufacture these components a superhigh-pure nonmagnetic vacuum-tight aluminium is used.

Vacuum ceramic chambers were assembled from segments up to 1000 mm long. The ceramic segments were soldered by fine-dispersed glass-ceramic solders, which provided vacuum tightness and required strength characteristics of the joint. The inner surface of the chamber was

metallized by molybdenum-content pastes with the following firing-on, as well as by using the method of vacuum or plasma spraying of metallic films from titanium, copper, niobium and other metals. With the chamber surfaces treated mechanically quality 3 and asperity according to $R_a V0.025$ were achieved.

Ceramic vacuum chambers with different cross-sections, wall thickness and length were manufactured. On the chamber ends metal adapters were soldered to provided joining with the flanges. Tests performed showed, that the chamber ensured the vacuum inside the volume of up to 10^{-12} torr without pre-training and warming-up.

Ceramics, stainless steel, copper conductors should be used in the structure of the vacuum-tight joint in such metalloceramic units, as current leads and decouplings. The elements in the ceramic units were joined both by metallic solders with plastic additives and various glass-fiber reinforced cements. Tests performed revealed, that the metalloceramic units preserved vacuum-tightness of joints at room and cryogenic temperatures.

IV. CONCLUSION

The properties of ceramic materials of a nitride class have been analyzed. Ceramics based on silicon nitride and aluminium oxide is proposed to be used as a turn-to-turn insulation for electromagnet coils. Metallic solders have been chosen for a rigid joint of structural elements of copper buses. The regime of aluminium bus anodizing has been developed making it possible to produce anode-oxide films of a large thickness (up to 100 μm) with an electric strength of more than 3 kV. The properties of impregnating and sealing compounds have been tested, which allow for a qualitative potting of structures with narrow deep gaps. The scale models of the coils with the chosen insulation materials have been manufactured and tested for electric strength. The materials satisfy the requirements for electric strength. The ceramic vacuum chambers with inner metallization, as well as various metalloceramic elements complying with the operation condition for accelerating facilities have been started to be manufactured.

The Advanced Light Source (ALS) Radiation Safety System*

Arthur L. Ritchie, Donald E. Oldfather, and Allan F. Lindner
Lawrence Berkeley Laboratory
University of California Berkeley, California 94720

Abstract

The Advanced Light Source (ALS) at the Lawrence Berkeley Laboratory (LBL) is a 1.5 GeV synchrotron light source facility consisting of a 120 keV electron gun, 50 MeV linear accelerator, 1.5 GeV booster synchrotron, 200 meter circumference electron storage ring, and many photon beamline transport systems for research. See figure 1.

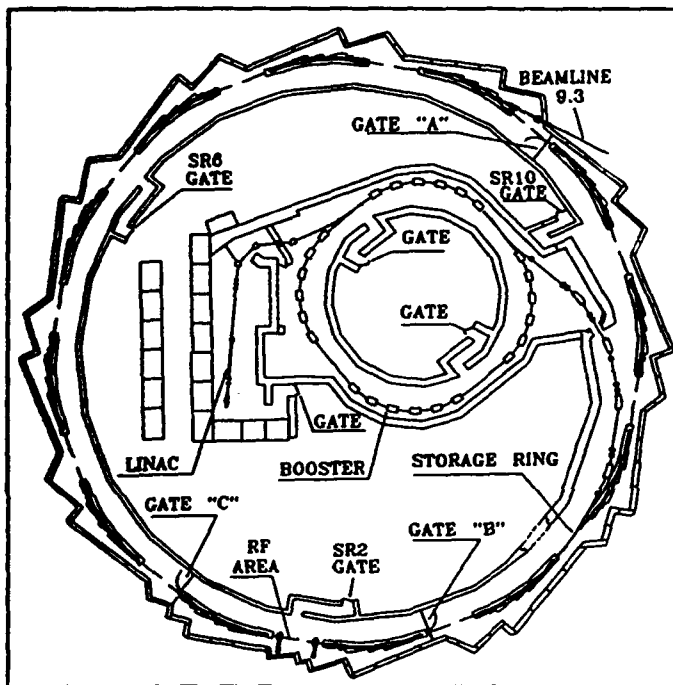


Figure 1 - ALS Floor Plan

The Radiation Safety System for the ALS has been designed and built with a primary goal of providing protection against inadvertent personnel exposure to gamma and neutron radiation and, secondarily, to enhance the electrical safety of select magnet power supplies

I Introduction

The initial review process called for a preliminary design review of the complete system followed some time later by a final design review but, because of the construction and operation schedule, it was decided to separate the project components into sub-areas and review each separately. These designs were subjected to many in-house ALS staff reviews,

*This work was supported by the Director, Office of Energy Research, Office of Basic Energy Sciences, Materials Sciences Division, of the U.S. D.O.E., under Contract No. DE-AC03-76SF00098.

followed by an LBL design review and, eventually, by an outside team of interlock safety professionals from other DOE labs. The DOE conducted overall project safety (fire, electrical, radiation, etc.) reviews as well. Throughout this process a number of recommendations for improvement were made and incorporated into the design.

II Design Considerations

A very important factor in designing the ALS radiation safety system was future component availability for maintenance spares and circuit expansion. With typical accelerator lifetimes of 30 to 50 years or more, circuit components with a high probability of being manufactured in the distant future narrowed the design process but the foremost factor in the component selection process was component reliability, failure modes, and predictability.

For all of these reasons, and others, a 24 volt direct current system using electrical-mechanical relays to perform the logic functions was selected. The 24 volts is well below the 50 volt level set by OSHA for hazardous working conditions requiring lock-out/tag-out or special safety equipment for "live" work. This voltage is also widely used in industrial and military control circuit designs, thus a large number of components are available from manufacturers to solve design problems. Because of the proliferation of relays in control and safety circuits dating back to the early part of this century, a long history exists regarding their ruggedness, reliability, and predictability. Solid state devices introduced in the late 1950's, quite often become obsolete and unavailable, and tend to fail in the unsafe (shorted) mode. Programmable devices often have software quality assurance and control problems. The broad worldwide use of electrical-mechanical relays and large number of manufacturers tends to guarantee future availability.

Except for short lengths at interlocked radiation monitors and beamline safety shutters, radiation safety system cables are routed in separate enclosed wireways or conduit apart from other accelerator wiring and not allowed in open ladder trays. An audio intercom system uses #20 AWG shielded twisted pair and a video system uses RG-59 coax cables, otherwise, all interlock cables are specified to have a minimum wire size of number 16 AWG, stranded, tinned copper, with an abrasion resistant, flame retardant, low smoke insulating jacket, and be listed and approved by the Underwriters' Lab with a type TC (tray cable) rating.

All switch and relay contacts have a minimum 5 amp rating at 24 volts dc and all relay coils must operate at 75 percent of their coil voltage rating. In an effort to prevent accidental

wiring errors or tampering all radiation safety equipment, cabinets and junction boxes are locked. All interlock chains are tested on a six month basis and all radiation monitoring equipment is calibrated quarterly.

III Access Control

The system permits three types of access control. The first being no access allowed during accelerator operations. Second is controlled access inside the shielding under certain conditions. After an area inside the shielding has been searched and secured, controlled access can be allowed back into that area. Accelerator operations are inhibited and guaranteed by requiring each person entering under controlled access to take a key from a "controlled access key cache" located outside each entrance gate. This key cache has redundant interlocks preventing accelerator operation until all keys are returned. This type of access control does not require the accessed area(s) to be searched and secured after a controlled access has been allowed. Any uncontrolled, inadvertent access or activation of any emergency crash-off push button switch in a previously searched area will interrupt accelerator operations and require a new search and secure of that area. The third type of access is uncontrolled access and occurs when the accelerator is shut down for modifications or maintenance and the access gates entering the shielding are propped open.

An audio and color video intercom system links the six shielding entrance gates with the control room and is used for controlled access activities. A commercial video and audio switching unit made by Pelco Inc. is located in the control room along with a color monitor and speaker/mic assembly.

IV Search and Secure

The search of a given area of the accelerator is done using keys and key-switches. The "search keys" are removed from key-switches in the main control room. Removal insures the safety of the search party. Areas to be searched have key switches that mate with the search keys. These key-switches must be reset in a prescribed sequence, and in some cases, an extra push button is installed whereby two switches must be operated in tandem, thus forcing a two person search. Accelerator operation is inhibited until the search keys are returned to the control room and turned to the operate position and a 60 second time delay occurs. During this 60 second delay, normal white lighting inside the shielded radiation areas is immediately turned off, red lighting is turned on and a two tone audible alarm inside the shielding is sounded. Backlit status indicator signs located in numerous locations change from "safe" to "operational" and after the 60 seconds has timed out, the indicator signs change to "unsafe leave area", the audible alarm ceases and red flashing beacons outside the entrance gates commence flashing. Controlled access entry turns the normal white lighting back on and turns the red lighting and flashing beacons off. After the person(s) has exited from a controlled access and returned

the keys to the key cache, the 60 second time delay sequence is re-initiated with the audible and visual warnings as described above.

V System Description

The interlock system consists of three main interlock chains each having a number of sub-chains; all with redundancy throughout. The first of the three main interlock chains is the linac chain which controls the 120 KeV electron gun as well as the 50 MeV linac. Both have redundant interlock controls. The electron gun, for example, has its ac main interrupted and the 120kV power supply external interlock turned off should an interlock be violated. The linac chain has three sub-chains capable of interrupting the electron gun/linac operation. A description of these sub-chains is as follows:

a) Because of thin shielding in the booster-to-storage ring beam transport area, a portion of the storage ring (between internal gates "A" and "B") is interlocked as a sub-chain to the linac chain, and occupancy of that portion of the storage ring is not allowed while the linac is operational. Shielding is adequate when backed up with these interlocks. These same interlock devices (gate/door micro switches, search switches, crash-off switches, etc.) in this storage ring area are also a part of the storage ring interlock chain described later. After the storage ring is filled and operated in a "stored beam" mode, and the linac is shut down, occupancy of this area is still prohibited because of the radiation produced by the stored electron beam. Access to this area is only permitted when both the linac and the storage ring are shut down. Controlled access to this area inhibits operation of both the linac and the storage ring.

b) The second sub-chain controlling the linac chain is the booster interlock chain. Originally the booster interlock chain was to be a separate interlock system allowing access to the booster while limited linac operations were permitted. Shielding design changes mandated the booster interlock system control the linac operation. Access to the booster through either of its two entrance gates or activation of any booster crash-off push button switch will inhibit the linac operation. As with the linac chain having sub-chains, the booster has a sub-chain consisting of active radiation monitors that eventually control the operation of the linac. Should gamma or neutron radiation above a preset trip level be detected outside the shielding, the radiation monitor will interrupt the linac operation indirectly via the booster chain. The tripped radiation monitor interlock is latched off and requires control room investigation and manual reset in the area of concern. These radiation monitors are commercially manufactured by Health Physics Instruments Inc. and are designed for pulse operations. In addition to an active interlock output, they have a number of features including analog and digital output signals for remote data collection of the radiation being detected.

c) The third sub-chain of the linac is another radiation monitoring system using the same type of detectors as described above for the booster sub-chain. These detectors

are located in areas just outside the linac shielding and if radiation above a preset trip level is detected, the linac operation will be inhibited. As with the booster radiation monitoring chain, the tripped monitor is latched off and requires control room investigation and reset before operations can resume.

The second main ALS interlock chain is the storage ring chain. It eventually becomes an input along with the third main ALS interlock chain (storage ring fill/run described later) to control the storage ring RF system and the booster-to-storage ring electron beam transport line B1 and B2 bending magnets. The inner storage ring shielding wall has three controlled access entrance gates. Inside the shielding are three internal gates dividing the storage ring into three zones. The outer wall has 12 hinged concrete doors for maintenance access. All of these doors and gates are interlocked. The operation of the storage ring chains and sub-chains is as follows:

a) The storage ring area between internal gates "A" and "B" as discussed earlier is a sub-chain of the linac and storage ring. The function of the interlock devices bounded by the two internal gates "A" and "B" are summed as a sub-chain at the storage ring sector 10 entrance gate safety racks and becomes an input for the main storage ring chain at the storage ring sector 6 entrance safety racks (as well as the linac described above).

b) The storage ring has two RF cavities installed in the straight section between sectors 2 and 3 that are powered by a 300kW klystron via a wave guide structure. To allow testing of this RF system and uncontrolled access to the remainder of the storage ring, a third internal gate (gate "C") was installed to form an interlocked area surrounding the cavities. The storage ring sector 2 entrance gate access this area and, along with two interlocked concrete doors, emergency crash-off switches, internal gates "B" and "C", and other devices, form a sub-chain allowing RF testing. As can be seen, internal gate "B" functions in two chains; the linac chain because of the storage ring area between gates "A" and "B" and also the storage ring RF test chain because of the area between internal gates "B" and "C". The interlock devices for the area between internal gates "B" and "C" are summed at the storage ring sector 2 entrance gate safety racks and becomes an input for the main storage ring chain at the storage ring sector 6 entrance racks.

c) The third zone of the storage ring consists of sectors 4 through 9 and is bounded by internal gates "A" and "C". This area is normally accessed via an entrance gate at sector 6 where safety racks bring together interlocked devices within this zone as well as the two other zones discussed above. Additional inputs from the storage ring RF system (indicating it is in an operate mode as opposed to test) and an interlocked utility tunnel transiting under the storage ring and linac appear at this location to form the main storage ring chain. The utility tunnel interlocks are also shared by the linac chain discussed earlier.

The third main ALS interlock chain is the storage ring fill/stored beam chain. It has two functions. It will inhibit filling of the storage ring if the beamline safety shutters are not inserted and it turns off the storage ring RF if a beamline hutch interlock is violated. Beamline interlocks for each sector are summed at that sector and then all sectors are brought together. In order to fill the storage ring, a global fill request is sent to all beamlines to close all beamline safety shutters. This request is one input to an interlock controlling the booster-to-storage ring beam transport line bending magnets B1 and B2. When all safety shutters are closed the interlock is then complete to allow operation of the B1 and B2 magnets. Should a safety shutter open during a fill procedure, the two magnets are disabled. After the storage ring has been filled the, global fill request is removed. This relinquishes control of the safety shutters to the beamline operating stations and reasserts the inhibit of operation for the B1 and B2 bend magnets. This prevents accidental beam transport from the booster during tune-up while the storage ring is in a stored beam mode and the position of beamline safety shutters is unknown. Active radiation monitors outside the storage ring shielding also control these two magnets and the storage ring RF. Should radiation outside the shielding be detected above the trip level, the B1 and B2 magnet power supplies and storage ring RF are turned off.

Normal access to an interlocked beamline hutch is via a request to a programmable logic controller (PLC). The PLC cycles certain machine protection equipment and outputs a command to close the beamline safety shutter. Redundant micro switches sense the shutter position and if the shutter is inserted, key(s) are allowed to be released from the beamline safety shutter control panel. Removal of a key operates an interlock switch that keeps the safety shutter inserted until the key is returned, regardless of any PLC activity to the contrary. These key(s) mate with key switches on the hutch doors that will release a hutch door and capture the key while in the released position. A search push button switch inside the hutch must be reset if the hutch door has been opened or the emergency crash-off push-button inside the hutch has been depressed. Hutchless beamlines are identical except for the hutch door release key(s) and the search requirement. The beamline control panel also allows the ALS beamline safety coordinator the capability of locking out any beamline not meeting ALS standards.

VI Operating Experience

After initial debugging during commissioning, the linac and storage ring interlock systems have performed very well. At the time of this writing, components for the beamline safety shutters and hutches are being fabricated and installed. Beamline operations are expected within the next two to three months.

RADIATION MEASUREMENTS DURING CAVITIES CONDITIONING ON APS RF TEST STAND*

D.M.Grudzien, R.L.Kustom, H.J.Moe, J.J.Song
Argonne National Laboratory, Argonne, IL 60439

Abstract

In order to determine the shielding structure around the Advanced Photon Source (APS) synchrotron and storage ring RF stations, the X-ray radiation has been measured in the near field and far field regions of the RF cavities during the normal conditioning process. Two cavity types, a prototype 352-MHz single-cell cavity and a 352-MHz five-cell cavity, are used on the APS and are conditioned in the RF test stand. Vacuum measurements are also taken on a prototype 352-MHz single-cell cavity and a 352-MHz five-cell cavity. The data will be compared with data on the five-cell cavities from CERN [1].

I. INTRODUCTION

The X-ray and vacuum measurements were made on various cavities with conditioning and without conditioning. The information obtained provides data for the final design of the radiation shielding on the APS RF stations.

II. EXPERIMENTAL SET-UP AND PROCEDURE

Measurements were made on the cavities that were installed in the APS RF test stand. The RF test stand block diagram and area layout are shown in Figures 1 and 2, respectively.

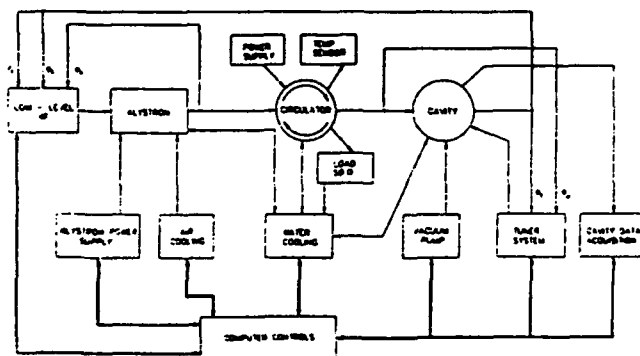


Fig. 1. RF Test Stand Block Diagram

*Work supported by U.S. Department of Energy, Office of Basic Science under contract W-31-109-ENG-38.

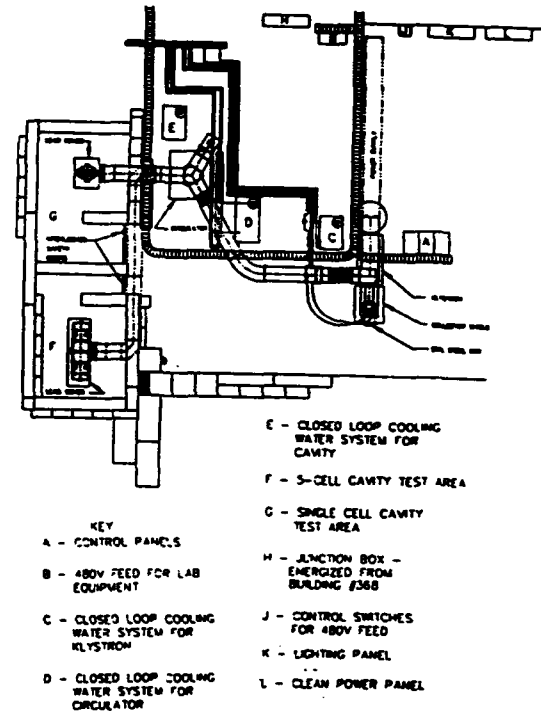


Fig. 2. RF Test Stand Area Layout

The RF system consists of a 250-kW Philips Klystron YK1350, a 351-MHz ANT circulator, a WR 2300 waveguide, directional couplers, coaxial water loads, and a 351.9-MHz single-cell [2] or a 351.9-MHz five-cell resonant cavity (LEP) type [3]. Directional couplers are located immediately after the klystron power and in each of the arms of the circulator to monitor both forward and reverse power.

The cavities are loop-excited using an input coupler from the WR2300 waveguide. The low-level RF system controls the amplitude and phase of the RF signal which drives the klystron amplifier. It also includes the phase regulation that maintains the cavity resonance point. The low-level RF system consists of an RF drive control loop for pulse or CW operation to set the operating level of the klystron in the linear or saturation region, and a frequency control loop to keep the cavity on resonance. The power supply is rated at 550 kW DC and produces 10 A at 55 kV or 8.6 A at 65 kV to feed the klystron. The cavities are tested at a vacuum limit of 5×10^{-7} Torr and more typically about 1 to 2×10^{-7} Torr. The base pressure of the single cell cavity is 10^{-8} Torr and the five-cell cavity is 10^{-10} Torr.

X-ray levels were measured with a Xetex Wide Area Monitor Model 510A-10 and film badges.

III. MEASUREMENTS

1) Single-Cell Prototype Cavity

After assembly the cavity was not baked. X-ray measurements were done with five film badges placed around the cavity. The radiation levels in millirads are shown in Table 1. The measurements were performed for two hours at power levels of 30 kW and 60 kW.

Table 1. Radiation measurements around a single-cell cavity (in mrd).

Radiation badge #	Position from the center of the cavity in the directions			30kW	60kW
	x	y	z		
1	-0.84	-0.28	+0.39	min	410
2	-0.84	+0.28	+0.39	min	400
3	-0.66	+0.28	+0.39	min	260
4	-0.66	-0.28	+0.39	min	260
5	0	0	+0.39	min	20

The single-cell cavity vacuum as a function of RF power is shown in Fig. 3.

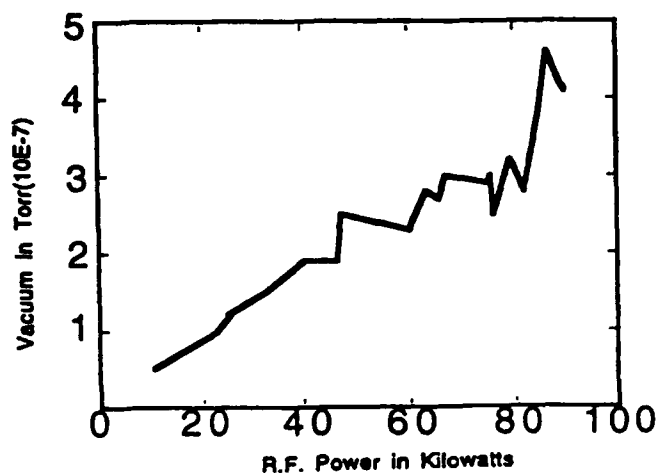


Fig. 3. Cavity vacuum as a function of RF power after 122 hours of conditioning.

2) Five-Cell Cavity #1

After assembly, the cavity was baked out at 150°C for 24 hours and then conditioned with RF power up to 100 kW in the RF test stand.

An X-ray radiation level of .14 mrd/h was found around the blockhouse at a 40-kW power level. Nothing was observed for low power levels. About this same level was observed on an Xetex X-ray monitor with its head sensor located in the blockhouse (Fig. 2). The radiation levels in millirads are listed in Table 2. At 100 kW measurements were taken for three hours with ten film badges placed around the cavity. This cavity was pumped with two 400-l/s turbo pumps.

Table 2. Radiation measurements around a five-cell cavity at 100 kW.

Radiation badge #	Position from the center of the cavity in the directions in m			Radiation level in mrd
	x	y	z	
1	-1.4	0	0	895
2	-1.1	-0.4	+0.4	95
3	0	-0.4	+0.4	50
4	+1.1	-0.4	+0.4	35
5	+1.4	0	0	120
6	+1.1	+0.4	+0.4	30
7	0	+0.4	+0.4	85
8	-1.1	+0.4	+0.4	125
9	-2.0	-2.0	-2.0	35
10	+2.0	+2.0	+2.0	15

The radiation level in mrd/h, the cavity vacuum in Torr, and RF power in kW are shown in Fig. 4.

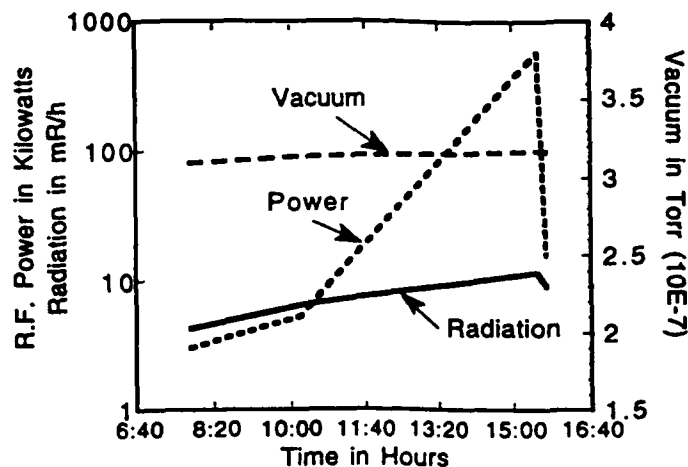


Fig. 4. Radiation level, cavity vacuum level, and RF power level as a function of time.

The five-cell cavity vacuum as a function of RF power after 42 hours of conditioning is shown in Fig. 5.

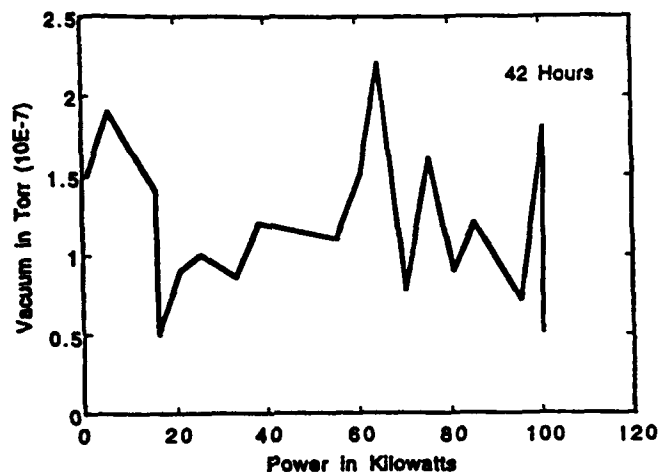


Fig. 5. Cavity vacuum as a function of RF power after 42 hours of conditioning.

3) Five-Cell Cavity #2

After assembly, the cavity was baked out at 150° C for 24 hours and then conditioned with RF power up to 100 kW in the RF test stand. At a power level of 100 kW measurements were taken for three hours with ten film badges placed around the cavity. This cavity was pumped one 400-l/s turbo pump.

Table 3 shows the radiation level in millirads.

Table 3. Radiation measurements around a five-cell cavity at 100 kW.

Radiation badge #	Position from the center of the cavity in the directions in m			Radiation level in mrd
	x	y	z	
1	-1.4	0	0	140
2	-1.1	-0.4	+0.4	40
3	0	-0.4	+0.4	60
4	+1.1	-0.4	+0.4	45
5	+1.4	0	0	500
6	+1.1	+0.4	+0.4	85
7	0	+0.4	+0.4	40
8	-1.1	+0.4	+0.4	70
9	-2.0	-2.0	-2.0	15
10	+2.0	+2.0	+2.0	Min

The radiation level in mrd/h, the cavity vacuum in Torr, and RF power in kW as a function of time are shown in Fig. 6 and the cavity vacuum as a function of RF power is shown in Fig. 7.

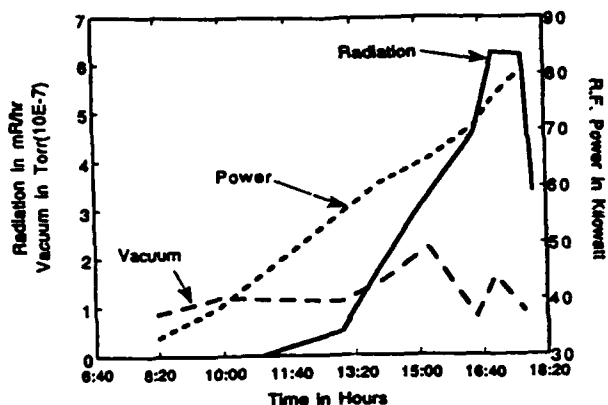


Fig. 6. Radiation level, cavity vacuum level, and RF power level as a function of time.

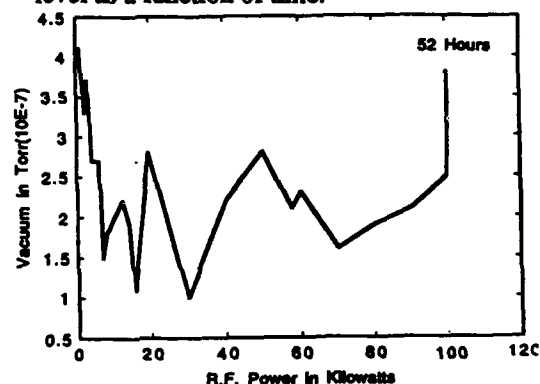


Fig. 7. Cavity vacuum as a function of RF power after 52 hours of conditioning.

IV. CONCLUSIONS

Since the prototype single-cell cavity was not baked out after assembly, the conditioning process was approximately two months long. High radiation levels of 895 and 500 mrd were measured on badges positioned close to the beam ports of the five-cell cavities.

V. ACKNOWLEDGMENTS

The authors wish to thank David Meyer, Donald Voss, and Edward Wallace who helped conduct the tests.

VI. REFERENCES

- [1] P. Brown, G. Geshonke, H. Henke and I. Wilson, *Proceedings 1989 Particle Accelerator Conf.*, pp. 1128-1130, (1989).
- [2] J.F. Bridges, J.M. Cook, R.L. Kustom, J.J. Song, *"Proceedings 1991 Particle Accelerator Conf."*, pp. 639-641 (1991).
- [3] Ian Wilson, H. Henke, "The LEP Main Ring Accelerating Structures," *CERN 89-09*, Nov. 8, 1989.

Application of a Simple Analytical Model to Estimate Effectiveness of Radiation Shielding for Neutrons

S. Frankle, D. Fitzgerald, R. Hutson, R. Macek, and C. Wilkinson

Medium Energy Physics Division, Los Alamos National Laboratory, Los Alamos, NM 87545 USA

Abstract

Neutron dose equivalent rates have been measured for 800-MeV proton beam spills at the Los Alamos Meson Physics Facility. Neutron detectors were used to measure the neutron dose levels at a number of locations for each beam-spill test, and neutron energy spectra were measured for several beam-spill tests. Estimates of expected levels for various detector locations were made using a simple analytical model developed for 800-MeV proton beam spills. A comparison of measurements and model estimates indicates that the model is reasonably accurate in estimating the neutron dose equivalent rate for simple shielding geometries. The model fails for more complicated shielding geometries, where indirect contributions to the dose equivalent rate can dominate.

I. INTRODUCTION

The assessment of radiation shielding for the Los Alamos Meson Physics Facility (LAMPF) and the Los Alamos Neutron Scattering Center (LANSCE) required a quick and simple method of estimating neutron dose equivalent rates (DER) for 800-MeV proton beam spills. An analytical model has been developed for this purpose. During the 1992 operating cycle, neutron DER measurements were performed in the switchyard area of LAMPF and at LANSCE. These results have been used to gauge the accuracy of the model to estimate the neutron DER (accuracy within a factor of 2-3 is desired). The analytical model is discussed, the 1992 beam-spill measurements performed are described, and a comparison with the model estimates is made.

II. ANALYTICAL MODEL FOR ESTIMATING NEUTRON DOSE EQUIVALENT RATES

The analytical model used to estimate the neutron DER is a combination of a Moyer Model [1,2] for lateral production angles and extended for 800-MeV proton beams and a Monte Carlo based formula for forward production angles [3]. The model has the following functional form:

$$D = \frac{H_0}{r^2} \exp(-\beta\theta) \exp\left(-\sum_i \frac{r_i}{\lambda_i}\right)$$

where D is the neutron dose equivalent rate, H_0 is the source term, r is the distance from spill to observation point, β is the angular relaxation parameter, θ is the production angle between the incident beam direction and the ray from spill to observation point, r_i and λ_i are the path length through and attenuation length for material i , respectively. The model parameters are listed in Table 1, which includes the attenuation lengths for concrete (2.42 g/cc), magnetite concrete (3.64 g/cc), natural iron (7.87 g/cc), and tuff (1.6

g/cc). For production angles of $30^\circ \leq \theta \leq 60^\circ$, DER estimates are made with both sets of parameters defining a range of possible values.

Table 1.
Analytical Model Parameters for Estimating Neutron Dose Equivalent Rates for 800-MeV Proton Beam Spills.

Parameter	$0^\circ \leq \theta \leq 30^\circ$	$60^\circ \leq \theta \leq 120^\circ$
H_0 (mrem·m ²)/(hr·μA)	856×10^6	296×10^6
β (rad ⁻¹)	2.14	2.3
λ concrete (m)	0.58	0.50
λ mag. concrete (m)	0.43	0.40-0.43
λ tuff (m)	0.77	0.66
λ nat. iron (m)	0.35	0.20

III. 1992 BEAM-SPILL MEASUREMENTS

A. Description of Beam-spill Measurements and Detector Locations

Beam-spill measurements were performed in the switchyard area of LAMPF and at LANSCE. The switchyard measurements were performed in Line D, the transfer line from the linac to the Proton Storage Ring that supplies beam to LANSCE. Measurements were made for two spill points in the Line D 89° bend, and for four spill points at LANSCE. Measurements for two detector/spill point combinations in the switchyard area and 25 detector/spill point combinations at LANSCE were compared to model estimates.

The neutron dose equivalent rates (mrem/hr) for various beam-spill tests were measured using HPI Pulsed Neutron Detectors Model 2080, referred to as Albatrosses. For each spill test, Albatross readings were taken after three time intervals; usually three, six, and nine minutes. This allowed each detector to come into equilibrium and established that it was consistent over time. The DER measurements for each spill test were then normalized by the beam current to the units mrem/(hr·μA).

B. Corrections to the Neutron DER Measurements

Albatrosses have a very low efficiency for detecting the contribution to the DER from neutrons with $E_n \geq 20$ MeV. Therefore, an estimate of the DER that was not measured by the Albatrosses must be made and a correction factor applied to the data. Neutron energy spectrum measurements were performed for two beam spill and detector locations in 1992. These, and previous spectrum measurements, indicate that the DER contribution from neutrons with $E_n \geq 20$ MeV is (34-

65% of the total, for a correction factor of $f=1.5-3.0$. A value of $f=1.5$ corresponds to a detector location where the indirect contribution to the DER is large, while a value of $f=3$ corresponds to detector locations where the indirect contribution is negligible. Since not every detector location has a corresponding spectrum measurement, a correction factor of $f=2.25$ has been applied and the neutron DER measurements are believed accurate to within a factor of 2 [4].

IV. COMPARISON OF MODEL ESTIMATES WITH MEASUREMENTS

A. Comparison for the LAMPF Switchyard Area

The LAMPF switchyard area has an overburden of tuff, with two penetrations, the personal access maze and the truck access. The truck access is filled with large concrete shielding blocks whose total length is ≈ 6.8 meters. A tungsten block was inserted between two bending magnets midpoint in the 89° bend and the upstream bending magnet was turned off, simulating a spill in one of the magnets. Two Albatrosses were located 6.3 meters along, and on top of, the concrete shielding blocks in the truck access. There was a total distance of (12-12.5) meters between spill and observation point, with a total of (6.4-7.2) meters of concrete shielding. Approximately 70% of the beam interacted within the magnets and tungsten block, with an equivalent natural iron path length of 0.1-0.2 m, and the remainder continued forward and struck the concrete shielding blocks. The production angle ranged from 12° to 29° . The [estimated: measured] values for the neutron DER for the two Albatross locations are [76:120] and [19:63]. The estimates are within a factor of 2-3 of the measured values, and are acceptable given the complexity introduced from the beam interacting at two locations.

B. Comparison for LANSCE

The LANSCE spill measurements include cases in which the DER is expected to be dominated by direct contributions as well as cases dominated by indirect contributions from scattered neutrons. The LANSCE experimental area is composed of adjacent two-story buildings. The beam enters on the upper floor (Service Area) of the first building and is bent 90° downwards into the neutron production target. The lower floor is Experimental Room 1 (ER1) and contains the neutron production target surrounded by a bulk shield with the horizontal neutron beam lines fanning out radially. As shown in Figure 1, steel shielding was added in the forward beam direction on the upper level. The second building is Experimental Room 2 (ER2). The spill points and detector locations are illustrated in Figure 1, and the corresponding model estimates and measured neutron DER are tabulated in Table 2.

The model accurately estimated the neutron DER for a number of spill and Albatross locations (**bold type**), but was unsuccessful for others. First, let us consider the three

Albatross locations A-C in ER2. Albatross A was located 6.8 m above the floor of ER2, while Albatrosses B & C were 2.4 m above the floor, all directly along the beam's line-of-sight. The model grossly underestimated the measured DER for Spills 1-3 for Albatross B and Spills 2-3 for Albatross C. This is because the model only estimates the direct line-of-sight contribution to the DER. The additional steel shielding, as well as the large amount of tuff, in the forward direction substantially reduces the direct contribution to the DER at locations B & C, so that scattering of low-energy neutrons from larger production angles and other indirect contributions dominate. To illustrate this point, consider the ratio of the difference between measured and estimated values for Albatrosses B & C to the measured values for Albatross A, where the indirect contribution to the DER is negligible. The

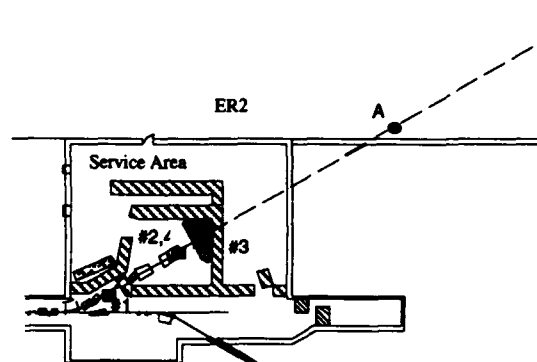


Figure 1.a. Plan view of the Service Area and the upper level of ER2.

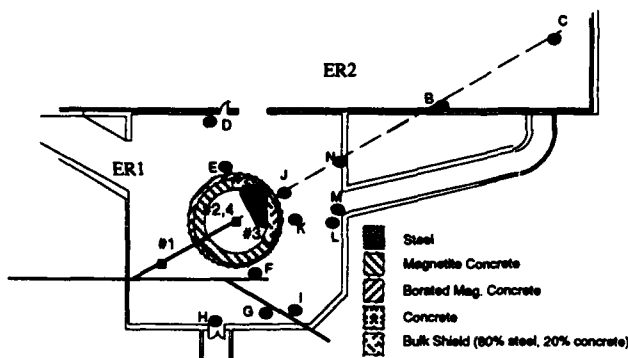


Figure 1.b. Plan view of ER1 and ER2.

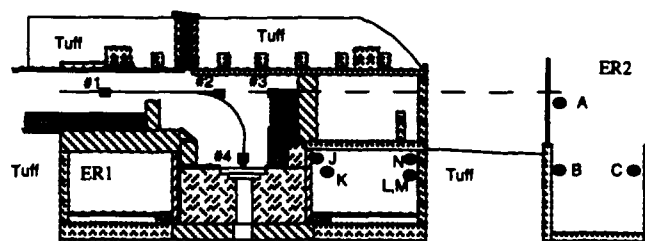


Figure 1.c. Vertical elevation view of the Service Area, ER1, and ER2.

Table 2.
Comparison of the Measured DER with the Model Estimate
for the 1992 Beam-Spill Tests at LANSCE.

Albatross	Spill #	Production Angle (°)	Measured DER	Estimated DER
A	1	3.2	13	---
	2	3.8	331	409
	3	4.6	522	706
	4	97	0.0	0.0
B	1	11	1.6	0.0
	2	13	54	0.0
	3	16	84	0.01
	4	86	0.0	0.0
C	1	9.5	6.1	6.9
	2	10	109	2.9
	3	12	163	9.7
	4	88	0.4	0.0
D	4	87	124	295
E	4	88	783	1067
F	4	88	859	1067
G	4	87	144	295
H	4	85	173	272
I	4	84	110	117
J	1	24	44	2.4
	2	37	713	15
	3	62	456	0.0
	4	75	6.1	0.04
K*	1	---	82	---
	2	---	1582	---
	3	---	498	---
	4	---	8.2	---
L*	1	---	50	---
	2	---	1074	---
	3	---	506	---
	4	---	9.0	---
M*	1	---	46	---
	2	---	946	---
	3	---	605	---
	4	---	3.8	---
N	1	16	16	0.4
	2	21	457	26
	3	29	683	40
	4	85	1.1	0.01

* Included for informational purposes only.

difference between measured and estimated DER is used in order to remove the direct contribution from the total. The ratio values for Albatross B to A are 0.125, 0.163 and 0.161 (mean=0.150). The ratio values for Albatross C to A are 0.329 and 0.293 (mean=0.311). These values are relatively constant and independent of spill location indicating that detector locations B and C will see an indirect contribution equal to 15% and 31% of the total DER at location A for all spill points. The large discrepancy between measurement and calculation indicates that indirect contributions can dominate

the total DER, particularly for locations where the expected direct line-of-sight contribution is small.

This is further illustrated by the comparison between measurement and model estimate for Albatross locations in ER1. No calculations have been performed for K, L, & M; these measurements are included for information purposes only. The analytical model was successful in estimating the DER for D, E, F, G, H & I and Spill 4. where the estimated DER was large. The model was unsuccessful for detector locations J & N. As stated previously, these two locations are directly shielded by the additional steel shielding. The other nine locations are mostly shielded by magnetite concrete only. The discrepancy between measured and estimated DER is considerably larger than was observed in ER2. This is most probably due to ER1 being a much smaller enclosed area, a large fraction of the room is occupied by equipment and shielding for the 12 neutron beam lines, and the room is enclosed on three sides by tuff. The backscattering of low-energy neutrons may play a greater role in this case.

V. SUMMARY

The analytical model was successful in estimating the neutron DER for those spill/observation point combinations where the shielding geometry was relatively simple. The model accurately estimated the DER for forward angles in the Line D switchyard and the ER2 crane area, at lateral angles at LANSCE where the shielding geometry was simple and/or where the estimated direct DER was dominant. The model was unsuccessful at forward and lateral angles for more complicated shielding geometries, particularly where the estimated direct contribution was small.

A simple analytical model can be used to estimate the neutron DER for many spill/observation point combinations allowing the user to perform a large number of calculations relatively quickly. However, the model must be applied discerningly and with a great deal of caution; the shielding geometry must be well understood so that it can be determined that indirect contributions to the DER are negligible.

VI. REFERENCES

- [1] G. Stevenson and R. Thomas, "Determination of Transverse Shielding for Proton Accelerators Using the Moyer Model," *Health Physics* 43, 13 (1982).
- [2] J. McCaslin, W. Swanson, and R. Thomas, "Moyer Model Approximations for Point and Extended Beam Losses," *Nucl. Instrum. Methods* A256, 418 (1987).
- [3] C. Wilkinson *et al.*, "Monte Carlo Based Formula For Radiation Shielding Assessment in the Forward Direction," these proceedings.
- [4] S. Frankle, "Neutron Energy Spectrum Measurements with Bonner Spheres and Neutron Dose Equivalent Rate Measurements Using Albatrosses," PSR Technical Note 93-005, LA-UR number to be assigned.

Monte Carlo Based Formula for Radiation Shielding Assessment in the Forward Direction

C. Wilkinson, D. Fitzgerald, S. Frankle, R. Hutson, and R. Macek

Medium Energy Physics Division, Los Alamos National Laboratory, Los Alamos, NM 87545 USA

Abstract

Monte Carlo simulations of 800-MeV proton beam spills in common shielding materials show that neutron dose equivalent rates in the forward direction can be characterized by a Moyer Model-like formula[1,2]. Particle transport codes were used to determine the neutron flux at depths up to 6 meters and for production angles from 0° to 30° for primary proton beam spills on cylindrical beam stops. The flux was then converted to dose equivalent rate as a function of depth and angle. The results for three common shielding materials were combined and the resulting fitted formula provides a quick method for estimating the dose equivalent rates and shielding effectiveness outside thick shielding at forward angles.

I. INTRODUCTION

The assessment of radiation shielding for the beam lines and experimental areas at the Los Alamos Meson Physics Facility (LAMPF) required a quick and simple method of estimating neutron dose equivalent rates for 800-MeV proton beam spills in the forward direction. Although some work has been done on simple formulas for forward production at energies above a few GeV[3], no useful formula exists at the intermediate energies found at LAMPF. Since the Moyer Model formula worked well for us for calculations in the transverse direction, it was our hope that we could fit a similar, simple formula to Monte Carlo results for dose equivalent rates in the forward direction.

II. MONTE CARLO SIMULATION

A. Particle Transport Codes and Computer

The particle transport codes LAHET[4] and MCNP[5] were used to simulate particle histories resulting from the interaction of a monochromatic 800-MeV proton beam in three common shielding materials: concrete, natural iron, and magnetite concrete. LAHET was used to create and track histories for protons above 1 MeV and neutrons above 20 MeV, while MCNP was used to track neutrons below 20 MeV and photons. No variance reduction techniques were used in the simulations. The simulations were run on an HP-730 workstation, which has been shown to be approximately equivalent in speed to a CRAY Y-MP in benchmark tests for these codes.

B. Simulation Geometry and Data Records

The Monte Carlo geometry simulated proton beam spills on three cylindrical beam stops made of the individual shielding materials. The beam-spill point was taken to be the center of the end face of each beam stop, with the incident beam parallel to the axis of the cylinder. See Figure 1. For

each of the shielding materials, the particle fluxes $\phi(E, \theta, r)$ as a function of energy E , production angle θ , and material depth r were recorded on several surfaces bisecting the cylinder normal to the incident beam direction. Each surface was divided into seven concentric annuli subtending production angles $\theta \pm 2.5^\circ$, where $\theta = 0^\circ, 5^\circ, 10^\circ, 15^\circ, 20^\circ, 25^\circ$, or 30° . The distance r was measured from the spill point to the midpoint of each annular ring, and θ was the production angle as measured from the incident beam direction. Dose equivalent rates $DER(\theta, r)$ were obtained by multiplying the flux by the energy-dependent ICRP[6] conversion factors and summing over energy for each θ and r .

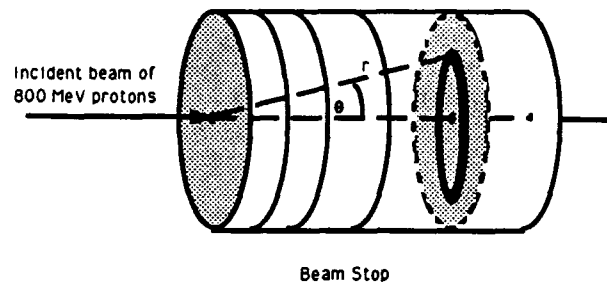


Figure 1. Cylindrical beam stop geometry used for Monte Carlo simulations. The spill point is the center of the incident face. Particle flux as a function of energy, production angle θ , and distance r from the spill point was recorded over annular areas on surfaces at several depths.

C. Removal of Backscatter and Minimal Contributions

Contributions to the total dose equivalent rate $DER(\theta, r)$ from photons were on the order of a few percent or less and were therefore ignored. Protons, however, contributed a substantial fraction to the calculated dose equivalent rate up to depths of several meters. By the time the DER had reached acceptable biological occupation levels, however, contributions by protons were a few percent and were ignored for the purposes of this study. Only neutron fluxes were used in the fit.

We were interested in the neutron dose equivalent rate outside the shielding. The neutron flux inside the cylinders, however, included contributions from internally backscattered neutrons. This internal backscattering component must first be removed before using the results from inside the cylinder. To do this, several additional Monte Carlo runs were performed with truncated cylinders whose end faces corresponded to the positions of some of the internal faces. A comparison of internal- and end-surface DER's allowed an estimate of the backscattered contributions to be made. For the three materials discussed here, the fraction of backscattered contributions for each material was essentially constant for all angles and all surfaces tested. Correction factors of 0.70 for concrete, 0.68 for magnetite concrete, and

0.40 for iron were applied to the dose equivalent rates for internal surfaces so that the fitted values would be accurate for calculations outside shielding.

III. SELECTION OF DATA SAMPLE

It was our intent to obtain adequate statistical samples in each material to depths of at least 7 radiation attenuation lengths, approximately the shielding thickness needed for our worst-case spills. A sufficient number of source protons, several million in the cases of both concrete and magnetite concrete, were started such that the final average statistical errors for the flux bins $\phi(E, \theta, r)$ up to depths of $r \approx 9\lambda$ were $\sim 11\%$. If the data at $\theta=0^\circ$ (the annulus with the smallest sampling area) were excluded, the average statistical errors on the fluxes were $\sim 6\%$. The iron data presented a slightly different picture: the average statistical error on the flux bins for depths up to 6λ was 19%. This number was influenced by a few bins at wide angles and large depths, as indicated by the fact that 90% of the flux was contained in bins with statistical errors of 5% or less. Slightly more than a million source protons were required to obtain this accuracy in iron. For the purposes of developing a simple formula for dose equivalent rates outside the shielding, we excluded data within two attenuation lengths of the spill point to get past the build-up of particles and into an equilibrium region that could be fitted simply. The data included in the fit are given in Table 1.

Table 1.

Input data for the weighted MINUIT fit of Monte Carlo dose equivalent rates and the parameters of the fit. Data for all angles between 0° and 30° were included. Numbers in parentheses give the depth in terms of attenuation lengths, λ .

Input Data to the Monte Carlo		
Material	Density gm/cm ³	Depth meters
Concrete	2.42	1.5 - 5.0 (2.6 - 8.6) λ
Iron	7.87	0.70 - 2.0 (2.0 - 5.7) λ
Magnetite Concrete	3.64	1.0 - 4.0 (2.3 - 9.3) λ

IV. RESULTS OF A WEIGHTED FIT TO MOYER MODEL FORMULA

The dose equivalent rates $DER(\theta, r)$ and statistical errors for the three materials, at all angles and at the depths listed in Table 1, were used to perform a global, weighted fit to a Moyer-type formula of the form

$$D = \frac{H_0}{r^2} \exp(-\beta\theta) \exp\left(-\frac{r}{\lambda}\right).$$

Here $D(\text{rem/hr-nA})$ is the neutron dose equivalent rate, $H_0(\text{rem-m}^2/\text{hr-nA})$ is the source term, $r(\text{m})$ is the distance from spill to observation point, $\beta(\text{rad}^{-1})$ is the angular relaxation parameter, $\theta(\text{rad})$ is the production angle between the incident beam direction and the ray from spill to observation point, and $\lambda(\text{m})$ is the attenuation length for a material. The fitted parameters H_0 , β , and the individual λ 's for concrete, iron, and magnetite concrete are given in Table 2.

Table 2.

Fitted parameters from a MINUIT fit to a Moyer-type formula. Units are $\text{rem-m}^2/\text{hr-nA}$ for the source term H_0 . Numbers in parentheses give the radiation attenuation lengths in gm/cm^2 .

H_0	β	λ_{conc}	λ_{iron}	λ_{magn}
856	2.14 rad ⁻¹	0.58 m (140.4)	0.35 m (275.5)	0.43 m (156.5)

The fitted values were insensitive to the inclusion of Monte Carlo data at greater depths than those listed in Table 1. When the fit was expanded to include additional data for depths up to 6 m in concrete, 3 m in iron, and 5 m in magnetite concrete, there was no significant change in the fit parameters, although the relative errors for the parameters increased several percent. The plots in Figures 2-4 show the Monte Carlo results at all depths, but the line representing the fit only includes the data listed in Table 1. It can be seen that the calculated values using the formula are still a good fit to the data at the greatest depths, but not for data in the build-up region at depths less than 2λ .

It should be noted that the fitted attenuation length $\lambda=0.35$ m for iron for forward-production angles is significantly longer than the value of 0.21 m normally quoted for use in the transverse Moyer Model. This is because the forward formula is fit to data that explicitly includes low energy neutrons. When neutrons with energy below 20 MeV are excluded from the forward fit to iron, an attenuation length of 0.21 m is obtained. This inclusion of the low energy data in the forward parameters and formula removes the need for the addition of hydrogenous material to obtain the calculated iron dose equivalent rate normally advised in the transverse case.

V. SUMMARY

A Moyer Model-like function provides a very good fit to the Monte Carlo results for neutron dose equivalent rates in the forward direction for beam spills by a monochromatic 800-MeV proton beam. This function can be used to estimate neutron dose equivalent rates outside radiation shielding in simple geometries where the contributions from indirect sources such as skyshine and backscattering from nearby structures are not significant. A comparison of estimated dose equivalent rates from the formula and measured values for

beams spills at LAMPF[7] shows that the formula gives a useful estimate of the neutron dose equivalent rate in cases with minimal indirect contributions.

VI. REFERENCES

- [1] G. Stevenson and R. Thomas, "Determination of Transverse Shielding for Proton Accelerators Using the Moyer Model," *Health Physics* 43, 13 (1982).
- [2] J. McCaslin, W. Swanson, and R. Thomas, "Moyer Model Approximations for Point and Extended Beam Losses," *Nucl. Instrum. Methods A256*, 418 (1987).
- [3] R.H. Thomas and G.R. Stevenson, "Radiological Safety Aspects of the Operation of Proton Accelerators," Technical Report Series No. 283, IAEA Vienna (1987).
- [4] R.E. Prael and H. Lichtenstein, "User Guide to LCS: The LAHET Code System," LA-UR-89-3014, Los Alamos (1989).
- [5] "MCNP - A General Monte Carlo Code for Neutron and Photon Transport," Version 3A, LANL Report LA-7396-M, Los Alamos (1986).
- [6] R.G. Jaeger, ed., "Engineering Compendium on Radiation Shielding," Volume I, IAEA Vienna (1968).
- [7] S. Frankle et al, "Application of a Simple Analytical Model to Estimate Effectiveness of Radiation Shielding for Neutrons" (to be published, these proceedings).

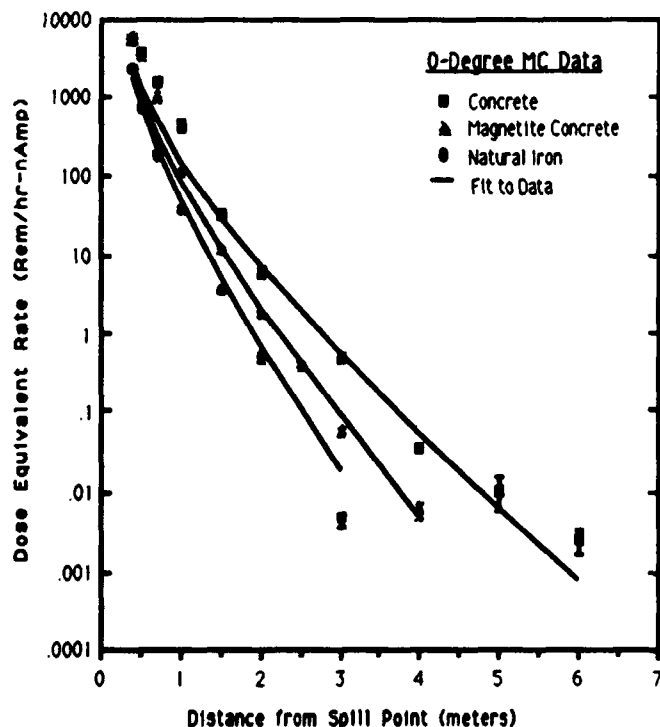


Figure 2. Comparison of Monte Carlo data and the fit to a Moyer-like formula for neutron dose equivalent rates at a production angle of 0 degrees.

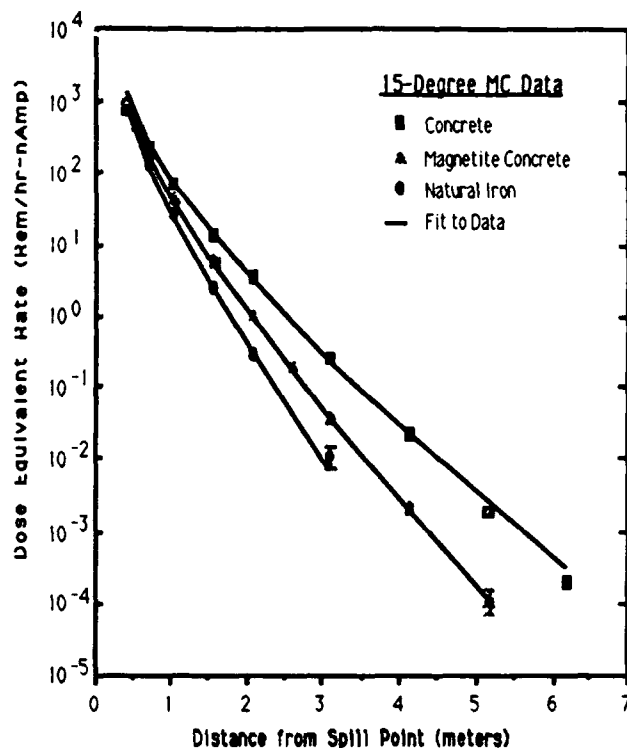


Figure 3. Comparison of Monte Carlo data and the fit to a Moyer-like formula for neutron dose equivalent rates at a production angle of 15 degrees.

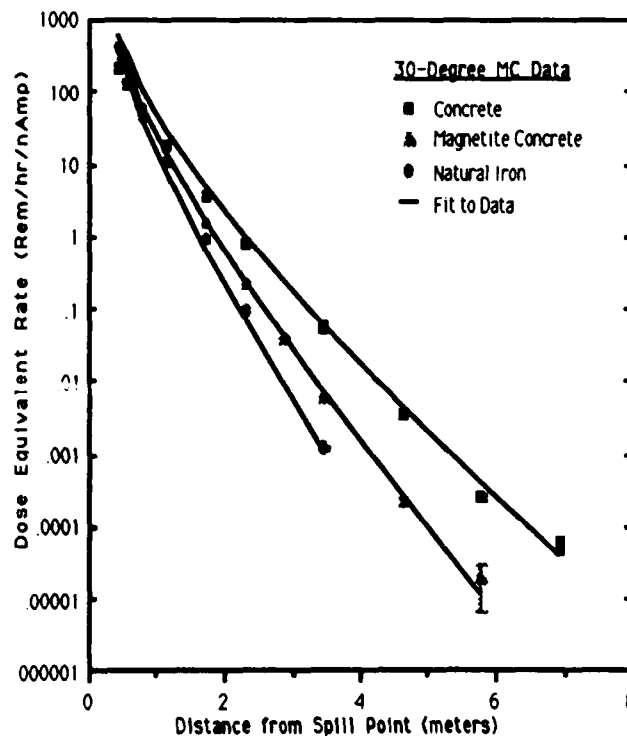


Figure 4. Comparison of Monte Carlo data and fit to Moyer-like formula for neutron dose equivalent rates at a production angle of 30 degrees.

A High Reliability Oxygen Deficiency Monitoring System

R. Parry, G. Claborn, A. Haas, R. Landis, W. Page, J. Smith
Superconducting Super Collider Laboratory
2550 Beckleymeade Avenue, Dallas, TX 75237 USA

Abstract

The escalating use of cryogenics at national laboratories in general and accelerators in particular, along with the increased emphasis placed on personnel safety, mandates the development and installation of oxygen monitoring systems to insure personnel safety in the event of a cryogenic leak. Numerous vendors offer oxygen deficiency monitoring systems but fail to provide important features and/or flexibility. This paper describes a unique oxygen monitoring system developed for the Magnet Test Laboratory (MTL) at the Superconducting Super Collider Laboratory (SSCL). Features include: high reliability, oxygen cell redundancy, sensor longevity, simple calibration, multiple trip points, offending sensor audio and visual indication, global alarms for building evacuation, local and remote analog readout, event and analog data logging, EMAIL event notification, phone line voice status system, and multi-drop communications network capability for reduced cable runs. Of particular importance is the distributed topology of the system which allows it to operate in a stand-alone configuration or to communicate with a host computer. This flexibility makes it ideal for small applications such as a small room containing a cryogenic dewar, as well as larger systems which monitor many offices and labs in several buildings.

I. INTRODUCTION

The Magnet Test Lab was constructed to perform acceptance and life tests on superconducting magnets. It is a complex of buildings and areas including: a compressor building, service building, main magnet test hall, control room, basement, and numerous lab areas and offices.

Cryogenics (liquid helium and nitrogen) flow through virtually all areas. A release of cryogenics can create an oxygen deficiency hazard. If the release is sufficiently large, the loss causes displacement of oxygen in the area to less than life-supporting levels. The MTL oxygen monitoring system consists of: 21 oxygen sensors, 20 global audio/visual alarm units for personnel notification and evacuation, and 2 ventilation fan controllers. The sensors are placed where the highest probability exists for a leak such as valves and connecting joints. If both helium and nitrogen are present, oxygen sensors are placed in pairs. One sensor is located near the ceiling to detect oxygen deficiencies due to a liquid helium leak (helium is lighter than air and rises), and the other is placed near the floor to detect deficiencies from a liquid nitrogen leak (cold nitrogen is slightly heavier than air and falls).

II. OXYGEN SENSORS

A. Measuring Oxygen

Several techniques may be used to measure oxygen. High accuracy methods are expensive, especially if a large number

of sensors are to be used in applications like the MTL where many sensors are installed to provide adequate coverage. Inexpensive electrochemical oxygen cells are a better choice to detect oxygen deficiencies in these applications. These cells act like an oxygen sensitive battery, the more oxygen the cell is exposed to, the higher the voltage output from the cell. Conversely, less oxygen yields a lower voltage.

Note that the term *cell* as used in this paper refers to the small electrochemical device that is used for sensing oxygen content. The term *sensor* is used to indicate the 9" x 9" unit containing *cells*, electronics, horn, and strobe.

B. High Reliability

For highest reliability the longevity of the sensor represents the greatest concern. Like a conventional battery, electrochemical oxygen cells have a finite life, typically 9 to 24 months. Experience has shown that the health of the cell is a major factor contributing to false alarms. Ailments range from infant mortality, to anomalous cell variations and ultimately to cell death. At first glance, using two cells would appear to be a solution. For example, if one cell drops below the safe level, we could switch to the other cell (one out of 2 voting). However, this is not a safe solution since an oxygen deficiency measured by one cell would not allow us to ascertain with certainty if the measured value is caused by an actual oxygen deficiency or a false alarm. The solution is to use three cells. Using a 2 out of 3 voting scheme allows one to differentiate between an actual oxygen deficiency and a single cell failure. Only if two cells agree does the system initiate an actual alarm. A single low reading sensor is voted out. In this way, false alarms are significantly reduced.

3 oo 3: Three cells are normal, select lowest value.

Cell A	Cell B	Cell C	Result	Example	Result
Norm	Norm	Norm	Norm	20, 21, 22	20

2 oo 3: Two cells are normal, select lowest value.

Cell A	Cell B	Cell C	Result	Example	Result
Norm	Norm	High	Norm	20, 22, 25	20
Norm	Norm	Warn	Norm	20, 22, 19	20
Norm	Norm	Alarm	Norm	20, 22, 15	20

1 oo 3: One cell is normal, select lowest value unless two are high, then select highest value.

Cell A	Cell B	Cell C	Result	Example	Result
Norm	High	High	High	20, 24, 25	25
Norm	High	Warn	Warn	20, 25, 19	19
Norm	High	Alarm	Alarm	20, 25, 15	15

0 oo 3: No cells normal, select lowest value unless there are three high, then select highest value.

Cell A	Cell B	Cell C	Result	Example	Result
High	High	High	High	24, 25, 26	26
High	High	Warn	Warn	24, 25, 19	19
High	High	Alarm	Alarm	24, 25, 15	15

The above table shows the 2 out of 3 voting logic integrated into the software of the controller. The basic voting rule is to error on the side of safety, specifically this means select the case would result in a state equal to or more severe than the suspected state. For example, an *alarm* state is a safer state than the warning state since it causes additional actions such as activating the ventilation fans.

The triplication also carries with it fault tolerance and ease of maintenance. Should a cell fail during a running period, the cell need not be replaced immediately. Two of the three cells remain functioning to provide safe oxygen monitoring. However should another cell fail, an alarm will be initiated. The system provides a remote alarm indication which signifies the failure of the cell. During a maintenance period, the failed cell may be replaced without interrupting operations. Another benefit of triplication is added cell longevity. While the actual life of the cell is not lengthened, a normal maintenance program that replaces cells before they fail (i.e., replace cells as they approach their life expectancy) need not be implemented. Cells may remain in use until they actually fail.

Other factors affecting cell reliability are temperature, barometric pressure, and humidity. To assure high reliability each of these factors should be addressed. Temperature is a major contributor to inaccuracy and poor reliability. It is compensated for within the cell by a temperature compensating resistor. Although humidity also affects oxygen measurements, compensation need not be introduced since high accuracy is not required for personnel oxygen measurements. Barometric pressure does significantly affect cell accuracy. At this writing pressure compensation is not provided, however as shown in the figure, a pressure transducer is included for a possible future version.

C. Set points

The normal partial pressure of oxygen at sea level is 158 mm Hg ($158 / 760 \text{ mm Hg} = 20.8\%$). Deleterious effects due to a lack of oxygen do not occur in healthy individuals until the partial pressure is less than approximately 135 mm Hg (17.8%). To insure that a warning is provided before this level is reached, 19.5% is defined as a safe level to indicate a possible hazard.

Based on this standard, several system states have been identified: *normal*, *warning*, *alarm*, and *malfunction*. The *normal* state is represented by oxygen levels between 19.5% and 23%. A *warning* exists anytime the oxygen level is less than 19.5% and greater than 18.0%. Personnel are notified of a *warning* by a intermittent horn. When the level falls below 18% an *alarm* state exists in which area horns, strobes, and ventilation fans are activated. The fans bring fresh air into the area. Measurements less than 0% or greater than 23% are considered system malfunctions since these measurements are considered erroneous in our application.

D. Calibration

The output of a typical electrochemical cell is 12 mv, but varies greatly between cells. Therefore the cells must be calibrated before installation and in the field if cells are replaced. Given the number of sensors and the precarious locations of many of the sensors, calibration must be simplified. The calibration method has been reduced to placing a "cup" connected to a calibrated reference gas (20.8%) over the cells and depressing a "calibrate" switch. Software within the controller makes specific checks and normalizes the sensor's output to 20.8%.

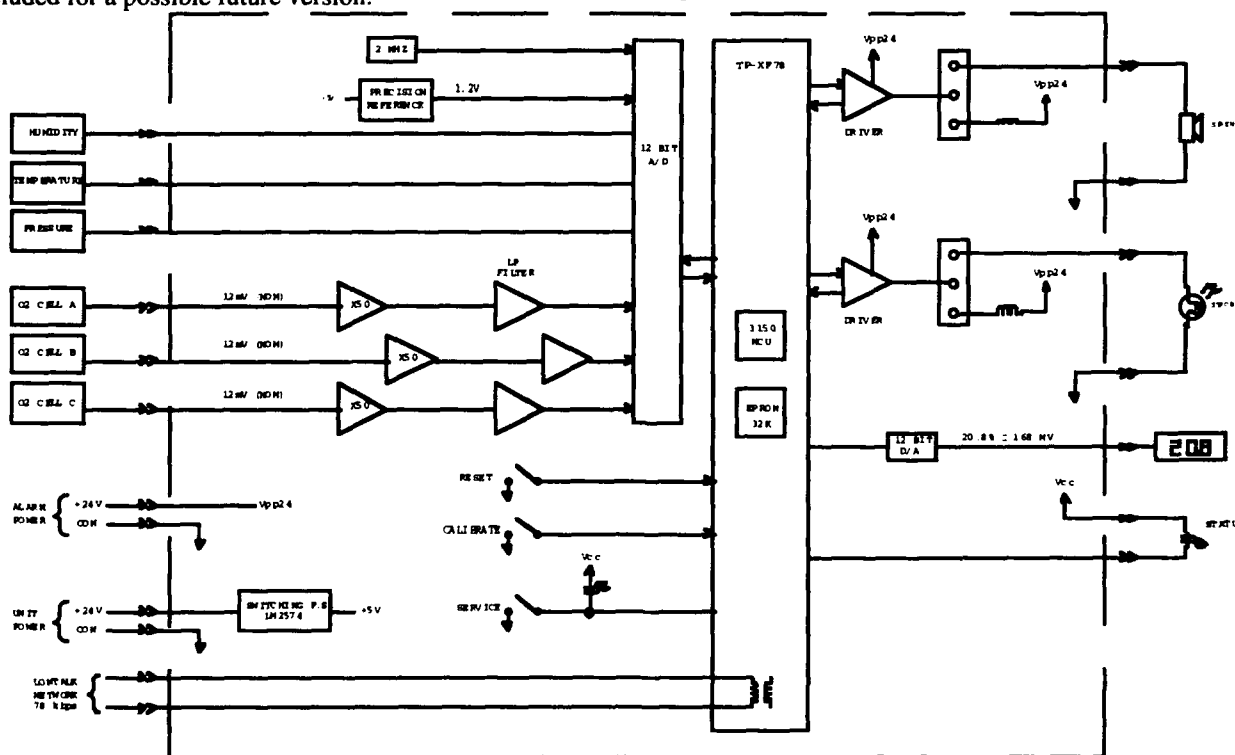


Figure 1. Block diagram of the oxygen monitor. The heart of the system is the Echelon 3150 Neuron Chip. The three oxygen cells are shown as A, B, and C. The humidity, temperature, and pressure transducer are not implemented in the present design. The unit is powered by a single 24 vdc supply. Alarm power for the horn and strobe is separate.

III. THE NETWORK

A. Features

Providing notification to personnel of a hazardous condition is of paramount importance. For this reason both visual and audible indications in the form of strobe lights and evacuation horns are provided. Additional alarms attached directly to the sensors indicate locally the status of the oxygen sensors and aid in locating the offending unit.

The analog level is digitally displayed on the front of the unit. This value may also be ascertained remotely via the operator interface console. The analog levels are also recorded at 15 second intervals. These data files are kept for 7 days which provides adequate historical records for purposes of analysis and fault reconstruction. Plotting software is available for easy and concise display of the data. Discrete state changes such as warning, alarm, and normal are time and date stamped and logged. This information proves valuable in ascertaining system reliability.

For non-operating periods of the MTL, remote notification of alarming events is provided in two forms. By way of the lab wide Ethernet network, EMAIL messages are broadcast to maintenance personnel. A dedicated VMAIL (Voice Mail) system initiates telephone calls to phones and/or pagers. This system also allows for call-in status requests from a remote location to ascertain oxygen levels of oxygen sensors.

B. Hardware

The need to provide adequate coverage requires many sensors in often precarious and/or remote locations. Some are suspended from a 30' high ceiling and others in pits or basements. Running cable and conduit to these locations represents a significant cost. The need to reduce cable complexity was answered by a new communication technology developed by Echelon® Corporation and embodied in the 3120 and 3150 Neuron integrated circuits manufactured by Motorola® and Toshiba®. A "multi-drop" network topology is used which allows for sensor communication over a single twisted pair cable. This has the advantage of also reducing conduit size and therefore further reducing installation costs. For our application 78 Kbps was used (1.25 Mbps is also available). Other communications media are available such as RF (4800 bps), power line (9600 bps), coax, IR, and optical fiber.

The Neuron is basically a standard microcontroller such as the Motorola 68HC11 and Intel 8051 with internal RAM, ROM, and EEPROM. What makes this chip unique is the powerful built-in communications capability, LonTalk™, a proprietary seven-layer network protocol. Peer to peer communications is easy to implement allowing any sensor to broadcast messages to any other sensor or for that matter any

device on the network. Error checking, packet assembly, acknowledgment and retries are implemented within the Neuron and are transparent to the programmer. A predictive Carrier Sense Multiple Access (CSMA) with optional collision detection is used for communications and provides high throughput even at high traffic rates. Transformer coupling provides additional fault tolerance to cell failures which may otherwise adversely affect the network.

C. Software

Software is required to implement the many features described. The software is written in Neuron C which contains several extensions to standard C which allows the programmer to easily take advantage of the Neuron's features. Neurons communicate with each other by the use of input and output network variables. In our application, the fan controllers and alarm units have input variables and the oxygen monitors, output variables. In order for a cell to control a fan, a connection between the nodes must be made. This process is called, "binding". Therefore the logic (program) that might normally be implemented in a single controller, is implemented in a database of bindings.

IV. CONCLUSION

Use of oxygen monitoring systems will continue to expand in use at national laboratories and represent a large subsystem at the SSCL. False alarms of such systems adversely affects humans and creates both operational and availability problems. Using triplicated cells provides increased reliability from several types of cell failures. In addition, the distributed control system described has great flexibility and saves on both cable and installation costs.

V. REFERENCES

- [1] J. Butler, "Embedded Controller Networking Alternatives," *Circuit Cellar INK*, April/May - 1992, issue #26.
- [2] K. Davidson, "Echelon's Local Operating Network," *Circuit Cellar INK*, April/May - 1991, issue #21.
- [3] R. Parry, "Personnel Access Safety Systems at the Superconducting Super Collider," *Proceedings of the Industrial Computing Conference*, Vol 2, page 437, ISA, 1992 - Paper #92-0467.
- [4] M. Zalenski, et. al, "Operational Considerations in Monitoring Oxygen Levels at the National Transonic Facility", *NASA Contractor Report 3953*, December 1985.
- [5] "LonBuilder™ User's Guide", Echelon® Corporation, Palo Alto, CA. USA.
- [6] "Neuron® C Programmer's Guide", Echelon® Corporation, Palo Alto, CA. USA.

Programmable Electronic Safety Systems

Richard R. Parry
Superconducting Super Collider Laboratory
2550 Beckleymeade Avenue, Dallas, TX 75237 USA

Abstract

Traditionally safety systems intended for protecting personnel from electrical and radiation hazards at particle accelerator laboratories have made extensive use of electromechanical relays. These systems have the advantage of high reliability and allow the designer to easily implement fail-safe circuits. Relay based systems are also typically simple to design, implement, and test. As systems, such as those presently under development at the Superconducting Super Collider Laboratory (SSCL), increase in size, and the number of monitored points escalates, relay based systems become cumbersome and inadequate. The move toward Programmable Electronic Safety Systems is becoming more widespread and accepted. In developing these systems there are numerous precautions the designer must be concerned with. Designing fail-safe electronic systems with predictable failure states is difficult at best. Redundancy and self-testing are prime examples of features that should be implemented to circumvent and/or detect failures. Programmable systems also require software which is yet another point of failure and a matter of great concern. Therefore the designer must be concerned with both hardware and software failures and build in the means to assure safe operation or shutdown during failures. This paper describes features that should be considered in developing safety systems and describes a system recently installed at the Accelerator Systems String Test (ASST) facility of the SSCL.

I. INTRODUCTION

Incidents at Bhopal, India and Chernobyl, Russia and much closer to home, the Challenger shuttle disaster are extreme cases of failures that make one appreciate the need for safety systems to control a process. Particle accelerators do not present the same level of hazard. However, the importance of careful design of such systems to protect personnel from those hazards typically found at accelerators such as electrical and radiation, cannot be overlooked. To aid in the design of such systems, the performance goal and requirements must be quantified using reliability engineering and compared to an acceptable level of risk. The question to ask is not, *is it safe?*, but *is it safe enough?*

Using availability to quantify safety system performance, a casual manager might specify an availability of 99.9% thinking this is surely safe enough. However, relating this to the real world would result in 16,000 pieces of mail lost every hour, 22,000 checks deducted from the wrong account every hour, two unsafe landings at Chicago's O'Hare airport everyday, and one hour of unsafe drinking water every month.¹ These examples may seem extreme but they show the importance of developing an acceptable performance level for the process in question.

¹ Is 99.9% Good Enough, *InTech*, 1989.

II. SAFETY SYSTEM DESIGN

A. Overt Failures

Several types of safety system failures have been identified which the designer must be concerned with and if possible prevent. An overt failure of a safety system results in a revealed, fail-safe action. At a particle accelerator this failure might take the form of a coil failure of a normally energized relay opening resulting in a critical power supply turning off. Since these failures result in a safe shut down of an accelerator, the system has failed-safe which is the first concern of the designer. However, these failures are costly as they directly affect accelerator availability. For reasons other than safety, these failure must be prevented.

Overt availability (A_O) can be defined using mean time between failure (MTBF) and mean down time (MDT).

$$A_O = \text{MTBF} / (\text{MTBF} + \text{MDT}) \quad (1)$$

Since an overt failure is self revealing (i.e., machine shuts down when failure occurs), MDT equals the mean time to repair (MTTR) resulting in the following relationship.

$$A_O = \text{MTBF} / (\text{MTBF} + \text{MTTR}) \quad (2)$$

B. Covert Failures

Covert failures on the other hand are far more dangerous and typically receive less attention. These failures are hidden and may not be found until a demand is put on the system or some unusual circumstance arises. Covert failures remain in the system and may only be revealed when the system needs to respond. Hopefully these failures are discovered during a system's test rather than an actual need for the system in which the system fails to respond.

Statistically speaking, faults can occur at any time between two successive tests, the average time of half the test interval (TI) must be factored into the equation resulting in the following equation.

$$A_C = \text{MTBF} / (\text{MTBF} + \text{MTTR} + 1/2 \text{ TI}) \quad (3)$$

Therefore the more frequently a system is tested, the higher the covert system availability. For this reason, frequent testing cannot be overemphasized to discover covert failures. Heretofore systems using simple electromechanical relay logic for control required manual testing (typically at 6 months intervals). Modern electronic systems give greater flexibility and allow frequent automated testing.

B. Common Mode Failures

If a single action can adversely affect the performance of a safety system, the potential for a hazard increases. A common mode failure can be defined as the failure of two or more independent items due to a common cause. Particle accelerator safety systems are typically redundant, but this does not make them immune to common mode failures. For example, two independent magnetically operated proximity switches used to sense an access door may fail to function properly when subjected to a single external stray magnetic field. Common mode failures may be prevented by using active parallel redundancy, in other words, completely independent systems. But even here a careful analysis of failure modes must be considered. For example, a simple solution to the failure of two magnetically operated switches is to use two different technologies for door sensing such as a simple mechanical switch and one magnetically operated proximity switch.

Other solutions include using active sensing rather than passive sensing devices. A conventional switch is static (passive) in sensing an access door's position. An electronic device that continually transmits signals and expects a response is an active solution that in essence "must work to work". This field device has the advantage of failing safe and failures are overt, they are discovered when they occur rather than during a system test that may detect only covert failures.

III. CONTROL TECHNOLOGIES

A. Electromechanical Relays

Heretofore, picking a control system for safety system applications was relatively simple since there were few solutions and it was often mandated that simple, reliable electromechanical relays must be used. Indeed relays have passed the test of time. These systems are unaffected by numerous types of interference, have a low initial cost, are easy to document, and, of utmost importance to safety system designers, they are 98% fail-safe with well understood failure modes.

However, the 98% fail-safe feature is a mixed blessing. It means relay based systems are prone to overt (nuisance) trips. In addition, they are inflexible. Inflexibility for safety systems is a plus, since errors are often introduced when changes are made and not properly tested or documented. However, the inflexibility also means that some useful, albeit unnecessary, changes that one may wish to implement are often not implemented due to the time and difficulty required.

B. Hardwired Solid State Controllers

Some of the deficiencies associated with relay based systems can be overcome by hardwired solid state systems. These systems consist of electronic logic devices hardwired in a specific configuration. In size and weight sensitive applications, these systems have an advantage over relay based systems and allow one to more easily develop redundant systems with low power consumption. Solid state controllers also allow on-line testing of input and output circuits either manually or automatically and therefore serve to increase covert (hidden) availability when tests are performed often.

C. Microprocessor

The microprocessor has come a long way since its initial introduction and has recently crossed the safety system barrier. Like hardwired solid state controllers, implementing automated testing of both the processor's internal health (i.e., memory tests etc.) and external field devices can be easily achieved. Adding an external "watchdog" timer (heartbeat monitor) is also easy to develop and serves as a guard of the overall system's integrity.

Programmable Logic Controllers (PLC) fall into the category of microprocessor based systems. In recent years these controllers have become very powerful and easy to use. Their use in industry for process control is widespread. In addition, these systems are at present in use or under development at several particle accelerator laboratories. However, not all PLCs are created equal and most are not suited for safety applications. Careful consideration must be given safety issues in selecting a specific PLC.

The microprocessor systems may be easily integrated into the main control system over a network. Amenities such as event data logging, simulated human speech announcements, and color graphic operator interface video displays can easily be implemented. Such extras could not economically be implemented in other technologies.

Microprocessors flexibility arises from its software programmability. This flexibility is both an asset and a major area of concern in safety applications. The safety system's designer has well founded fears relating to the reliability of software and its security. Numerous documented incidents of software failures have led to loss of life. Complicating the issue is that while well understood and accepted standards exist for evaluating hardware systems, there is no universally accepted standard for evaluating software reliability.

One solution to the problem of software reliability might be to develop two independent software programs for installation on redundant controllers. This approach has been adopted at the Continuous Electron Accelerator Facility (CEBAF) in Newport News, VA. and here at the SSCL (see Figure 1). The intent of such a philosophy is to prevent software failures, specifically common mode failures. Presumably a software error made by one programmer will not be made by another programmer. However, this method is not a solid solution. There is typically one requirements document developed for a system. One can make a cogent argument that a flaw existing in the specification, will flow into the both programs even though developed separately. Others argue that a careful review process of the software is a solution. Until a standard is developed the issue of software reliability will continue to be of great concern.

IV. ASST

A. Personnel Access Safety System

The Accelerator System String Test (ASST) facility is a surface enclosure measuring 626' in length located at the SSCL. The facility was developed to perform tests on a half cell of superconducting magnets. The hazards within the enclosure are electrical and cryogenic. The safety system consists of dual programmable logic controllers to monitor and control the myriad aspects of safety.

Two independent programmable logic controllers are on line at all times using 2 out of 2 voting (i.e., two of the two systems must be running for the system to be operational).

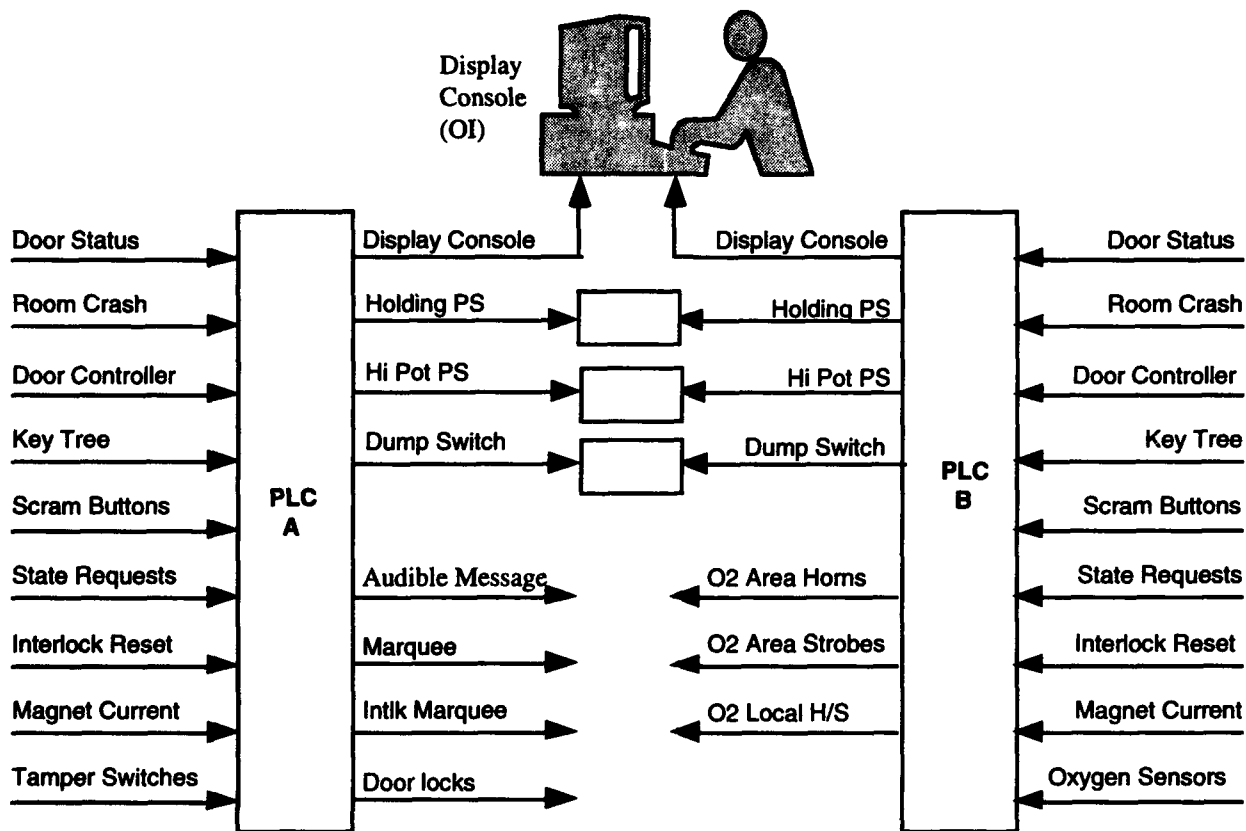


Figure 1. The system is comprised of dual redundant programmable logic controllers. Critical field devices such as personnel access door sensors are redundant. In those cases where two separate field devices are not practical, two signals are derived from a single point.

V. CONCLUSION

Numerous technologies exist today for the designer to solve complex safety problems. However, with the diverse number of solutions comes the need to systematically develop requirements appropriate for the hazards and their consequences. For this reason, a careful examination of availability requirements must be developed from the beginning giving careful consideration to overt, covert, and common mode failures. Equally important is the need to carefully select the technology appropriate for the application. If the solution uses programmable controllers, additional efforts must be given to the issues of software configuration management and reliability.

VI. ACKNOWLEDGMENTS

I wish to thank Jay Heefner and Henry Robertson at the CEBAF for their pioneering work in the use of Programmable Logic Controllers in personnel safety systems at particle accelerators.

Kudos also to Robert Landis, Joe Claborn, and Madhu Reddy of the SSCL for their great help in developing the ASST Personnel Access Safety System (PASS).

VII. REFERENCES

- [1] B. Balls, P. Gruhn, "Design Considerations for High-Risk Safety Systems", *Intech*, March 1991, p 28.
- [2] T. Fisher, "Control Systems Safety," *ISA Transactions*, The Quarterly Journal of the ISA, Volume 30 Number 1, 1991.
- [3] A. Frederickson, "Fault Tolerant Programmable Controllers for Safety Systems", *Programmable Controls*, March 1989, p 109.
- [4] P. Gruhn, "Risks With Using PLCs for Safety Protection", *C & I*, September 1990, p 53.
- [5] R. Parry, "Personnel Access Safety Systems at the Superconducting Super Collider," *Proceedings of the Industrial Computing Conference*, Vol. 2, p 437, ISA 1992 - Paper #92-0467.
- [6] PES - Programmable Electronic Systems in Safety-Related Applications, *Health and Safety Executive*, HMSO, London, UK, 1985.
- [7] R. Waterbury, "Fault-Tolerant / Fail-Safe Systems are Fundamental, *Intech*, April 1991, p 35.

A Pseudo Real Time Tune Meter for the Fermilab Booster

G. Wu, V. Bharadwaj,
J. Lackey, D. McGinnis, R. Tomlin
Fermi National Accelerator Laboratory
P.O. Box 500, Batavia, IL 60510

Abstract

A tune meter has been developed and installed for the Fermilab Booster. It is capable of measuring the tunes in two planes over the energy ramping cycle with an accuracy of 0.001 and measuring chromaticities in pseudo real time. For each plane this system uses one stripline pick-up type BPM and one single turn ferrite kicker. Data acquisition, processing and control is implemented in a VMEbus based system as an integrated part of the Fermilab Accelerator Controls Network (ACNET)¹ system. The architecture enables the tune measurement and control to be contained in one intelligent system. Here we will present architecture, software, results

I. INTRODUCTION

The Fermilab Booster² presently operates over an energy range of 200 MeV to 8 GeV at 15 Hz cycle. The nominal betatron frequencies in the horizontal and vertical planes are $\nu_x = 6.7$ and $\nu_y = 6.8$ respectively but vary substantially over the cycle because of changes in the synchrotron lattice functions. A correction-magnet assembly consisting of a horizontal and vertical dipole, a quadrupole and a skew quadrupole is placed in each short and each long straight section. The quadrupoles and skew quadrupoles are designed to accommodate the space-charge tune shift at injection and to control the tune against inherent resonances and the coupling resonance of the horizontal and vertical oscillations over the entire cycle. Historically tune control in the Booster has been a difficult job because the tune measurement is slow and unreliable. Also, the tune measurement and tune control was not implemented in an integrated system. The new tune meter described here measures both the horizontal and vertical tunes over the entire energy ramping cycle in pseudo real time. The new architecture provides tune measurement and control in an integrated system with the control system.

II. ARCHITECTURE

Fig. 1 is a block diagram showing architecture of the tune meter. A CAMAC controlled sub-system pulses the kicker at a programmed frequency, duration and amplitude to keep the beam excited throughout the cycle. The turn-by-turn beam position analog signals for the entire cycle, after passing a band-pass filter are captured and digitized in the ADC board³. The data for a whole cycle is moved to a DSP memory board and is Fourier transformed into frequency spectrum of consecutive windows. The DSP board also finds amplitudes and positions of peaks in the frequency spectrum. After this is done the results are buffered and the system is enabled again for

next beam cycle. All these activities are controlled by the VME host processor, a Motorola VME133XT, which is in

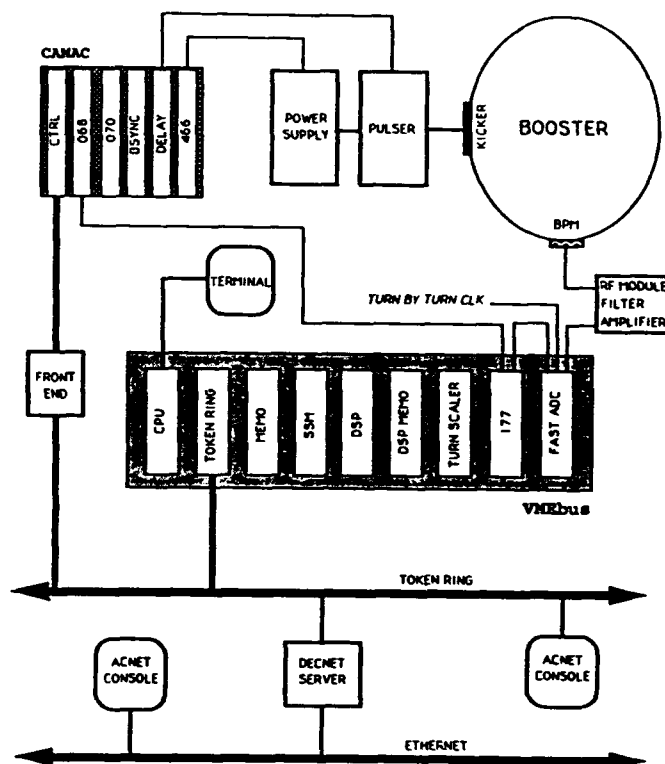


Fig. 1 The tune meter system diagram

turn commanded by an interactive application program running on one of ACNET consoles. Communications (commands, status information and data) between the console and the VME crate are done by the standard ACNET system.

III. SOFTWARE

Two user programs make the system function as desired. One is a micro-processor program which resides in the VME133XT and the other is an application program in a VAX console. Fig.2 shows the basic flow chart of the micro-processor program. The software environment of the tune meter consists of a standard set of tasks for data acquisition running under the MTOS operating system. The interface between these standard tasks and the micro-processor program written by the user is a protocol called Object Oriented Communications (OOC)⁴. The console program acts as a master while the micro-processor program is the slave. The micro-processor program performs sequential operations coordinating actions of all the VME boards: acquiring, processing and moving data according to commands received

from the console. The menu driven console program sends

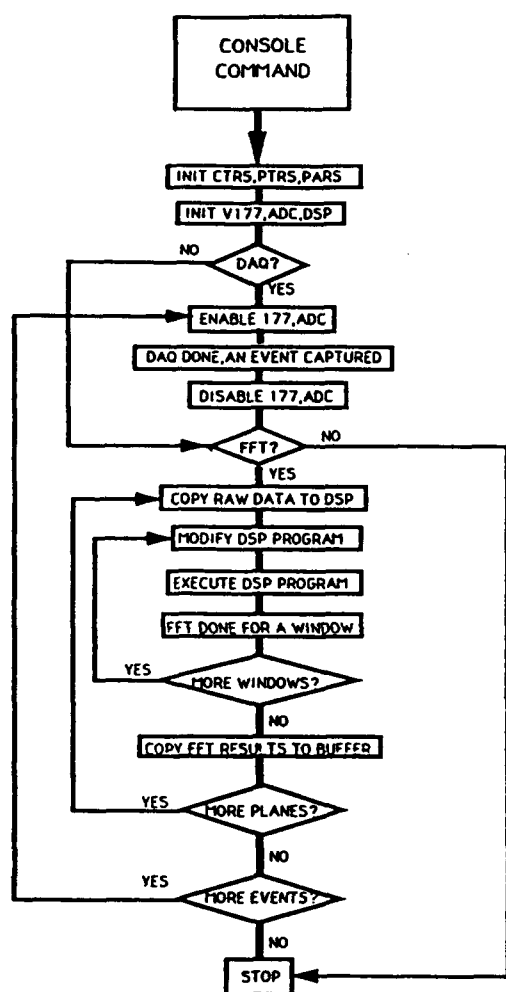


Fig. 2 The micro-program flow chart

command settings and reads status or data from the micro-processor program. Thus, the console program has access to control devices so it can control the kickers for tune measurements and change correction quadruples strength setting to excise tune control over the cycle.

IV. RESULTS

The tune meter is now being used regularly for measuring tune and chromaticity. Shown in Fig. 3 are on-line displays of the fractional tune in horizontal plane. In Fig. 3-a about 50 beam cycles were measured at the same beam conditions. For Fig. 3-b, as the beam intensity changed so did the tune. Fig. 3-c shows the tune responding to the changes in ramping current in the correction quadruples. For these measurements, the beam was kicked every 1 millisecond or about every 550 turns, the high voltages applied to the single turn kicker magnet was about .5 KV at the beginning of cycle and 1.5 KV at the end. With such kicker strength (about .87 Gauss at the beginning and 2.57 at the end) the effect on the beam transmission throughout the cycle is negligible. For each cycle of data (about 20000 turns), the DSP did the Fourier Transformations 40 times, each time 512 words to give one

tune measurement. The system's dead time, when operated

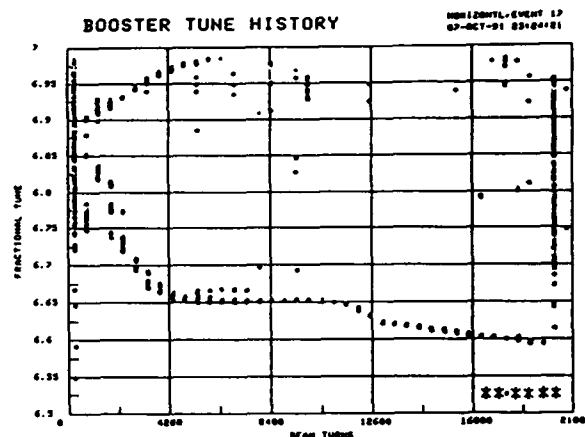


Fig. 3a on-line display of horizontal tunes,50 cycles

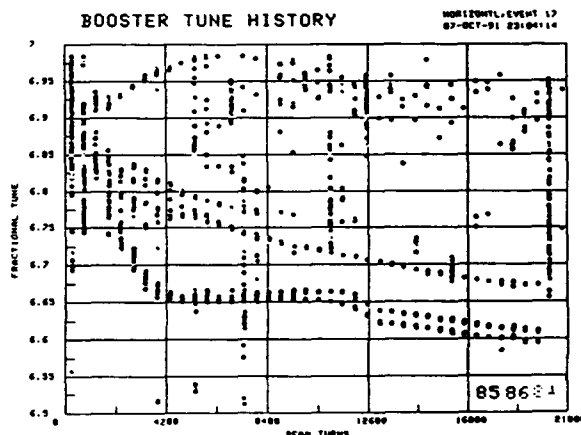


Fig. 3b Tune display as beam intensity changed

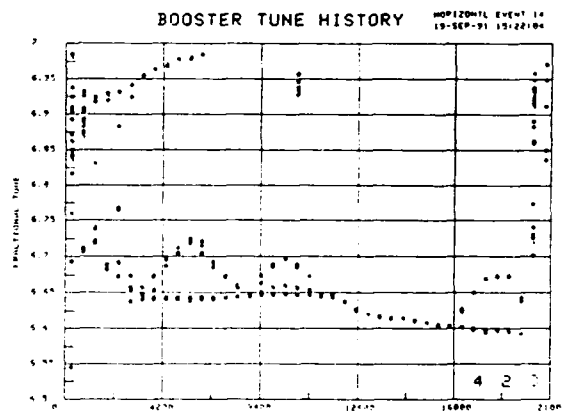


Fig. 3c On-line display of tunes responding to the changes in corrector ramping current.T.

under these conditions, is about one third of a second during which the DSP is processing data and the ADC is prohibited data taking for next beam cycle. While there are rooms for further optimizations, the quality of tune measured and speed of the measurements as shown are practically good enough for both tune measurements and controls

Fig 4 shows horizontal chromaticities throughout a Booster cycle, containing data for seven RPOS (a low level

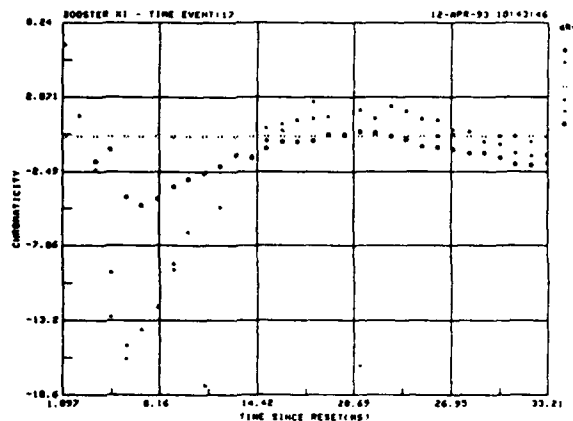


Fig. 4 On-line display of chromaticities.

RF program that controls radial beam position) curve settings. One notice that the data for two RPOS curve settings at extreme are standing apart from the rest. This is clearly an effect of higher order multiple fields where the beam were positioned. In a regular diagnostic measurement of chromaticity we need only take data for two RPOS curve settings, both are near normal orbits but one offset from the other.

V. ACKNOWLEDGEMENTS

The Authors give thanks to many people who helped the development of this system, especially among them: Charlie Briegel for his help in ACNET communications and Mike Shea for providing us with the quick ADC he designed.

VI. REFERENCES

- [1] P. Lucas, "Updated Overview of the Tevatron Control System", Control Systems for Experimental Physics, CERN 90-08, p71, 1987.
- [2] E. L. Hubbard(editor), "Booster Synchrotron", Fermilab internal report, TM405.
- [3] Mike Shea and Al Jones, "Fairly Quick VMEbus Digitizer", Fermilab internal report.
- [4] Lee J. Chapman, "An Object-Oriented Communication Protocol", *NIM* A293(1990) 347-351.

Measurement Techniques Using the Tektronix® 3052 DSP System

James M. Steinel Jr. & Dave McGinnis
Fermi National Accelerator Laboratory*
P.O. Box 500, Batavia, IL 60510 USA

Abstract

The Tektronix 3052 DSP System contains a 26MHz A/D converter and 1024 parallel digital bandpass filters. It allows a 10MHz wide spectrum to be viewed as a function of time with a maximum update rate of 1 spectrum per 200 μ s. This paper will illustrate the uses and limits of the device for the Fermilab Booster in applications such as tune measurement and coupled bunch mode diagnostics.

I. INTRODUCTION

This paper discusses the application of the Tektronix 3052 DSP System on the Fermilab Booster. The system provides a solution to many of the problems associated with tune and coupled bunch mode instability measurements of the Booster.

The Booster is a medium energy synchrotron accelerator. It accelerates a 200MeV proton beam to 8GeV where it is injected in to the Main Ring. The RF accelerating voltage must ramp from a frequency of 30MHz to 53MHz in a cycle time of 33ms. The non-linear frequency ramp has a peak slope of 2GHz/s near the beginning of the cycle.

Because of the fast frequency ramp, many of the standard methods for measuring tunes, chromaticities, and instabilities cannot be used on the Booster. A spectrum analyzer cannot sweep fast enough to see the Booster RF cycle, let alone see a change in tune. A digital scope with FFT capability only has enough memory to catch a small time window. It will not show a change in the frequency component as a function of time in the Booster cycle.

Before the 3052 was available, the only way to measure tunes in the Booster quickly was with a custom system[1]. The system is fast, but it is not very flexible once the hardware and programming are completed. The 3052 offers a fast, more flexible system to measure tunes and coupled bunch modes.

II. TEK 3052 FUNDAMENTALS

A. Functional Block Diagram

The functional block diagram of the 3052 is shown in Figure 1 [2]. A 10MHz low pass filter band limits the input signal. The signal enters a variable amplifier and attenuator before being over sampled by a 26.5MHz A/D converter. This digital data is split 1024 ways and enters a digital filter bank. The data from the filters is processed and relayed to the monitor.

*Operated by the University Research Association, Inc. under contract with the U.S. Department of Energy.

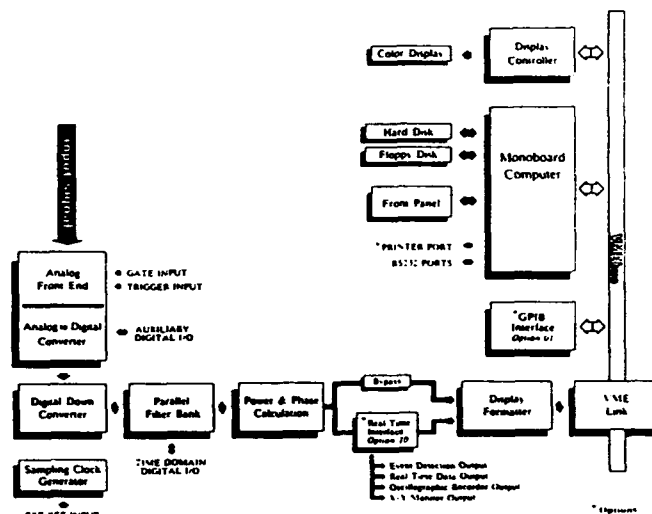


Figure 1. Tektronix 3052 Block Diagram

The data may also be processed by the monoboard computer. This computer operates under a UNIX operating system, and it can store data and C programs in its memory. Thus, a user can customize the data processing for each particular application of the system by calling an application program stored on disk.

B. Specifications

Table 1 shows some of the important specifications associated with the Tek 3052 [3].

III. BOOSTER TUNE MEASUREMENTS

A. Front End

A stripline pickup detects the transverse position of the Booster beam signal, and the difference signal is input in to the Tek 3052. The detector attenuates the first 10 MHz of beam signal because of its frequency response. To increase the signal level, the pickup signal is mixed with the RF signal from the VCO. This allows the 3052 to see the first 10MHz after the first RF harmonic, which has a higher pickup response.

The dynamic range of the input signal is very large. The RF component of the beam signal is more than 60dB greater than the betatron frequency component. An extra 10 MHz bandpass filter was added to the front of the 3052, because its internal filter does not roll off fast enough to keep the RF component from aliasing in to the frequency band.

B. Triggering

Booster beam is injected, accelerated, and extracted in a period of 33ms, and the video update rate of the 3052 is up to 350ms. Therefore, the data for a Booster cycle must be taken,

convenient for data in storage rings [4] because changes happen very slowly. None of these modes are convenient for triggering data acquisition in the Booster because of the quick cycle time and multiple frames. Thus, a custom application program triggers the 3052 to take a block of spectrum measurements for 33ms at the maximum rate of 5 kHz.

Table 1
Span Related Characteristics

Span	Bin Width/ Resolution Passband (0.05 dB Bandwidth)	Spectral Frame		Spectral Frame Rate / Resolution Passband	Sensitivity @ 1 MHz		
		Interval	Rate		dBm	dBv	dBmV
10 MHz	12.5 kHz	200 μ s	5 kHz	0.4	-107	-120	-60
5 MHz	6.25 kHz	200 μ s	5 kHz	0.8	-110	-123	-63
2 MHz	2.50 kHz	200 μ s	5 kHz	2.0	-114	-127	-67
2 MHz	1.25 kHz	200 μ s	5 kHz	4.0	-117	-130	-70
500 kHz	625 Hz	200 μ s	5 kHz	8.0	-120	-133	-73
200 kHz	250 Hz	1 ms	1 kHz	4.0	-124	-137	-77
100 kHz	125 Hz	1 ms	1 kHz	8.0	-127	-140	-80
50 kHz	62.5 Hz	1 ms	1 kHz	16.0	-130	-143	-83
20 kHz	25 Hz	5 ms	200 Hz	8.0	-134	-147	-87
10 kHz	12.5 Hz	5 ms	200 Hz	16.0	-137	-150	-90
5 kHz	6.25 Hz	5 ms	200 Hz	32.0	-140	-153	-93
2 kHz	2.5 Hz	25 ms	40 Hz	16.0	-144	-157	-97
1 kHz	1.25 Hz	25 ms	40 Hz	32.0	-147	-160	-100

Maximum Dynamic Range without Distortion = 58dB
Total Dynamic Range with Front End = 183dB

stored in memory, and displayed at some time after processing is complete. A trigger is required to synchronize the start of data acquisition with the start of the Booster cycle.

The 3052 has three triggering modes for data acquisition: start/stop, single, and continuous. The continuous mode is

C. Processing

Once the block of data is stored in memory, the data may be processed in any format the user desires. A C program processes the raw data from the tune measurements by shifting the frequency of each frame. The program uses a set function to determine the frequency shift as a function of time in the Booster cycle. An example of vertical tune measurement and processing is shown in Figure 3.

IV. COUPLED BUNCH MODE MEASUREMENTS

Another application of the Tek 3052 is the measurement of the amplitude and growth rate of coupled bunch modes. The 3052 spectrogram/spectrum analyzer mode measures the coupled bunch modes in the Booster using the same triggering scheme developed for tune measurements. In this display mode, the spectrum analyzer plot represents one frame of the spectrogram, and the frame displayed is set by the spectrogram marker. By adjusting the time coordinate of the

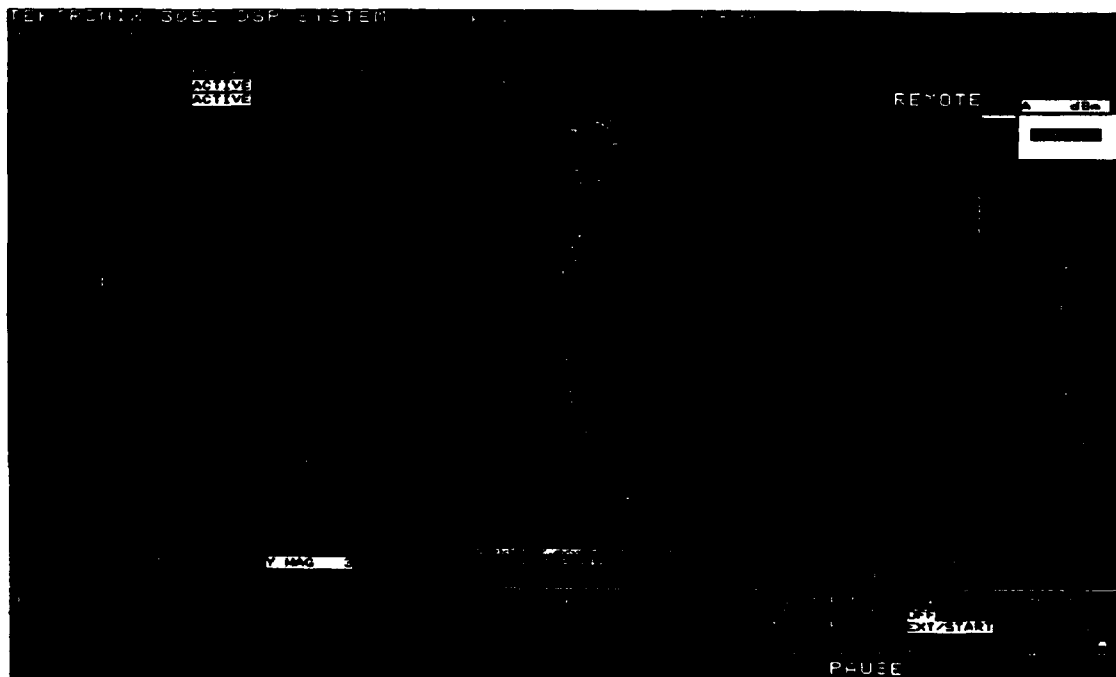


Figure 3. Processed vertical tune measurement in spectrogram display mode.

spectrogram marker, the change in coupled bunch mode amplitude can be seen on the spectrum analyzer plot.

A more convenient way to view the growth of the coupled bunch mode is to look at a collection of spectrum analyzer plots. The 3052 has a waterfall display mode illustrated in Figure 4 which gives a three dimensional plot of time, amplitude, and frequency. This format gives a better indication of the growth rate of the coupled bunch mode.

Unfortunately, because of the 10MHz bandwidth limit of the 3052, less than half of the possible modes are displayed.

V. ACKNOWLEDGMENTS

The authors would like to thank Mike Schnecker of Tektronix for providing the block trigger software used in the measurements.

VI. REFERENCES

- [1] G. Wu et al., "A Pseudo Real Time Tune Meter for the Fermilab Booster," *Proceedings of the 1991 AIP Accelerator Instrumentation Workshop*, pp. 276-284.
- [2] Tektronix Federal Systems, Inc., "3052 Digital Signal Processing System," 4.
- [3] Ibid., 5
- [4] K.J. Cassidy et al., "Development of a Model for Ramping in a Storage Ring," *Proceedings of the 1991 AIP Accelerator Instrumentation Workshop*, pp. 148-149.

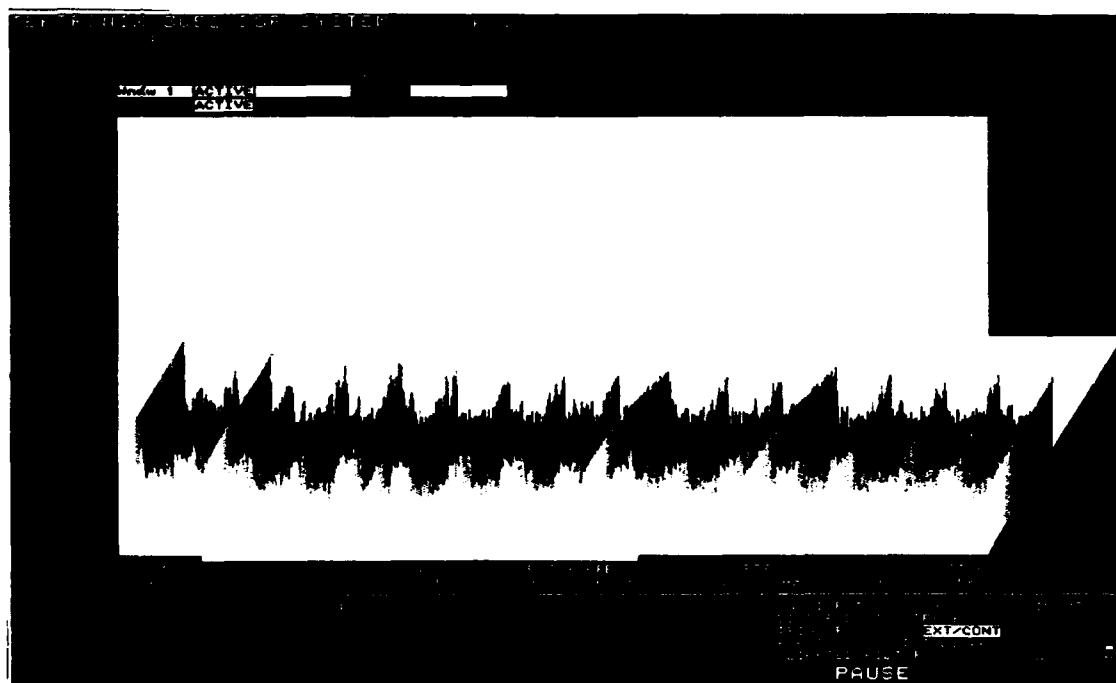


Figure 4. Waterfall display of transverse coupled bunch modes

USING TRANSIENT WAVEFORM RECORDERS TO MEASURE AND STORE BEAM PARAMETERS*

Robert E. Stege Jr., R. Keith Jobe, Marc Ross

Stanford Linear Accelerator Center, Stanford University, Stanford, CA 94305 USA

Abstract

Transient waveform digitizers are used to measure the tunes in the Stanford Linear Collider (SLC) damping rings. Since the beam injection and extraction from these rings occurs at a high rate (120 Hz) and because of the stringent extracted beam stability requirements, simpler asynchronous resonant excitation spectrum analyzer measurements are not possible. The beam position monitor signals are processed, digitized, and a Fast Fourier Transform (FFT) is applied to find the tunes. The coherent beam motion at injection, even though it damps quickly, is large enough to provide a strong tune signal. Recently, this technique has also been applied to several longitudinal signals [1]. The results from these monitors are recorded at six-minute intervals in the SLC control system history buffers [2]. This paper will describe the hardware setup and the software used to process the data, and will present some of the results.

I. INTRODUCTION

In the Stanford Linear Collider (SLC) two damping rings are used to achieve smaller beam emittances through radiation damping. The rings are both 35 m in circumference and operate at an energy of 1.21 GeV. During normal running, beams are injected and extracted at 120 Hz.

The Damping Rings turn-by-turn monitor (Fig. 1) is a modular digital signal processor system, using off the shelf CAMAC modules, and driven by the MATLAB [3] software package. It was originally installed to measure the ring tunes, but has recently been expanded to analyze other signals as well.

II. HARDWARE

The signals originate from four Beam Position Monitor (BPM) stripline detectors that are oriented at 45° with respect to the horizontal and vertical planes, and are brought out of the vault by four equally timed 1/2-inch heliax cables. These signals are combined in hybrid junctions to produce horizontal and vertical difference signals, ΔX and ΔY , as well as a sum signal (TMIT). Amplification or attenuation is provided by a LeCroy 6103 programmable CAMAC amplifier. The resulting beam position signals are digitized and recorded at each turn by DSP Technology 2008 transient waveform digitizers. The digitizers receive a clock pulse at each ring turn from a SLAC built Programmable Synchronization Unit (PSU), and they record data with eight bit resolution for up to 8192 turns. The clock is timed so that only one of the stored bunches per turn is recorded. The stored data is then read by the VAX computer and processed using the MATLAB software package to produce the FFT plots.

* Work supported by Department of Energy contracts DE-AC03-76SF00515 (SLAC).

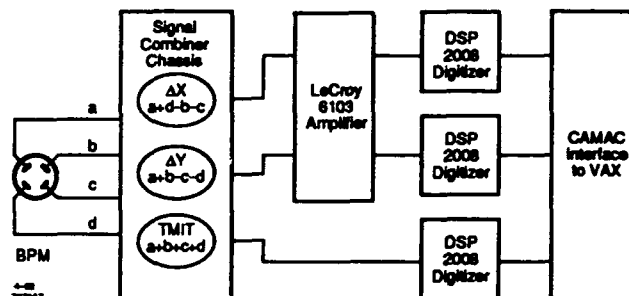


Figure 1. Block diagram of the Damping Rings turn-by-turn monitor.

III. SOFTWARE

The software used to process the data presented in this document is a prototype system that uses several existing software packages. To run the program, the user signs on to the VAX computer that is used to control the SLC and calls up a MATLAB program named "turns." This program is menu-driven and allows the user to select from several options, such as: set amplifier gains, select north or south ring, take data, calculate FFT, or print plots. An on-line help facility is also available. The MATLAB program then calls FORTRAN and other routines that control and read the hardware.

Recently, some of this software has been rewritten and integrated into the SLC control system. The new software makes better use of computer time and has a much-improved user interface. It is easily accessed by the SLC operators on the SLC console touch panels and displays.

IV. RESULTS

Figures 2 and 3 show the time domain and frequency domain (FFT) plots of typical data in the horizontal plane.

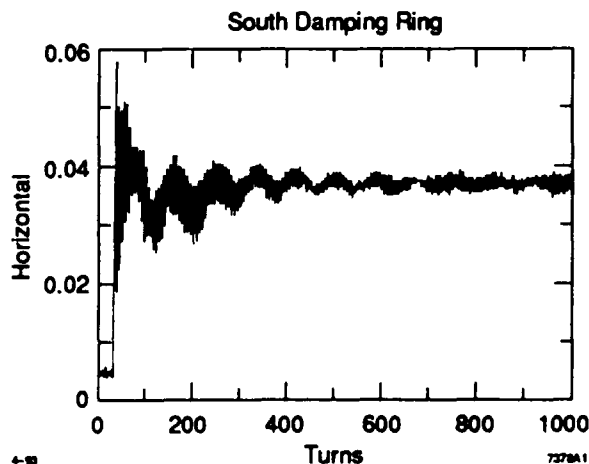


Figure 2. Raw data in the horizontal plane showing both the betatron tune and the lower frequency synchrotron tune.

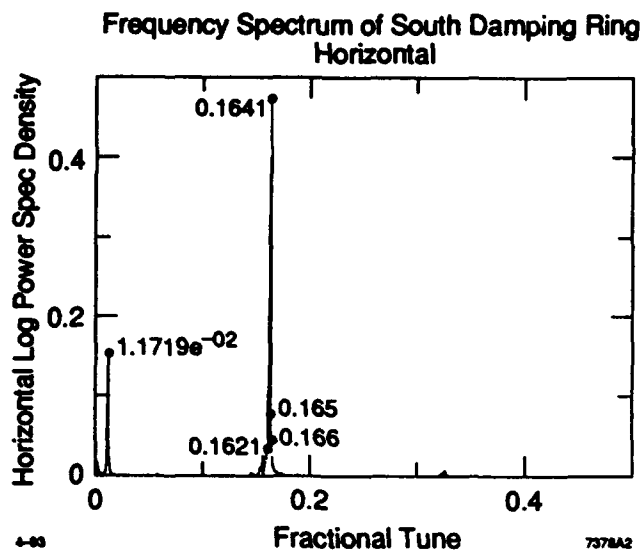


Figure 3. Fast Fourier Transform (FFT) of the horizontal data showing peaks at both the betatron tune and the synchrotron tune.

The strong synchrotron oscillations immediately after injection are readily apparent. The FFT of the data was taken from turn 200 through 1223 to somewhat suppress the strong synchrotron line on the frequency domain plot, see Figure 3.

The vertical axis in Figure 2 is in volt, where 20 mV represents approximately 760 μm . In Figure 3 the five highest points are labeled. The MATLAB routine allows choice of the number of points to be labeled.

Figures 4 and 5 illustrate the effectiveness of the system during startup, before stable beams have been established. This is a useful diagnostic tool in the event of a difficult startup.

During routine running, one of the quantities that it is important to monitor is Damping Ring transmission, or how much of the injected beam makes it through the ring. Figure 6

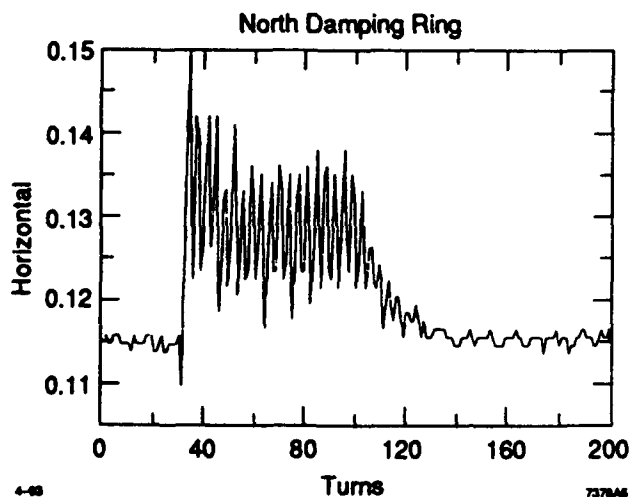


Figure 4. Raw data at the start of the cycle when less than 100 turns had been achieved.

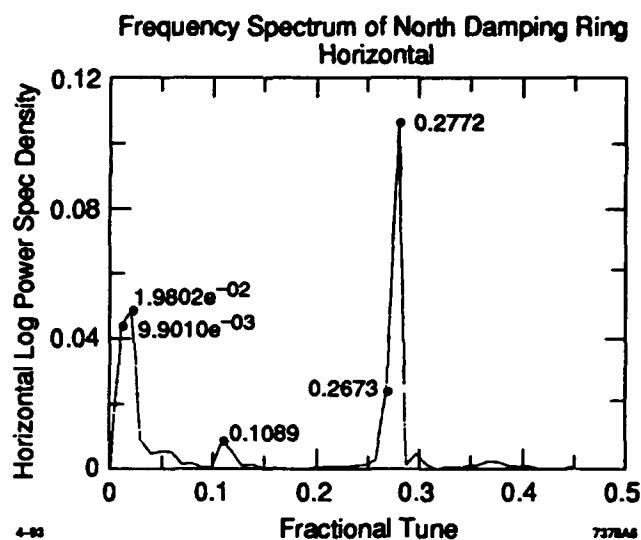


Figure 5. FFT of the data illustrating the systems ability to measure tunes when less than 100 turns is available.

shows a plot of the response of a fast toroid installed in the south Damping Ring indicating losses in early turns.

Figure 7 is an example of one of the longitudinal signals that have been digitized. This data is derived from a BPM sum signal that is proportional to the inverse of the bunch length. Precompression of the bunch length is accomplished using a so-called "bunch muncher" that shock excites a bunch length oscillation by modulating the rf amplitude [4]. The timing is set so that a minimum bunch length occurs just before extraction. The data in Figure 7 clearly shows extraction occurring after the minimum bunch length has occurred.

Figure 8 shows a history buffer plot of the tunes and TMIT for a 24 hour period. The value of the tune recorded in the history buffer is computed by a MATLAB routine that searches

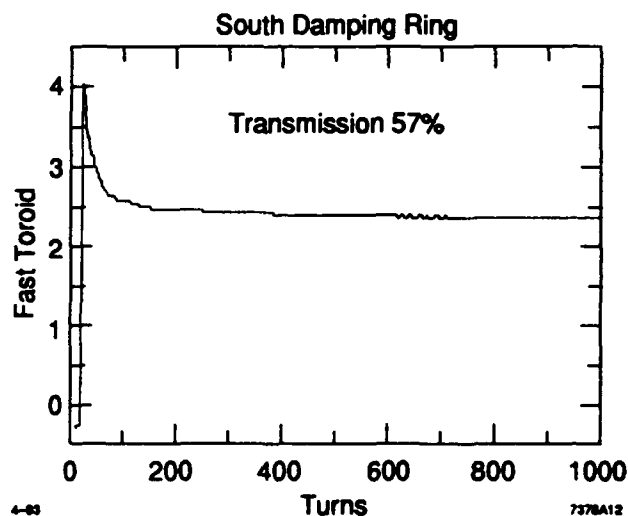


Figure 6. Measurement of beam loss in early turns using a fast toroid.

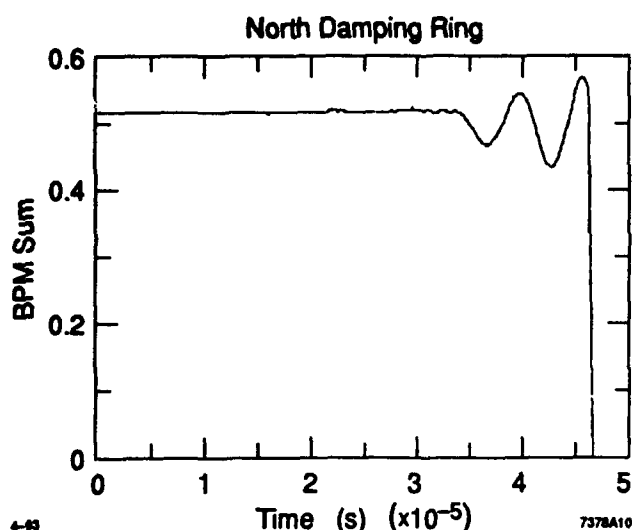


Figure 7. Data representing inverse bunch length just before extraction derived from a BPM sum signal.

for the highest peak within a specified range in the FFT data. The many routines available in MATLAB make it easy to choose and record in the history buffer the desired values from the digitized data.

Future plans for the system include adding the capability of synchronous data acquisition with other signals so that correlations can be made to diagnose sources of machine jitter.

REFERENCES

- [1] P. Krejcik, K. Bane, P. Corredoura, F.-J. Decker, J. Judkins, T. Limberg, M. Minty, R. Siemann, SLAC; F. Pedersen, CERN, "High Intensity Bunch Length Instabilities in the SLC Damping Rings," these proceedings.

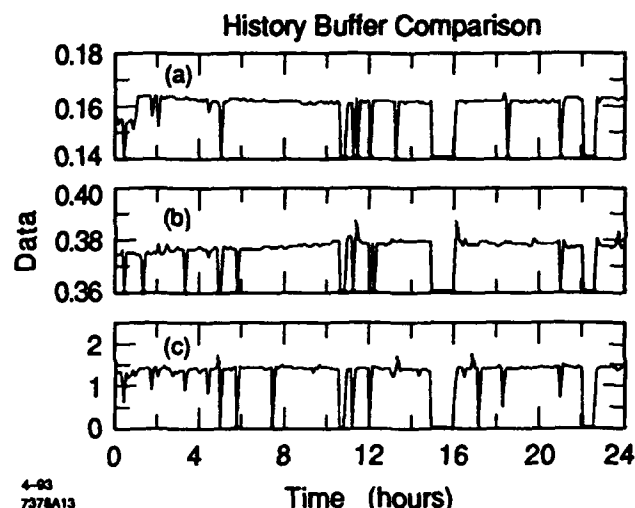


Figure 8. History buffer plot of the south damping ring: (a) horizontal tune, (b) vertical tune, and (c) TMIT for a 24 hour period.

- [2] R. Johnson, G. White, "History Data Facility in the SLC Control System," Conference Record of the 1991 IEEE Particle Accelerator Conference, Vol. 3, pp. 1540-1542.
- [3] MATLAB is a trademark of The MathWorks, Inc., Cochituate Place, 24 Prime Park Way, Natick, MA 01760-9889 (508) 653-1415.
- [4] F.-J. Decker, T. Limberg, J. Turner, "Precompression of Bunch Length in the SLC Damping Rings," Proc. Int. Conf on High-Energy Accelerators (HEPAC '92), Hamburg, Germany, July 20-28, 1992; SLAC-PUB-5871 (1992).

Tune Measurement in the APS Rings*

W. Sellyey, E. Kahana, and X. Wang
Argonne National Laboratory
9700 S. Cass Avenue, Argonne, IL 60439

I. INTRODUCTION

The APS system will contain three rings. The first is a positron accumulator ring (PAR). Its function is to coalesce 24, 30-ns-long positron bunches into one 290-ps bunch. The second is the injector synchrotron (IS). It accelerates the 450-MeV positron bunches to 7 GeV for injection into the storage ring (SR). Five IS bunches are accumulated into one SR bucket to produce 17.5-nC, 60-ps bunches. Twenty buckets will be filled in the SR to give a current of 100 mA. Additional important tune measurement related parameters for the three rings are shown in Table 1.

Table 1. Various Tune Related Frequencies

	PAR	IS (7 GeV)	SR
R.F. (MHz)	9.7757	351.93	351.93
Revolution (kHz)	9775.7	814.3	271.5
Fractional Tune (kHz)			
x	1662	620	60
y	2121	652	81.5
z	19.0/60.2	21.2	1.96
Line Width (Hz)			
x	96	741	220
y	78	741	220
z	136	1481	440

II. SYSTEM DESCRIPTION

Betatron and synchrotron motion frequently occurs in circular machines, without any deliberate excitation. However, the amplitudes of this motion cannot be predicted. Therefore, it is desirable to have controlled ways to excite these modes.

Two types of devices will be used to excite the beam. One will be a magnetic kicker or bumper. All rings already have these devices planned for the horizontal direction for injecting and extracting beams. Some of these magnets will be used for exiting horizontal betatron motion. In the storage ring, a special kicker will be installed to produce up to 1 mm amplitude motion in the vertical direction.

*Work supported by the U.S. Department of Energy, Office of Basic Energy Sciences, under Contract No. W-31-109-ENG-38.

Two 8.4-in striplines (SL) ($1/4$ wavelength at 352 MHz) will be installed on all rings. One stripline in each ring will be used to drive all three tunes, and the other stripline will be used as a pickup. In the PAR and IS, the pickup stripline will be in a dispersive region. This will allow observation of both betatron and synchrotron motions. In the SR, the stripline will be in a nondispersive region because it is not practical to install it in a dispersive region. To do synchrotron tune measurements in the SR, one of the button BPMs located in a dispersive region will be used.

Figure 1 shows the drive circuit for the stripline. The biphasic modulators will control the phase of the signal applied to the stripline. When all lines are in phase, the synchrotron tune can be excited. For x-betatron tune, the left pair of strips will be 180° out of phase with the right pair and for y-tune, the top and bottom pair will be out of phase. The amplifiers will be 500 mW for the PAR and 25 W for the IS and SR.

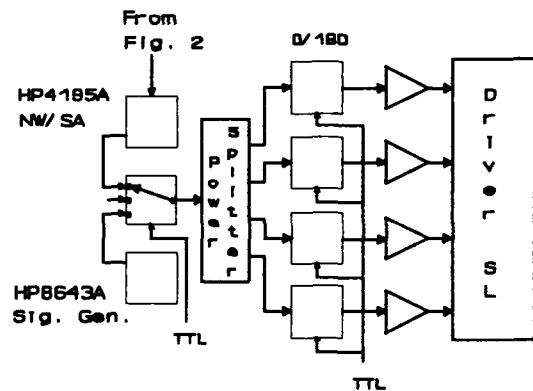


Figure 1. Stripline Driver Circuit

To minimize development effort, as much of the BPM system electronics as possible will be used in the tune measurement system [1]. The BPM electronics uses the AM/PM conversion technique. This system operates at 352 MHz. Thus, tune measurement components were also designed to operate at 352 MHz.

The two parts of the BPM system used here are the filter comparator (FC) and the monopulse receiver (MR). The FC inputs are the four beam pickup outputs. Hybrids are used to generate two signals proportional to the x and y beam displacement and the charge. A third signal is proportional to the total

charge. These signals are passed through matched 352-MHz filters of 10 MHz width. The filters are nearly phase constant over about 20 MHz. The MR converts these signals to a position signal which is independent of charge and depends on position only. A stable position signal exists at the monopulse receiver output for about 100 ns.

If the beam is exactly in the center of the position pickup and the pickups are perfect, the filter comparator difference outputs would be zero. In the real system, one expects offsets. This can make synchrotron motion tune measurements difficult. Thus, for tune measurement, the BPM filter comparators will be modified with a 3-db voltage-controlled attenuator in each of the input signal lines. These will be adjusted to minimize the offsets such that the beam always appears to oscillate near the center of the pickup.

Figure 2 shows the pickup system for the PAR. This, combined with components of Fig. 1, constitutes the entire PAR tune measurement system. The IS system is the same, except that there will be two digital signal processors (DSPs) and the network analyzer (NWA) will be an HP8711A. The SR system will be the same as the PAR system except that the pickup device will be switchable between the stripline and a button.

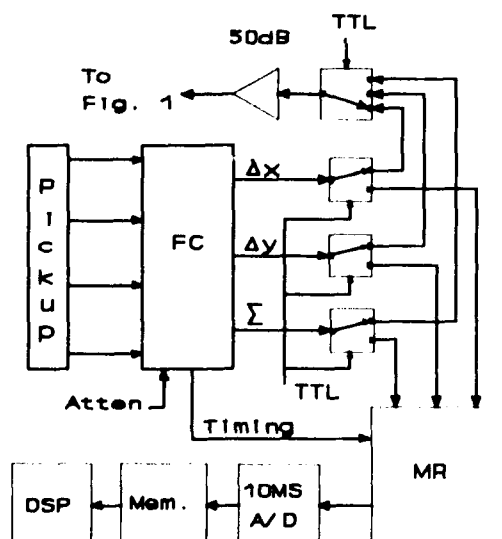


Figure 2. PAR Pickup System

III. OPERATION

Each tune measurement system will have several modes of operation. In one mode the spectrum analyzer will be used to look at bands inside the pass-band of the 352-MHz filters. The beam could be self-excited; it could be excited using the FM modulated

signal-generator, or the magnetic pinger could be activated. The IS acceleration time is 250 ms, and magnet-related tune constants are about 25 ms. Thus, this mode is not available in the IS during acceleration because no spectrum analyzer seems to be able to capture spectra in 25 ms or so.

A second mode of operation uses the network analyzer. In the IS, the HP8711A NWA will be able to take spectra over a 100-kHz span in 20 ms. However, it takes over 60 ms to read this information out, so no real time measurements can be made. However, different 20-ms sections of the acceleration process can be observed during successive IS cycles. Thus, a tune history can be generated in a few seconds.

The last mode of operation is the time domain mode. In this, the position of a bunch is observed on every revolution and recorded in memory. After sufficient data is collected, a digital signal processor does a fast Fourier transform (FFT), finds peaks, and passes the results on to the control system. In the IS, two DSPs will be able to obtain all tune frequencies every 20 ms. The excitation methods will be the same as for the spectrum analyzer mode.

Table 1 can be used to predict what a network or spectrum analyzer will see. The filter comparator limits signals to about 40 MHz around 352 MHz. In the PAR, there will be five revolution frequency lines in this band. These will be suppressed as much as possible by the attenuations in the filter comparator. In the x-direction above and below these, there will be one or more synchrotron lines separated by 19 or 60.2 kHz. Whether it is 19 or 60.2 depends on whether the 12th harmonic bunching cavity in the PAR is off or on [2]. Above and below each revolution line there will be an x-betatron line 1.662 MHz away. In y motion there will be a line 2.121 MHz away. The synchrotron line widths will be 136 Hz and the betatron width will be 96 Hz in the PAR. The IS and SR will have similar spectra, except that the line densities will be higher.

The time domain measurement with FFT effectively down converts the spectra to base-band, without losing the advantageous signal-to-noise ratio of working at 352 MHz. Half the sampling rate is the highest frequency one will be able to observe. Since the sampling rate is equal to the revolution frequency, one will need to contend with only one betatron line for each of x and y, and only one synchrotron band. The frequency resolution will be determined by the observation time. Thus, a 10-ms observation time will yield 100 Hz resolution. This should be adequate for most measurements.

Table 2 shows expected difference output power, voltage, and displacement at the tune measurement pickup sensor for the stated input power at the driver stripline. It is assumed that the driving frequency is near 352 MHz and corresponds to the exact frequency of one of the fractional tune lines discussed above. The

stated output power is that of the difference signal from a lossless filter comparator. The actual signal will be about 20 db less.

One of the important functions of the SR system is that it should be able to provide continuous tune monitoring. It is essential that the tune measurement process should not disturb the photon beam experiments. This is accomplished by keeping transverse beam motion below a few microns. An HP4195A was evaluated for this purpose. To do this, a crystal filter with 8.83 MHz central frequency and bandwidth of 500 Hz was put between a down and up converter pair. An adjustable oscillator running at around 343 MHz drove one side of each mixer. This produces an effective 500-Hz-wide filter with a control frequency of 352 MHz. The 4195 was used in a network analyzer mode to look at the passband of this filter. The 4195 was set up for an IF bandwidth of 100 Hz and a span of 80 kHz. It took 8.62 seconds to make a sweep. The power through the passband was adjustable using attenuators. Signal (S) was about equal to noise (N) when this power was -115 dbm. When a 50 db amplifier was added, S = N occurred at the -135-dbm signal level.

Table 2. Typical stripline input and resulting output.

Pin = power input per strip on drive stripline unit; Pout, Vout = power and voltage after pickup output passes through filter comparator; X = maximum displacement amplitude of beam bunch at pickup sensor. The pickup sensor is a stripline everywhere, except for the longitudinal SR results.

		<u>Transverse</u>	<u>Longitudinal</u>
PAR	Pin (mW, dbm)	.1 (-10)	10 (10)
	Pout (mW, dbm)	.09 (-10.5)	.1 (-10)
	Vout (mV)		95100
	X (μm)	.97	1.02
IS	Pin (mW, dbm)	10 (10)	25,000 (44)
	Pout (mW, dbm)	5×10^{-7} (-63)	1.26×10^{-6} (-59)
	Vout (mV)		.22.55
	X (μm)	13	21
SR	Pin (mW, dbm)	10 (10)	25,000 (44)
	Pout (mW, dbm)	7.14×10^{-4} (-31.5)	2.5×10^{-7} (-66)
	Vout (mV)		8.455.0
	X (μm)	16.5	9.8

From Table 1, for the SR transverse motion, .1 mW of drive power will result in 1.7 μm beam motion and -52 dbm of signal power. Assuming 20-db loss through the filter comparator, and a 50-db gain before the 4195 input, an S/N of 63 db should be obtained. For longitudinal motion, 2.5 W of drive power will result in 3 μm beam motion in the dispersive region

and an S/N of 39 db on the 4195. For commissioning, currents may be 1000 times lower, but beam motion can be larger. By using narrower IF bandwidths (10 Hz) and averaging, it should be possible to clearly see both betatron and synchrotron motion.

The time domain measurement system is expected to be particularly useful in the IS. To assure adequate beam motion, the FM-modulated signal generator will be used. It will typically be swept through 200 kHz every ms for betatron tune measurements. It is clear that the data of Table 2 is not directly applicable. To estimate how much power will be needed, it was assumed that the system can be represented as a driven oscillation with a resonant frequency equal to the fractional tune frequency. This shows that for a 200-kHz sweep around the resonant frequency, the average beam motion amplitude will be a factor of 50 less than what is shown in Table 2. To get 13 μm of motion, 2500 times more power will be needed (or 25 W). The single turn, noise-related rms error of the monopulse receiver system is 10 μm when the high signal levels from striplines are used. In a typical IS measurement, data will be collected for 10 ms, resulting in 8192 points and a frequency resolution of 100 Hz. Once the FFT is done, the fractional error at the fractional tune frequency will be $10/(13\sqrt{8192}) = .0085$. Thus, the tune signal will be clearly visible. The FFT and tune peak search will take about 10 ms. With two DSPs in the IS system, tune measurements will thus be made effectively in real time.

For synchrotron motion in the IS, similar results can be obtained but the swept frequency will need to be over a narrower range. In the PAR, the HP4195A network analyzer will be able to make 100 Hz resolution tune measurements in one to ten seconds. The time domain system will be able to collect 10^5 points in 10 ms, and the FFT will take about 300 ms. Thus, a tune measurement can be done in 310 ms. Increased beam motion and lower frequency resolution could be used to decrease measurement time by an order of magnitude.

In the SR, use of the time domain method will result in a tune measurement about every 15 ms. This method would ordinarily not be used during normal operation because the resulting beam motion would be excessive for the x-ray beam users.

IV. REFERENCES

- [1] E. Kahana, "Design of Beam Position Monitor Electronics for the APS Diagnostics," *Proceedings of the Third Annual Workshop on Accelerator Instrumentation*, Newport News, VA, October 1991, pp. 235-240.
- [2] M. Borland, "Update on the Argonne Positron Accumulator Ring," these proceedings.

Integrating Log-Ratio Position Processing for the Los Alamos Proton Storage Ring Extraction Line*

Thomas W. Hardek and Alan Band¹
Los Alamos National Laboratory
MS-H838, PO. Box 1663, Los Alamos, NM 87545 USA

Abstract

The Los Alamos Proton Storage Ring (PSR) is a compressor ring intended to accept 1-msec-long proton macropulses from the LAMPF linear accelerator and compress these pulses to 250 nsec in length. Beam position monitor sensors of the terminated strip-line design centered at 200 MHz are provided in the transport line from LAMPF, the PSR injection line, the PSR ring, and the extracted beam line. Strip-line sensors used in conjunction with phase processing are a good match for linac transport lines and PSR injection lines where there exists a strong 200-MHz frequency component but lead to difficulties in the ring and extracted beam line where this component tends to wash out. This paper describes the development of Integrating Log-Ratio processing techniques, which utilize the original strip line sensors to achieve a major improvement in position monitoring for the extracted beam line. The design concepts are discussed and the present hardware is described in detail. Operational difficulties encountered during the development process are discussed and actual beam-related results are provided.

I. INTRODUCTION

For the past several years, various alternatives to the existing 201-MHz amplitude-to-phase processing system have been investigated. In the PSR ring, the 201-MHz component is largely due to the most recently injected beam rather than stored beam, while the extracted beam lacks any appreciable 201-MHz component. In both cases, the present system performance is questionable. Many detectors, signal processing schemes, and position processing techniques have been evaluated as possible replacements [1], [2], [3], [4], [5].

We have placed the highest priority on extracted beam monitoring since the operation of our present system is

least adequate in this application. PSR extracted beam intensity varies from a few hundred milliamperes in tune-up mode to 25 amperes during production times (a dynamic range of 100:1). For extracted beam monitoring, it makes sense to observe the total charge that passes the sensors. Our most encouraging test results have led to the selection of an integrating log-ratio processing scheme, which can fulfill both of these extracted beam monitoring requirements.

II. ELECTRODE SELECTION

For economy and simplicity, our recent efforts have emphasized using the existing 50-ohm strip-line detectors along with wide-band signal processing. Initially we worked with unmodified pickups. The 50-ohm terminated strip-lines have about 30 pF of capacitance giving rise to a 1.5-nsec decay time constant. The PSR extracted beam pulse is approximately triangular with a base width of 250 nsec. The short time constant these terminated strip-line detectors exhibit differentiates the relatively long beam signal. An integration function is required to recover the beam signal. To observe the total charge that passes the sensors, another analog integration function is needed. The inherent low frequency gain of these integrating stages enhances system noise and limits the available dynamic range to about 10:1. Since a dynamic range in excess of 100:1 is needed to adequately monitor the extracted beam position [6], a decision was made to modify the existing pickups by removing the terminating resistors and padding the electrodes with capacitance to increase the time constant.

A standard extraction line detector is modified by removing its terminating resistors and adding 500 pF chip capacitors between each of its strip lines and ground. The capacitors are actually installed in matching boxes connected to the electrode signal ports. This effectively creates a capacitive pickup that only requires a single integration stage in the processing electronics. Wide-band (20 kHz to 30 MHz) RF transformers are used in a 5:1 voltage step-down (25:1 impedance ratio) to drive the existing 50-ohm coaxial cables. A series connected 1200-ohm resistor is inserted to provide back termination in the primary circuit, resulting in a time constant of 1.25 μ sec and giving 20% droop over the 250-nsec beam pulse. In addition to increasing the decay time

* Work performed under the auspices of the U.S. Department of Energy.

1. National Institute of Standards and Technology, NIST
Electron Physics Group, Building 220, Room B206
Gaithersburg, MD 20899 USA

constant, the transformers help reduce the system low frequency noise by breaking ground loops and limiting the low-frequency bandwidth [7]. A second transformer (wired in step-up configuration) is used at the receiving end of the cables to boost the signals back up to their original levels without degrading the signal-to-noise performance.

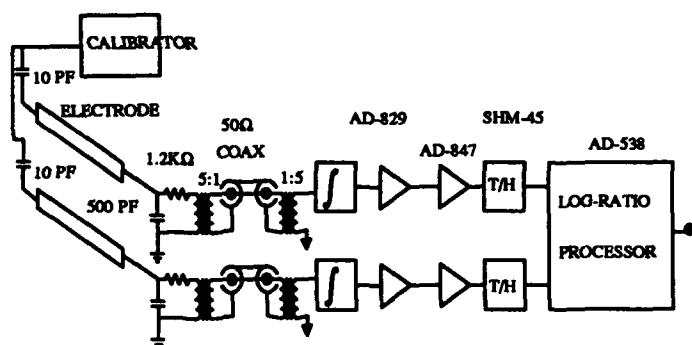


Figure 1: Integrating Log-Ratio Block Diagram.

III. CIRCUIT DESIGN

Figure 1 shows a block diagram of our Integrating Log-Ratio beam position monitoring system. A small matching box containing the shunting capacitor, series resistor, and cable matching transformer is placed at the electrode signal output ports. Calibrated test pulses may be injected at the electrodes to verify system integrity and perform active system calibration. One-hundred-foot-long 50-ohm coaxial cables transmit the beam signals to the remote processing electronics. Each processor signal path consists of the following elements: a 1:5 step-up transformer, a passive RC integrator, a low-noise gain stage ($A=10$), a switchable gain stage ($A=1$ or 10), a high-slew-rate track-and-hold amplifier, and the log-ratio processing circuit. The track-and-hold circuitry captures the signal peaks and holds these data for the relatively slow responding log-ratio position processors.

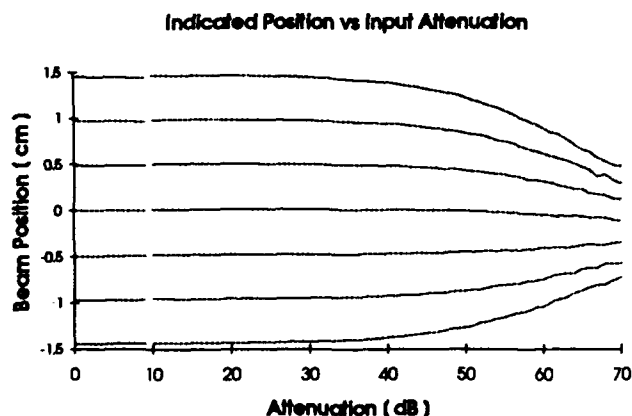


Figure 2: Processor Response vs Input Signal.

Figure 2 gives the response of our processor to varying input signal levels. The vertical axis is in cm and the input signal with no attenuation is a 3-volt peak triangular pulse 250 nsec at the base repeated at a 20-Hz rate. Adequate dynamic range is not available from the high-sensitivity range alone. We have included a low-sensitivity range to allow for future increases in PSR beam intensity and to extend system performance to cover the desired 40-dB range.

IV. HARDWARE DIFFICULTIES

We chose to incorporate a passive integrator in our final design. In an earlier design, we configured the first low-noise amplifier stage as an AC active integrator. Active integrators offer improved accuracy over passive circuitry but are difficult to implement in the high-frequency high-slew-rate range (in excess of 100 V/ μ sec) we operate in.

At low signal-levels, the Log-Ratio circuits are quite sensitive to noise and small offset voltages at their inputs. The topology of the signal processing section was chosen to minimize noise and DC offset effects. The AD829 High Speed, Low Noise Video Operational Amplifier is used as the first gain stage because of its excellent noise characteristics (1.7 nV and 1.5 pA / root Hertz at 1 kHz). AC coupling at the track-and-hold inputs removes DC offsets from the early gain stages with no loss of accuracy. The pedestal offset error common to fast track-and-hold circuits remains a problem. Figure 3 shows the resulting output of an ideal Log-Ratio processor with a 1-mV offset difference added to various common mode offset levels in the presence of an equivalent 1-cm beam displacement signal. Overall transfer gain has been adjusted to match our processor transfer gain.

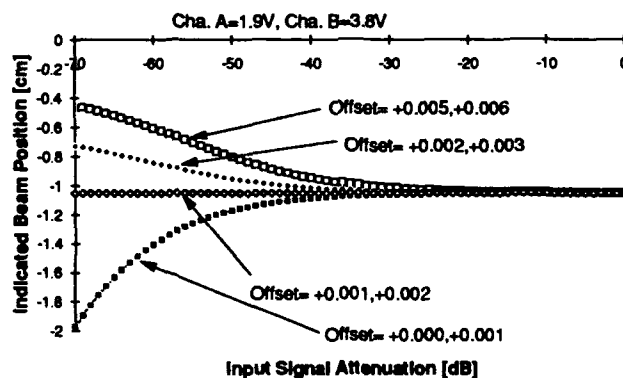


Figure 3: Effect of Small Offset Voltages at Log-Ratio Circuit Inputs.

Our search for a fast track-and-hold circuit with low pedestal offset initially led us to the SHM-30C/HA5330. This is a high-slew-rate track-and-hold circuit employing monolithic integrated circuit technology with an extremely low pedestal offset specification (0.5 mV). Bench testing revealed a strong slew-rate dependence on input signal amplitude, making this device a questionable candidate. We replaced it with an industry standard 4860 track-and-hold

circuit module, measured pedestal offset voltages, and corrected the resulting data to produce the live beam results of Figure 4. These data show apparent position shifts at the lowest input signal region. The pattern repeats with changes in beam position provided by upstream steering magnets. We believe this to be a real effect resulting from off-center injection of just a few beam bunches into the PSR.

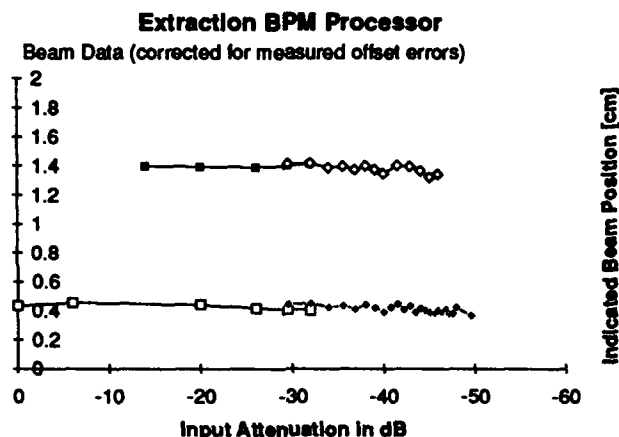


Figure 4: Beam Position Data with Offset Correction.

A second attempt to resolve the pedestal offset difficulty led us to the SHM-49 track-and-hold circuit. This is another monolithic integrated device offered as a high-slew-rate low-cost unit. No attempt has been made by the manufacturer to balance the pedestal offset, but an inverting input is available and a compensating charge may be coupled through a small capacitor into this input. We found the compensation to be temperature dependent largely due to the track-and-hold circuit and chose a negative-temperature-coefficient thermistor configured as a self-regulating heater to maintain a constant chip temperature. While bench tests yielded quite acceptable results, live beam results from three production processors resulted in one unit with unacceptable low-level response.

Our present preferred track/hold circuit choice is the SHM-45. This is a version of the 4860 with a single hold command input allowing the manufacturer to trim the circuit for a typical pedestal offset of less than 1 mV. The trimming is relatively insensitive to temperature fluctuations and with careful selection the SHM-45 will provide the desired results.

V. NOISE CHARACTERISTICS

Overall system noise will ultimately limit the usable dynamic range of any position processing system. Figure 5 gives the measured noise characteristics of our processing system. RMS displacement data for live-beam and bench tests for high-sensitivity and low-sensitivity settings are given. At

high input signal levels, the observed noise is at the limits of our measurement system.

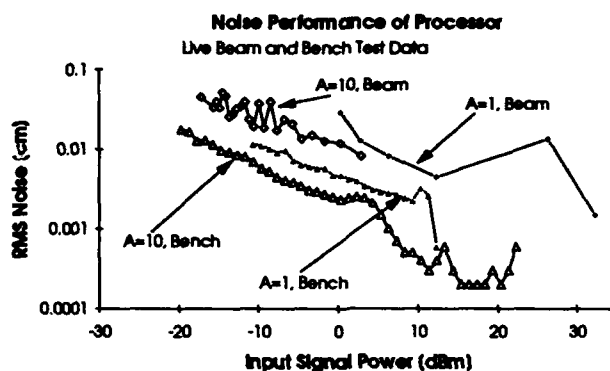


Figure 5: Processor Noise Performance.

VI. CONCLUSIONS

We have produced three versions of our Integrating Log-Ratio processor. Tests with live beam have been encouraging, resulting in an observed dynamic range in excess of the desired 40 dB. There remain some circuit difficulties, which we now feel can be controlled. We are constructing a full complement of processors and plan a complete conversion of the PSR extracted beam line in the near future.

VII. REFERENCES

- [1] G. Gelato, PSR Technical Note No.158, 159, and 160.
- [2] R. Shafer, Private Communication, "Cathode Follower Response Requirements for PSR Pickup Electrodes."
- [3] R. Shafer, Private Communication, "Proposal for PSR Extraction Line Beam Position Monitoring System."
- [4] A. Band, "PSR BPM Development, Feb. 89-July 89," PSR Technical Note, PSR-90-013.
- [5] R. E. Shafer et al., "Beam Position Monitor Upgrade For The Los Alamos Proton Storage Ring," *Proceedings of the 1989 IEEE Particle Accelerator Conference*, Vol. 3, pp. 1562 -1564.
- [6] A. Band, PSR BPM Development, August 1989 - October 1990," PSR Technical Note PSR-90-014, Nov. 1990.
- [7] David Brown notes from private discussion with Andrew Browman on Feb. 28, 1987.

Betatron "Ping" Tune Measurement System for the IUCF Cooler Synchrotron/Storage Ring*

Brett J Hamilton, Mark S. Ball, Timothy J.P. Ellison
The Indiana University Cyclotron Facility
2401 Milo Sampson Lane, Bloomington, IN 47405

Abstract

A system has been developed for nearly real-time measurement of the coherent betatron fractional tune, ΔQ , in the IUCF cooler synchrotron/storage ring. This system measures the horizontal and vertical beam position on a turn-by-turn basis for beam currents in the range from $< 1 \mu\text{A}$ to $> 1 \text{ mA}$. A fast Fourier transform of this position data is performed by a PC-based DSP module at a rate of 10 measurements per second yielding the betatron fractional tune. This tune information has been used to modify ramp parameters in order to minimize the tune shift. This paper describes the ping tune system's overall design principles, details of the various electronics systems, and compares the theoretical performance with the measured performance.

I. INTRODUCTION

The ping tune system, PTS, was developed in order

*Work Supported by the National Science Foundation under Grants PHY89-1440 and PHY90-15957.

to allow the operators to easily and quickly monitor and control the betatron tune[1]. The previous tune measurement method, rf knockout [2], works well for non-ramped beam; in this regime there is only a single tune to be measured and the machine cycle time can be made very short, $\ll 1 \text{ s}$. During ramped beam operation, however, many measurements (as a function of time) must be made and the machine cycle time can be very long ($> 10 \text{ s}$); in this regime rf knockout is excessively time-consuming.

A further advantage of the PTS is that it is nondestructive whereas rf knockout is destructive. The rf knockout system excites the beam with a transverse rf electric field; when the excitation frequency, f_{KO} , is equal to $\Delta Q \pm n f_0$ where n is an integer and f_0 is the revolution frequency, betatron oscillations with amplitudes exceeding the machine aperture can be excited. In practice, one varies f_{KO} until beam loss is observed. The PTS system, on the other hand excites small amplitude betatron oscillations which the electron cooling system can quickly damp.

The IUCF Cooler Synchrotron/Storage Ring is hexagonal with a circumference of 86.82 m. The relative

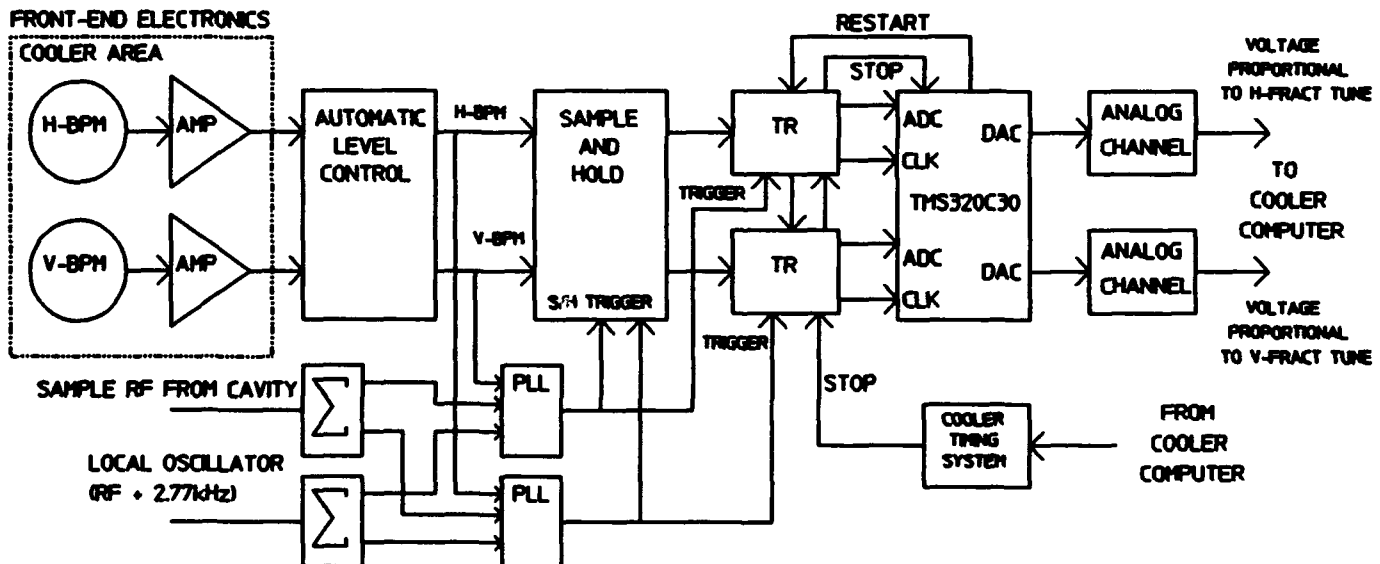


Figure 1. The ping-tune system is used to measure the betatron fractional tune of the IUCF cooler synchrotron/storage ring.

momentum spread of the beam is about ± 0.0001 FWHM. The rms normalized emittance of the electron-cooled proton beam can be much less than $0.1\pi \mu\text{m}$. The beam lifetime can be as long as hours. A typical operation mode is stripping injection and cooling accumulation of 90 MeV H_2^+ . The revolution period, T , for 45 MeV protons is 969 ns corresponding to an rf frequency of 1.03168 MHz. The typical full width at half maximum beam time spread, T_{FWHM} , ranges from 20 ns to 100 ns. Beam currents range from 0.1 to 1,000 μA . The bunching factor, BF , defined as the peak current divide by the average current, or $\approx T/T_{FWHM}$, can range from 1 for unbunched beam, to greater than 50 for highly bunched beams.

II. System description

The PTS consists of six major subsystems (Fig. 1): (1) the front-end electronics, (2) the automatic level control (ALC) with signal conditioning, (3) the sample and hold (S/H) module, (4) the phase-lock-loop (PLL), (5) the transient recorder (TR) and (6) the digital signal processor (DSP).

The front-end electronics consists of one horizontal and one vertical beam position monitor (BPM) electrode and amplifier [3]. The BPM electrodes are diagonally split cylinders. The electrode amplifiers produces two signals: one proportional to the beam linear charge density, and the other proportional to the product of the beam linear charge density and position relative to the center of the pickup. The first stage amplifier determines the system noise level; the electrode length, electrode and cable capacitance, and the intensity, velocity and BF of the beam determine the system signal level. We have evaluated both high input impedance field effect transistor (FET) buffer amplifiers and 50 Ω input bipolar junction transistors (BJT) amplifiers for this application. An FET input buffer amplifier was chosen as the first stage amplifier for this system because of the better low frequency response important for the relatively long (≈ 40 ns) T_{FWHM} encountered most often in machine operations.

The dynamic operating range is extended through the use of a solid state ALC. The heart of this circuit is a CLC520 wideband amplifier [4] with voltage-controlled gain. The CLC520 has a 160 MHz small signal bandwidth, 0.5 degree linear phase deviation (to 60 MHz) and 0.04% signal nonlinearity at 4 V_{pp} output. The peak detected beam intensity signal is used as the feedback signal in a loop which maintains a constant output level with varying input levels. This same intensity feedback is also used to control the gain of the position signal. A dynamic range of over 55 dB has been obtained using this circuit, corresponding to a beam intensity variation of close to 10,000 since for electron-cooled space-charge-dominated beams, $BF \sim 1/I^{1/3}$ [5].

After the ALC, the short pulses (20 - 100 ns in length) are peak-detected by an active operational amplifier

using a resistor in parallel with a capacitor (RC) in the feedback to stretch the pulse. Errors due to jitter and drift in the S/H timing signals are reduced by sampling this stretched pulse, rather than the very short unprocessed signals.

A CLC940 fast sampling, wideband track and hold amplifiers [4] is used to capture and hold both the intensity and position signals. This component has proven to be both reliable and easy to use. The CLC940 has a 150 MHz small signal bandwidth and a 12 ns track-to-hold time. The hold clock is derived from a rf cavity sample clock which has been locked in phase to the beam signal. This provides a reliable clock signal even with very low beam currents.

The PLL is necessary in order to track a single beam bunch as the beam energy, and consequently velocity and thus frequency, is changed. The changing frequency results in a phase shift due to non phase-matched cables. It is important to sample the BPM signal near its maximum amplitude during this energy ramping process. The PLL locks the trigger and beam signal by shifting the phase of the rf cavity sample clock in order to keep the relative phase near 90 degrees at all times. By locking the trigger circuitry in phase to the beam signals, no adjustments are required with varying beam velocity, bunching factor (the beam must be bunched) or intensity. This enables tune measurements to be made during the acceleration process where the beam velocity can change by over a factor of two.

The cooler ring revolution frequency can range from 1 to 2.5 MHz corresponding a beam energy ranging from 45 to 415 MeV. In order to digitize at these rates a high-speed TR is used. The DSP Technology Inc. 2012 TR [6] has 12 bit resolution, 8k memory, and can sample at rates up to 10 MHz. Once the TR buffer is full, the digitized data is replayed at a 100 kHz rate into a Spectrum TMS320C30 Real-Time System DSP board [7]. The DSP board performs a 1024 point fast fourier transform (FFT), which yields the tune information. A voltage proportional to the tune is then output by the DSP board. This information is displayed on the cooler control console as well as on a digital oscilloscope for observation during a cooler ramp cycle.

The DSP board resides in a personal computer (PC). All software changes can be made and compiled on the PC. The C programming language is used along with a set of SPOX application programming interface (API) high-level functions [8]. Using the provided high-level functions, complex operations such as FFT's become trivial one line function calls. The DSP board is a user-friendly system requiring little development time.

At the heart of the DSP board is a Texas Instruments TMS320C30 processor [9] running at 33.33 MHz with 32-bit memory and I/O busses. Analog interfacing is accomplished via two 16-bit, 150 kHz analog-to-digital converters and two 16-bit, 1.5 μs digital-to-analog converters.

III. System Operation and Performance

A. System Operation

A small coherent betatron oscillation is excited by a horizontal and/or vertical kicker magnet. A single measurement, or multiple measurements up to a rate of 10 measurements per second, can be made per ring cycle. The minimum measurement cycle time is limited by the 100 kHz transient recorder playback rate. A timing signal from the cooler computer controlled timing system initiates a measurement. This signal, via hardware logic, fires both kicker magnets and triggers the data acquisition system. The kick amplitude is set via the control console. The beam can be kicked in a single plane or in both planes at the same time. The beam loss due to the kick must be monitored. If the beam is kicked too hard, the beam current could fall below the data acquisition threshold level. If the beam is kicked too little the oscillation will be weak and the signal-to-noise ratio will be poor. A beam loss of approximately 1 dB seems to work very well for a single kick. An FFT of the first 1024 beam position points after the kick yields the fractional tune.

B. System Performance

A signal to rms noise voltage per channel ratio of 5 is necessary to ensure a 99.9% probability of detecting the correct tune. The signal voltage on one of the electrode pairs, V_s , is:

$$V_s = \frac{I B F L}{2 \beta c C} \frac{x}{R}$$

where I is the beam current, $L = 0.15$ m is the electrode length, $\beta = v/c$ and c is the speed of light, $C \approx 60$ pF is the input capacitance, and $x/R \approx 0.05$ is the kick amplitude over the pickup radius. The total voltage noise is ≈ 25 μ V due to the 4.6 nV/ $\sqrt{\text{Hz}}$ FET input voltage noise which is attenuated as $e^{-\alpha \text{ MHz}}$ due to cable loss. This noise power is distributed equally in each of the 1024 channels (yielding 0.79 μ V/channel). If the system noise were dominated by this white noise, then the tunes could be acquired with peak beam currents ($BF \cdot I$) as low as ≈ 6 μ A. In this system, however, we have found that coherent rfi limits the system performance, though accurate measurements can be made with peak currents as low as 20 μ A with $x/R = 0.05$.

Tune information has been obtained during an energy ramp cycle. A problem encountered during this measurement is beam current loss. A typical ramp time is 3 s, if the beam is kicked every 100 ms a substantial beam loss can occur since cooling does not occur during ramping. For this reason smaller kicks must be used when operating in this mode. At higher energies a larger kick is required to produce the same amplitude oscillation. Consequently, the tune is sometimes

not acquired toward the end of the ramp. This problem can be avoided by measuring smaller time intervals of the overall ramp and adjusting the kicker amplitude accordingly.

V. Conclusions

The PTS information has been used to modify the tune during an energy ramp from 45 MeV to 350 MeV as shown in Fig. 2. Using this system, tune information during an energy ramp can be obtained in a matter of minutes compared to hours with the rf knockout method. This system will better enable operators to duplicate machine performance and operating characteristics from one run to another.

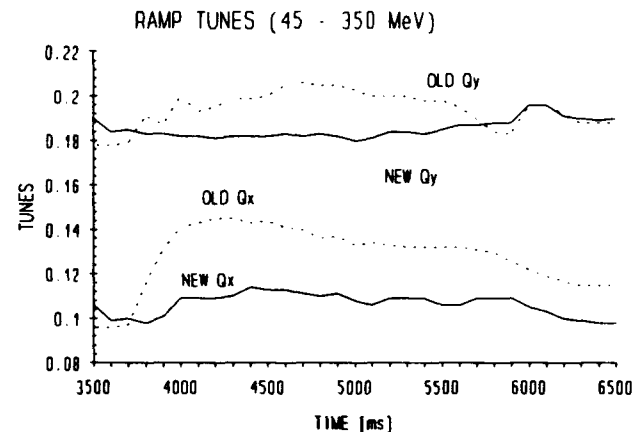


Figure (2). Reduction in tune variations during a ramp after 2 iterations.

IV. References

- [1] E.J.N. Wilson, "Proton Synchrotron Accelerator Theory", *Academic Training Programme of CERN 1975-1976*, CERN 77-07, 29 March 1977
- [2] L.W. Jones *et al.*, "Comparison of Experimental Results with the Theory of Radio-Frequency Acceleration Processes in FFAG Accelerators", *Proceedings of the Intern. Conf. on High-Energy Accelerators* - CERN 1959
- [3] Timothy JP Ellison, C. Michael Fox, Steven W. Koch, Liu Rui, "Nondestructive diagnostics for measuring the phase, position, and intensity of 15 nA beams for IUCF cyclotron", *Proc. 11th Int. Conf. on Cyclotrons and their Applications*, edited by M. Sekiguchi, Y. Yano, K. Hatanaka (Ionics, Tokyo, Japan, 1986)279-283.
- [4] Comlinear Corporation 1991 Databook, "Amplifiers and Data Conversion"
- [5] Timothy J.P. Ellison, Sergei Nagaitsev, Mark S. Ball, David D. Caussyn, Michael J. Ellison and Brett Hamilton, "Attainment Of Space-Charge Dominated Beams in a Synchrotron" *Phys. Rev. Lett.* **70**, 790., 8 Feb. 1993
- [6] DSP Technology, Inc., "Model 2012 Users Manual"
- [7] Spectrum Signal Processing Inc., "TMS320C30 System Board User's Manual"
- [8] Spectron Microsystems, "SPOX Application Programming Manual"
- [9] Texas Instruments, "TMS320C3x Users Manual"

Tune Measurement in the NSLS Booster Synchrotron*

E.B. Blum and R. Nawrocky
National Synchrotron Light Source
Brookhaven National Laboratory
Upton, NY 11973

Abstract

The NSLS booster synchrotron can accelerate an electron beam from approximately 80 to 750 MeV in 0.7 sec. The betatron tunes can change during acceleration by as much as 0.1 units, causing beam loss as they cross resonance lines. Precise measurements with a conventional swept spectrum analyzer have always been difficult because of the rapid variation of tune as the magnets are ramped. We are now using a system based on a Tektronix 3052 digital spectrum analyzer that can obtain a complete frequency spectrum over a 10 MHz bandwidth in 200 μ sec. Betatron oscillations are stimulated for the measurements by applying white noise to the beam through stripline electrodes. We will describe the instrumentation, our measurements of tune as a function of time during the acceleration cycle, and the resulting improvements to the booster operation.

I. INTRODUCTION

The injector for the electron storage rings at the National Synchrotron Light Source (NSLS) is a 77 - 750 MeV synchrotron called the booster [1]. It has a 28.35 m circumference and a 0.7 Hz repetition rate. The lattice consists of four superperiods, each containing two combined function bending magnets and two horizontally focusing quadrupoles. The vertical tune is determined primarily by the gradient in the bending magnets and the horizontal tune by the quadrupoles. Eight small, air-core trim quadrupoles are provided at positions in the lattice with large values of the vertical beta function for fine adjustment of the vertical tune. Each family of magnets is powered by its own programmable power supply.

The booster performance has always been very unstable. The electron current could vary by a factor of ten from one acceleration cycle to the next. It was known from measurements with a conventional spectrum analyzer that at a given point in the acceleration cycle, the betatron tunes could vary by as much as 0.1 on succeeding cycles. It was also known that injection required a tune just below the half-integer resonance. Apparently, the beam was lost when the horizontal tune wandered close to the half integer.

Because a conventional spectrum analyzers may need at least 20 msec to measure a frequency spectrum, it was always hard to see the rapid tune changes that occurred in the booster during acceleration. The spectra were distorted as the spectrum analyzers swept slowly through the measured frequencies and the number of points that could be measured while the beam was accelerated was small.

To understand the problems with the booster a way was needed to rapidly measure the tunes during a single acceleration cycle. Real time display of the results was desired to aid in adjusting the magnet ramps. This paper will describe a system based on the Tektronix 3052 Digital Signal Processing system [2], an instrument that can measure a complete frequency

spectrum from 0 - 10 MHz in a time of 200 μ sec, to simultaneously measure the horizontal and vertical tunes in the NSLS booster throughout the acceleration cycle [3].

II. TUNE MEASUREMENT SYSTEM

A. Spectrum Analyzers

Accelerator tune measurements are often made with a swept spectrum analyzer. This consists of a tunable bandpass filter whose center frequency $\omega_0(t)$ is swept over the frequency range of interest. The center frequency can not be changed by an amount equal to the bandwidth of the filter $\delta\omega$ in a time less than $O(1/\delta\omega)$ without distorting the spectrum. Additional time may also be needed by the instrument to process the data after the sweep is completed. In a rapidly cycling accelerator like the NSLS booster, the tunes can change appreciably during the sweep time which can distort the spectra and make them hard to interpret.

The Tektronix 3052 Digital Signal Processing System uses 1024 bandpass filters operating in parallel to obtain a frequency spectrum. All of the filters simultaneously measure the signal within their passbands to produce the entire frequency spectrum in one shot. The Tektronix 3052 takes 200 μ sec to measure a complete spectrum over a 2 MHz range to a resolution of 1/800.

A Fast Fourier Transform (FFT) spectrum analyzer operates in the time domain by sampling the incoming signal and then performing an FFT numerically to calculate the frequency spectrum. This technique is commonly used to measure accelerator tunes in the 100 KHz range but, for the 5 MHz spectral range required for the NSLS booster tune measurements, the FFT technique would be dominated by the numerical processing time, and could not be used.

B. System Details

Electrostatic pick-up electrodes are used to measure the beam position in the NSLS booster synchrotron. The betatron tune appears as sidebands on the harmonics of the revolution frequency. Because coherent betatron oscillations do not usually appear spontaneously, it is necessary to stimulate the beam with a driving force to provide a large enough signal to measure the tune. This is done by applying a deflecting field to the beam with a set of stripline electrodes.

With a conventional swept spectrum analyzer, an amplified signal from a tracking generator is used to drive the beam at the frequency being measured. A sustained response is only possible at the frequency of one of the beam's normal modes of oscillation; i.e. at one of the revolution harmonics or the betatron tune sidebands. The position signal is then connected to the input of the spectrum analyzer and the betatron tune lines are seen as a response of the beam to the deflecting signal.

Measuring the betatron tunes with a multiple receiver spectrum analyzer like the Tektronix 3052 or by FFT techniques is slightly more complicated. Because all of the frequencies in the range of interest are observed simultaneously, it is necessary to stimulate the beam at all of

*This work was performed under the auspices of the U.S. Department of Energy, under contract DE-AC02-76CH00016.

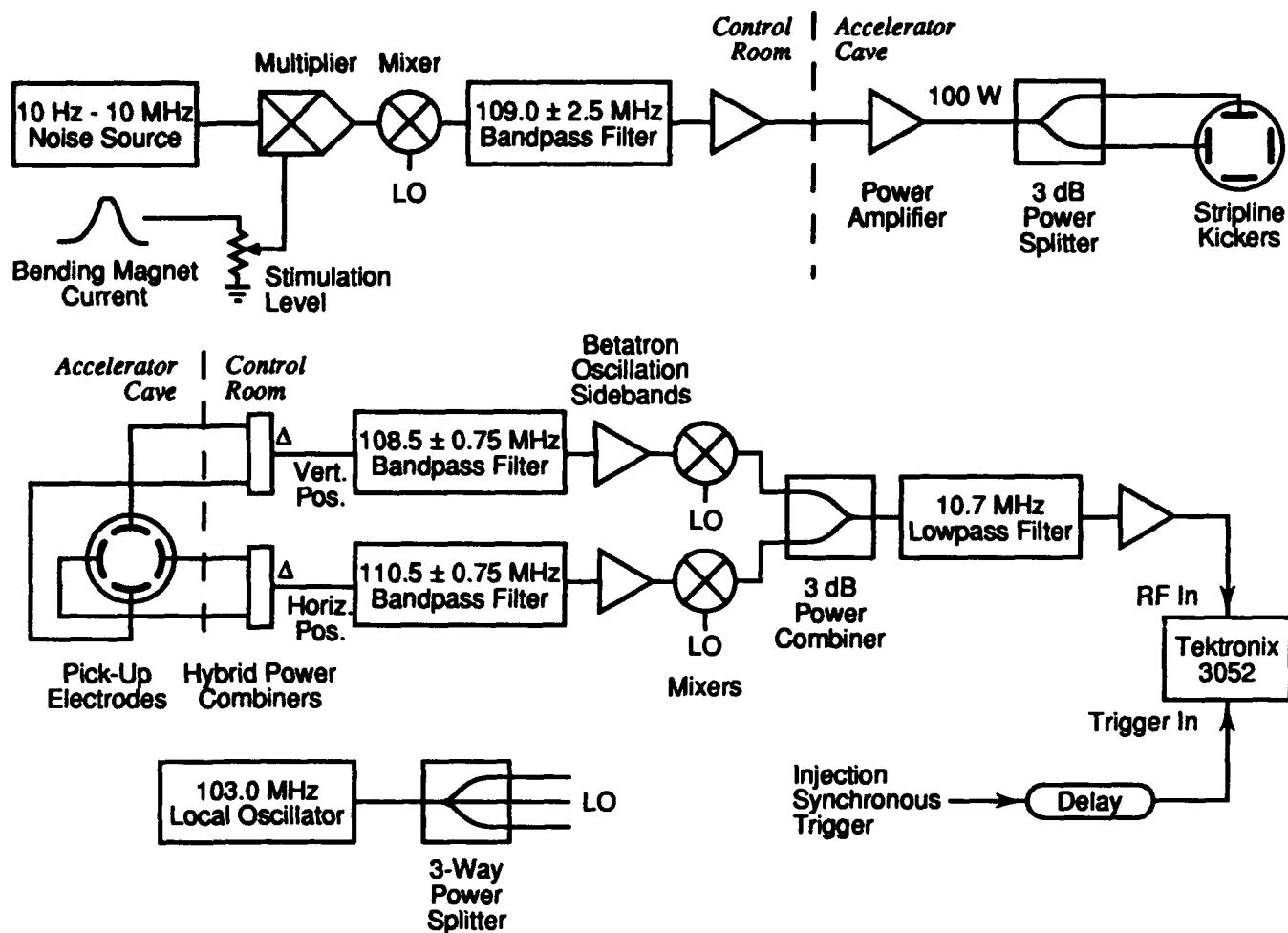


Fig. 1. NSLS booster tune measurement system block diagram.

the frequencies of the band simultaneously as well. This can be done by applying the signal from a broadband noise generator to a deflecting electrode.

A block diagram of the NSLS booster tune measurement system is shown in fig. 1. Horizontal and vertical tunes are measured simultaneously. The beam positions are obtained by subtracting the signals that are induced on pairs of electrostatic plates using hybrid power combiners. Deflecting forces are applied to the beam by signals on horizontally and vertically oriented stripline kickers. Both the position detectors and stripline kickers are most sensitive at frequencies near 100 MHz so we measure the betatron tunes at the upper sideband of the tenth harmonic of the 10.58 MHz revolution frequency. We heterodyne these signals down to the 0 - 10 MHz range of the Tektronix 3052.

The stimulating signal is obtained from a noise generator with a flat frequency spectrum from 10 Hz to 10 MHz. To provide a constant excitation at all beam energies, the noise source is scaled by a signal proportional to the current in the dipole magnet which, in turn, is proportional the beam energy. The signal is then mixed with the 103 MHz signal from a crystal controlled oscillator, the components in the 103.0 ± 2.5 MHz band are selected, amplified, and applied to the horizontal and vertical kickers.

From the design of the booster and from previous measurements with swept spectrum analyzers, we knew that the fractional horizontal tune was between 0.4 and 0.5, and the

fractional vertical tune was between 0.2 and 0.3. At the sidebands of interest, these correspond to frequencies near 110.5 MHz for the horizontal tune and 108.5 MHz for the vertical tune. We filter the signals from the position detectors at these frequencies to avoid saturating the electronics with extraneous noise. The horizontal and vertical betatron sidebands are separately mixed with a signal from the 103 MHz local oscillator, combined, and the difference signal is selected by a 10.7 MHz low pass filter. The result, containing the horizontal and vertical betatron tune information, is applied to the input of the Tektronix 3052.

After receiving a trigger corresponding to the injection of the electrons into the booster, the 3052 begins to collect a frequency spectrum every 200 μ sec. Every r^{th} spectrum is saved, where r is an integer that can be set by the user, and 501 spectra can be saved in the instrument's internal memory. A false color image showing the horizontal and vertical tunes as a function of time after injection is displayed after each booster cycle. An example of a color spectrogram can be seen in reference [3].

C. DATA ANALYSIS

The 3-D plots that are produced by the spectrum analyzer can be used for tuning the booster, but for analysis it is useful to extract 2-D plots of tune vs. time or horizontal vs. vertical tune. This information is extracted using the Motorola 68030 based, single board computer that is incorporated in the Tektronix 3052. The program is written in the "C" language.

Tunes are extracted from the raw data by a simple peak finding algorithm following exponential smoothing of the data at nearby frequencies to remove narrow-band electrical noise. (This is described in more detail in reference [3].) An ASCII file containing the the horizontal and vertical tune as a function of time is written to the spectrum analyzer's hard disk where it can later be examined or transferred to another computer via an RS-232 interface for further analysis. Performing the initial data reduction within the spectrum analyzer has the advantage of reducing the amount of data transmitted. Fig. 2 shows a plot of the horizontal and vertical tune during a typical booster acceleration cycle.

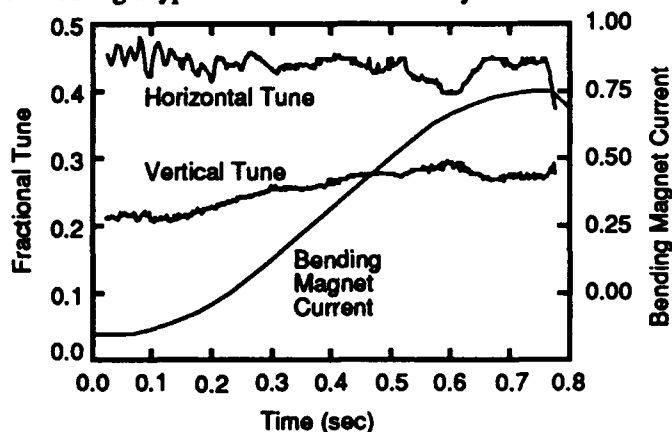


Figure 2. Horizontal and vertical tunes in the NSLS booster as a function of time during the acceleration cycle. Also shown is the booster bending magnet current which is proportional to beam energy.

III. RESULTS AND DISCUSSION

Together with the tune data, fig. 2 shows the booster bending magnet current, which is nearly proportional to the electron beam energy. The horizontal tune fluctuates at a frequency of approximately 60 Hz at low energy. The oscillation is caused by an instability in the regulation of the bending magnet power supply at low currents. The tune at any given time in the cycle also tends to vary from one cycle to the next due to slow drift in the power supply. On some cycles, the variation is enough to carry the peaks in the horizontal tune across the half-integer resonance causing beam loss. This explained an instability in booster operation that had been seen for many years but only incompletely understood.

In the long term the problem with the tune variation will be cured by replacing the booster power supplies [4] but for now, the instability was fixed in another way. A program had already been started to increase the energy of the linac that serves as an injector for the booster from 77 to 116 MeV. Observation of the tune instability provided impetus for completing the linac upgrade. At 116 MeV, corresponding to a time of approximately 0.15 sec in fig. 2, neither the rapid fluctuations nor the cycle to cycle variation in the horizontal tune are as severe. We used the same bending magnet ramp as for 77 MeV injection but delayed the injection time until the magnet currents reached the 116 MeV values. Booster operation is now much more stable. The cycle to cycle variation in the electron current is now less than 10%.

More recently, a new digital feedforward system [5] was connected to the bending magnet power supply to improve the low frequency response. This corrected the remaining cycle to

cycle tune variation. Because the new feedforward system changed the regulation of the power supply, it was necessary to adjust the magnet ramp to compensate. This was easily done, using the tune measurement system to monitor the tune in real-time. Similar adjustments in the past took weeks of work with a swept spectrum analyzer.

Fig. 3 shows a plot of the vertical tune as a function of the horizontal tune in the booster, derived from the mean data in fig. 2. Also shown are the resonance lines in the region plotted. As the beam is accelerated, it crosses the fourth order resonance $4q_y=1$ and later skirts back and forth along the third order resonance $q_x+2q_y=1$ but never crosses it. Although the fourth order resonance apparently does not effect the beam, the third order resonance does. This explains why the booster beam was lost if the vertical tune was increased. Raising it will carry it across the resonance line.

The vertical tune in the booster is controlled largely by the trim quadrupoles. Their power supply can only produce a limited current and can not be scaled with beam energy during the entire acceleration cycle. This explains the increase in vertical tune seen in fig. 2. The lack of control of the vertical tune has always been a problem: if the vertical tune is too low injection suffers but if it is too high the third order resonance is crossed. Now that the tunes were measured precisely, a new trim quadrupole power supply will be installed to correct the problem.

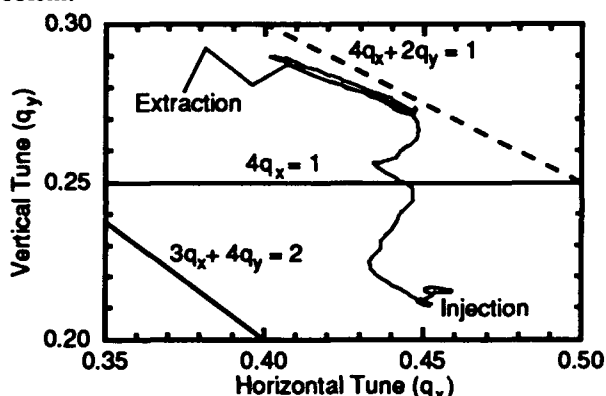


Figure 3. Horizontal vs. vertical tune in the NSLS booster obtained from the data in fig. 2, smoothed to eliminate rapid oscillations. The third and fourth order resonance lines in this region of the tune plane are indicated.

IV. ACKNOWLEDGEMENTS

The authors would like to thank Michael Schnecker of Tektronix Federal Systems Inc. for assistance with the Tektronix 3052 Digital Signal Processing System.

V. REFERENCES

- [1] J. Galayda, L. Blumberg, R. Heese, J. Schuchman, and A. van Steenberg, *I.E.E.E. Trans. Nucl. Sci.* NS-26 (1979) 3839.
- [2] Tektronix Federal Systems Inc., P.O. Box 4490, Beaverton, OR 97076, USA.
- [3] E.B. Blum and R.J. Nawrocky, *Nucl. Inst. and Meth. A*, to be published.
- [4] R. Olsen, J. Dabrowski, and J. Murray, Conf. Rec. of the 1992 IEEE Nucl. Sci. Sym. and Med. Imaging Conf., 572.
- [5] R. Olsen, J. Dabrowski, and J. Murray, "Control System for the Booster Power Supply Upgrade", these proceedings.

A Realtime Feedback Microprocessor for the TEVATRON

D.A. Herrup, L. Chapman, A. Franck, T. Groves, B. Lublinsky
*Fermi National Accelerator Laboratory**

*P.O. Box 500
Batavia, Illinois 60510*

Abstract

A feedback microprocessor has been built for the TEVATRON. Its inputs are realtime accelerator measurements, data describing the state of the TEVATRON, and ramp tables. The microprocessor includes a finite state machine. Each state corresponds to a specific TEVATRON operation. Transitions between states are initiated by the global TEVATRON clock. Each state includes a cyclic routine which is called periodically and where all calculations are performed. The output corrections are inserted onto a fast TEVATRON-wide link from which the power supplies will read the realtime corrections. We also store all of the input data and output corrections in a set of buffers which can easily be retrieved for diagnostic analysis. I will describe use of this device to control the TEVATRON tunes, and discuss other uses.

INTRODUCTION

In hadron colliders such as the Fermilab TEVATRON, the HERA p ring, the SSC and the LHC, a well-defined sequence of operations is needed to take the accelerator from an initial state, without stored beam, to a final state, with stored beam and collisions at the interaction points. There are many intermediate states (such as acceleration), during which accelerator parameters change. It is difficult to construct a single model of the accelerator which applies during all these states. Instead, it is convenient to consider each process separately and construct models for each state. The entire process may be thought of as a finite state machine, with each state corresponding to a different operation and having its own model of the accelerator. In addition, the time scales at which the accelerator parameters change vary from state to state. Changes in accelerator parameters lead to variations in the beam parameters such as the tunes, coupling, and chromaticities. If the beam parameters are not carefully controlled, beam quality will deteriorate. One of the principal challenges of collider operations is to maintain high beam intensities and low emittances through the chain of operations from injection to collisions.

The sequence of operations in the TEVATRON is illustrative of this process¹. Operations proceed through the following (simplified) set of states: p injection, energizing electrostatic

separators to create different helical orbits for p 's and \bar{p} 's, \bar{p} injection, acceleration, lattice modifications to produce low β^* 's at the interaction regions, and energizing additional separators to create head-on collisions at the two interaction regions. In p and \bar{p} injection, a closed orbit time bump moves the circulating orbit near an injection kicker, and back immediately after injection. Closed orbit changes may be accompanied by betatron tune and coupling changes caused by the non-linear fields of the bending dipoles and sextupoles. Energizing the separators has the same effect. During acceleration, all the magnetic elements are ramped. Although the linear lattice is kept constant, the multipoles change, affecting the tunes and coupling. The closed orbit may also vary. "Squeezing" is the term used to describe lattice changes to create small β^* 's at the interaction regions. In principle, only a restricted set of quadrupoles should be needed for this step. However, since the quadrupole strengths are not precisely known, the exact settings for the quadrupoles cannot always be calculated. The closed orbit may not pass through the centers of the quadrupoles, leading to closed orbit (and tune and coupling) shifts. If during these states the tunes and couplings are not kept away from harmful resonances, emittance growth and/or beam loss will result.

Closed orbit and quadrupole variations also affect the chromaticities. These effects are usually small and do not pose problems for beam stability. However, persistent current effects in the bending dipoles of superconducting accelerators have a large effect on the sextupole moment. During the 1-3 hour TEVATRON injection front porch, the chromaticities change by as much as 70 units. These changes are undone in the first seconds of acceleration. If the chromaticities are too low during these states, head-tail instabilities may develop. If they are too large, the chromatic tune spread may overlap harmful resonances. In both cases, emittance growth and/or beam loss may result.

In all of these cases it is necessary to have accurate tune and chromaticity control. This is usually accomplished with open loop control in the form of tables operating at breakpoints, with linear interpolation between breakpoints. However, this interpolation is often not accurate. The C'BA¹ system at Fermilab was constructed to provide tune control with realtime feedback loops. It operates as a finite state machine in which each state corresponds to a specific TEVATRON process. Feedback within a state is performed by periodic calls to the state's data acquisition and feedback routines. Each state also includes a set of buffers in which the measurements and calculations from the feedback routine are stored. All data are available through the Fermilab accelerator control system. We will describe the gen-

*Operated by the Universities Research Association under contract with the U. S. Department of Energy

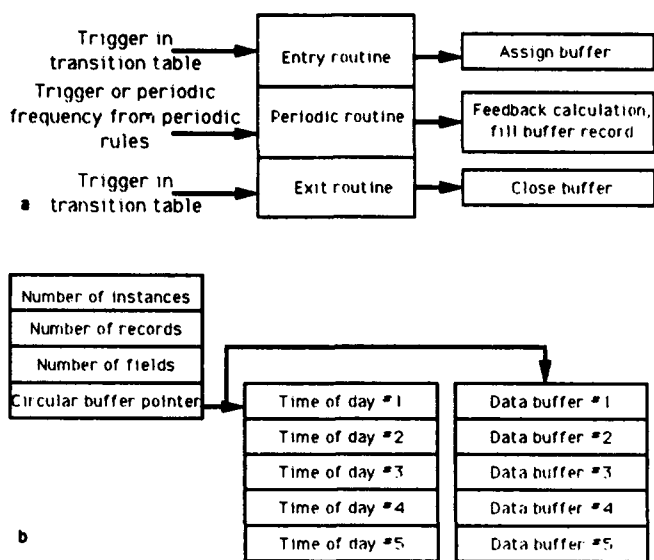


Figure 1: a CBA State Structures and b CBA Buffer Structures.

eral features of the microprocessor software, the way in which it has been incorporated into the TEVATRON control system, and some of the ways in which it has been used.

FEATURES OF THE CBA SYSTEM

The hardware standard chosen for CBA was the Intel Multi-bus II³ chassis using a Micro Industries 80386 processor card with 8 MBytes of DRAM. We use the MTOS⁴ operating system. All software is written in C.

The heart of the finite state machine is a set of states with a transition table and a set of periodic rules and buffers for each state. These structures are illustrated in Figure 1a and 1b. The transition table consists of a list of allowed transitions between states and the trigger which will cause a given transition. Each state can have transitions into up to 8 other states, although a given trigger signal can occur only once in the transition table for a state. The periodic rules consist of a specification of 8 frequencies and timing signals which will cause the periodic routine to be called. The frequencies vary from state to state, depending upon the accelerator processes occurring. For instance, during acceleration the persistent current effects are removed rapidly, and a frequency of several Hz is indicated, but during the squeeze the quadrupole circuits change very slowly and a frequency of 1 Hz is sufficient.

Associated with each state is a set of buffers. The buffer structures consist of a specification of the number of fields, number of records, number of instances of a state which may be buffered before they are overwritten, time-of-day stamps for each buffer, and the data buffers themselves. One buffer is filled for every instance of a state, and after the entire set has been filled, they are overwritten in a circular manner. The number of buffers for each state has been chosen to be large enough so that there is no danger of buffers being overwritten before they have been archived, if desired. The time-of-day stamp is the clock date and time at which the instance of the state occurred. It is stored in a separate circular buffer which maintains the one-

to-one correspondence with the data buffers. Each data buffer consists of fields into which the input data, accelerator parameters, and output data may be loaded. A new record consisting of data for all the fields is added to the buffer each time the periodic routine is called.

The computations for each state are performed in the entry, exit, and periodic routines. The entry routine allocates the next available buffer and zeroes the timer which counts time since the start of the state. The exit routine closes the buffer and zeroes the feedback output. The periodic routine consists of routines that read the beam and accelerator parameters, such as the betatron tunes and bending bus current. It also accesses the tables of desired values for beam quantities as a function of time since entry into the state. The desired values and measured values are inputs to the feedback routine, which calculates an error signal. The accelerator model is then used to calculate the feedback current required to null the error signal. These corrections are output in real time to the power supplies and are stored, along with the input data and whatever calculations are desired, in the buffer being used for the particular instance of the state.

TEVATRON IMPLEMENTATION

Figure 2 is a complete diagram of the system as implemented in the TEVATRON. The inputs are a set of phase lock loops whose input is the signal from a set of Schottky detectors⁵. These circuits provide a realtime measurement of the tune. The triggers for the transition tables are read from the global TEVATRON clock (TCLK) and other machine parameters (the bend bus current) are read from the global MDAT link⁶. The realtime corrections are transmitted to the power supply controllers over MDAT. Various control parameters (feedback gains, frequencies, on/off switches, etc.) are downloaded into CBA through the accelerator control network (ACNET). The data buffers are also available to the console system over ACNET.

We have conducted several closed loop tests of CBA. In one such test, we demonstrated that CBA can successfully compensate tune shifts caused by changes in TEVATRON parameters other than the tune circuits. We introduced a single horizontal dipole kick of varying magnitude at one location. In Figure 3a we plot the kick, the position measured on a beam position monitor, and the horizontal and vertical tunes. The kick leads to a maximum tune change of about 0.01. Figure 3b is the same plot with CBA turned on to perform active feedback. The tune shift has been successfully compensated to within 0.002.

CONCLUSIONS

We have built a general purpose microprocessor based feedback system which has been tailored to fit the finite state behavior of hadron collider operation. The system will work with any reliable realtime inputs and will provide feedback at up to 60 Hz. Each state has its own feedback routines which contains a model of that particular accelerator state. We have provided a buffer system which matches the states of the state machine and which contain all information describing the operation of the feedback loop. Closed loop corrections to the power supplies can be output on any accelerator-wide link. This system has been tested and shown to work in circumstances which are useful to accelerator operations.

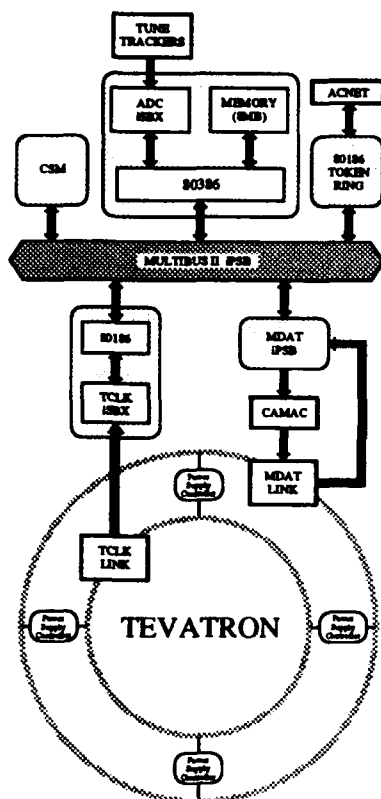


Figure 2: CBA implementation in the TEVATRON.

REFERENCES

- [1] G. Dugan, Particle Accelerators 26, 12 (1990).
- [2] CBA is an acronym for Colliding Beam Adrastus. See R. Graves, THE GREEK MYTHS, vol. 2, Viking Penguin Inc., New York, New York, 1955, p. 377. See also D. Herrup et. al., Real-Time Feedback Control of the Tevatron Tunes and Chromaticities, Proceedings of the 2nd European Particle Accelerator Conference, Nice, June 12-16, 1990, p. 898, and D. Herrup et. al., A Feedback Microprocessor for Hadron Colliders, to appear in Nuclear Instruments and Methods Section A.
- [3] Multibus is a trademark of the Intel Corporation.
- [4] MTOS is a trademark of Industrial Programming, Inc.
- [5] D. Martin et. al., A Resonant Beam Detector for TEVATRON Tune Monitoring, Proceedings of the 1989 IEEE Particle Accelerator Conference, March 20-23, 1989, Chicago, IL, and J. Fitzgerald and R. Gonzalez, Tune Trackers for the Fermilab TEVATRON, Proceedings of the 1991 IEEE Particle Accelerator Conference, May 6-9, 1991, San Francisco, CA.
- [6] D.G. Beechy and R.J. Ducar, Time and Data Distribution Systems at the Fermilab Accelerator, Nuclear Instruments and Methods in Physics Research A247 (1986), p. 231.

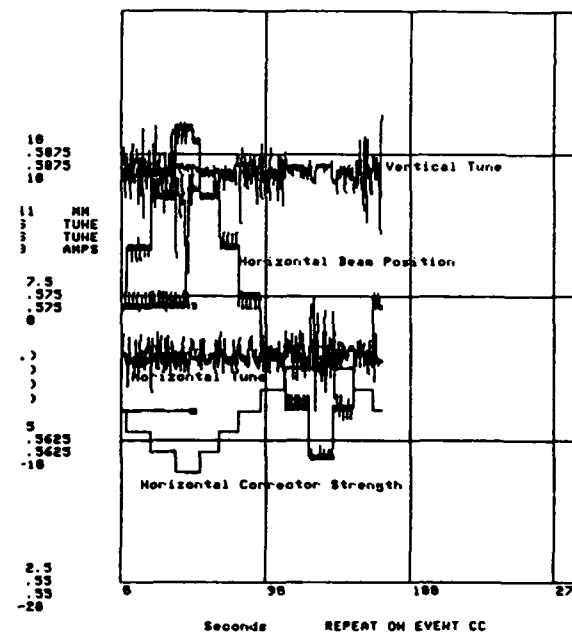
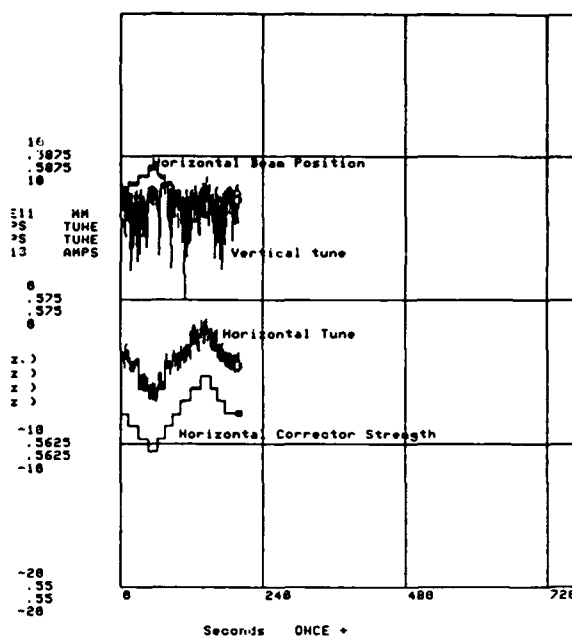


Figure 3: Plots of a horizontal correction dipole, horizontal beam position monitor, and the horizontal and vertical tunes with a CBA off and b CBA on.

A New Study of the Main Ring Physical Aperture

G. Wu, S. Pruss, D. Capista
Fermi National Accelerator Laboratory
P.O. Box 500, Batavia, IL 60510

Abstract

Changes made to the Fermilab Main Ring lattice and the Main Ring's future importance for the HEP program require a new study of its physical aperture. This task has been carried out using a computer program that automatically and systematically measures the available aperture around the ring. This program and its performance are described along with a preliminary analysis of the results. Further systematic analysis of aperture data is underway in preparation for modifications to be made in the coming summer shutdown.

I. INTRODUCTION

The random misalignments of Fermilab Main Ring elements are responsible for reduced transverse and momentum aperture and are the cause of high ramped dipole corrector currents. This has been one of sources of frequent power supply failures. In the past, aperture scanning, a process to measure physical apertures, has been done manually, and has involved tedious human intervention, precious beam time, and yet has resulted in incomplete information. The new automated aperture scan program is more than a convenience in that detailed and accurate aperture pictures can be achieved with minimum human interventions in a repetitive, reproducible process. In relatively short time, detailed 2-dimensional aperture pictures were obtained at all 216 beam position monitor(BPM) locations. Work to identify the locations in the Main Ring which should be modified or resurveyed during the upcoming summer shutdown is in progress.

II. THE PROGRAM

A goal in the program design is to relieve the operator of time consuming and error prone manipulations while achieving sufficiently detailed and accurate data within

limited time. This is largely facilitated by the now much improved Fermilab ACNET¹ utility software that interface data pool, central file sharing system, network communications, TV and graphics I/O. The core of the program is the coordinated control of reading and setting C453 ramp cards (CAMAC modules that control corrector currents), and reading beam intensities and BPMs. For a given location, it forms a local 3-bump in one plane and a 4-bump in the other plane. By resetting those C453 cards for the seven correctors involved, the beam is stepped in 2-dimensions from center toward the 'edge' of the aperture. The 'edge' is recognized when the beam intensity is reduced to a preset level. At each step, horizontal and vertical beam positions together with the beam intensity are displayed in a 2-dimensional aperture map. When one location is done all information including closure of the bumps are logged into a file and the scan of the next location is started. The program has proven to be fairly robust and reliable. When questions arise regarding losses at certain locations, one can review the aperture pictures on file or re-scan for a new map to aide in tuning the machine.

III. PRELIMINARY RESULTS

In the coming summer shutdown, some of the Main Ring beam line elements will be resurveyed based on these aperture maps. While systematic study and test are needed to understand all major problems, some problems are very obvious by just looking at the map. Fig. 1 is a typical normal map, whereas Fig. 2 to Fig. 4 are maps for problem locations. In the plot the numbers represent the percentage of surviving beam current measured at those coordinates. These problems may call for realignment of the lattice elements or require an investigation for obstacles in the beam tube. Some problem may be due to misalignments of the BPM detectors. To aide systematic study, multiple aperture maps can be plotted in order of their positions around the ring in one plot. Fig. 5 is

NR APERTURE AT VA21 84/28/93 8935

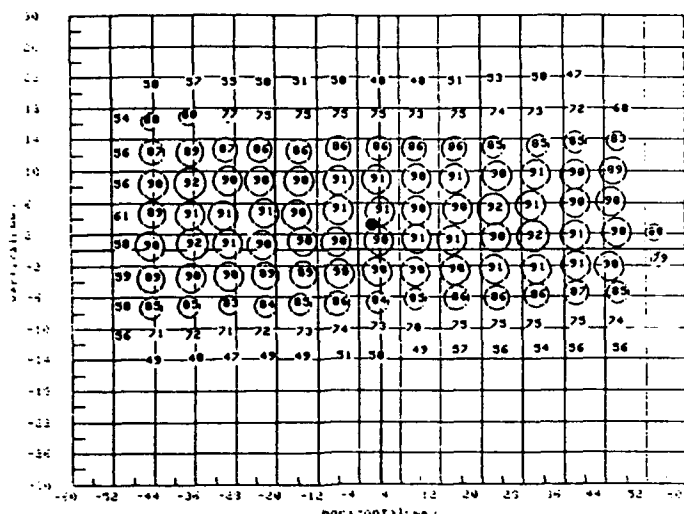


Fig. 1

NR APERTURE AT VF16 84/28/93 2383

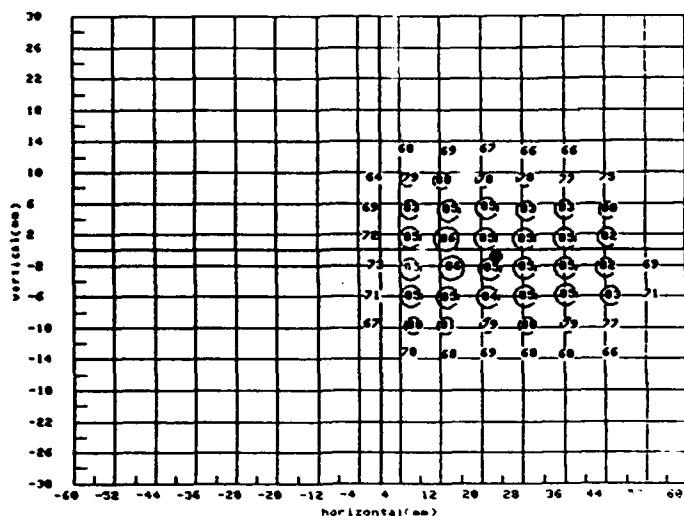


Fig. 2

NR APERTURE AT HD11 84/21/93 1639

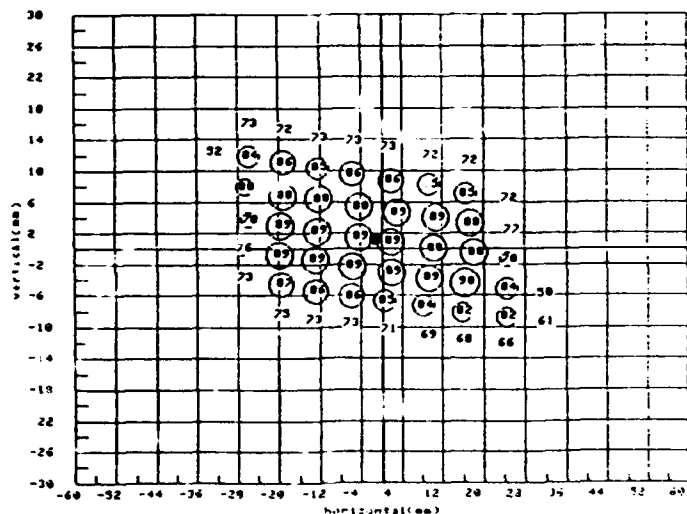


Fig. 3

NR APERTURE AT VF35 85/12/93 1545

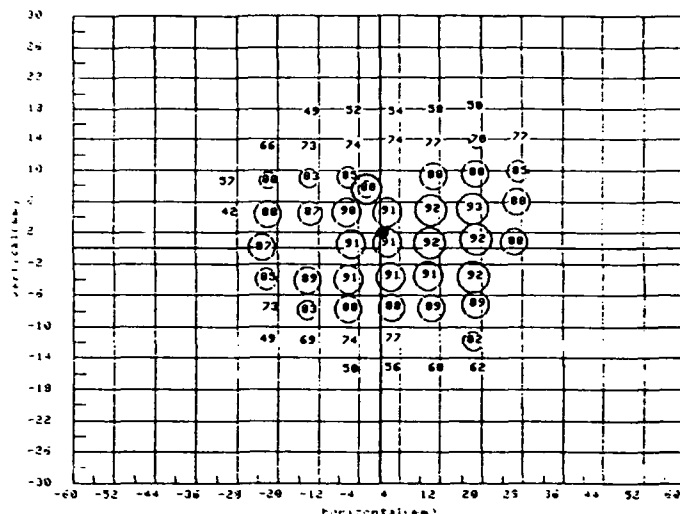


Fig. 4

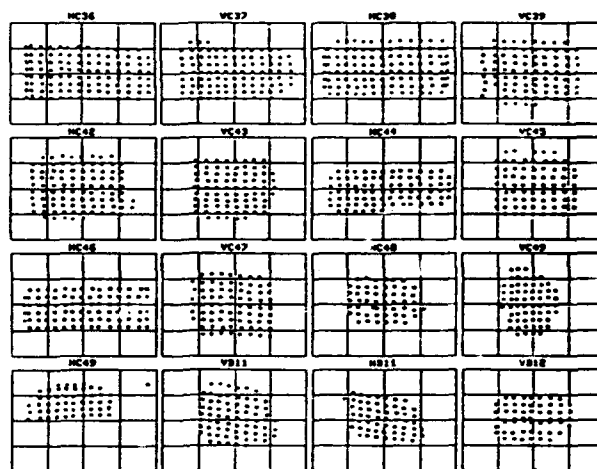


Fig. 5

such a plot in which beam intensities are indicated by different colors.

V. ACKNOWLEDGMENTS

The Authors would like to thank Gerry Jackson for his contributions to this work. Brian Hendricks has provided a great deal of guidance in the actual programming. We owe many thanks to him.

VI. REFERENCES

[1] P. Lucas, "Updated Overview of the Tevatron Control System", Control Systems for Experimental Physics, CERN 90-08, p71, 1987.

ELECTRON BEAM STABILITY AND BEAM PEAK TO PEAK MOTION DATA FOR NSLS X-RAY STORAGE RING*

Om Singh

National Synchrotron Light Source, Brookhaven National Lab, Upton NY 11973

Abstract

In the past two years, a significant reduction in electron beam motion has been achieved at the NSLS X-Ray storage ring. The implementation of global analog orbit feedbacks, based on a harmonics correction scheme, has reduced the beam motion globally. Implementation of six local analog feedback systems has reduced the beam motion even further at the corresponding beam line straight sections. This paper presents beam motion measurements, showing the improvement due to the feedback systems. Beam motion is measured using a spectrum analyzer and data is presented at various frequencies, where peaks were observed. Finally, some of the beam motion sources are discussed.

I. INTRODUCTION

The X-Ray storage ring at the National Synchrotron Light Source (NSLS) is now in its tenth year of operation. Amongst other developments[1 and 2], improvement in the orbit stability has been a major goal of the department, second only perhaps to the machine's operational reliability. The early part of this effort was devoted to improving and upgrading several key systems such as magnet power supply system, RF system. This contributed to a fair amount of beam stability improvement but far from the acceptable range. Next, local feedback systems[3] were implemented where each system kept the electron beam stable at the two ends of an insertion device straight section. Although, the results at these beamline met our expectations, the beam motion at bending magnet beamline user's locations was far from satisfactory.

In December 1989, a prototype analog global feedback in the UV storage ring[4] (2nd storage ring at NSLS) showed a significant improvement in beam stability. This system showed lot of promise for the X-Ray ring. A crash program was, therefore, put into effect for an operational system for the X-Ray ring. This was achieved in August 1991 with excellent results[5].

This paper presents analysis of the beam motion at all pue locations both in frequency as well as time domain and then identifies some of the sources of beam motion. Further, it tabulates beam position data quantitatively at all pue's locations.

*Work performed under the auspices of the U.S. Department of Energy under contract DE-AC02-76CH00016.

II. CHARACTERIZATION OF THE BEAM POSITION INSTABILITY

The single most important part of the beam instability is the "Orbit Drift" and is discussed in section 3. When the beam is originally centered or aligned by a dc orbit correction, an "Orbit Drift" is observed by as much as 0.5 mm horizontally and 0.2 mm vertically over the operational run of 12 to 24 hours (with no feedbacks implementation). In addition, a beam "bounce" or fast peak to peak motion about its nominal position exist which is characterized by analyzing the spectrum of the beam position. The amplitude and the frequency of the beam bounce depend on various factors and are discussed in section 4.

III. ORBIT DRIFT

Typical horizontal beam motion for an X-Ray operational run is shown at one pue location in fig. 1. This is a run of 8 hrs following a fill, where beam current decays from 200 ma to 100 ma (shown by the smooth curve). It can be seen that the majority of the drift occurs during the initial 2 to 3 hours period after the fill. The cause appears to be the coupling of the chambers to the magnet[6] due to uneven cooling. The cooling configuration of the vacuum chamber and the constriction of the vacuum chambers in the many magnets, distorts the vacuum chamber causing the main magnets to move and also the orbit as a function of the beam current.

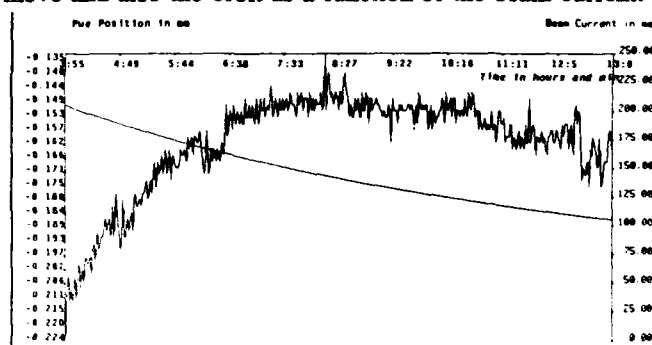


Fig. 1. Typical horizontal orbit drift at PUE 05

The orbit drifts in horizontal and vertical planes are tabulated in Table 1 at each pue location for an operation, indicating which pue is a part of local or global feedback systems. This same data is plotted in Figure 2. As expected, the least drift is noted at local feedback pue locations (shown by circled pues in figure 2), where feedbacks are implemented.

PUE #	Hor Drift (microns)	Hor Feedback	Vert Drift (microns)	Vert Feedback
3	57	-	10	-
4	38	-	26	-
5	99	Global	24	-
6	67	-	22	-
7	67	-	23	-
8	70	Global	24	Global
9	37	-	15	-
10	41	-	19	-
11	76	Global	45	-
12	48	Local(*)	46	Local(*)
13	50	Local(*)	19	Local(*)
14	85	Global	21	Global
15	57	-	28	-
16	63	-	30	-
17	68	Global	36	-
18	44	Local(*)	10	Local
19	38	Local(*)	5	Local
20	66	Global	22	Global
21	33	-	9	-
22	54	-	9	-
23	51	Global	27	-
24	39	Local(*)	17	Local(*)
25	56	Local(*)	14	Local(*)
26	84	Global	22	Global
27	68	-	24	-
28	49	-	22	-
29	42	Global	24	-
30	26	Local	7	Local
31	23	Local	8	Local
32	45	Global	24	Global
33	50	-	40	-
34	89	-	31	-
35	68	Global	24	-
36	51	-	19	-
37	46	-	29	-
38	79	Global	20	Global
39	49	-	42	-
40	50	-	47	-
41	26	Global	40	-
42	23	Local	9	Local
43	17	Local	8	Local
44	50	Global	25	Global
45	58	-	14	-
46	56	-	27	-
47	40	Global	32	-
48	17	Local	7	Local
49	20	Local	7	Local
50	41	Global	19	Global

* These local feedbacks were not implemented at the time of data taken

Table 1. Maximum orbit drift

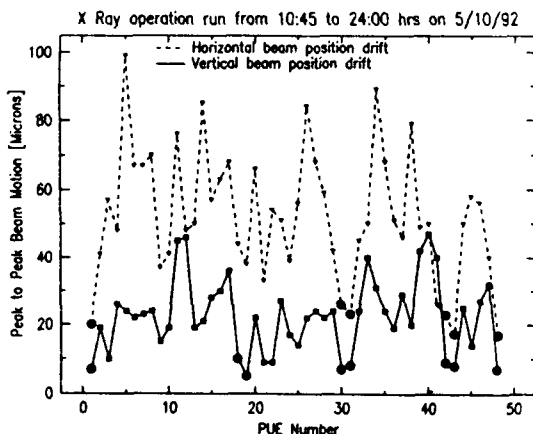


Fig. 2. Maximum orbit drift

Before the implementation of the feedback system, the orbit drifts were measured to be in the range of 200-500 microns horizontally and 50-200 microns vertically. Feedback systems reduce this motion to 17-100 microns horizontally and 7-50 microns vertically.

IV. BEAM "BOUNCE" OR FAST PEAK-TO-PEAK MOTION

Spectrum analysis of the beam motion, shown in figure 3,

reveals that there are several peaks from 0.5 hz to 500 hz, however the magnitude of these peaks depends on the external conditions. To explain, the spectrum is divided into 3 frequency ranges: a) 0.5 hz to 10 hz; b) 10 hz to 60 hz; c) 60 hz and its harmonics.

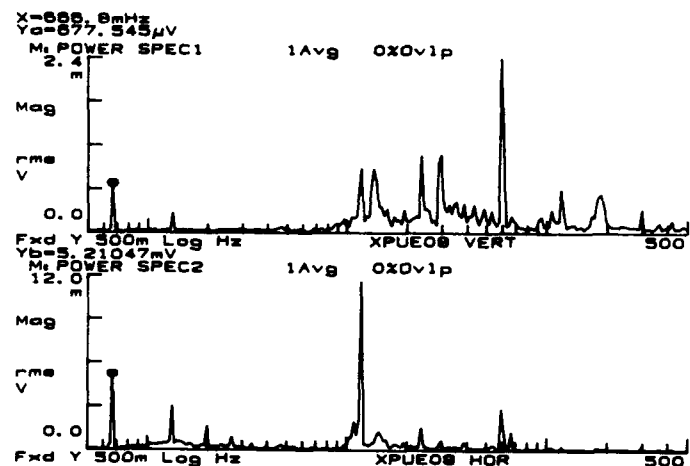


Fig. 3. Spectrum at PUE 08 - 1 mV rms ~ 5.6 microns p-p (measured on 5/3/93 - dry weather conditions)

The frequency range a) contains peaks at the fundamental frequency 0.67 hz and its harmonics which are present only when NSLS booster is on (ramp rate of 0.67 hz). This coupling occurs magnetically to the electron beam in the X-Ray ring. The figure 4 shows the horizontal displacements at the 2nd harmonic frequency (1.33 hz) due to NSLS booster, with global feedback off and on. The remaining bump towards pue 41 and 44 (with feedback on) in figure 4, tells us that this is the location where coupling occurs and where magnetic shielding should be attempted.

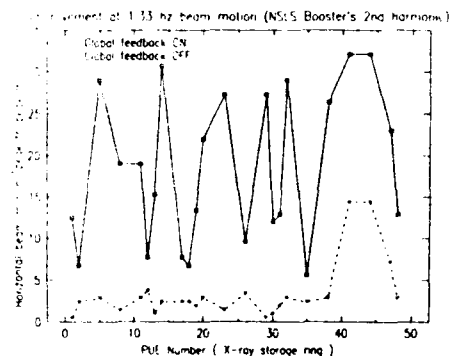


Fig. 4. Horizontal peak-to-peak beam motion at 1.33 hz.

The bounce components in the 10 hz to 60 hz range have been shown, mostly, to be related to several mechanical vibration modes of quadrupole girder support structure. After vibration evaluation[7], significant improvements in vibration reduction were achieved by performing: grout repairs on the magnet installation, removal of lead shielding from the magnet

(thus detuning the natural frequencies) and tightening the bolts holding the magnet structure. The predominant horizontal 11.89 hz peak in the bottom trace of figure 3 is excited by the action of a nearby High Flux Beam Reactor (HFBR) Helium compressor which is about 1000 feet away. Vibration measurement results[7], also show that this amplitude increases significantly (by a factor of 3 to 5) during periods of heavy rainfall. It supports the fact that transmissibility of soil vibration waves increases dramatically with moisture contents. During rainfall conditions, the amplitude at this frequency is in the range of 25 to 250 microns horizontally and 5 to 20 microns vertically. When HFBR compressor is off, the bounce component in the 10 to 60 hz frequency range is less than 50 microns horizontally and 10 microns vertically. Spectrum peaks with significant amplitudes are tabulated in table 2.

Higher frequency components occurring mainly at 60 hz and its harmonics are electrically induced, although their sources are not totally known. The amplitudes at 60 and 120 hz are given in table 2.

Figure 5 provides a typical beam motion, in time domain, at horizontal pue 8 measured during the wet conditions (4/21/91). The top trace shows the motion when both the NSLS booster and HFBR compressor are off. The middle trace shows the motion when NSLS booster is turned on with peaks occurring every 1.5 seconds. The bottom trace shows the motion with both NSLS booster and HFBR compressor on. It should be noted that p-p 11.89 hz motion in figure 5 is about 250 microns (5 boxes x 50 microns = 250 microns p-p). This motion is larger by a factor of 3.7 to that measured in figure 3 (12 mv rms x 5.6 microns/mv p-p = 67.2 microns p-p). This is due to the dry conditions that existed when the measurements were made for figure 3 (5/3/93).

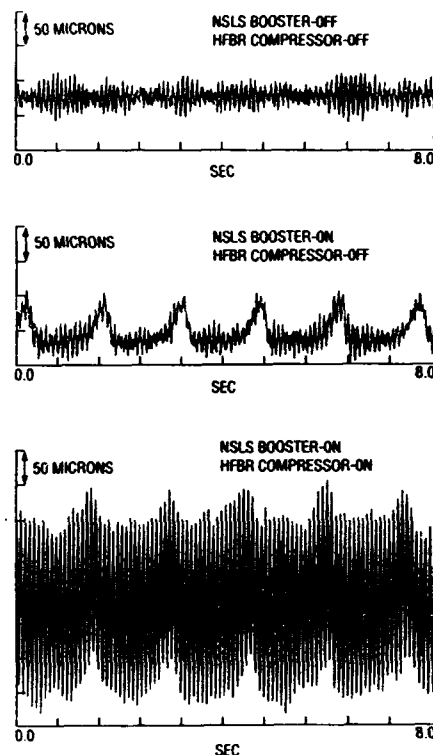


Fig. 5. Time domain beam motion at PUE 08 (measured 4/21/91 - heavy rainfall conditions)

ACKNOWLEDGEMENTS

I would like to thank Norman Fewell for his useful discussions and his comments.

REFERENCES

- [1] S. Krinsky et al., "Storage Ring Development at NSLS", AIP conference Proceedings 249 Volume 2, The Physics of Particle Accelerator.
- [2] A.M. Fauchet et al., "Lifetime, Stability and Accelerator Developments at NSLS", Nucl. Inst. and Meth. in Phys. Res., A319 (1992).
- [3] R.J. Nawrocky et al., "Automatic Steering of X-Ray beams for NSLS Insertion Devices Using Closed Local Orbit Feedback", IEEE Particle Accelerator Conference, Chicago, Ill. (1989).
- [4] L.H. Yu et al., "Real Time Closed Orbit Correction System", IEEE Particle Accelerator Conference, Chicago, Ill. (1989).
- [5] L.H. Yu et al., "Real Time Global Orbit Feedback System for NSLS X-Ray Ring", IEEE Particle Accelerator Conference, San Francisco, CA (1991).
- [6] E. Johnson, "Interim Progress on Monitoring of Beam and Water", Interim BNL memo dated 1/18/91.
- [7] Gilbert/Commonwealth, Inc. "Vibration Evaluation - Cold Neutron Facility, Helium Compressor", G/C report no. DR-05200-0414-1,3/1991.

X Ray electron beam p-p motion at various frequency (or frequency range) as measured at 48 pass around the ring					
Category	Frequency range	Horizontal (microns p-p)		Vertical (microns p-p)	
		Global fdbk off	Global fdbk on	Global fdbk off	Global fdbk on
a	0.5 Hz to 10 Hz (Booster Effect)	90-100	10-50	5-20	< 1
b	11.89 Hz (HFBR Compressor On)	25-250	10-100	5-20	2-10
	10 to 12 Hz (HFBR Compressor off)	10-50	2-10	1-5	< 1
	24.41 Hz	2-10	1-5	2-10	1-5
	29.85 Hz	2-10	1-5	2-10	1-5
	54.64 Hz	1-10	NI	< 1	NI
c	60 Hz	5-15	NI	5-15	NI
	120 Hz	1-5	NI	1-10	NI

NI - No improvement

Table 2. Peak-to-peak beam motion at various frequencies.

Test of Fast-Digital Beamline Feedback Control at the Photon Factory

Norio Nakamura and Tomotaro Katsura
KEK National Laboratory for High Energy Physics
Oho 1-1, Tsukuba-shi, Ibaraki-ken, 305 Japan

Abstract

A fast-digital feedback system stabilizing the photon beam position for a beamline was tested. A DSP (digital signal processor) board linked with 16-bit ADC and 14-bit DAC boards was used as a digital controller of the feedback system. The DSP system sampled the signals from a photon beam position monitor at a high rate of 10 kHz and set the magnet currents for a 3-magnet orbit bump steering system at the same rate. The system frequency response was easily compensated in gain and phase by programming. As a result, the feedback system well suppressed the beam motion up to 100 Hz.

I. INTRODUCTION

In the Photon Factory (PF), a local feedback system dedicated to a beamline should be so designed that it can cover a wide frequency range, because the frequency components of the photon beam motion at the beamline spread up to 100 Hz. The beam motion is caused by various disturbances such as ring building distortion due to thermal stress[1], temperature variations of the cooling water for the PF storage ring, stray magnetic field variations of the TRISTAN acceleration-deceleration cycle and floor vibrations[2].

The local feedback systems controlled by the analog circuits have been developed in many facilities[3-5] and also in the Photon Factory[6]. Although the analog controllers had a fast feedback speed, they generally had difficulty in high-level computation and easy modification of their transfer functions. Recently DSPs have made great progress in processing speed and come to be used as controllers of various fast feedback systems in place of analog circuits. In fact, a global orbit feedback system was designed by use of a DSP board[7]. Therefore we constructed a local feedback system digitally controlled by a DSP system and tested it at a beamline. In this paper, we present the feedback system and the test result.

II. SYSTEM DESCRIPTION

The feedback system is composed of a new fast-digital controller, existing photon beam position monitor, vertical steering magnets and power supplies. Figure 1 shows the block diagram of the feedback system. The controller is a DSP system (LORY ACCEL from mtu), which consists mainly of a 32-bit floating-point DSP (TMS320C30) board, a 4-channel ADC board with 16-bit resolution and an 8-channel DAC board with 14-bit resolution. The DSP board is linked with ADC and DAC boards through a DSP local bus in the system case and connected to the bus of a PC9801 microcomputer (from NEC). The photon beam position monitor[8]

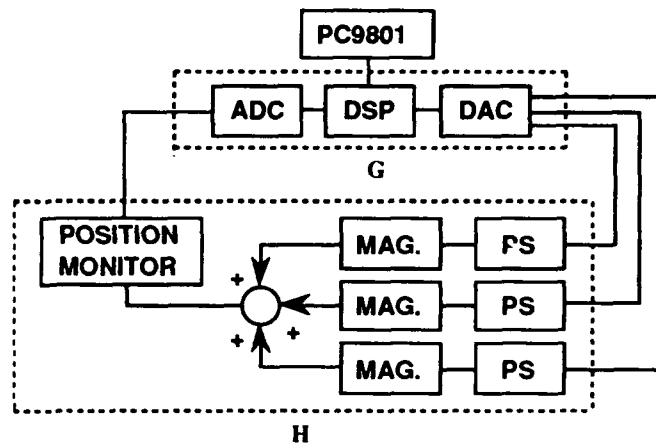


Figure 1. Block diagram of the feedback system.

is located at branch C of beamline 4 (BL-4C) and the three vertical steering magnets[9] near bending magnet 4 (BM4). The steering magnets make a closed orbit bump to cancel the beam position displacement detected by the monitor.

A control program is coded in C-language and compiled/linked with the PC9801 microcomputer, and then it is downloaded to the DSP. The feedback is switched on/off by the keyboard of the microcomputer and can be programmed. While the DSP system running, the microcomputer numerically and graphically monitors various parameters such as the photon beam position and the setting currents of the magnet power supplies. The sampling rate of the ADC data can be increased up to 10-20 kHz with normal action of the DSP system. The setting of the DAC data follows the sampling of the ADC data with a time lag of the sampling time. The upper limit of the sampling rate is basically decided by the I/O control time and also depends on the computation time. The sampling rate was set at 10 kHz during the test.

III. TRANSFER FUNCTION

The transfer function of the feedback system is divided into two components $G(z)$ and $H(z)$, which correspond to the controller and the rest including the magnets, power supplies and monitor. Although $H(z)$ is mainly dominated by eddy currents of the PF aluminium vacuum chamber, $G(z)$ is decided by the control program. Therefore the open-loop and closed-loop transfer functions of the feedback system defined by $G(z)H(z)$ and $1/(1+G(z)H(z))$ can be modified easily by programming.

The feedback system was tested for five different cases (Cases A to E) where the system has different transfer

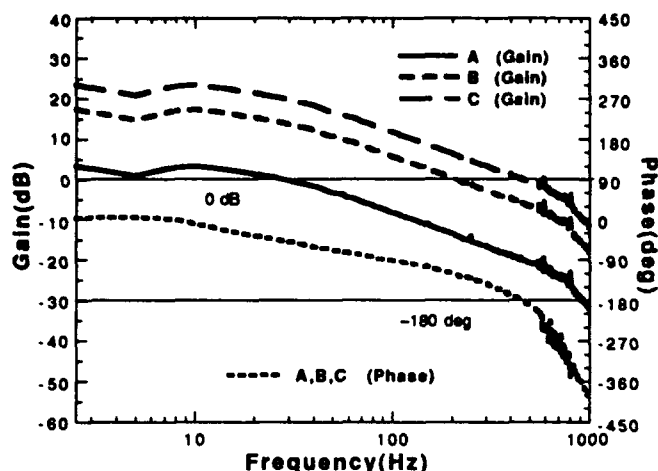


Figure 2. Open-loop frequency response curves for Cases A, B and C. In Case B and C, only the gain is compensated.

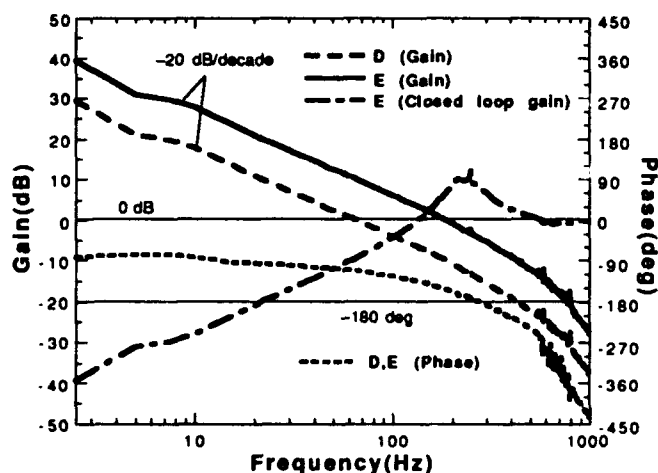


Figure 3. Open-loop frequency response curves for Cases D and E, and a closed-loop gain curve for Case E. In these cases, both the gain and phase are compensated.

functions. Figure 2 shows open-loop transfer functions for Cases A to C in terms of their frequency response curves. In Case A, the controller is programmed to simply set the currents of the power supplies which correspond to the DC bump strength cancelling the beam position displacement. In Cases B and C, a simple gain compensation is given in the control program. As a result, the system gets a higher open-loop gain by a factor of 5 (14 dB) and 10 (20 dB) than in Case A, though it still has the same phase response as in Case A. For these three cases, $G(z)$ is expressed with the frequency f and sampling time T_s ($= 100 \mu s$) for $f \ll 1/T_s$ as follows:

$$G(z) = K z^{-\frac{1}{2}} \quad (z = e^{2\pi j f T_s}). \quad (1)$$

Here j is an imaginary number ($j^2 = -1$). $K = 1$, $K = 5$ and $K = 10$ are taken for Cases A to C respectively. From this equation, the contribution of the controller to the whole transfer

function is estimated to be negligibly small (only 5.4-degree phase rotation at 100 Hz). In Case C, the open-loop gain response has no sufficient gain margin when the phase response curve crosses -180 -degree line. Therefore, the system was expected to be unstable with the loop closed.

Figure 3 shows open-loop frequency response curves for Cases D and E. In these cases, both gain and phase compensations are added to the control program. $G(z)$ is given by the following expression including two additional compensation terms:

$$G(z) = K z^{-\frac{1}{2}} G_c(z), \quad (2)$$

where

$$G_c(z) = \left\{ 1 + \frac{1+z^{-1}}{2(T_i/T_s)(1-z^{-1})} \right\} \times \frac{1 + (T_d/T_s)(1-z^{-1})}{1 + 0.1(T_d/T_s)(1-z^{-1})}. \quad (3)$$

$K = 0.0316$ and $K = 0.1$ are taken for Cases D and E. The first term with the integral time T_i ($= 100 \mu s$) in Eq. (3) has a gain curve with an approximate rate of -20 dB per frequency decade for $f \ll 1/T_i$ and improves the loop gain especially in the low frequency region. The second term with the differential time T_d ($= 5.3$ ms) suppresses the phase rotation due to $H(z)$ and the first term to guarantee sufficient gain and phase margins for the system stability. The computation time for these compensation terms is about $10 \mu s$ and much shorter than the sampling time.

IV. TEST RESULT

First the feedback loop was closed for the five different cases described in the previous section. Figure 4 shows the beam stability recorded by a chart recorder (bandwidth ~ 5 Hz) for Cases A, B, D and E. In Case A, the beam stabilization by the feedback system was clearly found to be incomplete. In Case B, the system gave better beam stability than in Case A, but the performance was not yet enough. The system in Case C became unstable as expected in the previous section. On the other hand, the system in both Cases D and E nicely suppressed the beam motion within a few μm . The good performance is produced by the high loop gain especially in the low frequency region.

Next the frequency spectra of the monitor signal were measured for Case E before and after the feedback loop was closed. In Case E, the system has the best transfer function, because it almost keeps the highest loop gain from 0 to 100 Hz without losing the system stability. Figure 5 shows the various frequency components with the loop open and closed. From this figure, the system was found to significantly suppress the frequency components peaking from 0 to 100 Hz. The 14.5 Hz component was reduced by ~ 24 dB and the 50 Hz component by ~ 12 dB. This was in good agreement with the closed-loop gain curve of the system for Case E shown in Figure 3.

V. CONCLUSIONS AND FURTHER DEVELOPMENT

The local feedback system controlled by the DSP system successfully stabilized the beam motion up to 100 Hz. The gain and phase compensations improving the beam stability could easily be added and modified. These facts mean that the feedback system has both good feedback performance and flexibility. However, further development must be done to use such a system for actual operation at some beamlines. The values of the compensation parameters T_i and T_d in Eq. (3) were properly chosen but not fully optimized. Further optimization will improve the feedback performance. The monitoring of interlock signals related to the system is also required for automatic feedback on/off. In addition, the DSP system should be applied to a 4-magnet orbit bump steering system with two position monitors to stabilize both the position and direction of the beam at a light source point.

VI. ACKNOWLEDGEMENTS

The authors would like to thank Dr. K. Haga, Dr. T. Mitsuhashi and Dr. T. Honda for the tuning and calibration of the position monitor.

VII. REFERENCES

- [1] K. Huke, "Low emittance and positron storage operation at the Photon Factory", *Rev. Sci. Instrum.*, 60, 1382 (1989).
- [2] K. Huke, "Correlation between the movement of the Light Source building and the vibration of the synchrotron radiation axis", *Jpn. J. Appl. Phys.*, 26, 285 (1987).
- [3] R. O. Hettel, "Beam steering at the Stanford Synchrotron Radiation Laboratory", *IEEE Trans. Nucl. Sci.* NS-30, No. 4, 2228 (1983).
- [4] R. J. Nawrocky, J.W. Biuner, Li Ma, H. M. Rarback, D. P. Siddons and L. H. Yu, "Automatic steering in the NSLS storage rings using closed orbit feedback", *Nucl. Instrum. Methods* A266, 164 (1988).
- [5] W. Brefeld, "Stabilization of synchrotron radiation beam at HASYLAB", *Rev. Sci. Instrum.*, 60, 1513 (1989).
- [6] T. Katsura, Y. Kamiya, K. Haga, T. Mitsuhashi, and R. O. Hettel, "Beam position monitoring and feedback steering system at the Photon Factory", *Proceedings of 13th International Conference on High Energy Accelerators*, Vol. 2, pp. 243-246 (1988).
- [7] D. Bulfone, A. Carniel, J-C. Denard, F. Iazzourene, R. Richter and A. Wrulich, "Design consideration for the ELETTRA beam position feedback system", *Proceedings of the 2nd European Particle Accelerator Conference*, pp. 895-897 (1990).
- [8] T. Mitsuhashi, K. Haga, and T. Katsura, "Construction of a synchrotron radiation position monitor by means of X-ray photoemission", *Proceedings of the 1987 IEEE Particle Accelerator Conference*, pp. 576-578.
- [9] T. Katsura, Y. Kamiya, K. Haga, T. Mitsuhashi, N. Nakamura, M. Katoh, and I. Abe, "Beam position stabilization at the Photon Factory", *Rev. of Sci. Instrum.*, 60, 1507 (1989).

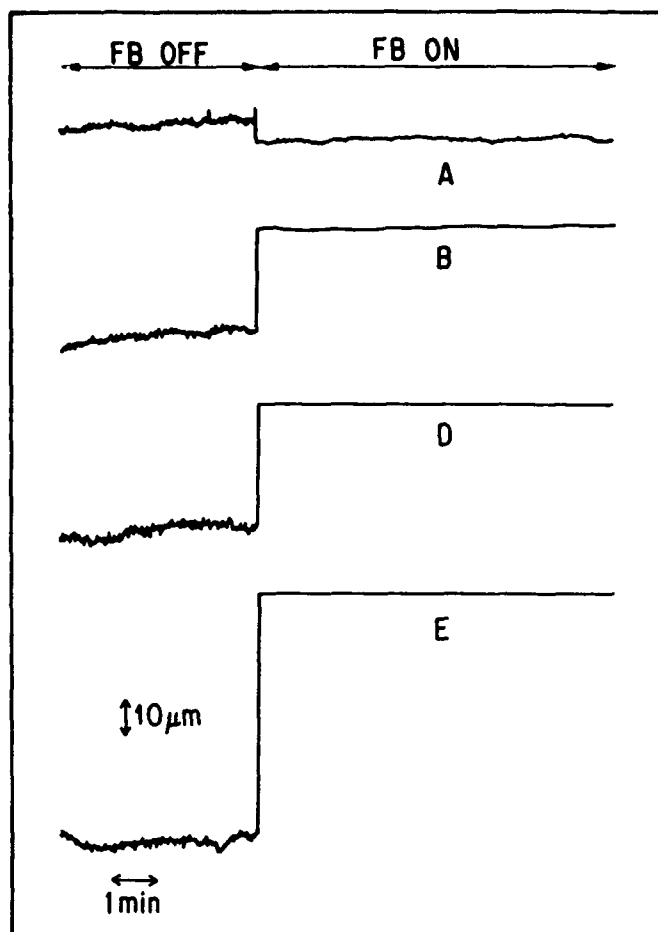


Figure 4. Typical chart recording without and with feedback for Cases A, B, D and E. In Case C, the system became unstable with feedback.

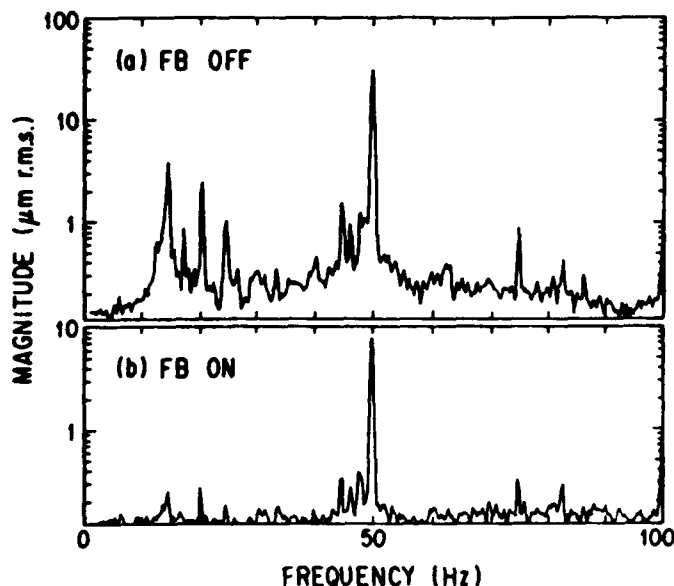


Figure 5. Frequency spectra of the position monitor signal without and with feedback for Case E.

Horizontal Movement of the Storage Ring Floor at the Photon Factory

Tomotaro KATSURA, Hajime NAKAMURA, Yukihide KAMIYA* and Yutaka FUJITA⁺

Photon Factory, National Laboratory for High Energy Physics, KEK,

**The Institute for Solid State Physics, The University of Tokyo,*

and ⁺Shimizu Corporation, JAPAN

Abstract

At the Photon Factory, the storage ring with an elliptic shape varies its size due to heat generated from many accelerator components and beamline instruments packed in the ring building as well as due to solar irradiation and atmospheric heat. We continuously measured the major axis length of the ring with a laser interferometer, and also measured temperatures at the building roof slab and on two floors of ring tunnel and experimental hall. It was found that the long-term variation in the major axis length is well reproduced by a computer simulation.

1. INTRODUCTION

The storage ring floor of the Photon Factory had been earlier reported to move both horizontally and vertically due to the external thermal stress on the building roof and walls. The vertical floor displacement was measured with a hydrostatic level measuring system [1]. On the other hand, the horizontal and diurnal floor movement was evaluated from the variations in the circumference and also in the major axis of the storage ring [2]. The circumference variation was given in terms of the RF frequency required to sustain the central orbit, while the major axis was measured with a system of laser interferometer.

However, it was found that there may be other sources of thermal stress which cause the ring building to be largely distorted [2]. Further accumulation of data for several months has made it clear that the floor movement is more precisely described by including internal thermal loads on the ring floor and experimental floor: the internal thermal loads may come mostly from the accelerator components such as ring magnets and cooling water pipes, and partly from the beamline components.

To ascertain that both external and internal thermal loads actually give rise to the major axis variation, we first calculated the expansion rate of the major axis to a unit thermal load (1°C temperature rise of structure) imposed on each of the roof slab, experimental hall floor and ring tunnel floor, three different parts of the building structure, where the measurement of temperature had also been made. Using the expansion rates, we next reconstructed the major axis variation from the measured temperatures. Indeed, the reconstructed variation in the major axis has a good agreement with the measured one, the data taken by the laser interferometer system.

2. MEASUREMENT OF MAJOR AXIS

The Photon Factory storage ring has an elliptic shape with a circumference of about 187 m. Its major axis of ellipse is about 68 m and the minor axis 50 m. Figure 1 shows a plan view of the storage ring building composed of the ring tunnel and the experimental hall. Since October 1991, the length variation in the major axis was being measured with the laser interferometer system, as illustrated in Fig. 1 (the overall measurement error of the laser system was estimated to be less than several microns [2]). At the same time, temperature data

were taken on the building roof with thermocouples and also on the floors of both ring tunnel and experimental hall with thermistors.

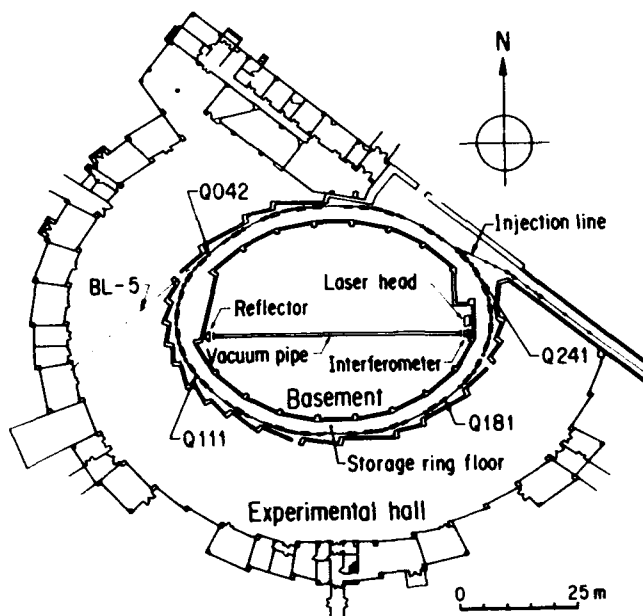


Figure 1. Plan view of the storage ring building of the Photon Factory; the ring tunnel and experimental hall. Also illustrated in the figure is the measurement system of the major axis length, which consists of a laser interferometer, vacuum pipe and reflector.

Figure 2 shows two typical examples of these measured data; one is data taken on February 29 to March 6 in 1992 (Data A) and the other on June 26 to July 7 (Data B). The roof temperature T_r is the average of the temperatures measured on the upper and lower surfaces of the roof slab. Filtered data denoted in the figure are "low-pass filtered" data in which short-term fluctuations with a period of less than a few days are filtered out, and the filtered. The filtered data of T_s and T_e in the figure are those of the averaged temperatures. For Data A, the ring first expanded and then contracted with the major axis variation of about $200\text{ }\mu\text{m}$. The data imply that the major axis variation tends to follow the temperature variations in the roof (coming from external thermal loads) and in the ring floor (mainly coming from internal loads), but that it is insensitive to the temperature at the experimental hall. On the other hand, in the latter half part of Data B the major axis variation seems to correspond to the temperature rise of the experimental hall.

3. SIMULATION

A computer simulation based on a finite element method has been carried out to evaluate the expansion of the major axis to unit thermal loads that are individually imposed on the roof slab and two floors of ring tunnel and experimental hall.

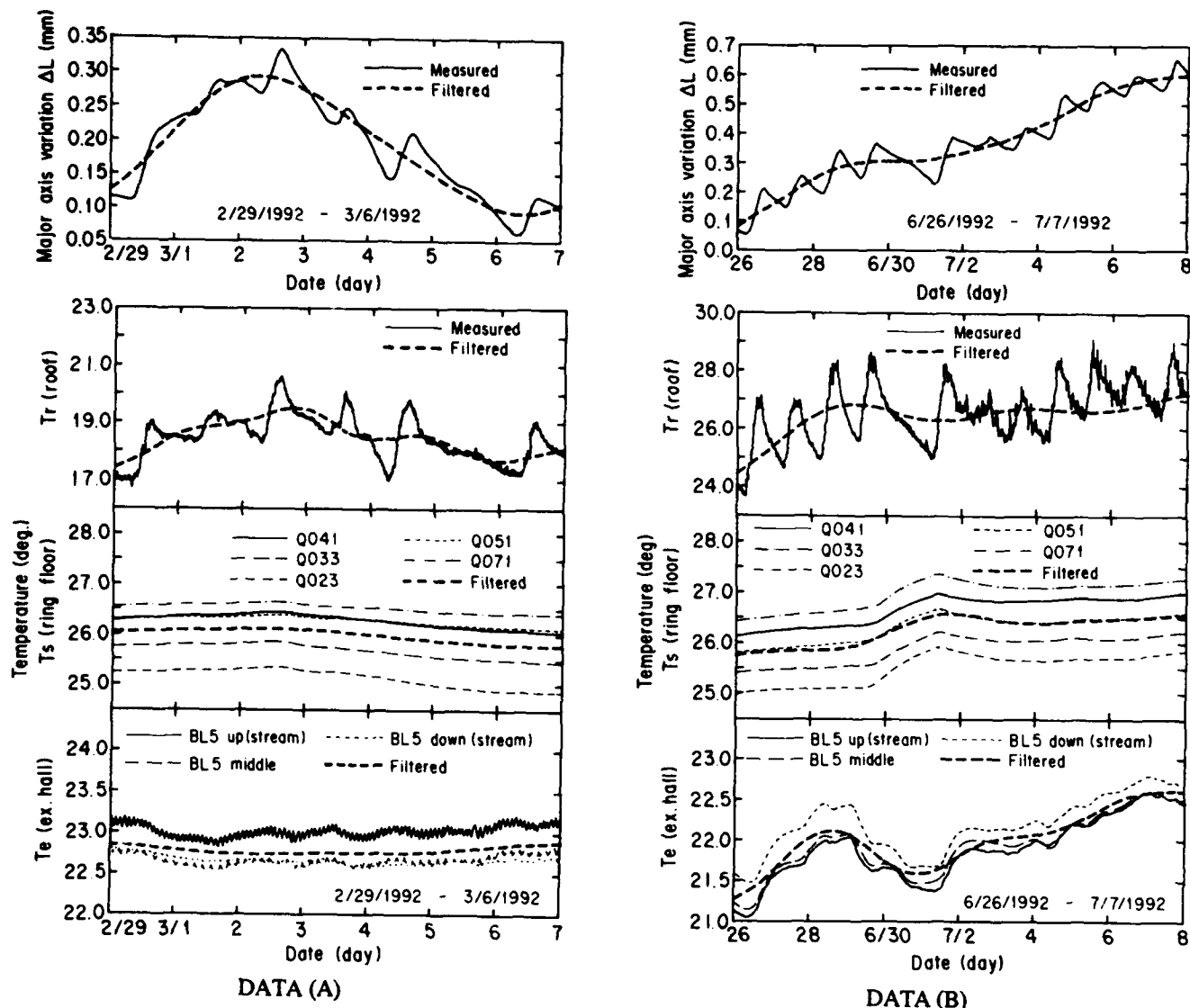


Figure 2. Variation in the major axis and temperatures in three different parts of the building structure. The T_s , T_r and T_e denote the temperatures at the storage ring floor, the roof and the experimental hall floor, respectively.

The structure modeling for simulation is already described in Reference [1] and [2]. Thereafter, the expansion rate of the major axis to a unit load is called thermal weighting factor. The result of simulation is shown in Fig. 3, where the ring expansion due to thermal loads is exaggeratedly depicted. As seen in the figure, the major axis of the ring is more susceptible to the temperature variation in the ring tunnel than in the other two.

Table 1 Thermal weighting factors of the major axis expansion

locations	weighting factors [$\mu\text{m}/^\circ\text{C}$]
Ring floor (C1)	220
Roof (C2)	86.7
Exp. floor (C3)	37.3

The thermal weighting factors defined above, which we can calculate from the simulation, are listed in Table 1. Hence the variation in the major axis may be written as,

$$\Delta L = C_0 + C_1 T_s + C_2 T_r + C_3 T_e, \quad (1)$$

where the C_0 is a constant to adjust the data offset and the other C 's are given in Table 1.

4. COMPARISON

To compare the measured variations in the major axis with the ones calculated using the temperatures at three different parts of the building structure, the following procedures were taken:

- (1) We take the average of temperatures measured at three points along a beamline in the experimental hall (see Fig. 2), and assume that the temperatures in the whole experimental hall be represented by the average. Similarly, we also take the average of temperatures measured at several points of the ring tunnel.
- (2) Then, all data, the measured variation in the major axis and the temperatures of the roof, experimental hall and ring tunnel, are low-pass filtered as described in Sec. 2, because we are mainly interested in a long-term behavior of the building distortion in this paper.

- (3) Finally, we substitute three filtered data of temperature into Eq. (1) to obtain an estimate of the major axis variation.

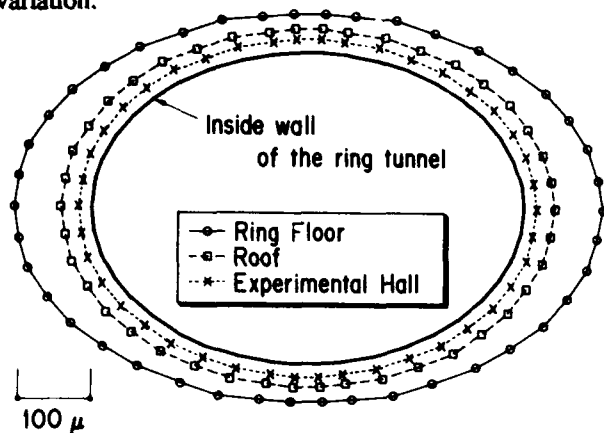


Figure 3. Simulated horizontal displacements of the storage ring for unit thermal loads, which are separately applied to three different parts of the building structure; roof, experimental hall floor and the ring tunnel floor.

Figure 4 shows the measured and calculated variations ΔL in the major axis of the ring for the same periods of time as in Fig. 2. The calculated ΔL well agrees with the measured one, though there is still a little amount of fluctuation in the calculated ΔL . We have also made a similar comparison for raw data of temperature, which is not presented here. In this case, not-filtered fluctuations of temperature, that is, diurnal and more rapid ones, directly reflect on the calculated ΔL , whereas raw data of the major axis have an amplitude of diurnal or rapid fluctuation by a factor of two or more smaller than the calculated one. This is probably because the true average of the roof temperatures is not accurately represented by the averaged data T_r , which include largely changeable temperature on the upper surface of roof. However, it is clear that the above procedures are valid enough to investigate long-term variations.

In conclusion, the long-term variation in the major axis length of the Photon Factory storage ring was well reproduced by a computer simulation using the measured temperatures, and it was found that both external and internal thermal loads give rise to the building distortion. As early reported, the long-term as well as short-term distortions of the ring closed orbit, whatever their cause is, have already been suppressed by an orbit feedback system. Since the Photon Factory ring is a second-generation synchrotron light source, however, both thermal loads may seriously affect the performance of a third-generation light source.

5. SUMMARY

The following is a summary of the results obtained from the above-mentioned measurement and analysis:

- (1) Thermal weighting factors of three different structure parts of the ring building were evaluated using a computer simulation model. The simulation showed that the weighting factor of the ring tunnel floor has a larger value than the other two, though the temperature itself is more stable at the tunnel floor.
- (2) Since the measurement of temperature is limited to some localized places in the whole building, there

might be some unknown sources that greatly affect the variation in the major axis. The measured variations in the major axis length, however, showed a good agreement with the calculated ones that were calculated only using three temperature data and the weighting factors evaluated from a computer simulation. Thus we may conclude that the temperature variations in three kinds of structure parts of the building, that is, roof, experimental hall and ring floor, are major sources for horizontal movement of the Photon Factory storage ring building.

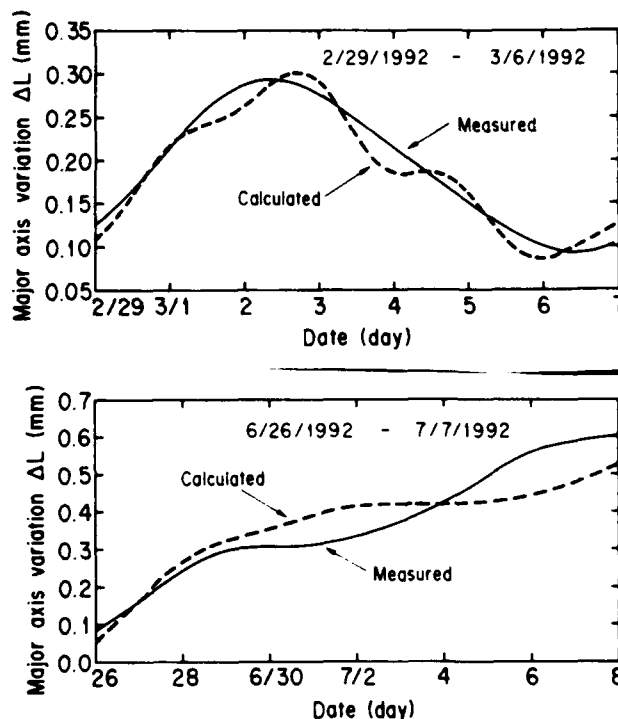


Figure 4. Measured and calculated variations of the major axis. Note that filtered data are treated here.

6. ACKNOWLEDGMENTS

Part of this work was supported by a collaboration program between National Laboratory for High Energy Physics and the Nuclear Power Division, Shimizu Corporation.

The authors sincerely thank Prof. H. Kobayakawa, Director of the Light Source Division of the Photon Factory for his useful advice and suggestions, and to the staff of the Division who kindly helped them to carry out the measurements. They are greatly indebted to the staff of the Nuclear Power Division, Shimizu Corporation for their valuable support. And one of the authors, Y. K., also thanks all staff of Synchrotron Radiation Laboratory, ISSP, Tokyo University for their support.

7. REFERENCES

- [1] T. Katsura and Y. Fujita, *Rev. Sci. Instrum.* 62(11), p.2550 (1991); T. Katsura et al., *Proc. of the 1991 IEEE PAC, San Francisco*, p.2682.
- [2] T. Katsura et al., *Proc. of the 3rd European Part. Accel. Conf., Berlin, Mar., 1992*.

Closed Orbit Correction Using Singular Value Decomposition of the Response Matrix*

Y. Chung, G. Decker, and K. Evans, Jr.
Argonne National Laboratory, Argonne, IL 60439

Abstract

A theory of global orbit correction using the technique of singular value decomposition (SVD) of the response matrix and simulation of its application to the Advanced Photon Source (APS) storage ring are presented. The response matrix relates beam motion at the beam position monitor (BPM) locations to changes in corrector magnet strengths. SVD reconfigures the BPMs and correctors into the same number of "transformed" BPMs (t-BPMs) and "transformed" correctors (t-correctors), each t-BPM being coupled to at most one t-corrector and vice versa with associated coupling strength which determines the efficiency of orbit correction. The coefficients of these linear transformations can be used to determine which BPMs and correctors are the most effective. Decoupling the weakly coupled pairs will enhance the overall correction efficiency at the expense of accuracy. The orbit errors at decoupled t-BPMs are conserved and the strengths of decoupled t-correctors can be adjusted appropriately to optimize the actual corrector strengths. This method allows for estimating the limitation on orbit correction with given sets of BPMs and correctors, as well as optimizing the corrector strengths without overloading the corrector magnet power supplies.

I. INTRODUCTION

The third generation synchrotron light sources, of which the Advanced Photon Source (APS) is one, are characterized by low emittance of the charged particle beams and high brightness of the photon beams radiated from insertion devices. Transverse stability of the particle beams is a crucial element in achieving these goals and the APS will implement extensive beam position feedback systems, which include 320 corrector magnets, 360 positron beam position monitors (BPMs) distributed around the storage ring, miniature BPMs for insertion device beamlines, and photon beam position monitors in the front end of X-ray beamlines.

The beam position feedback systems can largely be divided into the global and local feedback systems according to the extent of correction, and the DC and AC feedback systems according to the bandwidth of correction.

In this work, we will concentrate on the theory of DC global orbit correction and its application to the APS storage ring. We will show that the global response matrix relating the beam motion at selected BPMs and changes in steering

corrector strengths can be transformed into a diagonal matrix. The mechanism of this transformation is provided by the technique of singular value decomposition (SVD)[1-3] of matrices. Each diagonal element represents the correction efficiency of an orbit correction channel and the channels are independent of one another. The AC global orbit correction is then equivalent to a combination of the DC global correction algorithm and multiple non-interacting feedback systems. The analysis of a single-channel feedback system in frequency and time domains is treated in Ref. [4].

II. THEORY

Let us consider M BPMs and N correctors used for closed orbit correction in the storage ring. The i -th BPM has beta and phase functions (β_i, ψ_i) , and similarly, the j -th corrector has (β_{cj}, ψ_{cj}) . The response matrix R_{ij} corresponding to the beam motion at the i -th BPM per unit angle of kick by the j -th corrector is then given by [5]

$$R_{ij} = \frac{\sqrt{\beta_i \beta_{cj}}}{2 \sin \pi \nu} \cos(|\psi_i - \psi_{cj}| - \pi \nu). \quad (1)$$

ν is the betatron tune of the machine. The response matrix R_{ij} can be obtained from measurements by reading beam position changes while varying the corrector strengths one by one.

A. SVD Formalism

With the response matrix R thus obtained, we write R as a product of three matrices U , W , and V as [1]

$$R = U \cdot W \cdot V^T, \quad (2)$$

where U is an $M \times M$ unitary matrix ($U^T \cdot U = U \cdot U^T = 1$), W is an $M \times N$ diagonal matrix with positive or zero elements, and V is an $N \times N$ unitary matrix ($V^T \cdot V = V \cdot V^T = 1$). M is the number of BPMs and N is the number of correctors. This decomposition is unique only to a certain extent, and there are other ways of decomposing the matrix R . [2, 3]

Let us denote by Δx the global orbit change due to the corrector strength change $\Delta \theta$ and define

$$\Delta x' = U^T \cdot \Delta x \quad \text{and} \quad \Delta \theta' = V^T \cdot \Delta \theta. \quad (3)$$

Then, from Eqs. (2) and (3) we have

$$\Delta x' = W \cdot \Delta \theta'. \quad (4)$$

*Work supported by the U.S. Department of Energy, Office of Basic Energy Sciences, under Contract No. W-31-109-ENG-38.

Equation (3) is the rule of transformation for the BPMs and correctors. $\Delta x'$ and $\Delta \theta'$ are the vectors in the transformed BPM (t-BPM) space and transformed corrector (t-corrector) space, respectively. The columns of the matrices U and V are the orthogonal basis vectors $\{u_i\}$ and $\{v_j\}$. The elements of the matrix W is given by

$$W_{ij} = w_{\min(i,j)} \delta_{ij}. \quad (5)$$

We call these diagonal elements w_n (≥ 0 , $1 \leq n \leq \min(M, N)$) eigenvalues, which represent the coupling efficiency between the t-BPMs and t-correctors. The matrix R is singular if any of the eigenvalues are equal to zero. The basis vectors are related through the relation

$$R \cdot v_n = w_n u_n, \quad 1 \leq n \leq \min(M, N) \quad (6)$$

B. Matrix Inversion and Orbit Correction

Let Δx be the orbit error given by the difference between the reference orbit x_r and the current orbit x_m . That is,

$$\Delta x = x_r - x_m. \quad (7)$$

In order to bring the orbit to the reference orbit, we need to calculate $\Delta \theta$ such that

$$R \cdot \Delta \theta = \Delta x. \quad (8)$$

In case such solutions do not exist, we want the solution that minimizes the difference $|R \cdot \Delta \theta - \Delta x|$. SVD provides this solution as

$$\Delta \theta = R_{\text{inv}} \cdot \Delta x, \quad (9)$$

where

$$R_{\text{inv}} = V \cdot W_{\text{inv}} \cdot U^T. \quad (10)$$

W_{inv} is a diagonal matrix of dimension $N \times M$ and the elements are given by

$$W_{\text{inv},ij} = q_{\min(i,j)} \delta_{ij}, \quad (11)$$

where

$$q_n = \begin{cases} 0, & w_n \leq \epsilon w_{\max} \\ \frac{1}{w_n} & \text{otherwise.} \end{cases} \quad (1 \leq n \leq \min(M, N)) \quad (12)$$

ϵ is the singularity rejection parameter in the range $[0, 1]$. This parameter is determined primarily by the orbit correction needs and the corrector strength limits. Zero q_n 's correspond to decoupled channels which do not contribute to orbit correction.

When $\epsilon = 0$, all the non-zero eigenvalues are retained and the most accurate correction will result. However, this will require very robust power supplies for the correctors. On the other hand, if $\epsilon = 1$, R_{inv} is a null matrix and there will be no

orbit correction. Usually, ϵ is set to the smallest value such that none of the power supplies saturates.

For a given matrix R , we define $\epsilon_m(R)$ as

$$\epsilon_m(R) = \max \{ \epsilon \mid w_n > \epsilon w_{\max} \text{ for all } w_n \neq 0 \}. \quad (13)$$

That is, ϵ_m is the largest possible value for ϵ in order to retain all non-zero eigenvalues. The inverse matrix R_{inv} satisfies

$$R \cdot R_{\text{inv}} \cdot R = R \quad (\epsilon \leq \epsilon_m) \text{ and } R_{\text{inv}} \cdot R \cdot R_{\text{inv}} = R_{\text{inv}} \quad (\text{for all } \epsilon). \quad (14)$$

C. Minimization of Orbit Error

Orbit correction when the number of BPMs M is not larger than the number of coupled channels C ($\leq \min(M, N)$) is trivial since the solution that satisfies Eq. (8) always exists. Let us now consider the case when M is larger than C , the maximum number that does not saturate the corrector strengths, and let Δx be the initial orbit error. Then the new difference orbit $\Delta x'$ after applying the correction $\Delta \theta$ given by Eq. (9), using Eqs. (2) and (3), is

$$\Delta x' = (1 - R \cdot R_{\text{inv}}) \cdot \Delta x = U \cdot (1 - W \cdot W_{\text{inv}}) \cdot U^T \cdot \Delta x, \quad (15)$$

or, in the t-BPM space,

$$\Delta x'' = U^T \cdot \Delta x' = (1 - W \cdot W_{\text{inv}}) \cdot \Delta x'. \quad (16)$$

Since the transformation conserves vector norm, Eq. (16) gives

$$|\Delta x'| = |\Delta x''| = \left(\sum_{i=C+1}^M |\Delta x'_i|^2 \right)^{1/2}. \quad (17)$$

In Eq. (17), the position error $\Delta x'_i$ is reduced to zero for the coupled t-BPMs ($1 \leq i \leq C$) after correction, while it is conserved for the decoupled t-BPMs ($C + 1 \leq i \leq M$). Therefore, the orbit error cannot be reduced further than given by Eq. (17) unless C is increased by, e.g., optimizing the corrector strengths. This is also proven by showing that the corrector strengths are not changed any more. From Eq. (14),

$$\Delta \theta' = R_{\text{inv}} \cdot \Delta x' = (R_{\text{inv}} - R_{\text{inv}} \cdot R \cdot R_{\text{inv}}) \cdot \Delta x = 0. \quad (18)$$

Particularly, with C equal to N , Eq. (17) is the absolute minimum beyond which no further orbit correction is possible by any method. However, in reality, error in the measurement of the response matrix R , changes in the machine condition, and external perturbations cause residue in the closed orbit error. Correction of this error is done by AC orbit correction with appropriate bandwidth.

D. Optimization of Correctors

When the number of correctors N is larger than C , the number of coupled channels, the correctors can then be optimized in various ways. Between successive corrections of the closed orbit, some of the correctors can be close to saturation, thus preventing any further corrections. In this

case, if N is larger than C , the decoupled t-correctors can be used to relieve those correctors.

Let V_s be the submatrix of V that corresponds to the decoupled t-correctors. That is,

$$V_{sij} = V_{ij+C}. \quad (1 \leq i \leq N, 1 \leq j \leq N-C) \quad (19)$$

The desired corrector strengths change, $\Delta\theta_s$, is transformed in the subspace of t-correctors spanned by the corrector basis vectors v_j ($C+1 \leq j \leq N$) and then inverse-transformed. The resulting $\Delta\theta'_s$ given by

$$\Delta\theta'_s = V_s \cdot V_s^T \cdot \Delta\theta_s \quad (20)$$

will then be the closest to the $\Delta\theta_s$ while disturbing the orbit the least. As a special case, when $\Delta\theta_s = 0$, we have

$$|\Delta\theta| = |\Delta\theta'| = \left(\sum_{j=1}^C |\Delta\theta'_j|^2 \right)^{1/2} \quad (21)$$

since $\Delta\theta'_j = 0$ for the decoupled t-correctors ($C+1 \leq j \leq N$). That is, $|\Delta\theta|$ given by Eq. (21) is the minimum value possible. Particularly, when $C = N$, it is the absolute minimum among all solutions that satisfy Eq. (8).

In a similar manner, if θ is the current corrector strengths, θ' given by

$$\theta' = R_{inv} \cdot R \cdot \theta. \quad (22)$$

will minimize the overall corrector strengths. In case $N > C$, further optimization can be done by applying Eq. (20).

III. ANALYSIS OF THE APS STORAGE RING

In this section, we will analyze global orbit correction for the APS storage ring in the vertical plane. There are 40 sectors in the machine and each sector has nine BPMs (total 360) and eight correctors (total 320) available for global orbit correction. The distribution of BPMs and correctors is identical for all sectors.

Figure 1 shows the plot of the BPM basis vectors U_{i1} and U_{i2} as functions of the BPM index i . These vectors are mutually orthogonal and correspond to the largest eigenvalues w_1 and w_2 equal to 1.140×10^3 m/rad. They also have the same frequency as the integer tune ($\nu_v = 14.2987$) of the machine, which means that perturbation with the harmonic number 14 can be corrected the most efficiently. The first two corrector basis vectors V_{j1} and V_{j2} show similar behavior.

Figure 2 shows the eigenvalues w_n ($1 \leq n \leq 320$) in descending order when all BPMs and correctors are used. The maximum and minimum values are 1.140×10^3 and 9.126×10^{-2} ($\epsilon_m = 8.005 \times 10^{-5}$) in units of m/rad, respectively. The machine periodicity is exhibited in the discontinuous changes of w_n at every 40. The large decrease at $n = 240$ indicates that 80 of the correctors are redundant and therefore do not contribute much to orbit correction. These correctors have the smallest values of the function

$$E(j) = \sum_n w_n V_{jn}^2. \quad (1 \leq j \leq 320) \quad (23)$$

When those correctors are removed, ϵ_m becomes 6.656×10^{-4} .

The function $E(j)$ is a measure of the efficiency of the j -th corrector. A similar function can be defined for the BPMs and these functions can be used to select a subset of BPMs and correctors with the condition that ϵ_m be maximized.

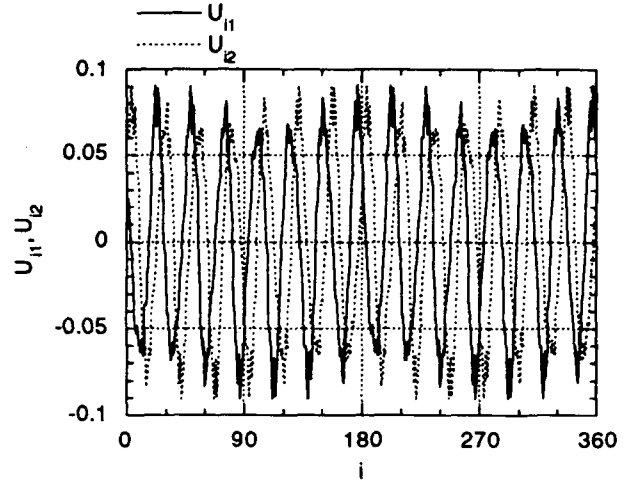


Fig. 1: The BPM basis vectors U_{i1} and U_{i2} ($1 \leq i \leq 360$) for the most strongly coupled channels ($w_1 = w_2 = 1.140 \times 10^3$ m/rad) in the vertical plane ($\nu_v = 14.2987$) for the APS storage ring.

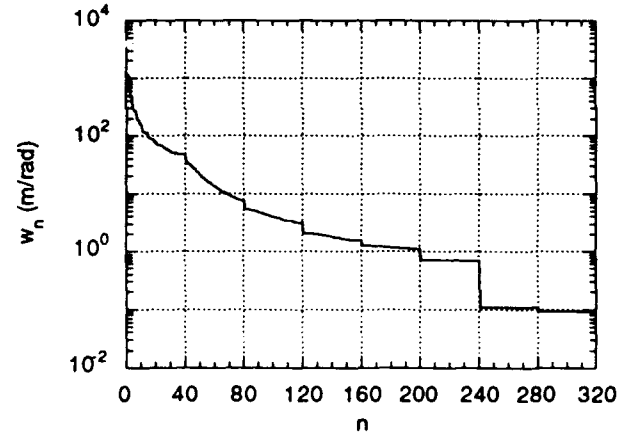


Fig. 2: Plot of the eigenvalues in descending order for the APS storage ring. $M = 360$, $N = 320$. $\epsilon_m = 8.005 \times 10^{-5}$.

IV. REFERENCES

- [1] *MATLAB™ User's Guide*, The Mathworks, Inc., p. 3-178, 1990.
- [2] W. Press et al., *Numerical Recipes in C*, Cambridge University Press, p. 60, 1989.
- [3] *Mathematica™*, Wolfram Research, Inc., p. 454, 1988.
- [4] Y. Chung, L. Emery, and J. Kirchman, "Compensation for the Effect of Vacuum Chamber Eddy Current by Digital Signal Processing for Closed Orbit Feedback," these proceedings.
- [5] M. Sands, "The Physics of Electron Storage Rings - An Introduction," SLAC-121, 1970.

Compensation for the Effect of Vacuum Chamber Eddy Current by Digital Signal Processing for Closed Orbit Feedback*

Y. Chung, L. Emery, and J. Kirchman
Argonne National Laboratory, Argonne, IL 60439

Abstract

The Advanced Photon Source (APS) will implement both global and local beam position feedback systems to stabilize the particle and X-ray beams. The relatively thick (1/2") aluminum storage ring vacuum chamber at corrector magnet locations for the local feedback systems will induce significant eddy current. This will reduce the correction bandwidth and could potentially destabilize the feedback systems. This paper describes measurement of the effect of the eddy current induced in the APS storage ring vacuum chamber by a horizontal/vertical corrector magnet and its compensation using digital signal processing at 4 kHz sampling frequency with proportional, integral, and derivative (PID) control algorithm for closed orbit feedback. A theory of digital feedback to obtain the linear system responses and the conditions for optimal control will also be presented. The magnet field in the vacuum chamber shows strong quadrupole and sextupole components varying with frequency, in addition to significant attenuation and phase shift with bandwidth (-3 dB) of 20 Hz for horizontal and 4 Hz for vertical fields relative to the magnet current. Large changes in the magnet resistance and inductance were also observed, as the result of reduced total magnetic energy and increased Ohmic heat loss.

I. INTRODUCTION

In the APS storage ring, an extensive beam position correction system will be implemented comprised of many corrector magnets (318 total) and beam position monitors (BPMs) monitoring the positions of the positron and photon beams. The AC corrector magnets, which will correct beam motion of up to 100 μ rad at 25 Hz, induce eddy current in the relatively thick (1/2") aluminum vacuum chamber of the storage ring for the local beam position feedback systems. This results in significant attenuation and phase shift of the magnet field even at frequencies as low as 5 Hz. The global orbit feedback system uses a thin stainless steel chamber and is not significantly affected by the eddy current effect.

In order to avoid the problems characteristic of analog circuits, e.g., drift, offset, and sensitivity to temperature change, we used digital signal processing (DSP) and closed loop feedback to control the magnet field in the vacuum chamber. A prototype of the storage ring sextupole magnet was used in this work, which has geometry similar to that of the six-pole horizontal/vertical corrector magnet. The effect

of the eddy current in the 0.025"-thick magnet laminations was measured and found to be negligibly small in a previous work. [1]

This paper will be largely divided into two parts. In the first part, we will overview Z-transform and theory of digital signal processing and in the second part, we will present measurement of eddy current effect and its compensation using a digital filter and closed loop feedback. [2, 3]

II. DIGITAL SIGNAL PROCESSING

In this section, theory of closed loop feedback using digital signal processing based on Z-transform [2] will be discussed.

A. Digital Filters

Given a discrete input sequence $\{x_n\}$ sampled at every $T (= 1/F_s)$, a digital filter produces an output sequence $\{y_n\}$ given by the difference equation

$$y_n = \sum_{k=0}^M a_k x_{n-k} - \sum_{k=1}^L b_k y_{n-k}, \quad (1)$$

where $\{a_k\}$ and $\{b_k\}$ are the filter coefficients. F_s is called the sampling frequency. The filter takes M previous inputs plus the current one and L previous outputs, and therefore, the filter is physically realizable or causal. Performing a Z-transform on Eq. (1), we obtain

$$Y(z) = H(z)X(z), \quad (2)$$

where $X(z)$ and $Y(z)$ are the Z-transforms of $\{x_n\}$ and $\{y_n\}$ and $H(z)$ is the filter function given by

$$H(z) = \frac{\sum_{k=0}^M a_k z^{-k}}{1 + \sum_{k=1}^L b_k z^{-k}}. \quad (3)$$

With $z = e^{-i\lambda}$ and $\lambda = \pi f/F_s$, the Z-transform is the digital analog of the Fourier transform.

The inverse of the filter $H(z)$ in Eq. (3) can be written as

$$\frac{1}{H(z)} = \frac{1}{a_0} \frac{\sum_{k=0}^L b_k z^{-k}}{1 + \sum_{k=1}^M \frac{a_k}{a_0} z^{-k}}. \quad (b_0 = 1) \quad (4)$$

*Work supported by the U.S. Department of Energy, Office of Basic Energy Sciences, under Contract No. W-31-109-ENG-38.

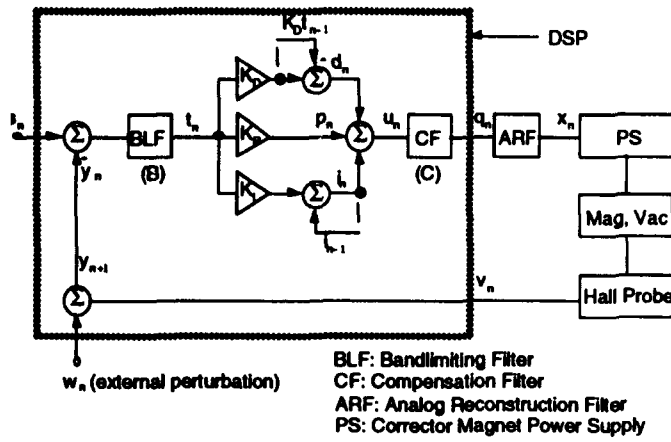


Fig. 3: Schematic diagram for the closed loop feedback with PID control.

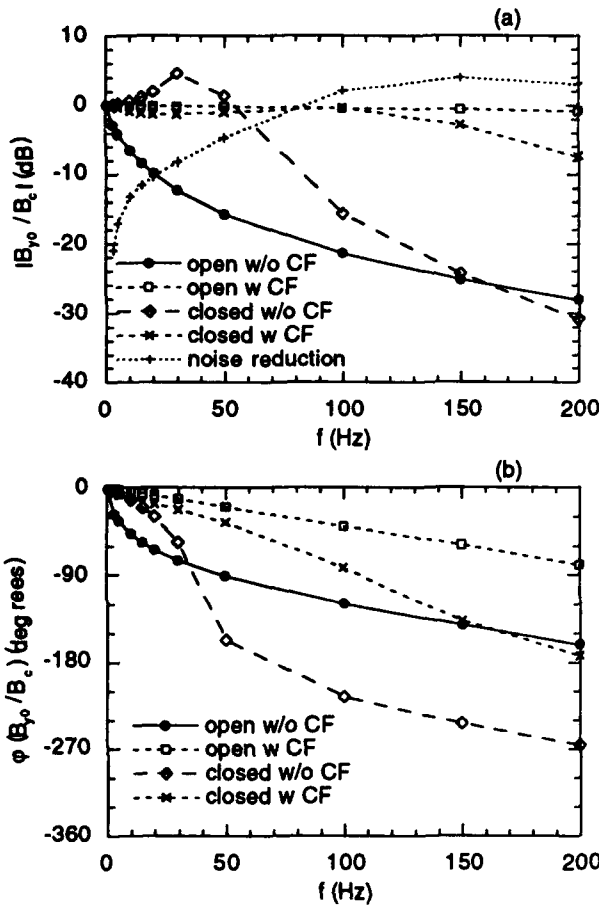


Fig. 4: Results of measurement on the closed loop feedback for corrector magnet field: (a) amplitude attenuation and (b) phase shift. The parameters used were: $F_s = 4$ kHz, $f_b = 30$ Hz, $K_p = 3$, $K_I = 0.05$, and $K_D = 0.5$.

high frequency components in the output from DSP. It was also intended to simulate the BPM, which will have finite bandwidth due to averaging over many turns. ARF was used only for closed loop measurements.

For the open loop measurements of the frequency response, the control signal is at either the input of the CF (u_n)

or the PS (x_n) in Fig. 3. For the closed loop measurements, the control signal is at the input of the DSP (s_n).

The digital compensation filter (CF) was obtained by inverting the digital filter representation of the vacuum chamber. Using the measurement results shown in Fig. 2(a), the best fit with four poles and four zeroes gives

$$q_n = 57.8 (u_n - 3.1575996823 u_{n-1} + 3.5206625349 u_{n-2} - 1.56793656962 u_{n-3} + 0.2048748912 u_{n-4}) + 1.60395604698 q_{n-1} - 0.276518570415 q_{n-2} - 0.30381547655 q_{n-3} - 0.023772023183 q_{n-4} \quad (8)$$

Since no future samples from either the input or output are needed to calculate the current output, the filter is physically realizable or causal.

The results of measurements on B_{y0}/B_c (B_c : control signal) with and without CF is shown in Fig. 4. Figure 5 shows time domain measurements of the magnet field B inside the vacuum chamber in response to the input square pulses of 15 Hz with the CF turned off and on.

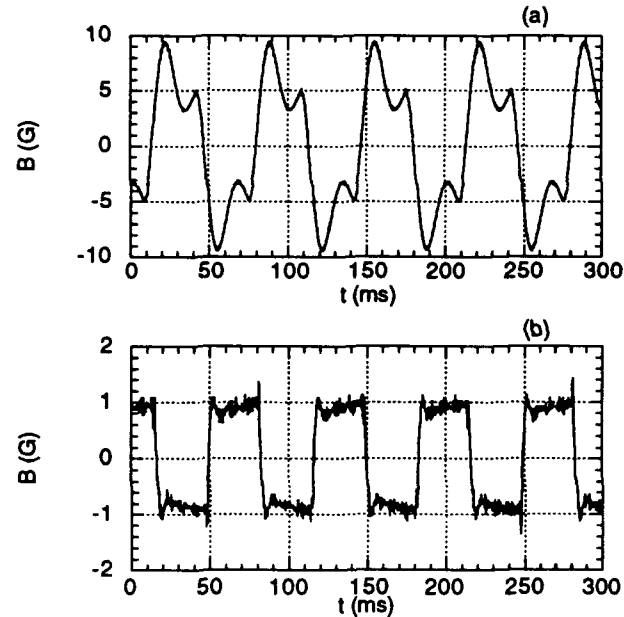


Fig. 5: Feedback system response in the time domain (a) without and (b) with eddy current compensation. The parameters used were: $F_s = 4$ kHz, $f_b = 30$ Hz, $K_p = 3$, $K_I = 0.05$, and $K_D = 0.5$. The control signal is a 15 Hz square wave.

IV. REFERENCES

- [1] Y. Chung and J. Galayda, "Effect of Eddy Current in the Laminations on the Magnet Field," LS Note 200, ANL, 1992.
- [2] A. Peled and B. Liu, *Digital Signal Processing*, John Wiley & Sons, 1976.
- [3] Y. Chung, L. Emery, and K. Kirchman, "Digital Signal Processing for Beam Position Feedback," LS Note 202, ANL, 1992.

The inverse filter in Eq. (4) can be used to compensate for analog devices if the corresponding filter coefficients $\{a_k\}$ and $\{b_k\}$ can be obtained by fitting the frequency response to Eq. (4) with $z = e^{-i\omega T}$. We will use this approach to compensate for the effect of eddy current in the vacuum chamber.

Closed Loop Feedback

In Fig. 1 is shown a simple closed loop feedback system with proportional control of open loop gain G . The bandlimiting filter (BLF) is inserted in the loop for stability reasons. It is a low-pass filter with bandwidth f_b and has the transfer function

$$B(z) = \frac{1 + z^{-1}}{1 + c + (1 - c)z^{-1}}, \quad c = \cot\left(\frac{\pi f_b}{F_s}\right) \quad (5)$$

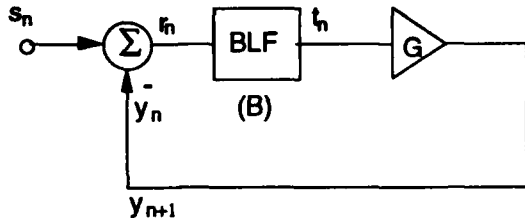


Fig. 1: Closed loop feedback with digital signal processing. BLF is the bandlimiting filter with bandwidth of f_b .

The response of the system in the form of a difference equation is given by

$$(1 + c)y_{n+1} + (1 - c + G)y_n + G y_{n-1} = G(s_n + s_{n-1}). \quad (6)$$

Assuming $F_s \gg f_b$, Eq. (6) can be converted to a second-order differential equation and Fourier analyzed. In general, a closed loop feedback system with k open loop poles can be presented as a filter of $k+1$ poles in the complex plane.

The system is stable if $G < 1 + c$ and, assuming $G \gg 1$, the bandwidth of the closed loop system is approximately equal to f_b . It can be shown that the condition for critically damped response is

$$\frac{F_s}{G f_b} \approx 20, \quad (7)$$

and therefore, the bandwidth of the optimally controlled feedback system is roughly equal to $F_s/20$.

III. MEASUREMENTS

In this section, we will present results of measurements of the effect of the eddy current in the vacuum chamber and its compensation using digital filters.

Magnet Impedance

The magnet resistance R and inductance L can be obtained by measuring the ratio of voltage and current on the magnet as function of frequency. The results show large changes both in R and L . For the horizontal field, they changed from 100

m Ω and 11.8 mH at DC to 920 m Ω and 8.2 mH at 200 Hz. For the vertical field, the changes were from 80 m Ω and 8.7 mH at DC to 460 m Ω and 4.9 mH at 200 Hz. These are mainly attributable to the eddy current in the vacuum chamber. While this has the effect of reducing the magnet time constant, it also increases power consumption.

B. Field Attenuation and Phase Shift

In Figs. 2(a) and 2(b) are shown the attenuation and phase shift of the field relative to the magnet current as functions of frequency at the center of the vacuum chamber ($x = 0$). The vertical field shows stronger attenuation and phase shift with frequency than the horizontal field, though the horizontal field appears to catch up in the high frequency region.

Spatially resolved measurement of the vertical magnet field in the vacuum chamber shows significant quadrupole and sextupole components. Below 20 Hz, the quadrupole component dominates ($|b_1| \approx 0.12 \text{ cm}^{-1}$ @ 20 Hz), while above 50 Hz the sextupole component becomes stronger ($|b_2| \approx 0.16 \text{ cm}^{-2}$ @ 100 Hz). This will cause bump closure error in the local feedback systems and interference among them as a result. The resolution of this effect will be done by the global feedback system.

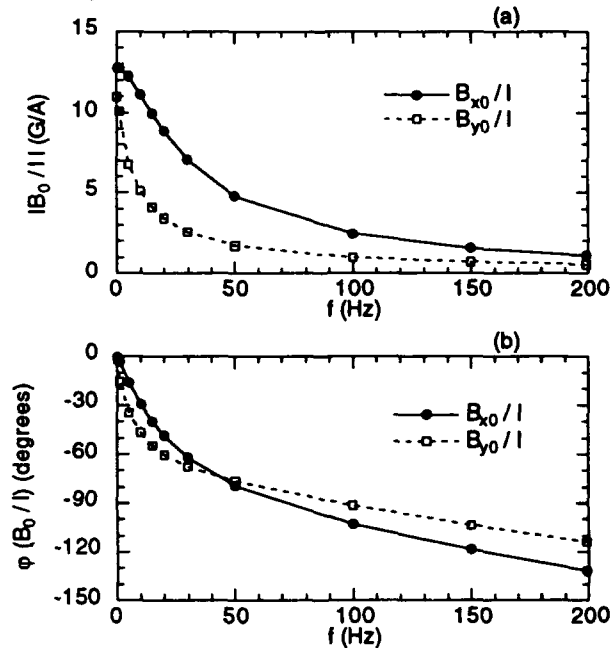


Fig. 2: (a) Attenuation of the field efficiency $|B_{x,y}/I|$ and (b) phase shift ϕ between the field and the current as functions of frequency at the center of the vacuum chamber ($x = 0$).

C. Closed Loop Feedback with PID Control

Figure 3 shows the schematic diagram for closed loop feedback with PID control for the magnet field in the vacuum chamber. A bandlimiting filter (BLF) of 30 Hz was used for these measurements. The analog reconstruction filter (ARF) is an analog low pass filter of 200 Hz bandwidth inserted in front of the power supply control input in order to eliminate

Dynamic Closed Orbit Correction

Yao Cheng

Synchrotron Radiation Research Center

No. 1 R&D Road VI, Hsinchu Science-based Industrial Park, Hsinchu 30077, Taiwan R.O.C.

Abstract

This paper discuss the high speed method of the orbit correction. The speed is affected by many time-constants such as vacuum chamber, magnet, position sensor, power supply, controller, and beam itself. The beam effect is the major concern of this paper. The damping effect implies that the transfer function of the orbit correction contains at least a pole. In the DC case, the transfer function becomes the response matrix of the closed orbit. In the fast feedback application, this pole has to be taken into account to avoid instability. If the zero-pole compensation is possible, the correction speed can be increased. On the other hand, the local bump method doesn't change the periodic boundary condition of the orbit. Therefore, the local bump responds immediately without damping transient. The linear combination of the local bump is fast, but less degree of freedom. The general method to increase the correction speed and the eddy current induced sextupole component are discussed.

I. Introduction

In the control system, the frequency response of each subsystem should be identified. The controller is then designed with proper gain and phase compensation to have a satisfactory dynamic response and accuracy. The modeling of the subsystem plays an important role in the design phase. In this paper, The model of the accelerator from the control point of view is discussed and treated with the beam position monitor (BPM) together. The transfer function between the input steering field and output reading of the beam position contains several time-constants, such as damping time and betatron frequency which are known by every accelerator physicists. Here, all of these physical nature is organized into a engineering presentation.

There are many methods to correct the beam position. The major concern is the frequency response of these methods. The speed means the fast setting and the high feedback gain. Both characters are wanted for the good dynamic response in a feedback control system. Two methods, bump and response matrix, are selected. The bump is fast in sense of accelerator response. Therefore, the controller increase the gain at high frequency region. The response matrix is accurate and suitable for the slow operation. The combined method joins the advantages and provides the fast and accurate feedback.

II. Kick Response

The betatron oscillation induced by a kick pulse is

$$x_{mn} = \sqrt{\beta_m \cdot \beta_n} \cdot \sin(\phi_m - \phi_n) \cdot \theta \quad \text{.....(1)}$$

where m,n are the location indices for the beta function and the phase in respect to the observation as well as the kick. θ is the strength of the kick. If we take the damping effect into account[1], the particle oscillation amplitude of the k th turn of a circular accelerator is written by

$$x_{mn}(k) = e^{-kT_0/\tau} \cdot \sqrt{\beta_m \cdot \beta_n} \cdot \theta \cdot \sin(2\pi\nu k + \phi_{mn}) \quad \text{.....(2)}$$

The damping factor $e^{-kT_0/\tau}$ express the time relationship between the revolution time T_0 and the damping time τ in average. ν is the characteristic tune of the accelerator, and $\phi_{mn} = \phi_m - \phi_n$. The observation, turns by turns, is actually a discrete form. We can find the z transform

$$X_{mn}(z) = \sum_{k=-\infty}^{\infty} x(k) \cdot z^{-k} \quad \text{.....(3)}$$

in a standard text book [2], with a general expression

$$H_{mn}(z) = \frac{X_{mn}(z)}{\theta(z)} = \sqrt{\beta_m \cdot \beta_n} \cdot \text{Im} \left[\frac{ze^{j\phi_{mn}}}{z - e^{-T_0/\tau} \cdot e^{j2\pi\nu}} \right] \quad |z| > e^{-T_0/\tau} \quad \text{.....(4)}$$

This transfer function is used to measure the betatron tune with the knock-out method. The betatron oscillation has a resonant amplitude when the excitation frequency approaches the betatron frequency. The name "knock-out" is no longer true for an electron machine with damping.

If the concerned frequency is much less than the revolution frequency, we take the short revolution time limit $T_0 \rightarrow 0$. The observation is treated as a continuous signal, whose corresponding Laplace transform is[2]

$$H_{mn}(s) = \sqrt{\beta_m \beta_n} \cdot \text{Im} \left[\frac{e^{j\phi_{mn}}}{s + \frac{1}{\tau} - j\omega_t} \right] \quad \text{.....(5)}$$

where $\omega_t = 2\pi\nu/T_0$ is the angular velocity of the betatron oscillation. In this continuous-signal approach, the kick pulse is becoming a δ -function $\theta\delta(t-t_0)$. The transfer function of the impulse response of the accelerator is just like a damped second order low-pass filter with a pair conjugate

poles at $\left(\frac{1}{\tau} \pm j\omega_i\right)$. The betatron frequency ω_i is the upper limitation of the feedback frequency, since the phase changes very fast when the excitation frequency approaches ω_i .

III. Response Matrix

We define the discrete unit step kick of the k th turn

$$u(k) = \begin{cases} 0 & k < 0 \\ 1 & k > 0 \end{cases} \quad \text{.....(6)}$$

The Z transform of this function is

$$u(z) = \frac{z}{z-1} \quad (|z| > 1) \quad \text{.....(7)}$$

The final state of the unit step response is obtained by using the final value theorem.

$$\begin{aligned} \lim_{k \rightarrow \infty} x_{mn}(k) &= \lim_{z \rightarrow 1} (z-1) \cdot H_{mn}(z) \cdot u(z) \cdot \theta \\ &= \sqrt{\beta_m \beta_n} \cdot \theta \cdot \text{Im} \left(\frac{e^{j\phi_{mn}}}{1 - e^{-T_0/\tau} \cdot e^{j2\pi\nu}} \right) \quad \text{.....(8)} \end{aligned}$$

Wiedemann has exact the same expression in the Chapter 7 of his book [1]. He took the short revolution time limit $T_0 \rightarrow 0$ to get the well known formulation of the response matrix.

$$A_{mn} = \frac{\sqrt{\beta_m \beta_n}}{2 \sin(\pi\nu)} \cos(\pi\nu + \phi_{mn}) \quad \text{.....(9)}$$

In many standard textbook, this formula is solved by the periodic boundary condition without damping effect[3]. It holds true as long as $T_0 \ll \tau$. In case of $T_0 \sim \tau$, the equation 8 has to be applied. For a super big synchrotron light source with many insertion devices, this condition may occur. With some rearrangement, we can prove that the denominator is always greater then zero.

$$\begin{aligned} 1 - 2e^{-T_0/\tau} \cos(2\pi\nu) + e^{-2T_0/\tau} \\ = 2e^{-T_0/\tau} \left(\cosh\left(\frac{T_0}{\tau}\right) - \cos(2\pi\nu) \right) > 0 \quad \text{.....(10)} \end{aligned}$$

It implies that the resonant line disappear. The damping effect has a positive contribution to avoid resonant.

IV. Local Bump

A local bump doesn't change the closed boundary condition[3]. Only the orbit inside the bump is changed. There is no betatron oscillation propagate to the next turn. Hence, the response of the step local bump is immediate

without oscillation and damping. The transfer function of the local bump is merely a matrix without poles and zeros.

$$H_{mi} = \sum_n \sqrt{\beta_m \beta_n} \sin(\phi_{mn}) \cdot a_{ni} \quad \text{.....(11)}$$

Where a_{ni} describes the tri-diagonal bump matrix

$$a_{ni} = \delta_{n,i-1} \frac{\sin(\phi_{i,i+1})}{\sqrt{\beta_{i-1}}} + \delta_{n,i} \frac{\sin(\phi_{i+1,i-1})}{\sqrt{\beta_i}} + \delta_{n,i+1} \frac{\sin(\phi_{i-1,i})}{\sqrt{\beta_{i+1}}} \quad \text{.....(12)}$$

Since the bump is created by three kicks, the column number is less than row number by 2. This also means that the degree of freedom for bump correction is less than for matrix.

V. BPM

The beam position monitor functions like a radio receiver. The signal coming from the buttons is mixed with local oscillation and filtered to low frequency. Then, we have the observation

$$O_{mn}(t) = \sum_{k=0}^{t/kT_0} f_b(t - kT_0) x_{mn}(k) \quad \text{.....(13)}$$

where $f_b(t - kt_0)$ is the impulse response of the BPM. This formula is rather difficult to evaluate. We try a first order low pass filter to make this calculation clearly. Assume that the low pass filter has the same time constant as the damping time constant of the accelerator. The observation of the equation 2 becomes

$$O_{mn}(t) = \sum_{k=0}^{t/kT_0} e^{-(t-kT_0)/\tau} \cdot x_{mn}(k) \quad \text{.....(14)}$$

For the low frequency application, we approximate again with the same limit $T_0 \rightarrow 0$.

$$\lim_{T_0 \rightarrow 0} O_{mn}(t) = e^{-t/\tau} A_{mn} \quad \text{.....(15)}$$

The transfer function of the observation turns out to be

$$H_{mn}^o = \frac{A_{mn}}{s + 1/\tau} \quad \text{.....(16)}$$

the response matrix with a first order low pass filter.

VI. Fast Feedback

A combined correction method of bump and response matrix is considered here to apply on the global feedback system. The fundamental idea is to use bump method at high speed and response matrix at low speed. The response matrix has more degrees of freedom, which allows a better correction of the closed orbit distortion. The local bump is usually applied at the local correction of the photon port with a high setting rate. We want to merge the bump method into global feedback system. From the analysis of last section, the betatron oscillation raised by corrector setting will not affect

the observation, if we use BPM filter to smoothing reading. However, the betatron is damped with the speed of the damping time constant which is independent of the smoothing time constant.

The concern is slow damping time, which is in the range of a couple of millisecond. The fast setting from the response matrix will activate the betatron oscillation. The photon beam position detectors will pick up the betatron oscillation and force the local bump at photon port to correct it. From this point of view, we have to reduce the correction gain at high frequency region (> 100 Hz), if the response matrix is applied. In the SRRC case, this attenuation will be contributed from the vacuum chamber.

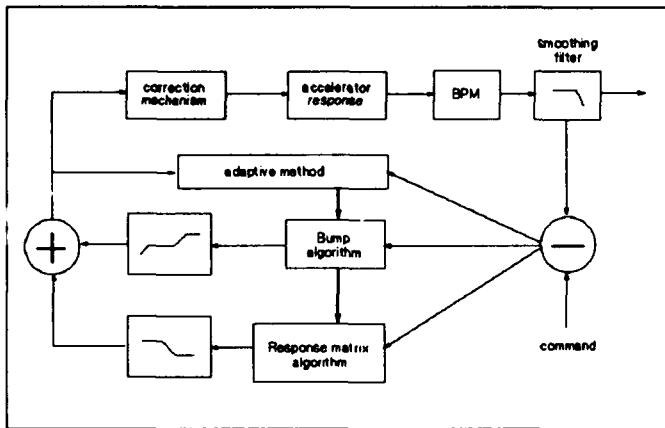


Figure 1. System Block Diagram

Figure 1. is the block diagram of this combined correction method. The BPM readings pass through the smoothing filter and are distributed to each correction algorithm. After the calculation, the setting values are compensated in the high frequency region for the bump method, and in the low frequency region for the response matrix. The sum of two setting values is send to the correction magnet. We compare the sum setting and the BPM reading to estimate the parameter changes. The new parameter values modify both algorithms with the adaptive method[4].

The compensation of the bump method starts with a high pass edge, since the DC accuracy of bump is worse than that of the response matrix. The gain at higher frequency region is enhanced by another rising edge, which attempt to compensate the attenuation from the vacuum chamber. This enhancement should be carefully adjusted in respect to he speed of the correction power supply. On the contrary, the setting from the response matrix is enhanced below the cut-off frequency raised from the vacuum chamber response.

The correction mechanism transfer the setting current of magnet to steering angle. The response contains two poles. One of them is coming from the vacuum chamber; the other depends on the character of the power supply to drive the inductive load. The modern MOS technology provides the high speed capability to fulfill this requirement.

VII. Vacuum Chamber

The eddy current is the energy dissipated part of the field equation when the alternative field penetrates a metallic chamber. The transfer function is more or less like a low pass filter of the first order. The time constant is proportional to the product $\Delta \cdot \sigma \cdot a$ of the thickness Δ , the conductivity σ and the perpendicular dimension "a" of the chamber in respect to the field[5]. This time constant is not the limitation of the feedback speed indeed, since the phase lag is stable and less than 90 degree. Driving over this cut-off frequency requires more power to keep the same field. However, the high frequency component of the feedback signal exists rarely because of the shield effect. The power consumption is small as long as the signal is small. The speed is acutely limited by the second pole of the correction power supply and the time delay of the controller.

The other concern is the sextupole component. We take a low order approximation of the lost field[6]

$$\Delta B(x) \approx \Delta B(0) \cdot \left(1 - \frac{x^2}{a^2}\right). \quad \dots (17)$$

The jitters of the beam is in the range of hundred μm . Its spectrum concentrates most in the region lower than the chamber cut-off frequency. Since the lost field is proportional to the jitters and its frequency, the contribution of the sextupole can be estimated by equation 17.

VIII. Reference

- [1] Wiedemann, H. Manuscript of the Particle Accelerator Physics, Springer Verlag.
- [2] Franklin, G. F., Powell, J. D. and Workman, M. L., Digital Control of Dynamic Systems, Addison-Wesley Publishing Company, 1980.
- [3] Wilson, E. "Transverse Beam Dynamics", *Proceedings Vol. I, CAS General Accelerator Physics, Gif-sur-Yvette, Paris, France, 3-14 September 1984.*
- [4] Cheng, Y. and Hsue C.-S., "Adaptive Closed Orbit Correction", in the *Proceedings of the 1991 IEEE Particle Accelerator Conference.*
- [5] Haus, H. A., Melcher, J. R., Chapter 10, Page 431, *Electromagnetic Fields and Energy, Prentice-Hall International, Inc. 1989.*
- [6] Hemmie, G. and Rossbach, J., "Eddy Current Effects in the DESY II Dipole Vacuum Chamber", DESY M-84-05, April 1984.

A Closed-Loop Photon Beam Control Study for the Advanced Light Source*

G. Portmann and J. Bengtsson

Lawrence Berkeley Laboratory, University of California
1 Cyclotron Road, Berkeley, CA 94720 USA

Abstract

The third generation Advanced Light Source (ALS) will produce extremely bright photon beams using undulators and wigglers. In order to position the photon beams accurate to the micron level, a closed-loop feedback system is being developed. Using photon position monitors and dipole corrector magnets, a closed-loop system can automatically compensate for modeling uncertainties and exogenous disturbances. The following paper will present a dynamics model for the perturbations of the closed orbit of the electron beam in the ALS storage ring including the vacuum chamber magnetic field penetration effects. Using this reference model, two closed-loop feedback algorithms will be compared -- a classical PI controller and a two degree-of-freedom approach. The two degree-of-freedom method provides superior disturbance rejection while maintaining the desired performance goals. Both methods will address the need to gain schedule the controller due to the time varying dynamics introduced by changing field strengths when scanning the insertion devices.

I. INTRODUCTION

The ALS is designed to store a 400 mA, 1.5 GeV, multi-bunch electron beam with a lifetime of 6-8 hours. The natural rms emittance is 3.4×10^{-9} m-rad with an estimated rms beam size at the center of the insertion device of 195 μ m horizontally and 37.4 μ m vertically. The lattice is based on a cell with a triple bend achromat, repeating twelve times. This leaves room for a maximum of ten insertion devices. The storage ring is optimized to produce photon beams in the VUV to soft X-ray spectral region.

In order to position the photon beams accurate to the micron level, a closed-loop feedback system on the electron beam is being developed. Potential error sources driving the electron beam include: environmental vibrations, magnetic field changes associated with insertion device scanning, magnet power supply ripple, and temperature drift. Steering of the photon beam is done by monitoring the position at two locations and correcting the position and angle of the electron beam through the insertion device. This is done by local correction using four dipole corrector magnets in each plane. The following paper integrates accelerator beam dynamics with feedback control theory for systematic controller design.

*This work was supported by the Director, Office of Energy Research, Office of Basic Energy Sciences, Material Sciences Division, of the U.S. Department of Energy under the U.S. DOE Contract No. DE-AC03-76SF00098.

II. ALS MAGNET LATTICE

In order to design a feedback control system for photon beam steering, one must have an accurate closed orbit beam dynamics model. Fig. 1 shows the magnetic lattice for two of the twelve sectors. Each sector is identical except for the type of insertion device. Using the two dipole corrector magnets on either side of the insertion device, the goal of the local bump system is to accurately steer the electron beam through the insertion device without perturbing the beam position outside the four magnet bump. This algorithm must account for focusing changes in the quadrupoles located between the corrector magnets and the field changes of the insertion devices during scanning.

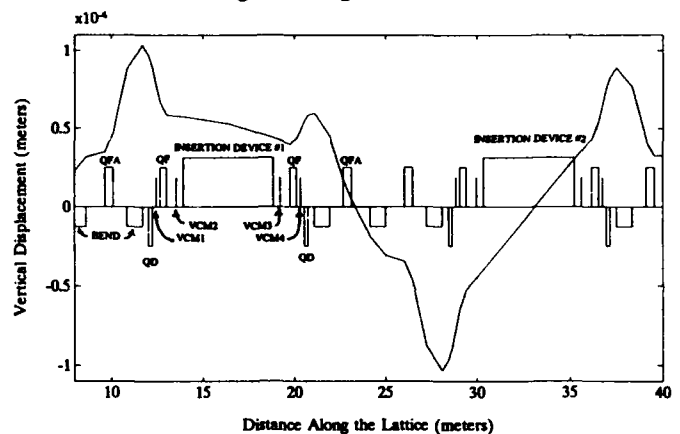


Fig. 1. Closed Orbit for a 10 μ -radian dipole kick at VCM1

Since only small perturbations about the equilibrium orbit are being considered, linear models are sufficient. If necessary, one can easily generalize to the nonlinear case by using automatic differentiation, [9].

The change of the phase space coordinates $\bar{x} = (x, p_x)$ between two points in the lattice is given by the transport matrix,

$$\bar{x}_j = M_{i \rightarrow j} \bar{x}_i. \quad (1)$$

Therefore, $M_{i \rightarrow j}$ is the one-turn matrix. Consider the closed orbit distortions for a single dipole kick, $\Delta \bar{x}_i = (0, \Delta \theta_i)$. The distortion at location i is then given by

$$\Delta \bar{x}_i^{\text{cod}} = [I - M_{i \rightarrow i}]^{-1} \Delta \bar{x}_i. \quad (2)$$

The distortions at other locations in the lattice can be computed from (1). Fig. 1 shows the distortions of the vertical closed orbit for a .01 milliradian kick from corrector magnet VCM1. By superposition, one can find the contributions to the closed orbit distortions from the four

corrector magnets to the center of the insertion device and VCM4. Introducing, $\Delta \bar{\Theta} = (\Delta \theta_1, \Delta \theta_2, \Delta \theta_3, \Delta \theta_4)$, one obtains the following system of equations

$$\begin{bmatrix} \Delta \bar{x}_{id} \\ \Delta \bar{x}_{vcm4} \end{bmatrix} = T \Delta \bar{\Theta} \quad (3)$$

If the new position and angle downstream of VCM4 is along the unperturbed closed orbit, then the bump will remain local. Hence, for open-loop steering of the photon beam, the corrector strengths can be found from T^{-1} with $\Delta \bar{x}_{vcm4} = (0,0)$. Although the position and angle of the electron beam at VCM4 was chosen, any position outside the bump would suffice. Also, equation (3) can easily be generalized to account for any coupling between the vertical and horizontal dimensions.

III. FEEDBACK CONTROL SYSTEM MODEL

Equation (3) provides the corrector strengths for static beam steering. However, due to modeling uncertainties and exogenous disturbances, a dynamic system is necessary. In order to "close the loop" on the photon beam position, an accurate model for entire control system needs to be developed. Shown in Fig. 2, the feedback control algorithm consists of a controller (to be developed in Sections IV and V), the beam dynamics compensation gain (T^{-1}), and vacuum chamber compensation filters. The transfer function for the accelerator (i.e. power supply inputs to photon beam position monitors) consist of the superposition of four decoupled corrector magnets systems. The dynamics of this system is dominated by the eddy currents effects of the aluminum vacuum chamber. The cutoff frequencies for the vacuum chamber at the correctors are (58Hz, 195Hz, 250Hz, 58Hz) vertically and (3 Hz, 55Hz, 66Hz, 3Hz) horizontally. The power supply and magnet bandwidths are approximately 500 Hz and 1000 Hz, respectively.

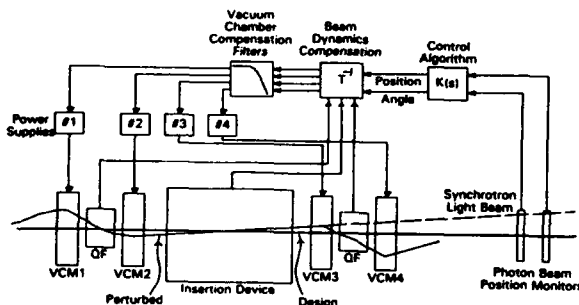


Fig. 2. Local Bump Control System Model

The power supply range is ± 100 amps vertically and ± 40 amps horizontally (accurate to 1 part in 10,000), which corresponds to a ± 3.2 milliradian change in the electron beam at 1.5 GeV. The photon beam position monitors

(PBPM), located 8 and 12 meters from the insertion device center, are accurate to ± 1 micron.

The inherent difficulty in designing a feedback control law for this system is due to the fact that only two position monitors are available when one is trying to control four decoupled corrector magnet systems. The fact that the states in each of the correctors are decoupled makes the plant unobservable. Lack of observability extremely limits feedback control design. As done in [5] and [6], essentially one has to take an open-loop control approach, then feedback on two PBPM signals with the assumption that the zero leakage condition is met. The problem with this approach is that closed-loop control only provide robustness to modeling uncertainties for the photon beam steering, and no robustness on the leakage condition. Hence, the controller performance and stability will be extremely sensitive to modeling errors.

The remainder of this paper will concentrate on the controller design, $K(s)$. The design example will be a four magnet local bump in the vertical dimension with a closed-loop bandwidth of 100 Hz. For simplicity, only an analog control design will be considered, however, the actual implementation will be digital for flexibility.

IV. CLASSICAL CONTROL DESIGN

The fundamental goal of a feedback control system is to track a given input command given actuator limitations, uncertainties in the dynamics model, sensor noise, and exogenous disturbances. A generic feedback control structure is shown in Fig. 3. The power supplies, magnets, and accelerator physics models are lumped into block $G(s)$ (the plant), with modeling uncertainties, $\Delta(s)$. The disturbances are external inputs not accounted for in the design model, e.g. vibration, power supply ripple, cross-talk errors, and temperature drift.

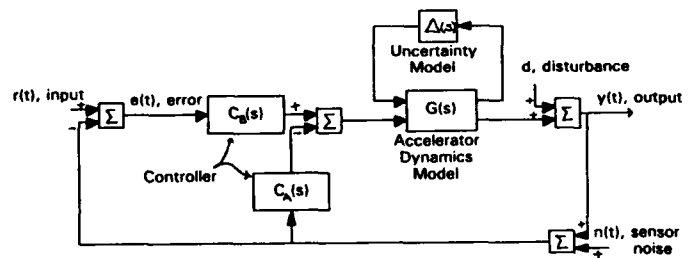


Fig. 3. Feedback Control System Structure

If $C_A=0$, then the equations of interest are the following.

$$y = GC_B (I + GC_B)^{-1} (r - \eta) + (I + GC_B)^{-1} d \quad (4)$$

$$\tilde{e} \equiv r - y = (I + GC_B)^{-1} (r - d) + GC_B (I + GC_B)^{-1} \eta \quad (5)$$

The sensitivity function is defined as the d to y transfer function, $S = (I + GC_B)^{-1}$, and the complementary sensitivity function is the r to y transfer function, $T = GC_B (I + GC_B)^{-1}$. The fundamental trade-off in classical control is that $|T+S|=I$ over all frequencies. $|S|$ "small" implies good tracking performance, however, it forces $|T|$ close to unity. Since G naturally rolls off at high frequency, this

would force K to increase which is destabilizing since the knowledge of the plant dynamics at high frequency is poor. This is discussed in detail in [2] and [4]. Classical PID control and lead-lag compensation can be used to adjust the trade-off. For the vertical local bump the following PI control law provides the necessary performance, $\tau = .0016$ seconds.

$$C_B(s) = \frac{1.4[s + 650]}{s}, \quad C_A(s) = 0 \quad (6)$$

V. A TWO DEGREE-OF-FREEDOM CONTROL DESIGN

By using two "handles", C_A and C_B , to adjust the control signal, [1], one can remove the fundamental trade-off in Section IV. Define,

$$C_A = \tilde{G}^{-1}Q(I - Q)^{-1} \quad (7)$$

$$C_B = K(I - Q)^{-1} \quad (8)$$

where \tilde{G} is the estimate of G . There are two cases of interest. If $\tilde{G} = G$, then the output and error transfer functions are the following.

$$y = (I + GK)^{-1}GKr + (I - Q)(I + GK)^{-1}d - (I + GK)^{-1}(Q + GK)\eta \quad (9)$$

$$\tilde{e} = (I + GK)^{-1}r - (I - Q)(I + GK)^{-1}d + (I + GK)^{-1}(Q + GK)\eta \quad (10)$$

Therefore, if the estimate of the plant is accurate, then the Q function acts as a scaling term to adjust the influence of the two error sources on the output and error. In the limit, if $Q = I$, then

$$y = (G\tilde{G}^{-1} + GK)^{-1}GKr - \eta \quad (11)$$

$$\tilde{e} = (G\tilde{G}^{-1} + GK)^{-1}G\tilde{G}^{-1}r + \eta \quad (12)$$

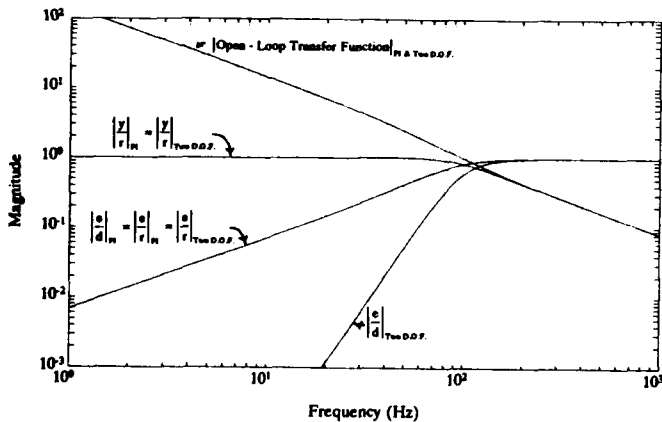


Fig. 4. Disturbance to Error and Reference Input to Error Transfer Functions.

Notice that the disturbance has been totally eliminated -- even when $\tilde{G} \neq G$. Given these facts, the design goal is to choose $Q \approx I$ inside the system bandwidth. The following design example will use a third order Butterworth filter with the cutoff frequency set at the system bandwidth, 100 Hz. K will be the same PI controller as in (6).

As shown in Fig. 4, the two degree-of-freedom approach has superior disturbance rejection over the simple PI controller -- 80 dB per decade versus 20 dB per decade. However, the reference input to error and closed-loop transfer functions are identical. As discussed in [1], the two degree-of-freedom controller can be formulated as a disturbance observer-based system. By estimating and canceling the disturbance, one will not only reduce environmental error sources but also the negative effects of cross-talk between the local bumps.

VI. CONCLUSION

The development of an accurate closed orbit model for the ALS is crucial for the success of the photon beam steering feedback system. The insertion devices will cause relatively large field perturbations when scanned. Since the quadrupole magnets will be adjusted to help compensation for the field changes, the local bump algorithm must continually update the lattice model in order to compute the proper dipole kicks, equation (3). The effects of field variations for the worst case (i.e. ten insertion devices) is currently being studied.

To minimize the effects of cross-talk due to modeling errors as well as environment error sources, a two degree-of-freedom control algorithm has been developed. This approach has superior performance over the classical PI controller. It has the added advantage that one can set the system bandwidth independent of the disturbance rejection "bandwidth". The only cost of these benefits is a more demanding computer throughput.

VII. ACKNOWLEDGMENTS

The authors would like to thank S. Chattopadhyay, the Center for Beam Physics, and H. Lancaster for their continued support and encouragement during this study.

VIII. REFERENCES

- [1] T. Umeno, Y. Hori, IEEE Trans. Industrial Electronics, Vol. 38, No. 5, Oct. 1991.
- [2] Doyle, G. Stein, IEEE Trans. Automatic Control, Vol AC-26, No. 1, Feb. 1981.
- [3] C. Chen, "Linear System Theory and Design," 1984.
- [4] G.F. Franklin, J.D. Powell, A. Emami-Naeini, "Feedback Control of Dynamic Systems," 1991.
- [5] R.J. Nawrocky, J.W. Bittner, Li Ma, H.M. Rarback, D.P. Siddons, and L.H. Yu, Nucl. Instr. and Meth., A266, pp.164-171, corrected Oct. 10, 1988.
- [6] R.O. Hettel, Nuc. Inst. & Methods in Phys. Res., A266, pp. 155-163, 1988.
- [7] E.D. Courant and H. S. Snyder, Ann of Phy. 3, 1958.
- [8] "1-2 GeV Synchrotron Radiation Source, Conceptual Design Report," PUB-5172 Rev., Lawrence Berkeley Laboratory, 1986.
- [9] J. Bengtsson, E. Forest, H. Nishimura, unpublished.
- [10] MATLAB Reference Guide.

Global DC Closed Orbit Correction Experiments on the NSLS X-ray Ring and SPEAR*

Y. Chung, G. Decker, and K. Evans, Jr.
Argonne National Laboratory, Argonne, IL 60439

J. Safranek, I. So, and Y. Tang
Brookhaven National Laboratory, Upton, NY 11973

W. J. Corbett and R. Hettel
Stanford Linear Accelerator Center, Stanford, CA 94305

Abstract

The global closed orbit correction experiments conducted on the NSLS X-ray ring and the SPEAR using the technique of singular value decomposition (SVD) are presented. The beam response matrix, defined as beam motion at beam position monitor (BPM) locations per unit kick by corrector magnets, was measured and then analyzed using SVD. The BPMs and correctors are reconfigured into "transformed" BPMs (t-BPMs) and "transformed" correctors (t-correctors), with each t-BPM coupled to at most one t-corrector and vice versa for orbit correction. The decoupled t-BPMs are used to estimate the limit on orbit correction, while the decoupled t-correctors are used to optimize the corrector strengths. As a result, the vertical r.m.s. orbit error at the BPM locations was reduced from 208 μm to 61 μm about an arbitrary reference orbit in the NSLS X-ray ring. In SPEAR, the vertical closed orbit was brought to the BPM centers at the selected BPM locations with an r.m.s. error of 215 μm reduced from the initial 780 μm .

I. INTRODUCTION

The third generation synchrotron light sources, of which the Advanced Photon Source (APS) is one, are characterized by low emittance of the charged particle beams and high brightness of the photon beams radiated from insertion devices. Transverse stability of the particle beams is a crucial element in achieving these goals and the APS will implement extensive beam position feedback systems, which include 320 corrector magnets, 360 positron beam position monitors (BPMs) distributed around the storage ring, miniature BPMs for insertion device beamlines, and photon beam position monitors in the front end of X-ray beamlines.

The beam position feedback systems can largely be divided into the global and local feedback systems according to the extent of correction, and the DC and AC feedback systems according to the bandwidth of correction.

In this paper, we will present the results of global DC beam position feedback experiments conducted on the X-ray ring of

the National Synchrotron Light Source (NSLS) and on SPEAR at Stanford Synchrotron Radiation Laboratory (SSRL). Integral control with full correction was used, and the technique of singular value decomposition (SVD) was used to invert the response matrix.

The rest of this paper will consist of a brief review of the theory of SVD applied to closed orbit correction in Section II, analysis of the response matrices in Section III, and presentation of the measurement results in Section IV.

II. THEORY

The mathematical formulation of the SVD of matrices is broadly available in the literature [1-4] and its successful application to closed orbit correction at Aladdin, SRC, was reported in Ref. [5]. A theoretical treatment and physical interpretation of the technique for closed orbit correction is presented in Ref. [6], including minimization of orbit error and optimization of corrector strengths. In this section, we will overview the SVD formalism in order to introduce the terminology used in following sections.

Suppose that there are M BPMs and N correctors used for closed orbit correction in the storage ring. Assuming linearity, the response matrix R_{ij} is defined as the beam motion at the i -th BPM per unit angle of kick at the j -th corrector. The orbit change Δx due to the corrector strength change $\Delta \theta$ is then given by

$$\Delta x = R \cdot \Delta \theta. \quad (1)$$

Using SVD, we write the response matrix R as [4]

$$R = U \cdot W \cdot V^T, \quad (2)$$

where U is an $M \times M$ unitary matrix ($U^T \cdot U = U \cdot U^T = 1$), W is an $M \times N$ diagonal matrix with positive or zero elements, and V is an $N \times N$ unitary matrix ($V^T \cdot V = V \cdot V^T = 1$).

From Eqs. (1) and (2) and the unitary property of U and V , we have

$$\Delta x' = W \cdot \Delta \theta', \quad (3)$$

*Work supported by the U.S. Department of Energy, Office of Basic Energy Sciences, under Contract No. W-31-109-ENG-38.

where $\Delta x' = U^T \cdot \Delta x$ and $\Delta \theta' = V^T \cdot \Delta \theta$ in the transformed (t-) BPM and corrector spaces. The matrix W is given by

$$W_{ij} = w_{\min(i,j)} \delta_{ij}, \quad (4)$$

where the diagonal elements w_n (≥ 0 , $1 \leq n \leq \min(M, N)$) are called eigenvalues. Each represents the coupling efficiency of the correction channel of a pair consisting of a t-BPM and a t-corrector. The matrix R is singular if any of the eigenvalues is zero.

Given an orbit perturbation Δx , the necessary corrector strength $\Delta \theta$ is the product of the inverse matrix R_{inv} given by

$$R_{\text{inv}} = V \cdot W_{\text{inv}} \cdot U^T \quad (5)$$

and Δx . W_{inv} is a diagonal matrix of dimension $N \times M$ and the elements are given by

$$W_{\text{inv},ij} = q_{\min(i,j)} \delta_{ij}, \quad (6)$$

where

$$q_n = \begin{cases} 0, & w_n \leq \epsilon w_{\max} \\ \frac{1}{w_n}, & \text{otherwise} \end{cases} \quad (1 \leq n \leq \min(M, N)) \quad (7)$$

ϵ is the singularity rejection parameter in the range $[0,1]$. For a given matrix R , we define $\epsilon_m(R)$ as

$$\epsilon_m(R) = \max \{ \epsilon \mid w_n > \epsilon w_{\max} \text{ for all } w_n \neq 0 \}. \quad (8)$$

That is, ϵ_m is the largest possible value for ϵ in order to retain all non-zero eigenvalues.

III. ANALYSIS OF RESPONSE MATRICES

In this section, we will analyze the response matrices of the NSLS X-ray ring and SPEAR in the vertical plane.

A. NSLS X-ray Ring

We used all of the 48 (M) BPMs and 39 (N) correctors available for orbit correction. The nominal vertical tune of the

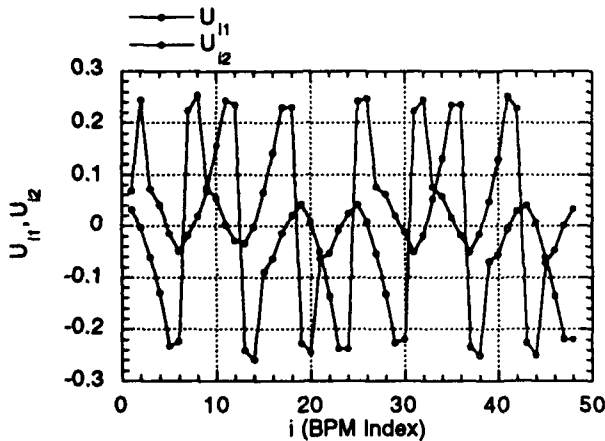


Fig. 1: The basis vectors U_{11} and U_{12} of the NSLS X-ray ring for the most strongly coupled channels.

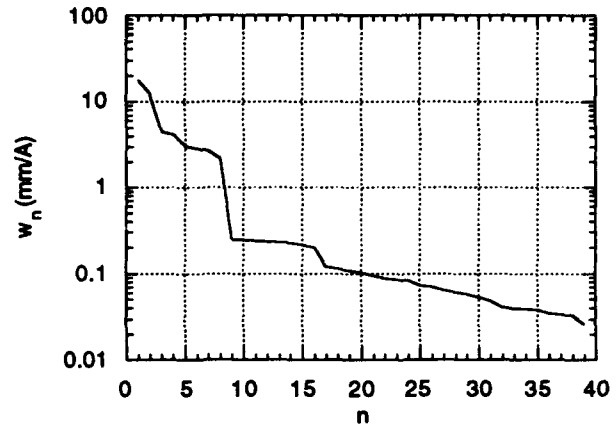


Fig. 2: Plot of the eigenvalues of the response matrix for the NSLS X-ray ring. $\epsilon_m = 1.47 \times 10^{-3}$.

machine is $\nu_v = 6.2$. The response matrix was measured as the ratio of the beam motion in mm and the applied current on the corrector magnets in amperes. The conversion to the angle is done using

$$\Delta \theta \text{ (rad)} = \begin{cases} 4.20 \times 10^{-5} \Delta I \text{ (A)}, & \text{V8 correctors} \\ 6.87 \times 10^{-5} \Delta I \text{ (A)}, & \text{others} \end{cases} \quad (9)$$

Figure 1 shows the BPM basis vectors U_{i1} and U_{i2} ($1 \leq i \leq 48$) for the most strongly coupled channels. These two vectors exhibit pseudo-periodicity of the integer tune 6 and are shifted in phase by approximately 90 degrees. This indicates that the two channels will mostly correct $m = 6$ harmonic mode. The eigenvalues w_n ($1 \leq n \leq 39$) are shown in Fig. 2. ϵ_m of the response matrix is 1.47×10^{-3} .

Table 1 summarizes the results of simulation of orbit correction on the initial r.m.s. orbit error of $207.8 \mu\text{m}$ using a different number (n_i) of eigenvalues. The theoretical limit on the residual error after correction is $46.6 \mu\text{m}$.

Table 1: Simulation of orbit correction in the vertical plane of NSLS X-ray ring using a different number (n_i) of eigenvalues.

n_i	$\Delta I_{\min} \text{ (A)}$	$\Delta I_{\max} \text{ (A)}$	$\Delta I_{\text{rms}} \text{ (A)}$	$\Delta y_{\text{rms}} \text{ (}\mu\text{m)}$
0	0.000	0.000	0.000	207.8
2	-0.010	0.011	0.007	183.2
6	-0.83	0.09	0.044	128.9
10	-1.01	0.13	0.30	108.8
20	-1.39	0.89	0.52	84.0
30	-2.90	1.81	1.01	68.9
34	-4.50	2.11	1.39	59.7
36	-4.88	3.03	1.65	52.2
38	-4.98	3.01	1.66	52.1
39	-5.40	3.78	1.93	46.6

B. SPEAR

As in the case of the NSLS X-ray ring, all of the 26 BPMs and 30 correctors available for orbit correction were used. The nominal vertical tune of the machine is $\nu_v = 6.72$. As shown in Fig. 3, the response matrix is nearly singular, and the weakest four channels ($n = 23 - 26$) may not be usable unless

the power supplies are very robust. ϵ_m of the response matrix is 4.43×10^{-4} .

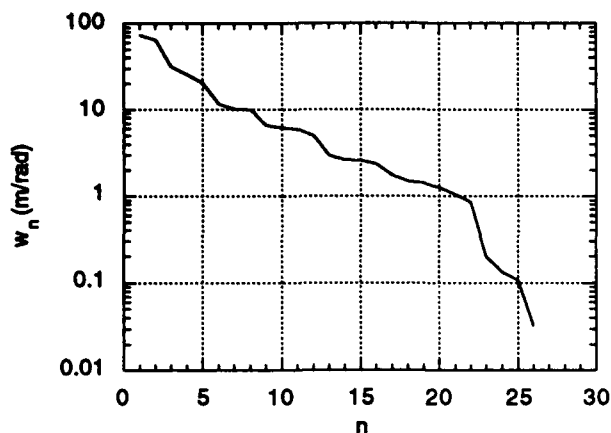


Fig. 3: Plot of the eigenvalues of the response matrix for SPEAR. $\epsilon_m = 4.43 \times 10^{-4}$.

IV. MEASUREMENT RESULTS

Figure 4 shows the result of orbit correction using 35 eigenvalues on the NSLS X-ray ring. The initial r.m.s. orbit error was $138 \mu\text{m}$, which was reduced to $61 \mu\text{m}$ after correction. A few iterations were necessary before the r.m.s. error settled down to this value, possibly due to changes in machine condition and error in the response matrix measurement. The corrector current changes ranged from -4.56 A to 2.45 A , with the r.m.s. value of 1.47 A . Some of the corrector power supplies got close to, but did not reach, saturation at the maximum current of 10 A . Including more eigenvalues would trip off some of the power supplies and was not tried.

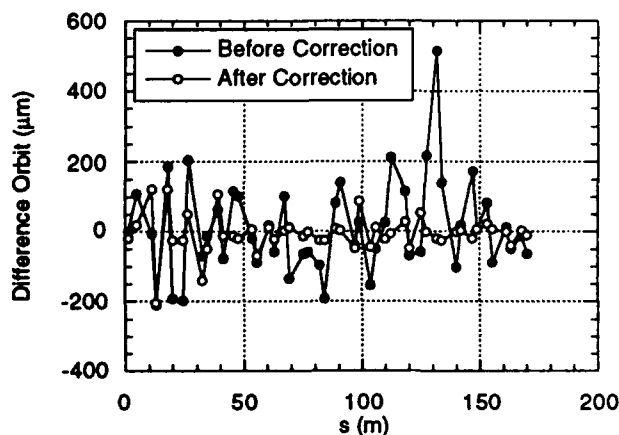


Fig. 4: DC Global orbit correction on the NSLS X-ray ring. The r.m.s. orbit error relative to the reference orbit is $137 \mu\text{m}$ and $61 \mu\text{m}$ before and after correction, respectively. Thirty-five eigenvalues out of 39 were used.

In the case of SPEAR, we tried to bring the orbit as close as possible to the electrical centers of the BPMs, which were used as the reference for orbit correction. After each correction, the RESOLVE [7] computer program was used to

fit the measured orbit to the machine model. This enabled us to locate some of the BPMs with significant offsets and remove them for orbit correction. Using this procedure, 9 out of 26 were removed, and the result is shown in Fig. 5. The r.m.s. orbit error was reduced from $780 \mu\text{m}$ to $215 \mu\text{m}$ at the locations of the 17 remaining BPMs using 15 eigenvalues. Two channels had to be decoupled to avoid power supply saturation resulting from the misalignment of a BPM with the center of an adjacent quadrupole. This led to the kink in the orbit between the 9th and 10th BPMs.

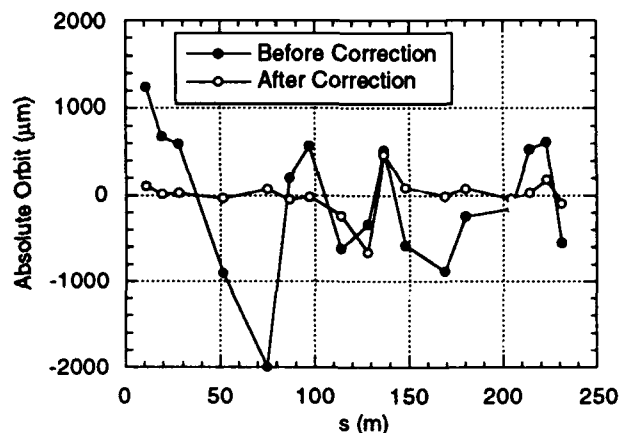


Fig. 5: DC global absolute orbit correction at SPEAR, SSRL. The r.m.s. orbit error relative to the vacuum chamber center is $780 \mu\text{m}$ and $215 \mu\text{m}$ before and after correction, respectively. Fifteen eigenvalues out of 17 were used.

V. REFERENCES

- [1] G. H. Golub and C. Reinsch, "Singular Value Decomposition and Least Squares Solutions," *Numer. Math.* 14, pp. 403-420, 1970, and references therein. Also in J. H. Wilkinson and C. Reinsch, *Linear Algebra*, vol. II of *Handbook for Automatic Computation*, Springer-Verlag, New York, 1971.
- [2] G. E. Forsythe, M. A. Malcolm, and C. B. Moler, *Computer Methods for Mathematical Computations*, Prentice-Hall, Englewood Cliffs, N.J., 1977.
- [3] J. J. Dongarra, et al., *LINPACK User's Guide*, Chapter 11, Society for Industrial and Applied Mathematics, Philadelphia, 1979.
- [4] *MATLAB™ User's Guide*, The Mathworks, Inc., p. 3-178, 1990.
- [5] K. J. Kleman, "Beam Diagnostics and Control at Aladdin," *Nuclear Inst. and Meth.*, A266, p. 172, 1988.
- [6] Y. Chung, G. Decker, and K. Evans, Jr., "Closed Orbit Correction Using Singular Value Decomposition of the Response Matrix," these proceedings.
- [7] W. J. Corbett, M. J. Lee, and Y. Zambre, "Automatic Beamline Calibration Procedures," *Proceedings of the 3rd European Particle Accelerator Conference*, Berlin, p. 753, 1992. Cf. M. J. Lee for information on RESOLVE.

FFT-Oriented Feedback

F.-J. DECKER

Stanford Linear Accelerator Center*, Stanford, California 94309

Abstract

In the SLC many feedback systems keep the beam under control. Here we concentrate on feedback systems which operate at 120 Hz or lower frequencies, so software can be used to make some decisions. The linac steering feedback uses beam position monitor data and corrects magnet settings to keep the beam orbit to the desired values (mostly flat). Looking at the Fast Fourier Transformation (FFT) of the data, a reduction in the zero and very low frequency component is observed, while on the other hand noise at higher frequencies is amplified. To improve this situation, the FFT can be used to alter the feedback so a flat spectrum can be achieved, indicating the lowest white noise level. If there is a spike at e.g. 2 or 7 Hz or another feedback is oscillating, this feedback would adjust itself till this spike is reduced to the white noise level (not beyond). Different simulation results for the frequency response are presented.

1 Introduction

At the Stanford Linear Collider (SLC) the beam position and angle is control by feedbacks at many different locations. A step function in the position of the injected beam into the linac would cause an over-correction if all the feedback would start to correct the situation in a simple way. One way is to link the feedback together and share the information in a cascaded way [1]. Here we will describe another approach. The history of the beam itself carries a lot of information, which can be used to predict the position (and angle) of the next pulse. Even if some upstream feedback is oscillating or there is a "time slot" separation (60 Hz oscillation), the fast Fourier transformation (FFT) shows which component is the highest and should be suppressed. The main idea is that the feedback should not have a fixed frequency response but vary its response due to the measured FFT spectrum. So instead of trying to reduce some zero-frequency component, which might not be there at the time, and amplifying e.g. some 2 Hz noise, the new FFT-oriented feedback would recognize the situation and would only reduce the highest peaks in the FFT spectrum.

Different insights of averaged response curves and their time behavior might be even interesting for the current cascaded feedback.

*Work supported by the Department of Energy contract DE-AC03-76SF00515.

2 General Feedback Issues

A feedback should keep a status, say the position of a beam, in a fixed state. Any deviations should be brought back as soon as possible, so the rms around this state is minimized. White noise cannot be reduced with a feedback, but any deviation like more low-frequency components can be suppressed. How a feedback works in general can be understood by looking at its frequency response.

2.1 Frequency Response

Let's take the position of beam pulses as an example. Many pulses jitter around zero or slowly drift away. The feedback tries to predict the position of the following pulse by using one or many pulse positions of the past. Applying the prediction might cause a reduction or amplification of the next position amplitude. This depends on the response type of the feedback and on the frequency. Fig. 1 shows a typical behavior of some simple feedbacks for mainly low frequency noise. Looking only at the last point, x_1 dotted, the feedback will reduce it to zero at low frequency, at $1/6 * 120 \text{ Hz} = 20 \text{ Hz}$ is the cross-over and the resulting amplitude will be twice as much at 60 Hz. For an average of the last two points, $(x_1 + x_2)/2$ dashed, the response doesn't overshoot that much, and so on till an average of the last six points, $(x_1 + x_2 + \dots + x_6)/6$ dashed again, has three oscillations.

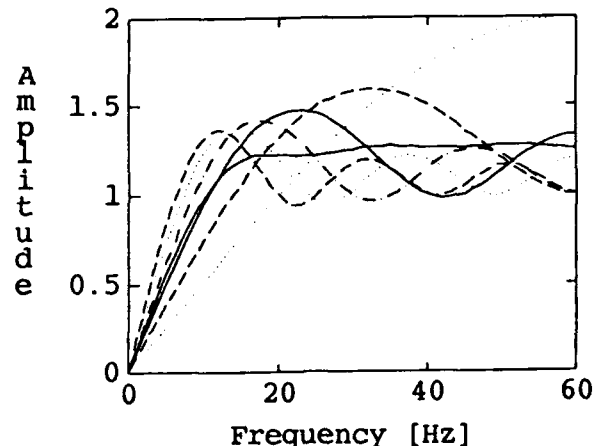


Figure 1: Feedback Response Function.

At 120 Hz all frequencies between 0 and 60 Hz can be recognized. Besides the wanted reduction at low frequency, a simple feedback looking at the last, or the last two, ... or the last six pulses gives always some oscillations. The average of these six possibilities (solid) shows a flat amplification.

An interesting behavior is an average of all these averages (solid), which is pretty flat for higher frequencies and doesn't show the overshoot directly after the first cross-over. This average gives additionally a time structure, later points are weighted stronger and earlier points are damped in such a natural way that the "necessary" overshoot is flat. This feedback would reduce any drifts up to about 10 Hz and amplify white noise above that by about a factor of 1.25; (60 pulses yield a reduction up to 3 Hz and an amplification of less than 4%).

2.2 Higher Frequencies

These feedbacks can be also used to reduce high frequency noise by changing the response function. Instead of predicting the last (x_1), the second last (x_2), ... or (x_4) top in Fig. 2, the feedback can guess minus the last, minus the second last, ... pulse (middle). By determining the frequency of the oscillation it would be possible to reduce any oscillation by just reacting on the last two points: For low frequencies up to 20 Hz x_1 is right, between 20 and 40 Hz x_2 (dashed middle) and between 40 to 60 Hz $-x_1$ will reduce all below the unit amplitude. By knowing the frequency f and taking $x_1 \cos \phi - x_2 \sin \phi$ with $\phi = 2 * \pi * f / 120$ Hz a reduction down to 0.55 or lower is achieved.

The goal is to obtain the frequency amounts by making an FFT or by other techniques and use the achieved information to adjust the response of a feedback that it can reduce all pulse to pulse variations to a flat white noise level (lowest possible amount).

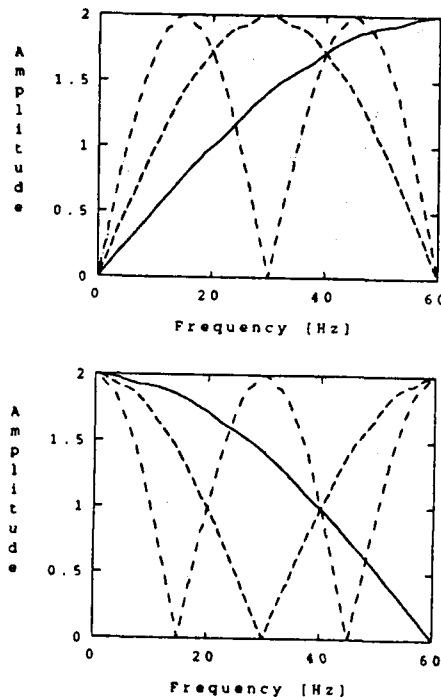


Figure 2: Other Response Functions.

Reacting on the last (x_1), second last (x_2), ... (top), or on minus the last, minus the second last, ... pulse (bottom) has different response functions.

3 Noise and Oscillations

The random white jitter noise of a beam position is difficult to improve, but any frequency component which sticks out in the Fourier transformation and is quite stable indicates some oscillation (or offset, drift for $f \approx 0$ Hz). Fig. 3 show a measurement of the beam angle at a linac feedback in the SLC.

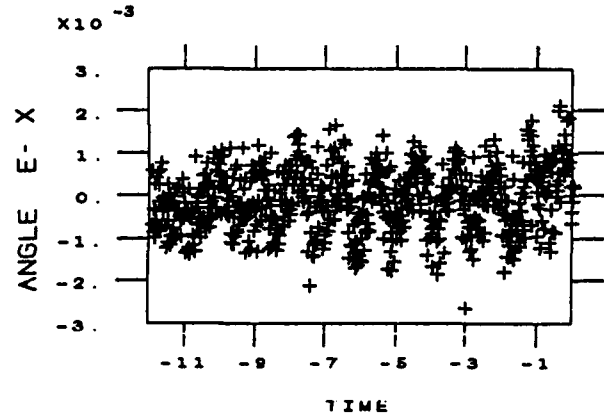


Figure 3: Oscillating Beam Angle.

Besides the noise jitter, the angle of the beam is oscillating with an amplitude of about one sigma of the noise increasing the rms. The sources are mainly feedbacks having too much amplification at these frequency.

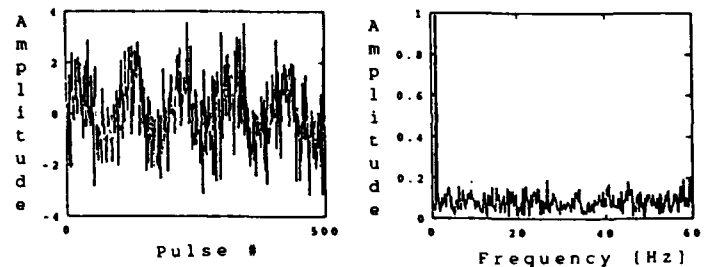


Figure 4: Simulation of Noise plus 1 Hz Oscillation.

The jitter noise and oscillation in the time frame (left) and its frequency amplitudes (right).

A simulation with a white noise jitter (Gaussian sigma = 1) and a 1 Hz oscillation (amplitude = 1) is shown in Fig. 4. The left shows the noisy oscillation for 500 pulses. The square-root of the FFT (not the power spectrum) is shown on the right and gives the amplitude of each of the 256 frequency bins. The 256 noise bins at about $A_f = 0.0625$ give an rms-amplitude

$$\sigma = \sqrt{\sum_{Bin} A_f^2} \quad (1)$$

of one. The oscillation would add about 1/2 "rms" in quadrature. But since the distribution of a sin is not Gaussian at all, but more like double horned corresponding to the two crests of the sin curve, the gaussian fit to the projection is about 30 % bigger, indicating that the single oscillation had about an 0.8 amplitude effect.

4 FFT-Orientation

The so far mentioned examples give some ideas how to implement the information of an FFT. Here some techniques and the comparison with Notch filters are given.

4.1 Simple Approach

Following the example with the last two pulses, here is a way to determine the weights of the desired correction. The last pulses $x_1, x_2 \dots x_n$ are multiplied by an $(n+1) \times n$ matrix M , which contains the information about the oscillation frequency

$$M_{mk} = \cos(\pi/n * (m-1) * k) * 2/n, \quad (2)$$

with $M = M/2$ if $m = 1$ or $m = n + 1$.

For $m = 0$ it is just an averaging over the last n pulses (no averages over different n to keep it simple); for $m = n$ it is $-x_1, +x_2, -, + \dots$, which would be a high number if there is a big time slot separation (60 Hz oscillation). The square of these numbers and a sin term are used as weights for the different predictions. This method can be compared with Notch-filters at zero, $f/2n, f/n, \dots f/2$ and a weight for each filter. An averaging like in Fig. 1 is also possible for a Notch filter.

4.2 FFT Weights

An FFT of the last n pulses results in also n numbers, which are the amplitudes and the phases at the corresponding $n/2(+1)$ frequencies. For instance, 6 pulses have an amplitude and phase value for 10, 20, 30, 40, 50 Hz and only an amplitude value for 0 and 60 Hz, since zero and Nyquist (60 Hz) frequency don't have a phase information. The amplitudes can directly be used as weights. Fig. 5 shows an example where eight+1 frequencies are totally suppressed.

The overshoot at low and high frequency needs more investigation, the rest is at least less than 55 % of the original amplitude. Going with this scheme to more pulses doesn't reduce these peaks dramatically but adds new points with total suppression. A time dependent averaging might reduce more the peaks, since the slope near the suppressed frequency is not as steep.

The interesting feature of this feedback is that it can suppress oscillations of any frequency below their initial amplitude. This means that the response of the feedback has no parts with amplification.

4.3 Future Work

The FFT-oriented feedback which adjusts the feedback response to the amounts in the FFT has a high goal to achieve. It should get the maximum out of the past pulses to achieve the lowest spread around the desired value.

The time dependent averaging should get the right damping. Also the behavior of higher order correction [2] may be considered. They achieve a flat curve at the suppressed frequency on the expense of a much worse amplification beyond the crossover point.

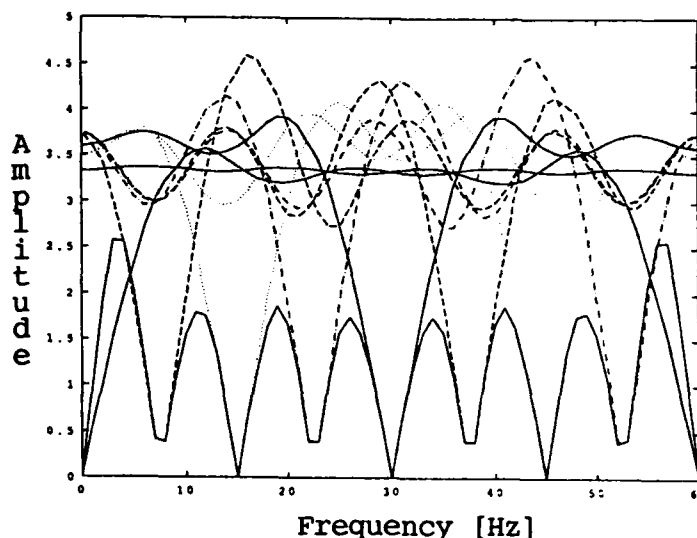


Figure 5: FFT-Oriented Feedback Response.

The lower solid curve shows the response by using the FFT information of oscillations with an amplitude of 3. The other curves are Notch filter type responses for eight pulses.

The response to steps or varying frequencies has to be checked. The many frequency components during a step may be ideally handled by an FFT-oriented feedback. But even whether it is good for frequent changes or better for stable oscillations can be adaptive: Taking many pulses into account slows down the response to fast changes, but these changes would tell the feedback to consider less pulses.

5 Conclusion

The study of a feedback which response is adjusted by the amount of the FFT of the last pulses has shown to reduce every single frequency component. Additionally averaging schemes were found which don't show oscillations in the amplification regime which should be more stable than the currently used response.

Acknowledgement

I would like to thank T. Himel and L. Hendrickson for many helpful discussions, and L. Hendrickson for reading the manuscript.

References

- [1] T. Himel, S. Allison, P. Grossberg, L. Hendrickson, R. Sass, H. Shoae, SLAC, *Adaptive Cascaded Beam-Based Feedback at the SLC*, PAC, Washington, May 1993.
- [2] R. Steining, *Sampled Feedback in the Linac Collider*, SLAC, CN-14, 1980.

Issues of the Transverse Feedback Systems Design at the SSC

W. Chou and J. Peterson
Superconducting Super Collider Laboratory*
2550 Beckleymeade Ave., Dallas, TX 75237

Abstract

The transverse feedback systems are needed at the SSC for several different reasons. The requirements of these systems are analyzed and specified. In addition to the general requirements (power, bandwidth and gain), specific attention is given to the noises in the systems, which need to be controlled in order to keep the emittance growth at a tolerable rate. A quantitative treatment is given to specify the allowable noise level in the feedback systems.

I. INTRODUCTION

The physics involved in the design of the SSC transverse feedback systems has been discussed in detail in Ref [1]. This paper is a brief overview of some selected issues. The feedback systems will serve four different purposes:

1. Correction of the injection errors:

At injection there are errors in the beam position, angle, energy and phase. These errors can lead to beam emittance growth if not corrected. Because the errors are relatively large (\sim mm), the feedback system needs high power.

2. Damping of the resistive wall instability:

The Collider beam tube is made of stainless steel with thin copper coating. At low frequencies (a fraction of the revolution frequency $f_0 = 3.441$ kHz), the skin depth is larger than the coating thickness Δ (~ 100 μ m). In this case, the resistive wall instability growth time is proportional to the product $\sigma_e \Delta$, where σ_e is the conductivity of copper under operation conditions. At the design value $\sigma_e \Delta = 2 \times 10^5 \Omega^{-1}$, the growth time is about 110 turns. Therefore, the feedback system needs a large gain.

3. Damping of the coupled bunch instability driven by the higher order modes (HOM) of the rf cavities:

The PEP 5-cell cavity is the original candidate for the Collider. Its HOM would cause both longitudinal and transverse coupled bunch instabilities. The growth is slow (in the order of seconds). But the feedback system needs a wide bandwidth. (This instability may be avoided if the single-cell cavity with HOM properly damped is to be used [2].)

4. Control of continuous emittance growth:

Because the radiation damping time of the protons in

the Collider is long (~ 13 hours), external perturbations will be remembered by the beam and lead to eventual emittance growth. A feedback system that keeps the coherent motion of the beam below certain allowable amplitude can effectively reduce the emittance growth rate. This system must be of low noise.

The noise of the feedback systems is a special concern of the SSC, because it may blow up the beam emittance. Previous experiences at the Tevatron and SPS show that the emittance dilution is increased when the transverse feedback system is on.

II. DAMPING PROCESS

Let us define a vector that represents the amplitude and phase of the collective beam oscillation:

$$\eta \equiv \frac{x}{\sqrt{\beta}} + i\left(\frac{\alpha x}{\sqrt{\beta}} + \sqrt{\beta}x'\right) \quad (1)$$

where α and β are the lattice functions. When a feedback system with gain g is applied, the amplitude $|\eta|$ will be decreased in one turn by:

$$\Delta|\eta| = -g|\eta|\cos^2\phi_1 \quad (2)$$

where ϕ_1 is the betatron phase at the pickup. Also, the phase angle is changed by:

$$\Delta\phi = -g\sin\phi_1\cos\phi_1 \quad (3)$$

Note that the fractional decrement in the amplitude is monotonic and on average is equal to $g/2$, while the change in phase angle oscillates and has a zero average. After N turns, we have:

$$|\eta(N)| = |\eta_0| \exp\left(-g\left(\frac{N}{2} + \frac{\sin(2\pi\nu(2N+1)) - \sin 2\phi_0}{4\sin 2\pi\nu}\right)\right) \quad (4)$$

Thus, the collective amplitude damps as an exponential with a characteristic period of $2/g$ turns, but the exponential also has some minor wiggles.

III. EMITTANCE GROWTH AT INJECTION

A. Emittance dilution due to injection errors

The magnitude of the coherent amplitude x_c due to injection position error δx and angle error $\delta x'$ in, say, the horizontal plane is:

$$|x_c|^2 = \delta x^2(1 + \alpha_x^2) + 2\alpha_x\beta_x\delta x\delta x' + \beta_x^2\delta x'^2 \quad (5)$$

*Operated by the Universities Research Association, Inc., for the U.S. Department of Energy under Contract No. DE-AC35-9ER40486.

For the case of an injection energy error $\delta E/E$, the resultant coherent amplitude is:

$$|x_c|^2 = \left(\frac{\delta E}{E}\right)^2 \left(D_x^2(1+\alpha_x^2) + 2\alpha_x\beta_x D_x D'_x + \beta_x^2 (D'_x)^2\right) \quad (6)$$

where D_x and D'_x are the dispersion function and its slope. The eventual fractional emittance increase produced by decoherence is:

$$\frac{\delta\epsilon_x}{\epsilon_x} = \frac{|x_c|^2}{2\sigma_x^2} \quad (7)$$

in which σ_x is the rms beam width.

B. Decoherence

The decoherence due to the chromaticity ζ and momentum spread σ_p/p and due to the non-linear magnetic fields has been analyzed in Ref [3]. The centroid of the bunch with an initial betatron amplitude a_0 has after N turns the amplitude $a(N) = a_0 A(N)$, where $A(N)$ is the decoherence factor. In the chromaticity case, one has

$$A(N) = \exp\left(-2\left(\zeta \frac{\sigma_p}{p} \nu_s^{-1} \sin(\pi \nu_s N)\right)^2\right) \quad (8)$$

where ν_s is the synchrotron tune. If ν_s is independent of synchrotron amplitude (linear approximation), the whole bunch decoheres and then perfectly re-coheres every synchrotron period. For the Collider at injection, $\sigma_p/p = 1 \times 10^{-4}$, $\nu_s = 2.2 \times 10^{-3}$, and for a residual chromaticity of 5, the linear decoherence factor oscillates between 1.0 and 0.90 at the synchrotron period of 455 turns and, therefore, does not significantly affect the feedback requirements.

In the non-linear fields case, simulations have shown for typical magnetic error distributions in the lattice that the horizontal tune is well represented by

$$\nu_x = \nu_0 - \mu x^2 \quad (9)$$

where ν_0 is the tune at zero betatron amplitude, x is the betatron amplitude, and μ is about $1.4 \times 10^{-4} \text{ mm}^{-2}$ [4]. The decoherence factor is:

$$A(N) = (1 + (2\pi\sigma_x N)^2)^{-1} \quad (10)$$

where $\sigma_x = 2\mu\sigma_x^2$ is the rms tune spread. From Eq. (10), one can define the decoherence time:

$$\tau_d = \frac{T_0}{\sigma_x} \quad (11)$$

where T_0 is the revolution time. For the Collider at injection, σ_x^{-1} is 1.8×10^4 turns.

IV. CONTINUOUS EMITTANCE GROWTH

A. Continuous emittance growth without feedback

Consider the beam in a storage ring in which there is a continuous, small emittance growth $\dot{\epsilon}_0$ due to small and random dynamic disturbances, such as, quadrupole motion or power-supply jitter. These disturbances continually produce small-amplitude collective betatron oscillations, which continually smear out through decoherence

and so transform into emittance growth. This growth rate can be expressed in terms of an average collective amplitude x_{av} and the decoherence time τ_d :

$$\dot{\epsilon}_0 = \frac{x_{av}^2}{2\beta} \cdot \frac{1}{\tau_d} \quad (12)$$

During the collision period, the decoherence is dominated by the beam-beam interaction, which produces a large tune spread. For a Gaussian bunch, the rms tune spread can be obtained from a numerical integration [5]:

$$\sigma_\nu \approx 0.2 \xi \quad (13)$$

in which $\xi = N_b r_p / (4\pi\epsilon_N)$ is the beam-beam parameter (N_b = protons per bunch, r_p = classical proton radius, ϵ_N = normalized rms beam emittance). For the Collider in nominal case σ_ν is 7.6×10^{-4} , giving a typical decoherence time of 1.3×10^3 turns.

B. Continuous emittance growth with feedback

From Eq. (4) one can define the feedback damping time:

$$\tau_f = \frac{2}{g} T_0 \quad (14)$$

The total emittance growth rate with feedback is [1]:

$$\dot{\epsilon}_f = \dot{\epsilon}_0 \left(\frac{2\sqrt{2}\tau_f}{\tau_d}\right)^2 = \dot{\epsilon}_0 \left(\frac{4\sqrt{2}\sigma_\nu}{g}\right)^2 \quad (15)$$

where $\dot{\epsilon}_0$ is defined in Eq. (12). Therefore, if the feedback gain is big enough such that $g > 4\sqrt{2}\sigma_\nu$, we will have $\dot{\epsilon}_f < \dot{\epsilon}_0$, i.e., the feedback will reduce the emittance growth rate.

C. Noises in the feedback system

If there are noises in the feedback system equivalent to a beam amplitude x_N at the pickup, then there is a contribution $f_0(gx_N)^2$ to the collective amplitude. Thus, Eq. (15) has to be modified and takes the form

$$\dot{\epsilon}_f = \left(\dot{\epsilon}_0 + \frac{f_0 g^2 x_N^2}{2\beta}\right) \cdot \left(\frac{4\sqrt{2}\sigma_\nu}{g}\right)^2 \quad (16)$$

Let ϵ_0 be the initial emittance, one may also define the emittance growth rate as

$$\frac{1}{\tau_c} \equiv \frac{\dot{\epsilon}_f}{\epsilon_0} \equiv \frac{1}{\tau_{ext}} + \frac{1}{\tau_{noise}} \quad (17)$$

in which

$$\frac{1}{\tau_{ext}} = \frac{\dot{\epsilon}_0}{\epsilon_0} \cdot \left(\frac{4\sqrt{2}\sigma_\nu}{g}\right)^2 \quad (18)$$

is the growth rate due to external sources, and

$$\frac{1}{\tau_{noise}} = \frac{1}{\epsilon_0} \frac{f_0 g^2 x_N^2}{2\beta} \left(\frac{4\sqrt{2}\sigma_\nu}{g}\right)^2 = 0.64 f_0 \left(\frac{x_N}{\sigma_x}\right)^2 \Delta\nu^2 \quad (19)$$

where we have converted σ_ν to the total tune shift $\Delta\nu$ (which equals ξ times total number of interaction points)

Feedback system	A	B	C
Purpose	Injection errors	Resistive wall instability, Emittance control	Coupled bunch instability
Gain	0.04	0.1	0.02
Damping time	50 turns	20 turns	100 turns
Maximum correction	± 2 mm	± 100 μ m	± 40 μ m
Kick angle	0.27 μ rad	0.04 μ rad	0.003 μ rad
Kicker length	4 m	4 m	4 m
Kicker voltage	1 kV	150 V	150 V
Kicker power	40 kW	0.9 kW	0.9 kW
Bandwidth	500 kHz	500 kHz	≥ 30 MHz
Noise level	-	≤ 2 μ m	≤ 1 μ m
Resolution limit	0.02 μ m	0.02 μ m	0.16 μ m

using Eq. (13). It is interesting to note that the emittance growth rate due to the noises in the feedback system is independent of the gain. It is also interesting to compare this result with that presented in Ref. [6], which was obtained using the well established stochastic cooling theory. Eq. (19) above differs from Eq. (8) in [6] by approximately a factor of 2.

V. FEEDBACK SYSTEMS

Three systems are required by the Collider: A. Injection error correction; B. Resistive wall instability and emittance control; C. Coupled bunch instability damping. System A has high power. It is used only during injection. Its bandwidth is determined by the batch spacing (1.7 μ s). System B needs large gain but low power. It has demanding low noise requirement. Its bandwidth is also determined by the batch spacing. System C has a wide bandwidth, which is determined by the bunch spacing (16.7 ns). It does not need much power or gain, but the noise level must also be low. (It may be possible to combine B and C into one system.)

All the three systems can share the same pickups. But at least two different kickers are needed — one for A (high power), the other for B and C (low power). Each system has its own signal processor. These systems will be located in the west utility region at the high β -function points. The pickups should avoid the dispersive region. Otherwise the beam loading induced coherent synchrotron oscillation may cause coherent betatron motion through dispersion.

The proposed 2-pickup, 2-turn scheme has certain advantages. By using two pickups, the performance of the systems will be independent of the betatron tune of the machine. By comparing the signals from two (or more) consecutive turns, one can reject the closed orbit signal that is not needed by the feedback systems.

The requirements of the power, bandwidth, gain and noise level are listed in the table above. The noise level is calculated by Eqs. (16)-(19), assuming the allowable emittance growth time τ_e is 24 hours, while the growth time τ_{ext} due to external excitations is 0.1 hour.

The theoretical limit of the pickup resolution comes from the thermal and electronic noises. It can be approximately expressed by:

$$\Delta x = \frac{2b}{I_{av} \sin(\frac{\omega \ell}{c})} \sqrt{\frac{k_B T \cdot \Delta f \cdot 10^{NF/10}}{Z}} \quad (20)$$

in which k_B is the Boltzmann constant, T the temperature, Δf the bandwidth, NF the noise factor (in dB), b the half distance between two pickup electrodes, Z the characteristic impedance, ℓ the length of the electrodes, c the velocity of light, and I_{av} the average beam current. The value of Δx must be smaller than x_N given by Eq. (16) in order to avoid the emittance growth problem.

There are several other error sources that are not included in this analysis but may also put a limit to the pickup resolution. These include the least significant bit (LSB) error if a digital system is used, and the mechanical vibration of the pickup. The LSB error may be significant. As an example, the Tevatron Super-damper utilizes an 8-bit digital system for signal processing. The full scale is about 5 mm, which is determined by the residual orbit error. Therefore, the maximum LSB error is about 20 μ m. It is much larger than the theoretical limit Δx and is a possible source of the emittance dilution increase discussed in Section I.

VI. REFERENCES

- [1] W. Chou and J. Peterson, "The SSC Transverse Feedback Systems," *Proc. Feedback System Workshop*, Erice, Italy, November 12-21, 1992; also see SSCL-623 (1993).
- [2] W. Chou, "Choice of the RF Cavity for the SSC Collider," this conference.
- [3] R. E. Meller et al., SSC-N-360 (May 1987).
- [4] G. Bourianoff, private communication.
- [5] V. A. Lebedev et al., INP Preprint 91-120 (1991).
- [6] D. Boussard, SL/Note 92-79 (RFS), CERN (1992).

A Digital Feedback System for Orbit Stabilization*

A. Friedman, E. Bozoki, O. Singh and J. Smith
National Synchrotron Light Source,
Brookhaven National Laboratory,
Upton, NY 11973

Abstract

We are reporting on the design and preliminary results of a prototype digital feedback system for the storage rings at the NSLS. The system will use a nonlinear eigenvector decomposition algorithm. It will have a wide dynamic range and will be able to correct noise in the orbit over a bandwidth in excess of 60 Hz. A Motorola-167 CPU board is used to sample the PUE's at a minimum rate of 200 Hz and an HP-742rt board is used to read the sampled signals and to generate a correction signal for the orbit correctors.

1 Introduction

In synchrotron radiation facilities the stability of the orbit (i.e. the time dependent changes in the orbit) is extremely important. An unstable orbit reduces the effective brightness of the photon source and increases the dynamic aperture of the beam thus reducing lifetime. Usually, the orbit can be stabilized with a feedback system. At present there are two feedback systems operating at the light source. A global feedback [1], using an harmonic correction algorithm, and a local feedback [2] that achieves higher beam stability at the insertion devices. The feedback systems are very successful at reducing beam noise at frequencies of up to 50 Hz. However, above 30 Hz there is a significant reduction of gain in the system.

After the present feedback systems were implemented, significant noise was observed at frequencies above 50 Hz. Thus, there is a need for a higher bandwidth of the feedback system. In addition, the present systems are based on analog hardware. Hence, they are not flexible to changes in the algorithm. It is therefore beneficial to develop a digital feedback system that will satisfy the present needs and will be flexible enough for future improvements.

2 Algorithm used

In implementing the digital feedback system, we are using the eigenvector decomposition based orbit correction method described in Refs. [3, 4]. This method will yield the 'minimum' kick vector required for a desired accuracy of orbit correction.

For any given circular machine, the response matrix A 'translates' between a $\tilde{\Theta}$ kick vector and the resulting \vec{X} orbit change:

$$\vec{X} = A\tilde{\Theta} \quad (1)$$

In general, the number of correctors and monitors are different, consequently the response matrix A is rectangular. Let λ_j be the eigenvalues and $\hat{\theta}_j$ the corresponding eigenvectors of the $A^T A$ matrix. The orbit change corresponding to the j -th eigenvector is:

$$\vec{x}_j = A\hat{\theta}_j \quad (2)$$

The \vec{X}_o orbit to be corrected is essentially decomposed in terms of these \vec{x}_j 'eigen' orbits:

$$\vec{X}_o = \sum_{j=1}^{N_c} c_j \cdot \vec{x}_j \quad (3)$$

where

$$c_j = \vec{X}_o \cdot \vec{x}_j \quad (4)$$

Substituting Eq. (2) into Eq. (3) we obtain

$$\vec{X}_o = A \sum_{j=1}^{N_c} c_j \hat{\theta}_j \quad (5)$$

that is, the kick vector which corrects the \vec{X}_o orbit, can be obtained from the eigenvector decomposition of this orbit as:

$$\tilde{\Theta} = \sum_{j=1}^{N_c} c_j \hat{\theta}_j / \sqrt{\lambda_j} \quad (6)$$

3 Architecture

3.1 Hardware

The system will rely, mostly, on existing hardware with several modifications. The basic layout is depicted in Fig. 1. There are four micros involved. The PUE micro will sample the PUE data at 200 Hz rate (but with sampling time of 2 msec). The data is then transferred to the feedback micro which calculates the orbit correction and optimizes it. The kick values are then transferred into the trim micro which, in its turn, sets the new values to the trims power supplies. The communication between the micros is done directly on the VME bus through shared memory. The most computational intensive task is that of the feedback micro. Hence, we chose an HP 742rt, which we estimate to run six times faster than a Motorola 167/162 for that kind of application. We have added a fourth micro (control micro) to the design in order to isolate the PUE and feedback micros from the general control

*Work performed under the auspices of the U.S. Dept. of Energy under contract no. DE-AC02-76CH00016.

network. These micros are expected to operate at close to full load. Thus, any requests addressed to them on the network may slow them down, reducing the feedback rate. The control micro will sample the PUE micro at 20 Hz and will make this data available to workstations for existing control programs [5] such as Real Time Orbit, Fast Orbit History, etc. This micro will also send commands to the feedback micro and display data on its status. If the need arises, it is possible that either the PUE micro or the feedback micro will write 200 Hz orbit history to a DAT tape.

In order to prevent aliasing problem the PUEs will be set up with an analog low pass filter of a 100 Hz.

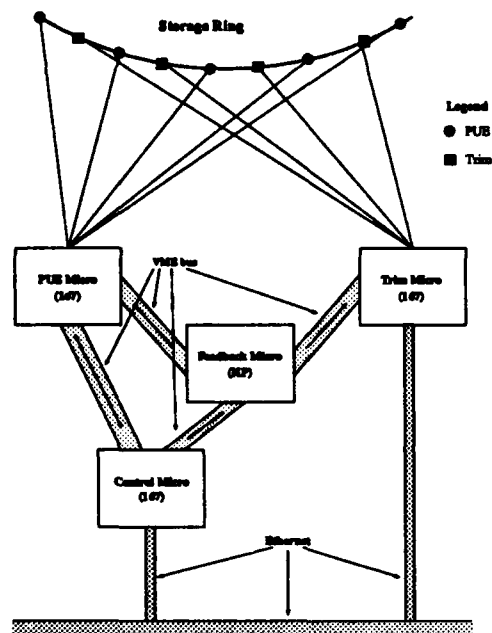


Figure 1
Layout of the feedback system.

3.2 Software

The PUE, trim and control micros will use the existing monitor [6]. Their programming will be modified to place the read points and set point into shared memory, and to synchronize data collection with the feedback micro. The device read points for the PUEs will be read through the control micro, and will be updated at a frequency of 20 Hz, which is the present PUE sampling frequency. A new monitor will be written for the feedback micro, based on the HP-RT operating system. The orbit correction code is a modification of the code that was used for orbit correction in Refs. [3, 4]. This is an object oriented code written in C++.

4 Preliminary studies

4.1 Algorithm

A preliminary study was performed on the NSLS VUV ring, using the existing global feedback system. The eigen-orbits and eigen-kicks [3, 4] were fed to the feedback system instead of the harmonic data. The result was a reduction of 17 db in the noise up to 20 Hz. It is expected that the future system will perform much better since it includes more trims and PUEs and it optimizes the kick values.

4.2 Timing

From preliminary study, we estimate the computation time in the feedback micro to be 1.5 msec/cycle. The sampling time of the PUEs is 2 msec and the writing time of the trims is 1 msec. It is, thus, possible to complete a cycle in 5 msec, which is the maximum time allowed in order to achieve 200 Hz rate. However, it is necessary to synchronize the operation of the three micros.

I. REFERENCES

- [1] L.H. Yu et al., Real Time Closed Orbit Correction System, Proc. IEEE PAC, p.1792, 1989.
L.H. Yu et al., Real Time Global Orbit Feedback System for the NSLS X-ray Ring, Proc. IEEE PAC, p.2542, 1991.
- [2] R.J. Nawrocky et al., Automatic Steering of X-ray Beams from NSLS Insertion Devices Using Closed Orbit Feedback, Proc. IEEE PAC, p.1856, 1989.
Om Singh, Electron Beam Stability and Beam Peak to Peak Motion Data for NSLS X-ray Storage Ring, In this proceedings.
- [3] Eva Bozoki and Aharon Friedman, Optimization Method for Orbit Correction in Accelerators, In this proceedings.
- [4] Aharon Friedman and Eva Bozoki, Use of Eigen Vectors in Understanding and Correcting Storage Ring Orbits, In preparation.
- [5] J. Smith, S. Ramamoothy, Y. Tang, J. Flannigan, S. Sathe, J. Kean, S. Krinsky, NSLS Control System Upgrade Status, In this proceedings.
- [6] S. Ramamoothy and J. Smith, NSLS Control Monitor and its Upgrade, In this proceedings.

Results From the AGS Booster Transverse Damper¹

D. Russo, M. Brennan, M. Meth, T. Roser
Brookhaven National Laboratory
AGS Building 911A, Upton, NY. 11973 USA

Abstract

To reach the design intensity of 1.5×10^{13} protons per pulse in the AGS Booster, transverse coupled bunch instabilities with an estimated growth rate of $1500s^{-1}$ have to be dampened. A prototype transverse damper has been tested successfully using a one turn digital delay and closed orbit suppression implemented in a programmable gate array. An updated damper, which includes an algorithm to optimize damping for a changing betatron tune, will also be presented.

I. INTRODUCTION

As the intensity of protons per pulse in the AGS Booster increases, the resistive loss in the vacuum pipe will induce a force on the beam which causes the beam's transverse oscillations to increase with time and ultimately results in beam loss. [1] Figure 1A illustrates the damping method used to prevent beam loss from such coupled bunch transverse instabilities. On every turn of a particular bunch, its position at a PUE sensor is measured and processed. The kick needed to dampen transverse oscillations, once calculated, is placed on a queue and is clocked out as the beam arrives at the kicker on the next turn.

The processing unit consists of several sub-blocks which are illustrated in figure 1.B. The sum and difference signals are normalized using an analog normalizer. The normalized voltage signal is then integrated, which results in a voltage level proportional to the transverse position of the beam with respect to pipe center. The horizontal and vertical beam position values are then digitized to an eight bit resolution. These two eight bit values are fed into a digital block which generates the proper kick to apply to the bunch as it passes through the kicker plates on the next turn.

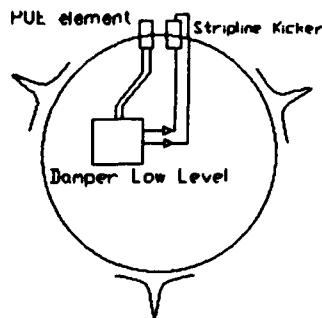


Figure 1A. Damper system in the AGS Booster



Figure 1B. Sub-blocks in the Damper low level system

II. DESIGN OF DAMPER SYSTEM

A. Damping Algorithm

The goal of the Damper is to reduce the coherent dipole motion of the beam. The coherent motion of the PUE can be expressed in terms of the Courant-Snyder invariant ϵ :

$$\epsilon = \pi(\gamma X^2 + 2\alpha XX' + \beta X'^2)$$

where α , β , γ are the Twiss parameters and X , X' are the position and angle of the beam at the PUE. A kick θ at the kicker location will change ϵ by:

$$\begin{aligned} \Delta\epsilon &= 2\pi(\alpha X + \beta X')\theta \\ &= 2\pi[(\alpha \cos(2\pi Q) - \sin(2\pi Q))X_1 + \beta \cos(2\pi Q)X'_1]\theta \end{aligned}$$

where the second line shows $\Delta\epsilon$ as a function of the position and angle of the previous turn; Q is the betatron tune. The expression for $\Delta\epsilon$ becomes particularly simple for $Q=4.75$:

$$\Delta\epsilon = 2\pi X_1\theta$$

Therefore, by making the kick proportional and opposite in sign to the previous turn, ϵ will be reduced monotonically. This mode of operation was used in the prototype system.

To accommodate a betatron tune other than 4.75, data for X'_1 must also be taken. In a future Damper implementation, the PUE position information from two turns previous to the kick, $X_{2,1}$ is used as well as $X_{1,1}$. $\Delta\epsilon$ is then:

$$\begin{aligned} \Delta\epsilon &= -G[(\cos(4\pi Q)/\sin(2\pi Q))X_{1,1} + (\cos(2\pi Q)/\sin(2\pi Q))X_{2,1}] \\ &= -G[C_1 X_{1,1} + C_2 X_{2,1}] \end{aligned}$$

where G is the loop gain and the coefficients C_1 and C_2 are tune dependent. They are shown in Figure 2. With these coefficients, the damping rate is independent of the betatron tune. Such a scheme will be implemented with a non-recursive digital filter.

¹This project was made possible through funding from the U.S. DOE.

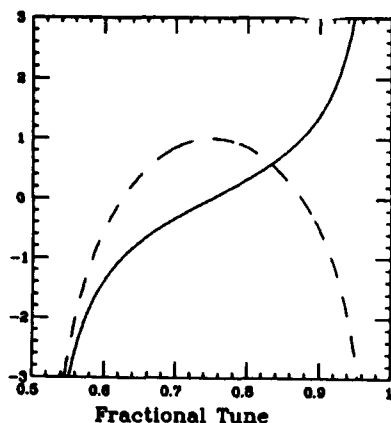


Figure 2. Coefficients for 2-turn damping algorithm. The solid line is C_2 and the dashed line is C_1 .

B. Analog normalizer

As was explained in the introduction, the PUE difference signal is normalized with the sum signal in order to obtain an intensity independent value for position. The schematic illustrated in figure 3 shows the analog normalizing circuitry used in the system. Essentially, the sum signal is the input to an auto-gain control circuit which keeps the output level of a voltage controlled amplifier constant for a changing sum intensity.

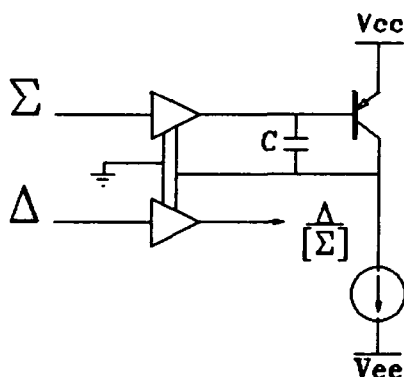


Figure 3. Schematic for Analog Normalizer

This is achieved by using the output from the amplifier to limit the charging of a capacitor. The voltage on the capacitor, in turn, feeds back to the gain control of the amplifier. Thus a feedback is established in which the charge on the capacitor, which is directly related to the time integral of the sum signal, controls the level of the output. As the intensity of the sum signal increases, less current is available to charge the capacitor, which results in less gain on the amplifier. Consequently, the output level is always held at a set level determined by the amount of dc current set to charge the capacitor. The result of this auto-gain control is that the voltage controlling the gain is related to the inverse of the time integral of the sum signal. By using this same

voltage to set the gain of a matched amplifier whose input is the difference signal, the desired normalization takes place. The advantage of this particular scheme is that a dual voltage controlled amplifier with a 40dB dynamic range could be utilized, resulting in a high level of sensitivity.

C. Fast Integrator

The output from the normalizing circuitry, must be integrated every rf period of the accelerator. In the case of the AGS Damper, the bunches have a maximum duty factor of .75 and a maximum frequency of 4.5 MHz. Also, it is true that the signals from the PUE are AC coupled, which means that no set zero baseline is available for integration. The schematic shown in figure 4. represents the scheme which is utilized in the damper system. The normalizer signal is split into two integrating channels, which effectively halves the bandwidth through either channel. This is achieved with the use of fast track and hold amplifiers. As a result of this scheme, one amplifier tracks the current bunch while the other holds the baseline level. Consequently, a zero baseline level is established by subtracting the held level from the channel signal. Once the integration is finished, the two channels are analog multiplexed to form a single channel which outputs an integral value for every beam bunch

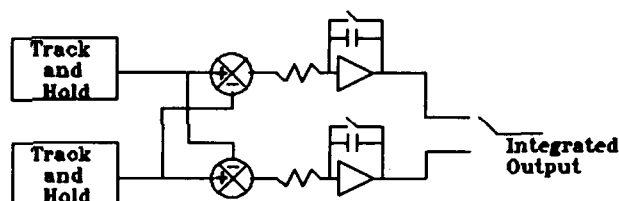


Figure 4. Fast Integrator Circuitry

D. Digital Kick Calculator

In section A. it was explained that, in the case of a fractional betatron tune of .75, the damping kick is directly related to the current position value. However, the closed orbit component of the position value was neglected. It is necessary, to subtract the portion of the position information which is due to the closed orbit. The block diagram illustrated in figure 5 demonstrates a way to digitally implement closed orbit suppression. Initially, all registers and memory is cleared. As position information is fed into the algorithm, a running average is taken. Also the values are stored on a circular buffer. In this implementation, an average of 32 bunches is taken. Once 32 values are stored in the buffer, the next bunch position information overwrites the earliest value in the buffer and an average of these 32 values is taken. Since 32 is a power of 2, averaging is done simply by using an accumulator whose output is shifted 5 bits, ie. divided by the number 32. Once this value is obtained, it is subtracted from the current position information. The value is then placed into

a register and is latched to the output at the appropriate time. The digital system is implemented using a programmable logic array, which integrates all the logical blocks illustrated in figure 5. except the 32x8 bit buffer. A fast static ram memory device was used to implement the buffer.

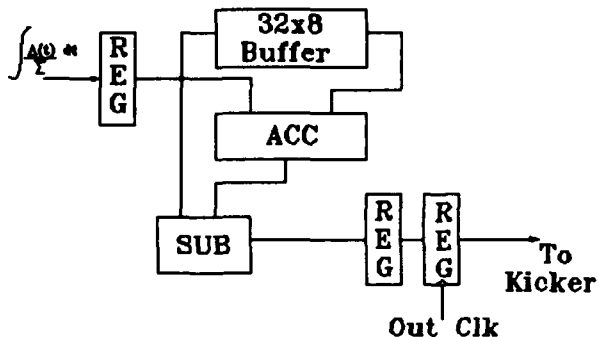


Figure 5 Digital Closed Orbit Suppression Logic

E. Timing Considerations

It is crucial for the proper operation of the AGS Booster damper system that retrieval of position information be synchronized with the beam and the damping kick be administered at the correct time with respect to the beam. Consequently, timing signals to the system must be synchronized with the Booster rf frequency. The rf low level system produces an rf signal which is phase locked to the accelerating bunches at the location on the ring where the damping system resides. This signal is used to control and synchronize all signals necessary for damper operation. One problem which arises is that there is a fixed output delay time from the moment of latching the output data to the time when voltage is developed on the kicker plates. This time delay corresponds to a phase shift which changes with rf frequency. In order to compensate for this delay, a second rf signal was sent to the damper system which is time advanced by the exact amount of output delay existing in the system. In this way, the voltage on the kicker plates is phase locked to the beam at all frequencies.

III. RESULTS OF PROTOTYPE SYSTEM

In order to simplify construction and experimentation, the first prototype system was constructed for damping in one transverse direction; the vertical plane was chosen due to the higher likelihood of instability in this dimension. Also, as was explained in section A, the prototype system was designed to operate with a betatron tune of 4.75. Making this tune assumption enables the simplification of the digital kick calculation, since at this tune the kick is proportional to the position value of the bunch on the previous turn. The prototype system allowed for switching the polarity of the

kicker voltage, which enabled both damping or antidamping. This was useful, since successful antidamping causes beam loss which can be seen on a current monitor. In order to show damping, a small kick was applied to produce transverse oscillations that slowly decayed with time when the damper system was off. With the damper system activated, the coherent oscillations could be dampened within about 1.5 ms. With anti-damping on, a persistent oscillation could be observed and, with increased loop gain, beam was lost.

IV. REFERENCES

- [1] E. Raka, "Damping the transverse resistive wall instability in the AGS Booster," AD Booster technical note No. 137, Brookhaven National Labs, New York, 1989.

Single Board Op-Amp Beam Position Monitors Electronics*

Mark Ball, Timothy JP Ellison, Brett J Hamilton
The Indiana University Cyclotron Facility
2401 Milo Sampson Lane, Bloomington, IN 47405

Abstract

A new approach has been developed for beam position monitors (BPM) [1] in the new 600 keV beamline [2]. A single four layer printed circuit board, attached with short (0.3 m) cables to the electrodes, processes the raw signals and outputs voltages proportional to the beam intensity, horizontal and vertical position, and quadrupole moment. Newly-available high-speed operational amplifiers are used exclusively instead of more conventional rf components. The rf input frequency can be as high as 36 MHz, and the IF frequency is 100 kHz. The output signals from each monitor will be digitized by the VME-based control system which will provide operator displays and use the information as feedback in automatic loops controlling the beam position, envelope, and dispersion. The signal processing at each BPM location eliminates the need for expensive multiplexing and routing of signals to a central processing location. The cylindrical electrode is split into four equal segments allowing both horizontal and vertical information to be obtained at each location thus minimizing the required beamline insertion length.

I. INTRODUCTION

The new high intensity polarized ion source (HIPIOS) [3] being commissioned at IUCF is designed to increase the

intensity of the polarized beams by an order of magnitude over that provided by the existing polarized ion source. The 30 m long beam transport system connecting the 600 kV ion source terminal to the cyclotron has been designed with the goal of increasing the transmission efficiency of the beams from the source to extraction from the main stage cyclotron from the present range of 4 - 10% to as high as 20 - 50%. The BUM system is the key diagnostic in this new beamline and will be used for non-destructive monitoring of the beam intensity and measurement and control of the beam position, dispersion, and envelope.

Each BUM electrode will have a dedicated set of electronics contained on a single four layer circuit board. This approach, although requiring more electronics, is more efficient and cost effective than a single processing approach. Radio frequency (rf) signals remain localized to the electrode location thus eliminating costly cable runs and multiplexing systems. The position and intensity information from any electrode is available to the computer at all times, thus eliminating timing complications and increasing the system bandwidth.

This approach is made possible by the use of newly available, low cost operational amplifiers and a custom, high density circuit board. The system (Fig. 1) consists of four major subsystems: (1) the pickup electrode, (2) the rf section, (3) the mixer/intermediate frequency (IF) section, (4) and the

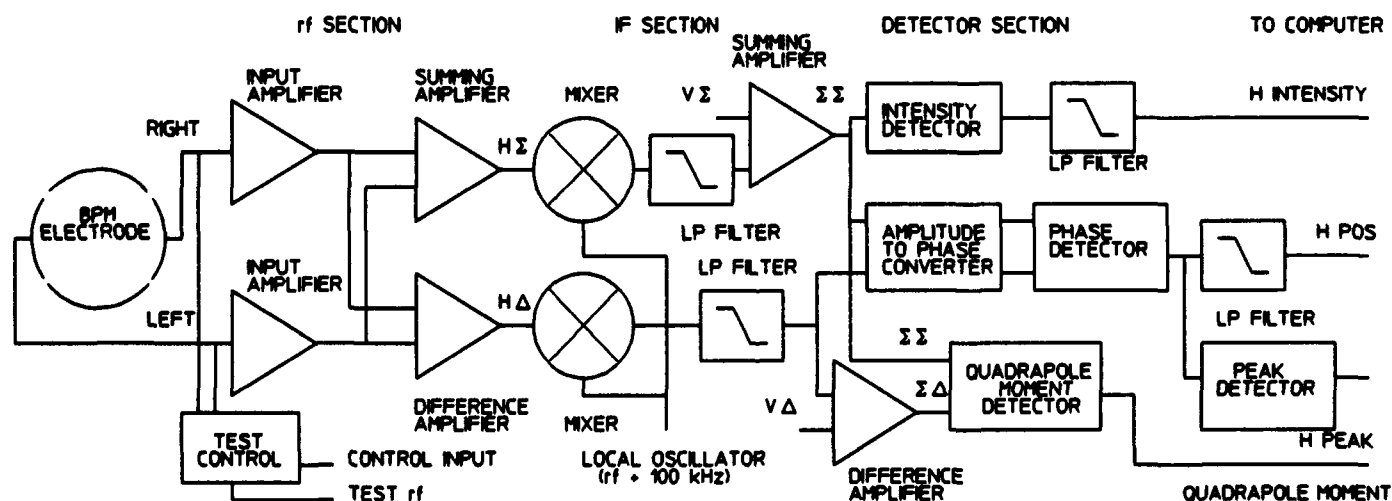


Figure 1. Block diagram of BPM electronics.

*Work supported by the National Science Foundation (Grant No. NSF PHY 90-15957).

detector section.

The system will operate at rf frequencies in the range from 27 to 35 MHz though operation in the range from < 1 to > 50 MHz is possible; the IF frequency was limited to 100 kHz to ease the gain-bandwidth requirements of amplifiers in the IF section. The four layer circuit board is 7.5 inches wide and 9 inches long. It houses 23 integrated circuit (IC) chips, 250 resistors, 130 capacitors and various other support components. The required supply voltages are ± 5 and ± 15 V. Each board has a local oscillator, split 4 ways, and 4 rf test inputs with control bits (left, right, up, and down). The output voltages are proportional to the beam intensity, horizontal and vertical position, and quadrupole moment. Two other outputs provide voltages proportional to the amplitude of low frequency modulation of the beam position in each plane.

II. SYSTEM DESCRIPTION

A. Pickup electrode and rf section

The electrode diameter, D , is 76 mm and length, L , is 50 mm. The total input capacitance, C , which is the sum of the electrode, input cable and amplifier capacitances, is ≈ 75 pF. The cable length from electrode to amplifier is as short as possible to minimize the capacitance and maximize the effective electrode impedance, Z , which is given by:

$$Z = \frac{L}{\beta c C} \quad (1)$$

where c is the speed of light and $\beta = v/c = 0.0357$ for 600 keV protons. Using the above values, we obtain a Z of 62 Ω .

The input buffer amplifier is a Comlinear CLC400, a fast settling, wideband, operational amplifier [3]. Its input noise is 6.3 nV/ $\sqrt{\text{Hz}}$. The noise voltage, V_{noise} , signal voltage, V_{signal} , and rms position resolution, δ , are given by:

$$\begin{aligned} V_{\text{noise}} &= 6.3 \frac{\text{nV}}{\sqrt{\text{Hz}}} \sqrt{BW} \\ V_{\text{signal}} &= \frac{IZ}{4} \\ \delta &= \frac{V_{\text{noise}} D}{\sqrt{2} V_{\text{signal}}} \end{aligned} \quad (2)$$

where I is the beam current which will be in the range from 1 to 100 μA , and BW is the output bandwidth (2.8 kHz). For beam currents in this range we expect δ to vary from 1.2 mm to 12 μm . Bunching factor is not included in Eq. 2 since the detector is tuned to a single harmonic of the fundamental frequency.

The left and right, or up and down, input signals are

both added and subtracted after the input buffer amplifiers. The sum, Σ , and difference, Δ , signals are then converted to IF signals.

Each BUM circuit board has an rf test signal input with computer on/off control. This test signal can be applied to any combination of the four electrode inputs. These signals are used as a system operational and diagnostic test as well as for initial calibration.

B. Mixer/IF section

The IF is derived by mixing the rf beam signal with a local oscillator signal having a frequency 100 kHz higher than the beam signal using a Mini-Circuits SRA-3H [4] level 17 mixer having a maximum rf input power level of 10 dBm. A 100 kHz low pass filter follows the mixer. The amplifiers used in the IF section are Elantec EL2424 high speed op-amps [5]. The EL2424 has a unity-gain bandwidth of 60 MHz. All of the amplifiers in the IF are also used as active filters to further reduce the level of higher frequency products from the mixers.

C. Position detector

The position detection is accomplished using the standard amplitude to phase conversion technique [6]. The two resulting signals are converted to digital signals, or leveled, using a Maxim, Max901 quad, high-speed, voltage comparator [7]. The phase is detected with an exclusive-or gate. The phase detector output is offset and amplified. The sensitivity is 0.26 V/mm, with a fullscale output of ± 10 V.

A system of 4 steerers operating at 10 Hz will move the beam along an ellipse having the same shape as the measured beam emittance at the beginning of the line. The peak detector section is used to measure the amplitude of the position modulation at each BUM consequently giving the operators an online measurement of the beam envelope. The computer will also use this data to optimize the strength of quadrupoles. The position signals are sent through half-wave rectifiers, then filtered and amplified to produce a dc signal proportional to the position modulation amplitude with less than 2% ripple.

The intensity output of the BUM is the rectified sum of the horizontal and vertical Σ channels. The intensity range is 1 – 100 μA .

The quadrupole moment is a test circuit yet unproven in design or usefulness. This circuit calculates the ratio of the difference in the Σ signals to the sum of the Σ signals using a circuit identical to the position measurement circuit.

III. SYSTEM PERFORMANCE

The dynamic range of the position detector is greater than 50dB. The normal range of operation is 1 – 100 μA . Within a 35 dB normal operating range, position gain errors of less than 300 μm (Fig. 2) and zero offset errors of less than

200 μm (Fig. 3) have been observed under bench test conditions. The output bandwidth of the position detector and intensity detectors are 2.8 and 1 kHz respectively.

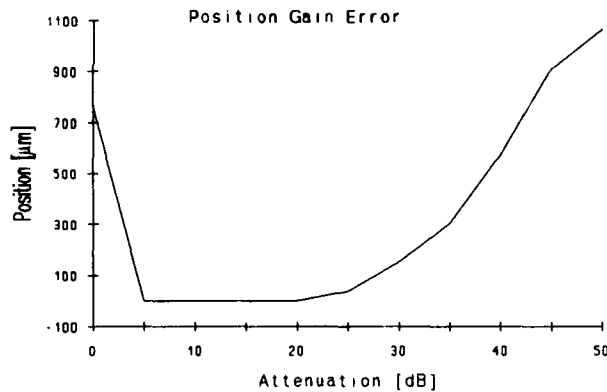


Figure 2. Position gain error (in μm) as a function of input level over a 50 dB range.

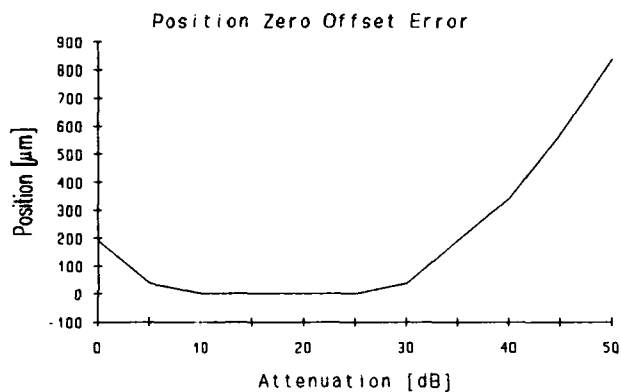


Figure 3. Zero offset error (in μm) as a function of input level over a 50 dB range.

IV. Conclusions

With the introduction of high speed, wide bandwidth, and low cost op-amps, design of accurate and reliable beam position detectors has been made simpler for. Although many of the ideas of beam position measurement have been used before in the laboratory they have not been carried out using this technology.

V. Acknowledges

We are grateful for the support of many staff members at IUCF especially John Collins, Bill Jones for beam optics calculation, and Gary East and the operations staff for help in fabricating and testing the electronics.

V. References

- [1] Timothy JP Ellison, C. Michael Fox, Steven W. Koch, Liu Rui, "Nondestructive diagnostics for measuring the phase, position, and intensity of 15 nA beams for IUCF cyclotron", *Proc. 11th Int. Conf. on Cyclotrons and their Applications*, edited by M. Sekiguchi, Y. Yano, K. Hatanaka (Ionics, Tokyo, Japan, 1986)279-283.
- [2] W.P. Jones, T.J.P. Ellison, M.S. Ball, J.C. Collins, D. DuPlantis, D.L. Friesel, B. Hamilton, J.W. Hicks, and P. Schwandt, "Beam Transport System For The IUCF High Intensity Polarized Ion Source", *Proc. 13th Int. Con. of Cyclotrons and their Applications*, edited by G.Dutto, M.K. Craddock, (Vancouver, B.C., 1992)609-611.
- [3] M. Wedekind, R. Brown, V. Derenchuk, J. Hicks, P. Schwandt, "The IUCF High Intensity Polarized Ion Source Project", these proceedings.
- [4] Comlinear Corporation 1991 Databook, "Amplifiers and Data Conversion"
- [5] Mini-Circuits 92/93 Databook, "RF/IF Designer's Handbook"
- [6] Elantec 1992 Databook, "High Performance integrated Circuits"
- [7] R.E. Shafer and R.E. Gerig, "Proc. of 12th Int. Conf. on High Energy Accel." (Fermilab, 1983),pg. 609
- [8] Maxim 1992 New Releases Databook, "1992 Analog Design Series"

A Single-Passage Beam-Position Monitor in the TRISTAN AR-to-MR Transport Lines

Takao Ieiri and Mitsuhiro Arinaga
KEK, National Laboratory for High Energy Physics
Goto 1-1, Tsukuba-shi, Ibaraki, 305 Japan

Abstract

A beam-position monitor (BPM) has been installed in the transport lines between the Accumulation Ring (AR) and the Main Ring (MR) of TRISTAN. This monitor comprises stripline and button electrodes, detectors and charge-sensitive ADCs. The detector is a homodyne type synchronous-receiver at 70 MHz with four channels corresponding to four electrodes. Operation software automatically displays the detected beam position and its charge on a TV screen after each passage of the beam. The system is stable and is used to monitor the drift of the beam position. This is a brief report on the monitor. Details are seen in ref.[1].

1. INTRODUCTION

The TRISTAN Main Ring (MR), an electron/positron collider, catches a bunch extracted from the Accumulation Ring (AR). This bunch is transported through a long line with a length of 170 m for injection into the MR. Before, we could not easily watch a bunch during the transfer. If some trouble occurred in the line, we had no useful tool to diagnose it. Thus, the efficiency of the transfer, defined as the injected beam charge in the MR divided by a circulating charge in the AR, was poor. In order to improve the efficiency and to clarify the transportation status, a nondestructive beam position monitor is required.

The transport lines [2] guide electron and positron beams of 8 GeV from an AR extraction point to an MR injection point. The AR accumulates an electron or positron beam of 2.5 GeV up to the required beam-current level. The magnetic field of the AR increases for a ramping beam energy of up to 8 GeV. The beam is then extracted from the AR. The magnetic field decreases after the extraction until the next beam. This AR cycle takes about 60 seconds, not constant, since the period depends on the required accumulated beam-current and other injection conditions. Thus the extraction is irregular. There are two symmetrical lines: one for an electron beam and the other for a positron beam. Each line is about 170 m long and comprises eighteen dipole magnets, twenty-four quadrupole magnets and some correction magnets.

2. DESIGN

An extracted beam from the AR is a single bunch with a charge of 1 - 25 nC. This charge depends on the beam current of the AR. The rms bunch length of a bunch is expected to be about 20 mm, or 67 ps. The beam position should be

detected in one passage of a bunch, since the period of the extraction is very long and irregular. The required specifications for a position measurement are:

accuracy	: 0.5 mm
resolution	: 0.1 mm
dynamic range	: 30 dB
number of monitor station	: 4 for each line.

In order to avoid external noise and to obtain a good S/N ratio, a simple homodyne receiver using a synchronous detector has been adopted, which directly rectifies an RF ringing signal without any frequency conversion. Since the noise spectrum of the kicker exists up to 30 MHz, the detected frequency should be greater than 30 MHz. When the frequency is greater than 100 MHz, however, it is technically difficult to rectify. The loss in a cable increases as the frequency increases. On the other hand, the transfer impedance of a pick-up electrode, such a stripline or a button, is proportionally increased as the frequency increases in the region below 100 MHz. Therefore, the detected frequency was chosen to be 70 MHz.

An expected peak voltage of the ringing using the narrow-band method is proportional to the bandwidth of a BPF, and is given as

$$V_p \cong 2 \cdot e N \cdot |Z_d| \cdot \Delta f \quad (1)$$

Here, $|Z_d|$ is the transfer impedance of a pick-up electrode and Δf is the full bandwidth of a BPF. Assuming $eN=1$ nC and $\Delta f=10$ MHz, the peak voltage picked up by the stripline is $V_p=40$ mV, when $|Z_d|=2\Omega$ at 70 MHz. In the case of the button, the peak voltage is one-order less than that of the stripline and is expected to be 2 to 4 mV. It is not difficult to detect the RF signal with the amplitude of several mV.

Two methods are considered to obtain the beam position. One is called an analog method, which generates the Δ/Σ function before the RF detection. This method requires hybrid junctions and a divider in an analog circuit. One may note some errors in the analog circuit and the coupling among the beam signals from the electrodes. The other is a digital method, where the digitization using a ADC is performed before the Δ/Σ function. The resolution of the ADC limits the dynamic range of the system. This is covered by a programmable attenuator. In order to avoid errors due to the coupling among channels, the one-to-one method has been adopted, where each beam signal picked up by each electrode is detected and digitized.

3. SYSTEM

Fig. 1 shows approximate locations of the monitor stations in the transport lines. The total number of the monitors is ten. Five monitors are installed for each line. The monitors are installed near quadrupole magnets, and are called E/P03, E/P04, E/P23 and E/P24. Letters E and P mean electron and positron line, and the following numbers called after quadrupole magnets also mean locations. The monitors at E21 and P21 are used to generate a timing pulse for detection. The monitors at E/P03 and E/P04 are mounted at the upper-stream side, and mainly watch the extracted beam from the AR. On the other hand, the monitors at E/P23 and E/P24 watch the injection condition to the MR.

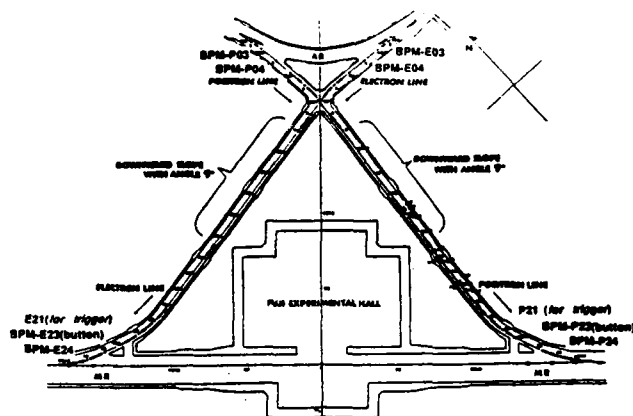


Fig. 1 Locations of the monitor chambers in the transport lines.

Fig.2 shows an outline of the system. The system comprises pick-up electrodes, cables, detectors and ADCs. The beam pulse picked up by each electrode is directly sent to the West-Room of the AR through a cable, where detectors and ADCs are mounted in a rack. The room temperature is kept constant. Before a beam pulse is fed to a detector, the pulse passes through a coaxial SPDT switch (single port double transport, Teledyne (CS-33S10)) and a programmable attenuator (Weinschel 3201). The switch is used to select either an electron or positron beam. The switches have 32 channels of inputs corresponding to each signal from the electrodes. The programmable attenuator can control the signal level in steps of 4 dB. The detector rectifies a 70 MHz component of a beam pulse. The ADC holds the charge of a beam pulse gated by a timing pulse. A beam signal picked up by E/P21 is bipolar, and is converted to a pulse with constant level of NIM and a width of 300 nsec by a zero-cross discriminator. This NIM-pulse is delayed by 1 to 2 μ s in order to overlap it on a crest of a detected pulse; it is fed to the gate input of the ADC. This closed system has advantages of being jitter-free and easy to maintain. The detector and the ADC are common for electron and positron beams for easy maintenance. Stored digital data are read by a computer network of TRISTAN.

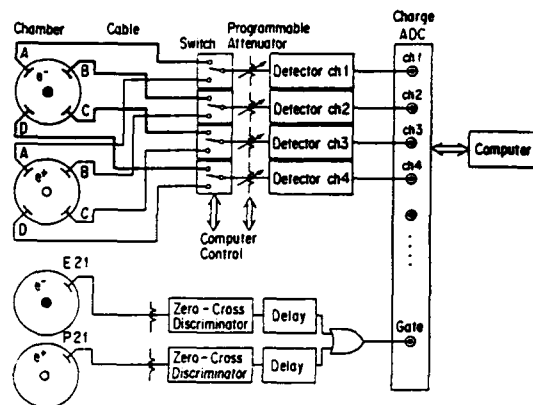


Fig. 2 Outline of the beam position monitor.

Fig. 3 shows a block diagram of one channel of a BPM detector. A beam pulse is stretched by a LPF (low-pass filter), the cut-off frequency of which is 100 MHz, and passes through a BPF. The center frequency of the BPF is 70 MHz, and the bandwidth is 10 MHz. The BPF converts a pulse to a ringing waveform with a frequency of 70 MHz. The duration of the ringing is 140 ns, and depends on the bandwidth, (10 MHz). In order to avoid any distortion in the ringing waveform, a SAW (surface acoustic wave, Murata SAF70MH00N) filter is used. The ringing waveform is amplified with a low-noise amplifier (NEC, 2SC3358, NF=1.1 dB) and is then sent to a synchronous detector. The bandwidth of the detector is determined by the cut-off frequency of the LPF, (500 kHz).

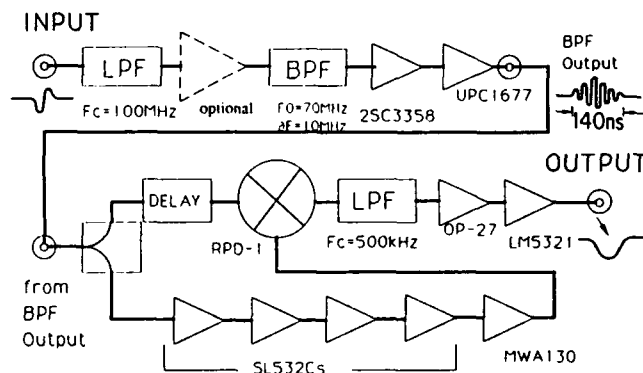


Fig. 3 Block diagram of the detector electronics.

4. PERFORMANCE

The resolution of the detection system was measured by repeatedly reading the position data about 100 times. Fig. 4 shows the standard deviation of the position data change as a function of the input charge. A standard deviation of 10 μ m was obtained at full scale. The standard deviation is roughly proportional to the input level. This means that the resolution of the detector is mainly determined by that of the ADC, where the ADC has 11 bits. However, it was found that the pedestal of the ADC fluctuated with 3 - 4 counts.

Therefore, the expected best resolution is about 8 μm , which agrees with the measured value.

The long-time stability was tested. A pulse with an amplitude of 70% of the maximum level was applied to the detector through a four-way divider. Position data were recorded every one hour. Both variations in the horizontal and vertical directions settled within $\pm 50 \mu\text{m}$. No drift was observed.

The nonlinearity of the detector produces a position shift which depends on the input level. In order to reduce the nonlinearity, the gain of the detector is changed from a fixed value to be a function of the input level. A correction curve, which is the difference between a linear line and the measured values, is obtained using a second-order polynomial. The correction is common among the four channels and the four detectors for simplicity. A position shift was also measured with an artificial imbalance of the input level. Attenuators of 6 dB were inserted at two channels, (the A & D channels of the detector). This imbalance produces a position offset of 6 mm. Fig. 5 shows the position deviation from the reference with and without a correction. The position shift is reduced to be less than 0.2 mm from 0.8 mm in the range of 20 dB.

Early during a beam test the system suffered from external noise. First, a noise was observed in a detected beam-pulse. It was found that this noise invaded through a power line of AC 100 V for a scope. A shielded transformer was inserted there in order to eliminate the noise. Next, the gate pulse generated by a beam-pulse was doubly triggered by reflections in the signal line. An attenuator made the reflections negligibly small.

The long-time stability was recorded during routine TRISTAN operation. The stored position data are useful for investigating the stability of the extraction components of the AR.

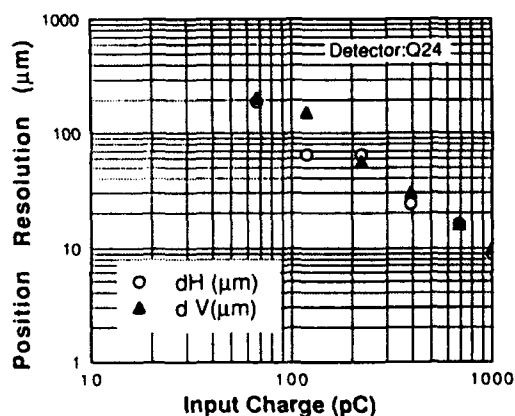


Fig. 4 Position resolution as a function of the input charge.

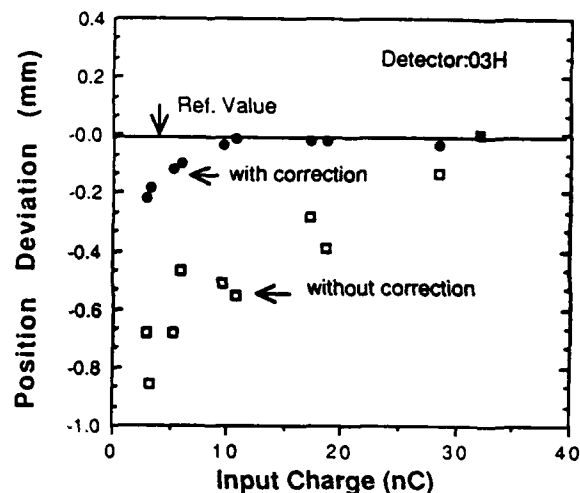


Fig. 5 Position deviation vs. input charge with a horizontal position offset of 6 mm.

5. SUMMARY

A BPM system has been installed in the transport lines. A homodyne receiver is used at 70 MHz in order to avoid any external noise. The system contributes to the diagnosis on the transfer process. The performance of the BPM system is summarized as follows:

- 1) The resolution of position is 10 μm rms value at the full scale.
- 2) The position accuracy is about 0.3 mm over a dynamic range of 16 dB.
- 3) The minimum detectable beam-charge is 1.0 nC. The dynamic range is more than 30 dB using a programmable attenuator.
- 4) The absolute value of beam-charge is unclear. A systematic error may exist.
- 5) Storing beam-position data is useful for monitoring its drift.

REFERENCES

- [1] T. Ieiri and M. Arinaga, A Single-Passage Beam-Position Monitor System for the TRISTAN AR-to-MR Transport Lines, KEK Report 93-02 (1993).
- [2] M. Kikuchi et al., Extraction system of TRISTAN accumulation ring and transport line to main ring, The 5-th Symp. on Accelerator Science and Technology, KEK, Japan (1984) p. 306.

Beam Position Monitoring System using PIN Diode Switches

Kenji SHINOE, Tadashi KOSEKI, Yukihide KAMIYA
Norio NAKAMURA*, Tomotaro KATSURA* and Takao IEIRI†

The Institute for Solid State Physics, The University of Tokyo,

**Photon Factory, †TRISTAN, National Laboratory for High Energy Physics, KEK, JAPAN*

Abstract

We have developed a BPM system that uses PIN diodes for switching and attenuating RF-signal, being intended as more high-speed and reliable than using mechanical switches instead. This system has already been working in the SOR-RING of ISSP. Large unevenness of BPM data that would unexpectedly occur in a case of mechanical switches has never been observed. Moreover, relative accuracy of the order of sub-micron has been attained with this system.

1. Introduction

A third-generation VUV ring with a low emittance of several nm·rad is being designed at the SRL of ISSP in close collaboration with the Photon Factory of KEK. In such a ring that can supply highly collimated synchrotron light to experimental stations, the beam position monitor (BPM) would take a more important role than ever, e. g., to measure a tiny drift of beam orbit and to correct it. As one of the R&D's for the future plan of the high-brilliant source, we have developed a BPM system that uses PIN diodes for switching and attenuating RF-signals from pickup electrodes. The purpose of using PIN diodes is to obtain more high-speed and reliable than using mechanical coaxial switches.

around 500 MHz. The operational status of SOR-RING and the machine study using the BPM system are reported in Ref. [1]. Given in this paper are the BPM system and its actual performance.

The BPM system includes four BPM's fixed on newly fabricated vacuum chambers for quadrupole triplets and each BPM consists of four pickup-electrodes of a button type. Four BPM's are located in narrow spaces between quadrupole magnets as seen in Fig. 1. We did not intend the BPM's to be precisely positioned in the ring, for example, much less than 0.1 mm, first because the aim of this BPM system is to test the performance of PIN diodes, and next because there is no good reference point for alignment. Before installing the BPM's into the ring, their sensitivity to the beam position was calibrated on a test bench. It was found from the calibration data that the physical position (x, y) of the beam center is well estimated with a fifth order polynomial of U and V. More details are described in Ref. [2]. Separately from the BPM calibration, a performance test of PIN diode switches and attenuators was made and their insertion losses were carefully measured. In addition, a little nonlinear response of the RF-signal detector was calibrated using a RF-signal generator and later using a real beam. The nonlinearity is compensated for on the BPM system computer when the detected RF-signals are processed.

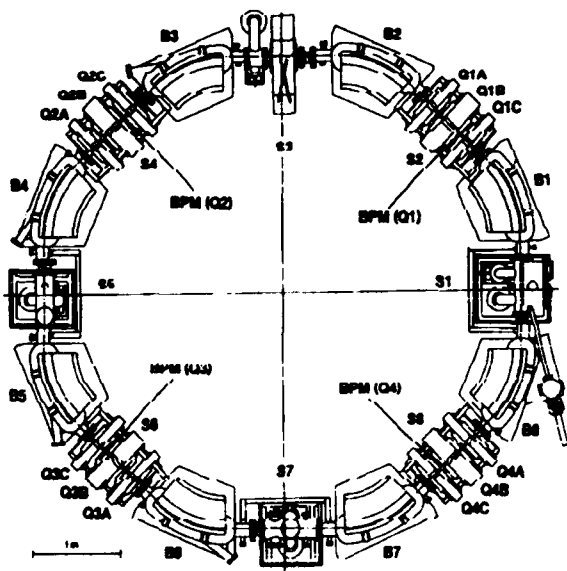


Fig. 1 Plan view of SOR-RING

This system has been installed into SOR-RING (Fig. 1) in the 1992 summer shutdown in order to test it with a real beam and to measure the closed orbit of the ring where there was no working BPM system until then. The present system has been designed to detect 120-MHz spectrum in RF signals from BPM's as the RF frequency of SOR-RING is about 120 MHz, while the RF frequency of the future ring will be

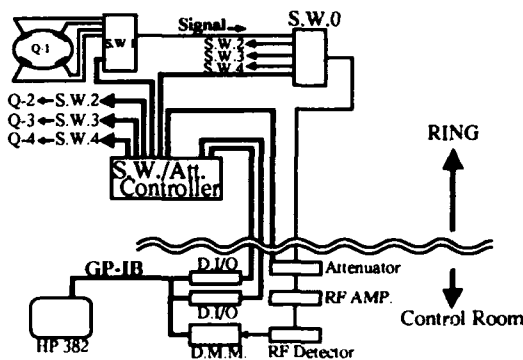


Fig. 2 Schematic of the BPM system

2. BPM System

A. Overview

Figure 2 shows a schematic of the whole BPM system that is working at SOR-RING to test its performance with a real beam. The first-stage PIN diode switches multiplex RF-signals from four pick-up electrodes of a BPM and the second-stage PIN diode switches (S.W.0) then multiplexes signals from four BPM's. The multiplexed signal is sent to a 120-MHz RF amplifier through an attenuator that also uses PIN diode switches. Finally, the signal is detected by a heterodyne detector (RF Detector) and read by a digital multimeter (DMM) that can remove noises with the power line frequency (CMR = 160 dB, NMR = 60 dB for > 1PLC (Power Line

Cycle)). The multiplexing PIN diodes and those used in the attenuator are controlled by a controller (S.W./Att. Controller) and two digital I/O modules. The multiplexing PIN diodes and S.W./Att. Controller are placed in the ring, while the other electronic modules are placed in the control room. The modules that treat RF-signals are connected each other by semi-rigid 50- Ω coaxial cables. A workstation, HP382, converts the data from DMM to the beam position (x,y) and displays it on the CRT. The whole BPM system is also controlled by the workstation.

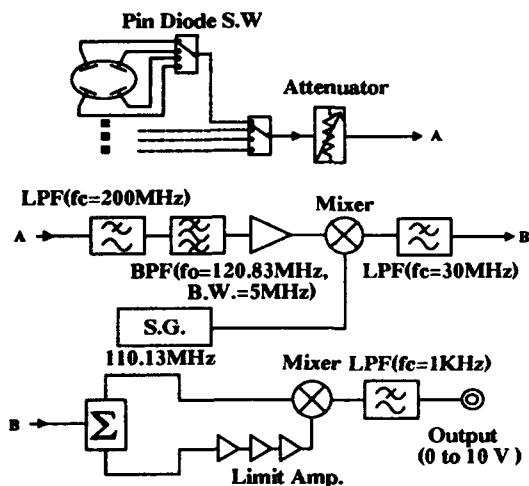


Fig. 3 Block diagram of RF circuit

A block diagram of the RF circuit is shown in Fig. 3. Before heterodyne detection, the RF-signal is filtered by LPF (low-pass filter) that rejects higher harmonics of RF frequency, and further filtered by BPF (band-pass filter) with a bandwidth of 5 MHz; the revolution frequency is about 17 MHz. After filtered by the final-stage LPF with a cutoff frequency of 1 kHz, the output DC signal is sent to a digital multimeter (DMM). By a bench test, it was found that the input/output response of the RF circuit is almost linear but with a small nonlinearity of 0.1 % in the range of the output voltage between 0.1 and 10 V.

B. PIN diode

We chose PIN diode switches, DAICO 100C 1248 SP4T, (four input signals, one output) as the switches to multiplex RF-signals from BPM. The PIN diode switches can be driven by a trigger with TTL level, and each input port is terminated with 50 Ω impedance when the port is switched off. The specifications of the PIN diode switches are; maximum switching speed = 2.5 μ sec, typical insertion loss = 0.8 dB for 20 - 200 MHz, minimum isolation = 85 dB for 20 - 200 MHz, VSWR = 1.1 at 120 MHz. The insertion losses were measured for the switches we purchased. Its result is listed in Table I. As the deviations of insertion loss from the average are small, we have not taken account of these data to compensate for the BPM data. The switching speeds were also measured, and it was proved that RF-signals may be multiplexed at 100 kHz without losing their accuracy.

We chose DAICO 100C1595 as the attenuator, the specifications of which are; the attenuation range = 63.5 dB with a setting step of 0.5 dB, typical insertion loss = 3.5 dB, typical switching speed = 5 μ sec, VSWR = 1.1 at 120 MHz.

We checked the reproducibility of attenuation. The standard deviation measured was about 0.001 dB. As the beam position is calculated from the ratio of detected signals, however, the quality would not affect the beam position.

So far, both PIN diode switches and attenuator are working well without any failure for several months.

3. Beam Test at SOR-RING

After the BPM system was installed in SOR-RING, we measured again the linearity of output response to input signals that were sent by a RF-signal generator from the input ports of PIN diode switches. The nonlinearity in the measured response is compensated for on the BPM system computer when the detected signals are converted to the beam position. The compensation curve is shown in Fig. 4. Just after the beam test began, we found that 120-MHz RF noise on the ground line got mixed in the BPM system and gave rise to false signals in it. This trouble was however fixed by isolating the RF circuit from the ground line.

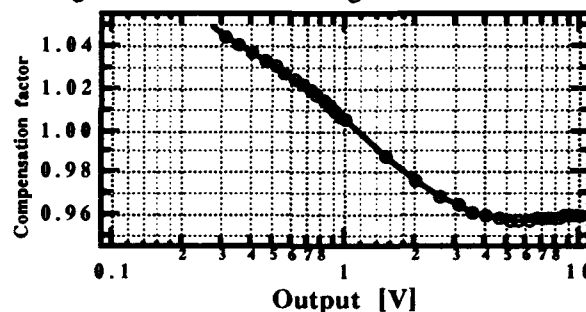


Fig. 4 Compensation curve of the BPM system

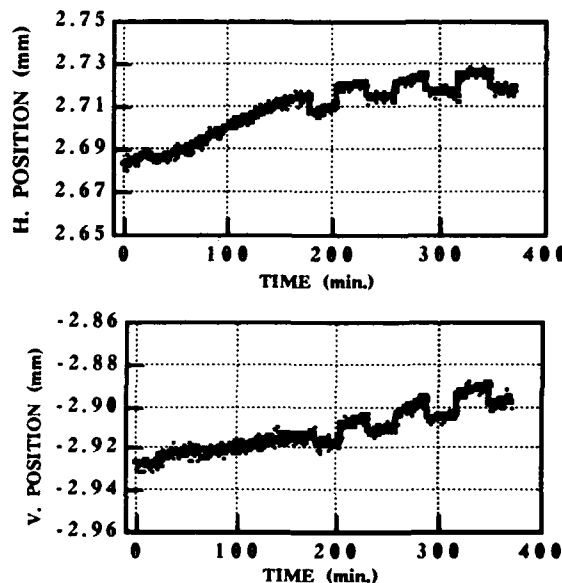


Fig. 5 Orbit drift of SOR-RING

(a): horizontal orbit of a BPM vs. time. (b): vertical orbit of BPM vs. time. The cause of rectangular changes has not been identified yet.

Horizontal C.O.D. measured with the BPM system has a maximum of 3 mm and vertical C.O.D. about 4 mm. The C.O.D.'s along the ring as well as the corrected ones are shown in Ref. [2]. Figure 5 shows an example of the orbit drift measured with the BPM system. The data were taken

during a normal user run with a high beam current. The measurement shows that the beam position of SOR-RING slowly drifts about a few tens of μm for the storage mode and jumps by a several tens μm at injection, unless there is no variation in the data caused by the system's drift. For such a user run at SOR-RING, the beam is continuously fluctuating due to a longitudinal instability and ion-trapping phenomena that give rise to an AC noise in the beam position signals.

Therefore, the data of orbit drift were taken at a low current less than several mA in order to check the relative accuracy (resolution) and long-term drift of the BPM system itself. The DMM that reads DC signals was set at the integration time of 10 PLC and the resolution of 7.5 digits. The measured data indicated that the orbit drift measured is actually caused by the beam itself but not by apparent drift in the BPM system. Deviations of measured data from the average taken in a short period were also displayed on a histogram. Figure 5 is an example of such a histogram. The standard deviations are about $0.3 \mu\text{m}$ in the horizontal direction and about $0.4 \mu\text{m}$ in the vertical direction. Thus we may conclude that the BPM system has the relative accuracy of sub-micron.

We also measured a low-frequency fluctuation in the beam position by inserting a hybrid circuit between a BPM and a PIN diode switch. This measurement is described in Ref. [2].

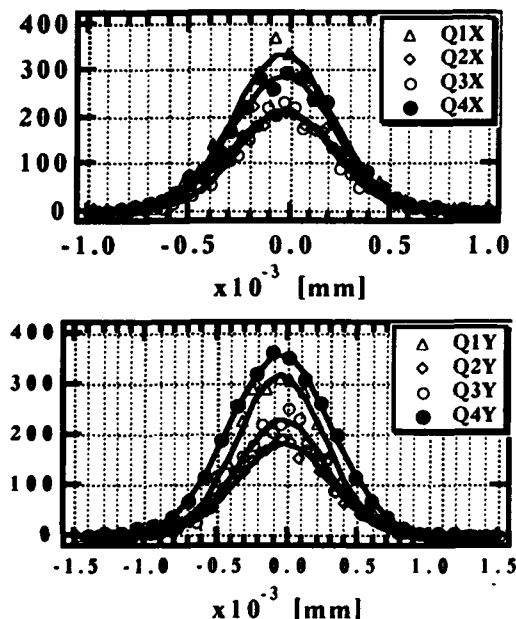


Fig. 6 Relative accuracy of the BPM system
(a): horizontal accuracy of BPM's. (b): vertical accuracy of BPM's. The data were taken for 500 minutes.

4. Summary

A BPM system using PIN diodes has been developed and tested with a real beam at SOR-RING. So far, we have obtained the relative accuracy of the order of sub-micron. Next step of the R&D is to make the data acquisition faster, but probably at expense of accuracy; this may be accomplished by improving the digital circuit and by replacing DMM with ADC.

5. Acknowledgements

The authors would like to thank Prof. T. Ishii, Director of Synchrotron Radiation Laboratory of ISSP, and the other staff members of the Laboratory for their continuous encouragement and valuable support. They also sincerely thank Prof. H. Kobayakawa, Director of Light Source Division of the Photon Factory, and all staff of the Division for their support to this study.

6. References

- (1) K. Shinoe et al.: *Design and Calibration of Pickup-electrodes for Beam Position Monitoring at SOR-RING*, in these proceedings.
- (2) H. Kudo et al.: *Measurement of the Orbit Parameters at SOR-RING*, in these proceedings.

Table I. Insertion losses of PIN Diodes

serial No.	J No.	Insertion loss [dB]
1316 (S.W.0)	1	0.4788
	2	0.48268
	3	0.48975
	4	0.50054
1317 (S.W.2)	1	0.50054
	2	0.48343
	3	0.48574
	4	0.47962
1318 (S.W.3)	1	0.48642
	2	0.46967
	3	0.47802
	4	0.49302
1320 (S.W.4)	1	0.49508
	2	0.49111
	3	0.47709
	4	0.47723
1321 (S.W.1)	1	0.47403
	2	0.48796
	3	0.48590
	4	0.48510

Performance of the CEBAF Arc Beam Position Monitors

A. S. Hoffer, B. A. Bowling, C. S. Higgins, P. K. Kloeppe, G. A. Kraft, K. L. Mahoney
The Continuous Electron Beam Accelerator Facility
12000 Jefferson Ave., Newport News, VA 23606

Abstract

The first three quarters of the first CEBAF arc have been instrumented with beam position monitors. Thirty-seven monitors (of 450) have been installed and their noise measured. Resolution of 100 μm was obtained at the lowest operating current of 1 μA . The update time of the system is 1 sec, limited by computer interfacing, with a potential bandwidth of greater than 10 kHz.

I. INTRODUCTION

The basic requirements for the beam position monitor system are dictated by the properties of the beam. In the accelerator arcs, the range of currents that should be accurately detected is from 1 μA to 200 μA . The beam size in these regions is approximately 100 μm rms. Therefore a system with 100 μm position resolution is appropriate. The BPMs should be useful both in CW mode, the standard operational mode for CEBAF, and in a pulsed low-power tune-up mode in which, for machine safety, the beam pulses are limited to about 100 μsec . The BPMs provide primary signals for feedback stabilisation purposes.

A basic schematic of the system is shown in Fig. 1 [1]. Starting on the beam line, the fundamental frequency of the beam is induced on each of four BPM wires and transmitted to a B0005 chassis, better known as the arc tunnel electronics. Here the signal is amplified and down-converted to 1 MHz for transmission to detection circuitry in the service buildings upstairs. Each of the 1 MHz signals from the B0005 box is sent to a separate channel of a B0007 board resident in a CAMAC crate upstairs. In the B0007 board, the amplitude of the 1 MHz signal is detected and digitised. The digitised voltage levels are then conveyed to the computer where the beam position is computed.

If there were no errors in the system, and if X_{\pm} and Y_{\pm} were proportional to the amplitude of the beam generated signal on each wire, the beam position before rotation could be calculated as

$$X' = k \frac{X_+ - X_-}{X_+ + X_-},$$

and likewise for Y' , where k is the sensitivity of the BPM at 1500 MHz.

Because of errors in the system, two software corrections are made. The first deals with the fact that the amplitude gains in the different channels might be different.

The second deals with the offsets that exist in the amplitude detector. The modified computation of the unrotated positions is

$$X' = k \frac{(X_+ - X_{\text{off}+}) - \alpha_X(X_- - X_{\text{off}-})}{(X_+ - X_{\text{off}+}) + \alpha_X(X_- - X_{\text{off}-})},$$

and likewise for Y' , where α_X , α_Y , $X_{\text{off}\pm}$, and $Y_{\text{off}\pm}$ are measured by the automatic calibration circuitry as follows:

- Using the zero wires facility in the software, measure the offset voltages $X_{\text{off}\pm}$ and $Y_{\text{off}\pm}$ with both the beam and calibration signal off,
- calibrate the X channels with a calibration signal on y_- , and
- calibrate the Y channels with a calibration signal on x_- .

The word "calibrate" means to find the relative gain ratios α_X and α_Y for the X and Y channels respectively. This is done by measuring the amplitude ratio when the beam is off and the calibration signal is on:

$$\alpha_X = \frac{X_+ - X_{\text{off}+}}{X_- - X_{\text{off}-}},$$

and likewise for α_Y .

The beam position, after rotation by 45°, is

$$\begin{pmatrix} X \\ Y \end{pmatrix} = \frac{1}{\sqrt{2}} \begin{pmatrix} 1 & -1 \\ 1 & 1 \end{pmatrix} \left[\begin{pmatrix} X' \\ Y' \end{pmatrix} - \begin{pmatrix} X'_{\text{off}} \\ Y'_{\text{off}} \end{pmatrix} \right],$$

where the offsets X'_{off} and Y'_{off} are used to save particular orbits as discussed below.

II. HARDWARE DESCRIPTION

A. Mechanical

The beam position monitors that are used in the CEBAF arcs are two models of the same basic design. They consist of four thin-wire quarter-wave pickup antennas, symmetrically placed at the corners of a square that is perpendicular to the beam and centered on the beam axis [2]. The pickups are parallel to the beam. The monitors in the first of the five beam passes must be accommodated to a larger beam pipe than the others, nominally 4.7 cm (the M20 monitor) as compared with 3.5 cm (the M15 monitor). The diameter of the outer shell is fixed by the requirement that the impedance be 200 Ω . Up to the present, most beam tests have been performed with M20 monitors; there is no evidence that the M15 monitors give substantially different results.

The pickup wires are approximately positioned in the manufacturing process. They are then individually positioned with the aid of an optical comparator to within 75 μm . When this process is completed, their electrical response is individually measured with a network analyzer to ensure that it is within acceptable limits. The monitors are

*Supported by U.S.DOE contract DE-AC05-84ER40150.

then cleaned and slow-baked, and finally are leak-tested. If accepted, they are released to be installed on the accelerator beamline. The BPM sensitivity k is measured for every monitor; the values usually are within 1% of 18.5 mm.

B. Electrical

The electronics portion of the arc BPM system is composed of a heterodyne front-end preamplifier located in the tunnel enclosure and a synchronous amplitude detector located in the service buildings.

The front-end B0005 electronics amplifies, and then downconverts each of the four position inputs from 1.5 GHz to 1 MHz. The 1 MHz signals are buffered and sent upstairs to be detected. An oscillator used in the calibration and testing of the BPM system is included in the front-end electronics; it is activated only during the calibration sequence. If both channels are working correctly the relative gain ratio should be approximately 1.

The B0007 detector card includes a programmable gain amplifier, synchronous detector, and analog-to-digital converter on each channel. The detection and conversion may be either internally (CW mode) or externally (pulse mode) triggered, selectable by the operator. The minimum detectable pulse width is governed by the synchronous detector and is on the order of 25 μ sec.

The synchronous detector system is used to provide an amplitude-detected signal for each channel. The instantaneous dynamic range of the detected signal is governed by two factors. First, the detector has a minimum threshold below which it cannot phase lock the incoming signal. Second, the detected signal is digitized using an 8-bit analog-to-digital converter which limits the signal range to 256 states. For this reason a programmable gain amplifier is included in the detector front end. The gain, adjustable over a 30 dB range, is set according to the expected value of the operating current of the accelerator.

Because the arc BPM is a linear difference-over-sum system, special attention is given to ensure sufficient dynamic range and signal-to-noise ratio in the preamplifier and detector subsystems. The CEBAF peak beam current ranges from 1 to 200 μ A, giving a signal level between -73 and -27 dBm on center. Care is taken to ensure sufficient signal-to-noise ratio through the detector. The front-end preamplifier establishes the system noise figure at approximately 4 dB.

III. SOFTWARE DESCRIPTION

The BPM software system, part of the TACL [3,4] control system, consists of an operator interface and software controls. The interface is comprised of three types of TACL display pages running on console computers. The software controls reside in user functions in TACL logic processed on front-end computers attached to CAMAC crates. Communication between the operator in the control room and the B0007 cards in CAMAC crates in the service buildings is managed by the software system.

The basic software organization is that one BPM user function accesses one B0007 card, but display pages may provide monitor and control capabilities for one or more BPMs. Various BPM operating modes, for example the calibration mode, are requested and monitored by the operator via display pages, and these requests are interpreted and passed by logic to the selected user functions. All signal and position information generated by the user function is calculated using ADC wire data acquired by logic from the B0007 card. Other CAMAC interactions required to initiate and terminate BPM operating modes are handled by the user function. The user function converts and calculates all of the data from the BPMs on the display pages.

The information from the BPM system is displayed in the control room in three ways. Beamline screens are used in daily operations and provide the relative position of the BPM on the beamline, the device name, and the calculated beam position in millimeters or the BPM status. Second, test screens provide the operational controls for the BPMs and display system information such as readbacks for wire signal values, position and wire offsets, calibration constants, and approximate beam current. Finally, "Red October" charts display all of the BPM positions in individual sonar-like displays.

During normal operations the user function converts filtered ADC wire values to positions. The normal mode of filtering collects one set of values at the same cycle rate as logic (3 to 8 Hz) and averages them continuously, giving position data that lag the machine state by 20 sec without degrading overall performance. This lag can be reduced to less than a second at the expense of front-end performance if logic reads the BPM crate many times per logic cycle and provides an averaged ADC value to the BPM user function. This second mode of filtering results in a reduction of overall front-end performance by a factor of three. Such filtering modes can be combined to achieve the best tracking response while minimizing the impact on performance. The normal filter mode can be applied globally to all the BPMs in the machine or can be specified for a subset of BPM modules. The CAMAC averaging scheme is specifically invoked for subsets of BPM modules. Because of the performance cost, it should be reserved for situations where tracking response time is a concern, as with automated optics setup software [5,6].

One of the capabilities of the user function is to define a "golden orbit" or position offset. The BPM electronics pick up noise from neighboring RF cavities and power sources as well as the beam signal, resulting in false or offset position readings. This can be eliminated by establishing an acceptable beam orbit and requesting the user functions to use the current positions as the zero reference. Once these offsets are recorded, they are subtracted from the calculated positions until a new "golden orbit" is defined. Currently, this option is used most with automated orbit correction algorithms which attempt to center positions in the BPMs [5].

During the recent series of pre-commissioning tests, the BPMs were most useful in initial manual beam threading efforts. In the user function the wire currents are summed together, providing an approximate beam current seen by the BPM. By watching the beam current values and the position readback on the test display screens, it is easy to determine whether or not the beam is passing through a specific BPM.

IV. RESULTS

Initial tests of the tunnel electronics uncovered two problems which have subsequently been remedied. The first was that the components selected for the microwave front-end amplifier were not ideally suited for 1497 MHz operation. Second, the tunnel electronics were susceptible to radiated interference from external sources. Both problems were addressed by redesigning the tunnel electronics using surface-mount technology. Initial tests of the redesigned board show measurable improvements in gain, noise immunity, and stability.

In Fig. 2, a graph of beam position as a function of time demonstrates the ability of the monitors to respond to weak currents. The jitter in position is the result of both electronics noise and actual beam motion. It is in any case less than about 0.1 mm rms at $0.5 \mu\text{A}$, and is smaller at high currents. For example, at $10 \mu\text{A}$ (not shown), the jitter is only about one-fourth as large. Whether the beam is diagnosed in CW or pulsed mode, the position fluctuation after averaging is the same.

Thirty seven complete systems were installed and operated simultaneously, extending throughout the spreader

and the first three quarters of the east arc. In normal operations, the software provided quick and reliable information, especially when the block reads were successfully implemented. The BPM test screens, through the calibration options, provided especially useful diagnosis of hardware problems.

V. CONCLUSIONS

The CEBAF arc beam position monitors have been successfully used to diagnose the CEBAF beam in the first spreader and east arc of the CEBAF electron accelerator. The monitors are the only means of steering in a large section of the machine, and this section of the machine was traversed the first time with little additional difficulty. They have operated under a wide dynamic range in addition to the standard tune-up setting of about $10 \mu\text{A}$ beam current. Experiments reported in several other papers in this conference required functional BPMs. In particular, the automatic steering routines [5], east arc commissioning [6], and the energy correction hardware/software [7] relied on the arc BPMs.

VI. REFERENCES

- [1] W. Barry, J. Heefner, and J. Perry, *Proc. 1990 Beam Instrumentation Conference*.
- [2] W. Barry, *Nucl Instrum Meth A301*, 407-416 (1991).
- [3] R. Bork *et al.*, *Proc. 1989 Part. Accel. Conf.*
- [4] M. Bickley, and J. Kewisch, these proceedings.
- [5] B. Bowling *et al.*, these proceedings.
- [6] Y. Chao *et al.*, these proceedings.
- [7] G. Kraft *et al.*, these proceedings.

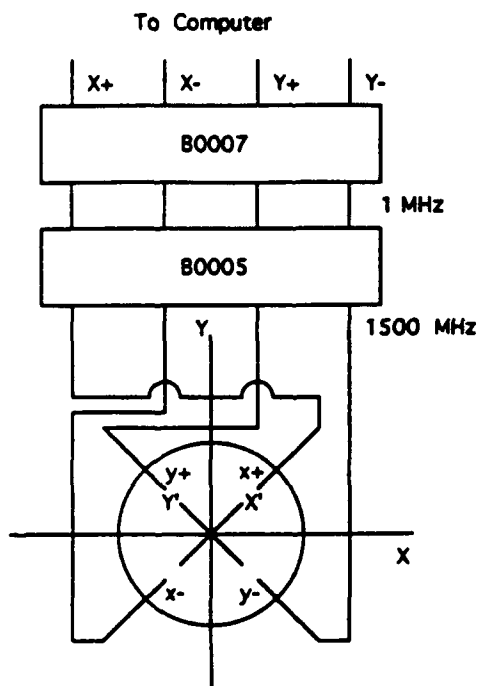


Figure 1. Block diagram of BPM electronics.

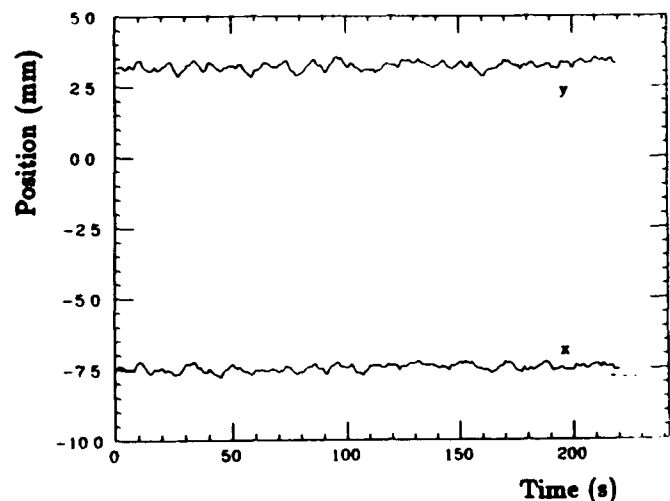


Figure 2. Position seen at $0.5 \mu\text{A}$.

The Million Turn Data Acquisition System BOSC

A. Burns, W. Fischer, H. Jakob, I. Milstead, F. Schmidt and L. Vos,
CERN

CH 1211 - Geneva 23

Abstract

The data acquisition system BOSC [1] has now reached a reliable operational stage after the phase of designing and debugging its complex hardware and software. The system consists of a VME-crate with a 68030 CPU-card, a timing module, a bunch selector card and 12 ADC cards each with two channels to acquire and store data of up to one million turns. The aim of the system is to measure a wide range of different signals each being recorded in one of the ADC channels. Three such crates are connected via Ethernet and Token Ring to Apollo workstations on the SPS site. Very flexible measurement requests can be sent to the crates in data-structures which are then filled with the requested data and sent back to the Apollo for processing. In the crate a complex control software running under OS9 has been developed, with several application software programs now running on the Apollo. One use of the system is for operational purposes such as tune measurements. Moreover BOSC has been the essential tool in conducting the delicate dynamic aperture experiments where the measurement needs are constantly changing.

I. HARDWARE DESCRIPTION

BOSC is designed as a turn by turn acquisition system. It was originally intended to be used in the SPS to measure the intensity and the position of the individual proton and anti-proton bunches over a full machine cycle. The signals are taken from homodyne receivers. These requirements and conditions lead to the actual properties of this system:

- each acquisition channel is backed with a 1MByte dynamic memory to allow the measurement turn by turn over a period of more than 20s in the SPS
- the bandwidth of the acquisition is 5MHz which is well matched to the bandwidth of the receivers
- the receiver also requires an input signal of level $\pm 5V$

The BOSC acquisition system in its final form is housed in a VME crate. It can handle up to 24 analog signals. They are organised in 12 dual channel electronic cards (*dual sampler*) which contain a memory for each channel and a logic

cell array common to both channels which acts as a slave to the crate central processor unit (68030). The system is mainly intended for the measurement of single bunches. The *bunch selector* picks a given bunch which circulates in the machine. The time resolution of this selection is determined by the bandwidth of the system and is at present at the order of 200ns. Special care has been taken to isolate the low power analog circuits from the high power digital circuitry. The connection between the two is made in the *VME bridge* module. The information concerning the machine cycle time is fed in the system by the *TG3* timing module.

At present three units are installed in the SPS:

- A first one is dedicated to turn by turn position measurements. It is used to derive the machine tunes. A number of channels are connected to 200MHz receivers completely in line with the original specifications. They are well adapted to measure single lepton bunches. However, they are also used to measure the SPS proton beams bunched at 200MHz. Special low frequency FET amplifiers of which the bandwidth is reduced to 5MHz to match the acquisition system are connected to a second set of channels. They allow the measurement of bunched and unbunched beams. The excitor for this measurement can either be a special fast kicker magnet or the deflector plates of the transverse feedback system. The excitation of the latter is controlled by BOSC using the *sequencer* unit.
- A second BOSC unit is devoted to single bunch intensity measurements. The signals are generated by 20MHz homodyne receivers.
- A third unit makes the acquisition of much slower signals generated by DC current transformers, collimators movements and scintillators.

II. CONTROL SOFTWARE

The control software [2], running under OS9 on the 68030 processor, has the following tasks: setting up the communication between the crate and the Apollo workstation, setting & changing some hardware parameters, taking measurement requests from an Apollo workstation, starting the data acquisition on the crate and sending the data

to the Apollo after an acquisition has been made. It is capable of handling several requests simultaneously on the same crate.

The communication is done over Ethernet and Token ring where sockets under TCP/IP are used. For the data transfer in any direction MOPS structures are used [3].

A schematic overview of the system consisting of the crate, the Apollo and the communication part is given in Fig. 1.

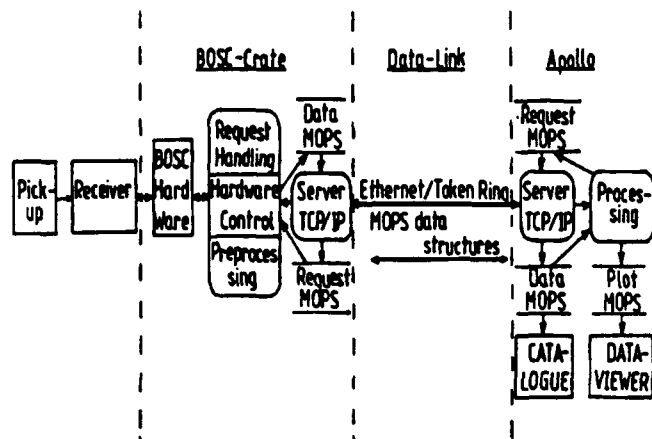


Figure 1: Setup of BOSC

It is possible to change some of the parameters controlling the hardware such as base addresses, gains and bunch selector settings. The use of base addresses allows the translation from physical to logical channel addresses, so as to freely choose channels without the need of swapping cables. The receiver gain can be changed from 14db to 70db in 14db steps, each ADC channel gain can be changed from 0db to 24db in 6db steps.

The MOPS data structure which is sent to start the measurement on the crate in one of its objects holds a coded request (9 integer numbers) which specifies the measurement parameters: on which BOSC crate to run the measurement, the number of super cycles to be measured, the start time of the measurement in the SPS super cycle, the time between blocks of acquisitions, the number of acquisition blocks, the time between sub-blocks of acquisitions, the number of sub-blocks in one block, the number of turns per sub-block and the channels to be used for the measurement. An example of the usage of some of these parameters can be found in Fig. 2. A server program is running on both ends to receive MOPS data structures with measurement requests or acquired data respectively. The data read from the ADC memory and hardware settings like timing information are added to the request MOPS data structure that has been sent from the Apollo.

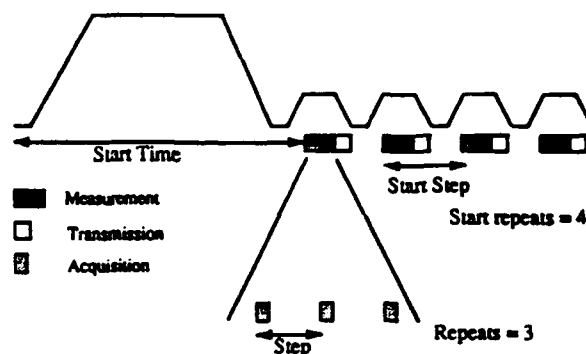


Figure 2: Structure of a measurement

III. APPLICATION SOFTWARE

The application software [4] is an interface for starting a measurement, displaying the data acquired, storing data and performing a detailed post-processing analysis. For displaying data the *dataviewer* program is used [5], the archiving is managed by a catalogue package [6]. BOSC is now used as an operational tool for tune measurement [7] as well as a tool for the dynamic aperture experiments performed on the SPS [8]. In the following we only report on the later application software package. There are two main types of measurements that can be performed:

- Lifetime measurements
- Phase space measurements

In the dynamic aperture experiments we want to investigate effects that influence the particle stability over long periods. It is therefore very convenient to have BOSC for following simultaneously and continuously beam intensity, scraper positions and loss monitor readings. Different phenomena leading to particle loss can thereby be easily distinguished (see Fig. 3). For a phase space measurement the position and intensity signals of one or more pick-ups can be recorded. After having applied a kick to the beam the Fast Fourier Transforms from the position signals give the tunes and the line spectra due to resonances. Fig. 4 shows how readings of two pick-ups separated by a multiple of 90 degrees allows one to depict phase space projections. Currently we take and analyze online two samples of up to 65000 turns, the repetition rate being 30s. This allows a very precise determination of the tune, but also linear coupling correction, chromaticity compensation and identification of high order resonances.

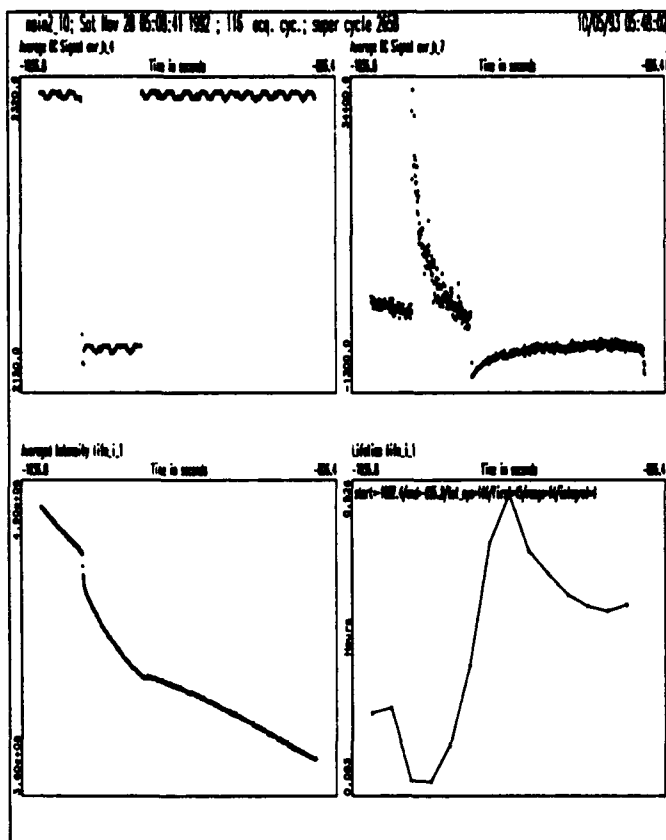


Figure 3: Lifetime measurement

The effect of moving a scraper (upper left) can be seen on the loss monitor, the beam intensity and the lifetime (upper right, lower left and lower right part respectively).

For phase space measurements there is a tool box which contains four programs. The *zero_stuff* program allows to set the position signals in a certain time range to zero. With this facility one can detect changes in the tunes, for instance due to power supply ripple. The *stroboscope* program plots only every n^{th} point in phase space thereby visualizing resonances in the horizontal, vertical and physical phase space projection. The *fake* program has the same functionality as *stroboscope* but uses the information of only one pick-up via relating $x(i)$ with $x(i + \text{skip_step})$. The *smear* program computes the horizontal and vertical decoherence, the decoherence corrected amplitude and the smear.

IV. CONCLUSIONS

BOSC can now be considered an operational tool, especially due to a considerable improvement in the control software part. Operational tasks like tune measurements are now in place. The more complicated requests for dynamic aperture or other experiments can be fulfilled, but there are still many of capabilities yet to be exploited.

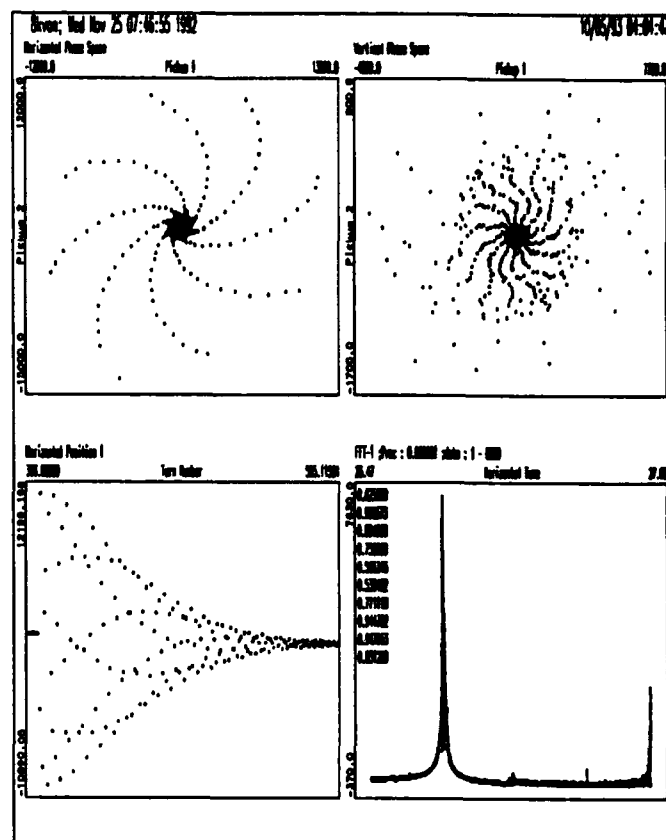


Figure 4: 8th order resonance

Motion is depicted close to a horizontal resonance (upper left) with the kicked and decohered beam and a FFT (lower left and lower right part respectively).

V. REFERENCES

- [1] A. Burns et al., *The BOSC Project*, CERN SL/90-68(AP).
- [2] I. Milstead, *SPS BOSC - Beam OSCillation Data Acquisition System for the SPS, System Users Guide*, Version 3.22, 1992.
- [3] W. Herr, *M.O.P.S. Users Guide for "C" programs*, CERN-SPS/88-43(AMS), 1992.
- [4] W. Fischer and F. Schmidt, *Application Software for the BOSC Data Acquisition System of the SPS, Users Guide*, CERN-SL Note, to be published.
- [5] A. Sweeney, *The Dataviewer Programmer's Guide*, LEP Controls Note 107, SPS/ACC Note 89-11.
- [6] Q. King, R. Schmidt, *The SPS Catalogue Data Structure*, CERN SPS/ABM/Note/88-12.
- [7] A. Sweeney, *Private Communication*.
- [8] W. Fischer et al., *Recent Results from the Dynamic Aperture Experiment at the SPS*, CERN SPS, presented at this conference.

Beam Position Monitor Calibration for the Advanced Photon Source*

Y. Chung, G. Decker, E. Kahana, F. Lenkszus, A. Lumpkin, and W. Sellyey
Argonne National Laboratory, Argonne, IL 60439

Abstract

This paper describes the sensitivity and offset calibration for the beam position monitors (BPMs) using button-type pickups in the injector synchrotron, storage ring, and insertion devices of the Advanced Photon Source (APS). In order to reduce the overall offset and to isolate the error ($\leq 100 \mu\text{m}$) due to the low fabrication tolerance in the extruded storage ring vacuum chamber, the electrical offset is minimized by carefully sorting and matching the buttons and cables according to the button capacitance and the characteristic impedances of the cable and the button feedthrough. The wire method is used for the sensitivity calibration, position-to-signal mapping, and measurement of resolution and long-term drift ($\leq 1 \text{ mV}$) of the processing electronics. The processing electronics was also tested at Stanford Synchrotron Radiation Laboratory (SSRL) using a real beam, with results indicating better than $25 \mu\text{m}$ resolution for the APS storage ring. Conversion between the BPM signal and the actual beam position is done by using polynomial expansions fit to the mapping data with absolute accuracy better than $25 \mu\text{m}$ within $\pm 5 \text{ mm}$ square. Measurement of the effect of button mispositioning and mechanical inaccuracy of the extruded storage ring vacuum chamber, including deformation under vacuum, will be also discussed.

I. INTRODUCTION

For beam position monitoring of the charged particle beam, button-type pickups will be used in the storage ring, injector synchrotron and insertion devices of the APS. In order to meet the requirements on the accuracy of the measured beam position as shown in Table 1, it is necessary that the BPMs are accurately calibrated for the offset and sensitivity.

The offset calibration of the BPMs will be done using the external method developed by G. Lambertson. [1-4] Since the APS storage ring vacuum chamber is subject to significant deformation under vacuum due to the photon exit channel, separate measurements of the offset are needed in air and vacuum. The measurement, however, can be affected by the button position error and the resulting calibration error needs to be estimated for proper application. In order to isolate the mechanical error and to minimize the overall offset error, the buttons and cables will be matched electrically.

The sensitivity calibration, on the other hand, requires the use of a wire, antenna, or charged particle beam whose

transverse position can be controlled. We will present results obtained using the wire in the lab and electron beam in SPEAR at Stanford Synchrotron Radiation Laboratory (SSRL). Comparison with the theory will be also discussed.

Table 1: APS Storage Ring BPM Specifications.

First Turn, 1 mA Resolution / Accuracy	200 μm / 500 μm
Stored Beam, Single or Multiple Bunches @ 5 mA Total Resolution / Accuracy	25 μm / 200 μm
Stability, Long Term	$\pm 30 \mu\text{m}$
Dynamic Range, Intensity	$\geq 40 \text{ dB}$
Dynamic Range, Position	$\pm 20 \text{ mm}$

II. BUTTON CHARACTERISTICS

Let C_p be the capacitance of a button and let Z_T be the terminating impedance at the instrument end for measurement of the button signal. Then gain coefficient g_c for the button and connecting cable at frequency ω can be written as [5]

$$g_c = \frac{S_{21}}{1 - S_{11} - i\omega C_p Z_T (1 + S_{11})} \quad (1)$$

where S_{11} and S_{21} ($= S_{12}$) are the reflection and transmission coefficients between the button and the terminating resistor Z_T , including the button feedthrough.

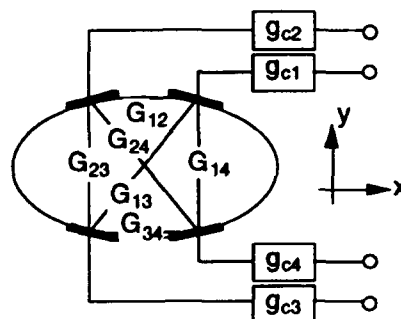


Fig. 1: The schematic of a BPM.

In terms of the capacitive coupling coefficient G between two buttons, the ratio V_{ij} of the voltage V_i detected on button i and the voltage V_j applied on button j can be written [1]

$$V_{ij} = \frac{V_i}{V_j} = 2 Z_T g_{ci} g_{cj} G_{ij} \quad (2)$$

*Work supported by the U.S. Department of Energy, Office of Basic Energy Sciences, under Contract No. W-31-109-ENG-38.

G_{ij} contains the geometric factors including the chamber deformation under vacuum.

Figure 1 shows the geometry of the positron beam chamber, the buttons, and associated g_c - and G -coefficients. The measured beam position (x, y) using linear approximation can be obtained from the button signals V_i ($1 \leq i \leq 4$) using

$$\frac{\Delta x}{\Sigma} = \frac{V_1 - V_2 - V_3 + V_4}{V_1 + V_2 + V_3 + V_4} = S_x (x + \Delta x_w), \quad (3)$$

and similarly for $\Delta y/\Sigma$. Δx_w is the x offset, and S_x is the sensitivity coefficient. The coordinate origin ($x = 0, y = 0$) may be conveniently identified with a position that can be referenced from an external fiducial mark.

The overall gain g_i for the i -th button is the product of g_{ci} and the electrical gain coefficient g_{bi} for beam-to-button coupling for the beam centered at origin. That is,

$$g_i = g_{bi} \cdot g_{ci}. \quad (4)$$

Then, the BPM offsets Δx_w and Δy_w can be expressed in terms of the g -coefficients in dB unit as

$$\Delta x_w = \frac{0.0288}{S_x} (g_1 - g_2 - g_3 + g_4), \quad (g_i \text{ in dB}) \quad (5)$$

$$\Delta y_w = \frac{0.0288}{S_y} (g_1 + g_2 - g_3 - g_4), \quad (g_i \text{ in dB}) \quad (6)$$

Approximation was made assuming that the gain differences are small. In the following discussions, we will use dB units for g - and G -coefficients and V_{ij} unless noted otherwise.

III. BPM SENSITIVITY AND 2-D MAPPING

A. BPM Sensitivity

The coefficients S_x and S_y determine the sensitivity of the BPM in detecting beam motion. We used a thin wire of 12-mil diameter suspended along the vacuum chamber for calibration of injector synchrotron and storage ring BPMs. Figure 2 shows the result for the storage ring BPM and Table 2 lists theoretical and measurement results obtained for various BPMs in the APS.

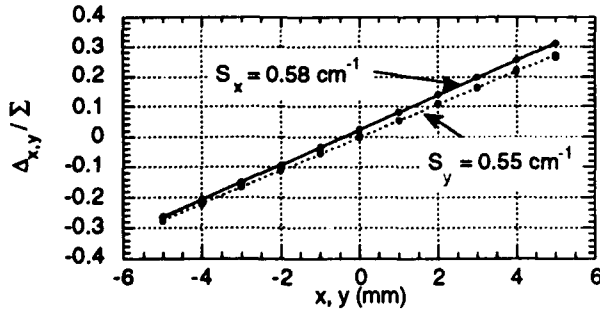


Fig. 2: Determination of the sensitivity coefficients S_x and S_y for the APS storage ring.

Table 2: Theoretical and measured sensitivities for the APS storage ring, injector synchrotron, and insertion device BPMs.

	Storage Ring	Injector Synch.	ID 12 mm gap	ID 8 mm gap
S_x	0.57 cm ⁻¹	0.70 cm ⁻¹	2.08 cm ⁻¹	3.44 cm ⁻¹
S_x^*	0.58 cm ⁻¹	0.70 cm ⁻¹	—	—
S_y	0.53 cm ⁻¹	0.58 cm ⁻¹	1.51 cm ⁻¹	1.47 cm ⁻¹
S_y^*	0.55 cm ⁻¹	0.57 cm ⁻¹	—	—

(*: measured)

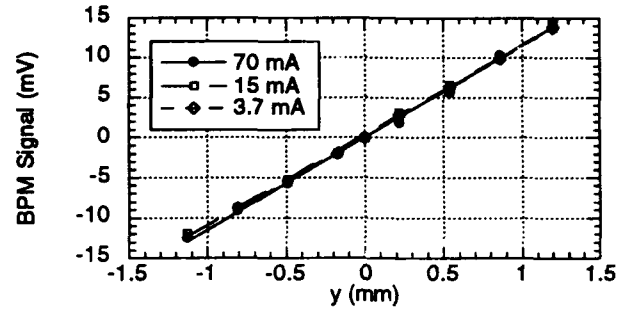


Fig. 3: BPM signal from the processing electronics measured on SPEAR, SSRL, for beam current of 70, 15, and 3.7 mA.

In Fig. 3 is shown the BPM signal from the prototype processing electronics measured on the electron beam in SPEAR at Stanford Synchrotron Radiation Laboratory (SSRL). The average sensitivity is 11.4 mV/mm. With additional gain of 6 for the final design, this translates to approximately 20 μ m resolution assuming 1 mV r.m.s. error.

B. 2-D Mapping

Figure 4 shows the 2-dimensional mapping (contour lines of $\Delta x,y/\Sigma$) of the APS storage ring BPM response in the region $|x| \leq 20$ mm and $|y| \leq 10$ mm. This data is used to obtain the polynomial coefficients for conversion between the BPM signal (V_x, V_y) and the beam position (x, y) ,

$$P: (V_x, V_y) \rightarrow (x, y). \quad (7)$$

With 8th order both in x and y , absolute accuracy better than 25 μ m within ± 5 mm square was obtained. This calculation is done by local processors in the VME crates for the BPMs in real-time.

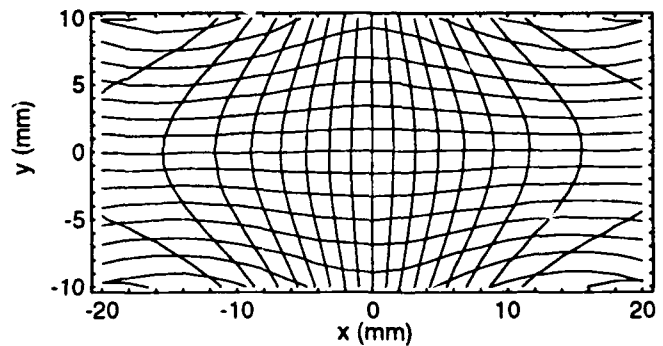


Fig. 4: 2-dimensional mapping of the APS storage ring BPM response. Grid spacing = 0.1.

The inverse of Eq. (7), which converts the beam position to BPM signal for the fast beam position feedback systems acting on the raw BPM signal to enhance speed, cannot be in general represented as polynomials. Instead, the polynomial functions

$$Q : (x, y) \rightarrow (V_x, V_y) \quad (8)$$

are used as the initial guess for the iterative search following the direction of the steepest change.

IV. OFFSET CALIBRATION

In this section, we will discuss calibration of the BPM offset using the external method applied on the APS storage ring. From Eq. (2) and putting $a = 20 \log(2 Z_T)$, we have

$$a + g_{ci} + g_{cj} + G_{ij} = V_{ij} = V_{ji}. \quad (9)$$

The offsets are determined in terms of V_{ij} as

$$\Delta x_e = \frac{0.0288}{S_x} (V_{14} - V_{23}),$$

$$\Delta y_e = \frac{0.0288}{S_y} (V_{12} - V_{34}). \quad (10)$$

Other combinations are also possible and they may be used for error-checking. In this work, we will use the expressions in Eq. (10) only. Equation (9) can in principle be used to determine the g_c - and/or G -coefficients. This, however, requires shuffling of the buttons and cables to get a large enough number of independent measurements.

A. Analysis of Calibration Error

The tooling ball located on top of the vacuum chamber is used as the fiducial mark for survey and alignment of the BPM relative to an adjacent quadrupole or sextupole. The offset calibration error can be defined as the BPM signal after calibration with the beam at the position referenced by the tooling ball. Let us consider the button position error (h_i and v_i , $1 \leq i \leq 4$) and the tooling ball position error (x_t and y_t) as the dominant error sources. h_i is the button position error along the mounting surface in the direction outward from the center and v_i is the error in the outward direction normal to the surface. The surface is sloped at 15.11° about the horizontal plane.

Using Eqs. (10) and (11) and the partial derivatives listed in Table 3, the offset calibration errors Δx_{err} and Δy_{err} for the APS storage ring are given by

$$\Delta x_{err} \approx 0.14 x_t - 0.22 (h'_1 - h'_2 - h'_3 + h'_4) + \Delta x'_w - \Delta x'_e, \quad (11)$$

and

$$\Delta y_{err} \approx 0.75 y_t + 0.20 (h'_1 + h'_2 - h'_3 - h'_4) + \Delta y'_w - \Delta y'_e, \quad (12)$$

where the prime (') denotes random error. It is to be noted that the vertical position error v_i does not contribute to the

calibration error. Equations (11) and (12) show that overall mechanical tolerance of a few mils is acceptable to achieve $100 \mu\text{m}$ (≈ 4 mils) of r.m.s. offset calibration error.

Table 3: Listing of the partial derivatives of the g - and G -coefficients in units of dB/mm. Analytical and numerical calculations were done in 2-D.

	$\frac{\partial G_{12}}{\partial h_1}$	$\frac{\partial G_{14}}{\partial h_1}$	$\frac{\partial g_{b1}}{\partial h_1}$	$\frac{\partial G_{12}}{\partial v_1}$	$\frac{\partial G_{14}}{\partial v_1}$	$\frac{\partial g_{b1}}{\partial v_1}$
Analytical	-0.83	-0.01	-0.45	-	-	-
Numerical	-0.74	0.07	-0.37	-2.9	-2.8	-2.8
Measurement	-	-	-	-3.4	-3.4	-3.4

B. Chamber Deformation under Vacuum

For the APS storage ring, BPMs are an integral part of the vacuum chamber with the buttons directly mounted on the machined surface of the chamber. When the chamber is put under vacuum, significant deformation of the chamber was observed. This effect led to approximately $400 \mu\text{m}$ shift in the x offset measured using the external method.

Assuming linearity, we found the relation

$$\Delta x_e = \Delta x_{ea} + k_v (\Delta x_{ev} - \Delta x_{ea}), \quad k_v \approx 0.65, \quad (13)$$

where Δx_{ea} and Δx_{ev} are the offsets measured in air and vacuum, respectively. The proportionality constant k_v was obtained with separate measurements using wire and simulation of vacuum pumpout by mechanical means.

Acknowledgment

R. Hettel at SSRL is to be thanked for his collaboration on measurements of the BPM response on SPEAR.

V. REFERENCES

- [1] G. R. Lambertson, "Calibration of Position Electrodes Using External Measurements," LSAP Note-5, Lawrence Berkeley Laboratory, May 6, 1987.
- [2] J. Hinkson, private communication.
- [3] G. Decker and Y. Chung, "Progress on the Development of APS Beam Position Monitoring System," *Proceedings of 1991 IEEE Particle Accelerator Conference*, pp. 2545 - 2547, 1991.
- [4] Y. Chung and G. Decker, "Offset Calibration of the Beam Position Monitor Using External Means," *Proceedings of 1991 Accelerator Instrumentation Workshop*, pp. 217 - 224, 1991.
- [5] Y. Chung, "BPM Button Characterization for Offset Calibration," LS Note 193, ANL, 1992.

Self Triggered Single Pulse Beam Position Monitor

J.L.Rothman and E.B. Blum

National Synchrotron Light Source

Brookhaven National Laboratory

Upton, New York 11973

Abstract

A self triggered beam position monitor (BPM) has been developed for the NSLS injection system to provide single pulse orbit measurements in the booster synchrotron, linac, and transport lines. The BPM integrates the negative going portion of 3 nS wide bipolar pickup electrode signals. The gated, self triggering feature confines critical timing components to the front end, relaxing external timing specifications. The system features a low noise high speed FET sampler, a fiber optic gate for bunch and turn selection, and an inexpensive interface to a standard PC data acquisition system.

I. INTRODUCTION

The BPM is designed as a stand alone, real-time diagnostic tool for tuning the linac, booster, and transport lines. High speed sampling units, located near the pick-up electrodes, process the short pulses and provide a signal readable by an inexpensive PC based data acquisition system. This allows the use of easy to use, well tested high level programming tools such as Visual Basic for DOS [1].

II. DESIGN

A. Specifications

The specifications for a single non-averaged measurement of a bunch with 10^9 electrons are as follows:

Beam current dynamic range:	30dB
Position dynamic range:	$\pm 30\text{mm}$
Resolution:	100uM
Accuracy:	$\pm 500\text{uM}$
Repetition rate:	.5s

B. System Design

The specifications are modest compared to the requirements of a storage ring beam position monitor therefore the design can be simplified and costs reduced. The system design is shown in figure 1.

* Work performed under the auspices of the U.S. Department of energy.

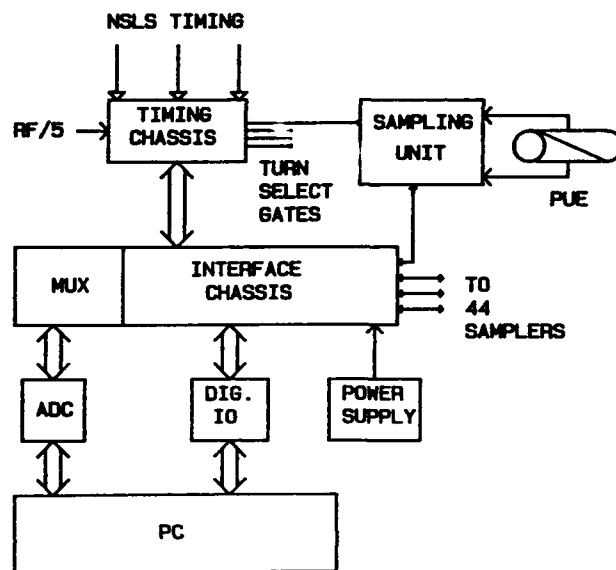


Figure 1
System block diagram

The timing chassis generates a gate corresponding to a selected turn in the booster. The timing chassis also interrupts the PC at the beginning of a data acquisition sequence. The sampling units self trigger within the turn select gates and transmit the result to the interface chassis via 4-20 mA current loops. The PC reads the data with a 12 bit data acquisition card. All 88 analog channels are routed to the card with multiplexers located in the interface chassis. The PC initializes the timing chassis and externally triggers the sampling units to measure the pedestal. The turn select gates are transmitted over fiber optic cables and all other digital signals use opto-isolators.

C: Sampling Units

The sampling units are built around thick film hybrid samplers [2] shown in figure 2. Q_1 is gated to trap the charge from the second half of a bipolar PUE signal. The input is effectively integrated by C_1 since the capacitance is large and very little voltage is developed. The charge then slowly transfers onto C_2 with a time constant $T = R_1 * C_1 = 6.8\mu\text{s}$. The op-amp and associated components function as a

gated charge sensitive amplifier. The track and hold samples the output of the op-amp. The hybrid sampler is well suited to measuring very short pulses that occur infrequently. The primary limitations are the 700pS turn on time for Q_1 and the 47uS required to drain C_1 by 99.9%.

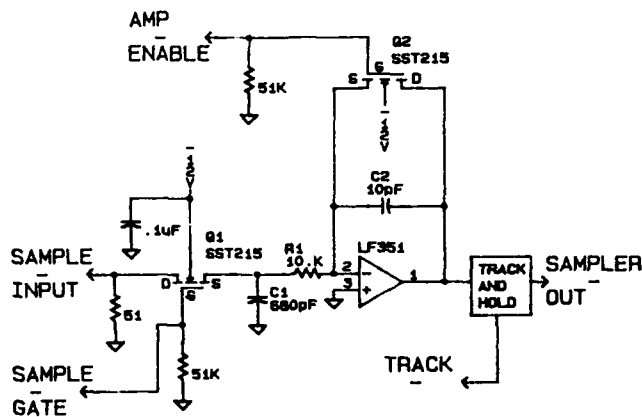


Figure 2
Thick film hybrid sampler schematic

The sampling unit block diagram is shown in figure #3. The rising edge of the turn select pulse triggers two one shots. The output of one shot #1 remains high 5uS longer than one shot #2 since the track and hold on the hybrid sampler must return to hold mode before the charge sensitive amplifier is reset. The zero crossing detector is reset for the length of the 100nS turn select pulse. The RF hybrid processes the pick-up electrode (PUE) signals and sends sum and difference signals to the inputs of the hybrid samplers via delay lines. The delay lines compensate for delays in the trigger circuit.

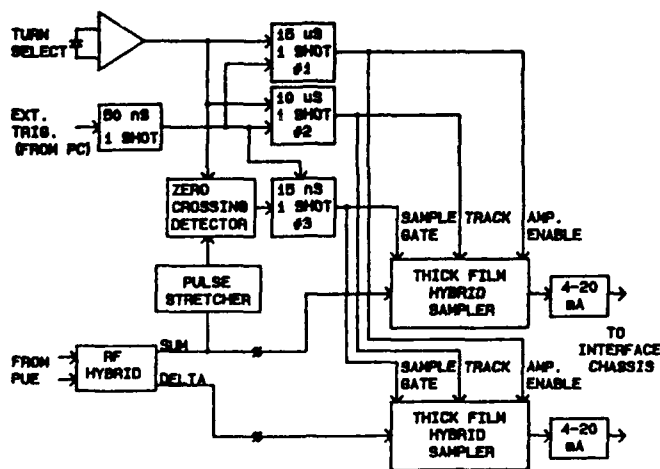


Figure 3
Sampling unit block diagram

The sum signal is split stretched and then run into the zero crossing detector. The output of the zero crossing detector rises when the input rises above 47mV and the output gives a falling edge when the input crosses zero. Since one shot #3 is negative edge triggered the sample gate is generated on the zero crossing, thereby making the timing of the sample gate insensitive to changes in the amplitude of the sum signal. The internal trigger functions as half of a constant fraction discriminator. Since the PUE signals are already bipolar it is not necessary to delay and recombine the pulse to generate a zero crossing. The external trigger generates precisely the same timing sequence as the internal trigger, allowing for an accurate pedestal measurement. The 4-20mA current loop drivers simply follow the output of the hybrid samplers.

III. PERFORMANCE

The prototype was tested using the circuit shown in figure 4. The monocyte generator produces bipolar pulses identical to those produced by the injection system PUEs. Attenuator 1 simulates changes in beam current while attenuators 2 and 3 simulate changes in beam position. Attenuators 2 and 3 are changed in such a way as to maintain a constant sum signal out of the RF hybrid.

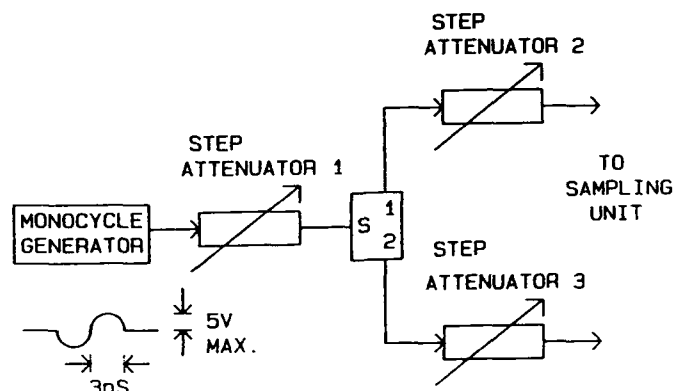


Figure 4
Test unit

Figure 5 shows the response of the sampling unit at three different currents. The amplitude of the sum signal is measured at the input to the hybrid sampler. While the output of the monocyte generator is 5V_{peak}, losses in the attenuators and splitters limit the sum test signal to 1.5V_{peak}. Also note that the delta/sum ratio is larger than one because the sum signal is split to provide the internal trigger. Changes in current have only a small effect on the position scale factor. The zero crossing detector minimizes timing walk. Since walk affects both the sum and delta samplers in the same way, the effect is normalized out. In precision applications the small scale factor change can be corrected in software.

30dB of current dynamic range is about the maximum practical without range switching. If additional dynamic range were needed, a stepped attenuator could be

placed ahead of the pulse stretcher. No attenuators would be needed in front of the hybrid samplers since they have been shown to have a dynamic range in excess of 80dB [2]. As it stands the cable lengths must be minimized and pads used to avoid reflections that would lead to multiple triggers.

VI. ACKNOWLEDGMENTS

Thanks to Charlie Nielson for technical support and to Bob Meller for useful discussions.

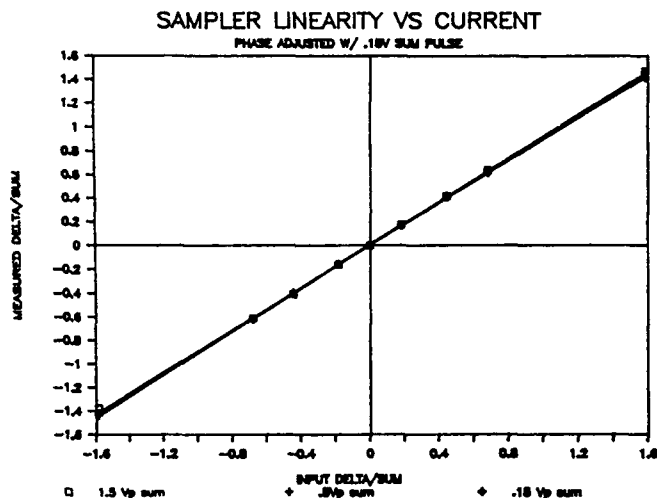


Figure 5
Sampler linearity

Resolution is limited by the 12 bit ADC. Linac beam position measurements show the same noise as measured on the bench. The resolution at the top of the dynamic range is $46.1\text{mm}/4096 = 11.25\text{ }\mu\text{m}$, where the PUE scale factor = 46.1mm.

IV. PACKAGING

The sampling unit electronics are housed in commercially available aluminum "Compac" boxes measuring 4" x 5" x 2". All timing components are on a motherboard with the hybrid samplers mounted vertically. Noise is minimized by connecting the sampling units to the PUEs with short RF cables, mounting sensitive components inside an RF tight enclosure, using fiber optics and opto-isolators on all digital signals, and by reading the current loops with differential receivers. The self triggering feature simplifies installation since all critical timing components are contained in the sampling units. The units will function properly as long as the PUE signal arrives at any time during the 100ns gate select pulse.

V. REFERENCES

- [1] Microsoft Corporation, "Visual Basic for Dos", One Microsoft Way Redmond, WA 98052-6399
- [2] R.E. Meller, C.R. Dunnam, "Beam Position Monitors for the CESR Linac" Proc. of the 1989 IEEE Particle Accelerator Conference.

A Prototype BPM Electronics Module for RHIC*

W. A. Ryan, T. J. Shea, P. Cerniglia, and C. M. Degen
Brookhaven National Laboratory
Upton, NY 11973 USA

Abstract

Prototype components of the VXI-based Beam Position Monitor Electronics for the Relativistic Heavy Ion Collider have been constructed and tested for accuracy, resolution and linearity. The detector, designed solely for single-bunch acquisition, consists of a homodyne detector followed by a sample and hold and Analog-to-Digital Converter. In the final modules, an on-board Digital Signal Processor will provide turn by turn data correction, continuously updated closed-orbit averaging, and circular buffer maintenance. A timing processor allows synchronization of modules to enable correlated data collection.

frequency (78 kHz) and digitally calculated closed orbit at the synchrotron frequency (less than a few hundred Hz). The design philosophy is to digitize as soon as possible in the processing chain, perform all data correction and position calculation digitally within the module itself, and store results in on-board memory. A Digital Signal Processor is being designed into the BPM electronics module for this purpose.

All RHIC BPM electronics modules will conform to the VXI (VME Extension for Instrumentation) specification for register based C-size modules. All memory will be directly mapped into the VXI memory address space, allowing stored data to be accessed at high speeds.

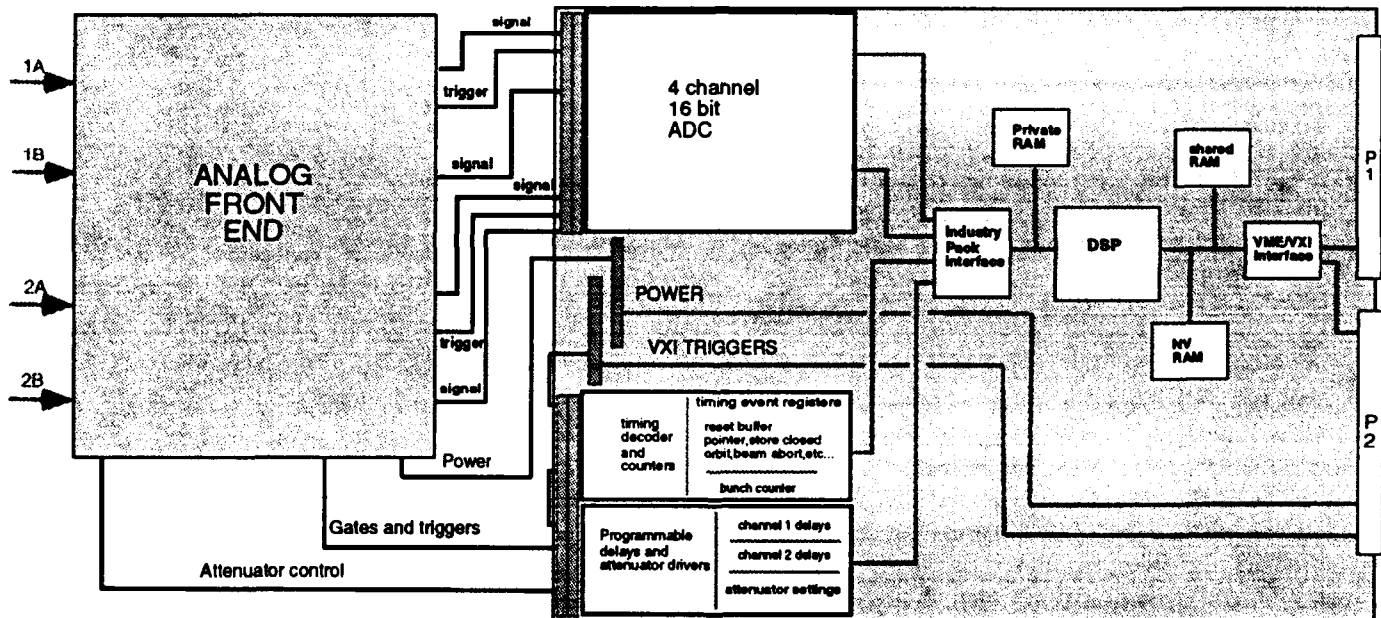


Figure 1. Block diagram of the position monitor electronics module

I. Introduction

As previously described^[1], the RHIC position monitor system will contain over 500 BPMs in the two storage rings and over 40 BPMs in the injection lines. Most monitors in the injection lines and regular arcs will measure in only in the plane of maximum beta. Others will measure in both planes. All monitors share a similar design based on shorted 50Ω strip-lines approximately 23 cm long^[2].

The RHIC BPM electronics are being designed to simultaneously provide single bunch acquisition at the revolution

As seen in Figure 1, the BPM electronics is being developed in two parts: the analog front end, which consists of a pulse detector mounted in the front half of the VXI module, and the digital acquisition section, which consists of the DSP-based VXI card with daughterboards containing the digitizers and timing interface circuitry. The analog front end has been through several prototypes with test results from the latest version reported here. The DSP and VXI interface design is being done in cooperation with the Brookhaven Instrumentation Division and first prototypes are due during the summer of 1993. Digitizer prototypes are under construction and the timing circuitry is currently being tested.

* Work supported by the U.S. Department of Energy

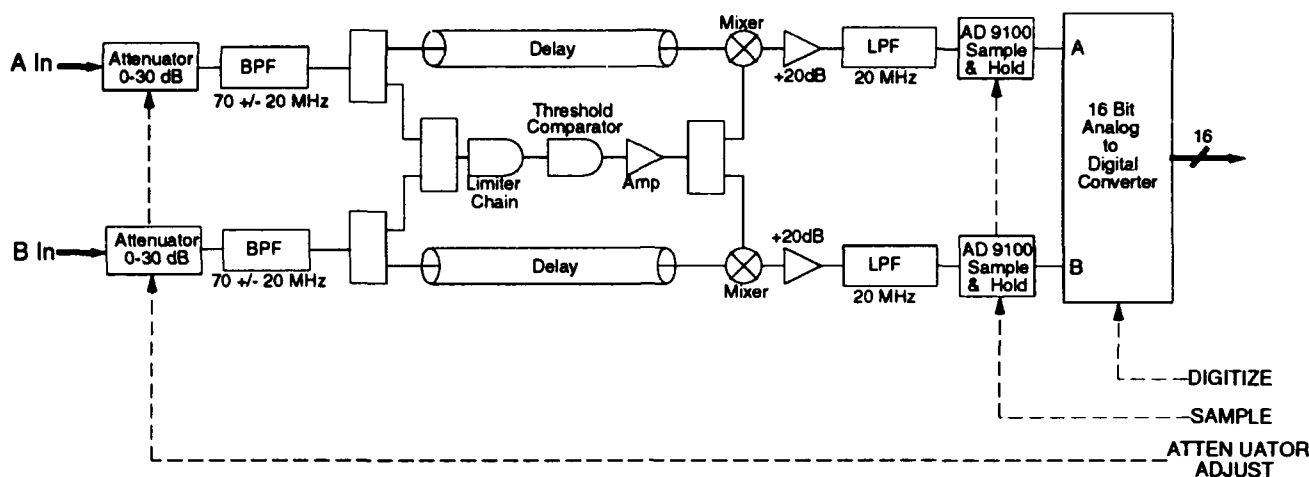


Figure 2. Block diagram of the synchronous detector prototype

II. Analog Front End

A. Beam characteristics

RHIC will contain relativistic beams of ions in the mass range from protons through fully ionized gold. The bunches will be accelerated in a 26.7 MHz accelerating RF system, and undergo a bunch rotation at top energy to allow clean transfer to a 196 MHz storage RF system. All ions except protons will pass through transition. Minimum bunch spacing is 110 ns with a single gap a few hundred ns long to accommodate for the extraction kicker risetime.

Table 1: Dynamic range requirements

Parameter	Min	Max	Effect on Common Mode Power
Intensity	10^{10} e/bunch	3×10^{11} e/bunch	30 dB
Bunch Length	1.2 m	5.1 m	9.5 dB
Position	-20 mm	+20 mm	7.5 dB
	-5 mm	+5 mm	4 dB

By using these beam characteristics in a system simulation^[3], the dynamic range required of the analog front end can be determined. A useful subset of the simulation results is shown in Table 1. For a fixed intensity, the full dynamic range of common mode power (total power transmitted through the two BPM cables) due to changes in beam position and bunch length is 17dB. This is the absolute minimum instantaneous dynamic range required of the analog front end, but for operational convenience much more will be provided.

B. Analog front end specifications

The following points summarize the specifications and design philosophy of the analog front end:

1. Single bunch acquisition.
2. Maximum bunch acquisition rate: 78 kHz (the revolution frequency).
3. Position uncertainty at center for entire system (BPM + electronics): $<0.13\text{mm}$.
4. Single bunch resolution for commissioning (single bunch, 10^{10} protons per bunch): $<1\text{mm}$.
For operating storage ($>10^{11}$ protons per bunch, or 10^9 gold ions per bunch): $<<0.1\text{mm}$
5. Bunch-to-bunch coupling: $<-60\text{dB}$
6. Instantaneous Dynamic Range: $>17\text{dB}$.
Programmable attenuation: $>30\text{dB}$.

C. Analog Front End Prototype

The analog front end, shown in Figure 2, is a homodyne detector optimized for single bunch acquisition, using band-pass filters on the input for pulse stretching, and adjustable attenuation for increased dynamic range. The bandpass filter has a 40MHz bandwidth, very wide for this type of application, which is necessary to keep the bunch-to-bunch coupling less than -60dB with the 8.9MHz bunching frequency. Due to the large amounts of power coupled through 40MHz bandwidth, 30dB of adjustable attenuation can be used to increase the dynamic range of the detector. The homodyne detector itself combines a limiter chain with a comparator threshold detector to generate the mixer LO signal. This arrangement gives $>50\text{dB}$ dynamic range while preventing oscillations in the detector loop. This is a necessity for single bunch acquisition, where a continuous signal and its ability to overcome loop oscillations does not exist.

One of the design goals for the analog front end was to make sure that the noise signal input to the S/H and digitizer was the same or slightly larger than the digitization output

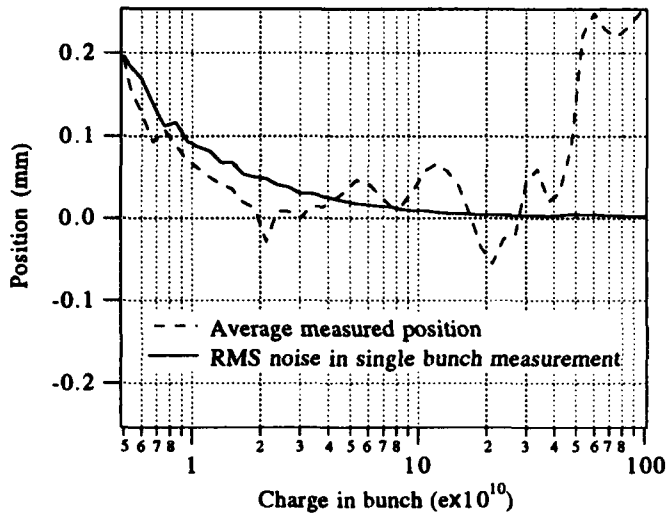


Figure 3. Single bunch performance

noise seen with a 50 Ω termination on the S/H input. This insures that the maximum signal to noise ratio is being achieved. Even with a 20dB gain block after the detector, this criterion is maintained.

The signal is then sampled with an AD9100 monolithic sample and hold, and for these bench tests only, it is digitized with a ICS-140 VME card, which uses two Crystal CS5101 16-bit digitizers for simultaneous acquisition. In the final implementation, the 16 bit ADCs will reside on a daughter card on the digital acquisition board. Results of single bunch bench tests are shown in Figure 3. For these tests, a bunch under storage conditions was simulated and a 20 dB input attenuator was used. For low intensity operation, the 20 dB attenuation would be switched out and similar performance would be expected for bunches with an order of magnitude less charge. Performance of the front end prototype under both CW and single bunch conditions is summarized in Table 2. The

Table 2: Performance of Prototype Front End

	70 MHz CW Detection	Single Bunch Detection
Accuracy	+/- 50 μ m	+/- 50 μ m
Dynamic Range	50dB	30dB
Resolution	<10 μ m RMS (40MHz BW)	<20 μ m RMS

dynamic range quoted is the instantaneous range for the given accuracy and does not take into account the availability of variable input attenuation. The immediate design goal is to increase the operating dynamic range for single bunch acquisition to approach that of CW operation. To achieve this, all components of the detector must be matched for transient operation.

III. Digital Acquisition Section

Table 3 summarizes the functionality of the digital acquisition section shown in Figure 1. The RAM (used mostly for

Table 3: Specification of the digital acquisition section

Feature	Specification
closed orbit buffer	10 second deep circular buffer; initialized, updated on globally distributed timing events, and stopped on abort event
turn by turn buffer	several synchrotron periods deep; initialized on a timing event and updated on a trigger locally delayed from a turn-by-turn event
timing decoder	decodes several timing events; counters provide synchronization with any bunch and programmable delay lines provide 2ns resolution
DSP software	perform within a single turn (12 μ s): acquire 4 digitized values, apply corrections, calculate position & charge, average closed orbit, and update buffers

the buffers), DSP, VXI interface, and Industry Pack (IP) interface are all provided on a board within the C-size module. Space for four industry packs is provided in each module and the ADCs and timing decoder reside on these IPs. Using IPs for the more specific circuit functions allows the same DSP board to be adapted for different applications, avoiding inefficient design reproduction.

IV. Calibration system

In-place calibration will be provided to test the electronics from the control room, as the hardware cannot be accessed while the machine is in operation. The calibration input to the BPM processing chain is a stripline directional coupler attached to the cryostat. This will couple a calibration signal, a simulated beam pulse generated in the equipment alcove, equally to both inputs of a BPM channel. Variation of the input attenuators will permit both offset and gain calibration. By injecting the pulses into the directional coupler during the extraction gap in the beam, calibration measurements can be made during machine operation.

V. References

- [1] T. J. Shea, Design Studies on the RHIC Position Monitor System, BNL-48048, AD/RHIC-114, 1992.
- [2] P. Cameron, M. Grau, T. J. Shea, R. Sikora, this conference.
- [3] W. A. Ryan and T. J. Shea, An Interactive Beam Position Monitor System Simulator, Workshop on Accelerator Instrumentation, Berkeley, October 1992

DYNAMIC RANGE EXTENSION OF BPM at the NSLS*

Mordechai Bordoley
NSLS Department, Brookhaven National laboratory
Upton NY 11973

Abstract

In order to overcome range limitations, the existing Beam Position Monitor (BPM) receiver was modified, extending the dynamic range from 35 dB to 60 dB. The modifications include the insertion of an RF PIN attenuator, RF amplifier, and control circuitry in line with the RF link to add an extra 25dB to the existing AGC loop. This stand alone 25dB RF gain control stage is integrated into the present system without any change to the existing receiver.

I. INTRODUCTION

The 30 to 35 dB dynamic range of the existing receiver is sufficient for normal operation of the VUV and XRAY rings. However, this limited range is insufficient for research which requires low currents in the rings, resulting in large errors in the receiver's position outputs. Since the useful ranges of the receivers do not exactly overlap the range of ring operation, an additional margin of receiver range would be useful. Three different approaches were considered:

1. Improve the 10.7 MHz IF section. This approach is time consuming in that it requires replacing an existing working board. This means deleting existing circuitry, installing new circuitry and finally, recalibrating and checking the new receiver.
2. Build a separate AGC at the 158.66 MHz, RF frequency. This approach has the advantage of minimizing the RF power range at the input to the mixer. This stand alone AGC need not be

extremely precise because the existing IF AGC will continue to operate, controlling the overall loop performance. The major drawback in this method is that it requires more complex circuitry and careful attention to ensure the two loops do not interfere with each other.

3. Insert a voltage control RF attenuator (PIN diode). This is the approach ultimately chosen (Figure 1). The control voltage to the PIN is derived from the existing 0-10v voltage that drives the IF AGC. The input-output for this box is in the form of SMA connectors that can be placed just before the 158.66 MHz band pass filter. This approach does not necessitate any modification to existing circuitry. Installation of this box is simple, so the overall upgrade is easily accomplished.

II. RF ATTENUATOR

The attenuator consists of Watkin Johnson G2 PIN diode attenuator with frequency range up to 1000 MHz, and attenuation range over 45 dB. The PIN attenuator is followed by a Watkin Johnson A81-2 RF amplifier which has 17dB gain and operates to 400 MHz.

At low current levels in the ring, the PIN diode is in its minimum attenuation level (insertion loss). The combination of the 2dB insertion loss of the PIN diode and the 17 dB gain of the RF amplifier actually improves the noise figure of the receiver at these low levels. The AGC input signal to the RF attenuator must be offset and gain adjusted in order to optimize the performance of the combined AGC. Figure 2 shows the RF AGC layout.

*Work performed under the auspices of the U.S. Department of Energy.

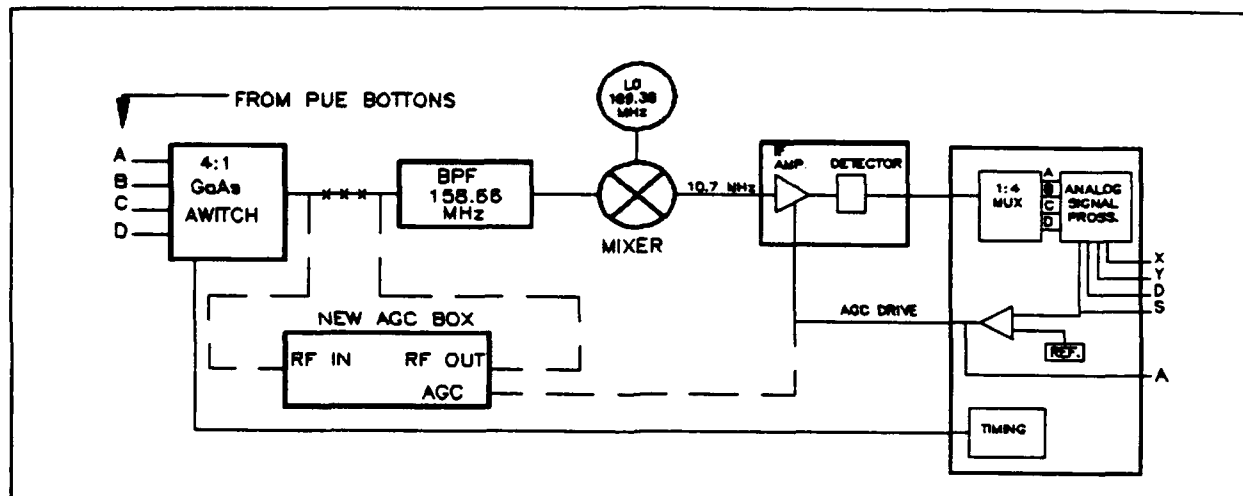


Figure 1. RF BPM receiver block diagram.

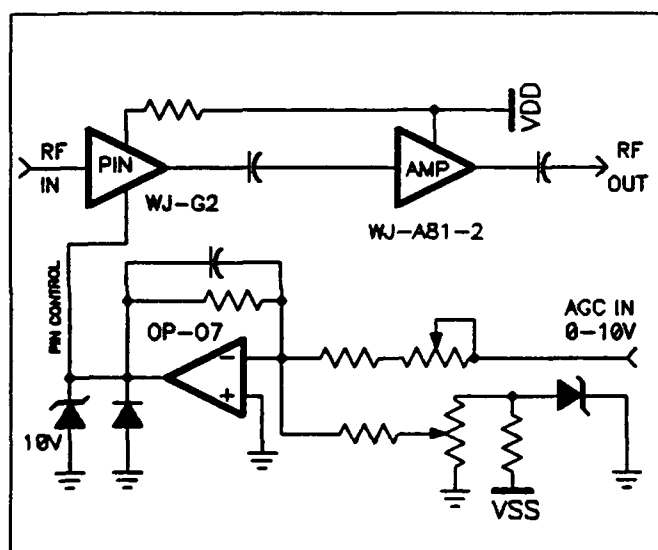


Figure 2. RF attenuator diagram.

III. RESULTS

Figure 3 shows a typical attenuation vs. control voltage characteristic of the WJ-G2 PIN diode. These diodes have greater than 40 dB dynamic range at 158 MHz. However, at low input voltages the non linearity is extremely severe, eliminating the usefulness of this range. The offset and gain potentiometers were adjusted in such a way that 0 to 10 volts at the input to the box resulted in 1.5 to 8 volts at the input to the PIN diode.

Figure 4 shows the PIN diode attenuator box characteristics. All units were calibrated this way, and showed little deviation from one to another. Thus far, 5 units have been integrated into the BPM receivers. The improved overall dynamic range is shown in Figure 5. The tight position control ranges close to 50 dB, and up to 60 dB with small deviations.

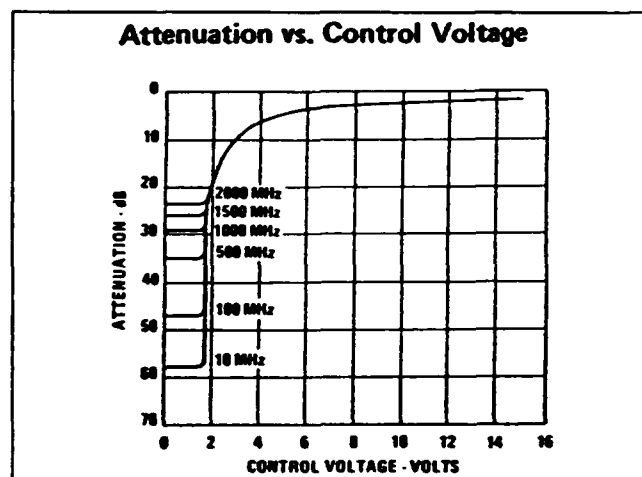


Figure 3. WJ-G2 diode characteristics.

IV. CONCLUSION

The addition of an RF voltage control attenuator to the existing BPM extends the dynamic range of the receiver by 25 dB. The integration into

the receivers proved to be simple, requiring very little adjustment. In three of the five units integrated, nothing more was required than to place The attenuator box in the receiver. Since each receiver is different, some adjustments and optimizations of the overall AGC loops should be expected.

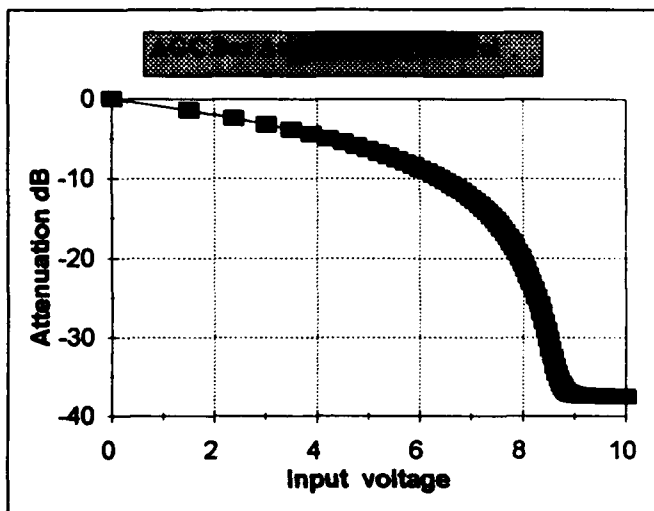


Figure 4. AGC box characteristics.

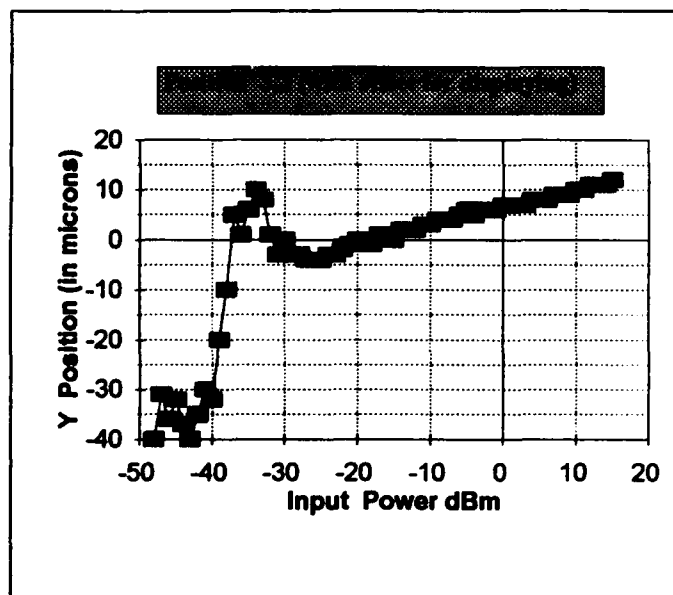


Figure 5. Y - Position variation (3,3 mm) vs. input power.

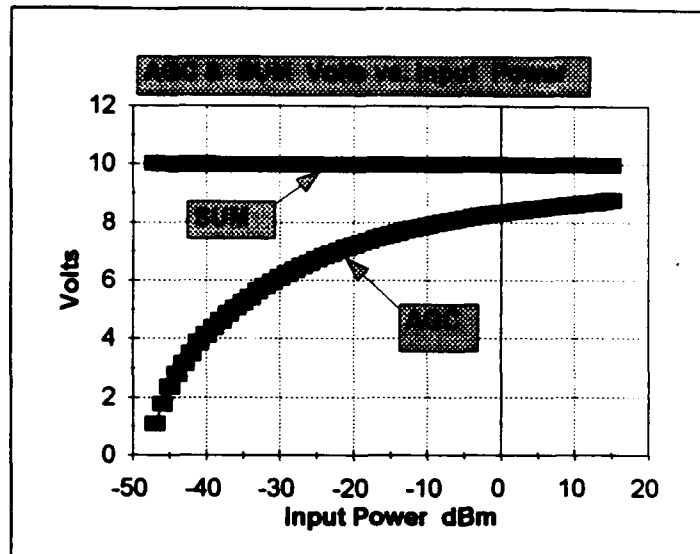


Figure 6. AGC and SUM variation vs. input power.

Beam Position Monitoring in the 100-MHz to 500-MHz Frequency Range Using the Log-Ratio Technique*

F. D. Wells, R. E. Shafer and J. D. Gilpatrick
Los Alamos National Laboratory, MS: H808
Los Alamos, NM 87545 USA

Abstract

A logarithmic-ratio beam position monitor (BPM) circuit has been designed that operates directly from radio frequency signals in the 100-MHz to 500-MHz frequency range. The circuit uses four logarithmic amplifiers, a pair for each channel. One amplifier per channel receives its signal input directly from a BPM electrode, while the second amplifier receives the same signal attenuated by 7-dB. The two outputs of each channel are summed together and the composite video outputs are applied to a differencing amplifier. The net result is the logarithmic-ratio position measurement derived from the two input rf signals. Paralleling the pairs of outputs from the amplifiers provides measurement accuracy that is comparable to other circuit techniques used for position measurement.

I. INTRODUCTION

Logarithmic-ratio processing of beam position monitor (BPM) signals is a viable circuit technique that has been described in several publications [1], [2], and [3]. Previously, however, an upper frequency limit of 100-MHz was imposed by the Analog Devices Model AD640 integrated circuit logarithmic amplifier that was employed for this application. Recent investigations have shown the feasibility of designing log-ratio circuits around the Plessey Semiconductor Company Model SL3522A logarithmic amplifier [4]. This device is a successive detection logarithmic/limiting, monolithic amplifier that produces a Log/Lin characteristic for input signals between +6 and -64 dBm with a linearity of 1-dB over the 100-MHz to 500-MHz frequency range. Comprising the circuit are six amplifier stages of 12-dB gain each, seven detector stages, a limiting rf output buffer and a video output amplifier. For the log-ratio application the rf output buffer is disabled.

II. AMPLIFIER CHARACTERISTICS

In Figure 1, the transfer curve for a typical SL3522A amplifier is shown. The figure also shows a plot of the difference between a straight line fit to the curve and the actual amplifier response. The difference curve illustrates the sinusoidal ripple that is present in the transfer function. This ripple is a side effect of the successive approximation technique used to achieve the logarithmic response.

When two amplifiers are employed in a log-ratio circuit a large amount of ripple is produced in the position measurement response. This is illustrated by the curves of

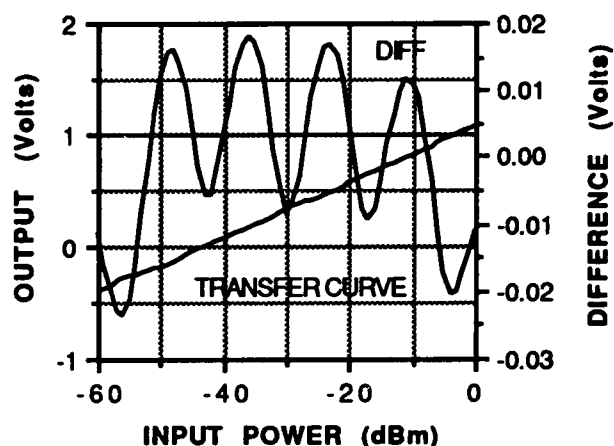


Figure 1. Transfer curve of a SL3522A amplifier and the straight line fit difference plot.

Figure 2. The measurement error resulting from this ripple ranges from 2% at the center of a cylindrical BPM probe to approximately 8% at one-fifth of the probe radius [4].

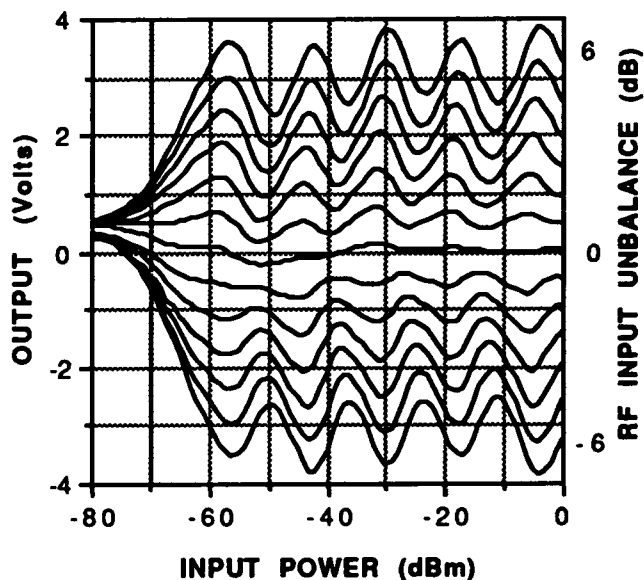


Figure 2. Response curves of the dual amplifier log-ratio circuit.

Work supported and funded by the US Department of Defense, Army Strategic Defense Command, under the auspices of the US Department of Energy.

A technique for suppressing the ripple has been suggested in Reference [3]. Two amplifiers are operated in parallel and their outputs are summed to give a composite response. One amplifier receives its signal directly from a BPM electrode, while the second receives the same signal attenuated by approximately one-half the intrastage gain, i. e., 6-dB. For this case 7-dB was found to produce the best results.

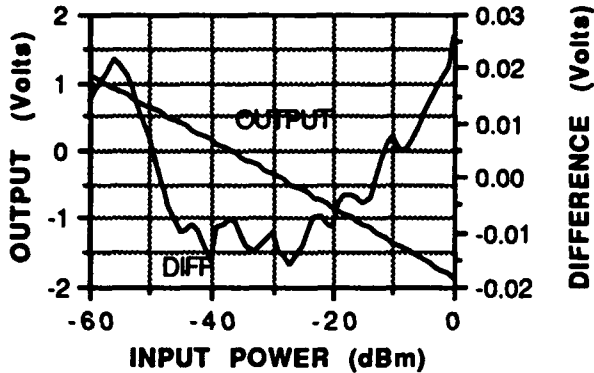


Figure 3. Transfer curve of a dual amplifier combination with the input to one amplifier attenuated 7-dB.

Figure 3 shows the transfer curve of the pair, along with the straight-line-fit difference curve. The transfer curve is more linear than that of a single amplifier and the ripple is suppressed.

To obtain the best results the circuit adjustments are important. Each amplifier has a gain and an offset adjustment. Care must be taken to match the gains and the offsets so as to equalize the transfer slopes.

III. THE QUAD-AMPLIFIER CIRCUIT

Figure 4 shows the circuit configuration for the log-ratio application. The four logarithmic amplifiers, two summing amplifiers and the differencing amplifier combine to produce a beam-position-output signal proportional to $\log(A/B)$.

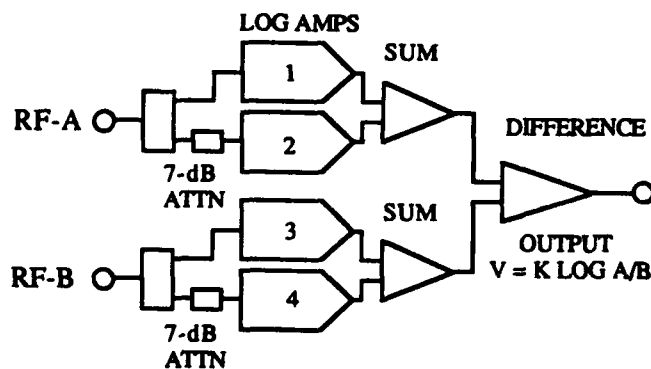


Figure 4. The quad-amplifier log-ratio circuit.

The response of the quad-circuit to 425-MHz rf signals is shown in Figure 5. On the horizontal axis, the rf input power to the A and B channels is plotted, ranging from -70 dBm to 0 dBm. The family of curves represents 13 position values corresponding to signal input ratio changes from -6-dB to +6-dB in 1-dB steps. The center trace results when the two signals are equal ($A=B$). The upper traces correspond to $A>B$, whereas the lower traces result when $A<B$. Ripple in these curves has been substantially reduced by use of the quad-amplifier technique. Best operation occurs in the range of -50 dBm to -10 dBm, corresponding to a dynamic range of 100:1 in beam current. The transfer factor for the circuit is about 0.5 volts per dB.

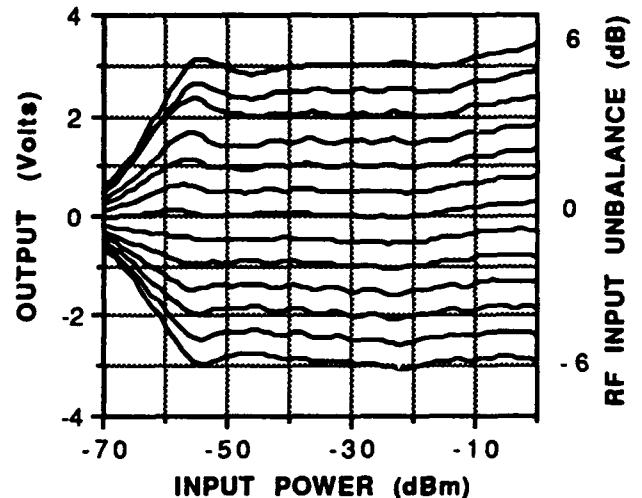


Figure 5. Response curves of the quad-amplifier log-ratio circuit.

IV. NOISE CONSIDERATIONS

Figure 6 shows the noise limited resolution characteristic of the circuit, along with a plot of the theoretical kTB resolution, for a circuit bandwidth of 2-MHz. Below -40 dBm the two curves have approximately the same slope and they

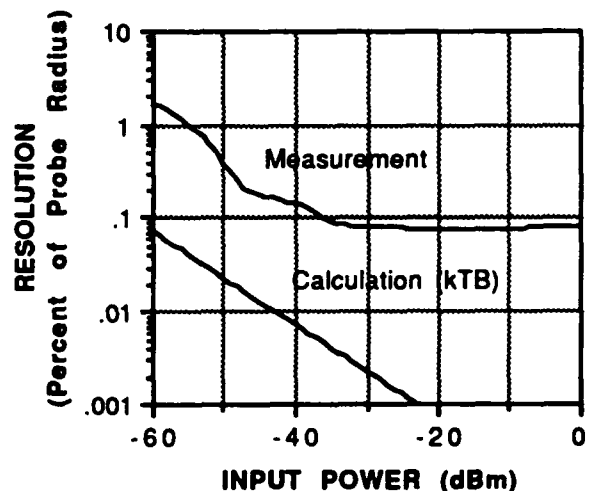


Figure 6. Resolution curve of the quad-amplifier log-ratio circuit.

are separated by about 25-dB of input power. For rf power inputs greater than -40 dBm the trend is toward a constant value of resolution. This flattening of the resolution curve is characteristic of log-ratio circuits [2], [3]. It may be caused by saturation effects that take place in the intrastage amplifiers and detectors as the input power increases.

V. CONCLUSIONS

The quad-amplifier log-ratio circuit is a viable candidate for beam position measurement in the 100-MHz to 500-MHz frequency range. Many accelerators operate at bunching frequencies in this range and they could benefit from beam position measurements using this equipment. The principle attribute of the circuit is that it can operate directly from BPM rf signals. No additional circuits such as down converters would be required.

VI. REFERENCES

- [1] F. D. Wells, R. E. Shafer, J. D. Gilpatrick and R. B. Shurter, "Log-Ratio Circuit for Beam Position Monitoring," AIP Conference Proceedings 229, Accelerator Instrumentation, pp. 308-314, 1990.
- [2] F. D. Wells, R. E. Shafer, J. D. Gilpatrick and R. B. Shurter, "Log-Ratio Circuit for Beam Position Monitoring," Conference Record of the 1991 IEEE Particle Accelerator Conference, pp. 1139 -1141.
- [3] G. R. Aiello and M. R. Mills, "Beam Position Monitor Electronics Using DC Coupled Demodulating Logarithmic Amplifiers," European Particle Accelerator Conference Record, 1992.
- [4] F. D. Wells, R. E. Shafer and J. D. Gilpatrick, "Log-Ratio Beam Position Monitoring at 425 MHz," 16th International LINAC Conference, 1992.

Beam Pinging, Sweeping, Shaking, and Electron/Ion Collecting, at the Proton Storage Ring*

T. Hardek, R. Macek, M. Plum, and T.-S. Wang
Los Alamos National Laboratory
MS-H838, PO. Box 1663, Los Alamos, NM 87545 USA

Abstract

We have built, installed, and tested a pinger [1] for use as a general diagnostic at the Los Alamos Proton Storage Ring (PSR). Two 4-m-long parallel-plate electrodes with a plate spacing of 10.2 cm provide kicks of up to 1.1 mrad. A pair of solid-state pulsers may be operated in a single-pulse mode for beam pinging (tune measurements) or in a burst mode at up to 700-kHz pulse rates for beam sweeping. During our 1992 operating period, we used the pinger for beam sweeping, for beam shaking, for measuring the tune shift, and we have used it as an ion chamber. Using the pinger as an ion chamber during production conditions has yielded some surprising results.

I. INTRODUCTION

In the past, we have measured the horizontal tune at high intensity by pulsing the extraction-kicker electrodes at reduced voltages. We have also acquired additional horizontal data by observing coherent motion produced by the charging operation for our Blumlein-configured extraction-kicker modulators; however, there has been no convenient way to make a similar measurement in the vertical plane. During a break in our 1992 operating period, we installed a set of vertical pinger electrodes [1] in section 3 of the PSR. We are now capable of pinging the beam vertically and observing vertical coherent motion.

In addition to beam pinging, we also have the ability of sweeping beam from the space between beam bunches. Operating at a maximum of 10 kV, our pulsers cannot remove all the beam in a single kick. We depend on several kicks timed to add up to an effective kick sufficient to completely remove the beam. In practice, we adjust the fractional tune to $1/6$ and kick every 6 turns. We have also operated with a vertical tune of $1/4$ with a kick every 4 turns.

The pinger electrodes may be DC biased and used as clearing electrodes to remove unwanted electrons and ions. A metering device may be added to use the electrodes as an ion chamber and measure the quantity of electrons and ions collected. Preliminary experiments have yielded some confusing results.

* Work performed under the auspices of the U.S. Department of Energy.

We present here an overview of some of the initial data we have collected in pinger and beam-sweeping experiments. We also present results from our measurement of the collected charge with the pinger plates operated as an ion chamber.

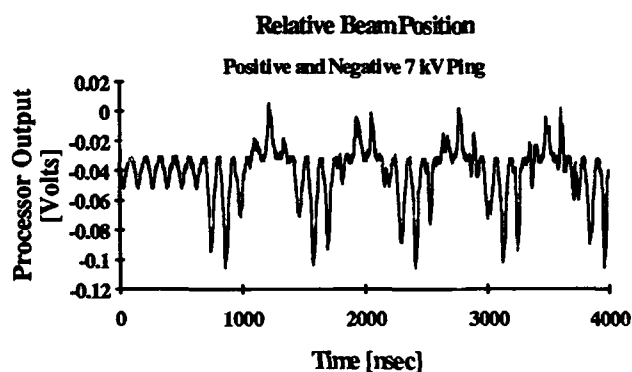


Figure 1: Coherent Beam Motion after a 7-kV Ping

II. BEAM PINGING

We can provide positive and negative 10-kV pulses timed to occur at any selected time within the PSR accumulation cycle. The pulse width is adjustable from 100 nsec to several μ sec in width and has rise and fall times of 20 nsec. For beam pinging, we adjust the pulse width to one PSR revolution period (360 nsec) and time the kick to occur as the beam bunch passes the pinger electrode. We can observe beam motion with a 30-MHz-bandwidth capacitive pickup system or with high frequency strip-line pickups (first maximum at 200-MHz for the normal electrode or 400-MHz for a short version). The strip-line pickups differentiate the beam signal, complicating analysis, so we generally utilize the capacitive pickup system. Figure 1 shows the capacitive pickup output for a single ping late in the injection cycle with full-intensity beam stored in the PSR (2.5×10^{13} stored protons). The processing electronics is not normalized to beam intensity so the output retains the shape of the beam bunches. In this trace, the circulating beam is offset toward the inner radius. The initial part of the waveform shows negative pulses, indicating the beam offset and the

oscillations after the ping are centered about the offset central orbit. A spectrum-analyzer scan taken with these conditions gives sidebands at 2.476 MHz and 3.144 MHz with a measured revolution frequency of 2.808 MHz. The resulting full-intensity vertical tune is 2.119, compared to a low-intensity single-injected-bunch measured tune of 2.134.

III. BEAM SWEEPING

In the beam sweeping mode, we can provide a 100-nsec-long 10 kV-kick at a maximum rate of 700 kHz. The revolution frequency is 2.8 MHz, so we can kick every four turns. For normal production, we set the vertical tune to 2.173. Only a minor change is necessary to alter the fractional tune to 0.166 and generate a kick every six turns, so we have chosen this scenario for our normal sweeping mode. The minimum available pulse width is 100 nsec (full width, half maximum). Figure 2 shows the result of several sequential sweeping pulses. We have set the injected beam bunch length to 100 nsec and have centered the kick on the beam bunch, allowing our sweeping pulse to remove all of the injected beam. We have not longitudinally confined the beam, so some beam remains at the leading and trailing edges of the kick.

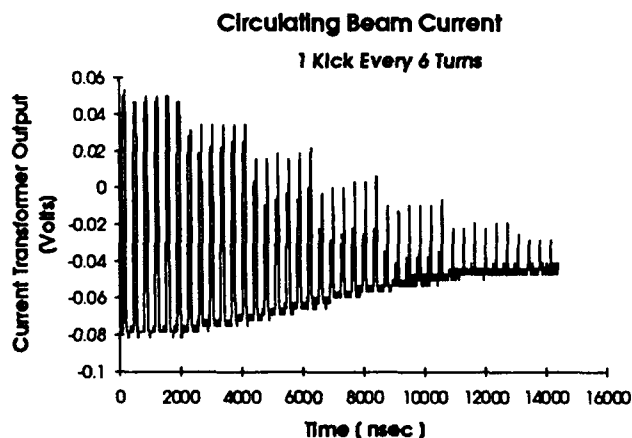


Figure 2: 100-nsec Beam Bunch Kicked Every 6 Turns

One intended use for our sweeping technique is to completely clear the space between bunches of protons. Only a small amount of protons in the gap between bunches is required to trap electrons and produce the unstable condition we observe at high intensity in the PSR. We have made several attempts to demonstrate stable operation with beam sweeping with varied success. The sweeping pulse is longer than the space between the bunches, so we always sweep out some circulating beam. We have been able to replace this lost beam and demonstrate stable operation. In our efforts to increase intensity with beam sweeping, we still observe a fast beam loss. We attribute this to an increase in electrons generated by the beam lost during sweeping, gap filling at rates exceeding

the sweeping rate, or some other mechanism we do not yet understand.

IV. BEAM SHAKING

During the 1990 run period, we were able to drive an extraction-kicker electrode with a continuous wave sinusoidal rf signal at a frequency near the lowest horizontal tune frequency. We observed an increase in the instability threshold of about five percent. We have now repeated this experiment using the pinger electrode and demonstrated a similar result for the vertical plane. Driving at about 25 MHz at the 100-watt level (into a 50-ohm load at one end of the electrode) resulted in an abrupt increase in vacuum chamber pressure. There seems to have been some sort of electrical breakdown at voltage levels well below the 10 kV-hold-off capability of our electrode system. We have yet to repeat the experiment without beam.

V. ION-CHAMBER RESULTS

We have also used the pinger electrodes as an ion chamber by biasing one or both electrodes and measuring the current thus collected. Ions and electrons from residual gas ionization usually comprise the primary contribution from such a measurement. Other contributions include secondary emission of electrons due to interactions of the beam with the beam pipe and pinger electrodes, and protons from the halo of the beam stopping in the electrodes. There are also strong (150 V peak-to-peak into 50 ohms) ac-coupled signals due to the beam passing by the electrodes. To minimize the effect of these signals, we carefully terminated each end of each electrode into 50 ohms, as shown in Figure 3.

We have tried various setups, including biasing one electrode and measuring the current on the other electrode, and biasing both electrodes with opposite polarities and measuring the current on one of them. We have also tried to suppress the strong ac-coupled signal, due to beam passing by the electrodes, by installing 1- μ F shunt capacitors at the vacuum feedthroughs. In all cases, we get the surprising results shown in Figure 4. For this figure, we have chosen two representative data sets, one with, and one without, the shunt capacitors installed at the vacuum feedthroughs. For both measurements, we have biased one electrode and measured the current on the other electrode. The two data sets were taken during production conditions, but on different days. We see that they are basically the same except for their relative amplitudes, but we cannot deduce much from this since we have observed large fluctuations in amplitude from one data set to another, apparently due to imperceptible variations in the exact tune of the linac, beam line, and PSR.

We do not fully understand the behavior of the data in the -50-V to +50-V region. The collected currents are huge. We have seen up to 15- μ A of average collected current which

is a large fraction of the 70- μ A average injected current. We expect just a few nA of current from residual gas ionization. We suspect some sort of secondary emission of electrons caused by the interactions of the residual gas ions and electrons with the beam pipe walls and pinger electrodes. The strong ac-coupled signals on the pinger electrodes due to the high-intensity beam pulses may contribute to the unusual peaks in these data. To eliminate this effect, we tried injecting low-current dc beam into the ring. Figure 5 shows the results of these measurements, taken at 4 Hz, with 200 μ s of accumulation and 500 μ s of storage. In this figure, the error bars represent the range of current readings observed over a 30-second interval. The setup was also a bit different from that shown in Figure 3. The bottom electrode was connected directly to a power supply, with no 50-ohm terminations at either end, and the low-pass filter on the picoammeter was slightly different. These data are about what one would expect, showing a gradual climb to a plateau at a couple thousand volts. We hope that additional measurements scheduled for this summer will shed some more light on our puzzling data.

VI. CONCLUSIONS

We have a new diagnostic tool to study PSR performance. We have thus far had only limited opportunities to explore the uses of this new tool and have generated some confusing but interesting results. This year we hope to clarify these results and complete additional beam experiments, possibly including a detailed beam transfer function measurement.

VII. REFERENCES

- [1] T. W. Hardek and H. A. Thiessen, "A Pinger System for the Los Alamos Proton Storage Ring," *1991 Particle Accelerator Conference Proceedings*, pp. 866-868.

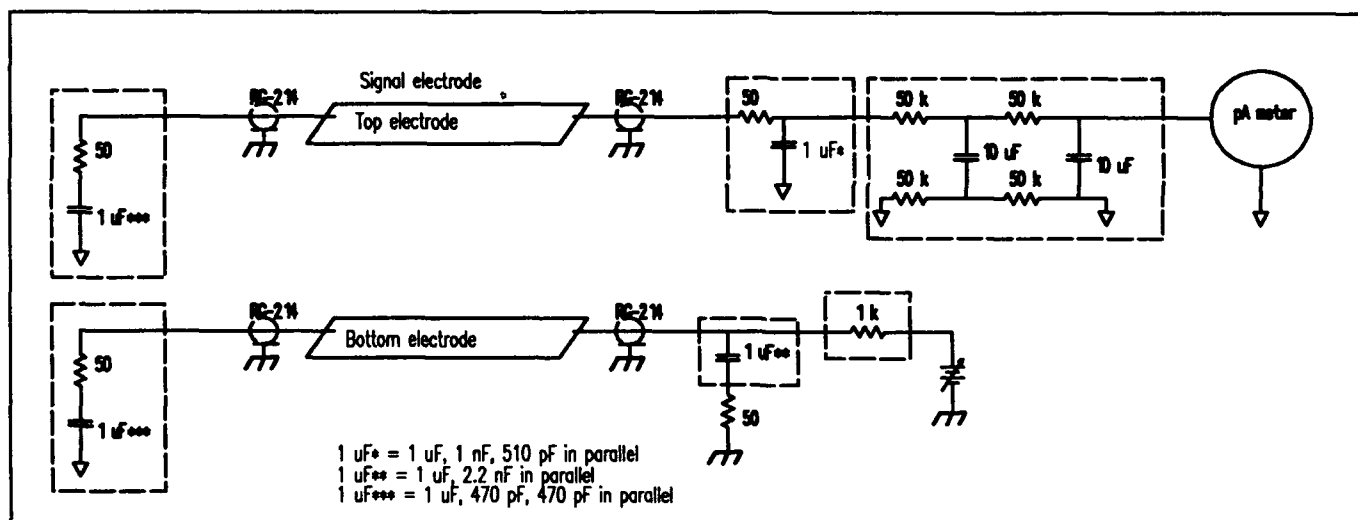
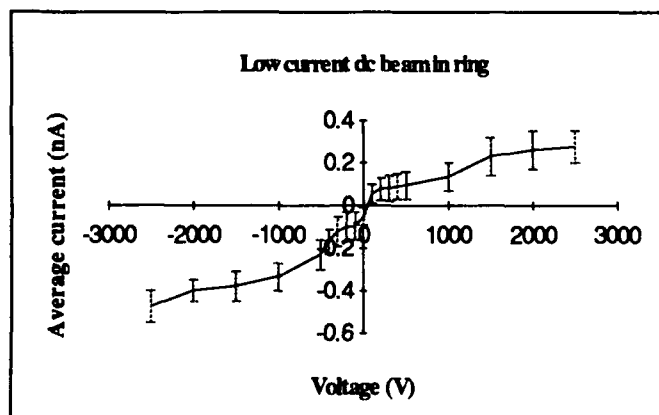
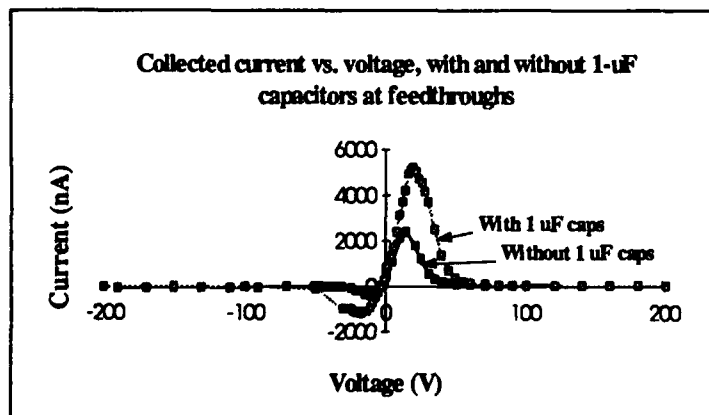


Figure 3: Pinger Electrode Connection for use as an Ion Chamber



Test Results of the SSC Log-Ratio Beam Position Monitor Electronics

G.R. Aiello, M.R. Mills, R.E. Gonzalez
Superconducting Super Collider Laboratory*
2550 Beckleymeade, MS-4005, Dallas, TX 75237 USA

Abstract

A working prototype of Beam Position Monitor (BPM) electronics, based on the log-ratio technique is described in this paper. Results of a test performed at the Fermilab Booster, comparing the existing Fermilab BPM system are also presented. A calibration technique has been used which corrects errors due to mismatched channels and electronics drift. The results are compared with bench measurements on the prototype circuit.

I. INTRODUCTION

The log-ratio technique for BPM electronics has recently been investigated at many laboratories and encouraging results have been obtained from bench testing. A test was performed at the Fermilab Booster in order to understand the performance limitations in the field. The machine the log-ratio electronics was tested on presents some interesting problems. The RF frequency is ramped from 30MHz to 53MHz in 33ms, and the average beam current increases during the acceleration cycle changing the signal amplitude presented at the input of the electronics. A test on this machine has a direct interest for the SSC because of the similar parameters of the Low Energy Booster. A direct comparison of the log-ratio BPM electronics, built at the SSC, with the Fermilab Booster AM/PM electronics is described in this paper. The signal from the BPM electrodes was split in order to provide a simultaneous source to both systems. The outputs were digitized by the same ADC module and later processed.

II. LABORATORY RESULTS

A. Position Characteristics

The log-ratio technique for BPM electronics is based on equation 1, [1], where S_x is the sensitivity in dB/mm, V_A and V_B the signal amplitudes at the output of the BPM electrodes.

$$x = \frac{1}{S_x} \times \left(20 \times \log \frac{V_A}{V_B} \right) \quad (1)$$

Bench performance is extensively described in previous publications [2], [3], [4]. The two plots which best summarize the performance are shown in figures 1 and 2.

Circuit linearity is an important consideration in measuring position over the complete range of beam current and to accurately measure displacement from center. The logamp electronics have demonstrated a linearity of 1% error over an input power dynamic range of 70dB.

A plot of simulated position vs. beam current was obtained by applying a source signal from a signal generator to both channels of the log-ratio electronics. Ramping the power level of the generator over the electronics dynamic range simulated a changing beam current. A simulation of beam displacement off center was accomplished by changing the power ratio of the two signals while again ramping the input power. The circuits dynamic range over a simulated beam displacement of ± 10 mm is demonstrated in figure 1. A sensitivity of 1dB/mm, which corresponds to a circular beam pipe of radius 33mm, was chosen for graph legibility.

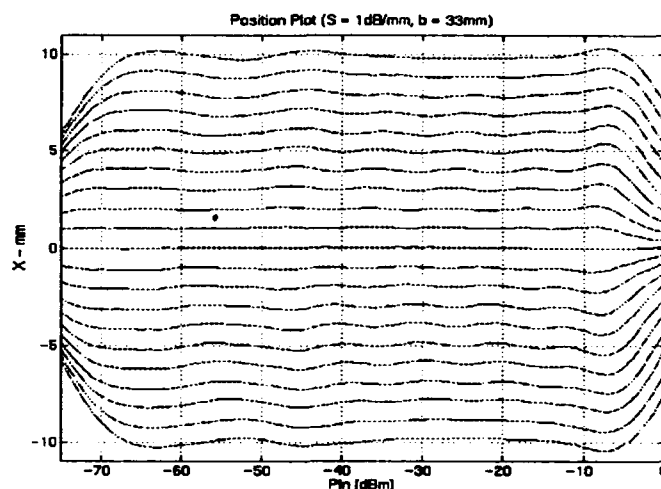


Figure 1. Simulated beam fluctuation.

B. Noise Characteristics

The resolution of the position measurement is limited by the signal to noise ratio, according to the following expression [1]:

$$\delta_x = \frac{b}{4} 10^{\left(\frac{P_N - P_S}{20} \right)} \quad (2)$$

where b is the beam pipe radius, P_N is the noise power and P_S is the signal power, both in dBm. The theoretical noise power is expressed by [5]:

$$P_N = 10 \log \left(\frac{KTB}{0.001} \right) + NF \quad (3)$$

where K [J/K°] is Boltzman's constant, T [K°] is temperature, B [Hz] the bandwidth and NF [dB] is the noise figure. The noise figure is derived by measuring the position resolution at a given signal power, and calculating the noise power at the measured conditions. The theoretical curve derived by equations 2 and 3, using $NF=0$, and the experimental curve of the logamp response is shown in figure 2. The noise figure is derived by

*Operated by the University Research Association, Inc., for the U.S. Department of Energy under contract No. DE-AC35-89ER40486

measuring the distance in the horizontal axis between the two curves, which is 15dB.

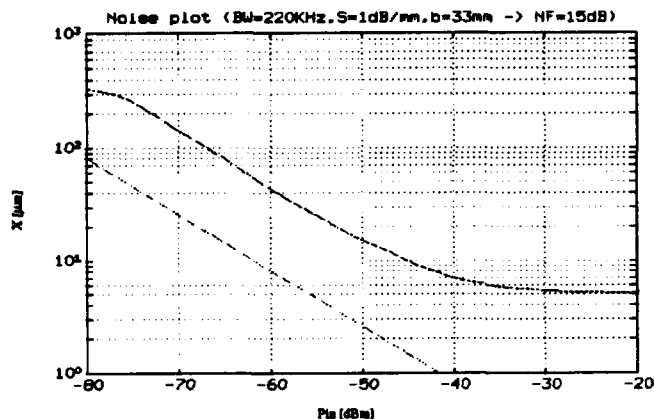


Figure 2. Beam position resolution as a function of input signal amplitude.

III. FERMILAB TEST RESULTS

Position measurements of the Fermilab Booster were taken with the test setup shown in figure 3. Signals A and B originated at a set of horizontal beam pickups. During normal operation, these signals would be terminated in Fermilab's RF module which incorporates the AM/PM method of beam detection [6]. The signals were split and sent to both the RF module and the log-ratio circuit. The outputs of both circuits were digitized by the same ADC module running at a sample frequency synchronized to the revolution frequency. The injection synchronization pulse arrives at the beginning of the Booster cycle and arms the ADC. The Trigger Generator produces a pulse

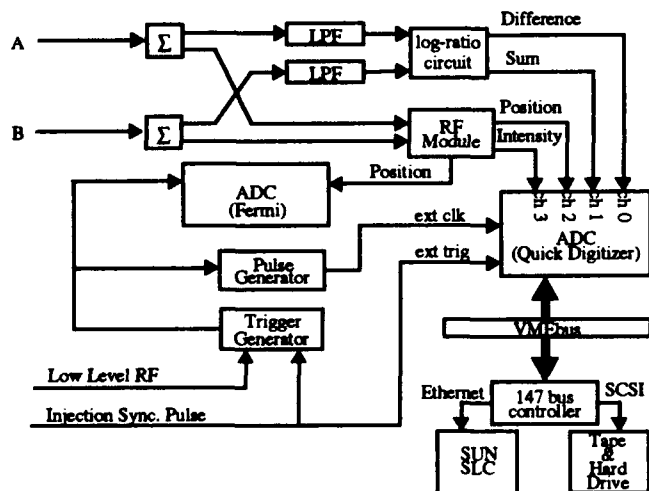


Figure 3. Block diagram of the log-ratio, AM/PM position test conducted at Fermilab.

which tracks the frequency sweep of the Booster with the low level RF. This signal triggers the Pulse Generator, which provides a signal for the ADC module, and triggers the digitizer on every fifth revolution, the quickest rate available.

A plot of the beam position vs. the number of turns, using the log-ratio circuit, is shown in figure 4. A corresponding plot of the beam position obtained with the RF module was used for comparison. The difference between the log-ratio circuit and the RF module positions is shown in figure 5.

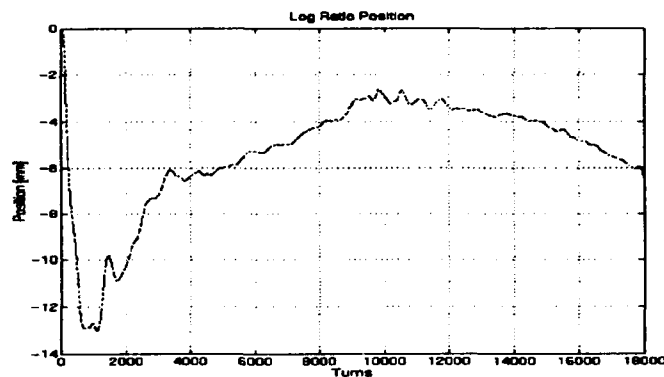


Figure 4. Measured position vs. number of turns through one acceleration cycle with the log-ratio circuit.

After the first 4000 turns, the results are as good as can be expected, considering the errors associated with the two systems. The typical offset for the Booster RF module is approximately 0.5mm. The error of the log-ratio circuit, due to ripple caused by saturating gain stages internal to the logamp, could be as high as ± 0.1 mm, with the Booster sensitivity of 0.52dB/mm. 12 bit ADC's are used in the digitizer. With a half bit of noise, $\pm 16\mu\text{m}$ could be realized with the log-ratio electronics and $\pm 165\mu\text{m}$ with the RF module. The position signal from the RF module was provided from its 20dB attenuation port, which would account for the greater displacement. These ADC resolutions causes the ripples seen in figure 5, not the general shape of the curve.

During the first 4000 turns several other factors must be considered in understanding the plot of figure 5.

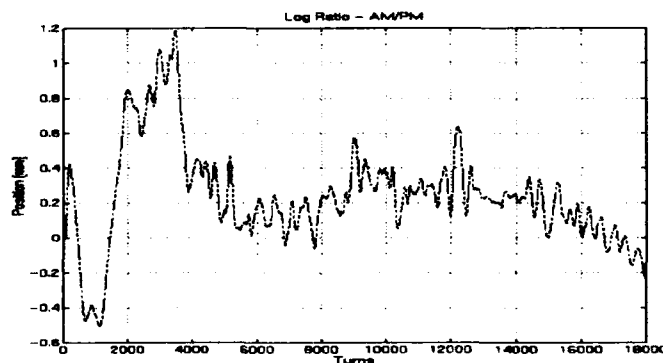


Figure 5. Difference of position between the log-ratio circuit and the RF module vs. number of turns.

The beam signal intensity increases by about 10dB and the revolution frequency sweeps from 30MHz to 47MHz in this early part of the cycle. The frequency as a function of the number of turns is shown in figure 6.

The contributions to the error plot of the log-ratio electronics is due to both amplitude and frequency. The electronics is

certainly processing the beam signal through its maximum range of linear response error, which appear as the ripples in figure 1, and corresponds to ± 0.1 mm. The amount of position deviation as a function of frequency expected is on the order of 0.08 mm. Both these numbers were verified by bench testing at the SSC.

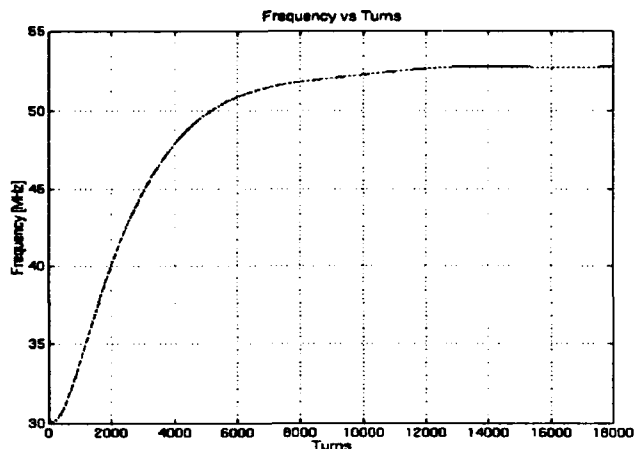


Figure 6. RF frequency vs. number of turns at the Fermilab Booster.

Errors due to the AM/PM electronics are a little harder to discuss because an RF module was not available for lab testing. However, there are a few factors which could account for at least part of the total error. During the early period of acceleration, the beam displacement is in the range of 7 mm to 13 mm off center. Considering the Booster sensitivity, this is in the range where the AM/PM response is becoming nonlinear. Although a correction formula was used to calculate position, there is still some amount of error associated with this nonlinearity. Important also is the error due to the frequency sweep. Down converters and limiters both contribute to the total error which could be as large as ± 0.4 mm [7].

The contribution of all the errors amounts to about 1 mm, which is not out of line with the plot of figure 5.

IV. CONCLUSIONS

The log-ratio design will be utilized in the SSC's Linac. This design will be implemented in conjunction with a frequency down-converter from 428 MHz to 60 MHz. The IF frequency was chosen with the intention of consolidating a design which may also be suitable for the other SSC machines.

Through incorporating relatively minor design changes, this log-ratio circuit will also be proposed for service in the SSC's Low Energy Booster (LEB). With the LEB sensitivity slightly greater than that of Fermilab's Booster, 0.72 dB/mm as opposed to 0.52 dB/mm, and a narrower frequency sweep from 47 MHz to 59 MHz, instead of 33 MHz to 53 MHz, frequency compensations won't be necessary. The experience at the Fermilab Booster has taught us to be careful here. It is critical that the input filters be well matched through this frequency sweep. An impedance mismatch as a function of frequency will result in a direct position error.

V. ACKNOWLEDGMENTS

The authors wish to thank Tony Hawkins and Tom Boone for providing test software support; Victor Brouk for providing data for the plot in figure 6; and Bob Webber for many useful discussions. Special thanks to Ed Barsotti for his help in assuring the testing at Fermilab to be smooth and productive.

VI. REFERENCES

- [1] R.E. Shafer, "Beam Position Monitoring", *AIP Conf. Proc.* 212 (1989), pp. 26-58.
- [2] F.D. Wells, J.D. Gilpatrick, R.E. Shafer, "Log-ratio Circuit For Beam Position Monitoring", *U.S. PAC* (1991), pp 1139-1141.
- [3] G.R. Aiello, M.R. Mills, "Preliminary Evaluation of AD640 Logamp Detector for BPM Electronics", SSCL-N-787 (Feb 1992).
- [4] G.R. Aiello, M.R. Mills, "Log-Ratio Technique for Beam Position Monitor Systems", *Accelerator Instrumentation Conference* (1992).
- [5] J. Bird, "An Introduction to Noise Figure", *RF design*, March (1993) pp. 78-83.
- [6] S.P. Jachim, R.C. Webber, R.E. Shafer, "RF Beam Position Measurement for Fermilab Tevatron", *IEEE Trans. Nucl. Sci.* 28, 2323 (1981).
- [7] R.C. Webber, private communication (1993).

RF Beam Position Monitors for the TESLA Test Facility

Ronald Lorenz

Technische Universität Berlin, EN-2, Einsteinufer 17, D-1000 Berlin 10, Germany

Abstract

For the TESLA Test Facility beam position monitors with a precision of about 10 μm are required. A circular cavity excited in the TM_{110} -mode by the off-axis beam provides a signal strong enough for various injectors. Expected signal to noise ratios and the theoretical resolution are estimated for a designed structure. A coaxial combiner was designed for common mode rejection. It is also foreseen to test different low-impedance monitors behind the injector. A structure using two coupled cavities is briefly described.

1. Introduction

For the alignment of the quadrupoles in the TESLA Test Facility (TTF) beam position monitors with a precision of about 10 μm are required. This has to be achieved for several bunch charges ([1]). The monitors will be attached to the quadrupoles within 50 μm mechanical alignment precision. Because of the desired precision and the limited

name	particles/bunch	frequency	bunch separ.
1b	$5 \cdot 10^8$	73 MHz	14 ns
2	$5 \cdot 10^{10}$	1 MHz	1 μs

Table 1: Injectors proposed for the TTF and TESLA

space we designed a TM_{110} -excited circular cavity. The resonant frequency $f_{110}=2.1\text{GHz}$ was chosen to avoid interferences from the accelerating cavities. In this paper we denote 'resolution' as 'precision limited by electromagnetic interference and circuit noise'.

Since monitors with lower impedances might be required for a multibunch Linear Collider it is also foreseen to test other structures like resonant buttons or a re-entrant cavity (see also [2]) behind the injector. A structure using two coupled coaxial cavities is briefly described here.

2. TM_{110} -Excited Circular Cavity

The simplest microwave BPM-structure is a circular cavity excited in the TM_{110} -mode by an off-axis beam.

Advantages

- * the TM_{110} -amplitude yields the desired signal directly; it is stronger than the signal given by other monitors
- * the cavity can be machined within micrometer tolerances
- * the structure itself does the subtraction - in principle no

additional combiners, less cable drift and unbalances

- * by measuring the amplitude of the fundamental mode we get a signal proportional to the bunch charge

Problems

- * the precision is limited by the finite Q ([4]); it can be increased by combining two symmetrical outputs in a hybrid
- * a common mode rejection of more than 120 dB with respect to the TM_{110} will be required for signal detection
- * an appreciable amount of power (common modes) might be extracted from the beam and stored in the cavity
- * the strong signal change requires a very wide dynamic range in power for the electronics; special problems arise for the first beam or in the case of a beam break-up

2.1. Estimated Resolution

The resolution of such a cavity-BPM is limited by:

- * the power out, signal to noise ratio (electronics).
- * the expected signal ratio due to the finite Q-values.

To estimate both limits we need the maximum voltage of the TM_{110} excited by a beam with a displacement δ_x ([3])

$$V_{110} = \frac{J_1'(0)}{J_1^{max}} \frac{a_{11} \cdot \delta_x}{r} V_{110}^{max} = \frac{J_1'(0)}{J_1^{max}} \frac{a_{11} \cdot \delta_x}{r} \cdot 2qk_{110} \quad (1)$$

with the Bessel function J_1 , its first root a_{11} , the cavity radius r and the longitudinal lossfactor k_{110} of the TM_{110} excited at one of its maxima.

Expected Power in the Dipole Mode

The power in the TM_{110} extracted from the beam can be estimated using impulse excitation of an equivalent circuit

$$P_{110} = \frac{V_{110}^2}{4 \cdot k_{110} \cdot T_p} = \delta_x^2 \cdot \frac{q^2}{T_p} \cdot \frac{k_{110}}{4} \cdot \left(\frac{a_{11}}{J_1^{max} \cdot r} \right)^2 \quad (2)$$

T_p is the time for the power to decay, q the bunch charge. With $k_{110}=\omega/4 \cdot (R/Q)_{110}$, N the number of particles per bunch and (1) we get

$$P_{110} = \delta_x^2 \cdot (N e \omega)^2 \cdot \frac{Z_0 \cdot l \cdot a_{11}}{4\pi \cdot r^3 \cdot Q_L \cdot (J_0(a_{11}))^2} \quad (3)$$

With $Q_L=2000$, $f_{110}=2.1\text{GHz}$, $r=81\text{mm}$, length $l=44\text{mm}$ this yields for $N=5 \cdot 10^{10}$

$$\frac{P_{110}}{W} = \left(\frac{\delta}{\mu\text{m}} \right)^2 \cdot 1.31 \cdot 10^{-16} \cdot N^2 \approx 3.3 \cdot 10^{-7} \left(\frac{\delta}{\mu\text{m}} \right)^2 \quad (4)$$

With numerical results (Table 2) for the $\frac{R}{Q}$ of a cavity with beam pipes and assuming a coupling factor $\beta=1$ we obtain

$$P_{out} \approx 2 \cdot 10^{-7} W / (\mu m)^2$$

This is much more than the expected thermal noise from the first stage of amplification ($P_{noise} \approx 10^{-12} W$).

length	Mode	frequency GHz	Q	$\frac{R}{Q}$ Ω	$\frac{k_0}{V/pC}$
l_1	TM_{010}	1.66	1901	48.60	0.127
l_1	TM_{110}	2.12	2537	71.83	0.237
l_2	TM_{010}	1.55	3989	86.62	0.209
l_2	TM_{110}	2.11	5471	100.70	0.332
geometry: $r=81mm$, $a=39mm$, $l_1=20mm$, $l_2=44mm$					
material: ring - Cu, endplates - CrNi					

Table 2: MAFIA-results for a cavity with beam pipes

Excitation of Common Modes

W. Schnell ([3], confirmed in [4]) estimated the voltage ratio of the beam driven TM_{110} and TM_{010}

$$S_1 = \frac{V_{010}(\omega_{010})}{V_{110}(\omega_{110})} \approx \frac{5.4}{\lambda_{110}} \cdot \delta_x \cdot \frac{k_{010}}{k_{110}} \quad (5)$$

For the spectral densities at ω_{110} he obtained

$$S_2 = \frac{v_{010}(\omega_{110})}{v_{110}(\omega_{110})} \approx S_1 \cdot Q_{110} \cdot \left(1 - \frac{\omega_{010}^2}{\omega_{110}^2}\right) \quad (6)$$

λ_{110} is the wavelength, Q_{110} the Q-factor of the TM_{110} . Including numerical results we obtain $\delta_x \approx 30\mu m$.

With a symmetry-reduction (combination of 2 outputs by a hybrid) we can get another 30 dB, which is limited by the finite isolation of a hybrid.

2.2. Design-study for the TTF

The prototype consists of the cavity itself and a coaxial ring-combiner to reject common modes.

TM₁₁₀-cavity

The number of modes trapped in the cavity should be as small as possible. This can be achieved with a short cavity and shifting the resonant frequency of the TM_{020} above the beam pipe cut-off. The resonant frequency $f_{110} \approx 2.1GHz$ was chosen to avoid interferences from the accelerating cavities (stop-band: 1.9 GHz - 2.38 GHz).

Since it is foreseen to measure individual bunches with the second injector Q_L has to be less than 2000. Hence the material was chosen as CrNi. First measurements on a brass modell confirmed the theoretical resolution of $10\mu m$ for brass. An improvement of the measurement accuracy is expected with a new experimental set-up.

Ring-Combiner

Since the theoretical resolution for our design is limited by the common-mode excitation (see results above) we designed a ring-combiner to reject these modes (Fig.1; also [5]). For $f_{110} = 2.1GHz$ the magnetic field of the dipole

mode adds whereas for the common modes it subtracts. We expect a symmetry rejection of more than 30 dB.

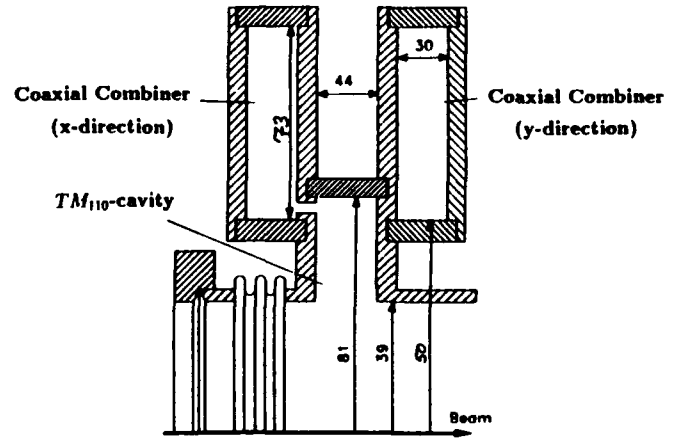


Figure 1: Cavity and coaxial ring-combiner

One problem is to avoid standing waves. We designed a coupling to a ridged waveguide via a slot in z-direction. However, it might be necessary to realize a stronger coupling with a selective coupler.

The TM_{010} will be used as a reference and for measuring the bunch charge. We investigate a selective coupler located at a point where the magnetic field of the TM_{110} (in the hybrid) will be zero. The combiner can be machined with micrometre tolerances, too.

2.3. Signal-Detection

We plan to realize two different schemes and to compare some parameters (e.g. resolution, stability, costs):

a) with a superheterodyne receiver, no damping

In a superheterodyne receiver the frequencies of the dipole

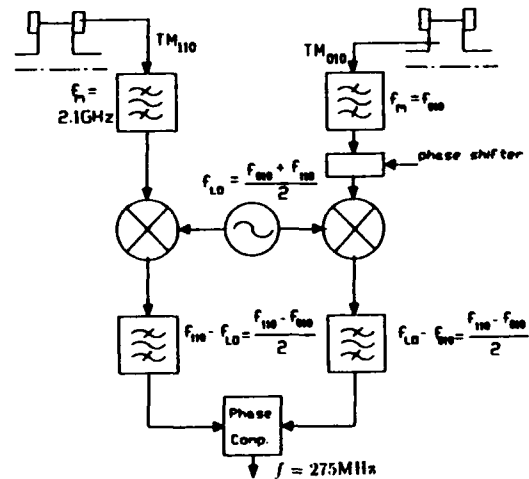


Figure 2: Signal detection using a heterodyne receiver

mode and a reference (smaller or equal the dipole mode frequency) are mixed down to an IF. Due to the difference between both frequencies we need only one stage, with an LO at $f_{LO} = \frac{f_{010} + f_{110}}{2}$. But the very high dynamic range required for the mixers causes problems.

b) with selective couplers and several filters
The problem mentioned above could be solved with a filter, rejecting all other modes except the TM_{110} . At the end log-amplifiers at 2.1GHz will be used to get the desired dynamic range. A possible scheme which requires several filters to get more or less than 120 dB rejection is given in Fig.3 (see also [6]).

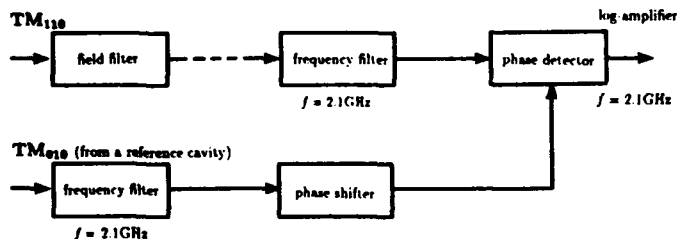


Figure 3: Signal detection using different filters

3. Coupled Zero-Mode Monitor

It might be necessary for the operation of a multibunch Linear Collider to use monitors with a lower impedance. We investigated three different structures, which are resonant to get the desired resolution. Resonant buttons, a monitor using a re-entrant cavity and measurements on prototypes are discussed in detail in [7]. Theoretically, with resonant buttons one can get a resolution of $10\mu\text{m}$ for $N=5 \cdot 10^{10}$ ($P_{noise} \approx 10^{-12}\text{W}$).

In another arrangement proposed by W. Schnell [3] the signal is superimposed as a modulation. Two identical cavities are weakly coupled to the beam by coupling slots. If the beam passes through the centre both cavities start oscillating at equal amplitudes and in phase with each other. The oscillation decreases in a smooth exponential. If the beam is displaced to the right, the left cavity will be given less energy than the right. A modulation by $f_s = f_0 - f_\pi$ (f_0 is the zero-mode and f_π the π -mode frequency) will be superimposed to the exponential decay of the output signal. Its amplitude yields the beam displacement, while the starting phase determines the sign.

However, the originally proposed arrangement is complicated and not very favourable for machining at micrometre tolerances. We investigated coaxial cavities as shown in Fig.4 and estimated the coupling between a coaxial cavity and the beam to get the power in the desired mode. For our design and $5 \cdot 10^{10}$ particles per bunch we expect a resolution of about $12\mu\text{m}$ (see also [7]).

The coupling between the cavities and hence the modulation frequency has been increased with additional slots in the common walls between the cavities. The whole BPM consists of two such cavities for x- and y-direction, respectively, and a reference cavity to get the starting phase.

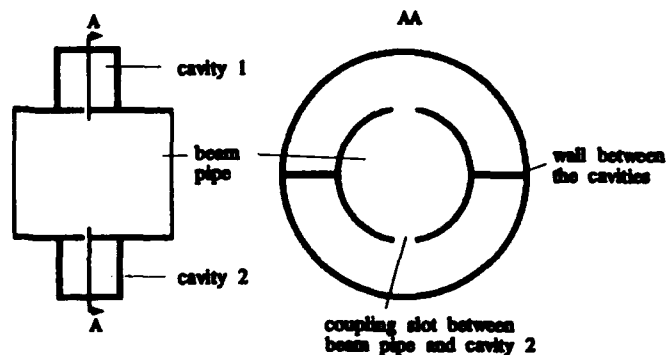


Figure 4: Coaxial coupled zero-mode monitor

Advantages

- * simple device, can be machined with μm -tolerances
- * the coupling to the beam is much weaker than for the TM_{110} -cavity, lower wakefields even with high Q-factors

Problems

- * f_0 and f_π are much closer than the frequencies in the cavity (using (8) we can estimate the spectral densities)
- * less power per μm displacement, smaller sensitivity
- * impossible to measure $10\mu\text{m}$ with injector 1b

5. Acknowledgements

The advice and help of H. Henke for the analytical calculations and helpful discussions is gratefully acknowledged.

References

- [1] Workshop on the TESLA Test Facility, at DESY Hamburg, 24-26 February, 1993
- [2] R. Bossart, *Microwave Beam Position Monitor Using A Re-Entrant Coaxial Cavity*, CERN PS 91-59 (LP)
- [3] W. Schnell, *Common-mode rejection in resonant microwave position monitors for linear colliders*, CLIC note 70, CERN-LEP-RF/88-41
- [4] J.P.H. Sladen et al., *The effect of finite Q on the precision of resonant beam position monitors*, CLIC note 185, 1993
- [5] H. Hayano et al., *Submicron Beam Position Monitor for the Japan Linear Collider*, presented at LINAC 92, Ottawa, 1992
- [6] V. Vogel, *BPM for VLEPP*, presented at the ECFA-workshop on e^+e^- Linear Colliders LC 92, Garmisch-Partenkirchen, 25 July - 2 August 1992
- [7] R. Lorenz, K. Yezza *Low Impedance Resonant Beam Position Monitors*, TESLA-Note, to be published

RHIC Beam Position Monitor Assemblies *

P.R. Cameron, M.C. Grau, W.A. Ryan, T. J. Shea, and R.E. Sikora
Brookhaven National Laboratory
Upton, NY 11973 USA

Abstract

Design calculations, design details, and fabrication techniques for the RHIC BPM Assemblies are discussed. The 69 mm aperture single plane detectors are 23 cm long short-circuited 50 ohm strip transmission lines subtending 80 degrees. They are mounted on the sextupole end of the Corrector-Quadrupole-Sextupole package and operate at liquid helium temperature. The 69 cm aperture was selected to be the same as that of the beampipe in the CQS package, the 23 cm length is a compromise between mechanical stability and electrical sensitivity to the long low-intensity proton and heavy ion bunches to be found in RHIC during commissioning, and the 80 degree subtended angle maximizes linear aperture. The striplines are aligned after brazing to maintain electrical-to-mechanical centers within 0.1 mm radius, eliminating the need for individual calibration. Because the cryogenic feedthrus isolate the UHV beam vacuum only from the HV insulating vacuum, and do not see liquid helium, a replaceable mini-ConFlat design was chosen to simplify fabrication, calibration, and maintenance.

I. Performance Requirements

The RHIC Design Manual specifies that the beam position measurement be accurate within 130 microns from the center of the sextupole field to the number displayed in the control room (because of the strong chromaticity correction in RHIC the most stringent position requirement for the BPM is relative to the sextupole). There are three main sources of error in the position measurement. First are errors from the center of the sextupole field to the position of the dowel holes in the plate upon which the BPM is mounted. Second are errors in the location of the BPM mechanical center (determined by the dowel pins) relative to the BPM electrical center¹ (determined by the geometry of the striplines). And finally, there are errors in the electronics². These errors add in quadrature, which suggests that error from each source should be less than about 100 microns. This accuracy in the position of the BPM electrical center relative to the mechanical center is easily accomplished using the bumping alignment technique described in Section III.

II. Design Details and Fabrication Techniques

A typical RHIC Beam Position Monitor is shown in Figure 1. The non-directional shorted stripline design minimizes vacuum penetrations, and adapts well to economical fabrication and alignment techniques.

* Work supported by the U.S. Department of Energy

A. Brazement

The brazement is constructed of type 316L stainless steel, which is copper brazed in a hydrogen furnace. Because the brazing temperature is above the annealing temperature for 316L, the mini-ConFlat flanges, the buffer volume bellows, and the tailpiece bellows are welded on after brazing. The mini-ConFlat flanges are TIG welded. The buffer volume and tailpiece bellows are EB welded to minimize thermal distortion.

The flange is machined from a 316L forging to eliminate the possibility of piping from the liquid helium buffer volume to the beam vacuum. Two alignment pins are pressed into the flange, and one of the two pins is a diamond pin to eliminate over-constraint.

The striplines are wire EDM cut from seamless 316L tube redrawn to size inside and out. The redrawing operation delivers a tube accurate enough to require machining on the circumference only at the braze joint, where tolerances are closely controlled to maintain between 13 and 38 microns radial clearance. A groove is machined in the stripline adjacent to the braze joint to concentrate stresses and localize yielding during the alignment bumping procedure. ANSYS 3D plastic analysis of this region is in progress. Stripline impedance was calculated to be 50 ohms using PE2D, ANSYS, HFSS, and EMAS.

The housing is progressively drawn to shape from 316L welded tubing. Again, the drawing operation delivers a part accurate enough to require circumferential machining only at the braze joint. The material thickness was selected to satisfy the ASME Boiler Code.

The buffer volume bellows mechanically isolates the BPM from displacements of the buffer volume during the 1.9 MPascal (275 psi) quench. Performance of this bellows during quench was analyzed using a program written³ specifically for bellows analysis. Several different geometries were ANSYS analyzed in this region before settling on the bellows.

Despite precise fixturing and good attention to welding technique, it has not been possible to maintain satisfactory alignment when accomplishing the BPM-to-beampipe weld. The beampipe has a 3 m long lever arm on the BPM. The convolutions in the tailpiece region provide a hinge which prevents the generation of excessive stresses and the resulting distortion. The annular space between the two bellows is ported to the insulating vacuum. The outer bellows is required by a RHIC design specification that insulating vacuum be interposed between beam vacuum and liquid helium at all welds. Both bellows are designed³ to resist quench pressure.

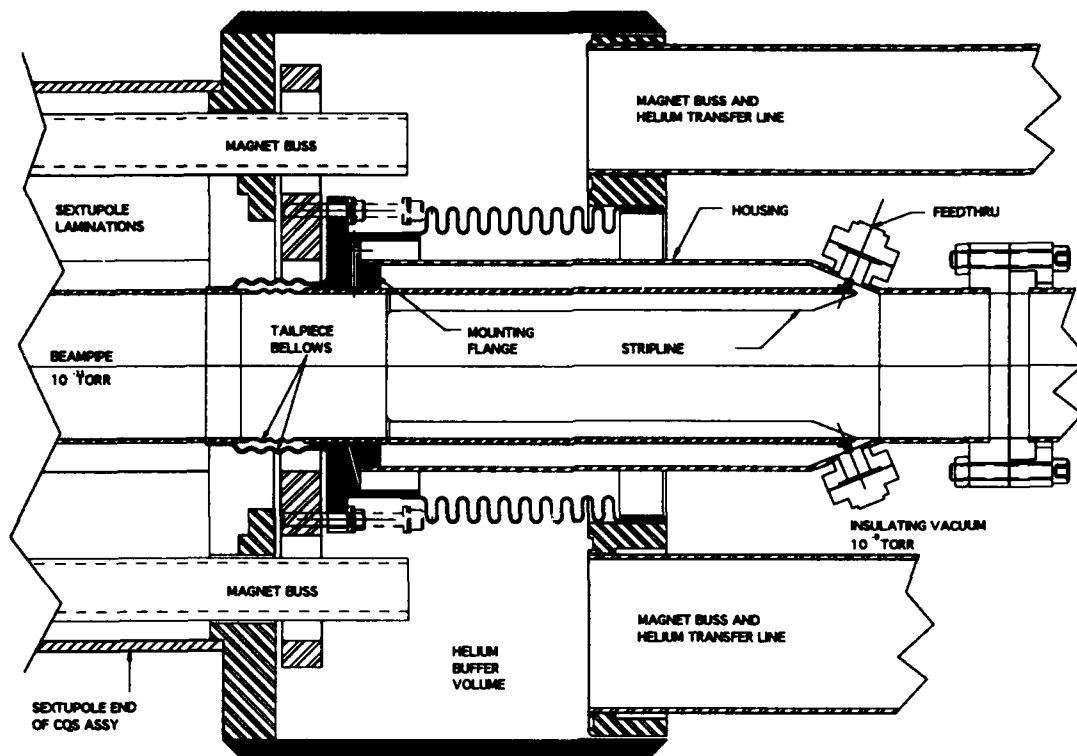


Figure 1. Typical BPM showing surrounding Buffer Volume and adjacent CQS Assembly

B. Contacts

The contact and feedthru geometry is shown in Figure 2. The bellows spring portion of the contact is gold plated electrodeposited sulfur free nickel, which is EB or laser welded to the stainless steel post. The spring rate of the bellows is 12.5 lb/in, the maximum compression is 1.8 mm, the working compression is 1 mm, and the contact force is 2.5 N (9 ounces). The maximum operating temperature is limited to 180 C by annealing of the nickel. While the impedance match to the feedthru is the responsibility of the manufacturer, some modelling was done using HFSS.

C. Feedthrus

The feedthru is incorporated into a mini-ConFlat package. Two different feedthru designs are being evaluated. The more conservative conventional design uses ceramic dielectric metallized and brazed to a thin kovar strain relief which is welded to the stainless steel flange. This design is relatively complicated and expensive, but is a proven performer. The newer design uses lithium silicate glass dielectric which is doped to match the expansion coefficient to stainless steel, and a glass-to-metal seal. This design is more simple and economical and has better RF properties, but has not yet been used in a major accelerator.

A total of 50 prototype feedthrus were purchased from four vendors, equally split between ceramic and glass dielectric. VSWR and S parameters were measured, in good agreement with HFSS calculations. Based upon these measurements and calculations, the specification for the production feedthru requires VSWR of less than 1.1 from DC

through 3 GHz. Reliability of the SMA connector was poor in some of the feedthrus, in some instances because the contact spring material appeared to have been annealed during manufacture, and in others because of poor contact geometry. Reliability of this connector will receive close attention during acceptance testing of the production feedthrus.

All of the prototype feedthrus were cryogenically tested by direct immersion in liquid nitrogen, followed by warming to room temperature in ambient air. Leak tightness was monitored throughout the cycle, and this cycle was repeated five times. No failures of the dielectric-to-metal bond were observed with either glass or ceramic. This thermal cycling will be part of the acceptance testing for all production feedthrus.

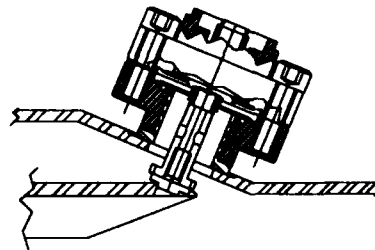


Figure 2. Contact and Feedthru Geometry

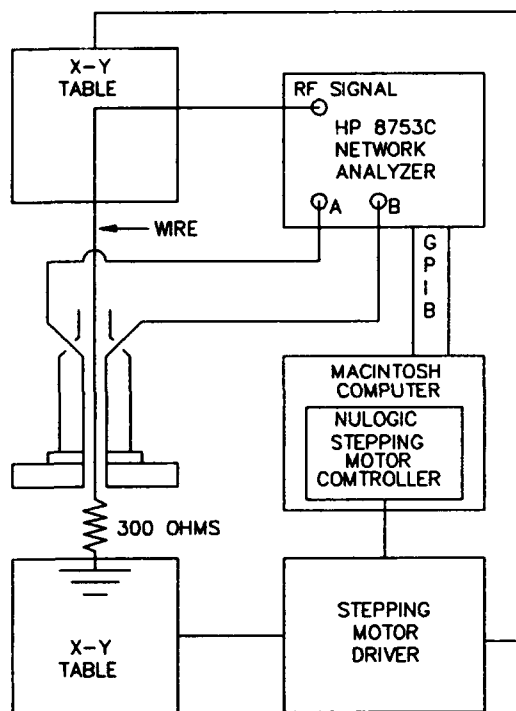


Figure 3. Block Diagram of the Mapping System

D. Cables

The cables must be radiation resistant, mechanically flexible, cryogenically compatible, have low heat leak and VSWR, and most important, have good electrical stability. In addition to minimal as-manufactured variations, the cable must be electrically stable when subjected to the above mentioned radiation, flexing, and temperature gradients. Dielectric materials under consideration include silicon dioxide, magnesium oxide, ultem(polyimide), silem, and tefzel. Silicon dioxide cables have been tested, and seem satisfactory. An experiment⁴ to measure the radiation damage characteristics of PEEK at liquid helium temperatures resulted in a violent explosion after a dose of about 0.5 gigarad. While this dose is much higher than any expected in accelerator operations, we are not presently actively pursuing this material.

III. Testing of the Assembly

A. Calibration of the BPM

A block diagram of the mapping system is shown in Figure 3. LabVIEW software running on the Macintosh computer controls the NuLogic stepping motor controller and the network analyzer. The position of the signal wire is initially established with a precision fixture aligned by the dowel holes on the mounting plate. The positions of the wire when it makes electrical contact with the fixture alignment points are recorded, then the fixture is rotated 180 degrees and the results of the two measurements are averaged. Using this method it is possible to position the wire with an accuracy of about 25 microns.

The alignment fixture is then replaced by the BPM, and the position of the electrical center of the BPM is measured relative to the mechanical center. The measured transfer function is about 0.7 dB/mm. The appropriate feedthru is then removed and replaced with an assembly consisting of a micrometer welded into a mini-ConFlat flange. The micrometer is cranked in to yield the stripline. Yielding begins at about 2 mm deflection. After bumping the feedthru is replaced and the position of the electrical center is remeasured. If necessary, the bumping procedure is repeated. Using this method the required 0.1 mm position tolerance is easily attained.

B. Thermocycling

Using a test setup similar to that shown in Figure 3, a prototype BPM was thermally cycled from room temperature to liquid nitrogen temperature and back to room temperature. Measurement of the impedance of the striplines indicates that movement of the striplines relative to the housing was less than 25 microns. This measurement will be repeated with a production BPM both at liquid nitrogen and at liquid helium temperatures.

IV. Conclusions

A simple, robust, accurate, and economical design for a cryogenic BPM has been developed. The possibility of making yet further gains in accuracy with improved survey techniques is under active investigation.

V. References

- [1] The possibility of greatly reducing the first two types of errors by surveying the BPM electrical center directly to the sextupole magnetic center is discussed in: M. Goldman, R. Sikora, and T. Shea, "Preliminary Studies on a Magneto-Optical Procedure for Aligning RHIC Magnets", these proceedings.
- [2] W. Ryan, T. Shea, P. Cerniglia, and C. Degen, "A Prototype BPM Electronics Module for RHIC", these proceedings.
- [3] C. M. Lac, private communication.
- [4] Bom Soon Lee, private communication.

operate in Ultra High Vacuum, minimize Higher Order Mode losses, and have a minimum insertion length. The stripline monitor is made of four approximately $1/4 \lambda$ (24.7mm) long. The length of the strip is designed for the 2856MHz fundamental. Each of the strips subtends 42° of the 60 mm aperture. Each strip sits in a pocket spaced 3° away from a solid spacer on either side. The strips ends are chamfered at 45° and the pin connectors are angled at 45° for impedance matching. Longitudinally, there is a 2mm space from the end of the strip to the body. Figure 2 shows a photo of the stripline unit and Figure 3 shows a design schematic drawing.

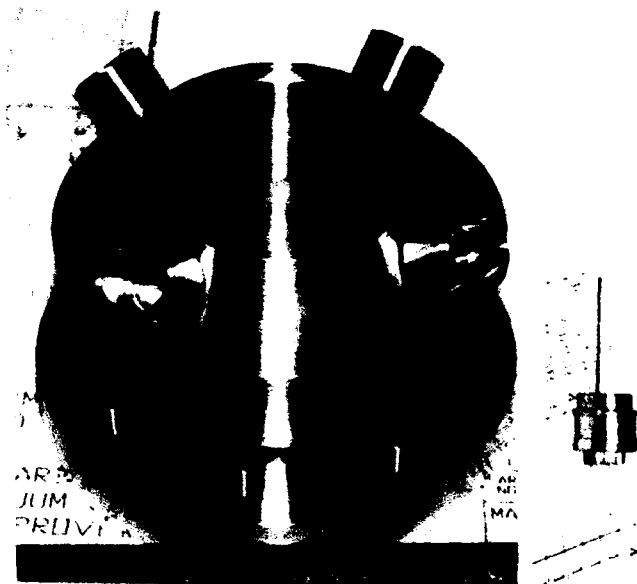


Figure 2. Photo of stripline BPM.

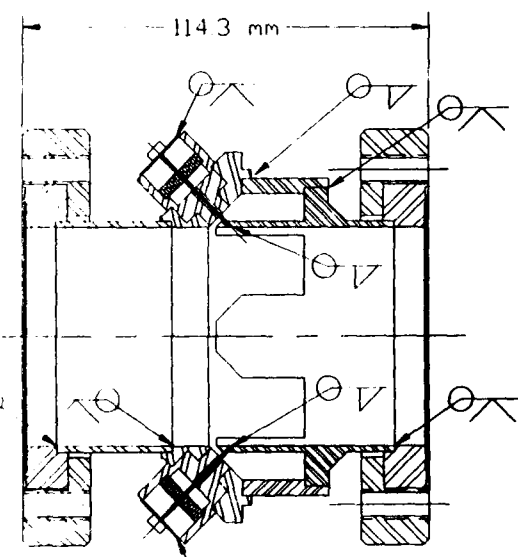


Figure 3. Stripline BPM Design.

The body is made by conventional machining methods from a 3.25" by 0.75" wall stabilized 316L seamless stainless steel tubing. After machining and cleaning, it is TIG welded and leak checked. The connectors are not demountable and are welded into the strips and body. Replacement requires machining. By the use of close tolerances and centering on machined surfaces, the electrical centers are reproducible within $\pm 0.025\text{mm}$. These tolerances were checked after welding. The stripline monitors reach pressures of 5×10^{-10} torr unbaked. They are designed to be baked to 150°C .

IV. Impedance Measurements

The transmission core coefficient [S21] was measured for a pulse transmitted through the BPM on a bead loaded 50Ω coaxial line. coefficient approximates the longitudinal coupling impedance of the device undergoing such tests. The measurement was performed using a network analyzer HP-8510 to obtain data in the frequency domain, which were FFT transformed to determine the two port S-parameters of the BPM. Tapered input and output sections with level response over a 10 GHz frequency range were designed and employed to minimize reflections at the BPM ports. Measurements were made with and without the transition section, higher order mode damper spacer inserts, and with and without a 50Ω output load line. Some results are shown in figure 4.

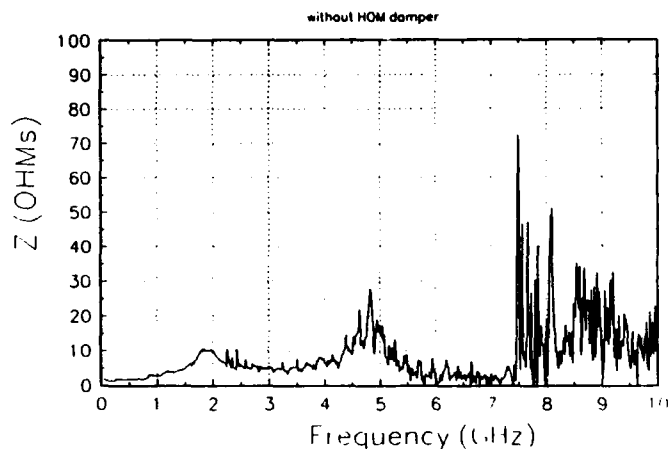
To investigate the impedance matching of the junctions of the feed-through and the stripline, time domain measurements were conducted using the network analyzer including the TDR option.

V. Stripline BPM Electronics

The Signal processing of the transducer signals is conducted in two stages, RF processing at 2856 MHz and an IF stage at 50 MHz. The RF stage consists of feeding the outputs of opposite strips into a 90° hybrid where the amplitude information is converted into phase information. As long as the difference in electrical lengths of the cables feeding the hybrids are small, no significant errors are introduced. The output of the hybrids goes through a phase matching section and possibly a circulator or attenuator, then into a mixer section, heterodyning the signals to 50 MHz. These

signals are summed with the other two strips to get a signal proportional to the beam current. The phase detector has an amplifier and analog multiplier, then a gain converting amplifier and line driver. These signals are then digitized by a flash ADC converter for signal processing. The bandwidth of the IF signal processing stage is 15 MHz.

Couplg. Imped. of New Version of Stripline BPM



Couplg. Imped. of New Version of Stripline BPM

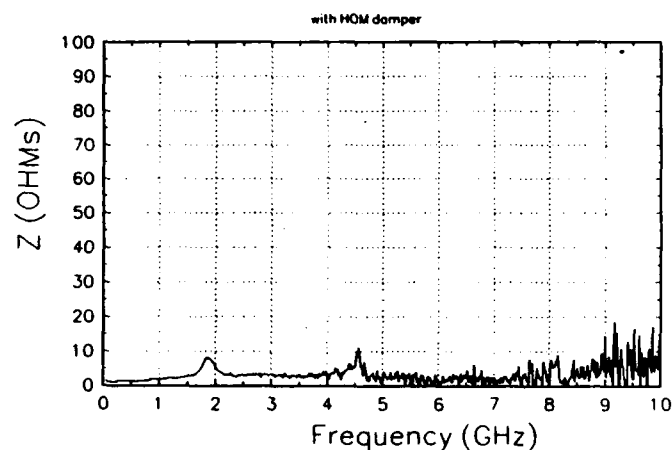


Figure 4. Stripline BPM Impedance measurements with and without spacer insert.

Calculations and measurements of noise levels show that the signal to noise ratio is high enough to get the .1mm resolution at 1ma of beam current. There are some problems with mismatches in the RF section, causing reflections which can introduce a large offsets in the output. Solutions to this problem will be the addition of attenuators or preferably circulators after the hybrids to kill the reflections.

V. Operation

Tests with beam have been conducted both in the beam switchyard beam line and the SHR. Figure 5 shows the beam position at a location in the SHR for several turns. The figure shows the beam current and beam position with betatron oscillation resulting from the beam trajectory being different from that of the closed orbit. (That is also the reason for the decreasing current.) At about 0.5mA the signal disappears. Measurements to 40 mA have been made with good results. The gains of the monitor electronics differ by as much as 5% from BPM to BPM, however they are measured and recorded in the computer data acquisition system. The BPMs and ancillary systems are designed for data acquisition in several modes [3].

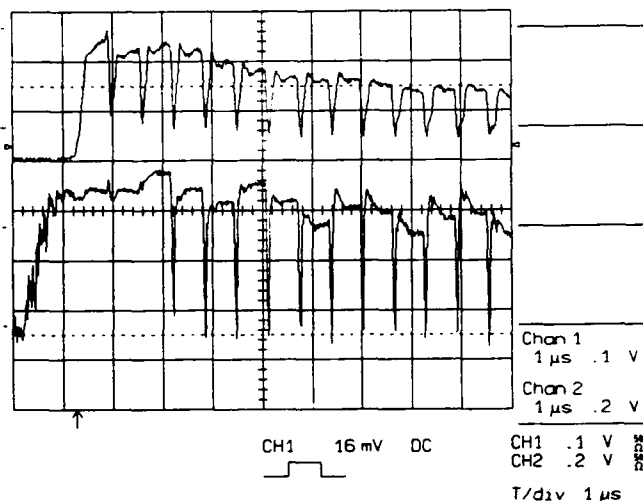


Figure 5. Beam Position Output from Stripline BPM.

VI. References

- * Work Supported by the U.S. Department of Energy
- [1] K.D. Jacobs, P.T. Demos, J.B. Flanz, A. Zolfaghari, J. Wurtele, X.T. Yu, and K. Balewski, Proceedings 1991 Particle Accelerator Conference, p1791, (1991).
- [2] T. Weiland, Part. Accel. 17, 227 (1985).
- [3] O. Calvo, T. Russ, and J. Flanz, Proceedings 1991 Particle Accelerator Conference, p1467 (1991).

Design and Operation of Button-Probe, Beam-Position Measurements

J. D. Gilpatrick, J. F. Power, R. E. Meyer, and C. R. Rose
Los Alamos National Laboratory
Los Alamos, NM 87545

Abstract

Beam position measurement systems have been installed on the Advanced Free Electron Laser (AFEL) facility at Los Alamos National Laboratory [1]. The position measurement uses a capacitive- or button-style probe that differentiates the beam-bunch charge distribution induced on each of the four probe lobes. These induced signals are fed to amplitude-to-phase processing electronics that provide output signals proportional to the arc tangent of the probe's opposite-lobe, signal-voltage ratios. An associated computer system then digitizes and linearizes these processed signals based on theoretical models and measured responses. This paper will review the processing electronics and capacitive probe responses by deriving simple theoretical models and comparing these models to actual measured responses.

I. INTRODUCTION

The goal of the AFEL was to demonstrate that a free electron laser (FEL) suitable for industrial, medical, and research application can be built. This goal has been achieved by accelerating an electron beam to 20 MeV with a bunching frequency of 108.3 MHz and transporting the beam into and out of a FEL. To have sufficient lasing efficiency from this wiggler-based laser, the electron beam position and trajectory angle must be known at the entrance and exit of the wiggler with resolutions and accuracies of a few tenths of a percent and a few percent of the beam pipe radius, respectively. Also, this beam position information must be known over as few microbunches as possible while maintaining at least a factor of ten in beam current dynamic range. To attain these measurement goals, the preferred measurement system choice was an integrated beam-position measurement system similar to those implemented on the Ground Test Accelerator (GTA) [2]. The AFEL beam position and intensity measurements consist of three basic components: a capacitive- or button-style probe, an amplitude-to-phase position processor, and associated linearization algorithms that reside in the control system.

Table 1

Specification of the AFEL Position and Intensity measurements

	Position	Intensity
Measurement Range	± 10 mm	460 to 1 A _{pk}
Dynamic Range (nC/bunch)	4.6 to 0.01	4.6 to 0.01
Resolution	± 25 μ m	± 1 A _{pk}
Accuracy	± 0.25 mm	± 10 A _{pk}
Bandwidth (MHz)	3.5	3.5

*Work supported by the US Department of Energy, Office of High Energy and Nuclear Physics.

Table 1 describes the specifications for the beam position and intensity measurement systems.

II. MEASUREMENT SYSTEM DESCRIPTION

Figure 1 shows a picture of the capacitive-style beam-position monitor (BPM) installed on the AFEL beamline. Each probe consists of four rectangular metal lobes whose dimensions are defined by the subtended lobe angle of 45° and a 3.2 mm length. The probe clear aperture is 2.34 cm with a lobe aperture of 2.54 cm. Alignment of the probe assembly with the accelerator beamline is achieved by using the four bosses located on the upstream probe vacuum flange (see Figure 1). These bosses are used in both a beamline alignment process and a probe taut-wire characterization fixture to find the absolute offsets and sensitivities to beam position. This alignment and probe characterization procedure provides sufficient information to make absolute beam position measurements to the nearest ± 0.25 mm.



Figure 1. The AFEL capacitive probe shown with its alignment stand and an associated coaxial transmission line.

The signal power from each lobe is calculated by assuming that the Gaussian-distributed beam image charge on each probe lobe is

$$\rho(z, t) = -\frac{\theta_0}{2\pi} \frac{eN}{\sqrt{2\pi}\sigma} e^{-\frac{(\beta ct - z)^2}{2\sigma^2}} \quad (1)$$

where $\rho(z)$ is the beam charge distribution, eN is the total charge per bunch, θ_0 is the subtended angle of the probe lobe, σ is the bunch length, and βc is the beam velocity. The beam image current induced on each of the probe lobes, Equation (2), is the integral of $\rho(z)$ in the z -dimension and the time derivative where τ is the rms temporal bunch length,

$$i_B(t) = -\frac{eN\theta_0}{\sqrt{2\pi}\tau} \left[e^{-\frac{t^2}{2\tau^2}} - e^{-\frac{(t-L/\beta c)^2}{2\tau^2}} \right] \quad (2)$$

and L is the length of the lobe. The beam-induced output voltage, $V_p(j\omega)$, at the input to the processing electronics is

$$V_p(j\omega) = \frac{\sigma(j\omega)I_B(j\omega)}{\sqrt{2}} \frac{Z_c}{1+j\omega Z_c C_p} \frac{1}{I_0\left(\frac{\omega R}{\beta\gamma c}\right)} \frac{2I_1\left(\frac{\omega r}{\beta\gamma c}\right)}{\left(\frac{\omega r}{\beta\gamma c}\right)} \quad (3)$$

where C_p is the probe capacitance, Z_c is the characteristic impedance of the transmission line and the input impedance of the processing electronics, and s is the cable attenuation [3]. The I_0 and I_1 terms are the zero- and first-order Bessel functions that describe the low-beam-velocity effects of the beam image-current longitudinal distribution caused by the probe radius, R , and the diffuse beam radius, r , respectively [4].

The measured beam-position and taut-wire probe characterization is the logarithmic ratio (in dB) of the opposite lobe signal amplitudes and may be expressed as

$$R_x(t) = 20 \log \left\{ \frac{1 + \frac{4}{\theta_0} \sum_{n=1}^{\infty} \frac{1}{n} \left(\frac{r_0(t)}{R} \right)^n \cos(n\phi(t)) \sin\left(\frac{n\theta_0}{2}\right)}{1 + \frac{4}{\theta_0} \sum_{m=1}^{\infty} \frac{1}{m} \left(\frac{r_0(t)}{R} \right)^m \cos(m\phi(t)) \sin\left(m\left(\pi + \frac{\theta_0}{2}\right)\right)} \right\} \quad (4)$$

where $R_x(t)$ is the ratio of the signal amplitudes of opposing lobes, and r_0 and ϕ are the polar coordinates of the beam position [5]. For an "ideal" probe, Equation (4) and its inverse may be reduced with minimal loss of information to include only offsets, first-, and third-order coefficients. This simplification yields a probe/beam position inverse transfer function of

$$x(t) = x_0 + S_x R_x(t) + S_x^3 R_x^3(t) + S_{xy}^2 R_x(t) R_y^2(t) \quad (5)$$

The S or "sensitivity" terms in Equation (5) are calculated based on two-dimensional, third-order polynomial least squares fit to the measured characterization-map BPM data. This characterization-based model provides $\pm 1\%$ accurate beam-position measurement inside 30% of the probe radius

(linear portion of a probe) and $\pm 4\%$ accurate beam-position measurements from 30% to 80% of the probe radius [5].

The position processor consists of an amplitude-to-phase converter followed by a phase-detection circuit [2], [6]. The amplitude-to-phase technique converts an input two-port amplitude ratio to a phase difference between output ports using vectorial processing techniques. This phase difference is then detected with a double balanced mixer. The low frequency output of the double balanced mixer is a voltage that is a function of the input signal power ratios. The transfer function describing the position processor is

$$V_{BP}(t) = \frac{4GA_{rf}}{\pi} \left[\tan^{-1} \left(10 \frac{R_x(t)}{20} \right) - \frac{\pi}{4} \right] \quad (6)$$

where $V_{BP}(t)$ is the output voltage, G is the output amplifier gain, and A_{rf} is the peak voltage driving the double balance mixer [6]. Figure 2 shows the Equation (6)-based least-squares fit to the measured values of an AFEL position processor. There is a 3% difference between the fitted equation and measured data when the measured values for the processor constants, G and A_{rf} , were substituted into the fit variable, $\frac{4GA_{rf}}{\pi}$.

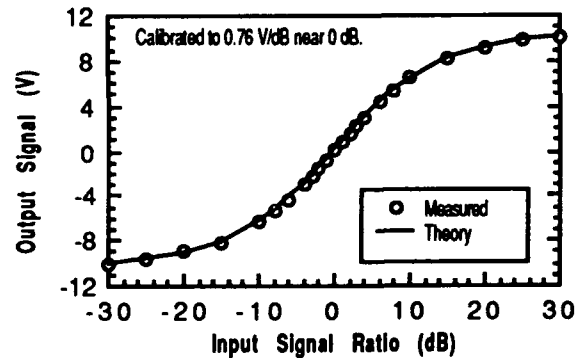


Figure 2. Measured data versus calculated theory [i.e., a least squares fit to Equation (6)] of the beam-position processor-transfer function.

The beam intensity measurement system processes the summation of the four lobe signals. It does this by synchronously detecting these summed signals with a double balanced mixer operating as a full-wave detector. The intensity transfer function, $V_I(t)$, is

$$V_I(t) = G_i G_o \frac{3.105}{\pi} i_B(t) \quad (7)$$

where $i_B(t)$ is the average beam current during the macropulse, G_o is the output amplifier gain term, and G_i is the input transconductance gain term that converts the electron beam current to the peak RF input voltage to the double balanced mixer [7].

The control system algorithms use the inversion of Equation (6),

$$R_x(t) = 20 \log \left[\tan \left(\frac{V_{BP}(t)\pi}{4GA_{rf}} + \frac{\pi}{4} \right) \right] \quad (8)$$

and the probe inverse transfer function [Equation (5)] for beam position, and the inversion of Equation (7) for beam intensity [8].

III. BEAM TEST RESULTS

Two beam tests were conducted to verify the operation of the beam position and intensity measurement system. The first test was the measurement of the capacitive-probe frequency response using the AFEL bunched beam. The second test was a position measurement test comparing the beam positions measured by the BPM system and an optical transition radiation (OTR) profile monitor [1].

The signal power model from Equation (3) was calculated based on the actual geometries of the AFEL BPMs. These calculated data were then compared to a set of acquired data (Figure 3) based on an independently measured bunch length and beam current. There is very good agreement between the probe model and measured data up to approximately 2 GHz. Past these frequencies, it is likely this simple model [Equation (3)] does not accurately describe the beam/probe interaction.

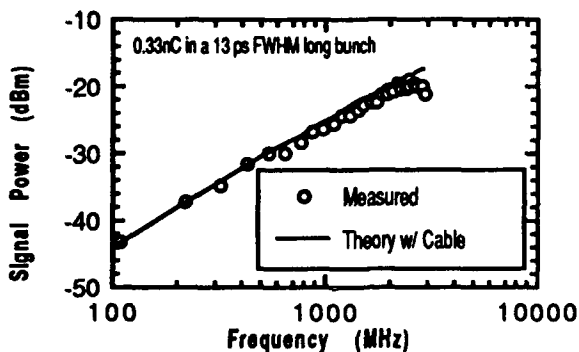


Figure 3. These signal-power data are the average of the top and bottom lobes' signal powers as a function of frequency from a centered electron beam. The theoretical model is the calculated signal power based on Equation (3).

The beam position data were acquired by steering the beam in both axes with a dipole magnet upstream of the OTR viewing screen and BPM. The beam positions were then acquired simultaneously with the BPM system and the OTR screen. Figure 4 shows the comparison between the OTR- and BPM-acquired data. There is good agreement between the two measurements in both axes, as can be seen by the 0.02% and 3.1% gain-term errors and the -0.164 and 0.245 mm offset errors. The larger vertical axis offset- and gain-term errors are most likely caused by the inaccurate angular alignment of the OTR view screen with respect to the vertical axis.

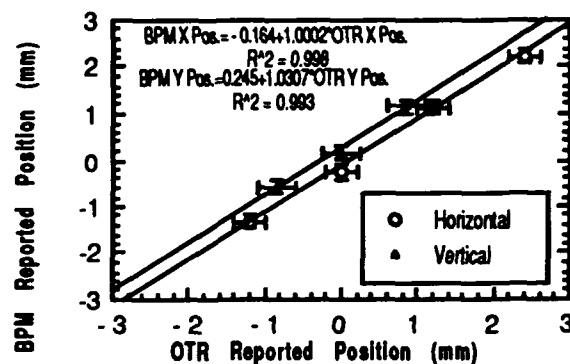


Figure 4. Horizontal and vertical beam position data show correlations between OTR and BPM data. The equations are least squares fit to these data and "R²" are X² values.

IV. CONCLUSION

A series of beam-position and intensity-measurement systems were installed and commissioned on the AFEL beamline. Analytic theoretical transfer functions for each system component were derived, calculated, and measured. There was good agreement between the theoretical component functions and measured system data. Also, beam data were taken and shown to agree with the measurement system models for change in both beam current and beam position. These systems are now operational and are providing valuable information to the AFEL researchers.

VI. REFERENCES

1. K. C. Dominic Chan, et al., "Compact free-electron laser at the Los Alamos National Laboratory," in *SPIE's International Symposium on Optical and Optoelectronic Applied Science and Engineering*, San Diego, CA (1991).
2. J. D. Gilpatrick, et al., "Measurements and Performance of a Microstrip Beam Probe System," in *IEEE Particle Accelerator Conference*, 91CH3038-7, 2, 1136 (1991).
3. J. D. Gilpatrick, et al., "Design and Operation of a Bunched Beam, Phase-Spread Measurement," in the *1992 Linear Accelerator Conference Proceedings*, Vol. 1, pp. 359-361.
4. J. H. Cuperous, "Monitoring of Particle Beam at High Frequencies," *NIM*145, 219-231 (1977).
5. J. Power, et al., "Characterization of Beam Position Monitors in Two Dimensions," in the *1992 Linear Accelerator Conference Proceedings*, Vol. 1, pp. 362-365.
6. J. D. Gilpatrick, et al., "Microstrip Probe Electronics," Los Alamos National Laboratory document LA-CP-89-488 (1989).
7. J. D. Gilpatrick and F. D. Wells, "Double Balanced Mixer Operation Used as Phase and Synchronous Detector as Applied to Beam Position and Intensity Measurements," Los Alamos National Laboratory document LA-UR-93-1622 (1992).
8. J. D. Gilpatrick, "Microstrip Measurement Algorithms," Los Alamos National Laboratory document LA-UR-93-1639 (1992).

Design and Calibration of Pickup-Electrodes for Beam Position Monitoring at SOR-RING

Kenji SHINOE, Norio NAKAMURA⁺, Tomotaro KATSURA⁺ and Yukihide KAMIYA

The Institute for Solid State Physics, The University of Tokyo,

and ⁺Photon Factory, National Laboratory for High Energy Physics, KEK, JAPAN

Abstract

Described in this paper are the design and calibration of button-type pickup-electrodes, which have been incorporated in the beam position monitoring system (BPM system) at SOR-RING. The BPM system that has been developed as an R&D for a third-generation VUV synchrotron light source is aimed at testing the key components of the system, PIN diode switches. This system is also aimed at measuring the beam position of SOR-RING and correcting it. In addition, briefly described in the paper are ion-clearing electrodes installed in the ring.

1. Introduction

A system of beam position monitors (BPM's) using PIN diode switches was installed in the SOR-RING of ISSP, Tokyo University [1]. Using this BPM system, the closed orbit was measured and then corrected for the first time since the ring construction had been completed in 1974 [2].

The system includes four BPM's fixed on newly fabricated vacuum chambers for quadrupole triplets (see Ref. [2]) and each BPM consists of four pickup-electrodes of a button type. Calibration measurement of BPM's was made on a test bench of the Photon Factory [3] and also with a method of S-parameters [4]. Using a method of BEM (Boundary Element Method) [5], we calculated the response of a BPM to electric field induced by the beam and also compared it with the measured result.

In addition, we designed ion-clearing electrodes and incorporated them into new vacuum chambers. The beam lifetime was found to increase by a factor of two when a few KV was applied to the ion-clearing electrodes [3]. However, the electrode's effect on the beam is not studied in detail.

2. Design and Fabrication

A. Pick-up Electrode

We first designed two types of test BPM's with short chambers; one is a cylindrical type (C-type BPM) and the other is the same type as the BPM's installed in SOR-RING (SOR-type BPM). The button diameter of 20 mm was chosen so as to fit the narrow vacuum chamber of SOR-RING. The diameter is much smaller than 10 cm, the rms bunch length of SOR-RING. At the RF frequency of 120 MHz the response of BPM is almost independent of the bunch length. A pick-up electrode consists of a vacuum feedthrough and a button. We chose the N-type as the vacuum feedthrough because of its robust connection. The tip of central conductor in the feedthrough was specially designed to have a small washer, to which the button was precisely welded. In order to mount the pick-up electrodes flush with the inside wall of a stainless steel block of BPM, a short piece of a ring shape was attached to the feedthrough's outer conductor by welding. The stainless steel block precisely machined to house the electrodes was in turn welded to the vacuum chamber. Figure 1 shows the cross-sectional views of both types of BPM's. The BPM's actually installed in SOR-RING were made almost in the same way as the test BPM's.

B. Selection of Feedthrough

We measured the capacitances of all feedthroughs with a LCR-meter and arranged four feedthroughs for a BPM to be equal in capacitance as far as possible. For test BPM's we also checked the capacitances of pick-up electrodes before and after attached on the vacuum chambers. Table I lists some data of measured capacitance.

Table I. Measured capacitance of test BPM

Feedthrough only (at 10kHz)				
	1-A	1-B	1-C	1-D
C[pF]	3.2	3.2	3.2	3.2
Pick-up electrode (at 10 kHz)				
	1-A	1-B	1-C	1-D
C[pF]	5.92	5.95	5.83	5.86

C. Ion-Clearing Electrode

The cross-sectional view of a pair of ion-clearing electrodes we designed is shown in Fig. 2. Each of four new chambers has a pair of ion-clearing electrodes. The electrodes and their high-voltage feedthroughs have been designed so that several KV can be easily applied to the electrodes. By using a BEM (Boundary Element Method) we calculated the electric field induced by a DC voltage of 1 KV on one electrode and -1 KV on the other electrode [see Fig. 3]. As mentioned in Sec. 1, these ion-clearing electrodes helped the beam lifetime to increase.

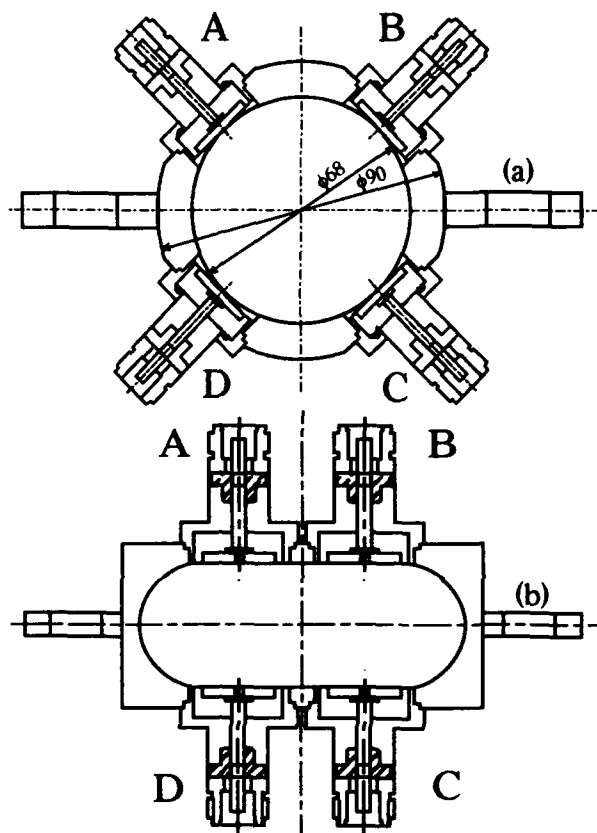


Fig. 1 Cross-sectional view of a BPM
(a) : cylindrical BPM (C-type)
(b) : BPM for SOR-RING (SOR-type)

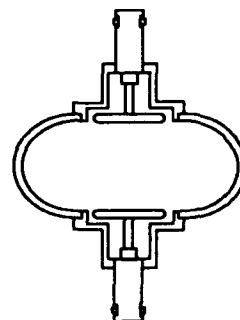


Fig. 2 Cross-sectional view of a pair of ion-clearing electrodes

D. Alignment of BPM

We did not intend to precisely position the BPM's in the ring, since there is no good reference point for alignment at SOR-RING and also the aim of this R&D is to test PIN diode switches incorporated in the BPM system. We also have to isolate the BPM's as well as vacuum chambers from the ground, since the ring is baked out by directly passing AC current through the vacuum chambers. The BPM blocks were therefore sandwiched between the magnet poles of quadrupoles with precisely machined insulators, as shown in Fig. 4. The alignment error of BPM to the center of quadrupole magnet was expected to be around 0.1 mm.

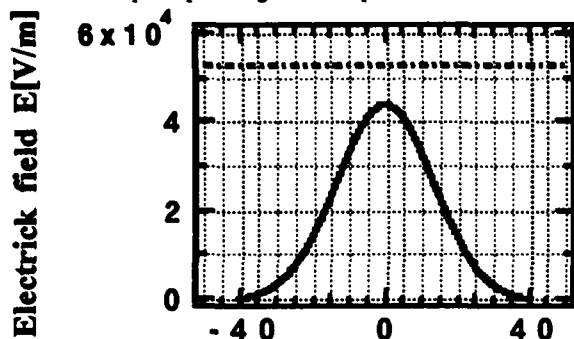


Fig. 3 Field calculation of ion-clearing electrodes
The dash-dotted line is for infinitely extended electrodes.

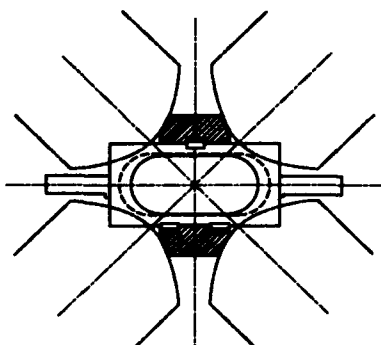


Fig. 4 Alignment of BPM chamber in a quadrupole magnet

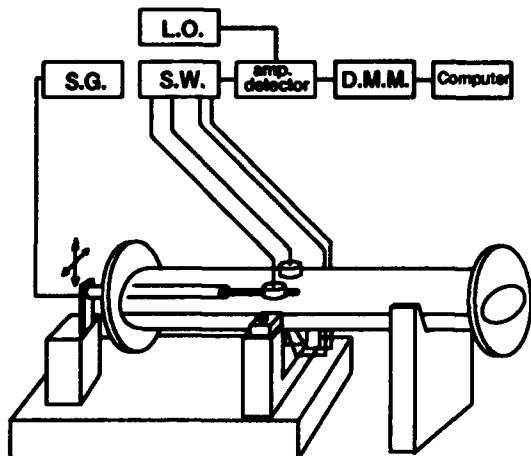


Fig. 5 Calibration setup for BPM

3. Calibration Measurement

A. Test BPM

Before fabricating the BPM's for SOR-RING, the position sensitivities of two types of test BPM's were measured by scanning an RF antenna on the BPM test bench of the Photon Factory [3], as shown in Fig. 5. Data were taken mainly at 120.83 MHz and 500 MHz. Presented in this paper are data for 120.83 MHz. The results of sensitivity measurement for the C-type BPM are shown in Fig. 6. This sensitivity map shows the transformation of the physical (x, y)-plane of the beam center to the (U, V)-plane and to the (U1, V1)-plane, where U and V are defined as,

$$U = \frac{(B+C)-(A+D)}{A+B+C+D}, \quad V = \frac{(A+B)-(C+D)}{A+B+C+D}$$

and U1 and V1 are also defined as,

$$U1 = \frac{(B-A)}{(B+A)} + \frac{(C-D)}{(C+D)}, \quad V1 = \frac{(B-C)}{(B+C)} + \frac{(A-D)}{(A+D)}$$

Here A, B, C and D stand for the detected voltages of the corresponding pickup-electrodes in Fig. 1. Figure 7 shows the sensitivity map in the case of the SOR-type BPM.

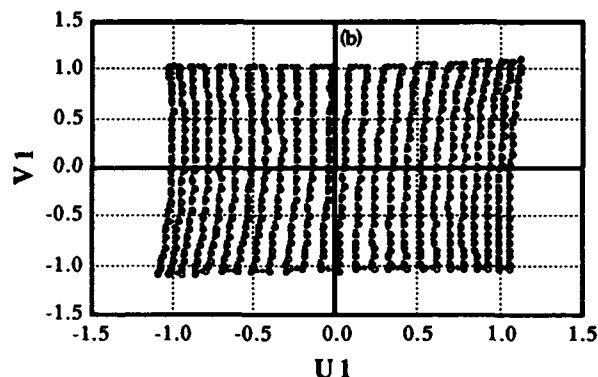
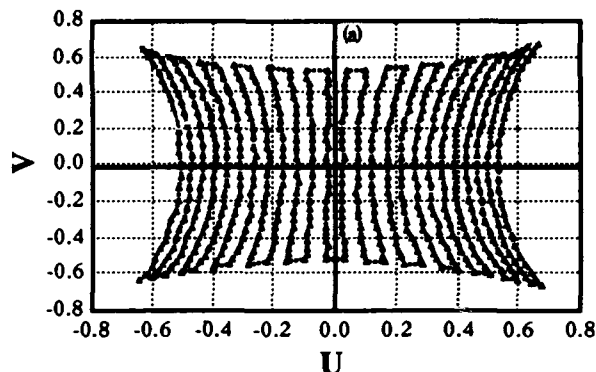


Fig. 6 Measured response of the cylindrical BPM

(a) : (U, V)-map, (b) : (U1, V1)-map

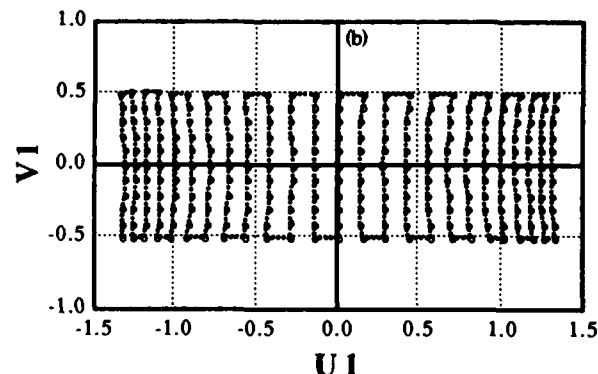
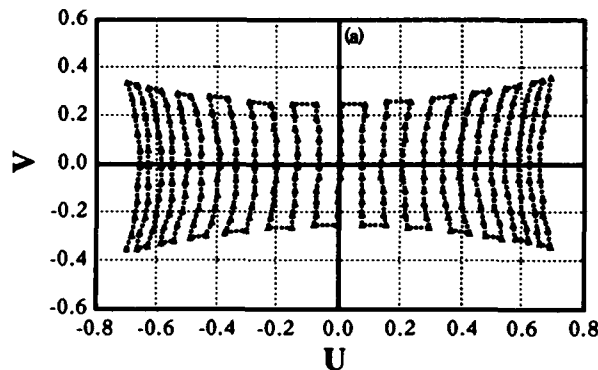


Fig. 7 Measured response of the SOR-RING's BPM

(a) : (U, V)-map, (b) : (U1, V1)-map

We carefully measured the electric offset of the center of the SOR-type BPM. Since the RF-antenna of the old test bench was slightly bent, we decided to measure the offset both for the normal setup of BPM and for the reverse setup in order to remove the position error of the antenna itself.

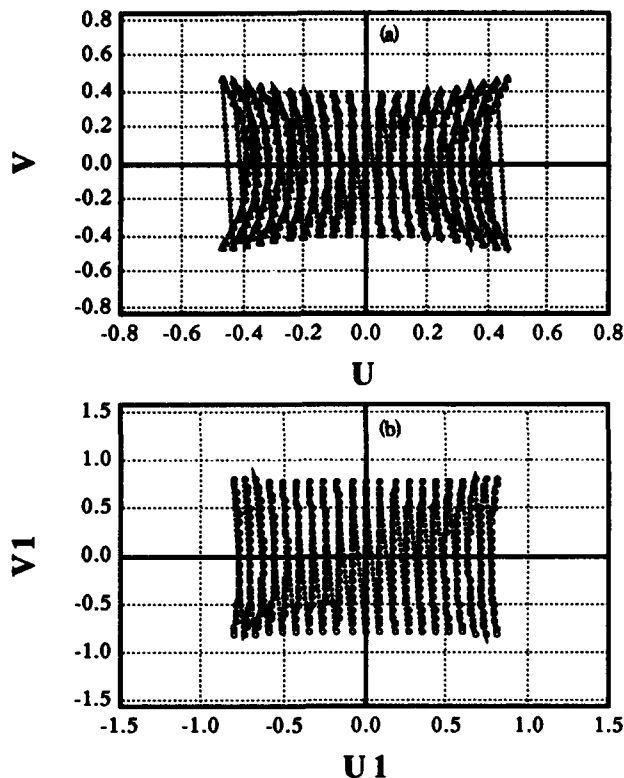


Fig. 8 Calculated response of the cylindrical BPM
(a) : (U,V)-map, (b) : (U1,V1)-map

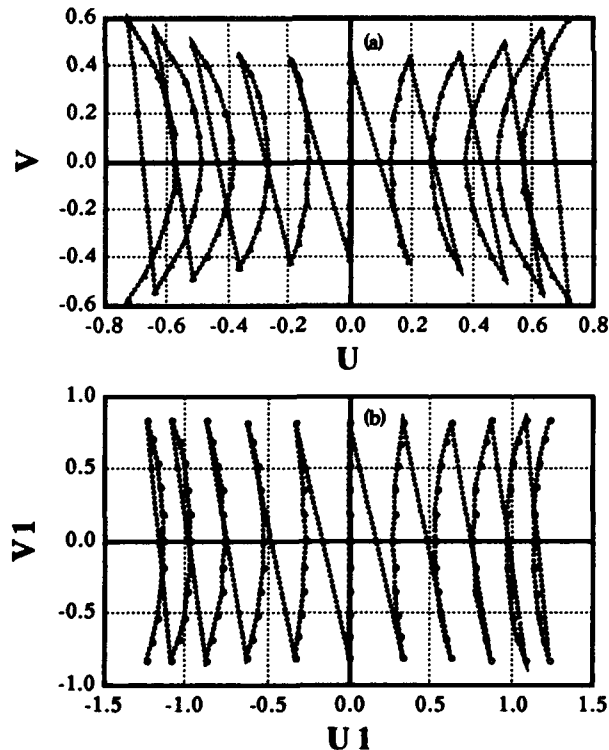


Fig. 9 Calculated response of the SOR-RING's BPM
(a) : (U,V)-map, (b) : (U1,V1)-map

We also made the measurement of the electric offset with the method of S-parameters [4]. These measured results are summarized in Table II.

Table II. Measured center-offset of test BPM

ΔX_a [mm]	ΔX_e [mm]	ΔX_s [mm]
0.064	0.087	0.081
ΔY_a [mm]	ΔY_e [mm]	ΔY_s [mm]
0.077	0.203	0.198

subscript a: antenna offset, e: electric offset(RF antenna)
s: electric offset (S-parameters)

B. BPM's for SOR-RING

Before installing the BPM's in SOR-RING, we took the data of sensitivities and offsets for all BPM's in the same way as for the test BPM's. It was found from the calibration data that the beam center position is well estimated with a fifth order polynomial of (U,V) or (U1,V1). At present, however, we make use of the (U,V)-coordinates to calculate the beam position (x, y), though the sensitivity map for (U,V)-coordinates is more deformed than for (U1,V1)-coordinates. The coefficients of the polynomials for all BPM's were stored on the BPM computer thereby to calculate the beam position. For example, the polynomials, x and y at a BPM, are written as,

$$\begin{aligned}
 x = & -0.078 + 14.17U - 0.24V + 0.09U^2 + 0.09V^2 - 0.26UV \\
 & + 4.97U^3 + 1.06V^3 + 0.53U^2V - 19.69UV^2 \\
 & - 0.21U^4 + 0.24U^3V - 0.14U^2V^2 - 0.08UV^3 + 0.13V^4 \\
 & + 10.45U^5 - 0.16U^4V + 12.35U^3V^2 - 0.68U^2V^3 - 8.59UV^4 - 4.68V^5, \\
 y = & 0.14 - 0.22U + 19.45V - 0.12U^2 + 0.44V^2 + 0.02UV \\
 & - 0.19U^3 + 9.3V^3 - 15.64U^2V + 0.63UV^2 \\
 & - 0.01U^4 - 0.08U^3V + 0.13U^2V^2 + 0.18UV^3 - 3.41V^4 \\
 & + 0.57U^5 + 7.13U^4V - 0.86U^3V^2 - 4.04U^2V^3 - 1.18UV^4 - 3.66V^5.
 \end{aligned}$$

C. BEM Calculation

We developed a two-dimensional computer code using the method of BEM. Then we calculated the response of BPM to the beam for both C-type and SOR-type. The calculated results are shown in Fig. 8 for C-type BPM and in Fig. 9 for SOR-type BPM. For C-type, both measured and calculated maps of sensitivity are alike in shape but slightly differ in scale. For SOR-type, they largely differ in the vertical direction. The discrepancy between measured and calculated results has not been solved yet; it is probably because the RF-antenna used in the measurement can not generate a field as truly two-dimensional as a relativistic beam does. However, this discrepancy is almost irrelevant to the center offset of BPM.

Acknowledgments

We would like to thank Prof. T. Ishii, Director of the Synchrotron Radiation Laboratory of ISSP, and Prof. H. Kobayakawa, Director of Light Source Division of the Photon Factory for their encouragement and support. We are also indebted to all staff of the Synchrotron Laboratory and the Light Source Division.

References

- [1] K. Shinoo et al.: *Beam Position Monitoring System using PIN Diode Switches*, in these proceedings.
- [2] H. Kudo et al.: *Measurement of the SOR-Ring Parameters*, in these proceedings.
- [3] T. Katsura and S. Shibata: *Beam Position Monitor for the Photon Factory Storage Ring*, KEK Report, KEK-79-27, Nov., 1979.
- [4] G. R. Lambertson: *Calibration of Position Electrodes Using External Measurements*, Lawrence Berkeley Laboratory, Advance Light Source, LSAP Note-5, May 6, 1987.
- [5] T. Shintake et al.: *Sensitivity Calculation of Beam Position Monitor using Boundary Element Method*, NIM A254, pp146-150, 1987.

The position monitor using stretched wire technique

T. Mimashi, S. Kuroda, H. Nakayama, K. Oide, R. Sugahara, N. Yamamoto

National Laboratory for High Energy Physics (KEK),
Tsukuba, Ibaraki 305, Japan

abstract

The position monitor using stretched wire method [1] is being developed as a component of the active alignment system for particle accelerator equipment, such as RF cavities and magnets. The RF voltage is supplied to the stretched wire and the monitor measures the change of capacitance between wire and pickup strip. Present resolution, limited by the electronics noise, is about 5nm.

I. Introduction

An alignment system using stretched wire technique is developed for the precision alignment of the accelerator components. The system will be used in the final focus section of KEK future project such as B factory [2] and Japan Linear Collider (JLC) [3].

In addition to the beam based alignment, another independent alignment system is necessary for the continuous monitoring of relative position of quadrupole magnets. Since the beam size at the final focus beam line of JLC is expected to be an order of a few nm - a few tens nm, the nano meter resolution alignment is required. The alignment system with the stretched wire and pickup electrodes is developed as one of the candidates.

According to the ground motion measurement, an amplitude of seismic motion becomes less than 1 nm above 3 Hz.[4] Though other artificial vibration such as the vibration caused by cooling water is expected, the basic idea is "reduce high frequency vibration with visolator, and measure only low frequency vibration and cancel out them with an actuator". The alignment system is designed to detect the vibration below 3 Hz.

II. Principle

In this alignment system, the position of all monitors are determined relative to the stretched wire. Monitors with pickup electrodes are equipped closed to the stretched wire. A sinusoid wave signal is supplied to the wire, and the induced charge on the two faced electrodes are amplified. By measuring the difference between the amplitude of signal from left and right electrodes, the monitor position relative to the wire can be measured.

In order to distinguish whether monitor or the wire support position is moving, two stretched wires are necessary. Fig. 1 shows one simple example. We assume the system consists of three monitors and two wires which are supported at four fixed points as shown in Fig. 1. Each monitor consists of two set of pickup electrodes which measure the vertical and horizontal position of two wires. Monitors and support points should move independently. Two wires are fixed at the same position on H1 and H4. Absolute position of H1 and H4 should be determined by other system, then both the position of fixed points H2, H3 and the position of pickup electrodes

which will be mounted for example on the quadrupole magnet, M1, M2 and M3 can be calculated from the output of signals from the 6 sets of pickup electrodes.

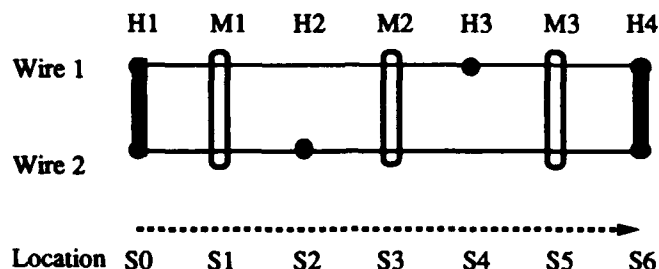


Fig. 1 An simple example of position measurement setup

III. System design

A copper-beryllium, 0.2 mm diameter wire is used as a reference stretched wire. The wire is surrounded by the grounded aluminum tubes. The sinusoid wave voltage signal, 3 KHz, 8 V peak to peak, is supplied to the wire. In order to reduce the noise, preamplifiers are mounted directly on the 1.6mm thick, epoxy-graphite card. The both side of this card is clad with 0.2 mm of copper. This copper cladding is etched to provide the readout strip. The dimension of the strip electrode is 12 mm long along the wire, 1 mm wide and 0.2 mm thick. The change of the sinusoid wave amplitude at the output of preamplifier corresponds to the 1 nm movement is calculated as a function of the displacement between the wire center and pickup electrode. (Fig. 2) The sensitivity increased rapidly at the short distance, so that the displacement between the wire and each electrode is set to about 1.5 mm.

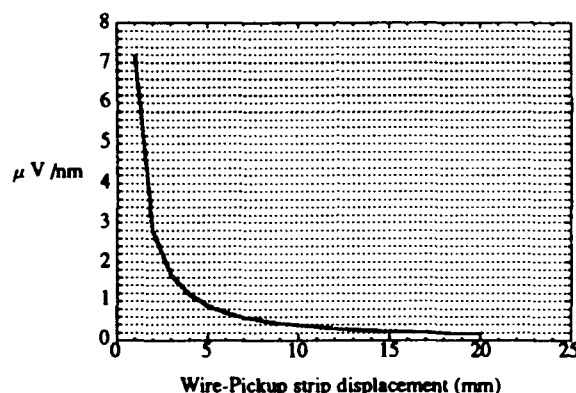


Fig. 2 The change of the sinusoid wave amplitude at the output of preamplifier corresponds to the 1 nm movement as a function of wire-pickup strip displacement.

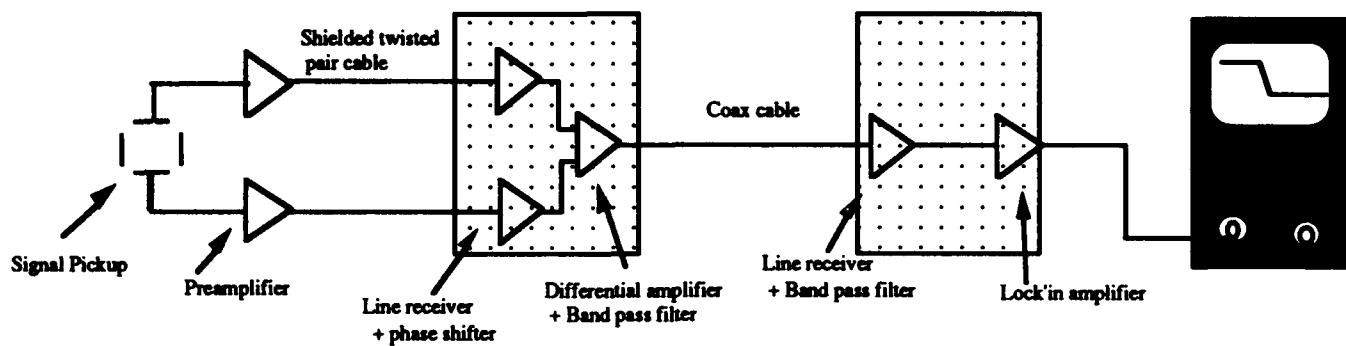


Fig. 3 A schematic of the front end electronics

IV. Electronics

A simple schematic of the front end electronics for the stretched wire alignment system is shown in Fig. 3. The system consists of preamplifiers directly mounted on the pickup electrode card, a main amplifier circuit and a lock'in amplifier. A main amplifier module is connected to the pickup electrode-preamplifier card by 1 m long shielded twisted pair cables. A coax cable is used to send the signal from main amplifier to a lock'in amplifier.

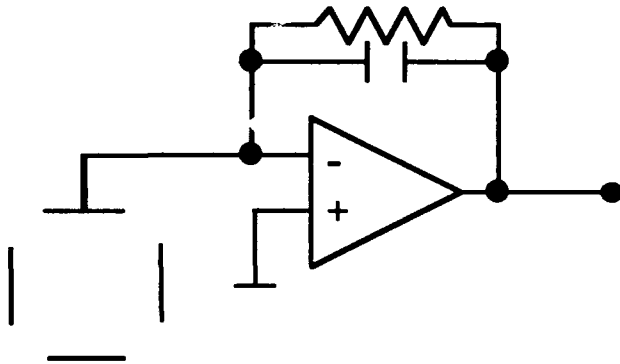


Fig. 4 Preamplifier circuit

A. Preamplifier

To get high gain and cancel out the coupling capacitance between two faced electrodes which loses the sensitivity a lot, a charge sensitive amplifier is chosen as a preamplifier. As shown in Fig 4, since the input of the operational amplifier is virtual ground, so that the voltage difference between two electrode is always 0. It means the effect of coupling capacitance between two faced electrode is canceled. The high impedance input, low noise operational amplifier (BB2604) is chosen.

B. Main Amplifier

A main amplifier circuit consists of line receivers, phase shifters, a differential amplifier with gain control trim resistor, bandpass filters, two inverting operational amplifiers. In order to cut ground loop noise, pulse transformers are used as line receivers. The phase shifters adjust the phase difference between signals from two faced electrodes. A differential amplifier amplifies the difference between two signals. A band pass filter is used to reduce the noise. And the signal is amplified so that 1 nm movement corresponds to the a few mV amplitude change.

C. Lock'in Amplifier

Each channel on the lock'in amplifier card consists of an operational amplifier receiver, two stages of band pass filter and phase detector. An analog signal passes through a linear amplifier whose gain is reversed by square wave reference signal controlling an analog switch. The output signal passes through a low-pass filter, RC. The response time is determined by this time constant. Totally, 1nm displacement corresponds 1.5 mV voltage change at the lock'in amplifier output.

V. Performance

The schematic drawing of the bench test setup is shown in Fig. 5. A copper-beryllium wire, 0.2 mm diameter and 1 m long, is stretched on the visolator table [5]. The Piezo-electric actuators which can move the detector in the horizontal direction in a few nm step, are adopted as precision mover. The Piezo system was bought from PI-Polytec CO., LTD. The system consist of Piezo actuator and the inductive gage position sensor. Using the signal from the inductive gage position sensor, the extension of Piezo actuator is controlled. The accuracy of the inductive gage is a few nano meter.

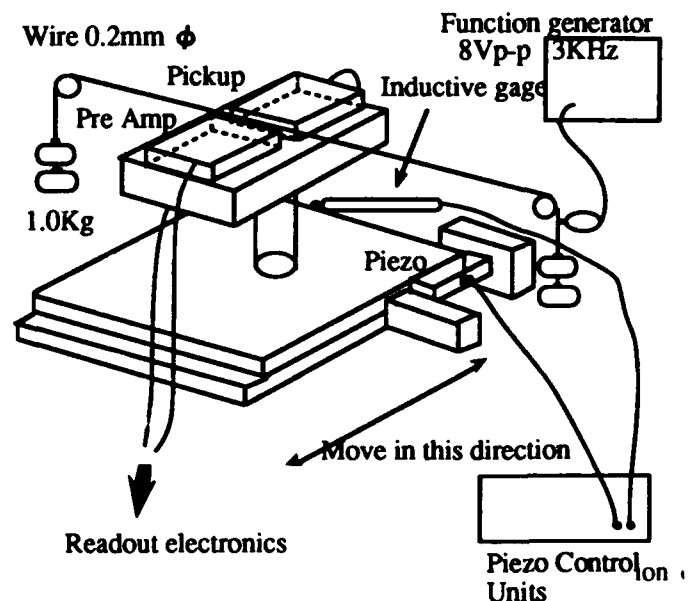


Fig. 5 The bench test setup for stretched wire alignment

Fig. 6 shows resultant output signal of the lock'in amplifier circuit. The sensitivity is set to 1.5 mV/nm at the output voltage of the lock'in amplifier.

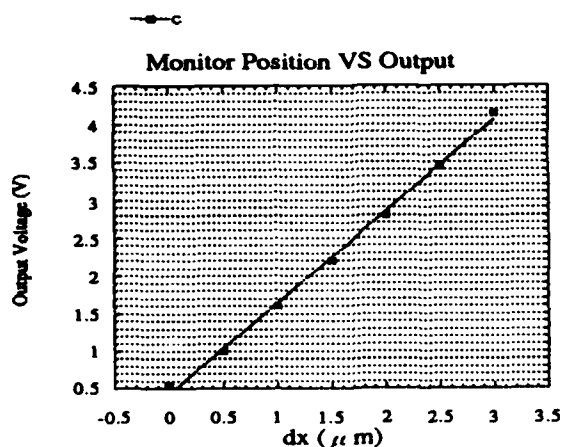


Fig. 6 Lock'in Amplifier output voltage as the function of displacement from reference point.

Fig. 7 shows the output voltage change related to the monitor movement. Each step corresponds 50 nm movement of the monitor. The resolution of this alignment system is around 5 nm.

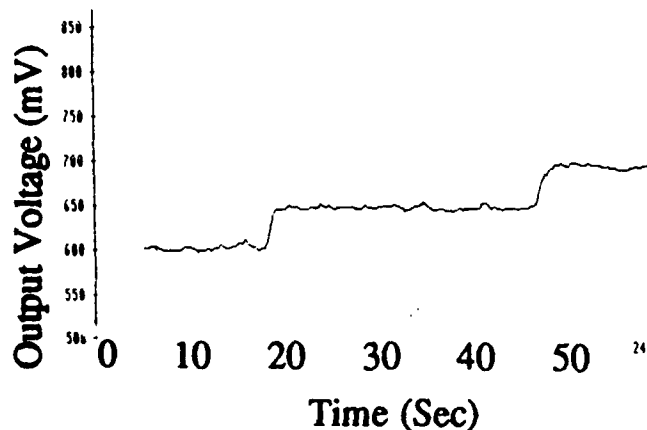


Fig. 7 The lock'in amplifier output voltage change when the monitor position is changed 50 nm step.

VI. Conclusion

The stretched wire technique is being developed as a precision alignment method. The electronics is designed that 1 nm displacement corresponds to 1.5 mV change at the lock'in amplifier output. The resolution is around 5 nm and the response time constant is set to 3 Hz.

We thank Dr. K.Taniguchi and Dr. Y.Fukushima for useful discussion about electronics circuit.

VII. References

[1] Private communication to Prof. Vladimir E Balakin

[2] S.Kurokawa et al., Accelerator design of the KEK B-factory, KEK Report 90-24, March 1991.

[3] Y.Kimura et al., JLC-I, KEK Report 92-16, December 1992.

[4] Private communication to Prof. S. Takeda

[5] Made by Herz Industry CO.,LTD.

AN OVER-MODED STRIPLINE BEAM POSITION MONITOR

J.G.Noomen, J.Bijleveld, F.Kroes, T.Sluijk.

NIKHEF-K

p.o.box 4395, 1009 DB, Amsterdam, The Netherlands

Abstract

The operating RF frequency of the AmPS stretcher ring is 2856 MHz. The beam pipe cross section is above cut-off for some modes of this frequency. This inhibits proper functioning of the stripline beam position monitors. The problem has been solved by applying particularly shaped high vacuum quality RF dampers.

Introduction

The 900 MeV AmPS stretcher ring has become operational in the middle of 1992 [1]. Two types of experiments will be enabled by this new facility. Physics with a high duty cycle (90%) extracted beam (stretcher mode) and internal target physics (storage mode).

The inner size of the beam pipe is determined by making the machine suitable for both types of experiments. For proper extraction the beam pipe should have a relative large width in the extraction area. From the optical design [2] it follows that also elsewhere in the ring the beam width will be large. The inner beam pipe height is determined by the requirement to store the beam at least one hour.

Therefore in the curves the inner beam pipe width is 8.0 cm and the height is 4 cm. In the straights the round beam pipe has an inner diameter of 9.2 cm.

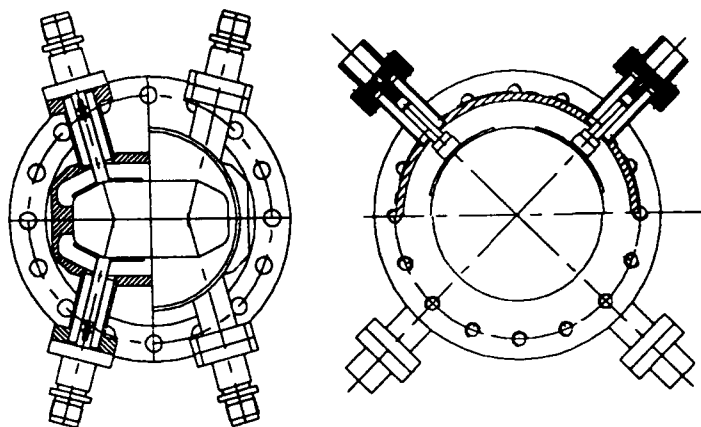
In stretcher mode the frequency of the RF power source in the ring is the same as the RF frequency of the 900 MeV injecting accelerator: 2856 MHz [3]. This is necessary to trap all injected bunches in the RF bucket, otherwise an intolerable loss of beam would occur.

The revolution time of the beam is 0.7 μ sec. For proper measurement of successive turns we decided that the bandwidth of a position monitor should be at least 15 MHz. For this purpose the 2856 MHz frequency component of the beam must be used and stripline position monitors based on this frequency have been developed [4]. The stripline monitors have the same cross section as the beam pipe, thus allowing the same beam clearance. As a consequence, the combination of this high RF frequency and large inner beam pipe size results in a over-moded beam position monitor. For instance the TE₀₁ mode is above cut-off in the curves and the TE₁₁ mode is above cut-off in the straights. Without any precautions the monitors wouldn't work due to disturbing wakefields.

Wakefields

The ring consists of four 90° bends connected by straights.

According to the two different beam pipe cross sections there are two types of stripline monitors fig.1.



Curve-type

Straight-type

Fig.1. Stripline Position Monitors

One with the cross section of the curve and one with the cross section of the straight. In each curve and each straight four monitors have been installed.

We expect wakefields mainly to be generated at strong alterations of inner beam pipe size. Propagation of these wakefields through the beam pipe is then possible by mode conversion into a mode above cut-off. Since the propagation of such a mode is not synchronous with the beam, the energy content of the propagating mode can not be further enhanced by the beam. Initially we thought it to be sufficient to put only RF damping material in the straights. The positions we had in mind were the transitions straight-curve and close to disturbing objects as kickers and septa. Beam measurements however showed that a proper response of the monitor could only be obtained if the monitor itself was sandwiched between RF damping material.

RF dampers

The RF dampers consist of pieces ceramic pipe coated with a resistive paint. The paint obtains its resistive property after a special bake out treatment. After this treatment the vacuum properties of the paint are excellent. The outgassing is comparable with a stainless steel surface [5]. We have investigated what resistive value gives the best result. For this purpose a stripline monitor in a beam line has been provided with dampers with resistive values between 10 and

1000 ohm per square (see beam tests). Also the attenuation of the dampers has been measured on a bench using the beam pipe as a waveguide. A resistive value of 140 ohm per square proved to be the best choice. It performed the best beam response as well as maximum attenuation.

The bench measurements were done by putting the damper in 1 m beam pipe terminated at the ends by tapering to S-band waveguide WR-284. For the selected 140 ohm dampers the attenuation was 6 dB for a complete (upper and lower part) 38 mm long curve type damper and 10 dB for a complete 75 mm long straight type damper. Over the important frequency range 2 to 4 GHz the attenuation showed to be quite constant.

RF damper assembly

In the straights the dampers are put directly in the pipe (fig.2) thus affecting the beam stay clear in vertical direction.

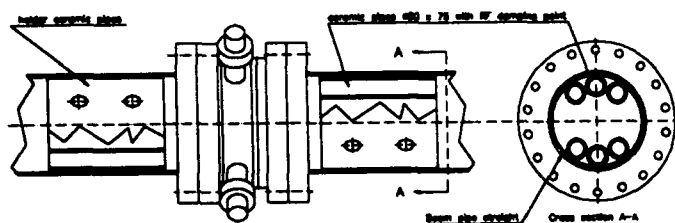


Fig.2. RF damper assembly, straight-type monitor.

This is allowed since the large beam pipe size is required in stretcher mode where the beam excursion is large in the horizontal direction only. One holder comprises six 20 mm diameter, 75 mm long ceramic pipes. Three at the upper side and three at the lower side of the beam pipe.

In the curves it was not allowed to decrease the beam clearance. The only possibility to fit dampers around the stripline monitors in the curves was to use the bellows of each monitor. In fig.3 is shown how this has been realised.

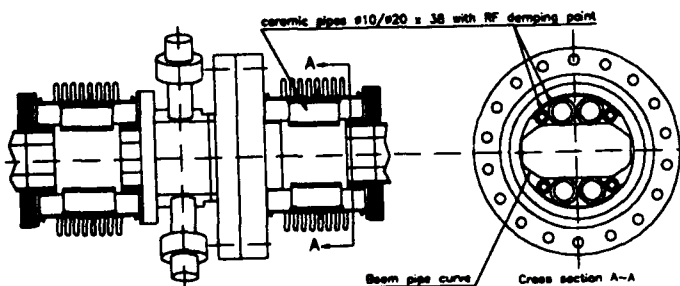


Fig.3. RF damper assembly curve-type monitor.

The original smoothing RF sleeves have been removed. Then the corrugated surface of the bellows has been covered with a metal foil. Hereafter the holders with the damping pipes have been positioned, one in the upper and one in the lower part of the bellows. Each holder comprises two 20 mm diameter ceramic pipes in the middle and two 10 mm diameter ceramic pipes at the sides. The length of the pipes is 38 mm giving the bellows 5 mm length clearance which is sufficient for alignment purposes.

It appeared to be difficult to reproduce the resistive value. Therefore the dampers are provided with ceramic pipes in such a way that the average values of upper and lower part of a damper were equal and close to 140 ohm.

Coupled beam impedance

We assume that the dampers only contribute to the broadband impedance. That means only the single bunch current threshold is affected by the RF dampers [6]. Applying the coaxial wire method [7] for beam impedance measurements, the sum of all dampers will contribute 2.8 ohm to the longitudinal broadband impedance Z/n in the frequency range 2 to 4 GHz. This value also includes RF dampers elsewhere in the ring, for instance at the straight-curve transitions. However this increase of the broadband impedance will not disable the original aimed maximum beam current in the ring (200 mA).

Beam tests

Prototypes have been tested in a 6 m long part of the beam line. The test sections comprised one or two stripline monitors and 6 m beam pipe with the same cross section as the monitor. As mentioned before a variety of resistive values for the RF dampers has been used. The best response was obtained with 140 ohm per square. Other resistive values performed lower sensitivities and distorted responses. The response on beam position with 140 ohm dampers is shown by the isoposition lines in fig.4. The X and Y output voltages are obtained after signal processing [4]. The average sensitivity constants (defined in [8]) were,

$$\begin{aligned} \text{curve type } K_x &= 24 \text{ mm} & K_y &= 25 \text{ mm} \\ \text{straight type } K_x &= 50 \text{ mm} & K_y &= 50 \text{ mm} \end{aligned}$$

After installation in the ring the centre position of the monitors has been calibrated by centring the beam in the quadrupoles (by wobbling) in between the monitor has been positioned. Also the sensitivities have been measured. The average centre offsets appeared to be $dx = -0.8 \text{ mm}$ and $dy = 0.7 \text{ mm}$ with standard deviations of $\sigma_x = 2.0 \text{ mm}$ and $\sigma_y = 5.4 \text{ mm}$. The average sensitivities were equal to those measured in the test section however with standard deviations of 33 % for x and 28 % for y.

This result is not as good as could be expected from the prototype tests. An explanation and possible cure requires more research but probably two effects can be blamed for it:

the generation of much stronger wakefields in the ring compared with the test section and the non-uniformity of the dampers with respect to the resistance and also slightly the geometry. Summarised the response of the stripline monitors is not ideal but they are suitable for position measurement if properly corrected for the individual deviations.

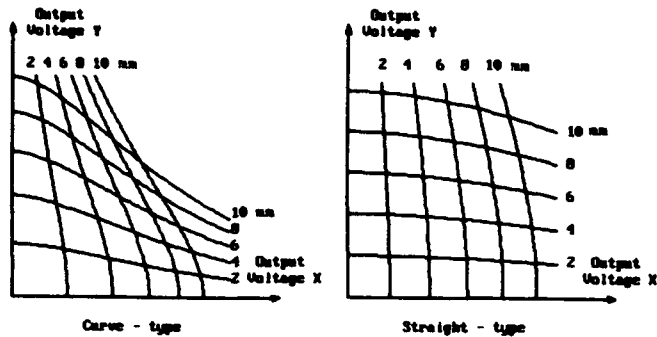


Fig.4. Beam position response, isoposition lines.

Acknowledgement

The work described in this paper is part of the research program of the National Institute for Nuclear Physics and High Energy Physics (NIKHEF), made possible by financial support from the Foundation for Fundamental Research on Matter (FOM) and the Netherlands Foundation for Scientific Research (NWO).

References

- [1] G.Luijckx et al., The Amsterdam Pulse Stretcher, First commissioning results, proceedings HEACC, 1993, Hamburg.
- [2] R.Maas and Y.Y.Wu, Optics of the Amsterdam Pulse Stretcher, IEEE proceedings of the Particle Accelerator Conference, 1989, Chicago, p 1698
- [3] F.B.Kroes et al., A fast amplitude and phase modulated RF source for AmPS, IEEE proceedings of the Particle Accelerator Conference, 1991, San Francisco, p 684
- [4] J.Noomen et al., A beam position monitor for AmPS, IEEE proceedings of the Particle Accelerator Conference, 1991, San Francisco, p 1148
- [5] F.Caspers et al., EPA beam vacuum interaction ion clearing system, EPAC vol2 (1988) 1324
- [6] M.S.Zisman et al., ZAP users manual, LBL, December 1986
- [7] F. Caspers, Beam impedance measurements using the coaxial wire method, CERN PS/88-59 (AR/OP)
- [8] C.R.Carman and J.L.Pellegrin, The beam positions of the spear storage ring, NIM 113 (1973) 423-432

Loss of precision in resonant beam position monitors due to finite Q

J. P. H. Sladen and W. Wuensch
CERN, Geneva, Switzerland

Abstract

The performance of resonant beam position monitors is limited in part by the presence of a symmetrical (common mode) excitation of the cavity. Due to finite Q, a centred beam will give a non-zero output at the observation frequency. This interference is analysed and general expressions are given for the electrical and magnetic spectral densities, split into the wanted resonant term and the "broad-band" unwanted signal, for a cavity with arbitrary shape. This analysis is particularly relevant to beam position monitor studies for the CERN linear collider (CLIC), where very precise measurement of transverse beam position is required. It is shown that a common mode position error of under 1µm is obtainable from a high Q 33GHz pill-box, even prior to the use of any external difference-taking elements.

Introduction

The performance of high precision resonant beam position monitors (BPM's) will be limited in part by the off-resonance excitation of common modes (E_{0m} modes in a cylindrical cavity). Due to finite Q, a centred beam will give a non-zero output at the frequency used for observation and this will remain after narrow-band filtering of the cavity output. The interference from the E_{010} mode in a cylindrical cavity BPM operating in the E_{110} mode has already been treated [1]. Here, the analysis is extended to include all interfering modes and an arbitrary cavity shape. General expressions are given for the electrical and magnetic spectral densities at the BPM operating frequency, split into the wanted resonant term and the "broad-band" interference.

This analysis is particularly relevant to BPM studies for the CERN linear collider (CLIC), where very precise measurement of transverse beam position is required. The BPM that has been proposed is a cylindrical cavity operating in the E_{110} mode at a

frequency of 33GHz [1,2]. This case is taken as an example and the position error is calculated for output coupling to the circumferential magnetic field.

Finally, measurements of common mode interference in a prototype BPM are described.

Cavity spectral density at resonance

The electric and magnetic fields due to a line current $Ie^{j\omega t}$ travelling through a cavity in the z direction with co-ordinates r_0, ϕ_0, z can be written as an expansion in terms of orthogonal modes [3,4]. For the electric field, both the zero divergence solenoidal set of modes E_n and the zero curl irrotational set F_n are required:

$$E = \sum_n \frac{-j\omega\mu_0 \left(1 + \frac{1-j}{Q_n}\right)}{k_n^2 - k^2 \left(1 + \frac{1-j}{Q_n}\right)} \int_0^d I e^{-jkz} E_{nz}(r_0, \phi_0, z) dz E_n + \sum_n \frac{1}{j\omega\epsilon_0} \int_0^d I e^{-jkz} F_{nz}(r_0, \phi_0, z) dz F_n \quad (1)$$

where d is the cavity length, E_{nz} and F_{nz} are the z direction components of E_n and F_n respectively and $k = \omega/c$. k_n is the n^{th} eigenvalue and Q_n is the quality factor. For the magnetic field, only the solenoidal set H_n is excited:

$$H = \sum_n \frac{k_n}{k_n^2 - k^2 \left(1 + \frac{1-j}{Q_n}\right)} \int_0^d I e^{-jkz} E_{nz}(r_0, \phi_0, z) dz H_n \quad (2)$$

E_n , F_n and H_n are real and satisfy:

$$\nabla \times E_n = k_n H_n \quad \nabla \times H_n = k_n E_n \quad \nabla \times F_n = 0$$

$$\int_V E_n \cdot E_n dV = 1 \quad \int_V F_n \cdot F_n dV = 1 \quad \int_V H_n \cdot H_n dV = 1$$

At the frequency of the p^{th} resonance, we can split the response into the wanted resonant term and the sum of the interfering modes. Assuming large Q_n and that we are far from resonances $n \neq p$:

$$\mathbf{E} = -\frac{Q_p}{\omega_p \epsilon_0} \int_0^d I e^{-jk_p z} E_{pz}(r_0, \phi_0, z) dz \mathbf{E}_p - \sum_{n \neq p} \frac{j\omega_p \mu_0}{k_n^2 - k_p^2} \int_0^d I e^{-jk_p z} E_{nz}(r_0, \phi_0, z) dz \mathbf{E}_n \quad (3)$$

$$- \sum_n \frac{1}{j\omega_p \epsilon_0} \int_0^d I e^{-jk_p z} F_{nz}(r_0, \phi_0, z) dz \mathbf{F}_n$$

$$\mathbf{H} = -\frac{jQ_p}{k_p} \int_0^d I e^{-jk_p z} E_{pz}(r_0, \phi_0, z) dz \mathbf{H}_p + \sum_{n \neq p} \frac{k_n}{k_n^2 - k_p^2} \int_0^d I e^{-jk_p z} E_{nz}(r_0, \phi_0, z) dz \mathbf{H}_n \quad (4)$$

These expressions are independent of the Q 's of the interfering modes. It should also be noted that all transit time factors are calculated at the frequency ω_p .

It is not possible to give a general expression for the position error resulting from the off-resonance terms since it is very much dependent on the output coupling.

Pill-box cavity

Equation (4) is now applied to a pill-box cavity operating in the E_{110} mode with output coupling to the circumferential magnetic field, through an iris into rectangular waveguide. Although the summation is in fact a triple series, interference comes only from the E_{0ml} common modes, as only these are strongly excited by a beam near the centre. In addition, we will omit all modes with $l > 0$ since these modes do not couple through the iris to the H_{10} mode in the rectangular output waveguide. For a cavity of radius a and length d , we have:

$$E_{110z} = \sqrt{\frac{2}{\pi d a^2 J_0^2(p_{11})}} J_1(p_{11} r/a) \cos \phi \quad (5)$$

$$H_{110\phi} = \sqrt{\frac{2}{\pi d a^2 J_0^2(p_{11})}} J_1(p_{11} r/a) \cos \phi \quad (6)$$

$$E_{0m0z} = \sqrt{\frac{1}{\pi d a^2 J_1^2(p_{0m})}} J_0(p_{0m} r/a) \quad (7)$$

$$H_{0m0\phi} = \sqrt{\frac{1}{\pi d a^2 J_1^2(p_{0m})}} J_1(p_{0m} r/a) \quad (8)$$

$$k_{nm0}^2 = (p_{nm}/a)^2 \quad (9)$$

where p_{nm} is the m^{th} root of J_n . For $r_0 \ll a$ and $\phi_0 = \phi = 0$, the circumferential magnetic field given by (4) is:

$$H_\phi = \frac{I}{jk_{110} \pi d a} (e^{jk_{110} d} - 1) \left(\frac{jQ_{110} r_0}{J_0(p_{11}) a} + \sum_m \frac{p_{0m}}{(p_{0m}^2 - p_{11}^2) J_1(p_{0m})} \right) \quad (10)$$

If we define the position error as the value of r_0 for which the magnitudes of the wanted and unwanted terms in (10) are equal, then:

$$\text{error} = \frac{J_0(p_{11}) a}{Q_{110}} \sum_m \frac{p_{0m}}{(p_{0m}^2 - p_{11}^2) J_1(p_{0m})} = 0.305 \frac{\lambda_{110}}{Q_{110}} \quad (11)$$

The error in a 33GHz cavity with a Q of 4000 is thus $0.69 \mu\text{m}$. For the CLIC BPM, this will be reduced by the symmetry rejection of a pair of diametrically opposed irises feeding a hybrid tee. A reduction by more than an order of magnitude is easily achievable.

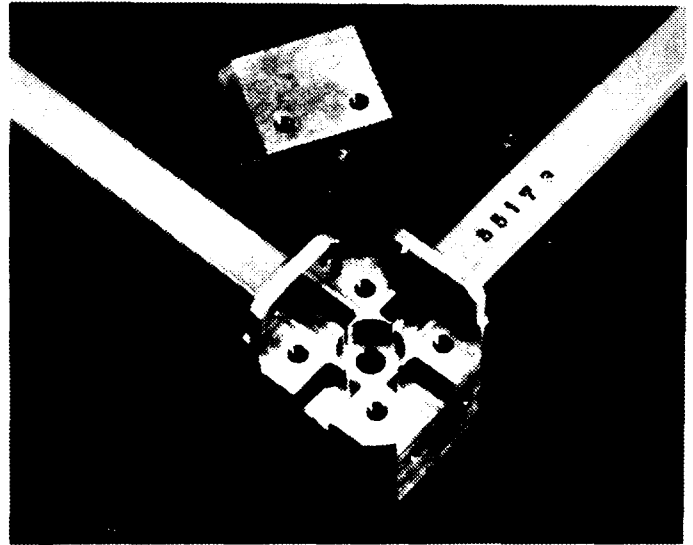


Fig. 1 Prototype dual axis BPM cavity.

Measurement of position error due to common modes

Common mode interference has been measured experimentally in a prototype 33GHz E_{110} pill-box BPM (Fig. 1). The cavity was excited by a 5mm long antenna placed in the beam hole 0.5mm outside the end-wall and a network analyser was used to measure the transmission through the antenna-cavity-output iris system. The antenna could be moved relative to the cavity using a precision translation stage with a nominal $0.1\mu\text{m}$ resolution. Fuller details of the experimental configuration have been given elsewhere [5]. For the present measurements, a brazed diamond machined cavity of diameter 10.600mm and with a loaded Q of 4000 was employed. A single cavity output port was used with no external symmetry rejection.

Again, we define the common mode position error as the value of displacement for which the magnitudes of the E_{110} resonant and the quadrature "broad-band" responses are equal. The experimental estimate of this error was $1.0\mu\text{m}$. It was found by firstly positioning the antenna at the null of the E_{110} transmission (flat response), and then moving it either side to where the transmission increased by $\sqrt{2}$, at the frequency of the E_{110} resonance. This value was reached at antenna positions of $\pm 1.0\mu\text{m}$ from the null, as is shown in Fig. 2.

Acknowledgements

We are most grateful to G. Dôme for his invaluable advice on this work. We would also like to thank R. Bossart, W. Schnell and I. Wilson for their aid and helpful comments.

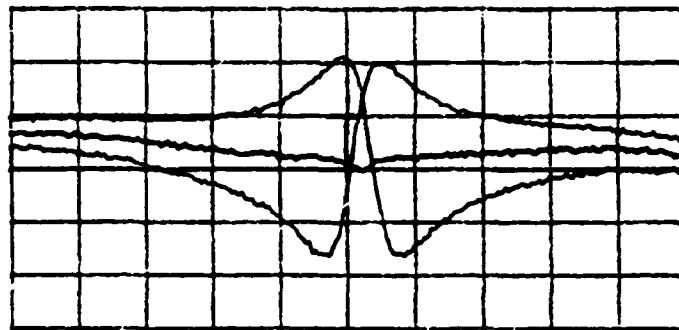


Fig. 2 Transmission through cavity at the E_{110} null and at $\pm 1\mu\text{m}$ either side. Vertical 2dB/div. Horizontal 10MHz/div, centre 32.8GHz.

References

- [1] Schnell, W., "Common-mode rejection in resonant microwave position monitors for linear colliders", CERN CLIC Note 70, 1988.
- [2] Sladen, J. P. H., 'Signal processing for the CLIC beam position monitor', Proc. 2nd European Particle Accelerator Conference, Nice, 12-16 June 1990, pp. 735-737.
- [3] Collin, R. E., *Field theory of guided waves*, IEEE press, 1991, page 394.
- [4] Dôme, G., "RF systems: waveguides and cavities", CERN SPS/86-24 (ARF).
- [5] Schnell, W., Sladen, J. P. H., Wilson, I. and Wuensch, W., "CLIC beam position monitor developments", 15th International Conference on High Energy Accelerators, Hamburg, 20-24 July 1992.

Simulation of the ALS Longitudinal Multibunch Feedback System*

John Byrd
Lawrence Berkeley Laboratory
Berkeley, CA 94720 USA

Abstract

Longitudinal coupled bunch growth rates in the Advanced Light Source (ALS), a 1.5 GeV electron storage ring for producing synchrotron radiation, indicate the need for damping via a feedback (FB) system. The design of the system is based on the proposed PEP-II longitudinal FB system which uses a digital filter to provide the required phase and amplitude response. We report the results of a detailed computer simulation of the FB system including single particle longitudinal beam dynamics, measured RF cavity fundamental and higher order modes, and response of major FB components such as the power amplifier and kicker. The simulation addresses issues such as required FB power and gain, noise, digital filter effects, and varying initial bunch conditions.

INTRODUCTION

The calculated longitudinal multibunch growth times resulting from interactions with the RF cavity higher order mode impedance[1] indicate the need for a multibunch FB system in order to maintain longitudinal beam stability. The longitudinal feedback (LFB) system proposed for the ALS is based on a design for the FB system proposed for PEP-II, a high-current, many-bunch storage ring proposed to be built a SLAC[2].

A time-domain computer simulation of the longitudinal motion of a multibunch beam[3] has been used in order to study the performance of the ALS LFB system under a variety of conditions. The simulation is useful for studying many issues which theoretical methods on coupled-bunch beam stability can only estimate. These include transients and growth rates for nonuniform bunch filling patterns, residual beam noise, nonlinearities, and power requirements. The simulation is also useful for examining electronic effects which can occur in the FB system such as amplifier saturation, limited frequency response, deviations from linear phase.

LONGITUDINAL SIMULATION[3]

Difference Equations

The simulation code models each bunch as a single macro-particle of charge q . The coordinates used for describing the longitudinal motion of each bunch are ΔE , the energy deviation from the reference energy, and ϕ , the phase of the RF clock at the arrival time of the bunch at the cavity.

*This work was supported by the Director, Office of Energy Research, Office of Basic Energy Sciences, Materials Sciences Division, of the U.S. Department of Energy under Contract No. DE-AC03-76SF00098.

The turn-by-turn difference equations for these coordinates can be written as

$$\Delta E_{i+1} = \Delta E_i + qV_g \sin \phi_i - U_{s,i} + qV_w + qV_{FB} + qV_{noise} \quad (1)$$

and

$$\phi_{i+1} = \phi_i + 2\pi\alpha h \frac{\Delta E_i}{E}. \quad (2)$$

V_g is the voltage in the cavity from an external generator, V_w is the wakefield voltage, V_{FB} is the voltage kick from the FB system, and V_{noise} is a noise source. $U_{s,i}$ is the energy lost to synchrotron radiation on turn i and is given by

$$U_{s,i} = U_0 + \Delta E_i \frac{\partial U}{\partial E} \quad (3)$$

where $U = U(E)$ is the energy lost to radiation for an electron of energy E .

To include effects from the fundamental mode such as Robinson damping and beam gap transients, it is necessary to apply standard beam-loading compensation to the RF voltage[4]. To do this, the fundamental mode is detuned from the RF frequency and V_g is adjusted to maintain a constant cavity voltage (V_c). The amount of frequency detuning is given by the relation

$$\Delta f_c = \frac{I_0 \cos \phi_s}{V_c} \left(\frac{R}{Q} \right) f_{rf}. \quad (4)$$

Including beam-loading compensation, Eq. 1 is modified as

$$\Delta E_{i+1} = \Delta E_i + qV_g \sin(\phi_i + \psi) - U_{s,i} + qV_w + qV_{FB}. \quad (5)$$

The generator voltage is given by

$$V_g = (V_c + V_{br}) \cos \psi \quad (6)$$

where

$$V_{br} = \frac{2I_0 R_s}{1 + \beta}$$

and the tuning angle, ψ , is given by

$$\tan \psi = \frac{2Q_0}{1 + \beta} \frac{\Delta f_c}{f_{rf}} \quad (7)$$

The beam-induced voltage in the fundamental mode is included in the wake voltage, V_w . It is initialized to its expected steady-state value at the start of a run in order to avoid transient problems.

The wakefield voltage is found by summing the voltage contribution from each cavity mode. All cavity modes are

assumed to be resonator-type impedances. The net wake voltage is given by

$$V_w(t) = \sum_{j=1}^M 2k_j q \cos(\omega_{r,j}t) e^{-\frac{\omega_{r,j}}{2Q}t} \quad (8)$$

where ω_r , Q , k are the resonator frequency, quality factor, and loss factor. The loss factor is related to the shunt impedance by

$$k = \frac{\omega_r R_s}{2Q} e^{-(\omega_r \sigma_r)^2} \quad (9)$$

Each resonator wake voltage is initialized to zero at the start of the simulation except for the fundamental mode.

Feedback Model[3]

The purpose of the LFB system is to process a measured bunch phase error and produce an energy correction with a 90° phase shift at the synchrotron frequency. In the proposed design of the system, a beam phase oscillations are detected at $6 \times f_{rf}$. This signal is digitized and a farm of digital signal processors (DSPs) computes an output using a digital filter with the desired frequency and phase response using a digital filter algorithm. The computed correction is then converted to a voltage and modulated to the operating frequency of the longitudinal kicker.

The digital filter used in the DSPs is a 5-tap finite impulse response (FIR) filter. To reduce the total amount of data processing, only the signal from every n th turn for a particular bunch is used to calculate the output. Because of the many (~ 110) turns per synchrotron oscillation, a reduced set of sampled signals is adequate to define the synchrotron oscillation for a given bunch. On turns where a new output for a given bunch is not calculated, the previous correction for that bunch is used. For the simulation, a downsampling factor of $n = 24$ was used, corresponding to roughly 5 samples per synchrotron oscillation.

The correction signal is calculated from the input phase error signal as a convolution given by

$$Y_k = \sum_{n=0}^{m-1} C_n X_{k-n} \quad (10)$$

where Y_k is the output of the filter on turn k , n is an index which sums over the last m phase error measurements of a particular bunch, C_n are the weighting coefficients of the filter, and X_{k-n} are the digitized input phase error measurements for the last m samples. The filter coefficients are chosen to pass signals at the synchrotron frequency with a 90° net phase shift and zero DC response. The filter coefficients for one of the 5-tap filters used in this simulation and the resulting frequency response is shown in Figure 1.

The simulation LFB model includes: 1) the properties of the phase detector, mixer, low-pass filter, low-pass filter, A/D and D/A conversion, 2) input noise, gain, and offset errors, 3) algorithm running DSPs to compute output response, 4) bandwidth limitations of amplifier, and kicker.

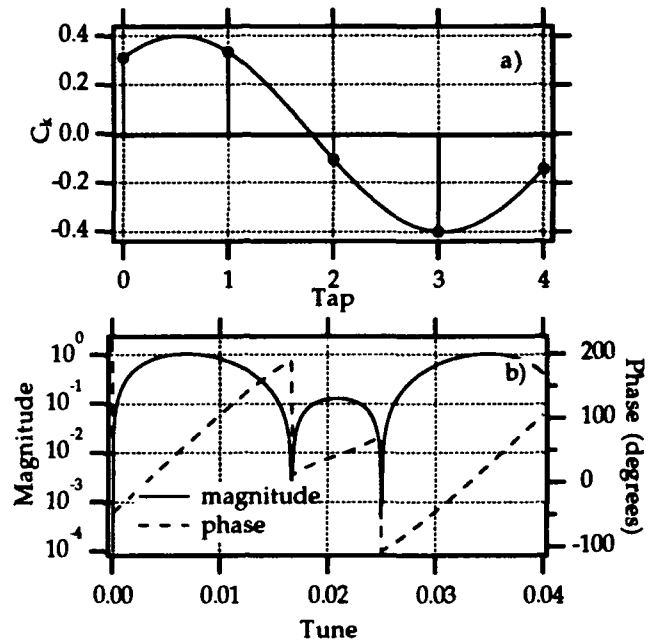


Figure 1: a) Filter coefficients used in FIR filter. b) Frequency response of FIR filter.

Digital filters were used to approximate the frequency response of the LFB system components in the simulation. A wide variety of filters were tried. For the results in this paper, a 20-tap FIR bandpass filter was used to approximate frequency response of the analog components in the system.

RESULTS

The ALS and FB parameters used for the simulation are shown in Table 1. The monopole RF cavity modes used were measured on a spare ALS cavity and are given in reference[5], in these proceedings. One of the consequences of the gap in the bunch filling pattern is a different synchronous phase angle for each bunch. This makes the zero

Parm.	Description	Value
E_b	Beam energy	1.5 GeV
C	Circumference	196.8 m
h	Harmonic number	328
N	Number of bunches	280
I_0	Total DC beam current	0.4 A
Q_s	Synchrotron Tune	0.009
τ_s	Rad. damping time	22500 turns
$\delta\phi_{inj}$	Inj. phase offset	0.20 rad
$(\delta E/E)_{inj}$	Inj. energy offset	0.002
$V_{FB,max}$	Maximum FB kick	1.5 kV
V_{noise}	RMS noise	50 V
τ_{CB}	Max. CB growth time	1500 turns
τ_{FB}	Max. FB damping time	600 turns

Table 1: ALS and LFB parameters used in the simulation.

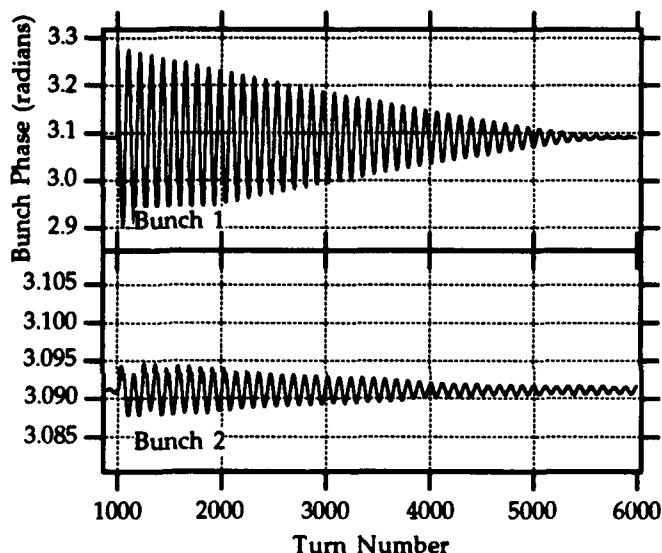


Figure 2: Transient response of two of the 280 bunches with feedback.

DC response of the FIR filter important. Since all bunches start at the same initial phase, the simulation is run for 1000 turns before an injection disturbance is applied in order to allow the beam to settle into its steady-state condition.

All simulation runs used ALS injection conditions. The injector system injects 4 bunches separated by 4 RF buckets into the storage ring at a 1 Hz rate. Each bunch has a maximum centroid energy and phase offset given in Table 1. Runs with the FB turned off show an exponential increase in the bunch phase up to an amplitude of ~ 0.3 rad whereupon the oscillation appears to self-limit. The limiting mechanism is not yet understood. The transient responses of an offset bunch (bunch 1) and a trailing bunch (bunch 2) with the FB on are shown in Figure 2. Bunch 1 is kicked at turn 1000 and is damped linearly while the FB voltage is saturated at 1.5 kV and exponentially in the proportional region. Bunch 2 is excited through wakefield coupling and is damped down to the sensitivity level of the FB input, which is determined by the least significant bit of the input A/D conversion. For the simulation, the sensitivity was 2 mrad.

Shown in Figure 3 is an expanded view of the bunch phase and the computed FB output kick for bunch 1. The stepping structure of the output is a result of the downsampling of the input signal. Note that the output is shifted by $\sim 90^\circ$ from the bunch phase and that the output has no DC component. The damping rate of the LFB system was set to be 2.5 times the largest calculated CB growth rate.

For the FB gain and external noise used, the system was always capable of damping the bunch phases to within the sensitivity level of FB input. The requisite voltage to damp the beam was also studied. The FB system was able to stabilize the beam for the above injection transients with $\sim 1/2$ the maximum FB voltage kick. Thus, the system could conceivably run with $\sim 1/4$ the specified power for

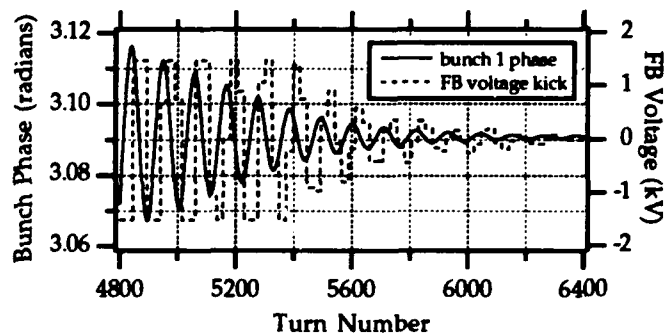


Figure 3: Transient response of bunch 1 and the FB output. The FB is saturated up to turn 4700.

the kind of injection disturbances expected.

The effect of shifts in the HOM frequencies on the ability of the FB system to damp the beam was also studied. We ran a series of simulation runs using the measured HOM parameters, where several of the high- Q HOM frequencies were varied randomly from run to run. The FB was able to damp the beam under all conditions except when the frequency strongest HOM landed on a frequency corresponding to an unstable coupled-bunch mode.

CONCLUSIONS

A simulation of the ALS longitudinal multibunch FB system has demonstrated that it is capable of damping coupled-bunch oscillations to acceptable levels for nominal operating conditions. The actual power requirements should be less than calculated.

The author would like to thank Kathy Thompson for providing the original multibunch simulation code and Don Briggs, Walid Hosseini, Haitham Hindi, and John Fox for providing the code for the FB model. Thanks also to Glen Lambertson for many useful discussions, Johan Bengtsson for assistance in deciphering the simulation code, and to members of the Center for Beam Physics at LBL for their general support and encouragement.

REFERENCES

- [1] J. Byrd and J. Corlett, *Study of Coupled-bunch Collective Effects in the ALS*, these proceedings.
- [2] *Design Update for PEP-II*, LBL PUB-5303 (1992).
- [3] D. Briggs et. al., *Computer Modelling of bunch-by-bunch feedback for the SLAC B-factory design*, *Proceedings of the 1991 IEEE Particle Accelerator Conf.* (1991).
- [4] See, for example, P. Wilson, *Proceedings of the 1982 Particle Accelerator School*, AIP Conf. Proc. 127 (AIP, New York 1982).
- [5] J. Corlett, J. Byrd, *Measurement of Higher-order Modes of the ALS 500 MHz Accelerating Cavities*, these proceedings.

Analysis of DSP-Based Longitudinal Feedback System: Trials at SPEAR and ALS*

H. Hindi, N. Eisen, J. Fox, I. Linscott, G. Oxoby, L. Sapozhnikov
Stanford Linear Accelerator Center, Stanford University, Stanford, CA 94309
and

M. Serio, INFN Laboratori Nazionali, Frascati, Italy

Abstract

Recently a single-channel prototype of the proposed PEP-II longitudinal feedback system was successfully demonstrated at SPEAR and ALS on single-bunch beams. The phase oscillations are detected via a wide-band pick up. The feedback signal is then computed using a digital signal processor (DSP) and applied to the beam by phase modulating the rf. We analyze results in the frequency- and the time-domain and show how the closed-loop transfer functions can be obtained rigorously by proper modeling of the various components of this hybrid continuous/digital system.

The technique of downsampling was used in the experiments to reduce the number of computations and allowed the use of the same digital hardware on both machines.

I. INTRODUCTION

It has been proposed that the longitudinal synchrotron oscillations in storage rings can be suppressed using a DSP-based bunch-by-bunch feedback system [1]. In the bunch-by-bunch approach, each bunch is treated as an individual oscillator driven by an unknown disturbance. The phase of each bunch is detected, a feedback signal particular to that bunch is computed using a digital signal processor, and is applied to that bunch on the following turn. The idea is that since this approach deals with each bunch on an individual basis, it can be extended to the multibunch case. The coupling would then be lumped into the unknown driving term. This technique would work if the coupling between the bunches is sufficiently weak. The programmable nature of the DSP-based feedback system and the technique of downsampling makes it possible to use the same digital hardware on different machines.

A single-channel prototype of this system was demonstrated successfully at SPEAR and, more recently, at ALS on single-bunch beams. We present some of the results of these experiments and show how they can be rigorously analyzed by appropriate modelling of the different components in the feedback system.

II. EXPERIMENTAL SETUP

The basic experimental setup used on both machines is shown in Figure 1. Since no wide-band kicker was available, the feedback was applied to the beam by phase modulating

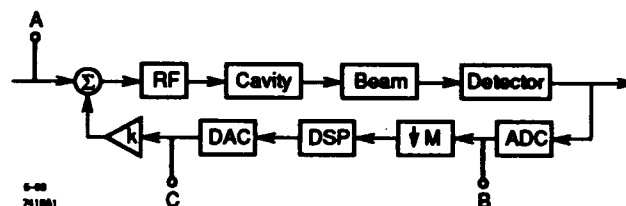


Figure 1: Experimental setup used at SPEAR and ALS.

the rf. A compensator (not shown) was included before the rf cavity to extend its bandwidth to beyond the frequency range over which the beam dynamics are interesting. The component k represents an attenuator that was used to vary the loop gain. The $\downarrow M$ represents downsampling¹. This process had very little effect on the experiment as a whole.

Points A, B, and C represent points in the system between which transfer function measurements were made.

III. MODEL OF SINGLE-BUNCH BEAM WITH FEEDBACK

In this section we obtain theoretical expressions for the transfer functions from points A to B,² $T_{A \rightarrow B}(s)$, and from B to C, $T_{B \rightarrow C}(s)$. From these expressions, the closed-loop transfer function is obtained. Due to the large number of components in the loop, the modelling of delays plays an important role.

A. Model of the Beam

We model the beam phase oscillations, τ , with respect to the rf as obeying the simple harmonic oscillator equation [4], except that we modify this equation to allow for a delay, T_{d1} , in the response:

$$\ddot{\tau} + 2\omega_o \zeta_o \dot{\tau} + \omega_o^2 \tau = -A u(t - T_{d1}) \quad (1)$$

where ω_o is the synchrotron frequency, ζ_o is the damping term, A is a gain constant, and $u(t - T_{d1})$ is the driving input to the system, delayed by T_{d1} . These parameters can be easily extracted from the plots of the open-loop transfer functions of the system. Laplace transforming equation (1) yields the open-loop beam transfer function:

$$B(s) \triangleq \frac{\tau(s)}{u(s)} = \frac{-A e^{-sT_{d1}}}{s^2 + 2\omega_o \zeta_o s + \omega_o^2} \quad (2)$$

¹This was used to reduce the number of computations by allowing only one out of every M data samples to get to the DSP, see [2]

²" s " here denotes the Laplace frequency variable.

*Work supported in part by U.S. Department of Energy contract DE-AC03-76SF00515.

We assume that, apart from contributing to the delay T_{d1} and to the gain A , the frequency responses of all the other components in the branch $A \rightarrow B$ are "flat" over the range of frequencies where the beam dynamics are of interest. Hence we take $B(s)$ to be our model for this branch, i.e., $T_{A \rightarrow B}(s) = B(s)$.

B. Model of the Feedback

The objective of the feedback is to measure τ and process it to produce a feedback signal u_{fb} that damps the synchrotron oscillations. Ideally, this could be done using differential feedback [3], that corresponds to filtering τ with a differentiator, $H(s) = -K_{diff}s$, where K_{diff} is a constant. However, ideal differentiators have the unfortunate property of amplifying high-frequency noise. Hence, the DSP was used to implement a finite impulse response (FIR) digital filter [5] that approximates a differentiator over a finite frequency range. The transfer function of the FIR filter is given by

$$H(s) = K_o \sum_{n=1}^N h(n) e^{-sT_s n}, \quad (3)$$

where K_o is the gain of the filter, $\{h(n)\}_1^N$ are the coefficients of the FIR filter, and T_s is the sampling rate. The coefficients used at SPEAR and ALS were given by:

$$h(n) = \sin\left(\frac{2\pi n}{N} - \Delta\right) \quad ; 1 \leq n < N. \quad (4)$$

Δ is an adjustable parameter which gives control over the phase response of $H(s)$. In this single-channel prototype, additional delays due to the hardware exist, so we modify $H(s)$ to allow for these:

$$H(s) = K_o \left(\sum_{n=1}^N h(n) e^{-sT_s n} \right) e^{-sT_{d2}}. \quad (5)$$

Once again, assuming that apart from contributing to a delay T_{d2} and to the gain K_o , the frequency responses of all the other components in the branch $B \rightarrow C$ are flat we can take $T_{B \rightarrow C}(s) = H(s)$. The only unknown parameters here are K_o and T_{d2} . These are obtained from measurements of the transfer function $T_{B \rightarrow C}(s)$.

C. Closed-Loop Response

Through the modelling process above, we have reduced the complicated system of Figure 1 to that shown in Figure 2.

Finding the closed-loop beam transfer function, $T_{A \rightarrow B}^{cl}(s)$, is now trivial: it is simply given by

$$T_{A \rightarrow B}^{cl}(s) = \frac{B(s)}{1 + k H(s) B(s)}. \quad (6)$$

RESULTS AND DISCUSSION

Since much more data was available from the trial at ALS than at SPEAR, we focus on those results here,

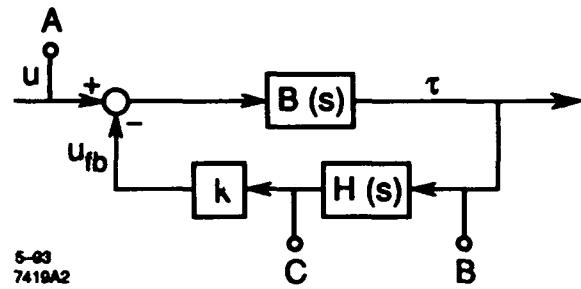


Figure 2: Model of the experimental setup used at SPEAR and ALS.

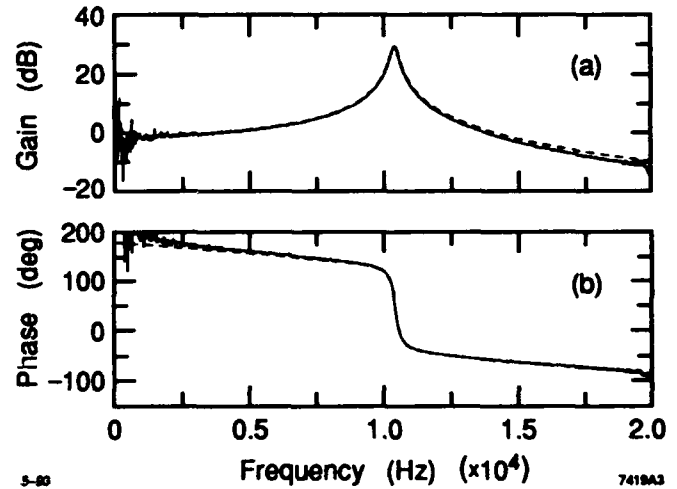


Figure 3: ALS measured versus fitted $T_{A \rightarrow B}(s)$.

though the results from both experiments were very similar. The ALS measured (solid) versus fitted (dashed) open-loop beam and DSP transfer functions are shown in Figures 3 and 4, respectively. In general, the agreement is good, except for the faster roll off of the measured responses. This roll off was probably due to the sample and hold of the DACs. The roll off at very low frequencies in the beam transfer function could have been the result of the response of any of the other components, whose frequency responses were assumed to be flat.

Figure 5 compares the ALS measured versus theoretical closed-loop responses, for several different loop gains. Notice that the damping (as measured by the width of the resonances) increases with loop gain for loop gains of -2 to -19dB. However, at the larger loop gains of 24 and 29dB, the feedback actually began to drive new resonances at other frequencies. Thus we conclude that the closed-loop system using FIR feedback is conditionally stable, i.e., it is stable only over a finite range of loop gains. This means that there is actually a limit to the amount of damping that this type of feedback can provide.

Figure 6 shows the impulse responses corresponding to the loop gains above, obtained by inverse Fourier transforming the frequency responses above. As expected, the

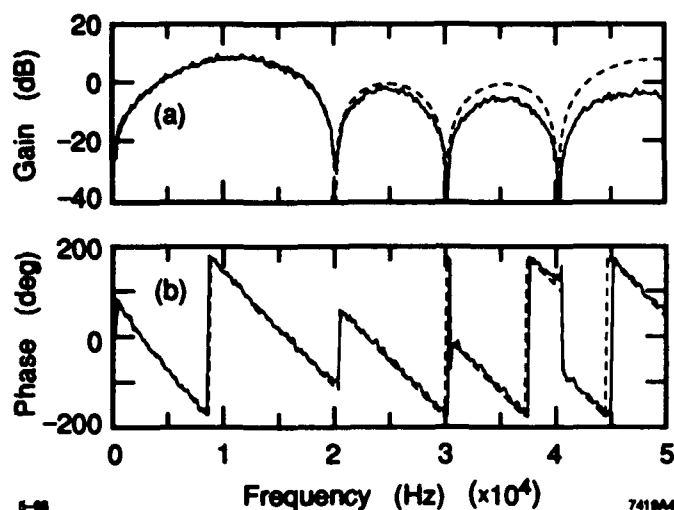


Figure 4: ALS measured versus fitted $T_{B \rightarrow C}(s)$.
 $N = 6, \Delta = 260^\circ$.

damping time constant is large for both very low and very high loop gains and is the shortest at 19dB (approximately two cycles), which is quite sufficient for accelerator physics purposes.

Despite their unusual appearance, these results were actually anticipated, as a result of an analysis similar to the one above.

In summary, we have presented an analysis of results from the trials of a single-channel feedback system on single-bunch beams at SPEAR and ALS. The results were analyzed by modelling each branch of the feedback system with a transfer function. The theoretical and measured closed-loop performance were in close agreement. Such a rigorous approach is necessary in the analysis, and more importantly, in the *design* of realistic feedback systems, such as the proposed PEP-II multi-bunch feedback system.

ACKNOWLEDGEMENTS

The authors would like to thank the ALS and SPEAR operations staff for their cooperation and enthusiasm during the machine physics runs, and Jean-Louis Pellegrin for his help and interest in the analysis.

REFERENCES

- [1] "PEP-II, An Asymmetric B Factory—Design Update," H. Hindi, et al., Conceptual Design Report Update, SLAC 1992.
- [2] H. Hindi et al., "Downsampled Signal Processing for a B Factory Bunch-by-Bunch Feedback System," Proc. of the 1992 European Particle Accelerator Conf., p. 1067.
- [3] "Feedback Control of Dynamic Systems," G. Franklin, Addison-Wesley, 1991.
- [4] "The Physics of Electron Storage Rings, An Introduction," M. Sands, SLAC-121 U-28, 1970.
- [5] "Discrete-Time Signal Processing," A. V. Oppenheim and R. W. Schaffer, Prentice-Hall, 1989.

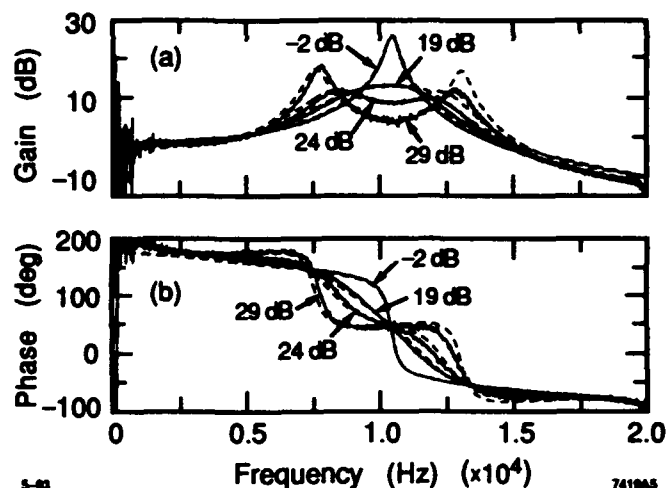


Figure 5: ALS measured versus fitted $T_{A \rightarrow B}^{cl}(s)$ for loop gains of -2, 19, 24 and 29dB.

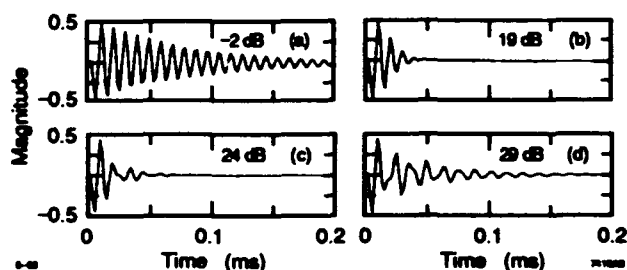


Figure 6: ALS closed-loop impulse responses for loop gains of -2, 19, 24 and 29dB.

VXI Based Low Level RF System for Fermilab Linac Upgrade

B.E. Chase, R.J. Pasquinelli,
Fermi National Accelerator Laboratory*
P.O. Box 500, Batavia, IL 60510

Abstract

A VXI-based Low Level RF (LLRF) system has been designed for the Linac Upgrade project at Fermilab.[1] The design includes not only amplitude and phase feedback around the 805 MHz Klystron and side coupled cavities, but also an adaptive feedforward circuit to compensate for beam loading. In this paper, we will concentrate on the advantages of the VXI environment as well as actual system performance.

I. INTRODUCTION

Accelerator RF systems have had higher demands placed on them in the last decade, both in performance and flexibility. This has led to the use of embedded microcomputers, which in turn creates the new problems of mixing computer and RF environments. Needs in the military and industry for high performance, compact Automated Test Equipment (ATE) drove the development of the VME Extensions for Instrumentation (VXI) standard in July 1987.[2] This standard addresses the issues of integrating a flexible instrumentation system. VXI has matured in the last 6 years to become a very "friendly" architecture for accelerator instrumentation.

We now have an operational RF system that is ready for commissioning later this year. The VXI based LLRF has proven to be flexible and reliable. VXI has also provided a smooth path for system evolution.

II. LLRF DESCRIPTION

The LLRF provides the necessary amplitude and phase feedback control for the 12 megawatt and 200 kilowatt linac stations. All operational levels are at the 100 milliwatt level or below. In addition, a feedforward loop has been added with the use of local VXI based computing power. Feedforward provides the extra level of amplitude and phase control that is required due to beam loading.

The LLRF also provides the capability of electronically adjusting the phase of each individual station for the proper phase advance of the beam. Waveguide to cavity phase is measured for the temperature regulation of the cavities. Figure 1 is a block diagram of the RF system.

The need for feedforward is most critical in the debuncher section. The debuncher is located after the beam chopper, so all beam that passes through it is injected into the Booster accelerator. In order to limit momentum spread, the beam-induced current vector in the cavity must be countered by RF power with exact timing, amplitude and phase.

The correct amplitude of the feedforward waveform is computed from the digitized error signals of the magnitude and phase loops. The average error during beam loading is subtracted from the average error before beam loading. This difference is multiplied by a gain factor and then filtered over many RF cycles to produce the amplitude of the pulse. The pulse timing is selected with 100ns resolution from the control system.

III. PLATFORM CONSIDERATIONS

One of our goals is to have a clean topology both in functionality and in physical hardware. Experience with trouble-shooting broken accelerators at all hours of the day and night defines the need for straight-forward signal flow, limited cabling and as many monitor points as possible. Other considerations are data way bandwidth, triggering, power supply, module size, cooling, electrical shielding, and integration into the accelerator control system. The two solutions proposed are a VME/NIM combination and VXI.

In the VME/NIM system, both the computation of the feedforward correction and data acquisition are done in VME. The RF circuitry resides in a NIM crate. This traditional solution is very workable, however, it requires large numbers of interconnections between the two crates of high-speed analog and digital signals.

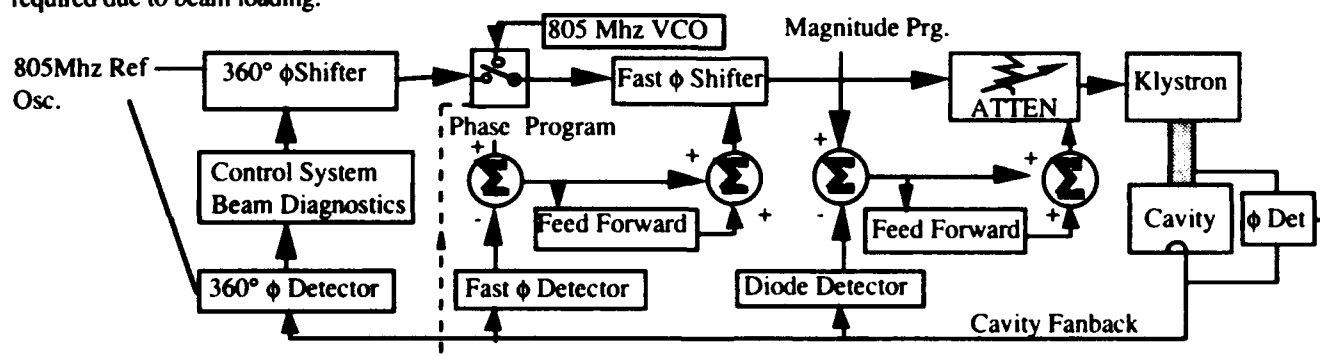


Figure 1. LLRF System Block Diagram

*Operated by the Universities Research Association
under contract with the U.S. Department of Energy

With the VXI platform, all system functions are provided in one crate, with a minimum of front panel connections. Much of the VXI backplane capabilities are utilized. The VME bus is used for high speed communication between the CPU and the RF modules. The 10 MHz ECL clock is locked between all stations in the linac. RF events are timed from the trigger bus. Software tasks are called by the interrupt bus. The Local Bus is used for both analog and digital signals between modules. The mod ID line is used by the resource manager to determine hardware configuration. By knowing the crate configuration, the CPU knows if it is controlling one or two RF stations. For two stations the first four modules are shared. A VXI crate has a total of thirteen slots, of which one station uses seven.

- HP1404A slot 0 crate controller
- Motorola MVME133 CPU
- 1MB Battery Backed RAM
- Vertical Interconnect: a fast link to the Linac Control System.
- 360 degree Phase Shifter/Detector
- LLRF Module (Shown in figure 2)
- Cavity Temperature Control Loop Phase detector and Startup VCXO

IV. MEASURED SYSTEM PERFORMANCE

Testing of the low level system with real beam loading can not be done until the system is commissioned later this year. For this reason, we built a test box to introduce an amplitude and phase step in the RF drive to the Klystron. While this cannot simulate effects such as cavity fill time or

Q shift, it does give us a good measurement of system loop gain and settling time.

Figure 3 shows the open loop response of the system to simulated beam loading. The dominant pole in the loop comes from the loaded Q of the cavity. The measured unloaded Q of the cavity is 20,000. If the waveguide was back-terminated into its characteristic impedance, the loaded Q would drop to 10,000. In this case, there is no circulator in the waveguide, hence much of the return energy from the cavity is reflected off of the Klystron to add in phase with the cavity voltage.

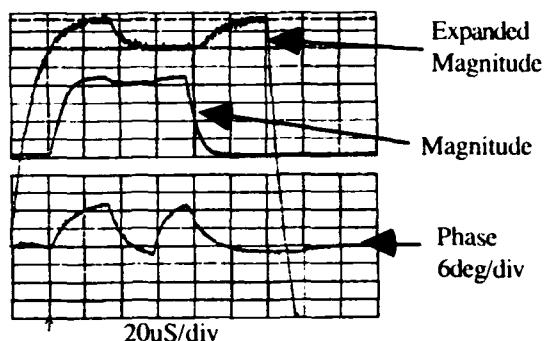


Figure 3. System open loop response to simulated 7.5% beam loading and 18 deg. phase shift. Klystron operating at 7.5 Mwatts.

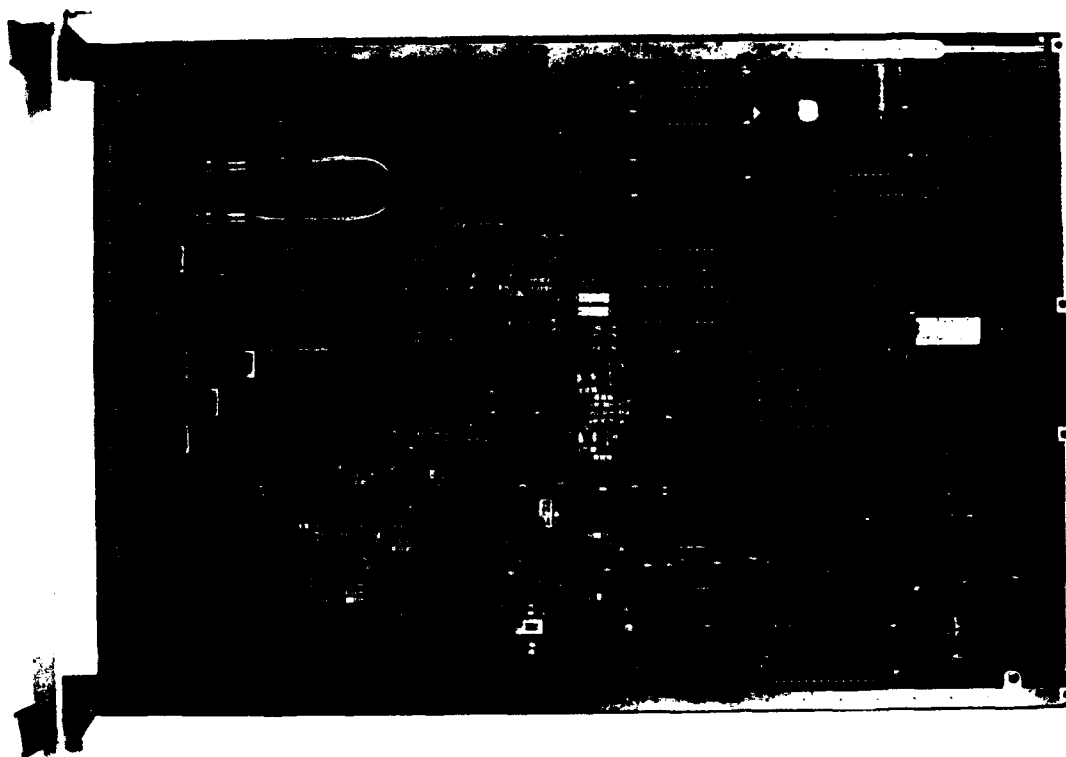


Figure 2. Linac Upgrade Low Level RF Module.

The lower power loss results in a Q of about 1300 and a baseband dominant pole of 32KHz for the magnitude and phase detector signals. This pole combined with the system group delay determine the maximum gain and bandwidth of the feedback loops.

Figure 4 shows the corrected cavity voltage waveform with feedback and feedforward on. Feedback loop gains are typically 15 dB while feedforward is unconditionally stable with loop gains of 46 dB.

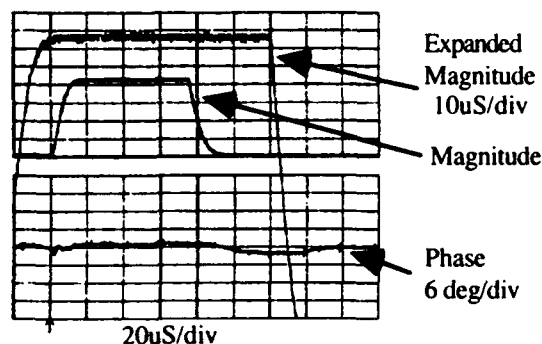


Figure 4. System response to simulated 7.5% beam loading and 18 deg. phase shift with feedforward on. Klystron is operating at 7.5 Mwatts.

The response of the IIR filter is shown in figure 5.

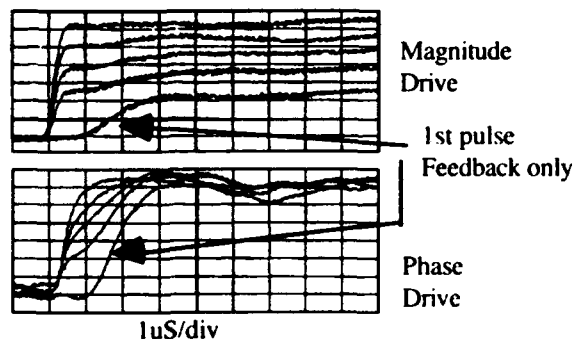


Figure 5. Phase Shifter and Mixer Drive Signals Feedforward "Learning" response to a 10% amplitude and 18% phase step.

V. SYSTEM EVOLUTION WITH VXI

When we started testing the RF system with a real Klystron and cavity, all the custom circuitry resided on one VXI module. We have since added two more custom modules. Most accelerator electronics are by nature development projects. Changes to the original concepts and the evolution of hardware are a natural part of good engineering practice. Therefore, it is important that the original design does not limit growth. VXI, by design, is very general in its architecture and has provided us with a seamless path for upgrades.

We designed much flexibility into the LLRF module. By having a high speed computer bus directly connected to the board, it is easy to put almost any parameter of interest under computer control. By building in a 16 channel ADC, we are able to monitor all signals of interest at any time during the RF cycle. Many variables in the feedforward program are parameters in the control system. Operation of the system relies on the easy access to control and monitor points.

During early running at the test station, a large shift in the resonant frequency of the cavities was found when the RF pulsed drive is turned off for even a few seconds. This is caused by the RF heating of the cavity nose cones and their short thermal time constant. With the cavity off resonance from the reference oscillator, there is a large amount of reflected power back to the klystron. This power is detected and trips the klystron protection system so that the cavities will never warm up. A local VCO was added to track the cavity resonant frequency until the nose cones were at operating temperature. At this point the reference oscillator is switched back in. The Cavity Temperature Control Loop Phase-detector and Startup VCXO module is fairly simple, requiring only a few channels of analog and digital I/O. To take advantage of existing hardware, the VXI local bus was used to route the needed signals to and from the LLRF Module.

Late last year there was a request from Beam diagnostics for a 360 degree Phase Shifter and Detector. For this module we took advantage of a commercial VXI interface daughter card.[4] The daughter card provides the VME bus interface as well as the VXI defined registers. This interface saved us much time in the design, layout, and trouble shooting of this card.

VI. CONCLUSIONS

A low level RF system is installed and tested for the Fermilab Linac Upgrade. The control of the LLRF has taken advantage of the VXI architecture. VXI provides both the analog/RF and control system interface environment in one packaging scheme. The response of the feedback loops to beam loading has been greatly improved by a learning feed forward algorithm. Two years of experience with the VXI platform has proven it to be well suited to accelerator instrumentation.

REFERENCES

1. Noble, R., "The Fermilab Linac Upgrade", Proc. of the 1990 Linac Conf., p.26, Los Alamos Publication LA-12004-C.
2. Tektronix Product Information, "VXI bus System Specification Revision 1.3"
3. Pasquinelli, R., Chase, B., "Linac Low Level RF Operating Procedure" Fermilab internal document.
4. Interface Technology, DT9110 Interface Daughter-Card. Pomona, CA.

Longitudinal Feedback in LEP

J. P. Boiteux, P. Brown, E. Ciapala, H. Frischholz, G. Geschonke, J. C. Juillard and E. Peschardt
CERN
CH-1211 Geneva 23

Abstract

Dipole coupled bunch oscillations were observed at an early stage of LEP commissioning for currents above about 150 μA per bunch. An improvised feedback system, acting on the phase of some of the accelerating cavities was developed and has been in operation for about three years. However, due to the small bandwidth of the RF cavities this system can only be used with four bunches or less per beam. With plans for eight bunch operation (the Pretzel scheme) the construction of a dedicated longitudinal feedback system was approved in 1991. The system operates at 999.95 MHz with phase modulation of a 200 kW klystron feeding four seven-cell cavities. The necessary bandwidth of 260 kHz is obtained by heavy over-coupling. With a total cavity voltage of 1.9 MV a damping rate of about 450 s^{-1} is obtained with phase excursions of one radian. The system has been in routine operation since July 1992 with a feedback cavity voltage of 1.2 MV and a damping rate of about 100 s^{-1} . Longitudinal feedback eases operation and usually increases the maximum currents which can be accumulated.

I. INTRODUCTION

Longitudinal instabilities were not expected in LEP before the current was approaching the design value of 0.75 mA per bunch. However, during the commissioning of the collider in 1989, coupled dipole oscillations were seen at currents above about 0.15 mA per bunch when LEP was operated with four bunches per beam. They were cured with an improvised feedback system [1] which acts on the beams via some of the accelerating cavities. A fundamental limitation of this system is the narrow bandwidth of these cavities. It can therefore only be used for beams with four bunches or less. With plans for eight bunch operation in LEP [2], a longitudinal feedback system using dedicated cavities was therefore prepared and finally approved in March 1991.

II. SYSTEM REQUIREMENTS

The cost of a high power RF system is mainly determined by the RF power requirement which is calculated from the necessary bandwidth and voltage. High frequency operation is advantageous because for a given bandwidth, cavity length and voltage, the required power decreases with frequency.

A. Bandwidth

In order for the energy error of each bunch to be corrected individually, the cavity field has to change in the time interval between the passage of two bunches. Therefore the longer this

time interval, the higher the cavity Q-value which can be used. In the case of two counter-rotating beams of eight bunches this time interval would be maximum if the feedback cavities were located 1/16th of the circumference from a collision point. In LEP this is not possible and the only free space available is located 435 m from the intersection points. At this position the minimum time between bunch passages is 2.9 μs . Assuming that in this time interval the cavity field should reach 90 % of the set value, the required cavity filling time is 1.26 μs with a resulting bandwidth of about 260 kHz.

With this bandwidth the system can be used with any even number of bunches up to 12 and if the cavity bandwidth is increased to 300 kHz, 18 bunch operation is also possible.

B. Frequency

By choosing a frequency of about 1 GHz, four cavities of a type developed and constructed by DESY can be used. Within their tuning range the exact frequency is determined by the revolution frequency and the number of bunches in LEP. If the harmonic number is a multiple of 360 the feedback system allows operation for all possible number of bunches which have been studied. The harmonic number is then found to be 88920 and the frequency 999.9497 MHz ($247/87 f_{\text{RF}}$). Using a frequency which is not an harmonic of the LEP RF frequency of 352.209 MHz complicates the frequency generation system but the functioning of the system is not effected.

C. Cavity Voltage

Four seven-cell cavities are used for the system. The 260 kHz bandwidth is obtained by lowering the loaded Q-value with strong over-coupling. A cavity voltage of 625 kV is expected for 40 kW at the input coupler. With a generator power of 200 kW and 20 % wave guide losses the total voltage for four cavities is about 2.5 MV.

For phase modulation with a modulation index of $\pi/2$ the relationship between feedback voltage, U_{FB} and feedback damping rate, α_{FB} is [3]:

$$U_{\text{FB}} = \frac{2\alpha_{\text{FB}}E_0}{ef_{\text{rev}}} \left(\frac{\Delta E}{E_0} \right)$$

where f_{rev} is the LEP revolution frequency, E_0 the energy and $\Delta E/E_0$ the maximum likely coherent energy oscillation. For $E_0 = 20 \text{ GeV}$ and $\Delta E/E_0 = 10^{-3}$ and if for linearity reasons the phase excursions are limited to one radian the feedback voltage is:

$$U_{\text{FB}} = 4.2 \times 10^3 \alpha_{\text{FB}}$$

giving a maximum damping rate of 600 s^{-1} .

III. SYSTEM DESCRIPTION

The dipole oscillations are detected by the system which was developed for the first feedback system [1] where the signal from a sum pick-up is phase compared with the RF frequency. The only addition required is a time multiplexing scheme which selects the signals from the positron and electron bunch oscillation detector in such a way that the signal from a particular bunch is applied to the cavities during the passage of the same bunch one turn later.

A schematic block diagram is shown in Figure 1. The feedback signal is applied to a fast phase shifter. Phase modulation has been chosen in order to operate the klystron with constant RF power. The drive level dependent phase shift in the klystron is then eliminated and the cavity tuning system is not disturbed.

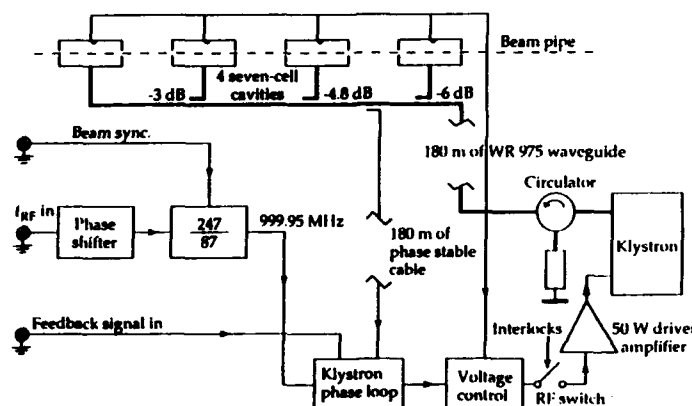


Figure 1. Block diagram of the feedback system.

The 1 GHz signal is generated in a voltage controlled crystal oscillator locked to the RF frequency (Figure 2). In addition because the frequency of the system is not a harmonic of the RF frequency, synchronisation to one of the beams is required. The latter is obtained from a sum pick-up signal processed to detect the beam polarity and with flip-flops (FF) used to reset a counter. When available, the positron bunches are used for this synchronisation, otherwise the system switches automatically to the electron bunches.

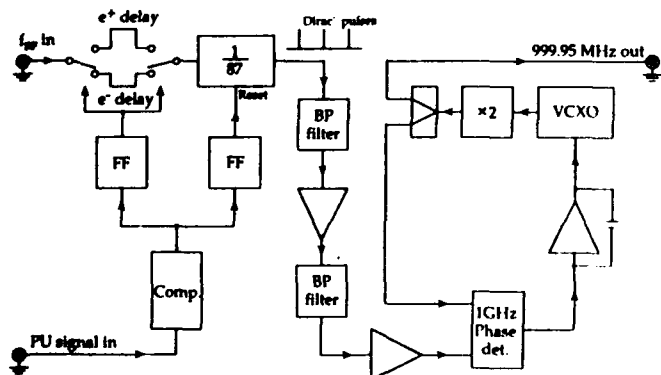


Figure 2. Schematic diagram of the frequency generator.

The distance between the power generation system and the cavities is about 180 m. The signal for the klystron phase loop which compensates for phase variations in the power generation system is returned from the cavity end through a special phase stable cable which has a delay stability better than 2 ppm/°C at 500 MHz.

B. RF Power Generation and Distribution

The cavities are powered by a 200 kW klystron, operating at 999.95 MHz. The -1 dB output bandwidth of this klystron is ± 2 MHz. A 60 W solid state amplifier drives the klystron via a short length of coaxial cable. The amplifier output is protected from any load mismatch by a circulator.

From the over-coupled cavities about 50 % of the incident power is reflected. In order to protect the klystron against these reflections a waveguide differential phase shift circulator is inserted in its output line. The rated power handling capability of the circulator is 400 kW with up to 75 % reflections at any RF phase angle. Ports three and four are terminated by coaxial water loads with maximum RF power dissipation ratings of 100 and 40 kW respectively.

The RF power is transmitted to the cavities via WR975 waveguides and three power splitters which comprise short-slot waveguide hybrids with coupling factors of -6, -4.77 and -3 dB, thus ensuring equal input power to all the cavities. The insertion loss of the 180 m long waveguide line is about 1 dB, which means that at 200 kW incident and 100 kW reflected RF power about 56 kW is dissipated in the waveguide walls. In order not to overload the air ventilation system of the LEP tunnel the waveguides must be water cooled. An extruded Al profile with a cooling water channel was therefore bolted on the centre line of both wide sides of each waveguide. At a water flow of 10 l/min in both cooling channels about 80% of the power dissipated in the waveguides is absorbed by the water, resulting in an average waveguide temperature increase of only 6 °C at the above mentioned RF power flows.

In April 1993 the vertical 200 kW Philips klystron V109SK was replaced by the horizontal EEV model K 3440 C which provides about twice the output power of the previously installed one.

C. Cavities

DESY generously supplied CERN with four copper accelerating cavities. Each cavity consists of seven pill box cells without nose cones, cell coupling via the beam hole. They were fully equipped with tuners in the third and fifth cells, centre-cell power coupler and field probes.

The required bandwidth was achieved by strongly over-coupling the power coupler. This was done by increasing its penetration by 25 mm and by altering the field distribution by means of a fixed tuner of 50 mm diameter, penetrating 21 mm into the centre cell. The loaded Q-values thus obtained are between 3250 and 3950, giving a bandwidth between 253 and 304 kHz. The unloaded Q-value was measured to be 27000.

After the modifications the accelerating field flatness in the seven cells was within $\pm 8\%$.

The RF input power couplers developed by DESY are a coaxial type with a brazed ceramic disk. The power handling capability was increased from its original design value of 40 kW to 70 kW by modifications to the air cooling system and by modifying the RF contacts on the inner conductor.

For the tuning system, wherever possible, equipment built for the LEP accelerating cavities was used. The system uses the phase between the forward travelling wave taken from a directional coupler in the wave guide feeder line directly in front of the cavities and the centre cell field probe for tuning and the amplitude ratio between the third and the fifth cell probes for field balancing. The tuners are driven with five-phase stepping motors. The tuning range is about 4.1 MHz.

Before installation in LEP all the cavities were individually conditioned to an RF power of 70 kW.

IV. SYSTEM PERFORMANCE

The phase of the feedback cavity voltage was adjusted with respect to the 352 MHz RF voltage by maximising the synchrotron frequency. From the increase of this frequency when the feedback voltage is switched on the actual voltage is found. For some reasons, possibly bad power calibrations, this voltage is about 20 % lower than expected.

A = 2 V 6.25ms

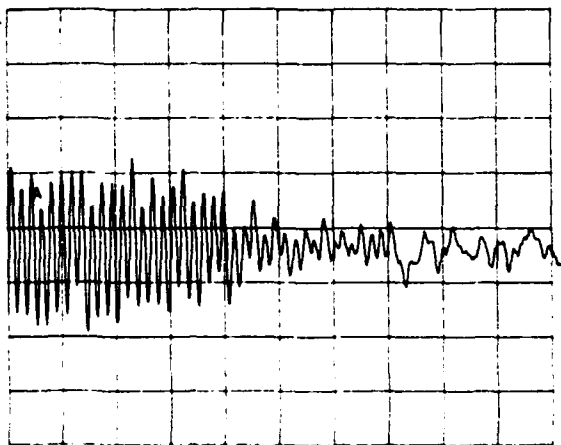


Figure 3. The decrease in amplitude of the dipole bunch oscillations when the feedback is switched on. The damping time constant was about 10 ms with a cavity voltage of 1.6 MV and a current of 100 μ A per bunch.

The modulation was then added and after a few adjustments the system damped all eight modes of the two eight bunch counter-rotating beams. Figure 3 shows the decrease in oscillation amplitude for a particular bunch when feedback is switched on. In this case the damping time was about 10 ms with a feedback cavity voltage of 1.6 MV. The rise time of the oscillations was for the same bunch about 50 ms.

The spectra shown in Figure 4 and 5 prove that all modes are damped.

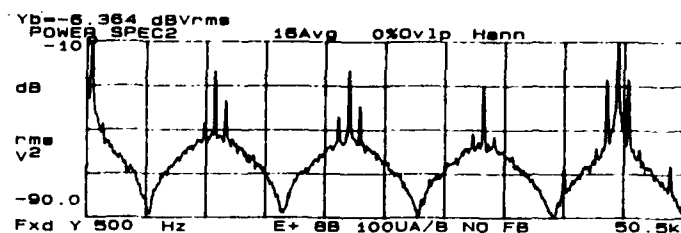


Figure 4. Spectrum of the dipole oscillations for an eight bunch positron beam of 100 μ A per bunch. The synchrotron frequency is 875 Hz and all eight modes are seen as sidebands to the revolution frequency of 11.25 kHz and its harmonics. The largest amplitude is measured on the mode 0 at 875 Hz, followed by mode 4 seen at 44.1 and 45.86 kHz.

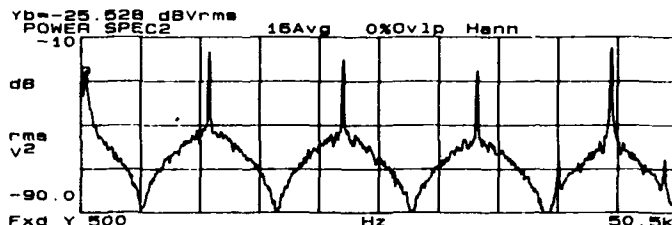


Figure 5. The spectrum seen in Figure 4 measured with longitudinal feedback and a voltage of 1.2 MV. All eight modes are damped. The remaining spectral lines are the revolution frequency and its first three harmonics.

The system is now used routinely during accumulation at 20 GeV with a feedback voltage of 1.2 MV which requires a klystron output power of 90 kW. After acceleration to the collision energy of about 45.6 GeV where longitudinal feedback is not required the system is switched off.

V. ACKNOWLEDGEMENTS

The rapid installation and commissioning of the longitudinal feedback system for LEP was due in large part to the use of cavities, waveguide pieces and klystron from the Deutsches Elektronen-Synchrotron (DESY) laboratory. The authors would like to thank the DESY laboratory for providing this equipment and also to thank the members of the DESY MHF group for their collaboration and support.

VI. REFERENCES

- [1] J. C. Juillard and E. Peschardt, "Damping of Longitudinal Coupled Bunch Oscillations in LEP", Proc. 2nd EPAC, Nice, June 1990, pp. 1554-56.
- [2] R. Bailey, J. M. Jowett, W. Kalbreier and D. Wang, "Commissioning and operation of the LEP Pretzel scheme", this conference, paper Pb5.
- [3] S. Myers, "A First Look at Longitudinal Feedback for LEP", LEP note 366.
- [4] P. Brown, E. Ciapala, S. Hansen, E. Peschardt and J. Sladen, "The LEP radio-frequency low power system", IEEE Trans. Nucl. Sci., NS-23, October 1985, pp. 2032-34.

Performance of the Upgraded Stacktail Momentum Cooling System in the Fermilab Antiproton Source

Ralph J. Pasquinelli, David McGinnis
Fermi National Accelerator Laboratory *
P.O. Box 500, Batavia, IL 60510

ABSTRACT

Major changes in the Stacktail Momentum Stochastic Cooling system have resulted in an improved stacking rate as well as the capability to stack larger quantities of antiprotons. Both these effects result in higher initial and integrated luminosity for colliding beam physics. An overview of the changes and actual system performance will be presented.

I. INTRODUCTION

Since our initial report in 1987 [1], a number of changes have been made to this cooling system. It was discovered early in the history of the Antiproton source that excessive transverse core heating by the stacktail system was limiting the maximum core size. A subset of four of the twenty kickers was implemented as transverse kickers to minimize this effect. The original twenty kickers have been totally replaced with sixteen new planar loop design kickers.

Although the superconducting notch filters performed admirably through their life, there was the added expense of the liquid helium. These filters were replaced with Bulk Acoustic Wave (BAW) filters [2] that save approximately \$200K in annual operations costs. A system equalizer was also designed to maximize the system bandwidth. Finally, even with the new kicker design there is still core transverse heating. A special hybrid [3] has been used for the same subset of transverse kickers, but now these same kickers are both longitudinal and transverse.

II. NEW PLANAR LOOP KICKERS

The purpose of Stack Tail Momentum Kicker Upgrade was to minimize the betatron heating of the core due to the stack tail momentum stochastic cooling system. Previous to implementing the upgrade, the gain of the stack tail system had to be reduced so as not to heat particles in the core orbit, essentially kicking them out of the machine. This condition was most prominent with a large number of particles in the core. The reduced gain of the stack tail system resulted in a decreased stacking rate. The betatron heating of the core is caused by a transverse component of kick given by the kicker electrodes. The transverse kick results from the fact that transverse pairs of kicker electrodes are not electrically identical and are not centered with respect to the beam.

To reduce the transverse kick, the entire kicker tank is aligned with respect to the core orbit. The previous stack tail system consisted of twenty kicker arrays contained in three

vacuum tanks. Each array was powered by a pair of TWT's. An exact cancellation of the transverse kick could not occur because the frequency response of the each TWT and the electrical center of each array was not identical. The upgraded system consists of sixteen arrays contained in eight vacuum tanks. Since the number of TWT's per vacuum tank is much lower, the variation of the transverse kick due to the variation in the frequency response of the TWT's was reduced.

The kicker arrays of the previous system were fabricated with three dimensional stripline electrodes [4]. The reproducibility of the electrodes was on the order of 0.030 inch. The electrodes were suspended mechanically into a tube of rolled stainless steel. Due to the mechanical nature of the rolled stainless steel tubes, the alignment of the arrays to beam center varied by as much as ± 0.020 inch along the length of the array.

As part of the upgrade, the three dimensional arrays were replaced with planar loop arrays. Planar loops were developed for use in Bunched Beam Stochastic Cooling in the TEVATRON [5]. The loops are fabricated on one side of a printed circuit board and the combiner board is placed on the other side. Because the arrays are etched using printed circuit techniques, the reproducibility of the electrodes is on the order of 0.001 inch. Since the printed circuit material is semi-flexible it can be supported with a machined aluminum backing to obtain an accuracy of alignment on the order of 0.001 inch. In addition, since the electrodes and the electrode combiner are on the same circuit card, the arrays can be made substantially smaller.

As in the previous system, four sets of kicker electrodes were wired in the transverse mode to compensate for the transverse kick of the rest of the kicker tanks. Each set corresponds to a different transverse plane and a different position in the lattice. The four sets of transverse electrodes are gain and phase adjusted to minimize the net transverse kick given by the entire stack tail system. However, since the frequency response of electrodes wired in the transverse mode is different from the net transverse kick of all the other electrodes, the transverse kick is not eliminated but is reduced by approximately 10 dB. Because the number of tanks was increased from three to ten, the space allocated for vacuum flanges and bellows in between tanks was increased. To accommodate for this added space, four kicker arrays were sacrificed in the upgrade. However, in the upgrade, the transverse compensating kickers were also driven in the sum mode to provide extra longitudinal kick. Thus the number of longitudinal kicker arrays before and after the upgrade was kept constant. The sum and difference mode hybrid used to combine the transverse and longitudinal kick had to have superb balance

*Operated by the Universities Research Association
under contract with the U.S. Department of Energy

in order to not add extra unwanted transverse kick from the sum mode ports[3].

III. NOTCH FILTERS

The original notch filters included the Traveling Wave Tubes (TWT's) as part of the third notch filter. This presented operational difficulty as the gain and phase of the TWT's and their driver amplifiers had to be very carefully matched. Every time one of these components required replacement, there was degradation in filter #3 performance, i.e. there is no such thing as an exact replacement. The original reason for doing this was to reduce odd order intermodulation products. Careful study showed that the reduction in intermodulation distortion did not warrant the added complexity of the filter. Because of the added active components within the correlator, vector gain balance was compromised and maximum notch depth was only 15 to 20 dB.

The new notch filters are three passive BAW devices that require only temperature stabilization for reliable performance. The number of kicker TWT's has been reduced from 40 to 16 further increasing system reliability. The maximum notch depth is 25 to 40 dB for this filter which is a marked improvement over the previous filter.

IV. SYSTEM EQUALIZER

With the availability of microwave simulation software [6] we were able to design a custom system equalizer to improve system bandwidth. An open loop measurement of the system was made that included both the electronic and beam transfer functions. This data was entered into the optimization software to develop a custom equalizer. The circuit is a stripline design that incorporates quadrature hybrids, coupled lines, and a Schiffman phase equalizer. Figure 1 shows the improvement in cooling bandwidth with the equalizer.

V. SYSTEM PERFORMANCE

Shortly after commissioning the new system, there was some skepticism as to how well it was functioning. Initial stacking rates were only 80% to 90% of the old system. After a couple of months of tuning the entire accumulator complex, stacking rates have exceeded 4.5×10^{10} per hour. Stacking rate is about double the best rate of the original system and closing in on the design book value of 1.0×10^{11} per hour. The current maximum stack size is 1.45×10^{12} . The design book value for this parameter was 4×10^{11} . The production efficiency of pbars from protons is consistently in the neighborhood of 15 parts per million now as opposed to 10 to 12 parts per million before the upgrades. (Figure 2) This number folds in all factors of accumulation showing a definite improvement in system performance. For comparison, 1988-89 collider run performance was a stack rate of 1.6×10^{10} per hour and a production efficiency of 6 parts per million. Figure 3 shows a comparison of stacking statistics for the present run and that of the 1988-89 collider run.

The main injector era requires improvement of source stacking rate to 1.5×10^{11} per hour and stack sizes of 2×10^{12} . At this time it is not clear if the present system can handle these requirements. Eighty-five percent of all pbars produced at the target are presently stacked. The main injector may eventually more than double the amount of available pbars hence potentially saturating the system. Before the end of the current run, we are proposing reversal of magnet polarity so that a careful study of stacking protons can be made in an attempt to find the maximum stack rate of the present system. (Targeting protons can easily simulate the expected new Pbar production rate.)

The improvement in stacking of pbars is also due to improvements made in the debuncher cooling systems. Since 1987, a new debuncher momentum cooling system has been installed and the transverse cooling systems have had their power doubled. Also the Bunch Rotation voltage of the Debuncher has been increased to 5.1 MVolts. The main ring is once again supplying 2×10^{12} protons per pulse to the target station.

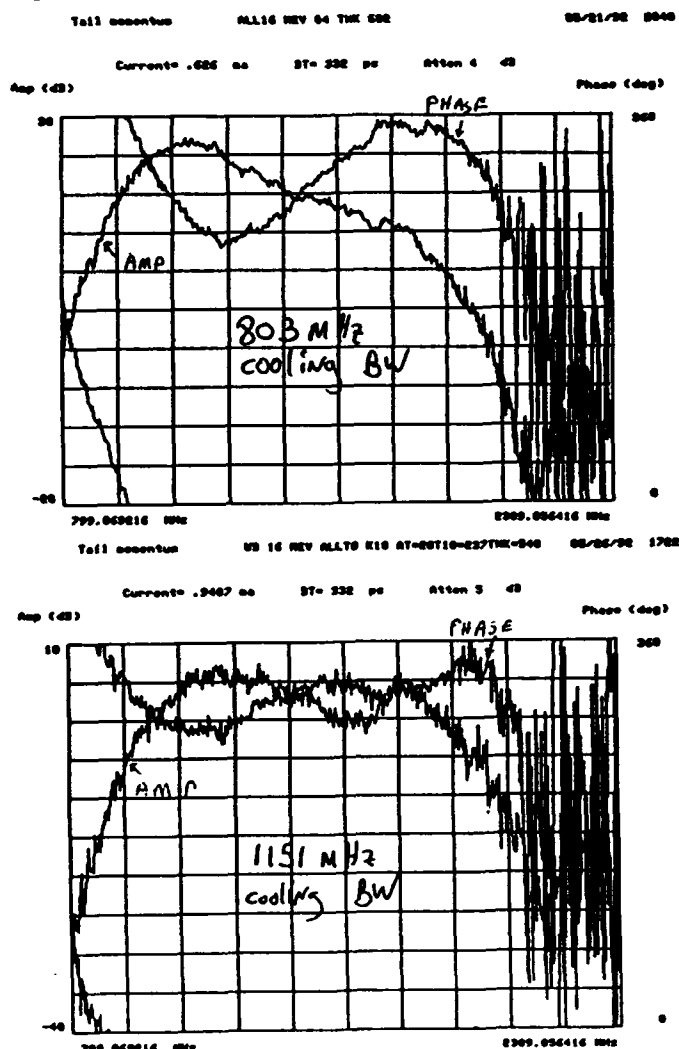


Figure 1. Open loop beam transfer function. Top: before equalizer system calculated cooling bandwidth is 803 MHz. Bottom: after equalizer system calculated cooling bandwidth is 1151 MHz.

Energy Vernier System for CEBAF*

G. A. Krafft, J. J. Bisognano, M. T. Crofford, J. C. Hovater, L. Merminga, S. N. Simrock, and S. D. Witherspoon
CEBAF
12000 Jefferson Avenue, Newport News, VA 23606
and
K. Kubo
KEK
Oho, Tsukuba-shi, Ibaraki-ken, 305, Japan

Abstract

The beam energy of CEBAF must be accurately controlled for precise physics experiments. In order to achieve a relative energy spread better than $\sigma_E/E = 2.5 \times 10^{-5}$, a feedback system is needed to stabilize the energy against phase and amplitude fluctuations in the individual cavities. In the energy vernier system, the energy deviation of the beam is measured at a location with high dispersion. The error signal controls the accelerating gradient of selected vernier cavities. The methods used to correct the energy will be discussed, as well as the noise sources in the system. The results of beam tests at the CEBAF north linac will also be reported.

I. INTRODUCTION

The functions of the energy vernier are to stabilize the average energy of the emerging beam and to set the RF phases in the cavities in a way that minimizes the energy spread. In this paper it is proposed that the first function is accomplished by a dedicated fast spectrometer-based feedback system. The second problem is solved using a low-noise phase shifter between the master oscillator and the phase reference line to optimize the overall linac phase.

A. Requirements of the Energy Vernier

Ideally, the RF system is timed so the bunches arrive synchronized with the RF; the bunch centroid (in phase) should coincide with the RF crest. Mathematically, the requirement is

$$\bar{\theta}_n = \int \theta f_n(E, \theta) dE d\theta = 0$$

where $f_n(E, \theta)$ is the single-particle longitudinal distribution function of the beam electrons as they enter the n th cavity, E is the kinetic energy, and θ is the phase with respect to the RF in the n th cavity. Performing the proper statistical average to obtain the rms relative energy spread at the end of the machine yields

$$T_{rms}^2/T^2 = E_{rms}^2/T^2 + \sigma_\theta^2/2$$

where T is the total energy, E_{rms} is the rms energy spread at injection and σ_θ is the rms phase spread. The beam

emerging from the ideal system has a finite energy spread because of the finite energy spread at injection and because of the finite bunch length. For CEBAF at full energy, the first term in the sum is negligible compared to the second term.

When errors derived from the RF system are included [1], and when it is assumed that the vernier operates perfectly, the relative energy spread is

$$T_{rms}^2/T^2 = E_{rms}^2/T^2 + \sigma_I^2/2 + \sigma_\delta^2 \sum_{n=1}^N (\phi_n - \Phi)^2/N^2 + \sigma_\delta^2(\sigma_\delta^2/2 + \sigma_I^2)/N + (\sigma_A/A)^2/N \quad (1)$$

assuming the fast errors in different cavities are statistically independent and

$$T_{rms}/T = \sqrt{E_{rms}^2/T^2 + (\sigma_I^2 + \sigma_\delta^2)^2/2 + (\sigma_A/A)^2} \quad (2)$$

assuming the fast errors are completely correlated. In these equations, σ_I denotes the rms phase spread emerging from the injector, σ_δ denotes the rms fast phase error in the field of the accelerating cavities (e. g., those in the RF controls), ϕ_n is the slow phase error of the n th cavity (e. g., those from thermal drift in the phase line), Φ is the phase introduced by the vernier to minimize the energy spread (usually $\Phi \approx \sum_{n=1}^N \phi_n/N$), σ_A/A is the rms relative amplitude fluctuation in the cavities, and N is the number of cavities.

To achieve the requisite energy spread, the following specifications were used in the CEBAF RF system design:

Table 1 RF Tolerances Yielding
 2.5×10^{-5} rms Relative Energy Spread [2]

	σ_I	0.27°
UNCORRELATED ERRORS		
σ_A/A		2.0×10^{-4}
σ_f		0.25°
σ_δ		2.6°
CORRELATED ERRORS		
σ_A/A		1.1×10^{-5}
σ_f		0.13°

Because a gradient error in the vernier is directly an energy error on the beam, the requirement on the gradient

*Supported by U. S. DOE contract DE-AC05-84ER40150.

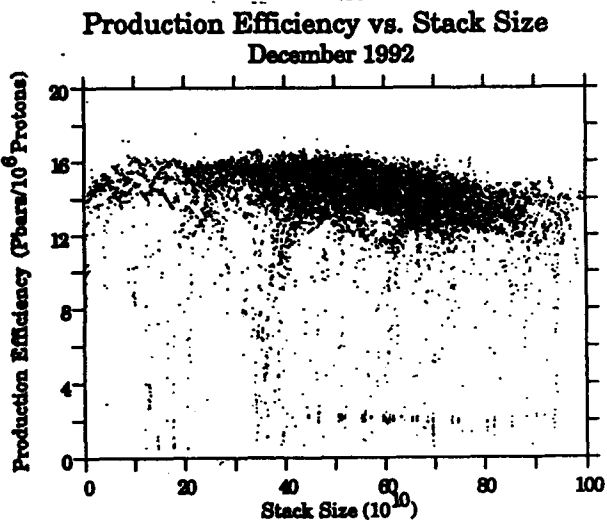
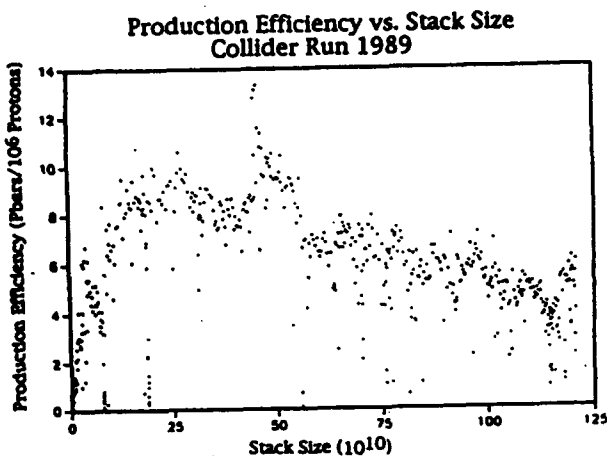


Figure 2. Comparison of production efficiency between 1989 collider run and present 1992-93 run.

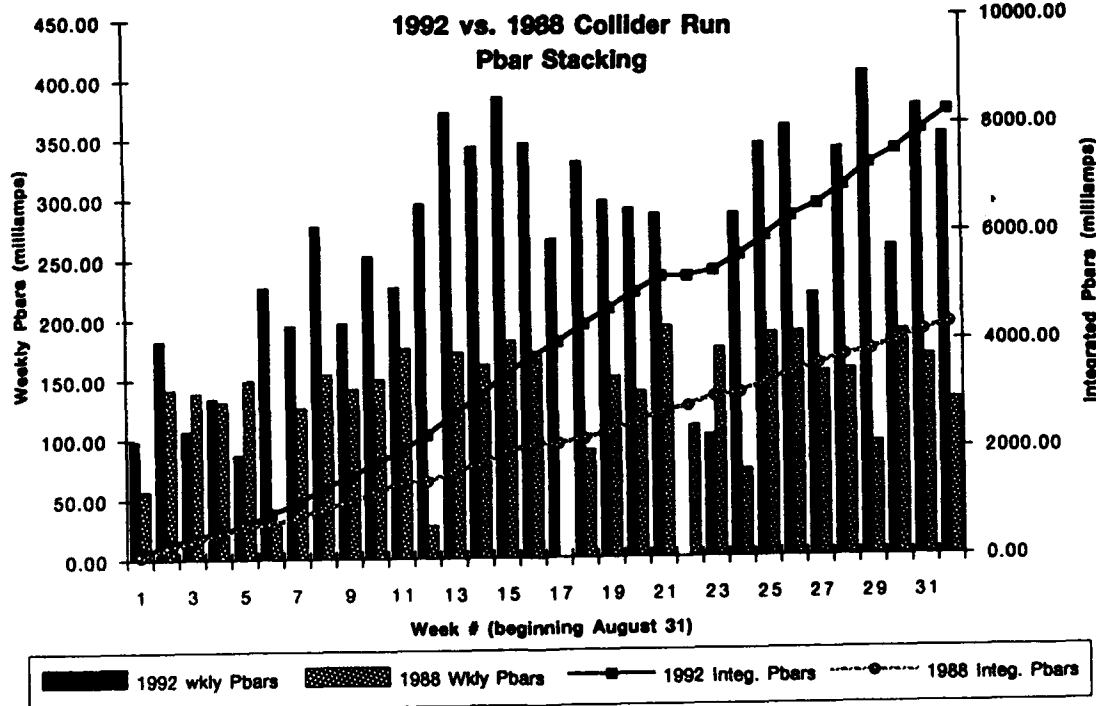


Figure 3. Comparison of stacking performance between present collider run and 1988 collider run.

The goal for peak luminosity in the Tevatron for the present collider run was 5×10^{30} . Due in large part to the ability to accumulate more antiprotons in a shorter time that goal was shattered. The present peak luminosity achieved is 9×10^{30} with new records being achieved weekly.

VI. ACKNOWLEDGMENTS

The improvements to the cooling system were a team effort by the members of the Antiproton source group, the mechanical support group, and other members of the Accelerator Division.

VII. REFERENCES

- [1] R.J. Pasquinelli, et al., "Stacktail Momentum Cooling in the Fermilab Antiproton Source", IEEE PAC 1987, Volume 2 pp. 1132-1134.
- [2] R.J. Pasquinelli, "Bulk Acoustic Wave (BAW) Devices for Stochastic Cooling Notch Filters, IEEE PAC 1991, Volume 3, pp. 1395-1397.
- [3] J. Petter, "Planar Slot Coupled Microwave Hybrids" U.S. Patent # 5,075,647. December 1991.
- [4] F. Voelker et al. "An Array of 1-2 GHz Electrodes for Stochastic cooling", IEEE Trans Nuclear Science NS-30, 1983, pp. 2262-2263
- [5] D. McGinnis et. al., "Design of 4-8 GHz Bunched Beam Stochastic Cooling Arrays for the Fermilab Tevatron", IEEE PAC 1991, Volume 3, pp.1389-1391.
- [6] EEsof Inc., "Touchstone", West Lake Village, CA.

vernier system is that the corrected energy error be less than the expected energy spread; choosing an rms error less than 1.0×10^{-5} gives less than 15% energy spread growth.

Because vernier phase errors appear like any other correlated phase error, the vernier must correct the average phase to under a bunch length; 0.05° is the design requirement chosen.

B. Basic Description the Energy Vernier

A schematic of the vernier scheme appears in Fig. (1). The gradient portion of the vernier system is based on a "spectrometer" that exists in the first CEBAF arc [3,4]. The beam produces a BPM signal at a location of high dispersion in the lattice. The signal is converted to base-band and compared to a BPM set voltage that is obtained from the computer control system. The difference signal is sent to the gradient set in the RF controls of two vernier cavities that have opposite coupler kicks.

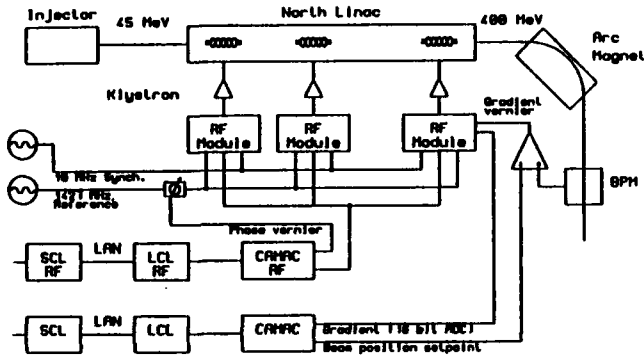


Figure 1 Schematic of Energy Vernier

The phase portion of the vernier system is based on a computer controlled electronic phase shifter. The low noise phase shifter shifts the phase of the phase line going to the individual linac sections. This has the effect of shifting the phases of all the cavities in the linac section with respect to the beam. Then, using the procedure outlined below, the correct offset phase is computed and updated through the computer control system.

II. VERNIER SYSTEM

A. Gradient Control

More detail on the feedback system is given in Fig. (2). The open-loop gain of the feedback system, G_{ol} , is

$$G_{ol} = N\alpha G_a G_d SD/E_0,$$

where N is the number of vernier cavities, α is the RF control module amplitude conversion ratio in MeV/V, G_a is any amplifier gain inside the loop, G_d is the differential gain of the position set amplifier, S is the sensitivity of the BPM in V/m offset, D is the dispersion at the BPM location in m, and E_0 is the total energy at the vernier. Numerical values consistent with the current CEBAF designs are $\alpha = 0.5$ MeV/V, $D = 10$ m, and $S = 140$ mV/mm.

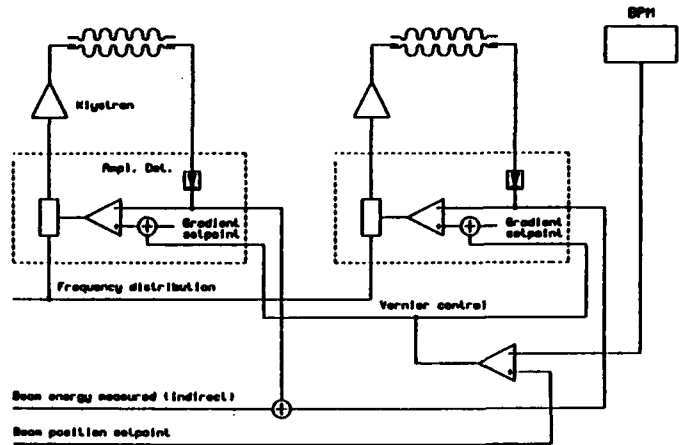


Figure 2 Detail on Gradient Vernier

The main noise source for this system is the energy error from the slow phase errors in the RF system, denoted by ΔE . As usual, the regulated energy gain error, δE , is suppressed relative to the noise by the closed-loop gain of the system,

$$\delta E = \frac{\Delta E}{(1 + G_{ol})}$$

The largest slow phase error that is expected is around 1.5° . To suppress the energy error generated by such a phase error to 1×10^{-5} requires an open-loop gain of 100. Such a gain is achieved with $G_a \cdot G_d \approx 40$ with two vernier cavities.

Two problems in this scheme might be anticipated. The first is that tilt misalignment of the vernier cavities would invalidate the approach. A tilt misalignment has the effect of mimicking the dispersion in measurements at a given BPM. A simple calculation gives

$$D_{eff} = D + M_{12}^1 \sin(\alpha_1) + M_{12}^2 \sin(\alpha_2)$$

where the M_{12} s are transfer matrix elements between the vernier cavities and the BPM and the α s are tilt misalignment angles [3]. However, if the dispersion is different, this has an effect only on the closed-loop gain of the feedback loop, which can always be increased as needed.

A more substantial problem is beam missteering which causes position errors in the BPM unrelated to the energy fluctuations. One way to solve this problem is to have an orbit lock before the spectrometer to guarantee that steering errors are corrected before entering the spectrometer. The high regulation of the arc dipole power supplies ensures that negligible error is introduced by the bend.

B. Phase Control

In more detail, the software phase control procedure is outlined in the flow chart in Fig. 3. After tuned beam is placed on the vernier BPM, the BPM reading is saved and used as an offset for subsequent calculations. The hardware and software control is activated. If the gradient control is activated, the beam remains fixed in the BPM.

The software can correct on the gradient control signal. The accuracy of the control is equal to the permitted range in the software loop. The response time of the system, at present limited by BPM acquisition time, is of order 5 sec.

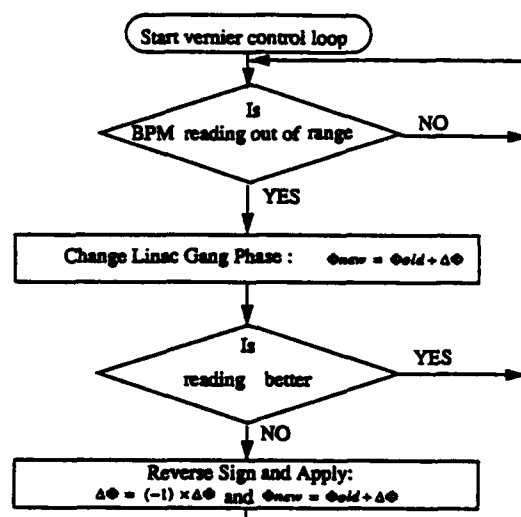


Figure 3 Software Phase Control Procedure for the Vernier

III. RESULTS

Initial tests were performed on both the hardware and software portions of the vernier system. Both tests were based on the BPM in the first spreader of the CEBAF accelerator. The test BPM was at a location where the dispersion is about 1.4 m.

In the hardware test, an energy modulation was introduced into the beam at cavity NL18-8. The square wave energy modulation had a frequency from 1 Hz up to 30 Hz. Cavities NL13-7 and NL13-8 were used as the vernier cavities. At 1 Hz modulation frequency, when the loop was closed the modulation was corrected by 20%. Saturation of a preamp in the feedback chain prevented higher loop gains from being achieved.

Two simple modifications of the hardware should yield substantial improvements on this result. First is to increase the amplitude conversion ratio in the RF control module. A factor of ten increase has been implemented in the vernier controls but not tested with beam. Secondly, when the arc is run in a high dispersion mode where $D \approx 10$, there should be another factor of seven improvement in gain, with no additional electronic noise.

A final factor of five should be possible by going to more sophisticated BPM front end electronics. Such electronics are being developed for this purpose, for fast orbit lock purposes, and also for fast time plots from the BPMs.

The software vernier was tested successfully. With the hardware system off, the software algorithm was used to correct the linac phase using the BPM output from the

same spreader BPM. The result was that the beam was held stably to under 0.5 mm by adjustments of the overall linac phase alone for periods of several minutes. With a dispersion of 1.4 m, this means the energy error was held to under 2.5×10^{-4} . The stability of the algorithm was also investigated by forcing the loop to go unstable by input parameter adjustment, and by restoring the correct input parameters. Energy errors up to 2.5×10^{-3} were induced and reproducibly corrected by the algorithm.

When the software is used to do energy corrections with the 10 m dispersion of the final system, the energy error will be under 2.5×10^{-5} , about a factor of two from the ultimate goal. It is thought that suitable optimisation of the feedback loop algorithm will allow us to achieve the final goal.

IV. CONCLUSIONS

A feedback system control scheme has been used for the energy vernier. The amplitudes of the vernier cavities are adjusted to produce a constant position in a BPM at a high dispersion point. To set the phase for minimum energy spread, a correlated phase shift is introduced into the section of linac to be phased, and the gradient signal in the vernier cavities responds with enough sensitivity to unambiguously determine the correct phase shift.

Prototype designs of the electronics for the energy vernier system have been completed. The resulting electronics have been tested with beam during the recent CEBAF run. The results were not entirely satisfactory because the dispersion at the BPM used in the studies was not as large as in the final system. Additionally, amplifier saturation limited the performance of the closed-loop system, but this problem should be solved during the next iteration, where the amplitude conversion constant of the RF controls is increased. After these improvements, achieving the energy specification will be possible.

The software phase correction algorithm was successfully implemented and tested on a low-dispersion BPM. The energy error was corrected to under 2.5×10^{-4} for drift times longer than a few seconds. When the experiment is repeated with a BPM at a higher dispersion location, the energy error will be under 2.5×10^{-5} .

More work needs to be done on orbit locking hardware and software to ensure that position offsets at the BPM are totally correlated with energy offsets.

V. REFERENCES

- [1] G. Kraft, J. Bisognano, and R. Miller, CEBAF-TN-0050 (1987).
- [2] G. A. Kraft, CEBAF-TN-90-0269 (1990).
- [3] G. A. Kraft and S. N. Simrock, CEBAF-TN-90-0280 (1990).
- [4] Y. Chao *et al.*, these proceedings.

A Digital Approach For Phase Measurement Applied To Delta-t Tuneup Procedure

G. Roberto Aiello
Superconducting Super Collider Laboratory*
2550 Beckleymeade, MS-4005, Dallas, TX 75237 USA

Abstract

Beam energy and phase in a Linac are important parameters to be measured in order to tune the machine. They can be calculated by the time of flight of a beam bunch over a known distance between two locations, and by comparing the phase of a cavity to the beam phase. The phase difference between two signals must be measured in both cases, in order to get the information required. The electronics to be used for this measurement must meet stringent requirements: high bandwidth, good accuracy and resolution have always been a challenge for classical analog solutions. A digital approach has been investigated, which provides a good resolution, accuracy independent on the phase difference value, good repeatability and reliability. Numerical analysis have been performed, showing the system's optimal performance and limitations. A prototype has been tested in the laboratory, which confirm the predicted performance, and proves the system's feasibility.

I. INTRODUCTION

The phase difference between the beam and the RF reference must be measured in order to get information for delta-t and phase scanning. Purpose of the delta-t measurement is to calculate the time of flight between two locations, to be compared with the model. This is done by switching a cavity OFF and ON and by calculating the difference between the two measurements. When two of these measurements are taken at two different locations, the difference between the two measured values gives information about the time of flight. The time can be then calculated using the following equation:

$$t = \frac{\Delta\phi}{\omega} \quad (1)$$

where $\Delta\phi = \Delta\phi_1 - \Delta\phi_2$, $\Delta\phi_1 = \phi_{1\text{ OFF}} - \phi_{1\text{ ON}}$, and $\Delta\phi_2 = \phi_{2\text{ OFF}} - \phi_{2\text{ ON}}$, with ϕ_{OFF} and ϕ_{ON} the phase difference between beam and RF reference at the locations 1 and 2, respectively when the cavity is OFF and ON.

Purpose of the phase scanning measurement is to changed the phase of the cavity respect to the RF reference, and to measure the phase variation of the beam with respect to the same reference. Since only phase differences are needed, none of the measurements requires absolute phase knowledge. The phase measurements requirements are shown in table 1.

Analog solutions have been used so far for these applications [1,2]. The problems connected with an analog system are well known: phase shifter linearity and temperature stability,

limiter phase linearity, phase detector dynamic range, video bandwidth etc... All these reasons induced the author to find an alternative solution which didn't present these problems.

Table 1
Phase measurement requirements.

Item	Value
Phase dynamic range	360 deg
Resolution (minimum phase difference)	0.5 deg rms
Repeatability (respect to RF reference)	0.5 deg rms
RF frequency	428 MHz
Beam current dynamic range	5 - 50 mA
Sample time	5 μ s - 35 μ s
Repetition rate	10 Hz

The architecture shown in figure 1 solves the problems given by limiters and phase shifter, and realizes a 360 degrees phase detector with 200 KHz video bandwidth. The video bandwidth is limited by the technology used for this particular system, given the requirements. The current technology would allow to reach more than 2 MHz video bandwidth.

II. GENERAL ARCHITECTURE

The two input signals are undersampled and the phase difference is calculated using a curve fitting algorithm.

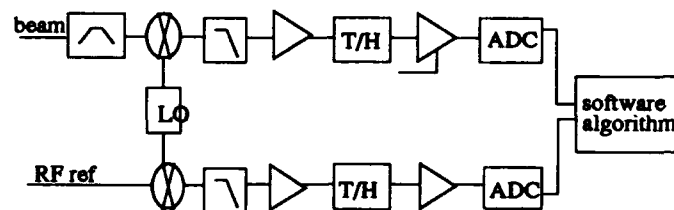


Figure 1. General architecture.

The main harmonic is selected and the signal is downconverted to a frequency compatible with the track and hold input analog bandwidth. The ADC's sampling rate is chosen in order to get a reasonable number of points in the measurement time interval. The software curve fits the two sampled signals with the best sinewave [3], and calculates the phase of the two signals. The phase difference is then computed.

The 428 MHz signals are downconverted to 60 MHz, the track and hold used is the Analog Devices AD9100, and the ADC is the Datel ADS118, a 12 bits ADC whose maximum sampling rate is 5 MHz. Two RF amplifiers are installed in front of the track and holds in order to provide the required

*Operated by the University Research Association, Inc., for the U.S. Department of Energy under contract No. DE-AC35-89ER40486

amplitudes in input. A variable gain amplifier after the track and hold in the beam signal channel compensates for the beam current fluctuations. The timing diagram of the sampling process is shown in figure 2.

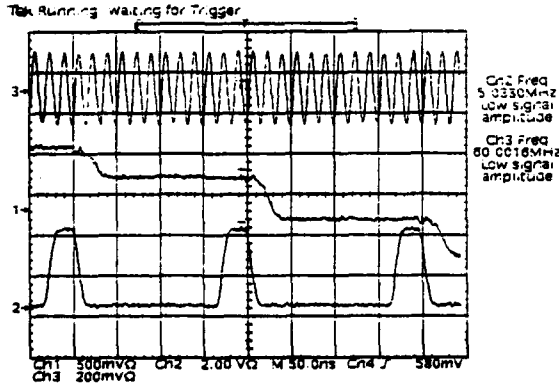


Figure 2. Timing diagram of the sampling process. Channel 3: input signal, channel 1: output data from the track and hold, channel 2: ADC sampling clock.

III. SOFTWARE ALGORITHM

A curve fitting algorithm fits the four parameters V_o , V_a , f_{in} and ϕ of a sinewave of form given in (2), by minimizing the error between the data points and the fit with successive approximations.

$$V_{in}(n) = V_o + V_a \cos(2\pi f_{in} n T_{sample} + \phi) \quad (2)$$

This expression can be rewritten as:

$$V_{in}(n) = V_o + V_a \cos(\omega_{in} T_n + \phi) \quad (3)$$

and using elementary trigonometric relations:

$$x_n = A \cos(\omega_{in} T_n) + B \sin(\omega_{in} T_n) + C \quad (4)$$

with $A = V_a \cos(\phi)$, $B = -V_a \sin(\phi)$ and $C = V_o$.

If the input frequency is known, eq. (4) can be rewritten as:

$$x_n = A \alpha_n + B \beta_n + C \quad (5)$$

with $\alpha_n = \cos(\omega_{in} T_n)$ and $\beta_n = \sin(\omega_{in} T_n)$, where the parameters to fit now are A, B, C. The advantage of this form respect to (2) is that there is a close form solution given by the algorithm described below.

Given a data record y_n of M samples, the total residual error ε of the measured data relative to the fit sine wave is:

$$\varepsilon = \sum_{k=1}^M (y_k - x_k)^2 = \sum_{k=1}^M (y_k - A \alpha_k - B \beta_k - C)^2 \quad (6)$$

Setting the partial derivatives with respect to the parameters being fit to zero gives:

$$\begin{cases} 0 = \frac{\partial \varepsilon}{\partial A} = -2 \sum_{k=1}^M (y_k - A \alpha_k - B \beta_k - C) \alpha_k \\ 0 = \frac{\partial \varepsilon}{\partial B} = -2 \sum_{k=1}^M (y_k - A \alpha_k - B \beta_k - C) \beta_k \\ 0 = \frac{\partial \varepsilon}{\partial C} = -2 \sum_{k=1}^M (y_k - A \alpha_k - B \beta_k - C) \end{cases} \quad (7)$$

with some algebra:

$$\begin{cases} \sum_{k=1}^M y_k \alpha_k = A \sum_{k=1}^M \alpha_k^2 + B \sum_{k=1}^M \alpha_k \beta_k + C \sum_{k=1}^M \alpha_k \\ \sum_{k=1}^M y_k \beta_k = A \sum_{k=1}^M \alpha_k \beta_k + B \sum_{k=1}^M \beta_k^2 + C \sum_{k=1}^M \beta_k \\ \sum_{k=1}^M y_k = A \sum_{k=1}^M \alpha_k + B \sum_{k=1}^M \beta_k + C M \end{cases} \quad (8)$$

The fit parameters are given by the solution to the linear equation $Y = UX$, which is $X = U^{-1}Y$, where:

$$X = \begin{bmatrix} A \\ B \\ C \end{bmatrix}; Y = \begin{bmatrix} \sum_{k=1}^M y_k \alpha_k \\ \sum_{k=1}^M y_k \beta_k \\ \sum_{k=1}^M y_k \end{bmatrix}; U = \begin{bmatrix} \sum_{k=1}^M \alpha_k^2 & \sum_{k=1}^M \alpha_k \beta_k & \sum_{k=1}^M \alpha_k \\ \sum_{k=1}^M \alpha_k \beta_k & \sum_{k=1}^M \beta_k^2 & \sum_{k=1}^M \beta_k \\ \sum_{k=1}^M \alpha_k & \sum_{k=1}^M \beta_k & M \end{bmatrix} \quad (9)$$

The phase is then calculated by:

$$\phi = \arctan\left(-\frac{B}{A}\right) + [1 - \text{sign}(B)] \frac{\pi}{2} \quad (10)$$

IV. PERFORMANCE

The results of the measurements in the laboratory are shown in figures 3-6, the measurement parameters in table 2. The phase was changed with a programmable delay line, and the value calculated by the system was compared with the phase measured with the Vector Voltmeter HP 8508. The Vector Voltmeter accuracy at the measurement's conditions is better than 0.4 deg. The absolute phase error versus the phase measured with the Vector Voltmeter is shown in figure 3.

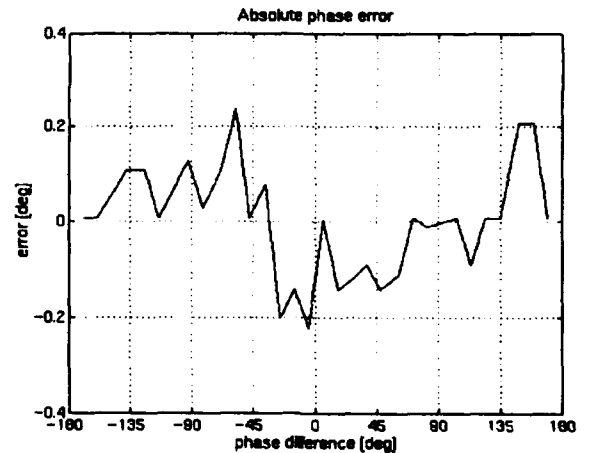


Figure 3. Absolute error versus phase difference.

The resolution of the system is shown in figure 4. Fifty measurements were taken at different phase angles, and the

standard deviation calculated. These values limit both the system resolution and repeatability.

Table 2

Laboratory measurement parameters.

Item	Value
Input signal frequency	60 MHz
ADC sampling rate	5.04 MHz
Input signal	-17 dBm
ADC dynamic range	11 bits
Number of samples	25
Number of loops	50

The measurement parameters are specified by the requirements at table 1. The number of bits and number of samples are the optimized values experimentally determined, compared with the numerical simulation.

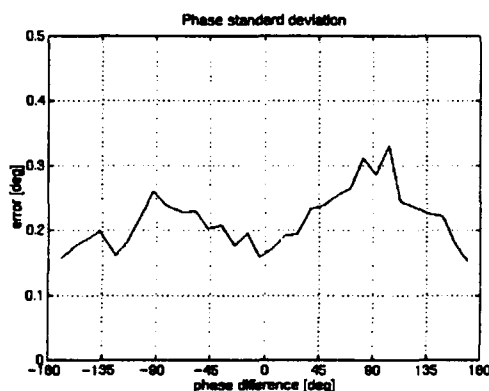


Figure 4. Standard deviation versus phase difference

The effect of the number of bits on the resolution is shown in figure 5, where experimental data are compared with the results of the simulation. The data points don't follow the theoretical plot, because of the noise on the ADC module used for the test. The digitized output shows 5 counts rms, when the analog input is terminated to ground.

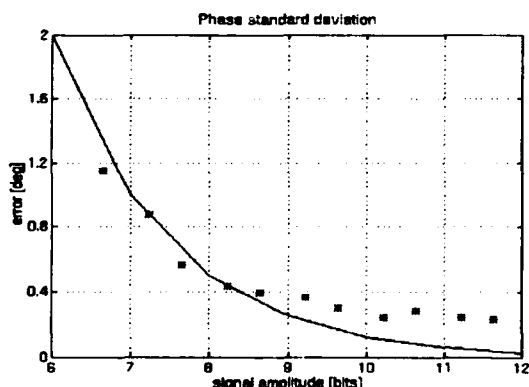


Figure 5. Standard deviation versus number of bits. Experimental data are compared to the simulation.

The algorithm chosen to calculate the phase proved to be very robust. The frequency value used for the curve fitting

doesn't need to be determined better than 1%, and the sampling clock jitter is also not so critical, as shown in figure 6.

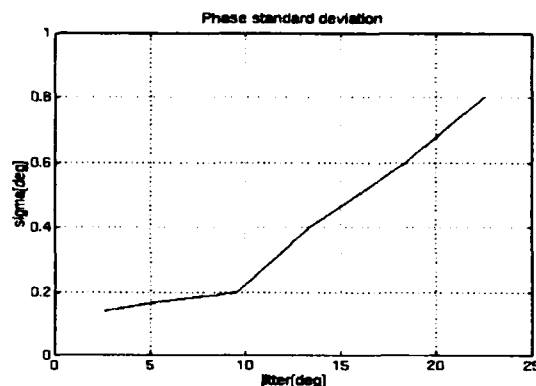


Figure 6. Phase standard deviation versus sampling clock jitter, expressed in degrees of the input frequency (60MHz).

The summarized system performance, shown in table 3, fully meet the system requirements. A better choice of the ADC module is expected to improve the system repeatability.

Table 3

Phase measurement performance.

Item	Value
Phase difference dynamic range	360 deg
Phase difference absolute accuracy	< 0.25 deg
Phase difference standard deviation	< 0.3 deg rms
Input signal dynamic range	-17 -52 dBm
Sample time	> 5 μ s

V. ACKNOWLEDGEMENTS

The author is grateful to Dave Beechy and G.G. Nadkarni for many useful discussions, and Mike Gargiulo and Tony Hawkins for their help in the laboratory.

VI. CONCLUSION

A digital approach for phase measurement has been investigated, which provides good resolution, accuracy independent of the phase difference value, good repeatability and reliability. The system doesn't present problems typical of analog solutions. Numerical analysis have been performed, showing the system's optimal performance and limitations. A prototype has been tested in the laboratory, which confirms the predicted performance, and proves the system's feasibility. This system will be installed in the SSC Linac starting October 1993.

VII. REFERENCES

- [1] K. R. Crandall, "The At Tuneup Procedure for the LAMPF 805-MHz Linac", LA-6374-MS (1979).
- [2] J.D.Gilpatrick, R.E.Meter, F.D.Wells, J.F.Power, R.E.Shafer, "Synchronous Phase and Energy Measurement System for a 6.7 MeV H- Beam", *Linac Conf. Proc.*, 134 (1988)
- [3] IEEE Std. 1057, "Digitizing Waveform Recorders" (1989)

RF Feedback for Beam Loading Compensation in the SLC Damping Rings*

P.Krejčík, P.Corredoura, M.Minty, R.Siemann, R.Tighe
Stanford Linear Accelerator Center
Stanford University, Stanford, California 94305

F.Pedersen
CERN, CH-1211 Switzerland

Abstract

An RF feedback around the cavities and klystron has been added to the SLC Damping Rings to provide stability under changing beam loading conditions. The beam loading changes in the cavity as a result of programming the RF voltage during the beam store time. The RF voltage is lowered to control the onset of bunch length instabilities, but without RF feedback the beam becomes unstable in the Robinson zero frequency mode. The steady state analysis of the beam loading with and without feedback is presented together with a description of the hardware implementation. Operational experience with the system during SLC running is described.

I. INTRODUCTION

The RF system for the SLC damping rings comprises one 60 kW klystron per ring, driving two two-cell cavities through a circulator and a magic-T. At a constant RF voltage totaling 1 MV nominally for the ring, the degree of RF over-coupling is optimized for RF matching of the klystron to the combined RF load of the cavity and beam at the design intensity of two bunches of $5 \cdot 10^{10}$ particles each. In order to control the onset of turbulent bunch lengthening and the associated "sawtooth" instability it is desirable to program the RF voltage during the beam store time[1]. The RF voltage is ramped down to a low value shortly after injection to prevent the bunch length from damping below the instability threshold.

We found that, when two bunches were present in the ring, it was not possible to ramp the voltage down without a beam loading or "Robinson like" instability occurring. This arises because the cavities are tuned for an optimum loading angle of zero when the voltage is at its maximum, but are then far from

optimum at low voltages. With the cavity tuning angle fixed during the beam store time the beam rapidly goes unstable as the condition is reached where the beam power exceeds the cavity dissipation power.

To overcome this limitation we have implemented a direct RF feedback system of a type also used in other beam loading dominated accelerators[2,3]. This feedback compensates the cavity loading to the extent of the maximum gain permitted in the feedback system and has allowed the programmable voltage ramp to operate down to much lower levels.

II. BEAM LOADING STABILITY CRITERIA

The stability analysis of the cavity and klystron with beam is based upon a model of the cavity as a resonator with a fundamental mode only, and driven by two current sources representing the generator (the klystron) and the beam, fig. 1. Using the notation in reference [5], these currents can be represented as phasors, as in fig. 2. The impedance angle, ϕ_Z , is determined by the cavity geometry, i.e. the frequency to which the cavity is tuned w.r.t. the RF. The beam phase angle, ϕ_B , is determined by the synchronous phase condition for the particle. In practice, we tune the cavity on the basis of the measured loading angle, ϕ_L , between the klystron current and the cavity voltage. The cavity tune that results will thus be a function of the beam current, I_B , and the generator current, I_G , supplied by the klystron.

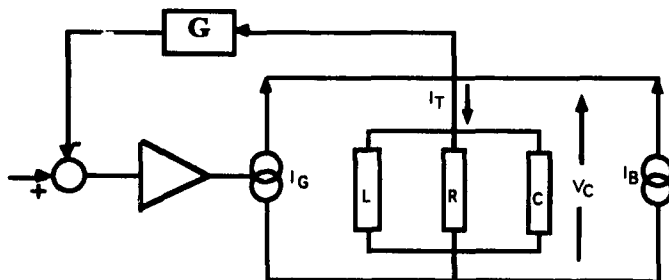


Fig. 1. Simple resonant cavity model driven by a generator and a beam current. RF feedback appears as a transform G of the cavity voltage summed with the klystron drive signal.

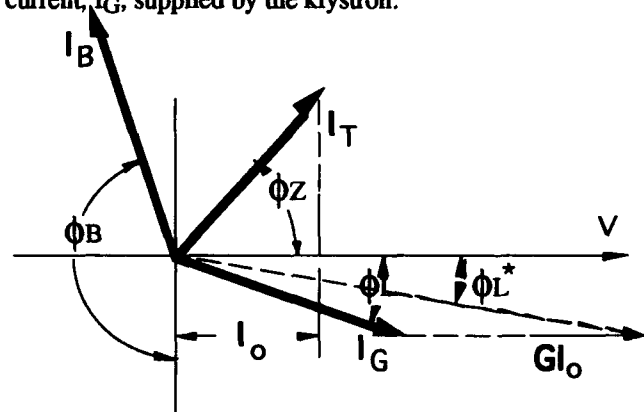


Fig. 2. The current from the generator, the beam and the total current are represented as phasors, referenced to the cavity voltage. The feedback contributes a term $G I_0$.

The beam loading ratio is defined as $Y = I_B / I_0$, where I_0 is the real part of the total current in the cavity, I_T , i.e. the component of I_T in phase with the cavity voltage, V . The

* Work supported by Department of Energy Contract DE-AC03-76SF00515.

vector relationship between these phasors can be described by the following:

$$I_G = \frac{I_0(1 + Y \sin \phi_B)}{\cos \phi_L} \quad (1)$$

$$\tan \phi_L = \frac{\tan \phi_Z - Y \cos \phi_B}{1 + Y \sin \phi_B} \quad (2)$$

The stability criterion derived by Robinson[4] can be expressed[5] as:

$$\frac{2 \cos \phi_B}{Y} < \sin 2\phi_Z < 0 \quad (3)$$

These stability boundaries are shown graphically in fig. 3, where the shaded region for positive ϕ_Z leads to antidamping of the synchrotron oscillations of the bunches; and the left hand shaded region corresponds to unstable exponential growth as the beam loading limit is exceeded. The actual working point on this diagram is determined by the choice of loading angle. Superimposed on fig. 3 is a curve, derived from eqn (2) representing the locus of points for which we choose ϕ_L to be zero, indicating how ϕ_Z must change for increasing beam loading. These curves are calculated for our nominal 1 MV RF voltage for which the synchronous phase is close to 170° .

If the voltage is ramped down to 250 kV during the store the synchronous phase changes to 140° and the stability limit drops as shown by the lighter shaded region in fig. 3. In our particular mode of operation the cavity tune stays constant as the voltage is ramped down. For an intensity of $2 \times 3.5 \cdot 10^{10}$ eqn (2) indicates that the loading angle changes to 36° as the voltage is ramped from 1 MV to 250 kV. The curve for $\phi_L = 36^\circ$ in fig. 3 confirms that we are far beyond the limits of stability with our fixed cavity tune. The ramp occurs on a time scale of milliseconds during which it is impossible to retune the cavity back to a more favorable loading angle. Instead we reestablish stability by implementing direct RF feedback through the klystron.

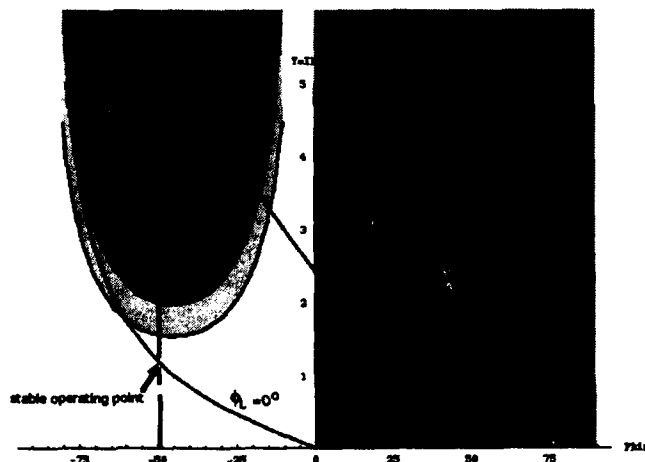


Fig. 3. Beam loading stability limit vs. impedance angle.

III. DIRECT RF FEEDBACK: GAIN VS. STABILITY

Direct RF feedback requires feeding back a portion of the cavity voltage and summing it with the drive signal to the klystron. The group delay around this loop determines the

maximum gain at which the loop can operate stably. To see this we look at the transformed impedance of the cavity plus feedback. The complex impedance of the resonator in fig. 1, tuned to a frequency ω_n and with a loaded quality factor Q_L and shunt impedance R_{SH} , is:

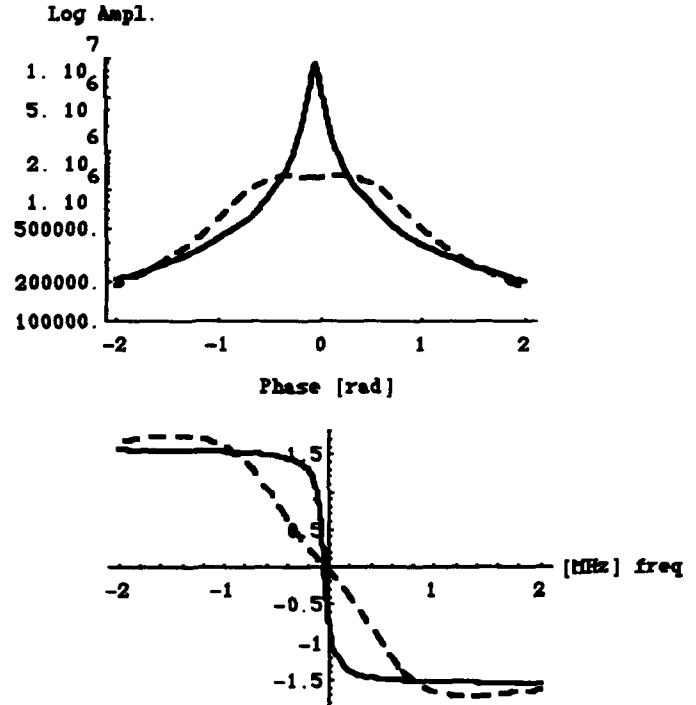


Fig. 4. Modelled phase and amplitude for the cavity impedance, with (dashed) and without (solid) feedback.

$$Z(j\omega) = \frac{j\omega \cdot \omega_n \frac{R_{SH}}{Q_L}}{(j\omega)^2 + j\omega \cdot \frac{\omega_n}{Q_L} + \omega_n^2} \quad (4)$$

This impedance function is shown in fig. 4 for our damping ring parameters.

The feedback transfer function, $G(j\omega)$, is given the product of a gain G_0 with a transductance $1/R_{SH}$ and a delay ΔT :

$$G(j\omega) = \frac{G_0}{R_{SH}} \cdot e^{-j\omega\Delta T} \quad (5)$$

The closed loop transfer function gives the impedance of the cavity plus feedback, as seen by the beam:

$$Z'(j\omega) = \frac{Z(j\omega)}{1 + G(j\omega)Z(j\omega)} \quad (6)$$

which is also plotted in fig. 4 for a group delay of 300 nS and a gain $G_0=6$.

At the cavity frequency, ω_n , we have $Z(j\omega_n)=R_{SH}$ and $G(j\omega_n)=G_0/R_{SH}$ so that the effective impedance is reduced as $Z'=Z/(1+G_0)$. The real part of the cavity current, I_0 , increases by $(1+G_0)$. The effect on our stability diagram in fig. 3 is to raise the boundary of the shaded, left hand zone by the amount $(1+G_0)$.

The effective impedance can not be reduced indefinitely by increasing the gain G_0 , as can be seen by applying the Nyquist

criterion to the magnitude of the open loop transfer function, which is required to be greater than -1,

$$|G(j\omega)Z(j\omega)| < 1 \quad (7)$$

Allowing for a 45° phase margin this leads to the limit:

$$1 + G_o < \frac{\pi Q_L}{2\omega_n \Delta T} \quad (8)$$

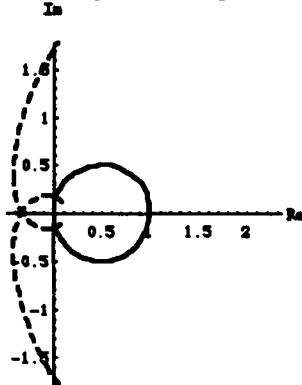


Fig. 5. Nyquist plot for the cavity impedance in fig. 4, illustrating the stability limit with feed back (dashed).

IV. DIRECT RF FEEDBACK IMPLEMENTATION

The klystron is located in the vault with the RF cavities so the signal path lengths are reasonably short for the feedback loop. The layout is shown schematically in fig. 5. The cavities have a two-cell structure which have a non-accelerating 0-mode close in frequency to the accelerating π -mode of the cavities. The cavity probe signals from the two cells are therefore combined with phase shifters and attenuators to ensure there is not excessive gain at the unwanted mode. The signals from the two cavities are further combined with appropriate phase shift and attenuation. A common phase shifter and attenuator in the loop is remotely operable through the SLC control system to tune the loop in the presence of beam. The measured open and closed loop response of the loop are shown in fig. 6.

V. PERFORMANCE WITH BEAM

The optimum setting for the feedback phase shifter is found empirically by observing the beam stability. Typically, an upper and a lower setting of the phase shifter will be found at which the beam is barely stable allowing us to find the midpoint of the stable range. In our analysis above, changing the phase shifter corresponds to a rotation about the origin of the dashed Nyquist curve in fig. 5. As the curve rotates it soon intercepts the stability boundary at -1. Increasing the gain G_o translates the curve to the left so we find that there is less range for rotation before hitting the boundary. As the stability constraint for the maximum gain depends on ΔT in eqn (8), we have worked on improving the contribution to the group delay from the klystron. This was done by changing the klystron cavities for broader bandwidth, at the expense of a reduced klystron gain.

With RF feedback it is now possible to operate the damping ring comfortably with a ramp from 1 MV down to 250 kV with a beam intensity of two bunches of $3.5 \cdot 10^{10}$ particles per bunch. This enhancement to the beam loading limitation in the rings is consistent with the predicted analysis above.

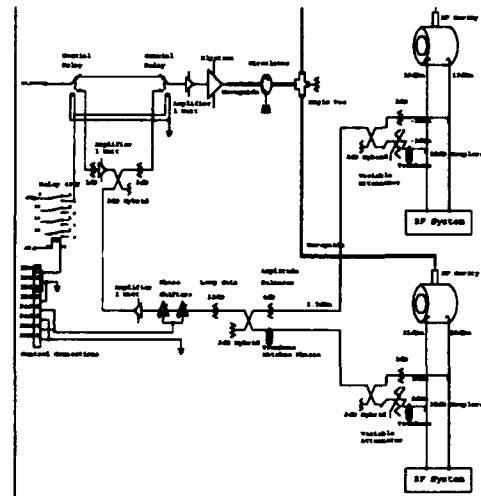


Fig. 5 Schematic of the direct RF feedback implemented around the klystron and two damping ring cavities.

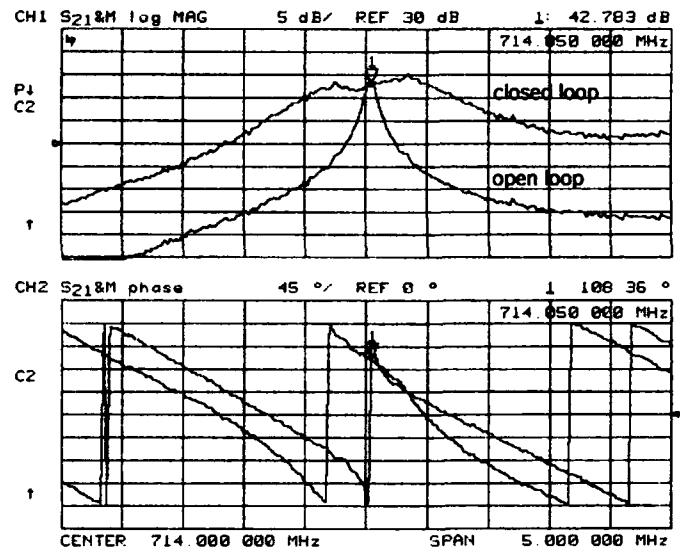


Fig. 6. Measured open and closed loop response of the system.

The limitations imposed by saturation effects of the klystron have not been discussed here. If the program gap voltage is too high for any given current the nonlinearity of the klystron drives the loop unstable.

The reduction in effective cavity impedance also reduces the damping rate of 0-mode dipole bunch oscillations, so some additional feedback is called for to damp injection transients.

VI. REFERENCES

- [1] P. Krejcik et al, "High Intensity Bunch Length Instabilities in the SLC Damping Rings", These proceedings.
- [2] F. Pedersen IEEE Trans. Nucl. Sci. NS-32, p.2138, 1985.
- [3] D. Boussard IEEE Trans. Nucl. Sci. NS-32, p.1852, 1985.
- [4] K.W. Robinson CEA Report no. CEAL-1010, 1964.
- [5] F. Pedersen IEEE Trans. Nucl. Sci. NS-22, p.1906, 1975.

Simulation and Analysis of RF Feedback Systems on the SLC Damping Rings

M. Minty, T. Himmel, P. Krejcik, R.H. Siemann, R. Tighe

Stanford Linear Accelerator Center, Stanford University, Stanford CA 94305 *

Abstract

The rf system of the SLC Damping Rings has evolved since tighter tolerances on beam stability are encountered as beam intensities are increased. There are now many feedback systems controlling the phase and amplitude of the rf, the phase of the beam, and the tune of the cavity. The bandwidths of the feedback loops range from several MHz to compensate for beam loading to a few Hz for the cavity tuners. To improve our understanding of the interaction of these loops and verify their expected behavior, we have simulated their behavior using computer models. A description of the models and the first results are discussed.

1. Introduction

During the 1992 SLC/SLD run, accelerator operation became sensitive to the microwave instability¹ at beam currents above 3×10^{10} particles per bunch. To avoid the onset of bunch lengthening at higher currents, an rf voltage ramp was implemented. However, the depth of the ramp was limited by a Robinson-like instability^{2,3}, which was corrected for using direct rf feedback^{3,4}. With these modifications, the parameter space has become more complex. Operating conditions must be adjusted and optimized such that the rf system operates stably under varying conditions. In particular, the system should be insensitive to injection phase errors and intensity jitter, repetition rate changes, and effects arising from klystron saturation.

Effects of heavy beam loading and rf feedback have been studied in detail by Pedersen^{2,3}, who has also studied the effect of adding more feedback loops. The dynamics become more complicated when the nonlinear effects of klystron saturation are considered. The purpose of our simulations is to understand the stability of the damping ring rf system with multiple feedback loops and a partially saturated klystron.

2. System Overview

A block diagram of the rf system is shown in Fig. 1. The coupling between the beam and cavities increases as the beam current is raised. Two cavities are driven by a single klystron. Surrounding the cavities and klystron are various feedback loops. The cavity voltage is regulated using the gap voltage control feedback. Other loops include a beam loading feedback, a beam phase loop, a klystron phase compensation loop, a synchrotron oscillation zero mode feedback, and cavity tuner loops.

The rf system is modelled by calculating the dynamics of the beam cavity interaction. These equations along with measured loop characteristics and klystron saturation data are then incorporated into numerical integration programs such as Matrix-x⁵ and Simulink⁶. These algorithms use state space representations of the system to solve the differential equations. The system can be analyzed in both the time and frequency domains.

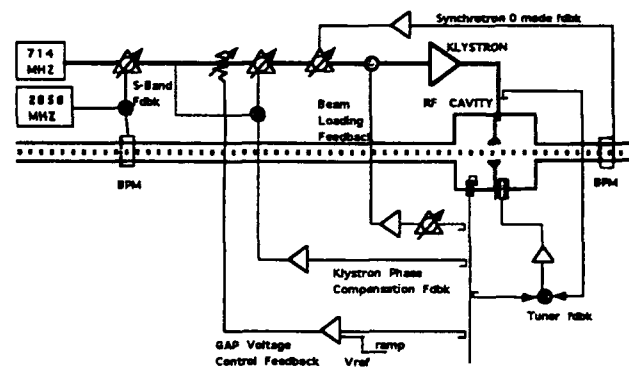


Figure 1. SLC damping ring rf system.

3. System Modelling

We first discuss the beam cavity interaction and the klystron. We then consider the various feedback loops.

A. Beam Cavity Interaction

The equations of motion for the beam cavity interaction are mixed to baseband for computational efficiency. Each cavity is modelled as a parallel RLC circuit. The dynamics are described by

$$\begin{aligned} \frac{dv_r}{dt} + \frac{1}{2Q} \frac{dv_i}{dt} + \frac{v_r}{2Q} \omega_{rf} + v_i(\omega_0 - \omega_{rf}) &= \frac{R\omega_{rf}}{2Q} I_r \\ \frac{dv_i}{dt} - \frac{1}{2Q} \frac{dv_r}{dt} + \frac{v_i}{2Q} \omega_{rf} - v_r(\omega_0 - \omega_{rf}) &= \frac{R\omega_{rf}}{2Q} I_i \end{aligned} \quad (1)$$

Here v_r and v_i are the real and imaginary parts of the cavity voltage and the approximation $\frac{dv}{dt} \ll v\omega_{rf}$ has been made. Also $Q = 6860$ is the loaded quality factor of the cavities, $\omega_{rf} = 2\pi \times 714$ MHz is the angular drive frequency, $R = 2.5$ M Ω is the shunt impedance, I_r and I_i are the real and imaginary parts of the total current, $I_t = I_g + I_b$, where I_g is the generator and I_b is the beam current. The resonant frequency, ω_0 , of the cavity is given by $\frac{\omega_0}{\omega_{rf}} = [1 - \frac{1}{2Q} \tan \phi_z]^{-1}$, where ϕ_z is the impedance angle between the total current and the cavity voltage.

*Work supported by the Department of Energy Contract DE-AC03-76SF00515

The equations for the beam current, expressed in polar coordinates, are $|I_b| = 2I_{dc}$, where I_{dc} is the dc beam current and, for the nonlinear phase equation,

$$\frac{d^2 \phi_b}{dt^2} = -\frac{\eta \omega_{rf}}{E_0 T_0} [V \sin \phi_b - (U_0 + U_{hom})], \quad (2)$$

in which ϕ_b is the beam phase angle, ϕ_c is the cavity phase angle, $\eta = -0.015$ is the slip factor, $E_0 = 1.19$ GeV is the beam energy, $T_0 = \frac{2\pi}{\omega_{rf}} = 117.65$ ns is the revolution period, and U_0 and U_{hom} are respectively the energy losses due to synchrotron radiation and higher order modes.

An example of the time dependence of the beam phase is shown in the insert of Fig. 2. With the impedance angle ϕ_z equal to -20 degrees, the damping time τ of the oscillations is compared with analytic calculation.

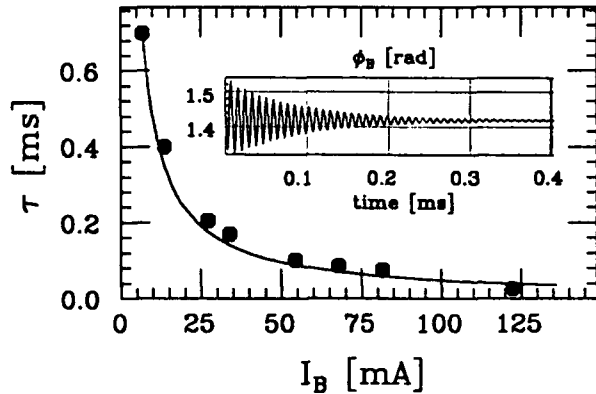


Figure 2. Damping time of phase oscillations as a function of beam current with $\phi_z = -20$ deg. A simulation output of the beam phase for $I_B = 68$ mA is also shown.

B. Nonlinear Klystron

To minimize the bunch length at extraction we operate the klystrons in the nonlinear region near saturation. The measured saturation characteristics of the klystron are shown in Fig. 3. The klystron becomes nonlinear in gain at an output power near 30 kW or at a cavity voltage of 550 kV when tuned for optimum coupling. In addition, the klystron produces a power dependent phase offset for output powers greater than 10 kW. These data are input into the model in the form of interpolation tables. The klystron bandwidth (5.3 Mhz at 3 dB) is modelled at baseband as a third order lowpass Butterworth filter. A 240 ns delay is also included. To compute the output current I_g we convert the input voltage V_{in} into input power P_{in} , use the saturation data to determine the output power P_{out} , and take into account the coupling to the cavity ($\beta = 2.5$). The transconductance, S , for which $I_g = SV_{in}$, is

$$S = \sqrt{\frac{4\beta}{(1+\beta)^2} \frac{1}{2R(50\Omega)}} \left(\frac{P_{out}}{P_{in}} \right) \quad (3)$$

The phase shift resulting from driving the klystron to saturation is also calculated from the input power.

The open loop Bode plot obtained by modulating the klystron input and detecting the amplitude controller output (see below) is shown in Fig. 4 and is compared with

online measurement. From the figure can be seen the additive effects of the cavities and the klystron as well as the controller and rf attenuator on the system gain and phase.

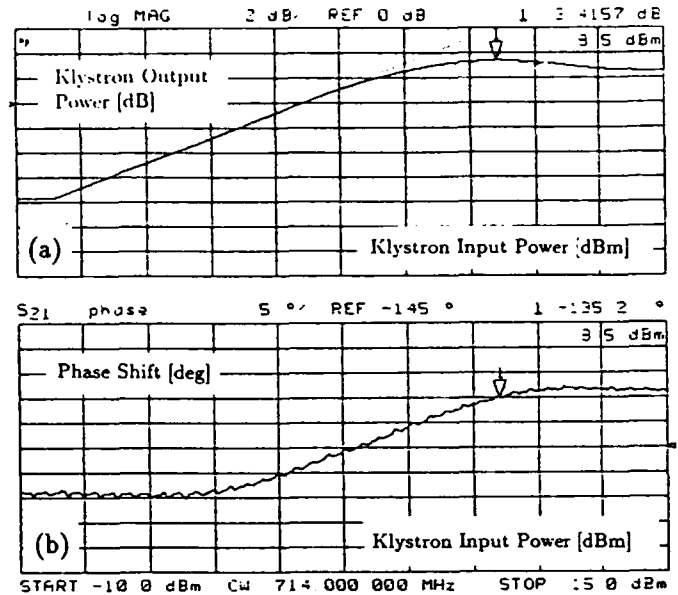


Figure 3. Measured gain (fig. 3a) and phase shift (fig. 3b) of klystron as a function of input power.

C. Feedback Loops

Beam Loading Feedback

The rf feedback loop is described in detail in Ref. 4. When this feedback is implemented, the Q of the cavity is reduced by $1 + G_0$, where G_0 is the feedback gain. In the model, we form the vector sum of the two cavity voltages and allow an overall phase shift of the feedback signal. A 120 ns delay is included for the waveguides and cable delays. Simulations to determine the threshold for unstable exponential growth of phase oscillations agree well with theory.

Amplitude Feedback Loop

The amplitude feedback loop is used to regulate the voltage ramp during the store cycle. Unlike the rf feedback, which uses the vector sum of the cavity voltages as the feedback signal, the amplitude loop feeds back on the sum of the magnitude of the two cavity voltages. The measured 3 dB bandwidth of the controller is about 600 Hz. A first order transfer function characterizes its frequency response. In addition, we model a series rf attenuator as a first order transfer function with the measured 3 dB bandwidth of 40 kHz. When the rf feedback loop is closed, the gain in the amplitude feedback is raised by $1 + G_0$ accordingly.

Phase Feedback Loop

The phase loop is used to lock the ring rf at extraction to the linear accelerator rf. We model it as a constant gain bandwidth amplifier and use a first order transfer function with a measured 3 dB bandwidth of 30 Hz.

Klystron Compensation Feedback Loop

This phase feedback loop is supposed to compensate for

slow variations in the AC power source for the klystron drive. The measured 3 dB bandwidth is about 10 Hz. Cavity Tuner Loop

The very slow (≤ 1 Hz) tuner loop is used primarily to control the initial conditions for the loading angle ϕ_l . The phase angle ϕ_z between the cavity and generator is fed back through a second order transfer function.

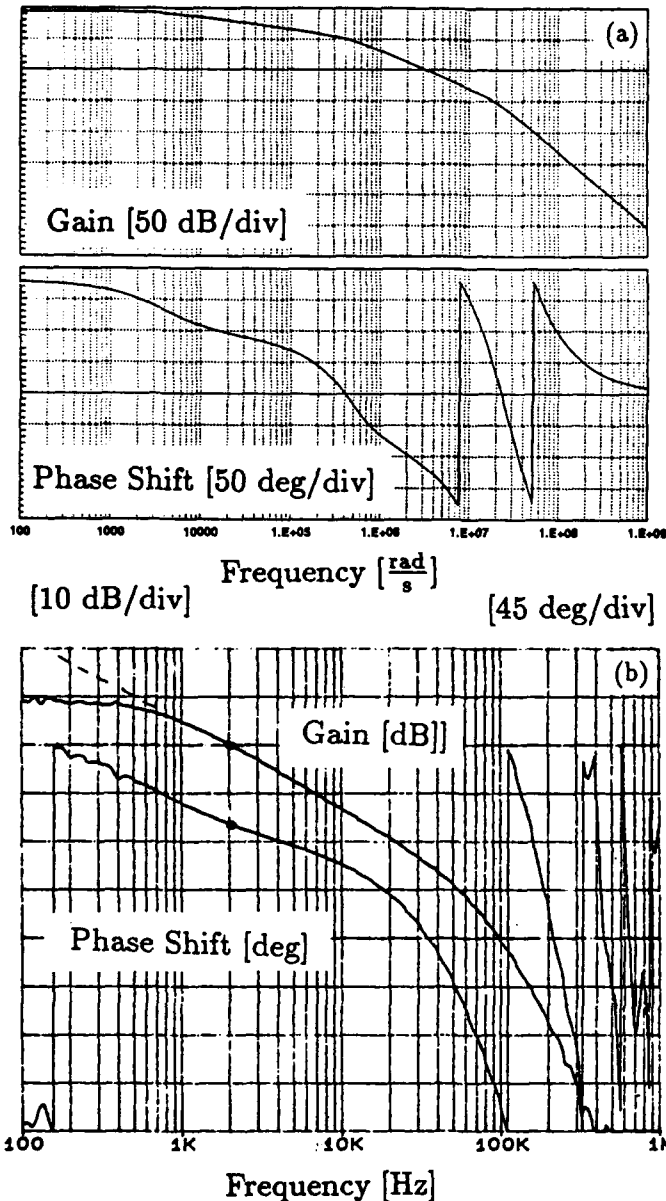


Figure 4. Calculated open loop response (fig. 4a) is compared with online measurement (fig. 4b)

4. Effect of Nonlinear Klystron

The saturation in the klystron reduces the stability threshold for the system as there is insufficient output power to compensate for heavy beam loading. Plotted in Fig. 5a is the ratio of the klystron output to input power as a function of the beam loading ratio, $Y = \frac{I_{beam}}{V}$, for different cavity voltages with all feedback loops off. The impedance angle was held fixed at -45 degrees while the loading angle was allowed to vary. A power ratio of 2.67×10^5 corresponds to a linear klystron. In Fig. 5b the threshold for beam

loading with $\phi_z = -45$ degrees is plotted as a function of cavity voltage. For a linear klystron the threshold is constant near 2.

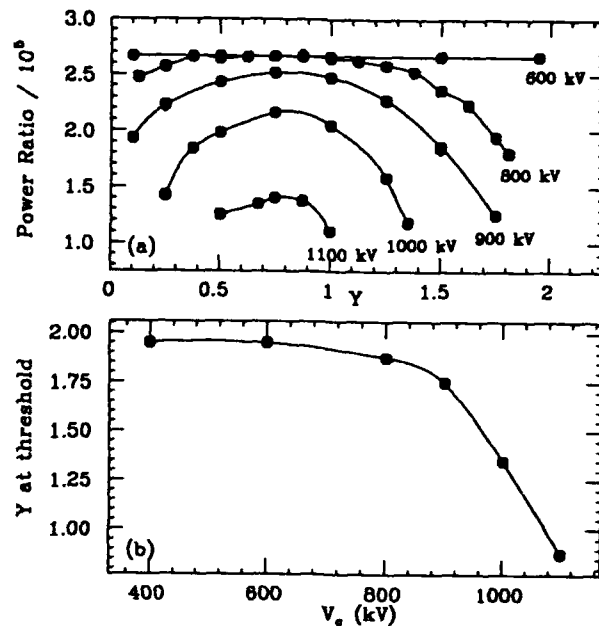


Figure 5. Ratio of the klystron output to input power as a function of loading ratio with $\phi_z = -45$ deg for different cavity voltages (fig. 5a) and stability threshold as a function of cavity voltage with $\phi_z = -45$ deg (fig. 5b). Higher order mode losses were assumed to be constant.

5. Conclusion

The equations of motion for the beam dynamics mixed to baseband were used to model the damping ring rf systems at the SLC. Measured feedback loop and klystron characteristics were included. Robustness of the simulations has been demonstrated by comparison to theory and experiment in the time and frequency domains. First results included a study of the nonlinear klystron. In the future we will study stability of the rf system with all the feedback loops closed.

The authors thank F. Pedersen of CERN, A. Hill, P. Correidoura, J. Judkins, and H. Schwartz of SLAC, and S. Karahan of Integrated Systems for their insights.

References

- 1 P.Krejci et al, "High Intensity Bunch Length Instabilities in the SLC Damping Rings", these proceedings
- 2 F.Pedersen, "Beam Loading Effects in the CERN PS Booster", IEEE Tran. on Nucl. Sci., NS-22, No. 3 (1975) 1906.
- 3 F.Pedersen, "A Novel RF Cavity Tuning Feedback Scheme for Heavy Beam Loading", IEEE Tran. on Nucl. Sci., NS-32, No. 3 (1985) 2138.
- 4 P.Krejci et al, "RF Feedback for Beam Loading Compensation in the SLC Damping Rings", these proceedings
- 5 Matrix-x by Integrated Systems, Santa Clara, CA
- 6 Simulink by Mathworks, Boston, MA

Improved Impedance Reduction in the CERN SPS Superconducting Cavities for High Intensity Proton Operation

D. Boussard – G. Lambert – T. P. R. Linnecar

European Organization for Nuclear Research (CERN), 1211 Geneva – Switzerland

I. INTRODUCTION

Two four cell superconducting cavities are installed in one bimodule in the SPS accelerator to provide accelerating voltage for leptons. The four 3.5 GeV-20 GeV lepton cycles are interleaved with a 14 GeV-450 GeV fixed target high intensity proton cycle, the composite supercycle being 14.4 s long. The extremely high impedance of the superconducting cavities is unacceptable for the high intensity proton beam and to maintain beam stability the resonances in the main cavity passband must be heavily damped. This damping is produced by an RF feedback system [1]. The limitations for this feedback system are due mainly to the proximity in frequency of the two upper resonances in the cavity and the loop delay. Typically a final, operationally reliable, impedance of $\approx 400 \text{ K}\Omega/\text{cavity}$ can be obtained. Measurements on the proton beams at high intensity have shown that with two cavities in the machine this impedance produces coupled bunch instabilities when $\approx 3 \times 10^{13}$ protons/pulse are accelerated. As there are plans to increase the proton intensity beyond this value, and since the possibility also exists of installing a second bimodule for lepton acceleration, it has become very important to study possible methods of further reducing the total impedance. Two methods have been studied, built and tested in machine development periods, both of these acting as a supplement to the existing RF feedback system. The first consists of a feedforward loop injecting a beam current signal into the feedback loop and the second consists of an additional feedback loop around the first, acting only at harmonics of the revolution frequency.

II. THE BIMODULE AND EXISTING FEEDBACK

Each superconducting cavity consists of four coupled cells producing four resonances in the main passband at 347, 349, 351 and 352 MHz. The latter, the π mode, is used for acceleration and has an R/Q of 230Ω ; the others interact to a much smaller extent with the beam. The extremely high Q_{ext} of each resonance, $\approx 3 \times 10^7$, is reduced by the RF feedback during proton operation to $\approx 2 \times 10^3$ giving an impedance on the π mode of $\approx 400 \text{ k}\Omega$. This feedback is shown schematically in Fig. 1a. The detailed design and functioning of the loop have been described previously [1]. For the present purposes, the transfer function of the ensemble from point A to point B is given by:

$$X(s) = \frac{Z(s)G_1(s) e^{-s\tau'}}{1 + Z(s)G_1(s) e^{-s\tau}}$$

where $Z(s)$ is the transfer function in-out of the cavity ($V(s)/I_g(s)$), τ the total loop gain, τ' the measurement path delay and $G_1(s)$ the amplifier gain (\approx constant for the upper two modes). The amplitude response of this closed loop is given in Fig. 2.

III. FEEDFORWARD COMPENSATION

A. Implementation

The principle is to cancel the voltage induced in the cavity by the beam current by injecting an equal and opposite current via the power amplifiers. The implementation is shown schematically in Fig. 1b. A signal proportional to the beam current is derived from a wideband monitor situated close to the superconducting cavity. Provision is made for adjusting both the phase and amplitude of this signal and a gate is incorporated to allow switching during the proton cycle. Since the bandwidth of the amplifier is significantly wider than that of the cavity, care must be taken to avoid loading the power amplifier unnecessarily. For this reason a bandpass filter is added in the chain. The bandwidth is a compromise between the amplifier requirements and the need for minimum delay since any delay in the feedforward path reduces the efficiency of the feedforward compensation at frequencies away from the centre. In practice the filter had a 2.8 MHz bandwidth (delay $\approx 150 \text{ ns}$).

The effective impedance of the cavity with feedforward is defined as:

$$Z_{\text{eff}}(s) = \frac{V(s)}{I_b(s)} = \frac{Z(s)[1 - G_2(s)e^{-s\tau''}]}{1 + Z(s)G_1(s)e^{-s\tau}}$$

where τ'' is the total delay in the feedforward path; i.e. the electronic delay from monitor through to cavity plus the beam delay cavity to monitor (which may be negative). $G_2(s)$ is the gain in the forward path.

B. Results with Beam

The phase and gain were adjusted using the signal of the beam induced voltage in the cavity. A spectrum analyzer was used to observe a few revolution frequency lines centred on the π mode, the feedforward being switched on just after transition energy during the proton cycle and switched off again just before extraction at 450 GeV. Fig. 3 shows a typical result, a reduction in impedance of $\approx 10 \text{ dB}$ being obtained. Observation on a much wider frequency bandwidth covering the two modes in the passband of the filter gives results shown in Fig. 4. The reduction in signal on the π mode is accompanied as expected by the emergence of the signal on the lower mode. Even for a perfect feedforward correction on the π mode, the observed signal $V(s)$ does not vanish completely at 352 MHz, because of the contribution of the other mode. Precise phase and amplitude settings of the feedforward path (which are independent of the RF feedback gain) are better adjusted with high Q separated resonances (low RF feedback gain). The total delay in the feedforward path was $\approx 530 \text{ ns}$. It is clear that with this delay the injected current changes phase by π between 351 and 352 MHz,

thus limiting the efficiency of the feedforward. However it will be improved significantly (reduction of 230 ns) by replacing the existing monitor by a dedicated monitor upstream of the cavity. Another limitation of the method is the residual R/Q of the other modes which cannot be corrected.

IV. ONE TURN DELAY FEEDBACK

IV.1 ONE CAVITY

B. Implementation

The delay in the main feedback loop combined with the proximity of the resonant frequencies forces a limitation in gain of the system and hence of impedance reduction. If we look at the transfer function on a network analyzer and unravel the response with a delay correction, negative, we see that the four cavity resonances can all be superimposed in the right half of the complex plane (Fig. 5a) and that therefore if such a delay could be inserted in series, a secondary feedback loop could be used to further reduce the impedance. In a synchrotron the frequencies where loop gain is beneficial occur at multiples of the revolution frequency, f_{rev} . If $f_{rev} \gg f_s$, the synchrotron frequency, then only a small bandwidth at each harmonic is important. A comb-filter in the feedback path can be used to select these bands and the total delay of the loop can be increased to $\tau_{rev} = 1/f_{rev}$ to rotate the phase by 2π between each harmonic [2] [3]. This produces, for these bands, the same result as the negative delay mentioned above. The cavity impedance with this extra loop is defined as:

$$Z_{eff}(s) = \frac{Z(s)}{1 + G_1(s)Z(s)e^{-s\tau} + G_1(s)G_3(s)Z(s)e^{-s(\tau + \tau'')}}}$$

τ'' is the "one-turn" loop delay and $G_3(s)$ is the loop gain which includes the comb-filter response:

$$H(s) = \frac{(1-k)e^{-s\tau_{rev}}}{1 - ke^{-s\tau_{rev}}}$$

The layout is given in Fig. 1c for this particular implementation. The signal at 352 MHz is mixed down in two stages to 5MHz, after which it is digitised. The signal then passes through the comb filter and delay, (bandwidth 0-10MHz), both realised in digital form [2], and then, after the DAC, is remixed to 352 MHz. Phase and amplitude adjustment are provided plus an RF switch and following amplification the signal is reinjected into the main loop. The delay phase and gain are adjusted in open loop using the network analyzer (the delay tolerance is found to be ± 25 ns). The two upper resonances are shown with delay correction in Fig. 5b and after the comb-filter in Fig. 5c. What remains is the non-linear phase response of the system. The closed loop response is given in Fig. 6. Here the "tails" on the response are due to these residual errors, which could be compensated if necessary using an equalisation filter. The spacing of the four resonances is not exactly the 1 MHz and 2 MHz quoted and consequently it is impossible to "place" all four resonances one on top of the other. With the delay

optimised for the upper two, the lower two would seriously reduce the maximum loop gain possible. For this reason, the lower two are rejected by notch filters [1].

B. Results with Beam

The combination of loops implemented on one cavity was tested using beam. The second cavity in the bimodule was used to render the beam unstable at top energy by reduction of the main feedback gain. The difference in gain values on this cavity for instability threshold when the single-turn feedback on the other cavity is ON or OFF gives a measure of the effective impedance reduction. A reduction of 5 x in impedance has been reliably obtained.

IV.2. TWO CAVITIES

A. Implementation

A one-turn feedback system can be used independently on each cavity in the bimodule. A more economic system is to make the vector sum of the signals from the cavities and correct via a single cavity. This is shown in Fig. 1d. Again provision is made for independent phase and amplitude control. The easiest way to adjust this was found to be to use a difference hybrid and set the controls for minimum beam-induced signal at the output. The introduction of 180° delay then produces the required sum signal. One point to note is the increased power requirement on the power amplifier used for feedback. Performance is limited by inaccuracies in the summation [4].

B. Results with beam

This technique has been tested on the SPS and its efficiency estimated by reducing the main feedback gain and searching for the instability threshold. An impedance reduction of ≈ 3 x is estimated.

V. CONCLUSIONS

It has been shown experimentally that a feedback system around a multi-cell cavity can be complemented in two ways by feedforward and single.turn feedback. It has also been shown that the impedance of two multi-cell cavities can be reduced by using the vector sum of the two as reference for the single turn feedback loop.

VI. REFERENCES

- [1] RF feedback Applied to a Multicell Superconducting Cavity. D. Boussard, H. P. Kindermann, V. Rossi. EPAC Rome 1988
- [2] Reduction of the Apparent Impedance of Wideband Accelerating Cavities by RF feedback, D. Boussard, G. Lambert, IEEE 1983 PAC Santa Fe
- [3] Design and Operational Results of a "One-Turn Delay Feedback" for Beam Loading Compensation of the CERN SPS Ferrite Cavities. F. Blas, R. Garoby, IEEC 1991 PAC San Francisco
- [4] RF Cavity Feedback, F. Pedersen, CERN PS/92-59

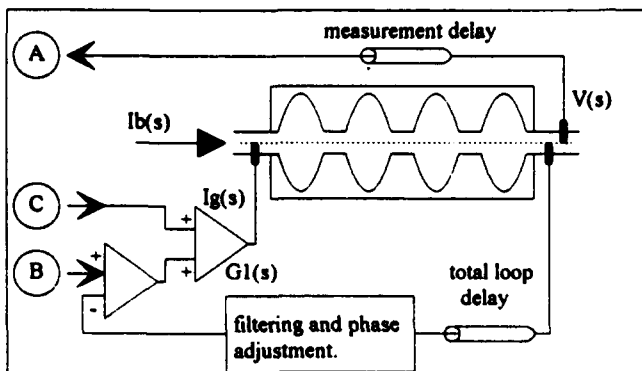


Fig. 1a RF feedback, normal operation.

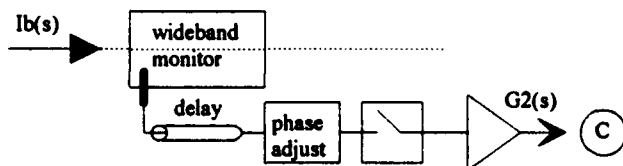


Fig. 1b Addition of feedforward.

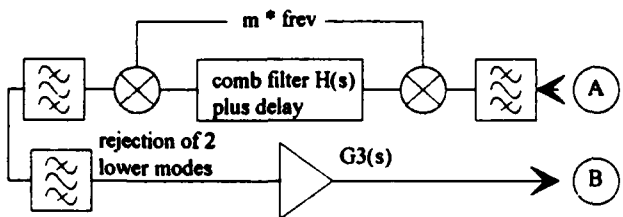


Fig. 1c Addition of one-turn feedback.

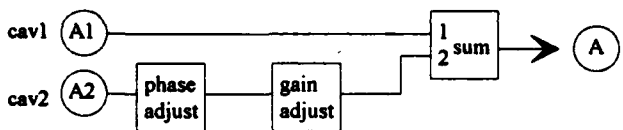


Fig. 1d Addition of 2 cavities to one turn feedback.



Fig. 2 4 resonances of damped cavity
349 MHz \pm 4 MHz (H); 10 dB/div (V)

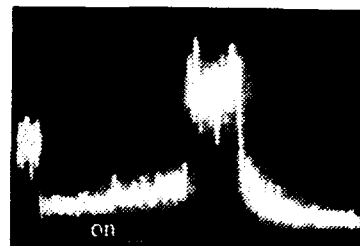


Fig. 3 Effect of feedforward
0.5 s/div (H)
5 dB/div (V)

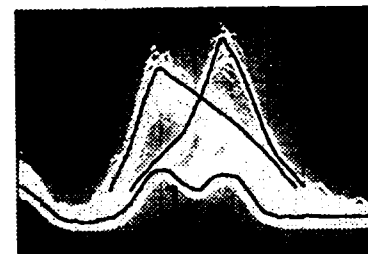


Fig. 4 Spectrum of feedforward
500 KHz/div (H)
5 dB/div (V)
1. System noise
2. Feedback off
3. Feedforward on

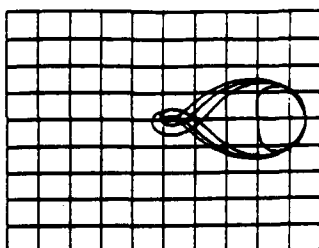


Fig. 5a Calculated response
4 resonances with delay correction

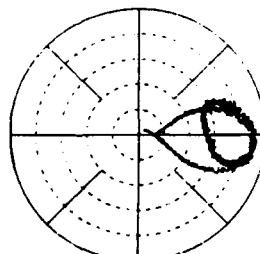


Fig. 5b Measured response
with delay correction, upper two modes

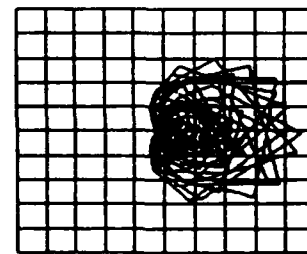
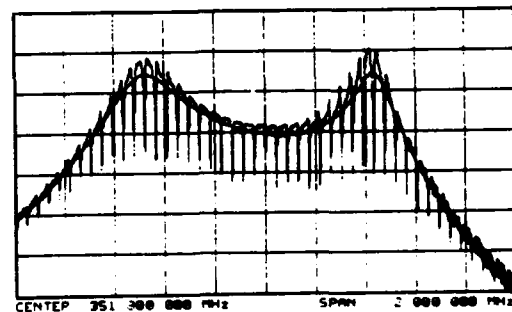


Fig. 5c With comb filter

Fig. 6 Response with and without one turn feedback



Damping of Phase Errors at Injection in the LHC

D. Boussard – E. Onillon

European Organization for Nuclear Research (CERN), 1211 – Geneva Switzerland

I. INTRODUCTION

Capture losses must be kept to an extremely small value in the superconducting, very high intensity (0.85 A per beam) LHC machine [1]. Bunches from the injector (the SPS accelerator) are fairly long (51 cm full length compared to the RF wavelength of 75 cm) and phase injection errors may bring the edge of the injected bunch very close to the separatrix. Following the SPS collider experience, it is therefore of prime importance to quickly damp any phase (or energy) error at injection in order to avoid capture losses as much as possible. The main LHC RF system is composed of eight single cell 400 MHz superconducting cavities [2], which are common to both beams and cannot be used to act independently on a newly injected batch. Dedicated cavities (or longitudinal kickers) working on each beam separately will provide damping of phase oscillations just after injection; they may also be used to suppress any coupled bunch longitudinal instability during coast.

II. PHASE ERRORS AT INJECTION

A. Phase Modulation in the LHC

As explained in ref [3], the equilibrium phase of the LHC bunches is not constant along one machine turn, due to the effect of transient beam loading. The RF waveform will be phase modulated via the reference voltage of the RF feedback circuits; this is in order to keep the required RF power within acceptable limits. When a new batch is injected, the equilibrium phase modulation changes immediately (Fig. 1). This means that the already injected bunches become out of phase with the new RF waveform and start phase oscillations. The maximum phase error $\delta\phi_{\max}$ occurs when the last batch is injected:

$$\delta\phi_{\max} = \frac{1}{2} \frac{R}{Q} \frac{\omega_0}{V} I_B \Delta t_0 \quad (1)$$

where $\frac{R}{Q} = 8 \times 43.5\Omega$ is the characteristic impedance of the eight RF cavities, $\omega_0/2\pi=400$ MHz the RF frequency, $V=8$ MV the RF voltage at injection, $I_B=1.25$ A the RF component of the injected beam current, $\Delta t_0=6.2\mu s$ the length of the injected batch and $T=1/f_0=89\mu s$ the revolution period. One finds $\delta\phi_{\max} = 0.42$ rad (24° RF phase).

B. Phase Modulation in the SPS

The SPS RF system is composed of four 200 MHz travelling wave structures [4], each 16 m long (4 sections). The accelerated batch for LHC, which occupies only a small fraction ($6.2\mu s$) of one SPS turn ($23\mu s$) induces in each accelerating structure a voltage $V_b = 1.40$ MV, almost in phase with the beam current. This beam induced voltage must be compensated by an increase of the RF input power in the structure from 560 kW ($I_B=0$) to 750 kW ($I_B=1.57$ A at 200 MHz). A straightforward way to achieve this is with a

feedforward technique: the I_B signal measured with a beam monitor is added to the cavity drive signal after one turn delay and proper phase and amplitude adjustments. Compensation cannot be perfect, however because of the limited bandwidth of the RF power amplifiers and of the different responses of the cavity to the beam and to the RF drive. For a simplified model of the cavity (transmission line equivalent) the transient beam induced voltage is parabolic with a response time of 560 ns. The correction from the amplifier has a rise time of about $1\mu s$ (combination of linear rise of 560 ns in the cavity and amplifier rise time) (Fig. 2). The maximum difference when the amplifier is slightly overpowered (max power 1 MW) can be kept below $V_b/4$, which corresponds to a residual phase modulation of $\pm 10^\circ$ at 200 MHz for a 2MV RF voltage per cavity.

In order to compress the bunches prior to ejection the SPS will be equipped with three superconducting single cell 400 MHz cavities providing an additional 6MV RF voltage, but with a negligible contribution to the machine impedance (with RF feedback). These cavities will be essentially beam driven at ejection, when the instantaneous RF frequency of the beam current is brought close to the s.c. cavity resonant frequency [5]. The residual phase modulation due to the travelling wave cavities will be reduced by the factor $h_1 V_1 / (h_1 V_1 + h_2 V_2)$ where V_1, V_2, h_1, h_2 are the voltages and harmonic numbers at 200 MHz and 400 MHz respectively. It follows that the residual 400 MHz phase modulation at ejection is $\pm 8^\circ$.

Due to the large bandwidth of the travelling wave structures, it is always possible to phase modulate the ejected batch to match the equilibrium phase slope in the LHC.

Finally, errors in the synchronization electronics between the two machines will result in a random (but constant for one batch) error estimated to $\pm 15^\circ$ at 400 MHz.

III. SIGNAL PROCESSING

A. Phase Detection

A classical double balanced mixer circuit will be used as a phase detector at 400 MHz between a reconstructed RF burst from the beam and the RF reference. A technique similar to that proposed for the SLAC B factory [6], but working at the RF frequency looks adequate. Each bunch will produce a 20 ns long 400 MHz burst (8 periods) at the output of an eight quarter wave couplers comb generator. In order to minimize the total length of the comb generator, the quarter wave couplers need not be spaced by one full wavelength provided the cable lengths to the combiner are properly selected. The output of the mixer is sampled at the bunch frequency (40 MHz) and converted to digital form for subsequent processing.

In order to avoid large offsets ($\approx 60^\circ$) which would considerably reduce the useful range of the phase detector, the RF reference applied to the mixer must be phase modulated like the reference applied to the RF cavities [2] [3].

B. Filtering

The phase error signal of each bunch should ideally be phase shifted by 90° at the synchrotron frequency and applied

to the same bunch as an additional feedback voltage V_f , after a delay of one or several turns. If the same processing is applied to every bunch, one obtains an overall periodic transfer function which repeats every f_0 [7] [8]. Within a $0-f_0/2$ interval the filter should exhibit a high gain and phase shift close to 90° at the synchrotron frequency f_s to get optimum damping with minimum RF power. Outside the range of f_s the gain should be low to limit noise power, in particular it must vanish at zero frequency to reject the phase detection offsets. For the particular case of fast damping of injection errors, it is important to quickly reject the injection offset; this takes a time of the order of $1/f_p$ where f_p is the frequency of the peak response of the filter ($0 < f_p < f_0/2$). For $f_p > f_s$ (differentiator case) the offset is rejected in less than one synchrotron period, which allows closing the damping loop very soon after each injection without saturation. Noise induced power outside the f_s band is unimportant at injection, as power requirements are completely determined by the initial phase errors.

The selected filter architecture is based on the difference of two recursive digital filters of the form:

$$H(\omega) = \frac{1 - K_1}{1 - K_1 \exp(-j\omega T)} - \frac{1 - K_2}{1 - K_2 \exp(-j\omega T)} \quad (2)$$

which can be realized with a limited memory capacity (3 times the number of bunches) and simple hardware (Fig. 3), especially if K_1 and K_2 are of the form $1/2^N$. In this case, only adders and subtractors are needed. The cycle time of the filter (two adders, truncation, memory access and latch) amounts to less than 20 ns, smaller than the bunch to bunch distance of 25 ns. Consequently neither multiplexing nor down sampling would be necessary. The same filter could be used in coast where $f_s = 20$ Hz is smaller by changing K_1 and K_2 ($K_1 = 7/8$, $K_2 = 15/16$). With $K_1 = 3/4$, $K_2 = 7/8$ and $K_1 = 7/8$, $K_2 = 15/16$ one obtains the curves $H(\omega)$ of Fig. 4. An additional memory will complement the filter to achieve an overall one turn delay. Fig. 5 shows how quickly the filter separates the useful f_s signal from the unavoidable offset at injection.

C. Post Processing

A further signal processing will be needed before applying the signal to the feedback cavities (longitudinal kickers). An equalization circuit is needed to compensate the cavity response at least up to a frequency corresponding to the fastest change of phase errors at injection (a few MHz). The feedback cavities will be equipped with RF feedback in order not to increase the machine impedance. Their closed loop transfer function including the loop delay is very similar to that of a second order system and can be compensated at the digital level by the inverse circuit.

Holes in the LHC bunch trains need special treatment, otherwise the step in the filter output signal at each new bunch following a hole will saturate the power amplifier during the passage of the first bunches of the batch. It is proposed to write in the last memory, instead of the non significant values of the hole, the value of the first following bunch. The step, which now appears at the beginning of the hole will saturate the chain during the hole instead of during the passage of bunches.

After digital processing, the feedback signal is translated in frequency by a double balanced mixer (rejected carrier) driven by the (phase modulated) RF.

IV. HIGH POWER EQUIPMENT

A. Feedback Voltage

For a damping time of three synchrotron periods and maximum phase error of 24° RF phase, the peak feedback voltage amounts to $V_f = 360$ kV. It will be provided by three 200 MHz "bar cavities" per beam, similar, but longer to those described in [1]. The total R/Q of the feedback cavities (525 Ω per beam) is comparable to that of the main cavities (348 Ω for the two beams), however their effect on transient beam loading can be made negligible with RF feedback (bandwidth ± 400 KHz). Each feedback cavity will be driven by one or several 200 MHz tetrodes. The transformation ratio between accelerating voltage and anode voltage should be approximately constant over the range of the bunch to bunch feedback system i.e ± 20 MHz. This means that the tetrode cavity distance must be as short as possible which is also beneficial for RF feedback.

B. Power Requirements

The peak power capability of the tube is determined by V_f (120 kV per cavity) and the maximum tube current I_g transformed at the cavity gap. During the passage of a batch $I_g \approx I_b = 1.25$ A (RF feedback effect) whereas during the hole preceding the newly injected batch (0.97 μ s long) I_g is needed to change V_f rapidly. In the worst case $\delta\phi = 24^\circ + 15^\circ$, one finds $I_g = 1.82$ A and finally an installed power of 110 kW per cavity.

In this scenario the very fast rate of change of V_f induced by the residual SPS phase modulation (8° in 200 ns) will be slow rate limited by the processing electronics, the result being a slower damping for the limited number of bunches concerned.

V. REFERENCES

- [1] The LHC Study Group, Design Study of the Large Hadron Collider, CERN 91-03 (May 1991).
- [2] D. Boussard, V. Rödel The LHC RF system, Proc. XV Int. High Energy Acc. Conf., Hamburg, July 1992.
- [3] D. Boussard, RF Power Requirements for a High Intensity Proton Collider, Proc. 1990, Part. Acc. Conf. San Francisco.
- [4] G. Dôme. The SPS Acceleration System, Travelling Wave Drift Tube Structure for the CERN SPS, Proc. 1976 Proton Linac Conference, Chalk River, Canada.
- [5] T. Bohl, D. Boussard, 400 MHz Superconducting Cavities in the SPS, CERN SL Note/ (in preparation).
- [6] D. Briggs et al., Prompt Bunch by Bunch Synchrotron Oscillation Detection Via a Fast Phase Measurement, Proc. 1990, Part. Acc. Conf. San Francisco, p 1404-1406.
- [7] F. Pedersen, RF Cavity Feedback CERN PS/92-59.
- [8] F. Pedersen, Multibunch Feedback, Filters and Signal Processing, INFN Eloisation Workshop, Feedback of Multibunch Instabilities, Erice (Italy) Nov. 1992.

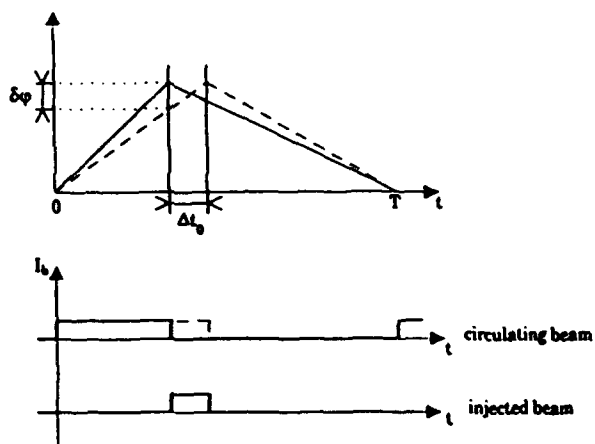


Fig. 1 Phase modulation at injection

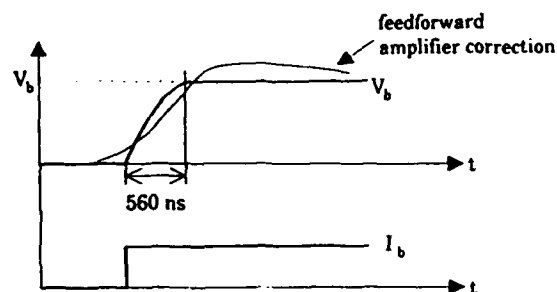
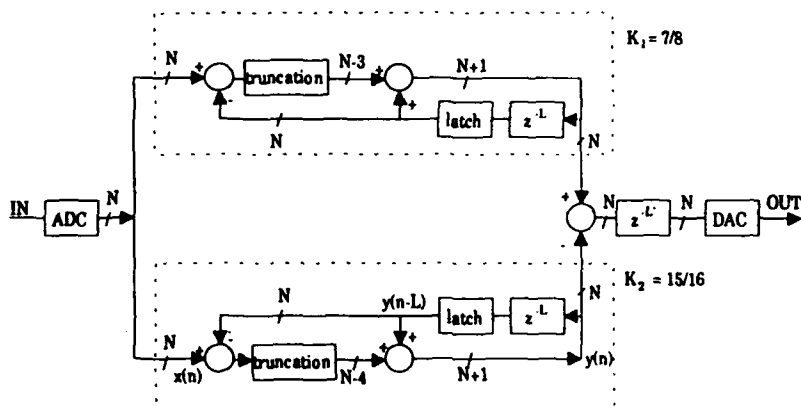


Fig. 2 Transient induced voltage in the SPS travelling wave structure



z^{-L} : delay of L clock periods (one turn)
 $z^{-L'}$: delay of L' clock periods (one turn minus a fixed delay)
 N : number of bits

Equation of the branch of the filter with $K=15/16$:
 $y(n) = y(n-L) + (x(n) - y(n-L))/16$ or
 $y(n) = 15/16 \cdot y(n-L) + x(n)/16$

Fig. 3 Architecture of the filter

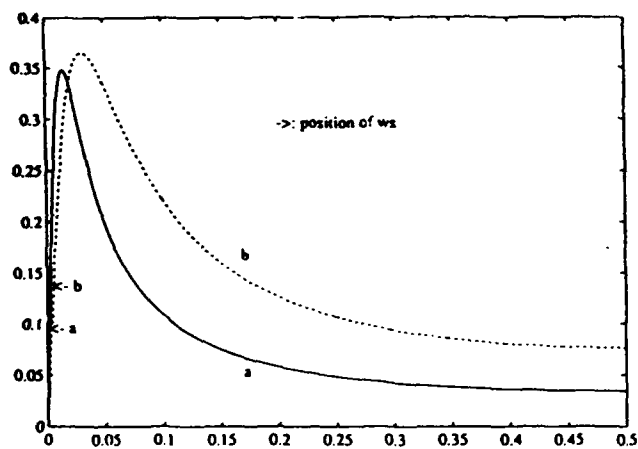


Fig. 4 Amplitude response of the filter
a: $K_1=7/8$, $K_2=15/16$
b: $K_1=3/5$, $K_2=7/8$

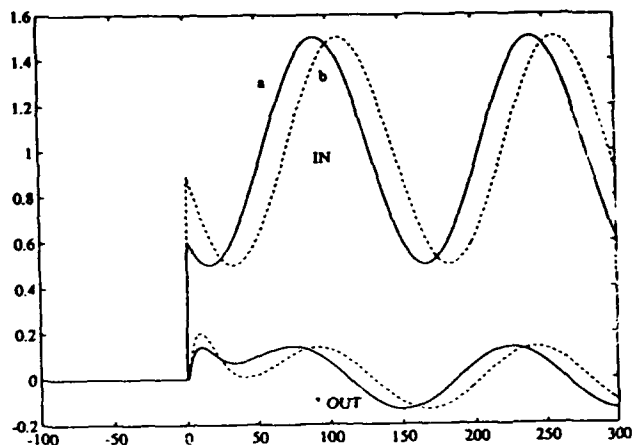


Fig. 5 Rejection of injection offset
top: f_s oscillation (2 phases a, b) superimposed on unit step offset
bottom: filter output

A Digital Beam Phase Loop for the Low Energy Booster

L.K. Mestha, V. Brouk, R.C. Webber, John Mangino and T. Uher
Superconducting Super Collider Laboratory*
2550 Beckleymeade, MS-4005, Dallas, TX 75237 USA

Abstract

The Direct Digital Synthesizers (DDS) have a proven record of high frequency stability in accelerator beam control. For the Low Energy Booster working in the frequency range of 47MHz to 60MHz, a highly stable, high resolution DDS can improve the longitudinal beam stabilities. With the DDS as the source it would be highly desirable to make the beam phase loop digital. In this paper we show the description of the loop hardware and a method to simulate the performance in the presence of loop delay using a control system simulation software called SIMULINK. Some experimental hardware based on DDS system which was used to accelerate the beam in the FNAL booster is discussed.

I. INTRODUCTION

Reason for going to digital as compared to analog in implementing phase loop is due to (1) the advent of super stable, high speed and high resolution direct frequency synthesizers and (2) the opening of new opportunities to implement complete real time processor control without additional hardware modifications.

A. Frequency source

For the Low Energy Booster the accelerating frequency is varying through the cycle from 47MHz to 60MHz and there are tough requirements to both frequency stability and spectral purity of the source. The rate at which the frequency varies is considerably high (2.5GHz/s). All this is within easy reach with the Gallium Arsenide technology. Using conventional analog circuits the super frequency stability is hard to satisfy. Recently developed high-speed Direct Digital Synthesizers are very promising as master oscillators. Such a device being completely digital, except for an output DAC, provides 32-bit (2×10^{-10}) frequency resolution with its stability completely defined by external fixed frequency oscillator. Off-the-shelf ready to use synthesizers have stability to the order of 10^{-8} or better. However, the spectral purity depends on the clock frequency and the operating frequency. The output signal is generated by the digital adder - phase integrator, and hence there are no reasons for phase discontinuity unless the digital circuit is malfunctioning. The main concern will be about the phase/frequency noise, creating sidebands with the synchrotron frequency and its harmonics near the fundamental and other

harmonics of the revolution frequency. There was also the fear about sidebands, generated due to stepwise frequency control during the cycle. This was calculated analytically for the LEB and was shown to be below -55dBc for a time step of 1.9 μ s so that all the dangerous components were insignificant.

B. Beam phase loop.

Even a perfect frequency source requires feedback in order to provide damping of dipole synchrotron oscillations. The block-diagram of phase loop together with the frequency source is shown in Fig. 1.

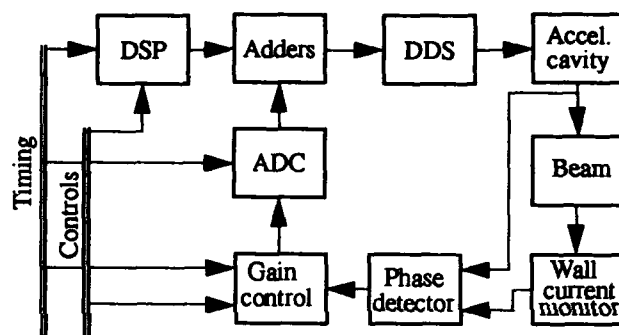


Fig. 1: Beam Phase Feedback Loop

In order to simplify the picture, radial position and synchronization loops are not shown. Digital signal processor (DSP) is used to provide the frequency profile, which is stored in its memory and the data is applied to the adder input with a rate of 500 kwords/s. A frequency down conversion based phase detector uses an intermediate frequency of 10.7MHz. The overall bandwidth is 300 kHz and linear angle range is $\pm 150^\circ$. Gain control allows programmable loop gain during the acceleration cycle. The ADC is 10Ms/s with 12 bit resolution. Its speed is an essential parameter, since it defines the effective delay and contributes to the overall loop performance. Fast digital adder circuits are needed to close the phase loop.

The basic requirement for the phase loop is associated with damping of the coherent dipole oscillations. To meet this general requirement effectively the open loop gain of the loop has to be designed more than 2 at the highest synchrotron frequency¹. For synchrotron frequency f_s and phase stability margin of 45° the limit of the total delay is: $t_{max} = 1/16f_s$, which gives 2.5 μ s and 2.1 μ s for the LEB and FNAL booster accordingly. This limitation becomes more tight if one will take into account phase shifts due to limited bandwidth of various parts of the loop, in particular - the phase detector and accelerating cavities. If we take into account the inevitable cable delays (0.5 - 1.5 μ s), the feasibility of digital signal processing for FNAL

*Operated by the University Research Association, Inc., for the U.S. Department of Energy under contract No. DE-AC35-89ER40486

booster becomes questionable. To proceed with this we started some experimental test on FNAL booster and also analytical and numerical investigation using SIMULINK/MATLAB software.

II. SIMULATION USING MATLAB SOFTWARE

In order to evaluate the loop performance in actual working conditions we have to build the complete hardware and then test with beam in the machine in the presence of other low level rf loops. On the other hand, if all the loops are decoupled, then the interaction between them is negligible. This allows us to independently design and simulate the loop by representing the hardware components as blocks with appropriate transfer functions. SIMULINK¹ is a good software package for modelling and simulating such control loops which is available in MATLAB. This software provides tools to investigate the behavior of nonlinear systems as well as systems with time varying parameters. The latter is particularly important for fast cycling boosters, where typical time of parameter variation is comparable with the period of the synchrotron frequency. Using SIMULINK it becomes easy to investigate the single particle behavior with a well known control terminology.

The loop is described using the set of standard as well as user-defined blocks (Fig. 2) and user-written command files. Fig. 3 shows the closed-loop frequency response of the phase loop for the LEB parameters with an effective delay of $1\mu s$. Fig. 4 shows the response of the same loop to the phase step for three different values of the loop gains. For the open loop gain at the synchrotron frequency equal to 3.0 the damping is insufficient (Fig. 4). While decreasing the gain lead to reduced oscillatory response on the natural frequency as shown in Fig. 5 for a gain of 0.5. In Fig. 6 the step response for the optimal gain of 1.5 is shown.

Further steps in the simulation could involve time varying parameters, which will increase the permissible delay. Both radial and synchronization loops can be added to investigate their interactions with beam. Beam-loading effects are also easy to simulate.

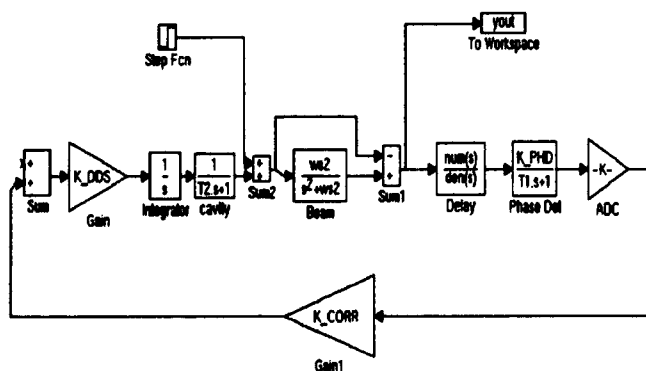


Fig. 2: SIMULINK model of the digital beam phase loop

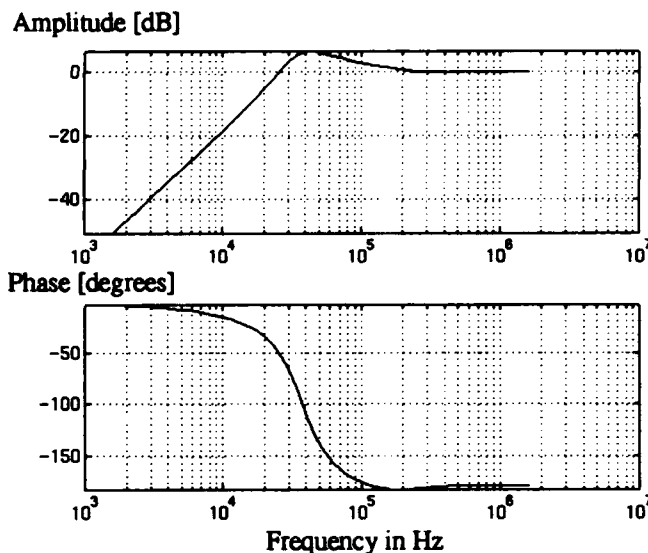


Fig. 3: Closed loop frequency response

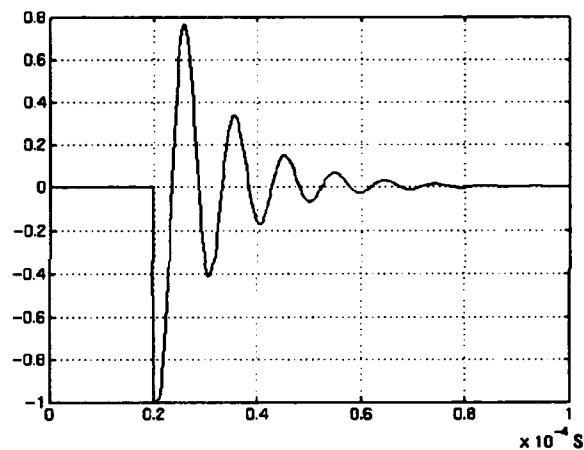


Fig. 4: Step response for $G_t = 3.0$

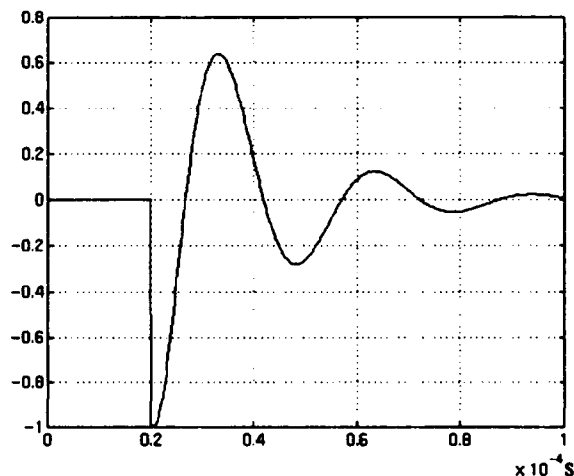


Fig. 5: Step response for $G_t = 0.5$

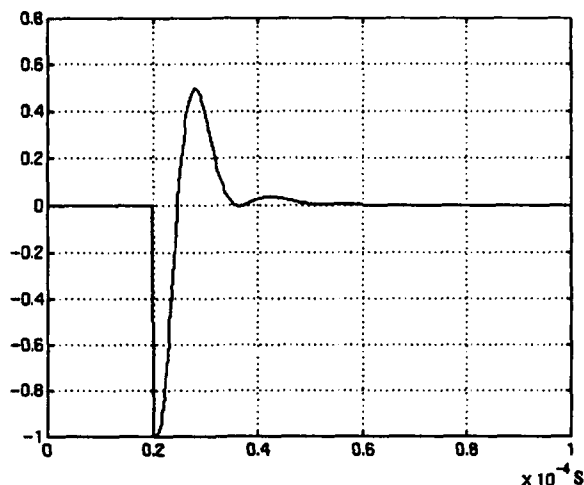


Fig. 6: Step response for $G_s = 1.5$

III EXPERIMENTAL STUDIES

Some experimental work on FNAL booster low level rf system was done to establish the feasibility of the Direct Digital Synthesizer based digital beam phase loop for a fast cycling machine. As a first step, which didn't require special beam time, the PLL loop, shown in Fig.7 for locking the DDS to the beam was assembled and investigated. Note that a cable delay of $1.4\mu s$ was introduced in the loop. The DDS was locked to the beam throughout the acceleration cycle with the phase error controlled to within 10° . The loop performance was completely defined by the effective loop delay and the processing algorithm in DSP#2. Digital processing time in DSP#2 contributed additional $1.2\mu s$ delay in the loop.

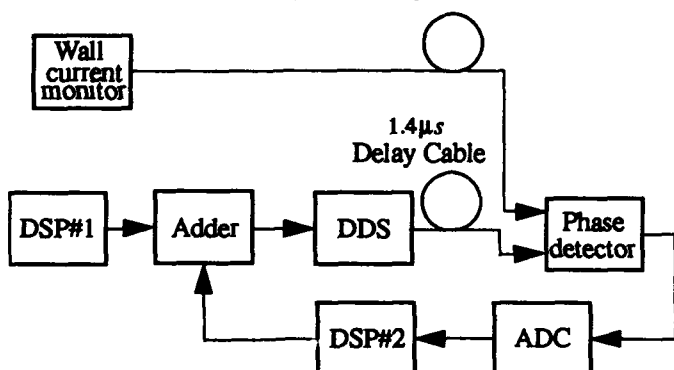


Figure 7. Experimental setup used at Fermilab

The second stage of the experiment was done by replacing existing VCO and part of the phase loop by the circuit shown in Fig. 7 with the exception of DSP#2. The DDS was made to drive the booster cavities to control the beam in the ring. After setting appropriate loop gain the acceleration was immediately obtained. All the qualities of the beam expected from a normal booster run was preserved during the operation with the DDS. The experiment was conducted upto full booster intensity. The accuracy of the DDS/DSP frequency profile was, as it was

expected, significantly better than that of the VCO. The delay contributed by the ADC, adder circuits and the DDS was about $0.6\mu s$. This was the first and complete proof of a digital frequency source together with partly digital phase loop which worked on an existing fast cycling machine. With this experience we believe that there are good opportunities which lie ahead to use the hardware for the LEB so that the reliability and the quality of beam can be greatly improved.

IV. CONCLUSIONS

Control systems-oriented SIMULINK software is a useful tool for the analysis of beam-control systems with time-varying parameters. Using SIMULINK a simple way of modelling and then the simulation of the practical digital beam phase loop is shown. Direct Digital Synthesizer has proved to be a precise RF source for the frequency range of 30MHz to 60 MHz and with a $df/dt \approx 3\text{GHz/s}$. So it can be used for the LEB as well as for the MEB and the HEB. As the time progress we can expect further growth in DDS technology which will allow us to use it at 360MHz for the collider. The possibility of using Digital Signal Processors in fast-cycling booster phase loop is limited by the loop time delay. LEB has a good layout of the RF cavities, wall current monitor and low-level RF equipment. So, the existing TMS320C40 DSP could be used while delay budget in the FNAL booster barely allows such things. Having a DSP directly in the phase loop as in Fig. 7 is useful to introduce active and passive filters with time-varying gains. Evidently, for larger and/or slower machines a complete digital RF sources and the feedback is an advantage.

V. REFERENCES

1. H.G. Hereward, "Open and Closed Loop Properties of an RF Accelerated Beam", CERN/PS/4497, 1960.
2. SIMULINK User's Guide, The MathWorks, Inc., Massachusetts, March 1992.

General Time-Varying State-Space Control Model and its Application for Transient Beam Loading Compensation

L. K. Mestha *, C. M. Kwan * and K.S. Yeung **

* Superconducting Super Collider Laboratory[†]

** The University of Texas at Arlington

Abstract

A time-varying state-space control model was presented and used to predict the functions required to cure the injection voltage transients. We discuss a novel method to calculate the feedforward functions. Simulation results are shown to validate the method.

I. INTRODUCTION

It is required in the LEB for proper bunching and acceleration that the cavity gap voltage transients are controlled to within specifications. The direct RF feedback and local phase and amplitude loops will no doubt be able to control the injection voltage transients. But before trying the feedback loops it is usual practice to consider some open loop techniques since the loops tend to affect the overall stability of the system. Some rf feedback [1] and feedforward [2] techniques are considered and used in proton accelerators in other Laboratories. Feedforward techniques were generally applied in combination with the local rf feedback loops so that the combined effect would cure the transients. Feedforward techniques require accurate prediction of the functions. In this paper, we have identified the time-varying terms effecting the voltage transients. Later we show a method to predict the compensating terms accurately for the parameters of the Low Energy Booster. We think this technique is applicable to similar proton machines elsewhere. The technique relies on the accuracy of the control model. Our particle tracking studies show that the voltage transients are kept to within specifications when the feedforward functions were realized in the absence of loops.

II. LINEAR STATE-SPACE MODEL

Let x_1 = synchronization phase error, x_2 = radial position error, x_3 = beam phase error, x_4 = cavity gap voltage error, x_5 = cavity gap phase error and x_6 = tuning error. Then a complete state-space model can be derived for a macro particle using the accelerating cavity as an equivalent RLC circuit. Development of a complete linear time-varying state-space model is well described in Reference 3. We simply reinstate the model below in terms of the system matrix A , the input matrix B and the disturbance matrix d .

$$\dot{x} = Ax + Bu + d \quad (1)$$

For a time-invariant system, the terms in d will be zero and the derivative of the synchronous phase, ϕ , is negligibly small. Equation 1 agrees with Pedersen's model of [4] and hence satisfies Robinson's stability criteria. For completeness, we include the exact expression of (1) below.

Equation 1 agrees with Pedersen's model of [4] and hence satisfies Robinson's stability criteria. For completeness, we include the exact expression of (1) below.

$$\begin{bmatrix} \dot{x}_1 \\ \dot{x}_2 \\ \dot{x}_3 \\ \dot{x}_4 \\ \dot{x}_5 \\ \dot{x}_6 \end{bmatrix} = \begin{bmatrix} a_{11} & a_{12} & 0 & 0 & 0 & 0 \\ 0 & a_{22} & a_{23} & a_{24} & a_{25} & 0 \\ 0 & a_{32} & a_{33} & a_{34} & a_{35} & a_{36} \\ 0 & a_{42} & a_{43} & a_{44} & a_{45} & a_{46} \\ 0 & a_{52} & a_{53} & a_{54} & a_{55} & a_{56} \\ 0 & 0 & 0 & 0 & 0 & a_{66} \end{bmatrix} \begin{bmatrix} x_1 \\ x_2 \\ x_3 \\ x_4 \\ x_5 \\ x_6 \end{bmatrix} + \begin{bmatrix} 0 & 0 & 0 & 0 & 0 & 0 \\ 0 & 0 & 0 & 0 & 0 & 0 \\ 0 & 0 & b_{33} & b_{34} & b_{35} & 0 \\ 0 & 0 & b_{43} & b_{44} & b_{45} & 0 \\ 0 & 0 & b_{53} & b_{54} & b_{55} & 0 \\ 0 & 0 & 0 & 0 & 0 & b_{66} \end{bmatrix} \begin{bmatrix} u_1 \\ u_2 \\ u_3 \\ u_4 \\ u_5 \\ u_6 \end{bmatrix} + \begin{bmatrix} 0 \\ 0 \\ 0 \\ c_4 \\ c_5 \\ c_6 \end{bmatrix} - \frac{d\phi}{dt}$$

The model was compared with the longitudinal particle tracking code to confirm its validity when the rf frequency and the cavity gap voltage were varied with time during the acceleration cycle. We see that the cavity gap voltage has a large initial voltage transients when there are no feedback loops. In Fig. 1 the cavity gap voltage error is plotted with time for the first 1 ms after injection. The transients have been identified to be due to the high rate of change of voltage at the beginning, just after injection, and due to the sudden appearance of the beam (Fig. 1). We have identified that the terms c_4 and c_5 in the state-space model constitute to the initial voltage transients. This was done by solving for the gap voltage error, x_4 , and gap phase error, x_5 , from the state-space model by setting terms c_4 and c_5 equal to zero (See Fig. 1). In Pedersen's model due to no direct RF feedback ($H=1$) and no time varying terms ($\dot{V}=0$ =derivative of the cavity gap voltage) c_4 and c_5 are zero. The terms c_4 and c_5 are shown below to gain some insight into their complexities.

[†]Operated by the University Research Association, Inc., for the U.S. Department of Energy under contract No. DE-AC35-89ER40486

$$c_4 = -F_{11}\sigma(H\dot{V} + \omega v \tan\phi_z^0) - F_{12}\omega(\dot{V} + \sigma HV) + F_{11}\sigma RK_g \omega(I_b \cos\phi^s - I_g \sin\phi_L) + F_{12}\sigma RK_g \omega(-I_b \sin\phi^s + I_g \cos\phi_L) + \sigma RK_g i_g (F_{11} \cos\phi_L + F_{12} \sin\phi_L) \quad (2)$$

$$c_5 = -F_{21}\sigma(H\dot{V} + \omega v \tan\phi_z^0) - F_{22}\omega(\dot{V} + \sigma HV) + F_{21}\sigma RK_g \omega(I_b \cos\phi^s - I_g \sin\phi_L) + F_{22}\sigma RK_g \omega(-I_b \sin\phi^s + I_g \cos\phi_L) + \sigma RK_g i_g (F_{21} \cos\phi_L + F_{22} \sin\phi_L) \quad (3)$$

F 's in (2) and (3) depend on machine parameters.

Clearly, the direct rf feedback alone must in theory be capable of reducing the rf voltage transients. This is however insufficient in many machines including the LEB (See Fig. 2) due to the limitation on the direct RF feedback strength, H , (for LEB, $H = 20$) which is restricted by the loop delays. In theory, the amplitude and phase loops would reduce the transients to zero (Fig. 2) but their gains are again restricted due to the overall stability limits and the cavity tuning conditions. Since the terms responsible for the transients are known we can develop an amplitude and a phase function for the generator current to reduce the voltage transients. Feedback can be applied later, if needed. This is done below.

3. TRANSIENT COMPENSATION WITHOUT FEEDBACK

When we say the transient compensation without feedback we mean without the fast loops such as the direct rf feedback, local amplitude and phase feedback. The cavity tuning loop is, however, a must for the LEB since it affects all other states (see Eqn. 1). To see the compensation method more clearly, at first we extract the cavity voltage and phase equations below.

$$\dot{x}_4 = a_{42}x_2 + a_{43}x_3 + a_{44}x_4 + a_{45}x_5 + a_{46}x_6 + b_{43}u_3 + b_{44}u_4 + b_{45}u_5 + c_4 \quad (4)$$

$$\dot{x}_5 = a_{52}x_2 + a_{53}x_3 + a_{54}x_4 + a_{55}x_5 + a_{56}x_6 + b_{53}u_3 + b_{54}u_4 + b_{55}u_5 + c_5 \quad (5)$$

The control ' u_3 ' is the frequency shift provided in the global low level rf beam control system which has the effect over the complete ring. Hence, we cannot use this term to generate the feedforward function local to the cavity. Whereas control quantities, u_4 - the generator current amplitude and u_5 - the generator current phase are affected local to each cavity station. Therefore, by rearranging u_4 and u_5 in Eqns. (4) and (5) such that their combined effect nullifies the effect of the terms c_4 and c_5 on x_4 and x_5 , we would obtain the compensating function. It is given by the following equation.

The parameters, b 's are shown in Reference 3. u_4 and u_5 are calculated from Eqn. (6) for the LEB machine parameters. The computed feedforward functions are

$$\begin{bmatrix} u_4 \\ u_5 \end{bmatrix} = \begin{bmatrix} b_{44} & b_{45} \\ b_{54} & b_{55} \end{bmatrix}^{-1} \begin{bmatrix} -c_4 \\ -c_5 \end{bmatrix} \quad (6)$$

shown in Figs. 3 and 4. The generator current amplitude function has steps due to the discrete nature of the cavity voltage we used in the program. Fig. 5 shows the gap voltage error with respect to time after applying the compensation. Clearly it is well within 1% of the gap voltage. A disadvantage with this type of compensation is due to the fact that u_4 and u_5 also affect the coherent beam phase oscillations (see Eqn. 1). Also the upper and lower limits of these quantities must be in a realizable form. In the simulation studies using the predicted values of u_4 and u_5 , we see a negligible effect on the beam phase oscillations since the cavity voltage amplitude and phase error diminishes with accurate feedforward function. The function u_4 and u_5 look within practical limits and can be realized in practice using function generators with the functions feeding to the same control points (See Fig. 6) where the local amplitude and phase loops were expected.

4. CONCLUSIONS

In this paper we have identified the terms affecting the injection gap voltage transients in proton synchrotrons using the linear time-varying state-space model derived in Reference 3. Mathematical model was derived with the assumption that the ring cavities are lumped and is a simple equivalent RLC circuit. Also, the fundamental of the beam current was considered to include the beam loading effects. Using the model, a method was described to calculate the local feedforward function to cure the voltage transients. We did not see the need of local amplitude and phase loops to cure only predictable voltage transients. However, the presence of direct RF feedback loop for the LEB, although not essential, would benefit in correcting for unpredictable voltage transients occurring in a cycle to cycle basis.

5. REFERENCES

- [1] S. R. Koscielniak, "Compensation of RF Transients During Injection into the Collector Ring of the TRIUMF KAON Factory," PAC, May 1991.
- [2] P. Barratt, I. Gardner, C. Planner, G. Rees, "RF System and Beam Loading Compensation on the ISIS Synchrotron," EPAC, June 12-16, 1990.
- [3] L. K. Mestha, C.M. Kwan and K.S. Yeung, "Interaction Between Beam Control and RF Feedback Loops for High Q Cavities and Heavy Beam Loading," SSCL Preprint-195, February 1993.
- [4] F. Pedersen, "Beam Loading Effects in the CERN PS Boosters," IEEE Transactions on Nuclear Science, Vol. 22, No. 3, 1975.

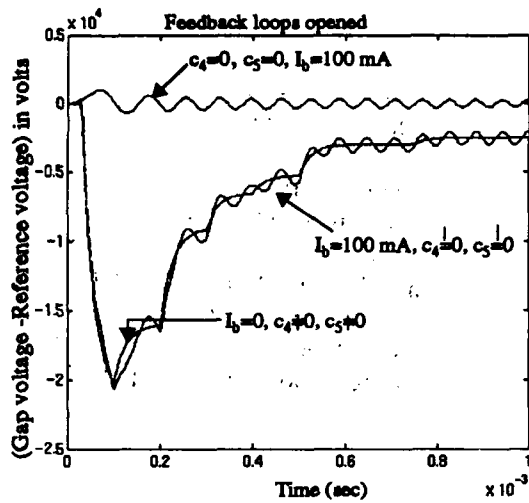


Fig. 1 : Cavity gap voltage error with time

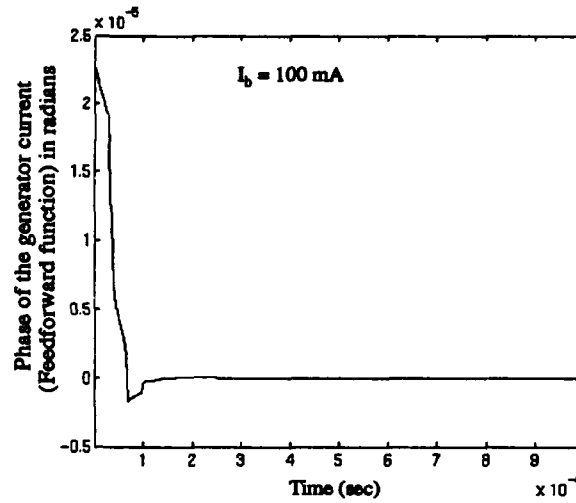


Fig. 4 : Generator current phase (Feedforward function)

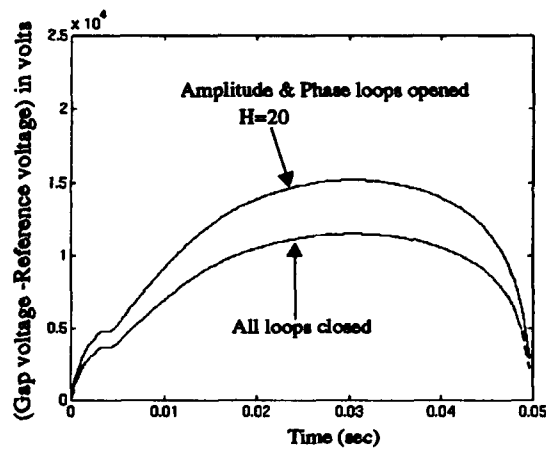


Fig. 2 : Cavity gap voltage error with time

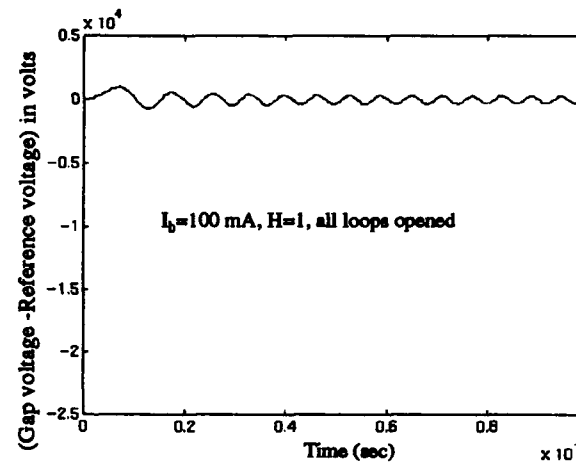


Fig. 5 : Cavity gap voltage error with feedforward correction

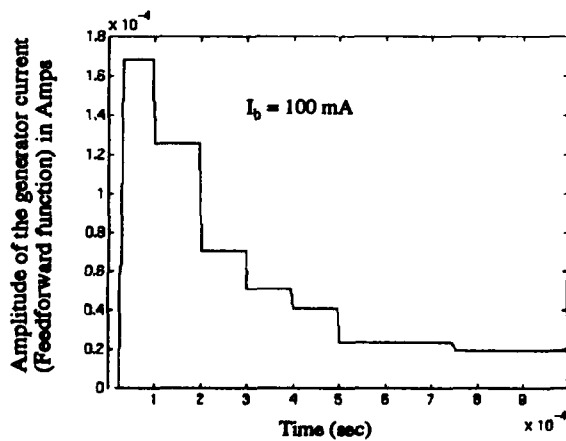


Fig. 3 : Generator current amplitude (Feedforward function)

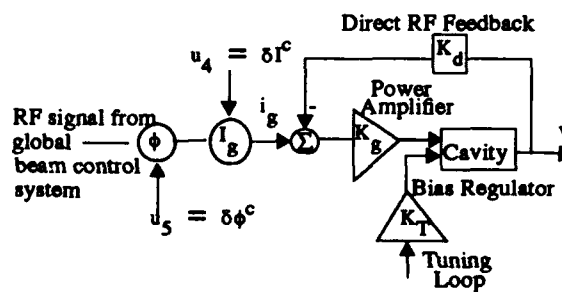


Fig. 6 Schematic representation of the control points for feedforward compensation system.

A Digital Phase and Amplitude Feedforward Correction System*

David Yu and Pat Conway
DULY Research Inc., Rancho Palos Verdes, CA

Abstract

We have designed and fabricated a phase and amplitude correction system¹ (PACS) using digital microelectronic circuitries and microstrip RF components with subnanosecond switching and response time. The control system uses a feedforward scheme to correct unwanted variations in phase and amplitude of a short (<100 ns) RF pulse which is generated repeatedly by an external RF source (e.g. relativistic klystron, FEL). Programmable or constant phase and amplitude (to within 0.5° and 0.1 dB, respectively) are achievable with the PACS. The system features a digitally programmable phase shifter and attenuator based on a direct RF digital-to-analog converter¹ (RFDAC).

Introduction

RF phase and amplitude stability is critically important for many accelerator applications. Devices for producing repeatable pulses of microwave energy at very high peak power typically include a pulsed microwave amplifier which amplifies an input signal produced by a low-power microwave generator. The energy required for signal amplification may be derived from a high energy electron beam directed into the amplifier. Klystrons, relativistic klystrons, free electron lasers and cyclotron auto-resonant masers are examples of pulsed microwave amplifiers of this kind. Amplitude and phase stability at the output of such pulsed microwave amplifiers is strongly dependent on the stability of the current and voltage, respectively, of the driving electron beam. For certain electron drivers such as linear induction accelerators, it is difficult to eliminate the current and voltage variations in a given pulse. Because of the physical sizes and resulting long signal paths of these devices, feedback correction techniques are not fast enough to correct variations in the phase and amplitude of the output *during* each pulse. An analog feedforward correction system² was considered earlier but was abandoned because, among other reasons, voltage-controlled phase shifters and analog output switches were too slow.

Our approach here is to use a fast digital feedforward correction system to incrementally reduce phase and amplitude variations in successive pulses. The apparatus comprises 1) a module which detects the phase and amplitude of an RF output pulse as a function of time, compares them with those of a reference, and converts the analog error signal into a sequence of 1-bit error data, 2) a module which stores and processes the phase and amplitude error data to generate two separate sequences of N-bit correction words, and 3) a module which uses the correc-

tion words to modulate the phase and amplitude of subsequent pulses. Since the pulse width (<100 ns) is typically much shorter than the time between pulses (>10 ms at moderate rep rate), the error detection and correction (modules 1 and 3) require very fast, accurate and reliable circuitry, while the error processing (module 2) can be done at a much slower clock rate between pulses. The system functions are synchronized by timing and control logic. The portable system is designed to mount in a standard 19 inch drawer, complete with power supply and self test logic. We plan to test this system soon on a high-power choppertron at Lawrence Livermore National Laboratory.

Description of the System

Fig. 1 is a functional block diagram of the phase and amplitude correction system (PACS). The system modifies the RF input signal based on error information obtained from the high power amplifier output. A portion of the RF CW input signal is used to provide a phase reference for the PACS. Another portion, after being modified by the PACS, is used to drive a high power amplifier such as a choppertron. The output frequency (11.4 GHz) of the LLNL choppertron is twice that of the input (5.7 GHz).

A small amount of the RF output pulse power is transported via a directional coupler to the PACS for processing. This signal is divided by a splitter and applied to a phase detector and an amplitude detector. The frequency of the phase detector reference is doubled to be coherent with the RF feedback pulse. An adjustable line stretcher is used to calibrate the phase detector.

An internal clock driven by a 1.5-GHz oscillator controls the timing bin width and the number of bins during a pulse. For the prototype PACS, we divide a pulse into 18 bins each having a bin width of 4 ns. The starting time of the first bin is within $1/3$ the bin width, or 1.33 ns.

Analog phase and amplitude error signals are converted to logic levels, bin-to-bin, by two separate comparators. Reference voltages or thresholds for the comparators are individually adjustable with potentiometers. The comparators may be considered to be 1-bit analog-to-digital (A/D) converters. A third comparator produces an input timing synchronization pulse. The amplitude error threshold is independent of the input timing threshold. A fourth comparator produces the output timing synchronization pulse. The input to the fourth comparator is provided by an external timing pulse. This pulse is timed so that its leading edge causes the phase and amplitude correction signals to arrive at the input of the high-power amplifier at the appropriate time to correct the output pulse.

The system corrects the phase and amplitude errors in parallel. Each pulse is divided into M bins. There are as many error (1-bit) words and correction (N -bit) words as there are bins. For the prototype, $M=18$ and $N=6$. Each of the 1-bit error data indicates whether the detected phase or amplitude in a time bin is higher or lower than the reference in the same time bin. The phase and amplitude errors are stored for each cycle and processed between pulses to generate the correction data for the next cycle. The algorithm for the mechanization is to either add one to a correction word, or subtract one from it, according to the sign of the corresponding error word. Shift registers are used for error and correction data storage. A timing signal consisting of M bursts of pulses are applied to write or read the M words of a pulse.

During the processing cycle, the error data in the storage banks is read out by applying slow clock bursts (approximately 1 MHz) of M pulses and processed by the correction logic. The results are stored in storage banks via a multiplexer. During the correction cycle, the correction data is shifted out of storage banks by applying the fast clock bursts, and applied separately to a programmable phase shifter or a programmable attenuator. The RF input is first corrected by the phase shifter, and is then coupled to the attenuator where the amplitude is corrected. The attenuation of the phase and amplitude correctors in the prototype system is chosen to provide a phase correction range of $\pm 30^\circ$ in approximately 0.5° steps, and an amplitude correction range of ± 3 dB in approximately 0.1 dB steps. Finally, the PACS output is applied to an external circuit as an RF input to a high power amplifier.

Timing and Control

The fundamental timing of the PACS is shown in fig. 2. The cycle is started by an output timing pulse. The correction cycle or fast output clock bursts are initiated by the leading edge of output timing pulse, and the processing cycle or slow clock bursts by the trailing edge. The output timing pulse is approximately 2 microseconds in duration to allow for completion of the correction cycle before starting the data processing cycle. The RF feedback pulse appears at the corrector system some time after the output fast clock bursts. The input timing pulse occurs when the RF output pulse is detected by the amplitude detector and comparator, triggering the input fast clock bursts. The fast output clock bursts can be delayed to compensate for differences in the phase and amplitude error detection paths.

The M slow clock bursts of the data processing cycle are initiated after the completion of the correction cycle. In the prototype PACS, the slow error processing logic block is time-shared by the phase and amplitude correctors.

The input timing logic and output timing logic are identical in generating the fast clock bursts of M pulses, but operate independently in time. They are driven by the high frequency clock generated by the 1.5-GHz oscillator.

The frequency of this clock is 6 times the bin rate. The bin-rate clocks are derived by dividing-down the frequency of this clock. Since the clock bursts are started on any cycle of the clock, the granularity of synchronizing the bin clocks with the actual bins is a fraction of a bin-time.

Programmable Phase Shifter and Attenuator

A feature of the present system is the provision of very fast bin-to-bin switching in the phase shifter and the attenuator. For this purpose we have conceived and implemented an RF digital-to-analog converter (RFDAC). The basic idea of the RFDAC¹ employs mixers that are digitally controlled as bi-phase modulators producing binary weighted outputs, which are then summed to produce the desired output amplitude. Schottky diodes possess the properties of high-speed switching and meet the drive requirements. The output voltage is an RF signal rather than the conventional DC. The RFDAC is thus an apparatus which produces the processed RF directly without intermediate analog steps. A schematic of a 6-bit RFDAC is shown in fig. 3. Leads 2 and 4 are RF input and output, respectively. Lead 3 is a digital input. Prior to assembling the phase and amplitude correctors, we dynamically staircase tested a 6-bit 5.7-GHz RFDAC breadboard, monitoring the RF waveform with a Tektronix 11802 sampling scope. A control logic circuit triggers a total of 64 steps in 180 ns (2.8 ns/step). A band-pass filter of 2.4 GHz bandwidth centering at 5.7 GHz is used to suppress logic noise feedthrough. The dynamic test setup is shown in Fig. 4 and the staircase test results are shown in fig. 5.

A simple way to implement a programmable attenuator using an RFDAC is shown in fig. 6. The RF input is split by a power splitter and applied to the input of an RFDAC and to a power combiner. The output of the RFDAC is applied to the same combiner. The RFDAC produces an RF output according to the state of the digital input. The output voltage of the combiner is equal to 0.7071 times the vector sum of its inputs (not accounting for insertion losses). Thus the output varies in amplitude according to the state of the digital input. The dynamic range of the attenuator is adjusted by setting the signal level of the RF DAC range. A programmable phase shifter is similarly constructed using a 90° combiner in place of the 0° combiner in the programmable attenuator. The range of phase shift is set by adjusting the signal level of the RFDAC range.

We thank T. Houck, K. Kawaguchi, J. Northland, J. Papalski, R. Stever, G. Westenskow and J. Vogler for their assistance.

*Work supported by DOE SBIR Grant No. DE-FG03-90ER80907.

¹U.S. patents pending (07/952,065, 08/055314).

²D. Hopkins, D. Yu, et al., Proc. IEEE Part. Acc. Conf., San Francisco, May 6-9, 1991, pp.1335-1337.

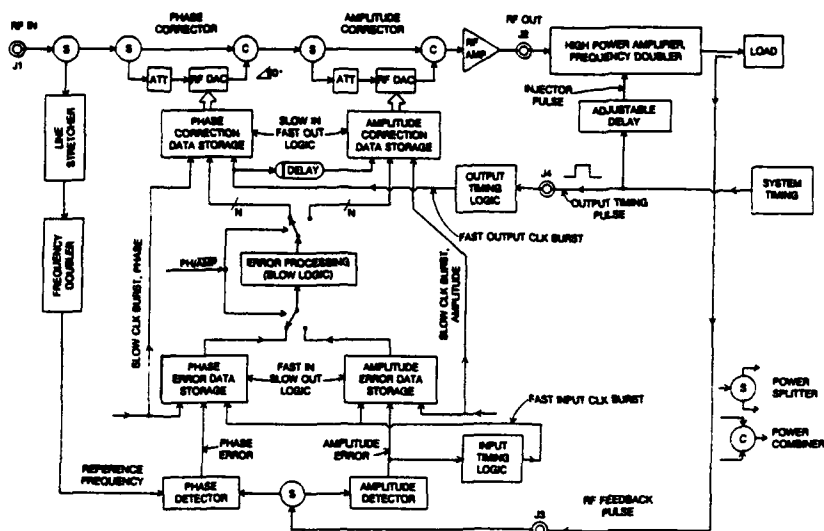


Figure 1 System Functional Block Diagram

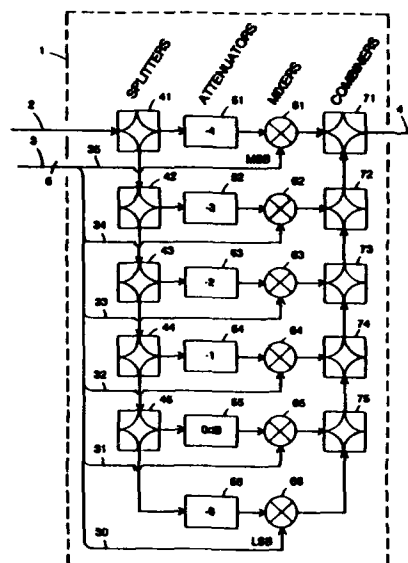


Figure 3 6-Bit RFDAC Schematic

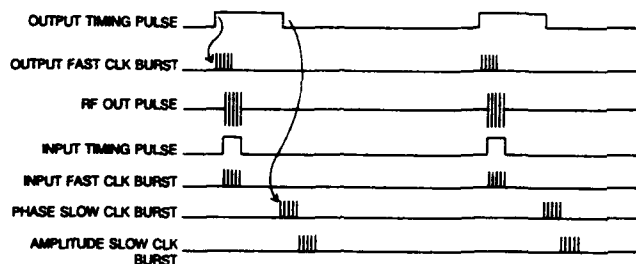


Figure 2 System Timing Pulses

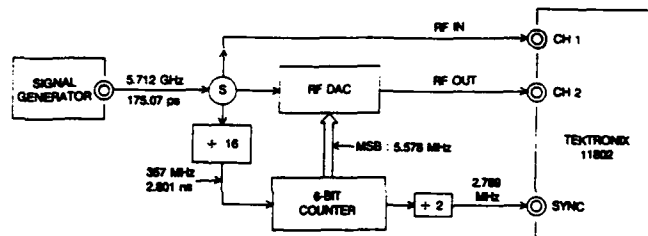


Figure 4 Dynamic Test Setup for an RFDAC Breadboard

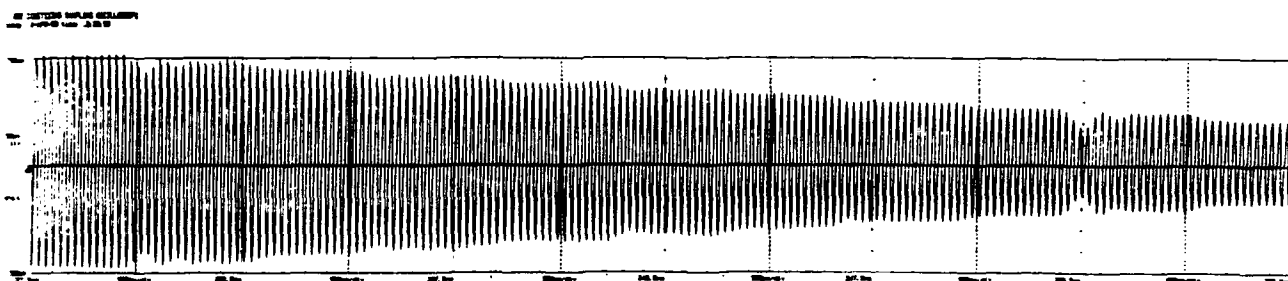


Figure 5 Staircase Test Results, 227.5 ns to 257.5 ns, in 2.8 ns Steps

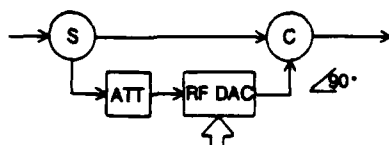


Figure 6 Programmable Phase Shifter/Attenuator

Results Of Adaptive Feedforward On GTA*

C. D. Ziomek, P. M. Denney, A. H. Regan, M. T. Lynch, S. P. Jachim, L. E. Eaton, E. F. Natter
MS-H827, Los Alamos National Laboratory, Los Alamos, NM 87545

Abstract

This paper presents the results of the adaptive feedforward system in use on the Ground Test Accelerator (GTA). The adaptive feedforward system was shown to correct repetitive, high-frequency errors in the amplitude and phase of the RF field of the pulsed accelerator. The adaptive feedforward system was designed as an augmentation to the RF field feedback control system and was able to extend the closed-loop bandwidth and disturbance rejection by a factor of ten. Within a second implementation, the adaptive feedforward hardware was implemented in place of the feedback control system and was shown to negate both beam transients and phase droop in the klystron amplifier.

I. INTRODUCTION

The GTA control system uses feedback to control the RF fields in the accelerating cavities. A simplified block diagram of the GTA RF control system is depicted in figure 1.

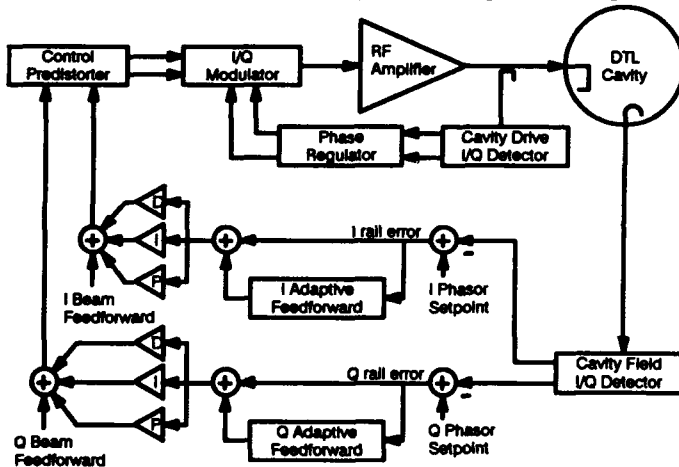


Figure 1. Simplified block diagram of GTA control system

Closed-loop bandwidths of a few hundred kHz have been demonstrated by the GTA RF control systems [1]. These bandwidths are limited by the physical properties of the high-Q cryogenic cavities, the high-power amplifier responses, and the long propagation delays due to the large physical distances between equipment. The amplitude and phase disturbances to the RF field that are beyond the closed loop bandwidth cause amplitude and phase errors in the accelerating field. A significant disturbance that occurs with every RF pulse is the beam turn-on transient. The fast rise-time of the beam causes the accelerating field to droop before the feedback system can compensate. The beam turn-on disturbance causes transient errors in the field amplitude and phase for a few microseconds as the feedback loop recov-

*Work supported and funded by the United States Department of Defense, Army Strategic Defense Command, under the auspices of the United States Department of Energy.

ers. Due to the repetitive nature of the beam transients, a feedforward correction function can be inserted into the drive signal that will predict the beam transient affects. This correction function is adaptively updated as the accelerator operates to optimize a correction function that negates the repetitive disturbances. The detailed theory of operation is described elsewhere [2-4]. This paper will focus on the experimental results of the hardware functioning on the first drift tube linac (DTL) cavity of GTA.

II. ENHANCEMENT TO FEEDBACK

The adaptive feedforward hardware was designed to operate as a modular addition to enhance the feedback control system. Figure 1 shows the experimental setup for the adaptive feedforward tests on the first 850 MHz DTL cavity of GTA. The operating conditions for the DTL consist of a gap voltage of 2.1 MV, a beam current of 30 mA with a -30° synchronous phase, and copper losses of 33 kW. From this, the beam loading calculates to be 62%.

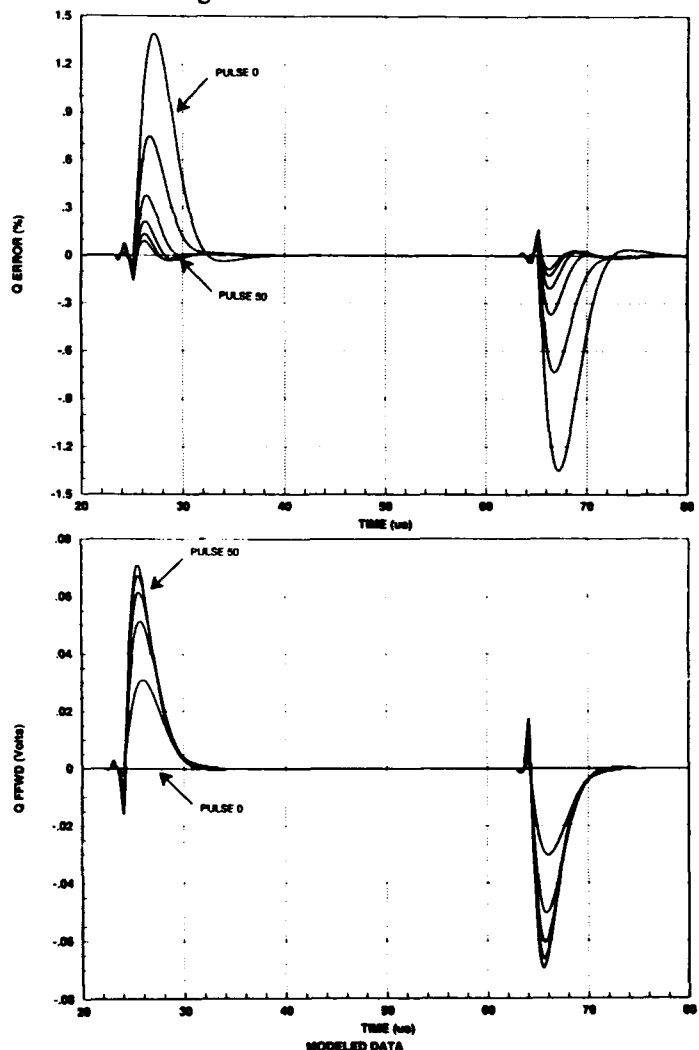


Figure 2. Modelled results of feedforward as enhancement

Figure 2 shows the predicted RF system performance determined with a sophisticated software model of the GTA RF system. The figure shows a sequence of five traces that depict the expected feedforward and error signals as the adaptation occurs over the course of 50 pulses. The feedforward correction function adapts to the transient errors in the RF field caused by the beam pulse turning on and off. Notice that the feedforward signal grows and the error signal is reduced as the hardware adapts. These traces depict the quadrature signals only, but the in-phase errors are simultaneously reduced as well.

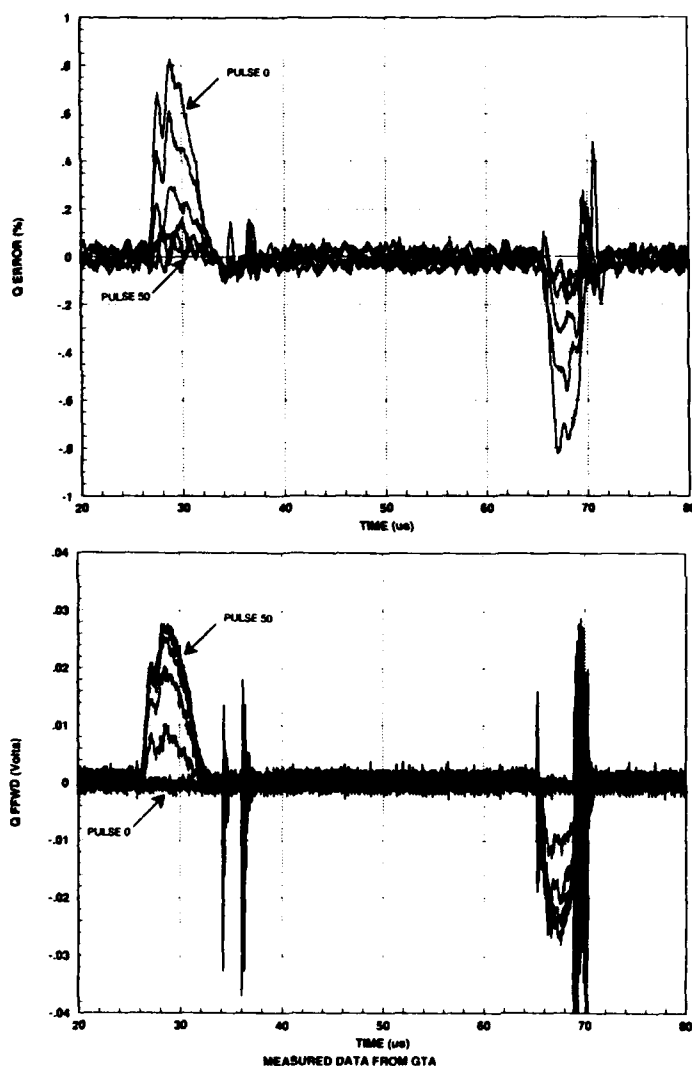


Figure 3. Measured results of feedforward on GTA

Figure 3 shows the measured data from an experiment on the first DTL cavity of GTA. Again, five feedforward and five error signals in a sequence of 50 pulses are shown. The errors are caused by the beam turn-on and turn-off transients. As the system operation progresses, the correction function improves and the error signal is reduced. Before adaptation begins (pulse 0), the magnitude of error in the quadrature component of the RF field is $\pm 0.8\%$. After 50 pulses of adaptation, the quadrature error is reduced to less than $\pm 0.1\%$. Notice that the measured DTL performance

closely matches the expected performance derived from the model.

III. REPLACING FEEDBACK

In addition to the intended implementation of the adaptive feedforward module, a second functional configuration was evaluated. Instead of using the device as a feedforward enhancement to the feedback control system, the module can be used as an adaptive controller, replacing the feedback control system entirely. Figure 4 shows the topology of this configuration, where the control output is provided

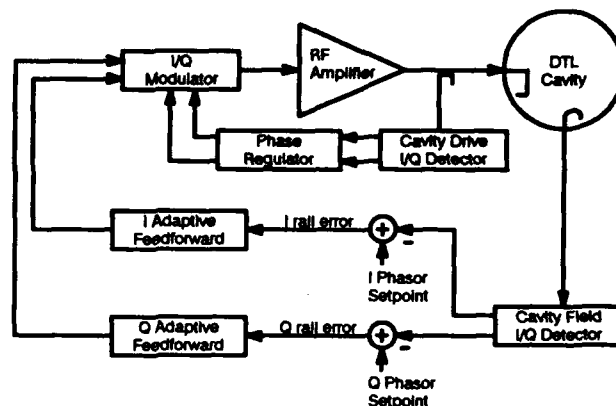


Figure 4. Diagram of adaptive control system (no feedback)

by the adaptive controllers. The measured parameters of past RF pulses are used to derive the control output for the current pulse. As system parameters vary over time, the adaptive controllers modify the control output. Any instantaneous changes in the system require a number of pulses for the control function to adapt, but the system does track slow changes very closely. As long as the time constants for the changes are significantly longer than the repetition rate for the pulsed accelerator, the field amplitude and phase can be accurately maintained. For the GTA DTL, the accelerator repetition period is hundreds of milliseconds, whereas the changes in the RF hardware performance occurs at very slow rates (many seconds or minutes). A drawback of this device is that the controller needs past data measurements in order to adaptively determine the control output. Consequently, when the system is turned on or the setpoint changes, a number of pulses occur before the field parameters settle to the operating point.

Figure 5 shows the measured results of using the device as an adaptive controller to maintain the amplitude and phase of the RF field in the accelerating cavity. These plots show 5 traces of the in-phase and quadrature errors for the entire RF pulse as the controller adapts for 50 pulses. Notice that before the adaptation begins (pulse 0), the field falls during the beam loading and there is a ramp in the quadrature error is due to the phase droop of the klystron amplifier. After 50 pulses of adaptation, the in-phase error is reduced from 0.8% to 0.1% , and the quadrature error is reduced from 2.8% to 0.1% . During this experiment, the adaptive controller was able to hold the RF field parameters within 0.2% of the operating point for many minutes of operation.

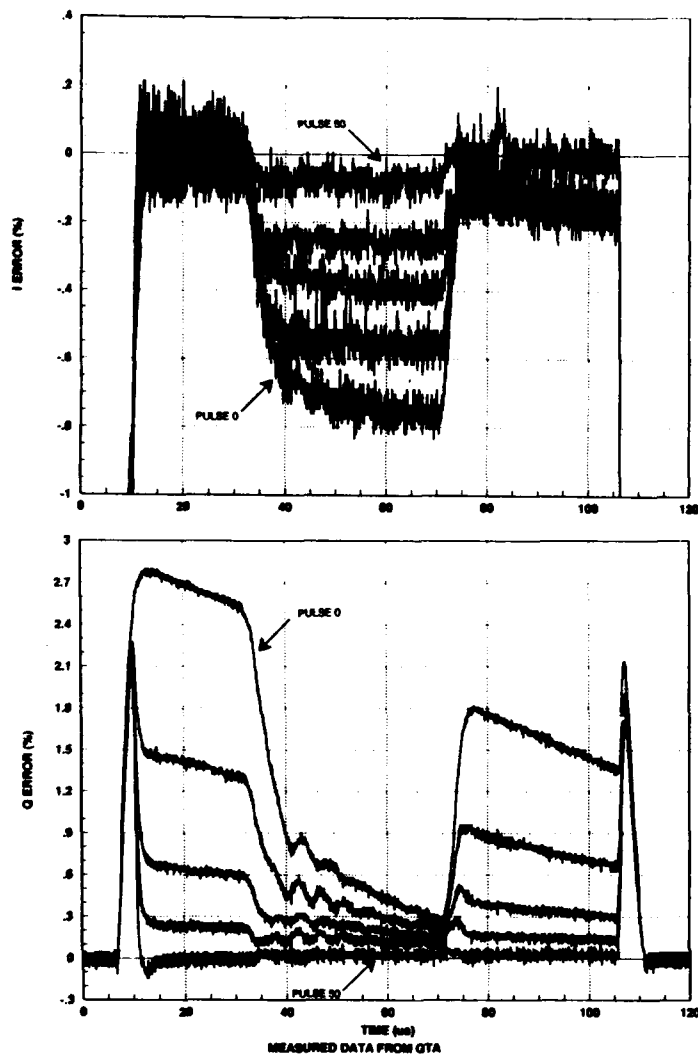


Figure 5. Measured results of adaptive control (no feedback)

IV. FUTURE WORK

These experiments proved extremely successful and verified the concept of adaptive feedforward as a viable solution to improving the field control performance for pulsed accelerators. In addition, some possibilities for additional work in the future were identified. As shown in figure 3, there are transient glitches that grow slowly as many pulses are accumulated. These glitches are a result of the adaptive algorithm used to accumulate the error functions for all past pulses with no way of eliminating some of the past data. Consequently, any circuit or computational glitches will eventually grow to become significant. A revision that incorporates a forgetting function has been designed. The algorithm governing the adaptive process remains

$$f_N(t) = \sum_{i=0}^{N-1} k_i \cdot e_i(t + \Delta T) \quad (1)$$

but whereas in the original implementation all the k_i values were equal, the revision incorporates exponential k_i values, creating a windowing or forgetting function. The forgetting function creates a sliding window that is used to

weight a finite number of past data values for accumulation into the correction function. Consequently the algorithm for the revision is described by the equation

$$f_N(t) = g \cdot f_{N-1}(t) + k \cdot e_{N-1}(t + \Delta T) \quad (2)$$

In this algorithm, the gain, k , corresponds to the adaptation gain which affects the sensitivity and adaptation time for the device. The gain, g , provides the forgetting function that is used to discard old data with an exponential decay. The preliminary tests with the new design show that by including the forgetting function, g , the adaptation gain, k , can be increased significantly. Thus, the new design allows more input sensitivity (more dynamic range) and provides a faster settling and tracking time.

The success of the adaptive controller configuration suggests additional applications for this type of device. An adaptive, stand-alone controller could be useful for many accelerator RF systems where conventional feedback control is impractical. For example, short-pulse-length accelerators typically do not have time for feedback corrections. The adaptive controller could adaptively predict the correct control output.

Currently, there is significant interest in evaluating the usefulness of the current design for other accelerator applications. Adaptive feedforward tests are scheduled for LANSCE II, University of Twente FEL, AFEL, and APLE. Each of these accelerators requires control bandwidths greater than a feedback system can provide. The adaptive feedforward is a viable solution to this common accelerator RF control requirement.

VI. REFERENCES

- [1] P. Denney, S. Jachim, "Measured performance of the GTA RF Systems" *Proc. IEEE Particle Accelerator Conference*. May, 1993.
- [2] C.D. Ziomek, "Adaptive feedforward in the LANL RF control system" *Proc. Linear Accelerator Conference*. August, 1992.
- [3] S.P. Jachim, et. al., "The Los Alamos VXI-based modular RF control system," *Proc. IEEE Particle Accelerator Conference*. May, 1993.
- [4] C. Ziomek, S. Jachim, E. Natter, "Design of a multivariable control system using gain-shaping in the frequency domain," *Proc. IEEE Particle Accelerator Conference*. May, 1991.

FAST BUNCH-TO-BUNCH CURRENT SAMPLING IN THE CORNELL ELECTRON-POSITRON COLLIDER

C. R. Dunnam

Laboratory of Nuclear Studies ♦
Cornell University, Ithaca, NY 14853

K. B. Unser

European Organization for Nuclear Research (CERN) - SL Division
CH-1211 Geneva 23, Switzerland

Abstract

Preliminary studies of a high resolution Cornell Electron-positron Storage Ring (CESR) bunch-to-bunch signal processing system are described. In these studies, a prototype inductive-integrating, sampling current monitor is evaluated for improved estimation of bunch lifetimes over a series of planned CESR luminosity upgrades. Initial test data indicate significant performance advantages over conventional electrostatic pickup systems in the areas of linearity, dynamic range and beam position sensitivity. Novel features of the fast bunch current monitor include its wideband passive integrating pickup, duplex filter section and high resolution bunch signal processor (BSP). Evaluation studies in CESR indicate this fast bunch monitor is potentially useful in colliders and other storage rings utilizing bunch-to-bunch or bunch train separations down to 80 nanoseconds. Proposed system revisions to permit fast, high resolution bunch train current measurements in future CESR operations are discussed. Commercial availability of several principal bunch-to-bunch current monitor components is noted.

Introduction

Fundamental revisions of CESR storage ring operating procedure are presently under consideration for increased luminosity via multibunch-train HEP operation¹. Preliminary investigations have demonstrated the utility of diagnostic techniques which provide accurate lifetime and reliable absolute charge measurements of individual trains. Applications for a CESR multichannel fast current monitor include injection studies, examination of differential loss near parasitic crossings and tune-up for high energy physics.

Accurate differential current measurements and lifetime prediction require current monitor signal-to-noise (SNR) performance not obtainable with electrostatic pickups, and absolute determination of bunch intensities demands linearity beyond the capability of conventional pulse stretchers. A series of evaluation studies² conducted at Cornell several years

ago in collaboration with CERN's LEP Division demonstrated the potential utility for CESR of a high resolution wideband passive-integrating bunch charge monitor. Since that time, further research and development at CERN^{3,4} and technology transfer to the commercial sector has led to evolution of several high performance standardized system components⁵. This paper describes a prototype system for CESR, based on these components, which is suitable for both multiple bunch and bunch-train measurements.

Evaluation Fast Bunch Processor System

A single-channel version of the proposed multichannel CESR fast bunch monitor (FBM), assembled for evaluation of principal components and initial diagnostic tests, is shown in Figure 1. Of principal interest are performance of the

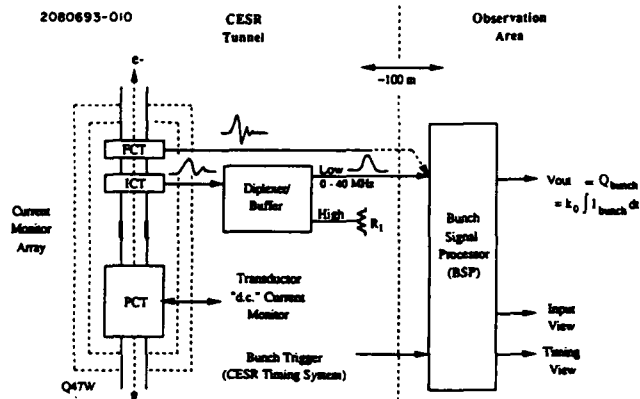


Figure 1. FBM evaluation system.

integrating current transformer (ICT), r.f. diplexer and BSP fast gated integrator subsystems. The ICT and BSP are commercial units (ref.: figure 2), while the r.f. diplexer is a proprietary lowpass filter device. For evaluation purposes, the prototype system's analog path is configured to resemble that of the proposed multichannel monitor, so that the ultimate dynamic range and linearity parameters of the proposed system may be accurately predicted by performance of the prototype. Only the ADC and I/O sections differ: for evaluation studies, a high resolution integrating voltmeter and

♦ Work supported by NSF grant PHY-9014664.

an IEEE-488 (GPIB) data bus have been substituted for the high resolution ADC's and CESR control system interface.

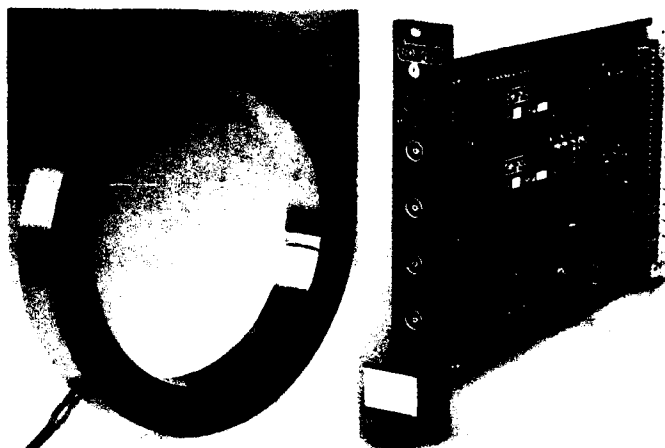


Figure 2. ICT and BSP system components.

As an electron or positron bunch traverses the CESR current monitor assembly, a fraction of its wakefield energy propagates through a capacitive gap in the ceramic beampipe section into a cavity which encloses the fast (FCT), ICT and PCT "d.c." current monitor transformers. Spectral components of the trapped electromagnetic field, in the range of d.c. to approximately 600 MHz, induce corresponding signals at the output of each transformer. The FCT output is a fast (.02 to 320 MHz @ -3 dB) single-turn diagnostic tool which can be used as a lower-resolution "backup" input to the fast bunch signal processing system if needed. For high resolution diagnostics, the spectrally-shifted ICT signal is required.

As a signal source for the fast bunch processor system, the ICT possesses a useful property of passive spectrum down-conversion⁶, transposing essentially all energy deposited by a passing bunch to a lower frequency range. The translated spectrum is now entirely within the upper band limit of the bunch signal processors' (BSP) precision gated differential integrator, yielding optimal system dynamic range and linearity. System waveforms are shown in Figure 3. The ICT output waveform of Figure 3a consists of a spectrum-shifted (i.e., stretched) pulse of around 35 nanoseconds with a ringing artifact superimposed by a broad, unavoidable cavity resonance. All but a few percent of the wideband input energy has been translated into a signal bandwidth of ≈ 0.1 to 20 MHz. Figure 3b demonstrates the 35 MHz diplexer lowpass filter section's effect in removing the ringing component. Pulse width broadening from the original 35 nanosecond value to around 50 nanoseconds occurs in the filter, but has no appreciable effect on system performance. Figure 3c shows

the timing sequence monitor signal available from the BSP bunch signal processor. Following a CESR timing system trigger, the processor first synchronizes, then initiates a signal integration period (70 nanoseconds for CESR), then integrates with opposite sign for a precisely equal time. In CESR, the desired bunch is acquired during the second timing window, with the corresponding baseline offset integral taken during the third window, after which the BSP resets to its quiescent state.

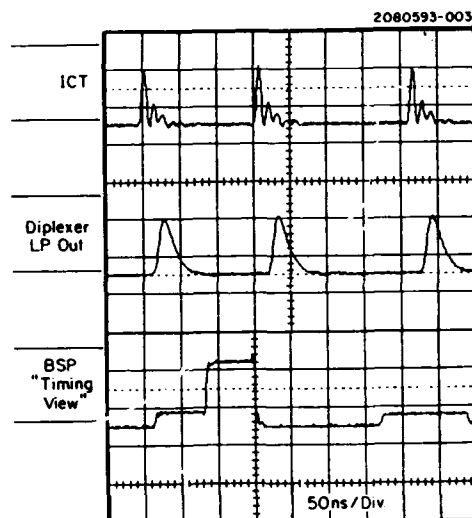


Figure 3. FBM signal and timing view waveforms.

Evaluation data

Signal-to-noise (SNR) performance, dynamic range and linearity are extracted from analysis of data collected at a fixed timing value. Results of the data analysis are presented in Table 1.

Resolution:	$Q_{Nrms} = 8.40E6 \text{ e}$
Maximum charge:	$Q_{max} = 9.03E11 \text{ e}$
Dynamic range:	$= 1.07E5$
Linearity:	$= 1.47E-3$

Table 1. Measured parameters.

These measurements indicate a CESR fast bunch resolution of approximately 1.3 pC (0.53 μA)—very good performance for the 167 ms averaging period under which the evaluation data were taken (a factor of 1.5 improvement is expected with a 0.5 sec/point data input rate of the proposed multichannel system). Saturation bunch charge has been calculated from the data scale factor; the dynamic range figure is based on the system saturation level and the calculated resolution. An upper bound on minimum linearity is derived from an exponential fit to the full data set.

Position sensitivity is a critical parameter which can strongly affect system resolution, due to the large transverse noise inherent in circulating lepton beams. Although the high prototype system resolution of Table 1 indicates little or no position sensitivity, a study of large deflections in both x and y transverse axes was conducted over a full range of possible CESR beam position offsets to verify the observation under worst-case conditions. From analysis of the data, we conclude that the ICT position sensitivity is less than 5×10^{-5} for a ± 10.0 mm deflection.

Proposed Systems

A proposed multichannel high resolution bunch-to-bunch current monitor for CESR is outlined in Figure 4. Its analog

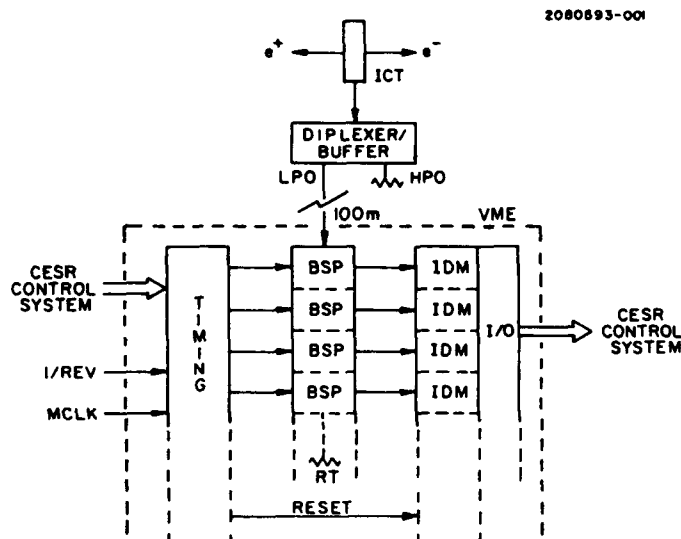


Figure 4. Proposed multichannel FBM

path is identical to the evaluation system, with the exception of signal division as needed for the parallel bunch signal processors. In the parallel system, triggers for the processors are generated locally and provision is made for interleaving (i.e., reassigning sampling times) as needed to best utilize the parallel BSP array. Interfacing to the CESR control system is effected through a parallel system of 20 bit integrating ADC's and a multiport control interface. All analog and digital subsystems will reside in a single VME crate.

In the near future, the multichannel system is expected to serve as a CESR multi-bunch train fast current monitor. Because the bunches in a CESR train will be separated by as little as 14 nanoseconds, the fast current monitor only provides charge integration over the duration of each of the 18 trains. This does not diminish overall diagnostic capability, however, since high resolution measurements of the integrated train charges will provide the same information

regarding differential loss and absolute intensity as before. Nonetheless, it is evident that the BSP internal timing will have to be substantially modified to accommodate multibunch-train operation, since the trains are longer than the inter-train separations. We anticipate that appropriate scaling and weighting of BSP integration window intervals and values will provide a viable capability for future multibunch-train studies in CESR.

Conclusions

Analysis of evaluation data collected from the Cornell prototype fast bunch-to-bunch current monitor indicates that the critical performance parameters of dynamic range and linearity have been met at the present 180 nanosecond CESR bunch spacing. Position sensitivity has been found to be at or below the system noise level for beam offsets well beyond the maximum CESR aperture at the ICT pickup location. The multichannel fast current monitor, with some revisions, is expected to remain useful over a series of CESR multibunch-train upgrades. Compared with button or stripline based fast current monitors, the integrating current transformer (ICT)-based bunch charge monitor appears to offer far superior dynamic range, negligible beam position sensitivity and relative system design simplicity.

Acknowledgment

We wish to thank Messrs. J. Bergoz and A. Charvet (BERGOZ, Crozet, France), who provided us with expert technical assistance in preparation for the CESR evaluation studies.

- ¹ D.H. Rice, invited paper, PAC'93, Washington, D.C., May, 1993.
- ² K.B. Unser, "Design and Preliminary Tests of a Beam Intensity Monitor for LEP", CERN/LEP/89-07, Particle Accelerator Conference, Chicago, IL, March, 1989.
- ³ K.B. Unser, "Measuring Bunch Intensity, Beam Loss and Bunch Lifetime in LEP", CERN/SL/90-27, EPAC'90, 2nd European Particle Accelerator Conference, Nice, France, June 1990.
- ⁴ G. Burtin et al, "Mechanical design, signal processing and operator interface of the LEP beam current transformers", CERN/SL/90-30, EPAC'90, 2nd European Particle Accelerator Conference, Nice, France, June 1990.
- ⁵ Product literature, "Integrating Current Transformer" and "Bunch Signal Processor", BERGOZ, 01170 Crozet, France, 33-50.41.00.89
- ⁶ K.B. Unser, "Design and Preliminary Tests...", p.2, §6.

A METHOD FOR MEASURING DARK CURRENT ELECTRON BEAMS IN AN RF LINAC*

X.K. Maruyama, T. Fasanello, H. Rietdyk
Naval Postgraduate School, Monterey, CA 93943

M.A. Piestrup
Adelphi Technology, Palo Alto, CA 94301

D.W. Rule, R.B. Fiorito
Naval Surface Warfare Center, Silver Spring, MD 20903

Abstract

X-ray fluorescence from thin foils inserted into the Naval Postgraduate School linac has been used to measure the integrated electron beam intensity when the accelerator is operating with dark current. The measured x-ray flux, the known inner shell ionization cross sections and radiative transition probabilities are used to obtain measurements of dark currents of the order of 10^{-14} Amperes. The same arrangement allows continuous, in-situ energy calibration of our SiLi detector in the electromagnetic noise environment of the linac. This technique was originally developed to perform absolute production efficiency measurements of parametric x-ray generation in the 5 - 50 keV range.

I. INTRODUCTION

The count rate for X-ray spectroscopy experiments are limited by detector characteristics and for large cross section events, the incident electron current must be considerably reduced. In our experiment to measure the characteristics of parametric x-radiation (Bragg scattering of virtual photons)¹, the electron beam from a pulsed s-band linac was restricted to dark current wherein the electron gun was turned off and average currents of the * order of 10^{-14} amperes were incident on target (10^{-14} A is approximately 1000 electrons per each 1 μ s macrobunch in our linac). Such small currents presented a challenge in determining the normalization for the absolute production efficiency of x-rays.

A second consideration is the energy calibration of the x-ray spectrum in the linac environment. The detector is energy calibrated against known sources in a static environment. However, x-rays are generated by electrons from a pulsed s-band rf linac wherein they are accelerated in 1 μ s macrobunches. For our

application, the microbunch structure is not a consideration since the detector resolving time is longer than the linac macrobunch time. During the interaction time of the electron with the target, there are sources of noise associated with the linac pulse structure which distort the energy calibration. These include klystron rf noise picked up by the detector preamplifier and ground loop currents. Physical corrections such as rf shielding and grounding of the detector system are only partially successful.

II. X-RAY FLUORESCENCE MEASUREMENTS

Both x-ray energy and electron fluence questions have been successfully addressed by the observation of K fluorescence photons from electron-excited atoms. K energies are well known. Since the electro-excited atomic lifetimes are much shorter than 1 μ s they may be considered to be created within the linac bunch duration. With the knowledge of electron interaction cross sections² and from radiative transition probabilities³, the fluorescent x-ray intensities may be unfolded to obtain the incident electron integrated current. Figure 1 presents a spectrum of fluorescence x-rays obtained from a foil target consisting of a sandwich of titanium, yttrium and tin. For this measurement, the target foil was rotated 30° from normal to the electron beam. 85 MeV electrons were made incident upon the foil targets and x-rays were measured with a Si(Li) detector placed at 45° with respect to the incident electron beam direction. We have also made measurements using other materials such as copper and indium to address other energy calibration markers. By identifying known emission line energies with observed peaks the measured spectrum could be calibrated.

The fluorescence was assumed to be isotropic. Care was made to order the target foils so that the x-rays were generated sequentially in tin, yttrium and titanium in order to insure that the softer x-rays suffered less attenuation. The targets were placed in a vacuum chamber and had to traverse a 25 μ m kapton window, a 1.3 cm air gap and a 50 μ m beryllium window before entering a 5 mm thick Si(Li) detector. Corrections for

* This work was partially supported by the Defense Nuclear Agency, the Naval Postgraduate School and USDOE SBIR Contract (No. DE-FG03-91ER81099).

attenuation⁴ in the intervening materials were made.

$$N_e = \frac{N_{ph} AW}{\sigma \left(\frac{\Omega_d}{4\pi} \right) \rho N_o f_{det} t_{eff} a \epsilon}$$

where,

- N_e = total number of electrons incident on target
- N_{ph} = Number of photons detected
- AW = Atomic Weight of target (g/mole)
- σ = electron interaction cross section (cm²)
- Ω_d = detector solid angle
- ρ = density of target material (gm/cm²)
- N_o = Avogadro's number
- f_{det} = radiative transition probability
- t_{eff} = effective target thickness (cm)
- a = total photon attenuation factor
- ϵ = detector efficiency

When two photons arrive within the resolving time of the detector, they are counted as a single photon with energy equal to the sum of the two photons. The inferred average currents when the ratio between linac machine pulses and events counted in the pulse height analyzer was 2:1 differ by over 30 %. When the ratio of machine pulses to observed counts is increased to 7:1, the range of inferred currents is reduced to a more consistent 13 %. The uncertainties presented in these tables mainly reflect the estimated uncertainties of 30 % for the electron-interaction cross section² and 10 % for the radiative transition probabilities³. These uncertainties reflect systematic errors for determination of the absolute integrated beam current.

III. APPLICATION

The method prescribed here was used to both energy calibrate and normalize the spectrum of x-rays from parametric x-radiation¹. Figure 2 presents an observed PXR spectrum. In this observation, a thin foil of tin was placed on the back of a mosaic graphite target from which the PXR peaks of interest were generated. The fluorescent x-rays and the parametric x-rays were measured under identical conditions. PXR peaks are located at integer multiples of the fundamental. By carefully selecting x-ray fluorescence calibration materials, the calibration peak may be made to not interfere with the measurement of the PXR peak. The tin x-ray peaks serves both as an energy marker and as an integrated beam current monitor.

IV. CONCLUSION

By measuring fluorescent x-rays simultaneously with photons generated from parametric x-radiation, an on-line energy and intensity calibration has been determined. This technique can be further exploited for special circumstances. With a soft x-ray detector contained in the same vacuum system as the electron beam, it would be possible to use the x-ray fluorescence from the parametric x-ray generation target. For example, with a crystalline silicon target, 1.8 keV x-rays would have to be detected. For heavier crystals such as silver, the present arrangement would suffice result in K_{α} x-rays of 22.16 and 21.99 keV and K_{β} x-rays of 24.9 keV.

The method described in this paper need not be confined to the measurement of parametric x-radiation, but can be extended to other sources such as channeling⁵ and transition radiation⁶.

	Tin	Yttrium	Titanium
N_{ph}	453±95	2553±194	1214±177
$N_e (10^8)$	9.67±3.67	9.48±3.13	8.57±2.99
$I(10^{-14} A)$	3.70±1.41	3.62±1.19	3.28±1.15

Table I. Number of observed photons, incident electrons and average current. Elapsed time was 4212 s.

V. REFERENCES

1. D.W. Rule, R.B. Fiorito, M.A. Piestrup, C.K. Gary and X.K. Maruyama, "Production of X-rays by the Interaction of Charged Particle Beams with Periodic Structures and Crystalline Materials", SPIE, 1552, p. 240 (1991). See also X.K. Maruyama et al., these Proceedings.
2. S.T. Perkins, D.E. Cullen and S.M. Seltzer, "Tables and Graphs of Electron-Interaction Cross Sections from 10 eV to 100 GeV", LLNL, UCRL-50400 Vol 31 (1991).
3. S.T. Perkins et al., "Tables and Graphs of Atomic Subshell and Relaxation Data Derived from the LLNL Evaluated Atomic Data Library (EADL), Z=1-100", LLNL, UCRL-50400 Vol 30 (1991).
4. J.H. Hubbell, "XCOM: Photon Cross Sections On a Computer", U.S. Department of Commerce, NBSIR 87-3597 (1991).
5. e.g., H. Uberall, B.J. Faraday, X.K. Maruyama and B.L. Berman, "Short-Wavelength Radiation Sources", 1552, p. 198 (1991).
6. e.g., C.I. Pincus et al., "Measurements of X-Ray Emission from Photoabsorption-edge Transition Radiation", J. Appl. Phys. 72,4300 (1992).

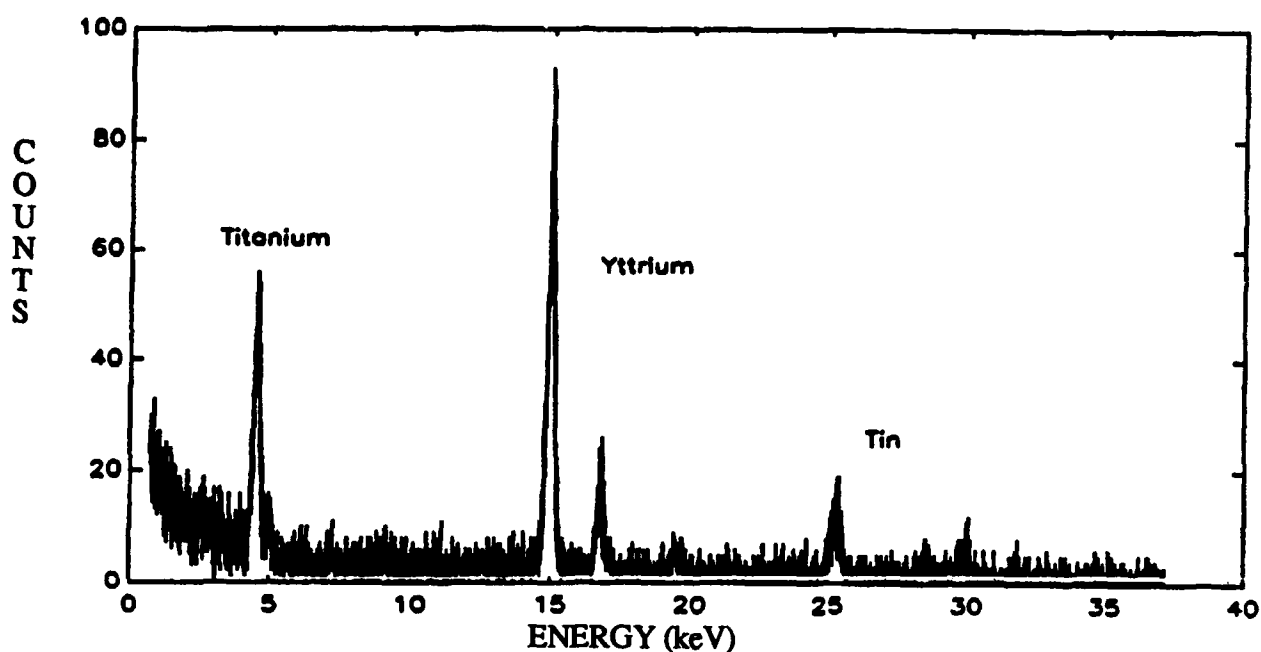


Figure 1. Pulse Height Analysis Spectrum of fluorescent x-rays from a sandwich foil of titanium, yttrium and tin. In Y and Sn the K_{α} and K_{β} lines are observed. Electron beam energy was 85 MeV.

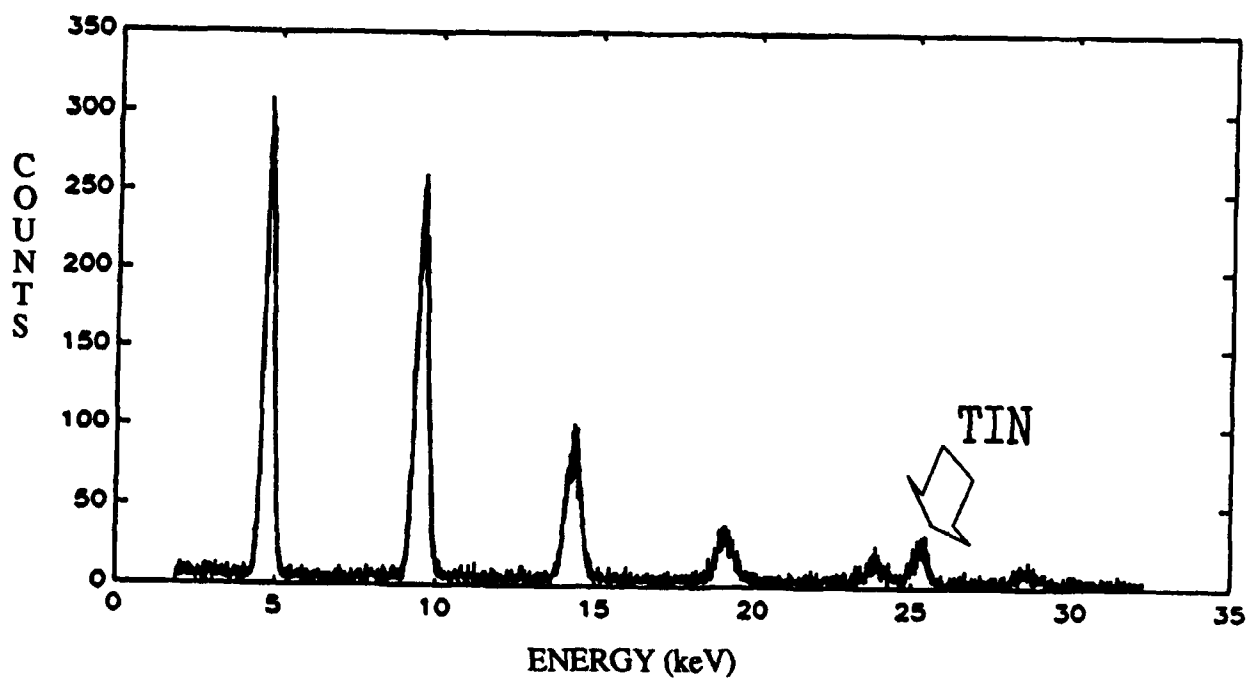


Figure 2. Observed spectrum of parametric x-radiation from a mosaic graphite target. A thin foil of tin behind the PXR target was used to create the calibration peak at 25.2 keV.

High Bandwidth Beam Current Monitor*

R. M. Baltrusaitis and C. A. Ekdahl
Los Alamos National Laboratory
P. O. Box 1663
Los Alamos, NM 87545

R. G. Cooper
EG&G Energy Measurements, Santa Barbara Operations
130 Robin Hill Road
Goleta, CA 93117

E. Peterson and C. E. Warn
EG&G Energy Measurements, Las Vegas Area Operations
P. O. Box 1912
Las Vegas, NV 89125-1912

Abstract

A stripline directional coupler beam current monitor capable of measuring the time structure of a 30-ps electron beam bunch has been developed. The time response performance of the monitor compares very well with Cherenkov light produced in quartz by the electron beam. The four-pickup monitor is now used on a routine basis for measuring the beam duration, tuning for optimized beam bunching, and centering the bunch in the beam pipe.

I. INTRODUCTION

The RF electron linear accelerator at EG&G/Santa Barbara Operations is used to develop and calibrate detectors sensitive to electron or gamma radiation pulses. The linac is typically operated at energies between 1 and 26 MeV, with peak currents between a few milliamperes and 200 A. Excellent beam bunching (50-ps wide pulse) has made it an especially useful tool for studying detector systems with bandwidths up to 1 or 2 GHz. However, as our detector system bandwidth has increased over the years into the multi-GHz range, the beam pulse waveform has become an appreciable contribution to the measured detector signal. Improved beam measurements are needed not only to correct detector data, but also to improve accelerator tuning. We began a project to develop a beam current diagnostic that would faithfully reproduce the time structure of the electron beam bunch. The goal was a clean response up to and above 10 GHz. Another objective was straightforward use as an everyday measurement, without special setup or checkout required.

The workhorse recorder for most measurements is a four channel sampling oscilloscope (20-GHz HP54120) with the sampling head a few feet from the detector being tested. For

our applications, a nonintercepting current monitor permanently installed in the linac vacuum pipe is ideal, because then beam current and detector measurements can be made simultaneously with the same instrument. After some investigation of resistive wall image-current monitors and B-dot probes, we settled on a stripline directional coupler as the most promising technique to achieve our goals of bandwidth and convenience.

II. THE STRIPLINE DIRECTIONAL COUPLER

The basic principle of the directional coupler monitor is illustrated in Figure 1. The pickup is a simple rod spaced just

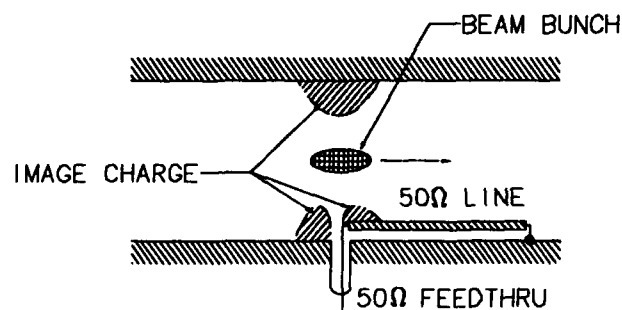


Figure 1. Schematic of beam bunch passing the pickup.

inside the beam pipe wall to create a 15-cm long 50- Ω transmission line, connected to the outside world at the upstream end with a 50- Ω vacuum feedthrough and shorted at the downstream end to the beam pipe itself. For an ultra-relativistic electron traveling inside the beam pipe, the electromagnetic field just inside the wall of the pipe is almost purely transverse, and can be thought of as a thin disk traveling along with the electron. More accurately, the FWHM duration of the fields from a point charge is $1.4 a/\gamma c$, where a is the radius of the pipe and γ is E/mc^2 . For our case, this time is much less than the FWHM of the beam pulse, so the duration of the electromagnetic pulse accurately reproduces the length of an electron beam bunch. As the

* This work is supported by the U.S. Department of Energy under Contracts No. W-7405-ENG-36 and DE-AC08-88NV10617.

field sweeps past the upstream end of the pickup rod, the magnetic flux threaded by the loop formed by the pickup rod and the pipe beam wall will rise up to a constant, illustrated in Figure 2. An oscilloscope connected to the coupler by the

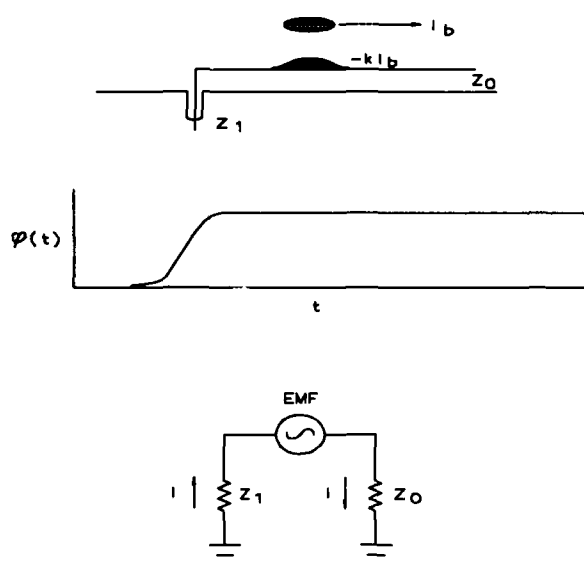


Figure 2. The magnetic flux producing the monitor pulse.

feedthrough detects the resulting EMF as a negative pulse proportional to the beam current. The proportionality constant, k , is approximately equal to the fraction of the beam pipe circumference subtended by the pickup rod. Because the downstream end of the transmission line is shorted, the pulse reflects and appears at the scope as an opposite polarity pulse delayed by twice the transit time.

In reality, of course, the directional coupler response is more complicated than this simple picture, especially at high

frequencies. The two main effects muddying the model are wakefields and local resonances associated with the coupling to the feedthrough. We use the term wakefields here very loosely to mean all of the beam-induced electromagnetic fields aside from the main TEM mode. Every discontinuity in beam pipe diameter (collimators, for example) and even the finite resistivity of the beam pipe will generate undesirable electromagnetic fields following the beam down the vacuum pipe waveguide. The directional coupler pickup responds without discrimination to any electromagnetic field, so the observed signal will happily reproduce all of the undesirable wakefields as well as the primary beam pulse. Our attempts (admittedly not exhaustive) to dampen the wakefields with RF-absorbing materials created other problems, either lowering the bandwidth of the primary response or creating new sources of wakefields themselves. The simplest solution for us is to ensure that wakefield frequencies are above the rolloff frequency of our recording system. The cutoff frequency of a cylindrical waveguide is inversely proportional to the radius (0.5 cm radius corresponds to a 17.5 GHz cutoff), so we constructed the directional coupler in a small diameter pipe. The 20-GHz recording system then acts as a low-pass filter for any propagating wakefields.

Particular attention was paid to the details of the feedthrough and its coupling to the pickup rod. For example, the exposed dielectric area at the feedthrough penetration of the beam pipe was minimized to avoid cavity resonances. Small diameter pickup rods were chosen to circumvent transverse resonances.

III. RESULTS

Figure 3 illustrates the method used to test some of the prototype direction couplers. The electron beam emerges

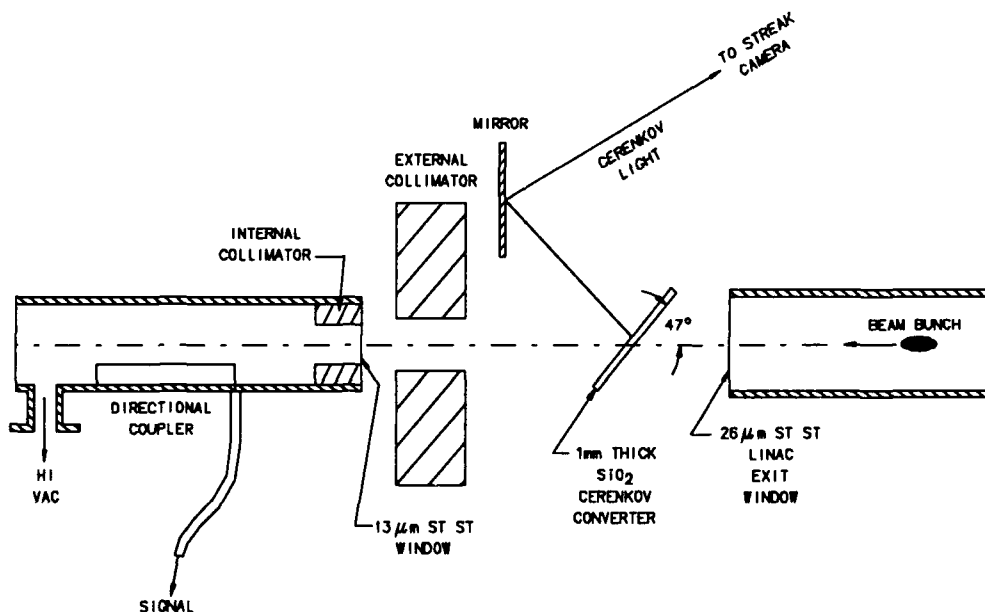


Figure 3. Experimental setup for comparison of directional coupler with Cherenkov light.

into the air through a thin window, and strikes a thin quartz disk at 47° , producing Cherenkov light. The disk is masked to a 4-mm slit to minimize time of flight spreading of the optical pulse, which is then reflected and focused into a Hamamatsu C1587 streak camera. After the streak measurement, the quartz is remotely moved out of the beam, and the directional coupler response is recorded on the sampling oscilloscope. Tests were also made with the directional coupler mounted to the linac exit port, with the quartz radiator at the downstream end of the coupler. Figure 4 shows a comparison of the streak and directional coupler responses. The FWHM of both is about 35 ps.

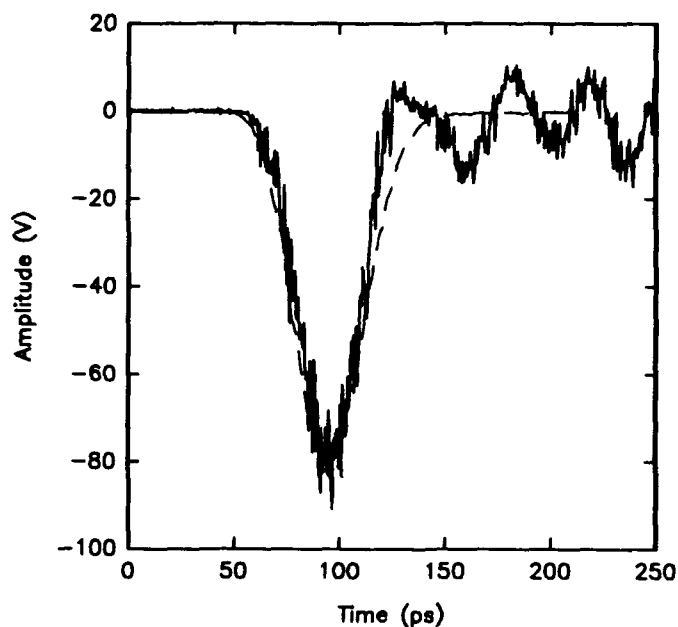


Figure 4. Directional coupler response (solid) and streak of Cherenkov light (dots).

Rapid Measurements of Two Dimensional Ion Beam Current Distribution for Pulsed Neutron Source

A.M. Tron

Moscow Engineering Physics Institute
Kashirskoe sh., 31, 115409 Moscow, Russia

Abstract

To monitor maximum current density and two-dimensional ion beam current distribution at the entrance of intense pulsed neutron source of INR the secondary electron monitor is considered. A new means is realized in this device. Two-dimensional primary beam current distribution is transformed into the corresponding distribution of secondary electrons. The electron distribution is transferred from the ion beam area, registered in discrete points and finally approximated. By means of the monitor one can detect with a high precision the current distribution practically within entire ion pipe during a time period that is not more than 10 ms.

I. INTRODUCTION

To prevent the termomechanical damage of first wall of the INR intense pulsed neutron source (INS) [1,2] as a result of proton beam action and to improve the using of this source a device for rapid monitoring of maximum proton beam current density j_m and measuring of two-dimensional beam current density distribution $j(x,y)$ at the entrance of INS is needed.

The $j(x,y)$ measuring system must satisfy a number of stringent requirements in this case. Rms error of j_m measurement must be not more than $\pm 5\%$ of indication and its measurement time - 20 ms. Radius of measurement area must be not less than 60 mm when the ion pipe aperture is 160 mm. The device must ensure its calibration without disassembling and must disturb the beam negligibly.

Our studies have shown that the known devices for $j(x,y)$ measurement [3,4,5] do not satisfy fully these requirements. However a secondary electron technique [6] has the best prospects. As for example the

secondary electron monitor described in [7] has been already successfully tested.

II. PRINCIPLE OF OPERATION

Figure 1 shows a layout of such monitor which satisfies the requirements mentioned above. All sizes are given in mm.

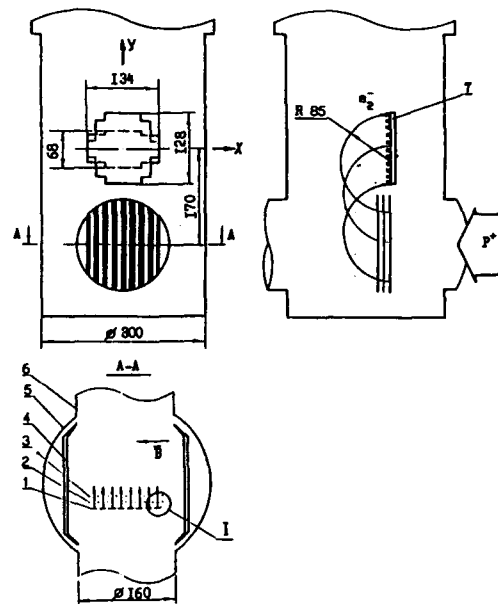


Fig.1. Layout of the beam monitor.

The monitor operation principle is the following. Electrons that have been produced as a result of interaction between the primary beam and thin striplike emitters (1), made of 0.01 mm tantalum foil, are accelerated on their path from the emitter with negative potential equal to -4 kV till the electrodes (3) under ground potential. The focusing of the electron flux in (x,z) plane was realized by installation of additional electrodes (2) with potential close to the emitter one. Then by semicircular focusing in uniform magnetic field the electrons are transferred from

the ion beam space to the plane of 64-channel collector (7). The magnetic field is highly uniform in a region of the electrons motion and it is produced by specially shaped poles (4). In this figure the current collector (7) maximum sizes are displayed by: solid line - for occasion of beam monitoring at the entrance of the beam trap, dashed line - at INS. The lock and screen grids are placed before the collector (7).

Figures 2,3 explain the electrostatic focusing in primary convertor (PC) and mutual position of the electrodes: fig.2 shows distribution of electrons potential energy in the electric field of the electrodes and fig.3 - the electrons trajectories and equipotential lines of the same electric field.

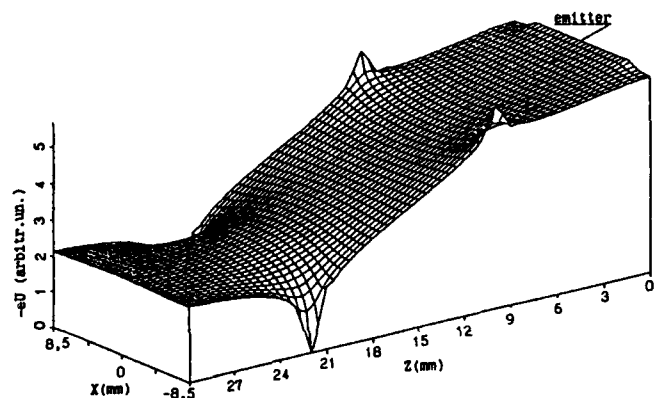


Fig.2. Distribution of electrons potential energy in electric field of PC.

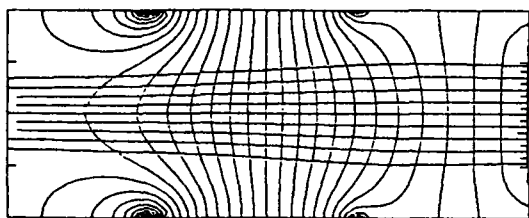


Fig.3. Electrons trajectories and equipotential lines of the electrodes field.

The distance between 15 mm wide emitters is 2 mm, the diameter of focusing electrodes and grids wires is equal to 0.1 mm. Leaving the emitter surface at the normal the electrons from 12 mm part are being focused into 0.2 mm wide strip at

the distance of 26 cm downstream. The electrons from other parts produce background that has current density more than two orders less than corresponding magnitude of major current.

111. RESOLUTION OF THE MONITOR

The monitor resolution accounting real initial energy-angle secondary electron distribution have been defined by numerical simulation. In this case HWHM secondary electrons distribution along y coordinate in the collector plane is 0,5 mm and along x - 4 mm that are smaller by a factor of 5 as rms sizes of the ion beam. The electrons initial distribution along y was assumed to be delta-function and along x as uniform within emitter strip width. The monitor resolution is inversely proportional to electrons velocity i.e. by raising emitter potential it may be extremely improved.

Focusing high quality that have been obtained in rather simple system allows one to define by approximation method two-dimensional distribution $j(x,y)$ with the demanded accuracy by use of its measurement in 64 discrete points. The two-dimensional Kotelnikov series technique was employed for approximation.

The PC electrostatic focusing system have been tested as model, a photo of which is shown in fig.4. A single strip thermoelectron current image width was less than 2 mm and this is in a good respect with calculations.

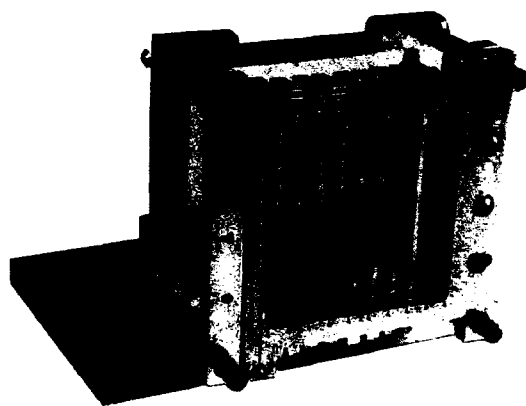


Fig.4. Photo of scale model PC.

To represent the results of two-dimensional ion beam current distribution measurements graphically both as isometric

picture and lines of equal current density in the transverse plane the corresponding software has been developed. Fig.5 illustrates the efficiency of two-dimensional reconstruction algorithm employing Kotelnikov series: fig.5(1) shows the initial two-dimensional beam current density distribution, fig.5(2) - the computer simulation of 64-channel collector charges measurement. The error of the measurement was supposed to be a random variable in the range $\pm 3\%$ of indication. The distribution reconstructed by means of two-dimensional Kotelnikov series is displayed in fig.5(3).

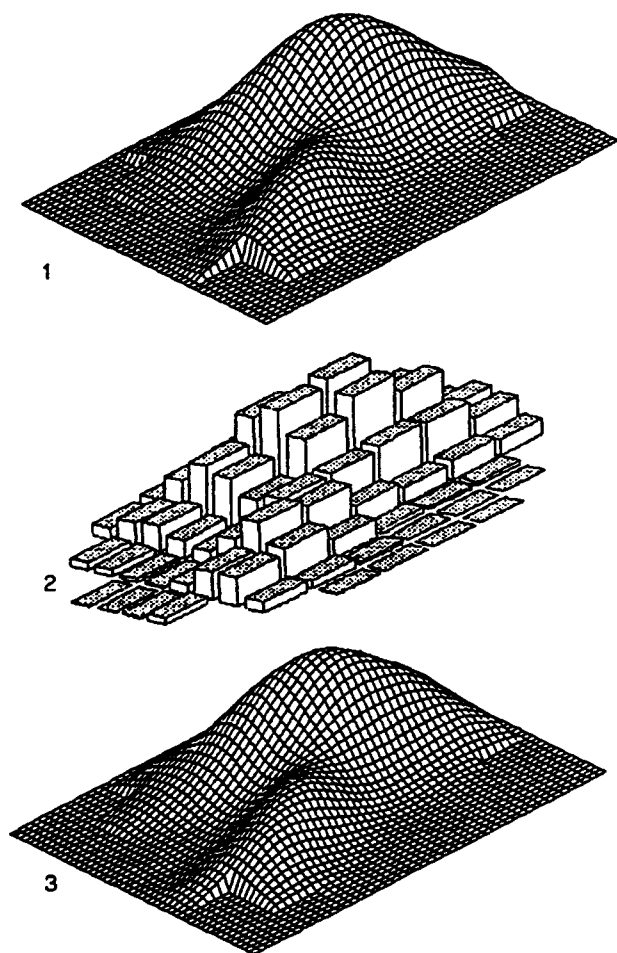


Fig.5. Results of simulation of $j(x,y)$ measurement.

IV. CONCLUSION

Estimations and model tests show that the time period necessary for registration of two-dimensional distribution and determination of j_m is less than 10 ms in

our case. The converter construction developed allows one to fulfill the detector operative calibration using the electrons of thermoemission.

Studies have shown that the monitor discussed can be successfully used with slight modification for monitoring of the same transverse size proton beam \dagger with pulsed beam current up to 15 A.

V. ACKNOWLEDGMENTS

Author expresses his acknowledgement to Yu.Ya.Stavissky for support of this work and to V.V.Shako and P.B.Vasilev for help in computer simulations.

VI. REFERENCES

- [1] Yu.Ya.Stavissky. Proc. of the XI Meeting of the ICANS-XI, KEK, Japan, Oct. 22-26, 1990, pp.87-99.
- [2] S.G.Lebedev. Preprint INR RAS P0356, 1984.
- [3] D.D.Chamberlin et al. IEEE Trans. Nucl. Sci., NS-28(1981), p.2347.
- [4] J.S.Fraiser. IEEE Trans. Nucl. Sci., NS-28(1981), p.2137.
- [5] Yu.P.Komissarov, V.G.Mikhailov, V.A.Rezvov, L.I.Yudin. 11 Vsesoyuznoe soveshanie po uskoritelyam zaryadzenykh tchastits (Dubna, 25-27 Oct. 1988). Dubna, R9-88-738, 1988, p.21.
- [6] A.M.Trone. V kn.: "Metody rastchota i experimentalnye issledovaniya sistem lineinykh uskoritelei". M., Energoatomizdat, 1987, pp.41-45.
- [7] A.M.Trone, P.B.Vasilev, Proc. 3 EPAC, Berlin, 24-28 March, 1992, Vol.2, pp.1124-1126.

Short Bunch Length Detector for Ion Beam with High Bunch Density

A.M.Tron, V.V.Shako

Moscow Engineering Physics Institute
Kashirskoe sh. 31, 115409 Moscow, Russia

Abstract

The secondary electron rf monitors for short ion bunch phase distribution measurement are presented. Construction particularities of the monitors, influence of space charge of both the primary and the secondary electron beams on the phase resolution, thermal regime of the target during beam-target interaction are considered.

I. INTRODUCTION

The secondary electron bunch longitudinal profile monitors have the best prospects for detailed study of the particles longitudinal dynamics, precise beam longitudinal matching and for setting up the rf parameters of cavity accelerators operating in a low or intermediate energy region especially.

These monitors have been designed during last about twenty years at MEPhI. Two monitors proposed and designed at MEPhI in 1978 and 1980 for ion linacs have been successfully tested respectively at IHEP in the I-100 injector (Protvino, 1980) and at INR (Troitsk, 1988). These monitors use low energy secondary electrons and their bandwidths were not less than 20 GHz.

In this report a short review of this activity relative to the monitors for L band ion linac with high bunch density similarly to project beam parameters of linacs at SSCL or INR is presented.

These monitors must satisfy the next major requirements as a rule their phase resolution has to be not worse than two degrees at the frequency of bunches. In many cases the detector size along the accelerator axis must be about 0.1 m. The detector must permit its inspection without disassembling. To use the same type detector for entire accelerator the major monitor parameters must be independent of the beam energy.

Our studies have shown that the secondary electron rf monitors satisfy the above mentioned requirements most completely. In these devices the phase distribution of the high energy primary beam is isochronously transferred into the same distribution of the low energy secondary beam. Then this secondary distribution is coherently transformed into transverse one through rf modulation allowing direct presentation on a low frequency display.

It is known that the secondary electron emission is divided into low energy and high energy components. The time dispersion of the former was found to be less than 6 ps [1], which is acceptable for measurements in L band linac. As to the latter, its dispersion may be made less than 0.1 ps [2,3]. Note that one of the first detectors with rf transverse scanning of low energy secondary electrons was that above [1].

II. PRINCIPLE OF OPERATION

The detectors for ion beam analysis consist of the primary converter (PC) and rf shutter (RFS) with single channel collector on its exit or rf-modulator (RFM) with multichannel collector.

PC is either a target unit with threadlike focusing electrodes or wire target without electrodes. In first case the target-emitter is a strip [3]. Fig.1,2 make the electrostatic focusing and relative position of the electrodes clear for this case.

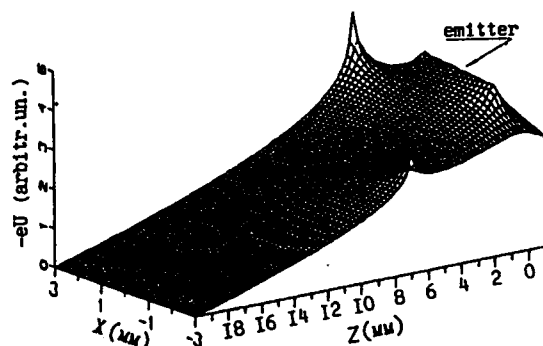


Fig.1. Distribution of electrons potential energy in electric field of PC.

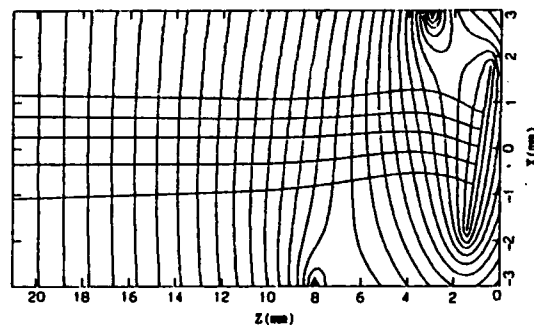


Fig.2. Electrons trajectories and equipotential lines of field as above.

RFS of longitudinal or transverse types are used. In the former the electrons are energy modulated by either the same or multiple rf used in the linac and then spatially separated with a spectrometer. The latter contains a rf scanner of the beam and the electron spatial separation is accomplished in a drift space with the slit collimator on its exit. Replacing in RFS the collimator and the single channel collector with the multichannel one and choosing the special monitor operation regime we get RFM and the corresponding monitor with resolution better than 2° over a range of entry phases not less than 90° [3]. In this case the rapid longitudinal profile measurements can be carried out.

The principle of the monitor operation consists in the following. By applying high negative voltage to the target and the focusing electrodes in PC the secondary electrons produced as a result of the primary beam-target interaction are accelerated and formed as a narrow beam at the entrance of rf resonator of RFS (or RFM) so that the axes of the electron and ion beams are orthogonal to each other. Only for some interval of input particle phases the electrons will pass through the RFS. Recording the collector output signal as a function of the RFS phase we get the bunch phase distribution averaged over the ensemble of the beam bunches. The monitor with RFM allows to record the bunch phase distribution of single bunch.

III. RESOLUTION OF THE DETECTORS

The monitor phase resolution is basically determined by the secondary electron phase debunching in PC and the RFS resolution. The phase debunching is mainly defined by the finite transverse spot sizes of the primary and secondary beams on the target and the initial secondary electron energy spread. By choosing geometry and potential of the target (for corresponding ion beam energy) the debunching caused by the finite transverse beam sizes may be reduced to negligibly small value in comparison with the latter [3]. Note the initial secondary beam spread in energy takes effect within the electron path length in the detector from the target to the half rf modulator gap length. To minimize the electron phase debunching caused by this last reason the distance between the target and the gap and also the electron path length in the rf modulator gap must be as small as possible. In the known detector [4] the rf modulator gap with length of about 5 mm is placed on the ion beam pipe boundary. It ought not to place the RFS gap in the accelerated beam area, otherwise the electrons will be modulated by resultant rf voltage one component of which is induced by the ion beam and another - by the RFS generator.

Using a toroidal cavity as the rf modulator of the electrons a suitable degree of uniformity of rf field in electron transit slot is achieved with the ration of the gap length to the entrance slit width not less than 5.

However, there are some other important effects which can lead to a degradation of monitor phase resolution.

IV. INFLUENCE OF SPACE CHARGE

The space charge forces of both the primary and the secondary electron beams disturb the electrons motion in the monitor. As a result of this interactions the electron beam was got an added broadening of momentum spectrum ($\delta, \%$), an additional angular divergence ($\Delta x', \text{rad}$), and added phase debunching ($\Delta\varphi$).

These parameters as function of equivalent target radius R_0 and distance x_r from target to the resonator wall are displayed in fig.3,4 where: for fig.3 - target potential $u_t = -4 \text{ kV}$, $x_r = 20 \text{ mm}$, distance from the ion beam axis to the wall is equal 20 mm; for fig.4 - $u_t = -4 \text{ kV}$. Proton beam parameters were: proton energy - 100 MeV, beam diameter - 5 mm, bunch phase length 10^{-3} of 0.2 GHz and pulsed beam current - 50 mA.

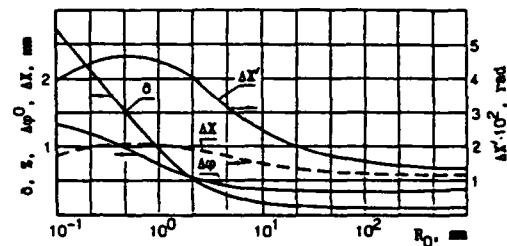


Fig.3. Dependences of $\delta, \Delta\varphi, \Delta x, \Delta x'$ vs the target radius R_0 .

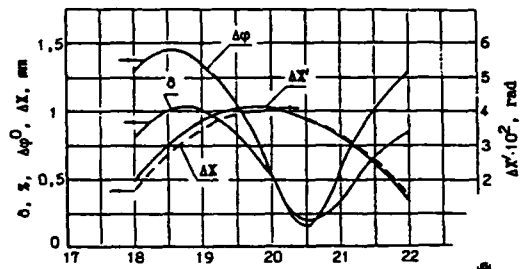


Fig.4. Dependences of $\delta, \Delta\varphi, \Delta x, \Delta x'$ vs the target position x_r relative to the resonator wall.

As it follows from these figures the radius R must be not less than 2 mm and the target have to be in maximum of the ion beam current density [3].

The influence of space charge of the secondary electron beams is illustrated in fig.5,6 where the electron phase debunchings $\Delta\varphi_2$ of 427.6 MHz as function of the target potential U_t and the gap length L_g are shown. In fig.5 for curves 1 and 2 the secondary electron bunch charges Q are 2 pC and 0.4 pC respectively and for 3,4,5 Q are equal to 38 pC, 25 pC and 7 pC. In the first case the bunch phase length $\Delta\varphi$ is 30° of 427.6 MHz and the primary beam energy $W = 2.5 \text{ MeV}$. In the second case $\Delta\varphi = 10^\circ$, $W = 70 \text{ MeV}$. The target material may be either carbon or tungsten or tantalum because the ion bunch charge is transferred into the secondary charge with corresponding coefficients are equal to the secondary electron coefficients for the above mentioned material. All curves in fig.6 are defined at the electron energy $W = 10 \text{ keV}$ but curve 1 - for $W = 4 \text{ keV}$ and $Q = 25 \text{ pC}$. The initial beam radius for all curves is 1 mm but for curve 5 of fig.5 one of the transverse bunch size is equal to 0.1 mm.

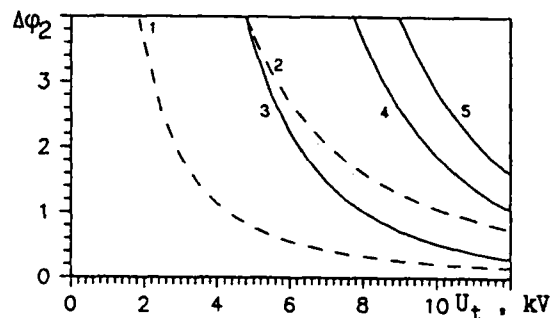


Fig.5. Dependences of phase debunching vs U_t .

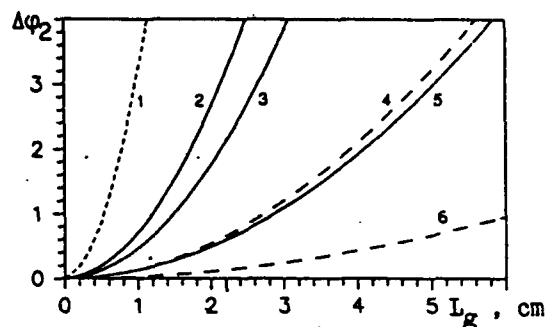


Fig. 6. Dependences of phase debunching vs L_g .

As it follows from these figures the target potential is to be about 10kV and the gap length - about 1cm.

V. BEAM HEATING OF EMITTER

The monitor emitter heating up to temperature when thermocurrent density can exceed 1% of corresponding secondary electron current density restricts the device range of operation. To determine time dependence of the emitter maximum temperature when it is being pulse beam heated an unstationary heat transfer equation with a radiant heat transfer term has been solved. Thermophysical coefficients for temperature profiles calculation have been taken from [5]. The beam current density distribution was taken Gaussian.

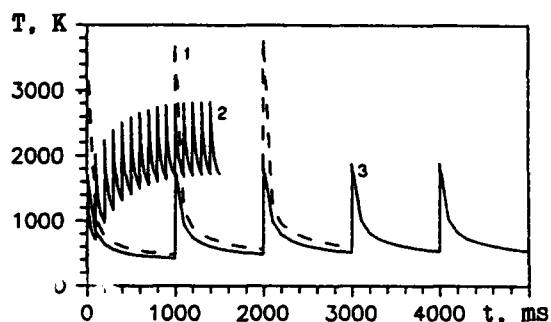


Fig. 7. Dependence temperature of wire-target vs time.

Fig. 7 shows tungsten temperature vs time at 2,5 MeV proton beam heating. Beam parameters for 7(1): beam impulse frequency $f = 1$ Hz, rms $r = 1$ mm; for 7(2): $f = 1$ Hz, rms $r = 0,5$ mm; for 7(3): $f = 10$ Hz, rms $r = 1$ mm. The emitter wire length - 30mm, radius - 0,05mm. Fig. 8 shows carbon strip-emitter maximum temperature vs time for the same ion beam: for 8(1) and 8(3) - rms $r = 1$ mm, for 8(2) rms $r = 0,5$ mm. For 1 and 2 curves the thickness of target is 0,1mm and for 3 - 0,2mm. The target geometry for fig. 8 is shown in fig. 2.

From these figures it is clear the strip target has advantage over the wire target.

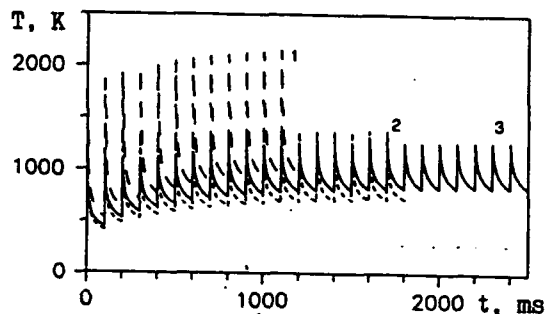


Fig. 8. Dependence temperature of strip-target vs time.

VI. CONCLUSION

Our consideration demonstrates the design of the monitor must take account of the influence of space charge of both the primary and the secondary beams and the thermal regime of the target on the monitor operation. Our studies shows the rf monitor using the low energy secondary electron can achieves its bandwidth up to 50 GHz.

VII. REFERENCES

- [1] E.W.Ernst, H.J.Von Foerster, J.Appl.Phys., Vol.26, No.6, 781 (1955).
- [2] A.M.Trön, VANT, Ser.Technika Fizicheskogo Experimenta, Kharkov, Vol.2 (19), pp.48-50 (1984).
- [3] A.M.Trön, Proc. 1990 Linear Accelerator Conf., September 10-14, Albuquerque, pp.477-479 (1990).
- [4] A.M.Trön, A.V.Feschenko, Proc. 7 All-Union PAC, (Dubna, October 14-16, 1980), Vol.2, pp.125-129 (1981).
- [5] Physico-khimicheskije svoistva elementov, Spravotchnik, Kiev, Naukova Dumka, 1965.

Measurement of Bunch Time-structure in KEK PF

M. Tobiyama*, T. Kasuga*, T. Takeo†, T. Obina*, K. Tamura
Faculty of Science, Hiroshima University, Higashi-Hiroshima 724, Japan
and
T. Katsura
National Laboratory for High Energy Physics, Tsukuba 305, Japan

Abstract

The time-structure of the bunches in the KEK-PF storage ring under the single bunch condition was measured by means of a photon counting system installed in beamline 21. When the jitter in the electronic system is negligible, the response of the whole system is finally determined by a transit time spread (TTS) of a photomultiplier (PMT). The TTS of the PMT was measured with a picosecond pulse laser system, pulse width of which was about 7 ps in FWHM. A current dependence of the longitudinal bunch shape was observed with the improved system and was found the increase of the asymmetry with the increase of the current.

1 Introduction

In a positron (electron) storage ring, the longitudinal bunch shape has a Gaussian distribution standard deviation of which is determined by the radiation damping and the quantum radiation excitation if the interaction between bunches and the vacuum chamber is negligible at a low current. However, when the beam current becomes large and the interaction increases, the longitudinal bunch shape deviates from the ideal or natural bunch shape. As one of the features of this effect, the bunch lengthening is widely investigated not only theoretically but also experimentally^[1]. Furthermore, it is also predicted that the longitudinal shape is deformed from the Gaussian distribution^[2].

We have installed a single photon counting system in beamline 21 in the KEK-PF. An excellent dynamic range is obtained when enough events are collected and high time resolution is achieved because the timing at which event occurs can be detected precisely with a fast photomultiplier and a constant fraction discriminator. A large dynamic range of the system gives us precise measurement of the single bunch impurity which is defined as a ratio of electron number in unwanted bunches to that in the main bunch.

*Present address: National Laboratory for High Energy Physics, Tsukuba 305, Japan

†Present address: Oita-Tsurusaki high school, Oita, 870-01, Japan

Table 1: Main Parameters of KEK-PF-Ring

Energy	E	2.5	GeV
Circumference	C	187.07	m
Betatron tune	ν_x	8.37	
	ν_y	3.39	
Revolution frequency	f_{rev}	1.6	MHz
Harmonic number	h	312	
Radio frequency	f_{rf}	500	MHz
Momentum compaction factor	α_p	0.0157	
Radiation damping time	τ_x	7.79	ms
	τ_y	7.82	ms
	τ_e	3.92	ms

Measured data do not show the longitudinal shape but convolutions of the response function of the system to the bunch shape. Therefore, if the response function is determined, we will be able to reconstruct the original bunch shape by the deconvolution. We have measured the response function of the system using a picosecond pulse laser system[†]. The determination of time response and its improvement are shown in Sec. 3. With a new electronic system, the bunch shape was measured as a function of beam current. The change of the shape of the bunch is discussed in Sec. 4. Related parameters of the KEK-PF storage ring is listed in Table 1.

2 Experimental Setup

The experimental setup has been described in refs.[3, 4] in detail, therefore only a brief outline is shown here. The system is shown schematically in Fig. 1. Photons from the nearest bending section (BM21) are led to a mirror chamber through a vacuum pipe and are reflected by a mirror made of SiC. The reflected visible light reaches a microchannel-plate type photomultiplier (MCP-PMT, Hamamatsu R2980U) through an ICF-70 view port, a Pb-acrylic glass of 22 mm thickness, light reducing filters and a precise horizontal slit. The intensity of photons is reduced to the level of one photon detection per about a hundred

[†]The picosecond pulse laser system, Faculty of Integrated Arts and Science, Hiroshima University

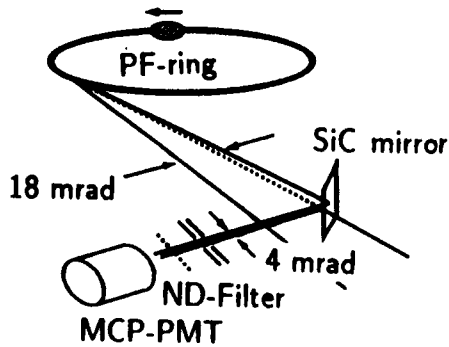


Figure 1: The photon counting system

revolutions of a bunch.

Pulses from PMT are amplified by two wideband amplifiers, then shaped by a constant fraction discriminator (CFD) and led to a time to amplitude converter (TAC). The time intervals between the shaped signal from the CFD and the synchronized signal to the bunch are converted to the pulse heights by the TAC. The outputs from the TAC are amplified with a DC-amplifier and the distribution of pulse heights is analyzed with a multichannel analyzer (MCA).

3 Time Response of the System

We determined the time response of the system using the picosecond pulse laser system. Figure 2 shows the measuring setup schematically. The laser pulse has the wave-

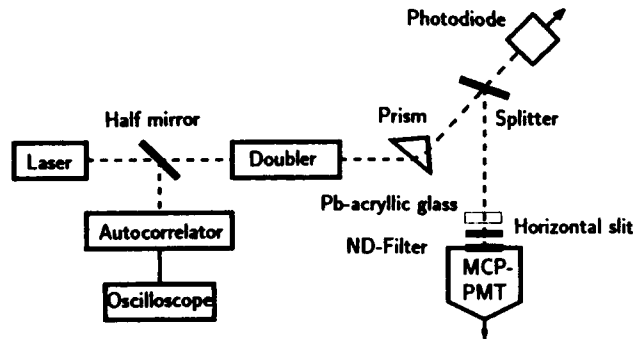


Figure 2: Time response measuring system with the picosecond pulse laser.

length of about 800 nm, the pulse width of about 7 ps in FWHM and the repetition of about 80 MHz. As the wavelength is somewhat longer than the sensitive region of the PMT, we employed an optical doubler and a prism to select the wavelength of 400 nm only. About a third of the blue light are reflected by a half mirror and led to the PMT block. The straight light enters a pin-photodiode (HP 4203) and makes a stop signal to the TAC through a CFD. The mean counting rate of the PMT was tuned to

be about 8 kHz.

The obtained shape was far wider than the reported transit time spread (TTS) of the PMT. We found that the CFD (Ortec 582) limited the time response and it was exchanged for a faster CFD (Tennelec TC 454). The time response was greatly improved as shown in Fig. 3, the FWHM of which was about 28.18 ps. In order to de-

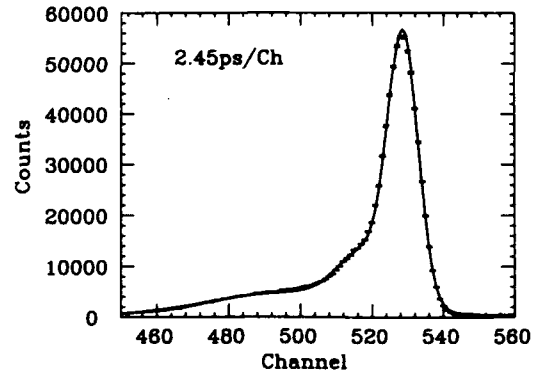


Figure 3: Time response of the system.

termine the jitter of the photodiode, we set a same type photodiode instead of the PMT and made a same measurement. It was about $18 \text{ ps}/\sqrt{2}$ in FWHM, small enough compared with the whole resolution of 28 ps. The effect of the Pb-acrylic glass for radiation shield was measured and no evident change was seen. The result at the wavelength of 800 nm is almost the same as that at 400 nm.

4 Bunch Shape

We express the response function of Fig. 3 with

$$g(x) = \sum_{i=1}^3 a_i \exp\left(-\frac{(x - O_i)^2}{2\sigma_i^2}\right)$$

by the least square method using a computer code MINUIT. The fitted results are shown in solid curve in the figure. Assuming the Gaussian as the original bunch shape, we tried to deconvolute the experimental data by fitting with the equation

$$f(x) = \int_0^\infty \frac{A}{\sigma\sqrt{2\pi}} \exp\left(-\frac{(x-t-\mu)^2}{2\sigma^2}\right) g(t) dt \quad (1)$$

where A , σ and μ are fitting parameters. Figure 4 (a, b) shows the result for $I_b=9.5 \text{ mA}$ and $I_b=49 \text{ mA}$ respectively, at the RF voltage of 1.3 MV. Time flies from right to left and statistical errors are also shown in the figure. The fits are not satisfactory as shown in the figure. The deviation of the fitted data from the observation is appreciable, especially around the peak. Judging from this fact, we conclude that the Gaussian bunch shape assumed in Eq. [1] is not adequate.

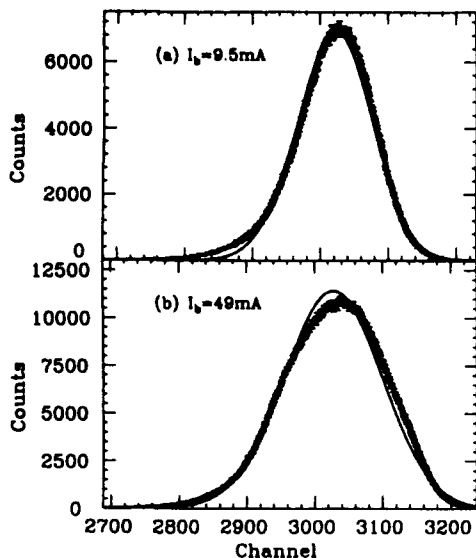


Figure 4: The shape of the main bunch and the calculated result assuming Gaussian distribution of the bunch at $I_b=9.5$ mA (a) and $I_b=49$ mA (b).

To express the asymmetry, we introduce a time dilatation factor τ and fit the experimental data with the equation

$$f'(x) = \int_0^\infty \frac{A'}{\tau\sigma\sqrt{2\pi}} \exp\left(-\frac{(x-t-\mu)^2}{2\sigma^2}\right) \exp\left(-\frac{t}{\tau}\right) dt, \quad (2)$$

neglecting the response function of the system. This function has no theoretical base but fits very well as shown in Fig. 5. The fitted σ and τ are shown in Fig. 6. Using this

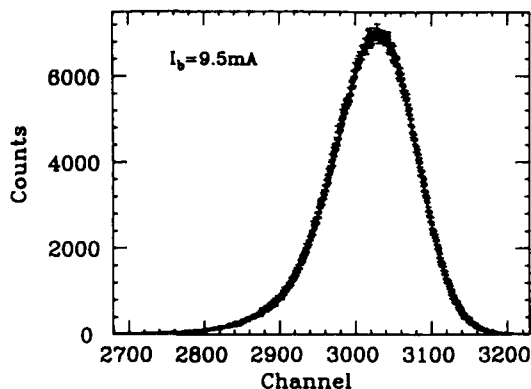


Figure 5: The fitted bunch shape.

σ , we fit the data by the potential well distortion formula (lower current side) and the microwave instability formula (higher current side). From the cross point of the two curves, we obtained the threshold current of microwave instability to be 27 mA. This fit becomes worse gradually above the threshold. We conclude that the behavior of the change in bunch shape varies above the threshold. More detailed experiment and analysis are necessary.

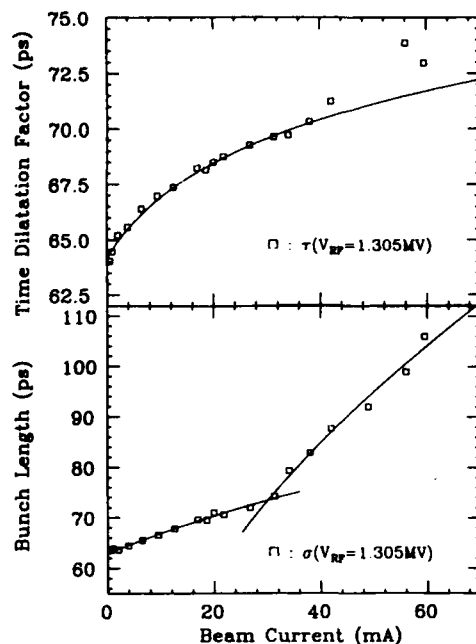


Figure 6: Current dependence of the bunch length σ (solid curve) and the time dilatation factor τ .

5 Summary

We have considerably improved the time response of the photon counting system installed at beamline 21 in the KEK-PF and determined the time response function of the system using the picosecond pulse laser system. With improved system, the change in the bunch shape as a function of the beam current has been measured. The longitudinal bunch shape is deformed when the beam current is high. Quantitative determination of the shape will be done in the near future.

The authors wish to express their sincere appreciation to Prof. H. Kobayakawa who supported us to make experiments in the PF ring. They acknowledge Prof. K. Ohbayashi of Faculty of Integrated Arts and Science, Hiroshima University who kindly gave us the opportunity to use the picosecond pulse laser system.

References

- [1] For example, see P. B. Wilson *et. al.*, IEEE Trans. Nucl. Sci. NS-24, 1221 (1977)
- [2] A. W. Chao, Proc. SLAC Summer School (AIP105, 1982) p. 353
- [3] M. Tobiyama *et. al.*, in Proceedings of 1991 IEEE Particle Accelerator Conference p.1338 (1991)
- [4] T. Obina *et. al.*, in Proceedings of the 8th Symp. on Accelerator Science and Technology, p.298 (1991)

A Fifth Harmonic RF Bunch Monitor for the ANL-APS Electron Linac*

A. Nassiri and A. Grelick

Argonne National Laboratory 9700 So. Cass Ave., Argonne, 60439

ABSTRACT

The function of a fifth harmonic (14.28 GHz) bunch monitor is to provide a signal which is proportional to the electron beam bunch size. The monitoring of the rf power signal at 14.28 GHz enables the operator to optimize the rf bunching of the beam at the end of the first accelerating section where the full bunching has been formed and remains mainly constant in size throughout the rest of the electron linac. A modified version of the SLAC original bunch monitor has been fabricated and its rf properties measured. This paper describes the design and the initial measurement results.

I. INTRODUCTION

Knowledge of the electron beam bunch size in a linear accelerator provides useful information about the beam energy spread. The electron beam bunch length in the APS electron linac is about 12° in phase or 12 ps after the first accelerating section where the beam energy is nominally 56 MeV . Bunch length of this size is too short to be measured directly by conventional timing techniques. In recent years several time-resolved imaging techniques have been developed and used to measure charged particle beam profiles (particularly e-beam) with very short time structures (typically $10 - 20\text{ ps}$) [1]. These techniques rely on the detected optical radiation in the visible region by optical transition radiation (OTR), Cherenkov radiation, and synchrotron radiation (SR) using gated or streak cameras. These methods have the distinct advantage of providing precise information about a detected charge distribution. For the APS electron linac operation, however, it is desirable to dynamically monitor the electron bunch length due to the changes in the low energy linac parameters (for example, rf power and phase variation of the pre-buncher and the buncher). An indirect measuring method, using an rf cavity resonant at the fifth harmonic of the SLAC main linac fundamental frequency (2856 MHz), was proposed by R. Miller [2] and successfully used to measure the bunch length at the SLAC main linac. The modified bunch monitor consists of only a single rf induction cavity resonant at 14.28 GHz . Figure 1 is a cross sectional view of the bunch monitor. As the beam traverses the bunch monitor, it excites the cavity. The rf power from the cavity is detected with a broad-band detector. The detected signal is then displayed on a scope. This signal is proportional to the second moment of the charge distribution in the bunch.

*Work supported by U.S. Department of Energy, Office of Basic Energy Sciences under Contract No. W-31-109-ENG-38.

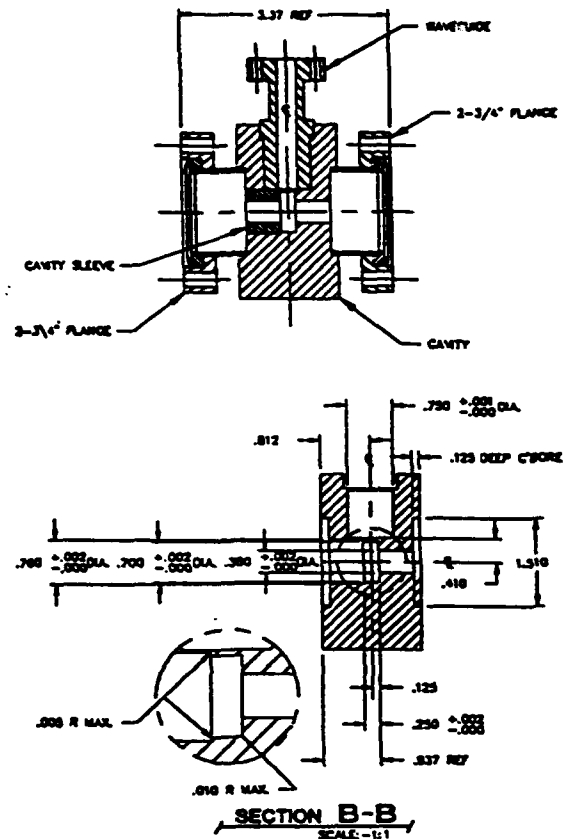


Figure 1
Bunch monitor cross section

II. ANALYTICAL DERIVATIONS

We give a brief derivation based on the moment method suggested by R. Miller [2]. If $I(t)$ is the instantaneous beam current, then the m^{th} moment of the current distribution is defined as

$$E_m(t^m) = \frac{1}{q} \int_{-\tau}^{+\tau} t^m I(t) dt \quad (1)$$

where q is the total charge per bunch

$$q = \int_{-\tau}^{+\tau} I(t) dt, \quad (2)$$

$\tau = \frac{1}{2f_s}$, and f_s is the linac fundamental frequency.

By definition, $E_0 \equiv 1$ and the origin of t is chosen so that

$$E_1(t) = \frac{1}{q} \int_{-\tau}^{+\tau} t I(t) dt = 0. \quad (3)$$

Assuming a Gaussian beam distribution, the half-width of the bunch is defined as

$$\sigma = \sqrt{E_2(t^2)}. \quad (4)$$

The beam current can be expressed by a Fourier series

$$I(t) = \sum_{m=-\infty}^{m=+\infty} I_m e^{im\omega_0 t} \quad (5)$$

where

$$I(\omega) = \frac{\omega_0}{2\pi} \int_{-\tau}^{+\tau} I(t) e^{-i\omega t} dt. \quad (6)$$

The n -th derivative of the current distribution, $I(\omega)$ evaluated at $\omega = 0$ is

$$\frac{d^n I(\omega)}{d\omega^n} = \frac{(-i)^n \omega_0}{2\pi} \int_{-\tau}^{+\tau} t^n I(t) dt \quad (7)$$

or

$$\frac{d^n I(\omega)}{d\omega^n} = (-i)^n I_0 E_n \quad (8)$$

where $I_0 = \frac{\omega_0 q}{2\pi}$. So $I(\omega)$ can be expanded in a Taylor series about $\omega = 0$:

$$I(\omega) = I_0 \left(1 - \frac{1}{2!} E_2 \omega^2 + \frac{1}{3!} E_3 \omega^3 + \frac{1}{4!} E_4 \omega^4 + \dots \right). \quad (9)$$

For low harmonics one can write:

$$|I_m| = I_0 \left[1 - \frac{\sigma^2}{2} (m\omega_0)^2 \right] \quad (10)$$

where m is the rf harmonic number (here, $m=5$). The beam-induced power from a cavity resonating at the m -th harmonic is

$$P_m = \frac{|I_m|^2}{2} R_m, \quad (11)$$

where R_m is the cavity shunt impedance. With the half-width of the bunch (in radians) defined as $\theta = \sigma\omega_0$, the beam-induced power can be expressed as

$$P_m = \frac{I_0^2 R}{2} |1 - \theta^2 m^2|. \quad (12)$$

Therefore, the power from the cavity is proportional to the second moment of the bunch, θ^2 . For $m = 5$, $\theta = 0.21$ radians, $I_0 = 6.8 \times 10^{-4}$ Amperes, and a shunt impedance of $1.3 \times 10^5 \Omega$, the power is

$$P_m \approx 3 \text{ mW}. \quad (13)$$

The choice of the fifth harmonic cavity was based on maximizing the resulting signal. For a tube size of about 1.0 cm, the fifth harmonic provides the highest signal which is sufficiently beyond the cutoff.

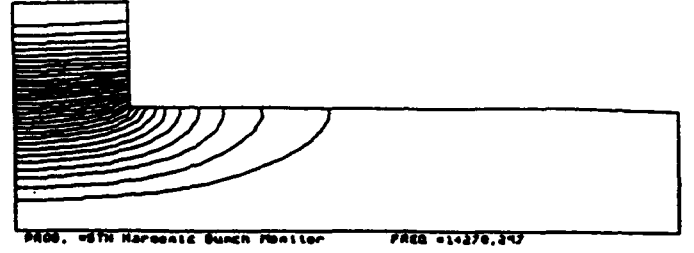


Figure 2
Bunch monitor cavity E-field plot

III. CAVITY DESIGN AND CONSTRUCTION

The initial SLAC two-cavity design was modified to include only a single rf induction cavity resonating at 14.28 GHz. The bunch monitor consists of three separate pieces- -copper cavity, copper rectangular waveguide, and drift tubes- -all copper brazed together after machining. The assembled structure was checked for leaks around the brazed joints with a helium leak detector. No leaks were found at a pressure of 2×10^{-10} Torr. A vacuum flange fabricated from 304 stainless steel was subsequently brazed to the rectangular waveguide to facilitate attachment of a ceramic vacuum window. The window is mounted in a standard brass WR-62 rectangular waveguide and the one-atmosphere side uses a standard waveguide flange. A standard WR-62 to SMA adaptor completes the basic assembly. When the bunch monitor is installed in the APS electron linac a coaxial attenuator and a zero bias schottky diode detector will also be used. The basic rf properties of the bunch monitor were determined using the SUPERFISH program. For the dimensions shown in Figure 1, SUPERFISH gives a resonant frequency of $f = 14.27$ GHz and a $Q = 3655$. Figure 2 is the E-field plot for this cavity.

IV. MEASUREMENTS

The cavity was excited with an antenna (E-probe) with about 10 mW of rf power ($\sim +10$ dBm) provided by the network analyzer. The signal coupled from the cavity through the WR-62 waveguide was displayed and the cavity resonant frequency and the quality factor, Q , was determined. Figure 3 shows a plot of the relative amplitude (dB) versus frequency (GHz). It can be seen from this plot that the dominant frequency (the cavity's fundamental resonant frequency) is 14.28 GHz. The cavity's quality factor, Q , was determined by finding the 3-dB points relative to the resonant frequency (see Figure 4). The 3-dB point half-bandwidth is $\Delta f = 2.0$ MHz. The Q -value is determined by

$$Q = \frac{f_0}{2\Delta f} = 3571.$$

Two other measurement attempts were made, unsuccessfully, to characterize the cavity by exciting it using a central wire. In the first setup, since the diameter of the central tapered rod (matched $50\ \Omega$) was comparable to the diameter of the fifth-harmonic cavity, all the cavity's modes were suppressed by the central rod and no signals (beyond the noise level) were observed either by using a short (45 ps) pulse source and reading the response on an HP-8562A spectrum analyzer or with an HP-8510 network analyzer. Nothing but noise was observed in the region of interest. Next, the central rod was replaced by a thin wire ($\sim 1\text{ mm}$ diameter) and the measurements were repeated. With the pulsed excitation there was still no signal observable above the noise. On the network analyzer, there was a slight rise in the region of interest but it had no resemblance to the predicted high Q response.

V. SUMMARY

An indirect bunch length monitor using an rf cavity is a simple and non-destructive method of providing on-line information about the relative longitudinal bunch length of the electron beam. In this paper we described the design of the bunch monitor and reported on the rf characterization of the rf cavity. Measurements with the network analyzer using an E-probe gave $f_0 = 14.28\text{ GHz}$ and $Q = 3571$ ($Q = 3655$ from SUPERFISH). No beam measurements have been made yet; however, the bunch monitor is being installed in the electron linac beamline. Final calibration tests will be done using the APS electron linac beam.

VI. ACKNOWLEDGEMENTS

The authors would like to thank M. White for her support, J. Song and J. Zhou for their help in the rf setup and measurements, and C. Gold for carefully assembling the bunch monitor several times. One of the authors (AN) is in debt to R. Miller of SLAC for fruitful discussion and helpful suggestions.

REFERENCES

- [1] A. Lumpkin, "Advanced, Time-Resolved Techniques for Electron-Beam Characterization," Second Annual Workshop on Accelerator Instrumentation, Batavia, IL, p.151, 1990.
- [2] R. Miller, private communication.

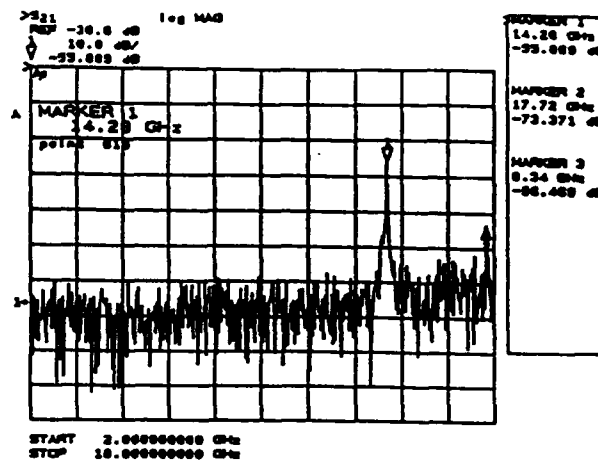


Figure 3
Frequency response

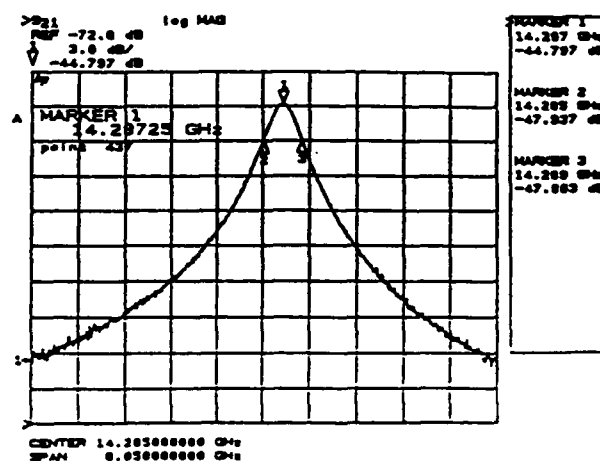


Figure 4
Resonant frequency

Characterization of Subnanosecond Heavy-Ion Bunches at the TASCC Superconducting Cyclotron

G.R. Mitchel and N.A. Towne
AECL Research, Chalk River Laboratories
Chalk River, Ontario, Canada, K0J 1J0

Abstract

The TASCC heavy ion facility produces beams at specific energies of 4 to 50 MeV/u. We report on the fine time structure of the beam, typically bunches of 150-500 ps FWHM, at a repetition rate of 31-62 MHz. Average beam currents range from 1 to 500 nA. The ratio between peak and dark current typically exceeds 5000:1, ideal for time-of-flight experiments. We also discuss measurements of absolute beam energy by bunch time-of-flight.

I. INTRODUCTION

The Chalk River Superconducting Cyclotron (SCC) is a $K=520$ machine, fully commissioned in Oct. 1991. Its two pairs of dees operate in 0-mode or π -mode, from 31-62 MHz. It accelerates beams from 3 Li to 238 U up to 50 MeV/u and 10 MeV/u, respectively. Extracted currents range from 1 to 500 nA. Here we discuss the timing properties of the beam, and energy measurement by bunch time-of-flight.

Figure 1 shows the TASCC facility layout. A Tandem accelerator serves as injector for the SCC. The Low Energy Buncher (LEB) uses an rf sawtooth (up to 2 kV across a grid) to pre-bunch the beam to about 1 ns ($10\text{-}20^\circ$ rf), focusing at the Tandem stripper to minimize straggling. The High Energy Buncher (HEB) is a double drift tube device that rebunches the beam to a focus at the SCC stripper foil. The beam is sent to the target areas through the time-of-flight energy measurement system (described in Section 3 below).

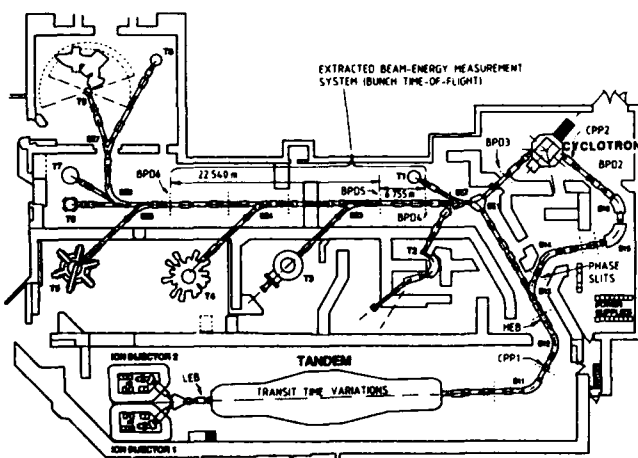


Figure 1. TASCC Facility Layout.

II. INJECTION TIMING

We have reported on the phase control system in a previous paper [1], but briefly re-cap here to point out recent

modifications. A capacitive pickup (CPP1) after the Tandem provides a signal to a phase shifter at the LEB to correct for transit time variations through the Tandem, typically of order $10\text{-}30^\circ$ rf. An analyzing magnet and slits after the HEB are used in another feedback loop to remove most of the unbunched current and to maintain energy stability at SCC injection by varying the HEB phase. The beam position is stabilized both vertically and horizontally using analog feedback at the object slits of the analyzer [2].

The HEB is operated the second or fourth rf harmonic, to ensure matching of the drift tube length to $\beta\lambda/2$ over the wide range of injected beams, and so not all HEB focusing buckets are filled. A recently-developed 'bucket control' computer program monitors the beam phase and coarsely resets the LEB phase to feed the desired HEB bucket after large phase shifts. These can occur after ion source or Tandem disruptions. Residual phase noise is reduced to typically $\pm 0.5^\circ$ rf at SCC injection, with current variations less than a few percent. Much recent effort has gone into noise control, improved sensitivity of capacitive phase probes [3] and development of linear, octave-bandwidth phase modulators [4]. Our ability to bunch and phase-control a Uranium beam of <10 nA was crucial to the commissioning of the SCC.

BEAM-PULSE WIDTH MEASURING SYSTEM

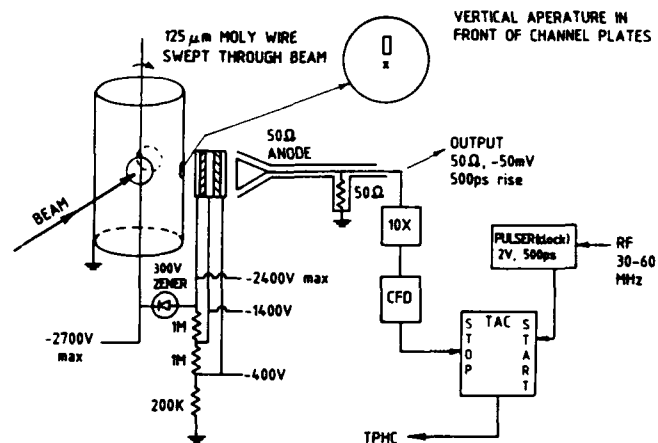


Figure 2. Beam Pulse Detector.

Bunch lengths are measured [5] with Beam Pulse Detectors (BPD) (shown in Figure 2). A 0.25 mm molybdenum wire at -2 kV is inserted into the beam. Ions hitting the wire produce primary electrons, with a (low) probability proportional to instantaneous beam current. They are accelerated through a small slot to a 'chevron' micro-channel plate to create secondaries with a gain of 10^4 and a

transit-time jitter of ~ 50 ps (manufacturer's data). Collected at a conical $50\ \Omega$ anode, they produce pulses of 500 ps risetime, and ~ 1 ns width. The overall detection efficiency is roughly 10^{-3} pulse per bunch. The electron pulse arrival time is strongly correlated with the instantaneous ion current, thus, a histogram of arrival time with respect to the rf clock represents the bunch shape in real-time. Data is accumulated over several seconds and includes residual phase noise. The electronic time resolution of the system is about 60 ps [5].

Figure 3 shows the time structure of the beam measured at SCC injection, with (a) the HEB alone (at 4^{th} harmonic), (b) the LEB alone and (c) both bunchers, with phase control properly set up. About 60% of the DC beam from the Tandem is bunched as shown. 72% of the bunched beam is in one of the HEB focusing buckets, with the rest divided between the defocusing HEB buckets and the out-of-phase focusing buckets. Typically 65-85% of the bunched beam is in the desired bucket, for an overall bunching efficiency of 40-50%. The bunch width measured at SCC injection is 200 ps FWHM, or about 2.4° rf at $f = 33.4$ MHz for a 24 Mg beam at 37.7 MeV. Typical injected bunch widths are in the range of 2.5 - 6° , depending on the frequency, the details of beam production in the ion source and straggling in the Tandem (straggling is worse for heavier beams).

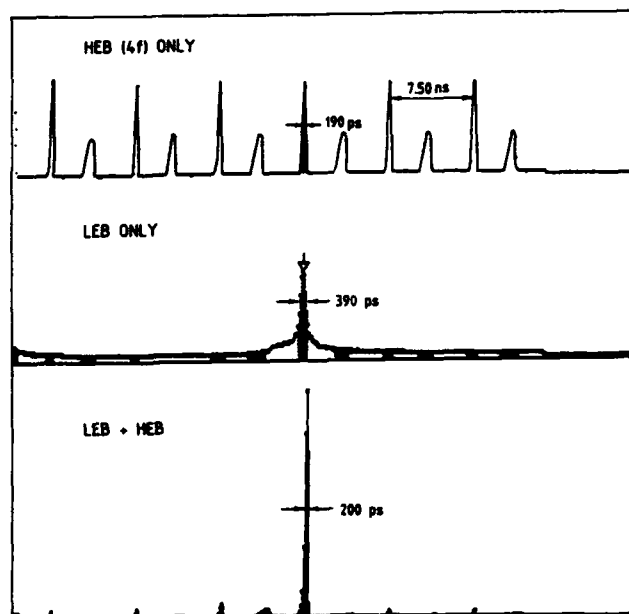


Figure 3. Injection Timing with Low and High-Energy Bunchers ^{24}Mg 37.7 MeV, $f = 33.4$ MHz.

Such narrow bunches produce well-separated turns in the SCC, making diagnostics easier. We use single-turn extraction, with a combination of (first harmonic) magnetic field shaping and electrostatic deflection. The energy spread of the beam is limited to a theoretical value of $1 - \cos(\text{HWHM}) \sim 3 \times 10^{-4}$ for a 3° bunch, assuming isochronism. Beam extraction efficiency is between 40% and 100%, depending on the electrostatic deflector gap and magnetic field details (e.g. there is loss of radial focusing at outer radius due to loss of isochronism).

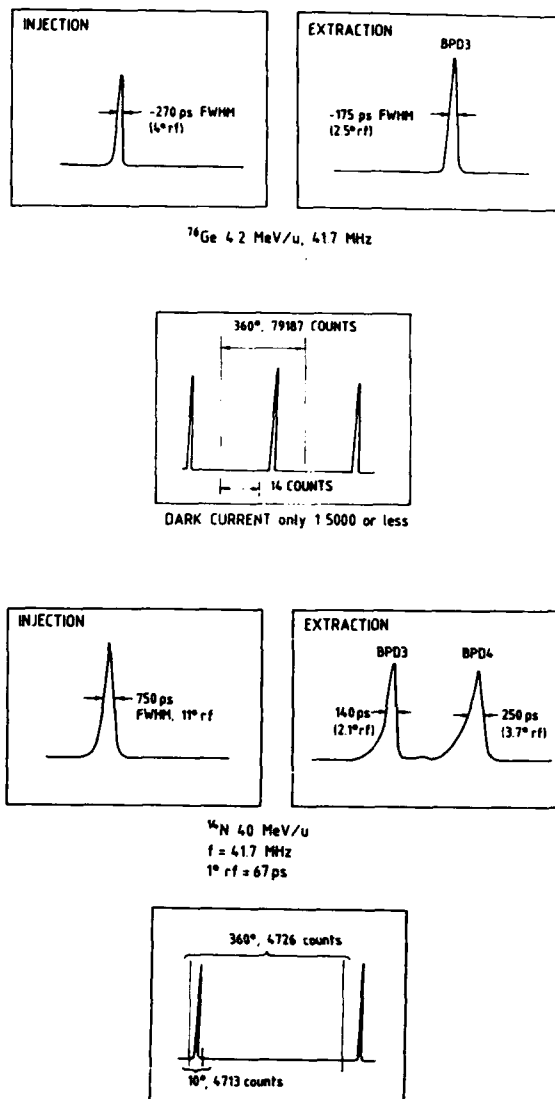


Figure 4. Bunch Widths and Current Contrast on Extraction.

The bunch length of the extracted beam is usually less than at injection, both because of the bunch compression due to the increasing DEE voltage with radius in the SCC itself [6,7] and because of aperture-clipping within the machine [8]. Figure 4 shows the bunch length for two different beams, at injection, on extraction (at BPD3), and analyzed at BPD4 in the target area. In the first case (76 Ge, 4.2 MeV/u, 41.71 MHz), the bunch length is 270 ps FWHM (4° rf) on injection, and 175 ps FWHM (2.5°) at extraction. In the second case (14 N, 40 MeV/u, 41.69 MHz), the injected bunches are purposely wide, 750 ps FWHM (11°) on injection, 140 ps (2.1°) at extraction (BPD3), and 250 ps FWHM (3.7°) at BPD4, after an additional 6 m drift and the dispersion of the analyzing magnet (BE1 in Fig. 1). The injected bunches were made wide and the current high to maximize output current. Extraction efficiency was low due to limited deflector voltage, with much of the accelerated

beam clipped on the deflector electrode. The deflector performance has since been greatly improved; this is reported in another paper in this conference [9]. In both cases, the bunch timing at extraction has an extraordinary level of time-contrast, that is, the ratio between instantaneous bunched current and the dark current between bunches, of at least 5000:1. This is of interest for time-of-flight experiments.

III. TIME-OF-FLIGHT ENERGY MEASUREMENT

We have built a system to measure the absolute beam energy [10] along the straight section of the extraction beamline (shown in Fig. 1). The bunch time-of-flight (BTOF) energy measurement system consists of an array of three Beam Pulse Detectors (BPD's) on the extraction beamline (BPD 4,5,6 in Fig. 1). The bunches are time-resolved by each detector, and from the time-of-flight over the 29m path length, the velocity and energy are calculated.

The system specifications and characteristics are as follows:

- specific energies 4 - 50 MeV/nucleon
- velocities β 0.09 - 0.32
- bunch repetition rate 31 - 62 MHz
- typical counting rate 5 - 100 KHz
- range of detectable currents 1 to > 100 enA
- flight path 6.755 m + 22.540 m (three detectors)
- time-of-flight 300 - 1100 ns
- transverse spatial resolution 0.25 mm (wire diam.)
- time-of-flight determined to ± 85 ps
- detector position surveyed to ± 2 mm
- **ACCURACY OF ENERGY MEASUREMENT:**
 $\delta E/E_{abs} \pm 3 \times 10^{-4}$ for 4 MeV/u, $\beta = .09$, 41.7 MHz
(e.g. Ge 4.2)
 $\delta E/E_{abs} \pm 9 \times 10^{-4}$ for 50 MeV/u, $\beta = .32$, 46.2 MHz
(e.g. C 50)

A representative result is shown in Fig. 5. The injected bunch pattern is shown in Fig. 5(a), with a FWHM of 330 ps, or 6.2° rf with a 'bucket efficiency' of 88%. For ^{127}I at 15 MeV/u, $\beta = .18$, 52.09 MHz, the bunches are $\beta\lambda \sim 1.03$ m apart in the beam-line. Each detector in the extraction array (BPD 4,5,6) produces a bunch footprint at 19.2 ns intervals, as shown in Fig. 5(b),(c). Using one pair of detectors, the velocity and energy can be determined to within $1/n$, where n is the number of bunches between the detectors. Using three detectors, n is determined uniquely, and the absolute energy found to within $\delta E/E < 10^{-3}$.

We have now done measurements of absolute energy of five beams, in seven runs, from 4.2 to 25 MeV/u. Small energy changes of order 10^{-3} can readily be detected and the SCC tuning corrected as needed.

The authors wish to acknowledge many fruitful discussions with H. Lindqvist.

IV. REFERENCES

- [1] G.R. Mitchel et al, "TASCC Bunch Injection and Phase Control System", Proceedings of the 12th Int. Conference on Cyclotrons, Berlin, 1989.
- [2] N.A. Towne, "Beam Position Stabilization System", TASCC internal report #162, 1993.

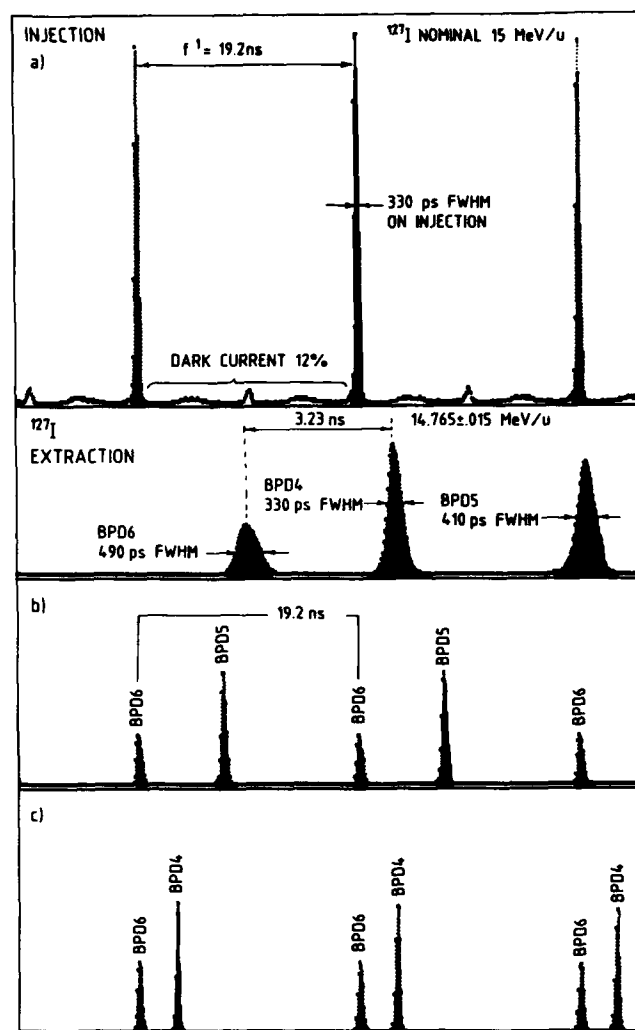


Figure 5. Injection and Extraction Timing, Bunch Time-of-Flight System.

- [3] N.A. Towne et al, "Improvement in Sensitivity of the Capacitive Phase Probes", TASCC internal report #153, 1992.
- [4] S. Kingsley-Jones, "Linear Phase Modulator", TASCC internal report #164, 1993.
- [5] G.R. Mitchel, "Subnanosecond Beam Pulse Detection System", TASCC internal report #69, 1989.
- [6] D. Bibet, M.H. Moscatello, "Cyclotron Tuning as a Rebuncher", Proceedings of the 13th Int. Conf. on Cyclotrons and their Applications, Vancouver, 1992.
- [7] R.W. Muller and R. Mahr, Nucl. Instr. and Meth. 86, 241, 1970.
- [8] D. Ramsay et al, "Production and Monitoring of Short Duration Beam Bursts from the TRIUMF Cyclotron", Nucl. Inst. Meth. A327, 265, 1993.
- [9] W.T. Diamond, "High Voltage Vacuum Insulation in Crossed Magnetic and Electric Fields", PAC Conference Proceedings, 1993.
- [10] G. Auger et al, "Absolute Measurement of the GANIL Beam Energy", GANIL preprint, 1993.

Design, Implementation, and Results from a Longitudinal Phase Space Tomography (PST) Monitor in the Fermilab Main Ring

G. Jackson
Fermi National Accelerator Laboratory*
P.O. Box 500 MS 341
Batavia, IL 60510

Abstract

In order to image the longitudinal phase space density distribution of a beam during complicated RF manipulations or during important points in the ramp such as transition, a Phase Space Tomography (PST) monitor has been installed in the Fermilab Main Ring. Based on tomography techniques normally used to image organs inside human beings, a 2-D map of the internal distribution of charge in longitudinal phase space is produced. The detector is simply a resistive wall monitor. Presented are descriptions of the monitor hardware, image reconstruction software, and results when the monitor is used to diagnose problems during the coalescing process.

I. INTRODUCTION

During commissioning and tuning of such longitudinal beam manipulations as coalescing [1], imaging enhancements can save time and allow the diagnosis of problems not readily identifiable by more traditional beam diagnostic techniques. This is especially true in the longitudinal plane where the shape and extent of the beam phase space distribution with respect to the separatrix are especially important parameters. One technique for producing such an image of the longitudinal phase space of the beam is the subject of this paper. The technique is very similar to that of medical CAT scans of human patients.

When a doctor needs to know the 2-dimensional size, shape, and position of an organ in a patient, a now common procedure is to put the person in a special X-ray machine. Instead of exposing a piece of photographic film to a single burst of radiation through the body, an array of X-ray tubes and electronic detectors are rotated around the patient, measuring the attenuation of each X-ray beam as a function of angle. This attenuation data is digitized and acquired by a computer.

In 1917 the Austrian mathematician J. Radon published a paper proving that any two-dimensional object can be reconstructed from the infinite set of its projections. Later mathematicians were able to show that a sufficient number of projections could reconstruct the two dimensional structure using some rather simple mathematical algorithms. Applying these same algorithms to the X-ray data, a computer can

generate a 2-dimensional density profile of the person on a grid of pixels. This technique is called tomography.

In the case of a particle beam it is relatively easy to measure only the temporal projection of a longitudinal phase space charge distribution. Sending the signal from a resistive wall monitor [2] into a fast digitizer is analogous to measuring the signals from an array of X-ray detectors from just one angle. But to carry the analogy between medicine and accelerator physics further, imagine that instead of rotating the X-ray tubes, the patient is rotated. This is called a synchrotron oscillation in the world of accelerators! By digitizing the output of the resistive wall monitor periodically during a synchrotron period, enough projections of longitudinal phase space can be accumulated to use the standard tomography reconstruction algorithms to image phase space.

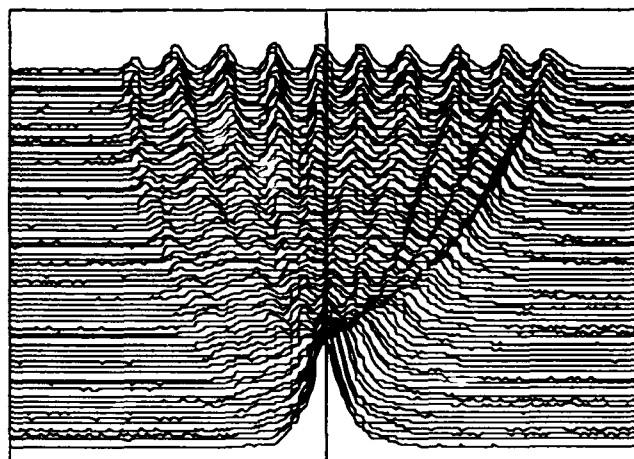


Figure 1: Mountain range plot of high intensity beam during the bunch rotation phase of coalescing. Note that the earlier bunches are debunching while the later ones preserve their shape.

II. SYSTEM DESIGN

The heart of the system is a Tektronix RTD720 transient digitizer linked via GPIB to the Fermilab control system. Capable of digitizing at a peak rate of 2 GS/sec, with a 500 MHz analog bandwidth, and with a segmented memory capable of more than 512 ksamples of storage, this device can be repeatedly triggered, filling a successive portion of memory each time. After acquisition is complete, the data stored in the digitizer memory is downloaded to the control system for processing. In the implementation aimed at diagnosing Main Ring coalescing, two of the channels of the digitizers are

*Operated by the Universities Research Association under contract with the U.S. Department of Energy.

utilized, each working at a 1 GS/sec sampling rate. While one channel is monitoring the beam signal, the other is digitizing the RF cavity fanback waveform. With a RF period of approximately 19 nsec and bunches which fill the RF buckets, enough resolution is attainable for tuning and diagnosis. With the memory segmented into 512 sample sections, 512 turns of data may be sampled, where the triggering is accomplished via a timing signal synchronized with the beam sent through a programmable +N counter.

The data is analyzed using a VAXstation computer, which is the standard console in the Fermilab control system. The first step of the reconstruction is to propagate each ray through the grid at its correct position and angle, adding the value of that digitizer bin to all of the grid squares that it traverses [3]. This summation method is a surprisingly good way to start the process, though for a small number of measured angles the contrast of the image suffers significantly. Given a finite number of colors or gray gradations, a background subtraction where pixels with values at or below zero are not plotted (or are black) can improve the contrast a bit.

A standard method for improving the fidelity of the phase space image relies on the convergence of an iterated algorithm. The resistive wall monitor data represents various projections through the actual longitudinal phase space density distribution. After applying the above summation method to an initially zeroed grid, perform a mock measurement through this distribution at the same positions and angles as the original measurements. For each ray, subtract the actual projection measurement from the grid projection measurement, and then distribute the difference across all of the intercepted grid points equally so that another projection measurement would agree with the original measurement. An optional step after each iteration which improves convergence is to find all pixels less than zero and setting them to zero. Repeat the entire process until the image does not change substantially any more.

III. SAMPLE MEASUREMENTS

As an example of the power of this phase space tomography, a phase space rotation during coalescing of high intensity protons is presented. Figure 1 shows the beam current data from the resistive wall monitor acquired every 80 revolutions of the Main Ring. The rotation RF voltage, which has a wavelength of 21 accelerating RF buckets, clearly changes the alignment of the bunches in phase space from the time axis to the energy axis, at which point the accelerating voltage is turned back on to recapture this new distribution in a single bucket. Calling the starting alignment 0° and assuming that recapture occurs at 90° , the data in figure 1 is used to reconstruct the phase space picture at recapture time. This phase space image is shown in figure 2. By writing a simulation program which creates mountain range images similar to figure 1, various tuning errors and intensity effects can be recognized and corrected. See figure 3.

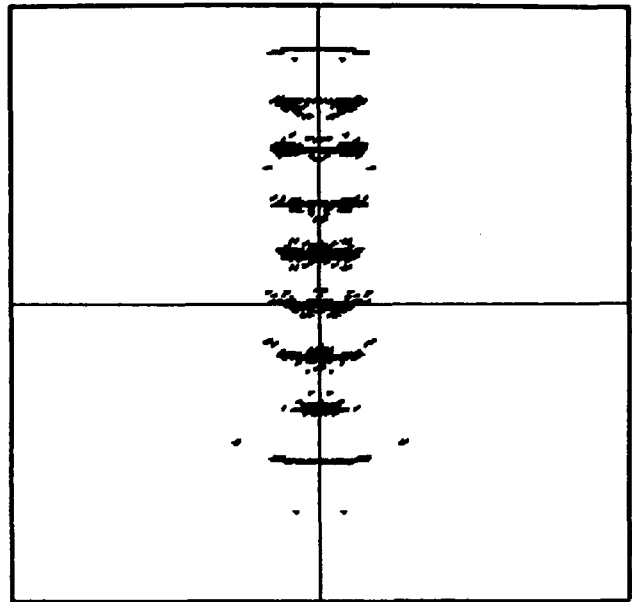


Figure 2: Phase space distribution of the beam reconstructed from the above Main Ring data and imaged at recapture time.

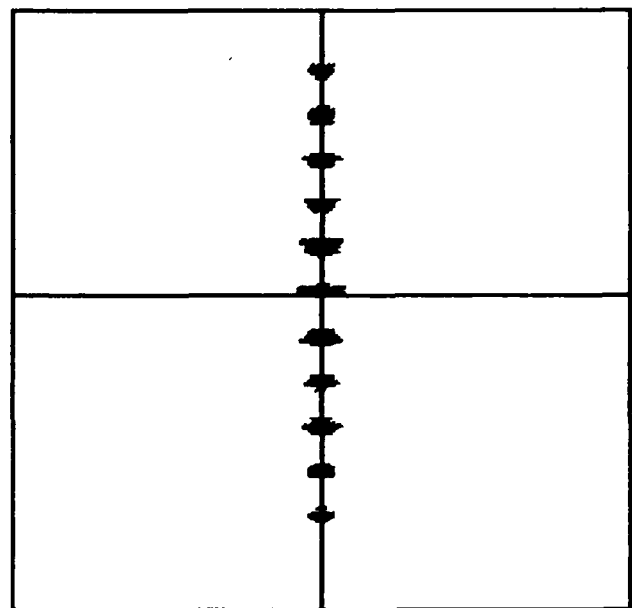


Figure 3: Phase space distribution of a low intensity beam which was coalesced after considerable tuning.

IV. REFERENCES

1. I. Kourbanis, G. Jackson, X. Lu, Proc. IEEE Part. Acc. Conf., Washington D.C. (1993).
P. Martin, K. Meisner, and D. Wildman, Proc. IEEE Part. Acc. Conf., Chicago (1989) 1827.
2. C.D. Moore, et. al., Proc. IEEE Part. Acc. Conf., Chicago (1989) 1513.
3. R. Gordon, G. Herman, and S. Johnson, Sci. Am., 233 No. 4 (October 1975) 56.

An Electrostatic Sweep Plate Device for Emittance Measurement of Ion Beams to 2 MeV*

T. W. Debiak, J. Porter, R. Heuer, and I. Birnbaum
Grumman Aerospace and Electronics Group
1111 Stewart Avenue, M/S B29-25, Bethpage, NY 11714 USA

Abstract

Electrostatic sweep plate devices have been used previously for the measurement of ion beam emittance.[1] These devices may be routinely designed with an ultimate angle resolution of ± 0.25 mrad or less. We have used a similar device for measuring the emittance of H^- and H^+ beams exiting an RFQ at 1 MeV. This scanner will be used to characterize the beam exiting a low-power DTL at energies up to 2 MeV. The physics design changes consist primarily of increasing the length of the deflection plates and decreasing their separation to obtain high electric field at low deflection plate voltage. The front face of the scanner was made thicker and designed for water cooling to withstand the beam power at up to 2 MeV. In this paper the design of the scanner is discussed. This includes the device angular resolution and maximum acceptable angle. The thermal analysis that led to the design of the water-cooled front face is shown. Data showing the performance of the device and resulting emittance measurements at 1 MeV are presented.

I. INTRODUCTION

For many accelerator applications, the most important parameter is the ion beam's transverse emittance. The device of choice for the highest precision emittance measurement is

an electrostatic sweep plate scanner[1]. We have been using such a device for H^- and H^+ beam emittance measurements at energies between 10 keV and 35 keV[2] on our ion source test stand and accelerator beamline.

We have installed an RFQ on our beamline and plan to install a matching section and DTL at the end of the RFQ. To characterize the beam at the output of the RFQ (1 MeV) and at the output of the DTL (1.76 MeV), the sweep plate scanner was redesigned. The design goal was to obtain a maximum sweep plate voltage of 2.5 kV while keeping the length of the deflection plates to a reasonable length. In addition the front face of the scanner was designed to withstand the 30- to 60-fold increase in beam power at the higher beam energies.

In the original design[2], the scanner was mounted on a ring that rotated through 90° . This permitted the measurement of emittance in both the horizontal and vertical beam directions using a single device. This ring assembly was made more rugged for the larger and heavier scanner. Figure 1 shows the side and front views of the new scanner mounted in the more rugged ring assembly. In this figure, the scanner is positioned for use in the horizontal direction. The scanner is guided on a lead screw that is driven by a pulley attached to a stepper motor.

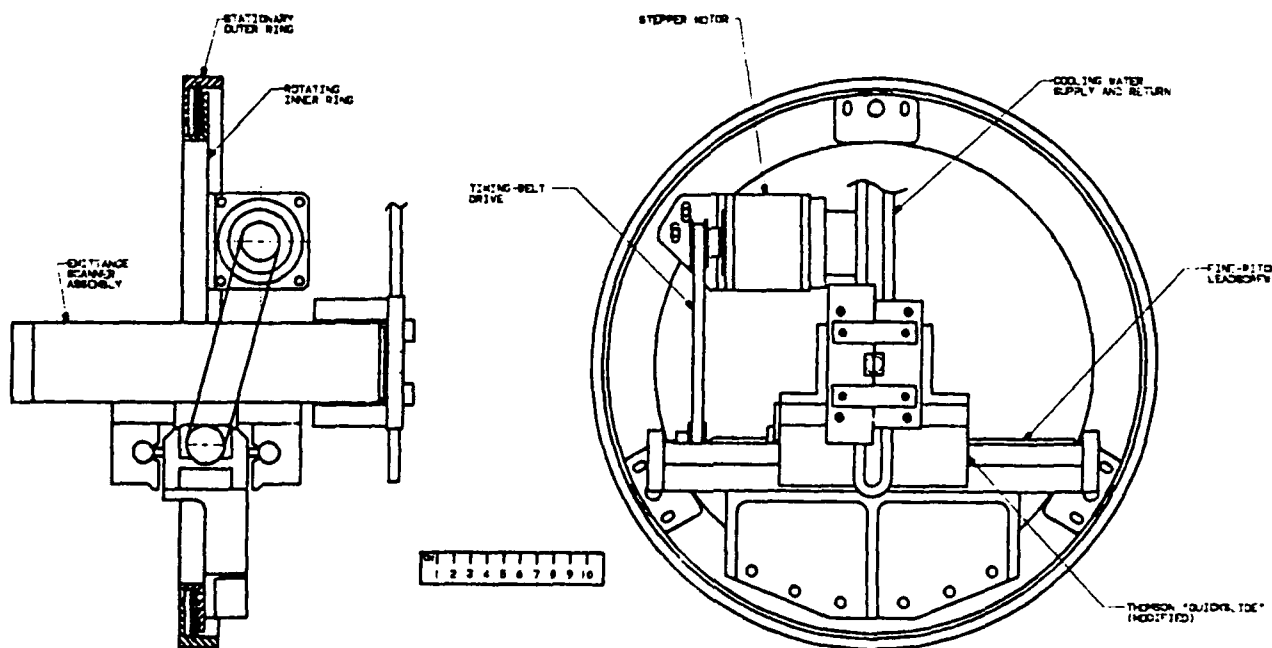


Figure 1. Front and side views of the ring assembly for the high-energy emittance scanner.

* This work was supported by Grumman IR&D project 7256-2709.

II. PHYSICS DESIGN

Since the energy of the beam downstream of the RFQ is two orders of magnitude higher than in the LEBT, the scanner deflection plates were made longer and their separation was made shorter. Fortunately, the beam divergence at the RFQ output is expected to be less than 45 mrad, compared with up to 130 mrad at the source output.

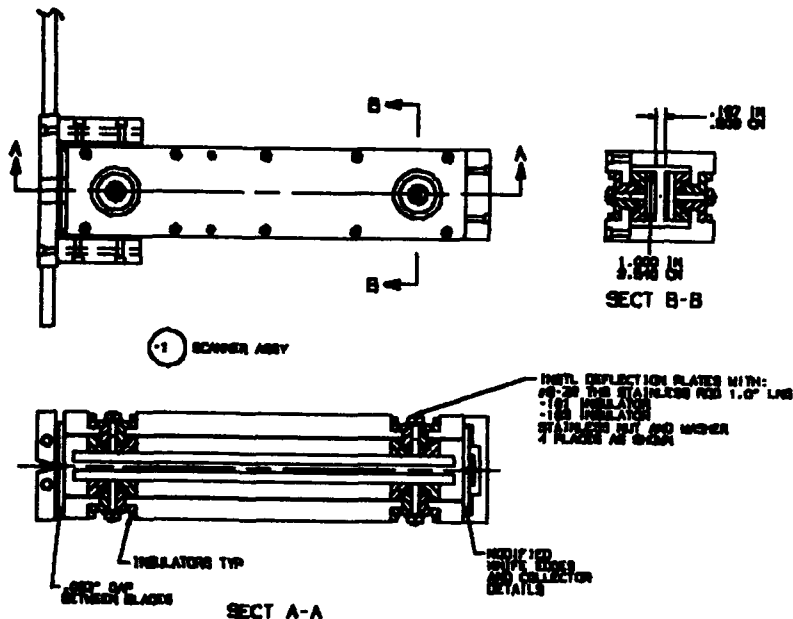


Figure 2. Top, side, and front views of the high-energy emittance scanner.

Figure 2 shows a three-view schematic diagram of the new scanner and Table 1 shows the critical dimensions of both the low- and high-energy scanners. The resulting relationship of deflection plate voltage vs. beam angle for the redesigned scanner is shown in Figure 3. Note that the maximum voltage that need be applied to the high-energy scanner is 2300 volts, compared with 123 volts for the low-energy scanner. The angle resolution for both scanners is shown. This was obtained by calculating the angular range of ions that would pass through the top and bottom extremes

Table 1
Comparison of Parameters for the Low- and High-Energy Emittance Scanners

	Low Energy Scanner	High Energy Scanner
Defl. Plate Separation (cm)	0.132	0.5
Defl. Plate Length (cm)	3.8	20
Field-Free Regions (cm)	0.16	0.5
Slit Opening (cm)	0.0025	0.0076
Nominal H ⁺ Energy (keV)	30	1013
Max. Analyzable Angle (mrad)	±59	±45
Max. Defl. Plate Voltage (V)	±123	±2300
Angle Resolution (mrad)	±0.62	±0.38

of the entrance and exit slits at constant deflection plate potential. This becomes ±0.62 and ±0.38 mrad for the low- and high-energy scanners respectively.

III. THERMAL DESIGN

A thermal/structural evaluation was performed to support the design of the high-energy scanner. The purpose of the study was to determine the maximum temperature of the protective front face and to determine the extent of the deformations of the knife blade assemblies during beam impact using various amounts of water cooling. The beam parameters used were 30 mA at 1% duty factor, 10 pulses per second (1ms pulse length). The analysis was performed using the finite element code, ANSYS. The resulting temperature distributions of the front face and knife blade are shown in Figure 4 assuming a water flow of 1.5 - 2.0 GPM. With these temperature distributions, the thermal stress due to temperature cycling of the molybdenum should not produce fatigue cracking.

Another thermal consideration was the vertical deflection of the knife blades due to beam heating. The analysis showed that, in the worst case, each knife blade should deflect (toward closing the slit opening) by 0.55 mils; therefore, a slit opening of 3 mils was chosen to permit a minimum slit opening of 1.9 mils.

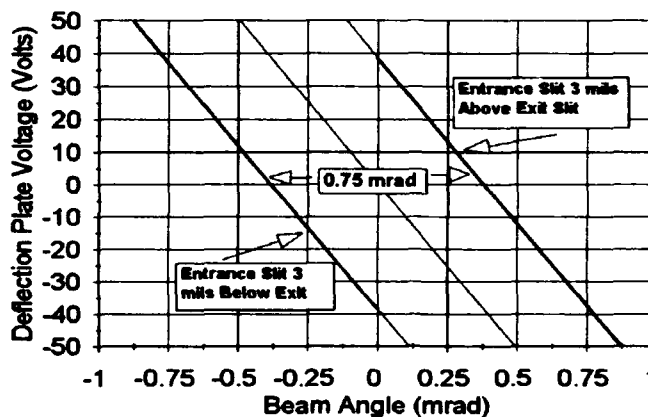


Figure 3. Voltage on each deflection plate (opposite polarity) as a function of beam angle. The angular resolution is the range of angles transported through the entrance and exit slits at constant deflection plate voltage.

Length Monitor for 1 mm SLC Bunches*

E. Babenko[#], R. K. Jobe, D. McCormick, and J. T. Seeman

Stanford Linear Accelerator Center
Stanford University, Stanford, California 94309 USA

Abstract

A non-intercepting RF bunch length monitor for $\sigma_z = 0.5$ to 2.0 mm long electron and positron bunches in the Stanford Linear Collider (SLC) has been built with a design similar to a previous device for longer bunches¹. For this device, fields from the beam pass through a ceramic gap, enter receiving cavities, are then measured with power detectors, and finally are recorded by the SLC control computer. The designs of the receiving cavities (25 and 36 GHz) are described as well as the choice of the RF power distribution and measuring systems. Beam measurements have been taken as a function of bunch compressor RF voltage, bunch intensity, and beam position. Long term bunch length measurements were recorded during SLC colliding beam operation indicating that the bunch length is constant to about 3%. Thus, 1 mm length monitors operating at 25 and 36 GHz have successfully monitored long term bunch length changes at the few percent level in the SLC.

Theory

We consider a highly relativistic electron (positron) bunch with a gaussian rms length nominally 1 mm traveling linearly along a vacuum chamber. The electric field lines of each charge in the bunch extend radially from the particle with a longitudinal angle of $1/\gamma$ where $\gamma = E/mc^2$. A integral over the longitudinal charge distribution gives the power spectrum of the bunch. For example, the power spectra for three representative bunch lengths and two shapes are shown in Fig 1. Using these plots frequencies of 20-40 GHz seem optimal.

Conversely, if the power spectrum is measured for a bunch then its length (distribution) can be deduced. In our system the bunch is made to pass by a ceramic gap in the vacuum chamber. The fields from the bunch radiate from the gap and enter a cavity through a small radial hole. The power in the cavity is then radiated out the entrance hole but also through a hole leading to a high frequency power meter after a length of rectangular waveguide. A schematic view of this arrangement is shown in Fig. 2. The frequencies of the cavity were chosen to optimally measure changes in the bunch length. For our case two cavities were made at frequencies of 25 and 36 GHz, allowing comparisons to be made.

In our situation the TM_{020} mode is used in the cavity and only one component is excited, namely H_ϕ . To obtain

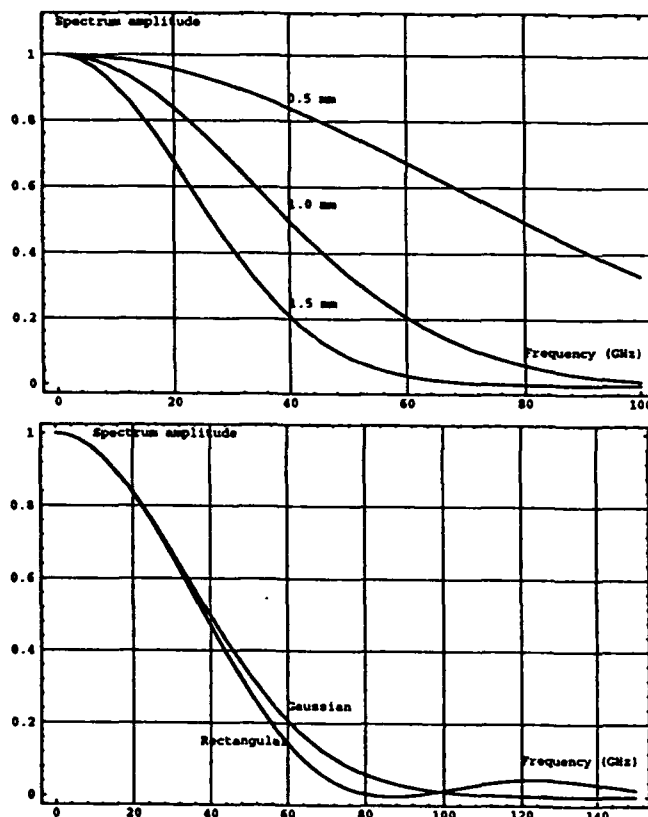


Figure 1 Theoretical beam power spectra for three different bunch lengths and two distributions.

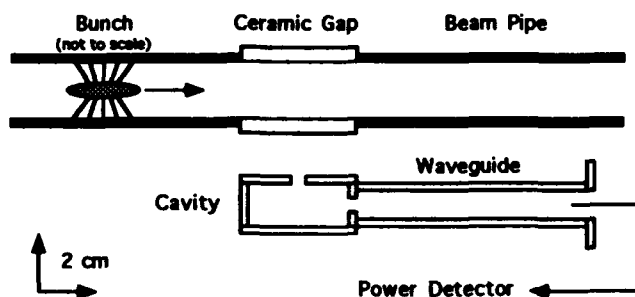


Figure 2 Layout of the bunch length monitor system.

the maximum power² one must consider the distance from the beam to cavity, the radius and depth of the coupling holes, the Q of the cavity, the ratio of the diameters of the input to output coupling holes (nearly equal is best), and the attenuation of the waveguide from the cavity to the power detector. The expected peak power P can be calculated²

* Work supported by the Department of Energy contract DE-AC03-76SF00515.

[#] Visitor from the Budker Institute of Nuclear Physics, Novosibirsk, Russia.

$$P_{\text{peak}} = d q^2 \exp(-\omega_0^2 \sigma_t^2) \exp(-\alpha y) \quad (1)$$

where ω_0 is the cavity frequency, σ_t is the bunch length in time, q is the bunch charge, α is the attenuation coefficient of the waveguide from the cavity to the detector at a distance y . The cavity design constants are included in d . The general parameters of the two cavities are listed in Table 1.

Table 1 Monitor Cavity Parameters for $3 \times 10^{10} e^-$.

Parameter	36 GHz	25 GHz
Cavity:		
Radius (cm)	0.73	1.05
Height (cm)	0.67	0.97
Distance to beam(cm)	3.8	5.0
Input hole diameter (cm)	0.3	0.45
Output hole diameter (cm)	0.35	0.4
Input Q Factor	490	750
Output Q Factor	700	1700
Pulse duration (ns)	1.2	3.2
Waveguide:		
Wide wall 'a' (cm)	0.71	1.07
Narrow wall 'b' (cm)	0.36	0.43
y length (m)	13.	13.
Attenuation constant	0.42	0.43
Detector peak power (mW)	12.7	3.3

SLC Hardware Configuration

Two cavities were built using the specifications in Table 1 and were brazed to short waveguide stubs. The finished units are shown in Fig. 3. Since the cavities are not used in vacuum the cover "side" plates are held in place by clamps. Both cavities were installed in the SLC in Sector 25 at the 2500 m location in the accelerator. At that location a ceramic gap had been installed with a 3 cm ID and 3.8 cm OD. The gap is about 1 cm long and is brazed to stainless steel tubes (2.5 cm diameter) on both ends. The cavities were installed one on each side of the gap. The distances from the beam to the cavities are listed Table 1. Here each bunch has an energy of about 42 GeV, has a transverse size of about 100 mm, and a repetition rate of 120 Hz.

The signals are transported out of the radiation enclosure through rectangular waveguides to respective Hewlett-Packard power detector diodes HP 8474E. A typical output signal is shown in Fig. 4. The signal levels are a few milli-watts, matching nicely the upper level capability of the detectors. The processed signals are then amplified, integrated by a gated ADC, and recorded in the SLC VAX control computer.

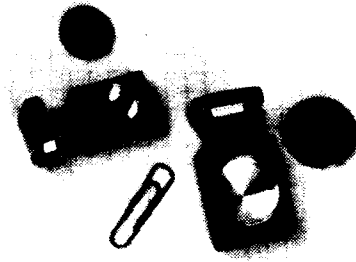


Figure 3 Photograph of the bunch length monitor cavities.

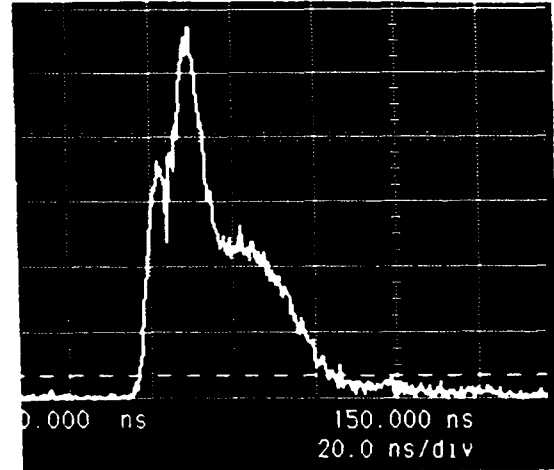


Figure 4 Measured signal from the 36 GHz monitor with $\sigma_z = 1.8$ mm and 3×10^{10} electrons. (Scale = 100 μ W / div.)

Observations

The first test of the system was to measure signal sensitivities to transverse position changes of the beam as indicated by nearby position monitors. Only a very weak dependence was observed. The signals changed less than 2% when the beam moved by 1 mm. The beam positions are typically stable to 100 μ m during long term operation.

The bunch length in the SLC is determined by the peak RF voltage of the compressor accelerator. The bunch length σ_z in the linac is given by³

$$\sigma_z^2 = \sigma_{dr}^2 [1 - 2\pi R_{56} f E_c / (E_{dr} \lambda)]^2 + R_{56}^2 (\sigma_E/E)^2 \quad (2)$$

where $E_{dr} = 1.19$ GeV, $\sigma_{dr} = 6 - 10$ mm, $E_c = 0 - 40$ MV (typically 29 MV), $R_{56} = 603$ mm, $\sigma_E/E = 1 \times 10^{-3}$, f is a calibration constant for the compressor RF voltage measurement, and $\lambda = 105$ mm. For the data below, $f = 0.94$. The minimum bunch length (about 0.5 mm) is obtained with $E_c = 36$ MV.

The length monitor signal was recorded as a function of compressor voltage (and bunch length). The resulting data are plotted in Fig. 5 for $3.3 \times 10^{10} e^-$. The solid line is the shape determined from Eqns. 1 and 2. The expectation matches the data. The nominal compressor voltage is 28.6 MV corresponding to a length of about 1.8 mm for $3 \times 10^{10} e^-$.

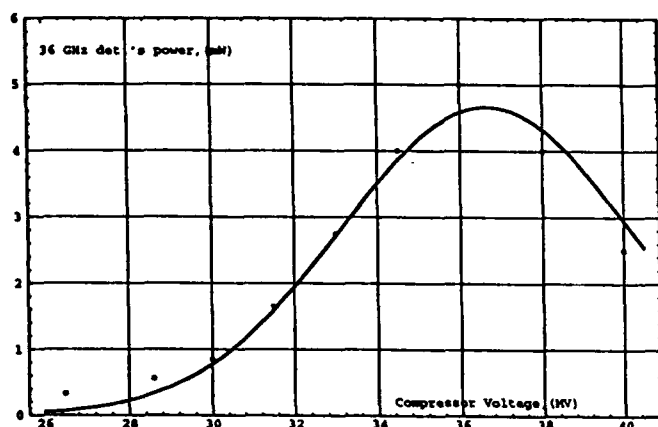


Figure 5 Signal (36 GHz) versus damping ring compressor voltage. The bunch length changes from 1.2 mm at 28.6 MV to 0.5 mm at 36 MV at low beam charge.

The length signal was measured as a function of bunch intensity as is shown in Fig. 6. From Eqn. 1 we expect a quadratic increase in signal with intensity, which is seen at low intensities. However, at high intensities the damping ring exhibits bunch lengthening⁴ which reduces the signal rise. Thus, the solid line in Fig. 6 is a calculation of the expected signal versus intensity including the lengthening effects in the damping ring. The data and the calculation are in good agreement.

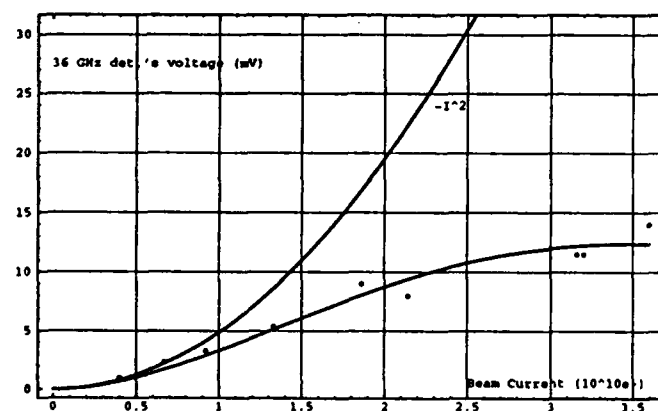


Figure 6 Signal (36 GHz) versus bunch charge. The solid line represents the power expected including bunch lengthening in the damping ring with current.

During colliding beam conditions the bunch length must be held constant. Any change in this length will affect the

energy gain in the accelerator from beam loading changes and, thus, change the emittance growth along the accelerator. The VAX control computer has been setup to record the bunch length signals as a function of time. One eight day history plot is shown in Fig. 7. Here we see that the bunch length is quite stable in time showing only small changes of order 3%, mostly diurnal. Some of the diurnal changes are due to temperature effects in the amplifiers (under investigation) and some of the step changes may be due to compressor voltage changes.

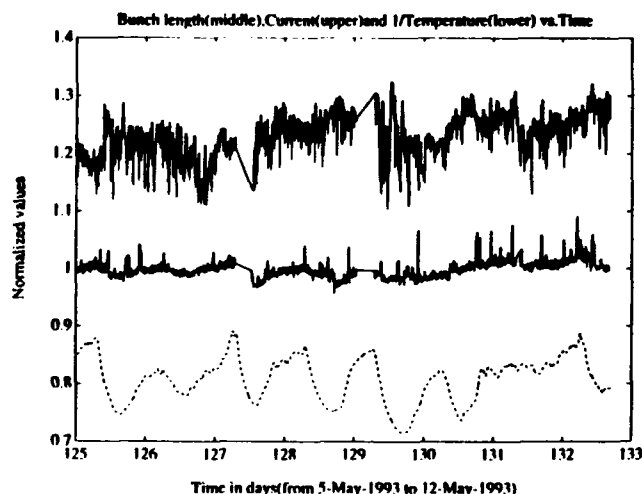


Figure 7 Long term signals for an SLC electron beam with 3×10^{10} particles and compressor amplitude of 28.5 MV. The center data are the fractional bunch length changes with time. Note only a few percent change over days. The lower plot shows the changes of temperature ($1/T$) with time on an arbitrary scale. Some temperature effects are seen in the length signal. The upper plot is the fractional change in the beam charge ($\times 1.2$ for clarity) versus time. The changes of bunch charge with time have been removed from the length data.

Acknowledgments

The authors wish to thank T. Himel, N. Phinney, and M. Ross for comments concerning this monitor and for assistance in setting up the long term history buffers.

References

1. A. Kulikov, *et al.*, "A Monitor of Single Bunch Lengths," SLAC internal note, April 1986 (unpublished).
2. E. Babenko, "Length Monitors for Single Bunches," SLAC internal note, March 1993 (unpublished).
3. L. Merminga, *et al.*, "Bunch Length Measurement in the Linac," SLC Experimental Report 116, January 1990, (unpublished).
4. K. L. F. Bane, "Bunch Lengthening in the SLC Damping Rings," Stanford, SLAC-PUB-5177 (1990).

Bunch Shape Monitor For SSCL Linac*

J. W. Hurd, G. M. Arbique, C. E. Crist, F. W. Guy, G. T. Lelfeste, D. Raparia, K. Saadatmand, D. A. Swenson
Superconducting Super Collider Laboratory
2550 Beckleymeade Avenue, Dallas, TX 75237

S. Esin, A. Feschenko, A. Stepanov, A. Mirzozan
Institute for Nuclear Research of the Academy of Sciences of Russia
Moscow, 117312

Abstract

The Superconducting Super Collider Laboratory and the Institute for Nuclear Research are collaboratively developing a Bunch Shape Monitor [1] diagnostics for commission the SSCL linac. The Bunch Shape Monitor is designed to measure the intensity of beam as a function of time over the micro-bunch of the beam. Design resolution for the SSCL monitors is approximately 7 psec. The first monitor will operate at the fundamental frequency of 428 MHz and will be used to measure the output beam of the RFQ Linac. First available results will be presented and compared with predictions. Further development will allow the monitors to fit in a standard SSCL beam box and one will operate at the third harmonic of 428 MHz. Proposals to use the Bunch Shape Monitor to measure the longitudinal phase space distribution of the beam will be discussed.

I. INTRODUCTION

The SSCL linac [2] consists of three major rf accelerators, a Radio Frequency Quadrupole that accelerates an H^- beam to 2.5 MeV, a Drift Tube Linac to 70 MeV, and a Coupled Cavity Linac to 600 MeV. The H^- beam is then stripped and injected into the Low Energy Booster, the first of four synchrotrons that accelerate the protons to 20 TeV [3].

To commission, tune, and monitor the SSCL linac, a set of diagnostics is being developed to measure the transverse and longitudinal characteristics of the beam [4]. The transverse set of diagnostics consists of the standard set of position monitors, wire scanners, and slit and collector emittance measurement units. The longitudinal diagnostics are the beam position monitors, energy absorber and collectors for low energy phase scans, and the Bunch Shape Monitor.

The phase information from the beam position monitors gives longitudinal phase centroid information about the beam. The bunch shape is used to measure the longitudinal width of the beam in the phase or time dimension. The bunch shape monitor measurements separated by some known transformation can be used much like three wire scanner measurements to reconstruct the longitudinal RMS emittance of the beam [5]. The first measurements of the beam's longitudinal characteristics have been made on the output beam from the 2.5 MeV RFQ.

* Operated by the URA for the USDOE, under contract No. DE-AC35-89ER40486.

II. DESCRIPTION

Bunch Shape Monitors have been built and successfully used at the Moscow Meson Factory, [6], [7], [8], and at the FNAL linac [9], [10]. The basic concept and development history leading to the SSCL version of the Bunch Shape Monitor was reviewed at the 1992 Workshop on Beam Instrumentation in Berkeley [11].

Figure 1 illustrates the concept of the Bunch Shape Monitor. The 428-MHz micro-bunches of the H^- beam hit the

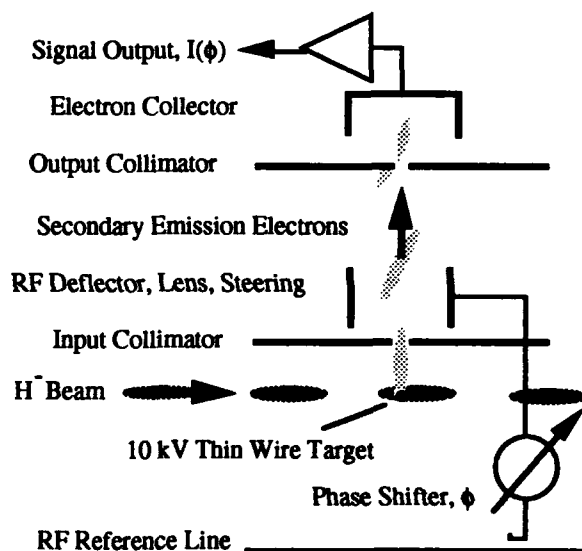


Figure 1. Functional diagram of Bunch Shape Monitor. Beam colliding with the target produces secondary emission electrons. The electrons have the same temporal structure as the beam. The rf deflector "time stamps" the secondary emission electrons which reach the electron collector.

target. The target is similar to a standard wire scanner with the wire at 10 kV. The H^- beam hitting the target produces a proportional amount of secondary emission electrons. These electrons are created with average energy of approximately 4 eV and are quickly accelerated radially by the target potential. A well defined beam of electrons is created by the input collimator. The electron bunches have the same longitudinal structure as the H^- beam. The beam passes into the rf structure. The rf deflector plates have a DC electrostatic field component which is used to focus the electron beam on the Output Collimator slit. The rf field sweeps the electron bunch across the Output Collimator slit. Only the thin slice

of beam with the correct phase passes through the slit to the Electron Collector. The charge in this slice is proportional to the analogous slice of H^- beam with the same relative phase. The Electron Collector is either a Faraday cup or an electron multiplier. The measured electron charge as a function of rf phase gives the bunch shape of the H^- beam. The resolution is calculated [12] to be approximately 7 picoseconds.

The new, compact design utilizes a quarter wave length parallel wire line deflector combined with electrostatic focusing and steering electrodes. The Bunch Shape Monitor has been designed to fit in the nominal standard beam box for the SSCL linac. Bunch Shape Monitors are being developed for the RFQ-to-DTL matching section, DTL-to-CCL matching section, and the 600-MeV Transport Line, as well as the Test model which will be used throughout the linac during commissioning.

III. THEORETICAL RESULTS

The first measurements of the bunch shape are on the output of the 428-MHz RFQ. The RFQ accelerates the H^- beam to 2.5 MeV. The H^- beam out of the RFQ has a nominal phase spread of 15 degrees and a longitudinal emittance of 0.13π MeV-degree (RMS). The drift from the end of the RFQ to the Bunch Shape Monitor target is 148 mm.

Theoretical results were obtained from simulations using PARMTEQ and PARMILA. Measured transverse emittances were used as the input beam. Longitudinal profiles were calculated at the bunch shape monitor. Earlier analysis had shown that image charges on the vanes did not contribute significantly for the SSCL RFQ. Therefore, the version of PARMTEQ we used had only space charge and multipole effects. Five thousand particles are used and the results are grouped in 3 degree wide bins. The calculated bunch shape at the nominal vane voltage setting is shown in figure 2. The bunch shape was determined for all the particles in transverse phase space while the measured data is for a limited set as sampled by the target wire.

Bunch shapes were calculated for vane voltages from 80% to 120% of design vane voltages in steps of 5%. The RMS width of the bunch shape and the change in phase center are calculated for each scan. The results are shown in figures 3 and 4 along with the measured data. To determine the design vane voltage, the transmission as a function of vane voltage was also calculated. The phase of the plot is relative to the synchronous particle.

IV. MEASUREMENT

The beam bunch shape was measured for vane voltages from 80% to 112% of the nominal vane voltages in steps of 2.5% and 5%. The nominal vane voltage was determined by measuring the knee of the transmission curve and by x-ray spectrum from electron traversing the RFQ gap. Figure 2

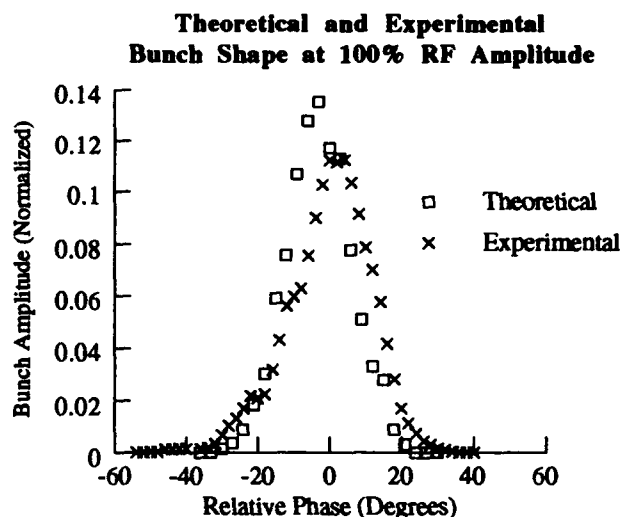


Figure 2. Theoretical bunch shape predicted by PARMTEQ simulation and experimental data as measured by the bunch shape monitor for nominal vane voltage. The intensity is normalized for a unit area.

shows the results of the measurement at the nominal vane voltage. The data is taken at a 1 MHz sample rate during the beam pulse. The experimental data shown is an average over 10 sets of data during the middle of the beam pulse. The data is normalized for an area of one and shifted for an average phase of zero. Figures 3 and 4 show the measured rms width and centroid for various RFQ vane voltages. The phase is relative to the RF drive line and is shifted from the cavity phase by an unknown constant. Therefore, to compare the measured and theoretical data, the phase of the experimental data is shifted such that the average is the same as the average of the theory.

V. COMPARISON

The RMS width and centroid compare well with the theory. Reproducibility at the 100% rf amplitude settings showed variations in the phase width and centroid of less than a few degrees. Error estimates have not been done for the simulations. The resolution of the measurement is expected to be approximately 1 degree. The sensitivity of the results to input phase space conditions for both the simulation and measurement have not been explored.

The actual bunch length measurement samples a thin line in transverse space. To get a meaningful number of particles in the results, the simulation uses all the particles across transverse space. Measurements must be performed across the beam width to determine the bunch shape transverse dependence.

VI. CONCLUSION

First results of measurements using the SSCL/INR Bunch Shape Monitor are shown. The results are compared to theory. More work is required to quantify the accuracy and errors associated with the measurement. The Bunch Shape Monitor is also capable of measuring the micro-bunch shape as a function of time along the macro-bunch. These studies will be carried out at a later date. Additional bunch shape monitor systems are being developed for commissioning of

the SSCL linac. They will be installed and tested in the matching sections into the DTL and CCL and at the end of the linac.

VII. ACKNOWLEDGMENTS

Olin B. van Dyck of Los Alamos National Laboratory and Elliot S. McCrory of Fermi National Laboratory are acknowledged for their support and effort on the bunch shape monitor diagnostic.

VIII. REFERENCES

- [1] A. V. Feschenko and P. N. Ostroumov, "Bunch Shape Measuring Technique and Its Application for an Ion Linac Tuning," *Proceedings of 1986 Linac Conference*, pp. 323-327.
- [2] L. W. Funk, "The SSC Linac, 1992 *Linear Accelerator Conference Proceedings*," Vol. 1, pp. 8-12.
- [3] *Site-Specific Conceptual Design Report*, SSCL Report SSCL-SR-1056, July 1990.
- [4] J. W. Hurd et. al., "Beam Diagnostic Layout Requirements for SSCL Linac," these *proceedings*.
- [5] Yu. V. Bylinsky et. al. "Longitudinal Emittance Measurement of the 100 MeV Proton Beam," *Conference Record of 1991 IEEE Particle Accelerator Conference*, pp. 3062-3063.
- [6] Yu. V. Bylinsky et. al., "Initial Operation of the First 20 MeV Tank of the INR Linac," *Proceedings of the 1989 IEEE Particle Accelerator Conference*, Vol. 3, pp. 1411-1413.
- [7] G. I. Batskich et. al. "Proton Beam Acceleration Up to 160 MeV at the Moscow Meson Factory Linac," *Conference Record of the 1991 IEEE Particle Accelerator Conference*, Vol. 5, pp. 3067-3069.
- [8] V. A. Andreev et. al., "Development of RFQ Accelerator for the MMF Linac," *Conference Record of the 1991 Particle Accelerator Conference*, Vol. 5, pp. 3109-3110.
- [9] E. McCrory et. al., "Use of an INR-Style Bunch-Length Detector," 1992 *Linear Accelerator Conference Proceedings*, Vol. 2, pp. 662-664.
- [10] E. McCrory, private communication of data and results of preliminary beam measurements using FNAL bunch shape monitor, Feb. 2, 1993.
- [11] A. V. Feschenko, "Bunch Shape Monitor Using Low Energy Secondary Electron Emission," proceedings of the Workshop on Beam Instrumentation, Berkeley, Oct. 1992.
- [12] A. V. Feschenko and S. K. Esin, "Bunch Shape Monitor for the SSCL Linac, Preliminary Design Review Report," Academy of Science of Russia, Institute for Nuclear Research, Sept. 1992.

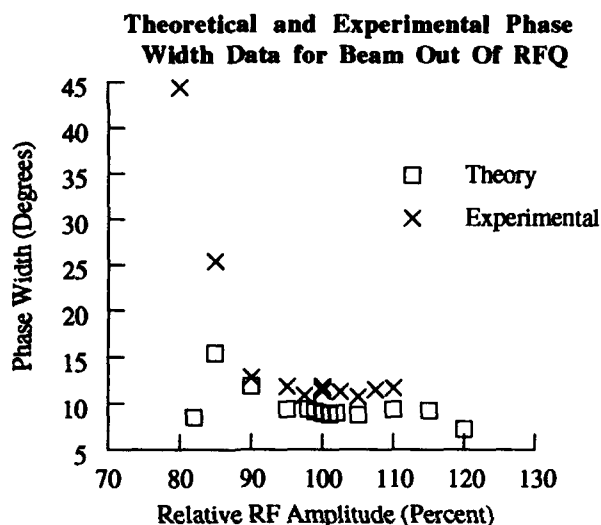


Figure 3. Measured and calculated RMS widths shown as a function of vane voltage. Widths are in degrees of 428 MHz.

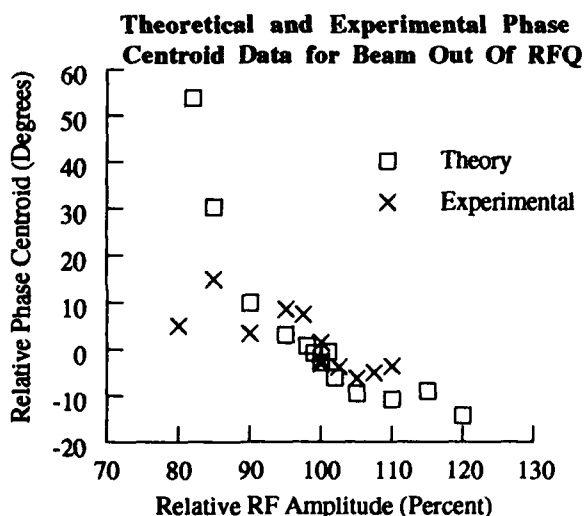


Figure 4. Measured and calculated micro-bunch centroids shown as a function of vane voltage. Widths are in degrees of 428 MHz. The centroid scale offsets are arbitrary. The zero for the theoretical data is defined by the centroid for the nominal (100%) vane voltage. The experimental data is shifted such that the average is the same as the theoretical data.

A Field-Based Technique for the Longitudinal Profiling of Ultrarelativistic Electron or Positron Bunches Down to Lengths of ≤ 10 Microns*

R. Tatchyn

Stanford Linear Accelerator Center, Stanford, CA 94305, USA

Abstract

Present and future generations of particle accelerating and storage machines are expected to develop ever-decreasing electron/positron bunch lengths, down to 100μ and beyond. In this paper a method for measuring the longitudinal profiles of ultrashort ($1000 \mu \sim 10 \mu$) bunches, based on: 1) the extreme field compaction attained by ultrarelativistic particles, and 2) the reduction of the group velocity of a visible light pulse in a suitably-chosen dielectric medium, is outlined.

I. INTRODUCTION

A number of widely known techniques for measuring the longitudinal density profiles of single-pass or recirculating particle bunches are employed on present-day particle accelerators and storage rings. Two basic approaches to this problem can be noted. The first involves passing the beam through axially distributed inductive or capacitive pick-up sensors [1,2,3]. In temporal-length regimes where the bandpass characteristics of the detectors and signal-processing electronics are sufficiently wide, Fourier analysis of the detector's spectral response can be used to resolve features of the bunch profile. The second involves: 1) passing the spontaneous radiation emitted by the particles in a bunch onto a streak camera [4] or fast photodiode [5,6], and 2) unfolding the longitudinal distribution from the streak camera or oscilloscope sweeps. Although techniques based on these approaches have generally kept pace with the measurement tasks dictated by evolving bunch parameters, the emerging introduction of advanced storage rings and linacs with emittances and longitudinal beam sizes [7,8,9] of 1-2 orders of magnitude smaller than those realized today can be expected to eventually start exceeding the capabilities of conventional methods of characterization.

In this paper a method with the capability of accurately characterizing the longitudinal profiles of charged-particle bunches down to lengths of 10μ and beyond is outlined [10,11]. It is based on essentially three conventional precepts: 1) the availability of high power visible/UV laser pulses with temporal lengths of 10fs or less; 2) the high compaction of an ultrarelativistic particle's transverse electric and magnetic fields; and 3) the modulation of a dielectric material's index of refraction by the combined fields of the laser and electron bunch fields. The following definitions will be employed:

E[GeV] = average energy of a charged-particle beam

* Supported by DOE Offices of Basic Energy Sciences and High Energy and Nuclear Physics and Department of Energy Contract DE-AC03-76SF0015.

- I [mA] ■ average current associated with a particle beam
- q ■ magnitude of the CGS unit of charge
- c [cm/s] ■ speed of light
- $m_e c^2$ [g] c^2 ■ electron (positron) rest energy in ergs
- $m_p c^2$ [g] c^2 ■ proton (antiproton) rest energy in ergs
- βc ■ speed of a relativistic particle
- $\gamma = \sqrt{1 - \beta^2}$ ■ relativistic contraction factor
- $\rho(z)$ [#/cm] ■ number density of a particle bunch vs. z
- N_C ■ total number of particles in a bunch
- $g(z) = \rho(z)/N_C$ ■ (normalized) Gaussian particle density
- $\sigma_x, \sigma_y, \sigma_z$ ■ standard deviations of random distributions of particle positions vs. x , y , and z directions
- N_B ■ total number of bunches in a storage ring

II. FIELD BASIS OF PROFILING METHOD

Consider a charged particle bunch with N_C particles traveling, on the average, along a locally rectilinear trajectory. Referring to Fig. 1, we take the axis of this trajectory

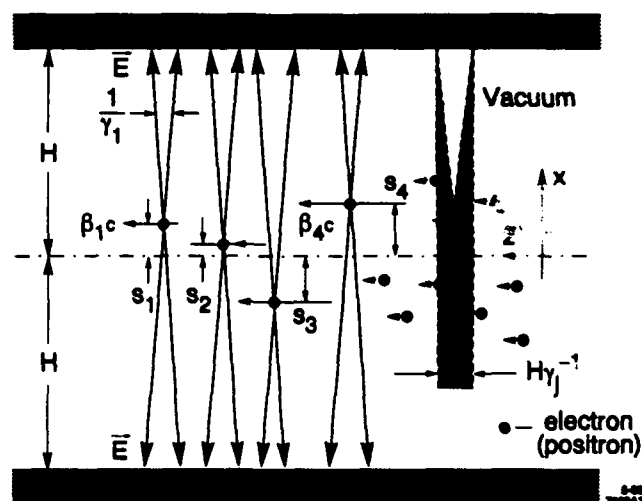


Figure 1. Parameters of particle bunch in vacuum.

to be coincident with the symmetry axis (z-axis) of a cylindrical (rectangular) duct of radius (half-width) H . For normally distributed particle positions, we associate the main bunch dimensions with the quantities $2\sigma_x, 2\sigma_y$, and $2\sigma_z$. For our present analysis we will take $\sigma_x, \sigma_y \ll H$. This restriction, valid whenever the maximum transverse radius of the bunch is much smaller than the duct diameter, allows the representation of the bunch by a filamentary distribution of charge. Of central importance is the instantaneous peak transverse field generated at the location $(x=H, z)$ by an electron j located at point (s_j, s'_j, z) , where s'_j is its

displacement vs. y . Under the assumed restriction, the transverse field magnitude at H can be expressed as

$$|\vec{E}(x=H, z)|_e \left[\frac{KV}{cm} \right] = \frac{0.3 \gamma_j q}{(H - s_j)^2 + (s_j')^2} = \frac{0.3 \gamma_j q}{H^2}. \quad (1)$$

Corresponding to the relativistic enhancement of the transverse field strength is a corresponding attenuation of the forward component by the amount γ_j^{-2} . Assuming, then, that most of the electron's field is concentrated within the angle γ_j^{-1} , it follows that the limiting resolution of its instantaneous z -position at $x=H$ is given by

$$\Delta z_e = H / \gamma_j. \quad (2)$$

An important quantity is the number of particles in the vicinity of electron j that also contribute significantly to the field at $(x=H, z)$. Assuming a minimal energy spread, we can drop the index and define the designated group of electrons by projecting the resolution segment H/γ from the point $(x=H, z)$ back toward the z axis. This yields

$$N_{1/\gamma}(z) = H \rho(z) / \gamma = \Delta z_e \rho(z). \quad (3)$$

For γ^{-1} sufficiently small, the magnitude of the total field at $(x=H, z)$ is given approximately by

$$|\vec{E}(x=H, z)| [KV/cm] = N_{1/\gamma} |\vec{E}|_e = \frac{0.3 q \rho(z)}{H}. \quad (4)$$

For the case of a Gaussian $\rho(z)$, designated by $N_C(g(z))$, the instantaneous transverse field profile can be re-expressed in terms of the total number of particles in the bunch by

$$|\vec{E}(x=H, z)| [KV/cm] = \frac{0.3 N_C q g(z)}{H}. \quad (5)$$

A graph displaying practical parameter ranges and attainable field strengths from charged-particle bunches in linacs or storage rings is shown in Fig. 2. First, we note the high energy regime required for proton (antiproton) beams for the method to be considered useful. Second, in order to obtain significant field strengths, there must be a sufficient quantity of particles within one electronic resolution length (H/γ) along the beam. This quantity, which should ideally be present in the sparsest region of the bunch to be measured, can be used to establish the minimum current levels at which the profiling technique can be applied. In applying the graph, different storage rings (or linear machines) are identified not by their species of particle or energy (which is assumed to exceed a well-defined minimal value), but by their average currents and interbunch intervals. For example, taking the average current in the LCLS [9] to be approximately $0.15 \mu A$, with an interbunch interval of $10^7 ns$ and a 150μ full bunch

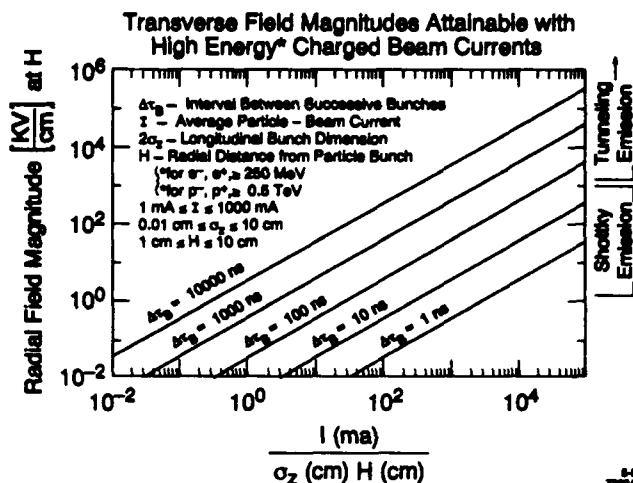


Figure 2. Field magnitudes obtainable from charged-particle bunches.

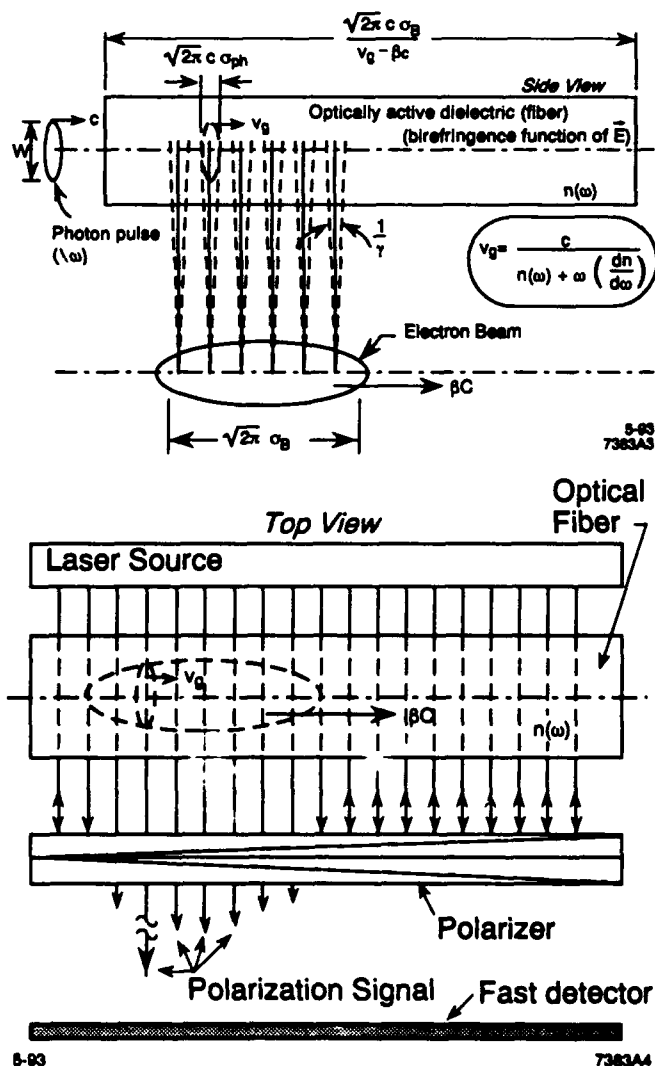


Figure 3. Parameters of a modulated-dielectric bunch profiler.

length, extrapolation of the curves in the graph indicates that field strengths in excess of 10^3 kV/cm could be attained at distances of the order of 1cm from the bunch axis.

III. FIELD SCANNING AND DETECTION

As schematized in Fig. 3, the essential component of the profiling method is the interaction of a probe photon pulse of full length $(2\pi)^{1/2} \sigma_{ph}$ with the particle bunch field as they both traverse a suitable dielectric medium. If we assume the group velocity, v_g , of the photon pulse to be different from βc , the particle bunch velocity, and $\sigma_{ph} \ll \sigma_B (= \sigma_z)$, it is evident that the photon pulse will "scan" the electron field profile in a time equal to the temporal length of the bunch dilated by the factor $1/(\beta - (v_g/c))$. A necessary condition to be fulfilled is that the dispersion inside the dielectric be small enough for the photon pulse to retain its shape (viz., length) without excessive loss of intensity during the scan. The physical basis for detection lies in the non-linear modulation of the dielectric material by the combined fields of the photon and particle bunches. Light from a tertiary source, e.g., a laser, is then instantaneously perturbed by the modulated index of refraction, and the perturbation is recorded. In principle, variations of intensity, scattering direction, polarization, or dielectric-boundary effects could be effected [12]. To minimize convolution blurring, an apparent constraint is that the thickness of the dielectric (e.g., the diameter of an optical fiber) should ideally be of the same order of size as the required resolution length. Thus, both the (instantaneous) length and thickness of the interaction region could each need to be made as small as several microns. In this limit, it is evident that the modulated fraction of photons from the tertiary source within one resolution interval could become extremely small, making the choice of radiation parameters for modulation and detection critical to the applicability of the method. We note that although the absolute number of modulated photons could be increased by enlarging the dielectric in the azimuthal direction, their net fraction will remain the same, necessitating a similar scaling of the output power of the tertiary photon source. Denoting the full, dispersion-dependent dielectric constant by n' (i.e., $n'=c/v_g$), selected dimensional and physical parameters that would be required to configure a profiling system for a typical storage ring energy are calculated in Table 1.

TABLE 1.
Bunch profiling system parameters for 5.11 GeV

n'	σ_B [μ]	σ_{ph} [μ]	Scan Time [fs]	Scan Time [ns]	Diel. Length [m]
1.001	3000	0.6	2	25	7.5
1.001	300	0.6	2	2.5	0.75
1.001	30	0.6	2	0.25	0.075
1.01	3000	0.6	2	2.5	0.75
1.01	300	0.6	2	0.25	0.075
1.01	30	0.6	2	0.025	0.0075

For the assumed indices of refraction, it is apparent that feasible dielectric lengths exist for which the tabulated laser pulse and particle bunch lengths are consistent. Further analytical studies are in progress to identify suitable dielectric materials and configurations with regard to n' and the magnitude and time scales of non-linear field effects.

IV. ACKNOWLEDGEMENTS

Useful discussions with Karl Bane and Roberto Coisson are acknowledged.

V. REFERENCES

- [1] C.-R. Carman and J.-L. Pellegrin, "The Beam Positions of the SPEAR Storage Ring," Nucl. Instrum. Meth. 113, 423(1973).
- [2] T. Katsura, Y. Kamiya, K. Haga, and T. Mitsuhashi, "A Beam Position Feedback System for Beam Lines at the Photon Factory," Proceedings of the 1987 IEEE Particle Accelerator Conference, IEEE Catalog No. 87CH2387-9, p. 538.
- [3] R. Webber, J. Fritz, S. Holmes, W. Marsh, J. Zagel, "A Beam Position Monitor System for the Fermilab Booster," p. 541.
- [4] R. Tatchyn, A. Toor, H. Kilic, J. Hares, J. Kilkenney, P. Csonka, H. Watanabe, A. Fuller, "On-axis streak camera measurements of undulator light on Beam Line V at SPEAR," SPIE Proceedings No. 733, 103(1987).
- [5] I. Munro and A. Sabersky, "Synchrotron Radiation as a Modulated Source for Fluorescence Lifetime Measurements and for Time-Resolved Spectroscopy," in Synchrotron Radiation Research, H. Winick and S. Doniach, eds., Plenum Press, New York, 1980, p. 323 ff.
- [6] D. R. Kania, R. J. Bartlett, and P. Pianetta, "Subnanosecond time resolved measurements of synchrotron x-ray pulses using photoconductive detectors," Nucl. Instrum. Meth. A246, 534(1986).
- [7] M. Cornacchia and H. Winick, eds., Proceedings of the Workshop on Fourth Generation Light Sources, SSRL, Feb. 24-27, 1992, SSRL Pub. 92/02.
- [8] T. Raubenheimer, "The Preservation of Low Emittance Flat Beams," this conference - B2, 1993.
- [9] J. Seeman, K. Bane, T. Raubenheimer, "Electron Transport of a Linac Coherent Light Source (LCLS) Using the SLAC Linac," this conference - Jb19, 1993.
- [10] R. Tatchyn, "A Field-Based Longitudinal Profiling Scheme for Short Charged Particle Bunches in High Energy Storage Rings," SSRL ACD-Note 119, February 24, 1992.
- [11] R. Tatchyn, "Field-Based Longitudinal Profiling Schemes for Short Charged Particle Bunches in High Energy Storage Rings," Proceedings of the Workshop on Fourth Generation Light Sources, M. Cornacchia and H. Winick, eds., SSRL, Feb. 24-27 1992, SSRL Pub. 92/02, p. 229.
- [12] R. R. Alfano, ed., The Supercontinuum Laser Source, Springer-Verlag, New York, 1989.

Performance limits of a Streak Camera in Real Time three-dimensional measurement of Bunch Oscillation in LEP

E. ROSSA, CERN, SL Division, CH-1211 Geneva, Switzerland
F. TECKER [1], RWTH Aachen, D-5100 Aachen, Germany
J.C. MATHAE, ARP, F-67088 Strasbourg, France

Abstract

A new method using a streak camera to observe the synchrotron radiation of LEP was developed for the bunch measurement. This allowed monitoring of the particle density distribution in three dimensions in space at successive bunch passages. The optical set-up allows to see the top view and side view of the bunch simultaneously. The software analyzes the density distribution in these two perpendicular planes and extracts online the σ and the center of gravity for the bunch length and also for transverse dimensions. We will give the experimental results of the resolution limits due to the streak camera in this application. The resulting influence of the transverse photon bunch dimension on the measured bunch length will be presented and compared with the calculation.

I. INTRODUCTION

Small wiggler magnets produce synchrotron radiation to monitor the shape of both LEP beams [2]. The density distribution in space of the emitted photon bunches is proportional to the density of the particles in the e^+ and e^- bunches. Two beryllium mirrors collect the light in the vacuum tube. Two achromatic lenses create the image of the source onto the double sweep streak camera (S.C.) in an underground optical laboratory [3, 4]. The optical set up allows observation of the side view and the top view of both bunches simultaneously. Up to 50 single successive bunch passages can be recorded on one image. The system visualizes instabilities in all three dimensions [5] and extracts the bunch length. Alternatively the front view of the bunches can be displayed.

The precise knowledge of the bunch length is essential to obtain the best performance of LEP.

II. OPTICAL SETUP

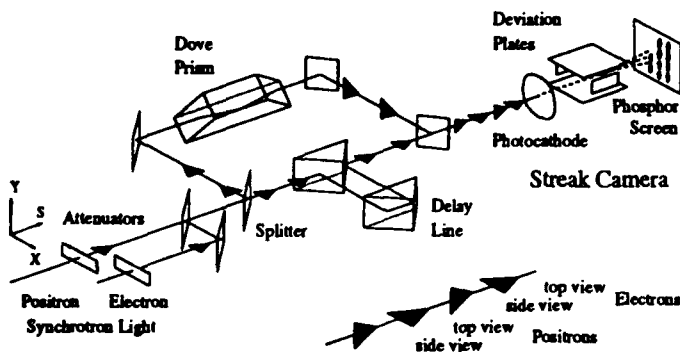


Figure 1: Optical setup to provide side and top view at the same time

The setup is shown schematically in Figure 1. The synchrotron radiation of the e^+ and e^- bunches arrives slightly separated in time (~ 500 ps). An automatic attenuation system of motorized continuously varying neutral density filters and a photomultiplier keeps the intensity of the light constant. A semi-transparent mirror divides the light and a dove prism rotates one bunch by 90° about the longitudinal axis with respect to the other. So the streak camera displays both top and side view which are the density projection of the beam in the horizontal and vertical plane, respectively [5]. The side- and top-view of both beams can be shown simultaneously in one streak of the camera. So a single sweep gives the following display on the computer screen (Fig 2):

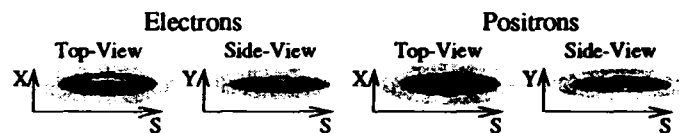


Figure 2: Views obtained in one single streak

Figure 3 shows an example of six successive bunch passages. The displayed profile shows the projection of the streak selected in the window.

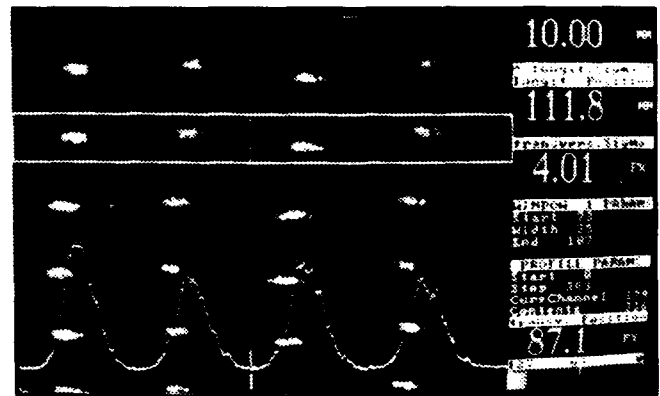


Figure 3: Stable beam at 45 GeV, $\sigma_S = 10$ mm

The software is tracking the bunches in real time at a frequency of 12.5 Hz and extracts the photon bunch length and transverse dimensions to a precision of better than 2%. Head-Tail-Effects in the horizontal or vertical plane appear very clearly on the image.

III. RESOLUTION LIMITS OF THE ENTIRE SYSTEM

The limit of resolution for the streak camera and the digitizing system is shown in Table 1.

X, Y transverse	< 15 μm
S (length)	< 0.8 mm
jitter fast sweep	< 2 ps
$\hat{=}$ center of gravity	< 0.6 mm
sensitivity _{max}	1 photon/count/pixel

Table 1: Resolution limits at the input photocathode plane

The spatial resolution limit of 15 μm in direction of the fast sweep and perpendicular to the direction has been obtained by measuring the smallest spot size possible.

A picosecond laser pulse measured with the S.C. has shown a F.W.H.M. of 6 ps which corresponds to $\sigma=0.8$ mm [3]. That means that the resolution of the S.C. itself is better than this.

The software calculates the center of gravity of the bunches in real time. We measure the trigger jitter, with a laser diode pulse of $\sigma=12$ ps, by taking the standard deviation of the center of gravity on the screen. Thus, the measured value of 2 ps includes the jitter of the laser diode. So this corresponds to the precision on the center of gravity of the bunches in the RF-phase.

The sensitivity is high enough to analyze profiles of some thousands photons per pulse.

IV. INFLUENCE OF SPOT SIZE

The streak camera in this application is used — in contrary to most other — without a slit in front of the photocathode to visualize the bunch size and instabilities in all dimensions. So there is a finite spot size in the direction of the fast sweep which broadens the measured bunch length. For a Gaussian distribution, with a dimension σ_X of the light spot on the phosphor screen of the streak camera, the broadening of the measured bunch length σ_{meas} is expected to be

$$\sigma_{meas} = \sqrt{\sigma_L^2 + \sigma_X^2}. \quad (1)$$

σ_{meas} is the length measured on the phosphor and σ_X the finite spot size there.

Hence the correction to achieve from the measured σ_{meas} the real σ_L is

$$\sigma_L = \sqrt{\sigma_{meas}^2 - \sigma_X^2}. \quad (2)$$

To verify this effect, the light pulse of a laser diode is projected by a lens onto the S.C. . The light is strongly attenuated in order to have no intensity effects as described later. The position of the lens is varied to achieve different spot sizes on the photocathode. The gain on the micro-channel-plate of the S.C. is adjusted to have a good signal/noise ratio. The spot size is measured in focus mode of the S.C. . Then the fast sweep is set to the maximum streak speed and the length of the pulse is measured. Fig. 4 shows the obtained result.

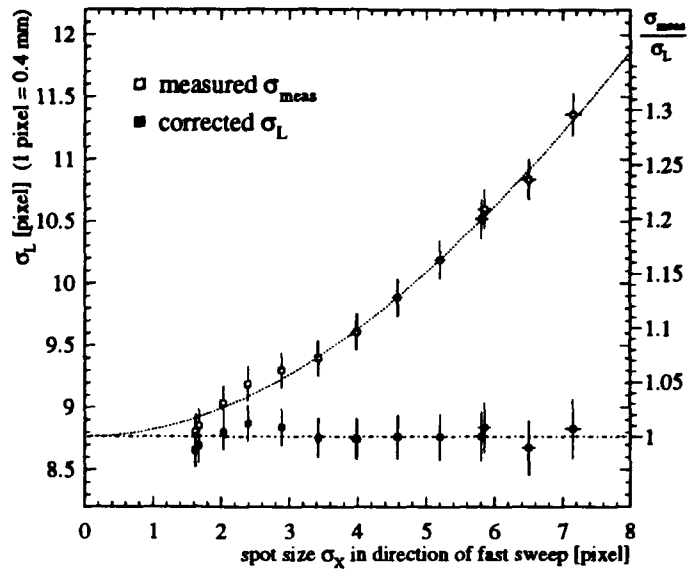


Figure 4: Influence of spot size on measured length

It proves that the correction according to (2) is valid for a wide range of spot sizes σ_X . Even when the spot dimension on the phosphor becomes comparable to the dimension of the bunch length profile the correction still yields the correct result.

It is preferable to choose a spot size not too small to maintain a good resolution of the transverse measurement.

V. INFLUENCE OF INTENSITY

It is known that the measured pulse length increases with higher intensity of the incident light pulse, especially for short pulses [6]. But this effect was only measured for constant slit which induces that there is always a proportionality between total intensity and intensity per unit area.

In our application it is necessary to know the influence of both. The precision we like to achieve is 5%. So we define the dynamic range to be the range where the deviation for the measured bunch length after spot size correction (2) is less than 5% (common for S.C.: 20%).

A. Influence of light intensity

The bunch length at a fix spot size is measured with different optical attenuators in front of the streak camera to vary the total intensity.

As in Ref. [6] we expect an increase of the measured bunch length due to space charge effects inside the camera tube. The result is plotted in Fig. 5. The lowest intensity is 10^{-15} J/pulse.

The measured length stays constant in a dynamic range of 30. According to common definition the dynamic range is 100. With longer pulses as coming from LEP ($\sigma \sim 30$ ps) the dynamic range should be even better than this [6].

Anyway, we can select the appropriate attenuation of the incoming light and it is kept constant with the automatic attenuation system. So the dynamic range in this application does not impose any limits.

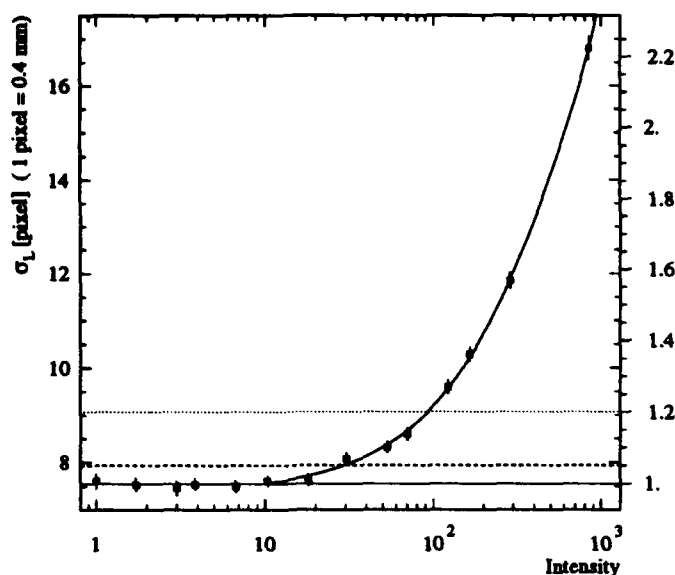


Figure 5: Influence of total intensity on measured length

B. Influence of photon flux

The measurement described in section IV. is repeated for a higher total intensity. The total intensity of the pulse is kept constant while the spot size on the photocathode is varied by moving the lens. Thus, the average photon flux is inversely proportional to the square of the spot size. The measured bunch length is corrected for spot size according to (2). Fig. 6 shows the results obtained at a total energy of $3.5 \cdot 10^{-14}$ J per pulse.

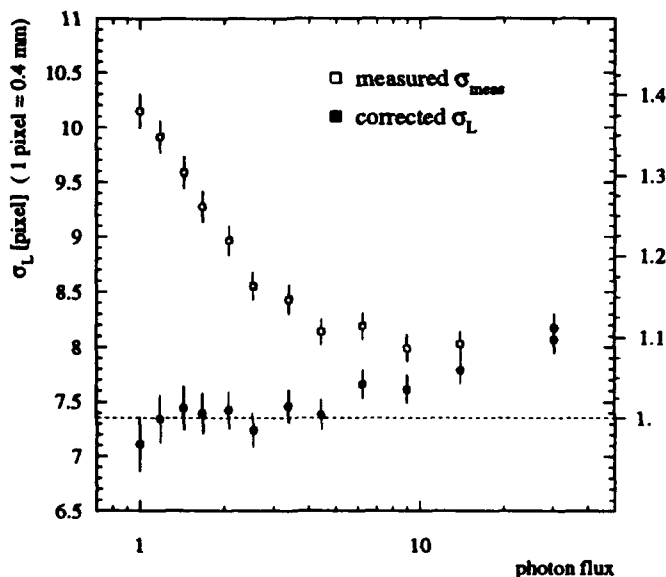


Figure 6: Influence of photon flux on measured length

The corrected bunch length varies less than 5% in a dynamic range of 13 for the photon flux. For higher fluxes the measured length increases.

As in the case of the total light intensity, we can choose an appropriate level of light not to be affected by this effect.

VI. OUTLOOK FOR REAL APPLICATION

Since two perpendicular views of one bunch can be displayed at the same time, length and both transverse spot dimensions (X, Y) are known.

The spot size perpendicular to the direction of the fast sweep measured with the fast sweep 'ON' corresponds with the spot size in focus mode better than 1.5%.

So the bunch length measured on the top view can be corrected in real time for spot size with the transverse dimension of the side view and vice versa.

The transverse emittance of the beam could be deduced after calibrating the transverse dimensions σ_x and σ_y precisely with the beam.

VII. CONCLUSION

We measure the density projection of single bunches in three views:

- front view (focus mode) \Rightarrow X, Y
- or
- side view \Rightarrow Y, S
- top view \Rightarrow X, S.

Thus the three dimensions and the center of gravity of the photon-bunches can be extracted in real time.

The presented way of correcting the measured bunch length for the spot size allows to determine in real time the bunch length very precisely without losing the possibility to observe all kinds of instabilities in the bunches of LEP.

VIII. ACKNOWLEDGMENTS

We would like to thank Mr. Tomasini and Mr. Roth from the firm A.R.P. for their cooperation and G. Baribaud, J.J. Savioz and P. Pivot for their contribution to the automatic light controller.

IX. REFERENCES

- [1] F. Tecker, *Evaluation of the performance of a Streak Camera at LEP*, Diplomarbeit, RWTH Aachen, Pitha 93-7, (in preparation)
- [2] C. Bovet, M. Placidi, *A dedicated synchrotron radiation source for LEP beam diagnostics*, LEP Note 532, April 1985
- [3] E. Rossa et al., *Double sweep streak camera for LEP*, Proc. EPAC 1990, p.783
- [4] G. Baribaud et al., *Three dimensional bunch observation in LEP*, CERN SL 92-33 (DI)
- [5] E. Rossa et al., *Real Time Measurement of Bunch Instabilities in LEP in three Dimensions using a Streak Camera*, Proc. EPAC 1992, Vol. 1, p.144
- [6] D.J. Bradley et al., *Intensity dependent time resolution and dynamic range of Photochron picosecond S.C., II. Linear photoelectric recording*, Rev. Sci. Instrum. 51 (6), Jun. 1980

Bunch Length Measurements in the SLC Damping Ring

F.-J. Decker, T. Limberg, M. Minty, M. Ross,

Stanford Linear Accelerator Center, Stanford, California 94309*

Abstract

The synchrotron light of the SLC damping ring was used to measure the bunch length with a streak camera at different times in the damping cycle. There are bunch length oscillations after injection, different equilibrium length during the cycle due to rf manipulations to avoid microwave instability oscillations, and just before extraction there is a longitudinal phase space rotation (bunch muncher) to shorten the bunch length. Measurements under these different conditions are presented and compared with BPM pulse height signals. Calibration and adjustment issues and the connection of the streak camera to the SLC control system are also discussed.

1 Introduction

Different techniques exist to measure the bunch length of $\sigma_z = 2$ to 25 mm. A bunch length measurement in the damping ring (DR) using the synchrotron light and a streak camera has the advantage that it is a non-invasive measurement and can be used at different times in the damping cycle. In contrast, a bunch length measurement with a screen in the dispersive region of the ring-to-linac (RTL) compression region is invasive (a wire might be suitable), measures only the extracted bunch length, and is limited by the non-linear RF slope for longer bunch length. We will discuss here the first technique. After describing the set up and calibration, we will present measurements during the store time and discuss their implications for longitudinal phase space.

2 Streak Camera Set Up

The synchrotron light for the DRs is guided with five mirrors and two achromatic lenses over 15 m to an optical table, where it is split for turn by turn size measurements with a gated camera [1] and for length measurements with a streak camera. The streak camera is manufactured by Hadland Photonics [2] with a IMACON 500 streak tube.

2.1 Resolution

The advertised resolution is 2 ps. The measured resolution is 6 ps (FWHM) [3] determined using a femto-second laser pulse. This corresponds to a σ -resolution of 0.8 mm and is

*Work supported by the Department of Energy contract DE-AC03-76SF00515.

sufficient for most of the measured bunch lengths between 2 and 25 mm (σ_z). The thickness of the cumulated lenses and windows of about 50 mm must also be taken into account. With no frequency filter a delta pulse with a wide spectrum of 400 to 800 nm produces about a 7 ps FWHM long signal. Achromats compensate this effect only slightly (actually they overcompensate), since they are in general not compensated to be isochronous.

2.2 Connection to SLC Control System

Since the normal one-dimensional analyser of the streak camera could be used only locally, the output of the streak camera was imaged to a gated camera (spare) which has a high gain so that even single photons are detected. With this set up we could see correlations between y and z at injection (or x and z) and use digitization techniques for a normal camera, which is supported by the SLC control system. These include calibration of the scales, projections in z (and y) and fitting with a gaussian (or other) distribution to the data, statistical averaging, correlation plots with other parameters (e.g. store time), etc.

2.3 Calibration

The inclusion of the gated camera made a calibration necessary. For slow sweep speeds the shift of the centroid in mm could be compared with the change in time (0.1 ns steps) of the variable delay unit (VDU). A correct calibration will give a slope of $A = 300$ mm/ns the velocity of light.

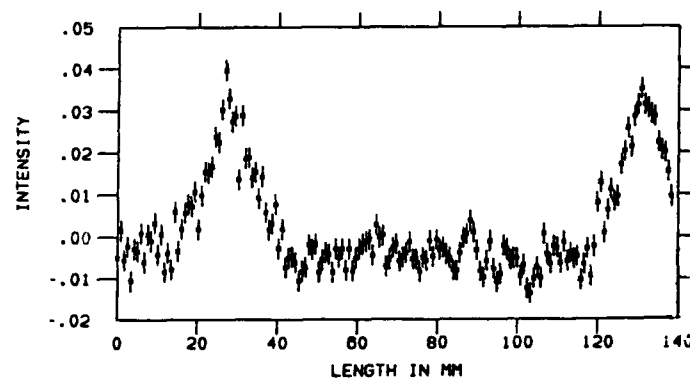


Figure 1: Calibration technique.

For the faster sweep speeds the light was splitted, delayed (105 mm) and combined. The double pulse (bottom) shows exactly this separation after the right calibration.

For faster sweep speeds this technique is not appropriate, since the timing jitter of 20 ps dominates the measurement. Therefore the light was split and combined after 105 ± 5 mm. The separation of this double pulse (Fig. 1) was measured with the streak camera and the calibration adjusted accordingly (15 % off from expected scaled value).

Tab. 1 summarizes the measured values.

Streak Camera Calibration			
Streak speed	Digitizer bin/mm(m)	Comparison ps/ch (old)	Resolution in mm
5 ns/mm	11.4	80.9	270
2 ns/mm	37.9	33.5	107
1 ns/mm	67.7	18.1	59
500 ps/mm	130.0	8.65	42
200 ps/mm	270.0	3.49	22
100 ps/mm	0.57	1.73	14
50 ps/mm	1.14	0.89	6.5
20 ps/mm	4.1(3.6)	0.31	≈ 2

Table 1: Calibration summary.

For each streak speed setting the video digitizer was calibrated. The inverse of the old calibration (in ps/channel) should correspond to the new one (exception: 20 ps/mm). The resolution is mainly limited by the slit opening and spatial camera resolution for the slow speeds and the streak tube itself (timing of electrons) for the fast speeds.

3 Bunch Length Measurements

Different times during the store cycle were studied corresponding to the different type of investigation. The first turn, injection oscillation, longer bunch length during the low rf voltage ("DR-ramp") and the pre-compression at the end of store time ("bunch muncher") were all studied.

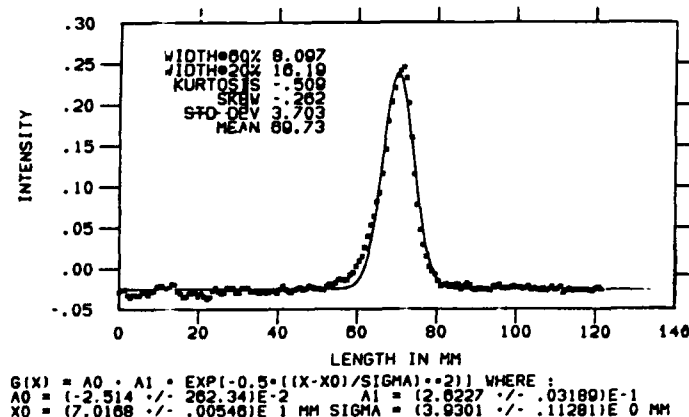


Figure 2: Bunch distribution after the first turn.

The bunch length is determined not only by the injected length but also by the length energy correlation, which was in this case pretty high causing a long bunch with a big asymmetry.

3.1 First Turn

After nearly one turn the first measurement can be done. Sizes of 2-4 mm (σ_z) were observed, correlations with y seen and asymmetries recognized (Fig. 2). Even pre- or postbunches, one S-band bucket away from the main bunch ($\lambda = 105$ mm) of up to 5 % were observed. This information was used to optimize injection parameters.

3.2 Injection Oscillations

Since the bunch length and the energy spread of the injected bunch is not matched to the longitudinal acceptance of the DR (this could be done with a "bunch muncher", see below), the beam performs bunch length oscillations with an amplitude of ± 13 mm around the equilibrium of 15 mm (σ_z). (Fig. 3). These decohere after about 0.3 ms or 2500 turns which seems long, but one has to consider that a partly filamented beam with for instance three peaks in the projected distribution (observed) will be fitted with only one Gaussian with a too small σ_z . The initial big value is mainly the resolution of the 2nd fastest sweep speed of the streak camera used for these mainly big sizes.

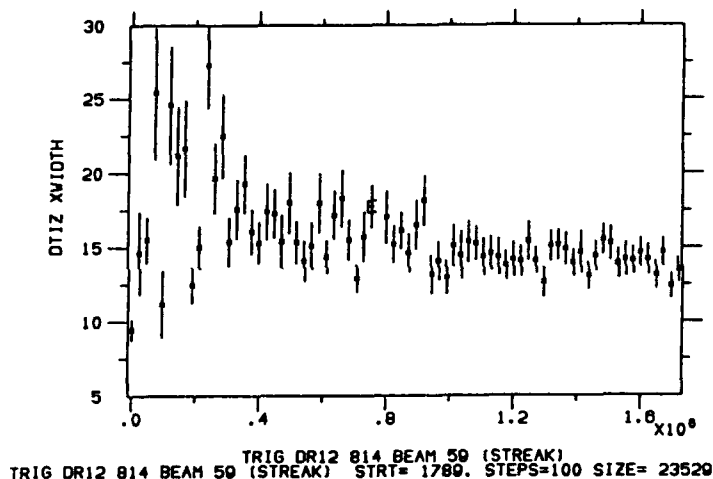


Figure 3: Injection oscillations of the bunch length.

The digitized bunch length (XWIDTH) in mm is plotted versus the time in 200 turn steps (23529.4 ns) directly after injection. The measured size includes the resolution (6.5 mm) which must be subtracted in quadrature.

3.3 DR RF Voltage Variation

After the injected beam is captured at high rf voltage ($V_{rf} = 800$ kV) the voltage is reduced to about 400 kV to achieve a longer bunch length which is insensitive to microwave instability oscillations [4]. The bunch length (resolution subtracted) changes from 11.0 to 17.0 and back to 10.5 mm (Fig. 4). It should be mentioned that the longitudinal phase space is not totally damped down at the extraction time and that the bunch length is much longer than the design value of 5 mm. The higher energy spread which turns into bunch length in the linac (with no bunch muncher) induced a bunch length variation which could not be detected directly.

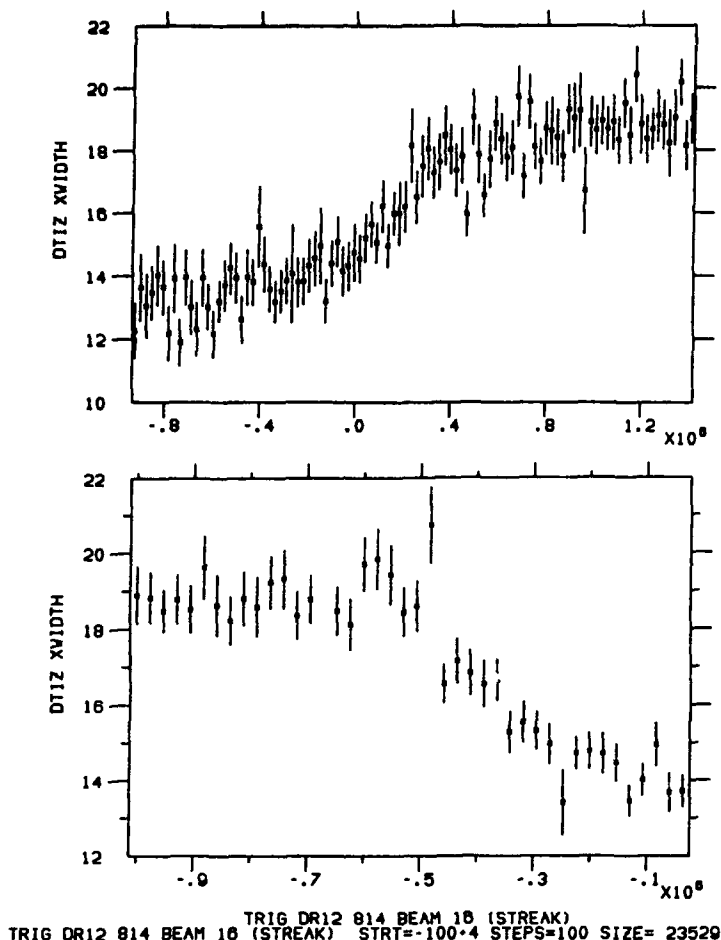


Figure 4: Bunch length during the DR RF ramp.

After about 2.5 ms (zero here) after injection the rf voltage in the damping ring is reduced by a factor of roughly two (top). Then about 5 ms later or 0.6 ms before extraction (bottom) the rf voltage is set to its nominal value and the bunch length starts to decrease but not totally to its equilibrium.

3.4 Pre-Compression (Bunch Muncher)

To reduce the extracted bunch length at the end of the store time, two $2.5 \mu\text{s}$ long dips in the rf-amplitude are applied. This excites a bunch rotation in longitudinal phase space [5]. A pre-compressed bunch length for injection into the RTL is achieved (Fig. 5).

4 Conclusion

After calibration the bunch length measurements with the streak camera give absolute values. Beyond the easier to use BPM peak signal, which could be also calibrated e.g. with the streak camera, the streak camera gives additional information about the asymmetry, the y - z (x - z) correlations and pre- or post-bunches.

Acknowledgement

We would like to thank all the people who have helped in the set up of the streak camera, the electronics and

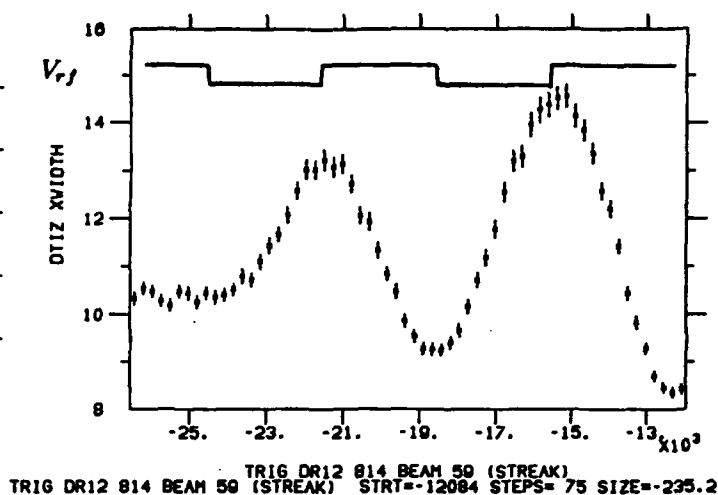


Figure 5: Pre-compression of the bunch length.

The measured (digitized) bunch length in mm is plotted against the last $15 \mu\text{s}$ before extraction. The pre-compression was set to 20 % $= (10.5 - 8.4) / 10.5$ (top). The inverse of the peak signal of a BPM ("sum-signal") shows a similar response (middle) while the phase (bottom) is mainly compensated.

software. Special thanks go to T. Himel for updating the video software.

References

- [1] M. Minty et al., *Using a Fast-Gated Camera for Measurements of Transverse Beam Distributions and Damping Times*, Accelerator Instrumentation Workshop, Berkeley, Oct. 1992.
- [2] Hadland Photonics, Sunnyvale, CA 94087.
- [3] J. Frisch, *private communication*.
- [4] P. Krejcik et al., *High Intensity Bunch Length Instabilities in the SLC Damping Rings*, PAC 93, Washington, May 1993.
- [5] F.-J. Decker, T. Limberg, J. Turner, *Pre-Compression of Bunch Length in the SLC Damping Rings*, HEACC'92, Hamburg, July 1992.

Virtual Photon Impulse of Bunch, Beampipe Response, Coherent RF Beamstrahlung; and BEPC Bunch Length, BES Jam, Virtual Acceleration

Jing Shen

Institute of High Energy Physics, Academia Sinica.
19 Yu Quan Road, P. O. Box 918, Bin 6, Beijing 100039 P. R. C

Abstract:

A brief EEE view of signal QED is presented. The research has been concentrated on the virtual photon modes of ultra relativistic shock wave in a bunch—beampipe system, and real photon modes of Coherent RF Beamstrahlung CRFB. Physically, the virtual photons emitted by a bunch were treated as a travelling pseudo wave packet in a flight coaxial cavity constructed by bunch—wakefield core and beampipe. Mathematically, it is a boundary solution of shock wave excited by ultra relativistic impulse of bunch. The new modes of solution: VTA, VTEM, VTM, VLE are virtual photon packets and RTE, RTM, RTE are real photon modes of CRFB. By these results we measured and corrected BEPC bunch length from signals of: (1) TOF reference of BES, (2) BPM of BEPC, (3) Colliding CRFB of BEPC—BES coupling signal, as well as (4) the ordinary method of Synchrotron Radiation. All results of the measured bunch lengths are in accordance with the design length of BEPC, and were verified by the BES data of vertex reconstruction of hadron events. We also found that CRFB is the unknown jam source of BES electronics. VLE virtual photons can accelerate particles.

I. Specialities of Bunch Signal and Dynamics

The known physics of accelerator, microwave, laser, Synchrotron radiation and Beamstrahlung, QED [1—4] can not explain bunch signal perfectly. The main variations are A. Boundary QED, B. Source Guiding Wave, C. Guiding Relativistic Shockwave, D. Virtual and Real Photon signal, E. Special Gauge Choise. The equations and quantization are:

$$\square^2 A_\mu = -\mu_0 J_\mu, \quad J_\mu = J_\mu^A + J_\mu^I \quad (1.1.1)$$

$$\square \cdot A_\mu = 0, \quad \nabla \cdot A = 0, \quad A_0 = 0, \quad A_3 = 0 \quad (1.1.2)$$

$$\square \cdot J_\mu = 0, \quad J_\mu = (v\rho, ic\rho), \quad \rho = \langle \psi | \psi \rangle \quad (1.1.3)$$

$$[\partial_t + u \cdot \nabla + a \cdot \nabla_u] \rho(R', u' + v, t') = 0 \quad (1.1.4)$$

$$|\psi\rangle \rightarrow |\psi\rangle \exp\left[-\frac{i}{\hbar} e\theta\right], \quad A_\mu \rightarrow A_\mu + \partial_\mu \theta \quad (1.1.5)$$

$$(1.1.1) \text{ is invariant, } \therefore p_\mu \rightarrow -i\hbar \partial_\mu - eA_\mu \quad (1.1.6)$$

II. Pseudo Waves of Virtual Photon

A. Virtual Photon Cloud in Bunch Beampipe System

A virtual photon of electron in bunch can travel at most a distance

$$\Delta R = c\Delta T = 2\pi c/\Delta\omega = 2\pi\hbar c/\Delta E \quad (2.1.1)$$

It carries the information of bunch shape, and can be absorbed by an electron in detector. The wave equations of a motional virtual photon package surrounding a bunch can be obtained by $\nabla \cdot A = 0$ gauge of (1.1.1).

$$\nabla^2 \Phi^V(R, t) = -\frac{1}{\epsilon_0} \rho(R', t') \quad (2.1.2)$$

$$\square^2 A^V(R, t) = -\mu_0 (J + \epsilon_0 \partial_t \nabla \Phi^V) = -\mu_0 J, \quad (2.1.3)$$

(2.1.2) is a Coulomb field in the bunch coordinate. (2.1.3) is a transvers real photon wave resulted from the transverse impulse of the bunch J_\perp .

B. Pseudo Transverse Electric Wave Packet — Bunch Field

In laboratory the Coulomb field Φ^V is travelling with the bunch by velocity v like a travelling wave package. ∇_\perp (2.1.1)

$$\nabla_\perp^2 E^V(R, t) = -\mu_0 c \nabla_\perp c \rho(R' + vt, t') \quad (2.2.1)$$

Transform from bunch coordinate to laboratory coordinate by

$$c \nabla_\perp c \rho(R' + vt, t') \rightarrow [c \nabla + \beta \partial_t] c \rho(R', t') \quad (2.2.2)$$

$$\nabla_\perp^2 \rightarrow [\nabla^2 - \frac{1}{v^2} \partial_t^2]_\perp \equiv [\square_\perp^2]_\perp \approx \square_\perp^2, \quad (v \approx c) \quad (2.3.3)$$

The right sides imply an image of the bunch at the origin to be the source of pseudo transverse wave.

$$\square^2 E^V(R, t) = -\mu_0 [\nabla + \beta \partial_t] c \rho^i(R', t') \quad (2.2.4)$$

C. Pseudo Magnetic Wave Packet— Wake Field

The impedance virtual photon package following the bunch can be obtained by the Hamilton gauge $A_0 = 0$ of (1.1.1).

$$\square^2 A^V(R, t') = -\mu_0 J^V(R', t') \quad (2.3.1)$$

$$\square^2 B^V(R, t') = -\mu_0 \nabla \times J^V(R', t') \quad (2.3.2)$$

D. Spin Potential Wave Equations of Bunch — Spin Field

The Third kind virtual photon is the Spin — Potential wave of polarized bunch in Axis gauge $A_3 = 0$ of (1.1.1).

$$\square^2 A^S(R, t) = -\mu_0 J^S(R', t') \quad (2.4.1)$$

In cylindrical symmetry, $A^S(R, t)$ is in the direction of v_z .

III. Virtual, Real Modes in Different Region

A. Separating Virtual and Real Photons

By (2.2.4), (2.3.2), (2.4.1); (1.1.1) is decomposed into [5—8]

$$\square^2 E^V(R, t) = -\mu_0 c \square_\perp c \rho^i(R', t') \equiv f^V \quad (3.1.1)$$

$$\square^2 c B^V(R, t) = -\mu_0 c \nabla \times v \rho^i(R', t') \quad (3.1.2)$$

$$\square^2 A^S(R, t) = -\mu_0 J^S(R', t') \quad (3.1.3)$$

$$\square^2 E^R(R, t) = -\mu_0 c \square_\perp c \rho(R', t') \equiv f^R \quad (3.1.4)$$

$$\square^2 c B^R(R, t) = -\mu_0 c \nabla \times v \rho(R', t') \quad (3.1.5)$$

B. Ahead Bunch Vacuum and Retard Wave Vacuum

The relativity makes field vanish ahead the bunch. The

causality makes the front of bunchstrahlung retard the bunch top head at a distance z apart from

$$z = H \lg \theta = H \cos \psi / 2 \quad (3.2.1)$$

z is beampipe axis. θ, ψ are the angles of $(z, R_s), (z, R)$. H is distance of detector from z .

C. Bunch Field Region of Guiding Relativistic Shock

$$f' = f_s H_0 + f_s z_0 \quad (3.3.1)$$

In the region of flight bunch, $f_s \gg f_i$ if $H \ll 2\sigma_s$; the TEM, TE modes are superiority. $f_s \approx f_i$ if $H \gg 2\sigma_s$; the TEM, TE modes are equal to TM, LE modes. Thus, $H \ll 2\sigma_s$ is much better for getting single mode signal for bunch size measurement.

D. Wake Field Region of Impedance Effect

In the region behind the bunch, where $\psi > \pi/2$, and $f_i > f_s$, thus, VLE and VTM modes become the superiority. It leads to a region of wake fields with $4\pi\sigma_s$ in length when $H \leq 2\sigma_s$. VLE mode fields can accelerate or decelerate the tail of the bunch. Practically wake fields have both LE and LM modes. Hence, they make the tail of the bunch rotate, and conduct the wall currents which carry the bunch size information precisely.

E. Transformation Region of Reaction

The wake field is actually charged by the δ impulse of bunch and input to the bunch—beampipe cavity which is flying with bunch called Fight Coaxial Cavity FCC. Hence, transformation region is the discharging region.

F. Radiation Propagation Region of Collision

Following the transformation region, there is the radiation region, where the real photons of (3.1.4), (3.1.5) are radiated by interactions of bunch—bunch, bunch—field. The typical radiation is SR and CRFB. [8]

IV. Waveform of Real and Virtual Photon

A. VTEM Mode Signals of Relativistic EM Shock Wave

In the case of ultra relativistic case the electric fields observed in laboratory coordinate is $E^V(R, t) = E^{+m} + E^V$, where $E^{+m} = E_R R_0$, $E_\theta = E_\phi = 0$, $i_k = \epsilon_0 \pi \sigma_s \sigma_y E^{+m}$ (4.1.1)

The relativistic transverse impulse f'_i solution of (3.1.1) with (3.3.1) is

$$E^{+m}(R, t) = \frac{1}{2c} \int_{-\infty}^t d\tau \int_{-\infty}^{t+\tau} d\zeta f'_i(\zeta, \tau) \quad (4.1.2)$$

Hence, it looks like a TEM transverse photon, and

$$i_k(0, t) = - \frac{NeS}{\sqrt{2\pi}} \rho(x, y) \frac{v^2 t}{\sigma_s^2} \exp\left[-\frac{v^2 t^2}{2\sigma_s^2}\right] \quad (4.1.3)$$

This is the waveform of BEPC bunch signal which we detected at TOF time reference electrode of BES [5–8]. After correction of the skin effect of the signal cable, the bunch length of BEPC is $\sigma_s = 5.4$ cm. (See Fig. 1)

B. VLE VTM Mode Signals of Wall Current and Wake Field

Because FCC impedance retards $[E, cB]$ and

$$E_\theta = B_\phi = 0 \quad (4.2.1)$$

Thus, the impulse width is $<$ the wake field length, then $\square_\theta \approx \nabla$, $\square^2 \approx \nabla^2$. Integrate (3.1.1), (3.1.2).

$$i_\omega(t) = \frac{Ne}{\sqrt{LC}} \exp\left[-\frac{R_\omega}{2L}t\right] \sin \sqrt{\frac{1}{LC}}t \quad (4.2.2)$$

$$R_\omega = R_\omega \cdot \frac{4\sigma_s}{2\pi H} = 3.26 \times 10^{-7} \sqrt{f} \frac{2\sigma_s \Omega}{\pi H} \quad (4.2.3)$$

Hence the risefront of $i_\omega(t)$ is resulted by bunch length

$$T_r = \frac{T}{4} = \frac{1}{4} \cdot \frac{2\pi}{\omega} = \frac{\pi}{2} \sqrt{LC} = 2\pi \sqrt{\epsilon_0 \mu_0} \sigma_s \quad (4.2.4)$$

$$\sigma_s = cT_r/2\pi = 4.775T_r \text{ (ns) cm} \quad (4.2.5)$$

The σ_s of BEPC obtained by (4.2.5) is 5.6 cm. [5–8] (See Fig. 2)

C. Boundary Free Mode Signal of Synchrotron Radiation

The readout waveform $S(t)$ of SR is a cascade convolution of electronic responses of $f_i(t)$. [5–8] (See Fig. 3)

$$S(t) = f_0(t) * f_1(t) * \dots * f_i(t) \dots \quad (4.3.1)$$

$$t[FWHM]^d = g t[FWHM]^d \quad (4.3.2)$$

We proved by the functional theory in Banach space, that

$$g = g_1 g_2 \dots g_i, \quad g_i = t[FWHM]^d / t[FWHM]^d \quad (4.4.3)$$

Hence, $\sigma_s = 6.16$ cm with respect to $t[FWHM]^d = 800$ ps.

D. RTEM Mode Signals of Coherent RF Beamstrahlung

When e^+ bunch travels in the wake field of e^- bunch after collision and vice versa, both radiate CRFB. In BEPC, it is a beat wave in beampipe. The wave length carries the information of bunch length. It has been observed by the readout electronics of sub-detectors of BES. $\sigma_s = 5.7$ cm. (See Fig. 4 and 5) All measured σ_s narrated above are proved by collision point reconstruction of BES event data. [9]

Thanks to Profs. M. H. Ye, S. X. Fang and Z. P. Zheng.

V. References

- [1] S. A. Heifets and S. A. Kheifets, "Coupling Impedance in Modern Accelerators", *Rev. Mod. Physics*, Vol. 63, No. 3, PP. 631–673, 1991
- [2] ANSI/IEEE std 100 – 1988. P. 556. 1988.
- [3] C. K. Kao, "Optical Fiber System: Technology, Design and Applications", McGraw-Hill, Inc, 1982.
- [4] B. L. Young, "Introduction to Quantum Field Theories", State Univ. of Iowa, Science Press, Beijing, 1987.
- [5] Jing Shen, "Bunch Crossing Signal Research on Time Reference of TOF/BES", *BEPC Engineering Documents* 02, 13, 7–5–8, July 1989.
- [6] Jing Shen, "Bunchstrahlung and Bunch Signal Dynamics (I) – (VI)", *BIHEP – DE – 90 – SJ07 to SJ12*, 1990.
- [7] Jing Shen, "Bunch Signal Analysis and Bunch Length of BEPC", *Proc. Symp. on Particle Accelerator Physics, PASC*, PP. 213–226, 1991.
- [8] Jing Shen, "Bunch Signal Dynamics with Quantum Theory, (I), (II)", *BIHEP – DE – 92 – 02 to 03*, 1992. Beijing
- [9] Jin Li and Z. P. Mao, *High Energy Phys. and Nucl. Phys.* Beijing, 15, P. 385, 1991.

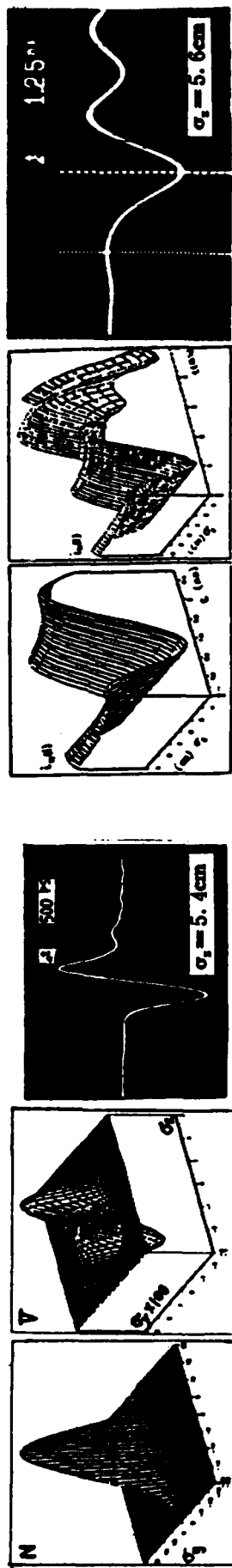


Fig. 1. VTEM Virtual Photon Signal of BEPC read out by TOF of BES

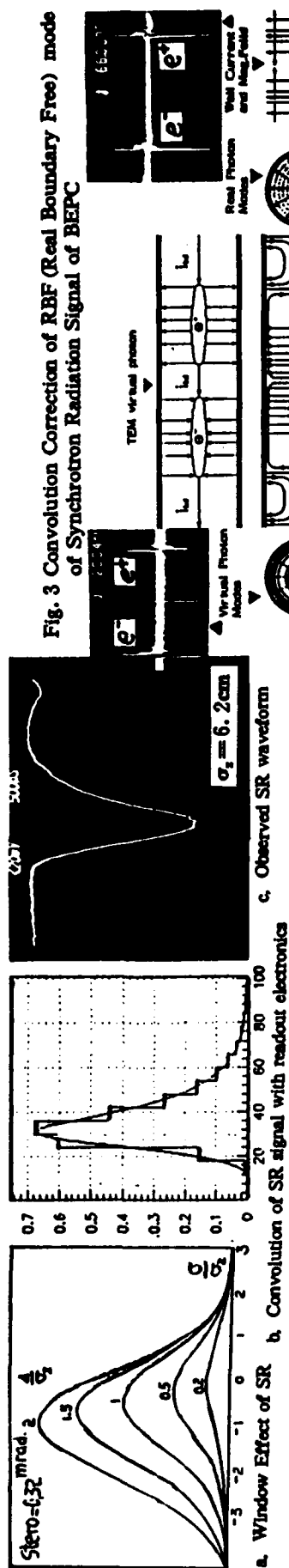


Fig. 2 VTM, VLE Virtual Photon Signal of BEPC read out by BPM

Fig. 3 Convolution Correction of RBF (Real Boundary Free) mode of Synchrotron Radiation Signal of BEPC

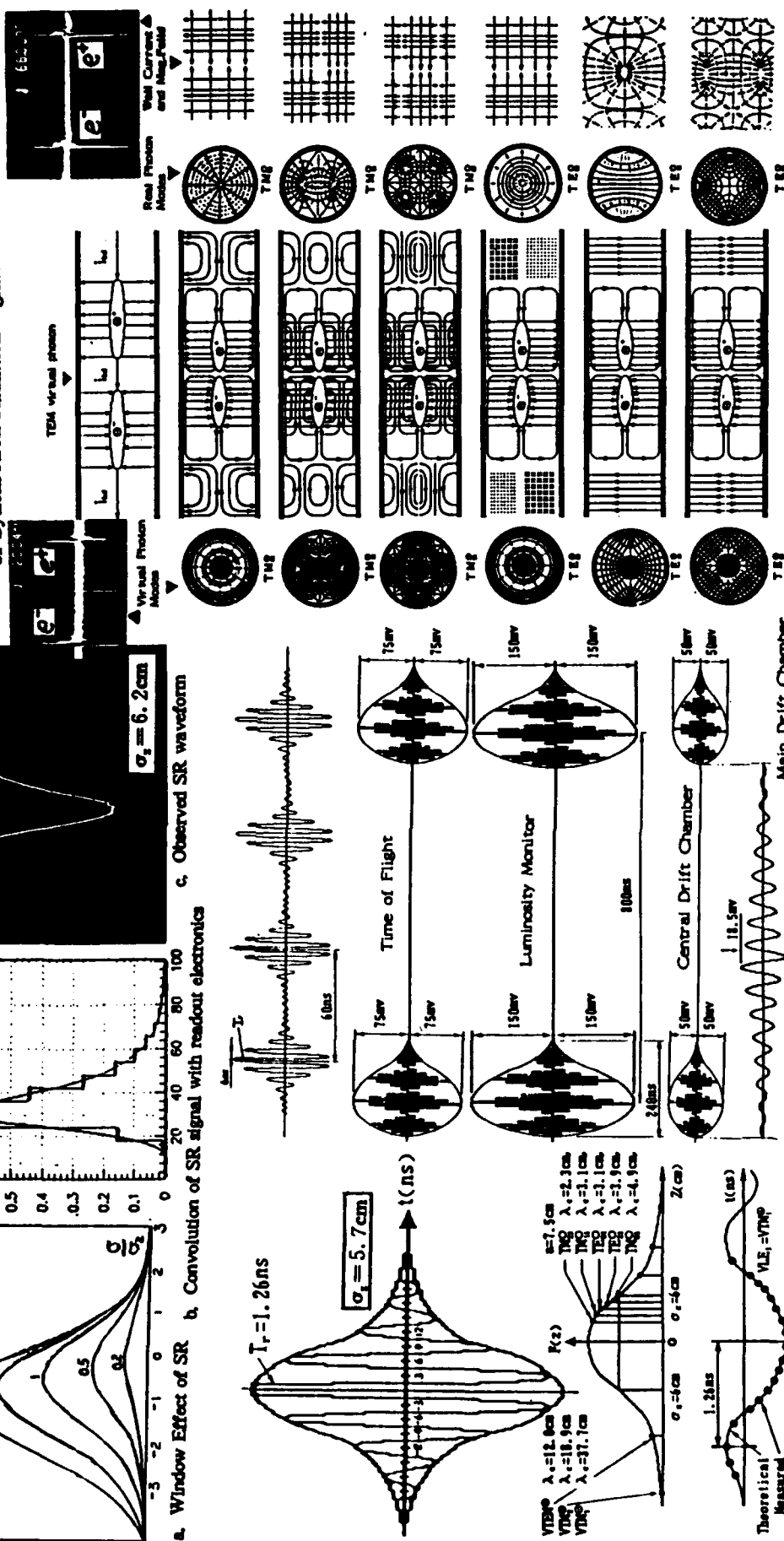


Fig. 4 RTEM model of Coherent Radio Frequency Beamstrahlung Signal of BEPC read out by Sub-detectors of BES

Fig. 5 Modes of Real and Virtual Photon

Development on Multistrip Monitor for Nonintercepting Measurement of Beam Geometric Moments

Yan Yin

TRIUMF, 4004 Wesbrook Mall, Vancouver, B.C., V6T 2A3

Abstract

The wall current distribution created by a charged particle passing through a beam pipe gives information on the beam profile moments [1]. A coordinate translation has been made to obtain beam centroid moments. The beam current, position and profile moments (in terms of $\sum_i \rho_i^n \cos n(\theta - \phi_i)$) can be obtained by performing a spatial Fast Fourier Transform on the wall current distribution of a cylindrical multistrip monitor [2].

Computer simulations of the measurement and their results are presented. The accuracy of the measurement is predicted to be better than 0.1%.

I. INTRODUCTION

Beam profile moments provide beam profile information and are very useful for beam emittance [1] and instability studies. A multistrip monitor provides a non-intercepting tool for that purpose. The derived parameters are moments, which not only depend on beam intensity, but also on beam shape and size.

Moment descriptors have various forms. Some examples of moments include geometric, complex, radial and orthogonal moments. For the particular problem studied here, which has rotational symmetries, radial moments are adopted in this paper; however, we shall introduce the subject with the more familiar geometric moments.

The definition of the two dimensional geometric $(p+q)$ th order moments of a density distribution function $\rho(x, y)$ in plane x, y is defined in terms of Riemann integrals [3] as:

$$M_{pq} = \iint x^p y^q \rho(x, y) dx dy, \quad p, q = 0, 1, 2, \dots \quad (1)$$

It is assumed that $\rho(x, y)$ is a piecewise continuous, bounded function, and that it can have non-zero values only in a finite part of the x, y plane; then moments of all orders exist and the uniqueness theorem can be proved.

Uniqueness Theorem: The double moment sequence M_{pq} is uniquely determined by $\rho(x, y)$; and conversely, $\rho(x, y)$ is uniquely determined by the set M_{pq} .

II. MOMENT MATCHING APPROACH

We could always obtain a continuous function $g(x, y)$, whose moments exactly match those of $f(x, y)$ up to a given order N_{max} , assuming that we have the set of moments M_{pq} [4]. The more higher order moments we have, the more accurate and closer to the original function $f(x, y)$ the $g(x, y)$ must be.

$$g(x, y) = g_{00} + g_{10}x + g_{01}y + g_{20}x^2 + g_{11}xy + g_{02}y^2 + g_{30}x^3 + g_{21}x^2y + g_{12}xy^2 + g_{03}y^3 + \dots \quad (2)$$

The coefficients g_{pq} should be determined so that the moments of $g(x, y)$ match the moments, M_{pq} , of $f(x, y)$, according to the following expression:

$$\int_{-1}^{+1} \int_{-1}^{+1} x^p y^q g(x, y) dx dy = M_{pq}. \quad (3)$$

So, if we have the whole set of the second or third degree moments, we could reconstruct the beam up to the accuracy of that order [4].

There are some other orthogonal polynomials that can be used for image reconstruction, which are more convenient than the moment matching approach [4].

III. WALL-CURRENT DISTRIBUTION AND MOMENTS

When a charged particle beam passes through a conducting pipe, an image current will be produced on the wall. If the particle is an ultra-relativistic one, or if the beam is very long, then the electrical field will be in a plane which is perpendicular to the direction of motion. The wall current distribution in the cross-sectional plane is a two-dimensional problem, and can be described with the field produced by a line current. The wall-current distribution is not only determined by the beam position, but also by the density distribution of the beam and the total beam current.

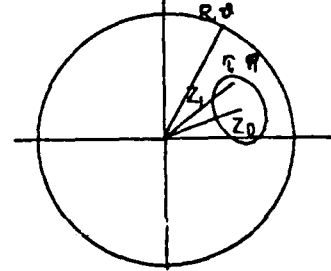


Fig.1: Wall current due to a line current in a conducting cylinder and coordinate translation.

For a delta function line current ρ_i , at point (r_i, ϕ_i) , the image current density, J , on a conducting cylinder of radius R at point (R, θ) (see Fig.1) is given by:

$$J_{image}(r, \phi, R, \theta) = \frac{\rho_i}{2\pi R} \frac{(R^2 - r_i^2)}{(R^2 + r_i^2 - 2Rr_i \cos(\theta - \phi_i))} \quad (4)$$

Expanding in powers of r_i/R gives:

$$J_{image}(r, \phi, R, \theta) = \frac{\rho_i}{2\pi R} \left[1 + 2 \sum_{n=1}^{\infty} \left(\frac{r_i}{R} \right)^n \cos n(\theta - \phi_i) \right]. \quad (5)$$

The above expansion represents a series of azimuthal components. The wavelength of the dipole component ($n=1$) is the circumference of the beam pipe $2\pi R$. The induced current density at one observed location on the wall will be the integral of the above equation over all the beam particles:

$$J_{image}(r, \phi, a, \theta) = \frac{1}{2\pi R} \left[\sum_i \rho_i + 2 \left(\sum_{n=1}^{\infty} \frac{\cos n\theta}{R^n} \times \sum_i \rho_i r_i^n \cos n\phi_i + \sum_{n=1}^{\infty} \frac{\sin n\theta}{R^n} \sum_i \rho_i r_i^n \sin n\phi_i \right) \right]. \quad (6)$$

The above equation shows that the wall-current density created by a beam passing through the pipe is actually

the sum of moments closely related in form to the radial moments with both degree and angular dependence of n . The FFT components of each order give the moments of that order in the forms of $\sum_i \rho_i^n \cos n\phi_i$ and $\sum_i \rho_i^n \sin n\phi_i$.

But the moments we obtained here are the moments around the center of the beam pipe (P_{nn}). Only the moments around the beam centroid have the property of invariance, and can be used to describe the beam.

IV. CENTROID MOMENTS

A coordinate translation has to be done to obtain the centroid moments, Fig. 1. Let us use the complex form to express the moments. From the FFT, the moments we obtained are: $P_0 = \sum_i \rho_i$

$$P_{nn} = \sum_i \rho_i r_i^n \cos n\phi_i + i \sum_i \rho_i r_i^n \sin n\phi_i = \sum_i \rho_i Z_i^n \quad (7)$$

where $Z_i = x_i + iy_i$ is the distance from the particle to the center of the pipe. $Z_0 = x_0 + iy_0$ is the distance from the centroid to the center of the pipe. So, the distance from the particle to the centroid is: $Z_i - Z_0$.

The centroid moments M_{nn} are:

$$M_0 = P_0 = \sum_i \rho_i \quad (8)$$

$$\begin{aligned} M_{nn} &= \sum_i \rho_i (Z_i - Z_0)^n = \sum_i \rho_i \sum_{k=0}^n \frac{n!(-1)^{n-k}}{k!(n-k)!} Z_i^k Z_0^{n-k} \\ &= (-1)^n Z_0^n P_0 + \sum_{k=0}^{n-1} \frac{n!(-1)^{n-k}}{k!(n-k)!} Z_0^{n-k} P_{kk} + P_{nn} \end{aligned}$$

V. THE BASIC BEAM INFORMATION FROM A CYLINDRICAL MULTISTRIP MONITOR

The wall-current distribution on a cylindrical multistrip monitor immediately yields basic beam parameters such as current, position, orientation and information related to size.

A. Phase angle of each higher order moment

The FFT of the wall current distribution only gives the value of $Re(M_{nn})$, $Im(M_{nn})$ and ϕ_n directly. Here, $Re(M_{nn})$ represents the real part of the second order moment, and $Im(M_{nn})$ represents the imaginary part.

Although the azimuthal moments are the sum of the density value at each point multiplied by its distance r_i^n and $\cos n\phi_i$ or $\sin n\phi_i$, where ϕ_i is the phase angle of the particle at that place, the collective effect of the sum is that the moment has a phase angle ϕ_n , which represents the orientation of the image component of that order. For example, for the quadrupole moment, ϕ_2 represents the orientation of the best-fit beam ellipse, and for the sextupole, ϕ_3 represents the orientation of the triangle, etc. So, from the FFT, $n\phi_n$ can be determined by $\tan^{-1}(Im(M_{nn})/Re(M_{nn}))$, and ϕ_n as well. In the following, we use ϕ_n to represent the phase angle in each FFT component of the corresponding order and use M_{nn} to represent the centroid moments.

B. DC component

The first component, i.e. zero order of the FFT, is a constant value, which represents the dc current of the beam with a factor of πR . The dc current is also called the zero degree moment.

C. Position

The first order component of the FFT is $\frac{1}{2\pi R^2} \sum_i \rho_i r_i \cos(\theta - \phi_i)$, which gives the first degree moment around the center of the pipe as $Re(M_{11}) = \sum_i \rho_i r_i \cos \phi_i$, $Im(M_{11}) = \sum_i \rho_i r_i \sin \phi_i$. ϕ_1 represents the phase angle in the FFT data, which is the total effect of the position shift of all the particles.

Therefore the position of the centroid in a polar coordinate is $r = (\sqrt{Re(M_{11})^2 + Im(M_{11})^2})/M_0$, and $\phi_1 = \tan^{-1}(Im(M_{11})/Re(M_{11}))$, or in the xy plane, $x = r \cos \phi_1$, $y = r \sin \phi_1$.

D. Quadrupole, sextupole and higher order moments

The second order component from FFT provides information about the best-fit ellipse. The third order component gives the sextupole moment; the fourth order gives the octupole moment. The number of moments that can be obtained depends on how many strips the monitor has. The moments are all in the form of:

$$Re(M_{nn}) = \sum_i \rho_i r_i^n \cos n\phi_i, \quad Im(M_{nn}) = \sum_i \rho_i r_i^n \sin n\phi_i \quad (9)$$

The coefficients of the second order component from the FFT give the second degree moments, i.e. quadrupole moments and phase. It also can be written as:

$$\begin{aligned} Re(M_{22}) &= \sum_i \rho_i r_i^2 (\cos^2 \phi_i - \sin^2 \phi_i) = \sum_i \rho_i x_i^2 - \sum_i \rho_i y_i^2 \\ Im(M_{22}) &= 2 \sum_i \rho_i x_i y_i, \quad \phi_2 = \frac{1}{2} \tan^{-1} \frac{Im(M_{22})}{Re(M_{22})} \end{aligned} \quad (10)$$

For a uniformly distributed elliptical beam whose principal axes are the same as x and y , the following formulae are valid:

$$\iint \rho x^2 dx dy = \frac{1}{4} \pi \rho a b^3, \quad \iint \rho y^2 dx dy = \frac{1}{4} \pi \rho a^3 b \quad (11)$$

where $2a$ and $2b$ are the long and short axes of the ellipse respectively, and $\iint \rho xy dx dy = 0$. So,

$$\frac{M_{22}}{M_0} = \frac{1}{4} (a^2 - b^2), \quad \frac{M_{20}}{M_0} = \frac{1}{4} (a^2 + b^2) \quad (12)$$

where M_{20} is the second degree moment with 0 angular dependence, i.e. $\sum_i \rho_i r_i^2$. The half-axis a and b can be determined therefore.

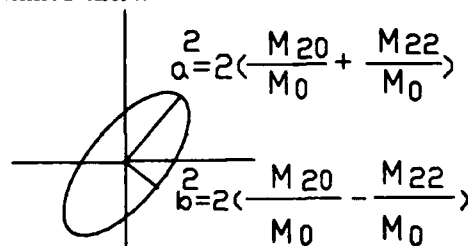


Fig. 2: Best-fit ellipse

E. Width signal

Although we have obtained M_{22} and the phase of the beam, M_{20} , which contains $a^2 + b^2$, is missing from our FFT data. A Monte Carlo computer simulation has been done with elliptical beams of uniform distribution. All had the same $a^2 - b^2 = 0.75$, but a/b varied from 1.5 to 2, 3

and 4. The wall-current distribution has been calculated for both centered and off center beams. As long as the positions and phases of the beams are the same, the difference between the corresponding wall-current distributions is of order 10^{-4} , which is at the level of statistical fluctuation of the Monte Carlo calculation. Therefore, M_{20} or a/b has to be measured with another method.

If the beam aspect ratio is known from the beam optics or some other measurement, then the best fit ellipse can be determined. With Teague's moment matching formulae or other orthogonal polynomials, one could reconstruct a beam shape to the accuracy of that order. For a thin beam, say, b is $1/3$ or even $1/4$ of a , $a^2 - b^2$ is approximately a^2 , so the width signal a can be obtained immediately.

A round beam does not have high order moments, so the cylinder multistrip monitor will indicate this. When a round beam is in the center of the pipe, the distribution on the wall is uniform.

VI. COMPUTER SIMULATION

A Monte Carlo calculation has generated an elliptical beam, which is 0.25 cm vertically off the center of the beam pipe with a size of 2 cm \times 1 cm and $\phi_2 = \pi/2$. Since the moments of each order can be calculated, the accuracy of the method can be determined. The comparison shows the accuracy can be better than 0.1%. Fig.3 is the reconstruction of the generated beam up to second degree moment.

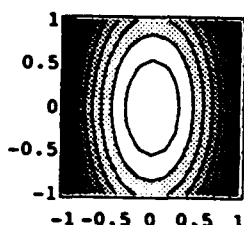


Fig.3: Reconstruction of computer generated beam.

The result of the computer simulation is listed in the following table for the first 6 orders:

Table: Monte Carlo Simulation Results

n	FFT Ampl	phase	ctr. moments	dir. calc.
1	0.2502696	1.570795	-7.96E-09	0.
2	0.2500159	3.12109	-0.18738	-0.1875
3	0.1564581	4.712302	-1.104E-04	0.
4	0.1446773	6.282875	0.070239432	0.0702232
5	0.1183089	1.570440	1.4728506E-05	0.
6	0.1101785	3.142132	-0.032884017	-0.0328926

VII. SENSITIVITY

The wall-current distribution formula [6] gives the amplitude of the second order component of the FFT as $\frac{1}{\pi R^2} \sum_i \rho_i r_i^2 \cos 2(\theta - \phi_i)$. The sensitivity to measuring this component is:

$$\frac{2}{R^2} \left[\frac{\left| \sum_i \rho_i r_i^2 \cos 2(\theta - \phi_i) \right|}{\sum_i \rho_i} \right] = \frac{(a^2 - b^2)}{2 R^2} \quad (13)$$

Assume a voltage across the resistor of the monitor is induced by a sizeless beam with same intensity, position, phase and time structure. If the aspect ratio of the measured beam is 2 and the short half axis b is $1/10$ of the pipe radius, then the signal we could pick up is 0.015 of

this voltage value, which not only depends on beam structure but also on the frequency response of the monitor. The signal amplitude also depends on the sensed current, which is determined by the width of the strip used.

If the wall-current monitor has the frequency response needed, and assuming that the peak current is 10 mA, with 10 ohm resistors, 16 strips, we will have about 6.25 mV across each resistor. With a 40 dB amplifier, the signal will be 625 mV. With an aspect ratio of 2, $b/R = 10$, we will have a signal changing from -9mV to +9 mV around 625 mV.

An advantage of the method is that because the variation in the amplitude of the signals depends on moments, we can get a measurable signal for a beam that is small in size but high in intensity.

VIII. ERROR DUE TO NOISE

In the pipe, there may be other sources of electrical charges, such as residual gas etc., which cause errors in the signal. Considered as white noise, their effect will be uniformly distributed in the area of the whole pipe. In the round pipe, this will give an extra uniform distribution to the wall-current, which only changes the zero degree moment, not the others. When we use the zero degree moments as a dc level for normalization to get beam size information, there will be an error.

There may be some other noise sources due to grounding or RF etc, and one should try to eliminate them before doing the FFT.

IX. SOME SUGGESTIONS

The FFT analysis of the wall-current distribution has a unique advantage; it can distinguish the moments of each order very clearly. A concern with some present BPM systems is correction for non-linearities. But if the beam pipe is round, using the FFT, it is very easy to obtain the position of the beam centroid without any non-linearities. Also, the zero order coefficient of the FFT gives the dc component right away. One does not need to do BPM mapping anymore, just place a round pipe antenna in the center of the pipe to calibrate the correction coefficients for all the pick-up strips. This will save a lot of work.

To avoid noise problems, some filtering, which usual electronics have already used, may be needed before doing the FFT.

X. ACKNOWLEDGMENTS

The author gives her thanks to Z.Y.Feng (Univ. Of Washington, Physics Department) for his help with Monte Carlo calculations, to Ray Burge for his constant support and valuable information, to R.Miller, Juwen Wang(SLAC) for helpful discussions, to Prof.Z.X.Xu (Victoria University), and to Bill Rawnsley (TRIUMF) for good discussions.

XI. REFERENCES

- [1] R.Miller et al: *Nonintercepting emittance Monitor*, Proc. XII High Energy Accelerator Conference, 1983, p602.
- [2] Yan Yin: *A multistrip beam profile high order moment monitor*, Proc. XVth Int. Conf. on High Energy accelerators, Hamburg, 1992, p260.
- [3] M.K.Hu: *Visual pattern recognition by moment invariant* IRE Trans. Info. Theory, IT-8, 179-187 (Feb. 1962).
- [4] Michael Reed Teague: *Image Analysis via the general theory of moments*, J. Opt. Soc. Am., Vol. 70, No. 8, 920-930, Aug. 1980.

Wire Scanner Data Analysis for the SSC Linac Emittance Measurement

C.Y.Yao, J.W.Hurd, J.Sage
Superconducting Super Collider Laboratory*

Abstract

The wire scanners are designed in the SSC Linac for measurement of beam emittance at various locations. In order to obtain beam parameters from the scan signal, a data analysis program was developed which considers the problems of noise reduction, machine modeling, parameter fitting and correction. This program is intended as a tool for Linac commissioning and also a part of the Linac control program. Some of the results from commissioning runs are presented.

I. INTRODUCTION

The SSC linear accelerator is a 600 MeV H^+ linac including a 35 KeV ion source, a low energy beam transport section, a 2.5 MeV RFQ acceleration section, a 70 MeV Drift Tube Linac and the final 600 MeV Coupled Cavity Linac. The required beam emittance is 0.37mm-mrad in both X and Y directions.

In order to achieve the desired goal, emittance growth control is important not only at the design and construction stage, but also during commissioning and operation.

The Wire scanner system is one of the main emittance measurement methods for the SSC linac. A total of 18 wire scanners are designed in the linac and transport line. They are located at different stages of beam acceleration and will be used for on line beam matching and optimization.

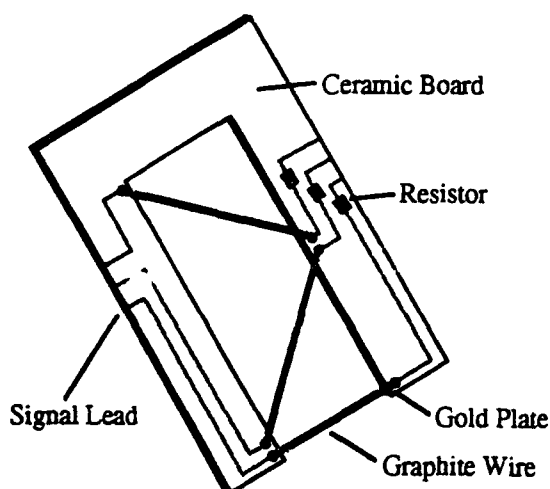


Fig.1 Schematic of SSC Wire Scanner

*Operated by the University Research Association, Inc., for the Department of Energy under Contract No. DE-AC35-89ER40486.

II. WIRE SCANNER FOR SSC LINAC

A schematic of the wire scanner is shown in Figure 1. The design is similar to the SLAC SLC wire scanner.

The wire is made of gold plated graphite fiber with a diameter of 33 micron. The frame is made of ceramic material plated for wire mounting. Three wires are mounted in such a way that the wires cross the beam in X, Y and at a 45° orientations in a complete scan.

The wire frame is driven by a stepping motor.

When the wires are struck by the beam, both secondary emission and forward scattering is produced which is reflected in the signals on the wire. The wire signals are brought to a sample amplifier and a 12 bit wave form digitizer to convert into digital wave form data. Wire signals are sampled by the amplifiers at about 5MHz rate to ensure adequate bandwidth for observation of longitudinal macro bunch structure.

III. DATA ACQUISITION SYSTEM

Wire scanner data acquisition is performed by the linac control system, which is a distributed control system consisting of SUN workstations, network servers and local control systems (IOC). Each IOC is a VME system running VxWorks operating system and EPICS.

Wire scanner signals are connected to a VME wave form digitizer module through a preamplifier and a multipurpose interface card. Wire motion is driven by a SMC controller board and the position is sensed by a LVDT. A complete scan contains about 200 position data scans each has 500 sampling points.

Data acquired by the IOC are read by a SUN workstation through Channel Access. The data is then sent to an Oracle database on the network which is accessible to all the workstations.

IV. DATA ANALYSIS PROGRAM

The wire scanner data analysis program is designed for commissioning and operation of the linac. The main requirements are effective and practical algorithm, friendly user interface, easy of operation and access. It is designed as a X/Motif application and can be run on any workstation on the linac control system network.

It mainly consists of four functional parts: user interface, wire data display, r.m.s. beam width calculation, and emittance fitting.

1. User Interface

A main window with menu button and text window provides program control and message display. A popup window provides various plot functions. Display options are selected by selection buttons.

2. Wire Data Display

The main function of the wire data display is to provide the operator with a direct view of the acquired data. Noises, hardware failure and other possible error will cause false data. By careful study of the original data, some problems can be diagnosed and treated.

The display program provides several views of the data. A longitudinal view gives the data variation with time which reveals the beam distribution along the longitudinal direction and signal spectrum generated by hardware or noises. Three dimensional view and single curve step through options are provided to allow observation with different respective. Background signal subtraction, filtering, averaging and smoothing are provided to aid diagnosis. Fig.3. shows a typical display.

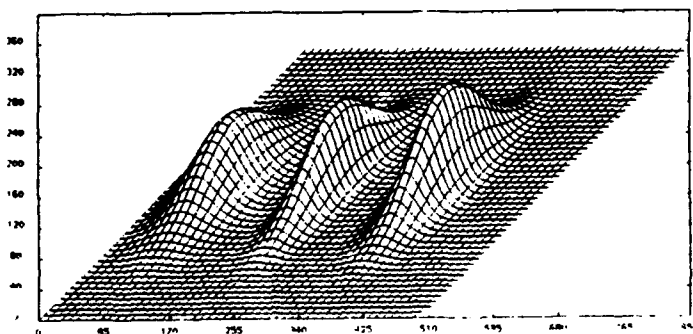


Fig.2 Wire Data Display

Data are also displayed in text format for careful review and a data editor is also incorporated to allow the operator to eliminate outliers due to interferences or hardware failure.

3. R.M.S. Width Calculation

It was shown that to first order, which this program is intended for, beam behavior could be well represented by an equivalent beam distribution with the same r.m.s. width. We choose Gaussian distribution to fit the beam profile. The transverse beam profile is defined by:

$$\rho_2 = \int \rho_4 e^{-x^T \sigma^{-1} x} dx' dy'$$

where X is four dimension phase space vector, σ is transverse emittance matrix, ρ_2, ρ_4 are real space and phase space beam distribution.

For single amplifier configuration, the beam signal is the sum of three signals from each of the wires. If the wire separations are large enough, the signals are easily separated. When the size of beam profile is comparable to the wire separations, signals become overlapped and a signal separation routine is developed.

Signal center and width are calculated through first and second moments calculation. A least square fitting routine is then used to do a final fitting. The program outputs position of the beam, signal amplitude, and r.m.s. beam width as well as bunch tilt angle. Fitting results are also graphically displayed.

Fig. 3 is a display of the fitting result.

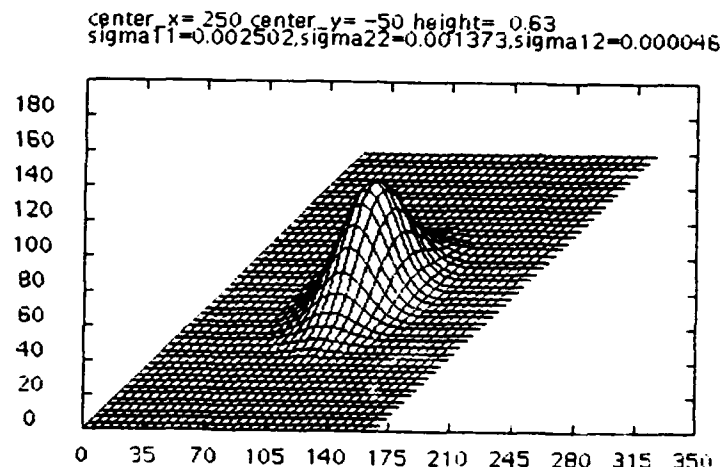


Fig.3 Display of Fitted Beam Profile

4. Emittance Fitting and Matching

Several methods can be used to measure transverse beam emittance. Here we only describe fixed optics method which is also suitable for on-line matching correction.

For a fully coupled beam, σ -matrix can be reconstructed by measurement of beam profile at 4 locations. For decoupled case three measurement are adequate. In the following description the decouples case is assumed.

Due to errors in the width measurement and errors in machine parameter and modeling, directly solving the linear equations may not give good results. We use a least square minimization to fit the σ -matrix which presents the r.m.s. emittance and Twiss parameters of the beam.

A series of wire scanners are used to reconstruct the r.m.s. emittance fitting and matching. Fig.4 outlines the algorithm. The iteration is needed because of the space charge effect at low beam energy.

First the σ -matrix are calculated using first order transformation which does not include space charge effects. Based on this σ -matrix new transformation matrices are generated which are used to make another σ -matrix fitting. This process is iterated until a convergence is reached.

The least square fitting process is described briefly here. Let $\sigma(0)$ denote the desired beam σ -matrix, $\sigma(n)$ for σ -matrices at wire scanner n and $R(n)$ for the transformation matrix from the point where $\sigma(0)$ is associated to the n th wire scanner location. The relation between $\sigma(0)$ and $\sigma(n)$ is given by:

$$\sigma(n) = R(n) \sigma(0) R^T(n)$$

The measured r.m.s. radius, $x(n)$, of the beam is related to the σ -matrix elements by

$$x_m(n) \propto \sqrt{\sigma_{11m}(n)}$$

here subscript m denotes measured values.

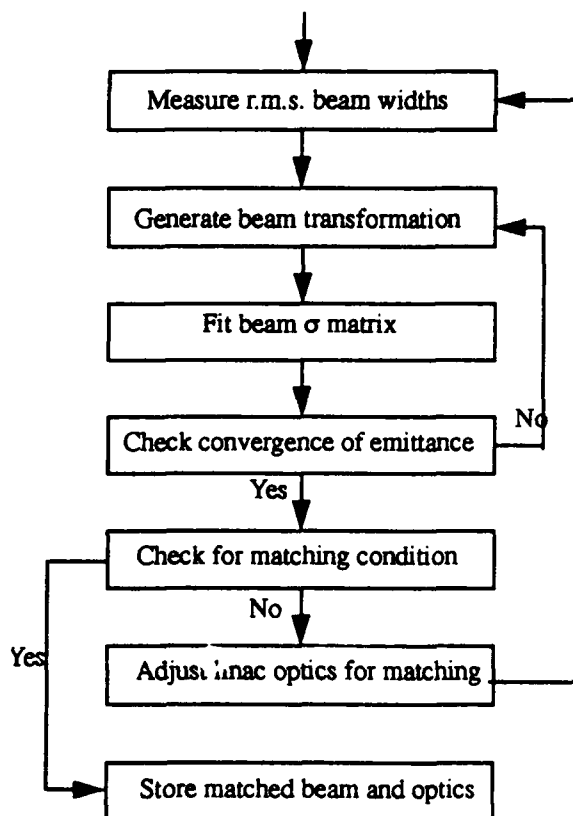


Fig.4 Fitting and Matching Algorithm

For each wire scanner n , we have

$$\sigma_{11}(n) = \sum_{i,j=1}^2 R_{1i}(n) \sigma_{ij}(0) R_{1j}(n)$$

The total error is minimized for

$$\chi^2 = \sum_{n=1}^N \left[\sigma_{11m}(n) - \sum_{i,j=1}^2 R_{1i}(n) \sigma_{ij}(0) R_{1j}(n) \right]^2$$

The least square minimization criteria is satisfied by solving the three equation given by

$$\sum_{n=1}^N \left[R_{1k}(n) \sigma_{11m}(n) R_{1l}(n) \right.$$

$$\left. - R_{1k}(n) R_{1l}(n) \sum_{i,j=1}^2 R_{1i}(n) \sigma_{ij}(0) R_{1j}(n) \right] = 0$$

for $kl=11,12,22$. This gives the element of $\sigma(0)$.

V. REFERENCES

- [1] K.L.Brown et. al., "Transport - A Computer Program for Designing Charged Particle Beam Transport Systems," Stanford Linear Accelerator Center report SLAC-91, May 1977
- [2] G. Swain et. al. "Generating Catalogs of Transverse Matching Solutions," Proc. of the 1989 IEEE Particle Accelerator Conference
- [3] K.R.Crandall, "Trace: An Interactive Beam-Transport Program," Los Alamos Scientific Laboratory Report LA-5332, October 1973
- [4] A.Burns et. al., "Wire Scanner News from the CERN-SPS," Proc. of 1989 IEEE Particle Accelerator Conference
- [5] M.C.Ross et. al., "Wire Scanners for Beam Size and Emittance Measurement at the SLC," Proc. of 1991 IEEE Particle Accelerator Conference

Real-Time Spot Size Measurement for Pulsed High-Energy Radiographic Machines*

Scott A. Watson

Los Alamos National Laboratory, M-4 Hydrodynamics
MS P-940, Los Alamos, NM 87545 USA

Abstract

The focal spot size of an x-ray source is a critical parameter which degrades resolution in a flash radiograph. For best results, a small round focal spot is required. Therefore, a fast and accurate measurement of the spot size is highly desirable to facilitate machine tuning. This paper describes two systems developed for Los Alamos National Laboratory's Pulsed High-Energy Radiographic Machine Emitting X-rays (PHERMEX) facility [1]. The first uses a CCD camera combined with high-brightness fluors, while the second utilizes phosphor storage screens. Other techniques typically record only the line spread function on radiographic film, while systems in this paper measure the more general two-dimensional point-spread function and associated modulation transfer function in real time for shot-to-shot comparison.

I. INTRODUCTION

A flash x-ray source is produced when a beam of high-energy electrons impinges on a heavy metal target producing bremsstrahlung radiation. The time-integrated spatial intensity distribution or spot size of this source degrades the resultant image. A radiographic experiment can be well modeled as a linear system in the following way [2]:

$$i(x,y) = o(x,y) * s(x,y) * f(x,y) \quad (1)$$

Where $i(x,y)$ is the resultant image, $o(x,y)$ is the object transmission characteristic, $f(x,y)$ is the film blur characteristic, and $s(x,y)$ is the two-dimensional point-spread function (PSF) of the source, and $*$ denotes convolution. Clearly, as $s(x,y)$ deviates from an ideal delta function, the resolution of the resultant image will be degraded. To evaluate a source for a given radiographic task, it is necessary to characterize the focal spot experimentally. We have adopted a definition proposed by Mueller [3] using the -3 dB point on the modulation transfer function (MTF) curve for reducing the source PSF to a single number spot size for performance comparison across machines.

II. SYSTEM DESIGN

A wealth of literature exists on the various techniques for source characterization [4-7]. The primary methods are illustrated in Table 1. Most of these techniques are applied to low energy machines with small spots and may require multiple pulsing to achieve the desired sensitivity.

Technique	Advantages	Disadvantages
Resolution Pattern	Scanner is not required.	Requires low contrast measurement. Difficult to interpret.
Pin Hole	Yields PSF. Self shielding	Requires multiple shots & large magnification. Hard to manufacture.
Particle Array	Yields PSF	Requires small opaque particles and computer. Poor at high energies.
Knife Edge	Common usage	Assumes isotropic source & yields only LSF. Requires computer.
Streak Camera	One-dimensional time-resolved data.	Assumes isotropic source. Difficult to use. Requires computer.
Large Pin Hole	Yields PSF. Self shielding.	Requires computer. Needs high quality data (i.e. good SNR).

Table 1. Common Spot Size Measurement Techniques

After testing these methods and several others (using type AA radiographic film with 1-mm lead screens), the large pin hole was chosen because it offers several advantages in a real time system. First, the large pin hole is self-shielding, and consequently lowers the scattered background radiation delivered to the CCD camera [8]. Furthermore, it can be used on a single pulse with relatively low magnification. Finally, it indirectly yields a two-dimensional PSF. A block diagram of a prototype system is shown below in Fig. 1.

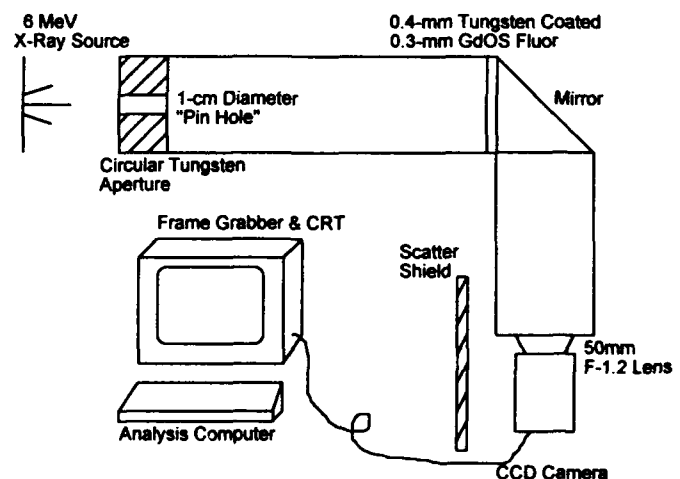


Figure 1. Real-Time Spot Size Camera System

This system images a 10-mm-diameter, 100-mm thick tungsten aperture onto a 0.3-mm thick Gd_2O_3 fluor coated onto a 0.4-mm tungsten intensifying screen. The resulting image is relayed to a VAX 3100 analysis computer by way of

*Work performed under the auspices of the U.S. Dept. Of Energy.

a front surface mirror, 50mm F1.2 camera lens, and a COHU RS-170 CCD camera with an Analogic DASM 8-bit frame grabber.

The aperture transfer function and the detector blur function are then deconvolved using a Wiener inverse filter [9] to yield the source PSF,

$$S(f) = \frac{I(f)}{O(f)F(f)} \quad (2)$$

Here $S(f)$, $I(f)$, $O(f)$, and $F(f)$ are Fourier transforms of the source PSF, resultant image, the opaque tungsten aperture (a zero-order Bessel function), and the spatial blur function respectively.

The CYLTRAN electron-photon transport code [10] was used to obtain a one-dimensional estimate of the detector blur function at the 6-MeV incident effective photon energy of PHERMEX. The resulting blur function is shown in Fig. 2 below. For our machines, this blur represents a small perturbation on the final result that can be made negligible by using radiographic magnifications greater than two [11].

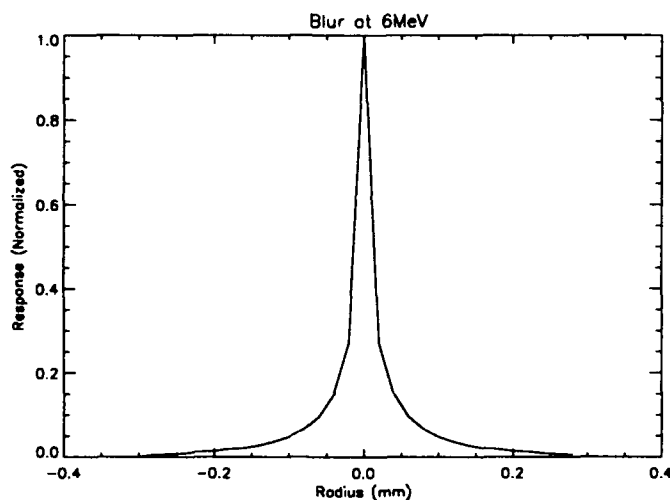


Figure 2. Gd_2O_2S Spatial Blur Function

Several types of commercially available fluors were tested, and the Gd_2O_2S type fluor was superior in all respects. (1) It has a green spectral response that matches the CCD camera spectral sensitivity, (2) has much higher speed than $CaWO_4$, $ZnCdS$, or $LaOBr$, (3) has low inherent blur, and (4) is highly resistant to radiation damage [11]. The final screen was specially fabricated by directly coating the Gd_2O_2S onto the tungsten intensifying screen using a lower binder ratio to increase the effective density (from 3.2 g/cc to 4.5 g/cc) and thus increase the speed and lower the inherent blur from secondary electron emission.

Our second approach uses the same basic large pin hole technique with a different imaging system. Rather than using transfer optics and a CCD array, the hole is directly imaged onto a storage phosphor screen, which is then read directly

using a 16-bit Molecular Dynamics laser-scanner with an on-board Intel-486 personal computer.

Both systems use in house software (written with the commercially available IDL image analysis package for VAX and IBM PC computers) which was calibrated using synthetic radiographs with known point spread functions.

III. EXPERIMENTAL RESULTS

Figure 3 below shows spline-fit data from a typical machine tune - spot size vs solenoid focus current. Notice the characteristic parabolic shape and the high sensitivity (better than 0.2 mm) of the camera system. The deviation from a parabola at lower focus currents was attributed to pre-collimation of the beam by a tapered beryllium collimator.

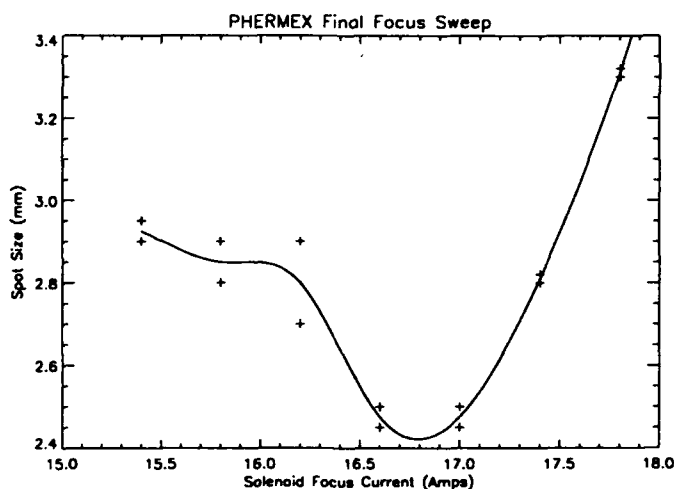


Figure 3. Spot Size vs Final Focus Magnet Current

The reconstructed point spread function (with 2-axis parametric least-squares Gaussian fits) is shown below in Fig. 4, along with the associated (radial-averaged) modulation transfer function in Fig. 5. These results are typical of both systems.

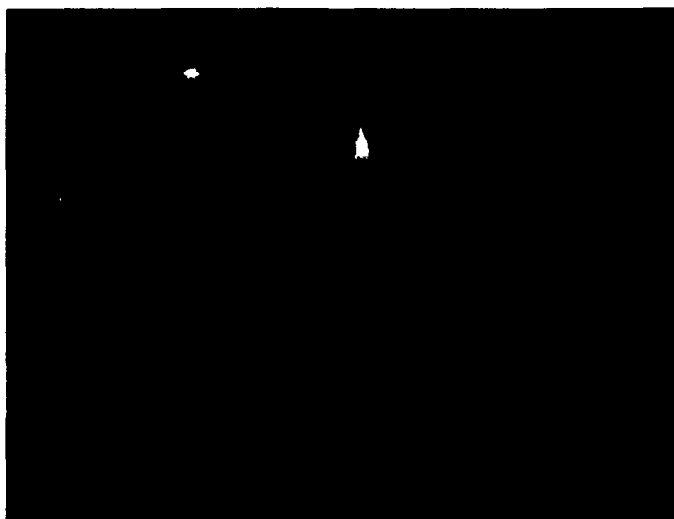


Figure 4. Typical PSF Reconstruction

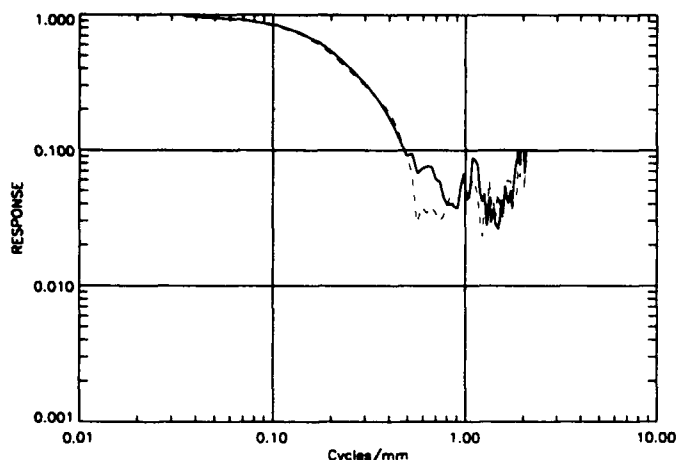


Figure 5. MTF's of Two Identical Pulses
Illustrating Machine Repeatability

Based upon our experiments, we estimate the following specifications for each system and for radiographic film [12]:

System-	CCD Camera	Phosphor	AA Film
Acquisition Time	1 min	8 min	2 hr
Sensitivity	0.1 mm	0.1 mm	0.1 mm
Resolution	2-9 mm	0.5-9 mm	0.3-9 mm
Required Dose	10 Rad at Fluor	0.1 Rad	1 Rad
Abs. Accuracy	0.4 mm	0.3mm	0.3 mm
Dynamic Range	8 bits	16 bits	11 bits
SNR (Typical)	13 dB	20 dB	20 dB
Image Size	256x256	512x512	512x512
Detector Cutoff	1.0 Cycle/mm	.2 Cycle/mm	.3 Cycle/mm
Analysis Time	0.5 min	2 min	2 min
Energy Range	0.1 - 30 MeV	0.1 - 50 MeV	0.1 - 50 MeV
Align. Error	0.2 mm	0.1 mm	0.1 mm
Magnification	1.5-2.5	3.0-5.0	2.0-5.0

Table 2. Estimated System Specifications

IV. CONCLUSIONS

Both systems performed well as a machine diagnostic to facilitate tuning. Previously, to obtain and analyze the data for a single shot took several hours. These systems both reduce this turnaround time to a few minutes, dramatically increasing the number and type of parameters that can be easily adjusted. The additional information conveyed by the two-dimensional PSF is also valuable whenever the beam is not isotropic.

The CCD system's primary advantage is the short turnaround time (less than 2 min), which makes it effectively "real-time". The storage phosphor's 16-bit dynamic range yields improved performance at the expense of processing time (typically 5-10 min per event). The quality of the data obtained with storage phosphors is as high as radiographic film. On the basis of our experience using both systems at a variety of radiographic facilities, we recommend the storage phosphor system using a large pin-hole because it offers the best compromise between quality, turnaround time, and ease of use.

V. REFERENCES

- [1] D. Venable, et al. "PHERMEX: A Pulsed High Energy Radiographic Machine Emitting X-Rays," *Los Alamos National Laboratory*. LA-3241. (1967).
- [2] J.C. Dainty & R. Shaw. "Image Science," *Academic Press Inc.* London. (1974).
- [3] K. H. Mueller. "Measurement and Characterization of X-Ray Spot Size," *Proceedings of the 1989 Flash Radiology Topical, American Defense Preparedness Association.* (1989).
- [4] S. A. Watson, et al. "Single-Shot Determination of Electron Beam Spatial Distribution with Radiographic and Streak Camera Techniques," *Los Alamos National Laboratory DARHT Tech. Note # 30.* (1992).
- [5] M. Trefler & J. Gray. "Characterization of the Imaging Properties of X-Ray Focal Spots," *Journal of Applied Optics*, Vol. 15, No. 12. (1976).
- [6] U. V. Gopala. "A New Method To Determine The Focal Spot Size of X-Ray Tubes," *Dept. of Radiology, John Hopkins University.* (1971).
- [7] J. U. Madsen. "Focal Spot Size Measurement for Microfocus X-Ray Sets," *ANDREX Radiation Products.* (1989).
- [8] G. J. Yates & B. T. Turko. "Circumvention of Radiation Induced Noise In CCD And CID Imagers," *26th Annual IEEE Conference on Nuclear and Space Radiation Effects.* (1989).
- [9] R. C. Gonzalez & P. Wintz. "Digital Image Processing," *Addison-Wesley Publishing Company.* 2nd Ed. (1987).
- [10] J. A. Halbleib et al. "Integrated TIGER Series of Coupled Electron/Photon Monte Carlo Codes," *Oak Ridge National Laboratory RSIC Computer Code Collection.* (1992).
- [11] K. H. Mueller. "Prediction of Radiographic System Resolution and Selection of Optimum Radiographic Magnification," *Los Alamos National Laboratory. M-4:GR:84-05.* (1992).
- [12] J. T. Seeman et al. "Beam Tests of Phosphorescent Screens," *SLAC Single Pass Collider Memo CN-290.* (1985)
- [13] S. A. Watson. "Real-Time Spot Size Camera For Pulsed High-Energy Radiographic Machines," *Los Alamos National Laboratory. M-4:GR-92-06.* (1992).

High Resolution Beam Monitoring with Optical Transition Radiation at 3 MeV Electron Energy

A. Specka, D. Bernard, R. Guirlet¹, F. Jacquet, P. Miné, B. Montès, R. Morano, P. Poilleux
(Laboratoire de Physique Nucléaire des Hautes Energies, IN2P3 - CNRS),
F. Amiranoff (Laboratoire d'Utilisation des Lasers Intenses),
J. Morillo (Laboratoire des Solides Irradiés, CEA/DTA/CEREM/DTM),
Ecole Polytechnique, 91128 Palaiseau, France

Abstract

In the framework of the *plasma beat wave accelerator* experiment at Ecole Polytechnique, high precision position and focussing monitoring of a 3 MeV electron beam is needed. A device is proposed that uses backward *optical transition radiation* (OTR) from a tilted metal foil held into the beam. For an electron energy of 3 MeV, OTR is emitted within a large solid angle (typical apex angle about 40°) around the direction of specular reflection. The design requirements are a *high resolution* of the imaging optics ($\approx 10 \mu\text{m}$), a *high sensitivity* ($\approx 10 \mu\text{A}$ beam current, not focussed), robustness, and low cost. A prototype has been constructed and successfully tested. A similar device will be used for adjusting a laser focal spot on an electron focal spot, and for monitoring the beam on entry and exit of a gas vessel.

1. Introduction

The need for ever increasing particle energies at reasonable accelerator size has led to numerous investigations of new techniques to increase the accelerating electric field. One of these techniques is the plasma beat-wave acceleration (PBWA) scheme, proposed by Tajima and Dawson [1].

In the PBWA experiment at Ecole Polytechnique two high-intensity Nd-laser pulses of slightly different wavelengths (YAG, 1064 nm and YLF, 1053 nm) are focussed in a vessel containing hydrogen gas at a pressure of 2 mbar (≈ 1.5 Torr) and create almost instantaneously a fully ionized plasma by multi-photo-ionization. The beating of the two light-waves provides a longitudinal electric force which oscillates with the frequency difference $\Delta\omega = \omega_2 - \omega_1$ of the two lasers. If the frequency difference is equal to the plasma frequency $\omega_p = \sqrt{e^2 n_e / \epsilon_0 m_e}$, this so-called ponderomotive force resonantly excites a longitudinal relativistic electron plasma wave (Lorentz-factor $\gamma = \omega_1 / \omega_p \approx 100$), i.e. spatial and temporal variations of the electron density n_e . The charge separation produces a longitudinal electric field of up to several GV/m. A relativistic electron with the right phase can catch the wave and, riding from the crest to the trough of the wave, gain energy from the potential difference [2].

So far, at Ecole Polytechnique the first two stages of the experiment, i.e. plasma creation and beat-wave generation have been studied [3]. The injection of 3 MeV electrons from a Van-de-Graaff accelerator is scheduled for 1994.

The laser beams are focussed to form a plasma of about 100 μm (FWHM) width and about one centimeter length.

¹Now at: DRFC, CEA Cadarache, France

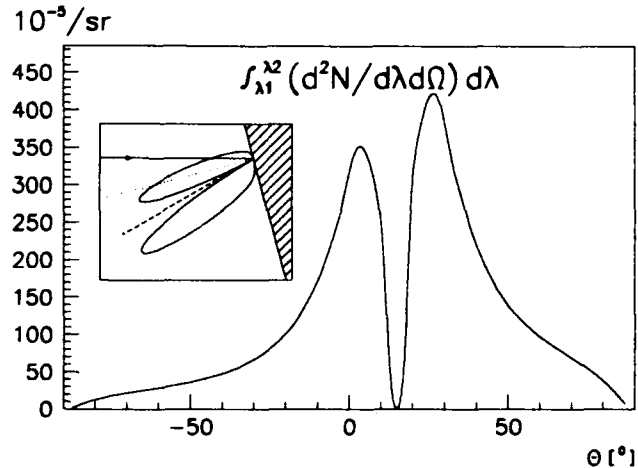


Figure 1: Angular photon distribution and corresponding emission pattern for 3 MeV electrons

Thus, the injected electron beam has to be focussed and positioned with high accuracy, i.e. spot position and size have to be monitored with a precision of order 10 μm .

In the past 20 years, beam spot visualization using backward optical transition radiation has proved to be a useful, simple and inexpensive method [4],[5], since conventional imaging optics and video (CCD) cameras can be used.

2. Transition radiation intensity

When a charged particle crosses the boundary between two media with different refractive indices, electromagnetic radiation is emitted. This phenomenon is called *transition radiation* (TR) [6]. The case where one of the media is the vacuum ($n=1$), and where the particle is relativistic ($\gamma = E/m \geq 2$) is generally considered. The spectral and angular distributions depend on whether the particles cross the boundary from medium to vacuum (forward-TR) or vice versa (backward-TR).

In the case of forward-TR, the photons emitted by an appreciably relativistic particle are mainly in the X-ray domain. The number of photons per wavelength interval shows a $1/\lambda$ rise up to a cutoff frequency $\omega_c = \gamma\omega_p$ where ω_p is the plasma frequency of the medium². The total number of emitted photons is then of the order of $\alpha\gamma$ where α is the fine structure constant.

On the contrary, the spectral photon density for backward-TR is proportional to the reflectivity of the medium, which drops to zero for frequencies above ω_p . It is also inversely proportional to the wavelength, and therefore emission takes place mainly in the visible and in

²For most metals, $\hbar\omega_p$ is of the order of 10–20 eV

the near UV (*optical transition radiation*, OTR). The total number of emitted photons is of the order of α .

The angular intensity distribution is centered around a nominal axis of emission. In the case of forward TR this direction is the particle trajectory itself. In the case of backward-TR it is the direction of specular reflection of the particle on the boundary. The emission vanishes in the nominal direction and is maximal on a cone around the nominal direction with a half apex angle γ^{-1} . In the case of normal incidence, the intensity distribution is symmetric around the nominal axis. For oblique incidence the pattern is dissymmetric, becoming symmetric only in the ultra-relativistic limit. In this latter case the (double differential) angular and spectral photon density for backward-TR is given by [4]:

$$\frac{d^2 N}{d\omega d\Omega} = \frac{\alpha}{4\pi^2} \cdot \frac{R(\omega)}{\omega} \cdot \frac{\beta^2 \sin^2(\theta + \psi)}{[1 - \beta \cos(\theta + \psi)]^2} \quad (1)$$

where θ is the angle of observation with respect to the normal to the boundary, $\beta = v/c$, ω is the frequency, and $R(\omega)$ is the reflectivity of the medium.

In the present application we monitor a 3 MeV electron beam ($\gamma = 6$) and the ultra-relativistic limit is not sufficiently accurate. Hence, we have used rather the exact and more complex expression given in [4]. The numerical results given here apply for backward-TR in oblique incidence at an angle of $\psi = 15^\circ$ on aluminum and for a spectral domain from 400 nm to 800 nm. Figure 1 shows the number of photons per unit solid angle as a function of θ in the plane of incidence. The corresponding emission pattern is included in the figure.

The quantity of collected OTR photons depends on the angle of observation θ and the numerical aperture³ $\Delta\theta$ of the imaging optics. Figure 2 shows the calculated dependence of the collected energy on the numerical aperture for various observation angles. Around the angles of maximum

³half apex angle of the aperture cone

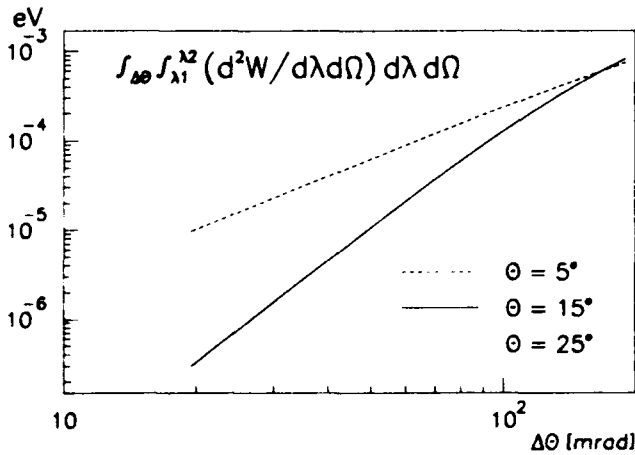


Figure 2: Dependence of collected TR energy per incident electron on numerical aperture for different angles of observation

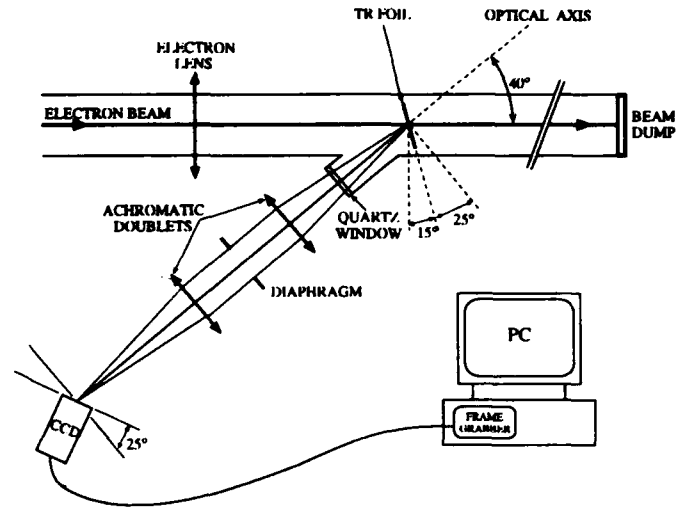


Figure 3: Experimental setup

emission $\theta_- = \psi - \gamma^{-1} \approx 5^\circ$ and $\theta_+ = \psi + \gamma^{-1} \approx 25^\circ$ the intensity grows with the square of $\Delta\theta$. Around the angle of minimal emission $\theta = \psi = 15^\circ$ the intensity grows with the fourth power of $\Delta\theta$.

The radiant energy for $\Delta\theta = 100$ mrad at $\theta = \theta_+$ is $0.29 \cdot 10^{-3}$ eV per electron or 0.29 nW per μA beam current. The photon yield is $0.13 \cdot 10^{-3}$ photons per electron or $8 \cdot 10^{11}$ photons per second and μA . Taking into account the spectral OTR distribution one obtains the corresponding luminous flux of $0.17 \cdot 10^{-9}$ lumen/ μA . A beam spot of 1 mm^2 size then has a luminous exitance of $0.17 \cdot 10^{-3}$ lux ($0.16 \cdot 10^{-4}$ footcandle) per μA beam current which gives sufficient light yield for high sensitivity CCD cameras for the range of currents in our application.

3. Experimental setup

Figure 3 shows the experimental setup used for the test of the prototype of the beam profile and position monitor (BPPM). A magnetic solenoid lens focusses the parallel continuous electron beam on a $1.5 \mu\text{m}$ thick aluminum foil which is tilted by 15° with respect to the beam axis. Beam current ranges up to $200 \mu A$. A fused silica window at 40° with respect to the beam axis allows observation of the spot at the angle of maximal emission, i.e. $\theta = 25^\circ$. A two-lens optics images the spot on the sensor of a CCD camera⁴. The video signal is read by a frame grabber card⁵ inside a PC for image processing.

Besides high resolution, the design of the imaging optics was governed by two other demands: high numerical aperture and a long working distance (about 200 mm). The size of the object field fixes the magnification at unity.

A symmetric system of two achromatic doublets of 200mm focal length located on both sides of an iris diaphragm was found to satisfy these demands. The cemented achromatic doublets⁶ are optimized for spherical aberration at infinite conjugates.

⁴COHU 6500

⁵EPIX 4MEG VIDEO, Aries, France

⁶Melles Griot LAO225

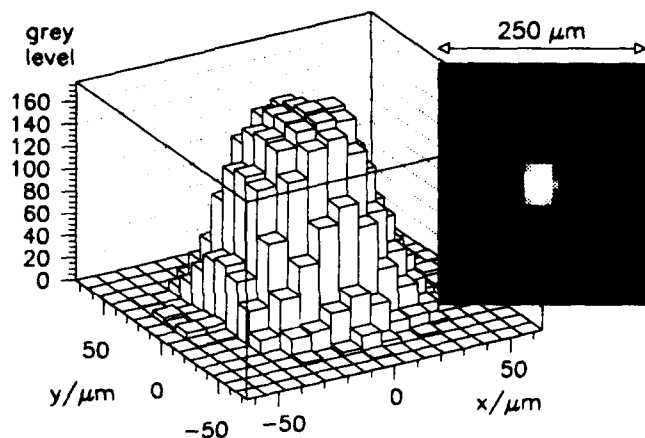


Figure 4: Focal spot ($125 \mu\text{A}$, 1 ms)

For unit magnification the object plane (i.e. TR foil) is at the front focus of the first lens, the image plane (CCD) at the back focus of the second lens, and the rays are parallel between the two lenses. In this case third order aberrations of odd order in image height cancel. The third order spherical aberration then dominates. For the extreme marginal ray at 90 mrad we calculate an aberration of about $50 \mu\text{m}$ at paraxial focus, giving about $8 \mu\text{m}$ standard deviation at best focus. Comparing this number to the pixel size (about $10 \mu\text{m}$) and to the diffraction limit (diameter of the Airy-disc, about $7 \mu\text{m}$ at 500 nm), we can state that the optical system is nearly diffraction limited and that its resolution is matched to the detector.

The optical axis is at an angle of 25° with respect to the normal to the foil. In order to maintain image sharpness over the entire field, we have tilted the image plane (CCD) as well. This introduces a slight but quite tolerable image distortion of less than 1% at field edge. The precision on the tilt angle is not critical to resolution.

4. BPPM performance

The sensitivity of the BPPM is sufficiently high to visualize the parallel beam spot (about 1 mm diameter) at $10 \mu\text{A}$ current at 20 ms exposure time. This is particularly useful during the beam alignment.

Figure 4 shows a typical focal spot at $125 \mu\text{A}$ and 1 ms exposure time. We found typically standard deviations of $20 \mu\text{m}$ for optimally focussed spots. As this is rather close to the estimated resolution limit of the system, actual spot sizes might even be smaller.

Before our test run, the motor turning the rubber belt of the accelerator has been magnetically shielded in order to suppress beam rotation. When operating the camera at 20 ms exposure time we have observed a residual rotation of the focal spot with an amplitude of about 0.3 mm . The movement is probably due to residual fields and still too large for the beat-wave experiment. By reducing the exposure time to 1 ms we were able to get one single image of a spot per video frame. In order to obtain a stable spot, we are thinking of pulsing the electron beam and synchronizing it with the oscillation of the residual field.

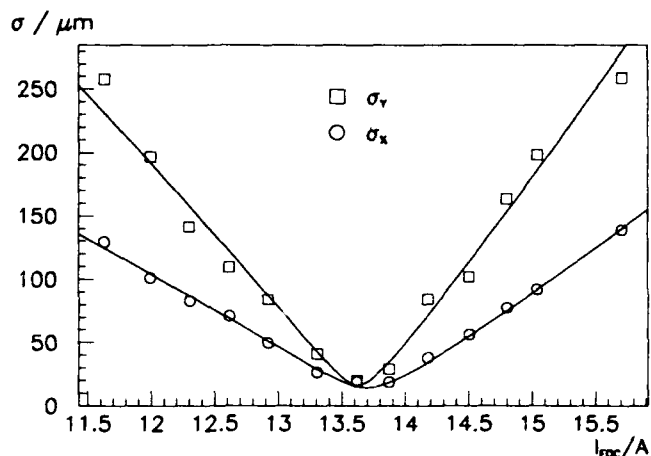


Figure 5: Spot sizes σ_x and σ_y as a function of the current in the magnetic lens. The curves are fitted theoretical beam envelopes. ($125 \mu\text{A}$, 1 ms)

By tracing the spot size as a function of the current in the focussing lens we can measure the beam emittance⁷(Figure 5). We obtained an upper limit for the emittance of $0.03 \text{ mm} \times \text{mrad}$.

The γ radiation noise was tolerable and could easily be subtracted, if present. No significant radiation damage to the camera (dead pixels) or the optics was observed.

5. Conclusion and future developments

Beam profile and position monitoring with OTR at 3 MeV has been successfully tested. It meets the specifications for the beat wave experiment of high resolution, high sensitivity, robustness and low cost. Focal spot sizes of $80 \mu\text{m}$ in diameter (4σ) have been measured.

A similar device will be used at the entrance of the gas vessel, and inside the gas vessel for the alignment of the laser and electron focal spots. Viewing the laser focus and the electron focus with the same apparatus will reduce systematic errors.

6. Acknowledgements

We would like to thank R. Chehab and L. Wartski for many fruitful discussions on the subject of TR. Very efficient technical support from the Van de Graaff crew (P. Lapiace et T. Perrin) and from the PNHE workshop is warmly acknowledged.

7. References

1. T. Tajima, J. M. Dawson, Phys. Lett. **43**, 267 (1979)
2. P. Mora, J. Appl. Phys. **71**(5), 2087 (1992)
3. F. Amiranoff et al., Phys. Rev. Lett. **68**, 3710 (1992)
4. J. Bosser et al., Nucl. Instr. and Meth. **A238**, 45 (1985)
5. X. K. Maruyama, R.B. Fiorito and D. W. Rule, Nucl. Instr. and Meth. **A272**, 237 (1988)
6. V. Ginzburg and I. Frank, JETP **16**, 15 (1946)

⁷We define the emittance as the product of the standard deviations of the spatial and angular intensity distributions measured at a focus. The surface of the phase space ellipse containing 95% of a Gaussian beam is $\approx 6\pi$ times higher.

Beam Profiling with Optical Transition Radiation

D. W. Rule and R.B. Fiorito
Naval Surface Warfare Center, Dahlgren Division
Silver Spring, MD 20903-5000

Abstract

One of the simplest applications of optical transition radiation (OTR) to accelerator beam diagnostics is beam profiling. We compare the limits of resolution of beam profiles made using OTR and profiles made using synchrotron radiation. We will discuss the physical basis for the limiting resolution in each case and show that the case of OTR yields essentially the same result as standard diffraction theory.

I. INTRODUCTION

During the last several years, we have developed a number of techniques for measuring the emittance of relativistic electron beams, in collaboration with colleagues at several accelerator facilities [1-4]. Our emittance measurement techniques, based on OTR, have been performed at energies up to about 110 MeV, to date. The emittance measurement involves the simultaneous observation of the OTR radiation pattern in the focal plane of a lens and the image of the beam profile at a beam waist [4]. The OTR radiation pattern from a single foil, or a two foil Wartski OTR interferometer [5], is used to determine the beam divergence. The polarization of the radiation patterns gives information on the horizontal and vertical emittances.

Gradually, OTR based beam diagnostics are beginning to be used more and more at accelerator facilities around the world; however we have become aware that some members of the beam diagnostics community mistakenly believe that OTR techniques are limited to relatively moderate energies because of a supposed self-diffraction effect [7]. The purpose of this brief paper is to discuss the physical basis for the limiting resolution of beam profiles using OTR. We will demonstrate that OTR can, in principal, be used for ultra relativistic beam diagnostics. OTR resolution will also be contrasted with the optics of imaging beams with synchrotron radiation (SR), which is well known. Some of the misunderstandings about the optics of OTR imaging comes from inappropriate analogies to SR's special optical properties.

II. OPTICAL PROPERTIES OF OTR

A. Angular Distribution

Two common misunderstandings regarding OTR's optical properties are: 1) that it is inherently "self-diffracting" because it is confined to angles of the order of $1/\gamma$, and 2) that it is "formed" over a length $L \sim \gamma^2 \lambda$. We will show why these concepts are wrong in this section.

In Reference [6], we used the model of a charge entering a perfect conductor to illustrate the properties of OTR. This model is excellent for optical wavelengths and the angular

distribution derived also applies to x-ray wavelengths.

Figure 1 illustrates the results of deriving the transition radiation properties using the method of image charges.

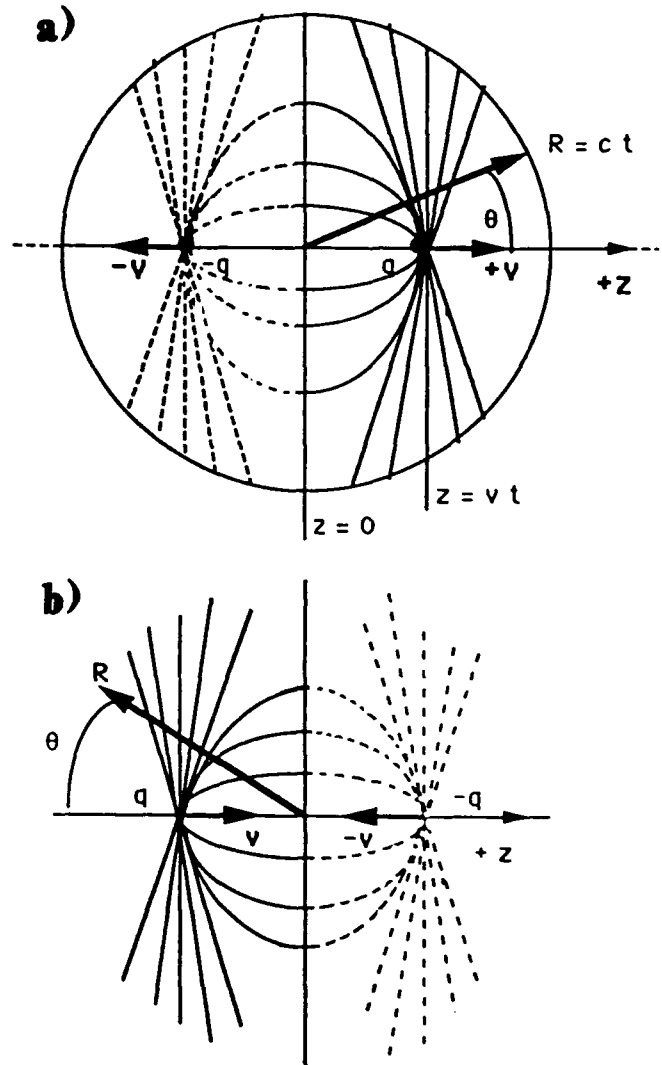


Figure 1. Coulomb and radiation fields generated by a charge q and its image $-q$: a) charge emerging from conductor, b) charge entering conductor. Radiation fields exist only on sphere of radius $R=ct$, when $t>0$.

Figure 1a shows the Lorentz contracted Coulomb fields of a relativistic charge emerging from a conductor as a bundle of field lines centered on q . The radiation field is on the sphere of radius $R=ct$ and the Coulomb fields are nonzero only inside this sphere. Figure 1b shows the situation for a charge q entering a conductor. In this case backward OTR appears on

the sphere of radius $R=ct$ and the Coulomb fields disappear at time $t=0$. The radiation is in phase everywhere on this sphere, however the field strengths are a function of θ , given by:

$$E_r = 0$$

$$E_\theta = B_\phi = \frac{2\beta q \sin\theta}{R(1-\beta^2 \cos^2\theta)} \quad (1)$$

where $\beta=v/c$. The peak fields occur at $\theta=\sin^{-1}(\beta\gamma)$, however, since the radiation is a spherical wave centered at $R=0$, there is no uncertainty in its position of origin. Note that it takes a finite time for the Coulomb fields to propagate along the surface of the conductor inside the radius R .

It has been suggested that, since the Fourier component of wavelength λ of the Coulomb fields of a relativistic particle in vacuum extend out a distance $\sim\gamma\lambda$ perpendicular to the velocity vector, there would be an uncertainty of this amount in the position of origin of the photon produced at a boundary. Further, it is incorrectly suggested that this will limit the resolution of OTR images to $\gamma\lambda$. The above discussion of Figure 1 shows that the presence of a boundary modifies the Coulomb fields in such away as to confine them inside the sphere whose boundary contains the radiation fields.

Another misunderstanding arises in connection with the concept of "formation length". The terminology is misleading because it refers to the distance along the z -direction in Figure 1 over which the radiation fields on the hemisphere at $R=ct$ remain in phase with the Coulomb fields centered on the charge q . When the charge has traveled a distance $Z \sim \gamma^2\lambda$, the radiation fields begin to get ahead of the particle fields. Note that the relative phase of the Coulomb fields, where they intersect the hemisphere, varies as a function of θ , thus the "formation length" is a function of θ , with maximum value at $\theta=0$. The formation length does not apply to backward OTR.

This characteristic length Z , associated with the phase between a particle field and co-moving radiation, is essentially the same as is found in the case of undulator and free electron laser radiation. It *does not* refer to a distance over which a photon is supposedly "formed" and therefore *cannot* be a basis for suggesting that OTR is subject to a depth of field limit to resolution similar to the synchrotron radiation depth of field problem discussed below.

Figure 2 shows the ratio of radiated OTR intensity per unit frequency contained inside a cone of half-angle θ_{\max} to the intensity integrated over the entire hemisphere. This ratio is plotted versus θ_{\max} in units of $1/\gamma$ for two energies of electrons, 1 and 10 GeV. Figure 2 demonstrates that, even for ultra relativistic electrons, a substantial portion of the OTR occurs at angles $\theta \gg 1/\gamma$; therefore the concept of a sharply limited angular distribution of order $1/\gamma$ and an associated "self-diffraction" effect is *not valid*.

B. Diffraction Limit of OTR Images

We have just discussed how the OTR production and its characteristic properties don't create any strange resolution limitations. Now we will summarize the result of a calculation of diffraction of OTR by a lens which focuses a spherical OTR wave front to a Gaussian image point on the optical axis of an optical system at a distance f from the aperture of radius a of the lens. The distance from the axis in the image plane is r , as shown in Figure 3. A point in the image plane at r subtends an angle $\theta = \sin^{-1}(r/f)$. As described in Reference [6], we have used standard scalar diffraction theory, assuming $f \gg a$, and $a \gg \lambda$; however, we replaced the usual constant pupil function with one with the angular behavior of E_θ of Eq (1), where now θ of Eq. (1) becomes α in Figure 3.

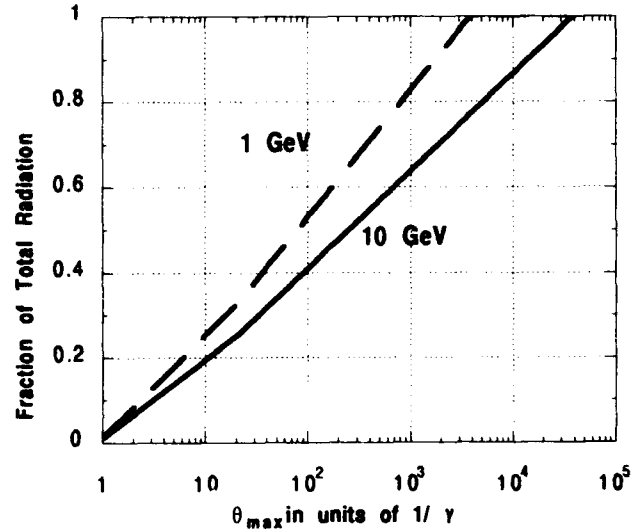


Figure 2. Fraction of total OTR radiation per unit frequency contained in cone of half-angle θ_{\max} as a function of θ_{\max} , in units of $1/\gamma$, for 1 and 10 GeV electrons.

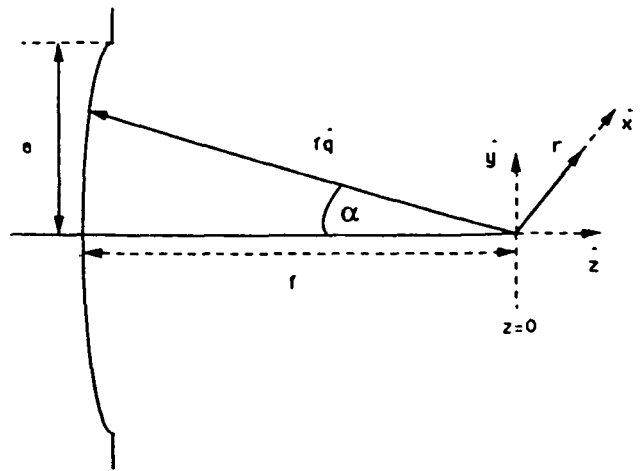


Figure 3. Diffraction of converging spherical waves at a circular aperture. Image plane is at $z=0$.

Figure 4 shows the results of the diffraction calculation for OTR, i.e. the diffracted amplitude of a point source imaged at $z=0$ in Figure 3 as a function of $x=ka \sin \theta$. For comparison, we show the standard plane wave diffraction result for a constant pupil function. Figure 4a is for the case of an aperture angle $\alpha_{\max} = 1/\gamma = 0.01$, while Figure 4b is for the case of $\alpha_{\max} \gg 1/\gamma$ and is valid for any value of γ . We see that when $\alpha_{\max} = 1/\gamma$, the diffraction is very close to the standard diffraction pattern, while it is only slightly broader when $\alpha_{\max} \gg 1/\gamma$, and resembles an apodized diffraction pattern. Therefore OTR diffraction limits are almost the same as the standard plane wave diffraction, i. e. this calculation shows that self-diffraction *does not* significantly alter the resolution of OTR images.

III. Comparison of OTR and synchrotron radiation

The properties of SR are summarized in Reference [8]. For the purpose of comparison to OTR, we will summarize those aspects of SR which affect the resolution of beam profiles imaged in SR. First, SR is formed at every point on the orbit in a bending magnet, therefore a horizontal limiting aperture is required to limit the length of the orbit which is imaged. Secondly, SR is more narrowly directed than OTR for frequencies $\omega < \omega_c$, the critical frequency. In contrast, the OTR radiation pattern is essentially independent of frequency. For an orbit of radius ρ and observed arc length $s=\rho\theta$, there is an apparent increase of the source width in the horizontal plane, which is

$$\Delta = \rho\theta^2/2 = s^2 / 2 \rho. \quad (2)$$

The diffraction limit to the resolution is

$$\delta x \sim \lambda/\theta. \quad (3)$$

Equating Eqs. (2) and (3) gives an optimum angle $\theta \sim (\lambda/\rho)^{1/3}$ which minimizes diffraction and depth of field distortion. Even the apparent beam size in the direction perpendicular to the orbit is increased by the depth of field. In practice, the vertical aperture dimension is chosen to match the natural opening angle of SR and x-ray wavelengths are used to increase the resolution. Since OTR is formed at the planar interface of the radiating foil, it does not suffer from the depth of focus problem and the aperture of the imaging system can be made large enough to obtain the required diffraction limited resolution in accordance with Figure 4.

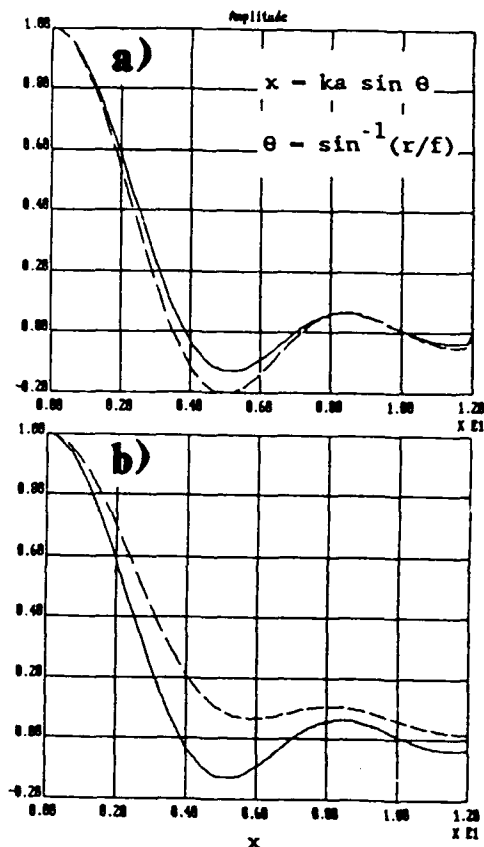


Figure 4. Comparison of standard (solid curve) and OTR (dashed curve) diffraction amplitudes for: a) aperture angle $\alpha_{\max} = 1/\gamma$ and b) $\alpha_{\max} \gg 1/\gamma$.

IV. REFERENCES

- [1] R. B. Fiorito et al., *Proc. 6th Int. Conf. on High Power Beams*, Kobe, Japan, 1986.
- [2] D. W. Rule, *Nucl. Instr. and Meth. B24/25*, 901 (1987).
- [3] R. B. Fiorito, D. W. Rule, J. S. Ladish, S. E. Caldwell, S. G. Iverson, and X. K. Maruyama, *Proc. European Particle Accel. Conf., June 1988, Rome*, p. 1078, Vol. 2 (World Scientific, New Jersey).
- [4] A. H. Lumpkin, R. B. Fiorito, D. W. Rule, D. H. Dowell, W. C. Sellyey, and A. R. Lowrey, *Nucl. Instr. and Meth. A296*, 150-158 (1990).
- [5] L. Wartski et al., *J. Appl. Phys.* 46, 3644 (1975).
- [6] D. W. Rule and R. B. Fiorito, p. 315, *AIP Conf. Proc. NO 229, "Accelerator Instrumentation"*, Batavia, IL 1990, Elliot S. McCrory, Ed. (AIP 1990).
- [7] K. T. McDonald and D. P. Russell "Methods of Emittance Measurement", *Proc. Joint US-CERN School on Observation, Diagnosis and Correction in Particle Beams*, Capri, Italy, October 20-26 1988.
- [8] S. Krinsky, M. L. Perlman and R. E. Watson, "Characteristics of Synchrotron Radiation and of Its Sources", *Handbook on Synchrotron Radiation, Vol. 1A*, Ernst-Eckhard Koch, Ed. (North Holland 1983).

Beam Emittance From Coherent Cherenkov Radiation in a Solid Dielectric*

R.D. Richardson[†] and R.C. Platt[†]

Science Applications International Corporation, Albuquerque, New Mexico
and

C.E. Crist[†]

Sandia National Laboratories, Albuquerque, New Mexico

Abstract

We report experimental results of a technique for direct measurement of the emittance in high energy beams. This technique is analogous to the well known "pepper pot" masking approach, but with no upper limit on particle energy. Single shot emittance profiles were obtained on the 10 kA, 4 MeV Sandia National Laboratories' electron Recirculating Linear Accelerator showing agreement with theory and with alternate emittance measurements. Coherent (i.e., not strongly scattered or diffused) Cherenkov radiation from a flat, transparent, range-thin dielectric foil was split by an array of mirrors in order to view the emission profile up to a divergence angle of 70°. The mirrors were imaged by a distant telescope attached to an intensified, 2 ns video framing camera. The relative intensity profiles of the multiple images were unfolded using the properties of classical Cherenkov emission and geometric optics to obtain directly, without precise knowledge of other beam parameters, the transverse velocity distribution in the viewing plane. In our case the rms emittance was directly proportional to the product of the beam diameter and the transverse velocity spread. This and prior research efforts indicate applicability over a wide range of high energy beam parameters.

I. INTRODUCTION AND BACKGROUND

Understanding the transport properties of high current (several kA), high energy (several MeV) electron beams is complicated by difficulties in experimental measurement of the beam phase space parameters. Several techniques¹ based on apertured masks have been developed that work well with repetitively pulsed or cw beam sources. However, the particle range in the mask material must be small compared to the working aperture size and the beam transverse temperature must be low enough to avoid collimation errors.

Our research into Cherenkov radiation based emittance measurements was motivated by the need for a diagnostic which could potentially operate at energies into the 100 MeV range and beyond, provide local measurements of emittance with nanosecond time resolution, and be minimally perturbing to the beam. We also expected to encounter difficult conditions such as plasma backgrounds, rotating hollow beams, and beams with large amplitude collective instabilities. In non-fluorescing materials Cherenkov emission dominates other radiation processes such as bremsstrahlung and transition radiation and has a time

response on the order of the particle transit time through the material. For range-thin converter foils there is minimal perturbation to the beam. Transparent FEP Teflon material was chosen for study due to its excellent performance as an optical Cherenkov radiator, its availability in large area thin films, and its relative ease of mechanical workability. The optical emission in the range of 400-700 nm from 2 mil thick foils exhibited strong peaking at the nominal Cherenkov angle, time dependence that tracked the beam current, and no evidence of fluorescence or radiation darkening. These results were obtained over a range of beam current densities from 1kA/cm² to 20kA/cm² and pulse lengths from 20 to 50 ns.

The emittance measurements were performed on the SNL Recirculating Linear Accelerator (RLA) injector in support of an ion focused regime (IFR) transport experiment. The RLA injector, referred to as IBEX, nominally produced a 10 kA, 4 MeV, 25 ns electron beam with a 1-2 cm radius at the measurement point. Emittance data were collected after 2m and 5m of linear transport along the ion focusing channel. These data were in good agreement with theoretical predictions of the emittance growth and also with emittance estimates obtained from a vacuum expansion technique. While Cherenkov witness plates have been used in other laboratories as optical current meters or as beam profile diagnostics², to the authors' knowledge, this represents the first emittance diagnostic for an IREB based entirely upon the directional properties of Cherenkov radiation.

II. DESCRIPTION OF THE DIAGNOSTIC

A. Essential properties of Cherenkov radiation

For a charged particle traveling at velocity v in a straight line through a dielectric medium with refractive index n , Cherenkov radiation is emitted in a thin cone centered on the trajectory with opening angle θ_c given by $\cos \theta_c = 1/\beta n$, where $\beta = v/c$ is the usual relativistic factor. The basic properties of this radiation are well described in the literature^{3,4}. The radiation power per kiloampere of current per millimeter of dielectric thickness in the visible spectrum $\lambda_1=400\text{nm}$ to $\lambda_2=700\text{nm}$ is found to be $P \approx 58 \text{ kW/kA-mm}$, where βn was chosen to be 1.4. Since this power is radiated into a small solid angle, the observed intensities can be quite strong even with very inefficient light collection optics.

Inside a linear, isotropic optical medium the angular thickness of the Cherenkov cone is determined mainly by Coulomb scattering and by the optical dispersive properties of the dielectric. Variation of θ_c due to slowing down of the particle may be neglected for range-thin converters. In this case it can be shown that the Cherenkov cone is broadened by less than a few milliradians in the visible spectrum for most optical materials. Now consider the radiation pattern, still within the dielectric, produced by a monoenergetic beam

* Work supported by Sandia National Laboratories, The U.S. Navy, the U.S. Air Force, and DARPA

[†] Present address Superconducting Super Collider Laboratory, Dallas, Texas

having a transverse temperature characterized by a thermal velocity $\beta_{\perp} = v_{\perp}/c$. We will use the following approximations: $\beta_{\parallel} = 1$ and $\tan \phi_i = \beta_{\perp i} / \beta_{\parallel} = \phi_i$, where the component $\beta_{\perp i}$ is the instantaneous transverse speed for the i th particle in the beam as the particle passes through the converter. Hence, there is a one-to-one correspondence between the distribution function of transverse velocities and transverse angles. The accuracy is better than two percent for $\beta_{\perp} < 0.2$. Since the Cherenkov cone angle is the same for all particles, the angular distribution of Cherenkov radiation intensity in a plane perpendicular to the beam cone will be directly proportional to the beam transverse velocity distribution. This simple result is the basis for the emittance diagnostic.

Outside the dielectric the physical and geometric optical properties of the converter will change this simple proportionality relation. The main distortion of the radiation distribution in the laboratory is due to simple geometric optics effects. Figure 1 illustrates the geometry by considering the ray optics of an optically flat slab converter.

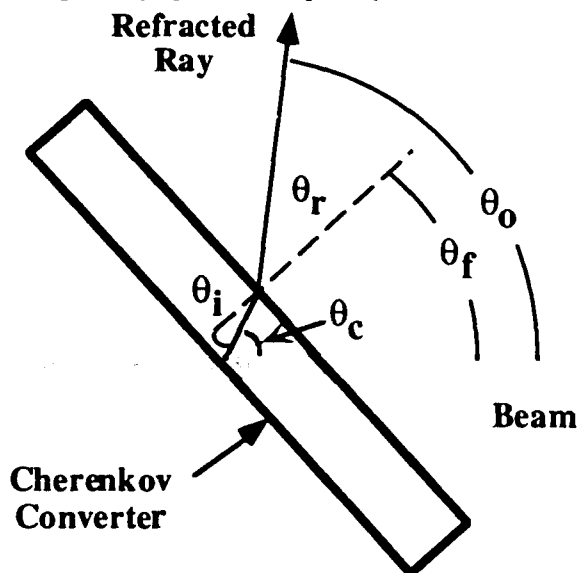


Figure 1. Basic geometry of a slab converter. θ_c , θ_i , θ_r , θ_f , and θ_o are the Cherenkov, internal incidence, external refracted, foil tilt, and observation angles, respectively.

The converter plane is shown tilted with respect to the particle trajectory to include this option explicitly in the analysis. Using Snell's law the observed angle of emission with respect to the beam axis is related to the angle of emission in the dielectric by the expression

$$\theta_o = \theta_r + \sin^{-1}[n \sin(\theta_c - \theta_r)], \quad (1)$$

where θ_o , θ_f , and θ_c are the observation, converter plane tilt, and Cherenkov angles, respectively. Internal reflection can become significant as the internal angle of incidence approaches the total reflectance angle given by $\theta_{\max} = \sin^{-1}(1/n)$. FEP Teflon has the desirable property of a low index of refraction of 1.345 which yields $\theta_c = 42^\circ$ and $\theta_{\max} = 48^\circ$. For ideal observation conditions the foil is tilted such that $\theta_c = \theta_f$ and the observation angle is equal to the principal Cherenkov angle, and this angle is normal to the foil surface. We use the term principal Cherenkov angle to refer

to the angle of emission for a particle in the beam having $\beta_{\perp i} = 0$. In the converter, by our approximations, the average angle of emission in the plane perpendicular to the beam cone is always the principal angle. The intensities must also be corrected for internal reflection effects. Cherenkov radiation is polarized with the polarization vector normal to the cone surface and to the direction of propagation. Hence, the p-wave transmission reflection coefficient given by

$$R = \frac{\tan^2(\theta_r - \theta_i)}{\tan^2(\theta_r + \theta_i)},$$

where θ_i is the internal angle of incidence and θ_r is the external angle of refraction, is appropriate. Summing the infinite series for total forward transmitted power yields

$$P_{\text{forward}} = \frac{P_0}{1 + R}. \quad (2)$$

B. Measurement technique

The method chosen to collect the intensity profiles was to image the converter foils at different angles and use the intensity ratio of the images to unfold the Cherenkov angular distribution inside the dielectric. Stray light sources such as intense sparks can easily be identified in this manner. Data acquisition was via a fast gated, intensified video camera with computer based image analysis. In order to obtain an angular discrimination of a few mrad the camera(s) must be placed at a large distance D from the converter such that $[2a+d]/D < 10^{-2}$, where d is the effective camera aperture size. For our experiments $D=30\text{m}$. The Cherenkov radiation lobe in the viewing plane was split into six different angular slices by using flat mirrors placed near the converter foil. Figure 2 shows the mirror and converter foil layout for the IBEX RLA measurements. The mirror holder consisted of an aluminum block with interference fit grooves machined at 10° intervals to correctly position each mirror in the array. The entire arrangement fitted inside a standard 8 inch vacuum cross. A 10 inch lucite plate served as the vacuum window.

Using a 600 mm focal length $f/5.6$ lens on the camera gave an angular resolution for this system of about 5 mrad which is on the order of the diffraction modified Coulomb scattering⁶ limit of the 2 mil FEP Teflon foil and is much less than the expected >200 mrad divergence of the refracted Cherenkov lobe.

C. data analysis

The corrected Cherenkov intensity profile in the dielectric was found, and then the data were fit to a Gaussian transverse velocity distribution. The Gaussian assumption was not necessary, but it was an excellent approximation in our case. Solving equation (1) for the emission angle θ_c^j in the dielectric in terms of the observation angle θ_j yields

$$\theta_c^j = \theta_r + \sin^{-1} \left[\frac{\sin(\theta_j - \theta_r)}{n} \right].$$

The intensity must be corrected for refractive broadening in the viewing plane given by differentiating equation (1)

$$\frac{d\theta_j}{d\theta_c^j} = \frac{n \cos(\theta_c^j - \theta_r)}{[1 - n^2 \sin^2(\theta_c^j - \theta_r)]}.$$

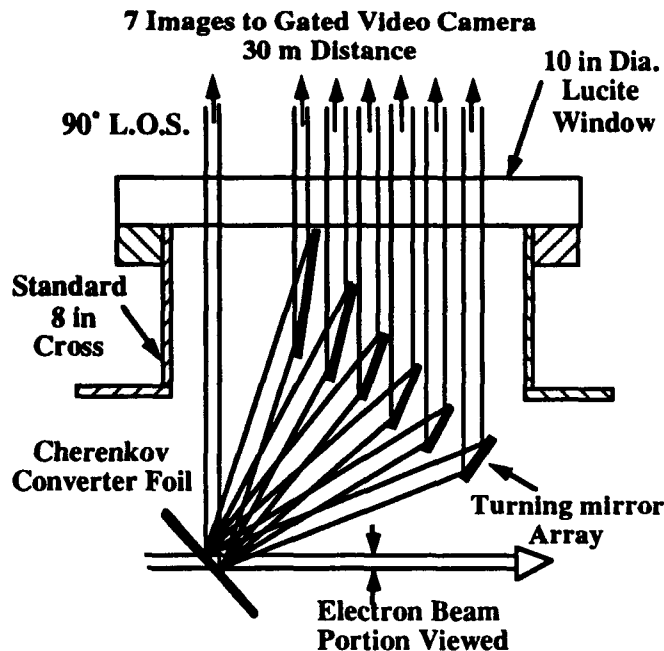


Figure 2. Cherenkov converter foil and turning mirror array arrangement shown as used inside the 8 in vacuum cross. Foil tilt angle was 42° from normal to the beam.

Including the effect of internal reflection from equation (2) the relative intensity I_j at the emission angle ϕ_j is related to the measured intensity F_j at the corresponding observation angle by

$$I_j = F_j \frac{d\theta_j}{d\theta_c} (1 + R_j) .$$

Fitting a Gaussian distribution to the I_j data yields β_{\perp} .

Transverse emittance ϵ_x may be defined to be $1/\pi$ times the area in xx' phase space, where x is a transverse coordinate and $x' = dx/dz$ is the conjugate angle. Using the definition of rms emittance⁵ it can be shown, for beams of radius a having azimuthal symmetry, that $\epsilon_{rms} = 2a\beta_{\perp}$.

III. EXPERIMENTAL RESULTS

Intensity profiles were taken after various lengths of IFR transport on IBEX. The Gaussian fit results are shown in Figure 3 for both 2m and 5m. The values of β_{\perp} obtained were 0.11 and 0.17, respectively. The combined error in this measurement technique is less than ten percent. For comparison the two intensity curves are normalized to the same peak value. Measurements based upon a vacuum expansion technique⁷ gave $\beta_{\perp} = 0.15$ after 5m of transport. Calculations using the beam envelope equation⁸ with the measured plasma channel densities and beam radii gave $\beta_{\perp} = 0.18$ for the 5m case.

The main problem encountered in this diagnostic was background light in the chamber due to diffusely reflected Cherenkov light seen as higher than baseline intensities between the mirrors. As the emittance became larger this problem became more noticeable. While not tested on our experiment, it should be straightforward to reduce the background levels using baffles and low reflectance coatings.

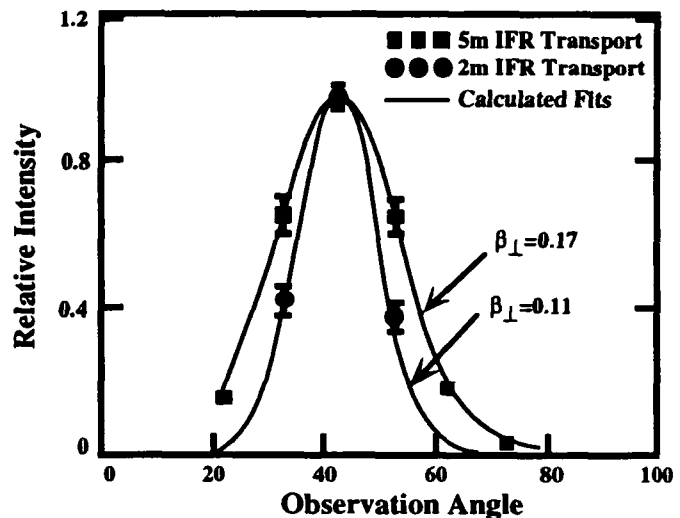


Figure 3. Gaussian fit to Cherenkov intensity profile data for the cases of 2m and 5m IFR transport.

IV. CONCLUSIONS

The angular dependence of Cherenkov radiation from range-thin, transparent, flat dielectric foils can be used to measure the transverse velocity distribution, and therefore the emittance, of a warm IREB. This diagnostic is capable of giving the local beam temperature for each point on the beam/foil intersection plane to an accuracy better than ten percent without detailed models or simulations of the beam transport conditions. Time resolved data is generally necessary. There is essentially no upper limit to the beam particle energy in this application. We have completed a basic feasibility study and a series of experiments culminating with the test of a fully operational emittance meter on the IBEX RLA experiment. Results are in agreement with theoretical predictions and an alternate measurement technique. There are few difficulties involved in fielding Cherenkov diagnostics on IREB machines. The fundamental limit to the angular resolution is diffraction modified Coulomb scattering.

Acknowledgment

Dr. Gordon Leifeste developed the fast gated video cameras and image analysis system and we would like to thank him for the use of the system in these experiments.

V. REFERENCES

- [1] C. Lejeune, J. Aubert, *Advances in Electronics and Electron Physics: Charged Particle Optics*, p159, A. Septier, ed., Academic Press, New York, 1983.
- [2] M. Buttram, R. Hamil, *IEEE Trans. Nucl. Sci.* **30**, 2216 (1983).
- [3] J.V. Jelley, *Cherenkov Radiation*, Pergamon Press, New York, 1958.
- [4] J.D. Jackson, *Classical Electrodynamics*, Wiley, New York, 1962.
- [5] P.M. Lapostolle, *IEEE Trans. Nucl. Sci.*, **NS-18**, 1105 (1971).
- [6] R.G. Dedrick, *Phys. Rev.*, **87**, 891 (1952).
- [7] K.W. Struve, F.W. Chambers, J.C. Clark, *IEEE Trans. Nucl. Sci.*, **30**, 1991 (1985).
- [8] H.L. Buchanan, *Phys. Fluids*, **30**, 221 (1987).

A. Wire Plane Construction- Strung Wire Design

The strung wire design uses conventional technology as demonstrated by the original TSEM [1] to create a wire plane by stringing 30 titanium wires (50 μm diameter) in a tightly tolerated pattern. The wires are strung at a center to center spacing of 125 μm in a central 1.9 mm wide region (16 wires) and at a center to center spacing of 250 μm in two 3.0 mm wide regions (7 wires each) to either side of the central region. This combination provides good resolution at the center and a larger outer area of monitor sensitivity for initial beam steering. The pattern is maintained by a machinable ceramic base plate (22.9 cm x 7.6 cm by 6.4 mm thick) into which two "V" shaped arrays of stainless steel pegs are inserted (see fig. 1). Each wire end is bent by 45 degrees around a peg and held in place by anchoring screws placed about the periphery of the ceramic base plate. The ends of the wires are crimped in standard stainless steel wiring lugs. One lug on each wire is connected directly to the appropriate anchoring screw while the other is connected to an anchored constant force (95 g/cm) spring. Each wire is sized to stretch the attached spring 2-5 mm to allow for elongations due to beam heating (see *Beam Heating* section). The guide hole patterns for alignment pegs are numerically machined in the ceramic base plate to a center to center tolerance of $\pm 10 \mu\text{m}$. A central hole in the ceramic base plate allows the proton beam to intersect the wires without interference.

Improvements over the previous strung wire design include easier alignment of the wires during the assembly process due to the closely machined ceramic base plate (versus the loose peg and template method used previously) and the use of crimped lug wire connections rather than the sometimes unpredictable spot welding method. This is evidenced by the short assembly time required for a new strung wire plane (typically 8 hours for stringing 30 wires).

This wire plane design results in individually tensioned 50 μm diameter titanium wires with a minimum center spacing of 125 μm . Observed error under microscope reveals an estimated positional error of $\pm 10 \mu\text{m}$ or 8% of the nominal wire spacing. The design is relatively robust and should not degrade in the harsh targeting environment.

B. Wire Plane Construction- Photoetched Design

The photoetched design utilizes exact photoetching technology to create a wire plane by chemically etching a 30 wire pattern from a 50 μm thick titanium (3A1-2.5V) foil bonded to a 7.6 cm by 7.6 cm by 4.8 mm thick ceramic support plate (see fig. 2). The pattern features signal read out pads around the periphery of the backing plate. Electrical signal connections to the wires are made by spot welding ceramic coated copper wires directly to the exposed titanium pad surfaces. The wire spacing and diameters are identical to those of the strung wire design.

The etching process was developed by Max-Levy Autograph of Philadelphia [2]. Initially, the 30 line pattern is etched halfway through the thickness of a complete piece of titanium foil. The partially etched foil is then bonded to the alumina backing plate, etched side down, with a sodium silicate inorganic binder. Care is taken to keep the foil flat over the central hole in the backing plate. After curing the bond, the delicate wire pattern is etched into the remaining

titanium foil thickness from the unetched side. This leaves the wire pattern intact on the ceramic plate including the unsupported lengths of wires directly over the central hole. Finally, a Cotronics ceramic paint [3] is layered over the visible wire pattern leaving only the access pads on the periphery and the wires in the central region exposed.

The final result is a one piece TSEM wire plane with 50 μm diameter titanium wires on a minimum center spacing of 125 μm . Observed error under microscope reveals an estimated positional error of $\pm 15 \mu\text{m}$ or 12% of the nominal wire spacing. Most of this error is due to a slight bowing of the wires over the central unsupported region. The bowing is believed to be caused by the extruded titanium foil stress relieving during the removal of much of its bulk during the etching process. In fact, bowing seems to be minimized when the extrusion marks apparent on the unetched foil are oriented perpendicular to the etched wire direction.

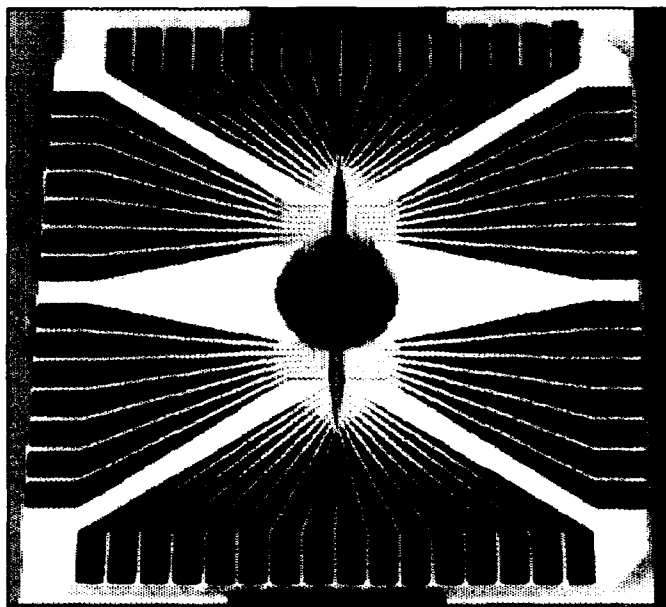


Figure 2. Photograph of photoetched wire plane design before applying ceramic over coat.

C. Vacuum Vessel Construction

Both designs utilize similar vacuum vessel designs consisting of two 33.7 cm diameter conflat type vacuum flanges. The flanges are modified to provide an enclosed area between the flanges 25.4 cm in diameter and 4.4 cm in depth. The chamber is equipped with 38 μm thick titanium foil beam windows. Electrical signals from the enclosed wire planes are passed from this interior space to atmosphere via ceramic coated copper wire and a conventional electrical feedthrough. The vessel is pumped with an 8 l/s ion pump attached permanently to the flange assembly. All materials used in both wire plane designs are vacuum compatible metals (titanium, 304 stainless steel and 6061 aluminum) and inorganic ceramics.

Two wire planes are mounted (one horizontally and one vertically) to the interior surface of one of the vessel flanges (see fig. 3). The mounting apparatus consists of four posts to capture and align the two wire planes to each other without over constraining the planes from thermal expansions and

A 10 μm Resolution Secondary Emission Monitor for Fermilab's Targeting Station

P. Hurh, S. O'Day, R. Dombrowski, and T. Page
Fermi National Accelerator Laboratory*, Batavia, Illinois 60510

Abstract

Improvement in focusing the proton beam onto the antiproton production target necessitates the development of a higher resolution beam profile monitor. Two designs for the construction of a multiwire profile monitor grid are presented. The first is a conventional strung and tensioned Ti wire design. The second is a photo etched Ti grid of wires bonded to a ceramic substrate. Both have a central wire spacing of 125 μm . The completed beam profile monitors are designed to operate in a 120 GeV beam pulse of 5×10^{12} protons with a 1.5 μs duration and will be installed in late 1993.

I. INTRODUCTION

Efficient antiproton production relies greatly on the precision with which a highly focused proton beam can be placed on target. Antiprotons are produced at the Antiproton Source Target Station by bombarding a 10 cm nickel target with a bunched proton beam from the Main Ring. The present intensity of this beam is 2.1×10^{12} protons per pulse and this will rise to 5.0×10^{12} protons per pulse with the future Fermilab upgrade to the Main Injector. At present, the targeting station utilizes a multiwire Target Secondary Emission Monitor (TSEM) with 250 μm spacing between wire centers to measure the targeted beam's profile and position [1]. This original monitor's design was based on a predicted rms proton beam size of 400 μm . With the present rms beam size at target (averaged over both horizontal and vertical planes) equal to 160 μm and smaller beam sizes expected in the near future, it is obvious that a higher resolution monitor is needed to ensure that the proton beam interacts with enough wires so that its width may be determined accurately. In addition, with the advent of increasing beam intensity, great care must be taken to ensure that higher resolution TSEM wires do not melt from their interaction with the proton beam.

II. DESIGN CRITERIA

Ideally, the wire size and spacing of a new refined resolution TSEM should be minimized while still ensuring the survivability of the wire planes in the TSEM's harsh operating environment and during the TSEM's delicate assembly process. In order to accurately fit a Gaussian distribution and determine the proton beam distribution's mean and sigma in both planes, the beam must interact with at least 4 wires. This implies a wire center spacing equal to at least the average beam rms size of 160 μm and an individual wire diameter considerably less than that is desired.

The TSEM's operating location is just upstream (approximately 25 cm) of the target. This results in a highly

radioactive environment. The TSEM must be constructed of inorganic materials resistant to high radiation doses (>5000 rad/hour) and resistant to the high temperatures expected from the beam heating of the TSEM wires (see *Beam Heating* section).

In addition, for optimum secondary emission effects, a vacuum environment for the wires and their associated electron collection foils is required. This demands use of vacuum compatible materials and design techniques to achieve a vacuum pressure on the order of 10^{-7} torr.

III. CONSTRUCTION

Two new designs of the TSEM have been developed to offer the needed resolution and satisfy the design criteria. Both designs are similar in all respects except for the method of wire plane construction. One design uses conventional strung wire technology while the other utilizes new photoetching techniques. Both result in 50 μm diameter wire planes with 125 μm wire centers, essentially doubling the resolution of the present TSEM.

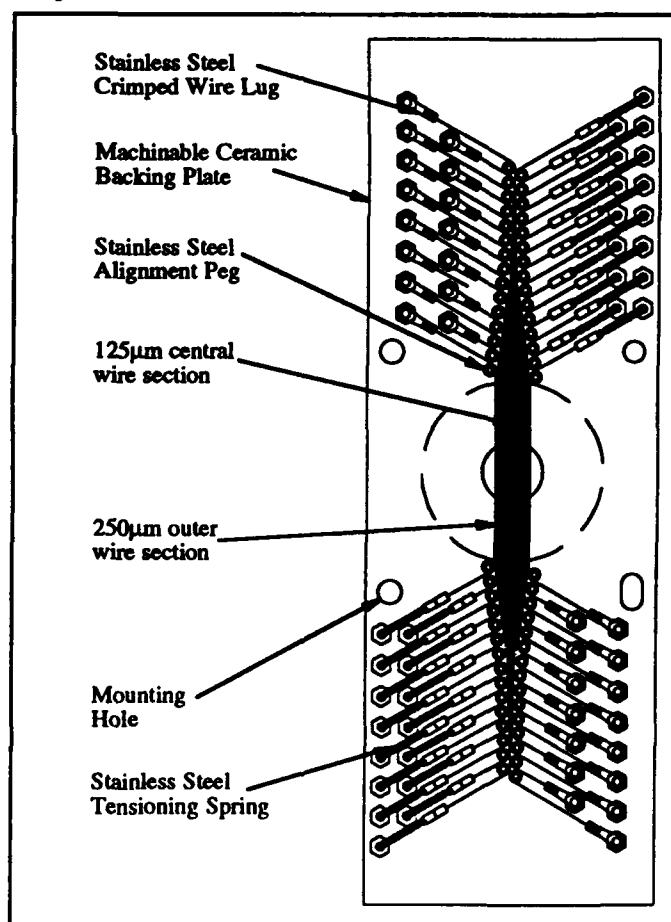


Figure 1. Schematic of new strung wire plane design.

*Operated by the Universities Research Association under contract with the U.S. Department of Energy

contractions. Surrounding the individual wire planes are 38 μm thick titanium electron collection foils to collect the electrons emitted from the struck wires and close the signal path to the integrating electronics. Mounting mechanisms are similar for both design types.

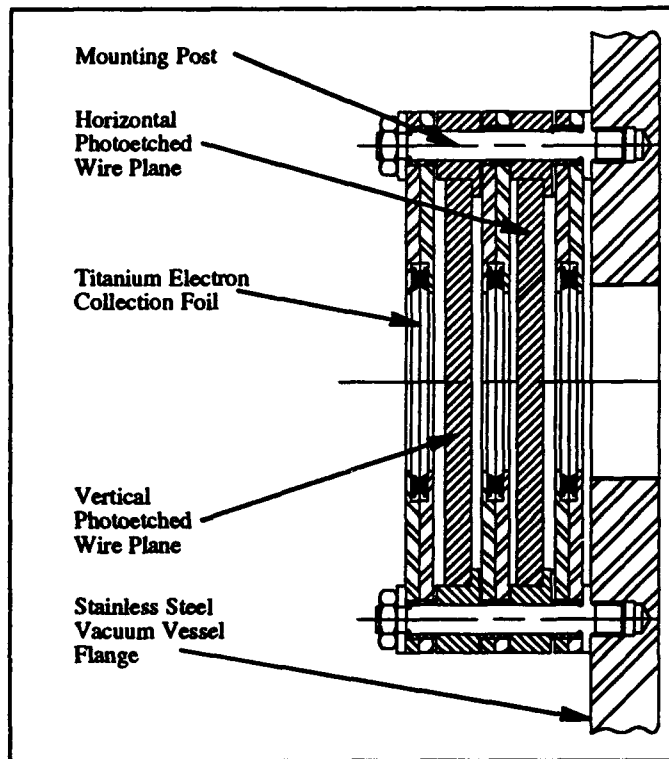


Figure 3. Schematic of wire plane mounting apparatus.

IV. BEAM HEATING OF WIRES

Heating of the TSEM's wires by the proton beam is important to investigate for two reasons. Overheating of the wire (near the wire material's melting point) could damage the wire integrity and thermal expansions could cause a wire to bow and short to a neighboring wire.

The instantaneous peak temperature of the section of wire that actually interacts with the proton beam is calculated by estimating the amount of energy deposited in the small volume of wire exposed to beam. If the critical incoming proton beam parameters are assumed to be equivalent to the current predictions of beam on target characteristics after the Main Injector comes on line several years in the future (5×10^{12} protons per pulse, 0.015 cm rms beam size), then for a 50 μm diameter titanium wire ($dE/dx = 1.50 \text{ MeV/g/cm}^2$), the instantaneous peak temperature can be calculated to be 1270°C.

Assuming a logarithmic transient cooling curve of the form e^{-U^2} and assuming the material and geometry are of the photo etched design, then after 1.5 sec (anticipated duty cycle of future Main Injector beam on target) the temperature will cool, by conduction only, to approximately 25°C. After several pulses the wire will most likely only cool to the temperature predicted by averaging the total heat input per pulse over the entire duty cycle, in this case, approximately 350°C.

The above calculations, however do not take into account that some of the energy transferred from the protons to the electrons in the wire material by Coulomb scattering will exit the wire with the higher energy electrons escaping the wires. Rough calculations show that this 'lost' energy is on the order of 51% of the total energy deposited normally calculated for titanium wire [4]. Taking this into account, instantaneous peak temperatures of central TSEM wires should be no more than 620°C and long term equilibrium temperatures should average around 170°C. Since the melting temperature of titanium is 1670°C; damaging the wire material by overheating is not a primary concern.

If we assume an average equilibrium temperature of 130°C as predicted above, then the elongation of the 1.6 cm long exposed section of wire (photoetched, untensioned design) is approximately 5.3 μm . If we assume a circular shaped bow in the wire due to this elongation, the amount of sag is 18 μm , more than enough to touch a neighboring wire. This situation should be addressed in future design modifications.

V. CONCLUSIONS

Nine photoetched TSEM wire planes have been constructed successfully. All specimens exhibit a high degree of precision wire alignment in a compact, radiation hard form. The wire planes have undergone electrical continuity, conductivity and vacuum compatibility testing without mishap. Future development of this photoetched design will concentrate on further strengthening the sodium silicate bonding techniques and producing a method to tension the unsupported wire lengths if found necessary. This method of wire plane construction offers a simple, radiation hard, one piece design coupled with delicate high precision wire placement.

Two strung wire TSEM wire planes are presently being constructed at Fermilab. The highly accurate wire placement and robust design of this construction technique have been proven through the successful completion of a six wire sample wire plane. Future development of this strung wire design is limited to modifications to improve the ease of assembly. This method of wire plane construction offers precision placed, individually tensioned wires coupled with a durable, radiation hard design.

Both wire plane designs will be mounted in TSEM vacuum vessel assemblies and an installation at the Antiproton Source Target Station will take place later this year. The designs will offer the high resolution and reliability necessary to satisfy the targeting effort requirements not only during the continuing Fermilab collider run but also into the Main Injector era.

VI. REFERENCES

- [1] J. Krider & C. Hojvat, "A Multiwire Secondary Emission Beam Profile Monitor With 20 μm Resolution," *Nuclear Instruments and Methods in Physics Research*, A247, pp. 304-308 (1986)
- [2] Max Levy Autograph, Inc., 220 W. Roberts Avenue, Philadelphia, Pennsylvania, 19144-4298, USA.
- [3] Cotronics Corporation, 3379 Shore Parkway, Brooklyn, New York, 11235, USA.
- [4] J. Bosser, et al., "The Micron Wire Scanner at the SPS," *European Organisation for Nuclear Research, CERN-SPS Division*, CERN SPS/86-26 (MS), December (1986).

Construction of a High Resolution Electron Beam Profile Monitor*

J. Norem, J. Dawson, W. Haberichter, W. Novak, L. Reed, X-F. Yang
Argonne National Laboratory, Argonne, IL, 60439, USA

Abstract

Bremsstrahlung from an electron beam on a heavy target can be used to image the beam profile using collimators and slits. The limiting resolution using this system is determined by Fresnel diffraction, and is $\sim \sqrt{\lambda d/2}$, where λ is the photon wavelength and d is determined by the linear dimensions of the system. For linear colliders this resolution could be a few nm. The highest resolution requires detectors which see only high energy, (small λ), photons, and this is accomplished by converting photons to pairs, and detecting Cherenkov light in a nearly forward angle with a CCD detector or streak camera. Tests are planned at the Argonne APS and SLAC FFTB.

I. INTRODUCTION

The next generation of linear colliders will require very small (1 - 100 nm) beam spots at the interaction point to produce significant luminosity, since the number of electrons which can be accelerated to high energy is limited by the available power, its cost, and the acceleration efficiency. Producing, maintaining and monitoring these spots will be difficult. [1]

We are building a bremsstrahlung beam profile monitor which uses nonimaging optics to measure beam position and density profile, ($\rho(y)$ or $\rho(y,t)$), at the final focus of a beamline or collider[2]. The ultimate resolution is roughly 5 - 30 nm, and 200 fsec, which should be sufficient to contribute to initial and final tune up, and online monitoring of beam position if active stabilization of seismic motions is required. Although the system is being developed using bremsstrahlung, backscattered photons from Compton scattering or beamstrahlung from e^+/e^- collisions could also be used.

The system, Figure 1, consists of a Bremsstrahlung radiator at the focus of the electron beam, a single sided collimator to produce a bremsstrahlung shadow, and a slit and detector system to measure the shape of the shadow edge. The diagnostic slit could be either tilted or parallel with the primary collimator. The sharpness of the shadow is inversely proportional to the size of the spot at the bremsstrahlung source. Shielding, and sweeping magnets, are not shown. Finally, the bremsstrahlung photons will be detected using a pair converter and Cherenkov radiator.

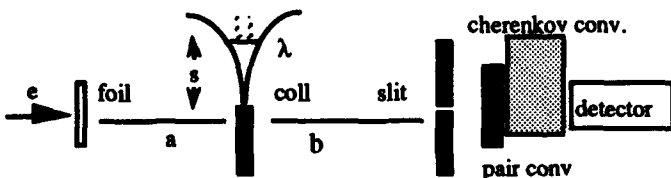


Figure 1. Bremsstrahlung radiator, single sided collimator, slit and detector.

*Work supported by the US Department of Energy, Office of High Energy and Nuclear Physics, Including Contract W-31-109-ENG-38

II. RESOLUTION

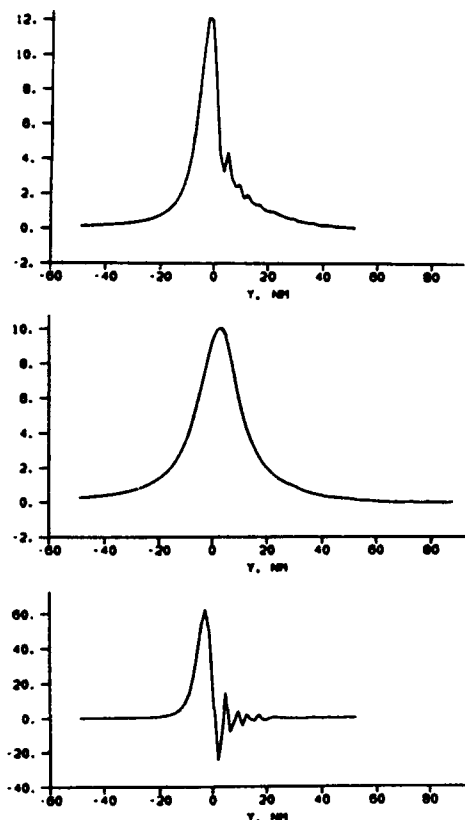
The ultimate resolution of this system is limited by Fresnel (circular wavefront) diffraction[3]. This limit can be approximated using Fraunhofer (plane wave) diffraction, by considering a virtual slit at the primary collimator location, where the virtual slit width, s , is such that the sagitta is equal to λ , the photon wavelength. If the source to collimator distance is a , the collimator to detector distance is b , and $b \gg a$, the expression for the sagitta $\lambda = s^2/2a$ gives the virtual slit width, $s = \sqrt{2\lambda a}$, (see Fig 1). The angular diffraction width is then λ/s and the limiting resolution at the foil is roughly $(\lambda/s)a \sim \sqrt{\lambda a/2}$, nearly the geometric mean of the beamline dimensions, (1 - 10 m), and the photon wavelength, ($\lambda \sim 10^{-16}$ m at 10 GeV). Improving the resolution requires reducing a , by moving collimators close to the target, or λ , by detecting the highest energy photons.

Accurate calculations require: 1) Fresnel optics, which is done for monochromatic light in most optics books, and 2) a complete photon spectrum which includes the actual detector acceptance function. The relevant spectra are bremsstrahlung, with $n_\gamma(y) \approx 1/y$, Compton scattering, with $n_\gamma(y) \approx \text{const}$, and $n_\gamma(y) \approx y^{-2/3} (1-y)^{1/3} e^{\kappa y/(1-y)}$, from beamstrahlung at the IP. Here $y = E_\gamma / E_{e,\text{max}}$, and $\kappa = 2/3Y$, and Y is the fractional energy lost to individual photons.[4] The acceptance of the detector has been evaluated using EGS4 and a more specialized monte carlo program which generates a bremsstrahlung spectrum, computes pair production and subsequently evaluates multiple scattering. The brems spectrum are shown in ref [2]. Integrating Fresnel diffraction patterns for the appropriate energy spectra gives the complete profile. This note defines a resolution function as the derivative of this sum of diffraction images, shown in Fig 2. This curve, which is nongaussian, is the effective shape of a beam at the bremsstrahlung radiator in the limit of a zero width slit at the detector.

An option for the bremsstrahlung detector is shown in Fig 1, with pair converter followed by Cherenkov radiator. Sweeping magnets may be required to reduce shower background. The number of Cherenkov photons detected should be on the order of 2000 / half width, which should be sufficient for the operation of a streak camera. Time resolution on the order of $\sigma = 200$ fsec should be obtainable with the Hamamatsu FESCA 500 streak camera[5], which should be able to examine structure within individual bunches. This resolution is only available with slit widths of 10 μm , which will be difficult.

Ionization of the bremsstrahlung radiator, motion of the target ions, multiple scattering, depth of focus, beam focusing by the plasma created in the radiator, and synchrotron radiation

by the primary electrons, should be detectable, and correctable, effects Multiple scattering and focusing should be small effects compared to the divergence of the primary beam. Synchrotron radiation should be detectable, at colliders, with fractional photon energy $Y=0.1$, but perhaps also at the FFTB as well, where $Y=0.002$. Ions will be focused by the beam, increasing the local density of the bremsstrahlung radiator, although this should be correctable.



Figures 2 Resolution functions for bremsstrahlung (top), beamstrahlung (middle) and Compton scattering (bottom) using possible linear collider conditions, ($E_e = 250$ GeV, $a = 10$ m, $b = 200$ m, $\theta = 2^\circ$). All are nongaussian

The thick foil in the beam will be a source of background in the experiment as well as an additional constraint on the shielding. In principle, since the emittance of the signal is so small, it should be possible to produce a reasonable signal/noise ratio, by moving detectors downstream to a more quiet environment.

III. COMPONENTS

The bremsstrahlung radiator will be thin, 0.1 mm foils. Possible materials would include Ta, W, Pt, U, and Au, all of which are sold in many thicknesses and sizes by Goodfellow Corporation[6]. Tungsten and tantalum have the highest heat of vaporization, which seems to be the best measure of their stability, but platinum, uranium or gold foils could also be useful. These materials would be locally destroyed on every pulse. Energy deposited in the foil due to dE/dx losses would be on the order of 0.6 mJ/pulse. This energy would be

sufficient to vaporize a hole 10 μm in radius in a tungsten foil. The foils would be moved after every pulse.

The collimators and slit edges have to be flat, and thick enough to stop the beam. Tungsten mirrors can be produced which are 3" in diameter, and optically flat, $\lambda/20 \approx (\sigma \approx 10\text{nm})$, for reasonable prices, with better surface quality possible at higher prices[7]. With a radiation length of about 0.31 cm, direct photons would be attenuated by 10^{-11} if they penetrate the collimator. Encoder motors or stepping motors are both sold which have setting errors of about $\sigma = 30$ nm, which should be sufficient. Finer motions can be achieved with piezomovers. Guard collimators, located in front of the primary collimator and slit, should be cooled.

The camera, shown in Figure 3 uses a Hamamatsu V4183U two stage, gated image intensifier which has single photon sensitivity, mechanically in contact with a Hamamatsu S3902 MOS linear image sensor[5]. Fiber optic exit and entrance windows permit high resolution. Measurements of single photons have shown that the resolution is very good, $\sigma \approx 25$ μm , depending somewhat on pulse height. The radiation sensitivity of this system has been tested and it should operate well in a 100 mR/hr environment. The manufacturer claims that the components should not be particularly sensitive to radiation damage.

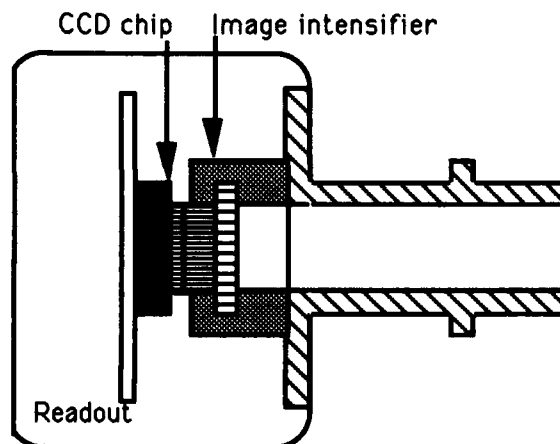


Figure 3. The camera.

The camera controller is a single width CAMAC module containing the circuitry for control and readout the CCD camera. Event In, a NIM level input, starts the cycle to read in the CCD. The video signal from the camera is buffered to an 8-bit analog to digital converter (ADC), which writes its output data into a 4K by 8-bit First In First Out (FIFO) memory. This memory can be written or read by the computer thru the CAMAC dataway. A crystal oscillator generates a clock (312.5 KHz) for the CCD readout and provides two other frequencies, 9.8 KHz and 76 KHz, which will be used for seismic sensing. An 8-bit status register keeps track of status conditions in the module as well as the condition of two NIM inputs. The status register can also be written or read from the computer.

The control computer, a 486 clone, uses LabWindows[8], and the code is written in C. It presently controls 8 encoder

motors, the printer and the camera. It will also control the seismic correction system and Ethernet communications when needed.

The collimators can be roughly aligned using transets and levels to about 100 μm . It is assumed that the slits can be opened and bremsstrahlung signals can be used to align the system from this point. For high precision measurements, seismic motions at the 50 - 150 nm level must be corrected. We plan to have a seismic correction system which can compensate these motions, and have ordered a Streckeisen STS-2 seismometer[9] which is very sensitive in the frequency range 0.1 - 10 Hz. The measured noise level of this device is two orders of magnitude below midcontinent nighttime ambient earth noise. Corrections could be made either on line with piezomovers, or off line by correcting the data.

IV. TESTS

The Argonne Advanced Photon Source (APS) is scheduled to be completed in 1995, and the electron/positron linac injector should be running in the summer of 1993. Parasitic bremsstrahlung from the positron production target can provide a useful test of the proposed system, because the electron beam energy is high enough to be detected (200 MeV), and high enough to produce a realistic shower background, and there seems to be space enough downstream of the positron linac to mount collimators, slits and detectors.

A more challenging test of the system would be to measure the properties of the $\sigma \approx 60$ nm beam spot at the SLAC/FFTB. The primary collimator would be located about 20 feet downstream of the dump line bending magnets and 28 m from the IP. In front of the primary single sided collimator would be a guard collimator system, consisting of two tungsten or tantalum blocks ground flat and spaced apart by 0.00025" - 0.001" with shims. The guard collimator would serve two purposes: minimizing beam heating and deflection of the primary collimator, and providing a "black" background against which the beam on target can be seen.

This system should permit measurements of the beam profile, $\rho(x,t)$, at the final focus, which might be used to study single or multibunch beam instabilities driven by wake fields, and possible nonlinearities due to beam optics. The high resolution should permit study of a variety of other effects, such as the Oide limit, where the $\sigma \propto e^{5/7}$ [1]

The technique should also be useful for plasma lens experiments where focusing is inherently nonlinear, due to inhomogenities in the transverse and longitudinal charge density, plasma response time, $1/\omega_p$, and uneven plasma ionization. Deconvolving beam shape and beam jitter also make single bunch measurements desirable.

V. CONCLUSIONS

Nonimaging optics should provide useful information about beam shapes at high energy electron accelerators and

colliders. Bremsstrahlung is the easiest source of high energy photons, however beamstrahlung in colliders should provide a passive method of looking at e^+/e^- collisions, and Compton backscatters could be used to produce higher energy photons and better resolution for single beam measurements.

We are building a system which should make it possible to study the technique experimentally at the Argonne APS and SLAC FFTB.

VI REFERENCES

- [1] R. B. Palmer, *Annu. Rev. Nucl. Part. Sci.* **40**, 529, ('90)
- [2] J. Norem, *Rev. Sci. Instrum.*, **62**(6), (1991), 1464
- [3] Jenkins and White, *Fundamentals of Optics*, Ch 18, Fresnel Diffraction, McGraw-Hill (1957)
- [4] P. Chen, P., *Phys. Rev. D*, **46**, (1992), 1186.
- [5] Hamamatsu Photonic Systems, Bridgewater, NJ, 08807
- [6] Goodfellow Corporation, Malvern, PA 19355
- [7] R Lowrey, Rockwell Power Systems, Albuquerque NM (private communication)
- [8] National Instruments, Austin, TX, 78730
- [9] Quanterra, Inc. Harvard, MA, 01464

Ian C. Hs , Tinge Hui Huang

*Institute of Nuclear Science, National Tsing-Hua University and
Synchrotron Radiation Research Center
Hsinchu, Taiwan 30043, R.O.C.*

Abstract

The electron beam profile is one of the most important parameters of a storage ring accelerator. This paper presented the design study of one type of beam profile monitor by using synchrotron radiation which was emitted by the electron beam. The beam profile monitor system needs an optical system to image the synchrotron light onto a high resolution image sensor. The system is intended for monitoring 100 mm beam size. Therefore, the aberrations of the system has been studied. Those include the calculation and the reduction of monochromatic and chromatic aberrations. The experimental setup for measuring those aberrations in order to calibrate the results of the beam measurement are presented. We also discussed the synchrotron radiation power consideration for choosing a suitable image sensor.

I. INTRODUCTION

Using the synchrotron radiation to observed the electron beam profile of a storage ring is a nondestructive measurement. For the electron beam with cross section around 100 μ m, the errors of the optical system will affect the results of the measurements. Therefore, we must calibrate the monochromatic aberrations, chromatic aberration and diffraction errors after designing the optical system for the measurements. Considering the power deposition and the radiation intensity change range , choosing a suitable photodiode array for measuring the exact beam profile is also important.

II. OPTICAL SYSTEM DESIGN

The visible light wavelength range of synchrotron radiation was chosen for the measurement to reduce the complexity of the measurement optical system. As the synchrotron radiation sweeping from the bending magnetic, the vertical natural opening angle is Ψ [1, 2]

$$\Psi = \frac{m_0 c^2}{E} \left(\frac{\lambda}{\lambda_c} \right)^{\frac{1}{3}}$$

where E , λ and λ_c are electron energy, observed wavelength and critical wavelength respectively. The sweeping angle θ depends on the slit size as shown in Fig. 1 where ρ and θ_s are the bending magnetic radius and the opening angle made by the slit. The sweeping angle θ equals to θ_s and there is a error δx coming from curved orbit

$$\delta x \approx \frac{\rho \theta^2}{8}$$

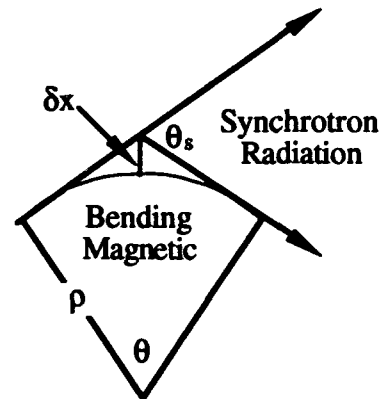


Fig. 1 Relations between the sweeping angle and the curved orbit error.

The diffraction limit d , related with the slit opening angle as the following equation,

$$d \approx \frac{\lambda}{\theta_s}$$

Increasing the sweeping angle will decrease the diffraction limit but it will also increase the depth of field, hence enlarge the error which comes from the curved orbit. The optimized sweeping angle θ_s was set by equating the diffraction limit d , and the curved orbit error dx .

$$\theta_s \approx 2 \left(\frac{\lambda}{\rho} \right)^{\frac{1}{3}}$$

If $\rho=3.245$ m and $\lambda=500$ nm, the optimized sweeping angle is about 10.46 mrad. The optical system for focusing synchrotron radiation is described as in Fig. 2. The slit determines the sweeping angle after the synchrotron radiation passing through the quartz window of the vacuum chamber. The filter (500 \pm 20nm) will allow a part of visible synchrotron radiation passing through it. The optical system was used to focus the synchrotron radiation and to form the image on the horizontal and vertical linear photodiode arrays by using a splitter. Before the synchrotron radiation arriving the vertical linear photodiode array, another splitter was used to split the light ray onto a 2-dimension photodiode array.

III. OPTICAL SYSTEM CALIBRATION

As the electron beam size is about 100 μ m, the aberrations of optical system must be considered. Taking the 100 μ m beam size, the theoretic value of the sum of the monochromatic and chromatic aberrations are about 8.72 μ m.[3] Other errors like curved orbit error and diffraction error will increase the total error. Thus, the study of the optical system is necessary. The calibration method of monochromatic aberration is described as in Fig. 3. Because the designed wavelength of the two focusing lenses is 546.1

nm. A green randomly polarized He-Ne laser was used as a light source. The chromatic aberration can be neglected in this case. The laser light after passing through the slit which has 105 μm width was used to simulate synchrotron radiation light source with a proper opening angle. The slit B will be covered by the central light beam of the diffraction laser light. After calculating the rms of the simulated light source size σ_s and assuming the vibration of optical table is $\sigma_{\text{vibration}}$, we will have the following relation.

$$\sqrt{\sigma_{\text{mono}}^2 + \sigma_{\text{vibration}}^2} = \sqrt{\sigma_{\text{measured}}^2 - \sigma_s^2}$$

where σ_{measured} is the beam profile measured by linear photodiode array.

The setup for the calibration of the chromatic aberration is shown in Fig. 4. The white light lamp was located at the focal plane in front of the lens ($f=100$ mm) in order to form the parallel light. The parallel ray after passing through the 105 μm slit will become the simulated synchrotron radiation light with a proper opening angle. Then, the chromatic aberration $\sigma_{\text{chromatic}}$ can be estimated by the following formula :

$$\sigma_{\text{chromatic}} = \sqrt{\sigma_{\text{measured}}^2 - \sigma_s^2 - (\sigma_{\text{mono}}^2 + \sigma_{\text{vibration}}^2)}$$

IV. MEASUREMENTS OF ELECTRON BEAM PROFILE

As measuring the electron beam profile, the slit B will produce a diffraction error $\Delta h \approx L\lambda/s$ in the horizontal direction as in Fig. 5.

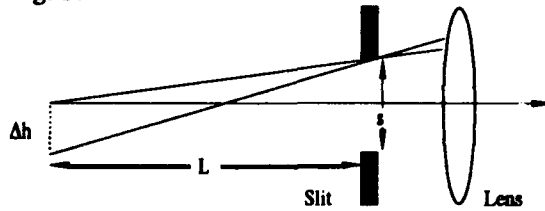


Fig. 5 Diffraction error due to the slit S.

Calculated the rms value of the diffraction error σ_{diff} of the diffraction error, the electron beam profile σ_e can be estimated by the following formula :

$$\sigma_e = \sqrt{\sigma_{\text{measured}}^2 - (\sigma_{\text{mono}}^2 + \sigma_{\text{vibration}}^2) - \sigma_{\text{chromatic}}^2 - \sigma_{\text{diff}}^2}$$

In the case which we discussed here, the diffraction error in the vertical direction is negligible.

V. PHOTON FLUX AND PHOTODIODE ARRAY ILLUMINATION LIMIT

The synchrotron radiation photon power per electron per turn is P_t [4]

$$P_t = \int_{\omega_1}^{\omega_2} \frac{4}{2 \cdot 3^3 \cdot \Gamma(\frac{1}{3})} \frac{r_0 m_0 c^2}{\rho} \left(\frac{\omega}{\omega_0}\right)^{\frac{1}{3}} d\omega$$

where $\omega = 2\pi/\lambda$ and ω_0, r_0 , are the angular revolution frequency and the classical electron radius. Two cases of different photon power on the photodiode array are calculated as in Table 1, where bending radius $\rho = 3.495$ m and $\omega_0 = 2\pi \times (2498.27 \text{ kHz})$. The results take the transmittance of optical elements into account. The illumination limit, Luxmin will provides the information for choosing a suitable photodiode array

$$\text{Lux}_{\min} = \frac{P_{\text{array}}}{4\sigma_v\sigma_h}$$

where P_{array} is total power deposited on the photodiode array and σ_h, σ_v are the horizontal and the vertical imaged beam sizes.

VI. CONCLUSION

Although the electron beam size is very small, the optical system should be capable to measure the beam profile exactly after error calibration. With different beam size simulation, we may overcome the difficulty that the vertical beam size is smaller then the resolution limit of the optical system.

VII. REFERENCE

- [1]. BNL 50595, Vol. 1 (1977)
- [2]. IEEE Transaction on Nuclear Science, Vol. NS-32, No. 5, Oct. 1985
- [3]. Miles V. Klein and Thomas E. Furtak, Optics, 1985, p.223-256
- [4]. Herman Winik and S. Doniach, Synchrotron Radiation Research, 1980, p.13

Supported by the National Science Council of ROC, Contract NSC 81-0417-E-007-545 and SRRC, ROC

Beam Current (mA)	*1 Number of Electron	*2 Parray (W)
200	5×10^{11}	1.169×10^{-3}
5 Multibunch Mode	1.25×10^{10}	2.924×10^{-5}
0.67 Single Bunch Mode	1.675×10^9	3.918×10^{-6}

*1 Number of Electron = Beam Current (mA) / (Revolution Freq. 1.6×10^{-19})

*2 Parray = $P_t \times (0.8) \text{ window} \times (0.6) \text{ filter} \times (0.008 / 2\pi) \text{ slit} \times (0.993) \text{ lenses} \times (0.45) \text{ splitter} \times (\text{Number of Electrons})$

Table 1 Power deposited on photodiode arrays for two different beam current.

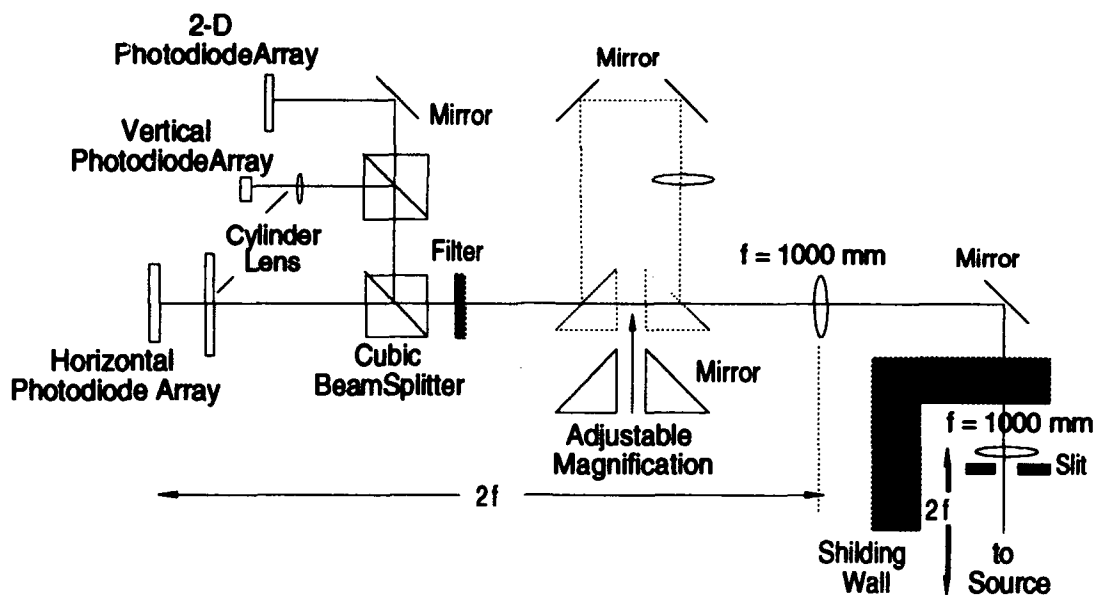


Fig. 2 The schematic drawing of the whole optical system.

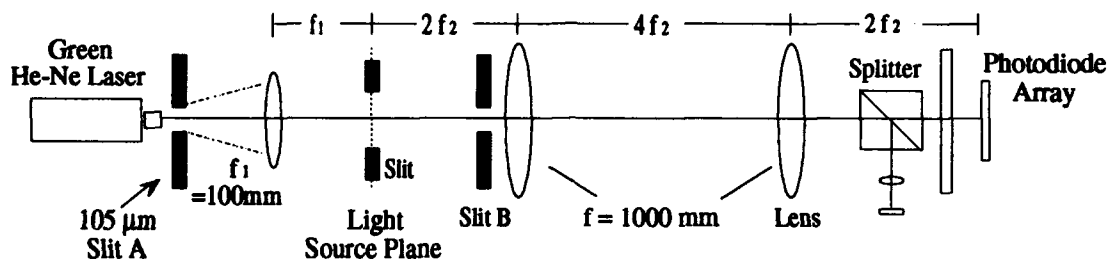


Fig. 3 The experimental setup for the calibration of monochromatic aberrations.

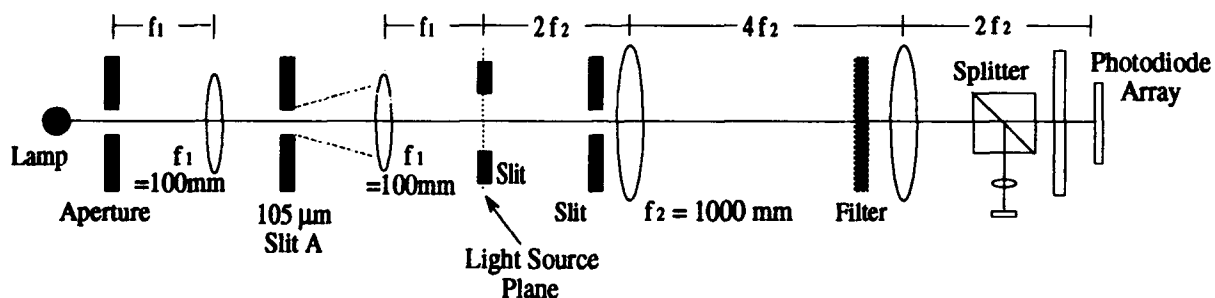


Fig. 4 The experimental setup for the calibration of chromatic aberration.

Limitations of a Residual Gas Ionization Beam Profile Monitor for the SSC Collider

R. Meinke, W. Nexsen, E. Tsyganov, and A. Zinchenko
Superconducting Super Collider Laboratory*
2550 Beckleymeade Ave., Dallas, TX 75237 USA

Abstract

A residual gas ionization beam profile monitor for the Superconducting Super Collider is considered in detail using the Monte Carlo simulation code. It is shown that a good spatial resolution could be obtained using a combination of strong electrical and magnetic fields.

A system of beam profile monitors that can control the beam emittance is a very important factor in the commissioning and reliable operation of the Superconducting Super Collider (SSC). The Conceptual Design of the SSC^[1] proposes flying-wire scanners and synchrotron-radiation light monitors for this purpose. Both methods have their own shortcomings, and some alternatives would be desirable. A residual gas ionization monitor to measure the collider beam profile is discussed below.

The characteristic parameters for the warm section and cold section of the collider are shown in Table 1.

Calculations indicate that the statistics are high enough to expect good spatial resolution for a residual gas ionization monitor. However, systematic effects could smear the resolution for the SSC beam. Electrons produced with velocity close to zero are affected by beam charge, and so the space information could be essentially lost. One can expect a better performance of such a monitor if strong external electrical and magnetic fields are applied.

A diagram of the residual gas ionization monitor using a dipole magnetic field is presented in Figure 1. Two compensating magnets are used to compensate for the influence of the magnetic field on beam dynamics. Electrons are accelerated up to the energy of about 30 KeV and are detected either by silicon microstrip detectors or by microchannel electron multipliers with a mult cathode readout. A similar detection system was proposed in Reference 4. One can achieve some magnification of the beam profile image using shaped magnetic and electrical fields.

Investigation of electron collection from the residual gas has been carried out using a computer simulation code, ZBEAM,^[5] which traces electrons and ions under the influence of applied electrical and magnetic fields. A two-dimensional Gaussian distribution with $\sigma_x = \sigma_y = 50 \mu\text{m}$ was used to describe a bunched beam; the bunch length was taken to equal 10 cm, and protons were uniformly distributed in the Z-direction. The number of protons in the bunch was 10^{10} . External electrical and magnetic fields directed along the Y-axis (perpendicular to the beam direction) were applied. Ion-electron pairs are produced in space according to the proton density in a bunch.

The energy spectrum of electrons was produced according to a $1/E^2$ dependence, beginning from $E_e = 3 \text{ eV}$ ^[3]. It was assumed that 90% of electrons will produce a good image of the beam, i.e., we neglect 10% of all electrons with recoil energy of more than 30 eV. The velocity vectors of the electrons were distributed isotropically in space. Finally, electrons were "collected" at the $Y = 2 \text{ cm}$ plane.

Table 1.
Parameters for Warm and Cold Sections of Collider.

Warm Section	
Pressure (nitrogen)	10^{-9} Torr ($1.65 \times 10^{-15} \text{ g/cm}^3$) ^[1]
Ionization losses of MIP in nitrogen	1.82 MeV/g/cm^2 ^[2]
Average energy loss of MIP to produce one primary electron-ion pair in nitrogen	196 eV ^[3]
Beam intensity	75 mA ($0.45 \times 10^{18} \text{ p/s}$)
Number of ionization electrons	$0.7 \times 10^7/\text{cm-s}$
Cold Section	
Hydrogen density	$3 \times 10^8 \text{ H}_2/\text{cm}^3$ ($1.0 \times 10^{-15} \text{ g/cm}^3$) ^[1]
Ionization losses of MIP in hydrogen	4.12 MeV/g/cm^2 ^[2]
Average energy loss of MIP to produce one primary electron-ion pair in hydrogen	65 eV ^[3]
Beam intensity	75 mA ($0.45 \times 10^{18} \text{ p/s}$)
Number of ionization electrons	$2.8 \times 10^7/\text{cm-s}$

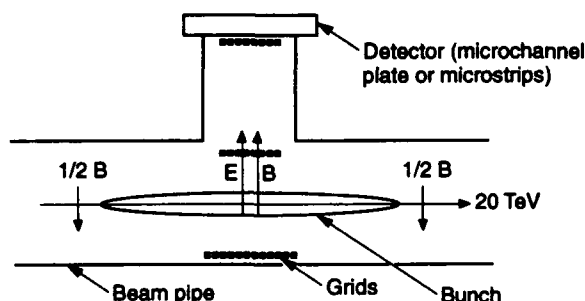


Figure 1. Residual Gas Ionization Beam Profile Monitor for the SSC.

*Operated by the Universities Research Association, Inc., for the U.S. Department of Energy under Contract No. DE-AC35-89ER40486.

Figure 2 illustrates the distribution of electrons arriving at the detector plane of the residual gas ionization monitor for a uniform magnetic field of 2 T and external constant electrical field of 10 kV/cm. Simulation data were taken at an X-coordinate of 50 μm . An rms spread of about 5 μm was obtained, and this satisfies the requirements for the SSC emittance monitors. Figure 3 shows the rms spread vs. X-coordinate, and Figure 4 presents possible systematical deviations of the measured X-coordinates from the true ones vs. the X-position. No significant dependence effects were found for the rms spread or the deviation.

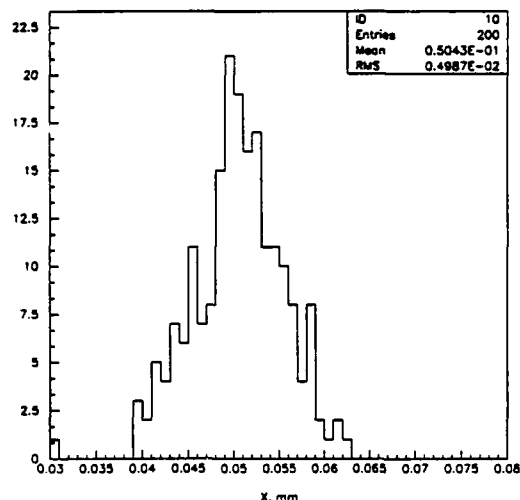


Figure 2. Distribution of the Coordinates of Electrons Arriving at Plane $Y = 2$ cm (the same we expect at the plane of the detector). Initial X-coordinate is 50 μm . Two hundred events are simulated, and Y and Z positions of ion-pair production are randomized, as are initial energies of electrons and their directions. The resolution of approximately 5 μm is achieved.

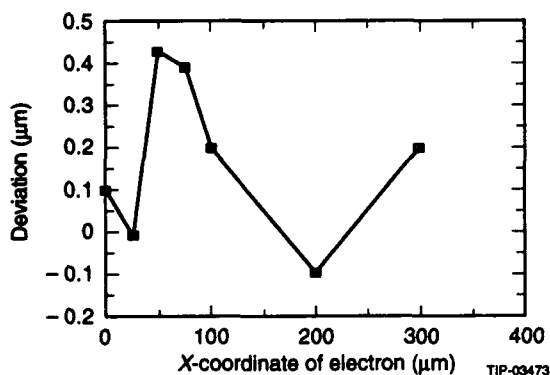


Figure 3. Space Resolution of the Device vs. Position of an Ionization Electron.

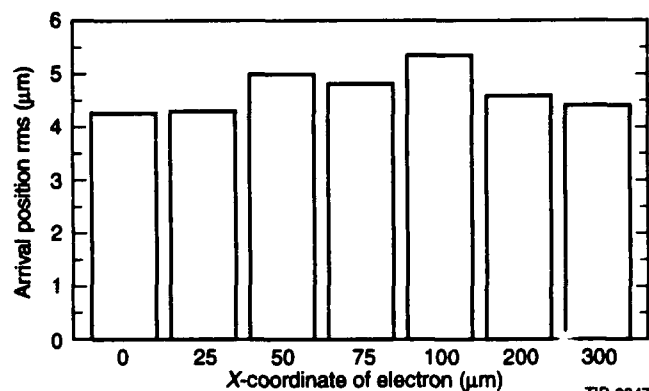


Figure 4. Deviation of the Average Positions of the Arriving Electrons for Different Starting Positions. Statistical accuracy is about 0.3 μm .

Some electron trajectories produced by the tracing code ZBEAM are presented in Figures 5–6.

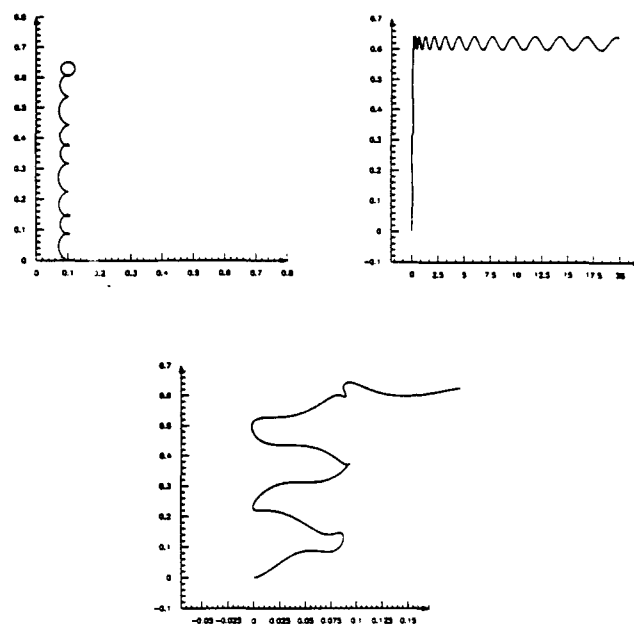


Figure 5. Motion of Zero Velocity Electron Near the 20-TeV Proton Beam in case of $E = 10$ kV, $B = 1$ T. Initial X-position of the electron is 100 μm . (a) in the X-Z plane; (b) in the Y-Z plane; (c) in the Y-Z plane, extended scale. Coordinates are in millimeters. In (c) one can see a kind of oscillation of the electron around some equilibrium position defined by the sum of the beam electrical field and the external electrical field applied. A bunch-occupied time is 0.3 ns, and full electron travel time is 0.8 ns.

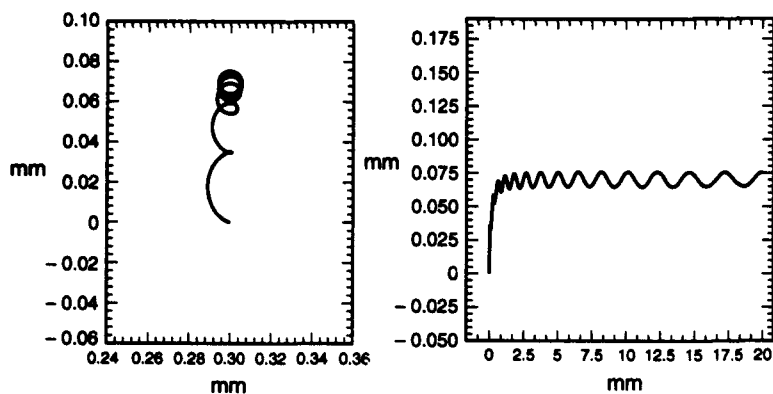


Figure 6. The same as in Figure 5, except the initial electron position is 300 μm . There are no oscillations.

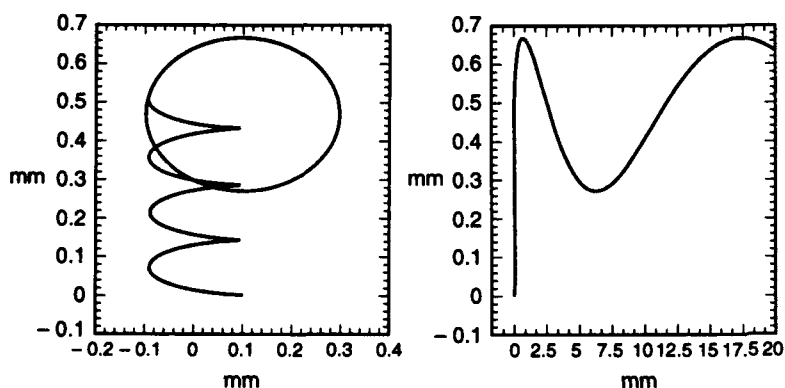


Figure 7. The same as in Figure 5, except $B = 0.1$ T.

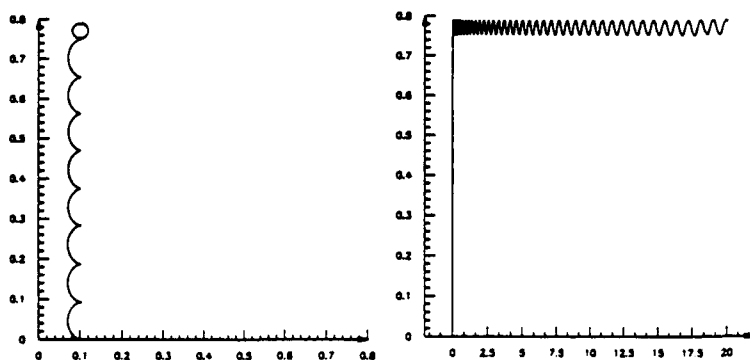


Figure 8. The same as in Figure 5, except $E = 1$ kV/cm.

Results of the analysis presented here demonstrate that even for the strict SSC requirements, construction of a residual gas ionization beam profile monitor with good space resolution looks feasible with the use of a strong magnetic field. In practice, a much lower magnetic field could be used with no significant degradation of the results. For example, in the utility region, where the rms beam size is about 150 μm , a monitor resolution of 20 μm is quite adequate, because it is added to the measured beam size in quadrature. Therefore, a 0.5-T magnetic field could be used, which is technically more attractive.

For the immediate future, a more detailed study of the electron drift process should be carried out, a corresponding read-out system should be constructed, and a prototype of the residual gas ionization beam profile monitor should be built and tested.

REFERENCES

- [1] *Site-Specific Conceptual Design*, SSCL-SR-1056, July 1990.
- [2] "Review of Particle Properties," *Phys. Rev. D*, 45 (1992).
- [3] F. Sauli, CERN 77-09, 1975.
- [4] A. G. Chilingarov *et al.*, "The Non-Destructive Ionization LEB Beam Profile Monitor," 1992.
- [5] E. Tsyganov and A. Zinchenko, "ZBEAM, charge tracing code for the SSC environment," in publication.

Full Cycle Beam Diagnostics with an Ionization Profile Monitor*

Arnold Stillman and R. E. Thern
Brookhaven National Laboratory, Upton, NY 11973

May 14, 1993

Abstract

The Alternating Gradient Synchrotron Booster at Brookhaven National Laboratory uses an ionization profile monitor to generate profiles of proton and heavy-ion beams. The profile monitor can acquire hundreds of profiles during an acceleration cycle, and then display and store them for analysis. Profiles appear in real time on an oscilloscope-type display, but other visualizations are available as well, namely mountain range and emittance displays. File storage of profile data is simple, as is the storage of moments and emittances.

I. INTRODUCTION

The Alternating Gradient Synchrotron (AGS) Booster at Brookhaven is both a proton accumulator and a heavy ion accelerator. The heavy-ion requirement of an ultra-high vacuum implies an ionization device with very high gain. The AGS Booster uses an ionization profile monitor (IPM) composed of a microchannel plate and multi-anode readout. A separate paper describes the profile monitor in detail [1]. This report is essentially a description of the user interface.

II. THE USER INTERFACE

The IPM can display profiles in real time at any particular trigger time during the cycle or show statistics from the profiles of a complete cycle, all at a glance and immediately after the acquisition of the final profile. Also useful and quite striking is the movie

mode, in which a sequence of profiles appears as fast as the program can display them. The apparent time in the movie is about a thousand times slower than real time. The movie display also makes great use of the magnet cycle. Correlations of beam motion and energy are clearly visible, since the magnet cycle appears in a contrasting color, with a moving dot indicating the displayed profile's occurrence in the cycle.

Several figures should serve to illustrate these points. The basic display in Figure 1 shows the horizontal and vertical profiles of a typical proton beam at 72.58 ms after injection. The time displayed in the center between the two profiles is the time during the cycle, but injection occurs at about 40 ms., so this set of profiles represents the beam at about 33 ms into the acceleration cycle. Below the graphical display is a collection of numerical data, which includes integration time, trigger time, statistical moments, raw amplitude minima and maxima, and various instrument readbacks. The most important numbers are the three moments of the Gaussian fit to the profile: M0, the total area.; M1, the centroid in mm.; M2, the 1σ width.

Obviously, we can not illustrate the movie display. However, some "frames" from a typical movie can give an idea of the display. In Figure 2, three separate frames show Au^{+33} profiles and the magnet cycle. An extraction bump is causing the beam to move radially outward. Some qualitative differences in beam motion are apparent on this time scale, but synchrotron motion is too rapid to resolve, even at our fastest scan rate.

More typical for accelerator operators is a mountain range display. Figure 3 shows a typical mountain range display, using proton profiles. Compare the motion in this figure with that of the motion in Figure 2.

*Work performed under the auspices of the U.S. Department of Energy.

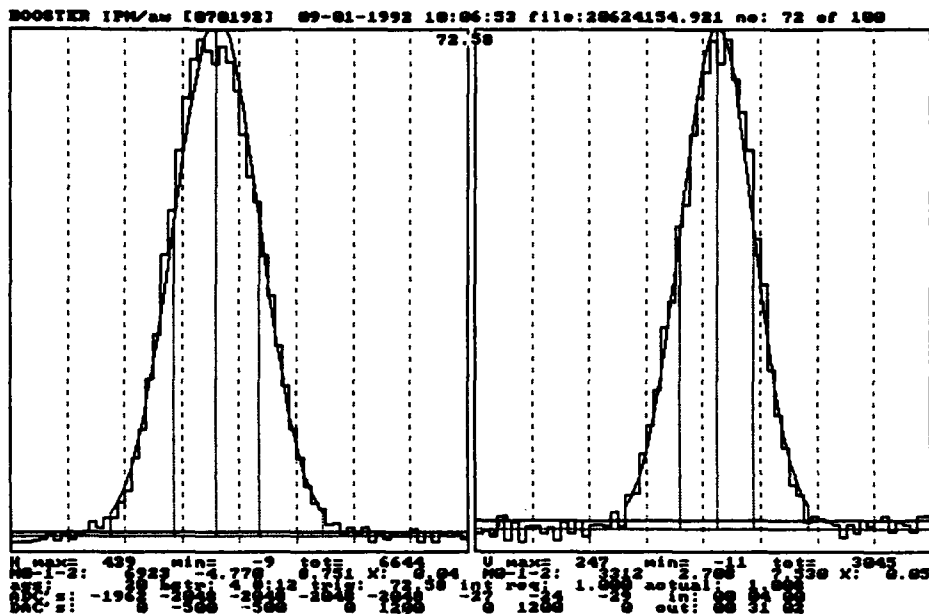


Figure 1: The Profile Display. Typical profiles of the proton beam in the AGS Booster. On the left is the horizontal profile and on the right, the vertical. The channel spacing is 1.4 mm and the vertical dashed lines occur every eight channels. Radially inward is to the right in the horizontal profile, and vertically upward is to the right in the vertical profile.

Finally, perhaps the most informative of the available modes is one in which the normalised emittance appears as a function of time in the cycle. In conjunction with the magnet cycle display, studies of emittance growth are now on-line operations. The definition of normalised emittance ultimately relies on the magnet cycle to determine β and γ (β and γ are the familiar relativistic v/c and $1/\sqrt{1-v^2/c^2}$). The specified error between the magnet programming function and the actual magnetic field in the magnets is on the order of 5%[2].

III. NULL SUBTRACTION

The AGS Booster has a mode of operation in which four short cycles of proton acceleration, preceded by a cycle with no beam, define a larger cycle, known in this case as User 1. User 1 provides a handy way to do null subtraction. First, however, we provide a description of the User structure of the Booster magnet cycle. There are up to four separate magnet cycles that are available during Booster operations. Each one is a User, in the sense that it serves a particular physics or beam studies user. A complete set of Users make up a Booster "supercycle." Although the number of Users is variable from one to four, anyone

operating a beam device, such as the IPM, only sees the display of the selected User. The timing selection software ignores unwanted Users.

To do null subtraction, we take advantage of the fact that the first pulse of User 1 is "empty" in the sense that the magnet cycle is present but there is no injected beam. This generates a pulse with all the systematic noise signals of the actual acceleration cycle, but none of the beam-induced signals. The IPM display program uses this empty pulse to generate null levels. Subtracting these null levels from the actual profiles produces extraordinarily clean signal data. For example, Figure 4 shows the same profile with the systematic background present and absent.

References

- [1] A. N. Stillman, R. Thern, and R. L. Witkover, *Rev. Sci. Instrum.* **63**, 3412 (1992)
- [2] A. Soukas, private communication.

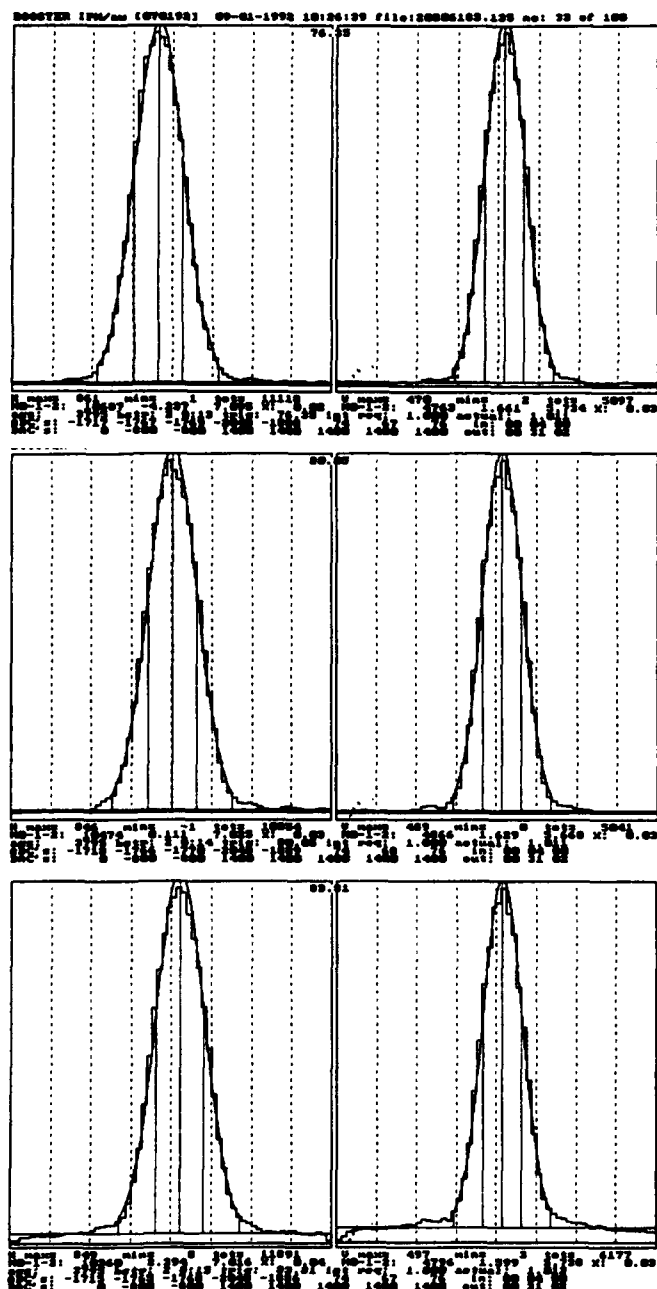


Figure 2: The Movie. Three frames from a movie of all the profiles in a full acceleration cycle. The display is of the same beam as in Figure 2. The spacing between profiles is about 3.5 ms.

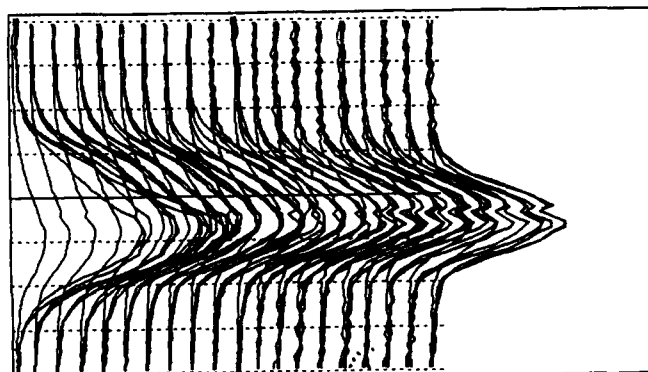


Figure 3: The Mountain Range. A typical mountain range display of the horizontal profiles of the beam in Figure 2. The time axis extends through the entire cycle.

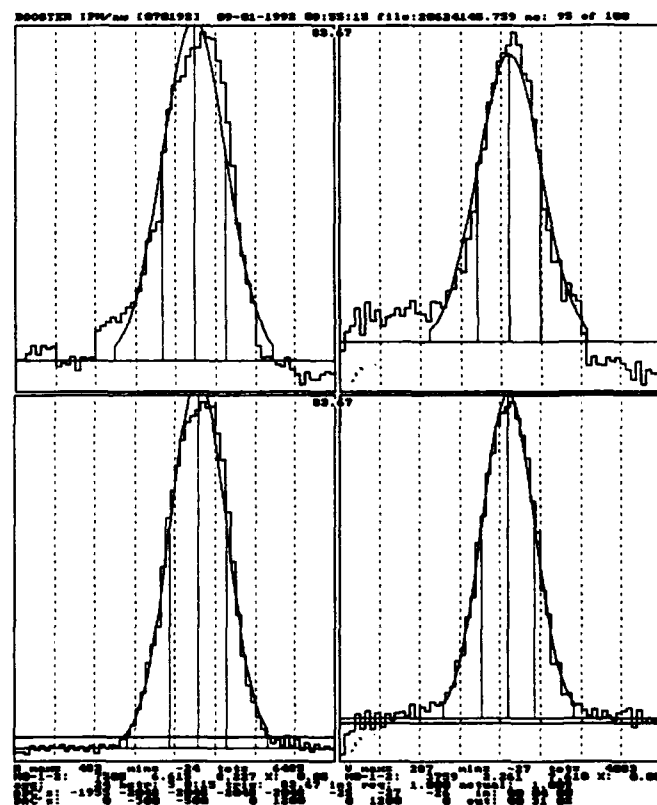


Figure 4: Null Subtraction a. A typical proton profile superimposed upon systematic noise. b. The same profile, but after removal of systematic noise with pre-sampled null values. The sampling of the null values occurs in an empty pulse, but at the same time in the pulse as the sampling of subsequent profile data.

Electron Beam Diagnostics by Means of Edge Radiation

O.V.Chubar, Russian Research Center - Kurchatov Institute, 123182 Moscow, Russia

E.S.Masunov, Moscow Engineering Physics Institute, 115409 Moscow, Russia

Abstract

Method for measurement of electron beam divergences and transversal sizes with visible range edge radiation (ER) is discussed. Intensity distribution of the ER generated by an infinitely thin electron beam at two adjacent bending magnet edges in a storage ring represents a system of concentric interference rings. The real beam divergences and transversal sizes smooth off the interference pattern; information on the extent of the smoothing off, being processed numerically, allows to determine the above-mentioned beam parameters. Precise computing technique of the ER intensity distribution with regard to finite beam emittance is presented. The results of simulations illustrating the application of the method for 450 MeV electron storage ring Siberia-1 are exhibited.

I. INTRODUCTION

Electromagnetic radiation generated by relativistic protons at bending magnet edges in synchrotron was already used for proton beam diagnostics: in Ref. [1] proton beam profile was measured with the visual range ER, the same way as electron beam profile is usually measured with visible synchrotron radiation (SR) [2], [3]. It was possible since in the proton synchrotron the ER intensity at $\lambda \ll \lambda_c$ (where λ_c is critical SR wavelength) greatly acceded the intensity of the standard SR.

It is proposed to use edge radiation for electron beam diagnostics by other means in this paper. It was shown both experimentally and theoretically [4] - [8], that ER intensity distribution in electron storage rings is very sensitive to beam divergences and transversal sizes. Calculations of the ER characteristics in the approximation of infinitely thin electron beam [7], [8] showed the intrinsic parameters of the ER angular distribution at $\lambda \gg \lambda_c$ to be the inverse reduced energy γ^{-1} and the value $[\lambda/(2l)]^{1/2}$, where l is inter-magnet distance. The first parameter results from angular distribution of single bending magnet ER, whereas the second one arises from the distribution of interfering radiation generated at two adjacent bending magnet edges. If λ belongs to visible region, these parameters are comparable with typical angular divergences of electron beam and the ratios of beam transversal sizes to observation distance in storage rings.

Experimentally, the method discussed consists in the measurement of the ER intensity distribution in the area adjacent to straight section axis (Fig.1). Monochromatic

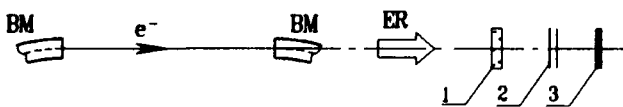


Figure 1. Edge radiation registration scheme.

1- neutral light filters, 2- monochromatic filter, 3- detector.

filter providing sufficiently narrow transparency band ($\Delta\lambda/\lambda \approx 10^{-2}$) should be used, since the radiation in wide spectral region smooths off the interference pattern, same as beam divergences and transversal sizes do.

The general point of the method is the technique for numerical processing of the measurement results, which allows to determine the parameters of emitting beam from intensity distribution of the ER being registered. This problem consists of two ones. The first is the computation of the ER intensity distribution with due regard for finite beam emittance; the second is the fitting of measurement results over the beam parameters, to be based on successive solution of the first problem. Effective least squares fitting algorithms are well-known; therefore only the method of computing the ER intensity distribution in view of finite beam emittance is discussed in this paper.

II. METHOD OF COMPUTATION

The expression for Fourier component of electric field emitted by single electron in its motion along the trajectory $\vec{r}(\tau)$ is readily obtainable from Fourier transformations of delayed potentials [9],

$$\vec{E}_\omega = \frac{ie\omega}{c} \int_{-\infty}^{\infty} \frac{\vec{\beta} - \vec{n}}{R} \exp[i\omega(\tau + R/c)] d\tau, \quad (1)$$

where $\vec{\beta} = \frac{1}{c} \frac{d\vec{r}}{d\tau}$ is relative velocity of electron, $\vec{n} = \vec{R}/R$, $\vec{R} = \vec{r}^* - \vec{r}$, $R = |\vec{R}|$, \vec{r}^* denotes observation point position, ω is radiation frequency; e is the charge of electron; c is the speed of light; i is unit imaginary number. The integration variable is time τ . Eq. (1) is valid at $\lambda/R \ll 1$.

Let the origin of coordinates be set in the middle of the straight section, y-axis be coincident with the straight section axis, x and z be horizontal and vertical ones.

The radiation of ultra-relativistic electron ($\gamma \gg 1$) is directed forward with respect to the particle motion; beam transversal dimensions are negligible as compared with observation distance. Therefore one can accept for transversal coordinates of observation point (x^*, z^*): $|x^*| = |(x^* - x)/R| \ll 1$, $|z^*| = |(z^* - z)/R| \ll 1$ (x, z are transversal coordinates of instantaneous electron position); it takes place in the trajectory region where the observed radiation is generated: $|\beta_x| \ll 1$, $|\beta_z| \ll 1$. In view of it, one can obtain the following for the phase in Eq.(1) by the corresponding expansion of R (from here on, the equilibrium trajectory length s is used as the integrating variable instead of τ),

$$\begin{aligned} \omega(\tau + R/c) &= \Phi_0 + \Phi(s); \\ \Phi(s) &\approx \frac{\pi}{\lambda} \left[s\gamma^2 + \int_0^s (x'^2 + z'^2) ds + \frac{(x^* - x)^2 + (z^* - z)^2}{y^* - s} \right], \end{aligned} \quad (2)$$

where Φ_0 does not depend on s , $x' = dx/ds \approx \beta_x$, $z' = dz/ds \approx \beta_z$; y^* denotes distance from the origin of coordinates to detec-

tor. Eqs. (2) include all the terms that may really contribute to the radiation intensity value in high-energy electron storage rings. It is worth noting that in this approximation the equilibrium trajectory length is coincident with longitudinal Cartesian coordinate of electron and transversal coordinates in the natural (connected with the beam) frame of reference coincide with those of the Cartesian frame.

In the approximation under consideration linear particle dynamics is commonly described by

$$\begin{cases} \begin{bmatrix} x \\ x' \end{bmatrix} = \begin{bmatrix} x_{eq}(s) \\ x'_{eq}(s) \end{bmatrix} + M_x(s) \begin{bmatrix} x_0 \\ x'_0 \end{bmatrix}; \\ \begin{bmatrix} z \\ z' \end{bmatrix} = M_z(s) \begin{bmatrix} z_0 \\ z'_0 \end{bmatrix}, \end{cases} \quad (3)$$

where $M_x(s)$ and $M_z(s)$ are 2×2 matrixes defined by magnet lattice characteristics; x_0, x'_0, z_0, z'_0 are initial values of particle trajectory; $x_{eq}(s)$ and $x'_{eq}(s)$ define equilibrium trajectory (supposed to be plane),

$$x'_{eq}(s) \approx -\frac{e}{mc^2\gamma} \int_0^s B_z(\hat{s}) d\hat{s}; \quad x_{eq}(s) = \int_0^s x'_{eq}(\hat{s}) d\hat{s}, \quad (4)$$

where $B_z(s)$ is vertical magnetic field. The ER intensity distribution depends on electron energy [6] - [8], but within small beam chromaticity this dependence is negligible.

In electron storage rings, if longitudinal bunch length is much larger than the wavelength of observed SR, the radiation emitted by different electrons is known to be incoherent. Spectral photon flux density of the radiation generated by the total electron beam may be represented as

$$\left(\frac{dN}{d\Omega d\omega} \right)_{incoh} = \frac{c^2 \alpha I}{4\pi^2 e^3 \omega} \int |\bar{E}_\omega(\bar{r}^*, x_0, x'_0, z_0, z'_0)|^2 F(x_0, x'_0, z_0, z'_0) dx_0 dx'_0 dz_0 dz'_0, \quad (5)$$

where I is electron current, α is the fine structure constant;

$|\bar{E}_\omega(\bar{r}^*, x_0, x'_0, z_0, z'_0)|^2$ is defined by

$$|\bar{E}_\omega|^2 = \frac{e^2 \omega^2}{c^4} \left| \int_{-\infty}^{\infty} \frac{\bar{\beta} - \bar{n}}{y^* - s} \exp(i\Phi) ds \right|^2 \quad (6)$$

and Eqs. (2) - (4). Integration in (5) is over all phase space. $F(x_0, x'_0, z_0, z'_0)$ is initial particle density distribution in phase space; in a much used approximation

$$F(x_0, x'_0, z_0, z'_0) = (B_x \Gamma_x - A_x^2)^{1/2} (B_z \Gamma_z - A_z^2)^{1/2} \pi^{-2} \times \exp(-\Gamma_x x_0^2 - 2A_x x_0 x'_0 - B_x x'^2_0 - \Gamma_z z_0^2 - 2A_z z_0 z'_0 - B_z z'^2_0), \quad (7)$$

where A, B, Γ are unnormalized parameters of phase ellipse.

If variations of magnetic field across the electron beam dimensions are negligible, then at $A_x=A_z=0$ $|\bar{E}_\omega|^2$ depends only on variable compositions $(x^*-x_0-y^*x'_0)$ and $(z^*-z_0-y^*z'_0)$ [10]. This allows to simplify Eq.(7). Though very useful for understanding the phenomena, this approximation is inapplicable for ER in strong-focusing synchrotrons. First, quadrupole lenses deflect particle trajectories, thus interference conditions for ER emitted at two bending magnet edges are different for different particles. Second, the elements of beam optics are the radiation sources providing unlike emission conditions at different x_0, x'_0, z_0, z'_0 .

In this paper, an alternative method for computing the incoherent radiation intensity with regard to finite beam emittance is proposed. In view of Eq.(6), relation (5) may be rewritten as

$$\left(\frac{dN}{d\Omega d\omega} \right)_{incoh} = \frac{\alpha \omega I}{4\pi^2 c^2 e} \iint_{-\infty}^{\infty} \frac{ds d\bar{s}}{(y^* - s)(y^* - \bar{s})} \times \int (\bar{\beta} - \bar{n}) \left(\frac{\bar{\beta} - \bar{n}}{\bar{\beta} - \bar{n}} \right) \exp[i(\Phi - \bar{\Phi})] F(x_0, x'_0, z_0, z'_0) dx_0 dx'_0 dz_0 dz'_0, \quad (8)$$

where $\bar{\beta}, \bar{n}, \bar{\Phi}$ depend on \bar{s} , while $\bar{\beta}, \bar{n}$ and Φ depend on s . Eq.(8) means six-fold integration, but in terms of Eqs. (2), (3), (5) and (7) the inner four-fold integration may be done analytically, thus only two-fold integral (over s and \bar{s}) should be computed. This method is valid for insertion devices as well as for any layout of electron beam optics.

III. COMPUTATION RESULTS

Computations of the ER intensity distribution at different beam divergences and transversal sizes were performed for the Siberia-1 (weak focusing) electron storage ring by the method based on Eq.(8). The following parameters were used in process: $\gamma=881$, $I=100\text{mA}$, bending radius $r_0=1\text{m}$, $|r_0(\partial B_z/\partial x)/B_z|_{x=0, z=0}=0.5$, inter-magnet distance $l=63\text{cm}$; function $B_z(s)$ was determined according to measurements made in the Institute of Nuclear Physics (Novosibirsk).

The computations were done for $\lambda=600\text{nm}$. Results are given for the traditional beam parameters $\sigma_x, \sigma'_x, \sigma_z, \sigma'_z$ at $A_x=A_z=0$.

Fig.2 compares the ER intensity distribution of infinitely thin electron beam with that of the beam at expected σ, σ' . The detector is offset by $y^*=572\text{cm}$. Since $\sigma_x > \sigma'_x, \sigma'_z > \sigma'_z$, the interference pattern is more smoothed off horizontally.

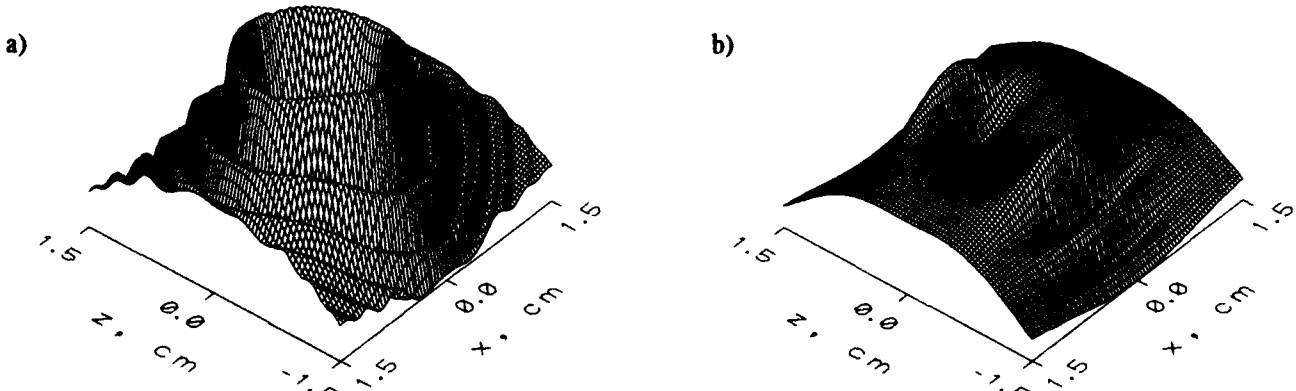


Figure 2. ER intensity distribution in detector plane: a) $\sigma_x=\sigma'_x=\sigma_z=\sigma'_z=0$; b) $\sigma_x=1.62\text{mm}$; $\sigma'_x=0.65\text{mrad}$; $\sigma_z=0.13\text{mm}$; $\sigma'_z=0.08\text{mrad}$.

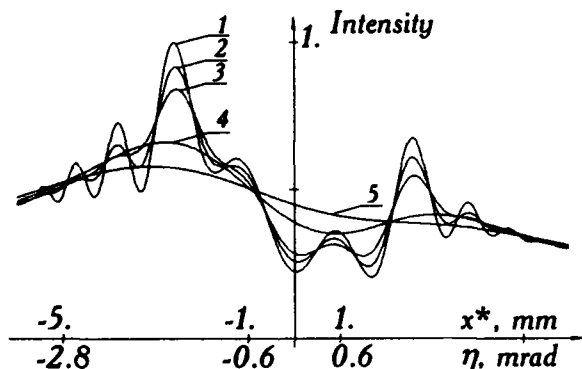


Figure 2. ER intensity distributions in median plane; η is horizontal angle relative to straight section axis.

1- $(\sigma'_x + \sigma_x/y^*)=0$; 2- $(\sigma'_x + \sigma_x/y^*)=0.17$ mrad; 3- $(\sigma'_x + \sigma_x/y^*)=0.28$ mrad; 4- $(\sigma'_x + \sigma_x/y^*)=0.91$ mrad; 5- $(\sigma'_x + \sigma_x/y^*)=1.54$ mrad.

The ER sensitivity to transversal dimensions and divergences of the beam is also clearly illustrated by Fig.2, where the intensity distributions in the median plane at different values of σ'_x and σ_x are exhibited ($\sigma'_z=0.08$ mrad, $\sigma_z=0.13$ mm and $y^*=181.5$ cm for each curve). Since the computations performed refer to the case of weak-focusing synchrotron, the effective parameters of the ER intensity distribution are the compositions $(\sigma'_x + \sigma_x/y^*)$ and $(\sigma'_z + \sigma_z/y^*)$ (similar to those discussed in previous chapter). Therefore one should make measurements at different distances y^* to distinguish contributions of σ' and σ (large y^* is preferable for distinct measurement of σ').

Fig.3 shows the intensity distributions in median plane computed at different y^* for finite beam parameters as well as for infinitely thin beam. The distribution at larger y^* is evidently less smoothed off (in consequence of the lesser contribution of transversal size); also, it is more symmetric. The distribution asymmetry is explained by the comparability of y^* and inter-magnet distance.

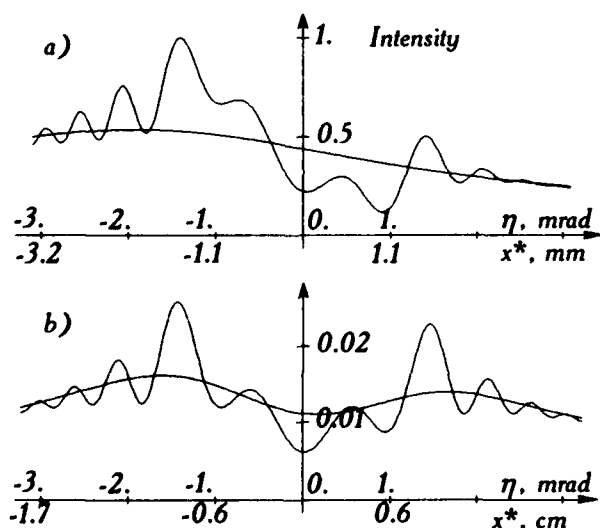


Figure 3. ER intensity distribution in median plane at $\sigma_x=1.62$ mm, $\sigma'_x=0.65$ mrad compared to one at $\sigma_x=\sigma'_x=0$:

a) $y^*=75$ cm; b) $y^*=572$ cm.

IV. SUMMARY

The effective computing the edge radiation with regard to finite beam emittance is supposed to allow the measurement of beam divergences and transversal sizes by means of the visible ER in electron storage rings. The method proposed, being very simple experimentally, may beneficially supplement the existing technique of electron beam diagnostics.

We would like to thank Dr. V.N.Korchuganov (Institute of Nuclear Physics, Novosibirsk) for magnetic field measurement results he kindly presented and Dr. N.V.Smolyakov (Russian Research Center - Kurchatov Institute) for fruitful discussions.

For more detailed information on the subject, please contact us by e-mail address chubar@ksrs.msk.su or use postal addresses given under the headline.

V. REFERENCES

- [1] R.Bossart, J.Bosser *et al*, "Proton beam profile measurements with synchrotron light", *Nucl. Instr. and Meth.*, Vol.184, Nos.2-3, 349 (1981).
- [2] A.P.Saberski, "Monitoring the beam in SPEAR with synchrotron light", *IEEE Trans. Nucl. Sci.*, NS-20, 638 (1973).
- [3] J.S.Mackay, "Electron beam profile, position systems and measurements on the Daresbury SRS", Preprint Daresbury Laboratory DL/SCI/P591A (1988), *Proceedings of the 1988 European Particle Accelerator Conference*.
- [4] M.M.Nikitin, A.F.Medvedev, M.B.Moiseyev, "Interference of synchrotron radiation", *Sov. Phys. JETP*, Vol.52, 388 (1980).
- [5] M.M.Nikitin, A.F.Medvedev, M.B.Moiseyev, "Synchrotron radiation from ends of straight-linear interval", *IEEE Trans. Nucl. Sci.*, Vol. NS-28, No.3, 3130 (1981).
- [6] Yu.A.Bashmakov, "Synchrotron radiation of electrons in the edge magnetic fields of storage rings", *Rev. Sci. Instrum.*, Vol.63, No.1, 343 (1992).
- [7] O.V.Chubar, N.V.Smolyakov, "VUV range edge radiation in electron storage rings", *J. Optics (Paris)*, Vol.24, No.1 (1993).
- [8] O.V.Chubar, N.V.Smolyakov, "Generation of intensive long-wavelength edge radiation in high-energy electron storage rings", these proceedings.
- [9] L.D.Landau, E.M.Lifshits, *The Classical Theory of Fields*, Pergamon, Oxford (1971).
- [10] K-J.Kim, "A new formulation of synchrotron radiation optics using the Wigner distribution", *SPIE Vol.583*, 2 (1985). *The 1985 International Conference on Insertion Devices for Synchrotron Radiation Sources*.

CEBAF Beam Viewer Imaging Software*

B. A. Bowling, C. McDowell
Continuous Electron Beam Accelerator Facility
12000 Jefferson Avenue, Newport News, VA 23606-1909 USA

Abstract

This paper discusses the various software used in the analysis of beam viewer images at CEBAF. This software, developed at CEBAF, includes a three-dimensional viewscreen calibration code which takes into account such factors as multiple camera/viewscreen rotations and perspective imaging, and maintaining a calibration database for each unit. Additional software allows single-button beam spot detection, with determination of beam location, width, and quality, in less than three seconds. Software has also been implemented to assist in the determination of proper chopper RF control parameters from digitized chopper circles, providing excellent results.

I. INTRODUCTION

CEBAF uses phosphorous beam viewer devices for initial beam setup and for visual observations of beam spot quality. The viewscreens, made of a chromium-doped alumina material, are inserted into the beamline using pneumatic plunger devices, with the resultant image being captured via a Sony vidicon CCTV camera, and displayed in the control room using closed-circuit monitors (fig. 1). The video signal is also fed into a 512x512 8-bit video frame grabber, which is operationally controlled from software.

Some viewscreens at CEBAF are oriented on the beamline in the familiar 45 degree angle relative to the beam axis, with the camera mounted 90 degrees facing the viewscreen. The majority of the viewscreens, however, in addition to the above geometry, are mounted at a 45 degree angle axially rotated relative to the beamline, and the camera is similarly rotated 45 degrees relative to the camera axis. The complex 3-dimensional rotations encountered by the digitized image due to these physical mountings, as well as pronounced depth-perception effects caused by the relatively close proximity of the cameras, ruled out the use of any of the available off-the-shelf imaging software known by the authors. It was therefore required to develop the calibration software in-house, which was customized for use with the viewscreens in use at CEBAF. This software allows for individual viewscreen positional calibration, with the results entered into a database for use by other application programs.

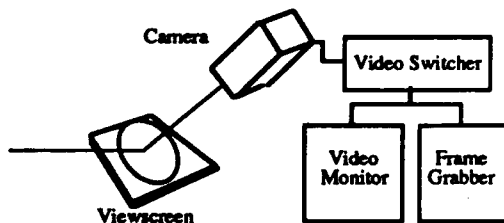


Figure 1. Camera System Diagram

* Supported by U. S. DOE contract DE-Ac05-84ER40150

Other imaging software developed and currently in use at CEBAF includes an automated beam spot detector, which when activated performs a digitization of the currently inserted viewscreen and determines spot centroid position, spot width, and spot quality. Another specialized code performs analysis of an image of the chopping ellipse, providing steering, amplitude and phase information directly applicable to the chopper controls.

II. CALIBRATION SOFTWARE

Each viewscreen used at CEBAF consists of a phosphorous plate contained in a stainless-steel retaining fixture, which exposes a circular area of phosphorous 1.125 inch in diameter. Each viewscreen is precisely CNC machined, and the pneumatic plunger device provides extremely accurate and reproducible placement of the screen within the beampipe. Similarly, the camera mounting on the beamline is very rigid, generating negligible movements in the cameras. This quality setup allows the frame of the viewscreen to be the calibration fiducial, greatly simplifying the calibration software.

An outline of the viewscreen frame was created within the calibration software. The calibration code provides an outline which is overlaid on the currently digitized viewscreen image. The outline can be translated, rotated, and/or adjusted for perspective imaging by the attached knob board. The rotation matrices used consists of rotations in the order of x , y , and z , and can be combined to yield:

$$R(\theta_x, \theta_y, \theta_z) = \begin{bmatrix} \cos \theta_z \cos \theta_y & -\cos \theta_z \sin \theta_y & \sin \theta_z & 0 \\ \cos \theta_x \sin \theta_z \sin \theta_y + \cos \theta_x \cos \theta_z & -\sin \theta_x \sin \theta_z \sin \theta_y & -\sin \theta_x \cos \theta_z & 0 \\ -\sin \theta_x \cos \theta_z \cos \theta_y + \sin \theta_x \sin \theta_z & \sin \theta_x \sin \theta_z \cos \theta_y + \cos \theta_x \sin \theta_z & \cos \theta_x \cos \theta_z & 0 \\ 0 & 0 & 0 & 1 \end{bmatrix}$$

Translation is handled by the following matrix:

$$T(T_x, T_y, T_z) = \begin{bmatrix} 1 & 0 & 0 & 0 \\ 0 & 1 & 0 & 0 \\ 0 & 0 & 1 & 0 \\ T_x & T_y & T_z & 1 \end{bmatrix}$$

The cameras are mounted relatively close to the beamline, accentuating perspective imaging effects^{1,2}. This is taken into account by the following perspective matrix:

$$P(x, y, z) = \begin{bmatrix} 1 & 0 & 0 & 0 \\ 0 & 1 & 0 & 0 \\ 0 & 0 & 0 & \frac{1}{f} \\ 0 & 0 & 1 & 0 \end{bmatrix}$$

The user acquires the image, which is automatically displayed on the computer screen as a gray-scale image and adjusts the rotation angle, translation, and perspective values until the viewscreen outline overlies the image properly. When the user is satisfied with the calibration, the save button is

activated, saving the angles, translations, and perspective values. These calibration values are maintained in a database file for each viewscreen, available for use by all imaging codes.

The camera calibration program also allows one to use the mouse arrow to point to a particular area on the viewplate image, displaying the equivalent beam coordinate in millimeters, using the pre-determined calibrations. An automated beam spot detection algorithm is also available in this code which determines spot location, width, and quality, which is described in the next section.

III. INSTAMATIC BEAM DETECTOR

To aid in the analysis of digitized beam spots, the INSTAMATIC automatic beam detection and analysis software was developed at CEBAF³. The design goal of this code was to quickly determine beam location on the currently-inserted viewscreen to aid in rough beam tune-up and beam analysis. With a single click of a button, the frame grabber captures the image and INSTAMATIC performs the spot analysis in less than three seconds, achieving the design goals

The spot detection algorithm starts by determining an intensity threshold in which the beam spot pixel must exceed in order to be considered. The digitized images exhibit speckle and slow intensity variations, which required a somewhat robust threshold determination. The threshold is determined from pixel values located around the outer perimeter of the viewplate, where the beam can never be present:

$$\langle I \rangle = \frac{\sum_{k=1}^n I_k}{n}$$

$$I_o = \langle I \rangle + 2 \left[\frac{1}{n-1} \left\{ \sum_{k=1}^n I_k^2 - \frac{\left(\sum_{k=1}^n I_k \right)^2}{n} \right\} \right]^{\frac{1}{2}}$$

The algorithm now determines the approximate location of the beam spot within the digitized grid array. One cannot simply seek out the brightest digitized grid value, due to the aforementioned speckle. The method implemented uses two pieces of information to determine the location of the spot; one looks at the intensity of a given pixel, choosing the pixel with the greatest intensity, and the other averages the eight neighboring pixels surrounding the given pixel, choosing favorably neighbors with little deviation. The two are combined to yield

$$G(i,j) = \frac{I(i,j)}{256} * \left(1 - \frac{\sum_{k=i-1}^{i+1} \sum_{l=j-1}^{j+1} (I(i,j)I(k,l)) * (1 - \delta(i,k)\delta(j,l))}{8(I(i,j) + 1)} \right)$$

This equation is performed for each pixel contained on the phosphorous area of the plate, and the value of G which is greatest is chosen as the spot location. This detection equation

performs very well, operates fast, and was simple to implement.

The above equation locates the spot in a general region. However, due to spot variations like speckle, this usually is not the centroid of the beam. The centroid pixel location is determined by a center-of-mass calculation which recursively spawns itself off within the spot, similar to a flood-fill graphics algorithm. Additionally, a center-of-area computation is performed determining the pixel which best lies in the center of the spot outline. The distance from the center-of-mass pixel to the center-of-area is defined as the quality factor; with perfect spots these two criteria are at the same pixel.

IV. GINSU CHOPPER CIRCLE ANALYZER

CEBAF utilizes a chopping system which consists of two identical RF cavities producing a transverse rotary motion in the beam. The beam is passed through a 60 degree aperture plate, to achieve the chopping. The aperture is removable and can be replaced by a viewscreen to allow a visual inspection of the rotary beam motion.

The size and centering of the chopping ellipse are very critical. In the past, mechanical means were used for determining proper elliptical parameters, such as the use of calipers on the image produced on the CCTV monitor. A more automated method was required for this setup, giving birth to the GINSU chopper alignment code⁴, developed at CEBAF. This program uses the frame grabber to snapshot a picture of the chopping circle and performs a least-squares fit to parametric equations defining the ellipse, determining the amplitude and relative phase slip in the digitized image. This information can be fed directly into the RF controls, performing a feedback in order to improve the ellipse.

When the image of the ellipse is acquired, the GINSU code starts its analysis by detecting the ellipse within the digitized data. This is accomplished by sending out rays at constant angular increments from the calibrated center of the viewscreen, comparing each pixel value and saving the location (pixel row and column) containing the brightest pixel. This produces a pair of x,y locations as a function of angle from the ray, tracing out a circle from 0 to 360 degrees, as in figure 2.

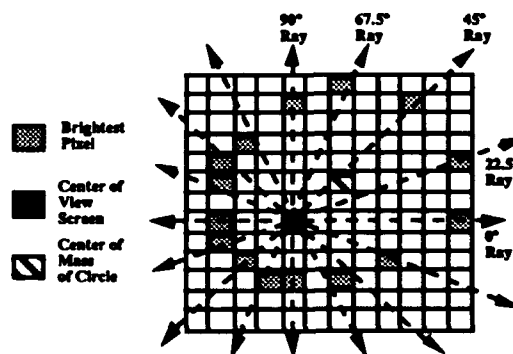


Figure 2. GINSU Ray Operation.

The rays are sent out with the calibration center being the point of origin. However, the ellipse may not be properly centered on the viewscreen, which will result in vastly unequal distances between data points (see fig. 2). From this, however, it is possible to determine the true center from a center-of-mass calculation, taking the irregular point spacings:

$$\langle X \rangle = \frac{\sum_{i=1}^n X_i \rho_i}{\sum_{i=1}^n \rho_i}; \quad \langle Y \rangle = \frac{\sum_{i=1}^n Y_i \rho_i}{\sum_{i=1}^n \rho_i}; \quad \rho_i = \sqrt{(X_i - X_{(i-1)})^2 + (Y_i - Y_{(i-1)})^2}$$

Once this location has been determined, the rays are sent out again using this new location as the center, and these final pixel row and column locations are used.

The chopping ellipse is generated by an RF cavity which is driven in both the horizontal and vertical planes, and which is described parametrically as:

$$X = A \cos(2\pi\alpha x) \\ Y = B \sin(2\pi\alpha x + \phi)$$

A least-squares fit can be performed on the digitized image using the following minimization criterion:

$$S = \sum_{\theta=0}^{2\pi} (B \sin(\theta + \phi) - Y(\theta))^2$$

This expression cannot be directly minimized due to the phase parameter within the transcendental function. However, a solution can be obtained by computing S for various values of ϕ and using the phase value which yield the best minimum, with B defined as:

$$B = \frac{\sum_{\theta=0}^{2\pi} Y(\theta) \sin(\theta + \phi)}{\sum_{\theta=0}^{2\pi} \sin^2(\theta + \phi)}$$

The computed values of B and ϕ can be directly applied to the RF control system to improve the ellipse. The determined centroid values provide relevant information about steering correction. The fitted amplitudes are within 20 percent, and the computed phase angle is usually within plus or minus 5 degrees. This accuracy generally results in one application of correction to the RF system to obtain a proper chopper ellipse.

During chopper setup using the viewscreen, it was noticed that the elliptical image would slowly drift and radially expand, which was due to charge deposition on the view plate from the beam. This results in erroneous steering computations, as well as distortions in the ellipse image with corresponding errors in the GINSU phase and amplitude results. This problem was alleviated by triggering the frame grabber off of the beam sync, which is generated by the gun interface module. The accelerator is operated in the single-shot mode, which provides the minimum amount of time

required to digitize the image, practically eliminating the charge deposition problem.

V. REFERENCES

- [1] P. K. Kloeppel, B. A. Bowling, and M. E. Wise, "Linearity Tests on the CEBAF Viewer System", CEBAF-TN-026(1991).
- [2] S. Jin, P. K. Kloeppel, "Error Analysis of the Beam Viewer System for Quantitative Measurements", CEBAF-TN-91-088(1991).
- [3] B. Bowling, C. McDowell, "Automatic Beam Spot Detection for the CEBAF Camera System", CEBAF-TN-012 (1992).
- [4] B. Bowling, P. K. Kloeppel, and G. Krafft, "Determining Chopper Alignment with the CEBAF Camera System", CEBAF-TN-91-108(1991).

Prototype Flying-Wire Beam-Profile Monitor*

David B. Barlow, Cliff M. Fortgang, John D. Gilpatrick
Ross E. Meyer, Armando M. Rendon, David S. Warren, and Mark D. Wilke
Los Alamos National Laboratory
Los Alamos, NM 87545

Abstract

A prototype flying-wire beam-profile monitor has been designed, fabricated, and tested to measure profiles of high-current high-duty electron beams. The device measures the beam's horizontal and vertical profiles with a pair of thin carbon filaments mounted on a wheel. The beam that intercepts the filaments, or wires, produces electrons by secondary emission in proportion to the incident beam current. The secondary electron signal is detected either by measuring the charge depletion current on the wires or by measuring the current collected on a pair of positively biased charge collectors. A servo motor is used to accelerate the wheel from rest to a speed of 25 RPS in less than half a revolution passing the wires through the path of the beam at a speed of ~ 10 m/s. The wheel is then decelerated back to rest before completing one full revolution. The precise timing requirements of this application led to the development of an indexer capable of controlling the servo motor position with less than 20 μ s of timing jitter.

I. INTRODUCTION

A prototype flying-wire beam-profile monitor, shown schematically in Figure 1, has been developed to measure profiles of high-current high-duty electron beams where the use of view screens or fixed-wire scanners is not practical. The system was designed for use on the Average Power Laser Experiment and High Powered Oscillator (APLE/HPO) electron accelerator under construction at Boeing Aerospace Corporation. The nominal APLE/HPO beam has an energy of ~ 18 MeV and current of about 0.2 A averaged over an 8 ms long macropulse. The width of the beam varies from 1 mm to 5 mm. The profile monitor measures the beam's horizontal and vertical profiles using a pair of 35 μ m diameter carbon filaments mounted perpendicular to one another on a wheel that sweeps them through the beam. The wheel diameter is 17 cm and the distance from the wheel's axis of rotation to the axis of the beam is 6.6 cm. The design minimizes the length of beam line occupied by the setup. The discontinuity in the beam pipe is kept to a gap of ~ 2 cm which helps reduce the deleterious effects caused by wake fields. Due to the high power density of the beam, it is not desirable to place any material, other than the wires, in the path of the beam. The single spoke design of the wheel allows the maximum angular range to accelerate the wheel

from rest to the operating velocity and back to rest before the spoke can pass through the path of the beam. The profile is determined by measuring either the charge depletion current of the wires or the charge collection current from a pair of positively biased charge collectors mounted concentric with the beam axis on either side of the wheel. The current signal from either the wires or collectors is converted to a proportional voltage signal which can be displayed on an oscilloscope or recorded by a transient digitizer.

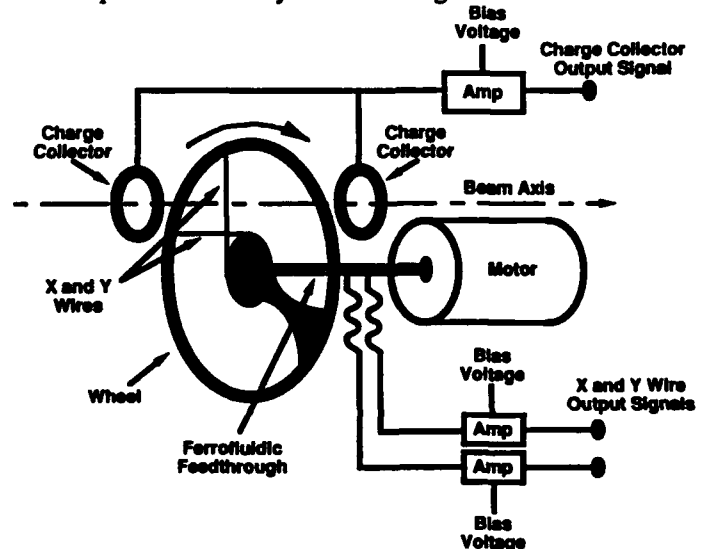


Figure 1 Schematic view of the prototype flying-wire beam-profile monitor.

II. SECONDARY EMISSION ELECTRONS

The beam profile is determined by measuring the secondary emission electron signal from the interaction of the beam with the wire. The secondary electron production rate for 30 MeV electrons on carbon has been measured to be about 3%.^[1] Assuming this rate, the secondary electron current is calculated to be on the order of 200 μ A for a 35 μ m wire in the center of a 1 mm diameter 0.2 A beam. Because the distribution of the secondary electrons falls off rapidly with energy, nearly all the secondaries can be attracted to a nearby collector biased at a few hundred volts.

III. BEAM HEATING

Heating of the wire during a single pass through the beam is a major concern when attempting to measure the profile of high average power electron beams. For this reason it is imperative that the wire pass through the beam quickly enough to prevent thermionic emission or breakage. The rise in temperature of the wire as it traverses the beam is proportional to;

* Work supported and funded by the US Department of Defense, Army Strategic Defense Command, under the auspices of the US Department of Energy.

$$\Delta T_{\text{wire}} \propto (I_{\text{beam}} dE/dx)/(C_s V_{\text{wire}} W_{\text{beam}}).$$

where, I_{beam} is the beam current, dE/dx is the energy loss of the electrons in the wire, C_s is the specific heat of the wire, V_{wire} is the velocity of the wire, and W_{beam} is the width of the beam. This does not take into account any heat loss due to thermal radiation or conductance. Of the many possible wire materials, carbon filament has the lowest ratio of dE/dx over C_s . Combined with its high tensile strength this material is well suited for use in flying-wire scanners. For a 1 mm diameter, 0.2 A beam, the carbon wire must be moved through the beam at a speed of at least 10 m/s to keep the calculated ΔT in the carbon wire below 2000 K. For wire temperatures above 2000 K thermionic emission and breakage become a concern.

IV. MECHANICAL DESIGN

The primary challenge of the mechanical design was to accelerate the motor and wheel from rest to the required velocity and back to rest in less than one revolution. The acceleration must be smooth and reproducible, with minimal timing jitter when the wire passed through the beam. A Compumotor model KS-230 servo motor with indexer position control was chosen for this system. The motor was selected to provide sufficient torque to accelerate the motor and wheel to a velocity of 25 RPS in less than half a revolution. The ideal velocity profile would have a trapezoid shape, i.e., constant acceleration from rest up to the desired operating speed, followed by a period of constant velocity as the wires pass through the beam, and finally constant deceleration back to rest. However the inertia of the motor and wheel combined with the rapid change in velocity makes it difficult to achieve the ideal velocity profile. Figure 2 shows a plot of an ideal velocity profile specified by the indexer and an actual profile measured by a tachometer mounted on the back of the motor. There is considerable overshoot in the measured velocity due to the inability of the servo motor's closed loop control system to react fast enough to keep the motor on the specified velocity profile. However the traversal time of the wire through the beam is less than 1 ms. Therefore the velocity can be considered constant during the measurement. The motor speed is recorded along with the signal data in order to determine the wire's velocity at the time of the measurement.

For the best performance the wheel must be both stiff and light weight. Of the several materials; aluminum, G-10 fiberglass epoxy, and VESPEL (a polyimide) that were tried, 1.6 mm-thick G-10 was found to best. Because the one-spoke wheel tends to distort a small amount during acceleration and deceleration, it is not possible to rigidly attach the wires to the wheel. Instead one end of each wire is attached to the wheel with a small spring which helps maintain a constant wire tension. Using the spring attachment the wires are able to survive over 10,000 cycles at a peak wheel speed of 25 RPS. The electrical contacts to the wires were routed through a hole in the shaft of the ferrofluidic feedthrough between the wheel in vacuum and the motor in air, and potted to maintain the vacuum seal. A short length of wire was left on the motor end of the ferrofluidic feedthrough to take up the slack as the motor rotated back and forth. Two small rings were mounted on either side of the wire-beam intersection point to act as the charge collectors. The

collector rings were connected in series to a vacuum feedthrough to an external connector.

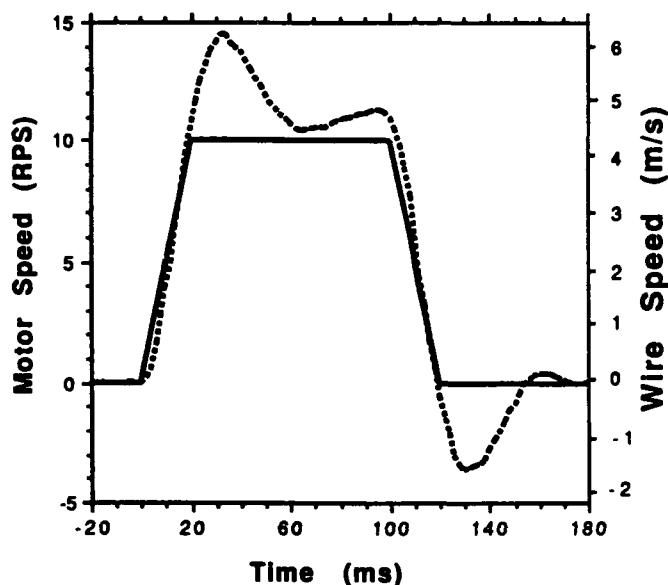


Figure 2. Specified and measured velocity profiles, (solid and dashed curves respectively).

V. ELECTRONICS

The servo motor is controlled by a prototype VME indexer, designed and built at LANL.^[2] This indexer was designed to replace commercially available indexers that tend to have timing jitter of up to a few ms due to the cycle time of their onboard microprocessors which must be interrupted to begin the control sequence. The LANL indexer has no onboard microprocessor. Instead the indexer has only memory which is loaded ahead of time with a bit pattern corresponding to the motor step sequence. Upon receipt of a trigger the bit pattern is immediately read out at a constant rate determined by a clock frequency. Using this indexer, the jitter between the trigger and the time the wheel rotates half a revolution, passing one of the wires through the beam center at a wheel speed of 25 RPS, was measured to be 20 μ s with respect to the external trigger.

A set of transimpedance amplifiers were designed and fabricated to convert the small secondary electron current to a voltage signal with a gain 20,000 volts per ampere. The transimpedance amplifiers could also isolate the input and apply either a positive or negative bias of up to 300 V.

VI. BEAM TESTS

The system was tested using the electron beam provided by the APLE Prototype Experiment (APEX) electron accelerator at LANL.^[3] The APEX beam is a low-duty 20 to 40 MeV electron beam with a typical beam current of 10 to 50 mA over a 5 to 20 μ s long macro pulse. The beam at the flying wire station was typically 2 to 4 mm in width. The short macro pulse length of the APEX electron beam ruled out the possibility of operating the system in the flying-wire mode. However the short macro pulse allowed the wires to be placed directly in the path of the beam without being overheated. The first goal of the APEX beam tests was to determine the

best means of detecting the secondary electron signal from the beam and wire interaction. The secondary electron signal measured from the charge depletion current on the wires had a typical signal to noise ratio of less than 10. The poor signal to noise ratio of the wires is attributed to the $\sim 1\text{k}\Omega$ resistance of the carbon wires which makes them good antennas for picking up noise. Applying a negative bias potential of a few hundred volts did not have any measurable effect the wire's signal to noise ratio. The signal to noise ratio of the charge collector was found to be almost an order of magnitude better than the wire's. However the charge collectors had a background level of about 10%. The source of the background is not completely understood but is believed to be due to secondary electrons produced by the interaction of the beam halo with the walls of the beam pipe. The background subtracted signal from the collectors was comparable to the signal measured from the wires, indicating that the collection efficiency was near 100%. The signal measured from the wires and collectors was consistent with a secondary emission rate of about 1% per incident electron.

The second goal of the APEX beam tests was to see how well the secondary electron signal from the wires could determine the beam profile. Because the macro pulse was too short to operate the system in the flying-wire mode, the wires were slowly stepped through the beam between macro pulses to map out the beam profile averaged over a number of macro pulses. An optical transition radiation (OTR) screen and video camera system was mounted 28 cm upstream of the flying wire setup to allow comparison between the flying-wire and video profile measurements. Figures 3 and 4 show OTR screen vs flying-wire profile measurements made in the same plane of two different width beams. The flying-wire profile measurements were made using the charge collection rings with the background subtracted. The width of the OTR profile has been normalized to match the width of the flying-wire profile to account for the expansion of the beam over the drift

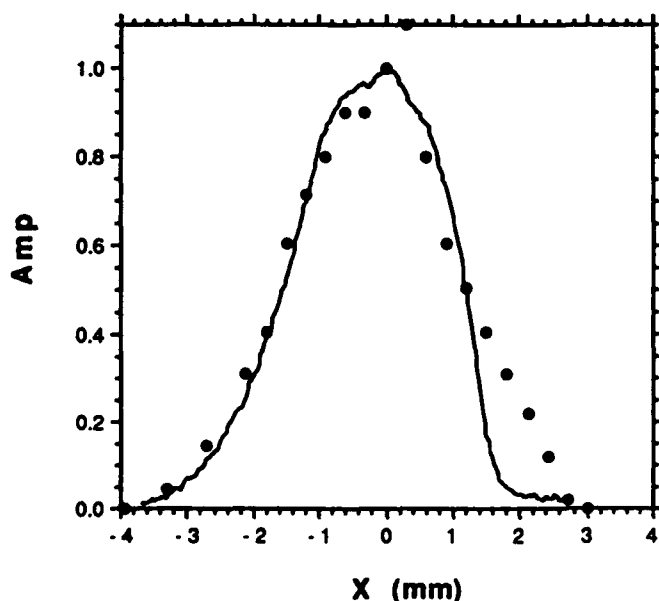


Figure 3. Wide beam profile measured by the flying wire (dots) compared to the profile measured by the OTR screen (solid curve).

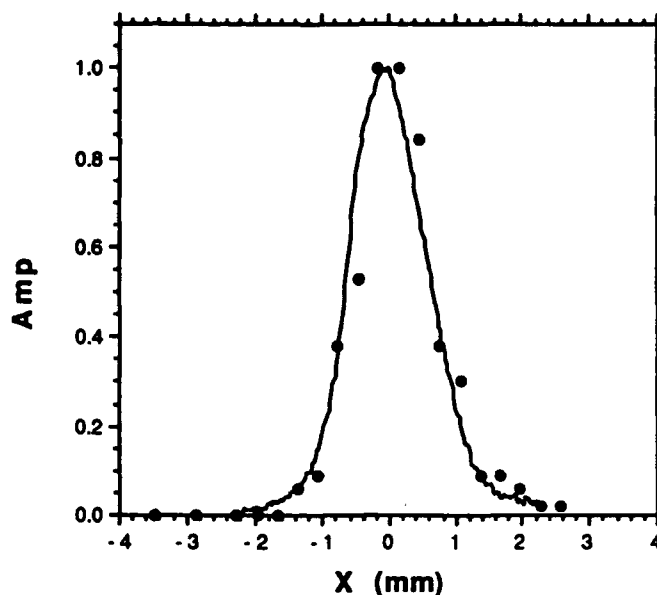


Figure 4. Narrow beam profile measured by the flying wire (dots) compared to the profile measured by the OTR screen (solid curve).

between the OTR screen and the flying-wire. The amplitude of both profiles has also been normalized to one, and both peaks have been centered at the origin. The flying-wire profile measurements show agreement with the normalized OTR profiles.

VII. CONCLUSIONS

The prototype flying-wire system performed well during bench tests of the mechanical assembly. The system was found to be capable of accelerating the wheel up to the required speed with very little timing jitter. The prototype flying-wire also performed well during beam tests. The beam tests indicated that the charge collectors had a significantly higher signal to noise ratio and were therefore the best method of detecting the secondary electron current signal from the beam and wire interaction. The use of charge collectors greatly simplify the setup by eliminating the electrical connections to the wires mounted on the rapidly moving wheel. Measurement of a beam profile, using the charge collectors, was in agreement with beam profiles observed on a near by OTR screen. Further refinements are being incorporated into the second generation system that will be put into service on the APLE/HPO beam line for a fully integrated test of the mechanical assembly, electronics, and control system. This system can be readily adapted to measure the profile of almost any charge particle beam providing its macro pulse length is sufficiently long for the wires to scan it, and its current density is low enough to not overheat the wires.

VIII. REFERENCES

- [1] R. Chehab et al., IEEE Transactions on Nuclear Science, Vol NS-32 No. 5, p 1953 (1985).
- [2] C. M. Fortgang, Los Alamos National Laboratory, LA-CP-90-466 (1990).
- [3] P. G. O'Shea et al., NIM A318, 52 (1992).

Emittance Measurement and Data Analysis for the SSC Linac Injector Lab

J.E. Hébert, P. Datte, F.W. Guy, N.C. Okay, K. Saadatmand, J. Sage, D.M. Wetherholt, W.A. Whittenberg
Superconducting Super Collider Laboratory*
2550 Beckleymeade Avenue, Suite 125
Dallas, TX 75237-3997

Abstract

The Superconducting Super Collider (SSC) ion source/LEBT produces and focuses a 35 keV 30 mA H⁺ beam into the RFQ. The beam emittance (ϵ_{rms}), and its other characteristics, are measured using a slit and collector diagnostic system. The resultant data is analyzed by two separate applications. Both the hardware and software involved will be discussed. Result examples will be presented.

I. Introduction

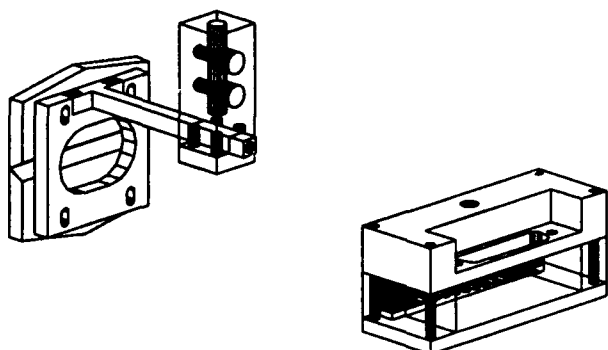


Figure 1 Downstream view of the SSC slit and collector

In the SSC Linac Injector Lab, a slit and collector diagnostic system is used to measure the transverse emittance of the H⁺ beam at the output of the ion source, LEBT, and RFQ¹. The beam conditions are quite diverse, depending on which system is being evaluated.

This paper will discuss the system hardware, the software used to control the hardware and make the measurements, and the software used to analyze the data. Finally, the performance of the system will be discussed with particular interest on certain techniques and algorithms which have significantly extended the limitations of the system.

II. Hardware

Slits

The slits used in this system were designed for use in a low energy (35 keV), highly divergent beam. The knife edges have a flat specified as $0.001'' \pm 0.0005''$. This allows very narrow gaps with very high angular acceptance.

Note in figure 1 that the slit design allows for longitudinal positioning. Note also that the beveled sides of the knife edges are opposite the beam incident surface. This is practical since thermal loading is not a concern at the

intended beam energy. These features allow the incident edges of the slit (the plane of measurement) to be positioned directly in the plane of interest. This is of particular significance at low energies where emittance growth due to space charge is most significant.

A final feature of the slit design is its ability to serve as a faraday cup. The slits are electrically isolated from the vacuum vessel by an insulating bracket. The slits are biased in the normal way, and the output is measured on an oscilloscope. Comparisons of this system to the solid faraday cup used previously have shown no measurable difference. This feature eliminates the need for an additional device in the beamline, and the associated hardware risks.

Collectors

The collectors are 48 channel devices, and were built at Los Alamos National Laboratory. Each channel consists of an 0.008" foil of copper, laminated with a 0.002" layer of insulating film. The signal produced on each channel is preamplified and fed into an 11 bit ADC.

III. Software

Measurement and Motion Control

The application used to control the slit and collector motion, and measure the beam, is named Emit. It was written in-house using TACL (Thaumatugic Automated Control Logic), which was developed at CEBAF.

During an emittance scan, the position of the slit (slit[i]) defines the X-axis coordinate of phase space, while the position of the collector (coll[i]) defines the X'-axis coordinate of each channel (or wire) of the collector. This gives rise to a finite plane of phase space covered by any given system. The X-axis limits are defined by the limits of travel of the slit. The limits of the X'-axis, however, are

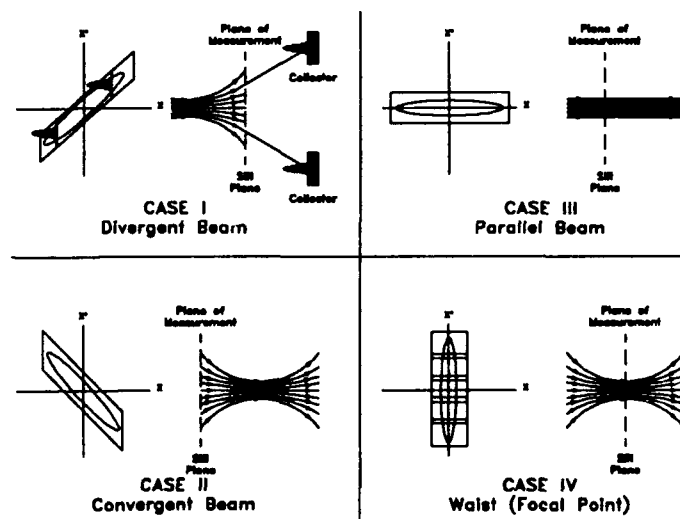


Figure 2 Examples of phase space ellipse orientations

* Operated by the University Research Association, Inc. for the U.S. Department of Energy, under contract No. DE-AC35-89ER40486.

defined by the angular acceptance of the slit, or the limits of travel of the collector, whichever is least.

Figure 2 shows four possible phase space ellipse orientations. Each case requires a different motion of the collector, relative to the slit, to sweep out that region of the plane.

Consider case I, a divergent beam. When the slit is at the first edge of the beam, the angular distribution of the ellipse is at a positive angle. At this point, the collector must be at a more positive position than the slit. When the slit has passed through the beam to the opposite edge, the angular distribution is at a negative angle, with the collector at a more negative position than the slit.

For this reason, the collector must traverse a greater distance than the slit. The algorithm used in this system, similar to that used by Los Alamos National Laboratory², defines the motion of the collector as a factor times the slit motion (or distance traversed). This factor is specified by the experimenter as the ratio of collector-to-slit motion, or simply the ratio.

In addition to the ratio (rat), the experimenter specifies a slit offset (s_off), a collector offset (c_off), a step size (step_sz), and the total number of steps (steps) the system is to make. From these parameters, the slit and collector motion is defined as follows:

$$\begin{aligned}\text{slit}[0] &= \text{s_off} + (\text{step_sz} * \text{steps}) / 2 \\ \text{coll}[0] &= \text{c_off} + \text{rat} * (\text{step_sz} * \text{steps}) / 2\end{aligned}$$

For $i = 1$ through steps

$$\begin{aligned}\text{slit}[i] &= \text{slit}[i-1] + \text{step_sz} \\ \text{coll}[i] &= \text{coll}[i-1] + \text{rat} * \text{step_sz}\end{aligned}$$

Notice that the motion of the slit and collector will sweep out a parallelogram in phase space centered about the slit and collector offsets. The ratio specified by the experimenter will determine the slope of the parallelogram. In case I the ratio would be positive. In case II, a convergent beam, the ratio would be negative. Case III would require a ratio of unity, and case IV is a special case which will be addressed later.

At each step, the system samples the beam for a time duration (gate), typically a few hundred nanoseconds, beginning at a specified time (delay). Both the gate duration and delay are specified by the experimenter. During this time, the signal from each channel will result in a digital count from 1 to 2048 in the associated ADC. These counts represent relative intensities which produce the angular distribution that makes up $\Delta\theta$ (any vertical slice of the ellipse). The X' coordinate of each channel is calculated as follows:

$$\begin{aligned}\text{For } j &= 0 \text{ through } 47 \\ \text{wire}[j] &= \\ \text{Tan}^{-1}\{((\text{coll}[i] - \text{slit}[i]) + ((24 - i) * \text{wire_sz})) / \text{drift_ln}\}\end{aligned}$$

where wire_sz is the thickness of each channel, and drift_ln is the drift length between the slit and collector.

Data Analysis

The measured data is initially analyzed with Emit.

These analyses are printed as a color contour plot where the relative intensities are color coded through six (6) standard deviations. The associated numeric data are included on this plot.

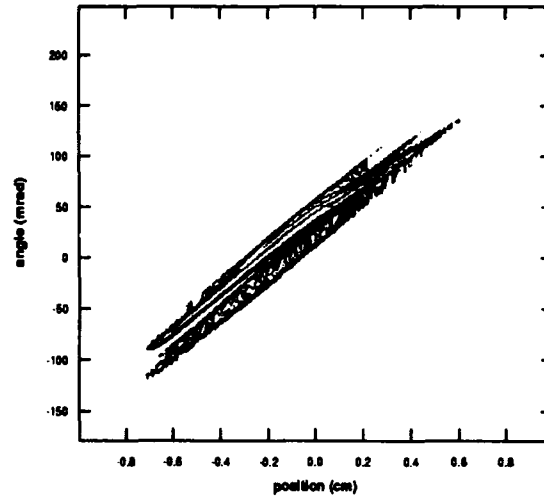


Figure 3 Plot of phase space data measured at the ion source (background subtracted).

The resultant data is then stored in a database from which it is extracted for further analysis off-line. This second analysis is performed with REANE analysis code, which was developed at, and provided by, Los Alamos National Laboratory. REANE provides the ability to plot the data as a set of six (6) contours corresponding to six (6) standard deviations, or as a set of percentiles of the total beam (see figure 3). The numeric data for REANE analyses are tabulated on a second printout.

Since background subtraction can't eliminate all extraneous signals from the data, REANE also allows the analyst to *cut out* the beam. Figure 3 shows an example of a raw data file after background subtraction, while figure 4 shows the same file after *cutting*.

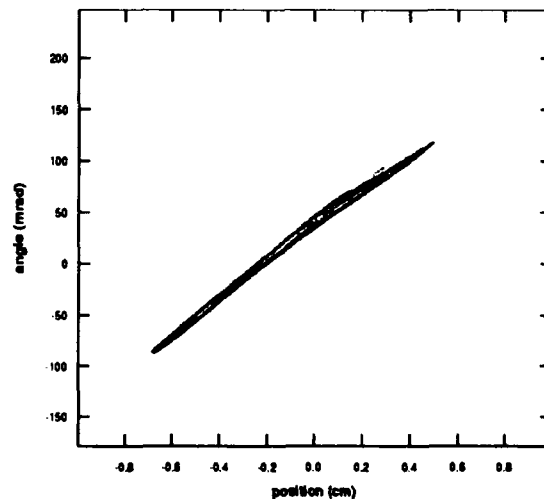


Figure 4 Plot of phase space data measured at the ion source (after cutting)

IV. System Performance

Ion Source Beam

Figures 3 and 4 are plots of a phase space measurement made at the ion source. In this case an extraneous ellipse appeared due to neutral particles. The collector channel amplifiers are biased negatively. As a result, secondary electrons generated by H^0 particles produce a measurable signal which must be dealt with. A positive bias may eliminate the unwanted signals, but it would also adversely affect the resolution of the H^+ signals since recaptured electrons would not necessarily return to the channel of their origin.

As seen in figures 3 and 4, this is not a significant problem in the vertical plane. The H^+ beam is deflected upwards slightly by the electron spectrometer. In the horizontal plane, however, both the H^+ and H^0 beams occupy the same phase space. To measure the horizontal axis of the ion source beam, a pair of electrostatic deflection plates were installed. With the plates grounded, the superimposed beams were measured. A second scan was made with ± 3.5 kV on the deflection plates. The H^0 particles were then measured, unperturbed by the E field, with all measurement parameters held constant. The H^0 data was then subtracted from the superimposed data, leaving only the H^+ data as the difference. As a check, the deflected H^+ beam was also measured. The integrated sum of the separated H^0 and H^+ data was within $\sim 5\%$ of the superimposed beam.

LEBT Beam

Refer back to figure 2. Note that case IV shows the waist of the beam as the measurement plane. Since the area of the ellipse is the emittance, a conserved quantity, and is approximately

$$\epsilon \approx X_{\text{envelope}} X'_{\text{envelope}}$$

the X' envelope must increase as the beam diameter decreases.

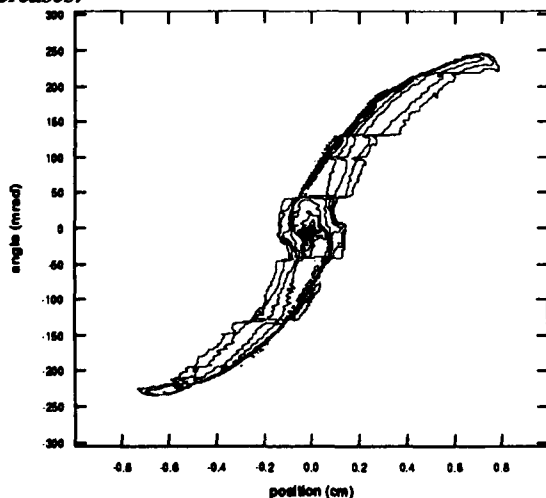


Figure 5 Plot of phase space data measured from the LEBT

Measuring the beam out of the LEBT was such a case. The focal point was the plane of interest, which is in fact a beam waist. The magnitude of the X' envelope made it

impossible to capture the beam in a single scan. Instead, a series of scans, as many as seven (7), were required to capture the entire beam. Each scan was made with a ratio of collector to slit motion of unity, but at different collector offsets leaving only a small overlap between scans.

Analysis of the resultant data was accomplished via a program written to combine the separate scans into a single data file. This utility currently allows a single degree of freedom, the collector offset, requiring all other parameters be held constant from scan to scan. In the future, this utility will be modified to allow a second degree of freedom, the slit offset.

Figure 5 shows a typical phase space plot of the LEBT beam. Once the beam is cut with REANE analysis code, the seams become all but indiscernible.

RFQ Beam

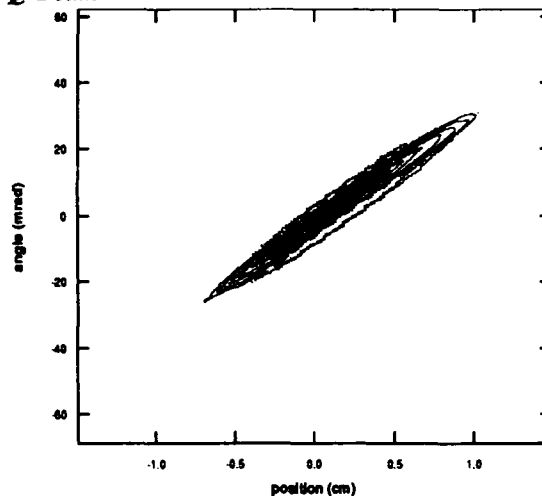


Figure 6 Sample emittance plot of beam out of RFQ

Measuring the RFQ beam posed a single challenge. The beam energy at the output of the RFQ is 2.5 MeV. To accommodate the thermal loading, new graphite plates for the slits were built. The knife edge flats were increased to 0.040" and the beveled faces were turned toward the beam. The rep-rate of the beam was reduced from 10 Hz to 5 Hz, and the current measuring capabilities of the slits were sacrificed in lieu of a thermally conductive path to the vacuum vessel.

Studies of the RFQ beam are ongoing, and the modified slit and collector system is performing exceptionally. Figure 6 is a typical emittance plot measured at the output of the RFQ.

V. References

- [1] Stanley Humphries, Jr., Charged Particle Beams, (Wiley, New York, 1990), p. 79 - 159.
- [2] Saadatmand, K., (private communication).

Automatic Emittance Measurement At The ATF *

X.J. Wang, R. Malone, K. Batchelor and I. Ben-Zvi
Brookhaven National Laboratory
Upton, New York 11973

Abstract

An automatic emittance measurement system to characterize the transverse emittance of the electron beam produced by the BNL photocathode electron gun is described. The system utilize a VAX workstation and a Spiricon beam analyzer. A operator window (created through the Vista control software package) controls the emittance measurement system and the graphic presentation of the results. Quadrupole variation method is used for the ATF automatic emittance measurement system. A simple emittance formula was derived to study the performance of the quadrupole variation method, and compared with the ATF experimental data is also presented.

I. VARIABLE QUADRUPOLE METHOD

The experimental program at the Brookhaven National Laboratory Accelerator Test Facility (ATF) requires rapid and accurate characterizing the electron beam produced by the ATF photocathode RF gun. An automatic emittance measurement system was developed at ATF to characterization of the electron beam transverse emittance at both 50 MeV and 4.5 MeV.

Using TRANSPORT notation, a 2-dimension transverse phase space of the uncoupled particle beam is described by the beam matrix σ ,

$$\sigma = \begin{pmatrix} \sigma_{11} & \sigma_{12} \\ \sigma_{21} & \sigma_{22} \end{pmatrix}. \quad (1)$$

where $\sigma_{12} = \sigma_{21}$, and σ is a positive definite matrix. The one- σ geometric emittance is,

$$\epsilon = (\sigma_{11}\sigma_{22} - \sigma_{12}^2)^{1/2}. \quad (2)$$

It can be seen from Eq. (2) that the emittance measurement usually involves determining three parameters. Several techniques ¹ have been widely used to measure the transverse emittance. The variable quadrupole method is one of them. It obtains the emittance by measuring beam sizes while varying an up-stream quadrupole magnet. The measured beam sizes ($\sqrt{\sigma_{11}^M}$) are connected to the beam matrix at the quadrupole through the transfer matrix R ,

$$R = \begin{pmatrix} R_{11} & R_{12} \\ R_{21} & R_{22} \end{pmatrix}. \quad (3)$$

and

$$\sigma_{11}^M = R_{11}^2 \sigma_{11}^Q + 2R_{11}R_{12}\sigma_{12}^Q + R_{12}^2 \sigma_{22}^Q. \quad (4)$$

where σ_{ij}^Q are elements of the beam matrix at the quadrupole.

* Work supported by U.S. DOE.

For n measurements ($n > 3$),² the Eq. (4) can be expressed,

$$\Sigma^M = A \Sigma^Q. \quad (5)$$

where

$$\Sigma^M = \begin{pmatrix} \sigma_{11}^{1M} \\ \vdots \\ \sigma_{11}^{nM} \end{pmatrix} \quad \text{and} \quad \Sigma^Q = \begin{pmatrix} \sigma_{11}^Q \\ \sigma_{12}^Q \\ \sigma_{22}^Q \end{pmatrix}$$

and

$$A = \begin{pmatrix} R_{11}^2(1) & 2R_{11}(1)R_{12}(1) & R_{12}^2(1) \\ \vdots & \vdots & \vdots \\ R_{11}^2(n) & 2R_{11}(n)R_{12}(n) & R_{12}^2(n) \end{pmatrix}.$$

Using the linear least squares fitting method, the solution of the beam matrix Σ^Q is,

$$\Sigma^Q = (A^T A)^{-1} A^T \Sigma^M. \quad (6)$$

II. ERROR ANALYSIS

Eq. (6) shows that the calculation of the beam matrix in the variable quadrupole method is fairly straight forward, it involves only matrix inversion and multiplication. We will study the possible sources which may affect the emittance obtained using the variable quadrupole method. **Error caused by the resolution of the beam width measurement.** For a Gaussian approximation of the beam width, the measured beam width σ_m can be expressed,³

$$\sigma_m^2 = \sigma_r^2 + \sigma_{sys}^2. \quad (7)$$

where σ_r is the ideal beam width while σ_{sys} is the system error of the beam width which includes optics and electronic errors. Then the measured emittance using the variable quadrupole method is:

$$\epsilon_m = \sqrt{\frac{\sigma_{11}^Q \sigma_{22}^Q}{R_{12}^2} + \epsilon_r^2}. \quad (8)$$

The above equation shows that the emittance error can be reduced either by decreasing the systematic error σ_{sys} , or increasing the the R_{12} , which is the drift distance after the quadrupole for a simple variable quadrupole method.

Error contributed by the transfer matrix. To simplify the calculation, the thin lens approximation will be used for the quadrupole. Then the transfer matrix R for the focusing plane is:

$$R = \begin{pmatrix} 1 & L \\ 0 & 1 \end{pmatrix} \begin{pmatrix} 1 & 0 \\ -\frac{1}{f} & 1 \end{pmatrix} = \begin{pmatrix} 1 - \frac{L}{f} & L \\ -\frac{1}{f} & 1 \end{pmatrix}. \quad (9)$$

where f is the focal length of the quadrupole, and L is the drift distance between the exit of the quadrupole and the screen of the beam profile monitor.

Considering only three different quadrupole settings, Eq. (5) can be rewritten,

$$\begin{aligned} \left(1 - \frac{L}{f_1}\right)^2 \sigma_{11}^Q + 2L \left(1 - \frac{L}{f_1}\right) \sigma_{12}^Q + L^2 \sigma_{22}^Q &= b_1 \\ \left(1 - \frac{L}{f_2}\right)^2 \sigma_{11}^Q + 2L \left(1 - \frac{L}{f_2}\right) \sigma_{12}^Q + L^2 \sigma_{22}^Q &= b_2 \\ \left(1 - \frac{L}{f_3}\right)^2 \sigma_{11}^Q + 2L \left(1 - \frac{L}{f_3}\right) \sigma_{12}^Q + L^2 \sigma_{22}^Q &= b_3. \end{aligned}$$

where b_i are squares of the measured beam sizes. Subtracting the third equation from the first and second equations eliminates the coefficients of σ_{22} from those two equations. The above equations can be written in matrix form $A\sigma = B$, where $\sigma^T = (\sigma_{11}, \sigma_{12}, \sigma_{22})$, $B^T = (b_1 - b_3, b_2 - b_3, b_3)$, and,

$$A = \begin{pmatrix} \left(2 - L \frac{f_1 + f_3}{f_1 f_3}\right) \frac{f_1 - f_3}{f_1 f_3} L & 2L^2 \frac{f_1 - f_3}{f_1 f_3} & 0 \\ \left(2 - L \frac{f_2 + f_3}{f_2 f_3}\right) \frac{f_2 - f_3}{f_2 f_3} L & 2L^2 \frac{f_2 - f_3}{f_2 f_3} & 0 \\ \left(1 - \frac{L}{f_3}\right)^2 & 2L \left(1 - \frac{L}{f_3}\right) & L^2 \end{pmatrix}.$$

Inverting the matrix A , the beam matrix σ_{ij} can be found by the matrix multiplication. The general expression is long and tedious. But If we choose three special points such that $f_1 = f_3 - \Delta f$, $f_2 = f_3 + \Delta f$, and $b_1 - b_3 = b_2 - b_3 = \Delta b$, then the emittance can be obtained by,

$$\epsilon = \frac{\sigma_{min}}{L^2} \left(\Delta b \frac{f_1 f_2 f_3}{\Delta f} \right)^{\frac{1}{2}}. \quad (10)$$

where $\sigma_{min} = \sqrt{b_3}$. In choosing three points satisfy above condition, b_3 is the minimum spot size when scanning the quadrupole. Eq. (10) shows that,

1. The measured emittance is linearly proportional to the measured minimum spot size. Fig. 1 was generated by changing only the minimum spot size using experimental data from ATF (courtesy of D.P. Russell). It agrees with the prediction of Eq. (10).
2. Eq. (10) shows the measured emittance also strongly depends on the focal lengths of the quadrupole. This dependency will affect mainly the accuracy of the measurement in the low energy situation. Our experience showed that the residual field of the magnet could also affect the experiment result.
3. Eq. (10) shows that the space charge could make the measured emittance smaller since stronger quadrupole (shorter focal length) will be used to compensate the defocusing force of the space charge.

Chromatic effect. The chromatic effect will also contribute to the error in the emittance analysis. Following simple formula⁴ can be used to estimate the chromatic effect:

$$\delta\epsilon = \frac{\sigma_{11}^Q}{f} \left(\frac{\delta p}{p} \right)_{rms}. \quad (11)$$

where $\delta p/p$ is the relative momentum spread. It can be seen from Eq. (11) that the chromatic effect will be smaller if a weaker quadrupole is used.

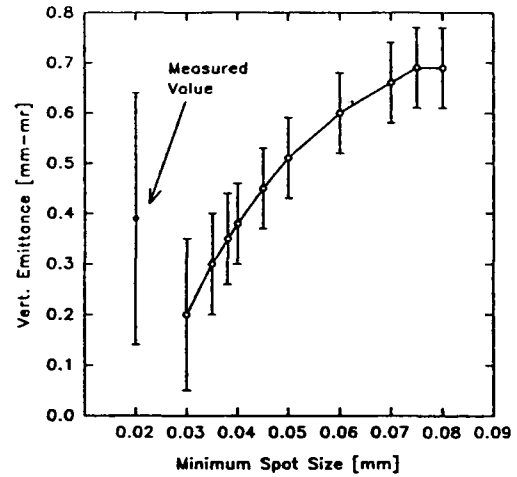


Figure 1: The relation between the emittance and minimum spot size.

III. THE ATF AUTOMATIC EMITTANCE MEASUREMENT SYSTEM

The variable quadrupole method was used for the ATF automatic emittance measurement system because its simplicity and versatility. The ATF automatic emittance measurement system is part of the ATF computer control complex. It is not only capable of processing the data and compute the emittance, but also monitor both the laser and electron beams.

Fig. 2 shows a schematic representation of the ATF emittance measurement system. The ATF control system was built around a VAX 4200 computer, which is connected CAMAC data acquisition hardware by serial highway. The Spiricon beam analyzer was connected to the VAX through a standard IEEE 488 interface card. Spiricon beam analyzer was designed for laser beam applications, it can also be used to process the electron beam images from the beam profile monitor (BPM). The ATF BPM⁵ has a resolution of 40 μm . The Spiricon beam analyzer is pre-triggered by the ATF master timing system, the video camera of the BPM (PULNiX TM-745E) is synchronized with the electron beam by the sync. signals generated by the Spiricon beam analyzer. The automatic emittance measurement system is controlled by an

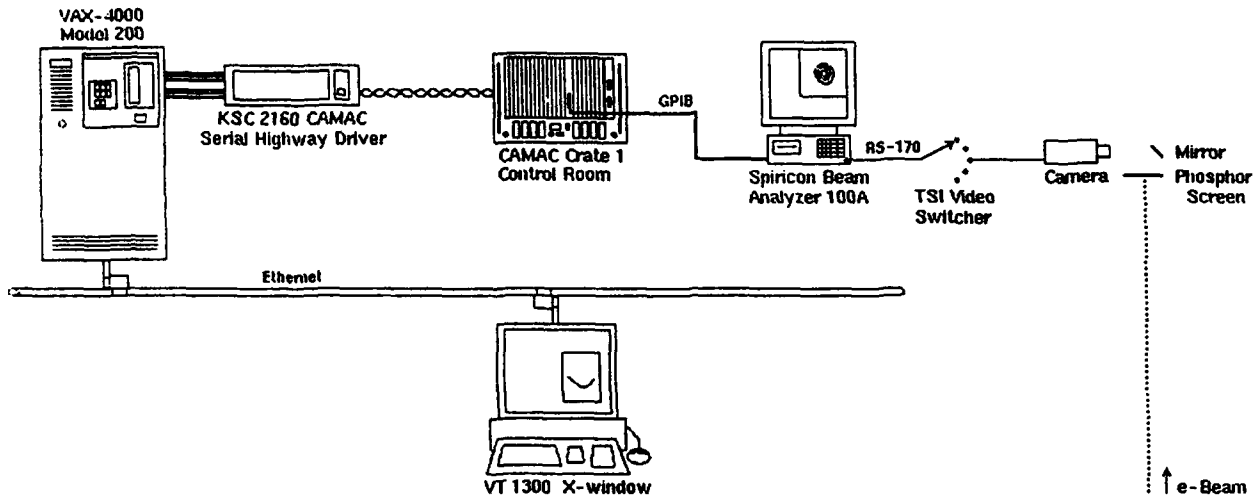


Figure 2: The schematic of the ATF emittance measurement system.

operator window, which was created using Vista control software package. For each emittance scan, the emittance measurement system step through the quadrupole magnet for a given range. It turns on and off the laser beam, acquires dark current and photoelectron beam images. The images are sent to the Spiricon beam analyzer to obtain photoelectron image only by subtraction. Then the Spiricon calculates the elliptical beam parameters for specified portion of the beam image. The Spiricon send the beam information to the VAX by hardware interruption. When data acquisition finished, the VAX calculates the beam matrix and emittance using the algorithm presented in the previous sections. The emittance measurement system also plots the data in real time (Fig. 3), and the beam matrix ellipse in the end.

The Spiricon can calculate the image in several manners, and performs Gauss fit.⁶ The calculation method used in the ATF emittance measurement system is Energy Method. It allows us to calculate elliptical beam parameters for different portions of the beam, and compare with the measured emittances with an ideal gaussian beam. For a gaussian distribution beam, the beam fraction F is given by,⁷

$$F = 1 - \exp\left(-\frac{\epsilon}{2\epsilon_{rms}}\right). \quad (12)$$

and the emittance of a fraction of a gaussian beam is,

$$\frac{\epsilon_{rms}(F)}{\epsilon_{rms}} = 1 + (1 - F) \ln(1 - F) / F \quad (13)$$

Using Spiricon beam analyzer's energy method, we can calculate the beam emittance of the different fractions of the electron beam, and determine the beam distribution by using Eq. (13).

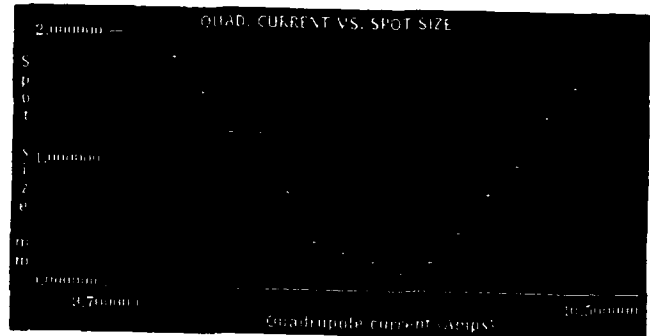


Figure 3: The beam sizes as function of the quadrupole strength.

IV. REFERENCES

1. K.T. McDonald and D.P. Russell, "Methods of Emittance Measurement", p. 122 - 132, Proceeding of the Joint US-CERN School on Observation, Diagnosis and Corrections in Particle beams(1988).
2. M.C. Ross *et al.*, p.725, Proceeding of Particle Accelerator Conference (1983).
3. M.C. Ross *et al.*, SLAC-PUB-4278.
4. X.J. Wang *et al.*, "THE BROOKHAVEN ACCELERATOR TEST FACILITY INJECTION SYSTEM", p. 307, Proceeding of Particle Accelerator Conference (1989).
5. D.P. Russell and K.T. McDonald, p. 1510, Proceeding of Particle Accelerator Conf.(1989).
6. Beam Analyzer Operator's Manual, Spiricon Inc., Logan, Utah.
7. O. Sander, "Transverse Emittance: Its definition, applications, and Measurement", AIP Conf. Proc. No.212, 127-155 (1989).

Electron Beam Emittance Monitor for the SSC

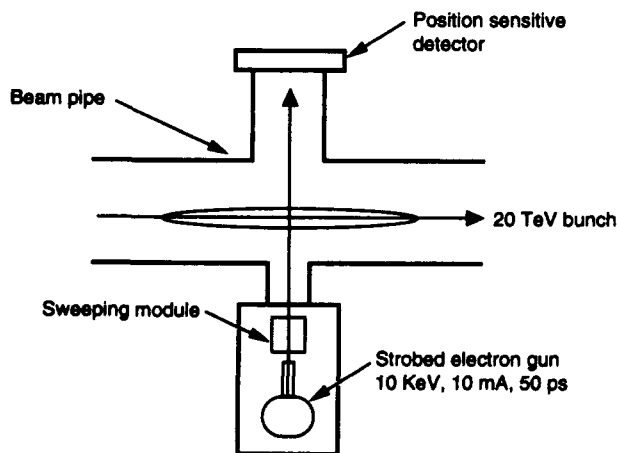
E. Tsyganov, R. Meinke, W. Nexsen, S. Kauffmann, A. Zinchenko, and A. Taratin
Superconducting Super Collider Laboratory*
2550 Beckleymeade Ave., Dallas, TX 75237 USA

Abstract

A nondestructive beam profile monitor for the Superconducting Super Collider (SSC) is presented using as a probe a low-energy electron beam interacting with the proton bunch charge. Results using a full Monte Carlo simulation code look promising for the transverse and longitudinal beam profile measurements.

Recently a low-energy electron beam was proposed [1] for nonperturbing diagnostics of high-energy electron beams, based on earlier works [2,3]. We studied a similar approach in connection with applications for the SSC collider and its transfer lines.

A diagram of the beam emittance monitor for the SSC using a low-energy probe electron beam is presented in Figure 1. A strobed electron gun directs the beam of 10-KeV electrons perpendicular to the proton beam. Deflected electrons are detected with a position sensitive detector. A silicon microstrip detector seems to be a perfect candidate for this. The monitor can use a well-focused electron beam sweeping through the proton beam, or a wide, parallel electron beam. Single bunch measurements are possible in the latter case, *i.e.*, when illuminating a bunch of high-energy particles by a wide parallel electron beam one can obtain a specific "shadow picture" of the proton bunch. The duration of the pulse of electrons in this case should be shorter than the duration of the proton bunch.



TIP-03533

Figure 1. Electron beam profile monitor for the SSC collider.

*Operated by the Universities Research Association, Inc., for the U.S. Department of Energy under Contract No. DE-AC35-89ER40486.

We used the ZBEAM simulation code described elsewhere [4,5] to trace probe electrons in the vicinity of a 20-TeV beam. Electrons were traced from $Y = -1$ cm to $Y = 2$ cm, Y is being the direction of the electron beam. The Z -direction corresponds to the direction of a proton beam. Deflection angles of electrons in the X - Y plane were calculated versus the probe beam position along the X -direction.

The bunch structure of the 20-TeV beam was taken into account. The bunch was considered as a moving charge equivalent to the charge of 10^{10} protons with three-dimensional Gaussian distribution in space. A Gaussian distribution with sigma equal to 5 cm was used in the Z -direction. Four beam sizes were considered with $\sigma_X = \sigma_Y$, for sigma being equal to 50 μ m, 100 μ m, 200 μ m and 500 μ m. The electrons were exactly synchronized with the proton bunch. In our case the Z -component of the electrical field of the bunch is rather small, and we neglect it.

It was found that the electron deflection angle is quite sensitive to the position of the electron beam inside the proton bunch. Figure 2 presents the scattering angle of the electron versus its distance from the center of proton beam (impact parameter) for different beam sizes. By measuring the deflection of the electron beam, it is possible to obtain the rms size of the beam with good precision. The probing electron beam would be swept across the main beam to obtain a full deflection profile. Electrons should be focused in the plane of the proton beam in a spot less than 10 μ m in size in order to not introduce any significant broadening to the measured beam size. Figure 3 demonstrates the sensitivity of the method to the shape of the charge distribution inside the bunch. Scattering angles versus impact parameter are presented for Gaussian and uniform charge distributions in the X - Y plane with the same rms, 50 μ m. In the Z -direction both distributions are Gaussian with sigma of 5 cm. An obvious difference between the two curves is seen.

A notable, and not entirely intuitive, feature of Figures 2 and 3 is the leveling off of the deflection angle for values of the impact parameter which exceed the X -extent of the beam. If the impact parameter b is beyond the X -extent of the beam, but still very small compared to the Z -extent of the bunch, it is reasonable to model the force felt by the probe electron as that due to an infinite line charge,

$$\vec{F}(\vec{R}) = \frac{-2eq_L\vec{R}}{|\vec{R}|^2}, \quad (1)$$

where e is electron's charge, q_L is the linear charge density of the idealized line charge, and \vec{R} is the two-dimensional vector (X , Y). Thus, after some calculations, we arrive to

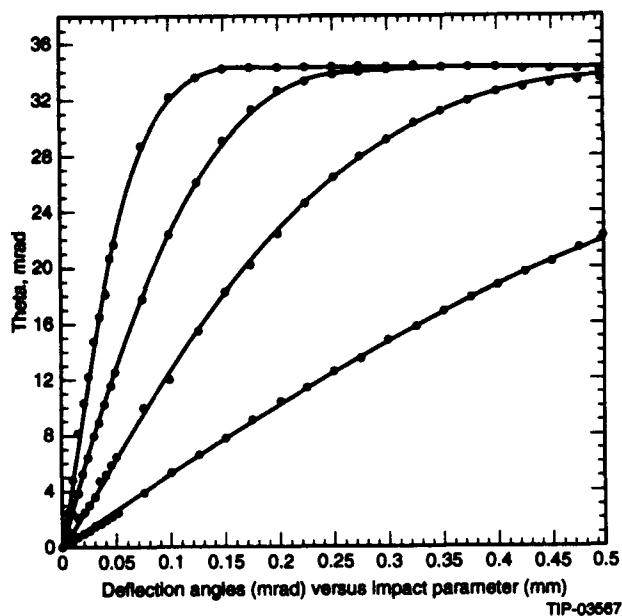


Figure 2. Deflection angles versus electron beam positions relative to the center of a proton bunch. Data for three-dimensional Gaussian distributions of the bunch charge with $\sigma_X = \sigma_Y$ equal to 50 μm , 100 μm , 200 μm and 500 μm . σ_Z is equal to 5 cm. Smooth curves represent a fit of data by error function.

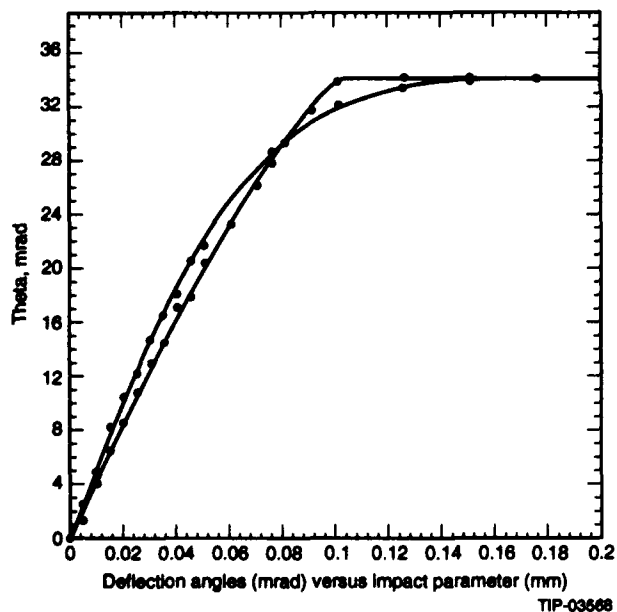


Figure 3. Scattering angle vs. impact parameter for two charge distributions with the same rms, 50 μm . Upper curve—uniform distribution of charge within a 100 μm radius of beam, lower curve—Gaussian distribution with sigma 50 μm . A difference between the two curves is seen.

$$\frac{d\theta}{db} = \frac{-4\pi e}{m\gamma v^2} \int_{-\infty}^{\infty} dY \rho_L(b, Y). \quad (2)$$

In other words, the derivative of the deflection angle as a function of impact parameter is proportional to the Y-integrated profile of the transverse beam charge distribution ρ_L . This happens to be precisely the same information as one obtains from a probe wire ("flying wire") which is passed perpendicular to the beam in the Y-direction (that of the probe electron) through the X-point corresponding to that electron's impact parameter b . The deflection functions shown in Figure 2, then, simply proportional to the indefinite b -integrals of the very "beam profiles" which are measured by "flying wires"!

Figure 4 presents the dependence of the X-position of a deflected electron at $Y = 2$ cm versus its initial X-position at $Y = -1$ cm. Electrons are "switched" in the X-direction by the proton bunch charge around the center of the proton beam, and the shape of this switching is defined by the proton beam profile. Note, that the shape of the curve presented defines not only the transverse shape of the proton beam, but also the longitudinal charge density at the center of the bunch.

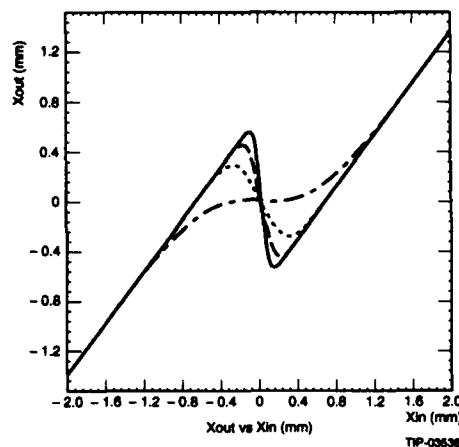


Figure 4. X-position of an electron at the plane $Y = 2$ cm versus its X-position at the plane $Y = -1$ cm. Solid line is for Gaussian beam with $\sigma_X = \sigma_Y = 50 \mu\text{m}$, dashed line—for 100 μm , dotted line—for 200 μm , dash-dotted line—for 500 μm .

Figure 5 presents the X-profiles of a 4-mm wide, parallel, uniformly distributed, electron beam at the $Y = 2$ cm plane for different proton beam sizes. In the Z-direction this beam could be as wide as 10 mm. 10^6 electrons were simulated for each distribution. It is easy to see that the shape of the electron beam profile resulting from interaction with the proton beam is very sensitive to the size of the proton beam. Similar data, but with a Gaussian angular divergence for the electron beam of 1 mrad, are presented in Figure 6. Sensitivity of the resulting electron beam profile to the size of the proton beam remains adequate.

In conclusion, the preliminary calculations presented here show that the emittance of a 20-TeV beam at the SSC can be effectively monitored with low energy electron beams in a

non-destructive technique. Further detailed studies of the process are needed, including construction of a prototype of the device and testing its performance on high energy beams.

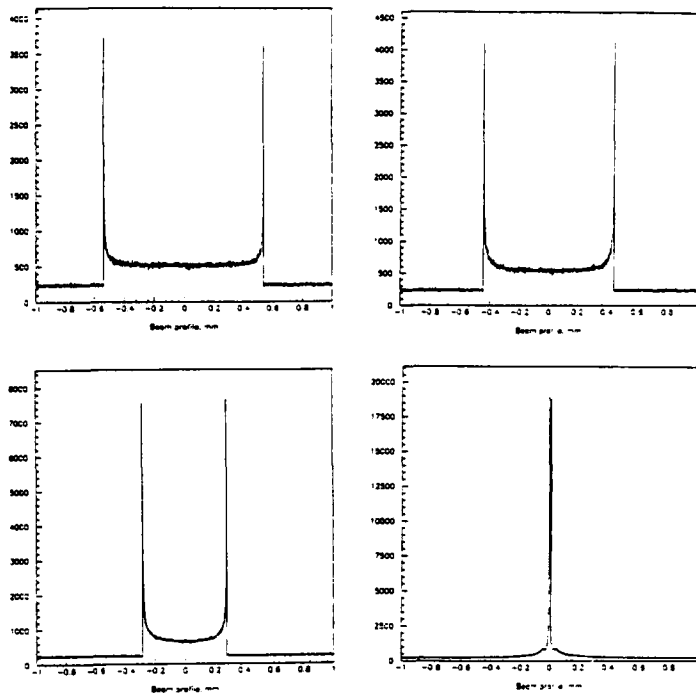


Figure 5. Electron beam profiles at the plane $Y = 2$ cm for different proton beam sizes. Upper left—for sigma $50 \mu\text{m}$, upper right—for sigma $100 \mu\text{m}$, lower left—for sigma $200 \mu\text{m}$, lower right—for sigma $500 \mu\text{m}$. Uniform distribution of the electron beam from -2 mm to $+2$ mm with no angular divergence is assumed at the plane $Y = -1$ cm. 10^6 electrons are used.

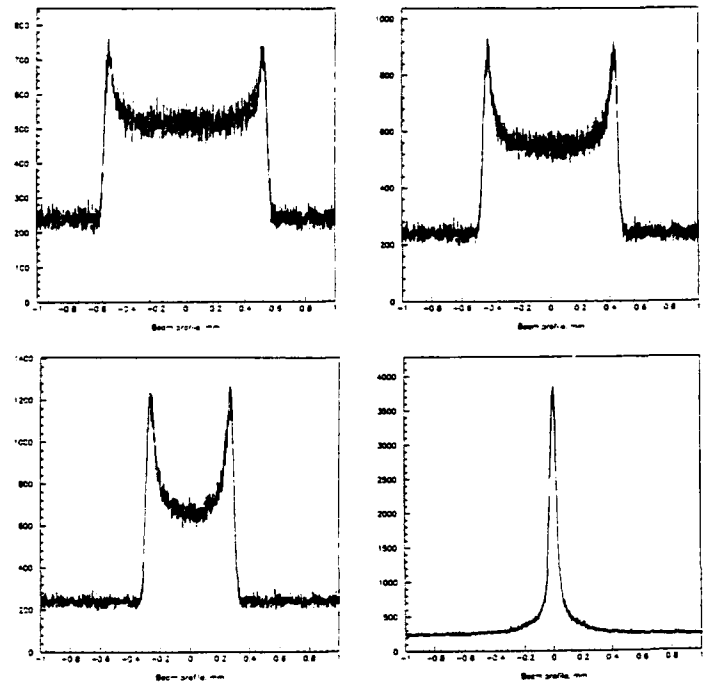


Figure 6. The same, as in Figure 5, but a Gaussian divergence with sigma of 1 mrad is used for the primary electron beam.

REFERENCES

- [1] V. Shestak et al., "An Electron Beam Probe for Ion Beam Diagnosis," TRIUMF Design Note, TRI-DN-87-36 Rev, (1987). J. Pasour and M. Ngo, "Nonperturbing Electron Beam Probe to Diagnose Charged-Particle Beams," *Rev. Sci. Instrum.* 63 (1992) 3027.
- [2] P. D. Goldan, *Phys. Fluids*, 13 (1970) 1055.
- [3] D. A. Swanson, B. E. Cherrington, and J. T. Verdeyen, *Phys. Fluids*, 16 (1973) 1939.
- [4] A. Maschke, W. Nexsen, E. Tsyganov, A. Taratin, A. Zinchenko, "Angular Divergence of 10 KeV Ar⁺ and CS⁺ Ions Due to Ion-Bunch Interaction," Internal Note of the SSCL Collider Group.
- [5] R. Meinke, W. Nexsen, E. Tsyganov, A. Zinchenko, "Limitations of the Residual Gas Ionization Beam Profile Monitor for the SSC Collider," SSCL-602, November 1992.

Measurement of Vertical Emittance at LEP from Hard X-Rays

H. Akbari, J. Borer, C. Bovet, Ch. Delmere, A. Manarin, E. Rossa, M. Sillanoli, J. Spanggaard,
CERN, SL Division, CH-1211 Geneva

Abstract

Two solid state detectors measure in real time the vertical profiles of both beams in LEP, from hard X-rays produced in normal machine dipoles. Each detector consists of 64 elements of CdTe photoconductor deposited with a pitch of 100 μm on a ceramic support. Profiles can be recorded at the rate of bunch passages (88 kHz) for 250 revolutions and are subsequently analysed. This paper describes the new readout electronics adapted to 8 bunch operation of LEP and the performance of detectors using the data acquired in 1992. From the r.m.s. size of these profiles and the knowledge of machine optics, emittance values are obtained.

1. INTRODUCTION

The goal of this instrument is to measure, in real time, at a repetition frequency of 88 kHz, the vertical emittance of electron and positron bunches in LEP. These particles radiate very large quantity of synchrotron X-ray, in the main dipole magnets [1]. This radiation strikes the detectors, placed in two special recesses [2], through a 0.4 mm Be window of the LEP vacuum chamber. There is no imaging of the synchrotron light and the vertical divergence is directly measured by an array of photoconductors (Fig. 1) with a pitch of 100 μm . Having the knowledge of the machine optics, emittance values can be estimated from the measured profiles [3].

A brief description of the detectors is followed by a presentation of the readout electronics and data acquisition system. The calibration and performance of the detectors are described using the data collected during 1992 LEP Operation. During this period the detector was mainly used to test its performance. All of the results (apart from emittance values) shown here are for the electron beam. Identical results were obtained for the positron beam.

2. DETECTORS

During the normal operation of LEP, where these detectors can be used in parasitic mode permanently, they may be exposed to dose of X-rays (10-100 keV) irradiation up to 10^{12} Sv per year. To meet such a requirement, a thin layer (4 μm) of polycrystalline CdTe [2] is deposited on ceramic substrate (127 μm thick) which can resist such severe irradiation. The bias line and 64 horizontal finger lines (50 μm wide) with a pitch of 100 μm , are made with vacuum deposited gold.

During the previous feasibility tests of detectors, they were exposed to an intense X-ray radiation (6 watts per mm^2) for a month. This resulted in a deposition of a carbon layer on the photoconductors due to residual gases. This carbon produces a shunt across the photoconductors and increases the dark

current. Currently new detectors are being fabricated with a protective SiO_2 isolating layer.

Movable mechanics supports the detector mounted on a water cooled aluminium block. It can be displaced vertically within a range of ± 10 mm and rotated for 45° . The movement allows for a proper alignment of the detector with the incident light and also to retract it from irradiation when no data is acquired. The detector is electrically isolated from its support and is contained in a vacuum tank (about 10^{-6} torr).

3. READOUT ELECTRONICS

In order to obtain the vertical profiles of each LEP beams at every passage of each bunch, the data readout, acquisition and pre-processing must be completed in less than 11 μs ; and the readout must be ready to register the next profile (with 8 bunches per LEP turn). Once the data are readout by the front-end electronics, they must be transferred to the data processors over 300 m of cable length. Thus to reduce costs (factor 8 about) and fulfil the time requirement for the readout, an analogue signal multiplexing solution has been chosen.

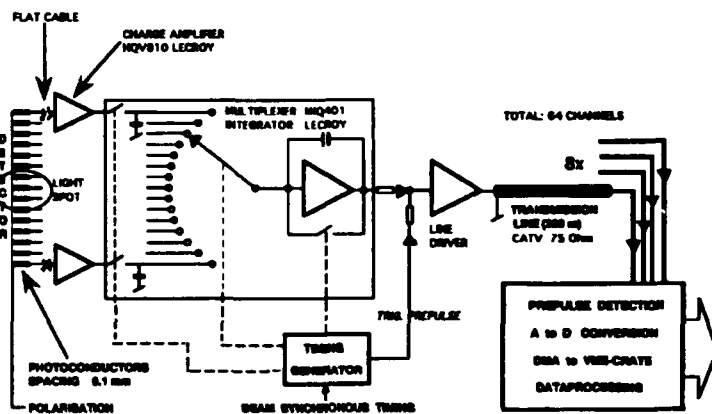


Fig. 1. Synoptic diagram of detector's electronics

Beside the usual difficulties due to mechanical motions in vacuum, a greater technological problem had to be solved: a flat cable with 66 conductors (100 μm wide and 250 μm pitch) and vacuum feed-through to interface the detector with the front-end electronics. The cable is a flexible stripline made with a multilayer of copper and Kapton. An additional external isolating layer avoids parasitic current in the front-end ground layer. The vacuum feed-through is obtained by sealing the flat cable with resin through a slotted flange. This first version was very difficult to connect to the ceramic detector and was fragile. A new version of high mechanical precision, with an intermediate connector and a total length of 2 m, is in preparation.

The low noise charge-preamplifier integrates for each line the current pulse proportional to the photoconductor illumination. The pulse reflections within the 50 ohms lines of the flat cable have no influence on the total integrated charge since the carrier lifetime in the CdTe is about 10 picoseconds. In such configuration, the photoconductors act as an open circuit and the cable as a capacitive memory. The hybrid circuits, LECROY MIQ401, time multiplexes 64 signals in 8 groups of 8 to form a pulse train within the delay of 11 μ s between bunches (fig. 1 and 2). A line driver sends the pulses on long distance cables (300 m) to the data acquisition crate. The time multiplexing is synchronised with turn clock pulses distributed by the Beam Synchronous Timing system which is phase locked to the LEP-RF [4] and delay controlled for selection of bunch.

4. DATA ACQUISITION SYSTEM

The data acquisition system is similar to that of the Beam Orbit Measurement system [5]. FADCs are self triggered by the incoming signal. In a sequence they sample first the base line values and second the pulse heights, thus allowing for DC restitution (fig. 2). The data pairs for each channel are stored in a buffer memory with a time sticker. A maximum of 250 beam revolutions can be stored within its depth of 32 kbyte. A secondary memory with smaller depth, 8 kbyte, is connected in parallel for other applications like real time observation.

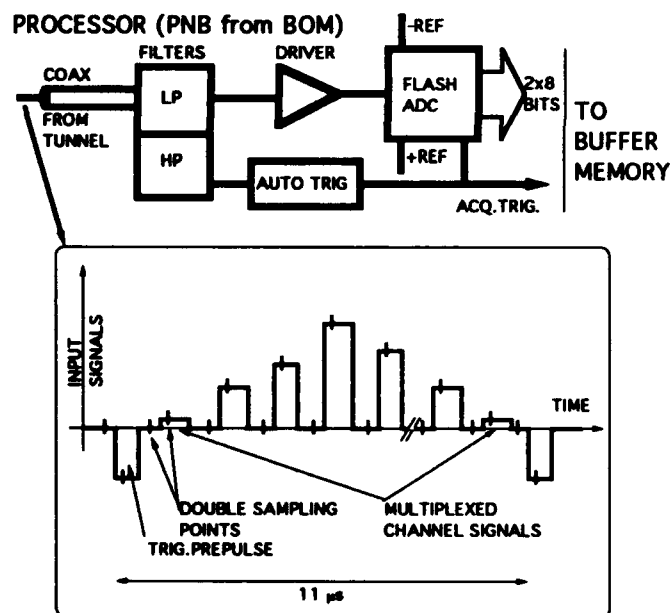


Fig. 2. Acquisition scheme with FADC and buffer memory

The FADCs are connected directly in parallel to the memory module input (VME module) for fast data transfer (about 130 ns). The local processor (Device Stub Controller) scans the data and orders them according to their reference position in the detector. The data are normalised with the coefficients obtained from the calibration of the detectors. The result is a file containing the measured vertical profile for each bunch for up to 250 revolutions. This file is then transferred to an Apollo computer for further processing.

The instrument is fully remote controlled: the detector movements, the power supplies, test generators and the analogue direct profile display for maintenance and performance optimisation purposes.

5. DETECTOR CALIBRATION

The response of photoconductors can be formulated as following :

$$R = A_0 + A_1\Phi + A_2\Phi V$$

where A_0 is the pedestal signal (noise) due to detector and readout electronics in the absence of polarisation voltage (V) and light (Φ); $A_1\Phi$ is due to the electrons leaving the surface of photoconductors which are exposed to an intense photon flux but have no polarisation voltage applied; $A_2\Phi V$ is the response of the photoconductors to light in presence of voltage.

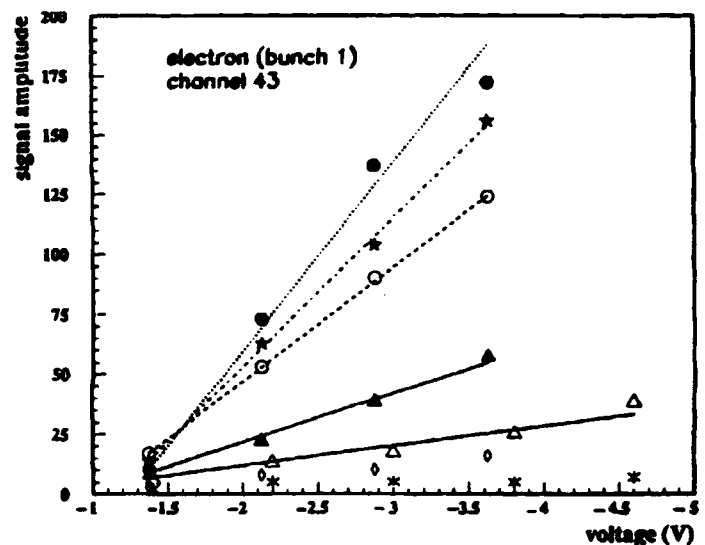


Fig. 3. Response of photoconductor channel 43 as a function of polarisation voltage for different light intensities

The response linearity of each photoconductor channel can be examined as a function of polarization voltage for different intensities of light. All photoconductor channels of both detectors have shown linear response similar to that of channel 43 in fig. 3.

The first step in calibration entails the measurement of A_0 for all channels when there is no beam. Then a relative calibration of the detector involves the determination of a constant proportional to $A_1 + A_2V$ for each channel as obtained for a given polarization voltage V . In order to obtain comparable illumination (Φ) for each photoconductor, the detector is displaced every 100 μ m to measure the vertical beam profile at each displacement. In this manner, ideally all photoconductors are exposed to the same light intensity allowing their gains to be compared with each other. Fig. 4 shows a typical measured profile before and after it is calibrated. The results obtained from such calibration are not

fully satisfactory because of variations observed on some channels due to unstable contact resistance.

6. PERFORMANCE

One of the interesting aspects of this detector is its capability to measure the beam profiles for each bunch over 250 turns. The variation of fitted Gaussian parameters for one bunch over six consecutive turns was examined. The mean position varied by $\pm 5 \mu\text{m}$ and the sigma, (typically $\sim 500 \mu\text{m}$) by $\pm 3 \mu\text{m}$. These values reflect the precision with which the detector can measure the beam profiles.

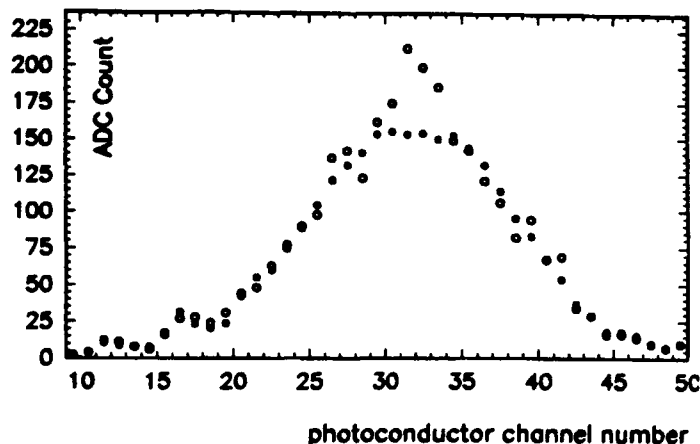


Fig. 4. A typical vertical profile before (o) and after (●) calibration

Once the vertical profile of the beam is measured, the vertical emittance can be easily calculated as following :

$$\epsilon_y = \frac{\sigma_m^2 - \delta_{ph}^2}{\beta_y}$$

where σ_m is the measured sigma, δ_{ph} is the correction due to photon beam divergence from the light source to the detector and β_y is the betatron function at the detector. The typical values measured for the sigma of profiles and vertical emittances during 1992 are given below

	e^+	e^-
$\sigma_m [\mu\text{m}]$	~ 570	~ 430
$\epsilon_y [\text{nm}]$	~ 3.1	~ 1.5

During 1992 operation of LEP, the electron and positron beams manifested a 50 Hz vertical oscillation. Such beam instability has been observed and measured by these detectors [6].

7. CONCLUSIONS

With the new electronics vertical profiles can be recorded for the sixteen bunches in LEP, at consecutive revolutions. The

signal to noise ratio allows good measurements as from the injection energy of 20 GeV/c. At 45 GeV/c a filter can be used to select the higher energy part of the X-ray spectrum which allows emittance measurements with an accuracy of 0.1 nm.

More work remains to be done in the hardware stripline connection to the detector and in the software calibration and data analysis programs. Also new photoconductors protected with a thin layer of silicon oxide have to be tested in the beam.

ACKNOWLEDGEMENTS

We would like to thank M. Cuzin [7] for the supply of CdTe photoconductors and J. Camas, D. Cocq, R. Cornali, B. Hominal, B. Jenny, for the hardware advice and assistance and also the Software Section for the acquisition program.

REFERENCES:

- [1] C. Bovet, J. Kishiro, "A Beam Profile Monitor using Synchrotron Light", LEP Note 492, 20th March 1984.
- [2] E. Rossa, C. Bovet, B. Jenny, J. Spanggaard, E. Jeanclaude, M. Cuzin, M.C. Gentet, C. Ravel, "X-Ray Monitors to Measure Bunch Length and Vertical Profile at LEP" Proc. EPAC Nice (France) 1990.
- [3] C. Bovet, E. Rossa, "Measurement of Vertical Emittance at LEP from Hard X-Rays". Workshop on Advance Beam Instrumentation KEK Tsukuba (Japan), 22-24 April 1991, Also CERN/SL/91-18(BI).
- [4] G. Barribaud et al, "The Beam Synchronous Timing System for the LEP Instrumentation", Int. Conf. on Accelerators and Large Experimental Physics Control Syst., Vancouver, Oct. 30-Nov. 3, 1989, Cern/LEP-BI/89-66.
- [5] J. Borer, "Instrumentation and Diagnostics Used in LEP Commissioning, with Accent on the LEP Beam Orbit Measurement System", American Inst. of Physics, Conf. proceedings no. 229, Accel. Instrumentation second Annual Workshop, Batavia, IL. 1990.
- [6] E. Rossa. "Streak Camera and BEXE". Proc. of Third Workshop on LEP Performance. Chamonix, January 10-16, 1993. Edited by J. Poole. CERN SL/93-19 (DI).
- [7] D. LETI, Institut de Recherche Technologique et de Developpement Industriel, C.E.A., 85 X- F.38041 GRENOBLE (FRANCE)

Performance and Operational Experience of the LEP Synchrotron Light Telescopes

G. Burtin, R.J. Colchester, J.J. Gras, R. Jung, J.M. Vouillot
European Organization for Nuclear Research (CERN)
CH-1211 Geneva 23, Switzerland

Abstract

The experience and performance over the past three and a half years of operation is reported. The dynamic range of the monitor has been increased by an improved cooling of the CCD chip with the help of Peltier cells. The contributions from the diffraction and the depth of field have been evaluated with precision in order to estimate the beam emittances. Comparisons and cross calibrations with the wire scanners have been started. A video frame grabber and fast projection calculation for real time beam size display has been implemented.

I. INTRODUCTION

There are four synchrotron radiation (SR) telescopes located around Intersection 8 of LEP. The system has been described in detail in [1]. The monitors have been in operation since the start-up in July 1989. Two monitors observe the electron beam and two the positron beam. For each type of particle, there is a monitor located at a near zero-dispersion location and one at a high dispersion point. The telescopes have a magnification of 1/5 between the beam and the detectors. Two detectors per telescope are in use. The first and most used one is a CCD chip which integrates the light coming from all bunches over a maximum period of 20 ms. The second is a gated intensifier and wavelength shifter coupled to a CCD which is able to acquire individual bunches at selected intervals. The effort over the past year was mainly directed towards the improvement of the precision on emittance measurements. For this, the dynamic range was increased and the contributions of the depth of field and diffraction were measured with better precision.

II. IMPROVEMENT OF THE DYNAMIC RANGE

The dynamic range of the monitor is first limited by that of the CCD chip. Charges of thermal origin, the so-called dark current, are collected in the CCD potential wells during the integration and readout periods. They decrease the dynamic range, introduce statistical non-uniformities on the signals and a slope on the vertical beam projection. The latter is generated by the difference in time spent in the CCD by the various pixel charges as a function of their origin. The dark current can be reduced by a shorter readout time and by cooling the CCD chip. For best geometrical precision, the CCD chip, of the frame transfer type, is read out pixel by pixel at a frequency up to 1 MHz, limited by the speed of the 12 bit ADC and the 500 m cable length from the camera head to the processing electronics. This readout can take up to 200 ms. A faster readout frequency would decrease the dark current but also increase the noise of the output stage and the charges lost during the many transfers to the output.

Experiments have been carried out at various temperatures of the CCD chip, at read-out frequencies of 450 kHz, 900 kHz and 7 MHz, in full darkness and with uniform illumination, in order to find optimum operating conditions. The CCD temperature was changed by connecting to its back face a Peltier effect cooling cell and by providing a cooled dry air circulation in the telescope. The chip temperature was lowered, starting from an estimated temperature of 60°C with the original closed camera [1]. The slope of the vertical projection was reduced from one hundred counts (out of 4096) to one count over the 288 useful lines as soon as a temperature below 15°C was reached. The noise of the two projections was FFT analysed. The dominant noise is the quantification noise of the 12 bit ADC both in darkness and with a uniform illumination. This justifies the use of an ADC of at least 12 bits if the conversion time is not a major issue. Switching from 450 to 900 kHz gave little improvement. The Dark Current Non Uniformity and the Photon Response Non Uniformity were estimated to be in the range of ± 1 count and the detector was found to be linear over 3500 counts. The charges lost during the numerous transfers to the output amplifier are characterised by the Charge Transfer Efficiency (CTE). At 450 kHz and near saturation, a CTE slope of $-2 \cdot 10^{-4}$ /pixel has been measured. It results in a maximum charge loss of 20%. This slope increases with frequency. As a consequence, all CCD cameras will be of the open frame type with one Peltier cooling cell and will be read at a frequency of 450 kHz, except for one detector which will be operated at 900 kHz for test purposes. Good projections are obtained in practice at a signal peak amplitude of one hundred counts. With the available neutral density filters the beam intensity dynamic range is extended to 3000, starting at a circulating current of 5 μ A with an integration time of 20 ms, a wavelength filter centred around 450 nm and present beam sizes.

III. DIFFRACTION AND DEPTH OF FIELD CONTRIBUTIONS TO THE MEASURED PROFILES

In order to calculate the beam size from the measured light spot, it is necessary to evaluate the broadening introduced by the depth of field and the diffraction.

The depth of field is limited by a horizontal slit of width w located in the focal plane of the focusing spherical mirror [1]. This slit is the main origin of diffraction in the horizontal plane. In the vertical plane, the only diffraction to be considered is that originating from the small aperture of the SR. The various contributions have been measured by varying the slit width w and the wavelength λ used. The evolution of the horizontal and vertical rms beam sizes as a function of the slit width w are given in Fig. 1.

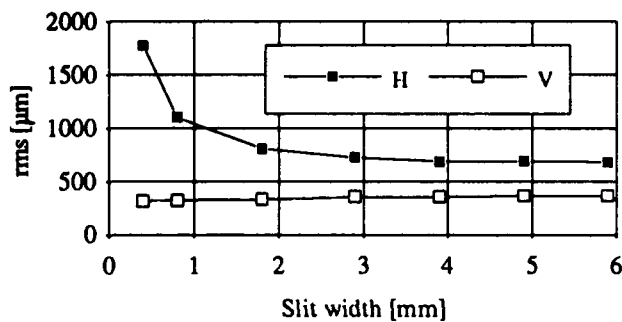


Fig. 1: Evolution of the horizontal and vertical rms beam sizes as a function of slit width w at 450 nm.

The vertical rms size of the light spot decreases slowly with the slit width w , whereas in the horizontal plane the size passes through a minimum before increasing sharply for low values of w . This is due to the combination of depth of field and diffraction acting in opposite ways. An operational slit width of 2 mm has been chosen as an acceptable compromise.

The natural diffraction contribution has been evaluated by measuring the vertical size of a beam at four different wavelengths, i.e. 450, 622 and 800 nm with the CCD and 254 nm with the intensifier coupled to the CCD: Fig. 2. A fifth point is given by a solar blind filter.

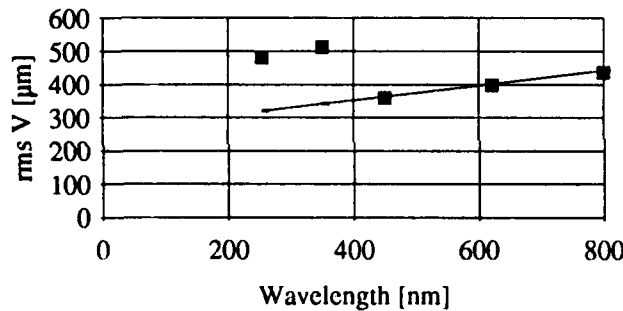


Fig. 2: Vertical light spot sizes measured at various wavelengths together with the expected spot size curve.

The spot size decreases with the wavelength as expected until the CCD is replaced by the intensifier, showing the additional spot broadening introduced by the intensifier. This broadening has been estimated to be 72 μm rms at the detector level, i.e. 360 μm at the beam level.

Correction coefficients for estimating the beam size have been calculated from these measurements. The rms contributions, expressed in μm , of the diffraction, σ_{DH} and σ_{DV} , and of the longitudinal acceptance σ_{LA} can be expressed as:

$$\begin{aligned}\sigma_{DH} &= 1.45 \lambda/w \\ \sigma_{DV} &= 3.9 \lambda^{2/3} \\ \sigma_{LA} &= 40 w\end{aligned}$$

where the slit size w is expressed in mm and the wavelength λ in nm. These contributions are subtracted quadratically from the measured light spot rms size. The main difficulty in measuring these correction coefficients is to have sufficient stable beam conditions. The broadening introduced by the gated intensifier-wavelength shifter is too large to permit precision beam size measurements. The calibration curve of the vertical light spot size versus emittance at the nominal operating parameters is given in Fig. 3.

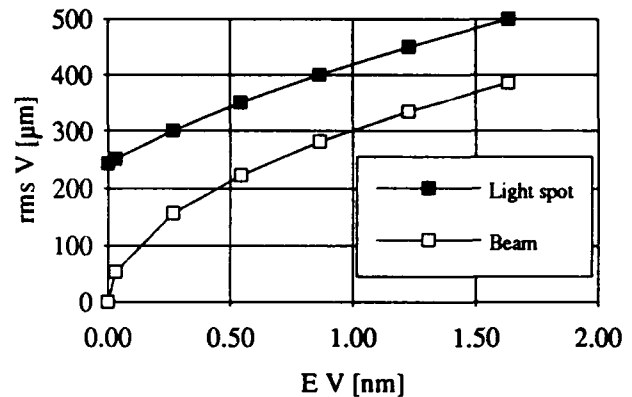


Fig. 3: Vertical Light spot size versus Emittance at zero dispersion: for $\beta_y=91\text{m}$, $\lambda=450\text{nm}$, $w=2\text{mm}$

A similar curve can be established for the horizontal case. As can be seen from this calibration curve, it is desirable to lower the wavelength at which the measurements are made for evaluating the present small beam emittances.

IV. OBSERVATIONS AND EMITTANCE ESTIMATIONS

A feature which became apparent during the previous measurements were small beam size excursions. By varying the CCD integration time from 2 to 30 ms with a stable beam, the variation of the spot sizes could be measured: Fig. 4.

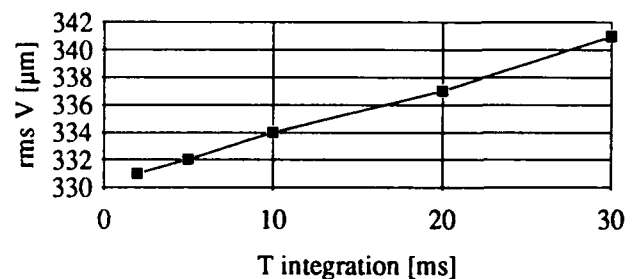


Fig. 4: Light spot size variations as a function of CCD integration time.

Variations of 4 μm of the horizontal projection and of 10 μm of the vertical projection, at beam level, were recorded. Unfortunately the integration time could not be increased beyond 30 ms to characterise more precisely the frequency of the phenomenon. Neither was it possible to get precise

enough information from the gated detector. The influence of these oscillations on estimated beam sizes is negligible in the horizontal plane but results in an enlargement of up to 2 % in the vertical plane for a 20 ms integration time. This "wobbling" has been observed also with the pick-ups [2] and is suspected to be of 50 Hz frequency and be caused by a power cable. This particular effect should disappear in 1993. Nevertheless the possibility to increase the integration period beyond 40 ms, actually up to 512 ms, in order to study similar phenomena will be implemented.

During the first two years of running, the LEP emittances were close to the original design values of 42 and 1.7 nm and the emittances provided by the telescopes were consistent with the experimental Luminosity figures. In 1993 a new optics with a 90° phase advance in both planes was introduced, resulting in much lower emittances, typically 12 and 0.5 nm. Despite the improvements implemented, the emittance figures provided by the telescopes for colliding beams were generally high, sometimes up to 40%, w.r.t the Luminosity figures. Several phenomena can be considered to explain it. The most likely ones are the lack of knowledge of the machine optical functions at the telescopes, beam instabilities during the integration period, and magnetic coupling resulting in beam tilts which give larger apparent vertical emittances in the detector frame.

Precision cross-calibrations with the wire scanners have been started [3]. Due to the different operating conditions and locations of the two monitors, the results of these tests are delicate to interpret. Beam tilts and limited knowledge of the machine optical functions increase the difficulty of these comparisons. A few good comparisons were made and are encouraging for the future. An upper limit on the precision of ± 0.5 nm on the horizontal emittance and ± 0.2 nm on the vertical emittance could be deduced. The relative accuracy is much better. Beam size changes of 5 μ m can be detected, see Fig. 4, and hence emittance changes of 2% are detectable with stable beams. Systematic comparisons with the X-ray vertical profile monitors [4] are also foreseen in 1993.

The facilities with the fast shutter were little used. This is mainly due to the additional enlargement of the spot size and to the late availability of display software for the control room workstations. This mode is useful to compare the sizes of the different bunches and to observe fast turn by turn beam instabilities with the "burst" mode [1]. The new display facilities show centre of gravity and beam size evolution over the eight acquired profiles, taken at intervals from one to 256 LEP turns.

As some measurements have indicated that the beam tails were not gaussian, preliminary tests to study these tails have been made by directing the beam light spot towards the edge of the CCD detector in order to increase its apparent dynamic range up to $1/10^5$. These tests will be continued.

The TV monitors with superimposed measurement results [1] are still the most used facility. For helping with the tuning of LEP, an eight bit frame digitiser with fast (40 ms)

hardware beam size calculations was installed. The results are averaged over ten measurements for noise rejection and displayed on a colour TV monitor in the control room: Fig. 5.

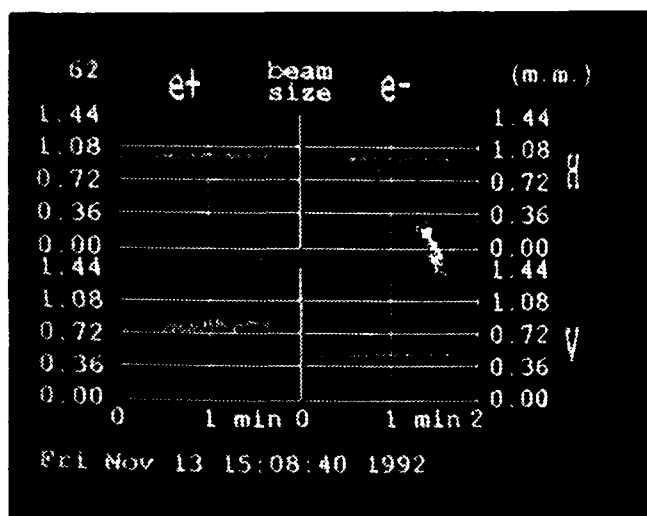


Fig. 5: Fast beam size display showing the evolution of the two beams over two minutes. It is updated every 600 ms.

V. PLANS FOR THE FUTURE

For 1993 it is foreseen to install:

- a phosphor coated CCD sensitive down to 200 nm to improve the precision of the beam size measurement,
- a set of finite width density filters for implementing a "corona"-type set-up to study the beam tails,
- a linear density filter set to keep automatically the beam signal close to its maximum during a whole run,
- to have all detectors equipped with Peltier cooling cells.

The system will be using a 68 030 CPU running under OS 9 and directly connected to Ethernet which will increase the processing speed and suppress a layer of the original control set-up.

ACKNOWLEDGEMENTS

Acknowledgements are due to J.P. Bindi who designed and installed the telescope cooling with Peltier cells, to L. Brunel for the CCD measurements, to G.F. Ferioli and J. Provost who provided the hardware for the fast video acquisition and display of the beam sizes, to A. Burns for the video display software, and to E. Hatziangeli for the workstations software.

REFERENCES

- [1] C. Bovet et al.: The LEP synchrotron light monitors, Proc. of the 1991 IEEE Acc. Conf., San Francisco
- [2] J. Borer et al.: Harmonic analysis of coherent bunch oscillations in LEP, Proc. of the 1992 EPAC, Berlin
- [3] J. Camas et al.: High resolution measurements of profiles with the LEP wire scanners, these proceedings.
- [4] E. Rossa et al.: Measurement of vertical emittance at LEP from hard X-rays, these proceedings

High Sensitivity Beam Intensity and Profile Monitors for the SPS Extracted Beams

J. Camas, G. Ferioli, R. Jung, J. Mann
European Organization for Nuclear Research (CERN)
CH-1211 Geneva 23, Switzerland

Abstract

Secondary Emission Monitors using caesium iodide coated thin aluminium foils have been installed in the SPS transfer channels to monitor the intensity of the extracted heavy ions beams. Tests have shown an increase by a factor twenty of their sensitivity with respect to bare aluminium foils. Luminescent screens viewed with TV cameras are used to monitor the position and the profiles of the extracted beams. Various luminescent screen materials have been tested. Results on chromium doped alumina, thallium doped caesium iodide and quartz are reported. A dynamic range of 10^3 in beam intensities can be achieved by using these three materials in turn in the usual three screen tanks. Intensifiers used together with CCD cameras and video frame grabbers with incorporated projection calculations are used in conjunction with these screens. Results with heavy ions in the transfer channels and with protons extracted from circulating beams in the SPS are given. Detection sensitivities down to a few tens of protons per video frame have been observed.

I. INTRODUCTION

Oxygen and sulphur ions have been accelerated in the SPS and delivered to the users of the experimental areas in the past, and the instrumentation had been adapted to this low intensity mode [1]. After the approval of the project to accelerate lead ions in the SPS complex from 1994 onwards, the instrumentation for the transfer channels was re-examined. The instruments discussed here are for intensity, position and profile measurements in the transfer lines. The intensities are measured traditionally with secondary emission foils covering the whole aperture (BSI), the position is taken from luminescent screens (BTV) and the profiles acquired with Secondary Emission Grids (BSG). The sensitivity of the BSIs had to be improved substantially. The same was done with a BSG for test purposes, but there was still the limited resolution, the risk of non uniformity from strip to strip and the inherent complexity of the monitor electronics. With the advent of high yield luminescent screens and intensified CCD cameras, it was decided to try to use also the luminescent screens for profile measurements. The output of all these monitors is proportional to the Z^2 of the ions observed.

II. HIGH SENSITIVITY INTENSITY MEASUREMENT

The usual aluminium foils used in Secondary Emission Monitors (SEM) have a yield of 5% at the SPS

beam energies. It has been known for some time that this sensitivity could be increased by coating the foils with CsI or KCl. These coatings were thick ones and experienced most of the time some hygroscopic effects and sensitivity degradation with time. As the monitors had to be used over long periods, a thin coating of CsI was tested. A 500 nm thick coating was deposited at CERN on 5 μm aluminium foils with a 100 nm Al evaporated coating. It demonstrated a yield of 100% and a relatively long lifetime. When analysed on the electron microscope, the CsI appears as approximately 0.5 μm droplets covering roughly 40% of the aluminium surface: Fig. 1.

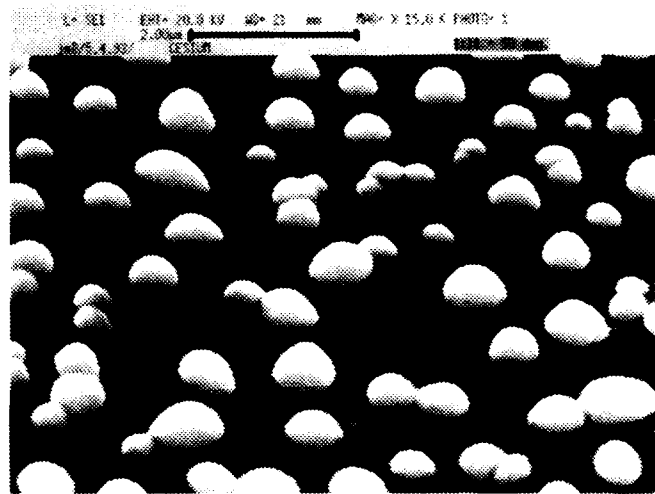


Fig.1: Electron microscope photography of a CsI coating on an aluminium foil. The reference bar at the top is 2 μm long.

Five BSI monitors were equipped with these foils for the sulphur run of 1991 and three more monitors were equipped for the 1992 run for monitoring the injection into the SPS and the ejections towards the North and West experimental areas. Together with a new high sensitivity front electronics, the system has a basic noise level of 10^5 charges with Sulphur, which is the limiting resolution. Studies were made during this period to define the sensitivity, as a function of the various beam parameters, and its variation in time. The gain factor of CsI decreases from a high value of twenty for low peak current beams down to a factor five for high peak intensity beams, the transition taking place around 1 mA peak. The foils which were not continuously submitted to high peak current proton beams of several Amperes, kept their amplification factor over the two years of experience. On the other hand, foils which had been submitted regularly to the traversal of high peak currents had their sensitivity lowered by approximately 20% from one year to the next.

III. BEAM PROFILE MONITORING

It is possible to measure beam profiles with luminescent screens. They have many advantages over SEM-Grids, i.e. high resolution with a minimum of cabling, good dynamic range, and low noise, essentially when CCD detectors can be used. The resolution is given in this case by the size of the picture elements or pixels of the chip. The CCD is a matrix of 604 x 294 pixels, 10 μm in square, made by Philips. For observing the low intensity signals associated with heavy ion operation, a DC intensifier is installed in front of the CCD camera. It has a gain which can be controlled by a low level signal, generated by a DAC under computer control and applied to the high voltage DC/DC converter. It can change the global gain from a low value of 400 up to a gain of 10^4 . The Intensifier is coupled to the CCD by two lenses mounted back to back: Fig. 2. The set-up is less compact and efficient in light transmission than a fibre optic coupling, but has the advantage to be far more economical.

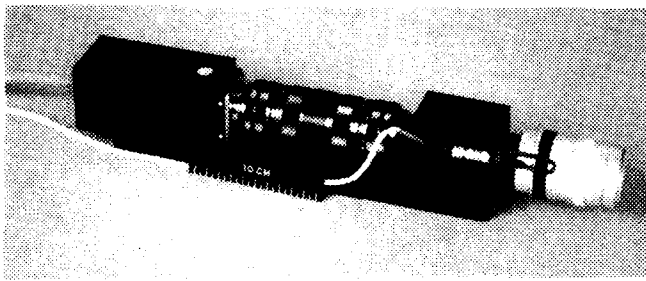


Fig. 2: Intensifier (at left) coupled by two back to back lenses to the CCD camera.

In order to use the screen information to measure beam profiles, the video signal in CCIR standard has to be digitised. As in beam monitoring the beam projections along the horizontal and vertical axis are to be used to calculate the beam emittances, a function which is not yet implemented in the commercial devices, it was decided to build a VME frame grabber module, which next to the digitisation calculates on board the two projections during two successive TV frames. The module has a windowing function, enabling to digitise and memorise a square area within the TV picture. The data reduction achieved permits to memorise several pictures and profiles until the image and profile memories are filled up, e.g. from one image of 256x256 pixels to six images of 100x100 pixels and up to 160 profiles over 100x100 pixels. This information is available for later retrieval. The digitisation is done by an 8 bit flash ADC converting at a rate of 7 MHz. A companion module allows to memorise the full TV image and to display it on the TV monitor until a reset pulse is received. This feature is interesting in the long cycles in use at the SPS. Four Intensified CCD cameras were installed for the 1991 heavy ion run. As they gave satisfactory results, five more were installed for the 1992 run.

The CCD cameras have to be replaced by tube cameras for the high intensity proton runs to avoid radiation damage.

To achieve the best sensitivity of the system, some effort was invested in the study of the luminescent screen material. Up to the heavy ion runs, three types of screen material were used: quartz for very high density beams, Cerium doped Lithium glass and Chromium doped Alumina, the light yield increasing in that order. Thallium doped Caesium Iodide crystals have interesting properties. This material has a better light yield than Al_2O_3 (Cr), is a thousand times faster which is interesting for time resolved profiles and emits light at 550 nm, in the sensitivity region of a normal CCD (450 to 1000 nm). The main disadvantage of CsI (Tl) is its softness which limits its size to a disk of 80 mm in diameter for a one millimetre thickness. The spectral emission curves for the four screens are given in Fig. 3, normalised for a 10^{13} proton beam.

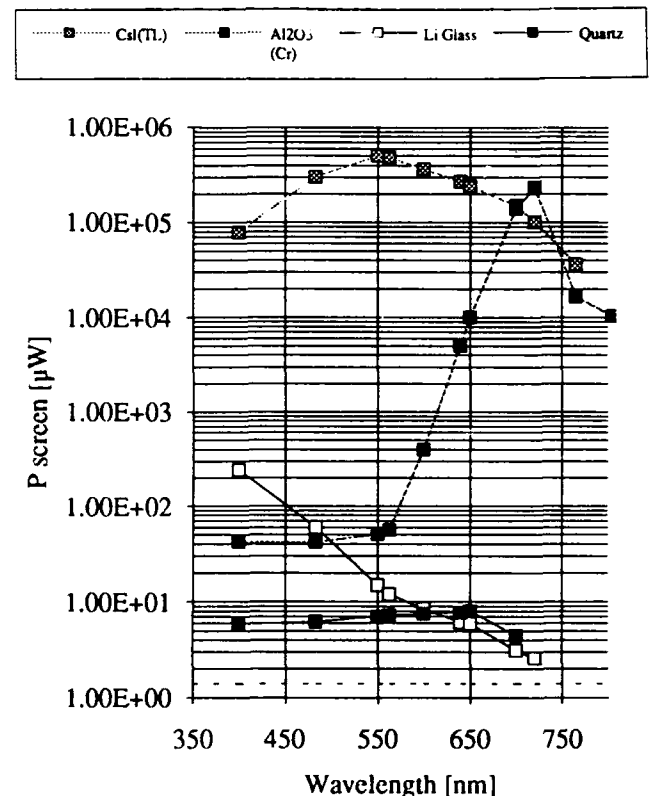


Fig. 3: Spectral emission curves of four screen materials

The lithium glass which is well adapted to TV tubes cannot be used with CCDs as it emits mainly outside the spectral sensitivity of these detectors. The properties of the three screens which are used with CCDs are collected in Table 1, where the sensitivities are given for protons beams of 2 mm diameter FWHM with a screen to CCD demagnification of 10.

Table 1: Screen material characteristics

Material	Activator	λ_c [nm]	decay	Sensitivity
Quartz	none	large	ns	1×10^8
Al_2O_3	Cr	700	ms	2×10^6
CsI	Tl	550	μs	7×10^4

Two Caesium Iodide screens were installed for test purposes in 1992. The results were promising and it was decided to install the previous three screen types in a maximum of monitors. The monitors have four positions, three for screens and an empty one for the free passage of beam: Fig. 4.

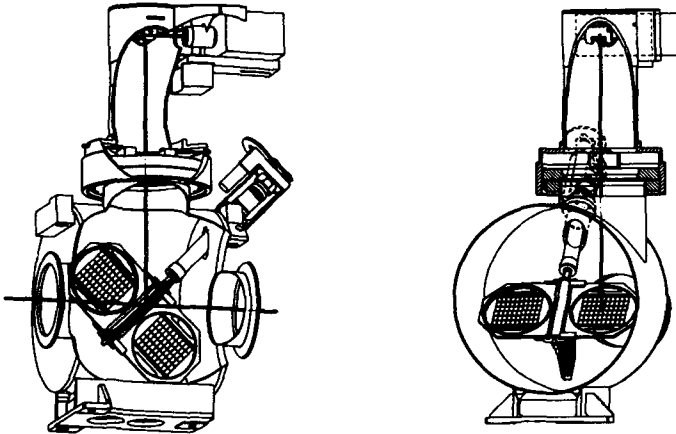


Fig. 4: Luminescent screen monitor with four positions, three for screens and one for the free passage of beam.

During the 1992 Sulphur run profiles of beams with 10^5 ions per profile were taken. A typical example is given in Fig. 5.

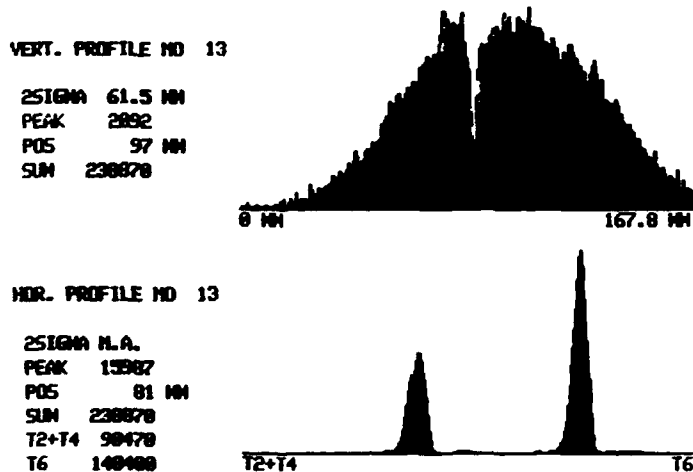


Fig. 5: Horizontal and Vertical profiles of 1.10^5 extracted Sulphur ions (in 20 ms) taken after splitter #1.

In the SPS ring, good quality profiles were also taken with the wire scanners, the signal being acquired with scintillators downstream of the wire.

IV. VERY HIGH SENSITIVITY PROFILE MONITORING.

Encouraged by the good results with heavy ions, a luminescent screen monitor was installed for the crystal extraction experiment in the SPS [2]. The monitor is comprised of a tank identical to that of Fig.4 located on the proton extraction path, under air, equipped with CsI(Tl) and Al_2O_3 (Cr) screens and with the standard Intensified CCD camera of Fig.2. It permits a direct observation of the extracted beam on a TV monitor over a wide dynamic range and the digitisation of the acquired images. A lego plot of such an acquisition is given in Fig. 6.

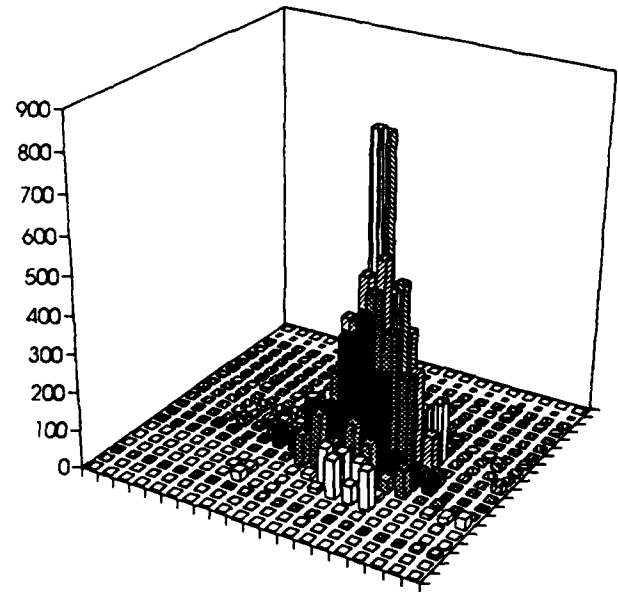


Fig. 6: Lego plot of protons extracted from the SPS by a bent crystal.

By making comparison with scintillator counters, it appears that sensitivities down to one proton per pixel can be obtained with the CsI(Tl) screen and Intensified CCD combination.

V. ACKNOWLEDGEMENTS

It is a pleasure to acknowledge the contribution of J. Provost to the design of the CCD acquisition system and of J. Koopman to various phases of the project.

REFERENCES

- [1] J. Bosser et al.: Beam Transfer Monitors for the Operation of the SPS with Oxygen, Proc. of the 1987 IEEE Part. Acc. Conf., Washington D.C.
- [2] S. Weisz et al.: Proton extraction from the CERN-SPS by a bent crystal, these Proceedings

High Density Harp For SSCL Linac

Craig T. Fritsche and Michael L. Krogh
AlliedSignal Inc., Kansas City Division*
P.O. Box 419159, Kansas City, MO 64141-6159

Charles E. Crist
Superconducting Super Collider Laboratory†
2550 Beckleymeade Ave., MS-1043, Dallas, TX 75237-3946

Abstract

AlliedSignal Inc., Kansas City Division, and the Superconducting Super Collider Laboratory (SSCL) are collaboratively developing a high density harp for the SSCL linac. This harp is designed using hybrid microcircuit (HMC) technology to obtain a higher wire density than previously available. The developed harp contains one hundred twenty-eight 33-micron-diameter carbon wires on 0.38-mm centers. The harp features an onboard broken wire detection circuit. Carbon wire preparation and attachment processes were developed. High density surface mount connectors were located. The status of high density harp development will be presented along with planned future activities.

INTRODUCTION

AlliedSignal Inc., Kansas City Division, and the Superconducting Super Collider Laboratory (SSCL) are developing a high density harp for use in the SSCL linac. The SSCL required a 128-wire harp with overall dimensions no greater than 80 mm X 80 mm X 50 mm (L X W X D). The carbon wires needed to be approximately 25 microns in diameter and spaced 380 microns on center¹. The harp must mount to the end of a SSCL actuator² using a 2.125-inch conflat flange.

To accomplish the SSCL's design goals, the Kansas City Division's experience in designing and manufacturing hybrid microcircuits (HMCs) was utilized.

Utilizing the technologies used to fabricate hybrid microcircuits, a harp can be produced with greater wire density than previously obtainable. The high density harp utilizes thick film conductor lines printed on a ceramic substrate. Since thick film networks (TKNs) can be

fabricated with 0.127-mm lines and spaces, carbon wires spaced 0.254 mm on center are possible.

A carbon wire attachment process was developed to bond carbon wires to gold TKN bond pads. The attachment was required to be a maximum of 0.254-mm wide to match the minimum TKN line spacing

HARP DESIGN

Figure 1 illustrates the design for a high density harp. The overall dimensions of this harp are 80 mm X 75 mm X 45 mm (L X W X D). This harp has been designed to mount to the SSCL actuator with a 2.125-inch conflat flange. Connection to the data monitoring circuitry³ is made within the 25.4 mm I.D. actuator arm by mating to the harp's four 37-contact high density surface mount connectors manufactured by Nanonics Corporation. These dual-row nanominiature connectors feature 0.635 mm contact spacing and measure only 11.43 mm X 5.72 mm X 3.18 mm (L X W X D).

The harp TKN is a 1-mm-thick alumina substrate printed with thick film conductor inks. Conductor inks used include gold for the wire bond pads and conductor lines and a platinum/gold composition for the connector pads. The platinum/gold composition allows the connectors to be surface mount soldered without leaching the pads off the substrate. The harp's TKN has six conductor layers printed on both sides. Printed dielectric layers separate the conductor layers. A 0.15 mm X 0.23 mm oval-shaped through-hole via geometry was developed to make the required 128 TKN front-to-backside connections in the available amount of space.

A benefit of utilizing a TKN for the harp network is that a 1 M-ohm resistor array can be printed directly on the harp substrate. This allows the incorporation of a broken wire

*Operated for the U.S. Department of Energy under Contract Number DE-ACO4-76-DP00613

†Operated by the University Research Association, Inc. for the U.S. Department of Energy, under contract No. DE-AC35-89ER40486

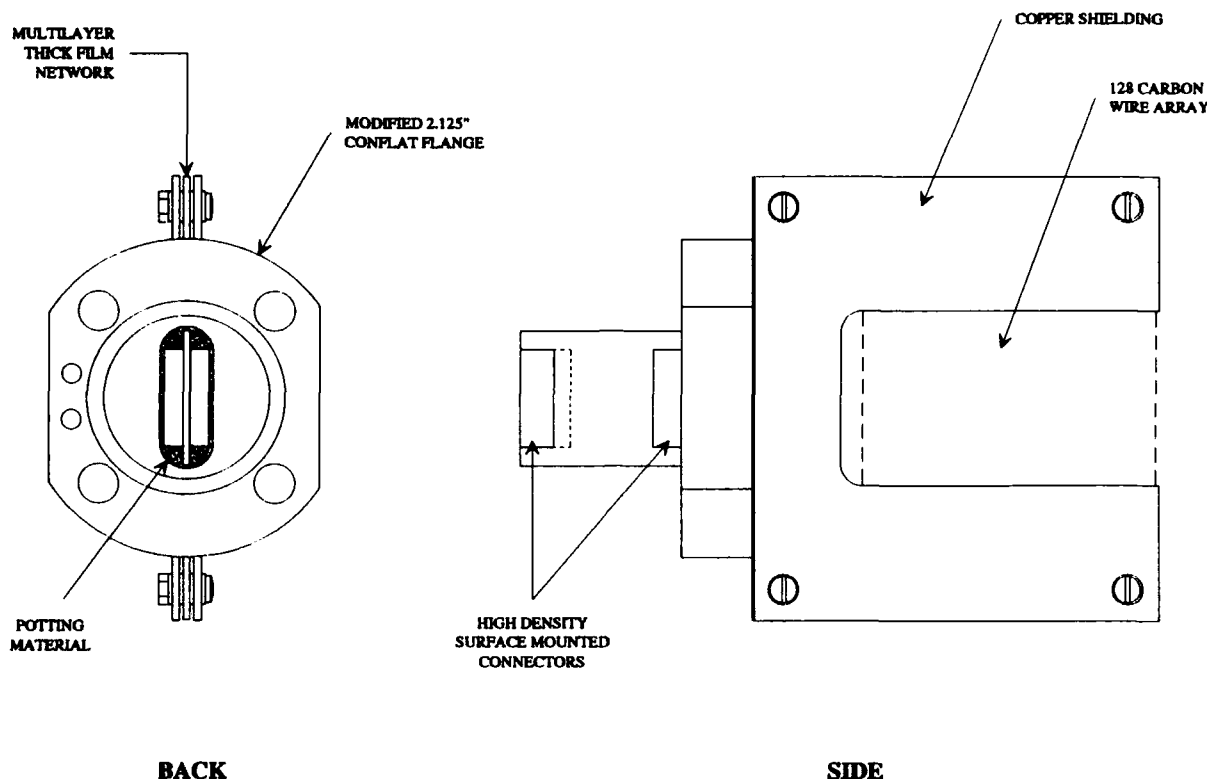


Figure 1. High density harp

detection circuit without increasing the harp's thickness or adding components.

To obtain a vacuum feedthrough with 128+ conductors, the harp thick film network was designed with a

necked-down region that may be potted into the conflat flange, forming a hermetic seal.

CARBON WIRE ATTACHMENT

The high density carbon wire array required the development of a bonding technique to attach the carbon wires to the harp TKN bond pads. The technique makes it possible to attach 33-micron-diameter carbon wires to 0.127-mm-wide metallized pads, providing mechanical and electrical connection.

Before carbon wires are bonded to the harp network, the ends of the wires are metallized with titanium, palladium, and gold. In preparation for the metallization process, the wires are epoxy-attached under tension to a metallized ceramic frame so that all of the wires are parallel to each other and properly spaced (Figure 2). The ceramic frame is made from standard herman-size (3.75 X 4.5-inches) ceramic to be easily accommodated by the Kansas City Division's processing equipment, a vacuum deposition chamber and a gold electroplating tank, without new fixturing.

The frame containing the carbon wires, masked to expose only the ends of the wires, is sputtered with

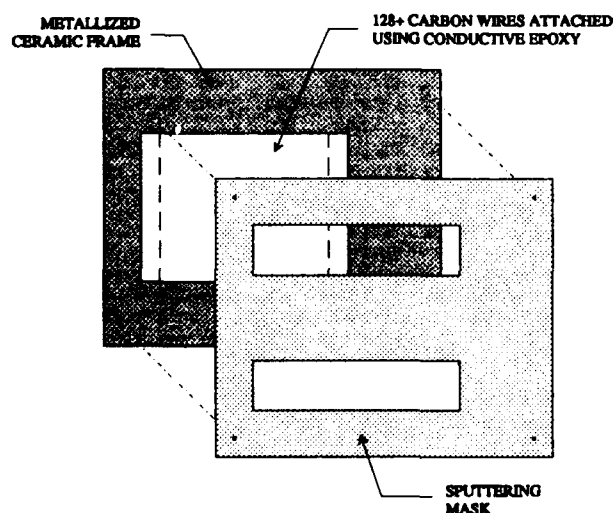


Figure 2. Wire preparation for Ti/Pd sputtering

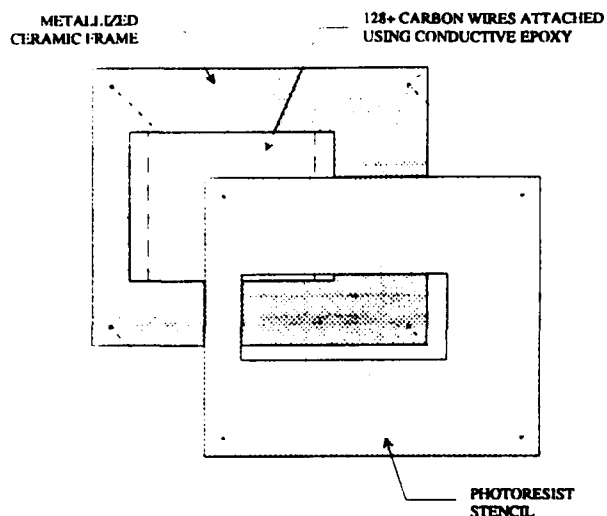


Figure 3. Wire preparation for gold electroplating

approximately 1,500 Å of titanium, followed by approximately 2,500 Å of palladium.

The frame is then overlaid with a stencil to apply photoresist to the center region of the wires (Figure 3), thereby preventing gold from adhering during the plating process. The photoresist-covered wires are then electroplated with approximately 500 microinches of gold.

The prepared carbon wires are positioned over the harp network bond pads in preparation for bonding. The end metallized carbon wires are bonded to the harp TKN bond pads using a parallel gap welding process. Figure 4 shows an example of an end metallized carbon wire bonded to a thick

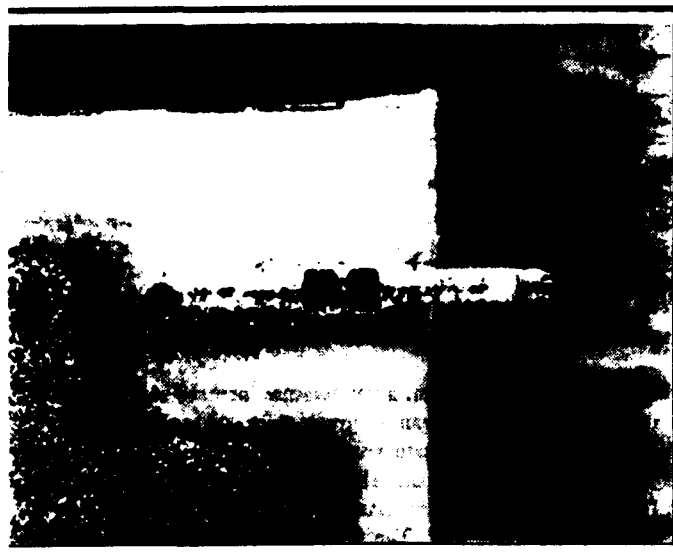


Figure 4. Bonded carbon wire

film gold bond pad. The process provides a strong mechanical bond, maintaining wire tension, without damaging the carbon wire.

STATUS

- A wire scanner has been designed and built utilizing a thick film network with welded carbon wires demonstrating the design features to be used on the high density harp.
- A potted vacuum feedthrough was demonstrated during the fabrication of a collector².
- A TKN test pattern has been designed and fabricated successfully demonstrating the 0.15 mm X 0.23 mm oval-shaped through-hole via geometry.
- Layout of the high density harp TKN is nearly complete. Fabrication of the high density harp is scheduled to be completed later this year.

REFERENCES

- ¹J. Hurd and others, "Physics Requirements of Commissioning Diagnostics for SSCL Linac," *Proceedings of the 1993 IEEE Particle Accelerator Conference*
- ²C. Crist and others, "SSCL Linac Commissioning Diagnostic Cart," *Proceedings of the 1993 IEEE Particle Accelerator Conference*
- ³A. VanDeusen and others, "High Density Data Monitoring for SSCL Linac," *Proceedings of the 1993 IEEE Particle Accelerator Conference*

High Resolution Measurements of Lepton Beam Transverse Distributions with the LEP Wire Scanners.

J. Camas, G. Crockford, G. Ferioli, C. Fischer, J.J. Gras, R. Jung, J. Koopman, J. Mann
CERN CH-1211 Geneva 23, Switzerland

Abstract

A large number of improvements were carried-out on the LEP Wire-Scanners in preparation for the 1992 running period. They include modifications of the monitors mechanics to decrease the vibrations and the heating of the wire by the beam generated electromagnetic fields, improvements of the detector chain and a software re-organization at the various levels for better noise rejection, improved user interface and "off-line" data analysis capabilities. It is now also possible to acquire the profiles of each of the sixteen circulating bunches, electrons and positrons, during the same sweep. As a consequence of these actions the quality of the collected data is much improved. The results are presented and discussed.

1. INTRODUCTION

Four wire-scanners are installed in LEP straight section 1 [1] to provide transverse distributions in both horizontal and vertical planes. Figure 1 gives the lay-out of the monitors together with their associated detectors.

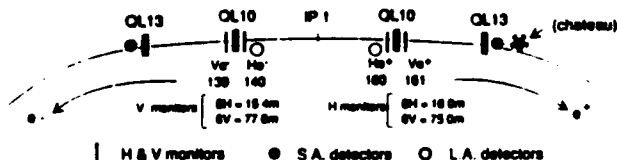


Fig 1: The LEP Wire-Scanners arrangement and Optics Parameters

One horizontal and one vertical monitor are symmetrically installed and are each associated with two detectors:

- a scintillator located behind a thin window, 75 meters downstream of the wire, receives the Bremsstrahlung resulting from the beam-wire interaction emitted at small angles (S.A.). It acquires the scan of the associated beam (i.e. e- profile from the monitors located on the e- injection side).

- a scintillator installed against the vacuum chamber near to the horizontal monitor collects the emission at large angles (L.A.) during the passage of the counter-rotating beam.

The signal received by the S.A. scintillators [1] is attenuated by 4 orders of magnitude before transmission to a photo-multiplier which has a gain 100 times smaller than that of the L.A. detectors.

II. THERMAL AND MECHANICAL OBSERVATIONS

Fourteen wires have been destroyed from 1989 to 1992, most of them in 1989 and 1990. With the exception of two 50 μ m Beryllium wires, they were 36 μ m thick carbon wires. The Be wires showed clearly [1] that the wire had melted over its full length, excluding beam energy deposition as the only destruction mechanism. This is confirmed by previous measurements at the SPS where the wires survived higher intensities at comparable speeds. Moreover, permanent wire average temperature monitoring has shown several interesting features (Figure 2):

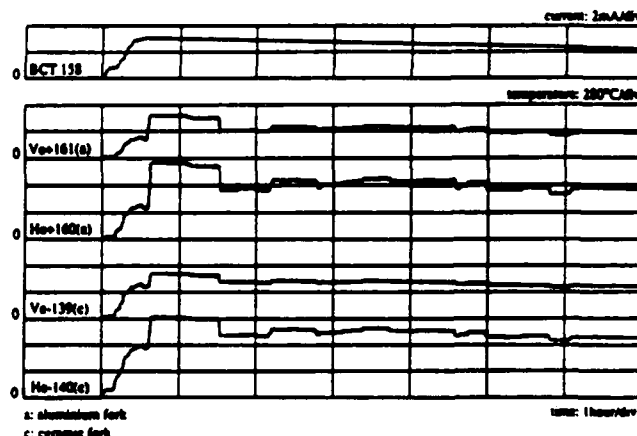


Fig. 2: Long term recording of wire resistance (temperature) and beam current with wires retracted in the parking position

The temperature of the wires increase with the stored current and the vertical wires temperature increases less than that of the horizontal ones. This indicates that the heating is of electromagnetic origin, due to the wake fields generated in the wire scanner tanks. The vertical wires heat up less because they are retracted in a rectangular tube functioning as a waveguide below cut-off. The second evidence in favour of electromagnetic heating is the fact that the wire temperature changes when beam manipulations modifying the bunch length take place at constant circulating beam intensity. Finally wire temperature recordings during scans provide other evidence of heating by electromagnetic coupling (Figure 3).

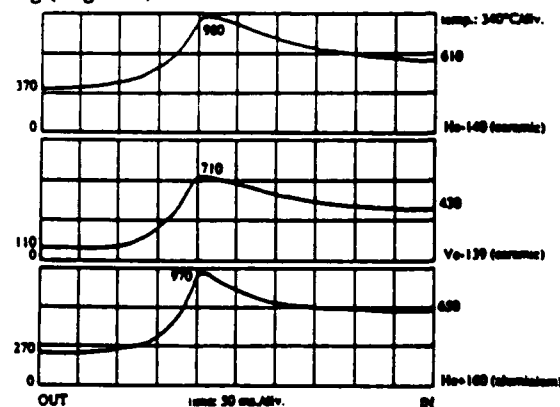


Fig. 3: Wire resistance change during scans of 300 μ A on 300 μ A circulating beams. Calculated temperatures are indicated.

As the wire approaches the beam, a temperature increase starts at approximately 40 mm from the beam centre, mainly due to coupling to the electric field. A steady state temperature is reached again when the wire is far from the beam. This results mainly from the magnetic field created by the beam passing in the loop formed by the wire and the supporting fork. The temperature increase of the

horizontal and vertical wires is inconsistent, the latter being too low compared to the former. Laboratory tests have shown that thermoemission starts at around 1000°C and shifts the resistance measurement towards lower equivalent temperatures. Electromagnetic heating of the wire being established, the fork construction was analysed for possible improvements. A coupling capacitance of a few pF was found between the wire and the fork; this was created between the aluminium arm, the wire supporting aluminium piece and the ceramic insulator (Figure 4). Two different types of supporting forks were installed in early 1991. The first design had a modified wire support piece and ceramic transition pieces to decrease the coupling capacitance (Figure 4).

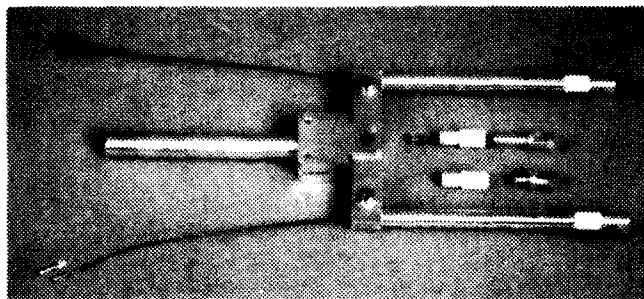


Fig. 4: Wire supporting fork with original (top) and modified (bottom) wire holding and ceramic isolating pieces.

A second design was implemented with the whole supporting tubes made of ceramic. In 1992, the wire length of the combined aluminium/ceramic forks was reduced from 55 to 29 mm. The vertical wire with this design broke twice in 1992. The temperature recording of the first incident showed that it happened at a circulating current of 2.8 mA; the temperature reached was 1280°C, uncorrected for thermoemission. For 1993, a 30 μ m quartz wire has been installed in place of the broken wire. The quartz wire will definitely break any current loop leading to heating but it may experience high voltage breakthroughs when passing through the beam. Since 1991, no wires with full ceramic arms were broken.

Scans taken in 1991 and 1992 are affected by a shift of the beam centre of charge between the IN and OUT directions of the order of 100 μ m. Laboratory tests have shown that it is due to an inertia induced movement of the driving screw [1]. This effect could be reduced in the laboratory from 70 to 10 μ m by using a counter-pin pushing on the free end of the driving shaft. This modification could not be implemented for the 1993 LEP start-up.

III. LOW LEVEL AND APPLICATION SOFTWARE

The basic software design used in 1992 was unchanged from 1991. Amongst the various data structures exchanged between the local equipment server and the application, the PROFILE structures (one per profile) hold all the signals relative to a given bunch received from the photo-multiplier. If their initial analysis (sigma processing within the server) is successful, these data are trimmed to ± 4 sigmas; otherwise the entire profile is stored for more detailed "off-line" analysis. An analysis failure usually occurs when all signals are hidden within the noise. However, even with a good signal level the fit results (mainly the standard deviation) are noise dependent. In order to cope with this, two different methods have been tested :

- a simple rms calculation over the whole profile followed by a second iteration over a limited window

- a more refined gaussian fit providing a chi-squared minimization on all data above 10% of the maximum amplitude.

The later technique is less noise sensitive but is also less accurate when the distribution is not gaussian. For the future runs the results of both the rms processing and the gaussian fit will be forwarded to the application for systematic comparisons.

The application interface has also been upgraded for 1993 owing to the availability of more powerful graphic tools. It will be possible to display simultaneously up to eight circulating bunch profiles (of the same beam or of the two e+/e- beams) and to display IN and OUT profiles relative to a given scan on the same plot. These modifications added to better "off-line" analysis facilities will ease the interpretation of results.

IV. RESULTS AND DISCUSSION

A scan is systematically performed in the IN (beam) and OUT (of beam) directions. As a result, two profiles are measured and can be compared each time a sweep is triggered in a given plane. The wire position (x axis) is in millimeters whereas the y scale unit is arbitrary and depends on the monitor gain setting.

HORIZONTAL PLANE:

In this plane the signal received by the S.A. detectors is excellent and provides good gaussian fits of the bunch profiles. This is illustrated on Figure 5 in the case of a positron bunch analysed with the monitor located on the positron side. Standard deviations from both scan directions are in agreement within $\pm 1.3\%$.

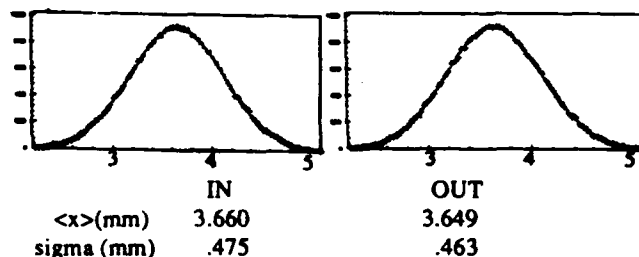


Fig 5: IN and OUT profiles and fit results of a positron bunch scanned with the He+ monitor and analysed with the S.A. detector at the window

Another S.A. detector (chateau) located fifteen meters downstream from the Bremsstrahlung radiation extraction window was also used in order to investigate eventual acceptance problems and effects of background close to the vacuum chamber. This detector was shifted radially which gave better shielding. Its response is given on Figure 6 for the same bunch.

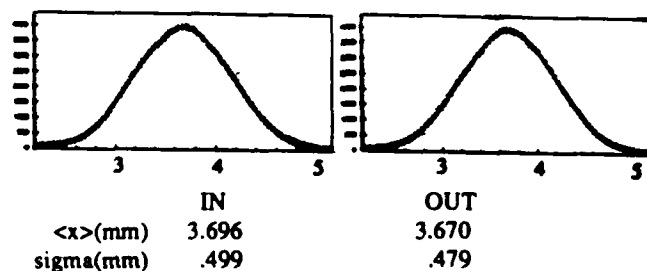


Fig 6: IN and OUT profiles and fit results of the same bunch from the S.A. detector located 15 meters downstream from the window

Between the IN and OUT directions the agreement is $\pm 2\%$ and both S.A. detectors give the same standard deviation within $\pm 2.1\%$

The response of the L.A. detectors is less good. The signal to noise ratio at large angle is less favourable and a compromise must be found between the shielding depth protecting the scintillator from background and the signal level to be analysed. In order to reduce the background noise 10 mm of Lead was necessary. However some saturation then started to affect the photo-multiplier in the peak region (Figure 7)

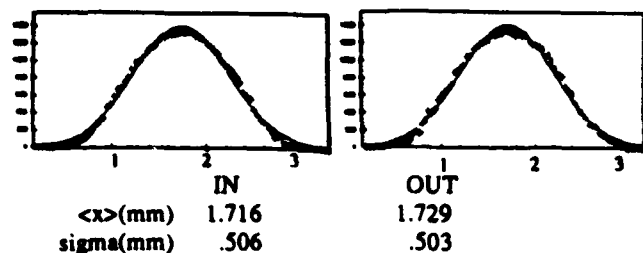


Fig 7: IN and OUT profiles and fit results of the same bunch scanned with the He-monitor and analysed with the L.A. detector.

The fit results provided by both directions agree very well but lead to standard deviations 5% higher than the S.A. detectors. The different average positions indicate that the beam trajectory is different at the e+ and at the e- monitors.

VERTICAL PLANE :

Typical profiles performed using the vertical monitors are shown on Figure 8 for the S.A. detectors.

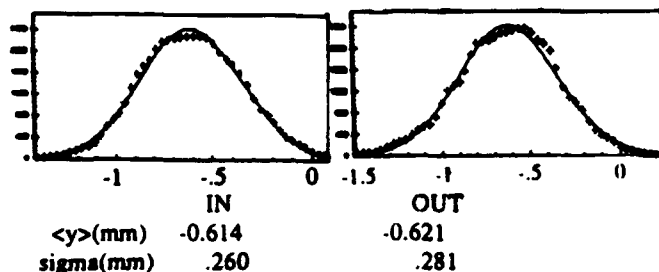


Fig 8: IN and OUT profiles and fit results of an electron bunch scanned with the Ve-monitor and analysed with the S.A. detector at the window.

Vertical profiles are usually affected by blow-up effects resulting from Coulomb Scattering of the beam through the wire. Taking the emittance ratio in LEP and the present monitor performances these effects can now be neglected in the horizontal plane at 46 GeV. They dilute mainly the second half of the vertical scan (positive and negative sides for respectively the IN and OUT directions) as can be seen on Figure 8. Hence, a direct gaussian fit provides a too pessimistic result. By modelling this effect and analysing the non-perturbed halves of the IN and OUT profiles [1], it is possible to reconstruct the initial distribution. An example of the results is given on Figure 9. A reduction of the rms value by 10% to 20% is then observed with respect to the fit of the entire measured distribution. However this method still suffers from the random mechanical effects (section II) and from timing imprecisions. Therefore it cannot be used systematically.

The L.A. detectors suffer from a lack of signal in the case of vertical profiles as they are located near to the H monitors (Figure 1) five meters downstream from the vertical ones.

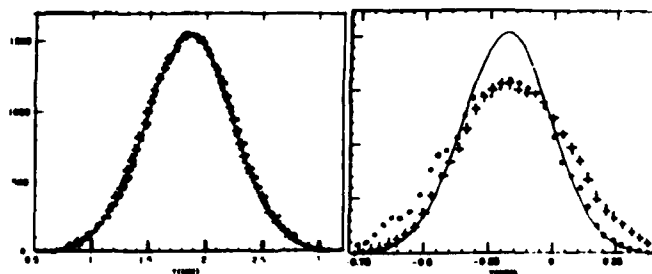


Fig 9: Initial distributions from IN and OUT profile analysis :
+: IN direction , o: OUT direction , —: fitted profile .

The gaussian fits of profiles from the S.A. detectors provide emittance values of 0.9nm to 1 nm in the vertical plane and 14nm to 15 nm horizontally. The precision achieved is a few per cent in the horizontal plane. Vertically the results are not so accurate as long as blow-up effects are not properly eliminated.

V. COMPARISON WITH S.R. MONITORS

These figures, can be used to calibrate the U.V. telescopes [2]. The agreement between the two devices is disturbed by parasitic effects which must be considered; they are at locations in the machine where the optics are not the same and where beam dynamical effects are different (for example coupling). This can account for discrepancies of around 20%. Some 50Hz noise also disturbs the two devices differently as they have different modes of acquisition

VI. FUTURE UPGRADES AND CONCLUSION

Several steps will be taken to improve wire-scanner performances in addition to the ones discussed in section II. The mechanics will be modified to reduce the shift between the two directions. It has also been considered to add to each monitor a wire rotated by 45 degrees. This will allow a better evaluation of the tilt effects. The electric noise level will be reduced in the wire scanners environment by installing filters on adjacent motorised devices. These improvements are foreseen for the 1994 runs. Both the S.A. and L.A. detectors have been modified. The former will have a better acceptance in particular close to the vacuum chamber whereas the shape of the later has been reconsidered to increase its acceptance and hence have better signal to noise ratio.

Several software modifications will be implemented apart from the availability of the new application (section III). An interlock will prevent any scans above a given circulating beam current and temperatures will be systematically recorded during wire sweeps. The timing will be upgraded so as to lower the uncertainty in the absolute position reference between IN and OUT scans from 50 μ m down to 10 μ m (rms). The wire status will also be monitored in permanence.

Resulting from these modifications we expect to have the same level of performance in both the horizontal and vertical planes.

VIII. REFERENCES

- [1] B.Bouchet et al., "Wire-Scanners at LEP", Proc. of the 1991 IEEE Part. Accel. Conf., San-Francisco, 6-9 May 1991 .
- [2] G. Burtin et al., "Performance and Operational Experience of the LEP Synchrotron Light Telescopes", these proceedings.

Beam Size Measurements with Noninterceptive Off-Axis Screens

F.-J. DECKER, R. BROWN, J.T. SEEMAN

Stanford Linear Accelerator Center*, Stanford, California 94309

Abstract

At the end of the Stanford Linear Accelerator the transverse distributions of small electron and positron beams ($\sigma \approx 100 \mu\text{m}$) are measured by profile screens. To avoid constant interception and emittance blow-up of the production beams, the beams are deflected with fast magnets on to off-axis screens. One in a 1000 pulses is deflected. The required and achievable resolutions are described in another paper [1]. Here we concentrate more on the magnets, the screen set-up, the readout, and signal processing of the video data. Together with the kicker magnet, two PCs, one for electrons, one for positrons, are triggered recording the next frame of the camera. Hardware and software process this information quickly producing a color-enhanced picture which is displayed in the control-room. With the resulting visual and digital information, the wakefield tails of the beam can be compensated using orbit oscillations. Minute by minute variations and slow drifts of the beam are recognizable.

1 Introduction

The transverse density distribution of a beam can be obtained from an image of a beam which hits a fluorescent screen. Normally a screen is moved into the beam line for observation disrupting the beam for the downstream use. Here we present a set up which routinely obtains the beam distribution without effectively disturbing the downstream operation of the accelerator. This is achieved by kicking one out of many beam pulses on to an off-axis screen.

2 Set Up of the Off-Axis Screens

The set up consists of kicker magnets, off-axis screens and the optical system to the remote cameras.

2.1 Kicker Magnets

At the end of the SLC-linac four "kicker" magnets are installed at betatron phase advances of 0° , 22.5° , 90° and 112.5° . A pulse with a peak current of 600 A and a rise and fall time of 1 ms each provides a beam offset of 6 mm at the downstream fluorescent screens which are about 2 to 3 mm off axis (Fig. 1).

*Work supported by the Department of Energy contract DE-AC03-76SF00515.

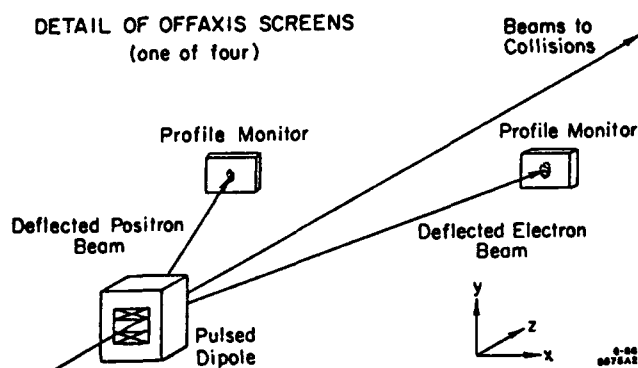


Figure 1: Principle Set Up of the Off-Axis Screens.

A pulsed dipole (kicker) magnet deflects one out of many beam pulses, going to interaction point for collision. This one pulse (electron and positron bunch) hits the nearby off-axis screens.

For one out of 960 pulses, this is every eight seconds at 120 Hz, one of the kickers bends the beams (electrons and positrons) onto two screens. Eight seconds later the next kicker fires and so on, till the beams have hit all eight screens. With the measured sizes the emittance ellipse in phase space can be calculated.

2.2 Screens

The self-supporting screens are $120 \mu\text{m}$ thick and made out of $\text{Al}_2\text{O}_3:\text{Cr}$ which emits light at 695 nm. They are tilted by an angle of 60° with respect to the beam so that the beam size is magnified by a factor of two. The tilt angle is either in z or y to enlarge the spot dimension with the smaller β -function. Holes of $340 \mu\text{m}$ diameter are drilled into the screens in a pattern of 3 by 2 mm for calibration purposes.

The resolution of the 12m long optical system is discussed in another paper [1], here we will give only a summary of the different sources contributing to the resolution (Tab. 1). The resolution of $50 \mu\text{m}$ is subtracted in quadrature. In the 60° case the beam showed that a $25 \mu\text{m}$ resolution is more reasonable. This indicates that the material is not as transparent under beam conditions as in the laboratory tests. This might come from high radiation damage.

For flat beams used in the current operation the expected vertical beam sizes are $\sigma_z = \sqrt{\epsilon_z \beta} = 30 (45) \mu\text{m}$, with $\gamma\epsilon_z = 0.3 \cdot 10^{-5} \text{ m-rad}$ and $\beta_{\text{min}, (\text{max})} = 25 (50) \text{ m}$. This is comparable with the resolution of the system.

	σ_c	σ_t	σ_o	σ_g	σ_Σ
0°	30	0	30	30	52
60°	15	45	15	15	52

Table 1: Resolution Contributions in μm .

Different components of an optical system contribute to the overall performance. Here the σ -resolution in beam sizes are shown for no angle and a 60° angle to the beam making most of the resolutions twice as good. The camera (c) has a line resolution. If the screen is transparent, the thickness (t) of the screen has a big effect. The diffraction limit of the optical system (o) and the granularity (g) of the screen gives further limitation. The overall resolution (Σ) is about 50 μm in both cases.

3 Cameras, Electronics and Computer

The images from the screens are processed with cameras, cables, combining boxes and readout computers.

3.1 Initial Set Up

The initial set up had eight RCA TC 2521U (Ultracon) cameras and two signal switching boxes each combining the four camera signals of one beam (e.g. electrons). The video signal was sent over two RG 59 cables to two PCs in the control room. In this system three problems occurred which could be localized to the switch box: (1) Non-linear signal behavior, (2) a non-synchronization to the beam arrival resulting in half the beam spot bright the other half dimmer in the vertical, and (3) a loss of half the video lines and therefore resolution.

This set up was changed to newer CCD cameras (COHU 4810), eight 1/2' solid shield aluminum CATV transfer cables and a multiplexed readout card in the computer. This system will be described further.

3.2 Cameras

The cameras should have sufficient spatial resolution, and a good linear or square root of amplitude ($\text{Gamma} = 0.5$) response over a wide dynamic range. One sigma of a Gaussian distribution corresponds to a modulation transfer function (MTF) value of about 60%. With 250 TV lines at that value and an image area of 8.8 * 6.6 mm a resolution of about 30 μm (6.6 mm/250) is achieved (similar to the old camera). The dynamic range or signal-to-noise ratio of 55 dB (compared to 44 dB) should give some improvements. Fig. 2 shows the response of an LED spot with linear and $\text{Gamma} = 0.5$ setting showing that the full dynamic range is achieved for the 0.5 value. Recent measurements have shown that for $\text{Gamma} = 0.5$ the response curve is not exactly the predicted one, giving different size for different intensities.

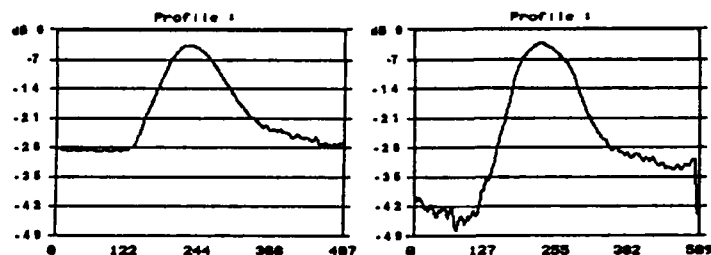


Figure 2: Signal Response for $\text{Gamma} = 1$ and 0.5.

An LED spot (asymmetric) on the camera was read out with a Gamma setting of 1 (linear) and 0.5 ($\sqrt{\text{intensity}}$). The intensity over the spot is plotted in logarithmic scale versus the pixel number. For a Gaussian spot this should give a quadratic behavior (or x^4 for $\text{Gamma} = 0.5$) down to the noise level.

3.3 Computers and Cards

The new cables to the computers reduced a frequency dependent loss of 7 dB down to less than 1 dB at higher frequency (10 MHz). The 8-channel video multiplexer (DT2859) from Data Translation [2] switches from one screen to the next one corresponding to a bit pattern from the kickers fed into the parallel input/output (printer) port of the 486 PC. The frame grabber (DT2861) in the PC is triggered externally to acquire a picture (or several consecutive) from the camera. An array processor card allows "hardware" calculations, for example averaging over the surrounding pixels (7 * 7 convolution) in 1.7 s. (This took 30 (3) min on a 386 PC without (with) a co-processor.)

3.4 Program

The program was written in C with DT-IRIS subroutines [2]. Since this package doesn't support printout from a stored picture another program, Image-Pro, is used. The initial program had many features to handle the hardware status: It had to decide which screen was hit, adjust the gain (varying combining box signal), judge from the size pattern whether it is an electron or a positron beam (this is still used), resynchronize if the beam went away (1 Hz suppresses the kicker trigger) and averaged over five video frames. Additionally, there are different test bits possible which generate design beam spots, take old saved raw data for processing or generate a movie like sequence were wakefield tails are developing in phase space.

The main design criteria for the program were the following features: It should provide a color enhanced video signal of four spots per beam which should show low intensity parts of the beam tails. It should also provide the sizes and emittances of the beams and display them.

Colored Display. The display consists of a color table with 16 colors and black lines in between. These lines have two advantages: They help visual acuity and also provide contour lines for a black and white printout like for this paper. With this table and a linear camera response the smallest recognizable level would be 6% of the peak value. Therefore the input table, which transforms the camera

signal heights into 255 numbers, was changed to square root of intensity (not necessary if Gamma = 0.5 at the camera). This should make tails and beam halos down to 0.5% visible. A further enhancement makes background noise like stripes and waves on the picture visible.

To suppress backgrounds one picture frame is acquired and a few frames later a background frame, which is subtracted from the first one. The result is scaled and convoluted over 6*6 pixels which reduces pixel noise and washes out the difference between the two interlaced fields of one frame (beam spot decays or camera changes gain). Additionally, the spots are centered in their respective quadrants of the video image and projections in x and y plotted, indicating also the center and the symmetric one sigma points.

Sizes and Emittance Values. The sizes are extracted out of the projections in x and y . Since the background subtraction is not perfect and the convolution produces non-zero values near the boundary, a simple rms calculation wasn't correct. A non-linear fit with a Gaussian (or asymmetric) function would have been the right thing if there were no constraints in speed. Therefore the following method is used. The peak center is defined as the average of all values 90% of the maximum and higher. From this center the right and left sigma is achieved by averaging all values between 48 and 72% on one side of the maximum (linear scale). This was checked with some generated distributions. It is very fast and also very robust to strange beam distributions. The σ of the beam is the average of the left and right sigmas minus the resolution of 50 (25) μm in quadrature. The results are displayed in the corners of the TV image in μm (SX= σ_x ,... see Fig. 3). The asymmetry or tails of the beam is given by:

$$T = \frac{\sigma_R - \sigma_L}{\sigma_R + \sigma_L} \quad (1)$$

for one spot. The numbers TX, TY give the average of the two top or two bottom spots. Positive numbers represent a tail to the top and right on the left screens (left on the right screens, mirror image).

The normalized "emittance" $\gamma\epsilon$ at each screen is calculated by

$$\gamma\epsilon = \gamma \frac{\sigma^2}{\beta}, \quad (2)$$

where β is the β -function at the screen and $\gamma = 90\,000$ the relativistic Lorentz factor. The results are shown in the middle of the left and right side in mm-mrad. This information indicates a mismatch of the beam or problems with the calibration of each camera. The arithmetic average of all four numbers will give Bmag*emittance since there are two pairs of two screens being 90° apart [3]. Bmag is a factor indicating the emittance blow-up of a mismatch after filamentation. These emittance numbers (EX, EY in mm-rad) are in the center of the display. Above them is an averaged number for x and y of 20 good measurements. These numbers, together with size and tail values, go to the VAX control computer via a DAC card in the PC. There they are put into history buffers.

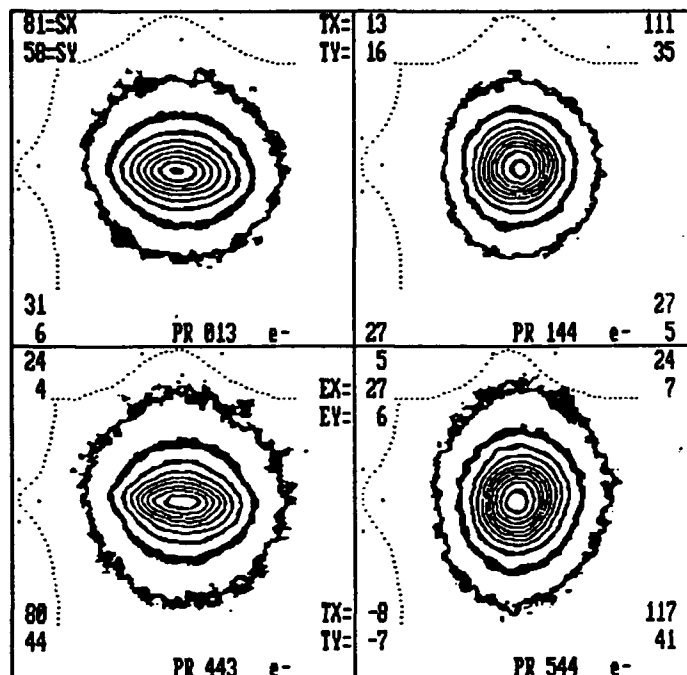


Figure 3: Flat Beam Spots.

The normally colored pictures show the transverse distribution of the electron beam at the end of the SLC-linac. The flat beam set up resulted in emittances of $\gamma\epsilon_{x(y)} = 27(6)$ mm-mrad (see center of picture).

4 Measurements

Fig. 3 shows an example for flat beams. The emittance ratio is about 5:1 at the end of the linac. This measurement was done with low currents ($\leq 2 \cdot 10^{10}$ particles) and a longer store time in the damping ring. This example is near the resolution limit for y .

Often one-sided asymmetries (wakefield tails) occur which can easily be seen on these screens. Control of the tail is made by introducing betatron oscillations with a certain phase and amplitude, so that no tails are visible [4].

5 Conclusion

Non-interceptive off-axis screens give a continuous information of the beam distribution, size and emittance at the end of the SLC-linac.

References

- [1] F.-J. Decker, *Beam Size Measurement at High Radiation Levels*, PAC, San Francisco, May 1992, p. 1192.
- [2] DATA TRANSLATION (R), *Product Handbook: Image Processing, Data Acquisition*, 1991, Tel. (508) 481-3700.
- [3] W.L. Spence, *Private communication*.
- [4] J.T. Seeman et al., *Introduction of Trajectory Oscillations to Reduce Emittance Growth in the SLC Linac*, HEACC'93, Hamburg, July 1993, p. 879.

Resolution Improvement in Beam Profile Measurements with Synchrotron Light

O.V.Chubar, Moscow Engineering Physics Institute, 115409 Moscow, Russia

Abstract

Numerical method for improving optical resolution in electron beam profile measurements with visible synchrotron radiation (SR) is proposed. Image formation of electron beam profile is described by integral convolution-type equation of the first kind – the diagnostic equation. Precise procedure of computing the equation kernel in terms of classical electrodynamics is presented. With this procedure special features of the SR emission and diffraction scheme peculiarities may be taken into account. Numerical regularized solution of the diagnostic equation is shown to lead to the resolution improvement. The technique is supposed to be beneficial in high-energy storage rings.

I. INTRODUCTION

Visible SR is much used as a tool for beam profile measurements in synchrotrons and storage rings [1] - [4]. Fig.1 shows traditional layout of the measurements. Also, an extracting mirror absorbing short-wavelength SR is optionally used.

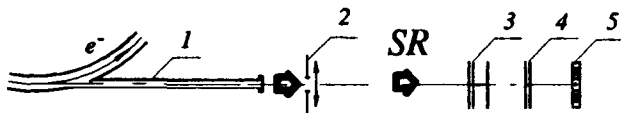


Figure 1. Scheme of measurements.

1- beamline; 2- focusing lens and limiting diaphragm; 3- neutral light filters; 4- monochromatic filter; 5- position-sensitive detector.

Unfortunately, in high-energy electron storage rings the diffraction-limited spatial resolution may be comparable with transversal beam dimensions [3], [4]. Beam profile image may also be distorted by aberrations, for example those resulting from thermal deformation of the extracting mirror.

If one can precisely describe the formation of beam profile image, then one can improve the optical resolution mathematically, by numerical processing of the measurement results. In this paper a diagnostic equation describing the image formation is treated. Technique for precise computation of the equation kernel is proposed. Results of simulation illustrating the numerical solution of the diagnostic equation are exhibited.

II. DIAGNOSTIC EQUATION

Detector response is proportional to the intensity of incident radiation. The visible SR emitted by different electrons is known to be dominantly incoherent in electron storage rings, if longitudinal bunch length is larger than micrometers. The beam profile image formed by focusing lens is insensitive to angular divergences of the emitting beam. Let x and z to be transversal Cartesian coordinates in the object plane (i.e., in the plane the lens is focused on),

and x^* , z^* to be coordinates of a point in the detector screen. In line with the assumptions made, if $n(x, z)$ is transversal distribution of particle density in the object plane, then the intensity distribution in the detector screen $I(x^*, z^*)$ is related with $n(x, z)$ as

$$\int_{-\infty}^{+\infty} \int_{-\infty}^{+\infty} n(x, z) K(x, z, x^*, z^*) dx dz = I(x^*, z^*), \quad (1)$$

where $K(x, z, x^*, z^*)$ is radiation intensity at observation point (x^*, z^*) in the detector screen, which results from passage of a single particle along trajectory intersecting the object plane at (x, z) .

Relations similar to (1) are commonly used in optics to describe image formation of extended incoherent source [5]. Function $K(x, z, x^*, z^*)$, being known from physical consideration, and $I(x^*, z^*)$, being determined by the detector, allow to treat relation (1) as the integral equation of the first kind with respect to $n(x, z)$ – the diagnostic equation. In practice $I(x^*, z^*)$ is averaged within detector exposure time, so $n(x, z)$ should be considered correspondingly.

To define the kernel $K(x, z, x^*, z^*)$, let us start from the Fourier transformation of electric field emitted by single electron in its motion along the trajectory $\vec{r}(\tau)$, the relation one can easily obtain from delayed potentials [6] for observation point $P(\vec{r}')$ in space before lens,

$$\vec{E}_\omega = \frac{ie\omega}{c} \int_{-\infty}^{+\infty} \frac{\vec{\beta} - \vec{n}}{R} \exp[i\omega(\tau + R/c)] d\tau, \quad (2)$$

where $\vec{\beta} = (d\vec{r}/d\tau)/c$ is relative velocity of electron, $\vec{n} = \vec{R}/R$, $\vec{R} = \vec{r}' - \vec{r}$, $R = |\vec{R}|$, ω is radiation frequency, e is the charge of electron, c is the speed of light, i is unit imaginary number. Eq. (2) is valid at $[c/(\omega R)] \ll 1$.

Two wave disturbances corresponding to σ - and π -components of \vec{E}_ω , may be sufficiently considered in wave zone. For ultra-relativistic particle, the general contribution to the integral (2) takes place at $|\beta_x| \ll 1$; the radiation is directed mainly forward ($|\ln_x| \ll 1$, $|\ln_z| \ll 1$) [6], [7]. Therefore the σ -component wave disturbance may be given by the expression

$$U_\sigma \approx C \int_{-\infty}^{+\infty} \frac{n_x - \beta_x}{R} \exp[i\omega(\tau + R/c)] d\tau, \quad (3)$$

where C is constant. Here and later on, the π -component expression is not presented: it may be readily written by direct analogy.

Eq. (3) may be regarded as superposition of disturbances from motionless coherent point sources arranged on the electron trajectory, each disturbance phase and magnitude

being defined by the position of corresponding hypothetical source. A diffraction integral (see [5]), which allows to calculate the source contribution to the total disturbance value at point $P(\bar{r}')$ on the detector screen, can be written for each source. The total disturbance is given by the expression

$$U_o^* = C^* \int_{-\infty}^{\infty} d\tau \int_{\Delta\Sigma} \frac{n_x - \beta_x}{R''S} \exp \left[ig(\tau) + \frac{i\omega}{c}(S - R'' + \Psi) \right] d\Sigma, \quad (4)$$

where function $g(\tau)$ describes individual initial phase of each source, the value adequate to the image space; R'' is reference sphere radius (see Fig.2); S is distance between the observation point P^* and point P' in the reference sphere; Ψ is total wave aberration; C^* is constant. The inner integration in Eq. (4) is on the reference sphere within lens diaphragm.

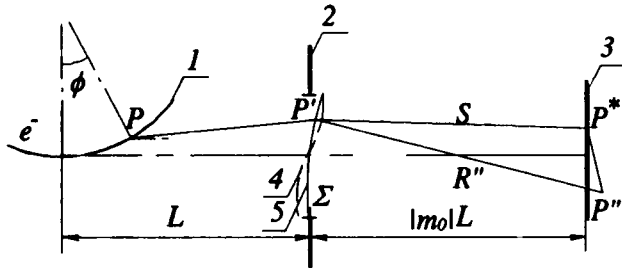


Figure 2. Diffraction scheme.

1- electron trajectory; 2- lens diaphragm plane; 3- detector plane; 4- wave front; 5- reference sphere.

If sufficiently narrow monochromatic filters are used, then the diagnostic equation kernel is defined as

$$K(x, z, x^*, z^*) = |U_o^*|^2 + |U_\pi^*|^2. \quad (5)$$

The functions involved in Eq.(4) may be determined from the measurement geometry. Using angular variables of reference sphere integration, horizontal one ξ and vertical one ζ , and applying the expansions of all the phase functions in Eq.(4) in terms of these small values, one can obtain for the radiation from bending magnet

$$U_o^* \approx C^{**} \int_{-\infty}^{\infty} d\phi \exp(if_0) \int_{-\bar{\xi}}^{\bar{\xi}} (n_x - \beta_x) \exp(if_\xi \xi + if_{\xi\xi} \xi^2) d\xi \times \int_{-\bar{\zeta}}^{\bar{\zeta}} \exp(if_\zeta \zeta + if_{\zeta\zeta} \zeta^2) d\zeta, \quad (6)$$

where the azimuth ϕ is used as angular integration variable instead of τ ; C^{**} is constant. The phase expansion coefficients $f_0, f_\xi, f_\zeta, f_{\xi\xi}, f_{\xi\zeta}, f_{\zeta\zeta}$ depend on ϕ .

Numerical estimations of high-order term contributions show that approximation (6) allows to compute the diagnostic equation kernel with a precision of order 0.5%.

According to Eq.(6), variables ξ and ζ are uncoupled under the external integration on ϕ if the limits $\bar{\xi}$ and $\bar{\zeta}$ are constants; that essentially simplifies computation. Eq.(6) was written in assumption of small lens aberrations. Nevertheless, even if a large ξ - independent aberration takes place (for instance, the aberration due to thermal

deformation of extracting mirror), the uncoupling structure of Eq.(6) retains.

The problem on optical resolution in beam profile measurements was discussed in [3], [4], where diffraction of synchrotron radiation and depth-of-field effect were considered separately. The method under discussion allows to treat these effects as single phenomena closely related with nature of synchrotron radiation.

In the computations discussed below, the coefficients $f_0, f_\xi, f_\zeta, f_{\xi\xi}, f_{\xi\zeta}, f_{\zeta\zeta}$ were determined from exact geometrical relations. But it would be well to consider approximate values of the coefficients. It is obtainable,

$$\begin{cases} f_0 \approx \frac{\omega}{2\omega_0}(\gamma^2\phi + \phi^2/3); & f_\xi \approx -\frac{\omega m_0}{2\omega_0}\phi^2 - \frac{\omega}{c}(x^* - m_0x); \\ f_\zeta \approx -\frac{\omega}{c}(z^* - m_0z); & f_{\xi\xi} \approx f_{\zeta\zeta} \approx \frac{\omega m_0^2}{2\omega_0}\phi, \quad n_x \approx m_0\xi, \quad \beta_x \approx \phi, \end{cases} \quad (7)$$

where ω_0 is cyclotron frequency, γ is the reduced energy of electron ($\gamma \gg 1$); m_0 is transversal optical magnification.

By analogy with unfocused SR, the cubic term in f_0 may be shown to prevail at $\omega \ll \omega_c$ ($\omega_c = 3\gamma^3\omega_0/2$ is critical SR frequency). Using the corresponding normalization in Eqs. (6), (7), one may see that if an acceptance angle is $|m_0|\bar{\zeta} \ll (\omega_0/\omega)^{1/3}$, then the vertical diffraction is Fraunhofer's one with the resolution of order $c/(\omega|m_0|\bar{\zeta})$, whereas at $|m_0|\bar{\zeta} \gg (\omega_0/\omega)^{1/3}$ the optical resolution has the order of $c/(\omega^2\omega_0)^{1/3}$.

Eqs. (5) - (7) show that

$$K(x, z, x^*, z^*) \cong \mathcal{K}(x^* - m_0x, z^* - m_0z), \quad (8)$$

i.e., to certain accuracy Eq.(1) may be treated as a convolution type integral equation. Numerical analysis shows the accuracy to be better than 1% for high-energy electron storage rings. Analytically the feature was studied in [8].

Relation (8) allows to apply effective methods based on the convolution theorem for the numerical solution of Eq.(1). The regularized solution of Eq.(1) may be written as follows [9], [10]:

$$n_o(x, z) = \frac{1}{(2\pi)^2} \iint_{-\infty}^{\infty} \frac{\tilde{\mathcal{K}}(-\omega_x, -\omega_z) \tilde{I}(\omega_x, \omega_z) \exp(-im_0x\omega_x - im_0z\omega_z)}{|\tilde{\mathcal{K}}(\omega_x, \omega_z)|^2 + \alpha M(\omega_x, \omega_z)} d\omega_x d\omega_z, \quad (9)$$

where $\tilde{\mathcal{K}}(\omega_x, \omega_z)$ and $\tilde{I}(\omega_x, \omega_z)$ are Fourier transformations of the kernel and the measured intensity; α is regularization parameter; function $M(\omega_x, \omega_z)$ suppresses high-frequency component of the detector noise. The solution may be found by iteration as well as directly (if certain *a priori* information on its behavior is known).

II. COMPUTATION RESULTS

Computations of the diagnostic equation kernel for bending magnet radiation of 2.5 GeV electron storage ring Siberia-2 were performed according to Eqs. (5), (6). The kernel $\mathcal{K}(x, z)$ computed for radiation wavelength $\lambda = 540\text{nm}$, bending radius $r_0 = 1960\text{cm}$, distance from object plane to

lens $L=700\text{cm}$, the lens diaphragm widths $d_x=2\text{cm}$, $d_z=6\text{cm}$; $m_0=-1$, is shown in Fig.3.

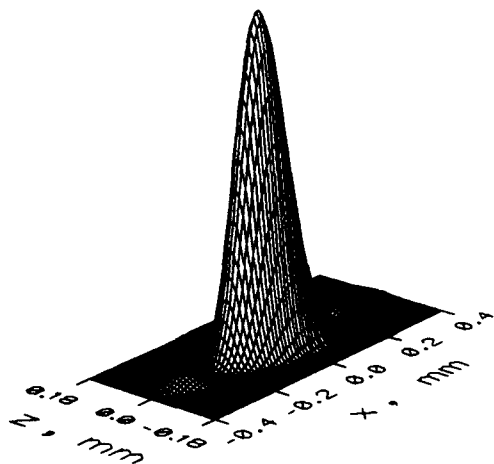


Figure 3. Diagnostic equation kernel.

The computation accounts only for the σ -component of SR. Secondary maxima inherent in Fraunhofer diffraction are recognizable in horizontal direction. Corresponding maxima are absent in vertical direction; the distribution is symmetric with respect to median plane. $\mathcal{K}(x,z)$ is sensitive to d_x/L , d_z/L , but with these values large enough the sensitivity eliminates; it correlates well with qualitative considerations given in previous chapter.

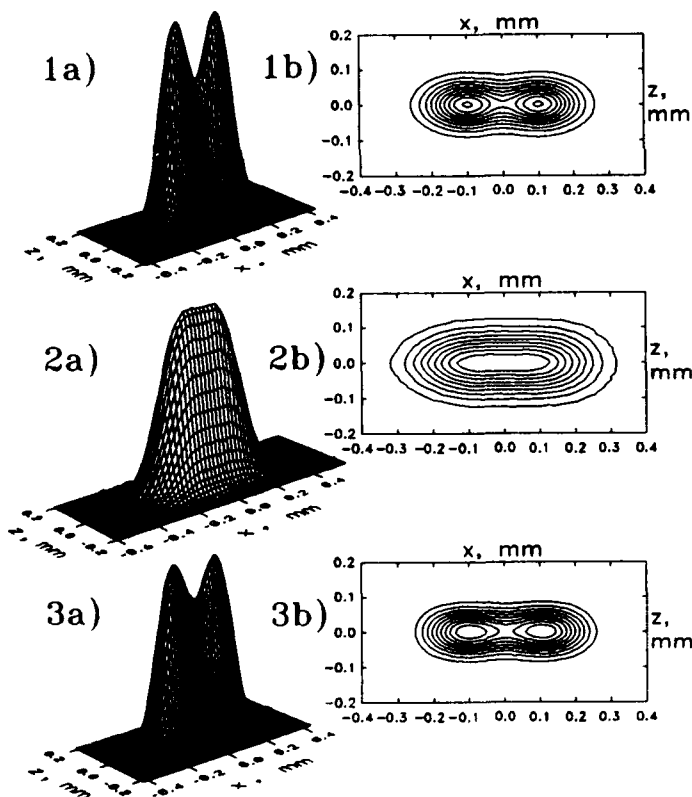


Figure 4. Results of simulation ((a)- surfaces, (b)- level lines): 1- $n(x,z)$; 2- $I(x,z)$ deviated by noise; 3- $n_a(x,z)$.

As an illustration to processing the data on beam profile measurements, Fig.4 gives the results of the corresponding simulation. The simulation was done according to the

following traditional algorithm: a function $n(x,z)$ modeling the transversal distribution of particle density was chosen; corresponding SR intensity distribution in the detector plane $I(x^*,z^*)$ was computed by Eqs. (1), (8); $I(x^*,z^*)$ was distorted by random noise assuming the detector dynamic range to be 100; the solution of diagnostic equation, $n_a(x,z)$ was found for the distorted intensity by Eq. (9) in accordance with regularization technique.

The procedure of regularized solution of the diagnostic equation is equivalent to the use of hypothetical measurement system providing higher spatial resolution. Simulations show the possibility of increasing the spatial resolution in beam profile measurements about 1.5 - 2.5 times and even more (the value depends on detector dynamic range, applied regularization algorithm, as well as the solution behavior).

III. SUMMARY

Proposed technique is expected to be efficient when optical resolution in beam profile measurements is comparable with actual beam dimensions, as it takes place in high-energy storage rings. The method proposed for computation of the diagnostic equation kernel allows to take into account practically all main distortion sources in the measurements. The technique may be easily adapted to particular experimental conditions.

I would like to thank M.M.Samorukov and N.V.Smolyakov (Kurchatov Institute, Moscow) for fruitful discussions.

Contact e-mail address: chubar@ksrs.msk.su

IV. REFERENCES

- [1] A.P.Saberski, "Monitoring the beam in SPEAR with synchrotron light", *IEEE Trans. Nucl. Sci.*, NS-20, 638 (1973).
- [2] J.S.Mackay, "Electron beam profile, position systems and measurements on the Daresbury SRS", Preprint Daresbury Laboratory DL/SCI/P591A (1988), *Proceedings of 1988 European Particle Accelerator Conference*.
- [3] A.Hofman, F.Meot, "Optical resolution of beam profile measurements by means of Synchrotron Radiation", *Nucl. Instr. and Meth.* Vol.203, 483 (1982).
- [4] Atsushi Ogata, "On optical resolution of beam size measurements by means of synchrotron radiation", *Nucl. Instr. and Meth.* Vol. A301, 596 (1991).
- [5] M.Born and E.Wolf, *Principles of Optics*, 6th ed., Pergamon, Oxford (1980).
- [6] L.Landau, E.Lifshits, *The Classical Theory of Fields*, Pergamon, Oxford (1980).
- [7] *X-ray Data Booklet*, edited by D.Vaughan (Lawrence Berkeley Laboratory, Univ. of California, 1986).
- [8] K-J.Kim, "A new formulation of synchrotron radiation optics using Wigner distribution", *SPIE*, Vol.582, 2 (1985).
- [9] A.N.Tikhonov, V.Ja.Arsenin, *Methods for solution of ill-posed problems*, Moskva, Nauka (1986) -- in Russian.
- [10] C.W.Groetsch, *The Theory of Tikhonov Regularization for Fredholm Equations of the First Kind*, Boston, Pitman Publ. Ltd. (1984).

The Orsay Spot Size Monitor for the Final Focus Test Beam

J. Buon, B. Delcourt, J. Jeanjean, F. Le Diberder, V. Lepeltier, and P. Puzo

Laboratoire de l'Accélérateur Linéaire, IN2P3-CNRS
et Université de Paris-Sud, F - 91405 Orsay Cedex

Abstract

The principle of the ionization spot size monitor built at Orsay and installed at the focal point of the FFTB line of SLAC is reviewed. Its constituents (pulsed gas target, MCP ion detector and electronics) and their performances are briefly described, together with preliminary background tests performed at Orsay.

I. INTRODUCTION

A beam size monitor of a new type [1] built at Orsay to measure the beam dimensions at the focal point of the Final Focus Test Beam [2] (FFTB) has been installed at SLAC. The goal is to measure a spot size of about one micron horizontally and that can be vertically decreased down to 60 nm r.m.s. in a flat beam operation. The principle of the measurement [3,4] is based on the transverse kick given to ions by the space charge field of the electron beam. The ions will be produced by ionization of a pulsed gas target at the focus. In a first measurement with an Argon gas, the heavy Ar^+ ions receive a kick proportional to the electric space charge field. The maximum velocity of these ions is proportional to the maximum field that is inversely proportional to the beam dimensions. The time of flight of the ions to reach a detector has a minimum value that scales linearly with the radius of a round beam (see Fig. 1). For a flat beam, this quantity is also slightly dependent on the beam aspect ratio.

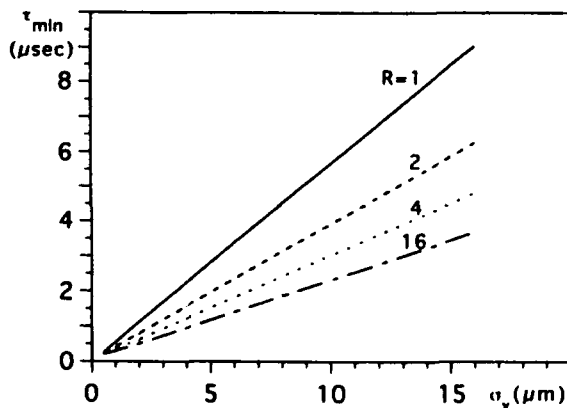


Figure 1: The minimum time of flight τ_{\min} of Ar^+ ions vs. the r.m.s. horizontal beam dimension σ_x for several aspect ratios $R = \sigma_x / \sigma_y$.

A second measurement, with a Helium gas, will allow to obtain the aspect ratio and to resolve the ambiguity of the first measurement. The light He^+ ions are trapped and oscillate in the space charge field during the passage of the beam pulse. In the case of a horizontally flat beam, the mean oscillation amplitude is larger in the horizontal direction than in the vertical one. After passage of the beam the ions are

emitted in the transverse plane with an azimuthal distribution peaked along the horizontal direction. On the contrary, the azimuthal distribution is isotropic in the case of a round beam. The anisotropy of the azimuthal distribution (see Fig. 2) will then give the beam aspect ratio.

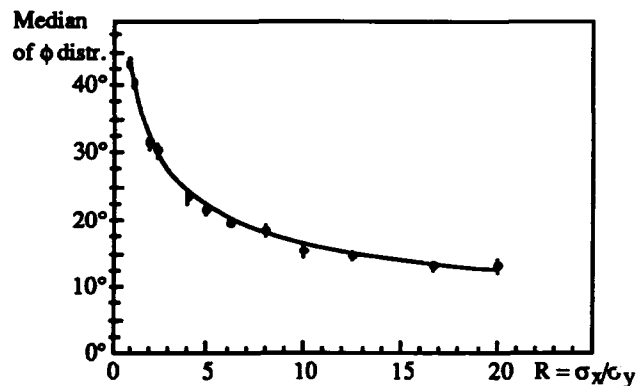


Figure 2: The median of the He^+ azimuthal ϕ -distribution between 0° (hor. direction) and 90° (vert. direction) in the transverse plane vs. the beam aspect ratio σ_x / σ_y , as given by a Monte-Carlo simulation.

Schematically, the Orsay beam size monitor comprises a pulsed gas injection and pumping device, and an array of multichannel plates with spatial and time resolution to detect the ions (see Fig. 3). Two gas inlets allow to inject Helium and Argon gas into the beam pipe at the focal point. The injected gas is pumped rapidly between two successive electron bursts. The ions kicked by the space charge field of the beam pass through a narrow slit inside a thick shielding. They hit an octagon of microchannel plate (MCP) detectors. The hit signals, collected on read-out anodes, are analyzed in time by fast ADC's. The anodes are divided in 8 strips, parallel to the electron beam, for each of 6 MCP detectors and 16 ones for the two MCP detectors hit by the ions emitted near the horizontal plane. The azimuthal distribution will be given by the counting rate of these 80 strips. The ions are also longitudinally deflected by an electric field applied between two small electrodes at the exit of the slit. The strips are made resistive and are read at each end so that the charge division of a signal between the two ends gives the longitudinal position and the deflection. Its correlation with the measured time of flight allows to discriminate ions of different electric charges.

II. THE PULSED GAS TARGET

The two gas injectors are modified fast valves of General Valve Co with a minimum opening time of about 150 μsec. Their shutter needles open two 1 mm diameter nozzles in the wall of the beam pipe. The injected gas expands in the pipe

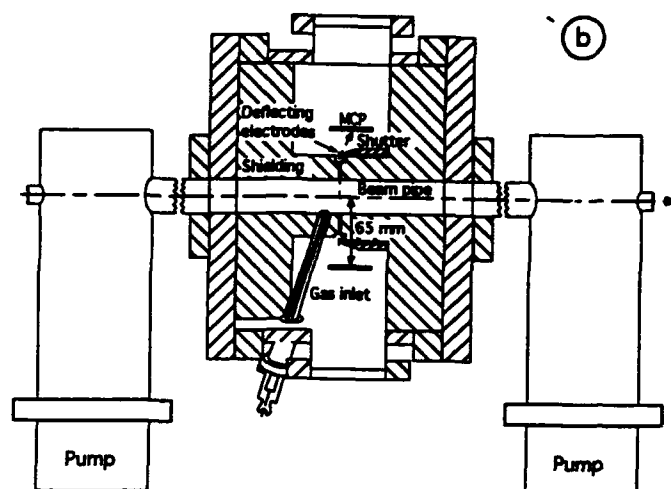
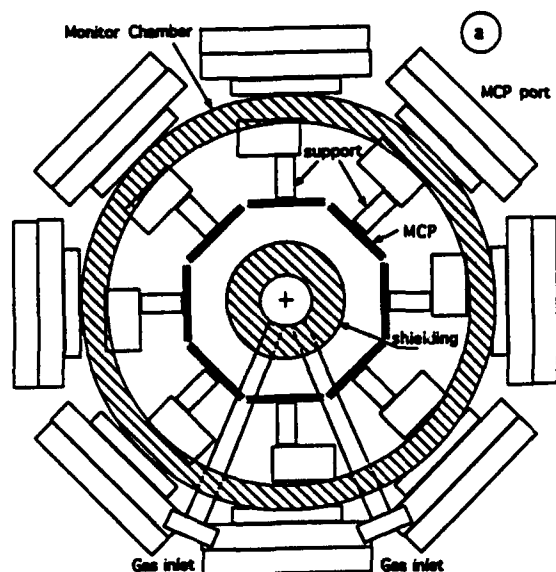


Figure 3: Schematic view of the beam size monitor : a) Transverse section at the FFTB focus, b) Longitudinal section along the beam line.

and its pressure reaches a maximum at the shutter closure when the electron bunch passes through. The maximum value is controlled by the opening time. It can be varied in the range 10^{-6} – 10^{-3} Torr. The upstream gas pressure is set around one bar. The pulse of gas is then pumped through the beam pipe by the two 150 l/sec turbopumps on each side of the monitor. The pressure decreases exponentially with a characteristic time of a few milliseconds (see Fig. 4). The mean increase of the pressure in the beam pipe has been measured, at the point where the pump pipes are connected, and has been found to be about a factor 200 lower than the maximum pressure at the focal point.

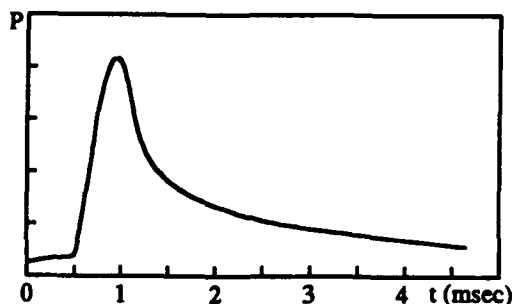


Figure 4: The variation of the pressure P (in arbitrary units) at the focal point in the beam pipe as a function of the time, when a pulse of Helium is injected. The pressure has been measured on a full-size model of the monitor with a fast gauge ($P_{\text{max}} = 1.4 \times 10^{-3}$ T, $P_{\text{upstream}} = 450$ T).

III. THE MCP ION DETECTOR

Each detector is made of 8 pairs of rectangular 40x50 mm MCP's from Hamamatsu Co. They deliver fast signals (~ 5 nsec) of a few picocoulombs. To calibrate them four radioactive α -sources will be located in front of the MCP's. Fig. 5 shows a pulse height spectrum obtained with these α -rays. The position of the peak is controlled by the high

voltage applied on the MCP's. It allows to adjust the gain and the electronic efficiency of the 8 pairs as required to obtain the ion azimuthal distribution.

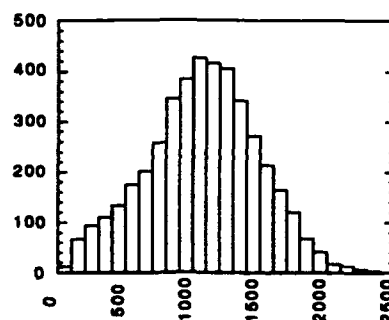


Figure 5: A pulse height spectrum (arbitrary units) of α -ray signals. The resolution is 77% FWHM.

Preliminary tests of the charge division between the two ends of each anode strip have indicated a longitudinal resolution of about 0.5 mm r.m.s. (see Fig. 6). It will be enough to discriminate ions of different charges that are separated by a few millimeters when a DC potential of about 1500 V is applied between the two small deflecting electrodes.

IV. ELECTRONICS AND ACQUISITION

Each of the 160 electronic channels (see Fig. 7) is made of a charge preamplifier located near the monitor followed by an amplifier and a shaper at a remote location. They have a smooth gain saturation that avoids long dead time, after the background pulse accompanying the beam (see Section 5), that would prevent the detection of the first ions arriving on the MCP's. The gain can also be rapidly changed by steps. The shaper pulses (30 nsec long) are sampled by HAMU chips [5] (analog pipelines) followed by 8-bit ADC's and

triggered at each electron burst. They run at 200 MHz, delivering 512 samples, each 5 nsec long. They give the time of each ion hit and the amplitude of its signal. A Macintosh microcomputer is used for data acquisition and treatment. It is also used to control the monitor hardware in connection with the general control of the FFTB line.

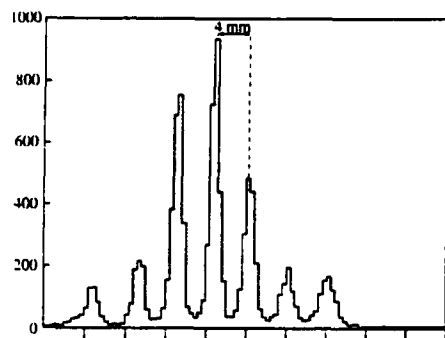


Figure 6: The spectrum of the longitudinal positions obtained with ions passing through thin slits 4 mm apart.

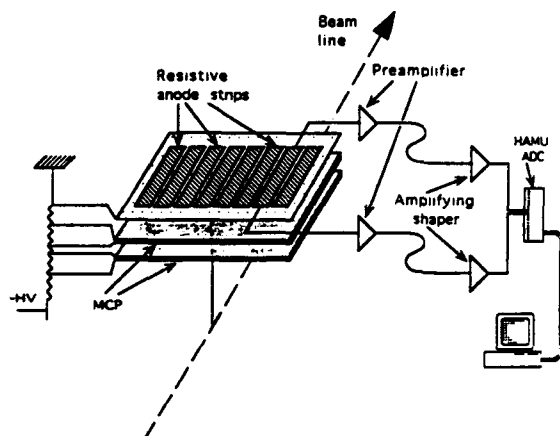


Figure 7: Schematic diagram of a MCP pair with the resistive anode strips and the associated electronics. Two read-out channels of only one strip are shown.

V. LINAC TESTS

The ability of MCP's to detect ions in the environment of a high-energy electron beam has been tested on the Orsay linac at 1 GeV and bursts of a few 10^8 electrons. The background conditions were severe, probably more severe than it can be expected at the FFTB. However, the background level in the MCP detection set-up has been found very small after the passage of an electron bunch. Ions were produced by the electron beam in a low-pressure gas target, composed of a residual gas with some addition of Helium. The beam space charge was negligible and a DC electric field was used to drift and collect the ions on a MCP. Figure 8 shows the time of flight spectrum of these ions, showing two peaks due to H^+ and He^+ ions respectively. The first peak at ≈ 200 ns is observed even without drifting field. It is attributed to background particles associated with the long tail of the beam, arriving after the applied cut off and extending up to ≈ 400 ns.

The only problem is the high background signal at the time of the bunch passage that is 10-100 times larger than an individual ion signal (see Fig. 9). It saturates the electronics

and can lead to a long dead time preventing to detect ions arriving 200 nsec later or less. Several means to reduce the dead time have been developed. The first one is to cut the gain of the MCP pairs during the passage of the beam by applying a blocking pulse between the two MCP's that reverses the potential on the gap between them. Most of the electrons getting out of the front MCP are repulsed and cannot reach the second MCP. It reduces the background signal by a factor 3. In another means, the preamplifiers have been designed to have a smooth saturation curve with nearly logarithmic increase of their gain up to an about 100 pC charge. Finally, the width of the shaper pulses has been reduced to 30 nsec FWHM. In conclusion, the electronic improvements made after the linac tests, show that even the fastest ions (arriving with a delay of about 70 nsec) could be detected if the background would be as high as at the Orsay linac.

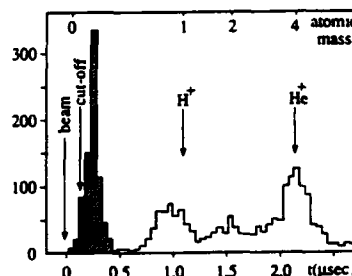


Figure 8: Time spectrum of MCP signals obtained with and without (hatched) a DC drifting voltage of 100 V.

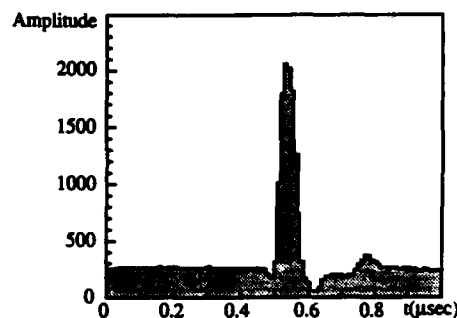


Figure 9: A record of a beam background pulse (≈ 50 pC) collected on a MCP anode after amplification, and digitized by a "HAMU" chip (The bin width is 10 nsec). The small pulse, arriving 240 nsec later and corresponding to about 1 pC, is due to an individual particle.

VI. REFERENCES

- [1] J. Buon et al., Nucl. Instrum. Methods A306 (1991) 93.
- [2] Final Focus Test Beam project design report, SLAC-Report-376 (1991).
- [3] P. Chen, D.L. Burke, M.D. Hildreth and R.D. Ruth : "A Plasma Beam Size Monitor", SLAC-AAS-41, 1988; presented at the International Workshop on the Next Generation of Linear Colliders, Stanford, 1988.
- [4] J. Buon : "Possibility to measure very small spot sizes using gas ionization at future linear colliders", Part. Accel. 31 (1990) 39.
- [5] D.R. Freytag et al., IEEE Trans. on Nucl. Science, 33 (1986) 81.

Beam Monitor Utilizing Transition Radiation

Yujiro Ogawa, Jae-Young Choi, Tsuyoshi Suwada, Takuya Kamitani, Takao Urano,
Kazuro Furukawa, Satoshi Ohsawa, Atsushi Enomoto and Isamu Sato
KEK, National Laboratory for High Energy Physics
Tsukuba, Ibaraki 305, Japan

Abstract

Beam monitors utilizing electromagnetic waves, especially visible light radiated by charged particles, have several excellent features for beam diagnostics in accelerators: they are essentially free from environmental electromagnetic noise and are characterized by a high-speed time response. A beam monitor based on transition radiation is one of the most promising monitors concerning positions, sizes, emittance, energy and time structures of bunches for high-intensity, short-pulse beams. We started to develop beam monitors utilizing transition radiation for the beam diagnostics of high-intensity electron beams. Bunch-length measurements were performed at the KEK 2.5-GeV linac with this monitor and a streak-camera system.

I. INTRODUCTION

Precise measurements of the beam parameters of an intense beam are indispensable for the stable operation of future accelerators. For instance, in the linac for the B-factory project proposed at KEK [1], it is required to accelerate an intense single-bunched beam of about 10 nC to a positron production target without any degradation of the beam quality; the beam-emittance growth due to a transverse-wake instability must be suppressed by precisely adjusting the beam position to the center of accelerating structures. In this case, beam-position monitors play an essential role. Bunch-length measurements become crucial for estimating the short-range wake fields, since their strength, especially the longitudinal type, strongly depends on the bunch shape. In any case, all of the beam parameters should be measured and evaluated not only precisely, but also reliably.

Beam monitors utilizing electromagnetic waves, especially visible light radiated by charged particles, have several excellent features for beam diagnostics in accelerators: they are essentially free from environmental electromagnetic noise and are characterized by a high-speed time response. Cherenkov radiation as well as synchrotron radiation is commonly used as input light for a beam-monitoring system; for example, the bunch length is measured at a good time resolution of less than several picoseconds by guiding the Cherenkov radiation into a streak camera. The handling of both systems, however, is generally not simple; in the case of

Cherenkov radiation, some special material or gas must be inserted into a beam line to generate radiation; there are also some problems regarding the radiation angles and the threshold energy of the radiation. Moreover, the optical system, for instance that which leads the light to the streak camera, may be complex, since the radiation source is essentially not point-like.

A beam monitor based on transition radiation [2-5] is one of the most promising monitors concerning positions, sizes, emittance, energy, and time structures of bunches for high-intensity, short-pulse beams. It has been noticed that transition radiation is generated from a point-like source under certain conditions, which makes it easier to arrange an optical system.

In this connection, we started to develop beam monitors utilizing transition radiation for the beam diagnostics of high-intensity electron beams. The fundamental concepts of the monitor are given and preliminary results concerning bunch-length measurements using this monitor with a streak camera is presented.

II. TRANSITION-RADIATION BEAM MONITOR

A. Principles

Transition radiation occurs during the uniform motion of a charged particle in a spatially inhomogeneous medium: for instance, when passing from one medium to another. For beam diagnostics, we utilize the radiation emitted from a vacuum-metal boundary; in practice, a thin metal foil is inserted into the beam line with an oblique angle to the beam direction of motion (Fig. 1). The radiation emitted by the metal surface is characterized by two features: a sharp angular directivity for relativistic particles, and a formation zone. The angular distribution of the radiated energy in a unit angular frequency (ω) is expressed as [2]

$$W(\omega, \theta) = \frac{e^2 \beta^2}{\pi^2 c} \frac{\sin^2 \theta}{(1 - \beta^2 \cos^2 \theta)^2},$$

where e is the electron charge, β the velocity of the charged particle divided by the velocity of light (c), and θ the angle of radiation (Fig. 1). The formation zone for radiation with a wavelength of $\lambda = 2\pi c / \omega$ is determined by the cylinder around the beam axis at a depth of d and a radius of ρ .

$$d = \gamma^2 \frac{\lambda}{2\pi} \quad (\text{in the vacuum side})$$

and

$$\rho = \gamma \frac{\lambda}{2\pi}.$$

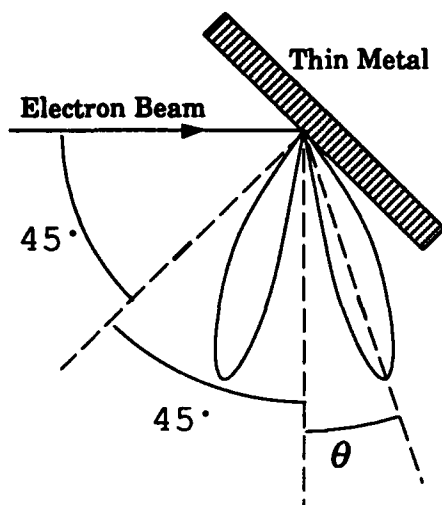


Fig. 1 Usual configuration of transition-radiation beam monitors. The radiation has sharp directivity.

Figure 2 shows the angular directivity pattern of transition radiation, indicating a narrow angular distribution with a characteristic angle of $\theta = 1/\gamma$ for two peaks, which allows easy installation of the light-guiding optics. The formation zone determines the fundamental resolution as a beam monitor; the formation radius provides position/size resolution for beam-profile monitors. The relativistic Lorentz factor (γ) appeared in the formation zone size, indicating the effectiveness of utilizing transition radiation in beam monitors at relatively low energy.

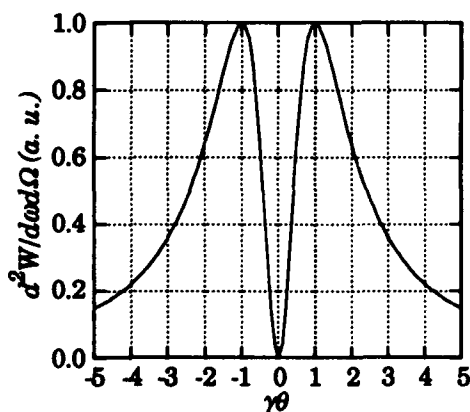


Fig. 2 Directivity pattern of transition radiation. It has two maximums at angles of $\theta = \pm 1/\gamma$.

B. Experimental

The experimental configuration for a transition-radiation monitor is shown in Fig. 3. A thin, polished mirror of stainless steel with a thickness of 2 mm is inserted into the beam line at the end of the first two accelerating guides after the bunching system of the KEK 2.5-GeV linac [6]. An electron beam with a peak current of 4 A and a pulse width of 15 ns hits the metal at an energy of about 50 MeV. The visible light emitted in a small angle from the thin metal is transported through an achromatic optical system to a CCD camera for beam-profile observations, as well as to the streak camera for bunch-length measurements. For the bunch-length measurements, the beam spot was adjusted to be about 3-4 mm in diameter, so as to optimize the light flux; at the input of the streak-camera system with a slit width of 30 μm , the photon number per bunch amounts to about 10^5 , which is measurable by a streak-camera system of Hamamatsu Photonics Ltd., Japan, with a time resolution of 2 ps for a single-shot measurement.

The alignment of the light-guiding system from the metal to the input of the streak camera was made by using a He-Ne laser placed at the other side of the light-extraction window (Fig. 3). The position and direction of the laser light was determined so that it simulated the transition radiation emitted at the metal surface.

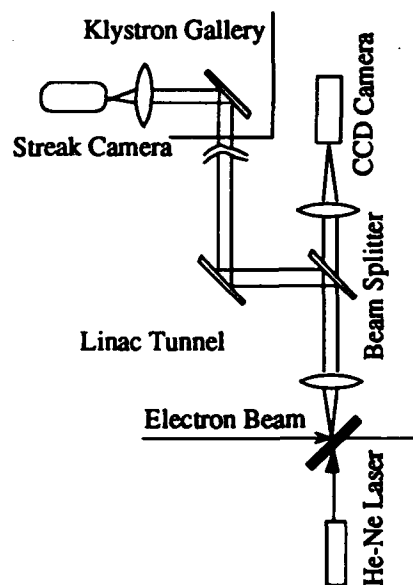


Fig. 3 Light-guiding system for streak camera.

The bunch shape for one of the bunches was observed with this system (Fig. 4). The bunch length was measured in two cases in order to demonstrate the system performance; the upper photograph of Fig. 4 indicates the bunch shape with a

width (FWHM) of about 12 ps when the bunching strength was set to a modest value; the lower shows a bunch length of about 9 ps under good bunching conditions.

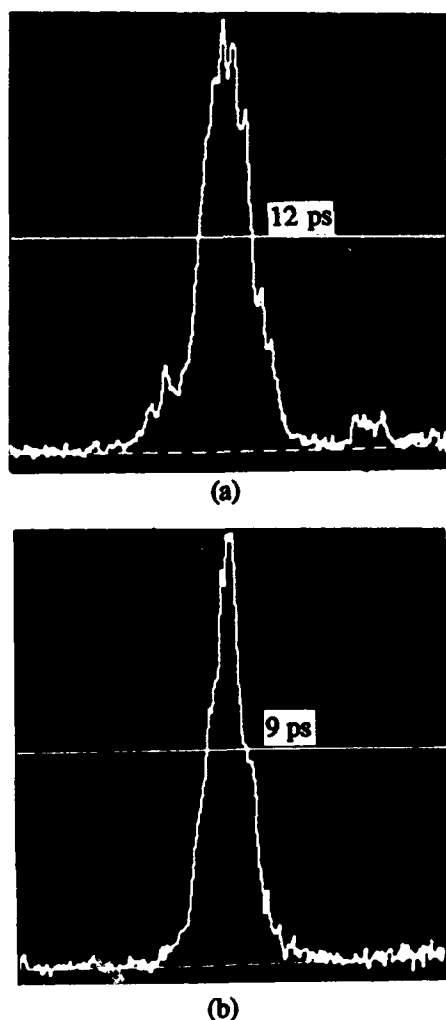


Fig.4 Demonstration of bunch-shape measurements by a transition-radiation monitor at the end of the first accelerating guides after the bunching section. (a) The prebuncher power is not optimized, and (b) optimized. The beam energy is about 50 MeV and the charge/bunch amounts to about 1 nC.

III. CONCLUSIONS AND DISCUSSIONS

A transition-radiation monitor has been developed for precise beam diagnostics of an intense beam. Among several excellent features of this monitor, we first applied its fast time response to bunch-length measurements. The preliminary results in the bunch-length measurement using transition radiation as a light source for a streak-camera system seems to indicate good performance of the monitor. Further elaboration as the bunch monitor and applications to the beam

position/size monitor for precise emittance measurements [7] will be made in the near future.

The fundamental resolution of the transition-radiation monitors is estimated by evaluating the formation zone mentioned above; in optical wavelengths (e.g. 500 nm) the depth of the formation zone for a beam energy of 50 MeV becomes about 0.8 mm, while the zone radius is about 8 μm , giving the position/size resolution.

The light-guiding system also causes some sort of aberration, which degrades the time resolution. A rough estimation gives 1-2 ps of time resolution in our system. We plan to improve the optical system by selecting a narrow band of visible light so as to decrease the chromaticity as well as to utilize single-mode fibers for easy light guiding.

IV. ACKNOWLEDGMENT

The authors would like to thank members of Linac for the stable operation of the machine during the experiments.

V. REFERENCES

- [1] B-Factory Accelerator Task Force, "Accelerator design of the KEK B-Factory", edited by S. Kurokawa, K. Satoh and E. Kikutani, February, 1991, KEK Report 90-24.
- [2] V. L. Ginzburg and V. N. Tsytovich, "Several problems of the theory of transition radiation and transition scattering", *Physics Reports*, **49**, 1 (1979).
- [3] L. Wartski, S. Roland, J. Lasalle, M. Bolore and G. Filippi, "Interference phenomenon in optical transition radiation and its application to particle beam diagnostics and multiple-scattering measurements", *J. Appl. Phys.* **46**, 3644 (1975).
- [4] M. Jablonka, J. Leroy, X. Hanus and L. Wartski, "Beam diagnostic using transition radiation produced by a 100 MeV electron beam", DPhN Saclay 91-32.
- [5] D. W. Rule, "Transition radiation diagnostics for intense charged particle beams", *Nucl. Instrum. Methods B24/25*, 901 (1987).
- [6] S. Ohsawa, I. Abe, S. Anami, J. -Y. Choi, A. Enomoto, K. Furukawa, H. Hanaki, K. Kakiyama, N. Kamikubota, T. Kamitani, H. Kobayashi, Y. Ogawa, T. Oogoe, I. Sato, T. Suwada, Y. Yamazaki, M. Yokota and A. Asami, "New pre-injector of the KEK 2.5-GeV linac and its performance", these proceedings.
- [7] R. Chehab, M. Taurigna and G. Bienvenu, "Beam emittance determination using optical transition radiation", *The Third European Particle Accelerator Conference*, Berlin, Germany, March 24-28, 1992, pp.1139-1141.

Fermilab Main Ring Low Level RF System Modifications For Focus Free Transition Beam Tests

R. G. Scala and K. Meisner

Fermi National Accelerator Laboratory*

P. O. BOX 500

Batavia, Illinois 60510

Abstract

A novel idea for crossing transition energy has been proposed for study in the Fermilab Main Ring accelerator. The idea has been named focus free transition crossing¹ and involves reducing the RF focusing force nearly to zero when the beam energy is near the transition energy by adding a third harmonic to the RF accelerating voltage, and then adjusting the accelerating phase angle to 90°. The modification of the accelerating voltage wave form shape and phase are accomplished by accurate program control of the amplitude and phase of the 53 Mhz RF cavities and a recently installed 159 Mhz cavity. The studies also require interrupting the normal LLRF system beam energy feedback loops in favor of a new energy control loop near the transition energy. This paper describes the functions of the LLRF system electronics recently installed to facilitate this control, and initial operational experience with the system.

Introduction

Focus free transition crossing (FFTC) may offer an improvement in Main Ring performance through reducing longitudinal emittance growth and beam loss as beam accelerates through the transition energy. The basic concepts of focus free transition crossing and performance improvements, plus some results of recent beam studies are described elsewhere.^{2,3} The Main Ring LLRF system modifications⁴ discussed here are to control the 53Mhz RF cavities and a recently installed 159Mhz RF cavity very accurately in amplitude and phase. This produces an accelerating voltage wave form with zero slope around 90°, and thus provides only the required accelerating voltage with no RF focusing force. This control occurs during the non-adiabatic period around transition, an interval of approximately 10 msec. The new LLRF system operating modes for focus free transition studies in no way compromise existing operation.

Background

Even without functionality required for FFTC studies, the Fermilab Main Ring LLRF system is a complex beam control system providing an interesting variety of control options for the Fermilab physics program. The LLRF system accommodates RF synchronous transfer of beam from

several machines, accelerates protons or antiprotons, operates on different MR ramp profiles and peak energies, and provides bi-directional beam transfers to specific RF buckets between MR and Tev at 150 Gev. The MR LLRF system uses a VCO and signals from two beam detectors to control the beam energy. Beam signal from a stripline longitudinal detector located at F11 is processed and serves as the master input to phase lock loop feedback which forces the VCO to follow the beam frequency and damp coherent energy oscillations at the synchrotron frequency. Signal from a horizontal position detector at F28 is processed to provide a beam radial position measurement (RPOS) that is compared to a desired position program (M3ROF). The resulting position error signal (RPERR) is processed and drives a phase shifter to control the beam accelerating phase angle and energy gain per revolution. When FFTC studies produce an accelerating voltage with zero slope, the radial position feedback loop can no longer use the accelerating phase angle to control the beam energy, and is abandoned in favor of a loop using the RF amplitude to control energy.

The MR LLRF also controls the RF bucket area for bunch shape manipulations at flat-top energies.^{5,6} These manipulations accomplish bunch rotation at 120 Gev for pbar production, and bunch coalescing at 150 Gev for Tev injection in the Fermilab colliding beams physics program. For bunch rotation and coalescing, the MR LLRF output and the RF cavities are divided into A and B groups, and the system independently controls A and B group amplitudes and phases. Application program T101 calculates voltage and phase programs and loads these into four sets of Camac 069/071 digital curve generators. The phase programs are a single 12 bit curve that input to the Counterphase Program Select module (CPPS), which receives timing information to select when programs play. The CPPS module 12 bit outputs drive two phase shifters called Counterphase A and B modules. The Counterphase modules are a specific application of hardware widely used at Fermilab called DF modules. They are digitally controlled, bi-directional, fully periodic RF phase shifters providing phase resolution of .09°. The existing T101 phase programs, the CPPS module, and Counterphase shifters equally retard and advance the A and B group phases respectively. This system also provides the operational transition phase jump. A CPPS digital input named M:TPJenn ("nn" is a MR cycle type) specifies a phase jump magnitude, and equally advances the A and B group phases at transition. FFTC studies require individual A and B phase programs to simultaneously counterphase A and B LLRF outputs while also advancing the A+B sum voltage phasor to 90°. Existing phase programming could not satisfy this requirement.

* Operated by Universities Research Association Inc., under contract with the U.S. Department of Energy.

Digital Adder module

The Digital Adder was designed to provide new A and B group phase programming for FFTC studies, and is in series between the existing CPPS and Counterphase modules. The adder has two channels of processing with two stages of ALUs in each channel. It combines three new digital phase control inputs with the two CPPS A/B phase programs. These 5 inputs produce 2 digital outputs which drive the Counterphase A/B shifters. Two of the new inputs are named M:PPGA and M:PPGB (Phase Program Group A and B). These provide unique A and B group program curves for FFTC studies and are generated in Camac 467 modules. Application program W48 derives required PPGA and PPGB phase programs and loads the curve generators⁷. The third new phase control input is named CPEFB, for CounterPhase Energy FeedBack. This input provides small counterphase angle modulation between the A and B groups to control the beam energy during the FFTC interval and will be discussed later.

The two Digital Adder phase control outputs and the resulting phase shifts generated by the counterphase A and B shifters are:

$$\Phi_A = -CPPSA + PPGA - CPEFB$$

$$\Phi_B = +CPPSB + PPGB + CPEFB$$

The sign convention is that positive $\Delta\Phi$ is phase advance.

The Digital Adder has the following features. All inputs and outputs are 12 bits and have an associated data valid strobe. All input and output data is latched in the Adder. The Adder asynchronously combines all active input data in a method which guarantees maximum throughput and correct output. The maximum throughput is when only one input is active and corresponds to a delay of 260 nsec. The slowest data output rate occurs when all three inputs are active with no timing overlap, corresponds to the largest delay between a first input data change and output update, and results in a delay of 780 nsec. The Adder does not have on/off gating, and includes no provision to reset output data. The system relies on Adder input data sources to properly reset Counterphase A/B shifter program inputs to appropriate values (generally 0°) when programs finish.

Digitize/Hold modules

The MR LLRF system has two Digitize/Hold modules which provide two (of four possible) channels of functionality required for FFTC studies. A Digitize/Hold module features two channels with input buffering and scaling options, track and hold, 12 bit 600 KHz ADC, digital output (Dout), and reconstructed analog output (Vout). The module provides true 12 bit resolution and all bits are used. Channel 1 accepts ± 10 volt signals and is scaled so $V_{out} = V_{in}$. Channel 2 accepts ± 2.5 volt signals and is also scaled so $V_{out} = V_{in}$. Channel encode rate can be separate or common, and the clock source can be internal or external. In the FFTC application, the digitize rate is common for both channels and is from an internal 500 KHz TTL clock oscillator. Each Digitize/Hold

channel accepts a TTL active high Hold control input gate. Module timing is designed so that Dout and Vout remain constant at their last value before the positive edge of the hold gate. The modules are used as accurate track and infinite hold circuits. Since the ADC always runs, Dout and Vout quickly reacquire V_{in} at the hold gate negative transition.

Counterphase Energy Feedback

The two Digitize/Hold channel V_{in} signals used for FFTC studies are both from the LLRF system radial position (energy) feedback loop. The ± 10 volt channels of two Digitize/Hold modules are used. One channel digitizes the loop output signal (M:PSHIFT) to the loop phase shifter. This digitizer is simply in series with the PSHIFT signal, and delivers Vout to the loop phase shifter. The second channel digitizes the RPERR signal from a point early in the Radial Position Feedback Loop Processor module. Dout from this Digitize/Hold channel is in 2's complement format and represents the beam energy error. At the beginning of the FFTC interval, a hold command is given to the PSHIFT digitizer. This holds M:PSHIFT and the RPOS loop contribution to the beam acceleration phase angle constant, establishes the initial conditions for subsequent phase programming, and effectively opens the energy feedback loop normally used during acceleration. PPGA and PPGB phase programs then counterphase the A and B RF cavity groups while advancing the acceleration phase angle to 90°. The typical initial counterphase angle is 55°, and is called the cone angle. Dout from RPERR is the CPEFB phase control summed by the Digital Adder into the Counterphase A/B shifter inputs. CPEFB modulates the cone angle between the A and B RF cavities and the amplitude of the flattened RF voltage wave form. This provides beam energy feedback during the FFTC interval.

The total cone angle modulation by the CPEFB loop input must never exceed the programmed cone angle between the A and B RF cavity groups. This would reverse the sign of the feedback loop and destroy the beam if allowed to adjust the beam energy gain per turn too much, and means the CPEFB loop contribution to A and B phase programs must be limited to one half the programmed cone angle.

Digital Limiter module

This module receives the digitized RPERR output data (Dout) from the CPEFB loop Digitize/Hold module. The Digital Limiter sets upper and lower limits on the CPEFB loop cone angle modulation to avoid positive feedback. The limits are currently set to $\pm 22.5^\circ$.

The circuit consists of PLS153 program logic array's which determine if the 12 bit input phase program is within allowed limits. Dual 4 - 1 data selectors/multiplexers (74LS153's) either pass the input or an upper or lower limit value. The final output stage uses 74LS541's output drivers. The module also outputs a data valid strobe to latch information into the Digital Adder. Module output data is active only when a TTL control gate input is high. The gate

is generated from system triggers named M:TCPFON and M:TCPFOF (CPEFB ON and OFF). At M:TCPFOF the Limiter module outputs 0° and a data valid to reset the CPEFB Digital Adder input.

RF Rephaser Module

This module receives the 53Mhz LLRF A and B group outputs from the Counterphase A/B phase shifter modules. Both inputs are amplitude limited and processed to produce an RF output that is constant amplitude, and at the phase of the vector sum of the A and B RF inputs. The advantage of the Rephaser output is that it represents the phase of the 53Mhz RF sum voltage by a large amplitude signal, even when the A/B shifters are programmed to counterphase the true sum vector amplitude to a very small value. The RF Rephaser output drives the 159 Mhz oscillator.

159 MHz Oscillator

This module receives the RF Rephaser module signal, amplitude limits the input with a 20 dB range AGC circuit, and triples the frequency. The module 159Mhz output drives the 159 Mhz amplifier system and RF cavity⁸. An input curve named M:HV3PG from a Camac 465 module programs the RF output amplitude and the cavity voltage. The RF output is turned on and off by a TTL gate controlled by system triggers named M:TH3ON and M:TH3OFF.

The 53 Mhz input from the Rephaser module is already constant amplitude, but to facilitate using the 159Mhz oscillator in other applications it has an input AGC circuit. The AGC circuit is an AD834 multiplier transformer coupled to a Comlinear current feedback operational amplifier. The amp output is AC coupled and drives a power splitter and simple diode detector. The detector output is viewed at a monitor called Vdet. Vdet is compared to Vset, an internal set voltage, and produces an error signal for a high gain feedback loop that controls the multiplier gain input.

The AGC circuit 53Mhz output drives a simple frequency tripler consisting of two power splitters, an RF amplifier, and two mixers. Mixing products are removed by a Trilithic 4BC159/10-3-CC tubular band pass filter.

The oscillator is capable of two types of feedback operating on the 159Mhz cavity voltage. The feedback is enabled by system timers M:TH3FON and M:TH3FOF. The first type is 159/53 Mhz amplitude ratio feedback. It forces the detected 159Mhz cavity voltage to equal a specified fraction of the detected 53Mhz cavity voltage. The second feedback type is direct feedback and forces the detected 159 Mhz cavity voltage to follow the amplitude input program HV3PG. This loop would compensate for gain changes in all components of the 159Mhz amplifier system. During FFTC studies the 53Mhz RF cavity voltage is modulated by the CPEFB loop and PPGA/B programming. The 159Mhz cavity must maintain the correct voltage ratio (approximately 13% of the 53Mhz) to optimize the RF wave form flatness. Selection of feedback loop type is via a jumper option. Ratio feedback is currently implemented.

Oscillator performance summary

Max. RF input:	+7 dbm
AGC stage RF input range:	-15 to +5 dbm
Input frequency:	500 KHz to 80 Mhz
Vset	- 1.563 volts
AGC stage RF output:	+ 3.4 dbm

Conclusion

All the hardware necessary for focus free transition crossing beam studies is implemented in the MR LLRF system. Curve generators and application program W48 are used to control the hardware with predicted accuracy and results. FFTC beam studies verify correct control of the MR 53Mhz and 159Mhz RF cavity amplitudes and phases. Control of the beam energy in the FFTC interval with the new feedback loop works well. A key signature of successful FFTC is bunch length increase (instead of shortening), and no beam loss through transition. This signature has been observed routinely during FFTC studies.

Acknowledgments

The authors wish to thank D. Klepec of FNAL and R. Gonzalez of SSCL for valuable assistance in developing the hardware presented in this paper.

References

- [1] James E. Griffin "Focus Free or Sliding Under Transition Crossing Fermilab TM-1700
- [2]. James E. Griffin " New Method For Control of Longitudinal Emittance Dilution During transition Crossing in Proton Synchrotrons" IEEE Particle Accelerator Conference (1993)
- [3] C. Bhat "Operating Experience with Third Harmonic RF for Improved Beam Acceleration through transition in the Fermilab Main Ring "IEEE Particle Accelerator Conference (1993)
- [4] K. Meisner "Main Ring LLRF System Modifications For Sliding Under transition Studies" Fermilab Operations Bulletin #1237, Nov., 1992
- [5] P. Martin "Performance Of The RF Bunch Coalescing System In The Fermilab Main Ring" IEEE Trans. Nucl. Sci Vol. NS-32. No. 5(1985)
- [6] D. Wildman " Bunch Coalescing in the Fermilab Main Ring" IEEE Particle Accelerator conference (1987)
- [7] M. A. Martens "Controlling The Third Harmonic Cavity During Focus Free Transition Crossing in the Fermilab Main Ring" IEEE Particle Accelerator Conference (1993)
- [8] J. Dey "The High Level RF System for Transition Crossing without RF focusing in the Main Ring at Fermilab" IEEE Particle Accelerator Conference (1993)

RF Synchronous Transfer Into Specific Buckets Between Fermilab Main Ring And Tevatron Accelerators

K. Meisner

Fermi National Accelerator Laboratory*

Abstract

I present a description of the design philosophy, hardware implementation, and operation of the system used to place beams transferred in either direction between the Main Ring and Tevatron accelerators into specified RF buckets of the receiving machine. The system provides reliable phase coordinate placement with $.09^\circ$ resolution without beam measurements of any kind. The system also controls the collision point in the Tevatron during the Fermilab colliding beams HEP program with $.689$ mm. resolution.

Introduction

During early preparations for the first Fermilab colliding beams operation, it was realized that a new method of RF synchronous beam transfer was required between the Main Ring (MR) and Tevatron (Tev) accelerators. Special functionality for these transfers includes accurate phase coordinate placement into specific RF buckets, minimal disturbance of beam previously injected, transparent bi-directional transfer operation, accommodating very low intensity beams of protons or antiprotons, the ability to completely test the system without beam, and remote control and diagnostic capability. In early 1984 a hardware system to accomplish these goals progressed from design to installation. It has since provided reliable operation and has become known as the Cogging LLRF system.

Principle of Operation

RF synchronous transfer is the correct beam to RF bucket phase at injection. Synchronization between any two Fermilab accelerators means both accelerator RF cavity systems have equal frequencies and a specific, adjustable phase relationship between them at beam transfer time. Fermilab LLRF systems traditionally use phase lock loops to synchronize one machine to another. Since the final conditions are achieved from arbitrary frequency offset and phase initial conditions, the phase lock loop approach can present problems when RF buckets contain beam. Fast RF bucket phase modulation from transient effects and loop initial conditions should be avoided. Beam momentum deviations also should be minimized.

The cogging system provides synchronization while avoiding these problems. The basic principle of the cogging system is to drive the RF cavities of both the MR and Tevatron accelerators from the same LLRF oscillator at transfer. The Tevatron LLRF oscillator is a synthesizer with an output frequency that is very stable and accurately programmed from a bend magnet current input, and is chosen to be the common RF drive source.¹ Accurate control of the relative phase between the drive signals to the RF cavities of each machine then

correctly places beam into the RF buckets in the phase coordinate. An output of the Tevatron LLRF oscillator that does not drive any RF cavity is frequency modulated to exactly match the MR LLRF output frequency and phase, and is then switched in to drive the MR RF cavities, with no observable effects on the MR beam. The modulation is generated digitally, and is relaxed in a very controlled manner.

After synchronization to an arbitrary RF bucket is complete, a process called transfer cogging aligns the beam to a specific bucket by again frequency modulating the Tevatron LLRF signal and MR RF cavities. This modulation produces any required integral bucket shift between MR and Tevatron. MR and Tevatron beam synch clock system (MRBS and TVBS) markers label the RF buckets of each machine.² These clock systems generate markers at the beam revolution frequency by continuously dividing RF outputs from the respective LLRF systems by the harmonic number. The MRBS marker is also used to synchronize MR beam injection to a specific RF bucket. Transfer cogging components of the cogging system measure and adjust MRBS and TVBS marker (bucket) displacement, and so do not require actual beam measurements for operation or system tests.

Frequency modulation of the Tevatron LLRF signal is accomplished by the MR Cogging Delta Frequency (MRCDF) module. This is one application of many DF module uses at Fermilab. DF modules are digitally controlled, bi-directional, fully periodic RF phase shifters. They can receive a 12 bit phase shift input program to produce $\Delta\Phi$, and they can receive a clock pulse train (Fclk) and sign control input to produce $d/dt(\Delta\Phi) = \pm \Delta F$. The Tevatron LLRF system also uses two DF modules, one each to control the drive signal phase shift to the Tevatron proton and anti-proton RF cavities. These are called Proton Cogging DF (PCDF) and Anti-Proton Cogging DF (APCDF) modules.

Figure 1 shows elements of the cogging system, the MRBS and TVBS systems, and the MR and Tevatron LLRF and RF cavities. Nine control sequences accomplish RF synchronization and transfer cogging. A tenth sequence adjusts the proton-antiproton collision point in the Tevatron, and is called collision point cogging. A module named the Cogging DF Controller (CDFC) accepts accelerator timing information and coordinates all cogging operation.

Cogging DF Controller

The CDFC module decodes TCLK to determine current MR cycle cogging requirements. Cogging control sequences begin and end when specific events are detected by the CDFC, and generally require arbitrary amounts of time for completion. The CDFC provides precise control of the MRCDF module and specifies the MRCDF phase with a resolution of $\Phi_{Lsb} = 360^\circ/4096 = .089^\circ$. The CDFC also controls the MRCDF $d\Phi/dt = \Delta F$ and $d^2\Phi/dt^2 = \Delta F \dot{}$ with resolutions of $.125$ Hz and $.250$ Hz/msec respectively.

The CDFC contains an accurate voltage to frequency converter (VFC) that can be driven by several input voltages.

* Operated by Universities Research Association Inc., under contract with the U.S. Department of Energy.

and selects which input runs the VFC with FET switches. Any selected input drives a comparator to obtain the sign of V_{in} . An absolute value circuit converts V_{in} to $-|V_{in}| \times \text{gain}$ in order to drive the VFC. Each VFC output pulse steps the MRCDF phase 1 Lsb when enabled by the CDFC.

The CDFC contains a 12 bit DAC that can also drive the VFC. A 12 bit counter (ΔF counter) loads the DAC, and provides knowledge of the MRCDF module ΔF magnitude. The ΔF counter can itself be clocked at a controlled rate, and therefore specify the MRCDF ΔF_{dot} . This clock rate is determined in the CDFC by an 8 bit $\div N$ circuit driven by a stable 500 KHz TTL oscillator.

The CDFC contains a 12 bit arithmetic logic unit (ALU) with selectable A and B inputs used for detecting control sequence start and end events ($A=B$), A versus B magnitude comparisons, and subtractions required in CDFC calculations. The CDFC also contains a 22 bit phase "tick" counter that sums MRCDF phase increments (VFC pulses) and counts MRCDF revolutions to an accuracy of 1 part in $M_{revolutions} \times 4096$.

Cogging Control Sequences

This section describes the ten cogging control sequences.

Sequence 1 occurs at Tclk event C1 once each Tevatron load cycle before any beam is injected. The CDFC clock decoder detects event C1 and presets Tev LLRF PCDF and APCDF modules to phases specified by host computer parameters T:PCDFP and T:APCDFP. This sequence resets fractional RF bucket collision point cogging from previous Tev cycles and specifies the Tev RF cavity phases for subsequent beam transfers.

In sequence 2, the MR LLRF system accelerates the beam to flattop. As the MR 150 Gev flattop begins, the MR LLRF system VCO and beam feedback loops are controlling the beam. The MRCDF module is off ($\Delta F=0$), and its output frequency equals the Tev LLRF oscillator programmed value. A Fermilab overlap phase detector (OPDET5) compares the MR LLRF signal to the Tev LLRF output of the MRCDF module and shows a beat frequency between the two signals. The Tev LLRF output can successfully drive the MR cavities only if it is very near the 150 Gev programmed frequency. Hardware called the Permit module reads the Tev energy program, compares it to the 150 Gev value, and inhibits or allows a trigger named M:LMRCDF (Lock MRCDF).

Sequence 3 and those which follow occur only if the LMRCDF trigger is passed to the CDFC by the Permit module. CDFC FET switches select OPDET5 Vout as the VFC analog input (V_t) to close a high gain phase lock feedback loop (PLL). This forces the MRCDF RF output into a constant phase relationship with the phase shifted MR VCO RF, and modulates the TLLRF frequency in whatever direction is required to equal the MRRF frequency. The CDFC ΔF counter and DAC are also preset to zero in this sequence.

Sequence 4 begins after the PLL has remained closed for 18 msec. The CDFC DAC is then ramped up from zero at a fixed rate of 62.5 Hz/msec. A sample of V_t is low pass filtered and compared to the DAC output (V_d). When a CDFC analog comparator detects $V_d=V_t$, the ΔF counter stops to hold V_d . OPDET5 Vout is disconnected from the VFC (V_t

decays to zero volts) and V_d is switched into the VFC. The CDFC latches and remembers the sign of ΔF , and applies this information to the MRCDF $\pm \Delta F$ control input. At this time the CDFC also pulses the select B input of two MRLRF system RF switches so that the MRCDF output drives the MRRF cavities, the MR beam, and the LLRF distribution system (the MRBS input source). The MRCDF output frequency and phase is identical to the VCO RF, but is derived from the Tevatron LLRF oscillator, and is precisely controlled by the ΔF counter, DAC, and VFC in the CDFC.

Sequence 5 begins the relaxation of the MRCDF frequency modulation. To make algorithms of sequence 6 a function of one independent variable, ΔF is programmed to 50Hz. The CDFC ALU compares ΔF to 50Hz (ΔF_{nom}) and ramps the ΔF counter up or down as required toward 50Hz at a $|\Delta F_{dot}|$ rate of 1.04 Hz/msec. The ALU monitors $\Delta F(t)$ and stops changing the ΔF counter when $|\Delta F|=50$ Hz.

In sequence 6 the CDFC calculates the ΔF_{dot} rate at which the MRCDF frequency must go from $\Delta F=50$ Hz toward $\Delta F=0$. The rate is derived by comparing the current MRCDF phase reading (Φ_r) to the desired stop phase (Φ_d). Φ_d is an input from the host computer named M:MRCDFP. As the MRCDF approaches $\Delta F=0$, the area of $\Delta F(t)\Delta T$ must be such that the integrated MRCDF phase steps (slippage) will smoothly approach $\Phi_d=M:MRCDFP$ from the MRCDF initial phase= Φ_r . The CDFC ALU finds $(\Phi_d-\Phi_r)$, and uses this to address prom tables that load N into the $\div N$ circuit to control the ΔF_{dot} rate.

In sequence 7 the CDFC ALU compares $|\Delta F(t)|$ with 1 Hz (ΔF_{lim}). When it detects $\Delta F=1$ Hz, the CDFC holds ΔF and continues reading $\Phi_r(t)$, the MRCDF phase. When $\Phi_r = \Phi_d = M:MRCDFP$, the CDFC inhibits further VFC tick pulses to the MRCDF and forces $\Delta F=0$. At the completion of sequence 7, the Tevatron and MR RF systems are driven by one oscillator and have exact relative phasing. RF synchronous transfer to an arbitrary RF bucket is possible. For the fixed target physics program (only one beam transfer per Tev cycle) sequence 7 is the final cogging system function. The Tev bucket which receives the first beam bunch is then labeled bucket 1 by a clock lock process in the TVBS system.

Tclk events E20, E2A, and E2B designate Main Ring cycles for the Fermilab colliding beams program. Sequence 8 and 9 provide transfer cogging, and occur on any of these cycles. Single MR bunches are loaded into the Tev on sequential MR acceleration cycles. At the start of sequence 8 the MR bunch azimuthal location with respect to the target Tev RF bucket is arbitrary on each cycle. The target bucket is unique for each cycle and bunches must be injected with roughly equal spacing around the Tev circumference. A bucket offset is applied on each injection cycle to the TVBS marker which labels bucket 1. The Cogging Zero Shifter (CZS) module applies the offset by shifting the the TVBS marker an interval specified by host computer parameters C:XCBO (transfer cog bucket offset). Transfer cogging then always brings the MRBS marker into alignment with the offset TVBS marker. The CDFC issues a pulse called CSBREQ (Cogging Smart Box Request) at the end of sequence 7. The pulse interrupts a micro processor in the Cogging Smart Box (CSB), which begins the following sequences to generate a $\Delta F(t)$ waveform to drive the CDFC VFC and MRCDF module:

1) Trigger the Cogging Phase Detector (CPD) to measure the bucket displacement between the MRBS and offset TVBS markers as PHASE=buckets to cog. Send PHASE as a digital word (CSBBS in figure 1) to the CDFC.

2) Calculate PHASE*GAIN/TIME. GAIN and TIME are CSB parameters input by front panel thumbwheel switches. This calculation determines the maximum amplitude of the $\Delta F(t)$ wave form.

3) Send a REPLY pulse to the CDFC to initiate transfer cogging. The CDFC selects the CSB output wave form as the VFC drive (V_t). The CDFC also presets its tick counter to PHASE and begins to count down with each VFC pulse sent to the MRCDF module.

4) The CSB outputs a word called Cogging Phase Detector Phase Compare (CPDPC) to the CPD and continues reading the RF bucket displacement (PHASE).

5) When PHASE = CPDPC, the CSB ramps the voltage wave form to a "vernier level", which is also a CSB input parameter. The CSB continues reading PHASE from the Cogging Phase Detector.

Sequence 9 begins when the CSB reads PHASE = 1 from the CPD and there is just 1 bucket left to cog. The CSB

then ramps its $\Delta F(t)$ output wave form to a small value that produces $|\Delta F| = 2\text{Hz}$. The CDFC tick counter keeps track of how many buckets the beam is actually cogged and will stop the MRCDF at exactly the correct phase ($\Phi_d = M:MRCDFP$) when the tick counter reaches 0. At this point RF synchronous transfer into the specified Tev bucket is possible.

Sequence 10 controls collision point cogging and occurs on interrupt from the host computer. Parameters T:ACPS and T:MCPS specify integer bucket and fractional bucket cogging shifts respectively. The CDFC selects a ΔF rate of $\pm 2\text{Hz}$ (or 2 buckets per second) and frequency modulates the Tev LLRF APCDF module and shifts the four anti-proton RF cavities and beam azimuthally relative to the protons. A one bucket shift via ACPS cogs the antiprotons a distance of the (orbit circumference $\div 1113$), the harmonic number, and moves the collision point one half that amount. Fractional cogging via MCPS provides 2^{-12} of a single bucket shift, which equals .689 mm. A parameter named C:COGSUM sums all collision point cogging displacements.

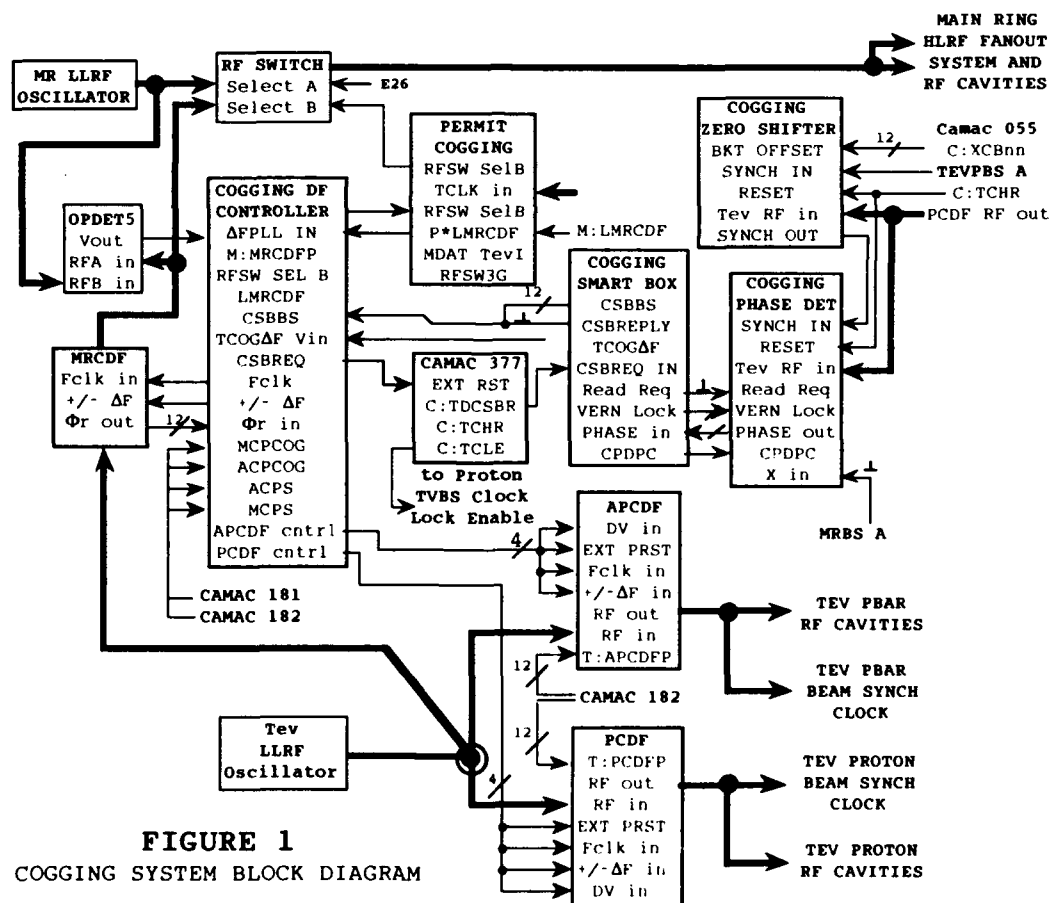


FIGURE 1
COGGING SYSTEM BLOCK DIAGRAM

References

- 1) K. Meisner, et al., "A Low Level RF System For The Fermilab Tevatron", IEEE PAC proceedings (1987)
- 2) D. Beechy and R. Ducar, "Time And Data Distribution Systems At The Fermilab Accelerator", Nuclear Instruments and Methods in Physics Research A247 (1986)

Main Ring Bunch Length Monitor

K. Meisner and G. Jackson

Fermi National Accelerator Laboratory¹, Box 500, Batavia, IL 60510

Abstract

Hardware to measure the Main Ring beam bunch length was installed in January of 1991. The system measures bunch length by comparing relative strengths of 53Mhz and 159Mhz components of signal from a beam detector. The output signal is proportional to bunch length, is scaled in nanosec., and has become a very useful diagnostic tool. Hardware design and operational performance are presented.

Introduction

The principle of operation for the Main Ring bunch length monitor (BLMON), motivation for it's design, choice of detector, and circuit components are given in detail elsewhere^{2,3}, and will be presented here only briefly. Electronics developed initially for BLMON early in 1990 produced unexpected noise on the output and exhibited useful operation over a small range of beam intensity. The emphasis of this paper is on a basic description of the electronics, improvements made to the original design and test procedures, and resulting performance.⁴

Measurement Principle

If N beam bunches with Gaussian longitudinal charge distribution pass through an ideal detector and are spaced by fixed time intervals, a signal V(t) is produced which is a function of σ_t , the rms. bunch length in time units, s, the detector sensitivity, I_n , the individual bunch currents, and $T_0 = \tau_{ff}$, the bunch to bunch time spacing. Taking the Fourier transform of V(t) gives V(ω), and allows evaluating the peak height of V(ω) at harmonics of T_0 . These harmonics dominate the beam signal spectrum. In the bunch length region of interest, the signal strengths at harmonics of $\omega_0 = 2\pi/T_0$ are:

$$V(m\omega_0) = 2V_{DC} e^{-\left[\frac{2\pi^2 m^2 \sigma_t^2}{T_0^2}\right]}, \text{ and}$$

$$V_{DC} = \frac{S}{4\sqrt{2}\pi} \sum I_n$$

V_{DC} is the DC response produced by the beam. Solving the equation for σ_t/T_0 at frequencies $m=1$ and $m=\lambda$, and subtracting $V(\lambda\omega_0) - V(\omega_0)$ gives the normalized bunch length as a function of the ratio of two harmonic signal strengths:

$$\text{EQN 1} \quad \frac{\sigma_t}{T_0} = \sqrt{\frac{-1}{2\pi^2(\lambda^2 - 1)}} \ln \left[\frac{V(\lambda\omega_0)}{V(\omega_0)} \right]$$

In the Main Ring accelerator, T_0 is nearly constant and the 95% interval of the beam distribution, referred to as the full bunch length $4\sigma_t$, is the quantity of interest.

A quarter wavelength coaxial stripline detector located in the Main Ring at E48 has resonances at $(2n+1) F_{rf}$. Signals from the upstream and downstream ends of the stripline are combined to allow detecting the beam current from both proton and antiproton beams. Detector output signals at the 53Mhz fundamental RF frequency and at the 159Mhz third harmonic give good sensitivity for detection of bunch lengths in the 1-12 nsec range of the Main Ring beam. These two frequencies are chosen for processing by BLMON electronics, which uses EQN 1 with $\lambda=3$.

BLMON Electronics Description

Figure 1 is a block diagram of the hardware. The beam RF input signal passes through a 7-bit digitally programmed attenuator with 127db range in 1db steps. For test purposes, the attenuator can be controlled locally. For normal operation, the attenuator is controlled remotely by system parameters named M:BUNnn, where "nn" designates one of the seven Main Ring accelerator cycle type Tclk reset events. Each of the cycle types can have unique beam type (proton or antiproton), bunch intensity, and fill factor. Early in the appropriate Main Ring beam cycle, the correct M:BUNnn parameter automatically switches into the attenuator control input and centers the input signal amplitude in the operating range of the BLMON hardware.

The attenuated beam input is then split into two channels. Trilithic Inc. tubular band pass filters with center frequencies of 53 and 159 MHz select the frequencies for processing by the first harmonic and third harmonic channels. The filters have matched bandwidths of 1Mhz to achieve comparable transient responses. Slight differences in the insertion loss of the filters and transmission loss of cabling is compensated for with a fixed attenuator at the input to the filter of the first harmonic channel.

Two stages of heterodyne receivers are used to detect each beam signal frequency component. The receivers offer good sensitivity and dynamic range. Intermediate frequencies (IF) of 10.7Mhz and 455Khz are used since commercial filters at these frequencies are readily available. Local oscillator (LO) RF signals used for down conversion to 10.7Mhz and 455Khz are derived from a Main Ring low level RF (LLRF) system input signal. The LLRF signal sweeps in frequency from 52.813Mhz to 53.103Mhz as the beam accelerates and remains synchronized with the beam RF input. The LLRF 53Mhz is mixed with a 10.7Mhz crystal oscillator output, band pass filtered at $F_c=42.3$ Mhz, band reject filtered at $F_c=10.7$ Mhz, and amplified to produce an LO signal near 42.3Mhz that correctly tracks the beam input first harmonic. The 42.3Mhz LO signal is mixed (1st mixer in figure 1) with the beam signal in a Mini Circuit Laboratories SRA-1 double balanced mixer to produce an

output at 10.7Mhz with amplitude proportional to the strength of the 53Mhz component of the beam signal.

In the 159Mhz receiver channel, the LLRF input drives a frequency tripler consisting of power splitters, SRA-1 mixers, RF amplifiers, and filters. The 159Mhz output is mixed with the 10.7Mhz crystal oscillator signal to produce an LO signal near 148.3Mhz. This LO signal mixes with the beam 159Mhz signal component to give a 10.7Mhz output with amplitude proportional to the strength of the 159Mhz component of the beam signal.

Subsequent processing of 10.7Mhz signals is identical for both frequency channels. Murata SFE 10.7 MA-Z band pass ceramic filters and RF amps drive the 10.7Mhz into the 2nd mixer stage RF input. A 10.245Mhz LO signal from a crystal oscillator down converts the 10.7Mhz to 455Khz. This IF signal is amplified and filtered by a Murata CFW 4558B ceramic filter with 22Khz bandwidth, and drives an operational amplifier and line driver.

The amplitudes of the 455Khz IF signals are proportional to the beam input signal strengths at the RF frequency first and third harmonics. A 455Khz coherent detector splits each 455Khz input into two signals, amplifies and limits one, and mixes this limited signal with the other in a MCL SRA-3 mixer. The outputs are filtered and amplified in an AD518 operational amplifier with offset and gain adjustments. The coherent detector outputs are labeled V₁ and V₃ in figure 1. They are available for local monitoring, and are read back by the host computer system as parameters M:BLM53 and M:BLM159. These signals are viewed when M:BUNAnn parameters are adjusted to place the input signal amplitude within the operating range of the electronics.

V₁ and V₃ also input to the normalizer circuit. Each voltage drives a Burr-Brown Corp. 4127 logarithmic amplifier. Log amp. outputs are subtracted by an operational amplifier and drive an AD534 four-quadrant multiplier in square root mode to produce the output voltage proportional to the beam bunch length as given by EQN 1. The output is scaled in the host computer database to convert the output to nanosec., and is named M:BLMON.

System Improvements

Beach tests of original hardware revealed noise on the BLMON output near 1.3Khz that was approximately equivalent to 2nsec. p/p bunch length modulation. The test procedure used the combined outputs of two crystal oscillators at 53 and 159Mhz to simulate a beam input signal. The 53Mhz oscillator also provided a LLRF input for generating LO signals. Since the two free running oscillator output frequencies were never exactly in the ratio of 3.00, this procedure introduced close in IM product sidebands at the offending frequency, especially on the 148.3Mhz LO source signal. These sidebands were well within the bandwidths of the filters intended to reject mixing products. The noise was easily eliminated by revising the test procedure to use only the 53Mhz crystal oscillator. It is a fifth overtone oscillator and its output is rich in harmonics. The harmonic at 159Mhz was selected with a bandpass filter, amplified to an appropriate level, and combined with the 53Mhz to provide a new test beam signal input. Like the actual beam signal, the

test signal 159 and 53 Mhz frequencies were then exactly a ratio of 3, and the output noise was completely eliminated.

After finding and replacing a significant number of broken electronic parts, the useful dynamic range of beam signal was only 14db. The output of an MWA-130 amplifier between the first and second mixer stages in the third harmonic channel showed a noise floor about 12db above that expected. At small beam signal levels, this noise dominated the coherent detector input. Grounding and power bypassing at the amp. were improved to achieve the expected output.

A signal at 455Khz and approximately -35dbm was measured at the coherent detector inputs even with no beam input. This signal would initially appear and then persist after once applying a beam input, and reduced the range of coherent detector linear operation. Fast edges of 455Khz in the coherent detector limiter circuit initiated the noise, which then regenerated itself as input signal through power supply coupling. Bypass capacitors at the 15 volt power inputs were increased at four places in the limiter and the unwanted signal was reduced to -74dbm.

IM products from mixing stages in the LO signal generator hardware also limited the dynamic range of BLMON. Trilithic tubular filters at 42 and 148Mhz with 5 and 10Mhz bandwidths respectively were installed on the outputs of these stages.

A precision voltage source was used to check and tune normalizer board log. amp. scaling and dynamic range. V₁ and V₃ stages were matched, and gave proper operation over 4 decades of input range.

Conclusion

Much of the design and construction work for the BLMON system was completed by 1990, but the hardware operation fell quite short of the expected performance for unknown reasons. Investigation of the system resulted in substantial improvements in test procedures and operation with regard to accuracy and dynamic range. Comparisons of the M:BLMON output with calculated bunch lengths and those observed from wide band resistive wall monitors show close agreement. Remote control of the BLMON system attenuator and remote viewing of signals proportional to 53 and 159Mhz beam signal strength facilitate adjustment for the variety of Main Ring accelerating cycles.

Acknowledgments

The authors debugged, refined, and installed the system after it was nearly complete. The original design and construction of the electronics was principally done by T. Ieiri of KEK, R. Gonzalez of SSCL, and D. Martin of SSCL.

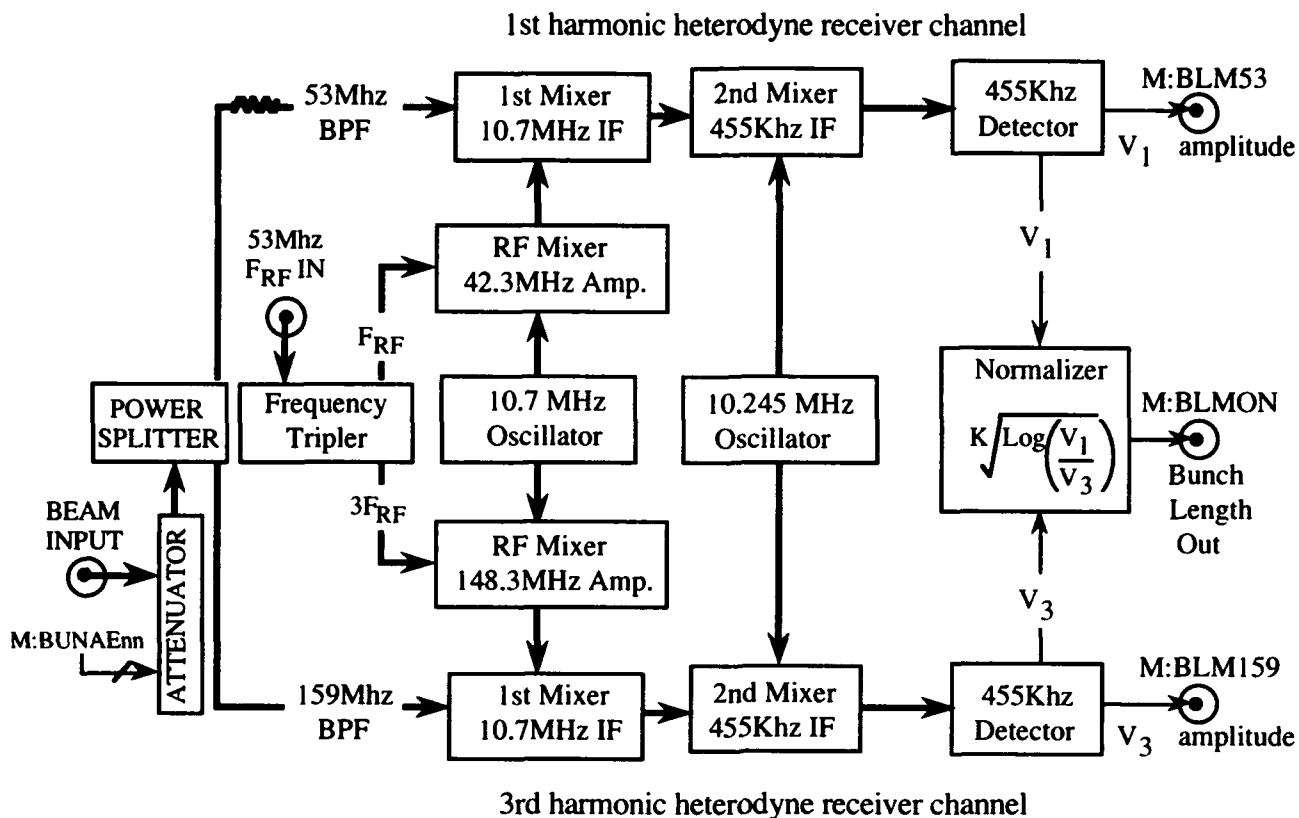


Figure 1: Bunch Length Monitor Block Diagram

Performance Summary

LLRF 53Mhz Input Level	+2 dbm
Beam Input Dynamic Range	40 db
Maximum 53/159Mhz Beam Input	-16 dbm
BLMON Frequency Response (-3db)	6 KHz
BLMON Accuracy (over 40db range)	+/- 2%

References

1. Operated by the Universities Research Association Inc., under contract with the U.S. Department of Energy.
2. G. Jackson and T. Ieiri, IEEE Trans. Nucl. Sci. NS-30, 863 (1989).
3. G. Jackson and T. Ieiri, Fermilab note TM-1600 (1989)
4. K. Meisner, Fermilab Operations Bulletin #1220, July 1991

A VXI/LabVIEW-based Beamline Tuner

Willem Blokland
Fermi National Accelerator Laboratory*
P.O. Box 500, Batavia, IL 60510 USA

Abstract

A general purpose beamline tuner is being developed to reduce betatron oscillations resulting from missteering during beam transfer. The tuner is based on VXI instruments controlled by a LabVIEW program running on a Macintosh computer. VXI digitizers take turn-by-turn data from beam position monitors followed by an analysis of the data in the time- and frequency- domains. The results, the phase and amplitude of the betatron oscillations, are communicated from LabVIEW to the control system over a tokenring network. An application program at a control console calculates the required changes in the correction elements from the phase and amplitude to reduce the oscillations. The beamline tuner is self-contained and easy to adapt to other beamlines. Early results indicate that the tuner outperforms the current system.

I. INTRODUCTION

During a collider run it is important to achieve the highest possible luminosity. Betatron oscillations of the beam result in a growth of the beam emittance which decreases the luminosity during beam-beam collision. The betatron oscillations occur when the beam is not injected onto the closed orbit. The task of a tuner, therefore, is to adjust the correction elements so that the beam is injected onto the closed orbit. An overview of injection tuning methods is given in [1].

The current Tevatron injection tuning system uses a method that measures the beam position signal of 13 consecutive beam position monitors (bpm) at the first turn and then subtracts the beam positions of the closed orbit at those locations. The resulting data represents the betatron oscillation to which a sinusoid is fitted to determine the phase and amplitude. To do a proper fit, the phase advances, the beta values and the dispersion values at each bpm location must be accurately known. Because the method assumes that all beta values are the same and ignores the dispersion, it introduces errors in the calculations. The current system also suffers from the limitation that it can handle only one bunch per ring. The digitizers trigger on beam intensity and multiple bunches in the ring would lead to triggering on a wrong bunch. This means that the tuning of the injection must be separate from the actual loading of the ring for a collision shot. The time from tuning to loading the last bunch is often more than an hour. Meanwhile the drift of various elements can invalidate the calculated corrections resulting in betatron oscillations of up to one millimeter. The injection tuning of the anti-protons is also done in a separate step. To avoid wasting precious anti-protons, protons are reverse injected from the Tevatron into the Main Ring. The correction method is the same as for pro-

ton or forward injection. The current system is described in [2].

An advantage of using many, e.g. 1024, turn-by-turn measurements for injection tuning is that the current betatron tune can be determined and unwanted frequencies as noise or synchrotron oscillations due to dispersion, can be filtered out. Also, only a single detector per plane is needed, eliminating the error due to inaccurate betafuncions and phase advances. The turn-by-turn method has already been successfully applied at Fermilab for the accumulator and is described in [3].

II. CONFIGURATION

The hardware centers around two Tektronix VX4240 digitizers, one for each plane. A 7.5 MHz clock for the digitizers is derived by a special CLOCK module from a beamsync signal. A V177 card decodes from the same beamsync signal an event that triggers the digitizers at a rate of 47 kHz, or once per turn. The digitizers sample on the first positive clock edge after a positive trigger edge. Since both the clock and trigger are derived from the beamsync signal, the beam is always sampled at the same point in the beam position waveform. Different bunches are selected by directing the V177 to change the delay of the trigger. To start the sampling on an injection, a V177 module decodes an injection event that arms the digitizers from the Tevatron Clock signal. To be able to look at Tevatron and at Main Ring injections, HP E1366A RF multiplexers switch the V177 cards between the Main Ring and Tevatron bpm signals and between the Main Ring beamsync and Tevatron beamsync signals.

A Macintosh IIci controls the VXI crate through a MXI interface. The Macintosh connects to the accelerator control's Tokenring network, enabling it to exchange information with an application program on a control console. An independent control signal can cycle the power to the Macintosh and VXI crate to perform a remote reboot. The configuration is shown in figure 1.

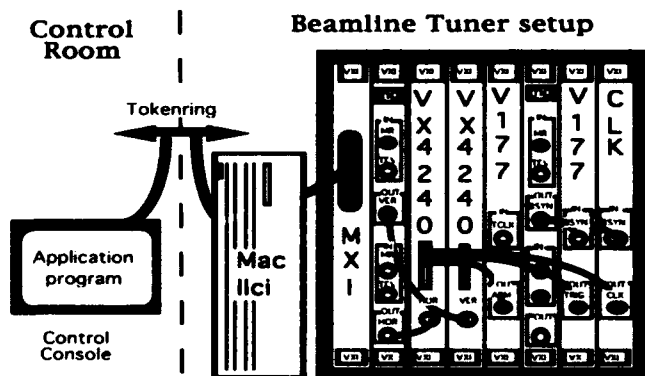


Figure 1. The configuration of the beamline tuner.

* Operated by the Universities Research Association under contract with the U.S. Department of Energy.

III. OPERATION

The Mac IICI runs the graphical programming language LabVIEW which includes a VXI library. All crate modules are controlled using this library. The Acnet (Accelerators Control Network) Interface library, developed in-house and described in [4], handles the communication from LabVIEW to the control system. At startup, the VXI modules are initialized and the Acnet interface is activated. After the injection and data has been taken, the analysis starts. The first step of the analysis is a Fourier transform of the turn-by-turn measurements. A peak search in a range around the expected betatron tune determines the current tune. If two peaks are found, the betatron oscillation is assumed to be coupled and a warning is given since the analysis assumes an uncoupled motion. The algorithm continues with the largest peak as the current tune. The next step is an inverse Fourier transform of only the frequencies within the range. This removes the dc offset, various noise sources, e.g. 60 Hz, and the synchrotron oscillation due to dispersion. The third step is to analyze the amplitude of the oscillation on damping due to decoherence and on additional oscillation due to coupling. The found damping coefficient is used to even the amplitude of the signal so that an undamped sinusoid can be fitted. A warning is given if coupling is found. The Levenberg-Marquardt algorithm from the LabVIEW analysis library does the fitting. Because the damping in both Tevatron and Main Ring reduces the oscillation to noise levels in less than 80 turns, only up to the first 30 turns are suitable for fitting. Currently, the fit uses only 15 turns in order to handle a small degree of coupling. The Tevatron runs in general with only a minimum of coupling which is not a problem for the analysis. The earlier calculated tune and amplitude are used as initial guesses for the fit. While a damped sinusoid could have been fitted, it would introduce one more parameter to estimate and lead to a slower or possibly wrong convergence. The results of the fit, figure 2, are communicated to an application program running on a control console under operator supervision.

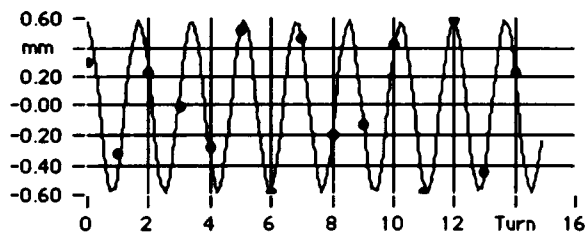


Figure 2. A fit by the beamline tuner.

The console application program then calculates and sends out the adjustments to the corrections elements. The application bases its calculations on the results of studies. These studies relate settings of corrector elements empirically to the estimated phase and amplitude. With this approach, the lattice functions were not needed. The left diagram of figure 3 shows the oscillation vector, the estimated phase and amplitude, move in a line as one of the correctors is changed. This is because only the amplitude is a function of the corrector setting while the phase depends on phase advance from the

corrector to the bpm. By using two correctors at different phase advances, the measured amplitude and phase can be decomposed in terms of the correctors' oscillation vectors. The right diagram of figure 3 shows the relation between the amplitude of the oscillation and the value of the setting. This relation, in combination with vector decomposition, yields the adjustments to the correction elements for any phase and amplitude of the betatron oscillation.

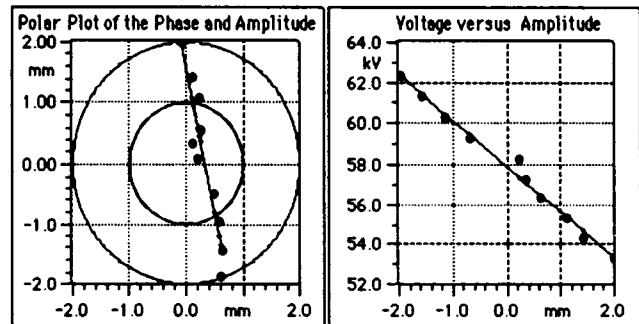


Figure 3. The results of the E17 injection kicker study.

The application program, shown in figure 4, provides the operator with a user-interface to control what bunch from what ring should be sampled and whether the calculated settings are sent out.

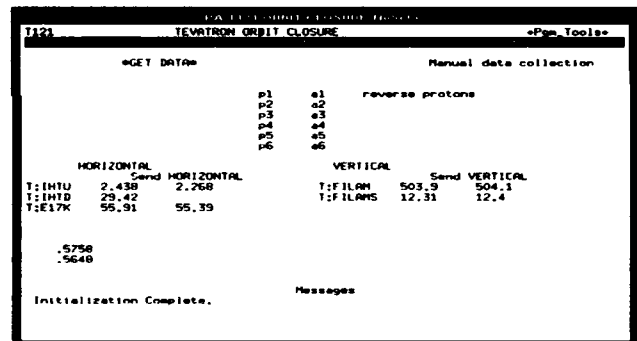


Figure 4. The console application program.

The functionality of man-machine interface could also have been implemented by directly displaying the Macintosh screen with the beamline tuner's menu on a control console using the application XGator or on a Macintosh using Timbuktu. However, providing the operator with a standard interface was more important than using only one programming platform. The remote display is being used though, for diagnostic purposes and expert adjustments to the operation of the beamline tuner, figure 5. The beamline tuner can store the measurements including the results and current algorithmic parameters in a file. This file can be uploaded using Appleshare, Timbuktu, or a FTP application. The data can then be analyzed with various parameter settings using an off-line version of the tuner. The same data transfer applications can download updates of the beamline tuner software made on a development system.

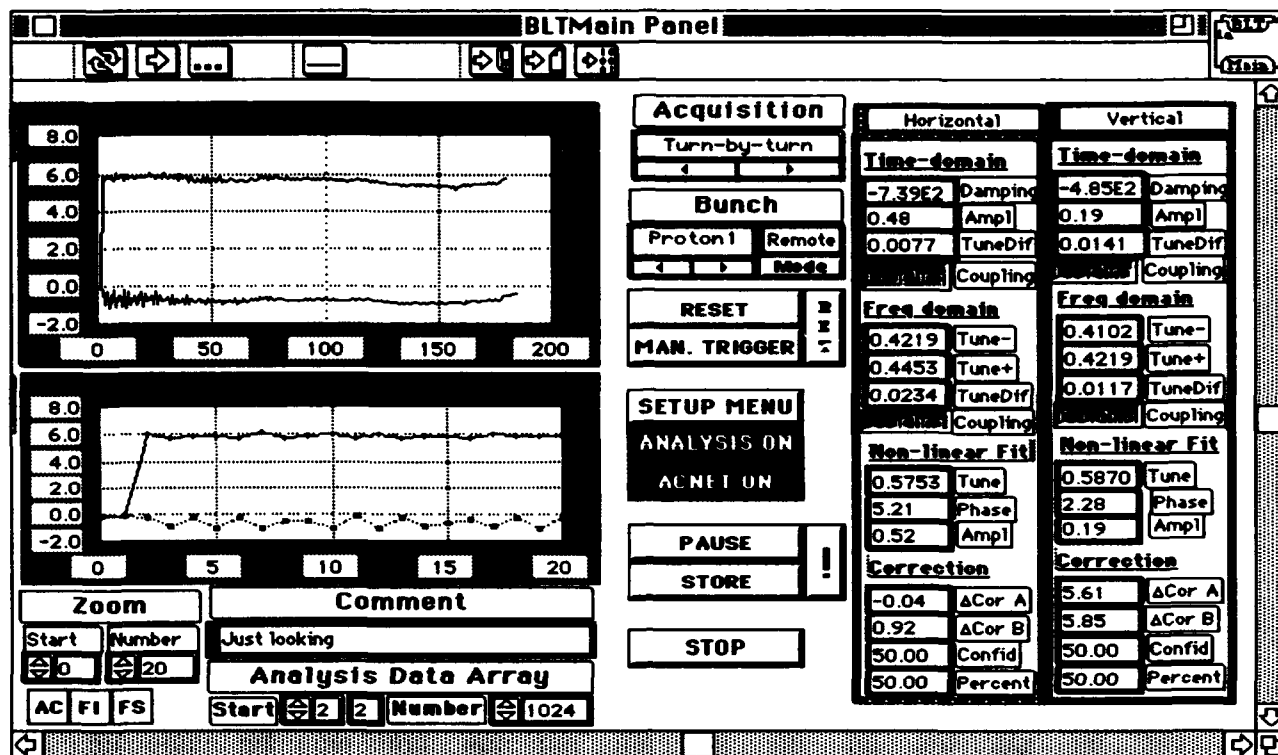


Figure 5. The beamline tuner's display and menu.

IV. CONCLUSIONS

Early experiences indicate that the beamline tuner can accurately correct betatron oscillation of 0.3 mm and larger. The old system often leads to oscillations of up to 1 mm in the horizontal plane for the last proton bunches because of the long wait between tuning and loading. The difference of a 0.3 mm compared to a 1 mm oscillation would reduce the emittance by about 20 percent.

The VXI/LabVIEW system operated in a reliable manner and proved to be easily adapted to enhancements in software and hardware. The off-line version proved very useful in determining the proper settings of the parameters of the algorithms. The additional direct access to the beamline tuner provided the expert with a wide variety of menu options to change the operation of the modules or algorithms or to diagnose the system on-line.

V. ENHANCEMENTS

Future enhancements are planned in order to reduce betatron oscillations to an amplitude of 0.1 mm. The beam position wave form of a single bucket bunch has only a 150 nsec wide range where its value represents the beam position. For a perfect bpm module this range is flat and it does not matter where it is sampled. In practice, however, the signal shows a slope or a small oscillation. Therefore it is important to always sample within nanoseconds on the same spot. The clock signal derived from the beamsync signal showed a jitter of up to 5 nsec. By applying a phase-locked loop, this jitter should be reduced to sub-nanoseconds. Another problem is

that the range is not always 150 nsec, but is smaller at some bpm's. With a 7.5 MHz clock the smallest step is 130 nsec. This means that in some cases samples are taken at the edge of the valid region. By using a fast delay generator, the clock signal can be skewed, giving control over the point of sampling in terms of nanoseconds. Another option is to use a faster digitizer, e.g. running at 53 MHz, thus reducing the delay step size. All options are currently implemented to compare the results.

VI. ACKNOWLEDGEMENTS

The author wants to recognize the contributions of Jerry Annala for helping with the studies and writing the console application program.

VII. REFERENCES

- [1] J.P. Koutchouk, "Trajectory and closed orbit corrections," CERN LEP-TH/89-2, (1989).
- [2] S. Saritepe, "Beam Transfer at E0: An Overview," FERMILAB-TM-1790 (1992).
- [3] D.J. Harding and A.W. Riddiford, "Automatic Steering Corrections to Minimize Injection Oscillation in the Fermilab Antiproton Source Rings," *Proc. of 1989 IEEE Particle Accelerator Conf.*, Chicago, pp 1663-1665.
- [4] W. Blokland, "An Interface from LabVIEW to the Accelerator Controls Network," *Conference Proceedings of the Accelerator Instrumentation Third Annual Workshop*, LBL, Berkeley (1992).

A Frequency-domain Directivity Enhancement of Beam Position Stripline Detectors

Edward L. Barsotti

Fermi National Accelerator Laboratory*
P.O. Box 500, Batavia, IL 60510 USA

Abstract

Stripline detectors are commonly used in beam position monitoring (BPM) systems and can be used as dual directional couplers for beams passing in opposite directions. Directivity between 21-26 dB is typical near the Tevatron operating frequency of 53.1 MHz, and these values are limited by mismatches on the upstream ports. Improvements to the directivity can be made with external corrections to these mismatches, but in the Tevatron the four ports (two striplines, proton upstream and downstream) are available only after a series of discontinuities (tapers, feedthroughs, cables) forming unknown frequency-dependent networks. A method has been developed to characterize the networks and compensate the mismatches, at a single frequency. No beam is needed, so this simplifies implementation. The technique can be applied to a narrowband BPM system operating in an approximately steady-state condition. Conditions for directivity, development of the method, and a large-scale implementation procedure are described with applicable results, including an explanation of shortcomings in a transient beam situation.

I. INTRODUCTION

The Tevatron BPM stripline detector [1]-[3] is designed to form a 50 Ω transmission line with the beam pipe. At each end of each stripline plate, a taper and feedthrough bring signals to 50 Ω cables and the rest of the system. This arrangement turns each stripline into a directional coupler, and its directivity is the ratio of upstream and downstream signal. Ideally, the upstream port has a doublet signal while the downstream port has none. The directivity is primarily determined by how well matched the upstream system is to the stripline. The signal is reflected by various discontinuities as it travels in time from the stripline towards the processing electronics upstairs: the taper, the feedthrough, cables, adapters, and finally the RF Module itself. In the frequency domain, all of these reflections combine as a function of frequency to form the impedance $Z_{upstream}(f)$. The mismatch between $Z_{upstream}$ and the characteristic impedance of the stripline, Z_{plate} , forms a frequency-dependent directivity. At 53.1 MHz, this directivity has been measured for the TeV BPM system to range between 21-26 dB, representing a mismatch of 5-10 Ω . To obtain a directivity of 40 dB, a match within 1 Ω would be required.

Directivity is important in the collider mode of the Tevatron, when protons and antiprotons coexist in counterrotating, separated helical orbits. Directivity should be as high as possible to prevent interference of one beam signal upon another, especially when trying to read the antiproton beam in the presence of the more intense proton beam. Any external correction to increase directivity must take place outside the vacuum enclosure, and in the Tevatron, there is a

half meter of cable and various discontinuities between the stripline and a vacuum flange.

In order to determine the correction, a method [4] was devised to characterize the discontinuities between the stripline detector plate and the vacuum flange ports. This process is now described.

II. CORRECTION DEVELOPMENT

In this case, 220 BPM detectors and vacuum enclosures were already in place, and only a single cable per stripline existed between the tunnel and the upstairs processing electronics. Thus, a relay per stripline is needed to switch between the two ports, and the directivity correction algorithm is performed in the tunnel (with no beam) and implemented with the relay circuitry. In summary, the external correction is derived by exciting one of the proton upstream flange ports and tuning a variable load until a minimum in forward coupling to the proton downstream port of the other stripline is obtained. This provides enough information about the unknowns inside the vacuum enclosure to compensate for them. The first step requires electrostatic knowledge of the coupled line system formed by the two stripline plates.

A. Even and Odd Mode Impedances

In a symmetric system with two coupled signal conductors, such as the BPM striplines, "self-capacitances" between each conductor and ground, C_a and C_b ($C_a=C_b$) exist along with mutual capacitance C_{ab} . For these coupled lines, three characteristic impedances can be defined: Z_{even} , for the even mode between the lines (both conductors at same potential); Z_{odd} , for the odd mode (conductors at opposite potentials); and Z_{plate} , the equivalent transmission line impedance for a single conductor in the presence of the second. The characteristic impedances are defined by

$$Z_{even} = \frac{1}{C_a v_p}, Z_{odd} = \frac{1}{(C_a + 2C_{ab}) v_p}, Z_{plate} = \frac{1}{(C_a + C_{ab}) v_p}. \quad (1)$$

where v_p is the velocity of propagation. Two programs, "Matrix Parameters for Multiconductor Transmission Lines" from Artech House and POISSON (with the author's post-processing program), were used to find the required capacitances. From the results, the assumed impedances were $Z_{plate} = 45\Omega$ and $Z_{even} = 50\Omega$.

B. Excitation of a Plate

Directivity as a function of terminating impedance was simulated for the coupled lines, using EEsof's Touchstone program. When one of the striplines is excited at its proton upstream port and directivity of the coupling to the other stripline is desired, the optimum termination at the ports is Z_{plate} . Backward-wave coupling is predominant for the coupled lines, just like the beam coupling to the striplines. The coupling from the upstream port of A to upstream B was -35 dB, highly independent of terminations. The amount of coupling from upstream A to downstream B is a combination

* Operated by the Universities Research Association under contract with the U.S. Department of Energy.

of two factors: 1) the upstream B signal, down 35 dB from upstream A, partially reflects back from upstream B due to its mismatch from Z_{plate} , and 2) the excitation signal from upstream A is partially reflected from downstream A, due to its mismatch from Z_{plate} , and then couples down 35 dB to downstream B.

C. Excitation by Beam, Systematic Directivity Decreases

When the striplines are excited by the centered beam, modeled by an ideal current source, only the even mode is present and the correct upstream terminating impedances for maximum directivity is Z_{even} . The amount of odd mode excitation, or the difference in the stripline currents for beam closer to one of the striplines, determines downstream magnitude when all ports are terminated in Z_{even} . Thus, directivity will change for beam displacement towards one stripline, but displacement in the orthogonal plane has negligible effect. For perfect Z_{even} terminations and a stripline current ratio of 1.25:1, corresponding to 3 mm off-center in the Tevatron detector, directivity is decreased from infinity to 40 dB. Another possibility for a systematic decrease in directivity is a difference between the beam propagation velocity and the plate transmission line propagation velocity. Directivity will decrease to 35 dB for a 3.5% mismatch and 27.7 dB for an 8% difference. As discovered in stochastic cooling work, these differences can be caused by the longitudinal gaps between beam pipe and pickup, as well as the finite width of the pickup plates.

D. Requirement for Solution

To best solve the directivity problem, given the systematic errors, the impedance Z_{even} needs to be applied at all frequencies to the correct "termination points" at the ends of the striplines. Since the nearest access point for each of the four ports is the N-type elbow connector on the flange, everything between the two points must be characterized at all frequencies. Broadband implementation becomes impossible, so here the characterization is restricted to the frequency of interest, 53.1 MHz. Finally, the desired mode for tuning, beam on and centered, prohibits tunnel access. The only measurement mode to "view" the striplines is the *Excitation of a Plate* case described above.

E. Attempt at a Broadband Solution

At first, an attempt was made to characterize the line between plate and flange over a broad frequency band. A flange-to-flange two-port S-parameter matrix measurement was taken over a wide frequency range. A model consisting of three transmission lines (two vacuum cables and the stripline) and four electrically "thin" lumped element models (two flange discontinuities and two vacuum cable-to-stripline transitions) was entered into EEsof's Touchstone program. The model could not be optimized to the data, due to the large number of variables and model breakdown over the large frequency range. Even artificially created [S] data from a known model solution would not converge. Because of the problems with a broadband solution, the need for a single frequency solution was more apparent.

F. Equivalent Transmission Line for Discontinuities

The complexity of the above problem was reduced by converting everything between the flange ports into two equivalent "uniform" transmission lines (consisting of the four

sets of discontinuities and two vacuum cables) and the stripline transmission line. This model works because 1) none of the discontinuities are too large at 53.1 MHz, and 2) the system is nearly 50Ω throughout. The goal of using this equivalent transmission line concept is the ability to use the formula for input impedance Z_{in} of a load Z_{load} propagated along a uniform transmission line,

$$Z_{in} = Z_0 \frac{Z_{load} + Z_0 \tanh(\gamma d)}{Z_0 + Z_{load} \tanh(\gamma d)}, \quad (2)$$

where Z_0 is the complex transmission line characteristic impedance, d is its length, and $\gamma = \alpha + j\beta$ is its propagation coefficient. Because of the different phasings of the discontinuities, there is a different Z_0 at each frequency. Also, under the above restrictions, S_{21} of a transmission line is approximately equal to $\exp(-\gamma d)$ and is cascaded with other lines by simply multiplying the S_{21} parameters together.

G. Applying Correct Terminating Impedance to Plates

If the equivalent uniform transmission line between flange and plate can be found, then the impedance Z_{load} can be selected and applied to the flange port to produce the terminating impedance $Z_{in} = Z_{even} = 50\Omega$ at the "termination point" at the stripline end. The variables Z , γ , and d can be defined for ports 1 (proton upstream for stripline A), 2 (downstream A), 3 (upstream B), and 4 (downstream B). As described above, the amount of coupling S_{41} from excitation of port 1 depends on the sum of the mismatches of ports 2 and 3 as

$$|S_{41}|_{dB} = |\rho_2 + \rho_3|_{dB} - 35, \quad \rho_{2,3} = \frac{Z_{in2,3} - Z_{plate}}{Z_{in2,3} + Z_{plate}}. \quad (3)$$

If the reflections from ports 2 and 3 cancel, or $\rho_2 = -\rho_3$, then S_{41} will be a minimum and (3) simplifies to

$$Z_{in2} Z_{in3} = Z_{plate}^2. \quad (4)$$

If a known load Z_{load2} is applied to flange port 2 and a variable load Z_{load3} on flange port 3 is tuned for a minimum in S_{41} , then (4) is true and can be expressed from (2) as

$$Z_{plate}^2 = Z_2 Z_3 \frac{Z_{load2} + Z_2 \tanh(\gamma_2 d_2)}{Z_2 + Z_{load2} \tanh(\gamma_2 d_2)} \frac{Z_{load3} + Z_3 \tanh(\gamma_3 d_3)}{Z_3 + Z_{load3} \tanh(\gamma_3 d_3)}. \quad (5)$$

From a measurement of S_{21} and S_{43} , the variables $\gamma_2 d_2$ and $\gamma_3 d_3$ can be estimated. The path of the S-parameter S_{21} consists of a cascade of three transmission lines, and so,

$$S_{21} = \exp(-\gamma_1 d_1 - \gamma_{plate} d_{plate} - \gamma_2 d_2). \quad (6)$$

From the plate dimensions, $\gamma_{plate} d_{plate}$ is known, and if the approximation $\gamma_1 d_1 = \gamma_2 d_2$ is taken, then for the various ports,

$$\gamma_1 d_1 = \gamma_2 d_2 = \frac{1}{2}(-\ln|S_{21}| - \gamma_{plate} d_{plate}), \quad (7)$$

and similarly for ports 3 and 4. This leaves two unknowns in (5), the characteristic impedances Z_2 and Z_3 . A second equation with a different Z_{load2} and Z_{load3} pair would be needed, but a lack of resolution prevents reasonable results from the root finder. The further approximation $Z_2 = Z_3$ must be taken for satisfactory results. Then, from (2),

$$Z_{load2,3} = Z_{2,3} \frac{Z_{in2,3} - Z_{2,3} \tanh(\gamma_{2,3} d_{2,3})}{Z_{2,3} - Z_{in2,3} \tanh(\gamma_{2,3} d_{2,3})}. \quad (8)$$

The method can be done for S_{23} to find Z_{load1} and Z_{load4} .

III. IMPLEMENTATION AND RESULTS

A. Circuitry

The tuning circuitry to implement the desired Z_{load} at the flange is housed in the tunnel along with a relay to select which of the two beams has its upstream port sent upstairs. The undesired beam's upstream port (the desired beam's downstream) has a tuned termination which presents Z_{load} at the flange, taking into account the cable between the module and the flange. The reflection off the tuned circuitry actually cancels, at the selected frequency, the signal created by the non-directive reflections between the stripline and flange. It trails the non-directional signal in time. The circuitry consists of discrete inductors, resistors, and capacitors, the latter two are adjustable for orthogonal tuning. Good beam impedance is ensured in two ways. First, a diplexer filter is included before the relay and the tune circuit, transmitting a 35 MHz bandwidth centered at 53.1 MHz while terminating the stopband in an external 50 Ω for higher power dissipation. Also, the tuning section includes a shunt resistor to provide a return loss of at least 13 dB at all the bandpass frequencies.

B. In-tunnel Tuning Procedure

To find the correct tunes for all of the in-place detectors, an automated procedure of the above algorithm was devised. A two-channel variable-load module was developed for this purpose. It consisted of two varactor diodes separated by a quarter-wavelength at 53.1 MHz for orthogonal tuning, plus the DACs to bias them. A Macintosh computer and a program using LabVIEW software controlled the tuner and an HP8753B vector network analyzer. The operator changed connections between the analyzer, the tuner, and the flange. First, S_{21} and S_{43} were measured. Then S_{41} was minimized for two different Z_{load3} settings, and the solutions were averaged. The procedure was repeated for S_{32} . A Mathematica program was used to find the roots to (5). The operator then performed the correction tune, using the network analyzer. With this procedure, the in-tunnel work was greatly reduced and a database of the detectors was created.

C. Measuring Directivity

The directivity with beam present was measured in two ways. First, a spectrum analyzer was used for fixed target operation, during which the vast majority of the ring's 53.1 MHz buckets are filled with beam bunches, resulting in most of the spectral content at 53.1 MHz and its harmonics. Second, the "intensity" output of the RF Module front-end electronics was viewed with an oscilloscope for both a beam structure of 20 consecutive bunches and also normal collider mode single-bunch operation. The signal, used to self-trigger the position signal digitizer, is down-converted to baseband from a 5 MHz bandwidth, 53.1 MHz bandpass filter.

D. Interpretation of Results

The directivity from the full ring case was measured for two detectors and four striplines, ranging from 31 to 38 dB. These results, especially the higher directivities, were considered good, considering the number of approximations and systematic errors. In the single-bunch case, however, the unwanted signal appeared in time as two large peaks, barely separated. Going to 20 bunches, the peaks remained at the signal's beginning and end, but between the peaks the

unwanted signal decreased to a level consistent with the full ring result.

It was concluded that the peaks were caused by the tune having a bandwidth less than the RF Module's 5 MHz bandwidth. Outside the tune bandwidth, directivity is actually worse than the original 21-26 dB. At the edges of a signal, when the RF Module's filters are charging, other frequencies are present. However, for a long train of 53.1 MHz buckets filled with beam, the filters are in a steady-state, and only the fundamental frequency is present.

During single-bunch collider operation, the results are unacceptable, for two reasons. First, when a proton and antiproton bunch are coincident at a detector, their signals interfere too much with each other and affect the position reading. Second, when reading antiprotons, the more intense proton bunches cause peaks comparable in amplitude to the desired antiproton intensity signal. Thus the digitizer can trigger on the unwanted proton signals. The latter problem is eliminated by a fast switch gated by the control system, currently being added to the system, removing the unwanted triggers as well as providing other improvements.

VI. CONCLUSION

A method to increase the directivity of beam stripline detectors has been devised and implemented for the Fermilab Tevatron. The technique enables external circuitry to correct for an unknown series of discontinuities causing the non-directivity. An in-tunnel (no beam) tuning algorithm has been developed. The correction method works best for narrowband signal processing approximating steady-state. This occurs from either a long sequence of RF buckets filled with beam, resulting in narrow spectral peaks at the RF harmonics, or a filter with a bandwidth smaller than the implemented tune.

IV. ACKNOWLEDGEMENTS

The author wants to recognize the many contributions of Rodolfo Gonzalez (now with SSC) and others in the Fermilab Accelerator Instrumentation Department.

V. REFERENCES

- [1] R. Shafer, "Characteristics of Directional Coupler Beam Position Monitors," *IEEE Trans. Nucl. Sci.* NS-32, No. 5, 1933 (1985).
- [2] R. Shafer, R. Webber, and T. Nicol, "Fermilab Energy Doubler Beam Position Detector," *IEEE Trans. Nucl. Sci.* NS-28, No. 3, 2323 (1981).
- [3] R. Shafer, R. Gerig, A. Baumbaugh, and C. Wegner, "The Tevatron Beam Position and Beam Loss Monitoring Systems," *Proc. XIIth Internat. Conf. on High-Energy Accelerators*, Fermi National Laboratory, 609 (1983).
- [4] E. Barsotti and R. Gonzalez, "Tev BPM PSD Module Description," Beam Position Monitor Design Note #27, internal Fermilab document (1992).

The Control System of ROSY I

T.Goetz, M.Picard

Physikalisches Institut der Universität Bonn, Nußallee 12, D-5300 Bonn 1, Germany

M.Plesko

Sincrotrone Trieste, Padriciano 99, 34012 Trieste, Italy

ROSY I is a planned synchrotron radiation light source with a number of straight sections for wigglers and undulators for photon energies in the range from 1 keV to 20 keV [1]. This paper describes the design principles of the fully distributed architecture of the ROSY control system, pointing out the extensive use of de-facto standards for both hardware and software such as UNIX, X11/Motif, VMEbus etc. Particular attention is given to the implementation of the man-machine-interface, the design of the distributed online database, the homogeneous communication architecture and the integration of data processing and feedback in the realtime environment of the process layer.

1 Introduction

Most modern accelerator control systems build on the same principles: a distributed architecture and standardisation towards open systems. The control system of the ROSY I synchrotron light source is no exception. It is specially designed for high bandwidth on all layers and, due to envisaged future upgrades and expansions, seamless extension in capacity and capability.

The architecture of the ROSY control system is inspired by the newly designed control system for the Storage and Stretcher Ring ELSA [2], which is under development at the physics institute of the University of Bonn.

2 Guidelines

The following guidelines were set for the design of the ROSY control system:

- The basis is a distributed system with several loosely coupled logical layers providing failsafe operation and allowing scalability. The intelligence and computing power for the handling of local tasks and computations is transferred to lower layers whenever possible.
- Transparent behaviour of the complete control system and in particular of the communications between the logical layers of the

control system from the viewpoint of both the user and the application developer.

- The widest possible use of standards for all hardware and software components allow for a minimal implementation time and simplify service and support.
- A common development platform for all software components on the workstations and use of development tools for software engineering and documentation.

3 Architecture

The architecture is made up of four logical layers (see figure):

The presentation layer consists of several UNIX RISC-workstations running the X11 and OSF/Motif windowing system. A man machine interface – based on the system developed at ELETTRA[3] – is providing the interactive control of all parameters. Other user oriented applications like orbit correction are also activated on the presentation layer.

The control layer is formed by several powerful UNIX RISC-computers. Each of them is in charge of the autonomous control of a subsystem of the accelerator complex. The architecture and software of the control system allows for the seamless addition of further computers for new subsystems. The control computers manage a distributed, memory resident online database, which

Control System Architecture

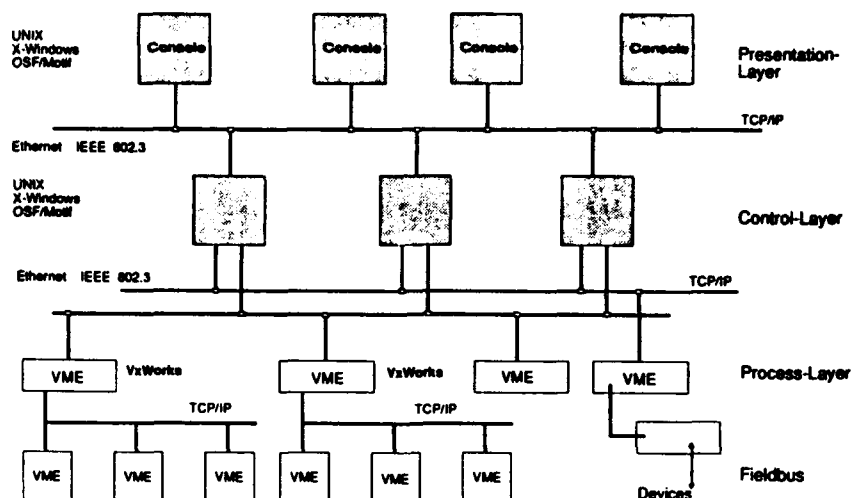


Figure 1
ROSY Control System Architecture

acts as a mirror image of the accelerator state. In addition, there are one or several server computers in the control layer, which provide disk storage, relational databases, printing and other central functions in the network.

The process control layer performs data reduction and runs control and measuring tasks. It is built of VME based components with MP68030/40 CPUs assisted by dedicated image processing boards and digital signal processors for fast beam diagnostics and digital feedback systems.

The fieldbus layer interfaces all the devices of the accelerator complex which do not require high data throughput and connects them to the process control layer. It is realized through low-cost VME components and/or possibly by use of a fieldbus system which has established itself in industry.

The process control and the fieldbus layer together form the process system. For both layers of the process system a real-time operating system will be used which must have excellent networking capabilities. At the present state of evaluation, the "VxWorks" kernel [4] is our favourite choice. All VME crates of the process system are diskless; they boot over the network from the computers of the control layer.

The communication system between the upper two layers and the process system is based on Ethernet (IEEE 802.3). The physical media is optical fibre; the topology of the network will enable a subsequent upgrade to the FDDI standard. The consistent realisation of the process system with VME components and a uniform operating

system allow for a homogeneous communication system based on standard protocols (TCP/IP) for the complete control system. The remote inter-process communication on all layers is realised through synchronous and/or asynchronous message exchange. High bandwidth data paths will be realised exclusively by using TCP socket data transfers, accompanied by data compression whenever necessary (e.g. for images and BPM signals).

4 Software

The efficiency and flexibility of a control system is mainly determined by its software. The software of the control system performs tasks which in many ways resemble the duties of a *distributed operating system*. The results arising from research in the field of distributed systems are therefore fundamental for the design of such an accelerator operating system [5][6].

4.1 Process Applications

The process system contains applications for data acquisition, equipment control, monitoring and alarms and for complex real-time tasks like feedbacks and ramping. Each application consists of a set of one or more concurrent threads synchronised by the VME operating system kernel. These applications send data to the control layer in regular intervals (e.g. tune monitoring), triggered by observed parameter changes (e.g. status conditions)

or perform a task on request (e.g. image acquisition and processing).

4.2 Rule Engines

Each control computer runs a "rule engine" (i.e. a set of processes fed with patterns of accelerator parameter changes) which elaborates abstract rules and correlates machine parameters. A set of rules will handle the algorithmic mapping from hardware dependent parameter sets to machine physics parameters. Other rules will implement heuristic recipes for easy management of complete subsystems. Rules may be activated or deactivated during normal operation.

4.3 High Level Applications

User oriented applications which run on the presentation layer have a common graphical user interface, built in accordance with the OSF/Motif guidelines. They consist of graphical objects (panels, menubars, knobs, etc.) of the Motif and X11 program library, which provide a completely event driven usage of the application. The structure of the control system allows for application programs to transparently access any of the controlled parameters through a common application interface which hides details of the control system from the application programmer.

4.4 The Man Machine Interface

The man machine interface (MMI) is the interactive tool from which the individual components of the ROSY accelerator complex are controlled. In order to avoid confusion and to minimise the learning time, the MMI builds on ergonomic and logical concepts which allow for an intuitive understanding of its operation and of the operation of the devices it controls.

The interaction between the user and the MMI is based on virtual navigation through the synopsis which is built as a plan view of the accelerator complex, using PHIGS for vectorial graphics. The elements to be controlled are represented by graphical objects which resemble their real appearance, arranged in accordance with the topology of the whole complex.

Virtual control panels allow users to operate on the graphical representations of a large set of de-

vices like switches, knobs, sliders, digital and analog indicators, whose behaviour is equivalent to that of the real instrumental devices. The panels can be generated interactively by means of a control panel editor in a menu driven way without writing a line of code. The connection with the online database and the underlying servers on the lower layers is automatic and completely transparent.

4.5 Databases

Each computer of the control layer is managing a memory resident online database representing one part of the accelerator complex. The set of online databases on the individual computers is linked via horizontal communication paths, such that only a single, distributed database is seen which allows for transparent access to all the informations pertaining the accelerator. The relation of given parameters to individual computers is not explicitly seen by high level applications and process layer software alike.

The offline storage of machine data is performed by a relational database system based on SQL. The control system relevant parts of ROSY are completely described by the offline database.

5 Acknowledgement

We are indebted to Prof. Dieter Einfeld and the Forschungszentrum Rossendorf for their support and interest in this work.

6 References

- [1] D.Einfeld et al., *The Synchrotron Light Source ROSY I*, these Proceedings.
- [2] D. Husmann, *The ELSA Stretcher Ring*, Lecture Notes in Physics No.234., Springer Verlag
- [3] F.Potepan, *The ELETTRA Man Machine Interface*, Sinctrotrone Trieste ST/M-91/2, March 1991.
- [4] *VzWorks Guide*, Wind River Systems Inc., Alameda, CA 94501
- [5] A. Goscinski, *Distributed Operating Systems - The logical design*, Addison-Wesley Publ.Comp. 1991
- [6] S. Mullender, Editor, *Distributed Systems*, ACM Press New York 1991

Measuring Emittance Using Beam Position Monitors*

Steven J. Russell and Bruce E. Carlsten
Group AT-7, MS H825, Los Alamos National Laboratory
Los Alamos, NM, 87545, USA

Abstract

The Los Alamos Advanced Free-Electron Laser uses a high charge (greater than 1 nC), low-emittance (normalized rms emittance less than 5π mm mrad), photoinjector-driven accelerator. The high brightness achieved is due, in large part, to the rapid acceleration of the electrons to relativistic velocities. As a result, the beam does not have time to thermalize its distribution, and its transverse profile is, in general, non-Gaussian. This, coupled with the very-high brightness, makes it difficult to measure the transverse emittance. Techniques used must be able to withstand the rigors of very-intense electron beams and not be reliant on Gaussian assumptions. Beam position monitors are ideal for this. They are not susceptible to beam damage, and it has been shown previously that they can be used to measure the transverse emittance of a beam with a Gaussian profile [1]. However, this Gaussian restriction is not necessary, and, in fact, a transverse emittance measurement using beam position monitors is independent of the beam's distribution.

I. INTRODUCTION

The Advanced Free-Electron Laser (AFEL) is a compact, computer-controlled FEL that is intended as a coherent light source, tunable from the infrared to the visible. The accelerator is driven by a photoinjector and produces a high-brightness, 20-MeV beam. In order for it to achieve lasing in the visible regime, the AFEL relies heavily on beam quality, i.e., low emittance, and on the high peak currents that are obtainable with a photoinjector.

Measuring the second-moment properties of electron beams from photoinjectors is not a trivial proposition [2]. At the present, the AFEL uses single-quadropole scans on an intercepting screen to measure the emittance. However, simulations indicate that this method underestimates the rms emittance by a factor of about four. In fact, this method seems to measure the instantaneous emittance at the center of the beam [2]. While this number is more important to the performance of the laser, the rms quantity is more important for beam transport through the beamline.

In this paper, we will discuss the possibility of using beam position monitors (BPMs) to measure the rms emittance of the AFEL electron beam. What we will show is that the numbers produced by this technique are independent of the beam distribution. Thus, the measurement gives true rms values whose meanings are clear.

II. IMAGE CHARGE DISTRIBUTION

Consider an electron beam pulse traveling down a beam

pipe. If, in its rest frame, this pulse has some distribution, $I(\rho, \phi, z)$, that is normalized to the total charge, q_{tot} , then the image charge distribution on the beam pipe is given by

$$\sigma(\phi, z, t) = -\frac{\gamma^2}{\pi a^2} \int_V I(\rho', \phi', \gamma(z' - \beta ct)) \\ \otimes \sum_{n=0}^{\infty} \sum_{m=1}^{\infty} a_n \cos[n(\phi - \phi')] \\ \otimes \frac{J_n\left(x_{nm} \frac{\rho'}{a}\right)}{J_{n+1}(x_{nm})} e^{-\frac{x_{nm}}{a} \gamma |z-z'|} d^3x', \quad a_n = \begin{cases} \frac{1}{2}, & n=0 \\ 1, & n \neq 0 \end{cases}$$

where a is the radius of the beam pipe, β and γ are the usual relativistic parameters, the J_n s are Bessel functions, the x_{nm} s are Bessel function zeros, and the volume of integration is the volume that contains the electron pulse. As γ becomes large, this simplifies to the expression,

$$\sigma(\phi, z, t) = -\frac{1}{2\pi a} \iint_{\text{area of pipe}} I'(\rho', \phi', z - \beta ct) \\ \otimes \left\{ 1 + 2 \sum_{n=1}^{\infty} \left(\frac{\rho'}{a}\right)^n \cos[n(\phi - \phi')] \right\} da',$$

where $I'(\rho', \phi', z - \beta ct)$ is the pulse distribution in the lab frame, also normalized to q_{tot} [3].

III. BPM SIGNAL

A beam position monitor consists of four electrodes placed around the beam pipe at 90° intervals, as shown in Fig. 1. They couple to the beam through the image charge, or wall current, produced on the beam pipe by the electron beam. Their signals can be expanded in powers of $1/a$. In general, the terms of this multipole expansion are dependent on the distribution of the electron beam. However, what we will show is that the terms important for measuring the emittance are distribution independent.

For the case where the electrodes have no angular width and the electron beam distribution is Gaussian, the first four terms of the multipole expansion have previously been determined [1]. It is a simple matter to extend this result to the case of electrodes with angular width (Fig. 1), which we have done. Table 1 gives the first three terms of the multipole expansion in this case, normalized to $q_{tot}/2\pi a$. From these the quantity $\sigma_x^2 - \sigma_y^2$ can be determined, and that determination leads to a method of measuring the emittance [1].

*Work performed under the auspices of the U.S. Department of energy.

Table 1: Multipole terms for Gaussian beam, normalized to $q_{tot}/2\pi a$

Electrode	R=Right ($\phi = 0$)	L=Left ($\phi = \pi$)	T=Top ($\phi = \frac{\pi}{2}$)	B=Bottom ($\phi = \frac{3\pi}{2}$)
Monopole	2α	2α	2α	2α
Dipole	$4 \sin \alpha \frac{\bar{x}}{a}$	$-4 \sin \alpha \frac{\bar{x}}{a}$	$4 \sin \alpha \frac{\bar{y}}{a}$	$-4 \sin \alpha \frac{\bar{y}}{a}$
Quadrupole	$2 \sin 2\alpha \left[\frac{\sigma_x^2 - \sigma_y^2}{a^2} + \frac{\bar{x}^2 - \bar{y}^2}{a^2} \right]$	$2 \sin 2\alpha \left[\frac{\sigma_x^2 - \sigma_y^2}{a^2} + \frac{\bar{x}^2 - \bar{y}^2}{a^2} \right]$	$-2 \sin 2\alpha \left[\frac{\sigma_x^2 - \sigma_y^2}{a^2} + \frac{\bar{x}^2 - \bar{y}^2}{a^2} \right]$	$-2 \sin 2\alpha \left[\frac{\sigma_x^2 - \sigma_y^2}{a^2} + \frac{\bar{x}^2 - \bar{y}^2}{a^2} \right]$

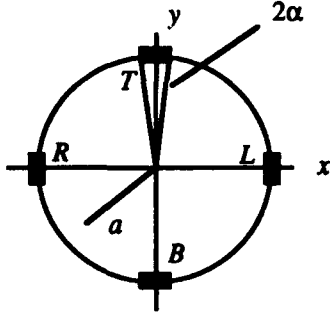


Fig. 1: BPM electrode positions.

Now consider the case of a general beam distribution. A BPM at some position z_0 along our beam pipe has electrodes placed as shown in Fig. 1, with length $2\Delta z$. Then the image charge on an electrode at angular position, ϕ , is

$$\begin{aligned}
 q(\phi, t) &= -\frac{1}{2\pi a} \int_{\phi-\alpha}^{\phi+\alpha} d\phi \int_{z_0-\Delta z}^{z_0+\Delta z} dz \iint_{\text{area of pipe}} I'(\rho', \phi', z - \beta ct) \\
 &\otimes \left[1 + 2 \sum_{n=1}^{\infty} \left(\frac{\rho'}{a} \right)^n \cos[n(\phi - \phi')] \right] da' \\
 q(\phi, t) &= -\frac{1}{2\pi a} \int_{z_0-\Delta z}^{z_0+\Delta z} dz \iint_{\text{area of pipe}} I'(\rho', \phi', z - \beta ct) \\
 &\otimes \left[2\alpha + 4 \sum_{n=1}^{\infty} \left(\frac{\rho'}{a} \right)^n \frac{\sin n\alpha}{n} \cos[n(\phi - \phi')] \right] \rho' d\rho' d\phi'.
 \end{aligned}$$

The integration over z is complicated by two things: the beam bunch is moving, so that the integration depends on t , and there is the possibility that the electrode length may be shorter than the beam pulse length. For simplicity, we will fix t so that the center of the charge, βct , corresponds to the center of the BPM, z_0 . This is the point at which the charge peaks. Also, we will assume that the electrode length is large enough relative to the bunch length that we can take $\Delta z \rightarrow \infty$. (For the AFEL, the electron pulses are about 3 mm long, so even 1-cm-long electrodes are adequate for this assumption to be good.)

The integration over ρ' and ϕ' can be changed to an integration over x' and y' . Since we have assumed no special distribution, it is perfectly acceptable to make the substitution

$$I'(\rho', \phi', z - \beta ct) \rightarrow I'(x' - \bar{x}, y' - \bar{y}, z - z_0).$$

This substitution indicates that we are now writing the beam distribution in Cartesian coordinates with the beam's center at (\bar{x}, \bar{y}, z_0) . Then we can use the expansion

$$\begin{aligned}
 2\alpha + 4 \sum_{n=1}^{\infty} \left(\frac{\rho'}{a} \right)^n \frac{\sin n\alpha}{n} \cos[n(\phi - \phi')] &= 2\alpha \\
 + 4 \frac{\sin \alpha}{a} (x' \cos \phi + y' \sin \phi) \\
 + 2 \frac{\sin 2\alpha}{a^2} [(x'^2 - y'^2) \cos 2\phi + 2x'y' \sin 2\phi] \\
 + \frac{4 \sin 3\alpha}{3} [(x'^3 - 3x'y'^2) \cos 3\phi + (3x'^2y' - y'^3) \sin 3\phi] \\
 + \text{higher order terms}
 \end{aligned}$$

to convert the rest of the integral to Cartesian coordinates [3].

The beam distribution is always zero outside the pipe; therefore, when integrating over x' and y' , we can make the limits of integration $+\infty$ and $-\infty$. Then the peak image charge on a BPM electrode is

$$\begin{aligned}
 q_{\text{peak}}(\phi) &= -\frac{1}{2\pi a} \int_{z_0-\infty}^{z_0+\infty} dz \iint_{-\infty}^{+\infty} I'(x - \bar{x}, y - \bar{y}, z - z_0) \\
 &\left\{ 2\alpha + 4 \frac{\sin \alpha}{a} (x \cos \phi + y \sin \phi) \right. \\
 &+ 2 \frac{\sin 2\alpha}{a^2} [(x^2 - y^2) \cos 2\phi + 2xy \sin 2\phi] \\
 &+ \frac{4 \sin 3\alpha}{3} [(x^3 - 3xy^2) \cos 3\phi + (3x^2y - y^3) \sin 3\phi] \\
 &\left. + \text{higher order terms} \right\} dx dy dz,
 \end{aligned}$$

where we have dropped the primes for convenience. Making use of the following integrals:

$$\int_{z_0-\infty}^{z_0+\infty} dz \iint_{-\infty}^{+\infty} I'(x - \bar{x}, y - \bar{y}, z - z_0) dx dy dz = q_{\text{tot}},$$

$$\begin{aligned}
& \int_{z_0}^{z_0+\infty} \int_{-\infty}^{+\infty} \int_{-\infty}^{+\infty} x I'(x - \bar{x}, y - \bar{y}, z - z_0) dx dy dz = q_{tot} \bar{x}, \\
& \int_{z_0}^{z_0+\infty} \int_{-\infty}^{+\infty} \int_{-\infty}^{+\infty} y I'(x - \bar{x}, y - \bar{y}, z - z_0) dx dy dz = q_{tot} \bar{y}, \\
& \int_{z_0}^{z_0+\infty} \int_{-\infty}^{+\infty} \int_{-\infty}^{+\infty} x^2 I'(x - \bar{x}, y - \bar{y}, z - z_0) dx dy dz \\
& = \int_{z_0}^{z_0+\infty} \int_{-\infty}^{+\infty} \int_{-\infty}^{+\infty} [(x - \bar{x})^2 + 2x\bar{x} - \bar{x}^2] \\
& \quad \otimes I'(x - \bar{x}, y - \bar{y}, z - z_0) dx dy dz \\
& = q_{tot} [(\langle x - \bar{x} \rangle)^2 + 2\bar{x}^2 - \bar{x}^2] \\
& = q_{tot} (\sigma_x^2 + \bar{x}^2), \quad (\sigma_x \text{ is the rms halfwidth in } x) \\
& \int_{z_0}^{z_0+\infty} \int_{-\infty}^{+\infty} \int_{-\infty}^{+\infty} y^2 I'(x - \bar{x}, y - \bar{y}, z - z_0) dx dy dz \\
& = q_{tot} (\sigma_y^2 + \bar{y}^2),
\end{aligned}$$

$q_{peak}(\phi)$ becomes

$$\begin{aligned}
q_{peak}(\phi) = & -\frac{q_{tot}}{2\pi a} \left\{ 2\alpha + 4 \frac{\sin \alpha}{a} (\bar{x} \cos \phi + \bar{y} \sin \phi) \right. \\
& + 2 \frac{\sin 2\alpha}{a^2} \left\{ [(\sigma_x^2 - \sigma_y^2) - (\bar{x}^2 - \bar{y}^2)] \cos 2\phi \right. \\
& + 2 \langle xy \rangle \sin 2\phi \left. \right\} + \frac{4 \sin 3\alpha}{3 a^3} \left\{ [(\langle x^3 \rangle - 3\langle x^2 y \rangle) \cos 3\phi \right. \\
& \left. + (3\langle x^2 y \rangle - \langle y^3 \rangle) \sin 3\phi \right\} + \text{higher order terms} \left. \right\}.
\end{aligned}$$

The angled brackets indicate an rms average. Substituting in $\phi = 0, \pi/2, \pi$, and $3\pi/2$, to get the peak charge for each electrode, one finds that the first three terms in the multipole expansion are identical to those for the Gaussian beam in Table 1.

IV. EMITTANCE MEASUREMENT

Measuring emittance using BPMs is difficult. Most often, it is the lack of an adequate signal to noise ratio that is the main cause for concern. However, we have discovered a further problem that we believe is associated with the very-short beamline of the AFEL and the nature of the measurement.

The matrix equation $\bar{Q} = \bar{M} \cdot \bar{\sigma}_1$, where

$$\bar{M} = \begin{bmatrix} (R_{11})_1^2 & (2R_{11}R_{12})_1 & (R_{12})_1^2 & -(R_{33})_1^2 & -(2R_{33}R_{34})_1 & -(R_{34})_1^2 \\ \vdots & \vdots & \vdots & \vdots & \vdots & \vdots \\ (R_{11})_n^2 & (2R_{11}R_{12})_n & (R_{12})_n^2 & -(R_{33})_n^2 & -(2R_{33}R_{34})_n & -(R_{34})_n^2 \end{bmatrix}.$$

is what we are setting up when we use BPMs to measure the emittance [1]. The elements of the vector \bar{Q} are the measurements, and the vector $\bar{\sigma}_1$ is what we wish to determine [1]. The R_{ij} s are the elements of the transfer matrix between the point where you want to know the emittance and the BPM that is making the measurement.

On the AFEL, the distance from the end of the linac to the BPM that we wish to use for our emittance measurement is about 1.5 m, with four quads along the way. Our first inclination was to vary one of those quads to generate our measurements. However, the matrix produced by doing this proved to be highly unstable. It had a condition number of about 10^4 , which means that any error in our measurements could be amplified by that factor when we solved our matrix equation. What we ended up having to do was use two or more quads in concert, so that our transfer matrix acted as a "filter." By setting the quads to appropriate values, we can make all but one of the numbers in a \bar{M} matrix row zero, or very small. This allows most of the terms in the vector $\bar{\sigma}_1$ to dominate a number of measurements. As a result, we can reduce the condition number of \bar{M} so that it is close to unity, which is as small as it can be.

Why do poorly conditioned matrices arise? For the AFEL, with its short beamline, that situation is partly a resolution problem. Mostly, though, it comes from the fact that not all the elements in one row of the \bar{M} matrix are independent. A long beamline will help, but it is not necessarily the answer. One must be careful when making measurements. In general, it has been our experience that adjusting quads at random produces very poorly conditioned matrices, even when more than one quad is turned on at the same time.

V. CONCLUSION

A photoinjector-driven accelerator presents unique challenges for emittance measurements. By using BPMs for this purpose, we circumvent the need for knowledge of the actual distribution. However, in order for this technique to work, we still need to improve the signal to noise ratio of the BPMs, and this is a problem we have not yet addressed.

VI. REFERENCES

- [1] R. H. Miller et al., "Nonintercepting Emittance Monitor," in *Proceedings of the 12th International Conference on High-Energy Accelerators*, Francis R. Cole and Rene Donaldson, Ed. (Fermi National Accelerator Laboratory, Batavia, Illinois, 1983), p. 602.
- [2] Bruce E. Carlsten, et. al, "Measuring Emittance of Nonthermalized Electron Beams From Photoinjectors," 14th International Free Electron Laser Conference, Kobe, Japan. August 23-28, 1992, Los Alamos National Laboratory document LA-UR 92 2561.
- [3] R. T. Avery et al., "Non-intercepting Monitor of Beam Current and Position," *IEEE Trans. Nucl. Sci.* NS-18, 920-922, June 1971.

On the Reliability of Measured Results by Non-Destructive Beam Profile Monitor

Tadamichi Kawakubo, Eiichi Kadokura and Tadaharu Ishida*

National Laboratory for High Energy Physics, 1-1, Oho, Tsukuba-shi, Ibaraki-ken, 305, Japan

*Mitsubishi Electric Company, 1-7-4, Iwamoto-cho, Chiyoda-ku, Tokyo-to, 101, Japan

Abstract

In KEK-PS, there is a pair of horizontal (H) and vertical (V) non-destructive beam profile monitor (NDPM) in the Booster, and two H- and one V-NDPM in the main ring. All NDPMs can measure the time dependence of beam profile within one acceleration period without beam destruction, and the combination of two H-NDPMs in the main ring can measure the time dependence of momentum spread. By the system with a scraper and orbit bump magnets we cross-checked the beam size. And by measuring the longitudinal bunch length and the RF characteristics, we also cross-checked the momentum spread. The half width by NDPM is apt to be wider than the width by the scraper method to the extent of some mm. The error becomes severe in the measurement of narrow beam width.

I. INTRODUCTION

The positive ion are produced by the collision of the circulating proton beam into residual gas in a synchrotron ring. Leading them to a sensor by a external collecting field, the position dependence of these ion currents shows circulating beam profile indirectly. We call this monitor as a non-destructive beam profile monitor (NDPM) [1]. Since the ion current signal is very low, we usually use a micro-channel plate (MCP) to amplify the signal. KEK-PS has five sets of NDPM by using a large rectangular area MCP with 32 anodes, two of which measure the time dependence of the horizontal and vertical booster beam profile, separately. In the main ring, one NDPM measures the vertical beam profile and a pair of two monitors measures not only horizontal beam profile but also momentum spread ($\Delta p/p$) [2]. When the beam intensity is high, the electric potential of the beam distorts the collecting field. Therefore, it needs to be checked by other measuring system that the measured data by NDPM is correct. The data of the horizontal and the vertical beam profile of the Booster and the vertical in the main ring were checked by the combination systems of a scraper and orbit bump magnets, and the data of the momentum spread in the main ring was

checked by the calculation from the bunch length and RF characteristics [3]. The beam width measured by NDPM is apt to be wider than the width by the scraper and orbit bump magnets system, especially in the the vertical beam with narrow width and high intensity.

II. CROSS-CHECK OF BEAM PROFILE

The measurement by the system with a scraper and orbit bump magnets is shown in Fig.1. The beam orbit is deformed by the bump magnets and some part of the beam is hit by the scraper. The dependence of the beam loss on the bump current (see Fig.2) is changed by the scraper position. By taking these dependence curves, the calibration constant between the bump current and the moved distance of the beam at the scraper position is obtained. Fig.3 shows the typical vertical beam profile in the Booster measured by NDPM (white circle) and the beam loss dependence on the bump current which is equivalent to the moving scraper position (black circle). The former profile is the projection of the beam density in the phase space along Y' axis as shown in Fig.4a, on the other hand, the later beam loss dependence shows the density dependence on the radius in the phase space as shown in Fig.4b. These position dependences of the signal show different meanings of the beam density distribution in the phase space with each other, however, it is safe to say that the half width at 5% height of these two profiles should be good agreement with each other. Fig. 5a and 5b show the dependence of the half vertical beam width at 5% height on the acceleration time of the Booster at low and high intensity, respectively. Fig.6 shows the horizontal case at medium intensity. The horizontal beam width by NDPM is fairly good agreement with one by the scraper and bump system (Fig.6). However, the vertical beam width by NDPM is wider than one by the scraper system, especially in the case with high intensity and narrow width (Fig.5b). All measurement were done under the sufficient high collecting field ($=30\text{kV}/120\text{mm}$).

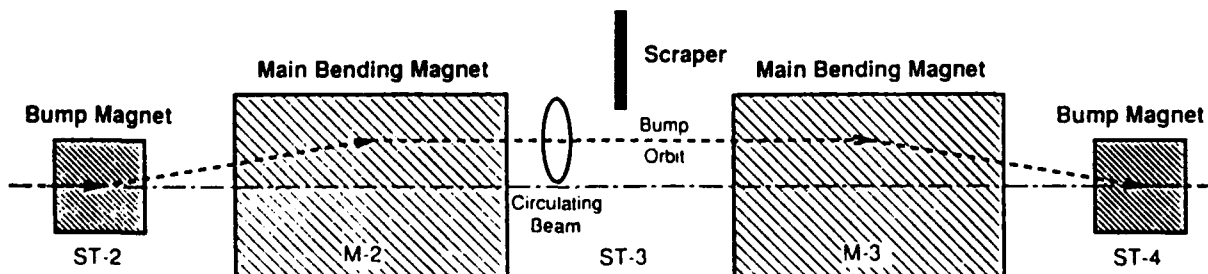


Fig.1 A scraper and two orbit bump magnets system.

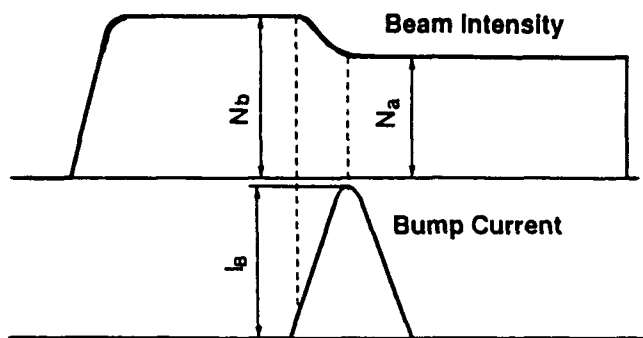


Fig.2 Beam loss generated by orbit bump current

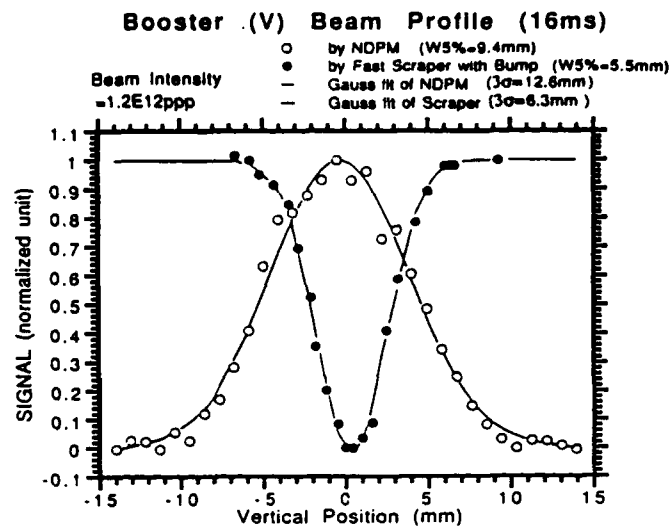


Fig.3 Typical Booster vertical beam profile by NDPM (white circle) and beam loss dependence on effective scraper position (black circle)

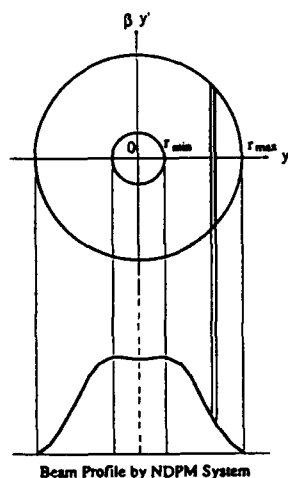


Fig.4a Relationship between output of NDPM and density distribution in phase space

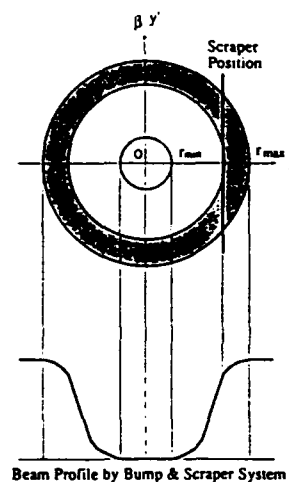


Fig.4b Relationship between output by scraper & bump system and density distribution in phase space

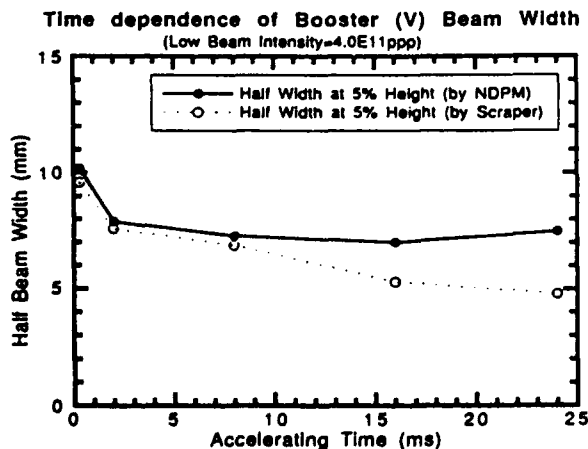


Fig.5a Time variation of half width at 5% height in Booster vertical beam profile (at low intensity)

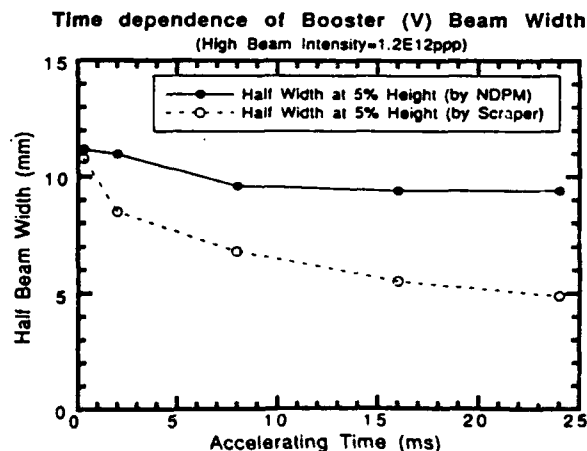


Fig.5b Time variation of half width at 5% height in Booster vertical beam profile (at high intensity)

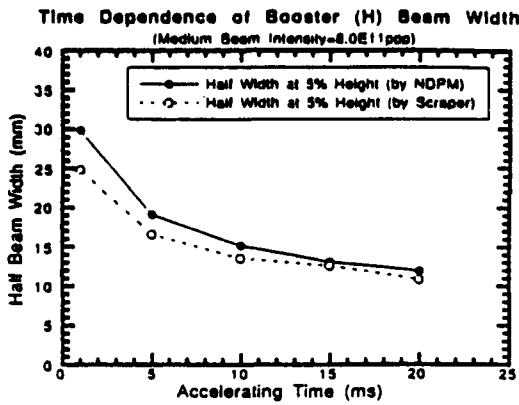


Fig.6 Time variation of half width at 5% height in Booster horizontal beam profile (at medium intensity)

III. CROSS-CHECK OF MOMENTUM SPREAD

A. Measurement by NDPM

Assuming that the intrinsic beam profile and momentum distribution have Gaussian shapes, the total half beam width (x) is,

$$x = (\beta\epsilon + (\eta \cdot \Delta P / P)^2)^{1/2}, \quad (1)$$

where β the Twiss parameter, ϵ the beam emittance, η the dispersion function, and ΔP the momentum spread. If two NDPMs are installed at locations with the Twiss parameter and dispersion function of (β_1, η_1) and (β_2, η_2) , respectively, the momentum spread is deduced from the above-mentioned equation to

$$\Delta P / P = \left(\frac{x_1^2 / \beta_1 - x_2^2 / \beta_2}{\eta_1^2 / \beta_1 - \eta_2^2 / \beta_2} \right)^{1/2}, \quad (2)$$

where x_1 and x_2 are the half beam width at the position of 1 and 2, respectively. The solid line in Fig. 7 shows the time dependence of the momentum spread in the main ring calculated by the half width at 5% height of beam profiles measured by two horizontal NDPMs.

B. Measurement by bunch length and RF characteristics

When the minimum longitudinal phase (ϕ_1) of the bunch circulating in a synchrotron ring is near $-\pi/2$ and the maximum (ϕ_2) is near $\pi/2$, the following equation is obtained approximately [3],

$$\Delta W = \left(\frac{eVPR}{\pi h \eta \Omega} \phi_B \right)^{1/2} \cos \phi_s \left(1 + \frac{\cos \phi_s - \frac{\pi}{2} + \phi_s \sin \phi_s}{\phi_B \cos^2 \phi_s} \right)^{1/2}, \quad (3)$$

where $\Delta W = \Delta E / \Omega$, eV is RF voltage (eV), cP is proton momentum (eV), R is radius of ring (≈ 54 m), $\Omega = 2\pi f$ (f is rotating frequency of proton beam in the ring), ϕ_B is the half bunch length, ϕ_s is the phase of the synchronous proton (r)

$$\text{and } \eta = \left| (1/\gamma_v)^2 - (1/\gamma)^2 \right|.$$

Momentum spread is deduced by above and following equations;

$$\Delta P / P = \frac{\Omega}{\beta^2 \gamma \cdot E_0} \cdot \Delta W, \quad (4)$$

where $E_0 = 9.38 \times 10^8$ (eV). The result is shown by cross mark in Fig.7. It can be said that the results by two different methods almost agree.

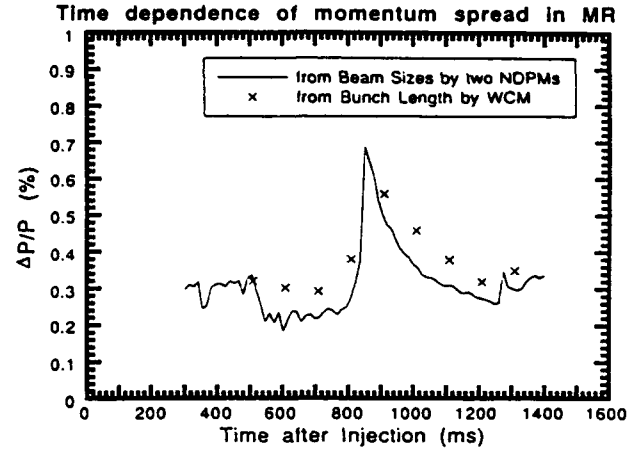


Fig.7 Time dependence of momentum spread in main ring by two horizontal NDPMs (solid line) by calculation from bunch length and RF characteristics (cross marks)

IV. CONCLUSION

It might be thought that the beam width measured by the system with a scraper and orbit bump magnets shows the real value. The half beam width obtained by NDPM is wider than real value to the extent of 3, 4 mm. The error is severe when the beam intensity is high and the width is narrow. As far as beam width is wide, the momentum spread measured by NDPM agrees well with the approximate calculation from the bunch length and RF characteristics.

V. ACKNOWLEDGMENT

The authors would like to acknowledge Dr.S.Ninomiya for his good comments to calculate the momentum spread from bunch length and RF characteristics. Thanks to him, we could cross-check the results measured by NDPM.

VI. REFERENCES

- [1] T.Kawakubo, T.Ishida, E.Kadokura, Y.Ajima and T.Adachi, "Fast data acquisition system of a non-destructive profile monitor for a synchrotron beam by using a micro channel plate with multi-anodes", N.I.M., A302 (1991), pp.397.
- [2] T.Kawakubo, E.Kadokura, T.Ishida, Y.Ajima and T.Adachi, "Non-destructive fast data taking system of beam profile and momentum spread in KEK-PS", Proceedings of the International Conference on Accelerator and Large Experimental Physics Control Systems, Nov., 11-15, 1991, KEK, Tsukuba, Japan, pp.399
- [3] private communication by Dr.S.Ninomiya.

Transverse Feedback System With Digital Filter

V. M. Zhabitsky

Joint Institute for Nuclear Research, 141980 Dubna, Moscow Region, Russia

I. L. Korenev and L. A. Yudin

Moscow Radiotechnical Institute, 113519 Moscow, Russia

Abstract

Main theoretical results for a transverse feedback system with a digital IIR-filter (infinite duration impulse response filter) and FIR-filter (finite duration impulse response filter) are described. The Z-transform method is used to solve the problem of the beam dynamics in the accelerator with a digital feedback. The analytical solution for the damping time and for the eigen frequencies are obtained and the system stability analyzed.

I. INTRODUCTION

The transverse feedback systems (TFS) are used in synchrotrons to damp the coherent transverse beam oscillations. In these systems the kicker (DK) corrects the beam angular according to the beam deviation from the closed orbit in the pick-up (PU) location at each turn. A classical TFS consists of one PU and one DK per plane. These systems have been used widely and provide an amplitude decrease of 25% per revolution [1]. In order to suppress fast resistive wall instability in UNK-1 (Serpukhov, Russia) [2] a more effective system is studied and developed [3]. It consists of two PU and two DK per plane connected by a feedback circuit with a digital filter and delay. The digital filters are used in a classical TFS [4] and designed for a fast TFS [5] to remove the revolution frequency harmonics. Feedbacks with digital filters have essential advantages for new large accelerators such as UNK, LHC, SSC where the revolution period is $70 \div 290 \mu s$ and the digital procedures for signal transformations can be realized with signal processors. This article is based on studies of TFS for UNK-1 [3, 5] and LHC [6].

II. BASIC EQUATIONS

A feedback system consists of PU and DK connected by circuit with a preamplifier, a filter, a power amplifier and a delay τ (Fig.1a). If bunch coupling, which happens due to resistive wall instability, is neglected, the matrix method

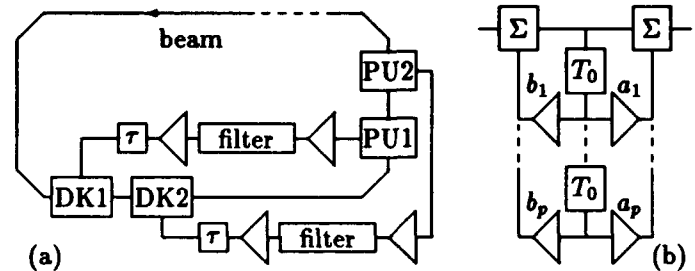


Figure 1: Feedback layout (a) and IIR-filter scheme (b).

becomes suitable for the beam motion description. Let the column matrix $\hat{X}[n, s]$ determine the beam state at the n -th turn at point s of the circumference C_0 . The first element of this matrix equals the beam deviation $x[n, s]$ from the closed orbit and the second one is $x'[n, s]$. After a short DK the x' value of the beam is changed by $\Delta x'[n, s_K]$ while deviation remains the same as before the DK at point s_K . Hence, after DK at point s_K^+ , the beam state is

$$\hat{X}[n, s_K^+] = \hat{X}[n, s_K^-] + \hat{T} \Delta \hat{X}[n, s_K],$$

where \hat{T} is the 2×2 matrix in which $T_{21} = 1$ and the other elements are zero. The kick is determined with column matrix $\Delta \hat{X}[n, s_K]$, where the first element equals $\Delta x'[n, s_K]$ and the second one has an arbitrary value.

If $\hat{M}(s_2, s_1)$ is the transfer matrix from s_1 to s_2 , then at the PU1 location at the $(n+1)$ -th turn the beam state is

$$\begin{aligned} \hat{X}[n+1, s_{P1}] &= \hat{M}_0 \hat{X}[n, s_{P1}] + \\ &+ \sum_{l=1}^M \hat{M}(s_{P1} + C_0, s_{Kl}) \hat{T} \Delta \hat{X}[n, s_{Kl}], \end{aligned} \quad (1)$$

where \hat{M}_0 is the unperturbed revolution matrix from point s_{P1} of the PU1 location and M is a number of kickers.

Let $\Delta x'[n, s_{Kl}]$ be proportional to the output voltage $V_{out}[n, s_{Kl}]$ in the feedback circuit during n -th crossing of the l -th kicker. The input voltage $V_{in}[n, s_{P1}]$ is assumed to be proportional to the beam deviation $x[n, s_{P1}]$ in the l -th pick-up. The kicker should change the angle of the same fraction of the beam that was measured by the PU. The delay $\tau = qT_0 + \eta$ is adjusted to provide such a synchronization (q is integer, T_0 is the revolution period, η is

the time of the particle flight between PUI and DKI). If the kick at the n -th turn depends on the beam state in the previous turns, then for the digital circuit we can write [7]:

$$V_{out}[n, s_{KI}] = u[n - q] \sum_{m=0}^{n-q} h[m] V_{in}[n - m - q, s_{PI}],$$

where $u[n]$ is the discrete unit step function [7] and the $h[m]$ coefficients are determined in accordance with the structure scheme of the feedback circuit. If $s_{KI} > s_{PM}$ and all feedback circuits are identical, then we have

$$\Delta \hat{X}[n, s_{KI}] = u[n - q] \times \sum_{m=0}^{n-q} \frac{|K| h[m]}{\sqrt{\beta_{PI} \beta_{KI}}} \hat{M}(s_{PI}, s_{PI}) \hat{X}[n - m - q, s_{PI}], \quad (2)$$

where β_{PI} and β_{KI} are the transverse betatron amplitude functions in the PU and DK locations and $|K|$ is the gain of the feedback without a filter.

Eqs.(1,2) fully describe the beam dynamics in the accelerator with the digital feedback system. These equations can be solved using Z -transform [7] for sequence $\hat{X}[n, s]$:

$$\begin{aligned} \hat{X}(z) &= \sum_{n=0}^{\infty} \hat{X}[n, s] z^{-n}; \\ \hat{X}[n, s] &= \frac{1}{2\pi i} \int_C \hat{X}(z) z^{n-1} dz = \sum_k \text{Res} [\hat{X}(z_k) z_k^{n-1}]. \end{aligned} \quad (3)$$

The motion of the particles will be stable if $|z_k| < 1$. The damping factor $D_k = |z_k|$ and the number of oscillations per turn $\{\text{Re} Q_k\} = \arg(z_k)/2\pi$ are fully determined by the singular points z_k . Using Z -transform for (1,2) we get:

$$\hat{X}(z) = \frac{z\hat{I} - \hat{M}^{-1}(z) \det \hat{M}(z)}{\det(z\hat{I} - \hat{M}(z))} z \hat{X}[0, s_{PI}], \quad (4)$$

$$\begin{aligned} \hat{M}(z) &= \hat{M}_0 + \\ &+ \sum_{l=1}^M \frac{K(z)}{\sqrt{\beta_{PI} \beta_{KI}}} \hat{M}(s_{PI} + C_0, s_{KI}) \hat{T} \hat{M}(s_{PI}, s_{PI}), \\ K(z) &= z^{-q} |K| H(z), \end{aligned} \quad (5)$$

where \hat{I} is the unit matrix; $\hat{X}[0, s_{PI}]$ is the initial beam state matrix; $K(z)$ is the transfer function for a feedback circuit with the delay τ and the filter system function $H(z)$ depending on $h[m]$. It is known [7] that in radiotechnical sense the circuit is stable if all the singular points of $K(z)$ lie inside the circle $|z| < 1$. If this condition is fulfilled, the singular points z_k in (4) are found from the equation [8]:

$$\begin{aligned} \det(z\hat{I} - \hat{M}(z)) &= z^2 - [2 \cos(2\pi Q) + \\ &+ K(z) \sum_{l=1}^M \sin(2\pi Q - \psi_{PIKI})] z + \det \hat{M}(z) = 0, \end{aligned} \quad (6)$$

where Q is the number of unperturbed betatron oscillations per revolution in transverse plane; ψ_{PIKI} is the betatron phase advance from PUI to DKI.

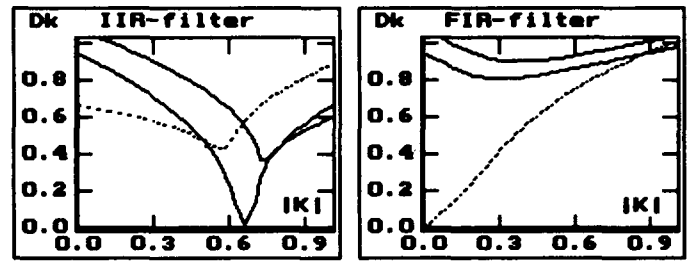


Figure 2: D_k for a classical feedback with IIR-filter (left) and FIR-filter (right). $\text{Re} Q = 70.3$; $|\text{Im} Q| = 0.01$.

When instability occurs, Eq.(6) will have the same form but the betatron phase advances must be calculated with a complex value of $Q(z)$ both for coasting [6] and bunched [9] beams.

III. FEEDBACK WITH FILTER

The digital IIR-filter (Fig.1b) consists of amplifiers a_m , b_m and delays T_0 ; the order of the filter is p . The system function for this filter is

$$H(z) = \left[1 + \sum_{m=1}^p a_m z^{-m} \right] \left[1 - \sum_{m=1}^p b_m z^{-m} \right]^{-1}. \quad (7)$$

The results for the filter of the first order ($p = 1$) and for $q = 0$ are shown bellow.

A. Classical Feedback

For a classical feedback we have $M = 1$ and

$$\det \hat{M}(z) = 1 - K(z) \sin \psi_{PK}.$$

Taking into account (5,7) we get in (6) a cube equation for z_k . If $|K| \ll 1$, then in linear approximation we obtain:

$$\begin{aligned} z_{1,2} &= \left(1 \mp \frac{i}{2} |K| e^{\mp i \psi_{PK}} \right) e^{\pm i 2\pi Q} - \frac{a_1 + b_1}{2} |K| \mu_{1,2}, \\ z_3 &= b_1 + (a_1 + b_1) |K| \mu_3, \end{aligned} \quad (8)$$

where μ_i are defined in [6]. Without a filter ($a_1 = b_1 = 0$) we have two solutions and a damping time τ_D is

$$\begin{aligned} \frac{T_0}{\tau_D} &= -\ln \text{MAX}|z_k| = \frac{1}{2} |K| \sin(\text{Re} \psi_{PK}) - 2\pi |\text{Im} Q| = \\ &= \frac{1}{2} \sqrt{\beta_P \beta_K} \left(\frac{\Delta x'_K[n]}{x_P[n]} \right) \sin(\text{Re} \psi_{PK}) - 2\pi |\text{Im} Q|. \end{aligned} \quad (9)$$

This decrement formula is well known [4]. However, for a feedback with a filter it is necessary to take into account three roots. Fig.2 shows $|z_k|$ dependencies on $|K|$ when the phase advance from PU to DK is adjusted closely to an odd number of $\pi/2$ radians ($|\sin \text{Re} \psi_{PK}| = 1$). The solid curves correspond to the oscillations with the tune in neighbourhood of Q . The dotted curve corresponds to

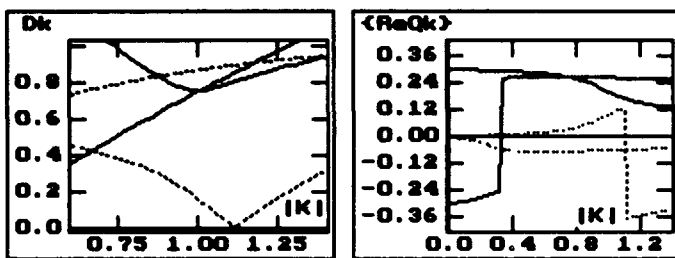


Figure 3: D_k and $\{ReQ_k\}$ for a fast feedback.

the third root. This new oscillation mode is conditioned with the filter structure, when the kick in DK depends on the beam state in the previous two revolutions. To provide the independence on $|K|$ of the feedback action on the closed orbit displacement and for a better suppression of noise it is necessary to set $a_1 = -1$ [6]. Optimization of b_1 value on the maximum damping rate gives $b_1 = 0.66$ for a feedback with the IIR-filter. It is seen from Fig.2 (left) that for $|K| > 0.65$ the damping rate is determined by third oscillation mode. For $b_1 = 0$ we have a notch filter (FIR-filter). The maximum decrement in this case (Fig.2, right) corresponds to $|K| = 0.38$. It is easy to see that a feedback system with a notch filter is slower and its stability region is narrower than the feedback system with the IIR-filter.

B. Fast Feedback

For a fast feedback we have $M = 2$. If $Re\psi_{P_2P_1} = Re\psi_{K_2K_1} = \pi/2$, then ¹

$$\det \hat{M}(z) = 1 - 2K(z) \sin \psi_{PK} + K^2(z).$$

After some transformations in (6) we get the equation:

$$z - [1 \mp iK(z) \exp(\mp i\psi_{PK})] \exp(\pm i2\pi Q) = 0. \quad (10)$$

Hence, for $K(z)$ in (5) with $H(z)$ from (7) the additional solutions z_k and, thus, the new eigen frequencies are obtained. This leads to modification of stability region, $|z_k| \leq 1$, especially when $|K| \geq 1$. The maximum damping rate is achieved by the fast feedback system at optimum positions of PU and DK ($|\sin Re\psi_{PK}| = 1$) connected via feedback without filter [3] and its value is

$$MAX(D_k) = |\sinh(2\pi ImQ)| \quad \text{for } |K| = \cosh(2\pi ImQ).$$

This means that without instability the fast TFS can damp the coherent oscillations in one turn. But in the UNK-1 it is expected that $|ImQ| = 0.1$. Hence, the stability region is not large. For this reason the PU and DK positions were taken as close to their optimum positions as possible. In Fig.3 the D_k and $\{ReQ_k\}$ dependencies on $|K|$ are shown for the feedback system with the IIR-filter. As it is mentioned above there are more than two ordinary eigen

frequencies for the feedback with a filter. In Fig.3 the solid curves correspond to the ordinary modes and the dotted curves are determined by the filter structure. For the same reasons mentioned above for a classical feedback it is necessary to set $a_1 = -1$. The filter parameter $b_1 = 0.61$ was chosen to provide the best damping conditions. The ReQ value for all these curves is 56.7. But with a different number of particles the coherent tune shift for ReQ may be about 0.09 for the horizontal and 0.41 for vertical betatron oscillations [2]. It means that $Re\psi_{PK}$ will differ from its optimum value. The particle motion is stable, if [3]

$$|\sin(Re\psi_{PK})| > |\sinh(2\pi ImQ)|.$$

Hence, the $Re\psi_{PK}$ deviation is not more than 0.2π radians in the UNK-1. As soon as this deviation is less than the coherent tune shift for vertical oscillations, then the tune must be corrected during injection in order to have an acceptable phase advance from PU2 to DK1.

It is necessary to emphasize that the optimum value of b_1 depends on Q . For this reason in the filter design it is useful to foresee a possibility to vary the b_1 .

IV. CONCLUSION

The matrix equations for a transverse feedback system with a digital filter have been obtained and the Z-transform method has been effectively used to solve them. The analytical solutions for the damping time and for the eigen frequencies obtained allow one to design feedback systems with digital filters and to optimize the damping rate and the amplifier gain in stability region.

ACKNOWLEDGMENTS

The authors would like to thank I.N. Ivanov (JINR) and D. Boussard (CERN) for help and many useful discussions.

REFERENCES

- [1] L. Vos. *CERN SL/91-40 (BI)*, Geneva, 1991.
- [2] V.I. Balbekov. *The IX All Union Conference on Particle Accelerators. JINR, Dubna*, vol.2, p.360, 1985.
- [3] V.M. Zhabitsky et al. *JINR P9-91-99*, Dubna, 1991.
- [4] E. Ebert et al. *DESY 91-096*, 1991.
- [5] V.M. Zhabitsky et al. *JINR P9-91-494*, Dubna, 1991.
- [6] V.M. Zhabitsky. *CERN SPS/RFS/91-14*, Geneva, 1991.
- [7] W.McC. Siebert. *Circuits, Signals, and Systems. The MIT Press*, 1986.
- [8] V.M. Zhabitsky. *JINR P9-92-910*, Dubna, 1992.
- [9] V.M. Zhabitsky et al. *JINR P9-92-909*, Dubna, 1992.

¹ The influence of deviations for phase advances from $\pi/2$ radians is analyzed in [8].

Conference Author Index

A

Aas, T. 2967
 Abbott, S. 3748
 Abe, I. 3087
 Abrahamsson, K. 1735
 Acerbi, E. 1524
 Ackerman, G. D. 3169
 Adam, S. R. 3639
 Adams, F. P. 829, 832, 835, 1039
 Adamski, J. 2967
 Adler, R. J. 1306
 Adney, J. 3745
 Adolphsen, C. 414, 417, 543, 2019, 3342
 af Ugglas, M. 1735
 Ahrens, L. 3633
 Ahrens, L. A. 3763
 Aiello, G. R. 2322, 2367
 Aiello, R. 2118
 Aizawa, K. 1468
 Akai, K. 769, 992, 3450
 Akbari, H. 2492
 Akchurin, N. 32
 Akemoto, M. 1309
 Akre, J. 1572
 Alberti, S. 2656, 2690
 Aleksandrov, A. 3243
 Alessandria, F. 1524
 Alexandrov, V. 2042
 Alimov, A. S. 2059
 Allen, C. K. 3145, 3648
 Allen, L. J. 1689, 1691
 Allen, S. L. 1551, 1554
 Alley, R. 3045, 3047
 Alley, R. K. 2978, 3027, 3036
 Allison, P. 3172
 Allison, S. 1884, 2106
 Alton, G. D. 2979
 Amidei, D. 2199
 Amiranoff, F. 2450
 Amiry, A. 173
 Anami, S. 590, 1163, 1193, 1416, 3087
 Anamkath, H. 608, 611
 Anashin, V. 3876
 Anashin, V. V. 2022
 Anders, A. 1390
 Anders, S. 1390
 Anderson, D. 3745
 Anderson, D. E. 1354
 Anderson, K. 3096, 3163
 Anderson, R. R. 2919
 Anderson, S. 1421
 Anderson, T. 2835
 Andler, G. 1735
 Ando, M. 1468
 Andreev, V. A. 3121, 3124
 Andreev, V. G. 980
 Andreev, V. V. 297
 Anerella, M. 2744, 2766, 2790
 Annala, G. 3808
 Annala, J. 354
 Anne, R. 1789, 1792

Anthouard, P. 670, 697
 Antoine, C. 798
 Antropov, V. 2042
 Aoki, T. 2039
 Aoyagi, H. 2978, 3036
 Arai, S. 1780, 1783, 1786
 Arakaki, Y. 41
 Araki, M. 1518
 Arbique, G. 827, 3127
 Arbique, G. M. 2124, 2426, 2986
 Arbuzov, V. 1226
 Archie, C. N. 480
 Arcioni, P. 772, 1524, 1569
 Arinaga, M. 2292, 3552
 Arkhipov, O. 2042
 Arnaudon, L. 44
 Arnold, D. E. 989
 Arnold, N. D. 1957, 1960
 Artiimov, A. S. 2166, 2169
 Artru, X. 3093
 Asami, A. 3087
 Askew, D. R. 1336
 Assang, A. 2187
 Asseev, A. A. 315, 318, 320, 322, 324
 Assmann, R. 44
 Åström, J. 2068
 Atkins, W. H. 1669
 Aurerbach, E. H. 1872
 Ausset, P. 858
 Austin, R. H. 2970
 Averbukh, J. 824
 Averill, R. 1372, 2054, 2331, 2868, 2871, 2874, 3851
 Awaji, N. 1515, 1518
 Ayvazian, H. 1750
 Azuma, O. 1202

B

Baartman, R. 3330
 Baba, H. 959
 Babenko, E. 2423
 Baccaglioni, G. 1524
 Bachman, D. A. 3190
 Bachmor, R. 1178
 Badano, L. 32
 Bagge, L. 1735
 Baglin, V. 2720
 Bai, X. 3237
 Baier, T. 3093
 Baier, V. N. 3093
 Baik, K. H. 679
 Bailey, J. 3757
 Bailey, R. 1937, 2001, 2013
 Baiod, R. 2826
 Baishev, I. S. 3109, 3772
 Bak, J. 581
 Bak, J. S. 593
 Balabin, A. I. 3675
 Balandin, V. 441, 444, 477
 Ball, M. 29, 224, 227, 420, 2289, 3745
 Ball, M. S. 2243, 3536
 Balleyguier, P. 1136
 Baltrusaitis, R. M. 2400
 Band, A. 2240
 Bane, K. 543, 1445, 3240, 3375
 Bane, K. L. 596
 Bane, K. L. F. 3339, 3342, 3432
 Baptiste, K. 1238
 Baranovsky, A. E. 682
 Barbier, M. M. 3102
 Bardy, J. 670, 697
 Barklow, T. 2019
 Barletta, B. 2638
 Barletta, W. 2010, 3836
 Barletta, W. A. 775, 1524, 1988, 3817
 Barlow, D. 1703
 Barlow, D. B. 2480
 Barnard, J. 703, 706
 Barnard, J. J. 712, 715, 733, 3612
 Barnes, M. J. 1148, 1181, 1330, 3402
 Barnes, P. 763, 886, 889, 892, 918, 921, 977, 995, 1399
 Barov, N. 561, 2617, 2623, 3216
 Barr, D. S. 2163
 Barranco-Luque, M. 2956
 Barry, W. 2109
 Barsotti, E., Jr. 3294
 Barsotti, E. L. 2531
 Bartalucci, S. 778
 Bartelson, L. 918, 1342
 Barth, W. 3142
 Barts, T. 3444
 Bar'yakhtar, V. 1480
 Bassetti, M. 2048
 Batchelor, K. 2486, 3000, 3012
 Batishchev, O. V. 2620
 Batskikh, G. 2717
 Batskikh, G. I. 980
 Batygin, Y. K. 50
 Bazzani, A. 273
 Be, S. H. 3845
 Bearzatto, C. 1184
 Beaufait, J. 3103
 Beckert, K. 1645, 1738
 Beebe, E. 1735
 Beechy, D. 2118
 Behrsing, G. 83
 Belk, A. 1937
 Belkacem, A. 3751
 Bell, R. A. 1039, 2010
 Bellomo, G. 775, 1001, 1524
 Belloni, F. 3839
 Belomestnykh, S. 1226
 Belomestnykh, S. A. 3669
 Belomestnykh, S. E. 2022
 Beloshitsky, P. 2042
 Belov, V. 2042
 Belov, V. P. 3820, 3822
 Belova, N. G. 664, 3546
 Bemes, M. 2967
 Benaroya, R. 3857
 Benes, S. J. 1957
 Benesch, J. 1016

- Benesch, J. F. 748, 781, 947
 Bengtsson, J. 567, 1488, 2272, 3312
 Benke, T. 1706
 Bennett, G. 2070
 Bennett, L. F. 667
 Bennett, M. 3748
 Bennett, P. 1916
 Benson, S. 3663
 Benvenuti, C. 806
 Ben-Zvi, I. 849, 1439, 1602, 2486, 2962, 3000, 3012
 Berg, J. S. 291
 Berg, W. 605
 Bergher, M. 3708
 Bergmann, U. 2145
 Bernard, D. 2450
 Bernard, M. 694
 Bernard, P. 806
 Bernardini, M. 3842
 Beroud, Y. 784
 Bertrand, P. 1789
 Bertsche, K. J. 1727
 Berz, M. 155, 164
 Bethel, S. 2967
 Bethke, S. 2172
 Betto, A. 1220
 Bhandari, R. 381
 Bharadwaj, V. 2228, 3806
 Bhat, C. M. 405, 787, 1223
 Biagini, M. E. 2048
 Bickley, M. 1835, 1895
 Bieniosek, F. 3096
 Bieniosek, F. M. 3163
 Bieri, R. L. 742
 Bieth, C. 1789
 Bijleveld, J. 2343
 Billan, J. 68
 Billen, J. 1712
 Billen, J. H. 790, 793
 Billquist, P. 1694
 Birattari, C. 1524
 Birnbaum, I. 2420
 Birnbaum, I. A. 3012
 Biscardi, R. 1419
 Biscari, C. 2048
 Bishop, D. 1148, 1181
 Bisoffi, G. 1747
 Bisognano, J. 512, 3663
 Bisognano, J. J. 179, 2364, 2929, 3246, 3473, 3515
 Bixio, A. 1063
 Bizek, H. 1485
 Blaker, G. 1300
 Blasche, K. 357, 3736
 Blaskiewicz, M. 3321, 3324
 Blell, U. 357
 Bleser, E. 3766
 Bleser, E. J. 3763
 Blewett, J. P. 2546
 Blind, B. 56
 Blockus, D. 2172
 Bloess, D. 806
 Blokland, W. 2528
 Blondel, A. 44
 Bloom, E. 3084
 Bluem, H. 1451
 Blum, E. 3579
 Blum, E. B. 1599, 2246, 2307
 Blumberg, L. N. 3579
 Bobin, J. L. 3202
 Bobyleva, L. 2042
 Boden, A. 2051
 Boers, J. E. 327
 Boeuf, J. P. 3039
 Bogacz, S. A. 74, 77, 2587
 Bogatov, N. 2769
 Bogaty, J. M. 1694
 Böge, M. 460
 Bogert, D. 3793
 Bohl, T. 2001
 Bohn, C. L. 838, 1715, 3666
 Boiteux, J. P. 2358
 Bollinger, L. M. 1694
 Bolme, G. O. 1669, 3118
 Bondarev, B. I. 980
 Boni, R. 611, 778
 Bonifacio, R. 1524
 Bonin, B. 798
 Bonnafond, C. 670, 697, 2115
 Bordoley, M. 1867, 2313
 Bordry, F. 44, 2001
 Bordua, M. 3748
 Borer, J. 2103, 2492
 Borisov, O. N. 518
 Borland, M. 285, 2028, 3015
 Bosch, F. 1645
 Bosch, R. A. 3369
 Boscolo, I. 1524
 Bosotti, A. 1524
 Bossert, R. 2769
 Bossingham, R. 3751
 Botlo, M. 128
 Botman, J. I. M. 1072, 1820, 2062, 2065, 2892, 2927, 3423, 3645
 Bourg, F. 2997
 Bourgarel, M. P. 1789
 Bourianoff, G. 128, 203, 515
 Boussard, D. 2376, 2379
 Bovet, C. 2492
 Bowling, B. A. 1895, 2298, 2477
 Bowling, S. 1669
 Boyce, R. 1445, 1608
 Boyce, R. F. 543
 Boyd, J. K. 463
 Boyes, J. 667
 Bozoki, E. 105, 2284, 3636
 Brabson, B. 29, 224, 227, 420
 Bracco, R. 1587
 Bradley, S. 2054
 Brandeberry, F. 824, 880
 Brandt, D. 3429
 Branson, B. H. 1220
 Brau, C. A. 1448
 Brauer, S. O. 1217
 Braun, A. 354
 Bravar, A. 32
 Brennan, J. M. 1241, 3763
 Brennan, M. 2286
 Bres, M. 1184
 Bressan, M. 772, 1524, 1569
 Bressler, V. E. 2736, 2950
 Briand, P. 2997
 Brianti, G. 3917
 Bridges, J. 285, 1013
 Bridges, J. F. 766, 910, 913, 1157, 1408, 1906
 Briegel, C. 1914
 Briggs, R. J. 3922
 Brindza, P. 3103
 Brinkgreve, P. 2892
 Brinkmann, R. 3742
 Brittain, D. L. 1169
 Broggi, F. 1524, 1569
 Brooks, T. 1154
 Broome, W. 1419
 Brouk, V. 2382
 Browman, A. 1683
 Browman, M. J. 3267
 Brown, B. 3757
 Brown, B. C. 351, 2829
 Brown, D. 2181
 Brown, D. J. 2664
 Brown, G. 2760
 Brown, I. 1390
 Brown, K. 384
 Brown, K. L. 333, 378
 Brown, N. 62
 Brown, P. 2358
 Brown, R. 2507, 3184
 Browne, M. 3045, 3047
 Brownman, M. J. 800
 Bru, B. 1789, 1792
 Brütsch, E. 2748
 Bruhwiler, D. L. 59, 3624
 Brumwell, F. 3757
 Brunelle, P. 1465
 Bruns, W. 904, 1133, 3714
 Bryant, H. 369
 Bu, S. 1411
 Buchanan, E. 3533
 Buda, S. 1419
 Budlong, J. 3533
 Budnick, J. 29, 224, 227, 420, 2865
 Budzko, A. 3642
 Budzko, A. V. 3784
 Builta, L. 3055
 Bull, J. 1369
 Buller, T. L. 1075
 Bulos, F. 3084
 Bultman, N. 1712
 Bulyak, E. 300, 1480
 Bulyak, E. V. 3512
 Buon, J. 469, 2513
 Burgett, W. 2731, 2757, 2763
 Burke, D. 2019
 Burke, D. L. 543
 Burkhardt, H. 2001
 Burnham, B. 2889
 Burns, A. 2103, 2301
 Burns, M. 3055
 Burns, M. J. 2944
 Burtin, G. 2495
 Burton, R. J. 829, 832
 Busch, G. 2967
 Bushuyev, A. 1226
 Butterworth, A. 1903
 Büttig, H. 1477
 Byrd, J. 2349, 3315
 Byrd, J. M. 2109, 3318, 3408
 Byrne, T. 567

C

- Cai, S. Y. 3075
 Cai, Y. 203, 2781
 Calabrese, R. 3243
 Calame, J. P. 2667, 2670
 Calderon, M. 3836
 Callahan, D. A. 730, 733, 3660
 Callin, R. 543, 620, 1106
 Calloway, D. 2172
 Calo, A. 3127
 Calvert, J. 1160, 3748
 Camas, J. 2498
 Cameron, P. 1166
 Cameron, P. R. 2328
 Campbell, B. 1402
 Campisi, I. E. 1115, 1220
 Capista, D. 2252
 Caporaso, G. 703
 Caporaso, G. J. 712, 715
 Cappi, R. 3570
 Cardito, M. 2154
 Cardman, L. S. 3246
 Carey, D. C. 47
 Carlé, P. 1735
 Carlini, R. 2136, 3103
 Carlisle, L. 1718
 Carlson, R. L. 661
 Carlsten, B. 2675
 Carlsten, B. E. 2537, 2664
 Carmel, Y. 2714
 Carpenter, J. 3757
 Carr, R. 1596
 Carroll, F. E. 1448
 Carron, G. 1066, 3426
 Carson, J. 2769
 Carter, A. 2054
 Carwardine, J. 1709
 Carwardine, J. A. 3210
 Caryotakis, G. 543, 1106, 1259
 Casella, R. 1277
 Caspers, F. 2157, 3381
 Cassel, R. 543, 1318
 Castellano, M. 573
 Castro, P. 2103
 Catani, L. 573
 Caussyn, D. 3745
 Caussyn, D. D. 29, 224, 227, 420, 3536
 Cavallari, G. 806
 Celata, C. M. 724, 3748
 Cerniglia, P. 2310
 Chabert, A. 1789
 Chae, Y. 282
 Chae, Y. C. 182
 Chamberlain, O. 2172
 Champion, M. 809, 918, 1127
 Champion, M. S. 989
 Chan, C. F. 3157, 3160
 Chan, K. D. C. 2970
 Chanel, M. 2157
 Chang, C. H. 1943, 2886
 Chang, C. R. 122, 812, 3585
 Chang, H. P. 1943
 Chang, J. S. 1345
 Channell, P. J. 38
 Chao, A. 3781
 Chao, A. W. 29, 224, 227, 420, 3345, 3348
 Chao, Y. 587
 Chapman, L. 1914, 2249
 Chappelier, J. 158, 161
 Charruau, G. 858
 Chase, B. E. 2355
 Chattopadhyay, S. 83, 2638, 3042
 Chautard, F. 267, 2720
 Chechetenko, V. 1480
 Chehab, R. 3093
 Chel, S. 855
 Chen, B. 3345, 3348
 Chen, C. 2656
 Chen, H. 2151
 Chen, J. 1095
 Chen, J. R. 1635
 Chen, J. S. 1878
 Chen, P. 617, 2638
 Chen, S. 200, 3255
 Chen, S. C. 2575, 2696, 2699
 Chen, S. J. 1878
 Chen, T. 3479
 Chen, Y. 303, 718, 2841
 Chen, Y. J. 703, 706
 Cheng, J. 2659, 2667
 Cheng, W. 221
 Cheng, Y. 1262, 1393, 2269
 Chepurinov, A. S. 2059
 Chesnokov, Y. A. 454
 Chester, N. 2826
 Chester, N. S. 2823
 Chevallier, M. 3093
 Chiaveri, E. 806, 849
 Chida, K. 41
 Chimenti, V. 3906
 Chin, J. 1572, 1584
 Chin, Y. H. 3347, 3414
 Ching, C. H. 3351
 Chiou, T. C. 2635
 Chirkov, P. 2769
 Chmielewski, A. G. 1890
 Cho, C. 2151
 Cho, M. 581, 1521
 Cho, M. H. 593, 1315
 Cho, Y. 399, 3757
 Cho, Y. S. 679
 Choi, B. H. 679, 3196
 Choi, J. 2516, 3273
 Choi, J.-Y. 3087, 3705
 Chojnacki, E. 815, 1844, 2596, 3061
 Chou, P. J. 3363
 Chou, W. 818, 2281, 3444, 3609, 3781, 3888
 Christensen, K. 1712, 2947
 Christiansen, C. F. 1098, 2139
 Christianson, M. 2757
 Chu, C. 306, 2841
 Chubar, O. V. 1626, 2474, 2510
 Chubarov, O. V. 2059
 Chugun, T. 2205
 Chung, K. H. 679, 3196
 Chung, Y. 188, 1814, 2112, 2263, 2266, 2275, 2304
 Chupp, W. W. 703, 3199
 Church, M. 330
 Chuvilo, I. V. 1675
 Ciapala, E. 1903, 2358
 Ciardullo, D. J. 1241
 Ciarlette, D. 285
 Ciarlette, D. J. 1814
 Cifarelli, F. 3099
 Ciullo, G. 3243
 Claborn, G. 2222
 Clark, D. 369, 3888
 Clark, D. J. 1724, 1727
 Clark, S. L. 543
 Clarke, J. A. 1494, 1638, 3594, 3672
 Claudet, S. 2956
 Claus, J. 2895
 Clay, W. 3888, 3891
 Clayton, C. 2976, 3003
 Clayton, C. E. 558, 2551, 3543
 Clayton, T. 1369, 2781
 Clément, M. 1363
 Clendenin, J. 3033
 Clendenin, J. E. 2978, 3027, 3036
 Clerc, G. 1184
 CLIC Study Group 540
 Clifft, B. E. 1694
 Cline, D. 2051, 2638
 Clout, P. 1801
 Clozza, A. 3906
 Coacolo, J. C. 3567
 Coadou, B. 798
 Cobb, J. K. 2838
 Codutti, A. 1587
 Cohen, S. 369
 Colby, E. 3021
 Colchester, R. J. 2495
 Cole, B. 128, 203
 Cole, M. 821, 3012
 Cole, R. 1669
 Coleman, P. 824
 Coleman, P. D. 1033, 1256, 3252
 Colestock, P. 3294
 Colestock, P. L. 3303, 3306, 3384, 3540
 Collet, G. J. 3030
 Collet, P. 1187
 Collier, P. 1937, 2001
 Collins, J. 29, 224, 227, 420
 Collins, J. P. 2823
 Colton, E. 3297
 Combs, C. 1703
 Combs, C. M. 846
 Conciauro, G. 1524, 1569
 Conde, M. E. 3042
 Condé, H. 1771
 Connolly, R. 1669
 Conte, M. 32, 438
 Conway, P. 2388
 Coombes, R. 2769
 Cooper, R. 3297
 Cooper, R. G. 2400
 Cooper, R. K. 3267
 Cooper, W. S. 3169
 Coosemans, W. 44
 Corbett, J. 173
 Corbett, W. J. 108, 114, 1483, 2275
 Cork, C. 1575
 Corlett, J. N. 2109, 3318, 3408, 3411
 Cornacchia, M. 173
 Cornelis, K. 2001, 3429

Cornelius, W. D. 2994
 Corredoura, P. 2370, 3240
 Corsini, R. 626, 1524
 Cottingame, W. B. 3118
 Courant, E. 3778
 Courant, E. D. 137
 Cover, R. 1605
 Craddock, W. 2638
 Crandall, K. R. 1042, 3585, 3657
 Crane, M. 1922, 1966
 Cravey, W. R. 739
 Crawford, A. 1223
 Crawford, C. 886, 918
 Crawford, C. A. 3540
 Crawford, J. F. 1771
 Crawford, K. 1925, 3757
 Crist, C. 2121
 Crist, C. E. 2124, 2130, 2426, 2456, 2501
 Crockford, G. 2504
 Crofford, M. 587
 Crofford, M. T. 2364
 Crosbie, E. 285, 1485
 Crosbie, E. A. 282, 506
 Crouch, R. 2199
 Cuevas, C. 1838, 3127
 Culwick, B. 1277
 Cuneo, M. E. 694
 Curbow, J. 941
 Curry, B. P. 375
 Curtin, M. 1154, 1244
 Cutler, R. 3509
 Cutler, R. I. 827, 1250

D

Dabrowski, J. 1274, 1855, 1858, 1861
 Daclon, F. 1378, 3842, 3873
 Dalesio, L. R. 1806
 D'Alsace, R. 1419
 Daly, R. 1960, 2142
 Damjanovich, R. 3175
 Damm, R. 1166
 Danared, H. 1735
 Danby, G. T. 2883
 Danilov, V. 3429, 3711
 Danly, B. G. 2575, 2656, 2690
 Dasbach, D. 1080
 Datte, P. 1703, 2118, 2483, 3127
 D'Auria, G. 953, 956, 1145
 D'Auria, J. M. 1641
 Dauvergne, J.-P. 2739
 Davidson, A. D. 1175
 Davis, K. 2967
 Davis, P. 561, 2976, 3003, 3216, 3543
 Davis, T. J. 2653, 2687
 Dawson, J. 2462
 Dawson, R. 1733
 Deadrick, F. 703
 Debiak, T. 821
 Debiak, T. W. 2420, 3193
 Decker, C. 2635
 Decker, F. 3582
 Decker, F.-J. 414, 2019, 2278, 2435, 2507, 3234, 3240, 3576

Decker, G. 188, 2196, 2263, 2275, 2304
 Decker, G. A. 1814
 Deckers, R. 1820
 DeFord, J. 3450
 Degen, C. M. 2310
 DeHaven, R. 1021, 1683
 Dehen, J. 3142
 Dehning, B. 44
 Deitinghoff, H. 3139, 3142
 de Jong, M. S. 829, 832, 835, 1039
 Dekkers, E. 2892
 de Lamare, J. 1318
 Delaunay, M. 2997
 Delayen, J. R. 288, 838, 1715, 3666
 Delchamps, S. W. 2769
 Delcourt, B. 2513
 Delhez, J. L. 1820, 2062, 2065, 3423
 Delikaris, D. 2739
 Dell, G. F. 171
 Delmere, C. 2492
 Delsart, P. 670, 697
 de Mascureau, J. 670, 697, 2115
 de Menezes, D. 858
 Demmel, E. 1178
 Demos, P. T. 829, 832
 Demroff, H. 2711
 Demroff, H. P. 2705, 2708
 Demsky, M. I. 682
 Deng, D. P. 1172
 Denney, P. 1154, 1669
 Denney, P. M. 1232, 2391
 Depaola, F. 1013
 Derenchuk, V. 29, 224, 227, 420, 3184
 de Rijk, G. 1937, 2001
 Deruyter, H. 543, 620, 907, 986, 1121
 Derwent, P. F. 2199
 De Salvo, L. 1524
 Desforges, B. 2001
 Despe, O. D. 1864
 Destler, W. W. 685
 Devin, A. 670, 697, 2115
 Devred, A. 2769
 deVries, G. J. 3169
 Dewa, H. 1697
 Dey, J. 405, 1223
 Diamond, W. T. 1381
 Dickey, C. 1339
 Didelez, J. P. 3093
 Didenko, A. A. 2022
 Dienel, S. 1477
 Dikansky, N. 3243
 Dikansky, N. S. 2022, 3684
 DiMarco, J. 2769
 DiMarco, J. N. 1021
 Di Massa, G. 2154
 Dinkel, J. 1357
 Dinova, K. 1620
 Diviaco, B. 1587, 1590, 1593
 Dmitrieva, I. 2769
 Do, S. H. 3196
 Dobeck, N. 587
 Doble, N. 1363
 Doi, M. 1783, 1786

Dolinsky, A. V. 3822
 Dolique, J.-M. 3567
 Dombek, T. 2731, 2757, 2763
 Dombrowski, R. 2459
 Donahue, J. 369
 Donald, M. 131
 Dong, W. W. 1448
 Dooling, J. 1709
 Doolittle, L. R. 748
 Doose, C. 2802, 2805
 Doose, C. L. 2799
 Dorfman, J. M. 2010
 Dortwegt, R. 3857
 Douglas, D. 587, 1895
 Douglas, D. R. 584, 2929
 Dovbnya, A. 1480
 Dow, K. 2054, 2868
 Dow, K. A. 2935, 2938, 2941
 Dowell, D. 2967
 Dreher, K. 2748
 Drew, M. M. 2705
 Drobot, A. 3267
 Drozhdin, A. I. 1360, 3109, 3772
 Drury, M. 841
 Ducar, R. 2199
 Dugan, G. F. 3717
 Dunbar, A. 1166
 Dunn, A. 2199
 Dunnam, C. R. 578, 2394
 Dutt, S. 29, 224, 227, 267, 420, 3609
 Dutto, G. 2991
 Duval, M. 1789
 Dvornikov, V. A. 844
 Dwinell, R. 3748
 Dwyer, S. 2760
 D'Yachkov, M. 3330
 Dykes, D. M. 3594, 3672
 Dylla, H. F. 748, 3867
 Dymnikov, A. 206, 3618
 Dyshkant, A. 454

E

Early, R. 620, 2025
 Early, R. A. 2880
 East, G. 29, 224, 227, 420
 Eaton, L. 1154
 Eaton, L. E. 2391
 Ebihara, K. 673
 Eden, J. R. 3485
 Edwards, D. A. 134
 Edwards, H. 918
 Edwards, H. T. 537
 Efimov, S. 300, 1480, 2057
 Egan-Krieger, G. V. 1887
 Ehrlich, R. 995
 Ehrnstén, K. 1735
 Eickhoff, H. 357, 1645, 1738
 Eidelman, Y. 450
 Einfeld, D. 149, 152, 1477
 Eisen, N. 2076, 2352
 Ekdahl, C. A. 2400
 Elayi, A. 3093
 Elia, R. 2172
 Elkins, J. 1160
 Elkonin, B. V. 849

Elliot, T. S. 2705
 Elliott, T. S. 2708, 2711
 Ellis, S. 1718
 Ellison, J. 423
 Ellison, J. A. 387, 3588
 Ellison, M. 29, 224, 227, 420
 Ellison, M. J. 3536
 Ellison, T. 29, 224, 420, 3745
 Ellison, T. J. P. 2243, 2289, 3536
 Elmgren, K. 1771
 Elsener, K. 1363
 Emery, L. 2266, 3360
 Emma, P. 116, 429, 635, 2019, 2160
 Emma, P. J. 98, 100
 Emoto, T. 546
 Endo, K. 1291
 Enegren, T. 846, 877, 941, 1703
 Enge, H. 2868
 Engels, O. 3139
 Engström, A. 1735
 Enomoto, A. 546, 590, 2516, 3087, 3705
 Eppley, K. 1106
 Eppley, K. R. 1190
 Erdman, K. 1733
 Erdt, W. K. 2956
 Erg, G. 1384
 Erickson, J. 1669
 Esarey, E. 2626, 2629, 2632
 Esin, S. 2426
 ESRF Project Team 1427
 Evans, D. 3127
 Evans, K., Jr. 188, 2263, 2275
 Evans, L. R. 1983
 Everett, M. 2551, 3003
 Evstigneev, A. 1384
 Eyharts, P. 670, 697
 Eyl, P. 670, 697
 Eylon, S. 703, 706, 709, 712, 3199

F

Fabbricatore, P. 1001
 Fabris, A. 953, 956, 1145
 Fabris, R. 1333, 1378
 Facco, A. 849
 Faehl, R. 2675
 Faehl, R. J. 2664
 Fahmie, M. 1869
 Faillon, G. 1184
 Fainberg, Y. B. 2620
 Faltens, A. 703, 721, 724
 Fan, J. Y. 1943
 Fan, M. 306, 1721, 2841
 Fang, J. 2578
 Fant, K. 543, 1106
 Fant, K. S. 620
 Farias, R. H. A. 1089
 Farkas, Z. D. 620, 1121, 1196, 1208
 Farkhondeh, M. 1372, 2054, 2868, 2935, 2938, 2941
 Fasanello, T. 2397
 Fathizadeh, M. 1288
 Faugier, A. 2001

Faure, J. 1465
 Faus-Golfe, A. 2045
 Fawley, W. M. 724, 1530
 Fazio, M. 2675
 Fazio, M. V. 2664
 Fedele, R. 209, 212
 Fedorov, V. 2769
 Fedotov, Y. S. 315, 318
 Feinberg, B. 2187, 3748, 3751
 Felker, B. 1551, 1554
 Fenstermacher, M. 1551
 Fenstermacher, M. E. 1554
 Ferguson, M. 1294
 Ferguson, S. W. 1551, 1554
 Ferioli, G. 2498, 2504
 Fero, M. 2172
 Ferrario, M. 573, 968, 3279
 Ferry, J. 3745
 Feschenko, A. 2426
 Fessenden, T. 703
 Ficklin, D. 1318
 Fieguth, T. 3084
 Fields, S. 1551
 Fields, W. F. 1554
 Filimonov, M. Z. 2208
 Filtz, M. 901, 1036
 Fink, C. L. 375
 Finley, D. A. 3721, 3806
 Fiorito, R. B. 1620, 2397, 2453
 Firebaugh, J. 1817, 1912
 Firjahn-Andersch, A. 3139
 Fischer, C. 2504, 3597
 Fischer, G. E. 44
 Fischer, J. 2929
 Fischer, R. 2632
 Fischer, W. 246, 2301
 Fisher, A. 2632
 Fisher, A. S. 2578
 Fishler, Y. 1297
 Fitzgerald, D. 366, 369, 2216, 2219, 3297
 Fitzgerald, D. H. 3739
 Flannigan, J. 1852
 Flanz, J. 2868, 2871, 2874, 3851
 Flanz, J. B. 1875, 2054, 2331
 Fleck, R. 1080
 Flora, R. 1914
 Flynn, T. 889
 Foelsche, H. W. 2895
 Foerster, C. 3836, 3876
 Foley, M. 852, 3294
 Fomin, M. 1226
 Fong, B. 1483
 Fong, K. 1139
 Fontana, J. R. 2614
 Force, R. 3748
 Forest, E. 131, 291
 Fortgang, C. M. 2480, 3118
 Fouaidy, M. 855
 Fougerson, C. 858
 Fowkes, R. 1106
 Fowkes, W. R. 620, 1259
 Fowler, W. 3793, 3796
 Fowler, W. B. 2823
 Fox, J. 2352
 Fox, J. D. 2076, 2109
 Fox, W. 995, 1712
 Fraivillig, J. 2790
 Franck, A. 2249, 2835

Franczak, B. 1645, 3736
 Frandsen, P. 2956
 Frandsen, P. K. 2739
 Frankle, S. 366, 369, 2216, 2219, 3297
 Franzke, B. 357, 1645, 1738
 Frias, R. 3748
 Friddell, K. 2967
 Friedman, A. 105, 703, 727, 730, 1599, 2284
 Friedrichs, C. 803, 824
 Friesel, D. 29, 224, 227, 420, 3184
 Frisch, J. 3045, 3047
 Frisch, J. C. 2978, 3027, 3036
 Frischholz, H. 1247, 2358
 Fritsche, C. T. 2501
 Fu, S. 1686
 Fugitt, J. 939, 1109
 Fuja, R. 605
 Fujita, H. 1697
 Fujita, Y. 2260
 Fukuda, S. 1193
 Fuller, R. 543
 Fullett, K. D. 3309
 Funakoshi, Y. 3497
 Funk, L. W. 812, 1700, 1706, 2130
 Funk, W. 1703, 1765, 3585
 Furman, M. A. 3485
 Furukawa, K. 2516, 3087, 3705
 Fuzesy, R. 2172

G

Gabella, W. 420, 2051, 2638
 Gabella, W. E. 233
 Gagliardi, P. 1063
 Gai, W. 2596, 3050
 Gallardo, J. C. 2578, 3012, 3081, 3615
 Gallo, A. 778
 Galloway, C. 620
 Galluccio, F. 209, 2154
 Galyaev, N. A. 454
 Gammel, G. 3193
 Ganetis, G. 2744, 2766
 Gannon, J. 1898, 2731, 2757, 3870
 Gao, J. 862, 865, 868
 Gao, S. 745, 3521, 3696
 Garavaglia, T. 3591, 3609, 3769
 Garber, M. 2744, 2766
 Gardelle, J. 626
 Garden, C. 3033
 Garden, C. L. 2978, 3027, 3036, 3039
 Gardner, C. 3633, 3763
 Gardner, M. 1439
 Gareyte, J. 246
 Garnett, R. 1712
 Garoby, R. 3570
 Garren, A. 2051, 3778
 Garren, A. A. 137
 Gath, B. 1572
 Gatignon, L. 1363
 Gattu, R. 2760

Gavrilov, N. 1226
 Gayet, P. 2956
 Geisik, C. 3172
 Gelbart, W. Z. 3099
 Gelfand, N. 2835
 Gelfand, N. M. 3790
 Geller, J. 1277
 Gemme, G. 775, 1001, 1524
 Genesio, F. 806
 Genin, R. D. 3018
 George, M. J. 661
 Georges, P. 3053
 Gerasimov, A. 3276, 3291
 Gerig, R. 267, 3558
 Gerig, R. E. 333
 Geschonke, G. 2358
 Gevchuk, A. 1480
 Ghosh, A. 2744, 2766
 Ghosh, A. K. 2742, 2790
 Giacuzzo, F. 3842
 Giannini, M. 1378
 Giardino, G. 3202
 Gierman, S. M. 2970
 Giguët, E. 2656
 Gilgenbach, R. M. 2693, 3351, 3354
 Gillespie, G. H. 86
 Gillier, R. 3900
 Gilpatrick, J. D. 1669, 2163, 2316, 2334, 2480
 Giovannozzi, M. 246, 273, 500
 Giove, D. 1524
 Girard, M. 2997
 Gjaja, I. 3387
 Gladkikh, P. 1480, 2057
 Gladkikh, P. I. 194
 Gläser, W. 1477
 Glass, H. D. 351, 2829, 2856, 2859
 Glenn, J. W. 3633, 3763
 Glock, H.-W. 614, 623
 Gluckstern, R. L. 221, 1545, 3219, 3387, 3390
 Godden, D. 1709
 Goderre, G. 354, 3482
 Godfrey, G. 3084
 Godwin, R. P. 3090
 Goetz, T. 1477, 2534
 Golceff, P. 3018
 Gold, S. 1318
 Gold, S. H. 2644, 2647
 Goldberg, D. A. 871, 874
 Goldin, L. 1771
 Goldman, M. 1166
 Goldman, M. A. 2916, 2919
 Goldstein, J. C. 3090
 Golubeva, N. 441, 444
 Gonçalves da Silva, C. E. T. 252, 390, 1454
 Gonczy, I. 2769
 Gonichon, J. 2575, 2696, 2699
 Gonzalez, R. E. 2322
 Goodwin, J. E. 2835
 Goren, Y. 824, 846, 877, 880, 883, 1703, 3405, 3888
 Gormley, M. 1127
 Gorniker, E. 1226
 Gould, H. 3751
 Gourber, J.-P. 68
 Gourlay, S. 2769
 Govil, I. M. 1753
 Gower, E. 1244
 Graber, J. 886, 889, 892, 918
 Grafström, P. 1363
 Granatstein, V. I. 2572
 Granatstein, V. L. 2667, 2670, 2673
 Gras, J. J. 2495, 2504
 Grau, M. C. 2328
 Gray, E. 1021
 Green, K. 998
 Greene, A. 2744, 2766
 Greenwald, Z. 3690
 Gregory, W. 3055
 Greiner, P. 798
 Greiser, M. 1747
 Grelick, A. 605, 2412
 Grenier, J. 626
 Gribov, I. V. 2059
 Griffin, J. 405
 Griffin, J. E. 408
 Grigor'ev, Y. 2057
 Grimm, T. 824, 1083
 Grimm, T. L. 3252
 Grippe, J. 827, 1250, 3213
 Grippe, J. M. 1169
 Grishanov, B. I. 2022
 Grossberg, P. 2106
 Grote, D. 703, 709
 Grote, D. P. 727
 Groupe d'Etudes des Cavités Supraconductrices 796
 Groves, T. 2249
 Grüneberg, H. 2748
 Grua, P. 670, 697
 Gruber, A. 1645
 Grudzien, D. M. 2213
 Grun, J. 2632
 Grusell, E. 1771
 Guharay, S. K. 3145, 3648
 Guidee, P. 1184, 1187
 Guidi, V. 3243
 Guigli, J. 1238
 Guignard, G. 3336, 3426, 3600
 Guirlet, R. 2450
 Guk, I. 2057
 Gulley, M. 369
 Gundersen, M. 3039, 3072, 3537
 Gundersen, M. A. 3066
 Günther, C. 3381
 Guo, Z. Y. 3237
 Gupta, R. 258, 2744, 2766
 Gupta, R. C. 2754, 2778
 Guratzsch, H. 1477
 Gurd, D. P. 1916
 Güsewell, D. 2956
 Gutscher, W. D. 1154
 Guy, F. 1703, 2986, 3585
 Guy, F. W. 122, 2124, 2127, 2426, 2483, 3130

H

Haber, I. 724, 727, 730, 3612, 3627, 3660
 Haberichter, W. 2462
 Habs, D. 1747
 Haebel, E. 806, 898
 Haenni, D. 2757
 Hafizi, B. 1560, 1623, 2584, 2644, 2647
 Hage-Ali, M. 1363
 Hagedoorn, H. L. 1072, 2062, 2065, 2892, 2927, 3423, 3645
 Hahn, A. 2193
 Hahn, K. 3285
 Hahn, R. v. 1747
 Hairapetian, G. 561, 2976, 3003, 3216, 3543
 Halbach, K. 1445, 1581, 1599, 1608, 1727
 Halbleib, J. A. 691
 Halka, M. 369
 Hall, J. 32, 1244
 Hall, T. 2865
 Halling, A. M. 472, 474, 2193
 Halling, H. 1253
 Halling, M. 3814
 Halliwell, J. 3748
 Hamilton, B. 29, 224, 227, 420, 3745
 Hamilton, B. J. 2243, 2289, 3536
 Hamm, C. 962
 Han, H. S. 2796
 Hanaki, H. 590, 1163, 3087
 Hancock, S. 3570
 Hanft, R. 2769
 Hanna, B. 354, 1357
 Hanna, S. 1419
 Hanna, S. M. 895, 1118
 Hansberry, E. 1154
 Hansen, S. 1229
 Hanson, D. L. 694
 Haraguchi, M. 1518
 Hardek, T. 2319, 3297
 Hardek, T. W. 2240
 Hardekopf, R. A. 3760
 Harding, D. J. 2823, 2826, 2829
 Harfoush, F. A. 342, 345, 348, 351, 2829
 Harkay, K. 3258
 Harkay, K. C. 3306
 Harkewicz, R. 1694
 Harmer, P. 1916
 Harms, E. 3533
 Harms, E., Jr. 3803
 Harris, K. 1318
 Hart, R. 1901
 Hartley, R. 1527
 Hartman, S. 575, 2976, 3003, 3357, 3543
 Hartman, S. C. 561, 3216
 Hartmann, B. 1477
 Hartog, P. D. 1709
 Hartung, W. 898, 921, 3450
 Haseroth, H. 2720
 Hashimoto, Y. 1780, 1783
 Hassenzahl, W. 1572
 Hassenzahl, W. V. 1575, 1584
 Hatton, V. 2001
 Hattori, T. 1783, 1786, 3115
 Haug, F. 2739

Hauviller, C. 3854
Hawkins, S. A. 739
Haworth, M. 1703, 2124, 2986
Hayashi, S. 2039
Hayes, T. 1241
Haynes, W. 2675
Hays, T. 3450
Hayward, T. D. 1075
Hayworth, M. D. 846
He, A. 2775
Hebert, J. 2986, 3151
Hébert, J. E. 2483
Heefner, J. 1838
Heese, R. 608
Heifets, S. 543, 3456, 3459
Heifets, S. A. 3462
Heinrichs, H. 995
Hellborg, R. 206, 3618
Heller, H. 2892
Helm, R. 92, 131, 185
Helser, A. 1399
Hemmer, F. M. 2919
Hendrickson, L. 1972, 2106
Hendry, G. O. 1730
Henestroza, E. 703, 709, 3199
Henke, H. 549, 901, 904, 1133, 2593, 3288
Henrichsen, K. 44
Henriot, C. 798
Herr, S. 2187
Herrlander, C. J. 1735
Herrup, D. 2199
Herrup, D. A. 2249
Herz, P. R. 3190
Hettel, R. 2275
Heuer, R. 1439, 2420
Heuer, R. L. 1527, 3012
Hewett, D. 703
Hewett, D. W. 706, 718
Heydari, H. 411
Hicks, J. 3184
Higgins, C. S. 2298
Higo, T. 1027, 3503
Hildreth, M. 2019
Hilke, J. 1735
Hill, B. W. 86, 1762
Hill, J. 1154
Hill, N. 3050
Hill, S. F. 3594, 3672
Hiller, M. 921
Hilleret, N. 806
Himmel, T. 1972, 1975, 2019, 2106, 2373
Himeno, Y. 546
Hindi, H. 2076, 2352
Hinkson, J. 2097, 2109
Hipple, R. 703
Hiramatsu, S. 673
Hiramoto, K. 309
Hirano, K. 546
Hirao, Y. 1291, 1686
Hirata, K. 466, 3491
Hirota, J. 309
Hirshfield, J. L. 2584
Hitz, D. 2997
Ho, C. 1844, 2596, 3050
Hoag, H. 543, 1106
Hoag, H. A. 620, 907, 1121
Hochadel, B. 1747

Hodgson, J. A. 1039
Hoeberling, R. F. 2664
HoeHN, M. 3739
Hoffberg, M. G. 1957
Hoffstätter, G. H. 164
Hofler, A. 587, 1895
Hofler, A. S. 2298
Hofman, J. M. A. 3423
Hofmann, A. 44, 173, 3429
Hogan, B. 2667, 2670
Hogan, M. 3494
Hogrefe, R. 2799, 2802, 2805
Holdener, F. 3836
Holmes, S. 3793
Holt, J. A. 80, 3806
Holtzapfle, R. 638
Holtzapfle, R. L. 3234, 3564
Honabarger, D. 3055
Honabarger, D. J. 2944
Honma, H. 1416
Hooper, E. B. 1551, 1554
Horan, D. 1294, 3757
Hori, T. 602
Hori, Y. 3903
Horton, T. E. 1413
Hou, Y. 2841
Houck, T. L. 2590, 2611
Hourany, E. 3093
Hovater, C. 587, 3515
Hovater, J. C. 2364
Howard, D. 1160, 3748
Howell, J. 1497, 1500
Hower, N. 2889
Hoyer, E. 1572, 1575, 1581, 1584, 2850
Hoyt, E. 3033
Hoyt, E. W. 2978, 3036, 3039
Hs, I. C. 2465
Hseuh, H. C. 3897
Hsieh, H. 611, 3906
Hsu, I. 2151, 2638
Hsu, K. T. 2031, 2091
Hsu, T. 3066, 3072
Hsue, C. S. 1943, 3369
Hu, K. H. 2091
Hu, Y. 2841
Huang, H. 29, 224, 227, 420, 432
Huang, T. H. 2465
Huang, Y. 3558
Hughes, E. 2172
Hughes, E. A. 3594, 3672
Hughes, T. 3055
Hughes, T. P. 661
Hui, M. 1160
Hui, Z. 1557
Hulsey, G. 803, 824, 877, 1083
Hulsey, S. 1551
Hulsey, S. D. 1554
Hülsmann, P. 614, 623
Humphrey, R. 543
Humphries, D. 1572, 1575, 1581
Humphries, S. J., Jr. 1199
Hunt, D. 3748
Hunt, S. 128, 1823, 1826, 1829, 1838
Hunter, T. 393
Hur, J. 1327
Hurd, J. 1703, 2986, 3127, 3509

Hurd, J. W. 122, 2124, 2127, 2130, 2426, 2444, 3130, 3585
Hurh, P. 2148, 2459, 3533
Husmann, D. 152
Hutcheon, R. M. 829, 832
Hutson, R. 363, 366, 369, 2216, 2219, 3297
Hutton, A. 527
Hwang, C. 1393
Hwang, G. J. 2886
Hyodo, K. 1468

I

Ieiri, T. 2292, 2295, 3333
Igarashi, Z. 1163
Ihloff, E. 2054, 2331, 2868, 2871, 2874, 3851
Iida, T. 1515
Ikegami, M. 1697
Ikezawa, M. 1614, 1617
Iliev, A. 3784
Imanishi, A. 1783
Ingalls, W. 3118
Ingalls, W. B. 1669
Ingold, G. 1439, 1602
Inoue, M. 1697
Irwin, J. 92, 95, 116, 119, 131, 185
Ishi, K. 1614, 1617
Ishida, T. 2540
Ishimaru, H. 3885
Ishizuka, H. 676, 1566
Ishkhanov, B. S. 2059
Itano, A. 1291, 1686
Ivanov, A. S. 555
Ivanov, P. M. 2022
Ivanov, S. 3561
Ivers, J. D. 1312, 2687
Iwashita, Y. 1697, 3154
Izawa, M. 930

J

Jach, C. 1297
Jachim, S. P. 1154, 1232, 2391
Jackson, A. 1432
Jackson, G. 402, 1366, 2148, 2418, 2525, 3021, 3363, 3366, 3533
Jackson, G. P. 3799
Jackson, J. W. 2883
Jackson, L. T. 1265
Jackson, M. C. 1554
Jacobs, K. 3851
Jacobs, K. D. 1875, 2054, 2331
Jacobsen, R. 44
Jacquet, F. 2450
Jaenker, P. 1019
Jaeschke, E. 1474, 1747
Jaffery, T. S. 2769
Jahnel, L. 390
Jain, A. 2744, 2766
Jain, A. K. 2754, 2778
Jakob, H. 2301

Jameson, R. 1683
 Jameson, R. A. 3926
 Jamieson, G. 1703, 2118, 2127
 Jan, G. J. 1878, 2091
 Janssen, D. 1477
 Jason, A. 1683
 Jason, A. J. 56, 3760
 Jean, P. 3093
 Jeanjean, J. 2513
 Jeansson, J. 1735
 Jejic, A. 3093
 Jenner, D. 1421
 Jensen, C. 1357
 Jensen, D. R. 2838
 Jensen, K. 1300
 Jerng, D. 3757
 Jia, H. 2841
 Jiang, B. 1327, 3078
 Jiang, S. 3390
 Jiao, C. 2841
 Jiao, J. 2841
 Jin, J. T. 3196
 Jobe, R. K. 2234, 2423
 Joh, K. 71, 89
 Johnson, A. 939
 Johnson, A. M. 1220
 Johnson, C. D. 626
 Johnson, D. 236, 378
 Johnson, J. 2109
 Johnson, K. F. 1669, 3118
 Johnson, P. 2967
 Johnson, R. P. 1451, 1949
 Johnson, R. R. 3099
 Johnstone, C. 1912
 Johnstone, J. 342
 Jones, A. 2118
 Jones, C. M. 1660
 Jones, R. M. 936
 Jones, T. A. 3063
 Jones, W. P. 29, 224, 227, 420
 Jonker, M. 2001
 Joshi, C. 561, 2551, 2976, 3003, 3216, 3543
 Jost, W. 998
 Jostlein, H. 2835
 Joubert, A. 1789, 1792
 Jowett, J. M. 2013
 Joyce, G. 1560, 2626
 Judd, D. 703
 Judkins, J. 3240
 Judkins, J. G. 1039
 Juillard, C. 3429
 Juillard, J. C. 2358
 Julian, J. 1238
 Junck, K. 3540
 Jung, J. 3654
 Jung, K.-S. 3196
 Jung, R. 2202, 2495, 2498, 2504
 Junk, T. 2172
 Junquera, T. 855
 Juras, R. C. 1660
 Jurgens, T. 852

K

Kadnikov, A. 564, 1348
 Kadokura, E. 2540

Kahana, E. 1814, 2112, 2237, 2304
 Kahn, S. 2744
 Kahn, S. A. 2754, 2766
 Kaiser, H. 944
 Kakigi, S. 1697
 Kakihara, K. 3087
 Kako, E. 992, 1024
 Kalbfleisch, C. 1823, 1826, 1829
 Kalbreier, W. 2013
 Källberg, A. 1735
 Kalnins, J. 3748
 Kalichev, D. 2042
 Kamada, S. 1468
 Kamikubota, N. 3087
 Kamitani, T. 590, 2516, 3087, 3705
 Kamiya, Y. 930, 1509, 2260, 2295, 2337
 Kanai, T. 1614, 1617
 Kanazawa, K. 3860
 Kanazawa, M. 1291, 1686
 Kang, B. K. 2751, 2796
 Kang, H. 1521
 Kang, Y. G. 1268
 Kang, Y. W. 549, 766, 910, 913, 1057
 Kapchinskiy, I. M. 1675
 Kapustin, A. A. 3822
 Karabekov, I. P. 457
 Karas', V. I. 664, 2620, 3546
 Karl, F. X. 2919
 Karlner, M. 824
 Karnaukhov, I. 1480, 2057
 Kasha, D. 1166
 Kashihi, V. S. 3822
 Kasproicz, T. B. 2708
 Kasuga, T. 2409
 Katalev, V. 916
 Katayama, T. 41, 1783, 1786
 Katkov, V. M. 3093
 Kato, R. 1614, 1617
 Kato, S. 3518
 Kato, T. 1291
 Kato, Y. 2556
 Katsouleas, T. 2635, 2638, 3543
 Katsura, T. 2257, 2260, 2295, 2337, 2409
 Kauffman, S. 267
 Kauffmann, K. 3609
 Kauffmann, S. 2489
 Kauffmann, S. K. 137, 197
 Kauppila, T. 3055
 Kawakubo, T. 2540, 2556, 3552
 Kawamura, M. 1163
 Kawamura, Y. 3006
 Kawasaki, S. 676, 1566
 Kawazu, S. 3115
 Kazacha, V. 2042
 Kazarezov, I. 2650
 Kazarinov, N. 2042
 Kazimi, R. 599, 939, 1109
 Kazmark, D., Jr. 2219
 Keane, J. 608, 1118, 1419, 1852
 Keating, P. 369
 Keeney, D. S. 706
 Kehne, D. 62, 65, 3282, 3627
 Keller, F. 2811
 Keller, R. 2910

Kelley, E. 279C
 Kellogg, N. 1160
 Kelly, E. 2744
 Kennedy, W. L. 838, 1042
 Kerns, C. 1214
 Kerns, Q. 1127, 1214
 Kersevan, R. 3842, 3848, 3888
 Kerslick, G. S. 1312, 2687
 Kersteins, D. 1669
 Kewisch, J. 1835, 1895
 Kheifets, S. 543, 635
 Kheifets, S. A. 3462
 Kick, R. 233
 Kiehlmann, D. 1080
 Kijima, Y. 1518
 Killian, E. 2744
 Kim, C. H. 2036
 Kim, D. E. 2751, 2796
 Kim, G. H. 2564
 Kim, J. 2593
 Kim, J. M. S. 1112
 Kim, J. S. 3288
 Kim, K. 2799, 2802, 2805, 2808, 2814
 Kim, K.-J. 83, 1445, 1533, 3042
 Kim, S. H. 2799, 2802, 2805, 2808, 2814
 Kim, W. 3196
 Kimura, T. 2690
 Kimura, W. D. 2564, 2581, 2614
 Kimura, Y. 673
 Kincaid, B. 1572, 1575, 1578, 1581
 King, R. 2172
 Kinross-Wright, J. 2664
 Kinross-Wright, J. M. 2970
 Kinsho, M. 3181
 Kipper, A. 3139
 Kirbie, H. C. 739
 Kirby, R. E. 2978, 3030, 3036
 Kirchgessner, J. 763, 769, 886, 889, 892, 918, 921, 977, 995, 1399, 2953, 3450
 Kirchman, J. 2266
 Kirk, H. G. 3012, 3615
 Kirkman, G. 1327, 3066, 3072, 3078
 Kirsch, R. 3093
 Kiselev, V. A. 2022
 Kishimoto, T. 1515, 1518
 Kishiro, J. 673
 Kitagawa, A. 1291
 Kitagawa, S. 1686
 Kitagawa, Y. 2556
 Klaisner, L. 3033
 Klaisner, L. A. 2978, 3027, 3036
 Klamp, L. 3384
 Kleb, R. 3757
 Kleeven, W. J. G. M. 1072, 2065, 3423
 Kneffner, C. M. 1747
 Klein, H. 614, 623
 Kleman, K. J. 924, 1235
 Klepper, O. 1645
 Kloeppel, P. K. 2298
 Kneisel, P. 927, 947, 1010, 1016, 1060, 3867
 Knobloch, J. 889
 Knott, J. 2720

Lee, S. Y. 6, 29, 102, 224, 227, 420, 432, 435, 2865, 3291
 Lee, T. 841, 1106, 1457, 3273
 Lee, T. G. 1259
 Lee, Y. Y. 360, 3633
 Leemans, W. 83, 567, 2638
 Lefrancois, M. 3900
 Legg, R. 587
 Lehrman, I. 1439
 Lehrman, I. S. 1527, 3012
 Leibfritz, J. 3864
 Leifeste, G. T. 2124, 2130, 2426
 Lemaitre, E. 798
 Lenisa, P. 3243
 Lenkszus, F. 1960, 2304
 Lenkszus, F. R. 1814
 Lennox, A. J. 1666, 1756
 Lenz, J. 2986, 3133
 Lenz, J. W. 3151
 Leonhardt, W. J. 3882
 Leonov, V. V. 1795
 Leontein, S. 1735
 Lepeltier, V. 2513
 Leroy, R. 1789, 1792
 Lessner, E. 1485, 3757
 Lessner, E. S. 399
 Le Taillandier, P. 670, 697
 Leung, K. 3888
 Leung, K. K. 1503, 2787
 Leung, K. N. 1727, 3169, 3190
 Leung, K.-N. 3042, 3160
 Level, M. P. 1465
 Levichev, E. 230, 564, 1384, 1506, 2793
 Levin, M. 2757
 Levitt, S. 1969
 Levy, C. D. P. 2991
 Lewis, S. 3748
 Lewitowicz, M. 1792
 LHC Machine Group 3917
 Li, C. Y. 1727
 Li, D. 29, 224, 227, 420, 1439, 2865, 3006
 Li, G. X. 3237
 Li, M. 38, 236
 Li, N. 2862
 Li, Q. 1620
 Li, R. 1909, 3473
 Li, T. 2841
 Li, X. 3527
 Li, Z. 179, 1721
 Liang, C. 2841
 Liang, C. F. 1792
 Liang, D. 3696
 Lidbjörk, P. 2068
 Liebmann, J. 1747
 Lien, E. 1106
 Liger, P. 3663
 Likhachev, V. 1480, 2057
 Liljeby, L. 1735
 Lima, S. 1892
 Limberg, T. 429, 2019, 2025, 2435, 3240
 Lin, K. K. 2031
 Lin, L. 252
 Lin, L. C.-L. 2575, 2696, 2699
 Lin, X. 3453
 Lindner, A. 1160
 Lindner, A. F. 2210

Linnecar, T. P. R. 2376
 Linnemann, J. 1477
 Linscott, I. 2076, 2352
 Liou, R. 2638, 3039, 3066, 3072, 3537
 Lipkin, I. M. 1675
 Lipnicky, M. 1151
 Lippmann, G. 944
 Lipsett, M. G. 1039
 Liska, D. 1718
 Littmann, B. 1133
 Litvinenko, V. N. 218, 1442, 2889
 Liu, B. 1611
 Liu, C. J. 688
 Liu, H. 279, 512, 1563, 3663
 Liu, H. C. 2886
 Liu, J. 182, 285, 2841
 Liu, K. 1262
 Liu, Y. 2151
 Liu, Y. C. 1635
 Liu, Z. 2070
 Lo, C. C. 1142, 1238, 3058
 Lobanov, N. R. 3187
 Lockner, T. R. 667
 Loew, G. 1445, 3084
 Loew, G. A. 543, 620, 644
 Logachov, P. 3243
 Loiselet, M. 1672
 Lom, C. 821, 2133
 Lombardi, A. 3121, 3606
 Lopez, F. 2922, 2924
 López, G. 200, 2784, 3255, 3467
 Lorello, M. 1709
 Lorenz, R. 1133, 2325
 Losito, R. 2154
 Low, K. 1823, 1826, 1829
 Lu, J. 2711
 Lu, J. J. 1303
 Lu, X. 3366, 3799
 Lu, X. P. 472
 Lublinsky, B. 1817, 2249
 Luccio, A. 438, 1872, 2175
 Luchini, K. 1265
 Ludewigt, B. A. 1759
 Ludmirsky, E. A. 315
 Ludwig, P. 2997
 Ludwig, T. 3139
 Luginsland, J. W. 3354
 Luijckx, G. 1998
 Lujan, R. 2947
 Lukasiewicz, J. 1890
 Lulevich, V. I. 2853
 Lumpkin, A. 2304
 Lumpkin, A. H. 2086, 2112
 Luo, G. 1211
 Lütkehaus, H. 2748
 Lutz, I. 1265
 Lyashchenko, V. 1480
 Lynch, D. 1439, 3000
 Lynch, M. T. 1683, 2391
 Lyons, S. 608, 611
 Lysenko, A. 3711
 Lysenko, W. P. 1669

M

Ma, Y. 1611

Maas, R. 1901, 1998
 Macek, R. 363, 366, 369, 2216, 2219, 2319, 3297
 Macek, R. J. 3739
 Macek, R. W. 3760
 Macha, K. 2929
 Machida, S. 176, 255, 3224, 3558
 Maciga, B. 3243
 Maciszewski, W. 1890
 Mackenzie, G. H. 372
 Mackenzie, R. 1966
 MacKenzie, R. 1969
 Mackerrow, E. 369
 MacLachlan, J. 405
 Maddocks, J. 3879, 3888, 3891
 Madduri, V. B. 2711
 Madey, J. M. J. 218, 1442, 2889
 Madlung, J. 3139
 Maeda, H. 676
 Magyaray, S. 1811
 Mahale, N. 423, 3769
 Mahale, N. K. 877
 Mahoney, K. L. 2298
 Maier, K. 3093
 Maillard, J. 3093
 Main, W. 2714
 Maisheev, V. A. 315, 322
 Majima, T. 1321
 Makarov, A. A. 3822
 Makarov, I. 2650
 Mako, F. M. 2702
 Makowski, M. 1551
 Makowski, M. A. 1554
 Makulkin, A. V. 3702
 Malitsky, N. 128
 Malone, R. 2486
 Malyshev, O. 3876
 Mammosser, J. 781, 947, 1016, 2929
 Manarin, A. 2492
 Manca, J. 608, 611, 1244
 Mane, V. 3435, 3438
 Mangino, J. 2382
 Manheimer, W. M. 2644, 2647
 Manini, P. 3839
 Mankofsky, A. 3267
 Mann, J. 2498, 2504
 Mao, N. 333
 Mapes, M. 3882, 3897
 Mariam, F. G. 384
 Marin, M. 1063
 Marin, P. 1465
 Marino, M. 3839
 Markov, V. 1480, 2057
 Marks, N. 2898
 Marks, S. 1572, 1575, 1578, 1581
 Marneris, I. 1277
 Maroli, C. 1524
 Marquardt, J. 3118
 Marquardt, N. 1471
 Marrufo, O. 827, 1169, 3213
 Marsden, E. 3127, 3213
 Marsden, S. 827
 Marsh, K. A. 558, 2551
 Marsh, W. 1912
 Marshall, J. 841, 1396
 Martens, M. 405
 Martens, M. A. 1963, 3300
 Martin, D. 1703, 2118, 3888

Knott, M. 1960
 Knowles, H. B. 1762
 Knox, A. 3757
 Knox-Seith, J. F. 255
 Ko, I. 581, 1521, 3654
 Ko, I. S. 593
 Ko, K. 936, 986, 1039, 1121
 Kobari, T. 3903
 Kobayashi, H. 3087
 Kobayashi, M. 3903
 Kobayashi, T. 3552
 Kobayashi, Y. 215, 1321
 Kobliska, G. R. 2823
 Kocur, P. 236, 1369
 Kodaira, M. 1515, 1518
 Kodama, R. 2556
 Koehlin, F. 798
 Koepke, K. 918, 1127
 Kohno, T. 1291, 1686
 Koiso, H. 3497
 Kokorin, A. M. 3822
 Kolomiets, A. A. 1675
 Kondakov, A. 1226
 Konecny, R. 815, 2596
 Kong, S. H. 2970
 Kononenko, S. 1480, 2057
 Koo, Y. M. 2751, 2796
 Koontz, R. 543, 620
 Koontz, R. F. 1318
 Koop, I. 3711
 Koopman, J. 2504
 Korchuganov, V. 230, 564, 1384, 2793
 Korenev, I. L. 2543
 Koscielniak, S. R. 3506, 3639
 Koseki, S. 1291
 Koseki, T. 930, 1509, 2295
 Koshelkin, A. V. 1629, 1632
 Kostas, C. 3267, 3270
 Kosyakin, M. 2769
 Kot, N. C. 3243
 Kotov, V. I. 454
 Koujbida, R. P. 2853
 Koul, R. 2922
 Koul, R. K. 2924
 Kourbanis, I. 35, 405, 3630, 3799
 Koutchouk, J. P. 44, 68
 Kovachev, V. 3888
 Kowalski, S. 2054
 Kowitt, M. 2172
 Kozchekin, M. A. 2853
 Kozin, V. 1480, 2057
 Kozub, S. 2769
 Kozyrev, E. 2650
 Krafft, G. A. 426, 587, 599, 1895, 2298, 2364, 3246, 3515
 Kraimer, M. 1960
 Krall, J. 2626, 2629, 2632
 Krämer, D. 1436, 1474
 Krasnopolsky, V. 2717
 Krasnopolsky, V. A. 933
 Krasnykh, A. 552, 2042
 Kraus, R. 1669, 1703
 Kraushaar, P. 2731, 2757, 2763, 3888
 Krauter, K. 1922
 Krawczyk, F. 1712
 Krebs, G. 2187
 Kreiser, H. 32

Krejcik, P. 2019, 2370, 2373, 3240
 Kreutz, R. 2748
 Krinsky, S. 492, 1439, 1491, 1545, 1599, 1602, 1852, 3375
 Krishnaswamy, J. 1527
 Kroc, T. K. 1689
 Kroes, F. 1998, 2343
 Krogh, M. 2124, 2130
 Krogh, M. L. 2501
 Kroll, N. 620, 936, 1039, 1121, 2559
 Kroll, N. M. 543, 983, 1196, 3453
 Kropachev, G. N. 3675
 Krueger, W. 1004, 3267
 Krug, H. 1477
 Krupnick, J. 83, 2850
 Krycuk, A. 939, 1109
 Krylov, Y. 564
 Kryshkin, V. I. 454
 Kuang, E. 2687
 Kubo, H. 1291
 Kubo, K. 992, 1027, 2364, 3503, 3515
 Kubo, T. 1163
 Kubota, C. 1163
 Kuchnir, M. 918
 Kudelainen, V. 3243
 Kudelainen, V. I. 2022
 Kudo, H. 1509
 Kudo, K. 1163
 Kudryavtsev, V. 916
 Kukhtin, V. P. 3205
 Kulikov, A. V. 2978, 3027, 3036
 Kulinski, S. 336, 573, 611, 968
 Kulipanov, G. 564, 1384
 Kulipanov, G. N. 2751
 Kumada, M. 1291, 1686
 Kumazawa, R. 2205
 Kunkel, W. B. 1727
 Kuo, C. C. 1635, 1943
 Kuo, C. H. 2091
 Kuo, T. 372
 Kuo, T. T. Y. 1730
 Kuprianov, A. P. 682
 Kuptsov, I. 1226
 Kuramoto, R. 1300
 Kurennoy, S. S. 3417, 3420
 Kurkin, G. 1226
 Kurochkin, I. A. 2190
 Kuroda, S. 2340
 Kurokawa, S. 294, 2004, 2073
 Kurz, M. 614, 623
 Kusche, K. P. 2564
 Kushin, V. V. 1798
 Kushnick, P. 1016
 Kuske, B. 1474
 Kuske, P. 1474
 Kustom, R. 285, 549, 1013, 1057, 1294, 3757
 Kustom, R. L. 766, 910, 913, 1217, 2213, 3393, 3396
 Kuzmin, I. A. 844
 Kuznetsov, G. 2650
 Kuznetsov, N. A. 2022
 Kuznetsov, S. 564, 1506, 1955
 Kvashonkin, I. 2042
 Kwan, C. M. 2385
 Kwan, J. W. 3169

Kwan, T. 2675
 Kwiatkowski, S. 824, 941
 Kwok, P. 2638
 Kwon, S. 1832
 Kwon, S.-I. 3042

L

Labrousche, J. 670, 697
 Lackey, J. 2228
 Lackey, S. 1912, 1914
 Laclare, J. L. 1427
 Lahey, T. 1969
 Lai, P. 2638
 Laird, R. J. 1814
 Lal, A. 2551
 Lamanna, G. 3243
 Lambert, G. 2376
 Lambertson, G. 1039
 Lambertson, G. R. 2109
 Lamm, M. J. 2769
 Lamont, M. 1937, 2001
 Lampel, M. 3009
 Lamzin, E. A. 3205
 Lancaster, C. 2967
 Landis, R. 2222
 Langdon, A. B. 730, 733, 3660
 Lange, F. 3864
 Langenbeck, B. 3736
 Langenbrunner, J. 1021
 Lanni, C. 3876
 Lanz, P. 1151
 Lapitsky, S. N. 2190
 Lapostolle, P. 3606
 Larsen, R. 2070
 Larsson, B. 1771
 Laslett, L. J. 724
 Lasnier, C. J. 1551, 1554
 Lath, A. 2172
 Latham, P. E. 2659, 2661, 2670, 2673
 Latushkin, S. T. 1795
 Lau, Y. Y. 3351, 3354
 Launspach, J. 670
 Launspach, J. 697
 Lavery, M. 1139
 Lavine, T. 543
 Lavine, T. L. 620, 1121, 1196, 1208
 Lawson, W. 2667, 2670
 Lawson-Chroco, L. 44
 Laxdal, R. E. 372
 Lazarev, N. V. 1675
 Lebedev, V. A. 2022, 3243
 Leblond, B. 3053
 Le Diberder, F. 2513
 Le Duff, J. 2045
 Lee, B. 2705, 2708, 2711
 Lee, E. P. 3678
 Lee, H. 581
 Lee, H. K. 2796
 Lee, H. S. 593
 Lee, J. C. 1943
 Lee, M. 173, 1483
 Lee, M. J. 108
 Lee, M. K. E. 2667, 2670

- Martin, K. 1914
 Martin, P. 3793
 Martin, R. 2913
 Martini, M. 3570, 3699
 Maruyama, T. 2172
 Maruyama, X. K. 1620, 2397
 Marziali, A. 950
 Mashiko, K. 602
 Maslennikov, I. 3876
 Massarotti, A. 953, 956, 1145
 Masuda, H. 1780, 1783
 Masullo, M. R. 2154
 Masunov, E. S. 1681, 2474
 Mathae, J. C. 2432
 Matheisen, A. 918
 Mathewson, A. G. 3828
 Mathieson, D. 1823, 1826, 1829
 Matsumoto, H. 959, 1124
 Matsumoto, S. 1291, 3491
 Matsuoka, M. 1024
 Matthews, H. W. 2667
 Matuk, C. 83
 Matumoto, M. 3903
 Matveev, Y. 1348, 1384
 Matz, W. 1477
 Mavrogenes, G. 549, 605
 May, R. 2184
 Mayoud, M. 44
 Mazarakis, M. G. 667
 Mazumdar, T. K. 2705, 2708, 2711
 Mazur, P. 2769
 Mazur, P. O. 2856
 McAllister, B. 2054
 McAllister, B. G. 1875
 McAshan, M. 2757
 McCammon, D. 1421
 McCauley, G. 1718
 McCormack, F. 2187
 McCormick, D. 1975, 2160, 2423
 McCrory, E. S. 1691, 1952
 McDonald, D. S. 3190
 McDowell, C. 2477
 McDowell, W. 1960
 McGhee, D. 1864, 3757
 McGhee, D. G. 1271, 2817
 McGill, J. 378, 381, 384
 McGill, J. A. 333
 McGinnis, D. 35, 2100, 2228, 2231, 2361, 3533, 3787
 McGinnis, K. 2124, 2130
 McInturff, A. 2731, 2763
 McInturff, A. D. 2757
 McIntyre, P. M. 2705, 2708, 2711
 McKenzie-Wilson, R. 1172
 McMahan, M. A. 2187
 McMichael, G. E. 1175
 McMurry, D. 1669
 McNeerney, A. 1166
 McNeerney, A. J. 1241
 McPherson, J. 32
 Meads, P. F., Jr. 3825
 Meddahi, M. 1488, 3312
 Medvedko, A. 1297
 Meigs, M. J. 1660
 Meinke, R. 203, 2468, 2489
 Meisner, K. 405, 2519, 2522, 2525
 Meitzler, C. R. 3148
 Melin, G. 2997
 Meller, R. E. 578
 Mellors, W. 1039
 Melnychuk, S. 3193
 Melton, J. G. 2944
 Mendelsohn, S. L. 1774
 Menegat, A. 543, 620, 1121, 1196, 1208
 Meng, W. 2883, 2904, 2907
 Menge, P. R. 2693, 3351
 Menninger, W. L. 2656
 Men'schikov, L. 552
 Mercier, E. 3202
 Merl, R. 2799, 2802, 2805
 Merle, E. 670, 697, 2115
 Merminga, L. 599, 2184, 2364, 3515
 Merz, W. 1841, 1898
 Meshcherov, R. 2717
 Mestha, L. K. 2382, 2385
 Meth, M. 1166, 1241, 2286
 Metty, P. 1244
 Metzger, D. 918, 995, 1399, 3450
 Meuth, H. 962, 1253, 3381
 Meyer, D. 3888
 Meyer, F. 1841, 1898
 Meyer, R. 1703
 Meyer, R. E. 2334, 2480
 Meyer, W. 1551
 Meyer, W. H. 1554
 Meyerhof, W. E. 3751
 Meyerhofer, D. D. 2638
 Mezentsev, N. A. 1494, 2751
 Michelotti, L. 80, 495
 Michizono, S. 1193
 Micklich, B. J. 1715
 Miele, G. 209, 212
 Miertusova, J. 3842, 3873
 Migdal, W. 1890
 Mihelic, R. 3888
 Milburn, J. E. 2796
 Miles, J. 44, 2001
 Militsin, B. L. 2022
 Militsyn, B. 3711
 Miller, E. 1972
 Miller, J. 3612
 Miller, R. 608, 608, 611, 611, 3084
 Miller, R. H. 543, 620, 3027, 3063
 Miller, W. 369
 Millich, A. 965, 3426
 Milliman, L. 2967
 Millo, D. 1587
 Mills, F. 285, 549, 3757
 Mills, F. E. 2817, 2922, 2924
 Mills, M. R. 2322
 Mills, R. S. 3657
 Millsom, D. 1966
 Milstead, I. 2301
 Milton, B. 1733
 Mimashi, T. 2340
 Miné, P. 2450
 Ministrini, M. 573, 968
 Minty, M. 224, 227, 447, 2019, 2370, 2373, 2435, 3240
 Minty, M. G. 29, 420
 Miram, G. 1106
 Mironov, V. 2042
 Mirzozan, A. 2426
 Mishin, A. V. 971
 Mishnev, S. I. 2022
 Mishra, C. S. 342, 345, 348, 351, 2829
 Mitchel, G. R. 2415
 Mitra, A. K. 974, 1303
 Mitsuhashi, T. 215
 Mitsui, H. 2205
 Miura, A. 959, 1124
 Miura, I. 1650
 Miwa, H. 1024
 Miyahara, Y. 653
 Mizuno, A. 602
 Mizuno, H. 1202, 1321
 Mocheshnikov, N. 1480, 2057
 Mock, R. C. 691
 Modéer, J. 2034
 Moe, H. 3757
 Moe, H. J. 2213
 Moerel, J. 2892
 Moffat, D. 763, 769, 886, 889, 892, 918, 921, 977, 995, 3450
 Moffeit, K. 2172
 Moiseev, V. A. 3249
 Mokhov, N. V. 1360, 1369, 3090, 3109, 3772
 Moller, J. 1551
 Moller, J. M. 1554
 Møller, S. P. 1363, 1741
 Molodkin, V. 1480
 Momose, T. 3885
 Mondelli, A. 1004, 3267, 3270
 Montès, B. 2450
 Montuclard, J. 3900
 Morales, G. 3888, 3891
 Morales, H. 3018
 Morano, R. 2450
 Moravec, K. 3864
 Morcombe, P. 1339
 Morduev, A. 1672
 Moretti, A. 1127, 1214
 Morgan, G. 2744, 2766
 Morgan, G. H. 2754
 Morgillo, A. 2744, 2766
 Mori, W. B. 2635
 Mori, Y. 2991, 3181, 3754
 Morillo, J. 2450
 Morishita, O. 1686
 Moritz, G. 3736
 Morpurgo, G. 2103
 Morse, W. 2070
 Mortazavi, P. 1419
 Morton, P. 1445
 Moshhammer, H. 131, 2025
 Moskalenko, V. 1480, 2057
 Mosnier, A. 629, 855
 Mottershead, C. T. 1669
 Mourou, G. 2632
 Moz, S. 1063
 Mroczkowski, T. T. 2919
 Mudiugin, B. 2042
 Mud'ugin, B. G. 3822
 Mukugi, K. 1515, 1518
 Mulholland, G. 2757
 Muller, H. 889, 918, 995, 2953
 Müller, R. 1887
 Munson, F. H. 1694
 Murakami, T. 1291, 1686

Muratore, J. 2744, 2766
 Murin, B. P. 980
 Murphy, J. B. 1477
 Murphy, K. 2967
 Murray, D. 1838, 2757
 Murray, J. 1274, 1855, 1858, 1861
 Musenich, R. 1001
 Mustaine, R. E. 1033
 Myae, E. A. 318, 322
 Mynk, J. 1250
 Mytsykov, A. 1480, 2057
 Myznikov, K. 2769

N

Nadji, A. 1465
 Nagaenko, M. 2057
 Nagafuchi, T. 2039
 Nagaitsev, S. 29, 224, 227, 420, 3524, 3745
 Nagaitsev, S. S. 3536
 Nah, Y. G. 2796
 Nakagawa, S. 1468
 Nakahara, Y. 1566
 Nakajima, K. 2556, 2638, 3552
 Nakajima, S. 676
 Nakamura, H. 2260
 Nakamura, K. 3537
 Nakamura, N. 2257, 2295, 2337
 Nakamura, T. 3464
 Nakanishi, H. 2556, 2638, 3552
 Nakao, K. 1193
 Nakayama, H. 2340
 Nakazato, T. 1614, 1617
 Nam, S. 581
 Nam, S. H. 593, 1315
 Namkung, W. 581, 593, 1315, 1521
 Nantista, C. 543, 620, 983, 1196
 Napoly, O. 632, 3347
 Nassiri, A. 605, 2142, 2412
 Nation, J. A. 1312, 2653, 2684, 2687
 Natter, E. F. 1154, 2391
 Nawrocki, G. J. 1957
 Nawrocky, R. 2246
 Nawrocky, R. J. 2145
 Nazmov, V. 3876
 Neil, G. 279, 3663
 Neil, G. R. 1563
 Nelson, E. M. 983, 1086
 Nelson, J. 1916
 Nelson, W. R. 185
 Nemoshkalenko, V. 1480
 Neri, F. 56
 Nesterenko, I. 3711
 Nesterov, N. A. 1798
 Nett, D. 611
 Neuffer, D. 2136, 3297, 3663
 Neumann, W. 1477
 Neuschaefer, G. 1683
 Newberger, B. S. 387, 3588
 Newman, W. 2133
 Newton, M. A. 739
 Nexsen, W. 2468, 2489
 Nezhevenko, O. 564, 2650
 Ng, C. K. 986, 1039, 2638, 3432

Ng, K. Y. 29, 35, 102, 224, 227, 405, 420, 3300, 3630
 Ng, L. S. B. 1949
 Ng, Y. 2133
 Nguyen, D. C. 2970
 Nguyen, T. K. 2997
 Nguyen-Tuong, V. 1007
 Nick, W. 2748
 Nicol, T. 3021
 Nicol, T. H. 989
 Nielsen, R. 3757
 Nightingale, M. P. S. 1777
 Niki, K. 1780, 1783, 1786
 Nikiforov, A. 2650
 Nilsson, A. 1735
 Nilsson, B. 1771
 Ninan, L. 599
 Nishi, M. 309
 Nishida, Y. 2556, 2638, 3552
 Nishimura, H. 111
 Noda, A. 41, 1291, 1697
 Noda, K. 1291, 1686
 Nodarse, F. F. 1892
 Noguchi, S. 992, 1024
 Nolden, F. 1645, 1738
 Nolen, J. A. 71, 89, 1694
 Nomura, M. 546
 Noomen, J. 1998
 Noomen, J. G. 2343
 Nordberg, E. 995
 Norem, J. 2462, 2638
 Nortier, F. 3099
 Nosochkov, Y. 125, 143, 239, 3778
 Novak, J. 1021
 Novak, W. 2462
 Nuhn, H.-D. 173, 1445, 1608
 Nurushev, S. B. 315
 Nusinovich, G. S. 2572, 2659, 2661, 2673
 Nyman, M. 3748

O

Oasa, K. 1554
 Obert, J. 1792
 Obina, T. 2409
 Ochsner, J. 2790
 O'Connell, J. S. 3657
 O'Day, S. 330, 2459, 3096
 Oeftiger, U. 2157
 Oehme, W. 1477
 Oganessian, R. 1672
 Ogata, A. 2556, 2638, 3552
 Ogawa, H. 1291, 1686
 Ogawa, Y. 2516, 3087, 3705
 Ogitsu, T. 2769
 Ogiwara, N. 1566
 Ogloblin, A. A. 1795
 Ogren, H. 2172
 Ogura, K. 2714
 Oguri, Y. 3115
 Oh, J. S. 593, 1315
 Ohkuma, H. 1509
 Ohmori, C. 3297
 Ohnuma, S. 3148, 3603
 Ohsawa, S. 2516, 3087, 3705

Ohsawa, Y. 2205
 Oide, K. 466, 2340, 3339
 Oikawa, Y. 3845
 Okamoto, H. 221, 1545, 1697, 3390
 Okamura, M. 3115
 Okay, N. 2986, 3151
 Okay, N. C. 2483, 3133
 Oku, Y. 1468
 Okuda, S. 650
 Olchowski, F. 32
 Oldfather, D. E. 2210
 Oliphant, V. 1706
 Olivier, R. 44
 Olivo, M. 3190
 Ollis, C. W. 739
 Olsen, D. K. 1660
 Olsen, R. 44, 1274, 1855, 1858, 1861
 Olson, R. E. 667
 Onel, Y. 32
 Onillon, E. 2379
 Onischenko, L. 2042
 Onischenko, L. M. 518
 Ono, M. 546, 1024, 1163
 Oogoe, T. 3087
 Oothoudt, M. A. 3106
 Oren, W. 2929
 Orlov, Y. 3488
 Orr, N. 1792
 Orris, D. 2769
 Orthel, J. L. 1762
 Orzechowski, J. 3099
 Oshita, H. 546
 Osipov, V. 3876
 Ostiguy, J. 2901
 Ostiguy, J.-F. 2829
 Ostreiko, G. 564
 O'Sullivan, M. 1925
 Otis, A. 1241
 Otter, A. J. 2898
 Ovchinnikov, V. P. 555
 Owens, T. L. 1689, 1691
 Oxoby, G. 2076, 2352
 Oyamada, M. 1614, 1617
 Ozaki, T. 673, 2205

P

Paál, A. 1735
 Padamsee, H. 763, 769, 886, 889, 892, 918, 921, 977, 995, 998, 1399, 3450
 Page, T. 2459
 Page, W. 2222
 Palkovic, J. A. 21, 3261
 Palmer, D. 620
 Palumbo, L. 212, 778
 Pan, C. 44
 Pang, Y. 2705, 2708, 2711
 Papash, A. 372
 Papash, A. I. 3822
 Pappas, G. C. 1336
 Papureanu, S. 962, 1747
 Pardo, R. C. 1694
 Paris, P. 1792
 Parish, D. J. 2790

Parisi, G. 3121, 3124
 Park, K. H. 2796
 Park, S. 561, 570, 2976, 3003, 3216
 Park, S. S. 593, 1315
 Parker, B. 1360, 3772, 3775
 Parkhomchuk, V. V. 2022, 2959
 Parodi, R. 775, 778, 1001, 1524
 Parry, R. 2222
 Parry, R. R. 2225
 Parsa, Z. 509, 2723
 Parshin, I. O. 1798, 3675
 Parzen, G. 483, 486, 489
 Pasotti, C. 953, 956, 1145
 Pasquinelli, R. 3533
 Pasquinelli, R. J. 2081, 2355, 2361
 Passardi, G. 2739
 Paterson, A. 2850
 Paterson, J. 1445
 Paterson, J. M. 543
 Patteri, P. 573
 Patterson, D. 2112
 Paulson, C. C. 1774
 Pauluhn, A. 270
 Pavlov, S. N. 3822
 Pawlak, T. 3793
 Paxson, V. 1940
 Payet, J. 1465
 Payne, A. N. 736
 Payne, J. 3870
 Pearce, W. J. 1949
 Pearson, C. 543, 907, 1106, 1259
 Pearson, C. C. 620
 Pedersen, F. 2370, 3240
 Peggs, S. 35, 168, 233, 258, 261, 351
 Peggs, S. G. 74
 Pei, X. 29, 224, 227, 420, 1421, 1424
 Peiniger, M. 1080
 Pekeler, M. 918
 Pellegrini, C. 173, 561, 570, 575, 1445, 1533, 1608, 2617, 2976, 3003, 3216
 Pelligrini, C. 3543
 Pendleton, R. P. 1039
 Penner, S. 381
 Penzo, A. 32
 Perelstein, E. 2042
 Perevedentsev, E. 3429, 3711
 Perkins, L. T. 3190
 Perregrini, L. 772
 Perret, R. 2202
 Perry, J. 587, 1925, 2184
 Persov, B. 2650
 Peschardt, E. 1903, 2358, 3429
 Peschel, H. 2748
 Pestrikov, D. 294
 Pestrikov, D. V. 3681, 3684, 3687
 Peter, W. 2702
 Peters, C. 703
 Petersen, D. 1551, 3836
 Petersen, D. E. 1554
 Peterson, D. 809, 3533
 Peterson, D. W. 3573
 Peterson, E. 2400
 Peterson, J. 203, 2281, 3769, 3781
 Peterson, T. 809

Petillo, J. 1004, 3267
 Petradza, M. 2172
 Petrov, E. 2042
 Petrov, S. 1297
 Petrov, V. 824, 1226
 Petrov, V. M. 877, 941
 Petrucci, G. 2820
 Pettersson, O. 1771
 Pewitt, E. G. 2823
 Peyromaure, J. 858
 Pfeffer, H. 918
 Philipchenko, A. 564, 1384, 2793
 Phillips, H. L. 1007
 Phillips, R. 543, 1106
 Phinney, N. 116, 2019
 Pianetta, P. 1445, 1536
 Picard, M. 1477, 2534
 Pickens, D. R. 1448
 Pierini, P. 1524, 1569
 Piestrup, M. A. 1620, 2397
 Pikin, A. 1735
 Pilat, F. 143, 203, 239, 515
 Pile, G. 1709, 3210
 Pimiskern, K. 944
 Pindyurin, V. 3876
 Pinkow, J. 357
 Piovela, N. 1524
 Pipersky, P. 1572
 Pirkel, W. 1172, 1241
 Pirozhenko, V. M. 3112
 Pisent, A. 32
 Pistoresi, D. 2967
 Pitchford, L. 3039
 Pivarc, J. 3894
 Placidi, M. 44
 Plate, D. 1572, 1575
 Platt, R. C. 2456
 Plesea, L. 3133
 Plesko, M. 149, 152, 1477, 2534
 Plink, O. V. 3112
 Plotnikov, S. V. 1798
 Plotnikov, V. K. 1675
 Plouffe, D. 2736
 Ployard, G. 2115
 Plum, M. 366, 2181, 2319, 3297
 Pogorelsky, I. 2564, 2614
 Poilleux, P. 2450
 Poirier, R. L. 753
 Poizat, J. C. 3093
 Poliakova, R. V. 1892
 Poll, D. 3533
 Pollock, D. 2760
 Poloni, C. 1587
 Pontonnier, M. 2997
 Poole, M. W. 1494, 1638, 3594, 3672
 Popkov, Y. 1480, 2057
 Popov, A. 2042
 Popov, Y. 552
 Popovic, M. B. 1214, 1689, 1691
 Porro, M. 3839
 Porter, J. 2133, 2420
 Portmann, G. 1572, 2272
 Postiau, N. 1672
 Potter, J. 1004
 Potts, C. 3757
 Potukuchi, P. N. 1045
 Poukey, J. W. 667, 691, 694
 Power, J. 1669, 1844, 2596, 3061

Power, J. F. 2334
 Powers, T. 1007, 1010, 1016
 Pozdeev, E. 3711
 Pradal, F. 3842
 Preble, J. 841, 1396, 2929
 Preger, M. A. 2048
 Priest, D. H. 1103
 Prescott, C. 3033
 Prescott, C. Y. 2978, 3027, 3036
 Price, E. 587
 Price, R. R. 1448
 Primdahl, K. 766, 1013, 1294
 Pripstein, D. 2172
 Proch, D. 758
 Prodell, A. 2744, 2766
 Pröhl, D. 1477
 Propp, A. 824, 941
 Prosnitz, D. 1445
 Prusakov, V. 552
 Pruss, S. 2252
 Pruss, S. M. 3802
 Ptitsin, V. 3711
 Puech, V. 3039
 Pullia, M. 1524
 Pusterla, M. 32
 Putaux, J. C. 1792
 Puzo, P. 2513

Q

Qian, G. 745, 3521, 3696
 Qian, Q. 2670
 Qin, J. 3237
 Qin, Q. 3237
 Qiu, X. Z. 1439
 Quinn, P. D. 1638, 3594, 3672
 Qunell, D. 1357

R

Raabe, P. 1645
 Raffone, G. 2048, 3906
 Rahn, J. 1887
 Raimondi, P. 98, 100, 116, 2019
 Rajagopalan, S. 2638, 3555
 Rakowsky, G. 1605
 Ramamoorthy, S. 1849, 1852
 Ramaswamy, K. 685
 Rambaldi, S. 273
 Ramirez, G. 1419
 Ramseier, G. 44
 Ranganathan, R. 1402
 Rao, M. G. 927, 3867
 Raparia, D. 122, 1765, 2127, 2426, 2986, 3130, 3151, 3509, 3585
 Rathke, J. 1709
 Ratner, L. 432
 Ratti, A. 1166, 1172
 Raubenheimer, T. 417, 1445, 2019
 Raubenheimer, T. O. 11, 596, 635, 2025, 2880
 Rauchas, A. 3757
 Rawlins, A. 1727
 RD22 Collaboration 26

Reece, C. 1007, 1016
 Reece, R. K. 1277, 3763
 Reed, L. 2462
 Rees, D. 3213
 Rees, D. E. 1169, 1199, 1205
 Rees, G. 3297
 Rees, G. H. 3731
 Reeve, P. A. 2898
 Reeves, S. 2817
 Regan, A. 1683, 3213
 Regan, A. H. 1154, 2391
 Reginato, L. 703, 1351
 Reginato, L. L. 656
 Rehak, M. 2744, 2766
 Reich, H. 1645
 Reid, C. 809
 Reilly, R. 1357
 Reimund, J. A. 1280
 Reinhardt, N. 1327, 3078
 Reiniger, K. W. 1112, 1283
 Reiser, M. 62, 65, 685, 2667,
 2670, 3145, 3282, 3627, 3648,
 3660
 Reist, H. 1771
 Reistad, D. 1744, 3745
 Remelius, D. 2967
 Remillieux, J. 3093
 Remondino, V. 68
 Remy, M. A. 1089
 Rendon, A. M. 2480
 Renou, G. 3093
 Rensfelt, K.-G. 1735
 Repnow, R. 1747
 Reusch, M. F. 59, 1527, 3624
 Rhee, M. J. 688
 Ricaud, C. 1789
 Rice, D. 1978, 3479
 Rice, D. H. 2007
 Richardson, R. D. 2456, 3772
 Richter, R. 1160
 Richter-Sand, R. J. 1306
 Ride, S. K. 1623
 Riedel, C. 3736
 Rietdyk, H. 2397
 Rieubland, J.-M. 2739
 Rifkin, J. 543
 Rimmer, R. 1039
 Rimmer, R. A. 871, 874, 3411
 Rinckel, T. 32
 Ringwall, A. 1703
 Ringwall, A. D. 846
 Riordon, J. 2118
 Risselada, T. 246
 Ritchie, A. L. 2210
 Ritson, D. M. 125, 143, 3778
 Riunaud, J. P. 3570
 Rivkin, L. 3429
 Rivoltella, G. 1524
 Rizzi, V. 1145
 Robb, A. 1575
 Robb, J. 2929
 Robertson, S. 2641
 Robin, D. 131, 173
 Robins, K. 1439, 1602
 Robins, K. E. 2742
 Robinson, W. 2731, 2757, 2763
 Roche, C. T. 1715
 Ródenas, J. 647
 Rodenburg, R. 2967

Rodenz, G. 2664, 3267
 Rodger, E. 2895
 Rodgers, J. 685
 Rodrigues, A. R. D. 1454
 Rodriguez, J. P. 798
 Rodriguez, R. 827, 1250
 Roecklein, J. C. 2919
 Rogdestvensky, B. V. 3822
 Rogers, J. D. 1033, 1256
 Romero, A. 128
 Rondeau, G. 420
 Rönqvist, T. 1771
 Root, L. 372
 Ropert, A. 1512
 Roques, A. 670, 697
 Rose, C. 1669
 Rose, C. R. 2334
 Rose, J. 1172
 Rosengård, U. 1735
 Rosenthal, S. E. 694
 Rosenzweig, J. 233, 561, 1445,
 1548, 2623, 2638, 2976, 3024,
 3216, 3357, 3494
 Rosenzweig, J. B. 3021
 Roser, T. 2286, 3207, 3633, 3763
 Rosier, L. 3093
 Rosing, M. 815, 2596
 Ross, M. 522, 1975, 2019, 2234,
 2435
 Ross, M. C. 1972, 2160, 3564
 Rossa, E. 2432, 2492, 3429
 Rossi, C. 953, 956, 1145
 Rossi, L. 1524
 Rossmanith, R. 32, 429, 457, 1477
 Rostamzadeh, C. 1405
 Rotela, E. 1497
 Roth, G. 3072
 Rothman, J. L. 2307
 Rouaud, C. 3900
 Roux, D. 2932
 Rowson, P. 2172
 Roy, A. 1045
 Rubin, D. 921, 3450, 3479
 Rubingh, M. J. A. 1072
 Rudchik, A. T. 3822
 Rudd, H. 65
 Rudenko, V. 552
 Rudolph, K. 1019
 Ruggiero, A. G. 700, 3530
 Ruggiero, F. 503
 Ruiz, E. 3405
 Ruland, R. E. 2736, 2950
 Rule, D. W. 1620, 2397, 2453
 Rullier, J. L. 2656
 Ruschman, M. 809
 Rusnak, B. 1021
 Russell, S. J. 2537, 2970
 Russell, T. 605
 Russell, T. J. 1324
 Russo, D. 2286
 Rusthoi, D. P. 1669, 3118
 Ruth, R. D. 291, 543, 620, 907,
 1196, 3693
 Rutkowski, H. 703
 Rutkowski, H. L. 706
 Ryan, W. A. 2310, 2328
 Rybakov, E. 2769
 Rybalko, V. 2717
 Rychagov, A. 2769

Ryckewaert, G. 1672
 Ryder, R. 3739
 Ryne, R. 3267
 Ryne, R. D. 3229
 Ryu, C. 581
 Rzaev, R. A. 454
 Rzezonka, B. 2748

S

Saadatmand, K. 2124, 2127,
 2426, 2483, 2986, 3127, 3130,
 3133, 3145, 3151
 Sacepe, B. 697
 Sachtschale, R. J. 1339
 Saeki, H. 3885
 Sáez, P. 3033
 Sáez, P. J. 2978, 3027, 3036
 Safranek, J. 1491, 2275
 Sagalovsky, L. 288, 838, 1715
 Sagan, D. 53, 3470, 3479
 Sage, J. 1838, 2444, 2483, 3127
 Saint Laurent, M. G. 1792
 Saito, K. 673, 1024
 Saito, Y. 1193
 Sajaev, V. 230
 Sakamoto, K. 1566
 Sakamoto, S. 676, 1321
 Sakanaka, S. 1027, 3503
 Sakaue, H. A. 3845
 Sakawa, Y. 2556
 Saladin, V. 2763
 Sale, K. E. 1663
 Salimov, A. 3876
 Sampayan, S. E. 1554
 Sampson, W. 1439, 1602, 2744,
 2766
 Sampson, W. B. 2742, 2904
 Sandberg, J. 1277
 Sander, O. R. 1669, 3118
 Sanders, R. 1241
 Sanders, R. T. 1166
 Sandoval, D. P. 1669
 Sandweiss, J. 2578, 2617
 Sanford, T. W. L. 691
 Sannibale, F. 611
 Sapozhnikov, L. 2076, 2352
 Sapp, W. 1372, 2054
 Sapp, W. W. 2832, 2935, 2938,
 2941
 Saraniti, D. 921
 Saritepe, S. 354
 Sarkar, S. 1841, 1898, 1916, 1919
 Sasaki, Y. 2039
 Sass, R. 2106
 Sass, R. C. 1946
 Sathe, S. 1846, 1852
 Sato, H. 1291
 Sato, I. 546, 590, 1193, 1416,
 2516, 3087, 3705
 Sato, K. 1291, 1686
 Sato, Y. 1291, 1686
 Satogata, T. 261
 Satoh, K. 3115
 Sauer, L. 3863, 3864
 Saulter, Q. 841
 Saunders, C. 1864

- Saversky, A. J. 1030
 Savord, T. 1914, 2731, 2757
 Sawada, K. 1686
 Sawyer, D. 2838
 Sazhin, V. 2717
 Scala, R. G. 2519
 Scandale, W. 16, 246
 Schachinger, L. 1940
 Schachter, L. 1312
 Schächter, L. 2567, 2653, 2684, 2687
 Schaefer, J. 907
 Schäfer, P. 2748
 Schaffer, G. 1033, 1256
 Schailley, R. 236, 378, 1360, 1369
 Scharlemann, E. T. 1530, 1533, 1551
 Scharlemann, T. 1445
 Scheer, M. 1474
 Schegolev, L. 1384
 Schellekens, P. H. J. 2927
 Schempp, A. 3139, 3142
 Schimmel, F. 1901
 Schlenk, R. 1477
 Schlueter, R. 1572, 1575, 1581
 Schlueter, R. D. 1727
 Schmalzle, J. 2790
 Schmickler, H. 2001
 Schmid, J. 2739, 2956
 Schmidt, C. W. 1655, 1689, 1691
 Schmidt, F. 246, 500, 2301
 Schmidt, R. 44, 2103, 2133
 Schmitt, D. R. 3172
 Schmor, P. W. 2991
 Schmöser, P. 886, 918
 Schnase, A. 962, 1253, 3381
 Schneider, J. D. 1669, 3166, 3172
 Schneider, L. X. 1354
 Schneider, W. 841, 1396
 Schneider, W. J. 2929
 Schoessow, P. 1844, 2596, 3050
 Scholz, T. 1036
 Schriber, S. O. 3760
 Schukeilo, L. A. 3822
 Schultz, D. 3033
 Schultz, D. C. 2978, 3027, 3036, 3039
 Schultz, S. 2559
 Schumm, B. 2172
 Schürmann, M. 264
 Schwalm, D. 1747
 Schwandt, P. 3184, 3745
 Schwarz, H. D. 1039
 Schweppe, E.-G. 1178
 Schwettman, H. A. 950
 Schwitters, R. 3781
 Sciutto, W. 1063
 Sears, J. 763, 769, 886, 889, 892, 918, 921, 977, 995
 Sebek, J. 3018
 Sedlacek, M. 3745
 Sedlyarov, I. 1226
 Seeman, J. 1445, 1608, 2019
 Seeman, J. T. 414, 596, 638, 2423, 2507, 3234, 3564
 Segalov, Z. 685
 Seidl, P. 721
 Seifrid, P. 3533
 Seleznev, V. S. 2190
 Selin, A. V. 2853
 Sellyey, W. 2112, 2237, 2304
 Selph, F. 83
 Semertzidis, Y. 2070
 Sen, T. 134, 137, 140, 143, 146, 239, 3778
 Senichev, Y. 3509, 3642
 Seo, H. S. 2751
 Serafim, P. 1560
 Serafini, L. 3024, 3279
 Serdobintsev, G. 564, 2650
 Serebrennikov, D. 2042
 Sereno, N. S. 3246
 Sergeeva, O. S. 2853
 Serio, M. 778, 2076, 2352
 Servranckx, R. 236, 255
 Servranckx, R. V. 167, 3784
 Sessler, A. 2638
 Sessler, A. M. 1530, 2593, 2608, 3288, 3527
 Sethi, R. 1703
 Settles, M. 2172
 Severgin, Y. 2057, 2769
 Severgin, Y. P. 2208, 3205, 3820, 3822
 Shafer, B. E. 1285
 Shafer, R. E. 2316
 Shaimerdenov, E. 564
 Shako, V. V. 2406
 Shalz, L. 3748
 Shan, J. 405
 Shan, J. P. 35, 74, 3787
 Shan'gin, V. 2769
 Shankland, L. W. 1175
 Shapiro, G. 2172
 Sharma, S. 1497, 1500
 Sharp, W. M. 733, 2593
 Shatunov, Y. 3711
 Shchedrin, I. S. 1030
 Shcherbakov, A. 1480, 2057
 She, K. 995
 Shea, T. 3438
 Shea, T. J. 2310, 2328, 2916
 Sheedy, E. 3012
 Sheehan, J. 1439, 1439, 1527, 3000
 Sheffield, R. L. 2970
 Sheikh, J. Y. 1175
 Shen, J. 2178, 2438
 Sheng, I. C. 1497, 1500
 Shepard, K. W. 1042, 1045, 1694
 Shephard, W. 821
 Sherman, J. D. 3166
 Sherwin, G. 1881
 Sheynin, S. 393
 Shi, J. 242, 243, 3603
 Shibata, H. 3552
 Shibata, Y. 1614, 1617
 Shidara, T. 590, 1416
 Shih, H.-J. 387, 3588
 Shiho, M. 676, 1566
 Shiltsev, V. D. 2959
 Shinoe, K. 1509, 2295, 2337
 Shintake, T. 1048, 1051
 Shiraga, H. 2556
 Shirai, T. 1697
 Shishido, T. 992, 1024
 Shiwaku, H. 1468
 Shoaee, H. 1946, 2106
 Shofstall, D. 2967
 Shoji, T. 2556
 Shoji, Y. 3633, 3763
 Shpak, A. 1480
 Shrader, M. B. 1103
 Shtirbu, S. 1934
 Shu, Q. S. 921, 2787
 Shu, Q.-S. 3888, 3891
 Shutt, R. 2744
 Shvedunov, V. I. 1069, 2059
 Shvets, G. 2635
 Sibley, C. 1372, 2054, 2868
 Siddons, D. P. 2145
 Siemann, R. 2019, 2370
 Siemann, R. H. 532, 2373, 3240
 Siergiej, D. 3482
 Sievers, W. 1916
 Siffert, P. 1363
 Sigov, Y. S. 2620
 Sikora, R. E. 2328, 2916
 Sillanoli, M. 2492
 Silva, J. 3093
 Sim, J. W. 2856
 Simmons, J. 3888
 Simpson, J. 815, 2596, 3050, 3061
 Simrock, S. 1925, 2184
 Simrock, S. N. 599, 1909, 2364, 3515
 Sims, R. E. 2769
 Sinclair, C. 3663
 Sinclair, C. K. 1109, 3246
 Singh, O. 2254, 2284
 Sissakian, A. 2042
 Skachkov, D. G. 3675
 Skachkov, V. S. 2853
 Skarpaas, K. 1039, 3030
 Sladen, J. P. H. 2346
 Sloan, T. 29, 224, 227, 420, 1421
 Sluijk, T. 2343
 Smellie, R. 2757, 2781
 Smirnov, Y. 2042
 Smith, B. H. 1175
 Smith, D. D. 2705, 2708, 2711
 Smith, D. L. 667
 Smith, D. R. 1075, 2559
 Smith, H. V., Jr. 3172
 Smith, J. 1852, 2222, 2284
 Smith, J. D. 1846, 1849
 Smith, J. R. 694
 Smith, K. S. 3178
 Smith, L. 3678
 Smith, M. 1669, 3118
 Smith, P. 1718, 2953
 Smith, S. L. 1494, 1638, 3594, 3672
 Smolucha, J. 1817, 1912
 Smolyakov, N. V. 1626
 Smythe, W. R. 1054
 Snee, D. 1013
 Snitchler, G. 3888
 Snyder, D. 1620
 Snydstrup, L. 3897
 So, I. 2275
 Sobczynski, S. 1372, 3851
 Sohn, Y. U. 2751
 Sokolov, S. V. 318, 320
 Sokolowski, J. S. 849
 Solensten, L. 2133

- Solheim, N. 2956
 Solomon, L. 1439, 1602, 1605
 Solomons, R. 3748
 Sommer, F. 2748
 Sommer, M. 1465
 Somov, L. 552
 Song, J. 1057, 2142
 Song, J. J. 2213, 3393, 3396
 Song, T. 2199
 Sortais, P. 1789, 1792
 Soukas, A. 1277, 3633
 Soukas, A. V. 1345
 Soundranayagam, R. 1360
 Spädtke, P. 1645, 1738
 Spalek, G. 1021
 Spanggaard, J. 2492
 Spata, M. 841
 Spataro, B. 611, 778
 Spataro, C. 2883
 Spayd, N. 880, 3405
 Specht, J. E. 1694
 Specht, V. 2670
 Specka, A. 2450
 Spence, W. 2019
 Spence, W. L. 3234, 3576
 Spencer, J. 543, 2025, 2638
 Spencer, J. E. 396
 Spencer, N. 1884, 1969, 1975
 Spencer, T. A. 2693
 Spinos, F. 2757
 Spitz, R. 1166, 1241
 Sprangle, P. 1560, 2584, 2629, 2632, 2647
 Sredniawski, J. 821, 2133, 3193
 Srinivasan-Rao, T. 3012
 Stagno, V. 775, 1524
 Stallard, B. 1551
 Stallard, B. W. 1554
 Stampke, S. 203, 2781
 Staples, J. W. 1759
 Stapleton, G. 2184
 Starker, J. 1735
 Starkovich, V. S. 1075
 Steck, M. 1645, 1738
 Steckmeyer, J. C. 1792
 Stefan, P. M. 895
 Stege, R. E., Jr. 2234
 Steimel, J. M., Jr. 2100, 2231
 Steinbach, C. 339
 Steiner, H. 2172
 Steinhauer, L. C. 2564, 2581, 2614
 Stelzer, J. E. 3172
 Stepanov, A. 2426
 Stepp, J. D. 1157, 1408, 1906
 Steski, D. B. 3178
 Stevens, J. 3357
 Stevens, R. R., Jr. 3166
 Stevenson, N. 1733
 Stevenson, N. R. 3099
 Stiening, R. 143, 239, 3778
 Stillman, A. 2471
 Stittsworth, D. 2124, 2130
 Stoker, J. 703
 Stover, G. 1351
 Strait, J. 2769
 Strakhovenko, V. M. 3093
 Strelkov, M. 1480, 2057
 Strelkov, M. A. 194
 Striffler, C. D. 2667, 2670, 3075
 Stringfield, R. 2675
 Stringfield, R. M. 2664
 Struckmeier, J. 1645
 Stuart, M. E. 1727
 Stucki, H. 339
 Stupakov, G. V. 197
 Su, G. 1411
 Su, J. J. 2638
 Subbotin, S. 552
 Sudou, M. 1291, 1686
 Suemine, S. 650
 Suenaga, M. 2904
 Sueno, T. 1291
 Suetsugu, Y. 3860
 Sugahara, R. 2340
 Suhring, S. 587
 Sulgin, I. 916
 Suller, V. P. 1494, 1638, 3594, 3672
 Sullivan, C. A. 2644
 Sullivan, M. 131
 Sulyaev, R. M. 454
 Summers, L. K. 1220
 Sun, D. 1127
 Sun, H. 3696
 Sun, N. 515
 Sun, T. 1411
 Sundelin, R. M. 1092
 Sundquist, M. 3745
 Surma, I. V. 2059
 Susta, J. 1060
 Suwada, T. 2516, 3087, 3705
 Suzuki, H. 2039
 Suzuki, K. 2556
 Suzuki, S. 602
 Suzuki, T. 1024
 Svandrik, M. 953, 956, 1145
 Svinin, M. P. 555
 Swartz, M. 2172
 Swenson, D. 1703
 Swenson, D. A. 812, 846, 2426
 Swenson, D. R. 3175
 Sychev, V. 2769
 Symon, K. 285
 Syphers, M. 29, 203, 224, 227
 Syphers, M. J. 38, 134, 137, 140, 146, 420, 3588
 Sytchevsky, S. E. 3205
 Sytnikov, V. 2769
 T
 Tacconi, E. J. 1098, 2139
 Tadokoro, M. 309
 Tagawa, S. 3552
 Tajima, T. 1024, 2556
 Takada, E. 1291, 1686
 Takada, Y. 1291
 Takahashi, N. 546
 Takahashi, S. 3845
 Takahashi, T. 1614, 1617
 Takaki, H. 1509
 Takamuku, S. 650
 Takasaki, E. 1163
 Takayama, K. 673, 2205
 Takeda, O. 3115
 Takeda, S. 1309
 Takeda, Y. 1783
 Takenaka, T. 1163
 Takeo, T. 2409
 Tallerico, P. 1683
 Tallerico, P. J. 1199
 Talman, R. 203, 236
 Tamezane, K. 602
 Tamura, K. 2409
 Tanabe, J. 2850
 Tanabe, T. 1291, 3006
 Tanabe, Y. 3115
 Tanaka, M. 360, 2907
 Tang, C. 1623
 Tang, H. 2978, 3027, 3033, 3036, 3039
 Tang, Y. 1852, 2275
 Tang, Y. N. 492, 1846
 Tanii, T. 2205
 Tantawi, S. 543, 936, 1106
 Tantawi, S. G. 620, 1121, 1130, 1196
 Tao, Q. 2841
 Taran, A. 2769
 Tarasenko, A. 1480, 2057
 Taratin, A. 2489
 Tarovik, M. N. 3822
 Tarrant, M. 1937
 Tatchyn, R. 1445, 1536, 1539, 1542, 1608, 2429
 Taylor, B. 1142, 1238
 Taylor, L. 824
 Tazzari, S. 573, 968
 Tazzioli, F. 573, 3279
 Tecchio, L. 3243
 Tecker, F. 2432, 3429
 Tekawa, M. 3748
 Telegin, Y. 1480, 2057
 Temkin, R. J. 2575, 2656, 2690, 2696
 Temnykh, A. B. 2007, 3476
 Tenenbaum, P. 2838
 Teng, L. 224, 285, 420, 1485
 Teng, L. C. 182
 Tepikian, S. 168, 420
 Terrien, J. C. 1187
 Terzi, F. 1063
 TESLA Collaboration 537
 Thern, R. E. 2471
 Thevenot, M. 670, 697
 Thiagarajan, V. 3372
 Thieberger, P. 3178
 Thielheim, K. O. 276
 Thiessen, H. 3297
 Thiessen, H. A. 1021, 3760
 Thivent, M. 339
 Thomas, M. G. 1419
 Thomas, P. 3053
 Thompson, K. 3757
 Thompson, K. A. 543, 3342, 3693
 Thompson, K. M. 2808, 2814
 Thompson, P. 2744, 2766
 Thompson, P. A. 2754
 Thorndahl, L. 1066, 3426
 Thuot, M. E. 1806
 Tidwell, S. C. 2564
 Tiefenback, M. 587
 Tiefenback, M. G. 426
 Tieger, D. 2054, 2871, 2874

Tieger, D. R. 2832, 2938
 Tighe, R. 2370, 2373
 Tigner, M. 769, 918, 921, 977,
 995, 3450, 3479, 3690, 3931
 Timmer, C. A. 2970
 Timmermans, C. J. 1072, 1820,
 2892, 2927, 3645
 Ting, A. 2629, 2632
 Titcomb, C. 2956
 Tiunov, A. V. 1069, 2059
 Tiunov, M. 2650
 Tkatchenko, A. 1465
 Tobiyama, M. 2409
 Todd, A. M. M. 1774, 1777
 Toge, N. 98, 100, 116, 3912
 Tojyo, E. 1783
 Tokuchi, A. 676
 Tokuda, N. 1783
 Tokumoto, S. 1202
 Toldo, F. 1241
 Tolstun, N. G. 555
 Tomassini, D. 1477
 Tomizawa, M. 41, 1780, 1783,
 1786
 Tomkins, J. C. 2769
 Tomlin, R. 2228, 3787
 Tommasini, D. 1375, 1378, 2820
 Tompkins, P. A. 1448
 Tooker, T. F. 1706
 Tool, G. 1405, 2731, 2757
 Tornoe, R. N. 1103
 Tosolini, P. 1333, 1378
 Towne, N. A. 2415
 Toyama, S. 546
 Toyoda, K. 3006
 Tran, H. J. 3402
 Tran, P. 173
 Tran-Ngoc, T. 829, 832, 1039
 Travier, S. 3053
 Travish, G. 561, 1445, 1533,
 1548, 3216
 Trbojevic, D. 102, 168
 Treas, P. 608, 611
 Tribendis, A. 977, 3450
 Tribouillard, C. 1792
 Trifonov, D. E. 682
 Tron, A. M. 2403, 2406
 Tronc, D. 1768
 Trost, H.-J. 2705, 2708, 2711
 Trotsenko, V. 1480
 Trotz, S. 2575, 2699
 Trzeciak, W. 285
 Tsai, H. J. 1943
 Tsang, K. T. 3270
 Tsarik, S. V. 454
 Tschalaer, C. 2054
 Tsiang, E. Y. 3621
 Tsoupas, N. 2895
 Tsuchidate, H. 1515
 Tsuchiya, M. 3845
 Tsumori, K. 650
 Tsyganov, E. 2468, 2489
 Tuckmantel, J. 806
 Tuli, M. 3888
 Tupa, D. 3175
 Turchetti, G. 273
 Turlington, L. 939, 1109
 Turner, J. L. 2978, 3027, 3036

Turner, L. R. 2799, 2808, 2814,
 2817
 Turner, W. 3876, 3888
 Turner, W. C. 3833
 Tyrroff, H. 1477
 Tyson, E. 2967

U

Ueda, A. 215
 Ueda, S. 3903
 Ueda, T. 3552
 Ueng, T. S. 2031
 Ueyama, Y. 2039
 Uggerhøj, E. 1363
 Uher, T. 2382
 Uhm, H. S. 2599, 2602, 2605,
 2678
 Ulc, S. 2578
 Umezawa, H. 1024
 Umstadter, D. 2632
 Underwood, K. 1884, 1969
 Unser, K. B. 2394
 Urano, T. 2516, 3705
 Urasawa, S. 1614, 1617
 Ushakov, V. 564, 1384
 Ushkov, V. 564
 Utino, K. 1291
 Utterback, J. 1928, 1931

V

Vaccarezza, C. 3906
 Vaccaro, V. 2154
 Vaidya, M. 1010
 Vakhrushin, Y. P. 682
 Valbuena, R. 2202
 Valicenti, R. A. 3133
 Val'kov, A. E. 3822
 van Asselt, W. 3633, 3763
 van den Berk, F. 1820
 van der Heide, J. A. 1072
 van der Laan, J. 1901, 1998
 van der Stok, P. D. V. 1820
 Vandeusen, A. 2124, 2130
 Van Deusen, A. L. 2121
 van de Vijver, Y. 1820
 van Dyck, O. 369
 Vanecek, D. 703
 van Garderen, G. 1901
 van Laar, J. 3645
 van Oers, W. T. H. 2991
 VanOlst, D. 1884
 van Steenbergen, A. 2578
 Van Straagen, P. K. 86
 Van Westrum, D. C. 1054
 van Zeijts, J. 587
 Variale, V. 775, 1524
 Varisco, G. 1524
 Vasil'ev, A. N. 315
 Vasiliev, A. 2717
 Vasserman, I. 3711
 Vaughn, G. 1669
 Vejcek, S. 2199
 Vella, M. C. 3157

Verdier, A. 158, 161, 249
 Verdú, G. 647
 Vergamini, A. 1205
 Vescovi, M. 611
 Veshcherevich, V. 977, 1226,
 3450
 Vetter, A. M. 1075
 Vignola, G. 611, 1993, 2048
 Villate, D. 670, 697, 2115
 Vinnik, V. 1297
 Vinokurov, N. A. 1442
 Viola, R. 2913
 Vishnevsky, I. N. 3822
 Visnjic, V. 3811, 3814
 Vliks, A. 543, 1106
 Vliks, A. E. 620, 1121, 1196,
 1208
 Vobly, P. D. 2751
 Vodopianov, F. A. 1078
 Vogel, H. 1080
 Volk, K. 3139
 Volzhev, A. A. 682
 Vong, F. C. 1906
 Vormann, H. 3139
 Vorobjov, I. A. 1675
 Voroshilov, A. N. 2022, 3669
 Vos, L. 2301
 Voss, D. 285
 Votaw, A. 2112
 Votaw, A. J. 1814
 Vouillot, J. M. 2495
 Vretenar, M. 3121
 Vulcan, W. 3103
 Vylet, V. 543, 1445

W

Wadlinger, E. A. 1669
 Wagner, W. 2838
 Wait, G. D. 1148, 1181, 1330,
 3402
 Wake, M. 2769
 Walend, D. 2953
 Walker, N. 2019
 Walker, N. J. 92, 95, 98, 100,
 116, 119
 Walker, R. P. 1587, 1593, 2844,
 2847
 Wallace, J. D. 1033, 1256
 Walling, L. 824, 877, 880, 1083,
 3405, 3888
 Walstrom, P. 1021
 Walter, M. 3351
 Walter, M. T. 2693
 Walz, D. 185
 Walz, H. V. 2838
 Wan, W. 155
 Wanderer, P. 2726, 2744, 2766
 Wang, C. 1575, 1578, 2608
 Wang, C. J. 1878
 Wang, D. 2013, 2331, 3429, 3851
 Wang, D. X. 62, 3282, 3627, 3660
 Wang, D. Y. 1451, 1949
 Wang, F. 378, 381, 1360
 Wang, J. G. 62, 3282, 3627, 3660
 Wang, J. M. 1419

Wang, J. W. 543, 620, 907, 1086, 1208
Wang, K. 3148
Wang, M. H. 1943
Wang, S. 1411
Wang, T. 3297
Wang, T. F. 883, 3500
Wang, T.-S. 2319
Wang, X. 2051, 2112, 2237
Wang, X. J. 2486, 3000
Wang, X. Q. 1033, 1256
Wang, Y. 29, 224, 227, 420, 3845
Wang, Y. L. 546
Wangler, T. P. 1712, 3606, 3657
Warn, C. E. 2400
Warner, D. 2760
Warnock, R. L. 291, 3378
Warren, D. S. 2480
Watanabe, A. 1566
Watanabe, K. 3845
Watanabe, M. 1515
Watanabe, S. 41, 1291, 2714
Watanabe, T. 41
Waters, G. 1148, 1181
Waters, J. W. 1448
Watson, S. 3055
Watson, S. A. 2447
Weaver, H. J. 2959
Weaver, J. 2714
Weaver, J. N. 3018
Webber, R. 2118
Webber, R. C. 2094, 2382
Weber, K. J. 1387, 2877
Webers, G. A. 2062, 2065, 2927, 3423
Wedekind, M. 3184
Wei, J. 258, 3527, 3651
Wei, K. 312
Weihreter, E. 1474
Weingarten, W. 806
Weisend, J., II 2757
Weiss, R. 1669
Weissenburger, D. 1439
Weisz, S. 26
Welbourne, L. A. 1494, 1638, 3594, 3672
Welch, D. R. 661, 3549
Welch, J. J. 2007, 3476
Wells, F. D. 2316
Wells, R. P. 1727, 3169
Weng, W. T. 3264, 3633, 3726, 3763
Weninger, J. 44
Werkema, S. J. 3303, 3309, 3573
Wesolowski, W. 605
Westenskow, G. 2638
Westenskow, G. A. 2611
Wetherholt, D. M. 2483
Wetzels, S. F. C. L. 2927
Wheat, R. M. 2664
Whelen, C. 2967
White, G. R. 1881
White, M. 605
Whitham, K. 608, 611, 1244
Whittenberg, W. A. 2483, 3130
Whittum, D. 2638, 3552
Whittum, D. H. 673, 3288, 3399
Wienands, U. 255, 393
Wiik, B. H. 1

Wildman, D. 405, 1223, 3258
Wilke, M. D. 2480
Wilkinson, C. 366, 369, 2216, 2219, 3297
Willeke, F. 3742
Willen, E. 2744, 2766, 2790
Williams, R. 2638
Williams, S. H. 2838
Wilson, D. C. 3090
Wilson, I. 641
Wilson, P. 2681
Wilson, P. B. 543, 620, 1208
Winans, J. R. 1957
Wines, R. 3103
Wingate, C. A. 3090
Winick, H. 173, 1445, 1608
Winkler, G. 2956
Wiseman, M. 841, 1060, 2929
Wisnivesky, D. 1089, 1454
Witherspoon, S. 599
Witherspoon, S. D. 2364
Won, S. C. 1832
Wood, F. 2118
Wood, R. 1551, 1712
Woodbury, K. 1912
Woodle, M. 1439, 2578, 3000
Woodley, M. 92, 95, 119, 2019
Woodley, M. D. 3576
Woods, M. 2172, 2978, 3036, 3045, 3047
Woods, M. B. 3027
Woods, R. 3760
Woodworth, E. 2184
Worm, T. 1363
Worth, G. T. 3118
Wright, B. 998
Wright, E. 1106
Wright, E. L. 1259
Wright, S. 2124, 2130
Wu, B. 1611
Wu, D. 173
Wu, G. 2228, 2252
Wu, X. 255, 393
Wu, Y. 218, 1901, 1998, 2889
Wuensch, W. 641, 2346
Wuppertal, U. 995
Wurtele, J. 2638
Wurtele, J. S. 2575, 2635, 2699, 3327, 3399
Wüstefeld, G. 1474
Wyss, C. 2016

X

Xi, B. 2892, 3645
Xie, M. 1445, 1533
Xiu, L. 3148
Xu, C. Y. 3845
Xu, G. 3237
Xu, Y. 3148

Y

Yakimenko, V. 450
Yakovlev, S. 824

Yakovlev, V. 2650
Yakovlev, V. P. 877, 941
Yamada, S. 1291, 1686
Yamada, T. 1291, 1686
Yamaguchi, S. 959
Yarakawa, T. 215, 1614, 1617
Yamamoto, N. 466, 2340
Yamamoto, T. 650
Yamashita, Y. 676
Yamazaki, Y. 3087
Yampolsky, I. 1327
Yan, C. 2136, 3103
Yan, Y. 236, 3402
Yan, Y. T. 29, 38, 224, 227, 242, 243, 420, 423, 515
Yanagi, Y. 3845
Yanagida, K. 602
Yandon, J. C. 1916
Yang, B. 3243
Yang, X.-F. 2462
Yao, C. G. 812
Yao, C. Y. 122, 2444
Yarba, V. 236
Yarosh, V. E. 1795
Yartsev, D. I. 1795
Yelk, J. 2070
Yen, E. 1460
Yeremian, A. 543
Yeremian, A. D. 2978, 3027, 3063
Yeung, K. S. 2385
Yin, Y. 2441
Yokomizo, H. 602, 2039
Yokota, M. 3087
Yokouchi, S. 3845
Yokoya, K. 3441
Yoneda, C. 620
Yonehara, H. 2039
Yoneyama, S. 2039
Yoon, J. R. 2796
Yoon, M. 3273
York, R. 236, 255, 393, 3739
York, R. L. 3175
Yoshida, K. 1780, 1783
Yoshida, Y. 3552
Yoshikawa, H. 602
Yoshioka, M. 1614, 1617
Yoshizawa, J. 1291, 1686
Yoshizawa, M. 41, 1783, 1786
Young, A. 1205, 1285
Young, A. T. 1727, 3042
Young, L. M. 790, 3136
Youngman, B. 543
Yu, D. 2388, 2681
Yu, D. U. L. 936
Yu, J. X. 1727
Yu, K. 2787, 3888, 3891
Yu, L. H. 1439, 1602
Yu, S. 703, 709, 3199
Yu, S. S. 712
Yu, X. T. 3327, 3399
Yuan, V. 1669
Yücel, A. 3879
Yudin, I. P. 191, 297, 1892
Yudin, L. A. 2543
Yudin, L. I. 1795
Yugami, N. 2556, 3552
Yule, T. 1709
Yule, T. J. 1777
Yunn, B. 3663

Yunn, B. C. 179, 1092, 1909
Yupinov, Y. 564
Yvlov, T. 2042

Z

Zach, M. 1151
Zagel, J. R. 2193
Zakhvatkin, M. N. 2022
Zaltsman, A. 1241
Zangrando, D. 1587, 2844, 2847
Zante, T. 608, 611
Zapalac, G. 2172
Zapolsky, V. N. 454
Zapryagaev, I. 2650
Zarccone, M. J. 3178
Zarucheisky, V. G. 454
Zatopek, J. 2757
Zbasnik, J. 2787, 3888, 3891
Zelanzy, M. 1884
Zelazny, M. 1966
Zelenski, A. N. 2991

Zelinsky, A. Y. 194, 1480
Zelynsky, A. 2057
Zenkevich, P. 2073
Zhabitsky, V. M. 2543
Zhang, B. 1001
Zhang, C. 312, 3237
Zhang, H. 2841
Zhang, M. 1411
Zhang, P. 176
Zhang, P. L. 29, 224, 227, 420
Zhang, Q. 1411
Zhang, R. 561, 575, 3009, 3216
Zhang, S. Y. 1277, 3264
Zhang, T. 306, 2556, 2841
Zhang, W. 2841
Zhang, X. 312, 1439, 1599, 1721, 2841, 3081
Zhang, X. L. 3237
Zhang, Z. 303, 1611
Zhao, Y. 1033, 1256
Zhao, Z. 2841
Zhao, Z. T. 3237
Zhmendak, A. V. 3822
Zholents, A. 131

Zhou, C. 2841
Zhou, J. 3396, 3772
Zhou, P. 3303, 3309, 3540, 3573
Ziemann, V. 98, 100, 108, 114, 116, 498, 1483, 3909
Zinchenko, A. 2468, 2489
Zinkann, G. P. 1694
Zinneman, T. 1709
Zinneman, T. E. 3210
Ziomek, C. 1154, 3213
Ziomek, C. D. 2391
Zisman, M. S. 2010
Zolfaghari, A. 829, 832, 2331, 3851
Zolfaghari, Z. 2054
Zolotorev, M. 2172, 3027, 3045
Zolotorev, M. S. 2978, 3036
Zoni, G. 1063
Zotter, B. 3347, 3429
Zu, D. 1095
Zumbro, J. 1021
Zumbro, J. D. 2832, 2941
Zyngier, H. 1465

